Computational Modelling of CONCRETE STRUCTURES

Editors:
Günther Meschke,
Bernhard Pichler & Jan G. Rots

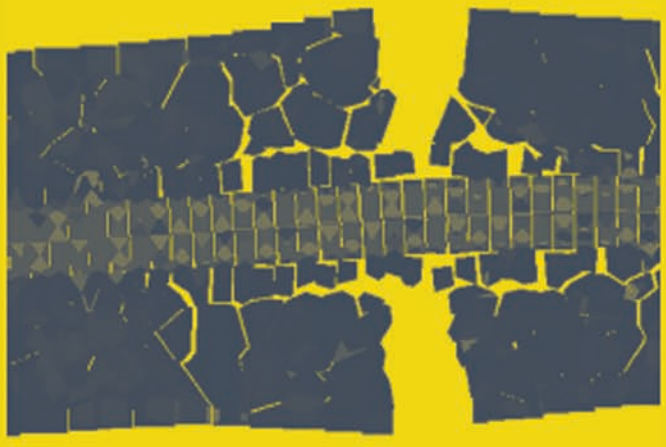

EURO-C 2018

CRC Press
Taylor & Francis Group
A BALKEMA BOOK

COMPUTATIONAL MODELLING OF CONCRETE STRUCTURES



Taylor & Francis
Taylor & Francis Group
http://taylorandfrancis.com

PROCEEDINGS OF THE CONFERENCE ON COMPUTATIONAL MODELLING OF CONCRETE AND CONCRETE STRUCTURES (EURO-C 2018), 26 FEBRUARY – 1 MARCH 2018, BAD HOFGASTEIN, AUSTRIA

Computational Modelling of Concrete Structures

Editors

Günther Meschke
Ruhr University Bochum, Bochum, Germany

Bernhard Pichler
Vienna University of Technology, Vienna, Austria

Jan G. Rots
Delft University of Technology, Delft, The Netherlands



CRC Press
Taylor & Francis Group
Boca Raton London New York Leiden

CRC Press is an imprint of the
Taylor & Francis Group, an **informa** business

A BALKEMA BOOK

CRC Press/Balkema is an imprint of the Taylor & Francis Group, an informa business

© 2018 Taylor & Francis Group, London, UK

Typeset by V Publishing Solutions Pvt Ltd., Chennai, India
Printed and bound in Great Britain by CPI Group (UK) Ltd, Croydon, CR0 4YY

All rights reserved. No part of this publication or the information contained herein may be reproduced, stored in a retrieval system, or transmitted in any form or by any means, electronic, mechanical, by photocopying, recording or otherwise, without written prior permission from the publisher.

Although all care is taken to ensure integrity and the quality of this publication and the information herein, no responsibility is assumed by the publishers nor the author for any damage to the property or persons as a result of operation or use of this publication and/or the information contained herein.

Published by: CRC Press/Balkema
Schipholweg 107C, 2316 XC Leiden, The Netherlands
e-mail: Pub.NL@taylorandfrancis.com
www.crcpress.com – www.taylorandfrancis.com

ISBN: 978-1-138-74117-1 (Hbk)
ISBN: 978-1-315-18296-4 (eBook)

Computational Modelling of Concrete Structures – Meschke, Pichler & Rots (Eds)
© 2018 Taylor & Francis Group, London, ISBN 978-1-138-74117-1

Table of contents

Preface xiii

Plenary lectures

Molecular dynamics-based structural mechanics of buildings' resilience 3
F.-J. Ulm, K. Keremidis, R.J.-M. Pellenq & M.J.A. Qomi

Century-long durability of concrete structures: Expansiveness of hydration and chemo-mechanics of autogenous shrinkage and swelling 15
Z.P. Bažant & S. Rahimi-Aghdam

Regularized continuum damage formulations acting as localization limiters 25
M. Jirásek

Erection of bridges and shells without formwork—challenges for the computational modelling 43
J. Kollegger, B. Kromoser & D. Suza

Network modelling of fracture processes in fibre-reinforced quasi-brittle materials 55
P. Grassl & A. Antonelli

New damage model to simulate ballistic impact on concrete targets 63
L. Pereira, L.J. Sluys & J. Weerheijm

Multiscale cement and concrete research: Experiments and modeling

Fishnet model for failure probability of nacre-like imbricated lamellar materials and Monte Carlo verification 73
Z.P. Bažant & W. Luo

Phase-field modeling of cement paste: Where particle physics meets continuum mechanics 79
T. Petersen & F.-J. Ulm

Towards a mesoscale model of geopolymers: Interaction potential from the molecular scale 87
F. Lolli & E. Masoero

Nanoscale simulations of cement hydrates precipitation mechanisms: Impact on macroscopic self-desiccation and water sorption isotherms 93
E. Masoero, I. Shvab, G. Di Luzio & G. Cusatis

Atomistic modeling of early hydration of C_3S 103
K.M. Salah Uddin & B. Middendorf

Modeling the evolution of C_3S-C_3S grain interface over hydration time 109
A. Alex & P. Ghosh

Fracture properties of cement hydrates determined from microbending tests and multiscale modeling 113
J. Němeček, V. Šmilauer, J. Němeček, F. Kolařík & J. Maňák

Testing and modelling of micro cement paste cube under indentation splitting 121
H. Zhang, E. Schlangen & B. Šavija

An adaptive concurrent two-scale FE model to predicting crack propagation in concrete 127
O.L. Manzoli, E.A. Rodrigues, L.A.G. Bitencourt Jr., T.N. Bittencourt & M. Sánchez

Multi-scale modelling of the mechanics of concrete based on the cement paste properties 137
G. Lifshitz Sherzer, E. Gal, E. Schlangen & G. Ye

Sensitivity estimation of cement paste properties in the microstructural characteristics 141
J.-S. Kim & T.-S. Han

Elastic-plastic multi scale approach for localization problems—the embedded unit cell 149
M. Grigorovitch & E. Gal

A continuum damage model for the simulation of concrete under cyclic loading 155
V. Kindrachuk, T. Titscher, V. Hirthammer & J.F. Unger

From slender columns to branching structures 165
R. Krč, J. Podroužek & R. Wan-Wendner

Aging concrete: From very early ages to decades-long durability

Assessing the flow characteristics of self-compacting concrete via numerical simulations of flow tests 173
S. Kulasegaram & B.L. Karihaloo

Mixing and extrusion of printing concrete 183
Y. Yuan & Y. Tao

Formulation, validation and application of a new shotcrete model 189
M. Neuner, M. Schreter, G. Hofstetter & T. Cordes

Aging behavior of normal and high strength concretes 197
L. Czernuschka, K. Nincevic, I. Boumakis, L. Wan-Wendner & R. Wan-Wendner

A multiscale framework for the prediction of concrete self-desiccation 203
M. Pathirage, D.P. Bentz, G. Di Luzio, E. Masoero & G. Cusatis

Effect of drying on the mechanical performances of concrete 209
F. Benboudjema, F. Soleilhet, X. Jourdain & F. Gatuingt

Temperature and humidity-driven ageing of the VeRCoRs mock-up 215
J.-P. Mathieu, L. Charpin, P. Sémété, C. Toulemonde, G. Boulant, J. Haelewyn, F. Hamon, S. Michel-Ponnelle, J.-M. Hénault & F. Taillade

Reassessment of the very long term basic creep of concrete 225
J.-M. Torrenti

Interaction between damage and time-dependent deformation of mortar in concrete: 3D FE parametric study at meso-scale 229
J. Ožbolt & S. Gambarelli

Prediction of air permeability in large RC structures using a stochastic FE THM modeling strategy 237
E.M. Bouhjiti, J. Baroth, F. Dufour & B. Masson

Simplified modelling strategy for the thermos-mechanical analysis of massive reinforced structures at early age 249
J. Mazars, M. Briffaut & S. Grange

Multiscale quantification of thermal expansion of concrete and thermal stresses of concrete structures 257
H. Wang, H.A. Mang, Y. Yuan & B. Pichler

Translating environmentally-induced eigenstresses to risk of fracture for design of durable concrete pavements 265
A. Louhghalam, T. Petersen & F.-J. Ulm

Simulation of permeable concrete to assess interrelationship between strength and permeability 275
P. Modi, M. Dave, A. Dodhiya, Y. Dadi, M. Mungule & M. Langhi

A coupled chemo-mechanical damage-healing model for cementitious materials 285
A.D. Jefferson & R.E. Davies

Flow in fibrous composite materials: Numerical simulations 289
J. Kang & J. Bolander

Modeling water absorption in cement-based composites with SAP additions 295
C. Romero Rodríguez, S. Chaves Figueiredo, E. Schlangen & D. Snoeck

Full coupling between diffusion and mechanical analysis in a discrete computational framework 305
F. Bousikhane, W. Li, G. Di Luzio & G. Cusatis

Alternative parameter to characterize pore distribution in cement paste, and its relation to mechanical properties 311
T.-S. Han & J.-S. Kim

Influence of air voids in multiphase modelling for service life prediction of partially saturated concrete 317
D. Eriksson & T. Gasch

Concrete frost damage due to cyclic environmental loading—experimental and numerical study 327
M. Koniorczyk, D. Gawin, A. Wieczorek & F. Pesavento

Computational modeling of combined frost damage and alkali-silica reaction to the durability of RC bridge decks 335
F. Gong, Y. Takahashi & K. Maekawa

Multiscale modelling of ASR induced degradation in concrete 345
T. Iskhakov, J.J. Timothy & G. Meschke

Nonlinear coupling models of alkali-silica reaction and multi-directional cracked reinforced concrete 353
Y. Takahashi, S. Ogawa, Y. Tanaka & K. Maekawa

Coupled C-M meso-scale model for ASR expansion in concrete 363
J. Liaudat, C.M. López & I. Carol

Numerical strategies for the modelling of reinforced concrete structures affected by internal swelling in variable thermo-hydric conditions 371
B. Nedjar & C. Rospars

A finite element implementation of delayed ettringite formation in concrete structures 377
M. Malbois, B. Nedjar, L. Divet, S. Lavaud & J.-M. Torrenti

Determination of critical anodic and cathodic areas in corrosion processes of steel reinforcement in concrete 387
J. Ožbolt, E. Sola & G. Balabanić

Challenges in corrosion detection based on numerical and experimental studies 395
M. Kwapisz, A. Vorwagner, A. Lechner & M. Rebhan

Advances in material modeling of plain concrete

Concrete mesoscopic failure analysis with the Virtual Element Method 403
G. Etse, M. Benedetto & A. Caggiano

A cyclic triaxial concrete microplane model with gradient regularization 413
I. Zreid & M. Kaliske

Simulation of cracking susceptibility in recycled concrete aggregate systems 421
A. Jayasuriya, M.J. Bandelt & M.P. Adams

On boundary layer arising from tessellation in discrete models 429
J. Eliáš

Size effect in concrete under splitting tension 437
J. Suchorzewski & J. Tejchman

Numerical prediction of deterministic size effect in concrete bars and beams 447
A. Wosatko, J. Pamin & A. Winnicki

Numerical investigations on early indicators of fracture in concrete at meso-scale 457
M. Nitka & J. Tejchman

Incremental sequentially linear analysis of a notched beam 465
C. Yu, P.C.J. Hoogenboom & J.G. Rots

Cohesive crack model in discontinuous Galerkin method 473
J. Jaśkowiec

Mesoscopic simulations of crack propagation in concrete using cohesive elements 481
W. Trawiński, J. Tejchman & J. Bobiński

Configurational forces for modelling cohesive fracture in concrete 491
C.J. Pearce, A. Amar & Ł. Kaczmarczyk

A constitutive law for concrete with smooth transition from continuous into discontinuous cracks' description 499
J. Bobiński & J. Tejchman

Nonlocal damage formulation with evolving internal length: The Eikonal nonlocal approach 509
G. Rastiello, C. Giry, F. Gatuingt, F. Thierry & R. Desmorat

Response scatter control for discrete element models 517
J. Podroužek, M. Marcon, J. Vorel & R. Wan-Wendner

Enhancement of multifiber beam elements in the case of reinforced concrete structures for taking into account the lateral confinement of concrete due to stirrup 525
N. Khoder, S. Grange & Y. Sieffert

Analysis of reinforced concrete structures

Modelling of the proof load test on viaduct De Beek 535
E.O.L. Lantsoght, A. de Boer, C. van der Veen & D.A. Hordijk

Organizing an international blind prediction contest for improving a guideline for the nonlinear finite elements analysis of concrete structures 545
A. de Boer, M.A.N. Hendriks, C. van der Veen & B. Belletti

Ultimate limit state design of three-dimensional reinforced concrete structures: A numerical approach 553
H. Vincent, M. Arquier, J. Bleyer & P. de Buhan

Computational buckling response of reinforcing bars embedded in Hybrid Fiber Reinforced Concrete (HyFRC) 561
I.D. Williams, C.P. Ostertag & C.A. Arteta

Analysis of RC frame corners using CDP model 569
M. Szczecina & A. Winnicki

Probabilistic cracking model for macrocrack propagation in reinforced concrete structures 579
P. Rossi, C. Nader & J.L. Tailhan

Numerical simulation of shear strength in a short reinforced concrete corbel strengthened with composite material compared with experimental results 585
I. Ivanova, J. Assih, V. Stankov & D. Dontchev

Computational modeling and experimental testing of shear and flexure performance of prestressing concrete T-shaped beams—safety formats 595
A. Strauss, B. Krug, O. Slowik, D. Novák & L. Novák

Characterising the shear behaviour of steel fibre-reinforced concrete 605
S. Zeranka & G.P.A.G. van Zijl

Shear behavior of full-scale RC slabs without shear stirrups in nuclear buildings: Experimental and numerical modeling 615
W.S.A. Nana, S. Limam, T.T. Bui, A. Limam & S. Abouri

Numerical lower bound analysis of plate bending problems containing requirements on shear capacity and shear-bending interaction 625
T.W. Jensen, P.N. Poulsen & L.C. Hoang

Simulation of reinforced HPFRCC deformation capacity under flexure- and shear-dominated stress states 633
M. Pokhrel & M.J. Bandelt

Computer-aided stress field analysis of discontinuity concrete regions 641
J. Mata-Falcón, D.T. Tran, W. Kaufmann & J. Navrátil

Investigations on strength and fracture in RC beams scaled along height or length 651
J. Suchorzewski, I. Marzec, J. Tejchman & E. Korol

Modeling of quasi-brittle materials cracking using a lattice discrete element approach 661
E. Zafati, C. Oliver-Leblond & F. Ragueneau

Evaluation of safety formats for structural assessment based on nonlinear analysis 669
J. Červenka, V. Červenka, M. Sýkora & J. Mlčoch

Modelling boundary conditions imposed by loads and supports in 3D D-regions 679
C. Meléndez & P.F. Miguel

Parameter identification as the basis for finite element simulations of ultimate limit states of concrete hinges 689
J. Kalliauer, T. Schlappal, H.A. Mang & B. Pichler

Rotational capacity of concrete beams using a crack process band 697
J.P. Ulfkjaer

An embedded rebar model for computational analysis of reinforced concrete structures with applications to longitudinal joints in precast tunnel lining segments 705
V.E. Gall, S.N. Butt, G.E. Neu & G. Meschke

Robust design of hybrid steel fiber reinforced concrete tunnel lining segments 715
G.E. Neu, V.E. Gall, S. Freitag & G. Meschke

Structural analysis of segmented tunnel rings: A combination of transfer relations with an interface law 725
J.L. Zhang, H.A. Mang, X. Liu, Y. Yuan & B. Pichler

Steel-concrete interaction, fiber-reinforced concrete, and masonry

Investigation of dowel action on a steel-concrete bond model for reinforced concrete structures 737
C. Turgut, L. Jason, L. Davenne & A. Pirard

Multi-scale tension stiffening approach for the minimum reinforcement of hybrid concrete beams 745
A.P. Fantilli, A. Gorino & B. Chiaia

Investigation of effect of local bond model on crack propagation in RC using 3D RBSM 755
L. Eddy, K. Matsumoto, K. Nagai & Z. Wang

Modeling of bond fatigue in reinforced concrete based on cumulative measure of slip 767
A. Baktheer & R. Chudoba

Fatigue life assessment of reinforced concrete members considering bond-slip 777
S. Bhowmik & S. Ray

Simulation of interface behavior between steel and concrete to study loss of bond due to reinforcement corrosion 785
B. Sanz, J. Planas & J.M. Sancho

Modeling of localization and softening behavior of passively confined concrete using coupled RBSM and nonlinear shell FEM 795
R. Mendoza Jr., Y. Yamamoto, H. Nakamura & T. Miura

Simulation of reinforced ductile cement-based composite beams under cyclic loads 805
S.L. Billington, Y. Shao, T.E. Frank, M.J. Bandelt & D.M. Moreno

The use of trilinear softening functions for modelling the cracking of fibre reinforced concrete 813
A. Enfedaque, M.G. Alberti & J.C. Gálvez

Model comparisons for a shell structure made of textile reinforced concrete 819
T. Senckpiel & U. Häussler-Combe

Finite element research of reinforced concrete structures strengthened with Textile Reinforced Concrete (TRC) 829
A. Schumann, R. Zobel & M. Curbach

Probabilistic multiple cracking model of elastic-brittle matrix composite reflecting randomness in matrix, reinforcement and bond 839
M. Vořechovský, R. Chudoba, Y. Li & R. Rypl

Numerical modelling of textile reinforced concrete sandwich panels 849
I.G. Colombo, M. Colombo & M. di Prisco

A two-phased and multi-scale finite element analysis of the tensile creep behavior of polypropylene fiber reinforced concrete 857
R. Vrijdaghs, E. Verstrynge, L. Vandewalle & M. di Prisco

Numerical simulation of the fracture behaviour of glass fibre reinforced cement: A cohesive crack approach 867
A. Enfedaque, M.G. Alberti & J.C. Gálvez

Multiscale modeling of steel fiber reinforced concrete based on the use of coupling finite elements and mesh fragmentation technique 877
L.A.G. Bitencourt Jr., Y.T. Trindade, T.N. Bittencourt, O.L. Manzoli & E.A. Rodrigues

Nonlinear finite element analysis of steel fiber-reinforced concrete coupling beams 889
S.-W. Kim, H.-D. Yun, S.-J. Jang, W.-S. Park, Y.-I. Jang & C.-S. Choi

Micromechanics based modelling of fibre reinforced cementitious composites 895
I.C. Mihai, A.D. Jefferson & P. Lyons

Tensile viscous response of Strain Hardening UHPFRC under high restraint and isothermal conditions 903
M.A. Hafiz & E. Denarié

A beam-particle model to identify constitutive laws for quasi-brittle materials under complex loading: From concrete to masonry 913
C. Oliver-Leblond, C. Giry, C. Limoge, M. Vassaux, E. Anglade & F. Ragueneau

The adobe delta damage model 921
T. Li Piani, J. Weerheijm, L. Koene & L.J. Sluys

Non-proportional loading for 3-D stress situations in sequentially linear analysis 931
M. Pari, J.G. Rots & M.A.N. Hendriks

Shear-sliding behavior of masonry: Numerical micro-modeling of triplet tests 941
F. Ferretti, C. Mazzotti, R. Esposito & J.G. Rots

Dynamic behavior: From seismic retrofit to impact simulation

Mechanical model of adhesive post-installed anchor subjected to combined force 955
Y. Takase, M. Mizoguchi & T. Wada

FEM analysis of post-installed adhesive anchors under combined stress 963
Y. Ishida, H. Sakata, Y. Takase, Y. Maida, Y. Shirai & T. Sato

Mechanical model of shear stress transfer of roughened concrete surface for R/C existing member 973
T. Isozaki, U. Musya, Y. Takase, T. Abe, K. Sakamoto, T. Hiwatashi & K. Katori

A practical design method to retrofit existing RC buildings with viscous dampers 983
R. Gobirahavan & A.C. Wijeyewickrema

An improved RSA procedure to compute shear force in tall RC shear wall buildings 993
K. Khy, C. Chintanapakdee & A.C. Wijeyewickrema

Introduction of shear warping in fibre beam elements for the computation of the nonlinear behaviour of concrete beams 1003
S. Capdevielle, S. Grange, F. Dufour & C. Desprez

Characterization of cracks of damaged concrete structures in dynamics 1009
R. Akiki, C. Giry & F. Gatuingt

High-dynamic strengthening of cementitious materials subjected to uniaxial compression 1017
E. Binder, H.A. Mang, Y. Yuan & B. Pichler

Modelling of reinforced concrete members for high impulsive loading 1023
Y. Lu & J. Xu

Author index 1031



Taylor & Francis
Taylor & Francis Group
http://taylorandfrancis.com

Computational Modelling of Concrete Structures – Meschke, Pichler & Rots (Eds)
© 2018 Taylor & Francis Group, London, ISBN 978-1-138-74117-1

Preface

EURO-C 2018 represents the continuation of a series of conferences on computational methods and numerical models for the analysis of concrete and concrete structures. EURO-C 2018 is dedicated to **Nenad Bićanić** († 2016), who was one of the founding fathers of this conference series and whose contributions significantly enriched the field of computational concrete modelling and whose influences are still felt today. Nenad was not only an inspirational scientist, but also a warm-hearted colleague and a dear friend. Ever since the first conference in 1984 in Split, Croatia, he was always curious about new trends in computational modelling. He enjoyed bringing together the concrete mechanics community by organizing unforgettable sessions, such as the "Betonstüberl" discussions, and the traditional EURO-C skiing races. Nenad's passing has been a great loss to his family and to all of us.





We are trying to keep his spirit alive! EURO-C 2018 will take place in Austria, in Bad Hofgastein, from February 26 to March 1, 2018, maintaining the tradition of previous successful conferences in the EURO-C conference series (Innsbruck 1994, Bad Gastein 1998, St. Johann im Pongau 2003, Mayrhofen 2006, Schladming 2010, St. Anton am Arlberg 2014). This series emerged as a joint activity, following early developments in nonlinear finite element analysis and softening models for concrete, generated at the time of the ICC 1984 conference in Split, the SCI-C conference in Zell am See and the two IABSE Concrete Mechanics Colloquia in Delft, 1981 and 1987.

The Proceedings of EURO-C 2018 comprise 6 papers of Plenary Lecturers as well as 112 contributed papers, grouped into 6 sections: (1) Multi-scale cement and concrete research: experiments and modelling, (2) Aging concrete: from very early ages to decades-long durability, (3) Advances in material modelling of plain concrete, (4) Analysis of reinforced concrete structures, (5) Steel-concrete interaction, fibre-reinforced concrete, and masonry, as well as (6) Dynamic behavior: from seismic retrofit to impact simulation. As compared to previous conferences, there are still many contributions on robustness and precision of numerical models at the structural scale. However, trends towards the materials scale with new fibres and 3D printable concretes, multi-scale and multi-physics frameworks, and life-cycle oriented models for ageing and durability of existing and new concrete infrastructure are clearly visible.

We are grateful to the members of the Scientific Advisory Committee (Zdenek Bažant, Sarah Billington, Gianluca Cusatis, Guillermo Etse, Dariusz Gawin, Christian Hellmich, Günter Hofstetter, Tony Jefferson, Milan Jirásek, Koichi Maekawa, Jacky Mazars, Javier Oliver, Chris Pearce, Gilles Pijaudier-Cabot,

Marco Di Prisco, Ekkehard Ramm, Victor Saouma, Bert Sluys, Jean-Michel Torrenti, Franz-Josef Ulm, Kaspar Willam, Yong Yuan) for their support and substantial efforts in the reviewing process of over 150 abstracts.

In addition to a special memorial session for Prof. Nenad Bićanić, the role of Prof. Zdenek Bažant as the founding father of concrete fracture mechanics and a key contributor to all previous EURO-C events will be recognized in the context of his 80th birthday.

We sincerely hope that the EURO-C 2018 Proceedings will serve as a major reference, stimulating new research directions in the field of computational modelling of concrete and its application to the analysis of concrete structures.

Günther Meschke, Bernhard Pichler & Jan Rots, Conference Chairmen
René de Borst & Herbert Mang, Honorary Chairmen

Bochum/Vienna/Delft/Sheffield/Vienna,
February 2018

Plenary lectures



Taylor & Francis
Taylor & Francis Group
http://taylorandfrancis.com

Computational Modelling of Concrete Structures – Meschke, Pichler & Rots (Eds)
© 2018 Taylor & Francis Group, London, ISBN 978-1-138-74117-1

Molecular dynamics-based structural mechanics of buildings' resilience

F.-J. Ulm, K. Keremidis & R.J.-M. Pellenq
Massachusetts Institute of Technology, Cambridge MA, USA

M.J.A. Qomi
University of California, Irvine, Irvine CA, USA

ABSTRACT: Making use of the tool-box of statistical physics, a Molecular Dynamics (MD) -based Structural Mechanics approach is proposed that is suitable for the assessment of resilience of buildings. The paper summarizes recent developments of the approach; namely Potential of Mean Force (PMF) expressions suitable for structural members for both two-body (stretch) and three-body (bending) interactions; an original potential parameter calibration procedure based on frequency spectra of structures; an illustration of the approach for a large-scale structure for the identification of the progressive structural collapse and fragility curves. It is shown that the proposed MD approach through its focus on interaction potentials is able not only to reproduce classical structural dynamics results. Most importantly, by redefining structural mechanics within the context of statistical physics, the approach provides a powerful means of determining a damage (bond-loss) inventory of buildings required for the assessment of resilience of buildings.

1 INTRODUCTION

With more than 75% of catastrophic losses in the United States in the period of 1993–2012 caused by windstorms (III 2016), there is an urgent need to enhance the resilience capacity of our built environment vis-à-vis windstorms. In particular, the 18 coastal states on the Atlantic Ocean and Mexican Gulf, and the majority of states east of the Rocky Mountains face wind vulnerability; 45% of the value of the US's built environment is in the 18 coastal states (Papadopoulos 2016). This economic impact calls for revisiting engineering approaches to structural and functional integrity of buildings. In fact, classical systems approaches, such as the Federal Emergency Management Agency's HAZUS-MH (FEMA 2016), or structural engineering approaches at building scale (see e.g., Barbato et al. 2013, Walker 2011), condense potential wind-damage into structural fragility curves for specific building types and components to evaluate the risk of damage and loss of functionality that occur due to, e.g., a windstorm, earthquake, flooding and so on. On a building element scale, structural mechanics approaches evaluate potential structural damage in relation to a code design limit state of structural members (see e.g. Yeo 2011). Thus, neither the system approach nor the case study approach provide a quantitative means to assess the actual partial loss of functionality of buildings due to failure of structural and non-structural members (incl. windows, roofs, etc.), and of the impact of this loss of functionality on residual robustness, rate of recovery, and the level of restoration of said functionality. This motivates the development of an approach that can address both the complexity of buildings and the loss of integrity at both the component and the system level.

At the core of our approach is the realization that the complexity of buildings is akin to molecular complexity, in which many strong and weak interacting atoms define the very physical properties of materials ranging from thermal properties to mechanical and structural properties. Thus, rather than considering a building as an ensemble of elements (beams, plates, walls), we propose to consider a building as an ensemble of discrete mass points ('atoms') that interact via effective bond-forces and moments, that capture all possible energy states of a building from the equilibrium state to failure when subject to load. With its focus on the interaction potentials, the approach aims at moving beyond the limitations of continuum-element-based structural mechanics approaches for the application to buildings composed of "strong" interacting members (structural elements), and "weak" interacting members (non-structural elements). The Molecular Dynamics-based structural mechanics approach is first presented, and a calibration scheme for the potential energy parameters are provided. The approach is then employed for

some sample structures showing both the commonality and the added value of the MD-based approach w.r.t. classical approaches for the assessment of fragility curves of buildings subject to wind loads.

2 MD-BASED STRUCTURAL MECHANICS APPROACH

Consider thus a structure discretized in mass points $i = 1, N$. The interaction energy between these mass points is written as a series expansion of functional terms of one, two, three,... mass points; so that the total (internal) energy of the system can be written as:

$$U = \sum_i^N U^i(\vec{r}_i) + \sum_{i,j}^N U^{ij}\left(\vec{r}_{ij} = \vec{r}_j - \vec{r}_i\right) + \sum_{i,j,k}^N U^{ijk}\left(\vec{r}_i, \vec{r}_j, \vec{r}_k\right) + \ldots \quad (1)$$

Herein, $U^i(\vec{r}_i)$ stands for the one-body term (the ground-state energy) of the energy of mass points $i=1, N$ defined by position vector $\vec{r}_i$; $U^{ij}(\vec{r}_{ij} = \vec{r}_j - \vec{r}_i)$ describes two-body interactions between mass points i and j; $U^{ijk}(\vec{r}_i, \vec{r}_j, \vec{r}_k)$ three-body interactions between i, j and k; and so on. The interaction potentials are assumed to carry all the relevant physics information to define the force vector at each mass point i satisfying the linear momentum balance equation:

$$\forall i = 1, N; m_i \frac{d^2\vec{r}_i}{dt^2} = \vec{F}_i = -\nabla_{\vec{r}_i} U\left(\vec{r}_{i=1,N}\right) \quad (2)$$

where m_i is the mass of mass point i. The key input to the approach are thus the two-body and three body interaction potentials, U^i, U^{ij} and U^{ijk}

2.1 *Potential-of-Mean-Force (PMF) approach*

2.1.1 *Two-body interactions*

With a focus on making a handshake of the molecular approach with structural mechanics theory, it is useful to concentrate all interactions between mass points into two body-interactions between mass point i and j, with two-body interactions defining the stretch potential between these mass points. The simplest form of interaction potentials is a harmonic potential that defines energy states around the equilibrium position, that is $\|\vec{r}_{ij}\|/l_{ij} = O(1)$, defined by the rest-length $l_{ij} = \|\vec{r}_{ij}^{\,0}\|$. It consists of a quadratic expansion of the displacement arguments of the form:

$$U^i + U_s^{ij} = -\varepsilon_i^0 + \frac{1}{2}\varepsilon_{ij}^n\left(\lambda_{ij}\right)^2 \quad (3)$$

where $-\varepsilon_i^0$ defines the well depth of the potential in the reference configuration, while ε_{ij}^n is the energy parameter activated by two-pair interactions due to the stretch $\lambda_{ij} = (1/l_{ij})(\vec{r}_{ij} - \vec{r}_{ij}^{\,0})\,\vec{e}_n^{\,ij}$ in the link direction $\vec{e}_n^{\,ij} = \vec{r}_{ij}/\|\vec{r}_{ij}\|$. The interaction force at point i is readily obtained from the r.h.s. of Eq. (3):

$$\vec{F}_i = -\sum_j^N \frac{\partial U_s^{ij}}{\partial \vec{r}_i} = \sum_j^N \frac{\varepsilon_{ij}^n}{l_{ij}} \lambda_{ij} \vec{e}_n^{\,ij} \quad (4)$$

We thus readily recognize that for a beam-type structure close to its equilibrium state $\varepsilon_{ij}^n / l_{ij}$ is nothing but the axial stiffness energy, EA (with E = Young's modulus and A = cross-section area). But the concept of potential of mean force (PMF) herein employed is far reaching, as it applies to any interactions that can be captured by energy expressions. For instance, the Taylor expansion of most non-linear expressions of potentials generate around the equilibrium state to harmonic expressions; for instance the Morse-Potential:

$$U^i + U_s^{ij} = \varepsilon_i^0 \left(\left(1 - \exp\left(-\beta_{ij}\lambda_{ij}\right)\right)^2 - 1\right) \quad (5)$$

where $\beta_{ij} = \left(\varepsilon_{ij}^n / \left(2\varepsilon_i^0\right)\right)^{1/2}$ is such that a Taylor expansion of Eq. (5) around the equilibrium state ($|\lambda_{ij}| \ll 1$) yields the harmonic expression (3); for details see e.g. Laubie et al. (2017a,b). This is illustrated in Figure 1. In turn, the force that derives from the Morse-potential is given by:

$$\vec{F}_i = -\frac{\partial U_s^{ij}}{\partial \vec{r}_i} = 4F_{i,\max}^j \exp\left(-\beta_{ij}\lambda_{ij}\right)\left(\left(1 - \exp\left(-\beta_{ij}\lambda_{ij}\right)\right)\vec{e}_n^{\,ij}\right) \quad (6)$$

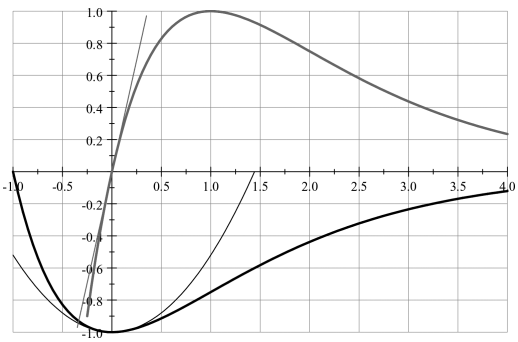

Figure 1. Normalized two-pair interaction energy, $\left(U^i + U_s^{ij}\right)/\varepsilon_i^0$ (bottom), and normalized force, $F_i^j / F_{i,max}^j$ (top), vs. normalized stretch, $\lambda_{ij}\beta_{ij}/\ln 2$, showing that around the equilibrium position the Morse potential (thick line) degenerates into a harmonic potential, associated with a linear force-stretch relation (thin lines).

where $F^{j}_{i,max} = \beta_{ij}\varepsilon^{0}_{i}/(2l_{ij})$ is the maximum force occurring at $\lambda_{ij} = \ln 2/\beta_{ij}$, which provides a link with strength and/or fracture behavior.

2.1.2 *Three-body interactions*

A similar approach can be employed for three-body interactions representing bending and torsional energy contribution of a link *i*, *j* and *k*. Such three-body interactions are nothing but (linear or non-linear) rotational springs defined along 3 orthogonal axis; so that the energy reads in the harmonic case as (see Appendix II):

$$U^{ijk} = \frac{1}{2}\vec{\vartheta}^{jk}_{i} \cdot \boldsymbol{C}_{\boldsymbol{ijk}} \cdot \vec{\vartheta}^{jk}_{i} \tag{7}$$

where $\boldsymbol{C}_{\boldsymbol{ijk}}$ is the second order tensor of rotational stiffness defined in the local orthogonal coordinate system of the three-body link system $(\vec{e}^{\,ij}_{n}, \vec{e}^{\,ij}_{b}, \vec{e}^{\,ij}_{t})$ and $(\vec{e}^{\,ik}_{n}, \vec{e}^{\,ik}_{b}, \vec{e}^{\,ik}_{t})$:

$$\boldsymbol{C}^{-1}_{\boldsymbol{ijk}} = 6\left[\frac{1}{\varepsilon^{b}_{ij}}\vec{e}^{\,ij}_{t}\otimes\vec{e}^{\,ij}_{t} + \frac{1}{\varepsilon^{t}_{ij}}\vec{e}^{\,ij}_{b}\otimes\vec{e}^{\,ij}_{b} + \frac{1}{\varepsilon^{b}_{ik}}\vec{e}^{\,ik}_{t}\otimes\vec{e}^{\,ik}_{t} + \frac{1}{\varepsilon^{t}_{ik}}\vec{e}^{\,ik}_{b}\otimes\vec{e}^{\,ik}_{b} + \frac{1}{2\kappa_{ij}}\vec{e}^{\,ij}_{n}\otimes\vec{e}^{\,ij}_{n} + \frac{1}{2\kappa_{ik}}\vec{e}^{\,ik}_{n}\otimes\vec{e}^{\,ik}_{n}\right] \tag{8}$$

with $(\varepsilon^{t}_{ij}, \varepsilon^{b}_{ij}, \kappa_{ij})$ and $(\varepsilon^{t}_{ik}, \varepsilon^{b}_{ik}, \kappa_{ik})$ the bending and torsional link energies of link *ij* and *ik*, respectively. For instance, for a straight beam element, $\varepsilon^{b}_{ij} = 12EI_{bb}/l_{ij}$, $\varepsilon^{t}_{ij} = 12EI_{tt}/l_{ij}$, $\kappa_{ij} = GJ/l_{ij}$, with E = Young's modulus, G = shear modulus, I_{bb}, I_{tt}, J the second-order (bending and torsional) moments of geometric inertia of the beam in the local coordinate system. Analogously to the pair-interaction, non-harmonic expressions can be employed for three-point interactions as well; e.g. a Morse potential:

$$U^{ijk} = \varepsilon^{0}_{i}\left(\left(1-\exp\left(-\beta_{ijk}\left\|\vec{\vartheta}^{jk}_{i}\right\|\right)\right)^{2}\right) \tag{9}$$

where $\left\|\vec{\vartheta}^{jk}_{i}\right\| = (\mathrm{tr}(\vec{\vartheta}^{jk}_{i}\cdot\vec{\vartheta}^{jk}_{i})^{1/2}$, with the Morse parameter $\beta_{ijk} = (\boldsymbol{C}_{\boldsymbol{ijk}} : \mathbf{1}/2\varepsilon^{0}_{i})^{1/2}$ chosen such that a Taylor expansion around the equilibrium state entails the harmonic expression (7). The contribution of the three-point interaction to the right-hand-side of Eq. (2) is readily found to be:

$$\vec{F}_{i} = -\sum_{j,k}^{N}\frac{\partial U^{ijk}}{\partial \vec{r}_{i}} = \sum_{j,k}^{N}\vec{M}^{jk}_{i}\cdot\frac{\partial\vec{\vartheta}^{jk}_{i}}{\partial\vec{r}_{i}};\ \vec{M}^{jk}_{i} = -\frac{\partial U^{ijk}}{\partial\vec{\vartheta}^{jk}_{i}} \tag{10}$$

with $\vec{M}^{jk}_{i}$ the moment vector, which is entirely defined by the PMF expression; for instance, in case of the Morse potential (9):

$$\vec{M}^{jk}_{i} = -m\frac{\vec{\vartheta}^{jk}_{i}}{\left\|\vec{\vartheta}^{jk}_{i}\right\|};$$
$$m = 4m_{\max}\exp\left(-\beta_{ijk}\left\|\vec{\vartheta}^{jk}_{i}\right\|\right)\left(\left(1-\exp\left(-\beta_{ijk}\left\|\vec{\vartheta}^{jk}_{i}\right\|\right)\right)\right) \tag{11}$$

where $m_{max} = \beta_{ijk}\varepsilon^{0}_{i}/2$ is the extremum of m at $\left\|\vec{\vartheta}^{jk}_{i}\right\| = \ln 2/\beta_{ijk}$, much akin to Eq. (6) and displayed in Figure 1.

2.2 *Calibration*

The potential-of-mean-force approach thus requires calibration of the energy parameters for each link; that is, the bond energy, ε^{0}_{i}, the stretch energy parameter, ε^{n}_{ij}, and the bending and torsion energy parameters $(\varepsilon^{(t,b)}_{ij}, \kappa_{ij})$, or the rotational stiffness values $\boldsymbol{C}_{\boldsymbol{ijk}}$. While for simple beam or truss-types structure, these energy parameters can be easily reconstructed from linear elastic free energy expressions, a more general approach is needed to generalize the approach for any structural discretization. In return, since ε^{n}_{ij} and $\boldsymbol{C}_{\boldsymbol{ijk}}$ are defined close to the (undeformed) equilibrium position, it is recognized that these parameters can be obtained from an analysis of the linear elastic response of the system. In return, the bond energy ε^{0}_{i} requires consideration of the rupture of the bonds, associated with fracture mechanisms.

2.2.1 *Elastic calibration from eigenfrequencies*

Consider thus a structure composed of N mass points. The system has thus 3 N degrees of freedom, associated with 3 N eigenfrequencies ω_{k} (k = 1,3 N) that can be determined from solving the eigenvalue problem considering harmonic potentials:

$$\det\left(\left[\boldsymbol{k}\right] - \omega^{2}_{k}\left[\boldsymbol{m}\right]\right) = 0 \tag{12}$$

where $[\boldsymbol{m}]$ and $[\boldsymbol{k}]$ stand for respectively the (3 N × 3 N) mass matrix and stiffness matrix that are obtained from the linear momentum balance equation (2), with $[\boldsymbol{k}]$ the Hessian matrix of the overall energy of the system evaluated around the equilibrium position:

$$\left[\boldsymbol{k}\right] = \frac{\partial^{2}U}{\delta\{\boldsymbol{u}\}^{2}}\Big|_{\vec{r}_{i}^{\,0}} \tag{13}$$

with $\{\boldsymbol{u}\}$ the vector assembling all displacement degrees of freedom of the mass points. Defined around the equilibrium position (for which non-harmonic potentials degenerate to harmonic expressions), $[\boldsymbol{k}]$ is thus a unique function of the local stretch and rotational energies; ε^{n}_{ij} and $\boldsymbol{C}_{\boldsymbol{ijk}}$.

Consider thus a 'measured' discrete frequency spectrum of a structure, $\omega_l^{exp}(l=1,M)$. This measurement can be obtained either from the Fourier analysis of actual dynamic measurements on the structure, or from a frequency analysis obtained by other continuum-element based linear-elastic analysis of a structure, such as Finite Element Method. Provided that the measured frequency spectrum has a sufficient number of frequencies, a minimization of the error between 'measured' and 'model' frequencies thus provides a means to calibrate 3 N local stretch and bending energies, ε_{ij}^n and $\boldsymbol{C}_{ijk}$:

$$\min_{\varepsilon_{ij}^n, \boldsymbol{C}_{ijk}} \sum_{m=1}^{3N} \left(\omega_m - \omega_n^{exp}\right)^2 \tag{14}$$

where ω_n^{exp} is the 'experimental' frequency associated with the n-th experimental eigenmode, for which the experimental eigenvector, $\vec{v}_n^{exp}$ pairs with the m-th model eigenvector $\vec{v}_m$; that is, making use of the orthogonality of eigenvectors:

$$n = argmax_{l=1,M}\left(\vec{v}_n^{exp} \cdot \vec{v}_m\right) \tag{15}$$

Since frequency values are integrated values that account for a large range of eigenmodes ranging from collective to local eigenmodes, the discretized structure thus captures the same frequency content as the "real" structure within the limits imposed by the level of mass point discretization. This approach for potential parameter calibration has much in common with what is known, in solid state physics, as the vibrational densities of state (or phonon density of state) at low temperatures (see e.g. Qomi et al. 2015). These collective harmonic vibrations, the so-called phonons, are closely related via the Hessian (i.e. Eq. 13) to the free energy of a molecular system, and thus to the energy parameters of the system. Which is why the frequency approach (Eqn. 14 and 15), employed here—by analogy—for structural systems, provides a convenient way to calibrate the energy parameters of the structural system that define the (close-to-) equilibrium state.

2.2.2 *Fracture property calibration*

When a link ruptures, the energy that is stored into the link between the equilibrium position and rupture is dissipated into the creation of fracture surface $\delta\Gamma^{ij}$, with $G_c\delta\Gamma^{ij}$ the dissipated energy per link rupture, entailing a release of the energy $U^i + U_s^{ij} \to 0$. That is, if the stretch potential expression is specified, the dissipated energy provides a means to define a link-fracture criterion. For purpose of illustration consider the harmonic expression (3). For $U^i + U_s^{ij} \to 0$, we readily obtain a stretch criterion for rupture; that is:

$$\lambda_{ij} \le \sqrt{2\frac{G_c\delta\Gamma^{ij}}{\varepsilon_{ij}^n}} = \sqrt{2\frac{\varepsilon_i^0}{\varepsilon_{ij}^n}} = \frac{1}{\beta_{ij}} \tag{16}$$

Similar stretch-based rupture relations can be derived for non-harmonic potentials; for instance, for the Morse potential, Eq. (5),

$$\lambda_{ij} \le -\frac{1}{\beta_{ij}}\ln(1-\alpha_i);\ \alpha_i = \sqrt{\frac{G_c\delta\Gamma^{ij}}{\varepsilon_i^0}} \tag{17}$$

Otherwise said, knowledge of the critical stretch and the (material) fracture energy provides a means to calibrate the ground-state energy ε_i^0 (noting that the two-body stretch energy ε_{ij}^n is known from the frequency calibration; see Section 2.2.1).

A similar approach can be employed for rupture of the three-body interactions leading to restricting the angle norm to a critical value; e.g. for a harmonic potential (7):

$$\left\|\vec{\vartheta}_i^{jk}\right\| \le \sqrt{2\frac{\varepsilon_i^0}{\boldsymbol{C}_{ijk}:\boldsymbol{1}}} = \frac{1}{\beta_{ijk}} \tag{18}$$

Similarly for the Morse potential (9):

$$\left\|\vec{\vartheta}_i^{jk}\right\| \le -\frac{1}{\beta_{ijk}}\ln(1-\alpha_i);\ \alpha_i = \sqrt{\frac{G_c\delta\Gamma^{ij}}{\varepsilon_i^0}} \tag{19}$$

2.3 *Examples*

The relevance of the PMF approach for structural elements is illustrated here for two types of structural elements, namely for bending moment bearing fastener connections employed in timber and steel structures; and steel-reinforced concrete sections.

2.3.1 *Timber-moment connections*

In timber structures, connections are critical structural elements which often limit the load bearing capacity of the members they connect. Such connections are achieved with different fastener techniques ranging from riveted nail connections (see Fig. 2), to dowels and bolted connections. Given the importance of these connections, a wealth of experimental research has been dedicated to assessing the moment-angle relations $(M^{exp} - \vartheta)$ of such connections (Hattar et al. 1995; Gehloff et al. 2010; Wang et al. 2015). In such tests, two timber members connected with a specific fastener are subjected to a bending moment and corresponding angles are recorded. A typical example is shown in Figure 2, together with the Morse-fit obtained from fitting the experimental energy

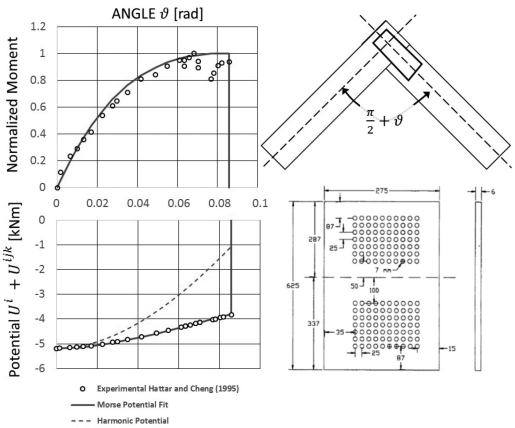

Figure 2. Illustration of Morse-fit of Moment-angle relationships for wood connections. Shown is a riveted connection (composed of a steel plate and nails, shown in the bottom right, lengths in mm) of two beams made of glued laminated Alberta spruce, tested by Hattar and Cheng (1995). The Morse parameters obtained by fitting the energy are $\beta_{ijk} = 8.47$; $\varepsilon_i^0 = 5.18$ kNm; $\alpha_i = 0.52$. The reported maximum experimental moment was max $M^{exp} = 22.0$ kNm [1 kNm = 1 kJ].

$U^{ijk} = \int M^{exp}\, d\vartheta$ to the Morse-potential expression (9). The fit provides values for the Morse-curvature parameter, β_{ijk}, from which the ground-state energy, $\varepsilon_i^0 = 2 \max M^{exp}/\beta_{ijk}$, and the dimensionless fracture parameter, $\alpha_i = 1 - \exp\left(-\beta_{ijk}\vartheta_c^{exp}\right)$, [with ϑ_c^{exp} the angle at failure], are obtained.

2.3.2 *Reinforced concrete sections*

It is common practice in reinforced concrete structural engineering to represent the moment-load bearing capacity in terms of non-linear moment-curvature relations. In contrast to moment-angle relationships which define the interaction at a specific structural connection, moment-curvature relations are section properties that encapsulate the non-linear stress-strain responses of the constituent materials; i.e. concrete and reinforcing steel in the case of reinforced concrete members. A typical example is shown in Figure 3, composed of an initial linear branch, followed by a monotonic increasing segment up to a maximum moment-section capacity and a descending branch before the section fails. For such section properties, it is appropriate to calibrate the Morse-potential by letting $\| \vec{\vartheta}_i^{jk} \| = \kappa l_{ij}^0$ in Eqn. (9) and (19), with κ the curvature. The Morse parameters which are thus obtained from fitting the three-body interaction energy $U^{ijk} = l_{ij}^0 \int M^{exp}\, d\kappa$ are the ground state energy per unit length, $\varepsilon_i^0 / l_{ij}^0 = 2 \max M^{exp}/(\beta_{ijk} l_{ij}^0)$, and the curvature parameter, $\beta_{ijk} l_{ij}^0$, where max M^{exp} is the maximum (experimental) section moment capacity. The calibrated values, $\varepsilon_i^0 / l_{ij}^0$ and $\beta_{ijk} l_{ij}^0$, are then rescaled, in structural simulations, for a specific mass-point discretization l_{ij}^0. The quality of such an energy calibration using the Morse potential is shown in Figure 3 as well.

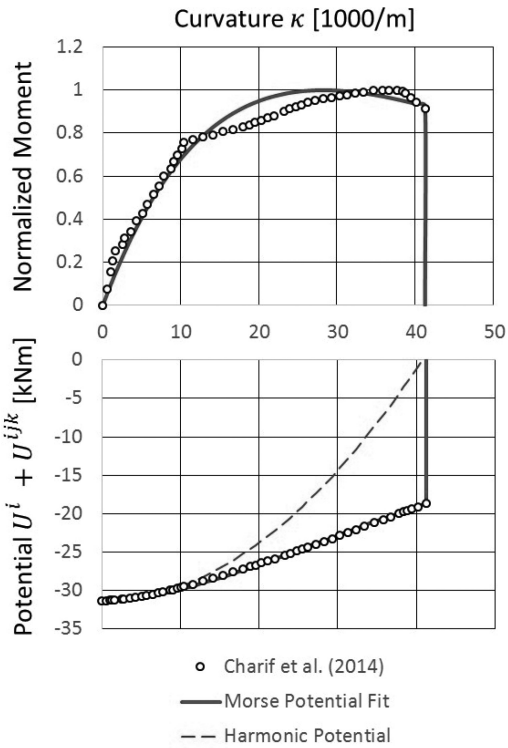

Figure 3. Moment-Curvature Relationship for a 0.4 × 0.4 m² concrete section of concrete compressive strength 25 MPa, steel reinforced with ρ = 3.5%, according to Charif et al. (2015). The Morse energy fit is obtained for $\beta_{ijk} l_{ij}^0 = 24.5$ m; $\varepsilon_i^0 / l_{ij}^0 = 31.3$ kN, and $\alpha_i = 0.64$. The maximum moment max $M^{exp} = 384$ kNm. [1 kNm = 1 kJ].

These examples thus illustrate that molecular potentials devised to capture the potential energy of interatomic bonds can be effectively employed for structural elements. Shown here for the harmonic case and the Morse potential, there is a wealth of other potential expressions to capture a large range of relevant structural behaviors.

3 APPLICATION

With a closed-system of relations for the calibration of the potential parameters thus established, this section aims at applying the MD-inspired structural mechanics approach to a resilience

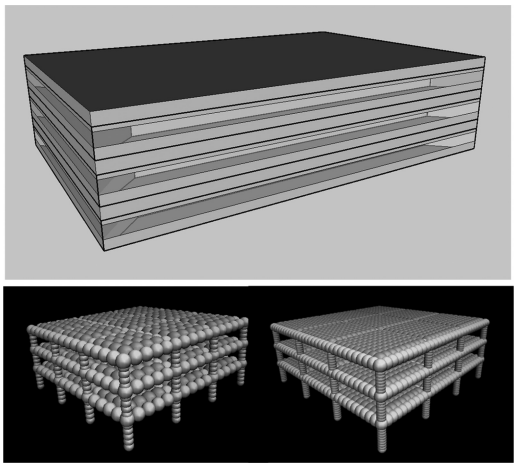

Figure 4. DOE-inspired office building (top) and different discretization levels (bottom), $N = h/l_{ij}^0 = 5$ and $N = 10$ (with h the storey height).

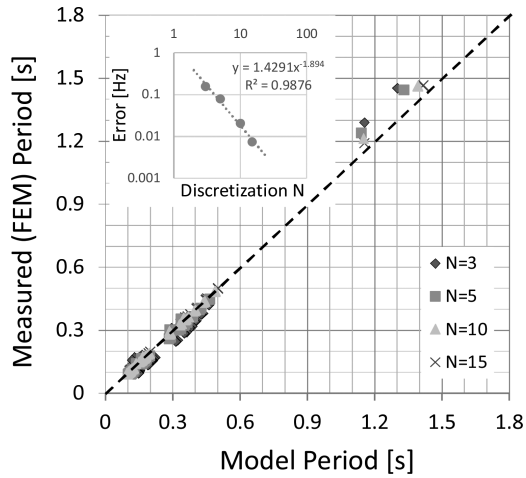

Figure 5. Frequency calibration of potential parameters of DOE-building: Model vs. 'measured' fundamental periods for different discretization levels, $N = h/l_{ij}^0$. 'Measured' frequencies were obtained from finite element simulations of the structure using beam elements for columns and plate elements (with both dispalcement and rotational degrees of freedom, and a FE-discretization of $N = 5$). The average quadratic error vs. discretization level of the calibration is displayed in the inlet, showing the convergence of the discrete approach with increasing mass discretization.

evaluation of a typical office building, inspired from the Department of Energy Reference Building Library for Medium Offices (Fig. 4): a 3-storey building of slab size 24×24 m^2, 0.1 m slab thickness, and storey height $h = 3.35$ m, resting on 16 columns of cross-sectional area 0.4×0.4 m^2. Different levels of discretization are herein employed to check the sensitivity and convergence of the discrete approach.

3.1 *Calibration*

The building is discretized considering 4 constant discretization lengths (columns and slabs): $N = h/l_{ij}^0 = 3,5,10$ and 15. For the elastic calibration, we consider, as 'experimental' frequency spectrum, the fundamental frequencies (eigenvalues and eigenvectors) obtained by Finite Element Analysis of the same structure discretized by beam and plate elements exhibiting both displacement and rotational degrees of freedom (in contrast to the discrete approach which has only displacement degrees of freedom defined by the position vector of each mass point).

Figure 5 displays the results of the frequency calibration procedure, Eqn. (14–15), together with the average quadratic error in function of the discretization level (inlet of Fig. 5). The error in frequency reduces with the discretization level close to $\sim N^{-2}$, showing the high convergence rate of the discrete approach with increase in discretization levels. That is, the discrete approach with $\sim 3N$ degrees-of-freedom accurately captures the frequency spectrum of a structure defined by $\sim 6N$ displacement and rotational degrees of freedom, showing the high efficiency of the MD-inspired approach compared to classical continuum-based approaches around the equilibrium state.

3.2 *Progressive collapse due to pressure loading*

Figure 6 displays a sample output of one MD-simulations, when the structure is subjected to a pressure load (modeled as concentrated forces on mass points with a load ramp fast enough to avoid a dynamic rebounce). The figure shows the evolution of the free energy U^{ijk} of all three-body interactions and of the external work achieved by prescribed pressure load along mass point displacements, as well as the deflection of the top floor in function of the potential energy. Following a quasi-linear load-displacement response which entails (1) a quadratic evolution of the potential energy in function of the prescribed forces respectively displacement, the structure reaches (2) its maximum capacity to store externally supplied work (by pressure forces) into recoverable free energy. As a consequence, bending bonds break leading to a successive drop of the bending interaction energy (curve labeled 'free energy'), which continues until elastic storage capacity is exhausted. This results in (3) the external work to approach the potential energy (1:1 – line).

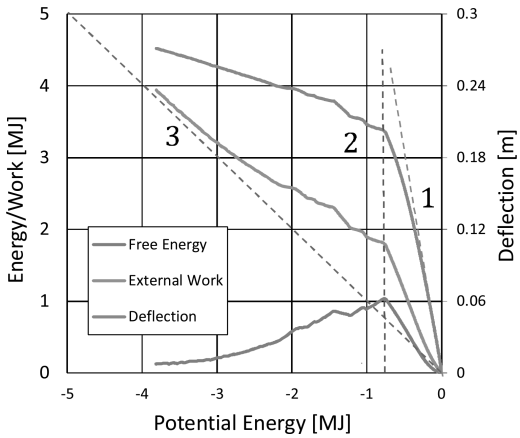

Figure 6. Sample output of MD-calculations in terms of free (bending) energy, external work by pressure forces applied to mass points, and deflection all in function of the overall potential energy of the structure.

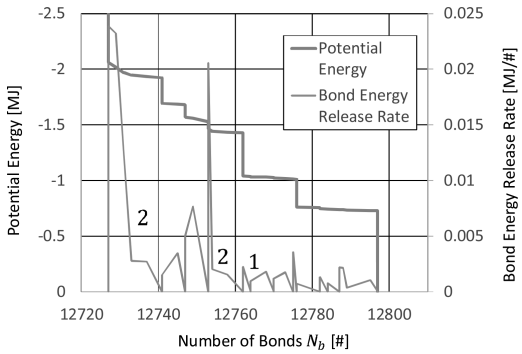

Figure 7. Progressive collapse analysis of structure: Potential energy and bond energy release rate vs. number of (unbroken) bonds. For $\mu > 0$, the bond-rupture process can be considered as (1) stable as long as the slope $\partial\mu/\partial N_b \geq 0$; and for (2) $\partial\mu/\partial N_b < 0$, is it unstable; which can be associated with a progressive collapse. (here for a potential energy $E_{pot} \approx 1.4$ MJ, thus well beyond the maximum free energy peak shown in Figure 6).

An important engineering question is what it is the load that defines the onset of progressive structural failure. In a first approach, it is of interest to analyze the evolution of the potential energy in function of the number of bonds, N_b. This is shown in Figure 7. To fully appreciate the displayed result, it is of importance to realize that the simulation are carried out in the so-called micro-canonical or NVE-ensemble, where N stands for the number of mass points, V for the volume of the simulation box and E for the overall energy, i.e. potential energy and kinetic energy; all assumed constant in the chosen NVE ensemble. Implicitly, this ensemble is the "engineering ensemble" of choice for structural dynamics simulations. In fact, a constant number of mass points simply means that no mass can leave the simulation box (closed system), even if all bonds to its neighbors are broken; a constant volume simply specifies the size of the box in which the structure resides; whereas a constant energy means that the sole source of internal energy dissipation is due to irreversible damage, fracture or plastic evolutions; and that the dissipated energy by bond breakage is transferred into kinetic energy. With this "engineering ensemble" definition in mind, it is of interest to consider two successive states, and calculate the internal dissipation due to bond breakage; that is—by analogy with classical fracture mechanics:

$$dD = -\mu dN_b \geq 0;\ \mu = \frac{\partial E_{pot}}{\partial N_b} \tag{20}$$

where μ (of dimension of energy) is recognized as the equivalent of the energy release rate in fracture mechanics, to which one can refer as bond energy release rate: it is the thermodynamic driving force of the bond breakage $dN_b \leq 0$, and derives from the systems potential energy $E_{pot} = F - W_F$ (with $F \approx U$ the Helmholtz free energy and W_F the work by prescribed forces along mass point displacements, $\vec{r}_i - \vec{r}_i^{\,0}$. Herein, we assume that the average kinetic energy of all mass points, E_k, is negligible as far as the evaluation of the free energy is concerned; that is, $F = U - TS \approx U$, with $T \sim E_k$ the temperature and S the entropy.) With a focus on the bending interaction energies, this is precisely what Figure 7 displays: the potential energy of the structure vs. the number of bonds, and the derived bond-energy release rate according to Eq. (20). It is then intriguing to push the fracture mechanics analogy, at the structural scale, one step further and define the rules of structural bond breakage by analogy with fracture mechanics in the form:

$$\mu - \mu_c \leq 0;\ dN_b \leq 0;\ (\mu - \mu_c)\, dN_b = 0 \tag{21}$$

where μ_c is the critical bond energy release rate (analogue of the fracture energy) at which bond breakage occurs. It is a structural property defining a structural energy dissipation capacity, such that $-\mu_c dN_b$ is the energy dissipated in the creation of broken bonds. Consider then a situation in which $\mu(N_b) = \mu_c$. For that any additional bond breakage, $N_b + dN_b < N_b$ occurs in a stable manner, it must be $\mu(N_b + dN_b) \leq \mu_c$; thus, considering a Taylor expansion:

$$\mu(N_b + dN_b) = \mu(N_b) + \frac{\partial \mu}{\partial N_b} dN_b \leq \mu_c \tag{22}$$

That is, much akin to the stability analysis of fracture processes (while noting that $dN_b < 0$):

$$\frac{\partial \mu}{\partial N_b} = \frac{\partial^2 E_{pot}}{\partial N_b^2} \geq 0 \tag{23}$$

As the bond-energy release rate thus increases in the process of bond rupture ($dN_b < 0$), the collapse can be considered to be progressive. This is shown in Figure 7.

3.3 *Fragility curves*

With a computationally efficient tool thus in place, it becomes possible to develop fragility curves by considering—for a typical class of structures—a variability of the bond energy input parameters. This is illustrated here for, respectively, a RC—and a wood structure, designed—deterministically-for similar limit loads. To obtain fragility curves, 400 simulations are carried out for each structure with randomly assigned, normally distributed limit angles for wood structures and limit curvatures for RC-structures; that is,

$$\left\| \vec{\vartheta}_i^{jk} \right\| \left(= \kappa l_{ij}^0 \right) \leq \epsilon \left(\vartheta_c, \sigma^2 \right) \tag{24}$$

where ϑ_c is the mean value defined by Eq. (19) calibrated from experimental data (Figs. 2 and 3),

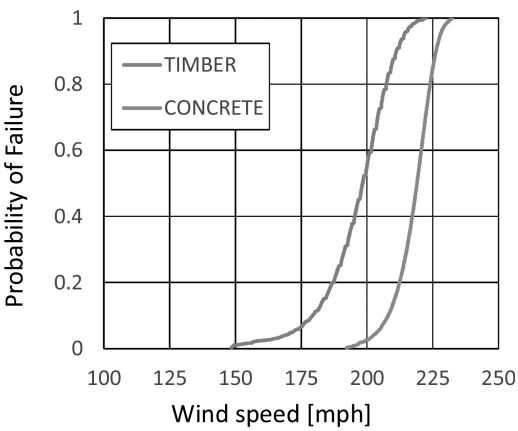

Figure 8. Example of fragility curves for a a reinforced concrete structure and a wood structure with timber-moment connections. The curves represents the cumulative distribution function (CDF) of the velocity corresponding to wind limit loads of the structures with randomly assigned normally distributed rupture angles (for wood) and rupture curvature (for RC-structures). [For reference, reported wind speeds of the September 19, 2017 Hurrican Maria that devastated Puerto Rico were 90–125 mph, with wind gusts of 175 mph].

whereas σ is the standard deviation. For purpose of example, we consider a coefficient of variation of CV = 50% for wood structure with, and CV = 30% for RC structures. The results are displayed in Figure 8, in terms of the cumulative distribution function (CDF) of the failure load, expressed here in corresponding wind-speeds $V \sim \sqrt{p}$. An interesting observation is that a CV of 30% for RC structures translates into a CV of the failure load of only 7% (wind speed CV = 7%); whereas a CV of 50% for wood structures entails a CV of the failure load of 13% (CV = 3%). This significant reduction in uncertainty from the bond-level to the structural scale highlights the capacity of the structural system to redistribute externally supplied energy (load) throughout the system, thus showing the value of heterogeneity on limit loads related to bond fracture. Similar results have been found for highly heterogeneous porous materials (Laubie et al., 2017b,c).

4 CONCLUDING REMARKS

The need for accurate predictions of resilience of buildings subject to extreme events requires a new generation of engineering tools that permit a damage assessment below the limit loads for which structures are classically designed. This damage of structures of both non-structural and structural members can be viewed as a sequence of bond breakage. The MD-inspired method here proposed addresses this bond breakage explicitly in a discrete way: rather than extending the classical realm of continuum based structural members into the non-linear regime, the MD-approach focusses on the elastic and in-elastic interactions between mass points that discretize the bulk of the structure. Provided a sufficient level of discretization, the MD-approach provides an efficient way to capture the energy transformations witnessed by a structure when subject to load. The following points deserves attention:

1. There are several advantages of the MD-method compared to e.g. Finite-Element-based continuum approaches; such as the absence of instabilities in MD, related in FEM to the loss of positive definiteness of the stiffness matrix and associated mesh-dependency issues; efficiency ($O(N)$ for MD vs. $O(N^2) \div O(N \log(N)$ of FEM; ease of bond removal etc., which makes the MD-based method highly efficient for large-scale recursive simulations required for e.g. fragility curve determination.
2. With a focus on internal interaction energy description, the MD-approach permits a straightforward link with other energy-based mechanics approaches, such as elasticity and linear and non-linear fracture mechanics. This

common denominator provides a clear path for calibration of the interaction potentials, from measured frequency spectra for energy parameters defining the equilibrium configuration, and from almost classical test data (such as moment-curvature curves) for bond energy parameters. Existing interatomic potential expressions are readily adapted to permit a representation of bond-forces and moments. Similarly, based upon thermodynamics derivations, the occurrence of progressive collapse mechanisms can be detected and used for structural optimization.

3. The simulation results presented in this paper were obtained within the context of NVE-ensemble simulations. This means that any form of energy dissipation is restricted to bond-breakage, and does not consider other sources of dissipation, such as viscous phenomena. The application of the proposed technique within the context of other ensembles is a natural extension. For instance, considering an NVT ensemble (where T stands for the temperature of an outside bath with which the system is in contact) would naturally entail consideration of a linear velocity-dependent damping in the equation of motion, which at "low enough prescribed temperature" would lead to the static response of the system (see Appendix I for temperature consideration). Here future work is needed in order to identify the link between engineering approach and physics approach enabled through a common language rooted in energy and dissipation representations; much akin to recent results obtained in the field of mesoscale poroelasticity of heterogeneous media (Monfared et al. 2017).
4. The fragility curves thus determined can be used in convolution expressions with probability of load occurrence to provide a rational criterion for the probability of failure of structures in specific environments (Noshadravan et al. 2017). These probabilities have become key to evaluate the resilience of structures and communities, and become now available for a much larger class of structures. Ultimately, we envision that such MD-based structural simulations can be used together with CFD simulations to evaluate the resilience of a city's building stock—an urgent task in view of the perils of global warming.

ACKNOWLEDGEMENT

This research was carried out by the Concrete Sustainability Hub (CSHub@MIT), with funding provided by the Portland Cement Association (PCA) and the Ready Mixed Concrete Research & Education Foundation (RMC E&F). The CSHub@MIT is solely responsible for content. Additional support was provided by ICoME2 Labex (ANR-11-LABX-0053) and the A*MIDEX projects (ANR-11-IDEX-0001-02) cofunded by the French program "Investissements d'Avenir," which is managed by the ANR, the French National Research Agency. All simulations were carried out with the open source code LAMMPS (Large-scale Atomic/Molecular Massively Parallel Simulator), distributed by Sandia National Laboratories, a US Department of Energy laboratory.

REFERENCES

Barbato M, Petrini F, Unnikrishnan VU, Ciampoli M. 2013. Performance-based hurricane engineering (PBHE) framework. Struct Saf 2013;45:24–35.

Charif A., Shannag M.J., Dghaither S. 2015. Ductility of reinforced lightweight concrete beams and columns. Lat. Am. J. Solids & Structures 2015, 11, 1251–1274.

Cimellaro GP, Reinhorn AM, Bruneau M. 2010. Framework for analytical quantification of disaster resilience. Eng Struct 2010;32:3639–49.

Federal Emergency Management Agency (FEMA), 2016. Hazus | FEMA.gov 2016. http://www.fema.gov/hazus

Gehloff M., Closen M., Lam F. 2010. Reduced edge distances in bolted timber moment connections with perpendicular to grain reinforcements. World Conference on Timber Engineering 2010, Paper 123.

Hattar C.P., Cheng, J.J.R. 1995. Development of moment connections in glued-laminated Alberta spruce and pine timber. Report A5020–121. Canadian Forest Service and Land and Forest Services, Edmonton, Alberta, Canada.

Insurance Information Institute 2016. Catastrophes: Insurance Issues | III 2016. http://www.iii.org/issue-update/catastrophes-insurance-issues.

Laubie, H., Monfared, S., Radjai, F., Pellenq R., Ulm, F.J. 2017a, Effective potentials and elastic properties in the Lattice-Element Method: Isotropy and Transverse Isotropy, J. Nanomech. Micromech. 7(3): 04017007.

Laubie, H., Monfared, S., Radjai, F., Pellenq R., Ulm, F.J. 2017b, Disorder-induced stiffness degradation of highly disordered porous materials, J. Mech. Phys. Solids 106207–228.

Laubie, H., Radjai, F., Pellenq R., Ulm, F.J. 2017c, Stress transmission and failure in disordered porous materials, Phys. Rev. Lett. 119, 075501.

Laubie, H., Radjai, F., Pellenq R., Ulm, F.J. 2017d, A potential-of-mean-force approach for fracture mechanics of heterogeneous materials using the lattice element method. Journal of the Mechanics and Physics of Solids 105, 116–130.

Monfared, S., Laubie, H., Radjai, F., Pellenq R., Ulm, F.-J. 2017, Mesoscale poroelasticity of heterogeneous media, J. Nanomech. Micromech. 7(4): 04017016.

Multihazard Mitigation Council 2005. NATURAL HAZARD MITIGATION SAVES: An Independent Study to Assess the Future Savings from Mitigation Activities Volume 1 -- Findings, Conclusions, and Recommendations. 2005.

Noshadravan, A., Miller T.R., Gregory J.G. 2017, A Life-cycle Cost Analysis of Residential Buildings Including

Natural Hazard Risk, Journal of Construction Engineering and Management 143 (7), 04017017.
Papadopoulos A. 2016. Resilience -- The Ultimate Sustainability -- Lessons from Failing to Develop a Stronger and Safer Built Environment. Resilience Action Fund.
Qomi MJA., Ulm F.J., Pellenq R. 2015. Physical origins of thermal properties of cement paste. Physical Review Applied 2015; 3, 064010.
Shinozuka M, Feng MQ, Lee J, Naganuma T. (2000) Statistical analysis of fragility curves. J Eng Mech 2000;126:1224–31.
Walker GR. 2011. Modelling the vulnerability of buildings to wind—a review. Can J Civ Eng 2011;38:1031–9.
Wang M., Song X., Gu X., Zhang Y., Luo L. 2015. Rotational behavior of bolted beam-to-column connections with locally cross-laminated glulam. J. Struct. Eng. 2015, 141(4), 04014121.
Yeo DH, Simiu E. 2011. High-Rise Reinforced Concrete Structures. Database-Assisted Design for Wind. J. Struct. Engrg 2011; 137(11): 1340–1349.

APPENDIX I: ON MASS-POINT DISCRETIZATION WITHIN THE LIMITS OF "CLASSICAL" MECHANICS

The employment of a molecular simulation approach within the framework of classical mechanics – as opposed to Quantum Mechanics – requires that the discretization respects the rules of classical mechanics (i.e. Newton's law (2)) as expressed by the de Broglie wavelength:

$$l_{ij}^0 \gg \lambda = \frac{h}{\sqrt{2\pi m k_B T}} \tag{A-1}$$

where l_{ij}^0 is the distance between mass points *i* and *j*, *h* is the Planck constant, *m* is the particle mass (typically $m = \rho A l_{ij}^0$ with ρ the mass density of the material and *A* the cross-sectional area of the structural member, k_B is the Boltzmann constant, and *T* the absolute temperature. It thus follows:

$$l_{ij}^0 \gg \frac{h^{2/3}}{\left(2\pi\rho A T\right)^{1/3}} \tag{A-2}$$

Considering $h = 6.626070040(81) \times 10^{-34}$ Js; $k_B = 1.38064852(79) \times 10^{-23}$ J/K; hence:

$$l_{ij}^0 \left(\frac{\rho A T}{\text{kg m}^2\text{K}} \right)^{1/3} \gg 1.7169 \times 10^{-15} \tag{A-3}$$

Eqn. (A-1) to (A-3) thus exclude simulations at (or close to) zero (Kelvin) temperature. A similar restriction applies to the Lattice Element Method (see Laubie et al. 2017d).

APPENDIX II: FROM 2-BODY BENDING INTERACTIONS TO 3-BODY INTERACTIONS—LINK WITH BEAM THEORY

There are different ways to account for three-body interactions related to bending, namely one that starts at the bond level *ij*, the other by considering jumps in angular variations at all mass points. The first approach forms much of the basis of classical beam theory; whereas the second is at the core of MD-type approaches, expressed e.g. by Eq. (7). This appendix shows the formal link between the two approaches in the context of harmonic potentials.

More specifically, the bond-level approach considers, in addition to the stretch potential, U_s^{ij}, a bending potential, U_b^{ij}, constructed in a way to satisfy per (mass-less) link *ij* the force and moment balance equations (Laubie et al. 2017a):

$$\vec{F}_i^{\,j} + \vec{F}_j^{\,i} = 0;\ \vec{F}_i^{\,j} = -\frac{\partial (U_s^{ij} + U_b^{ij})}{\partial \vec{\delta}_i} \tag{A-4}$$

$$\vec{M}_i^{\,j} + \vec{M}_j^{\,i} + \vec{r}_{ij} \times \vec{F}_j^{\,i} = 0;\ \vec{M}_i^{\,j} = -\frac{\partial U_b^{ij}}{\partial \vec{\vartheta}_i} \tag{A-5}$$

with $\vec{r}_{ij} = \vec{r}_j - \vec{r}_i$; $\vec{\delta}_i = \vec{r}_i - \vec{r}_i^{\,0}$ stands for the displacement vector of mass point *i*, and $\vec{\vartheta}_i$ for the vector of angular rotations. In order to satisfy (A-4) and (A-5), this requires to develop bending interactions in function of both lateral displacements $\theta_{ij}^b l_{ij}^0 = \vec{e}_b^{\,ij} \cdot (\vec{r}_{ij} - \vec{r}_{ij}^{\,0}) = \vec{e}_b^{\,ij} \cdot (\vec{\delta}_j - \vec{\delta}_i + \vec{r}_{ij}^{\,0} \times \vec{\vartheta}_i)$ and $\theta_{ij}^t l_{ij}^0 = \vec{e}_t^{\,ij} \cdot (\vec{r}_{ij} - \vec{r}_{ij}^{\,0}) = \vec{e}_t^{\,ij} \cdot (\vec{\delta}_j - \vec{\delta}_i + \vec{r}_{ij}^{\,0} \times \vec{\vartheta}_i)$ and angle variations, $\vartheta_{ij}^b = (\vec{\vartheta}_j - \vec{\vartheta}_i) \cdot \vec{e}_b^{\,ij}$ and $\vartheta_{ij}^t = (\vec{\vartheta}_j - \vec{\vartheta}_i) \cdot \vec{e}_t^{\,ij}$ in the link's local orthonormal basis $(\vec{e}_n^{\,ij}, \vec{e}_b^{\,ij}, \vec{e}_t^{\,ij})$; that is, in the case of harmonic expressions while neglecting torsion effects (Laubie et al. 2017a):

$$U_b^{ij} = \frac{1}{2}\varepsilon_{ij}^b \left[\left(\theta_{ij}^b\right)^2 - \vartheta_{ij}^t \theta_{ij}^b + \frac{1}{3}\left(\vartheta_{ij}^t\right)^2 \right] + \frac{1}{2}\varepsilon_{ij}^t \left[\left(\theta_{ij}^t\right)^2 - \vartheta_{ij}^b \theta_{ij}^t + \frac{1}{3}\left(\vartheta_{ij}^b\right)^2 \right] \tag{A-6}$$

Or, alternatively, in terms of the moment vectors:

$$U_b^{ij} = \frac{2}{\varepsilon_{ij}^b} \left[\left(M_i^{j,t}\right)^2 - M_i^{j,t} M_j^{i,t} + \left(M_j^{i,t}\right)^2 \right] + \frac{2}{\varepsilon_{ij}^t} \left[\left(M_i^{j,b}\right)^2 - M_i^{j,b} M_j^{i,b} + \left(M_j^{i,b}\right)^2 \right] \tag{A-7}$$

where ε_{ij}^b and ε_{ij}^t are bending interaction energy parameters, and $M_i^{j,l} = \vec{M}_i^{\,j} \cdot \vec{e}_l^{\,ij}$ and $M_j^{i,l} = \vec{M}_j^{\,i} \cdot \vec{e}_l^{\,ij} \left(l = t, b\right)$. If we let $\varepsilon_{ij}^b = 12EI_{bb} / l_{ij}$, $\varepsilon_{ij}^t = 12EI_{tt} / l_{ij}$, we readily recognize

that expressions (A-6) and (A-7) are nothing but the (free and complementary) bending energy of a linear elastic beam finite element with displacement and rotation degrees of freedom.

The previous 2-body bending interaction expressions can be recast in terms of a 3-body interaction energy of a mass point i connected to two other mass points j and k, when equating the energies of the two links:

$$U_b^{ijk} = \frac{1}{2}\left(U_b^{ij} + U_b^{ik}\right) = \frac{1}{2}\left(\vec{\vartheta}_i^{jk} \cdot \boldsymbol{C}_{\boldsymbol{ijk}}^b \cdot \vec{\vartheta}_i^{jk}\right) \tag{A-7}$$

where $\vec{\vartheta}_i^{jk} = \vec{\vartheta}_i^{j} - \vec{\vartheta}_i^{k}$ is the jump in angle at point i, whereas $\boldsymbol{C}_{\boldsymbol{ijk}}^b$ is the second order tensor of rotational stiffness that relates to the link energies $(\varepsilon_{ij}^b, \varepsilon_{ij}^t, \varepsilon_{ik}^b, \varepsilon_{ik}^t)$ by:

$$\left(\boldsymbol{C}_{\boldsymbol{ijk}}^b\right)^{-1} = 6\left[\frac{1}{\varepsilon_{ij}^b}\vec{e}_t^{\,ij} \otimes \vec{e}_t^{\,ij} + \frac{1}{\varepsilon_{ij}^t}\vec{e}_b^{\,ij} \otimes \vec{e}_b^{\,ij} + \frac{1}{\varepsilon_{ik}^b}\vec{e}_t^{\,ik} \otimes \vec{e}_t^{\,ik} + \frac{1}{\varepsilon_{ik}^t}\vec{e}_b^{\,ik} \otimes \vec{e}_b^{\,ik}\right] \tag{A-8}$$

If, in addition, harmonic torsion terms are considered in the link interaction potential [of the form $U_\tau^{ij} = \frac{1}{2}\kappa_{ij}(\vec{\vartheta}_j - \vec{\vartheta}_i)\cdot\vec{e}_n^{\,ij} = \frac{1}{2\kappa_{ij}}(M_i^{j,n})^2$ [with $M_i^{j,n} = \vec{M}_i^{\,j}\cdot\vec{e}_n^{\,ij} = -\vec{M}_j^{\,i}\cdot\vec{e}_n^{\,ij}$ the link's torsion moments satisfying momentum balance], one obtains expression (8) of the rotational stiffness tensor $\boldsymbol{C}_{\boldsymbol{ijk}}$.

Since the link energy expressions U_b^{ij} and U_τ^{ij} satisfy moment equilibrium (A-5), the global angular momentum is automatically satisfied; for which reason the MD-approach requires only satisfying the linear momentum (2) and thus the determination of the forces from Eqn. (6) and (10):

$$\vec{F}_i = -\sum_j^N \frac{\partial U_s^{ij}}{\partial \vec{r}_i} + \sum_j^N \frac{\partial U^{ijk}}{\partial \vec{r}_i} = \sum_j^N F_i^{j,n}\vec{e}_n^{\,ij} + \sum_j^N \vec{M}_i^{\,jk} \cdot \frac{\partial\, \vec{\vartheta}_i^{jk}}{\partial \vec{r}_i} \tag{A-9}$$

where $\vec{M}_i^{\,jk} = \boldsymbol{C}_{\boldsymbol{ijk}} \cdot \vec{\vartheta}_i^{jk}$; and, for small rotations (around the equilibrium position, for which harmonic expressions hold; see Fig. 1):

$$\vec{\vartheta}_i^{jk} \cong \frac{\vec{r}_{ij} \times \vec{r}_{ik} - \vec{r}_{ij}^{\,0} \times \vec{r}_{ik}^{\,0}}{\left\|\vec{r}_{ij}^{\,0}\right\| \left\|\vec{r}_{ik}^{\,0}\right\|} \tag{A-10}$$



Taylor & Francis
Taylor & Francis Group
http://taylorandfrancis.com

Computational Modelling of Concrete Structures – Meschke, Pichler & Rots (Eds)
© 2018 Taylor & Francis Group, London, ISBN 978-1-138-74117-1

Century-long durability of concrete structures: Expansiveness of hydration and chemo-mechanics of autogenous shrinkage and swelling

Zdeněk P. Bažant
Departments of Civil, Mechanical and Materials Science Engineering, Northwestern University, Evanston, USA

Saeed Rahimi-Aghdam
Department of Civil and Environmental Engineering, Northwestern University, Evanston, USA

ABSTRACT: Computations of long-time hygrothermal effects in concrete structures necessitate a physically based model for autogenous shrinkage and swelling of hardened portland cement paste. The present goal is to propose such a model. As known since 1887, the volume of cement hydration products is slightly smaller than the original volume of cement and water. However, this does not mean that the hydration reaction causes contraction of the cement paste and concrete. According to the authors' recently proposed paradigm, the opposite is true for porous cement paste as a whole. The growth of C-S-H shells around anhydrous cement grains pushes the neighbors apart and thus causes *volume expansion* of the porous cement paste as a whole, while the nanoscale volume contraction of hydration products contributes to porosity. The growth of ettringite and portlandite crystals may also cause additional expansion. On the material scale, the expansion always dominates over the contraction, i.e., the hydration per se is, in the bulk, *always expansive*, while the source of all of the observed shrinkage, whether autogenous or due to external drying, is the compressive elastic or viscoelastic strain in the solid caused by a decrease of chemical potential of pore water, with the corresponding decrease in pore humidity, increase of solid surface tension and, mainly, decrease of disjoining pressure. The low density C-S-H and high density C-S-H are distinguished in the proposed model. The selfdesiccation, shrinkage and swelling can all be predicted from one and the same unified model, as confirmed by comparisons with with the existing experimental evidence. The model is ready for use in finite element programs.

1 INTRODUCTION

The interaction of creep, shrinkage, pore humidity changes, water transport, and cement hydration is a complex problem, which has been debated for a long time. Although various useful models for particular phenomena have been developed, no comprehensive model capturing all these phenomena has been available until its general form was presented in Bažant et al. (2015).

One problem has been that most models assume the autogenous shrinkage, drying shrinkage and swelling to terminate with a horizontal asymptote. This assumption has been erroneous, caused by the widespread use of misleading plots in linear time scale and utter scarcity of long time tests. Nevertheless, there exist a few data (Persson 2002, Brooks & Wainwright 1983) whose logarithmic plots document that no asymptotic bound is in sight even after 30 years (Figs. 1a and 1b).

Here it is argued that they both the autogenous shrinkage and swelling will evolve logarithmically for decades, probably even centuries. What is the source of such behavior and how can it be modelled?

To answer this key question, let us begin with the autogenous shrinkage. Following Bažant et al. (2015), we consider its primary cause to be the decrease of pore relative humidity h due to selfdesiccation, no different to decrease of h due to external drying. According to RILEM TC 196-ICC (Kovler & Jensen 2007), the selfdesiccation is described as "the reduction of h in a sealed system when empty pores are generated". Obviously, the ultimate cause of selfdesiccation must be the hydration reaction.

However, the autogenous shrinkage, like drying shrinkage, must be getting prolonged by the *viscoelastic* behavior (i.e., creep plus elasticity, Bažant et al. 2015) of the solid skeleton of hardened cement paste loaded by pore pressure, reduced by a certain porosity factor. This is the second independent cause of long-term evolution of deformations.

The primary source of long-term autogenous shrinkage is the long-lived hydration process. Yet it has been widely believed that hydration terminates

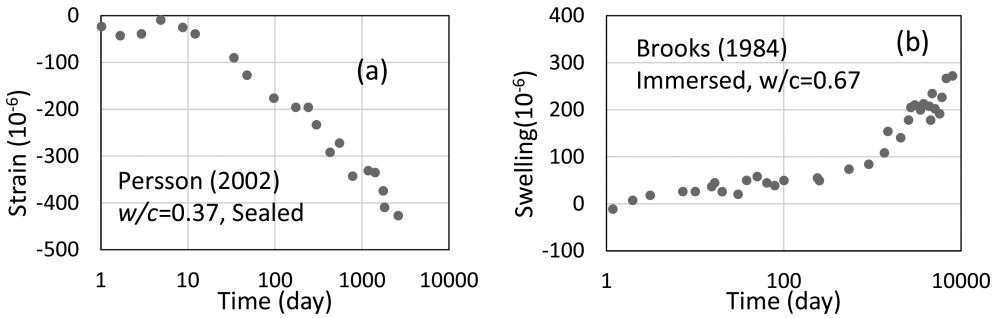

Figure 1. Long-term autogenous shrinkage and swelling experiments. a) autogenous shrinkage, b) swelling.

in about a year. But that is correct only in specimens thin enough to dry up uniformly within a year. In the cores of massive walls exposed to drying, high enough h may persist for decades, even centuries. What makes the hydration process long-lived and progressively slower is that, after the first day, the anhydrous cement grains become enveloped in contiguous shells of cement hydrate. The shells are highly impermeable and allow only a very slow transport of water toward the anhydrous grain interface. In addition, as these shell gradually thicken, the pore relative humidity h (and thus the chemical potential of water, μ) decrease, which slows down and further prolongs the hydration. This phenomenon was recently mathematically described by Rahimi-Aghdam et al. (2017).

As shown in this work, if h in the pores does not drop below about 0.7, the hydration reaction continues for several decades, probably even centuries. This must cause similar long-time evolution of autogenous shrinkage.

There is another phenomenon that doubtless prolongs greatly the autogenous shrinkage—the aging *viscoelasticity*, i.e., the creep plus elastic deformation. Maintaining local thermodynamic equilibrium requires equality of the chemical potential μ in all the phases of pore water. So a decrease of pore humidity h must produce tensile stress changes in all the phases of water (vapor, liquid, adsorbed and hindered adsorbed). These stress changes must be balanced by compressive stress changes, whichin turn must cause compressive elastic deformation and creep in the solid skeleton of cement paste.

In water immersion, most concretes are swelling. As several experiments show, the swelling is a also long-lived phenomenon. As documented by a few tests, concrete specimens immersed for a decade continue to expand logarithmically with no bound in sight. In immersed specimens, pores near the surface are saturated, $h = 1$, and those in the core undergo selfdesiccation until the saturation front arrives. From this it is clear that the expansion cannot be driven by pore humidity. Hence, it must be driven by chemical expansion during hydration. Since it is inconceivable for the hydration to be both expansive in water immersion and contractive without immersion, we have only two candidate hypotheses—the hydration is *always either contractive or expansive*.

If it were the former, the swelling under water immersion would not be physically explicable. But if it is the latter, the autogenous and drying shrinkage is explicable. Indeed, the tensile stress changes in pore water due to drying or selfdesiccation must be balanced by compression in the solid skeleton of cement paste, which will inevitably cause viscoelastic compressive strain in the solid skeleton. Although contrary to traditional thinking, this leads to a new paradigm (Bažant et al. 2015):

The deformation of porous hardened cement paste caused by the hydration process is always expansive.

At the dawn of cement research, it was established by Le Chatelier, and later confirmed by Powers and others, that the cement hydration reaction is always contractive, i.e., the volume of the cement gel produced by hydration is always smaller than the sum of the original volumes of anhydrous cement and water. But now we claim that this is true only on the level of nanoscale microscopic powder. In the bulk, with a sufficient pore volume growth and constant relative humidity in the pores, a porous material *must always expand*, even if the volume of solid in the material decreases.

In hardened portland cement paste, the growth of two contacting C-S-H shells around anhydrous cement grains must push the neighbors apart and thus cause volume expansion of the porous cement paste during hydration (Bažant, Donmez, Masoero, & Aghdam 2015). The compression force within each pair of contacting neighbors, akin the crystal growth pressure, must be balanced by overall tension in the solid skeleton of cement

paste. Like hydration, this tension evolves for decades, and so must the swelling. So the long-term hydration causes not only autogenous shrinkage, but also swelling. Furthermore, the long-time loading of the solid skeleton by pore pressure must, of course, produce not only elastic deformation but also creep.

It should be noted that several studies suggested that the source of swelling should be the growth of ettringite crystals (Taylor, Famy, & Scrivener 2001, Diamond 1996). But this could be only one minor contribution and can not be the basic cause of the long-term expansion, for two reasons. First, the ettringite crystals do not form with a delay of many years. Rather, they dissolve tn early age and thus cannot affect long-term swelling. Second, the long-term swelling can be seen in any type of cement regardless the amount of C_3A phase.

Therefore, even if we would admit the ettringite crystal growth to be cause swelling in the initial days, it could not explain the swelling in the long term. The final possible source of long-term swelling is Alkali-Silica reaction (ASR). Although ASR can cause considerable swelling, but only if the alkali-content of the cement paste be high enough and aggregates be reactive (Bažant & Rahimi-Aghdam 2016, Rahimi-Aghdam, Bažant, & Caner 2016) that is usually not the case in normal laboratory experiments.

2 EQUATIONS GOVERNING BOTH SHRINKAGE AND SWELLING

For normal saturated elastic porous material, the volumetric strain ϵ is related to the volumetric mean stress σ and the fluid pore pressure p through the equation:

$$\epsilon = \frac{\sigma_{eff}}{K} = \frac{\sigma + bp}{K} \tag{1}$$

where K is the bulk modulus of the dry skeleton and b is the Biot coefficient which is calculated as (Biot & Willis 1957):

$$b = 1 - \frac{K}{K_s} \tag{2}$$

Here K_s is the bulk modulus of the solid skeleton; for cement paste in particular, K_s is the bulk modulus of C-S-H gel and can be considered as K_s = 45 MPa (Nielsen 1991). The foregoing equations are valid only for saturated pores. In the cement paste and other partly saturated media, the equations need to be modified so as to consider several pore fluids. For instance, unsaturated cement paste contains liquid water, water vapor, adsorbed water and air. Usually, water vapor and air (gaseous phases) are considered together as one gas phase.

To deal with unsaturated case, we need the average pore fluid stress p^*. In the case of cement paste:

$$p^* = S_w p_w + S_g p_g \tag{3}$$

where p_g and p_w are, respectively, the pressure in gas and liquid water phases. The adsorbed water can be, for our purpose, ignored; S_w and S_g are the saturation degrees of liquid water and gas:

$$S_w = \frac{\phi_w}{\phi}; \quad S_g = \frac{\phi_g}{\phi} = 1 - S_w \tag{4}$$

where ϕ = total porosity, ϕ_w = porosity occupied by water and ϕ_g = porosity occupied by gas.

Drying caused a decrease of pressure, p_w, in the liquid phase in cement paste pores, which has three sources:

1. increase in capillary tension ($p_c < 0$) according to the Kelvin-Laplace (KL) theory,
2. decrease Δp_d of disjoining pressure p_d in nanopores (Bažant 1972, Bažant & Bazant 2012, Bažant & Jirásek 2017), and
3. decrease δp_s of pressure p_s caused by increase $\Delta\gamma$ of solid-fluid surface tension that results from a decrease of spreading pressure in adsorbed water layer on the surface on nano scale globules of C-S-H. Probably Δp_d is most important.

Fortunately, all the three sources of pressure decrease depend on the relative humidity, h, in a similar way, as follows:

$$p_i = C \ln h \tag{5}$$

Therefore, it is logical to consider p_w to depend on the relative humidity similarly:

$$p_w = C_w \ln h \tag{6}$$

Coussy et al. (2004) derived the modified relations for unsaturated cement paste, omitting cement paste aging and creep. Here we adopt their formulation but extend it to include the aging and creep. Based on Coussy et al. (2004), the variation of solid matrix free energy $\psi(\epsilon, \phi)$ can be calculated as,

$$\mathrm{d}\psi(\epsilon, \phi) = \sigma d\epsilon + \pi d\phi \tag{7}$$

where π is the equivalent pressure, which can be calculated as:

$$\pi = p^* - U; \quad U = \int_{S_w}^{1} (p_g - p_w)\mathrm{d}S_w \tag{8}$$

For normal saturated porous materials, the change of the free energy of solid can be calculated as,

$$\mathrm{d}\,\psi(\epsilon,\phi) = \sigma d\epsilon + p d\phi \tag{9}$$

Comparing Eqs. 9 and 7, we can conclude that the equivalent pressure π in an unsaturated medium acts the same way as the pressure p in a saturated medium. Using Eqs. 3, 4 and 8, the variation of equivalent pressure can be calculated as:

$$\mathrm{d}\pi = S_w \mathrm{d}p_w + S_g \mathrm{d}p_g \tag{10}$$

It should be noted that Coussy's use of p^* is a simplification of the physical reality, since the water molecules cannot pass from one pore to the next while remaining in the vapor or liquid state. Rather they must first enter the adsorbed water phase and pass to the neighboring capillary pore through nanopore necks filled by hindered adsorbed water (Bažant 1972, Bažant & Jirásek 2017). Thus, what really matters is the gradient of the spreading pressure (or chemical potential μ) along the hindered adsorbed water layer. Effectively, we assume this gradient to be proportional to grad p^* (or grad h, or grad μ). Note that, the better and more detailed method to consider the effect of pores with significantly different sizes is considering three-phase medium (Bažant, Chau, & Rahimi-Aghdam 2017).

For cement based materials, the pressure p_g usually remains close to atmospheric pressure that is significantly smaller than liquid water pressure p_w. Therefore, we can neglect p_g and, using equation 6, write:

$$\mathrm{d}\pi = S_w \mathrm{d}p_w = C_w S_w \frac{\mathrm{d}h}{h} \tag{11}$$

Now that we have the equation for equivalent pressure change, we can calculate the volumetric strain considering the creep:

$$\epsilon(t) = \int_0^t J(t-t')\mathrm{d}\sigma_{eff}(t') \tag{12}$$

where t' is the time of applying load increment $\mathrm{d}\sigma_{eff}(t')$ and J is the non-aging creep compliance function. Using Biot coefficient b and the equivalent pressure π, we can calculate $\mathrm{d}\sigma_{eff}$ as:

$$\mathrm{d}\sigma_{eff} = \mathrm{d}\sigma + b\mathrm{d}\pi = \mathrm{d}\sigma + bC_w S_w \frac{\mathrm{d}h}{h} \tag{13}$$

Until now we have not considered the effect of swelling due to the hydration process. To this end, we can consider an additional pressure (akin to crystal growth pressure) that is induced by the macro-expansive hydration process, σ_{hyd}. For simplicity, we can assume it to depend linearly on the hydration degree. Adding this pressure, we can rewrite equation 13 as:

$$\mathrm{d}\sigma_{eff} = \mathrm{d}\sigma + b\mathrm{d}\pi = \mathrm{d}\sigma + b\left\{C_w S_w \frac{\mathrm{d}h}{h} + C_{hyd}\mathrm{d}\alpha + \mathrm{d}\sigma_{cry}\right\} \tag{14}$$

where C_{hyd} is a calibration parameter and $\mathrm{d}\sigma_{cry}$ represents any possible additional pressure due to crystal growth. This study focuses on the swelling due to hydration, and so we assume $\mathrm{d}\sigma_{cry} = 0$.

It should be mentioned that aging has a considerable effect on the stiffness of cement-based materials. For simplicity, we consider the stiffness of cement paste to be related to the hydration degree linearly:

$$K(\alpha) = K_u\left(\frac{\alpha - \alpha_{set}}{\alpha_u - \alpha_{set}}\right) \tag{15}$$

The Biot coefficient depends on the bulk modulus K and can be calculated as

$$b(\alpha) = 1 - \frac{K(\alpha)}{K_S} \tag{16}$$

Finally, we must introduce a realistic equation for the creep compliance of solid skeleton, J, loaded by pore water pressure. This compliance is doubtless different from the creep compliance of the cement paste as a whole (which includes the load-bearing adsorbed water in nanopores). For limited time periods, we can ignore the aging due to hydration and, for lack of deeper information, we assume a simple power function:

$$J(t-t') = c_0 + c_1(t-t')^n \tag{17}$$

where c_0 corresponds to the instantaneous response; constant c_1 and exponent n are two calibration parameters.

Now we try to predict the autogenous shrinkage for cement pastes with different water-cement ratios, w/c. Their value changes not only the amount of selfdesiccation but also the strength and stiffness. Therefore, to predict the autogenous shrinkage correctly, we need a model that can predict the stiffness, E, for different cement pastes correctly. In the literature, there are several empirical models for predicting the stiffness of concrete from

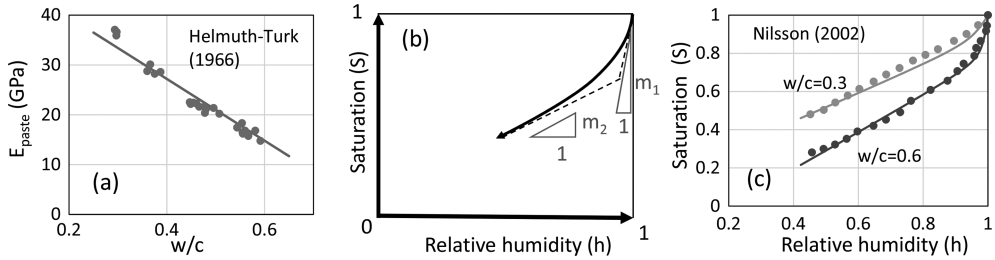

Figure 2. The stiffness of cement paste and desorption isotherm. a) Stiffness of cement paste with different water content, b) bi-linear desorption isotherm and c) experimental vs. simulated desorption isotherm for cement pastes with different water content.

its strength f_c', but they are not suitable for the hardened cement paste. Therefore, we propose the following simple, empirically calibrated, equation that can predict the stiffness of cement paste for different w/c (Figure 2a):

$$E = A - B\,w/c, \quad A = 52GPa, B = 62GPa \tag{18}$$

The Poisson ratio for cement pastes with different w/c is considered the same, $v = 0.2$.

3 DESORPTION AND ABSORPTION ISOTHERM

At constant temperature, the relation between evaporable water w_e and relative humidity h is known as the sorption isotherm. More specifically, the desorption isotherm describes w_e as a function of h at decreasing water content (or drying), while the absorption isotherm (sometimes called just the sorption isotherm) applies to increasing water content (wetting). The sorption isotherms exhibit pronounced hysteresis, which means that the absorption isotherm lies significantly below the desorption isotherm. Here we focus on drying and propose a simple equation for the desorption isotherm.

To have dimensionless parameters, the sorption isotherm is sometimes defined as a relation between the relative humidity, h, and the saturation degree, S (rather than the water content), which is what is adopted here. It makes it easier to compare the desorption isotherms for concretes with different water contents.

As shown by several studies (Nielsen 1991, Xi, Bažant, & Jennings 1994), the desorption isotherm is highly nonlinear and its shape depends significantly on the concrete properties. Based on experiments, the most important parameters are the water-cement ratio and age. In addition, some studies show that adding certain admixtures can change desorption isotherm significantly. Especially, adding silica fume makes the pore sizes more uniform and makes steeper the decrease of pore relative humidity at states below full saturation (Baroghel-Bouny, Mounanga, Khelidj, Loukili, & Rafaï 2006, Jiang, Sun, & Wang 2006). Various methods to obtain the desorption isotherm have been proposed, but either they are too complicated to use or necessitate several calibration parameters hard to determine.

This study proposes some simple empirical equations for the desorption isotherm. Based on experimental results, for high relative humidities (h > 50%) desorption isotherm can be fairly approximated by two straight lines. Accordingly, the isotherm is formulated as a smooth curve that has these two straight lines as asymptotes (see Fig. 2b), as follows:

$$\mathrm{d}h = k(h,\alpha)\mathrm{d}S \tag{19}$$

$$\frac{1}{k(h,\alpha)} = m_2 + (m_1 m_2)\frac{1}{1+\left(\frac{1-h}{1-h^*}\right)^2} \tag{20}$$

where $k(h, \alpha)$ is the inverse slope of the desorption isotherm; m_1 and m_2 are the slopes of the two straight lines (which can be more simply used to approximate desorption isotherm), and h^* is the intersection point of the two straight lines. These parameters can be empirically estimated as follows:

$$m_1 = \frac{f_\alpha}{c_{SF}}\left[2.4 + \left[\left(\frac{w/c - .13}{0.19}\right)^{1.5}\right]\right] \tag{21}$$

$$m_2 = c_{SF}^{0.5}\,1.18\,w/c^{0.4} \tag{22}$$

$$h_s = 1 - fc_{SF}\frac{0.03}{w/c^2} \tag{23}$$

$$f_\alpha = (\alpha_u - \alpha_0)/(\alpha - \alpha_0) \tag{24}$$

Parameter c_{SF} is included to account for possible addition of silica fume. In its absence $c_{SF} = 1$, and

generally, for a finite specific content ξ_{SF} of silica fume (mass of silica fume/mass of cement):

$$c_{SF} = 1 + 2\xi_{SF} \tag{25}$$

Fig. 2c compares the calculation results (solid curves) with the measured data using aforementioned equations. As it can be seen, the simulated desorption isotherms are in a good agreement with the experimental results. It should be mentioned that some studies showed some minor effect of temperature on isotherm, but for simplicity this effect has been neglected.

4 SELFDESICCATION

According to RILEM TC 196-ICC, the selfdesiccation is defined as "the reduction in the internal relative humidity of a sealed system when empty pores are generated". It can occur in any concrete cured under sealed conditions, but its effects are quite dependent on the sizes of the generated empty pores. The size of empty pores depends mainly on the water-to-cement ratio (w/c), the degree of hydration, the particle size distribution of cement, and the type of admixtures. The pore size is smaller for lower *w/c* and finer cements. A smaller pore size leads to more pronounced selfdesiccation. Furthermore, adding some fine admixtures such as the silica fume decreases the pore size and thus increases the value of selfdesiccation.

To calculate the selfdesiccation correctly, we should start with the hydration reaction and the amount of water that is used in this reaction. The ordinary portland cement (OPC) consists of various phases such as alite (C_3S), belite (C_2S), calcium aluminate (C_3A), tetracalcium aluminoferrite (C_4AF) and gypsum, as well as minor other phases (we use cement chemistry notation in which C, S, A and F stand, respectively, for CaO, SiO_2, Al_2O_3 and Fe_2O_3) (Taylor, 1997). C_3S and C_2S are two major components of OPC and their ratio depends on cement type. To measure the amount of consumed water in the hydration reaction, for simplicity we consider just C_3S and C_2S and we assume the cement to be composed of 8% C_3S and 20% C_2S. The nano-level hydration reaction of C_2S and C_3S can be summarized as (Qomi, Krakowiak, Bauchy, Stewart, Shahsavari, Jagannathan, Brommer, Baronnet, Buehler, Yip, et al. 2014),

$$C_2S + 2.1H \rightarrow \quad C_{1.7}SH_{1.8} + 0.3CH$$
$$C_3S + 3.1H \rightarrow \quad C_{1.7}SH_{1.8} + 1.3CH$$

where $C_{1.7}SH_{1.8}$ and H are, respectively, the typical C-S-H type found in OPC pastes and water. Table 1 summarizes the molar volume and density of different components in hydration reactions. Note that, in the aforementioned hydration reactions, the C-S-H pores were assumed to be empty, and so it is necessary to include additional water that is trapped in C-S-H pores.

Recently it became well established (Constantinides, Ulm, & Van Vliet 2003, Jennings 2000, Tennis & Jennings 2000) that two types of C-S-H are produced during hydration reaction; low density C-S-H (LD), with porosity 36%, and high density C-S-H (HD) with porosity 26%. Jennings and Thomas (2000) showed that, for different *w/c* values, the ratio between these two C-S-H types varies. For instance their model (JT model) predicted that for $w/c = 0.45$, there are 50% HD and 50%LD while for $w/c = 0.25$ there are 80% HD and 20% LD. Therefore, the average porosity of C-S-H, ϕ_{gp}, mainly depends on *w/c*. Here, for simplicity, we assume a linear relation limited by lower and upper bounds, as follows:

$$0.27 < \phi_{gp} = 0.28 + .2(w/c - 0.3) < 0.35 \tag{26}$$

The lower and upper bounds on ϕ_{gp} are introduced because considering only the LD or HD phases may be insufficient.

Having quantified the hydration relation and calculated the porosity of C-S-H, we can calculate the total volume of water, ξ_{gc}, per unit volume of cement, that is used in hydration to produce a C-S-H gel, the volume of empty pores, ξ_{bw}, and the volume of water that fills gel pores, ξ_{fp}:

$$\xi_{wc} = \xi_{bw} + \xi_{fp} \tag{27}$$

$$\xi_{bw} = w_{C_2S}\xi_{bw}^{C_2S} + w_{C_3S}\xi_{bw}^{C_3S} \tag{28}$$

$$\xi_{fp} = \phi_{gp}\xi_{gc}S_{gp} \tag{29}$$

where S_{gp} = saturation degree of gel pores; w_{C_2S} and w_{C_3S} = volume ratio of C_2S and C_3S respectively; $\xi_{bw}^{C_2S}$ and $\xi_{bw}^{C_3S}$ = volume of water that is consumed to hydrate one unit volume of C_2S and

Table 1. The molar volume and density of calcium-silicate phases present in the cement paste.

Phase	Molar volume (cm^3/mol)	Density (g/cm^3)
C_3S	72.9	3.15
C_2S	52.7	3.28
H_2O	18.0	1.0
C-S-H	110.1	2.05
CH	33.1	2.24

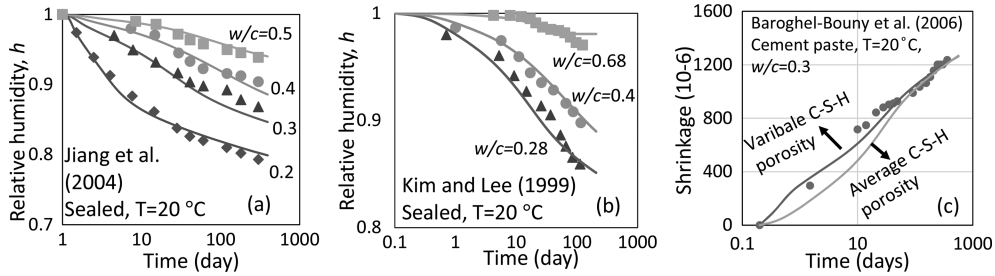

Figure 3. Self-desiccation and autogenous shrinkage. a) predicted vs. experimental relative humidity decrease in sealed specimens (self-desiccation) for experiment by Jiang et al. (2005), b) predicted vs. experimental relative humidity decrease in sealed specimens (self-desiccation) or experiment by Kim and Lee (2005), and c) predicted vs. experimental autogenous shrinkage using both average porosity and variable porosity.

C_3S, respectively, and produce C-S-H gel with empty pores. If we assume that 80% of cement is the C_3S and 20% C_2S, we have.

$$\xi_{bw} = 0.2(37.8/52.7) + 0.8(55.8/72.9) = 0.755$$
$$\xi_{gc} = 0.2(110/52.7) + 0.8(110/72.9) = 0.487$$

Since the gel pores are smaller than the capillary pores, in the literature the gel pores have always been considered as saturated. But Rahimi-Aghdam et al. (2017) show that this cannot be true and that some of the gel pores must be treated like unsaturated capillary pores. Otherwise the water in gel pores would always have a uniform chemical potential and we could not explain the stoppage of hydration at a certain low relative humidity. In this Study, we assume 33% of gel pores to have the same saturation degree as the capillary pores, and 67% the same as nanopores (which, at high relative humidities, are always saturated). Accordingly, for a high relative humidity, the saturation degree of capillary pores is:

$$S_{gp} = 0.67 + 0.33 S_{cp} \tag{30}$$

Fig. 3a,b show the predicted selfdesiccation using the aforementioned parameter. As it can be seen, the predictions agree with the experiments well. In spite of that, the predicted autogenous shrinkage curves show some delay (see Fig. 3c). This should be due to the fact that, initially, most of produced C-S-H gel is LD and, as hydration reaction goes on, the ratio of HD increases. This phenomenon may be formulated as,

$$\phi_{gp} = r_{LD}\phi_{LD} + r_{HD}\phi_{HD} = 0.36 r_{LD} + 0.26(1 - r_{LD}) \tag{31}$$

$$r_{LD} = \exp\left(-c_{w/c}\frac{\alpha}{\alpha_u}\right) \tag{32}$$

$$c_{w/c} = \frac{0.17}{(w/c - 0.05)^4} \tag{33}$$

where r_{LD} and r_{HD} are the volume fractions of the C-S-H gel produced. Using either the average porosity or a variable porosity C-S-H, one finds the predicted selfdesiccation curves to be almost the same but, as seen in Fig. 3c, the use of average porosity leads at early times to cause a delay in the prediction of autogenous shrinkage. Therefore, only the variable humidity method is employed here.

5 AUTOGENOUS SHRINKAGE PREDICTIONS

To check how good the predictions of the present model are, we begin with the experiments of Jiang et al. (2006), in which the autogenous shrinkage of cement pastes was measured for different water-cement ratios. Fig. 4a compares the calculated curves with the measured points. As seen, the agreement is good. Note that the model was calibrated only by matching of the measured bulk modulus of the cement paste with $w/c = 0.25$, and all the rest was predicted.

The second set of experiments considered here is a similar set by Baroghel-Bouny et al. (2005). As seen in Fig. 4b, the predicted results are in good agreement with the experimental ones except for the case of the highest water content, $w/c = 0.50$, in which the experimental results show a greater initial swelling than predicted. The reason for this error is probably the extra initial swelling due to growth of ettringite crystals, which is not considered in the present model.

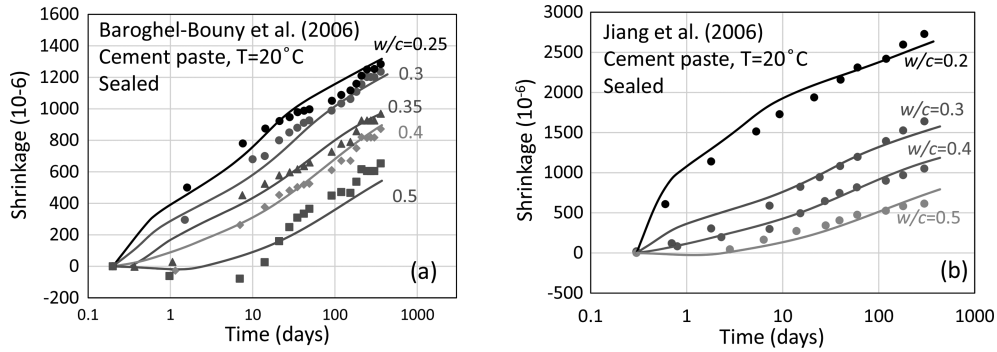

Figure 4. Comparison of predicted curves with measured values of autogenous shrinkage for cement pastes with different watercement ratios.

6 SIZE EFFECT ON SWELLING UNDER WATER, TRANSITING FOR LARGE SIZES TO SHRINKAGE

Despite lack of experimental evidence, it is here predicted that there must be a large size effect on the diffusion of water that gradually fills the self-desiccated pores to 100% humidity. This diffusion is much slower than drying. As shown in Bažant (1975) (see also (Bažant & Jirásek 2017)), the amount of water that needs to be delivered to the propagating front of wetting is large because the humidity at the selfdesiccated front must be raised to 100% before the wetting front can advance farther.

Thus the interface condition at the advancing wetting front gives a large interface sink of water, which greatly slows down the advance of the diffusion front of wetting. Note that a similar (negative) sink is absent at the front of drying which, therefore, propagates much faster.

The result is that structural members thicker than about 0.2 m must be expected to always shrink (autogenously) under water for at least a century (Miyazawa & Monteiro 1996), due to selfdesiccation of most of their interior volume. The swelling of the (relatively thin) surface layer is cancelled by inducing a compressive stress parallel to the surface, which is beneficial as it prevents the formation of surface cracks.

7 CONCLUSION

The new hypothesis that, on the porous material scale, the hydration reaction is always expansive (Bažant et al., 2015) allows grand unification of models for drying shrinkage, autogenous shrinkage and swelling under water immersion, and especially their long-time (multi-decade and century long) evolution. These diverse phenomena can all be predicted from one and the same material model, even for decade-long (and probably century -long) durations. When used in computer-aided design, this grand unification should be helpful for ensuring century-long durability, which is now seldom achieved for many large concrete structures.

ACKNOWLEDGMENT

Partial financial supports from the U.S. Department of Transportation, provided through Grant 20778 from the Infrastructure Technology Institute of Northwestern University, and from the NSF under grant CMMI-1129449, are gratefully appreciated.

REFERENCES

Baroghel-Bouny, V., P. Mounanga, A. Khelidj, A. Loukili, & N. Rafaï (2006). Autogenous deformations of cement pastes: part II. w/c effects, micro–macro correlations, and threshold values. *Cement and Concrete Research 36*(1), 123–136.

Bažant, Z. (1972). Thermodynamics of interacting continua with surfaces and creep analysis of concrete structures. *Nuclear engineering and design 20*(2), 477–505.

Bažant, Z. (1975). Pore pressure, uplift, and failure analysis of dams. In *Proc., Symp. on Criteria and Assumptions for Numerical Analysis of Dams (held at Univ. of Wales, Swansea). Brit. Nat. Committee on Large Dams*, pp. 781–808.

Bažant, Z., A. Donmez, E. Masoero, & S.R. Aghdam (2015). Interaction of concrete creep, shrinkage and swelling with water, hydration, and damage: Nanomacro-chemo. In *CONCREEP 10, 10th Int. Conf. on Mechanics and Physics of Creep, Shrinkage and Durability of Concrete and Concrete Structures, held in Vienna, Austria, Sept*., pp. 1–10. ASCE, Washington, D.C.

Bažant, Z.P. & M.Z. Bazant (2012). Theory of sorption hysteresis in nanoporous solids: part I: snap-through instabilities. *Journal of the Mechanics and Physics of Solids 60*(9), 1644–1659.

Bažant, Z.P., V.T. Chau, & S. Rahimi-Aghdam (2017). Three-phase cracked porous medium: Shale fracking and ASR damage. In *Poromechanics VI (Sixth Biot Conference on Poromechanics, held in Paris, France, July.)*, pp. 1–8. ASCE.

Bažant, Z.P. & M. Jirásek (2017). *Creep and Hygrothermal Effects in Concrete Structures*. Springer Verlag, 930 pp., in press.

Bažant, Z.P. & S. Rahimi-Aghdam (2016). Diffusioncontrolled and creep-mitigated ASR damage via microplane model. I: Mass concrete. *Journal of Engineering Mechanics 143*(2), 04016108.

Biot, M. & D. Willis (1957). The elastic coefficients of the theory of consolidation. *J. appl. Mech 24*, 594–601.

Brooks, J. & P. Wainwright (1983). Properties of ultrahigh-strength concrete containing a superplasticizer. *Magazine of Concrete Research 35*(125), 205–213.

Constantinides, G., F.-J. Ulm, & K. Van Vliet (2003). On the use of nanoindentation for cementitious materials. *Materials and structures 36*(3), 191–196.

Coussy, O., P. Dangla, T. Lassabatère, & V. Baroghel-Bouny (2004). The equivalent pore pressure and the swelling and shrinkage of cement-based materials. *Materials and structures 37*(1), 15–20.

Diamond, S. (1996). Delayed ettringite formation. Processes and problems. *Cement and Concrete Composites 18*(3), 205–215.

Jennings, H.M. (2000). A model for the microstructure of calcium silicate hydrate in cement paste. *Cement and concrete research 30*(1), 101–116.

Jiang, Z., Z. Sun, & P. Wang (2006). Internal relative humidity distribution in high-performance cement paste due to moisture diffusion and self-desiccation. *Cement and Concrete Research 36*(2), 320–325.

Kovler, K. & O. Jensen (2007). *Report 41: Internal Curing of Concrete-State-of-the-Art Report of RILEM Technical Committee 196-ICC*, Volume 41. RILEM Publications S.A.R.L. France, Bagneux.

Miyazawa, S. & P. Monteiro (1996). Volume change of high-strength concrete in moist conditions. *Cement and Concrete Research 26*(4), 567–572.

Nielsen, L.F. (1991). *A research note on sorption, pore size distribution, and shrinkage of porous materials*. Danmarks Tekniske Højskole. Laboratoriet for Bygningsmaterialer.

Persson, B. (2002). Eight-year exploration of shrinkage in high-performance concrete. *Cement and Concrete Research 32*(8), 1229–1237.

Qomi, M.A., K. Krakowiak, M. Bauchy, K. Stewart, R. Shahsavari, D. Jagannathan, D. Brommer, A. Baronnet, M. Buehler, S. Yip, et al. (2014). Combinatorial molecular optimization of cement hydrates. *Nature communications 5*(4960).

Rahimi-Aghdam, S., Z.P. Bažant, & F.C. Caner (2016). Diffusion-controlled and creep-mitigated ASR damage via microplane model. II: Material degradation, drying, and verification. *Journal of Engineering Mechanics 143*(2), 04016109.

Taylor, H., C. Famy, & K. Scrivener (2001). Delayed ettringite formation. *Cement and concrete research 31*(5), 683–693.

Tennis, P.D. & H.M. Jennings (2000). A model for two types of calcium silicate hydrate in the microstructure of Portland cement pastes. *Cement and concrete research 30*(6), 855–863.

Xi, Y., Z.P. Bažant, & H.M. Jennings (1994). Moisture diffusion in cementitious materials adsorption isotherms. *Advanced Cement Based Materials 1*(6), 248–257.



Taylor & Francis
Taylor & Francis Group
http://taylorandfrancis.com

Computational Modelling of Concrete Structures – Meschke, Pichler & Rots (Eds)
© 2018 Taylor & Francis Group, London, ISBN 978-1-138-74117-1

Regularized continuum damage formulations acting as localization limiters

M. Jirásek
Department of Mechanics, Faculty of Civil Engineering, Czech Technical University in Prague, Czech Republic

ABSTRACT: The aim of the present paper is to provide an overview of the main types of regularized continuum damage formulations that act as localization limiters, and to compare their localization properties by looking at the solutions constructed for a one-dimensional bar subjected to tension. Such a simple setting permits to demonstrate the principal concepts used by individual regularization techniques and to construct localized solutions based on relatively simple nonlinear ordinary differential (or integral) equations. Attention is paid to the onset of localization, seen as a bifurcation from a uniform state, as well as to the subsequent development of the damage profile up to complete failure. For each model, evolution of the size of active part of damage zone is documented and an equivalent cohesive diagram reflecting the relation between the stress and the inelastic part of bar elongation is constructed.

Inspection of the gallery of regularized damage formulations starts from integral-type nonlocal formulations, which incorporate weighted spatial averages of certain internal variables, and continues to gradient-enriched models in their explicit or implicit formats. Refined formulations with variable interactions are covered. Then, the focus shifts to regularization techniques that were initially developed outside the concrete mechanics community but recently have become widely popular. These formulations include variational damage models and phase-field models. Finally, the thick level set approach is described and analyzed. The results help to identify which regularization techniques are suitable for quasibrittle materials such as concrete.

1 INTRODUCTION

Under severe loading, dissipative deformation processes in concrete often concentrate in narrow bands. The thickness of such bands is controlled by the size and spacing of large aggregates, which represent the major heterogeneities in the material mesostructure. Localization of inelastic strain acts as a precursor to the development of the final failure pattern, ensuing from propagation and coalescence of microcracks and frictional slip segments.

More than 30 years ago, it was found that an objective description of strain localization phenomena requires special modeling and computational techniques, which can be based either on a replacement of the localized strain band by a strong discontinuity surface (representing a cohesive crack or slip surface) across which the displacement field has a jump, or on special enhancements of the underlying continuum theory. Models of the latter type introduce one or more parameters with the dimension of length, which reflect the heterogeneity of the material and control the size of the developed zone of localized strain. The enhancements that provide such desirable effects are known as localization limiters. From the mathematical point of view, they regularize the model by restoring well-posedness of the resulting boundary value problem.

2 LOCAL ISOTROPIC DAMAGE MODEL

In the literature, one can find a large variety of localization limiters formulated as enhancements of models based on plasticity and damage mechanics, including their combinations, and also of various smeared crack and microplane models. This short paper focuses on regularized formulations of damage models. For the present purpose, it is sufficient to start from the simplest version of such a model, with the stress-strain law in the form

$$\sigma = (1-\omega)\mathbf{D} : \varepsilon, \tag{1}$$

where σ is the stress tensor, ε is the strain tensor, $\boldsymbol{D}$ is the elastic stiffness tensor and ω is a scalar damage variable. Damage is considered as irreversible, driven by a scalar variable $\tilde{\varepsilon}$ that reflects the current level of strain and is called the equivalent strain. A frequently used formula for equivalent strain, first proposed by Mazars (1984), takes into account only the positive (tensile) part of strain.

Based on principal strains ε_I, $I = 1,2,3$, the Mazars equivalent strain can be evaluated as

$$\tilde{\varepsilon} = \sqrt{\sum_{I=1}^{3} \left\langle \varepsilon_I \right\rangle^2}, \tag{2}$$

where Macauley brackets $\langle \ldots \rangle$ denote the positive part.

Under monotonic loading, damage could be considered directly as a function of the current value of equivalent strain, $\omega = g(\tilde{\varepsilon})$. To cover the general case with possible unloading, it is useful to introduce a history variable κ, which represents the maximum previously reached level of equivalent strain and is formally defined by the loading-unloading conditions

$$\dot{\kappa} \geq 0, \quad \tilde{\varepsilon} - \kappa \leq 0, \quad (\tilde{\varepsilon} - \kappa)\dot{\kappa} = 0. \tag{3}$$

The damage variable is then evaluated from the damage law

$$\omega = g(\kappa), \tag{4}$$

where function g is a non-decreasing function with values between 0 and 1. A suitable form of the damage function g can be deduced from the uniaxial stress-strain diagram. For instance, to obtain linear elastic behavior followed by exponential softening, one needs to set

$$g(\kappa) = 1 - \frac{\varepsilon_0}{\kappa} \exp\left(-\frac{\langle \kappa - \varepsilon_0 \rangle}{\varepsilon_f} \right), \tag{5}$$

where ε_0 is the limit elastic strain and ε_f is another parameter that controls the post-peak slope of the stress-strain curve.

It is well known that, within the context of classical continuum mechanics, damage models with softening cannot provide an objective description of the failure process. Such models permit localization of damage into bands of arbitrarily small thickness. Consequently, numerical solutions obtained by the finite element method suffer by pathological sensitivity to the element size. As the mesh is refined, the response becomes increasingly brittle and the energy dissipated by failure is severely underestimated. Convergence to a physically meaningful solution can be restored only if the model is properly regularized, which is usually done by enhancements of the underlying continuum theory that incorporate a characteristic length and act as localization limiters.

This short paper provides an overview of various types of enhancements proposed in the literature as regularization techniques applicable to damage models. Their localization properties are illustrated and compared by looking at the onset of localization and subsequent evolution of the damage zone in the one-dimensional setting. Physically, the problem studied here can be interpreted as failure of a bar with uniform properties (sectional area and material parameters) under uniaxial tension. In the absence of applied body forces, the static equilibrium condition implies that the stress must be uniform along the bar, even after the onset of damage growth. Equation (1) can then be rewritten as

$$(1 - \omega(x,t))E\varepsilon(x,t) = \sigma(t), \tag{6}$$

where E is the Young modulus and t is the time variable, which parameterizes the deformation process but does not need to correspond to the real physical time, since the model is rate-independent and inertia effects are neglected. In the post-peak range, the test cannot be performed under load control, and a suitable control variable needs to be defined.

Consider a bar of initial length L, represented by the interval $\mathcal{L} = [-L/2, L/2]$. The change of length of the bar can be calculated as

$$\Delta L(t) = \int_{\mathcal{L}} \varepsilon(x,t)\,dx = \frac{\sigma(t)}{E} \int_{\mathcal{L}} \frac{dx}{1 - \omega(x,t)}. \tag{7}$$

Subtracting the change of length $\Delta L_e = L\sigma/E$ that would occur in a linear elastic bar subjected to the same stress, we obtain the part of ΔL caused by inelastic effects, which can be interpreted as the opening w of an equivalent fictitious crack. The inelastic part of bar elongation, representing an equivalent crack opening, is thus evaluated as

$$w(t) = \Delta L(t) - \frac{L\sigma(t)}{E} = \frac{\sigma(t)}{E} \int_{\mathcal{L}} \frac{\omega(x,t)}{1 - \omega(x,t)}\,\mathrm{d}x \tag{8}$$

and the graph that relates $\sigma(t)$ to $w(t)$ is the equivalent cohesive curve. For concrete, this curve is expected to have a convex shape with a relatively long tail.

For simplicity, in what follows we will not mark explicitly the dependence of individual variables on the spatial coordinate x and time t. Differentiation of (6) leads to the rate form of the stress-strain law,

$$\dot{\sigma} = (1 - \omega)E\dot{\varepsilon} - \dot{\omega}E\varepsilon = E_s\dot{\varepsilon} - E\varepsilon\dot{\omega}, \tag{9}$$

where superimposed dots denote rates (or infinitesimal increments) and $E_s = (1 - \omega)E$ is the secant (unloading) modulus, which remains positive for a partially damaged material and vanishes for a fully damaged material ($\omega = 1$). If a standard damage model with no enhancements is used, the evolution of damage is described by (4) and, in the rate format, we can write

$$\dot{\omega} = g_\kappa(\kappa)\dot{\kappa}, \tag{10}$$

where $g_\kappa \equiv \mathrm{d}g/\mathrm{d}\kappa$ is the derivative of the damage function g.

The rate of internal variable κ is $\dot{\kappa} = \dot{\varepsilon}$ during loading and $\dot{\kappa} = 0$ during unloading. In the case of unloading, (9) reduces to $\dot{\sigma} = E_s\dot{\varepsilon}$, , and in the case of loading we can link the stress rate to the strain rate by

$$\dot{\sigma} = E_s\dot{\varepsilon} - E\varepsilon g_\kappa(\varepsilon)\dot{\varepsilon} = E_{ed}\dot{\varepsilon}, \tag{11}$$

in which

$$E_{ed} = E_s - E\varepsilon g_\kappa(\varepsilon) = (1 - g(\varepsilon) - \varepsilon g_\kappa(\varepsilon))E \tag{12}$$

is the elasto-damage modulus, representing the slope of the tangent to the stress-strain curve. In the post-peak range, characterized by $\varepsilon g_\kappa(\varepsilon) > 1 - g(\varepsilon)$, this modulus becomes negative.

Suppose that the bar response remains uniform up to a certain strain level at which the solution bifurcates into a nonuniform one. For the standard (i.e., local) damage model, damage grows at points where $\dot{\varepsilon} > 0$ and remains constant at points where $\dot{\varepsilon} \le 0$. Since the stress is and must remain uniform along the whole bar, the equilibrium condition written for stress rates leads to

$$E_s\dot{\varepsilon}(x) = \dot{\sigma} \quad \text{if } \dot{\varepsilon}(x) \le 0, \tag{13}$$

$$E_{ed}\dot{\varepsilon}(x) = \dot{\sigma} \quad \text{if } \dot{\varepsilon}(x) > 0. \tag{14}$$

Since $E_s \ge 0$, the first condition implies $\dot{\sigma} \le 0$, and then the second condition can be satisfied only if $E_{ed} \le 0$. This is an expected result. Uniformity can be lost only if the tangent modulus becomes nonpositive. If the tangent modulus is negative, the distribution of strain (and damage) is piecewise constant, with $\dot{\varepsilon}(x) = \dot{\sigma}/E_s < 0$ in $\mathcal{I}_e$ and $\dot{\varepsilon}(x) = \dot{\sigma}/E_{ed} > 0$ in $\mathcal{I}_d$ Here, $\mathcal{I}_d = \{x \in \mathcal{L} \mid \dot{\omega}(x) > 0\}$ is the set of points at which damage grows, and $\mathcal{I}_e = \{x \in \mathcal{L} \mid \dot{\omega}(x) = 0\} = \mathcal{L} \setminus \mathcal{I}_d$ is the set of points at which damage remains constant.

3 INTEGRAL-TYPE NONLOCAL DAMAGE MODELS

3.1 *Formulation with constant internal length*

The first regularized damage model, proposed by Bažant (1987), was based on weighted spatial averaging of the damage-driving variable, which was initially chosen as the damage energy release rate. Later, other formulations with averaging of various internal variables appeared in the literature. The most widely used formulation is based on averaging of the equivalent strain. In conditions (3), the locally computed value of $\tilde{\varepsilon}$ is replaced by its nonlocal counterpart $\bar{\varepsilon}$, defined by the integral formula

$$\bar{\varepsilon}(\boldsymbol{x}) = \int_V \alpha(\boldsymbol{x},\boldsymbol{\xi})\tilde{\varepsilon}(\boldsymbol{\xi})\,dV(\boldsymbol{\xi}), \tag{15}$$

where V is the spatial domain occupied by the investigated solid body and α is a suitable nonlocal weight function. To satisfy the condition that a uniform local field is mapped onto a uniform nonlocal field, the weight function is often postulated in the form

$$\alpha(\boldsymbol{x},\boldsymbol{\xi}) = \frac{\alpha_0\left(\|\mathbf{x} - \boldsymbol{\xi}\|\right)}{\int_V \alpha_0\left(\|\mathbf{x} - \boldsymbol{\eta}\|\right)\,\mathrm{d}V(\boldsymbol{\eta})} \tag{16}$$

where $\alpha_0(r)$ is a distance-dependent function, usually decreasing with increasing distance r between points x and ξ. One possible form of this function is

$$\alpha_0(r) = \left\langle 1 - \frac{r^2}{R^2} \right\rangle^2, \tag{17}$$

where R is a material parameter with the dimension of length, called the nonlocal interaction radius.

Consider again the onset of localization in a bar. For the present nonlocal damage model, regions $\mathcal{I}_d$ (active part of damage zone) and $\mathcal{I}_e$ (zone in which damage does not grow) are characterized by $\dot{\bar{\varepsilon}} > 0$ and $\dot{\bar{\varepsilon}} \le 0$, respectively. The rate form of the stress-strain law (11) needs to be reformulated as

$$\dot{\sigma} = E_s\dot{\varepsilon} - E\varepsilon g_\kappa(\bar{\varepsilon})\dot{\bar{\varepsilon}} \tag{18}$$

and conditions (13)–(14) are replaced by

$$E_s\dot{\varepsilon}(x) = \dot{\sigma} \quad \text{if } \dot{\bar{\varepsilon}}(x) \le 0, \tag{19}$$

$$E_s\,\dot{\varepsilon}(x) + (E_{ed} - E_s)\dot{\bar{\varepsilon}}(x) = \dot{\sigma} \quad \text{if } \dot{\bar{\varepsilon}}(x) > 0 \tag{20}$$

Same as for the local model, condition (19) leads to $\dot{\varepsilon}(x) = \dot{\sigma}/E_s$ for $x \in \mathcal{I}_e$. It is convenient to rewrite (20) in terms of a transformed unknown function $\dot{\varepsilon}_d(x) = \dot{\varepsilon}(x) - \dot{\sigma}/E_s$, because then $\dot{\varepsilon}_d(x) = 0$ for $x \in \mathcal{I}_e$ and equation (20) can be transformed into a Fredholm integral equation of the second kind,

$$E_s\,\dot{\varepsilon}_d(x) + (E_{ed} - E_s)\int_{\mathcal{I}_d} \alpha(x,\xi)\dot{\varepsilon}_d(\xi)\,d\xi = \left(1 - \frac{E_{ed}}{E_s}\right)\dot{\sigma}, \tag{21}$$

which needs to be solved in $\mathcal{I}_d$ for the unknown function $\dot{\varepsilon}_d(x)$.

A careful analysis reveals that a nonuniform solution can exist only if $E_{ed} < 0$. The most interesting are those solutions for which A careful analysis reveals that a nonuniform is an inter-

val, i.e., damage is localized into one single band. The length of that interval, L_d, can be estimated analytically or evaluated numerically. It depends exclusively on the dimensionless ratio $-E_{ed}/E_s$. For sufficiently small values of this ratio, a good estimate is provided by the formula

$$L_d \approx \pi \sqrt{-\frac{2E_s}{E_{ed}} \frac{\int_0^\infty r^2 \alpha_0(r)\mathrm{d}r}{\int_0^\infty \alpha_0(r)\mathrm{d}r}}. \tag{22}$$

For a model with damage function (5), which corresponds to exponential softening, localization occurs immediately at the onset of damage, provided that the bar is sufficiently long, such that $L > L_d$. The subsequent evolution of strain and damage needs to be computed numerically. For a typical case with $\varepsilon_f = 5\varepsilon_0$, the resulting damage profile is plotted in Figure 1a and the equivalent cohesive stress-crack opening curve is shown in Figure 1c, in terms of dimensionless variables. In this example, nonlocal weight function (17) is used. The stress is normalized by the tensile strength, $f_t = E\varepsilon_0$, and the equivalent crack opening is normalized by the product $R\varepsilon_0$.

The graph in Figure 1c has a reasonable shape, and so the global response of the model characterized, e.g., by the load-displacement diagram, can be expected to properly reflect the response of concrete. The area under the cohesive curve is the fracture energy; if all other parameters are fixed, it is proportional to the nonlocal radius, R. The shape of the damage profile at initial stages of localization is also reasonable, but as the material degradation process proceeds, the profile becomes flat in its central part. Figure 1b shows the relation between the size of zone of growing damage, L_d, and the damage level attained at the center of that zone. The zone of growing damage slightly shrinks but does not tend to one point. Values of damage tend to 1 not only at the center of the process zone but in an entire interval of size $2R$ centered at that point. Thus, the material loses stiffness in a relatively wide band, which can lead to certain spurious effects in multi-dimensional simulations. The behavior would be even worse for nonlocal weight functions α_0 that remain positive for arbitrarily large distances r between interacting points, such as the Gaussian-type function. In such cases, the damage zone would, at very late stages of failure, expand and eventually spread over the whole domain of analysis.

Expansion of the damage zone is clearly nonphysical. It is desirable to construct a more realistic model for which damage would tend to 1 only at the center or the damage zone, since this could be interpreted as the formation of a macroscopic stress-free crack.

3.2 *Formulation with damage-dependent interaction*

Undesired expansion of the damage zone is caused by nonlocal interaction. At late stages of failure, local strain is highly localized and tends to infinity at the center of the damage zone. Spatial averaging with a fixed weight function makes the nonlocal strain grow at all points within the interaction radius, and the nonlocal damage law translates this into a growth of the damage variable. Physically, it is clear that mechanical interaction between points that are separated by highly damaged material should be weaker than if the material is in its virgin state. This consideration motivated the development of nonlocal models with evolving weight functions.

Desmorat & Gatuingt (2010) started from the assumption that the "strength" of nonlocal interaction between two points should depend not on their geometric distance but on the time needed for a stress wave to propagate from one point to the other. In a damaged medium, the wave speed is reduced by the factor $\sqrt{1-\omega}$ with respect to the elastic wave speed, and so the "effective interaction distance" should be inversely proportional to that factor. Since the damage distribution is in general nonuniform, the modification is applied to the differential of distance. In one spatial dimension, the effective distance r between points x and ξ is then evaluated as

$$r(x,\xi) = \int_{\min(x,\xi)}^{\max(x,\xi)} \frac{\mathrm{d}s}{\sqrt{1-\omega(s)}} \tag{23}$$

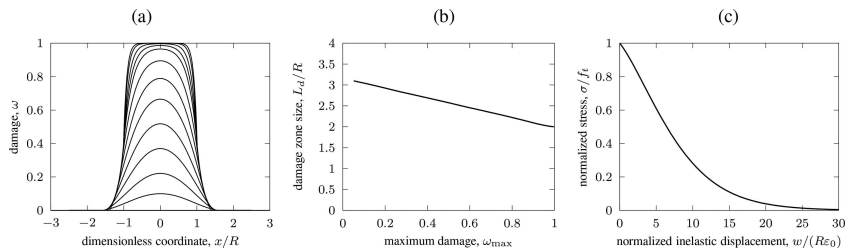

Figure 1. Integral-type nonlocal damage model: (a) evolution of damage profile, (b) evolution of damage zone width, (c) equivalent cohesive stress-crack opening curve.

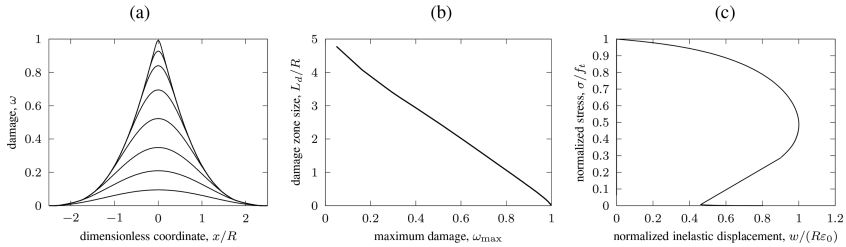

Figure 2. Integral-type nonlocal damage model with damage-dependent interactions: (a) evolution of damage profile, (b) evolution of damage zone width, (c) equivalent cohesive stress-crack opening curve.

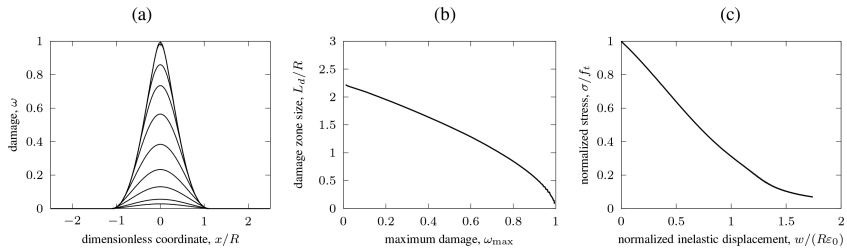

Figure 3. Integral-type nonlocal damage model with damage-dependent interactions and power-exponential damage function: (a) evolution of damage profile, (b) evolution of damage zone width, (c) equivalent cohesive stress-crack opening curve.

and this damage-dependent distance is used as the argument of the nonlocal weight function α_0 instead of the geometric distance, $|x-\xi|$.

Localization properties of this formulation were studied by Desmorat, Gatuingt,& Jirásek (2015). Figure 2 shows the numerically computed results obtained with $\varepsilon_f = 10\,\varepsilon_0$. The distribution of damage across the process zone tends to a final profile with values close to 1 concentrated near the center (Figure 2a) and the active part of the zone gradually shrinks to one single cross section (Figure 2b). The desired effect of the adjustment of nonlocal interactions is achieved but, unfortunately, the equivalent cohesive diagram has no longer a convex shape with a long tail (Figure 2c). This indicates that the global response becomes extremely brittle at late stages of the failure process and the resulting uniaxial load-displacement diagram would exhibit snapback even for very small specimens.

A partial remedy can be sought in adjustments of the form of the damage law. For instance, if the exponential damage function (5) is replaced by a power-exponential function

$$g(\kappa) = 1 - \frac{\varepsilon_0}{\kappa}\exp\left(-\frac{\langle \kappa^n - \varepsilon_0^n\rangle}{\varepsilon_f^n - \varepsilon_0^n}\right), \tag{24}$$

with a low exponent n, the shape of the cohesive diagram becomes more realistic. For $n = 0.1$ and $\varepsilon_f = 6\,\varepsilon_0$, the results are shown in Figure 3. The cohesive curve is seen to be initially almost linear and its final part has a short tail. Qualitatively, the global response is not so far from that obtained with the standard nonlocal formulation (Figure 1c), and the spurious spreading of damage is suppressed. However, implementation of the damage-dependent interaction distance in the framework of an integral nonlocal formulation is tedious, especially in multiple dimensions. Gradient formulations can be expected to lead to more efficient algorithms.

4 GRADIENT DAMAGE MODELS

4.1 *Explicit gradient damage model*

Motivated by an approximation of formula (15) based on the Taylor expansion of the local field κ in the vicinity of point x, Borst, Brekelmans, & de Vree (1996) proposed a possible regularized damage formulation with the damage-driving variable $\bar{\varepsilon}$ defined by the differential expression

$$\bar{\varepsilon} = \tilde{\varepsilon} + \ell^2 \nabla^2 \tilde{\varepsilon}, \tag{25}$$

where ∇^2 is the Laplace operator and ℓ is a model parameter with the dimension of length.

In the one-dimensional setting, the equivalent strain $\tilde{\varepsilon}$ is simply the strain, ε, and $\nabla^2\tilde{\varepsilon}$ reduces to the second spatial derivative of strain,

ε''. In the zone of growing damage, $\mathcal{I}_d$, we have $\kappa = \overline{\varepsilon} = \varepsilon + \ell^2\varepsilon''$ and the stress-strain law can be written as

$$(1 - g(\varepsilon + \ell^2\varepsilon''))E\varepsilon = \sigma. \tag{26}$$

Here, the second derivative of strain is contained in the argument of the damage function, g, which is in general nonlinear. Making use of the inverse function g^*, it is possible to convert (26) to a more convenient form

$$\varepsilon + \ell^2\varepsilon'' = g^*\left(1 - \frac{\sigma}{E\varepsilon}\right), \tag{27}$$

which is a nonlinear second-order differential equation for ε (recall that the stress, σ, is in the present case constant along the bar). Equation (26) is valid in the active part of damage zone, $\mathcal{I}_d$. In the unloading zone, $\mathcal{I}_e$, damage remains constant and thus strain can be directly expressed as

$$\varepsilon = \frac{\sigma}{E(1-\omega)}, \tag{28}$$

where ω is known based on the previous history. On the interfaces between the damaging and unloading zones, the strain must remain continuously differentiable.

Equation (27) always admits uniform solutions with $\varepsilon(x) = \text{const}$. For each value of ε, the corresponding stress is found by direct substitution into (26), with ε'' set to zero. The actual solution remains uniform at least during the linear elastic stage of the response. After the onset of damage, uniformity can get lost. The first bifurcation from a uniform state is described by the linear differential equation

$$E_{ed}\dot{\varepsilon} + (E_{ed} - E_s)\ell^2\dot{\varepsilon}'' = \dot{\sigma}, \tag{29}$$

which can be obtained by differentiating (27) with respect to time and taking into account the relations between the moduli E_{ed} and E_s and the damage function g. Equation (29) must be satisfied in $\mathcal{I}_d$, while in $\mathcal{I}_e$ the differentiation of (28) leads to $\dot{\varepsilon} = \dot{\sigma}/E_s$. Since $\dot{\varepsilon}' = 0$ in $\mathcal{I}_e$, continuous differentiability of strain implies that the solution of (29) describing the strain rate in $\mathcal{I}_d$ must satisfy conditions $\dot{\varepsilon}' = 0$ and $\dot{\varepsilon} = \dot{\sigma}/E_s$ imposed on the boundary of the damage zone, ∂I_d.

If the tangent modulus E_{ed} is positive, the general solution of (29) contains a constant function and a linear combination of two exponential functions, and no localized solution satisfying the boundary conditions exists. If E_{ed} is negative, the general solution of (29) reads

$$\dot{\varepsilon} = \frac{\dot{\sigma}}{E_{ed}} + C_1\cos\lambda x + C_2\sin\lambda x, \tag{30}$$

where

$$\lambda = \frac{1}{\ell}\sqrt{\frac{E_{ed}}{E_{ed} - E_s}}. \tag{31}$$

The particular solution satisfying conditions $\dot{\varepsilon}' = 0$ and $\dot{\varepsilon} = \dot{\sigma}/E_s$ on $\partial\mathcal{I}_d$ is given by

$$\dot{\varepsilon} = \dot{\sigma}\left[\frac{1}{E_{ed}} + \left(\frac{1}{E_{ed}} - \frac{1}{E_s}\right)\cos\lambda(x - x_0)\right] \tag{32}$$

and the damage zone $\mathcal{I}_d$ is an interval $(x_0 - L_d/2,\ x_0 + L_d/2)$, in which

$$L_d = \frac{2\pi}{\lambda} = 2\pi\ell\sqrt{\frac{E_{ed} - E_s}{E_{ed}}} \tag{33}$$

is the initial size of the localized damage zone and x_0 is the coordinate of the center of that zone (for a perfectly uniform bar, x_0 remains undetermined). The solution is consistent with the admissibility conditions $\dot{\varepsilon} + \ell^2\dot{\varepsilon}'' > 0$ in $\mathcal{I}_d$ and $\dot{\varepsilon} + \ell^2\dot{\varepsilon}'' \le 0$ in $\mathcal{I}_e$.

For the damage function given by (5), the ratio between the tangent and the secant modulus under monotonic loading is $E_{ed}/E_s = -\varepsilon/\varepsilon_f$, provided that the current strain has reached the limit elastic value, i.e., $\varepsilon \ge \varepsilon_0$. At damage initiation, the tangent modulus immediately becomes negative, and localization can occur if the bar is sufficiently long to accommodate the full process zone. The initial size of the localized damage zone obtained from (33) is $L_d = 2\pi\ell\sqrt{1 + \varepsilon_f/\varepsilon_0}$.

After the onset of localization, uniformity is lost and the subsequent evolution of strain is governed by nonlinear differential equation (27), valid in an evolving domain $\mathcal{I}_d$. The solution can be constructed numerically in an incremental fashion. The results obtained for $\varepsilon_f = \varepsilon_0$ are plotted in Figure 4. The initial size of the damage zone is $L_d = 2\sqrt{2}\pi\ell \approx 8.8858\,\ell$. Subsequently, the zone is slightly shrinking (Figure 4b) but damage grows to values close to 1 almost in the entire damage zone. The final distribution of damage, shown in Figure 4a, is even worse than for the integral-type nonlocal model with a fixed weight function. On the other hand, the equivalent cohesive diagram in Figure 4c has a very reasonable shape.

4.2 *Implicit gradient damage model with constant internal length*

Implicit gradient formulations define the nonlocal variable as the solution of a boundary value problem. A typical implicit gradient damage formulation proposed by Peerlings, de Borst, Brekelmans, & de Vree (1996) uses for this purpose differential equation

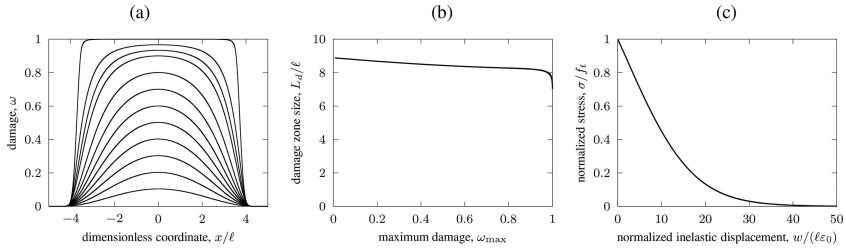

Figure 4. Explicit gradient damagemodel: (a) evolution of damage profile, (b) evolution of damage zone width, (c) equivalent cohesive stress-crack opening curve.

$$\bar{\varepsilon} - \ell^2 \nabla^2 \bar{\varepsilon} = \tilde{\varepsilon} \tag{34}$$

with the homogeneous Neumann boundary condition $\mathbf{n} \cdot \nabla \bar{\varepsilon} = 0$ imposed on the boundary of domain V. In the literature on regularized softening models, equation (34) is often referred to as the Helmholtz equation, but it differs from the actual Helmholtz equation by the sign of one of the terms on the left-hand side. In mathematical literature, equation (34) is called the screened Poisson equation.

A one-dimensional version of (34) combined with the stress-strain equation (6) and damage law $\omega = g(\bar{\varepsilon})$ leads to a nonlinear differential equation

$$\bar{\varepsilon} - \ell^2 \bar{\varepsilon}'' = \frac{\sigma}{E(1 - g(\bar{\varepsilon}))} \tag{35}$$

applicable in the damage zone, $\mathcal{I}_d$. Outside this zone, $g(\bar{\varepsilon})$ on the right-hand side must be replaced by known damage ω attained during the previous stages, and the governing equation is written as

$$\bar{\varepsilon} - \ell^2 \bar{\varepsilon}'' = \frac{\sigma}{E(1 - \omega)}. \tag{36}$$

At bifurcation from a uniform state, the rate form of (35) can be rewritten as the linear differential equation

$$E_{\mathrm{ed}} \dot{\bar{\varepsilon}} - \ell^2 E_{\mathrm{s}} \dot{\bar{\varepsilon}}'' = \dot{\sigma}. \tag{37}$$

In the unloading zone, $\mathcal{I}_e$, equation (37) needs to be replaced by

$$E_{\mathrm{s}} \dot{\bar{\varepsilon}} - \ell^2 E_{\mathrm{s}} \dot{\bar{\varepsilon}}'' = \dot{\sigma}, \tag{38}$$

which follows from the rate form of (36) with damage ω possibly nonuniform but constant in time.

The damage zone is characterized by $\dot{\bar{\varepsilon}} > 0$ and the unloading zone by $\dot{\bar{\varepsilon}} \le 0$. To preserve continuous differentiability of the solution, $\dot{\bar{\varepsilon}}$ must vanish on the boundary of the damage zone and its derivative from the left must be equal to its derivative from the right. These conditions combined with the boundary conditions permit the determination of integration constants and of the size of the damage zone. The analysis reveals that if damage growth localizes in one interval inside the bar (not adjacent to the boundary), the center of the damage zone must be exactly at the bar center. For a sufficiently long (theoretically infinite) bar, the rate of nonlocal strain is given by

$$\dot{\bar{\varepsilon}} = \begin{cases} \dfrac{\dot{\sigma}}{E_{\mathrm{ed}}} \left(1 - \dfrac{\cos \lambda x}{\cos \lambda L_{\mathrm{d}}/2} \right) & \text{for } |x| < L_{\mathrm{d}}/2, \\ \dfrac{\dot{\sigma}}{E_{\mathrm{s}}} \left(1 - \exp \dfrac{L_{\mathrm{d}} - 2|x|}{2\ell} \right) & \text{for } |x| \ge L_{\mathrm{d}}/2, \end{cases} \tag{39}$$

where

$$\lambda = \frac{1}{\ell} \sqrt{-\frac{E_{\mathrm{ed}}}{E_{\mathrm{s}}}}, \tag{40}$$

$$L_{\mathrm{d}} = \frac{2}{\lambda} (\pi - \arctan \lambda \ell). \tag{41}$$

Same as for the explicit gradient formulation, localization can occur as soon as the tangent modulus becomes negative, provided that the bar is sufficiently long. The subsequent evolution of nonlocal strain can be computed numerically using an incremental procedure, based on the solution of nonlinear equation (35) in the damage zone and of linear equation (36) with the right-hand side dependent on the previous evolution of damage in the currently unloading zone.

The results obtained for $\varepsilon_f = \varepsilon_0$ and for a bar much longer than the damage zone are plotted in Figure 5. The equivalent cohesive diagram has a reasonable shape (Figure 5c). The initial size of the damage zone is according to (40)–(41) equal to $L_{\mathrm{d}} = 2\ell(\pi - \arctan 1) \approx 4.7124\,\ell$. The active part of the zone first slightly shrinks but later starts expanding, as shown in Figure 5a,b. The behavior is similar to the integral nonlocal formulation with a fixed weight function, which is not by chance. It is well known that the implicit gradient model is

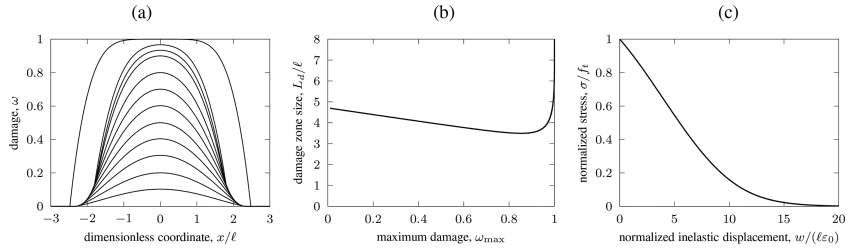

Figure 5. Implicit gradient damage model with constant internal length: (a) evolution of damage profile, (b) evolution of damage zone width, (c) equivalent cohesive stress-crack opening curve.

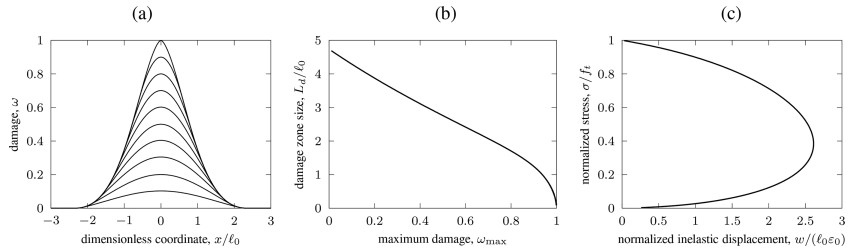

Figure 6. Implicit gradient damage model with damage-dependent internal length: (a) evolution of damage profile, (b) evolution of damage zone width, (c) equivalent cohesive stress-crack opening curve.

equivalent to an integral nonlocal model with a special weight function, constructed as the Green function of the boundary value problem that defines the nonlocal variable. In the present case, this weight function decays exponentially with increasing distance between interacting points but remains nonzero for an arbitrary distance. Therefore, the expansion of damage is even more dramatic than for the nonlocal model with weight function (17).

4.3 *Implicit gradient damage models with variable internal length*

To reduce the spurious expansion of damage at final stages of failure, Geers (1997) and Geers, de Borst, Brekelmans, & Peerlings (1998) proposed two modifications of the implicit gradient damage formulation, with the internal length ℓ treated no longer as a constant but as a function of the current state. One modification considered a dependence of internal length on damage and the other on strain. In both cases, the factor ℓ^2 multiplied the Laplacean of nonlocal equivalent strain, exactly as in the original formulation with a constant internal length.

For the formulation with damage-dependent internal length, it was suggested to use

$$\ell(\omega) = \ell_0 (1-\omega)^{n/2}, \tag{42}$$

where ℓ_0 is a reference value of internal length and n is a suitable exponent. In examples, n was set to 1. As shown in Figure 6a, this modification indeed leads to a substantial improvement of the final shape of the damage profile. The active part of the damage zone shrinks during the entire failure process and its size tends to zero (Figure 6b). Unfortunately, the resulting cohesive diagram, shown in Figure 6c, has a shape that is totally unrealistic for concrete and resembles the result that was obtained for the integral-type model with interaction distance modified by the factor $1/\sqrt{1-\omega}$. Indeed, there is a close relation between both formulations. For a uniformly damaged body, the reduction of nonlocal interactions based on (23) or (42) with $n=1$ would be fully equivalent.

For the formulation with damage-dependent internal length, it was suggested to use

$$\ell(\tilde{\varepsilon}) = \ell_0 \min\left(\sqrt{\tilde{\varepsilon}/\varepsilon_l}, 1\right), \tag{43}$$

where ε_l is an additional parameter. According to (43), the internal length ℓ is at low strain levels quite small and attains its maximum possible value ℓ_0 only if the local equivalent strain exceeds a given value, ε_l. At late stages of failure, the local strain tends to concentrate in a narrow core of the process zone and to decrease in the outer parts of the process zone. Reduction of internal length in these outer parts brings the nonlocal strain closer to the local one and limits the growth of damage that would otherwise be induced by the proxim-

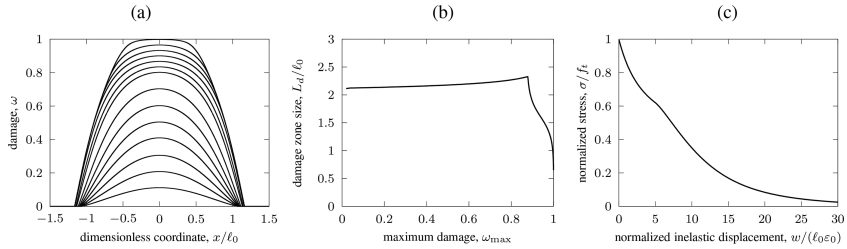

Figure 7. Implicit gradient damage model with strain-dependent internal length: (a) evolution of damage profile, (b) evolution of damage zone width, (c) equivalent cohesive stress-crack opening curve.

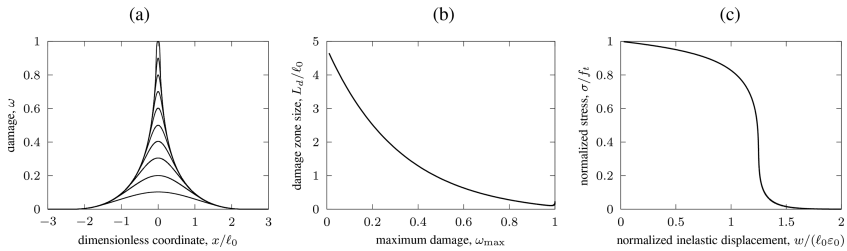

Figure 8. Implicit gradient damage model with decreasing interactions: (a) evolution of damage profile, (b) evolution of damage zone width, (c) equivalent cohesive stress-crack opening curve.

ity of the core with high local strains. Numerical results obtained for this model with $\varepsilon_l = 5\varepsilon_0$ and $\varepsilon_f = \varepsilon_0$ are shown in Figure 7. The damage zone first slightly expands, which is related to the growth of the internal length with increasing strain in the damage zone. The behavior changes abruptly after the maximum local strain exceeds the value ε_l and the corresponding internal length in the core of the damage zone attains its maximum value, ℓ_0. The active part of damage zone start shrinking and its size tends to zero (Figure 7b). This change of response is also reflected by a steeper descent of the equivalent cohesive diagram (Figure 7c). Overall, the behavior is acceptable, even though the abrupt change is certainly not favorable for numerical robustness of the model in application to multi-dimensional problems.

4.4 *Localizing gradient damage model with decreasing interactions*

An improvement of localization properties of the implicit gradient damage model has recently been reported by Poh & Sun (2017). They suggest to rewrite the governing equation (34) as

$$\bar{\varepsilon} - \nabla\cdot(\ell^2(\omega)\nabla\bar{\varepsilon}) = \tilde{\varepsilon} \tag{44}$$

and to use a damage-dependent internal length given by

$$\ell(\omega) = \ell_0\sqrt{\frac{(1-\rho)\mathrm{e}^{-\eta\omega} + \rho - \mathrm{e}^{-\eta}}{1-\mathrm{e}^{-\eta}}}, \tag{45}$$

where ρ and η are dimensionless parameters with typical values $\eta = 5$ and $\rho = 0.005$. As damage grows from 0 to 1, the internal length decreases from ℓ_0 to $\ell_0\sqrt{\rho}$. Consequently, the damage zone shrinks to a very narrow band, as illustrated in Figure 8a,b for the already mentioned values of parameters η and ρ and for $\varepsilon_f = \varepsilon_0$. Despite a dramatic reduction of the process zone size during the failure process, the resulting cohesive diagram does not exhibit the extremely brittle behavior found for a similar formulation with ℓ^2 proportional to $1-\omega$ and placed before the Laplacean. Still, the curve shown in Figure 8c is far from optimal, since it contains a steeply descending central part.

5 VARIATIONAL DAMAGE AND PHASE FIELD MODELS

5.1 *Variational damage formulations*

Mathematical treatment of gradient-enhanced models is facilitated if the governing equations (and inequalities) can be derived using a variational approach. As an instructive example, let us present the formulation developed by Jirásek & Zeman (2015) within the framework proposed by Mielke

(2005). This approach is based on an incremental minimization of the total energy, considered as the sum of potential energy and dissipated energy. For problems with loading imposed by prescribed displacements on the boundary, the total energy functional

$$\mathcal{E}(\boldsymbol{u},\omega) = \mathcal{E}_{\text{std}}(\boldsymbol{u},\omega) + \mathcal{E}_{\text{reg}}(\omega) + \mathcal{E}_{\text{dis}}(\omega) \tag{46}$$

is written as a sum of three terms:

$$\mathcal{E}_{\text{std}}(\boldsymbol{u},\omega) = \frac{1}{2}\int_V (1-\omega)\nabla_s \boldsymbol{u} : \mathbf{D} : \nabla_s \boldsymbol{u}\, dV, \tag{47}$$

$$\mathcal{E}_{\text{reg}}(\omega) = \frac{1}{2}\int_V g_f \ell^2 \left\|\nabla \gamma(\omega)\right\|^2 dV, \tag{48}$$

$$\mathcal{E}_{\text{dis}}(\omega) = \int_V D(\omega)\, dV. \tag{49}$$

Here, $\mathcal{E}_{\text{std}}$ is the standard expression for the energy stored in elastic deformation of a partially damaged body, $\mathcal{E}_{\text{dis}}$ is the dissipated energy and $\mathcal{E}_{\text{reg}}$ is an added regularization term. The symmetric part of the displacement gradient, $\nabla_s \boldsymbol{u}$, corresponds to the small-strain tensor. Function D describes the density of energy dissipated by increasing damage from zero to the current level ω. Constant g_f is introduced for the sake of dimensionality and can be set equal, e.g., to the density of elastically stored energy at the onset of damage. Constant ℓ is the internal length parameter and function $\gamma(\omega)$ defines a transformed variable computed from damage and used for regularization.

The total energy $\mathcal{E}$ is a functional dependent on the displacement field, $\boldsymbol{u}$, and on the damage field, ω. In each incremental step, the value of total energy at the end of the step is minimized over all admissible changes of these fields. Admissible displacement increments must satisfy the imposed Dirichlet boundary conditions, and admissible damage increments must be nonnegative. If the size of the increment is reduced, in the limit we obtain rates. A detailed analysis of optimality conditions leads to the usual equilibrium equation (with the stress-strain equation and strain-displacement equation incorporated),

$$\nabla \cdot ((1-\omega)\mathbf{D} : \nabla_s \boldsymbol{u}) = 0, \tag{50}$$

and to the damage law, which has a more complicated structure. It can be conveniently presented in the form

$$F(\nabla_s \boldsymbol{u}, \omega, \nabla^2\gamma(\omega)) \le 0, \quad \dot{\omega} \ge 0, \tag{51}$$

$$\dot{\omega} F(\nabla_s \boldsymbol{u}, \omega, \nabla^2\gamma(\omega)) = 0, \tag{52}$$

where F is an auxiliary function defined as

$$F(\varepsilon,\omega,G) = \tfrac{1}{2}\varepsilon : \mathbf{D} : \varepsilon + g_f \ell^2 \gamma_\omega(\omega) G - D_\omega(\omega). \tag{53}$$

Here, $\gamma_\omega \equiv \mathrm{d}\gamma/\mathrm{d}\omega$ and $D_\omega \equiv \mathrm{d}D/\mathrm{d}\omega$ are the derivatives of functions γ and D with respect to their argument, ω.

Equation (50) could be extended to the case with nonzero body forces, but this is not needed for the present purpose. In one spatial dimension, this equation reduces to $((1-\omega)Eu')' = 0$ and after integration we get $(1-\omega)Eu' = \sigma$ where σ is a constant that corresponds to the uniform stress along the bar and $u' = \varepsilon$ is the strain.

Conditions (51)–(52) can be interpreted as a damage law enhanced by a second-gradient term. Under uniform damage, the gradient term vanishes and F becomes a loading function dependent on the local strain and damage. The first term in the definition of F corresponds to the damage energy release rate, $Y(\varepsilon) = \varepsilon : \mathbf{D} : \varepsilon/2$. Condition $F \le 0$ then means that $Y(\varepsilon) \le D_\omega(\omega)$ and condition $\dot{\omega}F = 0$ means that damage can grow only if $Y(\varepsilon) = D_\omega(\omega)$. Here, Y plays the role of a "driving force" and D_ω is the current resistance against that force. If the equivalent strain is defined as $\tilde{\varepsilon} = \sqrt{2Y(\varepsilon)/E}$, condition $F = 0$ that remains satisfied during monotonic damage growth can be converted to the following equivalent conditions:

$$\tilde{\varepsilon} = \sqrt{\frac{2D_\omega(\omega)}{E}} \equiv g^*(\omega), \tag{54}$$

$$\omega = D_\omega^*\left(\frac{E\tilde{\varepsilon}^2}{2}\right) \equiv g(\tilde{\varepsilon}). \tag{55}$$

Here, D_ω^* denotes the function obtained by inverting function D_ω.

Relations (54)–(55) provide a link between the dissipation function D used in the variational formulation and the damage function g used in the standard form of the damage law (4). Thus, the dissipation function can be constructed such that the model response under uniform damage corresponds to a given local stress-strain law. One can even directly replace the "resistance" $D_\omega(\omega)$ in (53) by $Eg^{*2}(\omega)/2$ and the "driving force" $\varepsilon : \mathbf{D} : \varepsilon/2$ by $E\tilde{\varepsilon}^2/2$, and rewrite condition $F \le 0$ as

$$\tilde{\varepsilon}^2 + \frac{2g_f}{E}\ell^2 \gamma_\omega(\omega)\nabla^2\gamma(\omega) \le g^{*2}(\omega). \tag{56}$$

During damage growth, this condition is satisfied as an equality, and the resulting gradient damage law can be presented in the form

$$\omega = g\left(\sqrt{\tilde{\varepsilon}^2 + \frac{2g_f}{E}\ell^2 \gamma_\omega(\omega)\nabla^2\gamma(\omega)}\right). \tag{57}$$

This law has an implicit character because the expression on the right-hand side contains the

Laplacean of a damage-related variable γ. At uniform damage, (57) reduces to (55) and the growth of damage is driven by the equivalent strain, $\tilde{\varepsilon}$. In a general case, the damage field is nonuniform and damage growth is accelerated in regions where $\nabla^2\gamma > 0$ and slowed down in regions where $\nabla^2\gamma < 0$.

It has been shown that the dissipation function D can be deduced from the assumed shape of the local stress-strain diagram. The remaining ingredient of the model that needs to be specified is the relation between the damage variable ω and the variable γ that is used in the regularization term. The simplest choice is $\gamma = \omega$, which leads to the basic form of the model, with the regularizing part of energy related to the gradient of damage (Mielke & Roubíček 2006). Other choices may provide models with better localization properties. For instance, Jirásek & Zeman (2015) studied the performance of formulations with

$$\gamma(\omega) = \int_0^{\omega} \frac{1}{(1-\tilde{\omega})^p} \mathrm{d}\tilde{\omega}, \tag{58}$$

where p is a nonnegative exponent. The choice of $p = 0$ corresponds to the simplest formulation with $\gamma(\omega) = \omega$.

Localization of damage in a uniform bar under uniaxial tension can be analyzed by reducing (50)–(52) to one dimension. As already discussed, integration of the equilibrium equation (50) in 1D leads to (6). The damage law written for the damage zone, $\mathcal{I}_\mathrm{d}$, has the form of a nonlinear differential equation

$$\varepsilon^2 + \frac{2g_f}{E}\ell^2\gamma_\omega(\omega)(\gamma(\omega))'' - g^{*2}(\omega) = 0. \tag{59}$$

Based on (6), the strain can be expressed in terms of damage and subsequently eliminated from (59). This procedure leads to a differential equation

$$\frac{\sigma^2}{E(1-\omega)^2} + 2g_f\ell^2\gamma_\omega(\omega)(\gamma(\omega))'' - Eg^{*2}(\omega) = 0 \tag{60}$$

with a single unknown function, $\omega(x)$. Equation (60) should be satisfied in the damage zone, $\mathcal{I}_\mathrm{d}$, which is not known in advance but is characterized by a positive increment of damage. Outside this zone, damage remains constant and equal to the previously reached values, and the strain distribution easily follows from (6). The size of the damage zone must be in each step adjusted such that the damage distribution in space remains continuously differentiable.

Evolution of the localized damage profile computed for the formulation regularized by gradient of damage (i.e., with $\gamma(\omega) = \omega$) and with the dissipation function $D(\omega)$ that corresponds to damage function (5) with $\varepsilon_f = 9\varepsilon_0$ is shown in Figure 9a. The active part of the damage zone is shrinking and Figure 9b confirms that the size of this zone tends to zero as damage approaches its limit value 1 at the center of the zone. For comparison, the results are plotted here not only for $\varepsilon_f/\varepsilon_0 = 9$ but also for lower values of this ratio. The extreme case with $\varepsilon_f = 0$ corresponds to a model which would, in the absence of a regularizing term, behave as elastic–perfectly brittle. This is actually the original model considered by Mielke & Roubíček (2006). Interestingly, the present regularization technique works even in such an extreme case, which could not be treated by the explicit or implicit gradient formulations discussed in Section 4 because function g that should describe the dependence of damage on equivalent strain does not exist (while its "inverse", i.e., function g^* that describes the dependence of equivalent strain on damage, does exist and has a constant value, equal to the limit elastic strain ε_0). As shown in Figure 9c, the equivalent cohesive diagram exhibits snapback and returns to the origin when the failure process is complete. This is the case not only for the regularized elastic–perfectly brittle model but also for regularized forms of the model with exponential softening. When the "local ductility" is increased by increasing the ratio $\varepsilon_f/\varepsilon_0$, more energy is dissipated but the overall shape of the diagram remains the same.

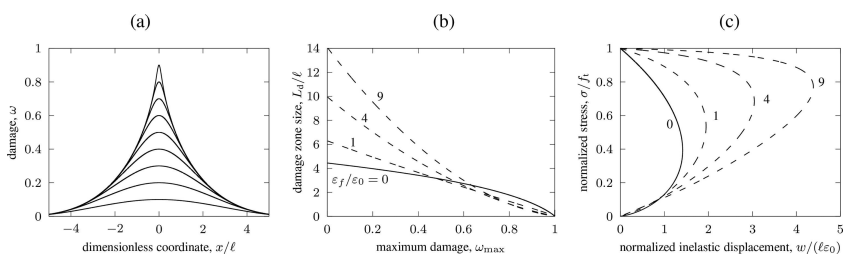

Figure 9. Damage model regularized by gradient of damage: (a) evolution of damage profile for $\varepsilon f = 9\varepsilon_0$, (b) evolution of damage zone width for various values of $\varepsilon f/\varepsilon_0$, (c) equivalent cohesive stress-crack opening curve for various values of $\varepsilon f/\varepsilon_0$.

The need for formulations that provide more realistic shapes of the equivalent cohesive diagram motivated the development of generalized regularization techniques that replace the gradient of damage by the gradient of another variable, γ, considered to be a unique function of the damage variable. The first step in this direction was the choice of the inelastic compliance variable $\gamma = \omega/(1-\omega)$, which corresponds to a special case of (58) with $p = 2$, and then the more general case with an adjustable exponent p was considered. It turned out that acceptable localization properties can be obtained for suitable choices of p and of the ratio $\varepsilon_f/\varepsilon_0$. For $p = 0.8$ and several values of $\varepsilon_f/\varepsilon_0$, the performance of the model is documented in Figure 10. For instance, for $p = 0.8$ and $\varepsilon_f/\varepsilon = 4$, the active part of the damage zone shrinks (except for the final stage of failure, when it slightly expands) and the equivalent cohesive diagram has a reasonable shape with a long tail. As shown by Jirásek & Zeman, replacement of $\nabla\omega$ by $\nabla\gamma(\omega)$ in the expression for regularization energy (48) is equivalent to a replacement of constant internal length ℓ by a function of damage, $\ell(\omega) = \ell_0\gamma_\omega(\omega)$.

5.2 *Crack field and phase field models*

The variational damage model used by Bourdin, Francfort, & Marigo (2000) was concieved as a regularized formulation of the variational formulation of brittle fracture by Francfort & Marigo (1998). In the initial work, the objective was to minimize an energy functional constructed as a sum of the standard elastically stored energy (without damage) and the product of the fracture energy G_c and the area of the crack, expressed as an integral over a surface Γ that can be placed anywhere in the body of interest. Such a functional depends not only on a vector field **u** but also on the choice of the crack surface Γ, and minimization with respect to all possible crack geometries is not an easy task.

To facilitate numerical implementation, Bourdin, Francfort, & Marigo (2000) developed a regularized formulation based on minimization of a functional defined as

$$E_\epsilon(\boldsymbol{u},s) = \int_V s^2\nabla_s\boldsymbol{u} : \boldsymbol{D} : \nabla_s\boldsymbol{u}\,dV + \\ + G_c\int_V \left\{\frac{(1-s)^2}{4\epsilon} + \epsilon\left\|\nabla s^2\right\|\right\}dV. \tag{61}$$

Here, S is called the *crack field variable*, and ϵ is a parameter with the dimension of length. The original formulation of Francfort & Marigo (1998) is attained in the limit of $\epsilon \to 0$, in the sense of Γ-convergence.

The model of Bourdin, Francfort and Marigo (BFM) can be cast into the format used in Section 5.1 if the internal length ℓ is set to 2ϵ, the generalized compliance variable is linked to damage by

$$\gamma(\omega) = 1 - \sqrt{1-\omega} \tag{62}$$

and the density of dissipated energy is linked to damage by

$$D(\omega) = \frac{G_c}{4\epsilon}(1-\sqrt{1-\omega})^2. \tag{63}$$

Essentially the same type of regularization technique was used by Miehe, Hofacker, &Welschinger (2010), with formal differences in notation and terminology. The added value of the model of Miehe et al. is that it introduces the split of elastic energy into parts attributed to tension and to compression, and the reduction caused by damage is applied to the tensile part only.

Localization properties of the BFM crack-field model are illustrated by the numerical results plotted in Figure 11. A particular feature of this model is that damage growth starts immediately (i.e., the elastic limit strain equals zero), but initially it is very slow and the stress-strain curve has a rising nonlinear branch. During the hardening stage, the solution of the one-dimensional bar problem remains uniform; see the dashed damage profiles in Figure 11a. In the post-peak range, uniformity is lost but the active part of damage zone is first very large and then its size gradually decreases to zero; see Figure 11b. The equivalent cohesive diagram

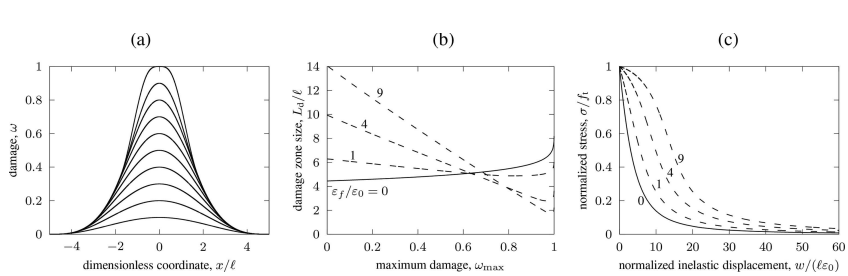

Figure 10. Damage model regularized by gradient of variable defined by (58) with $p = 0.8$: (a) evolution of damage profile for $\varepsilon f = 4\varepsilon_0$, (b) evolution of damage zone width for various values of "$\varepsilon f/\varepsilon_0$, (c) equivalent cohesive stress-crack opening curve for various values of $\varepsilon f/\varepsilon_0$.

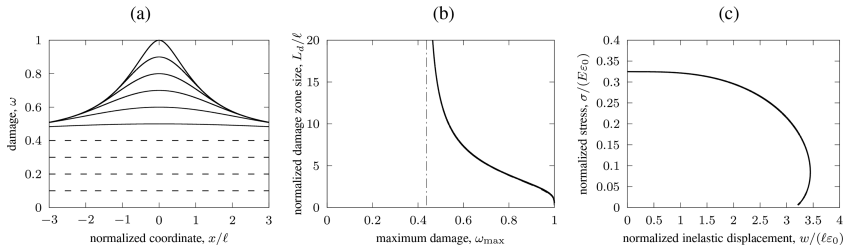

Figure 11. BFM crack field model: (a) evolution of damage profile, (b) evolution of damage zone width, (c) equivalent cohesive stress-crack opening curve.

plotted in Figure 11c is in this case extracted from the localized part of the response only. Its shape is not very realistic for concrete.

The one-dimensional version of the model of Karma, Kessler, & Levine (2001) (KKL) uses an energy expression that can be rewritten as

$$E = \int_{\mathcal{L}} \frac{1}{2} g_k(\varphi) E u'^2 \, dx + \int_{\mathcal{L}} \frac{1}{2} \kappa \varphi'^2 \, dx + \\ + \int_{\mathcal{L}} (1 - g_k(\varphi)) E_c \, dx, \tag{64}$$

where κ is a regularization parameter, φ is an auxiliary variable called the *phase field*, g_k is a suitable function (to be specified later), and $\mathcal{E}_c$ is a constant that represents a certain energy threshold. The first integral in (64) corresponds to the standard stored energy, $\mathcal{E}_{\text{std}}$, with $g_k(\phi)$ playing the role of the integrity factor $1-\omega$. The second integral corresponds to the regularization term $\mathcal{E}_{\text{reg}}$ defined by (48), with the phase field ϕ corresponding to the generalized compliance variable γ and with parameter $\kappa = g_f \ell^2$. The last integral in (64) represents the dissipated energy (it can also be interpreted as the energy stored in the creation of a new crack surface). Since $1 - g_k(\phi)$ corresponds to the damage variable ω, the dissipated energy density D is proportional to the damage and thus the underlying model is elastic-brittle, with dissipation given by $D(\omega) = \mathcal{E}_c \omega$ and with $\mathcal{E}_c$ representing g_f from (48); this parameter corresponds here to the energy per unit volume dissipated by total failure of the material (which is at the same time the elastic energy density at the limit elastic state).

In summary, the KKL model is in fact an elastic-brittle model with regularization based on the gradient of a certain variable ϕ obtained by transforming the usual damage variable ω. In the KKL model, ϕ is called the phase-field variable and is linked to damage by

$$\omega(\phi) = 1 - g_k(\phi). \tag{65}$$

If function g_k is invertible (and its inverse is denoted as g_k^*), we can also write the relation as

$$\phi = g_k^*(1-\omega) \tag{66}$$

and this is analogous to the definition of γ as a function of ω used in Section 5.1.

The specific form of function g_k used by Karma et al. is

$$g_k(\phi) = 4\phi^3 - 3\phi^4 \tag{67}$$

and the corresponding relation between damage and the phase field is described by

$$\omega = 1 - 4\phi^3 + 3\phi^4. \tag{68}$$

The phase-field variable ϕ is equal to 1 in the virgin state and decreases to 0 as the material stiffness is degraded. In contrast to that, the compliance variable γ used in Section 5.1 is supposed to be initially equal to 0 and then grow as the stiffness is degraded. The correspondence between the variational formulation from Section 5.1 and the KKL phase field model remains valid even if we set $\gamma = 1 - \varphi$ because the regularizing terms γ'^2 and φ'^2 (or, in multiple dimensions, $\|\nabla\gamma^2\|$ and $\|\nabla\varphi\|^2$ will still be the same. Therefore, equation (68) can be translated into the relation betwen the damage and generalized compliance,

$$\omega(\gamma) = 6\gamma^2 - 8\gamma^3 + 3\gamma^4. \tag{69}$$

In this case, the derivative

$$\frac{\mathrm{d}\omega(\gamma)}{\mathrm{d}\gamma} = 12\gamma - 24\gamma^2 + 12\gamma^3 \tag{70}$$

has a zero value at $\gamma = 0$. Consequently, the initial size of the damage zone tends to infinity. The KKL phase field model can thus be expected to lead, at early stages of the failure process, to a very large damage zone that gradually shrinks. This is confirmed by the numerical results plotted in Figure 12a,b. For small γ, equation (69) could be approximated by $\omega(\gamma) \approx 6\gamma^2$. This indicates that initially the phase field $\phi = 1 - \gamma$ evolves very fast

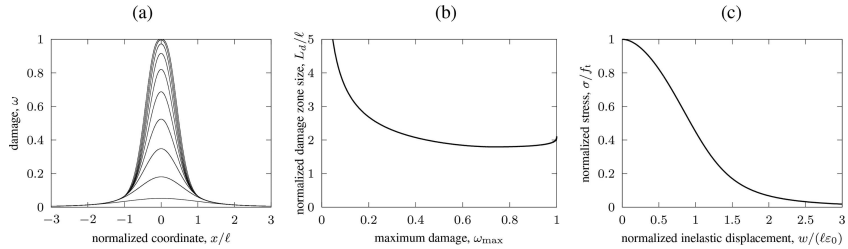

Figure 12. KKL phase field model: (a) evolution of damage profile, (b) evolution of damage zone width, (c) equivalent cohesive stress-crack opening curve.

as compared to damage, and damage gradients are strongly penalized by the term $\kappa\phi'^2$.

On the other hand, what matters most at late stages of the failure process is how ω approaches 1 when ϕ approaches 0 (complete failure), i.e., when γ approaches 1 from the left. For $\phi << 1$, the term with ϕ^4 in (68) becomes negligible compared to the term with ϕ^3, and (69) can be approximated by $\omega(\gamma) \approx 1 - 4(1-\gamma)^3$, which leads to

$$\gamma \approx 1 - \sqrt[3]{\frac{1-\omega}{4}} \qquad \text{as} \quad \omega \to 1^- \tag{71}$$

and

$$\frac{\mathrm{d}\gamma(\omega)}{\mathrm{d}\omega} \approx \frac{1}{12}\left(\frac{1-\omega}{4}\right)^{-2/3} \qquad \text{as} \quad \omega \to 1^-. \tag{72}$$

Inverse proportionality of the derivative $\mathrm{d}\gamma/\mathrm{d}\omega$ to $(1-\omega)^{2/3}$ is similar to the formulation with the relation between γ and ω given by (58) with exponent $p = 2/3$. It can therefore be expected that the KKL model shares some features with the elastic-brittle model regularized by the gradient of γ defined by (58) with $p = 2/3$. Indeed, the equivalent cohesive diagram constructed for the KKL model and plotted in Figure 12c has a tail similar to the solid curve in Figure 10c, obtained for $p = 0.8$.

5.3 *Thick level set models*

A recently developed special regularization technique directly enforces a certain shape of the localized damage profile along lines that correspond to the steepest descent of damage (Moës, Stolz, Bernard, & Chevaugeon 2011). Mathematical description and numerical implementation of such models rely on the level set technology, which was previously applied to the description of cracks, considered as displacement discontinuities. The location of a crack in a three-dimensional body can be conveniently described by a function Φ that is equal to zero on the internal surface that represents the crack, and has positive values on one side of the crack and negative values on the other side. Function Φ is usually defined as the signed distance from the crack surface, and then it satisfies the condition $\|\nabla\Phi\| = 1$. The set of points for which $\Phi = 0$ is called the zero level set of function Φ, and the function is referred to as the level set function.

Models based on the thick level set (TLS) approach aim at the description of localized damage bands of a finite thickness, and they consider a continuous transition between the intact and fully cracked states of the material, described by a damage variable ω that evolves from 0 to 1. A band of localized damage can be characterized by a level set function Φ which has zero values at the boundary of the band and positive values inside the band. It is again considered as a signed distance function, but this time the zero level set corresponds to points at which damage just starts to grow. The main idea is that the value of damage is directly linked to the value of the level set function Φ, i.e., to the distance from the boundary of the damage band. Full damage is supposed to be attained at points $\mathbf{x}$ for which $\Phi(\mathbf{x}) \geq \ell$ where ℓ is a characteristic length parameter.

The dependence of damage on the distance from the boundary of the band is prescribed by the condition

$$\omega = \Omega(\Phi), \tag{73}$$

where Ω is a given continuous non-decreasing function, equal to 0 for $\Phi \leq 0$ and equal to 1 for $\Phi \geq \ell$. The specific form of this function is to a large extent arbitrary, but it is assumed that the function is continuously differentiable for $0 < \Phi < \ell$. Function Ω directly controls the final shape of a fully developed damage profile. The damage band is formed by the points at which $\Phi \geq 0$, which can be interpreted as a "thick level set", hence the name of the approach. A parabolic shape of the fully developed damage profile is obtained by choosing

$$\Omega(\Phi) = \frac{2\Phi}{\ell} - \frac{\Phi^2}{\ell^2} \text{for } 0 \leq \Phi \leq \ell. \tag{74}$$

Fig. 13a shows several stages of the development of the damage profile in the one-dimensional setting.

Since the shape of the damage profile is prescribed, the evolution of damage cannot be governed by a local law applied separately at each material point. In fact, once the form of function Ω is selected, the distribution of damage inside the process zone is uniquely determined by the boundary of that zone, i.e., by the zero level set of function Φ. The law that governs the evolution of damage can be derived by incrementally minimizing the total energy. In contrast to the variational approach presented in Section 5.1, the higher-order term $\mathcal{E}_{\text{reg}}$ is omitted and regularization is achieved by imposing a constraint on the damage distribution.

In the one-dimensional setting, one can assume that damage localizes in an interval $\mathcal{I}_{\text{d}} = (L_{\text{d}}/2, L_{\text{d}}/2)$. The signed distance from the boundary of the damage band is then given by $\Phi(x; L_{\text{d}}) = L_{\text{d}}/2 - |x|$ and the damage distribution

$$\omega(x; L_{\text{d}}) = \Omega(\Phi(x; L_{\text{d}})) \tag{75}$$

is uniquely determined by the size of the band, L_{d}. The total energy $\mathcal{E}(u; L_{\text{d}})$ is obtained as the sum of $\mathcal{E}_{\text{std}}$ given by (47) and $\mathcal{E}_{\text{dis}}$ given by (49), with ω expressed according to (75). The resulting expression depends on the displacement field $u(x)$ and on variable L_{d}. Admissible increments of $u(x)$ must satisfy Dirichlet boundary conditions and admissible increments of L_{d} are those for which the damage increments are everywhere nonnegative, which is the case if $\Delta L_{\text{d}} \geq 0$. Optimality conditions then lead to the equilibrium equation in its usual form (50) and to conditions that govern the evolution of L_{d} (and thus of the entire damage profile). These conditions are conveniently written as

$$F(u'; L_{\text{d}}) \leq 0, \quad \dot{L}_{\text{d}} \geq 0, \quad \dot{L}_{\text{d}} F(u'; L_{\text{d}}) = 0, \tag{76}$$

where

$$F(\varepsilon; L_{\text{d}}) = \\ = \int_{\mathcal{L}} \left(D_{\omega}(\omega(x; L_{\text{d}})) - \frac{1}{2} E \varepsilon^2(x) \right) \frac{\partial \omega(x; L_{\text{d}})}{\partial L_{\text{d}}} dx. \tag{77}$$

Note that F is a functional dependent on the strain field, $\varepsilon(x)$, and on the damage zone size, L_{d}. The loading-unloading conditions (76) imply that damage can grow only if $F(\varepsilon; L_{\text{d}}) = 0$. This can be interpreted as an equality between the "nonlocal driving force",

$$\bar{Y}(\varepsilon; L_{\text{d}}) = \frac{1}{2} \int_{\mathcal{I}_{\text{d}}} E \varepsilon^2(x) \frac{\partial \omega(x; L_{\text{d}})}{\partial L_{\text{d}}} dx, \tag{78}$$

and the "nonlocal resistance",

$$\bar{g}^*_Y(L_{\text{d}}) = \int_{\mathcal{L}} D_{\omega}(\omega(x; L_{\text{d}})) \frac{\partial \omega(x; L_{\text{d}})}{\partial L_{\text{d}}} dx = \\ = 2D(\Omega(L_{\text{d}}/2)). \tag{79}$$

The nonlocal driving force, $\bar{Y}$, is obtained by weighted spatial averaging of the local damage energy release rate, $Y = E\varepsilon^2/2$, with $\partial\omega/\partial L_{\text{d}}$ used as the weight function. Damage grows if this nonlocal driving force becomes equal to the double of the density of energy that would be dissipated by the underlying local model if damage increased from zero to the level determined by the maximum damage at the center of the localized damage band, $\Omega(L_{\text{d}}/2)$.

The strain field can be eliminated from condition $\bar{Y}(\varepsilon; L_{\text{d}}) = 2D(\Omega(L_{\text{d}}/2))$ by substituting the usual expression $\varepsilon(x) = \sigma/(E(1-\omega(x)))$ where σ is constant along the bar and $\omega(x)$ is determined by L_{d}; see (75). The integral relation is thus converted into an algebraic relation between σ and L_{d}. The equivalent cohesive diagram that corresponds to the given local stress-strain law can then be constucted. As shown by Parrilla Gómez, Moës, & Stolz (2015), it is even possible to start from an assumed form of the cohesive law and to construct a TLS damage model that gives a macroscopically equivalent behavior, at least under uniaxial tension. This is illustrated in Figures 13–14. To obtain an exponential cohesive curve (Figure 13c), one needs to use a special form of dissipation function $D(\omega)$ shown by the solid curve in Figure 14a, which corresponds to the "local resistance" $D_{\omega}(\omega)$ shown by the dashed curve in Figure 14a and to

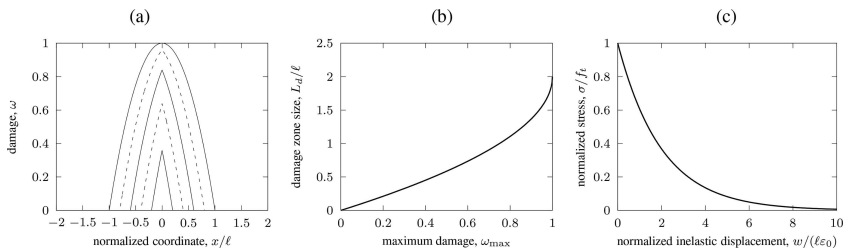

Figure 13. Thick level set model: (a) evolution of damage profile, (b) evolution of damage zone width, (c) equivalent cohesive stresscrack opening curve.

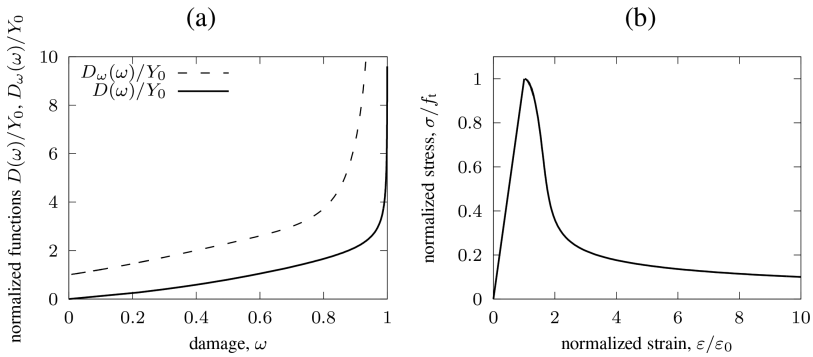

Figure 14. Thick level set model: (a) dependence of dissipation function D and its derivative D_ω on damage (both normalized by $Y_0 = E\varepsilon_0^2/2$), (b) stress-strain curve of the corresponding local damage model.

the local stress-strain diagram plotted in Figure 14b. The possibility to select directly the shape of the cohesive curve is an attractive feature of the TLS formulation.

6 CONCLUSIONS

In summary, it is not easy to construct a regularized damage formulation applicable to concrete that satisfies two basic requirements related to the behavior of localized solutions:

1. Ideally, the active part of the localized damage zone should gradually shrink and in the limit reduce to a crack surface. Alternatively, a limited expansion of the damage zone can be tolerated, provided that damage tends to 1 only at the center of that zone.
2. The cohesive diagram that describes the behavior of an equivalent fictitious crack should have a shape realistic for concrete, with a long tail.

These requirements are to a large extent contradictory and are hard to satisfy simultaneously. Traditional integral-type nonlocal formulations based on spatial averaging with a fixed distance-dependent weight function and explicit or implicit gradient damage formulations with fixed coefficients at the second-gradient enrichment term can satisfy requirement 2 but lead to wide bands of highly damaged material. Adjustments that reduce nonlocal interaction at late stages of the degradation process provide more realistic final damage profiles but may result into excessively brittle final parts of the equivalent cohesive curve. Certain types of variational damage models suffer by the same deficiencies. Nevertheless, by carefully combining model ingredients and tuning up parameters, one can obtain formulations that meet the above requirements. Promising results have been obtained for an integral-type model with damage-dependent nonlocal interaction combined with an extended tail of the local stress-strain curve, for a special form of the implicit gradient damage model with decreasing characteristic length, for variationally based damage models with a suitable choice of the regularizing variable, as well as for the thick level set approach.

The present study has been restricted to localization properties under uniaxial tension. Other aspects need to be taken into account when looking for a robust and efficient regularized formulation that provides physically realistic results in simulations of concrete structures. They will be discussed in the lecture at Euro-C 2018.

ACKNOWLEDGMENT

Financial support received from the Czech Science Foundation (GAČR project No. 17-04150 J) is gratefully acknowledged.

REFERENCES

Bourdin, B., G.A. Francfort, & J.-J. Marigo (2000). Numerical experiments in revisited brittle fracture. *Journal of the Mechanics and Physics of Solids 48*(4), 797–826.

Desmorat, R. & F. Gatuingt (2010). Introduction of an internal time in nonlocal integral theories. In *Computational Modelling of Concrete Structures*, pp. 121–128.

Desmorat, R., F. Gatuingt, & M. Jirásek (2015). Nonlocal models with damage-dependent interactions motivated by internal time. *Engineering Fracture Mechanics 142*, 255–275.

Francfort, G.A. & J.J. Marigo (1998). Revisiting brittle fracture as an energy minimization problem. *Journal of the Mechanics and Physics of Solids 46*(8), 1319–1342.

Geers, M.G.D. (1997). *Experimental analysis and computational modeling of damage and fracture*. Ph. D. thesis, Eindhoven University of Technology, The Netherlands.

Geers, M.G.D., R. de Borst, W.A.M. Brekelmans, & R.H.J. Peerlings (1998). Strain-based transient-gradient damage model for failure analyses. *Computer Methods in Applied Mechanics and Engineering 160* (1–2), 133–153.

Jirásek, M. & J. Zeman (2015). Localization study of a regularized variational damage model. *International Journal of Solids and Structures 69–70*, 131–151.

Karma, A., D.A. Kessler, & H. Levine (2001). Phase-Field Model of Mode III Dynamic Fracture. *Physical Review Letters 87*(4), 045501-1-045501-4.

Mazars, J. (1984). Application de la mécanique de l'endommagement au comportement non linéaire et à la rupture du béton de structure. Thése de Doctorat d'Etat, Université Paris VI., France.

Miehe, C., M. Hofacker, & F. Welschinger (2010). A phase field model for rate-independent crack propagation: Robust algorithmic implementation based on operator splits. *Computer Methods in Applied Mechanics and Engineering 199*, 2765–2778.

Mielke, A. (2005). Evolution of rate-independent systems. In C. Dafermos and E. Feireisl (Eds.), *Handbook of Differential Equations: Evolutionary Equations*, Volume 2, pp. 461–559. Amsterdam, The Netherlands: Elsevier B.V.

Mielke, A. & T. Roubíček (2006). Rate-independent damage processes in nonlinear elasticity. *Math. Models Methods Appl. Sci. 16*, 177–209.

Moës, N., C. Stolz, P.E. Bernard, & N. Chevaugeon (2011). A level set based model for damage growth: The thick level set approach. *International Journal for Numerical Methods in Engineering 86*, 358–380.

Parrilla Gómez, A., N. Moës, & C. Stolz (2015). Comparison between thick level set (TLS) and cohesive zone models. *Advanced Modeling and Simulation in Engineering Sciences 2*(1), 18.

Peerlings, R.H.J., R. de Borst, W.A.M. Brekelmans, & J.H.P. de Vree (1996). Gradient-enhanced damage for quasi-brittle materials. *International Journal for Numerical Methods in Engineering 39*, 3391–3403.

Pijaudier-Cabot, G. & Z.P. Bažant (1987).Nonlocal damage theory. *Journal of Engineering Mechanics, ASCE 113*, 1512–1533.

Poh, L. & G. Sun (2017). Localizing gradient damage model with decreasing interactions. *International Journal for Numerical Methods in Engineering 110*, 503–522.



Taylor & Francis
Taylor & Francis Group
http://taylorandfrancis.com

Computational Modelling of Concrete Structures – Meschke, Pichler & Rots (Eds)
© 2018 Taylor & Francis Group, London, ISBN 978-1-138-74117-1

Erection of bridges and shells without formwork—challenges for the computational modelling

J. Kollegger, B. Kromoser & D. Suza
TU Wien, Vienna, Austria

ABSTRACT: Construction methods have been developed at TU Wien, which enable the erection of bridges and shells without formwork. In the design of real structures on the basis of these construction methods only linear elastic finite element analysis were carried out. A linear elastic analysis, where the principle of superposition is applied and an automatic load case superposition is carried out, simplifies matters enormously during the design process. During the development of the bridge construction method, large scale experiments were carried out. In the paper the stress redistribution between the thin-walled plate elements and the filler concrete of a 30 m long post-tensioned girder over a period of seven years is studied using different material models and then compared to the experimental results. In the case of the reinforced concrete shell, the transformation process from the originally flat plate to a shell structure with double curvature was modelled using a nonlinear finite element program.

1 INTRODUCTION

For the erection of bridge and shell structures made of reinforced concrete a formwork is required when using conventional construction methods. In addition to the formwork a falsework or other support structures are needed to carry the weight of the formwork and the fresh concrete. The costs of the applied formwork and the falsework make up a huge portion of the construction costs of these engineering structures. In order to save on these costs construction methods have been developed at TU Wien during the last years, which enable an erection of bridges and shells without formwork. These erection methods will be explained in chapters 2 and 3 of this paper with an addition of shownapplications of these methods for recent structures.. It has to be admitted that the usage of nonlinear modelling techniques in the design of real structures is rarely required. Reinforced concrete structures have to be designed to fulfill serviceability limit state requirements, which means that they will remain uncracked or will show only limited cracking during later usage., therefore allowing a linear elastic analysis of the structures to be sufficient. A linear elastic analysis simplifies matters enormously for the designer, since the principle of superposition can be applied and an automatic load case superposition can be carried out.

Nonlinear effects like cracking, creep and shrinkage naturally have to be considered in the serviceability limit state. These nonlinear effects can be incorporated into a design by following the standard design rules, e.g. the length to depth ratio for a beam, or tmust be delt with using simplified engineering models.

In the ultimate limit state a sectional approach is usually applied. In the relevant cross-sections of a structure the fulfillment of the ultimate limit state is proven by showing that the member forces caused by the actions, which have to be multiplied by partial safety coefficients, are smaller then the member forces, which can be carried by the cross-section. In determining the resistance of a cross-section in the ultimate limit state nonlinear material models for concrete, reinforcing steel and post-tensioning tendons are applied.

While only linear analyses where carried out during the design process of the structures shown in chapters 2 and 3 of this paper, nonlinear computational models were established in order to study further improvements of the construction methods. In the case of the bridge structure the stress redistribution between the thin-walled prefabricated girders and the filler concrete was studied using commercial computer programs as well as a program developed at TU Wien. In the case at the reinforced concrete shell the transformation process from the originally flat plate to a shell structure with double curvature was modelled using a nonlinear finite element program.

2 BALANCED LIFT METHOD (BLM)

2.1 *Building bridges using the BLM*

In the conventional bridge construction methods the production of the bridge superstructure is carried out in horizontal position. By using the BLM, developed at TU Wien by Kollegger et al. (2014), the bridge girders are erected next to the pier in a vertical position and are subsequently rotated into the final horizontal position. In order to rotate the bridge girders, additional structural elements acting as compression struts are required. The compression struts then become an integral part of the finished bridge. The rotation of the bridge girders functions similarly to the opening of an umbrella, which is displayed in Fig. 1.

The example displayed in Fig. 1 is suited for valley bridges with high piers. The application of the BLM for bridges with piers of small height is possible, if an auxiliary pier is used as is shown in Fig. 2.

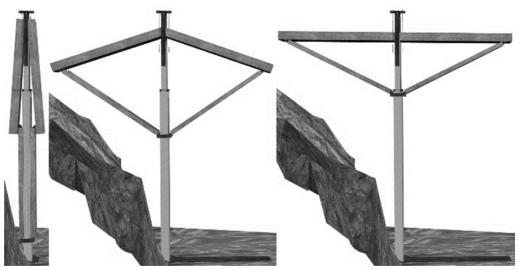

Figure 1. BLM for a bridge with a high pier.

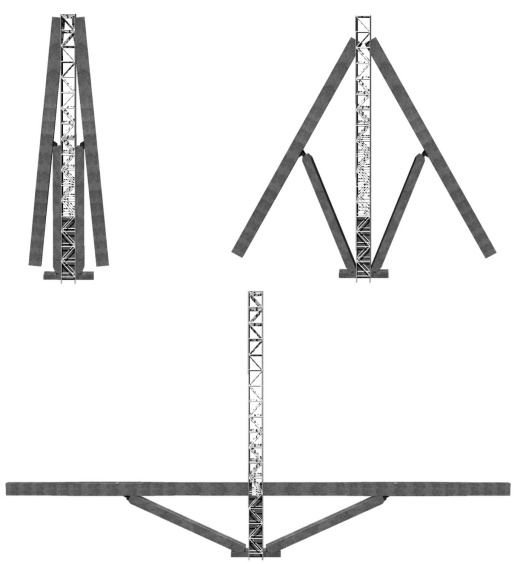

Figure 2. BLM for a bridge with an auxiliary pier.

The contribution of the BLM to the design of sustainable bridges is mainly based on the reduced material consumption. The mass of the bridge girders can be considerably reduced due to the action of the compression struts. In comparison to other bridge designs with compression struts, designs based on the BLM use the compression struts already during the construction phase which again results in savings of material for the completed structure.

2.2 *Practical application of the BLM*

The Austrian highway management company ASFINAG has commissioned an alternative design for four bridges on the S7 motorway, the Fürstenfelder Schnellstraße in the south-east of Austria, using the BLM. This alternative design was carried out by a joint venture of Kollegger GmbH and Schimetta Consult. The motorway bridges were originally intended to be built as steel and concrete composite structures erected by incremental launching (Fig. 3).

This construction method was proposed due to the fact that the site is protected for environmental reasons, restricting the access to the construction site to the central piers and the abutments.

By changing the design to post-tensioned concrete bridges erected using the BLM, the bridges are expected to cost 70% of the estimate calculated for the launching of the composite structures. The S7 bridges will each be built using the BLM for the central sections with a length of 72 m as shown in Fig. 4. The distance from the endpoint of the cantilevers to the abutments will be spanned by means of prefabricated beams with the same cross section as the balanced lift part. The deck structure will be completed by a conventional reinforced concrete deck slab, in the same way as a composite bridge. Construction of the bridges is scheduled for 2018.

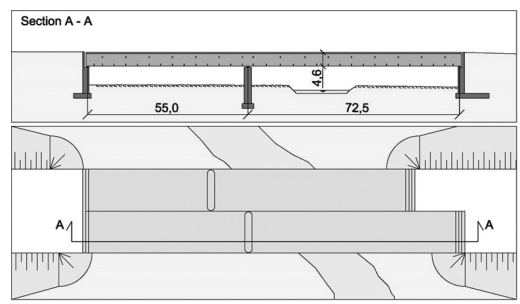

Figure 3. Original design for bridges on the S7 motorway with steel-concrete composite bridge girders.

2.3 *Large scale test structure*

A test structure with a total length of 50,4 m was built at the stockyard of an Austrian precasting company. The design of the test structure was based on a 70% scale of the design of the S7 bridges. To minimize the weight of the bridge parts which are moved during the balanced lift process, hollow reinforced concrete elements with small element thicknesses were prepared. For the 25 m long bridge girders, the side walls were 70 mm thick concrete elements like those that are often used as slab elements combined with cast in situ concrete for buildings (Fig. 5).

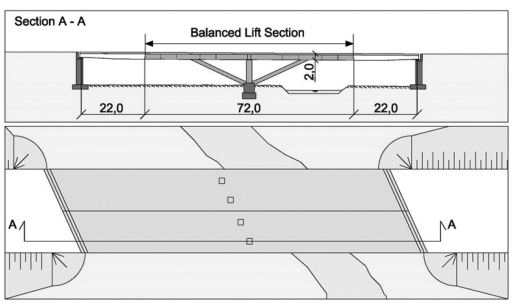

Figure 4. Bridge structures on the S7 motorway based on the BLM.

These elements were assembled on a steel form and then connected by a 120 mm thick slab of reinforced concrete. The height of the U-shaped sections of the 25 m long bridge girders was 1.26 m, with the width varying from 700 mm to 1.4 m; the larger width was required at the connection point between the beam and the compression strut.

This thin-walled bridge girder with its U-shaped cross section would have been too fragile for transport, assembly and the lifting process. Therefore, a truss made of reinforcing bars was welded to reinforcing elements protruding from the precast side wall elements at the top of the U-section. The U-section was hence converted to a box section which proved very robust in assembling and lifting operations. For the instalation of tendons, the bridge girders were equipped with transverse concrete beams for future post-tensioning operations. Two 25 m long sections of a tower crane, equipped with guide rails, served as an auxiliary pier. Fig. 6 shows the assembly of the compression struts in the vertical position. The lifting of the second bridge girder is shown in Fig. 7.

The lowering operations of the top points of the bridge with the aid of two mobile cranes are shown in Fig. 8. The maximum lifting force had been calculated to 270 kN, which corresponded well with the lifting force measured by the cranes. If this were a actual bridge construction the next step would have been the filling of the compression struts with in-situ concrete. In this case, where the



Figure 5. Production of prefabricated bridge girder.



Figure 6. Auxiliary pier and assembly of compression struts with the aid a mobile crane.



Figure 7. Assembly of the second bridge girder.



Figure 8. Lowering of top points of bridge girders with the aid of mobile cranes.

structure is intended as a demonstration project, only the node above the pier was filled with concrete to provide some wind resistance.

2.4 *Stress redistribution in a precast girder*

A stress redistribution experiment on a 30 m long precast girder was started in October 2010. The girder is a large-scale test of a real bridge girder used for the BLM. In order to demonstrate the feasibility of building bridges with thin precast concrete elements, a field test was realized with the aim of testing the behavior of the thin-walled elements under the load of the cast in-situ concrete and, at a later stage, the stress redistribution between prefabricated girder and filler concrete due to creep. A longitudinal section of the left half of the test girder is shown in Fig. 9.

The thickness of the wall elements was equal to 70 mm and the bottom plate had a thickness of 200 mm. The overall dimensions of the section amounted to a width of 700 mm and a height of 1440 mm. The experimental girder was pre-stressed by two 19-strand-tendons.

The three pre-fabricated parts were transported to the test site, placed on temporary supports, the ducts were connected and the 20 mm wide joints were filled with a high-strength grout. In the next step two tendons were stressed to 1500 kN each, which resulted in an upward movement of the central part of the test beam. Due to the upward movement the self-weight of the beam (g = 7,84 kN/m) was carried over the distance of 29,42 m between the supports by the beam itself.

Within a time difference of 24 hours, the filler concrete was placed in four layers, each with a thickness of 0,31 m. During the pouring of the concrete, the post-tensioning force was increased gradually up to 5300 kN. Details of the manufacturing procedure can be found in Kromoser (2011) and Wimmer (2015).

At the age of 181 days, two small cross beams were constructed in the middle of the span, in order to submit the examined beam to torsion testing. At the age of 568 days, the cross beams were enlarged for further loading tests. Elastic concrete strains caused by the dead load of the cross beam are visible in Figure 10 and Figure 11.

For a period of seven years the concrete strains of the experimental beam were measured using a mechanical extensometer with an accuracy of 0,001 mm. The measured points were fastened at the bottom of the precast girder in the same height as the post-tensioning tendons. For the concrete strain monitoring, it was sufficient to measure one side of the girder. After the hardening of the filer concrete inside the U-shaped pre-fabricated girder, the strains of these two different concretes were of the same magnitude. No slip in the reinforced concrete interface was measured. In order to separate the measured concrete strains from the temperature influence, the temperature of the air and the temperature of the experimental girder were continuously measured.

Regardless of the known temperature values, the analysis of the temperature of the composite cross-section is complicated due to the big difference of the air temperature and the temperature difference caused by sun exposure.

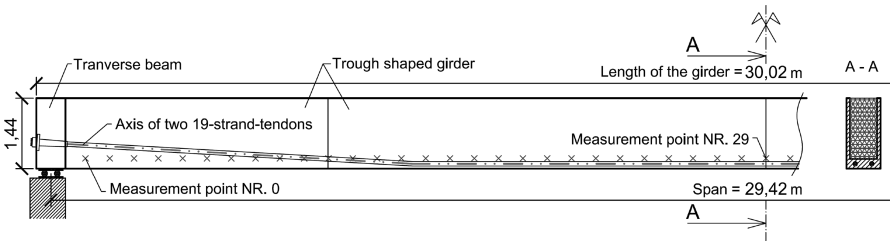

Figure 9. Longitudinal section of test beam.

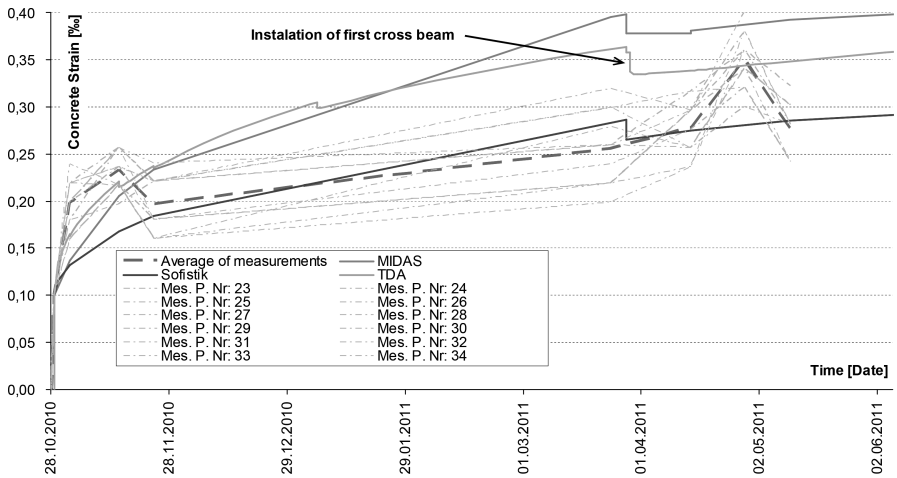

Figure 10. Comparison of measured and calculated concrete strains of test girder during the first seven mounths.

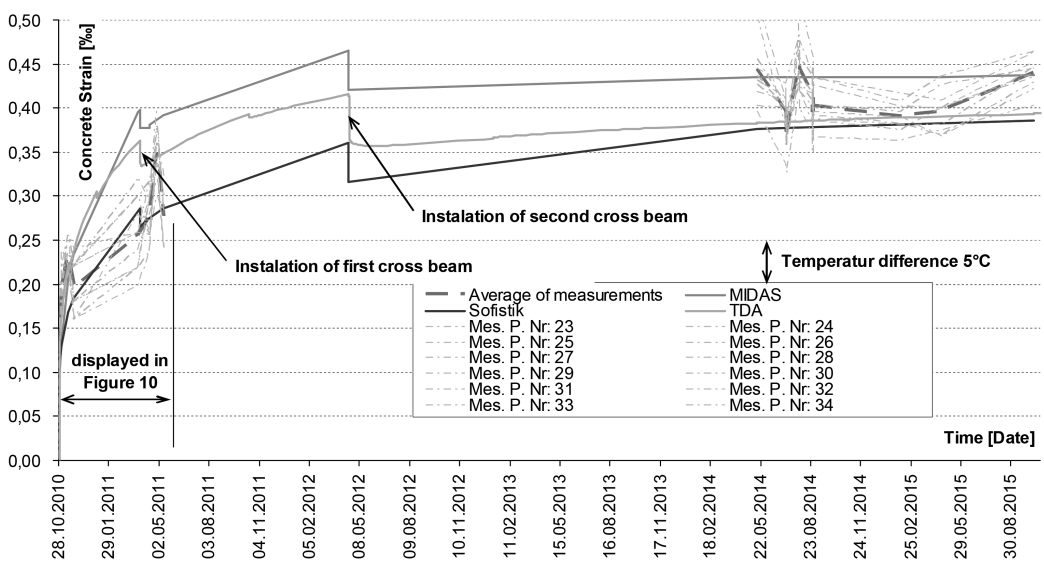

Figure 11. Five year measurement: comparison of measured and calculated concrete strains of test girder.

2.5 *Numerical simulation and comparison with experiment*

The measured concrete strains were compared to the results of three independent software calculations all using the same Code (EN 1992-1-1) and material model.

The calculation were carried out using two commercial programs—Sofistik 2014 from Germany and Midas Civil 2016 v2.1 from South Korea. The third program—TDA (Time Discretization Analysis) was programmed by Suza in Visual Basic for Application. The theory of the TDA was described by Navrátil (2014).

All these programs are suitable for calculating concrete composite girders assembled from different types of materials with different ages. It is possible to describe the loading history, the evolution of young concrete stiffness and the different curves of creep and shrinkage for all the section elements.

Time-dependent creep effects produce stress redistribution in the framework of existing composite cross-sections caused by all described influences. Based on creep capacity, the construction could redistribute the stresses until reaching a state as if the construction would have been cast in one construction phase. Time-dependent creep effects produce stress redistribution in the framework of existing composite cross-sections caused by all described influences. Based on creep capacity, the construction could redistribute the stresses until reaching a state as if the construction would have been cast in one construction phase.

A comparison of measured concrete strains and calculated concrete strains was carried out in order to assess the quality of the numerical simulations of the test girder. The results are shown in Figure 10 and Figure 11. The vertical axis displays total concrete strain [‰]. The thin grey dashed and dotted lines are the measured concrete strains. Measured points are positioned 100 mm from the bottom of the 30 m long experimental girder. The position of measured points corresponds to the position of the tendons. The displayed data is from the middle of the span (+/- 2 m).

The measured strains were corrected by the temperature influence. The girder temperature was assessed by the average daily temperature of the measurements. Regardless of the temperature corrections, an interference is still visible in the measured values. Differences of 5°C produce a concrete strain of 0,05 ‰. This is visible in Figure 10 and Figure 11 as the distance of two horizontal lines.

The dashed red line shows the average measured values. The dark blue and orange lines are strain results of the commercial programs Sofistik and Midas. The light blue line is the result of TDA (Time Discretisation Analysis).

All three programs proved good correlation of theoretical concrete strain evolution with the actual construction. Even though the initial

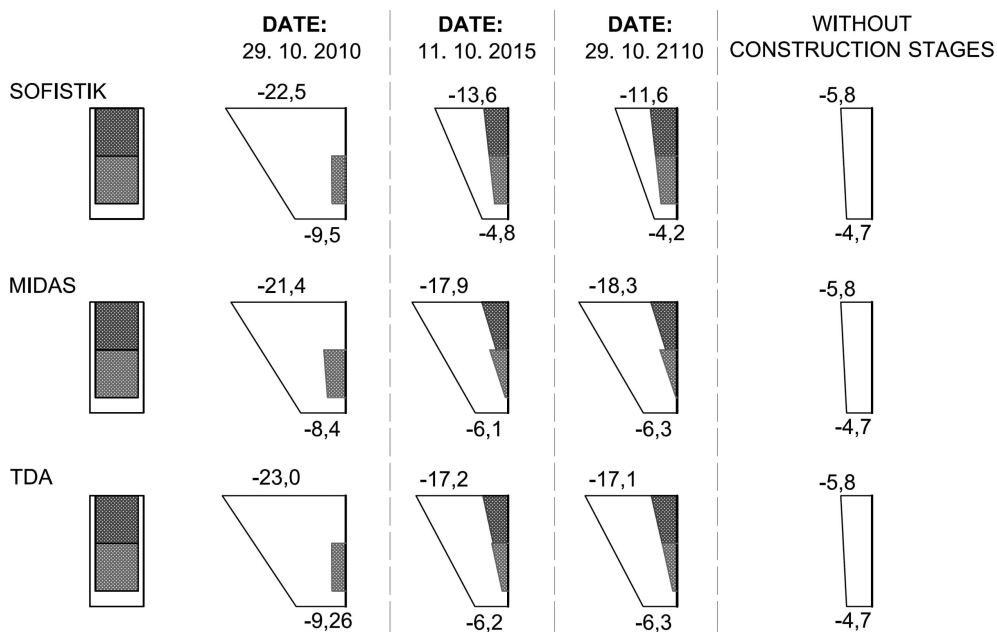

Figure 12. Comparison of calculated concrete stresses.

cross-section stresses were similar, and even though the programs used the same material models provided in the Eurocode 2 and the concrete strain developments were similar reaching a strain of 0,40 ‰, the stresses calculated by the programs did show some differences. Sofistik redistributes the stresses more than Midas and TDA. Results of Midas and TDA are similar (see Fig. 12). The Sofistik results show, that the initial upper stress (–22 MPa) and bottom stress (–9 MPa) of the U-shaped precast girder have decreased by almost 50% to this day (–13,6 MPa top fibers; –4,8 MPa bottom fibers). Sofistik solver expects that, redistribution will continue infinitely (100 years) and will further decrease (–11,55 MPa upper fibres; –4,23 MPa bottom fibres).

The Midas and TDA results have a good correlation with each other. The initial stresses of the U-shaped shape precast girder decrease up to 20–30% (see Fig. 7). Both models show that the present stresses of the girder should be similar to the stress at infinite time (100 Years).

None of the programs proved that the construction could have enough creep capacity to redistribute the stresses to the stage of an elastic calculation (that would be the case of a construction without construction stages).

All three programs Sofistik, Midas and TDA, provided a good match with measured strain values. Even though the results of Sofistik stresses are different to those of Midas and TDA, it is not unequivocally possible to determine which solution approximates the construction more accurately. It is important to know, that by using the same material models and the same codes, different results are obtained with different programs.

3 PNEUMATIC FORMING OF HARDENED CONCRETE (PFHC)

3.1 *Construction principle of PFHC*

The utilization of concrete as construction material can be increased sharply by optimizing the form of the structure according to the applied loads (Kromoser and Kollegger 2017b). For example, concrete shells represent such optimized forms. The particular forms found have a free formed geometry in most cases requiring a complex formwork and falsework to be produced. To address this problem, a new shell construction method was invented at the TU Wien with the name Pneumatic Forming of Hardened Concrete (PFHC). The idea is to simplify the production of such concrete shell structures by bending a thin flat hardened concrete plate to a double curved shell structure. The flat hardened concrete plate is lifted by inflating an air cushion placed underneath the concrete plate and by tensioning post-tensioning tendons mounted at the circumference as shown in Fig. 13. The functionality of the complete construction method could already be tested in two large scale experiments where a spherical concrete shell with 10.8 m diameter and 3.2 m height as well as a free formed concrete shell with the plan measurements of 17.6 × 10.8 m and a height of 2.9 m were erected as explained in Kromoser and Huber (2016). Both shells had a thickness of 50 mm. Currently, in the

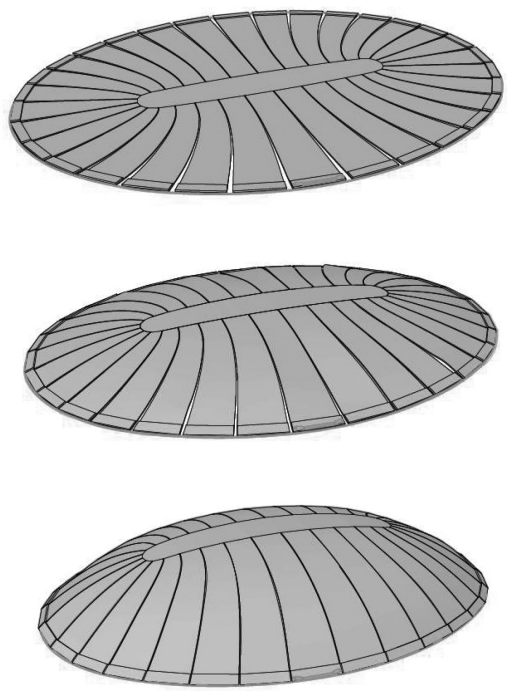

Figure 13. Construction principle PFHC: Erection of a concrete shell originating from a thin flat hardened concrete plate by the aid of an air cushion placed underneath the plate and tensioning a post-tensioning tendon mounted at the circumference (Kromoser and Kollegger 2017b).



Figure 14. Event canopy built with PFHC.



Figure 15. Shell bridge AM2 serving as deer pass (Picture taken during the construction works).

course of developing the construction method, the next step was to apply the method for the construction of two first buildings. On behalf of the Austrian Railways (ÖBB infrastructure) two shells, an event canopy (Fig. 14) and a shell bridge serving as deer pass (Fig. 15) were built in Carinthia in the south of Austria.

3.2 *The bending behavior of hardened concrete plates*

The core of the construction method is the bending process of the hardened concrete itself. The bending behavior of hardened concrete plates with 50 mm, 100 mm and 120 mm thickness, with different reinforcement types and reinforcement ratios could already be tested in extensive preliminary experiments as described in Kromoser and Kollegger (2014, 2015 and 2017). Fig. 16 shows a four point bending test with a 50 mm thick concrete plate with the dimensions of 2.5 × 0.5 m. In addition, Fig. 17 shows the four point bending test of a 100 mm thick concrete plate with the dimensions of 4.5 × 0.5 m. Stainless steel ropes with 7 × 19 wires and glass fiber reinforced polymer (GFRP) bars could be determined as best suiting reinforcement types as explained in Kromoser and Kollegger (2017a). Stainless steel ropes with 5 mm diameter were chosen as reinforcement for the construction of the two large-scale experiments mentioned above and described in Kromoser and Kollegger (2014 and 2015 b). GFRP rods with 6 mm diameter were used for the event canopy (Fig. 14) and GFRP rods with 8 mm diameter for the shell bridge built on behalf of the ÖBB. GFRP rods have the practical advantage that they can be installed in a conventional manner on construction site. In contrast, stainless steel ropes have a low stiffness and have to be prestressed into the formwork leading to a greater effort.

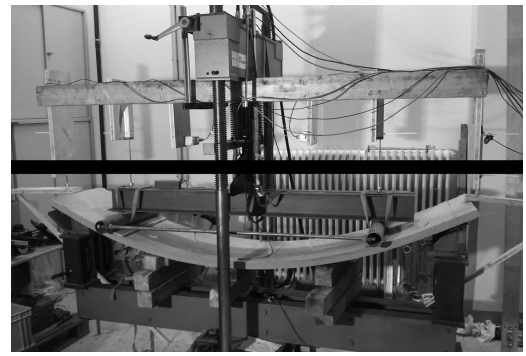

Figure 16. Bending experiment with a 50 mm thick concrete plate with the dimensions of 2.5 m × 0.5 m.

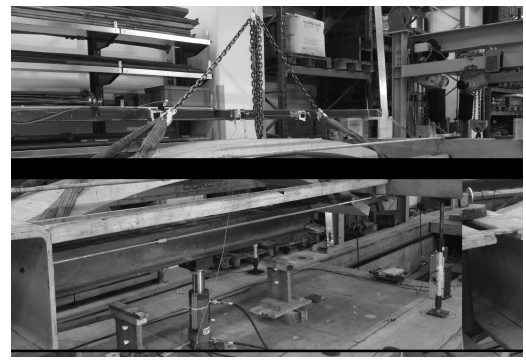

Figure 17. Bending experiment with a 100 mm thick concrete plate with the dimensions of 4.5 m × 0.6 m.

3.3 *Non-linear finite element calculations*

Non-linear finite element calculations using the calculation software Atena 3D from Cervenca Consult served to recalculate the deformation behavior of the thin concrete plates tested in the four point bending tests in a first step and to use the gathered knowledge to predict the transformation behavior from a flat plate to a double curved shell in a second step. The calculation model and the material properties were calibrated by using the results of the four point bending experiments. The main challenge was to realize the large deformations, which occur during the transformation process. For example, the flat plate of the shell bridge built in Carinthia with the plane dimensions of 56.0 × 43.0 m × 0.1 m was transformed to a shell with the dimensions 53.0 × 38.1 m and a middle height of 7.6 m. Due to the double symmetric geometry of the plate only a quarter of the flat plate (Fig. 18) was modelled for the non-linear finite element calculation. The finite-element mesh of the flat plate for the calculation of the construction of the shell bridge AM2 is shown

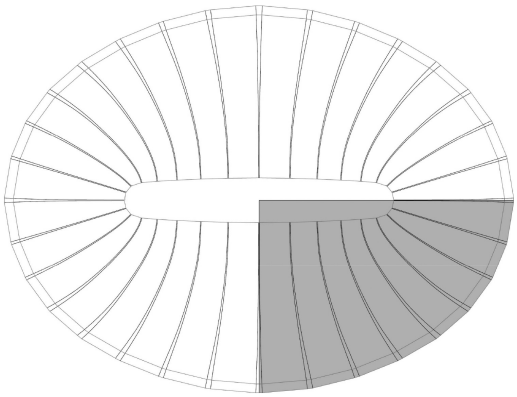

Figure 18. The non-linear finite element calculation was performed at a quarter of the structure.

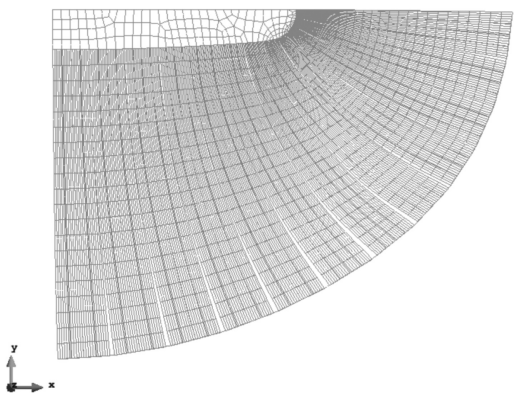

Figure 19. Mesh for the non-linear finite-element calculation for the prediction of the transformation behavior from a flat plate to a segmented shell.

in Fig. 19. The air pressure was modelled as distributed load. Quadratic hexahedron elements were used for the discretization. The element height was chosen with the thickness of the flat concrete plate (100 mm). The elements were formulated as shells. Stresses over the thickness were neglected. Each element has nine integration points in plane and eight over the thickness of the elements. In total, one element has 72 integration points. Shell elements have the advantage of significantly lower Integration points in comparison to volume elements leading to a lower calculation time. One-dimensional elements were used to simulate the reinforcement bars and the post-tensioning cables. The non—linear analysis was performed by using a newton Raphson calculation approach. The tangential stiffness matrix was calculated in each iteration step.

As convergence criteria following values were chosen:

1. Relative fault of the displacement: 0.01
2. Relative fault of the force-equilibrium: 0.01
3. Absolut fault of the force residuum: 0.01
4. Relative energy fault: 0.0001

3.4 *Results of the non-linear finite element calculations*

It was possible to simulate the transformation process with Atena 3D. The deformations in step 50, step 100 and step 166 are shown in Fig. 20–Fig. 22. The maximal calculated compressive strains in the concrete could be determined with 0.00106 as shown in Fig. 23. The maximum compression strain in the preliminary four point bending experiments could be determined with >0.003. Thus a safety factor of 3 can be observed The occurring strains were monitored in three different reinforcement bars as marked in Fig. 24. The development of the strains in these three bars during the transformation process are shown in Fig. 25. The maximal strains in the calculation was

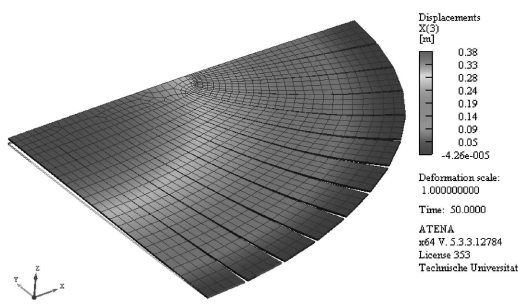

Figure 20. Step 50 of the non-linear finite element calculation of the transformation process during the construction of the shell bridge AM2.

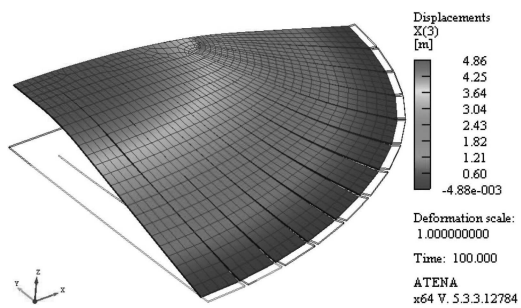

Figure 21. Step 100 of the non-linear finite element calculation of the transformation process during the construction of the shell bridge AM2.

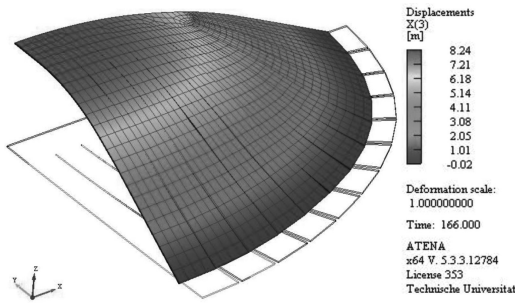

Figure 22. Step 166 of the non-linear finite element calculation of the transformation process during the construction of the shell bridge AM2.

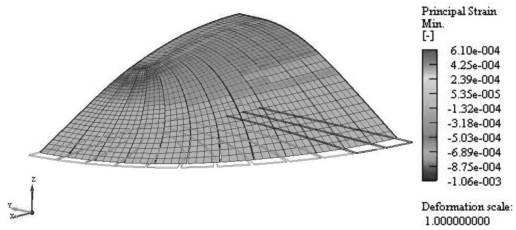

Figure 23. Principal strains of the concrete after finishing the transformation.

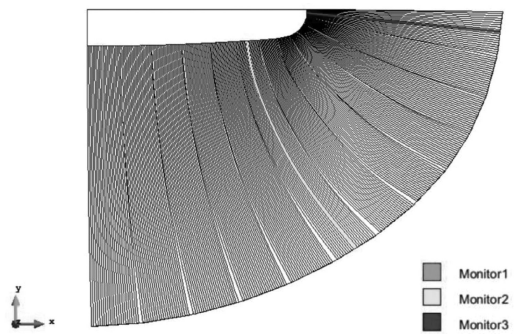

Figure 24. Monitored reinforcement.

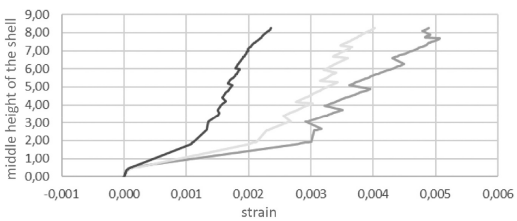

Figure 25. Strains in the monitored reinforcement bars.

0.005. The fracture strain of the bars is depending on the manufacturer but principally >0.0015. Here again a safety factor of 3 is given (GFRP rods have a linear elastic material behaviour right up to the moment of fracture). In comparison to the real transformation process on building site in Carinthia, the simulated form showed a higher curvature in the upper area close to the middle plate and lower curvature in the areas close to the outer rim. On construction site, an additional conventional reinforcement was assembled in the area of the middle plate and at the intersection of the middle plate to the elements. This led to a higher stiffness in these areas and to a slightly different geometry of the bridge in comparison to the calculation.

4 SUMMARY

Due to the constraints of available time and budget most designs of concrete structures are carried out using linear elastic models for the calculation of the response of these structures to the applied loads. However, advanced computational modelling procedures, which take into account the nonlinear behavior of reinforced concrete, are of great importance in the development of new construction methods. In this paper new construction methods for bridges and shells, which were developed during the last years at TU Wien, are explained and applications of these construction methods for real structures are shown. In the case of the bridge construction method (BLM) the stress redistribution of the highly prestressed prefabricated bridge segments to the filler concrete was investigated using nonlinear computational models. Further improvements of the economic advantages of the construction method will be possible, if this redistribution of stresses can be considered for real bridge projects. In the case of the shell construction method (PFHC) the transformation of the flat concrete plate to a shell structure with double curvature was modelled with the calculation program Atena 3D by taking into account the information obtained from previous experimental work on the bending of reinforced concrete plates.

ACKNOWLEDGEMENTS

The financial support of the experiment described in Section 2 by Austrian Research Promotion Agency (FFG), ASFINAG, ÖBB Infrastruktur AG and Vereinigung Österreichischer Beton- und Fertigteilwerke is gratefully acknowledged. In addition, the authors want to thank the project partners of the research project “Freiformflächen

aus Beton" (doka, ÖBB, Asfinag, Strabag, Porr, Alpine, Bilfinger, Habau, Swietelsky, Holcim, Lafarge, Wopfinger, Sika, and Festo) and the Austrian Research Promotion Agency (FFG) for the good collaboration and the financial support. The authors want to thank the Austrian railways (ÖBB) for the contract and the good collaboration in the course of the construction of the event canopy and the deer pass AM2 within the construction of the new built railway track Koralmbahn.

REFERENCES

Kollegger, J., et al 2014. Building bridges using the balanced lift method, *Structural Concrete: Journal of the fib, Vol. 15:* 281–291.

Kromoser, B. 2011. Brückenbau mit Fertigteilen—Großversuch zur Herstellung und zum Torsionswirkungsverhalten*, Masterthesis,* Vienna, Austria.

Kromoser, B., Kollegger, J. 2014. Herstellung von Schalentragwerken aus Beton mit der "Pneumatic Wedge Method" – Ein neues Bauverfahren für den Bau von zweifach gekrümmten Betonflächen, *Beton- und Stahlbetonbau 109, Heft 8*, p. 557–565.

Kromoser, B., Kollegger, J. 2015a. Application areas for pneumatic forming of hardened concrete, *Journal of the International Association for Shell and Spatial structures (IASS) Vol. 56, No. 3*, p. 187–198.

Kromoser, B. Kollegger, J. 2015b. Pneumatic Forming of Hardened Concrete—building shells in the 21st century, *Structural Concrete, Volume 16, Issue 2*, p. 161–171.

Kromoser, B., Huber, P. 2016. Pneumatic Formwork Systems in Structural Engineering, *Advances in Materials Science and Engineering, vol. 2016,* 13 pages.

Kromoser, B., Kollegger, J. 2017a. Aktives Verformen von ausgehärteten Betonelementen zur Herstellung von räumlich gekrümmten Betonflächen, *Beton- und Stahlbetonbau 112, Issue 2*, p. 106–115.

Kromoser, B., Kollegger, J. 2017b. How to inflate a hardened concrete shell with a weight of 80 t, *Proceedings of the IASS Annual Symposium 2017 "Interfaces: architecture. engineering. science",* September 25–28th, 2017, Hamburg, Germany.

Navrátil, J. 2014. Prestressed Concrete Structures, *VŠB—Technical University of Ostrava, Faculty of Civil Engineering,* Ostrava, Czech Republic.

Wimmer, D. 2015. Entwicklung eines neuen Brückenbauverfahren durch die Kombination von dünnwandigen Betonfertigteilen und Vorspannung, *Doctorthesis*, Vienna, Austria.



Taylor & Francis
Taylor & Francis Group
http://taylorandfrancis.com

Computational Modelling of Concrete Structures – Meschke, Pichler & Rots (Eds)
© 2018 Taylor & Francis Group, London, ISBN 978-1-138-74117-1

Network modelling of fracture processes in fibre-reinforced quasi-brittle materials

P. Grassl & A. Antonelli
School of Engineering, University of Glasgow, Glasgow, UK

ABSTRACT: Fracture processes in fibre-reinforced quasi-brittle materials were studied with a three-dimensional structural network approach. The geometry of the meso-structure was modelled as poly-dispersed ellipsoids and line segments. Here, ellipsoids and line segments represented aggregates and fibres, respectively. The position of the aggregates was mapped on an irregular network of structural elements. With the network elements, the responses of aggregates, matrix and interfacial transition zones between aggregates and matrix were modelled. Fibres were modelled as beam elements, which were positioned independently of the background network. They were connected to the nodes of the background network via link elements. The influence of aggregates and fibres on fracture processes in direct tensile tests of periodic cells was investigated. In particular, the response in the form of stress-displacement curves, dissipated energy and roughness of fracture patterns was studied. It was shown that already small volumes of fibres of low aspect ratio (typical for steel fibres) strongly increased energy dissipation. However, these small volumes of fibres had a small effect on strength and roughness.

1 INTRODUCTION

Many structures made of heterogeneous quasi-brittle materials exhibit failure processes which are influenced by the heterogeneity of the material at an intermediate (meso) scale. For instance, the type of coarse aggregates in concrete influences stiffness, strength and fracture energy of the material. For fibre reinforced cementitiuous materials, fibre type and geometry strongly influence the tail of the stress-crack opening curve. Only models that are designed based on a thorogu understanding of the governing failure processes can be used to predict the failure of structures outside the range of known experimental results. Therefore, detailed computational models, which consider the mechanical response of individual constituents are attractive, since they contribute to the understanding of failure processes.

Nonlinear fracture mechanics (NLFM) (Dugdale 1960, Barenblatt 1962) is commonly used to determine failure of structural concrete components of practical size, since the size of the fracture process zone is too large for Linear Elastic Fracture Mechanics (LEFM) tobe applicable. Here, fracture process zone is defined as the zone in which energy is dissipated during the fracture process. Numerically, NLFM is applied in structural analyses in the form of cohesive-crack and crack-band models. In cohesive-crack models, the displacement field across the fracture process zone is replaced by a displacement jump representing the crack opening (Hillerborg et al. 1976, Carol et al. 1997). Stresses are determined from a stress-crack opening law. In crack-band models, the displacement jumps are transformed into cracking strains, so that the stress is calculated using stress-strain laws taking into account the size of the regions in which strains localise. This size is usually a function of the element size (Bažant and Oh 1983, Jirásek and Bauer 2012), so that the load-displacement curves obtained with this approach are mesh-independent. Discrete approaches describe both elastic and inelastic responses by means of force-displacement relationships between discrete bodies (Schlangen and van Mier 1992b, Schlangen and van Mier 1992a, Bolander et al. 2000).

Continuum mechanics is an alternative to nonlinear fracture mechanics. In continuum mechanics, the fracture process zone is represented by a localised but regular field of displacements. This is achieved by including a length parameter in the continuum models, which is related to the width of the fracture processes zone (Pijaudier-Cabot and Bažant 1987, Bažant and Jirásek 2002). The value of this length parameter can strongly influence the numerically predicted peak load and deformation capacity of structures. Therefore, it is of interest to choose this length parameter so that the localised field of displacements matches the width of the fracture process zone of the material. Experimental studies for fracture in plain concrete in

(Mihashi et al. 1991, Mihashi and Nomura 1996, Otsuka and Date 2000) showed that the fracture process zone consists of a narrow band of high dissipation surrounded by a wider region of low dissipation. In (Grassl and Jirásek 2010, Xenos et al. 2015), information about the width of the fracture process zone was determined numerically using two-dimensional structural network approach for the meso-scale of concrete consisting of coarse aggregates embedded in a mortar matrix. The aim of this work was to obtain more information about fracture processes in fibre reinforced concrete by using a three-dimensional structural network model for fracture processes at the meso-scale of concrete containing coarse aggregates and fibres.

2 METHOD

The present numerical approach for obtaining information on fracture processes in fibre-reinforced quasi-brittle materials relied on periodic meso structure generation, periodic network modelling of the material response, and roughness evaluation of the fracture patterns obtained from the network modelling. In the following sections, the individual modelling techniques are described in more detail.

2.1 *Periodic meso-structure generation*

The meso-structure of concrete was modelled as coarse aggregates and fibres embedded in a mortar matrix. Aggregates and fibres were idealised as poly-dispersed ellipsoids and line segments, respectively. They were periodically arranged in a computational cell representing a unit of the material. For a given volume fraction of aggregates, Fuller's grading curve was used to determine the size distribution of aggregates. This distribution was used to divide the volume based on upper and lower sieves sizes m and $n = m/2$, respectively, which are commonly used for grading of aggregates. Here, m is smaller than or equal to the maximum sieve size $d_{\mathrm{a,max}}$ and n is greater than or equal to the minimum sieve size $d_{\mathrm{a,min}}$. Starting with the volume portion obtained with the largest pair of sieve sizes, aggregates were generated randomly with radii $s_3 > s_2 > s_1$ so that they fit through the square sieve size m, but not n (Slowik and Leite 1999, Leite et al. 2007, Mehrotra 2011). Steel fibres were assumed to be of uniform length l_{f} and diameter d_{f}. For a volume fraction ρ_f, the number of fibres was calculated as $n_{\mathrm{f}} = 4\rho_{\mathrm{f}} V/(\pi d_{\mathrm{f}}^2 l_{\mathrm{f}})$, where V is the volume of the unit cell. The input parameters for the meso-structure generation are the volume fraction of aggregates ρ_a, the maximum and minimum sieve sizes $d_{\mathrm{a,max}}$ and $d_{\mathrm{a,min}}$, respectively, the volume fraction of fibres ρ_{f}, fibre length l_{mf} and the diameter of fibres d_{f}. Here, ρ_a is the volume fraction of all aggregates including those that are assumed to be present in the mortar matrix. However, only aggregates greater than the sieve size $d_{\mathrm{a,min}}$ were generated.

Next, aggregates and fibres were placed in the periodic cell by a random sequential addition approach (Feder 1980) so that the centroids of aggregates and fibres are within the cell. For every randomly placed object, it was tested that there was no overlap with previously placed objects. If overlap was avoided, the object was placed in the cell and 26 mirror objects in the adjacent cells were generated by shifting the centroid of the object to the adjacent periodic cells. For the overlap check between aggregates, the algebraic equations in (Wang et al. 2001) was used. For a combination of fibres and aggregates, only possible overlap of aggregate and fibres was checked, but not overlap between fibres, since fibres were idealised as line element segments. For meso-structures consisting of a combination of aggregates and fibres, the coarsest aggregates were placed first, followed by the fibres and finally small aggregates. It was noticed that the presence of large aggregates influenced the arrangement of fibres, which were clustered in the spaces between large aggregates. Further statistical analysis is required to quantify the amount of clustering.

Examples of generations of aggregates with $d_{\mathrm{a,max}}$ = 16 mm, $d_{\mathrm{a,min}}$ = 8 mm and ρ_{a} = 0.8, and a combination of aggregates and fibres with $d_{\mathrm{a,max}}$ = 16 mm, $d_{\mathrm{a,min}}$ = 8 mm, ρ_{a} = 0.8, l_{f} = 30 mm and ρ_{f} = 0.01 are shown in Figure 1a and b, respectively, for a cell with an edge length of 100 mm. In these generations, the diameter of the fibres d_{f} did not influence the results, since the geometry of the fibres was idealised as line segments.

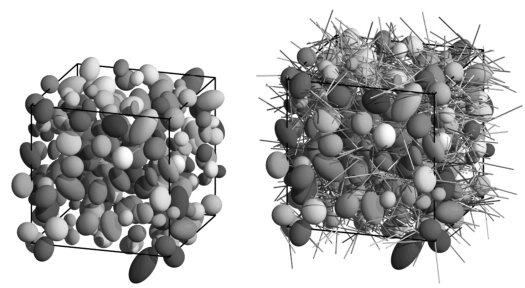

(a) (b)

Figure 1. Periodic meso-scale generation for (a) aggregates and (b) combination of fibres and aggregates.

2.2 *Periodic network modelling*

The fracture processes at the meso-scale were modelled for a periodic cell with a three-dimensional irregular network of discrete structural elements determined by dual Delaunay and Voronoi tessellations of a set of randomly placed points (Grassl and Bolander 2016) subject to a minimum distance $d_{\min}$. Periodicity with respect to the cell boundaries was introduced for both the network geometry and the displacements (Athanasiadis et al. 2017). For network elements crossing the cell boundaries, the displacements of nodes outside the cell were determined by means of displacements of the image node within the cell and six average strain components. This approach has the advantage that fracture planes could occur anywhere in the periodic cell (with the normal of the plane being the direction of loading) and were not influenced by the boundaries of the cell. Analyses of boundary value problems without the use of periodic displacements would require strengthening of the material close to the ends of the specimen to avoid fracture to occur at the boundaries. This method was originally proposed in two dimensions in (Grassl and Jirásek 2010) and then extended to three dimensions for coupled structural-transport analyses in (Athanasiadis et al. 2017).

The information of the spatial arrangement of aggregates was mapped onto the network. According to the position of network elements with respect to aggregates, network elements were given the properties of matrix, interfacial transition zone (ITZ) and aggregate. Network elements with both nodes positioned within an aggregate were given stiff elastic properties representing aggregates. Elements with both nodes located in the matrix were given properties of mortar with corresponding elastic properties, and strength and fracture energy. Finally, for elements with one node in an aggregate and another one in the matrix or another aggregate, the properties of ITZ were used, which were characterised by lower strength and lower fracture energy than those of the matrix. The stiffness of ITZ elements were determined by the harmonic mean of the stiffnesses of matrix and aggregate.

The response of aggregates, matrix and ITZs were modelled by linear elasticity and damage mechanics. The mid-cross-sections of the network elements were set equal to the common facets of the Voronoi cells associated with the element nodes (Yip et al. 2005). With this approach, the stress and strain fields were elastically homogeneous for zero Poisson's ratio, which was assumed in all analyses. The damage evolution was determined from an exponential softening stress-crack opening curve with tensile strength f_t and fracture energy G_F as input. The resulting load-displacement curves of tensile fracture simulations were independent of the element length, if the element length was chosen to be sufficiently small.

The fibres were idealised as linear elastic structural frame elements (McGuire et al. 2000), which were placed independently of the irregular network. Interactions between the fibres and the network representing matrix and ITZ were modelled by means of link elements as described in (Yip et al. 2005). This type of link elements was

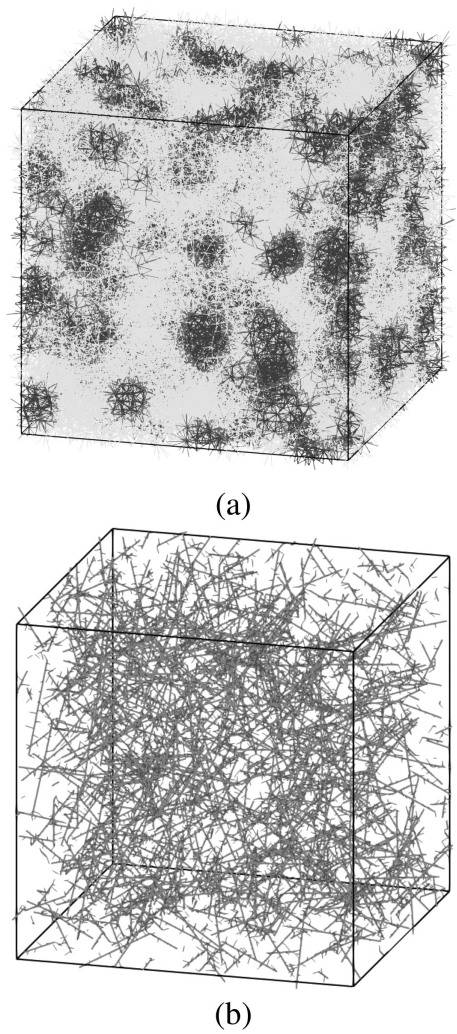

Figure 2. Network model: (a) Network of discrete elements representing matrix (light grey), aggregates (dark grey) and ITZs (medium grey). (b) Fibre beam elements (grey) arranged independently of background network and links (black) connecting fibres to network nodes.

originally used for the modelling of bond in reinforced concrete (Ngo and Scordelis 1967), and was more recently applied to network models in (Bolander and Saito 1997, Montero-Chacón et al. 2017). The present approach is computationally more intensive than the semi-discrete techniques proposed in (Kang et al. 2014, Kang and Bolander 2017), which incorporate important features of the fibre-matrix interaction, but do not model fibres by individual degrees of freedom. Reduction of the embedded length due to pullout of the fibres as analysed in (Naaman et al. 1991) was not modelled here, since only small displacements were considered.

An example of the network representing the three phases of matrix, aggregates and ITZ is shown in Figure 2a. Fibres with their corresponding link elements are shown in Figure 2b. The response of the periodic computational cell was controlled by six average strain components, which were chosen so that the cell was subjected to direct tension with monotonically increasing axial strain and zero lateral stress. Quasi-static analyses were performed with an incremental-iterative approach (de Borst, Crisfield, Remmers, & Verhoosel 2012). The iterative part was based on a modified Newton method using the secant stiffness for the damage model for matrix and ITZ, and the elastic stiffness for the elasto-plastic model for the links between fibres and background network.

2.3 *Roughness evaluation*

The fracture processes were analysed by evaluating the evolution of spatial distribution of dissipated energy. For the present evaluation, both dissipation due to damage in the structural network elements, as well as dissipation due to plastic slip in the link elements were considered. To each element in which energy is dissipated, a cross-sectional area with a centroid as shown in Figure 3 was associated.

Firstly, the mean of all heights of centroids of cross-sections was calculated as

$$\overline{z} = \sum_{i=1}^{N} w_i z_i \tag{1}$$

Here, z was measured in the direction of the applied tensile strain with the bottom of the cell used as the origin. Furthermore, w_i were the weights of the individual cross-sections, which were calculated as

$$w_i = \frac{A_i \Delta d_i}{\sum_{k=1}^{N} A_k \Delta d_k} \tag{2}$$

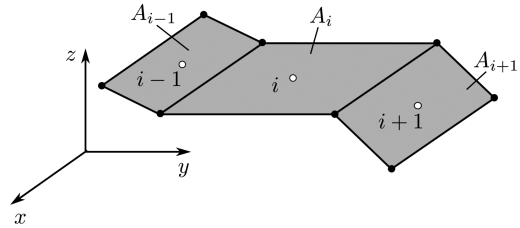

Figure 3. Evaluation of roughness from dissipated energy density of mid cross-sections of network elements. From (Xenos et al. 2015).

where A_i and Δd_i were the area and increment of dissipation per unit area, respectively, of the facet i. Then, the standard deviation Δh was calculated as

$$\Delta h = \sqrt{\sum_{i=1}^{N} w_i \left(z_i - \overline{z}\right)^2} \tag{3}$$

This standard deviation is a measure related to the width of the fracture process zone, which takes into account the intensity of the dissipation events. It is significantly smaller than the total width of the fracture process zone, which is defined as the zone in which energy is dissipated. For a localised crack surface with equal energy dissipation in all elements whose cross-sections form this surface, the measure used is equal to the standard deviation of the roughness distribution of the crack surface as described in (Xenos et al. 2015).

3 FRACTURE ANALYSES AND RESULTS

The network modelling approach described in Section 2.2 was applied to analyse fracture in cubic periodic cells. The cells with an edge length of 100 mm were subjected to direct tension in the axial direction, while keeping the average stress components in the other two directions equal to zero. The first analysis consisted of a network representing only matrix, aggregates and ITZs. The network was generated with a minimum distance $d_{\text{min}} = 3$ mm between the randomly placed points. The volume fraction of aggregates generated with the techniques described in Section 2.1 was $\rho_{\text{a}} = 0.8$ with a maximum sieve size of $d_{\text{a,max}} = 16$ mm. Only aggregates with a size above a minimum sieve size of $d_{\text{a,min}} = 8$ mm were mapped on the network. In the second analysis, fibres with a length $l_{\text{f}} = 3$ cm, a diameter $d_{\text{f}} = 0.75$ mm and a fibre volume fraction of $\rho_{\text{f}} = 0.01$ were used in addition to the aggregates. The input parameters for the different phases is shown in Table 1. For the links connecting the fibre

elements to the background network, the parameter f_t refers to the stress at which plastic slip occurs.

The stress-displacement curves for plain and fibre-reinforced concrete are shown in Figure 4 for one random meso-scale generation. For aggregates only, the stress-displacement curve exhibited the expected response of quasi-brittle materials with small nonlinearities in the pre-peak regime, followed by strong softening in the initial post-peak regime which then tails off at larger displacements at which the average stress approaches zero. The addition of fibres strongly altered the post-peak response. With fibres, the initial softening was less pronounced and a large residual stress was obtained. The pre-peak response was almost not at all influenced by the presence of the fibres. The peak stress for the fibre reinforced material was only slightly greater than for aggregates only. This small difference was due the low volume fraction and aspect ratio of fibres used.

The crack patterns in the form of mid cross-sections at which damage increases at this stage of analysis are shown in Figures 5 and 6 for threes stages marked in Figure 4. For both analyses, cracking was initially almost uniformly distributed at peak. Then, right at the beginning of the post-peak regime, both fracture zones were highly localised. The fibres had very little influence on the evolution of the fracture patterns.

The evolution of dissipated energy for the two analyses is shown in Figure 7. For both analyses, the dissipation in the pre-peak regime is very small. For aggregates only, the majority of dissipation occurs in the first part of the post-peak regime. For the analysis with fibres, the initial dissipation in the post-peak regime is slightly less than for the analysis without fibres. In the later stage of the post-peak regime, the fibres contribute significantly to the dissipation, so that the overall dissipation of the analysis of the fibre reinforced material is much greater than for aggregates only. Only fibres, which cross the localised crack shown in Figure 6, were loaded highly enough to contribute to the dissipated energy.

The measure of the width of the fracture process zone Δh obtained from the roughness evaluation in Section 2.3 versus displacement is shown in Figure 8. The roughness evolution for the two analyses is overall very similar. At the start of the analysis, no energy is dissipated, so that Δh is not defined. For the uniformly distributed cracking

Table 1. Input values.

Phase	E [GPa]	f_t [MPa]	G_F [J/m^2]
Matrix	30	3	100
Particle	90	–	–
ITZ	57.1*	3.25	50
Fibre	200	–	–
Link	3000	4	–

*The value E for ITZ is determined as harmonic mean of matrix and particle values.

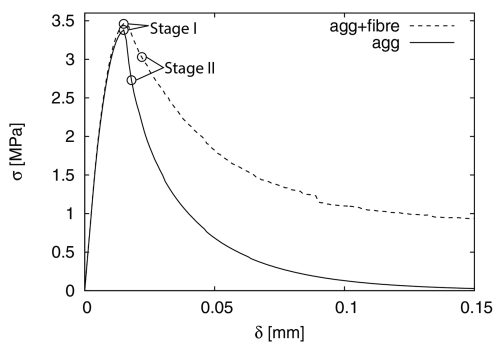

Figure 4. Meso-scale analysis: Stress versus displacement analyses with aggregates and aggregates with fibres. The symbols refer to stages for which the crack patterns are shown in Figures 5 and 6.

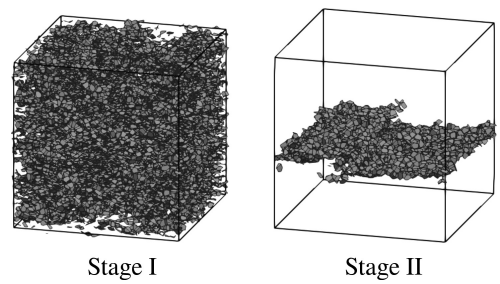

Figure 5. Meso-scale analyses: Crack patterns of direct tension analysis with aggregates at two stages marked in Figure 4. Grey polygons refer to mid cross-sections in which damage increases at this stage of the analysis.

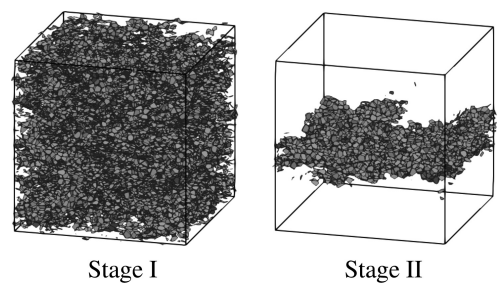

Figure 6. Meso-scale analyses: Crack patterns of direct tension analysis with aggregates and fibres at two stages marked in Figure 4. Grey polygons refer to mid cross-sections in which damage increases at this stage of the analysis.

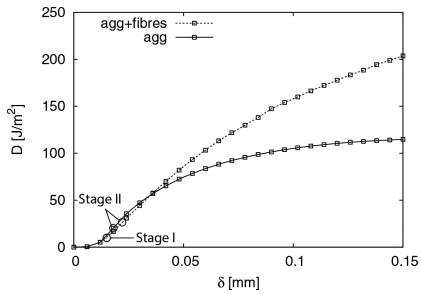

Figure 7. Meso-scale analysis: Dissipated energy D versus displacement δ for random analyses with aggregates, and with aggregates and fibres. The symbols refer to stages for which the crack patterns are shown in Figures 5 and 6.

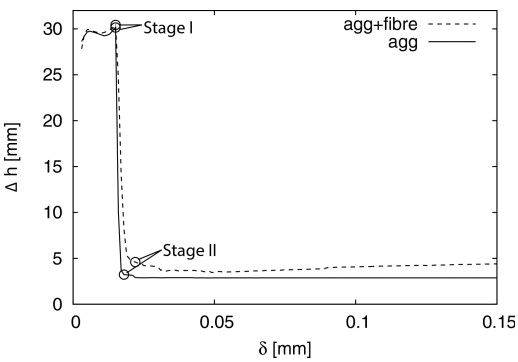

Figure 8. Meso-scale analysis: Measure of width of fracture process zone Δh versus displacement δ for random analyses with aggregates, and with aggregates and fibres. The symbols refer to stages for which the crack patterns are shown in Figures 5 and 6.

in pre-peak regime, Δh is approximately equal to 30 mm. This value agrees well with the theoretical value for the standard deviation of a uniform distribution over the interval from 0 to 100 mm, which is $100/\sqrt{12} = 28.9$ mm. At the start of the post-peak regime, the width of the fracture process zone dropped down to values less than 5 mm. This drop occurred at the beginning of the fracture process at very low values of dissipated energy. After the drop, the value of Δh for the analysis with aggregates and fibres is larger than for the analysis with aggregates only.

4 CONCLUSIONS

Network meso-scale analyses of fracture processes of periodic cells subjected to direct tension were performed. The meso structures consisted of quasi-brittle materials with aggregates, and with aggregates and low volumes of steel fibres. The presence of fibres strongly increases the energy dissipated at a later stage of the post-peak regime. However, the peak load is not much affected by the fibres. For both material configurations, the width of the fracture process zone reduces suddenly after the peak load to the width of a rough crack and then stays almost constant for the remaining part of the analysis. For the combination of fibres and aggregates, the roughness of the crack is greater than for the analysis with aggregates only.

ACKNOWLEDGEMENTS

The numerical analyses were performed with the nonlinear analyses program OOFEM (Patz´ak 2012) extended by the present authors.

REFERENCES

Athanasiadis, I., S.J. Wheeler, & P. Grassl (2017). Hydro-mechanical network modelling of particulate composites. *Accepted in International Journal of Solids and Structures, arXiv preprint arXiv:1707.09288.*

Barenblatt, G.I. (1962). The mathematical theory of equilibrium of cracks in brittle fracture. *Advances in Applied Mechanics 7,* 55–129.

Bažant, Z.P. & M. Jirásek (2002). Nonlocal integral formulations of plasticity and damage: Survey of progress. *Journal of Engineering Mechanics, ASCE 128*(10), 1119–1149.

Bažant, Z.P. & B.-H. Oh (1983). Crack band theory for fracture of concrete. *Materials and Structures 16,* 155–177.

Bolander, J.E., G.S. Hong, & K. Yoshitake (2000). Structural concrete analysis using rigid-body-spring networks. *J. Comp. Aided Civil and Infrastructure Engng. 15,* 120–133.

Bolander, J.E. & S. Saito (1997). Discrete modeling of shortfiber reinforcement in cementitious composites. *Advanced Cement Based Materials 6*(3–4), 76–86.

Carol, I., P.C. Prat, & C.M. López (1997). Normal/shear cracking model: Application to discrete crack analysis. *Journal of Engineering Mechanics 123*(8), 765–773.

de Borst, R., M. Crisfield, J.J.C. Remmers, & C.V. Verhoosel (2012). *Nonlinear finite element analysis of solids and structures.* John Wiley & Sons.

Dugdale, D.S. (1960). Yielding of steel sheets containing slits. *Journal of the Mechanics and Physics of Solids 8,* 100–108.

Feder, J. (1980). Random sequential adsorption. *Journal of Theoretical Biology 87*(2), 237–254.

Grassl, P. & J. Bolander (2016). Three-dimensional network model for coupling of fracture and mass transport in quasibrittle geomaterials. *Materials 9*(9), 782.

Grassl, P. & M. Jirásek (2010). Meso-scale approach to modeling the fracture process zone of concrete sub-

jected to uniaxial tension. *International Journal of Solids and Structures 47,* 957–968.

Hillerborg, A., M. Modéer, & P.E. Peterson (1976). Analysis of crack propagation and crack growth in concrete by means of fracture mechanics and finite elements. *Cement and Concrete Research 6,* 773–782.

Jirásek, M. & M. Bauer (2012). Numerical aspects of the crack band approach. *Computers and Structures 110–111,* 60–78.

Kang, J. & J.E. Bolander (2017). Event-based lattice modeling of strain-hardening cementitious composites. *International Journal of Fracture,* 1–17.

Kang, J., K. Kim, Y.M. Lim, & J.E. Bolander (2014). Modeling of fiber-reinforced cement composites: Discrete representation of fiber pullout. *International Journal of Solids and Structures 51*(10), 1970–1979.

Leite, J.P.B., V. Slowik, & J. Apel (2007). Computational model of mesoscopic structure of concrete for simulation of fracture processes. *Computers & Structures 85*(17), 1293–1303.

McGuire, W., R.H. Gallagher, & R.D. Ziemian (2000). *Matrix structural analysis.* New York: J. Wiley.

Mehrotra, S. (2011). Modelling the aggregate arrangement of concrete. Msc thesis, University of Glasgow.

Mihashi, H. & N. Nomura (1996). Correlation between characteristics of fracture process zone and tension-softening properties of concrete. *Nuclear Engineering and Design 165,* 359–376.

Mihashi, H., N. Nomura, & S. Niiseki (1991). Influence of aggregate size on fracture process zone of concrete detected with 3-dimensional acoustic-emission technique. *Cement and Concrete Research 21*(5), 737–744.

Montero-Chacón, F., H. Cifuentes, & F. Medina (2017). Mesoscale characterization of fracture properties of steel fiber-reinforced concrete using a lattice–particle model. *Materials 10*(2), 207.

Naaman, A.E., G.G. Namur, J.M. Alwan, & H.S. Najm (1991). Fiber pullout and bond slip. I: Analytical study. *Journal of Structural Engineering 117*(9), 2769–2790.

Ngo, D. & A.C. Scordelis (1967). Finite element analysis of reinforced concrete beams. *ACI Journal, Proceedings 64,* 152–163.

Otsuka, K. & H. Date (2000). Fracture process zone in concrete tension specimen. *Engineering Fracture Mechanics 65,* 111–131.

Patzák, B. (2012). OOFEM—An object-oriented simulation tool for advanced modeling of materials and structure. *Acta Polytechnica 52,* 59–66.

Pijaudier-Cabot, G. & Z.P. Bažant (1987). Nonlocal damage theory. *Journal of Engineering Mechanics, ASCE 113,* 1512–1533.

Schlangen, E. & J.G.M. van Mier (1992a). Experimental and numerical analysis of the micromechanisms of fracture of cement based composites. *Cement and Concrete Composites 14,* 105–118.

Schlangen, E. & J.G.M. van Mier (1992b). Simple lattice model for numerical simulation of fracture of concrete materials and structures. *Materials and Structures* 25, 534–542.

Slowik, V. & J.P.B. Leite (1999). Modellierung des mechanischen verhaltens von betonen auf der ebene des mesogefüges.

Wang,W., J. Wang, & M.-S. Kim (2001). An algebraic condition for the separation of two ellipsoids. *Computer aided geometric design 18*(6), 531–539.

Xenos, D., D. Grégoire, S. Morel, & P. Grassl (2015). Calibration of nonlocal models for tensile fracture in quasibrittle heterogeneous materials. *Journal of the Mechanics and Physics of Solids 82,* 48–60.

Yip, M., J. Mohle, & J.E. Bolander (2005). Automated Modeling of Three-Dimensional Structural Components Using Irregular Lattices. *Computer-Aided Civil and Infrastructure Engineering 20*(6), 393–407.



Taylor & Francis
Taylor & Francis Group
http://taylorandfrancis.com

Computational Modelling of Concrete Structures – Meschke, Pichler & Rots (Eds)
© 2018 Taylor & Francis Group, London, ISBN 978-1-138-74117-1

New damage model to simulate ballistic impact on concrete targets

L. Pereira
Portuguese Air Force Academy, Sintra, Portugal

L.J. Sluys & J. Weerheijm
Faculty of Civil Engineering and Geosciences, Delft University of Technology, Delft, The Netherlands

ABSTRACT: The development of realistic numerical tools to efficiently simulate the response of concrete structures to projectile impacts or near field explosions has been one of the major quests in defense research for decades. Under extreme loading conditions, dynamic pressure waves are locally transmitted to the target leading to complex failure modes, such as: (1) compaction, associated with pore collapse and comminution (i.e. fragmentation, crushing and pulverization) of the material in front of the impactor (front face); (2) spalling (tensile fracturing) at the rear face, upon reflection of the induced pressure wave; and (3) radial cracking around the penetration tunnel. So, the constitutive model used to simulate the dynamic response of concrete to impulsive impact loads must be able to cover all these failure mechanisms.

Modelling comminution of concrete has proven to be particularly challenging. In spite of the vast literature on impact and the subsequent dynamic fracture of quasi-brittle and brittle materials, most models used for macroscopic dynamic FEM analysis are inadequate to simulate the phenomenon as it is observed in front of the impactor. In this study, the material comminution and compaction under high pressure is phenomenologically represented by an additional (hydrostatic) damage mode linked with a confinement criterion. This new concept is combined with a recently developed effective rate-dependent damage model and used to simulate a series of high velocity impact experiments by Beppu et al. [Int. J. Imp. Eng, 35:12 (2008)]. This model reproduces the major phenomena associated to the dynamic failure of concrete under ballistic impacts. As a direct consequence of the stress-based nonlocal regularization scheme used, the results are mesh independent.

1 INTRODUCTION

Extraordinary actions such as blast loadings and high velocity impact are rare, but usually have devastating effects. Thus, making critical infrastructures, such as military and governmental facilities, power-plants, dams, bridges, hospitals, etc., more resilient against these hazards is one of the best ways to protect ourselves and our societies. Since concrete is probably the most commonly used construction material worldwide, the development of realistic numerical tools to efficiently simulate its failure under such extreme dynamic loading conditions is of paramount importance, but still a major challenge. Despite the considerable resources dedicated to the study of the dynamic behavior of concrete, very few of the models currently in use by engineers in finite element analysis are able to capture all failure mechanisms observed in concrete when subjected to such extreme dynamic loads. This paper presents a new phenomenological approach towards the numerical simulation of ballistic impact on concrete structures.

During high velocity impact, intense pressure waves are induced which, expand radially in front of the impactor, leading to a complex process of interfering stress waves which exposes the material to rapidly changing multiaxial stress states and strain rate conditions. This leads to different failure mechanisms which, depending on the impactor properties (shape and material) and velocity, as well as the thickness of the target, may be as complex as represented in Figure 1. The mechanisms include (Pereira et al. 2018): (1) compaction and crushing (hydrostatic damage) of the material in front of the impactor (strike face), associated with pore collapse and comminution (pulverization) of the material under pressure, leading to the formation of the Mescall zone; (2) radial cracking in front and around the impactor (mixed mode failure), caused by hoop stresses raised in the wake of the initial pressure wave; (3) spalling (dynamic tensile fracture) at the rear face, upon reflection of the pressure wave; and (4) formation/expansion of the crater due to spalling at the impacted face. The flow of the pulverized material around the penetrator allows it to cut through the target (cratering and tunneling). Under certain conditions, at the end of the deceleration phase of the impactor, conical punching failure (Hertzian cone) may occur as an extension of radial cracking. In a later stage, structural oscillations at moderate strain rates become

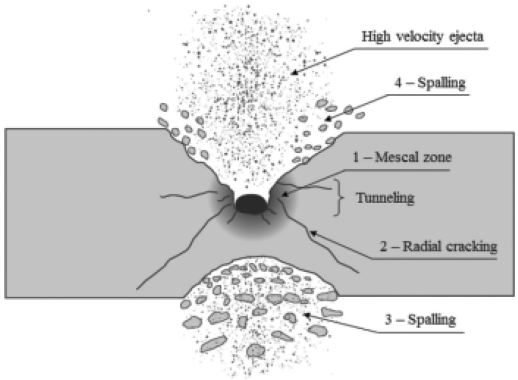

Figure 1. Failure mechanics in ballistic impact scenarios.

the leading loading condition, and the main cause for further material mechanical degradation, such as the formation of the radial cracks visible at the front and back surfaces of the target.

It has been shown that the evolution of failure of quasi-brittle materials is basically governed by three interdependent damage mechanisms (Mazars et al. 2010): (a) tensile (mode I) fracture; (b) compressive-shear (mode II and mixed-mode) failure; and (c) hydrostatic damage (crushing) of the cement matrix under compression, due to pore collapse during compaction. Furthermore, concrete is known to exhibit a significant dynamic increase of strength, stiffness and fracture energy in both tension and compression, due to the presence of water in the pores of the hardened cement past (Stefan effect), viscoelastic properties of the bulk material and inertia effects. A realistic representation of the dynamic failure of concrete has to capture all these failure modes. This paper proposes a new isotropic damage model to simulate the response of concrete under ballistic impact. This model is an enhanced version of the *effective rate-dependent* nonlocal damage model recently proposed by the authors (Pereira et al. 2017b). The effect of the hydrostatic damage (crushing) of the material matrix under pressure on the material stiffness as a function of confinement is added to the formulations which already described the dynamic failure of concrete under unconfined tension and compression-shear loading conditions. The proposed formulation has been developed and implemented as a *user defined material model* (UMAT) in LS-DYNA (Hallquist 2006) following an explicit computation scheme. After the description of the model in the following section, a set of high velocity impact tests, reported in Beppu et al. Beppu et al. (2008), is simulated to evaluate how the increase of energy absorption, provided by the added hydrostatic damage mode, contributes to a more realistic representation of the dynamic failure of concrete in ballistic impact situations.

2 CONSTITUTIVE LAW

The model presented here is an extension of the recently proposed *effective rate-dependent* nonlocal damage model, successfully used to simulate dynamic tensile failure (spalling) (Pereira et al. 2017a) and the dynamic propagation and branching of cracks in concrete (Pereira et al. 2017b). Two damage variables are considered to represent material failure under tension and compression-shear loading situations. Although the nonlinear response of the model is pressure dependent, as in the Drucker Prager model, the variation of strength or the deformation under compression cease to be realistic for high confining triaxial stress situations. To overcome these limitations, a hydrostatic damage variable is added to describe the damaging (crushing) of the cement matrix during compaction. The combined effect of the three damage variables ω_t, ω_c and ω_h, is assembled in a single variable according to the following formulation:

$$\omega = 1-(1-\omega_t)(1-\omega_c)(1-r_{conf}\,\omega_h) \tag{1}$$

where r_{conf} is the confinement factor which governs the effective contribution of ω_h to the degradation of the material stiffness.

$$r_{conf} = \min\left[\max\left(0, \frac{3\sqrt{3J_{\tilde{\sigma}}}}{-I_{\tilde{\sigma}}}\right), 1\right] \tag{2}$$

where $I_{\tilde{\sigma}}$ is the first invariant of the effective stress tensor and $\sqrt{3J_{\tilde{\sigma}}}$ is second invariant of the deviatoric effective stress tensor. Experimental evidences show that, even though the material matrix may be irreversibly damaged (crushed) during compaction, and concrete degenerates from a cohesive material into a granular material, it appears to become stronger, as long as it is kept confined. Only when confinement decreases ($\sqrt{3J_{\tilde{\sigma}}} > 0$), the damage developed during compaction progressively influences the global response of the material and leads to an effective degradation of the material stiffness. This is phenomenologically represented by r_{conf} which varies between zero, for a purely hydrostatic stress state, and one when the *confinement limit* is reached. The conceptual approach followed in the development of the model presented in this paper is schematically represented in Figure 2. It illustrates the fundamental parts of the model, in both deviatoric and hydrostatic spaces, as explained

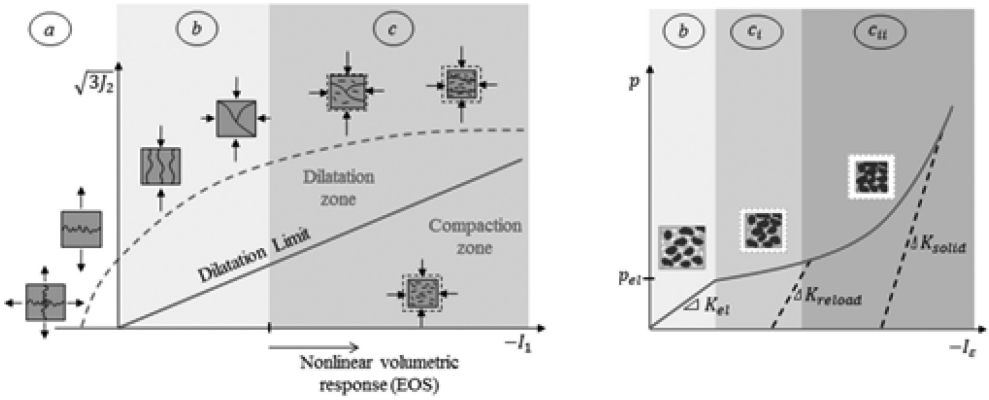

(a) (b)

Figure 2. Schematic representation of failure modes of concrete alongside the (a) ultimate strength (failure) envelope in the deviatoric space and (b) nonlinear volumetric response (EOS) in the hydrostatic space.

hereafter. Following a classical isotropic damage approach, the evolution of the material stiffness, and consequently the stress tensor, is simply described as follows:

$$\sigma = (1-\omega)\tilde{\sigma}, \tag{3}$$

where $\tilde{\sigma} = \varepsilon : C$ is the effective stress tensor defined as a function of the strain and elastic stiffness tensors.

3 TENSION AND COMPRESSION DAMAGE

The damage laws for tension and compression are defined as in the original Mazars model (Mazars and Pijaudier-Cabot 1989):

$$\omega_i = 1-(1-A_i)\frac{Y_{i0}}{Y_i} - A_i e^{-B_i(Y_i - Y_{i0})} \tag{4}$$

where A_i and B_i are material parameters and Y_{0i} are the equivalent strain damage thresholds. The index i in this and the following equations should be interpreted as t for tension and c for compression. The evolution of damage in time (t) is derived from two monotonic thermodynamic variables Y_t and Y_c:

$$Y_i(t) = \max_{t\geq\tau}[Y_{i0}, r_i\varepsilon_i, Y_i(\tau)] \tag{5}$$

where ε_i are the equivalent strains and r_i the internal variables which provide information on the actual loading state (Mazars et al. 2014). These variables were added to the formulation to weight the contribution of tension and compression to the nonlinear response of the material in mixed-mode stress conditions.

$$r = \frac{\sum_{I=1}^{3}\left\langle \tilde{\sigma}_I \right\rangle}{\sum_{I=1}^{3}|\tilde{\sigma}_I|}, \tag{6}$$

$$r_t = r^{\alpha} \quad \text{and} \quad r_c = (1-r)^{\alpha} \quad \text{with} \quad \alpha \leq 0.1 \tag{7}$$

where $\langle\tilde{\sigma}_I\rangle$ and $|\tilde{\sigma}_I|$ are the positive and absolute values of the principal effective stresses, respectively. The equivalent strains are scalar variables which characterize the local strain state in tension and compression, respectively:

$$\varepsilon_t = T_1 I_\varepsilon + T_2\sqrt{3J_\varepsilon} \tag{8}$$

$$\varepsilon_c = C_1 I_\varepsilon + C_2\sqrt{3J_\varepsilon} - C_3 I_\varepsilon^2 \tag{9}$$

where ν is the Poisson's ratio, and C_i and T_i are user-defined positive parameters which can be individually adjusted for calibration of the model. These quantities are defined in the deviatoric space, as a function of the first invariant of the strain tensor (I_ε) and the second invariant of the deviatoric strain tensor (J_ε).

3.1 *Hydrostatic damage and compaction*

When concrete is subjected to high confining pressures, compaction occurs by reducing the voids (air) in the mixture and the physical connections between aggregates are ruptured irreversibly. These two combined mechanisms lead to the observed nonlinear volumetric deformation of material and the variation of the compressive tangent stiffness

(i.e. bulk modulus K^*) from K_{el} to K_{solid} during compaction, see Figure 3(b). In the present study only the tangent stiffness is updated as a function of two volumetric strain dependent variables, ω_h and H_c, respectively describing the reduction of strength and stiffness associated with the loss of cohesion under pressure and the increase of stiffness due to compaction of the material. The current effective bulk modulus is determined by weight averaging the two effects, as follows:

$$K = \begin{cases} K_{new} = K_{el}(1-\omega_h) + K_{solid} H_c & \text{if} \quad \Delta\omega_h > 0 \\ K_{reload} = K_{el} + K_{solid} H_c & \text{if} \quad \Delta\omega_h = 0 \end{cases} \tag{10}$$

Please note that K^* is different in case of compaction (K_{new}) or in a reloading situation (K_{reload}). This feature is needed to capture the experimentally observed unloading-reloading bulk modulus, which is almost not affected in the early stages of compaction.

In the absence of a full understanding of when these processes start and finish, for simplicity, both hydrostatic damage and compaction are described by identical power laws with the only difference being the exponent.

$$\omega_h = \left(\frac{\mu_h - \mu_0}{\mu_{gran} - \mu_0} \right)^{\gamma_\omega} \quad \text{with} \quad \gamma_\omega < 0.5 \tag{11}$$

$$H_c = \left(\frac{\mu_h - \mu_0}{\mu_{gran} - \mu_0} \right)^{\gamma_c} \quad \text{with} \quad \gamma_c = 1 \tag{12}$$

where

$$\mu_h(t) = \max_{t \geq \tau} [\mu_0, \mu, \mu_h(\tau)] \tag{13}$$

and

$$\mu = -\varepsilon_v = -\varepsilon_{11} - \varepsilon_{22} - \varepsilon_{33}.$$

The powers $\gamma_i \varepsilon [0, 1]$ are user defined parameters and μ_h is the volumetric equivalent strain. The parameters μ_0 and μ_{gran} are the volumetric strain at the onset of damage and at the fully damaged (compacted) state, respectively. For simplicity, linear compaction of the material is assumed ($\gamma_c = 1$).

The implementation of this formulation takes advantage of the used explicit computation scheme to determine the evolution of the effective pressure ($\tilde{p}$) with the variation of K and $\Delta\varepsilon_v$:

$$\tilde{p} = \begin{cases} -K_{el}\varepsilon_v & \text{if} \quad (\varepsilon_v \geqslant 0 \text{ or } \omega_h = 0) \\ \max[0, \tilde{p}_{old} + \Delta\tilde{p}] & \text{if} \quad \text{otherwise} \end{cases} \tag{14}$$

with

$$\Delta\tilde{p} = -K^* \Delta\varepsilon_v \tag{15}$$

where $\tilde{p}_{old}$ is the pressure in the previous time step, and $\Delta\tilde{p}$ is the variation of the effective pressure determined as a function of the current bulk modulus K^*, which is respectively K_{new} or K_{reload} when ω_h is increasing or not. The final effective stress tensor is determined following the conventional decomposition in deviatoric (S_{ij}) and hydrostatic (p) stress tensor:

$$\tilde{\sigma}_{ij} = \tilde{S}_{ij} + \tilde{p}\delta_{ij} \tag{16}$$

with

$$\tilde{S}_{ij} = 2Ge_{ij} \quad \text{with} \quad e_{ij} = \varepsilon_{ij} - \tfrac{1}{3}\varepsilon_v$$

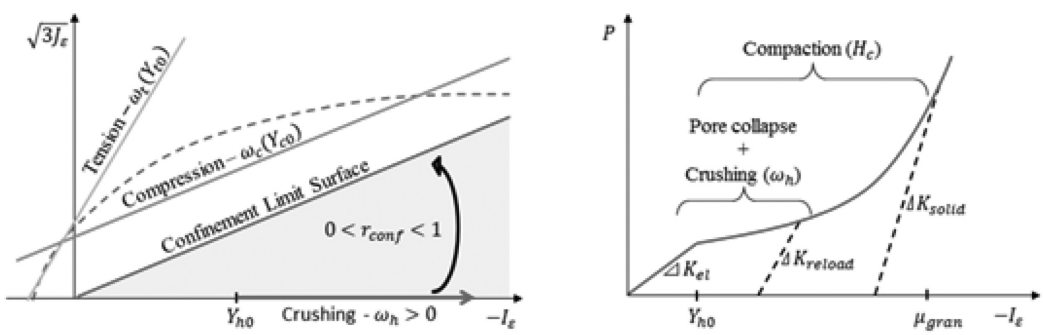

Figure 3. Schematic representation of damage variables and confinement criteria and compaction in the (a) deviatoric and (b) hydrostatic spaces.

3.2 *Rate enhancement*

As it is well known, concrete is a highly rate-dependent material. The observed variation of strength and fracture energy with rate is mainly caused by three phenomena (Pereira et al. 2017a): (*i*) change of fracturing process, associated with an increase of micro-cracking activation and consequently an increase of the effective fracture surface, with rate; (*ii*) viscous properties of the bulk material between cracks which lead to the retardation of cracking due to inertia (i.e. time-dependency of damage); and (*iii*) structural inertia forces. Only the latter phenomenon is naturally captured in continuum finite element modeling. The former two must be considered as inherent dynamic properties of the material and therefore, explicitly included in the constitutive relations.

From the three damage modes described by the model proposed above, only ω_t and ω_c describe mechanisms involving the propagation of cracks (i.e. cracking). Therefore, only these failure modes are considered to be rate dependent. Following common practice, the hydrostatic damage ($|omega_h$) and compaction (H_c) are considered rate independent phenomena. This is a simplification rather than physically objective, since experimental results suggest that the equation of state (EOS) is also rate dependent. As in a typical rate-dependent damage formulation, the variation of the material strength and strain-energy associated with cracking are dynamically updated as a function of rate. This is done by updating the damage threshold Y_{i0} and the parameter B_i in the damage evolution law (4):

$$Y_{i0}^{dyn} = Y_{i0}(1 + \zeta_i \, R_i^{\eta_i}), \tag{17}$$

$$B_i^{dyn} = B_i \left[1 - \delta_i \ln\left(\frac{R_i}{Y_0} \right) \right], \tag{18}$$

where ζ_i, η_i and δ_i are material constants, defined respectively for tension and compression. The parameter Y_0, represents the rate after which the loading is classified as dynamic. Consistently with the *fib* recommendation (MC2 2013), $Y_0 = 10^{-6}$ s^{-1} is assumed.

Unlike what is commonly done in *hydrodynamic* modeling, in this formulation, the material strength and energy are updated as a function of an *effective rate* (R) instead of the *instantaneous* strain rate ($\dot{\varepsilon}$). The *effective rate* is a time dependent quantity conditioned by the immediately preceding strain history which accounts for the time-dependency of cracking (Pereira et al. 2017a). In this model it is assumed that the effect of a variation of the strain rate takes some time (λ) to be experienced by the material and becomes effective. This is done by restricting the evolution of rate in case of a negative (R_{down}) or a positive (R_{up}) variation of the equivalent-strain rate ($\dot{\varepsilon}_i$), according to the following equations:

$$R_{down} = \max\left[\dot{\varepsilon}_i(\tau) e^{-\frac{t-\tau}{\lambda}}, \dot{\varepsilon}_i(t) \right] \text{ for } t \geq \tau \tag{19}$$

$$R_{up} = \min\left[\dot{\varepsilon}_i(\tau) e^{\frac{t-\tau}{\lambda}}, \dot{\varepsilon}_i(t) \right] \text{ for } t \geq \tau \text{ and } \omega > 0 \tag{20}$$

where λ is a user defined *characteristic time* of the material, t is the current time and τ is the last time that *strain rate* ($\dot{\varepsilon}_i$) was constant. In the current formulation, the *effective rate* is independently defined for tension and compression as the variation in time of the respective equivalent strains, i.e. $R_t(\dot{\varepsilon}_t)$ and $R_c(\dot{\varepsilon}_c)$. For more information about this model, the reader is referred to the work by Pereira et al. (2017a).

3.3 *Regularization model—stress based nonlocal*

To overcome spurious mesh sensitivity, typical for standard 'local' damage models, a regularization scheme is needed. In this study, an updated version of the stress-based nonlocal regularization scheme presented by Giry et al. (Giry, Dufour, & Mazars 2011) is used. As in any other nonlocal formulation of integral type, the stress response at a material Gauss point (x) is made dependent on its neighbors (ξ) by weight averaging a certain internal variable Z with the interaction domain Ω following eq. 21. The nonlocal update of the damage model is simply attained by replacing variable Z by its nonlocal counterpart $\left(\overline{Z}\right)$.

In this study, only the equivalent strain under tension is regularized, i.e. $Z = \varepsilon_t$. Although both equivalent strains (ε_t and ε_c) should be independently weight averaged, considering the bi-dissipative nature of the model, it was observed that the results are equivalent in both cases. So, for numerical efficiency, only one nonlocal variable (ε_t) was considered.

$$\overline{\varepsilon}_t(x) = \frac{\int_\Omega \alpha(x,\xi)\varepsilon_t(\xi)d\Omega}{\int_\Omega \alpha(x,\xi)d\Omega} \tag{21}$$

where $\alpha(x, \xi)$ is an arbitrary weight function, here considered to be the Gaussian function:

$$\alpha(x,\xi) = e^{-\left(\frac{2\|x-\xi\|}{l_r}\right)^2} \tag{22}$$

where l_r is the characteristic material length.

In a stress-based nonlocal formulation, the influence of the neighboring elements stress state is introduced in the description of the nonlocal interactions by updating the interaction length between

the Gauss point x and its neighbors ξ, $l_r = lx\xi_i$ in eq. 22, as follows:

$$l_{x\xi} = \rho(x,\xi) l_r \tag{23}$$

with

$$\rho^2 = \frac{1}{(f_t^{dyn})^2 \left(\frac{\sin^2\varphi\cos^2\theta}{\langle\sigma_1\rangle^2} + \frac{\sin^2\varphi\sin^2\theta}{\langle\sigma_2\rangle^2} + \frac{\cos^2\phi}{\langle\sigma_3\rangle^2} \right)} \tag{24}$$

where φ and θ are the angles between the eigenvectors of the principal stress tensor σ_I, with $I = 1$, 2 and 3, at point ξ defined in conventional spherical coordinates system. Considering that <·> are the Macaulay brackets, the expression between parentheses is the projection of the positive part of σ_I over the vector $x\xi$, $\langle\sigma_{x\xi}\rangle$. So, $\rho(x, \xi)$ is the ratio between $\langle\sigma_{x\xi}\rangle$ and f_t, which has a value between zero and one for tensile stresses and is equal to zero otherwise. A non zero interaction length must be used to prevent localization to occur in a zone smaller than the finite element, which is impossible and would lead to mesh dependency again. So, the interaction length between two points is allowed to vary between l_r and a minimum length l_{min}. For more information about this model and the computation scheme used for this research, the reader is referred to the works by Giry et al. (Giry, Dufour, & Mazars 2011, Giry, Oliver–Leblond, Dufour, & Ragueneau 2014) and Pereira et al. (Pereira, Weerheijm, & Sluys 2016, Pereira, Weerheijm, & Sluys 2017a).

4 HIGH VELOCITY IMPACT

For obvious practical reasons, when studying ballistic impact, researchers focus primarily on the influences of the concrete grade/quality, target geometry and impact velocity on the penetration depth or residual velocity of the projectile. The experimental work by Beppu et al. (2008) goes a step further and, in addition to the typical analysis of the post mortem specimens to determine the perforation depth and size of crater and spalling area, high speed video cameras were used to record the evolution of cratering and spalling. These authors conducted a systematic study designed to investigate how the local failure process on plane concrete plates change with projectile velocity and target thickness, during 'rigid' impact. Single steel mushroom-like projectiles were fired against a series of 500 × 500 mm² squared concrete plates with thicknesses ranging from 30 mm to 130 mm. Only impact normal to the plate surface was investigated, with velocities ranging between 200 m/s and 500 m/s. A set of the reported tests has been simulated for the numerical validation of the proposed model.

Although the targets are squared, the experiments were simulated with two dimensional axisymmetric models, as described in Figure 4. The problem was discretized with 2 mm quadrilateral linear finite elements, except for the mesh sensitivity analysis where different mesh sizes between 1 mm and 4 mm were considered for the target. The parameters used to simulate the concrete targets are summarized in Table 1. The damage laws, for tension and compression, and elastic properties were calibrated in order to have a realistic quasi-static representation of the concrete used in the experimental campaign (Beppu et al. 2008). The hydrostatic damage and compaction laws were calibrated in order to have a nonlinear volumetric response under pure hydrostatic deformation (EOS) similar to reference models in literature (Malvar et al. 1997, Hartmann et al. 2010, Gebbeken et al. 2006). The parameters in the rate dependent law for tension were calibrated to fit the modified dynamic increase factor (DIF) law proposed by Malvar and Ross (1998); and the parameters for compression were calibrated in order to reproduce only the first branch of the DIF function proposed by the *fib* model (CEB 1993).

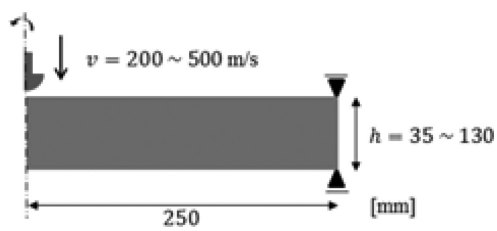

Figure 4. Schematic representation of experiment.

Table 1. Constitutive law parameters.

Symbol	Parameter	Symbol	Parameter
E	25.5 GPa	ρ	2315 kg/m³
ν	0.15	α	0.10
Y_{t_0}	9.8×1^{-5}	Y_{c0}	6.0×10^{-4}
A_t	1.0	A_c	1.0
B_t	10000	B_c	580
C_3	2.0	γ_ω	0.15
$l_r(l_{min})$	12(2) mm	K_{solid}	60 GPa
μ_0	0.003	μ_{gran}	0.25
η_t	0.80	η_c	0.30
ζ_t	0.35	ζ_c	0.20
δ_t	0.045	δ_c	0.030
λ_t	1.0 ms	λ_c	1.0 ms

The projectile was simulated as a bilinear elastoplastic material with $E_1 = 210$ GPa, $E_2 = 2.1$ GPa and σ_{yield} = 225 MPa. The interaction between impactor and target was modeled by a penalty-based contact algorithm with a coefficient of friction $\eta = 0.5$. Numerical erosion had to be taken into account, in order to avoid premature termination of the numerical analysis due to a negative Jacobian and to reduce the computation time, by removing the highly distorted elements. Two criteria were considered, with the deletion of an element being triggered when $\omega > 0.99$ and $\varepsilon_v \geq 0.2$. This is the lowest volumetric strain above which the effects on the damage evolution is negligible in all cases.

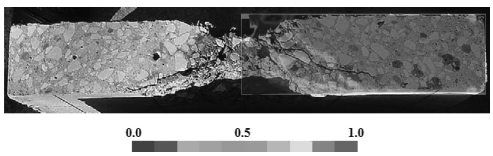

Figure 5. Comparison between experimental fracture patterns and the damage profile at t = 1.0 ms of a $h = 90$ mm thick plate impacted at $v = 420$ m/s.

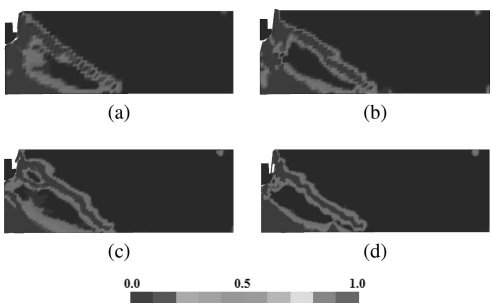

Figure 6. Damage profiles at $t = 0.25$ ms of a $h = 90$ mm thick plate impacted at v = 420 m/s considering different structured meshes: (a) 4 mm, (b) 3 mm, (c) 2 mm and (d) 1 mm.

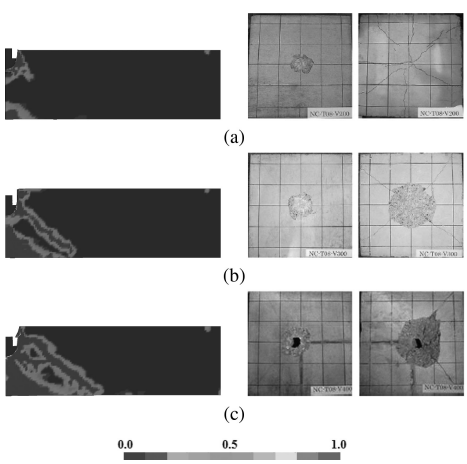

Figure 7. Damage profiles at $t = 0.25$ ms and the respective experimental results (impacted and back faces) of h = 80 mm thick plates impacted at different velocities: (a) v = 210 m/s, (b) v = 310 m/s and (c) v = 415 m/s.

Figure 5 depicts the damage profile of a h = 90 mm thick plate impacted at v = 420 m/s superimposed with the respective mid-section experimental fracture patterns. Except for the penetration depth, which is slightly overestimated, both the extension and shape of the crater and spalling are identical to the experiments. The predicted angle and extension of the conical crack is also very close to the visible crack. As it can be seen in Figure 6, these results are mesh objective upon refinement.

In this study, the effect of impact velocity and target thickness on the fracturing process was also evaluated. Figure 7 compares the numerical results of $h = 80$ mm plates impacted at different velocities with the respective experimental results. As it can be seen, all predictions are very realistic. Although

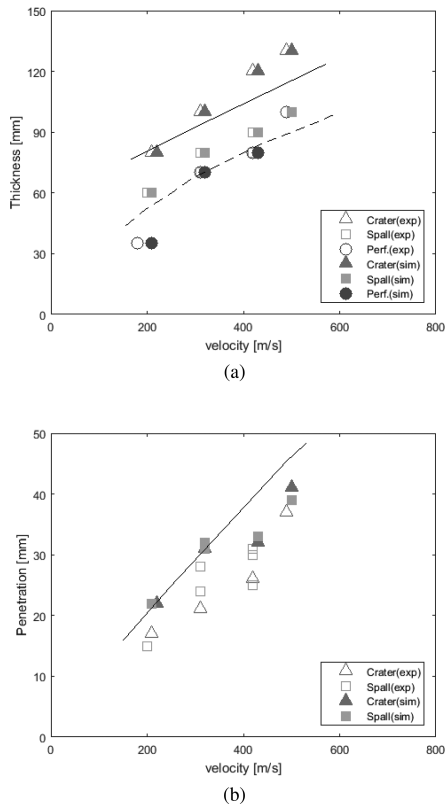

Figure 8. Comparison between experimental and numerical results. Evolution of (a) failure modes and (b) penetration depths with the impact velocity. (Note: simulated velocities are off +10 m/s).

limited spalling is predicted at the back face for the lower velocity impact, these results may be interpreted as realistic because, even though no spalling is observed in the experiments, it does not mean that the material at the back surface of the plate is not damaged. For the higher velocity example, although it is not evident from the damage state at $t = 0.25$ ms, as experimentally observed, perforation is predicted and the exit velocity is approximately 30 m/s.

Figure 8 summarizes all experimental and numerical results. Both the penetration depth and failure modes are compared to the modified NDRC formula (Kennedy 1976) predictions for the crater-spalling and perforation limits, respectively represented by the solid and dashed lines in the plots. As it can be seen in Figure 8(a), the simulated failure mechanisms agree very well with the experimental data. Only in case of the mm thick plate impacted at m/s a crater-spalling damage pattern is predicted while perforation was observed in the test. Notwithstanding, the simulation is in good agreement to the NDRC empirical formulation. In contrast to the good predictions of the failure modes, the model always overestimates the penetration depth (see Figure 8(b)). The use of numerical erosion is most likely the main cause for the increase of penetration depth. While in the model the damaged (crushed) material in front of the impactor is simply deleted, in reality this material flows around the impactor. This causes an extra pressure in the surrounding material, which would result in a local increase of confinement and consequently an increased resistance of the target.

5 CONCLUSION

In this contribution, a new isotropic damage model was used to investigate the dynamic response of concrete in ballistic impact situations. This formulation is an enhanced version of the *effective rate dependent* nonlocal damage model proposed earlier by the authors. To the already considered tensile and compressive damage modes, a new hydrostatic damage mode was added to the formulation in order to take the damage (crushing) of the material matrix as well as porosity reduction during compaction into account. This new damage mode, together with a compaction criterion, governs the nonlinear volumetric response of the material (EOS) and represents the deterioration of the material stiffness when confinement is reduced.

The proposed model can systematically predict the most significant failure modes (cratering, tunneling, spalling and radial cracking) observed during impact on a concrete plate as a function of the projectile velocity and the plate thickness.

REFERENCES

(2013). *fib Model Code for Concrete Structures 2010*. Ernst & Sohn.

Beppu, M., K. Miwa, M. Itoh, M. Katayama, & T. Ohno (2008). Damage evaluation of concrete plates by high-velocity impact. *International Journal of Impact Engineering 35*(12), 1419–1426.

CEB (1993). *CEB–FIB Model Code 1990. Design Code*. Lausanne, Switzerland: Thomas Telford Services Ltd.

Gebbeken, N., S. Greulich, & A. Pietzsch (2006). Hugoniot properties for concrete determined by full-scale detonation experiments and flyer-plate-impact tests. *International Journal of Impact Engineering 32*(12), 2017–2031.

Giry, C., F. Dufour, & J. Mazars (2011, dec). Stress-based nonlocal damage model. *International Journal of Solids and Structures 48*(25–26), 3431–3443.

Giry, C., C. Oliver-Leblond, F. Dufour, & F. Ragueneau (2014, jan). Cracking analysis of reinforced concrete structures. *European Journal of Environmental and Civil Engineering 18*(7), 1–14.

Hallquist, J. (2006). *LS-DYNA Theory manual*. Livermore, California: Livermore Software Technology Corporation.

Hartmann, T., A. Pietzsch, & N. Gebbeken (2010, dec). A Hydrocode Material Model for Concrete. *International Journal of Protective Structures 1*(4), 443–468.

Kennedy, R. (1976). A review of procedures for the analysis and design of concrete structures to resist missile impact effects. *Nuclear Engineering and Design 37*, 183–203.

Malvar, L., J. Crawford, J. Wesevich, & D. Simons (1997). A plasticity concrete material model for DYNA3D. *International Journal for Impact Engineereng 19*(9–10), 847–873.

Malvar, L. & A. Ross (1998). Review of strain rate effects for concrete in tension. *ACI Materials Journal 95*, 735–739.

Mazars, J., F. Dufour, C. Giry, A. Rouquand, & C. Pontiroli (2010). Concrete under various loadings, way to model in a same framework: damage, fracture and compaction. In N. Bicanic, R. de Borst, H. Mang, and G. Meschke (Eds.), *Computational Modelling of Concrete Structures*, pp. 45–58. Autria.

Mazars, J., F. Hamon, & S. Grange (2014). A model to forecast the response of concrete under severe loadings the μ damage model. *Procedia Materials Science 3*, 979–984.

Mazars, J. & G. Pijaudier-Cabot (1989). Continuum damage theory—application to concrete. *Journal of Engineering Mechanics 115*(2), 345–365.

Pereira, L., J. Weerheijm & L. Sluys (2016). A new rate-dependent stress-based nonlocal damage model to simulate dynamic tensile failure of quasi-brittle materials. *International Journal of Impact Engineering 94*, 83–95.

Pereira, L., J. Weerheijm, & L. Sluys (2017a). A new effective rate dependent damage model for dynamic tensile failure of concrete. *Engineering Fracture Mechanics 176*, 281–299.

Pereira, L., J. Weerheijm, & L. Sluys (2017b). A numerical study on crack branching in quasi-brittle materials with a new effective rate-dependent nonlocal damage model. *Engineering Fracture Mechanics 182*, 689–707.

Pereira, L., J. Weerheijm, & L. Sluys (2018). Simulation of compaction and crushing of concrete in ballistic impact with a new damage model. *International Journal of Impact Engineering 111*, 208–221.

Multiscale cement and concrete research: Experiments and modeling



Taylor & Francis
Taylor & Francis Group
http://taylorandfrancis.com

Computational Modelling of Concrete Structures – Meschke, Pichler & Rots (Eds)
© 2018 Taylor & Francis Group, London, ISBN 978-1-138-74117-1

Fishnet model for failure probability of nacre-like imbricated lamellar materials and Monte Carlo verification

Zdeněk P. Bažant
Department of Civil and Mechanical Engineering and Materials Science, Northwestern University, Evanston, USA

Wen Luo
Northwestern University, Evanston, USA

ABSTRACT: The conference paper reviews recent studies at Northwestern University, in which the connectivity in nacreous staggered lamellar systems is, for probabilistic analysis, represented as a fishnet pulled diagonally. The probability distributions of nacre, including its tail at 10^{-6} probability, turns out to be analytically tractable. The fishnet distribution is intermediate between those corresponding to the weakest link chain (series coupling) and fiber-bundle (parallel coupling). Millions of Monte Carlo simulations are presented to verify the analytical distribution, including its tail.

1 INTRODUCTION

In spite of their weak brittle constituents, nacre-like imbricated (staggered) lamellar structures can attain very high strength and fracture energy, exceeding by one to two orders of magnitude the strength or the constituents. The reasons have been clarified in a host of studies of the mechanics of failure [1, 2, 3, 4, 5, 6, 7, 8, 9, 10, 11, e.g.].

These studies, however, were mostly deterministic and provided only the mean behavior. For nacreous structures, no realistic probability distribution of the strength with the far left fail seems to exist at present, yet this is where the 'devil' resides. To capture the tail is the goal of this study (whose main ideas were compactly presented in [12] and developed in full detail in [13]).

To design safe structures with nacre-mimetic materials typically requires knowing their strength distribution up to the tail with failure probability of about $P_f = 10^{-6}$ (per lifetime), which requires determining the extreme value distribution [14, 15]. This is generally the level of safety required for engineering structures such as bridges, aircraft, MEMS, etc. It ensures the risks of engineering structures to be three orders magnitude lower than other risks that people willingly or inevitably take (e.g., car driving), and to be of about the same level as the risk of being killed, e.g., by a lightning of falling tree. Such low tail probabilities can hardly be determined by histogram testing of strength of many identical specimens of structures.

Consequently, one needs a realistic mathematical model for the strength distribution, to be verified only indirectly, by predictions depending on the tail. Here a diagonally pulled fishnet is proposed as the basis of such a model, providing a sufficiently realistic simplification of the connectivity of nacre's microstructure, for which the probability distribution is analytically tractable.

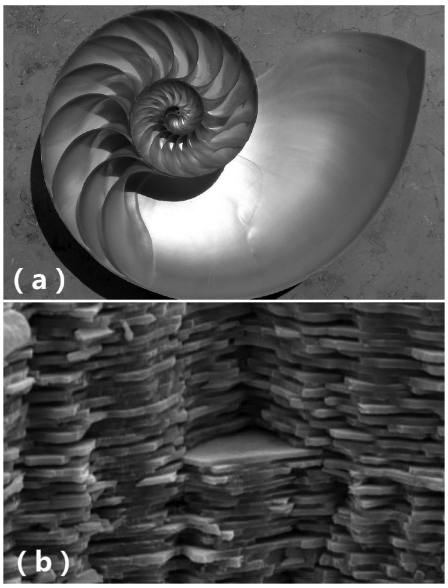

Figure 1. a) Nacre inside a nautilus shell; b) Electron microscopy image of a fractured surface of nacre (both images are from Wikipedia; https://en.wikipedia.org/wiki/Nacre).

The new idea of this article is to model the tail probability of strength of nacre-like structures by a square fishnet pulled along one of the diagonals. Same as the weakest-link model, the failure probability of fishnet, P_f, is obtained by calculating its counterpart—the survival probability, $1 - P_f$. As will be shown, these additional survival probabilities greatly enhance the strength for $P_f < 10^{-6}$, compared to the the weakest-link model.

The analytical predictions of failure probability are here verified by millions of Monte-Carlo simulations. Monte Carlo simulations of nacreous structures have previously been conducted with the random fuse model (RFM) [16, 5], in which the brittle bonds in the structure are simplified as a lattice of resisters with random burnout thresholds. The RFM simulates the gradual failure of resister network under increasing voltage. This is similar to the failure process of quasibrittle elastic material under controlled uniaxial load.

To calculate the maximum loads of the system of fishnet links, a simple finite element (FE) program for a pin-jointed truss is developed (in MatLab). For each of many shapes and sizes of the fishnet, the maximum loads are calculated for about 1 million input samples of randomly generated strengths of the links, based on the assumption that the link strength follows the grafter Gauss-Weibull distribution (see [15]). Running each set of about 1 million FE solutions takes a few days. With such a large number of random samples, the resulting strength histograms become visually indistinguishable from the theoretical cumulative probability density function (cdf) of failure probability P_f, derived in [13].

For the purpose of statistical analysis, the longitudinal load transmission must be realistically simplified. Almost no load gets transmitted between the ends of adjacent lamellae in one row, and virtually all the load gets transmitted by shear resistance of ultra-thin biopolymer layers between parallel lamellae. The links of the lamellae in adjacent rows many be imagined as the lines connecting the lamellae centroids, as marked in Fig. 2a.

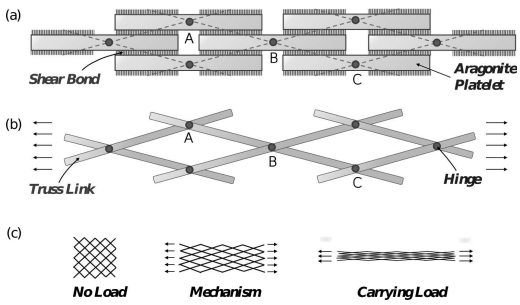

Figure 2. a) Microstructure of nacre; b) Equivalent fishnet structure with similar topology; c) Deformation mechanism of transversely unconstrained fishnet.

2 LOAD TRANSMISSION AND REDISTRIBUTION

The essence of load transmission may thus be characterized by a system of diagonal tensile links (Fig. 1b, which looks like a fishnet loaded in the diagonal direction and can be simulated by a finite element program for pin-jointed trusses. The transverse stiffness is found to be statistically unimportant, and is neglected. Thus the fishnet model is initially a mechanism in which all the links immediately collapse under longitudinal load into a single line (Fig. 2c) while retaining, crucially, the imbricated (or staggered) connections.

3 FAILURE PROBABILITY OF FISHNET MODEL

We consider the case of load control, for which the failure load is the maximum load, σ_{max}. We analyze rectangular fishnets with k rows and n columns, containing $N = k \times n$ links (Fig. 2c), loaded uniformly by uniaxial stress σ imposed at the ends of rows. Let $P_f(\sigma)$ be the failure probability of fishnet loaded by σ, and $X(\sigma)$ the total number of links failed at the end of experiment under constant load σ. This means that $X(\sigma)$ is measured when no more damages occur. The failed links may be contiguous or scattered discontinuously. The events $\{X(\sigma) = r\}, r = 1,2,3,...$ are mutually exclusive (or disjoint). So, to obtain the survival probability of the whole fishnet, the corresponding survival probabilities, $P_{S_r}(\sigma)$, must be summed;

$$1 - P_f(\sigma) = P_{S_0}(\sigma) + P_{S_1}(\sigma) + P_{S_2}(\sigma) + \cdots \quad (1)$$

$$+ P_{S_{k-1}}(\sigma) + \text{Prob}(\text{X}(\sigma) \geq \text{k and structure still safe}) \quad (2)$$

where $P_f(\sigma) = \text{Prob}(\sigma_{\max} \leq \sigma)$; σ_{max} = nominal strength of structure; and $P_{S_r}(\sigma) = \text{Prob}(\text{X}(\sigma)=r)$, $r = 0,1,2,....$

4 TWO-TERM FISHNET STATISTICS

To get a better upper bound, we now include the second term in Eq.(1), i.e., $1 - P_f(\sigma) = P_{S_0}(\sigma) + P_{S_1}(\sigma)$ where σ = average longitudinal stress in the cross section, the same in every section. For the sake of simplicity, we further assume that: 1) the stress redistribution affects only a finite number, v_1, of links in a finite neighborhood of the first failed

link in which $\lambda_i > 1.1$, and 2) factor λ_j is treated as constant, $\lambda_i = \eta_a^{(1)}$ (> 1) within this neighborhood, taken either as the weighted average of all redistribution factors (to get the best estimate), or as the maximum of these factors (to preserve an upper bound on P_f). With this simplification,

$$P_{S_1}(\sigma) = NP_1(\sigma)[1 - P_1(\sigma)]^{N-\nu_1-1}[1 - P_1(\eta_a^{(1)}\sigma)]^{\nu_1} \quad (3)$$

Here N means that failure can start in any one of the N links, which gives N mutually exclusive cases. The two bracketed terms mean that the failure of one of the N links must occur jointly with the survival of: (i) each of the remaining ($N - \nu_1 - 1$) links with stress σ, and of (ii) each of the remaining ν_1 links with redistributed stress $\eta_a^{(1)}$. Analysis shows that the second term of fishnet statistics P_{S_1} increases the terminal slope of strength probability distribution in Weibull scale by the factor of 2. Particularly important are the implications for structural safety. In Fig. 3b, the horizontal line for $P_f = 10^{-6}$ marks the maximum failure probability that is tolerable for engineering design.

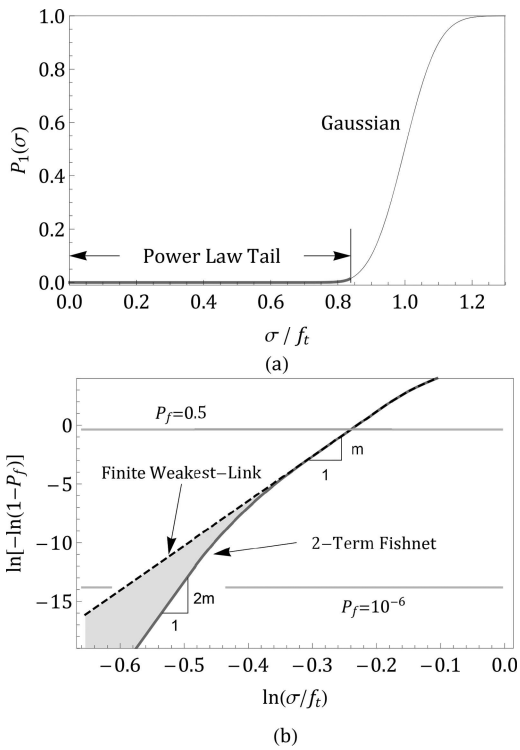

Figure 3. a) Cumulative distribution function (cdf) of failure for a single link with mean f_t = 10.016 MPa and CoV = 7.8%); b) Comparison of P_f (in Weibull scale) between the finite weakest-link model and the fishnet model with first 2 terms in the expansion of Eq. 1.

In this typical case, for constant N, the strength for $P_f = 10^{-6}$ is seen to increase by 10.5% when passing from the weakest-link failures to fishnet failures, while, at fixed strength, the P_f is seen to decrease about 25-times. The P_f decrease depends on the fishnet configurations and on P_1. but is generally more than 10-times greater. This is an enormous safety advantage of the imbricated lamellar microstructure, which comes in addition to the advantages previously identified by deterministic studies.

5 THREE-TERM FISHNET STATISTICS

Further improvement can be obtained by including the third term of the sum in Eq.(1). This term may be split into two parts, $P_{S_2} = P_{S_{21}} + P_{S_{22}}$, which are mutually exclusive, and thus additive. They represent the survival probabilities when the next failed link is, or is not, adjacent to the previously failed link. For detailed derivation, see [13].

6 MONTE CARLO FAILURE SIMULATIONS

A rectangular fishnet truss, with k rows and n columns of identical links, has been simulated by a finite element program (in MatLab). For computational stability, the fishnet is loaded under displacement control, by incrementing equal longitudinal displacements u_0 at the right boundary. At the left boundary, the horizontal displacement is zero. The boundary nodes slide freely in the transverse direction.

According to the arguments in [15, 17, 18, 19], based on nano-mechanics and scale transitions, the cumulative distribution function (cdf) of strength of each link, $P_1(\sigma)$, is assumed to be a Gaussian (or normal) distribution with a Weibull tail of exponent m grafted on the left at failure probability P_g (for $\sigma \to 0$, the cdf $\propto \sigma^m$). The strength of each of $N = k \times n$ links is generated randomly according to $P_1(\sigma)$. The autocorrelation length of the link strength field is assumed to be equal to the link size and, therefore, is not considered.

To verify the analytical two- or three-term statistics, respectively, the cases in which more than one, or two, links failed prior to the maximum load have been deleted from the set of about 1 million simulations of a fishnet having 16 × 32 links, CoV = 0.987 of P_1, and grafting point at $P_g = 0.09$. This is equivalent to omitting in Eq.(1) all the terms except the first two or three, respectively.

The remaining histograms ($\sigma_{max}^{(1)}$ and $\sigma_{max}^{(2)}$) are compared with the analytical cdf in Fig. 4b (Fig. 4a shows, for all simulations of σ_{max}, only the histogram). Despite simplifications, such as using a uniform redistribution ratio η and not

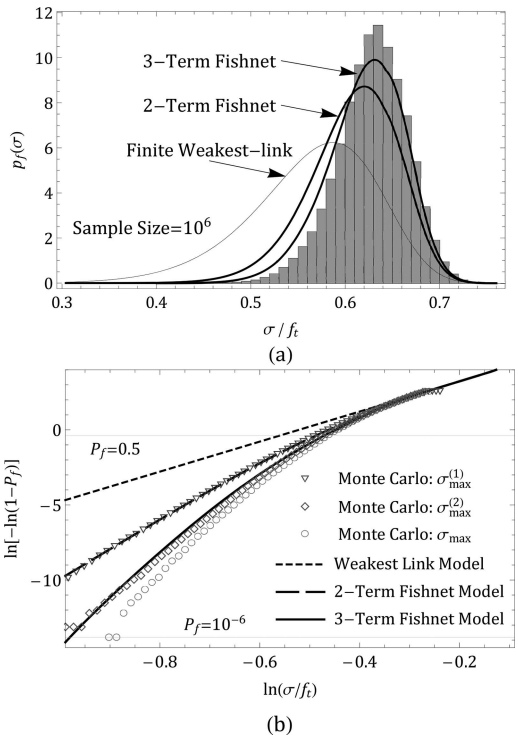

Figure 4. (a) Normalized histogram of 10^6 Monte Carlo realizations (σ_{max}) compared with the probability density functions of the weakest-link, 2-term fishnet and 3-term fishnet models; (b) The same data as well as the histogram of $\sigma^{(1)}_{max}$ and $\sigma^{(2)}_{max}$ converted into cumulative probability distribution and plotted on the Weibull paper. $f_t = 9.87$ MPa is the mean strength of one link and CoV = 9.87%.

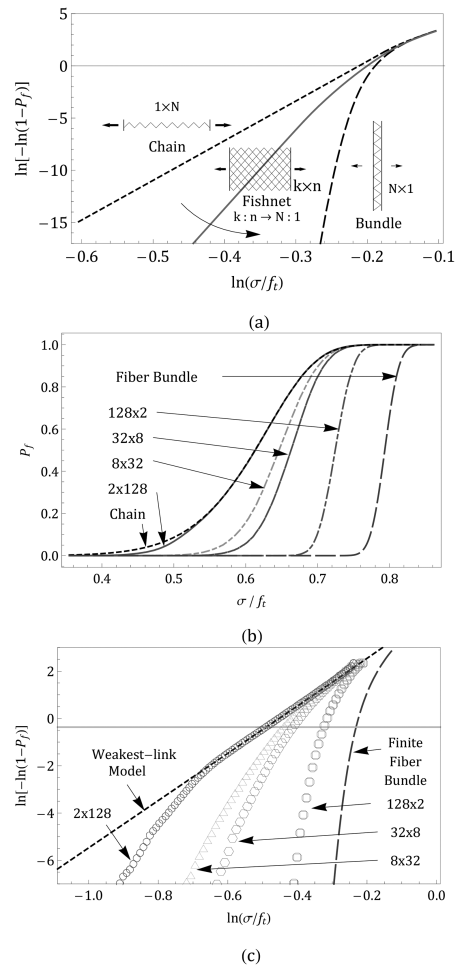

Figure 5. a) Change of failure probability of a fishnet pulled horizontally caused by varying the aspect ratio k/n gradually from 1:N to N:1 at constant number of links (Weibull scale); b) Monte Carlo simulations showing the transition of P_f as the aspect ratio of fishnet is changed from $1 \times N$ to $N \times 1$ ($N = 256$); c) The same data re-plotted on Weibull paper. $f_t = 9.87$ MPa is the mean strength of one link and CoV = 9.87%.

distinguishing link failures at the boundary from those in the interior, the agreement is excellent. This validates the analytical solution.

Fig. 4 shows, for comparison, also the histograms of all the Monte Carlo simulations, which correspond to the complete sum in Eq.(1). Note that, in this case, the three-term model, and even the two-term model, give a satisfactory estimate of fishnet cdf.

Shape Effect: Consider now the effect of the fishnet shape, or aspect ratio k/n. Fig. 5 shows the histograms obtained by random simulations (again about a million each) for fishnets with $N = 256$ links when their dimensions $k \times n$ are varied from 128×2, which represents the weakest-link chain (or series coupling), to 2×128, which represents the fiber bundle (or parallel coupling, with mechanics-based load sharing, i.e., equal extensions of all fibers). Obviously, the shape effect is very strong. However, fishnets with $k \gg n$ and rigid-body boundary displacements are not relevant to practical situations.

Fig. 4 shows the transition of P_f as the aspect ratio of fishnet is changed from $1 \times N$ to $N \times 1$ ($N = 256$). As expected, P_f gradually transforms from a Weibull distribution to Gaussian distribution as the shape of a fishnet changes from a chain to a bundle. Further note that this transformation from a chain to a bundle makes the fishnet stronger. Evidently, the weakest-link model and fiber bundle model give the upper and lower bound of P_f of all fishnets respectively.

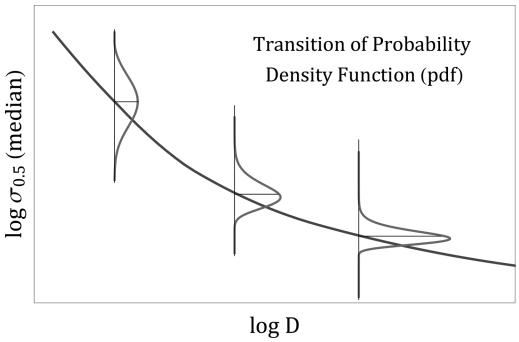

Figure 6. Statistical size effect on the median strength of quasi-brittle fishnet.

7 SIZE EFFECT

For simplicity, the effect of fishnet size D (chosen either as k or n) at constant shape k/n is here studied only for the median strength, $\sigma_{0.5}$, rather than the mean strength, $\bar{\sigma}$. Both analytical considerations and computer simulations show that the size effect curve in the plot of log $\sigma_{0.5}$ vs. log D is not a straight line, as in Weibull theory. Rather, the size effect curve descends at decreasing slope. Also, the CoV of $\sigma_{0.5}$ decreases with size D; see Fig. 6. This is all similar, but not identical, to the Type 1 size effect in fracture of concrete, rock, tough ceramics, fiber composites and other quasibrittle materials [20, 15].

8 CONCLUSIONS

1. The failure statistics of nacre-like material with imbricated (or staggered) lamellar microstructure under longitudinal tension can be approximately modelled by square fishnets pulled diagonally.
2. The probability distribution of fishnet strength, including the far-out left tail, can be calculated as a series of failure probabilities for maximum load occurring after the failure of one, two, three, etc., links. The series converges rapidly—the faster the greater the coefficient of variation (CoV) of scatter of each link.
3. The terms of this series represent various combinations of joint probabilities of survival and additive probabilities of failure for disjoint events. Near the zone of failed links, the link survival probabilities must be modified according to the mechanical stress redistribution due to previously failed links.
4. Compared to probability distribution for the finite weakest-link model developed for particulate materials and fiber composites, the strength at the failure probability level $P_f = 10^{-6}$ is about one to two orders of magnitudes higher, in terms of the ratio of strength to the mean strength. This ratio increases with increasing CoV of strength scatter of each link, but at the same time the mean strength decreases. Thus the combined effect at the level of $P_f = 10^{-6}$ can be strength decrease or increase.
5. There is no fixed-size representative volume element of material (RVE), in contrast to the weakest-link model for Type 1 quasibrittle failures of particulate materials. The size of the zone of failed links at maximum load grows with the CoV of link strength.
6. The size effect law is similar, though not the same, as in quasibrittle Type 1 finite weakest-link model. The nominal strength of fishnet at the same width-to-length ratio decreases significantly with the fishnet size.
7. The fishnet shape, i.e., the width-to-length aspect ratio, has a major effect on the probability distribution of strength, which contrasts with to finite weakest-link model for Type 1. The greater this ratio, the higher is the safety margin, i.e., the greater is the strength at the failure probability level $P_f = 10^{-6}$. As the aspect ratio is increased from 0 to ∞, the fishnet gradually transits for the weakest-link chain to the fiber bundle as the limit cases.
8. The fishnet model exhibits a strong size effect, similar to, though different from, the finite weakest-link model for Type 1 quasibrittle size effect characterizing particulate or granular materials and fiber composites. The evolution of cdf curves shows that, with increasing structure size, the cdf curves in Weibull scale get progressively steeper and cross each other. This is a qualitative difference from quasibrittle particulate materials or composites.
9. The fishnet model is verified by about a million Monte Carlo simulations of failure. The simulations were run for each of many different aspect ratios, link strength CoVs and fishnet sizes.
10. There now exist three basic, analytically tractable, statistical models for the strength of materials and structures:
    - the fiber bundle model (parallel coupling),
    - the weakest-link chain model (series coupling), and,
    - the fishnet model (mixed, or imbricated coupling).

    The third case includes the first two as the limit cases.
11. A similar steepening of the distribution slope at the lower end of Weibull scale plot can also

be achieved by the chain-of-bundles model, but only if a convenient intuitive non-mechanical load-sharing rule is empirically postulated for each bundle, and if the specimen length is subdivided by chosen cross sections into statistically independent segments of suitable length, corresponding to each bundle. However, the imbricated (staggered) lamellar connectivity cannot be captured.

ACKNOWLEDGMENT

Partial support from the Army Research Office Grant W911 NF-15-1-0240 is gratefully acknowledged. Some preliminary studies also drew support from NSF Grant CMS = 0556323.

REFERENCES

[1] Huajian Gao, Baohua Ji, Ingomar L Jäger, Eduard Arzt, and Peter Fratzl. Materials become insensitive to flaws at nanoscale: lessons from nature. *Proceedings of the national Academy of Sciences*, 100(10): 5597–5600, 2003.

[2] RZ Wang, Z Suo, AG Evans, N Yao, and IA Aksay. Deformation mechanisms in nacre. *Journal of Materials Research*, 16(9): 2485–2493, 2001.

[3] Xiaoding Wei, Tobin Filleter, and Horacio D Espinosa. Statistical shear lag model–unravelling the size effect in hierarchical composites. *Acta biomaterialia*, 18: 206–212, 2015.

[4] Yue Shao, Hong-Ping Zhao, Xi-Qiao Feng, and Huajian Gao. Discontinuous crack-bridging model for fracture toughness analysis of nacre. *Journal of the Mechanics and Physics of Solids*, 60(8): 1400–1419, 2012.

[5] Zsolt Bertalan, Ashivni Shekhawat, James P Sethna, and Stefano Zapperi. Fracture strength: Stress concentration, extreme value statistics, and the fate of the weibull distribution. *Physical Review Applied*, 2(3): 034008, 2014.

[6] Sina Askarinejad and Nima Rahbar. Toughening mechanisms in bioinspired multilayered materials. *Journal of The Royal Society Interface*, 12(102): 20140855, 2015.

[7] Roberto Ballarini and Arthur H Heuer. Secrets in the shell the body armor of the queen conch is much tougher than comparable synthetic materials. what secrets does it hold? *American Scientist*, 95(5): 422–429, 2007.

[8] F Barthelat and HD Espinosa. An experimental investigation of deformation and fracture of nacre–mother of pearl. *Experimental mechanics*, 47(3): 311–324, 2007.

[9] Abhishek Dutta, Srinivasan Arjun Tekalur, and Milan Miklavcic. Optimal overlap length in staggered architecture composites under dynamic loading conditions. *Journal of the Mechanics and Physics of Solids*, 61(1): 145–160, 2013.

[10] Abhishek Dutta and Srinivasan Arjun Tekalur. Crack tortuousity in the nacreous layer– topological dependence and biomimetic design guideline. *International Journal of Solids and Structures*, 51(2): 325–335, 2014.

[11] S Kamat, X Su, R Ballarini, and AH Heuer. Structural basis for the fracture toughness of the shell of the conch strombus gigas. *Nature*, 405(6790): 1036–1040, 2000.

[12] Wen Luo and Zdeněk P Bažant. Fishnet statistics for probabilistic strength and scaling of nacreous imbricated lamellar materials. *Journal of the Mechanics and Physics of Solids*, 109: 264–287, 2017.

[13] Wen Luo and Zdenek P Bazant. Fishnet statistics for strength scaling of nacreous imbricated lamellar materials. *arXiv preprint arXiv: 1706.01591*, 2017.

[14] Ronald Aylmer Fisher and Leonard Henry Caleb Tippett. Limiting forms of the frequency distribution of the largest or smallest member of a sample. In *Mathematical Proceedings of the Cambridge Philosophical Society*, volume 24, pages 180–190. Cjambridge University Press, 1928.

[15] Zdenek P Bazant and Jia-Liang Le. *Probabilistic Mechanics of Quasibrittle Structures: Strength, Lifetime, and Size Effect*. Cambridge University Press, 2017.

[16] Mikko J Alava, Phani KVV Nukala, and Stefano Zapperi. Statistical models of fracture. *Advances in Physics*, 55(3–4): 349–476, 2006.

[17] Zdeněk P Bažant and Sze-Dai Pang. Mechanics based statistics of failure risk of quasibrittle structures and size effect on safety factors. *Proceedings of the National Academy of Sciences*, 103(25): 9434–9439, 2006.

[18] Zdeněk P Bažant and Sze-Dai Pang. Activation energy based extreme value statistics and size effect in brittle and quasibrittle fracture. *Journal of the Mechanics and Physics of Solids*, 55(1): 91–131, 2007.

[19] Zdeněk P Bažant, Jia-Liang Le, and Martin Z Bazant. Scaling of strength and lifetime probability distributions of quasibrittle structures based on atomistic fracture mechanics. *Proceedings of the National Academy of Sciences*, 106(28): 11484–11489, 2009.

[20] Zdenek P Bazant. *Scaling of structural strength*. Butterworth-Heinemann, 2005.

Computational Modelling of Concrete Structures – Meschke, Pichler & Rots (Eds)
© 2018 Taylor & Francis Group, London, ISBN 978-1-138-74117-1

Phase-field modeling of cement paste: Where particle physics meets continuum mechanics

Thomas Petersen & Franz-Josef Ulm
Department of Civil and Environmental Engineering, Massachusetts Institute of Technology, Cambridge, MA

ABSTRACT: A phase-field model for the solidification and microtextural evolution of cement paste is introduced. In this mean-field approach the Gibbs free energy of the system defines the evolution of a set of reaction-diffusion equations that model the dissolution of a source phase and the precipitation and growth of Calcium-Silicate-Hydrates (C-S-H) as a density field of nanoparticles. Results for isothermal simulations at three temperatures are discussed with additional analyses focusing on the hydration kinetics, the coarsening of the pore structure, and the development of the elasticity. A tool scarcely explored by the cement science community, the potential of phase-field approaches to refine the current modeling capability of the nucleation and growth of C-S-H and to upscale information gleaned from its colloidal building-blocks are examined.

1 INTRODUCTION

Cement paste has long been identified as an hierarchically organized material, with multiple representative length scales (Feldman and Sereda 1968, Powers and Brownyard 1946). At the atomic scale, it is composed of calcium-silicates and bound water layers. At alarger scale, these semi-crystalline calcium-silicate-hydrates (C-S-H) form globular, colloidal masses that aggregate into an amorphous, cohesive, porous gel-network and provide the material the properties that make it an ideal binder for concretes (Jennings 2000a). And though much research has been dedicated to understanding the material behavior of C-S-H at the nanoscale, and cement paste at the meso- and macroscales, tools to bridge this understanding are scarce and often inadequate. The energy release rate during fracture presents perhaps the most striking discrepancy, where the surface energy created in cleaving the molecular structure of C-S-H was measured to be ≈ 0.5 J/m^2 (Bauchy et al. 2015) and nanomechanical scratch tests report values around ≈ 500 J/m^2 (Hoover and Ulm 2015): A 10^3-fold toughening between the respective representative elementary volumes (REVs). Of course, the challenges of upscaling and elucidating differences in mechanical measurements between constituent elements and bulk properties are not confined to cement systems. Particularly the formation of colloidal structures that settle into out-of-equilibrium configurations demand additional insight (Jennings 2000b, Ioannidou et al. 2016). Hence understanding and designing cement paste in the context of a reactive, hierarchical material necessitates progress on several fronts:

1. Further exploration of the complex material structure of cement paste, its changes in function of the mix design, and how thermodynamic conditions impact its hydration kinetics and morphology.
2. Advances by soft matter physicists in categorizing and describing the poly-disperse, out-of-equilibrium precipitation mechanisms of colloidal systems and their impact on the mechanics of cement paste.
3. The formulation of continuum scale models that homogenize the results of particle-based simulations into the relevant field equations.

The current proceeding is dedicated to the final challenge, whereby phase-field modelling, which has found success interpreting the microtextural evolution of other material systems, is proposed as a viable device to study the mechanics of the reactive cement system.

2 WHAT IS PHASE-FIELD MODELING?

Phase-field descriptions of material microstructures have allowed scientists to simulate a multitude of complex phenomena ranging from solidification and phase-transformation processes to stress-induced pattern formation and crack propagation (Chen 2002, Aranson et al. 2000). A phase-field model advances a set of field variables

by i) defining an homogeneous energy density with one or more minima separated by barriers, and ii) introducing gradient energy penalties that force the field variables to vary smoothly in space. Dependent on the height of the barrier and magnitude of the gradient penalty, a characteristic interface width and interfacial energy are established; Fig. 1 depicts such a diffuse interface for the field variable ϕ.

Because the nanogranular packing density of C-S-H particles has been established as the principal descriptor of the local mechanical behavior of cement paste, its evolving elasticity and strength can be predicted if we understand how the packing density varies in time and space. To advance this goal, the authors recently devised a phase-field model for the dissolution and precipitation reactions taking place during cement setting at the scale of 10^1–10^2 μm (Petersen et al. 2017). Under this directive, a free energy functional is defined for the system,

$$G = \int_V g^h(\phi,\psi,c) + \frac{\kappa_\phi}{2}|\vec{\nabla}\phi|^2 + \frac{\kappa_\psi}{2}|\vec{\nabla}\psi|^2\, dV, \quad (1)$$

and the homogeneous energy density g^h is made dependent on three field variables: the C-S-H packing density ϕ, an order parameter defining regions of source phase and pore space ψ, and a representative ion concentration of the pore solution $\tilde{c}$. The length scale of the pattern formation of the C-S-H is governed by the gradient energy coefficient for the packing density κ_ϕ, and the size of the dissolution region was controlled by adjusting κ_ψ.

Though the idea of incorporating diffuse interfaces for transformation was first introduced by van der Waals over a century ago (Waals 1894), use of the concept for reaction kinetics proliferated when Allen and Cahn formulated their equation for alloy coarsening in 1979 (Allen and Cahn 1979). This mean-field model is the ideal apparatus to upscale recent findings from coarse-grained particle simulations of C-S-H, whereby relevant physical properties are reduced to functions of ϕ and $\vec{\nabla}\phi$ and assimilated into the system's free energy (Eq.(1)). Once at hand, the driving force for the reaction kinetics is governed by minimizing G.

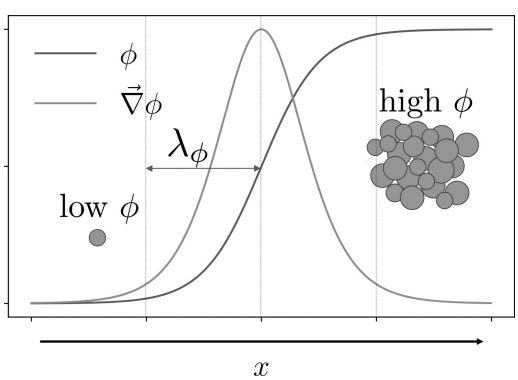

Figure 1. Sample 1D plot of a diffuse interface, where the phase-field variable ϕ and its gradient $\vec{\nabla}\phi$ vary continuously in space; ϕ increases from the low density to the high density value indicated by the minima in its energy functional.

3 A REACTIVE-DIFFUSION MODEL FOR CEMENT PASTE

The simplicity of phase-field approaches rests in unifying the free energy contributions of cement solidification into a single functional. At the micrometer scale, where dissolution and precipitation are to be accurately captured, the challenge persists in supplying physics-grounded expressions for the energy densities of C-S-H g^h_ϕ and the source phase g^h_ψ, where $g^h = g^h_\phi + g^h_\psi$. We continue by postulating possible forms of these potentials, and demonstrate how they may be used to drive the kinetics of the precipitation and dissolution reactions.

3.1 *Gibbs energy of the C-S-H nanoparticles*

To incorporate the Gibbs free energy of the C-S-H nanoparticles, a solution model akin to Flory and Huggins' theory for polymer mixtures is adopted with the following expression (Flory 1953, Huggins 1941):

$$g^h_\phi = \rho_\phi\{RT\left(\phi\ln(\phi)/m(\phi) + (\phi_\mathrm{m}-\phi)\ln(\phi_\mathrm{m}-\phi)\right) + \Omega\phi(\phi_\mathrm{m}-\phi) + E_\mathrm{p}\phi\}. \quad (2)$$

Above, ϕ_m is the maximum packing density, $m(\phi)$ is a parameter that accounts for the characteristic cluster size in course of densification, $\Omega(\tilde{c})$ is the particle interaction parameter, and $E_p(\tilde{c})$ is the precipitation energy (deeming either forward or backward reactions favorable).

The shape of this potential is plotted in (Fig. 1a) for increasing degrees of saturation. As is seen by the trend in $\tilde{c}$, the strength of the inter-particle attractive forces between C-S-H particles depends on the ion activity of the pore solution, whereby we adopt a linear relation for $\Omega = \Omega_0 + \Omega_1\tilde{c}$; this trend in increasing attractive forces is well supported by atomic-force-microscopy measurements between C-S-H surfaces at various salt concentrations (Plassard et al. 2005). Hence, Fig. 2(a) allows inference of the energetically favorable configurations,

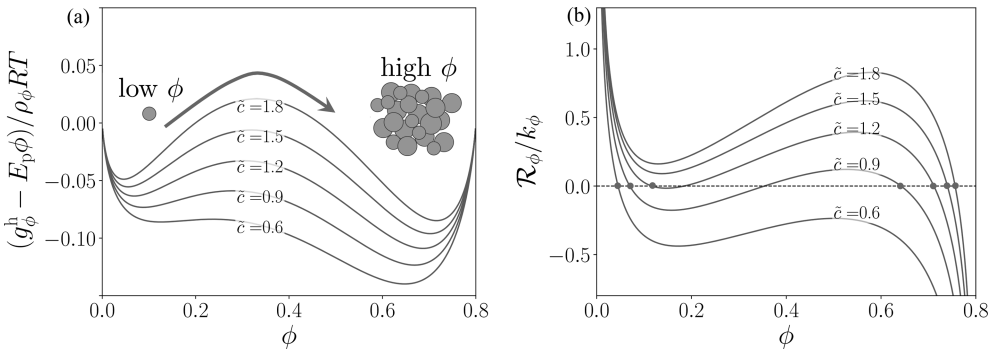

Figure 2. (a) Homogeneous Gibbs free energy pertaining to the configuration of the nanoparticles plotted for different values of the ionic concentration of the pore solution. (b) Reaction rate for the precipitation procedure of the C-S-H nanoparticles; the red dots indicate stable, stationary values in the reaction rate for a given $\tilde{c}$.

whereby phase separation and an increase in the miscibility gap—the difference between the low-ϕ and high-ϕ minima—is promoted at high Ω. This potential is plotted without regard to the chemical potential difference between nucleated and dissolved states of a nanoparticle, which is captured by E_{p}. As a result, dense regions—locations where g^{h} has achieved its HD minimum—develop only if the supersaturation of the pore solution exceeds a critical value, which enables the C-S-H to overcome its nucleation barrier.

3.2 *Gibbs energy of the source phase*

Next, the free energy of the source phase is modeled by

$$g_\psi^{\mathrm{h}} = \rho_\psi\{Wh(\psi) + E_d p(\psi)\}, \tag{3}$$

with $h(\psi) = 16\psi^2(1-\psi)^2$ and $p(\psi) = \psi^3(6\psi^2 - 15\psi + 10)$ being the barrier and interpolation functions used to create a double-well potential with minima at $\psi = 1$ and $\psi = 0$, here defining the solid and the porespace, respectively. This lends control in precisely defining regions eligible to ion diffusion and C-S-H precipitation. The dissolution energy $E_{\mathrm{d}}(\tilde{c})$ defines the difference between the energy minima of the source phase and the porespace, where $E_{\mathrm{d}} < 0$ causes the source phase to recede and locally increases the ion concentration. If $\tilde{c}$ reaches its saturation value w.r.t. the dissolution reaction, the chemical driving force ceases and $E_{\mathrm{d}} = 0$.

3.3 *Field-equations*

The evolution of the phase-field description of the cement microstructure is modeled using a simple set of reaction-diffusion equations. Herein, the dissolution rate of the source phase $\mathcal{R}_\psi$ and precipitation rate of the product phase $\mathcal{R}_\phi$ are modulated by the concentration of the pore solution. The dynamics are defined as follows:

$$\frac{\partial \phi}{\partial t} = \mathcal{R}_\phi\left(\frac{\Delta_{\mathrm{r}} G_\phi}{RT}\right) \tag{4a}$$

$$\frac{\partial \psi}{\partial t} = \mathcal{R}_\psi\left(\frac{\Delta_r G_\psi}{RT}\right) \tag{4b}$$

$$\frac{\partial(\varphi\tilde{c})}{\partial t} = \vec{\nabla}\cdot\left(D_c(\phi,\psi)\vec{\nabla}\tilde{c}\right) - \beta_\phi\mathcal{R}_\phi - \beta_\psi\mathcal{R}_\psi, \tag{4c}$$

It is noted that the mobility of the ionic species in general depends on the free volume ($\varphi = 1 - \phi$) and tortuosity of the pore network, effects incorporated into diffusion coefficient by the following expression:

$$D_c = D_0 p(\psi)\exp(-a\phi). \tag{5}$$

Above, $p(\psi)$ prevents any diffusion into the source phase and a is a positive constant that defines the slowing of the diffusion through the C-S-H solid.

The driving force $\Delta_r G_\phi\left(\Delta_r G_\psi\right)$ for $\mathcal{R}_\phi\,\mathcal{R}_\psi$ is given by the variational derivative of Eq.(1) w.r.t ϕ (ψ) (see Appendix A; details on the form of the reaction rates can be found in (Petersen et al. 2017)). In other words, $\Delta_{\mathrm{r}} G_\phi$ and $\Delta_{\mathrm{r}} G_\psi$ measure the change in the system's free energy due to infinitesimal variations in ϕ and ψ, respectively. The homogeneous reaction rate of the C-S-H precipitation $\mathcal{R}_\phi$, which neglects gradient energy contributions, is plotted in Fig. 2(b). Stable

stationary points in the reaction rate are marked by red circles, where the derivatives meet the requirements $\partial g_\varphi^{\mathrm{h}} / \partial \phi = 0$ and $\partial^2 g_\varphi^{\mathrm{h}} / \partial \phi^2 > 0$. It is thus the precipitation energy E_p that drives the reaction rate, where increases in $E_p(\tilde{c})$ vertically translate the curves in Fig. 2(b) upward (*i.e.*, an increase in the chemical potential difference between reservoir and solid promotes precipitation), whence curves of constant $\tilde{c}$ achieve a single high-ϕ stationary point. In an incremental approach to solving the reaction-diffusion equations, precipitating new particles locally consumes ions (reduces $\tilde{c}$), such that nuclei of high density regions form and only grow if afforded access to additional ionic species by the dissolution of the source phase. Early in the reaction process the microstructure depends largely on the ratio of the timescales of the precipitation and dissolution rates. For faster dissolution rates (at higher T), more homogeneous nucleation between the source phase particles is expected. At latter degrees of hydration, once C-S-H has precipitated along the boundaries of the source phase and this "hydration shell" has achieved a significant thickness, the reaction rate is controlled by the diffusion rate of the concentration field and it ability to maintain the solution's supersaturation.

4 RESULTS FOR TWO-DIMENSIONAL SIMULATIONS

This section of the proceeding is dedicated to the analysis of three sample simulations evolved at different temperatures T. Specifically, an investigation of the microtexture and its evolution in function of the hydration degree ξ is conducted and the ability of two-dimensional phase-field models to capture the hydration kinetics, the pore-structure, and the evolving elasticity is studied.

4.1 *Hydration kinetics*

Because direct access to the residual clinker phase is afforded, it is conveneient to define ξ at a time t by the ratio,

$$\xi(t) = \frac{\langle \psi(t) \rangle}{\langle \psi(t=0) \rangle} \tag{6}$$

where angled brackets indicate values averaged over the domain. Results for the hydration kinetics of the reaction-diffusion model at three different temperatures are portrayed in Fig. 3, where the rate of dissolution of the source phase $\langle d\psi / dt \rangle \sim \Delta_r G_\psi / RT$ shows close comparison to the rate of heat efflux from calorimetry measurements. As temperature is increased, the rate of

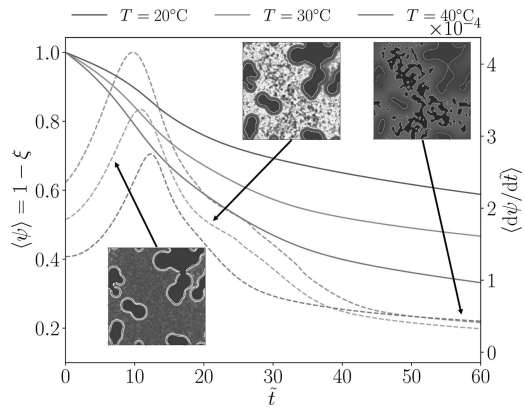

Figure 3. Plots of the source phase volume fraction, $\langle \psi \rangle = (1/V)\int_V \psi dV$ (primary, left-side axis), and the rate of dissolution of the source phase (secondary, right-side axis) in function of time and for different temperatures. Inset images depict the two-dimensional spatial distribution of the packing density for $T = 20°C$ at select stages of the hydration reaction; $\xi = 0.16, 0.33$ and 0.53.

reaction increases and the peak is placed earlier in the reaction process. The kinetics were also shown to be heavily influenced by the interfacial area of the source phase, where fine particles react more quickly than coarse particles given an equal initial volume fraction $\langle \psi(t=0) \rangle$ (Petersen et al. 2017).

4.2 *Pore structure*

To investigate the trends in the cement paste's structure, and more precisely, its porosity, the cement paste's packing density is summarized by key microstructural descriptors. For a given packing density, dense regions of C-S-H and regions of pore spaceare segmented via a threshold, such that an indicator function is defined by (Torquato 2013).

$$I(\phi) = \begin{cases} 1 \, \phi > \phi_s \, (\text{dense C-S-H}) \\ 0 \, \phi < \phi_s \, (\text{pore space / source}) \end{cases} \tag{7}$$

Fig. 4(b) demonstrates how this indicator functions acts on the packing density field represented in Fig. 4(a). As a consequence, a porosity at the length scale of the simulation box (pore sizes on the order of 10s of μm; here referred to as the macro porosity) is readily quantified by

$$p_{\text{macro}} = \left\langle \min\left\{ \mathcal{I}(\phi) + p(\psi), 1 \right\} \right\rangle, \tag{8}$$

and the remaining capillary pores (10nm – 50nm) and gel pores (<10nm) produce a porosity at a lower length scale measured collectively by

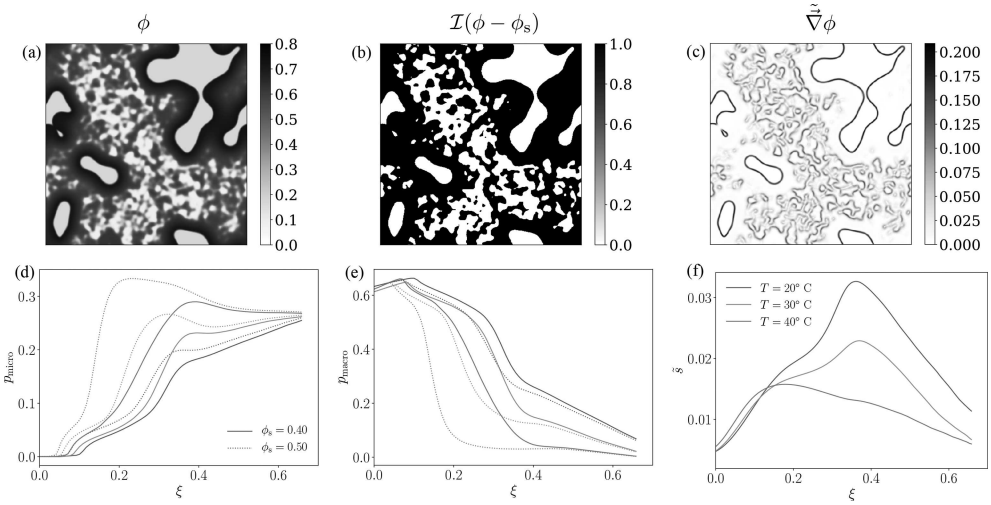

Figure 4. Top panel: Sample transformation of (a) the packing density to (b) its binary map indicating regions of solid and macro porespace, and (c) the indicator function for the interface; herein, $\phi_s = 0.5$ and $\xi = 0.42$ and the dimensions of the REV are $L \times L = 200\ \mu\text{m} \times 200\ \mu\text{m}$. Bottom panel: Plots of (d) the micro porosity, (e) the macro porosity, and (f) the non-dimensionalized specific surface $\left(\tilde{s} = sL\right)$ in function of the hydration degree.

$$p_{\text{micro}} = \left\langle \mathcal{I}(\phi)(1-\phi) \right\rangle. \tag{9}$$

The evolution of p_{macro} and p_{micro} are plotted as a function of ξ for two different threshold values $\phi_s = \{0.4, 0.5\}$ in Figs. 4(d,e). It is observed that the distinction between macro and micro porosity is extremely sensitive to ϕ_s at low ξ, before microstructural coarsening sharpens the boundaries between locations of high and low ϕ; much of the loss in p_{macro} by lowering ϕ_s is shifted to p_{micro}. As the reaction commences and interfacial regions become more defined, the two curves converge. Near the end of the reaction, the majority of the available macro porespace is occupied by densely precipitated C-S-H solid, and the vast majority of the porosity is found as small capillary and gel-pores. Here, it is noted that cement paste solidifying at higher temperatures produce more porosity, in line with experimental observations[1] (Gallucci, Zhang, & Scrivener 2013). Bentur, for instance, used mercury porosimetry and H_2O and N_2 adsorption to show a significant increase inpore volume for pore diameters less than $\approx 0.2\ \mu$m by raising the curing temperature from 25°C to 65°C (Bentur 1980). For higher temperatures, it is believed that an increase in the precipitation rate creates a less ordered structure.

Next, the specific surface between high density and low density regions—for 2D, the lineal distance of the interface per unit area of hydrating paste—is approximated by the volume average of the gradient of the packing density.

$$s = \frac{\left\langle \tilde{\vec{\nabla}}\phi \right\rangle}{\phi_m}. \tag{10}$$

The progression of the specific surface in function of ξ is shown in Fig. 4(f), where s initially increases as more solid mass precipitates, until no additional nuclei form and further growth would lead to the coalescence of locations of high-ϕ. As may be deduced from the earlier decline in p_{macro} for high T trial, increased temperature promotes an earlier peak in s.

4.3 *Mechanics*

The mechanics of the two-dimensional cement system are investigated under plane strain conditions using a linear elastic constitutive model

$$\sigma_{ij} = K\epsilon_{kk}\delta_{ij} + 2G\left\{\epsilon_{ij} - \frac{1}{3}\epsilon_{kk}\delta_{ij}\right\} \tag{11}$$

where σ_{ij} is the stress tensor, ϵ_{ij} is the infinitessimal strain tensor, $G(\xi, x_i)\left(K(\xi, x_i)\right)$ is the temporally and spatially varying shear (bulk) modulus, and δ_{ij} is the Kronecker delta. At the micrometer scale of the cement paste system, the local modulus depends critically on the local packing density, whereby an

[1]To reproduce the textural effects of hydration temperature on the gel pores and small capillary pores, a more refined model at lower length scales is necessitated.

empirical relation for attractive colloidal particles was suggested in the form (Trappe et al. 2001).

$$G(\phi,\psi) = G_0(\phi-\phi_0)^b + G_\psi p(\psi). \tag{12}$$

By setting the coefficient b to 3.5 and the reference modulus G_0 to 75 GPa, and assuming a constant Poisson's ratio of $\nu = 0.25$ (Constantinides and Ulm 2004), the trend in G agrees well with simulated and observed values of the indentation modulus in Ref. (Ioannidou et al. 2016). The function for the shear modulus of C-S-H is plotted in Fig. 5. The modulus and Poisson's ratio of the source phase are assumed time-independent, where $G_\psi = 52$ GPa and $\nu = 0.3$ (Acker et al. 2001). As a result, the local bulk modulus is given simply as $K = 2G(1+\nu)/3(1-2\nu)$, where $\nu = 0.25 + p(\psi)0.05$.

In all mechanical tests, homogeneous strain boundary conditions are applied, where the displacement vector u_i along the boundary ∂V is given by (Zaoui 2002).

$$u_i(x_j,\xi) = \epsilon_{ij}^{\text{hom}}(\xi)x_j \qquad x_i \in \partial V \tag{13}$$

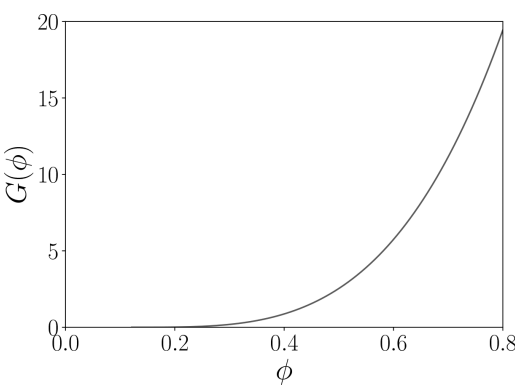

Figure 5. Shear modulus as a function of the local packing density ϕ.

and strain averaging over the REV recovers the homogeneous input value:

$$\langle \epsilon_{ij} \rangle = \frac{1}{V}\int_V \epsilon_{ij}(x_k,\xi)dV = \epsilon_{ij}^{\text{hom}}(\xi). \tag{14}$$

Thus, we measure

1. the homogenized shear modulus of a trial at fixed ξ by setting $\epsilon_{12}^{\text{hom}} = \epsilon_0$ (ϵ_0 being a constant reference strain) to obtain

$$G^{\text{hom}} = \frac{\langle \sigma_{12} \rangle}{2\epsilon_0} = \frac{\langle \sigma_{21} \rangle}{2\epsilon_0}. \tag{15}$$

2. and the homogenized bulk modulus by setting $\epsilon_{ij}^{\text{hom}} = \epsilon_0 \delta_{ij}$ and

$$K^{\text{hom}} = \frac{\langle \sigma_{kk} \rangle}{4\epsilon_0}. \tag{16}$$

Results for the evolution of the bulk modulus are plotted in function of t and ξ in Figs. 3(a) and (b), respectively. As is to be expected, simulations run at high T create more homogeneous nucleation and promote percolation at lower ξ. Whereas the the stiffening of the bulk modulus K^{hom} seems to plateau as a function of $\tilde{t}$, it shows a linear relation in function of ξ. Conversely, experimental micrometer scale indentation measurements have shown a ~ln(ξ) dependence of the stiffening (Hoover & Ulm 2015). Geometry may explain this discrepancy: i) Precipitation into three-dimensional, as opposed to two-dimensional, volumes leads to an earlier onset of the percolation of the solid network, causing more rapid initial gains in K^{hom}, and ii) for the same volume fraction of the source phase, more contact points exist between clinker grains in a 3D vs. 2D geometry. On the other hand, one should remark that strength measurements at different ξ and T reported in (Bentur,

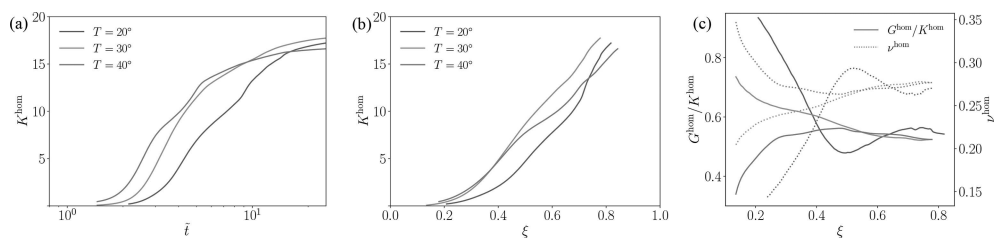

Figure 6. Plots of (a) the homogenized bulk modulus as a function of time and (b) hydration degree for varying temperatures $T = \{20°C, 30°C, 40°C,\}$ The right most figure shows (c) the homogenized shear-to-bulk modulus ratio (left, primary axis) and the Poisson's ratio (right, secondary axis) in function of ξ.

Berger, Kung, Milestone, & Young 1979) show similarity to the linear trend in the elasticity reported here. Additionally, both cases show a slower onset of the mechanical performance for paste's cured at lower T, which eventually exceeds the high T values at later ξ.

Finally, Fig. 3(c) compares the shear modulus to the bulk modulus, from which the Poisson's ratio ν^{hom} is defined; considering a drained specimen, values are only measurable beyond the percolation threshold ξ_0 $\left(K^{\text{hom}} = G^{\text{hom}} = 0 \text{ for } \xi < \xi_0\right)$. Interestingly, the plot indicates that the trend in ν^{hom} depends on temperature, and as a consequence, on how homogeneously the nucleation and growth proceeds in the REV. More porous microstructures (at the scale of the REV) tend to have lower ν^{hom}. For instance, the self-consistent scheme used in (Bernard et al. 2003) to upscale the elasticity to the cement paste scale shows that the compressibility of water plays an important role in predicting the trend of ν^{hom} at early ages. All simulations converge onto a final value of $\nu^{\text{hom}} \approx 0.27$.

5 CONCLUSIONS AND OUTLOOK

The current proceeding has displayed just a glimpse of the promise phase-field models possess in simulating the reaction kinetics and upscaling the mechanical properties of cement paste. In the preceding pages, a solution model for the Gibbs free energy of the C-S-H packing density was introduced, whereby the dissolution and precipitation processes were advanced by a reaction model similar to that pioneered by Allen and Cahn (Allen & Cahn 1979). By use of three sample simulations run at different temperatures, the model exhibited an ability to evolve the paste's microtexture and mechanics in time. Herein, enhanced temperatures play an important role in accelerating the reaction rates, coarsening the microstructure, and diminishing the late stage elasticity.

It is noted that much stands to be improved in the design of the reaction-diffusion model thus proposed. Further efforts to calibrate model parameters to experimental observations and/or define them from physics-based expressions can greatly assist in the predictive power of the model; for instance, additional connections to studies of cement paste at the nanometer scale should be made (Ioannidou, Krakowiak, Bauchy, Hoover, Masoero, Yip, Ulm, Levitz, Pellenq, & Del Gado 2016, Bonnaud, Labbez, Miura, Suzuki, Miyamoto, Hatakeyama, Miyamoto, & Van Vliet 2016, Masoero, Del Gado, Pellenq, Ulm, & Yip 2012).. Additionally, the current template allows additional field variables to be defined (*e.g.*, multiple ion concentrations, the calcium hydroxide phase) to enhance its fidelity w.r.t. the cement material, and realistic insights will demand fully three-dimensional simulations. And, of course, the technique is not limited to the micrometer scale: At the nanometer scale cement paste might be treated as a driven, open system (Bazant 2017). With these and other challenges still outstanding, the authors look forward to progressing phase-field models in the future to better describe cement paste's mechanical behavior across scales.

REFERENCES

Acker, P. et al. (2001). Micromechanical analysis of creep and shrinkage mechanisms. *Creep, Shrinkage and Durability Mechanics of Concrete and other quasibrittle Materials, Cambridge, MA,* 15–25.

Allen, S.M. & J.W. Cahn (1979). A microscopic theory for antiphase boundary motion and its application to antiphase domain coarsening. *Acta Metallurgica 27*(6), 1085–1095.

Aranson, I., V. Kalatsky, & V. Vinokur (2000). Continuum field description of crack propagation. *Physical review letters 85*(1), 118.

Bauchy, M., H. Laubie, M.A. Qomi, C. Hoover, F.-J. Ulm, & R.-M. Pellenq (2015). Fracture toughness of calcium–silicate–hydrate from molecular dynamics simulations. *Journal of Non-Crystalline Solids 419*, 58–64.

Bazant, M.Z. (2017). Thermodynamic stability of driven open systems and control of phase separation by electro-autocatalysis. *Faraday Discussions.*

Bentur, A. (1980). Effect of curing temperature on the pore structure of tricalcium silicate pastes. *Journal of colloid and interface science 74*(2), 549–560.

Bentur, A., R.L. Berger, J.H. Kung, N. Milestone, & J. Young (1979). Structural properties of calcium silicate pastes: Ii, effect of curing temperature. *Journal of the American Ceramic Society 62*(7–8), 362–366.

Bernard, O., F.-J. Ulm, & E. Lemarchand (2003). A multiscale micromechanics-hydration model for the earlyage elastic properties of cement-based materials. *Cement and Concrete Research 33*(9), 1293–1309.

Bonnaud, P.A., C. Labbez, R. Miura, A. Suzuki, N. Miyamoto, N. Hatakeyama, A. Miyamoto, & K.J. Van Vliet (2016). Interaction grand potential between calcium–silicate–hydrate nanoparticles at the molecular level. *Nanoscale 8*(7), 4160–4172.

Chen, L.-Q. (2002). Phase-field models for microstructure evolution. *Annual review of materials research 32*(1), 113–140.

Constantinides, G. & F.-J. Ulm (2004). The effect of two types of csh on the elasticity of cement-based materials: Results from nanoindentation and micromechanical modeling. *Cement and concrete research 34*(1), 67–80.

Feldman, R.F. & P.J. Sereda (1968). A model for hydrated portland cement paste as deduced from sorption-length change and mechanical properties. *Materials and structures 1*(6), 509–520.

Flory, P.J. (1953). *Principles of polymer chemistry*. Cornell University Press.
Gallucci, E., X. Zhang, & K. Scrivener (2013). Effect of temperature on the microstructure of calcium silicate hydrate (csh). *Cement and Concrete Research 53,* 185–195.
Hoover, C.G. & F.-J. Ulm (2015). Experimental chemo-mechanics of early-age fracture properties of cement paste. *Cement and Concrete Research 75,* 42–52.
Huggins, M.L. (1941). Solutions of long chain compounds. *The Journal of chemical physics 9*(5), 440–440.
In *Journal Proceedings,* Volume 43, pp. 101–132.
Ioannidou, K., K.J. Krakowiak, M. Bauchy, C.G. Hoover, E. Masoero, S. Yip, F.-J. Ulm, P. Levitz, R.J.-M. Pellenq, & E. Del Gado (2016). Mesoscale texture of cement hydrates. *Proceedings of the National Academy of Sciences 113*(8), 2029–2034.
Jennings, H.M. (2000a). A model for the microstructure of calcium silicate hydrate in cement paste. *Cement and Concrete Research 30*(1), 101–116.
Jennings, H.M. (2000b). A model for the microstructure of calcium silicate hydrate in cement paste. *Cement and concrete research 30*(1), 101–116.
Masoero, E., E. Del Gado, R.-M. Pellenq, F.-J. Ulm, & S. Yip (2012). Nanostructure and nanomechanics of cement: polydisperse colloidal packing. *Physical review letters 109*(15), 155503.
Petersen, T., P.-L. Valdenaire, R. Pellenq, & F.-J. Ulm (2017). A reaction model for cement solidification: Evolving the c-s-h packing density at the micrometer scale. *submitted.*
Plassard, C., E. Lesniewska, I. Pochard, & A. Nonat (2005). Nanoscale experimental investigation of particle interactions at the origin of the cohesion of cement. *Langmuir 21*(16), 7263–7270.
Powers, T.C. & T.L. Brownyard (1946). Studies of the physical properties of hardened portland cement paste.
Torquato, S. (2013). *Random heterogeneous materials: microstructure and macroscopic properties,* Volume 16. Springer Science & Business Media.
Trappe, V., V. Prasad, L. Cipelletti, P. Segre, & D.A.Weitz (2001). Jamming phase diagram for attractive particles. *Nature 411*(6839), 772–775.
Waals, J. v. (1894). van der: Arch. neerl. 28, 121 (1893); or. *Z. Phys. Chem 13,* 657.
Zaoui, A. (2002). Continuum micromechanics: survey. *Journal of Engineering Mechanics 128*(8), 808–816.

APPENDIX A

The variational derivatives of Eq. (1) w.r.t. the packing density ϕ and the order parameter ψ (also known as Euler-Lagrange equations) are written as

$$\frac{\Delta_r G_\phi}{RT} = \frac{1}{\rho_\phi}\left\{\frac{\partial g_\phi}{\partial \phi} - \vec{\nabla}\cdot\frac{\partial g_\phi}{\partial \vec{\nabla}\phi}\right\} \tag{17}$$

$$\frac{\Delta_r G_\psi}{RT} = \frac{1}{\rho_\phi}\left\{\frac{\partial g_\psi}{\partial \psi} - \vec{\nabla}\cdot\frac{\partial g_\psi}{\partial \vec{\nabla}\psi}\right\}. \tag{17b}$$

Table 1. Model parameters; $\tilde{x}$ indicates the variables non-dimensionalized value; k_ϕ and k_ψ are the reaction rate coefficients of the precipitation and dissolution rates, respectively.

Parameter	Value
$\tilde{t} = k_\phi t$	—
$\tilde{\vec{\nabla}} = L\vec{\nabla}$	—
$\tilde{\kappa}_\phi = \kappa_\phi / \rho_\phi L^2 RT$	0.38
$\tilde{\kappa}_\psi = \kappa_\psi / \rho_\psi L^2 RT$	2.0
$\tilde{E}_p = E_p / RT$	$-1.0\ln(\tilde{c})$
$\tilde{E}_d = E_d / RT$	$2.0\ln(\tilde{c})$
$\tilde{\Omega} = \Omega / RT$	$5.0\tilde{c} + 1.6$
$\tilde{W} = W / RT$	0.32
k_ϕ / k_ψ	0.05

Computational Modelling of Concrete Structures – Meschke, Pichler & Rots (Eds)
© 2018 Taylor & Francis Group, London, ISBN 978-1-138-74117-1

Towards a mesoscale model of geopolymers: Interaction potential from the molecular scale

F. Lolli & E. Masoero
School of Engineering, Newcastle University, Newcastle upon Tyne, UK

ABSTRACT: Geopolymers are alumino-silicate hydrates obtained by reaction of an alumino-silicate source (e.g. metakaolin or fly ash) with alkali solution. Geopolymer-based binders are less environmentally impacting than ordinary cement, but their implementation in the construction field is still limited and requires a better understanding of the nanoscale origin of their mechanical properties. This understanding can be advanced with new simulations based on interaction-driven aggregation of nanoparticles, similar to what has happened in the last decade in the field of traditional cement science. This paper introduces a pathway to develop such a model starting from recent molecular models of geopolymers, which allow to compute the interaction potentials needed for the larger mesoscale. Interaction potential parameters are presented in this work as a function of different particle sizes, targeting experimentally-observed ranges of particle sizes and porosity. Overall, this work opens new opportunities to understand the linkage between mesostructure and engineering properties of geopolymers, with the aim of supporting their commercialisation as alternative cements and, in this way, contributing to the development of a greener economy.

1 INTRODUCTION

Geopolymers are synthesised mixing alumino-silicate precursors (e.g. metakaolin, GGBS or fly ash) with highly alkaline solution, usually based on sodium or potassium. The alkali cations in solution (the focus in this work will be on sodium, e.g. Na^{+}) balance the anions of the raw material and start the geopolymerisation with a first dissolution of Si and Al atoms from the source material. The geopolymerisation process continues with two other main stages: reorganization and poly-condensation. The final result is a porous material with cementitius properties (Duxson et al. 2007). The macroscale mechanical properties of geopolymers are governed by the sodium-alumino silicate gel (N-A-S-H) formed during the geopolimerisation. The N-A-S-H is a cohesive matrix that can be modelled as an aggregate of nanoparticles and mesopores (viz. pores with characteristic size between 2 and 50 nm, Rouquerol et al. 1994). These heterogeneities have a primary role for the development of mechanical properties at the macroscale and this has already been shown by various authors working on the mesoscale modelling of ordinary cement hydrates (Masoero et al. 2012, Ioannidou et al. 2016, Yu and Lau 2015). Furthermore mesopores are crucial in controlling the interaction between the material and water in the environment, with key implications for transport properties and durability (Pinson et al. 2015).

A popular class of mesoscale models, in the field of modelling cementitious binders, is based on the aggregation of mechanically interacting nanoparticles. The key input of these simulations are the effective interaction potentials between particles, to be obtained from atomistic simulations at the smaller molecular scale (Bonnaud et al. 2016). These interactions are functions U(r) of potential energy, depending on the distance between nanoparticles (r), or otherwise defined in terms of interaction force $F(r) = -dU(r)=dr$. A pathway to compute such U(r) interactions is to start from stress-strain curves derived from molecular simulations of solid phases subjected to deformation. This approach has been followed in the field of traditional cement science (Masoero et al. 2012), where effective interaction potentials obtained from the stress-strain response of molecular models at the nanometre scale (Pellenq et al. 2009 and Manzano et al. 2013) have led to realistic predictions of mechanical properties at the larger mesoscale of *ca*. 500 nm. In the field of alkali activate materials the only mesoscale model to date has been developed by Yang and White (2016). In this model the coarsegrained units represent individual molecules rather than nanoparticles and the focus is on simulating the sequence of chemical reactions during polimerisation rather than on capturing mechanical properties. Nanoparticle-based simulation of geopolymer mechanics are still to be developed, especially because effective interactions

U(r), as well as the molecularscale inputs required for them, are still missing.

This paper introduces a methodology to derive effective interactions potentials and to obtain model structures for N-A-S-H geopolymers at the mesoscale between the nanometre and the micrometre. The NA-S-H gel is represented as an aggregate of nanoparticles randomly added to an initially empty simulation box using an efficient space filling algorithm. The effective interaction potential chosen is a modified Lennard-Jones which allows to model particles polydispersity, and which is parametrised from stressstrain curves derived from new molecular simulations of geopolymer mechanics.

2 METHODOLOGY

2.1 *Mesoscale model construction*

The mesoscale model is developed using the software LAMMPS (Plimpton 1995). The starting point is an empty simulation box of predefined dimensions, in which particles are added randomly. The range of possible particle sizes is chosen to be consistent with experimental results described in Section 3.1. The process to construct the model structures, such as the one in Fig. 1 a., is the following:

1. Particles with various diameters are added in groups of many hundreds at a time: this differs and turns out to be computationally more efficient than other space-filling algorithms where particles are added one at a time (Masoero et al. 2014, Ioannidou et al. 2014).
2. Each filling step is followed by energy minimization using the conjugate gradient method (Polak-Ribiere version) implemented in LAMMPS (Plimpton 1995); particle interactions are explained in Section 2.2.
3. When the system is sufficiently dense to display mechanical stability, the configuration is further stabilised by applying a pre-compressive stress to the box, followed by energy minimisation. The stress is then released by expanding the simulation box until zero pressure is recovered.
4. The entire process (partial space filling, compression, and relaxation back to zero pressure) is repeated until the desired packing density is obtained.

2.2 *Interaction potentials between particles*

The functional form of the effective interactions between nanoparticles is assumed to be a particle-sizedependent generalised Lennard-Jones (Mie potential, Avendano et al. 2011), developed by Masoero et al. (2014) to simulate the mesoscale mechanics of calcium silicate hydrates:

$$U_{ij}(r_{ij}) = 4 \in (\sigma_i, \sigma_j)\left[\left(\frac{\bar{\sigma}_{ij}}{r_{ij}}\right)^{2\alpha} - \left(\frac{\bar{\sigma}_{ij}}{r_{ij}}\right)^{\alpha}\right] \quad (1)$$

$U_{ij}(r_{ij})$ is the potential energy of an interaction between two particles i and j at a distance r_{ij} from one another and with diameters σ_i and σ_j. The depth of the energy well is governed by the parameter $\in(\sigma_i, \sigma_j)$ and α determines the narrowness of the energy well. $\bar{\sigma}_{ij}$ is the average diameter of the two particles. Shear forces are not transferred between particles. Following the same calculation explained by Masoero et al. (2014) and adapted to the results obtained with a molecular model of geopolymers (see Section 2.3) it is possible to identify:

$$\in(\sigma_i, \sigma_j) = f(\alpha) M \beta_{ij}(\sigma_i, \sigma_j) \bar{\sigma}_{ij}^{3} \quad (2)$$

where M is the indentation modulus, *viz*. the initial slope of the axial stress versus axial strain graph

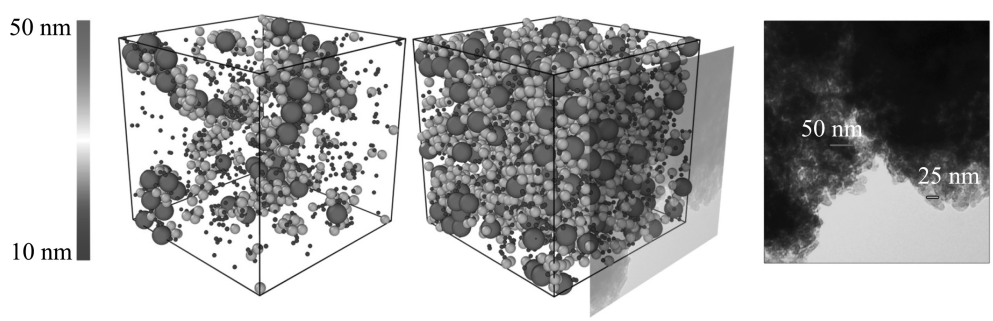

Figure 1. a) Snapshots of the packing process. b) Transmission Election Microscope micrograph of geopolymer metakaolin paste.

Table 1. Interaction potential parameters depending on the particle size.

M		σ_i	σ_j	$\overline{\sigma_{ij}}$	$\in(\sigma_i, \sigma_j)$
GPa	α	Å	Å	Å	eV
75.18	6	50	50	50	1,035
75.18	6	50	100	75	3,107
75.18	6	50	500	275	56,973
75.18	6	50	1000	525	217,536
75.18	6	100	100	100	8,287
75.18	6	100	500	300	124,306
75.18	6	100	1000	550	455,790
75.18	6	500	500	500	1,035,888
75.18	6	500	1000	750	3,107,665

obtained at the molecular scale, when the simulation box is not allowed to contract nor expand in the directions perpendicular to the direction of loading (see Section 2.3). β is a corrective factor for the different size of the two interacting particles. $f(\alpha)$ is a numerical constant that depends on the mapping between interaction potential and linear elastic properties (Masoero et al. 2014). α is calculated considering the ultimate strain obtained with the same stress-strain curve from the molecular scale and applying Eq. 3.

$$\in_{ult} = \frac{\sqrt[\alpha]{\frac{4\alpha+2}{\alpha+1}} + \sqrt[\alpha]{2}}{\sqrt[\alpha]{2}} \tag{3}$$

Therefore, the potential in Eq. 1 is entirely determined by two molecular-scale mechanical parameters only: $\in_{ult}$ and M.

2.3 *Reference mechanical parameters from the molecular model*

At the molecular scale geopolymers are constituted by sodium-aluminate-silicate hydrate (N-A-S-H), characterized by a nanocrystalline network embedded in an amorphous alumino-silicate gel (Provis, Lukey, & van Deventer 2005). This definition finds its origin in experimental evidence showing features typical of both amorphous and crystalline structures. XRay diffraction (XRD) of metakaolin geopolymers is characterised by a broad hump corresponding to $2\theta = 25°$ to $35°$ which is typical of amorphous materials, but the same experiment identifies also crystalline zeolites peaks corresponding to sodalite and faujasite (Fernández-Jiménez et al. 2008). In the X-ray pair distribution function the amorphous region is identified with broad peaks beyond 5 Å r-correlation function (White et al. 2013), but at shorter distance higher peaks are typical of crystalline domains. A molecular model that could be used to extract mechanical properties and inform the mesoscale potential in Eq. 1 has been developed only very recently by Sadat et al. (2016). This model, however, assumes a fully amorphous molecular structure of geopolymer and therefore, in this paper, another reference molecular structure is used in order to compute mechanical properties. This structure, recently developed by the authors of the present paper (details in a separate paper, currently under preparation), is intermediate between crystalline and amorphous and built by introducing defects into a crystalline structure of the sodalite type. Two different structures are developed, with Si:Al molar ratios of 1.5 and 2. The desired Si:Al ratio is obtained starting from a Si-only defective sodalite framework and substituting Si with Al while respecting the Lowenstein's rule and avoiding the formation of edge-sharing O-Si-O or O-Al-O tetrahedra. Na atoms and water molecules are packed randomly using Packmol (Martinez et al. 2009) applying periodic conditions in all three directions. The resulting structures respect charge neutrality: Na cations balance Al negative charges and Al tetrahedra are linked to four Si tetrahedra (Davidovits 1991). The fully polymerised defective structures are then analysed and subjected to large-strain tensile test to obtain stress-strain curves shown in Section 3 using LAMMPS (Plimpton 1995). During the simulation, each deformation step imposes an extension of 1% of the length in one direction, until rupture. From these tests it has been possible to calculate the indentation modulus (M) and the strain at failure $\in_{ult}$ required to parametrise the mesoscale potential, as per Section 2.2.

3 RESULTS

3.1 *Definition of the particle size distribution*

Geopolymers are widely described as mesoporous materials (Provis et al. 2015, Duxson et al. 2006), *viz*. materials with pore diameters between 2 and 50 nm as per IUPAC classification. Benavent et al. (2016) analysed the pore structure of geopolymers with different techniques, such as small-angle X-ray scattering, BET and MIP. Results describe a mean pore size between 5 and 15 nm, with a mesoporous network mainly open with only 1.2% to 2.7% of closed porosity, depending on the type of activator used. On the same line Kriven et al. (2004) studied the geopolymer gel with Transmission Electron Microscopy (TEM) identifying particles and pores in the order of 5 to 10 nm. Fig. 1b. shows a TEM micrograph of a metakaolin geopolymer paste in which it is possible to distinguish the amorphous geopolymer matrix with a grain size ranging between 10 and 50 nm. Therefore the N-A-S-H gel can be described as an aggregate of

nanoparticles ranging from 5 to 50 nm with a mesoporous network ranging from 2 to 50 nm.

3.2 *Mechanical parameters at the molecular scale*

Fig. 2 shows the stress—strain curves obtained from the molecular model of the defective structures with Si:Al 1.5 and 2. The mechanical behaviour displayed is similar for both structures with a ductile rupture, *i.e.* the tensile stress doesn't present a sudden drop after reaching its maximum value (strength). The ultimate tensile strain, *viz.* the strain corresponding to the maximum tensile stress, defined as a reference to calculate the parameter α is $\in_{ult} = 11.47\%$. The indentation modulus M is 75.18 GPa for the structure with Si:Al = 2.

3.3 *Interaction potential parameters*

Table 1 collects interaction potential parameters for different particle sizes identified as most characteristic for the mesoscale model (from 5 to 100 nm). $\alpha = 6$ leads to $f(\alpha) = 0.0154$. Fig. 3 illustrates two

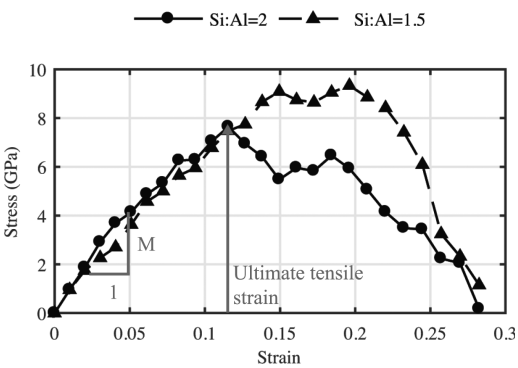

Figure 2. Stress strain graphs for two molecular structure with different Si:Al ratio.

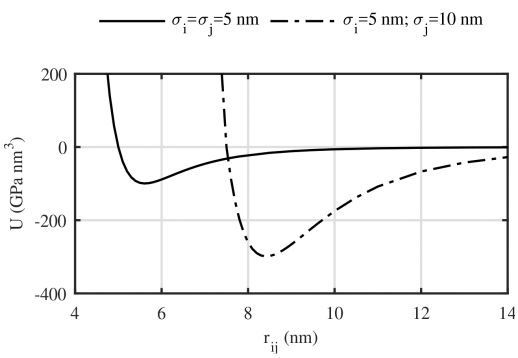

Figure 3. Interaction potential between two particles with same diameter of 5 nm and between two particles with different sizes.

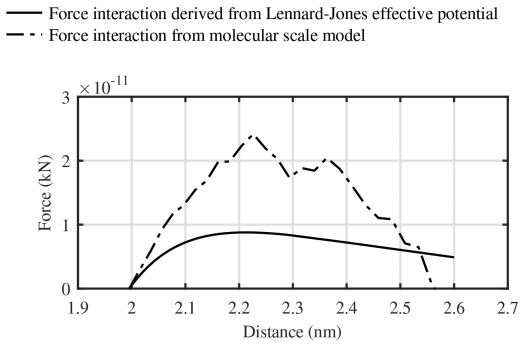

Figure 4. Force distance relationship obtained from the molecular model with Si:Al = 2 and from the derivative of the effective interaction potential.

curves for interaction potential between particles with same size and with different size. The depth of the potential well for particles with same size is lower than for particles with different size. This is due to the fact that the depth correlates to the strength of the interaction and a deeper potential well indicates that more energy is required in order to deform the structure. Fig. 4 compared the effective forces computed as the derivative of the Lennard-Jones potential in Eq. 1, and the integral of the stress-strain graph at the molecular scale over the contact area between two particles with diameter of 2 nm. The figure shows that the initial slope of the force-displacement curve, which is related to the indentation modulus M, is indeed well captured by the generalised Lennard-Jones functional form in Eq. 1. Also the interparticle distance corresponding to the maximum interaction force, which is related to the strain at failure $\in_{ult}$, is well captured. On the other hand, the effective Lennard-Jones potential underestimates force over most of the interaction range, hence the functional form in Eq. 1 may not be the optimum one to describe the mechanical interactions in a nanoparticle-based model of geopolymer. This indicates that the Lennard-Jones potential is not the optimum solution for this fitting. A possible alternative could be to develop a suitable effective potential in LAMMPS, obtained by directly tabulating the interaction force and energy as a function of interparticle distance obtained from the molecular simulations.

4 CONCLUSIONS

In this work a first polydisperse mesoscale model of geopolymers is presented. This model is based on mechanical properties obtained at the molecular scale. The effective pair interaction potentials are computed between particles ranging from 5 to

100 nm, with particle size distribution based on experimental results at different scales. It is also shown that a generalized Lennard-Jones functional form of the interaction potential captures some key features of the mechanics at the molecular scale, but it would also significantly underestimate the interaction forces at the mesoscale. By linking molecular scale mechanics with mesoscale structure and properties, the proposed model allows investigating the role of particle size distributions and different packing densities for a range of Si:Al molar ratios, types of activators, and water contents. The effective interactions presented here create the conditions to simulate for the first time the mechanical behavior of geopolymer binders at the mesoscale, with the aim of providing fundamental informations on the failure mechanism and deformations of these materials.

REFERENCES

Avendano, C., T. Lafitte, A. Galindo, C.S. Adjiman, G. Jackson, & E.A. Muller (2011). Saft-γ force field for the simulation of molecular fluids. 1. a single-site coarse grained model of carbon dioxide. *The Journal of Physical Chemistry B 115*(38), 11154–11169.

Benavent, V., F. Frizon, & A. Poulesquen (2016). Effect of composition and aging on the porous structure of metakaolin based geopolymers. *Journal of Applied Crystallography 49*(6), 2116–2128.

Bonnaud, P.A., C. Labbez, R. Miura, A. Suzuki, N. Miyamoto, N. Hatakeyama, A. Miyamoto, & K.J. Van Vliet (2016). Interaction grand potential between calcium-silicate-hydrate nanoparticles at the molecular level. *Nanoscale 8*, 4160–4172.

Davidovits, J. (1991). Geopolymers. *Journal of thermal analysis 37*(8), 1633–1656.

Duxson, P., A. Fernández-Jiménez, J.L. Provis, G.C. Lukey, A. Palomo, & J.S.J. van Deventer (2007). Geopolymer technology: the current state of the art. *Journal of Materials Science 42*(9), 2917–2933.

Duxson, P., G.C. Lukey, & J.S.J. van Deventer (2006). Evolution of gel structure during thermal processing of nageopolymer gels. *Langmuir 22*(21), 8750–8757.

Fernández-Jiménez, A., M. Monzó, M. Vicent, A. Barba, & A. Palomo (2008). Alkaline activation of metakaolin and fly ash mixtures: Obtain of zeoceramics and zeocements. *Microporous and Mesoporous Materials 108*(13), 41–49.

Ioannidou, K., K.J. Krakowiak, M. Bauchy, C.G. Hoover, E. Masoero, S. Yip, F.J. Ulm, P. Levitz, R. J.M. Pellenq, & E. Del Gado (2016). Mesoscale texture of cement hydrates. *Proceedings of the National Academy of Sciences 113*(8), 2029–2034.

Ioannidou, K., R.J.M. Pellenq, & E. Del Gado (2014). Controlling local packing and growth in calcium-silicate-hydrate gels. *Soft Matter 10*, 1121–1133.

Kriven, W.M., M. Gordon, & J.L. Bell (2004). Geopolymers: Nanoparticulate, nanoporous ceramics made under ambient conditions. *Microscopy and Microanalysis 10*(S02), 404–405.

Manzano, H., E. Masoero, I. Lopez-Arbeloa, & H.M. Jennings (2013). Shear deformations in calcium silicate hydrates. *Soft Matter 9*(30), 7333–7341.

Martinez, L., R. Andrade, E. Birgin, & J. Martinez (2009). Packmol: A package for building initial configurations for molecular dynamics simulations. *Journal Of Computational Chemistry 30*(13), 2157–2164.

Masoero, E., E. Del Gado, R.J.M. Pellenq, F.J. Ulm, & S. Yip (2012, Oct). Nanostructure and nanomechanics of cement: Polydisperse colloidal packing. *Phys. Rev. Lett. 109*, 155503.

Masoero, E., E. Del Gado, R.J.M. Pellenq, S. Yip, & F.-J. Ulm (2014). Nano-scale mechanics of colloidal c-s-h gels. *Soft Matter 10*, 491–499.

Masoero, E., H.M. Jennings, F.J. Ulm, E. Del Gado, H. Manzano, R.J.M. Pellenq, & S. Yip (2014). Modelling cement at fundamental scales: From atoms to engineering strength and durability. In *Computational Modelling of Concrete Structures, Vol 1*.

Pellenq, R.J.M., A. Kushima, R. Shahsavari, K.J. Van Vliet, M.J. Buehler, S. Yip, & F.J. Ulm (2009). A realistic molecular model of cement hydrates. *Proceedings of the National Academy of Sciences 106*(38), 16102–16107.

Pinson, M.B., E. Masoero, P.A. Bonnaud, H. Manzano, Q. Ji, S. Yip, J.J. Thomas, M.Z. Bazant, K.J. Van Vliet, & H.M. Jennings (2015). Hysteresis from multiscale porosity: Modeling water sorption and shrinkage in cement paste. *Phys. Rev. Applied 3*, 064009.

Plimpton, S. (1995). Fast parallel algorithms for short-range molecular dynamics. *Journal of Computational Physics 117*, 1–19.

Provis, J.L., G.C. Lukey, & J.S.J. van Deventer (2005). Do geopolymers actually contain nanocrystalline zeolites? a reexamination of existing results. *Chemistry of Materials 17*(12), 3075–3085.

Provis, J.L., A. Palomo, & C. Shi (2015). Advances in understanding alkali-activated materials. *Cement and Concrete Research 78, Part A*, 110–125.

Rouquerol, J., D. Avnir, C.W. Fairbridge, D.H. Everett, J.M. Haynes, N. Pernicone, J.D.F. Ramsay, K.S.W. Sing, & K.K. Unger (1994). Recommendations for the characterization of porous solids (technical report).

Sadat, M.R., S. Bringuier, A. Asaduzzaman, K. Muralidharan, & L. Zhang (2016). A molecular dynamics study of the role of molecular water on the structure and mechanics of amorphous geopolymer binders. *The Journal of Chemical Physics 145*(13), 134706.

White, C.E., K. Page, N.J. Henson, & J.L. Provis (2013). In situ synchrotron x-ray pair distribution function analysis of the early stages of gel formation in metakaolin-based geopolymers. *Applied Clay Science 73*, 17–25.

Yang, K. & C.E. White (2016). Modeling the formation of alkali aluminosilicate gels at the mesoscale using coarse-grained monte carlo. *Langmuir 32*(44), 11580–11590.

Yu, Z. & D. Lau (2015). Nano- and mesoscale modeling of cement matrix. *Nanoscale Research Letters 10*(1), 1–6.



Taylor & Francis
Taylor & Francis Group
http://taylorandfrancis.com

Computational Modelling of Concrete Structures – Meschke, Pichler & Rots (Eds)
© 2018 Taylor & Francis Group, London, ISBN 978-1-138-74117-1

Nanoscale simulations of cement hydrates precipitation mechanisms: Impact on macroscopic self-desiccation and water sorption isotherms

E. Masoero & I. Shvab
School of Engineering, Newcastle University, UK

G. Di Luzio
Dipartimento di Ingegneria Civile e Ambientale, Politecnico di Milano, Milan, Italy

G. Cusatis
Department od Civil and Environmental Engineering, Northwestern University, USA

ABSTRACT: Recent experiments show that the nanoscale morphology of cement hydrates can be tuned *via* solution chemistry and curing conditions. However, it is not known to what an extent a nano-tailored morphology of cement hydrates may translate into improved macroscale properties. This question is addressed here, focussing on water-content-dependent durability properties, in particular self-desiccation and water sorption isotherms. Nanoparticle-based simulations provide the starting point to create model hydrates structures at the micrometre scale, whose formation mechanisms and resulting morphologies depend on solution chemistry and interaction forces at the nanoscale. These nanoscale mechanisms and morphologies are then used to inform a simple model of cement hydration that predicts pore size distribution, water content, internal relative humidity and thus self-desiccation and water sorption isotherms at the macroscale. The results show that the nanoscale morphology of cement hydrates has indeed an important impact on the above-mentioned durability properties, and that hydrates precipitation in current ordinary cements follows a mechanism that is intermediate between the two frequently used models of homogeneous hydrogelation and boundary nucleation and growth.

1 INTRODUCTION

The high environmental impact of cement production, alongside its increasing demand, are challenging the target of an 80% reduction of greenhouse gas emissions by 2050. This is stimulating empirical research on new chemical formulations, but the industrial deployment of new cements is hindered by the uncertainties that surround their largely untested mechanical performance, especially in relation to long-term durability-related processes such as creep and shrinkage. This is in turn stimulating theoretical research on developing models to predict the engineering performance of a cement paste starting only from knowledge of their chemical composition, curing conditions, and environmental exposure during service. These models are necessarily multiscale, aiming to link the nanometre scale of molecular structures and chemical reactions, with the macroscale of engineering properties (Di Luzio and Cusatis 2009, Davie and Masoero 2015, Bažant et al. 2015, Cusatis et al. 2018).

In the multiscale modelling of cement chemo-mechanics, a crucial range of length-scales is the "mesoscale" between 1 nm and 1 μm. These are the length-scales at which the cement hydrates, precipitating from an aqueous solution during hydration, start to organise themselves into a nanoporous structure. The resulting network of nanopores controls largely the macroscopic interaction between cement paste and water, which is critical for the long-term mechanics (Jennings et al. 2013). Experimental research has shown that, depending on solution chemistry and curing conditions, cement hydrates with similar chemical compositions can precipitate into a wide range of sub-micrometre structures with different morphologies and nanopore networks. This hasbeen shown in particular for calcium–silicate–hydrate (C–S–H), which is the main binding phase in portland cement pastes (Tajuelo Rodriguez et al. 2015). The implication is that it may be possible to tune the sub-micrometre structure of cement paste and concrete in order to maximise the engineering

properties at the macroscale. However, this vision can be realised only by: (i) developing new theoretical tools to guide the experiments—these tools should help identify chemical formulations and curing conditions that may lead to the most desirable nanoscale features; (ii) proving that the submicrometre, nanoporous structure of C–S–H and other hydrates actually has a significant impact on the macroscopic properties of a paste.

This paper is divided in two main sections addressing the two challenges mentioned just above. First, results from recent nanoparticle simulations of C–S–H precipitation are presented (Shvab et al. 2017), focussing on two precipitation mechanisms: (i) radial growth of compact, emispherical, mesoporous domains of C–S–H, which is the nanoscale version of the Boundary Nucleation and Growth (BNG) mechanism (Thomas 2007), and (ii) precipitation and aggregation of C–S–H nanoparticles (hydrogelation) (Ioannidou et al. 2014). The mesoscale morphology evolutions resulting from these two different mechanisms are then taken as inputs for a simple model of cement hydration at the macroscale, which predicts the evolution of porosity and self-desiccation in the cement paste (Masoero et al. URev). The results of the combined simulations indicate that the experimentally observed self-desiccation of low-alkali cement pastes can be captured by a nanoscale precipitation mechanism that is intermediate between BNG and hydrogelation. The impact of the different precipitation mechanisms and nanoscale morphologies on the water sorption isotherm is also presented and discussed.

2 METHODS

2.1 *Nanoparticle simulations of precipitation*

In the last decade, simulations of nanoparticle nucleation and aggregation have started to clarify the relationship between mesoscale morphology and experimentally observed structural features and mechanical properties at the sub-micrometre level (González-Teresa et al. 2010, Masoero et al. 2012, Masoero et al. 2013, Masoero et al. 2014, Ioannidou et al. 2016). Only very recently, though, first nanoparticle simulations have been developed where the rates of particle nucleation and dissolution are quantitatively related to the chemical composition of the surrounding aqueous solution and to the mechanical interaction energy between particles (Shvab et al. 2017). These simulations provide a new framework to incorporate key experimental variables, such as solution chemistry and curing conditions, into the nanoparticle simulations. Only several key features of such simulations will be presented here, in order to let the reader appreciate the origin of the nanoscale morphologies presented later. The interested reader can find more details in (Shvab et al. 2017).

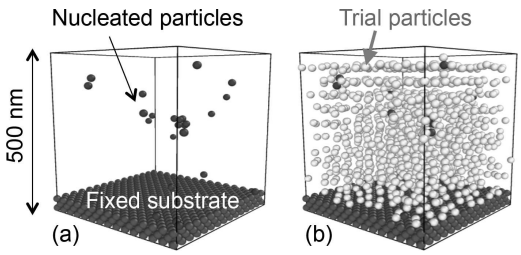

Figure 1. (a) Nanoparticle simulation box containing a fixed substrate and several nucleated particles. (b) Same configuration with also M trial particles for nucleation visualized.

The simulations in (Shvab et al. 2017) are based on the Kinetic Monte Carlo (KMC) method. The starting configuration is an empty simulation box, of characteristic size of *ca.* 500 nm (see Figure 1). The box is periodic in the horizontal plane, closed at the bottom by a disordered layer of nanoparticles representing a surface of tricalcium silicate (C_3S in cement notation, with C = CaO and S = SiO_2), and with a closed fixed boundary at the top. The particles forming the bottom layer are kept fixed during the simulation, *i.e.* they cannot dissolve nor move, but they do interact mechanically with the C–S–H particles that nucleate and aggregate inside the box.

The KMC simulations consist of a series of events, which can be the nucleation of a new C–S–H particle or the deletion of an existing one. The C–S–H particles have fixed diameter of *ca.* 10 nm, with a small polydispersity to avoid crystallisation. The chemistry of the solution is fixed and, for the purpose of this paper, it is entirely described by its supersaturation β with respect to C–S–H precipitation. The simulations presented later will consider two scenarios: one with β fixed in time, and the other with β decreasing with time following a realistic evolution for cement hydration from the literature (Bullard et al. 2015). In reality, the evolution of β is determined by the relative rates of C–S–H precipitation and C_3S dissolution, but here for simplicity $\beta(t)$ is given directly as an input and C_3S dissolution is not simulated: only C–S–H precipitation is considered. The simulations also do not account for: partial growth or dissolution of the C–S–H particles, anisotropy of the C–S–H particles, phases other than C–S–H (for example, calcium hydroxide), or diffusion of ions in solution leading to a spatial field of supersaturation. All these features could be incorporated in the simulations, but for now C–S–H nucleation/deletion will suffice to obtain several mesoscale morphologies to inform a larger-scale hydration model.

At each step, the KMC algorithm selects the next event that takes place from a list of *all* possible C–S–H nucleation and deletion events. Building this list can be tricky. If one considers a generic state with N C–S–H particles already nucleated, then the complete list will certainly include N possible deletion events (each C–S–H particle can be deleted). For the list of possible nucleation events, instead, one should consider the nucleation of a new C–S–H particle in every possible position, and there is an infinity of those. To overcome this problem, one can (Shvab et al. 2017):

1. discretise the simulation box with a rectangular lattice of M sites;
2. place only one trial particle in each lattice site;
3. search for a minimum of interaction energy U between each trial particle and the other N existing particles, by letting the generic trial particle sample different positions only within its lattice cell.

This approach ensures convergence of the overall precipitation mechanisms and precipitation rates, as the lattice spacing is reduced, *viz.* as M is increased (Shvab et al. 2017).

Once the list of N possible deletion event and M possible nucleation events is constructed, the KMC requires that a rate is associated to each of those events. (Shvab et al. 2017) proposed coarse-grained expressions for the rates of particle nucleation and deletion that are based on the assumption of a mechanism of classical growth at the molecular scale. According to this molecular mechanisms, a particle nucleation event implicitly represents a single molecule of C–S–H to which a series of n other molecule attach in all radial directions, until the desired diameter of *ca.* 10 nm, is reached (the opposite for particle deletion). By modelling each of the n molecular reactions with Transition State Theory (Lasaga 2014), the resulting effective rates become:

$$R^{in} = k r_0^* \beta a^2 \left\{ \sum_{i=1}^{n} \exp\left(\chi \frac{\gamma_i \Delta\Omega_{i-1}^{i} + \Delta U_{i-1}^{i}}{k_B T} \right) \right\}^{-1}, \quad (1)$$

$$R^{del} = r_0^* a^2 \left\{ \sum_{i=n}^{1} \exp\left[(1-\chi) \frac{\gamma_i \Delta\Omega_{i}^{i-1} + \Delta U_{i}^{i-1}}{k_B T} \right] \right\}^{-1}, \quad (2)$$

R^{in} and R^{del} are respectively the nucleation and deletion rate of a generic particle. They both depend on:

- r_0^*, which is the intrinsic rate of the basic chemical reaction driving precipitation and dissolution. For the case of C–S–H with calcium-to-silicon ratio of 1, this reaction may be:

$$Ca^{2+} + H_2SiO_4^{2-} + 3H_2O \rightleftharpoons C-S-H; \quad (3)$$

- a, which is characteristic the size of a C–S–H molecule (*ca.* 0.65 nm);
- n, which is the number of C–S–H molecules to be added in a generic radial direction to go from one C–S–H molecules to the radius of a C–S–H nanoparticle (here, *ca.* 5 nm);
- γ, which is the interfacial energy between solid C–S–H and aqueous solution;
- k_BT, which is the product between Boltzmann constant and temperature in Kelvin degrees;
- $\Delta\Omega$, which is the change of particle surface when its radius goes from size n · (i – 1) molecules to size n · i molecules in R^{in}, vice versa in R^{del};
- ΔU, which is the change in total interaction energy in the system caused by the radius of the considered particles increasing or decreasing by one molecule. In (Shvab et al. 2017), this change in energy is simplified and expressed as a direct function of the change in energy caused by inserting or deleting a full particle. Of course, ΔU depends on the spatial locations of a particle, and the process of local minimisation described at point 3 above impact this value in the rates.

Besides these common features, R^{in} also depends on the supersaturation β of the solution and on a prefactor k which is directly proportional to the volume of the lattice cell associated to the trial particle being considered for insertion. Finally the χ factor, which can be between 0 and 1, quantifies how much one should consider the intermediate transition state, between molecules in solution and solid molecule, to be already solid in terms of displaying surface energy and mechanical interactions. Classical Nucleation and Growth Theory (CNGT) assumes $\chi = 1$, hence $\Delta\Omega$ and ΔU matter only for the dissolution rate. However, CNGT is not meant to describe series of chemical reactions, nor it consider explicitly insertion and deletion, but rather the net rates of nucleation given by R^{in} minus R^{del}. If one assume $\chi = 1$ in the KMC simulations proposed here, then particles could form on top of existing ones (because their very unfavourable interaction ΔU would be neglected in R^{in}), but at the very next step the same particle would be immediately deleted due to the very large ΔU in R^{del}. Overall this would result in very inefficient calculations and unphysical kinetics. Therefore, we prefer to use instead an intermediate value of $\chi = 1$, which is analogous to what is usually done in the field of non-Newtonian fluid mechanics (Shvab et al. 2017).

Once the list of rates is known for all N+M possible events, the KMC algorithms selects one event randomly, with a probability that is proportional to its rate. The event is realised, thus a particle is inserted at a specific location or deleted, and the

time is advanced in proportion to the inverse of the cumulative rate of all N+M possible events.

2.2 *Macroscale hydration model*

The nanoscale simulations described in the previous section provide possible morphological evolutions of C–S–H domains, precipitating from solution during cement hydration. The model in this section will take those morphologies as inputs and predict their impact on the macroscopic processes of self-desiccation during cement hydration and water sorption isotherms.

Self-desiccation is the drop of internal relative humidity (iRH) in a cement paste caused by the consumption of water, due to its reaction with Ca and Si to produce C–S–H (eq 3) and calcium hydroxide. Water sorption isotherms instead quantify the amount of absorbed water when the sample is equilibrated with an environment at given relative humidity (RH). Both self-desiccation and sorption isotherms, therefore, involve the relationship between water content and RH. For pores larger than 1–2 nanometres, such relationship can be quantified using the Kelvin equations, which relates the size of the largest saturated pore with the RH.

The model in this section relates the degree of hydration (DOH) of a cement paste with: (i) the amount of consumed water, assuming hydration in sealed conditions; (ii) the total volume of pores in the paste, decreasing with the DOH, and (iii) the evolving pore size distribution. Assuming equilibrium conditions, one can thus compute the size of the largest saturated pore and thus the corresponding internal RH, to predict self-desiccation. Furthermore, at each DOH, one can use the pore size distribution and compute the amount of water that would be adsorbed at each RH between 0 and 1, *viz.* the water sorption isotherm. This section will present only an overview of the most important features of this model. The interested reader will find more details in a dedicated article by the same authors as this one, currently under review (Masoero et al. URev).

The hydration model starts from a statistical description of C_3S grains suspended in water, similar to (Masoero et al. 2014). The solution-filled space between the grains is assumed to be discretised with cylinders of height $D/2$ and diameter D, which represent the capillary pores (see Figure 2). The lateral surface of the cylinders is in contact with C_3S grains, thus the total lateral surface of all cylinders must equal the surface area of the cement paste. The initial size distribution of the capillary pores is entirely described by the size distribution of these cylinders, which can be assumed to be a power-law with many small cylinders, and few large

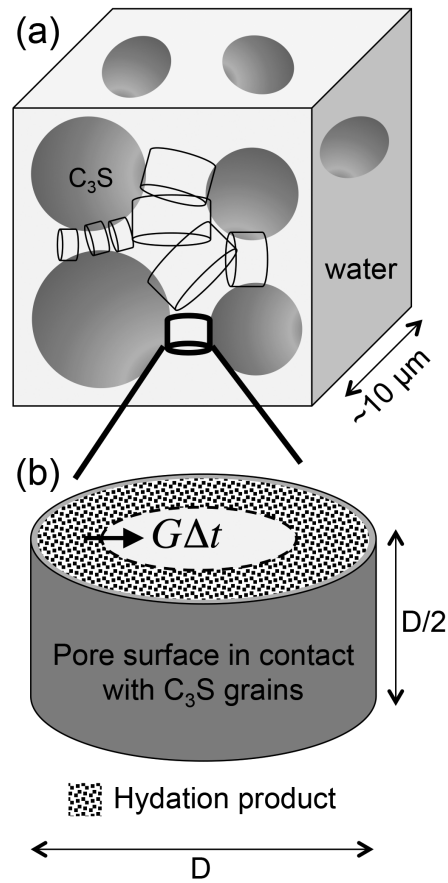

Figure 2. (a) Suspension of cement grains in water, and discretisation of the space between grains using cylinders with different sizes. (b) Formation of hydration product in a pore.

ones, in order to represent flocculation of the C_3S grains. Fixing the minimum and maximum D to reasonable values, *e.g.* $D = 1$ μm as minimum size (a typical resolution of cement hydration models) and $D \approx 10$ μm as maximum size, the cylinder size distribution is fully determined by two variables: the total number of cylinders, and the exponent of the power law. These two variables can be determined in order to match the surface area of the cement grains and the water-to-cement ratio, both of which are typical design variables for a cement paste.

The model always assumes stoichiometric balance between reactants (water and C_3S) and hydration product (C–S–H and calcium hydroxide). The hydration product grows radially starting from the outer surface of each cylindrical pore inward, with a linear growth rate G (see Figure 2b). Upon

increasing the hydration time by Δt, a certain volume of hydration product is produced in each cylinder, depending on its size (small cylinders may get entirely filled with product, stopping precipitation there). This causes a change of capillary pore size distribution over Δt, since the remaining capillary pores are only the inner parts of the partially filled cylinders. The volume of newly formed hydration product can be converted into mass and, by stoichiometric balance, into mass of dissolved C_3S and of consumed water, thus providing the change in DOH as well as the new water content of the paste. However, converting from volume of hydration product into mass requires knowledge of the nanopore volume per unit volume inside the hydration product: this is where the nanoscale morphologies from the previous section are needed as input.

The hydration model allows considering a solid volume fraction (η, complement to 1 of the nanopore volume fraction) that is either fixed and constant in time, or increasing in time from a minimum to a maximum value. Since the above-mentioned change of DOH during Δt depends both on G, on η of the newly formed hydration product and, if densification is assumed, on the change of η of the previously precipitated product, it is possible overall to quantify these parameters and their evolution in time in order to match the experimentally observed hydration rate, *e.g.* measured from calorimetry (Bullard et al. 2011). In this manuscript, however, we will only consider the relationship between DOH and RH (*via* the water content and pore size distribution). In such a case, time is just an internal variable for the simulation to progress, but the actual timescale will not influence the results that depend only on "configuration" and not on time.

The last point to clarify is how the average solid fraction η is related to the size distribution of the nanopores inside the hydration product. In principle, one could measure the pore size distribution directly from the morphologies in the previous section. For now, however, it is sufficient to interpolate and extrapolate pore size distributions that have already been published for homogeneously nucleated particle aggregates with $\eta = 0.33$ and 0.52 (Ioannidou et al. 2016). The details of the interpolation and extrapolation will be given elsewhere (Masoero et al. URev).

Overall, the hydration model outlined here provides a series of DOH and, for each of them, the total volume of capillary pores, the total volume of nanopores in the C–S–H gel, the total volume of water, and the size distributions of both capillary and gel pores. With these data, one can compute self-desiccation and water sorption isotherms as functions of the DOH, for a paste with given water-to-cement ratio and specific surface area of the grains, and for a given nanoscale morphology of the C–S–H.

3 RESULTS

3.1 *High-density and low-density C–S–H morphologies from nanoscale simulations*

Figure 3 shows two different mesoscale mechanisms of precipitation obtained with the nanoparticle-based KMC simulations presented in section 2.1. Both simulations use a pairwise Lennard-Jones interaction potential, with interaction strength ε, which quantifies the amount of energy required to completely separate two particles that were originally in contact.

The BNG mechanism in Figure 3a emerges when: (i) ε is in the order of the solid-solution surface energy γ multiplied by the cross sectional area of a particle, and (ii) the interaction between nucleated particles andparticles forming the substrate is slightly weaker than the interaction between nucleated particles only. Under such conditions, the first particle nucleates on the substrate, whereas subsequent particle nucleate on top of other previously nucleated particles. This leads to the hemispherical growth of a well-packed domain of nanoparticles, which is typical of a BNG mechanism. The local density inside the precipitated domain is always high (random close packing), and not changing during the precipitation process.

The evolution of precipitation rate corresponding to this BNG mechanism is shown in Figure 3b, for two different evolutions of the solution chemistry. In one case, the supersaturation of the solution with respect to C–S–H precipitation, β, is assumed to change in time, following a decreasing trend that is typical of bulk cement solutions (Bullard et al. 2015). In the other case, β is assumed to stay constant in time, which may be a realistic scenario in the vicinity of the interface between unhydrated cement and solution, *viz.* near the substrate in the simulations (Del Gado et al. 2014). Figure 3b shows that a decreasing β leads to an initial acceleration of the precipitation process, followed by deceleration: this is the typical trend of hydration rate expected for ordinary cement pastes (Bullard et al. 2011). By contrast, assuming a constant β leads to an unrealistic rate evolution, with initial acceleration followed by a constant rate.

The homogeneous mechanism in Figure 3c emerges when one considers much weaker interactions compared to the BNG case (approximately 100 times weaker). Under such conditions, the influence of the interaction energy U on the rate is small, and particles tend to nucleate everywhere in the solution, to then aggregate a bit. As a result,

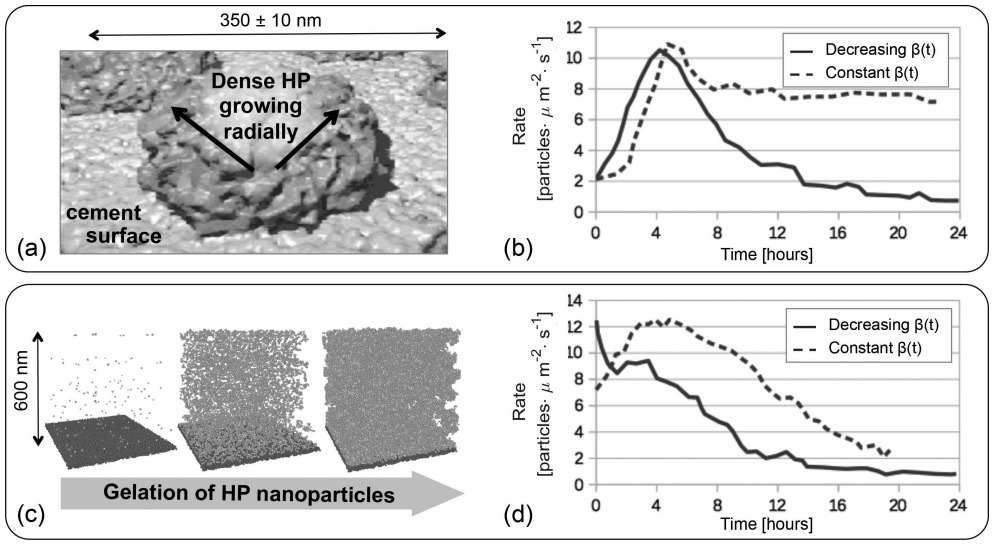

Figure 3. (a) Boundary Nucleation and Growth (BNG) precipitation mechanism, obtained when particle-particle and particle-substrate interactions are strong. (b) Predicted rates corresponding to the BNG mechanism: cases for a solution supersaturation β that decreases with time, as typical for bulk cement solutions, or constant in time. (c) Homogeneous nucleation mechanism, obtained when the interaction forces are weak. (d) Predicted rates corresponding to the homogeneous mechanism, again for decreasing and constant β.

the precipitated domain immediately covers the entire simulation box and the local density, which was always high in the BNG model, is now increasing with time within the precipitated domain. This densification has implications that will be important for the discussion of self-desiccation and sorption isotherms later in this paper.

The precipitation rate corresponding to the homogeneous mechanism is shown in Figure 3d. A β decreasing with time leads to an always-decreasing rate, without initial acceleration, in contrast with the experiments that always show acceleration. This happens because the interaction energy U is small and therefore the nucleation rate in eq 1 is governed by the temporal evolution of β. If β is kept constant, the rate shows some sign of initial acceleration and subsequent deceleration: the initial acceleration in this case is due to the weak aggregation processes that take place homogeneously in the solution. In any case, the homogeneous precipitation mechanism entails that the number of precipitated particles per unit of substrate is proportional to the space available for nucleation in the direction perpendicular to the substrate. In other words, the rate in Figure 3d increases linearly with the height of the simulation box, and this entails a proportionality between rate and water-cement ration that is not observed in the experiments (Shvab et al. 2017). The only way to reconcile the homogeneous "gelation" mechanism with the experimental results is to assume that the precipitation of C–S–H is confined to a limited region near the surface of the cement grain (Del Gado et al. 2014), a so-called "reaction zone" that several authors have quantified in the range of 400 nm to 1 μm (Masoero et al. 2014), consistent with the 600 nm box considered here.

3.2 *Self-desiccation as a function of nanoscale morphology*

Figure 4 shows the self-desiccation predicted by the hydration model in section 2.2. Three mechanisms of nanoscale morphology evolution are considered, and their impact on self-desiccation is compared with an experimental result for a low-alkali cement paste with water-to-cement ratio of 0.4, Blaine fineness (cement surface area) of 400 m^2/g, and hydrating in sealed conditions (Muller et al. 2013, Muller 2014). The considered nanoscale mechanisms are: (i) the BNG mechanism from Figure 3a, modelled by considering that the hydration product in Figure 2b precipitates immediately with solid fraction η = 0.655, constant in time; (ii) the homogeneous (gelation) mechanism in Figure 3c, modelled by considering that hydration product initially forms with very low solid fraction η = 0.01, which increases linearly with time towards a maximum value of 0.74; (iii) a case intermediate between the previous two, *viz.* a BNG

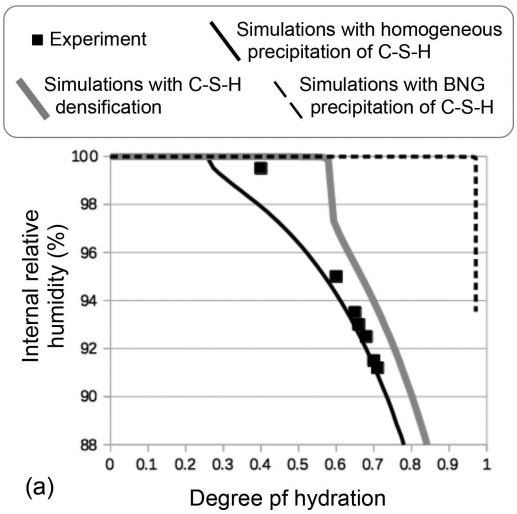

Figure 4. Self-desiccation of a low-aalkali paste hydrating in sealed conditions: comparison between experiment and simulations with different assumptions regarding the precipitation mechanisms of C–S–H at the sub-micrometre scale.

mechanisms where η increases in time from a minimum of 0.195 to a maximum of 0.74. This last mechanisms is indeed suggested by nuclear magnetic resonance measurements of C–S–H density on the same paste as in the self-desiccation experiment (Muller et al. 2013, Muller 2014).

The results in Figure 4 show that the BNG mechanisms largely overestimate the degree of hydration at which the internal relative humidity starts to decrease: *ca.* 0.99 compared to the *ca.* 0.4 from the experiment. The reason is that the Kelvin equation predicts a significant drop of humidity only when pores of *ca.* 100 nm or smaller get desaturated. A large mass of C–S–H in needed before the dense hydration product of the BNG mechanism fills the capillary pores to the extent of leaving only pores smaller than 100 nm saturated.

By contrast, the homogeneous gelation mechanism implies that the whole capillary porosity is immediately filled with a very-low-density hydration product. This product has nevertheless an internal pore network with sub-micrometre average pore size (see Figure 3c). As water is consumed during hydration, some of these small pores are immediately desaturated and, according to Kelvin equation, the internal relative humidity starts to drop at degrees of hydration well below the experimental 0.4. The prediction with this gelation mechanism gets increasingly similar to the experimental data while the degree of hydration increases. This is because at 0.4 degree of hydration, the experimental pastes have most of their capillary pores filled, which is the same conditions described by the gelation mechanism. Thus, from degree of hydration 0.4 onward, the configuration of filled capilary pores with a densifying gel in them, represented by the gelation mechanism, is realistic. On the other hand, the gelation mechanism still entails the issue of predicting a too-early onset of self desiccation and a linear dependnece of the degree of hydration on the water-to-cement ratio (see section 2.1).

The intermediate mechanism (low-density BNG plus densification) leads to results that are indeed intermediate between the homogeneous and BNG mechanisms. The degree of hydration corresponding to the onset of self-desiccation is overestimated compared to the experiment: 0.6 instead of 0.4. However, the issue related to a dependence on the water-to-cement ratio is removed, and overall the prediction of self-desiccation is satisfactory, especially if one considers the uncertainties related to the very simplistic hydration models employed in this work.

3.3 *Water isotherms as functions of nanoscale morphology*

Figure 5 shows water sorption isotherms at two different degrees of hydration (0.1 and 0.75) for simulations with the three mechanisms of nanoscale precipitation already discussed in relation to the self-desiccation results in Figure 4. In all cases, the isotherms show an increase of absorbed water with increasing degree of hydration for RH ≤ 0.99, whereas a closer look at Figure 5 shows that the final absorbed water at RH = 1 decreases with increasing degree of hydration. The reason for these trends is that the Kelvin equation associates the water adsorbed at RH ≤ 0.99 with pore diameter of *ca.* 100 nm or less, which are mainly

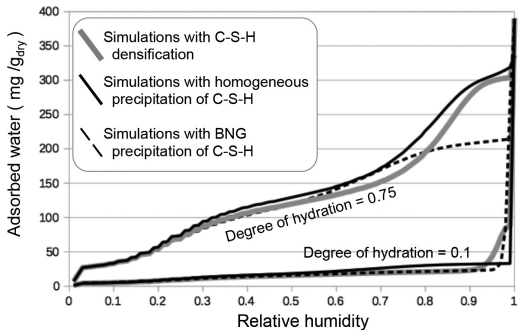

Figure 5. Water sorption isotherms for model cement pastes whose hydration has been simulated using different assumptions regarding the nanoscale mechanisms of C–S–H precipitation.

inside the C–S–H gel. An increasing degree of hydration corresponds to an increasing volume of C–S–H in the paste, and therefore to an increasing amount of water adsorbed in its pores. Vice versa, the water adsorbed at RH = 1 accounts for all the pores in the system: leftover capillary pores plus nanopores inside the C–S–H. An increasing degree of hydration causes the filling of some capillary pores, thus the maximum volume of water that can be adsorbed in the capillary plus the nano pores decreases overall.

For the BNG mechanism in Figure 5, the solid volume fraction of the C–S–H domains and the nanopore volume fraction in the C–S–H not change with time. This dense C–S–H has only small pores, smaller than the particle diameter of 10 nm because the particles are closely packed: as a result the isotherm has a clear finite slope only at RH between 0.2 and 0.7, which the Kelvin equation associates to pore sizes between 1 and 10 nm. The isotherm is then almost flat for RH > 0.8, which is unrealistic because experimental water sorption isotherms always display a finite slope also for RH>0.8 (Baroghel-Bouny 2007).

The homogeneous gelation mechanism and the densification mechanisms yield instead similar and more realistic results, in that both contain a wide range of pore sizes within the C–S–H between the nanometre and the micrometre, which evolve during hydration. This suggest that a gel densification mechanisms is necessary in order to predict realistic water sorption isotherms and related pore size distributions.

4 CONCLUSION

Nanoparticle-based simulations have indicated two different mechanisms of C–S–H precipitation: a homogeneus nucleation and growth (gelation) leading to a low density but densifying morphology, and a boundary nucleation and growth (BNG) leading to a high density hemispherical morphoology. These two mechanisms have been employed in simple macroscale simulations of cement hydration, which provide the evolution of water content and pore size distribution in the paste as hydration progresses.

The results show that the nanoscale morphology of the C–S–H has a significant impact on self-desiccation and water sorption isotherms. In particular, the BNG mechanism predicts no self desiccation until an unrealistically high degree of hydration is reached. The homogeneous gelation mechanism instead predicts realistic self-desiccation at sufficiently large degrees of hydration, *ca.* 0.4 and above, but has two shortfalls: firstly, it predicts an early onset of self-desiccation at too low degree of hydration (*ca.* 0.25 instead of the experimental 0.4), secondly, it entails proportionality between degree of hydration and water to cement ratio, also not recorded in the experiments. The results thus point to an intermediate mechanism, with the C–S–H forming initially at low density but following the heterogeneous nucleation of BNG, and then densifying in time in a similar manner as observed in the homogeneous gelation mechanisms. This intermediate mechanism, informed by experimentally measured evolutions of C–S–H density during hydration and implemented in a simple hydration model, realistically predicts both self-desiccation and water sorption isotherms.

Overall, these results indicate that: (i) macroscopic simulators of cement hydration should account for the nanoscale morphology and precipitation mechanisms of the hydration products; (ii) the nanoscale mechanisms and morphology of the C–S–H may be tuned to nanoengineer the interaction between cement paste and water, with potential for improving our control on the durability of concrete.

REFERENCES

Baroghel-Bouny, V. (2007). Water vapour sorption experiments on hardened cementitious materials: part I: essential tool for analysis of hygral behaviour and its relation to pore structure. *Cem. Concr. Res*. 37(3), 414–437.

Bažant, Z., A. Donmez, E. Masoero, & S.R. Aghdam (2015). Interaction of concrete creep, shrinkage and swelling with water, hydration, and damage: Nano-macro-chemo. In *CONCREEP 10*, pp. 1–12.

Bullard, J.W., H.M. Jennings, R.A. Livingston, A. Nonat, G.W. Scherer, J.S. Schweitzer, K.L. Scrivener, & J.J. Thomas (2011). Mechanisms of cement hydration. *Cem. Concr. Res. 41*, 1208–1223.

Bullard, J.W., G.W. Scherer, & J.J. Thomas (2015). Time dependent driving forces and the kinetics of tricalcium silicate hydration. *Cement and Concrete Research 74*, 26–34.

Cusatis, G., M. Pathirage, G. Di Luzio, E. Masoero, & D. Bentz (2018). A multiscale framework for the prediction of concrete hygral, thermal, and mechanical properties. In *Computational Modelling of Concrete and Concrete Structures*.

Davie, C. & E. Masoero (2015). Modelling damage from the nano-scale up. In *CONCREEP 10*, pp. 613–620.

Del Gado, E., K. Ioannidou, E. Masoero, A. Baronnet, R.-M. Pellenq, F.-J. Ulm, & S. Yip (2014). A soft matter in construction–statistical physics approach to formation and mechanics of c–s–h gels in cement. *The European Physical Journal Special Topics 223*(11), 2285–2295.

Di Luzio, G. & G. Cusatis (2009). Hygro-thermo-chemical modelling of high performance concrete. i: Theory. *Cement and Concrete composites 31*(5), 301–308.

González-Teresa, R., V. Morales-Florez, H. Manzano, & J. Dolado (2010). Structural models of randomly

packed Tobermorite-like spherical particles: A simple computational approach. *Materiales de Construcción 60*(298), 7–15.

Ioannidou, K., K.J. Krakowiak, M. Bauchy, C.G. Hoover, E. Masoero, S. Yip, F.-J. Ulm, P. Levitz, R.J.-M. Pellenq, & E. Del Gado (2016). Mesoscale texture of cement hydrates. *Proceedings of the National Academy of Sciences 113*(8), 2029–2034.

Ioannidou, K., R.J.-M. Pellenq, & E. Del Gado (2014). Controlling local packing and growth in calcium–silicate–hydrate gels. *Soft Matter*, 1121–1133.

Jennings, H.M., E. Masoero, M.B. Pinson, E.G. Strekalova, P.A. Bonnaud, H. Manzano, Q. Ji, J.J. Thomas, R.J.-M. Pellenq, F.-J. Ulm, et al. (2013). Water isotherms, shrinkage and creep of cement paste: hypotheses, models and experiments. In *Mechanics and Physics of Creep, Shrinkage, and Durability of Concrete: A Tribute to Zdeňek P. Bažant*, pp. 134–141.

Lasaga, A.C. (2014). *Kinetic theory in the earth sciences*. Princeton University Press.

Masoero, E., G. Cusatis, & G. Di Luzio (URev). CSH gel densification: the impact of the nanoscale on self desiccation and sorption isotherms.

Masoero, E., E. Del Gado, R.J.-M. Pellenq, F.-J. Ulm, & S. Yip (2012). Nanostructure and nanomechanics of cement: Polydisperse colloidal packing. *Physical Review Letters 109*(15), 155503.

Masoero, E., E. Del Gado, R.J.-M. Pellenq, S. Yip, & F.-J. Ulm (2014). Nano-scale mechanics of colloidal C–S–H gels. *Soft Matter 10*, 491–499.

Masoero, E., H. Manzano, E. Del Gado, R. Pellenq, F. Ulm, & S. Yip (2013). Kinetic simulation of the logarithmic creep of cement. In *Mechanics and Physics of Creep, Shrinkage, and Durability of Concrete: A Tribute to Zdenek P. Bažant*, pp. 166–173. ASCE.

Masoero, E., J.J. Thomas, & H.M. Jennings (2014). A reaction zone hypothesis for the effects of particle size and water-to cement ratio on the early hydration kinetics of C3S. *Journal of the American Ceramic Society 97*(3), 967–975.

Muller, A., K. Scrivener, A. Gajewicz, & P. McDonald (2013). Use of bench-top NMR to measure the density, composition and desorption isotherm of C–S–H in cement paste. *Microporous and Mesoporous Materials 178*(0), 99–103.

Muller, A.C.A. (2014). *Characterization of porosity & CSH in cement pastes by 1H NMR*. Ph.D. thesis, Ecole Polytechnique Federale De Lausanne.

Shvab, I., L. Brochard, H. Manzano, & E. Masoero (2017). Precipitation mechanisms of mesoporous nanoparticle aggregates: off-lattice, coarse-grained, kinetic simulations. *Crystal Growth & Design 17*(3), 1316–1327.

Tajuelo Rodriguez, E., I. Richardson, L. Black, E. Boehm- Courjault, A. Nonat, & J. Skibsted (2015). Composition, silicate anion structure and morphology of calcium silicate hydrates (csh) synthesised by silica-lime reaction and by controlled hydration of tricalcium silicate (c3 s). *Advances in Applied Ceramics 114*(7), 362–371.

Thomas, J.J. (2007). A new approach to modeling the nucleation and growth kinetics of tricalcium silicate hydration. *J. Am. Ceram. Soc 90*, 3282–3288.



Taylor & Francis
Taylor & Francis Group
http://taylorandfrancis.com

Computational Modelling of Concrete Structures – Meschke, Pichler & Rots (Eds)
© 2018 Taylor & Francis Group, London, ISBN 978-1-138-74117-1

Atomistic modeling of early hydration of C_3S

K.M. Salah Uddin & B. Middendorf
Department of Structural Materials and Construction Chemistry, University of Kassel, Kassel, Germany

ABSTRACT: Hydration mechanism, especially early hydration of cement clinkers at atomistic scale are not fully understood yet due to limitations of experimental techniques. Within the last decade computational methods have been expanded to the description of cementitious materials. Reactive force field ReaxFF has shown great potential and allowed to study the hydration mechanism at atomistic scale. In this work we use ReaxFF coupled with metadynamics to understand the early hydration of C_3S as well as insight the dissolution pathways of calcium from different surfaces of C_3S at different temperature (RT and 50°C). We explain the reactivity of (100) surface is higher compare to the (001) surfaces of C_3S from calculated free energy surfaces as a function of selected collective variable (distance). In addition, we show the reaction path for the dimerization of silicate in pore solution at different temperature.

1 INTRODUCTION

Concrete is the world's most used construction material due to its durability, versatility and relatively low cost. Cement is one of the key ingredients of concrete, which is composed of mainly a solid mixture of different clinker phases. Tricalcium silicate (C_3S, alite, Ca_3SiO_5) is the major constituent and relatively most reactive phases compare to other clinker phases in ordinary Portland cement (Hewlett, 2003). Therefore, many experimental studies have been done in order to investigate the hydration mechanism by using tricalcium silicate (C_3S) as a model system. Hydration of cement is a complex reaction and it is very difficult to monitor the reaction in the material interface at nanoscale by experiments. Calcium silicate hydrate (CSH) is the main hydration product responsible for strength development of concrete (Richardson, 2004). Therefore, the hydration mechanism, especially early hydration at atomistic scale are not fully understood yet. Atomistic simulation using Reactive Force Fields, i.e. ReaxFF, can be an effective solution to study the chemical reactions at material interfaces with sufficient accuracy. ReaxFF has been successfully implemented in order to describe the chemical reactions of hydrocarbons (Van Duin et al., 2001) metal oxides (Si/SiO_2) (Fogarty et al., 2010), metal hydrides (Cheung et al., 2005), polymer chemistry (Chenoweth et al., 2005) and many other systems. Typically, molecular dynamic simulation using ReaxFF requires femtosecond (i.e. 10^{-15} seconds) time steps in order to get correct integration of equations of motion. Though ReaxFF is time efficient method, sometimes it becomes computationally expensive during the calculation of interesting event (i.e. transition state) which often takes place at larger timescale. To minimize the simulation cost a large variety of methods have been implemented over the last few years. Metadynamics (metaD) is one of the powerful algorithms that can accelerate observing the rare events by introducing a biased potential that acts on a selected number of degrees of freedom named as collective variables (CVs) (Barducci et al., 2011). MetaD is able to enhance the sampling by reconstructing the free energy surfaces (FES). The bias potential is applied as a sum of Gaussians continuously growing during MD simulation by acting directly on the microscopic coordinates of the system (Bonomi et al., 2009). Therefore, ReaxFF coupled with metaD is an ideal combination to calculate the reaction path with reasonable computing times. Hydration of cement involves dissolution, the reaction in pore solution and precipitation. Manjano et al. have explained the absorption of water on the C_3S surfaces successfully by using ReaxFF (Manzano et al., 2015). Unfortunately, the authors lacked to study the reaction pathways for the dissolution of calcium and the polymerization of silicate during hydration which is not elucidated yet.

In this work, a multistep approach has been taken in order to get a clear picture about the reactivity of different surfaces of C_3S from the dissolution of calcium. First, we allowed the hydration of both (100) and (001) surfaces of C_3S for 600 picoseconds. Later on, both pre-hydrated surfaces were used to study the dissolution mechanism of calcium by using ReaxFF coupled with metaD. Afterwards, the reactivity of both surfaces was compared with the dissolution profile (free energy surface) of calcium. Polymerization of silicate is the key reaction

for CSH formation. Therefore, the dimerization mechanism of silicate in pore solution at different temperature (RT and 50°C) were elucidated using the combination of ReaxFF and metaD.

2 COMPUTATIONAL DETAILS

Even though quantum chemistry (QC) methods, like density functional theory (DFT), has been applied to calculate the geometry and vibrational energy for the small molecules with high accuracy, it is not practically applicable to study the molecular dynamics of the larger molecules. Therefore, well-parameterized force field theory can easily predict many dynamic properties of the large molecules such as force, geometry, the heat of formation, charge, conformational energy differences etc. Nevertheless, those conventional force field theories cannot describe the chemical reaction. Only Brenner FF theory is able to describe bond breaking but the van der Waals and Coulomb interactions are not considered in this theory (Brenner, 1990). On the other hand, the Bond Energy Bond Order (BEBO) method has been applied mainly describe the proton transfer reaction, however, it is limited to explain the complex reaction.

The reactive force field theory (ReaxFF) has successfully employed in order to describe the chemical reaction with sufficient accuracy. It is able to describe both bond formation and bond breaking applying the binding contributions by forces as a function of bond order. ReaxFF has been applied in cementitious systems by merging the two parameter sets (Si-O-H and Ca-O-H) developed independently by Fogarty et al. (Fogarty et al., 2010) and Manzano et al. (Manzano et al., 2012), respectively. This combined parameter set yields excellent results for the investigation of mechanical properties of amorphous, crystalline CSH (calcium silicate hydrate) and the hydration mechanism of C_3S (Manzano et al., 2015).

The computer simulations were carried out by using reactive force field theory (ReaxFF) in LAAMPS (Large-scale Atomic/Molecular Massively Parallel Simulator) platform. The latest version of LAMMPS is very efficient in parallel computing and it uses a special decomposition technique where the simulation domain is partitioned to the 3D small domain and the atoms are distributed equally to the all processors used for simulation. The equal task for each processor saves simulation time (Plimpton, 1995).

2.1 *Model construction*

The C_3S orthogonal periodic simulation cell $(36.49 \times 34.39 \times 37.06) \times 10^{-30}$ m^3 composed of 3240 atoms was constructed by Avogadro. The geometry has been optimized using energy minimizations with Hessian-free truncated Newton algorithm (hftn) where the cutoff tolerances for energy and force were 4.18×10^{-4} and 4.18×10^{-8} kJ mol^{-1} respectively. Maximum iterations for minimizer were 100. Later on, an additional 2.54×10^{-26} and 2.51×10^{-26} m^3 periodic cell filled with water was added to the both (100) and (001) optimized C_3S surfaces respectively using packmole. The number of water molecule matched a density of 1000 kg m^{-3} with a random distribution. The simulation cells were equilibrated to 298 K and 1 atm for 150 picoseconds with 0.5 femtoseconds time steps using canonical ensemble (nvt) with a Nose–Hoover thermostat, integrating the non-Hamiltonian equations of motion. Subsequently, they were hydrated for 600 picoseconds using Nose–Hoover barostat (npt) with all three diagonal component of the pressure tensor to be coupled together (iso). A periodic boundary condition was applied during the simulation.

The last geometry of both (100) & (001) hydrated (after 600 picoseconds) surfaces of C_3S were taken to calculate the dissolution mechanism of calcium using the combination of metaD and ReaxFF. The metaD simulations are performed by using the PLUMED package (Laio and Gervasio, 2008) as an extension of LAMMPS. It speeds up the simulation using history dependent biased potential. A calcium (Ca-2920 from (100) surface and Ca-1957 from (001) surface) located in between two silicates of the hydrated C_3S surface is selected and a well-tempered metaD scheme was applied in order to remove calcium from surface to pore solution. The distance (collective variable) between the center of mass (COM) and the selected calcium atom is computed by adding biased potential as a Gaussian with frequency 40. Furthermore, Gaussian hills with a height of 6.28 kJ/mol and a full width at half-maximum of 0.2×10^{-10} m are added every 0.02 picoseconds. The metaD coupled with ReaxFF are performed for 500 picoseconds (till converged) with NPT ensemble at temperature 298 K and the energies are averaged over the entire period to compute free energy of dissolution. The dissolution pathways (free energy surface) of calcium are computed for both surfaces of C_3S and compared the surface reactivity by analyzing the activation energy and free energy change (ΔG) during dissolution.

The hydration of C_3S is believed to base upon the dissolution of silicate and Ca ions into the pore solution. In this context, a $(20 \times 20 \times 20) \times 10^{-30}$ m^3 cubic simulation cell filled with water, four calcium atoms and two silicate monomers is constructed by Avogadro and packmol. The calcium atoms were added to encounter the negative charge of silicate

monomers which is required to get a charge neutral simulation cell. In addition, the number of water molecule matched a density of 1000 kg m^{-3} in the simulation cell with random distribution and the Ca/Si ratio is 2. The simulation cell was equilibrated by ReaxFF to 298 K for 100 picoseconds using NVT and additional 100 ps using NPT with 0.5 femtoseconds time steps temperature program. The equilibrated structure was used to study the dimerization of silicate in pore solution using metaD. Total three collective variables (1 coordination number and 2 distances) were used to calculate the dimerization of silicate. The coordination number (number of contacts) of bridging Oxygen with both silicons are computed with neighbor list cut off 5×10^{-10} m. The neighbor list is updated in every 10-time steps in order to achieve faster calculation. In addition, the distance between Si (2) and bridging oxygen as well as leaving Oxygen is computed by adding biased potential as a Gaussian with frequency 40. Furthermore, Gaussian hills with a height of 2.10 kJ/mol and a full width at half-maximum of 0.2×10^{-10} m are added every 0.02 picoseconds. The metaD coupled with ReaxFF are performed for 1 nanosecond (till converged) with NPT ensemble at temperature 298 K and the energies are averaged over the entire period to compute free energy of dimerization.

3 RESULTS AND DISCUSSION

3.1 *Hydration of C_3S*

In order to understand the interaction between C_3S surface and water bulk, we have followed the dynamics of the system for a period of 600 picoseconds at room temperature (298 K) and pressure. The periodic boundary condition was applied to all three directions to avoid unnecessary atom loss during simulation. Hence, when an atom passes one side of the cell, it reappears on the opposite side with the same velocity. A periodic dimension can change in size due to constant pressure boundary conditions. In addition, 0.5 fs (femtosecond) time step were used for entire simulation due to the presence of very small and lighter element hydrogen in the system. The lighter atom usually vibrates so fast and if we increase the time steps the distance between two atoms increases. As ReaxFF consider bond order at a higher distance these atoms considered as a non-bonded which provide wrong results. According to our observation, at the very initial stage, the water molecules interact with the surfaces of C_3S and dissociate to hydroxyl pair by protonating the free oxygen on (100) surface and un-hydrated silicate. Afterwards, the proton transfer (hopping process) from the hydroxyl to inner oxygen by leaving the

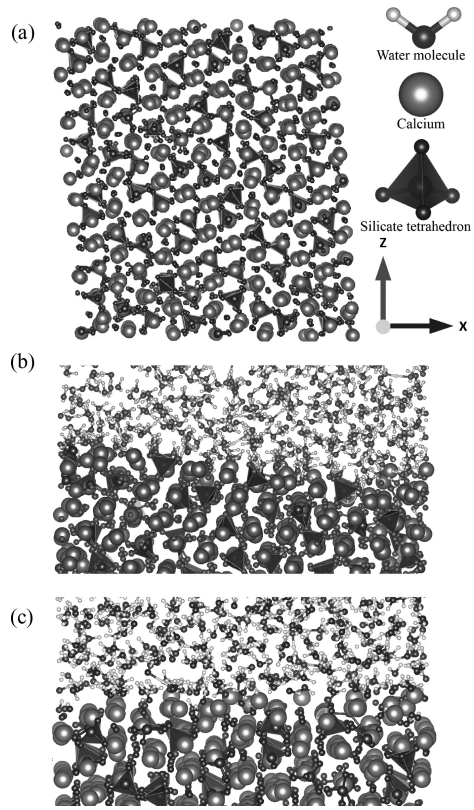

Figure 1. Orthogonal simulation cell of C_3S (a). Comparison of reactivity between the (100) surface along the x-axis (b) and (001) surface along the z-axis (c) during hydration for 600 picoseconds at 298 K.

first oxygen free for further reaction as described by Manzano et al (Manzano et al., 2015). Hydration is carried out only for 600 picoseconds in order to avoid polymerization of silicate.

The hydration of C_3S is exothermic in nature. The clinker (C_3S) surfaces normal to the *x*-axis (Fig. 1b) shows higher reactivity during hydration compared to the surface normal to the *z*-axis (Fig. 1c) due to water tessellation at the z-normal surface which prevents water from penetration into the crystal and the dissolution of calcium ions from the surface. The free oxygen of (100) surface is one of the influential factors for increasing the reactivity compare to (001) surface. This is in good agreement with the results from Manzano *et al.* for a larger system. However, further study is required to get a clear overview about the different reactivity of two different crystalline planes. The dissolution profile of calcium using metadynamics coupled with ReaxFF from both surfaces of C_3S is able to deliver proper explanation about

the reactivity by comparing the total free energy changes during dissolution. Therefore, both hydrated surfaces were used as an input to investigate the reaction path of the dissolution of calcium.

3.2 *Dissolution of calcium from C_3S*

Free energy difference calculations have received a significant importance in molecular dynamics (MD) simulation for a proper understanding of reaction mechanism including transition state.

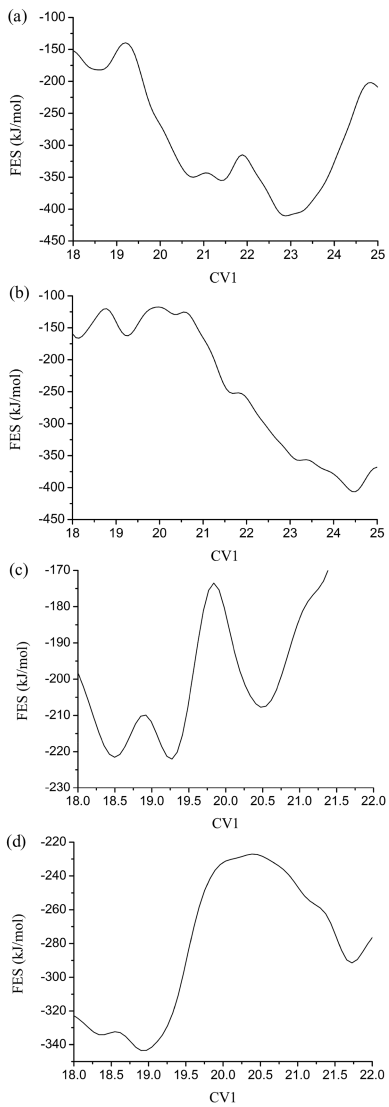

Figure 2. Dissolution mechanism (free energy profile) of Calcium from (100) and (001) surfaces of C_3S at RT (298 K) (a, c) and 50°C (323K) respectively (b, d) (where CV1 is collective variable (distance $\times 10^{-10}$) m).

A straightforward traditional sampling approach is often not possible in order to get FES due to the higher barrier. Well-tempered MetaD is able to force the system to overcome the free energy barriers by selecting the correct collective variable. It offers to control and compute the region of FES that we are interested in. MetaD simulations were performed to investigate the dissolution mechanism of calcium from hydrated (100) and (001) surfaces of C_3S. Figure 2a represents the metaD results for dissolution of calcium from (100) surface of C_3S at 298 K, once using a single collective variable (the difference between the center of mass and Ca-2920 distances). The free energy profile (Fig. 2a) obtain from 500 ps metaD run represents the movement of calcium from between the silicates to on the surface by overcoming the first energy barrier of 46.00 kJ/mol at 19×10^{-10} m. After a small fluctuation, it overcomes the electrostatic interaction with the oxygen of silicate and dissolute completely into the pore solution by passing the energy barrier of 37.60 kJ/mol at 22×10^{-10} m. The total free energy change (ΔG) of −225.90 kJ/mol and −238.50 kJ/mol at 298 K and 323 K respectively have indicated the process is exothermic and thermodynamically favorable. In contrast, complete dissolution of Ca-1957 from (001) surface has required overcoming the barrier of 12.50 kJ/mol at 19×10^{-10} m and 50.30 kJ/mol at 20×10^{-10} m. The total free energy change (ΔG) of +16.70 kJ/mol and +58.50 kJ/mol at 298 K and 323 K respectively. Hence, the dissolution of Ca from (001) plane is endothermic in nature and thermodynamically unfavorable which explains the less reactivity and water tessellation on the (001).

3.3 *Dimerization of silicate in pore solution*

Dimerization of silicate is a condensation reaction and it involved two-step. In the first step, a Si-O-Si bond evolves between two hydrated silicates. A five-fold oxygen coordinated silicon forms intermediately. The second step dimer forms by removing a water molecule (the proton from bridging oxygen is taken by the leaving O-H) to form a stable silicate dimer. Figure 3 compares the free energy profile of dimerization of silicate in water at different temperatures. It proves the exothermal nature of the reaction. The reaction is almost barrier less (2.40 kJ/mol) at 298 K, and the activation barrier increase to 49.70 kJ/mol at a higher temperature (323 K). In addition, the free energy for the reactions are −81.00 kJ/mol and −1.30 kJ/mol at 298 K and 323 K respectively. Hence, we can explain the early hydration where dimerization of silicate is less favorable at a higher temperature. In contrast, the barrier less dimerization of silicate at room temperature indicate the possibility dimer formation in the dormant period during hydration.

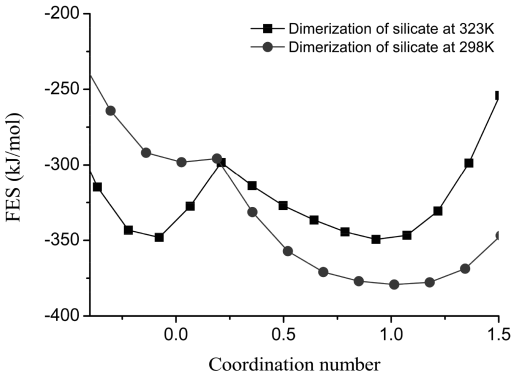

Figure 3. Free energy profile from metaD calculations as a function of reaction coordinates along the reaction path for the dimerization of silicate at 298 K and 323 K.

4 CONCLUSION

Through this work, we have combined the reactive force field and metadynamics to understand the early hydration and dissolution mechanism of calcium of model C_3S. First, we analyzed the reactivity of different surfaces of C_3S. The dissolution mechanism of calcium can be summarized as (100) surface of C_3S is more reactive compared to the (001) surface. In addition, water tessellation process is inhibiting hydration on (001) plane because of the dissolution of Calcium is thermodynamically unfavorable.

The dimerization of silicate in pore solution is involved 5 oxygen coordinated silicon intermediate. Moreover, the barrier less dimerization process at room temperature (Ca/Si is 2) has explained the dimer formation in the dormant period during hydration.

REFERENCES

Barducci, A., Bonomi, M. & Parrinello, M. 2011. Metadynamics. *Wiley Interdisciplinary Reviews: Computational Molecular Science,* 1, 826–843.

Bonomi, M., Branduardi, D., Bussi, G., Camilloni, C., Provasi, D., Raiteri, P., Donadio, D., Marinelli, F., Pietrucci, F. & Broglia, R.A. 2009. Plumed: A portable plugin for free-energy calculations with molecular dynamics. *Computer Physics Communications,* 180, 1961–1972.

Brenner, D.W. 1990. Empirical potential for hydrocarbons for use in simulating the chemical vapor deposition of diamond films. *Physical Review B,* 42, 9458.

Chenoweth, K., Cheung, S., Van Duin, A.C., Goddard, W.A. & Kober, E.M. 2005. Simulations on the thermal decomposition of a poly (dimethylsiloxane) polymer using the ReaxFF reactive force field. *Journal of the American Chemical Society,* 127, 7192–7202.

Cheung, S., Deng, W.-Q., Van Duin, A.C. & Goddard, W.A. 2005. ReaxFFMgH reactive force field for magnesium hydride systems. *The Journal of Physical Chemistry A,* 109, 851–859.

Fogarty, J.C., Akutulga, H.M., Grama, A.Y., Van Duin, A.C. & Pandit, S.A. 2010. A reactive molecular dynamics simulation of the silica-water interface. *The Journal of chemical physics,* 132, 174704.

Hewlett, P. 2003. *Lea's chemistry of cement and concrete*, Butterworth-Heinemann.

Laio, A. & Gervasio, F.L. 2008. Metadynamics: a method to simulate rare events and reconstruct the free energy in biophysics, chemistry and material science. *Reports on Progress in Physics,* 71, 126601.

Manzano, H., Durgun, E., Lopezoo-Arbeloa, I.I. & Grossman, J.C. 2015. Insight on Tricalcium Silicate Hydration and Dissolution Mechanism from Molecular Simulations. *ACS applied materials & interfaces,* 7, 14726–14733.

Manzano, H., Pellenq, R.J., Ulm, F.-J., Buehler, M.J. & Van Duin, A.C. 2012. Hydration of calcium oxide surface predicted by reactive force field molecular dynamics. *Langmuir,* 28, 4187–4197.

Plimpton, S. 1995. Fast parallel algorithms for short-range molecular dynamics. *Journal of computational physics,* 117, 1–19.

Richardson, I. 2004. Tobermorite/jennite- and tobermorite/calcium hydroxide-based models for the structure of CSH: applicability to hardened pastes of tricalcium silicate, β-dicalcium silicate, Portland cement, and blends of Portland cement with blast-furnace slag, metakaolin, or silica fume. *Cement and Concrete Research,* 34, 1733–1777.

Van Duin, A.C., Dasgupta, S., Lorant, F. & Goddard, W.A. 2001. ReaxFF: a reactive force field for hydrocarbons. *The Journal of Physical Chemistry A,* 105, 9396–9409.



Taylor & Francis
Taylor & Francis Group
http://taylorandfrancis.com

Computational Modelling of Concrete Structures – Meschke, Pichler & Rots (Eds)
© 2018 Taylor & Francis Group, London, ISBN 978-1-138-74117-1

Modeling the evolution of C_3S-C_3S grain interface over hydration time

Aleena Alex & Pijush Ghosh
Indian Institute of Technology Madras, India

ABSTRACT: The hydration states of Tricalcium silicate is modeled using the microstructural information obtained from Electron Imaging. The mechanical properties of individual phases determined using Nanoindentation is superimposed to the processed image to obtain the stiffness of individual grain-grain connectivity. This collective stiffness is then used in the Representative Volume Element (RVE) corresponding to the specific state of hydration.

1 INTRODUCTION

Strength of cement largely depends on the formation of Calcium Silicate Hydrate (C-S-H) which imparts cohesive property to the hydrating mix. Cement hydration being a complex phenomenon (Kondo & Udea 1968, Bullard et al. 2011, Scrivener et al. 2011, Scrivener et al. 2015), the hydration of Tricalcium Silicate (C_3S), the major constituent in cement has often been used as an approximation (Pommersheim et al. 1979, Pommersheim et al. 1982, Kumar et al. 2012). Most of these hydration models, which are used to design the performance of cement, have been developed at a larger length scale. Material heterogeneities and porosity at lower length scales have largely been ignored or approximated. However emerging techniques such as high resolution Electron Microscopy and Nanoindentation makes it possible to capture such microstructural and mechanical features at length scales lower than micrometer. Properly exploited, these methods will give us a deeper insight into the complexities of hydration. In this work we employ SEM and Nanoindentation to build a 2-Dimensional C_3S-C_3S grain interface model.

Hydrating C_3S observed via SEM shows the development of radially growing needles of Calcium Silicate Hydrate (outer product C-S-H). Grain interfaces of C_3S are observed as an intertwining network of these C-S-H needles (Thomas et al. 2011). Such needles have been reported to develop for Dicalcium Silicate (C_2S) as well. Nanostructure and nanomechanics of this C-S-H is well researched (Mosoero et al. 2012, Mosoero et al. 2014). However detailed information differentiating the morphology and microstructure of C-S-H formed from C_3S and C_2S is not available. By stopping the hydration at different points of time using solvent exchange method, it is possible to study the growth and development of these interfaces at various stages of C_3S hydration. The final strength of C_3S can be approximated as the cumulative effect of a complex 3-Dimensional network formed by such interfaces. The properties of these interface varies over time primarily due to two reasons: 1) The microstructure of the interface changes because of the formation of denser and longer needles. 2) The mechanical properties changes due to the conversion of High density inner phases to Low Density outer phases.

Grid indentation techniques have been well established to evaluate the mechanical properties of individual phases in hydrated cement (Constantinides et al. 2006, Constantinides et al. 2007, Ulm et al. 2007, Mondal et al. 2007, Hu et al. 2015). However most of these studies have been conducted on fully hydrated cement (after 28 days of hydration). In this work, we use grid indentation and statistical decoupling to evaluate the mechanical properties of partially hydrated C_3S at different stages of hydration (2 day, 7 day, 14 day etc). This is particularly challenging at the early stages of hydration as conventional sample preparation for grid indentation may not be suitable at this stage. Also early stage gelation and mechanical property development is still not very well understood (Ioannidou et al. 2016, Ionnidou et al. 2016).

In this work we try to accommodate the evolution of microstructure and mechanical properties into a single hydration model. The Young's Modulus obtained from Nanoindentation is fitted into a Finite Element model developed from the SEM images of hydrating C_3S interfaces on the corresponding day of hydration. The 2-D Finite Element interface model is then tested under different loading conditions (Tension, Compression etc.) This 2-D model can be extended to a 3-D network model to develop a Representative Volume Element (RVE) for C_3S.

The major objectives of the present work are:

a. Determine the mechanical properties and distribution of volume of different hydrate phases in C_3S over a period of 2 days to 28 days.
b. Develop a Finite Element model of C_3S-C_3S grain interface superimposing mechanical properties determined from Nanoindentation on SEM images of the interface.
c. From the FE model, determine the mechanical strength of C_3S-C_3S grain interface, under tensile and compressive loading.

2 METHODOLOGY

2.1 *Sample preparation and imaging*

Triclinic form of pure Tricalcium silicate was procured from SARL Mineral Research Processing, France. The powder is mixed well with 50% wt. water. The paste is then poured to cylindrical moulds. The moulds are sealed and placed in the dessicator for the required number of days at which the hydration is to be stopped (2 and 14 in this case). Once the desired hydration state is reached, the samples are removed from the mould and cut to slices of 0.5 mm thickness. These slices are further placed in Isopropyl alcohol (IPA) for 3 days. The IPA removes the water from the sample by the principle of solvent exchange, thus stopping further hydration. The samples are then removed and stored in desiccators for further testing.

The samples used for nanoindentation need to be polished before indentation. Since the samples are highly porous, first they are impregnated with epoxy and then polished. Coarse polishing is done using Silicon carbide sheets which bring down the RMS roughness to 500 nm. It is further subjected to fine polishing using diamond spray of particle sizes 6 μm, 3 μm and 1 μm. This gives are very good surface finish with a roughness in the order of 50–100 nm. These samples are used for Nanoindentation and grid indentation is performed. 10 × 10 grids are used and each sample is indented in at least 5 locations. The results of Nanoindentation have been reported in another article (Alex & Ghosh 2017). Nanoindentation results provide information on (a) the individual elastic properties of different phase constituents in hydrating C_3S. Volume fraction of each phase present in the matrix.

The samples before impregnation are used for SEM Imaging. It is observed that C-S-H develops from C_3S as radially developing needles that intertwines with neighboring grains to form a 3D network which imparts mechanical strength to the matrix. The length and density of these interfaces depends on the stage of hydration and it can be quantified by image analysis.

2.2 *Image analysis and processing*

The images are first cropped to contain 2 grains and the interface that is formed between them. Using a suitable threshold the image is converted to a binary form. The matrix generated from the binary image consisting of 1s and 0s in which 1s correspond to the cementitious phases and 0s correspond to the pores. The mechanical properties of individual phases obtained from nanoindentation are distributed to this matrix according to their volume fraction. This matrix of young's modulus values is used in the Finite Element Analysis to determine the stiffness of single grain-grain connectivity (Figure 1).

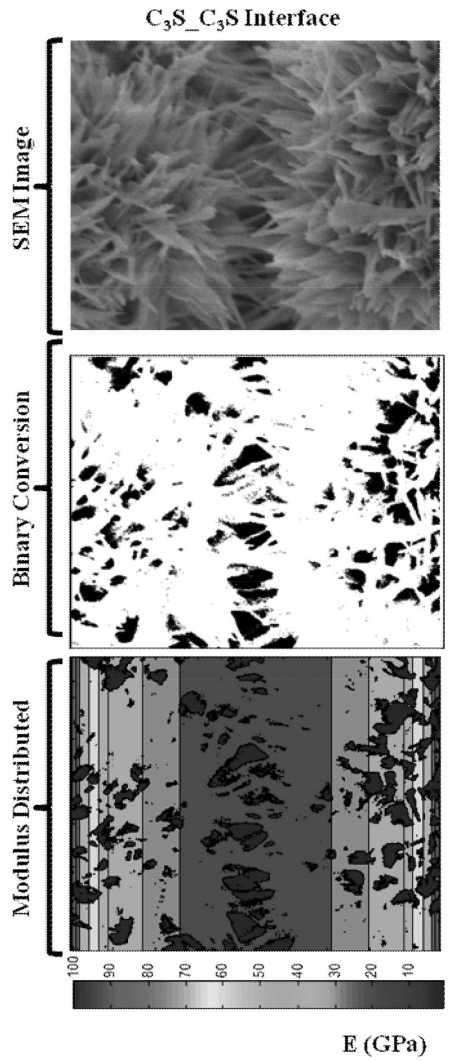

Figure 1. The steps followed for the determination of C_3S-C_3S grain stiffness.

2.3 *Finite element analysis*

Plane stress method is used to construct the global stiffness matrix from the E matrix obtained after the distribution. Poisson's ratio of all phases is assumed to be 0.3. Uniformly distributed tensile load is applied at one end of the system fixing the other end. The displacement at the end is obtained as the mean of the displacement of the end nodes where force was applied. E of the entire system is determined as $E = PL/A\delta$ and the stiffness K is determined as $K = AE/L$ where P is the total end load applied, L is the length of the system, A is the cross sectional area and δ is the mean end displacement.

2.4 *Representative volume element*

Once the individual grain-grain stiffness is determined, these values are used to construct an RVE of balls and springs where the stiffness of spring is obtained from FE Analysis. In this study, the balls are all of equal size, equally spaced and have equal stiffness's. It is subjected to displacement controlled tensile loading. The force along the direction of loading is determined from the summation of individual spring stiffness as $F = \sum K(r\text{-}r_0)$ where r_0 is the equilibrium distance between the grains. The modulus of the RVE is determined from the slope of load vs. displacement plot.

3 RESULTS AND DISCUSSION

3.1 *Interface length and stiffness*

Figure 2 shows the distribution of interface lengths measured from 15–20 images for each state of hydration. In each image of Interface the length is measured at 8–10 different points. It can be seen that for 14 day hydrated sample the distribution averages at 2.2 μm which is 1 μm greater than the distance at 2 day hydrated state. This information can be carried over to the construction of an RVE with randomly distributed grains. In case of 14 day only those grains which are at a distance of 2.2 μm or lower are considered to be connected. This in turn will lead to higher connectivity and higher stiffness to the same initial packing of 14 day hydrated state compared to 2 day hydrated state. However, in this work the RVE considered has not been refined to include this feature as the grains are in equally spaced grid structure. This refinement will be brought in the future works.

After the analysis of all the inter grain connectivity images using the method described in Section 2.2 we obtain a set of values corresponding to the Elastic Modulus (E) and Stiffness (K) of these models. The average and standard deviation of these values are used to construct a normal distribution plot as shown in Figure 3. It is observed

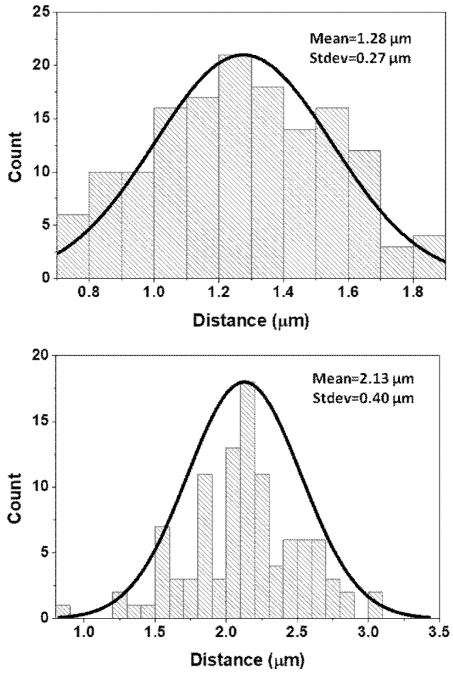

Figure 2. Distribution of C_3S grain-grain connectivity distances for 2 day and 14 day hydrated sample.

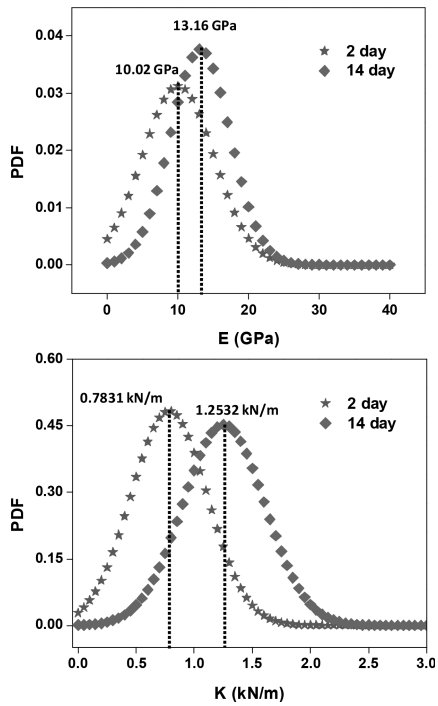

Figure 3. Normal distribution of Elastic Modulus and Stiffness of single grain-grain connectivity.

that both E and K average at higher values for 14 day hydrated sample. This is in spite of the fact that in the modulus value distribution obtained from indentation, the 14 day sample shows a reduction in higher density phases. This shows that the dense and long needles that develop for the 14 day hydrated sample creates an interface with lower porosity leading to the higher mechanical property. For a similarly constructed RVE this higher stiffness value will thus give a higher modulus to the 14 day hydrated state.

The RVE is constructed in a $10 \times 10 \times 10$ grid form with grains at the nodes and each grain is connected to the adjacent one. The spacing between individual grains is taken as 4μm. Supplying the two stiffness values to this system the Elastic Modulus of 2 day hydrated state is obtained as 4.16 GPa and that of 14 day hydrated state is 6.66 GPa. Even though this gives a rough estimate of the modulus value it needs to be further refined to include multiple complexities of the system.

4 CONCLUSION

From the images of grain-grain interfaces at different stages of hydration, it is possible to develop a multi-scale model of hydrating C_3S and determine the mechanical properties. This work successfully determines the stiffness of individual grain-grain connectivity at two states of hydration. The determined stiffness can be incorporated in an RVE to determine the overall Elastic Modulus. However in this work many complexities have not been included in the final RVE. Such finer refinements include incorporating random arrangement of particles and dynamic assignment of connectivity and spring stiffness based on the state of hydration, incorporating particle size distribution etc. This will be pursued in future works.

REFERENCES

Alex, A. & Ghosh. P. 2017. Temporal Evolution of Microstructure, Chemical and Mechanical Properties of Tricalcium Silicate. Proc. *ICACMS. 3–8 September 2017*. Chennai: India.

Bullard, J.W., Jennings, H.M., Livingston, R.A., Nonat, A., Scherer, G.W., Schweitzer, J.S., Scrivener, K.L. & Thomas, J.J. 2011. Mechanisms of cement hydration, *Cem. Concr. Res.*, 41(12): 1208–1223.

Constantinides, G. & Ulm, F.-J. 2007. The nanogranular nature of C–S–H. *J. Mech. Phys. Solids*. 55(1): 64–90.

Constantinides, G., Ravi Chandran, K.S., Ulm, F.J. & Van Vliet, K.J. 2006. Grid indentation analysis of composite microstructure and mechanics: Principles and validation. *Mater. Sci. Eng. A*. 430(1–2): 189–202.

Hu, C. & Li, Z. 2015. A review on the mechanical properties of cement-based materials measured by nanoindentation. *Constr. Build. Mater*. 90: 80–90.

Ioannidou, K., Kanduč, M., Li, L., Frenkel, D., Dobnikar, J. & Del Gado, E. 2016. The crucial effect of early-stage gelation on the mechanical properties of cement hydrates. *Nat. Commun*. 7: 12106.

Ioannidou, K., Krakowiak, K.J., Bauchy, M., Hoover, C.G., Masoero, E., Yip, S., Ulm, F.-J., Levitz, P., Pellenq, R.J.-M. & Del Gado, E. 2016. Mesoscale texture of cement hydrates. *Proc. Natl. Acad. Sci*. 113(8): 2029–2034.

Kondo, R. & Ueda, S. 1968. Kinetics and Mechanisms of the Hydration of Cements. *Proceedings of the Fifth International Symposium on the Chemistry of Cement*, Tokyo: Japan.

Kumar, A., Bishnoi, S. & Scrivener, K.L. 2012. Modelling early age hydration kinetics of alite. *Cem. Concr. Res*. 42(7): 903–918.

Masoero, E., Del Gado, E., Pellenq, R.J.M., Ulm, F.J. & Yip, S. 2012. Nanostructure and nanomechanics of cement: Polydisperse colloidal packing. *Phys. Rev. Lett*. 109(15).

Masoero, E., Jennings, H.M., Ulm, F.J., Del Gado, E., Manzano, H., Pellenq, R.J.M. & Yip, S. 2014. Modelling cement at fundamental scales: From atoms to engineering strength and durability. *Comput. Model. Concr. Struct*. 1: 139–148.

Mondal, P., Shah, S.P. & Marks, L. 2007. Short communication A reliable technique to determine the local mechanical properties at the nanoscale for cementitious materials. *Cem. Concr. Res*. 37: 1440–1444.

Pommersheim, J.M. & Clifton, J.R. 1979. Mathematical modeling of tricalcium silicate hydration. *Cem. Concr. Res*. 9: 765–770.

Pommersheim, J.M., Clifton, J.R. & Frohnsdorff, G. 1982. Mathematical modeling of tricalcium silicate hydration. II. Hydration sub-models and the effect of model parameters. *Cem. Concr. Res*. 12: 765–772.

Scrivener, K.L. & Nonat, A. 2011. Hydration of cementitious materials, present and future. *Cem. Concr. Res*. 41(7): 651–665.

Scrivener, K.L., Juilland, P. & Monteiro, P.J.M. 2015. Advances in understanding hydration of Portland cement. *Cem. Concr. Res*. 78: 38–56.

Thomas, J.J., Biernacki, J.J., Bullard, J.W., Bishnoi, S., Dolado, J.S., Scherer, G.W. & Luttge, A. 2011. Modeling and simulation of cement hydration kinetics and microstructure development. *Cem. Concr. Res*. 41(12): 1257–1278.

Ulm, F.J., Vandamme, M., Bobko, C., Alberto Ortega, J., Tai, K. & Ortiz, C. 2007. Statistical indentation techniques for hydrated nanocomposites: Concrete, bone, and shale. *J. Am. Ceram. Soc*. 90(9): 2677–2692.

Computational Modelling of Concrete Structures – Meschke, Pichler & Rots (Eds)
© 2018 Taylor & Francis Group, London, ISBN 978-1-138-74117-1

Fracture properties of cement hydrates determined from microbending tests and multiscale modeling

J. Němeček, V. Šmilauer, J. Němeček & F. Kolařík
Faculty of Civil Engineering, Czech Technical University, Prague, Czech Republic

J. Maňák
Institute of Physics Academy of Sciences, Prague, Czech Republic

ABSTRACT: The paper shows experimental results received from bending tests performed on micro-beams fabricated with focused ion beam milling. The micro-beams were bent by nanoindenter and load-displacement curves recorded. From that, tensile strength and fracture energy were deduced for individual cement paste constituents at the level of a few micrometers. The tensile strength of the C-S-H rich inner product reached 700 MPa while the supremum of fracture energy was in the range 4–20 J/m^2. The experimentally obtained values served for verification of the multi-scale numerical model that was built for scales starting from C-S-H globules (1–100 nm) to cement paste level (up to 1–100 μm). Simulation of random packing of C-S-H globules reproduced well experimental data, yielding cohesive stress of the globule as 2500 MPa. A weak size effect was found on the scale of C-S-H up to 1000 nm, signalizing high ductility and weak strain localization. Further extension to cement paste was proposed, introducing defects responsible for further strength reduction on scaling.

1 INTRODUCTION

Many material characteristics like elastic modulus, tensile strength or fracture energy belong to basic mechanical properties in fracture mechanics models. Traditionally, the properties are assessed on centimeter to meter sized samples whose dimensions are far above the size of microstructural heterogeneities. Thus, microstructure-based predictions that take microlevel heterogeneity into account need experimentation at a substantially smaller scale, i.e. at the level of micrometers. Moreover, cementitious materials exhibit quasi-brittle behavior on all considered scales. In this paper, we focus our attention to the basic microscopic level of cement paste which spans the range from 1 μm to approximately 100 μm and which forms the binder of all cementitious systems.

First, we introduce a unique experimental method that allows cutting out a micrometer sized cantilever beam using the Focused Ion Beam (FIB) milling technique from a heterogeneous composition of cement paste. High precision geometry of the beams is reached with FIB. The beam is loaded in bending with the help of a nanoindenter and mechanical response is determined. Careful selection of homogeneous-like regions allows assigning results to dominant chemical phases, particularly the inner product and the outer product that are rich of C-S-H and Portlandite (CH) rich regions. From these tests, it is able to determine tensile strength of the individual phases and, in some cases, fracture energy needed to break the cantilever. The experimental part is a stepping stone for the development for up-scaling and down-scaling models for fracture properties.

Thus, at second, we propose a three level numerical model for prediction of cement paste tensile strength. In the down-scaling direction, identification of cohesion of a C-S-H globule was done. Smeared crack model with strain-softening was used in the framework of damage mechanics. In the up-scaling direction, the tensile strength of C-S-H products is described well in accordance with experimental evidence gained on micro-beams. The tensile strength of cement paste is further reduced by internal defects whose size is beyond our experiments as shown at the end of the paper.

2 EXPERIMENTAL PART

2.1 *Samples and material microstructure*

Samples of well hydrated cement paste were prepared from pure Portland cement CEM-I 42,5R with a standard chemical composition given by Table 1. Water to cement ratio used for prepartion of the paste was 0,4. Samples were casted into small cylindrical moulds and stored in water for 7 years, thus the degree of hydration approaches 100%. Then, samples were cut into 5 mm thick

Table 1. Chemical composition of cement.

	CaO	SiO_2	Al_2O_3	Fe_2O_3	MgO	TiO_2
wt.%	63.77	20.51	4.74	3.3	1.05	0
	K_2O	Na_2O	SO_3	MnO	free Ca	
wt.%	0.95	0.15	3.07	0.09	0	

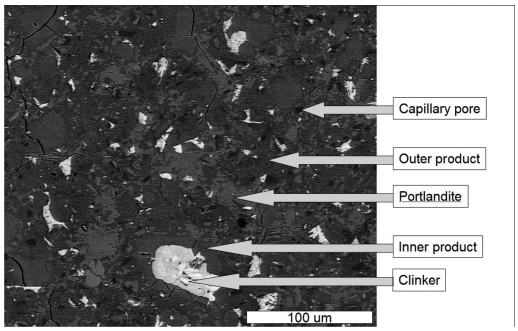

Figure 1. Microstructure of cement paste.

slices and prepared with a metallographic procedure (Němeček, Šmilauer, Polívka, & Jäger 2016) to get a flat and smooth surface with the roughness of several tens of nm. Such sufrace is suitable for nanoindentation and FIB analyses. After polishing samples were stored in an inert gas (argon) to limit carbonation besides testing times when samples were exposed to ambient lab humidity 20–40%.

At the level of hydrates (i.e. below 100 μm) the samples are characterized with a heterogeneous microstructure composing mainly of the inner and outer products that are rich in C-S-H gels and amorphous nano-crystallites of $Ca(OH)_2$, then larger Portlandite crystals and a small portion of unhydrous grains of clinker minerals, see Fig. 1. Also, the capillary porosity with the main pore radii in the level of 10^{-2} –10^{-1} μm as measured by MIP (Němeček, Šmilauer, Polívka, & Jäger 2016) is present at this scale.

2.2 *SEM and FIB*

After polishing samples were scanned and small micro-beams prepared with the FIB technology. FEI Quanta 3D FEG dual beam instrument combining SEM and FIB was used for fabrication of all samples. The FIB technique uses a finely focused beam of gallium ions for precise milling of microscopic samples with various geometries. For our purposes, the sample geometry was chosen to be a cantilever beam of 20 μm length and triangular cross-section with approximate dimensions of 3–4 μm in height and width. The final milling step was done at an accelerating voltage of 30 kV and

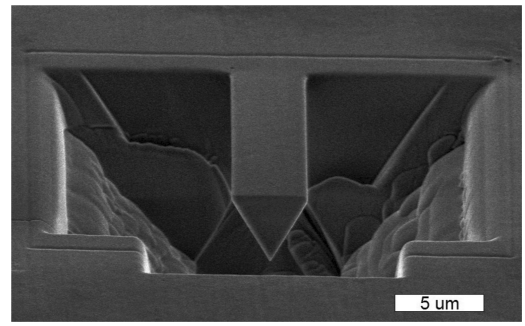

Figure 2. Microbeam fabricated in an outer product.

a current of 1 nA. Details on the fabrication can be found in (Němeček, Šmilauer, Polívka, & Jäger 2016). After FIB milling, the micro-beams were observed by SEM to scan their actual dimensions and position in a particular microscopic phase. An example of the milled beam is shown in Fig. 2.

2.3 *Nanoindentation*

Nanoindenter Hysitron Tribolab-700 system was used for characterization of mechanical response of micro-beams in two ways. First, standard imprints were performed in the vicinity of the beams to reveal elastic properties of the tested phase. Secondly, the indenter was used as a loading tool to bend cantilevers and record the force-displacement diagram in the displacement controlled regime. From the diagrams, both tensile strength f_t and fracture energy G_f^{sup} have been calculated as

$$f_t = \frac{F_{max} L}{I_y} \frac{h}{3} \tag{1}$$

$$G_f^{sup} = \frac{1}{A_f} \int_0^{w_{max}} F dw \tag{2}$$

where F_{max} is the maximum force measured by the nanoindenter, L is the cantilever length, I_y the cross-sectional second moment of inertia, h the height of the triangular beam cross-section, w_{max} is the peak deflection and A_f is the fracture area (i.e. $A_f = \frac{1}{2} bh$ for the triangle). Note that the fracture energy was computed as the supremum estimate based on the assumption that the micro-beam behavior shows neither snap-back nor softening and that the maximum force corresponds to the maximum energy release rate with a limiting stablecrack propagation.

2.4 *Results of microbending tests*

Results of the micro-bending tests as recorded by nanoindenter and recalculated into non-dimensional

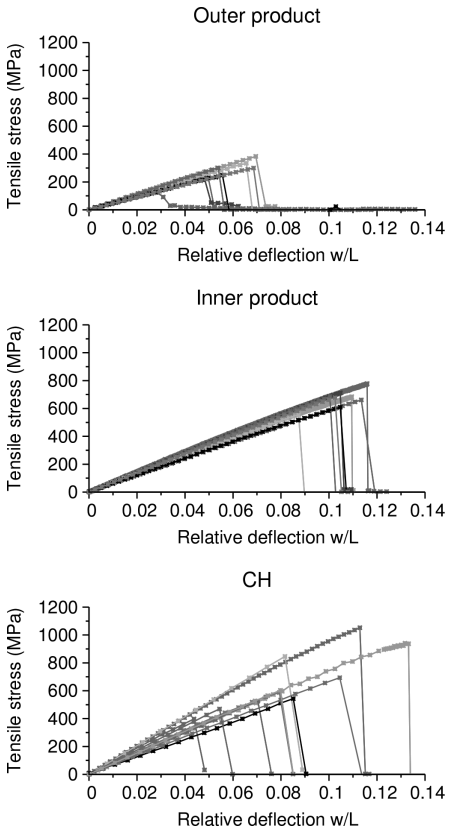

Figure 3. Results of micro-bending tests for individual phases.

stress and relative deflection quantities are shown in Fig. 3. It can be seen in the figure that the beams behave approximately linearly up to the break and the steep brittle fracture like unloading branch. Althought the machine is depth controlled the stability of the post-peak control is not well maintained and must be treated as approximate only. The tensile strength is, therefore, captured well while the fracture energy estimate was calculated as the supremum estimate, Eq. 2. The results agree well with previously obtained results of elastic properties of individual cement paste constituents (Němeček, Králík, & Vondřejc 2013) and also with energy calculations derived from bulk nanoindentation (Němeček, Hrbek, Polívka, & Jäger 2016).

3 MODELING PART

A four-scale fracture model was previously formulated and validated for compressive strength of cement paste with w/c $\in \langle 0.157, 0.68 \rangle$ after approximately 1 day of hydration (Hlobil, Šmilauer, & Chanvillard 2016). The basic assumption of the model was that the tensile failure of C-S-H globules leads to progressive failure on higher scales. At that time, downscaling approach identified apparent uniaxial tensile strength of the C-S-H_{HD} as 107 MPa, which is almost 7 × lower than tensile strength measured from microbending tests.

Recently, a molecular dynamics model of C-S-H gel, formulated as cohesive polydisperse particles, yielded tensile strength as C-S-H_{LD} = 550 MPa and C-S-H_{HD} = 720 MPa (Davie & Masoero 2015). Those values are comparable with microbending tests in Table 2, considering that outer product contains certain portion of capillary porosity. AFM nanoscale investigation of C-S-H cohesion (modified C-S-H_{LD} from alite hydration) yielded 930 MPa, which is again comparable with microbending results (Plassard, Lesniewska, Pochard, & Nonat 2005).

In order to match current C-S-H experimental data with the previous multiscale fracture model, strength scaling needs further improvement. In this regard, we propose three levels, see Figure 4, where each level represents

Table 2. Results from nanoindetation and microbending tests.

	Outer product	Inner product	CH
E	24.9 ± 1.3	33.6 ± 2.0	39.0 ± 7.1
f_t	264.1 ± 73.4	700.2 ± 198.5	655.1 ± 258.3
G_f^{sup}	4.4 ± 1.9	19.7 ± 3.8	19.9 ± 14.4
n.t.	8	8	11

Legend: E = Young's modulus (GPa); f_t = tensile strength (MPa); G_f^{sup} = supremum of fracture energy (J/m^2), n.t. = number of evaluated tests.

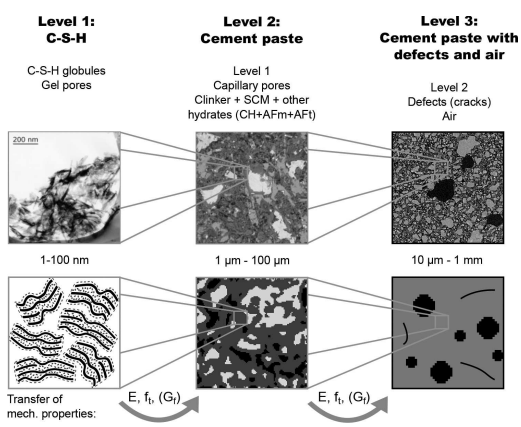

Figure 4. Three-level hierarchical multiscale model. Microstructure images from E. Lachowski, P. Stutzman, D.P. Bentz et al.

- Level 1: CSH. C-S-H globules are intermixed with gel pores
- Level 2: Cement paste. Level 1 acts with capillary porosity, other hydration products, unreacted clinker, unreacted SCMs.
- Level 3: Defects. Level 2 is enriched with defects in the form of cracks and air voids.

3.1 *Material model for compressive and tensile failure*

Material model describing compressive of tensile failure at each level is based on fracture/damage mechanics. Damage mechanics uses the concept of an equivalent strain, $\tilde{\varepsilon}$, as a descriptor of damage evolution. Damage becomes initiated when the equivalent strain, $\tilde{\varepsilon}$, exceeds strain at the onset of cracking, $\varepsilon_0 = f_t/E$, where E is the elastic modulus. The Rankine criterion for tensile failure defines $\tilde{\varepsilon}$ as

$$\tilde{\varepsilon} = \frac{\sigma_1}{E},\ \sigma_1 > 0 \tag{3}$$

where σ_1 is the maximum positive effective principal stress of undamaged-like material. Figure 5 elucidates the mechanism.

Under uniaxial compressive stress, crack initiation occurs under a different mechanism. A homogeneous material experiences only one negative principal stress and deviatoric stresses. Cracking in diagonal, shear band zone, is often encountered on cementitious specimens, however, the physical mechanism is again tensile microcracking in voids and defects in the underlying microstructure (Bažant & Planas 1998, pp. 297). Such a behavior has already been described in the work of Griffith (Griffith 1924), and McClintock and Walsh (McClintock & Walsh 1962), and we briefly review this theory and extend it with an equivalent strain to be used in the framework of damage mechanics.

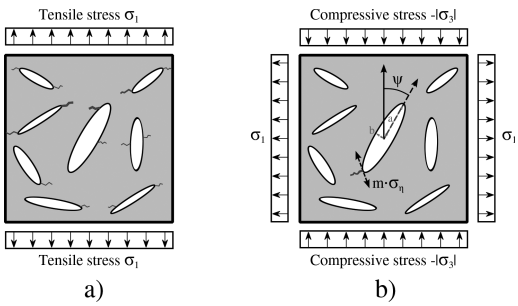

Figure 5. Crack evolution during (a) uniaxial tensile stress and (b) compressive stresses. The material contains randomly oriented elliptical voids with negligible area.

It is assumed that a material contains randomly oriented 2D elliptical flat voids with various aspect ratios $m = b/a$. The voids have a negligible area and only represent stress concentrators and internal defects in a material. Under macroscopic biaxial stress, the maximum tensile stress among all voids, $m \cdot \sigma_\eta$, appears on a critically inclined elliptical void under a critical angle ψ

$$\cos 2\psi = \frac{\sigma_3 - \sigma_1}{2(\sigma_3 + \sigma_1)},\ \frac{\sigma_1}{\sigma_3} \geq -\frac{1}{3} \tag{4}$$

$$m \cdot \sigma_\eta = \frac{-(\sigma_1 - \sigma_3)^2}{4(\sigma_1 + \sigma_3)} \tag{5}$$

Crack formation occurs when the tangential tensile stress, $m \cdot \sigma_\eta$, equals to the tensile strength of the matrix. Since σ_η and the crack geometry, m, cannot be measured directly, it is reasonable to relate their product to the uniaxial macroscopic tensile stress, $\overline{\sigma_1}$, as proposed by Griffith (Griffith 1924).

$$\overline{\sigma_1} = \frac{m \cdot \sigma_\eta}{2} \tag{6}$$

The material starts to crack when $\overline{\sigma_1}$ equals to the uniaxial macroscopic tensile strength f_t. Note that the tensile strength of the homogeneous matrix (intrinsic strength) and the crack geometry remain unknown separately and we can assess only apparent macroscopic tensile strength f_t.

Plugging Equation (5) into Equation (6) and further into Equation (3) leads to the definition of the equivalent strain, $\tilde{\varepsilon}$, under compression-dominant loading

$$\tilde{\varepsilon} = \frac{1}{E} \cdot \frac{-(\sigma_1 - \sigma_3)^2}{8(\sigma_1 + \sigma_3)} \tag{7}$$

An interesting feature of the Griffith model is that the ratio of the uniaxial compressive-to-tensile strength equals to 8

$$|f_c| = 8 f_t \tag{8}$$

This can be verified when plugging $\sigma_1 = f_t$ into Equation (3) which leads to $\tilde{\varepsilon} = f_t/E$. Plugging $\sigma_1 = 0$, $\sigma_3 = -8 f_t$ into Equation (7) leads to the same equivalent strain.

Since the equivalent strain may arise from the Rankine of Griffith criterion, it is necessary to compare both Equations (3) and (7) and to select the higher equivalent strain. Since the damage evolution law has a small effect on the computed macroscopic strength simple linear softening is

assumed in the simulations. The linear cohesive law takes the form

$$\sigma = f_t\left(1-\frac{w}{w_f}\right) \tag{9}$$

where w is a crack opening and w_f is the maximum crack opening at zero stress. According to the formulation of the isotropic damage model, the uniaxial tensile stress obeys the law

$$\sigma = (1-\omega)E\tilde{\varepsilon}. \tag{10}$$

with ω being the isotropic damage parameter, $\omega \in \langle 0;1 \rangle$.

Let us consider the fracture energy in mode I, G_f, and the effective thickness of a crack band h, which corresponds to the finite element size in the direction of the maximum principal strain (Bažant & Planas 1998). This ensures objective results, independent on finite element size (Jirásek & Bažant 2002). Notice that $w = h\omega\tilde{\varepsilon}$ and $w_f = 2G_f/f_t$. The evolution of isotropic damage is obtained by combining Equations (9) and (10).

$$\omega = \left(1-\frac{\varepsilon_0}{\tilde{\varepsilon}}\right)\left(1-\frac{hE\varepsilon_0^2}{2G_f}\right)^{-1} \tag{11}$$

3.2 *Model for fracture properties of C-S-H globules*

Nanoindentation experiments carried out previously (Constantinides & Ulm 2004) identified elastic properties of C-S-H and limit packing densities as $\eta_{\text{C-S-H}_{\text{LD}}} = 0.63$ and $\eta_{\text{C-S-H}_{\text{HD}}} = 0.76$ (Constantinides & Ulm 2007). Our model used 2D and 3D images for different packing densities. Figure 6 provides such examples for C-S-H_{LD} and C-S-H_{HD}.

In order to match uniaxial tensile test, periodic boundary conditions occur on horizontal surfaces and uniform static boundary conditions with zero normal stress belong to vertical surfaces. Vertical eigenstrain loads 2D unit cell and uniaxial macroscopic tensile stress recovers.

Figure 7 displays the evolution of the C-S-H tensile strength with regards to packing density, as determined from 200 × 200 nm microstructures. Fracture energy 2 J/m^2 was assigned to the globule. Analytical approximation reads.

$$f^0_{t,\text{C-S-H}} = f_{t,glob}\exp\left(\frac{1.293(\eta_{glob}^{\ 13.011}-1)}{\eta_{glob}}\right) \tag{12}$$

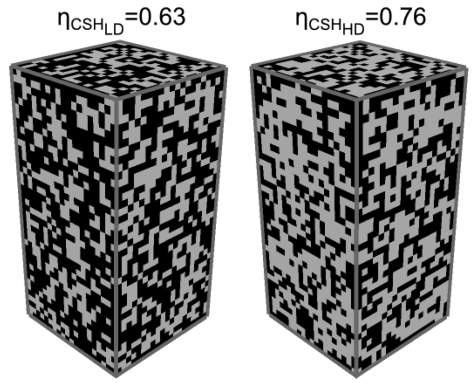

Figure 6. Unit cells for C-S-H_{LD} and C-S-H_{HD}, 20 × 20 × 40 brick elements (size 100 × 100 × 200 nm).

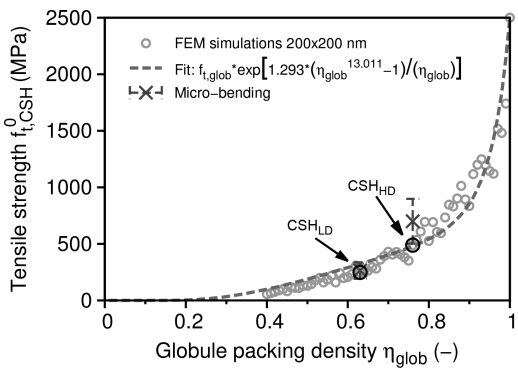

Figure 7. Tensile strength scaling in C-S-H gel with various packing density of globules.

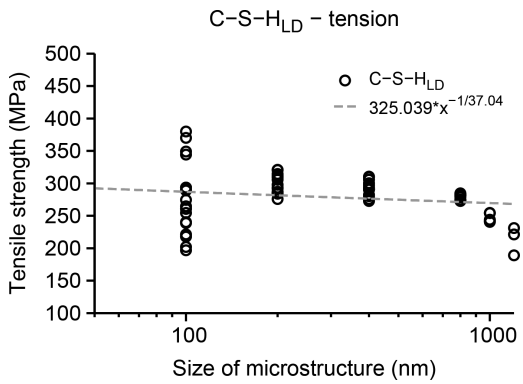

Figure 8. Tensile strength scaling on C-S-H_{LD} gel depending on size of microstructure.

where instrinsic cohesion of a globule was found as $f_{t,glog} = 2500$ MPa. This yields tensile strength $f^0_{t,\text{C-S-H}_{\text{LD}}} = 247.6$ MPa and $f^0_{t,\text{C-S-H}_{\text{HD}}} = 489.3$ MPa,

being comparable with molecular dynamics data and microbending tests.

Further, we explored strength scaling with the size of a unit cell. In perfectly plastic materials and parallel configuration of load-bearing phases, no size effect occurs as opposed to brittle materials or to serial configuration. Weak size effect was found on C-S-H_{LD} up to 1000 nm signalizing that C-S-H globules are ductile enough to redistribute stress during strain softening (Figure 8). Weak statistical size effect occurs after 1000 nm signalizing random nature of C-S-H packing with increasing brittleness.

3.3 *Model for level of cement paste*

Ordinary cement paste with low w/c attains flexural strength up to approximately 12 MPa (Taplin 1959). This can be significantly increased by hot-cured, compacted cement pastes with amorphous C-S-H where compressive strength 690 MPa was reached (i.e. the tensile strength of about 690/8 = 86 MPa can be assumed) (Gouda & Roy 1976). It was shown previously that significant decrease of strength from C-S-H to paste level is caused by presence of capillary porosity, spatial gradient of C-S-H, and stress concentration around elastic inclusions (unreacted cement clinker, crystalline hydration products, unreacted supplementary cementitious materials) (Hlobil, Šmilauer, & Chanvillard 2016). However, those effects are still insufficient for strength scaling from C-S-H to cement paste. Thus, further reducing mechanisms happen. They can be in the form of interfaces (Qian, Schlangen, Ye, & van Breugel 2012) or additional defects introduced at level 3.

Defects at level 3 can arise from several causes; shrinkage during water consumption, rearrangement of hydrates, internal stresses etc. It is obvious that size of those defects must lay above the size of our experimental cantilever beams, i.e. above ≈5 μm. LEFM can estimate the bottom size of internal defects if considered as a crack of length a in perfectly brittle material. For illustration, let us consider cement paste with E = 15 GPa, $G_{f,CSH}$ = 2 J/m^2, f_t = 10 MPa

$$f_t = \sqrt{\frac{EG_{f,CSH}}{\pi a}}, \tag{13}$$

$$a = \frac{EG_{f,CSH}}{\pi f_t^2} \approx \frac{15 \cdot 10^9 \cdot 2}{\pi (10 \cdot 10^6)^2} = 95 \cdot 10^{-6}\,\text{m}. \tag{14}$$

Such estimation is consistent with (Ghebrab & Soroushian 2010) who used $a \geq 50$ μm arguing that large portlandite crystals are responsible for stress concentration and crack propagation. However, simulations need to prove this hypothesis and validate experimental data.

4 CONCLUSIONS

The following conclusions can be drawn on experimental and numerical parts:

- Micro-bending tests on beams prepared with FIB give access to local fracture properties of cement paste constituents. Tensile strength of inner product, outer product and CH were found in the range of 260–700 MPa. Supremum of fracture energies lie in the range 4–20 J/m^2 for the respective constituents.
- Cohesion of C-S-H globule was identified as 2500 MPa. When intermixing C-S-H globules with gel porosity, experimentally measured strengths are approximately recovered for both C-S-H_{HD} and C-S-H_{LD}. Also, the results from molecular dynamics are consistent.
- Preliminary findings show that microcracks or internal defects as long as 100 μm exist and they control strength of cement pastes. The origin of those defects, their formation and description need further research.

ACKNOWLEDGEMENT

Financial support of the Czech Science Foundation's project 17-18652S is gratefully acknowledged.

REFERENCES

Bažant, Z.P. & J. Planas (1998). *Fracture and Size Effect in Concrete and Other Quasibrittle Materials*. CRC Press.

Constantinides, G. & F.-J. Ulm (2004). The effect of two types of C-S-H on the elasticity of cement-based materials: Results from nanoindentation and micromechanical modeling. *Cem. Concr. Res. 34*(1), 67–80.

Constantinides, G. & F.-J. Ulm (2007). The nanogranular nature of C-S-H. *Journal of the Mechanics and Physics of Solids 55*, 64–90.

Davie, C. & E. Masoero (2015). Modelling damage from the nano-scale up. In *10th International Conference on Mechanics and Physics of Creep, Shrinkage, and Durability of Concrete and Concrete Structuresg.*

Ghebrab, T. & P. Soroushian (2010, June). Mechanical Properties of Hydrated Cement Paste: Development of Structureproperty Relationships. *International Journal of Concrete Structures and Materials 4*(1), 3743.

Gouda, G.R. & D.M. Roy (1976). Characterization of hotpressed cement pastes. *Journal of the American Ceramic Society 59*(9–10), 412–414.

Griffith, A. (1924). Theory of rupture. In C. Biezeno and J. Burgers (Eds.), *First International Congress for Applied Mechanics, Delft*, pp. 55–63.

Hlobil, M., V. Šmilauer, & G. Chanvillard (2016). Micromechanical multiscale fracture model for compressive strength of blended cement pastes. *Cement and Concrete Research 83*, 188–202.

Jirásek, M. & Z.P. Bažant (2002). *Inelastic analysis of structures*. John Wiley & Sons, Ltd.

McClintock, F. & J. Walsh (1962). Friction of griffith cracks in rock under pressure. In Proc. *Fourth U.S. National Congress of Applied Mechanics*, New York City, pp. 1015–1021.

Němeček, J., V. Hrbek, L. Polívka, & A. Jäger (2016). Combined investigation of low-scale fracture in hydrated cement assessed by nanoindentation and fib. In V. Saouma, J. Bolander, and E. Landis (Eds.), *9th International Conference on Fracture Mechanics of Concrete and Concrete Structures, FraMCoS-9*.

Němeček, J., V. Králík, & J. Vondřejc (2013). Micromechanical analysis of heterogeneous structural materials. *Cement and Concrete Composites 36*, 85–92.

Němeček, J., V. Šmilauer, L. Polívka, & A. Jäger (2016). Tensile strength of hydrated cement paste phases assessed by microbending tests and nanoindentation. *Cement and Concrete Composites 73*, 164–173.

Plassard, C., E. Lesniewska, I. Pochard, & A. Nonat (2005). Nanoscale experimental investigation of particle interactions at the origin of the cohesion of cement. *Langmuir 21*(16), 7263–7270. PMID: 16042451.

Qian, Z., E. Schlangen, G. Ye, & K. van Breugel (2012). Multiscale lattice fracture model for cement-based materials. In *4th International Conference on Computational Methods (ICCM 2012)*, Gold Coast, Australia.

Taplin, J.H. (1959). A method for following the hydration reaction in Portland cement paste. *Australian J. Appl. Sci. 10*, 329–345.



Taylor & Francis
Taylor & Francis Group
http://taylorandfrancis.com

Computational Modelling of Concrete Structures – Meschke, Pichler & Rots (Eds)
© 2018 Taylor & Francis Group, London, ISBN 978-1-138-74117-1

Testing and modelling of micro cement paste cube under indentation splitting

H. Zhang & E. Schlangen
Department of Structural Engineering, Delft University of Technology, Delft, The Netherlands

B. Šavija
Structural Reliability, TNO Technical Sciences, Delft, The Netherlands

ABSTRACT: Cement paste is the glue that holds concrete together and any improvements in material performance will come from its microstructure. For better understanding and predicting its elastic properties and fracture performance, more and more studies are carried out based on micromechanics simulations. However, the predicted results can be hardly verified experimentally due to the technical limitations. This paper presents a procedure for validating micromechanics simulation by making, testing and modelling deformation and fracture of micro cement paste cube (100 μm × 100 μm × 100 μm). The micro scale specimens were produced by a micro dicing saw which is commonly employed in the semiconductor industry and fractured by a commercial cylindrical wedge tip mounted on a nano-indenter equipment. A combination of X-ray computed tomography technique and a discrete lattice fracture model was applied to simulate the deformation and fracture performance of the micro scale specimen under indentation. Mechanical properties of local phases are the input for this fracture simulation, which are taken from the previous study by the authors, wherein a micro scale experiment is developed to calibrate these values. Load-displacement curve and crack pattern from the simulation show a good agreement with those obtained experimentally. The proposed technique forms the basis for experimental validation of simulation tools that are used in a multi-scale framework at every scale.

1 INTRODUCTION

As the basic binding material in concrete, cement paste has generated considerable research interest. It is generally accepted that fracture of conventional concrete material starts from micro cracks of cement matrix where local tensile stress exceeds its tensile strength. Understanding the deformation and fracture performance (i.e. tensile strength and elastic modulus) of cement paste at micro scale is therefore of significant practical importance and scientific interest.

As an effective tool, nanoindentation has been implemented for quantification of local properties like elasticity and hardness of micro level components in the matrix (Constantinides & Ulm 2004, Hu & Li 2014). This technique provides a meaningful experimental input for analytical and numerical models to calculate the global micromechanical properties of cement matrix (Sanahuja, Dormieux, & Chanvillard 2007, Pichler, Hellmich, Eberhardsteiner, Wasserbauer, Termkhajornkit, Barbarulo, & Chanvillard 2013, Luković, Schlangen, & Ye 2015, Zhang & Jivkov 2016) which can be further used as input for a multi-scale framework to simulate the macroscopic mechanical performance of concrete (Pichler & Hellmich 2011, Hlobil, Šmilauer, & Chanvillard 2016, Qian, Schlangen, Ye, & van Breugel 2017, Zhang, Šavija, Figueiredo, & Schlangen 2017). For the past decades, a lot of valuable micromechanical information is obtained to set a basis for understanding and improving the macroscopic mechanical performances. However, for a number of reasons that include problems with producing and measuring miniaturized mechanical samples, these predicted micromechanical properties can be hardly verified experimentally.

In this paper a method on producing and testing micro cement paste cube is reported. The micro scale specimens are produced by a micro dicing saw and fractured by a commercial cylindrical wedge tip mounted on a nano-indenter equipment. In parallel with the experiments, a discrete lattice model is introduced here to simulate the deformation and fracture performance of these micro scale specimens under indentation. The simulated crack pattern and load displacement diagram are then compared with the experimental observations.

2 EXPERIMENTAL

In the experimental program, a grid of micro-cubes ($100 \times 100 \times 100 \times 100$ μm) was produced a method developed by the authors (Zhang, Šavija, Chaves Figueiredo, Lukovic, & Schlangen 2016) and tested by the nano-indenter equipment. The method is shortly presented here. 28-day cured cement paste specimens with 0.4 water-to-cement ratio were first glued on top of a glass substrate. The specimen thickness was then made equal to the desired thickness (100 μm), and this was done using a Struers Labopol-5 thin sectioning machine. The micro-cube grid was then fabricated using a precise diamond saw (MicroAce Series 3, Loadpoint, Swindon, UK) which is commonly employed in the semiconductor industry to create silicon wafers. In the machine, a 260 μm thick blade was run in two perpendicular directions over the specimen and the glass substrate (Figure 1). The procedure results in a grid of micro-cubes ($100 \times 100 \times 100 \pm 4$ μm) that are used for micromechanical testing (Figure 2a).

For testing of the micro-cubes, the nanoindenter is employed. For the purpose of this splitting test, a diamond cylindrical wedge tip (radius 9.6 μm, length 200 μm, see Figure 2b) was used in order to apply the load across the middle axis. The experiments were run using displacement control with a loading rate of 50 nm/s up to the failure of micro-cube (Figure 2c). Force and displacement data were acquired using the continuous stiffness measurement (CSM) technique (Li & Bhushan 2002) and the applied CSM settings were: 2 nm amplitude, 45 Hz frequency and 100 N/m surface detection.

A typical load-displacement curve recorded by the nano-indenter is shown in Figure 3. Clearly two regimes as well as the maximum load point at failure stage can be distinguished from this curve. In regime (I), the load on sample increases monotonically until reaching the maximum load. Once the load exceeds maximum load, the system transitions from a stable regime (I) towards an unstable regime (II). The maximum load can be further used to estimate splitting tensile strength of these micro-cubes (Šavija, Zhang, & Schlangen 2017). The horizontal line in regime (II) indicates an overshoot behaviour of the wedge indenter tip towards the substrate because of the structural collapse of

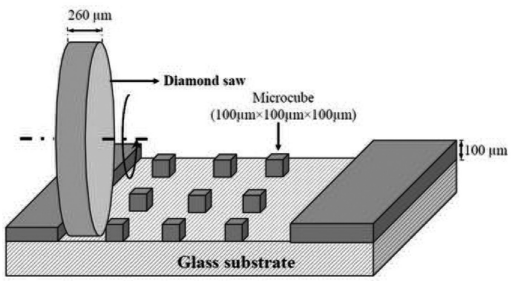

Figure 1. Schematic view of the specimen preparation procedure.

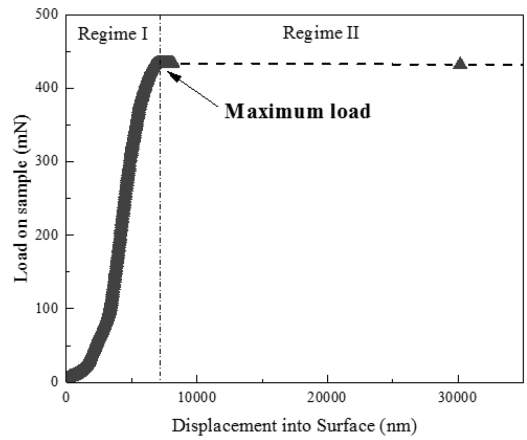

Figure 3. A typical load versus displacement response measured in the micro-cube splitting test.

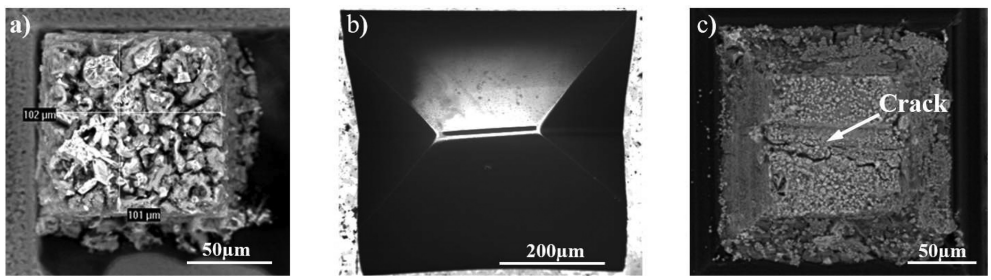

Figure 2. Environmental scanning electron microscope image of (a) small cement paste cube on glass plate (b) cylindrical wedge indenter tip and (c) damaged cement paste cube.

the micro-cube. Since displacement control of the nano-indenter is not fast enough, it is not possible at present to capture the post peak-peak behaviour of the specimen.

3 MODELLING

In the modelling part, fracture simulations with a lattice model (Schlangen & Garboczi 1997) were performed on voxel-based cement paste specimens with the same dimension (Figure 4). These specimens were generated by X-ray computed tomography (XCT) with a resolution of 2 μm^3/voxel, and consists of four phases including pore (P), anhydrous cement grain (A), inner hydration product (I) and outer hydration product (O). More information about the experiments, reconstruction and image segmentation procedure can be found in (Zhang, Šavija, Chaves Figueiredo, Lukovic, & Schlangen 2016).

In the lattice model, the material is assembled by a set of beam elements having linear elastic behaviour. Then, a set of linear elastic analyses is performed by calculating the nodal responses of the lattice network for an external boundary displacement. At every analysis step, a unit displacement is applied, a critical beam element with the highest stress/strength ratio is labelled and removed from the mesh, thereby introducing a small crack. This procedure is then repeated with the updated geometry and stiffness of the whole lattice network until structural failure happens. As a consequence, the fracture pattern of the investigated material volume at each step can be obtained as well as their load-displacement response which can be further converted to the laboratory observed load-displacement diagram of the specimen under loading.

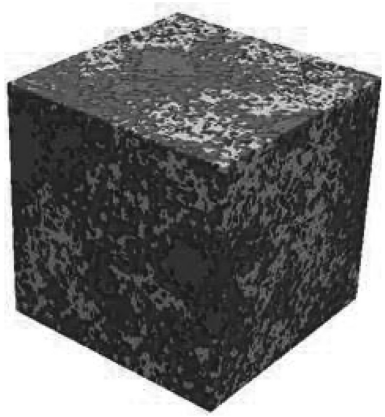

Figure 4. Microstructure of cement paste with size 100 μm × 100 μm × 100 μm at the curing age 28 days and 0.4 water-to-cement ratio from XCT experiments (grey-anhydrous cement; red-inner product; yellow-outer product; blue-pore).

As shown in Figure 5, the voxel-based specimen is discretized as a lattice mesh. The microstructure of the material can be mapped onto these beam elements by assigning them different properties, depending on the phase type of connected two voxels by the beam element. Three solid phases in the microstructure result in six types of lattice elements. Elasticity modulus of beam element was ascribed with the harmonic average of the connected two phases, while the strength assigned as the lower value in between. The mechanical parameters of each single phase used in this study are presented in Table 1. Elastic moduli are assumed equal to the nanoindentation measurements for individual phases (Hu & Li 2014). The tensile strengths are taken from a previous study by the authors (Zhang, Šavija, Chaves Figueiredo, Lukovic, & Schlangen 2016), wherein a micro scale experiment is developed to calibrate these values. The compressive strength of each phase is

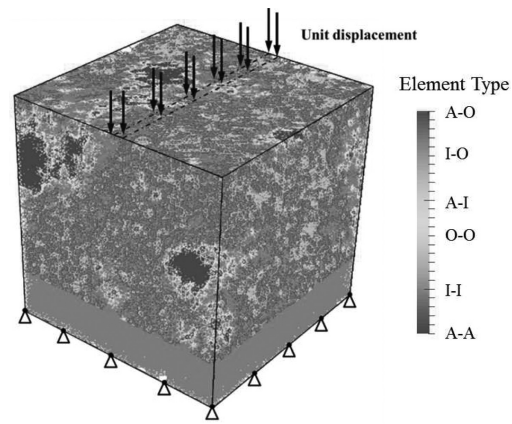

Figure 5. Computational splitting test on lattice mesh of micro cement paste cube.

Table 1. Assigned local mechanical properties of individual phases.

Phase	Modulus (GPa)	Tensile strength (GPa)	Compressive strength (GPa)
Pore	0.0	0.00	0.00
Anhydrous cement	99.2	0.68	13.2
Inner product	31.2	0.09	1.8
Outer product	25.2	0.06	1.2

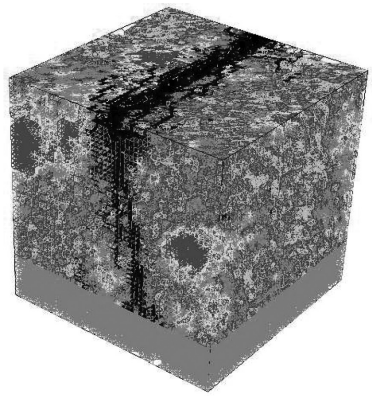

Figure 6. Damaged specimen in the final failure state under indentation splitting (black-crack).

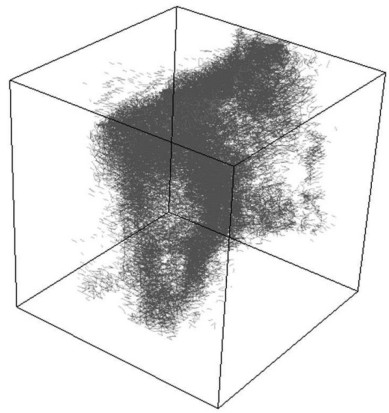

Figure 7. Simulated crack pattern in the final failure state.

estimated 20 times as high as its tensile strength. The lattice elements (coloured grey in Figure 5) located below 20 μm from the bottom were set as glue element with a low elastic modulus of 3 GPa (measured by a grid nano-indentation test) to represent the glue layer between cement paste and glass substrate. These elements were not allowed to fail in the simulation (i.e. they remain linear elastic). For the boundary conditions in the simulation it was assumed that the displacement of the nodes at bottom surface was fixed in all directions to represent the glued sample on the glass plate. A vertical displacement was applied on nodes in the two lines closed to the middle axis of the top surface to mimic the indenter load.

The damaged specimen and crack pattern are presented in Figure 6 and Figure 7 respectively. It can be clearly seen that the simulated fracture pattern is comparable to the experimental observation. A lot of damage occurs under the loading points, and the final crack pattern results in one main crack under the indenter. The simulated load-displacement curve is plotted in Figure 8 together with several experientially measured curves. As the post-peak behaviour of specimen cannot be captured due to current technical limitation, validation of the numerical model was restricted only in regime (I). The simulated load-displacement curve and one of the experimentally measured cures show a high degree of consistency on the peak load and stiffness (slope of the load displacement curve). Due to the fact that some slip occurs at the beginning of the experiments, the measurements are slightly shifted, but the slope remains similar to the one in simulated load displacement curve. It is observed that the test results still show a high variability which is induced by the inherent heterogeneity of this material. Therefore, it is suggested that

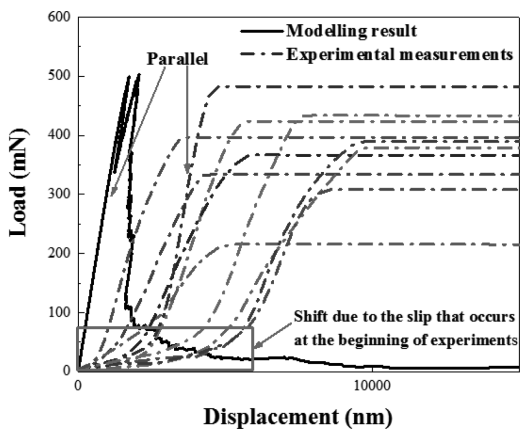

Figure 8. Comparison between simulated load displacement diagrams and experimental results.

in future investigation, multiple voxel-based specimens need to be generated and testedto obtain statistical results on the micromechanical properties.

4 CONCLUSIONS

In this paper the failure mechanism in cement paste specimens at micro scale was studied by a combination of experimental technique using nano-indenter equipment and a modelling technique using discrete lattice model. The input for the simulation are mechanical properties of the individual local phases, which are calibrated from the previous study by the authors, wherein a micro scale experiment is developed to calibrate

these values. The simulated fracture pattern and load-displacement curve are compared with the experimental observations of same size specimens. It is showed that these input local mechanical properties can be applied to fracture simulations under different boundary conditions and have satisfactory results. With the method presented in this paper the framework for validation of the modelling results at micro scale is created. This method forms also a basis for validation of multi-scale modelling results at every scale.

REFERENCES

Constantinides, G. & F.-J. Ulm (2004). The effect of two types of csh on the elasticity of cement-based materials: Results from nanoindentation and micromechanical modeling. *Cement and concrete research* 34(1), 67–80.

Hlobil, M., V. Šmilauer, & G. Chanvillard (2016). Micromechanical multiscale fracture model for compressive strength of blended cement pastes. *Cement and Concrete Research 83*, 188–202.

Hu, C. & Z. Li (2014). Micromechanical investigation of Portland cement paste. *Construction and Building Materials 71*, 44–52.

Li, X. & B. Bhushan (2002). A review of nanoindentation continuous stiffness measurement technique and its applications. *Materials characterization 48*(1), 11–36.

Luković, M., E. Schlangen, & G. Ye (2015). Combined experimental and numerical study of fracture behaviour of cement paste at the microlevel. *Cement and Concrete Research 73*, 123–135.

Pichler, B. & C. Hellmich (2011). Upscaling quasi-brittle strength of cement paste and mortar: A multi-scale engineering mechanics model. *Cement and Concrete Research 41*(5), 467–476.

Pichler, B., C. Hellmich, J. Eberhardsteiner, J. Wasserbauer, P. Termkhajornkit, R. Barbarulo, & G. Chanvillard (2013). Effect of gel–space ratio and microstructure on strength of hydrating cementitious materials: An engineering micromechanics approach. *Cement and Concrete Research 45*, 55–68.

Qian, Z., E. Schlangen, G. Ye, & K. van Breugel (2017). Modeling framework for fracture in multiscale cement-based material structures. *Materials 10*(6), 587.

Sanahuja, J., L. Dormieux, & G. Chanvillard (2007). Modelling elasticity of a hydrating cement paste. *Cement and Concrete Research 37*(10), 1427–1439.

Šavija, B., H. Zhang, & E. Schlangen (2017). Influence of microencapsulated phase change material (pcm) addition on (micro) mechanical properties of cement paste. *Materials 10*(8), 863.

Schlangen, E. & E. Garboczi (1997). Fracture simulations of concrete using lattice models: computational aspects. *Engineering fracture mechanics 57*(2), 319–332.

Zhang, H., B. Šavija, S. Chaves Figueiredo, M. Lukovic, & E. Schlangen (2016). Microscale testing and modelling of cement paste as basis for multi-scale modelling. *Materials 9*(11), 907.

Zhang, H., B. Šavija, S. C. Figueiredo, & E. Schlangen (2017). Experimentally validated multi-scale modelling scheme of deformation and fracture of cement paste. *Cement and Concrete Research 102*, 175–186.

Zhang, M. & A. P. Jivkov (2016). Micromechanical modelling of deformation and fracture of hydrating cement paste using x-ray computed tomography characterisation. *Composites Part B: Engineering 88*, 64–72.



Taylor & Francis
Taylor & Francis Group
http://taylorandfrancis.com

Computational Modelling of Concrete Structures – Meschke, Pichler & Rots (Eds)
© 2018 Taylor & Francis Group, London, ISBN 978-1-138-74117-1

An adaptive concurrent two-scale FE model to predicting crack propagation in concrete

O.L. Manzoli & E.A. Rodrigues
Department of Civil Engineering, UNESP—São Paulo State University, Bauru, Brazil

L.A.G. Bitencourt Jr. & T.N. Bittencourt
Polytechnic School, USP—University of São Paulo, São Paulo, Brazil

M. Sánchez
Zachry Department of Civil Engineering, Texas A&M University, College Station, USA

ABSTRACT: Finite element analysis including explicitly the details of the heterogeneities (finer-scale) can dramatically increase the numerical effort and memory demand. To minimize these drawbacks, a new concurrent adaptive multiscale model for concrete in two different scales of representation is proposed. In this approach, the macroscale stress is used as an indicator to properly update the model from the macro to the mesoscale model in the critical regions. The concrete is initially modeled as a homogenous material and then is gradually replaced by a heterogeneous representation, consisting of three phases: coarse aggregates, mortar matrix and Interfacial Transition Zone (ITZ). The use of Coupling Finite Elements (CFEs) is proposed to enforce the continuity of displacements between the non-matching meshes corresponding to the two different scales. These CFEs can ensure the connection between the finer and coarser scales without increasing the number of degrees of freedom of the problem. The mesoscopic scale is constructed using a mesh fragmentation technique in order to simulate the crack propagation process. This technique is based on the insertion of standard finite elements with high aspect ratio between all regular finite elements of the mortar matrix and in between the mortar matrix and aggregate elements, representing the ITZ. In the limit case, when the thickness of interface elements tends to zero and consequently the aspect ratio tends to infinite, these elements present the same kinematics as the Continuum Strong Discontinuity Approach (CSDA), being suitable to represent the formation of discontinuities associated to cracks, using a continuum tensile damage constitutive model. Numerical examples with complex crack patterns are carried out to validate the proposed adaptive multiscale model and show its efficiency and accuracy when compared to the full mesoscale model.

1 INTRODUCTION

One of the main challenges of numerical analysis of heterogeneous materials in mesoscale is the computational power limitation. The discretization of the material's internal structures generates very large systems of equations to be solved, which increase dramatically the numerical effort and memory demand.

To circumvent this problem, only small specimens are simulated or the mesoscale is only modeled in a restrict region where the fracture process is expected using multiscale models (Cusatis & Cedolin 2007, Nguyen et al. 2012, Etse & Caggiano 2012, Oliver et al. 2015, Roubin et al. 2015, Toro et al. 2016, Oliver et al. 2017).

Despite the good results obtained with this kind of multiscale modeling, in general, the region where the damage localization may take place cannot be known a priori, making the numerical analyses more difficult from a computational point of view. Thus, to circumvent this problem, adaptive failure approaches have been proposed (Ghosh et al. 2001, Unger & Eckardt 2011, Lloberas-Valls et al. 2012, Vernerey & Kabiri 2012, Sun & Li 2016).

In this paper, an alternative adaptive concurrent multiscale model is proposed. In the context of the finite element method (FEM), the analysis is initially carried out using a coarse finite element discretization, representing the macroscale model, with effective homogenized elastic properties for the entire structural member. For each load step of the analysis, an indicator based on the principal stress of the coarse mesh is tested. Once the indicator reaches the adaptive threshold, the corresponding coarse finite elements and the elements in their

vicinity, are replaced by a mesostructure discretization (Rodrigues et al. 2018).

To model the crack initiation in the ITZ and crack propagation through the matrix, the mesh fragmentation technique (MFT) proposed by Sanchéz et al. (2014) and Manzoli et al. (2016) is used. This technique is based on the use of degenerated solid finite elements (three-node triangular) with a very high aspect ratio (ratio of the largest to the smallest dimension), with the smallest dimension corresponding to the thickness of the element. Manzoli et al. (2012) demonstrated that as the aspect ratio increases, the element strains also increase, approaching the kinematics of the strong discontinuity, as is the case of the CSDA (Oliver et al. 1999, Oliver & Huespe 2004). Therefore, a continuum damage constitutive relation between strains and stresses, compatible with the CSDA, can be used to describe the nonlinear behavior of these interface elements, representing the crack formation process. The main advantage is that the analyses can be carried out integrally in the context of the continuum mechanics and complex crack patterns, even involving crack face bridges, can be simulated.

To couple the non-matching meshes (macro and mesoscale meshes), special coupling four-node triangular finite elements are used (Bitencourt et al. 2015). In this case, the fourth node of the coupling element coincides with the node of the mesoscale elements, while the other three nodes coincide with the nodes of the adjacent macroscale elements. This technique ensures compatibility of the displacements between the two independent meshes.

The advantage of this adaptive approach is that it does not require a periodic cell neither Lagrange multipliers for coupling the non-conforming meshes. Therefore, the mesostructure constituents can then be generated randomly with arbitrary geometry. Furthermore, since only the critical region is resolved in mesoscale, the computational cost is lower compared with the direct numerical simulation in mesoscale (DNS-M).

2 GENERAL DESCRIPTION OF THE METHODOLOGY

2.1 *Mesh Fragmentation Technique*

The Mesh Fragmentation Technique (MFT) proposed by Sánchez et al. (2014) and Manzoli et al. (2016) is based on the use of Interface Solid Elements with high aspect ratio, called here for simplicity Interface Elements (IEs) (Manzoli et al. 2012). The method consists in reassembling the original mesh in such a manner that the regular elements are first transformed into independent elements by replicating the shared nodes, and then a very small reduction is imposed on each element, creating narrow spaces between then. After that, the gaps between two neighboring modified elements are filled out by pairs of triangular finite elements with high aspect ratio, as illustrated in Figure 1.

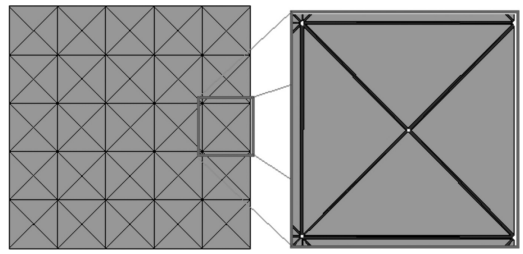

Figure 1. Example of a fragmented FE mesh.

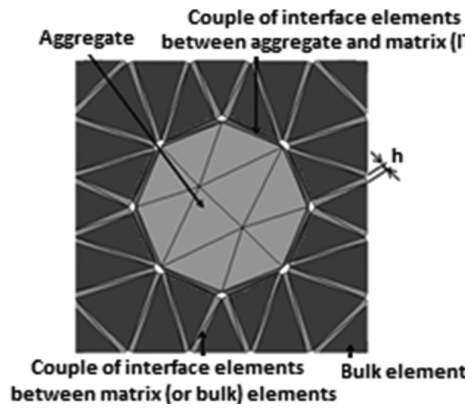

Figure 2. Mesoscale FE levels representation.

2.2 *Mesoscale modeling of concrete*

The coarse aggregates are randomly generated into the concrete sample taking into account a grading curve (Wriggers & Moftah 2006). Therefore, employing the MFT, the concrete in mesoscale can be represented as a three-phase material, consisting of coarse aggregate, mortar-matrix and ITZ, as showed in Figure 2. Details about this mesoscale model for concrete can be found in Rodrigues et al. (2016).

2.3 *Interface element formulation*

Following the standard finite element approximations, Manzoli et al. (2012) demonstrated that the strain tensor of the element illustrated in Figure 3 can be divided into two parts as:

$$\boldsymbol{\varepsilon} = \tilde{\boldsymbol{\varepsilon}} + \hat{\boldsymbol{\varepsilon}} = \underbrace{\tilde{\boldsymbol{\varepsilon}}}_{\text{Bounded}} + \underbrace{\frac{1}{h}\left(\mathbf{n} \otimes \left[\left[\mathbf{u}\right]\right]\right)^{s}}_{\text{Unbounded}} \tag{1}$$

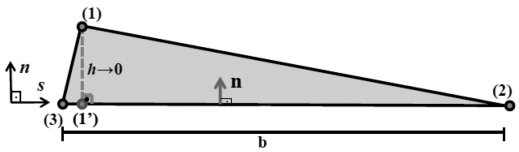

Figure 3. Interface solid element.

where the notation $(\bullet)^s$ refers to the symmetric part of $(\bullet)$; $\mathbf{n}$ is the unit vector normal to the element base; $\otimes$ denotes a dyadic product; and $[[\mathbf{u}]]$ is the vector of the components of the relative displacement between node 1 and its projection on the base of the element (1'), which according to the local coordinate system (n,s), are, respectively, the normal and tangential components of the relative displacement, $[[\mathbf{u}]]_n$ and $[[\mathbf{u}]]_s$.

In the limit situation where $h \to 0$, the node (1) and its projection tend to the same material point. Thus, the relative displacement $[[\mathbf{u}]]$ becomes the measure of a displacement discontinuity (strong discontinuity) and, consequently, the structure of the strain field described in equation (1) corresponds to the typical kinematics of the CSDA. Therefore, the kinematics of CSDA can be obtained with triangular finite elements with high aspect ratio (IEs). Details about this demonstration can be found in Manzoli et al. (2012).

2.4 *Tensile damage model*

The constitutive damage model employed is based on the effective elastic stress, $\bar{\boldsymbol{\sigma}}$, and has its damage criterion written in terms of the tension stress component normal to the base of the IE, $\bar{\sigma}_{nn}$. The current stress tensor is calculated applying the damage variable to degrade all components of the effective stress tensor, only if the normal stress is positive $(\bar{\sigma}_{nn} > 0)$. Table 1 summarizes the equations of this constitutive model.

In Table 1, $\mathbf{C}$ is elastic tensor and $\boldsymbol{\varepsilon}$ is strain tensor. The strain-like internal variable, r, assumes the maximum value that the effective stress $\bar{\sigma}_{nn}$ reaches during the loading process, starting from the initial tensile strength, f_t, of the material. The parameter A is related to the fracture energy, G_f, $A = (f_t^2)/(G_f E)$, where h is the thickness of the IE.

The mesoscale cracking can induce numerical instability, since multiple cracks can be simultaneously formed in the dissipative zone. To circumvent this problem and improve the stability and robustness of the simulations, the implicit-explicit integration scheme, IMPL-EX (IMPL → implicit, EX → explicit), is used to integrate the constitutive model. More details about the benefits provided by IMPL-EX can be found in Oliver et al. (2008).

Table 1. Equations of the tensile damage model.

Continuum model	
Effective stress	$\bar{\boldsymbol{\sigma}} = \mathbf{C} : \boldsymbol{\varepsilon}$
Equivalent stress	$\bar{\tau} = \bar{\sigma}_{nn}$
Damage criterion	$\bar{\varphi} = \bar{\tau} - r \le 0$
Evolution law for the strain-type variable	$r(t) = r = \max_{s\in[0,t]} \left[\bar{\sigma}_{nn}(s), f_t \right]$
Damage evolution	$d(r) = 1 - \frac{f_t}{r} e^{A h \left\{1 - \frac{r}{f_t}\right\}}$
Constitutive relation	$\boldsymbol{\sigma}_{n+1} = \begin{cases} (1-d)\bar{\boldsymbol{\sigma}} & \text{if } \bar{\sigma}_{nn} > 0 \\ \bar{\boldsymbol{\sigma}} & \text{if } \bar{\sigma}_{nn} \le 0 \end{cases}$

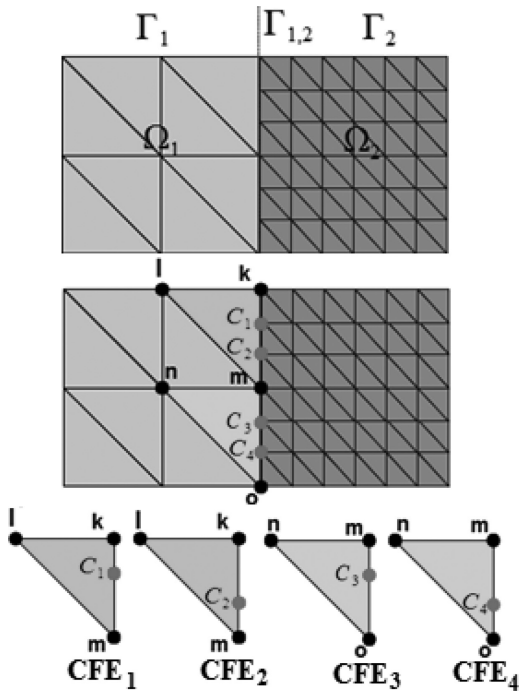

Figure 4. CFE scheme for two different subdomains.

2.5 *Coupling finite element*

To illustrate the coupling technique, Figure 5 shows a representative situation where two subdomains, Ω_1 and Ω_2, are discretized with independent meshes, forming the domain $\Omega = \Omega_1 \cup \Omega_2$ and the common boundary $\Gamma_{1,2} = \Gamma_1 \cap \Gamma_2$. This independence and different mesh refinement introduce four loose nodes (C_1, C_2, C_3 and C_4) in $\Gamma_{1,2}$. Therefore, according to the technique proposed by Bitencourt et al. (2015), the same number of coupling finite elements (CFEs) must be generated to couple the non-matching meshes (see Figure 5).

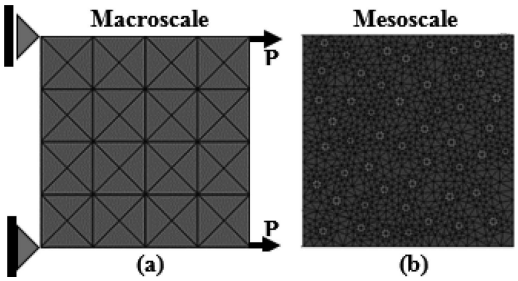

Figure 5. Two different FE levels of representation.

Coupling is enforced by a penalization of the relative displacement, [[u]], between the additional coupling node, D_{nn+1}, and its corresponding material point, $\mathbf{x}_C$, The penalization can be obtained assuming a linear relation to describe the elastic reaction force due to this relative displacement, as:

$$\mathbf{F}\left(\left[\left[\mathbf{U}\right]\right]\right) = \mathbf{C}\left[\left[\mathbf{U}\right]\right] = \mathbf{C}\underbrace{\sum_{i}^{nn}\bar{N}_i\left(\mathbf{X}_C\right)\mathbf{D}_i - \mathbf{D}_{nn+1}}_{\left[\left[\mathbf{U}\right]\right]} = \underbrace{\mathbf{C}\mathbf{B}_e\mathbf{D}_e}_{\left[\left[\mathbf{U}\right]\right]} \tag{2}$$

where $\mathbf{D}_i\left(i=1:nn\right)$ is the nodal displacement vector, $\sum_{i}^{nn}\bar{N}_i\left(\mathbf{X}_C\right)\mathbf{D}_i$ are the interpolated displacements of the extra node material point calculated from the nodal displacements using the regular shape functions $\bar{N}_i$, $\mathbf{D}_{nn+1}$ are the extra node displacements. Therefore, the matrix $\mathbf{B}_e$ can be written as:

$$\mathbf{B}_e = \left[\bar{\mathbf{N}}_1\left(\mathbf{X}_C\right)\bar{\mathbf{N}}_2\left(\mathbf{X}_C\right)\ldots\bar{\mathbf{N}}_{nn}\left(\mathbf{X}_C\right)-\mathbf{I}\right] \tag{3}$$

where I is the identity matrix. The vector $\mathbf{D}_e = \left\{\mathrm{D}_1,\mathrm{D}_2,\ldots,\mathrm{D}_{nn},\mathrm{D}_{nn+1}\right\}^T$ collects all the displacement components of the coupling finite element, so that the last components correspond to the extra node, and $\mathbf{C}$ is the elastic matrix, so that a rigid coupling between the non-match meshes can be obtained assuming high values for the elastic constants, i.e.;

$$\mathbf{C} = \begin{bmatrix}\tilde{C} & 0 & 0\\ 0 & \tilde{C} & 0\\ 0 & 0 & \tilde{C}\end{bmatrix} \tag{4}$$

where $\tilde{C}$ represents a high elastic stiffness, which plays the rule of a penalty variable on the relative displacement. According to Equation (2), since the reaction force must be bounded, the relative displacement must tend to zero as this elastic stiffness increases.

Considering the Equation (2), the CFE local internal forces and the stiffness matrix can be written as:

$$\mathbf{F}_e^{\mathrm{int}} = \mathbf{B}_e^T\mathbf{F}\left(\left[\left[\mathbf{U}\right]\right]\right) = \mathbf{B}_e^T\mathbf{C}\mathbf{B}_e\mathbf{D}_e \tag{5}$$

$$\mathbf{K}_e = \frac{\partial\mathbf{F}_e^{\mathrm{int}}}{\partial\mathbf{D}_e} = \mathbf{B}_e^T\mathbf{C}\mathbf{B}_e \tag{6}$$

According to the CFE technique, for mm different subdomains, $\Omega_j\left(j=1:mm\right)$, the global internal force vector and stiffness matrix can be calculated as:

$$\mathbf{F}^{\mathrm{int}} = \mathrm{A}_{e=1}^{nel\Omega_1}\left(\mathbf{F}_e^{\mathrm{int}}\right)_{\Omega_1} + \cdots + \mathrm{A}_{e=1}^{nel\Omega_j}\left(\mathbf{F}_e^{\mathrm{int}}\right)_{\Omega j} + \mathrm{A}_{e=1}^{nelC}\left(\mathbf{B}_e^T\mathbf{C}\mathbf{B}_e\mathbf{D}_e\right)_{\Omega_C} \tag{7}$$

$$\mathbf{K} = \mathrm{A}_{e=1}^{nel\ \Omega_1}\left(\mathbf{K}_e\right)_{\Omega_1} + \cdots + \mathrm{A}_{e=1}^{nel\ \Omega_j}\left(\mathbf{K}_e\right)_{\Omega_j} + \mathrm{A}_{e=1}^{nel\ \Omega_C}\left(\mathbf{B}_e^T\mathbf{C}\mathbf{B}_e\right)_{\Omega_C} \tag{8}$$

where A stands for the finite element assembly operator. Note that in Equations (7) and (8) the last terms are related to the introduction of the CFEs to connect the distinct subdomains $\left(\Omega_1+\cdots+\Omega_j\right)$.

3 ADAPTIVE MULTISCALE SCHEME

3.1 *Main feature of the adaptive method*

The adaptive multiscale model proposed is based on the generation of two initially independent meshes, representing the distinct physical levels, as illustrated in Figure 5.

The coarse mesh represents the macroscale, in which homogenized effective elastic properties are assumed, and where the initial boundary conditions are applied (Figure 5a). The refined mesh represents the mesoscale heterogeneities of the concrete (Figure 5b), which is initially deactivated. During the analysis, the continuum macroscopic elements can be replaced by the explicit continuum mesoscopic elements, when a given criterion is violated. The CFEs are used to couple the hanging nodes (or loose nodes) of the non-matching meshes, ensuring displacement compatibility between the meshes.

3.2 *Adaptive mesh criterion*

The criterion of the adaptive model is based on the maximum positive principal stress of the macroscopic mesh, giving by Equation (9),

$$F\left(\sigma_{\max}, Ft_{adap}\right) = \sigma_{\max} - Ft_{adap} < 0 \tag{9}$$

which is checked for each integration point of macroscopic elements during the analysis. Thus,

the element that violates this criterion is deactivated, giving place to the corresponding mesoscopic elements that have at least one node inside the domain of this deactivated macroscopic element. To enforce equilibrium between the two distinct meshes, coupling finite elements are used to connect the remained macroscopic mesh with those mesoscopic elements that have been activated. These CFEs are prepared in advance, in a pre-process step, for only the nodes of those mesoscopic elements that have nodes in different macroscopic finite elements, since only they are potential boundary nodes between the activated mesoscale mesh and the remaining active macroscopic mesh.

Once the elements of the coarse mesh are deactivated and the mesoscopic elements are activated, they remain in this condition until the end of the analysis. On the other hand, the coupling elements need to be activated or deactivated, according to the new boundary transition between the meshes that evolves during the analysis.

In this way, degrees of freedom can be removed and added to the system of equations during the analysis. Therefore, the global internal forces and the stiffness matrix, written in Equations (7) and (8), can be rewritten as assembling of the contributions from the macroscale (M), the mesoscale (m) and the coupling elements (C) as:

$$\mathbf{F}^{\text{int}} = \underbrace{\mathop{\mathrm{A}}_{e=1}^{nel(\mathrm{M})}\left(\mathbf{F}_e^{\text{int}}\right)_{(\mathrm{M})}}_{\text{Macroscopic elements}} + \underbrace{\mathop{\mathrm{A}}_{e=1}^{nel(\mathrm{m})}\left(\mathbf{F}_e^{\text{int}}\right)_{(\mathrm{m})}}_{\text{Mesoscopic elements}} + \underbrace{\mathop{\mathrm{A}}_{e=1}^{nel(C)}\left(\mathbf{B}_e^T\mathbf{C}\mathbf{B}_e\mathbf{D}_e\right)_{(C)}}_{\text{Coupling elements}} \tag{10}$$

$$\mathbf{K} = \underbrace{\mathop{\mathrm{A}}_{e=1}^{nel(\mathrm{M})}\left(K_e\right)_{(\mathrm{M})}}_{\text{Macroscopic elements}} + \underbrace{\mathop{\mathrm{A}}_{e=1}^{nel(\mathrm{m})}\left(K_e\right)_{(\mathrm{m})}}_{\text{Mesoscopic elements}} + \underbrace{\mathop{\mathrm{A}}_{e=1}^{nel(C)}\left(\mathbf{B}_e^T\mathbf{C}\mathbf{B}_e\right)_{(C)}}_{\text{Coupling elements}} \tag{11}$$

4 NUMERICAL RESULTS

4.1 *Three-point bending test*

In this example the influence of the adaptive mesh predictor on the amplitude of the mesoscale mesh activated during the analysis are studied. A notched beam loaded in three points is simulated, assuming the hypothesis of the plane stress condition, varying the predictor value of the adaptive model. Figure 6 and Figure 7 illustrate the two independent meshes generated for the concrete in macro and mesoscale, respectively, with the dimensions of the beam and the boundary condition applied.

The parameters adopted for the homogenized concrete and for each phase of the concrete in mesoscale are summarized in Table 2. The different adaptive mesh predictors assumed are: $\mathrm{Ft}_{\mathrm{adap}}$ = 0.5, 1.5, 2.5, 3.5, 4.2 and 5.0 MPa, varying from a value much smaller than the ITZ tensile strength to a value higher than the matrix-matrix tensile strength.

Figure 8 presents the final region occupied by the mesoscopic mesh for each values of the adaptive predictor used. Assuming an adaptive predictor much smaller than the ITZ strength, the mesoscale mesh will be activated long before any failure occurs. In this case, a very large region of the macroscopic mesh is replaced by the FEs of the mesoscopic mesh, minimizing the benefit of the adaptive model in terms of computational efficiency (Figure 8a, b).

On the other hand, for values close to the tensile strength of the ITZ or between the tensile strength of the ITZ and the matrix-matrix interface tensile strength, the mesoscopic mesh can be activated in a more restricted region (Figure 8c, d and e). However, for values very close (or equal) to or higher than the tensile strength of the matrix, the mesoscale damage process may be already in

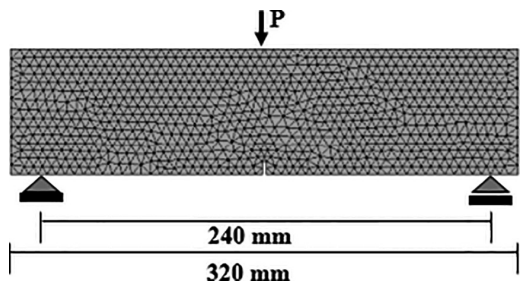

Figure 6. Macroscopic mesh with the boundary conditions.

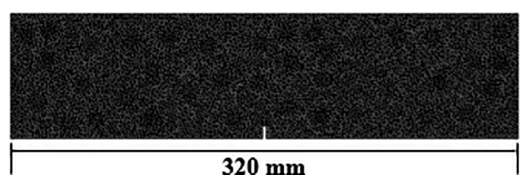

Figure 7. Mesoscopic mesh with explicitly representation of the aggregates, matrix and ZTIs.

Table 2. Material parameters of the beam test.

Materials	Elastic modulus (GPa)	Poisson's ratio	Fracture energy (N/mm)	Tensile strength (MPa)
Concrete	27.3	0.2	–	–
Aggregate	40.0	0.2	–	–
Matrix	20.0	0.2	–	–
Matrix's interface	20.0	0	0.076	4,2
ITZ	20.0	0	0.021	2,5

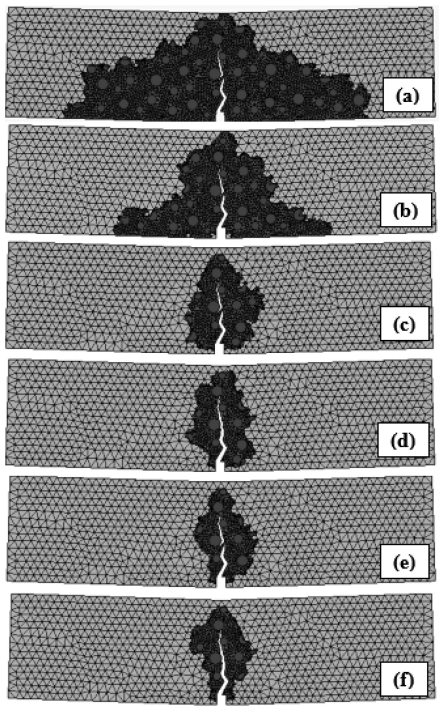

Figure 8. The activated mesoscale mesh for different adaptive predictor: Ft_{adap} = 0.5 MPa, Ft_{adap} = 1.5 MPa, Ft_{adap} = 2.5 MPa, Ft_{adap} = 3.5 MPa and Ft_{adap} = 4.2 MPa and 5.0 MPa.

an advanced stage when the mesoscale mesh is activated. This may negatively affect the prediction of the failure process, producing a spurious difference in the structural curves, as illustrated in Figure 9. Assuming very higher values (higher than the tensile strength of the matrix) may even compromises the convergence of the FE solution.

Therefore, the adaptive predictor should preferable assume values close to the tensile strength of the ITZ or between the ITZ and matrix strengths. In this case, when the mesoscopic mesh is activated the ITZs are still intact or in the initial stage of dam-

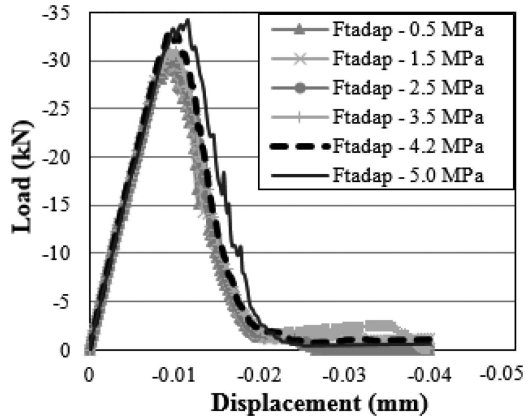

Figure 9. Structural curves for different adaptive indicators.

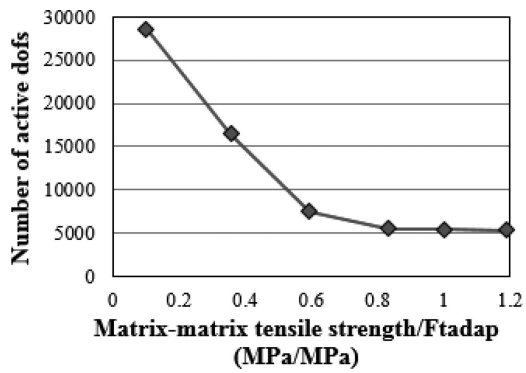

Figure 10. Number of activated dofs versus the ratio of the matrix-matrix interface tensile strength to the adaptive indicator.

age process. Note that, as the value of the adaptive predictor approximates the tensile strength of the matrix, the number of activated FE of the mesoscale mesh becomes smaller, as shown in Figure 10. However, according to the results obtained, values greater than the matrix are not recommended.

4.2 *L-shaped specimen*

This second example illustrates the performance of the adaptive concurrent multiscale approach for an L-shaped specimen.

The coarse scale domain of the specimen is discretized using a structured mesh of triangular finite elements and the fine scale is modeled using an unstructured mesh of triangular elements. Figure 11 illustrates the macroscopic mesh with the boundary conditions and the mesoscopic discretization. The properties assumed for the adaptive

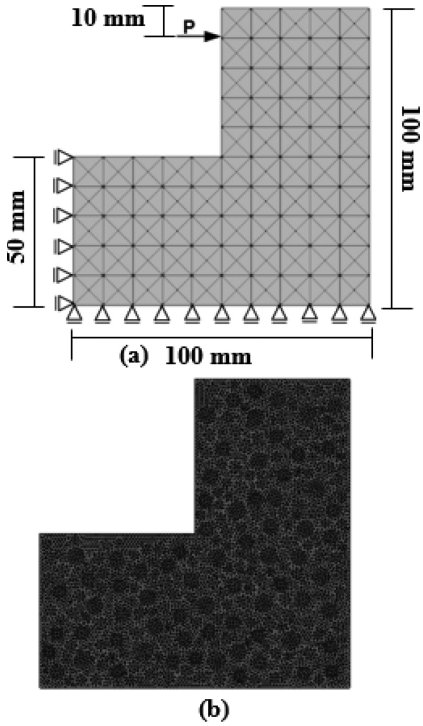

Figure 11. L-shaped specimen: a) macroscopic mesh and boundary conditions and b) initially inactivated mesoscopic mesh.

Table 3. Material parameters of the panel.

Materials	Elastic modulus (GPa)	Poisson's ratio	Fracture energy (N/mm)	Tensile strength (MPa)
Concrete	20.5	0.2	–	–
Aggregate	37.0	0.2	–	–
Matrix	18.5	0.2	–	–
Matrix's interface	18.5	0	0.10	4.2
ITZ	18.5	0	0.07	3.2

multiscale analysis are listed in Table 3. The adaptive mesh predictor assumed is $Ft_{adap} = 3.5$ MPa.

Figure 12 shows the deformed configuration of the specimen for four different loading stages, where the activated mesoscale mesh can be observed. The crack initiates at the corner and propagates toward the other side of the specimen, and, consequently, the mesoscopic mesh is activated following this crack propagation direction. The crack patterns obtained with the adaptive multiscale simulation (AMS) and with the direct numerical simulation in mesoscale (DNS-M) are

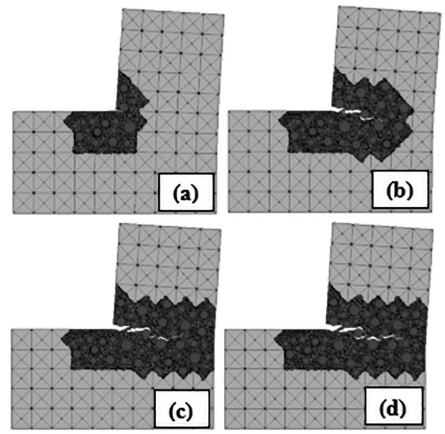

Figure 12. Deformed configuration of the specimen for different percentage of load: a) 15%, b) 30%, 50% and 100% of the total load.

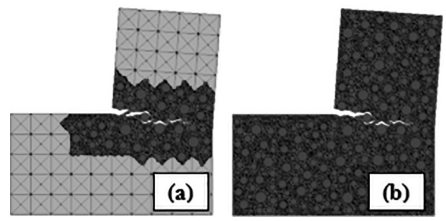

Figure 13. Adaptive multiscale and DNS crack patterns.

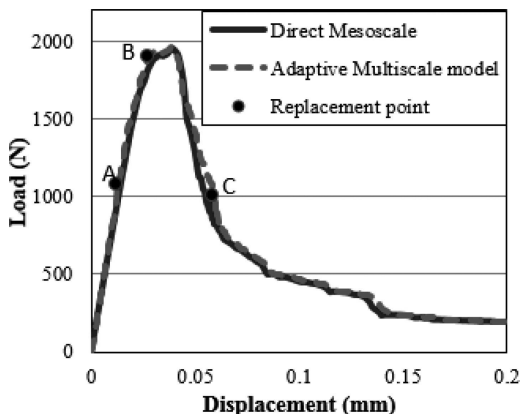

Figure 14. Load – displacement curves for direct simulation in mesoscale and adaptive multiscale model.

shown in Figure 13. As can be seen the crack paths are very similar.

Figure 14 presents the curves of the applied load against the displacement, obtained with the adaptive multiscale model and with the DNS-M model. Note that the difference between the curves

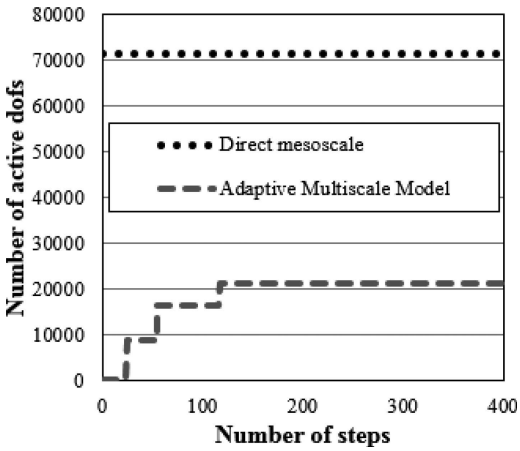

Figure 15. Number of active dofs (starts with 324 and finishes with 21,210 dofs) as function of the analysis steps.

is not significant. On the other hand, the history of the activated degrees of freedom (dof) during the analysis, shown in Figure 15, demonstrates the drastically reduction of the computational effort that the proposed adaptive model provides in comparison with the DNS-M model.

4.3 *Notched beam tested by Grégoire et al. (2013)*

In this third example, a notched beam experimentally tested by Grégoire et al. (2013) is simulated, using both DNS-M and AMS.

The beam has height and depth of 50 mm. Figure 16 illustrates the macroscopic mesh, containing 849 elements, the boundary conditions, as well as the mesoscopic mesh with 22,641 elements.

Table 4 shows the properties assumed in the numerical analysis, in which the elastic parameters were obtained performing an inverse analysis, using the theoretical model based on the rule of mixture so-called model of Counto (1964) in parallel. For this case, the adaptive mesh predictor assumed is $Ft_{adap} = 3.5$ MPa.

More details about the parameters and about the mesoscale modeling adopted for the beam, such as the aggregate generation, diameters and volume fraction, can be found in Rodrigues et al. (2016).

Figure 17 presents the deformed configuration of the beam for five different loading stages, where the progressively activation of the mesoscale mesh can be observed. A macro-crack initiates at the notch and propagates toward the point load. Thus, mesoscopic mesh is progressively activated in this direction. The crack patterns obtained with

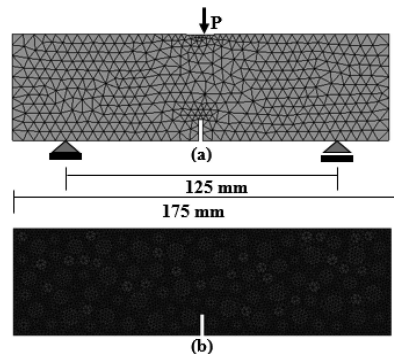

Figure 16. L-Beam in bending: a) macroscopic mesh and boundary conditions and b) initially inactivated mesoscopic mesh.

Table 4. Material parameters of the beam.

Materials	Elastic modulus (GPa)	Poisson's ratio	Fracture energy (N/mm)	Tensile strength (MPa)
Concrete	37.0	0.2	–	–
Aggregate	50.0	0.2	–	–
Matrix	30.2	0.2	–	–
Matrix's interface	30.2	0	0.10	5.2
ITZ	30.2	0	0.05	2.6

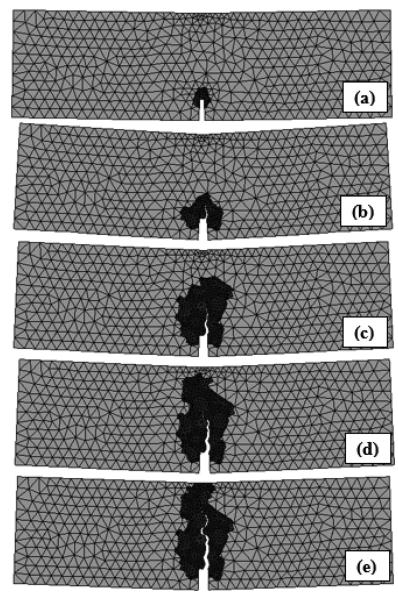

Figure 17. Deformed configuration of the beam at different stages of load: a) load-step 20 (scaling factor of 200), b) load-step 70 (scaling factor of 200), c) load-step 100 (scaling factor of 100), d) load-step 130 (scaling factor of 70) and load-step 230 (scaling factor of 30).

the AMS and DNS-M models are illustrated in Figure 18. The crack paths differ a little, possibly due to the high mesh resolution of the entire domain of the DNS-M model.

The applied load versus displacement curves obtained with the AMS and DNS-M are compared with the experimental curve in Figure 19.

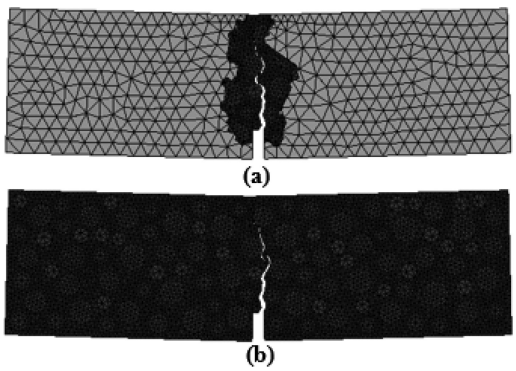

Figure 18. AMS and DNS-M crack patterns.

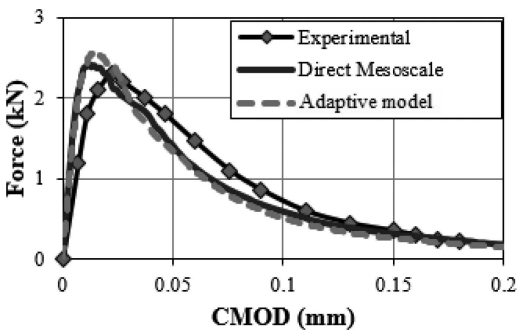

Figure 19. Force-CMOD curves for the experimental and numerical results.

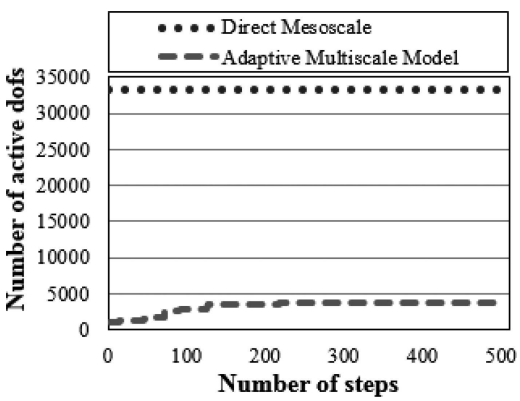

Figure 20. Number of active dofs by the analysis steps.

Table 5. Computational time in seconds.

	DNS-M (s)	AMS (s)
Number of degree of freedoms (DOF's)	33,315	965–3,783
First step solving time	11.67	3.81
Last step solving time	11.64	10.07
Total elapsed time for the 500 steps	5,831	4,308

The structural curves obtained are very close and agree well with the experimental result, showing the ability of the proposed model to predict the crack formation and propagation for composite materials like concrete.

The history of the activated degree of freedom (dof) during the analysis, shown in Figure 20, demonstrates the drastically reduction of the computational effort provided by the proposed adaptive model in comparison with the DNS-M model.

Table 5 shows the computational time (cputime) for the DNS-M and AMS models. These analyses were performed on a laptop with Intel Core i5 CPU M 450 @ 2.40 GHz, with 4 GB of installed RAM using 64-bit operating system.

The computation time of the AMS is less than the DNS-M, confirming the efficiency of the AMS in terms of computational time and memory demands.

5 CONCLUSIONS

An efficient adaptive multiscale approach is presented, which is able to deal with cases in which the region where the nonlinear behavior associated with crack propagation cannot be estimated in advance. The macroscopic finite element mesh is replaced by the mesoscopic one, when the adaptive mesh predictor based on the maximum positive principal stress exceeds an imposed limit. As illustrated in the second and third examples, the adaptive approach is able to provide results similar to the results obtained using full mesoscale model but with reduced computational cost. Some important strategies and techniques used in the presented multiscale approach are:

- The mesh fragmentation technique (MFT), which is based on the use of the solid elements with high aspect ratio in between all regular elements of the mortar matrix and between the elements of the mortar matrix and aggregate, modeling the ITZ.
- A simple continuum damage constitutive model based on the tensile stresses normal to the base of the interface elements that, along with the MFT,

showed to be appropriate to predict the complex process of propagation of cracks without the need of special schemes to track the crack paths during the analysis. This approach showed to be very attractive to describe the dissipation process involving the initiation of cracks in the ITZs, their propagation through the mortar matrix and the coalescence process leading to the formation of a predominant macro-crack path.
- The coupling mesh technique to ensure displacement compatibility on the transition between the macro and the mesoscale meshes, as proposed by Bitencourt et al. (2015). This technique is based on the definition of coupling finite elements (CFEs), which can ensure the continuity of displacement between non-matching meshes, in cases of non-overlapping and overlapping meshes, without increasing the total number of degrees of freedom of the problem.

REFERENCES

Bitencourt, Jr., L.A.G., Manzoli, O.L., Prazeres, P.G.C., Rodrigues, E.A. & Bittencourt, T.N. 2015. A coupling technique for non-matching finite element meshes. *Comput. Methods Appl. Mech. Engrg*. 290: 19–44.

Counto, U.J. 1964. The effect of the elastic modulus of the aggregate on the elastic modulus, creep and creep recovery of concrete. *Mag. Concr. Res.* 16(48): 129–138.

Cusatis, G., Cedolin, L. 2007. Two-scale study of concrete fracturing behaviour. *Eng. Fract. Mech.* 74: 3–17.

Etse, G. & Caggiano, A. 2012. Multiscale failure analysis of fiber reinforced concrete based on a discrete crack model. *International Journal of Fracture* 178: 131–146.

Grégoire, D.; Rojas-Solano, L.B. & Pijaudier-Cabot, G. 2013. Failure and size effect for notched and unnotched concrete beams. *Int. J. Numer. Anal. Meth. Geomech.* 37:1434–1452.

Ghosh, S., Lee, K. & Raghavan P. 2001. A multi-level computational model for multi-scale damage analysis in composite and porous materials. International journal of solids and structures 38: 2335–2385.

Lloberas-Valls, O., Rixen, D.J., Simone, A. & Sluys, L.J. 2012. Multiscale domain decomposition analysis of quasi-brittle heterogeneous materials. *International Journal for Numerical Methods in Engineering* 89: 1337–1366.

Manzoli, O.L., Gamino, A.L., Rodrigues, E. A. & Claro, G.K.S. 2012. Modeling of interfaces in two-dimensional problems using solid finite elements with high aspect ratio. *Computers and Structures* 94–95: 70–82.

Manzoli, O.L., Maedo, M.A., Bitencourt Jr., L.A.G. & Rodrigues, E.A. 2016. On the use of finite elements with a high aspect ratio for modeling cracks in quasi-brittle materials. *Engineering Fracture Mechanics* 153: 151–170.

Nguyen, V.P., Stroeven, M. & Sluys, L. J. 2012. Multi-scale failure modeling of concrete: Micromechanical modeling, discontinuous homogenization and parallel computations. *Comput. Methods Appl. Mech. Engrg.* 201–204: 139–156.

Oliver, J., Cervera, M. & Manzoli, O.L. 1999. Strong discontinuities and continuum plasticity models: the strong discontinuity approach. *Int. J. Plast*. 15(3): 319–351.

Oliver, J. & Huespe, A.E. 2004. Continuum approach to material failure in strong discontinuity settings. *Computer Methods in Applied Mechanics and Engineering* 193(30–32): 3195–3220.

Oliver, J., Huespe, A. E. & Cante, J. C. 2008. An implicit/explicit integration scheme to increase computability of non-linear material and contact/friction problems. *Computer Methods in Applied Mechanics and Engineering* 197(21–24): 1865–1889.

Oliver, J., Caicedo, M., Roubin, E., Huespe, A. & Hernández, J. 2015 Continuum approach to computational multiscale modeling of propagating fracture. *Comput. Methods Appl. Mech. Eng*. 294: 384–427.

Oliver, J., Caicedo, M., Huespe, A.E., Hernández, J.A. & Roubin, E. 2017. Reduced order modeling strategies for computational multiscale fracture. *Comput. Methods Appl. Mech. Eng.* 313: 560–595.

Rodrigues, E.A., Manzoli, O.L., Bitencourt Jr, L.A.G. & Bittencourt, T.N. 2016. 2D mesoscale model for concrete based on the use of interface element with a high aspect ratio. *International Journal of Solids and Structures* 94–95: 112–124.

Rodrigues, E.A., Manzoli, O.L., Bitencourt Jr, L.A.G., Bittencourt, T.N. & Sánchez, M. 2018. An adaptive concurrent multiscale model for concrete based on coupling finite elements. *Comput. Methods Appl. Mech. Engrg*. 328: 26–46.

Roubin, E., Vallade, A., Benkemoun & Colliat, J.B. 2015. Multi-scale failure of heterogeneous materials: A double kinematics enhancement for Embedded Finite Element Method. *International Journal of Solids and Structures* 52: 180–196.

Sánchez, M., Manzoli, O. & Guimarães, L. 2014. Modeling 3-D desiccation soil crack networks using a mesh fragmentation technique. *Comput. Geotech.* 62 (0): 27–39.

Sun, B & Li, Z. 2016. Adaptive concurrent three-level multiscale simulation for trans-scale process from material mesodamage to structural failure of concrete structures. *International Journal of Damage Mechanics*. 25(5): 750–769.

Toro, S., Sánchez, P.J., Blanco, P.J., de Souza Neto, E.A., Huespe, A.E. & Feijóo, R.A. 2016. Multiscale formulation for material failure accounting for cohesive cracks at the macro and micro scales. *International Journal of Plasticity* 76, 75–110.

Unger, J. F. & Eckardt, S. 2011. Multiscale modeling of concrete. *Archives of Computational Methods in Engineering* 18:341–393.

Vernerey, F.J. & Kabiri, M. 2012. An adaptive concurrent multiscale method for microstructured elastic solids. *Comput. Methods Appl. Mech. Engrg.* 241–244: 52–64.

Wriggers, P. & Moftah, S.O. 2006. Mesoscale models for concrete: homogenization and damage behaviour. *Finite Elements in Analysis and Design* 42:623–636.

Computational Modelling of Concrete Structures – Meschke, Pichler & Rots (Eds)
© 2018 Taylor & Francis Group, London, ISBN 978-1-138-74117-1

Multi-scale modelling of the mechanics of concrete based on the cement paste properties

G. Lifshitz Sherzer & E. Gal
Department of Structural Engineering, Ben-Gurion University in The Negev, Beer-Sheva, Israel

E. Schlangen & G. Ye
Faculty of Civil Engineering and Geo-science, Delft, The Netherlands

ABSTRACT: The mechanical response of concrete is complex and as other composite materials, multiscale modelling has the potential for modeling its macroscopic behavior. This paper presents an upscaling methodology for the modelling of the concrete mechanical properties. The suggested formulation starts from a known chemical and mechanical set of parameters of the cement paste, which are used to evaluate the mechanical properties of the LDPM (Lattice Discrete Particle Model) concrete mechanical parameters. The parameters are divided to groups, which are related to different damage modes such as: pore collapse and material compaction, cohesive behavior, and shear behavior. For each group of parameters, a set of microscopic simulations are performed to complete the up-scaling methodology.

1 INTRODUCTION

Concrete is a material that shows significant differences in the behavior of the stress-strain diagram under various combinations of loads. As concrete is considered as a composite material, the stress state within a specimen is strongly heterogeneous, even for homogeneous macroscopic loading situations. The concrete under tensional loads performs a softening behavior after the fracture strength is reached. Therefore, the specimen does not collapse instantaneously but the stress decreases gradually for increasing deformation. The softening behaver is strongly depended on the microstructure changes, for example change in the mineral composition, water to cement (w/c) ratio, change in the components of the elastic material stiffness, see also Z. Qian (2012). According to G. Hofstetter (1995), approximately at 60% of the maximum load, microcracks form through the Interface Transition Zone (ITZ) between aggregates and mortar matrix. By increasing the load, the interface cracks form through the mortar matrix and additional microcracks initiate within the mortar matrix. However, the damage of concrete under compression starts at very low strain-levels leads to failure in a progressive way, consequently the pre-critical crack growth is much larger than in tension.

For the behavior of concrete under high levels of confinement begins with initial peak point due to collapse of the material porous microstructure and followed by a hardening behavior due to closure of the pores. X. Vu et al. (2009) focus on the effects of the (w/c) ratio, entering the fresh concrete composition, on hardened concrete behavior under very high confinement. The finding of that work was that a drop-in (w/c) ratio pushes the confinement threshold higher, however beyond a critical mean stress, the limit state curve becomes independent of (w/c) ratio.

The damage of concrete under shear loads, appears as a mechanism induce tensile stresses in the concrete near the crack. Once the tensile strength of the concrete in these regions is reached, existing flexural cracks propagate in a diagonal direction or new cracks are created.

This paper deals with the development of a methodology for upscaling the cement scale response to obtain the mechanical parameters at the concrete scale. The evaluation of mechanical LDPM's parameters was achieved from the lower scale models under different load combinations that is suitable to represent the failure mechanism of the parameters. In this paper, we achieved from the suggested upscaling method, the flowing parameters; two cohesive, one shear and six pore collapses under compaction, while two elastic and four remaining parameters were achieved by macroscopic calibration.

The suggested methodology is based on a multiscale analysis procedure, in which material properties at the macro scale are evaluated based on lower scales. The cement paste scale is characterized by cement products prior to and following

the hydration process; the cement grain particle size range is 1–50 μm. For this scale, we suggest analysis using a lattice model Z. Qian *et al.* (2012). For the mortar-s scale including the cement paste as a matrix, sand as inclusion, and an (ITZ); the sand particle size range is 1.2–0.5 mm. For this scale, we suggest using the Anm and lattice models Z. Qian et al. (2016), Z. Qian et al. (2012). The mortar-a4 scale includes the combination of mortar-s as a matrix, with aggregates smaller than 4 mm as inclusions and an interface layer between them; the aggregate size range is 2.36–4 mm. The designation mortar-a4 was given to emphasize the fact that the aggregates are smaller than 4 mm. For this scale, we suggest using the Anm and lattice models Z. Qian et al. (2016), Z. Qian et al. (2012). The concrete scale includes aggregates larger than 4 mm (and usually up to 20 mm) and mortar-a 4 as a matrix; we consider this scale to be the concrete scale. For this scale, we suggest using the LDPM.

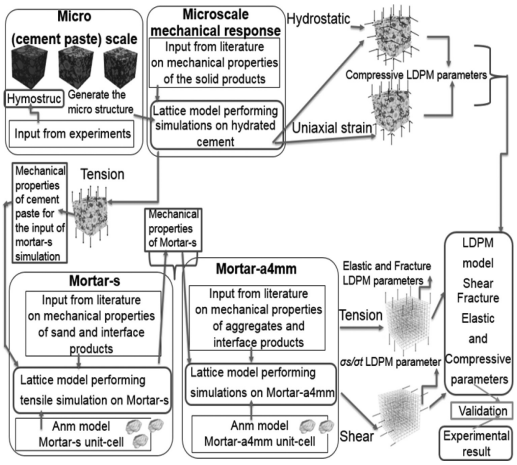

Figure 2. Flowchart of the suggested upscaling procedure.

2 METHODOLOGY OF RESEARCH

The upscaling suggested procedure bridges between the scales from the properties of the lower scales. Each LDPM parameters relate to a different failure modes and can therefore, be derived from a different set of simulations G. Cusatis, et al. (2011A, B) of the lower scales. The constitutive equations of the LDPM represent the mechanical behavior at the facets in which the mortar is located; therefore, it can be assumed that the facet failure modes can be characterized by a unit cell of the mortar, which includes aggregates smaller than 4 mm. As depicted in Figure 1 we assumed that the mortar-a4 scale is suitable to represent the unit cell of the facet, however to represent the failure criterion of the pore collapse mode, we assumed that it can be characterized by a unit cell of the cement paste, since only at that scale porosity is consider. The flowchart of the suggested methodology is depicts in Figure 2.

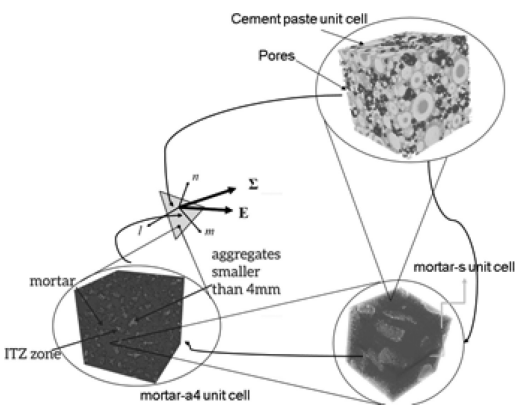

Figure 1. The LDPM facet and the lower scale unit cells.

For convenience, we divided the LDPM parameters (for more details see G. Cusatis et al. (2011), Z.P.; Bazant (1989)) to the following groups:

2.1 *Elastic parameters*

Two elastic parameters, which obtained at this stage of the research using macroscopic calibration:

1. E_0, the normal elastic modulus.
2. α the shear-normal coupling parameter.

2.2 *Fracture parameters*

Two fracture parameters, which represent the tensile mode:

1. σ_t, tensile strength
2. l_t, modified characteristic length

These two parameters were achieved using the suggested methodology as depicted in Figure 2.

2.3 *Pore collapse parameters*

Six pore collapse and material compaction parameters, which represent the compression behavior:

1. σ_{co} the yielding compressive stress.
2. E_D/E_0 the densification ratio.
3. H_{co}/E_0 the initial hardening modulus ratio.
4. k_{co} the transitional strain ratio.

5. k_{c1} nonlinear evolution parameter.
6. k_{c2} nonlinear evolution parameter.

These two parameters were achieved using the suggested methodology as depicted in Figure 2.

2.4 *Shear parameters*

Two shear parameters representing the interaction between shear and tensile behavior.

1. n_t, shear softening exponent parameter, at this stage of the research obtained using macroscopic calibration.
2. σ_s/σ_t is the shear-to-tensile strength ratio. These parameters were achieved using the suggested methodology as depicted in Figure 2.

3 RESULTS

For validation, we compare the numerical results obtained using the suggested methodology with experimental results (see Sherzer et al. (2015)), as shown in Figure 3. Figure 3, shows a comparison of the longitudinal and transverse displacement components measured from uniaxial compression test of a 100 mm × 100 mm × 100 mm concrete specimen. The input of the cement paste scale is given in Table 4 and 5. The Up-scaled LDPM parameters using the suggested methodology and

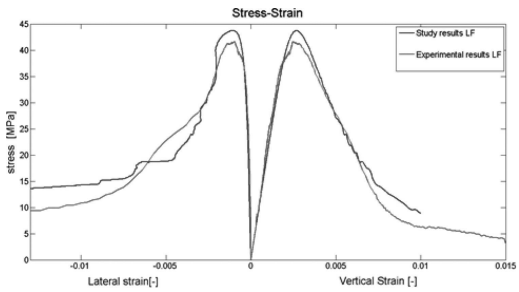

Figure 3. Uniaxial compression test; experimental and numerical results.

Table 1. Concrete Mix-design parameters.

Parameters	Units Kg/m^3	–	Units mm
C	391	–	–
w/c	–	0.567	–
a/c	–	2.2532	–
d_o	–	–	4
d_a	–	–	14
N_F	–	0.425	–

Table 2. Up-scaled LDPM parameters.

Parameters	Calibrated MPa	–	Up-scaled MPa	–
σ_t	4.03	–	4.259	–
G_t	32.32	–	29.62	–
σ_s/σ_t	–	2.7	–	2.63
σ_{co}	70	–	81.09	–
Hco/E_0	0.4	–	0.35	–
K_{c0}	–	2	–	2.72
K_{c1}	–	1	–	1
K_{c2}	–	5	–	0.4975

Table 3. Calibrated LDPM parameters.

Parameters	Calibrated MPa	–
E_0	30150	–
α	–	0.38
n_t	–	0.5
μ_o	–	0.2
μ_∞	–	0
σ_{No}	–	600

Table 4. Chemical properties of the cement.

Characteristic	Inputs specification
Mineralogical composition (%)	C3S: 54.9, C2S: 19.1, C3A: 4, C4AF: 8.8
Chemical composition (%)	Al_2O_3: 6.41, SiO_2: 20.39, MgO: 1.08, CaO: 58.58, Fe_2O_3: 3.92, SO_3: 2.92, Na_2O: 0.22, K_2O: 0.44
Minimum particle diameter	1 μm
Cement fineness (Rosin–Rammler distribution)	n = 1.05771, b = 0.04282
Curing temperature	20°C

the calibrated LDPM parameters are presented in Table 2 and Table 3 respectively, while the concrete mixture properties are presented in Table 1.

The stress-strain curves that is presented in Figure 3, demonstrates that the discrepancy between the experimental results and the numerical results as excellent were 8 parameters were obtain from the lower scale properties. Therefore, we conclude that the proposed method of bridging the scales is an effective way to provide accurate results. More details can be found in Sherzer et al. (2017A, B).

Table 5. Mechanical Properties of the Cement Paste Constituents (see Z. Qian (2012)).

No.	Element type	Young modulus E GPa	Shear modulus G GPa	Tensile strength *ft* GPa	Compression strength *fc* GPa
1	Unhydrated cement	135	52	1.8	–18
2	Interface Unhydrated and Inner	49	20	0.24	–24
3	Inner product	30	12	0.24	–24
4	Interface Inner and Outer	25	10	0.15	–1.5
5	Outer product	22	8.9	0.15	–1.5
6	Interface Outer and CH	26.4	10.6	0.15	–1.5
7	(CH) Calcium Hydroxides	33	13.2	0.264	–2.64
8	Interface Unhydrated and Outer	38	15.2	0.15	–1.5
9	Interface Inner and CH	31.5	12.6	0.24	–2.4

4 DISCUSSION AND CONCLUSION

This paper presents a methodology for evaluating the nonlinear properties of concrete based on the cement paste chemical and mechanical properties.

The tensile and the shear parameters obtained from microscopic simulations of the cement paste, sand and mortar scales, while the compression parameters obtain from microscopic simulations of the cement paste scale. Further research is required to enable upscaling the full set of the LDPM parameters related to the friction and interaction phenomena.

This methodology provide the basis for a powerful design tool, which illuminate the influence of the lower scales on the concrete macroscopic strength.

ACKNOWLEDGMENTS

This research was supported by the Israel Ministry of Science, Technology and Space, Government of Israel; COST Action TU1404; and Nesher-Israel Cement Enterprises.

REFERENCES

Bažant, Z.P.; Pijaudier-Cabot, G. Measurement of characteristic length of nonlocal continuum. J. Eng. Mech. 1989, 115, 755–767.

Cusatis, G.; Pelessone, D.; Mencarelli, A.: Lattice discrete particle model (LDPM) for failure behavior of concrete. I: Theory. Cement and Concrete Composites. 33 (9), 881–890 (2011).

Cusatis, G.; Mencarelli, A.; Pelessone, D.; Baylot, J.: Lattice Discrete Particle Model (LDPM) for failure behavior of concrete. II: Calibration and validation. Cement and Concrete composites. 33 (9), 891–905 (2011).

Garboczi, E.J.; Bentz, D.P.: Computer simulation and percolation theory applied to concrete. Annual Reviews of Computational Physics VII. 85 (1999).

Hofstetter, G.; and H. Mang, Computational mechanics of reinforced concrete structures: Vieweg + Teubner Verlag, 1995.

Poinard, C.; Malecot, Y.; Daudeville, L.: Damage of concrete in a very high stress state: experimental investigation. Materials and Structures. 43 (1–2), 15–29 (2010).

Qian, Z.; Schlangen, E.; Ye, G.; Van Breugel, K.: Multiscale lattice fracture model for cement-based materials. IN: ICCM 2012: 4th International Conference on Computational Methods, Gold Coast, Australia, ICCM: Gold Coast, Australia, 2012; pp. 25–28.

Qian, Z.; Multiscale modeling of fracture processes in cementitious materials. Ph.D. Thesis, Delft University of Technology, Delft, The Netherlands, 2012.

Qian, Z.; Garboczi, E.; Ye, G.; Schlangen, E. Anm: A geometrical model for the composite structure of mortar and concrete using real-shape particles. Mater. Struct. 2016, 49, 149–158 (2016).

Sherzer, G.; Marianchik, E.; Cohen, R.; Gal, E.; Development, Calibration, and Validation of Lateral Displacement for a Concrete Uniaxial Compression Test. In CONCREEP 10„ Vienna University of Technology, Austria, 2015 pp. 1420–1429.

Sherzer, G.; Gao, P.; Schlangen, E.; Ye, G.; Gal, E.; Upscaling Cement Paste Microstructure to Obtain the Fracture, Shear, and Elastic Concrete Mechanical LDPM Parameters. Materials. 10 (3), 242 (2017).

Sherzer, G.; Gao, P.; Schlangen, E.; Ye, G.; Gal, E.; Microstructure Upscaling to Obtain the Compressive Mechanical Parameter of the Lattice Discrete Particle Model. Presented at the The 4th MC meeting of the COST Action TU1404 in conjunction with the 2nd International RILEM/COST Conference on Early Age Cracking and Serviceability in Cement-based Materials and Structures, Brussels, Belgium 2017.

Vu, X.H.; Malecot, Y.; Daudeville, L.; Buzaud, E.: Effect of the water/cement ratio on concrete behavior under extreme loading. International Journal for Numerical and Analytical Methods in Geomechanics. 33 (17), 1867–1888 (2009).

Van Breugel, K.; Numerical simulation of hydration and microstructural development in hardening cement-based materials (I) theory. Cement and Concrete Research. 25 (2), 319–331 (1995).

Ye, G.; Van Breugel, K.; Fraaij, A.: Three-dimensional microstructure analysis of numerically simulated cementitious materials. Cement and Concrete Research. 33 (2), 215–222 (2003).

Computational Modelling of Concrete Structures – Meschke, Pichler & Rots (Eds)
© 2018 Taylor & Francis Group, London, ISBN 978-1-138-74117-1

Sensitivity estimation of cement paste properties in the microstructural characteristics

J.-S. Kim & T.-S. Han
Department of Civil and Environmental Engineering, Yonsei University, Seoul, Republic of Korea

ABSTRACT: The porosity of cement paste affects its mechanical and thermal properties. Even when two specimens have the same degree of porosity each other, the void distribution considerably affects the behavior of material. To evaluate the material properties of cement pastes statistically, a sensitivity analysis using a First-Order Second-Moment (FOSM) method can be used. This is a probabilistic method to determine the probability distribution of output variables with random input variables. The porosity(ϕ) and continuity of void (L_p area, Ω) are selected as input variables, and the thermal conductivity and stiffness of cement paste are selected as output variables. When a virtual specimen is generated from micro-level computerized tomographic (μ-CT) images of a real cement paste specimen, the specimens that have objective microstructures can be obtained using a reconstruction process. In this study, statistical distributions of input variables are from 64 virtual specimens and output variables are estimated from reconstructed specimens using finite element analysis. Based on sensitivity analysis, sensitivity measures of material properties on both characterizations are evaluated. From this results, the probability distributions of the responses can be estimated and the relation between input and output variables can be evaluated.

1 INTRODUCTION

Concrete is a composite material and is composed of aggregate, cement paste, and water. Among them, the cement paste is a matrix that binds and fills spaces between aggregates. The mechanical, thermal or permeability properties of cement paste are generally related to its microstructural characteristics (Mindess et al. 2003). To characterize the microstructure of cement paste, it is possible to divide the cement paste into two subphases: void and solid. The void distribution or clustering is strongly related to the properties of cement paste. Even if two or more samples of cement paste have the same porosity, their mechanical or thermal properties may be different according to the continuity and connectivity of the void. When new cementitious material is under the development, it is important to determine design parameters for designing the material for the intended use.

Microstructural characterizations can be estimated using two-points correlation functions (Torquato 2002, Chung et al. 2015, Tewari et al. 2004). Among several types of functions, a lineal path function is the probability that a line with length r is entirely located inside the same phase. The physical meaning of this function is the level of continuity of voids inside the material, and the area of the function can be used for the quantified measure of continuous void clustering (Singh et al. 2008). In some studies, the lineal path function is widely used to characterize the microstructure of a material (Zhang and Jivkov 2016, Gokhale et al. 2005, Neithalath et al. 2010). However, few studies have been conducted on the relation between the microstructural characteristics and material properties using the lineal path function.

When evaluating the structural responses, the uncertainty of the material responses or properties is one of the most important considerations. Likewise, in micro-level, the material responses are related on the material characteristics, so that the uncertainty of material characteristics can be concerned for evaluating the material response. By assessing a probabilistic distribution of material characterizations, a probabilistic distribution of material properties can be determined using the statistical method. The First-Order Second-Moment Method (FOSM) predicts the probability distribution of a function (or output variable) from a probability distribution of input variables. This method is widely used for several fields of research that need to consider the uncertainty and to use stochastic approaches (Lee and Mosalam 2005, Kunstmann et al. 2002). However, this method is not widely used to predict properties from material characterizations. The reason is that it is difficult to quantify the microstructural characteistics of the material, as well as to obtain their statistical distributions. For instance, several studies have been conducted on the uncertainty of material parameters (e.g., stiffness, strength) for

steel, concrete and even on seismic motions (Lee & Mosalam 2005). However, at the micro-level, it is difficult to obtain the statistical distribution of material characteristics and even to characterize the microstructure (Wang & Hsu 2009).

To estimate microstructural characterization, μ-CT, one of the non-destructive tests, can be used to determine the microstructure of the cement paste. By stacking cross-sectional versions of CT images, a three-dimensional virtual specimen is generated for finite element analysis, and microstructural characterizations can be obtained using the lineal-path function. Many researchers have studied these CT images in many research fields (Chotard et al. 2003, Gallucci et al. 2007, Lu et al. 2006, Chung et al. 2013, Bossa et al. 2015). In some cases, generating a reconstructed virtual specimen that has a target characteristics of a microstructure is required. The stochastic optimization (Chung et al. 2015, Kumar et al. 2006) can be applied to reconstruct the virtual specimen. That the microstructural characteristics and the property of the reconstructed virtual specimen are the same as the original must be guaranteed.

In this study, the effect of sensitivities of thermal conductivity and stiffness of the cement paste on porosity and void clustering are estimated using the FOSM method. The μ-CT images are used to generate the virtual specimen, and the reconstructed specimens are used to evaluate the properties of the material using the FOSM method. Because few studies have conducted sensitivity analysis of properties on the microstructural characteristics of cement paste, this study offers a methodology for applying to sensitivity analysis on the material level.

2 METHODOLOGY

2.1 *Sensitivity analysis*

The First-Order Second-Moment Method (FOSM) is used to evaluate the effect of the microstructural characteristics of cement paste on the thermal conductivity and stiffness of the material. The FOSM method is one of the sensitivity analyses used to obtain the distribution of outputs from that of input variables. This is a simple approach to predict the uncertainty of responses as compared to the Monte Carlo simulation method (Kunstmann et al. 2002, Lee and Mosalam 2005). For FOSM method, two specimens that satisfy the target microstructural characteristics are needed. In this study, this kind of specimen is called as a target specimen. If the target specimens can be generated, the probabiliistic distributions of responses can be determined only by using two target specimens and without a large numbers of calculations as in the Monte Carlo simulation. In this study, the porosity (ϕ) and continuity of void (Ω) were selected as input random variables, and the thermal conductivity and stiffness were evaluated as output random variables. A schematic of FOSM method is shown in Fig. 1.

The FOSM method is an approximate probability approach used to determine the mean (μ) and standard deviation (std, σ) of outputs from the distribution of input variables. To estimate the effect of porosity (ϕ) and void clustering (Ω) on the properties of a cement paste specimen, the FOSM method was used in this study. The mean and standard deviation of the thermal conductivity and stiffness, which are highly related to the microstructure, were evaluated from the distribution of the input variables as follows:

$$\mu_Y = g(\mu_X) \tag{1}$$

$$\sigma_Y^2 \approx \nabla^T g(\mathbf{X}) \mathrm{cov}[\mathbf{X}] \nabla g(\mathbf{X}) \tag{2}$$

or

$$\sigma_Y^2 \approx \sum_{i=1}^{n} \sum_{j=1}^{n} \frac{\partial g(\mu)}{\partial x_i} \frac{\partial g(\mu)}{\partial x_j} \mathrm{cov}(X_i, X_j) \tag{3}$$

where $\mathbf{X}$ is a random input variable (in this study, the porosity and void continuity) having a mean (μ_X) and a variance (σ_X^2), $\mathbf{Y} = g(\mathbf{X})$ is the system using $\mathbf{X}$ as the input variable (thermal conductivity and stiffness were selected as $\mathbf{Y}$), n is the number of input variables, and cov[·] is the covariance matrix related to the input variables. The gradient of the system function (∇g or $\frac{\partial g}{\partial x}$) is estimated by the central differences method as shown in Eq. 4, as the system $g(X)$ is a result of a finite element simulation performed in this study.

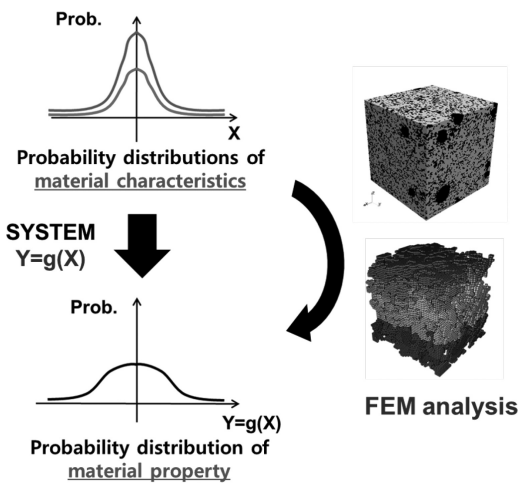

Figure 1. Schematic of FOSM method.

$$\frac{\partial g(\mu)}{\partial x_i} \approx \frac{g(\mu+\Delta x_i)-g(\mu-\Delta x_i)}{2\Delta x_i} \quad (4)$$

In Eq. 4, Δx can be selected as the standard deviation of the input variable. In this study, the system (g) is a finite element analysis, so that the outputs (**Y**) such as thermal conductivity and stiffness are obtained from simulation. The results of system (g) at each point, $\mu \pm \Delta x_i$, can be evaluated, and finally the probabilistic distribution of output can be estimated. The coefficient of variations (CV) is used as the sensitivity measure of the output. The CV is the ratio of the standard deviation to mean, and it is effective to compare the sensitivity of outputs that have different mean values.

2.2 *Microstructural characteristics*

Although cement paste is a multiphase material, the void can be one of the most important phases related to the material property at both the micro and macro levels. Even with the same porosity of two or more samples, their thermal conductivity and stiffness can be different because of the characterization of complex microstructures (Chung et al. 2016). In this study, the void distributions are selected as the microstructural characterization, so that the effect of the void distribution on the material response can be evaluated.

A lineal path function is the probability that a line with length r is completely in the same phase (Torquato 2002). The probability of a line with length r existing within the pore is referred to as L_p in this study. Using this probabilistic function, we can estimate the amount of pores (porosity) and the level of void continuity along a certain direction inside the material. A shape of the lineal path function L_p can mimic the exponential function described in the Eq. 5. Two parameters exist that fit the discrete probability of the virtual specimen.

$$L_p = ae^{br} \quad (5)$$

where a and b are fitting parameters and r is the length of the line. As shown in Fig. 2, a y-intercept of the lineal path function (i.e., a) refers to the porosity of the material. The area of this function is a scalar factor to quantify continuous phases inside the material. In this study, the porosity of cement paste (ϕ) and the L_p area (Ω) are selected as microstructural characteristics.

2.3 *Material property*

The thermal conductivity (k_c) of the cement paste is highly related to the porosity and void distribution. As the porosity of cement paste increases, the heat

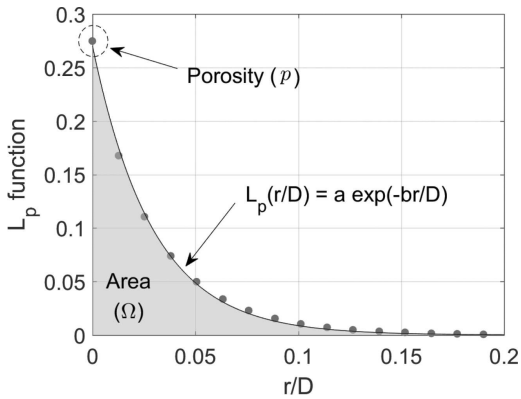

Figure 2. Example of fitted L_p function by exponential function.

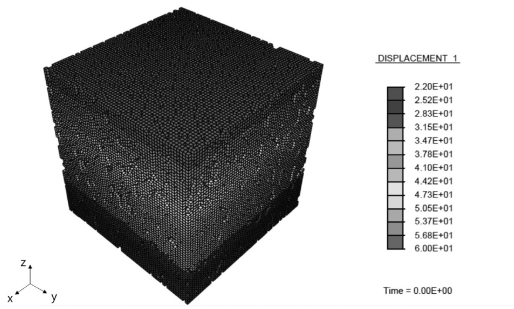

Figure 3. Finite element mesh after the thermal analysis (Note: the temperature of top surface is 60°C and that of the bottom is 22°C).

conductivity decreases and less heat is lost generally. The pore continuity also affects the heat flow. A finite element analysis using FEAP is conducted to estimate the mateiral properties (Taylor 1987). The thermal conductivity of cement paste itself (solid phase) is assumed to be as 1.8 $W \cdot m^{-1} \cdot K^{-1}$. To evaluate the thermal conductivity, thermal analysis is conducted using Fourier's law, as shown in the Eq. 6.

$$q = k_c \Delta T \quad (6)$$

where q is thermal flux (W), k_c is thermal conductivity ($W \cdot m^{-1} \cdot K^{-1}$), and T is temperature (K or °C). A steady state analysis is performed and z-directional heat flow is assumed. The temperature (T) of 60°C is applied to the entire top part of the mesh, and the temperature of the bottom part is restrained to T = 22°C, as shown in Fig. 3. The effective k_c of the specimen is calculated from the simulationresults with obtained heat flux (q).

The stiffness of material (k_s, GPa) is selected as the other material response. The young's modulus

of solid phase is 20 GPa and the elastic stiffness is evaluated along the z-direction. In general, the stiffness of a specimen according to porosity is inversely related to its thermal conductivity. To develop the material in terms of heat conductivity quality and durability, both properties (k_c, k_s) having an inverse relationship to the microstructure must be optimized. Therefore, the sensitivity analysis of material properties can be used to provide a guideline for controlling the microstructural characteristics during the material development process.

3 MODELING FOR VIRTUAL SPECIMEN

3.1 *CT image process*

A virtual specimen is generated from micro-level computerized tomography (μ-CT) images of a real cement paste specimen. The μ-CT images are obtained from a synchrotron accelerator in Pohang, Korea. Because we focus on the characterization of pore distribution in this study, the original reconstructed CT image with 16 bits is converted to binary images after a median filter is applied. The black (0) and white (1) parts in the binary CT images represent void and solid phases, respectively. The three-dimensional virtual specimen is generated by stacking binarized images along the z-direction. The specimen is cement paste having a 0.5 water-cement ratio after 28 days of curing. The porosity of the specimen is assumed to be the value derived from Powers equation (porosity ≈ 0.28) (Powers 1598).

3.2 *Reconstruction of virtual specimen*

For the sensitivity analysis, the virtual specimens that has target microstructural characterizations were required. As mentioned in Section 2.1, to obtain the sensitivity of the material property related on porosity, we need two target samples with porosity values near the mean value ($\mu \pm \Delta x$), whereas the L_p area is fixed to its mean value (Fig. 4). Likewise, when we conduct the sensitivity analysis of material properties on the L_p area, the other input parameter of the specimen (i.e., porosity) has to be fixed at its mean, and two L_p areas ($\mu \pm \Delta x$) are assumed.

The specimens with objective functions can be generated using the stochastic optimization method. The basic idea of the reconstruction is that a virtual energy function (E), which is a summation of errors between the objective function and the function from the reconstructed specimens, is minimized. The stochastic optimization equation is as follows (Eq. 7):

$$E = \sum_{\alpha} \sum_{r} \left[\hat{f}_{\alpha}^{\,L_p}(r) - f_{\alpha}^{\,L_p}(r) \right]^2 \tag{7}$$

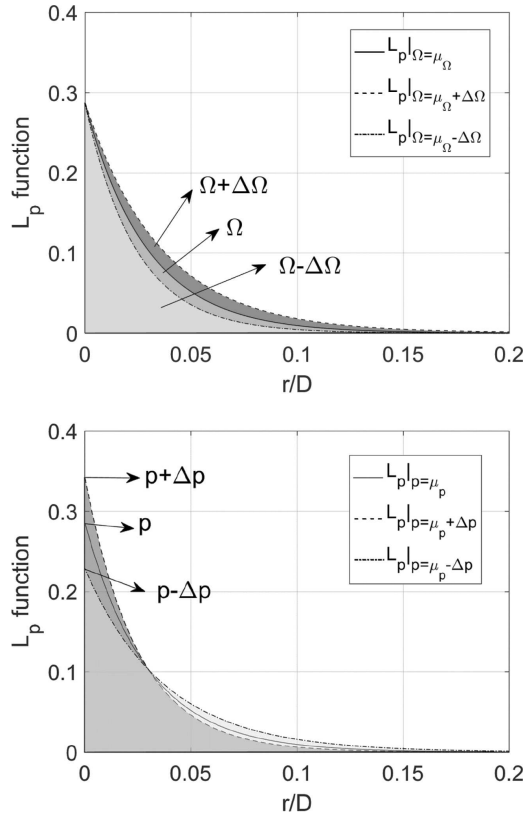

Figure 4. Comparison of objective function and function from reconstructed virtual specimen.

where $\hat{f}_{\alpha}^{\,L_p}(r)$ is a lineal path function of the virtual specimen, $f_{\alpha}^{\,L_p}(r)$ is an objective lineal path function, r is a distance between two random points, and α is a direction (z-direction in this study). Through several iterations of interchanging two elements with different phases, the virtual energy function E progresses into tolerance, and then a target specimen with the objective function can be reconstructed. From this reconstruction process, objective specimens for the sensitivity analysis are obtained.

4 ANALYSIS

4.1 *Probability distributions*

The statistical distribution of material response can be predicted based on the probability distribution of microstructural characterizations. As previously mentioned, the input variables (characterizations) are selected as the porosity (ϕ) and L_p area (Ω), and output variables are material properties such as

thermal conductivity (k_c) and stiffness (k_s). From the probability distribution of input variables, that of output variables is estimated based on Eq. 3.

The virtual specimen produced from the CT images is used to obtain the input values. Using a large specimen with a porosity of 0.28, several specimens are generated by dividing the large specimen into four pieces in each direction. From this process (as shown in Fig. 5), 64 specimens are used to estimate the probability distribution of ϕ and Ω.

The sensitivity measure is calculated using the CV (coefficient of variations). The CV is the ratio of the standard deviation to mean. As shown in Table 1, the CV of porosity and L_p area are 9.92% and 17.04%. respectively. The reconstructed specimens with objective characteristics are generated, and property evaluation is conducted by FE analysis. The probability distribution of material properties ar estimated based on the values from virtual specimens (μ, σ) and those derived from analysis of reconstructed specimens ($g(X)$, $\nabla g(\mathbf{X})$).

4.2 *Sensitivity: porosity (ϕ) versus responses (k_c, k_s) and L_p area (Ω) versus responses (k_c, k_s)*

When the porosity is selected as an input variable, the other parameter has to be fixed. In this case, the L_p area is fixed as the mean values of the L_p area (μ_Ω). To apply the FOSM method, two samples with different porosities are required. Through the reconstruction process, each sample has different porosity ($\mu_\phi \pm \sigma_\phi$) *with the same* L_p area (μ_Ω). To keep generality, five reconstruction specimens are generated; the CV for several specimens at the same objective is less than 0.1% for all cases.

The most important advantage of the FOSM method is that the effect of several input variables on outputs can be separated. In other words, because of the fixed Ω, we could ignore the effect of void continuity on thermal conductivity or stiffness and instead focus on the effect of porosity on the material response. The sensitivity measure (CV) of the thermal conductivity and stiffness are estimated as shown in Table 2. The CV of thermal conductivity according to porosity was 1.57%, whereas that of stiffness is approximately 6.58%. The stiffness is more sensitive to porosity than to thermal conductivity.

By contrast, the sensitivity of responses on the L_p area (Ω) is 0.64 and 0.47%, respectively. The L_p area is relatively less sensitive to material responses than is the porosity. In other words, the L_p area (Ω) can be used to fine-tune the parameter. Even with a slight change in porosity, the properties show considerable changes, whereas a small or notable change in properties can be controlled by a large L_p area. From this point of view, utilizing the L_p area to control the objective properties is desirable.

The probability functions fitted by Gaussian distribution curves are shown in Fig. 6. The probability distributions are obtained from the two reconstructed specimens, which has different porosities (L_p area) with the same L_p area (porosity). The main reason using the FOSM method for sensitivity analysis is that the probability distribution can be evaluated using only two objective samples. When the porosity $g(X_\phi)$ is controlled, both material properties have higher standard deviations and wider distribution than those when the L_p area is controlled. Based on this result, we focus on the independent effect of each material microstructural characterization on thermal conductivity and stiffness. When a restraint is imposed on the porosity under the material development, this result can be utilized effectively.

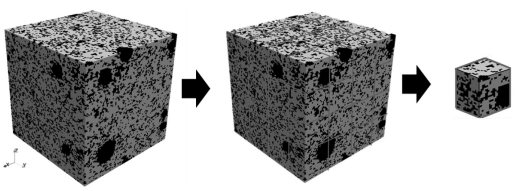

Figure 5. Process of generating specimens.

Table 1. Probability distribution of microstructural characterizations.

	Probability distribution		
Characterization	mean (μ_X)	std (σ_X)	CV (%)
Porosity (ϕ)	0.2866	0.0284	9.92
L_p area (Ω)	0.0113	0.0019	17.04

4.3 *Sensitivity: both characterizations (ϕ, Ω) versus responses (k_c, k_s)*

The porosity and L_p area are closely related. The correlation coefficient (r) between two characterizations is nearly 0.84, which is calculated from the 64 virtual specimens. The higher the correlation coefficient ($r \leq 1$), the more relevant is each parameter. In reality, seperating the effect of two characteris-

Table 2. CV of material responses according to microstructural characterizations.

	Input variables		
Material response	porosity	L_p area	Both
Thermal conductivity (k_c)	1.57	0.64	1.42
Stiffness (k_s)	6.58	0.47	6.34

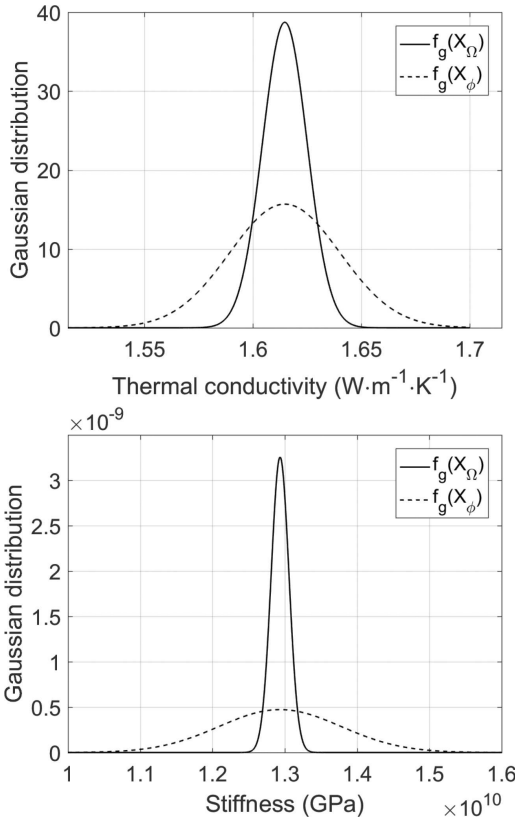

Figure 6. Gaussian distribution of thermal conductivity and stiffness estimated from sensitivity analysis. Here, f(·) is the probability density function.

tics (ϕ, Ω) is difficult. In order to distinguish their effects on the material response, the reconstructed specimens are generated and evaluated for their effect on each of two characteristics on the material properties. When we consider the both on the sensitivity analysis simultaneously, the Eq. 3 is recalled in order to estimate the standard deviation of output variables. Considering the cov (X_i, X_j), the sensitivity measures of thermal conductivity and stiffness are 1.42 and 6.34%. These values are determined between the sensitivity measures of each property on the porosity and L_p area, but are much closer to the sensitivity when only porosity is changed. The reason the sensitivity decrease when both are considered together, is that the signs of ∇g or $\frac{\partial g}{\partial x}$ on porosity and L_p area were different. Therefore, the term that is calculated by multiplying both in the Eq. 3 becomes negative (Table 3).

When this kind of sensitivity analysis is conducted using two randomly selected specimens without reconstruction, the material response

Table 3. Sign of ∇g or $\frac{\partial g}{\partial x}$ according to each input variables.

	Sign of ∇g or $\frac{\partial g}{\partial x}$	
Material response	porosity	L_p area
Thermal conductivity (k_c)	–	+
Stiffness (k_s)	–	+

according to the microstructural characterizations may not be consistent. For instance, a specimen with higher porosity can have larger stiffness. This is because the L_p area referring to the continuity of voids is not controlled. The microstructure possesses randomness. Therefore, without the reconstruction process, the sensitivity estimation of each or both of characterizations is not reasonable. Even though the Monte Calro simulation can give the comparable results, the cost of analysis is much higher than FOSM method. From this sensitivity analysis of material responses on both microstructural characterizations, the probability distributions of the response can be estimated and the relation between input and output variables can be evaluated.

5 CONCLUSION

In this study, the sensitivity of the mechanical and thermal properties of microstructural characterizations of a cement paste specimen are estimated using the FOSM method. The most important advantage of this method is that the effect of several input variables on outputs can be separated or combined together. The porosity (ϕ) and continuity of voids (L_p area, Ω) of a cement paste specimen are selected as input variables and the thermal conductivity (k_c) and stiffness (k_s) are evaluated as output variables using FE analysis. To estimate the probability distributions of output variables, those of input variables are obtained using 64 specimens generated from μ – CT images. To perform the FOSM method, two specimens with objective microstructural characteristics are reconstructed. The sensitivity (CV) of thermal conductivity and stiffness on each input variation is measured using reconstructed specimens. Both output variables are relatively more sensitive to porosity than to the L_p area. This means that the L_p area can be used as a fine-tune parameter. Because the cement paste has highly random microstructure, the reconstruction process is necessary to estimate the sensitivity of the material response based on each characterization. Considering both characterizations (ϕ, Ω) for sensitivity analysis, the sensitivity measures of thermal conductivity and stiffness

decrease slightly compared to that of porosity. From this result, the tendency of the material properties according to microstructural characterizations can be predicted and the probability distributions of the material response can be estimated using only a few specimens. This study can be used as a methodology or guideline for estimating the sensitivity at the material level.

ACKNOWLEDGMENTS

This research was supported by a Korea Research Foundation Grant funded by the Korean Government (NRF–2015K1A3A1A59073929 and NRF–2016R1D1A1B03931635).

REFERENCES

Bossa, N., P. Chaurand, J. Vicente, D. Borschneck, C. Levard, O. Aguerre-Chariol, & J. Rose (2015). Micro- and nano-x-ray computed-tomography: A step forward in the characterization of the pore network of a leached cement paste. *Cement and Concrete Research 67*, 138–147.

Chotard, T., M. Boncoeur-Martel, A. Smith, J. Dupuy, & C. Gault (2003). Application of x-ray computed tomography to characterise the early hydration of calcium aluminate cement. *Cement and Concrete Composites 25*(1), 145–152.

Chung, S.Y., M. Elrahman, D. Stephan, & P. Kamm (2016). Investigation of characteristics and responses of insulating cement paste specimens with aer solids using x-ray micro-computed tomography. *Construction and Building Materials. 118*, 204–215.

Chung, S.-Y., T.-S. Han, & S.-Y. Kim (2015). Reconstruction and evaluation of the air permeability of a cement paste specimen with a void distribution gradient using CT images and numerical methods. *Construction and Building Materials 87*, 45–53.

Chung, S.-Y., T.-S. Han, T. Yun, & K. Youm (2013). Evaluation of the anisotropy of the void distribution and the stiffness of lightweight aggregates using ct imaging. *Construction and Building Materials 48*, 998–1008.

Gallucci, E., K. Scrivener, A. Groso, M. Stampanoni, & G. Margaritondo (2007). 3d experimental investigation of the microstructure of cement pastes using synchrotron x-ray microtomography (μct). *Cement and Concrete Research 37*(3), 360–368.

Gokhale, A., A. Tewari, & H. Garmestani (2005). Constraints on microstructural two-point correlation functions. *Scripta Materialia 53*(8), 989–993.

Kumar, H., C. Briant, & W. Curtin (2006). Using microstructure reconstruction to model mechanical behaviour in complex microstructures. *Mechanics of Materials 38*(8), 818–832.

Kunstmann, H., W. Kinzelbach, & T. Siegfried (2002). Conditional first-order second-moment method and its application to the quantification of uncertainty in groundwater modeling. *Water Resources Research 38*(4).

Lee, T.-H. & K. Mosalam (2005). Seismic demand sensitivity of reinforced concrete shear-wall building using fosm method. *Earthquake engineering & structural dynamics 34*(14), 1719–1736.

Lu, S., E. Landis, & D. Keane (2006). X-ray microtomographic studies of pore structure and permeability in portland cement concrete. *Materials and Structures 39*(6), 611–620.

Mindess, S., J. Young, & D. Darwin (2003). *Concrete*. Prentice Hall.

Neithalath, N., M. Sumanasooriya, & O. Deo (2010). Characterizing pore volume, sizes, and connectivity in pervious concretes for permeability prediction. *Materials characterization 61*(8), 802–813.

Powers, T. (1598). Structure and physical properties of hardened portland cement paste. *Journal of American Ceramic Society 41*, 1–6.

Singh, H., A. Gokhale, S. Lieberman, & S. Tamirisakandala (2008). Image based computations of lineal path probability distributions for microstructure representation. *Materials Science and Engineering: A 474*(1), 104–111.

Taylor, R. (1987). *FEAP-ein finite element analysis programm*. Ing.-Gemeinschaft Klee & Wrigges.

Tewari, A., A. Gokhale, J. Spowart, & D. Miracle (2004). Quantitative characterization of spatial clustering in three-dimensional microstructures using two-point correlation functions. *Acta Materialia 52*(2), 307–319.

Torquato, S. (2002). *Random heterogeneous materials: Microstructure and macroscopic properties*. Springer-Verlag.

Wang, S.-J. & K.-C. Hsu (2009). The application of the first-order second-moment method to analyze poroelastic problems in heterogeneous porous media. *Journal of Hydrology 369*(1), 209–221.

Zhang, M. & A. Jivkov (2016). Micromechanical modelling of deformation and fracture of hydrating cement paste using x-ray computed tomography characterisation. *Composites Part B: Engineering 88*, 64–72.



Taylor & Francis
Taylor & Francis Group
http://taylorandfrancis.com

Computational Modelling of Concrete Structures – Meschke, Pichler & Rots (Eds)
© 2018 Taylor & Francis Group, London, ISBN 978-1-138-74117-1

Elastic-plastic multi scale approach for localization problems—the embedded unit cell

M. Grigorovitch & E. Gal
Department of Structural Engineering, Ben-Gurion University in The Negev, Beer-Sheva, Israel

ABSTRACT: This paper presents theoretical research of multi scale analysis of wide variety of composite materials, such as aluminum alloy or cement matrix with fibers or cement mass containing aggregates. We propose analysis approach, called Embedded Unit Cell (EUC), based on milestones of homogenization theory. The developed mathematical formulation was implemented using the Finite Elements Software package Simulia Abaqus.

The aim of the EUC approach is to evaluate the response of composites using the solution sequence of homogenization theory, but to enhance the applicability of classical homogenization to structure zones that can't be analyzed using classical homogenization due to method restrictions, such as the essential periodicity assumption.

The verification studies include several selected cases, such as Local Global problem or boundary zones of homogeneous structure. The mathematical formulation as well as the numerical and thus software implementation are compatible with physical cases containing pure elastic and combined elastic plastic types of response. For the approach validation purposes, the selected examples can be mostly solved using classical homogenization, since they are based on heterogeneous material with periodic structure. Nevertheless, the benefit of the presented approach is in accurate evaluation of mechanical response in zones, where both or any of geometrical and material periodicity can't be assumed.

1 INTRODUCTION

The multi-scale analysis of composite materials is widely investigated and numerous methods were proposed over the years providing different levels of solution and analysis Hashin & Shtrikman (1963), Aboudi (1991), Chajes, Finch Jr et al. (1996), Van der Sluis, Schreurs et al. (2000), Gal, Yuan et al. (2007), Oskay & Fish (2008), Gibson (2011). Composite materials often include material level behavior, which is essential for proper understanding of the structure response. The advantage of multi-scale analysis is by separating the view on material and structure scales, yet maintaining the information passing between the scales.

The material scale analysis has major impact on material properties evaluation, characterizing the interaction between numerous microscopic components. The microscopic behavior, in turn, is used to prescribe the overall response of macroscopic structure subjected to external loading Budiansky (1965), Takano, Zako et al. (2000), Terada & Kikuchi (2001), Gal & Fish (2008), Gal, Ganz et al. (2008), Valenta, Sejnoha et al. (2010).

One of the most commonly used methods of evaluating structure behavior in multiple scales is homogenization Sanchez-Palencia (1983), Allaire (1992), Gonella (2007), Ghosh, Bai et al. (2009), Fan, Yuan et al. (2010), Mei & Vernescu (2010), Nguyen, Lloberas-Valls et al. (2011), Gal, Suday et al. (2013). Using the asymptotic approximation, complicated cases can be evaluated by solution of several more simplified cases. In two scale example, the macroscopic scale is solved using equivalent material properties, whilst the actual material properties are zoomed in at the microscopic scale.

The application of homogenization theory presumes existence of mechanically representative and geometrically repetitive zone, called Unit Cell. Based on this assumption, the equivalent microscopic material properties are primarily evaluated and then are used to analyze the overall macroscopic structure using much more simplified numerical model.

Since precise analysis of composite materials might require demanding computational resources, utilizing the homogenization theory to implement multi-scale analysis found very useful to shorten valuable processing times.

Despite the benefits of homogenization theory in analyzing homogeneous structures, the applicability to cases where either the structure or the response is not strictly periodic found to be constrained. Significant preprocessing was often proposed

by researchers in order to be able to apply the classical homogenization in the non-periodic cases Dvorak, Bahei-El-Din et al. (1994), Chaboche, Kruch et al. (2001), Gal & Fish (2008), Michel & Suquet (2009).

The proposed EUC formulation presents approach of enhancing the applicability of classical homogenization to boundary and stress concentration zones, preserving the accuracy of the evaluated response.

2 METHODOLOGY

2.1 *EUC Methodology*

As mentioned beyond, the applicability of classical homogenization is restricted to cases, where both the geometric structure and the mechanical response are strictly periodic. This paper presents an approach that enhances the applicability of homogenization theory by avoiding the essential periodicity constraint. The presented approach adopts the special unit cell, called Embedded Unit Cell, in order to use the homogenization theory despite the non-periodic neighbourhood/ conditions.

The schematic description of a macroscopic body and zones of interest are described in Figure 1. The macroscopic domain Ω includes both type of problems that the EUC is challenged with: the homogeneous structure that consists of periodic composite material (Figure 1,(a)) and zone with local materials that are different from Global homogenous materials matrices (Figure 1(b)). Along with the unit cell under test Θ_{Yi}, the Embedded Unit Cell includes the area adjacent to the evaluated unit cell Θ_{Si}, described as surrounding continuum domain, which purpose is to interface between the non-periodic unit cell and presumed strictly periodic rest of the structure.

Moreover, alternative boundary condition Γ_Y are introduced in order to constrain the non-periodic unit cell and properly describe the interface between the internal microscopic unit cell and the surrounding macroscopic domain. Those boundary conditions are derived from the developed non-periodic formulation based on separating the solution to pair of simplified cases.

The multi scale procedure was applied using the Finite Elements software package ABAQUS, while the extended functionality, such as defining user materials, alternative boundary conditions, concurrent and sequential information passing between multiple scales, was achieved using the Abaqus user subroutines based on Fortran platform, such as UMAT and MPC, in addition with Python scripts controlling the analysis procedure.

Both pure elastic and combined elastic–plastic modes of structure were evaluated using complicated programming both in Python and Fortran.

2.2 *EUC numerical implementation*

The verification studies include Local Global case, which is characterized by small areas Θ_{Yi} where material properties differ comparing to the rest of the structure (see Figure 2) Grigorovitch & Gal (2015). Such zones are often expected to develop higher stress fields. In the EUC implementation for the matter of simplicity, we defined them as holes. These stress concentration zones are defined as unit cells evaluated at micro scale and replaced by single finite element with equivalent material properties (without a hole) in the simplified macroscopic model.

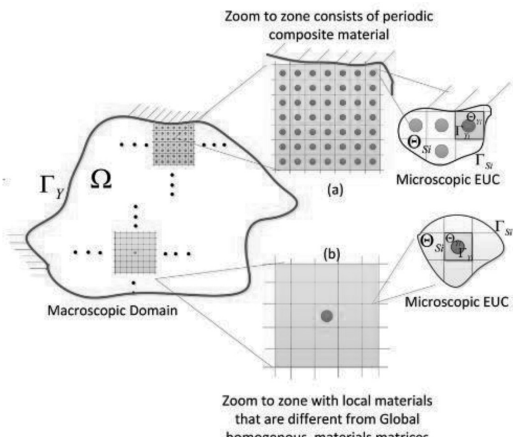

Figure 1. Embedded unit cell for stress concentration problems and boundary effects.

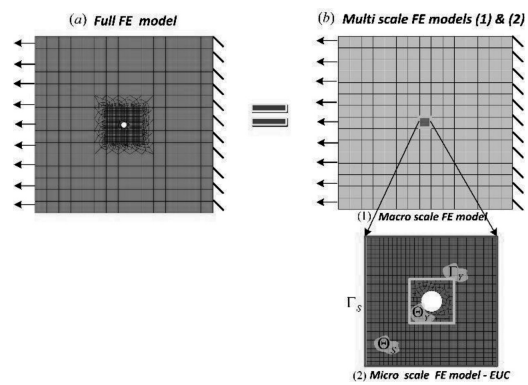

Figure 2. FE modeling based on EUC approach. (a) Full FE model of the plate (reference); (b) macro scale FE model; (c) micro scale FE model of the EUC. Grigorovitch & Gal (2015).

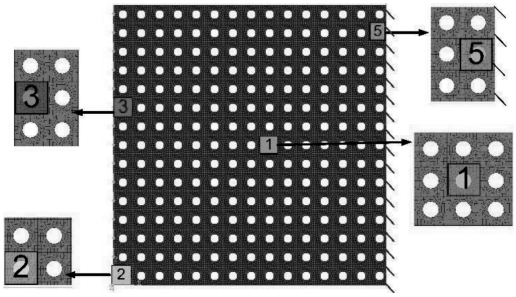

Figure 3. Description of different types of embedded unit cell depending on their macroscopic locations. Grigorovitch & Gal (2017).

Another example used in this research for verification purpose is classical homogenization case (see Figure 3), while the EUC emphasizes the precise modelling and solution of boundary zones Grigorovitch & Gal (2017). The geometry of these zones is not periodic with the rest of the structure, which disqualifies them from being solved using classical homogenization. In order to handle the variety of different geometries, we defined the library of microscopic unit cells including the appropriate boundary conditions and surrounding domain.

The mentioned above examples were verified both in pure elastic type of response and the plastic response. The implementation of procedure supporting the plastic response was involved with developing complicated computational infrastructure using the Newton-Raphson method to evaluate the nonlinear response of the structure. The sequential calculation procedure of macroscopic and microscopic scales appropriates for elastic response had to be changed to concurrent procedure appropriate to plastic response, where material properties and microscopic response differ from one macroscopic load increment to another.

The non-periodic response might be associated with either stress concentration in specific area or vicinity to macroscopic boundary. Assuming that both linear and non-linear response can occur depending on the characteristics of the loading, the proposed non-periodic formulation is separated to multiple paths of solution, as described on EUC procedure flow diagram at Figure 4.

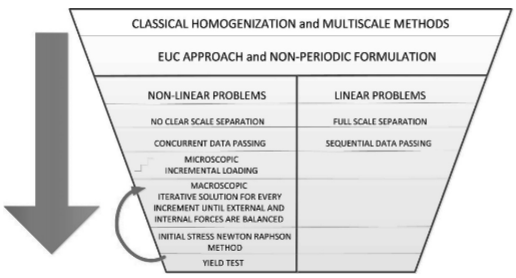

Figure 4. EUC procedure flow diagram.

3 RESULTS

Several numerical examples were verified by applying the EUC approach, such as fixed plate subjected to vertical and horizontal loading, number of beams with variety of boundary conditions.

Selected results are presented below including both pure elastic and elastic–plastic response of the structure. The following are some of the results for different boundary conditions, geometry, loads and different types of response (elastic and elasto plastic) Grigorovitch & Gal (2015).

Figures 5a and 5b depict the reference and the macroscopic model of plate (width and length are both 60 mm) with a small hole (radius r = 1 mm), located at the centre of the plate. The right side of the plate is fixed, and horizontal unit pressure load of 1 N/m is applied to the left side.

Figure 5c shows a comparison of the stress field in the vicinity of the hole using the suggested EUC approach and the reference FEM solution.

First row of images at Figure 5c are from the proposed EUC, while those in the second row represent the reference solution. The columns contain the horizontal stress components and the Von-Mises stress index.

These results show the good agreement between the proposed EUC solution and the reference FEM solution. In contrast, the results obtained using the classical homogenization theory are not satisfying compared to the reference solution (in critical zones, error is exceeding 33%), since the assumption of periodic response of the unit cell is not valid for this problem.

In the next numerical examples we consider beam (60 mm × 420 mm) and circular holes of radius r = 1 mm as shown in Figure 6 Grigorovitch & Gal (2017). The beam is fully supported on its bottom vertices. A constant distributed vertical load of 1 N/m is applied on the upper edge of the beams.

From the stress results at element #15, we conclude that the EUC provides a precise evaluation of maximal stresses and reflects the non-periodic distribution of stresses, which cannot be captured using the classical homogenization theory. The EUC error in the stress values compared to the reference solution is about 3%, while the error using the classical homogenization theory exceeds 15%.

The last example comes to present the elasto plastic type of response, that was evaluated using

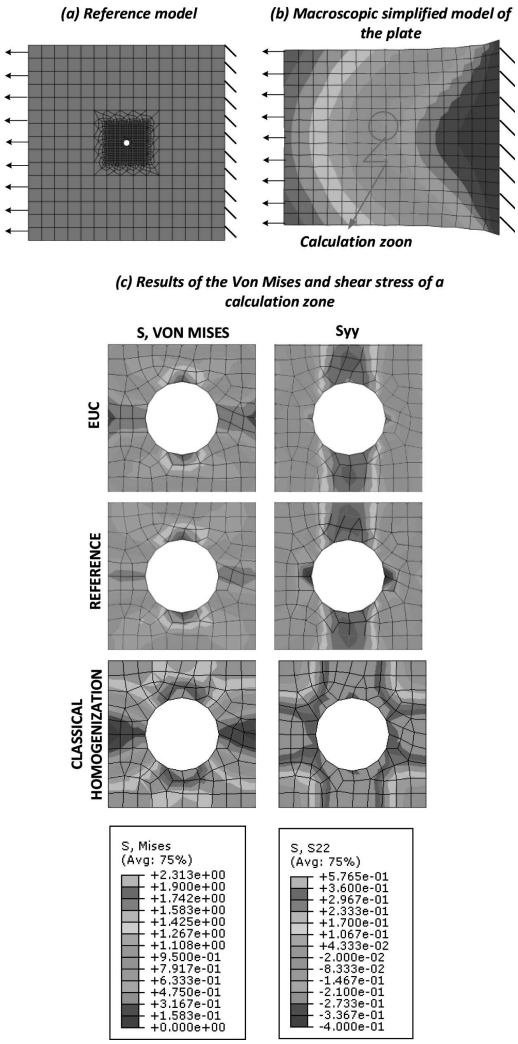

Figure 5. Stresses – a plate with a hole subjected to axial load.

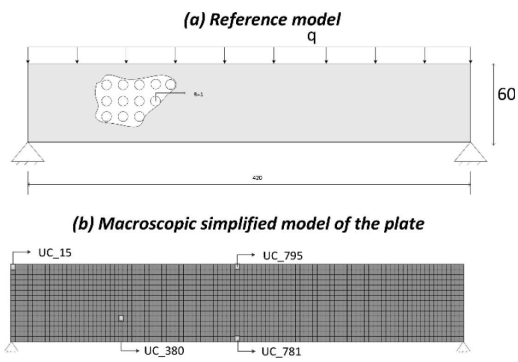

Figure 6. A plate with a hole subjected to axial load.

the suggest EUC approach. The method was applied on plate with small hole that was presented in Figure 2 earlier, but in this case the presented results reflect the response to vertical load (Figure 7) Grigorovitch & Gal (2017). The material is assumed to be elastic-plastic with an elastic modulus of 210 MPa, a Poisson's ratio equal to 0.3 and Von-Misses yield stress of 1.5 MPa.

Figure 9 presents result of increment 11, where the evidence of plastic response can be observed. The deflection result of macroscopic and reference model and the zooming in on the stress concentration zone near the hole are compared.

We can observe a good correspondence between the deflection and stress results of both models.

In addition, the transition between linear and non-linear response of EUC and referents models, is conveniently demonstrated on the Figure 9 presenting development of plastic stress as a function of incremental loading.

Non-linear response at the selected node is obtained at load increment #11, where the response becomes mostly plastic.

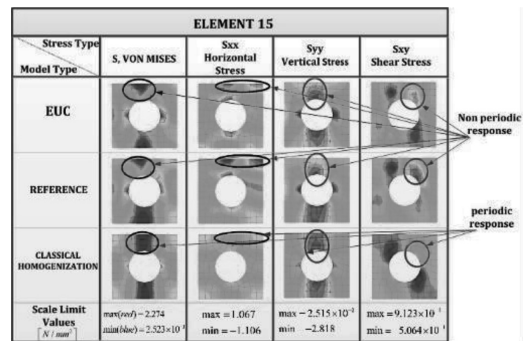

Figure 7. Stresses – a plate with a hole subjected to axial load.

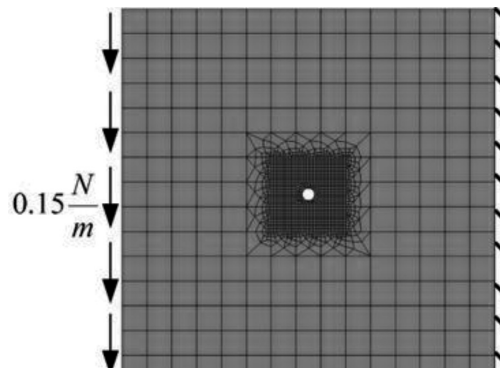

Figure 8. Finite element model of a plate with a small hole.

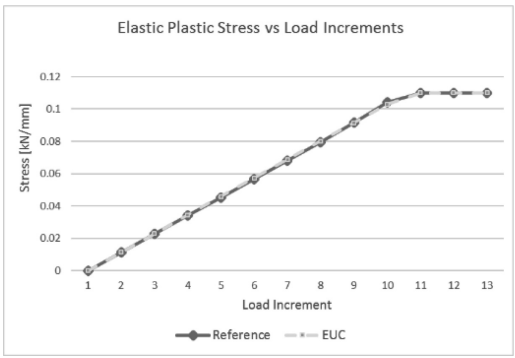

Figure 9. Elastic-plastic response, Step 11 of solution using Newton Raphson method.

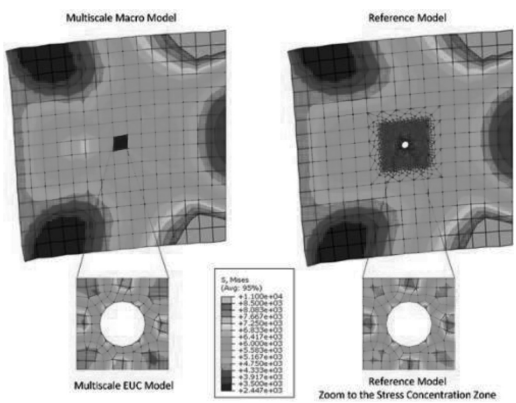

Figure 10. Stress response of selected node – reference and multi-scale models comparison.

Results obtained using EUC method and reference model have excellent agreement.

In addition to that, the horizontal deflection at a corner node on the left loaded side of the plate is presented in Figure 10.

CONCLUSION

This research, the Embedded Unit Cell, has been focused so far on performing analysis of mechanical response, verified in pure elastic and elastic-plastic modes of operation. The suggested approach allows the applying of classical homogenization methods in the non-periodic zones, by proposing the non-periodic homogenization formulation.

Multiple examples were modeled and tested in order to verify the accuracy of proposed multi-scale technique. The achieved results had shown good compliance compared to the reference finite elements model.

The Embedded Unit Cell approach has been successfully validated in boundary zones as well as in the stress concentration zones, which might occur after accidental structure damage. The next step of this research is to apply the EUC for the analysis of concrete structures.

ACKNOWLEDGMENTS

This research was supported by the Israel Ministry of Science, Technology and Space, Government of Israel.

REFERENCES

Aboudi, J. (1991). "Mechanics of composite materials- A unified micromechanical approach (Book)." Amsterdam and New York, Elsevier (Studies in Applied Mechanics. 29).

Allaire, G. (1992). "Homogenization and two-scale convergence." SIAM Journal on Mathematical Analysis 23(6): 1482–1518.

Budiansky, B. (1965). "On the elastic moduli of some heterogeneous materials." Journal of the Mechanics and Physics of Solids 13(4): 223–227.

Chaboche, J., S. Kruch, J. Maire and T. Pottier (2001). "Towards a micromechanics based inelastic and damage modeling of composites." International Journal of Plasticity 17(4): 411–439.

Chajes, M.J., W.W. Finch Jr, T.F. Januszka and T.A. Thomson Jr (1996). "Bond and force transfer of composite-material plates bonded to concrete." ACI structural journal 93(2).

Dvorak, G., Y. Bahei-El-Din and A. Wafa (1994). "The modeling of inelastic composite materials with the transformation field analysis." Modelling and Simulation in Materials Science and Engineering 2(3 A): 571.

Fan, R., Z. Yuan and J. Fish (2010). "Adaptive Two-Scale Nonlinear Homogenization." International Journal for Computational Methods in Engineering Science and Mechanics 11(1): 27–36.

Gal, E. and J. Fish (2008). "Anisotropic Micromechanical creep damage model for composite materials: A reduced-order approach." International Journal for Multiscale Computational Engineering 6(2).

Gal, E., A. Ganz, L. Hadad and R. Kryvoruk (2008). "Development of a concrete unit cell." International Journal for Multiscale Computational Engineering 6(5).

Gal, E., E. Suday and H. Waisman (2013). "Homogenization of materials having inclusions surrounded by layers modeled by the extended finite element method." International Journal for Multiscale Computational Engineering 11(3).

Gal, E., Z. Yuan, W. Wu and J. Fish (2007). "A multiscale design system for fatigue life prediction." International Journal for Multiscale Computational Engineering 5(6).

Ghosh, S., J. Bai and D. Paquet (2009). "Homogenization-based continuum plasticity-damage model for ductile failure of materials containing heterogeneities." Journal of the Mechanics and Physics of Solids 57(7): 1017–1044.

Gibson, R.F. (2011). Principles of composite material mechanics, CRC Press.

Gonella, S. (2007). Homogenization and bridging multiscale methods for the dynamic analysis of periodic solids, Georgia Institute of Technology.

Grigorovitch, M. and E. Gal (2015). "The local response in structures using the Embedded Unit Cell Approach." Computers & Structures 157: 189–200.

Grigorovitch, M. and E. Gal (2017). "Homogenization of non-periodic zones in periodic domains using the embedded unit cell approach." Computers & Structures 179: 95–108.

Hashin, Z. and S. Shtrikman (1963). "A variational approach to the theory of the elastic behaviour of multiphase materials." Journal of the Mechanics and Physics of Solids 11(2): 127–140.

Mei, C.C. and B. Vernescu (2010). Homogenization methods for multiscale mechanics, World scientific.

Michel, J.-C. and P. Suquet (2009). "Nonuniform transformation field analysis: a reduced model for multiscale nonlinear problems in solid mechanics." Multiscale Modelling in Solid Mechanics-Computational Approaches, edited by U. Galvanetto and F. AliabadiImperial College Press (Imperial College Press, London., 2009): 159–206.

Nguyen, V.P., O. Lloberas-Valls, M. Stroeven and L.J. Sluys (2011). "Homogenization-based multiscale crack modelling: From micro-diffusive damage to macro-cracks." Computer Methods in Applied Mechanics and Engineering 200(9): 1220–1236.

Oskay, C. and J. Fish (2008). "On calibration and validation of eigendeformation-based multiscale models for failure analysis of heterogeneous systems." Computational Mechanics 42(2): 181–195.

Sanchez-Palencia, E. (1983). Homogenization method for the study of composite media. Asymptotic Analysis II—, Springer: 192–214.

Takano, N., M. Zako and M. Ishizono (2000). "Multiscale computational method for elastic bodies with global and local heterogeneity." Journal of computer-aided materials design 7(2): 111–132.

Terada, K. and N. Kikuchi (2001). "A class of general algorithms for multi-scale analyses of heterogeneous media." Computer methods in applied mechanics and engineering 190(40): 5427–5464.

Valenta, R., M. Sejnoha and J. Zeman (2010). "Macroscopic constitutive law for mastic asphalt mixtures from multiscale modeling." International Journal for Multiscale Computational Engineering 8(1).

Van der Sluis, O., P.J.G. Schreurs, W.A.M. Brekelmans and H.E.H. Meijer (2000). "Overall behaviour of heterogeneous elastoviscoplastic materials: effect of microstructural modelling." Mechanics of Materials 32(8): 449–462.

Computational Modelling of Concrete Structures – Meschke, Pichler & Rots (Eds)
© 2018 Taylor & Francis Group, London, ISBN 978-1-138-74117-1

A continuum damage model for the simulation of concrete under cyclic loading

V. Kindrachuk, T. Titscher, V. Hirthammer & J.F. Unger
Federal Institute for Materials Research and Testing, Berlin, Germany

ABSTRACT: A continuum damage model for concrete is developed with a focus on fatigue under compressive stresses. This includes the possibility to model stress redistributions and capture size effects. In contrast to cycle based approaches, where damage is accumulated based on the number of full stress cycles, a strain based approach is developed that can capture cyclic degradation under variable loading cycles including different amplitudes and loading frequencies. The model is designed to represent failure under static loading as a particular case of fatigue failure after a single loading cycle. As a consequence, most of the material parameters can be deduced from static tests. Only a limit set of additional constitutive parameters is required to accurately describe the evolution under fatigue loading. Another advantage of the proposed model is the possibility to directly incorporate other multi-physics effects such as creep and shrinkage or thermal loading on the constitutive level. A multiscale approach in time is presented to enable structural computations of fatigue failure with a reduced computational effort. The damage rate within the short time scale corresponding to a single cycle is computed based on a Fourier based approach. This evolution equation is then solved on the long time scale using different implicit and explicit time integration schemes. Their performance and some limitations for specific loading regimes is discussed.

1 INTRODUCTION

1.1 *Motivation*

Lifetime aspects including fatigue failure of concrete structures were traditionally only of minor importance due to the limited amplitude of the applied cyclic loads compared to the constant dead load. However, because of the growing interest in maxing out the capacities of high performance concrete, its fatigue failure under compression has become an important issue. Typical examples are offshore wind energy plants, which undergo extreme loading conditions of non-uniform amplitudes arising from wind and waves or fatigue loading of bridges with a steady increase of traffic weight. However, a variety of interacting phenomena such as e.g. loss of prestress, degradation due to chemical reactions or creep and shrinkage influence the fatigue resistance. As a consequence, a pure experimental investigation to determine all interactions is extensive. Furthermore, failure due to cyclic loads is generally not instantaneous, but characterized by a steady damage accumulation. This is illustrated in Figure 1, where based on measurements with piezoelectic sensors the evolution of the speed of sound as a function of the fatigue lifetime is plotted. Apart from the initial and the final period, there is a significant part of the lifetime with an almost constant change of the speed of sound- the latter being directly related to the Youngs modulus and thus the damage evolution. Therefore, a reliable numerical model to predict the performance of concrete over its lifetime is required, which accurately captures order effects, the full three-dimensional stress state.

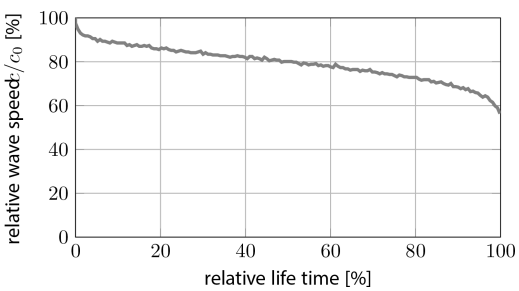

Figure 1. Evolution of the wave speed within a concrete specimen during fatigue loading according to (Thiele, Bäßler, Rogge, & Pirskawetz 2011).

Many mechanical models are currently available, which are applicable for specific loading regimes (monotonic, creep, temperature), different time scales (seconds to years) and different resolution scales (nano-, micro-, meso- to macroscale). However, a key limitation of those models is that they generally do not address issues related to fatigue on a structural level. Very few models can be found in the literature that reproduce deterioration

of concrete under repeated loading-unloading cycles. Additionally, these models describe only the material response (that is on the level of integration points) and not the structural behavior. This is due to the computational effort necessary to explicitly resolve every cycle which exceeds the currently available computational resources. For fatigue problems, the time scale for a single loading cycle can be in the order of seconds, whereas the expected overall lifetime spans over 50–100 years. As a consequence, most models use empirical approaches which define a reduction of the relevant material properties. One typical example is the subcritical crack growth rate of a notched specimen. This rate correlates with the stress intensity factor as empirically given by the Paris' law. For unnotched specimens, fatigue is generally modeled with Wöhler-curves, which describe the bearable stress level as a function of the lifetime in terms of number of cycles N_f. Based on the Wöhler-curves and a single elastic simulation, the lifetime of a structure under fatigue loading can be estimated. In situations with general load amplitudes, a damage accumulation theory is used, e.g. the Palmgren-Miner rule, which postulates a linear damage accumulation. This is in contrast with experimental data, where sequence effects, i.e. influence of the order of loading, have been measured. Therefore, many nonlinear cumulative damage rules have been proposed (Fatemi & Yang 1998) in order to remedy the deficiencies of postulating a linear damage accumulation. Nevertheless, the fundamental difference of such approaches compared to a realistic constitutive model is that only a phenomenological model is used for the approximation of the lifetime—a realistic degradation of the material with reduced stiffness and strength, and permanent deformations are not taken into account. Consequently, there is no option to include additional effects such as thermal loading, water intrusion, creep and shrinkage, strain rate effects, the ongoing hydration (aging) or interaction of these phenomena. Size effects observed for short term mechanical loading are also present in fatigue problems (Bažant 1991). As a consequence, it is often not meaningful to generalize a fatigue model calibrated from experiments for one specimen size to real structures without considering the influence of the fracture process zone, i.e. the characteristic length. Algorithms to include the influence of the mean stress, not present in the standard Wöhler approach, have been developed (Lemaitre & Plumtree 1979), but the generalization of the Wöhler concept to multiaxial stress states is not straightforward.

1.2 *Constitutive models for quasi-static loading*

A number of constitutive models have been developed for the numerical simulation of concrete, which primarily differ in the way softening is captured. Examples are models with strain-softening gradient plasticity (Jirásek & Rolshoven 2009a, Jirásek & Rolshoven 2009b), microplane models (Bažant & Ozbolt 1990, Bažant, Caner, Carol, Adley, & Akers 2000), models with damage (Mazars & Pijaudier-Cabot 1989, Jirásek & Grassl 2008) and coupled damage-plasticity formulations (Lemaitre & Desmorat 2006, Voyiadjis, Taqieddin, & Kattan 2008, Omidi & Lotfi 2013).

The major challenge for constitutive models with softening is the mesh sensitivity of the FE solution. In order to resolve the strain localization and mesh dependence, the material models can introduce a length scale in the local formulation (Bažant & Planas 1997). An alternative are gradient-enhanced formulations (Peerlings, de Borst, Brekelmans, & de Vree 1996) or concepts with non-local averaging (Jirásek 1998).

Concrete has a different behavior in tension and in compression due to microcracks opening under tension and their closure under compression. In order to adequately characterize damage in concrete during tensile and compressive loadings, the Cauchy stress tensor (nominal or effective) is often decomposed into positive and negative parts using the spectral decomposition technique leading to complex models (Lemaitre & Desmorat 2006, Voyiadjis, Taqieddin, & Kattan 2008). The different behavior in tension and in compression can also be modeled through separate scalar damage variables (Burlion, Gatuingt, Pijaudier-Cabot, & Daudeville 2000). The tensile damage due to microcracking can be governed by the reversible strain (Mazars criterion) or stress (Rankine), whereas the compressive damage due to microvoid growth or collapse is governed by plastic strains and respective yield surfaces. Mixed models using spectral decomposition of the stress tensor and two damage variables are also known (Wu, J. Li, & Faria 2006).

1.3 *Constitutive models for cyclic loading*

Models where damage progresses as soon as a certain criterion is fulfilled, for example the stress reaches the damage/yield surface in the space of principal stresses, can accurately simulate the constitutive behavior of concrete under static tension and compression. However, they do not necessarily predict deterioration during repeating loading-unloading cycles—the applied maximum stress will be inside the damage/yield locus already within the first reloading. Indeed, from a physical point of view, damage evolution under small amplitude stress cycles (like in high-cycle fatigue) or quasi-brittle failure may happen microscopically, even if the macroscopic load remains well below the yield or failure stress. The microscopic local stresses can be high enough because of structural inhomogeneity.

This scale phenomena was captured by (Desmorat, Ragueneau, & Pham 2007). The model is able to reproduce realistic Wöhler curves for specific choices of the parameters.

Another alternative to the damage/yield surface concept is the loading/unloading irreversibility criterion. It presumes energy dissipation even for loading states below the damage/yield surface and allows therefore for irreversible cyclic alterations. Furthermore, different evolution equations can be prescribed for loading and unloading. Avoiding any yield surfaces and hence avoiding to solve the consistency conditions, the loading/unloading criterion was applied to soils (Pastor, Zienkiewicz, & Chan 1990), initially formulated within the framework of generalized plasticity (Zienkiewicz & Mroz 1984). Applications for simulation of fatigue of quasi-brittle materials are also known (Alliche 2004, Mai, Le-Corre, Foret, & Nedjar 2012), where the damage variables evolve solely during the loading phase and are governed by the positive part of the strain tensor. The experiments in (Kim & Kim 1996) clearly demonstrate a significantly different fatigue behavior of normal and high strength concretes: a substantial increase of the lifetime with decreasing concrete strength for the same relative stress level was observed. Another model to simulate concrete failure under fatigue using a continuum model under compression was proposed by (Breccolotti, Bonfigli, D'Alessandro, & Materazzi 2015), but the application of the model was only shown for one dimensional stress strain curves as well as quasi-1D formulations through fiber elements on the structural level. A fatigue model for normal strength concrete under compressive loading conditions has been developed in (Kindrachuk, Thiele, & Unger 2015). In contrast to existing fatigue models for concrete, which use a rate-independent formulation, the derived model is based on a rate-dependent Duvaut-Lions flow law and formulated within the theory of multisurface continuum damage mechanics.

1.4 *Multiscale models in time*

The Large Time Increment Method (LATIN) (Boisse, Bussy, & Ladeveze 1990, Ladevéze, Passieux, & Néron 2010) introduced by Ladeveze is well suited for complex time loadings and nonlinear mechanical behavior, described by internal variables. The method provides an iterative procedure that solves the whole loading process in a single step. The initial mechanical problem is reformulated and decoupled into a linear global equilibrium sub-problem and a local, generally non-linear, sub-problem derived from constitutive equations. Each iteration is composed of two stages, sequentially satisfying the local and global sub-problems until both are fulfilled. This approach suffers from extensive discretization efforts, since the total number of unknowns is the product of the number of spatial and temporal unknowns.

A decomposition of the temporal scale for fatigue problems into macro- and micro-chronological scales was proposed in (Oskay & Fish 2004, Fish & Oskay 2005). The response fields and internal variables are decomposed into homogenized components that depend on the macro-chronological time only, and oscillatory components that depend on both chronological scales. The initial boundary value problem (IBVP) is split into an IBVP for the homogenized components and another one for the oscillatory components. The micro- and macro-chronological IBVPs are coupled only through the constitutive relationships. Thus, the damage increment within a single cycle is the solution of the micro-chronological IBVP. It is then transferred to the macro-chronological problem for a large time increment using adaptive algorithms like jump techniques. The benefit of this approach is its applicability to commercial finite element codes. However, the noticeable drawback is related to the permanent considerable data transfer between both IBVPs.

An easy to implement Direct Cycle Jump approach was introduced in (Cojocaru & Karlsson 2006, Moslemian, Karlsson, & Berggreen 2011). They calculate several cycles at the beginning of the time increment in order to determine the damage growth rate per cycle. Based on an extrapolation with an Euler forward procedure, the damage state at the end of the large time increment is estimated. Due to the extrapolation, the IBVP is no longer exactly fulfilled and the extrapolated solution has to be equilibrated. An adaptive procedure with a variable time increment is developed in the extrapolation scheme to balance the error introduced in the Euler forward procedure. It can properly deal with a nonlinear response of the structure during fatigue.

In the paper, a short introduction to a local continuum damage model for concrete is presented. Afterwards, a multiscale approach in time is discussed to allow the method to be efficiently used also for structural computations. Finally, some examples and an outlook are given.

2 CONTINUUM DAMAGE MODEL FOR CONCRETE

2.1 *Local damage model*

The initial boundary value problem for body in the domain Ω is given by

$$\rho \ddot{\boldsymbol{u}} = \nabla \cdot \sigma, \tag{1}$$

$$\sigma \cdot \boldsymbol{n} = \overline{\boldsymbol{f}} \text{ on } \partial\Gamma_{\sigma}, \boldsymbol{u} = \overline{\boldsymbol{u}} \text{ on } \partial\Gamma_{u}, \tag{2}$$

$$\sigma = \sigma(\varepsilon, s), \varepsilon = \frac{1}{2}\left(\nabla \mathbf{u} + (\nabla \mathbf{u})^T\right), \tag{3}$$

$$\dot{s} = g(\varepsilon, s), s(0) = 0. \tag{4}$$

Body forces are neglected and small deformations are assumed. Conditions (2) prescribe tractions and displacements on the boundary segments $\partial\Gamma_\sigma$ and $\partial\Gamma_u$, respectively. The constitutive equation (3) relates the stress to the strain and the set of history variables s in each material point. This set of history variables might also include plastic or viscous strains. Extension to other multiphysics problems (e.g. using water volume fraction to account for coupled shrinkage models) is straightforward. The evolution of these history variables is given by the ordinary differential equations (ODE) in (4) with initial conditions.

In a simplified approach, a local damage model regularized by the element length is used. The stress σ is thus computed as a product of a scalar damage variable ω, the linear elasticity tensor $\mathbb{C}$ and the strain tensor ε

$$\sigma = (1 - \omega(\kappa))\mathbb{C} : \varepsilon. \tag{5}$$

The damage variable is a function of a history variable κ using on an exponential softening function (Oliver, Cervera, Oller, & Lubliner 1990, Mazars & Pijaudier-Cabot 1989)

$$\omega(\kappa) = \begin{cases} 0 & \kappa < \kappa_0 \\ 1 - \frac{\kappa_0}{\kappa} \exp\left[-\frac{f_{ct}}{G_f}(\kappa - \kappa_0)\right] & \text{otherwise.} \end{cases} \tag{6}$$

The parameter $\kappa_0 = f_{ct}/E$ corresponds to a damage initiation threshold below only an elastic formulation is used. The parameters f_{ct} and G_f are the tensile strength and the fracture energy of the material. For regularization purposes, the latter is scaled with the inverse of the element length.

The evolution of the history variable κ that corresponds to the maximum equivalent strain in the history of a material point is obtained from the Karush-Kuhn-Tucker (KKT) conditions

$$\dot{\kappa} \geq 0 \quad \varepsilon_{eq} - \kappa \leq 0 \quad \dot{\kappa}(\varepsilon_{eq} - \kappa) = 0 \tag{7}$$

with the equivalent strain ε_{eq} computed from the strain-based modified von Mises criterion

$$\varepsilon_{eq}(\varepsilon) = \frac{k-1}{2k(1-2\nu)} I_1 + \frac{1}{2k}\sqrt{\left(\frac{k-1}{1-2\nu} I_1\right)^2 + \frac{2k}{(1+\nu)^2} J_2}, \tag{8}$$

with I_1 the first invariant of the stress tensor and J_2 the second invariant of the deviator. The paramater k controls the ratio between the uniaxial compressive and tensile strength.

2.2 *Extension to fatigue*

The standard model described in the previous section is able to represent concrete failure in tension as well as in compression under quasi-static loading. For subcritical fatigue cycles below the tensile or compressive strength, no damage accumulation is obtained. As a consequence, the original model is not able to reproduce experimental Wöhler lines. In the proposed extension, the history parameter κ is no longer the maximum equivalent strain ever reached in the history of a material point, but evolves with every positive change in the equivalent strains (Marigo 1985)

$$\dot{\kappa} = \begin{cases} \dot{\varepsilon}_{eq} & \text{if } \varepsilon_{eq} = \kappa \\ |\dot{\varepsilon}_{eq}| f(\sigma) & \text{otherwise.} \end{cases} \tag{9}$$

Physically, this corresponds to a damage accumulation during sliding of crack faces. The function $f(\sigma)$ is introduced to represent larger damage accumulations for larger stresses and vanishing damage accumulation in cracks with stresses below a threshold σ_∞

$$f(\sigma) = A \frac{\langle \sigma_{eq}(\sigma) - \sigma_\infty \rangle_+}{f_{ct}}. \tag{10}$$

The material parameter A is a scalar value that characterizes the damage rate under subcritical conditions. The only parameters to be calibrated for fatigue simulations are A and σ_∞, all other parameters are derived from quasi-static tests. Note also that quasi-static loading is a special case of the proposed model. The stress-strain relation for different loading scenarios are illustrated in Figure 2. The fatigue response is always bounded by the quasi-static model. For load controlled experiments (low stress cycles/high stress cycles), the damage is accumulated in each loading cycle until the quasi-static envelop and thus failure is reached. In a displacement-controlled/strain controlled loading regime, the specimen is loaded well above its strength. In the post-peak part, additional fatigue cycles lead to an accumulation of damage.

2.3 *Nonlocal fatigue model*

An alternative regularization technique to scaling the fracture energy is using a nonlocal formulation. In particular, the gradient-enhanced damage

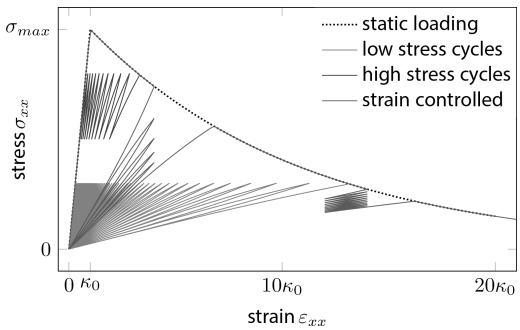

Figure 2. Stress-strain relation for the fatigue damage model under variable loading/unloading regimes.

model (Peerlings, de Borst, Brekelmans, & de Vree 1996) is applied here, such that κ in (7) and thus damage are governed by a nonlocal counterpart $\bar{\varepsilon}_{\text{eq}}$ of the equivalent strain ε_{eq}

$$\bar{\varepsilon}^{eq} - c\nabla^2 \bar{\varepsilon}^{eq} = \varepsilon^{eq} \text{ in } \Omega, \tag{11}$$

$$\nabla \bar{\varepsilon}^{eq} \cdot \boldsymbol{n} = 0 \text{ on } \partial\Gamma. \tag{12}$$

The damage variable is assumed to be directly driven by the nonlocal equivalent strain. The damage evolution law (6) can be represented in the rate form

$$\dot{\omega} = \frac{\mathrm{d}\Phi(\bar{\varepsilon}_{\text{eq}})}{\mathrm{d}\bar{\varepsilon}_{\text{eq}}} \dot{\kappa}. \tag{13}$$

The fatigue formulation is obtained similarly to (9)

$$\dot{\kappa} = \begin{cases} \left\langle \dot{\bar{\varepsilon}}_{\text{eq}} \right\rangle_+ & \text{if } \bar{\varepsilon}_{\text{eq}} = \kappa \\ \left\langle \dot{\bar{\varepsilon}}_{\text{eq}} \right\rangle_+ \left(\frac{\bar{\varepsilon}^{eq}}{\kappa} \right)^n & \text{otherwise.} \end{cases} \tag{14}$$

Combining (13) and (14) results in

$$\dot{\omega} = \frac{\mathrm{d}\Phi(\bar{\varepsilon}^{eq})}{\mathrm{d}\bar{\varepsilon}^{eq}} \left(\frac{\bar{\varepsilon}^{eq}}{\kappa} \right)^n \left\langle \dot{\bar{\varepsilon}}^{eq} \right\rangle +, \tag{15}$$

where $\kappa = \Phi^{-1}(\omega)$ and function Φ is adopted from (Fish, Yu, & Shek 1999)

$$\Phi(\bar{\varepsilon}^{eq}) = \frac{\arctan \frac{\bar{\varepsilon}^{eq} - e_0}{e_f} + \arctan \frac{e_0}{e_f}}{2\arctan 1 + \arctan \frac{e_0}{e_f}}. \tag{16}$$

The initial value of κ is zero $\kappa(0) = \Phi^{-1}(0) = 0$. In this simplified consideration fatigue is assumed to proceed at any level of loading provided that $\dot{\bar{\varepsilon}}^{eq} > 0$.

3 TEMPORAL MULTISCALE MODEL

The computation of the continuum damage model discussed in the previous section requires to integrate the constitutive equation over time. Using standard time integration schemes such as backward Euler (or Newmark schemes when including the inertia terms) requires to subdivide each cycle into at least ten time steps. For realistic simulations of fatigue failure with up to 10^6 cycles until failure, the computational effort is significant. In order to use this approach for realistic structural problems, a multiscale approach in time can avoid these extensive computations.

The standard cycle jump approach is based on the idea of calculating for a single cycle the damage rate (or any other history variable) for each quadrature point. Based on this rate of change and the assuming that the damage rate is constant for a given number of subsequent cycles, an extrapolation of these history variables can be performed. Thus, the number of single cycles that are fully integrated to compute the damage rate can be significantly reduced.

The computational efficiency of this approach can be even further increased. First, the damage rate within single cycle (microchonologial problem) is computed by transforming the problem into the frequency domain, and second an adaptive error control and implicit schemes for the macrochronological integration are discussed.

3.1 *Computation of the damage rate in a single cycle*

The idea is based on the assumption that in the secondary fatigue phase, the damage growth within a single cycle is small and thus does not influence the stress distribution (Kindrachuk & Unger 2017). It is assumed that the loading scenario (either load-controlled with prescribed external forces $\bar{\boldsymbol{f}}$ or displacement controlled with prescribed displacements $\bar{\boldsymbol{u}}$) can be described by a Fourier series with angular frequency $\omega = 2\pi/T$ and period T

$$\bar{\boldsymbol{u}} = \sum_{k \in \mathbb{Z}} \bar{\boldsymbol{u}}_k(x) e^{ik\omega t}, \; x \in \partial\Gamma_u \tag{17}$$

$$\bar{\boldsymbol{f}} = \sum_{k \in \mathbb{Z}} \bar{\boldsymbol{f}}_k(x) e^{ik\omega t}, \; x \in \partial\Gamma_\sigma. \tag{18}$$

For complex loading scenarios, a Fouries transformation of the time-dependent signal has to be performed. For pratical applications, the number of Fourier modes is very small and can often be approximated by only a single relevant frequency.

Discretizing the weak form of (1)–(18) results in the following system of equations

$$\boldsymbol{M}\ddot{\boldsymbol{u}} + \boldsymbol{F}^{int}(\boldsymbol{u}, s) = \sum_{k\in\mathbb{Z}} \boldsymbol{F}_k^{ext} e^{ik\omega t}, \tag{19}$$

$$\bar{\boldsymbol{u}} = \sum_{k\in\mathbb{Z}} \bar{\boldsymbol{u}}_k(x) e^{ik\omega t}, x \in \partial\Omega_u \tag{20}$$

where $\boldsymbol{u}$ denotes the displacements and $\boldsymbol{M}$ is the mass matrix. The internal force vector $\boldsymbol{F}^{int}$ is computed from the stress field (3) and depends thus on displacements and history variables. The external force $\boldsymbol{F}_k^{ext}$ represents the traction component $\bar{\boldsymbol{f}}_k$ from (18)

$$\boldsymbol{F}^{int}(\boldsymbol{u}, s) = \int_\Omega \boldsymbol{B}^T \sigma(\varepsilon, s) d\Omega, \tag{21}$$

$$\boldsymbol{F}_k^{ext} = \int_{\partial\Omega_\sigma} \boldsymbol{N}^T \bar{\boldsymbol{f}}_k d\Gamma, \tag{22}$$

with interpolation matrix $\boldsymbol{N}$ containing the shape functions and the strain-displacement matrix $\boldsymbol{B}$ containing the derivatives of the shape functions.

Under the assumption that the evolution of history variables within a single cycle is small, the displacement field can also be approximated by a Fourier series

$$\boldsymbol{u}(\mathcal{T}, \tau) = \sum_{k\in\mathbb{Z}} \boldsymbol{u}_k(\mathcal{T}) e^{ik\omega\tau}. \tag{23}$$

The cyclic displacement field (23) satisfies the temporal separation of scales since its Fourier coefficients evolve only on the long time scale $\mathcal{T} \gg T = 2\pi/\omega$ with the microchonologial time $\tau \in [0, T]$. In particular, $\boldsymbol{u}_0$ corresponds to the displacement that only depends on the macrochronological time and is thus constant within a single cycle.

The internal force (21) can be expressed as a linear superposition of the constant internal force vector at the beginning of the cycle $\boldsymbol{F}_0^{int}(\boldsymbol{u}_0, s(\mathcal{T}))$ that depends on the history variables related to the macrochronological time and an oscillating part that can be approximated by a Taylor series expansion with the elastic stiffness matrix $\boldsymbol{K}(\mathcal{T})$ related to the history variables at the beginning of the cycle

$$\begin{aligned}\boldsymbol{F}^{int}(\boldsymbol{u}, s) = \boldsymbol{F}_0^{int}(\boldsymbol{u}_0, s(\mathcal{T})) \\ + \boldsymbol{K}(s(\mathcal{T})) \sum_{k\in\mathbb{Z}\setminus\{0\}} \boldsymbol{u}_k(\mathcal{T}) e^{ij\omega\tau}.\end{aligned} \tag{24}$$

Substitution into (19) yields

$$\begin{aligned}\sum_{k\in\mathbb{Z}} \boldsymbol{F}_k^{ext} e^{ik\omega\tau} - \boldsymbol{F}_0^{int} = -\boldsymbol{M}\omega^2 \sum_{k\in\mathbb{Z}\setminus\{0\}} k^2 \boldsymbol{u}_k(\mathcal{T}) e^{ik\omega\tau} \\ + \sum_{k\in\mathbb{Z}\setminus\{0\}} \boldsymbol{K}(\mathcal{T}) \boldsymbol{u}_k(\mathcal{T}) e^{ik\omega\tau}.\end{aligned} \tag{25}$$

Due to the uniqueness of the Fourier coefficients $\boldsymbol{u}_k$, a decoupling of equation (25) is possible.

$$\boldsymbol{F}_0^{ext} - \boldsymbol{F}_0^{int}(\boldsymbol{u}_0, s(\mathcal{T})) = 0, k = 0, \tag{26}$$

$$\left(\boldsymbol{K}(s(\mathcal{T})) - \omega^2 k^2 \boldsymbol{M}\right) \boldsymbol{u}_k(\mathcal{T}) = \boldsymbol{F}_k^{ext}, k \neq 0, \tag{27}$$

$$\boldsymbol{u}_k(\mathcal{T}) = \bar{\boldsymbol{u}}_k \text{ on } \partial\Omega_u, k \in \mathbb{Z}. \tag{28}$$

The number of required Fourier coefficients is completely determined by the number of Fourier modes required for accurate representation of the oscillatory boundary conditions (17) and (18). In the simplest case, only a constant term related to the mean displacements ($k = 0$) and an amplitude related to the oscillatory part ($k = 1$) have to be used, which results in solving two decoupled systems. This approach allows for an efficient simulation of a single fatigue cycle, provided that the current state of history variables is known at the beginning of the cycle.

Based on the solution of the displacement field within a single cycle, the evolution rate of the history variables can be calculated. The key simplification of the proposed procedure is that the solution for all quadrature points is now decoupled. Discretizing the cycle into $n + 1$ substeps $\tau_j \in [\tau_0 = 0, \tau_1, .., \tau_n = T]$ the total strains for any quadrature point can be computed by

$$\boldsymbol{u}_j = \boldsymbol{u}(\mathcal{T}, \tau_j) = \sum_{k\in\mathbb{Z}} \boldsymbol{u}_k(\mathcal{T}) e^{ik\omega\tau_j}, \tag{29}$$

$$\varepsilon_j = \varepsilon(\mathcal{T}, \tau_j) = \boldsymbol{B}\boldsymbol{u}(\mathcal{T}, \tau_j). \tag{30}$$

Utilizing the backward Euler method to integrate the evolution equation (4)

$$s_{j+1} = s_j + \Delta\tau\, g(\varepsilon_{j+1}, s_{j+1}), s_0 = s(\mathcal{T}), \tag{31}$$

where the initial conditions are obtained from the macrochronological solution $s(\mathcal{T})$. Note that this does not require to solve a macroscopic system of equations, but only requires to solve the evolution equations for each quadrature point separately. The change of the history variables and thus the approximated rate of change with respect to the macrochronological time scale can be obtained from

$$\Delta_c s(\mathcal{T}) = s_n - s_0 \tag{32}$$

$$\frac{\partial s}{\partial \mathcal{T}} \approx \frac{\Delta_c s(\mathcal{T})}{T}. \tag{33}$$

The procedure to compute the rate of change of history variables for a single cycle is summarized in Figure 3.

This approach is easily implemented in a standard FE-software, since no substantial modifications of the framework are required. Combining the history data s of all quadrature points into a vector $\boldsymbol{s}$, the above procedure describes an ODE

- with initial history data $s(\Upsilon)$ solve for the coefficients u_k using equations (26) and (27)
- using the prescribed displacements within a single cycle, integrate the evolution of history data using equation (31)
- compute the rate of change of history variables using equation (33)

Figure 3. Computation of the damage rate.

for the evolution of the history data on the macrochronological time scale Υ

$$\dot{\boldsymbol{s}}(s,\Upsilon) = F(s,\Upsilon) \tag{34}$$

where the function F is calculated according to the procedure summarized in Figure 3.

3.2 *Cycle jump formulation*

The time integration of the macrochronological evolution equation (34) can be performed with different time integration schemes. The choice depends in general on the model. An important influence has the applied loading. For strain-controlled test usually used for low-cycle fatigue tests with large amplitudes, the stress within the specimen decreases during the lifetime, and thus damage growth also decreases. In contrast, for load-controlled tests usually used for high-cycle fatigue tests, the strains are constantly increasing with an acceleration of the damage growth—since the effective stress is constantly increasing. The latter problem is significantly more difficult to accurately integrate, since due to the error propagation an exponential growth is obtained.

The standard approach, often labeled as cycle jump method, is a standard Euler forward integration scheme

$$\boldsymbol{s}^{(n+\Delta n)} = \boldsymbol{s}^{(n)} + \dot{\boldsymbol{s}}(s,\Upsilon)\Delta n, \tag{35}$$

where n is the current cycle and Δn is the number of cycles for the extrapolation (step length). Note that implicit quadrature schemes are difficult to implement, since the corresponding Hessian matrix $\frac{\partial F(s,\Upsilon)}{\partial s}$ required for the solution procedure is a full square matrix with the dimension of the number of integration points (for a single scalar history variable such as damage ω).

For the determination of the step length, different approaches can be pursued. Straigthforward ideas are the limitation of the change of history variables due a prescribed maximum. In this approach, the step length Δn is determined from the relative change of the internal force vector $\boldsymbol{F}_u^{int}$ within a single cycle

$$\Delta_c \boldsymbol{F}_u^{int}(\Upsilon) = \boldsymbol{F}_u^{int}(s(\Upsilon) + \Delta_c s) - \boldsymbol{F}_u^{int}(s(\Upsilon)), \tag{36}$$

where $\Delta_c s$ is the change of history variables (damage) within a single cycle. This force characterizes the change in the internal force vector due to the damage evolution within a single cycle. Based on this difference, a limit for the cyclic evolution is introduced

$$q := \frac{\left\| \Delta_c \boldsymbol{F}_u^{int}(\Upsilon + \Delta\Upsilon) - \Delta_c \boldsymbol{F}_u^{int}(\Upsilon) \right\|_\infty}{\left\| \Delta_c \boldsymbol{F}_u^{int}(\Upsilon) \right\|_\infty} \leq tol, \tag{37}$$

where $tol > 0$ is the specified relative error, norm $\|\cdot\|_\infty$ returns the maximum absolute component of the force vector. This error definition limits the difference between the rate of changes in the first cycle compared to the rate of change in the final extrapolated cycle. The denominator in (37) is never zero for the presented fatigue model, since in the present model there is always at least in one quadrature point an evolution of the history variables—otherwise no fatigue failure would be obtained. If the criterion is fulfilled, the subsequent step size can be increased

$$\Delta\Upsilon \rightarrow \sqrt{\frac{tol}{\epsilon}}\Delta\Upsilon, \text{if } q \leq tol, \tag{38}$$

where $\epsilon = \max\{q, tol/4\}$ limits the maximum increase by a factor of two. If (37) is violated, the macrochronological step has to be repeated with a smaller step size

$$\Delta\Upsilon \rightarrow \frac{3}{4}\sqrt{\frac{tol}{q}}\Delta\Upsilon, \text{if } q > tol. \tag{39}$$

These adaptive empirical rules have been successfully used earlier for accelerated simulations of fatigue in visco-plastic solids (see (Kindrachuk & Unger 2017)).

In order to achieve better convergence rates, higher order explicit time integration schemes can be adopted in a straightforward manner. In addition to the explicit Euler method discussed above, higher order methods can be implemented and are discussed in a subsequent paper.

4 EXAMPLES

4.1 *Wöhler lines on the integration point level*

Wöhler lines relate the stress level of fatigue experiments with the number of loading cycles until the

material breaks. In the corresponding stress-strain curve (see Figure 2), this corresponds to reaching the static hull curve.

Figure 4 shows Wöhler lines of the present model in comparison to experimental data from (Kim & Kim 1996). Their experiments consist of sinusoidal loading between $\sigma_{\min} = 0.25 f_c$ and varying a $\sigma_{\max}$. This experiment is reproduce with the present fatigue model. The parameter A controls the shift of the resulting Wöhler lines and σ_∞ controls their slope.

4.2 *Wöhler lines on the structural level*

A three dimensional specimen with the material parameters from Table 1 is loaded under cyclic compression with the maximum amplitude $\sigma_{\max}$. Two sets of Wöhler lines are calculated that only differ in the loading setup. A uniaxial stress state is obtained when the horizontal displacements of the specimens at the loading platens are not constrained. This can be reproduced on the integration point level. The more common loading with clamped supports results in a complex stress state including strain localization, as shown in Figure 5.

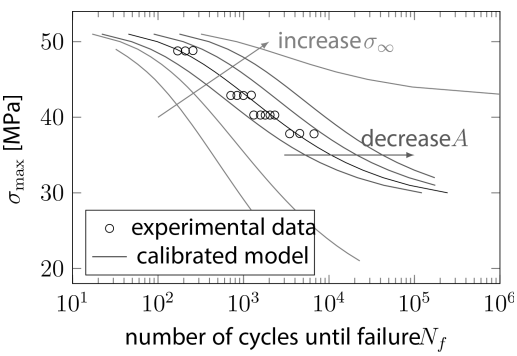

Figure 4. The calibrated Wöhler line of the present model ($A = 0.8$, $\sigma_\infty = 14$ MPa) is in good agreement with the experimental data ($f_c = 52$ MPa) from (Kim & Kim 1996).

Table 1. Material parameters for the three-dimensional fatigue compression test.

Young's modulus E	30000 MPa
Poisson's ratio ν	0.2
Tensile strength f_t	4 MPa
Compressive strength f_c	40 MPa
Global fracture energy G_f	0.2 Nmm^{-1}
Fatigue parameter A	1
Endurance stress σ_∞	4 MPa

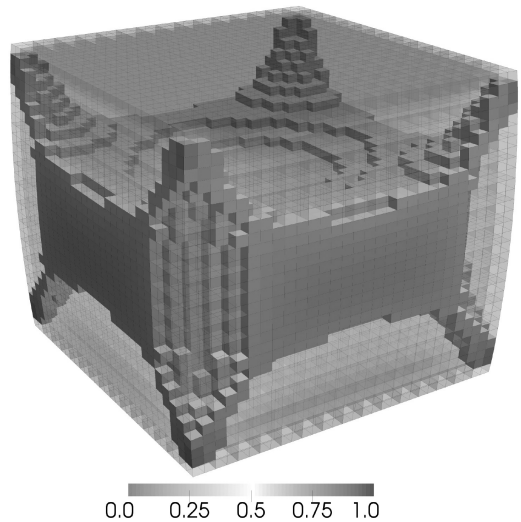

Figure 5. Damage plot (opaque elements with damage $\omega > 0.5$) of a 3D fatigue simulation. The amplified displacements (× 100) are shown for the clamped support at the top and bottom surface.

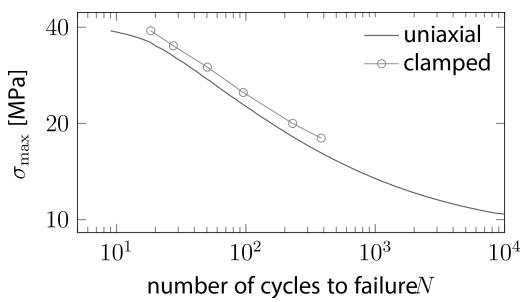

Figure 6. Comparison of Wöhler curves for different clamping conditions.

The resulting Wöhler lines in Figure 6 indicate a slight difference in the fatigue behavior. This has to be considered when calibrating the models—it has to be performed on the lab specimen level and not on only on the constitutive level. This is also true for the parameters related to the static tests.

4.3 *Performance multiscale in time*

Simulation of the fatigue response in a 2D specimen with holes, as depicted in Figure 7, is considered for validation of the temporal multiscale integration scheme. The sides of the specimen have length of 250 mm, whereas the used material parameters are listed in Table 2. The specimen is constrained on the bottom boundary. An oscillating

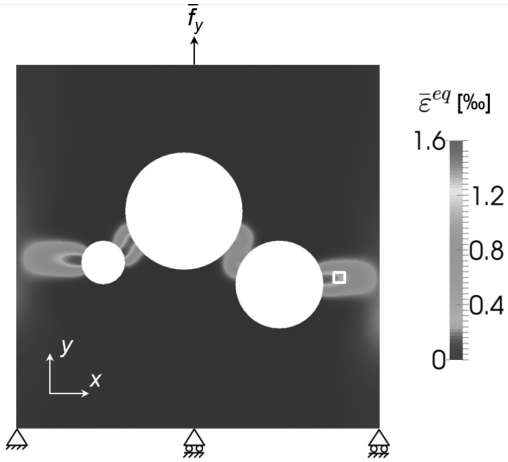

Figure 7. Distribution of the nonlocal equivalent strain at 90% of the lifetime. The selected place is used for the demonstration of performance of the cycle jump method, see figure 8.

Table 2. Material parameters for the two-dimensional fatigue test.

Young's modulus E	40000 MPa
Poisson's ratio ν	0.2
gradient parameter c	10 mm^2
e_0	0
e_f	3.5 10^{-4}
fatigue exponent n	2
Endurance stress	0 MPa

vertical traction is applied as a triangle wave function on the top boundary

$$\bar{f}_y(\boldsymbol{x},t) = \bar{f}_0 + \frac{8}{\pi^2}\bar{f}_1 \sum_{k=1,3,\ldots}^{7} \frac{(-1)^{\frac{k-1}{2}}}{k^2} \sin k\omega t. \qquad (40)$$

The loading results in the initiation of damage on the highly stressed locations near the boundaries of the holes. The damaged region expands during the fatigue loading history until failure occurs. The performance of the multiscale cycle jump method is evaluated due to comparison of the predicted fatigue response with the reference solution obtained by the direct numerical simulation. Figure 8 demonstrates a perfect match between the predicted damage evolution and the reference solution. The cycle jump method requires only 7.1% of the reference simulation time. Further decrease of the simulation time is possible, however it is accompanied with a decrease of the cycle jump accuracy due to higher values of the error tolerance *tol*.

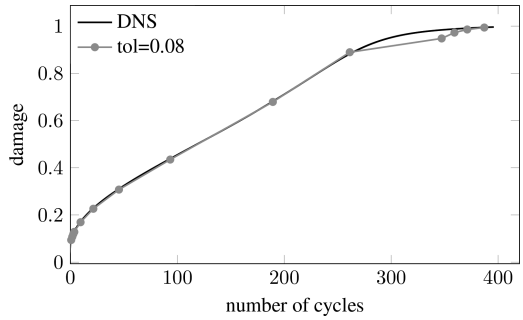

Figure 8. Evolution of the damage variable in the marked place of the specimen, see figure 7. The cycle jump method with a tolerance value $tol = 0.02$ predicts a solution which very accurately reproduces the damage variable as obtained by the direct numerical simulation.

5 CONCLUSION

The paper presents a continuum damage model for concrete under fatigue loading. The model is able to accurately represent experimental Wöhler lines. The advantage compared to traditional models based on the Palgren-Miner rule is that an interaction with other phenomena (such as creep, shrinkage, thermal expansion) is easily possible by extending the continuum model. The direct numerical simulation of this model for a large number of fatigue cycles requires significant computational resources. A multiscale method in time is presented to accelerate the computation on the structural level. As a result, these methods can also be applied to real stuctures taking into account load redistributions, environmental conditions and the evolution of material properties.

REFERENCES

Alliche, A. (2004). Damage model for fatigue loading of concrete. *International Journal of Fatigue 26*(9), 915–921.

Bažant, Z. & J. Ozbolt (1990). Nonlocal microplane model for fracture, damage, and size effect in structures. *Journal of Engineering Mechanics 116*(11), 2485–2505.

Bažant, Z. & J. Planas (1997). *Fracture and Size Effect in Concrete and Other Quasibrittle Materials*. New Directions in Civil Engineering. Taylor & Francis.

Bažant, Z., F. Caner, I. Carol, M.D. Adley, & S.A. Akers (2000). Microplane model M4 for concrete I: Formulation with work-conjugate deviatoric stress. *Journal of Engineering Mechanics 126*(9), 944–953.

Bažant, Z.P. (1991). Why continuum damage is nonlocal: micromechanics arguments. *Journal of Engineering Mechanics 117*(5), 1070–1087.

Boisse, P., P. Bussy, & P. Ladeveze (1990). A new approach in non-linear mechanics: The large time increment

method. *International Journal for Numerical Methods in Engineering 29*(3), 647–663.

Breccolotti, M., M.F. Bonfigli, A. D'Alessandro, & A.L. Materazzi (2015). Constitutive modeling of plain concrete subjected to cyclic uniaxial compressive loading. *Construction and Building materials 94*, 172–180.

Burlion, N., F. Gatuingt, G. Pijaudier-Cabot, & L. Daudeville (2000). Compaction and tensile damage in concrete: constitutive modelling and application to dynamics. *Computer Methods in Applied Mechanics and Engineering 183*(3–4), 291–308.

Cojocaru, D. & A. Karlsson (2006). A simple numerical method of cycle jumps for cyclically loaded structures. *International Journal of Fatigue 28*(12), 1677–1689.

Desmorat, R., F. Ragueneau, & H. Pham (2007). Continuum damage mechanics for hysteresis and fatigue of quasi-brittle materials and structures. *International Journal for Numerical and Analytical Methods in Geomechanics 31*(2), 307–329.

Fatemi, A. & L. Yang (1998). Cumulative fatigue damage and life prediction theories: a survey of the state of the art for homogeneous materials. *International Journal of Fatigue 20*(1), 9–34.

Fish, J. & C. Oskay (2005). A nonlocal multiscale fatigue model. *Mechanics of Advanced Materials and Structures 12*(6), 485–500.

Fish, J., Q. Yu, & K. Shek (1999). Computational damage mechanics for composite materials based on mathematical homogenization. *International Journal for Numerical Methods in Engineering 45*(11), 1657–1679.

Jirásek, M. & P. Grassl (2008). Evaluation of directional mesh bias in concrete fracture simulations using continuum damage models. *Engineering Fracture Mechanics 75*(8), 1921–1943.

Jirásek, M. & S. Rolshoven (2009a). Localization properties of strain-softening gradient plasticity models. part i: Straingradient theories. *International Journal of Solids and Structures 46*(11–12), 2225–2238.

Jirásek, M. & S. Rolshoven (2009b). Localization properties of strain-softening gradient plasticity models. part ii: Theories with gradients of internal variables. *International Journal of Solids and Structures 46*(11–12), 2239–2254.

Jirásek, M. (1998). Nonlocal models for damage and fracture: Comparison of approaches. *International Journal of Solids and Structures 35*(31–32), 4133–4145.

Kim, J.-K. & Y.-Y. Kim (1996). Experimental study of the fatigue behavior of high strength concrete. *Cement and Concrete Research 26*(10), 1513–1523.

Kindrachuk, V., M. Thiele, & J. Unger (2015). Constitutive modeling of creep-fatigue interaction for normal strength concrete under compression. *International Journal of Fatigue 78*, 81–94.

Kindrachuk, V.M. & J.F. Unger (2017). A Fourier transformation-based temporal integration scheme for viscoplastic solids subjected to fatigue deterioration. *International Journal of Fatigue 100, Part 1*, 215–228.

Ladevéze, P., J.-C. Passieux, & D. Néron (2010). The LATIN multiscale computational method and the proper generalized decomposition. *Computer Methods in Applied Mechanics and Engineering 199*(21–22), 1287–1296.

Lemaitre, J. & A. Plumtree (1979). Application of damage concepts to predict creep-fatigue failures. *Journal of Engineering Materials and Technology – Transactions of ASME 101*(3), 284–292.

Lemaitre, J. & R. Desmorat (2006). *Engineering Damage Mechanics: Ductile, Creep, Fatigue and Brittle Failures*. Springer.

Mai, S., F. Le-Corre, G. Foret, & B. Nedjar (2012). A continuum damage modeling of quasi-static fatigue strength of plain concrete. *International Journal of Fatigue 37*(0), 79–85.

Marigo, J. (1985). Modelling of brittle and fatigue damage for elastic material by growth of microvoids. *Engineering Fracture Mechanics 21*(4), 861–874.

Mazars, J. & G. Pijaudier-Cabot (1989). Continuum damage theory-application to concrete. *Journal of Engineering Mechanics 115*(2), 345–365.

Moslemian, R., A. Karlsson, & C. Berggreen (2011). Accelerated fatigue crack growth simulation in a bimaterial interface. *International Journal of Fatigue 33*(12), 1526–1532.

Oliver, J., M. Cervera, S. Oller, & J. Lubliner (1990). Isotropic damage models and smeared crack analysis of concrete. In N. Bićanić and H. Mang (Eds.), *Computer Aided Analysis and Design of Concrete Structures*, pp. 945–957. Pineridge Press, Swansea.

Omidi, O. & V. Lotfi (2013). Continuum large cracking in a rate dependent plastic–damage model for cyclic-loaded concrete structures. *International Journal for Numerical and Analytical Methods in Geomechanics 37*(10), 1363–1390.

Oskay, C. & J. Fish (2004). Fatigue life prediction using 2-scale temporal asymptotic homogenization. *International Journal for Numerical Methods in Engineering 61*(3), 329–359.

Pastor, M., O.C. Zienkiewicz, & A.H.C. Chan (1990). Generalized plasticity and the modelling of soil behaviour. *International Journal for Numerical and Analytical Methods in Geomechanics 14*(3), 151–190.

Peerlings, R., R. de Borst, W.M. Brekelmans, & J.H.P. de Vree (1996). Gradient enhanced damage for quasi-brittle materials. *International Journal for Numerical Methods in Engineering 39*, 3391–3403.

Thiele, M., M. Bäßler, A. Rogge, & S. Pirskawetz (2011). Schädigungsevolution in beton unter hochzyklischen ermüdungsbeanspruchungen. In *52. DAfStb-Forschungskolloquium*.

Voyiadjis, G., Z. Taqieddin, & P. Kattan (2008). Anisotropic damage-plasticity model for concrete. *International Journal of Plasticity 24*(10), 1946–1965.

Wu, J., J.Li, & R. Faria (2006). An energy release rate-based plastic-damage model for concrete. *International Journal of Solids and Structures 43*(3–4), 583–612.

Zienkiewicz, O. & Z. Mroz (1984). Generalized plasticity formulation and applications to geomechanics. In C. Desai and R. Gallaher (Eds.), *Mechanics of Engineering Materials*, pp. 655–679. Wiley.

Computational Modelling of Concrete Structures – Meschke, Pichler & Rots (Eds)
© 2018 Taylor & Francis Group, London, ISBN 978-1-138-74117-1

From slender columns to branching structures

R. Krč
Faculty of Civil Engineering, Brno University of Technology, Brno, Czech Republic

J. Podroužek
Christian Doppler Laboratory, University BOKU, Vienna
Faculty of Civil Engineering, Brno University of Technology, Brno, Czech Republic

R. Wan-Wendner
Christian Doppler Laboratory, University BOKU, Vienna

ABSTRACT: The first part of this paper reviews current approaches and methods used for modelling of structural concrete columns. Several methods are presented and their benefits and drawbacks are discussed. In the second part, a transition between traditional shapes and organic forms is described together with an example of a real structure. An insight for design and assessment of members with organic geometrical forms is then given, including a proposal for an inner bio-inspired filing of the structural member itself.

1 INTRODUCTION

With the development of technology and computers science, new possibilities for structural design occur. In these days, engineers are not limited by hand calculations and simplified approaches when designing a civil structure. Advanced numerical methods are available and new trends are regularly discussed on scientific conferences worldwide (Bicanic et al., 2014). With various software packages, that took months and years of intense development and testing, engineers are capable of performing a precise structural design and assessment within a moment (Navrátil et al., 2017; Subramani and Manivannan, 2014). Also, new technology such as additive manufacturing will most likely change the shape of civil engineering as new possibilities will become available (Bos et al., 2016). In this paper, past and current methods for designing concrete columns will be discussed. In the second part, the potential of organic shapes will be introduced and possible approaches will be reviewed.

2 CURRENT ENGINEERING APPROACHES

For massive columns, a simple calculation of internal forces followed with cross-section assessment is sufficient. According to Eurocode, columns with flexural slenderness $\lambda < \lambda_{lim}$ can be considered massive (European Committee for Standardisation, 2004). This condition is, however, rather limiting and most tall columns will not fulfil it and will be considered slender. In those cases, a different approach is required. We can either reduce the strength of the material for cross-section assessment or increase the design internal forces to account for second order effects. This can only be done if the slenderness parameter is close to the limit slenderness. For very slender columns their behaviour is rather non-linear and this should be considered in the model. Reduced interaction diagrams exist but are still just another simplification since the loading path for slender columns is rather non-linear. Considering this, the whole column has to be modelled non-linearly and limit strain and strength of material assessed accordingly. It can be done in most modern FEM programs like ANSYS, ATENA or IDEA StatiCa (ANSYS, 2017, ATENA, 2017, IDEA StatiCa, 2017).

As for calculation convergence, the widely used Newton-Rhapson method with load control performs quite well unless there is a sudden drop of structural resistance. In that case, the N-R method shows so-called 'snap-through' behaviour and finds another convergence point only and if the structure resistance increases again. To avoid this, an option is the Newton-Rhapson method with displacement control, which however suffers from so-called 'snap-back' behaviour, or the Arc-length method (Vasios, 2015). The latter one proceeds with constant steps no matter how the structural stiffness changes and therefore, finds convergence even for post-critical behaviour. The method was originally introduced by Riks (Riks, 1979) as a

system of equations, that was not very efficient to be algorithmized. An alternative was later introduced by Crisfield (Crisfield, 1981), who modified the system of equations into one, known as the 'arc-length' equation, that was easy to be implemented in any commercial software using Newton's method (Vasios, 2015). This can be rather useful for very slender columns or for fire loading when the behaviour is not straightforward.

Even though the arc length method is very efficient to find convergence after the limit point is reached, it also suffers from a major drawback. The method will always yield two solutions since the circle used for each step intersects the diagram in two points. This can cause divergence, especially in the first iteration since the direction of solution cannot be predicted with certainty. Another issue is the relatively slow solution for the linear part of the curve, compared to Newton's method. Therefore, it is not unusual that in commercial software both methods are combined. At first, the Newton method is used and once it diverges the Arc-length method is applied. As of arbitrarily shaped branching structure, the code recommendations are yet to be formulated.

3 TRANSITION TO BRANCHING STRUCTURES

Development of technology gives us more options how to reliably design non-prismatic columns. One reason is, that software packages used for design and assessment, can be, if properly used, much more precise than simplified approaches suitable for hand calculation. Another aspect is construction feasibility. Contemporary expansion of additive manufacturing, commonly known as 3D printing or fused deposition modelling (FDM), has caused, that this technology is finding its way even to traditional areas such as civil engineering.

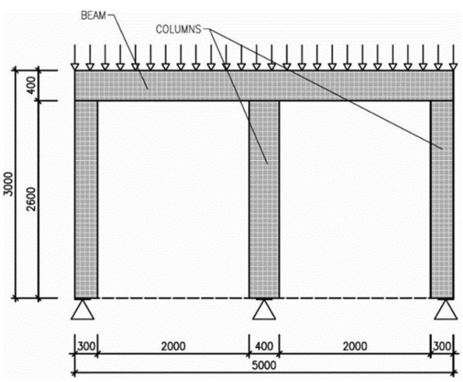

Figure 1. Classical approach to transmitting the uniformly distributed load to supports.

Currently, this method is still under development and a large amount of research has to be done before it will be ready to be massively used for construction. However, for the places, which are remote from classical resources, the additive manufacturing may eventually be the best option. Building outposts on the Moon or Mars from the local material may be significantly more efficient than carrying that material from the Earth (Benvenuti et al., 2013). This technology can also be attractive for prefabricated construction, since large-scale printers with other necessary equipment can be placed inside a factory itself (Lim et al., 2012).

To get an insight how these organic shapes should look like, an inspiration can be taken from nature where plenty of structures are already optimized by millions of years of evolution. A good example is a tree—seemingly very light structure capable of withstanding even strong winds. However, this shape cannot be directly applied to structural columns since the tree is meant to carry only its own weight not much greater dynamic loads from above. Another example is long bones like the femur, capable of transmitting much greater loads than their own weight. This bone is very slender and almost cylindrical in its cross-section, with sponge-like inner structure, mostly visible around its ends. Research showed, that this shape is adapted to carry maximal load with minimal material requirements (Brekelmans et al., 1972).

One way how to design such organic shapes is by using topology optimization. It is a method that optimizes material for given load and boundary condition, which usually yields in non-prismatic organic-like shape. An experiment was performed in structural software IDEA StatiCa (IDEA StatiCa, 2017). A rectangle wall with dimensions $5.0 \times 3.0 \times 0.2$ m was loaded with a uniformly distributed line load on its top edge. The wall was then supported by three-point supports with bearing plates 0.2 m wide. A topological optimization was performed with a target volume of 20% of the original structure. The result showed rather complex branching structure, that would be optimal to transmit the load to the supports.

This example demonstrates the possible transfer from current rectangular systems with prismatic members to more complex bio-inspired structures. With the development of additive manufacturing engineers can design complex organic shapes with a non-solid inner structure that can also be optimized to more efficient shapes for any given load case. Static vertical loads require different column shapes than dynamical loading from various directions, which yields a multiscale problem, for which the solution depends on scale considered. The final optimal structure will, therefore, be different for

each loading case. During the production process (3D printing), the material can also be deposited along the lines of principle stress instead of horizontal layers in order to maximize structural performance (Liu and Yu, 2017).

4 PERIODIC CONFIGURATION OF INNER STRUCTURE

When analysing these organic structural members, we need to keep in mind that it is a multi-scale problem and the structure can be analysed on three levels. On a structural level, the overall shape of the structural member is designed using some optimization method such as topology optimization mentioned above (Fig. 2). The inner spatial structure (Fig. 3) is analysed on a macro level as the cross-section does not need to be solid using additive manufacturing. There are shapes known as minimal periodic surfaces that can be an option for the microstructure. Great advantage of these surfaces is, that they do not contain any sharp edges causing peaks in stress flow. Finally, we also need to consider the material level where the performance depends on the parameters of the used material and technology.

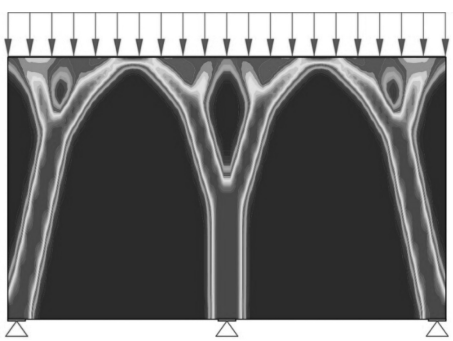

Figure 2. Topological optimization in IDEA StatiCa Detail: Red parts require more material, blue parts require no material.

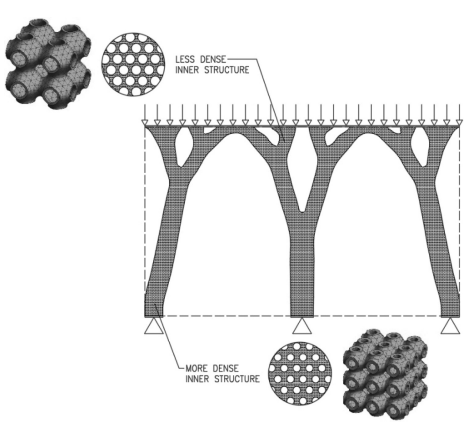

Figure 3. Wall example – proposed optimal structure with variable density.

There are many materials that can be used for additive manufacturing. In commercial sectors, thermoplastic polymers, such as polylactic acid (PLA) or polycarbonate (PC), are usually used for small-scale printing. For large scale application in civil engineering, a possible material option is concrete (Robert Bogue, 2013). Required parameters of concrete used for large-scale 3D printers is flowability and fast strength gain. Given the fact, that the standard reinforcement bars can only be inserted manually during the print (Features and perspectives of 3D-printing, 2017), or can be inserted by another robotic arm, the concrete can either be plain (for small structures) or reinforced by steel or polymer fibres.

4.1 *Geometrical configuration*

There is a great number of minimal periodic surfaces that can be used as shapes for inner structure of columns and other structural members. A research by NASA (Schoen, 1970) has already been done in 1970 to show the potential of such shaped materials for the space industry. A research on selected six of these minimal periodic surfaces was performed for the sake of this paper, to get an insight into their basic properties. Points in a given cube matrix with a base size of 4π were generated using the parametric equations shown in Table 1 in order to obtain a representative volume element (RVE).

The tolerance parameter t used in the equations correlates with the thickness of the surfaces walls

Table 1. Equations of surveyed minimal periodic surfaces.

Name	Equation
Gyroid	$(0 - t) < \sin(x)\cos(y) + \sin(y)\cos(z) + \sin(z)\cos(x) > (0 + t)$
Gyroid Squared*	$(1 - t) < (\sin(x)\cos(y))^2 + (\sin(y)\cos(z))^2 + (\sin(z)\cos(x))^2 > (1 + t)$
Gyroid Tripled*	$(0 - t) < (\sin(x)\cos(y))^3 + (\sin(y)\cos(z))^3 + (\sin(z)\cos(x))^3 > (0 + t)$
Schwarz P	$(0 - t) < \cos(x) + \cos(y) + \cos(z) > (0 + t)$
Schwarz D	$(0 - t) < \sin(x)\sin(y)\sin(z) + \sin(x)\cos(y)\cos(z) + \cos(x)\sin(y)\cos(z) + \cos(x)\cos(y)\sin(z) > (0 + t)$
Neovius	$(0 - t) < 3(\cos(x) + \cos(y) + \cos(z))^3 + 4\cos(x)\cos(y)\cos(z) > (0 + t)$

* These minimal periodic surfaces were developed for the sake of this paper from gyroid.

– the higher t, the thicker the walls and the denser the RVE.

Visualizations of the selected point clouds are shown in Figure 4.

Table 2 shows input parameters and Table 3 output parameters of the six minimal periodic surfaces. With relative volumes spanning from 14% to 29% of the solid cube, the resulting RVE mass is down to 330 kg/m^3 to 680 kg/m^3 (compared to 2360 kg/m^3 for regular concrete, 1400–1800 kg/m^3 for lightweight concrete or 650–700 kg/m^3 for ultra-lightweight concrete). A significant portion of the load carried by concrete structural members stems from the dead weight of the structure itself. Therefore, even small changes in the performance ratio (strength/volume mass) can lead to more efficient and cheaper structures. Also, the structure can be tuned for the static and dynamic response, have custom failure modes or tailored acoustic and thermal properties. The concrete formed into the shape of periodic surfaces with relatively thin walls can also have different shrinkage and creep behaviour than in the solid form.

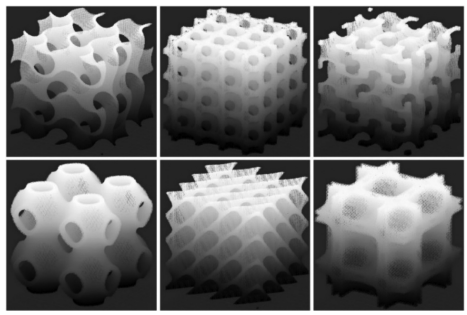

Figure 4. Generated shapes (from upper left): (a) Gyroid, (b) Gyroid Squared R, (c) Gyroid Tripled, (d) Schwarz P, (e) Schwarz D, (f) Neovius.

Table 2. Input parameters of surveyed minimal periodic surfaces.

Name	Base size	Tolerance t	Step
Gyroid	4π	0.20	0.10
Gyroid Squared	4π	0.10	0.10
Gyroid Tripled	4π	0.20	0.10
Schwarz P	4π	0.30	0.10
Gyroid	4π	0.25	0.10
Gyroid	4π	0.80	0.10

Table 3. Calculated parameters of surveyed minimal periodic surfaces.

Name	Locations	Points	Density
Gyroid	1 953 125	252 421	12.92%
Gyroid Squared	1 953 125	568 458	29.11%
Gyroid Tripled	1 953 125	441 405	22.60%
Schwarz P	1 953 125	335 627	17.18%
Gyroid	1 953 125	401 500	20.56%
Gyroid	1 953 125	679 057	34.77%

Research has to be done to find the optimal geometrical configuration of inner structures for different loading patterns, materials or structural parts. Even small changes in the parametric formulation will result in substantially different structure and, thus, different RVEs with different optimum parameters. An experiment on 3D printed minimal periodic cubes was recently performed e.g. by MIT (Chandler, 2017). It showed, among others, that the resistance and deformation capacity may be strongly influenced by the shell thickness only.

In terms of inner structure optimization, there are five aspects to consider in general. These are the periodic implicit formulation, its period length, shell thickness, shell density, and systematic/random spatial variation of the aforementioned. By considering different optimization goals (structural, thermal, acoustic, durability, costs, aesthetic) in combination with the five optimization aspects mentioned above, the dimensionality of the problem may clearly become prohibitive from optimization point of view. As seen often in nature, the fractal principle may be also applied to the shell thickness and density, where solid infill is not preferable and standard infill patterns (rectangular, triangular, honeycomb, etc.) should be applied to optimize production (3D printing) speed, among others.

4.2 *Numerical and experimental investigation*

A way has to be found to safely and efficiently design and analyse branching structural members consisting of non-solid spatial materials. Since the structure of the minimal periodic surface is rather fine, compared to the size of the whole structural member, it would be inefficient to model whole structures as precisely. Provided the parameters of the periodic surfaces are known, one possible way is to homogenize the structure (Palmieri and De Lorenzis, 2014). Parameters such as compressive strength or volume mass have to be either measured or calculated on a small scale and transferred to standard finite or discrete element formulations on the macro-scale.

When characterizing structural concrete, or any other heterogeneous random material, for numerical assessment, the statistical and spatially variable properties of aggregates, pores or fibre reinforcement (Wang, Yang, Yates, Jivkov, & Zhang, 2015) may be computationally intensive. The proposed periodic implicit formulation, on the other hand, may represent possible advantage, as the RVE can be

directly linked to selected period (scale), without the need for costly analysis. As for the nature and complexity of the resulting structures, a possible way how to model these in small scale is to use specialized computational software like MARS (MARS, n.d.). Among others, this software implements the recently introduced Lattice Discrete Particle Model (LDPM), which uses a discrete framework (particles) to model displacement field (Cusatis et al., 2011). Contrary to the traditional Finite Element Method (FEM), where the continuous framework is used, LDPM is ideally suited for modelling post-limit fracturing and the shattering of material.

Once the properties on the microscale are defined, whole structural members can be designed. Using concrete for 3D printed civil structures would be the first option since it can be formed into various shapes. It is the periodic geometrical form that may be advantageous over the solid one.

To get initial insight into the behaviour resulting from a periodic inner structure, a compression test on a cylindrical gyroid sample with diameter of 150 mm printed from PLA was performed. The parametric equation of gyroid can be found in Table 1. Young's modulus of typical PLA spans between 3.5 to 6.5 GPa (Farah et al., 2016) and compressive strength between 18 to 90 GPa ("PLA and ABS Strength Data," n.d.) compared to Young's modulus between 32 to 44 GPa and strength between 30 to 90 MPa for typical concrete. Sample before compression test is shown in Figure 5. The load-displacement diagram shown in



Figure 5. Gyroid sample printed from PLA before a compression test.

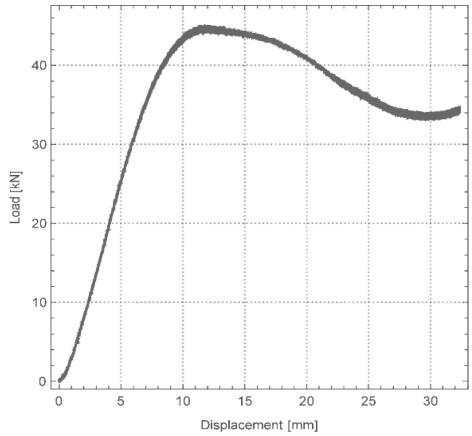

Figure 6. Load-displacement diagram of the gyroid sample printed from PLA.



Figure 7. Gyroid sample printed from PLA after the compression test.

Figure 6 reveals a steady linear load increase up to 85% the of peak strength. After the maximum load capacity was reached at the load of 44 kN, the sample showed a small drop in resistance followed by large deformation capacity before it was completely crashed. Before the end of the experiment, resistance of the sample increased again. This was caused by the fact, that crushed shells locked into each other, filling the previously empty space and, therefore, supporting the whole structure.

5 SUMMARY

The introduction of additive manufacturing into civil engineering gives new opportunities and

options for civil engineers and architects to design organic-like structures with complex inner geometry. A possible transition to bio-inspired shapes by methods such as topological optimization was discussed in this paper. Several shapes created from existing or modified minimal periodic surfaces, which can be used for the inner spatial structure were presented together with their basic parameters.

Using additive manufacturing not only allows the use functionally optimized overall column shapes but also for complex inner structures, yielding a multiscale problem with the target to reach an optimized streamlined geometry with variable density. Some of the advantages of using periodic shapes inside the structural members are better control over the overall material randomness, tuned static and dynamic response, custom failure modes or optimized acoustic and thermal properties.

Extensive research still needs to be undertaken before it will be possible to use such technology for large-scale civil concrete structures. The design approach must be able to deal with the multiscale nature of the proposed bioinspired structures and yield reliable results. In a next phase, experimental investigations and nonlinear multi-physics simulations of real 3D printed models of various minimal periodic surfaces will be performed to an attempt to promote the use of such spatial materials as an inner filling for concrete structural members.

ACKNOWLEDGEMENT

The financial support by the Austrian Federal Ministry of Economy, Family and Youth and the National Foundation for Research, Technology and Development is gratefully acknowledged, as well as the support of the project No. LO1408 "AdMaS UP – Advanced Materials, Structures and Technologies", supported by Ministry of Education, Youth and Sports under the "National Sustainability Programme I".

REFERENCES

ANSYS, 2017. ANSYS, Inc.

ATENA, 2017. Červenka Consulting s.r.o.

Benvenuti, S., Ceccanti, F., De Kestelier, X., 2013. Living on the moon: topological optimization of a 3D-printed lunar shelter. *Nexus Netw*. J. 15, 285.

Bicanic, N., Mang, H., Meschke, G., Borst, R. de, 2014. Computational Modelling of Concrete Structures. *CRC Press.*

Bos, F., Wolfs, R., Ahmed, Z., Salet, T., 2016. Additive manufacturing of concrete in construction: potentials and challenges of 3D concrete printing. *Virtual Phys*. Prototyp. 11, 209–225. doi:10.1080/17452759.2016.1209867.

Brekelmans, W.A.M., Poort, H.W., Slooff, T., 1972. A new method to analyse the mechanical behaviour of skeletal parts. *Acta Orthop*. Scand. 43, 301–317.

Chandler, D.L., 2017. Researchers design one of the strongest, lightest materials known [WWW Document]. MIT News. URL http://news.mit.edu/2017/3-d-graphene-strongest-lightest-materials-0106 (accessed 8.15.17).

Crisfield, M., 1981. A fast incremental/iterative solution procedure that handles "snap-through." *Comput. Struct.* 13, 55–62.

Cusatis, G., Pelessone, D., Mencarelli, A., 2011. Lattice discrete particle model (LDPM) for failure behavior of concrete. I: Theory. *Cem. Concr. Compos.* 33, 881–890.

European Committee for Standardisation, 2004. EN 1992-1-1: Eurocode 2: Design of concrete structures – Part 1-1: General rules and rules for buildings.

Farah, S., Anderson, D.G., Langer, R., 2016. Physical and mechanical properties of PLA, and their functions in widespread applications — A comprehensive review. *Adv. Drug Deliv. Rev., PLA biodegradable polymers* 107, 367–392. doi:10.1016/j.addr.2016.06.012.

Features and perspectives of 3D-printing, 2017. Apis Cor.

IDEA StatiCa, 2017. IDEA RS s.r.o.

Lim, S., Buswell, R.A., Le, T.T., Austin, S.A., Gibb, A.G.F., Thorpe, T., 2012. Developments in construction-scale additive manufacturing processes. *Autom. Constr.* 21, 262–268. doi:10.1016/j.autcon.2011.06.010.

Liu, J., Yu, H., 2017. Concurrent deposition path planning and structural topology optimization for additive manufacturing. *Rapid Prototyp*. J. 23, 930–942. doi:10.1108/RPJ-05-2016-0087.

MARS, n.d. ES3.

Navrátil, J., Kabeláč, J., 2017. Nonlinear analysis of reinforced and composite columns in fire. Frat. Ed Integrità Strutt. 72.

Palmieri, V., De Lorenzis, L., 2014. Multiscale modeling of concrete and of the FRP–concrete interface. *Eng. Fract. Mech. 1*31, 150–175. doi:10.1016/j.engfracmech.2014.07.027.

PLA and ABS Strength Data, n.d.

Riks, E., 1979. An incremental approach to the solution of snapping and buckling problems. *Int. J. Solids Struct*. 15, 529–551.

Robert Bogue, 2013. 3D printing: the dawn of a new era in manufacturing? *Assem. Autom.* 33, 307–311. doi:10.1108/AA-06-2013-055.

Schoen, A.H., 1970. Infinite periodic minimal surfaces without self-intersections.

Subramani, T., Manivannan, R., 2014. Crack Identification in Reinforced Concrete Beams Using Ansys Software. *Int. J. Eng. Res. Appl.* 4, 133–141.

Vasios, N., 2015. Nonlinear Analysis of Structures The Arc Length Method: Formulation, Implementation and Applications.

Wang, X.F., Yang, Z.J., Yates, J.R., Jivkov, A.P., Zhang, C., 2015. Monte Carlo simulations of mesoscale fracture modelling of concrete with random aggregates and pores. *Constr. Build. Mater.* 75, 35–45. doi:10.1016/j.conbuildmat.2014.09.069.

Aging concrete: From very early ages to decades-long durability



Taylor & Francis
Taylor & Francis Group
http://taylorandfrancis.com

Computational Modelling of Concrete Structures – Meschke, Pichler & Rots (Eds)
© 2018 Taylor & Francis Group, London, ISBN 978-1-138-74117-1

Assessing the flow characteristics of self-compacting concrete via numerical simulations of flow tests

S. Kulasegaram & B.L. Karihaloo
Cardiff School of Engineering, Cardiff University, Cardiff, UK

ABSTRACT: Due to the demand for highly durable concrete structures, Self-Compacting Concrete (SCC) with its unique characteristics (flow-ability, passing ability and stability) has been developed, and is increasingly replacing Vibrated Concrete (VC) in various structural applications. SCC, which is characterised in its fresh state by high flow-ability and rheological stability, has excellent applicability for structural elements with complicated shapes and congested reinforcement. An incompressible mesh-less Smooth Particle Hydrodynamics (SPH) methodology has been implemented in this simulation and a suitable Bingham-type constitutive model has been coupled with the Lagrangian momentum and continuity equations to model the flow of SCC in its fresh state. The aim of this numerical simulation was to investigate the capabilities of the SPH methodology in predicting the flow of SCC mixes. To confirm that a mix flows homogeneously, the distribution of large coarse aggregates in the mixes has also been simulated.

1 INTRODUCTION

In concrete construction, insufficient filling of formwork and de-airing and segregation of conventional vibrated mix components give rise to serious durability problems. The impact of such problems has increased sharply as complex formwork and/or dense reinforcement is being used. Self-compacting concrete (SCC) which flows and consolidates under the action of gravity, without external vibration, while maintaining homogeneity has been developed to overcome these problems (Okamura et al. 2003). It ensures proper filling of formwork and produces a high quality finish in heavily reinforced structural members and inaccessible areas even in the most complex formwork. It has rationalised the construction process by offering several economic and technical advantages over vibrated concrete.

Various tests are performed to evaluate the fresh properties of SCC, including its flowing and filling ability, passing ability, and resistance to segregation (EFNARC 2005). These tests are labour intensive, time-consuming and therefore expensive. Moreover, observations made from tests under one set of conditions are not always unconditionally applicable to other circumstances in which dissimilar materials and mix proportions than the test mixes may be used. Thus, new tests are required in such circumstances. Repeated experimental tests can be avoided by performing a cost-effective computational simulation to save cost, time, effort and materials. It can also provide a thorough understanding of the SCC flow behaviour, particularly in complex formworks, which is essential to achieving high quality finish. Indeed, modelling has brought insight into the significance of the rheology as a tool for the optimisation of mix composition and the processing techniques to fulfil the levels of engineering properties required for the intended civil engineering applications (Roussel et al. 2007).

Since the main characteristic of SCC is its flow-ability, its fresh property cannot be thoroughly comprehended without understanding its rheology. The quality control and accurate prediction of the SCC rheology are crucial for the success of its production. The accurate prediction of the SCC flowing behaviour is not a simple task, particularly in the presence of heavy reinforcement, complex formwork shapes and large size of aggregate. In this regard, the indispensable and inexpensive approach offering considerable potential is the numerical simulation of SCC flow. This approach will deepen the understanding of the SCC mix flow behaviour and evaluate its ability to meet the necessary self-compacting criteria of passing ability and segregation resistance (i.e. homogeneous distribution of coarse particles in the matrix).

From a computational point of view, choosing the right strategy for the simulation is an important issue, and several approaches have been tried to simulate the flow (Baaijens et al. 2001, Wu et al. 2010, Švec et al. 2012). Of these approaches, the one offering considerable potential is the smoothed particle hydrodynamics (SPH). Identifying SCC as a homogeneous fluid that consists

of particles of different sizes and shapes, the particle based method SPH is an ideal computational method to represent its rheological behaviour with an acceptable level of accuracy. This methodology can also assist in proportioning SCC mixes, thus improving on the traditional trial and error SCC mix design (Deeb & Karihaloo 2013, Abo Dhaheer et al. 2016a). It has also been used and proved to be efficient and accurate in modelling the flow and monitoring the movement of large aggregates and/or short steel fibres of SCC in the cone slump flow and L-box tests (Deeb et al. 2014a,b,c). The SPH simulation methodology also provides a useful tool for predicting the yield stress (τ_y) of SCC mixes accurately in an inverse manner from the flow spread (Badry et al. 2016). This is particularly relevant to the characterisation of an SCC mix because the measurement of τ_y by rheometers is inconsistent and fraught with inaccuracies.

The aim of this paper is to investigate numerical simulation of the flow of SCC in the J-ring, L-box and V-funnel tests. This methodology will provide a thorough understanding of whether or not an SCC mix can satisfy the self-compactibility criterion of passing ability through narrow gaps in reinforcement besides the flow-ability criterion. The capabilities of the SPH methodology will be validated, in terms of flow pattern and flow time recommended according to BS EN (2010) and EFNARC (2005).

2 DEVELOPMENT OF THE MIXES

An extensive laboratory study was conducted to produce different SCC mixes, with nominal 28-day cube compressive strengths of 30, 40, 50, 60, 70 and 80 MPa. These mixes were designed according to the rational mix design method proposed in Abo Dhaheer et al. (2016a,b). The compositions of all mixes are given in Table 1. In order to ensure that all mixes met the flowing and passing ability criteria without segregation (SCC requirements), slump flow, J-ring, L-box and V-funnel tests were conducted according to BS EN (2010) and EFNARC (2005). The experimental results of slump flow, J-ring and L-box tests are listed in Table 2.

Table 1. Mix proportions of test SCC mixes, kg/m^3.

Constituents	SCC mix designation by compressive strength (MPa)					
	30	40	50	60	70	80
Cement[a]	240	262.5	281.25	315	345	367.5
ggbs[a]	80	87.5	93.75	105	115	122.5
Limestone powder[b]	156	147	139	125	123	125
Water	201.6	199.5	198.8	197.5	184.0	171.5
Super-plasticiser	1.6	1.7	2.1	2.4	2.8	3.0
Fine aggregate[c]	788	775	760	735	735	735
Coarse aggregate[d]	840	840	840	840	840	840

a: cementitious materials.
b: super–plasticizer. Figures in brackets refer to increase in SP needed for satisfying passing ability.
c: limestone powder < 125 µm.
d: fine aggregate < 2 mm (Note: a part of the fine aggregate is the coarser fraction of the limestone powder, FA**125 µm –2 mm, whereas FA*** refers to natural river sand < 2 mm).
e: coarse aggregate < 20 mm.

Table 2. Flow and passing ability test results of SCC mixes.

Mix	Slump flow test		J-ring flow test		L-box test		
	Spread mm	t_{500} s	Spread mm	$t_{500\,J}$ s	t_{200} s	t_{400} s	H_2/H_1
30	685	0.5	650	0.7	0.5	1.1	0.91
40	730	0.6	700	0.8	0.5	0.9	0.92
50	675	1.2	640	1.4	0.7	1.4	0.86
60	665	1.2	665	1.5	0.8	1.5	0.89
70	700	1.4	690	2.0	1.3	2.7	0.88
80	730	1.9	700	2.8	1.5	3.1	0.93

3 NUMERICAL MODELLING

3.1 *Governing equations*

In view of its shear rate-dependent response, SCC can be regarded as a non-Newtonian incompressible fluid. Its rheology is best described by a Bingham type model which contains two material properties, the yield stress τ_y and the plastic viscosity η. It is known however that the yield stress of SCC mixes is very low (around 200 Pa) in comparison with normal vibrated concretes (thousands of Pascal) and remains nearly constant over a wide range of plastic viscosities (Ghanbari & Karihaloo 2009). From a practical computational point of view, it is expedient to approximate the bilinear Bingham constitutive model with a kink at zero shear strain rate $\dot{\gamma} = 0$ by a scalar continuous function (Papanastasiou 1987).

$$\tau = \eta\dot{\gamma} + \tau_y\left(1 - e^{-m\dot{\gamma}}\right) \tag{1}$$

in which m is a very large number m = 10^5. This smooth function is practically indistinguishable

from the original bi-linear relation. Equation (1) is applicable to each of the three independent shear components of the stress tensor.

The Bingham type constitutive model of the mixes is coupled with the Lagrangian continuity and momentum equations to model the flow of SCC mixes. The isothermal, Lagrangian form of mass and momentum conservation equations are:

$$\frac{1}{\rho}\frac{D\rho}{Dt} + \nabla.\mathbf{v} = 0 \tag{2}$$

$$\frac{D\mathbf{v}}{Dt} = -\frac{1}{\rho}\nabla P + \frac{1}{\rho}\nabla.\boldsymbol{\tau} + g \tag{3}$$

where ρ, t, $\boldsymbol{v}$, P, g and $\boldsymbol{\tau}$ represent the fluid particle density, time, particle velocity, pressure, gravitational acceleration, and shear stress tensor, respectively. Below we shall consider flows in which the density is constant, so that the first term in Equation (2) vanishes.

A projection method based on the predictor-corrector time stepping scheme has been adopted to track the Lagrangian non-Newtonian flow (Chorin 1968, Koshizuka 1998). The prediction step is an explicit integration in time without enforcing incompressibility. Only the viscous stress and gravity terms are considered in the momentum Equation (3) and an intermediate particle velocity v^*_{n+1} is obtained as:

$$\mathbf{v}^*_{n+1} = \mathbf{v}_n + \left(g + \frac{1}{\rho}\nabla.\boldsymbol{\tau}\right)\Delta t \tag{4}$$

Then the correction step is performed by considering the pressure term in Equation (3):

$$\frac{\mathbf{v}_{n+1} - \mathbf{v}^*_{n+1}}{\Delta t} = -\left(\frac{1}{\rho}\nabla P_{n+1}\right) \tag{5}$$

where v_{n+1} is the corrected particle velocity at the time step n+1.

The intermediate velocity v^*_{n+1} is usually not divergence-free but this condition is imposed on the corrected velocity v_{n+1} by enforcing the incompressibility condition from Equation (2):

$$\nabla.\mathbf{v}_{n+1} = 0 \tag{6}$$

Hence the intermediate velocity can be projected on the divergence-free space by writing the divergence of Equation (5), using (6), as

$$\nabla.\left(\frac{1}{\rho}\nabla P_{n+1}\right) = \frac{\nabla.\mathbf{v}^*_{n+1}}{\Delta t} \tag{7}$$

Since the density of particles remains constant in the present simulations, Equation (7) can be rewritten as:

$$\nabla^2 P_{n+1} = \frac{\rho}{\Delta t}\nabla.\mathbf{v}^*_{n+1} \tag{8}$$

where ∇^2 is the Laplacian.

Once the pressure is obtained from Equation (8), the particle velocity is updated by the computed pressure gradient (see Equation (5)):

$$\mathbf{v}_{n+1} = \mathbf{v}^*_{n+1} - \left(\frac{1}{\rho}\nabla P_{n+1}\right)\Delta t \tag{9}$$

And finally, the instantaneous particle position is updated using the corrected velocity:

$$\mathbf{x}_{n+1} = \mathbf{x}_n + \mathbf{v}_{n+1}\Delta t \tag{10}$$

The time step Δt is chosen based on the relevant stability conditions for the given problem. In the case of Bingham-type SCC fluid flow, the time step is primarily controlled by the effective plastic viscosity. Therefore, the time step size is generally decided by:

$$\Delta t = \min\left(\frac{\alpha_1 r_0}{V_{\max}}, \frac{\alpha_2 r_0^2 \rho}{\mu}\right) \tag{11}$$

where r_0 is the initial particle spacing, V_{max} is the maximum particle velocity, and α_1 and α_2 are the coefficients usually in order of 0.1. These coefficients depend on the choice of SPH kernel functions and the nature of the engineering application.

3.2 *Boundary conditions*

Mainly two types of boundary conditions namely, the rigid wall boundaries and the free surface boundaries need to be considered in the numerical modelling of SCC flow. For example, in the simulation of J-ring test these boundary conditions are: (1) the pressure on the free surface vanishes, and (2) the normal component of the particle velocity and the pressure gradient vanish at the wall of the cone, at the J-ring bars and on the bottom plate, as shown in Figure 1a. The zero pressure gradient is used only for solving the second-order pressure Poisson Eq. (8). In the simulations, the technique based on arrays of rigid dummy particles is used to implement the boundary conditions on the cone wall, J-ring bars and base plate, as shown in Fig. 1b. For realistic simulations, the friction between the SCC mix and the contacting surfaces needs to be taken into consideration, as

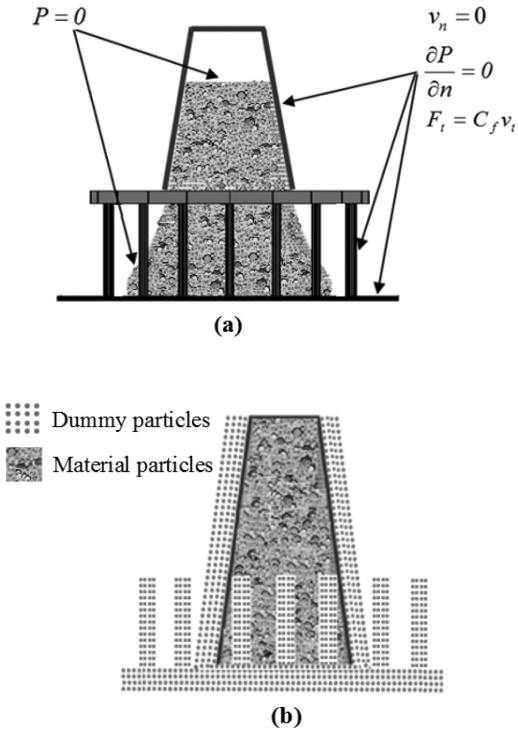

Figure 1. (a) J-ring test boundary conditions, (b) dummy particles for enforcing boundary conditions.

this contributes a force that resists the flow. The coefficients of kinematic friction (C_f) between the mix and the steel base plate and the J-ring bars are 0.55 and 0.48 N s/m, respectively. The former was determined previously (Deeb et al. 2014) by matching the t_{500} (the time when the mix spread reaches 500 mm) in slump cone test conducted in the same laboratory with the simulated results. The latter was chosen by matching the $t_{500\,J}$ in the J-ring test with the simulated results of Mix 50 in the present study. These calibrated coefficients of kinematic friction were then held unchanged for all other 5 mixes simulated in the present study. In line with these procedures, appropriate boundary conditions were employed in the case of L-box and V-funnel tests.

3.3 *Treatment of coarse aggregates*

Tracking the coarse aggregate particles during the flow of SCC gives an indication of whether or not they are homogeneously distributed in the mix. In order to be able to compare the simulated distribution of coarse aggregates equal to or larger than 8 mm in size with the distribution in the actual test specimen after the flow had stopped, the coarse aggregates in the size ranges G ≥ 20, 16 ≤ G <20, 12 ≤ G < 16 and 8 ≤ G < 12 mm used in some test mixes were colour coded with non-toxic non-water-soluble paints (Figure 2). As a result, the outlines of the aggregate particles can be clearly identified in the cut sections after SCC had hardened. To clearly illustrate this, the procedures adopted in the case of L-box test (Figure 3) are detailed below.

To investigate the coarse aggregate distribution in the SCC mix, the cut sections of the slab in the horizontal leg of the L-box after it had hardened is examined. In order to retrieve the slab from the horizontal section of the box, the front end plate of the horizontal section of the L-box was hinged (Figure 3(a)). Two SCC mixes of 40 and 60 MPa were cast with colour-coded coarse aggregates and tested in the L-box (Figure 3(b)). When the mix had flowed into the horizontal section of the L-box, the two steel bars were unscrewed and removed. After 24 h, the hinged end plate was dropped and the solid slab was carefully removed from the L-box and placed in a water tank for



Figure 2. Colour coded coarse aggregates (Yellow 8 ≤ *G* < 12, Green 12 ≤ *G* <16, Red 16 ≤ *G* < 20, White *G* ≥ 20).

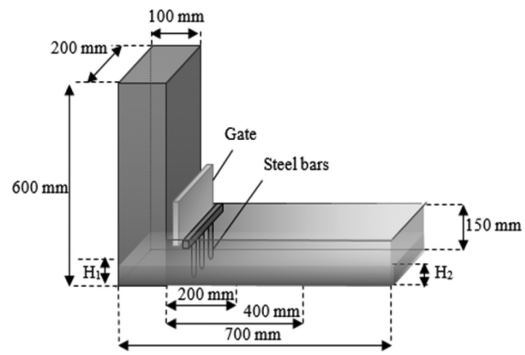

Figure 3. L-box configuration.



Figure 4. (a) Hinged end plate of L-box apparatus (b) 60 MPa SCC mix with colour-coded aggregates.

curing until needed for cutting. Each specimen was cut along two longitudinal sections using a diamond saw (Figure 5(a)).

The number of aggregates in the different size ranges (according to their different coloured outlines; Figure 5(c)) was counted in each of the two surfaces made by the cut. Table 3 lists the number of different size aggregates (the average of the two surfaces) counted along the two longitudinal sections of the L-box test slab in the two test mixes.

Coarse aggregates need to be homogeneously distributed in SCC mixes. Therefore, an important requirement of SCC mixes is that heavier aggregate particles do not segregate from the paste but stay homogeneously distributed during the flow. In order to be able to monitor the velocity and position vectors of aggregates of different sizes, as well as those of the fluid particles representing the paste, the particles were represented with distinct colours, as shown in Figure 6.

In the case of L-box test simulation, the total number of particles (Np) used in the 3D simulation was 59568 to represent the volume of the SCC mix in the L-box (129×10^5 mm^3), giving a resolution of 216.56 mm^3 per particle, if all particles have the same density as the viscous continuum. Thus, in all the SCC mixes, large aggregates that can be distinguished from the homogeneous mass must have an assigned volume (V_a) exceeding this minimum. It is for this reason that only aggregates of size 8 mm and above could be distinguished as discrete identities (Table 4). According to the volume fractions (obtained by sieve analysis), the masses of the SPH particles representing different coarse aggregate particles in the mix were calculated (Table 4). All particles representing the mix were generated randomly. Particles representing the mortar as well as the coarse aggregates form a homogeneous mass and possess the same continuum properties except for their assigned volumes. Throughout the simulation, particles representing the coarse aggregates based on their assigned

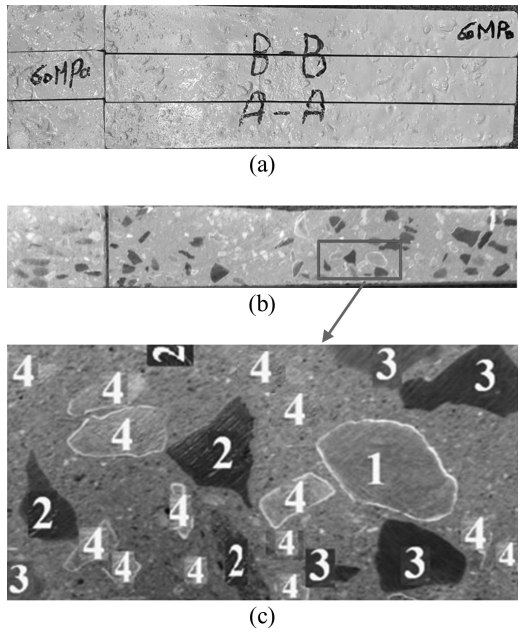

Figure 5. (a) Two longitudinal sections of hardened slab (mix. 60 MPa). (b) One of the two surfaces made by the longitudinal cut. (c) Outlines of coloured coarse aggregates clearly visible in the cut surface: coarse aggregates with white outlines are labelled 1, with red 2, with green 3 and those with yellow 4.

Table 3. Average number of coarse aggregate particles in different size ranges (G) in the two surfaces made by each of the two longitudinal cuts of hardened L-box slabs of 40 MPa and 60 MPa mixes.

Mix (MPa)	Section	G ≥ 20 (mm)	16 ≤ G < 20 (mm)	12 ≤ G < 16 (mm)	8 ≤ G < 12 (mm)
40	A–A	6	30	35	90
	B–B	5	34	40	95
60	A–A	6	30	37	95
	B–B	5	32	40	102

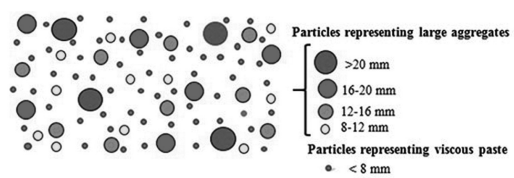

Figure 6. Schematic illustration of particle representation in the simulated mixes.

Table 4. Volume fractions and assigned volumes of aggregate particles in 3D L-box test (SCC mix 40 MPa).

	Particle size range (mm)	Representative particle diameter (mm)	Density (kg/m^3)	Volume fraction (%)	Number of particles (N_p)	Assigned volume per particle V_a (mm^3)
Aggregates ≥ 8 mm	G ≥ 20	20	2800	1.28	39	5097
	16 ≤ G < 20	18	2800	7.20	305	3716
	12 ≤ G < 16	14	2800	4.20	373	1748
	8 ≤ G < 12	10	2800	7.90	1953	637
Particles < 8 mm	G < 8		2173	79.0	56898	170
Total			2302	100	59568	

volumes were tagged (Figure 6) in order to monitor their velocity vectors and positions.

4 SIMULATION RESULTS

Due to space restriction, only some of the key simulation results of L-box, J-ring and V-funnel tests are presented below. Further, to clearly emphasize the importance of this research (and to avoid the repetition of information), the simulation and results of one of the tests (i.e. L-box test) are elaborated in more detail compared to other tests.

The plastic viscosity of a mix used in numerical simulation was calculated using the micromechanical procedure described in Ghanbari & Karihaloo (2009), based on the plastic viscosity of the paste (i.e. cement, ggbs, water, super-plasticiser and entrapped air). The latter was estimated from viscometer measurements of similar pastes reported in the literature (Nehdi et al. 2004, Sun et al. 2006). The estimated viscosity values are presented along with the J-ring test results in Table 7. The yield stress (τ_y) was predicted in an inverse manner using the SPH simulation of slump flow test (Badry et al. 2016). Over the wide range of SCC mixes (30–80 MPa) simulated, it has been found in Badry et al. (2016) that the τ_y varies only marginally from 175 to 190 Pa. Therefore, the same range was used for τ_y of the mixes in the present study.

4.1 *L-box test*

In the case of L-box test, the simulated profiles of the free-surface flows at several distances from the gate and the final profile are compared with the profiles obtained in the experiments of the test mixes. Figure 7 compares the free surface profile at two different instances of L-box simulation with mix designed to achieve 60 MPa strength. The profiles of the free surfaces of the simulated mixes look similar to those observed in the laboratory tests. Moreover, it was found that the ratio of the SCC mix height at the end of the horizontal section of the L-box to the height of the remaining concrete in the vertical section in the simulated flow was more than the minimum recommended value of 0·8 (EFNARC, 2005); these simulated results correlate very well with the experimental results.

The distribution of large aggregates (≥ 8 mm) in two simulated SCC mixes (40 and 60 MPa) was examined using two approaches, and the results were compared with the test results. In the first approach, the simulated L-box mix after the flow had stopped was cut along two longitudinal sections (A–A and B–B Figure 7(b)). One of the two surfaces made by each of the two cuts is shown in Figure 8.

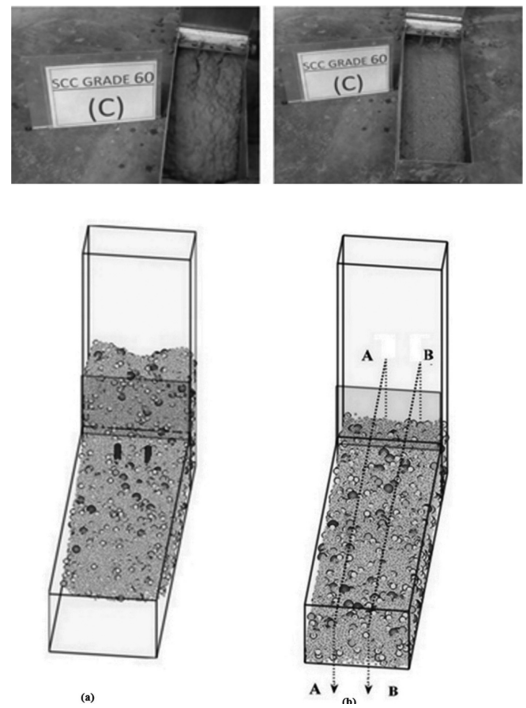

Figure 7. (a) Profile of free surface of experimental (upper photo) and simulated (lower figure) SCC mix 60 MPa at approximately 400 mm from the gate. (b) The final profile of free-surface flow after the flow had stopped; A–A and B–B show the sections along which cuts were later made.

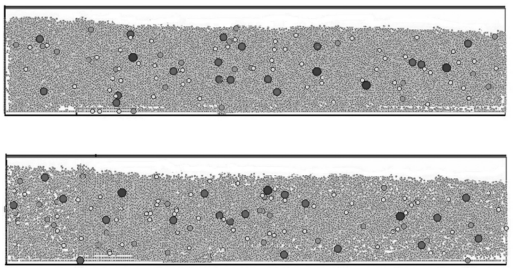

Figure 8. One of the two surfaces made by longitudinal cut (a) A–A and (b) B-B of the simulated SCC (mix 60 MPa).

The number of large aggregates of different size ranges in each of the two surfaces was counted and the average numbers in the two sections are listed in Table 5. As the volume fractions of the coarse aggregates of different size ranges (but not their actual numbers) were the same in the test mixes and simulations, their numbers in the cut sections of the L-box test and the simulated L-box flow must necessarily be correlated. This correlation may, for instance, be revealed by considering the ratio of the average number of aggregates of a certain size range to the number of aggregates of the largest size. This was done for the test and simulated L-box flows, and the ratios are reported in the last two columns of Table 6: it can be seen that the relative numbers of aggregates of different size ranges were indeed nearly the same.

Furthermore, the larger aggregates were homogeneously distributed along the two sections with no visible settlement of the larger aggregates (≥ 8 mm) (Figure 9), as in the actual test. This observation is in good agreement with a recent study conducted by Badry et al. (2016), who found that the SPH methodology is capable of accurately predicting the distribution of large coarse aggregates in simulated slump cone test.

In the second approach, a statistical analysis was performed using the Weibull cumulative distribution function (CDF) to compare the distribution of coarse aggregates in the experimental and simulated L-box specimens along sections A–A and B–B. The histograms (Figures 9 and 10) reveal that the average number of larger coarse aggregates in the simulated sections was almost identical to the average number of those in the experimental sections for both SCC mixes (40 and 60 MPa).

Table 5. Average number of coarse aggregate particles in different size ranges (G) in the simulated L-box along two surfaces made by each of the two longitudinal sections (cuts).

Mix (MPa)	Section	G ≥ 20 (mm)	16 ≤ G < 20 (mm)	12 ≤ G < 16 (mm)	8 ≤ G < 12 (mm)
40	A–A	4	17	21	56
	B–B	3	18	25	60
60	A–A	3	17	24	60
	B–B	4	19	21	58

Table 6. Average number of coarse aggregates along two longitudinal sections of mixes 40 MPa and 60 MPa.

Mix (MPa)	Size range (mm)	Average number		Ratio of average number to average number of size 20 mm	
		Experiment	Simulation	Experiment	Simulation
40	G ≥ 20	5.5	3.5	1.0	1.0
	16 ≤ G < 20	32.0	17	5.82	5.0
	12 ≤ G < 16	37.5	23.5	6.82	6.57
	8 ≤ G < 12	97.0	58.0	17.6	16.57
60	G ≥ 20	5.5	3.5	1.0	1.0
	16 ≤ G < 20	31.0	18.0	5.64	5.14
	12 ≤ G < 16	38.5	22.5	7.0	6.43
	8 ≤ G < 12	98.5	59.0	17.91	16.86

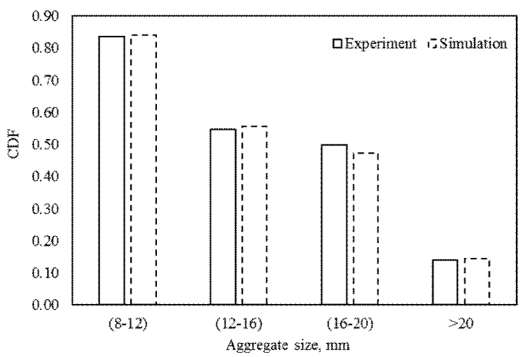

Figure 9. Histogram of the average number of larger coarse aggregates in SCC (Mix 40 MPa).

4.2 *J-ring test*

To investigate how efficient the SPH is to predict the flow of SCC mixes through gaps in the reinforcing bars, different SCC mixes were three-dimensionally simulated in the J-ring apparatus. The experimental and simulated flow patterns of selected SCC mixes (Mix40 and Mix60) at different times during the

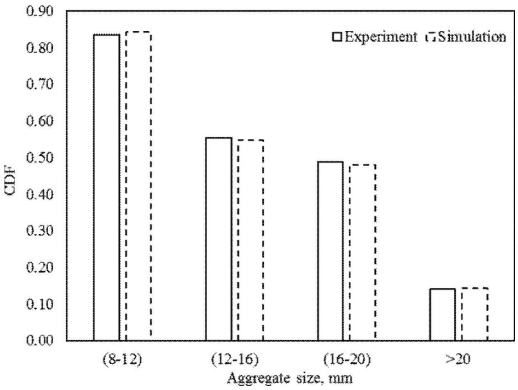

Figure 10. Histogram of the average number of larger coarse aggregates in SCC (Mix 60 MPa).



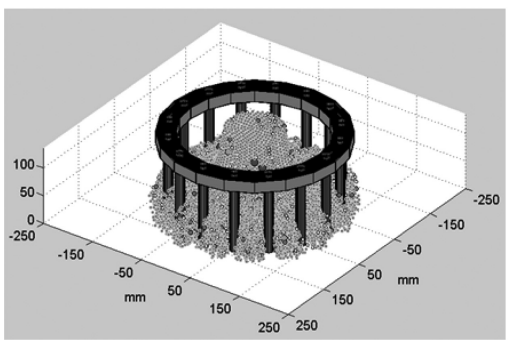

Figure 11. Flow pattern of SCC Mix40 just after passing through the gaps in J-ring bars (at 0.3 sec).

flow are shown in Figures 11 and 12. The simulations are found to be well correlated with the experimental results. From Figure 11 it can be noticed that the shape and the free surface profile of the simulated mix around the J-ring bars is similar to that observed in the test. The spread at 500 mm diameter also looks very similar to that observed

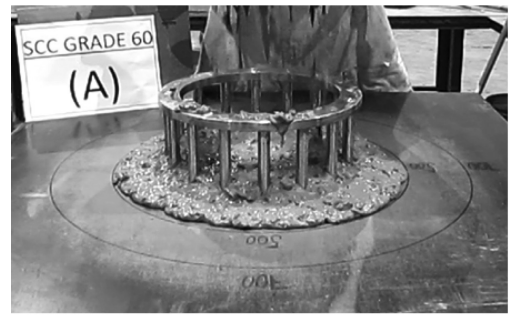

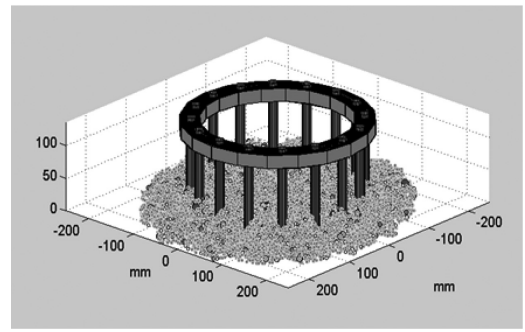

Figure 12. Flow pattern of SCC Mix60 at t_{500J} (at 1.5 sec).

Table 7. Simulation and experimental results for SCC mixes.

Mix designation	Viscosity, Pa s	Yield stress, Pa	t_{500J} (s)		Spread (mm)	
			Experimental	Simulated	Experimental	Simulated
30	4.63	175	0.7	0.7	650	640
40	6.82	175	0.8	0.9	700	680
50	7.84	180	1.4	1.4	640	640
60	8.18	175	1.5	1.6	665	655
70	9.32	180	2.0	2.0	690	695
80	10.47	190	2.8	2.7	700	700

in the laboratory test (Figure 12). Moreover, it can be observed (Table 7) that SPH can predict very well the time needed for flow to reach the spread at 500 mm diameter, t_{500J} for all the test mixes.

4.3 *V-funnel test*

In the three-dimensional numerical simulation of the flow through the V-funnel, each SCC mix has been represented by a limited number of particles

(53,846) to investigate its flow characteristics and compare with the corresponding experimental results. This number of particles has been chosen to provide adequate accuracy in a reasonable time. The simulation also reveals the distribution of the large components in SCC mixes (coarse aggregate size G, ≥ 8 mm) so that it can be ascertained whether these heavier aggregates remain homogeneously distributed in the viscous mix during the flow.

The flow patterns of two representative test mixes obtained from the numerical simulation at various time steps are shown in Figs. 13 and 14. The experimental discharge times of all six mixes agree well with the simulated ones from SPH as reported in Table 8. The slight difference between the experimental and simulated discharge time ($t_{v\text{-}funnel}$) may be due to two possible reasons. Firstly, the assumption that the SCC particles are spherical in shape and secondly, the slight time delay in opening the bottom gate. The delay is the greater the higher the pressure on the gate, i.e. the higher the density of the mix. Thus, the difference is the least in the 30 MPa mix because it is the lightest (density 2307.1 kg/m^3) and it is the largest in the 80 MPa mix because it is the heaviest (density 2365.5 kg/m^3).

It is worth stressing that the only free variable that has been altered in the simulation to get this excellent fit was the kinematic coefficient of friction between one SCC mix and the V-funnel sidewalls. The value that gave this agreement with the experimental result was equal to 0.55 N s/m. This value was held constant for all the remaining five mixes. It can be observed from the simulated flow illustrated in Figs. 13 and 14 that the larger aggregates appear to remain homogeneously distributed in the mix at various times during the flow and do not settle downwards. This has been confirmed by statistical analysis of the mix collected from the V-funnel exit (Alyhya et al. 2017).

Table 8. Experimental and simulation results by SPH of V-funnel discharge time.

Mix designation (MPa)	Discharge time ($t_{v\text{-}funnel}$) (s)	
	Experimental	Simulation
30	2.45	2.35
40	3.10	2.95
50	3.60	3.40
60	4.05	3.80
70	4.95	4.55
80	6.10	5.60

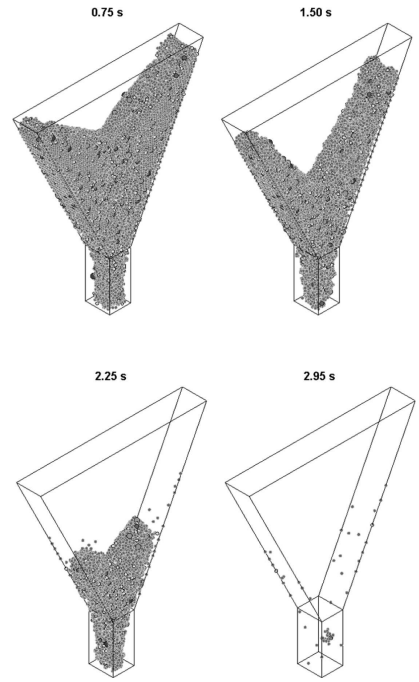

Figure 13. Simulated flow patterns of 40 MPa mix at different time steps.

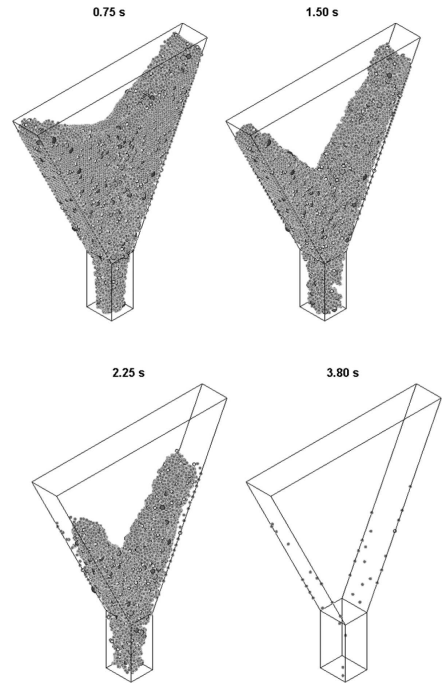

Figure 14. Simulated flow patterns of 60 MPa mix at different time steps.

5 CONCLUSIONS

The capabilities of the SPH simulation methodology to predict the SCC flow in L-box, J-ring and V-funnel tests were successfully assessed by comparing the results of different SCC mixes. The comparison showed that the simulations were in very good agreement with experimental results for all six mixes.

SPH allows tagging of the large aggregate particles in order to track their locations during the flow and after it has stopped. This allows the distribution of large aggregates in the mixes to be examined in order to ensure that they have not segregated from the mortar.

The SPH simulation methodology can indeed replace the time-consuming laboratory L-box, J-ring and V-funnel tests, thereby saving time, effort and materials.

REFERENCES

Abo Dhaheer, M. Al-Rubaye, M.M. Alyhya, W.S.B.L. Karihaloo, B.L. Kulasegaram, S. 2016a. Proportioning of self-compacting concrete mixes based on target plastic viscosity and compressive strength: part I—mix design procedure, J. Sustain. Cem. Mater. 5:199–216.

Abo Dhaheer, M. Al-Rubaye, M.M. Alyhya, W.S. B.L. Karihaloo, B.L. Kulasegaram, S. 2016b. Proportioning of self-compacting concrete mixes based on target plastic viscosity and compressive strength: part II—experimental validation, J. Sustain. Cem. Mater. 5:217–232.

Alyhya, W.S. Kulasegaram, S. Karihaloo, B.L. 2017. Simulation of the flow of self-compacting concrete in the V-funnel by SPH, Cem. Concr. Res. 100:47–59.

Baaijens, F.P.T. 2001. A fictitious domain/mortar element method for fluid-structure interaction, Int. J. Numer. Methods Fluids 35:743–761.

Badry, F. Kulasegaram, S. Karihaloo, B.L. 2016. Estimation of the yield stress and distribution of large aggregates from slump flow test of self-compacting concrete mixes using smooth particle hydrodynamics simulation. Journal of Sustainable Cement-Based Materials 5(3): 117–134.

BS EN 12350–12:2010. Testing Fresh Concrete, Part 12: Self-compacting Concrete, Jring Test.

BS EN 12350–9:2010. Testing fresh concrete: Self-compacting concrete-V-funnel Test.

BS EN 206–9: 2010 Concrete. Part 9: Additional rules for Self-compacting concrete (SCC).

Chorin, A.J. 1968. Numerical solution of the Navier-Stokes equations, Mathematics of Computation 22:745–762.

Deeb, R. Karihaloo, B.L. 2013. Mix proportioning of self-compacting normal and high strength concretes, Mag. Concr. Res. 65:546–556.

Deeb, R. Kulasegaram, S. Karihaloo, B.L. 2014a. 3D modelling of the flow of self-compacting concrete with or without steel fibres. Part I: slump flow test, Comput. Part. Mech. 1:373–389.

Deeb, R. Kulasegaram, S. Karihaloo, B.L. 2014b. 3D modelling of the flow of self-compacting concrete with or without steel fibres. Part II: L-box test and the assessment of fibre reorientation during the flow, Comput. Part. Mech. 1:391–408.

Deeb, R. Kulasegaram, S. Karihaloo, B.L. 2014c. Reorientation of short steel fibres during the flow of self-compacting concrete mix and determination of the fibre orientation factor, Cem. Concr. Res. 56:112–120.

EFNARC guidelines, 2005. The European Guidelines for Self-compacting Concrete; Specification, Production and Use p. 63.

Ghanbari, A. Karihaloo, B.L. 2009. Prediction of the plastic viscosity of self-compacting steel fibre reinforced concrete, Cem. Concr. Res. 39:1209–1216.

Koshizuka, S. Nobe, A. Oka, Y. 1998. Numerical analysis of breaking waves using moving particle semi—implicit method, Int. Journal for Numerical Methods in Fluids 26:751–769.

Nehdi, M. Rahman, M.A. 2004. Estimating rheological properties of cement pastes using various rheological models for different test geometry, gap and surface friction, Cem. Concr. Res. 34:1993–2007.

Okamura, H. Ouchi, H. 2003. Self-compacting concrete, J. Adv. Concr. Technol. 1:5–15.

Papanastasiou T.C. 1987. Flows of materials with yield, Journal of Rheology 31:385–404.

Roussel, N. Geiker, M.R. Dufour, F. Thrane, L.N. Szabo, P. 2007. Computational modeling of concrete flow: General overview, Cem. Concr. Res. 37:1298–1307.

Sun, Z. Voigt, T. Shah, S.P. 2006. Rheometric and ultrasonic investigations of viscoelastic properties of fresh Portland cement pastes, Cem. Concr. Res. 36:278–287.

Švec, O. Skoček, J. Stang, H. Geiker, M.R. Roussel, N. 2012. Free surface flow of a suspension of rigid particles in a non-Newtonian fluid: a lattice Boltzmann approach, J. Non-Newtonian Fluid Mech. 179–180:32–42.

Wu, J. Shu, C. 2010. An improved immersed boundary-lattice Boltzmann method for simulating three-dimensional incompressible flows, J. Comput. Phys. 229:5022–5042.

Computational Modelling of Concrete Structures – Meschke, Pichler & Rots (Eds)
© 2018 Taylor & Francis Group, London, ISBN 978-1-138-74117-1

Mixing and extrusion of printing concrete

Yong Yuan
Department of Geotechnical Engineering, Tongji University, Shanghai, China
State Key Laboratory of Disaster Reduction in Civil Engineering, Tongji University, Shanghai, China

Yaxin Tao
Department of Geotechnical Engineering, Tongji University, Shanghai, China

ABSTRACT: 3D concrete printing gains great attention in recent years because it is labor-saving and free of formwork. The workability of printable concrete is of vital importance because it would change during 3D printing process. The printable concrete should be easy to convey in pipelines and well set in a short period of time after extrusion. The paper simulates the process of mixing and extrusion of printable concrete, with the means of CFD approach. Mixing processes are modelled on a predefined concrete mixture. The rheological behavior of the fresh mixture is expected to be given. For modelling extrusion flow of pumped fresh concrete is supposed through Archimedes auger. Where liquid Flash Setting Admixture (FSA) in liquid state is merged in. Simulating the distribution of liquid FSA aims at finding the way to inject it uniformly before printing concrete out of jet head. This study could provide hints to the design of printing schedule.

1 INTRODUCTION

The quality of printable concrete is related to the mixing and extrusion process. The viscosity of fresh concrete is expected to moderate swiftly in the jet head to meet the requirements of both pumpability in pipe lines and buildability after extrusion. Liquid flash setting admixture (FSA) is of great use to regulate the viscosity of printable concrete (Gosselin, 2016). The schematic diagram of 3D printing setup is shown in Figure 1.

Numerical simulation provides an effective way to analysis the printing process. In this paper, the simulation contains two major processes, the process of mixing liquid FSA with fresh concrete and the process of reaction between FSA and concrete.

However, the research on the mixing and reaction process of fresh concrete and liquid FSA is rare. This paper is based on the following research. There are many research topics on the flow of fresh concrete. Computational Fluid Dynamics (CFD) method was used to simulate the flow of self-compacting concrete under gravity (Li, 2013). Volume of Fluid (VOF) model was used to simulate the rheological properties and the flow form of fresh concrete based on the Bingham model (Zhou, 2014). The relation between the rheological parameters and related experimental parameters is established at the same time. The research on reaction simulation is diversified. Liquid flow field and mixing process was analyzed in a solid-liquid reactor (Kasat, 2008). Mixing time of a multistage impeller stirred tank was got with a smaller middle gap by the means of CFD method. The results are in good agreement with experiments (Ochieng, 2008). CFD method was used to predict the flow filed in the mixing reactor with single-spindle agitating paddle. A conclusion is given that the numerical simulation results is essentially the same as the flow filed measured by LDV method (Kelly, 2003).

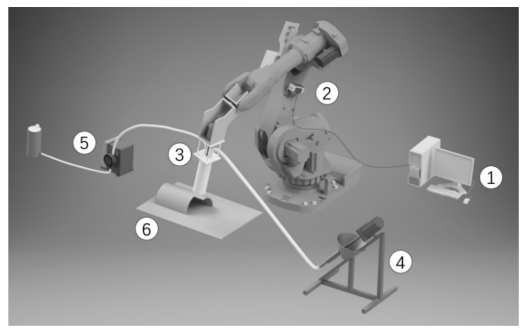

Figure 1. Schematic of the 3D printing setup: 1. Robot controller; 2. Robotic arm; 3. Printhead; 4. Peristaltic pump for concrete; 5. FSA pump; 6. 3D printed object.

CFD method is adopted in this paper to analyze the viscosity moderation of fresh concrete after mixed with liquid FSA. The rheological behavior of the fresh mixture is expected to be given. Velocity field in the jet head, degree of mixing and reaction is shown. Besides, viscosity change of fresh concrete is expected to be simulated.

2 MODELLING PROCEDURE

2.1 *Hydrodynamic model*

Fresh concrete is treated as continuous material. During the mixing process, the inertia force of fresh concrete is a main factor affecting the field and the flow state would be unstable. Coupled with rotary blades, the flow would be more disorder. RNG k-e model is a model related to the Reynolds time-average method. This model is a two-equation turbulence model, which is suitable for strong turbulence and strong eddy current. According to the calculation content and conditions, RNG k-e model is adopted in this paper.

2.2 *Transportation and reaction model*

Fresh concrete and liquid FSA are mixed in the jet head. The Component Transportation Model could be used to simulate diffusion and transmission of fluid flow. Mixture density of fresh concrete and liquid FSA follows the volumetric weighted average law, and viscosity of the mixture is based on the quality weighted average law.

It is certain that viscosity of fresh concrete would increase sharply after mixed with liquid FSA. The Reaction Model could be adopted to simulate the interaction between liquid FSA and fresh concrete. The Eddy Dissipation Model is adopted to simulate the interaction between liquid FSA and fresh concrete.

3 EXPERIMENTAL CASES

3.1 *Model parameters*

There are two main parts in this model. Mixing part is composed of cross-frame rotary blades. Extrusion part is an Archimedes auger. The cross-frame blades and auger are rotary at the same speed. Fresh concrete and liquid FSA enters from different inlet. In order to make sure that the extruded concrete is continuous, the size of the outlet is smaller than that of the main part. Schematic diagram of the jet head is shown in Figure 2. The design of blades is shown in Figure 3. External dimensions are shown in Table 1. And internal dimensions are shown in Table 2.

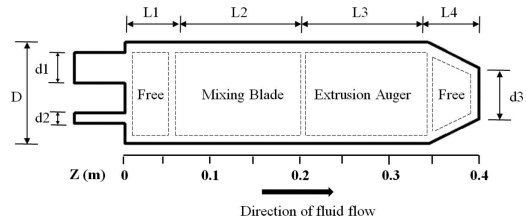

Figure 2. Schematic diagram of the jet head.

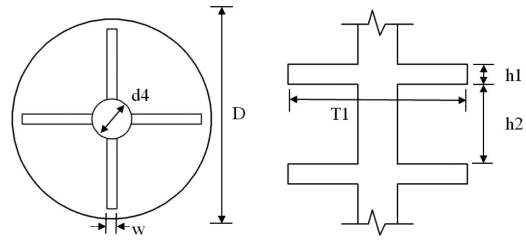

Figure 3. Schematic diagram of the axis.

Table 1. External dimensions of jet head.

Geometrical parameters	Length
Inner diameter (D)(mm)	100
Length of free part (L1)	D/2
Length of mixing part (L2)	3D/2
Length of extrusion part (L3)	3D/2
Length of nozzle (L4)	D/2
Diameter of concrete inlet (d1)	2D/5
Diameter of FSA inlet (d2)	D/10
Diameter of outlet (d3)	D/2

Table 2. Internal dimensions of blades and auger.

Geometrical parameters	Length
Impeller diameter (T1)	9D/10
Diameter of axis (d4)	D/5
Impeller blade width (w)	D/20
Length of Mixing blade (h1)	T/10
Length between impellers (h2)	D/2
Auger diameter (D2)	4D/5
Pitch of Auger (h3)	D

3.2 *Domain and mesh*

Compared with Single Reference Frame (SRF), Multiple Reference Frame (MRF) in the CFD method can be used to define different reference frames for different grid blocks and models with both stationary and rotary domains. Two

fluid domains are defined in this simulation. The external domain is static and the internal domain is rotary at the same speed as the rotary blades and Archimedes auger. The diameter of rotary domain is the same as that of Archimedes auger. Interfaces are defined between two domains to transfer data.

Considering the complex shape of the rotary blades and Archimedes auger, grids in rotary domain was refined. Schematic diagram of two fluid domains are shown in Figure 4.

3.3 *Material properties*

Aluminum sulfate, the main reaction component of the liquid FSA, can promote the formation of ettringite to accelerate the setting of fresh concrete (Paglia, 2004). The mechanism of inorganic acid-based FSA was studied by analyzing the chemical composition of cement and the amount of gypsum (Maltese, 2007). Similarly, after mixed with cement and water, Al^{3+} in alkali-free FSA reacted with C_3A and Ca^{2+} rapidly to produce ettringite.

Viscosity of fresh concrete increases after mixed with liquid FSA. In this simulation, mass ratio is 1:60. Fresh concrete is divided into two parts. 30% of fresh concrete can participate in the reaction and the rest part can't. Similarly, 20% of liquid FSA can participate in the reaction and the rest can't. In the setting process, ettringite, which is a new material of lager viscosity, is generated.

Mixing and extrusion process is shown in Figure 5.

Material properties are shown in Table 3.

3.4 *Boundary conditions*

The boundaries include two inlets, one outlet, outer wall of the stationary domain, inner wall of the rotary domain and interfaces between rotary domain and stationary domain. Fresh concrete enters from inlet 1 while liquid FSA enters from inlet 2. The velocity inlets and the pressure outlet are adopted, while the pressure of the outlet is atmospheric pressure. Total inflow is fixed as 9 L/min. Outer wall of the stationary domain is static wall with default setting function. Inner wall of the rotary domain is dynamic wall with active motion. Rotary speed is fixed as 60 rpm. Roughness height of the wall is 0.0001 m and the roughness is 0.5.

3.5 *Time step*

Time step is related to the cycle time of the fluid flow. Besides, time step is proportional to the reciprocal of the rotary speed. Generally, time step value is less than 1/10 of the reciprocal of the rotary speed. To keep the computational stability, time step is taken as a fixed value of 0.05 s.

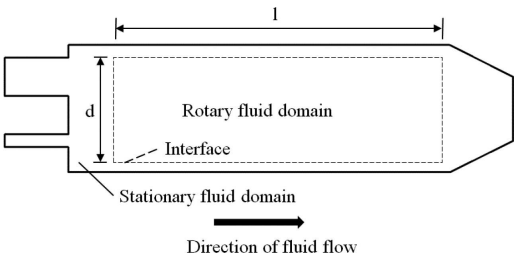

Figure 4. Fluid domains.

Table 3. Material properties.

Material	Density (kg/m^3)	Viscosity (Pa·s)
Concrete (non-react)	2314	40.0
Concrete (react)	2314	40.0
FSA (non-react)	1000	0.1
FSA (react)	1000	0.1
Product	2339	120.0

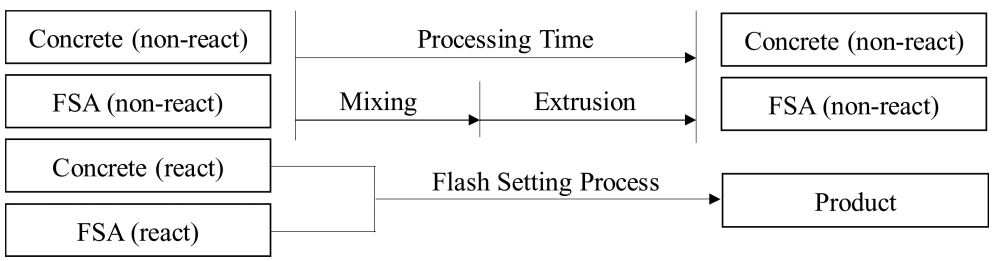

Figure 5. Mixing and extrusion process.

4 RESULTS AND DISCUSSION

4.1 *Velocity field*

The positive direction of z axis is parallel to the direction of fluid flow. Position of inlet is defined as z = 0 and outlet is defined as z = 0.4 m. The coordinate diagram is shown in Figure 6.

Figure 7 shows the contours of velocity in different sections. The mixing part ranges from z = 0.05 to z = 0.2 and the extrusion part ranges from z = 0.2 to z = 0.35.

In the mixing part, the following features can be observed. Velocity of flow near blade tips is higher than other area and the velocity near the internal wall of the stationary domain tends to be zero. Furthermore, velocity varies significantly from planes with rotary blades (z = 0.075 m, z = 0.125 m and z = 0.175 m) to planes without blade (planes between two blades. It could be seen that the rotary speed is higher than the flow velocity of the fluid along the z axis. In the extrusion part, velocity near auger is higher than other areas.

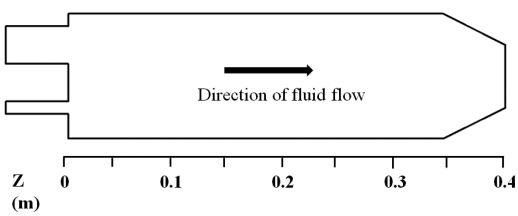

Figure 6. Coordinate diagram.

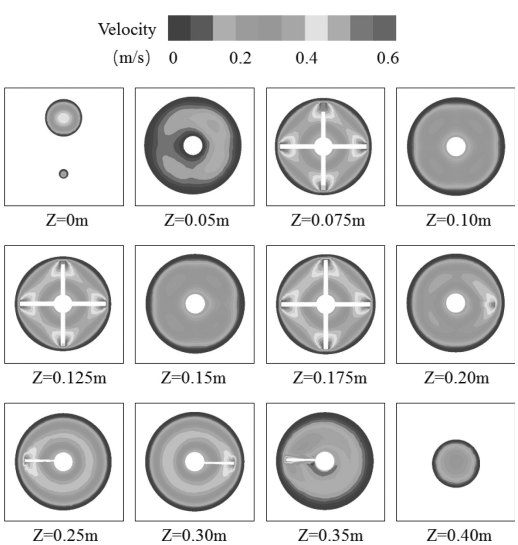

Figure 7. Contours of velocity.

4.2 *Mixing and reaction process*

The distribution of the mixture is characterized by the standard deviation of the mass fraction of part liquid FSA that do not participate in the reaction. Meanwhile, the degree of reaction is also characterized by the ratio of product.

As is shown in Figure 8, that standard deviation of mass fraction of liquid FSA tends to be lower along the direction of flow indicating that the mixture gradually becomes uniform. That standard deviation of mass fraction of FSA tends to be zero indicating that the mixing process is basically complicated. It can be seen in Figure 8(a) that fresh concrete and FSA are basically completely mixed in the mixing part (z = 0.05 m to z = 0.20 m). It can be seen in Figure 8(b) that ratio of product reaches 34.22% in the position of z = 0.02 m and 94.97% in the position of z = 0.35 m. Fresh concrete and liquid FSA are completely mixed in the mixing part, while the reaction is relatively delayed. The reaction is basically finished in the extrusion part.

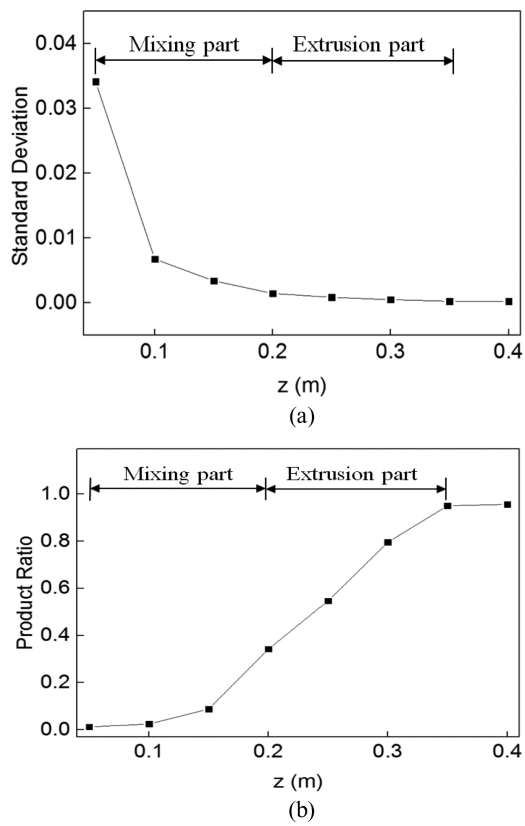

Figure 8. Standard deviation (a) and product ratio (b) along the direction of flow.

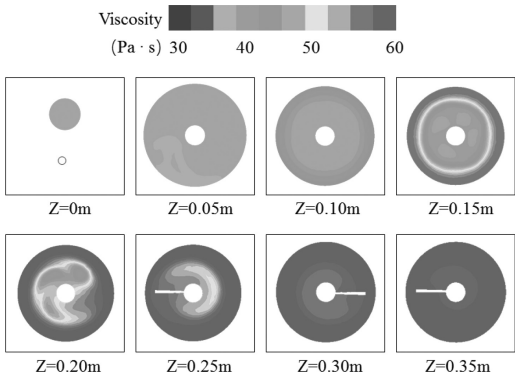

Figure 9. Contours of Viscosity.

Because of the reaction between fresh concrete and liquid FSA, viscosity of fresh concrete increases gradually in the jet head. Contours of viscosity in different sections are shown in Figure 9.

As is shown in Figure 9, viscosity continuously changes in the jet head. In the mixing part (from z = 0.05 m to z = 0.20 m), viscosity of fresh concrete near the outer wall of stationary domain increases first. In the extrusion part (from z = 0.20 m to z = 0.35 m), viscosity near the inner wall of rotary domain increases progressively. After mixing and extrusion process, the reaction is basically completed and the viscosity of fresh concrete is uniformly distributed.

5 CONCLUDING REMARKS

Conclusions are shown as follows: 1) Component transportation-reaction model is adopted in this paper. This model is proved to be effective to simulate the mixing and reaction process between fresh concrete and liquid FSA. 2) Under the given conditions, fresh concrete and liquid FSA can be basically mixed and reacted in the jet head. The change of viscosity meets the requirements of printing.

REFERENCES

Gosselin, C., Duballet, R. & Roux, P. (2016) Large-scale 3D printing of ultra-high performance concrete-a new processing route for architects and builders. *Materials & Design*, 100:102–109.

Kasat, G.R., Khopkar, A.R. & Ranade, V.V. (2008) CFD simulation of liquid-phase mixing in solid–liquid stirred reactor. *Chemical Engineering Science*, 63(15):3877–3885.

Kelly, W., Gigas, B. (2003) Using CFD to predict the behavior of power law fluids near axial-flow impellers operating in the transitional flow regime. *Chemical Engineering Science*, 58(10):2141–2152.

Li, J.Q. & Xu, W. (2013) A CFD Simulation of Self-Compacting Concrete Based on Herschel-Bulkley Rheological Model. *Engineering Mechanics*, 2013, 30(1):373–377.

Maltese, C., Pistolesi, C. & Bravo, A. (2007) Effects of setting regulators on the efficiency of an inorganic acid based alkali-free accelerator reacting with a Portland cement. *Cement & Concrete Research*, 37(4):528–536.

Ochieng, A., Onyango, M.S. & Kumar, A. (2008) Mixing in a tank stirred by a Rushton turbine at a low clearance. *Chemical Engineering & Processing Process Intensification*, 47(5):842–851.

Paglia, C.S.B., Wombacher, F.J. & Böhni, H.K. (2004) Influence of alkali-free and alkaline shotcrete accelerators within cement systems: Hydration, microstructure, and strength development. *ACI Materials Journal*, 101(5):353–357.

Zhou, Y. (2014) *Test Method and Inversion Technique of Self-Compacting Concrete's Rheological Parameters With L-Box Based on Bingham Model*. [Lecture] University of South China, 15th December.



Taylor & Francis
Taylor & Francis Group
http://taylorandfrancis.com

Computational Modelling of Concrete Structures – Meschke, Pichler & Rots (Eds)
© 2018 Taylor & Francis Group, London, ISBN 978-1-138-74117-1

Formulation, validation and application of a new shotcrete model

M. Neuner, M. Schreter & G. Hofstetter
Unit for Strength of Materials and Structural Analysis, Institute of Basic Sciences in Engineering Sciences, University of Innsbruck, Innsbruck, Austria

T. Cordes
BBT Brenner Basetunnel SE, Innsbruck, Austria

ABSTRACT: The complex material behavior of shotcrete is characterized by the time-dependent evolution of material properties due to hydration, hardening and softening, creep and shrinkage. Unlike to normal concrete, only a few advanced material models for shotcrete, representing the highly nonlinear, time-dependent material behavior, have been proposed in the literature so far. Recently, in (Neuner, Gamnitzer & Hofstetter 2017) a new constitutive model for shotcrete, based on a combination of the theory of plasticity, the theory of continuum damage mechanics, and a modified version of the solidification theory (Bažant & Prasannan 1989) was presented. In the present contribution, the new shotcrete model will be compared with two selected earlier models, i.e., the viscoplastic model, described in (Meschke 1996), and the viscoelastic-plastic model proposed in (Schädlich & Schweiger 2014). The capabilities of the three shotcrete models are evaluated by experimental data from the literature (Huber 1991, Müller 2001) and from a new experimental program on shotcrete specimens taken at a construction site of the Brenner Basetunnel. The performance of the three investigated shotcrete models will be evaluated by finite element simulations of the advance of a stretch of the Brenner Basetunnel, for which in-situ measurement data is available. In particular, the predicted evolution of stresses in the shotcrete shell and of deformations along the tunnel lining during the excavation process as well as the predicted long term behavior of the shotcrete shell will be examined.

1 INTRODUCTION

During tunneling according to the New Austrian Tunneling Method (NATM), a shotcrete lining, installed immediately after an excavation step, serves as a supporting structure for stabilizing the surrounding rock mass. For a realistic representation of this shotcrete shell in numerical simulations, accurate constitutive models for describing the time-dependent, nonlinear material behavior, and, in addition, experimental data for calibrating these models are necessary.

Recently, in (Neuner, Gamnitzer, & Hofstetter 2017) selected constitutive models for shotcrete, i.e., the model by Meschke (1996), the model by Schädlich and Schweiger (2014), and a novel damage plasticity model, denoted as the SCDP model, were compared. The models were calibrated and validated by experimental test results from the literature, i.e., the test data presented by Huber (1991) and Müller (2001). Building on this, the three material models were applied to a structural benchmark example, derived from a stretch of the Brenner Basetunnel, and an assessment of the models was presented in (Neuner, Schreter, Unteregger, & Hofstetter 2017).

However, the experimental tests by Huber and Müller were conducted on shotcrete compositions with low compressive strength. To account for the improved shotcrete compositions with higher compressive strength, a new experimental program was designed and presented in (Neuner, Cordes, Drexel, & Hofstetter 2017). The performance of modern shotcrete compositions compared to those older compositions investigated by Huber and Müller was demonstrated.

The present contribution gives an overview of the recent developments in the field of constitutive modeling of shotcrete, and places these recent insights in a new context by presenting the application of the calibrated material models to the benchmark example presented in (Neuner, Schreter, Unteregger, & Hofstetter 2017).

2 EXPERIMENTAL PROGRAM

A new experimental program on the time-dependent material behavior of a shotcrete composition (manufacturer designation *Sp C25/30/(56)/ÜK3/J2/XC4/XF3/GK8* according to the Austrian guideline for shotcrete (ÖVBB 2009)) was designed and

presented in (Neuner, Cordes, Drexel, & Hofstetter 2017). The program focused on the evolution of the Young's modulus and the uniaxial compressive strength, as well as shrinkage and creep tested on sealed specimens to exclude drying effects. Specimens for the lab tests were sampled at the construction site of the Brenner Basetunnel employing two different techniques: For tests on shotcrete younger than 24 hours, sprayed specimens, directly sampled from tubular molds were used, while for tests on shotcrete older than 24 hours both *sprayed* specimens as well as drill cores sampled from spray boxes were used. Sprayed specimens could already be unmolded 6 hours after casting, and experimental tests on the evolution of the uniaxial compressive strength were started immediately after. Sprayed specimens turned out as a suitable alternative to drill cores, if the spraying direction is nearly coaxial with the axis of the tubular mold in order to minimize the number of faulty specimens due to shotcrete rebound and air pockets.

Both the Young's modulus and the uniaxial compressive strength were tested up to a material age of 28 days. Figure 1 shows the mean values of the Young's modulus determined between 24 hours and 28 days, and the uniaxial compressive strength between 6 hours and 28 days, as well as the respective standard deviations (SD). Comparing the evolution of the Young's modulus and the uniaxial compressive strength, it can be seen that the ultimate Young's modulus is already attained at a material age of 7 days, while a substantial increase of material strength is still observed between 7 days and 28 days.

Shrinkage and creep tests were started simultaneously at three different ages of the material, i.e. 8 hours, 24 hours and 27 hours, and lasted for 56 days each. During the shrinkage and creep tests, the time-dependent strain was determined by measuring the time-dependent displacements at the center of the specimens over a distance of 200 mm, using three displacement transducers, which were arranged along the perimeter of each specimen. Creep tests were conducted on a hydraulic creep test bench (Figure 2), and the magnitude of the applied compressive load was chosen ensuring linear viscoelastic material behavior only. Accordingly, the specimens tested at 8 hours, 24 hours and 27 hours where loaded with compressive stresses of 1.9 MPa, 2.9 MPa and 2.7 MPa. After application of the load, it was held constant throughout the complete testing period.

From the experimental results of the creep tests, the material compliance functions, defined as time-dependent, load induced strain per unit stress, can be computed. Figure 3 shows the compliance functions computed from experimental results.

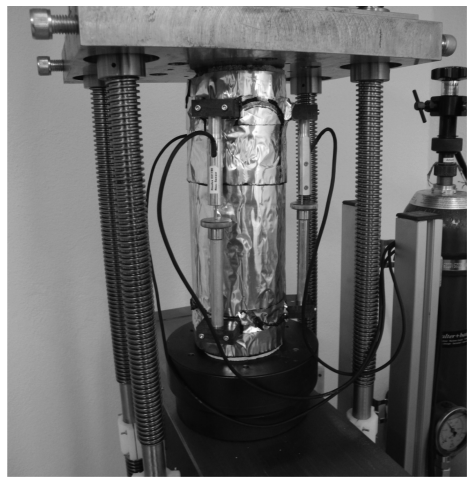

Figure 2. Sealed specimen during a creep test in the hydraulic creep test bench.

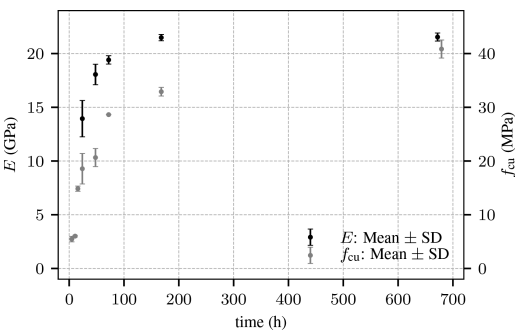

Figure 1. Time-dependent evolution of the Young's modulus (E) and the uniaxial compressive strength (f_{cu}): Mean values and standard deviations (SD) between a shotcrete age of 6 hours and 28 days.

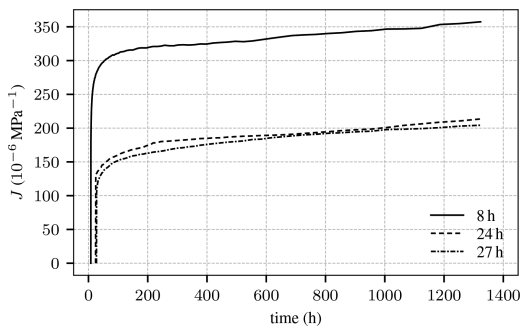

Figure 3. Compliance functions, computed from the three creep tests started at material ages of 8 hours, 24 hours and 27 hours.

3 MATERIAL MODELS

In the following, the employed shotcrete models are described briefly.

3.1 *SCDP model by Neuner et al.*

The SCDP model (Neuner, Gamnitzer, & Hofstetter 2017) is based on three constituents which are (i) the damage plasticity model by Grassl and Jirásek (2006) to describe hardening and softening inviscid material behavior, (ii) the shrinkage model by Bažant and Panula (1978), and (iii) the solidification theory by Bažant and Prasannan (1989) to describe the evolution of material stiffness and nonlinear creep. The latter model is incorporated into the framework of coupled plasticity theory and continuum damage mechanics, and modified by means of a time transformation function to account for the faster hydration of shotcrete compared to concrete.

The stress–strain relation in total form is expressed as

$$\boldsymbol{\sigma} = (1-\omega)\,\mathbb{C} : \boldsymbol{\varepsilon}^{\mathrm{el}}, \tag{1}$$

with

$$\boldsymbol{\varepsilon}^{el} = \boldsymbol{\varepsilon} - \boldsymbol{\varepsilon}^{\mathrm{p}} - \boldsymbol{\varepsilon}^{\mathrm{ve}} - \boldsymbol{\varepsilon}^{\mathrm{f}} - \boldsymbol{\varepsilon}^{\mathrm{shr}}. \tag{2}$$

In (1), $\boldsymbol{\sigma}$ denotes the nominal stress (force per total area), $\boldsymbol{\varepsilon}^{\mathrm{el}}$ is the instantaneous elastic strain, ω is the isotropic scalar damage parameter and $\mathbb{C}$ is the fourth order stiffness tensor, and in (2), $\boldsymbol{\varepsilon}$ denotes the total strain, $\boldsymbol{\varepsilon}^{\mathrm{p}}$ is the plastic strain, $\boldsymbol{\varepsilon}^{\mathrm{ve}}$ is the viscoelastic strain, $\boldsymbol{\varepsilon}^{\mathrm{f}}$ is the flow (viscous) strain, and $\boldsymbol{\varepsilon}^{\mathrm{shr}}$ is the shrinkage strain.

The evolution of the plastic strain is described by non-associated plasticity employing a smooth, single yield surface, and the evolution of ω is driven by the evolution of an equivalent plastic strain-like internal variable. The evolution laws for the elastic strain, the viscoelastic strain and the flow strain are adopted from the solidification theory for concrete aging and creep (Bažant & Prasannan 1989). Since they are incorporated into the damage plasticity model, they are formulated in the effective stress space:

$$\begin{aligned}
\dot{\boldsymbol{\varepsilon}}^{\mathrm{el}}(t) &= q_1 \mathbb{C}_v^{-1} : \dot{\bar{\boldsymbol{\sigma}}}(t), \\
\dot{\boldsymbol{\varepsilon}}^{\mathrm{ve}}(t) &= \frac{F\left(\bar{\boldsymbol{\sigma}}(t)\right)}{v(\tau(t), q_2, q_3)} \int_0^t \dot{\Phi}(t-t')\, \mathbb{C}_v^{-1} : \mathrm{d}\bar{\boldsymbol{\sigma}}(t'), \\
\dot{\boldsymbol{\varepsilon}}^{\mathrm{f}}(t) &= \frac{q_4 F(\bar{\sigma}(t))}{t}\, \mathbb{C}_v^{-1} : \bar{\boldsymbol{\sigma}}(t).
\end{aligned} \tag{3}$$

Therein, $\bar{\sigma}$ is the effective stress, $\mathbb{C}_v$ the fourth order unit stiffness tensor, $v(\tau(t), q_2, q_3)$ denotes the solidified volume, which is modified by the time transformation function $\tau(t)$ to account for the hydration behavior of shotcrete, $\dot{\Phi}(t-t')$ is the unit viscoelastic compliance rate, q_1 to q_4 are compliance parameters, and $F(\bar{\boldsymbol{\sigma}}(t))$ is an amplifying function dependent on the effective stress to account for nonlinear creep. Time transformation function $\tau(t)$ is calibrated by the Young's modulus at the age of 1 day to represent the experimentally determined early age behavior of shotcrete. In addition, empirical evolution laws are employed to describe the evolution of material strength and ductility.

3.2 *Viscoplastic model by Meschke*

In the viscoplastic model by Meschke (1996) nonlinear mechanical behavior of shotcrete is described on the basis of associated multisurface viscoplasticity theory. A hardening Drucker-Prager model is used for predominantly compressive stress states and mixed stress states, and a softening Rankine criterion for tensile stress states. The evolution of stiffness is modeled by hyperelastic constitutive relations, employing empirical time functions. Aging of shotcrete is considered by empirical evolution functions for the Young's modulus, the uniaxial compressive strength and the uniaxial tensile strength. Shrinkage of shotcrete is taken into account on the basis of the model proposed by Bažant and Panula (1978), and creep of shotcrete is modeled by a Duvaut-Lions type viscoplastic formulation.

3.3 *Viscoelastic-plastic model by Schädlich and Schweiger*

In the shotcrete model by Schädlich and Schweiger (2014) hardening and softening material behavior of shotcrete is described on the basis of multisurface non-associated plasticity, employing a hardening and softening Mohr-Coulomb model for predominantly compressive stress states and mixed stress states, and a softening Rankine criterion for tensile stress states. Aging of shotcrete is considered by empirical time functions for stiffness and strength. Shrinkage of shotcrete is taken into account on the basis of the model proposed by the ACI committee 209 (ACI Committee 209 1992), and nonlinear creep of shotcrete is modeled on the basis of the theory of viscoelasticity, derived from the model proposed in (EN 1992-1-1 2004).

3.4 *Calibration of the material models*

The parameter identification procedure for the three shotcrete models is described in (Neuner, Gamnitzer, & Hofstetter 2017), and the identification from the data of the present experimental program is reported in (Neuner, Cordes, Drexel,

Table 1. Identified material parameters for the SCDP model.

q_1 (Mpa^{-1})	q_2 (MPa^{-1})	q_3 (MPa^{-1})	q_4 (MPa^{-1})	ν (–)	$E^{(1)}$ (MPa)	$f_{cu}^{(1)}$ (MPa)	$f_{cu}^{(28)}$ (MPa)	f_{cy}/f_{cu} (–)
42.2×10^{-6}	41.1×10^{-6}	3.03×10^{-6}	33.95×10^{-6}	0.21	13943	18.56	40.85	0.1
f_{cb}/f_{cu} (–)	f_{tu}/f_{cu} (–)	$\varepsilon_{\infty}^{shr}$ (–)	k_h (–)	τ_{shr} (d)	$\varepsilon_{cpu}^{p(1)}$ (–)	$\varepsilon_{cpu}^{p(8)}$ (–)	$\varepsilon_{cpu}^{p(24)}$ (–)	$G_{fl}^{(28)}$ (N/mm)
1.16	0.1	–0.002	1.0	4082	–0.03	–0.007	–0.007	0.1

Table 2. Identified material parameters for the Meschke model.

$E^{(1)}$ (Mpa)	$E^{(28)}$ (MPa)	ν (–)	$f_{cu}^{(1)}$ (MPa)	$f_{cu}^{(28)}$ (MPa)	f_{cy}/f_{cu} (–)	f_{cb}/f_{cu} (–)	f_{tu}/f_{cu} (–)
13943	21537	0.21	18.56	40.85	0.1	1.16	0.1
η (h)	$\varepsilon_{\infty}^{shr}$ (–)	k_h (–)	τ_{shr} (d)	Δt_E (h)	t_E (h)	$G_{fl}^{(28)}$ (N/mm)	
5	–0.002	1.0	4082	6	8	0.1	

Table 3. Identified material parameters for the Schädlich model.

$E^{(1)}$ (Mpa)	$E^{(28)}$ (MPa)	ν (–)	ψ (°)	t_{50}^{cr} (h)	φ^{cr} (–)	$f_{cu}^{(1)}$ (MPa)	$f_{cu}^{(28)}$ (MPa)	$f_{tu}^{(28)}$(MPa)	f_{cy}/f_{cu} (–)
13943	21537	0.21	0	36	2.62	18.56	40.85	4.08	0.1
f_{cfn} (–)	f_{cun} (–)	F_{tun} (–)	$\varepsilon_{\infty}^{shr}$ (–)	t_{50}^{shr} (h)	$\varepsilon_{cpu}^{p(1)}$ (–)	$\varepsilon_{cpu}^{p(8)}$ (–)	$\varepsilon_{cpu}^{p(24)}$ (–)	$G_{fl}^{(28)}$ (N/mm)	$G_c^{(28)}$(N/mm)
0.1	0.1	0.1	–0.0019	8645	–0.03	–0.007	–0.007	0.1	30

& Hofstetter 2017). The resulting material parameters are listed in Tables 1, 2 and 3. For the sake of brevity, a detailed description of the parameters is omitted here.

The evolution of the Young's modulus is predicted by all models very well, although it is slightly underestimated between a material age 1 day and 28 days predicted by all models.

The evolution of the uniaxial compressive strength and the computed values are shown in Figure 5. It can be seen that both the Schädlich model and the SCDP model are in good agreement with the experimental results, while the compressive strength is overestimated by the Meschke model between 1 day and 28 days.

The experimental results from the creep test on a sealed specimen loaded at a material age of 27 hours with a compressive stress of –2.7 MPa are shown together with the predicted results in Figure 6. It can be concluded that the creep behavior is represented better by the Schädlich model and the SCDP model compared to the Meschke model. However, this is attributed to the viscoplastic formulation and the low applied stress level, as explained in (Neuner, Cordes, Drexel, & Hofstetter 2017). For this reason, the default viscosity parameter $\eta = 5$ h as proposed in (Meschke, Kropik, &

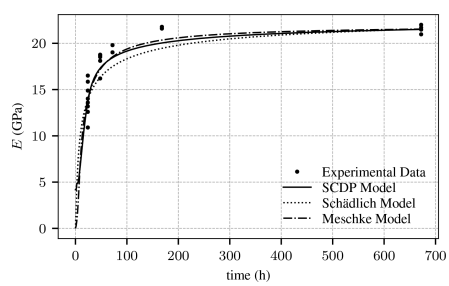

Figure 4. Measured and computed time-dependent evolution of the Young's modulus.

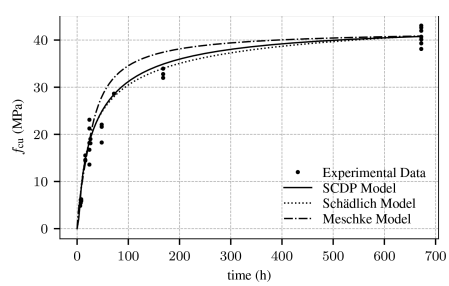

Figure 5. Measured and computed time-dependent evolution of uniaxial compressive strength.

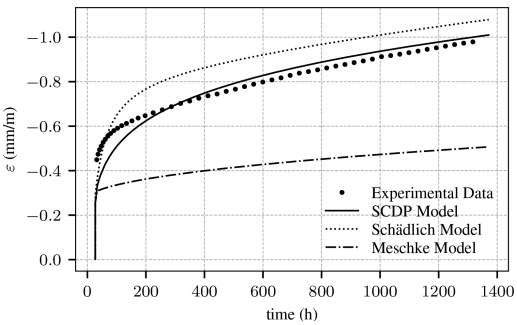

Figure 6. Measured and computed time-dependent evolution the total strain during the creep test on a sealed specimen loaded at a material age of 27 hours.

Mang 1996) is assumed for the subsequent numerical simulations.

4 APPLICATION

A structural benchmark example for assessing the mechanical response of the shotcrete shell in numerical simulations was presented in (Neuner, Schreter, Unteregger, & Hofstetter 2017). The example is derived from a stretch of the Brenner Basetunnel, for which in-situ measurement results of deformations in the surrounding rock mass during tunnel advance are available. The investigated stretch is characterized by a circular full face excavation profile with a diameter of 8.5 m, an overburden of 950 m measured from the tunnel axis, and an installed shotcrete shell with a thickness of 0.2 m.

The problem is idealized by a 2D finite element model, assuming plane strain conditions. The surrounding rock mass is described using the linear elastic perfectly-plastic Hoek-Brown criterion (Hoek & Brown 1980), calibrated to represent the material behavior of Innsbruck Quartz-phyllite (Schreter, Neuner, Unteregger, Hofstetter, Reinhold, Cordes, & Bergmeister 2017), characteristic for this specific stretch. The employed material parameter of the Hoek-Brown model are listed in Table 4.

Due to the geometry, boundary conditions, an assumed initial hydrostatic geostatic stress state, and full face excavation, axisymmetry can be exploited, leading to a reduced finite element model consisting of a single element row. The rock mass and the shotcrete shell are discretized by 8-node quadrilateral continuum elements, the latter by four elements through the thickness. Homogeneous Dirichlet boundary conditions are assumed perpendicular to the remaining part of the boundary of the single row of finite elements. The full 2D model and the reduced model (highlighted in black) are illustrated in Figure 7.

Table 4. Material parameters for the Hoek-Brown model for representing the rock mass.

E (MPa)	ν (–)	f_{cu} (MPa)	m_0 (–)
56,670	0.21	42	12
Ψ (°)	e (–)	GSI (–)	D (–)
11.6	0.51	40	0

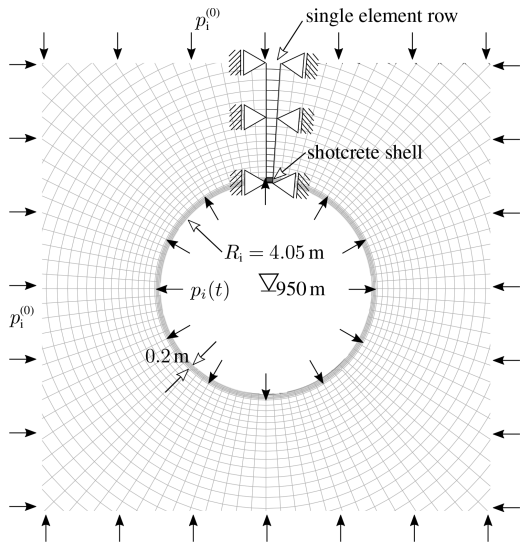

Figure 7. Schematic view of the benchmark example together with the 2D axisymmetric finite element model.

Then, in the numerical simulations the arising displacements of the shotcrete shell are restricted to radial displacements, and bending moments in the shotcrete shell are excluded. Obviously, this is a simplification of the actual deformations of the shotcrete shell during tunneling, however it allows for an easy comparison of the shotcrete models.

In the numerical simulations, an initial hydrostatic stress state in the rock mass of $p_i^{(0)} = 25.7$ MPa is assumed. The excavation of the investigated cross section is modeled by reducing an equivalent fictitious internal pressure $p_i(t)$ acting on the tunnel lining by means of a stress release ratio $\lambda(t)$ ranging from 0% (no reduction) to 100% (full removal), expressed as

$$p_i(t) = (1 - \lambda(t))\, p_i^{(0)}. \tag{4}$$

Before installing the shotcrete shell in the numerical simulations, the stress is released according to an initial stress release ratio. Subsequently, the shotcrete shell is installed and the remaining

fictitious internal pressure is removed employing a stepwise, time-dependent stress release function representing the sequence of *drill*, *blast and idle periods* during the further tunnel advance. This stepwise stress release layout follows a parabolic decline, as suggested by Pöttler (1990). In total, 9 excavation steps are considered, separated by idle periods of 8 hours. After the last excavation step, an additional time period of two weeks, i.e. 336 hours, is investigated for observing the relaxation behavior of the shotcrete shell.

Two different initial stress release ratios are considered: 85% and 95%. Both were derived according to the in-situ measured range of predeformations in the rock mass, as reported in (Neuner, Schreter, Unteregger, & Hofstetter 2017) and (Schreter, Neuner, Unteregger, Hofstetter, Reinhold, Cordes, & Bergmeister 2017).

The time-dependent mechanical response of the shotcrete shell is assessed by comparing the time-dependent evolution of the radial displacement of an arbitrary node at the inner surface of the shotcrete shell, as well as the time-dependent evolution the stresses in circumferential and longitudinal direction. The stresses are taken at an integration point close at the inner surface of the shotcrete shell. As already pointed out in (Meschke 1996) and confirmed in (Neuner, Schreter, Unteregger, & Hofstetter 2017), the stress state in the shotcrete shell can be classified as nearly biaxial, and, thus, the radial stress in thickness direction of the shotcrete shell is neglected in the present assessment.

The predicted time-dependent evolution of the radial displacement, the circumferential stress and the longitudinal stress for both initial stress release ratios are shown in Figure 8. The radial displacement consists of the instantaneous displacement of the unsupported rock mass due to initial stress release, the instantaneous displacements due to the 9 excavation steps after installation of the shotcrete shell, and the displacements due to the time-dependent deformations due to shrinkage and creep of shotcrete. Comparing the obtained radial displacements for the initial stress release ratio of 85%, it can be seen that during the first excavation steps the predicted responses by the Schädlich model and the SCDP model are very similar, with slightly larger displacements predicted by the Schädlich model during the

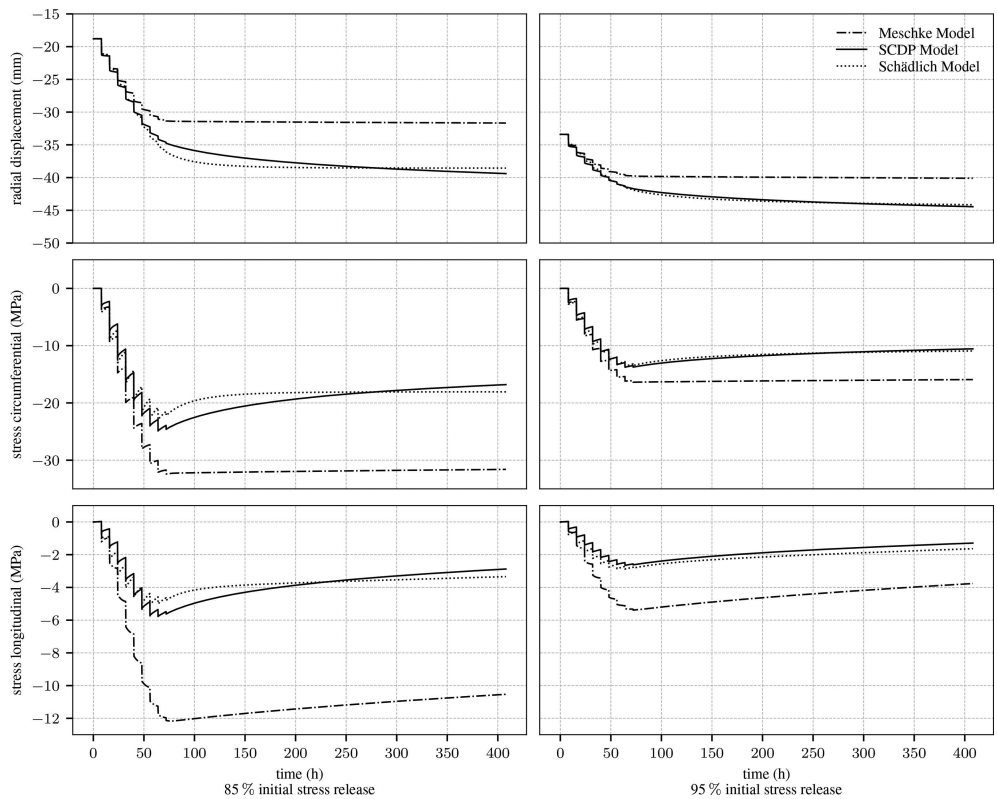

Figure 8. Time-dependent evolution of the radial displacement (top), circumferential stress in the shotcrete shell (center) and longitudinal stress in the shotcrete shell (bottom).

last excavations steps. However, larger displacements due to creep are predicted by the SCDP model, resulting in the largest radial displacement predicted at the end of the investigated time period. A stiffer material behavior, and thus smaller radial displacements are predictated by the Meschke model throughout the complete investigated time period. As explained in (Neuner, Schreter, Unteregger, & Hofstetter 2017), this is attributed to the viscoplastic formulation of the Meschke model.

The stronger relaxation predicted by the SCDP model results in the lowest circumferential and longitudinal stresses at the end of the investigated time period. Both the circumferential and longitudinal stress predicted by the Meschke model are considerably higher, which again is a consequence of the employed viscoplastic formulation, neglecting creep in the elastic domain.

For the initial stress release of 95%, nearly identical displacements and stresses are predicted by the Schädlich model and the SCDP model, and again, a stiffer response is predicted by the Meschke model due to the viscoplastic formulation.

Moreover, an interesting detail can be observed for the Meschke model: In contrast to the SCDP model and the Schädlich model, no relaxation of the longitudinal stress during the idle periods occurs, but conversely, it is increasing. This is a consequence of the employed associated viscoplastic formulation, assuming dilatant material behavior during creep.

5 CONCLUSIONS

A new experimental program on a state-of-the-art shotcrete composition used for the Brenner Basetunnel within the New Austrian Tunneling Method was presented. The investigated material phenomena comprise the evolution of stiffness and strength, shrinkage and creep. Moreover, three advanced constitutive models for shotcrete, i.e. the model by Meschke, the model by Schädlich and Schweiger, and the SCDP model were applied to a structural benchmark finite element example, employing material parameters which were identified from the experimental data.

On the basis of the benchmark example, it was shown that despite of the different formulations for evolution of stiffness and strength, hardening material behavior, shrinkage and creep, very similar displacements and stresses are predicted by the Schädlich model and the SCDP model.

REFERENCES

ACI Committee 209 (1992). 209r-92: Prediction of creep, shrinkage, and temperature effects in concrete structures.

Bažant, Z. & L. Panula (1978). Practical prediction of time-dependent deformations of concrete. *Mater. Struct. 11*, 307–328.

Bažant, Z. & S. Prasannan (1989). Solidification theory for concrete creep. i: Formulation. *J. Eng. Mech. 115*(8), 1691–1703.

EN 1992-1-1 (2004). *Eurocode 2: Design of concrete structures*. European Committee for Standardization.

Grassl, P. & M. Jirásek (2006). Damage-plastic model for concrete failure. *Int. J. Solids Struct*. 43(22–23), 7166–7196.

Hoek, E. & E.T. Brown (1980). Empirical strength criterion for rock masses. *J. Geotech. Eng. Div. ASCE 106*(GT9), 1013–1035.

Huber, H.G. (1991). Untersuchungen zum Verformungsverhalten von jungem Spritzbeton im Tunnelbau. Diplomarbeit, Leopold-Franzens-Universität Innsbruck.

Meschke, G. (1996). Consideration of aging of shotcrete in the context of a 3d-viscoplastic material model. *Int. J. Num. Meth. Eng. 39*(18), 3123–3143.

Meschke, G., C. Kropik, & H. Mang (1996). Numerical analysis of tunnel linings by means of a viscoplastic material model for shotcrete. *Int. J. Num. Meth. Eng. 39*(18), 3145–3162.

Müller, M. (2001). Kriechversuche an jungen Spritzbetonen zur Ermittlung der Prameter für Materialgesetze. Diplomarbeit, Montanuniversität Leoben.

Neuner, M., T. Cordes, M. Drexel, & G. Hofstetter (2017). Time-Dependent Material Properties of Shotcrete: Experimental and Numerical Study. *Materials 10*(9), 1067.

Neuner, M., P. Gamnitzer, & G. Hofstetter (2017). An extended damage plasticity model for shotcrete: Formulation and comparison with other shotcrete models. *Materials 10*(1), 82.

Neuner, M., M. Schreter, D. Unteregger, & G. Hofstetter (2017). Influence of the Constitutive Model for Shotcrete on the Predicted Structural Behavior of the Shotcrete Shell of a Deep Tunnel. *Materials 10*(6), 577.

ÖVBB (2009). *Richtlinie Spritzbeton - 2009*. Österreichische Vereinigung für Beton und Bautechnik.

Pöttler, R. (1990). Time-dependent rock-shotcrete interaction—a numerical shortcut. *Comput. Geotech. 9*, 149–169.

Schädlich, B. & H. Schweiger (2014). A new constitutive model for shotcrete. In *Numerical Methods in Geotechnical Engineering: 8th European Conference on Numerical Methods in Geotechnical Engineering*, pp. 103–108. CRC Press Taylor & Francis Group.

Schreter, M., M. Neuner, D. Unteregger, G. Hofstetter, C. Reinhold, T. Cordes, & K. Bergmeister (2017). Application of a damage plasticity model for rock mass to the numerical simulation of tunneling. In *Proceedings of the 4th International Conference on Computational Methods in Tunneling and Subsurface Engineering (EURO:TUN 2017)*, pp. 549–556.



Taylor & Francis
Taylor & Francis Group
http://taylorandfrancis.com

Computational Modelling of Concrete Structures – Meschke, Pichler & Rots (Eds)
© 2018 Taylor & Francis Group, London, ISBN 978-1-138-74117-1

Aging behavior of normal and high strength concretes

L. Czernuschka, K. Nincevic, I. Boumakis, Lin Wan-Wendner & Roman Wan-Wendner
Christian Doppler Laboratory LiCroFast, Institute of Structural Engineering, University of Natural Resources and Life Sciences, Vienna, Austria

ABSTRACT: Due to increasing demands concerning the durability, the design as well as the sustainability of concrete structures, it becomes more relevant to gain fundamental understanding of the material. Especially the long-term performance as well as the aging behavior is of main interest. As a result, processes, which influence the aging of material have to be captured and understood. The main source of aging is the hydration of the cement paste, which is known to have an influence on the time dependent properties such as shrinkage as well as on the evolution of the mechanical properties. Consequently, it is mandatory to have a computational framework, which is able to capture all aging related phenomena. In this contribution, the framework for the chemo-mechanical coupling only is presented, i.e. how the time-dependence of the local mechanical properties is formulated.

1 INTRODUCTION

The safety and durability of concrete structures is a crucial necessity in modern engineering. Therefore, the long-term performance of the used construction materials has to be studied in detail. As widely known, concrete is a material, which changes its behavior throughout time. The main source of this phenomena is the hydration of cement, which depends strongly on the environmental conditions and the mix design. Current design codes suggest empirical equations for the evolution of mechanical properties. Nevertheless, these equations describe the evolution of concrete's mechanical properties as a function of time and not as a function of the reaction degree. Furthermore, spatial variabilities caused by the boundary conditions are not taken into an account. This can be problematic for mass concrete, showing significant gradients towards the inside. In order to study the phenomenon aging in detail a very strong computational framework is required, which is able to capture all the involved mechanisms. In this study a computational framework is presented consisting of (1) a multi-physics model, which simulates the hydration of concrete under given boundary conditions and (2) a mechanical damage model, simulating the failure of concrete at meso-scale. The chemo-mechanical coupling is done by a set of aging functions developed by Wan et al. for ultra high performance concrete (Wan, Wendner, Benliang & Cusatis 2016, Wan, Wendner & Cusatis 2017) and also applied for normal strength concrete by (Wendner, Nincevic, Boumakis & Wan 2016).

2 STATE OF THE ART

Current design codes give empirical equations for the determination of concrete properties based on the mean 28 day compressive strength f_{cm} (CEN 2009). The evolution of compressive strength is given by Equation 1:

$$f_{cm}(t) = \beta_{cc}(t) \cdot f_{cm}, \tag{1}$$

with

$$\beta_{cc}(t) = exp\left\{ s\left[1 - \left(\frac{28}{t} \right)^{0.5} \right] \right\}, \tag{2}$$

where the time function β_{cc} describes the relative development with respect to the reference value 1 at 28 days and includes the dependency on the cement type with parameter s.

Furthermore, an aging function (Equation 3) for the evolution of tensile strength is suggested. Herein, α is 2/3 after 28 days.

$$f_{ctm} = \beta_{cc}(t)^{\alpha} \cdot f_{ctm} \tag{3}$$

The aging function for the modulus in dependency of the compressive strength is given by Equation 4:

$$E_{cm}(t) = \beta_{cc}(t)^{0.3} E_{cm} \tag{4}$$

Further the tensile characteristic length l_t, describes the brittleness of the material and thus

gives sound information about the fracture mechanical aging. Throughout time the material gets more brittle and the tensile characteristic length decreases. The equation for the tensile characteristic length, developed by (Hilleborg 1985) is given:

$$l_{ch} = \frac{EG_F}{f_t^2}, \tag{5}$$

with the total fracture energy G_F, the modulus E and the tensile strength f_t.

3 EXPERIMENTAL CAMPAIGN

3.1 *Mechanical properties*

In order to calibrate the aging framework and to evaluate the code based functions for the aging of mechanical parameters, an extensive experimental campaign was carried out. The experiments comprised tests of the mechanical behavior of the material such as compressive strength, tensile strength and fracture energy. Therefore, compressive strength tests on cylinders and cubes, modulus measurements on cylinders, Brazilian splitting tests, as well as fracture tests on notched three point bending tests were undertaken. In total 5 different mixes reaching from normal strength to high strength concretes were tested. The exact mix design for one of the tested concretes and the ages tested can be found in Tables 1 and 2.

3.2 *Time dependent behavior*

Apart from the tested mechanical properties, also the time dependent behavior of the material was studied in detail. For that matter, drying and autogenous shrinkage tests, basic and drying creep tests and measurements of internal humidity and temperature were performed. In order to obtain information about the hydration kinetics and to have valuable input for the model, isothermal calorimeter measurements for the used cement mixes were conducted.

3.3 *Curing conditions*

All tested specimens for mechanical properties are cured in water saturated with lime shortly before testing at a temperature of approximately 23°C. The specimens for the evaluation of the long-term behavior are stored in a room with controlled environmental boundary conditions, specifically a temperature of 20°C and a relative humidity of 0.60.

3.4 *Experimental results*

The results of the aging tests on mechanical properties for one concrete mix can be seen in Figure 1 and Figure 2. The data in both cases follow, as expected, a s-shape type function. For the used cement mix a s value of 0.20 for compressive and tensile strength is suggested by the codes. Taking the functional form of the modulus evolution into account, the optimum value would be $0.2 \cdot 0.3$. For fracture energy no suggestions for the evolution in time are given. For a first approximation the compressive strength aging function is adopted for fracture energy. In both figures two different fits are done (1) with an s-value based on the codes

Table 1. Experimental aging study—mechanical tests.

Tests	Tested ages (d)
Compressive strength cyl.	2, 7, 15, 17, 22, 29, 52, 87, 155
Compressive strength cube	3, 8, 29, 134
Three point bending	2, 7, 15, 17, 22, 28, 52, 87, 155
Brazilian splitting	9, 30, 52

Table 2. Mix design of concrete used for numerical study.

Component	Amount
Aggregate content [kg]	1979
Cement content [kg]	237
Water content [kg]	197
w/*c* ratio	0.83
a/*c* ratio	8.35

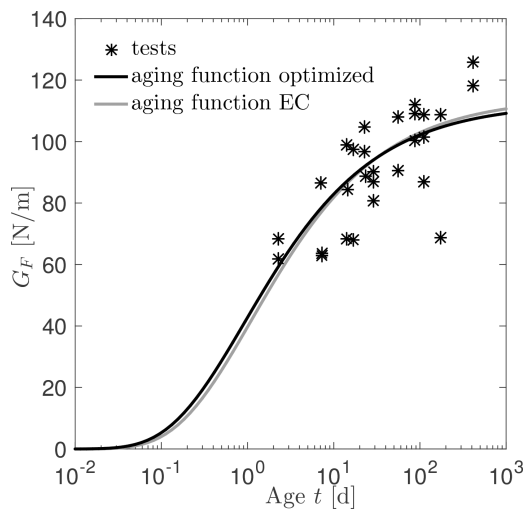

Figure 1. Time evolution of total fracture energy.

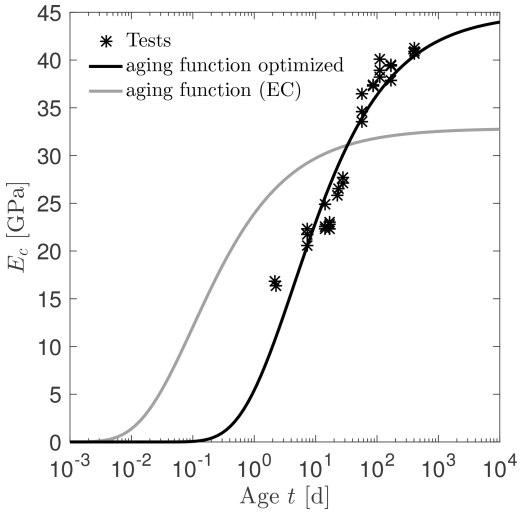

Figure 2. Time evolution of modulus.

(2) with an optimized *s*-value. The results are in a very good agreement with fracture energy for both fits with a difference of 0.02. However, the fit based on the codes differs significantly in case of the modulus with an optimized *s*-value of 0.40 instead of 0.06 (as given by the codes).

4 COMPUTATIONAL FRAMEWORK

To study the aging behavior of concrete material, a powerful numerical tool is used. This is comprised by a multiphysics model for the hydration process and a multiscale mechanical model for simulating the concrete failure at meso-scale. The last part of the aging framework is the chemo-mechanical coupling, which links the results of both independent models by a set of aging functions. These aging functions relate the hydration degree to the mechanical properties of the material.

4.1 *Multi-physics model*

The hygro-thermo-chemical model developed by Di Luzio et al captures the evolution of internal humidity, internal temperature and the hydration degree (Di Luzio & Cusatis 2009a, Di Luzio & Cusatis 2009b). The model solves the mass-heat balance equations, as well as equations describing the moisture transport and the hydration kinetics. Also the model can account for secondary reactions such as silica fume reaction. The development of temperature and internal humidity is given by Equation 6 and 7:

$$\nabla\cdot(D_h\nabla h)-\frac{\partial w_e}{\partial h}\frac{\partial h}{\partial t}-\frac{\partial w_e}{\partial \alpha_c}\dot{\alpha}_c-\frac{\partial w_e}{\partial \alpha_s}\dot{\alpha}_s-\dot{w}_n=0, \quad (6)$$

$$\nabla\cdot(k\nabla T)-\rho c_t\frac{\partial T}{\partial t}+\dot{\alpha}_c c\tilde{Q}_c^{\infty}+\dot{\alpha}_s s\tilde{Q}_s^{\infty}=0, \quad (7)$$

with the permeability D_h, the evaporable water w_e, the non evaporable water w_n, the hydration degree α_c, the heat conduction coefficient k, the temperature T, the concrete density ρ, the relative humidity h, the hydration enthalpy $\tilde{Q}_c^{\infty}$, the cement content c_t, the silica fume reaction degree α_s, the silica fume content s and the silica fume reaction enthalpy $\tilde{Q}_s^{\infty}$.

The multiphysics model results in spatial time dependent fields of internal humidity h, temperature T and reaction degree α_c.

Also other aging related phenomena such as shrinkage and creep, affect the long-term performance of the material. Hydration is an exothermal reaction which consumes water. This leads to the so-called autogenous shrinkage, due to self dessication. On top of the shrinkage caused by the chemical reaction, also a volume reduction by diffusion is caused (drying shrinkage). On the other hand, this is strongly influenced by the boundary conditions. Further, an influence of the temperature on the speed of the chemical reactions is given, which has an effect on the mechanical properties.

As literature states, the development of material properties is not only dependent on the degree of hydration, but is also influenced by the curing history of the specimen (e.g. temperature conditions) (Di Luzio & Cusatis 2013). With the same hydration degree, one specimen, cured at lower temperatures typically shows a higher strength, than one, cured at higher temperatures. In order to account for this phenomenon the aging degree is introduced (Equations 8 and 9):

$$\dot{\lambda}=\left(\frac{T_{max}-T}{T_{max}-T_{ref}}\right)^{n_\lambda}(B_\lambda-2A_\lambda\alpha)\dot{\alpha} \quad (8)$$

$$B_\lambda=[1+A_\lambda(\alpha_\infty^2-\alpha_0^2)/(\alpha_\infty-\alpha_0)] \quad (9)$$

Here A_λ and n_λ are aging parameters which are calibrated on experimental data. Further, the maximum temperature, under which concrete is hardening, the ambient temperature and the point in time when the concrete is set, are taken into account.

4.2 *Damage model*

The concrete failure at meso-scale is simulated with the well established lattice discrete particle model developed by Cusatis et al. In this model (LDPM) the interaction of the aggregates is simulated. Herein, the aggregates are assumed to

be spheres and are embedded in a cementitious matrix. The concrete is generated by randomly placing these particles in the concrete specimen following a Fuller curve. To each aggregate an amount of cement paste is allocated, resulting in polyhedral cells with triangular facets. The vectorial constitutive equations are applied on the facets of neighboring cells. A detailed model explanation can be found in Cusatis et al (Cusatis, Pelessone & Mencarelli 2011a, Cusatis, Pelessone & Mencarelli 2011b).

4.3 *Chemo-mechanical coupling*

The chemo-mechanical coupling is done by a set of aging functions, which link the curing degree to the local material properties. The formulated spatial variable formulations are listed in Equations 10 to 12. Here the modulus is assumed to have a linear relationship with the aging degree λ. Furthermore, the tensile strength is defined in a power law type relationship. The characteristic length is, as the modulus in a linear relationship.

$$E_0(x,y,z,t) = E_0^{\infty} \cdot \lambda(x,y,z,t) \tag{10}$$

$$\sigma_0(x,y,z,t) = \sigma_0^{\infty} \cdot \lambda(x,y,z,t)^{n_a} \tag{11}$$

$$l_t(x,y,z,t) = l_t^{\infty}(k_a(1-\lambda(x,y,z,t)^{n_a})+1) \tag{12}$$

As already mentioned before, the assumed aging functions are developed for UHPC at early age by Wan et al, which predicted the brittle behavior very well. Further, it was found that fracture energy is not an independent material property and as a result not suitable for the formulation as an aging law. In order to describe the evolution of fracture mechanical behavior, the tensile characteristic length was adopted, taking the modulus and the tensile strength into account.

5 CALIBRATION OF THE AGING FRAMEWORK

5.1 *Hygro-thermo-chemical model*

The first step of the model calibration is the calibration of the hydration kinetics. Therefore, isothermal calorimeter measurements were performed. The hydration parameters are calibrated in order to reproduce the experimental results as accurate as possible. The good agreement of the experiments with the numerical simulations can be seen in Figure 3. Further, the heat capacity and heat conductivity of the material have to be calibrated. This is done by fitting parameters to measurements of internal temperature for different positions inside a concrete specimen. The last part of the HTC calibration is the calibration of the

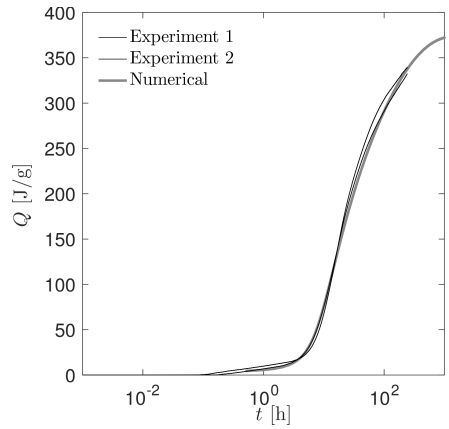

Figure 3. Calibration of hydration kinetics.

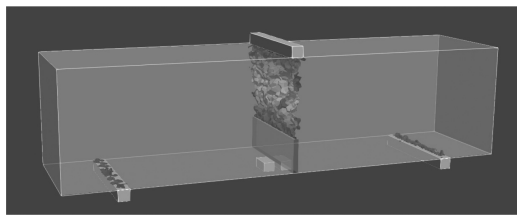

Figure 4. Crack development in LDPM three point bending model.

permeability parameters. The input parameters are defined in a way to reproduce experimental data, specifically the evolution of humidity inside a concrete specimen.

5.2 *Lattice discrete particle model*

The calibration of the mechanical response is at first done for individual ages. The input parameters, which are typically meso-scale tensile strength, normal modulus and tensile characteristic length, are chosen that, the response of all tests, can be captured with the same set. Below the crack development in a notched three point bending test can be seen. The results of the individual calibration is shown for the age of 28 days in Figures 5 and 6.

5.3 *Chemo-mechanical coupling*

After calibrating the multiphysics part and the mechanical part of the framework the aging parameters (as defined in Section 4) have to be calibrated. As discussed previously the calibration of the aging degree is done by the assumption of a linear relationship between modulus and aging degree λ. The best fit obtained is shown in Figure 7. After calibration of the aging parameters, the parameters k_a

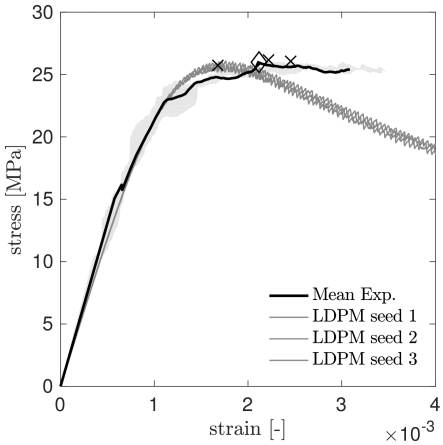

Figure 5. LDPM cube compressive strength calibration for 28 days.

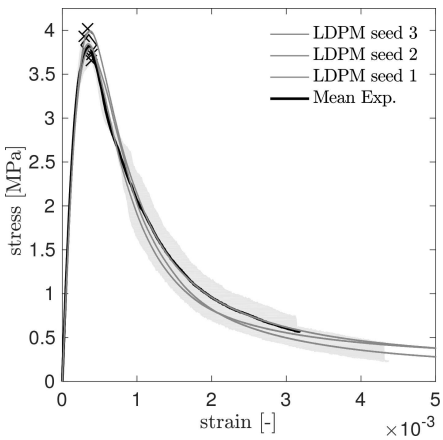

Figure 6. LDPM three point bending calibration for 28 days.

and n_a are calibrated based on strength and fracture data. As can be seen in Figures 8 and 9 the tensile strength follows, as proposed, a power law type function. The tensile characteristic length, as described in the aging function, is linear decreasing with the aging degree, which mirrors the growing brittleness in course of time.

The aging functions for the three involved parameters, which are tensile strength, tensile characteristic length and modulus are calibrated on the full aging experimental data set. Subsequently, the prediction of stress-strain curves for the different tests is possible without changing any of the parameters as shown in Figures 10 and 11. Here, the stress-strain curves for cube compressive strength at 134d and for three point bending at 156d are shown.

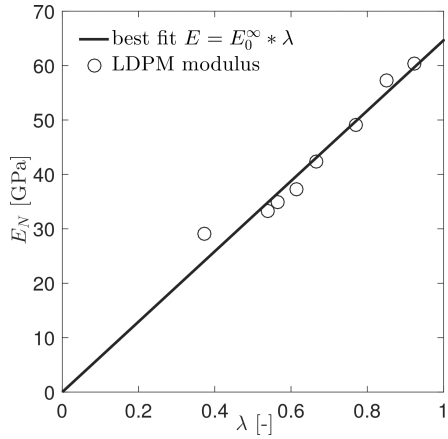

Figure 7. Calibration of normal modulus E.

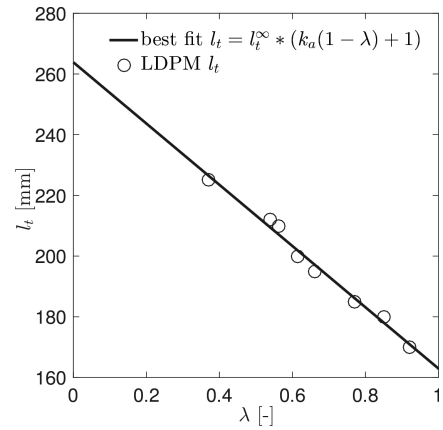

Figure 8. Relation tensile characteristic length—aging degree.

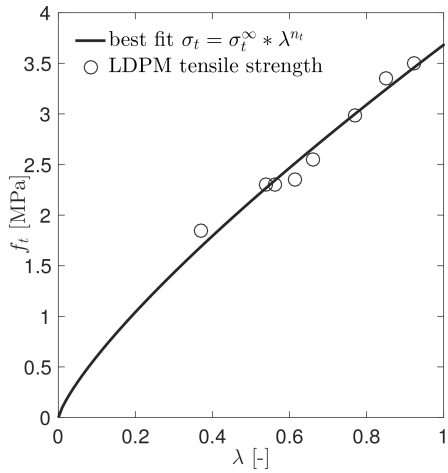

Figure 9. Relation tensile strength—aging degree.

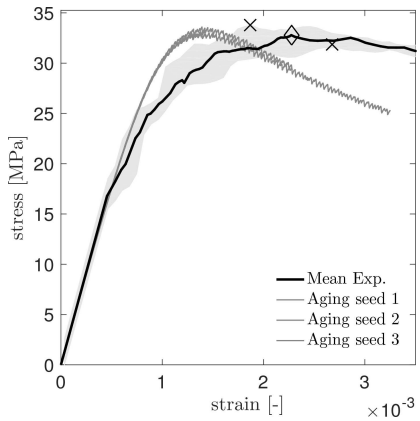

Figure 10. Results aging framework cube compressive strength tested at 134 days.

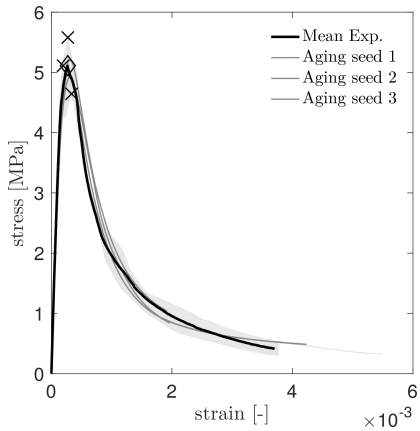

Figure 11. Results aging framework notched three point bending tested at 155 days.

6 CONCLUSIONS

In this contribution the aging behavior of normal strength concrete is investigated both experimentally and numerically. Following conclusions can be drawn:

- As it is shown by the experimental data, different material properties age at different rates, leading to an inconsistency in the fits to the code based aging functions
- The modulus follows, as assumed in the literature, a linear trend with the aging degree
- The tensile strength is in a power law type relationship with the aging degree
- The tensile characteristic length is a linear decreasing function of the aging degree. The decrease over time mirrors the growing brittleness of the material.
- The assumed aging functions for UHPC are applicable for normal strength concrete.

The application to high strength concretes (C50/60) is still an ongoing study, which is in it's finalization process.

ACKNOWLEDGEMENTS

The financial support by the Austrian Federal Ministry of Economy, Family and Youth and the National Foundation for Research, Technology and Development is gratefully acknowledged. The computational results presented have been achieved [in part] using the Vienna Scientific Cluster (VSC).

REFERENCES

CEN (2009). *Eurocode 2: Design of concrete structures—Part 1–1: General rules and rules for buildings,* Volume BS-EN-1992-1-1:2009. Eurpoean Committee for Standardization.

Cusatis, G., D. Pelessone, & A. Mencarelli (2011a). Lattice discrete particle model (LDPM) for failure behavior of concrete. i: Theory. *Cement and Concrete Composites 33*(9), 881–890.

Cusatis, G., D. Pelessone, & A. Mencarelli (2011b). Lattice discrete particle model (LDPM) for failure behavior of concrete. ii: Numerical implementation, calibration and validation. *Cement and Concrete Composites 33*(9), 891–905.

Di Luzio, G. & G. Cusatis (2009a). Hygro-thermo-chemical modeling of high performance concrete. I: Theory. *Cement and Concrete Composites 31*(5), 301–308.

Di Luzio, G. & G. Cusatis (2009b). Hygro-thermo-chemical modeling of high-performance concrete. II: Numerical implementation, calibration, and validation. *Cement & Concrete Composites 31*(5), 309–324.

Di Luzio, G. & G. Cusatis (2013). Solidification-microprestressmicroplane (smm) theory for concrete at early age: Theory, validation and application. *International Journal of Solids and Structures 50*(6), 957–975.

Hilleborg, A. (1985). The theoretical basis of a method to determine the fracture energy gf of concrete. *Materials and Structures 18*(4), 291–296.

Wan, L., R. Wendner, L. Benliang, & G. Cusatis (2016). Analysis of the behavior of ultra high performance concrete at early age. *Cement and Concrete Composites 74,* 120–135.

Wan, L., R. Wendner, & G. Cusatis (2017). Size effect and fracture characteristics of ultra high perfomance concrete at early age. *J Cem Concrete Composites (in press) arXiv pre-print 1608.08786/doi: 10.1016/j.cemconcomp.2017.09.010.*

Wendner, R., K. Nincevic, I. Boumakis, & L. Wan (2016). Agedependent lattice discrete particle model for quasi-static simulations. *Key Engineering Materials 711*, 1090–1097.

Computational Modelling of Concrete Structures – Meschke, Pichler & Rots (Eds)
© 2018 Taylor & Francis Group, London, ISBN 978-1-138-74117-1

A multiscale framework for the prediction of concrete self-desiccation

M. Pathirage
Department of Civil and Environmental Engineering, McCormick School of Engineering and Applied Science, Northwestern University, Evanston, IL, USA

D.P. Bentz
Engineering Laboratory, National Institute of Standards and Technology, Gaithersburg, MD, USA

G. Di Luzio
Department of Civil and Environmental Engineering, Politecnico di Milano, Milan, Italy

E. Masoero
School of Civil Engineering and Geosciences, Newcastle University, Newcastle upon Tyne, UK

G. Cusatis
Department of Civil and Environmental Engineering, McCormick School of Engineering and Applied Science, Northwestern University, Evanston, IL, USA

ABSTRACT: Cement hydration in concrete and mortar has been studied thoroughly over the past 50 years. To fully understand hydration in concrete and predict the evolution of the hygral, thermal, and mechanical properties at the structural level, one needs to studynot only the reaction kinetics but also the development of the microstructure. Many models have been developed for this purpose, some of them looking only at the micro-scale or at the macro-scale and others tackling the fundamental nature of the issue, which can be qualified as a multiscale problem. This paper proposes a novel approach that consists of combining a cement hydration model at the microstructural level, the CEMHYD3D model, with a macroscopic hygro-thermo-chemical model, the HTC model. The coupling is performed by post-processing the output of the CEMHYD3D model, in particular with reference to cement hydration degree, silica fume reaction degree, and amounts of evaporable water and chemically bound water in order to identify through a curve fitting routine the parameters of the HTC formulation. This approach allows the possibility of predicting concrete behavior at multiple scales based on the actual chemical and microstructural evolution, thus enhancing the capabilities of the so-called HTC-CEMHYD3D model. This paper focuses on 1) introducing the concepts behind the formulation of self-desiccation and 2) demonstrating the predictive capabilities of the coupled model using some available experimental data.

1 INTRODUCTION

The behavior of concrete in terms of its mechanical, hygral, and thermal properties has always been of a great interest to researchers and engineers, and many computational models have been proposed.

Models at the micro-scale level are numerous. The first model that described the hydration kinetics and development is the Jennings and Johnson microstructure simulation model (Jennings & Johnson 1986). Cement particles are represented as spheres, and hydration is simulated through a concentric growth of Calcium-Silicate-Hydrate (CSH) layers surrounding unhydrated particles. The model is able to capture key hydration features, including particle size distribution and evolution of volume due the formation of reaction products and the consumption of reactants. However, several model limitations must be cited. For example, the model is only capable of simulating hydration of tricalcium silicate (C3S), and does not take into account transport phenomena.

The HymoStruc model (Van Breugel 1995, Koenders & Van Breugel 1997, Ye, Van Breugel, & Fraaij 2003) appeared as a continuation of this effort. It uses the same approach as in Jennings and Johnson's model, and statistical analysis is introduced. However, the previous limitations on transport phenomena, as well as the actual chemistry in the pore solution are still constraints to an extensive use of this model.

The CEMHYD3D model (Bentz 1997, Bentz & Garboczi 1990, Garboczi & Bentz 1992, Bentz 2005) proposed a new approach that is based on cellular automata algorithm. CEMHYD3D stands for Cement Hydration in three dimensions and was developed at the National Institute of Standards and Technology (NIST). This open-source code is a digital image-based model and uses fundamental knowledge about hydration reactions and products. The model starts with an initial 3D microstructure, reconstructed from information on the actual cement powder via a scanning electron microscope (SEM) image for the phase distribution and the measured particle size distribution. Hydrating cement paste is represented by a cube of voxels. Each voxel is associated with a phase and can move and transform into another phase based on an iterative process through cycles. A database of cement types is available such that one needs only to calibrate a single parameter controlling the relationship between cycle lengths and real time. This model was successfully used in the literature and captures all aspects of the microstructure development, from chemical reactions to transport phenomena. It was legitimately pointed out (Thomas et al. 2011) that the parameter mapping the cycle lengths to the real time does not have a physical meaning and that the particle size limit of 1 voxel (1 μm^3) in the CEMHYD3D model brings a limitation. The HydratiCA model (Bullard 2007a, Bullard 2007b) and μic model (Navi & Pignat 1996, Bishnoi & Scrivener 2009) were developed in response to the aforementioned constraints. However, it is discussed later in this paper that such limitations have little or no effect on the proposed multiscale approach developed here. At the macro-scale, several models can be found in the literature that simulate not only cement hydration but also hygro-thermo-mechanical properties of concrete. Among others, the models of Ulm & Coussy (1995) and De Schutter & Taerwe (1996) are able to describe strength increase due to cement hydration. The temperature effect on hydration is taken into account in the work of Cervera, Oliver, & Prato (1999). More complex models provide better predictive capabilities in terms of hydration process, flow phenomena,chemical shrinkage and self-desiccation (Gawin, Pesavento, & Schrefler 2006a, Gawin, Pesavento, & Schrefler 2006b, Pan et al. 2017, Rahimi-Aghdam, Bažant, & Qomi 2017). Di Luzio & Cusatis (2009) proposed a hygro-thermo-chemical model, called the HTC model, that takes into account moisture transport governing the porerelative humidity and heat transfer. It also accounts for the heat released by hydration, silica fume reaction and cement hydration degrees, adsorption/desorption isotherms (by estimating the chemically bound water and the evaporable water), and concrete permeability. This model is considered in this paper.

It must be noted that in most of these models, the use of empirical or semi-empirical formulations at the macro-scale do not allow a fundamental description of physics and chemistry at a lower scale. Moreover, for almost all the models, lengthy and sometimes complex calibration processes are needed, which limit the use of such models to cases in which available and up-to-date experimental data exist.

The present study introduces a multiscale approach, coupling the CEMHYD3D model to the HTC model, that overcomes the aforementioned limitations.

2 THE HTC-CEMHYD3D MODEL

2.1 *Overview of the CEMHYD3D model*

The model considers the cement particles as digitized spherical elements. These spheres are created to replicate the measured particle size distribution and phase distribution obtained from SEM analysis on a generic volume of one million cubic micrometers. Each of the spheres are made of adjacent one micrometer cube voxels that represent either cement clinker phases, calcium sulfates, or supplementary cementitious materials. All the particles lie in water, also represented with voxels; the microstructureis then computed to form a representative volume element. The hydration process is computed through a cellular automata algorithm, where cement phase voxels dissolve, then diffuse where capillary water exists, and collide with other reactants to produce solid hydration products. This process occurs in a series of cycles that cumulatively represent the termination time of the simulation. The volume stoichiometry is conserved for the hydration reactions in the unit volume, and periodic boundaries are used to ensure an overall homogeneous distribution of reactants and hydration products. To control the kinetics of the chemical reactions, a real time is mapped to the number of hydration cycles through a parameter that usually needs to be calibrated from experimental data on hydration degree or non-evaporable water content over time. In order to make the model parameter-free, a commonly used conversion factor of 0.00035 hours/cycle[2] (Bentz 2005) is taken and fixed for all the simulations shown later inthe study.

2.2 *Self-desiccation formulation in the HTC model*

The HTC model is a macro-scale model. It considers the moisture transport and heat transfer through coupled diffusion equations (Di Luzio & Cusatis 2009). The present work focuses only on

self-desiccation, which involves the adsorption/desorption isotherms, thecement hydration degree α_c, evaporable water w_e, and non-evaporable water w_n. Silica fume reaction degree α_s is also taken into account. Since the gradient of temperature and humidity in space are minimal or zero regarding the size of the samples used to study self-desiccation, one can formulate the following moisture mass balance equation at any time t as

$$\frac{\partial w_e}{\partial h}\frac{\partial h}{\partial t}+\frac{\partial w_e}{\partial \alpha_c}\dot{\alpha}_c+\frac{\partial w_e}{\partial \alpha_s}\dot{\alpha}_s+\dot{w}_n=0 \tag{1}$$

where h is the internal moisture or relative humidity. The cement hydration degree is formulated as

$$\dot{\alpha}_c=A_{c1}(A_{c2}+\alpha_c)\left\langle \alpha_c^{\infty}-\alpha_c\right\rangle e^{-\frac{\eta_c\alpha_c}{\alpha_c^{\infty}}}e^{-\frac{E_{ac}}{RT}} \tag{2}$$

$$\alpha_c^{\infty}(h)=\alpha_c^{\infty,sat}\gamma(h) \tag{3}$$

$$\gamma(h)=e^{h_c^0\left(1-\frac{1}{h}\right)} \tag{4}$$

where A_{c1}, A_{c2} = 0.005, η_c and h_c^0 are material parameters, α_c^{∞} is the asymptotic hydration degree, $\alpha_s^{\infty,sat}$ is the asymptotic hydration degree at complete saturation, E_{ac} is the hydration activation energy, R is the universal gas constant. One can notice that in equation 2, the term $\alpha_c^{\infty}-\alpha_c$ can be negative when h is small enough, which would lead to an unphysical reduction in hydration degree over time. To ensure a positive rate of cement hydration degree, the Macaulay brackets $\langle.\rangle$ = max (0,.) are used.

The silica fume reaction degree is written in a similar functional form as

$$\dot{\alpha}_s=A_{s1}(A_{s2}+\alpha_s)\left\langle \alpha_s^{\infty}-\alpha_s\right\rangle e^{-\frac{\eta_s\alpha_s}{\alpha_s^{\infty}}}e^{-\frac{E_{as}}{RT}} \tag{5}$$

$$\alpha_s^{\infty}(h)=\alpha_s^{\infty,sat}\gamma(h) \tag{6}$$

$$\gamma(h)=e^{h_s^0\left(1-\frac{1}{h}\right)} \tag{7}$$

where A_{s1}, A_{s2} = 0.05, η_s and h_s^0 are material parameters, α_s^{∞} is the asymptotic hydration degree, $\alpha_s^{\infty,sat}$ is the asymptotic hydration degree at saturation, and E_{as} is the silica fume reaction activation energy. The notation $\langle.\rangle$ is once again used in equation 5 to avoid an unphysical decrease of silica fume reaction degree over time.

The cement hydration degree and the silica fume reaction degree are taken into account in a single formulation, namely the total reaction degree (Di Luzio & Cusatis 2013) as

$$\alpha=\frac{\alpha_c c\tilde{Q}_c^{\infty}+\alpha_s s\tilde{Q}_s^{\infty}}{c\tilde{Q}_c^{\infty}\alpha_c^{\infty}+s\tilde{Q}_s^{\infty}\alpha_s^{\infty}} \tag{8}$$

where $\tilde{Q}_c^{\infty}$ and $\tilde{Q}_s^{\infty}$ are the latent heat of hydration reaction and silica fume reaction, respectively, per unit of hydrated cementitious material, c and s are respectively the cement and silica fume contents. The chemically bound water is commonly formulated as $w_n=\kappa_c\alpha_c c$, where κ_c is the mass ratio of non-evaporable water at full hydration and c is the cement content. Furthermore, one can define w_e, the evaporable water, which is the resultant of two contributions, i.e., the evaporable water present in the CSH gel w_e^{gel} and the capillary water w_e^{cap}: $w_e=w_e^{gel}+w_e^{cap}$. They are formulated as

$$w_e^{gel}=g_2\alpha\left(c\alpha_c^{\infty}+s\alpha_s^{\infty}\frac{\tilde{Q}_s^{\infty}}{\tilde{Q}_c^{\infty}}\right)\left[1-e^{-10\alpha_c^{\infty}(g_1-\alpha)h}\right] \tag{9}$$

where g_1 = 1.5 and g_2 are material parameters. The capillary water is computed through a mass balance

$$w_0+\Delta w=w_e^{gel}+w_e^{cap}+w_n \tag{10}$$

where w_0 is the initial water content. Δw is defined as the mass of water to be supplied to compensate chemical shrinkage and maintain saturated conditions. It can be written as

$$\Delta w=X_c\left[\left(1-\frac{\tilde{Q}_c^{\infty}}{\tilde{Q}_s^{\infty}}\right)c\alpha_c+s\alpha_s\right] \tag{11}$$

where X_c is a material parameter. The equation 1 constitutes the governing equation and is discretized and solved using an implicit Crank-Nicolson method.

2.3 *Multiscale identification of the HTC model parameters*

Relevant outputs of the CEMHYD3D model are post-processed, and the material parameters of the HTC model listed earlier are automatically fitted. The identification procedure is performed under saturated and sealed conditions.

At saturation, i.e., h = 1, the parameters A_{c1}, η_c, $\alpha_c^{\infty,sat}$ in Equations 2 and 3 and A_{s1}, η_s, $\alpha_s^{\infty,sat}$ in Equations 5 and 6 are identified from the curves for cement hydration and the silica fume reaction degrees versus time obtained by the CEMHYD3D model. The activation energies for silica fume and cement reactions are the ones used in the micro-scale model. $\tilde{Q}_c^{\infty}$ and $\tilde{Q}_s^{\infty}$ in Equation 8 are identified by computing the initial masses of the different clinker phases and silica fume. In addition, one can compute the non-evaporable water by assuming that, for each cement clinker phase, the mass of chemically bound water produced is

proportional to the mass of reacted phase, through constant coefficients (Molina 1992). This allows the identification of κ_c. The evaporable water in the gel is computed from the CEMHYD3D model, along with the chemical shrinkage, allowing the identification of the parameters g_2 and X_c. The capillary water content is then evaluated from Equation 10, knowing w_0.

Last, the CEMHYD3D model evaluates the cement hydration and silica fume reaction degrees curves in time for the sealed condition. This enables the identification of the two remaining parameters h_c^0 and h_s^0 in Equations 4 and 7.

3 PREDICTION RESULTS

The HTC-CEMHYD3D model was used to predict experimental data on self-desiccation (Persson 1996, Persson 1997, Persson 1998). Three different concrete mixes were used, with a wide range of water to cement ratios, i.e., w/c = 0.22, w/c = 0.36, and w/c = 0.48 and a constant silica fume to cement mass ratio of s/c = 0.1. Concrete specimens were sealed and the relative humidity was measured at 28, 90, and 450 days after casting. For the mix design, a low alkali cement was used, which was replicated by using a similar cement type in the HTC-CEMHYD3D model. Table 1 shows the material parameters that were identified using the CEMHYD3D model and transferred to the HTC model.

Results are shown in Figure 1. The predictions are in agreement with the experimental data and able to capture the decrease in humidity at various concrete ages. At 28 days, the absolute differences between experiments and simulations are 1.77%, 5.92%, 3.05% respectively for the mixes with w/c = 0.22, w/c = 0.36, and w/c = 0.48. The predictions improve as time goes. Indeed, for the mix with w/c = 0.22, the absolute differences are 0.70% and 0.81% respectively at 90 and 450 days. Similarly for the mix with w/c = 0.36, one can report differences of respectively 2.61% and 0.34%, whereas for the mix with w/c = 0.48, one gets 0.40% and 1.17% respectively at 90 and 450 days.

Table 1. Identified HTC model parameters from CEMHYD3D.

HTC parameters		$w/c = 0.22$ $s/c = 0.1$	$w/c = 0.36$ $s/c = 0.1$	$w/c = 0.48$ $s/c = 0.1$
A_{c1}	[1/h]	9.67×10^6	5.76×10^6	2.78×10^6
η_c	[–]	4.42	5.49	6.62
$\alpha_c^{\infty,sat}$	[–]	0.38	0.55	0.83
E_{ac}	[kJ/mole]	40.00	40.00	40.00
h_c^0	[–]	0.20	0.40	0.50
A_{s1}	[1/h]	1.17×10^{14}	9.97×10^{13}	7.71×10^{13}
η_s	[–]	0.84	2.08	1.86
$\alpha_s^{\infty,sat}$	[–]	0.49	0.76	0.84
E_{as}	[kJ/mole]	83.14	83.14	83.14
h_s^0	[–]	1.50	0.55	0.40
$\tilde{Q}_c^\infty$	[kJ/kg]	506.74	508.04	506.52
$\tilde{Q}_s^\infty$	[kJ/kg]	780.00	780.00	780.00
κ_c	[–]	0.27	0.26	0.25
g_2	[–]	0.32	0.29	0.24
X_c	[–]	0.22	0.21	0.23

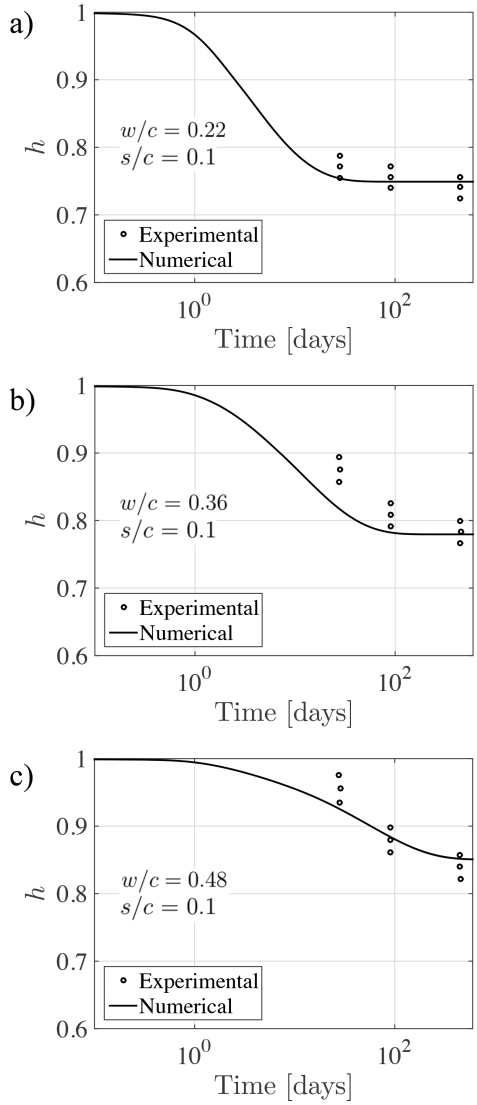

Figure 1. Prediction of self-desiccation in three different concretes. Upper and lower data points represent respectively +/-5% in humidity (absolute). Experimental data is from Persson, 1996, 1997, 1998.

4 CONCLUSIONS

A multiscale parameter-free framework to simulate hydration in concrete has been presented, including the modeling of the cement microstructure (CEMHYD3D model) and mathematical formulations modeling the macro-scale hygro-thermo-chemical properties of concrete, in particular self-desiccation. The model results were also compared to experimental data. This preliminary study showed the following:

- It is possible to simulate self-desiccation using model predictions from the micro-scale without additional parameters from the experiments.
- The model is capable of accurately predicting the drop in internal humidity in time at ages of 90 days and beyond.
- The model can take into account a wide range of water to cement ratios and the inclusion of silica fume.

ACKNOWLEDGMENT

The work of the first and last authors was sponsored by the U.S. Army Engineer Research and Development Center (ERDC) under Contract Number W912HZ-17-C-0027. Permission to publish was granted by the director of the ERDC Geotechnical and Structures Laboratory.

REFERENCES

Bentz, D. (2005). Cemhyd3d: A three-dimensional cement hydration and microstructure development modeling package. version 3.0.

Bentz, D.P. (1997). Three-dimensional computer simulation of portland cement hydration and microstructure development. *Journal of the American Ceramic Society 80*(1), 3–21.

Bentz, D.P. & E.J. Garboczi (1990). Digitised simulation model for microstructural development. *Ceram. Trans. 16*, 211–226.

Bishnoi, S. & K.L. Scrivener (2009). μic: A new platform for modelling the hydration of cements. *Cement and Concrete Research 39*(4), 266–274.

Bullard, J.W. (2007a). Approximate rate constants for nonideal diffusion and their application in a stochastic model. *The Journal of Physical Chemistry A 111*(11), 2084–2092.

Bullard, J.W. (2007b). A three-dimensional microstructural model of reactions and transport in aqueous mineral systems. *Modelling and Simulation in Materials Science and Engineering 15*(7), 711.

Cervera, M., J. Oliver, & T. Prato (1999). Thermo-chemomechanical model for concrete. i: Hydration and aging. *Journal of engineering mechanics 125*(9), 1018–1027.

De Schutter, G. & L. Taerwe (1996). Degree of hydration-based description of mechanical properties of early age concrete. *Materials and Structures 29*(6), 335.

Di Luzio, G. & G. Cusatis (2009). Hygro-thermo-chemical modeling of high performance concrete. i: Theory. *Cement and Concrete composites 31*(5), 301–308.

Di Luzio, G. & G. Cusatis (2013). Solidification–microprestress–microplane (smm) theory for concrete at early age: Theory, validation and application. *International Journal of Solids and Structures 50*(6), 957–975.

Garboczi, E. & D. Bentz (1992). Computer simulation of the diffusivity of cement-based materials. *Journal of materials science 27*(8), 2083–2092.

Gawin, D., F. Pesavento, & B.A. Schrefler (2006a). Hygrothermo-chemo-mechanical modelling of concrete at early ages and beyond. part i: hydration and hygro-thermal phenomena. *International Journal for Numerical Methods in Engineering 67*(3), 299–331.

Gawin, D., F. Pesavento, & B.A. Schrefler (2006b). Hygrothermo-chemo-mechanical modelling of concrete at early ages and beyond. part ii: shrinkage and creep of concrete. *International Journal for Numerical Methods in Engineering 67*(3), 332–363.

Jennings, H.M. & S.K. Johnson (1986). Simulation of microstructure development during the hydration of a cement compound. *Journal of the American Ceramic Society 69*(11), 790–795.

Koenders, E. & K. Van Breugel (1997). Numerical modelling of autogenous shrinkage of hardening cement paste. *Cement and Concrete Research 27*(10), 1489–1499.

Molina, L. (1992). *On predicting the influence of curing conditions on the degree of hydration*. Cement och Betong Institututet.

Navi, P. & C. Pignat (1996). Simulation of cement hydration and the connectivity of the capillary pore space. *Advanced Cement Based Materials 4*(2), 58–67.

Pan, Y. et al. (2017). Lattice modeling of early-age behavior of structural concrete. *Materials 10*(3), 231.

Persson, B. (1996). Hydration and strength of high performance concrete. *Advanced Cement Based Materials 3*(3), 107–123.

Persson, B. (1997, Nov). Moisture in concrete subjected to different kinds of curing. *Materials and Structures 30*(9), 533–544.

Persson, B. (1998). Seven-year study on the effect of silica fume in concrete. *Advanced cement based materials 7*(3), 139–155.

Rahimi-Aghdam, S., Z.P. Bažant & M.A. Qomi (2017). Cement hydration from hours to centuries controlled by diffusion through barrier shells of csh. *Journal of the Mechanics and Physics of Solids 99*, 211–224.

Thomas, J.J. et al. (2011). Modeling and simulation of cement hydration kinetics and microstructure development. *Cement and Concrete Research 41*(12), 1257–1278.

Ulm, F.-J. & O. Coussy (1995). Modeling of thermo-chemomechanical couplings of concrete at early ages. *Journal of engineering mechanics 121*(7), 785–794.

Van Breugel, K. (1995). Numerical simulation of hydration and microstructural development in hardening cement-based materials (i) theory. *Cement and Concrete Research 25*(2), 319–331.

Ye, G., K. Van Breugel, & A. Fraaij (2003). Three-dimensional microstructure analysis of numerically simulated cementitious materials. *Cement and Concrete Research 33*(2), 215–222.



Taylor & Francis
Taylor & Francis Group
http://taylorandfrancis.com

Computational Modelling of Concrete Structures – Meschke, Pichler & Rots (Eds)
© 2018 Taylor & Francis Group, London, ISBN 978-1-138-74117-1

Effect of drying on the mechanical performances of concrete

F. Benboudjema, F. Soleilhet, X. Jourdain & F. Gatuingt
LMT-Cachan/ENS-Cachan/CNRS, Université Paris Saclay, France

ABSTRACT: Drying of cement-based materials induces drying shrinkage, which may cause prestress loss or/and cracking if strains are restrained. Due to the slow rate of drying, a strong gradient occurs rapidly leading to tensile stresses at the surface and compressive stresses in the core. Since, drying shrinkage occurs only in cement paste, tensile stresses occur in the cement paste. The prediction of these self–stress state needs the take into account of creep. Besides, capillary pressure, disjoining pressure and surface tension lead to mean compressive stresses in the solid skeleton that can increase the strength of concrete. In order to unveil the contribution of each phenomena, experiments (not presented here) have been carried out on drying, drying shrinkage and mechanical properties after drying or in saturated conditions. Numerical simulations are performed and presented in order to study the effect of drying on mechanical performance of concrete.

1 INTRODUCTION

Cement-based materials are highly sensitive to water. As soon as the surrounding relative humidity is lower than the one in the material, drying occurs which leads to shrinkage and cracking. Shrinkage is related to the rise of capillary pressure, disjoining pressure and surface energy which creates internal compressive stresses in the solid skeleton. Cracking is due to two mechanisms:

- Differential drying shrinkage between the core and the surface;
- Strain incompatibilities between cement paste (subjected to drying shrinkage) and stiff aggregates.

In parallel, a mean triaxial compressive state of stress in the solid skeleton may increase the mechanical performance of concrete.

A lot of experimental data and models are available concerning drying and induced cracking, but few on the effect of drying on mechanical performance. Regarding the Young's modulus, most authors report a decrease of between 4 and 30% as concrete dries (e.g. Brooks ad Neville, 1977; Yurtdas et al., 2006). Conversely, there is no consensus concerning the compressive and tensile strengths: regarding compressive strength, some authors report an increase (e.g. Brooks ad Neville, 1977; Yurtdas et al., 2006) while others report a decrease (e.g. Philajavaara, 1974; Hanson, 1968). Concerning tensile strength, a slight increase was found in a splitting test (Hanson, 1968) while an initial decrease followed by a progressive increase up to zero percent relative humidity was observed in bending (e.g. Philajavaara, 1974). A decrease followed by an increase was also measured in direct tensile tests (De Larrard and Bostvirronois, 1991).

Therefore, In order to predict drying shrinkage, induced cracking and effect on mechanical performance, it is important to dispose of a predictive relevant model. The objective of this study is to combine experiments (not presented here, see Soleilhet et al., 2016) and numerical simulation in order to investigate the effect of drying on mechanical performance of concrete.

2 MODELLING

2.1 *Drying process*

The drying of cement-based materials is a complex phenomenon. Several, more-or-less coupled, mechanisms are involved: permeation, diffusion, adsorption-desorption and condensation-evaporation. Drying can be analysed through the resolution of liquid water, vapour and dry air mass balance equations. The use of several hypotheses (e.g. Thiery et al., 2007) allows for considering only the mass balance equation of liquid water:

$$\frac{dS_l}{dP_c}\frac{dP_c}{dt} = div\left(k_{rl}\left(S_l\right)\frac{K}{\mu_l\phi}grad\left(P_c\right)\right) \quad (1)$$

where S_l, P_c, ϕ, K, k_{rl} and μ_l are, respectively, the saturation degree, the capillary pressure, the porosity, the intrinsic permeability, the relative permeability and the viscosity of the liquid water.

It is shown (e.g. Thiery et al., 2007) that this equation is sufficient for an accurate prediction of the drying of ordinary and high-performance concretes at 20°C with a relative humidity greater than 50%. The capillary pressure and the relative permeability are related to the degree of saturation through van Genuchten's relation (van Genuchten, 1980):

$$S_l = \left(1 + \frac{P_c}{P_0}\right)^{1-\gamma} \tag{2a}$$

$$k_{rl}(S_l) = S_l^{nk}\left(1 - \left(1 - S_l^{\frac{1}{\beta}}\right)^{\beta}\right)^2 \tag{2b}$$

where nk, P_0 and β are materials parameters.

Depending on the studied sample, the modelling was based on 2D or 3D meshes. Drying at surfaces were modelled using a convection-type approach. In addition, it was found numerically that the evolution of humidity conditions in the climatic chamber did not have a significant impact on the evolution of drying, with respect to the assumption of a constant relative humidity (disregarding hysteresis effects). Therefore it was not taken into account and an average value was used. Finally, an inverse identification tool was implemented to determine *nk*, *K*, P_0 and β values thanks to experimental mass lost results.

2.2 *Drying shrinkage*

Following experimental results, the (free) drying shrinkage rate $\dot{\varepsilon}_{ds}$ may be taken as proportional to the water content variation (e.g. Carlson, 1936):

$$\underline{\underline{\dot{\epsilon}}}_{ds} = k_{ds}\dot{w}\underline{\underline{1}} \tag{3}$$

where k_{ds} is a hydrous compressibility factor and $\underline{\underline{1}}$ is the unit matrix.

It is possible to find alternative approaches but in this present work this modelling approach was chosen. It is easy to implement and give satisfactory results in our case. Moreover, the modelling of the drying shrinkage takes into account basic and drying creep. These allow a relaxation of the stresses decreasing the damage induced by the drying gradients.

2.3 *Basic and drying creep*

The model used for basic creep strain evolution is based on the microprestress theory proposed by Bazant et al. (1997) which has been enhanced in order to predict that basic creep depends on the internal relative humidity (Bazant et al., 1976). This model turns out to be particularly accurate when considering a very long time creep (which is the case here), and is in good accordance with experimental results (cf. the experimental campaign by Brooks (2005) for 30 years creep). The evolution of irreversible creep reads:

$$\frac{d\varepsilon_{bc_i}}{dt} = \tilde{\sigma}\frac{\alpha}{t}S_l^n \tag{4}$$

where α is a material parameter. The last right term, depending upon saturation degree, takes into account that the viscosity increases rapidly as drying occurs, leading to a decrease of basic creep strains as previously aforementioned.

In order to reproduce the (partial) reversible part of basic creep, a Kelvin-Voigt chain is used:

$$\frac{\tilde{\sigma}}{k} = \varepsilon_{bc_r} + \tau_{KV}\frac{d\varepsilon_{bc_r}}{dt} \tag{5}$$

where k is the stiffness of the spring, τ_{KV} is the characteristic time of the Kelvin-Voigt chain.

The most used model for (intrinsic) drying creep is probably the stress-induced shrinkage one, proposed by Bažant and Chern (1985), which is based on experimental observations. It has been used in this study:

$$\dot{\varepsilon}_{dc} = \mu\left|\dot{h}\right|\boldsymbol{\sigma} \tag{6}$$

where μ is a material parameter. Creep is extended to multiaxial state of stress by the use of a creep Poisson ratio, which has been taken equal to the elastic one.

2.4 *Cracking model*

The model is based on the developed by Mazars (1984): a scalar mechanical damage variable is associated to the mechanical degradation process of concrete induced by the development of microcracks. The relationship, between apparent stress $\boldsymbol{\sigma}$, effective stress $\tilde{\boldsymbol{\sigma}}$, damage D (depending also on tensile strength f_t), elastic stiffness tensor $\mathbf{E}$, elastic strain $\boldsymbol{\varepsilon}_e$, creep strain $\boldsymbol{\varepsilon}_c$ (sum of basic and drying creep), drying shrinkage $\boldsymbol{\varepsilon}_{ds}$, and total strain $\boldsymbol{\varepsilon}$, reads:

$$\boldsymbol{\sigma} = (1-D)\tilde{\boldsymbol{\sigma}} = \dot{\tilde{\boldsymbol{\sigma}}} = \mathbf{E}\dot{\boldsymbol{\varepsilon}}_{\mathbf{e}} = \mathbf{E}\left(\dot{\boldsymbol{\varepsilon}} - \dot{\boldsymbol{\varepsilon}}_{\mathbf{c}} - \dot{\boldsymbol{\varepsilon}}_{\mathbf{ds}}\right) \tag{7}$$

Softening behaviour of concrete may lead to non-unity of solutions and mesh dependency. Energetic regularization prevents these difficulties and has been used here (Hillerborg. et al., 1976).

Finally, a random field on the tensile strength generated by the Turning Band Method (Matheron,

1976) is used in order to take into account the variability of the material. The chosen parameters are:

- A variation coefficient equal to 10%;
- A correlation length taken three times bigger than the biggest aggregate.

2.5 *Calculation of crack openings*

To get crack openings, models rely on two main classes of techniques. Either post process cracks of a continuous damage field (Matallah and La Borderie, 2010) or the use of discontinuous models (XFEM, discrete or cohesive elements for instance). As part of this work, a post cracking method based on the damage field of the continuous model presented in the previous section, taking into account delayed deformations was used.

We can consider a strain partition as it is developed in (8) with ϵ^e_{Maz} the mechanical strain given by the Mazars' model (see Figure 1).

$$\epsilon_{ij} = \epsilon^e_{Maz} + \epsilon^{drying}_{kl} + \epsilon^{creep}_{kl} + \dots \tag{8}$$

This total mechanical strains is given by the equation (9) coming from equation (5):

$$\epsilon^e_{Maz} = \left((1-D)C_{ijkl}\right)^{-1}\sigma_{ij} \tag{9}$$

with D the damage, C_{ijkl} the stiffness matrix and σ_{ij} the strength. We can easily find the elastic strain, which is link to the strength by the stiffness matrix (equation (10)). We can make the assumption that the total strains can be divided into two parts. An "elastic" part and an other "inelastic".

$$\epsilon^e_{Maz} = \epsilon^{elas}_{kl} + \epsilon^{an}_{kl} \tag{10}$$

It is thus possible to calculate the various strains necessary for the quantification of the crack opening. The "elastic" strains is given by (11) while the "inelastic" strains is given as the difference between the total deformation field and the "elastic" deformation field (12).

$$\epsilon^{elas}_{kl} = C_{ijkl}{}^{-1}\sigma_{ij} \tag{11}$$

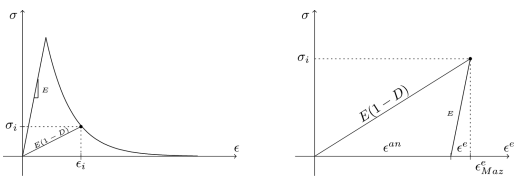

Figure 1. Uniaxial tension test schematic representation.

$$\epsilon^{ane}_{kl} = \epsilon^e_{Maz} - \epsilon^{elas}_{kl} \tag{12}$$

Final the crack opening is the product of the strains times the size of the element.

$$U_k = \epsilon^{ane}_{kl}.h_l \tag{13}$$

3 NUMERICAL SIMULATIONS

The results presented in this section tend to simulate the behaviour of 10 × 10 × 84 cm specimens tested in three point bending. They were kept under drying conditions (50% RH under a temperature of 21°C) for 70 days before testing. Parallel to this, other test pieces (similar in terms of geometry as well as concrete used) are kept in wet conditions. The results are then compared to characterize the impact of drying.

3.1 *Drying process*

The specimens' drying conditions (i.e. 50% RH) allow to only take into account the permeation in the modelling process. After an identification of the drying parameters by an inverse method based on the mass loss curves, the specimens are characterized with respect to the drying. The experimental mass losses as well as the gradients within the test pieces are obtained.

The relative mass variation is well predicted (Figure 2). The gradient of moisture within the test piece (Figure 3) is strong in the first moments and then tends to decrease over time. This difference between the core of the sample and the edge will therefore generate differential strains which will induce microcracking. In addition, a structural effect will be brought about by the non-homogeneity of the concrete with respect to moisture. This difference will generate additional resistance

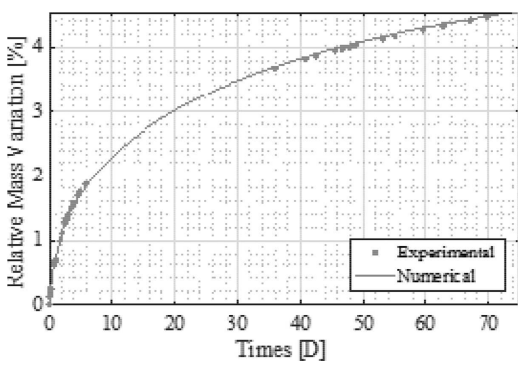

Figure 2. Evolution of relative mass variation.

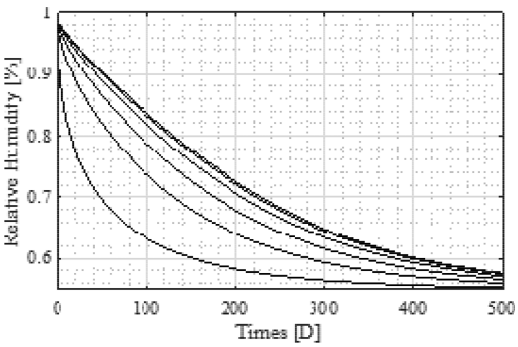

Figure 3. Evolution of RH gradient along the sample thickness.

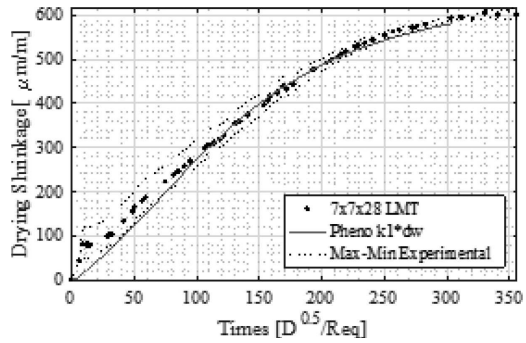

Figure 4. Evolution of drying shrinkage.

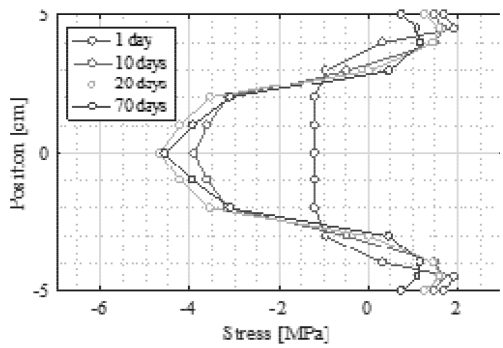

Figure 5. Evolution of normal stress along the center line.

3.2 *Drying shrinkage*

Phenomenological modelling of the drying shrinkage is based on the determination of water content gradients. The latter are obtained from the moisture gradients determined by the modelling of the drying process. Thus, the drying shrinkage and the state of internal stresses generated are obtained.

The drying shrinkage is calibrated on 7 × 7 × 28 cm specimens. The phenomenological model can correctly predict the evolution of drying (Figure 4). The final value is consistent, nevertheless the initial part at the short term seems wrongly predicted. This is mainly due to the mistake made in the prediction of drying. Indeed, the short-term behaviour is strongly impacted by the boundary conditions, difficult to characterize and rather variable depending on the case

If one is interested in the state of initial stresses (Figure 5), in the short term (1 day), tensile areas on the edge of the sample appear. The stresses are strong initially then the areas impacted by tension are damaged and the stress decreases in the short time. As time goes by, the thickness impacted by drying increases and the compressive stress at the centre tends to increase. The internal stresses imposed on the mechanical model correspond to the state of stress after 70 days. The section is visibly not at equilibrium.

3.3 *Effect of drying on the mechanical properties in bending*

Finally, the mechanical modelling is divided into two parts. It is started by the identification of the models parameters on wet beams' experimental curves and followed by the modelling of the drying process on similar beams exposed to drying.

It is shown in Figure 7 that taking into account the state of initial stresses due to drying strongly influences the macroscopic behaviour. If only drying shrinkage (D + S) is taken into account, the resulting damage is overestimated. Non-linearities appear very quickly, decreasing stiffness as well as peak strength. However this state is not representative of the phenomenon, the creep will reduce the stresses within the sample and at the same time reduce the damage, which will give a stronger behaviour (D + S + TC). Finally, within the material, the desaturation of the pores will lead to capillary phenomenon, which will lead to an increase in the overall strength. The case (D + S + TC + CP) takes this phenomenon into account. The overall behaviour appears to be better represented, however, an underestimation of the initial stiffness is still observed.

To illustrate the crack opening routine based on post-processing the damage, one can look at the cracking map obtained after 70 days of desiccation (Figure 6). There are no other stresses than those imposed by drying

With regard to the distribution of the cracks, it is noted that they are distributed around the circumference of the sample. This is easily justified by the fact that these areas are most affected by the hydric gradient. As for the size of the openings,

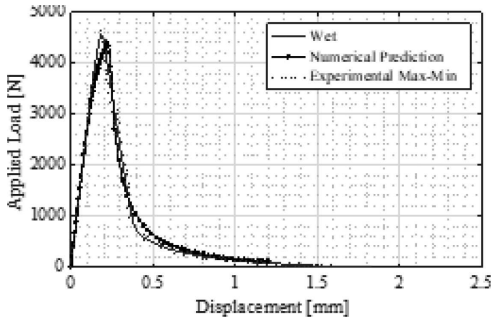

Figure 6. Calibration of model parameters in bending test (no drying).

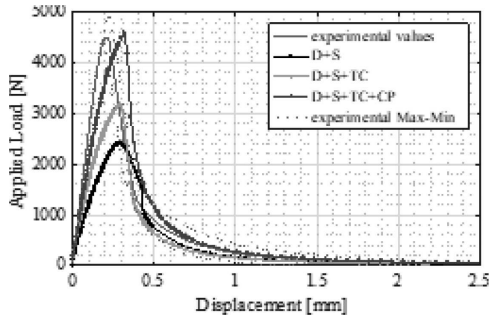

Figure 7. Prediction of the behaviour in bending after drying.

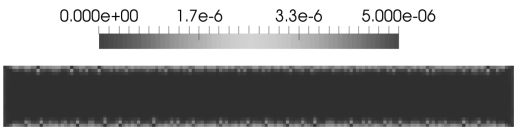

Figure 8. Crack map due to drying shrinkage [m].

they do not exceed the order of ten micrometres. This cracking is diffuse on the edges of the specimen nevertheless it remains superficial.

4 CONCLUSION

The drying phenomenon of cementitious materials is a major importance for understanding and forecasting long-term behaviour. Whether in terms of mechanical strength, behaviour (more or less brittle) or even transfer (fluid flux by permeation evolved with the cube of the crack opening), an impact of drying is observed experimentally. Although relative to all structures, drying is not much studied. The results found in the literature are sometimes inconsistent but can be explained by the different phenomena involved. Indeed, in the process three main phenomenon can be distinguished. The capillary pressure which stiffens the structure, the microcracking induced by the gradient of moisture and finally the strains incompatibilities.

The numerical approach presented in this paper is based on a four steps procedure which is concerned firstly with characterizing the water state of the material. This subsequently allows to quantify the delayed strains in order to then assume the internal state of stresses generated by drying shrinkage. These stresses are then took as initial value of the mechanical computation to finally obtain cracking pattern. They can be characterized regarding transfer phenomena by a external model not presented in this paper. The results presented here show that, as experimentally, the drying behaviour is strongly impacted by the drying shrinkage. Nevertheless, taking into account the phenomenon of capillary pressure and creep make it possible to approach a more realistic behaviour. In the modelling protocol there is no regard concerning strains incompatibilities. Some authors have proposed model to take this phenomenon into account but it is not widespread and it is still difficult to calibrate models' parameters.

Finally, the model presented allows to simulate the behaviour of large structure under drying from the hydric characterization to the hydric transfer. And it has the advantage on relying on a model regularize in fracture energy which makes it suitable for large scale modelling.

REFERENCES

Bažant Z.P., Asghari A., Scamiot J. 1976 *Materials and Structures* 9: 279–290.

Bažant Z. P., Chern J. C., 1985 *Materials and Structures* 18:1–20.

Bažant Z.P., Hauggaaed A.B., Baweja S., Ulm F.J., *Journal of Engineering Mechanics* 123:1188–1194.

Brooks J.J., Neville AM. 1977 A comparison of creep, elasticity and strength of concrete in tension and in compression. *Magazine of Concrete Research* 29(100):131–141.

Brooks J.J. 2005 *Magazine of concrete research* 57: 545–556.

Carlson, RW. 1937 Drying shrinkage of large concrete members. *J of the Am Concrete Inst* 33:327–336.

De Larrard F, Bostvirronois JL. 1991 On the long term losses of silica fume high strength concretes. *Magazine of Concrete Research* 43(155):124–129.

Hanson JA. 1968 Effects of curing and drying environments on splitting tensile strength of concrete. *Journal of the American Concrete Institute* 65(7):535–543.

Hillerborg A, Modéer M, Petersson P-E. 1976 Analysis of crack formation and crack growth in concrete by means of fracture mechanics and finite elements. *Cem Concr Res* 6:773–81.

Matallah, M., La Borderie, C. 2010 A practical method to estimate crack openings in concrete structures. *International Journal for Numerical and Analytical Methods in Geomechanics* 34:1615–1633.

Matheron, G. 1973 The intrinsic random functions and their applications. *Advances in applied probability*: 439–468.

Mazars, J. 1984. Application de la mécanique de l'endommagement au comportement non linéaire et à la rupture de béton de structure, Thèse de doctorat d'état, Paris VI.

Philajavaara SE. 1974 A review of some of the main results of a research on the aging phenomena of concrete: effect of moisture conditions on strength, Shrinkage and creep of mature concrete. *Cement and Concrete Research* 4(5):761–771.

Soleilhet, F., Benboudjema F., Jourdain X, Gatuingt F. 2016 Experimental and numerical investigation of drying effects on concrete's mechanical properties in International RILEM Conference on Materials, Systems and Structures in Civil Engineering.

Thiery, M., Baroghel-Bouny 2007 Modélisation du séchage des bétons: analyse des différents modes de transfert hydrique. *Revue Européenne de Génie Civil* 11:541–577.

van Genuchten M Th. 1980 A closed-form equation for predicting the hydraulic conductivity of unsaturated soils. *Soil Science Society of America* 44:892–898.

Yurtdas I, Peng H, Burlion N, Skoczylas F. 2006 Influences of water by cement ratio on mechanical properties of mortars submitted to drying. *Cement and Concrete Research* 36:1286–1293.

Computational Modelling of Concrete Structures – Meschke, Pichler & Rots (Eds)
© 2018 Taylor & Francis Group, London, ISBN 978-1-138-74117-1

Temperature and humidity-driven ageing of the VeRCoRs mock-up

J.-P. Mathieu, L. Charpin, P. Sémété & C. Toulemonde
Department Matériaux et Mécanique des Composants (MMC), EDF R&D, EDF Lab Les Renardières, France

G. Boulant
Department PErformance et prévention des Risques Industriels du parC par la simuLation et les EtudeS (PERICLES), France

J. Haelewyn, F. Hamon & S. Michel-Ponnelle
Department ElectRotechnique et MEcanique des Structures (ERMES), EDF R&D, EDF Lab Paris-Saclay, France

J.-M. Hénault & F. Taillade
Department Performance, Risque Industriel, Surveillance pour la Maintenance et l'Exploitation (PRISME), EDF R&D, EDF Lab Chatou, France

ABSTRACT: VeRCoRs is a 1/3 scale mock-up of a double walled concrete containment building that has been built by EDF to study the effect of ageing on the loss of pre-stress of the post-tensioned inner wall, and its subsequent effect on the leak rate evolution. This paper briefly introduces the industrial context around the mock-up, and the important effort that has been made on the aspects of (i) material characterization, (ii) instrumentation, (iii) numerical simulations. The solutions chosen to address the issue of dealing with a large amount of experimental data and to compare them with multi-physics simulation are highlighted. Then, it allows to easily compare three successive instances of the modelling of VeRCoRs ageing and to discuss their respective forecasting capacities. In such a predictive approach, thermal and hydric boundary conditions are essentials and their simplification although necessary, should not be too important as not to deviate too much from representativeness.

1 INTRODUCTION

1.1 *Industrial context*

EDF operates a large fleet of Nuclear Power Plants (NPPs). Safety in case of accidental situations relies for each French reactor on three barriers: fuel cladding, primary circuitry integrity, and reactor containment building leak-tightness. For some of these events, such as Loss Of Cooling Accident (LOCA), safety requirements impose a maximal leakage rate of the containment building. It is checked and validated periodically during every 10-yearly outage programmes (Periodic Safety Reviews), where the success of the Integrated Leakage Rate Test (ILRT) is mandatory to continue the plant operation.

24 of EDF French containment buildings are double-walled containments (DWCs) whose leak-tightness is primarily dependent on the inner Pre-stressed Reinforced Concrete Containment Building (PRCCB). The post-tensioning of tendons is calibrated in order to ensure that in case of an accident the concrete remains in compression (Masson 2015). However, due to delayed strains of concrete, this effect can decrease in time. Tendons are grouted on these containments so that increasing post-tension is not an option (not to mention the inherent difficulty of such an operation). Therefore, EDF has acquired a long experience of repair solutions that are thoroughly tested and qualified. The in situ feedback is positive but their operational implementation remains complex. Efficient and best safety are sought, so that the maintenance policies require a detailed knowledge about (i) the behavior of the concretes used in the containment buildings, in order to be able to predict (ii) the future evolution of their delayed strains and (iii) their subsequent effects on leak-tightness.

1.2 *Research efforts done at EDF*

Civil engineering community has been quite active in the last decades on the topics of concrete drying and delayed strains. EDF collaborations in several research projects and works has been decisive to improve its recent understanding of physical phenomena (Charpin et al. 2015, Sémété et al. 2017) and to achieve their modelling at different scales (Lavergne et al. 2015, Mazars et al. 2015, Foucault

et al. 2012). Measurements and instrumentation are also important topics (Courtois et al. 2011), and coupled to modelling approaches it can provide new insights in concrete large structure monitoring.

Experimental programs have also been conducted in order to substantiate these knowledge (Jason and Masson 2014, Herrmann et al. 2018) and to demonstrate their ability to fulfil a leakage prediction on mock-ups structurally representative of containment buildings. These projects are presented in (Galenne et al. 2014) along with a review of EDF's recent efforts in computational methods dedicated to civil engineering research topics. The previous paper ends with an evocation of the research program VeRCoRs. EDF R&D's recent work in this program will be the subject of this paper.

First, the mock-up will be briefly introduced as will be the accompanying program concerning concrete material, instrumentation, modelling and the setup of an informational system required for the exploitation of the massive dataset produced within the project. The objective is to build a so-called "digital twin" that will be used for forecasting the mock-up behaviour. The Finite Element (FE) simulation that concretizes this digital twin will then be exposed. Three successive sets of input parameters and Boundary Conditions (BCs) chosen or identified manually according to the available information will be discussed and used as an input. This will allow to focus on the respective influence of (i) a proper representation of the temperature and moisture fields and BCs and (ii) a precise calibration of the constitutive law on laboratory experiments on the prediction of delayed strains.

2 VERCORS, A UNIQUE MOCK-UP

VeRCoRs (***V**érification **R**éaliste du **C**onfinement des **R**éacteurs* / realistic assessment of reactors containment) is a 1/3 scale mock-up (Fig. 2) of a PRCCB that has been built at EDF Lab Les Renardières research facility, near Paris. An overview of the project as well as details and lesson learned from the first benchmark dedicated to modelling of the mock-up in its early age phase can be found in (Corbin and Garcia 2016).

2.1 *VeRCoRs construction and planned exploitation*

In order to achieve faster ageing, and according to the assumption that drying will be the main phenomenon causing delayed deformation, VeRCoRs has been built with the expectation of an accelerated ageing factor on deformations. To ease the transfer of the results to full-scale containment, several design choices were made (Corbin and Garcia 2016). Pre-stress and reinforcement designs are scaled to the largest practical extent: rebar length and overlapping were not scaled due to practical reasons and cables have fewer strands rather than scaling them. The 1/3 scale was thus chosen as the best compromise between scalability of construction and acceleration of ageing.

The mock-up construction started in 2013, inner containment raft foundation was concreted in July 2014, and the dome was finished in April 2015. Pre-stressing started after 28 days of curing and was completed in august 2015. The first ILRT (so-called "pre-operationnal") was conducted on the 5th November 2015. Since all phenomena do not follow the same similarity rules as drying, some specific measures were taken. The haunch between raft foundation and cylindrical part (gusset) was post-heated shortly after concreting to increase its temperature during hydration as it would raise in a 3 times thicker one. On the contrary, inner containment internal surface was kept wet until the end of the tendons post-tensioning operations to avoid excessive surface cracking due to differential shrinkage.

At the end of the construction, two auxiliaries air-conditionning units were started to impose realistic relative humidity and temperature inside and outside the inner containment and simulate the drying effect of regular operation of a nuclear reactor. ILRTs are conducted on a regular basis (approximately every 13 months according to observed delayed strain acceleration).

2.2 *Material characterization program*

In order to predict the evolution of the VeRCoRs mock-up, it is of paramount importance to have thorough information about the material behaviour of its constituents. The main constituent is the VeRCoRs concrete which is an OPC concrete with a water to cement ratio of 0.52 designed in order to exhibit creep in the same magnitude as concrete used in actual NPP containment buildings. Base materials have been selected to be as much as possible similar than the ones used for construction of full scale containments; concrete class is 34/37 MPa. Grain size fraction has been adapted in terms of its maximal aggregates size, although it was not possible to achieve full 1/3 scaling.

A very large experimental program has been designed and performed at EDF, in partner labs, or in the project MACENA www.agence-nationale-recherche.fr/ProjetIA-11-RSNR-0012. Also, the VeRCoRs project interacts with the COST action TU1404 www.tu1404.eu (Serdar et al. 2017) where the VeRCoRs concrete has been used (except for slight differences in the cement composition).

The material characterization program on concrete is detailed in Table 1.

Moreover, pull-out tests are performed on rebars embedded in concrete and relaxation tests are

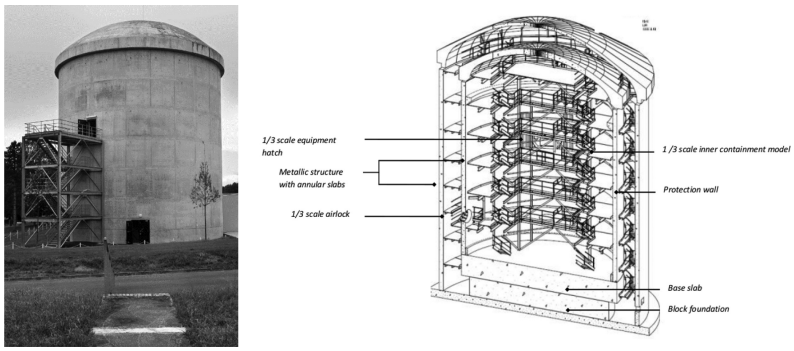

Figure 1. Outer containment wall of the VeRCoRs mock-up and sectional schematic view (Corbin and Garcia 2016).

Table 1. Experimental material characterization program on VeRCoRs materials.

– measurements of Youngś modulus, compressive and tensile strength, porosity, capillary absorption for every lift
– adiabatic calorimetry, thermal capacity, and thermal conductivity
– development of Young's modulus and strength depending on the curing temperature
– measurement of desorption isotherms
– EMM-ARM experiment (Azenha et al. 2012)
– characterization of drying, creep and shrinkage in sealed and drying conditions at 20°C, 40°C, 70°C. At 20°C biaxial tests are performed (Charpin et al. 2015)
– creep at high temperatures (100C)
– characterization of the effect of curing temperature on creep and shrinkage
– early-age properties (Delsaute et al. 2016)
– permeability, Young's modulus and strength dependence on temperature and humidity (Kallel et al. 2016)
– effect of load on permeability (Ezzedine El Dandachy et al. 2017)
– fracture energy
– creep on pre-stressed beams

performed on pre-stressing tendons (Toumi Ajimi et al. 2016). Through the COST action, various tests (quantitative XRD, calorimetry, shrinkage and creep, strength, …) are also performed.

This very large experimental program will yield a consistent set of data which will be used to improve and calibrate the phenomenological models applied to simulate the concrete containment buildings (Charpin et al. 2017), and also physics-based models aiming at understanding deeply the concrete behaviour (Sanahuja et al. 2017).

In order to deal with the large amount of data produced by the VeRCoRs project, a new data capitalization tool developed at EDF R&D called CADEEX is used. This tool can be called directly when performing the simulations in order to use experimental results for the constitutive models, for example.

2.3 *Instrumentation & monitoring*

An important effort has been made about measurements so that VeRCoRs is equipped with a large amount of sensors dedicated to the direct or indirect measurements of temperature, water content and strain in the concrete. The Table 2 providesan overview of the techniques used.

All the strain measurements shown in this paper will be representing the true strain. In order to obtain this strain, strains sensors like the vibrating wire sensors need to be corrected in order to remove the effect of their own thermal expansion effect during temperature variations. However, the effects of the materials thermal expansions around such as concrete or steel are included in the experimental data, coming from on-site measurements. On the other hand, for comparison with simulations, the thermo-mechanical strain will be extracted from the computations.

Water content measurements are considered as of primary importance on VeRCoRs for a better prediction and understanding of the delayed strains (Courtois et al. 2017).

Many of the sensors were embedded in concrete, and started recording data during the early age phase of the construction. Typical frequencies of data acquisitions are several per weeks during standard ageing phases and several per days during exceptional events (early age, ILRTs for instance). Most of the data acquisitions are automated. When the sensor technologies are already operated in the EDF's surveillance program of containment buildings, data are recorded directly in the existing databases (KOALA, operated by EDF DTG). For other ones (water content, OF), a dedicated database was built: the VeRCoRs Accompanying System (SAV).

2.4 *EDF efforts toward a digital twin of VeRCoRs*

Since KOALA and CADEEX database were already existing tools in EDF at VeRCoRs project

Table 2. Permanent sensors installed on the VeRCoRs mock-up in comparison with those installed on EDF's DWCs. More information about the sensors technologies used can be found in (Courtois et al. 2011, Courtois et al. 2017, Henault et al. 2012, Martinot et al. 2015).

Measured	Sensor	VeRCoRs	EDF
variable	type	mock-up	fleet
temperature	PT100 probes	>200	30
strain	vibrating wires	>300	50
diameter variation	plumb-lines	4	4
length variation	invar wires	4	4
rebar strain	strain gages	80	–
water content	TDR	20	–
water content	Pulse	20	–
strain & temperature	optic fiber (OF)	2 km	–

start, it was decided to comply with their standards for capitalization and to use their Application Programming Interfaces (APIs) to access them through the SAV tool.

Thus the SAV is set-up to capitalize, manage, centralize and easily access to a large amount of heterogeneous data about VeRCoRs:

- construction facts;
- materials data;
- ageing monitoring data;
- other data (like those obtained during ILRTs),

and to provide a dialog interface with existing tools currently in operation at EDF. These tools can be existing databases, so that SAV pulls-out information from them, or other tools that will pull-out data from the SAV as illustrated in Figure 2.

EDF R&D also developed a simulation and research toolbox (ARMORIC) in order to capitalize and improve the quality of: (i) advanced monitoring systems, (ii) numerical studies, and (iii) prediction tools related to VeRCoRs.

On the other hand, a web-based application (CERVIN) is also under construction that allows civil engineers to directly observe and extract online data about VeRCoRs that are stored in the SAV. The SAV, by providing data models for every aspects of VeRCoRs, can be seen at its Building Informational Model (BIM) dedicated to research and modelling.

All this Information System is illustrated in Figure 2, and constitutes a so-called "digital twin". This concept is derived from Product Life Management approaches. It emphasizes the underestimated difficulty to achieve a full data assimilation loop even once experimental data and modelling are capitalized and handled correctly. Since VeRCoRs will be operated for more than 7 years, this approach seems mandatory to allow everyone in the VeRCoRs project to work on consistent datasets. VeRCoRs is

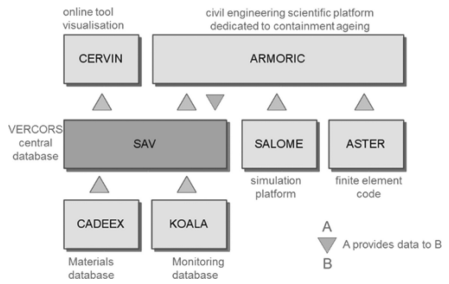

Figure 2. Illustration of the software ecosystem around VeRCoRs digital twin.

seen by authors as a great opportunity for EDF to adapt such methodologies to its existing fleet.

Several use-cases of these tools are envisaged in the future. The "best-estimate" simulation conducted with the ARMORIC platform is systematically post-processed in it, to produce a "virtual" series of measurements comparable with the "real" ones obtained during VeRCoRs ageing and stored in the SAV database. All the figures in the section 4 are thus obtained with ARMORIC tools through the use of several functions of the ARMORIC platform:

1. building three simulation cases A, B and C;
2. launching their computation on EDFs cluster;
3. launching a standard post-treatment on the resulting simulations;
4. building the graphics to compare several case outputs to SAV hosted values.

3 MODELLING OF THE MOCK-UP AGEING

The numerical model of the VeRCoRs mock-up is focused on the inner pre-stressed concrete containment building. The outer concrete containment building is not represented in this study since it has no explicit mechanical role neither in the ageing process of the inner containment nor in its subsequent leak-tightness. The mesh used for thermal and hydric computations is composed of 331962 nodes and 304928 hexahedral linear elements, while the mesh used for the mechanics computation is composed of 211776 nodes and 40656 hexahedral quadratic elements (Figure 3). For the latter case, the mesh is refined at the surface of concrete in order to correctly capture the drying gradients. In the cylindrical part, the wall thickness is discretized using 12 elements which size vary between 2 cm and 6 cm.

The pre-stress cables are individually modelled using bar elements which are kinematically linked to the solid concrete elements through Lagrange multipliers (Figure 3). Their deviations around the

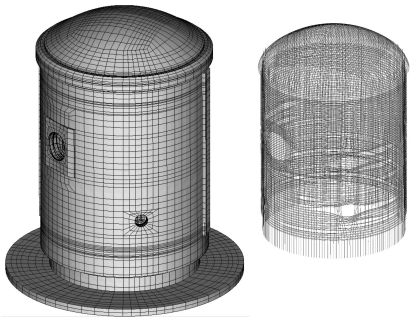

Figure 3. Solid hexahedral mesh used for the mechanical computations of reinforced concrete (left) and bar mesh used to represent the tendons (right).

access hatch and other passages through the walls are explicitly taken into account. The metal elements closing the through-wall passages (pipes, hatches) are also explicitly modelled in 3D in order to correctly take into account their role during the ILRT.

All computations are performed with Code_Aster which is an open-source FEM solver developed at EDF R&D www.code-aster.org. Three computations are performed sequentially: thermal, hydric and mechanical computations.

3.1 *Thermal history*

Thermal computation is performed using a linear heat diffusion equation (Haelewyn 2010):

$$\rho C_p \frac{\partial T}{\partial t} = \mathrm{div}[\lambda \nabla T] \tag{1}$$

Where ρ is the density of concrete, C_p is its thermal capacity, and λ is the thermal diffusion coefficient.

The boundary conditions are the fixed temperatures imposed at the surface of concrete (convection conditions have also been attempted but these computations are not shown here). The choice of the imposed temperatures is of importance, as will be discussed in section 3.4 concerning the temperature on the internal face and the outer face of the mock-up inner containment.

3.2 *Drying model*

Drying is modelled using the non-linear diffusion equation developed in (Granger 1995) from (Mensi et al. 1988) available in Code_Aster under the name SECH_GRANGER.

A non-linear diffusion equation governs the evolution of the water concentration C (L/m^3):

$$\frac{\partial C}{\partial t} = \mathrm{div}[D(C,T)\nabla C] \tag{2}$$

In isothermal conditions, the diffusion coefficient simply writes $D(C,T_0) = A\exp(BC)$ (Mensi et al. 1988). The dependence on the temperature is described by the following equation:

$$D(C,T) = D(C,T_0)\frac{T}{T_0}\exp\left[-\frac{Q}{R}\left(\frac{1}{T}-\frac{1}{T_0}\right)\right] \tag{3}$$

The temperatures are expressed in Kelvin. Parameter A governs the kinetics while B governs its dependence on the water concentration. Another important parameter is the boundary condition C^{eq} which is imposed as a fixed water concentration at the boundary. It represents the water concentration of the concrete at the relative humidity of the test room.

For the drying model, the boundary conditions need to be expressed in terms of water content C, which is achieved thanks to the choice of a boundary relative humidity and the knowledge of the desorption isotherm of the material. In the present simulations, fixed water content conditions were used. Exchange conditions were also attempted but are not described here.

The choice of the value of the boundary relative humidity as well as that of the material parameters A and B is of paramount importance and will be detailed in section 3.4.

3.3 *Mechanical model*

The mechanical model results from developments made in (Granger 1995), (Benboudjema 2002) and continued at EDF R&D (Foucault et al. 2012) following ideas from (Sellier and Buffo-Lacarrière 2009). It is available in Code_Aster under the name BETON_BURGER (Bottoni 2015). It is based on an additive decomposition of the strain in four main contributions: elastic strain, drying shrinkage strain, basic creep strain, and desiccation creep strain. In addition to these contributions the thermal strain is also accounted for.

Drying shrinkage The drying shrinkage is performed using the command ELAS_FO of operator DEFI_MATERIAU. The drying shrinkage is assumed proportional to the water concentration variation, which writes:

$$\varepsilon^{shr} = -k^{shr}(C^0 - C(t))\mathbf{1}, \tag{4}$$

where $\mathbf{1}$ is the second order identity tensor, C^0 is the initial water content and k^{shr} is a parameter to identify.

Elasticity and basic creep The combination of elastic and basic creep strains is formed as a Burgers rheological model (see Figure 4). Elasticity and basic creep are isotropic and hence, the Burgers model is

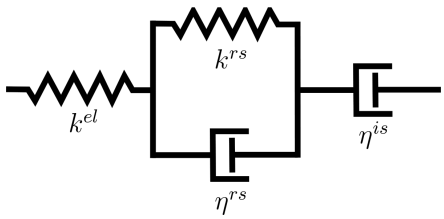

Figure 4. Burgers model (spherical chain).

duplicated in deviatoric and spherical chains[1]. For each chain (*d* relates to deviatoric and *s* relates to spherical), the strain is composed of elastic strain (ε_s^{el} and ε_d^{el}), reversible basic creep modelled by the Kelvin-Voigt element (ε_s^{rbc} and ε_d^{rbc}) and irreversible basic creep modelled by the Maxwell element by using a viscosity which is not constant in time (ε_s^{ibc} and ε_d^{ibc}): $\varepsilon^{bc} + \varepsilon^{el} = (\varepsilon_s^{el} + \varepsilon_s^{rbc} + \varepsilon_s^{ibc})\mathbf{1} + (\varepsilon_d^{el} + \varepsilon_d^{rbc} + \varepsilon_d^{ibc})$.

For any tensor, the spherical part is computed as $t_s = \text{tr}\, \boldsymbol{t}/3$ while the deviatoric part is computed as $\boldsymbol{t}_d = \boldsymbol{t} - t_s\mathbf{1}$.

The equations related to this Burgers model are now recalled for the spherical chain (the deviatoric can be obtained by replacing *s* by *d* and using tensors instead of scalars). The elastic strain is simply proportional to the stress: $\varepsilon_s^{el} = \sigma_s/(3k^{el})$. The basic creep strains are assumed proportional to the relative humidity *h*. The reversible basic creep is governed by Equation 5:

$$h\sigma_s = k^{rs}\varepsilon_s^{rbc} + \eta^{rs}\dot{\varepsilon}_s^{rbc} \tag{5}$$

while the irreversible one follows Equation 6:

$$h\sigma_s = \eta^{is}\dot{\varepsilon}_s^{ibc} \tag{6}$$

The viscosity of the irreversible contribution is assumed variable in time and writes:

$$\eta^{is} = \eta_0^{is}\exp\frac{\|\varepsilon^{ibc}\|_{max}}{\kappa}, \eta^{id} = \eta_0^{id}\exp\frac{\|\varepsilon^{ibc}\|_{max}}{\kappa} \tag{7}$$

where $\|\varepsilon^{ibc}\|_{max}$ is the maximum value since the beginning of the life of the sample of the norm of the irreversible basic creep strain:

$$\|\varepsilon^{ibc}\|_{max} = \max\left(\|\varepsilon^{ibc}\|_{max}, \varepsilon^{ibc} : \varepsilon^{ibc}\right) \tag{8}$$

This feature introduces some kind of ageing under loading and irreversibility in the model and at the same time ensures that the very long term (meaning for $t \gg \eta^{rs}/k^{rs}$ and $t \gg \eta^{rd}/k^{rd}$) creep is logarithmic.

1. Note that coefficients relative to the creep part of the Burgers model where not defined rigorously equivalently to elastic ones. To do so, one would have to replace k^{rs} by $3k^{rs}$, η^{rs} by $3\eta^{rs}$, k^{rd} by $2k^{rd}$ and so forth in the equations.

Therefore, a large number of parameters is introduced: k^{el}, μ^{el}, k^{rs}, k^{rd}, η^{rs}, η^{rd}, η_0^{is}, η_0^{id}, and κ. However, assuming that the basic creep Poisson's ratio is constant, the number of independent parameters can be reduced. The elastic Poisson's ratio writes: $\nu^{el} = (3k^{el} - 2\mu^{el})/(2(3k^{el} + \mu^{el}))$. Equivalently, $k^{el}/\mu^{el} = (2(1+\nu^{el}))/(3(1-2\nu^{el}))$. Similarly, the basic creep parameters can be related through the equations $\eta^{is}/\eta^{id} = \eta^{rs}/\eta^{rd} = k^{rs}/k^{rd} = (1+\nu^{bc})/(1-2\nu^{bc})$ where ν^{bc} is the basic creep Poisson's ratio.

Desiccation creep Finally, the desiccation creep is computed according to a modified version of a law called Bažant's law, relating the excess of strain rate during drying to the rate of change of the water concentration (Bažant and Chern 1985). The desiccation creep strain exhibits, in this version of the model, a zero Poisson's ratio and a similar behaviour in drying and water uptake:

$$\dot{\varepsilon}^{dc} = |\dot{h}|\frac{1}{\eta^{dc}}\boldsymbol{\sigma} \tag{9}$$

Other options have also been tested but are not presented here, such as the possibility to use a constant Poisson's ratio for this term (Charpin et al. 2017).

3.4 *Boundary conditions and model parameters*

The focus of this article is to show how improving the boundary conditions and the parameters used in the modelling of the VeRCoRs mock-up improved the results of the simulations when compared to on-site measurements. To illustrate this evolution of the structural model, three computations will be presented, and their results will be compared. They can be characterized by their sets of simulation input data (denoted *A*, *B*, and *C*) representing 3 milestones in the continuous process of calibration improvement and experimental data enrichment (e.g. creep tests can last for several months).

It is one of the numerous objective for EDF within the VeRCoRs project to increase its ability to manage such an evolving simulation that will have to accompany an existing structure during its lifespan. In this example only input parameters are prone to changes, but the same needs arise concerning more complex data types like the type of constitutive laws or the type of boundary conditions used.

Case A The thermal properties (density, thermal capacity and thermal diffusivity) were measured on VeRCoRs concrete.

The drying properties (parameters *A* and *B* of the drying law) were calibrated using a drying test performed on VeRCoRs concrete at 24 h in a 20°C and 50% RH atmosphere, using $B = 0.5$ as proposed in (Granger 1995). The thermal activation of drying was taken into account using the value of the activation energy proposed by (Granger

1995). The desorption isotherm was assumed linear (based on the knowledge of the saturation at 100% RH and at 50% RH determined from the drying test) since at that time no measured desorption isotherm was available.

Concerning the mechanical properties, the Young's modulus measured on concrete cylinders made during the construction was used, but the Poisson's ratio as well as the thermal dilation coefficient were not available, so typical literature values were used. The basic creep law coefficients were calibrated using 6 month of basic creep test performed at 20°C and 50% RH (these tests are also used in (Charpin et al. 2017)), whereas the drying shrinkage as well as desiccation creep coefficients were not calibrated but typical values used for other concretes at EDF were used. The assumption of a basic creep Poisson's ratio equal to 0.2 (which is slightly different from the elastic one) was used.

The mechanical properties of the steel of the tendons were typical values from the literature.

About the thermal boundary conditions, two different periods were considered, because at some point, the outer containment was sealed and an Air Conditioning (AC) system was started, with the aim to regulate the internal temperatures and humidities (inside inner containment and between outer and inner containment) of the mock-up. The temperature of the outer face of the inner containment building was assumed equal to 15°C, while the internal temperature was assumed equal to 15°C before the start of the AC system, and 35°C subsequently. The ground temperature was assumed equal to 10°C.

The hydric boundary conditions were fixed on three different periods. In the first period, the concrete was constantly kept moist using a water spraying system. During this period the boundary RH is supposed equal to 100%. Once this system was stopped and until the start of the AC system, the RH is assumed equal to 60% both on the internal and external faces of the mock-up according to average meteorological observations. Then, the internal boundary RH is assumed to lower to 25% as imposed by the AC system.

The mechanical boundary conditions are also quite schematic, since the displacements at the bottom of the raft (which is a very thick concrete slab) are assumed to be zero.

Case B This second computation is similar to computation A except for variations in the thermal and hydric boundary conditions.

First, concerning the phase were the outer containment was wide open to the outside, assuming constant temperatures and hydric conditions despite large seasonal variations (which are known thanks to a meteorological station placed close to the mock-up) was considered too crude so that an averaged seasonal temperature evolution was used. Second, an imposed temperature is used as a BC for thermal modelling, and using values measured with surface temperature sensors on the concrete allowed to refine the boundary conditions in comparison with the direct use of measured air temperature. However, the differences of temperature along the vertical axis inside the mock-up were still not accounted for.

The hydric boundary conditions were also changed to better account for the effect of starting the AC system. Differences between case A and B can be observed in Figure 5.

Case C Finally in the third computations, BCs were kept identical as in case B but the drying properties of concrete were changed using a new set of parameters for the drying law identified using a drying tests starting at 90 days (instead of 24 hours previously). This test is considered more representative of the drying of the mock-up concrete which has been kept moist for a long period of time before the start of drying. Despite this change, the parameters of the mechanical model were kept identical.

Difference between cases A, B and C is briefly summed up in Table 3.

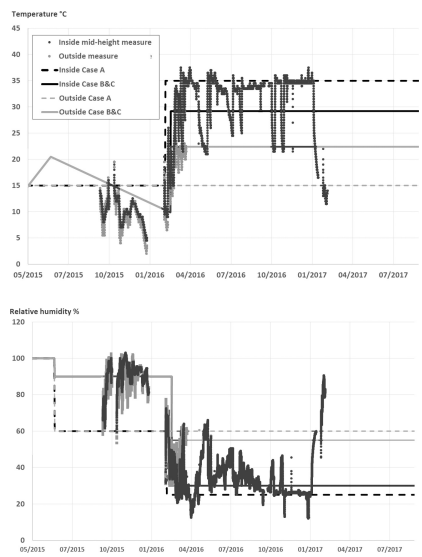

Figure 5. Temperature and Relative Humidity measured and boundary conditions applied for cases A, B and C. Some experimental data is missing because it could not be extensively validated.

Table 3. Differences between the 3 cases simulated.

Case	Temperature & RH	Drying test
A	ambient + no account for seasonal variations	24 hours aged
B	surface + account for seasonal variations	24 hours aged
C	surface + account for seasonal variations	90 days aged

3.5 *Phases of the mechanical computations*

The evolution of the thermal and hydric boundary conditions has been described earlier. The mechanical computations include various phases. First, the pre-stress cables are put in tension. Various groups are dealt with together, following the sequence used on the construction site. Then, while the drying, shrinkage and creep of the mock-up progress, every 13 months a pressure test is performed by pressurizing the inner face of the mock-up (concrete and metal parts). The pressure reaches 4.2 relative bars during these tests.

4 RESULTS AND DISCUSSION

It should be noted that the following results will not present some quantitative data in order to preserve the interest of the current benchmark concerning VeRCoRs ageing modelling: (https://fr.xing-events.com/EDF-vercors-project.html).

4.1 *Drying*

The results obtained in terms of computed saturation in the 3 simulations cases are compared to experimental values in Figure 6. This results shows that the adjustments made to improve the representativeness of the thermal and hydric BCs for simulations B and then C are not completely satisfying. For instance in the gusset zone, one can observe that if the last values in mid-2017 are closer to experimental results in the simulation C, this improvement comes at the cost of a loss of agreement in the first period of comparison.

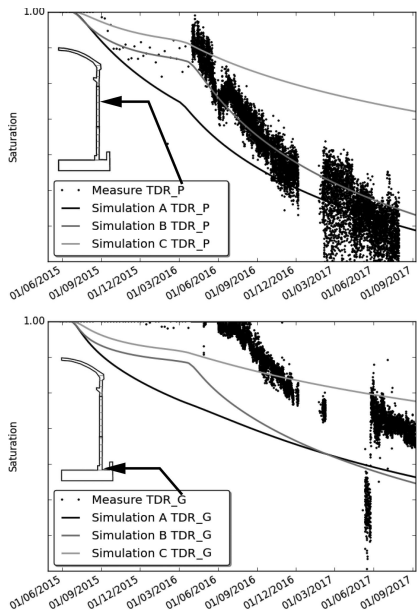

Figure 6. Comparison between measured saturation using TDR sensors and their equivalent in simulation cases A, B and C. Sensor TDR_P is placed in the cylindrical part far from any singularities and close to the inner surface. TDR_G is implemented at mid-thickness in the so-called "gusset", the larger section joining the basement raft and the cylindrical part.

4.2 *Delayed strains*

Figure 7 illustrates the comparison between the three simulations in terms of tangential strain in the same zone which was discussed before. This figure shows that the accordance is better for the last simulation (data-set C), but that the inadequate description of saturation provokes a discrepancy in the [january 15 – june 16] period. This is in complete accordance with the physical understanding of delayed strains and their close relationship with water content in the concrete structure (Courtois et al. 2017).

On the other hand the discrepancies between modelling and experience have to be discussed: one can observe in Figure 8 the same comparison only for simulation case C, but for tangential strain at the location of three similar sensors in the zone of the cylindrical part that is far from any singularities, including tendons deviations. This illustrates in

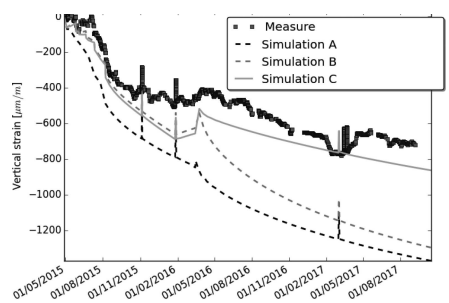

Figure 7. Comparaison between measured vertical strains and simulations at one point close to TDR_G in Figure 6.

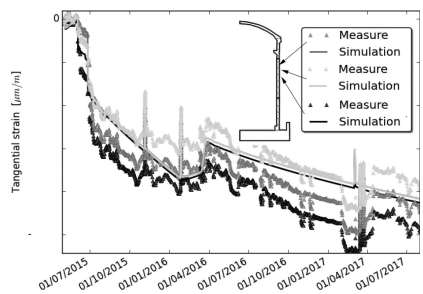

Figure 8. Comparison between measured tangential strain at three different altitudes far from any singularities for simulation C.

a zone that is considered homogeneous in terms of saturation and consecutive strains during the ageing, that the measurements can be different. The figure shows that the discrepancy appears during the post-tensioning phase, which is not captured by the simulation. Several reasons can be found but some experimental work is currently done at EDF CEIDRE TEGG to analyse the effect of vibrating wire location inside the reinforced concrete (i.e. the proximity of reinforcement) on the value it will capture during further loadings. On the other hand, simulations done at a smaller scale (representative patterns see (Charpin et al. 2017)) could also help to explain these effects in the future.

Figure 9 shows similar comparison close to the material hatch for three vertical strains. In this case the presence of the hatch—that can be seen as a "large elastic inclusion" in the cylindrical part of VeRCoRs submitted to creep—has an important effect that is quite well captured by the simulation, and it can be observed that simulation C provide a global improvement in the prediction of strains in this zone.

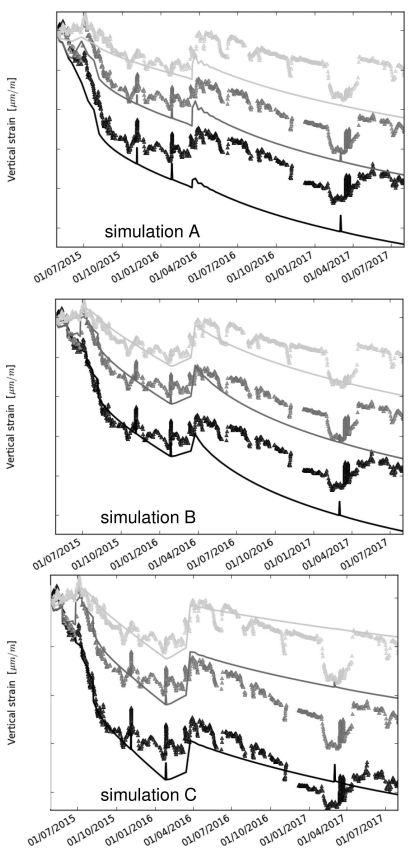

Figure 9. Comparison between measured vertical strain at three different point close to the material hatch for each simulation case.

On should notice that the results discussed above are based on a purely "predictive" approach, since no calibration of the constitutive laws has been done on the mock-up. The parameters have only been calibrated on laboratory tests on concrete samples produced on the construction site or in test laboratories.

One of the first difficulty to address with VeRCoRS for EDF with such a predictive approach was to find out an organization that allows to deal with hundreds of sensors and to compare their measurements with large scale simulations. It is believed that the digital twin solutions set-up for VeRCoRS is a convenient way to produce many local analyses in a fluid manner as presented above, and with a high degree of quality insurance and repeatability.

5 CONCLUSION AND PROSPECTS

The VeRCoRs mock-up is a large civil engineering experimental project that will help EDF to improve its knowledge of the effect of CCBs ageing on their subsequent leak-tightness. VeRCoRs is a 1/3 scale mock-up of a double-walled CCB that will undergo delayed strains approximately nine time faster than a real CCB. VeRCoRs is equipped with a large amount of sensors and will undergo ageing conditions comparable to a real containment (operating phases and ILRTs). A software ecosystem (the so-called digital twin) has been developed around the mock-up to address the issues of managing such an amount of data and to produce and update simulations associated to ageing studies. The first results are encouraging on predictive simulation although they emphasize the primary importance of dealing with multi-physics aspects in order to better capture the cross effects of temperature, relative humidity and pre-stress on delayed strains. The next step at EDF will be to understand the discrepancies between the predictive approach and the reality, and to reduce the gap by improving the model calibration (with a priority on thermal activation of creep), the boundary conditions (to account for the vertical temperature gradient in the mock-up for example), and the models themselves.

Data assimilation at the level of the structure (global approach) and sub-modelling (local approach) will also certainly help EDF to improve its understanding of the CCBs' ageing underlying phenomena in the near future.

REFERENCES

Azenha, M., L.F. Ramos, R. Aguilar, & J.L. Granja (2012). Continuous monitoring of concrete e-modulus since casting based on modal identification: A case study for in situ application. *Cement and Concrete Composites 34*(7), 881–890. *p. 3*.

Bažant, Z. & J. Chern (1985). Concrete creep at variable humidity: constitutive law and mechanism. *Materials and structures 18*(1), 1–20. *p. 6*.

Benboudjema, F. (2002). *Modélisation des déformations différées du béton sous sollicitations biaxiales. Application aux enceintes de confinement de bâtiments réacteurs des centrales nucléaires*. Ph. D. thesis, Université de Marne la Vallée. *p. 5.*

Bottoni, M. (2015). Relation of behavior BETON_ BURGER_FP for the creep of the concrete. Code_ Aster Documentation R7.01.35, EDF R&D. *p. 5.*

Charpin, L., J.-P. Mathieu, & T. Sow (2017). Stress concentrations induced by active and passive reinforcements in a concrete containment building. In *23ème Congrès Français de Mécanique*, Lille, France. *p. 3 and 9*.

Charpin, L., T. Sow, X. d'Estève de Pradel, F. Hamon, & J.-P. Mathieu (2017). Numerical simulation of 12 years long biaxial creep tests. Efficiency of assuming a constant Poisson's ratio. In *6th BIOT conference, Champs sur Marne, France. p. 6 and 7.*

Charpin, L., Y. Le Pape, E. Coustabeau, B. Masson, & J. Montalvo (2015). EDF study of 10-year concrete creep under unidirectional and biaxial loading: Evolution of the poisson coefficient under sealed and unsealed conditions. In *CONCREEP 10*, pp. 1381–1390. *p. 2 and 3.*

Corbin, M. & M. Garcia (2016). International benchmark vercors 2015 – overview, synthesis and lessons learned. Technical report, EDF SEPTEN. *p. 2 and 3.*

Courtois, A., F. Taillade, & D. Placko (2017). Pourquoi mesurer la teneur en eau des bétons ? *In 23ème Congrès Français de Mécanique, Lille*, France. *p. 3 and 8.*

Courtois, A., J.-M. Henault, A. Simon, Y.-L. Beck, & J. Salin (2011). La surveillance en exploitation des enceintes de confinement et des aéroréfrigérants à tirage naturel du parc nucléaire d'EDF. *Revue Générale Nucleaire 2011–2*, 49–59. *p. 2 and 3.*

Delsaute, B., J.-M. Torrenti, & S. Staquet (2016). Monitoring and modeling of the early age properties of the vercors concrete. *p. 3.*

Ezzedine El Dandachy, M., M. Briffaut, S. Dal Pont, & F. Dufour (2017). Effect of creep in traction on concrete permeability. In *23ème Congrès Français de Mécanique*, Lille, France. *p. 3.*

Foucault, A., S. Michel-Ponnelle, & E. Galenne (2012). A new creep model for NPP containment behavior prediction. In *Proc. SSCS, Aix-en-Provence, France. p. 2 and 5.*

Galenne, E., S. Michel-Ponnelle, J. Salin, G. Moreau, J. Sanahuja, & C. Toulemonde (2014). The aim of computational methods for managing concrete structures in nuclear power plants. In *Proc. of EURO-C 2014 conference,* pp. 51–60. CRC Press. *p. 2.*

Granger, L. (1995). *Comportement différé du béton dans les enceintes de centrales nucléaires: analyse et modélisation*. Ph. D. thesis, Laboratoire Central des Ponts et Chaussées, France. *p. 5 and 6.*

Haelewyn, J. (2010). Algorithm of linear thermics transitory. Code_Aster Documentation R5.02.01, EDF R&D. *p. 5*.

Henault, J.-M., M. Quiertant, S. Delepine-Lesoille, J. Salin, G. Moreau, F. Taillade, & K. Benzarti (2012). Quantitative strain measurement and crack detection in rc structures using a truly distributed fiber optic sensing system. *Construction and Building Materials 37*, 916–923. *p. 3.*

Herrmann, N., H.S. Müller, S. Michel-Ponnelle, B. Masson, & M. Herve (2018). The PACE-1450 experiment–investigations regarding crack and leakage behaviour of a pre-stressed concrete containment. In *High Tech Concrete: Where Technology and Engineering Meet*, pp. 1487–1495. Springer. *p. 2.*

Jason, L. & B. Masson (2014). Comparison between continuous and localized methods to evaluate the flow rate through containment concrete structures. *Nuclear Engineering and Design 277*, 146–153. *p. 2.*

Kallel, H., H. Carré, C. Laborderie, B. Masson, & N.C. Tran (2016). Effects of the hygrothermal conditions on the fracture energy of the concrete. In *Key Engineering Materials*, Volume 711, pp. 397–403. Trans Tech Publ. *p. 3.*

Lavergne, F., K. Sab, J. Sanahuja, M. Bornert, & C. Toulemonde (2015). Investigation of the effect of aggregates' morphology on concrete creep properties by numerical simulations. *Cement and Concrete Research 71*, 14–28. *p. 2.*

Martinot, F., G. Martin, J.-M. Henault, G. Moreau, E. Buchoud, Y.L. Beck, & A. Courtois (2015). Distributed fiber optic sensors in concrete of a nuclear containment. In *Proc. International Conference on Structural Health Monitoring of Intelligent Infrastructure. p. 3.*

Masson, B. (2015). La durée de fonctionnement des enceintes de confinement. *Revue Générale Nucleaire 2015–3*, 64–68. *p. 1.*

Mazars, J., F. Hamon, & S. Grange (2015). A new 3d damage model for concrete under monotonic, cyclic and dynamic loadings. *Materials and Structures 48*(11), 3779–3793. *p. 2.*

Mensi, R., P. Acker, & A. Attolou (1988). Séchage du béton: analyse et modélisation. *Materials and structures 21*(1), 3–12. *p. 5.*

Sanahuja, J., S. Huang, L. Dormieux, B. Bary, E. Lemarchand, & M. Hervé (2017). Porous materials undergoing timedependent phase transformations: Effective ageing viscoelasticity. In *Poromechanics VI, Champs sur Marne, France. p. 3.*

Sellier, A. & L. Buffo-Lacarrière (2009). Vers une modélisation simple et unifiée du fluage propre, du retrait et du fluage en dessiccation du béton. *European Journal of Environmental and Civil Engineering 13*(10), 1161–1182. *p. 5.*

Serdar, M., S. Staquet, I. Gabrijel, O. Cizer, S. Nanukuttan, V. Bokan-Bosiljkov, E. Rozière, A. Šajna, D. Schlicke, & M. Azenha (2017). COST Action TU1404: recent advances of the Extended Round Robin Test RRT+. In *Early Age Cracking and Serviceability in Cement- Based Materials and Structures,* Brussels, Belgium. *p. 2.*

Sémété, P., B. Février, Y. Le Pape, J. Delorme, J. Sanahuja, & A. Legrix (2017). Concrete desorption isotherms and permeability determination: effects of the sample geometry. *European Journal of Environmental and Civil Engineering 21*(1), 42–62. *p. 2.*

Toumi Ajimi, W., S. Chataigner, & L. Gaillet (2016). Influence of temperature on the behavior of steel reinforcement in prestressed concrete nuclear containement structures. In *TINCE 2016, 3rd Conference on Technological Innovations in Nuclear Civil Engineering*, Paris, France, pp. 10p. Société Française d'Energie Nucléaire. *p. 3*.

Computational Modelling of Concrete Structures – Meschke, Pichler & Rots (Eds)
© 2018 Taylor & Francis Group, London, ISBN 978-1-138-74117-1

Reassessment of the very long term basic creep of concrete

J.-M. Torrenti
University Paris-Est, Ifsttar, France

ABSTRACT: The prediction of delayed deformations of concrete at very long term is particularly important for prestressed structures such as nuclear power plant containments. The basic creep, which corresponds to the deformation of the concrete under load, without exchange of water with the environment, is a major component of the delayed strains. The analysis of several experimental results indicates that this component can be expressed in a logarithmic form. However, Brooks very long term tests (more than 30 years) seem to indicate a deviation from this trend and an acceleration of creep after 3 years of testing. This could be due to a non-linear behavior but these deviations can also be explained by experimental artefacts. In the case of Brooks tests, because the sample were stored in renewed water, calcium leaching could explain the evolution of the behavior on the very long term. Assuming a simple model for leaching and that the leached part of the sample does not sustain stress, it is possible to estimate the evolution of the stress within the core of the sample. Using the creep model fitted on the first part of the tests (before 1000 days) and in the framework of the superposition principle, it is possible to show that leaching indeed could explain the very long term behavior.

1 INTRODUCTION

Predicting very long-term delayed deformation in concrete is particularly important for prestressed structures such as nuclear power plants because it can affect their service life. Analysis of the behavior of this type of structure shows that delayed deformations are not asymptotic (Benboudjema and Torrenti 2015). The delayed deformation of these structures results from the relaxation of the steel and the delayed deformation of the concrete. Conventionally, the latter is expressed by means of four components: endogenous shrinkage, desiccation shrinkage, basic creep and desiccation creep.

The consensus with regard to basic creep seems to be that the compliance, which consists of both the elastic deformation and the basic creep deformation, can be expressed in the following way:

$$J(t_0,t-t_0)=\frac{1}{E(t_0)}+\frac{1}{\beta_1 C}log\left(1+\frac{t-t_0}{\beta_2\tau(t_0)}\right) \qquad (1)$$

where t_0 is the age of loading, E is the Young's modulus, C is a parameter which is independent of t_0, τ is a time depending on t_0, and β_1 and β_2 are adjusted parameters with default values equal to 1.

This relationship, which is similar in structure to that proposed for the fib Model Code 2010 (Muller et al., 2013), has been compared with many experimental results and provides an accurate representation of the behavior observed in most of the available tests (Le Roy, F. Le Maou and J.M. Torrenti, 2017), (Torrenti and Le Roy, 2017). However, in the very long term (after 1000 days), some experimental results seem to deviate from this relationship, exhibiting deformation that is greater than that predicted by Equation 1 (see Figures 1 and 2). The aim of this article is to analyze the possible causes of this deviation that result from the material itself: we assume that the system maintains a constant load and that the deformation measurement system is not responsible. In addition, in the case of basic creep, the possible effect of carbonation shrinkage is not considered.

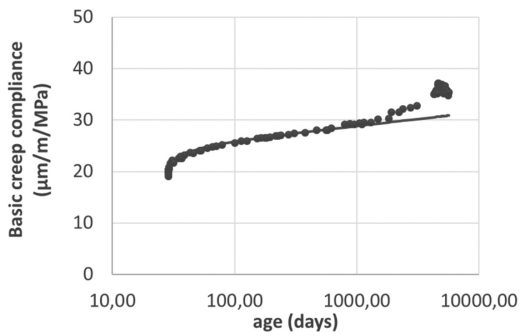

Figure 1. Basic creep: concrete B2 (W/C = 0.33) loaded after 28 days (Le Roy, F. Le Maou and J.M. Torrenti, 2017). Comparison between experimental results and modelling with equation 1 (solid lines).

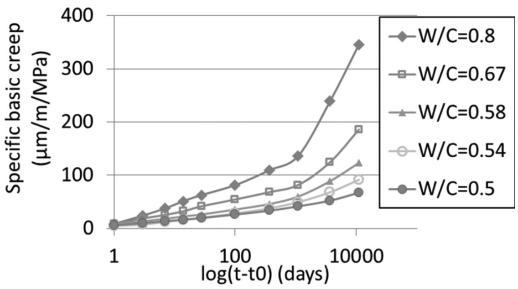

Figure 2. Specific basic creep: Brooks' tests, North Notts aggregates (Brooks, 2005). The test lasted for 30 years and reveals an acceleration of deformation with respect to the logarithm of time in the very long term, especially for the highest W/C ratios.

2 ANALYSIS OF THE POSSIBLE CAUSES

2.1 *An intrinsic cause?*

If a parasitic phenomenon is not involved (see the next paragraph), the acceleration in the basic creep may be due to an intrinsic phenomenon, for example a redistribution of CSH stresses to aggregates leading to nonlinearities (Šmilauer, Leps & Gregorova, 2013) or creep damage coupling linked to creep-induced microcracking (Rossi et al., 2012), (Torrenti et al., 2008), (Torrenti, 2017). For both approaches, it is possible to calibrate the parameters of the models in order to obtain this acceleration. However, this acceleration is not apparent in real structures: overall behavior seems to change with the logarithm of time (Bazant, Hubler & Yu, 2011), and if the current models in the codes cannot simulate this behavior it is because they predict bounded asymptotic behavior. It is therefore important to assess whether or not the observed behavior is an artefact.

2.2 *A defect in the basic creep test?*

When carrying out a basic creep test, two main approaches could be applied in order to prevent the concrete from drying: the samples are either covered with a sealing layer or kept in water. It should be noted that these two test conditions are not equivalent because for low water-to-cement ratios in particular—therefore for high strength and very high strength concretes—self-desiccation due to hydration reactions leads to internal moisture levels that are as low as 75% (Yssorche & Ollivier, 1999), which can limit hydration (Flatt, Scherer & Bullard, 2011). However, obviously, in the case of storage in water, the relative humidity remains at 100%. We will examine the phenomena that may affect long-term behavior in both cases.

3 ANALYSIS OF THE POSSIBLE ARTEFACTS

3.1 *Test with a sealing coating*

In this test, the samples are protected from desiccation by a surface coating. Several techniques are possible such as the application of a resin or self-adhesive aluminum sheets, or even a combination of both. However, maintaining tightness over a long period still poses serious difficulties (Attolou, Belloc & Torrenti, 1989). In the case of two layers of self-adhesive aluminum, (Toutlemonde & Le Maou, 1999) found that water loss accelerates over time and measured a loss of mass of approximately 0.4% after about 2 years.

Since creep is the result of the difference between total deformation and shrinkage, if shrinkage is measured at the same time as creep and the test pieces have the same protection for both tests, the subtraction eliminates any drying shrinkage. But very often the endogenous shrinkage test is stopped before the end of the creep test. This was the case for Le Roy's tests (Le Roy, F. Le Maou & J.M. Torrenti, 2017), where the endogenous shrinkage test was stopped after 1300 days while the creep tests were continued for more than 5000 days. Also, due to drying, the results of the basic creep test are affected by a proportion of the drying creep. The difference that can be seen in Figure 1 between a logarithmic relationship ($t-t_0$) and the measurements is of the order of 4 10^{-6}/MPa (for a period between 1000 days and 5000 days approximately) and this value is compatible with deformation due to drying shrinkage and desiccation creep.

3.2 *Test with storage of the samples under water*

In this type of test, the specimens are stored in water. The observed acceleration cannot therefore be due to drying. On the other hand, conservation in water can result in the progressive leaching of hydrates, beginning with portlandite and followed by C-S-H. Of course, this phenomenon is very slow and is not noticeable in a very short test. Similarly, if the water is not changed, it becomes saturated with calcium and leaching slows down greatly. Brooks' articles, unfortunately, do not mention if the water was changed. However, through personal contacts with Professor Forth (who works in the same laboratory as Brooks) we have established that the water in the basic creep tests was changed every 3 months or so. Leaching is therefore certain to have occurred. In this case, coupling with the creep exists (Torrenti et al., 2008) and since the radius of the Brooks test specimens was only 38 mm, it is likely that leaching had a major impact.

To estimate this effect, we have assumed that the leached zone no longer plays a role in the mechanical equilibrium of the cross-section. When the material leaches, the stress applied to the core material increases, which results in apparent nonlinearity of the creep and possibly, when the leached depth becomes very great, in nonlinearity due to coupling with damage (Torrenti et al., 2008). If the leached depth x_d is expressed by the following equation:

$$x_d = k\sqrt{t} \tag{2}$$

The stress applied to the core material changes as follows:

$$\sigma(t) = \sigma(t_0)\frac{\pi R^2}{\pi\left(R - k\sqrt{t}\right)^2} \tag{3}$$

where R is the radius of the sample and $\sigma(t_0)\pi R^2$ is the force applied to the sample, which is assumed to be constant. Using equation 1 to establish the creep and applying the principle of superposition to take account of the change in stress, the effect of leaching may be modelled:

$$\varepsilon(t,t_0) = \int_{t_0}^{t} J(\tau, t-\tau)\, d\sigma(\tau) \tag{4}$$

where $\varepsilon(t,t_0)$ is the strain corresponding to elastic and creep deformations and J is the compliance expressed in equation 1.

Kamali et al. (2008) have proposed an equation that expresses the parameter k in equation 2 as a function of the water to cement ratio W/C:

$$k = k_0 \ln\left(8.6\frac{W}{C}\right) \tag{5}$$

The parameter k_0 in this equation must be corrected to take account of the tortuosity effect of aggregates (Nguyen et al., 2006) and is adjusted to a value of 0.1 in line with the Brooks tests.

The simulation of the Brooks tests assumes that, based on Equation 1, the value of the basic creep parameters can be established on the initial part of the curves i.e. before 1000 days. Table 1 gives the basic creep parameters for the tests we have used. Beyond this time limit, leaching must be taken into account by recalculating the stress at each time step and applying the principle of superposition. Figure 3 shows that the leaching, with a set of parameters that is compatible with those found in the literature, explains the non-linearity of the basic creep in the very long term.

Table 1. Parameters of the basic creep for Brooks' tests.

W/C	β_1	β_2
0,8	0,025	1
0,67	0,037	1
0,58	0,055	1
0,54	0,070	1
0,5	0.080	1

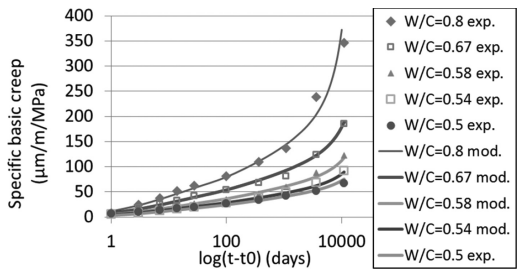

Figure 3. Comparison of Brooks' experimental results and creep modeling taking into account the leaching of concrete. $k_0 = 0.1$.

4 CONCLUSIONS

The basic creep of the concrete can be expressed as a logarithmic function of the time that has elapsed since the start of loading. Differences observed in the very long term, namely the acceleration of creep after 1000 days, can be explained by other physical phenomena related to the storage conditions: undesired drying in the case of preservation under a water-tight coating and leaching in the case of storage in water. In the latter case, a simple leaching model and the use of the superposition principle for creep have been applied to show that observed behavior can be reproduced with a plausible set of parameters.

REFERENCES

Attolou A., Belloc A., Torrenti J.M., "Méthodologie pour une nouvelle protection du béton vis à vis de la dessiccation", Bulletin de Liaison des LPC, n°164, Nov.–Dec. 89.

Bazant Z.P., Hubler M.H., Yu Q., «Excessive Creep Deflections: An Awakening», Concrete International, August 2011, p. 44–46.

Benboudjema F., Torrenti J.M., On the very long term delayed behaviour of biaxially prestressed structures: the case of the containments of nuclear power plants, Concreep10 conference, Vienna, 2015.

Brooks J.J. (2005) 30-Year creep and shrinkage of concrete. Mag. Concr. Res. 57(9):545–556.

Flatt R.J., Scherer G.W., Bullard J.W., Why alite stops hydrating below 80% relative humidity, Cement and Concrete Research 41 (2011) 987–992.

Kamali S., Moranville M., Leclerq S., Material and environmental parameter effects on the leaching of cement pastes: Experiments and modelling, Cement and concrete research, (2008) 38 (4), 575–585.

Le Roy R., Le Maou F., Torrenti J.M., Long term basic creep behavior of high performance concrete. Data and modelling, Materials and structures, (2017) 50:85, DOI 10.1617/s11527-016-0948-8.

Muller, H., Anders, I., Breiner, R., & Vogel, M. (2013). Concrete: Treatment of types and properties in fib Model Code 2010. Structural Concrete, 14, 320–334.

Nguyen V.H., Nedjar B., Colina H., Torrenti J.M., A separation of scales omogenization analysis for the modelling of calcium leaching in concrete, Comput. Methods Appl. Mech. Engrg. 195 (2006) 7196–7210.

Rossi P., Tailhan J.L., Le Maou F., Gaillet L., Martin E., Basic creep behavior of concretes investigation of the physical mechanisms by using acoustic emission, Cement and Concrete Research 42 (2012) 61–73.

Sellin J.P., Barthelémy J.F., Torrenti J.M., Bondonet G., Delayed deformations of segmental prestressed concrete bridges: the case of the Savines Bridge, Proceedings of the Intern. Conference on Ageing of Materials & Structures, Delft 26–28 May 2014.

Šmilauer V., Leps M. & Gregorova M., Updating B3 model for long-term basic creep, Life-Cycle and Sustainability of Civil Infrastructure Systems—Strauss, Frangopol & Bergmeister (Eds), 2013 Taylor & Francis Group.

Torrenti J.M., Nguyen V.H., Colina H., Le Maou F., Benboudjema F., Deleruyelle F., Coupling between leaching and creep of concrete, Cement and concrete research, 38 (2008) 816–821.

Torrenti J.M., Basic creep of concrete—Coupling between high stresses and elevated temperatures, European Journal of Environmental and Civil Engineering, 2017, DOI: 10.1080/19648189.2017.1280417.

Torrenti J-M, Le Roy R., Analysis of some basic creep tests on concrete and their implications for modeling. Structural Concrete. 2017; doi: 10.1002/suco.201600197.

Toutlemonde F., Le Maou F., Protection des éprouvettes de béton vis-à-vis de la dessiccation—Le point sur quelques techniques de laboratoires. Bulletin des laboratoires des Ponts et Chaussées, 1999, 203:105–119.

Yssorche M.P., Ollivier J.P., La microfissuration d'autodessiccation et la durabilité des BHP et BTHP, Materials and Structures, vol. 32, 1999, p. 14–21.

Computational Modelling of Concrete Structures – Meschke, Pichler & Rots (Eds)
© 2018 Taylor & Francis Group, London, ISBN 978-1-138-74117-1

Interaction between damage and time-dependent deformation of mortar in concrete: 3D FE parametric study at meso-scale

J. Ožbolt & S. Gambarelli
Institute of Construction Materials, University of Stuttgart, Stuttgart, Germany

ABSTRACT: Creep of concrete can be partly attributed to the time-dependent deformation of cement paste and partly to the interaction between load-induced damage of mortar (hardened cement paste) and its non-elastic deformations. The heterogeneity of concrete and related interaction between load-induced damage and non-elastic deformation of mortar can have significant influence on the long-term response of concrete. Some aspects of the problem are here investigated through 3D Finite Element (FE) analysis of a concrete cylinder at meso-scale. The concrete is treated as a bi-phase composite material, consisting of coarse aggregate and mortar matrix. The constitutive law for mortar is based on the microplane theory, while the aggregate is assumed to be linear elastic. For different levels of applied uniaxial compressive load the influence of basic creep and shrinkage of mortar is investigated. It is shown that with higher loading level the increase of time deformation of concrete becomes progressive. This is related to the interaction between the load-induced damage of mortar and its non-elastic deformations, especially shrinkage. This contribution to the creep of concrete can be higher than the contribution related to the creep of hardened cement paste.

1 INTRODUCTION

Research interest in time-dependent deformation of concrete, such as creep and shrinkage, has been largely increased over the years. This is due to the great number of concrete and RC structures that are sensitive to these effects in terms of structural damage and failure. Better understanding of concrete behavior under environmental conditions is important to guarantee its durability and to prevent a critical deterioration.

Creep is manifested as slow increase of deformation under sustained load while shrinkage is defined as the strain that occurs in absence of applied load (stress-independent deformation) and is related to drying and aging of hardened cement paste. Different theories for creep of hardened cement paste exist (Powers 1968, Feldman & Sereda 1968, Reutz 1968, Wittman 1970, Bažant et al. 1997), however, it seems that the main reason is the relative slip (micro-sliding) between Calcium-Silicate-Hydrate (C-S-H) sheets that is controlled by the amount and state of pore water (Tamtsia & Beaudoin 2000). Principally creep of cement paste can be divided in two parts, basic creep, which is measured at constant temperature and humidity, and drying creep, which is an additional creep associated with moisture content variation between C-S-H sheets. If the stress level is relatively low, then basic creep is approximately linear proportional to stress. However, at higher load level basic creep becomes non-linear with stress, which is a consequence of interaction between basic creep, shrinkage and damage of cement paste.

Due to inhomogeneity of concrete, creep of concrete becomes even more complex than the creep of hardened cement paste. Namely, similar to the interaction at micro structure of cement paste (e.g. basic creep, shrinkage and damage) in concrete there is a similar interaction between non-elastic deformation of cement paste (e.g. basic creep, shrinkage, temperature and humidity variation) and load-induced damage of mortar which can, in addition to the time-dependent deformation of cement paste, strongly effect time deformation of concrete. In the literature a number of studies can be found dealing with creep and shrinkage of concrete (Ross 1958, L´Hermite et al. 1965, Neville & Dilger 1970, Neville 1973, Bažant 1975, Bažant & Wittmann 1982, Bažant & Baweja 1995, Brooks 2005, Bažant & Li 2008a), where the influence of temperature is also considered. However, fewer studies (Fahmi et al. 1972, Santini-Bell & Sipple 2009, Burde 2010, Hedegaard et al. 2016) are focused on the long-term behavior of concrete under variable temperature and humidity, e.g. cyclic variation of thermal strains induced by changes in the environment temperature and humidity. This aspect, which is not investigated in the present work, is important, since many real structures are subjected to daily and seasonal temperature and humidity variations.

During the years, a gradual change of concrete properties is induced by the continuous hydration process of cement paste (aging), which never becomes complete. Several experimental tests have been performed in the past to identify the parameters governing the concrete behavior under environmental conditions. From the obtained results it is clear that time-dependent strains of concrete are influenced by many factors, which can be classified as intrinsic factors, fixed once and for all components when concrete is casted, and extensive factors that can vary after casting. The former are the properties of the aggregate, e.g. the strength, Young´s modulus and its volumetric fraction in concrete, the maximum aggregate size and shape. The extensive factors (also called state variables), such as load level, temperature, degree of hydration and pore water content, strongly influence time-dependent behavior of concrete (Bažant & Wittmann 1982). The influence of age at loading on creep has been experimentally investigated by many researchers (Hanson 1953, Ross 1958, L´Hermite et al. 1965, Neville 1973) and in all cases it was found that creep is lower if the age at loading is higher. As shown in (L´Hermite et al. 1965, Neville & Dilger 1970, Neville 1973) creep is accelerated if concrete is drying simultaneously with creep, and rapid heating, as well as rapid cooling also accelerates creep (Bažant 1975).

Another important aspect is the influence of high stress level on concrete long-term behavior. It is known that under stress exceeding about 40% of the uniaxial compressive short-time strength, the time-dependent strains of concrete become progressively non-linear with stress increase and this non-linearity is mainly caused by the gradual propagation of microcracks (Fahmi et al. 1972). The topic was first studied by Rüsch et al. (1968) who defined a "failure limit" and a "creep limit" for concrete under sustained loads. His experimental tests showed that for high stress level (≥ 80% of the short-term strength) the strong interaction between creep and cracking results in concrete failure after a finite time interval (tertiary creep, Neville, 1973). It is worth noticing that the specimens tested by Rüsch, cured for 7 days at 20°C, were exposed to drying at relative humidity of $h = 0.65$ before applying the load (at age of 56 days). This aspect greatly influences creep of concrete, which is higher than creep at constant environmental conditions (basic creep).

The combined effect of creep and damage of concrete under compressive loads has been investigated by many researchers (Ožbolt & Reinhardt 2001, Mazzotti & Savoia 2003, Ruiz et al. 2007, Zheng & Li 2010). In Ožbolt & Reinhardt (2001) the microplane model is coupled into a series with a linear creep model (generalized Maxwell chain model) to simulate creep-cracking interaction in concrete. Mazzotti & Savoia (2003) used strain-based isotropic damage model and a modified version of solidification theory to simulate damage and (non-linear) creep of concrete. In the recent study (Omar et al. 2009) the coupled effect of creep and damage has been experimentally studied on bending beams of various sizes. Moreover, the measurements on a number of structures, especially bridges (Bažant et al. 2011, 2012), show that the time-deformation continuously increase in time and do not converge to a certain limit.

The aim of the present study is to bring more light into the interaction between different processes related to the time-dependent deformation (creep) of concrete. Apart from the time-dependent deformation of hardened cement paste (basic creep and shrinkage), the question is how the load induced-damage and non-elastic deformations of mortar interact in concrete and how they affect the time-dependent deformation of concrete. Therefore, in the present study the time-dependent behavior of concrete is numerically investigated through 3D meso-scale finite element analysis of concrete cylinder for different levels of applied uniaxial compressive load. To filter out only the influence of the load induced-damage of mortar on time-dependent response of concrete, it is assumed that there is no interaction between basic creep and shrinkage of mortar (cement paste), i.e. only mechanical interaction between load induced-damage of mortar and non-elastic deformation of mortar is considered. The interaction is investigated for basic creep and shrinkage of mortar. Since the analysis is performed at the meso-scale the interaction should naturally come out from the analysis.

2 RANDOM AGGREGATE STRUCTURE IN CONCRETE

To randomly distribute the coarse aggregate inside the concrete cylinder (with ratio diameter/height = 100/200 mm) a simple generation procedure (implemented in Matlab R2013b) is used. The procedure is based on a minimum distance criterion, which prevents any intersection between spherical particles. Based on the information of a known concrete mix, the size distribution of the coarse aggregate is determined by using the Fuller curve and the following steps are performed (Gambarelli et al. 2016): (1) The centers of the aggregate particles are randomly generated avoiding any intersection between the particles; (2) Solid spheres (with a given diameter) are generated from the corresponding particle centers; (3) All the spheres are subtracted from the external solid to obtain the two distinct phases of the concrete specimen, coarse aggregates and mortar matrix. The generated meso-scale

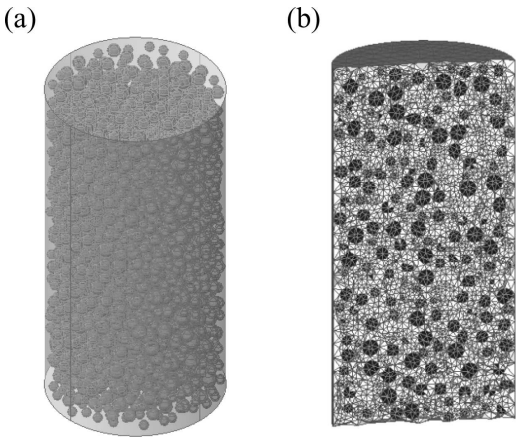

Figure 1. Meso-scale structure of concrete: (a) geometry and (b) FE model.

model is shown in Figure 1a, where 22% of the coarse aggregate (5 mm ≤ D ≤ 10 mm) is reproduced.

The geometry of the created meso-model is finally imported into the 3D FE code MASA (Ožbolt 1998) used for the simulations and meshed with solid four-node finite elements (Fig. 1b).

3 CONSTITUTIVE LAW AND FE DISCRETIZATION

In the meso-scale finite element analysis the constitutive law for mortar is based on the microplane model (Ožbolt et al. 2001), while the aggregate is considered as linear elastic, with Young's modulus of 90 GPa and Poisson's number 0.18. Perfect connection between mortar and aggregate is assumed. The macroscopic mechanical properties of mortar are reported in Table 1 and the corresponding constitutive law for uniaxial compression and tension is shown in Figure 2. Note that these properties were assumed to be constant in the transient finite element analysis, i.e. the increase of mechanical properties due to the further hydration of cement was not accounted for in the mechanical part of the model (microplane model), however, it was accounted in the computation of basic creep of mortar (Maxwell chain model).

Basic creep of mortar matrix is simulated based on the linear rate-type creep law (generalized Maxwell chain model) with eight age-dependent units (Ožbolt & Reinhardt 2001). It is coupled into a series with the microplane model (see Fig. 3).

The total strain tensor (ε_{tot}) is decomposed into elastic (ε_{el}) and damage (ε_{dam}) strains (microplane) and time-dependent non-elastic components (basic creep (ε_{bcr}) and shrinkage ((ε_{shr})):

Table 1. Mechanical properties of mortar at age of 28 days.

Secant modulus of elasticity, E [GPa]	23.0
Poisson' ratio, ν	0.18
Uniaxial compressive strength, f_c [Mpa]	32.0
Tensile strength, f_t [Mpa]	3.2
Fracture energy, G_F [J/m^2]	25.0

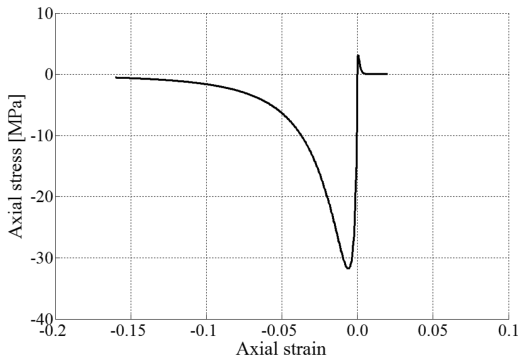

Figure 2. (a) Mechanical properties of mortar matrix and (b) Uniaxial compressive and tensile stress-strain response from microplane model.

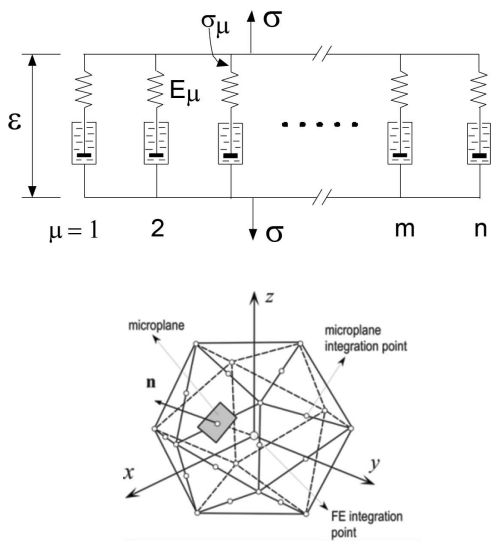

Figure 3. Serial coupling of microplane model (left) and generalized Maxwell chain model (right).

$$\varepsilon_{tot} = \varepsilon_{el} + \varepsilon_{dam} + \varepsilon_{bcr} + \varepsilon_{shr} \quad (1)$$

Basic creep of mortar matrix is simulated using the linear rate-type creep law (generalized Maxwell

chain model) with eight age-dependent units (Ožbolt & Reinhardt 2001). It is coupled into a series with the microplane model (see Fig. 3). The linear creep factor (ϕ_{lin}) for mortar is set equal to 4, which is relatively high compared with those typically assumed for concrete (Bažant & Wittman 1982). Note that basic creep of mortar is linear with stress.

Shrinkage of mortar matrix is modeled by an algebraic formula (Eq. 2a) that indicates the mean shrinkage of the cross section of a test specimen (Bažant et al. 1976):

$$\varepsilon_{sh}(\hat{t},t_0) = \varepsilon_{sh\infty} k_h S(\hat{t}) \tag{2a}$$

$$S(\hat{t}) = [\hat{t} / \tau_{sh} + \hat{t})]^{1/2} \tag{2b}$$

$$k_h = 1 - 0.95h^3 - 0.25h^{200} \tag{2c}$$

where t_0 is the curing time (in days), $\hat{t} = t - t_0$ is the duration of drying (in days), t is the current age of concrete, $\varepsilon_{sh\infty}$ is the ultimate shrinkage (humidity 0%), k_h is the humidity coefficient, h is the environmental relative humidity, S is a function of $\hat{t}$ giving the shape of the shrinkage curve and τ_{sh} is the shrinkage square half-time. In this study, the ultimate shrinkage of mortar ($\varepsilon_{sh\infty}$) is assumed equal to 0.002. This parameter has been calibrated through shrinkage analysis of the concrete cylinder, to reproduce a realistic shrinkage value for concrete that is approximately equal to 0.0008 (Bažant & Wittmann 1982). The environmental relative humidity (h) is set equal to zero (perfectly dry environment), with consequent unit value for the humidity coefficient (k_h). The shrinkage square half-time ($\tau_{sh} = 200$) has been calibrated in order to approach the final asymptotic value for shrinkage ($\varepsilon_{sh\infty}$) after 5 years.

The spatial 3D finite element discretization of the two concrete phases is shown in Figure 4. Fixed boundary conditions are imposed at the top and at the bottom of the specimen. The vertical load is applied at the top of the cylinder, either through displacement control (instantaneous loading) or through load control (sustained load). To assure results independent of the element size the regularization technique based on the simple crack band approach is used (Bažant & Oh 1983).

4 NUMERICAL RESULTS AND DISCUSSION

4.1 *Uniaxial compressive test*

As a first step a uniaxial compressive test has been performed on the concrete cylinder to evaluate the maximum compressive load and to check whether the model predicts a realistic material response.

The obtained results, in terms of axial stress-strain curve and concrete failure mode, are shown in Figure 5. It is possible to infer from Figure 5 that the meso-scale model is able to correctly reproduce

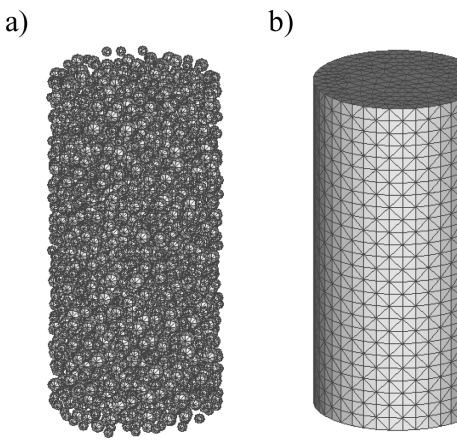

Figure 4. FE model: (a) coarse aggregate and (b) mortar matrix.

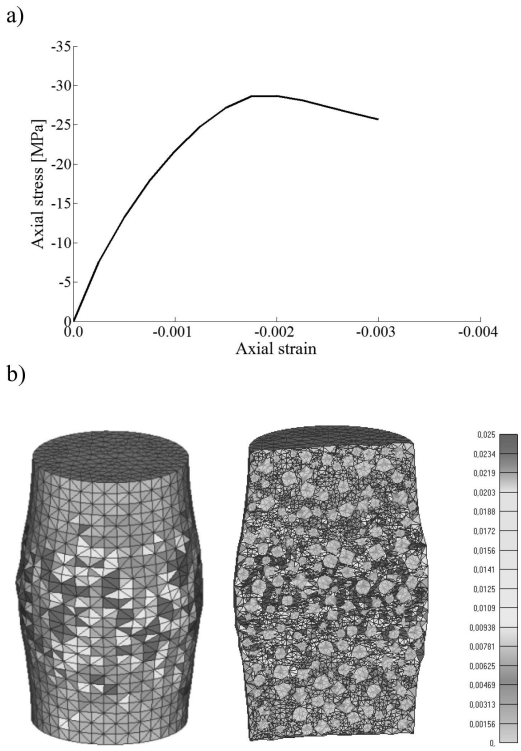

Figure 5. Uniaxial compressive test: (a) stress-strain curve and (b) concrete failure mode.

the typical compressive curve of normal strength concrete (f_c = 28 MPa, ε_c = 0.002, E_c = 27 GPa), in both pre and post-peak regions (Fig. 5a). Concrete failure mode is shown in Figure 5b in terms of maximum principal strains. The red zones correspond to a crack opening of 0.12 mm. As can be seen damage localizes in the central part of the specimen with several vertical and inclined cracks. To show the internal damage distribution the specimen is cut off at mid-section.

4.2 *Time-dependent analysis*

For different levels of the applied uniaxial compressive load (10%, 40%, 60% and 80% of the short-term strength), the influence of the following parameters has been investigated: (i) basic creep of mortar and (ii) shrinkage of mortar. Finally, to account for the interaction between these variables, the effect of their combination has been also studied.

4.2.1 *Basic creep of mortar*

The results obtained for basic creep, considering linear creep factor for mortar (φ_{lin}) equal to 4, are shown in Figure 6. The average axial strain, measured along the specimen height, is plotted against time (in semi log-scale). It can be seen that with increase of the applied uniaxial compressive load there is a progressive increase of non-elastic (creep) strains. However, the interaction between damage and basic creep is not very strong, even for relatively high load level (80% of the short-term strength). It seems that basic creep alone is not responsible for the markedly non-linear behavior of concrete observed in engineering practice.

In fact, as confirmed by several experimental studies (L´Hermite et al. 1965, Neville & Dilger 1970, Neville 1973), creep becomes more critical when concrete is drying simultaneously with creep (drying creep effect).

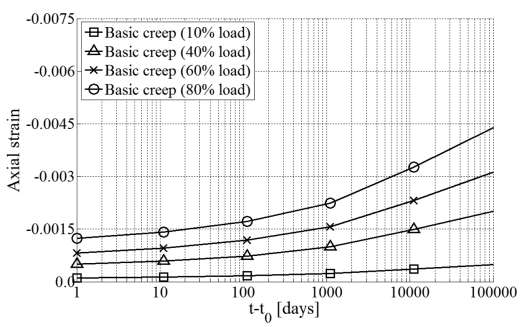

Figure 6. Axial average strain of concrete for: Load + Basic creep of mortar (φ_{lin} = 4).

4.2.2 *Shrinkage of mortar*

As a first step of the study, shrinkage analysis of the concrete specimen (without load) has been performed to clarify the influence of shrinkage of mortar (maximum assumed to be 0.002) on the time-dependent behavior of concrete. The predicted shrinkage curve of concrete is shown in Figure 7. The final shrinkage value obtained for concrete (0.0008) is evaluated considering a perfectly dry environment (h = 0), which is an extreme case, but still it is in agreement with typical values for concrete (Bažant & Wittmann 1982). It is worth noticing that the final shrinkage of concrete (0.0008) is relatively low with respect to the final value assumed for mortar (0.002). This result is justified by the presence of the coarse aggregate, which restraints the specimen volume changes, due to their rigidity.

The corresponding concrete damage due to shrinkage of mortar is shown in Figure 8 in terms of maximum principal strains. Maximum crack

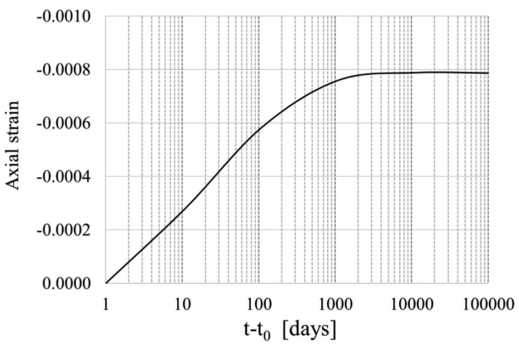

Figure 7. Shrinkage strain of concrete ($\varepsilon_{sh\infty}$ = 0.002).

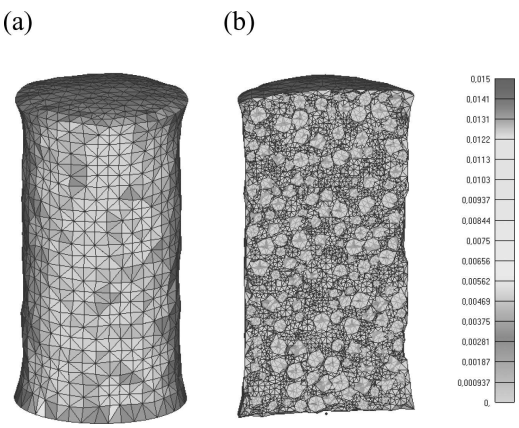

Figure 8. Damage of concrete due to shrinkage of mortar (27 years of drying).

width due to shrinkage at the concrete surface far from boundaries is approximately equal to 0.05 mm.

The results obtained from the shrinkage analysis at different load levels are shown in Figure 9.

It can be seen that with increasing the applied load there is significant increase of non-elastic strains of concrete, i.e. there is a strong interaction between shrinkage of mortar and damage induced by load. Even for the lowest load level, the total deformation after 27 years is more than double compared to the shrinkage of not loaded cylinder.

Damage of concrete for different load levels after 27 years is shown in Figure 10. It can be seen that already for the load level of 60% significant damage can be observed. This clearly indicates very strong interaction between the load-induced damage and shrinkage of mortar.

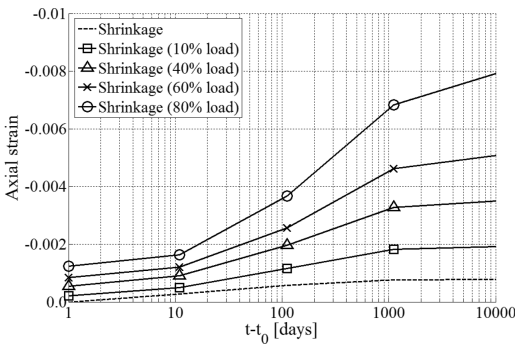

Figure 9. Axial average strain of concrete for: Load + Shrinkage of mortar ($\varepsilon_{shr\infty} = 0.002$).

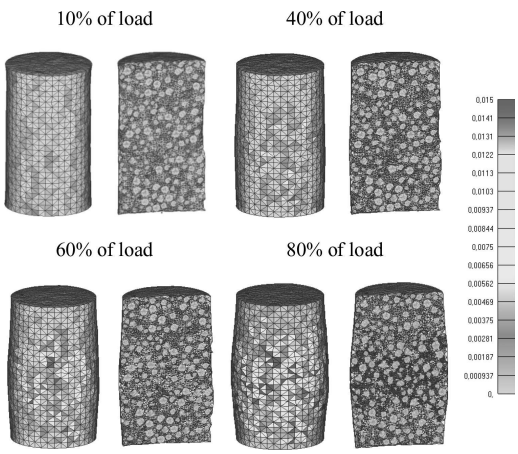

Figure 10. Damage of concrete for different load levels: Load + Shrinkage of mortar (after 27 years).

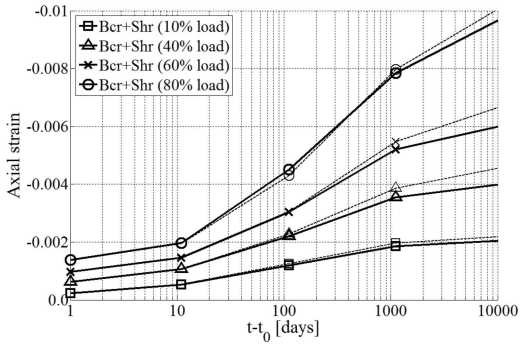

Figure 11. Axial average strain of concrete for: Load + Basic creep of mortar ($\phi_{\text{lin}} = 4$) + Shrinkage of mortar ($\varepsilon_{shr\infty} = 0.002$).

4.2.3 *Combination of creep and shrinkage*

The combined effect of basic creep and shrinkage of mortar has been numerically simulated to investigate the interaction between load-induced damage and basic creep and shrinkage of mortar.

Note that here no interaction between basic creep and shrinkage of mortar is accounted for. In the model, creep and shrinkage of mortar are activated after the application of load (28 days). The numerical results at different load levels are shown in Fig. 11. The curves obtained by simultaneous action of basic creep and shrinkage (continuous lines) are depicted together with those obtained by superimposing the separate contributions from Figs. 6 and 9 (dotted lines).

The interaction between the load-induced damage and time-dependent non-elastic strains of mortar (basic creep + shrinkage) leads to strong non-linear response of concrete. As can be seen, the total deformation after 27 years is slightly smaller than that obtained by simple superposition of deformations due to separate action of basic creep and shrinkage. This suggests that there is no strong interaction between basic creep and shrinkage on the total deformation of concrete.

5 DISCUSSION OF THE RESULTS

Figure 12 shows the numerically predicted relative effective creep factor of concrete ($\phi_{eff}/\phi_{eff,10\%}$) for all simulated cases as a function of load level, for load duration of 27 years. It is calculated as:

$$\phi_{eff,rel} = \phi_{eff} / \phi_{eff},10\% \tag{3a}$$

with:

$$\phi_{eff} = \frac{\varepsilon_{tot} - \varepsilon_{dam} - \varepsilon_{shr,inf}}{\varepsilon_{el} + \varepsilon_{shr,inf}} \tag{3b}$$

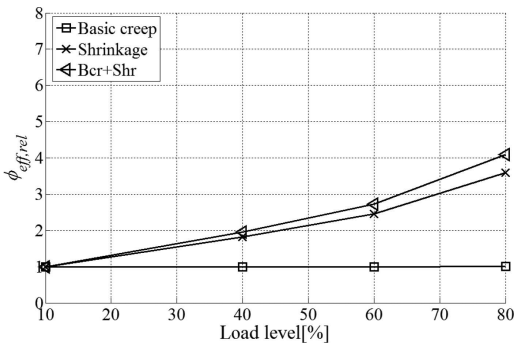

Figure 12. Predicted creep factor as a function of load level for all simulated cases.

in which $\phi_{eff,10\%}$ is effective creep factor for the lowest load level (10% of the short-term strength), ε_{tot} is total strain at the end of loading (27 years), ε_{el} and ε_{dam} are elastic and damage deformations of concrete cylinder at the application of load, respectively, and $\varepsilon_{sh,inf}$ is shrinkage deformation of load free concrete cylinder at $t = \infty$ (in the present study approximately 0.0008, see Fig. 7). The effective creep factor represents the increase of time deformation of concrete compared to the initial elastic deformation of concrete and shrinkage, if considered.

For basic creep ϕ_{eff} is approximately equal to the creep factor of mortar ($\phi_{\text{lin}} = 4$). As can be seen from Figure 12, $\phi_{eff,rel}$ for basic creep is almost independent of the stress level. This suggests that basic creep of concrete is linear proportional to the stress and that it is independent of the stress level. The relative effective creep factor for shrinkage is increasing from 1.0 (10% of load) to approximately 3.6 (80% of load). As already mentioned before, this indicates very strong interaction between the load-induced damage and shrinkage of mortar. Similar tendency can be observed for the simultaneous contribution of all non-elastic strain components.

Based on the presented numerical results, it is interesting to observe that there is no strong interaction between load-induced damage and non-elastic deformation of mortar if non-elastic deformations are coaxial with the stresses, e.g. basic creep. However, the interaction becomes very strong if non-elastic strains are not coaxial with the stresses, e.g. shrinkage. Note that coaxiality means that principal stresses coincide with principal non-elastic strains.

6 CONCLUSIONS

Creep of concrete consists of two contributions: (i) The contribution of creep of hardened cement paste and (ii) The contribution that is a consequence of the interaction between the load-induced damage of hardened cement paste (mortar) and its non-elastic strain deformations. In the present study some aspects related to the second contribution are addressed and investigated through the 3D FE study of the concrete cylinder at meso-scale. From the obtained numerical results, the following can be concluded: (1) Increase of the applied load level leads to the increase of non-elastic strains (creep) of concrete. This is related to the interaction between the load-induced damage of mortar and its non-elastic time-dependent deformations; (2) Results for the influence of basic creep of mortar show that its effect alone cannot reproduce the markedly non-linear creep of concrete at high stress level. However, the response becomes critical when basic creep of mortar is combined with shrinkage of mortar; (3) The results suggest that the mechanical interaction between the load-induce damage of mortar and its non-elastic time-dependent deformations strongly influence time-dependent response of concrete. This contribution to the creep of concrete can be larger than the contribution of time deformation of hardened cement paste. It can be attributed to the heterogeneity of concrete with the consequence that in practice the time-deformation of concrete (creep) constantly increases and do not converge to certain limit.

REFERENCES

Bažant, Z.P. & Baweja, S. 1995. Creep and shrinkage prediction model for analysis and design of concrete structures: Model B3, *Mater. Struct.*, 28(6): 357–367.

Bažant, Z.P. & Oh, B.H. 1983. Crack band theory for fracture of concret, *Materials and Structures*, RILEM 16(93): 155–177.

Bažant, Z.P. & Wittmann, F.H. 1982. *Creep and Shrinkage in Concrete Structures*, Chapter 7, Chicester, New York, Brisbane, Toronto, Singapore: John Wiley & Sons.

Bažant, Z.P. 1975. *Theory of Creep and Shrinkage in Concrete Structures: A Précis of Recent Developments*, in 'Mechanics Today', Vol. 2, pp. 1–93, Pergamon Press, Oxford: S. Nemat-Nasser.

Bažant, Z.P., Hauggrad, A.B. Baweja, S. & Ulm, F. 1997. Microprestress-solidification theory for concrete creep: I. Aging and drying effects, J *Eng. Mech.*, 123(11), 1188–1194.

Bažant, Z.P., Mija, H.H. & Yu, Q. 2011. Pervasiveness of Excessive Segmental Bridge Deflections: Wake-Up Call for Creep, *ACI Structural Journal*, 108(6).

Bažant, Z.P., Osman, E. & Thonguthai, W. 1976. Practical formulation of shrinkage and creep of concrete, *Materials and Structures* (RILEM, Paris), 9(54): 395–406.

Bažant, Z.P., Yu, Q. & Li, G-H. (2008a). Comprehensive database on concrete creep and shrinkage, *ACI Mater. J.*, 105(6): 635–639.

Bažant, Z.P., Yu, Q. & Li, G-H. 2012. Excessive Long-Time Deflections of Prestressed Box Girders. I: Record-Span Bridge in Palau and Other Paradigms, *Journal of Structural Engineering*, ASCE 138(6).

Bažant, Z.P., Yu, Q. & Li, G-H. 2012. Excessive Long-Time Deflections of Prestressed Box Girders. II: Numerical Analysis and Lessons Learned, *Journal of Structural Engineering*, ASCE 138(6).

Brooks, J.J. 2005. 30-year creep and shrinkage of concrete, *Mag. Concr. Res*. 57(9), 545–556.

BS EN 1992-1-2:2004. Design of concrete structures. General rules. Structural fire design.

Burdet, O.L. 2010. Thermal effects in the long-term monitoring of bridges, *34th International Symposium on bridge and structural engineering*, Venice.

Fahmi, H.M., Polivka, M., & Bresler, B. 1972. Effect of sustained and cyclic elevated temperature on creep and concrete, *Cement and Concrete Res. 2*: 591–606.

Feldman, R.F. & Sereda, P.J. 1968. A model for dydrated Portland cement paste as deduced from sorption-length change and mechanical properties, *Mater Struct*, 1(6): 509–520.

Gambarelli. S., Nisticò, N. & Ožbolt, J. 2016. Mesoscale modeling of concrete: microplane-based approach, *9th International Conference on Fracture Mechanics of Concrete and Concrete* Structures, FraMCoS-9, Berkeley, California.

Hanson, J.A. 1953. A 10-year study of creep properties of concrete, *concrete laboratory report No.Sp-38, U.S. Department of the Interior*, Bureau of reclamation, Denver, Colorado.

Hedegaard, B.D., French, C.E.W. & Shield, C.K. 2016. Effects of cyclic temperature on the time-dependent behavior of post-tensioned concrete bridges, *J. Struct. Eng*., 142(10).

L´Hermite, R., Mamillan, M. & Lefèvre, C. 1965. Nouveaux résultats de rcherches sur la deformation et la rupture du béton, *Annales de l´Institut technique du batiment et des travaux publics*, 18: 325–360.

Mazzotti, C. & Savoia, M. 2003. Non-linear creep damage model for concrete under uniaxial compression, *Journal of Engineering Mechanics* 129 (9).

Neville, A.M. & Dilger, W. 1970. *Creep of concrete: plain, reinforced, prestressed*, Amsterdam: North-Holland publishing company.

Neville, A.M. (1973). *Properties of concrete,* 2nd ed., New York: Wiley.

Omar, M., Loukili, A., Pijaudier-Cabot, G. & La Pepe, Y. 2009. Creep damage coupled effects: experimental investigation on bending beams with various sizes, *Journal of Materials in Civil Engineering*, American Society of Civil Engineering 21(2): 65–72.

Ožbolt, J. & Reinhardt, H.W. 2001. Creep-cracking of concrete-three dimensional finite element model, *Proc. Concreep 6,* Z.P. Bažant, F-J. Ulm, and F.H. Whitmann, eds., Cambridge, England, Elsevier, Amsterdam: 221–228.

Ožbolt, J. (1998). MASA – Macroscopic Space Analysis. *Internal Report*, Institute für Werkstoffe im Bauwesen, Universität Stuttgart, Germany.

Ožbolt, J., Li, Y. & Kožar, I. 2001. Microplane model for concrete with relaxed kinematic constraint, *International Journal of Solids and Structures* 38: 2683–2711.

Powers, T.C. 1968. *Mechanisms of shrinkage and reversible creep of hardened portland cement paste*, Proc. of Int. Conf. on the Structure of Concrete, Cement and Concrete Assoc., London, England, 319–344.

Reutz, W. 1968. *A hypothesis for the creep of hardened cement pasteand the influence of simultaneous shrinkage*, Proc. of Int. Conf. on the Structure of Concrete, Cement and Concrete Assoc., London, England, 365–387.

Ross, A.D. 1958. Creep of concrete under variable stress, *American Concrete Institute Journal* 54: 739–758.

Ruiz, M.F., Muttoni, A. & Gambarova, P.G. 2007. Relationship between non-linear creep and cracking of concrete under uniaxial compression, *Journal of advanced concrete technology* 5(3): 1–11.

Rüsch, H., et al. 1968. Festigkeit und Verformung von unbewehrtem Beton unter konstanter Dauerlast, *Deutscher AusschrlSs lilrStahibeton Heft 198*, W. Ernst, Berlin; see also Amer. Concrete Inst. J. 57 (1960): 1–28.

Santini-Bell, E.M. & Sipple, J.D. 2009. Accounting for the impact of Thermal Loads in Nondestructive Bridges Testing, *Proceedings form the TRB 2009 Annual Meeting*, *Transportation Research Board*. Washington D.C., January 11–15.

Tamtsia, B.T. & Beaudoin, J.J. 2000. *Basic creep of hardened cement paste A re-examination of the role of water*, Cement and Concrete research, 30, 1465–1475.

Wittman, F.H. 1970. *Influence of moister content on the creep of hardened cement*, Reol. Acta, 9(2), 282–287.

Zheng, D. & Li, W.W. 2010. Coupled damage and creep behavior of concrete under sustained loading, *9th International Conference on Fracture Mechanics of Concrete and Concrete Structures, FraMCoS*-7, Korea concrete Institute, Seoul.

Computational Modelling of Concrete Structures – Meschke, Pichler & Rots (Eds)
© 2018 Taylor & Francis Group, London, ISBN 978-1-138-74117-1

Prediction of air permeability in large RC structures using a stochastic FE THM modeling strategy

E.M. Bouhjiti
Grenoble INP Partnership Foundation—Chair PERENITI (EDF SEPTEN/DTG/CIH), Grenoble, France

J. Baroth
CNRS, University Grenoble Alpes, Grenoble INP, F-38000 Grenoble, France

F. Dufour
Chairholder of the Industrial Chair PERENITI (EDF SEPTEN/DTG/CIH), Grenoble, France

B. Masson
Electricité De France (EDF-SEPTEN), Lyon, France

ABSTRACT: In this contribution, a global random FE modeling strategy is proposed to account for the observed cracking state during the pre-operational phase of nuclear containment buildings whilst computing the long-term ageing effect on the concrete's air tightness evolution. The global behavior of concrete (drying and creep) is computed using a weakly coupled thermo-hydro-mechanical model whereas local behavior (cracking) is described according to a stochastic local strain-based damage model. From the obtained cracking and saturation profiles, concrete's air permeability is computed based on the known distinction of Darcy's and Poiseuille's flow modes. And the transition from one mode to the other is defined by a new strain-based matching law to account for a non-null residual permeability during the unloading phase. The global strategy is eventually applied to the VeRCoRs gusset and leads to an estimation of the lower and upper bounds of air leakage rates at the structural scale.

Keywords: RC structures; THM behavior; random cracking; air tightness

1 INTRODUCTION

The assessment of large concrete structures' durability and serviceability requires a recurrent and proper investigation of concrete's damage state and cracking patterns. This is evidently more crucial in the case of strategic buildings with a containment role such as dams or nuclear containment buildings where the safety issues are of the highest concern. Indeed, cracked or damaged zones in concrete are more permeable and represent preferential leakage paths jeopardizing the structural tightness. In such conditions, operators launch heavy maintenance and repair operations in order to meet with regulatory limits of the leakage rates and ensure a safe environment. Therefore, being able to predict the occurrence of random cracking patterns and their evolution in time is a key step for the real time evaluation of the structure's serviceability leading to anticipative and optimized repair actions.

Such objective can be reached using numerical clones if the following conditions are met: (1) Using physical and accurate modeling strategies that can reproduce both global and local behavior of concrete (2) Identifying properly concrete properties at the specimen scale and the applied loads at the structural scale (3) Enhancing the model's predictiveness by updating its response based on the observed and gathered in situ data.

Several models exist in the literature covering thermal, hydric and viscoelastic behavior of concrete for both early-age and long term phases (Corbin & Garcia 2015) when subjected to realistic operational loads. With that regard, the weakly coupled Thermo-Hydro-Mechanical (THM) modeling strategy (Figure 1) has been demonstrated to provide accurate results when it comes to concrete global behavior (thermal, drying and creep strains) within the Serviceability Limit State (Boucher 2016). As for the local aspect of damage and cracking, the modeling of size effects is still a subject of controversy amongst the scientific community especially when the scale of modeling tends towards the macroscopic one (in opposition to the

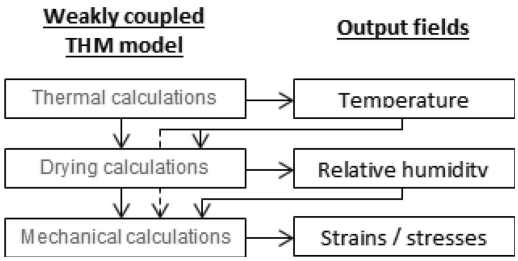

Figure 1. Global THM modeling strategy.

mesoscopic scale). In a previous study (Bouhjiti et al. 2017b), it has been shown that, for homogeneous and macroscopic modeling of concrete, the use of spatially correlated random fields coupled with probabilistic size effect laws (Bažant 1999 and Sellier & Millard 2014) induces a variation of the cracking patterns but requires a considerable number of realizations to obtain tail-distribution scenarios. Also, based on a 1st order sensitivity analysis, numerical results showed that the sensitivity of the obtained cracking patterns to the tensile strength (particularly its associated Weibull modulus) distribution is more pronounced compared to the rest of parameters and to the random field itself. This led to the suggestion of considering random fields to describe the Young's modulus spatial variation and facilitate localization under homogeneous tensile loads whereas the tensile strength is considered constant spatially but its mean value is associated with a Weibull probability density function. Consequently, as the tensile strength varies as an input so does the obtained cracking patterns. Since all uncertainties are associated with the tensile strength, such strategy would probably require some *a posteriori* adjustments to account for the uncertainties of the rest of the mechanical properties based on in-situ observations.

Eventually, once the hydric, damage and cracking states are defined throughout the structure's lifetime, concrete permeability can be numerically post-processed depending on the concrete's saturation and damage levels (Mozayan et al. 2013). Particularly, for low and diffuse damage values, the increase of concrete's permeability is governed by Darcy's flow mode whereas for high and localized damage, it is rather the Poiseuille's flow mode that is of interest. However, the evolution from one mode to the other seems to lack experimental investigation and raises the questions of (a) equivalence between damage and its associated crack opening and (b) the threshold from which concrete state changes from microcracked to macrocracked. Still, attempts have been made to match the two extreme modes (low diffuse and high localized damage states) using log-pondered damage-permeability laws (Pijaudier-Cabot et al. 2009 and El Dandachy 2016). Though, it is strain-dependent, the previous law cannot be used for unloaded concrete as its residual permeability tends to zero and needs, therefore, to be improved in order to be used for structures that can undergo loading and unloading cycles. As a consequence, two issues are addressed in this contribution: (1) the transition from Darcy's to Poiseuille's flow modes and (2) the effect of random cracking patterns on the leakage rate evaluation at the structural scale.

First, the global THM modeling strategy is recalled along with the main framework of size effects modeling. Second, the dependence of the concrete's air permeability on the hydric and mechanical results is detailed and discussed before introducing a new strain-based matching law to ensure a continuous and physical transition between Darcy's and Poiseuille's modes under both loading and unloading conditions. At last, the modeling strategy is applied to the first lift of a 1:3 scale Nuclear Containment Building's (NCB) gusset in an attempt to predict its leakage rate during pressurization tests. In this part, cracking patterns are directly issued from in situ observations whereas their evolution in time is blindly predicted. The effect of the cracking patterns randomness on the computed leakage rate is assessed using the classical Monte Carlo Method.

2 GLOBAL MODELING STRATEGY

2.1 *Global THM model*

The weakly coupled THM modeling strategy (Figure 1) consists of computing first the thermal behavior of concrete according to the classical heat equation (presented under its general form in Equation 1). Second, the thermal field is used as an input for concrete drying calculations (Equation 2&3).

$$\dot{\beta}(T) - \nabla \cdot (\lambda_c \nabla T) = Q \quad (1)$$

where $\dot{\beta}(T)$ = the variation of the enthalpy over time, λ_c = the thermal conductivity, T = the temperature and Q = the source term needed to account for the exothermic hydration reaction at early age (Ulm & Coussy 1998).

The thermo-activated diffusivity factor D_w associated with the chemically unbounded water particles in the concrete's porosity is expressed using a phenomenological approach (Mensi et al. 1988) and boundary conditions are expressed in terms of Relative Humidity RH (Granger 1995) related to the water content by the desorption curve in Equation 4 (Thierry et al. 2007). The correlation between the ambient RH and ambient temperature is defined according to the Magnus law.

$$\dot{C}_w = \nabla \cdot \left(D_w \nabla C_w \right) \tag{2}$$

$$D_w\left(C_w, T\right) = A_w e^{B_w C_w} \frac{T}{T_{ref}^{dr}} e^{-\frac{E_a^w}{R}\left(\frac{1}{T} - \frac{1}{T_{ref}^w}\right)} \tag{3}$$

where C_w = the water content, (A_w,B_w) = Diffusivity parameters to be adjusted in line with experimental results, E_a^w = the activation energy and T_{ref}^W = the reference temperature at which experimental identification is performed.

$$C_w = C_{w,0}\left(1 + \left(-a_w \ln\left(RH\right)\right)^{\frac{1}{1-b_w}}\right)^{-b_w} \tag{4}$$

where $C_{w,0}$ = the initial water content and (a_w,b_w) = fitting parameters depending on experimental results.

Finally, once the evolutions in time of the normalized hydration rate (at early-age), the RH and the temperature are known, their induced endogenous, thermal and drying shrinkages are computed (Equation 5–7) in addition to the viscoelastic concrete behavior (Basic creep ε_{BC} and drying creep ε_{DC} in Figure 2) according to the water migration theory (Foucault et al. 2012 and Benboudjema 2002).

$$\boldsymbol{\varepsilon_{ES}} = \alpha_{ES} < \alpha - \alpha_0 >_+ \mathbf{I_d} \tag{5}$$

$$\boldsymbol{\varepsilon_{TH}} = \alpha_{th}\left(T - T_0\right)\mathbf{I_d} \tag{6}$$

$$\boldsymbol{\varepsilon_{DS}} = \alpha_{DS}\left(C_w - C_{w,0}\right)\mathbf{I_d} \tag{7}$$

where α_{th} = the Coefficient of Thermal Expansion (CTE), α_{ES} = the coefficient of endogenous shrinkage, α = the normalized hydration rate (between 0 and 1), α_{DS} = the drying shrinkage coefficient and I_d = the identity tensor.

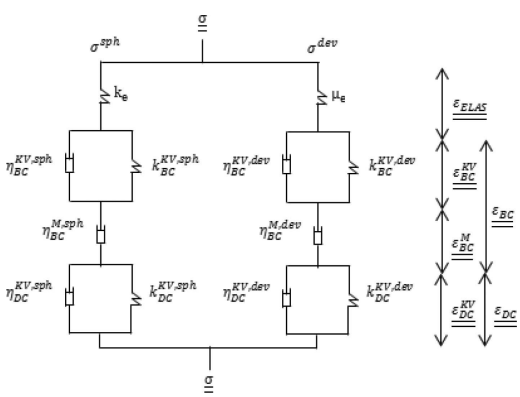

Figure 2. Burger rheological model associated with concrete basic and drying creep (distinguishing the deviatoric Xdev and spherical Xsph parts of a tensor X).

2.2 *Regularized strain-based local damage model*

Given our interest in concrete local behavior at the structural scale, local damage models seem less time consuming compared to non-local ones. In this work, a strain-based isotropic unilateral damage model is used (Mazars et al. 2015). The unilateral effect is essential in the case of structures that can undergo loading and unloading cycles so as to still be able to sustain loading under compressive loads even though tensile damage has been developed. Practically, the μ-Mazars damage model distinguishes two damage variables one for tensile and the other for compressive induced strains. The activation of each damage variable is directly related to the stress state in concrete. Being based on the evolution of a scalar "equivalent strain", the model's isotropy leads however to equal loss of stiffness (Equation 8) in all the principle directions which is critical in the case of diffuse damage and is less problematic when damage localizes along a defined path. In this last case, the orthotropic behavior is obtained at the structural scale even if the model is isotropic at the elementary level.

$$\mathbf{C} = \left(1 - d\right)\mathbf{C_0} \tag{8}$$

where d = the damage variable, $\mathbf{C}$ = the effective stiffness tensor and $\mathbf{C_0}$ = the initial stiffness tensor when d = 0.

To account for the contribution of creep under tensile stresses, the so-called equivalent strain $\varepsilon_{ea,t}$ is computed using Equation 9 where a portion of creep strain ε_{BC} is considered (Torrenti et al. 2008).

$$\varepsilon_{eq,t} = \left\| \boldsymbol{\varepsilon_e} + \beta_{coupl}\, \boldsymbol{\varepsilon_{BC}} \right\|_t \tag{9}$$

Another issue related to local damage models is their mesh-dependency if not properly regularized. Indeed, for every Gauss point, the implemented tensile behavior law (σ,ε) (the same thing can be said about compressive loads) needs to be representative of concrete damage regardless of the considered spatial discretization. Accordingly, the Hillerborg energy-based regularization (Hillerborg 1988) is performed to ensure the constancy of both the dissipated fracture energy G_F and the tensile strength f_t independently from the used spatial discretization. In the case of the exponential softening law used in the μ-Mazars damage model, the Hillerborg criteria lead to the system of equation in Equation 10. One can notice that for refined mesh sizes, the implemented law requires a damage threshold $\varepsilon_{d0} \leq f_t / E$

to meet the energetic criterion. This induces a hardening behavior until the tensile strength is reached (from a numerical point of view) and also a premature initiation of damage compared to the case where ε_{d0} is set to f_t/E. Moreover, the damage law cannot be used for macro-elements of which the size exceeds $2G_F E / f_t^2$. It is worth noting that when a local model is used the spatial discretization needs to be as close as possible to the dimension of the considered Fracture Process Zone (FPZ) for the hypothesis "each element can only contain one and only one crack" to be verified. Otherwise, a refined mesh would lead to an overestimation of the maximum cracks' number and a larger mesh would lead to its underestimation.

$$B_t = \frac{\varepsilon_{d0} + \sqrt{\frac{4G_F}{E\,h} - \varepsilon_{d0}^2}}{2\left(\frac{G_F}{E\,h} - \frac{\varepsilon_{d0}^2}{2}\right)}$$

$$\varepsilon_{d0} = \begin{cases} \dfrac{\ln\left(\dfrac{f_t}{E}B_t\right)+1}{B_t} \le \dfrac{f_t}{E}; h_{c,min} < h \le \dfrac{2}{5}\dfrac{G_F E}{f_t^2} \\ \dfrac{f_t}{E} \qquad\qquad ; \dfrac{2}{5}\dfrac{G_F E}{f_t^2} \le h \le 2\dfrac{G_F E}{f_t^2} \end{cases} \tag{10}$$

where (ε_{d0}, B_t) = two damage model parameters defining the post-peak softening law, h = the equivalent mesh size, E = the Young's modulus.

Finally, an additional post-processing step is required to define "equivalent" crack openings from the developed strains. The term equivalent is herein emphasized to underline the correspondence between a real crack in a discontinuous domain and its equivalent one in a continuous media. The formula presented in (Mattalah et al. 2010) is generalized in Equation 11 to a 3D configuration and accounts for creep contribution to crack openings as well.

$$u_{ck} = h * \left\| \varepsilon_e - \frac{(1+\nu)\sigma - \nu\, tr(\sigma)\underline{\underline{I}}}{E} \right\| + \left\| \beta_{coupl}\, \varepsilon_{BC} \right\| \tag{11}$$

where ν = the Poisson ration, $\mathbf{I}$ = the identity tensor and $\|X\| = \max(X_I, X_{II}, X_{III}, 0)$ with X_I, X_{II}, X_{III} are the Eigen values of a given tensor X.

2.3 *Modeling of size effects*

A two-step process is herein defined to deal with concrete's statistical and energetic size effects (Bouhjiti et al. 2017b). The first consists of defining the tensile strength as a function of the loaded volume and the second uses random fields to describe the spatial distribution of the mechanical properties:

Step 1: According to the Weibull theory, the tensile strength of concrete is related to the considered volume as shown in Equation 12 (Bažant 1999).

$$\frac{f_t\left(V_{eff}\right)}{f_{t,ref}} = \left(\frac{D_{eff}}{D_{ref}}\right)^{-\frac{n}{m}} \tag{12}$$

where m = the Weibull modulus directly related to the coefficient of variation associated with the tensile strength $cv_{f_t} = \sigma_{f_t}/\mu_{f_t}$, $f_{t,r,e,f}$ = the tensile strength measured on a given reference dimension D_{ref}, D_{eff} = the effective structural dimension under tensile loads and n = a dimensional factor (n = 1 for 1D,2 for 2D or 3 for 3D).

Hereafter, the 3D configuration is considered (but similar developments can be derived for the 1D and 2D cases). Generally speaking, the effective volume writes:

$$V_{eff}\left(\mathbf{x}_0\right) = \int_\Omega \psi\left(\left|\mathbf{x} - \mathbf{x}_0\right|, l_c, \left\|\sigma_+\left(\mathbf{x}\right)\right\|\right) d\Omega \tag{13}$$

where ψ is a weight function defining the zone of influence on a given point x_0 depending on an internal length l_c and the surrounding tensile stresses σ_+.

In the case of local damage model, however, it is possible to simplify the previous equation under generalized and homogeneous to quasi-homogeneous loads into Equation 14 which is only descriptive of the distribution of defaults and voids in the volume and its effect on the tensile strength reduction (stress distribution effects overlooked).

$$V_{eff}\left(\mathbf{x}_0\right) = \int_\Omega \psi\left(\left|\mathbf{x} - \mathbf{x}_0\right|, l_c\right) d\Omega \tag{14}$$

with $\psi = \exp\left(0.5\left|x - x_0\right|^2 l_c^{-2}\right)$ chosen arbitrarily as a Gaussian function (Sellier & Millard 2014).

Step 2: The heterogeneousness of concrete and its effect on the spatial scattering of the mechanical properties is modeled by spatially correlated random fields. They can be associated with either the Young's modulus and/or the tensile strength. The two however do not seem to follow the same probabilistic distribution as the Young's modulus follows rather a lognormal law (de Larrard et al. 2010) and the tensile strength a Weibull distribution type (Rossi & Wu 1992). Moreover, they are correlated as expressed in most of the regulatory design codes. In this study, the spatial variability is associated with the Young's modulus and the

tensile strength is considered constant (spatially). This choice is mainly motivated by the simplicity of the spatial correlation of normal and lognormal distributions using the Karhunen-Loève decomposition (Ghanem & Spanos 1991) compared to other non-normal-like distributions for which a normalization transformation is required. The lognormal random field, descriptive of the Young's modulus spatial variability, is firstly generated without considering the spatial correlation. Then, the spatial correlation is computed to take into account the effect of neighboring areas on the zone of interest following the principle that two close areas have more similarities than two distant ones. The autocorrelation function ρ_{ac} (Equation 15) is herein considered arbitrarily Gaussian as well (Bouhjiti et al. 2017b). Other choices might be better suiting depending on the performed (variogram statistical function based) experimental investigation to identify the spatial distribution properties (Baroth et al. 2011).

$$\begin{aligned} C(\boldsymbol{x},\boldsymbol{x}_0) &= \sigma_E^2\, \rho_{ac}(\boldsymbol{x},\boldsymbol{x}_0,l_{ac}) \\ \rho_{ac}(\boldsymbol{x},\boldsymbol{x}_0,l_{ac}) &= \exp\left(-l_{ac}^{-2}\left|\boldsymbol{x}-\boldsymbol{x}_0\right|^2\right) \end{aligned} \tag{15}$$

where l_{ac} = the autocorrelation length, C = the covariance function and σ_E^2 = the variance associated with the Young's modulus variable.

By randomizing the Young's modulus distribution, one can notice that the implemented behavior law becomes random as well and so does the crack initiation time and position (Bouhjiti et al. 2017a&b). By considering additionally an associated distribution with the tensile strength (that is spatially constant), one can obtain a distribution of the cracking patterns by performing several simulations with various tensile strength values.

3 PERMEABILITY OF CONCRETE

3.1 *Air leakage flow modes*

As mentioned in the introductory part, there are two modes of permeability which have been extensively studied:

- Low and diffuse damaged medium: Several models are available based on experimental results fitting (Choinska 2007 and Picandet et al. 2009). They relate directly the damage variable d (d < 15%) to the apparent intrinsic permeability denoted k_D (D in k_D stands for Darcy's mode). Hereafter, the expression (Equation 16) suggested by (Choinska 2007) is retained so as not to overestimate the permeability of concrete as the damage variable increases.

$$k_D = k_0\left(1+\sum_{n=1}^{3}\frac{(\alpha d)^{n\beta}}{n!}\right) \tag{16}$$

where (α, β) = fitting parameters and k_0 = the intrinsic permeability of (dry) concrete.

- High and localized damage: The Poiseuille's law (Equation 17) is usually used to describe permeability through a macrocrack (Rastiello 2016 and El Dandachy 2016).

$$k_P = \xi\frac{u_{ck}^2}{12} \tag{17}$$

where $\xi \leq 1$ is a factor accounting for the roughness and shape effects of the through crack domain (Equation 18). According to (Rastiello 2016) the factor ξ writes:

$$\xi = (\alpha_w u_{ck})\beta_w \tag{18}$$

with (α_w, β_w) = fitting parameters and u_{ck} the crack opening (Equation 11).

From a numerical point of view however, a macrocracked finite element domain sized h contains a macrocrack of an opening u_{ck} and also a microdamaged area around this given crack. The permeability through the crack only then writes:

$$k_F = k_P\varepsilon_{ck} = k_P\frac{u_{ck}}{h} \tag{19}$$

3.2 *New strain-based matching law*

Permeability matching laws intend to describe the evolution of the permeability from a microdamaged state which is only valid for low and diffuse damage values (d < 15%) to a macrocracked state gouverned by Poiseuille's law. As experimental investigation of this intermediate domain remains lacked, several matching strategies have been proposed based on simple mathematical extrapolation between Darcy's and Poiseuille's modes. Herein, the one suggested in (Pijaudier-Cabot et al. 2009 and El Dandachy 2016) is retained for comparison purposes (Equation 20). This law has the advantage of ensuring a smooth transition between the two modes without overestimating the permeability at low damage values in comparison with linear laws (Choinska 2007).

$$k = k_D^{1-d}k_F^d \tag{20}$$

Nevertheless, it has two main drawbacks (Figure 3): the first is that it is not strictly increas-

ing with the damage variable (especially when roughness effects are considered in Equation 18) and, second, for a closed crack (d = 1 and $u_{ck} = 0^+$) it gives a residual permeability equal to zero ($k = k_F = 0^+$).

To ensure the continuous increase of permeability with damage, the permeability matching can be performed between Darcy's flow and the sum of Darcy's and Poiseuille's flow as shown in Equation 21.

$$k = \left(k_D + k_F\right)^d k_D^{1-d} \tag{21}$$

For a different mathematical law, a new fitting of the experimental parameters is required. For example, the pair values (α, β) identified in (Choinska 2007) change from (11.3, 1.64) to (11.3, 0.82) in order to match the experimental data for d < 15%. The suggested matching law is also more accurate for the permeability of an unloaded element (whether the unilateral effect is accounted for or not): the residual permeability for a close crack ($u_{ck} = 0^+$) is equal to k_D(d = 1) in Equation 16. This result is qualitatively in line with experimental results since cracks' closure is never perfect once developed and the resulting permeability cannot be associated with a Poiseuille's flow in the absence of a clear macrocrack path.

3.3 *Air leakage descriptive equation*

The mass conservation equation in the case of a compressible fluid writes:

$$\frac{\partial P}{\partial t} - div\left(\frac{k}{\mu} Pgrad\left(P\right)\right) = 0 \tag{22}$$

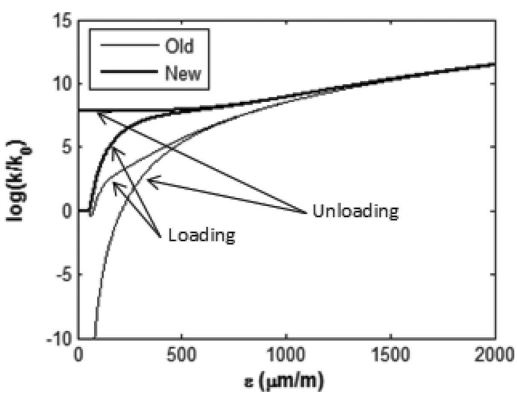

Figure 3. New (Equation 21) vs. old (Equation 20) strain-based permeability matching laws with h = 6 cm, f_t = 3 MPa, E = 36 GPa, G_F = 77 N/m and $k_o = 10^{-17}$ m².

where P = the fluid's pressure, k = the considered permeability and μ = the fluid's dynamic viscosity.

The permeability k is described using Equation 21 where k_D is generalized to the case of unsaturated concrete (Verdier 2001) and accounting for the Klinkerberg effect (Klinkenberg 1941):

$$k_D\left(S_r\right) = k_D\left(1 + \frac{\beta_K}{P}\right)\sqrt{1 - S_r}\left(1 - S_r^{\frac{1}{b}}\right)^{\frac{1}{2b}} \tag{23}$$

where S_r = the saturation rate, β_k = the Klinkenberg coefficient and b = fitting parameter. It is worth noting that for a macrocracked element the hypothesis of a dry medium is considered and maintained even after crack's closure.

4 APPLICATION TO NCB'S GUSSET

4.1 *Overview*

VeRCoRs is a 1:3 scale mock-up of double walled NCBs (Corbin & Garcia 2015 and VeRCoRs Project 2018). The inner wall is made out of reinforced and prestressed concrete (Figure 4) and ensures most of the static containment role. In this article, only the behavior of the first lift of the containment wall (the gusset in Figure 5) is of interest. During the early age phase, tensile stresses develop in the gusset volume because of (a) the cooling of concrete after hydration ends, (b) the strain gradient in the concrete thickness due to endogenous and thermal shrinkages and (c) the restrained strains due to the presence of a lower massive already erect base slab. Eventually, the risk of cracking in this area of the NCB is higher and requires an in-depth analysis to study its contribution to the global leakage rate under pressurization loads.

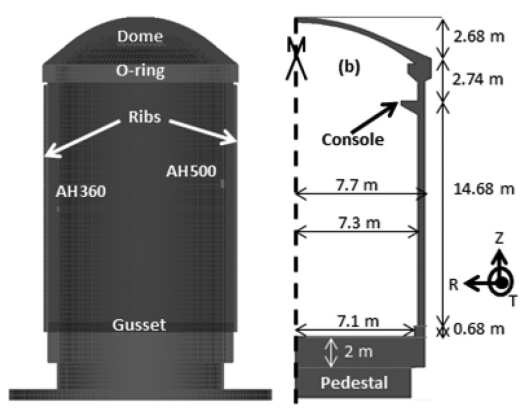

Figure 4. 3D and 2D-AXIS view of the VeRCoRs mock-up.

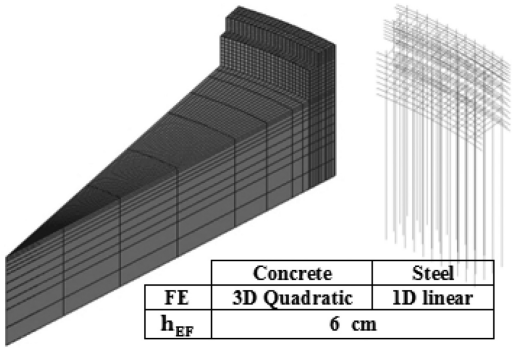

Figure 5. 3D view of the gusset's model (15° revolution angle).

The numerical model accounts for the presence of reinforcement bars, pre stressing cables and stirrups using elastic 1D elements whereas the size of the finite elements is defined so as to be equal to the size of the theoretical FPZ (≈3*maximum aggregates' size). Calculations are performed at the scale of the RSV of which the angular revolution is defined so as to fully cover the domain of variation associated with the Young's modulus property.

The applied boundary conditions are the following:

– Thermal: the applied temperature is the one directly measured on site (VeRCoRs Project 2018) for the past period of VeRCoRs' lifetime and is considered on the intrados side equal to 35°C during the forthcoming operational phase (predictive analysis). On the extrados side, temperature is supposed less by 15°C. During the programmed pressurization tests, dry air is purposely injected inside the NCB at 20°C.
– Hydric: The RH is defined from the temperature profiles according to the Magnus law using a mixing ratio of 6.31 g/kg.
– Mechanical: Throughout the analysis, axisymmetric boundaries are applied to the lateral edges. At early age, the upper surface of the gusset is supposed free to move and the formwork effect is overlooked. As the second lift is casted, the upper surface is supposed to have uniform vertical displacement which prevents also localization of damage around the anchors as cables are pre stressed. The values of tension in cables are defined by inverse analysis from in situ strain observations. They show a considerable variation along the tangential direction and a non-negligible gradient along the vertical one which suggests a dominance of the restrained effects due to the presence of the base slab compared to instantaneous prestressing losses along the cables. However, it can be assumed that for the considered RSV tangential loads are constant given the local notion of an RSV compared to the whole gusset. Finally, during the pressurization tests, radial, vertical and tangential tensile stresses are applied as if the containment wall were a closed hollow cylinder (see radial pressure in Figure 6).

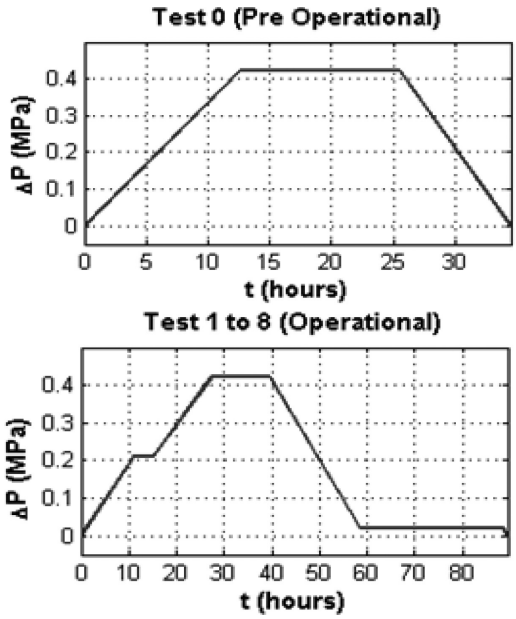

Figure 6. VeRCoRs dry air pressurization tests (expressed in terms of relative pressure).

As for the computational time, and for a full THM-L modeling (Thermo-Hydro-Mechanical with a Leakage estimation), one simulation lasts 3 days using a 14-core node with Code_Aster and Mfront numerical solvers.

4.2 *Model's inputs and random distributions*

The initial cracking patterns before the operational phase are directly issued from in situ observations 12 days after casting. They are considered as an input for the operational phase simulation. In Figure 7, one can see that the observed cracking patterns differ between the intrados and extrados sides and cannot show whether a crack is developed throughout the gusset or not. Given that the number of cracks is not the same for both sides, leakage paths remain difficult to assess visually especially in the presence of in-depth defects such as stirrups, rebars and prestressing cables which can be preferential paths as well.

However, from a numerical point of view the obtained early age cracks remain vertical (Bouhjiti

et al. 2017a&b) given the tangential nature of the restrained shrinkages. For that reason, the considered initial cracks are supposed vertical in the model. As shown by the leakage map after the first pressurization test (Figure 7), the leaking defects are eventually different than the ones identified at 12 days which underlines the limitation of visual inspection for small crack openings (less than 100 μm). Their number per RSV differs according to scenarios depicted in Figure 8 ranging from 0 to 3 cracks. Moreover, in situ observations show the existence of porosity lines along concrete joints (VeRCoRs Project 2018). Their existence can be associated with a probability density function as well (Figure 9) defining the amount of the concrete joint that has a higher porosity compared to the rest of the volume.

Eventually, the RSV finite elements can either be:

- Sound: the evolution of concrete permeability is due to drying only (Equation 23 with d = 0, $k_0 = 3.5\ 10^{-17}$ m^2 and $\beta_k = 0.15$ MPa).

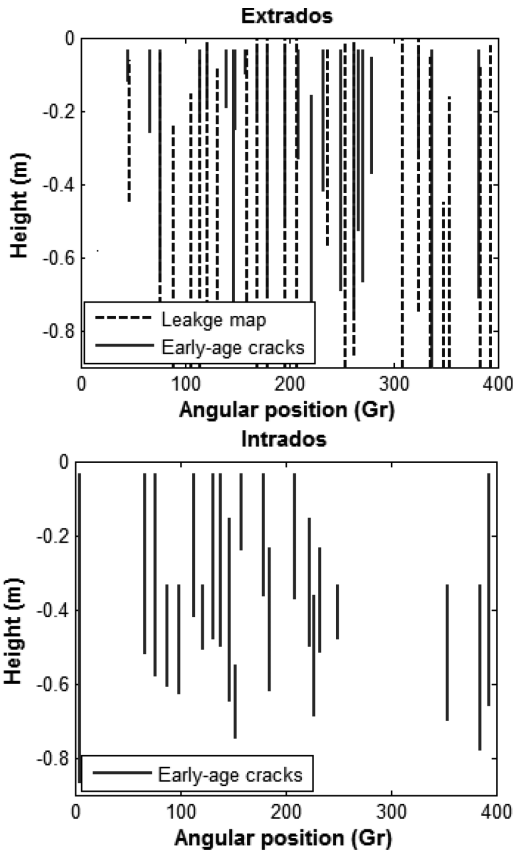

Figure 7. Cracking pattern at the gusset level 12 days after casting and the leakage map during the first pressurization test.

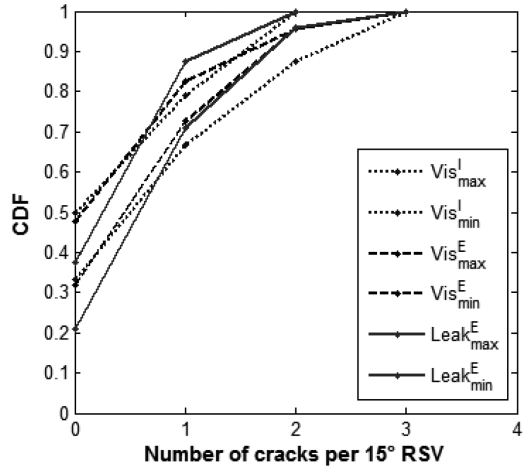

Figure 8. cdf of the number of cracks per RSV based on visual inspections (VIS) and the leakage map (Leak) from the intrados (I) and extrados (E) sides.

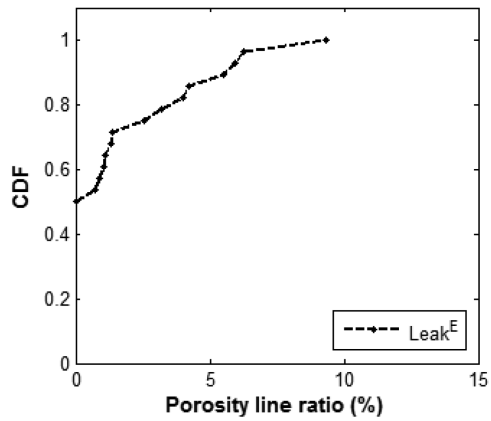

Figure 9. cdf of the porosity lines in concrete joints (expressed in% of the gusset's perimeter).

- Cracked: concrete permeability is defined using Equation 21 with d = 1. The crack opening is blindly computed as it depends only on the loading state after concrete is prestressed and not its early-age opening. The tangential prestressing load is considered equal to 0.5 MPa (mean value based on in situ strain measurements). And the coefficients in Equation 18 are considered from the work of (Rastiello 2013): $(\alpha_w, \beta_w) = (3726.71, 1.19)$. As for the rest of parameters in the matching law, $(\alpha, \beta) = (11.3, 0.82)$ are considered from the work of (Choinska 2007).
- Porosity line: based on experimental results, the leakage rate through the porosity lines seem

to stabilize after two pressurization tests. This suggests that their hydric equilibrium has been reached and their permeability is expected to be constant in the absence of any mechanically induced damage. However, this hypothesis is questionable as the origin of the porosity lines remains unclear and the contributions of early age damage, drying and ageing phenomena remains non-quantified. Consequently, the permeability along the porosity lines is considered constant in time and equal to 10^{-15} m² (mean value from in situ measurements).

4.3 *Results at the RSV and gusset scale*

The variable of interest is the maximum normalized leakage rate during the pressurization test denoted Q_{max} and expressed in Nm³/h (Normo-cubic meters per hour). It describes the equivalent volumetric flow at 20°C and 1 bar. One is reminded that the number of cracks (Figure 8) and the occurrence of porosity lines (Figure 9) are the only random inputs. Before moving to the gusset structural scale, the principle of superposition is verified first at the RSV scale (Equation 24). For that purpose two series of simulations are performed: one when only one of the three flow modes is considered and the second where all modes are simultaneously accounted for (Figure 10).

$$\begin{aligned} Q_{max}\left(N_{ck}, p_{lp}, q_{Darcy}\right) &= N_{ck} Q_{max}^{ck} + p_{lp}\, Q_{max}^{lp} + Q_{max}^{Darcy} \\ Q_{max}^{ck} &= Q_{max}\left(N_{ck}=1, p_{lp}=0, q_{Darcy}=0\right) \\ Q_{max}^{lp} &= Q_{max}\left(N_{ck}=0, p_{lp}, q_{Darcy}=0\right) \\ Q_{max}^{Darcy} &= Q_{max}\left(N_{ck}=0, p_{lp}=0, q_{Darcy}\right) \end{aligned} \tag{24}$$

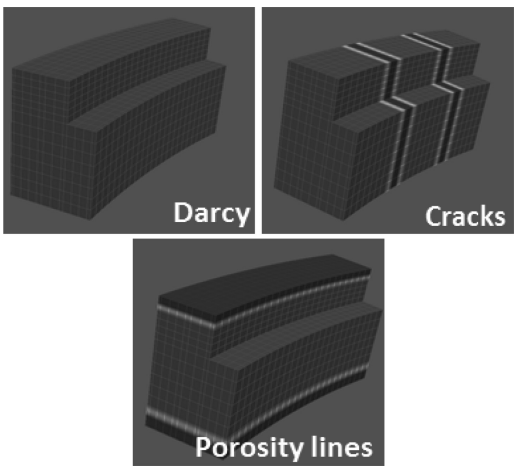

Figure 10. Air flow modes through the concrete volume at the RSV scale.

One can observe from Figure 12 that the superposition principle is applicable in the case of the outflow and induces an overestimation of the inflow. Indeed, inflow pressure profile is more sensitive to the presence of singularities compared to the outflow which still evolves during the transitional phase (the stationary state is hardly reached). Moreover, in the case of the gusset, the flow through joints and sound concrete is at most 10% of the flow through a single crack which highlights the criticality of early-age cracks for the leakage rate prediction. Focusing on the outflow which is the one of interest, the

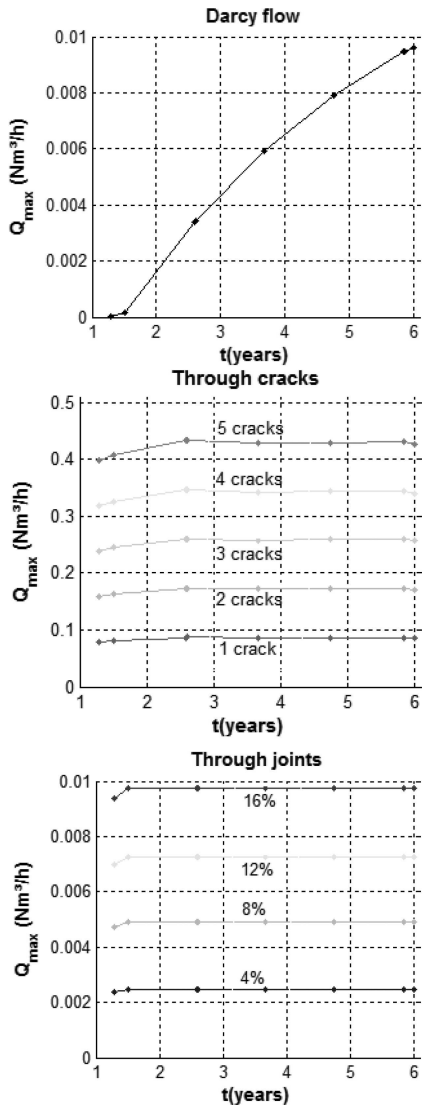

Figure 11. Elementary outflow leakage rates through the gusset's RSV volume.

variation of the cracks' number and porosity line ratio using cumulative density functions (cdf) in Figures 9 and 10 lead to a random flow Q_{max} (fitted to a normal cdf). To simplify the visualization of numerical results only the mean value and coefficient of variation evolution in time are depicted (Figure 13). One can easily notice that the gusset is composed of 24 RSVs of a 15° angle of revolution. The total leakage rate can therefore be computed as a sum of a 24-sample elementary leakage rates from the ones obtained in Figure 12. This leads to a global leakage rate evolution shown in Figure 13. Three configurations have been considered (Figure 9): (a) results of in situ observations at early age from the extrados side (b) from the intrados side and (c) the actual leakage map obtained after the first pressurization test (most realistic one).

Generally speaking, the observed increase in time is mostly due to the prestressing losses in the cables due to concrete drying and creep which lead to higher crack openings in time under the same pressurization loads. The experimental leakage rate during the first pressurization test is within the predicted upper and lower bounds (Figure 13). However, in terms of the mean response, the model underestimates the increase of the leakage rate between the first two tests. It is worth noting that prestressing losses are highly sensitive to the applied mechanical loads and to the water content evolution (which are constant in this study). Particularly, the higher the prestressing is the higher creep strains get and the longer it takes for a crack to reopen. On the other hand, the lower RH gets the sooner cracks would reopen and the higher their opening values become (Bouhjiti et al. 2017a). Such effects are being investigated as a part of an ongoing global stochastic analysis of the leakage rate of the VeRCoRs mock-up which is expected to improve the obtained cdf.

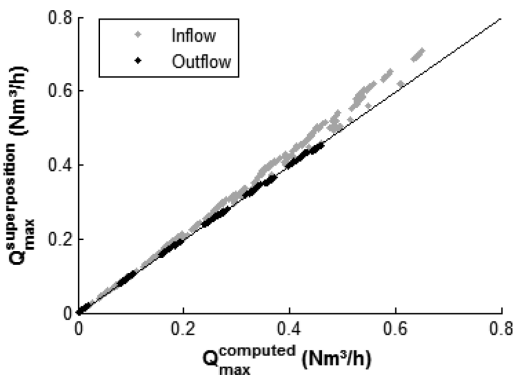

Figure 12. Comparison of the computed leakage rate accounting for all singularities and the one deduced by applying the superposition principle.

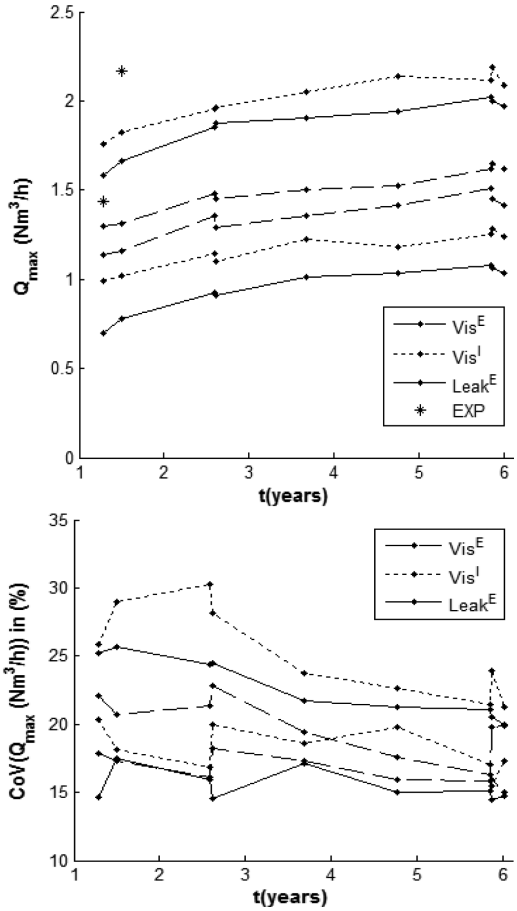

Figure 13. Evolution of the leakage rate at the gusset scale in terms of the mean and coef. of variation values of the associated normal law when visual inspection (VIS) results and leakage map (Leak) results are considered for intrados (I) and extrados (E) sides.

Coming back to the effect of random cracking on the leakage rate, the obtained mean values range from 1 to 1.5 Nm³/h during the first test and reach values from 1.6 to 2.1 Nm³/h towards the end of VeRCoRs lifetime with a mean coefficient of variation of 20%. Also the visual observations performed on the intrados side show closer results to the ones from the leakage map. This suggests that visual inspection should be performed from the intrados side whenever possible to identify the number of defects at the origin of the leakage rate.

5 CONLUSIONS

In this work, a random and weakly coupled THM modeling strategy is proposed to analyze and

predict the evolution of early age cracks of concrete in time and also define their effect on the computed leakage rates of NCBs. By using a new strain based damage-permeability matching law, the RSV-based methodology led to accurate estimations of the upper and lower bonds of leakage rates in comparison with in situ observations at the gusset level of the 1:3 scaled NCB. Moreover, it has been demonstrated that for cracked structural parts: (a) the air flow mainly goes through the macrocracks rather than through the unsaturated concrete volume or concrete joints (b) the principle of superposition can be applied (c) the stationary state is not reached for the considered pressurization tests duration and (d) the consideration of random cracking patterns induces up to 30% variation of the computed leakage rate. A forthcoming work shall include the effects of the prestressing loads and water content field variation to obtain a global cdf of the gusset's critical leakage rate and better characterize its evolution in time.

ACKNOWLEDGMENTS

This work was supported by EDF-SEPTEN/DTG/CIH within the Chair PERENITI agreement with the Grenoble INP Partnership Foundation. The author is grateful to EDF-SEPTEN for the provided in situ measurements. The Chair PERENITI partners shall not in any circumstances be deemed liable for the content of this publication which is only binding its author. The 3SR lab is part of the LabEx Tec 21 (Investissements d'Avenir–Grant agreement n°ANR-11-LABX-0030).

REFERENCES

Baroth, J. Breysse, D. Schoefs, F. 2011. Construction Reliability: Safety, Variability and Sustainability. *Wiley-ISTE eds. ISBN: 978-1-84821-230-5.*

Bažant, Z.P. 1999. Size effect on structural strength: a review. *Arch. of Appl. Mech. 6*9(9): 703–725.

Benboudjema, F. 2002. Modélisation des déformations différées du béton sous sollicitations bi axiales. Application aux enceintes de confinement de bâtiments réacteurs des centrales nucléaires (in French). *PhD thesis of UMLV.* France.

Boucher, M. 2016. Analyse de la corrélation spatio-temporelle des déformations entre le coeur d'un ouvrage épais en son parement (in French). *PhD thesis of UGA.* France.

Bouhjiti, E.M. Baroth, J. Dufour, F. & Masson B. 2016. Damage analysis and prediction of air leakage rate in nuclear reactor containment structures: Numerical model validation based on the VERCORS mock-up. *Proc. Int. Conf. on TINCE, Paris, 05–09 September.* France.

Bouhjiti, E.M. Baroth, J. Dufour, F. & Masson B. 2017a. Sensitivity analysis of the Thermo-Hydro-Mechanical parameters affecting double walled Nuclear Power Plants behaviour. *Proc. Int. Conf. on SMIRT, Busan, 20–25 August.* South Korea.

Bouhjiti, E.M. Baroth, J. Dufour, F. & Masson B. 2017b. Sensitivity analysis of cracking in large reinforced concrete structures: Case of the VeRCoRs mock-up. *Proc. 23rd CFM, Lille, 28 August - 01 September.* France.

Bouhjiti, E.M. Briffaut, M. Baroth, J. Dufour, F. & Masson B. 2017c. Thermo-mechanical modeling of the early age behavior of concrete in Nuclear Containment Buildings. *Proc. RILEM/COST Int. Conf. on EAC, Brussels, 12–14 September.* Belgium.

Choinska, M. 2006. Effet de la température, du chargement mécanique et de leurs interactions sur la perméabilité du béton de structure (in French). *PhD thesis ECN*, France.

Corbin, M. and Garcia, M. 2015. Benchmark VeRCoRs report *(conference-service.com/edf-VeRCoRs/welcome.cgi)*.

de Larrard, T. Colliat, J. B. Benboudjema, F. Torrenti, J. M., Nahas, G. 2010. Effect of the young modulus variability on the mechanical behaviour of a nuclear containment vessel. *Nuc. Eng.& Des.* 240(12):4051–4060.

Ezzedine El Dandachy, M. 2016. Characterization and modelling of permeability of damaged concrete: Application to reinforced concrete structures. *PhD thesis UGA,* France.

Foucault, A. Michel-Ponnelle, S. Galenne, E. 2012. A new creep model for NPP containment behaviour prediction. *Proc. Int. Conf. on SSCS, Aix-en-Provence, 29 May-1 Jun.* France.

Ghanem, R. Spanos, P. 1991. Stochastic finite elements—A spectral approach. *Revised ed. in Dover Publications, INC.* New York. USA.

Granger, L. 1995. Comportement différé du béton dans les enceintes de centrales nucléaires (in French). *PhD thesis of ENPC 1995.* France.

Hillerborg, A. 1988. Application of fracture mechanics to concrete: summary of a series of lectures. *Report TVBM Vol. 3030, Div. of Buil. Mat., Lund University*.

Klinkenberg, L. J. 1941. The permeability of porous media to liquids and gases. *Dril. and prod. Prac., American Petroleum Inst*. 200–213.

Mensi, R., Acker, P. & Attolou, A. 1988. Séchage du béton: analyse et modélisation. *Mat. & struc.* 21(3): 3–12.

Mozayan Kharazi, M. Davenne, L. & Ghavamian, S. 2013. A modeling methodology in predicting the leakage tightness of a pressure containment vessel without liner. *Proc. Int. Conf. on SMIRT, San Francisco, 18–23 August 2013.* USA.

Picandet, V. Khelidj, A. Hervé, B. 2009. Cracks effects on gas and water permeability of concretes. *Cem. and con. Res.* 39(6): 537–547.

Pijaudier-Cabot, G. Dufour, F. Choinska, M. 2009. Permeability due to the increase of damage in concrete: From diffuse to localized damage distributions. *Eng. Mech., American Society of Civil Engineers* 135(9): 1022–1028.

Rastiello, G., Desmettra, C., Tailhan, J.L., Dal Pont, S. 2016. Modeling of fluid leakage through multi-cracked RC structural elements using a numerical

probabilistic cracking approach. *Mat. & Struc.* 49(8): 3095–3108.

Rossi, P. Wu, X. 1992. Probabilistic model for material behaviour analysis and appraisement of concrete structures. *Mag. of Con. Res.* 44(161): 27–280.

Sellier, A. Millard, A. 2014. Weakest link and localization WL^2: a method to conciliate probabilistic and energetic scale effects in numerical models. *EJECE* 18(10): 1177–1191.

Thiery, M. Baroghel-Bouny, V. Bourneton, N. Villain, G. Stefani, C. 2007. Modélisation du séchage des bétons. Analyse des différents modes de transfert hydrique. *Rev. Euro. de GC* 11: 541–577.

Torrenti, J.M. Nguyen, V. H. Colina, H. Le Maou, F. Benboudjema, F. Deleruyelle, F. 2008. Coupling between leaching and creep of concrete. *Cem. and conc. Res.* 38(6): 816–821.

Ulm, F.-J., Coussy, O. 1998. Couplings in early-age concrete: From material modeling to structural design. *Sol. & Struc.* 35(31):4295–4311.

VeRCoRs Project. 2018. Data available in: www.conference-service.com/EDF-VERCORS-BENCHMARK-2018/welcome.cgi

Verdier, J. 2001. Contribution à la caractérisation de l'évolution du taux de fuite des enceintes de confinement du parc nucléaire. *PhD thesis UPS, Toulouse* France.

Computational Modelling of Concrete Structures – Meschke, Pichler & Rots (Eds)
© 2018 Taylor & Francis Group, London, ISBN 978-1-138-74117-1

Simplified modelling strategy for the thermos-mechanical analysis of massive reinforced structures at early age

J. Mazars & M. Briffaut
CNRS, University Grenoble Alpes, Grenoble INP, F-38000 Grenoble, France

S. Grange
University Lyon, INSA-Lyon, GEOMAS, F-69621 Villeurbanne Cedex, France

ABSTRACT: The aim of this work was to propose a complete and efficient modelling approach for simulation of the entire loading program of the RG8 test (restrained shrinkage part and mechanical part) performed in the framework of the French national program CEOS.fr. This was made possible by using a multifiber beam discretization including a THM model coupled with a unilateral concrete damage model. Due to the massive character of the structure, the scale effect required to be taken into account. This was done here through the use of a Weibull law that allows the measured mechanical characteristics of concrete to be transposed from a standardized test piece to the scale of the beam tested. The results of the in-situ measurements show the relevance of the approach.

1 INTRODUCTION

The work carried out in France by the national program CEOS.fr allows to highlight the importance of taking into account, from the design stage, the THM effects in massive structures (CEOS.fr group, 2016). This program included experiments on large test samples on which was based an international benchmark dealing with the modelling of the behaviour of the tested beams. The results have been published in a report (Lacarriere et al., 2011) and some of them, in a special issue of the EJECE journal (Mazars, 2014).

The experimental program included beams under restrained shrinkage during concrete maturation, by means of two steel struts (test RG8, see Fig. 1).

Based on extensive instrumentation, measurements were performed continuously for several weeks after casting and, in a second phase, the beam was tested in bending to determine the effects of THM processes on the mechanical response of the structure.

The aim of the present study is to propose a complete and efficient modelling for simulation of the entire loading program of the RG8 test.

The problem to solve includes a lot of coupled phenomena (temperature increase, progressive maturation of concrete, creep, restrained shrinkage effects, scale effects,…).

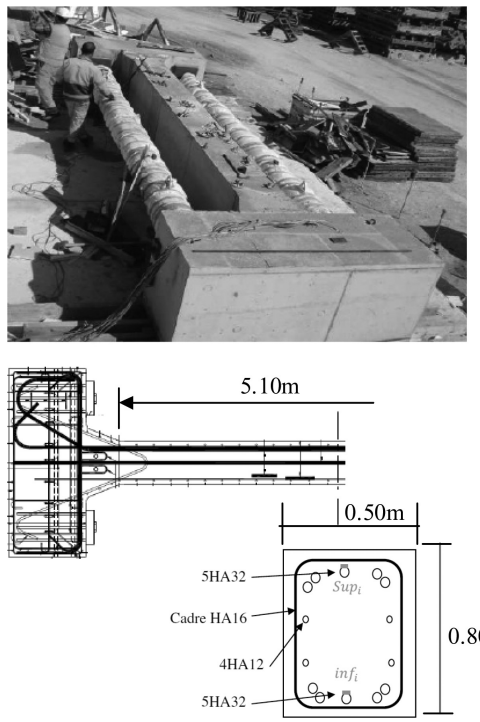

Figure 1. General view of the RG8 beam and detail of the reinforcement.

Treated with a classical FEM description this leads to heavy numerical simulation (Sellier et al., 2011). In order to reduce strongly the size of the modelling a simplified description based on multifiber beam discretization is used, including a THM model (Briffaut et al., 2011) coupled with a unilateral concrete damage model (Mazars and Grange, 2015) and, due to the massiveness of the structures, scale effect is taken into account. This is done here through the use of a Weibull law (Mazars et al., 1991).

In this framework the comparison between experimental and numerical results obtained on the RG8 test demonstrates the efficiency of the approach.

2 THE RG8 TEST

Only few experimental results related to large or massive structures are available in the literature. This is why the CEOS.fr program focused on such large scale specimens (beams and walls) with well identified boundary conditions and accurate crack pattern monitoring (see CEOS.fr group, 2016 for details).

2.1 *Blocks subjected to restrained shrinkage*

Three blocks (RG8, RG9 and RG10) have been designed in order to study the restrained shrinkage of massive concrete structures at early age. Made with the same concrete (C50/60), RG8 was the reference, in RG10 the thickness of the concrete cover was increased (5 cm instead of 3 cm) and in RG9 reinforcement ratio was deceased (0.56% instead of 2%).

The RG specimens were divided into three parts (see Fig. 1 showing the RG8 sample):

- a central block (5.10 m × 0.80 m × 0.50 m) plus a transition zone on each side of 0.4 m with a progressive increase of the width, which constitutes the test specimen;
- two heads (0.9 m × 2.2 m × 0.9 m);
- two steel struts, which restrain strain.

Due to hydration effects, the evolution of temperature and shrinkage was substantial in such a massive element. The two metallic struts restrain the contraction of the central part of the beam and consequently cause cracking at early age (Fig. 1).

All specimens were fully instrumented (9 internal temperature sensors, 24 vibrating cords, 3 internal optical fibers, 12 strain gages on rebar, etc., (Laccariere et al, 2011, Kolani et al, 2012). The external temperature and the solar exposition of the specimen were also measured during the test.

3 MODELS

3.1 *Multifiber beam modelling*

To decrease the number of degrees of freedom, 3D Timoshenko multifiber beam elements have been used (Kotronis et al., 2005).

The main advantage of such a description is that the behaviour is based on a 1D non-linear model for both, concrete and reinforcement bars. Compared to classical 3D FEM this technique reduces significantly the size of the problem, however the counterpart is that kinematic constraints have to be guaranteed between two elements with regard to the continuity of displacements and to the fact that sections remain plane during loading.

Concrete: The useful part (5.1 m) was modeled with 51 elements of 0.10 m in length. The section was divided into 5 × 8 fibers of 0.10 m side. The beam was completed on both sides by a part with a variable cross-section up to the support of the struts (see Fig. 2). On both sides, supports are considered as partial embedment allowing to describe the end heads effects.

Reinforcements: only the longitudinal reinforcements are represented by bar elements located in accordance with the reinforcement mapping of the beam (Fig. 1).

Struts: they are represented with bar elements respecting the characteristics of the real struts (length = 5,90 m and section = $2 \times 3.556\ 10^{-2}$ m^2). Struts and reinforcement bars are connected to the same embedment as the concrete beam.

3.2 *Models for concrete*

As mentioned above, at early age the phenomena are strongly coupled. Here the following phenomena are distinguished:

- Maturation of concrete;
- Evolution of performance with maturation;
- Autogenous shrinkage of concrete;

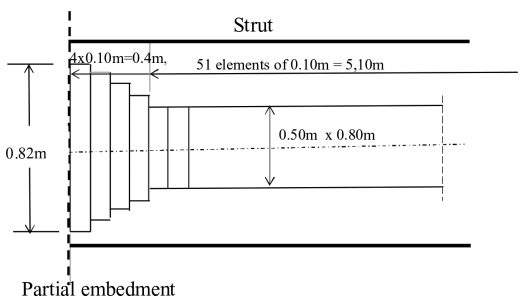

Figure 2. Multifiber beam mesh and boundary conditions.

– Basic creep of concrete;
– Thermal deformation of concrete and steel;
– Elasto-damaging behaviour of concrete;
– Elasto-plastic behaviour of reinforcement;
– Scale effects due to the massiveness of the structure.

3.2.1 *Thermal model for early age*

Hydration is a thermo-activated phenomenon. Thus, the structure heats up under the effect of internal heat sources, especially since it is massive. Exhaustion of the reaction and external exchanges lead to cooling, until gradually reaching balance. At the same time the material is subject to various volumetric variations and the mechanical performance increases.

At this stage two strong assumptions were made:

– the thermal problem was treated independently of the mechanical problem;
– the temperature variations were assumed to be identical in each section of the beam (independence with respect to the longitudinal axis x).

The three main following equations must to be solved in this problem (Briffaut et al., 2011).

* The energy balance equation:

$$C\dot{T} = \nabla(k\nabla T) + L\dot{\xi} \tag{1}$$

$\dot{X} = dX/dt$, T is the temperature (K), k is the thermal conductivity (W.M^{-1}.K^{-1}), L *is* the latent hydration heat (J.m^{-3}) and C is the volumetric thermal capacity (J.m^3 K^{-1}).

*The Arrhenius equation, from which is deduced the hydration degree ξ:

$$\dot{\xi} = A(\xi)\exp(-\frac{E_a}{RT}) \tag{2}$$

$A(\xi)$ is the chemical affinity (s^{-1}), which is a polynomial expression of ξ; E_a is the activation energy (J.mol^{-1}), R is the ideal gas constant equal to 8.3145 J.K^{-1}.mol^{-1}.

*The external exchange, which is solved as follows:

$$\varphi = h\left(T_s - T_{ext}\right)n \tag{3}$$

φ is the heat flux (W.m^{-2}), n is the vector normal to the surface, T_s is the surface temperature (K) and T_{ext} the external temperature (K). h is the exchange coefficient (W.m^{-2}.K^{-1}), whose value changes when the mould is removed.

Fig. 3 shows the results obtained, after identifying the parameters (see Briffaut et al., 2011 for details), for the evolution of temperature at the center of the beam. A good comparison is obtained with measurements performed in situ.

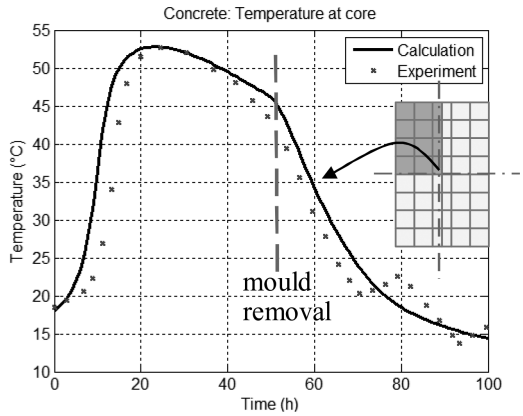

Figure 3. Temperature evolution at the center of the beam (experiment—calculation comparison).

3.2.2 *Mechanical model*

The basis is the μ damage model (Mazars & Grange, 2015). Thanks to the use of Timoshenko multifiber beams and related section kinematic assumptions, this model can be used in its 1D version. In that framework the related equations are, for tension and compression respectively:

$$\sigma = E(1-d_t)\varepsilon_t$$
$$\text{with } d_t = 1 - \frac{(1-A_t)\varepsilon_{0t}}{Y_t} - A_t\exp(-B_t(Y_t - \varepsilon_{0t})) \tag{4}$$

$$\sigma = E(1-d_c)\varepsilon_c$$
$$\text{with } d_c = 1 - \frac{(1-A_c)\varepsilon_{0c}}{Y_c} - A_c\exp(-B_c(Y_c - \varepsilon_{0c})) \tag{5}$$

Y_t = Sup(ε_{0t}, maxε_t), ε_{0t} is the tensile strain threshold. Y_c = Sup(ε_{0c}, max-ε_c), ε_{oc} is the compressive strain threshold. Generally ε_{0t} corresponds to the tensile strain at peak, then it can be written: $\varepsilon_{0t} = f_t/E$ (f_t being the tensile strength). Fig. 4 shows the corresponding uniaxial response with a specific loading path, from OAB in tension to ODF in compression while highlighting the range of evolution in stiffness due to crack opening and closure (unilateral effect).

3.2.3 *Thermo-chemo-mechanical coupling*

The mechanical performances progressively increase with the hydration process. To describe the state of the medium, the maturity M is introduced (Mazars et al., 1998):

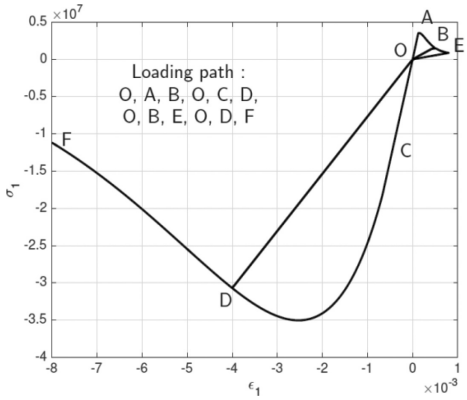

Figure 4. Uniaxial behaviour for concrete exhibiting unilateral effect.

$$\text{for } \xi > \xi_0 \quad M = \left\langle \frac{\xi - \xi_0}{\xi_\infty - \xi_0} \right\rangle_+ \tag{6}$$

ξ_0 is the percolation threshold (close to 0) and ξ_∞ the hydration degree when the hydration reaction is over (#0.83, from previous experiments). M evolves between 0 (beginning of the process) and 1 (end of hydration) and is used in a simple way to forecast:

- the Young modulus: $E = ME_\infty$, E_∞ being the value when $M = 1$ (matured concrete);
- the tensile strength of concrete: $f_t(M) = E(M)$. ε_{0t} (ε_{0t} is constant whatever is maturity).

These relations are a specific case of the ones proposed by de Shutter (1999).

From this it is easy to describe the non-linear beha-viour of the material. With i = t in tension and i = c in compression, it comes:

$$\text{for } \varepsilon_1 > \varepsilon_{0i} \quad \sigma = E_\infty M(1 - d_i)\varepsilon_i \tag{7}$$

3.2.4 *Scale effect*

From the Weibull theory, it has been shown by Mazars et al. (1991) that the tensile threshold for a uniform tension is:

$$\varepsilon_{t0} = \left(\frac{W_0}{V_t}\right)^{1/m} \tag{8}$$

m is the Weibull coefficient, W_0 is a material parameter.

Then, the ratio between the tensile threshold value coming from a laboratory test (volume V_{td}) and the tensile threshold which must be use on the RG8 test is given by:

$$\frac{\varepsilon_{t0}^{td}}{\varepsilon_{t0}^{RG}} = \left(\frac{V_{RG}}{V_{td}}\right)^{1/m} \tag{9}$$

Assuming that $\varepsilon_{t0} = f_t / E_0$ in both case, it has been shown that the ratio between the related tensile strengths (f_{td} / f_{tRG}) is about 1.5 and, about 2, between the nominal splitting strength and the tensile strength which must be used in the RG8 test.

3.2.5 *Global description of the problem*

This description is based on the following strain superposition (Briffaut et al., 2011):

$$\varepsilon = \varepsilon_e + \varepsilon_{bc} + \varepsilon_{au} + \varepsilon_{th} \tag{10}$$

From which, the global behaviour is written:

$$\dot{\tilde{\sigma}} = E(M)\dot{\varepsilon}_e = E(M)\left(\dot{\varepsilon} - \dot{\varepsilon}_{bc} - \dot{\varepsilon}_{au} - \dot{\varepsilon}_{th}\right) \tag{11}$$

$\tilde{\sigma}$ is the effective stress, $\tilde{\sigma} = \sigma/(1-d)$, then (10) introduces damage in the whole process.

ε_{th} is the thermal strain $\quad \varepsilon_{th} = \alpha T$ (12)

α being the thermal dilation coefficient (K^{-1})

ε_{au} is the autogenous shrinkage $\quad \varepsilon_{au} = -\kappa_\infty M$ (13)

κ_∞ being the final shrinkage (μm/m).

Creep is described by a series of three Kelvin–Voigt models and the behaviour of each model is given by:

$$\tau_{bc}^i \ddot{\varepsilon}_{bc}^i + \left(\tau_{bc}^i \frac{\dot{k}_{bc}^i(M)}{k_{bc}^i(M)} + 1\right)\dot{\varepsilon}_{bc}^i = \frac{\dot{\tilde{\sigma}}}{k_{bc}^i(M)} \tag{14}$$

ε_{bc} is the basic creep.

The stiffness of each spring is on the form $k_{bc}(M) = A(M)\, k_{bc\infty}$ and $\tau_{bc} = \eta/k$ is the characteristic time of a given Kelvin–Voigt model.

4 APPLICATION TO RG8 TEST

4.1 *Thermo-chemo-mechanical loading*

Loading is related first to temperature evolution, this evolution concerns both concrete andrebar.

Two main stages have been observed:

- From 0 to 120 hours, temperature variation is mainly due to the hydration effects.

  Thanks to the energy balance equation (1) this evolution has been evaluated and Fig. 2 shows a good agreement with the measurement performed in situ for the center of the beam section.

– From 120 hours to 700 hours (time corresponding to the remove of the struts), temperature variation is mainly due to external temperature evolution (day-night changes). Due to the massiveness of the beam, this change concerns only material close to the surface and, in order to simplify, calculation has been performed using a constant temperature of 12°C.

4.1.1 *Shrinkage and creep*

As for temperature, due to the massiveness of the structure and the relative brevity of the experiment (one month) drying is not considered in the structure.

In this context:

– Autogenous shrinkage was calibrated on previous tests performed on samples ($\kappa_{\perp} = 110$ µm/m).
– Basic creep model was also calibrated on previous laboratory tests and, in order to cover in an optimized way the whole duration of the test, the characteristic times of the three Kelvin–Voigt models were: $\tau_1 = 0.1$ day, $\tau_2 = 1$ day, $\tau_3 = 10$ days.

4.1.2 *Maturity and mechanical performance of concrete*

From equations (2) and (6) and the temperature evolution, $M(t)$ is calculated. From equation (7) Young modulus and tensile strength can be determined at a given time. It was shown that results obtained are in good adequacy with those obtained on tests performed on laboratory samples.

4.1.3 *Mechanical loading*

From 0 to 700 hours struts were active, in tension during the first 50 hours due to the thermal dilation of concrete, then in compression due to the shrinkage of concrete. At the same time struts are submitted to the external evolution of temperature: a 24 hours cyclic evolution with an average value of 12°C and an amplitude of 6°C is assumed. From the moment of removal of the mould (Fig. 3), the gravity load was assumed to be active all along the beam. A few days after the struts were removed and the beam was tested on a test bench. Supports were 5.1 m spaced and located at the end of the part of the beam where the section was constant. Loading was a four point bending one (spacing between the loads was 1.6 m – see Fig. 6).

4.2 *Example of results*

Due to the complexity of the phenomena a lot of results have been obtained, but only the main results are presented here. The experimental results can be found in (Kolani et al. 2012) and (Cheops data, 2017).

4.2.1 *From 0 to 700h: restrained shrinkage loading*

*Relative forces *developed in the central section*: in a given section, three main structure elements were considered: concrete, rebar and struts. For these three elements, it was easy to determine the global force developed at a given time from the measured data and from the calculation.

The evolutions of these three global forces were compared in Fig. 5a.

One can emphasize that:

– Due to equilibrium, at each time the sum of the three forces was zero. The comparison between calculation (solid line) and experiment (dashed line) is good.
– After a period where the struts are in tension and concrete and rebar are both in compression, at about 50 hours the sign of the forces changes and a first crack appears on concrete (#71h measured and #76h calculated).

Due to bending related to the gravity load, cracking is located is in the central section of the

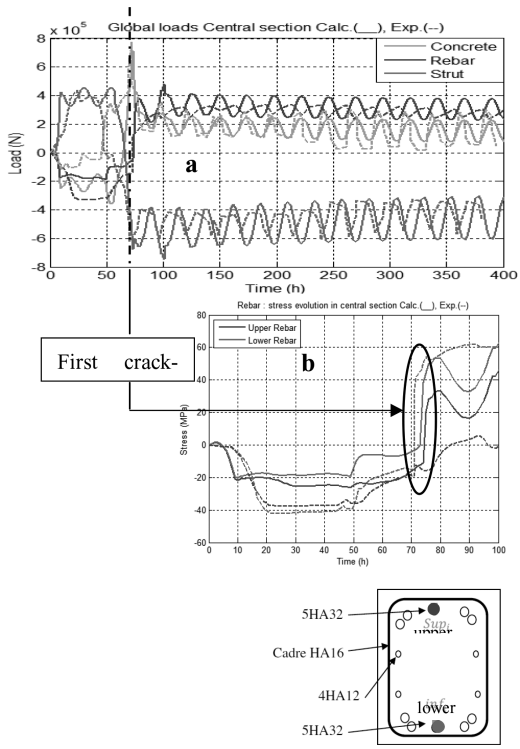

Figure 5. RG8 results in the central section (dashed line: experiment—solid line: calculation), a/ global force evolutions (struts, concrete, rebar); b/ local stress on the upper and lower rebar.

beam. This phenomenon creates a peak on the concrete force followed by a sudden decrease of this force and, at the same time, there is an increase of the one related to the rebar. Calculation forecasts a second series of cracking (outside of the central section) at about 103 hours (a peak corresponding to this point is visible on the calculation curves Fig. 5a). The second cracking process was observed experimentally at about 167 hours.

*Local stress *evolution in the rebar*. Along this restrained shrinkage process, the rebar remained elastic.

Fig. 5b gives the stress evolution with time corresponding to the upper rebar (blue line) and the lower rebar (red line) in the central section during the first 100 hours.

The jump related to the loading of the rebar due to the first cracking is clear.

For the lower rebar this jump is correctly predicted and the difference obtained for the upper one is the counterpart due to the use of the Timoshenko beam approach (plane section remains plane, which is not the case in practice).

4.2.2 *Final stage: 4 point bending loading*

With regard to the global behaviour of the beam, Fig. 6a compares three curves,

- the experimental one (dashed black line); the beam was loaded only up the serviceability limit state (SLS),
- the calculated one for the beam after the restrained shrinkage loading program (blue curve) and,
- the calculated one for the same beam considered sound (red curve).

One can observe that:

- the RG8 calculated curve is in good compliance with the experimental one;
- the two calculated curves (RG8 and sound beams) are very close in the most part of the loading evolution;
- a great difference is observed between the two original stiffness (ratio estimated at 0.55, see zooming Fig. 6b).

The main conclusions which can be drawn are:

- the final strength of the beam is not affected by the restrained shrinkage treatment;
- the initial stiffness is strongly affected by the restrained shrinkage loading (55% decrease) and the first mode of vibration is equal to 31.7 Hz instead of 59.2 Hz for the sound beam, which leads to a very different dynamic response. This fact must be taken into account in the case of a dynamic loading such as an earthquake.

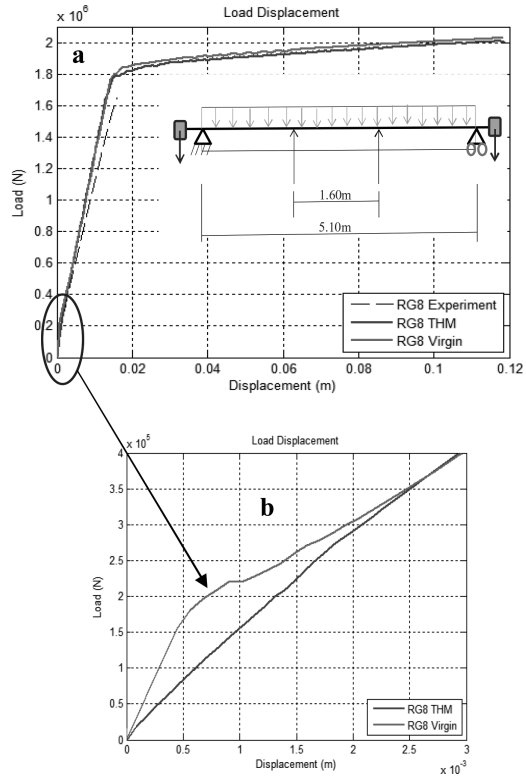

Figure 6. RG8 results Four point bending test, a/ total force-displacement responses, b/ zoom on the first 3 mm displacement showing the large difference between the two original stiffness (RG8 and sound beam).

5 CONCLUSIONS

The aim of the present study was to propose a complete and efficient modelling approach for the simulation of the entire loading program for the RG8 test.

The problem to solve includes a lot of coupled phenomena (temperature increase, progressive maturation of concrete, creep, restrained shrinkage effects, etc.) and it is proved here that it can be done using simplify modelling approach based on a multifiber beam description implementing adequate non-linear models.

The simulation allows to retrieve the main observed phenomena, particularly the triggering of the first crack (# 75h) and the subsequent behaviour over 700 hours are correctly reproduced.

Numerous other results have been obtained, especially in relation to the local behaviour (strain, damage, openings of cracks, etc.).

With regard to the mechanical flexural behaviour which follows the early age phase, simulations show that the THM phase strongly affects the initial stiffness (drop of the order of 55%) without jeopardizing the final static strength.

Thus, it can be concluded that the THM effects on a large test body, generates premature cracking which has two major types of consequences:

- on the durability of the structure;
- on its mechanical response; especially in dynamics loading, such as earthquake (in the present case the first natural frequency was reduced by nearly 50%).

Moreover, the modeling strategy, based on 1D non-linearity descriptions, leads to a calculation of high stability and low cost on the software platform ATL4S (Grange, 2015).

ACKNOWLEDGEMENT

the authors would like to thank the French national program CEOS.fr for its financial support and for providing the experimental results.

REFERENCES

Briffaut *et al.*, 2011. Numerical analysis of the thermal active restrained shrinkage ring test to study the early age behaviour of massive concrete structures, *Engineering Structures*, Vol. 33 (4), 1390–1401.

CEOS.fr group 2016. Control of cracking in reinforced concrete structures—Research project CEOS.fr, series editor Jacky Mazars, ISTE—Wiley, London 2016.

De Schutter G., 1999. Degree of hydration based Kelvin model for the basic creep of early age concrete, *Materials and Structures*, pp. 260–265, Vol.32.

Grange, S., 2015. ATL4S—A Tool and Language for Simplified Struct. Solution Strategy, Intern. report, 3SR, Grenoble. http://www.ceosfr.irex.asso.fr/en/, Cheops data (last accessed May 2017).

Kolani B., Lacarriere L., Sellier A., (2012) Exploiting the results of the THM test of RG structures, CEOS.fr report.

Kotronis, P. and Mazars, J., 2005. Simplified modelling strategies to simulate the dynamic behaviour of R/C walls, *Journal of Earthquake Engineering*, 9(2), 285–306.

Lacarriere L. et al., Intern. benchmark ConCrack—synthesis of the results, work. Concrack 2, Paris 2011.

Mazars J., Grange S., 2015. Simplified Modelling of Reinforced Concrete Structures for Engineering Issues, *Computers and Concrete*, 16(5) 683–701.

Mazars J., Bournazel J.P., 1998. Modelling of damage processes due to volumic variations for maturing and matured concrete, in *Concrete from Material to Structure*, Rilem, 43–54.

Mazars J., Pijaudier-Cabot G., Saouridis C., 1991. Size effect and continuous damage in cementitious materials, *International Journal of Fracture* 51, 159–173.

Mazars J. editor of "Control of cracking of RC structures: CEOS.fr international benchmark", *Europ. Journal of Environ.. and Civil Engineering,* special issue, 18 (7–8), 2014.

Sellier, A., and Lacarrière, L., 2011. Towards a simple and unified modelling of basic creep, shrinkage and drying creep of concrete. *Eur. J. of Envir. & Civil Eng.*, 13(10), 1161–1182.



Taylor & Francis
Taylor & Francis Group
http://taylorandfrancis.com

Computational Modelling of Concrete Structures – Meschke, Pichler & Rots (Eds)
© 2018 Taylor & Francis Group, London, ISBN 978-1-138-74117-1

Multiscale quantification of thermal expansion of concrete and thermal stresses of concrete structures

H. Wang & H.A. Mang
Institute for Mechanics of Materials and Structures, TU Wien—Vienna University of Technology, Vienna, Austria
College of Civil Engineering, Tongji University, Shanghai, China

Y. Yuan
College of Civil Engineering, Tongji University, Shanghai, China

B. Pichler
Institute for Mechanics of Materials and Structures, TU Wien—Vienna University of Technology, Vienna, Austria

ABSTRACT: The mechanical behavior of concrete structures subjected to temperature changes is significantly influenced by hygro-thermal processes occurring at the nanoscopic material scale. In order to quantify this relation exemplarily, a multiscale structural analysis of a simply supported concrete beam subjected to sudden cooling at its top surface is carried out. The overall analysis is organized in three steps. The first step refers to upscaling of thermoelastic properties of concrete by means of a multiscale model. It uses measured "hygrothermic coefficients" as input. They quantify the change of the internal relative humidity resulting from a temperature change. The multiscale model links temperature-induced changes of effective pore pressures in *nanoscopic* gel and capillary pores to the *macroscopic* thermal expansion behavior of the cement paste and the concrete. In the present contribution, this upscaling approach is validated by comparing model-predicted thermal expansion coefficients of cement paste with measured counterparts. The second step of the overall analysis consists of a macroscopic thermoelastic Finite Element analysis of the aforementioned concrete beam. These simulations are based on the homogenized elastic stiffness and the homogenized thermal expansion coefficient of concrete obtained in the first step. The simulations deliver distributions of the temperature and of the macroscopic stresses inside the analyzed concrete beam. In the third step, the obtained macroscopic stresses of concrete and the corresponding temperature changes are downscaled to average stress states of the cement paste matrix and of the aggregate inclusions, respectively. This way, it is shown that the significant mismatch of the thermal expansion coefficients of cement paste and aggregates results in microscopic tensile stresses of cement paste, which are significantly larger than the macroscopic tensile stresses experienced by concrete.

1 INTRODUCTION

When steel-reinforced concrete structures are subjected to temperature changes, all material constituents exhibit thermal eigenstrains. Given that the thermal expansion coefficients of steel and concrete are similar, there is no significant mismatch of thermal eigenstrains. However, the concrete constituents "cement paste" and "aggregates" do exhibit significantly different thermal expansion properties.

- Concrete aggregates exhibit thermal expansion coefficients ranging between $4 \cdot 10^{-6}/°C$ and $12 \cdot 10^{-6}/°C$, mainly depending on the mineral composition.
- The cement paste exhibits thermal expansion coefficients ranging between $8 \cdot 10^{-6}/°C^{-1}$ and $24 \cdot 10^{-6}/°C$, mainly depending on the internal relative humidity (Emanuel & Hulsey 1977). This dependence is typically attributed to the experimentally measured increase of the internal relative humidity, ΔRH, resulting from a temperature increase, ΔT. In this context, the ratio $\Delta RH/\Delta T$ is referred to as the "hygrothermic coefficient".

The described experimental observations suggest that thermal expansion of concrete is a multiscale thermo-hygro-poro-mechanical problem. This calls for multiscale structural analysis of concrete structures, which combines multiscale modeling of concrete with structural simulations.

The multiscale model of concrete used in the present contribution reflects the hierarchical organization of concrete based on four different matrix-

inclusion composites, introduced at four different scales of observation, see also (Wang et al. 2017b, Wang et al. submitted) and Figure 1. Concrete is considered to consist of a cement paste matrix and of spherical aggregate inclusions Figure 1.

The multiscale model renders two types of scale transition possible.

- Bottom-up homogenization of the elastic stiffness and of the thermal expansion properties of concretes.
- Top-down calculation of microscopic stress states inside the concrete constituents "cement paste" and "aggregates".

Both types of scale transitions turn out to be important for multiscale structural analysis of a thermally loaded concrete beam subjected to a sudden temperature change. This analysis is structured as follows:

1. An analytical solution of the heat conduction problem is presented. This involves a series solution of the temperature field history.
2. Thermo-mechanical Finite Element simulations of the concrete beam are performed. They use calculated temperature fields, the homogenized stiffness and the homogenized thermal expansion coefficient of concrete as input. The macroscopic simulations deliver thermal stresses in the homogenized concrete.
3. Microscopic stresses of cement pastes and aggregates are calculated based on the multiscale model, using the temperature field (from item 1) and the macroscopic concrete stresses (from item 2) as input.

The present contribution is organized as follows. Section 2 contains a brief overview over the multiscale model of concrete. Section ? deals with the multiscale structural analysis of a concrete beam subjected to a sudden temperature change. Section 3 contains conclusions.

2 THERMO-HYGRO-PORO-MECHANICAL MULTISCALE MODEL OF CONCRETE

2.1 *Modelling of gel and capillary pore spaces*

Both gel and capillary pores are considered to be spherical, with pore radii r following exponential distributions (Huang et al. 2015)

$$\phi_k^{pdf}(r) = \frac{1}{R_k}\exp\left(-\frac{r}{R_k}\right), \tag{1}$$

with $k \in [gpor; cpor]$. In Eq.(1), $R_{gpor} = 12\,nm$ and $R_{cpor} = 12\,nm$ denote the characteristic radius of the gel and the capillary pores, respectively (Wang et al. 2017b).

Considering partially saturated conditions, pores with radii smaller than r_{lg} are filled by porewater, while larger pores are occupied by air. Thereby, r_{lg} denotes the curvature of the menisci between liquidfilled and gas-filled domains. The curvature is a function of both the absolute temperature T and the internal relative humidity RH, as described by the Kelvin-Cohan equation (Neimark & Ravikovitch 2001).

$$r_{lg} = \frac{2\gamma^{lg} v_m \cos\theta}{\ln(RH)RT} + t, \tag{2}$$

where R, γ^g, θ, and v_m denote the universal gas constant, the surface tension prevailing in a liquid-gas interface, the contact angle of porewater, and the molar volume of water, respectively. Also in Eq. (2), t denotes the thickness of water layers which are adsorbed to the pore surfaces. It increases with increasing relative humidity, as quantified by Badmann et al. (1981),

$$t = 0.385\ \text{nm} - \ln[-\ln(RH)] \cdot 0.189\ \text{nm}. \tag{3}$$

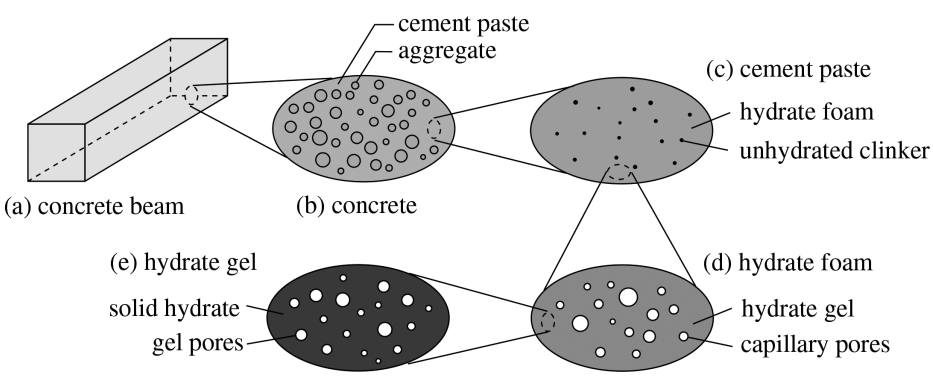

Figure 1. Multiscale representation of a concrete structure.

2.2 *Effective pore pressures relevant for homogenization*

The solid skeleton around the pores is subjected to so-called "effective pore pressures", combining the influence of the fluid pressure and of the surface tension. Considering that porewater is a perfectly wetting fluid, the effective pore pressures p(r) can be written as (Wang et al. 2017b)

$$p(r) = \begin{cases} \ln(RH)\dfrac{RT}{vm} & \cdots \quad r \le r_{lg}, \\ -\dfrac{2\gamma^{lg}}{r-t} & \cdots \quad r > r_{lg}. \end{cases} \tag{4}$$

Average effective pore pressures of gel and capillary pores, p_{gpor} and p_{cpor}, are relevant for upscaling of the pore-size-dependent effective pressures, see Eq. (4), to the material scale of concrete, see (Pichler & Dormieux 2010). With reference to Eq. (1), they read as

$$p_k = \frac{1}{R_k}\int_0^\infty p(r)\exp\left(-\frac{r}{R_k}\right)\mathrm{d}r, \tag{5}$$

with $k \in$ [*gpor*; *cpor*].

2.3 *Further phase input for homogenization*

Homogenization of the thermoelastic properties of the matrix-inclusion composites shown in Figure 1 is carried out in the framework of the Mori-Tanaka scheme. Each representative volume element (RVE), V, is subdivided into a matrix phase and an inclusion phase, occupying the domains V_m and V_i, respectively, where *m* stands for "matrix" and *i* for "inclusion". Both material phases $k \in$ [*m*; *i*] exhibit a specific elastic stiffness C_k and a specific eigenstress $\boldsymbol{\sigma}_k^e$,

$$\forall \underline{x} \in V_k : \begin{cases} \mathbb{C}(\underline{x}) = \mathbb{C}_k, \\ \boldsymbol{\sigma}^e(\underline{x}) = \boldsymbol{\sigma}_k^e, \end{cases} \tag{6}$$

as well as a specific volume fraction f_k, given as

$$f_k = \frac{V_k}{V}. \tag{7}$$

The phase stiffness tensors C_k, the phase eigenstress tensors $\boldsymbol{\sigma}_k^e$, and the phase volume fractions f_k, are described in the following three paragraphs.

The elastic stiffness tensors $\mathbb{C}_k$ of all material phases of concrete are considered to be isotropic. Therefore, they may be expressed in terms of phase bulk moduli, *k*, and phase shear moduli, μ, (see Table 1):

$$\mathbb{C}_k = 3k_k \mathrm{II}_{vol} + 2\mu_k \mathrm{II}dev. \tag{8}$$

In Eq. (8), II_{vol} and II_{dev} are the volumetric and the deviatoric part, respectively, of the symmetric fourthorder identity tensor II, i.e. $\mathrm{II} = \mathrm{II}_{vol} + I_{dev}$, see, e.g. (Wang et al. 2017b) for more details.

The eigenstress tensors $\boldsymbol{\sigma}_k^e$ of the pore phases are equal to the effective pore pressures defined in Eq. (5)

$$\boldsymbol{\sigma}_k^e = -pk\mathbf{1}, \tag{9}$$

with $k \in$ [*gpor*; *cpor*]. As for the solid phases, the eigenstresses are induced by the thermal eigenstrains

$$\boldsymbol{\sigma}_k^e = -\mathbb{C}_k : \varepsilon_k^e = -\mathbb{C}_k : \alpha_k \Delta T \mathbf{1}, \tag{10}$$

with $k \in$ [*hyd*; *cem*; *agg*].

The volume fractions of the concrete constituents are functions (i) of the initial composition, quantified in terms of the aggregate-to-cement mass ratio *a*/*c* and the initial water-to-cement mass ratio *w*/*c*, and (ii) of the maturity of the material, quantified in terms of the hydration degree ξ. At the concrete scale, the volume fractions of the cement paste and the aggregates read as (Pichler & Hellmich 2011):

$$f_{cp}^{con} = \frac{\dfrac{a/c}{\rho agg}}{\dfrac{1}{\rho_{cem}} + \dfrac{w/c}{\rho \mathrm{H_2O}} + \dfrac{a/c}{\rho_{agg}}}, \quad f_{agg}^{con} = 1 - f_{cp}^{con}, \tag{11}$$

where ρ_{agg} = 2648 kg/m³, ρ_{cem} = 3150 kg/m³, and $\rho\mathrm{H_2O}$ = 1000 kg/m³ are the mass densities of aggregates, cement, and water, respectively. At the cement paste scale, the volume fractions of the hydrate foam and the residual cement grains read as (Pichler & Hellmich 2011):

Table 1. Bulk and shear moduli of the material phases of concrete.

Phase	Bulk modulus *k* [GPa]	Shear modulus μ [GPa]	Sources
Solid hydrate	31.8	19.1	Ulm et al. (2004)
Cement	116.7	53.8	Pichler & Hellmich (2011)
Aggregate	22.2	16.7	Gudmundsson (2011)

$$f_{hf}^{cp} = \frac{w/c + 0.32\xi}{w/c + 0.32}, \quad f_{cem}^{cp} = 1 - f_{hf}^{cp}. \tag{12}$$

At the hydrate foam scale, the volume fractions of the hydrate gel and the capillary pores read as (Pichler & Hellmich 2011):

$$f_{gel}^{hf} = \frac{0.68\xi}{w/c + 0.32\xi}, \quad f_{cpor}^{hf} = 1 - f_{gel}^{hf}. \tag{13}$$

At the hydrate gel scale, the volume fractions of the solid hydrates and the gel pores read as (Ulm et al. 2004):

$$f_{hyd}^{gel} = 0.72, \quad f_{gpor}^{gel} = 1 - f_{hyd}^{gel}. \tag{14}$$

2.4 *Homogenization of thermoelastic properties of all involved matrix-inclusion composites*

The elastic behavior of any matrix inclusion composite can be expressed by means of the generalized Hooke's law as

$$\Sigma_{\text{hom}} = \mathbb{C}_{\text{hom}} : \mathrm{E}_{\text{hom}} + \Sigma_{\text{hom}}^{e}, \tag{15}$$

with Σ_{hom} denoting the homogenized stress tensor, $\mathbb{C}_{\text{hom}}$ standing for the homogenized stiffness tensor, E_{hom} denoting the homogenized strain tensor, and Σ_{hom}^{e} standing for the homogenized eigenstress tensor. The homogenized stiffness tensor reads as (Hill 1963)

$$\mathbb{C}_{\text{hom}} = f_m \mathbb{C}_m : \mathbb{A}_m + f_i \mathbb{C}_i : \mathbb{A}_i. \tag{16}$$

The homogenized eigenstress tensor reads as (Levin 1967)

$$\Sigma_{\text{hom}}^{e} = f_m \boldsymbol{\sigma}_m^{e} : \mathbb{A}_m + f_i \boldsymbol{\sigma}_i^{e} : \mathbb{A}_i. \tag{17}$$

Thereby, $\mathbb{A}_m$ and $\mathbb{A}_i$ are the phase strain concentration tensors of the matrix and of the inclusions, respectively. The corresponding Mori-Tanaka estimates read as (Mori & Tanaka 1973, Benveniste 1987)

$$\mathbb{A}_k = \left[\mathrm{II} + \mathbb{P} : (\mathbb{C}_k - \mathbb{C}_m)\right]^{-1} : \left[\sum_{j=m,i} f_j [\mathrm{II} + \mathbb{P} : (\mathbb{C}_j - \mathbb{C}_m)]^{-1}\right]^{-1}, k \in [m\,;i], \tag{18}$$

with $\mathbb{P}$ as the fourth-order Hill tensor for spherical phases.

As for the homogenization of the thermal expansion coefficient, α_{hom}, the composite is subjected to temperature change ΔT, and it is allowed to deform freely, such that the macroscopic stress tensor vanishes, i.e. $\Sigma_{\text{hom}} = 0$. In such a scenario, the homogenized strain tensor E_{hom} is equal to the homogenized thermal expansion coefficient α_{hom} multiplied by the second-order identity tensor 1, i.e.

$$\mathrm{E}_{\text{hom}} = \mathrm{E}_{\text{hom}}^{e} = -\mathbb{C}_{\text{hom}}^{-1} : \Sigma_{\text{hom}}^{e} = \alpha_{\text{hom}} \Delta T \mathbf{1}. \tag{19}$$

By inserting Eqs. (16) and (17) into Eq. (19), the homogenized thermal expansion coefficient of the matrix-inclusion composite can be determined.

2.5 *Bottom-up homogenization of concrete*

Analytical upscaling of the elastic stiffness of concrete, see Eq. (16), and of its eigenstress tensor, see Eq. (17), is carried in four subsequent steps, starting with the hydrate gel scale and continuing with the hydrate foam scale, the cement paste scale, and, finally, with the concrete scale, see Table 2.

As for the exemplary validation of these developments, model-predicted thermal expansion coefficients of mature cement pastes are compared with corresponding measurements. Hygrothermic coefficients, measured by Grasley & Lange (2007), see Figure 2, together with the initial water-to-cement mass ratios of the tested cement pastes serve as input for the multiscale model. The model-predicted thermal expansion coefficients of cement pastes agree quite well with independent measurements, also reported by Grasley & Lange (2007), see Figure 3. This underlines the satisfactory performance of the developed multiscale model.

2.6 *Top-down stress concentration*

After a structural simulation, the macroscopic stress tensors of concrete, Σ_{con}, and the temperature changes ΔT are known at every point of the structure. Top-down stress concentration aims at quantifying microscopic stress states inside both the cement paste matrix and the aggregate inclusions.

This task is accomplished by explicit consideration of the underlying Eshelby problems. At first, the macrostrain is calculated from the macrostress and the temperature change as

$$\mathrm{E}_{con} = \mathbb{C}_{con}^{-1} : \Sigma_{con} + \alpha_{con} \Delta T \mathbf{1}. \tag{20}$$

The macrostrain allows for quantification of the auxiliary strain E_{∞}, representing the remote loading of the underlying Eshelby problems (Zaoui 2002).

$$\mathrm{E}_{\infty} = \left\{ f_{cp} \mathrm{II} + f_{agg} \left[\mathrm{II} + \mathbb{P} : (\mathbb{C}_{agg} - \mathbb{C}_{cp}) \right]^{-1} \right\}^{-1} : \{ \mathrm{E}_{con} + f_{agg} \left[\mathrm{II} + \mathbb{P} : (\mathbb{C}_{agg} - \mathbb{C}_{cp}) \right]^{-1} : \mathbb{P} : (\boldsymbol{\sigma}_{agg}^{e} - \boldsymbol{\sigma}_{agg}^{e}) \}. \tag{21}$$

Table 2. Input and outputs of the step-by-step homogenization of the concrete.

RVE	Constituent	Volume fraction	Stiffness	Eigenstress	Homogenized Stiffness	Homogenized Eigenstress
hydrate gel	solid hydrates	f_{hyd}^{gel}	$\mathbb{C}_{hyd}$	$-\mathbb{C}_{hyd} : \alpha_{hyd}\Delta T\mathbf{1}$	$\mathbb{C}_{gel}$	Σ_{gel}^{e}
	gel pores	f_{gpor}^{gel}	0	$-p_{gpor}\mathbf{1}$		
hydrate foam	hydrate gel	f_{gel}^{hf}	$\mathbb{C}_{gel}$	Σ_{gel}^{e}	$\mathbb{C}_{hf}$	Σ_{hf}^{e}
	capillary pores	f_{cpor}^{hf}	0	$-p_{gpor}\mathbf{1}$		
cement paste	hydrate foam	f_{hf}^{cp}	$\mathbb{C}_{hf}$	Σ_{hf}^{e}	$\mathbb{C}_{cp}$	Σ_{cp}^{e}
	cement	f_{cem}^{cp}	$\mathbb{C}_{cem}$	$-\mathbb{C}_{cem} : \alpha_{cem}\Delta T\mathbf{1}$		
concrete	cement paste	f_{cp}^{con}	$\mathbb{C}_{cp}$	Σ_{cp}^{e}	$\mathbb{C}_{con}$	Σ_{com}^{e}
	aggregates	f_{agg}^{con}	$\mathbb{C}_{agg}$	$-\mathbb{C}_{agg} : \alpha_{agg}\Delta T\mathbf{1}$		

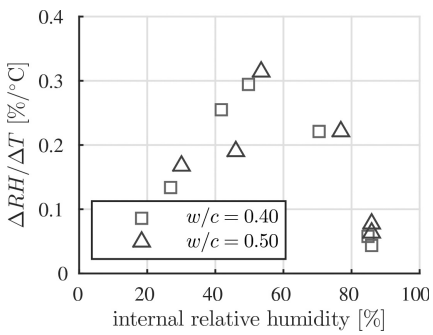

Figure 2. Experimentally determined hygrothermic coefficients $\Delta RH/\Delta T$ by Grasley & Lange (2007) for mature cement pastes with an initial water-to-cement mass ratio $w/c \in [0{:}40; 0{:}50]$.

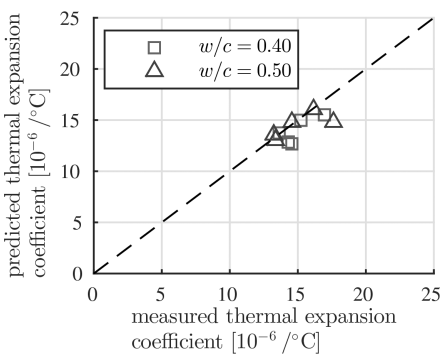

Figure 3. Comparison of model-predicted and measured thermal expansion coefficients of the cement paste with initial water-tocement mass ratios $w/c \in [0.40; 0.50;]$ the hydration degrees ξ of the mature pastes are set equal to 80%.

The microscopic strains of the cement paste and of the aggregates, $\boldsymbol{\sigma}_{cp}$ and $\boldsymbol{\sigma}_{agg}$, are quantified as (Zaoui 2002)

$$\begin{aligned} \boldsymbol{\varepsilon}_{cp} &= \mathrm{E}_{\infty}, \\ \boldsymbol{\varepsilon}_{agg} &= \left[\mathrm{II}+\mathbb{P}:\left(\mathbb{C}_{agg}-\mathbb{C}_{cp}\right)\right] \\ &\quad :\left[\mathrm{E}_{\infty}-\mathbb{P}:\left(\boldsymbol{\sigma}_{agg}^{e}-\boldsymbol{\sigma}_{agg}^{e}\right)\right]. \end{aligned} \tag{22}$$

The microscopic stresses of the cement paste and of the aggregates, $\boldsymbol{\sigma}_{cp}$ and $\boldsymbol{\sigma}_{agg}$, finally follow as

$$\begin{aligned} \boldsymbol{\sigma}_{cp} &= \mathbb{C}_{cp} : \left(\boldsymbol{\varepsilon}_{cp} - \boldsymbol{\varepsilon}_{cp}^{e}\right), \\ \boldsymbol{\sigma}_{agg} &= \mathbb{C}_{agg} : \left(\boldsymbol{\varepsilon}_{agg} - \boldsymbol{\varepsilon}_{agg}^{e}\right). \end{aligned} \tag{23}$$

3 MULTISCALE STRUCTURAL ANALYSIS OF A CONCRETE BEAM SUBJECTED TO SUDDEN COOLING AT THE TOP SURFACE

The object of the following multiscale thermo mechanical structural analysis is a simply-supported concrete beam with a rectangular cross section, see Figure 4. In the initial configuration, the beam exhibits a uniform reference temperature Tref

$$T(z, t<0) = T_{ref}. \tag{24}$$

At time instant $t = 0$, the top surface of the beam is considered to be flooded by ice-water.

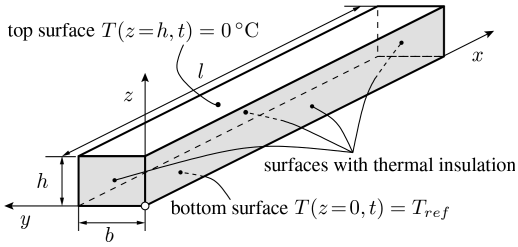

Figure 4. One-dimensional heat conduction along the height of a simply supported concrete beam with a rectangular cross section.

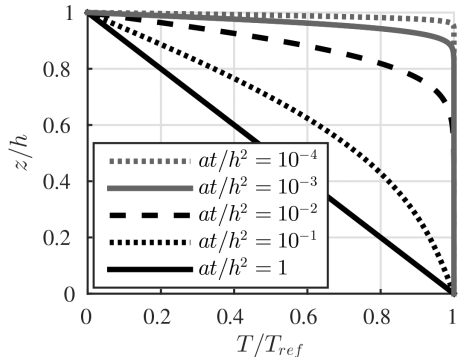

Figure 5. Distributions of the temperature along the height of the beam for different values of the dimensionless time parameter at/h^2.

The temperature at the top surface decreases instantaneously to zero degrees centigrade and remains constant thereafter

$$T(z=h;\,t)=0°\mathrm{C}. \tag{25}$$

The temperature at the bottom surface of the beam, in turn, remains constant at the reference temperature

$$T(z=0,t)=T_{ref}. \tag{26}$$

All other surfaces of the beam are considered to be perfectly insulated, such that one-dimensional heat conduction along the height of the beam, i.e. along the z-direction, takes place.

3.1 *Solution of the heat conduction problem*

One-dimensional heat conduction in z-direction is described by the following partial differential equation

$$\frac{\partial T}{\partial t}=a\frac{\partial^2 T}{\partial z^2}, \tag{27}$$

where a represents the thermal diffusivity of concrete. The analytical solution of the heat conduction problem defined in Eqs. (24) – (27) reads as (Binder et al. 2018, Wang et al. 2017a)

$$T(z,t)=T_{ref}\left[\left(1-\frac{z}{h}\right)+\sum_{n=1}^{\infty}\frac{2(-1)^{n-1}}{n\pi}\sin\left(\frac{n\pi z}{h}\right)\exp\left(-\frac{n^2\pi^2 at}{h^2}\right)\right]. \tag{28}$$

Distributions of the temperature along the height of the beam are shown in Figure 5, for specific values of the dimensionless time instant at/h^2. The temperature distribution along the height of the beam during the instationary heat conduction is nonlinear. Specifically, large temperature gradients are observed close to the top surface, where the sudden cooling is applied. Steady-state heat conduction has been already reached at the dimensionless time instant $at/h^2 = 1$, resulting in a linear distribution of the temperature field along the height of the beam.

3.2 *Macrscopic thermal stress analysis based on finite element simulations*

A three-dimensional Finite Element model of a simply-supported beam, with the dimensions $l\times h\times b=2\,\mathrm{m}\times 0.3\,\mathrm{m}\times 0.4\,\mathrm{m}$, is established for macroscopic thermo-mechanical analysis. The basis for two different types of input is as follows:

- Knowledge of the volume fractions, elastic properties, and thermal expansion coefficients of the cement paste and the aggregates gives access to the corresponding thermo-mechanical properties of the concrete following Eqs. (16) and (19), see also Table 3.
- Temperature distributions at the dimensionless time instants $at/h^2\in[10^{-2},10^{-1},1]$, are calculated according to Eq. (28). Thereby, the reference temperature, T_{ref}, and the thermal diffusivity of concrete, a, are set equal to $20\,^{\circ}C$ and to $4.73\times10^{-7}\ \mathrm{m^2/s}$, respectively.

Simulation results are the distributions of the normal stress along the height of the cross section, $\Sigma_{xx}(z)$, at midspan of the beam, see Figure 2. Right after the sudden cooling, significant tensile stresses occur at and in the vicinity of the top and the bottom surface of the beam, while compressive stresses prevail at the middle part of the beam. Notably, because of the overall equilibrium of the structure, in the absence of mechanical loads, the stress resultants, in the form of the normal forces and the bending moments, vanish at all times.

Table 3. Thermoelastic properties of the cement paste, the aggregates, and the homogenized concrete.

Material	Volume fraction	Elastic modulus	Poisson's ratio	Thermal expansion coefficient
cement paste	0.33	18 GPa	0.2	$15.0 \cdot 10^{-6}$/°C
Aggregates	0.67	40 GPa	0.2	$8.5 \cdot 10^{-6}$/°C
concrete	—	30 GPa	0.2	$10.0 \cdot 10^{-6}$/°C

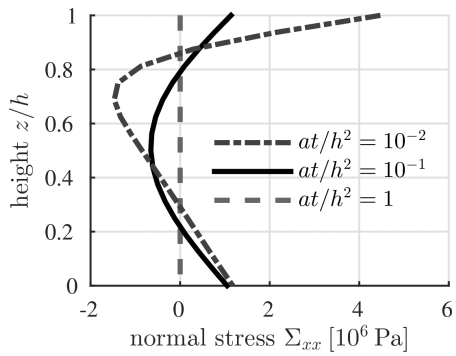

Figure 6. Evolution of the distribution of the macroscopic normal stress Σ_{xx} along the height of the cross-section at the middle length of the beam with heat conduction.

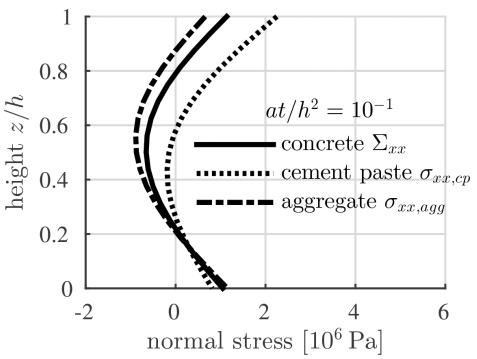

Figure 7. Distribution of the macroscopic stresses of concrete and of the microscopic stresses of the cement paste and the aggregates along the height of the cross section at midspan of the beam at the dimensionless time instant $at/h^2 = 10^{-1}$.

The temperature-induced stresses are gradually decreasing. Finally they vanish as the temperature profile along the height of the beam approaches the linear distribution which refers to the steady-state heat conduction.

3.3 *Top-down quantification of stress states in the cement paste and the aggregates*

The microscopic stresses in the cement paste and the aggregates are quantified on the basis of the presented multiscale model. The calculated macroscopic stress states of concrete and the temperature distribution along the height of the beam serve as input. The microscopic stresses in the cement paste matrix and in the aggregate inclusions at the dimensionless time instant $at/h^2 = 10^{-1}$ are shown in Figure 3. Because of the mismatch of the thermal expansion of the cement paste and the aggregates, the tensile stresses prevailing within the cement paste are larger in comparison to those within the aggregates and the concrete.

4 SUMMARY AND CONCLUSIONS

A multiscale thermo-hygro-poro-mechanical model for concrete was developed and applied to the multiscale structural analysis of a concrete beam.

- Bottom-up homogenization was used to upscale hygrothermic coefficients to the thermal expansion coefficients of the cement paste and the concrete.
- The homogenized stiffness and the thermal expansion coefficient were used as input for a three dimensional Finite Element simulation of a simply supported concrete beam subjected to sudden cooling at the top surface.
- Top-down stress concentration was used to quantify the microscopic stresses of the cement paste matrix and the aggregates.

This analysis has led to the following conclusions:

- The homogenization approach for thermal expansion coefficients was exemplarily validated in Subsection 2.5, where measured hygrothermic coefficients were upscaled to effective thermal expansion coefficients of different mature cement paste. The model-predicted thermal expansion coefficients agree very well with the measured counterparts. This is strong evidence of the predictive capabilities of the presented multiscale model.
- The overall multiscale structural analysis has shown that considerable macroscopic thermal stresses arise right after sudden cooling. These stresses gradually decrease and finally vanish, once heat conduction has reached the steady-state regime.
- Top-down stress concentration was carried out explicitly considering the mismatch of the

thermal expansion coefficients of the cement paste and the aggregates. This way, it could be shown that the tensile stresses in the cement paste are significantly larger than the ones at the concrete scale. This proves that the risk of cracking of concrete is larger than estimated on the basis of the tensile stresses quantified at the macroscopic scale of concrete.

ACKNOWLEDGEMENTS

Financial support by the Austrian Science Fund (FWF), provided within project P 281 31-N32 "Bridging the Gap by Means of Multiscale Structural Analyses" is gratefully acknowledged. The first author also gratefully acknowledges financial support by the China Scholarship Council (CSC).

REFERENCES

Badmann, R., N. Stockhausen, & M.J. Setzer (1981). The statistical thickness and the chemical potential of adsorbed water films. *Journal of Colloid and Interface Science 82*(2), 534–542.

Benveniste, Y. (1987). A new approach to the application of Mori-Tanaka's theory in composite materials. *Mechanics of Materials 6*(2), 147–157.

Binder, E., H. Wang, T. Schlappal, J. Zhang, Y. Yuan, B. Pichler, & H. Mang (2018). Bridging the gap between concrete microstructures and tunnel linings. In *Advances in Computational Plasticity*, pp. 23–44. Springer.

Emanuel, J.H. & J.L. Hulsey (1977). Prediction of the thermal coefficient of expansion of concrete. *Journal of the American Concrete Institute 74*(4), 149–155.

Grasley, Z.C. & D.A. Lange (2007). Thermal dilation and internal relative humidity of hardened cement paste. *Materials and Structures 40*(3), 311–317.

Gudmundsson, A. (2011). *Rock fractures in geological processes*. Cambridge University Press.

Hill, R. (1963). Elastic properties of reinforced solids. *Journal of Mechanics and Physics of Solids 11*(5), 357–372.

Huang, Q., Z. Jiang, X. Gu, W. Zhang, & B. Guo (2015). Numerical simulation of moisture transport in concrete based on a pore size distribution model. *Cement and Concrete Research 67*, 31–43.

Levin, V. (1967). Coefficients of temperature expansion of heterogeneous materials. *Mechanics of Solids 2*, 88–94.

Mori, T. & K. Tanaka (1973). Average stress in matrix and average elastic energy of materials with misfitting inclusions. *Acta Metallurgica 21*(5), 571–574.

Neimark, A.V. & P.I. Ravikovitch (2001). Capillary condensation in MMS and pore structure characterization. *Microporous and Mesoporous Materials 44*, 697–707.

Pichler, B. & C. Hellmich (2011). Upscaling quasi-brittle strength of cement paste and mortar: A multi-scale engineering mechanics model. *Cement and Concrete Research 41*(5), 467–476.

Pichler, B. & L. Dormieux (2010). Cracking risk of partially saturated porous media—Part I: Microporoelasticity model. *International Journal for Numerical and Analytical Methods in Geomechanics 34*(2), 135–157.

Ulm, F.J., G. Constantinides, & F. Heukamp (2004). Is concrete a poromechanics materials? – A multiscale investigation of poroelastic properties. *Materials and Structures 37*(1), 43–58.

Wang, H., C. Hellmich, Y. Yuan, H. Mang, & B. Pichler (submitted). Does reversible water uptake/release by hydrates govern the thermal expansion of cement paste? – A scale transition analysis. *Cement and Concrete Research*.

Wang, H., H. Mang, Y. Yuan, & B. Pichler (2017b). Microporomechanical modeling of thermal expansion of cement pastes. In *Poromechanics 2017 - Proceedings of the 6th Biot Conference on Poromechanics*, Paris, France, pp. 746–753.

Wang, H., M. Ausweger, H. Mang, Y. Yuan, & B. Pichler (2017a). Multiscale quantification of thermal stresses in concrete linings resulting from accidental sudden heating or cooling. In *Proceedings of the IV International Conference on Computational Methods in Tunneling and Subsurface Engineering*, Innsbruck, Austria, pp. 781–788.

Zaoui, A. (2002). Continuum micromechanics: Survey. *Journal of Engineering Mechanics (ASCE) 128*(8), 808–816.

Computational Modelling of Concrete Structures – Meschke, Pichler & Rots (Eds)
© 2018 Taylor & Francis Group, London, ISBN 978-1-138-74117-1

Translating environmentally-induced eigenstresses to risk of fracture for design of durable concrete pavements

A. Louhghalam
Department of Civil and Environmental Engineering, University of Massachusetts Dartmouth, Dartmouth, MA, US

T. Petersen & F.-J. Ulm
Department of Civil and Environmental Engineering, Massachusetts Institute of Technology, Cambridge, MA, US

ABSTRACT: Different mechanical loading or environmental stressors can cause cracks in concrete structures. These cracks can dramatically affect the durability of concrete, as they increase the potential for penetration of aggressive chemicals and accelerate the deterioration process. A model is developed here to predict the risk of fracture in concrete pavements. The pavement is modeled as an Euler-Bernoulli beam on a Winkler foundation and cracks are modeled by including additional compliance. The contribution of axial force and bending moment to the energy release rate are considered and used in a linear elastic fracture mechanics framework to predict the risk of fracture. A concrete pavement section under thermal cycles is examined, by way of illustration, and the proposed model is utilized to find the risk of fracture. Scaling relationships are developed between the thermal eigenstresses and material and structural properties of pavement and sub-grade. The applicability of information obtained from the scaling relationships in providing insights for the design of fracture resistant and durable pavements both at material and structural levels is also discussed.

1 INTRODUCTION

Using durable pavements in roadway networks reduces the cost and environmental footprint associated with pavement maintenance and rehabilitation. This is crucial due to the increasing demand for road transportation in the United States and the large cost associated with pavement construction, maintenance and rehabilitation (NHPN 2017). In addition pavement degradation alters the structural and surface characteristics, which has been shown to increase vehicle fuel consumption (Zaabar and Chatti 2010, Pouget et al. 2011, Louhghalam et al. 2013, Louhghalam et al. 2015) and network level greenhouse gas emissions (Louhghalam et al. 2017).

Concrete pavements are subjected to environmental distresses such as early-age autogenous shrinkage, drying, thermal cycles, alkali silica reaction and freeze-thaw cycles. The distress mechanisms result in physical and/or chemical evolution at smaller scales that, in turn, manifest themselves in the form of thermo- chemo- and hygro-mechanical self-balanced stress fields (eigenstresses) within the concrete. When a pavement is constrained by the subgrade and adjacent sections, the integrated impact of these eigenstresses at the continuum, structural scale—*i.e.* the scale of the pavement sections—can lead to tensile cracks. These cracks are a major source of deterioration of concrete and must be avoided when durability is the primary design criterion. Here a model is developed that expresses the risk of fracture, in terms of the eigenstresses within the pavement sections using linear elastic fracture mechanics (LEFM). When considering structural durability, the aim of this model is to shift the design paradigm from strength-based criteria, which do not account for the risk of cracking, to fracture-based criteria.

To provide a first order estimate of the risk of fracture, the pavement is modeled as an Euler-Bernoulli beam on an elastic foundation representing the subgrade with periodic cracks partially passing through pavement thickness. The existence of cracks changes both the axial and flexural stiffnesses of the beam. This is modeled by adding a set of springs to the beam, for which the compliance is a function of the crack depths. The total energy release rate of the system is then determined and compared to the that of a break-through crack (used to provide a zeroth-order estimate of the risk of fracture) given in Louhghalam and Ulm (2016).

The results are subsequently used in a linear elastic fracture mechanics framework to estimate the risk of fracture andcrack propagation. By way of example, the risk of pavement fracture for a section subjected to thermal cycles is investigated, and a scaling relationship between the allowable temperature change and material/structural characteristics of the pavement is obtained.

2 FRACTURE-BASED MODEL FOR PAVEMENT DURABILITY

Here, we model a pavement as an elastic Euler-Bernoulli beam—where we assume shear deformation is negligible—on an elastic foundation. The elastic foundation represents the subgrade's resistance to longitudinal and transversal deformations of the beam, modeled as line-springs in both the horizontal and vertical directions. The force corresponding to a horizontal spring is applied at the neutral axis, assuming that beam's thickness is small compared to its length, such that the moment caused by the horizontal spring action can be disregarded.

2.1 *Energy release rate*

The concrete beam is subjected to environmentally-induced eigenstresses (σ^p). These are self-balanced stresses that built up within our infinitely long pavement system. While they do not perform any mechanical work, the resulting axial forces and moments—due to restraints or eigenstress gradients—can lead to tensile cracking if the energy release rate $\mathcal{G}$ reaches the fracture energy of the material $\mathcal{G}_c$ (Griffith 1921, Irwin 1957):

$$\mathcal{G} = -\frac{d\varepsilon_{pot}}{d\Gamma} = \frac{1}{2}\int_\Gamma \underline{T}^0 \cdot \frac{d[[\underline{u}]]}{d\Gamma} da \le \mathcal{G}_c. \tag{1}$$

In the above ε_{pot} is the potential energy, Γ is the crack surface, $\underline{T}^0 = \sigma^p_{xx}\underline{e}_x$ is the traction vector due to the induced eigenstress σ^p at the initial equilibrium state, and $[[\underline{u}]]$ is the displacement discontinuity due to fracture at the final thermodynamic equilibrium state. Using the Navier-Bernoulli beam formulation, the displacement discontinuity can be decomposed into an axial discontinuity of the neutral axis $[[\underline{u}_0(x)]] = [[u]]\underline{e}_x$ and a rotational discontinuity of the beam $[[\underline{\omega}(x)]] = [[\omega(x)]]\underline{e}_y$, i.e. $[[\underline{u}]] = [[\underline{u}_0(x)]] + [[\underline{\omega}(x)]] \times \underline{x}_S$, where $\underline{x}_S = (z - z_c)\underline{e}_z + y\underline{e}_y$ is the position vector of the crack surface, with z and z_c respectively denote the coordinate along the beam's thickness, and the coordinate of the neutral axis of the uncracked beam. The energy release rate is therefore:

$$\mathcal{G} = \frac{1}{2}\int_\Gamma \sigma^p_{xx}\left(\frac{d[[u]]}{d\Gamma} + (z - z_c)\frac{d[[\omega]]}{d\Gamma}\right) da \le \mathcal{G}_c. \tag{2}$$

Integrating the above along the crack surface one can write:

$$\mathcal{G} = \frac{1}{2}\left(N^p \frac{d[[u]]}{d\Gamma} + M^p \frac{d[[\omega]]}{d\Gamma}\right) \le \mathcal{G}_c, \tag{3}$$

where

$$N^p = \int_S \sigma^p_{xx}(\underline{x})\, da \tag{4}$$

and

$$M^p = \int_S (z - z_c)\sigma^p_{xx}(\underline{x})\, da, \tag{5}$$

are respectively the beam's axial force and bending moment due to the initial eigenstress field σ^p_{xx}, and S is the beam's cross sectional area.

2.2 *Partial cracks*

The existence of crack reduces both the axial and bending stiffnesses of the beam. To consider this effect, an infinite beam with an edge cracks of depth a is modeled as two semi-infinite beams connected at the crack location with springs that account for the beam's additional compliance (Rice and Levy 1972, Hong et al. 1997, Roesler and Khazanovich 1997). The enhanced opening displacement and rotational discontinuity can be expressed as:

$$[[u]] = C_{tt}N^p + C_{tm}M^p \tag{6}$$

$$[[\omega]] = C_{tm}N^p + C_{mm}M^p. \tag{7}$$

In the above, C_{tt} and C_{mm} are respectively the additional axial and bending compliances due to the introduction of the crack, whereas C_{tm} accounts for the bending-axial coupling effect. After substituting the above displacements into (3), the total energy release rate can be expressed in terms of the derivatives of the springs' compliance functions with respect to the crack depth:

$$\mathcal{G} = \frac{1}{2}\left(\frac{dC_{tt}}{d\Gamma}(N^p)^2 + 2\frac{dC_{tm}}{d\Gamma}M^pN^p + \frac{dC_{mm}}{d\Gamma}(M^p)^2\right). \tag{8}$$

The compliance coefficients are evaluated by using the Irwin relationship between the energy release rate and the stress intensity factor. To this end, the stress intensity factors $\mathcal{K}_I$ and $\mathcal{K}_{II}$ for a plane-strain strip with an edge crack subjected

respectively to an axial force N^p and a bending moment M^p at far-field are written as

$$\mathcal{K}_t = \frac{N^p}{bh^{1/2}} g_t(\xi) \qquad \mathcal{K}_m = \frac{6M^p}{bh^{3/2}} g_m(\xi), \tag{9}$$

where $g_t(\xi)$ and $g_m(\xi)$ are the dimensionless stress intensity factors in functions of crack depth to thickness ratio $\xi = a/h$ for a notched strip of infinite length in the plane-strain condition and are given by (Tada et al. 1973, Benthem and Koiter 1973, Gross and Srawley 1965):

$$g_t(\xi) = \frac{\sqrt{2\tan\frac{\pi\xi}{2}}\left(0.752 + 2.02\xi + 0.37\left(1-\sin\frac{\pi\xi}{2}\right)^3\right)}{\cos\frac{\pi\xi}{2}} \tag{10}$$

and

$$g_m(\xi) = \frac{\sqrt{2\tan\frac{\pi\xi}{2}}\left(0.923 + 0.199\left(1-\sin\frac{\pi\xi}{2}\right)^4\right)}{\cos\frac{\pi\xi}{2}}. \tag{11}$$

Considering an infinite notched strip solely subjected to an axial force N^p at far-field and using Eqs (8) and (9) and the Irwin formula, one can write

$$\frac{dC_{tt}}{d\xi} = \frac{2hg_t^2}{SE}, \tag{12}$$

and determine the compliance coefficient C_{tt} in function of the dimensionless crack depth ξ as

$$C_{tt} = \frac{2hF_t(\xi)}{SE}, \tag{13}$$

where $F_t(\xi) = \int_0^\xi g_t^2(\xi)d\xi$. Similarly, considering an infinite strip with an edge crack subjected to a far-field bending moment M^p, the variation of the bending compliance associated with the crack is obtained as

$$\frac{dC_{mm}}{d\xi} = \frac{6hg_m^2}{EI} \tag{14}$$

Subsequently, the bending compliance coefficient of the spring reads

$$C_{mm} = \frac{6hF_m(\xi)}{EI}, \tag{15}$$

with $F_m(\xi) = \int_0^\xi g_m^2(\xi)d\xi$. The additional compliance corresponding to the axial-bending coupling action is determined by considering the notched strip subjected to both an axial force and bending moment at far-field. Using the superposition principle of the stress intensity factorsand substituting (12) and (14) into (8) one can write

$$\frac{dC_{tm}}{d\Gamma} = \frac{2\mathcal{K}_t\mathcal{K}_m}{M^pN^pE} = \sqrt{\frac{dC_{mm}}{d\Gamma}\frac{dC_{tt}}{d\Gamma}}. \tag{16}$$

It is observed that these compliance coefficients are monotonically increasing functions of the crack depth. Finally substituting (12)-(16) into (8) we arrive at the famous Irwin relation

$$G = \frac{\mathcal{K}^2}{E} = \frac{\left(\mathcal{K}_t + \mathcal{K}_m\right)^2}{E}. \tag{17}$$

3 BEAM ON ELASTIC FOUNDATION– WITH PERIODIC PARTIAL CRACKS

Consider an infinite beam on an elastic foundation having periodic partial cracks with spacing ℓ and crack depth a. We decompose the problem into axial and bending problems, and use translational and rotational springs as illustrated in Figure 1 to represent the additional compliance due to the existence of cracks when respectively an axial force N^p and a bending moment M^p are separately applied to the system. By way of the superposition principle, the total stress intensity factor is the sum of the stress intensity factors corresponding to the tensile and bending contributions. The total energy release rate is subsequently determined using the Irwin relationship.

3.1 *Axial contribution*

For a pavement subjected to initial axial force N^p, the internal axial force in the translational spring in Figure 1(a) is $N = [[u]]/C_{tt}$. The translational crack opening $[[u]]$ can be determined by solving the differential equation for the axial deformation of the neutral axis from the following equation:

$$\frac{d^2u}{dx^2} - \lambda_t^2 u = 0, \tag{18}$$

where $\lambda_t = \sqrt{k_H/ES}$, E is beam Young's modulus and k_H is subgrade horizontal stiffness. The solution is expressed as $u_i = B_i \exp(\lambda_t x) + C_i \exp(-\lambda_t x)$ with $i = 1,2$ representing the axial deformation at the left and right sides of the crack. We study the incremental risk of crack propagation, where initial and final elastic equilibrium states are partially cracked beams with dimensionless crack depth respectively equal to ξ and $\xi + d\xi$. The cracks are modeled as springs with an initial

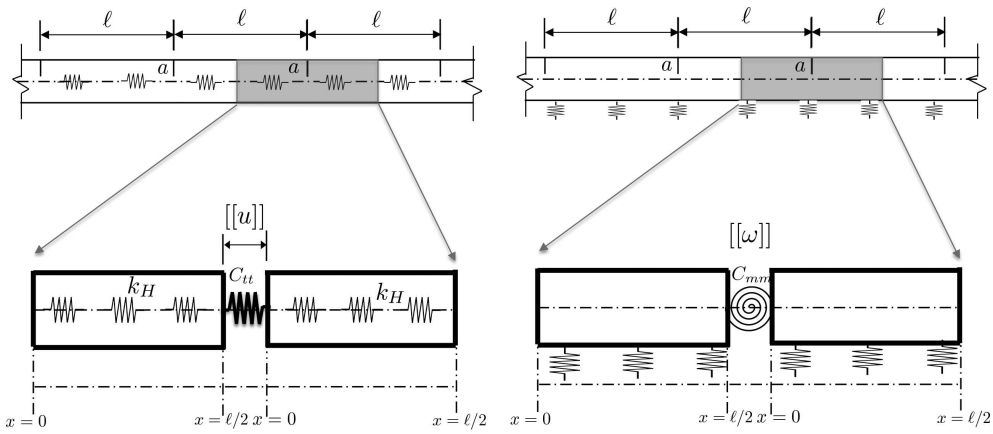

(a) (b)

Figure 1. Beam model with partial crack; cracks modeled as springs accounting for the increase in beam's compliance. (a) axial problem, (b) bending problem.

compliance of C_{tt}. The partially cracked beam is initially subjected to an axial force N^p, induced by the eigenstress σ^p. We make use of the symmetry condition at the mid distance between the cracks along with the boundary condition $ESu_i'(x)+N^p=\left(u_2(0)-u_1(\ell/2)\right)/C_{tt}$, $i=1,2$ at the two crack surfaces, i.e. $u_1(\ell/2)$ and $u_2(0)$, to determine the unknown coefficients B_i and C_i and subsequently evaluate the axial crack opening by $[[u]]=2C_{tt}N^p/(\lambda_t ESC_{tt}\coth(\lambda_t\ell/2)+2)$. The energy release rate and stress intensity factor corresponding to the axial force respectively read as

$$\mathcal{G}_{[[u]]}=\frac{N^p}{2S}\frac{d[[u]]}{d\xi}=\frac{h}{2E}\left(\frac{N^p}{S}\right)^2\times\mathcal{U} \tag{19}$$

and

$$K_{[[u]]}=\frac{N^p}{S}\sqrt{\frac{h}{2}\times\mathcal{U}}, \tag{20}$$

with the dimensionless energy release rate $\mathcal{U}$ given by

$$\mathcal{U}=\frac{4ES}{\left(2+\lambda_t ESC_{tt}\coth(\lambda_t\ell/2)\right)^2}\frac{dC_{tt}}{hd\xi}. \tag{21}$$

Substituting the spring compliance and its derivative from (13) and (12) the above is expressed as

$$\mathcal{U}=\frac{2g_t^2(\xi)}{\left(\lambda_t hF_t(\xi)\coth(\lambda_t\ell/2)+1\right)^2} \tag{22}$$

and illustrated in Figure 2 for different dimensionless crack depths ξ and spacing ℓ/h. It can be observed that $\mathcal{U}$ increases with crack depth and as $\lambda_t\to 0$ it approaches its maximum value, which is asymptotically expressed as

$$\mathcal{U}\to\frac{2g_t^2(\xi)}{\left(1+2F_t(\xi)h/\ell\right)^2}\left\{1-\frac{(\lambda_t\ell)^2}{3}\frac{F_t(\xi)h/\ell}{2F_t(\xi)h/\ell+1}\right\}, \tag{23}$$

and presented in Figure 3. The total potential energy that is released due to a crack with dimensionless depth ξ reads

$$\int_0^\xi\mathcal{G}_{[[u]]}d\xi=\left(\frac{N^p}{S}\right)^2\frac{SC_{tt}}{\lambda_t ESC_{tt}\coth(\lambda_t\ell/2)+2}, \tag{24}$$

and as ξ goes to unity approaches the dimensionless energy released rate of a break-through crack $\left(N^p/S\right)^2\times 1/(E\lambda_t\coth(\lambda_t\ell/2))$ given in Louhghalam & Ulm (2016).

3.2 *Bending contribution*

A similar analysis is performed to examine the energy release rate corresponding to bending action by considering an Euler-Bernoulli beam on an elastic foundation. Periodic partial cracks increase the bending compliance of the system. This is modeled by adding a rotational spring of compliance C_{mm} at crack locations as shown in Figure 1(b). The internal moment in the rotational spring is $M=[[\omega]]/C_{mm}$, with $[[\omega]]$ the angular crack opening. Similar to the axial problem, here we

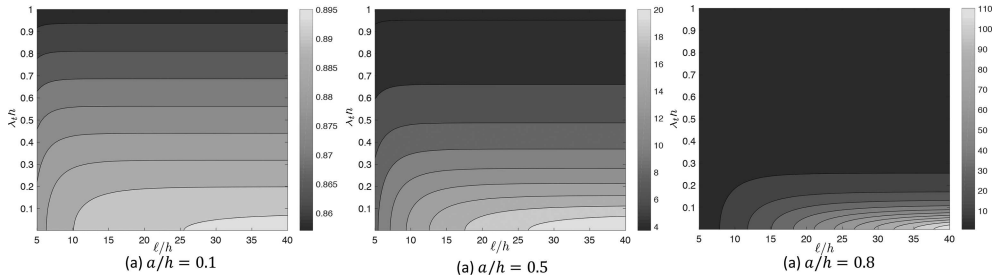

Figure 2. Contour plots of dimensionless energy release rate versus ℓ/h and $\lambda_b h$ for (a) $\xi = 0.1$, (b) $\xi = 0.5$ and (c) $\xi = 0.8$. The maximum value of $\mathcal{U}$ occurs for small $\lambda_b h$.

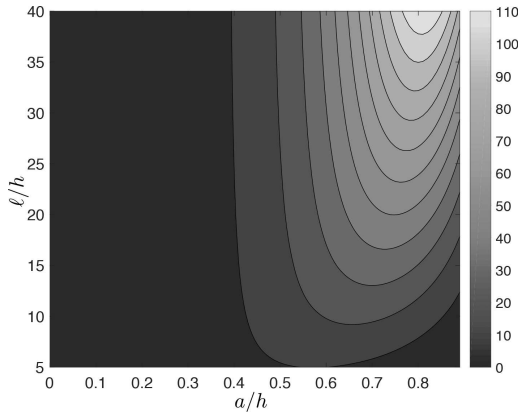

Figure 3. Dimensionless energy release rate for small values of $\lambda_b h$.

examine the incremental risk of crack propagation for the case where both initial and final elastic equilibrium states are partially cracked beams. In the initial equilibrium state, cracks of dimensionless depth ξ are subjected to an eigenstress-induced moment M^p. As cracks advance to the depth $\xi + d\xi$, their compliance increase to $C_{mm} + dC_{mm}$. The rotational discontinuity of the crack surface is determined by finding the transversal deformation of the beam by solving the following differential equation:

$$\frac{d^4 w}{dx^4} + \lambda_b^4 w = 0, \tag{25}$$

where $\lambda_b^4 = k_V/EI$, I is the beam's moment of inertia and k_V is the subgrade's vertical stiffness. The solution to the differential equation can be expressed as

$$\begin{aligned} w_i &= \exp(\lambda_b x)\left(A_i \sin\lambda_b x + B_i \cos\lambda_b x\right) \\ &\quad + \exp(-\lambda_b x)\left(C_i \sin\lambda_b x + D_i \cos\lambda_b x\right), \end{aligned} \tag{26}$$

with w_1 and w_2 respectively denoting beam's deformation at the left and right sides of the crack. The unknown coefficients A_i, B_i, C_i and D_i are determined by satisfying continuity of displacement and shear force and the boundary conditions $EIw_i''(x) + M^0 = \left(w_2'(0) - w_1'(\ell/2)\right)/C_{mm}$, i = 1,2 at the crack surfaces (i.e. $w_1(\ell/2)$ and $w_2(0)$). In addition, the symmetry conditions, i.e. zero slope and shear force, are satisfied at the mid distance between the cracks, and the rotational discontinuity of the beam is obtained as $[[\omega]] = 2w_2'(0) = 2M^p C_{mm}/\left(\lambda_b EIC_{mm} S(\lambda_b \ell) + 2\right)$, where $S(\lambda_b \ell) = (\sinh\lambda_b \ell + \sin\lambda_b \ell)/(\cosh\lambda_b \ell - \cos\lambda_b \ell)$. The energy release rate thus reads as

$$\mathcal{G}_{[[\omega]]} = \frac{M^p}{2S}\frac{d[[\omega]]}{d\xi} = \frac{h}{2E}\left(\frac{M^p}{\sqrt{SI}}\right)^2 \times \mathcal{W}, \tag{27}$$

and the stress intensity factor is

$$\mathcal{K}_{[[\omega]]} = \frac{M^p}{\sqrt{SI}}\sqrt{\frac{h}{2}\times\mathcal{W}}, \tag{28}$$

with the dimensionless energy release rate $\mathcal{W}$ given by

$$\begin{aligned} \mathcal{W} &= \frac{4EI}{\left(\lambda_b EIC_{mm} S(\lambda_b \ell) + 2\right)^2}\frac{dC_{mm}}{hd\xi} \\ &= \frac{6g_m^2(\xi)}{\left(3\lambda_b h S(\lambda_b \ell) F_m(\xi) + 1\right)^2}, \end{aligned} \tag{29}$$

which is illustrated in Figure 4. Similar to the axial energy release rate, the maximum $\mathcal{W}$ occurs at small λ_b with an asymptotic value of

$$\mathcal{W} \to \frac{6g_m^2(\xi)}{\left(1 + 6F_m(\xi)h/\ell\right)^2}\left\{1 - \frac{\lambda^4 \ell^4}{15}\frac{F_m(\xi)h/\ell}{1 + 6F_m(\xi)h/\ell}\right\}. \tag{30}$$

The above is illustrated in Figure 5 in terms of the dimensionless crack depth and crack spacing.

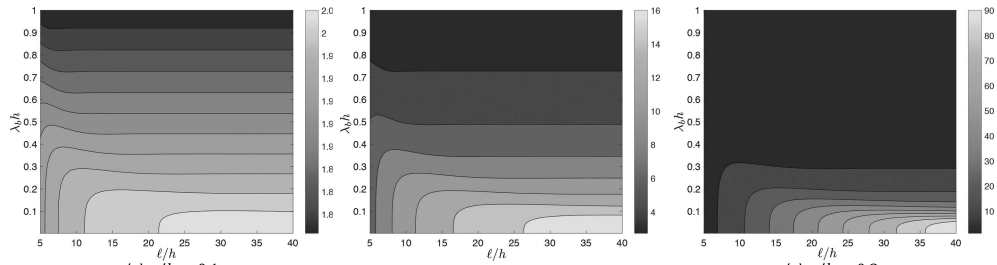

Figure 4. Contour plots of dimensionless energy release rate $\mathcal{W}$ versus ℓ/h and $\lambda_b h$ for (a) $\xi = 0.1$, (b) $\xi = 0.5$ and (c) $\xi = 0.8$. The maximum value of $\mathcal{W}$ occurs for small $\lambda_b h$.

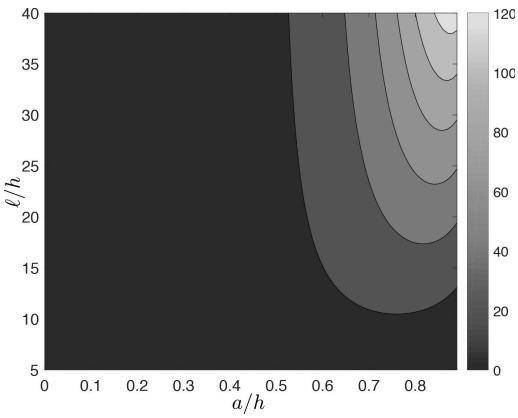

Figure 5. Dimensionless energy release rate for small values of $\lambda_b h$.

It is observed from both figures that $\mathcal{W}$ increases for increasing crack depth. As ξ goes to one, the total potential energy released,

$$\int_0^{\xi} \mathcal{G}_{[[\omega]]} d\xi = \left(\frac{M^p}{\sqrt{SI}}\right)^2 \frac{IC_{mm}}{\lambda_b EIC_{mm}\mathcal{S}(\lambda_b \ell) + 2}, \tag{31}$$

approaches the dimensionless energy release rate of a break-through crack $(M^p/\sqrt{SI})^2/E\lambda_b \mathcal{S}(\lambda_b \ell)$ presented in Louhghalam & Ulm (2016).

3.3 *Total contribution*

Using the procedure described in Section 2, the total energy release rate of a partially cracked beam on an elastic foundation subjected to eigenstresses in the form of axial forces and bending moments is determined as follows:

$$\mathcal{G} = \frac{h}{2E}\left(\frac{N^p}{S}\right)^2 \left(\mathcal{U} + \left(\frac{M^p}{N^p}\right)^2 \frac{S}{I}\mathcal{W} + 2\frac{M^p}{N^p}\sqrt{\frac{S}{I}\mathcal{U}\mathcal{W}}\right) \tag{32}$$

Finally using the Irwin formula the stress intensity factor reads:

$$\mathcal{K} = \frac{N^p}{S}\sqrt{\tfrac{h}{2}}\left(\sqrt{\mathcal{U}} + \frac{M^p}{N^p(h/6)}\sqrt{\tfrac{\mathcal{W}}{3}}\right) \tag{33}$$

4 APPLICATION: CONCRETE PAVEMENT SUBJECTED TO TEMPERATURE GRADIENT

By way of example, we examine the risk fracture in Portland Cement Concrete pavements due to thermal cycles. The average thermal expansion coefficient of a concrete mix is about 10×10^{-6} per degree Celsius, which can result in a significant change of length in concrete pavements of large size that are subjected to temperature changes of 40° or more. Since the motion of pavement sections are confined by the subgrade action as well as the neighboring sections, the developed thermal eigenstresses can lead to tensile cracks. We consider a pavement section that is initially at temperature T_0, and is exposed to an external surface temperature $T_{ext} < T_0$ at time zero. To investigate the temporal variation of the risk of fracture and examine the impact of the transient conditions, we solve the one-dimensional heat equation:

$$\frac{\partial T}{\partial t} = D_\theta \frac{\partial^2 T}{\partial Z^2}, \tag{34}$$

where D_θ is the thermal diffusivity, for which concrete has a typical value of $D_\theta = 4 \times 10^{-3}$m^2/h (Ulm & Coussy 2001). We define the characteristic time of heat diffusion $\tau = h^2/D_\theta$ – on the order of 10 hours for a typical concrete pavement of thickness h = 0.2 m–and disregard the heat exchange between the pavement and the subgrade. Using dimensionless parameters for depth $\bar{z} = Z/h$, temperature $\bar{T} = (T - T_{ext})/(T_0 - T_{ext})$ and time $\bar{t} = t/\tau$, the heat equation is expressed in the following dimensionless form:

$$\frac{\partial \bar{T}}{\partial \bar{t}} = \frac{\partial^2 \bar{T}}{\partial \bar{z}^2}. \tag{35}$$

The initial and boundary conditions of the problem can also be expressed in terms of the above dimensionless variables:

$$\bar{T}(\bar{z},0) = 1$$
$$\frac{\partial \bar{T}}{\partial \bar{z}}(\bar{z}=1,\bar{t}) = 0 \qquad \bar{T}(\bar{z}=0,\bar{t}>0) = 0. \tag{36}$$

For cooling pavement sections, where $\bar{T}(\bar{z}=1,\bar{t}) \le 1$, the solution reads

$$\bar{T} = \frac{4}{\pi}\sum_{n=0}^{n=\infty} \frac{\sin\left(\frac{(2n+1)\pi\bar{z}}{2}\right)\exp\left(-\frac{(2n+1)^2\pi^2\bar{t}}{4}\right)}{(2n+1)}. \tag{37}$$

For times that are large compared to the characteristic time of thermal diffusion ($\bar{t} \to \infty$), the temperature profile approaches a steady-state temperature profile of $\bar{T} = 0$, equal to a constant temperature of T_{ext} over the thickness. The axial, thermal eignestress in the pavement is then

$$\sigma_{th}^p = \frac{N_\infty^p}{S} = -\alpha_T E(T_{ext} - T_0), \tag{38}$$

with α_T the thermal expansion coefficient. Using the LEFM criterion in Eq. (20) one can write $\sigma_{th}^p \sqrt{h}/K_c \le \sqrt{2/\mathcal{U}}$, with $\mathcal{U}$ given by Eq. (22). We note that the critical case, i.e. when $\mathcal{U}$ is a maximum, corresponds to small values of λ_t. Therefore, from a design point of view, the asymptotic expression in Eq. (23) must be used to find the allowable thermal stress:

$$\frac{\sigma_{th}^p \sqrt{h}}{K_c} \le \frac{2F_t(\xi)h/\ell + 1}{g_t(\xi)} \tag{39}$$

For large values of ℓ/h the right hand side approaches $\mathcal{F}_{\ell\infty} = 1/g_t(\xi)$ and the allowable temperature change can be expressed in function of the crack spacing ℓ and the dimensionless crack depth ξ:

$$\langle T_0 - T_{ext} \rangle \le \frac{K_c}{\alpha_T E\sqrt{h}} \mathcal{F}_{\ell\infty} \times (2F_t(\xi)h/\ell + 1). \tag{40}$$

The allowable temperature change scales with $h^{-1/2}$ for large joint spacing and with $h^{1/2}$ for small joint spacing. This is also observed in Figure 6, where the allowable temperature change is presented as a function of ℓ/h. For instance, to increase the allowable temperature change, for a fixed crack depth a, one needs to increase the pavement thickness for large values of ℓ/h, and decrease the thickness for small values of ℓ/h. In addition, an increase in the allowable temperature change can be achieved by increasing the joint spacing and/or the horizontal subgrade stiffness. From a material design perspective, the maximum allowable temperature change can be improved by increasing the ratio of the concrete's fracture toughness to its Young's modulus. Note that one only needs to account for the risk of fracture when $T_0 > T_{ext}$ (where beam is under a tensile axial force).

The above analysis provides an estimate for the allowable temperature change in the steady-state condition by only considering eigenstresses that act as axial forces. However, the temperature gradient in the transient condition gives rise to eigenstressesthat manifest themselves as moments as well. To examine the risk of fracture in this case, we study the combined effect of axial forces and bending moments as a function of dimensionless time $\bar{t}$. We start with Eq. (4) and Eq. (5), use a change of coordinate $Z = h/2 - z$ and express the forces and moments in terms of the dimensionless parameters to arrive at

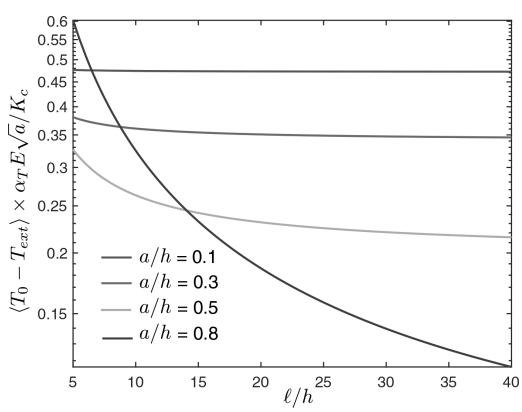

Figure 6. Dimensionless allowable temperature change in function of ℓ/h at different dimensionless crack depth a/h for negligible subgrade horizontal stiffness.

$$N^p(\bar{t}) = N_\infty^p \int_0^1 \left(1 - \bar{T}(\bar{z},\bar{t})\right) d\bar{z} \tag{41}$$

and

$$M^p(\bar{t}) = \frac{N_\infty^p h}{2} \int_0^1 (1-2\bar{z}) \left(1 - \bar{T}(\bar{z},\bar{t})\right) d\bar{z}. \tag{42}$$

Substituting the dimensionless temperature from Eq. (37) into Eqs. (41) and (42), the normalized eigenstress axial force and moment are obtained:

$$\frac{N^p(\bar{t})}{N_\infty^p} = 1 - \sum_{n=0}^{n=\infty} \frac{8 \exp\left(-\frac{(2n+1)^2\pi^2}{4}\bar{t}\right)}{\pi^2(2n+1)^2} \tag{43}$$

$$\frac{M^p(\bar{t})}{N_\infty^p h/2} = \sum_{n=0}^{n=\infty} \left(\frac{4(-1)^n}{\pi(2n+1)} - 1 \right) \frac{8 \exp\left(\frac{-(2n+1)^2\pi^2\bar{t}}{4}\right)}{\pi^2(2n+1)^2}. \tag{44}$$

The axial force increases until it reaches its steady state value at large $\bar{t}$, while the bending moment increases from zero right after the temperature change, to a maximum and then decreases until it completely vanishes at the steady-state condition. To find the transient risk of fracture, one needs to take into account the combined effect of axial forces and bending moments, as well as their coupled effect according to Eq. (32). The normalized total energy release rate is obtained by dividing Eq. (32) by the energy release rate at the steady state condition $(\mathcal{G}_\infty = h/2E \times (N_\infty^p/S)^2 \mathcal{U})$, written as

$$\frac{\mathcal{G}(\bar{t})}{\mathcal{G}_\infty} = \left(\frac{N^p(\bar{t})}{N_\infty^p} + \sqrt{3\varpi} \frac{M^p(\bar{t})}{N_\infty^p h/2} \right)^2, \tag{45}$$

where $\varpi = \mathcal{W}/\mathcal{U}$. The variation of the normalized energy release rate in function of time is plotted in Figure 7 for different ratios of $\varpi = \mathcal{W}/\mathcal{U}$. For values of ϖ larger than 4, the ratio $\mathcal{G}(t)/\mathcal{G}_\infty$ has a peak that surpasses unity, indicating that the energy release rate of a pavement under transient conditions, where the combined effect of bending moments and axial forces must be taken into account, surpasses the energy release rate of its steady state; engineers should design against this worst-case scenario.

To investigate the energy release rate in the transient condition, we utilize the closed-form approximations for the normalized axial force and bending moments developed in Louhghalam & Ulm (2016). For times right after the temperature change ($\bar{t} < 0.16$), the temporal variation of the normalized eigenstress axial forces and moments respectively read

$$\frac{N^p(\bar{t})}{N_\infty^p} \approx \sqrt{\frac{4\bar{t}}{\pi}} \tag{46}$$

$$\frac{M^p(\bar{t})}{N_\infty^p h/2} \approx \sqrt{\frac{4}{\pi}\bar{t}} - 2\bar{t}. \tag{47}$$

The normalized energy release rate at small $\bar{t}$ can thus be expressed as

$$\frac{\mathcal{G}(\bar{t})}{\mathcal{G}(\infty)} = \frac{4\bar{t}}{\pi} \left\{ 1 + \sqrt{3\varpi} \left\{ 1 - \sqrt{\pi\bar{t}} \right\} \right\}^2. \tag{48}$$

For small $\bar{t}$, when transient conditions prevail and the risk of fracture must be assessed by considering the combined effect of axial and bending contributions, the ratio $\mathcal{W}/\mathcal{U}$ must be constrained

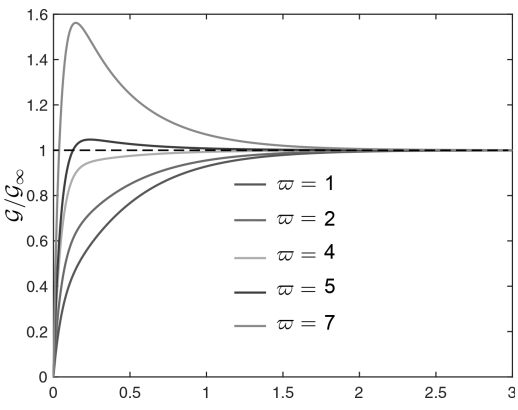

Figure 7. Ratio of the energy release rate in transient condition as a function of time to that of steady state condition for different ratios of $\mathcal{W}/\mathcal{U}$.

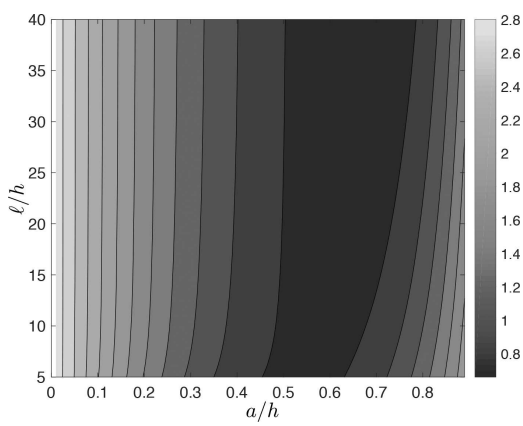

Figure 8. Ratio of dimensionless energy release rate for small values of λ_t and λ_b.

to values below 4. Figure 8 shows the ratio $\mathcal{W}/\mathcal{U}$ as a function of dimensionless crack spacing and depth for the case of negligible subgrade stiffness. It can be observed that $\varpi < 3$ and thus the energy release rate associated with the transient condition is less than that of the steady-state condition, and Eq. (40) can be used to find the crack/joint spacing of the pavement.

4 CONCLUSIONS

A model is developed that relates the risk of fracture in concrete pavements to its material and structural characteristics. The proposed approach is used to investigate the risk of fracture of a concrete pavement subjected to thermal cycles. The following points deserve attention:

- The allowable temperature change $\Delta T_a = \langle T_0 - T_{ext} \rangle$ in steady-state conditions decreases with increasing joint spacing. Furthermore, a transition in scaling of ΔT_a with thickness is observed from $\Delta T_a \propto h^{1/2}$ for small joint spacing to $\Delta T_a \propto h^{-1/2}$ for large joint spacing.
- From the material perspective, increasing the fracture toughness and decreasing the elastic modulus of concrete would increase the allowable temperature change.
- The energy release rate in the transient condition that accounts for both the axial an bending actions is shown not to surpass the energy release rate of the steady state condition for typical values of subgrade stiffness and joint spacing.

It is shown through this example how the development proposed in the above sections can be conveniently utilized to minimize the risk of fracture of concrete pavements and ensure their durability. The presented model aims at shifting the paradigm of designing durable structures from strength-based to fracture-based design. The proposed method can also be used to examine the performance of pavement sections that are subjected to eigenstresses caused by other physical, chemical and hygral evolutions due todifferent distress mechanisms.

REFERENCES

Benthem, J. & W. Koiter (1973). Asymptotic approximations to crack problems. In *Methods of analysis and solutions of crack problems*, pp. 131–178. Springer.

Griffith, A.A. (1921). The phenomena of rupture and flow in solids. *Philosophical transactions of the royal society of london. Series A 221*, 163–198.

Gross, B. & J.E. Srawley (1965). Stress-intensity factors for single-edge-notch specimens in bending or combined bending and tension by boundary collocation of a stress function. Technical report, DTIC Document.

Hong, A.P., Y.N. Li, & Z.P. Bazant (1997). Theory of crack spacing in concrete pavements. *Journal of Engineering Mechanics 123*(3), 267–275.

Irwin, G.R. (1957). Analysis of stresses and strains near the end of a crack traversing a plate. *Journal of Applied Mechanics 24*, 361–364.

Louhghalam, A., M. Akbarian, & F.-J. Ulm (2013). Flügge's conjecture: Dissipation vs. deflection induced pavementvehicle-interactions (pvi). *Journal of Engineering Mechanics*.

Louhghalam, A., M. Akbarian, & F.-J. Ulm (2017). Carbon management of infrastructure performance: Integrated big data analytics and pavement-vehicle-interactions. *Journal of Cleaner Production 142*, 956–964.

Louhghalam, A., M. Tootkaboni, & F.-J. Ulm (2015). Roughness-induced vehicle energy dissipation: Statistical analysis and scaling. *Journal of Engineering Mechanics*, 04015046.

Louhghalam, A. & F.-J. Ulm (2016). Risk of pavement fracture due to eigenstresses at early ages and beyond. *Journal of Engineering Mechanics 142*(12), 04016105.

NHPN (accessed 2017). United states department of transportation, federal highway administration's national highway planning network.

Pouget, S., C. Sauzéat, H.D. Benedetto, & F. Olard (2011). Viscous energy dissipation in asphalt pavement structures and implication for vehicle fuel consumption. *Journal of Materials in Civil Engineering 24*(5), 568–576.

Rice, J. & N. Levy (1972). The part-through surface crack in an elastic plate. *Journal of Applied Mechanics 39*(1), 185–194.

Roesler, J. & L. Khazanovich (1997). Finite-element analysis of portland cement concrete pavements with cracks. *Transportation Research Record: Journal of the Transportation Research Board* (1568), 1–9.

Tada, H., P.C. Paris, & G.R. Irwin (1973). The stress analysis of cracks. *Handbook, Del Research Corporation*.

Ulm, F.-J. & O. Coussy (2001). What is a massive concrete structure at early ages? some dimensional arguments. *Journal of engineering mechanics*.

Zaabar, I. & K. Chatti (2010). Calibration of hdm-4 models for estimating the effect of pavement roughness on fuel consumption for us conditions. *Transportation Research Record: Journal of the Transportation Research Board 2155*(1), 105–116.



Taylor & Francis
Taylor & Francis Group
http://taylorandfrancis.com

Computational Modelling of Concrete Structures – Meschke, Pichler & Rots (Eds)
© 2018 Taylor & Francis Group, London, ISBN 978-1-138-74117-1

Simulation of permeable concrete to assess interrelationship between strength and permeability

P. Modi, M. Dave, A. Dodhiya, Y. Dadi, M. Mungule & M. Langhi
Department of Civil Engineering, Institute of Infrastructure Technology Research and Management (IITRAM), Ahmedabad, India

ABSTRACT: Granular materials ranging from concrete to sand (graded soil) have substantially influenced our choices for construction materials. Such materials are desired to satisfy aspects such as permeability and strength as per requirement. Increased urban activity, frequent occurrence of floods owing to limited drainage area compelled researchers to look for alternate ways of absorbing surface runoff. Permeable concrete pavement being projected as a possible solution is practiced with limited success because increased permeability harms mechanical properties restricting its use. Permeable concrete with desired mechanical properties can be developed if its geometry and behaviour at granular level can be exploited. Computational modelling of concrete provides us with the window through which tapping into concrete at granular level can be achieved. Present study is an attempt towards development of numerical model aimed at analysing strength and permeability of permeable concrete which is achieved over two stages. In first stage, concrete is modelled as a granular material and further Sequential Packing Algorithm is used to accomplish requisite particle packing efficiency, followed by application of Cellular Particle Rejection System (CPRS) to identify voids and then its interconnection is analysed. In second stage, random discretization of homogenized space is achieved through Voronoi diagram and Delaunay triangulation. Granular model developed in first stage is superposed on the discretized model to incorporate heterogeneity into the system. The triangulation elements form a skeletal structure resembling concrete mix is then analysed under loading pattern to simulate mesoscopic response of the system. The response is analysed in terms of structural capacity, failure pattern and the dependence on the relative variation in the properties of mesoscopic phases. The resemblance between computational and actual concrete is acquired by maintaining composition entropy examined at mesoscale by using gradation curve based on Fuller maximum density. The developed model permits large scale testing of virtual concrete with varying composition to analyse influence on strength, permeability, pore network and failure pattern at granular level.

1 INTRODUCTION

Precipitation received in the catchment area of urban habitat is collected through piped network representing storm water drainage systems or is clubbed with existing sewage network. A sustainable system that is at the centre stage of urban planning, aims at reducing the wastage of precious natural resources governing our design for water transport systems. Irrespective of storm water drains, large influx of people towards urban areas causing unplanned expansion reducing available permeable surfaces, accumulation of dust and dirt in vicinity of storm water draining openings leading to partial or full blockage. With increased urbanization, traditional drainage systems with meager footprint and increased load and often suboptimal locations pose as most inefficient in terms of surface runoff, conveyance and maintenance. The problem is more acute in developing countries wherein unplanned urbanization along with suboptimally designed traditional drainage systems is widely unsuccessful and clogs the drains even at lowest downpour resulting in occurrence of urban floods.

The major consequence of urbanisation is the increase in impervious area leading to increase in direct runoff coupled with decreased infiltration. In rural areas with permeable surfaces, nearly 50% of the rainwater gets infiltrated through the soil to ground water while in urban areas with impermeable surfaces, only 15% of rainwater infiltrates through soil (Hingorani & Hingorani 2012). Increased impervious surfaces along with lack of sufficient and efficient drainage works increases the probability of urban flooding. To control urban flooding, huge economic investments are made to construct flood control measures.

In absence of such measures, urban flooding creates huge economic loss and damage to property. The pertinent question to address is the fact that flooding is caused by reduction in pervious surfaces and hence any solution to address the problem shall be aimed at restoring the desired degree of pervious land area. Since, urbanisation and development of support infrastructure is an irreversible process, attempts are being made towards development of intelligent alternatives that would permit the absorption of precipitation on one hand and ground water recharge on the other (Scholz & Grabowiecki 2007). Roads that occupy a substantial chunk of built up area (10%–30%) can act as a potential location for enhancing the perviousness of urban areas (Tennis, Lemming & Akers 2004). Thus, scientists have targeted paved surfaces as a preferential location and developed several models of permeable pavement systems (Pindado, Aguado & Josa 1999, Andersen, Foster & Pratt 1999, Schluter & Jefferies 2004). Although the research in the area is at nascent stage, serious efforts would be required to realize the full potential of permeable pavements. Permeable pavements can act as a sink to absorb the entire precipitation and can route the flood through underground network of pipes to desired target area. Limited to no human interaction would prevent clogging of drains thus enabling full potential of storm water network. However, the task is challenging as enhanced permeability would entail increased porosity requirement and is reported to have adverse effects on the mechanical characteristics of the material. Further, the problem is complicated with the fact that the atmospheric pollutants can potentially settle and clog the pores thus rendering the solution futile.

Figure 1 compares range of sizes in atmospheric pollutants and pore diameters in conventional concrete reflecting the narrow range of pore size available for development of permeable concrete

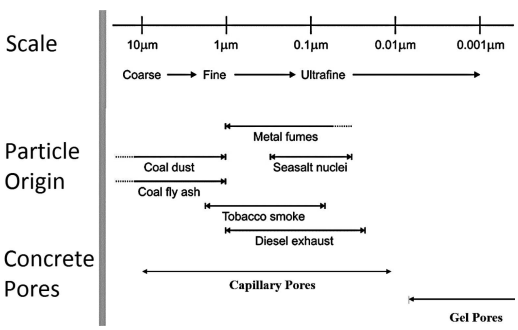

Figure 1. Comparison for size of particulate matter and concrete pores.

(Christian, Rothen-Rutishauser, Blank, Vanhecke, Ochs & Gehr 2008, Kumar & Bhattacharjee 2003). This limited window of possible pore size distribution is quite difficult to be engineered for the case of heterogeneous materials like concrete. For very small size pores, the material becomes impervious whereas for larger size it increases the risk of clogging by dust and particulate matters.

Another important aspect associated with concrete structures is that it is designed to permit limited porosity with unconnected voids. Several experimental studies have exhibited inverse relationship between strength of concrete and its porosity (Chen, Wu & Zhou 2013, Ghafoori & Dutta 1995). However, in case of permeable systems pores must be interconnected to permit drainage and shall be strong enough to sustain heavy vehicular loads. Development of feasible permeable systems is thus posed with constraints in terms of engineering porosity and strength and shall entail all possible means namely numerical, experimental and analytical study in quest towards development of such project.

In line with the challenges, experimental investigations conducted to test suitability of permeable concrete has focused on strength and permeability characteristics (Fortez, Merighi & Banderia 2006). In comparison with conventional concrete, permeable concrete was observed to possess lower unit weight as well as lower elastic modulus (Ghafoori & Dutta 1995, Suzuki, Yahiro, Koseki, Kagaya & Tokuka 1994). Further, permeable concrete possessed lower values of compressive, tension and flexure strengths (Ghafoori & Dutta 1995, Chen, Wu & Zhou 2013). On brighter side, it had lower shrinkage and higher thermal insulation. Experimental measurements of permeability varied in the range of 0.2–0.54 *cm/s* (Legret, Colandini & LeMarc 1996). The corresponding values of porosity in the said concrete ranged between 15%–25% (Tennis, Lemming & Akers 2004). The lower range of permeability values if linearly related with precipitation indicates ability to absorb rainfall in excess of 700 *cm/hr*. In tropical regions, an ability to absorb rainfall little over 50 *cm/hr* shall suffice in most cases. This indicates that optimal permeable pavements can be designed with substantially lower values of permeability than reported in the literature. The reduced permeability requirement if optimally engineered may yield desired values of compressive and flexural strength. Exploitation of composition that enables development of permeable concrete with minimal influence on mechanical characteristic is the motivation of the present work.

In this study, numerical analysis of factors influencing design of permeable pavement systems is performed. Discrete element modelling of permeable concrete is done to analyse properties

pertaining to strength and permeability. The strength assessment is done based on the assumption that macroscopic strength is influenced by mesoscopic composition represented in terms of aggregate, matrix and interface. For permeability, the mesoscopic representation is retained and 3*D* pore network model is studied as are presentative of permeability. The influence of pore geometry on permeability is well documented in the literature (Sumanasooriya & Neithalath 2011).

2 SIMULATION OF POROUS CONCRETE

Granular materials ranging from cement/cement composites to sand substantially influence performance of concrete. To ensure performance, it mandates hydraulic capability, structural adequacy and minimum clogging potential. For porous concrete, parameters influencing properties of interest includes water cement ratio, aggregate geometry and geometric characteristics of pores and is also reported in literature (Yang & Guoliang 2003, Cosic, Korat, Ducman & Netinger 2015, Ibrahim, Mahmoud, Mohammed & Patibandla 2014). Laboratory evaluation provides a direct means to assess these variables and their effects but deters gauging influence of each parameter due to its multi-phase component structure and inherent heterogeneity of its constituents. In numerical modelling for concrete, individual components can be realistically simulated incorporating the microstructure representing aggregate, mortar matrix (sand) and interfacial transitional zones (ITZ). To acquire in-depth knowledge of complex heterogeneous material such as concrete, it is essential to impede further progress on experiments and enhance the understanding of the numerically developed multiscale model. Zaitsev & Wittmann (1981) simplified the concept of multiscale modelling by dividing the inhomogeneities developed at each level. Mechanical properties of concrete vary with coarse aggregates at the macroscopic level, fine aggregates at mesoscopic level, pores in the mortar matrix at the microscopic level and capillary pores in hardened cement paste at the nanolevel. Enhancement in computational ability permits mesoscopic analysis of geometrically realistic concrete samples. Many researchers including Bazant, Tabbara, Mohammad & Pijaudier-Cabot (1990), Schlangen & Van Mier (1990), Schorn & Rode (1991), Wang, Kwan & Chan (1999) and Wittmann, Roelfstra & Sadouki (1985) have developed mesoscopic models with similar characteristics commonly called as 'Take and Place' Method, while Schutter, Geert & Taerwe (1993) to achieve higher packing density used divide and fill. Numerical simulation of concrete requires representation and identification of mesoscopic phases namely aggregate, matrix and interface. This can be achieved by presuming an enclosed space to represent matrix followed by addition of inclusions that represent aggregate phase. In conventional concrete, aggregates contribute 60%–80% of total volume and can substantially influence mechanical properties of concrete whereas, in permeable concrete, fine aggregate content is limited to increase the number of pores while the coarse aggregate is kept to a narrow gradation to achieve higher packing density (Tennis, Lemming & Akers 2004). The aggregate particles are assumed spherical resembling the dimensions of aggregate particle in real concrete and is placed at randomly generated points.

2.1 *Particle packing and aggregate size distribution*

The particle size distribution for simulating aggregates is chosen from a library of optimum particle distribution curves with different exponential factors to achieve desired packing density. Equation-based models on the other hand, follows the theoretical approach of calculating overall packing density based on the geometry of aggregated particle groups (Jones, Zheng & Newlands 2002). One prominent approach for choosing particle size distribution was presented by Fuller-Thompson-Andreason (Fuller & Thompson 1907) in a series of curves for packing of aggregates as described in Equation 1.

$$P_i = \left(\frac{d_i}{d_{max}}\right)^n * P_k \tag{1}$$

where, P_i is percentage particles passing through a sieve of diameter d_i, d_{max} indicates maximum size of aggregate, n is the exponent of equation (0.45–0.70) and P_k is desired packing density. Figure 2 represents ideal packing curves with the maximum

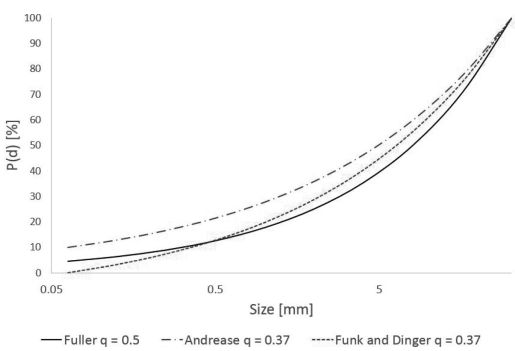

Figure 2. Optimal Fuller grading curves.

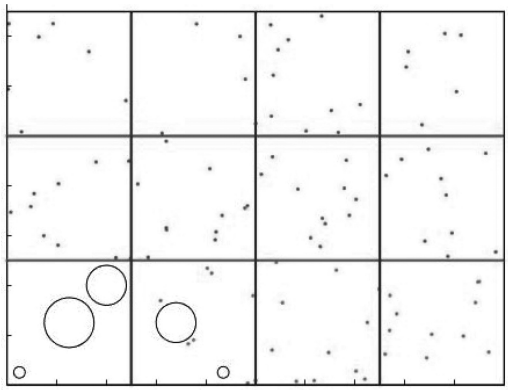

Figure 3. Periodic boundaries.

particle diameter of 32 *mm* and a minimum particle diameter of 63 μm.

The order of packing particles can be prescribed considering either a number of large particles dominating the particle structure and smaller particles accommodated into their voids or the larger particles are embedded in a matrix of smaller particles. In this study, the elementary volume of the confined specimen is well approximated by packing the spherical particles within a rigid boundary such that the centre of the spherical particles are randomly located in $3D$ space. To achieve desired packing density and enhance computational efficiency, the confined specimen is further partitioned using periodic boundaries thereby creating small cubes representing concrete. Use of periodic boundary condition makes it easier to check non-overlapping criterion for aggregates. An illustration of this is represented in Figure 3.

2.2 *'Take and Place' process*

Fuller grading curve with an exponent of 0.7 is adopted to compute number of aggregate particles of a given diameter to be simulated so as to achieve desired packing density. Diameter of simulated aggregates discretized over 14 segments varied in the range of 2–15 *mm*. The mesoscopic model generates random configuration for aggregate position defined by Cartesian coordinates (x,y,z) with reference to a datum point. In present study, virtual concrete with a dimension of $0.15 * 0.15 * 0.15$ *units* ($150 * 150 * 150$ *mm*) is simulated with an assumed maximum aggregate particle to specimen side ratio as 1/10. The confined cubical specimen is further divided into smaller subdomains using periodic boundary conditions based on similar size to side ratio. The elementary volumes (that of aggregate and sand) is well approximated to the volume in a confined specimen as per the required packing density. Thereafter the random configuration is adopted through Mersenne Twister algorithm. The numbers obtained ranges from 0 to 1 which is further multiplied by the specimen dimensions to get the position of randomly generated points. The particles are packed by divide and fill method in small cubicles formed by periodic boundaries. The new spherical particles are sequentially packed with decreasing radius after examining the locations and space availability with respect to previously packed particles in each cubicle. The centre of new spherical particles is fixed such that overlapping is avoided and the central distance is greater than their radial sum. Figure 4 represents mesostructure developed using estimated aggregate packing densities of 50%, 60% and 70%.

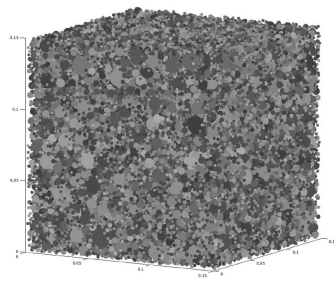

(a) Aggregate packing of 42.6% achieved with 50% packing density

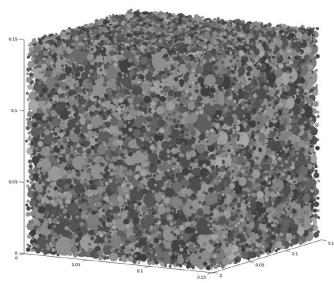

(b) Aggregate packing of 47% achieved with 60% packing density

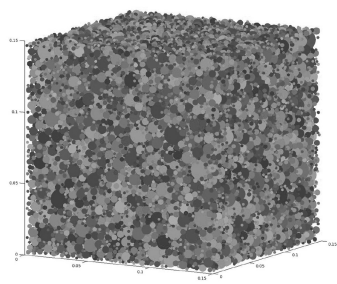

(c) Aggregate packing of 51.2% achieved with 70% packing density

Figure 4. Percentage packing achieved for given packing density.

Figure 4a represents a packing density of 42.6% against a 50% targeted packing density. This is because generating smaller particles in larger number enhances computational effort due to larger rejection rate. The packing density varies with the rejection rate. The ratio of the number of generated random points to the number of particles to be packed is termed as rejection rate. The proximity to the required value increases with the rejection rate. At a rejection rate of 3, it is possible to achieve 42.6% packing density for provided 50% of volume fraction. To achieve proximal packing density, the rejection rate can be 10 or higher. Figure 4a nearly consists of 53591 aggregate particles with an increasing number of aggregate particles in each gradation segment from 2 *mm* to 15 *mm*. Figure 4b and 4c represents the mesostructure with 60% and 70% targeted packing density with actual packing density up to 47% and 51.2% consisting of 39569 and 35418 aggregate particles respectively with a rejection rate of 2.

3 STRENGTH MODELLING OF CONCRETE

The characteristic feature of concrete is its randomness in microstructure for a given composition. Concrete is assumed to be continuum however its discrete representation in the form of lattices represented as a network of beam/truss elements offers a simplified approach for incorporating heterogeneity (Hrennkioff 1941). Apart from incorporating heterogeneity, geometric arrangement of lattice is an equally important factor that needs attention. Certain geometries of lattice may reflect mechanisms that are intrinsic to the chosen geometry and is not the reflection of material being modelled. For example, regular rectangular gird of lattice elements used to represent bar subjected to axial force would reveal substantial part of loads being carried by members oriented along longitudinal axis of the member whereas along perpendicular axis lattice members would largely remain in relaxed state. In present case, pseudo random approach is adopted to avoid impact of lattice geometry on material behaviour. This makes it necessary to introduce such randomness in lattice model generation in the computational model. Inclusion of this feature helps in obtaining a model which shows strong resemblance to real concrete.

3.1 *Lattice generation*

In order to analyse the failure pattern of any heterogeneous material and to identify the weak links of the constitutional composition at granular level, most suitable way is to convert the constituent arrangement into frame structure and solve the obtained frame under predefined load pattern. This can be done with the help of discretization, by considering the edges of discretized space as the elements of the frame structure. In this process, triangular pattern of discretization is opted as it is considered most appropriate lattice pattern. A 2*D* lattice generation is done based on Voronoi diagram and Delaunay triangulation. Delaunay triangulation works on the principle of forming triangles between the points such that there will be no other point in the circumcircle of the triangle formed. This avoid the formation of triangles with skewed angles to some extent in terms of edge lengths for the given triangle, however it requires some refinement to maintain the aspect ratio of triangulation. In order to refine the mesh, criteria to be satisfied are below.

- Aspect ratio should be maintained between 2 to 3; Aspect ratio = (Largest edge length)/(Shortest edge length)
- Generation of points on which triangulation to be carried out should be random
- Skewed angles in the triangles should be avoided
- Size of elements should be such that mesoscopic properties of the concrete phases can be properly incorporated (less than 1/3*rd* of least particle size)

Generation of lattice structure is initiated with development of well distributed pseudo random points in the domain of interest. In this approach, a loop is created to generate boundary points at defined interval for given dimensions of the plane and another loop is created to generate quasi random points around pre-defined grid pattern. This is done by generating single random point in the circles centred at the grid points with user defined radius such that it maintains the aspect ratio between 2 and 3. As generation of random points is dependent on the predefined grid points, it can be considered as quasi random discretization rather than fully random discretization. User has control over discretization in terms of identifying the desired geometry and also number of lattice points by choosing appropriate values for circle radius. One of the desired outcomes of this model is to observe and track crack or failure initiation and pattern.

This is attained by inserting a notch in the lattice system which acts as minute crack and provides the system with weak zone for failure propagation and is used to enhance stress concentration thus predefining crack path. Figure 5 represents the geometry of beam discretized into random lattice structure and a magnified view in the vicinity of notch.

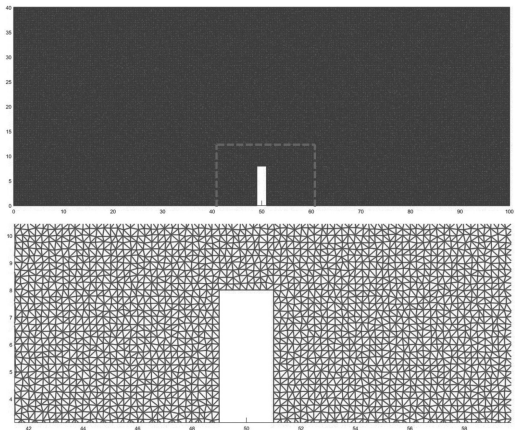

Figure 5. Random discretization of beam with lattice elements along with its magnified view.

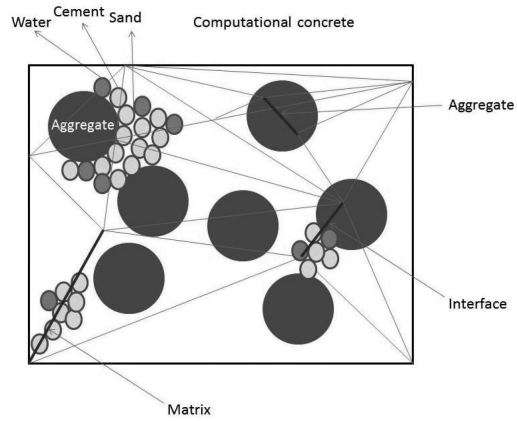

Figure 6. Schematic representation of discrete lattice overlaid on numerical concrete.

3.2 *Heterogeneity incorporation and material models*

To simulate heterogeneous nature of concrete at granular level, the lattice model obtained from pseudo-random approach is superposed over the microstructure obtained from particle packing algorithm. When concrete is modelled by incorporating the mesoscale features into its composition, the complexities gets reduced as the interface bonding, matrix and aggregates are converted into beam elements as shown in Figure 6 and the resulting space frame is analysed.

In virtual concrete, a lattice element with both ends in aggregate phase would be assigned the properties of aggregate, if the two ends are outside aggregate it would be assigned the properties of matrix whereas if one end falls inside aggregate and the other outside it, then it would be referred as interface elements. To generalise results obtained from such study, mapping of real and virtual concrete is of utmost important. This can be achieved by comparing percentage elements representing aggregate phase with its composition in real concrete. For example, concrete mix proportion given as 1:2:4 with 0.5 as water cement ratio resembles an aggregate proportion of 53.33%. Having classified lattice elements into phases corresponding to mesoscopic representation of concrete, the next step shall be defining material laws governing the behaviour of each of these phases.

Figure 7 shows the result of algorithm that differentiates the elements into 3 distinct phases of mesoscopic concrete. Assuming each mesoscopic phase to be linear and elastic, material law for a given phase would be restricted to definition of elastic modulus, poisson's ratio and limiting strain

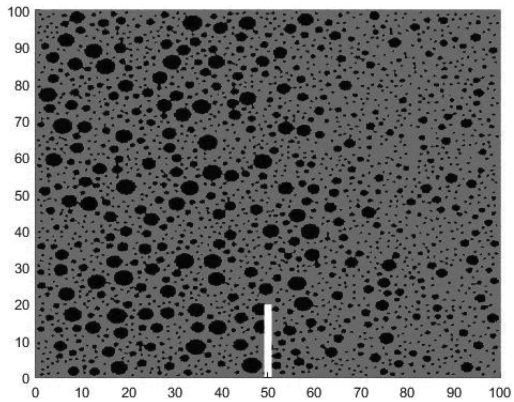

Figure 7. Virtual concrete.

values. Geometric properties for each phase shall remain constant and is defined as a function of length of lattice elements to maintain constant L/d ratio. Having defined material and geometric properties for each lattice element in the structure, space frame analysis is performed under varied external load and boundary conditions.

4 PORE NETWORK AND ESTIMATION OF POROSITY

CPRS (Cellular Particle Rejection System) is a tool to analyse the share of voids in the particulate assemblies. Detection of voids help in assessing the transport mechanism and the mechanical properties. Identifying the voids throughout the granular structure corresponding to the empty

space neither occupied by aggregate and sand can give an average permeable porosity of the specimen by identifying its void ratio. The particles are packed into a confined volume through sequential packing algorithm at randomly generated points to acquire the required packing density as per the Fuller particle distribution curve. The confined specimen is refined into smaller cubicles by applying multiple downscaling factors. Downscaling factors can be referred to as division of confined volume into smaller cubicles to quickly and accurately identify voids. Multiple downscaling factors reduces the computational time in contrast to single downscaling factor. The primary downscaling factor depends on maximum particle size while the secondary downscaling factor depends on the minimum particle size. Lesser the value of downscaling factor leads to more accurate estimation of voids in the concrete specimen. The combination of primary and secondary downscaling factors can estimate the number of voids in the concrete specimen. The process adopted in CPRS module can be summarized into following steps:

1. After the required packing density is achieved in a concrete specimen, the global list augments positions of the aggregate particle and sand micro-cubicles which is used as reference to estimate the voids.
2. The primary and secondary downscaling factors are provided as an input based on the optimal scaling ratio.
3. The confined specimens are partitioned into small cubicles/cells depending on the downscaling factors. The cells overlapping with the spherical particles are eliminated. This process of estimating the non-overlapping particles through rejection by distance criteria is termed as cellular particle rejection system.
4. Optimizing scaling ratio by applying different combinations of downscaling factors. Identifying the void ratio by evaluating the ratio of non-overlapping cubicles to overlapping particles.

5 RESULTS AND DISCUSSION

The distribution of aggregate particles based on Fuller curve gave an optimal packing of aggregate particles in a confined volume and consequently led to higher packing density relative to the volume fraction. The generation process and the void identification further dictates the efficiency of concrete in permeating water. Figure 8 represents the pore network in a confined volume with 50% targeted volume fraction (with 42.6% packing density) at a primary downscaling factor of 15 and secondary downscaling factor of 20. The primary downscaling factor (15) converts the confined volume ($150 * 150$ *mm*) into cubicles of volume $10 * 10 * 10$ *mm* each, while the secondary downscaling factor (20) further converts each into $0.5 * 0.5 * 0.5$ *mm*. This cubicles are identified as voids and constitute to 6.8% of the total volume. The percentage of voids varies with change in downscaling factor demonstrating increased/decreased capacity to identify voids. Size of cubicles after downscaling may vary from $1 * 1 * 1$ *mm* capturing 1.48% of voids to $0.2 * 0.2 * 0.2$ *mm* capturing 46% of voids.

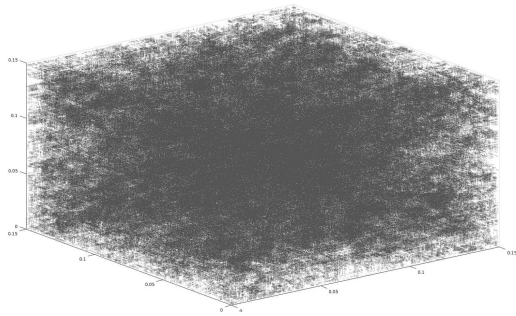

Figure 8. 3*D* pore network with particle packing density of 42.6%.

Figure 9 represents the sectional 2*D* pore network in YZ plane with reference to datum axis. Figure 9a, 9b and 9c represent the sectional pore network at 25 *mm*, 75 *mm* and 125 *mm* from the datum axis. At 25 *mm* distance the percentage of voids captured is 6.3% which constitutes of 5678 cubicles as voids from a total of 90000. Similarly at 75 *mm* and 125 *mm* the percentage voids captured is 6.8% and 6.74% which constitutes of 6106 and 6071 cubicles respectively as voids from a total of 90000.

Following the results obtained from the aspect of porosity, the same model is tested from strength perspective and the simulations carried out for the same are as follows.

To understand influence of the type of system in accordance with its phases (single, double and three phase). Simulations for one phase, two phase and three phase system are carried out for given composition, packing and lattice model. On the basis of these simulations, comparisons on its influence over characteristics strength and number of elements failed before achieving its maximum capacity is obtained.

Results obtained from above mentioned simulations are discussed hereafter.

The graph shown in Figure 10 clearly depicts that the number of elements failing increases drastically once maximum capacity is achieved. The post-peak undulations observed, are results of computational inefficiency as stiffness matrix moves towards becoming singular.

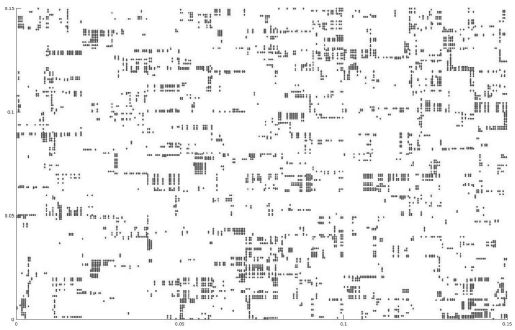

(a) Sectional pore network at 25 mm from YZ plane

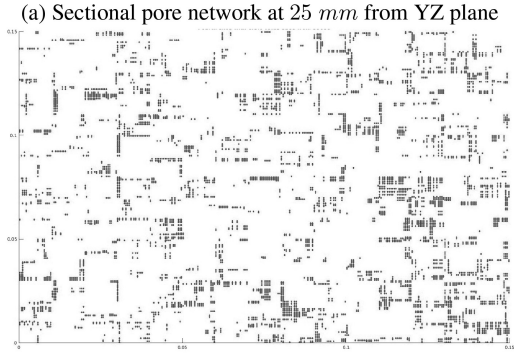

(b) Sectional pore network at 75 mm from YZ plane

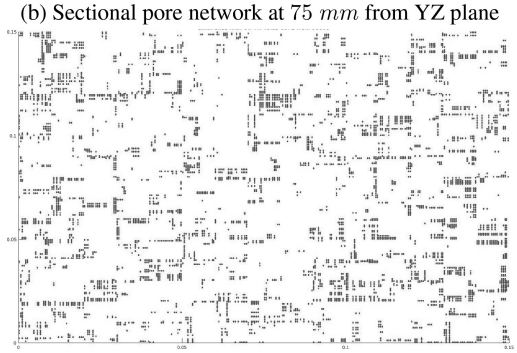

(c) Sectional pore network at 125 mm from YZ plane

Figure 9. Sectional pore network of the modelled concrete specimen.

Table 1. Specimen specifications.

Specimen size	10 $cm * 10$ cm
Particle size range	1.2 cm – 4.8 cm

The plot shown in Figure 11 represents the comparison of load deformation behaviour for one phase, two phase and three phase system. It is clearly observed that one phase system shows maximum capacity and three phase system shows the least, with two phase system being in the middle. However, it is also observed that three phase system is less brittle as compared to one phase system.

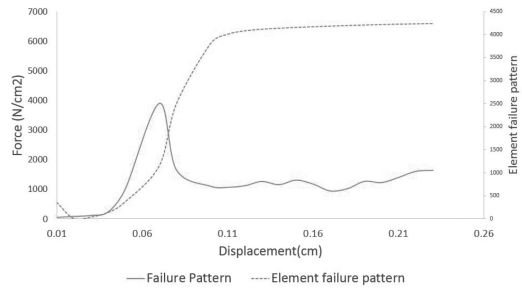

Figure 10. Load deformation and failure pattern for two phase system.

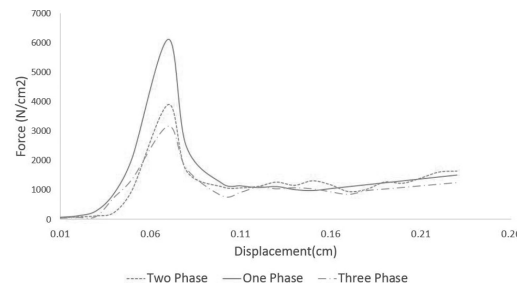

Figure 11. Comparison of one phase, two phase and three phase system w.r.t. load deformation.

This is evident from the behaviour of deformation curve for three phase system showing slow reduction in its capacity after failure when compared to one phase system.

The graphs represented in Figures 12 and 13 depicts the comparison between one phase, two phase and three phase system with subject to their failure pattern. It is evident from the results that number of elements failed before achieving peak value of strength increases with increase in number of phases (15% in one phase, 10% in two phase and 7% in three phase). From this, it is can be deduced that the amount of strain energy consumed by the system before failing is more in one phase system as compared to two phase and three phase system. This is implied by the fact that strain energy is function of strain values or E values assigned to elements, hence, more failed elements represent more strain energy consumption.

In this study, the main purpose is to understand how porosity affects the strength of concrete, so that an overall idea about engineering a concrete with desired properties can be attained. In order to do so, a condition similar to porous concrete is simulated keeping the composition constant as it was in conventional concrete. This was done by deleting the lattice elements falling into matrix class uniformly from the system to simulate pores. The comparison of load deformation pattern

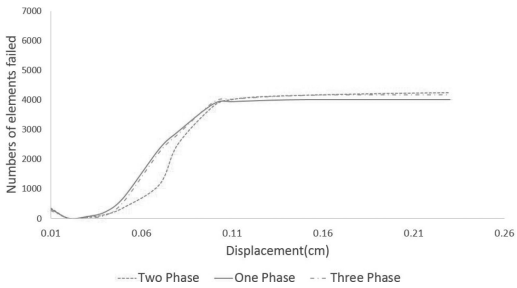

Figure 12. Element failure pattern comparison for different system.

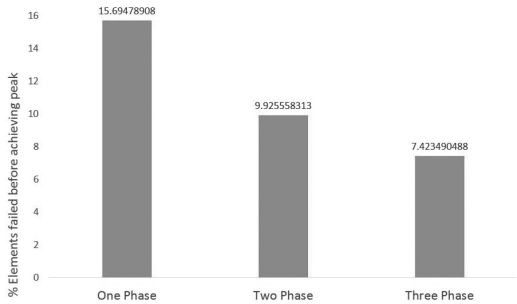

Figure 13. Percentage element failing before achieving maximum capacity.

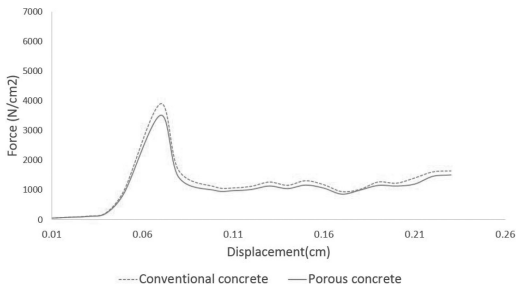

Figure 14. Load deformation comparison between conventional and porous concrete.

between conventional and porous concrete based on the results obtained is depicted in Figure 14. The plot clearly shows that there is reduction in strength of porous concrete then that of conventional concrete. However, this variation is nearly insignificant as it is of the order of 10.0072%.

6 CONCLUSIONS

Based on the results, it can be concluded that the particle packing models followed by identification of voids helped achieve higher packing density upto 51.2% based on the rejection rate of 2 which can be amplified to nearly 56% with a rejection rate of 10. The void identification through CPRS module meticulously identifies the voids upto 6.8% further delineating and portraying the pore network. From the comparison of different phase systems in accordance with their load deformation behaviour and failure pattern, it can be inferred that, interface proves to be the weak link causing the initiation of failure process as three phased concrete shows lower capacity. However, it represents more ductile behaviour and also the energy required for the failure of such system is higher. An important conclusion from the results obtained by comparing conventional and porous concrete is that the reduction in strength due to introduction of porosity of the order of 8% to 10%, is not very significant. This further implies that a concrete with desired porosity and strength can be engineered given the required infiltration capacity can be satisfied keeping reduction in strength minimal. It can be concluded that the results obtained from permeability as well as strength aspect have been positive, which suggests that there is scope for further exploration resulting in deeper understanding of the study.

REFERENCES

Andersen, C., I. Foster & C. Pratt (1999). The role of urban surfaces (permeable pavements) in regulating drainage and evaporation: Development of laboratory simulation experiment. *Hydrological processes 13(4)*, 597–609.

Bazant, Z.P., M. Tabbara, K.T. Mohammad & G. Pijaudier-Cabot (1990). Random particle model for fracture of aggregate or fibre composites. *Engineering Mechanics 116.8*, 1686–1705.

Chen, X., S. Wu & J. Zhou (2013). Influence of porosity on compressive and tensile strength of cement mortar. *Construction and Building Materials 40*, 869–874.

Christian, M., B. Rothen-Rutishauser, F. Blank, D. Vanhecke, M. Ochs & P. Gehr (2008). Interactions of nanoparticles with pulmonary structures and cellular responses. *Am J Physiol Lung Cell Mol Physiol 294*, L817–L829.

Cosic, K., L. Korat, V. Ducman & I. Netinger (2015). Influence of aggregate type and size on properties of pervious concrete. *Construction and Building Materials 78*, 69–76.

Fortez, R.M., J.V. Merighi & A.A. Banderia (2006). Laboratory studies on performance of porous concrete. *10th International Symposium on Concrete Roads*.

Fuller, W.B. & S.E. Thompson (1907). The laws of proportioning concrete transactions. *American Society of Civil Engineers (ASCE) 59*, 67–143.

Ghafoori, N. & S. Dutta (1995). Building and non-pavement application of no-fines concrete. *Materials in Civil Engineering*.

Hingorani, A. & S. Hingorani (2012). Storm water management: Retrofitting our urban streets for sustainable drainage. Technical report, Oasis Design Inc., Delhi, India.

Hrennkioff, A. (1941). Solution of problems of elasticity by the framework method. *Applied Mechanics 12*, 169.

Ibrahim, A., E. Mahmoud, Y. Mohammed & V.C. Patibandla (2014). Experimental study on portland cement pervious concrete mechanical and hydrological properties. *Construction and Building Materials 50*, 524–529.

Jones, M.R., L. Zheng & M.D. Newlands (2002). Comparison of particle packing models for proportioning concrete constituents for minimum void ratio. *Materials and Structures 35.5*, 301–309.

Kumar, R. & B. Bhattacharjee (2003). Porosity, pore size distribution and in situ strength of concrete. *Cement and Concrete Research 33*, 155–164.

Legret, M., V. Colandini & C. LeMarc (1996). Effect of porous pavement with reservoir structure on the quality of runoff water and soil. *Science of the total environment 190*, 335–340.

Pindado, M., A. Aguado & A. Josa (1999). Fatigue behavior of polymer modified porous concretes. *Cement and Concrete Research 29(7)*, 1077–83.

Schlangen, E. & J.G.M. Van Mier (1990). Simple lattice model for numerical simulation of fracture of concrete materials and structures. *Materials and Structures 25.9*, 534–542.

Schluter, W. & C. Jefferies (2004). Modelling the outflow from a porous pavement. *Urban Water 4(3)*, 245–53.

Scholz, M. & P. Grabowiecki (2007). Review of permeable pavement systems. *Building and Environment 42*, 3830–3836.

Schorn, H. & U. Rode (1991). Numerical simulation of crack propagation from micro cracking to fracture. *Cement and concrete composites 13.2*, 87–94.

Schutter, D., Geert & L. Taerwe (1993). Random particle model for concrete based on delaunay triangulation. *Materials and Structures 26.2*, 67–73.

Sumanasooriya, M.S. & N. Neithalath (2011). Pore structure features of pervious concretes proportioned for desired porosities and their performance prediction. *Cement and Concrete Composites 33*, 778–787.

Suzuki, T., M. Yahiro, H. Koseki, M. Kagaya & H. Tokuka (1994). Considerations of consistency test and properties of porous concrete for pavement. In *Theme-II of the 9th International symposium on concrete roads*, Istanbul, Turkey.

Tennis, P.D., M.L. Lemming & D.J. Akers (2004). Pervious concrete pavements. Serial No. 2828, Portland Cement Association.

Wang, Z.M., A.K.H. Kwan & H.C. Chan (1999). Mesoscopic study of concrete i: Generation of random aggregate structure and finite element mesh. *Computers and Structures 70.5*, 533–544.

Wittmann, F.H., P.E. Roelfstra & H. Sadouki (1985). Simulation and analysis of composite structures. *Materials Science and Engineering 68.2*, 239–248.

Yang, J. & J. Guoliang (2003). Experimental study on properties of pervious concrete pavement materials. *Cement and Concrete Research 33*, 381–386.

Zaitsev, Y.B. & F.H. Wittmann (1981). Simulation of crack propagation and failure of concrete. *Materials and Structures 14.5*, 357–365.

Computational Modelling of Concrete Structures – Meschke, Pichler & Rots (Eds)
© 2018 Taylor & Francis Group, London, ISBN 978-1-138-74117-1

A coupled chemo-mechanical damage-healing model for cementitious materials

A.D. Jefferson & R.E. Davies
Cardiff University School of Engineering, UK

ABSTRACT: A model is described for representing simultaneous damage and healing behaviour in cementitious structural elements that contain embedded autonomic healing systems. The model uses a crack-healing cohesive zone formulation in which damaged and healed proportions of the cohesive zone can both grow and diminish, with no restrictions placed on the number or timing of these damage-healing events. The cohesive zone sub-model is implemented in a finite element with strong discontinuity and is coupled to both capillary flow and chemical curing model components. The flow model simulates the transport of healing agents within discrete cracks as well as through micro-cracked regions within the fracture process zone. An important aspect of the damage-healing component of the model is the way that permanent strains are computed so as to satisfy the second law of thermodynamics. This is accomplished with the assumption that the stress in a component of healing agent is zero at the moment of solidification, which applies to both null and non-zero displacement fields. The new coupled model is assessed using some recent data obtained from a number of experiments undertaken at Cardiff University. These tests were conducted on both reinforced and unreinforced specimens, and encompass a range of cracking scenarios. The paper shows that the model accurately predicts the flow of healing agents within discrete cracks and that it is able to represent the mechanical behaviour associated with multiple and simultaneous damage-healing events with good accuracy.

1 INTRODUCTION

Researchers have shown that it is possible to produce cementitious materials with self-repairing properties (Joseph et al., 2011; van Tittelboom & De Belie, 2013; Van Belleghem et al., 2017). Some of the healing techniques developed to-date enhance natural 'autogenous' healing mechanisms (Ahn et al. 2010; van Tittelboom & De Belie, 2013; Lee et al., 2016), whilst others employ 'autonomic' -or manufactured- healing techniques (Dry, 1994; Giannaros et al., 2016).

In addition to the experimental research directed at developing new self-healing cementitious materials (SHCMs) there has been another strand of research work aimed at developing numerical models for self-healing materials. A significant number of models have been developed using continuum damage-healing mechanics (Barbero et al., 2005; Voyiadjis et al., 2012; Mergheim and Steinmann, 2013; Alsheghri and Abu Al-Rub, 2016) whilst others have employed micro-mechanical theories (Zhou et al. 2016; Davies and Jefferson, 2017).

Most existing damage-healing numerical models have been built on restrictive assumptions. These assumptions have included; healing always takes place under zero-strain conditions; healing and damage are never concurrent; healed material cannot re-damage; and healed material can only re-damage once (Barbero et al., 2005; Voyiadjis & Kattan; Mergheim and Steinmann, 2013; Alsheghri & Abu Al-Rub, 2016). There are real damage-healing scenarios that are consistent with some of these assumptions. For example, if damage in a structure occurred as the result of a single short-term extreme loading event and subsequently the loading returned to a relatively constant moderate level, a single event healing model would be appropriate. By contrast, damage from cyclic transient actions, be they environmental or mechanical, could result in multiple occurrences of damage and healing. In general, simultaneous damage and healing tends to occur when damage and healing rates are similar. Thus, a comprehensive damage-healing model should be able to represent simultaneously and multiple damage–healing events without any of the above restrictions.

The coupled model described in present paper brings together a formulation for simulating the capillary flow of healing agents in discrete cracks with a mechanical damage-healing model component.

2 CAPILLARY FLOW MODEL

Capillary flow in discrete cracks is simulated using a model proposed by Gardner et al (2014) that is

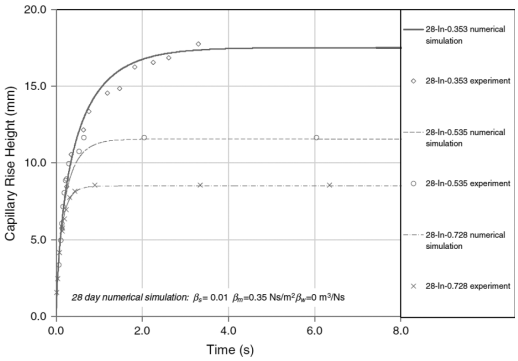

Figure 1. Capillary rise height data at 28 days for inclined planar crack configuration.

based on a modified Lucas-Washburn equation. The approach simulates flow in tortuous cracks of varying cross-section and accounts for stick-slip behaviour, frictional resistance at the moving front and wall slip. The approach has been validated against experimental data for a range of healing agents. The flow rate at the meniscus is given by equation (1);

$$\dot{z} = \left(p_{c0}(1-\beta_s) - \rho g z \sin(\varphi)\right) \Big/ \left(\frac{2\beta_m}{b(z)} + \eta\right) \tag{1}$$

where

$$\eta = A(z) \int_0^z 1 \Big/ \left(\frac{b(x)\beta_w}{2} + \frac{k(x)}{\mu}\right) A(x)\,dx$$

and in which the superior dot denotes the time derivative, z is the capillary rise height; $b(x)$ is the channel (crack) opening; β_w, β_s and β_m are the wall, stick-slip and meniscus correction parameters respectively; φ is the capillary inclination angle; ρ is the density of liquid; g is the gravitational acceleration; μ is the dynamic viscosity; t is the capillary rise time (s); effective permeability term $k = b^2/12$, and α is the inclination of the capillary wall.

An example set of validation data for the flow of healing agents in natural cracks in concrete specimens is given in Figure 1 (Gardner et al., 2014). This shows that the modified Lucas-Washburn equation is able to represent the capillary flow of cyanoacrylate in discrete cracks in concrete with good accuracy.

3 DAMAGE-HEALING MODEL

The damage-healing part of the model is applied to a 'crack-plane', which is defined as the mid-surface of a narrow band of material that contains a macro-crack or an array of micro-cracks. The model relates the crack-plane traction vector $(\tilde{\boldsymbol{\tau}})$ to the relative displacement vector $(\tilde{\mathbf{u}})$, for which the damage-healing constitutive relationship is as follows:

$$\tilde{\tau} = (1-\omega)\tilde{\mathbf{k}}^e\tilde{\mathbf{u}} \; + \; h\,\tilde{\mathbf{k}}^h\left(\tilde{\mathbf{u}} - \tilde{\mathbf{u}}_h\right) \tag{2}$$

in which $\omega \in [0,1]$ is the damage parameter, $h \in [0,\omega]$ is the proportion of healed material and $\tilde{\mathbf{u}}_h$ is the permanent healing relative-displacement that ensures that the healing material forms in a stress-free state.

$\tilde{\mathbf{k}}^e$ and $\tilde{\mathbf{k}}^h$ are elastic constitutive matrices for the original and healed material respectively. The inelastic component of $\tilde{\mathbf{u}}$ is computed from equation (3).

$$\breve{\mathbf{u}} = \tilde{\mathbf{u}} - \left(\tilde{\mathbf{k}}^e\right)^{-1}\tilde{\boldsymbol{\tau}} \tag{3}$$

The crack opening at any position is assumed to be equal to the normal component of $\breve{\mathbf{u}}$, which is denoted by the scalar u_f.

The cohesive zone model has been applied to a 4-noded element with embedded strong discontinuity within a research finite element program developed at Cardiff University.

4 HEALING AGENT CURING

It is assumed that curing of the healing agent employed in the present work (i.e. cyanoacrylate) can be reasonably represented by the following cuing function (ϕ);

$$\phi(t,t_0) = 1 - e^{\frac{-\langle t-t_0\rangle}{\tau_h}} \tag{4}$$

in which t and t_0 represent the current and initial time respectively, and τ_h is a healing time parameters. $\langle\rangle$ is a McCauley bracket, defined as $\langle x\rangle = 0$ if $x \le 0$ and $= x$ if $x > 0$.

A comparison between equation (4) and some experimental data measured by the Cambridge Polymer group (2004) for the curing of a droplet of cyanoacrylate on glass is shown in Figure 2.

The volume of cured material (v_{cured}) is obtained from the following convolution integral

$$v_{cured} = \int_{t_0}^{t} \phi(s,t_0)\frac{dv}{ds}\,ds \tag{5}$$

During a time increment, new healing material may arrive, healed material may damage and damaged material may re-heal. To account for these

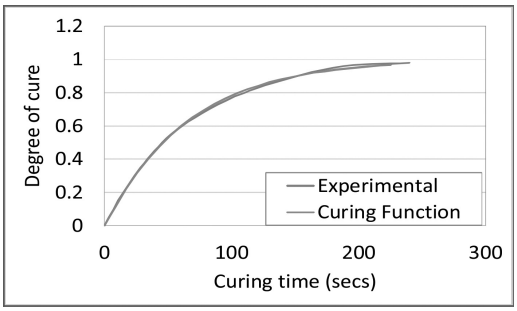

Figure 2. Comparison between curing function (4) and experimental data from reference Cambridge Polymer Group (2004).

factors the relative area of curing and cured material (a) at a particular point is given by;

$$a = a + \Delta a_c - \Delta a_{redam} + \Delta a_{rec} \tag{6}$$

in which Δa_c is the incremental area of virgin filled crack, Δa_{redam} is the incremental area of re-damaged material and Δa_{rec} is the incremental area of re-filled cracks; noting that $a = v/u_f$.

The total relative proportion of healed material is then computed from equation (7).

$$h = h \cdot e^{-\Delta t/\tau_h} + a \cdot (1 - e^{-\Delta t/\tau_h}) \tag{7}$$

A much fuller description of the model, including full details of the damage model, a description of the element with strong discontinuity, the method used to track the increments of material arriving and curing, the function used to compute $\tilde{\mathbf{u}}_h$ and the computational details of the coupled non-linear solution procedure will be provided in a forthcoming journal paper on the model. A further aspect discussed is the tendency of such a model to predict 'over-filling' during multiple damage-healing cycles (i.e. a or h becomes greater than ω). It is noted that a specific solution to this problem has been found.

5 EXAMPLE

The coupled model has been used to consider a set of experiments undertaken recently in Cardiff by PhD student Tharmesh Selvarajoo, which will be the subject of a forthcoming publication.

The test setup, illustrated in Figure 3, comprised a notched mortar beam with embedded channels that were used to supply healing agent to a crack. The beam was loaded such that the crack mouth opening displacement (CMOD) increased at a rate of 0.001 mm/s. The healing agent was supplied throughout the duration of the test. Each self-healing test set was undertaken three times and the specimens considered here were denoted SH7 to 9. In addition a control test was undertaken in which no healing agent was supplied.

The full experimental series encompasses a number of test arrangements and investigates healing at different loading rates, curing conditions, crack openings and crack geometries. The arrangement shown in Figure 3 was used in a test series that employed four loading rates which ranged from a CMOD increase rate of 0.0002 mm/s to 0.002 mm/s. The test set employed here (at 0.001 mm/s) involved continuous and overlapping healing and damage, and is thus considered suitable for validating the model.

The component of the deformed mesh around the central crack is shown in Figure 4. This shows the extent of cracking, healing agent and curing healing agent at a time of 60 seconds after the start of the test when the CMOD had reached 0.08 mm.

A comparison between the model predictions and experimental data is provided in Figure 5. It may be seen that the coupled model provides a reasonable representation of the experimental behaviour.

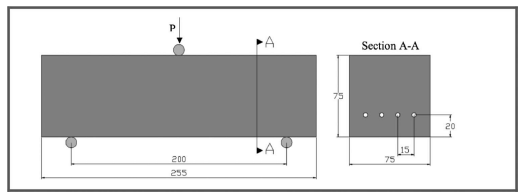

Figure 3. Experimental arrangement.

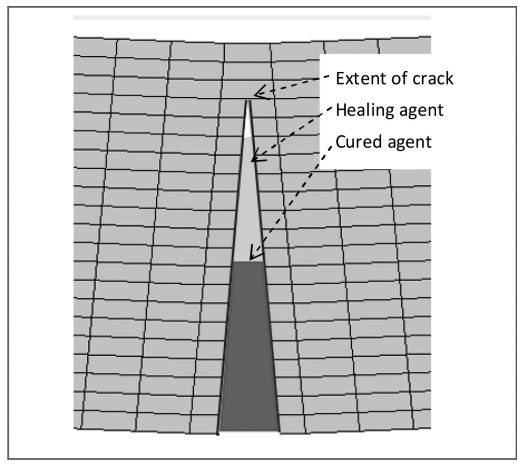

Figure 4. Finite element mesh in deformed configuration.

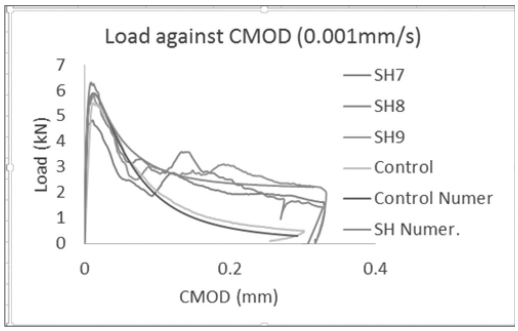

Figure 5. Comparison between experimental and numerical results.

6 CONCLUDING REMARKS

The simulation presented in this paper provides an indication that the model is able to represent combined damage-healing behaviour when the two processes are simultaneous and continuous over a period of time. The full study on the model includes simulations of a number of control and self-healing samples loaded at different rates. Based on the results obtained to date from this full study, the authors believe that the model presented here is able to simulate the type of continuous and simultaneous damage-healing behaviour described in the introductory section of this paper with good accuracy.

REFERENCES

Ahn, T.H., Kishi T. (2010) Crack self-healing behaviour of cementitious composites incorporating various mineral admixtures. J. Adv. Concr. Technol. 8, 171–186.

Alsheghri A.A., Abu Al-Rub R.K. (2016). 'Finite element implementation and application of a cohesive zone damage-healing model for self-healing materials'. Engineering Fracture Mechanics 163, 1–22.

Barbero E.J., Greco F. and Lonetti P. (2005). Continuum Damage-Healing Mechanics with Application to Self-Healing Composites, International Journal of Damage Mechanics, 14: 51–81.

Cambridge Polymer Group (2004) http://www.campoly.com/files/9213/5216/6060/001.pdf, accessed 20/10/2017.

Darabi M.K., Abu Al-Rub R.K., Little D.N. (2012). A continuum damage mechanics framework for modeling micro-damage healing. International Journal of Solids and Structures, 49, 492–513.

Davies R.E. and Jefferson A.D. (2017). 'Micromechanical modelling of self-healing cementitious materials'. International Journal of Solids and Structures, 113–114, 180–191.

Dry C.M. (1994). Matrix cracking repair and filling using active and passive modes for smart timed release of chemicals from fibers into cement matrices. Smart Mater. Struct. 3, 118–123.

Gardner D.R, Jefferson A.D., Hoffman A., Lark R.J. (2014). Simulation of the capillary flow of an autonomic healing agent in discrete cracks in cementitious materials, Cement and Concrete Research, 58.

Giannaros P., Kanellopoulos A. and Al-Tabbaa A. (2016). Sealing of cracks in cement using microencapsulated sodium silicate. Smart Mater. Struct. 25. (12 pp).

Joseph C., Jefferson A., Isaacs B., Lark R. and Gardner D. (2010). Experimental investigation of adhesive-based self-healing of cementitious materials. Magazine of Concrete Research 62(11), 831–843.

Lee H.X.D., Wong H.S. and Buenfeld N.R. (2016). Self-sealing of cracks in concrete using superabsorbent polymers. Cement Concr. Res. 79, 194–208.

Mergheim J., Steinmann P. (2013). Phenomenological Modelling of Self-Healing Polymers Based on Integrated Healing Agents. Computational Mechanics 52(3), 681–92.

Van Belleghem B., Van den Heede P., Van Tittelboom K., De Belie N. (2017). Quantification of the Service Life Extension and Environmental Benefit of Chloride Exposed Self-Healing Concrete. Materials 2017, 10(1), 5; doi:10.3390/ma10010005.

Van Tittelboom K., and De Belie N. (2013). 'Self-Healing in Cementitious Materials—A Review'. Materials 6(6): 2182–2217.

Voyiadjis G.Z. and Kattan P.I. (2012) Mechanics of damage processes in series and in parallel: A conceptual framework. Acta Mechanica 223(9): 1863–1878.

Zhou S., Zhu H., Yan Z., Ju J.W., Zhang L. (2016). A micromechanical study of the breakage mechanism of microcapsules in concrete using PFC2D, Construction and Building Materials 115, 452–463.

Computational Modelling of Concrete Structures – Meschke, Pichler & Rots (Eds)
© 2018 Taylor & Francis Group, London, ISBN 978-1-138-74117-1

Flow in fibrous composite materials: Numerical simulations

Jingu Kang & John Bolander
Department of Civil and Environmental Engineering, University of California, Davis, USA

ABSTRACT: A lattice model is developed to simulate steady-state flow in fibrous composite materials. The local contributions of individual fibers to flow are represented, such that the influences of fiber dispersion on flow can be studied in a straightforward manner. Fibers can be placed in the material volume irrespective of the background mesh representing the matrix phase of the composite material. Fiber additions do not alter the number of system degrees of freedom, so the modeling approach is computationally efficient. Accuracy of modeling approach is demonstrated through comparison with other simulation results, in which the fibers have been fully discretized within the material volume. Basic capabilities of the approach are shown through simulations of flow through materials containing differing amounts of fibers.

1 INTRODUCTION

The structural and non-structural properties of cement-based composites can be improved through the addition of fibers. With respect to mechanical performance, fibers are typically added to improve resistance to cracking and increase material toughness. The ability to restrict crack opening is of central interest in achieving durable concrete structures and repair schemes. Through proper selection of the type, size, and volume fraction of the fibers, and relevant properties of the matrix (e.g., tensile strength and its affinity for bonding with the fiber), such fiber-reinforced cement composites exhibit strain-hardening behavior. Material toughness is achieved through the formation of fine, distributed cracking during the process of strain-hardening. Both physical and computational experimentation with these strain-hardening cement composites (SHCC) has indicated there is a strong dependence of strength, toughness, and cracking behavior on the distribution of fibers. Regions with fewer fibers can act as defects, increasing crack opening and reducing both strength and toughness of the composite material. Of particular interest are models that explicitly represent the influences of individual fibers on both local and composite behaviors (Radtke et al. 2010, Cunha et al. 2011, Kunieda et al. 2011, Schauffert and Cusatis 2012, Montero-Chacón et al. 2015, Kang and Bolander 2016, Kang and Bolander 2017).

There have been many applications of fibers to develop or enhance non-structural properties. Electrically conductive fibers, including carbon fibers and carbon nanotubes, can be used to provide concrete with self-sensing capabilities. The resistivity of such materials changes under loading, such that strain can be accurately measured (Azhari and Banthia 2012). The addition of carbon nanotubes improves the shielding properties of concrete with respect to electromagnetic waves (Wang et al. 2013). Damage sensing skins have been made from carbon nanotube composites, based on mappings of conductivity produced from electrical impedance tomography (Loh et al. 2009). Carbon nanotubes have been mixed into concrete for bridge deck deicing applications (Galao et al. 2016). With respect to these and other non-structural applications, as well, the distribution of fibers is thought to affect the performance of the composite material.

In this paper, the influences of individual fibers on steady-state flow are modeled using a lattice framework. Herein, the term "potential" serves as a general reference to the aforementioned field quantitites (e.g., voltage, temperature, relative humidity). Two key features of the modeling approach are: 1) fibers can be placed within the computational domain irrespective of the discretization of the matrix phase; and 2) supplementary degrees of freedom are not introduced with the addition of fibers to the matrix. Due to the latter of these two features, the approach is computationally inexpensive. Accuracy of the approach is assessed through comparisons with model results for the case of fully discretized fibers, where the fibers possess degrees of freedom. Thereafter, the proposed approach is used to study the effects of fiber content and dispersion on potential values within the material domain.

2 MODELING APPROACH

Lattice models, as a class of discrete models, have been used to simulate the mechanical behavior of quasi-brittle heterogeneous materials, such as concrete or rock (Bažant et al. 1990, Schlangen and van Mier 1992). Such lattice models are composed of one-dimensional elements, interconnected on regularly or irregularly positioned nodes. The Delaunay/Voronoi dual tessellation of the nodal point set is an effective means for defining element connectivity and stiffness properties. In particular, based on the Rigid-Body-Spring concept (Kawai 1978), such discretizations render the lattice model elastically homogeneous (Asahina et al. 2017) and allow for fracture analyses that are objective with respect to mesh size and geometry (Bolander and Sukumar 2005). Variants of the Rigid-Body-Spring concept have been used to represent continuous or short-fiber reinforcement within the lattice modeling of the matrix (Bolander and Saito 1997).

In an analogous way, lattice models can be used to simulate various forms of potential flow. The one-dimensional elements can be viewed as conduits that transport the field quantity between nodes. When conduit connectivities and cross-section areas are based on the Delaunay/Voronoi dual tessellation, potential flow can be simulated without spurious effects associated with mesh size or geometry. By using coincident nodal points, this form of flow lattice easily couples to the structural lattice for the analyses of multi-field problems, such as those associated with the durability mechanics of structural concrete (Bolander and Berton 2004).

The work presented herein focuses on the extension of the flow lattice to account for the effects of short fibers. The approach is analogous to one used to represent stiffness contributions of short fibers within fiber-reinforced composites. In particular, the effects of short fiber reinforcement are realized without increasing the number of degrees of freedom of the model. The basic approach for modeling flow through the matrix is described first. Afterwards, that same approach is used to simulate flow local to a single fiber, where the fiber possesses its own degrees of freedom. Those simulation results serve as a benchmark for assessing the accuracy of the proposed approach.

2.1 *Matrix phase*

A planar model of the matrix phase is presented in Fig. 1a, where discretization is based on the Delaunay/Voronoi dual tessellation of the nodal point set. Each conduit element *ij* connects nodes *i* and *j* along a Delaunay edge (Bolander and Berton 2004). A semi-discrete form of the governing field equation serves as the basis for the lattice modeling of potential flow.

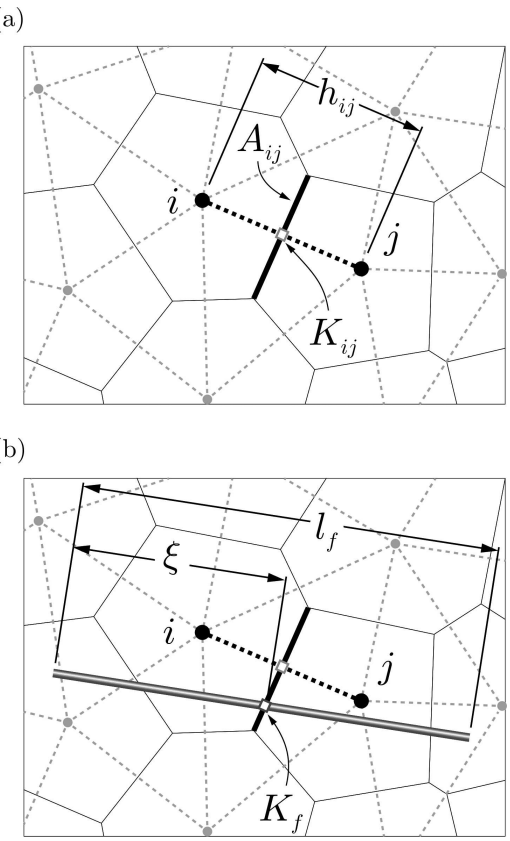

Figure 1. Delaunay/Voronoi tessellations for potential flow analysis: (a) conduit element along Delaunay edge *ij*; and (b) fiber inclusion and fiber element configuration.

$$\mathbf{KU} = -\mathbf{Q} \tag{1}$$

where **U** is the vector of nodal potentials; **Q** is the vector of discretized source or sink terms; and **K** is the conductivity matrix, assembled from its respective elemental contributions:

$$\mathbf{K}_{ij} = \left(\frac{KA}{h}\right)_{ij} \begin{bmatrix} 1 & -1 \\ -1 & 1 \end{bmatrix} \tag{2}$$

in which A_{ij} is the area of the Voronoi facet associated with nodes *i* and *j*, h_{ij} is the distance between the nodes, and K_{ij} is conductivity of the material represented by element *ij*.

2.2 *Fiber phase*

Analogous to the Rigid-Body-Spring construction of the fiber lattice elements in the mechanical problems (Bolander and Saito 1997), we have developed an approach for modeling the effects of fibers on

steady-state flow within fibrous composite materials. As noted, fibers can be placed within the computational domain irrespective of the background lattice representing the matrix. A fiber element is formed wherever a fiber intersects a Voronoi facet. For example, the fiber shown in Fig. 1b contributes to the conductivity between nodes i and j.

$$\mathbf{K}_{ij}^{\mathbf{f}} = K_f \begin{bmatrix} 1 & -1 \\ -1 & 1 \end{bmatrix} \tag{3}$$

where K_f can be derived from the differential equation expressing flow transfer across the fiber-matrix interface.

$$\frac{dQ_f}{d\xi} = -\psi H(U_f - U_m) \tag{4}$$

in which Q_f is the flow in the fiber; $U_f - U_m$ is the potential difference between the fiber and matrix; ψ is the perimeter of the fiber; ξ is the distance of the crossing point from the fiber end; and H is an interface conductivity coefficient. For any additional fiber crossing A_{ij} in Fig. 1, an additional conductivity contribution will be made to pathway between nodes i and j according to Eq. 3. All fiber contributions relate to the matrix nodes, such that the number of system degrees of freedom does not change upon the addition of fibers.

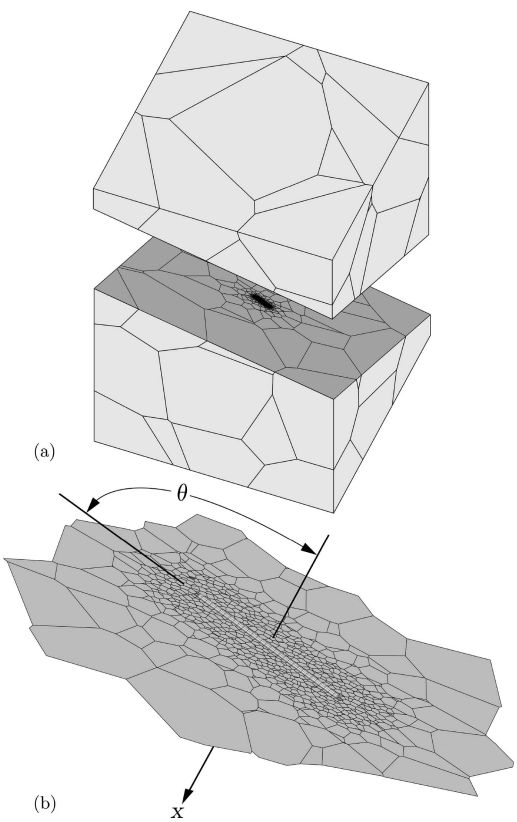

Figure 2. Discretization of single fiber within mortar matrix: (a) cross section through fiber; and (b) enlarged view of fiber (Saka et al. 2009).

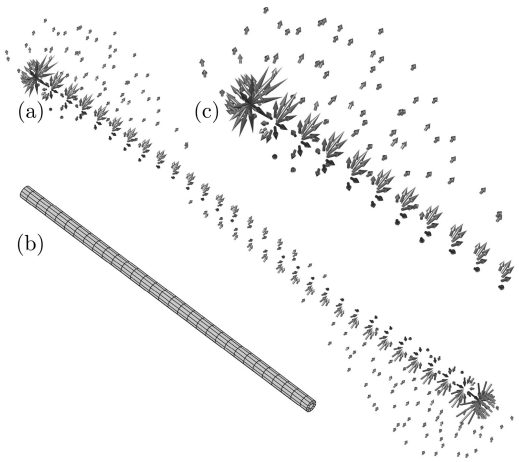

Figure 3. (a) Nodal flux vectors local to fiber channel; (b) discretization of fiber-matrix interface (shown at smaller scale); and (c) enlarged view of downstream flow conditions (Saka et al. 2009).

Equation 4 expresses flow transfer between the fiber and matrix, including the effects of the fiber-matrix interface. The nature of the flow transfer can be visualized by simulations (Saka et al. 2009), in which a fully discretized fiber is placed in a homogeneous matrix, as shown in Fig. 2. A positive potential difference is specified between the $-x$ and $+x$ faces of the model, causing flow in the $-x$ direction. The volume taken by the fiber is assumed to be empty, as an approximation of conditions during high temperature loading of polypropylene fiber-reinforced concrete, i.e., the fiber material has decomposed due to high temperature. The empty fiber channel is oriented at angle $\theta = 3\pi/8$ to the general flow direction. Under these conditions, flow is largely inward near the upstream end of the fiber, whereas flow leaves the fiber channel near the downstream end, as shown in Fig. 3.

3 NUMERICAL EXAMPLES

3.1 *Single fiber inclusion*

The influence of a single fiber inclusion is simulated using two different approaches: 1) the fiber is fully discretized according to the approach of Section 2.1, as shown in Fig. 4a. The boundary between the fiber, assumed to be cylindrical,

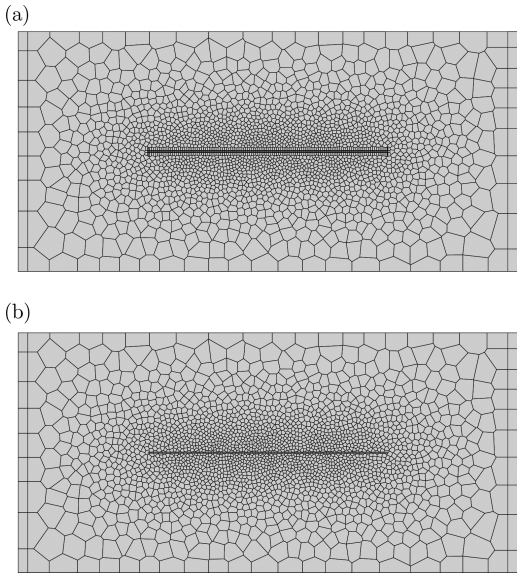

Figure 4. Lattice modeling of single-fiber inclusion: (a) fully discretized fiber inclusion and (b) semi-discretized fiber inclusion.

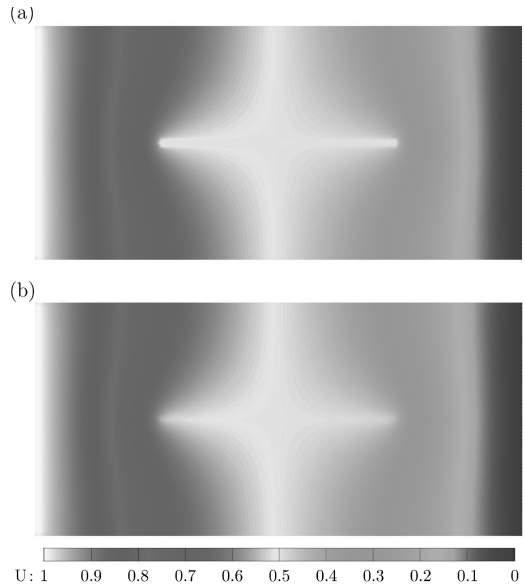

Figure 5. Potential distributions based on: (a) fully discretized fiber; and (b) semi-discretized fiber. Conductivity of the fiber is much greater than that of the matrix.

and the matrix has been discretized and the fiber possesses degrees of freedom; and 2) the fiber is represented by the semi-discrete approach of Section 2.2, as shown in Fig. 4b. For the second case, close inspection reveals the fiber is positioned within the material domain without association to the background mesh representing the matrix. For that case, the fiber does not have degrees of freedom. The density of nodal points is graded to reduce computational expense and demonstrate the solution (away from the fiber) does not depend on mesh size and geometry.

For both cases, the nodes along the left and right boundaries of the domain are assigned potential values of 1 and 0, respectively. The top and bottom boundaries are assumed to be insulated from the environment. The aspect ratio of the fiber is $l_f/d = 100$, where d is the fiber diameter. The fiber/matrix conductivity ratio is assumed to be 1×10^6. That is, the fiber is highly conductive relative to the matrix, as it would be when considering the electrical conductivity of carbon fiber reinforced cement composites. The conductance of the interface, H, is assumed to be the same as that of the fiber.

Contour maps of nodal potential are presented in Fig. 5a and b, for the cases of the fully discrete and semi-discrete modeling of the fiber, respectively. The nodal potentials in both cases are similar and show a strong influence of the fiber. The outline of the fiber is more apparent in the fully discrete representation of the fiber, since the finite widths of the fiber and its interface with the matrix are discretized. For the semi-discrete representation, the fiber and its interactions with the matrix occur along the fiber centerline, where it intersects with the Voronoi facets of each corresponding ij pair of nodes. The finite width of the fiber is not represented, but the general influence of the fiber on the flow field is captured well.

3.2 *Multiple fiber inclusions*

Following the methodology outlined in Section 2.2, the semi-discrete approach is used to simulate flow for varying amounts of fiber inclusions. The same material parameters and dimensions are assumed, as for the preceding examples of a single fiber inclusion, except the length of the fibers has been reduced by a factor of 2. The fibers have been placed using coordinates produced by a random number generator. Alternatively, the fiber locations could be determined experimentally, e.g., using computed tomography (Smith et al. 2014), or via computational fluid dynamics simulations (Žirgulis et al. 2016).

Contour maps of nodal potential are presented in Fig. 6. For the case without fiber inclusions, potential varies linearly over the length of the domain. Here, too, it is clear that the solution is independent of the irregular geometry of the lattice model. As the amount of fibers in the domain increases, the influence of individual fibers becomes less apparent; much of the domain has a potential value that is roughly equal to the average of the two end values, 1 and 0. It should be noted,

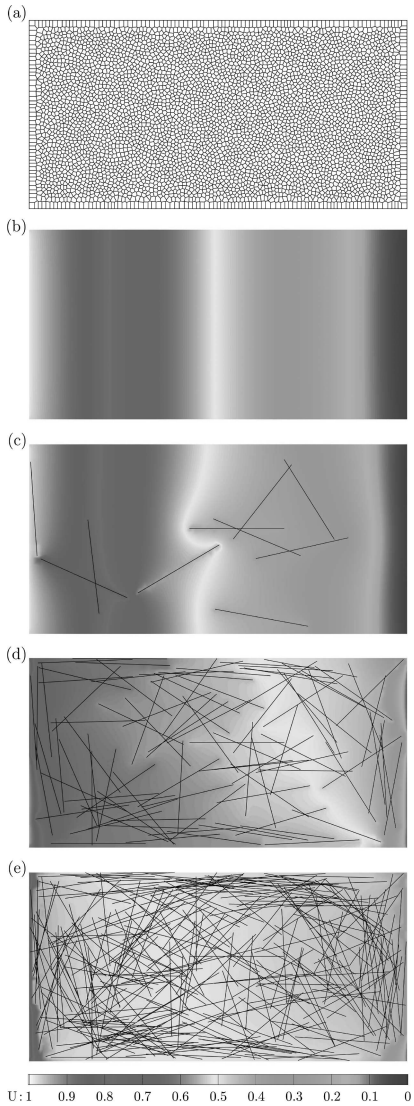

Figure 6. Contours of nodal potential: (a) discretized domain; (b) without fibers; (c) 10 fibers; (d) 100 fibers; and (e) 300 fibers.

however, that use of a planar lattice facilitates percolation of the highly conductive fibers. Furthermore, nodal density also influences the formation of percolation clusters. Coarser meshes tend to connect fibers that are otherwise isolated from one another. Such issues need further study.

4 CONCLUSIONS

This paper presents a novel approach for simulating steady-state flow in fibrous composites. Key features of the approach include the abilities to: 1) place fibers in the domain without consideration of the background lattice representing the matrix; and 2) represent the influence of fibers on flow without assigning degrees of freedom to the fibers. The approach is therefore computationally inexpensive, enabling multiscale simulations of actual fiber-reinforced materials. Simulations were run for the case of highly conductive fibers in a poorly conductive matrix. Good agreement is obtained between maps of nodal potential made with the proposed approach and those based on fully discretized fibers. As the number of fibers in the computational domain increases, the local effects of individual fibers become less apparent. Beyond these basic simulations, efforts are underway to validate the proposed model through comparisons with physical test results.

Recently, dual-lattice models have been proposed to improve the simulation of flow in fractured media (Nakamura et al. 2006, Grassl and Bolander 2016). For these models, the connectivity of the flow lattice is defined by the Voronoi (rather than the Delaunay) edges of the dual tessellations. Connectivity of the structural lattice lattice is defined by the Delaunay edges, as per usual. The simulation of flow along crack paths, and from the crack surfaces into the bulk material, is more realistic. We anticipate the approach for modeling the effects of fibers on flow, as proposed herein, can also be applied to such alternative flow networks.

REFERENCES

Asahina, D., K. Aoyagi, K. Kim, J.T. Birkholzer, & J.E. Bolander (2017). Elastically homogeneous lattice models of damage in geomaterials. *Computers and Geotechnics 81*, 195–206.

Azhari, F. & N. Banthia (2012). Cement-based sensors with carbon fibers and carbon nanotubes for piezoresistive sensing. *Cement and Concrete Composites 34*(7), 866–873.

Bažant, Z.P., M.R. Tabbara, M.T. Kazemi, & G. Pijaudier-Cabot (1990). Random particle model for fracture of aggregate or fiber composites. *Journal of Engineering Mechanics 116*(8), 1686–1705.

Bolander, J.E. & S. Berton (2004). Simulation of shrinkage induced cracking in cement composite overlays. *Cement and Concrete Composites 26*(7), 861–871.

Bolander, J.E. & S. Saito (1997). Discrete modeling of shortfiber reinforcement in cementitious composites. *Advanced Cement Based Materials 6*(3–4), 76–86.

Bolander, J.E. & N. Sukumar (2005). Irregular lattice model for quasistatic crack propagation. *Physical Review B 71*(9), 094106.

Cunha, V.M.C.F., J.A.O. Barros, & J.M. Sena-Cruz (2011). An integrated approach for modelling the tensile behavior of steel fibre reinforced self-compacting concrete. *Cement and Concrete Research 41*(1), 64–76.

Galao, O., L. Bañón, F. Baeza, J. Carmona, & P. Garcés (2016). Highly conductive carbon fiber reinforced concrete for icing prevention and curing. *Materials 9*(4), 281.

Grassl, P. & J.E. Bolander (2016). Three-dimensional network model for coupling of fracture and mass transport in quasibrittle geomaterials. *Materials 9*(9), 782.

Kang, J. & J.E. Bolander (2016). Multiscale modeling of strain-hardening cementitious composites. *Mechanics Research Communications 78*, 47–54.

Kang, J. & J.E. Bolander (2017). Event-based lattice modeling of strain-hardening cementitious composites. *International Journal of Fracture 206*(2), 245–261.

Kawai, T. (1978). New discrete models and their application to seismic response analysis of structures. *Nuclear Engineering and Design 48*(1), 207–229.

Kunieda, M., H. Ogura, N. Ueda, & H. Nakamura (2011). Tensile fracture process of strain hardening cementitious composites by means of three-dimensional meso-scale analysis. *Cement and Concrete Composites 33*(9), 956–965.

Loh, K., T.-C. Hou, J.P. Lynch, & N.A. Kotov (2009). Carbon nanotube sensing skins for spatial strain and impact damage identification. *Journal of Nondestructive Evaluation 28*, 9–25.

Montero-Chacón, F., E. Schlangen, H. Cifuentes, & F. Medina (2015). A numerical approach for the design of multiscale fibre-reinforced cementitious composites. *Philosophical Magazine 95*(28–30), 3305–3327.

Nakamura, H., W. Srisoros, R. Yashiro, & M. Kunieda (2006). Three-dimensional network model for coupling of fracture and mass transport in quasi-brittle geomaterials. *Journal of Advance Concrete Technology 4*, 147–158.

Radtke, F.K.F., A. Simone, & L.J. Sluys (2010). A computational model for failure analysis of fibre reinforced concrete with discrete treatment of fibres. *Engineering Fracture Mechanics 77*(4), 597–620.

Saka, T., J.E. Bolander, & P. Grassl (2009). Spalling potential of fire exposed structural concrete: Numerical simulation of the effects of polypropylene fibers. In F. Dehn and E. Koenders (Eds.), *Concrete Spalling due to Fire Exposure*, pp. 510–518. MFPA Institute Leipzig.

Schauffert, E.A. & G. Cusatis (2012). Lattice discrete particle model for fiber-reinforced concrete. I: theory. *Journal of Engineering Mechanics 138*(7), 826–833.

Schlangen, E. & J.G.M. van Mier (1992). Experimental and numerical analysis of micromechanisms of fracture of cementbased composites. *Cement and Concrete Composites 14*(2), 105–118.

Smith, J., G. Cusatis, D. Pelessone, E. Landis, J. O'Daniel, & J. Baylot (2014). Discrete modeling of ultra-high-performance concrete with application to projectile penetration. *International Journal of Impact Engineering 65*, 13–32.

Wang, B., Z. Guo, Y. Han, & T. Zhang (2013). Electromagnetic wave absorbing properties of multi-walled carbon nanotube/cement composites. *Construction and Building Materials 46*, 98–103.

Žirgulis, G., O. Švec, E. Sarmiento, G.M.R., A. Cwirzen, & T. Kanstad (2016). Importance of quantification of steel fibre orientation for residual flexural tensile strength in FRC. *Materials and Structures 49*(9), 3861–3877.

Computational Modelling of Concrete Structures – Meschke, Pichler & Rots (Eds)
© 2018 Taylor & Francis Group, London, ISBN 978-1-138-74117-1

Modeling water absorption in cement-based composites with SAP additions

C. Romero Rodríguez, S. Chaves Figueiredo & E. Schlangen
Department of Structures, Microlab, Delft University of Technology, Delft, The Netherlands

D. Snoeck
Department of Structural Engineering and Architecture, Magnel Laboratory for Concrete Research, Ghent University, Ghent, Belgium

ABSTRACT: The ability of Superabsorbent Polymers (SAP) to block water flow through cracks in cement-based materials has become an attractive feature of these admixtures. The diminution of flow rates in such composites are attributed to the capacity of the SAPs to absorb water and swell in the crack, but little work has been done to indicate one or the other cause. On the other hand, the SAPs present in the bulk matrix might act as distributed sinks through which water is absorbed (water that otherwise would have continued its path into the matrix). In this paper a preliminary effort is made to numerically model the effect of SAPs on the water absorption by mortar. A lattice-type model is proposed to predict both the bulk water absorption and the resulting penetration depth of water into the cementitious matrix. The results of the simulations point out the mechanisms of water absorption in mortar containing SAPs.

1 INTRODUCTION

Cement-based materials are largely used for construction purposes due to their relatively high compressive strength and low costs. Nevertheless, the porous structure of this composite allows the ingress of harmful species into the material. Eventually, these species degrade the matrix or the reinforcement leading to irreversible damage in the material if left without intervention. Such consequences can be further aggravated when cracks form during the service life of concrete elements, providing preferential paths through which the external deleterious agents penetrate into the material. In all cases, water is necessary for the transport of the external substances (chlorides, sulfates, CO_2, etc.).

In order to block water penetration into the matrix when cracks are present, Superabsorbent Polymers (SAP) have been proposed in literature to potentially obtain a self-sealing effect in the crack (Kim & Schlangen 2010). SAP are polyelectrolite gels which can absorb and retain large quatities of water with respect to their own weight. The swelling of these particles is driven towards the achievment chemical and physical equilibrium of the polymeric chains when in contact with a solution. The individual particle swells until the sum of all acting pressures upon it is zero (Vervoort 2006). In a polyelectrolite gel the main pro-swelling pressures are of osmotic nature, related to the repulsive Coulomb forces between charged chains, etc.. On the other hand, the counteracting pressures might be of an elastic nature within the gel, due to external forces, etc.

Many experimental studies have been performed regarding hydrogel formation inside cracks in cementitious materials. Permeation tests performed by Hong and Choi (2017) on SAP containing mortars showed reductions of 75% and 63% of the water flow rates for crack widths of 250 and 350 μm, respectively, on mortars with 1% of SAPs by weight of cement. In a work of Snoeck et al. (2012) Neutron Imaging was performed during water absorption tests in mortars with SAPs of different types and in various dosages. The results presented in the study show reduced depths of penetration of the wetting front in mortars with SAPs with respect to the plain reference mortars, in both horizontal and vertical directions. Such mixtures had no additional water. Snoeck et al. (2015) also demonstrated the reduction in porosity of the same cementitious matrices containing SAPs due to their internal curing effect. Despite all evidence regarding the reduced permeability and capillary absorption provided by these admixtures in cracked cement-based materials, the experimental methods used do not clarify the mechanisms of crack self-sealing by SAPs. Reduced capillary absorption in the densified matrix and consequent flow instabilities in the crack or swelling and absorption in the SAPs might

also be the causes of such an effect. It is interesting to investigate the influence of each mechanism on the sealing ability to optimize the material through numerical models.

In this work, a numerical model is presented to predict the capillary absorption of mortar with SAP admixtures. As a basis for modeling the overall physical problem, the well-established Richards equation is used to describe the capillary absorption in the bulk matrix, in combination with the exponential law for the hydraulic diffusivity in cement-based materials. In parallel, a diffusive-type law for the water uptake of SAPs is implemented as sink term in the diffusion equation. A lattice approach is used for the discretization of the domain. Heterogeneity of transport properties is explicitly modeled with this method, not only through the discrete distinction between SAPs and mortar but also through the use of an irregular lattice mesh for the simulations. The model was validated through available experimental data, first of the capillary absorption in plain mortar and secondly of mortar containing SAPs. On one hand, input parameters for the modeling of water absorption in mortar were also available for the different validating data sets. On the other hand the parameters needed for the description of water uptake by SAPs were missing, therefore a loose fitting procedure was implemented for this purpose.

The focus of this paper is on the qualitative validation of the presented model. The obtained results enable the use of the diffusive-type law of water absorption by SAPs inside the matrix and its use as a starting point for modeling the crack self-sealing by SAPs, as long as the necessary input parameters are available. Conclusions could be drawn for the mechanisms of water absorption in mortar with SAP admixtures.

2 FORMULATION OF THE PHYSICAL PROBLEM

In this section a brief derivation is offered of the governing equations for the studied problem. First, we introduce the simplified equation for the unsaturated flow in porous media and the empirical laws used for the derivation of its parameters in porous building materials. In the second part, the equation for the swelling kinetics of a single spherical SAP particle is reported.

2.1 *Theory of unsaturated water movement in sound cement-based composites driven by capillary absorption*

Starting from the two mass balance equations for air and water and Darcys extended law for the flow velocity, one can arrive at the two-phase formulation of immiscible flow in a homogeneous porous media. The complicated resulting system can be simplified if certain conditions are met, leading to the Richards equation for the unsaturated water flow in porous media (Szymkiewicz 2013). The conditions for the validity of Richards equation in cementitious materials have been reported in (Szymkiewicz 2013). In sum, isothermal conditions around 20 ensure the correctness of the assumption of uncoupling the water and air transport if they are assumed to be continuous throughout the pore space. Below, the potential form of such equation is reported:

$$C(\theta)\frac{\partial \phi}{\partial t} = \nabla(K(\theta)\cdot\nabla\phi) + S(\theta,t) \tag{1}$$

where ϕ is the hydraulic potential [L], sum of the water head (h), capillary (ψ) and gravitational (z) potentials; $S(\theta, t)$ contains sinks or sources; $K(\theta)$ [LT^{-1}] is the unsaturated permeability function and $C(\theta)$ [L^{-1}] is the so-called capacity or storage coefficient defined as:

$$C(\theta) = \frac{d\Theta}{d\phi} = (\Theta_s - \Theta_i)\frac{d\theta}{d\phi} \tag{2}$$

where $(\Theta_s - \Theta_i)$ represents the difference between volumetric water content at saturation and at the start, which in a way represents the porosity accessible to water of the material [–] and θ is the water saturation [–].

If gravitational and waterhead potentials are considered to be negligible with respect to the capillary potential and the hydraulic diffusivity, $D(\theta)$ [L^2T^{-1}], is defined as:

$$D(\theta) = \frac{K(\theta)}{C(\theta)}\nabla\phi \tag{3}$$

Equation 1 can be transformed into:

$$\frac{\partial \theta}{\partial t} = \nabla(D(\theta)\cdot\nabla\theta) + s(\theta,t) \tag{4}$$

The advantage of the PDE formulated as in equation 4 lies on the fact that $D(\theta)$ can be approximated as (Hall & Ho 2009):

$$D(\theta) = D_0 e^{n\theta} \tag{5}$$

where n has been proven to lay between 6–8, varying little among materials. In this work, n is assumed to have value 6, unless otherwise specified. D_0 can be estimated from sorptivity experiments

with good results, as proposed by Lockington et al. (1999):

$$D_0 = \frac{n^2 S^2}{(\Theta_s - \Theta_i)^2 [e^n (2n-1) - n + 1]} \quad (6)$$

And the Sorptivity S being defined as the slope of the best-fit line of the curve Cumulative water penetration vs. $[T^{1/2}]$.

The system of equations describing the water absorption in unsaturated cement-based materials results then in the parallel implementation of Equations 4 and 5.

The problem of water absorption in the studied material, to be implemented in 3D, has the following Boundary and Initial Conditions:

$$\begin{aligned} &\theta = 1 \quad \text{on } \Gamma_1 \\ &\frac{\partial \theta}{\partial n} = 0 \quad \text{on } \Gamma_2 \\ &\theta(t=0) = \theta_{initial} \quad \text{in } \Omega \end{aligned} \quad (7)$$

2.2 *SAP swelling kinetics*

Esteves (2011) and Sweijen et al. (2017) described the swelling kinetics of spherical SAP particles as a diffusion-governed process depending only on their diameter, provided a certain ionic composition of the solution and a certain type of SAP. Esteves (2011) validated such a model by monitoring the change in time of SAP's diameters. The differently sized particles were immersed in a micro-bath and observed under an optical microscope. In particular, Esteves assumed the hydrostatic pressure of the microbath negligible to the swelling pressure and a constant particle density to calculate the water uptake.

The swelling law (in Equation 8) was presented by the author in terms of the swelling capacity at equilibrium, Q_{max}, and at a given time t, Q.

$$\frac{dQ}{dt} = k(Q_{max} - Q) \quad (8)$$

The constant rate k, dependent on the particle diameter ϕ_{SAP}, is shown in Equation 9.

$$k = r_1 \varphi_{SAP}^{-r_2} \quad (9)$$

The constants r_1 $[L^{-r_2}/T]$ and r_2 [–] depend on the swelling medium and the SAP type under consideration. Their values should be fitted from experiments carried out like in the work mentioned above while monitoring as well the amount of absorbed water.

Since for the problem of resolving water absorption in mortar with SAP particles the interest is on the amount of absorbed water in time by the SAP rather than their change in dimensions, the authors hypothesized an extension of the swelling kinetics law to the volume of absorbed water instead. Herein, we assumed that the volume of the particle at equilibrium, $V_{SAP_m,max}$, is as follows:

$$V_{SAP_m,max} = \frac{Ab_{sol}\rho_{dry}}{\rho_{sol}} V_{SAP,dry} \quad (10)$$

where Ab_{sol} is the absorption capacity of the SAP in the solution, ρ_{dry} and ρ_{sol} are the densities of the dry SAP and the solution, respectively and $V_{SAP,dry}$ is the volume of the dry SAP particle.

3 NUMERICAL AND EXPERIMENTAL METHODS

In this section we briefly summarize the numerical methods used to model the problem of water absorption in unsaturated mortar. In addition, a brief explanation of the simulated experiments is offered, although no experiments were specifically carried out purposely for the validation of the model presented here.

3.1 *Mesoscale lattice network model*

Lattice network models have been successfully implemented to simulate mechanical behavior of cementitious materials (Schlangen & van Mier 1992). Lately, they have also found applications in mass and ionic transport in such materials (i.e. moisture, water, chlorides) (Šavija, Pacheco, & Schlangen 2013; Wang, Bao, & Ueda 2016). These types of models consist in an assembly of discrete two-nodes elements (lattice beams) that represents a continuum. For the modeling of transport, the lattice approach treats the transport as occurring along the beam elements in the lattice mesh. Other studies (Grassl & Bolander 2016) defend the implementation of the transport in cracked materials occurring along the facets of the Voronoi poligons (in 2D). Herein, the transport is regarded as along the lattice beams.

For the discretization of the domain, the nodes are placed pseudo-randomly inside each cubic cell of a quadrangular grid. The specified sub-cell dimension with respect to the cubic cell determines the randomness of the set of nodes. For the mesh generation, we choose a randomness coefficient of 0.5. Subsequently, a Voronoi tessellation is performed with respect to the previously placed nodes in the domain. Nodes belonging to adjacent

Voronoi cells are joined by lattice beams as schematized in Figure 1.

The advantage of lattice-type models for unsaturated flow in cement-based materials is, among others, the explicit implementation of heterogeneities in the material. Sound cement paste, cracked domain, aggregates, SAP particles, Interfacial Transport Zone (ITZ) and other interfaces are assigned different lattice phases and corresponding transport properties. A schematic of such implementation for concrete in 2D is shown in Figure 2.

In this work, only mortar, regarded as one phase, and SAP phases are explicitly implemented in the mesh of the SAP mortar, as well as their interface. Anm model (Qian, Garboczi, Ye, & Schlangen 2016) was used for parking irregular-shaped SAPs into a 5 mm cube with fully periodic boundaries. The cube was later used as primary cell in the creation of a specimen with larger dimensions. Such a procedure reduced drastically the computational time. The simulated SAP particles had the dimensions of the macropores left by the desorption of the SAP.

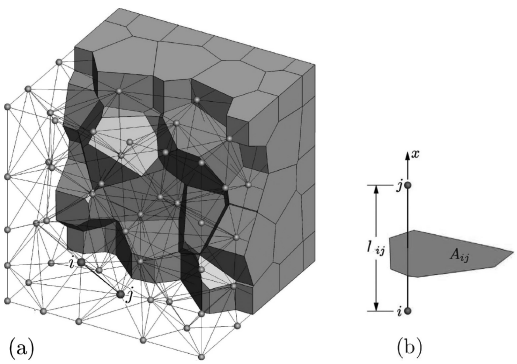

Figure 1. Schematics of spatial discretization with Voronoi Tessellation (Pan, Prado, Porras, Hafez, & Bolander 2017).

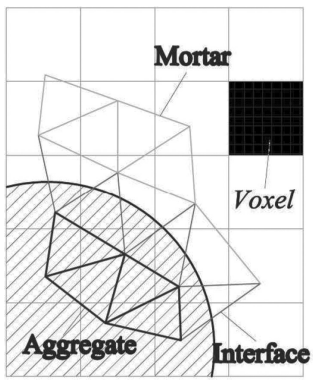

Figure 2. Heterogeneity implementation in a 2D lattice mesh (Savija 2014).

The binary tomography was used to discriminate between mortar and SAP phases in the mesh by overlapping both grids: nodes in the lattice mesh inside a cell belonging to a certain phase are tagged with such a phase. Similarly, beam elements with nodes belonging to the same phase were tagged as such, while elements bridging both faces were distinguished as interface elements. Although, since the transport properties of the interface zone between SAPs and the surrounding mortar were unknown, similar properties to the mortar were assigned with good approximation since the SAPs provide internal curing.

3.1.1 *Numerical implementation*

If Equation 4 is discretized by using Galerkin method, in the context of lattice model its weak formulation in matrix form results:

$$M\frac{\partial \theta}{\partial t} + K\theta = F \tag{11}$$

where the M and K are the mass and diffusivity matrices, respectively. F is the forcing vector, in which the Neumann-type boundary conditions and any sink/source terms are dumped. The elemental matrices and vectors described above are reported in Equations 12, 13 and 14 for the ij element in its local reference system:

$$m_{ij} = \frac{A_{ij} l_{ij}}{6\omega}\begin{bmatrix} 2 & 1 \\ 1 & 2 \end{bmatrix} \tag{12}$$

$$k_{ij} = \frac{D_{ij}(\theta) A_{ij}}{l_{ij}}\begin{bmatrix} 1 & -1 \\ -1 & 1 \end{bmatrix} \tag{13}$$

$$f_{ij} = \begin{bmatrix} f_i \\ f_j \end{bmatrix} \tag{14}$$

A_{ij} and l_{ij} are the elemental area and length. While ω is a correction parameter for the volume of the single element. It has been proven that, being ω the ratio between the sum of all elements volume in the mesh and the volume enclosed by the mesh boundaries, its value results 3 for three-dimensional meshes (Asahina et al. 2014).

Crank–Nicholson scheme is used for the time discretization.

$$(M + \frac{1}{2}\Delta t K^{n-1})\theta^n = (M - \frac{1}{2}\Delta t K^{n-1})\theta^{n-1} + \Delta t f \tag{15}$$

An iterative algorithm is avoided by calculating θ of the current time step (n) using the K matrix

calculated at the previous step (n–1). Although an error is introduced in the solution of the system, it is small for appropriately short time steps. Such a procedure was used by Luković et al. (2016) to model the drying of cementitious materials with good results.

3.1.2 *SAPs water absorption: Sink term or high transport properties?*

On one hand, SAPs are regarded as sinks for the current physical problem. On the other hand, from the moment that SAPs are considered as another phase in the modeled mortar, transport properties need to be assigned to the the beam elements corresponding to the SAP domain. Roughly saying, the following statement applies: water that does not get in cannot be absorbed. The hydraulic diffusivity of SAP beam elements for the current time step n was then approximated as: d for the current saturation of the element, per unit length of the discrete element under consideration.

$$D_{ij,SAP_m}^{n} = \frac{k_{SAP_m}(V_{m,max} - V_m^{n-1})}{l_{ij}} \tag{16}$$

In a similar fashion the sink term was implemented as follows. The volume of water absorbed by the node i – at the current time step was estimated as:

$$f_{i,SAP_m}^{n} = \frac{k_{SAP_m}(V_{m,max} - V_m^{n-1})}{\sum_{i \in m} V_{cell,i}} V_{cell,i} \tag{17}$$

where $V_{cell,i}$ is the volume of the Voronoi cell associated to node i –.

3.2 *Capillary absorption experiments and input parameters*

Different procedures are used in the laboratory for the measurement of the sorptivity of cementitious materials (ASTM 2008; CEN 2002). Basically, the methods differ on the preconditioning of the samples prior to the test, aimed to achieve an even moisture distribution inside the sample with prescribed dimensions.

In any case, the samples lateral surface is waterproofed and the top surface is loosely covered to avoid the buildup of pressure that may hinder the unidirectional flow of water in the sample while preventing moisture exchange at that boundary. The samples are placed on narrow supports inside a container and the water level is kept constant at 2–3 mm from the bottom of the sample. The mass increase of the sample is monitored over time throughout the test, more frequently during the first hours as the bulk of the water absorption occurs in this interval of time. The results are presented as a plot of the weight per unit of area exposed to saturation against the square root of time. S is determined as the slope of the best fit line in the first 4–6 hours since afterwards the gravitational forces start balancing the capillary forces, etc. resulting in a flattened curve. A schematic of the test is shown in Figure 3.

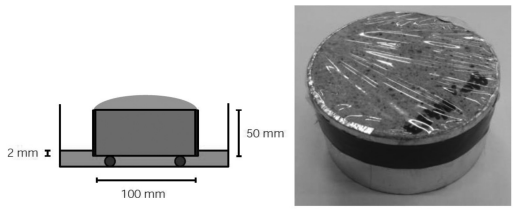

Figure 3. Capillary absorption test setup (Snoeck 2015).

For the imposition of the initial conditions, the internal moisture content must be known. Also the sorptivity S and the porosity of the material accessible to water are needed for the calculation of D_0. The latter must be known also for the quantification of the absorbed water.

Regarding the SAPs, the input parameters needed for the model are their size distributions at the dry state and at the swollen state during mixing, their absorption during mixing and their dry density. In addition, ideally the constants describing the swelling kinetics of used SAPs should be obtained from the experiment described in (Esteves 2011).

4 MODEL VALIDATION

In this section, the numerical model described in the previous section was validated with available experimental data. The validating procedure consisted of two parts. In the first part, simulations of capillary absorption in sound plain mortars were compared to available experimental data. In the second part, simulations on the coupling of capillary absorption in porous mortar matrix and water absorption by SAPs embedded in it were compared to the experimental results of sorptivity tests performed on SAP mortar.

4.1 *Mesh sensitivity analysis*

For the sake of optimizing computing speed, the influence of the cell size on the goodness of the simulation results was investigated. Voxel sizes of 0.25, 0.5 and 1.0 mm were used to discretize a mortar prism 20 mm high and square base with 10 mm

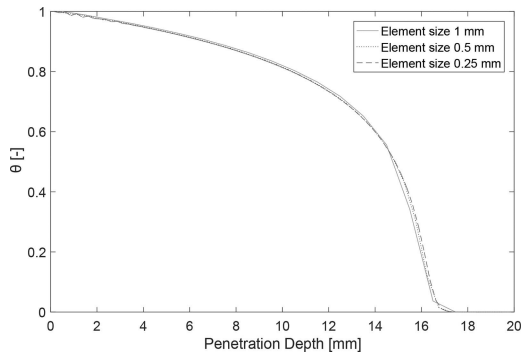

Figure 4. Saturation profiles along the direction of flow for different mesh sizes.

side. Consequently, simulations were carried out on meshes with 128000, 16000 and 2000 nodes, respectively. The resulting amount of beam elements was 942874, 111653 and 12480, respectively. D_0 was set as 0.0231 mm^2/min and the initial saturation null. The simulations were carried out with a time step of $\Delta t = 0.25$ min and total time $t = 60$ min.

The results in Figure 4 show little differences between the different meshes for the orders of magnitude of the given hydraulic diffusivity and mesh sizes. As follows, the simulations will be carried out with element lengths of approximately 1 *mm*, with exception of the simulations on SAP mortar, where SAPs dimensions require a refinement of the mesh.

4.2 *Capillary absorption simulations in plain mortar*

The numerical model regarding only capillary absorption of water was applied to simulate two different experiments, the results of which are available in literature, as well as the necessary input parameters.

Experimental data obtained from the measurement of moisture profiles in initially dry mortar with Nuclear Magnetic Resonance (NMR) were performed by Hall (1989). The mortar specimen had dimensions of 235 x 33 x 33 *mm*. In the experiment, one of the bases of the prism was brought into contact with a water reservoir and the water content distribution was measured at a series of elapsed times. The porosity accessible to water was estimated as 0.27, the sorptivity, measured in the experiments as well, was 2.57 $mm/min^{1/2}$ and the diffusivity from it calculated was 0.736 mm^2/min. Figure 5 shows the simulation results versus the data points provided by the author. Overall, the simulation results matched very well with the experimental ones, hence the model provides a good prediction of the water spatial distribution and content over time.

In yet a similar experiment, Van Belleghem et al. (2016) used X-ray radiographs to monitor the advancement of the wetting front and the water content distribution in unsaturated mortar. The study also presented the results of the sorptivity test in terms of global water uptake by the mortar over a time interval of 100 h. The authors obtained the necessary transport properties from the latter experiment and numerical fitting as $D_0 = 0.006$ mm^2/min and $n = 6.4$. Porosity of 0.1977 and initial saturation of 0.25 were determined experimentally prior to the absorption test. The first four hours of the sorptivity experiment were simulated with such input data by using the lattice model proposed herein. Figure 6 shows the

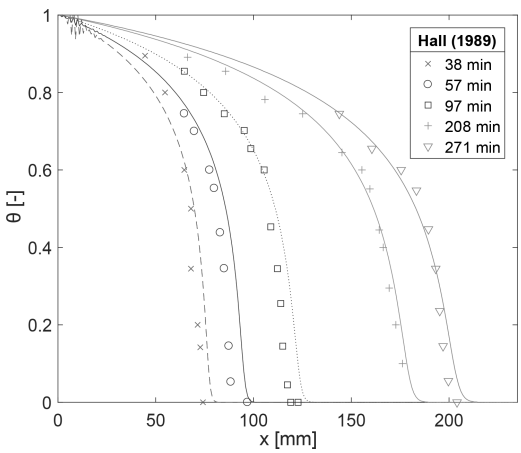

Figure 5. Comparison of saturation profiles between simulated (continuous lines) and NMR profiles (data points) after 38, 57, 97, 208 and 271 min of water absorption.

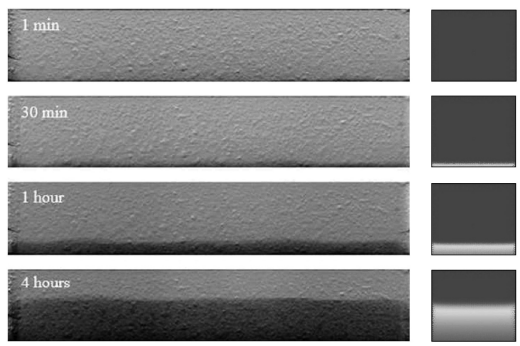

Figure 6. Comparison between X-ray radiographs (Van Belleghem et al. 2016)(left) and simulated water absorption (right) at 1 min, 30 min, 1 h and 4 h.

comparison between the transient water content distributions obtained through X-ray measurements and the simulated counterpart. It can be noted how both results are in good agreement with exception of the local effects that in the model are not explicitly taken into consideration.

4.3 *Plain Mortar vs. SAP mortar: Water absorption*

Sorptivity test results are reported in (Snoeck 2015) for SAP mortars and their reference mixtures with the same effective water to cement ratios. The author also provided information on the apparent porosity and initial water content of the specimens. These input parameters are summarized in Table 1. In this paper, only SAP B series was used for the qualitative validation of the model, namely B1.0, with 1% of SAPs by weight of cement, and the plain references R0.46 and R0.50, with the same effective water-to-cement ratio and with the same total water-to-cement ratio, respectively.

In a previous work (Snoeck et al. 2015), the data attaining to the swelling properties of SAP B, used in the above experiments, were determined experimentally. SAP B were cross-linked potassium salt polyacrilates with diameters in the range of $477 \pm 53\ \mu m$ at the dry state. The absorption capacity during mixing was determined experimentally by the author by means of vapor sorption experiments. The absorption capacity during mixing was also used as the maximum nominal absorption capacity during the capillary absorption test. The latter choice is motivated by the fact that each SAP particle is constrained by the boundaries of the macropore containing it. The absorption capacity was then set as $8.9\ g/g_{SAP}$.

For the sake of obtaining a qualitative validation, two prisms with dimensions $20 \times 5 \times 5\ mm$ were simulated for the studied mixtures. For the calculations of maximum volumes of water absorbed by the SAPs, the particles were assigned diameters of the equivalent spheres with same surface area as the irregular SAP particles simulated with Anm.

Table 1. Input parameters for the mortar phase used in the simulation of capillary absorption in Plain and SAP mortars.

	Transport properties		Physical parameters	
Mixture	$S[\frac{mm}{min^{1/2}}]$	$D_0[\frac{mm^2}{min}]$	Porosity	$\theta_{initial}$
R0.50	0.0341	0.0016	0.077	0.16
R0.46	0.0186	0.00097	0.068	0.18
B1.0	0.0186	0.001	0.064	0.19

The mortar phase in the SAP mortar was assigned transport properties based on the sorptivities of the reference plain mortars with similar porosity. The latter simplification is accurate enough since all the mixtures were tested under the same conditions and the initial moisture content was very similar among the different mixtures (Hall 1989).

The simulated and measured absorption of water per unit area normalized to the density of water for the different mixtures are shown in Figure 7 for different elapsed times in an interval of 6h from the moment of first contact with water. The constant of the of swelling kinetics law were loosely fitted as $r_1 = 2000\ \frac{\mu m^{1.267}}{min}$ and $r_2 = -1.267$ and the motivation is explained further in this section.

With regards to the mortars with embedded SAPs, one can observe in the graph that there is a deficiency in the water absorption of the simulated specimens in the first 20 minutes of the time-dependent analysis with respect to the measured ones. The cause for this abnormality might be the lack of SAPs at the boundary in contact with water and the low sorptivity of the matrix which leads to a delayed first contact of the lower SAPs with the upcoming water. Nevertheless, the model is able to capture similar slopes as in the experimental data for the studied time interval. After the first SAPs start absorbing water, a steeper increase on the water absorption is observed at the beginning with respect to the reference due to the uptake of water by the SAPs reached by the wetting front. As the SAPs left behind by the water front get saturated, their rate in water absorption decreases while the new ones, being reached by the water rising in the pores, start absorbing faster, overcompensating for the latter decrements. After the first 3 hours of the simulation, the deficiency in water absorption in the simulation is switched and the simulated results grow faster than those of the experimental data.

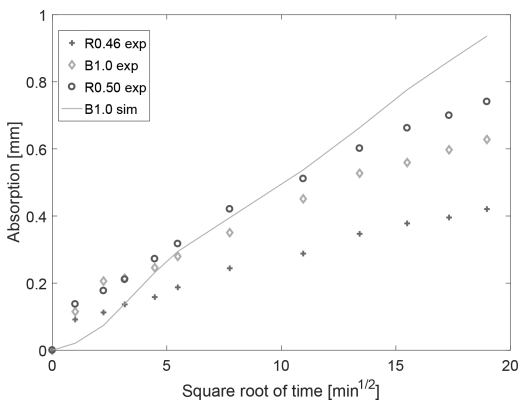

Figure 7. Absorption of water per unit area of Plain and SAP mortars.

The authors believe that the porosity of the mortar matrix has been overestimated, due to the high density of SAP macropores.

In order to validate this hypothesis the estimated water absorption of the SAPs was calculated from the simulations and compared to the absorption of SAPs that would has been obtained from the experimental data for different values of the sorptivity of the matrix. In Figure 9 the latter is reported for the best fit found, being the corresponding sorptivity, 0.006 $mm/min^{1/2}$, three times smaller than the one estimated from the measured apparent porosity. Although the overall behaviour of the absorption curve agrees with the square root law for the sorptivity found in the experiments, the fitted rates in the SAP swelling kinetics law are by no means correct due to the shift in water absorption of the SAP and the uncertainty on the correctness of the chosen value of the sorptivity.

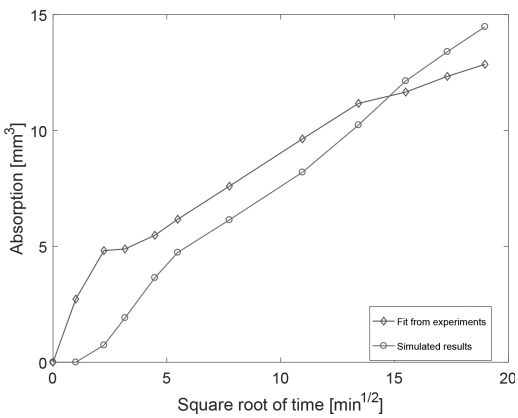

Figure 8. Amount of water absorbed by SAPs overtime in the simulations and fitted from the experimental results for $S = 0.006\ mm/min^{1/2}$.

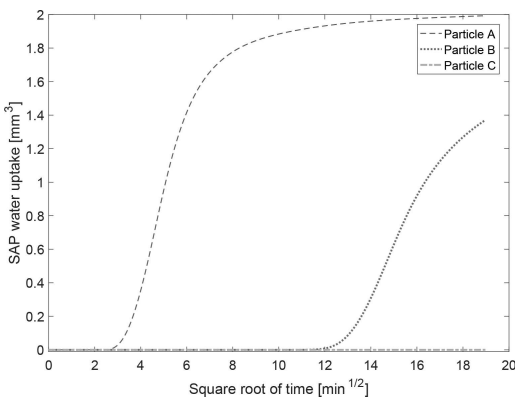

Figure 9. Absorption of water by individual SAPs at different heights along the sample.

Evidence of the role of SAP water absorption on the curve behavior can be observed in Figure 8. The Absorbed water vs. the square root of time is reported for three identical particles placed at different heights in the simulated sample. Particle A is positioned at 1.675 mm height from the boundary subjected to contact with water, B is at 6.775 mm and C at 11.65 mm. At time $t = 180\ min$ the wetting front is located at 7.5 mm circa from the bottom of the sample and the surroundings of the particles have saturation of 0.94, 0.39 and 0.19 (equilibrium), respectively.

5 ADDITIONAL CONSIDERATIONS

Since the mortars studied in the previous section present low levels of porosity, the rise of the wetting front was very slow as well as the absorption of the SAPs. In this section, a hypothetical case study is presented on the comparison of two mortars with the same porosity, one containing 1% (by weight of cement) of a hypothetical SAP with fast rates of water uptake and one plain mortar. The objective is to obtain information regarding the entity of the penetration depths at different elapsed times during absorption for the sake of comparison.

Same geometry of prisms as in Section 4.3 was used. The hydraulic diffusivity, the porosity and the initial water content of the mortar phase were the same for both materials: 0.012 mm^2/min, 0.15 and 0.19, respectively. For the SAPs, same properties as in the previous section were assigned while the rates are now $r_1 = 2.7 \times 10^5 \frac{\mu m^{1.267}}{min}$ and $r_2 = -1.267$.

Figure 10 shows the results of the simulations for Plain (a,c,e) and SAP (b,d,f) mortars at different times during the water absorption simulations (10, 60 and 120 min).

During the first 10 min, both materials behave similarly. As seen in Section 4.3, when water

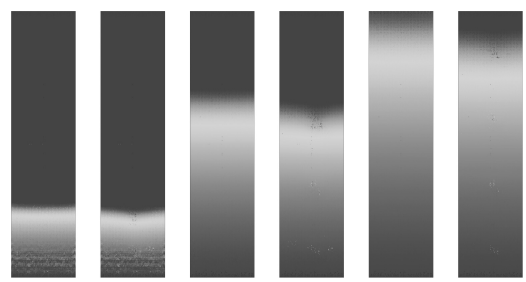

Figure 10. Penetration depths at different elapsed times during sorptivity simulations of plain (a,c,e) and SAP (b,d,f) mortars.

encounters the first SAPs, these start absorbing water with a fast rate but since they don't occupy entirely the volume of the macropore, water can also flow out of the cavity, therefore behaving like semi-permeable inclusions. As the SAPs get saturated, they stop absorbing water and act as impermeable inclusions (Asahina, Kim, Li, & Bolander 2014), similar to the effect of aggregates on fluid transport in concrete. At this stage, water has to turn around the macropore, elongating its path upwards.

6 CONCLUSIONS

In this work, an attempt has been made to model the water absorption in unsaturated mortars with and without SAPs. First, the authors derived the mathematical and numerical formulations and motivated the assumptions made. In the second part, a validating procedure was performed by using available experimental data. Last, the model was used to formulate conclusions regarding the mechanism of water absorption of mortars containing SAPs.

In particular:

1. The numerical model regarding the capillary absorption of water by plain sound mortars agreed very well with the experimental results published by different authors. Although it was not implemented in the plain mortar simulations, the model can account for the presence of heterogeneity in the material, i.e. porous reinforcement interface, aggregates, ITZ, etc. as seen for the SAP mortars where SAP particles are another phase in the mesh.
2. A diffusion-controlled law for the SAPs swelling kinetics was extended to the SAPs water absorption during sorptivity simulations in mortars. Although the absorption vs. square root of time of simulated and experimental data did not fit perfectly, the overall behavior of the curve was captured in the simulations, validating the appropriateness of the law for the description of the water uptake of SAPs embedded in a cementitious matrix.
3. The model is very sensitive to the value used for the sorptivity. The results suggest that the porosity of the SAP mortar was overestimated and therefore the assumption of interpolated sorptivity of the mortar phase with respect to the porosity of the reference mixtures failed. In particular, the sorptivity was re-estimated to be one third of the one used in the simulations.
4. Finally, some considerations were made regarding the role of SAP particles in the absorption of water in mortar. At first, the particles act as semi-permeable inclusions that attract the flow of water towards it due to the higher hydraulic diffusivity. When the particle has uptaken a certain amount of water, the diffusivity of the phase drastically decrease and the particle starts behaving as an impermeable particle. The simulation results suggest that although the material under study uptakes more water globally with respect to its plain counterpart, it does reduce relatively the water rise. The latter conclusion should be explicitly validated.

ACKNOWLEDGEMENTS

This research is supported by a grant (17SCIP-B103706-03) from Construction Technology Research Program funded by Ministry of Land, Infrastructure and Transport of Korean Government. The financial support of this institution is gratefully acknowledged. Also, the authors wish to acknowledge Dr. Branko Šavija and Dr. Zhiwei Qian for their highly appreciated help.

REFERENCES

Asahina, D., K. Kim, Z. Li, & J.E. Bolander (2014). Flow field calculations within discrete models of multiphase materials. *Composites Part B: Engineering 58*, 293–302.

ASTM (2008). C 1585 04 Standard Test Method for Measurement of Rate of Absorption of Water by Hydraulic-Cement Concretes. Technical report, ASTM.

CEN (2002). EN 13057 Products and systems for the protection and repair of concrete structures—Test methods—Determination of resistance of capillary absorption. Technical report.

Esteves, L.P. (2011). Superabsorbent polymers: On their interaction with water and pore uid. *Cement and Concrete Composites 33* (7), 717–724.

Grassl, P. & J. Bolander (2016). Three-dimensional network model for coupling of fracture and mass transport in quasi-brittle geomaterials. *Materials 9* (9), 1–18.

Hall, C. (1989). Water sorptivity of mortars and concretes: a review. *Magazine of concrete research 41* (147), 51–61.

Hall, C. & W. D. Hoff (2009). *Water Transport in Brick, Stone and Concrete* (2nd ed.), Volume 25. Spon Press.

Hong, G. & S. Choi (2017). Rapid self-sealing of cracks in cementitious materials incorporating superabsorbent polymers. *Construction and Building Materials 143*, 366–375.

Kim, J.S. & E. Schlangen (2010). Super Absorbent Polymers To Stimulate Self Healing in ECC. In *2nd International Symposium on Service Life Design for Infrastructure*, Number 1, pp. 849–858.

Lockington, D., J.-Y. Parlange, & P. Dux (1999). Sorptivity and the estimation of water penetration into

unsaturated concrete. *Materials and Structures 32* (5), 342.

Luković, M., B. Šavija, E. Schlangen, G. Ye, & K. van Breugel (2016). A 3D lattice modelling study of drying shrinkage damage in concrete repair systems. *Materials 9* (7).

Pan, Y., A. Prado, R. Porras, O. Hafez, & J. Bolander (2017). Lattice Modeling of Early-Age Behavior of Structural Concrete. *Materials 10* (3), 231.

Qian, Z., E. Garboczi, G. Ye, & E. Schlangen (2016). Anm: a geometrical model for the composite structure of mortar and concrete using real-shape particles. *Materials and Structures 49* (1–2), 149–158.

Savija, B. (2014). *Experimental and Numerical Investigation of chloride ingress in cracked concrete.* Phd dissertation, TU Delft.

Šavija, B., J. Pacheco, & E. Schlangen (2013). Lattice modeling of chloride diffusion in sound and cracked concrete. *Cement and Concrete Composites 42,* 30–40.

Schlangen, E. & J.G.M. van Mier (1992). Experimental and Numerical Analysis of Micromechanisms of Fracture of Cement-Based Composites. *Cement & Concrete Composites* (14), 105–118.

Snoeck, D. (2015). *Self-Healing and microstructure of cementitious materials with micro_bres and superabsorbent polymers*. Phd dissertation, Ghent University.

Snoeck, D., S. Steuperaert, K. Van Tittelboom, P. Dubruel, & N. De Belie (2012). Visualization of water penetration in cementitious materials with superabsorbent polymers by means of neutron radiography. *Cement and Concrete Research 42* (8), 1113–1121.

Snoeck, D., L.F. Velasco, A. Mignon, S. Van Vlierberghe, P. Dubruel, P. Lodewyckx, & N. De Belie (2015). The effects of superabsorbent polymers on the microstructure of cementitious materials studied by means of sorption experiments. *Cement and Concrete Research 77*, 26–35.

Sweijen, T., C. van Duijn, & S. Hassanizadeh (2017). A model for diffusion of water into a swelling particle with a free boundary: Application to a super absorbent polymer particle. *Chemical Engineering Science 172*, 407–413.

Szymkiewicz, A. (2013). *Modelling Water Flow in Unsaturated Porous Media*, Volume 9.

Van Belleghem, B., R. Montoya, J. Dewanckele, N. Van Den Steen, I. De Graeve, J. Deconinck, V. Cnudde, K. Van Tittelboom, & N. De Belie (2016). Capillary water absorption in cracked and uncracked mortar - A comparison between experimental study and finite element analysis. *Construction and Building Materials 110*, 154–162.

Vervoort, S. (2006). *Behaviour of hydrogels swollen in polymer solutions under mechanical action.* Phd dissertation, Ecole Nationale Sup erieure des Mines de Paris.

Wang, L., J. Bao, & T. Ueda (2016). Prediction of mass transport in cracked-unsaturated concrete by mesoscale lattice. *Ocean Engineering 127* (August), 144–157.

Computational Modelling of Concrete Structures – Meschke, Pichler & Rots (Eds)
© 2018 Taylor & Francis Group, London, ISBN 978-1-138-74117-1

Full coupling between diffusion and mechanical analysis in a discrete computational framework

F. Bousikhane & W. Li
Department of Civil and Enviromental Engineering, Northwestern University, Evanston, IL, USA

G. Di Luzio
Department of Civil and Enviromental Engineering, Politecnico Di Milano, Milan, Italy

G. Cusatis
Department of Civil and Enviromental Engineering, Northwestern University, Evanston, IL, USA

ABSTRACT: Nowadays durability and sustainability are two major priorities in the structural design and numerous models have been developed along these lines in different disciplines. Even though in reality, observed phenomena in concrete structures such as corrosion are the results of multi-physics, most models adopt a single disciplinary approach. Recently, advanced multi-physics computational framework have been proposed and successfully used to model: 1) the mechanical behavior of concrete, including visco-elasticity, long-term behavior, cracking and damage, and hygro-thermal deformations; 2) heat transfer and moisture variation/diffusion associated with environmental exposure and self desiccation; 3) aging that is the evolution of the mechanical and physical material properties. However, the current developed framework is not fully coupled between the mechanical and diffusion model.

1 INTRODUCTION

Many concrete structures suffer from environmental conditions where moisture can be the source of multiple deterioration mechanisms such as corrosion, chloride and sulfate attacks, alkali-silica reaction and freeze/thaw cycles. However, in classical complex engineering cases, one-way approaches can be limiting to accurately describe phenomena such as the interaction between diffusion phenomena and mechanical properties, which actually plays a major role when it comes to durability. One alternative to successfully characterize and model the mechanics and diffusion-based phenomena is to adopt a full coupling between them. This approach shows great potential for multi-physics applications where mechanical and diffusion equations cannot be solved independently. For example, in concrete constructions, cracks formation is a common occurrence, which allows for water ingress and the transport of multiple aggressive chemical compounds. Modeling the entire system naturally requires to couple the mechanical behavior and moisture transport.

In classical fracture flow approaches, the considered fluid is water which happens to be a double edge sword for cementitous materials. Indeed, water is a catalyst in cement hydration (Neville 1997, Taylor 1997) which governs concrete setting, strengthening, and aging. However, high level of stresses as well as volume changes due to drying (autogenous and exogenous) and/or thermal shrinkage lead to the formation of damage and localized cracks. Well known in the field of structural engineering and infrastructure materials, fractures behave like hydraulic conductors, increase significantly permeability and happen to be easy pathways to reinforcements for water ingress. At this level, the integrity of the concrete structures is always questionable and developing coupled models that can characterize fracture-flow behavior in cementitious materials becomes essential.

Pei, Schuster, & Wan (2011) and Villani, Busso, Ammar, Forest, & Geers (2011) developed continuous models that simulate the interactions between fluid and structure based on the classical Navierstokes equation for the fluid flow modeling. Based on a continuous approach, these models simulate material deformations but cannot capture crack initiation nor propagation. Such models are not suitable for fracture-flow analyses of concrete structures as cracks effect needs to be taken into account in the model to achieve great accuracy in the the analysis. Grassl (2008) proposed a hybrid discrete-continuum modeling of fracture-flow in concrete where respectively, the mechanical and

diffusion analysis are performed using a discrete and continuous model. However, combinations between discrete and continuum modelings can be the source of numerous bugs in the algorithms leading to instabilities. Recently, Grassl & Bolander (2016), proposed a dual three-dimensional networks of structural and transport elements to model the effect of fracture on mass transport in quasi-brittle materials. However, a simplified transport model were adopted for cement-based materials.

The present work describes recent developments of the Lattice Discrete Particle Model (LDPM Cusatis, Pelessone, & Mencarelli (2011)), a discrete model, for coupled fracture-flow analyses of cementitious materials. The Lattice Discrete Particle Model (LDPM), a three-dimensional mesoscale discrete model, is employed to simulate concrete mechanical response. LDPM simulates concrete at the level of coarse aggregate pieces and is capable of characterizing strain localization, distributed cracking in tension and compression and to reproduce post peak softening behavior. The LDPM features have been significantly perfected by the integration of early age concrete mechanical behavior (Di Luzio & Cusatis 2013), ASR modeling Alnaggar, Cusatis, & Di Luzio (2013, Alnaggar, Di Luzio, & Cusatis (2017), fiber effects Schauffert & Cusatis (2011), dynamic testing Smith & Cusatis (2016).

The Lattice Discrete Particle Model (LDPM) by Cusatis, Pelessone, & Mencarelli (2011) mesostructure is used to construct the edges (the elements of the flow lattice) which are along the triangular facets of the mesostructure, where the polyhedral cells are in contact. This creates a dual lattice model, fracture analyses are performed on the structural lattice, whereas diffusion/flow analyses are performed on the flow lattices. To couple the fracture and flow analyses, the amount of crack opening of each structural element which exhibits fracture, is used to evaluate the permeability increase of the surrounding flow lattice elements, in accordance with theory or experimental observations. The capabilities of this model are demonstrated further by simulating experimental data relevant to water diffusion in cracked concrete.

2 THE MECHANICAL DISCRETE MODEL (LDPM)

Recently, the Lattice Discrete Particle Model (LDPM), a meso-scale discrete model has been developed to simulate (Cusatis et al. 2011) the mechanical behavior of concrete. The LDPM is capable of mimicking the mechanical interactions between coarse aggregates ingrained in a cementitious matrix. The material parameters of the model control directly the nature of the interactions between the particles of an assemblage of grains.

Figure 1 illustrates the steps in the generation process of concrete internal structure. As concrete has a granular internal structure, coarse aggregates, modeled by perfect spheres are randomly distributed within a given volume. The application of boundary conditions is here facilitated by distributing infinitely small aggregates (*radius* = 0) on the external surface.

The topology of the grains is defined through Delaunay tetrahedralization that discretizes a given volume into a 3D mesh of tetrahedras. Then, a 3D domain tessellation integrated to the Delaunay tetrahedralization allows for the creation of a 3D polyhedral-cells system. Within this system, the adjacent polyhedral-cells interact through triangular facets, assumed to be the location of the potential concrete failure. Figure 2 illustrates an aggregate representation in the LDPM, a perfect sphere embedded in a cementitious matrix.

LDPM constructs the geometrical representation of concrete meso-structure through the following steps. 1) The coarse aggregate pieces, whose shapes are assumed to be spherical, are introduced into the concrete volume by a try-and-reject random procedure. 2) Zero-radius aggregate pieces (nodes) are randomly distributed over the external surfaces to facilitate the application of boundary conditions. 3) A three-dimensional domain tessellation, based on the Delaunay tetrahedralization of the generated aggregate centers, creates a system of polyhedral cells (see Figure 2a) interacting through triangular facets and a lattice system composed by the line segments connecting the particle centers. Figures 2b and c represent spherical particle and corresponding polyhedral representations of a typical dog-bone specimen. In LDPM, rigid body kinematics is used to describe the deformation of the lattice/particle system and the displacement jump, $[\![\mathbf{u}_C]\!]$, at the centroid of each facet is used to define measures of strain as

$$e_N = \frac{\mathbf{n}^T [\![\mathbf{u}_C]\!]}{\ell}; \quad e_L = \frac{\mathbf{l}^T [\![\mathbf{u}_C]\!]}{\ell}; \quad e_M = \frac{\mathbf{m}^T [\![\mathbf{u}_C]\!]}{\ell} \qquad (1)$$

where ℓ = interparticle distance; and $\mathbf{n}$, $\mathbf{l}$, and $\mathbf{m}$, are unit vectors defining a local system of reference attached to each facet.

Next, a vectorial constitutive law governing the behavior of the material is imposed at the centroid of each facet. In the elastic regime, the normal and shear stresses are proportional to the corresponding strains: $t_N = E_N e_N^* = E_N (e_N - e_N^0)$; $t_M = E_T e_M^* = E_T (e_M - e_M^0)$; $t_L = E_T e_L^* = E_T (e_L - e_L^0)$, where $E_N = E_0$, $E_T = \alpha E_0$, E_0 = effective normal modulus,

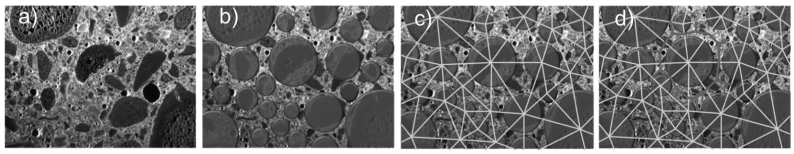

Figure 1. (a) Concrete material; (b) Supporting particles for grain generation; (c) Delaunay tetrahedralization; (d) Laminated structure model.

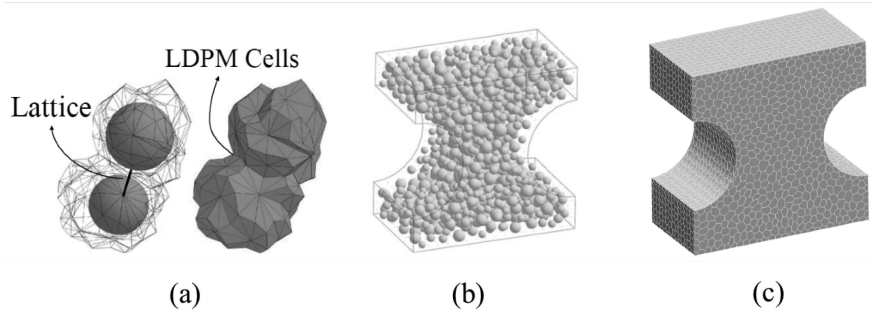

Figure 2. (a) LDPM polyhedral cell enclosing spherical aggregate pieces. (b) Spherical particle and (c) polyhedral cell representations of a typical dogbone specimen.

and α = shear-normal coupling parameter; and e_N^0, e_M^0, e_L^0 are mesoscale eigenstrains that might arise from a variety of phenomena such as, but not limited to, thermal expansion, shrinkage, and ASR expansion.

For stresses and strains beyond the elastic limit, LDPM mesoscale nonlinear phenomena are characterized by three mechanisms as described below.

3 THE DIFFUSION DISCRETE MODEL

3.1 *Geometry and topology*

To build a 3D diffusion network for concrete, the meso-scale geometry initially generated by the LDPM are here used to construct a 1D transport lattice. Figure 1c presents tetrahedrons (triangles in 2D) generated in Delaunay tetrahedralization according to the mesh generation described in the Section. Each tetrahedron interacts with four adjacent tetrahedrons creating a total of 5 interconnected tetrahedrons identifying the preferential diffusion path of moisture in the heterogenous structure of cement-based materials. To create the transport lattice network, the face-points (located a the centroid of triangular facets) and the adjacent tetrahedron-points (located at the center of the tetrahedrons) are directly connected. The face-points and tetrahedron-points constitute the 1D transport lattice network nodes and are used for the full tessellation of the 3D domain. By interacting with the mechanical lattice, the transport lattice can be used to simulate a coupled fluid flow associated with the deformation and cracking. The described model has shown superior capability in simulating similar mechanical and diffusional (moisture and heat) behaviors for material with similar internal structures such as rocks, mortar or limestones.

As can be seen from figure 3a the 1D lattice fluid flow element is characterized by the following geometrical features: A_c is the edge area of cracked material, A_e represents the edge area for uncracked material, l_e the element lengththat corresponds the intersection of the facet with the face, and w_{Ni} is the crack opening in the normal direction.

3.2 *Mass conservation*

The equation of mass conservation in a single lattice element can be written as

$$\frac{\partial v_u}{\partial t} + \frac{1}{A_e}\frac{\partial m_c}{\partial t} = \frac{\partial}{\partial x}\left(D_h(h,t)\frac{\partial h}{\partial x}\right) + \frac{1}{A_e}\frac{\partial Q_c}{\partial x} \qquad (2)$$

where $h = p/p_{sat}(T)$, v_u represents the mass of fluid in the uncracked material per unit volume, see (Di Luzio and Cusatis 2009a); m_c represents the mass of water in the crack per unit length; Q_c is the flux through the cracked material A_c and $D_h(h,t)\frac{\partial h}{\partial x}$ the flux through the uncracked material A_e.

3.2.1 *Flow across uncracked material*

The formulation of mass conservation, in equation 2, couples the diffusion in a single element considering the transport through the undamaged (uncracked) material with an area A_e and transport through the cracked areas of a tetrahedron-face of an area A_c on the all. More specifically, the fluid flow across the uncracked material is modeled using the Hygro-Thermo-Chemical (HTC) model (Di Luzio and Cusatis 2009a, Di Luzio and Cusatis 2009b). As the uncracked material represents more than 95% of the tetrahedron-face area, precise and reliable modeling of the fluid and temperature transport within the material internal structure becomes essential. This model is capable of computing the spacial and temporal evolution of temperature T, relative humidity h, and cement hydration degree α_c. Within the volume of interest, h and T fields are computed by imposing, respectively, moisture mass balance and enthalpy equation

$$\overline{D}_{unc}\frac{\partial^2 h}{\partial^2 x}-\overline{C}_{unc}\frac{\partial h}{\partial t}-\overline{S}_{unc}=0 \tag{3}$$

where $\overline{D}_{unc}=D_h$, $\overline{C}_{unc}=\partial w_e/\partial h$ and $\overline{S}_{unc}=(\partial w_e/\partial \alpha_c)\dot{\alpha}_c+(\partial w_e/\partial \alpha_s)\dot{\alpha}_s+\dot{w}_n$, in which D_h is the moisture permeability and $\dot{w}_n$ is the rate of non evaporable water. The moisture permeability D_h is formulated as a non linear function of the relative humidity.

3.2.2 *Flow through cracked material*

Mass of water in the cracks. Water can be found in the cracked area under three different states (solid, liquid or gas). Estimating accurately the portion of each water state is challenging as few resources are available on this topic. For the sake of simplicity in this formulation, the mass of water is calculated through a power law function of the relative humidity as follows:

$$m_c=k_\rho\rho_w A_c\phi(h) \tag{4}$$

where $\phi(h)=h^n$ a power law function of the relative humidity, A_c is the edge area of cracked material, ρ_w represents the fluid density, k_ρ and n are parameters to calibrate. Figure 3b displays the plot of equation 4 with $n=2$ and $k_\rho=10^{-13}$.

By deriving equation 4 with respect to time, the mass of water rate per unit length can be expressed as follows

$$\frac{1}{A_e}\frac{\partial m_c}{\partial t}=\overline{C}_{mc_h}\frac{\partial h}{\partial t}+\overline{S}_{mc} \tag{5}$$

with $\overline{C}_{mc_h}=(k_\rho\rho_w A_c/A_e)(\partial\phi/\partial h)$ and $\overline{S}_{mc}=(k_\rho\rho_w\phi A_c)/A_e$

Formulation of Poiseuille flow in the cracks. Fluid flow through the cracks of materials is classically modeled using Poiseuille flow. To establish the fluid mass balance in the crack per unit time (Q_c), a pressure p and crack of width w are considered as shown in Figure 3c. In this paper, a single phase flow at full saturation conditions is considered. As far as the fluid, the classical assumptions of laminar flow at any point and uncompressible Newtonian fluid are also assumed valid. More generally, the mass flux is a measurement of the amount of mass passing in or out of a control volume. Through a control volume, the discrete fluid flow rate is calculated by integrating the velocity field over the crossed surface of the cracks ($\Sigma_{i=1}^3 l_i w_i^3 h^m$, see also Figure 3a) and formulated as follows

$$Q_c=-\overline{D}_{crk_h}\frac{\partial h}{\partial x}+\overline{D}_{crk_T}\frac{\partial T}{\partial x} \tag{6}$$

with $\overline{D}_{crk_h}=(k_\rho\rho_w P_{sat}\sum_{i=1}^3 l_i w_i^3 h^m)/(12A_e k_\mu\mu_w)$ and $\overline{D}_{crk_T}=(k_\rho\rho_w h/12A_e k_\mu\mu_w h^m)(dP_{sat}/dT)$ where Q_c represents the flux of water in the crack per unit time, μ_w corresponds to the water viscosity and $k_\mu=10^{-4}$ is a fitting parameter.

Governing equation. The final governing equation characterizing the fluid flow through a discrete lattice element can be obtained by substituting equations 3, 5 and 6 into equation 2 and it leads to

$$\overline{C}\frac{\partial h}{\partial t}=\frac{\partial}{\partial x}\left(\overline{D}_h\frac{\partial h}{\partial x}\right)+\frac{\partial}{\partial x}\left(\overline{D}_T\frac{\partial T}{\partial x}\right)+\overline{S} \tag{7}$$

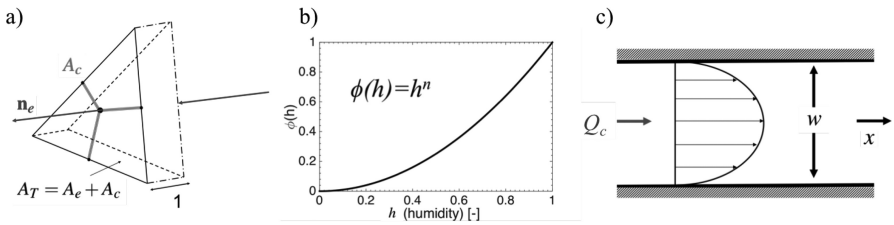

Figure 3. (a) Mass conservation sketch across tet face. (b) Plot of water mass in the cracks versus relative humidity. (c) Poiseuille flow modeling.

with $\overline{D}_h = \overline{D}_{unc_h} + \overline{D}_{crk_h}$, $\overline{D}_T = \overline{D}_{crk_T}$, $\overline{C}_h = \overline{C}_{unc_h} + \overline{C}_{mc_h}$ and $\overline{S} = \overline{S}_{unc} - \overline{S}_{mc}$

The unidimensional final governing equation characterizes the mass equilibrium of one transport lattice. To build a three dimensional diffusion network for concrete, the meso-scale geometry generated by the LDPM described initially is used to construct a 3D transport lattices. The three dimensional discrete implementation is performed according to the work of Bolander & Berton (2004).

4 THE DISCRETE DIFFUSION MODEL VERIFICATIONS

4.1 *Model verifications*

This part of the paper introduces simple problems designed to allow model verifications and insure that the updated governing equations implemented were leading coherent solutions. The performed work consisted in simulating a $160 \times 160 \times 160\ mm^3$ cubic concrete specimen subjected to a different boundary conditions. The material parameters of the LDPM for the mechanical behavior were picked from Cusatis, Mencarelli, Pelessone, & Baylot (2011). As far as the diffusion parameters, they were selected as suggested in Di Luzio & Cusatis (2009b).

4.2 *Verification 1: Crack effect on permeability*

Some preliminary results reported in Figure 4 demonstrate the capability of the proposed formulation to capture efficiently the effect of cracks on moisture diffusion. In this set of simulations, the diffusion parameter D_h used in equation 3 is set to zero to isolate the effect of cracks on drying. As far as boundary conditions, one lateral surface of the cube was exposed to a 50% relative humidity and the other sides were sealed to insure 1D moisture diffusion as show on Figure 4d and 4f. Generating cracks in the sample was achieved by applying a linear displacement (constant strain) on the nodes of one face of the cubic sample prior to drying. Three cases associated with three different levels of applied strain were here considered. As shown on Figure 4e, due to cracking, the moisture permeability increases significantly and drying occurs faster. The results

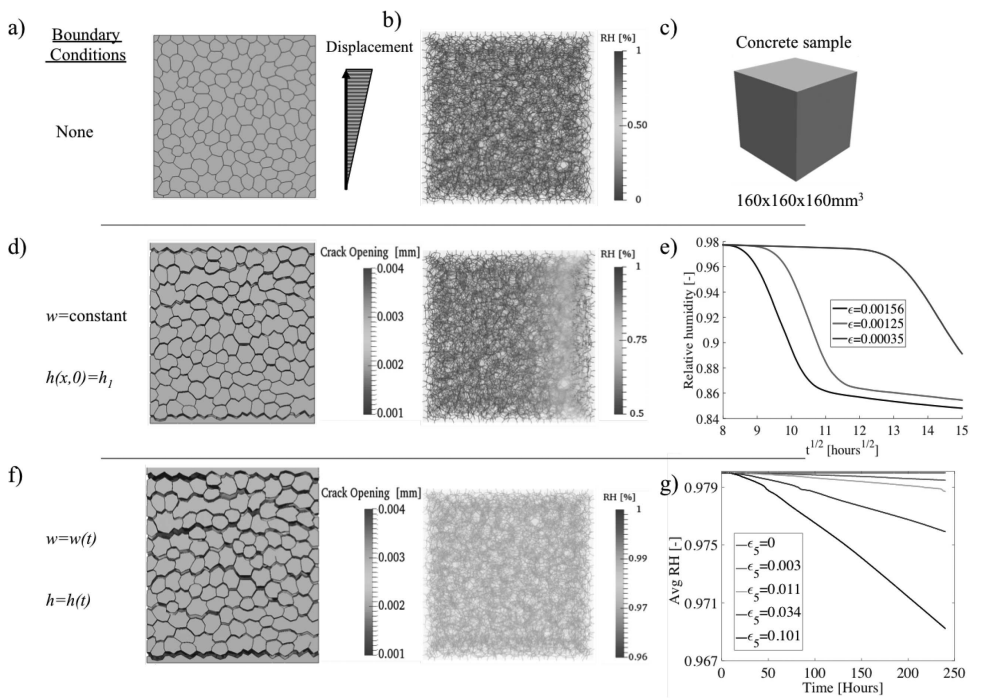

Figure 4. a) LDPM mesh. b) Transport lattice mesh. c) Sample geometry. d) Velocity and relative humidity profile for cracked concrete samples drying on one face. e) Plot of relative humidity versus the square root of time for 3 samples submitted to 3 constant strains and drying on one face at 50 percent relative humidity. d) Velocity and relative humidity profile for sealed cracked concrete samples. f) Plot of relative humidity versus the square root of time for 3 samples submitted to 5 constant strains under sealed conditions.

also show that for smaller strains (smaller cracks), the drying process is slower than for larger strains which is consistent with what is expected.

From the analytical solution of the governing equation for this problem, the square root of the permeability ($\sqrt{D}$) has to be proportional to the crack opening as confirmed in Figure 4e.

The results of this initial study show that the model is now effectively capable of model crack effects on concrete permeability.

4.3 *Verification 2: Volume change effect on relative humidity*

The second problem consisted in qualitatively evaluating the relative humidity evolution in a sealed concrete sample subjected to different levels of cracking as shown on Figure 4f. This part has for principal objective to evaluate the influence of the source term $\bar{S}$. To isolate the effect of the source term associated with the cracked material, the source term related to the uncracked material was set to zero. The method described earlier to generate cracks remains valid for this reused. The plot of Figure 4g shows that within the sealed sample, a decrease of the relative humidity is observed as the sample is being subjected to larger strains. This result is expected as by increasing the volume, the pressure within this given volume decreases automatically in sealed conditions. Also, the linear relationship between relative humidity h and pressure p given in the definition of h suggests that if the pressure decreases, then the relative humidity should decrease as well. This explains how the model captures the relative humidity sensitivity to volume change (cracking) as well. Once more, the preliminary results of this second study show that the model effectively simulates crack effects (volume change) on relative humidity distribution.

5 CONCLUSION

A discrete formulation for moisture flow in both intact and damaged material has been proposed in this paper. The model has been introduced in a discrete numerical framework and coupled with the LDPM (mechanical model). The results of the numerical simulations qualitatively confirm the reliability of the proposed model also in the presence of cracks.

ACKNOWLEDGEMENTS

The work of the first and last authors was supported under the National Regulatory Comission grant NRC-HQ-60-14-FOA-0001 to Northwestern University.

REFERENCES

Alnaggar, M., G. Cusatis, & G. Di Luzio (2013). Lattice discrete particle modeling (ldpm) of alkali silica reaction (asr) deterioration of concrete structures. *Cement and Concrete Composites 41*(Supplement C), 45–59.

Alnaggar, M., G. Di Luzio, & G. Cusatis (2017). Modeling timedependent behavior of concrete affected by alkali silica reaction in variable environmental conditions. *Materials 10*, 471.

Bolander, J.E. & S. Berton (2004). Simulation of shrinkage induced cracking in cement composite overlays. *Cement and Concrete Composites 26*, 861–871.

Cusatis, G., A. Mencarelli, D. Pelessone, & J. Baylot (2011). Lattice discrete particle model (ldpm) for failure behavior of concrete. ii: Calibration and validation. *Cement and Concrete Composites 33*, 891–905.

Cusatis, G., D. Pelessone, & A. Mencarelli (2011). Lattice discrete particle model (ldpm) for failure behavior of concrete. i: Theory. *Cement and Concrete Composites 33*, 881–890.

Di Luzio, G. & G. Cusatis (2009a). Hygro-thermo-chemical modeling of high performance concrete. I: Theory. *Cement and Concrete Composites 31*(5), 301–308.

Di Luzio, G. & G. Cusatis (2009b). Hygro-thermo-chemical modeling of high performance concrete. II: Numerical implementation, calibration, and validation. *Cement and Concrete Composites 31*(5), 309–324.

Di Luzio, G. & G. Cusatis (2013). Solidification-Microprestress-Microplane (SMM) theory for concrete at early age: Theory, validation and application. *International Journal of Solids and Structures 50*(6), 957–975.

Grassl, P. (2008). A lattice approach to model flow in cracked concrete. *Archives on condensed matter 09*.

Grassl, P. & J. Bolander (2016). Three-dimensional network model for coupling of fracture and mass transport in quasibrittle geomaterials. *Materials 9*(9), 782.

Neville, A. (1997). *Properties of concrete*. New York: John Wiley and Sons.

Pei, J., S. Schuster, & B. Wan (2011). Comparison of one-way and two way coupling methods for numerical analysis of fluid structure interactions. *Journal of Applied Mathematics 2011*, 16.

Schauffert, E.A. & G. Cusatis (2011). Lattice discrete particle model for fiber-reinforced concrete. i: Theory. *Journal of Engineering Mechanics, ASCE 12*, 826–833.

Smith, J. & G. Cusatis (2016). Numerical analysis of projectile penetration and perforation of plain and fiber reinforced concrete slabs: Numerical analysis of projectile penetration and perforation of plain and fiber reinforced concrete slabs. *International Journal for Numerical and Analytical Methods in Geomechanics 07*.

Taylor, H. (1997). *Cement Chemistry*. London: Thomas Telford.

Villani, A., E. Busso, K. Ammar, S. Forest, & M. Geers (2011). A fully coupled diffusional mechanical formulation: numerical implementation, analytical validation, and effects of plasticity on equilibrium. *Archive of applied mechanics 84*(9–11), 1647–1664.

Computational Modelling of Concrete Structures – Meschke, Pichler & Rots (Eds)
© 2018 Taylor & Francis Group, London, ISBN 978-1-138-74117-1

Alternative parameter to characterize pore distribution in cement paste, and its relation to mechanical properties

T.-S. Han & J.-S. Kim
Department of Civil and Environmental Engineering, Yonsei University, Seoul, Republic of Korea

ABSTRACT: Porosity has been used widely as an index for the void volume fraction within the microstructure of cement paste. However, the porosity has its limitations as a scalar parameter so that alternative measures could help further identifying the characteristics of pore microstructure and better correlating microstructure with properties.

The lineal-path function has been shown its potential to describe the characteristics of complex microstructures. In this study, the centroid of the lineal-path function is investigated as a supplement or alternative parameter to porosity for characterizing pore microstructure and correlating the characteristics with mechanical properties. In particular, the parameter is used to determine the diffusive crack length parameter, one of the material modeling parameters of the crack phase field model.

The centroid of the lineal-path function identifies the bimodal distribution of the pore microstructures within cement paste, which cannot be captured with porosity. The evaluated mechanical properties such as stiffness and tensile strength using the crack phase field model whose parameter is determined from the centroid of the lineal-path function are in the range of expected values. It is shown that the centroid of the lineal-path function has a potential as an alternative or supplement parameter for microstructure characterization and for determining the modeling parameter of the crack phase field model.

1 INTRODUCTION

The properties of cement paste are strongly dependent on the pores within the microstructure. Porosity has been used widely to indicate the void volume fraction embedded in the microstructure of cement paste. The mechanical responses such as stiffness and strength have been successfully correlated to the parameter. However, the porosity has its limitations as a scalar parameter so that alternative measures could help further identifying the characteristics of pore microstructure and better correlating microstructure with properties.

The lineal-path function, one of the low-order probability functions (Torquato 2002), has been shown its potential to describe the characteristics of complex microstructures. In this study, the centroid of the lineal-path function is investigated as a supplement or alternative parameter to porosity for correlating microstructural characteristics with mechanical properties.

The crack phase field model has gained a momentum for solving challenging problems with complex geometry and multiphysics phenomenon. The model has been applied for solving cementitious materials such as concrete and cement paste (Nguyen et al. 2015), and extended to incorporate the cohesive zone model to accurately address the behavior after post-peak strength (Wu 2017). In Nguyen et al. (2016), the crack phase field model related parameters g_c and l are determined by fitting the macro-scale compressive stress strain curve using optimization technique. However, the proposed method requires stress-strain curves, and it is difficult to apply such technique to cement paste at micro-scale since such experimental data is difficult to obtain.

We further investigate the correlation between the microstructural characteristics, the centroid of the lineal-path function, and the diffusive length parameter l for crack phase field model for evaluating mechanical properties of cement paste. For modeling the crack propagation in the cementitious materials, the diffusive crack length l is reported as a material parameter rather than a pure modeling parameter only for crack regularization (Nguyen et al. 2016, Wu 2017). When the complex void phase microstructure exists, there is a potential that the diffusive crack length parameter l is influenced by the pore microstructures characterized by the lineal-path function. It is found that the centroid of the lineal-path function can effectively characterize pore microstructure where the porosity cannot, and has a potential relationship with the mechanical responses.

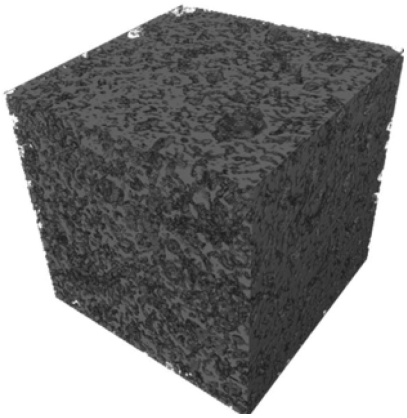

Figure 1. Hydrated cement paste specimen obtained from synchrotron μ-CT in PAL (Pohang Accelerator Laboratory) in Korea. (Side length: 130 μm).

2 CHARACTERIZATION

2.1 *Cement paste microstructures*

In this study, a synchrotron μ-CT (PAL, Korea) is used to obtain the 3D microstructures of the cement paste specimen of a water cement ratio (w/c) of 0.5. The cement paste specimens were prepared from the ordinary Portland cement (Type I), and were cured for 28 days until μ-CT scans were performed. The 39 cubic specimens from μ-CT are selected as a collection of representative volume element (RVE). The construction process of the specimens from the raw μ-CT images are elaborated in Chung et al. (2016). Each specimen has the side length of 130 μm, which is considered to be larger than the RVE of the cement paste (Luković et al. 2015, Zhang et al. 2016, Haecker et al. 2005).

Due to the random nature of the cement paste specimen, the porosity varies among specimens. The mean value of the porosity (ϕ) is 0.295, and the standard deviation is 0.0124, which can be considered to be small enough so that the selected side length satisfies the size of RVE. To investigate the random nature of the pore microstructures in detail, the lineal-path function from the specimens were extracted from the specimens. The lineal-path function and the parameter derived from the function is described next.

2.2 *Lineal-path function*

The mechanical responses such as stiffness and strength are dependent on the porosity of the cement paste. This is not surprising because the amount of void embedded in the microstructure should affect the mechanical properties. In the pioneering work presented in Powers (1958), the compressive strength was represented by the gel/space or capillary pore ratio, and the concept has been widely accepted for correlating material characteristics with properties. Although the porosity provides valuable information despite its simplicity, the porosity alone cannot sometimes explain material behavior with complex geometry due to its limitation as a scalar parameter. To overcome its shortcoming, alternative parameters could be used to further characterize the pore microstructures which can be linked to its complex mechanical responses.

The cement paste possesses random pore distributions so that one of the alternative characterization approaches is the probabilistic representation. Among such class of methods, the low-order probability functions have been found to be effective (Torquato 2002). The two-point correlation function, the lineal-path function, and the two-point cluster function are the ones which are most frequently used among the low-order probability functions. Here, the lineal-path function is further investigated because it provides long-range microstructural characteristics and is known to be closely linked to mechanical responses (Lu & Torquato 1992, Yeong & Torquato 1998).

The lineal-path function for a pore microstructure, L_p, is the probability of placing an entire line of length r within the void phase, as shown in Fig. 2(a). In the figure, three possible L_p lines, which contribute to construct the lineal-path function for the void phase, are shown for an arbitrary length r with an arbitrary direction. An example of the lineal-path function for the pore microstructure is illustrated in Fig. 2(b). The limits of L_p are

$$\lim_{r\to 0} L_p = \phi \quad \text{and} \quad \lim_{r\to\infty} L_p = 0 \tag{1}$$

where ϕ is the porosity.

A parameter introduced in this study is the centroid of the area under the L_p function in the r direction. The parameter r_c is obtained by taking the first moment of the L_p area divided by the L_p area:

$$r_c = \frac{\int_0^\infty r L_p(r)\, dr}{\int_0^\infty L_p(r)\, dr}. \tag{2}$$

The parameter is the average of the line length weighted by the probability of placing the line of length r in the void phase. r_c does not have a direct physical meaning, but the value of r_c, which is the length parameter, should possess aspects of microstructural features. The r_c is related to the mean void cluster size. Because r_c is a length parameter that characterizes the mean void cluster, this

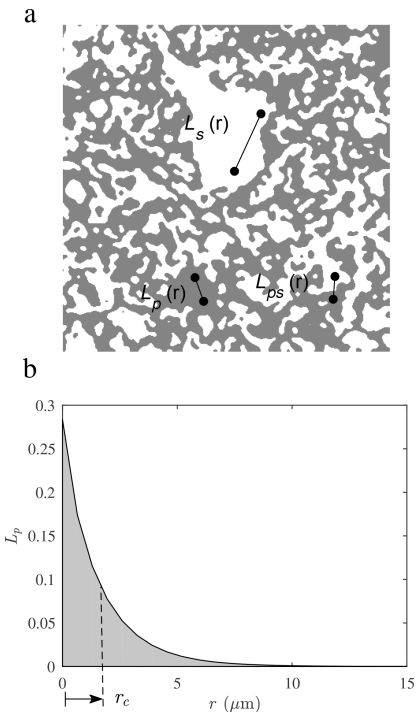

Figure 2. Schematic of lineal-path function: (a) Three possible cases of the lineal-path function at an arbitrary distance r are shown. The line L_p resides entirely in the pore or void phase. (Dark region: void; Light region: solid), (b) An example of L_p. The centroid of the area under the L_p function in the r direction is defined as r_c.

parameter is compared with the diffusive crack length parameter l for the crack phase field model. The r_c distribution of the 39 specimens from the μ-CT is bimodal, and illustrated in Fig. 3.

The bimodal distribution of the r_c values suggests that there are two distinct pore microstructural characteristic lengths present in the cement paste microstructure. The identification of two length characteristics are possible by adopting lineal-path function for characterization. Although not shown here, the bimodal characteristics are not captured using the porosity and the porosity data is approximated by the normal distribution well.

With this in mind, the r_c distribution is compared with the length-related input parameter for modeling. As a parameter with a more concrete physical interpretation, the mean chord-length can be obtained by taking the first moment of the chord-length density function, which is closely related to the lineal-path function (Torquato 2002). The chord-length function can be directly linked to the stereology parameters, and was also used to describe air voids in concrete (Mayercsik et al.

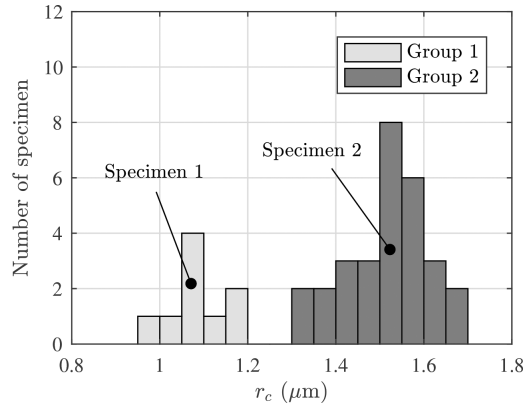

Figure 3. Bimodal r_c distribution obtained from L_p. Specimens 1 and 2 are the samples with the mean r_c value for corresponding void cluster group.

2014). However, considering the potential to reconstruct virtual microstructures where the lineal-path function is effectively utilized, the parameters derived from the lineal-path function are investigated here without introducing alternative probability functions.

3 MODELING

3.1 *Crack phase field model*

The mechanical responses, i.e. stiffness and strength, of the 39 specimens from the 3D μ-CT scans are evaluated using the crack phase field model under direct tension. The formulation of the model is consistent with the finite element framework proposed in Miehe et al. (2010), and only the strong form of the governing equations is presented here for brevity.

The crack phase field model solves an additional equation for the crack phase field by using the equation for the deformation field. The governing differential equations are

$$\mathrm{div}[\boldsymbol{\sigma}] + \rho_m \boldsymbol{b} = 0 \tag{3}$$

$$\eta \dot{d} - g_c l \nabla^2 d + \left(\frac{g_c}{l} + 2\mathcal{H} \right) d - 2\mathcal{H} = 0 \tag{4}$$

where ρ_m is the material density, $\boldsymbol{b}$ is the body force, η is a viscosity parameter used for the regularization process, g_c is the critical fracture energy, l is a length parameter related to the crack diffusivity, and $\mathcal{H}$ isa historical variable corresponding to the maximum positive free energy ψ_0^+ to enforce the crack irreversibility condition for material degradation. The system of equations are solved with

the proper boundary conditions as also elaborated in Miehe et al. (2010). The strong form of the equations are converted to weak form, and discretized to formulate finite element equations following the standard Bubnov-Galerkin method.

The viscosity η is set to 1.0×10^{-3} Ns/m^2 to stabilize the solution process without affecting the overall results. Among the material modeling parameters, the Young's modulus is set to 29 GPa and Poisson's ratio to 0.21 (Mindess et al. 2003) for the solid phase of the cement paste. The fracture related parameters are the fracture energy g_c and the diffusive crack length l. The fracture energy is set to 1.2 J/m^2 considering resolution of the μ-CT as well as the values from molecular dynamics (Bauchy et al. 2015) and experimental results (Němeček et al. 2016). Another fracture related material modeling parameter is the diffusive crack length l. Due to the complex pore microstructure in cement paste, it could be hypothesize that the diffusive crack length parameter can be influenced by the pore microstructure to incorporate the crack propagation at the micro-scale cement paste. The diffusive crack length is selected as 5 μm considering the geometric parameter r_c from the lineal-path function. The determination process is elaborated next in detail.

3.2 *Diffusive crack length l*

The diffusive length parameter l is considered to be a material modeling parameter as suggested and confirmed in previous studies (Miehe et al. 2015, Miehe and Mauthe 2016, Nguyen et al. 2016, Nguyen et al. 2016). When the complex microstructural features are present including the random voids, it should be reasonable to think that the diffusive crack length parameter could be dependent on the characteristic length of the void distribution. In this study, the crack diffusive length parameter is assumed to be only dependent on the void distribution characteristics.

The crack phase field (d) topology, if represented in 1-D, is approximated by a exponential function (Miehe et al. 2010):

$$d(x) = e^{-|x|/l} \tag{5}$$

where x is the distance measured from the center of the crack ($x = 0$), and l is the crack diffusive length parameter (Fig. 4). The crack phase field d ranges from 0 (no crack) to 1 (complete crack development).

To determine the value of the diffusive length parameter l, the crack is assumed to be developed when $d \geq 0.9$, i.e., the crack is assumed to be developed when d reaches 90% of the complete crack growth ($d_c = 0.9$). Then, the half width of the crack (x_c) when $d = d_c = 0.9$ is selected as 0.5 μm. This value is about the half of $r_c = 1.08$ μm, calculated

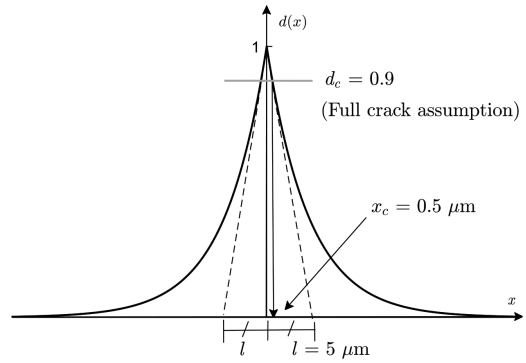

Figure 4. Diffusive crack topology in one dimension. Assuming a full crack of $d_c \geq 0.9$ and a diffusive crack length l of 5 μm, the half crack width (x_c) becomes 0.5 μm from Eq. 5.

from the first moment of the L_p, for the smaller void cluster in the bimodal r_c distribution (Section 2.2). The diffusive length l is calculated by substituting the pair of parameters (x_c, d_c) = (0.5 μm, 0.9) into Eq. (5), and it is approximated as 5 μm.

4 ANALYSIS

4.1 *Mechanical responses*

Using the aforementioned modeling parameters, stress vs. strain responses under direct tension of two representative specimens are presented in Fig. 5. Specimens 1 and 2 are selected from each group of r_c clusters (Fig. 3) with the mean r_c value of each cluster. The initial stiffness from Specimens 1 and 2 are 14.6 GPa and 13.1 GPa, and the peak stresses are 16.9 MPa and 15.2 MPa, respectively. Theses values are within the range of mechanical responses for cement paste at the micro-scale. The stiffness and strength of Specimen 1 are higher than those of Specimen 2, which are consistent with r_c values. The larger r_c value means the larger pore size, which results in reduction in stiffness and strength. The r_c and porosity for Specimen 1 are 41.7% and 2.6% lower than those for Specimen 2. This indicates that the r_c is much more sensitive to the pore microstructure than the porosity is, and r_c has a potential to describe the pore microstructure in detail.

Although the further in depth analysis is needed, especially comparison with the experimental results, the selected material modeling parameters including diffusive crack length parameter l provide a good estimate of the mechanical stiffness and strength.

The crack pattern of Specimen 1 at the end of simulation is presented in Fig. 6. The multiple crack initiations and propagations resulted in non-planar crack surfaces are observed. The crack patterns

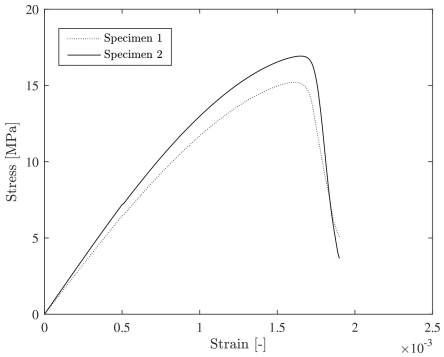

Figure 5. Macro-scale stress vs. (applied) strain under direct tension.

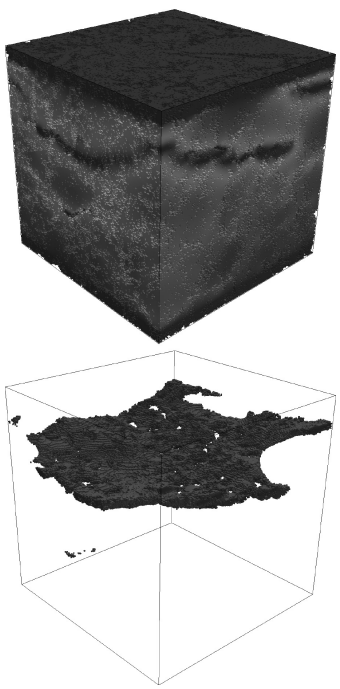

Figure 6. Crack pattern of Specimen 1 after the failure (applied strain: 1.9×10^{-3}) under direct tension. (Upper: phase field on surface, Lower: phase field over 0.9 ($d \geq 0.9$)).

show the potential of crack phase field for evaluating the mechanical responses of materials with complex microstructures including cement paste.

4.2 *Significance of r_c from lineal-path function*

The pore microstructure characterized by the lineal-path function, the centroid of the lineal-path function (r_c) in particular, captured the bimodal distribution of the inherent pore microstructures. Among the modeling parameters which need to be determined, the diffusive crack length parameter l is assumed to be related to r_c. An example of selecting l from r_c value is presented in Section 3.2. More in-depth analysis should be performed to confirm the direct relationship between r_c and l, but it is shown in this study that the r_c is in the same order as l and it has the potential as a parameter to determine the material modeling parameter l.

Of course, the porosity can represent the void phase characteristics to a certain degree, but r_c derived from the lineal-path function could identify the bimodal distribution of the pore distribution characteristics. With this information, it is expected that there is a potential to correlate the pore microstructure with mechanical properties in detail.

In this study, the energetic criteria formulation is adopted for the crack phase field model (Miehe et al. 2015). In this category of the model, the macro-scale peak strength decreases as the crack diffusive length increases when keeping the fracture energy constant. As l increases, the same amount of energy is dissipated from the broader regularized crack width, which results in strength reduction. On the other hand, when the stress criteria formulation is used for the model proposed in (Miehe et al. 2015), the macro-scale peak strength increases as l increases. This is because the material peak strength is maintained as the diffusive crack length is increases which has the outcome of increasing the fracture energy.

Either way, the determination of l for cement paste is expected to be related to r_c value, and r_c could be used as a supplementary or alternative parameter to porosity for characterizing the pore microstructure. The calibration process for the stress criteria formulation may be different from the energetic criteria formulation, but the stress criteria formulation is worth looking into because the cementitious materials are known to be peak strength sensitive. The relation between the pore characteristics with the cohesive behavior of materials could be further investigated.

5 CONCLUSIONS

Cement paste specimens obtained from the synchrotron μ-CT were characterized by r_c, the centroid of the lineal-path function. The r_c distributions showed the bimodal characteristics, while the porosity data from the same set of specimens followed the normal distribution.

The crack phase model was used to evaluate the mechanical properties (stiffness and tensile strength) of the representative specimens with distinct r_c values. Material modeling parameters such as Young's modulus, Poisson's ratio, and fracture energy (g_c) were obtained from the values avail-

able in the literature. However, determination of the diffusive crack length parameter l for cementitious material such as cement paste at micro-scale had not been investigated extensively. In this study, the hypothesis on relationship between r_c and l was proposed, and the potential of using r_c to determine l was shown.

Using the selected material modeling parameters, the crack phase field model was able to predict the initial stiffness and peak tensile strength in the reasonable range. It is concluded that the lineal-path function and its derived parameters could be used as alternative or supplementary parameters to conventional parameters such as porosity.

The evaluation of mechanical properties of cement paste at the micro-scale using experiment still remains a challenging task. Although further calibrations would be needed, the crack phase model showed a potential to be used as a synergistic tool combined with experimental approaches for property evaluation.

ACKNOWLEDGMENT

This research was supported by a grant from the Korea Research Foundation, funded by the Korean Government (NRF-2015K1A3A1A59073929 and NRF-2016R1D1A1B03931635). Parallel computation in this work was supported by the PLSI supercomputing resources of the Korea Institute of Science and Technology Information and the resources of the UNIST Supercomputing Center. The μ-CT images were obtained from the synchrotron operated by the Pohang Accelerator Laboratory (PAL) in Korea. Authors gratefully acknowledge Mr. Xiaoxuan Zhang and Prof. Chritian Linder at Stanford University for sharing their knowledge and implementation of the crack phase field model.

REFERENCES

Bauchy, M., H. Laubie, M. Qomi, C. Hoover, F.-J. Ulm, & R. Pellenq (2015). Fracture toughness of calciumsilicate- hydrate from molecular dynamics simulations. *J. Non-Cryst. Solids 419*, 58–64.

Chung, S.-Y., T.-S. Han, S.-Y. Kim, J.-H. Kim, K. Youm, & J.-H. Lim (2016). Evaluation of effect of glass beads on thermal conductivity of insulating concrete using micro CT images and probability functions. *Cem. Concr. Compos. 65*, 150–162.

Haecker, C.-J., E. Garboczi, J. Bullard, R. Bohn, Z. Sun, S. Shah, & T. Voigt (2005). Modeling the linear elastic properties of portland cement paste. *Cem. Concr. Res. 35*, 1948–1960.

Lu, B. & S. Torquato (1992). Lineal-path function for random heterogeneous materials. *Phys. Rev. A 45*, 922–929.

Luković, M., E. Schlangen, & G. Ye (2015). Combined experimental and numerical study of fracture behavior of cement paste at the microlevel. *Cem. Concr. Res. 73*, 123–135.

Mayercsik, N., R. Felice, M. Ley, & K. Kurtis (2014). A probabilistic technique for entrained air void analysis in hardened concrete. *Cem. Concr. Res. 59*, 16–23.

Miehe, C., M. Hofacker, & F. Welschinger (2010). A phase field model for rate-independent crack propagation: Robust algorithmic implementation based on operator splits. *Comput. Meth. Appl. Mech. Eng. 199*, 2765–2778.

Miehe, C. & S. Mauthe (2016). Phase field modeling of fracture in multi-physics problems. Part III Crack driving forces in hydro-poro-elasticity and hydraulic fracturing of fluid-saturated porous media. *Comput. Meth. Appl. Mech. Eng. 304*, 619–655.

Miehe, C., L.-M. Schänzel, & H. Ulmer (2015). Phase field modeling of fracture in multi-physics problems. Part I: Balance of crack surface and failure criteria for brittle crack propagation in thermo-elastic solids. *Comput. Meth. Appl. Mech. Eng. 294*, 449–485.

Mindess, S., J. Young, & D. Darwin (2003). *Concrete*. Prentice Hall.

Nguyen, T., J. Yvonnet, M. Bornert, & C. Chateau (2016). Initiation and propagation of complex 3D networks of cracks in heterogeneous quasi-brittle materials: Direct comparison between in situ testing-microCT experiments and phase field simulations. *J. Mech. Phys. Solids 95*, 320–350.

Nguyen, T., J. Yvonnet, Q.-Z. Zhu, M. Bornert, & C. Chateau (2015). A phase field method to simulate crack nucleation and propagation in strongly heterogeneous materials from direct imaging of their microstructure. *Eng. Fract. Mech. 139*, 18–39.

Nguyen, T., J. Yvonnet, Q.-Z. Zhu, M. Bornert, & C. Chateau (2016). A phase-field method for computational modeling of interfacial damage interacting with crack propagation in realistic microstructures obtained by microtomography. *Comput. Meth. Appl. Mech. Eng. 312*, 567–595.

Němeček, J., V. Králík, V. Šmilauer, L. Polívka, & A. Jäger (2016). Tensile strength of hydrated cement paste phases assessed by micro-bending tests and nanoindentation. *Cem. Concr. Compos 73*, 164–173.

Powers, T. (1958). Structure and physical properties of hardened portland cement paste. *J. Am. Ceram. Soc. 41*, 1–6.

Torquato, S. (2002). *Random heterogeneous materials: Microstructure and macroscopic properties*. Springer-Verlag.

Wu, J.-Y. (2017). A unified phase-field theory for the mechanics of damage and quasi-brittle failure. *J. Mech. Phys. Solids 103*, 72–99.

Yeong, C. & S. Torquato (1998). Reconstructing random media. *Phys. Rev. E 57*, 495–506.

Zhang, H., B. Šavija, S.C. Figueiredo, M. Lukovic, & E. Schlangen (2016). Microscale testing and modeling of cement paste as basis for multi-scale modelling. *Materials 9 (907)*, 1–14.

Computational Modelling of Concrete Structures – Meschke, Pichler & Rots (Eds)
© 2018 Taylor & Francis Group, London, ISBN 978-1-138-74117-1

Influence of air voids in multiphase modelling for service life prediction of partially saturated concrete

D. Eriksson & T. Gasch
Department of Civil and Architectural Engineering, KTH Royal Institute of Technology, Stockholm, Sweden

ABSTRACT: The purpose of this study is to show the influence and significance of including water filling of air pores when studying moisture conditions in concrete structures cast with air-entrained concrete and in contact with free water. Especially if the aim is to assess the risk for frost damages in different regions of the structure, based on a critical degree of saturation, in order to ultimately perform a service life prediction. A hygro-thermo-mechanical multiphase model that includes the effect of water filling in air pores, recently presented by the authors, is briefly described and applied in two numerical examples. The results show moisture distributions that would not be possible to capture without the air pore filling included in the model. More importantly, the general shape of these distributions complies well with measured distributions in real concrete structures as well as with distributions obtained in laboratory measurements.

1 INTRODUCTION

Durability of concrete structures is of major concern in all parts of the world. The most important deterioration mechanisms for a concrete structure mainly depend on the properties of the constituents in the concrete material, the microstructure as well as on the ambient conditions at site. In cold climates where freezing temperatures are common, degradation due to frost actions is often one of the major threats to the durability. Therefore, structures are often cast with air-entrained concrete that contains an artificially created network of large air voids (also denoted as air pores throughout this study) to reduce the risk for frost damages. The reason for the reduced risk can be explained by Powers (1945) hydraulic pressure theory, which states that frost damages are caused by the transport of expelled water from smaller pores into the surrounding cement paste as the water volume increases approximately 9% upon freezing. If the larger air pores are not completely saturated, they will act as extra reservoirs in which the excess water can enter and freeze without exerting high pressures. When a concrete surface comes into contact with water, the smaller pores are rapidly filled with water due to capillary suction. However, the larger air pores are water filled through another process where trapped air dissolves in the surrounding pore water and diffuses toward a free surface. The dissolved air is then replaced by water. This process is significantly slower and it might take several decades before reaching complete saturation. In a study performed by Fagerlund (1977), it was shown that there exists a certain critical degree of saturation above which frost damages inevitably occur. The magnitude of this threshold value normally means that the air pores are partially saturated, at least for air-entrained concretes.

To assess the risk for frost damages in a structure that is in contact with free water and cast with air-entrained concrete, it is apparent that the water filling process of air pores must be considered. Several studies have regarded this water filling process, but as completely decoupled from other mass transport processes (e.g. Fagerlund 1993, Fagerlund 2004, Liu 2016). The unsaturated flow in concrete has been extensively studied in the literature and there exist a number of different models with varying complexity that can be used to describe this. The more recent approach is to treat concrete as a multiphase porous medium, where it usually is divided into three phases: solid, liquid and gas. Several studies have shown that this type of model yield results that comply well with measurements for various conditions (e.g. Gawin et al. 1995, Gawin et al. 2006, Baroghel-Bouny et al. 2011). However, models that combine both the air pore filling process and unsaturated flow are scarce in the literature.

With regards to frost damage, multiphase models have successfully been used to describe the deformation of concrete upon freezing (e.g. Koniorczyk, et al. 2015, Coussy & Monteiro 2008). It has also been shown that they can account for the effect of air pores during freezing, at least when modelling single air pores surrounded by a

shell of cement paste (elementary cells). However, to establish a model that can be used for service life predictions of real concrete structures in contact with water, it is necessary to combine the freezing process with unsaturated flow models that include water filling of air pores.

The purpose of this study is to show the significance of including the air pore filling process in heat and mass transport models when for example dealing with frost damage assessments for service life prediction of concrete structures that are in contact with water and cast with air-entrained concrete. This is achieved by utilising a hygro-thermo-mechanical multiphase model that includes the effect of air pore filling, recently developed by Eriksson et al. (subm.). The multiphase model is validated by simulating an absorption test of air-entrained concrete. In addition, the model is used in a second numerical example that aims at resembling a concrete wall in a waterway, e.g. located in connection to a hydropower dam. Both examples are limited to the absorption of water and do, therefore, not consider any wetting-drying cycles nor the hysteresis effect.

2 ABSORPTION OF WATER IN CONCRETE

The absorption of water in concrete largely depends on its pore structure. There is a wide range of pore sizes and normally the pores are divided into at least three categories: gel, capillary and air pores. The limits between the three categories are somewhat arbitrary but following Jennings et al. (2015), pores with a radius of 2 to 8 nm are categorised as gel pores while a radius of 8 nm to 10 μm correspond to capillary pores. However, herein these two categories are lumped together and called capillary pores. All pores having a radius greater than 10 μm are considered as air pores. The moisture storage capacity of porous materials in equilibrium with the ambient air is usually described by sorption isotherms, but these also reflect the poresize distribution of the material. A schematic sorption isotherm for concrete containing a significant volume fraction of air pores is shown in Fig. 1.

2.1 *Concrete in contact with free water*

When a concrete surface comes into contact with free water, the empty capillary pores start to fill with water due to capillary suction. The driving potential is determined by the smallest capillary pores not yet filled with water and arise due to the menisci that are formed between air and water

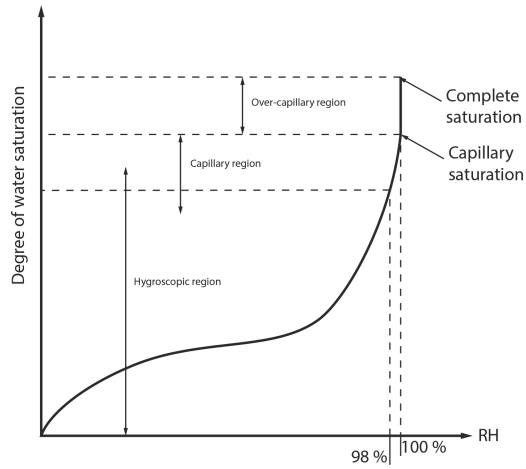

Figure 1. Schematic sorption isotherm for a concrete material containing a significant volume fraction of air pores, reproduction from Fagerlund (2004).

inside the pores. The magnitude of this potential is governed by the Young-Laplace equation

$$p^c = \frac{2\sigma}{r} \tag{1}$$

where p^c is the capillary pressure, σ the surface tension between air and water and r the pore radius. As the material continues to absorb water, larger capillary pores are being filled, and consequently the driving potential decreases. When the water reaches the larger air pores, which are surrounded by finer capillary pores, the suction potential becomes almost zero and the air gets trapped (Fagerlund 1993, Hall & Hoff 2012). This moisture state is denoted capillary saturation in Fig. 1. Even though the capillary suction potential is zero by definition at this state, the air pores continue to slowly fill with water up to complete saturation but due a different mechanism described in the following section 2.2. The critical degree of saturation, above which frost damages occur, normally varies between 0.75 to 0.90. For air-entrained concrete, this usually means that the air pores are at least partially saturated (Fagerlund 1977). Therefore, it is important to also consider this other water filling mechanism when assessing the risk for frost damage in structures that are constructed with air-entrained concrete.

2.2 *Long-term water absorption*

The water filling of air pores is a significatively slower process than the capillary suction of water,

and it might take several decades to reach full saturation. The basic mechanism can be explained by the dissolution of trapped air into the surrounding pore water. This dissolved air then diffuses toward larger pores and eventually to a boundary surface. As the air diffuses to the boundary of the material, it is replaced by water though suction from the reservoir (Fagerlund 1993, Hall & Hoff 2012).

The trapped air inside the air pores is subjected to an overpressure due to the menisci that are formed at the air-water interfaces. This overpressure is denoted del ΔP_{ap} and is determined by the Young-Laplace equation. Furthermore, Henry's law states that the concentration of dissolved air in water is proportional to the absolute gas pressure. In this particular case, the concentration of dissolved air is described by

$$c_{\mathrm{a}} = (P_0 + \Delta P_{\mathrm{ap}})k_{\mathrm{H}} = P_{\mathrm{ap}}k_{\mathrm{H}} \tag{2}$$

where c_a is the concentration of air in the pore water, P_0 a reference pressure, k_{H} the solubility constant and P_{ap} the absolute gas pressure inside the air pores. From this, it follows that the dissolved air diffuses from smaller pores toward larger pores.

Fagerlund (1993) derived two models to estimate the degree of saturation in air pores as a function of time from air pore size distributions. Both models are based on the local diffusion process between neighboring air pores of different sizes but differs in one assumption. In the first model, called Model 1, it is assumed that all air pores are filled simultaneously and at the same rate. Thus, a smaller air pore will be completely water filled before a larger air pore, which only will be partially saturated at this state. In the second model, Model 2, it is instead assumed that the air pores are consecutively filled with water, starting from the smallest air pore. Model 2 is more reasonable from a thermodynamic perspective since it represent a stateof lower free energy in the system.

In this study, the long-term water absorption is instead described by a global diffusion model. As proposed by Eriksson et al. (subm.), the concentration gradient of dissolved air is determined by an averaging procedure, where the air pore gas overpressure is averaged over the air pores not yet filled with water. Furthermore, based on Fagerlund's Model 2, it is assumed that the air pores are consecutively filled with water. Using a cumulative pore size distribution and the Young-Laplace equation, the average air pore gas overpressure is determined by

$$\Delta\overline{P}_{\mathrm{ap}}(r) = \frac{\int_r^\infty \frac{\mathrm{dV_{ap}}}{\mathrm{dr}}\frac{2\sigma}{r}\mathrm{dr}}{\int_r^\infty \frac{\mathrm{dV_{ap}}}{\mathrm{dr}}\mathrm{dr}} \tag{3}$$

where r is the radius of the smallest air pore not filled with water and V_{ap} the cumulative pore size distribution. It is also necessary to establish a relationship between the degree of gas saturation and the radius of the smallest pores not yetfilled with water. This relationship reads

$$\hat{S}_a^{\overline{g}}(r) = \frac{\int_r^\infty \frac{\mathrm{dV_{ap}}}{\mathrm{dr}}\mathrm{dr}}{\int_{r_{\min}}^\infty \frac{\mathrm{dV_{ap}}}{\mathrm{dr}}\mathrm{dr}} \tag{4}$$

where $\hat{S}_a^{\overline{g}}$ is the degree of gas saturation in the air pores and $r_{\min}$ the minimum considered air pore radius. Combining Eqs. (2) and (3) yields a relationship between the degree of gas saturation in the air pores and the average overpressure, which can be utilised in the diffusion model. A description of the diffusion model and the implementation of it in the hygro-thermo-mechanical multiphase model is given in section 3.

3 MULTIPHASE MODEL

Following Eriksson et al. (subm.), concrete is herein modelled as a porous material consisting of the three phases: solid (s), liquid water (w) and gas (g). Furthermore, the gas phase is considered as an ideal gasmixture of the species: vapour (W) and dry air (D). To account for the long-term absorption of water, the total degree of liquid water saturation and gas saturation is split between capillary pores and air pores according to

$$S^{\overline{f}} = \sum_\gamma S_\gamma^{\overline{f}} = \sum_\gamma \hat{S}_\gamma^{\overline{f}}\eta_\gamma \tag{5}$$

where $S^{\overline{f}}$ is the total degree of saturation of fluid phase $f \in (w, g)$ γ denotes either air pores (a) or capillary pores (c), η_γ the pore volume fraction of pore type γ while S_γ^f and $\hat{S}_\gamma^{\overline{f}}$ are the weighted and unweighted degree of saturation of fluid f in pore type γ, respectively. By definition, the sum of all weighted degrees of saturation is always equal to one.

The balance equations of mass, energy and momentum for each considered phase are obtained using the macroscopic balance equations for a generic porous medium derived with the TCAT

as a basis (Gray & Miller 2014). The chosen state variables of the multiphase model are: capillary pressure (p^c), gas pressure (p^g), temperature (T) and displacements (d).

The mass balances for liquid water and vapour are summed to obtain one mass balance equation for the total water content, which reads

$$\begin{aligned}&\frac{\partial\left(\hat{S}_c^{\overline{\omega}}\eta_c\,\epsilon\,\rho^{\omega}\right)}{\partial t}+\frac{\partial\left(\hat{S}_c^{\overline{g}}\eta_c\,\epsilon\,\rho^{w\overline{g}}\right)}{\partial t}+\frac{\partial\left(\hat{S}_a^{\overline{\omega}}\eta_a\,\epsilon\,\rho^{\omega}\right)}{\partial t}\\&+\frac{\partial\left(\hat{S}_a^{\overline{g}}\eta_a\,\epsilon\,\rho^{w\overline{g}}\right)}{\partial t}+\nabla\cdot\left[\left(\hat{S}_c^{\overline{\omega}}\eta_c\,\epsilon+\hat{S}_a^{\overline{\omega}}\eta_a\,\epsilon\right)\rho^{\omega}\mathbf{v}^{\overline{\omega s}}\right]\\&+\nabla\cdot\left[\left(\hat{S}_c^{\overline{g}}\eta_c\,\epsilon+\hat{S}_a^{\overline{g}}\eta_a\,\epsilon\right)\rho^{w\overline{g}}\mathbf{v}^{\overline{gs}}\right]\\&+\nabla\cdot\left[\left(\hat{S}_c^{\overline{g}}\eta_c\,\epsilon+\hat{S}_a^{\overline{g}}\eta_a\,\epsilon\right)\rho^{w\overline{g}}\mathbf{u}^{\overline{\overline{W}_g}}\right]\\&+\nabla\cdot\left(\hat{S}_c^{\overline{\omega}}\eta_c\,\epsilon\,\rho^{\omega}\mathbf{v}^{\overline{s}}\right)+\nabla\cdot\left(\hat{S}_a^{\overline{\omega}}\eta_a\,\epsilon\,\rho^{\omega}\mathbf{v}^{\overline{s}}\right)\\&+\nabla\cdot\left(\hat{S}_c^{\overline{g}}\eta_c\,\epsilon\,\rho^{w\overline{g}}\mathbf{v}^{\overline{s}}\right)+\nabla\cdot\left(\hat{S}_a^{\overline{g}}\eta_a\,\epsilon\,\rho^{w\overline{g}}\mathbf{v}^{\overline{s}}\right)=0\end{aligned}\tag{6}$$

where ϵ is the total porosity, ρ^{α} density of phase α, $\rho^{i\alpha}$ the mass concentration of species i in phase α, $\mathbf{v}^{fs}$ the relative velocity between fluid phase f and the solid skeleton S, $\mathbf{u}^{i\alpha}$ the diffusive velocity of species i in phase α and $\mathbf{v}^{\bar{\alpha}}$ the velocity of phase α. The mass balance equation of the dry air has the same form and is written as

$$\begin{aligned}&\frac{\partial\left(\hat{S}_c^{\overline{g}}\eta_c\,\epsilon\,\rho^{D\overline{g}}\right)}{\partial t}+\frac{\partial\left(\hat{S}_a^{\overline{g}}\eta_a\,\epsilon\,\rho^{D\overline{g}}\right)}{\partial t}\\&+\nabla\cdot\left[\left(\hat{S}_c^{\overline{g}}\eta_c\,\epsilon+\hat{S}_a^{\overline{g}}\eta_a\,\epsilon\right)\rho^{D\overline{g}}\mathbf{v}^{\overline{gs}}\right]\\&+\nabla\cdot\left[\left(\hat{S}_c^{\overline{g}}\eta_c\,\epsilon+\hat{S}_a^{\overline{g}}\eta_a\,\epsilon\right)\rho^{D\overline{g}}\mathbf{u}^{\overline{\overline{D}_g}}\right]\\&+\nabla\cdot\left(\hat{S}_c^{\overline{g}}\eta_c\,\epsilon\,\rho^{D\overline{g}}\mathbf{v}^{\overline{s}}\right)+\nabla\cdot\left(\hat{S}_a^{\overline{g}}\eta_a\,\epsilon\,\rho^{D\overline{g}}\mathbf{v}^{\overline{s}}\right)=0\end{aligned}\tag{7}$$

The mass balance equation of the solid phase is written in a different form than the other two equations, and instead expresses the rate of volume fraction change in the solid phase as

$$\frac{\partial\epsilon^{\overline{s}}}{\partial t}=-\frac{1}{\rho^s}\left[\epsilon^{\overline{s}}\frac{\partial\rho^s}{\partial t}+\nabla\cdot\left(\epsilon^{\overline{s}}\rho^s\mathbf{v}^{\overline{s}}\right)\right]\tag{8}$$

where $\epsilon^{\overline{s}}$ is the solid phase volume fraction, defined by $\epsilon^{\overline{s}}=1-\epsilon$. The momentum balance equation of the complete porous medium is obtained through summation of the three considered phases and reads

$$\nabla\cdot\mathrm{t}-\rho\mathrm{g}=0\tag{9}$$

where **t** is the total stress tensor, g the body forces due to gravity and ρ the total density of the porous medium, calculated as the average density of the three phases. The heat balance equation of the complete porous medium is obtained through summation of the three phases and can be written as

$$\begin{aligned}&(\rho C_p)_{\mathrm{eff}}\frac{\partial T}{\partial t}-\nabla\cdot\mathrm{q}+\Delta H_{\mathrm{vap}}M_{\mathrm{vap}}\\&+\left[\left(\hat{S}_{\mathrm{c}}^{\overline{w}}\eta_{\mathrm{c}}\,\epsilon+\hat{S}_{\mathrm{a}}^{\overline{w}}\eta_{\mathrm{a}}\,\epsilon\right)\rho^{\omega}C_p^{\omega}\mathbf{v}^{\overline{ws}}\right]\cdot\nabla T\\&+\left[\left(\hat{S}_{\mathrm{c}}^{\overline{g}}\eta_{\mathrm{c}}\,\epsilon+\hat{S}_{\mathrm{a}}^{\overline{g}}\eta_{\mathrm{a}}\,\epsilon\right)\rho^{g}C_p^{g}\mathbf{v}^{\overline{gs}}\right]\cdot\nabla T\end{aligned}\tag{10}$$

where ΔH_{vap} is the latent heat of evaporation, q the conductive energy flux, C_p^{α} the specific heat capacity of phase α and M_{vap} the mass exchange due to phase changes between vapour and water. The latter term is obtained by deriving the mass balance equation of the water phase. The effective heat content $(\rho C_p)_{\mathrm{eff}}$ of the porous medium is determined as the average heat content of the three phases.

The system of governing equations introduced above must be complemented with a set of constitutive relationships and constants in order to close the system. For brevity, only the most important constitutive relationships for the current study are covered herein, but a thorough presentation of all relationships are given by Eriksson et al. (subm.). Section 3.1 describes the relationships for advective and diffusive mass flux and section 3.2 the global diffusion model describing the long-term water absorption into air pores.

3.1 *Advective and diffusive mass flux*

The advective mass flux is quantified by the relative velocity vel-fs of the fluid phases, which here is described by the generalised Darcy's law according to

$$\epsilon\left(\hat{S}_{\mathrm{c}}^{\overline{f}}\eta_{\mathrm{c}}+\hat{S}_{\mathrm{a}}^{\overline{f}}\eta_{\mathrm{a}}\right)\mathrm{v}^{\overline{fs}}=-\frac{k_r^f\mathrm{k}}{\mu^f}\left(\nabla p^f-\rho^f g\right)\tag{11}$$

where k is the intrinsic permeability tensor, μ the dynamic viscosity and k_r^f the relative permeability of fluid phase f. The relative water and gas permeability is described with the relationship proposed by van Genuchten (1980) and here reads

$$k_r^w=\left(S^{\overline{\overline{w}}}\right)^{0.5}\left\{1-\left[1-\left(S^{\overline{\overline{\omega}}}\right)^m\right]^{\frac{1}{m}}\right\}^2\tag{12a}$$

$$k_r^g=\left(1-\hat{S}^{\overline{\overline{w}}}\right)^{0.5}\left[1-\left(\hat{S}_c^{\overline{\overline{\omega}}}\right)^{\frac{1}{m}}\right]^{2m}\tag{12b}$$

where m is a model parameter that is obtained through fitting another analytical expression proposed by van Genuchten to the sorption isotherm

$$\hat{S}_{\mathrm{c}}^{\overline{w}} = \left[1 + \left(\frac{p^c}{l}\right)^{\frac{m}{1-m}}\right]^{-\frac{1}{m}} \tag{13}$$

where l is a fitting parameter. For the relative gas permeability, the unweighted degree of water saturation in capillary pores has been chosen as independent variable instead of the total degree of water saturation. The reason for this choice is that the gas phase is not continuous at capillary saturation since the air is trapped inside the air pores. Consequently, there is no advective flux of gas and by making this choice this is also achieved in the model.

Diffusive mass flux of the two species vapour (W) and dry air (D) through the gas phase is only considered below capillary saturation. The flux is quantified through the diffusive velocity $\mathbf{u}^{\overline{ig}}$ and described by Fick's law

$$\mathbf{J}^{\overline{ig}} = \epsilon \rho^{\overline{ig}} \left(\hat{S}_{\mathrm{c}}^{\overline{g}} \eta_{\mathrm{c}} + \hat{S}_{\mathrm{a}}^{\overline{g}} \eta_{\mathrm{a}}\right) \mathbf{u}^{\overline{ig}} = -\rho^g \mathbf{D}_d^{ig} \nabla \frac{\rho^{\overline{ig}}}{\rho^g} \tag{14}$$

where $\mathbf{D}_{\mathrm{d}}^{ig}$ is the diffusivity tensor and $\mathbf{J}^{\overline{ig}}$ the diffusive mass flux. From Dalton's law it can be shown that $\mathbf{D}_{\mathrm{d}}^{\mathrm{Wg}} = \mathbf{D}_{\mathrm{d}}^{Dg}$ as well as that $\boldsymbol{J}^{\overline{Wg}} = -\boldsymbol{J}^{\overline{Dg}}$. The diffusivity tensor of vapour is defined according to relationship given by Gawin et al. (1999)

$$\mathbf{D}_{\mathbf{d}}^{Wg} = \epsilon^{A_d} \left(1 - \hat{S}_{\mathrm{c}}^{\overline{w}}\right)^{B_d} f_s D_{\mathrm{v0}} \left(\frac{T}{T_0}\right)^{C_d} \frac{p_0}{p^g} \mathbf{I} \tag{15}$$

where $\mathbf{I}$ is a unity tensor and D_{v0} the bulk diffusivity of vapour in air at a reference pressure p_0 and temperature T_0. The tortuosity of the porous network is accounted for by the parameter f_s, which also considers the Knudsen effect. The remaining parameters $A_{\mathrm{d}}, B_{\mathrm{d}}$ and C_{d} are model parameters.

3.2 *Diffusion model for long-term water absorption*

The diffusion of dissolved air towards a free surface can be described by Fick's second law of diffusion. Utilising the relationship between the degree of gas saturation in air pores and the average air pore overpressure established in section 2.2 as well as Henry's law, the diffusion model can be written as

$$\frac{\partial\left[\hat{S}_{\mathrm{a}}^{\overline{g}}\left(\overline{P}_{\mathrm{ap}}\right)\epsilon_{\mathrm{a}}\rho^g\right]}{\partial t} + \nabla\cdot\left[-\tau\,\mathbf{D}_{\mathrm{aw}}\kappa_{\mathrm{H}}\nabla\left(k_{\mathrm{H}}\overline{P}_{\mathrm{ap}}\right)\right] = 0 \tag{16}$$

where $\hat{S}_{\mathrm{a}}^{\overline{g}}(\overline{P}_{\mathrm{ap}})$ is the relationship from section 2.2, τ a tortuosity factor, $\mathbf{D}_{\mathrm{aw}}$ the diffusivity tensor of air in water $\overline{P}_{\mathrm{ap}}$ the average absolute air pore pressure defined by $\overline{P}_{\mathrm{ap}} = \Delta\overline{P}_{\mathrm{ap}} + P_0$. The air inside the air pores does not get trapped before capillary saturation is reached in the material. Before this state, no extra air is dissolved in the pore water and, hence, it is assumed that the concentration gradient is zero for such states. The term κ_{H} governs when the trapped air starts to dissolve and is defined as

$$\kappa_{\mathrm{H}} = \begin{cases} 0 & \text{if } \hat{S}_{\mathrm{c}}^{\overline{w}} < 1 \\ 1 & \text{if } \hat{S}_{\mathrm{c}}^{\overline{w}} = 1 \end{cases} \tag{17}$$

This mass balance equation requires its own state variable, but it is here denoted as an internal variable to separate it from the state variables of the multiphase system. Following from Eq. (16), the natural choice is the average absolute air pore pressure $\overline{P}_{\mathrm{ap}}$. By introducing this constitutive relationship into the system of governing equations of the multiphase system through the split of the total degrees of saturation between air pores and capillary pores, it is possible to also account for the long-term absorption of water into air pores.

4 NUMERICAL EXAMPLES

Two numerical examples are presented, where the first aims to validate the hygro-thermo-mechanical multiphase model. The second aims at showing the influence and significance of including air pore filling when studying moisture conditions in concrete structures cast with air-entrained concrete. Especially if the purpose is to assess the risk for frost damages in different regions of a structure based on the concept of critical degree of saturation.

The system of governing equations is solved with the commercial FE-code Comsol Multiphysics (COMSOL 2016). The governing equations are converted to weak form and integration by parts and the divergence theorem are applied to reduce the order of differentiation. The weak form equations are then discretized using the Galerkin method. Time integration of the discretized system is done with the fully implicit backward differentiation formula (BDF), while the non-linear equations are solved using a damped version of the Newton-Raphsons method.

4.1 *Example 1: Absorption test*

To validate that the proposed model can describe both the rapid initial capillary suction of water as well as the long-term water absorption into air pores, an absorption test performed by Liu & Hansen (2016) is simulated. The measurements

were performed on concrete specimens with a water-cement (w/c) ratio of 0.45 containing approximately 10.2% capillary pores and 5.0% air pores. The specimens were 12 mm thick and had a cross sectional area of 100 × 100 mm^2. All specimens were preconditioned by drying in an oven at a temperature of 50°C until a constant weight was reached, which approximately corresponds to an internal relative humidity of 11% at 20°C. The lateral sides and the top of the specimens were then sealed whereas the bottom surface was immersed into 5 mm of water. They also measured the pore size distribution of the air pore system, which can be described with the relationship

$$V_{\mathrm{ap}} = \epsilon_{\mathrm{a}} e^{-\left(\frac{\chi}{D}\right)^{\xi}} \tag{18}$$

where D is the air pore diameter. In Eq. (14), Ξ and ξ are two fitting parameters that for the current distribution are 86.6 μm and 0.987, respectively. The absorption isotherm was not measured for the tested concrete and consequently it has to be estimated. This was done using the model developed by Xi et al. (1994). It was then fitted to Eq. (13), where the values 16 MPa and 2.4 were obtained for the two fitting parameters l and m, respectively. It should be noted that the absorption isotherm only describes the moisture storage capacity up to capillary saturation due to the split of the total degree of saturation between capillary pores and air pores introduced in section 3. The chosen constitutive relationships for the relative permeabilities in section 3.1 mean that they depend on the absorption isotherm. Since it is estimated in this case, the intrinsic permeability must be fitted to obtain adequate results and a value of $1.1 \cdot 10^{-18}$ m^2 was found suitable. However, this value comply well with measured intrinsic permeabilities of air-entrained concrete containing a comparable volume fraction of air pores (Wong et al. 2011). The bulk diffusivity of air in water is set to $D_{\mathrm{aw}} = 2.0 \cdot 10^{-9}$ m^2/s whereas the tortuosity factor is set to τ = 0.25 (Hall & Hoff 2012). No deformations of the solid skeleton are considered in this example. For brevity, only the main material parameters were presented here, the complete set of parameters are given by Eriksson et al. (subm.).

The geometry of the specimens is discretized using an axisymmetric formulation where the radius is set to give an equivalent surface area as the top and bottom surfaces of the specimens. All model boundaries except the bottom surface are sealed or part of a symmetry line, wherefore Neumann boundary conditions equal to zero flux of liquid water and gas are applied on these boundaries. A temperature of 20°C is applied on all boundaries as Dirichelt conditions, except on the symmetry line where zero heat flux is imposed. Dirichelt type boundary conditions are applied on the bottom surface where the capillary pressure p^c, gas pressure p^g and absolute average air pore pressure P_{ap} are set to 0 Pa, 1 atm and 1 atm, respectively. The initial absolute average air pore pressure is obtained from the relationship between the degree of gas saturation in air pores and the average air pore overpressure discussed in section 2.2 for $\hat{S}_{\mathrm{a}}^{g} = 1$, which in this case corresponds to a value of 104.8 kPa. The initial temperature, relative humidity and gas pressure are set to 20°C, 11% and 1 atm, respectively. Kelvin's equation is used to convert the relative humidity to a corresponding capillary pressure. The results from the simulation are compared to the measurements in Fig. 2, plotted as the volume of absorbed water per cross sectional area of the specimens in contact with water and as a function of the square-root of time. The first steep part of the curve corresponds to the fast initial capillary suction of water whereas the second part corresponds to the long-term absorption of water into the air pores. As seen, the proposed model is capable of describing both parts of the water absorption accurately.

4.2 *Example 2: Concrete wall in a waterway*

The risk for frost damages to occur in concrete is closely related to the total degree of water saturation within the material. Most concrete structures located in cold climates and in contact with free water contain a considerable volume fraction of air pores to increase the resistance against frost damages. This example aims at showing the significance of also considering the long-term water absorption into air pores when studying moisture conditions in such structures. Especially if the purpose is to assess the risk for frost damages in different regions of the structure.

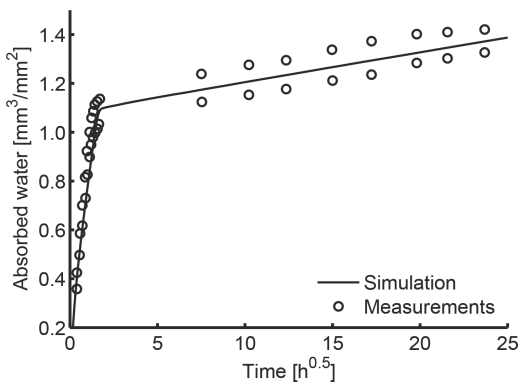

Figure 2. Comparison of simulation results and measured water absorption in Example 1.

The studied case aims at resembling the geometry and ambient conditions of a concrete wall in a waterway, e.g. located in connection to a hydropower dam. The assumed geometry of the wall as well as the assumed average ambient conditions over a year are shown in Fig. 3. However, some clarifications are needed. As seen in the figure, the bottom part of the wall is subjected to water pressure which arises due to cracks in the foundation. It is assumed that the ground water level on the right side lies 0.50 m above the foundation level, wherefore the soil is saturated. Also notice that boundary E stretches from the upper soil level on the right side to the upper water level on the left side of the wall. The geometry is discretized with second order quadrilateral elements. The average element size is 1.5 cm but the mesh is slightly denser close to the boundaries.

The concrete is assumed to have a w/c ratio of 0.50, whereas the capillary porosity ϵ_c and air porosity ϵ_a are assumed to be 19% and 5%, respectively. All other parameters are the same as in Example 1, except that deformations of thesolid skeleton also are considered in this example. A linear elastic material behaviour is assumed, where Young's modulus and Poisson's ratio are set to 30 GPa and 0.20, respectively.

The magnitudes of the applied boundary conditions are specified in Fig. 3. Dirichlet type boundary conditions are used for the gas pressure p^g and the absolute air pore pressure P_{ap} on all boundaries as well as for the water pressures applied on boundary A to C. The displacement conditions applied on boundary B are also of Dirichlet type. Convective type boundary conditions (Mixed type) are used on all boundaries for the heat transport, whereas this type is only used on boundaries D and E for the mass transport. The heat and moisture transfer coefficients are estimated based on the relationships given by Incropera et al. (2007). The initial temperature, gas pressure, relative humidity and average air pore pressure in the wall are set to 8°C, 1 atm, 90% and 104.8 kPa, respectively.

4.2.1 *Results and discussion*

Contour plots of the unweighted degree of water saturation in air pores are shown in Fig. 4. As discussed in section 2.2, the water filling of air pores is a slow process and after one year only the outermost layer of the concrete wall has absorbed water into the air pores. With increasing time, the saturation front continues to penetrate the wall but at a very low rate. Even after 50 years of contact with free water on two sides, there is a large region in the bottom part of the wall that has not reached complete saturation. Another interesting observation is that the region of partially and completely saturated air pores spreads above the water line and continues to extend with the time of exposure. Similar observations is reported by e.g. Rosenqvist (2016), who measured the degree of water saturation in specimens of air-entrained concrete exposed to free water up to mid height on one side as well as in an existing hydropower dam. It has also been observed that concrete in contact with water and simultaneously subjected to freeze-thaw

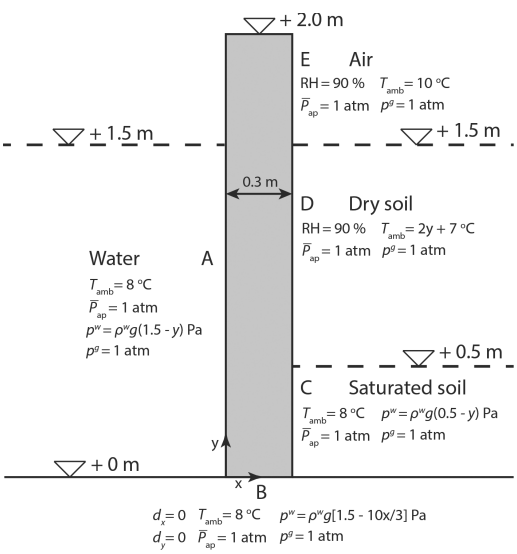

Figure 3. Geometry of the studied wall and applied boundary conditions.

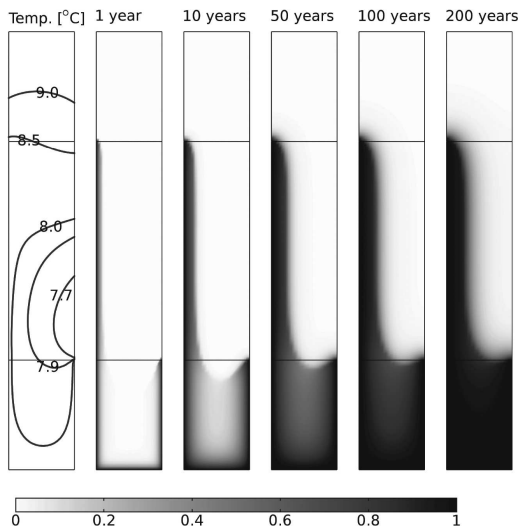

Figure 4. Plots of temperature distribution after 200 years (leftmost plot) and unweighted degree of water saturation in air pores $\hat{S}_a^w$ for increasing time in the wall.

cycles absorbs even more water (Rosenqvist 2016, Sandström 2010), but this effect is not considered herein. The temperature distribution after 200 years shown in Fig. 4 has reached a steady-state. The colder region in the lower part of the wall toward the right side arises due to the evaporation of moisture at the surface on this side. The cooling effect is larger closer to the ground water level since the moisture content in this region is higher than in the upper parts of the wall.

The critical degree of saturation can be used to identify the regions susceptible to frost damages. Assuming a critical value of 0.90, the regions having a total degree of water saturation S^w above this value have been plotted with grey color in Fig. 5 for increasing time. After one year of absorption, only the outer layer of the wall is likely to show frost damages if freezing temperatures arise. The region around the water line is the most susceptible to surface frost damagessince it is in direct contact with the ambient air. In addition, the water level in the waterway normally fluctuates over the year and if a lowered water level coincide with a cold period, the critical region of course increases. But it should be pointed out, that the concrete surface will start to dry as soon as the water level is lowered which means that the risk for frost damage is reduced. With increasing time, the saturation front continues to penetrate the wall and the risk for internal frost damages becomes higher. It should be noted that the wall might be subjected to freezing temperatures from the right side due to ground frost. As a consequence, frost damages might occur in the interior of the wall, which is not easily discovered during an inspection of the structure. Furthermore, surface spalling have been observed on the upstream side on several hydropower dams and might also occur in this case if the temperature on the right side of the wall becomes low enough. The mechanism of this damage type in hydraulic structures has been studied by Rosenqvist et al. (2016) and is believed to be caused by macroscopic ice lens growth.

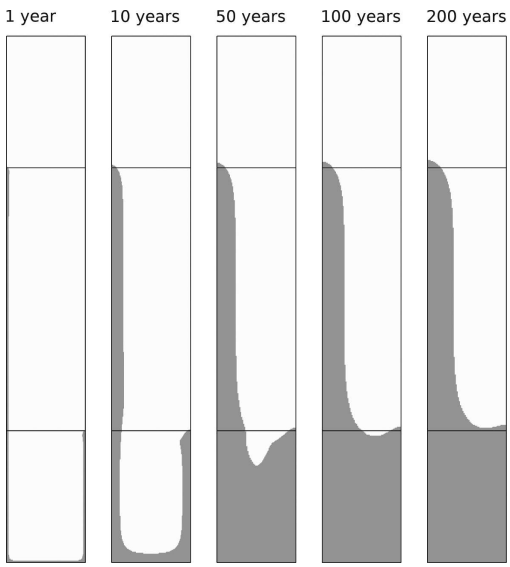

Figure 5. Regions in the wall having a total degree of water saturation S^w above 0.90 are plotted in grey.

Fig. 6 shows moisture profiles over the wall thickness at mid height. As seen, capillary saturation is reached relatively quickly in the left part of the wall, while the air pore filling rate is significantly lower. It can also be observed that the moisture gradient is steep close to the left surface in the beginning but decreases as the time of absorption increases. This general moisture distribution shape has been observed in in-situ measurements of an existing hydropower dam constructed with air-entrained concrete by Rosenqvist (2016) as well as in laboratory measurements of other porous materials containing pores in which air might get trapped during water absorption, see e.g. Hall (2007). Due to the slow nature of the air pore filling process, it also takes a considerable amount of time before a steady-state condition is reached. Even after 200 years, the saturated front continues to penetrate the wall but at a lower rate than earlier. In terms of advective and diffusive water flow through the wall, it is interesting to notice that advective flow of liquid water dominates in a relatively large region of the wall (region with $S^w > 0.79$), at least after more than 1 year. This observation complies rather well with a conceptual model of moisture flow through concrete structures subjected to a single sided water pressure, presented by Hedenblad (1994). As pointed out by Hall & Hoff (2012), this advective flow of

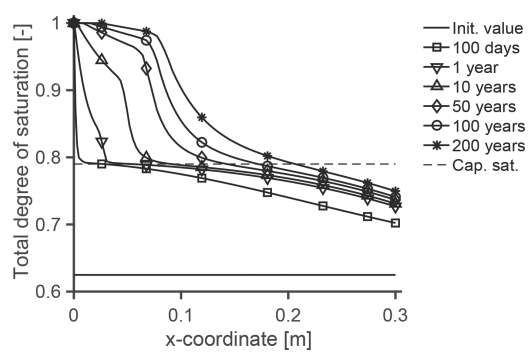

Figure 6. Moisture profiles showing the total degree of water saturation S^w over the thickness of the wall at mid height (y = 1.0 m) for increasing time.

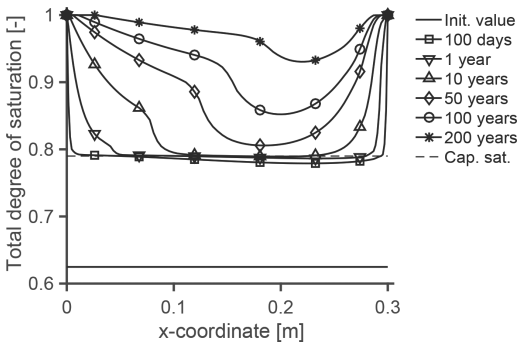

Figure 7. Moisture profiles showing the total degree of water saturation S^w S-w over the thickness of the wall at the ground water level ($y = 0.5$ m) for increasing time.

water might also remove some of the dissolved air, but this effect is not included in the current model. Moisture distributions over the wall thickness are also shown at the ground water level in Fig. 7. Even though the wall is subjected to free water on both sides, it is not completely saturated after 200 years of water absorption. It would of course take even longer time to reach complete saturation in this region if the wall was thicker, since the length of the diffusion paths toward the free surfaces increase. The asymmetry of the moisture distribution over the wall thickness is due to the different water pressures that act on each side of the wall.

5 CONCLUSIONS

A hygro-thermo-mechanical multiphase model recently developed by Eriksson et al. (subm) was used in two examples to demonstrate the influence and significance of considering water filling of air pores when studying heat and mass transfer in concrete structures cast with air-entrained concrete. The first example aimed at validating and showing the capabilities of the model by simulating an absorption test. The model was also applied in an academic example, which aimed at resembling a concrete wall constructed with air-entrained concrete and located in a waterway. The final goal of the simulation was to identify regions within the wall that are susceptible to frost damages after different times based on a critical degree of saturation.

The obtained moisture profiles within the wall showed sharp moisture gradients that could be attributed to the water filling process of air pores. Hence, it it is evident that the obtained moisture distributions in the wall would not be possible to capture without the air pore filling mechanism included in the multiphase model. This is further strengthened by the fact that similar moisture profiles have been measured by several researchers for cases similar to the case studied herein.

The critical degree of saturation for frost damage in air-entrained concrete is often higher than the degree of water saturation corresponding to capillary saturation. Thus, if the aim is to asses the risk for frost damage, it is necessary to consider the air pore filling mechanism. This is highlighted by the second example, showing that the multiphase model can serve as an aid when performing such assessments in different regions of a structure cast with air-entrained concrete, and ultimately provide better service life predictions. However, for certain regions subjected to wetting-drying cycles, e.g. in the water line of the current example, it might be necessary to also consider the hysteres is effect to obtain more accurate predictions of the frost risk.

ACKNOWLEDGEMENTS

The research presented was carried out as a part of Swedish Hydropower Centre—SVC. SVC has been established by the Swedish Energy Agency, Energiforsk and Svenska Kraftnät together with Luleå University of Technology, KTH Royal Institute of Technology, Chalmers University of Technology and Uppsala University. www.svc.nu.

REFERENCES

Baroghel-Bouny, V., M. Thi´ery, & X. Wang (2011). Modelling of isothermal coupled moisture-ion transport in cementitious materials. *Cement and Concrete Research 41*(8), 828–841.

COMSOL (2016). *COMSOL Multiphysics ver 5.2a Documentation*. Stockholm: COMSOL AB.

Coussy, O. & P.J.M. Monteiro (2008). Poroelastic model for concrete exposed to freezing temperatures. *Cement and Concrete Research 38*(1), 40–48.

Eriksson, D., T. Gasch, & A. Ansell (subm.). A hygro-thermomechanical multiphase model for long-term water absorption into air-entrained concrete. *Submitted to International Journal of Heat and Mass Transfer*.

Fagerlund, G. (1977). The international cooperative test of the critical degree of saturation method of assessing the freeze/thaw resistance of concrete. *Matriaux et Construction 10*(4), 231–253.

Fagerlund, G. (1993). The long time water absorption in the airpore structure of concrete. TVBM-3051, Lund University, Lund.

Fagerlund, G. (2004). A service life model for internal frost damage in concrete. TVBM-3119, Lund University, Lund.

Gawin, D., P. Baggio, & B.A. Schrefler (1995). Coupled heat, water and gas flow in deformable porous media. *International Journal for Numerical Methods in Fluids 20*(8–9), 969–987.

Gawin, D., C. Majorana, & B. Schrefler (1999). Numerical analysis of hygro–thermal behaviour and damage of concrete at high temperature. *Mechanics of Cohesive–frictional Materials 4*(1), 37–74.

Gawin, D., F. Pesavento, & B.A. Schrefler (2006). Hygro-thermo—chemo-mechanical modelling of concrete at early ages and beyond. Part I: Hydration and hygro-thermal phenomena. *International Journal for Numerical Methods in Engineering 67*(3), 299–331.

Gray, W.G. & C.T. Miller (2014). *Introduction to the thermodynamically constrained averaging theory for porous medium systems*. Switzerland: Springer International Publishing.

Hall, C. (2007). Anomalous diffusion in unsaturated flow: Fact or fiction? *Cement and Concrete Research 37*(3), 378–385.

Hall, C. & W.D. Hoff (2012). *Water transport in brick, stone and concrete* (2nd ed.). New York: Spon Press.

Hedenblad, G. (1994). Moisture flow through concrete structures subjected to lateral water pressure (in Swedish). TVBM-7082, Lund University, Lund.

Incropera, F.P., D.P. Dewitt, T.L. Bergman, & A.S. Lavine (2007). *Fundamentals of Heat and Mass Transfer* (6th ed.). Hoboken: John Wiley & Sons.

Jennings, H.M., A. Kumar, & G. Sant (2015). Quantitative discrimination of the nano-pore-structure of cement paste during drying: New insights from water sorption isotherms. *Cement and Concrete Research 76*, 27–36.

Koniorczyk, M., D. Gawin, & B.A. Schrefler (2015). Modeling evolution of frost damage in fully saturated porous materials exposed to variable hygro-thermal conditions. *Computer Methods in Applied Mechanics and Engineering 297*, 38–61.

Liu, Z. & W. Hansen (2016). A geometrical model for void saturation in air-entrained concrete under continuous water exposure. *Construction and Building Materials 124,* 475–484.

Powers, T.C. (1945). A working hypothesis for further studies of frost resistance of concrete. *Journal of the American Concrete Institute 16*(4), 245–272.

Rosenqvist, M. (2016). *Frost-induced deterioration of concrete in hydraulic structures: Interactions between water absorption, leaching and frost action*. PhD thesis, Lund University, Lund.

Rosenqvist, M., K. Fridh, & M. Hassanzadeh (2016). Macroscopic ice lens growth in hardened concrete. *Cement and Concrete Research 88,* 114–125.

Sandström, T. (2010). *Durability of concrete hydropower structures when repaired with concrete overlays*. Lic. thesis, Luleå University of Technology, Luleå.

van Genuchten, M. (1980). A closed-form equation for predicting the hydraulic conductivity of unsaturated soils. *Soil Science Society of America Journal 44*, 892–898.

Wong, H.S., A.M. Pappas, R.W. Zimmerman, & N.R. Buenfeld (2011). Effect of entrained air voids on the microstructure and mass transport properties of concrete. *Cement and Concrete Research 41*(10), 1067–1077.

Xi, Y., Z.P. Bažant, & H.M. Jennings (1994). Moisture diffusion in cementitious materials—adsorption isotherms. *Advanced Cement Based Materials 1*(6), 248–257.

Computational Modelling of Concrete Structures – Meschke, Pichler & Rots (Eds)
© 2018 Taylor & Francis Group, London, ISBN 978-1-138-74117-1

Concrete frost damage due to cyclic environmental loading—experimental and numerical study

M. Koniorczyk, D. Gawin & A. Wieczorek
Lodz University of Technology, Lodz, Poland

F. Pesavento
University of Padua, Padua, Italy

ABSTRACT: The relationship between transport phenomena and frost damage of concrete is established. The permeability is an important factor influencing degradation of concrete durability. The experimental study concerns the frost damage of an ordinary concrete with two different water to cement ratio (w/c equal to 0.5 and 0.4). The evolutions of permeability and elasticity modulus during repeating freeze-thaw cycles have been analyzed. The damage is characterized by the relative reduction of elasticity modulus. The changes of permeability, compressive strength and Young modulus of concretes were investigated after 0, 50, 100 and 150 freeze-thaw cycles. The model of moisture and heat transport considering kinetics of water crystallization is presented. The effective stress concept is introduced to take into account the crystallization pressure. The delayed damage model was applied to calculate the progress of ice-induced damage of concrete.

1 INTRODUCTION

Concrete is the most commonly used construction material and its durability is a key factor for its application. It depends mainly on the environmental conditions, in which it will be exploited, and its composition. In cold climates frost–induced damage is one of the most significant problems (Pigeon & Pleau 1995). Water solidification in pores leads to a stress resulting from bigger volume of ice comparing to the water one and surface forces in the interface zone (Powers 1975). Internal microstructure, mechanical and transport properties of concrete are affected by cyclic water freezing. On the other hand the concrete properties determine water migration and therefore the ice formation in the pore system.

The knowledge about physical and mechanical properties and their evolution due to the environmental loading is necessary for a more profound knowledge about damage phenomena. Understanding how the frost action influences transport and mechanical properties is crucial for development of more durable materials and more accurate simulation models. It will help to create materials that are able to serve for many years. Moreover, it will be possible to reduce the repair costs of deterioration caused by frost damage. Obtained results will also help to predict the lifetime of a concrete structure.

The paper consists of two parts. The first one concerns the experimental research, where we focus on the examination how the frost-induced damage affects the cement-based composites microstructure. We also determine the relation between gas permeability and damage parameter for concrete with two different water/cement ratio. The damage parameter is determined based on the change of elasticity modulus. The gas permeability is measured using Cembureau method (RILEM TC 116-PCD 1999).

The second part is devoted to numerical model of thermo-hydro-mechanical phenomena in porous materials considering water solidification and its influence on the durability of concrete. We consider the kinetics of water phase change and we apply the kinetic damage law in order to predict ice-induced damage of concrete.

2 EXPERIMENTAL STUDY

Concrete specimens with water to cement ratio equal to 0.5 and 0.4 were used in the experimental study. Concrete recipes are given in Table 1. The Portland cement CEM I 42.5 N-NA was used. The samples were stored in a freeze-thaw chamber, where the temperature varied between −18°C and +18°C. One freezing-thawing cycle lasted 8 h.

Table 1. Concrete compositions.

Mix ingredients [kg/m³]	C-1	C-2
Cement CEM I 42.5 N-NA	425	425
Water	212	170
Coarse aggregate, 8–16 mm	524	556
Medium aggregate, 2–8 mm	648	686
Sand, 0–2 mm	576	612
Plasticizer	–	2.12
w/c	0.50	0.40

The compressive strength of reference samples stored in water and the samples stored in the climatic chamber, after 50, 100 and 150 freeze-thaw cycles, were measured. The test was performed for three specimens of each series. Additionally, the error defined as the maximum difference between the results obtained for particular specimens and their average value, are given in Table 2.

Tested samples were loaded by axial compression and theie stresses and strains were recorded. The mean value of compressive strengths was used to determine the maximum stress level. The load was applied according to the standard EN 12390-13:2013, i.e. the stress varied between 0.5 MPa and 30% of the compressive strength. The elastic modulus was calculated using the stress-strain curves obtained at the end of the third loading-unloading cycle. Table 3 presents the evolution of elasticity modulus during the freezing-thawing cycles. The test was performed for three specimens of each series and the considered number of freeze-thaw cycles. The presented results are the average of three measurements.

Using the results concerning the change of the elastic modulus due to frost damage and applying a linear damage law, the damage parameter, d, was calculated from the equation (Pijaudier-Cabot et al. 1998):

$$d = (E_o - E_d) / E_o \tag{1}$$

where E_o is the modulus of elasticity for reference samples, and E_d is the modulus of elasticity obtained for concrete after succeeding freezing-thawing cycles (Wardeh et al. 2010).

After the measurements of the elastic modulus, three concrete discs were cut off from the central part of the cylindrical specimens. The thickness of each disc was 48 mm. The lateral sides of the sample were sealed with silicon in order to ensure one-dimensional gas flow. All specimens were dried at 60°C to a constant mass, then they were cooled for 48 h in a desiccators at 20°C. After drying the gas permeability test was performed using Cembureau method, which is recommended by RILEM

Table 2. Compressive strength of reference samples and after the freeze-thaw cycles.

	Number of freeze-thaw cycles			
	50	100	150	
Concrete	Compressive strength [MPa]			Control samples
C-1	54.0 ± 5.9	52.4 ± 3.7	50.1 ± 2.6	67.3 ± 2.1
C-2	75.8 ± 1.8	65.6 ± 2.6	64.9 ± 8.9	77.3 ± 4.5

Table 3. Elasticity modulus of reference samples and after the freeze-thaw cycles.

	Number of freeze-thaw cycles			
	50	100	150	
Concrete	Compressive strength [GPa]			Control samples
C-1	31.3 ± 0.3	19.1 ± 4.8	15.8 ± 3.2	31.7 ± 0.2
C-2	32.5 ± 0.2	32.3 ± 1.0	31.7 ± 1.0	33.3 ± 0.5

(RILEM TC 116-PCD. 1999). One-dimensional gas flow was imposed in the sample. The apparent gas permeability, k_a, was calculated at a given pressure according to the Hagen-Poiseuille equation for laminar flow under steady-state conditions:

$$k_a = (2 \cdot p_0 \cdot Q_i \cdot L \cdot \mu) / [A \cdot (p_i^2 - p_0^2)] \tag{2}$$

where p_i and p_0 are the inlet and outlet pressure, Q_i is the volumetric flow rate, L the thickness of the sample in the direction of the gas flow, A the area of the sample cross-section, and μ the viscosity of oxygen.

The apparent gas permeability was obtained for three different inlet pressures: 0.2, 0.25 and 0.3 MPa. To consider Knudsen flow, an intrinsic coefficient of permeability, k_v, was calculated using Klinkenberg relationship (Klinkenberg 1941):

$$k_a = k_v \cdot [1 + (b/p_m)] \tag{3}$$

where b is the Klinkenberg coefficient and $p_m = (p_i + p_o)/2$ is the mean gas pressure. The intrinsic permeability of concrete subjected to a laminar gas flow was obtained by a linear regression of the apparent permeabilities at infinite average pressure. The obtained results of intrinsic permeability of concrete samples after different number of freeze-thaw cycles are presented in Table 4.

The results concerning relationship between intrinsic permeability (Table 4) and damage parameter of the frost damaged concrete, calculated by means of Eq. (3) from the data in Table 3, are graphically presented in Figure 1. As may be observed,

Table 4. Intrinsic permeability of reference samples and after the freeze-thaw cycles.

	Number of freeze-thaw cycles			
	50	100	150	
Concrete	Intrinsic permeability [10^{-17} m^2]			Control samples
C-1	3.18 ± 0.67	4.67 ± 1.40	92.3 ± 37.0	–
C-2	0.85 ± 0.17	0.91 ± 0.25	0.95 ± 0.28	1.04 ± 0.27

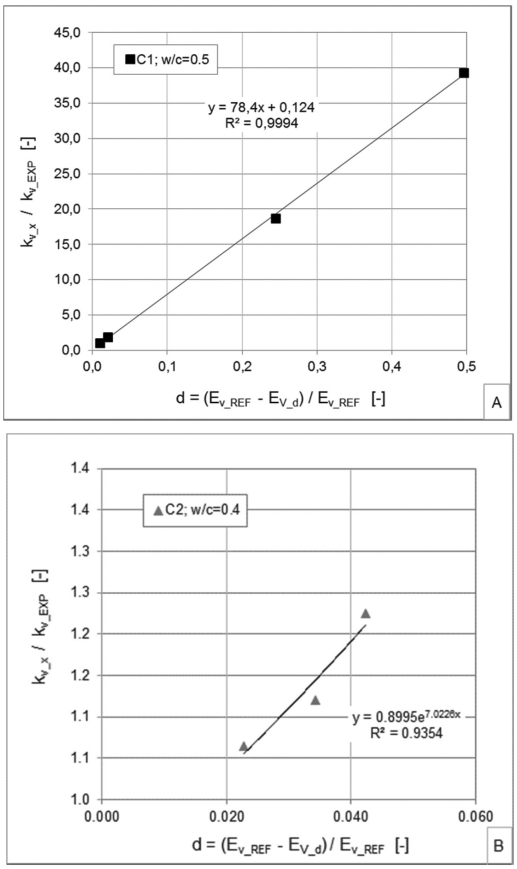

Figure 1. Relation between the increase of permeability and the damage value for concrete with water to cement ratio equal to 0.5 (a) and 0.4 (b).

a linear relationship between the permeability and damage parameter for frost deteriorated concrete was obtained for the both analyzed materials.

3 NUMERICAL MODEL

The mathematical model used in this work is based on Multiphase Porous Media Mechanics (MPMM), so concrete is treated as a porous material composed of a solid skeleton (considered as a single-component part) and water. The latter phase is formed of water in liquid and solid state (i.e. ice).

We assume to have fully saturated conditions that means the voids of the material are filled with liquid water or liquid water plus ice, i.e. $\eta_L + \eta_C = 1$.

The set of state variables is the following: liquid water pressure, p^L, temperature, T, and displacement vector, $\boldsymbol{u}$. These are supplemented by two internal variables, ice saturation degree, η_C, and mechanical damage parameter, d which are related to the corresponding evolution equations describing the freezing and damaging processes.

After neglecting convective heat transfer and considering the energy sink/source related to water phase change, the energy conservation equation for the multi-phase system reads,

$$\left(\rho C_P\right)_{ef} \frac{D^S T}{Dt} = div\left(\lambda_{ef} grad T\right) + \dot{m}_{L\to C} \Delta H_{fr} \tag{4}$$

where $(\rho C_p)_{ef}$ and λ_{ef} are the effective values of thermal capacity and thermal conductivity of the multiphase material and ΔH_{fr} is the volumetric latent heat of water freezing.

The mass balances of liquid water, ice and solid skeleton are described following system of coupled PDEs,

$$\frac{D^S\left(n\eta_L\rho^L\right)}{Dt} + div\left(n\eta_L\rho^L\mathbf{v}^{LS}\right) + n\eta_L\rho^L div\mathbf{v}^S = -\dot{m}_{L\to C} \tag{5}$$

$$\frac{D^C\left(n\eta_C\rho^C\right)}{Dt} = \dot{m}_{L\to C} \tag{6}$$

$$\frac{D^S\left(1-n\right)\rho^S}{Dt} + \left(1-n\right)\rho^S div\mathbf{v}^S = 0 \tag{7}$$

where D^κ/Dt ($\kappa = S, L, C$) means the material time derivative with respect to κ-phase, ρ^κ the real density of κ-phase ($\kappa = S, L, C$), $\mathbf{v}^\kappa$ and $\mathbf{v}^{LS}$ the velocity of κ-phase and velocity of liquid water with respect to solid skeleton, $\dot{m}_{L\to C}$ the volumetric mass source of ice due to water solidification.

After summing up equations (5) and (6), introducing constitutive relationships defining the densities of liquid water, ice and solid skeleton, and deriving the material derivative of porosity, one obtains the mass balance equation for water.

The rate of water freezing is calculated according to the following evolution equation:

$$\dot{\eta}_C = \frac{v_L}{RT}\frac{\Sigma_m\left(T_m - T\right) - \gamma_{C,L}\kappa_{C,L}}{\tau_{fr}} \tag{8}$$

where v_L is the molar volume of water, R the universal gas constant, Σ_m the ice melting entropy, $\gamma_{C,L}$ the crystal-liquid interface energy, $r_{C,L}$ the curvature of the crystal-liquid interface, τ_{fr} is the characteristic time of the freezing process. $T_m(\kappa_{C,L})$ is the ice melting temperature, which is dependent on the microstructure of a porous material. The latter relationship might be determined experimentally, e.g. using differential scanning calorimetry (DSC), see (Koniorczyk et al. 2015).

The linear momentum balance equation for the multiphase medium, after neglecting the inertial terms, has the following form (Koniorczyk et al. 2015):

$$div\,\mathbf{t}^{\text{total}} + \mathbf{g}\left[(1-n)\rho^S + n\eta_L\rho^L + n\eta_C\rho^C\right] = 0 \tag{9}$$

The total stress of a saturated material, $\mathbf{t}^{\text{total}}$, consists of the effective stress, $\mathbf{t}'$, transferred by the solid skeleton and a part, which accounts for pressure exerted by the phases occupying the pores, p^S:

$$\mathbf{t}^{\text{total}} = \mathbf{t}' - b\,p^S\mathbf{I} \tag{10}$$

where $b = 1 - K_T/K_S$ is Biot's coefficient, with K_T the bulk modulus of the porous material and K_S the bulk modulus of solid skeleton. The pressure exerted by the phases occupying pores on the solid skeleton might be given in the simplified form as:

$$p^S = \eta_L p^L + \eta_C p^C \tag{11}$$

For the damage law, a linear form is adopted, so the damage is proportional to the change of modulus of elasticity. Material damage parameter, d, due to external load and/or internal one (e.g. crystallization pressure) is described here by means of delayed damage model proposed in (Alix & Deu 1997). The rate form of the model has the following form,

$$\dot{d} = \frac{1}{\tau_c}\left[1 - \exp\left(-a\left\langle g(\gamma) - d\right\rangle\right)\right] \tag{12}$$

where τ_c is the characteristic time, representing the inverse of the maximum damage rate, a is a second model parameter, and $g(\gamma)$ has the following form,

$$g(\gamma) = \begin{cases} 0 & if\ \gamma \le \varepsilon_0 \\ 1 - \dfrac{\varepsilon_0}{\gamma}\exp\left(-\dfrac{\gamma-\varepsilon_0}{\varepsilon_f}\right) & if\ \gamma \ge \varepsilon_0 \end{cases} \tag{13}$$

where ε_0 the strain in the elastic limit, ε_f the parameter controlling the post-peak slope of stress-strain curve and $\gamma(t) = \max_{\tau \le t} \tilde{\varepsilon}(\tau)$ is the maximum strain reached in the loading history up to the given time t (Pijaudier-Cabot et al. 1998).

Finally, the mathematical model consists of three balance equations: for water mass, Eqs. (5) + (7), linear momentum, Eq. (9), and energy of the multiphase medium, Eq. (4), which are complemented with two evolution equations: for water freezing, Eq. (8), and mechanical damage, Eq. (12). The model equations, after introducing the constitutive relationships and space discretization with Finite Element Method, may be written in the matrix form as follows:

$$\begin{bmatrix} C_{LL} & C_{LT} & C_{L\mathbf{u}} \\ C_{TL} & C_{TT} & 0 \\ 0 & 0 & 0 \end{bmatrix} \begin{Bmatrix} \dot{\bar{\mathbf{p}}}_L \\ \dot{\bar{\mathbf{T}}} \\ \dot{\bar{\mathbf{u}}} \end{Bmatrix} + \begin{bmatrix} K_{LL} & 0 & 0 \\ 0 & K_{TT} & 0 \\ K_{\mathbf{u}L} & K_{\mathbf{u}T} & K_{\mathbf{uu}} \end{bmatrix} \begin{Bmatrix} \bar{\mathbf{p}}_L \\ \bar{\mathbf{T}} \\ \bar{\mathbf{u}} \end{Bmatrix} = \begin{Bmatrix} f_L \\ f_T \\ f_{\mathbf{u}} \end{Bmatrix} \tag{14}$$

where the terms of the above matrices are given in detail in (Koniorczyk et al. 2015).

After applying the fully implicit scheme of Finite Difference Method to approximate the time derivatives in Eq. (14), the set of governing equations may be written in the compact form as,

$$\mathbf{C}_{ij}(\mathbf{x}_{n+1})\frac{\mathbf{x}_{n+1} - \mathbf{x}_n}{\Delta t} + \mathbf{K}_{ij}(\mathbf{x}_{n+1})\mathbf{x}_{n+1} - \mathbf{f}_i(\mathbf{x}_{n+1}) = \mathbf{0} \tag{15}$$

where $i,j = L,T,\mathbf{u}$; $\mathbf{x} = [\bar{\mathbf{p}}_L, \bar{\mathbf{T}}, \bar{\mathbf{u}}]$, subscript n means the number of time step, Δt the time step length. The nonlinear equation set (14) is solved by means of a monolithic Newton-Raphson type iterative procedure. On the basis of the above described numerical model, the research computer code was developed.

The numerical model presented above was further generalized for partially saturated porous materials in (Gawin et al. submitted), where kinetic model of water solidification, expressed in terms of capillary pressure and based on nonequilibrium thermodynamics, was used (Pesavento & Gawin 2016).

4 MODEL VALIDATION

For the validation of presented here, kinetic model of water—ice phase change, a comparison between the numerical results and the experimental results of (Sun & Scherer 2010), is shown. The model validation, based on the DSC experiment, was previously presented in (Koniorczyk et al. 2015).

The experimental test used here for the model validation was performed by means of a differential mechanical analyser (DMA) by Sun and Scherer (2010). It is based on the measurements of strains during freezing and thawing of cement mortars made of ordinary Portland cement, with two different water/binder ratios (0.4 and 0.5) and three entrained air contents (0%, 3% and 6%). These results exhibit a hysteresis in the material behaviour caused by freezing—thawing of a moist material, in this case concerning strain vs. temperature performance.

The microstructure and some physical properties of the tested mortars have been extensively examined by Sun and Scherer (2010) by means of mercury intrusion porosimeter (MIP), nitrogen adsorption-desorption (NAD) and differential mechanical analyser (DMA). The details concerning the samples composition, preparation and conditioning, as well as testing of the mortar's physical properties, can be found in (Sun and Scherer, 2010). The main material parameters assumed in our simulations, are based on these data, see Table 5. During the DMA tests all the samples were initially fully saturated with water. The samples used for DMA tests had a diameter of 5 mm and 15 mm height. No visible frost damage was observed during the tests.

All the simulations in this section were performed for the same mesh of 75 (5 × 15) eight-node axisymmetric FEs of equal size and BCs shown in Table 6, using variable time step (from 1 s up to 15 s), dependent on the stage of process evolution (smaller during phase change).

Sun and Scherer measured strains of the mortars with 0%, 3% and 6% air, exposed to two different cooling—heating (with the rate of 0.25 K/min) temperature cycles: 1) with 12°C ≥ T ≥ –15°C; 2) with 20°C ≥ T ≥ –40°C. For validation of the present model the strain data for mortars with 0% and 6% air, exposed to cycle 1 are used.

Table 5. Main material properties (at T = 20°C) assumed in the simulations of the tests performed by Sun and Scherer (2010).

Material property	0% air	6% air
Porosity, n [%]	26.8	33.3
Water intrinsic permeability, k_o [m^2]	10^{-17}	10^{-17}
Young modulus, E [GPa]	20.1	16.0
Thermal conductivity, λ [W/m·K]	1.5	1.5
Specific heat, C_p [J/kg·K]	1019	1019
Thermal expansion coefficient α [1/K]	1.241×10^{-5}	1.241×10^{-5}

Table 6. Mesh and boundary conditions assumed in the simulations of DSC and DMA tests performed by Sun and Scherer (2010).

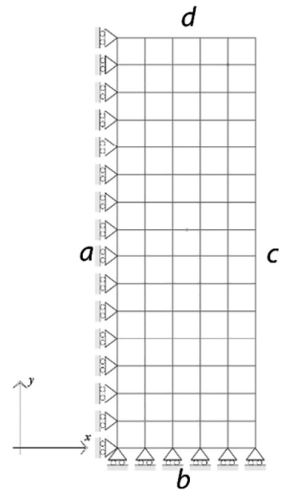

Side	Variables	Values and coefficients	B.C. type
a	u_x	$u_x = 0$	I
	p^L	$q^L{}_x = q^L{}_x = 0$	II
	T	$q^T{}_x = 0$	II
b	u_y	$u_y = 0$	I
	p^L	$q^L{}_y = q^L{}_y = 0$	II
	T	$q^T{}_y = 0$	II
c,d		sealed	II
	P^L	convective with: α_c = 30 W/(m^2 K);	
	T	$T(t)$ – according to Sun and Scherer (2010)	III

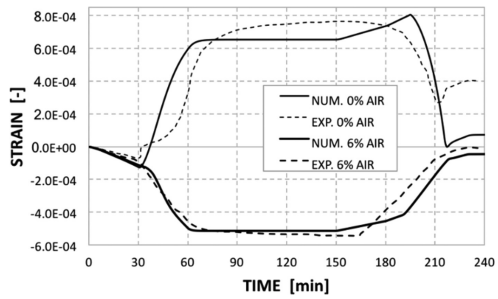

Figure 2. Comparison of the time evolutions of strains for the cement mortars with 0% and 6% air, cooled to –15°C, obtained from simulations and experiments (Sun & Scherer, 2010).

The results of simulations performed for the two mortars are compared with the experimental results of (Sun & Scherer 2010) in Figures 2

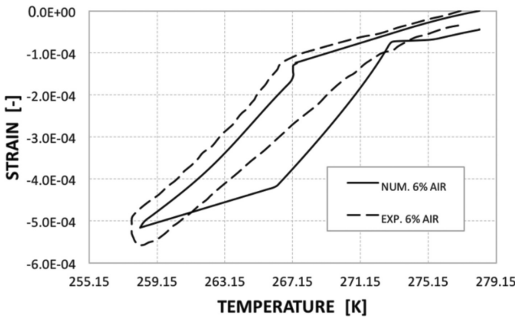

Figure 3. Comparison of the strain vs. temperature evolution for the cement mortar with 6% air, cooled to –15°C, obtained from simulations and experiments (Sun & Scherer, 2010).

and 3. A good agreement of the simulation and experimental results concerning time evolutions of the strains can be observed in Figure 2. Due to different pore microstructure, the mortar with 0% air experienced expansion, while the mortar with 6% air shrunk, what was properly predicted by the present model. The evolution of strain vs. temperature for the mortar with 6% air exhibits a hysteresis, which is reasonably well predicted by the simulations, Figure 3.

5 FROST DAMAGE IN A CONCRETE WALL

In the following, a numerical example concerning gradual frost damage of concrete structure is shown.

The simulation deals with a concrete wall exposed to variable external temperature causing cyclic material freezing-thawing. In particular, the hydro-thermal behavior and the stress-strain field in the water saturated concrete wall were analyzed, resulting in its frost damage. The analyzed domain was divided into 100 quadrilateral finite elements of equal size. The main material parameters were assumed as follows: $n = 6\%$, $E = 25$ GPa, $f_{ct} = 3.0$ MPa, $\lambda = 1.5$ W/(m·K), $k = 3 \cdot 10^{-21}$ m^2. The convective (Robin) boundary conditions are assumed for heat transport with heat transfer coefficient $\alpha = 8$ W/(m^2 K). The ambient temperature was changing according to:

$$T = \begin{cases} 293.15 - 8t\,[K], t \in [0h, 5h) \\ 253.15\,[K], t \in [5h, 10h) \\ 253.15 + 8(t-10)\,[K], t \in [10h, 15h) \\ 293.15\,[K], t \in [15h, 20h] \end{cases} \quad (16)$$

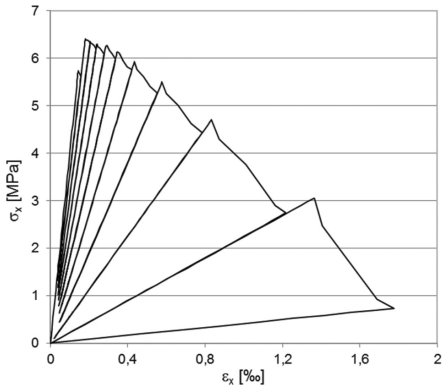

A

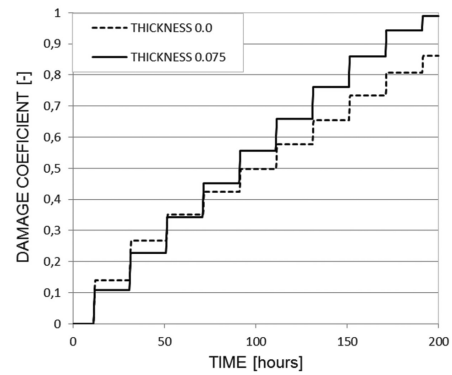

B

Figure 4. (a) Stress-strain relation and (b) the change of damage parameter in two selected points of the wall.

The 10 cycles of temperature, given by the above equation, were analyzed, thus the total simulation time was equal to 200 h. The results considering the stress-strain curve and the progress of damage parameters are presented in Figure 4.

As may be seen in Figure 4, a pronounced increase of frost damage after consecutive water freezing cycles was obtained, what is in agreement with experimental observations in laboratory. Application of the delayed damage model allowed to predict this phenomenon properly (Koniorczyk et al. 2015).

6 CONCLUSIONS

The research presented in the paper considers the ice-induced damage of concrete. The experimental study allowed to estimate the relation between permeability and damage parameters for concrete with two water-cement ration. The

numerical model, outlined in the second part of the manuscript, is based on the assumption that material is a multiphase medium and that the phases overlap. The kinetics of phase change was assumed. The effective stress concept was introduced to account for the pressure exerted by the phases occupying pores. Such a complex approach allows to predict the progress of ice-induced damage of concrete.

REFERENCES

Allix O. & Deu, J.F. 1997. Delay-damage modelling for fracture prediction of laminated composites under dynamic loading, *Engineering Transactions* 45: 29–46.

EN 12390-13:2013. *Testing hardened concrete–Part 13: Determination of secant modulus of elasticity in compression.*

Gawin, D., Pesavento, F., Koniorczyk, M. & Schrefler, B.A. submitted. Non-equilibrium modeling of water freezing-thawing with hysteresis in partially saturated porous media, submitted to *International Journal Solids and Structures*.

Klinkenberg, L.J. 1941. The permeability of porous media to liquid and gases. In *Drilling and Production Practice*: 200–213, American Petroleum Institute.

Koniorczyk, M., Gawin, D. & Schrefler, B.A. 2015. Modeling evolution of frost damage in fully saturated porous materials exposed to variable hygro-thermal conditions, *Computer Methods in Applied Mechanics & Engineering* 297: 38–61.

Pesavento, F. & Gawin, D. 2016. Modeling freezing of cementitious materials by considering process kinetics, In: Hasholt M.T., Fridh K. & Hooton R.D. (Eds.), *Proc. Int. RILEM Conf. on Materials, Systems and Structures in Civil Engineering. Frost Action in Concrete*, 22–23 August 2016, Technical University of Denmark, Lyngby, 101–110.

Pigeon, M. & Pleau, R. 1995. *Durability of concrete in cold climates*. Milton Park, Abingdon, Oxon: Taylor & Francis.

Pijaudier-Cabot, G., Gerard, B. & Molez, L. 1998. Damage mechanics of concrete structures subjected to mechanical and environmental actions, In de Borst R., Bicanic N., Mang H. & Meschke G. (eds.), *Computational Modelling of Concrete Structures—Euro-C 1998 Proceedings*: 567–576, Rotterdam: A.A. Balkema Publishers.

Powers, T.C. 1975. Freezing effects in concrete, In: *Durability of concrete*, American Concrete Institute, Special Publication 47: 1–12.

RILEM TC 116-PCD. 1999. Recommendation of TC 116-PCD: Tests for gas permeability of concrete—Preconditioning of concrete test specimens for the measurement of gas permeability and capillary absorption of water—Measurement of the gas permeability of concrete by the RILEM—CEMBUREAU method—Determination of the capillary absorption of water of hardened concrete. *Materials and Structures* 32: 174–179.

Sun, Z. & Scherer, G.W. 2010. Effect of air voids on salt scaling and internal freezing, *Cement and Concrete Research* 40: 260–270.

Wardeh, G., Mohamed, A.S.M. & Ghorbel, E. 2010. Analysis of concrete internal deterioration due to frost action, *Journal of Building Physics* 35 (1): 54–82.



Taylor & Francis
Taylor & Francis Group
http://taylorandfrancis.com

Computational Modelling of Concrete Structures – Meschke, Pichler & Rots (Eds)
© 2018 Taylor & Francis Group, London, ISBN 978-1-138-74117-1

Computational modeling of combined frost damage and alkali-silica reaction to the durability of RC bridge decks

F. Gong, Y. Takahashi & K. Maekawa
The University of Tokyo, Tokyo, Japan

ABSTRACT: A strong coupling between Freeze/Thaw Cycle (FTC) and Alkali Silica Reaction (ASR) is modelled on the basis of micro-structural level and up-scaled to macro-structural stage by considering non-uniform environmental and mechanistic conditions of confinement. Deformation and damage patterns are simulated for RC bridge decks under coupled FTC and ASR, and a remaining fatigue life under moving loads after different sources of damage is investigated. It is shown that ASR driven expansion is mainly governed by the arrangement of reinforcing bars, while the FTC damage is mainly initiated from corners, edges and surfaces of members, and closely relies on water supply. It is also found that ASR could be occasionally beneficial for bridge decks under moving traffic loads due to gel-filled cracks and chemical pre-stressing. However, if cracks are empty or filled by condensed liquid water, overall fatigue life will be significantly reduced.

1 INTRODUCTION

Deterioration process of concrete is of high complexity since structural concrete usually suffers from coupled mechanistic and multiple ambient actions, such as high cycle fatigue loads, alkali silica reaction (ASR), freeze-thaw cycles (FTC), carbonation and steel corrosion. In addition, when the coupled damage occurs in real RC structures, it is difficult to distinguish how much proportion of damage comes from which impact, then making the assessment of current situation as well as prediction of future performances difficult. Considering the complexity of durability problems in terms of chemical, physical and mechanical processes, a multi-scale modeling system has been developed (Maekawa *et al.*, 2003a), and successfully applied to several solo or coupled durability problems (Maekawa and Fujiyama, 2013, Gebreyouhannes and Maekawa, 2016, Takahashi *et al.*, 2016, Gong *et al.*, 2017).

FTC and ASR damages take place together to concrete of many cases, and alternately in winter and summer seasons. In addition, the deicing salt has been widely sprinkled on roads and bridge decks where the frost damage could happen, the remaining salt will also accelerate the ASR in summer season (Kawamura *et al.*, 1994). The deterioration mechanisms by each single event have been widely investigated in the past decades. While for the interactions between two impacts, previous experiments show that ASR gel can flow into entrained air bubbles, which can delay or reduce the ASR expansion (Jensen *et al.*, 1984) at early stage, but it will increase the risk of frost damage on the contrary. The ASR gel can also flow into pre-existing cracks (Maraghechi *et al.*, 2012), which will affect the water permeation in the crack system. These events are strongly and mutually coupled with each other.

In this paper, an integrated simulation approach is presented to simulate the coupled processes and their mechanical impacts to RC slabs. The coupling between FTC and ASR will be modelled from the micro-structural level, considering the ice formation and ASR gel intrusion into capillary pores, as well as the effect of entrained air. Then, based on the poromechanics, the mixed pore pressure and deformation of concrete skeleton will also be formulated by considering the multi-phase flows in pores. Finally, different sequences of combined FTC and ASR expansion will be simulated and discussed based on a FEM simulation for RC slabs, as well as their remaining fatigue lives under moving loads.

2 MULTI-SCALE MODELING

2.1 *Multi-scale simulation scheme*

The multi-scale integrated simulation scheme has been briefly summarized in Fig. 1. Starting from the hydration kinetics at nano-scale, chemo-physical reactions of cement phase are simulated (Kishi and Maekawa, 1995). Then, the hydration products together with cement particles form the complex micro pore structures, within which the moisture transport and thermodynamic equilibrium can be formulated. The multi-ionic transport and its equilibrium for ASR as well as the phase change

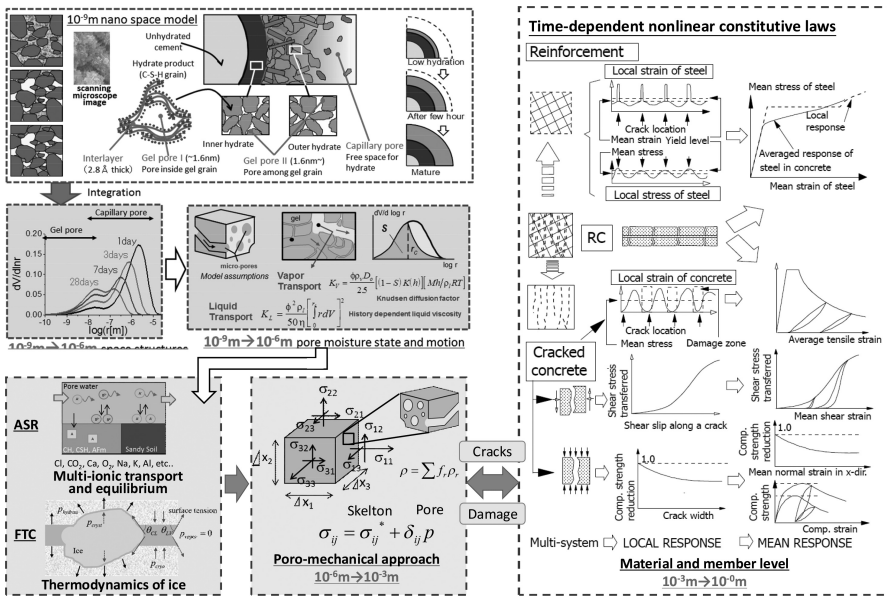

Figure 1. Multi-scale simulation scheme of ASR and FTC induced deformation (Maekawa et al., 2008).

of water-ice are considered as well at this scale (Takahashi *et al.*, 2016, Scherer and Valenza II, 2005). Since both ASR and ice formation will cause volume increase inside micro-pore substances, the mechanical interaction between pore substances (ice, liquid water, ASR gel) and concrete skeleton will be considered for both non-cracked and cracked conditions. On the frame of poro-mechanical modelling, condensed liquid water kinetics and silica gel migration are also calculated under the pressure gradient. Finally, mechanical responses of cracked concrete skeleton are taken into account based on the time-dependent nonlinear constitutive laws (Maekawa et al., 2006).

2.2 *Micro-mesoscale coupling model*

The coupled FTC and ASR effect will be investigated from the micro-pore structure level, and upscaled to the structural meso-stage in terms of the space-averaged kinetics. Figure 2 shows the representative volume element (RVE) for this multi-scale problem.

Considering a RVE at meso-scale (1 mm to 1 cm) which contains aggregate, cement paste, entrained air and meso-cracks, ASR gel will be created in and around aggregates, while the solidified ice will form in meso-scaled cracks (if cracks are filled by free liquid water before phase change). The semi-liquid alkali silica gel can flow into the meso-cracks and entrained air through micro-pore systems (Jensen *et al.*, 1984, Maraghechi *et al.*, 2012), the silica gel in meso-cracks can reduce the water transport and ice formation, which is beneficial to frost resistance. However, if the entrained air bubbles are filled by the ASR gel, they may also lose their function in preventing the frost damage.

At the micro-pore structure level (10 μm to 100 μm), the ice will be formed from larger capillary pores converging to the smaller ones, but if the greater capillary pores are already occupied by ASR gel, the ice formation will be delayed with less amount, and finally result in a smaller frost expansion. The amount of intruded ASR gel in capillary pores also relies on the tensile capacity of concrete matrix, which can be affected by the damage level and kinetic confining conditions like steel reinforcement. The aforementioned events are sensitive to the surface tension of ASR gel, for which more experimental investigations are required.

ASR is formulated based on the chemical process, and the total created ASR gel volume (V_{ASR_TOTAL}) is formulated as a function of alkali concentration, updated free water and the content of reactive aggregates. Environmental variable such as temperature and relative humidity have also been considered as control factors to affect the gel generation rate (Takahashi et al., 2016).

The coupling problem at microscale closely relies on the pore size distribution, which can be described by a simplistic Raleigh-Ritz (R-R) distribution function as follows (Maekawa et al., 2008):

$$\phi(r) = \phi_{fr} + \phi_{gel}\left(1 - \exp(-B_{gel}r)\right) + \phi_{cap}\left(1 - \exp(-B_{cap}r)\right) \quad (1)$$

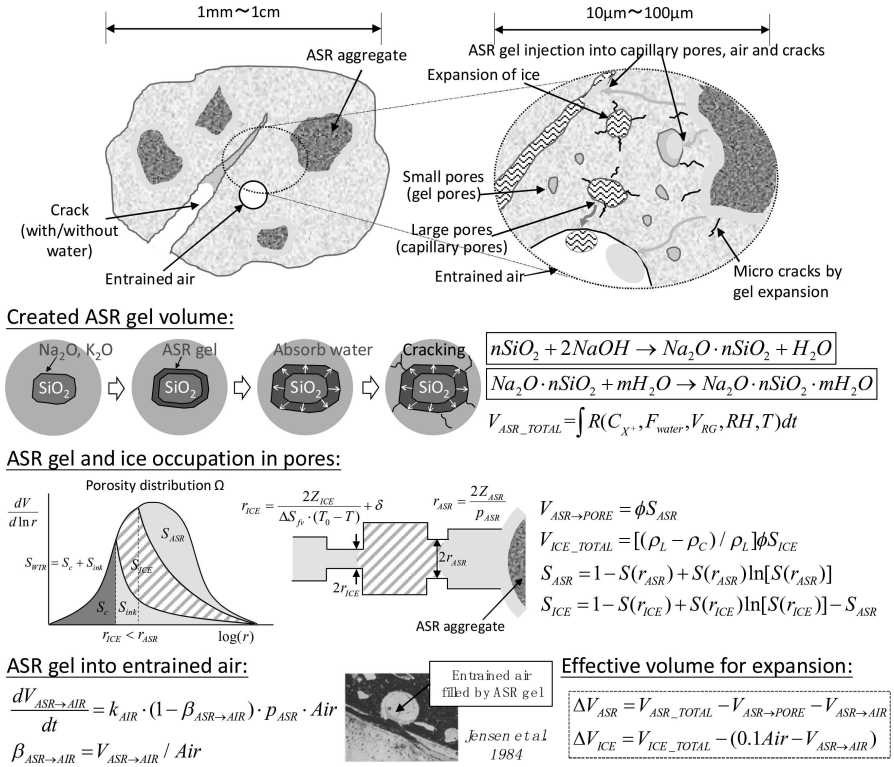

Figure 2. Micro-meso-scale coupled ASR expansion and ice formation (Gong et al., 2017).

where $\phi(r)$ is the cumulated porosity whose radii are less than r, ϕ_{lr}, ϕ_{gel} and ϕ_{cap} are the porosity of interlayer, gel and capillary pores, respectively, B_{gel} and B_{cap} are the solo porosity distribution parameter for gel and capillary pores. The critical radius (r_{ASR}) of the pore into which ASR gel can intrude under a gel pressure (p_{ASR}) can be determined as:

$$r_{ASR} = \frac{2Z_{ASR}}{p_{ASR}} \tag{2}$$

where $Z_{ASR} = \gamma_{ASR}\cos\theta_{ASR}$, γ_{ASR} is the specific energy of ASR gel and θ_{ASR} is the contact angle between ASR gel and concrete skeleton. The parameter $Z_{ASR} \approx 0.4$ is determined based on the sensitivity analysis using the free expansion data from Muranaka and Tanaka (2013). Similarly, the ice occupation of different size of pores depends on the thermodynamic equilibrium (Scherer and Valenza II, 2005):

$$r_{ICE} = \frac{2Z_{ICE}}{\Delta S_{fv}\cdot(T_0 - T)} + \delta \tag{3}$$

where $Z_{ICE} = \gamma_{ICE}\cos\theta_{ICE}$, $\gamma_{ICE} \approx 0.04$ J/m^2 is the specific energy of ice/water interface, $\theta_{ICE} \approx 0$ is the contact angle between ice and pore wall, $\Delta S_{fv} \approx 1.2$ J/(cm^3·K) is the molar entropy of fusion, $T < 0$°C is the local temperature in Celsius, T_0 is the freezing point of free water (0°C), $\delta \approx 0.9$ nm is the thickness of unfrozen water layer between ice and pore wall.

It is obvious that when ASR happens first, the ice will not start to form until $r_{ICE} < r_{ASR}$, as shown in Fig. 2. The so-called "ink-bottle" effect needs to be considered for both ice formation and ASR gel intrusion, which is caused by the differences in size between pore entry and pore body. This part of the pore volume can be evaluated as (Maekawa et al., 2008):

$$\begin{aligned} S_{ink} &= \int_{\min(r_{ICE}, r_{ASR})}^{\infty} f_r \Omega dr = \int_{\min(r_{ICE}, r_{ASR})}^{\infty} \left(\frac{S_c}{V}\right) dV \\ &= -S_c \ln(S_c) \end{aligned} \tag{4}$$

where S_{ink} is the ratio of the trapped water to the total pore space, Ω is the normalized pore size distribution, S_c is the equilibrium water content even when no water is trapped, $f_r = S_c/V$ is the probability that the water can be trapped by the ink bottle effect. It is obvious that S_{ink} will depend on the minimum value of r_{ICE} and r_{ASR} (Fig. 2).

Other than the micro-pores, the entrained air bubbles are also important to the frost damage and ASR expansion. The air bubbles can hold the expanded ASR gel, but at the same time, the filled bubbles will no longer prevent the frost damage. A simplistic rate-dependent model of ASR gel flow is assumed as:

$$\frac{dV_{ASR\to AIR}}{dt} = k_{AIR}\cdot(1-\beta_{ASR\to AIR})\cdot p_{ASR}\cdot Air \qquad (5)$$

where $dV_{ASR\to AIR}/dt$ is the speed of gel flow into air bubbles, k_{AIR} is a constant which can be determined by the sensitivity analysis (3×10^{-9} Pa^{-1} s^{-1}), $\beta_{ASR\to AIR} = V_{ASR\to AIR}/Air$ is the ASR gel occupying ratio in the air bubbles (0 to 1), Air is the total air content (entrained and entrapped air). The functional air bubbles for the frost resistance is roughly around 10% of the total air volume (Gong et al., 2017, Promentilla and Sugiyama, 2010). Thus, if the ASR gel occupation ratio is larger than 10%, the frost resistance from entrained air will totally disappear.

Finally, the effective volume of ASR gel (ΔV_{ASR}) and ice expansion (ΔV_{ICE}) which can contribute to the poro-mechanical expansion are:

$$\Delta V_{ASR} = V_{ASR_TOTAL} - \phi S_{ASR} - V_{ASR\to AIR} \qquad (6)$$

$$\Delta V_{ICE} = 0.09\phi S_{ICE} - \max(0.1Air - V_{ASR\to AIR}, 0) \qquad (7)$$

2.3 *Poromechanical modeling of mixed pore substances*

The strong coupling between ASR and FTC is considered at both the global scale and local scale as shown in Fig. 3. For the coupling at global scale, the deformation of concrete matrix is interacted with the mixed pore pressures at the macro scale, while the pore pressures will push the pore substances into capillary pores and entrained air at micro scale, and these micro-events will affect the total pore pressures and matrix deformation reciprocally. Then, at the local scale of liquid flow in pores and cracks, different phases of flow are also coupled together.

Based on the two-phase model in previous studies (Maekawa et al., 2008, Biot, 1963), the governing equations are extended to the multi-phase case. First, the averaged density (ρ) of whole material becomes:

$$\rho = (1-n)\rho_s + \sum_{r=1}^{N_1} f_r n\rho_r + \sum_{r=N_1}^{N_2} f_r n\rho_r \qquad (8)$$

where $1-n$ and ρ_s are the volume ratio and density of concrete skeleton, f_r is the proportion of each solid/liquid substance in pores and $\Sigma_{r=1}^{N_2} f_r = 1$, N_2 is the total number of pore substances, N_1 is the number of liquid phase in pores, ρ_r is the density of each pore substance.

The movement of each pore liquids denoted by $U_i^{(r)}$ is expressed by the space-averaged displacement of concrete skeleton u_i and the substantial relative displacement of each pore liquid phase ($w_i^{(r)}$) as,

$$U_i^{(r)} = u_i + \frac{w_i^{(r)}}{f_r n} \qquad (9)$$

The total stress (σ_{ij}) is composed of effective stress on the concrete skeleton (σ_{ij}^*), the stress caused by solid pore substances (s_{ij}), and the isotropic pore pressure (p):

$$\sigma_{ij} = \sigma_{ij}^* + s_{ij} + \delta_{ij}p \qquad (10)$$

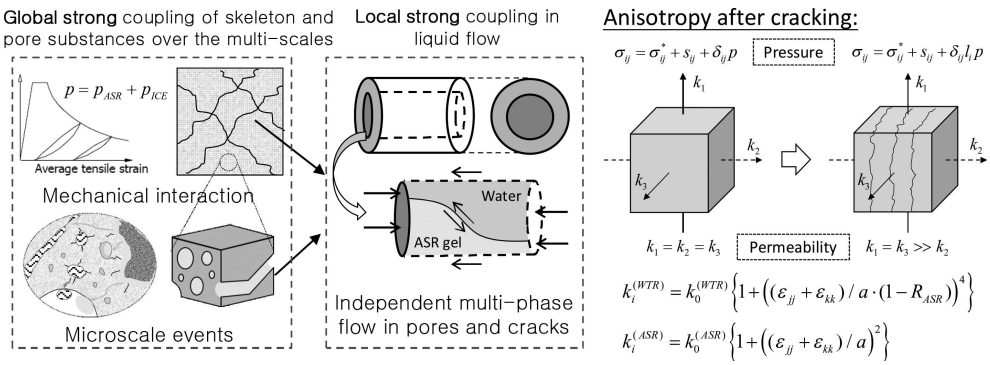

Figure 3. Poromechanics coupling of skeleton and pore substances considering multi-phase local flow and anisotropy after cracking.

where δ_{ij} means the Kronecker's delta ($\delta_{ij}=0$ if $i \neq j$; $\delta_{ij}=1$ if $i=j$). The total pore pressure p is a sum of all the partial pressures of each liquid phase:

$$p = \sum_{r=1}^{N_1} p^{(r)} \tag{11}$$

The dynamic equilibrium equations of the concrete skeleton and each pore liquid in cracks can be formulated as follows:

$$\sigma_{ij,i} = \rho(u_{i,tt} - g_i) + \sum_{r=1}^{N_1} \rho_r w_{i,tt}^{(r)} \tag{12}$$

$$p_{,i}^{(r)} = \rho_r(u_{i,tt} - g_i) - \rho_r w_{i,tt}^{(r)} / (f_r n) - (1/k_i^{(r)}) w_{i,t}^{(r)} \quad r = 1 \ldots N_1 \tag{13}$$

where g_i is the gravity and the last term of Eq. (13) represents the dragging action of each pore liquid based on Darcy's law, $k_i^{(r)}$ is the permeability of pore liquid r in each i-direction through concrete pore and crack gaps. The subscript t and tt denotes the first and second-degree differentiations with respect to time.

The total liquid and solid pore pressure in pores and crack system can be calculated as an extension of previous models (Maekawa and Fujiyama, 2013, Gebreyouhannes and Maekawa, 2016) as follows.

$$p = K_f^* \sum_{i=1}^{3} \left(\sum_{r=1}^{N_1} w_{i,t}^{(r)} + (1-\beta)\varepsilon_{ii} \right) \tag{14}$$

$$s_{ij} = 3\delta_{ij} K_f^* (a_{ii} + \beta \varepsilon_{ii}) \tag{15}$$

$$K_f^* = \left(\frac{1-n}{K_s} + \sum_{r=1}^{N_2} \frac{f_r n}{K_r} \right)^{-1} \tag{16}$$

where K_f^* is the average bulk modulus of the whole composite assuming a volumetric linearity, ε_{ii} is the strain of concrete skeleton based on the space averaged path and time dependent constitutive equation rooted in the multi-directional crack modeling, a_{ii} is the amount of all generated solid pore substances, β is the ratio of the solid phase of pore substances.

The anisotropy of cracking can affect both liquid pore pressures and the liquid permeability (Maekawa et al., 2013). Once the cracks are generated, the liquid pressure inside the crack gaps will act perpendicularly to a pair of parallel crack planes (Fig. 3) as,

$$\sigma_{ij} = \sigma_{ij}^* + s_{ij} + \delta_{ij} l_i p \tag{17}$$

where l_i is the unit directional vector normal to a crack plane.

The crack opening will also result in an anisotropy in the permeation of pore liquids (Fig. 3). For a multi-directional cracking system, the permeability enlargement depends on the crack opening width of other two directions, which has been proposed as (Maekawa et al., 2013),

$$k_i = k_0 \left\{ 1 + \left(\frac{\varepsilon_{jj} + \varepsilon_{kk}}{a} \right)^b \right\} \tag{18}$$

where k_i is the permeability in direction i, k_0 is the intrinsic permeability for different kinds of liquid, $\varepsilon_{jj}+\varepsilon_{kk}$ is the transverse in-plain strain of projection, a is a constant meaning the threshold of the crack opening (= 100 μ in this study), b is a constant related to the liquid type. Based on the experimental data from Wang et al. (1997), $k_0 = 10^{-9}$ cm/s, $b = 4$ for liquid water, while for the liquid ASR gel, the sensitivity analysis (Takahashi et al., 2016) based on measured ASR expansion shows $k_0 = 10^{-18}$ cm/s, $b = 2$. When both ASR gel and liquid water are existed in cracks, the water motion will be retarded due to the partially filled crack path by ASR gel.

3 COUPLED DETERIORATION FOR RC SLAB

3.1 *RC slab and moving load fatigue test*

The RC slab simulated in this study is based on the experiments by Maeshima et al. (2016), as shown in Fig. 4. Half model is used for the FEM mesh, and the smeared RC elements are adopted based on the nonlinear constitutive models (Maekawa et al., 2003b). After different kinds of environmental exposure, repeated wheel load is applied on the center of top surface. The basic material properties of concrete and reinforcement follows the experiments (Maeshima et al., 2016). The water

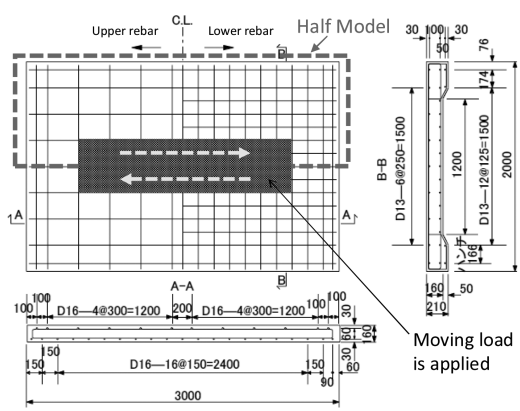

Figure 4. Simulated RC slab (Maeshima et al., 2016).

Table 1. Exposure and loading conditions.

Level	FTC*	ASR**	Fatigue
1	20 cycles (closed)	0.75 mol/L	without water
2	20 cycles (open)	1.5 mol/L	water on top
3	150 cycles (open)	3.0 mol/L	submerged in water

*Initially saturated, with/without water supply on stop surface.
**180 days of exposure at 40°C, with different initial NaOH concentration in pore solution.

to cement ratio is set as 0.65 and the air content is chosen as 1.5% for the comparison purpose.

The exposure conditions and loading conditions are listed in Table 1. For each category, three levels of deterioration are selected, and indexed as "FTx-ASRx-Fatix". For example, FT1-ASR3-Fati2 means first exposed to 20 cycles of FTC under closed moisture condition, then followed by ASR exposure with initial NaOH concentration of 3.0 mol/L, and finally tested with moving loads with free water on the top.

3.2 *Deformation under FTC*

The frost damage level in RC structures varies place by place significantly, not only depending on the lowest temperature that the particular location can reach, but also relying on the steel confinement.

Given the temperature history in Fig. 5, their profile of the RC slab can be calculated by solving the 3D thermal conductivity and conservation equations. The periodical cyclic temperature change in the slab may converge to stability after one or two FTC, and the amplitude of temperature variation decreases from the corners, edges, surfaces and finally the center. Thus, the ice expansion in each cycle and the damage accumulation during large numbers of FTC will be much reduced when the distance to the boundary becomes larger.

Referring to the principle strain as shown in Fig. 6, it can be seen that the frost expansion and damage start from the corners, edges and surfaces, while the inner core part is less affected. This is mainly due to the uneven temperature distribution as shown in Fig. 5. Just FT1 exhibits the temperature effect due to the closed moisture condition. However, if the stagnant water is supplied at the top surface, even under the same FTC, much deformation develops especially at the top surface (see FT2). This is caused by liquid water which flows into the generated crack spaces when the ice melts. Thus, more ice will form in the next FTC and result in a more subsequent expansion. As the number of FTC continuously increases, the expansive damage near

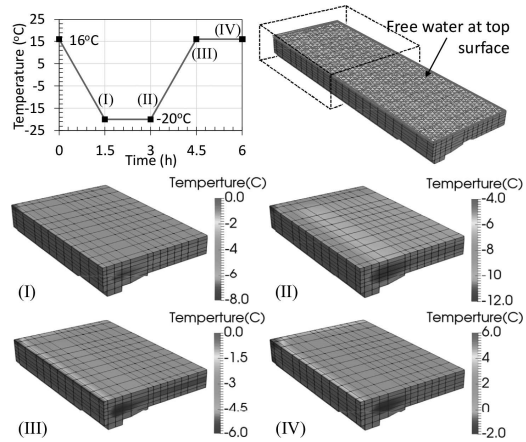

Figure 5. Temperature profile during one FTC.

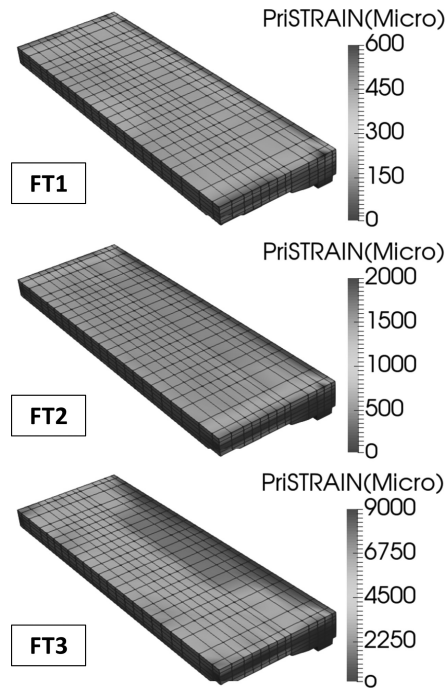

Figure 6. Expansion under different FTC conditions.

the central top surface becomes more dominant (see FT3). This is because the central top part has a lower confinement in the vertical direction (see Fig. 4), and greater horizontal cracks can be generated and the damage accumulation during FTC gets faster.

3.3 *Deformation under ASR*

The ASR expansion with different initial NaOH concentration in pore solution is shown in Fig. 7.

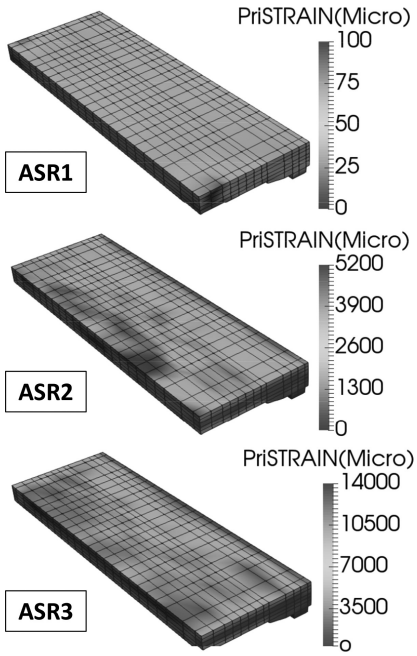

Figure 7. Expansion under different ASR conditions.

Here, 180 days of exposure under 40°C and humid environment is chosen to ensure the completed reaction and consumption of alkali. Therefore, the total created ASR gel volume should be proportional to the NaOH concentration, that is, 1:2:4 among ASR1, ASR2 and ASR3. However, due to the confinement by reinforcing bars, more created semi-liquid ASR gel can flow into capillary pores and entrained air bubbles. And just the rest part may contribute to the apparent expansion and damages. Since the majority of created ASR gel in ASR1 has been consumed by capillary pores and air bubbles for example, the less apparent expansion develops. If we assume the same consumed volume of ASR gel among ASR1-3, the effective gel volume which is associated with substantial expansion should be 0:1:3, which is similar with the magnitude in Fig. 7.

The ASR expansion profile is mainly controlled by the rebar arrangement in this analysis, giving the uniform temperature field and sufficient moisture supply. As a result, the top surface of the slab has much larger expansion than the bottom side due to less horizontal reinforcement. Similarly, the expansion of the slab's central part is bigger than the edges because of the absence of vertical reinforcing bars.

3.4 *Deformation under coupled ASR and FTC*

The sequentially coupled FTC and ASR is analyzed in this section. Both the medium levels of deterioration are selected (FT2 and ASR2) and applying the same environmental and boundary conditions as the single effect. The final deformations of two coupling sequences are shown in Fig. 8.

For the case of FT2-ASR2, the strain profile is closer to the single FT2 as shown in Fig. 6, but the final expansion is much bigger than the sum of two single effects. This is explained such that once a certain cracking system is created by FTC, the following semi-liquid ASR gel will flow into those crack spaces and expand subsequently.

Besides, the gel pressure in the damaged zone is always smaller than that in the undamaged zone. Then, the pressure gradient will also drive the ASR gel to the weak zone and accumulate there. Therefore, the final deformation profile basically follows single FTC case. Finally, due to the reduced tensile capacity after FTC, less ASR gel can be self-consumed by capillary pores and entrained air. Thus, the bigger proportion of created gel will contribute to the expansion.

When the ASR exposure comes first, the final coupled deformation profile is closer to single ASR case in Fig. 7, because the ASR-damaged zone is also more vulnerable during FTC. In addition, the entrained air bubbles may fully lose their function in frost resistance after filled by ASR, thus the additional expansion caused by FTC is also much bigger than single FTC case.

In sum, for this simulation case (w/c = 0.65, Air = 1.5%), the coupled cracking pattern is basically and primarily determined by the first ambient durability impact, and much higher final damage develops than the simple summation of two single effects, regardless of the coupling sequence. This is a strong coupling.

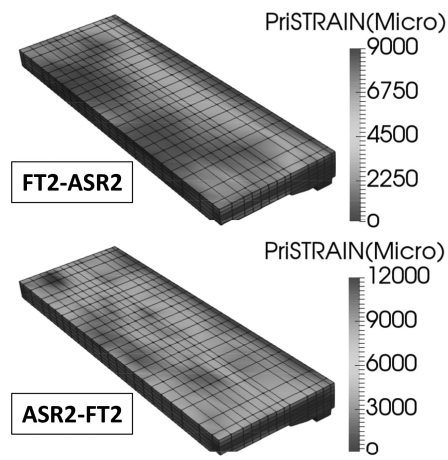

Figure 8. Final deformation after coupled FTC and ASR.

4 FATIGUE LIFE UNDER MOVING LOAD

4.1 *Fatigue behavior with/without condensed water*

The progressive deflection and deformation of the undamaged RC slab are shown first as the control group. It has been proved both experimentally (Matsui, 1987) and numerically (Maekawa and Fujiyama, 2013) that the moisture states under high cycle repetition of moving loads accompanying the principal stress rotation will greatly affect the fatigue life of RC slabs.

As shown in Fig. 9, if the top surface of the slab has stagnant condensed water (Fati2), the fatigue life is dramatically reduced in comparison with the dry case (Fati1). If the whole slab would be submerged in liquid water during fatigue loading (Fati3), the life will be much more reduced. It is mainly attributed to the rapid crack opening/closing which may cause pore pressure with high amplitude owing to the viscosity of water. Then, the great expansive pore pressure will act on the micro-pore structures and cause disintegration in cement particles. In fact, capillary pores develop densely nearby the interface between aggregates and cement binders.

4.2 *Fatigue behavior after FTC*

Following the FTC exposure tests as stated in Section 3.2, the fatigue behaviors of the RC slab with different levels of frost damage are simulated with comparison as shown in Fig. 10 and Fig. 11. Two moisture conditions (Fati1 and Fati2) are selected. It can be seen that the greater frost damage reduces the fatigue life more, and the rate of reduction in the wet fatigue test is much higher than that of the dry test.

A little bit difference can be found between FT1 and FT2 as shown in Fig. 10. Because, for both cases, the frost damage levels in the loading area

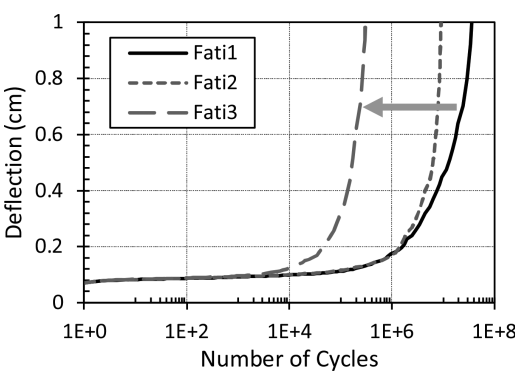

Figure 9. Deflection of undamaged slab with different moisture conditions during loading.

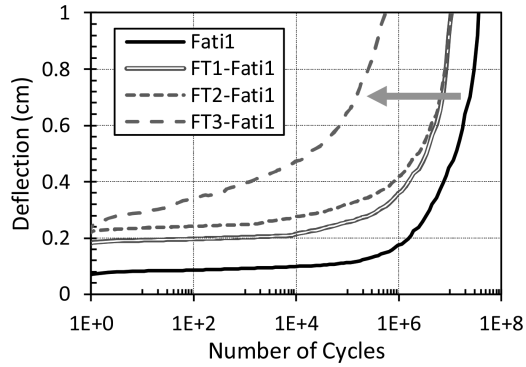

Figure 10. Deflection of FTC damaged slab in dry fatigue test.

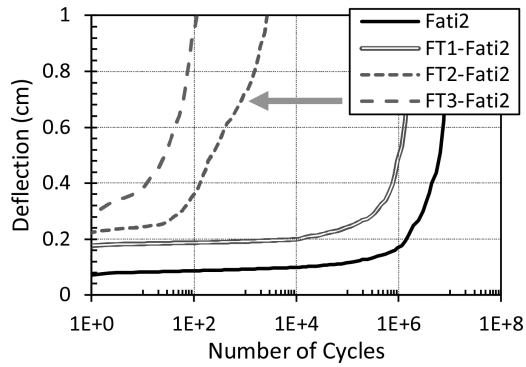

Figure 11. Deflection of FTC damaged slab in wet fatigue test.

are relatively small and similar (see Fig. 6), but as the central part gets more seriously damaged by FTC (FT3). Then, the fatigue life is thought to be reduced significantly.

When the condensed free water is supplied on the slabs as stagnant during the moving load tests (Fig. 11), more pre-stored cracks will lead to the greater disintegration in the micro-pore structure. Thus, the reduction in fatigue life is much more significant than the dry loading test.

4.3 *Fatigue behavior after ASR*

Although the ASR damaged slabs hold even greater expansion and damage (Fig. 7) than the FTC ones, the trend of varying fatigue life is opposite (see Fig. 12 and Fig. 13). Different from the FTC damage slab, the created ASR gel remains in cracks, which will hinder the condensed water in motion and bear a certain level of normal and shear forces. Then in the dry fatigue test (Fig. 12), all the ASR damaged slabs show a greater ductility

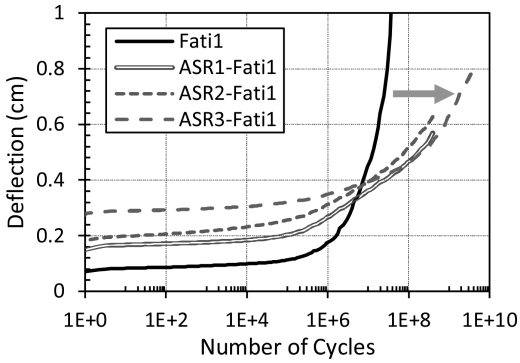

Figure 12. Deflection of ASR damaged slab in dry fatigue test.

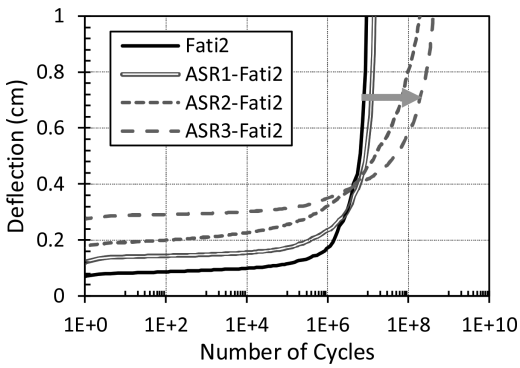

Figure 13. Deflection of ASR damaged slab in wet fatigue test.

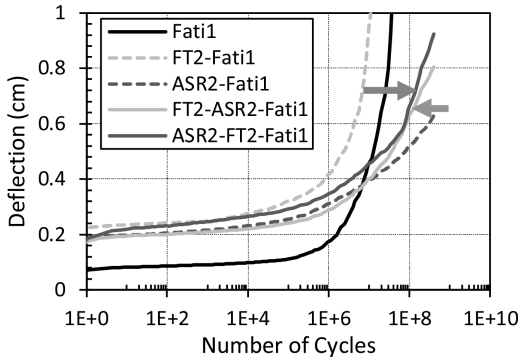

Figure 14. Deflection of single and coupled damaged slab in dry fatigue test.

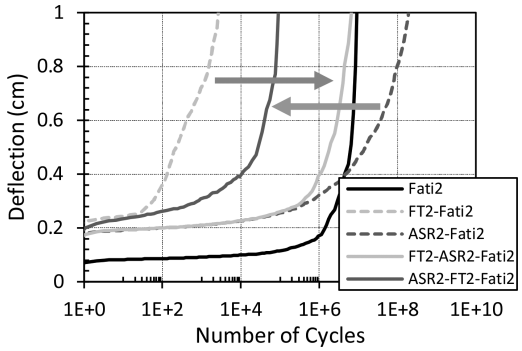

Figure 15. Deflection of single and coupled damaged slab in wet fatigue test.

and longer fatigue life, which is consistent with the past experiments (Maeshima *et al.*, 2016). However, the strengthening effect is not sensitive to the ASR damage level.

Under the wet condition, as shown in Fig. 13, the fatigue life will still increase but shorter than the dry fatigue tests, due to the water-driven disintegration in newly created cracks. The existing ASR gel in cracks can retard the condensed water motion, but depends on the gel amount. For example, since the majority of created gel in the case of ASR1 is self-consumed by capillary pores and entrained air, only a small proportion remains in the crack system. Thus, condense water motion through cracks cannot be reduced efficiently. When more silica gel exists in cracks, water motion can be retarded more. Thus, the longer fatigue life is realized.

4.4 *Fatigue behavior after coupled ASR and FTC*

Figure 14 and Figure 15 show the deflection in progress under high repetition of fatigue loads after coupled deterioration of ASR and FTC, and those in both dry and wet moisture conditions. All the cases show that the ASR gel can strengthen the cracked RC slabs and increase in its fatigue life (yellow lines in Fig. 14 and Fig. 15).

On the contrary, preceding FTC action will always create new crack opening which had never been filled yet by ASR gel. Thus, the fatigue life of the damaged decks will be shortened as blue lines in Fig. 14 and Fig. 15. Both the aforementioned strengthening and damaging effects of opposite impact will become much more significant when loading under the wet moisture condition is produced, because the disintegration effect is rather sensitive to the cracking level.

5 CONCLUSIONS

The strong coupling model of ASR and FTC has been developed considering both the micro-chemo-physical and meso-poro-mechanical coupling, which can take the solid pressures, liquid pressure

and liquid transportation into consideration. The expansion and damage under single and coupled FTC and ASR are analyzed for the RC slab, as well as their remaining fatigue lives under the moving load. The detailed conclusions are as follows:

The deformation profiles show that the FTC expansion is controlled by temperature field at the beginning, but as the FTC continuously goes on, the arrangement of reinforcing bar become more important. Besides, the accessibility of additional water is important for the frost damage accumulation during numbers of FTC. The ASR expansion profile is mainly determined by the rebar arrangement.

The coupled deformation is much bigger than the sum of two single process due to the micro-physical interactions between ASR and FTC. The final crack pattern is basically determined by the first deterioration stage.

As FTC damage becomes bigger, the remaining fatigue life becomes shorter. On the contrary, the ASR damage can increase the fatigue life due to the gel filling in crack system. In the coupling problem, still ASR always show a strengthening effect while FTC has a damaging effect.

Compared to dry fatigue test, the wet fatigue behavior is more sensitive to the crack opening condition and gel filling ratio in cracks, thus both the strengthening and damaging effects will be much bigger under the wet loading condition.

The effects of ASR and condensed water on the fatigue behavior of RC slab have been already verified experimentally, further verification will be conducted including the FTC effect.

ACKNOWLEDGEMENTS

This study was financially supported by Council for Science, Technology and Innovation, "Cross-ministerial Strategic Innovation Promotion Program (SIP), Infrastructure Maintenance, Renovation, and Management" granted by Japan Science and Technology Agency.

REFERENCES

Biot, M.A. (1963) Theory of stability and consolidation of a porous medium under initial stress. *Journal of Mathematics and Mechanics,* 12, 521–541.

Gebreyouhannes, E. & Maekawa, K. (2016) Nonlinear gel migration in cracked concrete and broken symmetry of corrosion profiles. *Journal of Advanced Concrete Technology,* 14, 271–286.

Gong, F., Takahashi, Y. & Maekawa, K. (2017) Strong coupling of freeze-thaw cycles and alkali silica reaction-Multi-scale poro-mechanical approach to concrete damages. *Journal of Advanced Concrete Technology,* 15, 346–367.

Jensen, A.D., Chatterji, S., Christensen, P. & Thaulow, N. (1984) Studies of alkali-silica reaction—part II effect of air-entrainment on expansion. *Cement and Concrete Research,* 14, 311–314.

Kawamura, M., Takeuchi, K. & Sugiyama, A. (1994) Mechanisms of expansion of mortars containing reactive aggregate in NaCl solution. *Cement and concrete research,* 24, 621–632.

Kishi, T. & Maekawa, K. (1995) Multi-component model for hydration heat of portland cement. *Journal of JSCE,* No.526/V-29, 97–109.

Maekawa, K. & Fujiyama, C. (2013) Rate-dependent model of structural concrete incorporating kinematics of ambient water subjected to high-cycle loads. *Engineering Computations,* 30, 825–841.

Maekawa, K., Ishida, T., Chijiwa, N. & Fujiyama, C. (2013) Multiscale coupled-hygromechanistic approach to the life-cycle performance assessment of structural concrete. *Journal of Materials in Civil Engineering,* 27, A4014003.

Maekawa, K., Ishida, T. & Kishi, T. (2003a) Multi-scale modeling of concrete performance. *Journal of Advanced Concrete Technology,* 1, 91–126.

Maekawa, K., Ishida, T. & Kishi, T. (2008) *Multi-scale modeling of structural concrete*, CRC Press.

Maekawa, K., Okamura, H. & Pimanmas, A. (2003b) *Non-linear mechanics of reinforced concrete*, CRC Press.

Maekawa, K., Soltani, M., Ishida, T. & Itoyama, Y. (2006) Time-dependent space-averaged constitutive modeling of cracked reinforced concrete subjected to shrinkage and sustained loads. *Journal of Advanced Concrete Technology,* 4, 193–207.

Maeshima, T., Koda, Y., Iwaki, I., Naito, H., Kishira, R., Suzuki, Y., Ohta, K. & Suzuki, M. (2016) Influence of Alkali Silica Reaction on Fatigue Resistance of RC Bridge Deck. *Journal of Japan Society of Civil Engineers, Ser. E2 (Materials and Concrete Structures),* 72, 126–145.

Maraghechi, H., Fischer, G. & Rajabipour, F. (2012) The role of residual cracks on alkali silica reactivity of recycled glass aggregates. *Cement and Concrete Composites,* 34, 41–47.

Matsui, S. (1987) Fatigue strength of RC-slabs of highway bridge by wheel running machine and influence of water on fatigue. *Proceedings of JCI,* 9, 627–632.

Muranaka, M. & Tanaka, Y. (2013) Development of Physical and Chemical Model for Concrete Expansion due to Asr Based on Reaction Mechanism. *Journal of Japan Society of Civil Engineers, Ser. E2 (Materials and Concrete Structures),* 69, 1–15.

Promentilla, M.A.B. & Sugiyama, T. (2010) X-ray microtomography of mortars exposed to freezing-thawing action. *Journal of Advanced Concrete Technology,* 8, 97–111.

Scherer, G.W. & Valenza II, J.J. (2005) Mechanisms of frost damage. *Materials Science of Concrete.* American Ceramic Society.

Takahashi, Y., Ogawa, S., Tanaka, Y. & Maekawa, K. (2016) Scale-dependent ASR expansion of concrete and its prediction coupled with silica gel generation and migration. *Journal of Advanced Concrete Technology,* 14, 444–463.

Wang, K., Jansen, D.C., Shah, S.P. & Karr, A.F. (1997) Permeability study of cracked concrete. *Cement and Concrete Research,* 27, 381–393.

Computational Modelling of Concrete Structures – Meschke, Pichler & Rots (Eds)
© 2018 Taylor & Francis Group, London, ISBN 978-1-138-74117-1

Multiscale modelling of ASR induced degradation in concrete

T. Iskhakov, J.J. Timothy & G. Meschke
Institute for Structural Mechanics, Ruhr University Bochum, Germany

ABSTRACT: In this contribution, we present a multiscale approach to model Alkali-Silica Reaction (ASR) induced degradation in concrete. The model is characterized by a synthesis of a multi-scale semi-analytical model describing the mechanics of microcracking and a finite element model for describing the physics of diffusion and kinetics involved in the Alkali-Silica Reaction. The mechanics of ASR induced deterioration of a Representative Elementary Volume (REV) of concrete containing reactive aggregates is modelled using continuum microporomechanics. At the microscale, ASR gel-pressure induced microcrack growth in the reactive aggregates and in the cement paste is modelled using the framework of linear elastic fracture mechanics. Mean field homogenization across multiple scales is used to obtain the overall expansion and degradation of the material. Experimental data for concrete degradation as a function of the macroscopic expansion is found to lie within the theoretical upper and lower bounds that characterize the distribution of the gel in the aggregate or the cement paste. The diffusion processes and the kinetics involved in the alkali-silica reaction is described by a second-order reaction-diffusion equation solved by means of the finite element method. The chemical reaction as well as alkali, moisture and gel transport are taken into account to obtain a gel mass distribution in the concrete microstructure. The evolution of the gel volume is coupled to the aforementioned semi-analytical model for microcracking induced deterioration and expansion. Comparisons of model predictions with experimental data suggest, that the connectivity of the initial pore structure and microcracks in the aggregate has a significant influence on the overall expansion of concrete.

1 INTRODUCTION

Concrete structures, such as pavements, dams and bridges, which contain reactive aggregates and sufficient moisture in the pore space, are susceptible to damage caused by the Alkali-Silica Reaction (ASR) (Stark & Wicht 2000). Degradation of concrete due to Alkali-Silica Reaction (ASR) occurs when alkali and hydroxyl ions in the pore fluid break the silanol and siloxane bonds in the reactive aggregates, forming a hydrophilic alkali-silica gel. This gel fills the existing voids and microcracks both in the aggregates and cement paste. In the presence of moisture, the gel swells and induces an internal pressure that generates stresses leading to the propagation of the microcracks. This microfracturing process causes degradation as well as the expansion of the concrete at the macroscale (Voland 2016). Such deterioration process involves the interaction of multiple physical phenomena across multiple scales. In order to characterize this complex process, a multiscale approach for ASR induced damage prediction is proposed to substitute existing phenomenological approaches (e.g. Ulm Coussy, Li, & Larive 2000, Bangert, Kuhl, & Meschke 2004). In this work first we review the micromechanics model for ASR degradation and expansion recently developed in (Iskhakov, Timothy, & Meschke 2018), focusing on the role of internal pressure generated by ASR gel expansion in pre-existing microcracks in the aggregates and the cement paste (see Figure 2). Furthermore, we extend the model by accounting

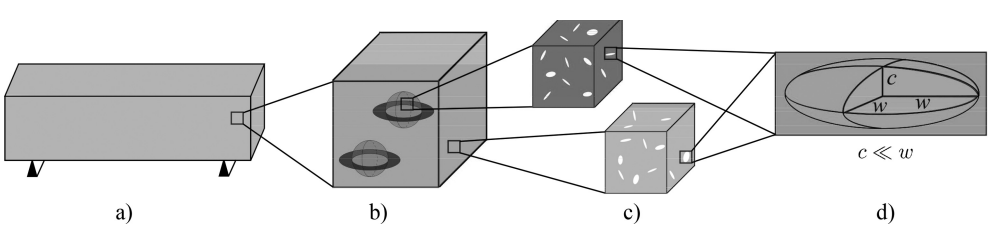

Figure 1. Multiscale characterization of concrete: a) structural level; b) concrete REV (Representative Elementary Volume) consisting of the cement matrix with embedded spherical aggregates; c) cement paste and aggregate REV containing distributed penny-shaped microcracks; d) penny-shaped microcrack.

for the kinetics of Alkali-Silica Reaction by means of finite element simulation. The paper structure is as follows: In Section 2 we present a multiscale micro-poro-mechanical model to characterize the overall expansion of concrete due to deterioration induced by microcracking in reactive aggregates and the cement paste. In Section 3 we develop a reaction-diffusion finite element model based on second-order reaction kinetics for the formation and diffusion of the expansive gel in and around the reactive aggregates. Finally in Section 4, we combine both sub-models to obtain a model for the time-dependent expansion and deterioration of concrete due to ASR. In Section 5 we summarize the findings reported in the paper and provide conclusions.

2 MICROCRACKING OF CONCRETE DUE TO INTERNAL PRESSURE

We consider REVs (Representative Elementary Volume) at two scales of observation (see Figure 1): At the concrete level, the REV is characterized by distributed spherical aggregate particles embedded in the cement paste matrix, and at the level of individual aggregates and the cement paste, the REV is characterized by microcracks embedded in the intact homogeneous aggregate and the cement paste. The microcracks are assumed to be penny-shaped with crack radius w and crack width c $(c \ll w)$ that may evolve due to an internal pressure induced by swelling ASR gel. We assume that these penny-shaped microcracks represent the void space in the aggregate and the cement paste. The microcrack volume fraction can be calculated as

$$V_c^i = \frac{4}{3}\pi n^i (w^i)^2 c^i, \tag{1}$$

where i denotes the component (aggregate: $i = a$, cement paste: $i = c$), n^i is the density of the microcracks, which is assumed to be constant. The stiffness tensors of the aggregate and the cement paste containing distributed microcracks can be calculated from

$$\mathbb{C}^i = \mathbb{C}^i_{solid} - V_c^i \mathbb{C}^i_{solid} : \mathbb{A}^i, \tag{2}$$

where $\mathbb{C}^i_{solid}$ is the stiffness tensor of the solid skeleton (containing no voids or microcracks) and $\mathbb{A}^i$ is the averaged strain concentration tensor.

The internal pressure leading to stable microcrack propagation is computed from the Griffith energy balance (Dormieux, Kondo, & Ulm 2006) :

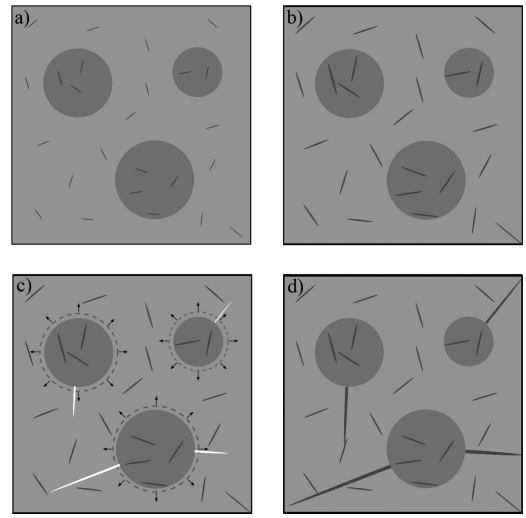

Figure 2. Mechanism of ASR induced microcracking in concrete: a) The void space of cement paste and aggregates is represented by microcracks, which are partially filled with ASR gel; b) swelling of ASR gel induces internal pressure causing microcrack growth; c) expansion of aggregates leads to formation of new microcracks located in their vicinity in the cement paste; d) the expanding ASR gel fills newly formed microcracks and leads to their propagation.

$$p^i = \sqrt{-\frac{4\pi}{3}\frac{G_f^i}{w^i}\left[\mathbb{D}^i : \frac{\partial \mathbb{C}^i}{\partial \epsilon^i} : \mathbb{D}^i\right]}^{-1/2}, \tag{3}$$

where G_f^i is the fracture energy, $\mathbb{D}^i$ is the compliance tensor, and ϵ^i is the crack density parameter. In order to obtain the volumetric expansion of the aggregate and the cement paste caused by the growth of pre-existing microcracks, the calculated pressures are inserted into the microporomechanics state equation (Dormieux, Kondo, & Ulm 2006).

$$\sigma^i = \mathbb{C}^i : \varepsilon^i - \mathbf{B}^i p^i. \tag{4}$$

Here, $\mathbf{B}^i$ is the Biot tensor. Considering the absence of external loading, these expansions can be viewed as *Eigenstrains* of the aggregate particles and the cement paste, which can be upscaled using Levin's theorem to obtain the overall stress-free expansion of the concrete at the macroscale. The stiffness of concrete at the structural level can be determined using the framework of mean field homogenization (Dormieux, Kondo, & Ulm 2006, Timothy & Meschke 2016a), assuming spherical aggregates with stiffness $\mathbb{C}^a$ embedded in the cement paste matrix with stiffness $\mathbb{C}^c$.

2.1 *Damage induced in the cement paste induced by aggregate expansion*

In addition to concrete deterioration due to growth of pre-existing microcracks, the aggregate expansion induces additional tensile stresses in the cement paste that could further lead to formation of new cracks in the cement paste. The tensile stresses around the aggregates can be computed using the exterior point Eshelby tensor. For the case of expanding spherical aggregates, without considering applied external loads or constraints, the stresses in the cement paste matrix around the aggregates are uniform. However, we now consider an applied load in order to determine the initiation point and shape of the crack which could form around the expanding aggregate. Imagine one expanding spherical particle embedded in the cement paste matrix. On the boundaries of the matrix, tensile (Figure 3a) and compressive (Figure 3d) loads are applied. The location of maximum principal stresses, i.e., the presumable location of crack initiation, is shown in Figures 3b and 3e. Comparison of the micromechanical predictions with explicit numerical simulations (Figure 3c and 3f), using a variational interface model (Khisamitov & Meschke 2018), are in good agreement. Moreover, the results obtained numerically suggest an annular crack morphology forming around the expanding aggregates. Without any external loads or constraints, the annular cracks can form at any point around the aggregate, since the stress state is theoretically uniform as was mentioned before. For simplicity, we assume the annular cracks to be aligned along the three orthogonal directions x, y, z. Here it should be noted, that crack formation mechanisms around expanding and non-expanding aggregates are different. As an example, the location of crack initiation and crack path around non-expanding aggregate are shown in Figure 4.

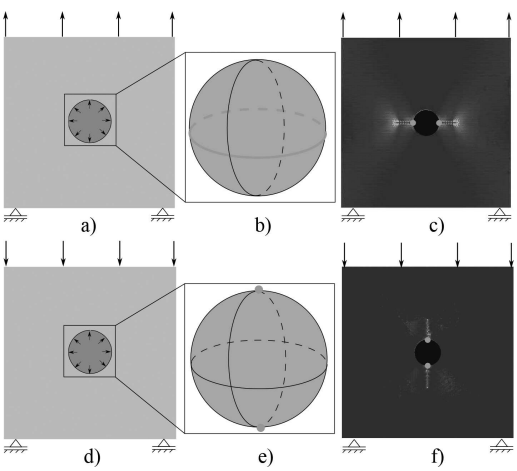

Figure 3. Crack initiation and propagation around an **expanding** aggregate subjected to uniaxial tension (a-c) and uniaxial compression (d-f). Figures a) and d) show the geometry and loading conditions, b) and e) show the micromechanical model predictions of the position of crack initiation while c) and f) show the crack path obtained from a numerical crack analysis using an interface fracture model. Green points and lines denote the location of crack initiation.

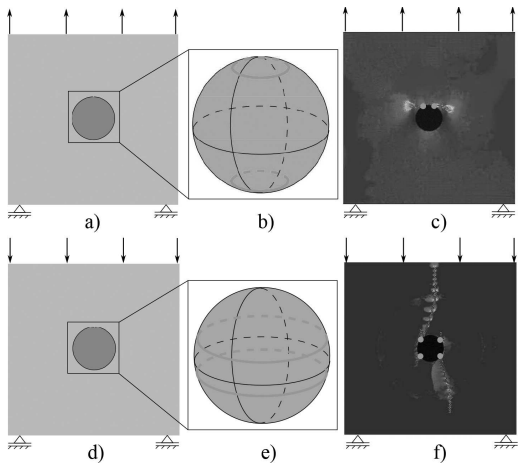

Figure 4. Crack initiation and propagation around a **non-expanding** aggregate subjected to uniaxial tension (a-c) and uniaxial compression (d-f). Figures a) and d) show the geometry and loading conditions, b) and e) show the micromechanical model predictions of the position of crack initiation while c) and f) show the crack path obtained from a numerical crack analysis using an interface fracture model. Green points and lines denote the location of crack initiation.

2.2 *Formation and propagation of annular cracks around the aggregates*

The aforementioned concept of annular cracking is employed in the proposed micromechanics model as follows: First, the tensile stresses in the cement paste caused by aggregate expansion (Figure 5a) are calculated using the Exterior Point Eshelby tensor. These tensile stresses lead to the formation of annular cracks of size s (Figure 5b), which can be found by calculating the stress intensity factor for an annular crack propagating from the aggregate surface into the cement paste matrix (Fett & Rizzi 2007) and comparing with the fracture toughness of the material K_{Ic}

$$K_I(s) = K_{Ic}. \tag{5}$$

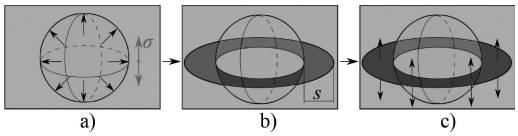

Figure 5. Formation and propagation of annular crack: a) Tensile stresses in the cement paste around the aggregate due to its expansion; b) initiation of annular crack of size *s*; c) ASR gel fills and pressurizes the annular crack leading to its growth.

K_{Ic} is the critical stress intensity factor for the cement paste. Thereafter, the ASR gel is assumed to i) fill the formed annular crack, ii) swell and iii) generate an internal pressure which drives annular cracking (Figure 5c). Finally, given the size of the annular crack, the additional expansion and additional degradation (Sevostianov 2003) of cement paste matrix are computed.

2.3 *Comparison with experimental data*

The model predictions for concrete behavior at the macroscopic scale are compared with experimental findings (Voland 2016, Lindgård 2013, Swamy & Al-Asali 1988, Sargolzahi, Kodjo, Rivard, & Rhazi 2010). Figure 6 presents the relation between ASRaffected concrete expansion and degradation. Experimental data from various authors are compared with model predictions for a realistic range of material parameters and microstructural geometrical properties (Iskhakov, Timothy, & Meschke 2018), which are included in Figure 6 as upper and lower bounds (solid and dashed lines). The upper bound corresponds to microcracking that originates only in the aggregates followed by annular microcracking in the cement paste described by the kink in Figure 6, while the lower bound corresponds to microcracking only in the cement paste marix (representing microcracking as a consequence of gel diffusion into the immediate neighbourhood of the reactive aggregates). A parametric study and a complete comparative analysis of experimental and simulation data can be found in (Iskhakov, Timothy, & Meschke 2018).

3 KINETICS OF ASR

In this section we discuss the modeling of the kinetics of the Alkali-Silica Reaction. We describe the reaction process in three steps. The first step consists of a hydrolysis of reactive silica by hydroxyl ions described by the following reaction: Si-O-Si + ROH$\rightarrow^{k_1}$ Si-O-R + H-O-Si. In the second step, silicic acid reacts with hydroxyl ions

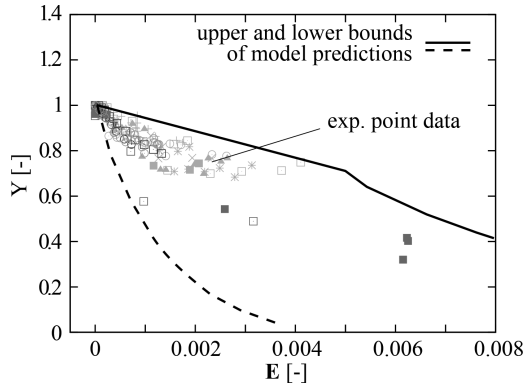

Figure 6. Macroscopic concrete expansion **E** vs. the normalized Young's modulus Y: Comparison of experimental data with bounds obtained from the micromechanics ASR model.

resulting in: H-O-Si + ROH$\rightarrow^{k_2}$ Si-O-R + H_2O The third step represents the process of gel swelling due to the moisture present in the concrete pores: Si-O-R + $nH_2O\rightarrow^{k_3}$ $Si\text{-}O^- + (H_2O)_n + Na^+$. Denoting the concentrations of reactants and reaction products by capital letters (A – siloxane, B – hydroxyl ions, C – intermediate reaction product, D – silicic acid, E – water, F – expanded ASR gel) the aforementioned chemical process can be described as:

$$\begin{aligned}
\frac{dA}{dt} &= -k_1 A(t) B(t), \\
\frac{dB}{dt} &= -k_1 A(t) B(t) - k_2 D(t) B(t), \\
\frac{dC}{dt} &= k_1 A(t) B(t) + k_2 D(t) B(t) - k_3 C(t) E(t), \\
\frac{dD}{dt} &= k_1 A(t) B(t) - k_2 D(t) B(t), \\
\frac{dE}{dt} &= k_2 D(t) B(t) - k_3 C(t) E(t), \\
\frac{dF}{dt} &= k_3 C(t) E(t),
\end{aligned} \tag{6}$$

where t is the time and k_1, k_2, k_3 are the rates of the aforementioned three reactions. According to (Saouma, Martin, Hariri-Ardebili, & Katayama 2015) the reaction rate values normalized with respect to $k_1 = 1$ can be taken as k_1: k_2: k_3 = 1:30:60.

Solving the system of equations (6), we obtain the evolution of the Alkali-Silica Reaction in time, which is depicted in Figure 7. Here the three components (siloxane, hydroxyl ions and water) drive the reaction. Their initial values will be discussed in Section 3.1. As can be seen in Figure 7, the concentrations of each reactant and reaction product approach asymptotically to finite values associated

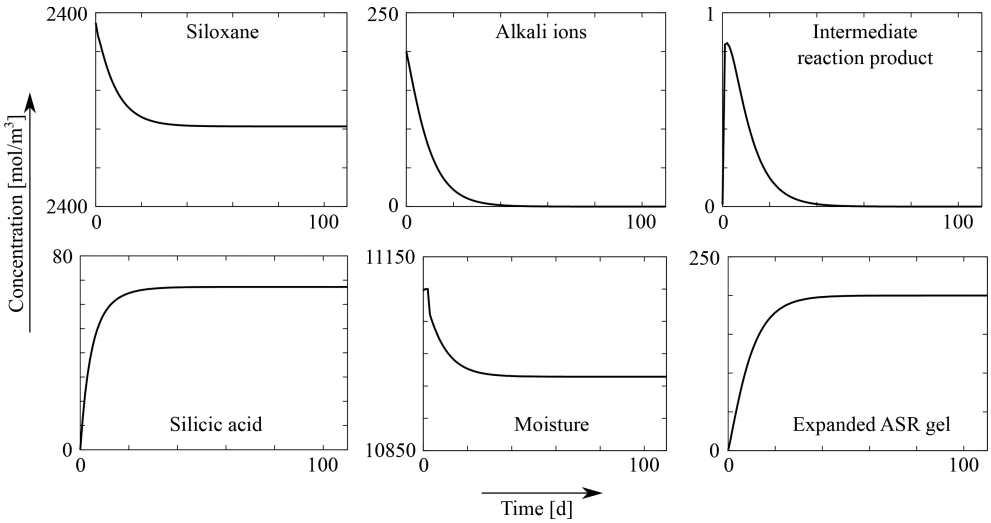

Figure 7. Evolution of Alkali-Silica Reaction in time. Figures present the concentrations (over time) of reactants and intermediate products involved in ASR as well as the concentration of expanded ASR gel which is assumed to cause microcracking.

with chemical equilibrium. Their concentration evolutions stop simultaneously indicating the termination of the Alkali-Silica Reaction. It can be observed that the reaction stops because there are no more alkali ions available for production of ASR gel.

3.1 *Reaction-diffusion equations of ASR*

In order to describe the spatial diffusion of the products and the reactants in a concrete REV, we add a diffusion term into equations (6)

$$\begin{aligned}
\frac{dA}{dt} &= -k_1 A(t) B(t) + D_A^{eff} \Delta A, \\
\frac{dB}{dt} &= -k_1 A(t) B(t) - k_2 D(t) B(t) + D_B^{eff} \Delta B, \\
\frac{dC}{dt} &= k_1 A(t) B(t) + k_2 D(t) B(t) - k_3 C(t) E(t) + D_C^{eff} \Delta C, \\
\frac{dD}{dt} &= k_1 A(t) B(t) - k_2 D(t) B(t) + D_D^{eff} \Delta D, \\
\frac{dE}{dt} &= k_2 D(t) B(t) - k_3 C(t) E(t) + D_E^{eff} \Delta E, \\
\frac{dF}{dt} &= k_3 C(t) E(t) + D_F^{eff} \Delta F,
\end{aligned} \tag{7}$$

where D_j^{eff} is the effective diffusion coefficient of reaction component $j = A;B;C;D;E;F$ in concrete and Δ is the Laplace operator. The effective diffusivity is given by (Timothy & Meschke 2016b):

$$D_j^{eff} = D_j \phi / \tau, \tag{8}$$

where D_j is the intrinsic diffusivity of the j-th component, ϕ is the porosity and τ is the tortuosity of material in which the diffusion takes place. For the aggregate we assume $\phi^a = 1[\%], \tau^a = 170$; and for the cement matrix $\phi^c = 20[\%], \tau^c = 170$. The diffusivities of reactants and reaction products are given in Table 1.

To characterize the ASR development at the aggregate level, we solve the set of Equations (7) discretized in 3D on the mesoscale of concrete (Figure 8). Here, the aggregate is assumed to be of spherical shape and covered with a layer of cement paste. The whole composite structure also is idealized by a spherical shape. The diameter of the aggregate is assumed to be 10 [*mm*]. The cement matrix thickness is taken so that the aggregate volume fraction is equal to 50 [%].

We assume that siloxane is initially available only in the aggregate and the alkali ions and moisture available only in the cement matrix. The initial concentration of siloxane can be found as

$$c_{SiO_2} = m_{SiO_2} \cdot \rho a / M_{SiO_2} = 2637[mol/m^3], \tag{9}$$

where $m_{SiO2} = 9.4$ [% *by mass*] is the soluble silica content of aggregate (Multon, Cyr, Sellier, Leklou, & Petit 2008), $\rho_a = 1700$ [kg/m^3] is the aggregate density and M_{SiO2} is the molar mass of silica. The initial concentration of silica ions in the cement matrix can be found in the following manner:

$$c_{Na+} = 2 \cdot m_{Na_2O} / M_{Na_2O} = 200[mol/m^3], \tag{10}$$

Table 1. Diffusion coefficients of reactants and reaction products (Values are given in [$m^2 = s$]).

D_{Si_2O}	$7.42 \cdot 10^{-12}$
D_{Na+}	$1.334 \cdot 10^{-9}$
D_{H-O-Si}	$2.2 \cdot 10^{-9}$
D_{H_2O}	$2.3 \cdot 10^{-9}$

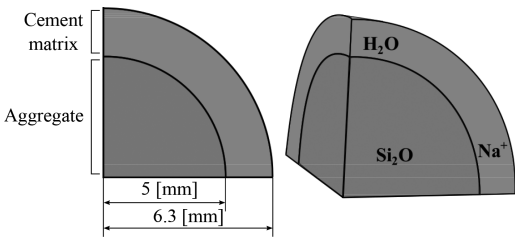

Figure 8. Left: Mesoscale model used for the description of the ASR kinetics process. Right: The spherical aggregate is assumed to contain silica, the cement paste layer is assumed to contain moisture and alkali ions.

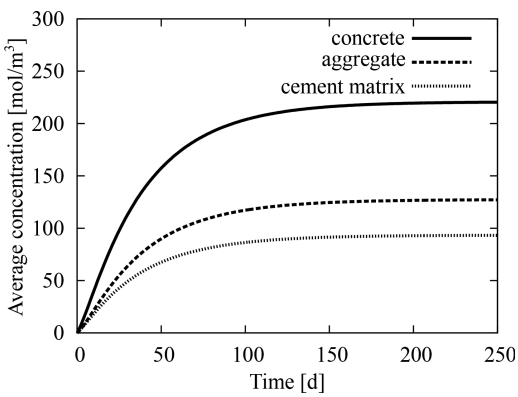

Figure 9. Evolution of the average concentration of swelling ASR gel in spherical aggregates and the surrounding cement paste (see Figure 8). The sum gives the concentration in the concrete.

where $m_{Na_2O} = 6.2\left[kg/m^3\right]$ is the equivalent alkali content in cement matrix and M_{Na_2O} is the molar mass of equivalent alkali. For the calculation of the initial moisture concentration, we assume that the pore-space of the cement matrix is fully saturated:

$$c_{H_2O} = \phi_c \cdot \rho_{H_2O} / M_{H_2O} = 11099\left[mol/m^3\right], \qquad (11)$$

where $\phi_c = 20$ [%] is the porosity of cement matrix, ρ_{H_2O} and M_{H_2O} is the density and molar mass of water, respectively.

By solving the system (7), the evolution of Alkali–Silica Reaction in concrete in space and time is obtained. Figure 9 presents the average concentration of expanded ASR gel in aggregate, cement matrix and the concrete composite (aggregate and the cement matrix). In the following section, we use these time dependent evolution of the gel concentrations to calculate the concrete expansion at the structural level.

4 MACROSCOPIC ASR INDUCED EXPANSION

In this section, we combine the models presented in Sections 2 and 3 in order to determine the time dependent macroscopic expansion of concrete due to ASR. Given the spatio-temporal evolution of the expanded ASR gel $V^i_{gel}(i,t)$ and the initial microcrack volume fraction $V^i_c(i,t)$ the microcracks do not grow if the volume of gel $V^i_{gel} < V^i_c$. For $V^i_{gel} > V^i_c$ the updated microcrack size can be obtained from:

$$V^i_{gel} = V^i_c = \frac{4}{3}\pi n^i \left(w^i\right)^2 c^i. \qquad (12)$$

The above expression neglects the influence of the compressibility of the gel. A simple analysis of a penny shaped crack under internal pressure due to an expanding ASR gel gives the following expression for the update of the microcrack size as:

$$V^i_{gel} = V^i_c\left(a^i\right)\left(1 + \frac{K_{Ic}}{2K_g}\sqrt{\pi / a^i}\right). \qquad (13)$$

K_g is the bulk modulus of the expanded ASR gel, a_i is the equilibrium microcrack size and K_{Ic} is the stress intensity factor. According to (13), the term $\left(1+\frac{K_{Ic}}{2K_g}\sqrt{\pi/a^i}\right)$ is significant only if the initial microcrack size is in the order of a few nanometers assuming the bulk modulus of the ASR gel is $34GPa$ (Moon, Speziale, Meral, Kalkan, Clark, & Monteiro 2013). After updating the microcrack radius, the macroscopic concrete deterioration and expansion is obtained according to the equations given in Section 2.

4.1 *Comparison with experimental data*

Using the average concentrations of expanded ASR gel from Section 3 and the molar volume of ASR gel M_{gel} = 21.5 [cm^3/mol] (Perruchot & Massard 2000), the produced volume of expanded ASR gel is determined. Further, it is inserted into equation (12) in order to describe the evolution of microcrack-

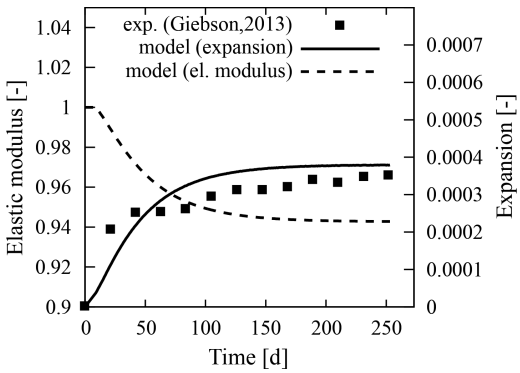

Figure 10. Model predictions of ASR induced expansion and deterioration of concrete at the structural level. The expansion curve is compared with experimental data.

ing in the cement matrix and the aggregate and the consequent expansion of concrete at the structural level. But results obtained with the aforementioned material and model parameters reveal that there is no microcrack propagation because the produced volume of expanded ASR gel (≈ 2 [mm^3]) does not exceed the initial microcrack volume fraction. This is a consequence of the assumption, that the microcracks initially present in the aggregates are fully connected. Assuming, that only part of all microcracks can be filled with the gel (here we set it equal to 5[%]), we obtain the model predictions which are in a good agreement with the experimental data (Giebson 2013) presented in Figure 10. The figure shows the macroscopic ASR induced concrete expansion and deterioration over time. As can be seen during the first ten days, no microcracking occurs and the elastic modulus stays unchanged. This is the "filling period" within which the ASR gel fills the microcracks and induces the pressure on crack faces, which is lower than the critical value. However, after the critical pressure is reached, the microcracks start growing and we observe the degradation of concrete stiffness.

5 CONCLUSIONS

In this paper, a multiscale model for ASR induced degradation in concrete based on a micromechanics damage model accounting for microcracking in the aggregates and the cement paste together with a computational diffusion reaction model based on the kinetics of the alkali silica reaction has been presented. Additional deterioration of cement paste due to aggregate expansion was accounted for by adopting the annular crack concept, which has been investigated analytically and numerically. with good mutual agreement. The upscaling of concrete expansion and deterioration over multiple scales was performed using mean field homogenization. The kinetics of the ASR has been analyzed by solving the reaction-diffusion equations at the mesoscale level. It was found, that consideration of the connectivity within the aggregates is a relevant aspect, which shall be investigated and accounted for in the modeling of the swelling gel induced microcracking in the aggregates and the cement paste. Adopting plausible assumptions, the model predictions of concrete expansion and degradation at the structural level correlate well with experimental measurements.

ACKNOWLEDGEMENTS

This work has been partially supported by the German Research Foundation (DFG) in the framework of Subproject 3 of the DFG-Research Group FOR 1498. This support is gratefully acknowledged.

REFERENCES

Bangert, F., D. Kuhl, & G. Meschke (2004). Chemo-hygromechanical modeling and numerical simulation of concrete deterioration caused by alkali-silica reaction. *International Journal for Numerical and Analytical Methods in Geomechanics 28,* 689–714. (invited paper, Special Issue on Computational Modelling of Concrete Structures).

Dormieux, L., D. Kondo, & F. Ulm (2006). *Microporomechanics.* Wiley & Sons.

Fett, T. & G. Rizzi (2007). *Weight Functions and Stress Intensity Factors for Ring Shaped Cracks.* Forschungszentrum Karlsruhe.

Giebson, C. (2013). *Die Alkali-Kieselsäure-Reaktion in Beton für Fahrbahndecken und Flugbetriebsflächen unter Einwirkung alkalihaltiger Enteisungsmittel.* Ph. D. thesis.

Iskhakov, T., J.J. Timothy, & G. Meschke (2018). Expansion and deterioration of concrete due to asr: micromechanical modeling and analysis.

Khisamitov, I. & G. Meschke (2018). Variational approach to interface element modeling of brittle fracture propagation. *Computer Methods in Applied Mechanics and Engineering 328*(1), 452–476. in print.

Lindgård, J. (2013). *Alkali-silica reaction (ASR)–Performance testing.* Ph. D. thesis.

Moon, J., S. Speziale, C. Meral, B. Kalkan, S.M. Clark, & P.J. Monteiro (2013). Determination of the elastic properties of amorphous materials: case study of alkali–silica reaction gel. *Cement and Concrete Research 54,* 55–60.

Multon, S., M. Cyr, A. Sellier, N. Leklou, & L. Petit (2008). Coupled effects of aggregate size and alkali content on asr expansion. *Cement and Concrete Research 38*(3), 350–359.

Perruchot, A. & P. Massard (2000). Experimental evaluation of composition and volume variability of ca-si gels, first products of alkali silica reaction (asr)[c]. In *Proc. of 11th International Conference on Alkali-Aggregate Reaction.*

Saouma, V.E., R.A. Martin, M.A. Hariri-Ardebili, & T. Katayama (2015). A mathematical model for the kinetics of the alkali–silica chemical reaction. *Cement and Concrete Research 68,* 184–195.

Sargolzahi, M., S.A. Kodjo, P. Rivard, & J. Rhazi (2010). Effectiveness of nondestructive testing for the evaluation of alkali–silica reaction in concrete. *Construction and Building Materials 24*(8), 1398–1403.

Sevostianov, I. (2003). Explicit relations between elastic and conductive properties of materials containing annular cracks. *Philosophical Transactions of the Royal Society of London A: Mathematical, Physical and Engineering Sciences 361*(1806), 987–999.

Stark, J. & B. Wicht (2000). *Zement und Kalk: der Baustoff als Werkstoff.* Baupraxis.

Swamy, R. & M. Al-Asali (1988). Engineering properties of concrete affected by alkali-silica reaction. *ACI Materials Journal 85*(5), 367–374.

Timothy, J.J. & G. Meschke (2016a). A cascade continuum micromechanics model for the elastic properties of porous materials. *International Journal of Solids and Structures 83,* 1–12.

Timothy, J.J. & G. Meschke (2016b). A micromechanics model for molecular diffusion in materials with complex pore structure. *International Journal for Numerical and Analytical Methods in Geomechanics 40*(5), 686–712.

Ulm, F.-J., O. Coussy, K. Li, & C. Larive (2000). Thermochemo-mechanics of asr expansion in concrete structures. *Journal of Engeneering Mechanics (ASCE) 126,* 233–242.

Voland, K. (2016). *Einfluss der Porosität von Beton auf den Ablauf einer schädigenden Alkali-Kieselsäure-Reaktion.* Ph. D. thesis.

Computational Modelling of Concrete Structures – Meschke, Pichler & Rots (Eds)
© 2018 Taylor & Francis Group, London, ISBN 978-1-138-74117-1

Nonlinear coupling models of alkali-silica reaction and multi-directional cracked reinforced concrete

Y. Takahashi, S. Ogawa, Y. Tanaka & K. Maekawa
The University of Tokyo, Tokyo, Japan

ABSTRACT: This research aims to investigate the mode of mechanistic coupling of alkali silica reaction (ASR) and the cracks induced by external forces on reinforced concrete (RC). The effects of preceding flexural cracks on the following ASR-induced expansion in RC beams are studied by means of analysis and experiments. It is shown that preceding cracks may affect the magnitude of 3D confinement and the alkali transport, which can influence on the 3D expansion. Complex interactions of multi-directional cracks, ASR-expansions and fatigue lives of structural concrete are discussed under moving fatigue loads on RC bridge deck slabs. Analytical studies are conducted in comparison with the literature on multi-scale modeling and it is recognized that the mechanical properties such as tension transfer by ASR-gel injected inside cracks may possibly affect the overall fatigue performance of RC slabs.

1 INTRODUCTION

1.1 *Background*

The alkali silica reaction (ASR) is one of the major mechanisms leading to the deterioration of structural concrete composites and many researches have been conducted to predict and suppress the expansion (e.g. Kawabata *et al.* 2013; Sannoh and Torii 2014; Costa *et al.* 2014).

Mechanical performances of ASR damaged concrete and its behavioral prediction by modelling has been also studied (e.g. Bažand and Steffens 2000; Grimal, *et al.* 2010; Multon and Sellier 2016; Saouma *et al.* 2015; Liaudat *et al.* 2015; Bangert *et al.* 2004; Timothy *et al.* 2016). In some studies, the multi-chemo physics is taken into account to simulate the progress of ASR expansion and its fractures. Multon and Sellier (2016) propose the coupling models of transports/fixations of alkalis into aggregate, mass balances and ASR gel pressure generations. With their coupling model, the effect of alkali leaching on the ASR expansion can be expressed successfully. Timothy *et al.* (2016) illustrate the computational flow as shown in Figure 1, which are the coupling of transports, reaction kinetics, phase field models and crack propagations. The enhanced permeability for alkali flows by micro-cracks are installed in their transport model. Thus, the effect of micro-cracks on the ionic transport and the kinetics about ASR are tried to be considered in concrete material scale.

This study tries to enhance these chemo-physics approaches to the structural scale (Takahashi *et al.* 2016) in order to predict the structural performances of RC damaged by ASR. Here, chiefly focused is the mutual interaction of macro cracks and ASR expansions. In many experimental studies, only the effect of preceding ASR expansion on structural performances of concrete has been discussed, even though, inversely, cracks by the loads can affect the mass transport and the rate of ASR. The effects of macro cracks on the progress of ASR in structural scale should be further studied in view of full coupling.

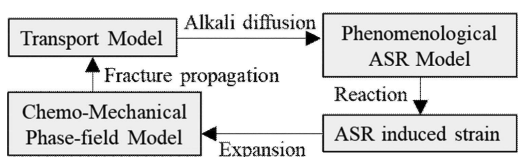

Figure 1. The example of multi-chemo physics scheme about ASR modelling (Timothy *et al.* 2016).

In this study, the mutual interaction of ASR in progress and force-induced cracks are discussed. First, the effect of preceding cracks on ASR expansion is analytically and experimentally studied with RC beams. Initial flexural cracks are introduced and then environmental actions for accelerated ASR is applied. The trade-off of stress release and fast-tracked ion transport is discussed. Next, structural performances of RC bridge decks are studied. In previous studies, some successful simulation was reported. Throughout these studies, key factors of importance are summarized in terms of ASR expansion and multi-directional cracks in finite domains.

1.2 *Multi-scale modelling*

The authors use the multi-scale chemo-hygral computational system (*DuCOM-COM3*, Maekawa *et al.* 2008; Maekawa and Ishida 2002), which is summarized in Figure 2 and conducts a three-dimensional multi-scale analysis of structural concrete. The moisture and other ion transports are simultaneously solved so that internal moisture state and alkali distributions can be taken into account (Elakneswaran and Ishida 2014). Among them, potassium and sodium ions in pore solution can be linked with the reaction model of silica gels.

This model is integrated with the chemical reaction model for alkali silica gel generation and its poro-mechanical model by Takahashi *et al.* (2014, 2015). The basic models to calculate the alkali silica gel generation as well as the isotropic/anisotropic pressures induced by created gels of volumetric inflation are summarized in Figure 3. The generated silica gel around aggregates is formulated based on the chemical equations. The rate of ASR is formulated as a function of the alkali concentration, updated free water and the content of reactive aggregates.

The thermodynamic variables of temperature and relative humidity have also been considered to affect the gel generation rate. As the reaction goes on, both alkali and free water will be consumed, and the reduced alkali and water will affect the chemical reaction rate, reciprocally. After gel volume is obtained, the deformation of concrete skeleton is calculated in consideration of the gel migration through cracks under the gradient of gel pressure as follows.

The generated alkali silica gel is thought as a semi-liquid substance and its total pore pressure is composed of both isotropic pressure by liquid gel and anisotropic one by the solidified phase of gel. In order to express the solid-liquid coexisting states, parameter β is introduced, which is the ratio of the solid phase to the total alkali silica gel generated. The proposed model has been verified by ASR related experiments for both the uniform expansion under the unconfined state and the non-uniform expansion with confinements (Takahashi *et al.* 2016).

In the previous studies by Takahashi *et al.* (2016) and Ogawa *et al.* (2017), it was shown that the ASR gel migration through cracks has an important role to express 3D ASR expansion. Figure 4 shows the analytical results of the expansion with the different sizes of mortars. In considering the proper permeation for ASR gel (1.0E-18 m/s), we have successful simulation of scale dependency. ASR gel leaching from the specimen's surfaces releases the internal pressure by expanded gel, which leads to the smaller expansion in smaller specimens.

No matter how large the size of concrete is and gel-leaching hardly affects the final ASR expansion,

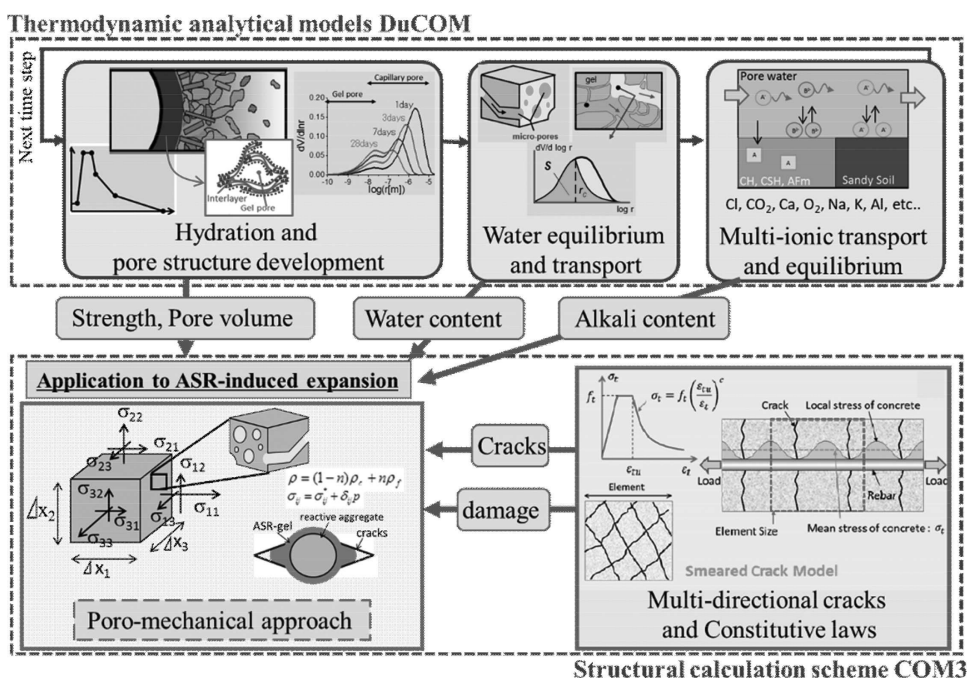

Figure 2. Multi-scale chemo-hygral computational scheme.

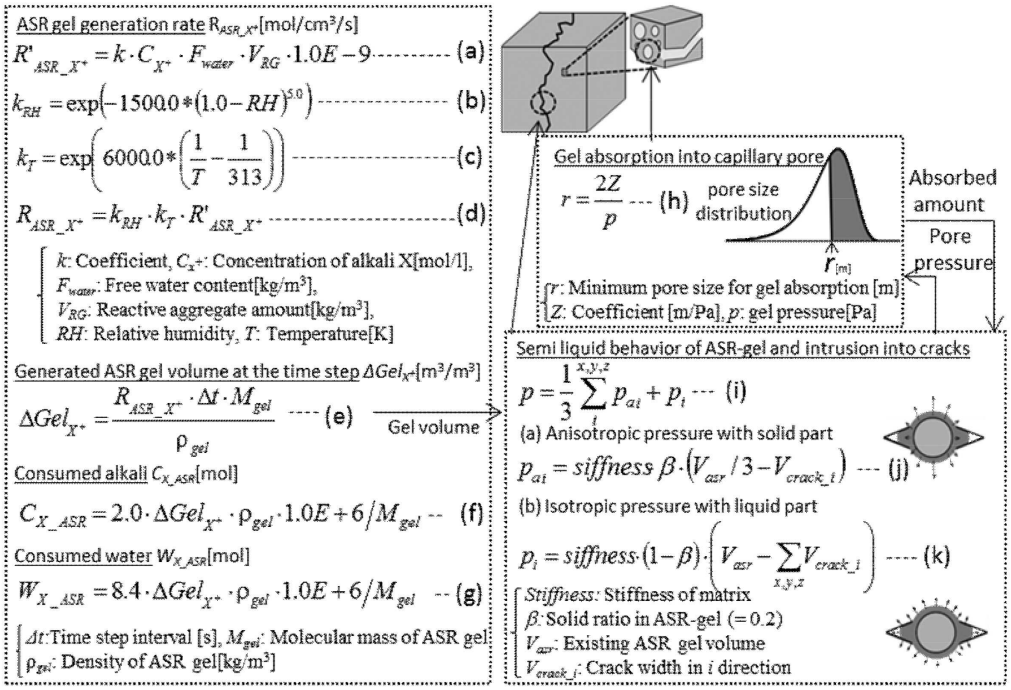

Figure 3. Chemical and physical models for ASR.

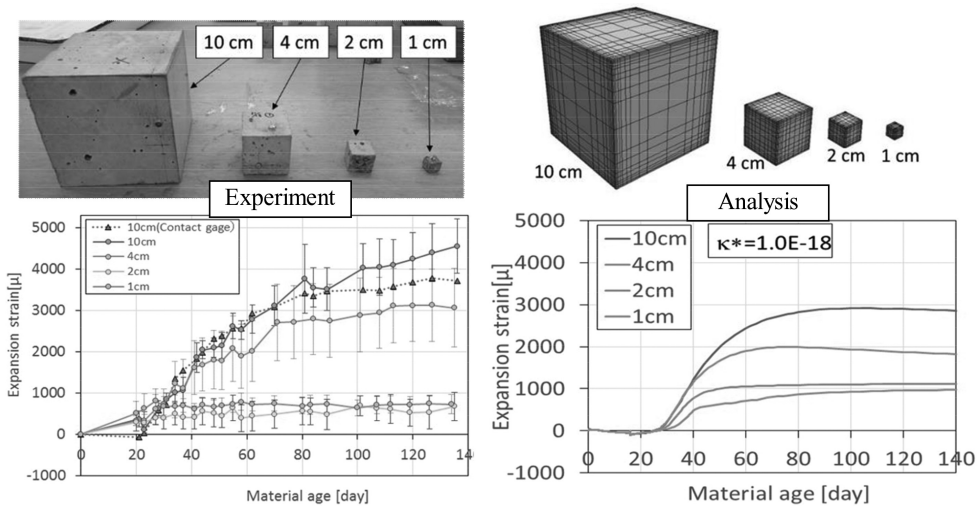

Figure 4. Scale dependent ASR expansion in experiment and its analyses with proper gel permeability.

the gel migration through cracks may affect ASR expansion if there are preceding cracks. Preceding cracks and damages may also affect confinement as well. In the next chapter, the effects of preceding cracks on expansion of RC members are discussed.

2 EFFECT OF PRECEDING CRACKS ON ASR EXPANSION

2.1 *Analytical studies*

Using the analytical scheme introduced in the previous section, the authors have conducted analyses

to get the effects of preceding cracks on ASR expansion (Ogawa *et al.* 2017). With the finite element discretization of RC beam as shown in Figure 5, the initial flexure and following ASR expansion are simulated. By taking advantage of the symmetry, only half of the beam is modeled and preceding cracks are generated by the static loading of 19.6 kN at the span center. 19.6 kN is 50% of the static capacity of the beam. In Figure 6, we have the identical distributed cracks by pre-loading.

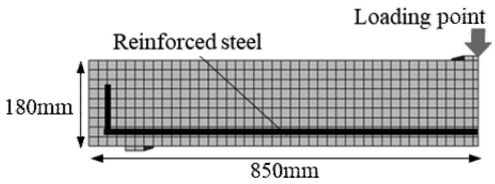

Figure 5. Finite element mesh for RC beam analysis.



Figure 6. Normal strain distribution in longitudinal direction after loading.

Afterwards, ASR gel is uniformly generated at 100 days computationally.

Figure 7 shows the normal strain profiles in the longitudinal and vertical directions after ASR. In both cases, longitudinal expansion is small because of the confinement by the steel, and the expansion in vertical direction gains on one hand. The difference of strains of two analytical cases is also shown in Figure 7. With preceding cracks, magnitude of expansion in the longitudinal direction around upper center of the beam gets greater than that of no preceding cracks. Near the preceding crack, strain along reinforcement decreases and increases in plain concrete zones. The strain in the vertical direction changes oppositely to the longitudinal one owing to the anisotropic gel migration like liquid.

From these analysis, it is thought that preceding cracks may affect confinement leading to 3D expansion. Further study is needed to verify this structural performance. In these cases of analyses, ASR-gel migration through preceding cracks has dominant effects in regard to expansion under greater confinement or small crack spacing under the assumption that the rate of reaction would not be changed.

2.2 *Experimental procedures*

It is foreseen that the effect of preceding flexural cracks on ASR expansion might exist. To see the real extent of these effects, the following experimental study with RC beams is worthy of execution.

The dimensions of targeted RC beams are shown in Figure 8, i.e., $150 \times 150 \times 1500$ mm and SD 295 A

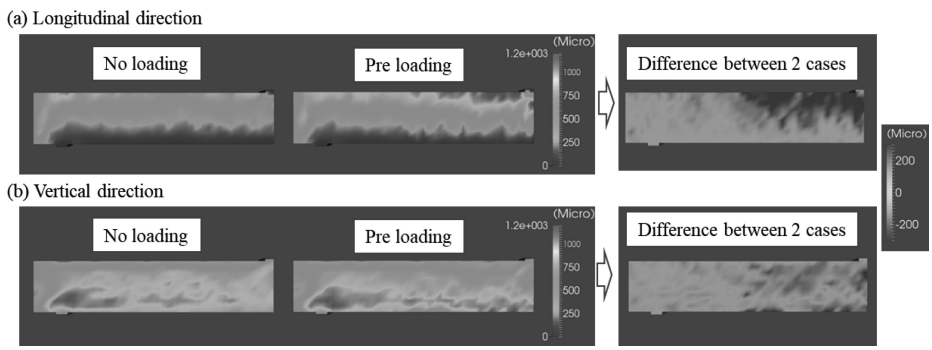

Figure 7. Normal strain profiles after ASR expansion and strain difference between 2 cases.

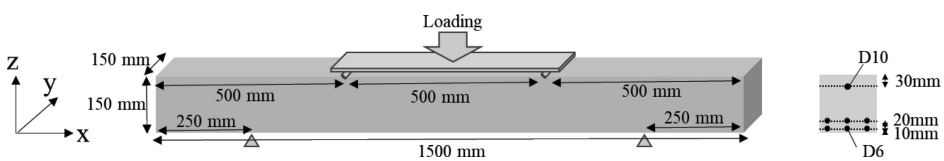

Figure 8. Dimensions, bar arrangement of beam specimen and loading condition.

type of D10 and D6 re-bars are arranged. To control the spacing of flexural cracks, cover depth is set to 10 mm. Mix proportion of concrete is listed in Table 1. Reactive andesite was used as coarse aggregate and 12.90 kg/m^3 of sodium hydroxide was added to mixture to accelerate ASR expansion. Three specimens were made with the same dimension and the mix proportion. Specimen A is for the static capacity. After 20 days sealed curing, 4 point loads were applied by the load control as shown in Figure 8. Specimen B is no preceding crack case; after casting, the specimen was sealed for 20 days and soaked into 3% sodium chloride solution whose temperature was kept constant as 40 °C. Specimen C is with preceding crack case; after casting, the specimen was sealed for 19 days and pre-loading was applied.

Loading level of the pre-loading to introduce flexural cracks was set up as 60% of static capacity. After introducing cracks, the specimen was soaked into the same sodium chloride solution as Specimen B to accelerate ASR. During the accelerated ASR period, length changes were measured by the handy contact gauge. Figure 9 illustrates the positions at which the length changes in different directions were measured on all surfaces over the constant bending moment zone. Longitudinal and vertical strains (X' and Z' in Figure 9) at the other area were measured on the side surface as well. Figure 10 shows the view of ASR acceleration in sodium chloride solution.

Table 1. Mix proportion of beam specimens.

Water-to-cement ratio (%)		65.0
Na_2O equiv. content (kg/m^3)		10.0
Unit weight (kg/m^3)	Water	175
	Cement	269
	Sand	827
	Gravel (reactive)	988
	NaOH	12.90
Ware reducing agent (% of cement)		1.6
Air entrained agent (% of cement)		0.004

2.3 *Experimental results*

Figure 11 shows the load-displacement curves of Specimen A and Specimen C. The static capacity by Specimen A was 80.7 kN. Thus, 48 kN (60% of the static capacity) was applied as pre-loading for Specimen C to introduce structural cracks. Consequently, flexural cracks as shown in Figure 12 developed. The crack spacing due to pre-loading was about 7–8 cm over the constant moment zone.

Regardless of preceding cracks, ASR acceleration was conducted and length changes were

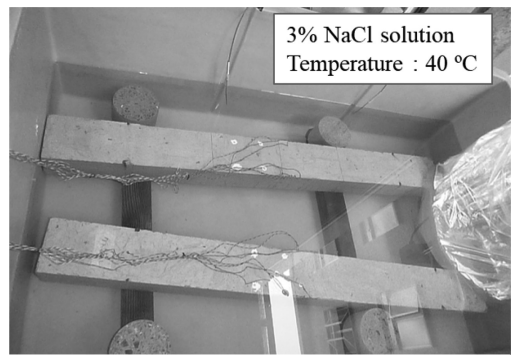

Figure 10. Overview of ASR acceleration method.

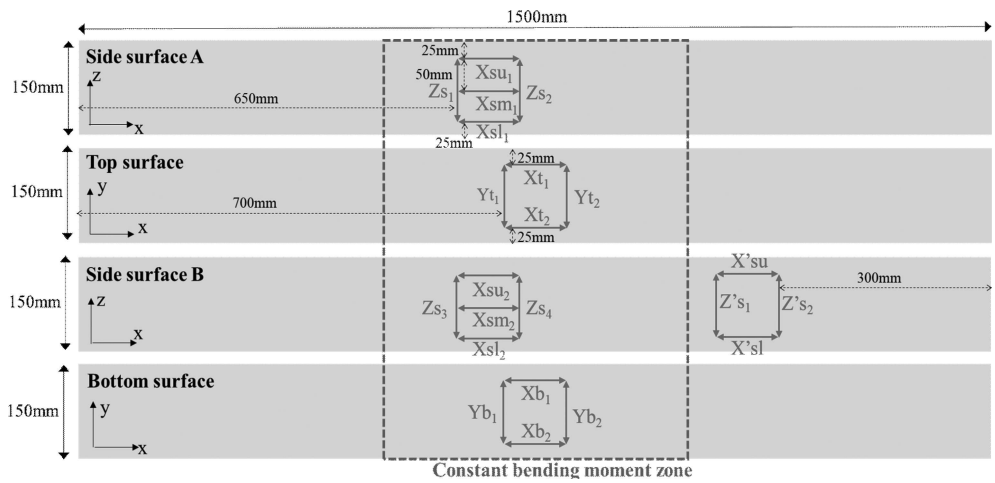

Figure 9. Measurement positions on RC beam specimens B and C.

measured. Figure 13 shows the strain development measured up to 100 days of ASR acceleration. In the longitudinal direction (X direction), the expansions are restrained by steel and it is observed only on the top surface (Xt). Xt of Specimen C is larger than the one of Specimen B, which are similar to the results of analyses as shown in Figure 7. The confinement in the longitudinal direction can be reduced due to preceding cracks. In other directions at the area of constant bending moment (Yt, Yb, Zs), length changes of Specimen C are larger than that of Specimen B.

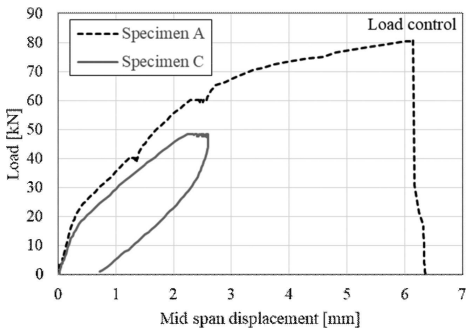

Figure 11. Load-displacement curves of RC beams.

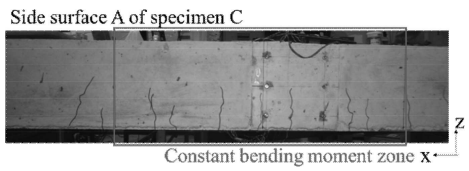

Figure 12. Crack distribution after pre-loading.

This trend is opposite to the prediction as shown in Figure 7. This might be caused by the accelerated alkali supply through cracks, which was not considered in the analysis. The preceding cracks not only release the pressure of alkali silica gel, but also accelerate the alkali transport from outside. These two factors have the opposite effects on overall ASR expansion.

Here, the rate of alkali supply has the dominancy in overall ASR progress. The fact that the expansion in constant moment area (Zs of Specimen C) is greater than no crack area (Z's of Specimen C) may attribute to the accelerated alkali supply as well. The trade-off of ASR gel pressure release and the alkali supply is a key factor. As the reactivity of the aggregate used in this study was not so high, the alkali transport might be a dominant factor on ASR expansion. The authors plan to conduct additional experiment with highly reactive aggregate, where other behaviors might appear as expansion will be faster and the gel generation could be dominant.

3 FATIGUE LIVES OF BRIDGE DECKS

3.1 *Experimental procedures*

Eguchi *et al.* (2016) and Maeshima *et al.* (2016) conducted experimental studies on the fatigue lives of RC slabs, as shown in Figure 14. In these studies, the coupled effects of moving fatigue loads and ASR expansions on fatigue performance of RC bridge decks were studied experimentally. Dimensions of the slab specimens are 3000 mm length, 2000 mm width and 160 mm thickness as shown in Figure 15. Double layered deformed bars were arranged with 30 mm of cover depth. SD 295 A

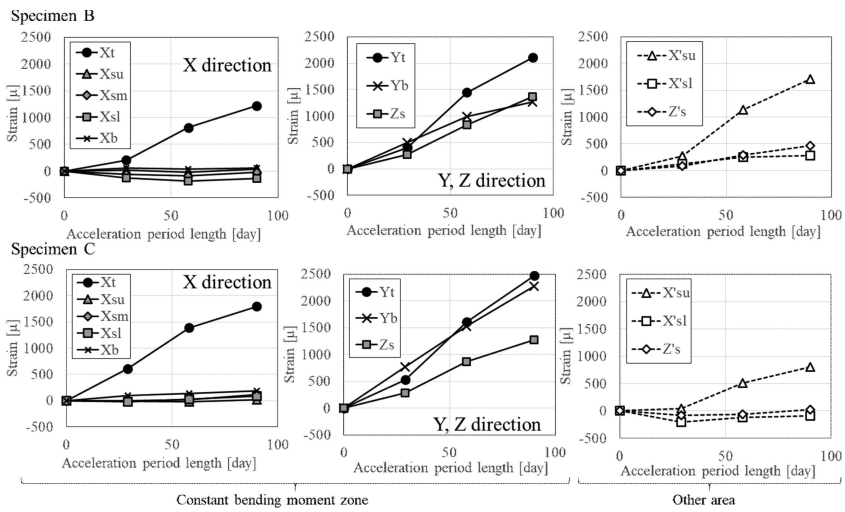

Figure 13. Length changes in three dimensions of specimen B and C.

type of D16 and D13 deformed reinforcing bars were placed in both longitudinal and transverse directions, respectively.

Spacing of reinforcing bars in the lower layer are 150 mm and 125 mm in each direction, and that of the bars in the upper layer is double of its lower one. Four experimental series as shown in Table 2 can be referred from the previous studies (Eguchi *et al.* 2016; Maeshima *et al.* 2016) to discuss the effect of preceding multiple cracks by preloadings. RC slabs with the same dimensions were exposed to each loading and the ASR acceleration condition listed in Table 2. During the moving load tests, condensed water was supplied on the surface of the specimen which has "w" in the name (Wet condition). The specimen of d-A-w has 100,000 cycles of fatigue loading before ASR. By comparing the result of d-A-w case with A-w case, we may discuss the effect of pre-loading and preceding cracks.

Table 3 shows the mix proportion of concrete used. Ordinary Portland cement, two types of crashed sand, crashed gravel, water reducing admixture and deforming agents were used. Tight sand stone (Sand 1) and granite (Sand 2) were selected as fine aggregates and they are both non-reactive. The gravel was andesite and it is known to be reactive for ASR. Additional 18.9 kg/m^3 of sodium chloride was included to mixture to accelerate ASR.



Figure 14. Overview of wheel type loading.

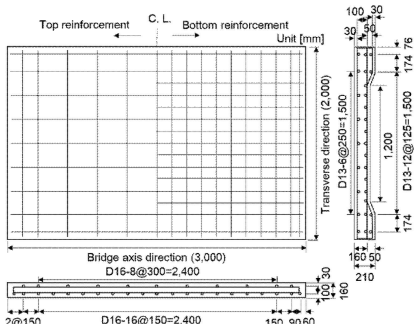

Figure 15. Dimensions and bar arrangement of slab.

After casting, four different curing processes were applied as shown in Figure 16. During the ASR acceleration period, the specimen was stored in the control room of environments which were kept 50 °C and RH 80% and its top surface was covered by saturated sodium chloride solution. After

Table 2. Experimental conditions.

Specimen	Pre-loading	ASR acceleration	Loading
N-d	No	No	Dry
A-d	No	Yes	Dry
A-w	No	Yes	Wet
d-A-w	Dry	Yes	Wet

Table 3. Mix proportion of slab specimen.

Water-to-cement ratio (%)		65.0
Air content (%)		4.5 ± 1.5
Unit weight (kg/m^3)	Water	175
	Cement	269
	Sand 1	413
	Sand 2	405
	Gravel (reactive)	1032
	NaCl	18.9
Water reducing agent (% of cement)		1.5
Deforming agent (% of cement)		0.006

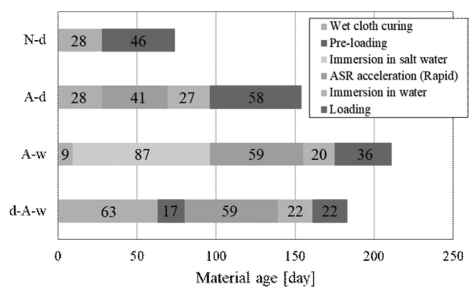

Figure 16. Curing and ASR acceleration processes.

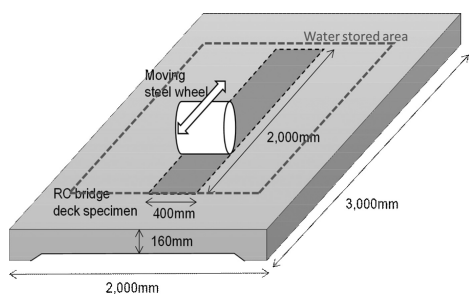

Figure 17. Position of moving wheel load.

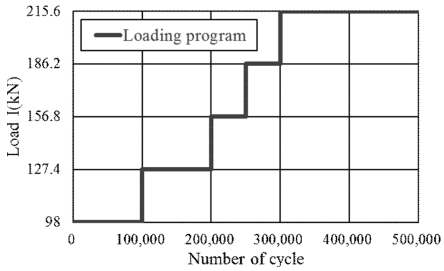

Figure 18. Loading program of wheel running load test.

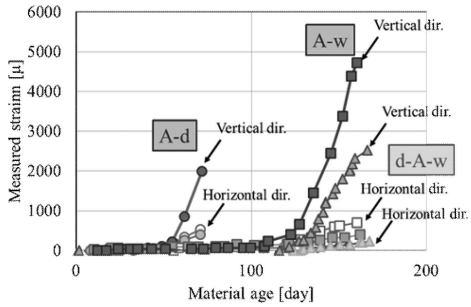

Figure 19. Measured anisotropic expansion.

curing of each specimen, the steel wheel whose width is 400 mm was set up at the span center as shown in Figure 17. Traveling distance of the steel wheel was 2000 mm. The initial wheel load was set as 98 kN which coincides with the allowable wheel load specified in the Japanese specification for road bridges (Japan Road Association 2012). In order to accelerate the experiment, the magnitude of the load was increased step by step as shown in Figure 18, and their traveling cycles were converted to equivalent ones with regard to 98 kN load-level by using Miner's law (Matsui 1996). The details of loading conditions can be referred to the previous study (Maeshima *et al.* 2016; Tanaka *et al.* 2017)

3.2 *Experimental results and discussions*

Figure 18 shows the measured expansion in progress of A-d, A-w and d-A-w specimens. We have the clear anisotropy in ASR expansion, the vertical direction of which is the greatest among three directions and it is almost 3–5 times larger than the other two horizontal directions. In association with arranged re-bars in the specimens, 3D anisotropic confinement against ASR expansion develops and it leads to the well-known anisotropy of deformation (Saouma *et al.* 2015). Figure 20 shows the chemical pre-stress forces calculated from the strains of embedded reinforcement. Induced stress in d-A-w case is smaller than A-w case. The pressure release may occur because of the preceding fatigue loadings.

Figure 21 shows the live-load deflection curve with regard to the equivalent traveling cycles. The live load deflection unceasingly increased in accordance with the loading cycles. Though the live load deflection at the first cycle in the ASR case is larger than the case of no-ASR, the fatigue life is one-order (10 times) longer in the ASR case than the one of non-ASR. It was mentioned that chemical pre-stress may partly restrain the deflection under live loads (Maeshima *et al.* 2016). The effect of stagnant water is not so significant for the ASR cases when we compare the results of A-d and A-w, although it is known that the existence of water generally

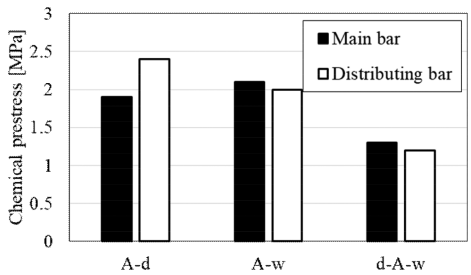

Figure 20. Chemical pre-stress in experiment.

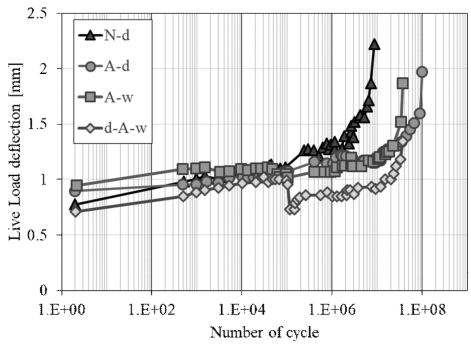

Figure 21. Experimental results of live load deflections.

reduces fatigue life dramatically in the no-ASR concrete cases (Hiratsuka and Maekawa 2015).

In the pre-loading case (d-A-w), ASR acceleration period was inserted after 100,000 cycles of pre-loading. We can see from Figure 21 that the live load deflection of d-A-w case reduces after ASR expansion, and the fatigue life of d-A-w case is almost the same as A-w case. ASR expansion of about 2000 μ doesn't cause the obvious deterioration on the pre-fatigued RC slabs. The induced chemical pre-stress in d-A-w case is smaller than A-d and A-w case. Thus, we cannot explain these behaviors only by the chemical pre-stressing effect. It is supposed that the ASR-gel filling process into cracks have somehow effect like quasi-viscosity on the structural performance of RC slabs against fatigues.

3.3 *Simulations and modellings*

With the calculation scheme explained in Section 1.2, fatigue lives of RC slabs with ASR were estimated. The silica gel volume of 0.003 [m^3/m^3] is built during the alkali silica reaction, which leads to 3D expansions. The expansions were approximately 2000 μ in the transverse direction, and 500 μ in the in-plane horizontal directions, due to the confinement by dispersed reinforcement. Figure 22 shows the calculated chemical pre-stress of A-d, A-w and d-A-w cases. The chemical pre-stress in main-bar direction reduces with pre-loading. Thus, the pressure release in RC slab is successfully reproduced.

Figure 23 shows the simulated fatigue performance of RC slabs. The absolute deflection at mid-span of the slabs is indicated in the figure. As for A-d and A-w cases, the multi-scale calculation scheme may capture the fatigue life of RC slabs with ASR within the variation of about 50% of the reality. The case of d-A-w has similar fatigue life to the one of A-w case as well.

However, the transient stiffness during the reaction differs from the experiment. In the simulation as shown in Figure 23, the elastic stiffness of the slab decays and the mid-span deflection increases through the process of ASR, while the real stiffness was recovered (Figure 21). As the mechanism of the stiffness recovery is not well understood, some sensitivity analysis is executed.

ASR gel injected in between crack planes is assumed not to transfer viscous tension (negative pressure in solid-liquid two phase model; Gray line in Figure 24), but it may bear pressure in compression. Although this assumption would be reasonable

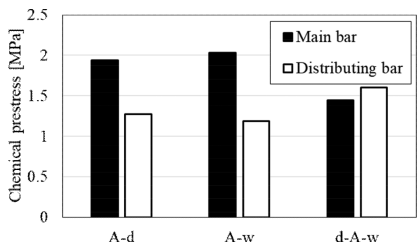

Figure 22. Chemical pre-stress in analyses.

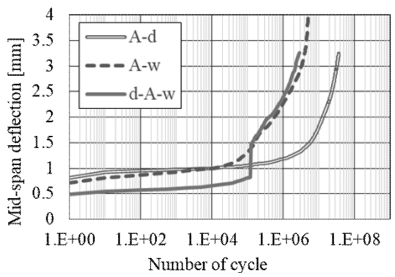

Figure 23. Mid span deflections in analyses.

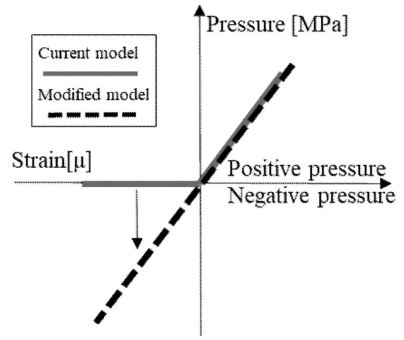

Figure 24. Pressure transfer model of ASR-gel.

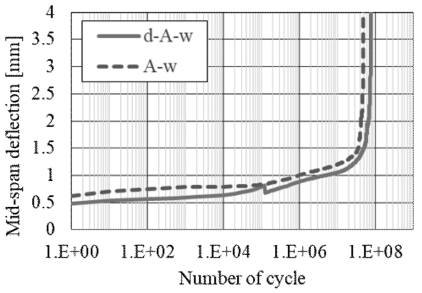

Figure 25. Mid span deflections in analyses considering negative pressure of ASR-gel.

for condensed liquid water with phase change, the silica gel is thought to bear negative pressure. Then, the model for ASR gel pressure is modified as trial to allow negative pressure (see Figure 24). In the modified model, the ASR-gel can resist somehow against crack openings.

With the modified model, the fatigue analyses of the damaged RC slab are conducted again. Figure 25 shows the simulated fatigue performance of A-w and d-A-w cases. Due to the tension transfer of ASR-gel, the stiffness of RC slabs increases and the fatigue life is prolonged as the reality. It is remarkable that the stiffness reduction due to ASR expansion in d-A-w case disappear in the simulation with the modified model.

From this analytical study, it is realized that the mechanical properties, especially, the tension of ASR gel should be considered to predict the long-term structural performance of RC in high reliability. Detailed behavior of ASR-gel in cracks has not been well-understood, thus the further experimental verification from material level would be needed in near future.

4 CONCLUSION

This research aims to understand the mutual relationships between the progress of alkali silica reaction and

the cracks induced by mechanical loads on reinforced concrete.

The effects of preceding flexural cracks in RC beams on following ASR-induced expansion are studied by means of analysis and experiment. It is pointed out that the preceding cracks may affect the three dimensional confinement and additional alkali supply which can change the 3D expansion, provided that the same chemical reaction would develop.

Complex interactions of multi-directional cracks, ASR-expansion and fatigue lives are discussed based under the moving fatigue load tests of RC bridge deck slabs. With the analytical studies simulates the previous experiments, it is computationally recognized that the mechanical properties such as tension transfer by ASR-gel injected inside cracks might have an important role on the fatigue performance of RC slabs.

ACKNOWLEDGMENT

This study was financially supported by JSPS KAKENHI Grant No. 15H05531 and the authors express their gratitude to engineers who join the intensive discussion in the scheme of Cross-ministerial Strategic Innovation Promotion Program (SIP).

REFERENCES

Bangert, F., Kuhl, D. and Meschke, G. 2004. Chemo-hygro-mechanical modeling and numerical simulation of concrete deterioration caused by alkali-silica reaction. *International Journal for Numerical and Analytical Methods in Geomechanics*, 28: 689–714.

Bažant, Z.P. and Steffens, A. 2000. Mathematical model for kinetics of alkali-silica reaction in concrete. *Cement and Concrete Research*, 30: 419–428.

Costa, U., Mangialar, T. and Paolini, A. 2014. Assessment of blended cements effectiveness against ASR by mortar and concrete expansion tests. *Journal of Advanced Concrete Technology*, 12: 266–278.

Eguchi, Y., Yoshida, T., Maeshima, T. & Iwaki, I 2016. Fatigue performance of RC road bridge decks damaged by coupled alkali silica reactions and fatigue loads, In: *Proceedings of JSCE Tohoku Branch Annual Conference*, V-23, *Iwate, 5th March 2016.* (in Japanese)

Elakneswaran, Y. and Ishida, T. 2014. Development and verification of an integrated physicochemical and geochemical modelling framework for performance assessment of cement-based materials. *Journal of Advanced Concrete Technology*, 12: 111–126.

Grimal, E., Sellier, A., Multon, S., Le Pape, Y. and Bourdarot, E. 2010. Concrete modelling for expertise of structures affected by alkali aggregate reaction. *Cement and Concrete Research*, 40: 502–507.

Hiratsuka, Y. and Maekawa, K. 2015. Multi-scale and multi-chemo-physics analysis applied to fatigue life assessment of strengthened bridge decks, In: E. Onate, D.R.J. Owen, D. Peric and M. Chiumenti (Eds.), *XIII International Conference on Computational Plasticity. Fundamentals and Applications*: 596–607, *Barcelona, 1–3 September 2015.*

Japan Road Association. 2012. Specifications for highway bridge, Part III Concrete bridges.

Kawabata, Y., Yamada, K., Ogawa, S. and Sagawa, Y. 2013. Prediction of ASR expansion of field-exposed concrete based on accelerated concrete prism test with alkali-wrapping. *Cement Science and Concrete Technology*, 69: 449–455.

Liaudat, J., Martínez, A., López, C. and Carol, I. 2015. Numerical modelling of ASR expansion in concrete. In: C. Hellmich, J. Kollegger, B. Pichler, *Proceedings of CONCREEP10*: 445–454, *21–23 September, Vienna.*

Maekawa, K. and Ishida, T. 2002. Modeling of structural performances under coupled environmental and weather actions. *Materials and Structures*, 35(10): 591–602.

Maekawa, K., Ishida, T. and Kishi, T. 2008. *Multi-Scale Modeling of Structural Concrete.* Taylor & Francis.

Maeshima, T., Koda, Y., Iwaki, I., Naito, H., Kishira, R. Suzuki, Y., Ohta, K. and Suzuki, M. 2016. Influence of alkali silica reaction on fatigue resistance of RC bridge deck, *Journal of Japan Society of Civil Engineers,* 72(2): 126–145.

Matsui, S. 1996. Life time prediction of bridge, *Journal of Japan Society of Civil Engineers*, 30(6): 432–440.

Multon, S. and Sellier A. 2016. Multi-scale analysis of alkali-silica reaction (ASR): impact of alkali leaching on scale effects affecting expansion tests. *Cement and Concrete Research*, 81: 122–133.

Muranaka, M. and Tanaka, Y. 2013. Development of physical and chemical model for concrete expansion due to ASR based on reaction mechanism. *Journal of Japan Society of Civil Engineers*, E2/V-69(1): 1–15.

Ogawa, S., Tanaka, Y., Takahashi, Y. & Maekawa, K. 2017. Effect of preceding cracks on ASR expansion of concrete and its poro-mechanical modeling, In: *Proceedings of Sixth Biot Conference on Poromechanics*: 778–786, *Paris, 9–13 July 2017.*

Sannoh, C. and Torii, K. 2014. The suppressing effect of fly ashes on alkali-silica reaction of RC specimens exposed on seashore. *In: Proceedings of Asian Concrete Federation-2014*: 1093–1096, *Seoul, 17–19 September, 2014.*

Saouma, V.E., Martin, R.A., Hariri-Aredebili, M.A. and Katayama, T. 2015. A mathematical model for the inetics of the alkali-silica chemical reaction. *Cement and Concrete Research*, 68: 184–195.

Takahashi, Y., Ogawa, S., Tanaka, Y. and Maekawa, K. 2016. Scale-dependent ASR expansion of concrete and its prediction coupled with silica gel generation and migration*, Journal of Advanced Concrete Technology,* 14(8): 444–463.

Takahashi, Y., Shibata, K. and Maekawa, K. 2014. Chemo-hygral modeling and structural behaviors of reinforced concrete damaged by alkali silica reaction. In: *Proceedings of Asian Concrete Federation-2014*: 1274–1281, *Seoul, 17–19 September, 2014.*

Takahashi, Y., Tanaka, Y. and Maekawa, K. 2015. Chemo-hygral model for ASR expansion and its effects on fatigue lives of bridge slabs. In: E. Onate, D.R.J. Owen, D. Peric and M. Chiumenti (Eds.), *XIII International Conference on Computational Plasticity. Fundamentals and Applications*: 944–955, *Barcelona, 1–3 September 2015.*

Tanaka, Y., Takahashi, Y. and Maekawa, K. 2017. Remaining fatigue life assessment of damaged RC decks -Data assimilation of multi-scale model and site inspection-, *Journal of Advanced Concrete Technology*, 15(7): 328–345.

Computational Modelling of Concrete Structures – Meschke, Pichler & Rots (Eds)
© 2018 Taylor & Francis Group, London, ISBN 978-1-138-74117-1

Coupled C-M meso-scale model for ASR expansion in concrete

J. Liaudat, C.M. López & I. Carol
Department of Civil and Environmental Engineering, Universitat Politècnica de Catalunya, Barcelona, Spain

ABSTRACT: As part of an ongoing development, this paper presents a brief description of a new Chemo-Mechanical (C-M) model for the expansions due to Alkali-Silica Reaction (ASR) in concrete. This model has been formulated at the meso-scale level (major aggregate fraction and cementitious matrix of cement paste or mortar). The chemical and the mechanical problems are solved by means of two different Finite Element (FE) codes coupled via a staggered implementation. Both codes use the same FE mesh, which can include zero-thickness interface elements in between continuum elements in order to simulate localized cracks. The chemical model consists of the three main diffusion/reaction field equations for the concentrations of aqueous Alkali, Calcium and Silicate ions in the pore solution, complemented by a number of chemical kinetics and chemical equilibrium equations. The volume fraction distribution of the solid constituents of the hardened cement paste, the aggregates and the reaction products (ASR gel) evolve with the progress of the reaction. Diffusion-reaction process can occur in both continuum and interface elements. The meso-mechanical model for concrete has the distinctive feature of considering lines in the FE mesh as potential crack lines, via the systematic use of zero-thickness interface elements, equipped with traction-separation constitutive models based on principles of non-linear fracture mechanics, while the matrix phase is considered elastic or linear viscoelastic. The proposed coupled model has been applied to some simple verification examples. The results show the good performance of the model and the individual physical consistency and reasonable interaction among the variety of ingredients (mechanical, chemical, etc.) involved.

1 INTRODUCTION

The mechanisms of concrete expansions due to Alkali-Silica Reaction (ASR) are not yet completely understood. In particular, the effect of the stress state on the magnitude and direction of the induced expansions is a controversial aspect that has deserved increasing attention in recent years and to which the authors have devoted some efforts in the context of a research project. This project includes both experimental (Liaudat, Carol, López, & Saouma 2017) and numerical modelling work. In relation to the latter, and as part of an ongoing development, this paper presents a brief description of a new Chemo-Mechanical (C-M) model formulated at the meso-scale level, together with some preliminary results. The model includes some original features such as the localized diffusivity in opened cracks, the precipitation of reaction products within in opened cracks, and the compressibility of the ASR gel. Previous versions of this model can be found in Liaudat, López, & Carol (2013), Liaudat, López, & Carol (2014), Liaudat, Martínez, López, & Carol (2015) and Liaudat, López, & Carol (2016).

2 MODELLING OF ASR EXPANSIONS IN CONCRETE

2.1 *Coupling Scheme*

The model is implemented via two different Finite Element (FE) codes. One code deals with the reactive transport problem and the other with the mechanical problem. Both codes are coupled in a staggered scheme in order to reproduce mechanisms such as:

- The generation of internal mechanical pressures due to the formation of expansive reaction products, both within cement/aggregate pores and within cracks.
- The localized diffusion of reactants along opened cracks.
- The change of concrete transport properties due to dissolution/precipitation of solids.

In order to ease the exchange of information both codes use the same FE mesh which can include zero-thickness interface elements in between continuum elements. Similar implementations has been used for modelling other coupled problems

in concrete such as external sulphate attack (Idiart, López, & Carol 2011a), drying shrinkage (Idiart, López, & Carol 2011b), and high temperature (Rodríguez, López, & Carol 2017).

2.2 *Meso-scale mechanical model*

The basic meso-mechanical model was originally proposed to represent the behavior of concrete under mechanical loads. In this model, the largest aggregate particles are represented explicitly, and it has the distinctive feature of considering lines in theFE mesh as potential crack lines, via the systematic use of zero-thickness interface elements equipped with traction-separation constitutive models based on principles of non-linear fracture mechanics (Carol, Prat, & López 1997, Carol, López, & Roa 2001), while the matrix phase isconsidered elastic or linear visco-elastic. With this conceptually simple model, the mechanical behavior of concrete was successfully reproduced under a variety of uniaxial, biaxial and triaxial conditions, creep, and differential temperature expansions (Carol, López, & Roa 2001, Caballero, López, & Carol 2006, López, Carol, & Aguado 2008, Pérez, Rodriguez, Lopez, & Carol 2013).

2.3 *Diffusion-reaction model*

As mentioned before, the ongoing research project includes also experimental work. These experiments have been performed using crushed recycled soda-lime (SL) glass as reactive aggregate. In order to model these experiments, a particular version of a more general diffusion-reaction model under development has been implemented. In this version, some particularities of SL glass as reactive aggregate such as the lack of porosity (impermeability) and the congruent dissolution at high pH (Maraghechi, Rajabipour, Pantano, & Burgos 2016) have been assumed.

For the sake of simplicity, in this first version of the model, temperature and water content are assumed to remain constant throughout the simulations.

2.3.1 *Reaction mechanism*

The reaction mechanism proposed is schematically summarized in Fig. 1. The interfacial zone between Hardened Cement Paste (HCP) and a cracked SL glass aggregate in concrete is represented. The HCP is assumed to be porous and fully saturated with water at all times during the reaction. Immediately after casting, the HCP content of portlandite and the pore water content of aqueous calcium (Ca) and alkalis (R) are assumed known. Note that sodium (Na) and potassium (K) are treated here indifferently as alkalis (R). The intact glass is assumed to be impervious and composed only by SiO_2 (76.7 wt%), CaO (14.1 wt%) and Na_2O (9.2 wt%).

The SL glass in contact with the highly alkaline (pH >12) pore solution of the HCP, both at the Interfacial Transition Zone (ITZ) and within pre-existent glass cracks, dissolves into silicate ($SiO_4H_3^-$), calcium (Ca^{2+}) and alkali (R^+) ions.

Wherever (within cracks in the glass, at the ITZ or in the HCP) the three reactants (aqueous calcium, alkali and silicate) are available in sufficient concentration, a reaction may occur forming a Calcium-Alkali-Silicate-Hydrate (C-R-S-H) of variable composition, depending on the relative concentration of the reactants. The composition, in turn, determines the molar volume and the maximum swelling pressure of this product. The effect of the remaining chemical species usually

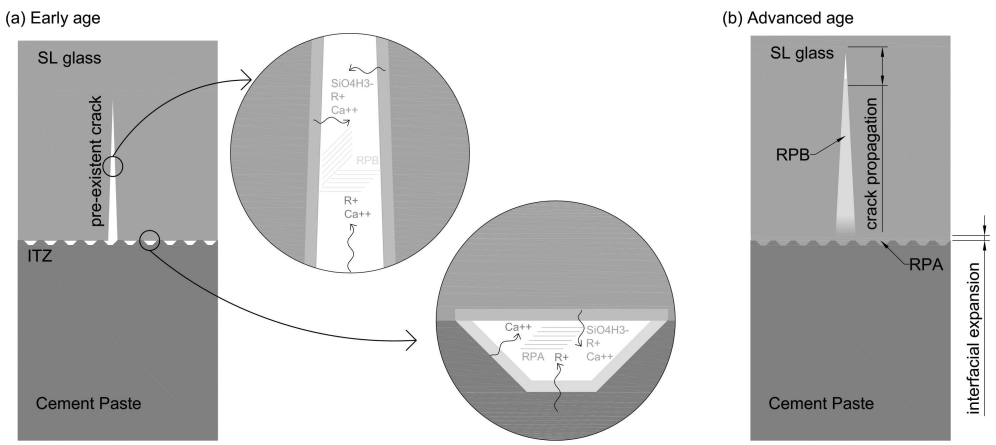

Figure 1. Schematic representation of ASR mechanism in concrete.

present in concrete on the development of ASR is neglected.

The variability of the composition is guaranteed by considering two separate reactions, each one with a fixed stoichiometry and its own kinetic law, one reaction forming C-R-S-H rich in calcium called Reaction Product A (RPA) and the other forming a C-R-S-H poor in calcium called Reaction Product B (RPB). The RPA has a composition similar to that of pozzolanic C-S-H and is mainly formed in contact with the HCP, where calcium from portlandite dissolution is readily available. The RPB, in contrast, is mainly formed separated from the HCP, i.e. within cracks in the crushed SL glass particles. Based on the works of Rajabipour, Maraghechi, & Fischer (2010), Maraghechi, Shafaatian, Fischer, & Rajabipour (2012), and on our own experimental observations, we assign to this reaction products different swelling pressures, high (around 10 MPa) for low-calcium RPB and low (around 2 MPa) for high-calcium RPA.

At a given location, the volume balance of the solid constituents, namely reactive silica, portlandite, RPA and RPB, determines the transport properties and the volume of pore solution. If the volume of precipitated reaction products is greater than the available space in capillary pores plus the additional space liberated by silica and portlandite dissolution, a localized internal pressure is induced.

It is assumed that the described mechanism can be suitably represented by considering the following five chemical reactions:

$$\underbrace{(SiO_2)(CaO)_{0.20}(R_2O)_{0.12}}_{\text{SL glass}} + 1.68H_2O \rightleftarrows SiO_4H_3^- + 0.2Ca^{2+} + 0.24R^+ + 0.36H^+ \quad (1)$$

$$Ca(OH)_2 \rightleftarrows Ca^{2+} + 2OH^- \quad (2)$$

$$RPA \rightleftarrows SiO_4H_3^- + 1.5Ca^{2+} + 0.2R^+ + 2.2OH^- \quad (3)$$

$$RPB \rightleftarrows SiO_4H_3^- + 0.3Ca^{2+} + 0.3R^+ + 0.1H^+ \quad (4)$$

$$H_2O \rightleftarrows H^+ + OH^- \quad (5)$$

where the first four reactions are dissolution / precipitation reactions correspondent to solid SL glass, portlandite, RPA, and RPB, respectively, while the last one correspond to water self-ionization.

2.4 *Formulation*

Assuming that the diffusion of aqueous species in the pore solution obeys Fick's diffusion law, averaging it in the saturated porous medium and establishing the corresponding mass balance equation, the following diffusion-reaction equations for the continuum porous medium are obtained

$$\begin{cases} \dfrac{\partial(\varphi c^s)}{\partial t} = \nabla^T\left(D^s \nabla c^s\right) + q^s \\ \dfrac{\partial(\varphi c^c)}{\partial t} = \nabla^T\left(D^c \nabla c^c\right) + q^c \\ \dfrac{\partial(\varphi c^r)}{\partial t} = \nabla^T\left(D^r \nabla c^r\right) + q^r \end{cases} \quad (6)$$

where the superscripts *s*, *c* and *r* indicate silicate, calcium and alkali, respectively, ϕ is the total porosity; c^β [mol/m^3] is the concentration of aqueous β-species in the pore solution expressed in moles per unit volume of pore solution, D^β [m^2/s] is the effective diffusivity of aqueous β-species in the porous medium (assumed isotropic), $\nabla = \left[\frac{\partial}{\partial x} \quad \frac{\partial}{\partial y}\right]^T$, and q^β [mol/(m^3.s)] is the rate of production/consumption of β-species per unit volume of porous medium, which in turn is a function of the concentration of aqueous silica, calcium and alkalis, i.e. $q^\beta = q^\beta(c^s, c^c, c^r)$.

Analogous expressions are obtained for the localized diffusion-reaction processes occurring in a discontinuity, such as a crack or and ITZ, of width *w* [m] and local orthogonal coordinates (*l*, *n*),

$$\begin{cases} \dfrac{\partial(w\varphi_{mp}c^s_{mp})}{\partial t} = \dfrac{\partial}{\partial l}\left(T_l^s \dfrac{\partial c^s_{mp}}{\partial l}\right) + wq^s_{mp} \\ \dfrac{\partial(w\varphi_{mp}c^c_{mp})}{\partial t} = \dfrac{\partial}{\partial l}\left(T_l^c \dfrac{\partial c^c_{mp}}{\partial l}\right) + wq^c_{mp} \\ \dfrac{\partial(w\varphi_{mp}c^r_{mp})}{\partial t} = \dfrac{\partial}{\partial l}\left(T_l^r \dfrac{\partial c^r_{mp}}{\partial l}\right) + wq^r_{mp} \end{cases} \quad (7)$$

where the under-script *mp* indicates that the concentration, the porosity and the sink/source rate are considered at the mid-plane of the discontinuity; T_l^β [m^3/s] is the effective longitudinal diffusivity of β-species in the discontinuity. The transversal passing fluxes j_n^β are given by

$$j_n^s = D_n^s \check{c}^s_{mp}; \quad j_n^c = D_n^c \check{c}^c_{mp}; \quad j_n^r = D_n^r \check{c}^r_{mp} \quad (8)$$

where D_n^s [m/s] is the effective transversal diffusivity of aqueous and $\check{c}^\beta_{mp}$ [mol/m^3] is the difference of concentration of β-species in pore solution between the two surfaces of the discontinuity. For a detailed discussion of diffusion processes through discontinuities refer to the work of Segura & Carol (2004).

A general expression of the production rate of β-species, q^β, is given in Eq. (14) as a function of the net rates of production of solid species resultant from Reactions (1) to (4), multiplied by the corresponding stoichiometric coefficient,

$$q^\beta = -\sum_\alpha x_\alpha^\beta \Gamma^\alpha(c) \quad (9)$$

where x_α^β is the dimensionless stoichiometric coefficient of β-species in the formation reaction of solid α-species, Γ^α [mol/(m^3.s)] is the reaction rate of solid α-species per unit volume of porous material (positive for solid formation, negative for solid dissolution), which is a function of the vector of local concentration of aqueous species $\mathrm{C} = \left[c^s \quad c^c \quad c^r \right]$, expressed in moles per unit volume of pore solution.

The calculation of the sink/source terms q^β according to Eq. (9) requires establishing the kinetic laws for Reactions (1) to (4) in order to obtain the corresponding reaction rates Γ^α. To do so, it is assumed that the driving force of the dissolution/precipitation reaction of reactive solid α-species is [1 – 2 exp (ψ^α ln2)], where ψ^α is the saturation index of the pore solution with respect to solid α-species. Dissolution and precipitation reactions are assumed not to occur simultaneously but alternately depending on ψ^α. If $\psi^\alpha > 1$ the solution is over-saturated with respect to α-species and, consequently, the reaction progresses in the precipitation direction. If $\psi^\alpha < 1$, the solution is under-saturated and solid dissolution occurs. If $\psi^\alpha = 1$, the solid and the solution are in thermodynamical equilibrium.

In order to determine the activities of the chemical species intervening in the kinetics laws described above, it is essential to determine the equilibrium concentrations of H^+ and OH^- for given concentrations of silicates (c^s), calcium (c^c) and alkalis (c^r) in the solution. This is achieved by solving a non-linear system of equations given by the equilibrium equation of Reaction (5) as well as the electric charge balance equation of the pore solution.

It has been found that by restricting the dissolution/formation reactions (1) to (4) to occur only at the ITZ and opened cracks (represented by means of interface elements), it is possible to substantially reducethe computational cost while obtaining sufficiently accurate results. With this simplification, the dissolution of glass and portlandite are assessed as dissolution fronts which move off the mid plane of the interface elements as the dissolution processes progress. In this approach, the continuum elements in between the interface elements only take part as diffusion media for the aqueous species.

The mass balance equation of solid α-species is given by

$$\frac{\partial M^\alpha}{\partial t} = \frac{(\partial \mathcal{U} \mathcal{N}^\alpha)}{\partial t} = \mathcal{U} \Gamma^\alpha \tag{10}$$

where M^α [mol] is the total quantity of solid α-species in the Representative Elementary Volume (REV), $\mathcal{U}$ [m^3] is the current volume of the REV, $\mathcal{N}^\alpha$ [mol/m^3] is the concentration of solid α-species per current unit volume of continuum porous medium or discontinuity.

The total volume of the REV of porous medium or discontinuity, $\mathcal{U}$, is given by

$$\mathcal{U} = \mathcal{U}^{cp} + \sum_\vartheta \mathcal{U}^\vartheta + \sum_\alpha \mathcal{U}^\alpha \tag{11}$$

where $\mathcal{U}^\vartheta$ is the volume of inert solid ϑ-species, $\mathcal{U}^\alpha$ is the volume of reactive solid α-species, and $\mathcal{U}^{cp}$ is the part of the REV volume not occupied by the solid phases and which is assumed to be filled with free water. In the porous medium $\mathcal{U}^{cp}$ is strictly the volume of capillary pores, but in discontinuities it also represents the empty volume created by a crack aperture. The volume of solid α-species is obtained as

$$\mathcal{U}^\alpha = \omega^\alpha M^\alpha ; \omega^\alpha = \frac{\eta^\alpha}{1 - \phi^\alpha} \tag{12}$$

where ω^α [m^3/mol] is the apparent molar volume, η^α [m^3/mol] is the 'specific' molar volume, and φ^α $\left[\mathrm{m}^3_{\mathrm{ps}} / \mathrm{m}^3 \right]$ is the intrinsic porosity of solid species α. Intrinsic porosity is defined as the ratio between gel water volume and total apparent volume of solid phase α. Note that for glass and portlandite the intrinsic porosity is null.

The $\mathcal{U}^{cp}$ in discontinuities and the continuous porous medium is calculated with

$$\mathcal{U}^{cp} = \left\langle U^* - \sum_\vartheta U^\vartheta - \sum_\alpha U^\alpha \right\rangle \tag{13}$$

where the operator $\langle X \rangle$ stands for 'the positive part of X', i.e. if $X < 0$, $\langle X \rangle = 0$ otherwise $\langle X \rangle = X$, and

$$U^* = 1 \qquad \text{for continuous medium} \tag{14}$$

$$U^* = w^{ITZ} + a_n \qquad \text{for discontinuities} \tag{15}$$

where w^{ITZ} [m] is the (equivalent) width of the ITZ, which is null for discontinuities in bulk aggregate or HCP, and a_n [m] is the normal aperture of the discontinuity. In a coupled analysis, a_n is obtained by solving the mechanical problem as explained in Section 2.2.

Since concrete is assumed to be fully saturated with water, the total volume of pore solution $\mathcal{U}^{ps}$ in the REV, which includes free and gel water, is equal to the total volume of pores and clean crack aperture, i.e.

$$\mathcal{U}^{ps} = \mathcal{U}^{cp} + \sum_\alpha \phi^\alpha \mathcal{U}^\alpha + \sum_\vartheta \phi^\vartheta \mathcal{U}^\vartheta \tag{16}$$

Finally, the total porosity ϕ is given by

$$\phi = \frac{\mathcal{U}^{ps}}{\mathcal{U}} \tag{17}$$

Eventually, the volume of reaction products may grow to a point in which the available space is exhausted, i.e. $\mathcal{U}^{cp} = 0$. From this point on, any additional amount of reaction products will impose an internal pressure on the solid skeleton surrounding the reaction site. The magnitude of this pressure will depend on the adopted mechanical constitutive laws both for the solid skeleton and for the ASR products.

3 PRELIMINARY MODELLING RESULTS: ASR CRACK PROPAGATION

The proposed model has been used for qualitatively reproducing the propagation of a crack due to ASR in concrete made with SL glass and subjected to external loading.

3.1 *Model description*

With this aim, an idealized geometry consisting in a 10 mm square of non-reactive mortar with a 3 mm circular inclusion of SL glass in its centre was considered (Fig. 2). At the four sides of the mortar square, loading plates were placed in order to impose suitable boundary conditions for the mechanical analysis. This geometry was discretized by means of 1180 linear triangular elements and 208 zero-thickness interface elements, a total of 866 nodes. The interface elements, indicated with thick lines in Fig. 2, were introduced within the mortar/glass domain in order to establish potential crack paths and chemical interfaces (such as the ITZ). The interface elements in between the loading plates and the mortar square, in contrast, were introduced only for simulating frictionless contacts.

For the mechanical analysis, a very stiff elastic material was assigned to the loading plates. The frictionless contacts were simulated by means of elastic interface elements with very high normal stiffness and very low tangential stiffness (see Table 1). The left and bottom plates were fixed, while the top and right plates were allowed to move only in their normal direction. The bulk mortar and glass were represented with linear elastic continuum elements with Poisson's coefficient of 0.20 and elastic moduli of 25 GPa and 74 GPa, respectively. The constitutive law proposed by Carol et al. (1997) was used for the zero-thickness interface elements representing potential crack paths. The relevant material parameters adopted for the interface elements are summarized in Table 1. Note that the pre-existing crack in the glass particle was represented with the same constitutive law as the crack paths in the sound glass, but with

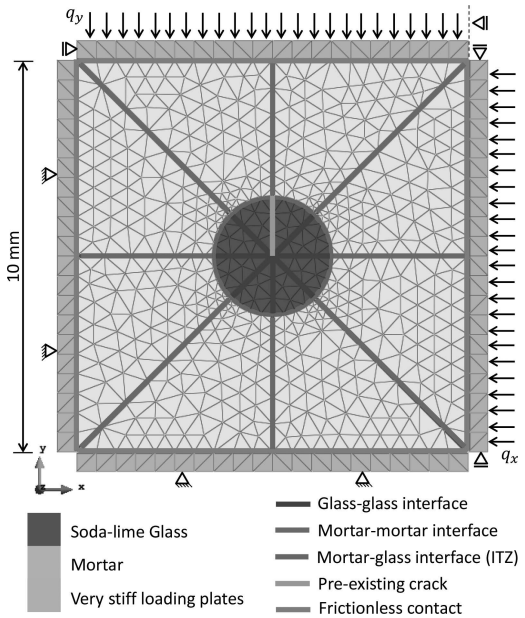

Figure 2. Model geometry, boundary conditions, and FE mesh.

Table 1. Relevant material parameters used in the simulations for zero-thickness interface elements. k_n: normal stiffness; k_t: tangential stiffness; $\mathcal{X}$: tensile strength; ϕ: friction angle; G_f^I: specific fracture energy in mode I; G_f^{IIa}: specific fracture energy in mode IIa.

Description	k_n [MN/m]	k_t [MN/m]	$\mathcal{X}$ [MPa]	c [MPa]	tan ϕ	G_f^I [MN/m]	G_f^{IIa} [MN/m]
Glass-Glass	1.00E+09	1.00E+09	3.00	9.00	0.70	2.50E-06	2.50E-05
Mortar-Mortar	1.00E+09	1.00E+09	3.00	9.00	0.70	1.00E-05	1.00E-04
Mortar-Glass	1.00E+09	1.00E+09	1.50	4.50	0.70	5.00E-06	5.00E-05
Pre-existent crack	1.00E+09	1.00E+09	0.01	0.015	0.70	5.00E-04	5.00E-03
Frictionless contact	1.00E+09	1.00E+00	n/a	n/a	n/a	n/a	n/a

much lower tensile strength. This artefact allowed the model to simulate contact forces between the two sides of the pre-existing crack when horizontal pressure (q_x in Fig. 2) was applied.

With regard to the diffusion-reaction analysis, the continuum mortar elements were assumed to be porous, with a total porosity of 0.48 and effective diffusion coefficients of 4.64, 3.12 and 5.28×10^{-8} m^2/h for silicate, calcium and alkali ions, respectively. The continuum glass elements were assumed to be impervious and without porosity. The zero-thickness interface elements within the glass particle and mortar matrix corresponding to potential crack paths had no initial 'volume', i.e. they remained chemically inactive unless a mechanical aperture had occurred due to cracking. In contrast, initial equivalent widths of 1.00×10^{-8} m and 1.00×10^{-7} m were assigned to the zero-thickness interface elements corresponding to the ITZ and the pre-existing crack, respectively, therefore allowing the reactions to occur within them since the beginning of the simulations regardless of whether there was or not any mechanical opening resulting from the mechanical analysis. The test temperature was considered to remain constant at 60 C, and the corresponding saturation product constants for reactions (1) to (4) were adopted to be 4.01×10^{-6}, 6.83×10^{-3}, 500 and 8.50×10^{-3}, respectively. The relevant chemical kinetic constants adopted for the zero-thickness interface elements are given in Table 2. A constant concentration of alkalis in pore solution of 1 mol/L was imposed at the mortar square boundaries. For calcium and silicate ions in pore solution, the square boundaries were considered to be impervious.

Table 2. Dimensionless chemical kinetic constants adopted for zero-thickness interface elements in the simulations. k_d^S, K_d^C : dissolution kinetic constant of glass and portlandite, respectively; k_f^{RPA}, k_f^{RPB} : formation kinetic constant of RPA and RPB.

Description	k_d^S	k_d^C	k_f^{RPA}	k_f^{RPB}
Glass-Glass	2.4E-09	0.0E+00	2.0E+03	1.0E+02
Mortar-Mortar	0.0E+00	4.0E-02	2.0E+03	1.0E+02
Mortar-Glass	1.2E-09	2.0E-02	2.0E+03	1.0E+02
Pre-existent crack	2.4E-09	0.0E+00	2.0E+03	1.0E+02

3.2 *Results*

Three different loading cases are studied: a) without any external load, b) with uniform vertical pressure of 10 MPa, and c) with uniform horizontal pressure of 10 MPa.

In Fig. 3 the deformed FE mesh after 112 days at 60 C are presented for the three loading cases considered. In the first and second cases, the pre-existing crack in the glass propagates into the mortar, while in the third case the horizontal pressure does not allow the crack propagation. Note also that no cracks can be observed at the ITZ in none of the three cases. The energy spent in fracture is plotted in Fig. 4, confirming the remarks made for the deformed meshes in Fig. 3.

In Fig. 5, the volume of ASR gel formed within the ITZ and in opened cracks are indicated. Complementarily, Fig. 6 displays the profiles of Ca/Si molar ratio of the formed ASR gel. At the beginning of the simulation, in the three cases, a uniform layer of calcium-rich ASR gel is formed at the ITZ around the aggregate, until the moment when the pressure exerted by the surrounding mortar matrix is high enough to inhibit the process. For the first and second loading cases, highly-expansive low-calcium ASR gel is formed within the aggregate making the pre-existent crack to propagate through the glass particle and into the mortar. In the third case, low-calcium ASR gel is also formed within the pre-existent crack, but in this case the pressure exerted by the gel is not high enough to overcome the applied horizontal pressure of 10 MPa.

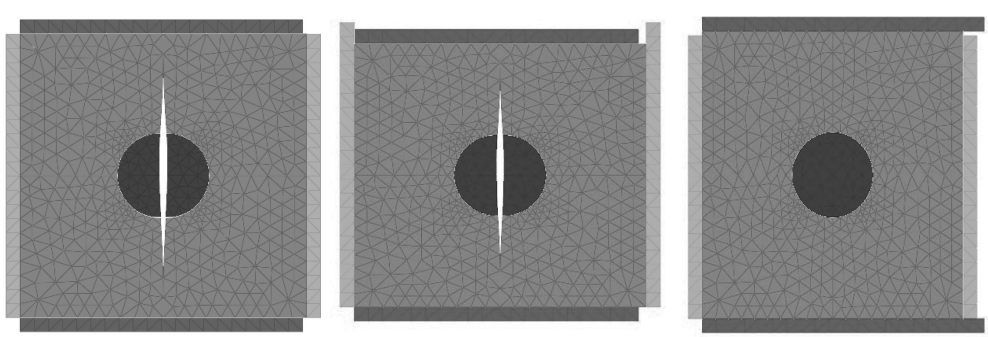

Figure 3. Deformed FE mesh (x200) after 112 days of ASR. (a) $q_x = q_y = 0$; (b) $q_x = 0$, $q_y = 10$ MPa; (c) $q_x = 10$ MPa, $q_y = 0$.

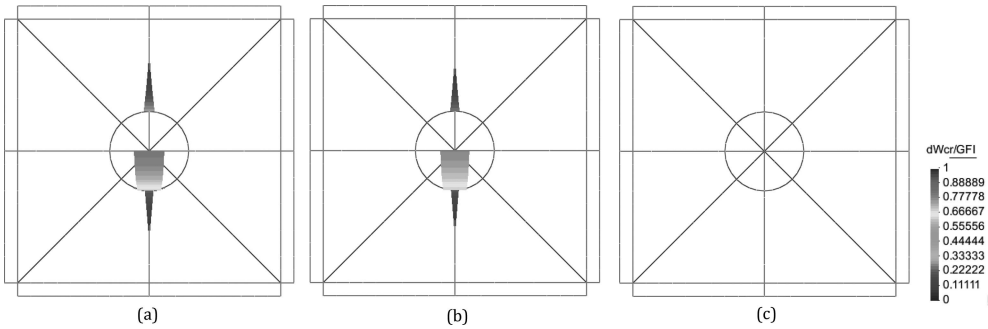

Figure 4. Energy spent in fracture after 112 days of ASR, expressed as a fraction fo the specific fracture energy of the material in mode I. (a) $q_x = q_y = 0$; (b) $q_x = 0$, $q_y = 10$ MPa; (c) $q_x = 10$ MPa, $q_y = 0$.

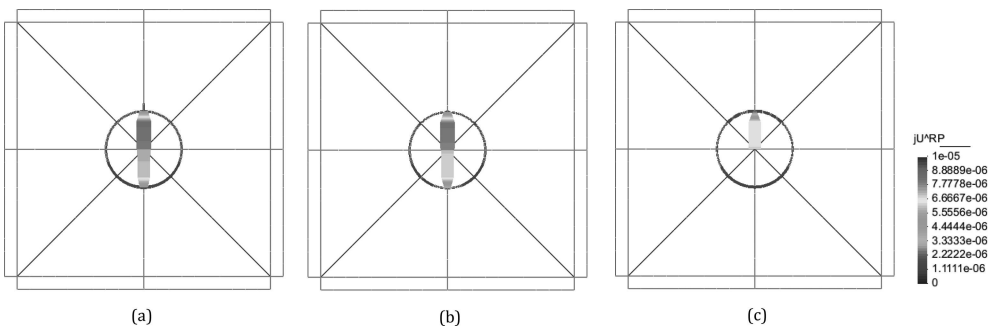

Figure 5. Volume [m] of reaction products in interface elements after 112 days of ASR. (a) $q_x = q_y = 0$; (b) $q_x = 0$, $q_y = 10$ MPa; (c) $q_x = 10$ MPa, $q_y = 0$.

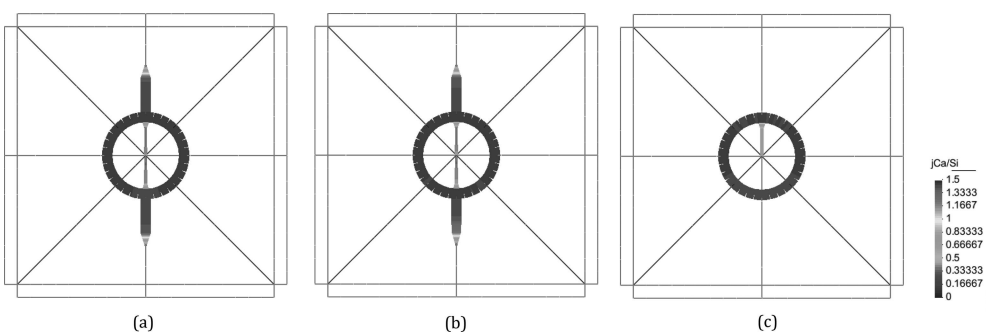

Figure 6. Ca/Si molar ratio of reaction products in interface elements after 112 days of ASR. (a) $q_x = q_y = 0$; (b) $q_x = 0$, $q_y = 10$ MPa; (c) $q_x = 10$ MPa, $q_y = 0$.

4 CONCLUDING REMARKS

As part of an ongoing research project, a coupled chemo-mechanical model for the simulation ASR expansions in concrete at the meso-scale has been briefly described and some preliminary results presented.

The model seems capable of reproducing the propagation of cracks due to the formation of ASR products, as well as the effect of applied stresses observed experimentally.

Some original features of the model such as the localized diffusivity in opened cracks, the precipitation of reactions products within in opened cracks,

and the compressibility of the ASR gel, turn out essential to reproduce experimental observations.

Ongoing work is aimed at the simulation of full size concrete specimens (multiple reactive aggregates) in order to reproduce the experimental expansion curves obtained by the authors with specimens under true triaxial confinement (Liaudat et al. 2017).

ACKNOWLEDGEMENTS

This work was partially supported by research grant BIA2016-76543-R from MEC (Madrid), which includes European FEDER funds and by AGAUR/Generalitat de Catalunya (Barcelona) through project 2014SGR–1523.

REFERENCES

Caballero, A., C.M. López, & I. Carol (2006). 3D meso-structural analysis of concrete specimens under uniaxial tension. *Computer Methods in Applied Mechanics and Engineering 195*(52), 7182–7195.

Carol, I., C.M. López, & O. Roa (2001). Micromechanical analysis of quasi brittle materials using fracture based interface elements. *International Journal for Numerical Methods in Engineering 52*, 193–215.

Carol, I., P.C. Prat, & C.M. López (1997). Normal/Shear Cracking Model: Application to Discrete Crack Analysis. *Journal of Engineering Mechanics 123*(8), 765–773.

Idiart, A.E., C.M. López, & I. Carol (2011a, mar). Chemomechanical analysis of concrete cracking and degradation due to external sulfate attack: A meso-scale model. *Cement and Concrete Composites 33*(3), 411–423.

Idiart, A.E., C.M. López, & I. Carol (2011b, jun). Modeling of drying shrinkage of concrete specimens at the meso-level. *Materials and Structures 44*(2), 415–435.

Liaudat, J., A. Martínez, C.M. López, & I. Carol (2015). Numerical Modelling of ASR Expansions in Concrete. In C. Hellmich, B. Pichler, and J. Kollegger (Eds.), *10th International Conference on Mechanics and Physics of Creep, Shrinkage, and Durability of Concrete and Concrete Structures (CONCREEP 10)*, pp. 445–454. Vienna, Austria: American Society of Civil Engineers.

Liaudat, J., C.M. López, & I. Carol (2013). Diffusion-reaction model for alkali-silica reaction in concrete. In E. Oñate, D. Owen, D. Peric, and B. Suárez (Eds.), *Computational Plasticity XII - Fundamentals and Applications* (First ed.)., pp. 479–489. Barcelona: International Center for Numerical Methods in Engineering (CIMNE).

Liaudat, J., C.M. López, & I. Carol (2014). Diffusion-reaction model for ASR: formulation and 1D numerical implementation. In N. Bicanic, H. Mang, G. Meschke, and R. de Borst (Eds.), *Computational Modelling of Concrete and Concrete Structures* (First ed.)., Number 2, pp. 639–648. St. Anton am Arlberg, Austria: CRC Press.

Liaudat, J., C.M. López, & I. Carol (2016). Numerical and Experimental study of ASR in concrete at the meso-level. In V. Saouma, J. Bolander, and E. Landis (Eds.), *The 9th Inter national Conference on Fracture Mechanics of Concrete and Concrete Structures (FraMCoS 9)*.

Liaudat, J., I. Carol, C.M. López, & V.E. Saouma (2017). ASR Expansions in Concrete under Triaxial Confinement. *Submitted for publication*.

López, C.M., I. Carol, & A. Aguado (2008). Meso-structural study of concrete fracture using interface elements. I: numerical model and tensile behavior. *Materials and Structures 41*, 583–599.

Maraghechi, H., F. Rajabipour, C.G. Pantano, & W.D. Burgos (2016). Effect of calcium on dissolution and precipitation reactions of amorphous silica at high alkalinity. *Cement and Concrete Research 87*, 1–13.

Maraghechi, H., S.-M.-H. Shafaatian, G. Fischer, & F. Rajabipour (2012, jan). The role of residual cracks on alkali silica reactivity of recycled glass aggregates. *Cement and Concrete Research 34*(1), 41–47.

Pérez, A., M. Rodriguez, C.M. Lopez, & I. Carol (2013). 3D Meso-mechanical analysis of cracking and spalling of concrete subject to high temperatures. In E. Oñate, D. Owen, D. Peric, and B. Suárez (Eds.), *Computational Plasticity XII - Fundamentals and Applications*, pp. 1015–1025. Barcelona, Spain: International Center for Numerical Methods in Engineering (CIMNE).

Rajabipour, F., H. Maraghechi, & G. Fischer (2010). Investigating the alkali-silica reaction of recycled glass aggregates in concrete materials. *Journal of Materials in Civil Engineering 22*(12), 1201–1208.

Rodríguez, M., C. L´opez, & I. Carol (2017). Modelling of heat and moisture transfer in concrete at high temperature. In E. Oñate, D. Owen, D. Peric, and M. Chiumenti (Eds.), *Computational Plasticity XIV Fundamentals and Applications*. Barcelona, Spain: International Center for Numerical Methods in Engineering (CIMNE).

Segura, J.M. & I. Carol (2004, aug). On zero-thickness interface elements for diffusion problems. *International Journal for Numerical and Analytical Methods in Geomechanics 28*(9), 947–962.

Computational Modelling of Concrete Structures – Meschke, Pichler & Rots (Eds)
© 2018 Taylor & Francis Group, London, ISBN 978-1-138-74117-1

Numerical strategies for the modelling of reinforced concrete structures affected by internal swelling in variable thermo-hydric conditions

B. Nedjar & C. Rospars
IFSTTAR/MAST, Université Paris-Est, Cité Descartes, France

ABSTRACT: Internal Swelling Reactions (ISR) can affect long term duration of Reinforced Concrete (RC) structures by causing cracking and expansion of concrete material. These pathologies mainly consist in Alkali Aggregate Reaction (AAR) and/or Delayed Ettringite Formation (DEF). Thus, it is necessary to provide robust predictive numerical models able to re-assess the mechanical state of affected structures. A new numerical strategy is proposed in this paper to compute the evolution of the ISR reaction from intrinsic parameters to be identified for the reactive concrete. Based on Larive's model, evolution of the chemical strain is written in order to assume the irreversibility of the mechanisms and to take into account time history of the Relative Humidity and Temperature supported by the concrete specimen. An effective time is proposed to store history of the reactive concrete and to be able to compute evolution of the chemical strain.

1 INTRODUCTION

The Internal swelling reactions can affect long term duration of reinforced concrete (RC) structures by causing cracking and expansion of concrete material. These pathologies mainly consist in Alkali Aggregate Reaction (AAR) and Delayed Ettringite Formation (DEF). AAR is an internal swelling reaction, which can affect concrete and occur over time. It is due to progressive formation of an expansive amorphous gel that involves silica from reactive aggregates and alkalis of the concrete pore solution. This expansive process leads to the macroscopic effects mainly consisting in materials swelling, cracking and decreasing of the mechanical properties, which can cause structural disorders due to unexpected strain and thus additional stresses in concrete. DEF consists in late Ettringite crystallization within concrete after hardening that may occur in material subjected to a heating above 65°C at early age and to high humidity. Thus, it is necessary to provide robust predictive models able to re-assess the mechanical state of affected structures, such as dams, bridges, tunnels, or nuclear power plant and nuclear waste storage. Long-term management of civil engineering concrete structures needs finite element models able to demonstrate the reliability of these RC structures over time.

Moreover concrete, even non-reactive, presents delayed strain, which control its long-term mechanical behaviour. In main models, the total delayed strain are splitted into autogenous shrinkage, drying shrinkage, dessiccation, basic and drying creep, and if AAR and/or DEF occurs in an additional chemical strain. Within the framework of the methodology written for the reassessment of ISR affected concrete structures, a calculation method has been developed. Several models describing the mechanical phenomenology of AAR or DEF affected structures have been published by LCPC and then IFSTTAR (Larive 1998; Ulm et al. 2000; Baghdadi et al. 2008; Capra & Sellier 2003 and more recently and Martin et al. 2013, and Al Shamaa et al. 2015). Based on calibrating the parameters of the expansion laws that describe the chemical evolution of ISR reaction, an algorithm of the resolution was proposed and implemented in CESAR-LCPC (Ulm et al. 2000, Baghdadi et al. 2008, Multon et al. 2008). It is known as "RGIB" operator. Herein, a new numerical strategy is proposed to compute chemical expansion strain independently of other delayed strains. The evolution of the ISR reaction is obtained from intrinsic parameters to be identified for the reactive concrete. Identification of parameters could be done using results of residual expansion tests on cores stored in a 100% Relative Humidity atmosphere in the case of AAR and immersed in water in the case of DEF. Based on Larive's model, see for example (Larive, 1998), evolution law of the chemical strains is written in order to assume the irreversibility of the mechanisms and to take into account time history of the Relative Humidity supported by the concrete specimen. An effective time is then proposed to store history of the reactive concrete

and to be able to compute evolution of the chemical strain. As creep and shrinkage can affect long-term behaviour of RC structure, all delayed strains will be compute if necessary.

2 MODELLING STRATEGIES FOR CONCRETE

2.1 *Numerical model*

Concrete presents an elastic brittle behavior in tension and its heterogeneities and porous characteristics leads to complex physico-chemical phenomena that must be describe through the mechanical model. Besides, the objective is the re-assessment of RC structures, that can be massive structures such as dams and massive concrete walls, all the major mechanisms must be introduced in the modeling. As a consequence, numerical model targeted for non-reactive concrete must be properly written before implementation of chemical delayed phenomenon.

The kinematic choice is as usual based on an additive split of the total strain tensor ε into an elastic part ε^e and complementary parts, each one corresponding to a phenomenon. To be as clear as possible, let us start by considering the simplest choice:

$$\varepsilon = \varepsilon^e + \varepsilon_{th} + \varepsilon_{hyd} + \varepsilon_x + \varepsilon_c + \ldots \tag{1}$$

where ε_{th} and ε_{hyd} are respectively the thermal and hydric dilatations, and ε_x the chemical expansion tensor, and ε_c the creep strain tensor, and so on, if another delayed strain must be introduced in the computation.

Using this kinematic choice, each strain can be assessing using a classical formulation. ε_{th} and ε_{hyd} are given using the classical relations:

$$\varepsilon_{th} = \alpha (T - T_0)\mathbf{1} \tag{2}$$
$$\varepsilon_{hyd} = \beta (S_r - Sr_0)\mathbf{1}$$

where α and β are respectively the thermal and hydric dilatation coefficients, $\boldsymbol{I}$ being the second-order identity tensor. Recall that T_0 and S_{r0} are the initial temperature and saturation, respectively, and notice that a form based on the relative humidity can be used instead of $(2)_2$.

From the estimation of the total strain ε, the elastic strain can be deduced and then a constitutive law can be derived in the classical standard mechanical framework. The kinematic decomposition (1) must be embedded into a constitutive relation. At this point, knowing all delayed strain (ε_x, ε_c, … for example), and knowing the thermo-hydric dilatations, the simplest choice is o consider an elastic relation for the reversible behavior. We then write:

$$\sigma = \boldsymbol{C} : \varepsilon^e \tag{3}$$

where σ is the stress tensor and the elastic part of the strain tensor is the one that has been used in the decomposition (1). $\mathbf{C}$ is the fourth-order elasticity tensor that can in turn be affected by damage as:

$$\boldsymbol{C} = (1 - d)\ \boldsymbol{C}_0 \tag{4}$$

This damage variable d can be chemical damage and/or mechanical damage, and $\mathbf{C}_0$ is the elastic modulus for the undamaged concrete. d is then an internal damage variable in the sense of continuum damage mechanics. This internal variable can be driven from stress or strain state, any existing damage model in the literature, or from evolution of chemical strain in case of chemical damage. In case of mechanical damage, its estimation depends on a damage law to be written separately.

Using such kinematic solution it is a numerical framework to derive each strain separately and then estimate elastic strain on which elastic relation (3) is applied. This framework will allow introducing mathematical formulation to model the effect of each thermo-hydric strain and additional delayed strain. It is then easy to write mathematical formulation for creep evolution (ε_c) and chemical evolution (ε_x) in case of ISR.

In this paper we focus on the resolution of thermic and hydric dilatation and then in the last paragraph on the basic chemical law derive from Larive's model to deal with ISR affected concrete.

2.2 *Water diffusion and drying in concrete*

Due to the high couplings between moisture and expansions, previous authors had pointed out the need to propose reliable assessment of the water content to predict realistic expansions, see for instance (Seignol et al. 2006; Grimal 2007). To deal with the thermo-hydric diffusion, an operator has been developed for linear as well as non-linear transient analyses, i.e. hydric diffusion and early age hydration. For thermal diffusion, the basic equation is used. The boundary-value problem will be solved iteratively to extend its use for nonlinear transient problems. For a coupled thermo-hydric problem, the two sub-problems are uncoupled during the numerical procedure. That is, the thermal field is solved first, followed then by the hydric diffusion. From the calculation of thermal hydration, we append the possibility to compute a field of the chemical strain potential. This strain potential (denoted ε_∞^0), depending on the thermal early age history, can enter into the phenomenological

modeling of DEF swelling if, after maturation, concrete is subjected to humidity.

For hydric problem, the principal unknown of the problem is chosen to be the field of concentration, or water content, denoted here by $C(x,t)$ of dimension l/m^3, and governed by:

$$\frac{\partial C}{\partial t} + div\left[-D(C;T)\nabla C\right] = 0 \tag{5}$$

where $D(C;T)$ is the hydric diffusion coefficient (m^2/s) that depends on both of the unknown C and the temperature T. In this model, we use the following expression that have been proposed by Granger (1995):

$$D(C;T) = Ae^{(BC)} \times \frac{T}{T_r} \times e^{\left\{-\frac{Q_s}{R}\left(\frac{1}{T}-\frac{1}{T_r}\right)\right\}} \tag{6}$$

where A (m^2/s), B, T_r in °K are material parameters. For instance, a usual value for the latter is $Q_s/R \approx 4700$°K. This form (6) is a combination of the Mensi-Acker et al. (1988) law and a thermo-activation proposed by Bazant (1972). At the end of a hydric computation, the result is plotted in terms of the saturation S_r defined as:

$$S_r(x,t) = \frac{C(x,t)}{C_{100}} \tag{7}$$

This resolution of water diffusion and drying in concrete is addressed to normal concrete. From the resolution of this two uncoupled sub-problems, thermal field and the water content field histories are computed for the whole structure.

2.3 *Numerical simulation scheme*

The French Institute of Science and Technology for Transport and Civil Engineering (IFSTTAR, formerly LCPC) developed a model allowing re-assessing AAR and DEF affected structures since Larive (1998). An algorithm of resolution was implemented in CESAR-LCPC Finite Element (F.E.) software and known as "RGIB" calculation modulus. It consists in an evolution of a pre-existing modulus "ALKA" which concerns the recalculation of concrete structures affected only by AAR, extended to DEF. This embedded modulus RGIB proved its efficiency in the re-assessment of concrete affected structures like dams (Metalssi et al. 2014). The concrete behavior is supposed to be linear elastic; endogenous creep is not fully represented, except its long-term value that is taken using EC2 prevision. Besides, its full-encapsulated algorithm leads to limitation in evolution laws. Recently, R.P. Martin et al. (2013) questioned about the necessity to better take into account coupling between transfer properties in internal swelling reaction. Coupling between creep and chemical strain is questionable too. As a consequence, if modeling results on small specimen give good predictions comparing to experimental response, simulation of ISR-affected large beams (AAR or DEF) is not totally satisfactory. The deflection of DEF beam is initially predicted to develop much faster than experimentally. In the AAR case, strain tends to be underestimated at the end of the monitoring period (R.P. Martin et al. 2013).

To deal with this challenge a rewritten of this modulus RGIB is being done in this work using the kinematic choice presented in section 1. Separation and then superposition of delayed strains to estimate the total strain, and thus the elastic strain, allows addressing standard evolution laws for each delayed strain.

Another interest of this numerical strategy is to propose a numerical framework able to deal with non-reactive concrete in addition to reactive concrete. The mechanical behavior of normal concrete, i.e. elastic damage model can be then fully modeled. Moreover, delayed strains, shrinkage and creep, participate to the behavior of the whole structure since early age and remain during all the concrete structure life duration. Some are specifically initiated during early age:

- early age shrinkage (endogenous shrinkage link to hydration and thermic shrinkage),
- drying shrinkage obtained with the modeling of concrete drying.

Which need specific algorithm for their calculation. As the response at early age is a key issue in the design of massive structures, especially in the core because of the heat released by hydration, modeling of early age need to be completely done. Then from maturation, endogenous creep and desiccation creep appear when concrete is submitted to stress. All these delayed strains can be dealt separately using proper equations. It concerns non-reactive concrete as well as reactive concrete. For reactive concrete (ISR affected concrete) an additional chemical strain (expansion) must be calculated. A good prediction of all these delayed strain, from early age, provide better understanding of the thermo-chemical phenomena occurring during experimental strain measured on specimens and beams.

Within this numerical framework, from the thermo-hydric diffusion obtained (see section 2.2), we first implemented the calculation of the chemical extension tensor (ε_x). For affected concrete this delayed chemical expansion is the major phenomenon observed with expansion of almost 0.2% for AAR to more than 2% for DEF.

3 CHEMICAL EXPANSION OF ISR AFFECTED CONCRETE

3.1 *Constitutive equations and mechanical balance*

This formulation is devoted to the expansion of reactive concrete and the mechanical coupling related to chemical expansions due to AAR and/or to DEF. The kinematical choice is as usual based on an additive split of the total strain as mentioned in section I. In this section, we focus on the chemical strain evolution. If we consider a purely volumetric chemical expansion, we write:

$$\boldsymbol{\varepsilon}_x = \varepsilon_x \mathbf{1} \tag{8}$$

where the scalar functional $\varepsilon_x(S_r, T, t, \ldots)$ is the so-called free chemical expansion, the expression of which depends on the humidity, the temperature, and of course on the time as well. In fully saturated conditions ($S_r = 1$ all the time), one has the nowadays well-known expression used for both of ISR (AAR or DEF) expansion phenomena. Following Brunetaud (2005), Baghdadi (2008) or Martin (2010):

$$\varepsilon_\chi = \varepsilon_\infty^0 \frac{1 - e^{\left(-\frac{t}{\tau_c}\right)}}{1 + e^{\left(-\frac{t-\tau_L}{\tau_C}\right)}} \left(1 - \frac{\varphi}{1+\delta}\right) \tag{9}$$

where ε_∞^0 is the potential chemical strain that constitutes an amplitude of expansion, τ_c and τ_L are respectively the characteristic and latent times, and ϕ and δ are parameters that control the long term kinetics. They are such that $\delta > \phi$. When ϕ is set to zero, the equation (9) reduces to Larive's law (1998). Whatever the exact formulation used, irreversibility of the expansion must be insured.

3.2 *Effective time*

A notion of effective time is introduced to control the amount of water (humidity) during time. This extends the applicability of the expansions models not only for cases of full saturation, but for variable conditions as well. The interest is to control the irreversibility of the chemical expansion and to block evolution of expansion when hydric condition decreased beyond a threshold. Above the threshold, swelling strongly depends on the relative humidity as well as on the temperature.

For the case of an AAR analysis, ε_∞^0 is a given parameter that depends on the concrete class, while for a DEF analysis, it depends of the thermal history at early age. To fix the ideas the following definition has been used:

$$\varepsilon_\infty^0 = \dot{\varepsilon}_m \int_0^{t_m} \begin{cases} 0 & T \le T_{def} \\ e^{\left[-\frac{E_0^{def}}{R}\frac{1}{T - T_{def}}\right]} & T > T_{def} \end{cases} dt, \tag{10}$$

where $\dot{\varepsilon}_m$ is a stain-rates-like material parameter that represents the material properties influencing the swelling pathology (cement grade, aggregates, concrete class,…), T_{def} is the threshold of temperature above which DEF can be generated, E_a^{def} is the activation energy relative to DEF expansion, and t_m is the maturation time.

The field $\varepsilon_\infty^0(x)$ is known during the mechanical analysis, and this fact plays a crucial role in the algorithmic design for the numerical approximation. Now to take into account the influences of both the thermal and hydric conditions, relation (9) must be adapted.

Variable thermal conditions: It has been shown experimentally that the ambient temperature has an influence on the kinetics of expansion (Poyet, 2003). Among other choices we can consider that the two characteristic times be thermo-active with the forms:

$$\tau_L = \overline{\tau}_L e^{\left[-\frac{U_L}{R}\left(\frac{1}{T} - \frac{1}{\overline{T}}\right)\right]}, \quad \tau_C = \overline{\tau}_C e^{\left[-\frac{U_C}{R}\left(\frac{1}{T} - \frac{1}{\overline{T}}\right)\right]} \tag{11}$$

as suggested in Larive (1998) for AAR. Here $\overline{\tau}_L$ and $\overline{\tau}_C$ are reference characteristic times for a reference temperature $\overline{T}$, and U_L and U_C are activation energies. Notice that, even possible, the amplitude ε_∞^0 is not thermo-activated here because of the lack of experimental evidence.

Variable hydric conditions: Experimental evidences have also shown that the expansion stops below a certain threshold of humidity. In terms of saturation, denoting this latter by $\overline{S}_r$, we can write:

$$\begin{cases} \dot{\varepsilon}_\chi = 0, & if\ S_r \le \overline{S}_r \\ \dot{\varepsilon}_\chi > 0, & if\ S_r > \overline{S}_r \\ \varepsilon_\chi\ is\ given\ by\ (9), & if\ S_r = 1 \end{cases} \tag{12}$$

Now for $\overline{S}_r < S_r < 1$, we need to establish a continuous link between the extreme situations. We introduce for this an effective time that we denote by $\tilde{t}$ and such that:

$$\dot{\tilde{t}} \equiv \dot{\tilde{t}}(S_r, t, \ldots) \in [0,1] \tag{13}$$

with the possible choice:

$$\dot{\tilde{t}} = \left(\frac{\langle S_r - \overline{S}_r \rangle_+}{1 - \overline{S}_r}\right)^m \Rightarrow \tilde{t} = \int_0^t \left(\frac{\langle S_r - \overline{S}_r \rangle_+}{1 - \overline{S}_r}\right)^{\overline{m}} dt \tag{14}$$

where the exponent parameter most probably depends on the saturation, $\bar{m}$ is function of S_r, and $<.>_+$ denotes the Macauley brackets. Hence, by replacing the real time t by effective time into the expression (9), we obtain a free expansion law that covers the requirements (12) for variable humidity.

Furthermore, and besides on the above features, if the final expansion amplitude depends on the level of saturation, i.e. $\varepsilon_\infty^0 \equiv \varepsilon_\infty^0(S_r)$, a possible choice could be:

$$\varepsilon_\infty^0 \equiv \varepsilon_\infty^0(S_r = 1) \times S_r^{m_\infty} \tag{15}$$

with m_∞ is a material parameter that can be identified from free expansion tests at different levels of saturation, keeping in mind that no expansion occurs when $S_r < \bar{S}_r$.

4 A NUMERICAL EXAMPLE

We consider the example of a beam made with a concrete that potentially develops DEF expansion. This beam mimics the experimental procedure developed in Martin et al. (2013) where a very reactive concrete has been choosen for the purpose of their experimental campaign, see also Martin (2010). Before going on, we first need to characterize the intrinsic behavior of the reactive concrete with regards to its DEF expansion.

4.1 *Free swelling on concrete samples*

We consider (11 × 22) cm cylindrical samples submitted to variable humidity conditions at a constant temperature T = 38°C. We choose the following set of parameters with regards to the relation (9):

$\tau_c = 13$ days, $\tau_l = 89$ days,
$\phi = 18$ days, $\delta = 120$ days,
$\bar{S}_r = 0.95$, $\varepsilon_\infty^0(S_r = 1) = 1.3110^{-2}$,

and $\bar{m} = 1 + 42.5S_r + 1750S_r^2$ for the exponent parameter in (14).

The results of the computations are shown in Figure 1 where one can notice the extreme sensitivity of the expansion kinetics for hydric conditions between the threshold $\bar{S}_r = 0.95$ and full saturation ($S_r = 1$).

4.2 *Free swelling of the concrete beam*

The above concrete is now used for the free swelling of a beam of 3 m length, 0.5 m height, and 0.25 m depth. For the finite element computation, the mesh discretization is shown in Figure 2.

For the thermal conditions, a uniform temperature of 38°C is imposed throughout the history so

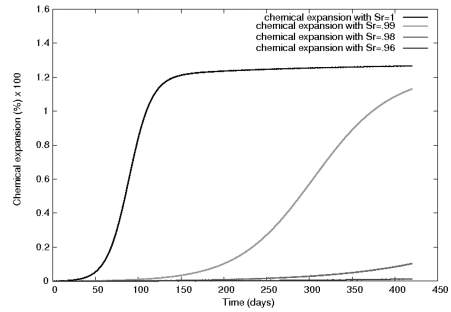

Figure 1. Free expansions of concrete samples at different saturation conditions.

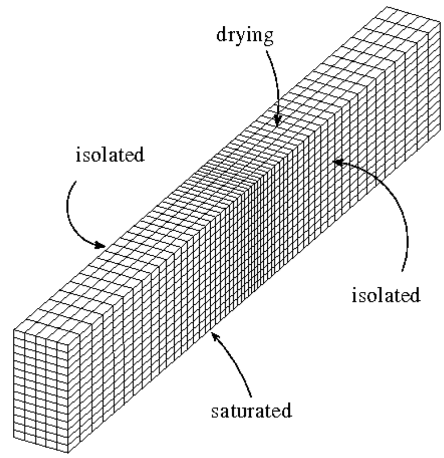

Figure 2. Free swelling of a concrete beam. Finite element mesh and hydric boundary conditions.

that the coefficient of thermal dilatation α is useless in the present example, equation $(2)_1$.

For the hydric conditions, the bottom face is continuously saturated at $S_r = 1$ and the top face is continuously dried at a saturation below threshold, here at $S_r = 0.3$, and the lateral faces are hydrically isolated so as to produce a gradient of humidity along the vertical direction of the beam. The initial condition of the saturation is $S_r = 0.9$ and the coefficient of hydric dilatation β, see equation $(2)_2$:

$\beta = 0.9 \times 10^{-3}$.

Last, the beam is simply supported on its bottom smallest edges.

Figure 3 shows the deformed configuration of the beam after 420 days. Notice the large expansion at the neighborhood of the bottom face where full expansion has been reached while at the level of the top face no expansion occurs. This causes a

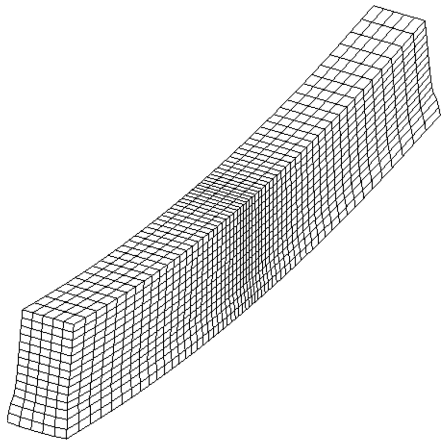

Figure 3. Free swelling of a concrete beam after 420 days.

non negligible bending of the whole beam. In all cases, further testing need to be performed that takes into account the self-weight of the specimen together with the influence of the both of the chemical and mechanical damage on the overall response. This work is still ongoing.

5 CONCLUSION

This paper presents a model based on continuum damage mechanics to re-assess reinforced concrete structure. The kinematic choice is based on an additive split of the total strain tensor ε into an elastic part ε^e and complementary parts, each one corresponding to a delayed phenomenon. The mechanical behavior of normal concrete, i.e. elastic damage model can be then fully modeled using constitutive equations. Moreover, delayed strains, shrinkage and creep, are separately evaluated. The thermo-hydric diffusion is calculated using an operator developed for linear as well as non-linear transient analysis. For reactive concrete (ISR affected concrete) an additional chemical strain (expansion) is then computed. Within this numerical framework, from the thermo-hydric diffusion obtained, we first implemented the calculation of the chemical extension tensor (ε_x). Based on Larive's model, evolution of the chemical strain is written in order to assume the irreversibility of the mechanisms and to take into account time history of the Relative Humidity and Temperature supported by the concrete specimen. An effective time is then proposed to store history of the reactive concrete and to be able to compute evolution of the chemical strain.

This numerical strategy is able to model the behaviour of ISR affected concrete and give a numerical framework for additional coupling between phenomena like transfer properties and expansion. An application of this numerical strategy is given in the Malbois et al. 2018.

REFERNCES

Al Shamaa M, Lavaud S., Divet L., Nahas G., Torrenti JM, Influence of relative humidity on delayed ettringite formation, Cement & Concrete Composites 58 (2015) 14–22.

Baghdadi N;, Seignol JF, Toutlemeonde F., Chemo-mechanical model describing the expansion due to internal sulphate attack: numerical simulation, International RILEM symposium on concrete modelling CONMOD'08. Delft, The Netherlands: 2008. P. 291–98.

Bazant Z.P., Nonlinear water diffusion in nonstaurated concrete. Materiaux et Constructions, 5(25):3–20, 1972.

Capra B., Sellier A., Orthotropic modelling of alkali-aggregate reaction in concrete structures: numerical simulations, Mechanics of Materials, 35 (2003) 817–830.

Granger L., Comportement différé du béton dans les enceintes de central nucléaire: Analyse et modélisation. PhD thesis, ENPC, 1995.

Grimal E., Caracterization des effets du gonflement provoqué par la reaction alkali-silice sur le comportement mécanique d'une structure en béton. PhD thesis, Université Paul Sabatier, France, 2007.

Larive C., Apports combinés de l'expérimentation et de la modélisation à la comprehension de l'alkali-réaction et de ses effets mécaniques. ERLPC OA 28 (LCPC, 1998).

Martin R.P., Experimental analysis of the mechanical effects of delayed Ettringite Formation on concrete strcutures. PhD thesis, Université Paris Est, 2010.

Martin RP, Metalssi O, Toutlemonde F., Importance of considering the coupling between transfer properties, alkali leaching and expansion in the modelling of concrete beams affected by internal swelling reactions, Construction and Building Materials 49 (2013) 23–30.

Metalssi O, Seignol JF, Rigobert S., Modeling the cracks opening-closing and possible remedial sawing operation of AAR-affected dams, Engineering Failure Analysis 36 (2014) 199–214.

Multon S., Barin FX, Godart B, Toulemonde F., Estimation of the residual expansion of concrete affected by alkali silica reaction, J Mater Civ Eng 2008: 20(1): 54–62.

Poyet S., Etude de la degradation des ouvrages en béton atteints par la reaction alkali-silice: Approche expérimentale et modélisation numérique multi-échelle des degradations dans un environement hydro-chemo-mécanique variable. PhD thesis, Université de Marne La Vallée, 2003.

Seignol J.F., Ngo TT., Toutlemonde F., Modelling of the coupling between moisture and ASR in concrete. In: Euro-C conference. Mayrhofen, Austria: 2006 p. 639–46.

Ulm FJ, Coussy O., Kefei L., Larive C., Thermo-chemico-mechanics of ASR expansion in concrete structures. J Eng. Mech 2000: 126(3): 233–42.

Computational Modelling of Concrete Structures – Meschke, Pichler & Rots (Eds)
© 2018 Taylor & Francis Group, London, ISBN 978-1-138-74117-1

A finite element implementation of delayed ettringite formation in concrete structures

M. Malbois
Laboratoire de Mécanique et Technologie—ENS Cachan, Cachan Cedex, France

B. Nedjar, L. Divet, S. Lavaud & J.-M. Torrenti
IFSTTAR/MAST, Université Paris-Est, Marne-la-Vallée Cedex 2, France

ABSTRACT: Delayed Ettringite Formation (DEF) in concrete is likely to develop in massive civil engineering structures such as bridges, nuclear plants, and dams with major security issues. DEF pathology can lead to swelling and cracking which may significantly impact mass transfer and mechanical properties. It is then of major importance to build predictive tools for engineering conceptions and expertizes. In this contribution, the chemical swelling evolution is integrated within the overall constitutive law of concrete that, besides, can experience other phenomena such like damage, plasticity, and long term creep, not all considered here. On another hand, as DEF is activated by environmental humidity above a certain threshold, we use a notion of effective time that takes into account the cumulative exposition above this threshold. Hence, a special care is taken with regards to the chemical irreversibility, together with the humidity-drying cycles. The computations are used to calibrate the model parameters with the help of results from an experimental compaign where two kinds of concretes were studied; one with siliceous aggregates, and one with calcious aggregates. We show the efficiency of the developed numerical tool through a series of examples.

1 INTRODUCTION

Delayed ettringite formation (DEF) in concrete can have significant impact on the long term behaviour of massive concrete structures. Ettringite is a crystal that has been chraracterised in the 1970s by Moore & Taylor (1970) and its formation controls the concrete hardening, and the material workability at young age as well. Under a particular set of conditions, ettringite formation could be delayed and could lead to degradations of the material. The swelling induced by the development of delayed ettringite generates cracking and so can affect the durability of the concrete structures. The economic impact of DEF can then be potentially significant due to maintenance and repairing, or even destruction fees. It is then of major importance to build numerical tools that can simulate this expanding kinematics and its consequences on the structural serviceability.

It is unanimously admitted that DEF develops under peculiar conditions:

- High temperature during curing due to the cement hydration process or to thermal treatments undergone by pre-casted concrete. For instance, Kchakech (2015) took an interest in defining the impact of the duration and temperature of the thermal treatment on DEF.
- Humid environment: DEF develops when concrete is at high humidity conditions or in contact with water, see for example (Heinz, Ludwig, & Rüdiger 1989, Martin 2010, Older & Chen 1995, among others), due to the departure of alkalines and the pH drop.
- Cement composition: Pavoine, Brunetaud, & Divet (2012) studied the impact of sulphates, aluminates and alkalis, and the cement fineness on DEF as well.
- Aggregate mineralogy nature and size: (Monteiro & Mehta 1986, Grattan-Bellew, Beaudoin, & Vallee 1998, Brunetaud 2005, Al Shamaa, Lavaud, Divet, Colliat, Nahas, & Torrenti 2016, among others) have demonstrated that sand and aggregates can impact the DEF in terms of kinetics as well as in amplitude.

From the mathematical point of view, extensive research has been conducted to model expansions caused by DEF, see for example (Baghdadi 2008, Brunetaud 2005, Kchakech 2015, Martin 2010, among others), and further developments are nowadays still ongoing. The models are mostly based on phenomenological approaches formulated in

terms of internal variables. The expansion is in general characterized by two important ingredients:

(*i*) An amplitude that depends on the temperature history at early age due to hydration and/or on heating conditions if a curing process is employed such as for pre-casting;

(*ii*) A kinetics that depends on the time, more precisely on the cumulated time, of exposure in contact with water.

Of interest in this work is the use of a notion of *effective* time, that we denote throughout by $\tilde{t}$, and that controls the amount of water (humidity) during time and, consequently, influences the kinetics of expansion, i.e. the above ingredient *(ii)*. This extends the applicability of the existing expansion models not only for cases of full saturation, but for varying conditions as well. Among others, the effective time depends on a threshold below which the swelling process stops, and above which swelling strongly depends on humidity as well as on temperature.

Within the continnum, the effective time is an internal field variable since each material point x has its own humidity history during the real time t; $\tilde{t} \equiv \tilde{t}(x,t)$. Hence, in the context of the finite element method, its update and storage are performed at the level of the integration points. This procedure is appended to the classical numerical thermo-hydro-mechanical treatment of concretes subjected to DEF expansions.

An outline of the remainder of this paper is as follows: we first recall the basic constitutive equations together with the simplest kinematical assumption we adopt in this work. The notion of effective time is then motivated and detailed. Then, focus is made on the most relevant points involved by the present formulation within the context of the finite element method. Finally, we present a set of numerical simulations to illustrate the effectiveness of the proposed framework that compare satisfactorily against experimental data from an experimental compaign and from results in the literature.

2 SWELLING KINEMATICS

The kinematical choice is as usual based on an additive split of the *total* strain tensor $\boldsymbol{\varepsilon}$ into an elastic part $\boldsymbol{\varepsilon}^e$ and complementary parts, each one corresponding to a phenomenon. To be as clear as possible, let us consider the simplest choice,

$$\boldsymbol{\varepsilon} = \boldsymbol{\varepsilon}^e + \boldsymbol{\varepsilon}_{th} + \boldsymbol{\varepsilon}_{hyd} + \boldsymbol{\varepsilon}_{\chi}, \tag{1}$$

where $\boldsymbol{\varepsilon}_{th}$ and $\boldsymbol{\varepsilon}_{hyd}$ are respectively the thermal and hydric dilatations, and $\boldsymbol{\varepsilon}_{\chi}$ the chemical expansion tensor, in our case due to DEF. We can use the classical relations for the formers as:

$$\boldsymbol{\varepsilon}_{\text{th}} = \alpha(T - T_0)\mathbf{1}, \quad \boldsymbol{\varepsilon}_{\text{hyd}} = \varpi(S_r - S_{r0})\mathbf{1}, \tag{2}$$

where T is the temperature, S_r is the saturation, α and ϖ are respectively the thermal and hydric dilatation coefficients, assumed constant for simplicity, and 1 is the second-order identity tensor. Here T_0 and S_{r0} are the initial temperature and the initial saturation, respectively. Notice that a form based on the relative humidity can be used instead of $(2)_2$ as well.

Now if we consider a purely volumetric chemical expansion, we write:

$$\boldsymbol{\varepsilon}_{\chi} = \varepsilon_{\chi}\mathbf{1}, \tag{3}$$

where the scalar functional $\varepsilon_{\chi} \equiv \varepsilon_{\chi}(S_r, T, t \ldots)$ is the so-called free chemical expansion, the expression of which depends on the humidity, the temperature, and of course on the time as well. In fully saturated conditions ($S_r = 1$ all the time), one has the nowadays well known expression used for both of DEF and Alkali-Agregate Reaction (AAR) expansions phenomena, see for example (Brunetaud 2005, Baghdadi 2008, Martin 2010, among others):

$$\varepsilon_{\chi} = \varepsilon_{\infty}^0 \frac{1 - e^{\left(-\frac{t}{\tau_c}\right)}}{1 + e^{\left(-\frac{t-\tau_l}{\tau_c}\right)}} \left(1 - \frac{\phi}{1+\delta}\right), \tag{4}$$

where ε_{∞}^0 is the potential chemical strain that constitues an amplitude of expansion, i.e. ingredient *(i)* in the Introduction Section. τ_c and τ_l are respectively the characteristic and latent times, and ϕ and δ are parameters that control the long term kinetics such that $\delta > \phi$. Equation (4) reduces to Larive's law (Larive 1998) when the parameter ϕ is set to zero.

For the case of a DEF analysis, ε_{∞}^0 depends on the thermal history at *early-age*. To fix the ideas the following definition has been used, see (Baghdadi 2008, Seignol, Baghdadi, & Toutlemonde 2009, among others):

$$\varepsilon_{\infty}^0 = \dot{\varepsilon}_{\text{m}} \int_0^{t_{\text{m}}} \begin{cases} 0, & T \le T_{\text{def}} \\ e^{\left[-\frac{E_a^{\text{def}}}{R}\frac{1}{T - T_{\text{def}}}\right]}, & T > T_{\text{def}} \end{cases} \text{d}t, \tag{5}$$

where $\dot{\varepsilon}_{\text{m}}$ is a material parameter, T_{def} is the threshold of temperature above which DEF can be generated, E_a^{def} is the activation energy relative to DEF expansion, and t_{m} is the maturation time.

The field $\varepsilon_{\infty}^0(x)$ is assumed known during the mechanical part of the analysis, and this fact plays a crucial role in the algorithmic design for

the numerical approximation. Now to take into account the influences of both of the thermal and hydric conditions, relation (4) must be adapted. We can assume the following choices.

2.1 *Variable thermal conditions*

It has been shown experimentally that the ambient temperature has an influence on the kinetics of expansion. We can for instance consider that the two characteristic times be thermo-activated as

$$\tau_l = \overline{\tau}_l e^{\left[-\frac{U_l}{R}\left(\frac{1}{T}-\frac{1}{\overline{T}}\right)\right]}, \qquad \tau_c = \overline{\tau}_c e^{\left[-\frac{U_c}{R}\left(\frac{1}{T}-\frac{1}{\overline{T}}\right)\right]}, \tag{6}$$

as suggested in (Larive 1998, Poyet 2003) for AAR. Here $\overline{\tau}_l$ and $\overline{\tau}_c$ are reference characteristic times for a reference temperature $\overline{T}$, and U_l and U_c are activation energies. Notice that, even possible, the amplitude ε_∞^0 is not thermo-activated in our DEF case because of the lack of experimental evidence. So that, at this point, the characteristic times τ_l and τ_c are assumed constant.

2.2 *Variable hydric conditions*

Experimental evidences have also shown that the expansion stops below a certain threshold of humidity, see (Al Shamaa, Lavaud, Divet, Nahas, & Torrenti 2015). In terms of saturation, denoting this threshold by $\overline{S}_r$, we can formally write:

$$\begin{cases} \dot{\varepsilon}_\chi = 0, & \text{if } S_r \le \overline{S}_r, \\ \dot{\varepsilon}_\chi > 0, & \text{if } S_r > \overline{S}_r, \\ \text{and } \varepsilon_\chi \text{ is given by (4)}, & \text{if } S_r = 1. \end{cases} \tag{7}$$

Now for $\overline{S}_r < S_r < 1$, we need to establish a *continuous* link between the extreme situations $(7)_1$ and $(7)_3$. We introduce for this an *effective* time that we denote by $\tilde{t}$ and such that,

$$\dot{\tilde{t}} \equiv \dot{\tilde{t}}(S_r, t, \ldots) \in [0,1]. \tag{8}$$

A possible choice would be:

$$\dot{\tilde{t}} = \left(\frac{\langle S_r - \overline{S}_r \rangle_+}{1-\overline{S}_r}\right)^{\overline{m}}$$

$$\Rightarrow \qquad \tilde{t} = \int_0^t \left(\frac{\langle S_r - \overline{S}_r \rangle_+}{1-\overline{S}_r}\right)^{\overline{m}} dt, \tag{9}$$

where the exponent parameter most probably depends on the saturation, i.e.

$$\overline{m} \equiv \overline{m}(S_r), \tag{10}$$

and $\langle\cdot\rangle_+$ denotes the Macauley brackets.

Hence, by replacing the real time t by the effective time $\tilde{t}$ into the expression (4), we obtain a free expansion law that covers the requirements (7) for variable humidity. Furthermore, and besides on the above features, if the final expansion amplitude depends on the level of saturation, i.e. $\varepsilon_\infty^0 \equiv \varepsilon_\infty^0(S_r)$, a possible choice could be

$$\varepsilon_\infty^0 = \varepsilon_\infty^0(S_r = 1) \times S_r^{\mathrm{m}_\infty}, \tag{11}$$

where m_∞ is a material parameter that can be identified from free expansion tests at different levels of saturation, keeping in mind that no expansion occurs when $S_r < \overline{S}_r$.

3 CONSTITUTIVE EQUATIONS AND MECHANICAL BALANCE

The kinematic decomposition (1) must now be embedded into a constitutive relation. At this point, the simplest choice is to consider an elastic relation for the reversible behaviour:

$$\boldsymbol{\sigma} = \mathbf{C} : \varepsilon^e, \tag{12}$$

where $\boldsymbol{\sigma}$ is the stress tensor and the elastic part of the strain tensor $\boldsymbol{\varepsilon}^e$ is the one that has been used in the decomposition (1). $\mathbf{C}$ is the fourth-order elasticity tensor that can in turn be affected by chemical damage as

$$\mathbf{C} = (1 - d_\chi)\mathbf{C}_0, \tag{13}$$

where $\mathbf{C}_0$ is the elastic modulus for the undamaged concrete and d_χ is a damage variable in the sense of contiuum damage mechanics. Intuitively, this latter can be driven by the chemical expansion itself, then explicitly given as a function of the quantity ε_χ, for instance, the following form as adopted in (Baghdadi 2008, Seignol, Baghdadi, & Toutlemonde 2009):

$$d_\chi = 1 - e^{\left[-\omega\langle \varepsilon_\chi - \varepsilon_{\mathrm{trs}} \rangle_+\right]}, \tag{14}$$

where $\varepsilon_{\mathrm{trs}}$ is the strain-like chemical damage threshold, and $\omega \ge 0$ a convenient parameter, i.e. no chemical damage takes place if we set $\omega = 0$.

With (12) we have a minimalist modelling framework with the simplest possible resolution procedure. The mechanical balance is linear since the thermal and hydric fields are a priori known at every time step. At the actual time t_{n+1} for instance, its weak form is given by:

$$\int_{\mathcal{B}} \nabla^s \delta\boldsymbol{u} : \mathbf{C}_{n+1} : \nabla^s \boldsymbol{u}_{n+1} \, \mathrm{d}V = G_{n+1}^{ext}(\delta\boldsymbol{u}) + \int_{\mathcal{B}} \nabla^s \delta\boldsymbol{u} : \mathbf{C}_{n+1} : (\mathcal{E}_{\mathrm{th}_{n+1}} + \mathcal{E}_{\mathrm{hyd}_{n+1}} + \mathcal{E}_{\chi_{n+1}}) \mathrm{d}V, \tag{15}$$

which must hold for any displacement variation δu, and where $\nabla^s(.)$ is the symmetric gradient operator. Here G^{ext}_{n+1} is a short hand notation for the virtual work of the external loads embedding both of the volumetric forces in the body $\mathcal{B}$ and traction forces on part of its boundary $\partial_t\mathcal{B} \subset \partial\mathcal{B}$ applied at time t_{n+1}.

Equation (15) is to be solved for the actual displacement field $\boldsymbol{u}_{n+1}$. However, care must be taken in evaluating the chemical strain $\varepsilon_{\chi_{n+1}}$ on the right hand-side of (15). Indeed, this latter is computed with the effective time $\tilde{t}_{n+1}$ that is updated locally at each time step as:

$$\tilde{t}_{n+1} = \tilde{t}_n + \left(\frac{\left\langle S_{r_{n+1}} - \overline{S}_r \right\rangle_+}{1 - \overline{S}_r} \right)^{\overline{m}_{n+1}} \Delta t, \tag{16}$$

where $\Delta t = t_{n+1} - t_n$ is the *real* time increment, and the exponent parameter $\overline{m}_{n+1}$ is evaluated with $S_{r_{n+1}}$, i.e. $\overline{m}_{n+1} \equiv \overline{m}(S_{r_{n+1}})$ in the form (10).

Consequently, the effective time is treated as an internal field variable; $\tilde{t} \equiv \tilde{t}(\boldsymbol{x},t)$.

4 OUTLINES OF THE FINITE ELEMENT APPROXIMATION

Notice that, beforehand, a thermo-hydric analysis must be performed. For the first step, the thermal computation is classical if we consider a linear analysis. Within a solid domain $\mathcal{B}$, the thermal field $T(\boldsymbol{x},t)$ at any point $\boldsymbol{x} \in \mathcal{B}$ and at any time t is governed by the following evolution equation:

$$\rho c \frac{\partial T}{\partial t} + \text{div}[-k \nabla T] = 0, \quad \text{in } \mathcal{B}, \tag{17}$$

where ρ is the mass density, c is the specific heat capacity, and k is the thermal conductivity. In general, these latter quantities are assumed constant in our applications. div[.] is the divergence operator and, without loss of generality, internal heat sources are not considered at this point for the sake of simplicity.

To this equation, one must append an initial condition for the thermal field at a reference time t_0:

$$T(\boldsymbol{x}, t = t_0) = T_0(\boldsymbol{x}), \tag{18}$$

together with boundary conditions over time of the Dirichlet-type on a part $\partial_T\mathcal{B}$ of the boundary $\partial\mathcal{B}$, and/or of the Neuman-type on the complementary part $\partial_q\mathcal{B} = \partial\mathcal{B} \backslash \partial_T\mathcal{B}$. We write these latter generically as,

$$\begin{cases} T(\boldsymbol{x},t) &= \overline{T}(\boldsymbol{x},t) \quad \text{on } \partial_T\mathcal{B}, \\ -k \nabla T.\boldsymbol{n} &= \overline{q}(\boldsymbol{x},t) \quad \text{on } \partial_q\mathcal{B}, \end{cases} \tag{19}$$

where $\boldsymbol{n}$ is the unit outward normal to the boundary $\partial\mathcal{B}$. The given scalar functions $\overline{T}(\boldsymbol{x},t)$ and $\overline{q}(\boldsymbol{x},t)$ are assumed known. Linear and nonlinear exchange conditions can easily be adapted by replacing in $(19)_2$ the function $\overline{q}$ by an adequate expression of the form $\overline{q}(\boldsymbol{x},T(t),t)$. For the case of a (linear) Fourier condition, one has

$$\overline{q} = h(T(\boldsymbol{x},t) - T^{\text{ext}}(\boldsymbol{t})), \tag{20}$$

where $T^{\text{ext}}(t)$ is the known external temperature, and h is the coefficient of exchange by convection.

In the next step, the hydric diffusion must be solved for. The principal unknow of the problem is chosen here to be the field of concentration, or *water content*, denoted by $C(\boldsymbol{x},t)$ of dimension $[C] = l/m^3$, governed by,

$$\frac{\partial C}{\partial t} + \text{div}[-D(C;T) \nabla C] = 0, \quad \text{in } \mathcal{B}, \tag{21}$$

where $D(C;\ T)$ is the hydric diffusion coefficient that depends on both of the unknown C and the temperature T, and $[D] = m^2/s$. Here we use the following expression that have been proposed by Granger (1995):

$$D(C;T) = A\, e^{(BC)} \times \frac{T}{T_r} \times e^{\left(-\frac{Q_s}{R}\left(\frac{1}{T} - \frac{1}{T_r}\right)\right)}, \tag{22}$$

where A (with $[A] = m^2/s$), B, T_r in $°K$ and the fraction Q_s/R in $°K$ are material parameters. For instance, a usual value used for the latter is $Q_s/R \approx 4700°K$. The form (22) is a combination of the law of Mensi, Acker, & Attolou (1988) and a thermoactivation proposed by Bazant (1972).

Equation (22) is supplemented by an initial condition $C_0 = C(\boldsymbol{x},\ t_0)$ at the reference time t_0 introduced above and by boundary conditions of the Dirichlet- and/or Newman-types.

Now coming back to the resolution of the mechanical balance, in the finite element context, the displacement field is defined at the nodes as

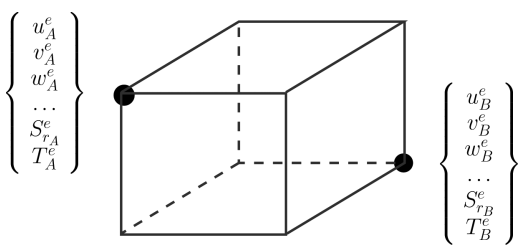

Figure 1. Typical finite element with nodal *dof*s in the mechanical analysis.

well as for the temperature and hydric fields, these latter being stored on a nodal data-base from the former steps of the Thermo-Hydro-Mechanical computation, see Figure 1 for an illustration. The interpolations of the reference geometry and the above fields over a typical element $\mathcal{B}_e$ take the form

$$\begin{aligned}
\boldsymbol{X}_e(\zeta) &= \sum_{A=1}^{n^e_{\text{node}}} N^A(\zeta)\boldsymbol{X}^e_A,\\
\boldsymbol{u}_e(\zeta) &= \sum_{A=1}^{n^e_{\text{node}}} N^A(\zeta)\boldsymbol{u}^e_A,\\
S_{r_e}(\zeta) &= \sum_{A=1}^{n^e_{\text{node}}} N^A(\zeta)S^e_{r_A},\\
T_e(\zeta) &= \sum_{A=1}^{n^e_{\text{node}}} N^A(\zeta)T^e_A,
\end{aligned} \tag{23}$$

where $\boldsymbol{X}^e_A \in \mathbb{R}^{n_{\text{dim}}}, \boldsymbol{u}^e_A \in \mathbb{R}^{n_{\text{dim}}}, S^e_{r_A} \in \mathbb{R}$ and $T^e_A \in \mathbb{R}$ denote, the reference position, the displacement vector, the saturation, and the pore temperature, respectively, associated with the element node A. $n_{\text{dim}} = 2$ or 3 is the space dimension, and $N^A(\zeta)$ are the classical isoparametric shape functions.

The element contribution to the stiffness matrix associated with the element is similar to an elastic linear analysis. From (15) we have:

$$\boldsymbol{K}^{AB}_e = \int_{\mathcal{B}_e} \mathbb{B}^T[N^A]\mathbf{C}_{n+1}\mathbb{B}[N^B]\mathrm{d}V_e, \tag{24}$$

where $A, B = 1, \ldots n^e_{\text{node}}$, and $\mathbb{B}[.]$ is the discrete symmetric gradient operator. At each time step, the elastic modulus $\mathbf{C}_{n+1}$ is computed from (13) where the chemical damage $d_{\chi_{n+1}}$ is computed from the function (14) evaluated with the help of the actual free chemical expansion $\varepsilon_{\chi_{n+1}}$ which, in turn, is evaluated with the updated effective time $\tilde{t}_{n+1}$, see below.

For the contribution to the vector of nodal forces, we have:

$$\begin{aligned}
F^A_e = {} & F^{\text{ext}\,A}_e\\
& + \int_{\mathcal{B}_e} \mathbb{B}^T[N^A](\mathbf{C}_{n+1} : \mathcal{E}_{\text{th}_{n+1}})\mathrm{d}V_e\\
& + \int_{\mathcal{B}_e} \mathbb{B}^T[N^A](\mathbf{C}_{n+1} : \mathcal{E}_{\text{hyd}_{n+1}})\mathrm{d}V_e\\
& + \int_{\mathcal{B}_e} \mathbb{B}^T[N^A](\mathbf{C}_{n+1} : \mathcal{E}_{\chi_{n+1}})\mathrm{d}V_e,
\end{aligned} \tag{25}$$

for $A = 1, \ldots n^e_{\text{node}}$, and $F^{\text{ext}\,A}_e$ is a shorthand notation for the discrete nodal forces relative to the external volumetric and surfacic loadings.

Last, the update (16) of the effective time $\tilde{t}_{n+1}$ and its storage are performed locally at the level of the integration points.

5 SIMULATIONS OF DEF EXPANSIONS FOR IMMERSED SAMPLES

In order to trigger DEF expansions, concrete samples were designed for their known expansive behaviour when heat-treated and immersed in water after casting. The concrete formulation used is detailed in Table 1. The Portland cement CEMII/A L with 6% of calceous additions (42.5 MPa) is used with a 0.57 water-cement ratio. Furthermore, two kinds of aggregates were used: siliceous (Palvadeau aggregates) and calcareous (Boulonnais aggregates).

In order to simulate the heating induced by cement hydration in massive structures, the samples undergo a thermic treatment detailed in Figure 2: temperature was increased from 20°C to 80°C in 24 h, then maintained at 80°C for three days, then decreased from 80°C to 20°C in three days. After this treatment, samples are immersed in water at 20°C; those with siliceous aggregates, and half of those with calcareous aggregates. The other half will undergo saoking and drying cycles. In all cases, 11 × 22 cm cylindrical samples have been used.

Table 1. Concrete composition.

Materials	Composition
Cement	350 kg
Water	210 kg
Sand (0–5 mm)	858 kg
Aggregates (5–12.5 mm)	945 kg
Viscosity modifying admixture	6.6 kg
W/C	0.57
A/S	1.1
Density	2354 kg/m^3

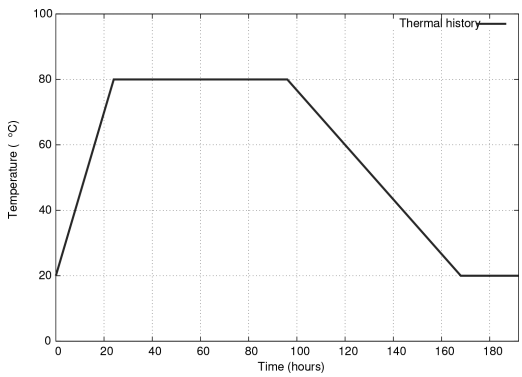

Figure 2. Heating treatment of the 11 × 22 cm cylindrical samples during first hours after curing.

5.1 *Simulations for siliceous-based concrete*

The experimental evolution of the mean expansions for samples made with siliceous aggregates is presented in Figure 3, with square-dot-points. It displays a complete profile of DEF expansion and is stabilized after one year with a maximum relative swelling of 0.959%. Curve fitting with the free-expansion law (4) gives the parameters summarized in Table 2. Here we observe that the law by Larive (1998) is sufficient for the modelling of expansion (Equation (4) with $\phi = 0$).

With these values, the simulated expansion is superposed in Figure 3 where good agreement is to be noticed. Here for the sake of simplicity, uniform temperature and uniform water content have been imposed, this later was set at the saturation $S_r = 1$ during the whole computation. In this case, the effective time is equal to the real time, i.e. $\tilde{t} = t$ for all the material points of the cylindrical sample, and swelling is governed by the property $(7)_3$.

5.2 *Simulations for calcareous-based concrete*

In Figure 4 we present similar results, this time for the sample made with the calcareous aggregates. The experimental data are shown in square-dots-points. Here the curve only just left the latent phase

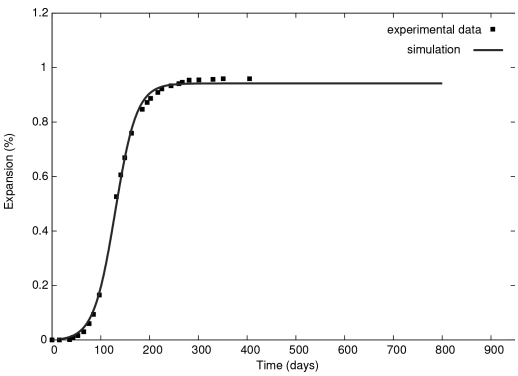

Figure 3. Swelling of concrete samples with siliceous aggregates. Experimental data and numerical simulation.

Table 2. Material parameters with the expansion law (4) for the siliceous-based concrete.

Definition	Identified values
Expansion amplitude $\mathcal{E}_\infty^0$	0.94%
Latent time τ_l	129.4 days
Characteristic time τ_c	22.05 days
Parameter ϕ	0
Parameter δ	0

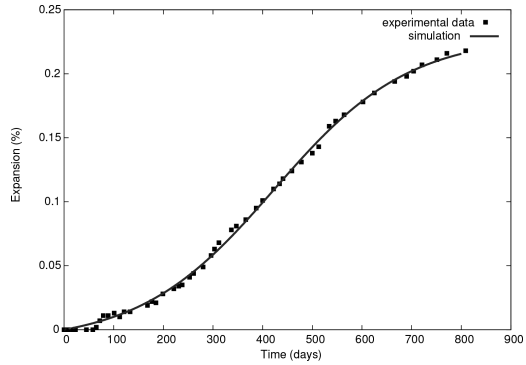

Figure 4. Swelling of concrete samples with calcareous aggregates. Experimental data and numerical simulation.

Table 3. Material parameters with the expansion law (4) for the calcareous-based concrete.

Definition	Identified values
Expansion amplitude $\mathcal{E}_\infty^0$	0.23%
Latent time τ_l	423.5 days
Characteristic time τ_c	135.48 days
Parameter ϕ	0
Parameter δ	0

and is beginning the asymptotic phase. Observe further that the use of calcareous aggregates generates less swelling than with siliceous aggregates, i.e. about 0.2 to 0.22% maximum expansion.

Curve fitting with the free-expansion law (4) gives this time the parameters summarized in Table 3 still Larive's law is sufficient with $\phi = 0$. Among others, we observe here that the latent and characteristic times are much higher than the ones with the former concrete, while the expansion amplitude is almost four times lesser.

With these values, the simulated expansion is superposed in Figure 4 where, here again, a good agreement is to be noticed. As the samples are immersed during the whole time, uniform saturation $S_r = 1$ is taken and, consequently, the effective time is identical to the real time here again.

5.3 *Simulations of the effect of soaking-drying cycles on DEF*

A second set of samples with the above calcareous aggregates was submitted to cycles of drying (at 50% of relative humidity and 20°C) alternated with soaking (at 20°C) to represent a more realistic environment of some structures which are not permanently in contact with water.

The swelling monitoring of this new study is plotted in Figure 5 (the dashed line with circle

dots), and compared to the previous experimental curve of Figure 4 with the samples kept continuously immersed in water (square-dots-points curve). One can notice that the drying cycles restrict the delayed ettringite formation in the material and have an important impact on the expansion kinetics.

From the modelling point of view, this falls within the scope of the properties $(7)_1$ for drying, and $(7)_3$ for soaking. For the material parameters of the expansion law (4), we use the ones of Table 3. And for the effective time (9), we fix the saturation threshold to $\overline{S}_r = 0.95$. Here the computation is independent of the exponent parameter $\overline{m}$ since:

$$\dot{\tilde{t}} = \begin{cases} 1 & \text{for soaking, with } S_r = 1, \\ 0 & \text{for drying, since } S_r \ll \overline{S}_r. \end{cases} \tag{26}$$

In the numerical computation, uniform saturation $S_r = 1$ is taken during the first 72 days, then cycles of drying for 13 days at $S_r = 0.48$ followed by soaking for 19 days at $S_r = 1$ are prescribed. In total, the sample is immersed 514 days and dried 295 days.

The simulated expansion is superposed in Figure 5 where good agreement is again observed. Notice further that the expansion after 809 days of alternate soaking/drying cycles is almost the same as the 514 days' expansion in continuous immersion conditions.

6 SIMULATIONS OF THE INFLUENCE OF THE RELATIVE HUMIDITY ON DEF EXPANSIONS

In this section we present simulations with regards to experimental tests given in (Al Shamaa, Lavaud, Divet, Nahas, & Torrenti 2015) on the study of the influence of relative humidity on expansion associated with DEF in concrete.

Different 11 × 22 cm cylindrical samples made with a siliceous-based aggregate concrete were heat-treated as given in Figure 2, and then separated in different groups, each group submitted to a controled constant relative humidity RH:

- Samples that have been stored at 94%, 96%, 98% and 100% RH, respectively denoted by RH94, RH96, RH98 and RH100;
- Samples that have been immersed continuously, denoted by IM;
- Samples that have been stored at 91% RH and then immersed in water at the age of 334 days, denoted by RH91-IM.

The experimental results are shown in Figure 6 where interesting observations must be pointed out. Among others:

- Expansions under continuous immersion and RH100 (no shown here) are almost identical;

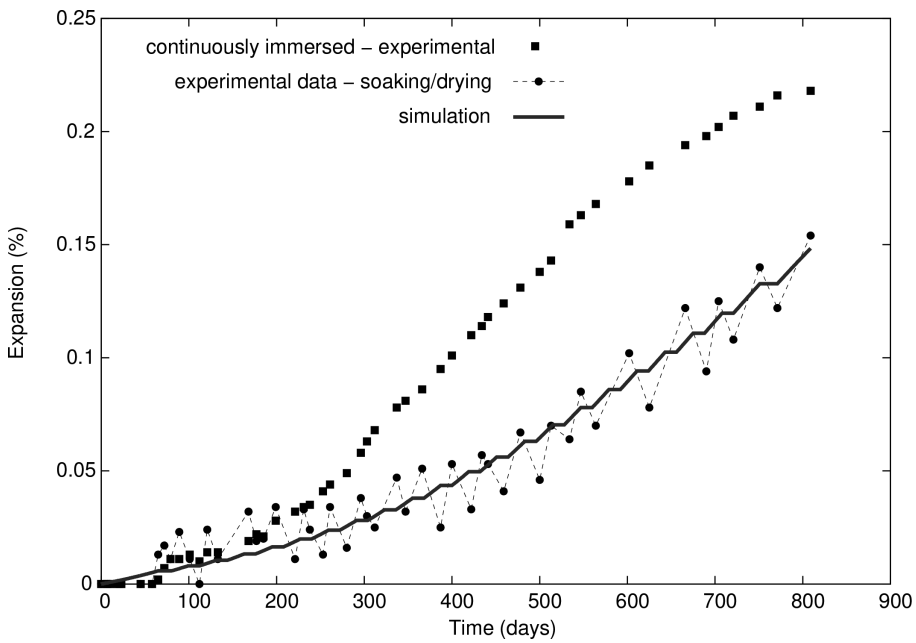

Figure 5. Impact of drying cycles on the swelling of concrete samples with calcareous aggregates. Experimental data and numerical simulation.

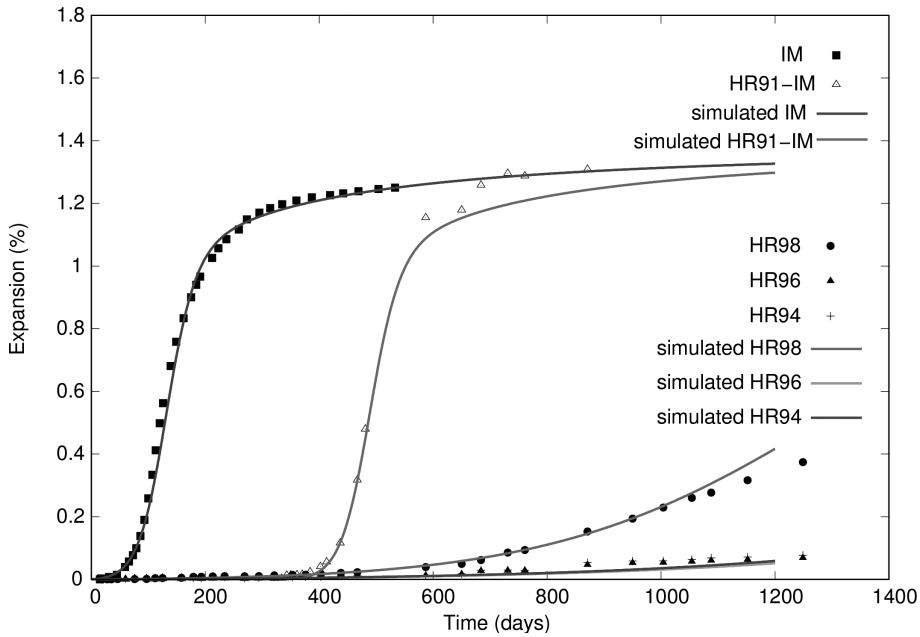

Figure 6. Expansions of all concrete specimens. Experimental results from (Al Shamaa & al., 2015). Superposition with the results of the numerical simulations.

Table 4. Material parameters with the expansion law (4) for the siliceous concrete of Figure 6.

Definition	Identified values
Expansion amplitude $\mathcal{E}_\infty^0$	1.4%
Latent time τ_l	128 days
Characteristic time τ_c	25 days
Parameter ϕ	68 days
Parameter δ	100 days

– With a relative humidity of 91%, the saturation is under the threshold $\bar{S}_r$;
– Above the saturation threshold, the expansion is very sensitive to the ambiant humidity, i.e. from 94 to 100% RH.
– The expansion amplitude is of the same order than that of the previous compaign with siliceous aggregates, here about 1.2%.

From the curve obtained at saturation $S_r = 1$ that correspond to the case of 100% RH or immersion, we can identify the parameters of the free-expansion law (4). They are summarized in Table 4 where the asymptotic parameters ϕ and δ are this time used for a better description of the long term expansion kinetics.

For the effective time, the property $(7)_2$ is active in this example, so the expression (9) must be used. We take $\bar{S}_r = 0.93$ for the saturation threshold, and the exponent parameter $\bar{m}$ has the form (10) chosen here as a quadratic function given by,

$$\bar{m}(S_r) = 1 + 42.5(S_r - \bar{S}_r) + 1750(S_r - \bar{S}_r)^2. \qquad (27)$$

With this set of parameters at hand, we show in Figure 6 the numerical results for the different exposures to water superposed with the corresponding experimental curves where good agreement is to be noticed.

7 CONCLUSIONS

In this study, we have presented and numerically tested an efficient tool for the modelling of the influence of relative humidity on the development of DEF expansions. The simple notion of effective time implicitly takes into account the amount of water during time in variable environmental conditions that strongly influence the kinetics of DEF expansions.

From the numerical point of view, we have presented a numerical design within the context of the finite element method for a simple update of this quantity, i.e. at the integration points level. Indeed, the effective time is history-dependent at each material point and, hence, is treated as an internal field.

Numerical simulations have shown good agreements with the experimental results issued from an experimental compaign, and others from the literature. However, further studies are ongoing to include this notion within more detailed formulations.

REFERENCES

Al Shamaa, M., S. Lavaud, L. Divet, J.B. Colliat, G. Nahas, & J.M. Torrenti (2016). Influence of limestone filler and of the size of the aggregates on def. *Cement and Concrete Composites 71*, 175–180.

Al Shamaa, M., S. Lavaud, L. Divet, G. Nahas, & J.M. Torrenti (2015). Influence of relative humidity on delayed ettringite formation. *Cement and Concrete Composites 58*, 14–22.

Baghdadi, N. (2008). *Modélisation du couplage chimicomécanique d'un béton atteint d'une réaction sulfatique interne*. Phd thesis, Université Paris-Est.

Bazant, Z. P. (1972). Nonlinear water diffusion in nonsaturated concrete. *Matériaux et constructions 5(25)*, 3–20.

Brunetaud, X. (2005). *Etude de l'influence de différents paramétres et de leurs intéractions sur la cinétique et l'amplitude de la réaction sulfatique interne*. Phd thesis, Ecole Centrale de Paris.

Granger, L. (1995). *Comportement différé du béton dans les enceintes de centrale nucléaire: Analyse et modélisation*. Phd thesis, ENPC.

Grattan-Bellew, P.E., J.J. Beaudoin, & V.G. Vallee (1998). Effect of aggregate particle size and composition on expansion of mortars bars due to delayed ettringite formation. *Cement and Concrete Research 28(8)*, 1147–1156.

Heinz, D., U. Ludwig, & I. Rüdiger (1989). Delayed ettringite formation in heat treated mortars and concretes. *Concrete Precasting Plants and Technology 11*, 56–61.

Kchakech, B. (2015). *Etude de l'influence de l'échauffement subi par un béton sur le risque d'expansions associées à la réaction sulfatique interne*. Phd thesis, Université Paris-Est.

Larive, C. (1998). *Apports combinés de l'expérimentation et de la modélisation à la compréhension de l'alcali-réaction et de ses effets mécaniques*. Laboratoire Central des Ponts et Chaussées, OA 28.

Martin, R. P. (2010). *Experimental analysis of the mechanical effects of Delayed Ettringite Formation on concrete structures*. Phd thesis, Université Paris-Est.

Mensi, R., P. Acker, & A. Attolou (1988). Séchage du béton: analyse et modélisation. *Materials and Structures 21*, 3–10.

Monteiro, P.J.M. & P.K. Mehta (1986). The tranzition zone between aggregate and type k expansive cement. *Cement and Concrete Research 16*, 111–114.

Moore, A.E. & H.F.W. Taylor (1970). Crystal Structure of Ettringite. *Acta Crystallographica 26(4)*, 386–393.



Taylor & Francis
Taylor & Francis Group
http://taylorandfrancis.com

Computational Modelling of Concrete Structures – Meschke, Pichler & Rots (Eds)
© 2018 Taylor & Francis Group, London, ISBN 978-1-138-74117-1

Determination of critical anodic and cathodic areas in corrosion processes of steel reinforcement in concrete

J. Ožbolt & E. Sola
Institute of Construction Materials, University of Stuttgart, Stuttgart, Germany

G. Balabanić
Faculty of Civil Engineering, University of Rijeka, Rijeka, Croatia

ABSTRACT: Chloride-induced corrosion of steel reinforcement in concrete is one of the major reasons for deterioration of reinforced concrete (RC) structures. In the present paper the coupled 3D chemo-hygro-thermo-mechanical model for concrete is used to study the influence of the anode/cathode surface ratio on the corrosion rate and corrosion induced damage. It has been demonstrated that the position and size of anode and cathode strongly influences the crack pattern and the corrosion rate (Ožbolt et al., 2012, 2014). Currently there is no algorithm which can predict the combination between anode and cathode surfaces on reinforcement that results to the highest corrosion rate. Therefore, to investigate this influence the expression for maximum entropy production, deduced from irreversible thermodynamics, is formulated. The entropy is produced by dissipative processes, which are in this special case the flow of ions through the electrolyte, the anodic and cathodic polarization and the diffusion oxygen process. Through several numerical examples, in which the size and position of anodic and cathodic surfaces are varied, is demonstrated that maximum entropy leads to maximum corrosion rate.

1 INTRODUCTION

Deterioration of reinforced concrete structures caused by chloride-induced corrosion is one of the major concerns for durability of RC structures (Tuutti, 1993; Cairns, 1998). Consequences of chloride-induced corrosion of steel reinforcement have negative effects on structural behavior and involve several aspects related to the life cycle of the structure, such as serviceability, safety and structural performance. The main effect of the corrosion attack is manifested as cracking and spalling of concrete cover, due to the expansion of corrosion products, which have greater volume than the steel. Direct and indirect costs of maintenance and repair are very high. Therefore, it is important to develop and improve numerical tools which can realistically predict the corrosion processes and the related mechanism of deterioration in RC structures.

Before depassivation of reinforcement a surface layer of ferric oxide covers and protects the steel in concrete. Depassivation of the protective layer can occur by reaching a critical threshold concentration of free chloride ions near the reinforcement bar surface or as a consequence of carbonation of concrete (Tuutti, 1993). Corrosion of steel in concrete is an electrochemical process dependent on the electrical conductivity of the concrete and steel surfaces and the concentration of dissolved oxygen in the pore water near the reinforcement (Bažant, 1979; Glasstone, 1964; Page and Treadway, 1982). The recently developed 3D chemo-hygro-thermo-mechanical model, which is employed in the present numerical simulations, couples the above mentioned physical and electrochemical processes with mechanical behaviour of concrete (damage). The model can simulate processes before and after depassivation of steel reinforcement in concrete under natural or accelerated corrosion conditions (Ožbolt et al., 2010, 2011, 2012, 2014; Oršanić, 2015). In order to predict the rate of rust production and related effects, it is necessary to simulate the following physical, electrochemical and mechanical processes: (1) Transport of capillary water, oxygen and chloride through the concrete cover; (2) Immobilization of chloride in concrete; (3) Drying and wetting of concrete as well as related hysteretic property of concrete; (4) Transport of OH-ions through electrolyte in concrete pores; (5) Cathodic and anodic polarization; (6) Transport of corrosion products in concrete and cracks; (7) Creep and shrinkage of concrete and (8) Damage of concrete due to mechanical and non-mechanical actions.

In general case, to compute the corrosion rate and the related induced damage it is necessary to assume position of anode and cathode on the reinforcement

surface. The influence and the effect of their distribution is a complex aspect of the modelling of corrosion which is still not solved. Therefore, to bring more light into the effect of different anode/cathode surface positions several combinations on a typical RC beam are numerically simulated. Based on the principle of maximum entropy production, deduced from irreversible thermodynamics, it is possible to find out which anode-cathode combination results to the highest corrosion rate and damage. The entropy is produced by dissipative processes which are the flow of ions through electrolyte, the anodic and cathodic polarization and the diffusion oxygen process. The first part of the paper gives a short overview of the 3D chemo-hygro-thermo-mechanical model as well as the formulation of the total rate of energy dissipation in a given volume of the corrosion cell and electrode surfaces. In the second part numerical simulations on a multi-rebar RC beam are performed, by changing anodic and cathodic regions along the rebar length and over the circumference. The results are compared and conclusions are drawn out.

2 GOVERNING EQUATIONS AND ENERGY DISSIPATION ANALYSIS

In current computations of corrosion rate of steel in concrete cathodic and anodic areas are determined in advance. If these areas cannot be determined experimentally, the corrosion rate cannot be calculated properly without additional conditions. Such additional conditions could be deduced from irreversible thermodynamics using the principle of maximum entropy production (or the principle of maximum dissipation of energy) generated in the dissipative processes such as mass transfer through porous media, the flow of ions through the electrolyte and cathodic and anodic polarization. Assuming that the temperature of the domain under consideration is uniform over entire domain (isothermal problem), the energy dissipation due to heat transfer through the porous media is not considered. Based on the above assumptions in the following the mathematical formulation of the processes relevant for the propagation stage of steel corrosion in concrete is presented.

Transport of oxygen through the concrete cover is considered as a diffusion problem only. It is defined by the following equation:

$$\frac{\partial C_o}{\partial t} = D_o(S_w, p_{con})\nabla^2 C_o \tag{1}$$

where C_o is oxygen concentration in pore solution (kg of oxygen/m^3 of pore solution), $D_o(S_w, p_{con})$ is effective oxygen diffusion coefficient (m^2/s), S_w is degree of water saturation of concrete, which has great influence on oxygen diffusivity (Tuutti, 1982) and p_{con} is concrete porosity. The convective part is neglected due to the assumption that water saturation of concrete is uniform (Ožbolt et al., 2010).

The oxygen consumed at cathode surface is supplied from concrete by oxygen diffusion. The oxygen diffusion flux at the cathode surface, j_o^c (kg/m^2 s) can be calculated as:

$$j_o^c = D_o(S_w, p_{con})\left.\frac{\partial C_o}{\partial n}\right|_{cathode} \tag{2}$$

where n is the outward normal to the cathode surface.

The oxygen consumption at the cathodic and anodic surfaces can be calculated as:

$$D_o(S_w, p_{con})\left.\frac{\partial C_o}{\partial n}\right|_{cathode} = -k_c i_c \qquad k_c = 8.29\times10^{-8}\,\frac{\text{kg}}{\text{C}} \tag{3a}$$

$$D_o(S_w, p_{con})\left.\frac{\partial C_o}{\partial n}\right|_{anode} = -k_a i_a \qquad k_a = 4.14\times10^{-8}\,\frac{\text{kg}}{\text{C}} \tag{3b}$$

where i_c and i_a are cathodic and anodic current density (A/m^2), respectively. The constants k_c and k_a are calculated using the stoichiometry of chemical reactions and Faraday's law.

The electric current through the electrolyte is a result of motion of charged particles and, if the electrical neutrality of the system and the uniform ions concentration are assumed, can be written as:

$$i = -\sigma\nabla\Phi \tag{4}$$

where **i** is electric current density vector, σ is electrical conductivity of concrete and Φ is electric potential. If electrical neutrality is accounted for and electrical conductivity of concrete is assumed as uniformly distributed, the equation of electrical charge conservation reads (Ožbolt et al., 2011):

$$\nabla^2\Phi = 0 \tag{5}$$

For a given boundary conditions, $\mathbf{n}\cdot\mathbf{i} = 0$ on all surfaces of the concrete body, the solution of Eq. (5) determines the electric potential distribution, and using Eq. (4) the corrosion current density can be calculated.

According to Butler–Volmer kinetics, in the present model kinetics of reaction at the cathodic and anodic surface can be estimated from:

$$i_c = i_{0c}\frac{C_o}{C_{ob}}e^{-2.3\eta_c/\beta_c}\quad i_a = i_{0a}e^{2.3\eta_a/\beta_a} \tag{6}$$

where C_{ob} is oxygen concentration at surface of concrete element exposed to seawater (kg/m^3), η_a and η_c are the anodic and cathodic overpotential, respectively, i_{0c} and i_{0a} are the exchange current density of the cathodic and anodic reaction (A/m^2), β_c and β_a are the Tafel slope for cathodic and anodic reaction (V/dec), respectively.

In order to calculate rate of energy dissipation per unit volume of corrosion cell and energy dissipation per unit surface of anode and cathode, first the differential equations (1) and (5) have to be solved. Then, knowing the scalar fields for each time step (oxygen concentration and electrical potential) and their gradients, using Eq. (6), the source terms of energy dissipation rate can be evaluated. According to Naterer et al. (2006), Hansen and Kjelstrup (1996) and Kjelstrup and Bedeaux (2008), the specific energy dissipation rate in the corrosion cell is composed of energy dissipation rate due to oxygen diffusion, ohmic losses and anodic and cathodic polarization:

$$\dot{Q} = \dot{Q}_{diff} + \dot{Q}_{ohm} + \dot{Q}_{polar,a} + \dot{Q}_{polar,c} \tag{7}$$

The first term, which represent volumetric energy dissipation rate due to oxygen diffusion, can be written as follows:

$$\dot{Q}_{diff} = -\mathbf{j}_o\nabla\mu_T. \tag{8}$$

where $\mathbf{j}_o = -D_o\nabla C_o$ is oxygen flux vector and $\mu_T = RT\ln C_o f + const$ is chemical potential at constant temperature (R is universal gas constant, T is temperature and f activity coefficient) (Kjelstrup and Bedeaux, 2008; Ožbolt et al., 2017). The expression for the chemical potential is obtained assuming that the activity is equal to the product of concentration of the solution and the activity coefficient. Furthermore, the solution behaves approximately ideally for low concentration, therefore the activity coefficient $f \approx 1$. After converting moles into kg and short computation, taking into account the above, Eq. (8) can be written as:

$$\dot{Q}_{diff} = D_o RT\frac{1000}{32}\frac{(\nabla C_o)^2}{C_o}. \tag{9}$$

The electrical resistance of the corrosion cells depends on its geometry, electrical conductivity of the electrolyte and electrode. Since the electrical conductivity of metals is significantly higher than the electrical conductivity of the electrolyte and that the electrodes of the corrosion cells are located next to each other, the ohmic resistance through the anode and cathode will be assumed as negligible, i.e. the second term which is the volumetric energy dissipation rate due to the flow of ions through the electrolyte can be expressed as:

$$\dot{Q}_{ohm} = -\mathbf{i}\nabla\Phi = \sigma(\nabla\Phi)^2. \tag{10}$$

A non-equilibrium thermodynamics can be defined for surface where the excess properties of the surface are essential in defining equations governing dissipated energy. For the electric current density $\mathbf{i}$ at the electrode—solution interface, such an excess of the normal component of the electric field may occur and can be identified with overpotential η. In electrochemistry, this phenomenon is known as polarization. The value of the overpotential can be considerably higher than the potential difference over a comparable distance in the bulk regions.

The third and the fourth terms in Eq. (7) relate the rate of energy dissipation due to the polarization of the anode and cathode. They can be written, using Eq. (6), as (Hansen and Kjelstrup, 1996):

$$\dot{Q}_{polar,a} = i_{na}\eta_a = \frac{\beta_a}{2.3}i_{na}\ln\left\{\frac{i_{na}}{i_{0a}}\right\}. \tag{11}$$

$$\dot{Q}_{polar,c} = i_{nc}\eta_c = -\frac{\beta_c}{2.3}i_{nc}\ln\left\{\frac{i_{nc}}{i_{0c}}\cdot\frac{C_{ob}}{C_o}\right\}. \tag{12}$$

where i_{na} and i_{nc} is the normal component of the electric current density at the anode and cathode surface, respectively.

The total rate of energy dissipation in a given volume of corrosion cell and electrode surfaces Q_V is computed by integrating all contributions (Sciacovelli, 2010):

$$\dot{Q} = D_O RT\frac{1000}{32}\int_V\frac{(\nabla C_O)^2}{C_O}dV + \sigma\int_V(\nabla\Phi)^2 dV + \frac{\beta_a}{2.3}\int_{A_a} i_{na}\ln\left\{\frac{i_{na}}{i_{Oa}}\right\}dA - \frac{\beta_c}{2.3}\int_{A_c} i_{nc}\ln\left\{\frac{i_{nc}}{i_{Oa}}\cdot\frac{C_{ob}}{C_o}\right\}dA. \tag{13}$$

where V is the volume of corrosion cell, A_a and A_c are anodic and cathodic surface, respectively. Note that the expression for the rate of energy dissipation can be written as $Q = TS$ where S is entropy production rate. Therefore the above considerations can also be applied to the production of entropy.

By considering total rate of energy dissipation as objective function, the geometrical parameters such as cathodic and anodic areas and its position, can be generally determined in a way to maximize the objective function, namely:

$$\dot{Q}(\xi, A_a, A_c) = \max. \tag{14}$$

where ξ represents the spatial coordinates. As the procedure of the objective function (14) maximization is mathematically highly demanding, cathodic and anodic areas are determined in a way that for different proportion of these areas it was found the one which maximizes the objective function.

3 NUMERICAL IMPLEMENTATION

By using the finite element method to solve the partial differential equations of the mathematical model, the strong form has to be rewritten into a weak form. The weak form of the system of partial differential equations is carried out by employing the Galerkin weighted residual method (Belytschko et al., 2000). This is then implemented into a non-commercial 3D finite element code MASA, developed at the University of Stuttgart (Institute of Construction Materials). The non-mechanical part of the problem is solved by using a direct integration method of implicit type (Belytschko et al., 2000). To solve the mechanical part, Newton-Raphson iterative scheme is used. As the constitutive law for concrete the microplane model based on the relaxed kinematic constraint is used (Ožbolt et al., 2001). To avoid mesh size dependency, as a regularization method the crack band approach is employed (Bažant and Oh, 1983). In the finite element analysis, the band corresponds to a row of finite elements. The width of the band is equal to the effective element size h. The crack width (opening) is calculated by multiplying maximum principal strain, which is perpendicular to the direction of crack propagation, with the element size h. As already mentioned, the coupling between the mechanical and non-mechanical parts of the model is performed by continuous updating of the governing parameters during the incremental transient finite element analysis using a staggered solution scheme. For more detail see Ožbolt et al. (2010, 2011, 2012).

One-dimensional corrosion contact elements are employed to account for the inelastic strains due to the expansion of corrosion products. They are placed radially around the reinforcement bar surface and their main function is to simulate the contact between reinforcement and the surrounding concrete. These contact elements can take up only shear forces, in the direction parallel to the reinforcement axis, and compressive forces perpendicular to the adjacent surface of the reinforcement. The inelastic radial expansion due to corrosion, Δlr, is calculated as:

$$\Delta l_r = \frac{m_r}{A_r}\left(\frac{1}{\rho_r} - \frac{r}{\rho_s}\right) \tag{15}$$

where ρ_r and ρ_s are densities of rust and steel, respectively, r is the ratio between the mass of steel (m_s) and the corresponding mass of rust (m_r) over the related surface of the reinforcement Ar that corresponds to the contact element. Note that the ratio between densities of steel and rust depends on the type of the corrosion products and can vary from 2 to 7 (Bažant, 1979; Cornell & Schwertmann, 1996; Sola, 2017).

4 NUMERICAL CASE STUDY

4.1 *Multi-rebar RC beam*

Recent applications of the above presented 3D chemo-hygro-thermo-mechanical model (Ožbolt et al. 2010, 2011, 2012, 2014) showed that the model is able to realistically replicate processes before and after depassivation of reinforcement as well as the corrosion induced damage. It has been demonstrated that the position of anodic and cathodic regions over the surface of reinforcement bars influences the corrosion of reinforcement and the crack pattern (Ožbolt at al., 2012, 2014). In the following numerical parametric study the model is used to investigate the critical combination of the anode/cathode position by employing the principle of maximum entropy production. The parametric study for several different geometric parameters determining the position of the anode and cathode and its area ratio is performed for a multi-rebar reinforced concrete beam (Dong et al., 2011; Oršanić, 2015), which is a typical application from the engineering practice. The study is performed assuming that for the given boundary conditions, oxygen diffusivity and electrical conductivity of concrete, such geometrical relationship between anode and cathode is possible for the selected reinforced concrete element. Because of the complexity of the problem, only a beam segment of 130 mm is discretized (see Fig. 1). The three longitudinal reinforcement bars with diameter of 16 mm and spacing of 60 mm are investigated. The lateral and the bottom covers are 52 mm and 32 mm, respectively. Concrete and reinforcement bars are discretized using eight-node solid finite elements. The expansion due to the corrosion products is simulated by means of one-dimensional (1D) radially oriented corrosion contact finite elements.

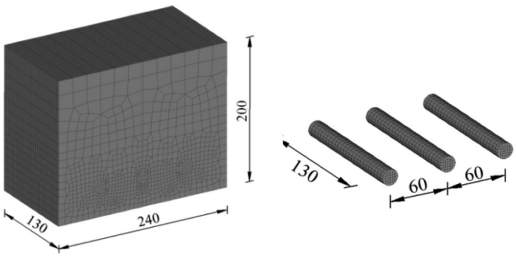

Figure 1. FE model of the beam section used in the numerical analysis (all in mm).

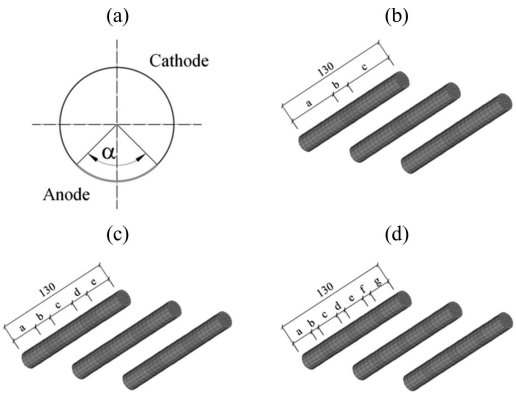

Figure 2. Assumed distribution of the anodic and cathodic part: (a) over the circumference; along the reinforcement bar: (b) configuration A, (c) configuration B and (d) configuration C (Ožbolt et al., 2017).

Since the aim of the parametric study is to investigate the influence of the position of the anodic and cathodic regions along the reinforcement bar length and across the section circumference on the entropy production and corrosion induced damage, different arrangements are examined. Three different longitudinal configurations are assumed (see Fig. 2). In the configuration A only one anodic region along the longitudinal direction is assumed and the rest of the reinforcement is considered as cathode. The configuration B and C have multiple anodic regions, subdivided in two and three portions, respectively. As already mentioned, in all of the three configurations different extent of the anodic area along the reinforcement length and over the circumference is investigated. These cases are chosen in order to find out which combination has the highest influence on the energy dissipation (entropy production) and, consequently, on the corrosion induced damage in concrete. The summary of the investigated cases can be found in Table 1. In total 26 different combinations are investigated.

Table 1. Summary of the investigated cases according to the extent of the anodic and cathodic area.

		Anodic and cathodic regions (mm)						
Conf.	α(°)	a	b	c	d	e	f	g
A-1	180	65	5	60	–	–	–	–
A-2	180	55	20	55	–	–	–	–
A-3	180	50	30	50	–	–	–	–
A-4	180	40	50	40	–	–	–	–
A-5	180	30	70	30	–	–	–	–
A-6	180	15	100	15	–	–	–	–
A-7	180	0	130	0	–	–	–	–
A-8	360	65	5	60	–	–	–	–
A-9	360	55	20	55	–	–	–	–
A-10	360	50	30	50	–	–	–	–
A-11	360	40	50	40	–	–	–	–
A-12	360	30	70	30	–	–	–	–
B-1	45	30	20	30	20	30	–	–
B-2	90	30	20	30	20	30	–	–
B-3	135	30	20	30	20	30	–	–
B-4	180	30	20	30	20	30	–	–
B-5	360	30	20	30	20	30	–	–
B-6	360	25	25	30	25	25	–	–
B-7	360	20	35	20	35	20	–	–
C-1	45	25	10	25	10	25	10	25
C-2	90	25	10	25	10	25	10	25
C-3	135	25	10	25	10	25	10	25
C-4	180	25	10	25	10	25	10	25
C-5	360	25	10	25	10	25	10	25
C-6	360	20	15	20	20	20	15	20
C-7	360	15	25	15	20	15	25	15

Computational modeling and solution of Eq. (14) is a challenging task, especially considering the interaction between the transport processes, the complexity of the geometry and the external boundary conditions. Therefore, the processes before depassivation of reinforcement are here not computed. It is assumed that at the start of the analysis the reinforcement is already depassivated and positions of anode and cathode as well as their surfaces are specified in advance. In total 26 combinations are calculated in which α and the size of the anodic and cathodic regions ($a - g$) are varied (Table 1). For each combination the total rate of energy dissipation at steady state is calculated using Eq. (13). Moreover, the related phenomena such as corrosion induced damage of concrete and related current intensity are calculated as well.

The adopted mechanical properties of concrete are: modulus of elasticity E_c = 26.2 GPa, Poisson's ratio ν_c = 0.18, uniaxial compressive strength f_c = 31 MPa, tensile strength f_t = 1.92 MPa and fracture energy G_F = 40 J/m^2. Steel is assumed to behave linear elastic with modulus of elasticity E_s = 200 GPa and Poisson's ratio ν_s = 0.33. As mentioned before, the analyses are carried out

Table 2. Parameters used in the numerical simulations.

Parameters	
Anodic exchange current density, i_{0a} (A/m^2)	1.875×10^{-4}
Cathodic exchange current density, i_{0c} (A/m^2)	6.25×10^{-6}
Anodic equilibrium potential, Φ_{0a}(V vs. SCE)	–0.780
Cathodic equilibrium potential, Φ_{0c}(Vvs. SCE)	0.160
Tafel slope for anodic reaction, β_a (V/dec)	0.06
Tafel slope for cathodic reaction, β_c (V/dec)	0.16

only considering the processes after depassivation of reinforcement for an un-cracked good quality concrete (w/c = 0.4) assuming a constant degree of water saturation of 50%, electrical conductivity and diffusivity of oxygen are taken as $\sigma = 0.20$ 10^{-3} Ω^{-1} m^{-1} and D_o = 1.55 10^{-8} m^2/s, respectively (Tuutti, 1982; Gjørv et al., 1977). The initial concentration of dissolved oxygen is taken as 0.0085 kg/m^3 of pore solution. This corresponds to the values at the free boundaries of the beam, assuming the beam is fully saturated with oxygen. The other relevant parameters used in the computations of corrosion current density are listed in Table 2. The active corrosion phase is computed for a time period t = 7 years.

4.2 *Results and discussion*

The steady state energy dissipation rates computed using Eq. (13) are plotted for case C in Fig. 3 as a function of the ratio between anodic and cathodic areas. The comparison of different contributions shows that the contribution of the cathodic polarization and ion flow through electrolyte are dominant. On the contrary, the contribution of the anodic polarization and oxygen molecular diffusion represent as maximum only 8.5% of the total energy dissipation.

The numerical results show that with the increase of the ratio between anodic/cathodic areas the total energy dissipation increases up to a certain critical value (Fig. 4a). With further increase of the ratio energy dissipation decreases. This effect is more pronounced for configurations B and C, and less for the case A (Fig. 4a). The maximum entropy production is reached for the anodic/cathodic area ratio of 0.63, 0.44 and 0.30, for the configuration A, B and C, respectively. The absolute maximum of energy dissipation is obtained for the case C (C-5, see Table 1). Furthermore, the different area distribution along the longitudinal bars strongly influences

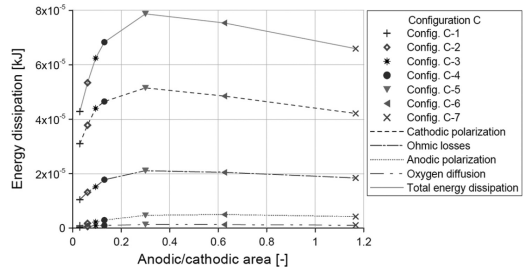

Figure 3. Contribution of different dissipative processes to entropy (case C) as a function of the anodic/cathodic area ratio.

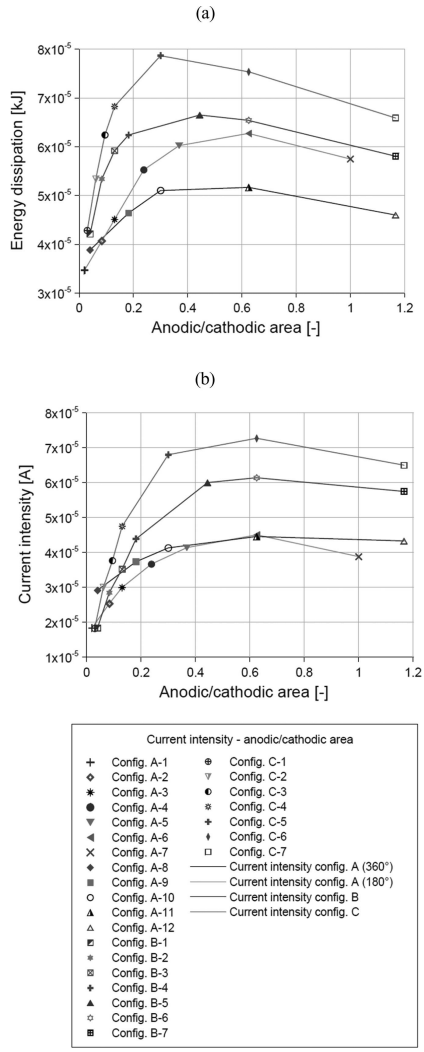

Figure 4. (a) Energy dissipation and (b) current intensity as function of the anodic/cathodic area ratio.

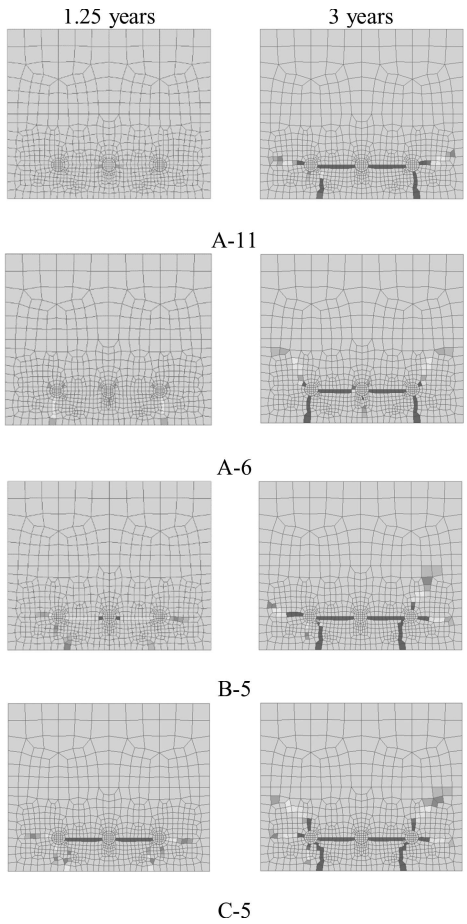

Figure 5. Predicted corrosion induced crack pattern in the beam cross section, 1.25 and 3.0 years after depassivation, for the configurations which exhibit the highest energy dissipation: A-6, A-11, B-5 and C-5 (red = critical crack opening of 0.10 mm).

the contribution of cathodic polarization and ion flow through electrolyte. It is also important to note that for the same area ratio, the distribution of anodic area over the circumference and length has a strong influence on the total energy dissipation.

In Fig. 4b the calculated current intensity is also plotted for all analyzed cases as a function of the anodic/cathodic area ratio. As can be seen, the current intensity exhibits similar trend as the dissipated energy. However, except for the configuration A, the peak values of current intensity do not coincide with the peak values of dissipated energy. The maximum current intensity is observed for the case C (C-6, see Table 1), similar as for the entropy. It is interesting to observe that the maximum current intensity is for all configurations obtained for the same anodic/cathodic area ratio (0.63). In contrary to this, maximum of dissipated energy for different configurations depends also on the anodic/cathodic area ratio. With increasing a number of cathodic zones the ratio at which entropy production reaches maximum decreases, i.e. it moves from 0.63 to 0.30.

The effect of changes in the anodic/cathodic area ratio on the corrosion rate is determined by the type of governing of the corrosion process. If governing is mixed, as in here presented model, the change in corrosion rate (or entropy production) due to the change in the anodic/cathodic area ratio, depends on the contribution of anodic, cathodic and the ohmic governing mode as well as the geometry of the system.

In engineering practice, the criteria based on the maximum current intensity is generally accepted as the relevant criteria for the measure of the highest corrosion rate of reinforcement in concrete (Ghods et al., 2007). However, from the theoretical point of view the criteria based on the maximum entropy production should be relevant (Bažant, 1979). The results of the present numerical study confirm this and indicate that the criterion for the most critical corrosion rate based on the current intensity does not always apply.

To demonstrate the effect of distribution of cathodic and anodic areas on the corrosion induced damage in concrete, development of the corrosion induced damage (crack patterns) for the cases A-6, A-11, B-5 and C-5 are shown in Fig. 5. It can be seen that the distribution of the anode/cathode regions significantly influences time of the appearance of the first visible crack. Crack patterns for these four cases after 1.25 and 3.0 years are similar, however, the level of the corrosion induced damage is significantly different. Comparing the four cases, it can be seen that the numerical results show good agreement with the principle of maximum entropy production. It can be observed that maximum damage of concrete after 3 years coincide with the maximum of dissipated energy.

5 SUMMARY AND CONCLUSIONS

The mathematical formulation of the entropy production in corrosion cells and its relative relation with corrosion rate and corrosion induced damage is discussed. The formulation is based on the recently proposed 3D chemo-hygro-thermo-mechanical model for concrete. The numerical study is performed on RC multi-rebar reinforced beam without stirrups. Based on the results of the study the following is concluded.

The computation of entropy production is carried out assuming that the main dissipative processes are: ion flow through electrolyte, anodic and cathodic polarization and oxygen diffusion process.

The results of the study show that among these four dissipative processes the contribution of cathodic and ohmic heating to entropy production is dominant whereas the contribution due to oxygen diffusion and anodic polarization are much lower.

It is typically observed that for all investigated configurations the entropy production first increases with the increase of the anodic/cathodic surface ratio up to the maximum value and subsequently there is a decrease. For the assumed boundary conditions and geometry, the entropy production and anodic/cathodic ratio at which dissipation is maximum depends on the assumed position of cathodic and anodic surfaces. Generally it is shown that the entropy production increases with increasing number of anodic and cathodic regions.

Comparing the corrosion induced damage of concrete it can be concluded that maximum entropy production directly correlates with the highest corrosion induced damage in concrete member.

It is shown that the shape of the relationship between current intensity vs. anodic/cathodic surface ratio is similar with the relationship between entropy production vs. anodic/cathodic surface ratio. Moreover, maximum of current intensity is obtained for the same anode-cathode combinatios (Case C). However, it is interesting to observe that maximum of current intensity for all investigated cases is obtained for the anodic/cathodic surface ratio of approximately 0.60 whereas the same ratio for the entropy energy production depends on the geometry, i.e. it is different in all three here investigated cases (A, B and C).

It should be pointed out that for each geometry and boundary condition there are an infinite number of possible anodic-cathodic combinations and to find the critical one is a rather demanding task. However, the main aim of the present study was to demonstrate that maximum entropy production coincides with the maximum of corrosion induced damage of concrete. Therefore, the principle of maximum entropy production can be considered as an important theoretical tool to find the most critical combination between anodic and cathodic surfaces of reinforcement.

REFERENCES

Bažant, Z.P. 1979. Physical model for steel corrosion in concrete sea structures – theory, *Journal of the Structural Division, ASCE* 105: 1137–1153.

Bažant, Z.P. & Oh, B.H. 1983. Crack band theory for fracture of concrete. *Mater Struct*, 16(93): 155–177.

Belytschko, T., Liu, W.K. & Moran, B. 2000. *Nonlinear finite elements for continua and structures*. New York: Wiley.

Cairns, J.W. 1998. *State of the art report on bond of corroded reinforcement*. Tech. Report No. CEB-TG-2/5, CEB.

Cornell, R.M. & Schwertmann, U. 1996. The Iron Oxides: Structure, Properties, Reactions, Occurrences and Uses, Wiley, 1996.

Dong, W., Murakami, Y., Oshita, H., Suzuki, S., & Tsutsumi, T. 2011. Influence of Both Stirrup Spacing and Anchorage Performance on Residual Strength of Corroded RC Beams. *Journal of Advanced Concrete Technology* 9(3): 261–275.

Ghods, P., Isgor, O.B. & Pour-Ghaz, M. 2007. A practical method for calculating the corrosion rate of uniformly depassivated reinforcing bars in concrete, *Materials and Corrosion* 58: 265–272.

Gjørv, O.E., Vennesland, Ø.E. & El-Busaidy, A.H.S. 1977. Electrical resistivity of concrete in the oceans. In: *Ninth Annual Offshore Technology Conference: Proceedings, New York*, 582–588.

Glasstone, S. 1964. An introduction to electrochemical behaviour of steel in concrete. *ACI Journal* 61: 177–188.

Hansen, E.M., & Kjelstrup, S. 1996. Application of non-equilibrium thermodynamics to the electrode surfaces of aluminum electrolysis cells. *Journal of the Electrochemical Society* 143(11): 3440–3447.

Kjelstrup, S. & Bedeaux, D. 2008. *Non-equilibrium thermodynamics of heterogeneous systems.* World Scientific.

Naterer, G.F., Tokarz, C.D., & Avsec, J. 2006. Fuel cell entropy production with ohmic heating and diffusive polarization. *International journal of heat and mass transfer* 49(15): 2673–2683.

Oršanić, F. 2015. *Chemo-hygro-thermo-mechanical model for simulation of corrosion induced damage in reinforced concrete*. Dissertation. Stuttgart.

Ožbolt, J., Li, Y. & Kožar, I. 2001. Microplane model for concrete with relaxed kinematic constraint. *Int J Solids Struct*, 38(16): 2683–2711.

Ožbolt, J., Balabanić, G., Periškić, G. & Kušter, M. 2010. Modelling the effect of damage on transport processes in concrete. *Constr Build Mater* 24(9): 1638–1648.

Ožbolt, J., Balabanić, G. & Kušter, M. 2011. 3D Numerical modelling of steel corrosion in concrete structures. *Corros Science* 53(12): 4166–4177.

Ožbolt, J. Oršanić, F., Balabanić, G. & Kušter, M. 2012. Modeling damage in concrete caused by corrosion of reinforcement: coupled 3D FE model. *Int J Fract*, 178(1–2): 233–244.

Ožbolt, J., Oršanić, F. & Balabanić, G. 2014. Modeling pull-out resistance of corroded reinforcement in concrete: Coupled three-dimensional finite element model. *Cement and Concrete Composites* 46: 41–55.

Ožbolt, J., Balabanić, G. & Sola, E. 2017. Determination of critical anodic and cathodic areas in corrosion processes of steel reinforcement in concrete. *Materials and Corrosion* 68(6): 622–631.

Page, C.L. & Treadway, K.W.J. 1982. Aspects of the electrochemistry of steel in concrete. *Nature* 297: 109–15.

Sciacovelli, A. 2010. Thermodynamic optimization of a monolithic-type solid oxide fuel cell, *Int. J. of Thermodynamics* 13(3): 95–103.

Sola, E. 2017. *Experimental and numerical study of chloride induced corrosion in reinforced*. Dissertation. Stuttgart.

Tuutti, K. 1993. *Corrosion of steel in concrete*. Tech. Report, Swedish Cement and Concrete Research Institute, Stockholm.

Tuutti, K. 1982. *Corrosion of steel in concrete*. Report No. 4. Stockholm.

Computational Modelling of Concrete Structures – Meschke, Pichler & Rots (Eds)
© 2018 Taylor & Francis Group, London, ISBN 978-1-138-74117-1

Challenges in corrosion detection based on numerical and experimental studies

M. Kwapisz, A. Vorwagner & A. Lechner
Austrian Institute of Technology, Vienna, Austria

M. Rebhan
Technical University Graz, Graz, Austria

ABSTRACT: Unannounced collapses of retaining walls in the alpine regions in the last few years raised a need for new assessment methods of existing walls which is the main challenge within the research project "SIBS". Investigations on the collapsed walls showed that these constructions suffered from corrosion damage along the horizontal construction joint between the foundation and the vertical concrete wall. The focus of the project is the development of new measurement technics and numerical investigations which should be confirmed by experimental studies. The presented work shows numerical simulations of corrosion progression and its partial validation with dynamic load tests. The results of the dynamic test seemed to be promising, as a significant drift of the Eigenfrequency due to corrosion is possible to detect. Nevertheless, the influence of temperature, ground saturation and earth stiffness might hide this shift making it difficult to keep apart. Therefore the static methods were considered more adequate, but are still under estimation.

1 INTRODUCTION

1.1 *Motivation*

The main topic of this study was a numerical simulation of a cantilever retaining wall affected by corrosion. It became of interest after a recent unannounced collapses (Figure 1) caused by reinforcement deterioration along the horizontal construction joint on the backfill side. Direct methods of corrosion detection in such a case are at present unreliable or costly, due to difficult accessibility. Therefore the potential of non-direct approaches using fixed or mobile sensors was evaluated. To the common static methods assessing the wall performance belong deformation, inclination and concrete strain measurements on the road side.

This paper concentrates on the computational methods used to assess the condition of the retaining walls and to the results of the dynamic tests on prefabricated small-scale elements. Planned big-scale tests are still under investigation.

The intention of the authors is not only to show the final successful computational method, but also to describe and discuss the aborted efforts. One of those was a way to model the loss of area of the reinforcing bars during the corrosion process which at first caused numerical instabilities. Another was a use of shell elements which would normally be a natural choice for such a wall, but turned out to be inadequate for a given task.



Figure 1. Failure of the highway retaining wall in Austria, Marte et al. (2014).

1.2 *Evaluation of the static assessment methods*

In order to assess the efficiency of the non-direct corrosion detection approach concerning deflection, inclination and concrete strain measurements, a sensitivity study was carried out. Simulations of different corrosion scenarios at the critical construction joint were taken into account and applied on the several retaining walls. The parameter set

of the investigation included a variation of wall thickness, different bond laws, corrosion rates and affected areas. The interaction with the earth pressure which is controlled by the deformation of the retaining wall was also exemplarily taken into account. The study demonstrates the possibilities and limitations of damage detection of those critical construction elements, based on the three dimensional nonlinear analysis. The computations were done using a commercial software ANSYS 17® with volume elements for concrete, link Elements for reinforcing bars and springs to simulate the bond in between.

1.3 *Dynamic load test*

Another common method for damage detection is a monitoring of eigenfrequency changes of the structure. Its potential was investigated based on numerical and experimental study on prefabricated test specimens with different reinforcement ratio to simulate the change of stiffness according to the loss of steel due to corrosion. It was carried out for a cracked cross section backfilled with gravel and for the alone standing wall without backfill as a comparison. The numerical model used for this assessment was far less sophisticated as the specimens were simplified and the bond loss between reinforcement and concrete was not applied.

2 NUMERICAL MODEL

2.1 *Choice of element types*

The most suitable elements in terms of accuracy and efficiency for a wall-like structure are shells. As the requirements for thickness to length ratio were fulfilled, it was also a first choice in this case. One of the downsides of using them for RC structures is that the bond between reinforcement and concrete cannot be explicitly modelled and thus the reinforcement must be considered as fixed to concrete. This assumption is true for most of the applications, as the slip of reinforcement only very slightly influences the results. As the bond degrades during the corrosion process, a comparison on a simple structural member was done to examine that influence. The deviation of results done with volume and shell elements indicated the need to use of much more complicated in modeling and computing times volumes.

If the corrosion would take place regularly over the length of the retaining wall, a plain strain state would occur. Shell elements might therefore still have been used in connection with link and spring elements for bond. In this study force redistribution due to unsymmetrical corrosion was an issue, so a full 3D model was required.

2.2 *Material models*

2.2.1 *Reinforcement*

For the reinforcing steel, a simple bilinear elastic-plastic model has been used. It was the intention of the authors not to use a multilinear with a given ultimate strain in order to capture several possible solutions for different ultimate strains within one computation. The maximum strain was monitored and reaching the ultimate limit state was afterwards defined in post processing of the simulation data. The reason for it was that the ultimate strain turned out to be a crucial parameter as no other failure has been priorly observed.

Additionally, it has been reported by Wenjun et al. (2017), that the corrosion might severely decrease the ultimate strain. This matter was planned to be a subject of additional tests, results of which might be used in the future assessment.

2.2.2 *Concrete*

Material model for concrete was taken from additional ANSYS® package Multiplas and was a fracture energy based Combined Rankine and Drucker-Prager model described in Model Code (2010) and Multiplas (2016). The Rankine yield surface exclusively represent tensile failure (cracking) and Drucker-Prager cone models the compressive yield surface. As a result, the hardening-softening function can be clearly assigned. This was meant to represent the cyclic behavior of the concrete correctly, but in authors' opinion not always performed well. It was especially inconvenient for elements that develop vast cracks, as the stress distribution in the following cycles seemed unrealistic. For this reason the calculation were limited to single—load only.

2.3 *Modelling of corrosion*

According to the examinations of the existing retaining walls, corrosion is expected in the connection joint on the backfill side of the wall. It had often a local character in both height of the affected bars

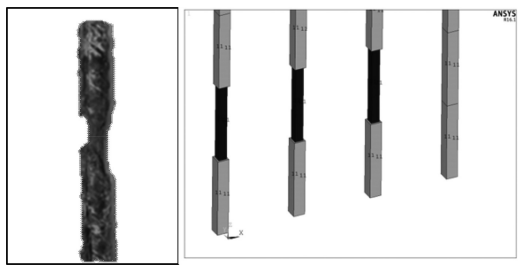

Figure 2. Corroded bar (Marte et al. (2014)) and its numerical representation.

and extension over the length (Figure 2). Not only was the decrease of the reinforcing bars cross section taken into account but also the loss of the bond.

2.3.1 *Reinforcement*

Simulation of the decrease of the reinforcement cross section area due to corrosion unexpectedly appeared to be a vital problem. The logical way of analysis that would be the closest to reality was to load the retaining wall at a given level and then implement the corrosion. The first try of doing it was as follows: for each pair of nodes, where the corrosion should take place, 10 link elements were created. Each of them had a different area, sorted decreasingly with the step of 10% (Figure 3 left). At first all the elements were deactivated using the birth/death capability of elements, apart from the one with full cross section. In the following step this one was killed, and the one with 90% cross section areas was alived, and so on. Those killed elements remained in the model but contributed a near-zero stiffness value to the overall matrix and nothing to the overall mass matrix.

The redistribution of forces between each corrosion step turned out to be time—consuming so a similar but more optimal solution was found: the elements between considered nodes had now 1/10 of the healthy cross section each and at the beginning (healthy wall) all were activated (Figure 3 right). With increasing corrosion there were then killed (deactivated) one after another. It did bring an improvement in the computation performance, but turned out to be unstable as soon as the reinforcement reached a plastic range. It would be therefore sufficient only for the elastic representation of the steel.

This behavior was also confirmed by the Ansys documentation (2016). It was unacceptable to stop the calculations at this stage as post-elastic behavior was the important part of the study. For this reason this approach had to be aborted. A stable solution in which the already loaded retaining wall get continuously damaged could not be found in spite of a significant effort involved. Therefore the whole procedure of corrosion application needed to be modified as described in the Chapter 4.2.

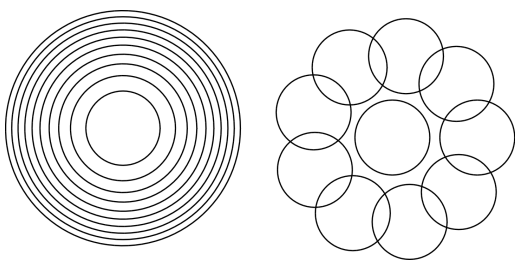

Figure 3. Sets of elements to model corroded bars.

2.3.2 *Bond*

The bond between link and volume elements were simulated by a spring elements according to the working lines described in model code 2010. It was done only for the main reinforcement and only in the longitudinal direction. The transversal directions were fixed by coupling of the coincidental nodes of the link and volume elements. In the corroded areas the spring stiffness was decreased according to Bhargava et al. (2010).

The differences in the literature concerning the bond deterioration are mostly visible in the beginning range of corrosion up to 15–20%. The authors of this study concentrated themselves on higher ranges due to the fact that at the beginning of corrosion process no indirect detection methods would be successful. It is widely agreed, that at corrosion rages above 30% the bond in the affected area practically disappears.

2.4 *Simplified model for the dynamic tests*

All the previously described models were used for assessment of the static methods for the existing walls. For the preparation of the experimental dynamic tests simplified calculations were carried out. Their purpose was, to precise the measurement set up and evaluate the accuracy of such a prediction.

The model was simplified into a linear 2D shell with predefined discrete crack and reinforcement throughout the crack represented with spring elements. The stiffness of the earth backfill was likewise done with springs without consideration of its mass.

3 DYNAMIC TESTS

3.1 *Measurement—layout*

The purpose of the measurement was to capture the Eigenfrequency change in dependency of corrosion progression. In order to simulate the corroded and healthy wall, two types of specimens were fabricated: Type A had 1% reinforcement ratio and Type B 0.2%. To introduce the crack, the precast elements were preloaded.

The measurement was equipped with 4 accelerometers, 1 inclination sensor and 1 laser vibrometer. The source of excitation was either an impulse hammer or a long stroke shaker mounted on the top (Figure 4). The force induced by the shaker was applied in steps with increasing intensity to capture the wall behavior for different amplitudes. It was expected that bigger crack opening would lead to lower frequency which was confirmed by the measurement.

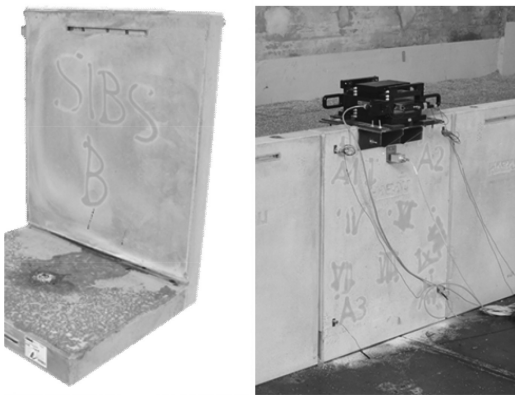

Figure 4. Precast element. Left: freestanding; right: backfilled. The long stroke shaker is mounted on top.

Table 1. Measured eigenfrequency [Hz].

	Maximum force spectrum		
Specimen type	25%	50%	100%
Healthy, non-cracked	74.0	74.0	74.0
Healthy, cracked	69.0	66.5	64.5
Corroded, cracked	66.25	60.0	57.25

Table 2. Margin settings for A4 size paper and letter size paper.

	Ground stiffness		
Specimen type	Week	Hard	Average
A Healthy, non-cracked	53.5	108.0	80.75
A Healthy, cracked	43.25	106.25	74.75
B Corroded, cracked	42.25	106.0	74.12

3.2 *Results: Simulation versus measurement*

The measurement evaluation of the cracked, alone standing, not backfilled walls resulted in the first three eigenfrequencies having almost the same mode shape. The first two had values laying far below the expected from the calculations. After careful examination, it could be identified that the first two frequencies must have been influenced by uneven underground and classified as a rigid body motion. It was not very clear to detect it, as the accelerometers were placed on bottom and on top of the wall and thus the bending form was hard to tell from rotation. Retrospectively, to avoid such tilting the specimens could be prestressed to the ground or situated on elastic bearings. Alternatively additional accelerometers could have been used in the middle of the wall height to ensure easy assignment of eigenmodes.

More meaningful results were those with a backfill, for which the tilt was indistinct, but also present. Table 1 present the first eigenfrequency for different applied force spectrums and for non-cracked, cracked with full reinforcement and cracked with only 20% reinforcement. There was a tremendous shift of frequency between each state, especially for high force spectrums, which indicated a promising method for damage detection.

On the other hand, consideration of the output of the beforehand made calculations presented in Table 2 showed a huge dispersion of the expected results. Due to unknown backfill to the time of calculation two extreme values for its stiffness—week and hard—were assumed. The average value of the two extremes was located coincidentally not far from the measurement. In general though, the uncertainty connected with boundary conditions at this stage of knowledge would cover completely the influence of the corrosion.

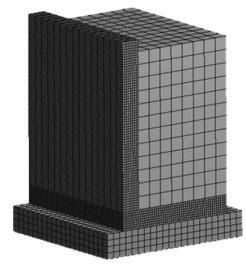

Figure 5. Updated FE model used for recalculation.

3.3 *Simulation results—recalculation*

The simple 2D modal analysis was afterwards recalculated using volume elements and updated gravel properties (Figure 5). In order to capture the effective contact area between specimen and underground, perturbation modal analysis was done. In the first step a static analysis with the maximal head displacement was carried out in order to obtain the status of the compression-only contact elements on the interaction surface. The crack size could be estimated in the same manner. This state was then transferred to second step where modal analysis was done.

It was possible to reproduce the measured results, also for the torsional and second bending modes. It must be stated though, that forecasting the dynamic properties of the retaining walls remains a challenging task due to numerous uncertainties involved in calculation and measurement.

Thus it is still improvable for practical corrosion detection.

4 STATIC METHODS

4.1 *Mobile measurement system*

For fast scanning of the retaining wall surfaces a mobile mapping system has been tested. It consisted of a laser scan mounted on car roof, gathering the data during a normal passing by with the speed of up to 80 km/h. It was also collecting GNSS Positions, inertial data and radar sensor to determine the absolute position and spatial orientation. Its precision and reliability has not yet been fully evaluated, but numerous test trips have been carried out—SIBS Endbericht (2016 unpubl.).

4.2 *Calculation procedure*

As the most realistic way of loading of the wall and implementing the damage afterwards needed to be aborted due to numerical problems (see chapter 2.3.1) a new approach had to be implemented. The basic idea was that each corrosion state would be separately modelled and loaded until failure. Having done that, the deformation, inclination and strain have been read for different earth pressure levels and compared with each other (see horizontal lines in Figure 6).

4.3 *Sensitivity analysis*

Several wall configurations have been taken into account with different thickness, corrosion extent, reinforcement ratio, corrosion height and wall length. It has been done to obtain the sensitivity of each parameter in regard to corrosion detection. Detailed results have already published by Kwapisz et al. (2017) and Rebhan et al. (2017).

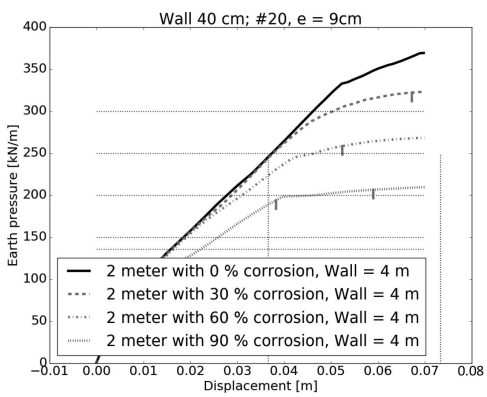

Figure 6. Earth Pressure—displacement diagram for different corrosion levels.

4.4 *Temperature compensation*

Adding an infrared temperature measurement of the surface might in addition to the numerical simulation reduce the uncertainty connected with the temperature influence on the retaining wall. According to Usamentiaga & Garcia (2017) its implementation to the already existing system during the pass byes might be possible despite the relative movement of the wall. It could be compensated using the knowledge of the motion that otherwise significantly decreases the accuracy of such a measurement.

This was not was not yet implemented in the measurement system and is only held as an option if the temperature—induced deflections should become an important issue.

5 CONCLUSIONS

The paper presented two approaches, static and dynamic, for corrosion detection in the retaining walls. It focused on the analysis methods rather than on the resulting applications, especially for the already partially published static methods. It described different possibilities of corrosion modelling and characterized its use for varying purposes.

Dynamic small-scale tests proved on one hand a huge potential, as a frequency shift due to crack and corrosion of up to 17 Hz was measured. At the same time the uncertainty connected with modelling and measuring would not allow a reliable assessment at present.

ACKNOWLEDGEMENT

This research was conducted within the scope of a national research Project managed and supported by the Austrian Federation of Drilling-, Well Construction- and Special Foundation Contractors (VÖBU) and is founded by the Austrian Research Promotion Agency FFG.

REFERENCES

Ansys Documentation. 2016. Release 17.

Bhargava K., Ghosh A., Mori Y., Ramanujam S. 2010. Corrosion-induced bond strength degradation in reinforced concrete – Analytical and empirical models. *Nuclear Engineering and Design* 237(2007) 1140–1157.

Dr. Vollenweider. Gefährdung von Winkelstützmauern durch Korrosion – Technischer Bericht Untersuchung des Bruchverhaltens – Phase 2, *Schweizereidgenossenschaft Bundesamt für Strassen ASTRA*.

Dynardo. 2015. Multiplas: Elastoplastic Material Models for ANSYS. General Multisurface Plasticity.

FIB, Model Code for Concrete Structures. 2010.

Kwapisz M., Vorwagner A., Rebhan M., Tschuchnigg F. 2017. Investigation on existing concrete cantilever walls subjected to reinforcement corrosion. Fib Symposium.

Model Code 2010.

Marte, R., R. Kienreich, F. Scharinger, Ch. Stadler, Überprüfung und Bewertung des Ist-Zustandes älterer Stützbauwerke im Straßennetz der ASFINAG, Beiträge zum 29. Christian Veder Kolloquium – Stützmaßnahmen in der Geotechnik, Technische Universität Graz, Gruppe Geotechnik Graz, 24–25 April 2014, ISBN: 978-3-900484-68-2.

Rebhan M., Vorwagner A., Kwapisz M., Marte R., Tschuchnigg F., Burtscher S. 2017. Safety assessment of existing retaining structures. *Geomechanics and tunneling 10.*

SIBS, *Endbericht Forschungsprojekt SIBS – Forschungsjahr 1 – 2016*, unpublished.

Usamentiaga R., Garcia D. 2017. Infrared Thermography Sensor for Temperature and Speed Measurement of Moving Material. *Sensors*, 17(5), 1157.

Wenjun Z., Raoul F., Chi Sun P., Jian-Guo D. 2017. Influences of corrosion degree and corrosion morphology on the ductility of steel reinforcement. *Construction and Building Materials,* Volume 148.

Advances in material modeling of plane concrete



Taylor & Francis
Taylor & Francis Group
http://taylorandfrancis.com

Computational Modelling of Concrete Structures – Meschke, Pichler & Rots (Eds)
© 2018 Taylor & Francis Group, London, ISBN 978-1-138-74117-1

Concrete mesoscopic failure analysis with the Virtual Element Method

G. Etse, M. Benedetto & A. Caggiano
INTECIN-CONICET, University of Buenos Aires and University of Tucumn, Argentina

ABSTRACT: Numerical simulations of fracture processes in cementitious materials are approached by combining a discrete crack approach, based on the use of zero-thickness Interface Elements (IEs), and the Virtual Element Method (VEM), which allows very efficient and effective spacial discretizations and numerical procedures. The proposed methodology is used for simulating the non-linear mechanical response and cracking process of cement-based composites at the mesoscopic level of observation. The potentials of VEM for realistically representing complex geometries such as those characterizing composite inclusions are used for discretizing domains of coarse aggregates which are composed by arbitrary number of edges (not necessarily convex). In this regard, the use of VEM allows to easily handle hanging nodes, flat angles and/or collapsing nodes while retaining the same approximation properties of FEM. Stress-crack opening processes are modeled by means of classical zero-thickness IEs which are placed in between the solid virtual elements. Numerical results are presented to demonstrate the soundness and capabilities of the proposed novel approach.

1 INTRODUCTION

During last decades, significant interest of the international scientific community in computational mechanics was advocated to the simulation of fracture and failure processes in composite materials and, moreover, to the optimization of the involved numerical tools for analyzing such a complex phenomenon. Accurate macroscopic failure analyses of engineering materials and composites necessarily require the explicit consideration of their meso- and microscopic structures as their involve interfaces, crack evolutions and field discontinuities.

Some relevant proposals in the available literature are aimed at solving the implicit complexity involved in computational failure analysis of engineering brittle and quasi-brittle materials, such as the embedded strong discontinuities approach (E-FEM) (Oliver 1996, Oliver et al. 2008) modelling,oliver2008two, the extended finite element method (X-FEM) (Zhang et al. 2013, Mohammadnejad and Khoei 2013), lattice models (Lilliu and van Mier 2003), particle approaches (Cusatis et al. 2011), the discrete element method (DEM) (Donzé et al. 2009) and the so-called discrete models based on zero-thickness interfaces (Caballero et al. 2006, Rodrigues et al. 2016).

Among the available approaches, those based on interface elements (formulated in terms of contact stresses versus opening relationships) have the relevant advantage of requiring the simplest numerical procedures and, therefore, are the most friendly to be used in numerical simulations of complex material failure processes. Nevertheless, the drawback of interface-based approaches is the imposed fix crack path which may suppress the cracking evolution through other more critical paths. To suppress or bypass this inherent shortcoming of the interface models, sufficiently dense meshes with interfaces in all connections between solid elements shall be considered.

Numerical approaches based on interfaces have been efficiently employed for simulating material contacts problems (Wriggers and Zavarise 2002), bond phenomena (Baky et al. 2012) and crack evolutions in quasi-brittle materials like concrete (Xie and Jr. 2006, Ciancio et al. 2013). One of the most frequent applications of interface elements in computational analyses of solid materials mechanical behavior, is related to mesoscopic failure simulations of quasi-brittle composites like concrete. Thereby, the use of non-linear interfaces can be limited to model only the aggregate-mortar joints (Stankowski et al. 1993) or, alternatively, also the mortar-mortar joints while linear elastic materials are considered for the continuum mortar elements (Lopez et al. 2008a, Lopez et al. 2008b).

In this work, the recently-developed Virtual Element Method (VEM) is combined with Interface Elements (IEs) for analyzing fracture responses and crack evolutions in concrete meso-specimens. The non-linear approach based on zero-thickness interfaces for discrete crack analysis of concrete is one of the most extensively considered strategy for such purpose. However, IEs have

never been combined before with VEM for simulating failure processes of quasi-brittle materials like concrete. This methodology represents the key novelty of this work. As already followed in classical finite element procedures, the VEM also adopts a Galerkin-based scheme for its formulation and implementation. VEMs have been firstly introduced by Beirão da Veiga et al. (2013) and applied in some simple two-dimensional elasticity (Da Veiga et al. 2013) and 2D plate problems (Brezzi and Marini 2013). The VEM represents a further extension of the classical mimetic finite difference method (Shashkov and Steinberg 1996, Brezzi et al. 2005). Particularly, VEM uses local spaces of test and trial functions that, in addition to all the polynomials of the chosen degree, contain some additional functions. These latter represent the solutions of suitable partial differential equations, inside of each considered element. In this respect VEMs represents a generalization of three methods: the finite elements on polygons, the polygonal finite element methods and the extended finite element methods (Ahmad et al. 2013).

After this introduction and literature review, the paper is organized as follows: Section 2 deals with the mathematical framework and the main ingredients of the VEM. Then, Section 3 summarizes the meso-scale approach adopting for taking into account the composite nature of concrete giving also some practical information behind the implementation of the proposed approach. Section 4 highlights the numerical applications and some examples for assessing the predictive capability of the proposed approach. Concluding remarks and future research lines are finally reported in Section 5.

2 THE VIRTUAL ELEMENT METHOD IN ELASTIC PROBLEMS

This section provides an overview of the main equations governing the Virtual Element Method (VEM). For the sake of brevity, few details are given in this work concerning the formulation and implementation of VEM. A comprehensive study of the method can be found in available works, see e.g. Brezzi et al. (2013, Beirão da Veiga et al. (2015, Artioli et al. (2017, Chi et al. (2017, Gain et al. (2014, Andersen et al. (2017). It has been shown in scientific literature that VEs are less sensitives to mesh distortion (Artioli et al. 2017), making the use of VEM a very attractive approach for complex and irregular meshes such as those characterized by mesoscopic length scales of cementitious composites such as concrete and mortar.

In the framework of the classical elasticity problem, represented in a given domain $\Omega \subset \mathbb{R}^d$ (d = 2,3), the goal is to find a displacement field, $\mathbf{u}: \Omega \rightarrow \mathbb{R}^2$, such that

$$\begin{cases} -\text{div}\,\sigma &= \mathbf{f} & \text{in}\,\Omega \\ \mathbf{u} &= 0 & \text{on}\,\Gamma_D \\ \sigma \cdot \mathbf{n} &= 0 & \text{on}\,\Gamma_N \end{cases} \tag{1}$$

where σ is the Cauchy stress tensor, $\mathbf{f}$ is the volumetric load, Γ_D and Γ_N are the Dirichlet and Neumann boundaries, respectively, while $\mathbf{n}$ is the normal vector to Γ_N. Non homogeneous boundary conditions are dealt analogously as in standard FEM.

Given a discretization of the domain (restraining in this work the discussion for the case of 2D) into a polygonal mesh τ_h of arbitrary and not necessarily convex polyhedral elements, with h being the mesh parameter, the lowest order local space V_h^E for an element $E \in \tau_h$ is defined as

$$V_h^E = \left\{ \mathbf{v}_h \in [\mathrm{H}_0{}^1(E) \cap C^0(E)]^2 : \mathbf{v}_{h|\partial E} \in C^0(\partial E), \mathbf{v}_{h|e} \in \mathbb{P}_1(e) \forall e \subset \partial E, \Delta \mathbf{v}_h = 0 \right\} \tag{2}$$

being $\mathbb{P}_1(e)$ the polynomial first order space on E. The definition of the shape functions is implicit, thus the name 'virtual'. The Degrees Of Freedom (DOF) are vertex values as usual in standard FEM, and shape functions are explicitly known only on the element boundary, while unknown and harmonic in its interior. The global space can be accordingly defined as

$$V_h = \left\{ \mathbf{v}_h \in [\mathrm{H}_0^1]^2(\Omega) : \mathbf{v}_h |_E \in V_h^E \forall E \in \tau_h \right\}. \tag{3}$$

The variational form of the problem reads: finds the allowable displacement field $\mathbf{u}$ which verifies the following relationship:

$$a(\mathbf{u}, \mathbf{v}) = l(\mathbf{v}) \quad \forall \mathbf{v} \in [\mathrm{H}_0^1(\Omega)]^2, \tag{4}$$

where

$$a(\mathbf{u}, \mathbf{v}) = \sum_{E \in \tau_h} \int_E \sigma(\mathbf{x}, \nabla \mathbf{v}(\mathbf{x})) : \nabla \mathbf{v}(\mathbf{x}) \, \mathrm{dS} \tag{5}$$

and

$$l(\mathbf{v}) = \sum_{E \in \tau_h} \int_E \mathbf{f}(\mathbf{x}) \mathbf{v}(\mathbf{x}) \, \mathrm{dS}\,. \tag{6}$$

The equilibrium equation in Eq.(1) can be completed by introducing a given constitutive rule, at every point $\mathbf{x}$ in the domain, $\sigma = \sigma(\mathbf{x}, \nabla \mathbf{u})$. This latter is dependent on the strain states based on the so-called compatibility equations and may also

consider the history of the material in case on formulation of non-linear constitutive models.

The basic idea behind the VEM formulation for elasticity problems is to employ a certain projector aimed at finding a patch-test satisfying approximation of the strain field, which adopts a constant strain values for each strain component. For this reason that for lowest orders of discretization and elasticity the VEM elements have convergence properties analogous to the classical CST (constant strain triangle).

The definition of the projector Π_E: $V_h^E \longrightarrow \mathbb{P}_1(E)$, satisfies the following conditions:

$$\begin{cases} a_h(\Pi_E(\mathbf{u}_h),\mathbf{p}) & = a_h(\mathbf{u}_h,\mathbf{p}) \quad \forall p \in \mathbb{P}_1(E) \\ \frac{1}{N_v^E}\sum_{i=1}^{N_v^E}\Pi_E(\mathbf{u}_h(v_i)) & = \frac{1}{N_v^E}\sum_{i=1}^{N_v^E}\mathbf{u}_h(v_i) \\ \frac{1}{N_v^E}\sum_{i=1}^{N_v^E}v_0\times\Pi_E(\mathbf{u}_h(v_i)) & = \frac{1}{N_v^E}\sum_{i=1}^{N_v^E}v_0\times\mathbf{u}_h(v_i) \end{cases} \tag{7}$$

where v_i, $i=1,...,N_v^E$ are the element vertices, while E and v_0 the coordinates of the barycenter. The last two equations of 7 are used to guarantee the unicity of the projection since they impose conditions for rigid motions, whose strains are null. This projection is explicitly computable only with the knowledge from the DOF. The discrete bilinear form can defined as follows

$$\begin{aligned} &\hat{a}_h(\mathbf{u}_h,\mathbf{v}_h) = \\ &\quad \sum_{E\in\tau_h}\int_E \sigma(\mathbf{x},\Pi_E(\nabla\mathbf{v}_h)(\mathbf{x})):\Pi_E(\nabla\mathbf{v}_h)(\mathbf{x})\mathrm{dx} = \\ &\quad \sum_{E\in\tau_h}|E|\,\sigma(\Pi_E(\nabla\mathbf{v}_h)):\Pi_E(\nabla\mathbf{v}_h). \end{aligned} \tag{8}$$

while the complete global bilinear ones becomes (for $\mathbf{u}_h,\mathbf{v}_h \in V_h$)

$$a_h(\mathbf{u}_h,\mathbf{v}_h) = \hat{a}(\mathbf{u}_h,\mathbf{v}_h) + \tau(\mathbf{u}_h)S_h(\mathbf{u}_h,\mathbf{v}_h) \tag{9}$$

being $\tau > 0$ a parameter which depends on the material model and the current state. Under the hypothesis of linearly elastic materials and small strains/displacements, some further decomposition of Eq.(9) can be developed. Particularly, from the generalized Hooke constitutive laws, for linearly elastic materials, based on the fourth order constitutive tensor $\mathbb{C}$, it can be written

$$\sigma(\mathbf{u}) = \mathbb{C}\epsilon(\mathbf{u}) = \lambda\mathrm{tr}(\epsilon)1\otimes 1 + 2\mu\mathbb{I}, \tag{10}$$

where $\epsilon(\mathbf{u}) = \frac{1}{2}(\nabla\mathbf{u} + \nabla^T\mathbf{u})$ is the linear strain tensor, $(1,\mathbb{I})$ are the $2nd$ and the $4th$ order unitary tensors, respectively, and $(\lambda,\ \mu)$ are the Lamé parameters of the material.

By replacing Eq. (10) in Eq. (9), the bilinear form becomes

$$\begin{aligned} a_h(\mathbf{u}_h,\mathbf{v}_h) &= 2\mu\int_E(\mathbf{u}_h):(\mathbf{v}_h)\mathrm{dS} \\ &\quad + \lambda\int_E \mathrm{div}(\mathbf{u}_h)\mathrm{div}(\mathbf{v}_\mathbf{h})\mathrm{dS} \\ &= 2\mu(\underbrace{-\int_E \mathbf{u}_h\cdot\mathrm{div}((\mathbf{v}_h))\mathrm{dS}}_{\mathrm{I}} \\ &\quad + \underbrace{\int_{\partial E}\mathbf{u}_h\cdot((\mathbf{v}_h)\cdot\mathbf{n}_E)\mathrm{dl}}_{\mathrm{II}}) \\ &\quad + \lambda\underbrace{\int_E \mathrm{div}(\mathbf{u}_h)\mathrm{div}(\mathbf{v}_\mathbf{h})\mathrm{dS}}_{\mathrm{III}}, \end{aligned} \tag{11}$$

while the integration by parts was used to obtain the last equality. Each of the terms I, II and III is can be computed in the local VEM space.

For the loading term associated with the linear form, the approximation is based on a quadrature rule on vertex values, for the VEM function $\mathbf{v}$,

$$l(\mathbf{v}_\mathbf{h}) = \sum_{E\in\tau_h}\mathbf{f}^E\overline{\mathbf{v}_\mathbf{h}}^E, \tag{12}$$

where

$$\mathbf{f}^E = \frac{1}{|E|}\int_E \mathbf{f}\,\mathrm{dx}, \tag{13}$$

and

$$\overline{\mathbf{v}_\mathbf{h}}^E = \frac{1}{N_v^E}\sum_{i=1}^{N_v^E}\mathbf{v}_\mathbf{h}(v_i), \tag{14}$$

which is the average over an element with N_v^E vertices.

3 MESOSCOPIC MESHING BASED ON VEM AND INTERFACES

The procedure implemented to analyze the cracking simulation of concrete composites based on continuous virtual elements and zero-thickness interfaces is proposed in this section. Geometric generation, meshing and interface addition in mesoscopic elements modeled with VEs and IEs are presented in some details.

3.1 *Geometry and mesh*

Polyhedral geometries for mesoscale generations were obtained using a modified version of Polymesher (Talischi et al. 2012), a random mesh-generator

Matlab algorithm. This algorithm hinges on Voronoi diagrams starting from a randomly perturbed point distribution, called "seeds". Modifications were introduced in the code to allow for some bias in the random selection of the element. The initial polyhedral mesh is usually rough and uneven and becomes smoother through iterations, tending to a regular hexagonal mesh.

Meso-scale simulations of cementitious composites are characterized by explicitly considering the response of the different components and the possible iterations between them. It is important to remark that meso-scopic discretizations with triangular elements, although it is the most used discretization type in 2D analysis, are characterized to have some relevant difficulties such as the presence of small angles and edges and elements with bad aspect ratios. This complication can be avoided using arbitrary polyhedral elements that do not require any further discretizations between aggregates and, therefore, do not lead to the aforementioned mesh defects. Since meshing complex aggregate geometry is no longer needed, there will be an improvement in element quality. Each aggregate was thus discretized by means of a single Virtual Element. In a given polyhedral mesh, the ratio of aggregate volume to total volume is set. The selection of finite elements representing the aggregates is random, so the results of the analysis vary within a certain range depending on discretization parameters such as the aggregate Mean Element Size (MES), shape, aggregate density and distribution, material parameters, etc. The limitation for selecting aggregates is that they should not share an edge with other aggregates nor lie on the boundary, though these limitations may be removed if desired. Voids in the specimen can be inserted analogously. Samples of meso-scale heterogeneous meshes obtained using this procedure are presented in 1, where bulk elements are depicted in blue and aggregates in red. The presence of matrix-matrix and matrix-aggregate interface elements are similarly represented with brighter colors. Finally, in the case that independently obtained meshes need to be compatibilized, full advantage is taken from the VEM feature to work with hanging nodes. Different meshes can be merged into a globally conforming mesh by sharing all nodes on the common boundary, with the only consequence of an increased number of edges for the affected elements.

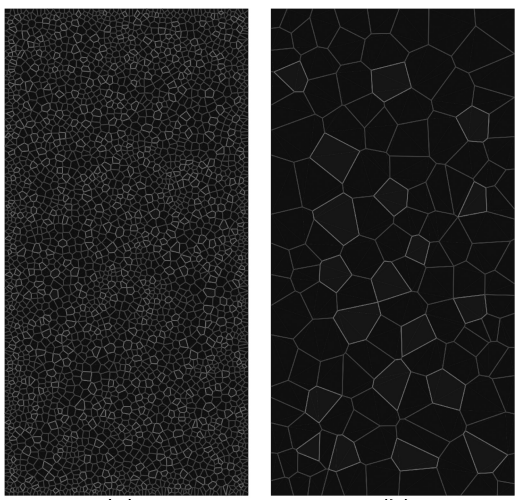

Figure 1. Mesoscopic geometries with fixed aggregate volume fraction (15%): (a) high number of aggregates and low MES and (b) low number of aggregates and high MES.

3.2 *Interface elements and constitutive rule*

Traditional IEs are added on edges of the VE mesh. These interfaces can be introduced regardless of the shape of the VE, and since the functions in the local VEM spaces are polynomials on the boundaries of the element (see Section 2), the insertion of IEs when the polynomial degree in the interface and the VEM discretization agrees is the same as with standard FEM.

IEs that do not form a closed path on the mesh are not acceptable, since that would result in a non-propagating crack path which is physically inconsistent. Therefore, two procedures for inserting interface elements were developed. The first one deals with closed paths, in which interfaces are added following the path until the last interface finishes either at the beginning of the first interface or at the boundary. In the latter case, it is required that the interface also begins at the boundary. This approach allows to introduce the minimum required amount of IEs to follow the crack path, although it requires a priori knowledge of the path. The second approach allows inserting IEs surrounding any element, and therefore a closed loop is always determined. This becomes specially useful when one needs to surround a particular element with interfaces (e.g., aggregates in cement matrices), because since the process is done locally on the element, few modifications to the meshing data structures are needed. Figure 2 illustrates both alternatives above described, showing the nodes duplication and interface creation, where element colouring indicates the number of edges comprising each Virtual element.

In the framework of discontinuous mechanics approaches which account for explicitly considered cracks, the governing equations including the equi-

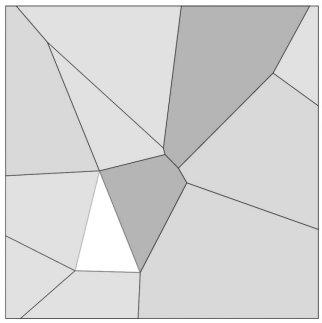

(a) Original mesh

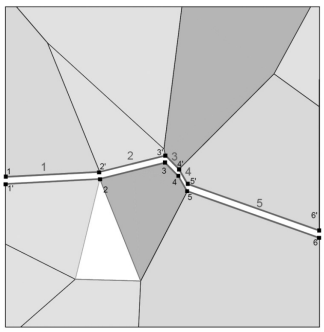

(b) Closed path

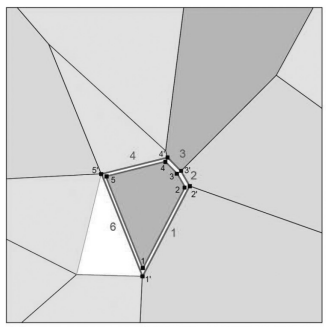

(c) Surrounding an element

Figure 2. Inserting interface elements into a virtual element mesh: (a) mesh without interfaces, (b) closed path insertions and (c) interfaces surrounding an inclusion.

librium equation, the natural and essential boundary conditions as highlighted in Eq. (1), are completed with the traction continuity at the crack surface

$$\begin{cases} \sigma \mathbf{n}_d^+ &= \mathbf{t}_c^+ \\ \sigma \mathbf{n}_d^- &= \mathbf{t}_c^- \ \text{on} \Gamma_d \\ \mathbf{t}_c^+ &= -\mathbf{t}_c^- \end{cases} \tag{15}$$

being $\mathbf{t}_c$ is the cohesive traction across the crack line Γ_d and $\mathbf{n}$ its unit normal vector. The above relationship is valid for any kind of discontinuous approach employed for discrete crack analyzes, not only for interface elements.

In the framework of the flow theory of plasticity, adopted for solving the non-linear discontinuous response of the interface model, the following equations can be written in rate format

$$\dot{\mathbf{u}} = \dot{\mathbf{u}}^{el} + \dot{\mathbf{u}}^{cr}, \tag{16}$$

where $\dot{\mathbf{u}} = [\dot{u}, \dot{v}]^t$ is rate of the relative displacement vector, across the interface, while $\dot{\mathbf{u}}^{el}$ and $\dot{\mathbf{u}}^{cr}$ are the elastic and cracking (inelastic) rate components, respectively.

The interface elastoplastic constitutive equation can be expressed as

$$\begin{aligned} \dot{\mathbf{u}}^{el} &= \mathbf{C}^{-1} \cdot \dot{\mathbf{t}} \\ \dot{\mathbf{t}} \quad &= \mathbf{C} \cdot \left(\dot{\mathbf{u}} - \dot{\mathbf{u}}^{cr} \right) \end{aligned} \tag{17}$$

being $\dot{\mathbf{t}} = [\dot{\sigma}_N, \dot{\sigma}_T]^t$ the interface stress rate vector and $\mathbf{C}$ the elastic stiffness matrix.

The rate of normal and tangential interface stresses is derived through the rates of relative displacement vector as:

$$\dot{\mathbf{t}} = \mathbf{C}^{ep} \cdot \dot{\mathbf{u}} \tag{18}$$

where $\mathbf{C}^{ep}$ is the tangential elastic-plastic operator which is dependent on the adopted constitutive model employed to model the non linear stress-crack opening response (failure criterion, damage surface, softening description, flow rules, etc.).

3.3 *Cohesive interface constitutive model*

A potential-based model proposed by Park, Paulino, & Roesler (2009) and Park & Paulino (2012) was chosen as the traction separation law in the so-called cohesive zone.

Normal and tangential stresses (σ_N and σ_T) vs. relative opening displacements u and v describe a constitutive rule which depends on the following parameters: fracture energy for pure modes I and II (ϕ_n, ϕ_t), post-peak behavior (brittle/ductile), critical/maximum stress and ratio between critical and final opening (λ_n and λ_t). δ_{nf} and δ_{tf} are the final normal and tangential openings, respectively, which establish the limits for the available interface stiffness. δ_{nc} and δ_{tc} represent the normal and tangential critical opening, respectively, for peak interface strength. Coupling between normal and tangential displacements is inherently incorporated in the model, thus stress response and tangent stiffness is dependent on both relative displacements so that,

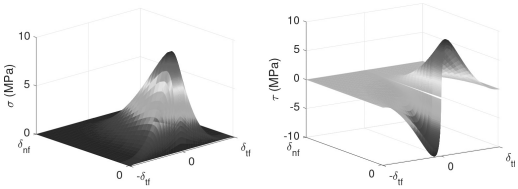

(a) Normal stress response at the interface

(b) Tangential stress response at the interface

Figure 3. Traction separation law.

for instance, fracture energy consumed in the tangential direction affects the response in the normal direction, and viceversa. Interfaces following the intrinsic approach, as in this work, exhibit a high initial stiffness to minimize the altering response for nearly closed interfaces. The model used here incorporates a smoothly varying tangent stiffness that is initially very high until critical opening.

4 NUMERICAL EXAMPLES

To show the potentials of the proposed method, uniaxial tests of concrete samples are evaluated at the mesoscopic level of observation. In these examples, the aggregate volume ratio was fixed at 22% while the rest of the selected material properties are given in Table 1. For each simulation, a generated mesh with randomly selected aggregates was generated following the guidelines given in Section 3.1. The considered meshes range between 200 to 2000 elements. The specimens were subjected to a uniform vertical displacement u until a 0.4% mean strain was reached. Minimal boundary conditions under plane stress condition were considered. All test were performed with an in-house VEM-based code using Matlab.

In the following, selected results are shown that provide a sample of the numerical simulations performed for this work. They are as plotted in Figure 4, where the final states of samples of different MES can be observed.

Figure 5 highlights the overall specimens behavior up to failure in the tensile test and in terms of mean axial stress vs. normalized axial displacement. Based on these results, the following conclusions can be figured out: (i) post-peak response seems to not depend on MES nor on aggregate distribution, under consideration of same aggregate volume ratio; moreover (ii) the peak strength lies, for all considered cases, within a small margin of variation: this is also largely validated in experimental observations published in the scientific literature; (iii) the numerical predictions deal with

Table 1. Interface model parameters for the uniaxial tests.

Bulk	Volume ratio	E (MPa)	ν
Matrix	72%	25000	0.2
Aggregate	22%	100000	0.2
Interface	Matrix	Matrix-Aggregate	
λ_n	1/50	1/50	
λ_t	1/50	1/50	
ϕ_n (N/mm)	1	0.4	
ϕ_t (N/mm)	1	0.4	
σ_{max} (MPa)	8	4	
τ_{max} (MPa)	8	4	

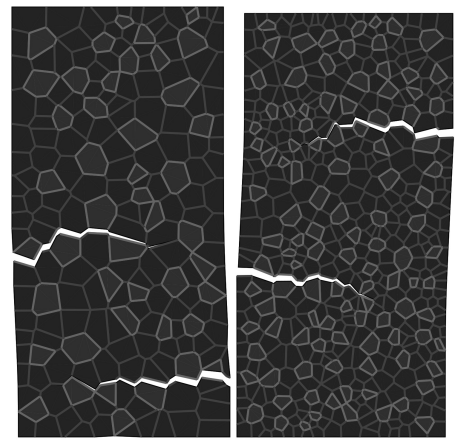

(a) Final state - 200 elements

(b) Final state - 500 elements

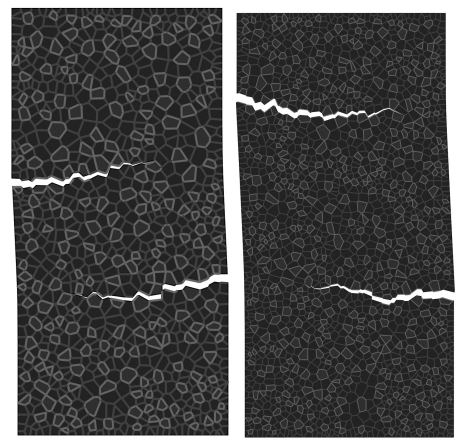

(c) Final state - 1000 elements

(d) Final state - 2000 elements

Figure 4. Comparison of the observed fracture paths for a specimen with varying MES and randomly selected aggregates (magnification factor = 10).

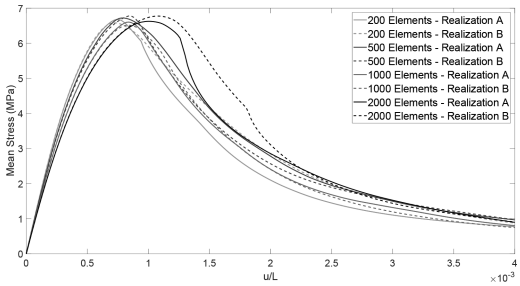

Figure 5. Average force versus normalized displacement for varying MES.

strong mesh failure localizations, which are in line with the well-known concrete (and other cohesive-frictional brittle materials) fracture behavior under uniaxial tensile tests.

In all analyzed tests can be observed that failure and fracture response are qualitatively very similar across all MES in terms of both stress-displacement responses and crack paths/evolutions. These results actually encourage the use of this approach based on combinations between IEs and VEM which, even with less discretized meshes and involving few elements, is able to provide very reasonable predictions of the non-linear and discontinuous behavior of specimens loaded under mode I type of fracture.

Figure 6 presents a comparison of final stages that can be observed with fixed test parameters and fixed MES, while only varying the aggregate distribution and the corresponding mesh. As expected, due to the lower strength of matrix-aggregate interfaces with respect to matrix-matrix ones, failure paths strongly depend on aggregate distribution. Furthermore, both single- and double macro-fracture paths can be observed. It is interesting to note how the post-peak behavior, represented in the diagrams of Figure 7, varies when a single macro-crack controls the specimen failure instead of two macro-cracks. Particularly, it can be clearly seen that when one single crack develops across the entire width of the sample, no residual strength appears while the softening response, starting from the peak strength, becomes much steeper.

It can be finally concluded, in this section, that several other variables can be incorporated in the analysed simulations with little additional effort. For example, the role of sample size in the response can provide valuable information to assess how representative a given sample may be. It is also possible to introduce sets of aggregates of different sizes. Pores as a percentage of the total volume of the sample can be added, simply by repeating the procedure of the aggregates and assigning

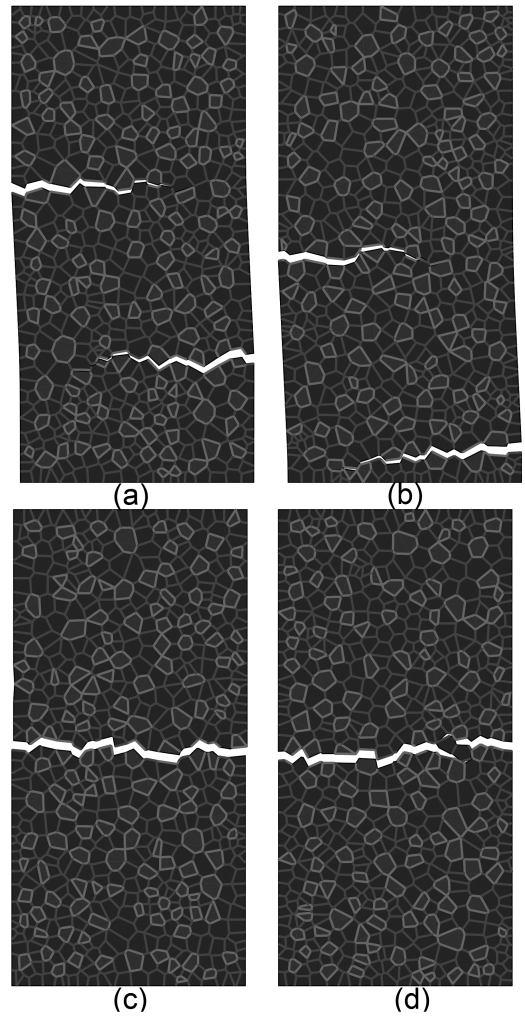

Figure 6. Comparison of observed fracture paths for a specimen with 667 elements and randomly selected/distributed aggregates (magnification factor = 10).

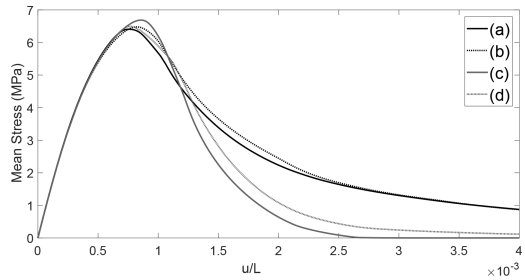

Figure 7. Average force versus normalized displacement for fixed MES and different aggregate distributions.

them with a zero or negligible stiffness. Different cohesive behaviors at the interface can be examined as well as a non linear (continuous) model for the bulk and aggregate elements. Further, interesting insight could be obtained from a statistical analysis to study the influence of the variation of the test parameters and the randomness of the mesh.

5 CONCLUSIONS

A novel methodology was described that combines solid Virtual Elements with Interface Elements in a discrete failure approach. The advantages of using arbitrary polyhedral meshes when discretizing heterogeneous material were highlighted and numerical results were presented to demonstrate the potentials of the proposed approach, particularly regarding mesoscopic failure analyses of quasi-brittle composites like concrete. Many future research paths based on the presented ideas appear promising, such as introducing non-linear bulk behavior, higher order discretizations, fracture evolution, 3D problems, etc. All these studies are currently ongoing and represents the future research lines followed by the authors of this paper.

ACKNOWLEDGMENTS

The authors would like to thank the SUPERCONCRETE Project (www.superconcrete-h2020.unisa.it) funded by the European Union within the Horizon 2020 Framework Programme (H2020-MSCA-RISE-2014 n645704). Moreover, the third author wishes to acknowledge the Alexander von Humboldt-Foundation for funding his two-year position at the Institut fur Werkstoffe im Bauwesen of TU-Darmstadt under the research grant ITA-1185040-HFST-P (2CENERGY project).

REFERENCES

Ahmad, B., A. Alsaedi, F. Brezzi, L.D. Marini, & A. Russo (2013). Equivalent projectors for virtual element methods. *Computers & Mathematics with Applications 66*(3), 376–391.

Andersen, O., H.M. Nilsen, & X. Raynaud (2017). Virtual element method for geomechanical simulations of reservoir models. *Computational Geosciences*, 1–17.

Artioli, E., L. Beirão da Veiga, C. Lovadina, & E. Sacco (2017, Jun). Arbitrary order 2d virtual elements for polygonal meshes: part ii, inelastic problem. *Computational Mechanics*.

Artioli, E., S. de Miranda, C. Lovadina, & L. Patruno (2017). A stress/displacement virtual element method for plane elasticity problems. *arXiv preprint arXiv:1702.01702*.

Baky, H.A., U. Ebead, & K. Neale (2012). Nonlinear micromechanics-based bond slip model for frp/concrete interfaces. *Engineering Structures 39*(0), 11–23.

Beirão da Veiga, L., C. Lovadina, & D. Mora (2015). A virtual element method for elastic and inelastic problems on polytope meshes. *Computer Methods in Applied Mechanics and Engineering 295*, 327–346.

Beirão da Veiga, L., F. Brezzi, A. Cangiani, G. Manzini, L.D. Marini, & A. Russo (2013). Basic principles of virtual element methods. *Mathematical Models and Methods in Applied Sciences 23*(01), 199–214.

Brezzi, F., L. Beirão da Veiga,, & L.D. Marini (2013). Virtual elements for linear elasticity problems. *SIAM Journal on Numerical Analysis 51*(2), 794–812.

Brezzi, F., K. Lipnikov, & M. Shashkov (2005). Convergence of the mimetic finite difference method for diffusion problems on polyhedral meshes. *SIAM Journal on Numerical Analysis 43*(5), 1872–1896.

Brezzi, F. & L.D. Marini (2013). Virtual element methods for plate bending problems. *Computer Methods in Applied Mechanics and Engineering 253*, 455–462.

Caballero, A., C. López, & I. Carol (2006). 3d meso-structural analysis of concrete specimens under uniaxial tension. *Computer Methods in Applied Mechanics and Engineering 195*(52), 7182–7195.

Chi, H., L.B. da Veiga, & G. Paulino (2017). Some basic formulations of the virtual element method (vem) for finite deformations. *Computer Methods in Applied Mechanics and Engineering 318*, 148–192.

Ciancio, D., I. Carol, & M. Cuomo (2013). A method for the calculation of inter-element stresses in 3d. *Computer Methods in Applied Mechanics and Engineering 254*(0), 222–237.

Cusatis, G., D. Pelessone, & A. Mencarelli (2011). Lattice discrete particle model (ldpm) for failure behavior of concrete. i: Theory. *Cement and Concrete Composites 33*(9), 881–890.

Da Veiga, L.B., F. Brezzi, & L.D. Marini (2013). Virtual elements for linear elasticity problems. *SIAM Journal on Numerical Analysis 51*(2), 794–812.

Donzé, F.V., V. Richefeu, & S.-A. Magnier (2009). Advances in discrete element method applied to soil, rock and concrete mechanics. *Electronic Journal of Geotechnical Engineering 8*(1), 44.

Gain, A.L., C. Talischi, & G.H. Paulino (2014). On the virtual element method for three-dimensional linear elasticity problems on arbitrary polyhedral meshes. *Computer Methods in Applied Mechanics and Engineering 282*, 132–160.

Lilliu, G. & J.G. van Mier (2003). 3d lattice type fracture model for concrete. *Engineering Fracture Mechanics 70*(7), 927–941.

Lopez, C.M., I. Carol, & A. Aguado (2008a). Meso-structural study of concrete fracture using interface elements. i: numerical model and tensile behavior. *jms 41*(3), 583–599.

Lopez, C.M., I. Carol, & A. Aguado (2008b). Meso-structural study of concrete fracture using interface elements. ii: compression, biaxial and brazilian test. *jms 41*(3), 601–620.

Mohammadnejad, T. & A. Khoei (2013). An extended finite element method for hydraulic fracture propagation

in deformable porous media with the cohesive crack model. *Finite Elements in Analysis and Design 73*, 77–95.

Oliver, J. (1996). Modelling strong discontinuities in solid mechanics via strain softening constitutive equations. part 2: Numerical simulation. *International journal for numerical methods in engineering 39*(21), 3601–3623.

Oliver, J., D. Linero, A. Huespe, & O. Manzoli (2008). Twodimensional modeling of material failure in reinforced concrete by means of a continuum strong discontinuity approach. *Computer Methods in Applied Mechanics and Engineering 197*(5), 332–348.

Park, K. & G.H. Paulino (2012). Computational implementation of the ppr potential-based cohesive model in abaqus: Educational perspective. *Engineering Fracture Mechanics 93*, 239–262.

Park, K., G.H. Paulino, & J.R. Roesler (2009). A unified potential-based cohesive model of mixed-mode fracture. *Journal of the Mechanics and Physics of Solids 57*(6), 891–908.

Rodrigues, E.A., O.L. Manzoli, L.A. Bitencourt Jr, & T.N. Bittencourt (2016). 2d mesoscale model for concrete based on the use of interface element with a high aspect ratio. *International Journal of Solids and Structures 94*, 112–124.

Shashkov, M. & S. Steinberg (1996). Solving diffusion equations with rough coefficients in rough grids. *Journal of Computational Physics 129*(2), 383–405.

Stankowski, T., K. Runesson, & S. Sture (1993). Fracture and slip of interfaces in cementitious composites. I: Characteristics, II: Implementation. *ASCE—J. Engrg. Mech. 119*(2), 292–327.

Talischi, C., G. Paulino, A. Pereira, & I. Menezes (2012). Polymesher: a general-purpose mesh generator for polygonal elements written in Matlab. *Structural and Multidisciplinary Optimization 45*(3).

Wriggers, P. & G. Zavarise (2002). *Computational contact mechanics*. Wiley Online Library.

Xie, D. & S.B.B. Jr. (2006). Progressive crack growth analysis using interface element based on the virtual crack closure technique. *Finite Elements in Analysis and Design 42*(11), 977–984.

Zhang, S., G. Wang, & X. Yu (2013). Seismic cracking analysis of concrete gravity dams with initial cracks using the extended finite element method. *Engineering Structures 56*, 528–543.



Taylor & Francis
Taylor & Francis Group
http://taylorandfrancis.com

Computational Modelling of Concrete Structures – Meschke, Pichler & Rots (Eds)
© 2018 Taylor & Francis Group, London, ISBN 978-1-138-74117-1

A cyclic triaxial concrete microplane model with gradient regularization

Imadeddin Zreid & Michael Kaliske
Institute for Structural Analysis, Technische Universität Dresden, Dresden, Germany

ABSTRACT: A coupled plasticity-damage microplane model for concrete is formulated and an implicit gradient enhancement is used to regularize the model. The coupling of damage and plasticity enables the modeling of the cyclic response of concrete, where both permanent deformation and reduction of stiffness is observed during unloading and reloading curves. Plasticity is governed by a smooth three-surface microplane cap yield function, which covers the full range of possible stress states. The yield function is based on the Drucker-Prager yield function, but supplemented with tension and compression caps. Additionally, the smoothness of the surface provides a stable algorithmic implementation for the return mapping and the tangent operator within an implicit finite element scheme. The damage formulation includes a tension compression split in order to account for the transition of stress state between compression and tension. Moreover, the numerical instability and the pathological mesh sensitivity, associated with strain softening, are handled by an implicit gradient enhancement. This enhancement makes the model strongly nonlocal by introducing the nonlocal fields as extra degrees of freedom governed by an additional partial differential equation. The result of this enhancement is a system of coupled fields which is solved by a simultaneous fully coupled scheme without the need of spatial averaging and explicit sharing of information between elements. The proposed model is implemented into a 3D finite element code and several numerical examples on plain and reinforced concrete are carried out to illustrate the capabilities of model.

1 INTRODUCTION

While concrete structures are usually designed using elastic analysis, inelastic deformations are expected in many cases. A nonlinear analysis enables the estimation of the failure load and crack patterns, as well as the degradation of the material at different loading stages, and thus can be advantageous especially for unconventional design cases. However, two main challenges hold back a broader use of nonlinear analysis for concrete structures. The first issue is the difficulty in formulating a widely applicable constitutive law for concrete. This is due to the complex heterogeneous nature of concrete, which results in a very distinct responses under different triaxial stress states and loading histories. The second issue is the higher cost of nonlinear simulations, not only due to the typical higher requirements for the nonlinear analysis, but also to the numerical instabilities caused by the nature of concrete constitutive laws, which involves strain softening and localization. Thus, dealing with both issues at the same time is necessary to create robust computational concrete models.

Most concrete models in the literature have been formulated either using plasticity theory or continuum damage mechanics, where the former depends on the concept of permanent deformation, while the latter depends on the degradation of the material stiffness. Both approaches can capture softening of concrete under monotonic loading, but to account for unloading and reloading behavior, a combination of both is required. The classical way of establishing material laws in these models is to use the strain and stress tensors directly, which means dealing with a second and fourth order tensor functions. An alternative way is the microplane approach where the constitutive laws are established between vectors on a randomly oriented plane. This means simplifying the constitutive laws to vectorial relationships and enabling the incorporation of induced anisotropy in a natural manner.

The response of concrete under tensile and low confined compression are characterized by strain softening. In terms of the governing differential equations, this leads to an ill-posed system, which in turn causes numerical instability and pathological mesh dependency in the finite element solution. One of the robust remedies for this problem are the nonlocal methods, which include integral type and gradient type formulations. In general, these methods introduce a length scale for nonlocal interaction such that the material response at one point will depend on a region surrounding that point.

The aim of this paper is to introduce a microplane concrete model based on a coupled damage plasticity formulation. The yield function for plasticity is a smooth three surface cap model, which

allows a stable return mapping and a consistent tangent algorithm. The damage variable is driven by the plastic strain and is split into compression and tension damage variables to account for the transition of loading from tension to compression and vice versa. Regularization of the model is achieved by an over-nonlocal implicit gradient formulation. Finally, the model is used to simulate both plain and reinforced concrete, in order to demonstrate the capabilities of the model in terms of agreement to experiments as well as the mesh objectivity.

2 COUPLED PLASTICITY-DAMAGE MICROPLANE MODEL

The basic components of the model could be summed up in the following stress-strain formula

$$\sigma = \frac{3}{4\pi}\int_{\Omega}\left(1-d^{mic}\right)\left[K^{mic}\boldsymbol{V}\left(\epsilon_V-\epsilon_V^{pl}\right) + 2G^{mic}\,\boldsymbol{Dev}^{T}\cdot\left(\epsilon_D-\epsilon_D^{pl}\right)\right]d\Omega, \tag{1}$$

where ε_V and ε_D are the volumetric and deviatoric microplane strains, respectively, and *pl* indicates the plastic part. The microplane strains are related to the macroscopic strain tensor as follows

$$\epsilon_V = V:\epsilon, \quad \epsilon_D = \boldsymbol{Dev}:\epsilon, \tag{2}$$

where $\boldsymbol{V}$ and $\boldsymbol{Dev}$ are projection tensors defined in terms of the normal vector to each microplane $\boldsymbol{n}$ as

$$\boldsymbol{V} = \frac{1}{3}1, \quad \boldsymbol{Dev} = \boldsymbol{n}\cdot\mathbf{I}^{dev} = \boldsymbol{n}\cdot\mathbf{I}^{sym} - \frac{1}{3}\boldsymbol{n}\cdot 1\otimes 1, \tag{3}$$

where $\mathbf{1}$ is the second order identity tensor, $\mathbf{I}$ is the fourth order identity tensor and $\mathbf{I}^{sym} = \frac{1}{2}\left[\mathbf{I}+\mathbf{I}^{T}\right]$ is its symmetric part. K^{mic} and G^{mic} are the microplane bulk and shear moduli, respectively. The homogenized quantities are calculated by numerical integration over a sphere. All the simulations in this work are performed with 42 microplanes, which due to symmetries can reduce to only 21 independent planes,

$$\frac{3}{4\pi}\int_{\Omega}(\bullet)\,d\Omega = \sum_{mic=1}^{21}(\bullet)\,w^{mic}, \tag{4}$$

where w^{mic} is the weight for each integration point, see (Bažant & Oh 1986, Zreid & Kaliske 2014). The plastic strains evolve according to the following flow rules

$$\dot{\epsilon}_V^{pl} = \dot{\lambda}m_V, \quad \dot{\epsilon}_D^{pl} = \dot{\lambda}\boldsymbol{m}_D, \tag{5}$$

where $\dot{\lambda}$ is the plastic multiplier and m_V, $\boldsymbol{m}_D$ are the flow directions, which considering an associated flow rule are derived from the yield function f^{mic} as follows

$$m_V = \frac{\partial f^{mic}}{\partial \sigma_V^e}, \quad \boldsymbol{m}_D = \frac{\partial f^{mic}}{\partial \sigma_D^e}, \tag{6}$$

and the microplane effective stresses σ_V^e and σ_D^e are defined as

$$\sigma_V^e = K^{mic}\left(\epsilon_V-\epsilon_V^{pl}\right), \quad \sigma_D^e = 2G^{mic}\left(\epsilon_D-\epsilon_D^{pl}\right). \tag{7}$$

2.1 *Microplane cap yield function*

The representation of the very distinct response of concrete under different stress states requires a yield function with multiple surfaces, which complicates the numerical implementation. A yield function with smooth transitions between the different surfaces avoids the numerical difficulties on the edges. The yield function used in this paper is shown in Fig. 1. It is based on the work of (Schwer & Murray 1994) and could be written as

$$f^{mic}\left(\sigma_D^e,\sigma_V^e,\kappa\right) = \frac{3}{2}\sigma_D^e\cdot\sigma_D^e - f_1^2\left(\sigma_V^e,\kappa\right)f_c\left(\sigma_V^e,\kappa\right)f_t\left(\sigma_V^e,\kappa\right). \tag{8}$$

The superscript *e* represents the effective stress, thus the yield function is evaluated without considering the damage. The function f_1 is the Drucker-Prager yield function with hardening (Zreid & Kaliske 2016),

$$f_1 = \sigma_0 - \alpha\sigma_V^e + f_h(\kappa). \tag{9}$$

Furthermore, f_c is the compression cap and f_t is the tension cap. The multiplication of f_c with f_1^2 results in a modified cap, which has the same slope as f_1 at the intersection point with f_1. In a similar manner, the tension cap gets the slope of f_1 at the

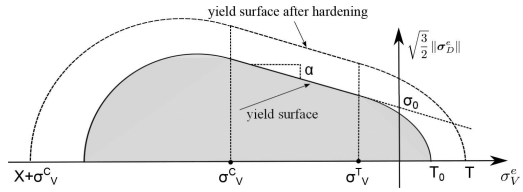

Figure 1. Smooth microplane cap yield function.

intersection point, and thus, the overall yield surface has a continuous derivative. The compression cap is given as

$$f_c = 1 - H_c\left(\sigma_V^C - \sigma_V^e\right)\frac{\left(\sigma_V^e - \sigma_V^C\right)^2}{X^2}, \tag{10}$$

$$X = Rf_1\left(\sigma_V^C\right), \tag{11}$$

where the material constant σ_V^C is the abscissa of the intersection point between the compression cap and the Drucker-Prager yield function, and R is the ratio between the major (volumetric) and minor (deviatoric) axes of the cap. Moreover, the tension cap reads

$$f_t = 1 - H_t\left(\sigma_V^e - \sigma_V^T\right)\frac{\left(\sigma_V^e - \sigma_V^T\right)^2}{\left(T - \sigma_V^T\right)^2}, \tag{12}$$

$$T = T_0 + R_t f_h\left(\kappa\right), \tag{13}$$

where σ_V^T, R_t, and T_0 are material constants. σ_V^T is the abscissa of the intersection point between the tension cap and the Drucker-Prager yield function, and T_0 is the initial intersection of the cap with the volumetric axis. Hardening causes T to increase and this increase is governed by parameter R_t. The Heaviside functions H_c and H_t activate the caps only when the stress state is within their domains. Lastly, the hardening is defined by a linear function,

$$f_h\left(\kappa\right) = D\kappa, \tag{14}$$

where D is a material constant and the evolution law for the hardening variable κ is given simply as

$$\dot{\kappa} = \dot{\lambda}. \tag{15}$$

2.2 *Damage evolution*

The initiation and growth of damage in concrete is different in compression and tension. In tension, softening starts directly after the elastic limit and the concrete is more brittle, while in compression some hardening is observed before eventual softening. Moreover, under cyclic loading, if a transition from tension to compression happened, the stiffness degraded by tensile cracking is recovered, due to crack closure. However, the damage sustained under compression persists upon transition to tension. This behavior could be captured using the damage split introduced in (Lee & Fenves 1998), where damage is decomposed into compression d_c^{mic} and tension d_t^{mic} parts as follows

$$1 - d^{mic} = (1 - d_c^{mic})(1 - r_w d_t^{mic}), \tag{16}$$

and exponential damage laws are used

$$d_t^{mic} = 1 - \exp\left(-\beta_t \gamma_t^{mic}\right), \tag{17}$$

$$d_c^{mic} = 1 - \exp\left(-\beta_c \gamma_c^{mic}\right), \tag{18}$$

where β_t and β_c are material constants, and the equivalent strain rate is a function of the volumetric plastic strain rate as follows

$$\dot{\eta}_t^{mic} = \begin{cases} r_w \dot{\varepsilon}_V^{pl} & \dot{\varepsilon}_V^{pl} > 0 \\ 0 & \dot{\varepsilon}_V^{pl} \le 0 \end{cases}, \tag{19}$$

$$\dot{\eta}_c^{mic} = \begin{cases} (1 - r_w)\dot{\varepsilon}_V^{pl} & \dot{\varepsilon}_V^{pl} > 0 \\ 0 & \dot{\varepsilon}_V^{pl} \le 0 \end{cases}, \tag{20}$$

$$r_w = \frac{\sum_{I=1}^{3}\left\langle \varepsilon^I \right\rangle}{\sum_{I=1}^{3}\left|\varepsilon^I\right|}. \tag{21}$$

The variable r_w is the damage split weight factor and has a range from 1 for total tension to 0 for total compression. ε^I are the principal values of the strain tensor and $\langle \bullet \rangle$ is the positive part function. The condition to limit the growth of damage to the case where $\dot{\varepsilon}_V^{pl} > 0$ prevents damaging of concrete under high confining pressure. Moreover, the factor r_w plays two rules. The first is dividing the equivalent strain to compression and tension, and the second is switching of the tension damage under compression. The variable γ^{mic} is calculated from the equivalent strain history as follows

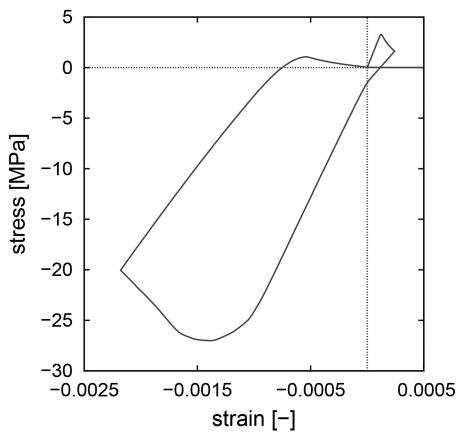

Figure 2. The behavior of the model under tension-compression cyclic loading.

$$\gamma_t^{mic} = \begin{cases} \eta_t^{mic} - \gamma_{t0} & \eta_t^{mic} > \gamma_{t0} \\ 0 & \eta_t^{mic} \le \gamma_{t0} \end{cases}, \tag{22}$$

$$\gamma_c^{mic} = \begin{cases} \eta_c^{mic} - \gamma_{c0} & \eta_c^{mic} > \gamma_{c0} \\ 0 & \eta_c^{mic} \le \gamma_{c0} \end{cases}, \tag{23}$$

where γ_{t0} and γ_{c0} are the damage thresholds for tension and compression, respectively.

3 IMPLICIT GRADIENT REGULARIZATION

Standard strain softening continuum models such as the one explained in the previous sections are afflicted with pathological mesh sensitivity and numerical instability. These adverse features are mathematical of the governing equations of the system, such as the nonlocal formulations. The implicit gradient enhancement is a type of nonlocal approaches, which calculates a nonlocal average of a local variable by considering the nonlocal field as an extra degree of freedom. This spatial averaging introduces a length scale in the equations, which keeps that the deformation field smooth and prevents displacement discontinuities. Hence, beside the balance of linear momentum,

$$\nabla \cdot \boldsymbol{\sigma} + \boldsymbol{f} = 0, \tag{24}$$

a modified Helmholtz equation is introduced to control the nonlocal field

$$\bar{\eta}_m - c\nabla^2 \bar{\eta}_m = \eta_m, \tag{25}$$

with the homogeneous Neumann boundary condition,

$$\nabla \bar{\eta}_m \cdot \boldsymbol{n}_b = 0, \tag{26}$$

where $\boldsymbol{\sigma}$ is the Cauchy stress tensor and $\boldsymbol{f}$ is the body force vector. Moreover, ∇ is the divergence, ∇ is the gradient and ∇^2 is the Laplace operator. Furthermore, c is material parameter and $\boldsymbol{n}_b$ is the normal to the outer boundary. Besides, η_m is the local variable to be enhanced and $\bar{\eta}_m$ is its nonlocal counterpart. In this model, the enhanced variables are equivalent strains η_t^{mic} and η_c^{mic}. However, not all the microplanes are considered independently, but a homogenized value as follows

$$\eta_m = \begin{bmatrix} \eta_{mt} \\ \eta_{mc} \end{bmatrix} = \begin{bmatrix} \frac{1}{4\pi}\int_\Omega \eta_t^{mic} d\Omega \\ \frac{1}{4\pi}\int_\Omega \eta_c^{mic} d\Omega \end{bmatrix}, \tag{27}$$

which means that two extra degrees of freedom are required. A full regularization of plastic damage models are achieved by the over-nonlocal formulation (Grassl & Jirásek 2006, Poh & Swaddiwudhipong 2009), where the over-nonlocal variable $\hat{\eta}^{mic}$ is evaluated as a linear combination of local and nonlocal variables,

$$\hat{\eta}_t^{mic} = m\bar{\eta}_{mt} + (1-m)\,\eta_t^{mic}, \tag{28}$$

$$\hat{\eta}_c^{mic} = m\bar{\eta}_{mc} + (1-m)\,\eta_c^{mic}. \tag{29}$$

The material parameter m should be larger than 1 in order to achieve regularization. This enhanced variable is now used instead of the local equivalent strains in Eqs. (22) and (23) as follows

$$\gamma_t^{mic} = \begin{cases} \hat{\eta}_t^{mic} - \gamma_{t0} & \hat{\eta}_t^{mic} > \gamma_{t0} \\ 0 & \hat{\eta}_t^{mic} \le \gamma_{t0} \end{cases}, \tag{30}$$

$$\gamma_c^{mic} = \begin{cases} \hat{\eta}_c^{mic} - \gamma_{c0} & \hat{\eta}_c^{mic} > \gamma_{c0} \\ 0 & \hat{\eta}_c^{mic} \le \gamma_{c0} \end{cases}. \tag{31}$$

The solution of the system follows the standard procedure for coupled field problems using a monolithic simultaneous scheme. The weak forms of Eqs. (24) and (25) are obtained by the help of weight functions $\delta\mathbf{u}$ and $\delta\bar{\eta}_m$,

$$\int_{\partial\mathcal{B}} \mathbf{t}_e \cdot \delta\mathbf{u}\, da - \int_{\mathcal{B}} \boldsymbol{\sigma} : \nabla\delta\mathbf{u}\, d\upsilon + \int_{\mathcal{B}} \delta\mathbf{u} : \boldsymbol{f}\, d\upsilon = 0, \tag{32}$$

$$\int_{\mathcal{B}} \delta\bar{\eta}_m \bar{\eta}_m\, d\upsilon + \int_{\mathcal{B}} \nabla\delta\bar{\eta}_m \cdot c\nabla\bar{\eta}_m\, d\upsilon = \int_{\mathcal{B}} \delta\bar{\eta}_m \eta_m\, d\upsilon. \tag{33}$$

The fields are interpolated over the sub-domains as follows

$$\mathbf{u} = \boldsymbol{N}\boldsymbol{d}^e, \quad \bar{\eta}_m = \bar{\boldsymbol{N}}\boldsymbol{E}^e, \tag{34}$$

where $\boldsymbol{N}$ denotes the shape functions for the displacement field and $\bar{\boldsymbol{N}}$ for the nonlocal field, and the gradient of the fields are given as

$$\nabla\mathbf{u} = \partial_x \boldsymbol{N}\boldsymbol{d}^e = \boldsymbol{B}\boldsymbol{d}^e, \nabla\bar{\eta}_m = \partial_x \bar{\boldsymbol{N}}\boldsymbol{E}^e = \bar{\boldsymbol{B}}\boldsymbol{E}^e, \tag{35}$$

where $\boldsymbol{d}^e$ are the nodal displacements and $\boldsymbol{E}^e$ are the nodal nonlocal field. The residual expression for the previous differential equations may be written a

$$\boldsymbol{R}^e = \begin{bmatrix} \mathbf{R}_u^e \\ \mathbf{R}_{\bar{\eta}}^e \end{bmatrix}, \tag{36}$$

where

$$\boldsymbol{R}_{u,i}^e = \int_{\mathcal{B}} \boldsymbol{B}^T \boldsymbol{\sigma}\, d\upsilon - \int_{\mathcal{B}} \boldsymbol{N}^T \boldsymbol{F}\, d\upsilon - \int_{\partial\mathcal{B}_e} \boldsymbol{N}^T \boldsymbol{t}_e\, da, \tag{37}$$

$$\boldsymbol{R}^{e}_{\bar{\eta},i} = \int_{\mathcal{B}} \bar{\boldsymbol{B}}^{T} c \bar{\boldsymbol{B}} \boldsymbol{E} d\upsilon + \int_{\mathcal{B}} \bar{\boldsymbol{N}}^{T} \left[\bar{\boldsymbol{N}} \boldsymbol{E} - \eta_{m} \right] d\upsilon, \tag{38}$$

and the fully coupled simultaneous solution takes the form

$$\begin{bmatrix} \mathbf{K}^{e}_{uu,i} & \mathbf{K}^{e}_{u\bar{\eta},i} \\ \mathbf{K}^{e}_{\bar{\eta}u,i} & \mathbf{K}^{e}_{\bar{\eta}\bar{\eta},i} \end{bmatrix} \begin{bmatrix} \Delta \boldsymbol{d}^{e}_{,i+1} \\ \Delta \boldsymbol{E}^{e}_{,i+1} \end{bmatrix} = - \begin{bmatrix} \mathbf{R}^{e}_{u,i} \\ \mathbf{R}^{e}_{\bar{\eta},i} \end{bmatrix}, \tag{39}$$

where $i+1$ is the current time step. As can be seen, the total tangent is unsymmetric due to the coupling terms and thus, an unsymmetric solver is required.

4 NUMERICAL EXAMPLES

In the following numerical examples, the elastic microplane material constants are related to the macroscopic elastic constants as follows

$$K^{mic} = \frac{E}{(1-2\nu)}, \qquad G^{mic} = \frac{E}{2(1+\nu)}, \tag{40}$$

and the yield function constants are related to the concrete uniaxial strength f_{uc} and biaxial strength f_{bc} as

$$\alpha = \frac{\sqrt{3}\left(f_{bc} - f_{uc}\right)}{2 f_{bc} - f_{uc}}, \tag{41}$$

$$\sigma_{0} = \left(1/\sqrt{3} - \alpha/3\right) f_{uc}. \tag{42}$$

A value of $f_{bc} = 1{:}15\, f_{uc}$ is used, and the tension cap constants are taken as,

$$\sigma^{T}_{V} = -f_{uc}/3, \qquad T_{0} = f_{ut}/3. \tag{43}$$

For the visualization of results, a homogenized quantities are computed as

$$d^{hom} = \frac{1}{4\pi} \int_{\Omega} d^{mic} d\Omega, \qquad k^{hom} = \frac{1}{4\pi} \int_{\Omega} k^{mic} d\Omega. \tag{44}$$

4.1 *Cyclic tension compression test*

Tension compression cyclic loading is applied to a notched concrete specimen (Cornelissen, Hordijk, & Reinhardt 1986). The geometry and boundary conditions of the test are shown in Fig. 3. Due to symmetry, a quarter of the specimen is simulated and the used parameters are listed in Table 1. Displacement control is used to apply the cyclic loading with increasing amplitude as given in Fig. 3. The numerical results are compared to the experimental results in Fig. 4 a), where the stress is calculated as the force divided by area between the notches and the displacement is the difference in deformation between the 35 mm length of the gauge as shown in in Fig. 3. It is observed that the stiffness recovery in Fig. 4, when the loading changes from tension to compression, is due to tensile cracks closure. Furthermore, a comparison of the numerical results obtained by three different mesh refinements demonstrates the objectivity of the mesh achieved by the implicit gradient enhancement, see Fig. 4 b) and Fig. 5.

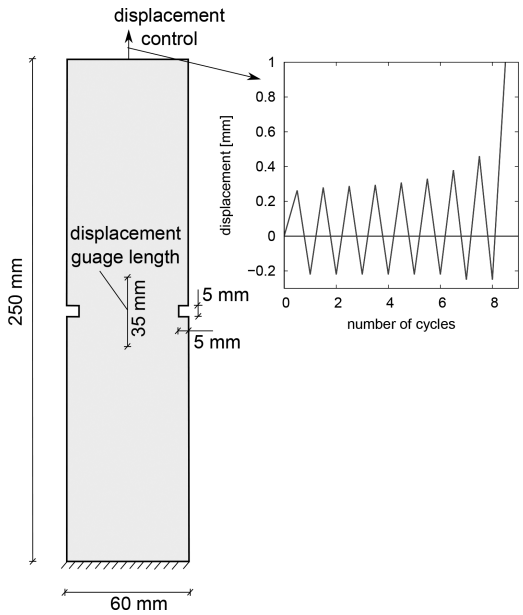

Figure 3. Geometry and boundary conditions for the cyclic test.

Table 1. Material parameters for the cyclic test.

E [MPa]	24000
ν	0.2
f_{uc} [MPa]	40
D [MPa]	6×10^{4}
R_{t}	4
σ^{C}_{V} [MPa]	−50
R	2
γ_{t0}	0
γ_{c0}	2×10^{-4}
β_{t}	7×10^{3}
β_{c}	5×10^{3}
c [mm^2]	36
m	2.5

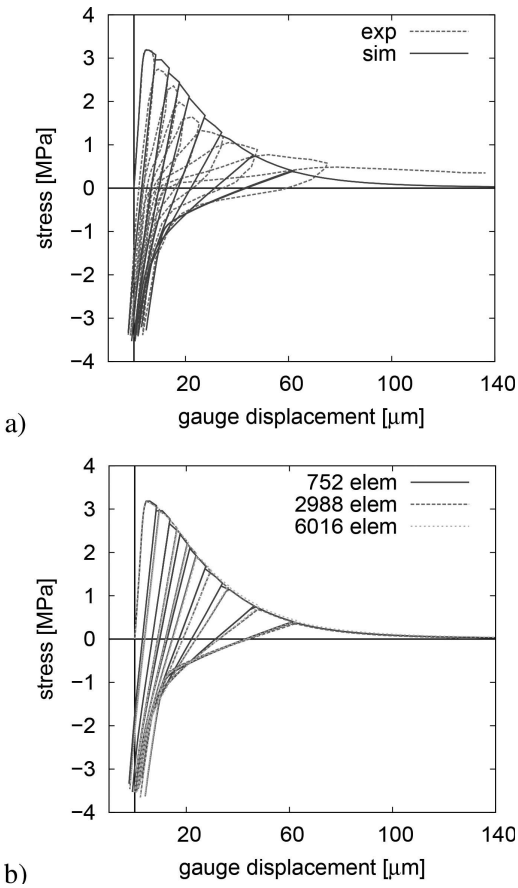

Figure 4. Comparison of experiment and simulation results with three discretizations for the cyclic bending test.

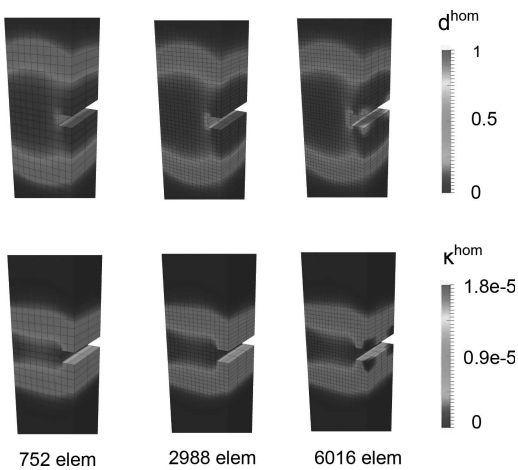

Figure 5. Cyclic test: damage profiles and plastic hardening distribution for three mesh sizes.

4.2 *High strength reinforced concrete column*

A reinforced concrete column is tested with different types of concrete to study the effect of intersecting high strength concrete columns with weaker slabs (Shin, Yoon, Cook, & Mitchell 2016). Fig. 6 shows the geometry and the reinforcement details. Three types of specimens are modeled: C50, C100 and C100-S50. The reinforcement is simulated using truss elements and von Mises plasticity with linear hardening. The rebar truss elements and the concrete brick elements are connected by shared nodes. The material constants for the steel are $E = 190 \times 10^3$ MPa, $\nu = 0.3$, the yield stress $f_u = 500$ MPa and the hardening parameter $H = 10.5 \times 10^3$ MPa. For the concrete, the material constants are given in Table 2. The specimens C50 and C100 were run first and material constants were found, then the same parameters were used to run the C100-S50 specimen. The discretizations is shown in Fig. 6, where a quarter of the column

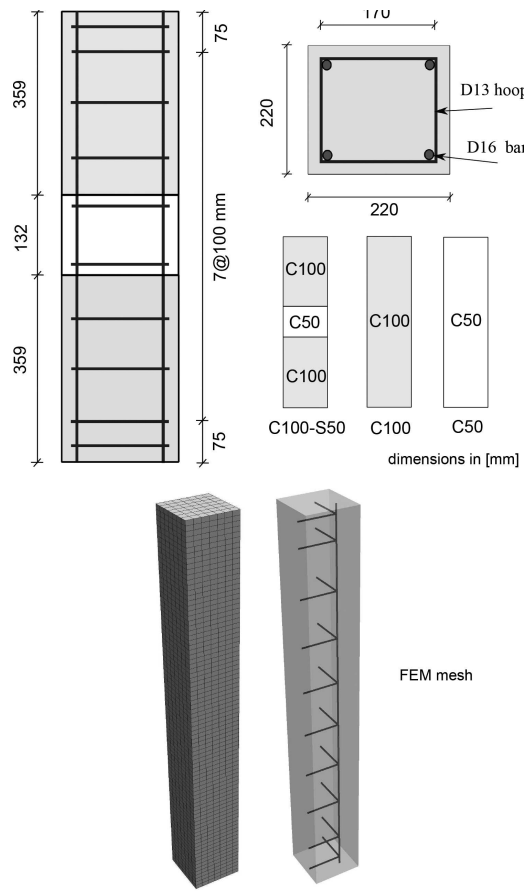

Figure 6. Geometry and reinforcement details for the RC column test.

Table 2. Material parameters for the RC column test.

	C50	C100
E [MPa]	29000	40000
v	0.2	0.2
f_{uc} [MPa]	50	130
D [MPa]	6×10^4	6×10^4
R_t	1	1
σ_V^C [MPa]	−35	−95
R	2	2
γ_{t0}	0	0
γ_{c0}	4×10^{-4}	5×10^{-4}
β_t	2×10^3	3.5×10^3
β_c	1.5×10^3	2.5×10^3
c [mm^2]	1200	1200
m	2.5	2.5

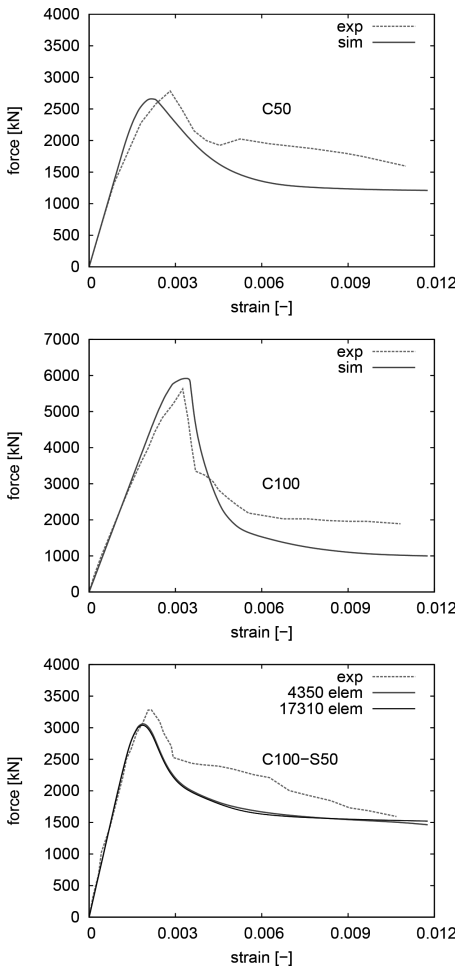

Figure 7. Comparison of experiment and simulation results for the RC column test.

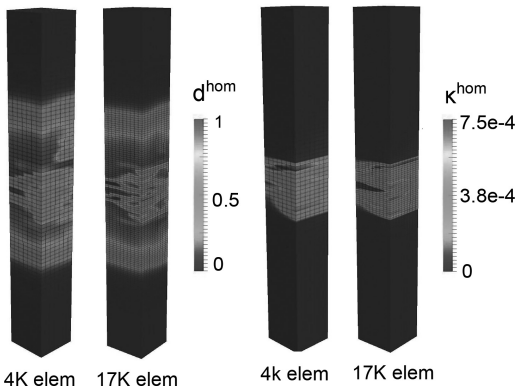

Figure 8. Damage profiles and plastic hardening distribution for the RC column test.

is modeled due to symmetry. In Fig. 7, the simulation results are compared to their corresponding experimental results. Moreover, damage and plastic hardening contours are given in Fig. 8 for two different discretizations.

5 CONCLUSIONS

A microplane model for concrete is introduced, which handles both the constitutive description of concrete as well as the numerical regularization. Based on a coupled plasticity-damage approach, the cyclic triaxial response of concrete is described. The smooth cap yield surface allows a robust implementation within an implicit finite element code. The damage part of the model is regularized with an over-nonlocal implicit gradient enhancement. Numerical examples both of plain and reinforced concrete are simulated with good correspondence to experiments. Pathological mesh sensitivity and numerical instabilities are eliminated.

REFERENCES

Bažant, Z. & B.H. Oh (1986). Efficient numerical integration on the surface of a sphere. *Zeitschrift für Angewandte Mathematik und Mechanik 66*, 37–49.

Cornelissen, H., D. Hordijk, & H. Reinhardt (1986). Experimental determination of crack softening characteristics of normalweight and lightweight concrete. *HERON 31*, 45–56.

Grassl, P. & M. Jirásek (2006). Plastic model with non-local damage applied to concrete. *International Journal for Numerical and Analytical Methods in Geomechanics 30*, 71–90.

Lee, J. & G.L. Fenves (1998). Plastic-damage model for cyclic loading of concrete structures. *Journal of Engineering Mechanics 124*, 892–900.

Poh, L.H. & S. Swaddiwudhipong (2009). Over-nonlocal gradient enhanced plastic-damage model for concrete. *International Journal of Solids and Structures 46*, 4369–4378.

Schwer, L.E. & Y.D. Murray (1994). A three-invariant smooth cap model with mixed hardening. *International Journal for Numerical and Analytical Methods in Geomechanics 18*, 657–688.

Shin, H.-O., Y.-S. Yoon, W.D. Cook, & D. Mitchell (2016). Enhancing the performance of uhsc columns intersected by weaker slabs. *Engineering Structures 127*, 359–373.

Zreid, I. & M. Kaliske (2014). Regularization of microplane damage models using an implicit gradient enhancement. *International Journal of Solids and Structures 51*, 3480–3489.

Zreid, I. & M. Kaliske (2016). An implicit gradient formulation for microplane drucker-prager plasticity. *International Journal of Plasticity 83*, 252–272.

Computational Modelling of Concrete Structures – Meschke, Pichler & Rots (Eds)
© 2018 Taylor & Francis Group, London, ISBN 978-1-138-74117-1

Simulation of cracking susceptibility in recycled concrete aggregate systems

A. Jayasuriya, M.J. Bandelt & M.P. Adams
John A. Reif, Jr., Department of Civil and Environmental Engineering, New Jersey Institute of Technology, Newark, NJ, USA

ABSTRACT: This paper presents an investigation into the cracking susceptibility of concrete made with recycled concrete aggregates through two-dimensional numerical finite element simulations. Due to the limited experimental data on the performance of Recycled concrete Aggregate Concrete (RAC) in both compression and tension, a series of finite element simulations were performed on a RAC systems with a range of adhered mortar contents for a regular 100 mm RAC cube. The finite element simulation was performed for 0%, 2%, 4%, 10%, 20%, 50%, and 100% adhered mortar contents in order to examine the compressive and tensile behavior of the RAC cube under monotonic loading. Experimental image analysis was used to map the physical geometry of each materialto the finite element model. Loading conditions were prescribed as a strain deformation for the monotonic loading, and sequential crack initiation and crack propagation were also explored. Simulated compressive strengths decreased by 11% between 0% and 50% adhered mortar contents, simulated tensile strengths remained consistent across adhered mortar contents, and modulus of elasticity degraded with adhered mortar content. Both compressive and tensile stress-strain behaviors have showed a slight increase in strain at cracking with increasing adhered mortar content, highlighting an apparent deformability in RAC systems. Stress concentrations were observed near the adhered mortar and interfacial transition zone boundaries, which emphasizes the fact that the fracture path initiates within the new interfacial transition zone.

1 INTRODUCTION

Recycled concrete aggregate (RCA) is an aggregate made from the recovery of demolished concrete which can be used as either a coarse aggregate or a fine aggregate. Concretes made of RCA have been used to address economic, environmental, and material constraint concerns related to production of normal concrete (Winfield and Taylor 2005). Many environmental challenges can be minimized by introducing RCA into the concrete production such as destruction of natural habitats of species, top-soilerosion, loss of ground water storage capacity, dust pollution and excessive greenhouse gas emission (Abbas et al 2007). During normal concrete production, greenhouse gases accumulate from mining, processing, and transporting aggregates (Abbas et al. 2007). Therefore, there is a need to alleviate these environmental impacts by reducing the amounts of natural aggregates used in concretes, and shifting towards recycled aggregates where the impact of mining and transportation can be minimized. Over 373 million tons of concrete demolition waste is produced each year (Environmental Protection Agency 2016), as such, an ample amount of RCA is available that could be used as a replacement material to the natural aggregates, such that the adverse environmental effects can be minimized.

Recycled concrete aggregate concrete (RAC) consists of five different materials that have unique mechanical properties. The five materials are natural aggregate, new interfacial transition zone, adhered mortar, old interfacial transition zone, and cement-paste matrix. A schematic diagram of an aggregate in the RAC system is shown in Figure 1. Although the response of each material is well understood, the composite RAC system is a complex heterogeneous material. In general, RAC has lower strength, lower elastic modulus, and higher peak strain compared to conventional concrete (Etxeberria et al. 2007). The adhered mortar consists of a highly porous cementitious material which makes it less strong (Malešev et al. 2010) than an ordinary mortar. This is due to the microcracks that are induced in the adhered mortars during the crushing operations (Padmini et al. 2009). RAC systems can achieve higher peak strains than ordinary concrete because a large volume of hardened adhered mortar exists in the RAC system (Liu et al. 2011). Peak strains can be higher in RAC systems compared to normal concrete systems due

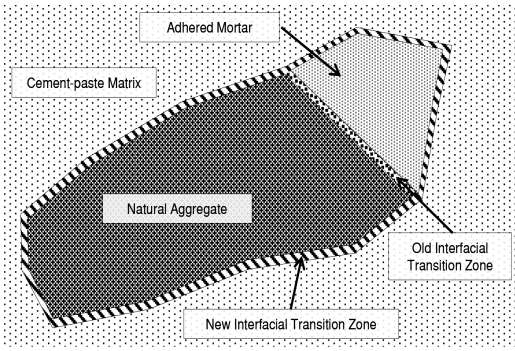

Figure 1. Schematic diagram of an aggregate in the RAC system.

to the high roughness index of the adhered mortar surface which can increase the friction between cement-paste matrix and adhered mortar in the concrete continuum (Malešev et al 2010. Further, RAC has been observed to have a higher cracking resistance due to the presence of adhered mortar from shrinkage testing results of RAC and traditional concrete systems (Adams et al. 2016). Strengths of RAC can be improved through the use of superplasticizers to maintain an appropriate effective water-to-cement ratio and offset the workability issues that are often seen when RCA is used in concrete (Padmini et al. 2009, Sagoe-Crentsil et al. 2001).

RAC crack patterns can be affected by the properties and content of adhered mortar, resulting in different failure patterns as the adhered mortar influences internal deformations (Padmini et al. 2009). This deformation and fracture process are tied together with the progressive failure through crack initiation, crack propagation, and coalescence of micro-cracks (Xiao et al. 2013). In RAC, most of the crack propagations occur either through new interfacial transition zone or old interfacial transition zone, as this interfacial transition zone is considered to be the weakest link in the concrete (M.G. Alexander 1996). Generally, the average thickness of the new interfacial transition zone and old interfacial transition zone varies from 20–50 μm (Tasong et al. 1999).

Stress concentrations can occur in a concrete system due to a difference in modulus of elasticity between two materials (e.g., aggregate and cement-paste matrix) (Bremner & Holm 1986). In RAC systems, the problem of relative stiffnesses is high due to the number of different individual materials (e.g., adhered mortar, aggregate, cement-paste matrix, etc.). This study focuses on the stress-strain relationships of RAC, in both compression and tension, with different amounts of adhered mortar. While experimental studies have been used to examine the influence of adhered mortar in the past, the numerical approach presented herein identifies internal deformations and propagation of damage until material softening occurs. The results can be used to understand how incremental changes in adhered mortar influence overall mechanical properties.

2 MODEL GEOMETRY AND MATERIAL BEHAVIOR

2.1 *Description of simulation setup*

In this study, the uniaxial compressive and tensile response of a 100 mm × 100 mm × 100 mm sample was simulated. The model geometry used a sample of concrete with a maximum aggregate size of 20 mm. A 100 mm × 100 mm cross section of a known RAC system was selected from prior research (Abbas et al. 2009). The selected image was then manually mapped onto a finite element model with four-noded quadrilateral elements that were 0.5 mm × 0.5 mm in size. Detailed boundaries of the aggregate and the cement-paste matrix were defined for a 0% adhered mortar content system (i.e., a system with only natural aggregates).

The area of each aggregate was computed, and then representative areas of natural aggregates were replaced with corresponding adhered mortar contents. In total, seven model geometries were developed with varying levels of adhered mortar contents. Figure 2 depicts the meshed models for each of the seven adhered mortar contents simulated in this study (0%, 2%, 4%, 10%, 20%, 50%, and 100%).

Each node along the bottom of the model was restrained in the vertical direction, and the node located at the bottom-left of the model was restrained in the horizontal direction to maintain equilibrium. A unit vertical displacement was applied along the nodes at the top of the model, allowing the computational model to be loaded in compression or tension. Figure 3 illustrates the boundary conditions orientation of the computational model.

2.2 *Material models, properties and parameters*

A total strain-based fixed cracked constitutive model (Feenstra et al. 1998) was implemented in this study. Since the load was applied using a prescribed deformation monotonically, it was expected that the principle compressive and tensile strains would remain fixed in direction, and therefore, a fixed crack model was implemented.

A parabolic softening behavior was used to simulate the compressive response of each material (Feenstra 1993). This parabolic softening model is based on the fracture energy properties as determined by

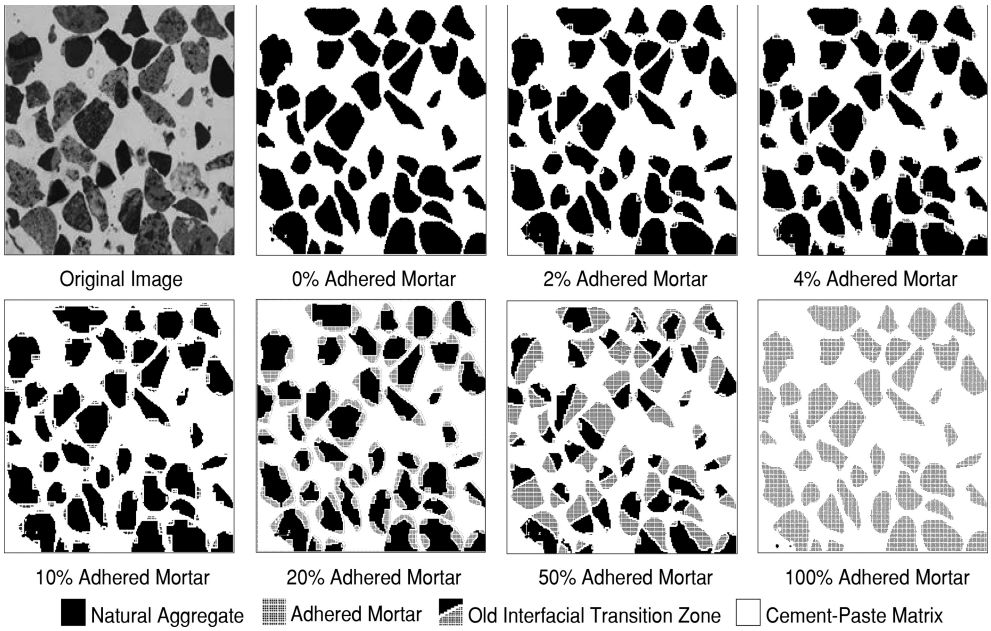

Figure 2. Mapping of RAC model.

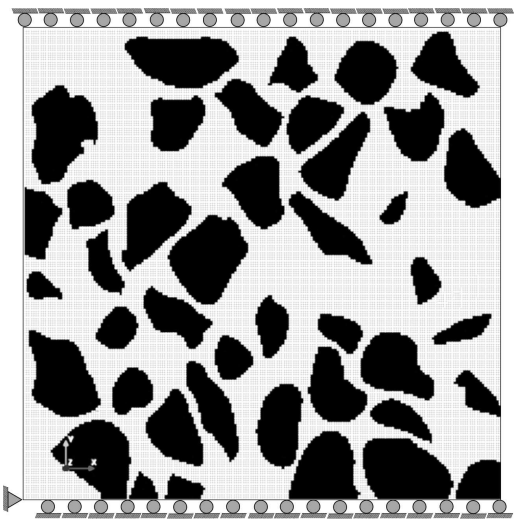

Figure 3. Nodal boundary conditions for the computational model.

uniaxial compressive experiments of each material. An exponential softening behavior was implemented to simulate the tensile response of each material based on fracture energy. A 1% of shear retention factor was allowed in the simulation to allow for some shear stiffness after crack formation.

As discussed in the introduction, each material type in RAC has different material properties that need to be defined in the simulation. Based on prior experimental research, the elastic moduli of natural aggregates, adhered mortar, and cement-paste matrix were obtained using nano-indentation techniques with recycled concrete aggregates and reported values are used in Xiao et al. (2013). Poissons ratio of the aforementioned materials were obtained from laboratory experiments (Xiao et al. 2013). Further, the moduli of elasticity and Poisson's ratios of the new interfacial transition zone and old interfacial transition zone had been previously tested and the appropriate values were used in this study (Ramesh et al. 1996). Additional mechanical properties for aggregate were determined from Winkler (1974). A detailed summary of the material properties are shown in Table 1.

2.3 *Loading conditions and analysis procedure*

Vertical deformation was prescribed to the specimen along the top nodes of the model in 0.001 mm increments. Therefore, each step constitutes a strain deformation of 10 microstrains ($\mu\varepsilon$) in both compression and tension. A modified Newton-Raphsons iteration technique was used as the convergence approach. The convergence tolerances for energy, displacements, and force norms were considered to be 0.01%, 0.1%, and 1% respectively. In certain simulations, the displacement step size was

Table 1. Material properties.

Material type	Modulus of elasticity MPa	Compressive strength MPa	Tensile strength MPa	Poisson's ratio	Fracture energy N/mm
Aggregate	80000	144.0	9.60	0.16	0.1628
Adhered mortar	25000	45.0	3.00	0.22	0.0509
Cement-paste matrix	23000	41.4	2.76	0.22	0.0468
Old ITZ*	20000	36.0	2.40	0.20	0.0407
New ITZ*	18000	33.1	2.21	0.20	0.0371

*Note: ITZ – Interfacial Transition Zone.

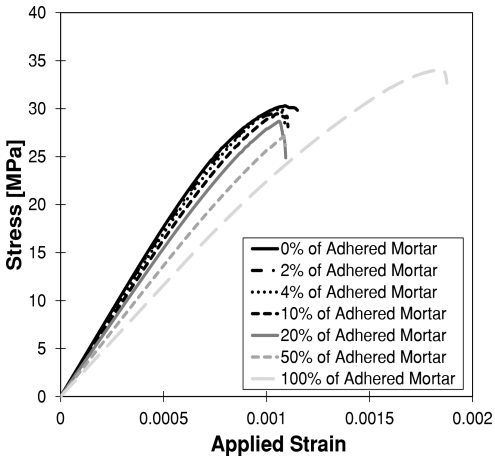

Figure 4. Stress-strain relationship in compression.

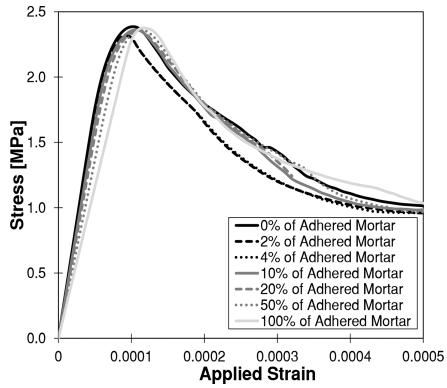

Figure 5. Stress-strain relationship in tension.

reduced to 0.0001 mm in order to improve convergence criteria during the softening response of the simulation.

3 SIMULATION RESULTS AND DISCUSSION

3.1 *Compressive behavior*

The simulation results were obtained for compressive softening behavior of different adhered mortar contents. The relationship between the mechanical characteristic (stress-σ) versus the deformation characteristic (strain-ε) in compression was also obtained for each adhered mortar content. Based on the stress-strain relationship depicted in Figure 4, it is clear that the increasing amount of adhered mortar content greatly affected the overall stiffness of the material resulting degrading elastic moduli. Due to the increasing amounts of adhered mortar contents in the RAC system from 0% to 100%, there was a 35.2% of reduction observed in modulus of elasticity. Further, the corresponding degradation of modulus of elasticity showed a negative nonlinear association.

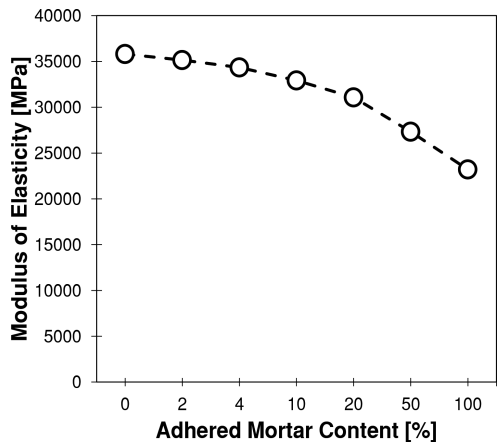

Figure 6. Modulus of elasticity vs. adhered mortar content.

The average peak stresses with adhered mortar contents between 0% and 50% was 29.2 MPa with a standard deviation of 1.2 MPa. The 100% adhered mortar content had a peak stress of 34.1 MPa, which was a 16.8% increase compared to the average peak stress which was obtained from the simulation results for 0% to 50% adhered mortar contents. This result shows that a 100% adhered mortar system can experience higher applied stresses under monotonic loading due to the low difference of material stiffness, preventing stress concentrations between adhered mortar and cement-paste matrix in the absence of natural aggregates. Furthermore, the peak strain of 100% adhered mortar content was 74.3% higher than the mean peak strain of adhered mortar contents from 0% to 50%. The standard deviation of peak strain was 2×10^{-5} for adhered mortar contents from 0% to 50%.

Contours of principal compressive strains are illustrated in Figure 7 where the strains lead to stress concentrations of deformation in the RAC system. The strain variation across the RAC specimens was not uniform due to the heterogeneity of the system. Results showed that strains for adhered mortar contents less than 50% had reached local strains of 0.003 before 50% or 100% adhered mortar simulations. When the amount of adhered mortar increased, less deformation concentration was observed as the relative stiffness between the adhered mortar and cement-paste matrix were

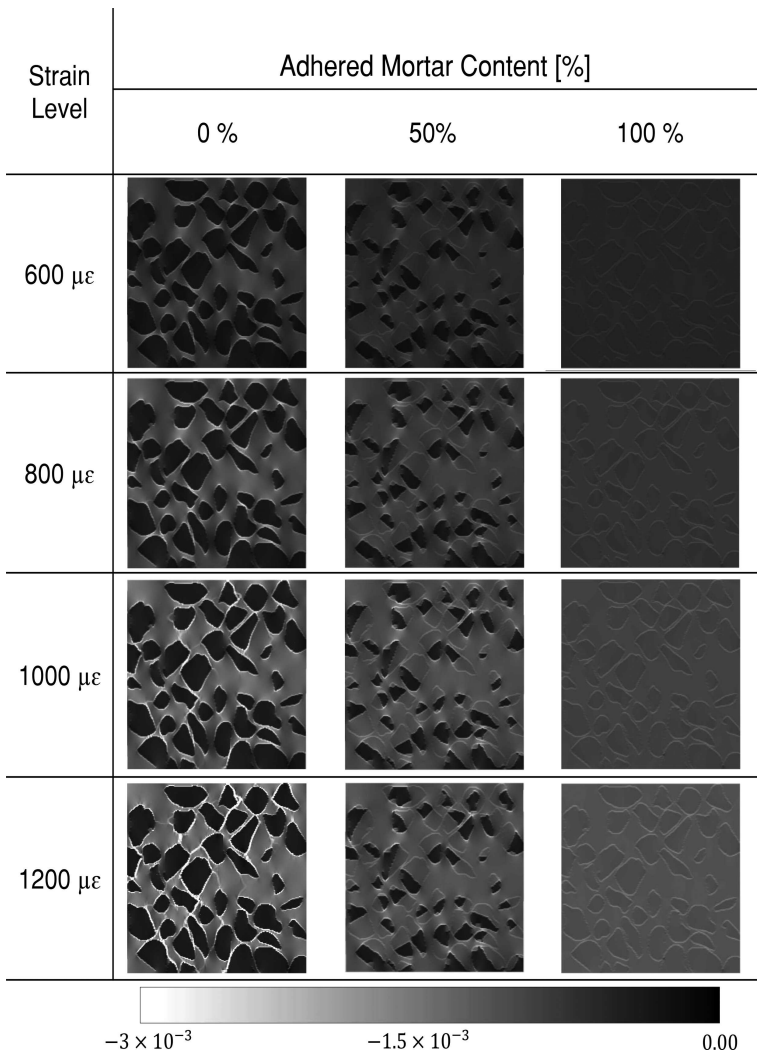

Figure 7. Principal compression strain contours from compression loading.

similar. For 100% adhered mortar contents, majority of the materials had similar mechanical properties as there was no effect from the natural aggregates. Therefore, stress and strain concentration around aggregates was minimized.

3.2 *Tensile behavior*

The tensile behavior was obtained from the simulation results for all adhered mortar contents. As shown in Figure 5, the average peak stress of seven sets of simulations was 2.35 MPa with a standard deviation of 0.027 MPa, indicating a small amount of variation in tensile strength based on adhered mortar content. Similar to the compressive response, the adhered mortar content significantly affected the stiffness as well as in tension. Variation of the elastic modulus against the amount of adhered mortar showed a negative nonlinear association. And it was found that moduli of elasticity varied in a similar manner for both compressive and tensile responses. The degradation of modulus of elasticity is plotted against the amount of adhered mortar content in Figure 6. The modulus of elasticity was calculated between the point of zero stress and strain, and the point at 40% of the maximum compressive, or tensile stress.

Figure 8 shows contours of principal tensile strain at strain increments for different adhered

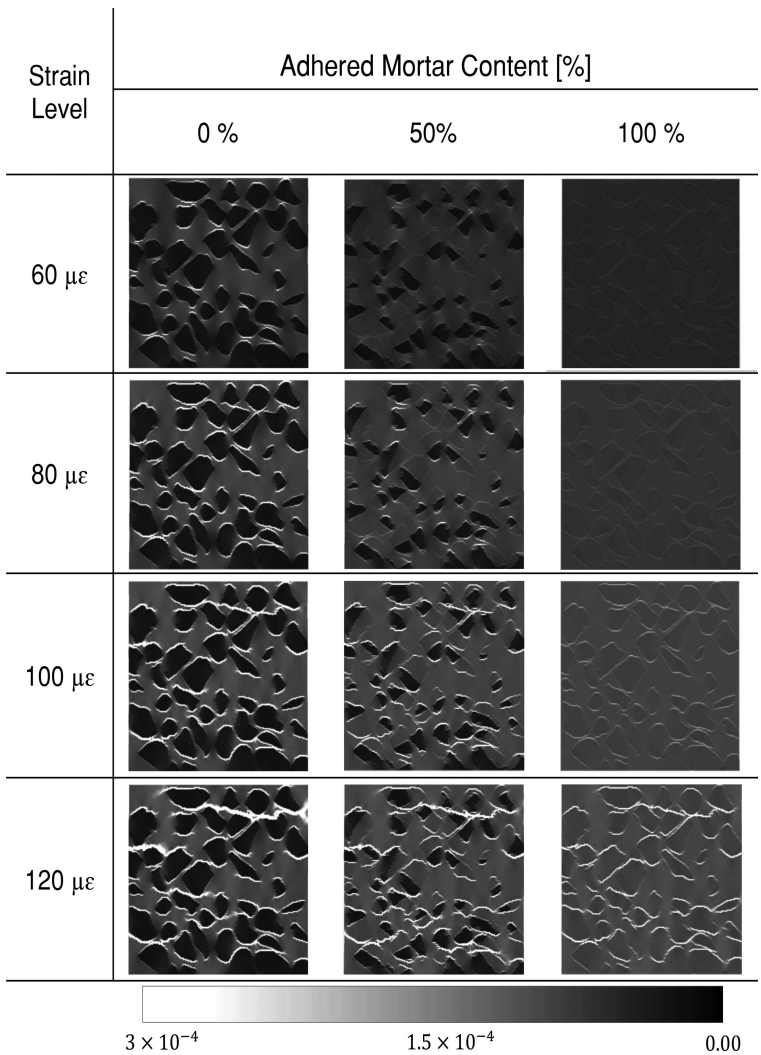

Figure 8. Principal tension strain contours from tension loading.

mortar contents. The amount of adhered mortar content affected the overall strain concentration behavior of the RAC specimen. The results showed that the tensile strain capacity of 0.0003 (which is about 10% of the compressive strain capacity in concrete) was reached at a faster rate for those which had adhered mortar contents lower than 50%. Strain concentrations were generally observed near the new interfacial transition zone.

3.3 *Crack initiation, propagation, and coalescence of cracks*

Cracks initiated in the RAC system when the stress was equivalent to the tensile capacity of the material. The simulation results showed that the stress concentrations occurred within the new interfacial transition zone. As the strain deformation increased further, the tensile stresses reached the tensile capacity of the new interfacial transition zone and created cracks near the interfacial transition zone boundary. Further, when the deformation was increased, a clear fracture path was created around thenatural aggregate. This was a common characteristic where damage was observed to initiate around the aggregate in both compression and tension. At larger strain deformations, the cracks further propagated and coalesced into the old interfacial transition zone.

4 CONCLUSION

Nonlinear finite element simulations were carried out on RAC subjected to monotonic loading for different adhered mortar contents. The simulation results in both compression and tension showed that the amount adhered mortar content had a significant affect on overall modulus of elasticity, peak stresses, strain at failure, location of damage concentration, and propagation of cracking.

Regardless of the loading criteria (i.e., tension or compression), the elastic modulus was reduced by increasing the adhered mortar content. Results showed that the reductions of moduli of elasticity for both compressive and tensile responses were in similar trends with the increasing adhered mortar contents from 0% to 100%. The elastic modulus decreased as a function of adhered mortar content showing a negative nonlinear correlation.

The mean peak stress in compression was 29.2 MPa with a standard deviation of 1.2 MPa for adhered mortar contents from 0% to 50%, and the highest peak stress of 34.1 MPa was observed in the 100% adhered mortar content. The tensile response showed a mean peak stress of 2.35 MPa with a standard deviation of 0.027 MPa for all the adhered mortar contents. Peak strain contours showed that RACs with higher adhered mortar contents have less deformation concentration around aggregates when compared with RACs with lower adhered mortar contents. Thus, the numerical findings presented here confirm the hypothesis of Adams et al. (2016) that concrete produced with RCA has an increased cracking resistance compared to concrete incorporating natural aggregates.

Simulation results showed that the strain localization can be occurred due to the large difference between each material stiffnesses in the RAC system during the load transfer. And it showed that, based on the relative difference in material properties and amounts of adhered mortar contents in the RAC system, distinct damage locations were observed near the adhered mortar and new interfacial transition zone boundaries. Damage was further propagated through the old interfacial transition zone at higher strain levels until the cube specimen reached its ultimate strain capacity.

Additional work is underway to simulate the response of RAC with stochastic distributions of material properties. Experimental work is also concurrently being conducted to validate numerical results.

ACKNOWLEDGEMENT

The authors gratefully acknowledge the support of the John A. Reif, Jr. Department of Civil and Environmental Engineering. All simulations were performed using the finite element software DIANA Release 10.0.

REFERENCES

Abbas, A., G. Fathifazl, B. Fournier, O.B. Isgor, R. Zavadil, A.G. Razaqpur, & S. Foo (2009). Quantification of the residual mortar content in recycled concrete aggregates by image analysis. *Materials Characterization 60*(7), 716–728.

Abbas, A., G. Fathifazl, O.B. Isgor, A.G. Razaqpur, B. Fournier, & S. Foo (2007). Environmental benefits of green concrete. *2006 IEEE EIC Climate Change Technology Conference, EICCCC 2006*.

Adams, M.P., T. Fu, A.G. Cabrera, M. Morales, J.H. Ideker, & O.B. Isgor (2016). Cracking susceptibility of concrete made with coarse recycled concrete aggregates. *Construction and Building Materials 102*, 802–810.

Bremner, T. & T. Holm (1986). Elasticity, Compatibility and the Behavior of Concrete. *ACI Mater J 83*(83), 244–50.

Environmental Protection Agency (2016). Advancing Sustainable Materials Management: 2014 fact sheet. Technical report.

Etxeberria, M., E. Vázquez, A. Marí, & M. Barra (2007). Influence of amount of recycled coarse aggregates and production process on properties of recycled aggregate concrete. *Cement and Concrete Research 37*(5), 735–742.

Feenstra, P., J. Rots, A. Arnesen, J. Teigen, & K. Hoiseth (1998). A 3D Constitutive Model for Concrete based on a co-Rotational Concept. In *Computational Modelling of Concrete Structures. Proceedings of the Euro-C 1998 Conference on Computational Modelling of Concrete Structures*, Badgastein, Austria. Brookfield.

Feenstra, P.H. (1993). *Computational Aspects of Biaxial Stress in Plain and Reinforced Concrete*. Ph. D. thesis, Delft University of Technology,.

Liu, Q., J. Xiao, & Z. Sun (2011). Experimental study on the failure mechanism of recycled concrete. *Cement and Concrete Research 41*(10), 1050–1057.

Malešev, M., V. Radonjanin, & S. Marinkovi´c (2010). Recycled concrete as aggregate for structural concrete production. *Sustainability 2*(5), 1204–1225.

M.G. Alexander (1996). The Effects of Ageing on the Interfacial Zone in Concrete, Interfacial Transition of Concrete. Technical report.

Padmini, A.K., K. Ramamurthy, & M.S. Mathews (2009). Influence of parent concrete on the properties of recycled aggregate concrete. *Construction and Building Materials 23*(2), 829–836.

Ramesh, G., E. Sotelino, & W. Chen (1996). Effect of transition zone on elastic moduli of concrete materials. *Cement and Concrete Research 26*(4), 611–622.

Sagoe-Crentsil, K.K., T. Brown, & A.H. Taylor (2001). Performance of concrete made with commercially produced coarse recycled concrete aggregate. *Cement and Concrete Research 31*(5), 707–712.

Tasong, W.A., C.J. Lynsdale, & J.C. Cripps (1999). Aggregatecement paste interface: Part I. Influence of aggregate geochemistry. *Cement and Concrete Research 29*(7), 1019–1025.

Winfield, M. & A. Taylor (2005). Rebalancing the Load: The Need for an Aggregate Conservation Strategy for Ontario. Technical report, Pembina Institute, Toronto, ON.

Winkler, E. (1974). Stone: Properties, Durability in Man's Environment. *Environmental geomorphology and landscape conservation 2*(Springer-Verlag, New York), 230.

Xiao, J., W. Li, D.J. Corr, & S.P. Shah (2013). Simulation Study on the Stress Distribution in Modeled Recycled Aggregate Concrete under Uniaxial Compression. 25(April), 504–518.

Xiao, J., W. Li, Z. Sun, & S.P. Shah (2013). Crack Propagation in Recycled Aggregate Concrete under Uniaxial Compressive Loading. (109), 451–462.

Computational Modelling of Concrete Structures – Meschke, Pichler & Rots (Eds)
© 2018 Taylor & Francis Group, London, ISBN 978-1-138-74117-1

On boundary layer arising from tessellation in discrete models

J. Eliáš
Faculty of Civil Engineering, Brno University of Technology, Brno, Czech Republic

ABSTRACT: The discrete meso-scale model developed for simulation of concrete behavior with geometry based on Voronoi tessellation is studied. It is shown that the model exhibits geometrical bias in a boundary region due to modification of the tessellation when the boundary is present. The geometrical bias the the boundary layer further influences elastic and inelastic model behavior. The boundary layer effects are analyzed by simulating concrete prisms under tension (in elastic regime) and three-point bending (in inelastic regime). The results demonstrate that the the boundary layer becomes stiffer for positive and more compliant for negative Poisson's ratio. In inelastic regime, the boundary layer is weaker and less ductile compared to the interior of the domain.

1 INTRODUCTION

Material in the vicinity of the boundary often differs in mechanical properties from bulk material due to various effects. One of the main effect in concrete is that the boundary layer contains less large and more small mineral aggregates compared to the interior (Bažant and Planas 1997). Thickness of the boundary layer is independent of the size of the specimen/member and is dictated by concrete sieve curve. The presence of the boundary layer may affect elastic and inelastic mechanical behavior of concrete members.

The paper focuses on a discrete meso-scale model of concrete with random geometry of meso-scale structure. The meso-scale geometry is generated via Voronoi tessellation (Bolander and Saito 1998, Grassl and Bolander 2016). Every model node with 6 (3) degrees of freedom in 3D (2D, respectively) represents one larger aggregate and surrounding matrix. This type of model is often called a *particle* model (Zubelewicz and Bažant 1987, Bažant et al. 1990). Its advantage, compared to the detailed classical lattice models of concrete (Schlangen and van Mier 1992, Man and van Mier 2008, Eliáš and Stang 2012), is substantial reduction in computational time.

Creation of a boundary in the Voronoi tessellation affects distribution of contact normals in its vicinity. While the elements inside the specimen are oriented with the same probability in any direction, the boundary layer has more elements oriented alongthe boundary. This orientation bias consequently affects mechanical behavior of the boundary layer, it becomes anisotropic. When straining along the boundary, the boundary layer becomes more compliant than the bulk material for a negative Poisson's ratio, while for a positive Poisson's ratio, it becomes stiffer. In the nonlinear regime, the boundary layer is weaker and less ductile than the interior material.

The effect of the boundary layer can be easily removed by changing constitutive behavior at the contacts. Recently, an iterative technique capable of removing both elastic stress fluctuations and the elastic effects of the boundary layer has been developed (Asahina et al. 2015, Asahina et al. 2017). The boundary layer might still have an effect in the nonlinear regime, depending on the applied inelastic constitutive relation. Another approach with similar consequences uses a constitutive law based on the volumetric-deviatoric split of strain tensor (Cusatis et al. 2017). Both of the mentioned approaches transfer the rich meso-scale model into a homogeneous macro-scale formulation. Though it might be beneficial in many applications, several important features (such as splitting forces under compression) are lost.

Using the discrete particle model as a meso-level model mimicking a real material structure, the aforementioned boundary layer might be viewed as realistic, i.e. corresponding to the real boundary layer in concrete. However, the underlying origin of it iscompletely different in the numerical model and a real heterogeneous solid. Because there are no experiments known to the author that evaluate the boundary layer effect, it is not possible to determine its appropriateness in the model.

The contribution is partly shortened and partly extended version of Eliáš 2017. The original text provides all the detailed derivation omitted here.

2 DISCRETE MODEL

The model is based on rigid-body-spring network with geometry produced by Voronoi tessellation

(Bolander & Saito 1998). Initially, the domain is filled with randomly placed nuclei generated sequentially. New nucleus is accepted only when its distance to all previously placed nuclei is greater than l_{min}. Parameter l_{min} dictates the internal length of the material. Delaunay triangulation and Voronoi tessellation is performed to obtain connectivity between the nodes and shape of the rigid bodies (Fig. 1).

The boundaries are created by mirroring the nuclei across the boundary plane before performing the tessellation (Fig. 2). Voronoi tessellation then creates body shapes that exactly represent the specimen shape (at least for convex domains).

Each nucleus is understood as one model node with three (two in 2D) translational, u, and three (two in 2D) rotational, θ, degrees of freedom. The associated body obeys the rigid body motion according to the nodal translations and rotations assuming that the rotations are small ($\tan\theta \approx \theta$). The movement of rigid bodies gives rise to displacement discontinuity vector between them. It is denoted Δ and measured in the centroid of contact facet (Fig. 1). Based on the displacement jump, contact strains are evaluated.

$$e_N = \frac{n \cdot \Delta}{l} \qquad e_T = \frac{\Delta}{l} - e_N n \tag{1}$$

where l is a distance between nodes in contact and n is a normal vector. Normal strain, e_N, is a scalar

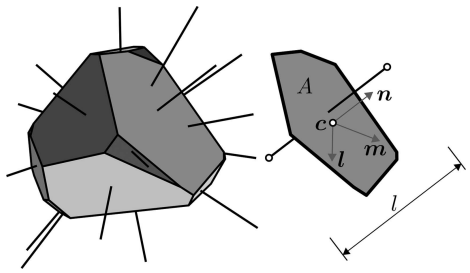

Figure 1. One rigid body of the model created by Voronoi tessellation and one contact facet with centroid c, normal direction n and tangential directions m and l.

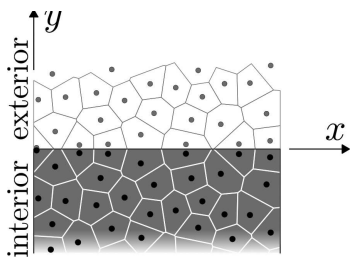

Figure 2. Boundary region in 2D sketch. Boundaries are imposed in Voronoi tessellation via mirroring of the interior nuclei outside the domain.

while the shear strain, e_T, is a vector perpendicular to the normal.

Contact stresses are evaluated from contact strains

$$s_N = (1-D)E_0 e_N \qquad s_T = (1-D)E_0 \alpha e_T \tag{2}$$

where E_0 and α are two elastic material parameters of the model and D is a damage variable at the contact within interval from 0 (healthy material) to 1 (completely disintegrated material). Evolution of the damage parameter is dependent on straining direction and governed by two additional model parameters: meso-level tensile strength, f_t, and fracture energy in tension, G_t.

The detailed description of the calculation of the damage variable is omitted here for sake of simplicity. It is taken from (Cusatis et al. 2006, Cusatis and Cedolin 2007) and simplified. Complete description of both linear and nonlinear constitutive equations, model kinematics and the creation of the model geometry is provided in Eliáš 2016. The interested reader is kindly asked to find all additional model-related information there. The only important feature of the nonlinear model for this text is that the more shear is involved, the stronger is the contact and the more energy is dissipated. The weakest and least ductile behavior is observed for contacts with purely tensile straining.

The response of the model is calculated based on equilibrium equations assuming no time dependence. In inelastic regime, Newton iteration scheme is implemented.

3 ANGULAR DEVIATION

The directional preference in elemental orientation can be beneficial ni case of anisotropic materials (Yao et al. 2016), but for isotropic materials such as concrete, the model should have the same probability of occurrence for all possible normal directions. It will be shown that this is true for interior, but there is a layer in the vicinity of boundaries that exhibit orientation bias. The elemental direction in the boundary layer is strongly biased towards normals aligned with the boundary. It is simply caused by the effort to create the boundary by the tessellation and there is no way known to the author how to get rid of it.

The directional bias is demonstrated by angular deviation of the contact normal from the direction of the x axis (Fig. 3). The deviation is denoted γ. In case of no directional preference, γ should have the following probability density (pdf)

$$f_\gamma(\gamma) = \begin{cases} \begin{cases} 2/\pi & \text{for } \gamma \in (0, \pi/2) \\ 0 & \text{otherwise} \end{cases} & \text{2D} \\ \begin{cases} \sin(\gamma) & \text{for } \gamma \in (0, \pi/2) \\ 0 & \text{otherwise} \end{cases} & \text{3D} \end{cases} \tag{3}$$

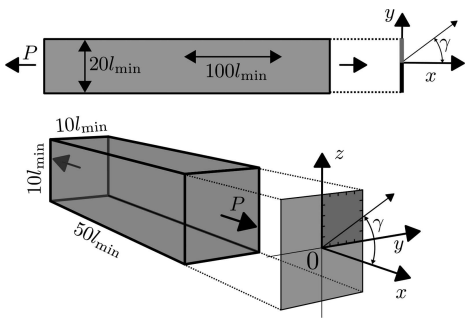

Figure 3. Two and three dimensional domains loaded in pure tension along the x axis, dimensions and definition of the angular deviation γ.

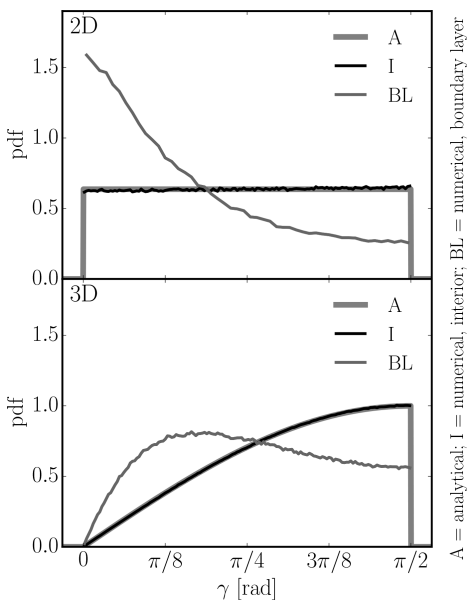

Figure 4. Probability distribution of the angular deviation from the x direction in 2D & 3D.

The angular deviation is statistically analyzed using 2D and 3D prisms shown in Fig. 3. The prisms were generated 500 × in 2D and 3000 × in 3D with different random seed and therefore different rigid body network geometry. Angular deviation γ was analyzed in the interior and in the boundary vicinity (distance to some boundary parallel with the x axis is lower than $l_{\min}$). The probability distributions of γ in these two regions are plotted in Fig. 4 together with the theoretical ideal distribution from Eq. (3). The interior comply with the ideal theoretical distribution, while the boundary layer exhibit strongly biased behavior with more elements aligned with the boundary.

4 ELASTIC BEHAVIOR

The prisms from the previous section were strained in the x direction (ε_{11}), while deformations in the y and z direction were unconstrained. Such loading results in a single macroscopic tensorial stress component σ_{11} and the following strain components

$$\begin{aligned} &\text{3D} \\ &\text{2D, plane stress} \end{aligned} \quad \varepsilon = \frac{\sigma_{11}}{E}\begin{pmatrix} 1 & 0 & 0 \\ 0 & -\nu & 0 \\ 0 & 0 & -\nu \end{pmatrix} \tag{4}$$

$$\text{2D, plane strain} \quad \varepsilon = \frac{\sigma_{11}(1+\nu)}{E}\begin{pmatrix} 1-\nu & 0 \\ 0 & \nu \end{pmatrix}$$

The macroscopic strain can be related to contact stresses between rigid bodies using assumption that all the rotations are zero ($\theta = 0$). The displacement discontinuity between bodies a and b is then simply (Kuhl et al. 2000)

$$\Delta = u_b - u_a = \varepsilon \cdot (x_b - x_a) \tag{5}$$

where x_i are coordinates of the ith node. Assuming perpendicularity of the facet area to the element ensured by Voronoi tessellation, Eq. (5) is simplified

$$\Delta = L\varepsilon \cdot n \tag{6}$$

Based on this equation, virtual work equivalence between a discrete system and a macroscopic elastic solid provides relations between elastic constants of the homogeneous elastic solid (elastic modulus E and Poisson's ratio ν) and elastic constants of the discrete system E_0 and α (Eliáš 2017)

$$\begin{aligned} \nu &= \frac{1-\alpha}{3+\alpha} \quad E = E_0 \frac{2+2\alpha}{3+\alpha} && \text{2D, plane stress} \\ \nu &= \frac{1-\alpha}{4} \quad E = E_0 \frac{5+4\alpha-\alpha^2}{8} && \text{2D, plane strain} \\ \nu &= \frac{1-\alpha}{4+\alpha} \quad E = E_0 \frac{2+3\alpha}{4+\alpha} && \text{3D} \end{aligned} \tag{7}$$

The assumption of zero rotations is correct only for $\alpha = 1$ (i.e. zero Poisson's ratio). Consequently, Eq. (7) is exactly valid only for $\alpha = 1$, for all other α values there is some deviation.

Combining Eqs. (1), (2), (4), (6) and (7), the normal and tangential stress magnitude can be expressed

$$s_N = \varepsilon_{11} E_0 \left(1 - \frac{4}{3+\alpha}\sin^2\gamma\right) \tag{8}$$

$$\|s_T\| = \frac{2}{3+\alpha}\varepsilon_{11}E_0\alpha\sin 2\gamma \tag{9}$$

The limit values of γ are 0 and $\pi/2$ This postulates limits in normal and tangential stress. On interval $(0,\pi/2)$ the maximum and minimum value of the stress is theoretically

$$\max\left(\frac{s_N}{\varepsilon_{11}E_0}\right) = 1 \quad \text{at} \quad \gamma = 0 \tag{10}$$

$$\min\left(\frac{s_N}{\varepsilon_{11}E_0}\right) = -\frac{1-\alpha}{3+\alpha} \quad \text{at} \quad \gamma = \pi/2 \tag{11}$$

$$\max\left(\frac{\|s_T\|}{\varepsilon_{11}E_0}\right) = \frac{2\alpha}{3+\alpha} \quad \text{at} \quad \gamma = \pi/4 \tag{12}$$

$$\min\left(\frac{\|s_T\|}{\varepsilon_{11}E_0}\right) = 0 \quad \text{at} \quad \gamma \in \{0,\pi/2\} \tag{13}$$

To evaluate the cumulative distribution function (cdf) of the normal and tangential stress, the following calculation is performed

$$\begin{aligned} F_{s_N}(t) &= P(s_N < t) = P\left(\varepsilon_{11}E_0\left(1-\frac{4}{3+\alpha}\sin^2\gamma\right) < t\right) \\ &= P\left\{\gamma > \arcsin\sqrt{\frac{3+\alpha}{4}\left(1-\frac{t}{\varepsilon_{11}E_0}\right)}\right\} \\ &= 1 - F_\gamma\left\{\arcsin\sqrt{\frac{3+\alpha}{4}\left(1-\frac{t}{\varepsilon_{11}E_0}\right)}\right\} \end{aligned} \tag{14}$$

$$\begin{aligned} F_{\|s_T\|}(t) &= P(\|s_T\| < t) = P\left(\frac{2}{3+\alpha}\varepsilon_{11}E_0\alpha\sin 2\gamma < t\right) \\ &= 1 + F_\gamma\left\{\frac{1}{2}\arcsin\frac{t(3+\alpha)}{2\varepsilon_{11}E_0\alpha}\right\} \\ &\quad - F_\gamma\left\{\frac{\pi}{2} - \frac{1}{2}\arcsin\frac{t(3+\alpha)}{2\varepsilon_{11}E_0\alpha}\right\} \end{aligned} \tag{15}$$

Now, we need to integrate the probability density function (pdf) of gamma to get the its cdf within interval $(0,\pi/2$

$$F_\gamma(t) = \int_{-\infty}^{t} f_\gamma(x)dx = \begin{cases} \int_0^t \frac{2}{\pi}dx = \frac{2t}{\pi} & \text{2D} \\ \int_0^t \sin(x)dx = 1-\cos(t) & \text{3D} \end{cases}$$

We can now apply it in Eqs. (14) and (15) and obtain cdf of s_N on interval $\left(\varepsilon_{11}E_0\frac{\alpha-1}{3+\alpha}, \varepsilon_{11}E_0\right)$ and $\|s_T\|$ on interval $\left(0, \varepsilon_{11}E_0\frac{2\alpha}{3+\alpha}\right)$

$$F_{s_N}(t) = \begin{cases} 1 - \frac{2}{\pi}\arcsin\sqrt{\frac{3+\alpha}{4}\left(1-\frac{t}{\varepsilon_{11}E_0}\right)} & \text{2D} \\ \sqrt{1-\frac{3+\alpha}{4}\left(1-\frac{t}{\varepsilon_{11}E_0}\right)} & \text{3D} \end{cases} \tag{16}$$

$$F_{\|s_T\|}(t) = \begin{cases} \frac{2}{\pi}\arcsin\frac{t(3+\alpha)}{2\varepsilon_{11}E_0\alpha} & \text{2D} \\ 1-\cos\left(\frac{1}{2}\arcsin\frac{t(3+\alpha)}{2\varepsilon_{11}E_0\alpha}\right) & \text{3D} \\ \quad +\sin\left(\frac{1}{2}\arcsin\frac{t(3+\alpha)}{2\varepsilon_{11}E_0\alpha}\right) & \end{cases} \tag{17}$$

Differentiating cdf with respect to t provides pdf of the normal stress and shear stress magnitude on the same intervals

$$f_{s_N}(t) = \begin{cases} \frac{\alpha+3}{\pi\sqrt{(\alpha+3)(\varepsilon_{11}E_0-t)((\alpha+3)t+(1-\alpha)\varepsilon_{11}E_0)}} & \text{2D} \\ \frac{\alpha+3}{4\varepsilon_{11}E_0\sqrt{\frac{t(\alpha+3)}{\varepsilon_{11}E_0}-\alpha+1}} & \text{3D} \end{cases} \tag{18}$$

$$f_{\|s_T\|}(t) = \begin{cases} \frac{\alpha+3}{\pi}\sqrt{\alpha^2\varepsilon_{11}^2E_0^2 - \frac{(\alpha+3)^2t^2}{4}} & \text{2D} \\ \frac{\frac{1}{2}(\alpha+3)(\cos H+\sin H)}{\sqrt{4\varepsilon_{11}^2E_0^2\alpha^2-(\alpha+3)^2t^2}} & \text{3D} \\ \quad where H = \frac{1}{2}\arcsin\frac{t(3+\alpha)}{2\varepsilon_{11}E_0\alpha} & \end{cases} \tag{19}$$

Having the theoretical distribution of stresses in structure with no orientation bias, one can compare them to the numerical results. Figs. 5 and 6 shows the comparison with stresses extracted from the strained prisms for twodifferent values of parameter α. One can see that the case $\alpha = 1$ exactly corresponds to the theoretical distribution in the interior, confirming no directional bias. The boundary layer prefers elements aligned with the boundary and so with the straining direction. One can therefore see statistically more higher values of normal stress. For cases when $\alpha = 0.29$ (3D) or $\alpha = 1/3$ (2D), the theoretical distribution deviates. As the system already involves rotations, the stress state is different from the one calculated analytically using the assumption of no rotations. Nevertheless, the same shift for more higher normal stresses is seen in the boundary layer.

The tensorial stress worth investigating as well. The fabric stress tensor is evaluated for each body k (L. Rothenburg 1989, K. Iwashita 1999).

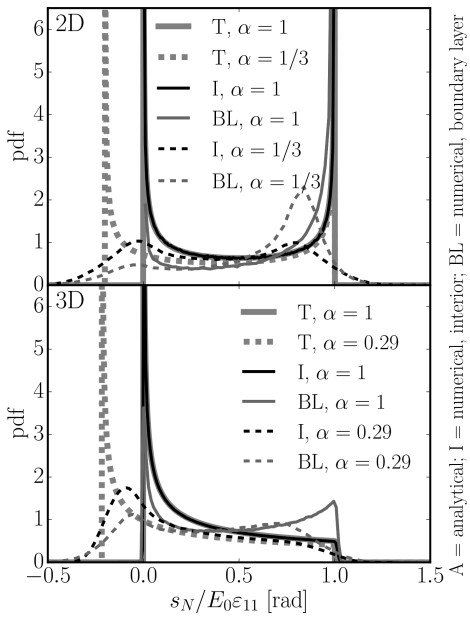

Figure 5. Probability distribution of the normal stress (normalized by $E_0\varepsilon_{11}$) in 2D & 3D for two values of α.

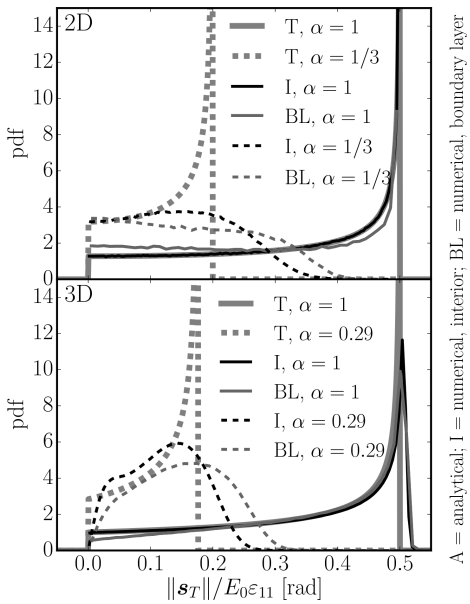

Figure 6. Probability distribution of the shear stress magnitude (normalized by $E_0\varepsilon_{11}$) in 2D & 3D for two values of α.

$$s^k = \frac{1}{V_k}\sum_{p=1}^{n_k} f^p \otimes (c^p - x^k) \tag{20}$$

where V_k is volume of the kth body, n_k is number of contact facets of the body, f^p is force vector from the pth contact with centroid c^p.

Calculating the tensorial stress s_{11} in the direction of straining in all the rigid bodies in all the prisms, the average value dependent on location in the cross section can be plotted. One can see this value normalized by specimen cross section area S and applied force P in Figs. 7 and 8 for 2D and 3D cases. Starting with $\alpha \neq 1$, one can clearly see the boundary layer with increased stress (in 3D emphasized in the corner) and the interior with normalized stress equal to 1. The increase is

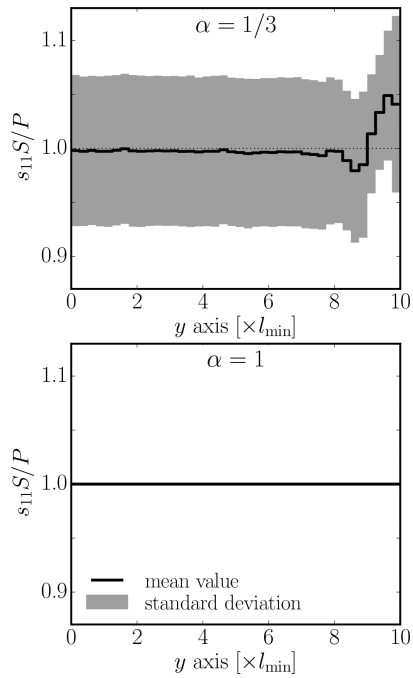

Figure 7. Tensorial stress component s_{11} in the cross section of two dimensional prism for two values of α. Only symmetrical half of the cross section is shown.

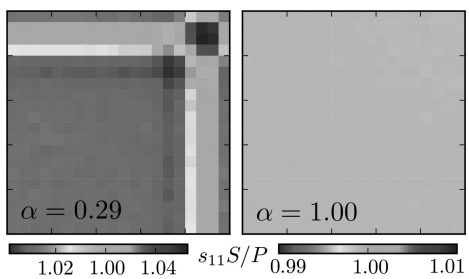

Figure 8. Tensorial stress component s_{11} in the cross section of three dimensional prism for two values of α. Only symmetrical quarter of the cross section is shown.

caused by elements with normal orientation biased towards straining direction. These elements therefore transfer the load mostly by normal force. Since $\alpha < 1$, the normal response is stiffer than shearing, hence the stress increase. The situation would be reverted, i.e. with tensorial stress decrease in the boundary layer, if $\alpha > 1$. For $\alpha = 1$, the tangential and normal response of the contact is the same implying that there is no dependence of the stiffness on the contact orientation and therefore no boundary layer effect.

5 INELASTIC BEHAVIOR

Inelastic behavior is studied using (3D only) beam model loaded in three-point-bending. The simulation represents experimental beam tested by Grégoire et al. 2013. Dimensions are: depth 200mm thickness 50 mm and span 500 mm. Identified material parameters are:E_0 = 60GPa, α = 0.29, f_t = 2.2 MPa and G_t = 35J/m^2; $l_{\min}$ = 10 Two versions of the model geometry around boundaries are studied, the basic version used previously in the elastic analysis (referred to as A), and alternative version B, where nuclei are randomly sampled in a region larger that the specimen domain.

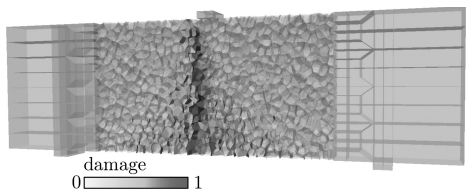

Figure 9. Macrocrack localized in the model of specimen loaded in three-point-bending.

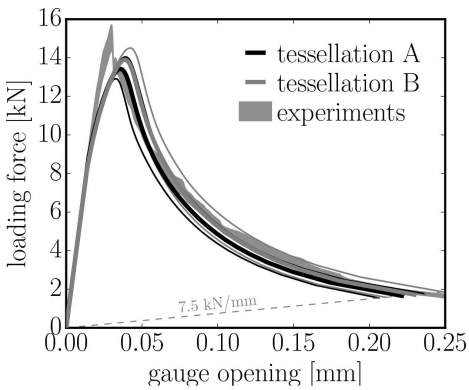

Figure 10. Averaged responses of the model of three-point-bending test with restricted (A) and unrestricted (B) sampling of nuclei compared with the experimental data.

After the extended domain is saturated, all the nuclei protruding the true specimen domain are removed. Then, the standard mirroring across the boundaries is used. Types A and B differ only in location of nodes close to the boundary. In the case A, the presence of the boundary influence al ready the location of nuclei, while in the case B, only the shape of the bodies is affected. The small change in the boundary layer geometry, that occupies only approx. 1/50 depth of the specimen, can lead to substantial difference in model response.

The calculation was performed 30 times for every model type. An example of crack localized in the model is shown in Fig. 9. Averaged responses of the model are shown in Fig. 10. The model version B is stronger than version A by 4% and dissipates 7% more energy.

6 CONCLUSIONS

Discrete meso-scale models based on Voronoi tessellation are investigated. The ideal isotropic geometry of the model is found in the interior of the domain, while existence of a boundary layer that strongly prefers contacts parallel with the boundary is reported. Behavior of the boundary layer in the elastic and inelastic regime is studied.

The boundary layer is found stiffer when straining parallel with the boundary in models with positive Poisson's ratio ($\alpha < 1$) and more compliant when negative Poisson's ration ($\alpha > 1$) is used. In nonlinear regime, the boundary layer (for materials that are weaker in tension than in shear) exhibit weaker and more brittle behavior (as demonstrated in Eliáš 2017 An example of three point bending shows that the geometrical structure of the boundary layer may have large impact on the overall nonlinear model response.

ACKNOWLEDGEMENT

Financial support provided by the Czech Science Foundation under project 16-22230S and the Ministry of Education, Youth and Sports of the Czech Republic under project LO1408 "AdMaS UP– Advanced Materials, Structures and Technologies" is gratefully acknowledged.

REFERENCES

Asahina, D., K. Aoyagi, K. Kim, J.T. Birkholzer, & J.E. Bolander (2017). Elastically-homogeneous lattice models of damage in geomaterials. *Comput. and Geotech. 81*, 195–206.

Asahina, D., K. Ito, J. Houseworth, J. Birkholzer, & J. Bolander (2015). Simulating the poisson effect in lattice models of elastic continua. *Comput. and Geotech. 70,* 60–67.

Bažant, Z.P. & J. Planas (1997). *Fracture and Size Effect in Concrete and Other Quasibrittle Materials.* CRC Press.

Bažant, Z., M. Tabbara, M. Kazemi, & G. Pijaudier-Cabot (1990). Random particle model for fracture of aggregate or fiber composites. *J. Eng. Mech. - ASCE 116*(8), 1686–1705.

Bolander, J. & S. Saito (1998). Fracture analyses using spring networks with random geometry. *Eng. Fract. Mech. 61*(5–6), 569–591.

Cusatis, G. & L. Cedolin (2007). Two-scale study of concrete fracturing behavior. *Eng. Fract. Mech. 74*(12), 3–17.

Cusatis, G., R. Rezakhani, & E.A. Schauffert (2017). Discontinuous cell method (DCM) for the simulation of cohesive fracture and fragmentation of continuous media. *Eng. Fract. Mech. 170*(1), 1–22.

Cusatis, G., Z.P. Ba˘zant, & L. Cedolin (2006). Confinementshear lattice CSL model for fracture propagation in concrete. *Comput. Method. Appl. M. 195*(52), 7154–7171.

Eliáš, J. & H. Stang (2012). Lattice modeling of aggregate interlocking in concrete. *Int. J. Fracture 175,* 1–11.

Eliáš, J. (2016). Adaptive technique for discrete models of fracture. *Int. J. Solids Struct. 100–101,* 376–387.

Eliáš, J. (2017). Boundary layer effect on behavior of discrete models. *Materials 10,* 157.

Grassl, P. & J. Bolander (2016). Three-dimensional network model for coupling of fracture and mass transport in quasibrittle geomaterials. *Materials 9*(9), 782.

Grégoire, D., L. Rojas-Solano, & G. Pijaudier-Cabot (2013). Failure and size effect for notched and unnotched concrete beams. *Int. J. Numer. Anal. Met. 37*(10), 1434–1452.

K. Iwashita, M.O. (1999). *Mechanics of Granular Materials: An Introduction.* Boca Raton, FL, USA: CRC press.

Kuhl, E., G.A. D'Addetta, H.J. Herrmann, & E. Ramm (2000). A comparison of discrete granular material models with continuous microplane formulations. *Granul. Matter 2*(3), 113–121.

L. Rothenburg, R.B. (1989). Analytical study of induced anisotropy in idealized granular materials. *Geotechnique 39*(4), 601–614.

Man, H.-K. &J.G. van Mier (2008). Influence of particle density on 3D size effects in the fracture of (numerical) concrete. *Mech. Mater. 40*(6), 470–486.

Schlangen, E. & J. van Mier (1992). Experimental and numerical analysis of micromechanisms of fracture of cement-based composites. *Cement Concrete Comp. 14*(2), 105–118. Special Issue on Micromechanics of Failure in Cementitious Composites.

Yao, C., Q. Jiang, J. Shao, & C. Zhou (2016). A discrete approach for modeling damage and failure in anisotropic cohesive brittle materials. *Eng. Fract. Mech. 155,* 102–118.

Zubelewicz, A. & Z. Bažant (1987). Interface element modeling of fracture in aggregate composites. *J. Eng. Mech. -ASCE 113*(11), 1619–1630.



Taylor & Francis
Taylor & Francis Group
http://taylorandfrancis.com

Computational Modelling of Concrete Structures – Meschke, Pichler & Rots (Eds)
© 2018 Taylor & Francis Group, London, ISBN 978-1-138-74117-1

Size effect in concrete under splitting tension

J. Suchorzewski & J. Tejchman
Gdansk University of Technology (GUT), Gdansk, Poland

ABSTRACT: The size effect is a fundamental phenomenon in concrete materials. It denotes that both the nominal structural strength and material ductility always decrease with increasing element size under tension. In the paper splitting tensile tests on cylindrical concrete specimens with the different diameter were carried out. Two types of the loading strip (plywood board and steel cylinder) were used. The concrete strength and ductility decreased with increasing specimen diameter. For large concrete specimens a clear snap-back occurred. The experiments were simulated with the spherical Discrete Element Method (DEM) under two-dimensional conditions. In the calculations, concrete was assumed as a four-phase composite material including aggregate, cement matrix, Interfacial Transitional Zones (ITZs) and macro-voids. The process of micro- and macro-cracking was studied in detail for various failure modes. The macroscopic curves and shapes of cracks were directly compared with the laboratory test outcomes.

1 INTRODUCTION

The size effect is a fundamental phenomenon in concrete elements and denotes that both the nominal structural strength and material ductility (ratio between the energy consumed during the loading process after and before the stress-strain peak) always decrease with increasing element size under tension (Bažant & Planas 1998, Tejchman & Bobiński 2013). Thus the results of laboratory tests on concrete which are scaled versions of the actual structures cannot be directly transferred to them. Concrete becomes ductile on a small scale and perfectly brittle on a sufficiently large scale. The physical understanding of size effects is of major importance for civil engineers who try to extrapolate experimental outcomes at laboratory scale to actual structures of practical size range. Since large structures are strongly beyond the range of testing in laboratories, their design has to rely on a realistic extrapolation of testing results with smaller element sizes.

Two size effects are of a major importance: energetic (or deterministic) and statistical (or stochastic) one. A deterministic size effect is caused by the formation of a region of intense strain localization with a certain volume (micro-crack region—called also fracture process zone FPZ) which always precedes discrete macro-cracks. Strain localization volume is not negligible to the cross-section dimensions and is large enough to cause significant stress redistribution in the structure (energy absorption in localized failure zones and energy release in remaining unloading regions). The size of localized zones with respect to the specimens cannot be appropriately scaled in laboratory tests. The first statistical theory has been introduced by Weibull (1951) (called also the weakest link theory) which postulates that a structure is as strong as its weakest component. The structure fails when its strength is exceeded in the weakest spot (when the stress redistribution is not considered). A combination of the energetic theory with the Weibull statistical theory led to the general energetic-statistical theory for geometrically similar structures (Bazant et al. 2007).

The splitting tensile tests (also known as the Brazilian tests) are the most popular laboratory tests on concrete to determine its uniaxial tensile strength due to their loading and specimen shape simplicity. This test consists of applying a distributed compressive force along the length of a concrete cylinder, which induces a primarily tensile stress perpendicular to the loading plane of the specimen's cross-section with a sharp compressive stress near the points of load application. The splitting tensile strength is generally greater than the direct tensile strength and lower than the flexural strength. The recommended standard cylindrical specimen sizes are: diameter $D = 0.15$ m and length $L = 0.3$ m. The tests are however sensitive to boundary conditions related to the width (Rocco et al. 1999), shape (Kuorkoulis et al. 2013) and stiffness (Miguel et al. 2016) of the loading strip. With growing loading strip width b, the concrete strength increased (Rocco et al. 1999). The shape's change of the loading strip from a rectangular strip to a curved one made the specimen strength higher by increasing the contact surface (Kuorkoulis et al. 2013). The loading strip stiffness turned out to be significant for $b/D < 0.25$ (very stiff loading strip

increased the strength in experiments (Miguel et al. 2016)). The effect of boundary conditions on the initial global stiffness and post-peak behaviour of concrete specimens (strength-displacement curve, fracture) has not been investigated in detail yet.

The fracture process in the splitting test with standard loading strips consists of two main stages: (1) a main macro-crack formation in the central vertical zone and (2) secondary cracks connecting the main vertical crack with edges of loading plates (Miguel et al. 2016). The American standard (ASTM C 496/C 496M-04) proposes loading strips of plywood that are $b = 25$ mm wide and $t = 3.2$ mm thick.

In addition, the laboratory test outcomes indicate a size effect, expressed by a decrease of both the nominal strength and ductility with increasing specimen diameter. The size effect in pure concrete during splitting tensile tests on cylindrical specimens was investigated by several researchers (Kadlecek V. et al. 2002, Carmona et al. 1998, Bažant et al. 1991, Hasegawa et al. 1985, Torrent 1997) who mainly focused on the tensile strength change with the varying cylindrical specimen diameter D. The specimen diameter varied from 2 cm (Bažant et al. 1991) up to almost 3 m (Hasegawa et al. 1985). The experimental results in Fig. 1 show a clear size effect in concrete, i.e. a reduction of the maximum tensile stress $\sigma = 2P_{max}/(\pi DL)$ with increasing specimen diameter D (P – the vertical splitting force along the specimen length L) except of 2 experimental results by Carmona et al. (1998) for a small specimen.

Our experimental and theoretical research works are aimed now at understanding the concrete behaviour at the meso-scale during different failure modes in quasi-static splitting tension, depending upon the specimen diameter. Based on preliminary laboratory experiments, a quasi-brittle concrete behaviour took place with small specimen diameters ($D = 5$ cm). For larger diameters ($D = 10$ cm), a brittle concrete behaviour occurred. Finally, for large diameters ($D = 15$ cm), a snap-back instability was observed (that is described by a positive slope in a stress-strain softening branch) (Bažant et al. 1987). This instability is typical for large and slender concrete structures, low fracture toughness and high tensile strength. In these cases, the energy absorption in localized failure zones is smaller than the energy release in remaining unloading regions under decreasing load (Tanabe et al. 2004).

In this paper we describe in detail the experimental results on concrete cylinders with the diameter of $D = 150$ mm and theoretical results on the size effect using 2 different specimen diameters ($D = 150$ mm and $D = 50$ mm). During laboratory tests the snap-back instability occurred with $D = 150$ mm. The vertical load was transferred to

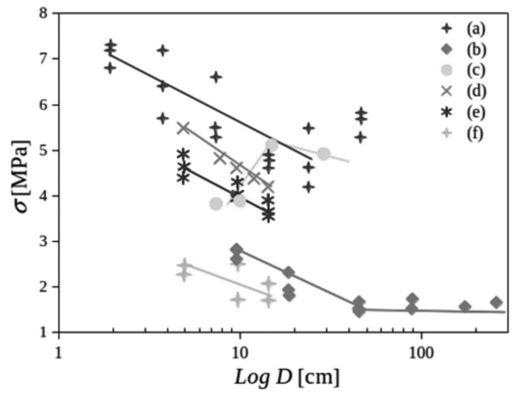

Figure 1. Relationship between tensile stress $\sigma = 2P/(\pi DL)$ and specimen diameter in logarithmic scale log D in splitting tensile tests on concrete by: a) Bažant et al. 1991, b) Hasegawa et al. 1995, c) Carmona et al. 1998, d) Kadlecek et al. 2002 and e) and f) Torrent 1997 (continuous lines are trend lines) (P – vertical splitting force, D – specimen diameter, L – specimen length).

concrete specimens through: 1) a plywood board (in the form of a surface contact) according to ASTM and 2) a steel cylinder (in the form of a line contact) to eliminate the effect of boundary conditions. Fracture was monitored using a high resolution and non-destructive technique in the form of the 3D x-ray micro-computed tomography system (using Skyscan 1173 (Skarżyński & Tejchman 2016). In addition, the 2D scanning electron microscope (SEM) Hitachi TM3030 and manual 2D digital microscope 'Scalar' were used. The discrete element method (DEM) was applied to describe a non-linear response of concrete during splitting tension under 2D conditions. In this method concrete was considered at the meso-scale as a 4-phase material (aggregate, cement matrix, macro-voids and interfacial transitional zones (ITZs)). The geometry of concrete microstructure at the meso-level was incorporated into DEM from real concrete specimens by means of x-ray micro-tomographic images. The model was successfully applied to concrete under bending (Skarżyński et al. 2015) and uniaxial compression (Suchorzewski et al. 2017). The calculation outcomes evidently showed that it was of importance to take into account the shape and position of aggregate particles and strength and number of ITZs for a realistic reproduction of concrete fracture. ITZs due to a porous structure acted as attractors for cracks and thus significantly influenced the strength and brittleness of concrete. DEM was also used to the fracture description in concrete by other researchers (Chen & Konietzky 2014, Dupray et al 2009, Groth et al.

2011, Hentz et al. 2004). The splitting tensile test for quasi-brittle materials was mainly simulated within continuum mechanics (e.g. (Miguel et al. 2016, Zhu & Tang 2006, Benkemoun et al. 2016).

The main goal of the paper is threefold: 1) to check the capability of DEM for simulating size effect under quasi-static splitting tension in concrete specimens at the meso-level by taking the snap-back instability into account, 2) to check the effect of different boundary conditions on the strength and fracture (expressed by the different loading/supporting strip type) and 3) to investigate in detail the concrete behaviour during quasi-static splitting tension at the meso-scale level. The numerical outcomes were directly compared with the experimental results with respect to the measured stress-strain curves and observed crack patterns based on 3D μCT-images. The evolution of contact forces, broken contacts, internal energies and crack displacements at the aggregate level were also investigated by DEM. The innovative point is to the use of a 4-phase concrete mesoscopic model for fracture investigations based on the real internal concrete structure based on μCT. In the future the DEM calculations may replace laboratory tests to investigate the influence of the concrete meso-structure on its global behaviour.

2 EXPERIMENTS

2.1 *Strength*

The splitting tensile experiments were performed in the static loading machine ZWICK Roaller Z400 (Fig. 2). The machine was equipped with a crack opening extensometer (Sandner EXR10-2x) within the measurement range of 2 mm with the maximum error of 2%. The extensometer base was equal to 40 mm. The extensometer was located at the mid-height of the concrete specimen and glued to the specimen front side (Fig. 2). The quasi-static tests were performed under the CMOD-control (CMOD – crack mouth opening displacement) with the displacement rate of 0.00001 (1×10^{-5}) mm/s. Two types of loading/supporting strips were used: deformable plywood boards with the thickness of t = 3 mm and width of b = 25 mm (Fig. 2b) (as recommended by ASTM) and rigid steel loading/supporting cylinders with the diameter of 20 mm (Fig. 2a). Thus the vertical load was respectively transferred to specimen through a surface or line.

Concrete was prepared in the weight proportion 3:1.6:7.1:12.6 (cement 32.5R, water, sand, aggregate). The minimum aggregate diameter was d_a^{min} = 2 mm, maximum aggregate diameter was d_a^{max} = 12 mm and mean aggregate diameter d_a^{50} = 5 mm. The

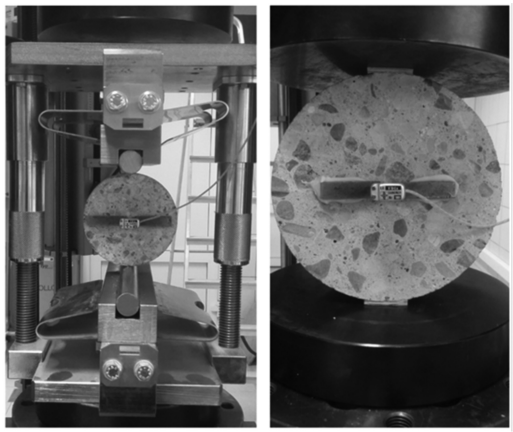

a) b)

Figure 2. View on loading machine Zwick Z400 with cylindrical concrete specimen of diameter D = 150 mm and length L = 60 mm for quasi-static splitting tensile tests: a) specimen loaded through steel cylinder and b) specimen loaded through plywood board.

volumetric aggregate sieve content was 31.2% (diameter 2–8 mm) and 16.6% (diameter 8–12 mm). Thus, the aggregate volumetric content was 47.8%. The total particle volumetric content (including sand and aggregate) in concrete was 75%. The concrete specimens with the diameter of D = 150 mm were used. The minimum specimen length was assumed $L = 60$ mm ($= 5 \times d_a^{max}$). The mean standard compressive strength of concrete tested on 3 cubic specimens $150 \times 150 \times 150$ mm^3 was equal to $f_{c,cube}$ = 49.6 MPa and mean standard modulus of elasticity tested on 3 cylindrical specimens D = 150 mm and length L = 300 mm was E_c = 33.1 GPa.

Several splitting tests on concrete were carried out. Figure 3A presents the representative experimental stress versus CMOD curves for concrete specimens using two types of the loading/supporting contact along the specimens (steel cylinder and plywood board).

The CMOD evolution during loading was perfectly linear in time. The splitting tensile strength, calculated as $\sigma = 2P_{max}/\pi DL$ (P_{max} – the maximum vertical piston force), varied between 3.26 MPa (P_{max} = 47.2 kN, v = 0.45 mm, CMOD = 18 μm) and σ = 3.64 MPa (P_{max} = 51.2 kN, v = 1.15 mm, CMOD = 22 μm) for the steel loading/supporting cylinders (line contacts) and plywood loading/supporting boards (surface contacts), respectively. Thus, the splitting tensile strength was higher by about 10% for the plywood board. Looking at the curve of the stress σ versus CMOD (Fig. 3A), initially concrete elastically behaved up to 70% of the maximum tensile stress σ and later slightly

non-linearly up to the peak load. After pronounced material softening occurred up to the residual state to failure. The residual stress was reached for $\sigma = 2.3$ MPa (plywood boards) and $\sigma = 1.9$ MPa (steel cylinder) for CMOD = 110 µm. When considering the experimental stress-vertical piston displacement diagram $\sigma = f(v)$ (Fig. 3B), a clear snap-back instability occurred for $v = 1.15$ mm (plywood loading board) and $v = 0.45$ mm (steel loading cylinder), expressed by a simultaneous reduction of the stress and displacement. Shortly before the test end, the displacement v slightly increased due to the specimen defragmentation.

In all tests the main vertical macro-crack first occurred at the mid-height of the specimen in the central vertical zone. Then it propagated towards both the specimen top and bottom. Later depending upon the loading and support strip type it reached the top and the bottom of the specimen or branched to form a wedge directly under the plywood board.

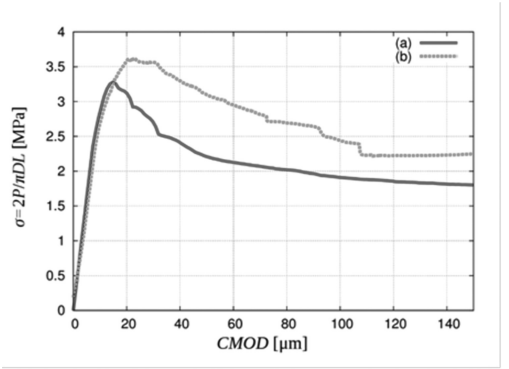

A)

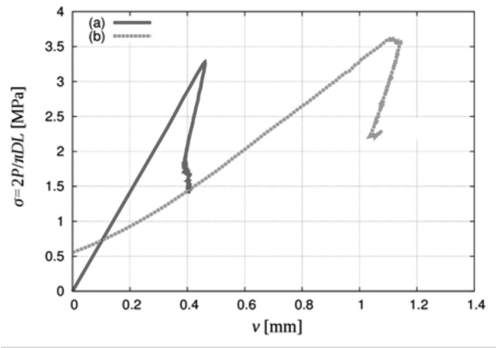

B)

Figure 3. Experimental curves for concrete specimens with diameter $D = 0.15$ m): A) splitting tensile stress $\sigma = 2P(\pi DL)$ versus CMOD and B) splitting tensile stress σ versus piston vertical displacement v for 2 different loading systems a) steel cylinder and b) plywood board (P – vertical force, L – specimen length).

Finally at failure, the concrete specimen was divided into two halves.

3 DISCRETE ELEMENT METHOD FOR CONCRETE

The 3D spherical discrete element model YADE takes advantage of the so-called soft-particle approach (i.e. the model allows for particle deformation that is simulated as an overlap of particles) (Kozicki & Donze 2013). A linear normal contact model under compression was used. Aggregate grains were modelled as clusters composed of spheres. The interaction force vector representing the action between two spherical discrete elements in contact was decomposed into a normal and tangential vector, respectively. The normal forces acting on spheres were modelled by an elastic law with cohesion. The normal and tangential forces were linked to the displacements through the normal stiffness K_n and the tangential stiffness K_s.

The stiffness parameters were computed with the aid of the modulus of elasticity of the grain contact E_c and two neighbouring grain radii R_A and R_B (to determine the normal stiffness K_n) and with the aid of the modulus of elasticity E_c and Poisson's ratio υc of the grain contact and two neighbouring grain radii R_A and R_B (to determine the tangential stiffness K_s), respectively (Kozicki & Donze 2013). The contact tangential forces F_s and normal forces F_n satisfied the cohesive-frictional Mohr-Coulomb equation using the inter-particle friction angle µ (Kozicki & Donze 2013). The normal force might be negative down to the minimum value of F_n^{min} if there was no a geometrical contact between elements. If this minimum normal force between spheres F_n min was reached, the contact was broken. Moreover, if any contacts between grains reappeared, cohesion between them was not taken into account. A crack was considered as open if cohesive forces between grains disappeared when a critical threshold was reached. A choice of a very simple linear elastic normal contact was intended to capture on average various contact possibilities in real concrete. One assumed that the cohesive force and tensile force were a function of the cohesive stress C (maximum shear stress at pressure equal to zero), tensile normal stress T and sphere radius R. To dissipate excessive kinetic energy in a discrete system, a simple local non-viscous damping scheme was adopted which assumed a change of forces by using the damping parameter.

Concrete was described in DEM computations as a four-phase material composed of aggregate, cement matrix interfacial transitional zones (ITZs) and macro-voids. The numerical analyses were performed on concrete specimens with the same

aggregate location and shape as in experiment. In the first step, two-dimensional simulations were performed to significantly reduce the computation time. Thus the crack curvature along the specimen length was not taken into account. The 3D analyses significantly increase computation times but do not significantly affect the results except of a small reduction of material brittleness. The macro-voids were modelled simply as empty regions with a real shape. In order to create the real aggregate shape in 2D calculations (2 mm ≤ d_a ≤ 12 mm) based on images of the polished specimen surface and μCT scan, the clusters composed of spheres with the diameter of d = 1.0 mm connected to each other as rigid bodies were used. One aggregate particle, depending upon its diameter, included 5–500 spheres. Based on experiments all aggregate grains with the diameter in the range of 2 mm < d_a < 12 mm included ITZs. The cement matrix was modelled by spheres with the diameter 0.35 mm ≤ d_{cm}< 2 mm without ITZs. ITZs were simulated for the sake of simplicity as contacts between aggregate and cement matrix grains. Thus they had no a physical width in contrast to experiments. Note that simulation of the width of ITZs (0.010–0.025 mm) requires of the use of very small spheres. In 2D calculations, the specimen length L included one row of aggregate and cement matrix particles. The specimen preparation process consisted of 2 stages. Initially aggregate particles and clusters simulating voids were created. Later smaller particles were added until the final specimen was filled in 98.4% in order to realistically the experimental micro-porosity was measured with μCT as 1.6% (Section 2.2). After the cement matrix was created, the particles at the place of voids were removed. Next all contact forces due to the particle penetration were deleted.

The following five main local material parameters were nee needed for our discrete simulations: E, υ, μ, C and T. In addition, the particle radius R, particle mass density ρ and damping parameters α_d were required.

The following parameters of the cohesion and tensile strength were used in all DEM analyses: cement matrix ($E_{c,cm}$ = 15 GPa, C_{cm} = 140 MPa and T_{cm} = 25 MPa) and ITZs ($E_{c,ITZ}$ = 12 GPa, C_{ITZ} = 112 MPa and T_{ITZ} = 20 MPa) based on our earlier calculations (Nitka & Tejchman 2015)). ITZs were obviously the weakest phase. The ratio $E_{c,ITZ}/E_{c,cm}$ = 0.8 was chosen based on the experiments. The remaining ratios were also assumed as 0.8: C_{ITZ}/C_{cm} = 0.8 and T_{ITZ}/T_{cm} = 0.8 due to the lack of experimental results. Note that there were no contacts between aggregate grains (d_a ≥ 2 mm). The remaining parameters were constant for all phases and regions: υ_c = 0.2 (Poisson's ratio of grain contact), μ = 18° (inter-particle friction angle), α_d = 0.08 (damping parameter) and ρ = 2.6 kG/m^3 (mass density). The prescribed damping parameter α_d and velocity did not affect the results during bending (Skarżyński et al. 2015). In the case of α_d < 0.08, the too excessive kinetic energy was always created during fracture (the tensile numerical test could not be performed without numerical damping due to excessively high velocities of particles (see also (Nitka & Tejchman 2015)). In turn, the effect of the αd-value on global results for α_d ≥ 0.08 became insignificant. The calculated mean nominal inertial number I for the maximum vertical load (which quantifies the significance of dynamic effects) was <10^{-4} that always corresponded to a quasi-static regime. The 2D concrete specimen under tensile splitting included in total about 20'000 spheres. The calculation time was about 1–2 days using PC with CPU 2.8 GHz. The material constants were assumed based on the test on concrete not on the cement matrix (due to the lack of the detailed information on properties of ITZs). With the material constants assumed, the uniaxial compressive strength of the 2D four-phase concrete specimen (15 × 15 cm^2) was about 45 MPa and elastic modulus E = 30 GPa (as in the experiments, Section 2.1).

4 DEM RESULTS

4.1 *Loading-strip type*

The 2D cylindrical concrete specimens of the diameter D = 150 mm obtained using DEM with two different loading/supporting systems as compared to real specimens were modelled. The deformable strip of the plywood board at the top and bottom of the specimen was created from 240 spheres assembled together with the 50% lower stiffness than concrete (with this value the same global elastic stiffness was calculated as in the experiment). It had a full contact with the concrete specimen without wall friction. The rigid cylinder of steel at the top and bottom of the specimen was created by a single sphere of the diameter of 20 mm with the 10-times higher stiffness than concrete. The deformation was induced by prescribing the vertical top displacement in such way that the changes of CMOD were approximately linear in time (as in experiments). CMOD was calculated as a horizontal displacement at the specimen mid-height between mid-points of two regions with the area of A = 5 × 15 mm^2 (based on preliminary calculations). The mid-points were at the distance of 40 mm as in the experiment (Fig. 2). If the calculated CMOD was larger than the assigned CMOD growth (v_{CMOD} = 1 × 10^{-5} mm/s), the difference was multiplied by the earlier calibrated proportional parameter n = 1.5 since the

inertia of the discrete system was different than this of the testing machine (ut + 1 = n × ut ($CMOD_{assigned}$ - $CMOD_t$)). A too small averaging area A mainly contributed to excessive displacement oscillations. In addition in order to diminish the excessive kinetic energy after the contact breakage between the areas A, larger local damping was assumed in calculations ($\alpha_d^{local} = 0.05$) if the single grain velocity vt was larger than 0.001 m/s. Next this velocity was reduced in the next step down to $v_t + 1 = \alpha_d \bullet v_{t0}$. In calculations, the time step dt was equal to $dt = 10^{-8}$ s.

Figure 4 presents the DEM results of the strength compared to the experiments. The strength's σ evolution versus CMOD and v was satisfactorily reproduced (Figs. 4A and 4B). The calculated maximum tensile stress was by 2% too low for the steel loading cylinder and by 10% too high for the plywood loading board than in experiments. The calculated residual tensile stress was the same for the steel loading cylinder and by 30% too high for the plywood board. The calculated rate of softening was similar for the steel cylinder and too small for the plywood board. The differences between numerical and experimental results are probably caused by the different stiffness of the plywood board than in experiments and some slight deviations between the calculated and theoretical CMOD evolution.

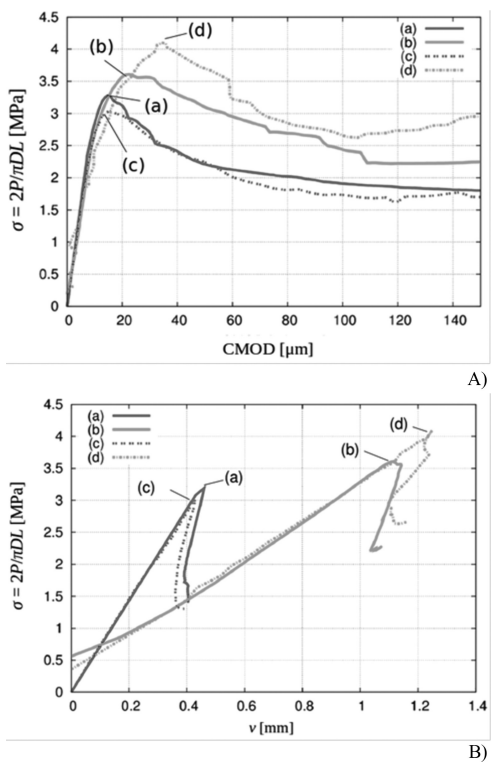

Figure 4. Calculated DEM results against experimental ones: A) strength σ against CMOD, B) strength σ against piston vertical displacement v (B) (curves 'a' and 'b' – experiments, curves 'c' and 'd' – DEM, red lines – steel loading cylinder, green lines – plywood loading board) in experiment (a) and DEM (b) (continuous lines – experiments, dashed lines – DEM).

The calculated crack patterns were very similar to the experimental ones (Fig. 5). In DEM calculations with the plywood strip (Fig. 5Bb), the macro-crack followed exactly the same path as in experiments (Fig. 5Ba). It also branched into rigid wedges at the same height (25% of D from the top and bottom). However, the crack shape in the wedge often followed the other side of the aggregate particle. In DEM calculations with the steel cylinder (Fig. 5Ab), the macro-crack was more curved than in experiments (Fig. 5Aa) and followed the opposite edges of aggregates in the lower specimen half. The large aggregate grain at the specimen bottom crushed in the experiment in contrast to DEM outcomes (our model has not included grain crushing yet).

In DEM simulations, initially several single micro-cracks occurred in the entire specimen. The broken contacts first occurred always in ITZs at corners of aggregate particles wherein tensile forces were the largest (Fig. 6Aa). Later micro-cracks started to concentrate in the vertical central zone at the specimen mid-height. Afterwards they

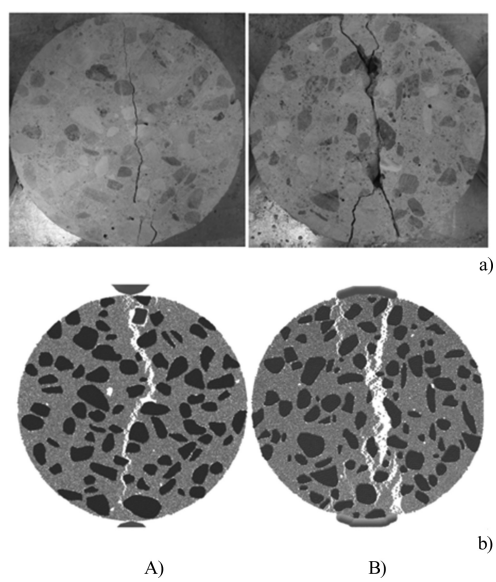

Figure 5. Experimental and calculated fractured specimens at residual state for CMOD > 150 μm: a) experimental cracks and b) calculated cracks by DEM for A) steel loading cylinder and B) plywood loading board.

connected with each other in the cement matrix by bridging and created a discrete macro crack in the vertical central zone (similarly as in the experiment) (Fig. 6Ac). The crack propagated towards the top and bottom of the specimen for CMOD = 30 μm. At the top and bottom, it branched by creating a clear wedge under the loading strip. At the test end (CMOD > 150 μm), the specimen was symmetrically de-fragmented. The macro-cracks were always created by bridging interfacial micro-cracks (Fig. 7).

Figure 6B presents the evolution of inter-particle normal contact forces. The blue lines indicate tensile and red lines compressive forces. The line thickness is proportional to the force magnitude. The external vertical splitting force was transmitted via a network of normal contact forces which formed force chains. They carried the majority of the loading and transmitted it on the entire system

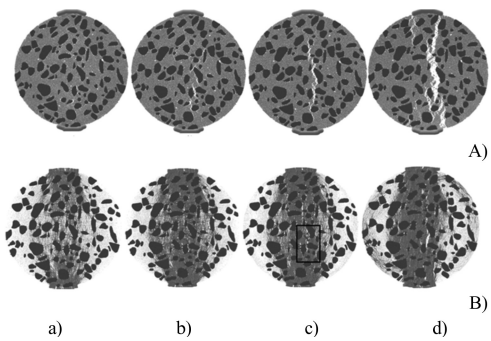

Figure 6. DEM: A) evolution of cracking in concrete specimen and B) inter-particle tensile (blue lines) and compressive (red lines) normal contact forces for concrete specimen with plywood loading board versus CMOD: a) CMOD = 10 μm, b) CMOD = 20 μm, c) CMOD = 30 μm and d) CMOD > 150 μm (green colour denotes small contact forces).

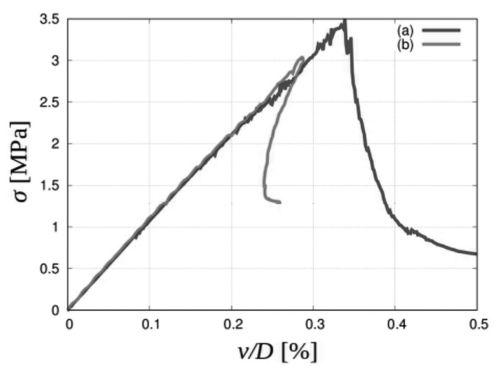

Figure 7. DEM: tensile stress σ versus normalized piston displacement u/D for specimen diameter D = 50 mm (a) and D = 150 mm (b).

and were the predominant structure of internal forces at micro-scale. Initially large vertical compressive normal contact forces were created in the almost entire specimen (Fig. 6Ba). Tensile normal forces occurred in a perpendicular (horizontal) direction. In the boundary regions compression obviously dominated over tension. Before the peak of the vertical force, the compression and tensile forces increased, however some single tensile forces started to break due to the contact damage (Fig. 6Bb). After the load peak the horizontal tensile forces started to reduce (Fig. 6Bc). When a vertical macro-crack occurred in the specimen, the compressive forces concentrated in the specimen mid-region whereas the tensile forces became located mainly along the specimen circumference due to the compression of two separated specimen halves (Fig. 6Bd).

4.2 *Size effect*

The concrete specimen with the diameter of D = 50 mm was cut out from the central part of specimen D = 150 mm for investigating the energetic size effect. The DEM simulations with D = 50 mm were carried out with the same parameters as for D = 150 mm (Section 3). The vertical displacement along the specimen top was prescribed (D = 50 mm).

The concrete tensile splitting strength was higher by 15% in the specimen D = 50 mm (Fig. 7). The normalized vertical displacement v/D corresponding to the maximum vertical force was greater by 15%. The specimen behaviour was quasi-brittle. Thus the failure mode changed from a very brittle (with the snap-back instability) for D = 150 mm to a quasi-brittle with a positive softening slope for D = 50 mm.

The evolution of the total energy E was analysed during the continuing deformation process for both specimens sizes (test with the steel loading cylinder) (Fig. 8).

For specimen D = 150 mm at the vertical top displacement v corresponding to the peak load P_{max} (v = 0.46 mm) (Fig. 8A), the elastic internal energy was equal to 75% (normal energy – 52%, tangential energy – 23%), plastic dissipation was equal to 1%, energy from removed cohesive contacts was equal to 2%, kinetic energy was equal to 0.5% and numerical damping was equal to 21.5% of the total energy. At the failure (v = 0.40 mm), the elastic internal energy was 42%, plastic dissipation was 2.5%, energy from removed cohesive contacts was equal to 5%, kinetic energy was 0.5% and numerical damping was 50% of the total energy. Due to the snap-back instability, the total internal energy reduced by 15%, the elastic normal internal energy reduced by 60% and the elastic tangential internal energy reduced by 20%

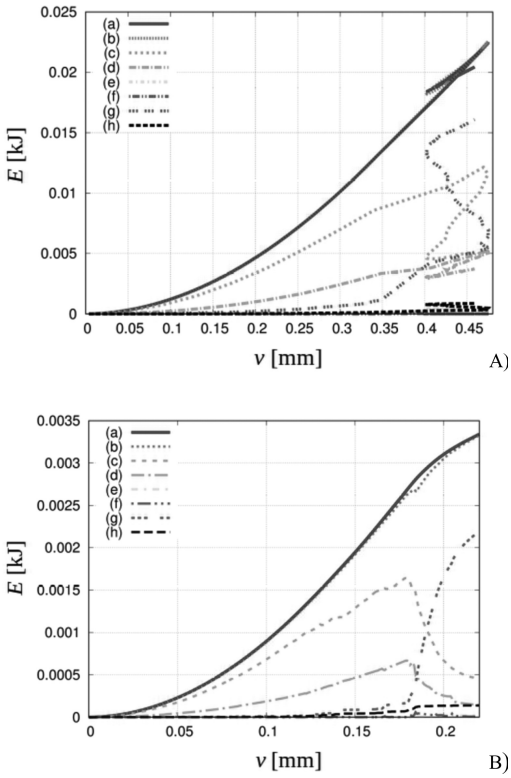

Figure 8. Energy evolution E in 2D concrete specimen with steel loading cylinder versus vertical top displacement v for specimen $D = 150$ mm (A) and $D = 50$ mm (B) using DEM: a) external work, b) internal work, c) normal elastic energy, d) tangential elastic energy, e) plastic dissipation, f) kinetic energy, g) numerical damping and h) broken contacts energy.

(Fig. 8A). In turn, the plastic dissipation, numerical damping and elastic energy from removed cohesive contacts increased by the factor 2.5, 2 and 2.5, respectively.

For specimen $D = 50$ mm at the peak load P_{max} ($v = 0.18$ mm), the elastic internal energy was equal to 85% (normal energy – 62%, tangential energy – 23%), plastic dissipation was equal to 0.2%, energy from removed cohesive contacts was equal to 4%, kinetic energy was 2% and numerical damping was 8.5% of the total energy. At the residual state ($v = 0.22$ mm), the elastic energy decreased to 27%, plastic dissipation was 0.2%, contact breakage 5%, kinetic energy was 1.8% and numerical damping increased to 66%.

The internal energies for specimens $D = 150$ mm and $D = 50$ mm changed mainly with respect to the normal elastic energy, numerical damping and energy from removed cohesive contacts. For the small concrete specimen ($D = 50$ mm), the relative elastic normal energy was higher by 10% at the peak load and the relative energy from removed cohesive contacts was higher by 3% at the peak load. The relative numerical damping was smaller at the peak load by 12% and higher at the residual state by 16%.

The total energy for the specimen $D = 150$ mm decreased after the peak load due to a large energy release in elastic unloading regions beyond the macro-crack that was higher than the energy absorption in the macro-crack. In the specimen $D = 50$ mm, the energy absorption in the macro-crack was however higher than the elastic energy release beyond it.

In order to improve the numerical results with respect to the experiments, the DEM model will be enhanced by aggregate crushing, width of ITZs and 3D analyses. The experiments and DEM calculations will be continued for the different specimen diameters ($D = 5$–30 cm).

5 CONCLUSIONS

The type of the loading strip significantly affected the concrete behaviour. The strength was smaller by 10%, CMOD corresponding to the strength was smaller by 20% and displacement corresponding to the strength was smaller by 300% when a line loading contact was prescribed at the top. In experiments with the specimen diameter of $D = 150$ mm, a snap-back phenomenon occurred. A clear compressive wedge took place when plywood loading/supporting boards was used that caused the strength's increase.

The macro-crack was curved along the specimen height and length due to a stochastic distribution of aggregates. It was initiated in the central region at the mid-height. Initially micro-cracks always occurred in ITZs and then propagated through a bridging mechanism. Several aggregates crushed during experiments. The width of ITZs was about 10–25 μm.

DEM proved its capability to model concrete fracture in detail by taking the snap-back instability into account. The agreement of calculated stress-displacement results and crack shapes with experimental ones was satisfactory. A decrease of the strength of ITZs and minimum particle diameter in the mortar caused the reduction of both the splitting tensile strength and material brittleness.

DEM demonstrated its applicability for concretes to calculate the size effect with respect to both the strength and brittleness. The calculated tensile strength increased and brittleness decreased with decreasing specimen diameter. The failure mode changed from very brittle to quasi-brittle with decreasing specimen diameter.

The external vertical splitting force was transmitted via a network of normal contact forces

which formed clear force chains. Some compressive forces appeared also along the macro-crack edge due to aggregate inter-locking.

Due to the snap-back instability (D = 150 mm), the total internal energy reduced by 15%, the elastic normal internal energy reduced by 60% and the elastic tangential internal energy reduced by 20%. The plastic dissipation, numerical damping and elastic energy from removed cohesive contacts increased by the factor 2.5, 2 and 2.5, respectively.

The relative normal elastic energy was greater at the peak load by 10% in the small specimen (D = 50 mm).

ACKNOWLEDGEMENTS

The research work has been carried out within the project "Experimental and numerical analysis of coupled deterministic-statistical size effect in brittle materials" financed by the Polish National Science Centre NCN (UMO-2013/09/B/ST8/03598).

REFERENCES

ASTM, Standard Test Method for Splitting Tensile Strength of Cylindrical Concrete Specimens, C496M-04, 2004.

Bažant, Z.P. & Planas, J. 1998. Fracture and Size Effect in Concrete and Other Quasibrittle Materials. CRC Press LCC, Boca Raton.

Bazant, ZP, Pang, SD, Vorechovsky, M, Novak, D. Energetic-statistical size effect simulated by S6FEM with stratified sampling and crack band model. Int. J. for Numerical Methods. in Engineering 2007; 71(11): 1297–1320.

Bažant, Z.P. Kazemi, M.T. Hasegawa, T. & Mazars, J. 1991. Size Effect in Brazilian Split-Cylinder Tests: Measurements and Fructure Analysis, *ACI Material Journal* 325–332.

Bažant, Z.P. Pijaudier-Cabot, G. & Pan, J.-Y. 1987. Ductility, snapback, size effect and redistribution in softening beams and frames. *ASCE Journal of Structural Engineering* 113(12): 2348–2364.

Benkemoun, N. Poullain, Ph. & Al Khazraji, H. et al. 2016. Meso-scale investigation of failure in the tensile splitting test: Size effect and fracture energy analysis. *Engineering Fracture Mechanics* 168: 242–259.

Carmona, S. Gettu, R. & Aguado, A. 1998. Study of the post-peak behaviour of concrete in the splitting-tension test, Fracture Mechanics of Concrete Structures, Proceedings FRAMCOS-3, Aedificatio Publishers, D-79104 Freiburg, Germany 111–120.

Chen, W. & Konietzky, H. 2014. Simulation of heterogeneity, creep, damage and lifetime for loaded brittle rocks, *Tectonophysics* 633:164–175.

.Dupray, F. Malecot, Y. Daudeville, L. et al. 2009. Mesoscopic model for the behaviour of concrete under high confinement. *International Journal for Numerical and Analytical Methods in Geomechanics* 33:1407–23.

Groh, U. Konietzk, H. Walter, K. et al. 2011. Damage simulation of brittle heterogeneous materials at the grain size level. *Theoretical and Applied Fracture Mechanics* 55: 31–38.

Hasegawa, T. Shioya, T. & Okada, T. 1985. Size effect on splitting tensile strength of concrete, Proceedings, Japan Institute 7th Conference 309–312.

Hentz, S. Daudeville, L. & Donze, F. 2004. Identification and validation of a Discrete Element Model for concrete. *Journal of Engineering Mechanics ASCE* 130(6): 709–719.

Kadlecek Sr., V. Modry, S. Kadlecek Jr., V. 2002. Size effect of test specimens on tensile splitting strength of concrete: general relation. *Materials and Structures* 35: 28–34.

Kozicki, J. & Donze, F.V. 2013. A new open-source software developer for numerical simulations using discrete modeling methods. *Computer Methods in Applied Mechanics and Engineering* 197: 4429–4443.

Kuorkoulis, S.K. Markides, Ch.F. & Chatzistergos, P.E. 2013. The standarized Brazilian disc test as a contact problem, *International Journal of Rock Mechanics & Mining Sciences* 57: 132–141.

Miguel, L.F.F. Riera, J.D. Iturrioz, I. & Aráoz, G.F. 2016. Influence of the width of the loading strip in the Brazilian tensile test of concrete and other brittle materials. *Journal of Materials in Civil Engineering* 28(11).

Nitka, M. & Tejchman, J. 2015. Modelling of concrete behaviour in uniaxial compression and tension with DEM. *Granular Matter* 17(1): 145–164.

Rocco, C. Guine, G.V. Planas, J. & Elices, M. 1999. Size effect and boundary conditions in the Brazilian test: experimental verification, *Material and Structures* 32: 210–217.

Skarżyński, Ł. & Tejchman, J. 2016. Experimental investigations of fracture process in concrete by means of x-ray micro-computed tomography. *Strain* 52: 26–45.

Skarżyński, Ł. Nitka, M. & Tejchman, J. 2015. Modelling of concrete fracture at aggregate level using FEM and DEM based on X-ray CT images of internal structure. *Engineering Fracture Mechanics* 147: 13–35.

Suchorzewski, J. Tejchman, J. & Nitka, M. 2017. Discrete element method simulations of fracture in concrete under uniaxial compression based on its real internal structure. *International Journal of Damage Mechanics*. DOI: 10.1177/1056789517690915.

Tanabe, T. Itoh, A. & Ueda, N. 2004. Snapback failure analysis for large scale concrete structures and its application to shear capacity study of columns. *Journal of Advanced Concrete Technology* 2(3): 275–288.

Tejchman, J. and Bobiński, J. 2013. Continuous and discontinuous modeling of fracture in concrete using FEM. Springer, Berlin-Heidelberg (eds. W. Wu and R. I. Borja).

Torrent, R.J. 1997. A general relation between tensile strength and specimen geometry for concrete—like materials, *Material Structures* 10: 187–196.

Weibull, W. 1951. A statistical distribution function of wide applicability. *Journal of Applied Mechanics* 18(9): 293–7.

Zhu, W.C. & Tang, C.A. 2006. Numerical simulation of Brazilian disk rock failure under static and dynamic loading. *International Journal of Rock Mechanics and Minining Science* 43: 236–52.



Taylor & Francis
Taylor & Francis Group
http://taylorandfrancis.com

Computational Modelling of Concrete Structures – Meschke, Pichler & Rots (Eds)
© 2018 Taylor & Francis Group, London, ISBN 978-1-138-74117-1

Numerical prediction of deterministic size effect in concrete bars and beams

Adam Wosatko, Jerzy Pamin & Andrzej Winnicki
Faculty of Civil Engineering, Cracow University of Technology, Cracow, Poland

ABSTRACT: The paper presents the results of simulations of deterministic size effect in concrete bars and beams. Two established material models are employed in the study: the consistency viscoplasticity and the gradient damage model. For direct tension of a double-edge notched bar three sizes are considered. For three-point bending of a beam without a notch four sizes are examined and the response is compared with experimental results taken from a paper by Grégoire et al. The results confirm that the regularized models exhibit size effect not only in the post-peak regime, but also in the nominal strength. It is more pronounced for the gradient damage model.

1 INTRODUCTION

It is well-known that size effects can have a purely mechanical nature. In brittle and quasi-brittle materials such deterministic size effect is more important than the one originating from the randomness of material strength (Bažant 1992). There is extensive experimental evidence of the deterministic size effect in concrete, see e.g. (Shah et al. 1995, Bažant et al. 1992, van Vliet 2000, van Mier 2013). Since the development of fracture mechanics the knowledge of size effect laws has also matured, cf. (Bažant and Planas 1998, Bažant and Yu 2009).

Classical, local models (e.g. plasticity or damage) do not incorporate any size effect (i.e. the strength is constant), which seems acceptable for small sizes of macroscopic models. Linear elastic fracture mechanics gives a simple approximation of size effect for very large specimen sizes. In between there is a range of sizes for which the nonlinear response seems to be represented by a power size effect law of Bažant (Bažant 1992, Bažant and Planas 1998).

The physical nature of the deterministic size effect can be different in cases when a specimen geometry produces a stress singularity (notched specimens) and in cases when initial stress distribution is smooth. Therefore, originally different size laws were proposed for those two cases (Bažant and Planas 1998). More recently, the so-called Universal Size Effect Law (USEL) has been introduced with intention to capture size effect properly in the quantitative sense for both notched and unnotched specimens (Bažant and Yu 2009). The extensive experimental campaign carried out by (Grégoire et al. 2013) on plain concrete specimens in three point bending (height of specimens in range from 50 mm to 400 mm, unnotched and with different notch depths) has confirmed the validity of USEL.

Since concrete is a quasi-brittle material which exhibits softening, its constitutive model should be equipped with a localization limiter. This can be achieved in three manners: the simplest approach is to relate the softening model with finite element size (so-called fracture energy trick or crack band model), the second is to make the constitutive description non-local (in either integral or gradient format), and the last concept is to include rate-dependence. Usually only the first or the third option is available in commercial FE codes. A general alternative is to use discontinuous models, either at the macro-scale (XFEM) or meso-scale (lattice models), but this aspect is not addressed in the paper.

If one uses a nonlocal model without the fracture energy G_f and an internal length parameter l scales the nonlocal or gradient effect, then the larger it is, the more ductile the response, and hence the strength grows. On the other hand, if one adopts G_f as a material constant and computes the area under the stress-strain diagram at the point level as $g_f = G_f / w$, where w is the crack band width related to internal length l, then the fracture energy governs the load-displacement diagrams. The reason is that if one takes a larger w then the nonlocal interaction is more extensive (providing additional ductility), but simultaneously g_f is smaller (giving a more brittle relation at a point), and the two effects may neglect, so that the global response does not depend on w unless the localization mode changes.

This is observed for one size of a structure and changing internal length. If we now keep all parameters constant and decrease the specimen size L then a similar response is observed, since it

depends on the ratio l/L. In other words, a nonlocal continuum reproduces the size effect due to the internal length parameter which ensures that the fracture process zone has the same width irrespectively of the structural size L, and the dissipated elastic energy depends on L.

In modelling of concrete there have been several attempts to reproduce size effects, see e.g. (Le Bellégo et al. 2003, Georgin et al. 2004, Grégoire et al. 2013, Havlásek et al. 2016, Korol et al. 2017). The influence of gradual crack or damage growth (e.g. due to notches) and nonlocality on the size effect in the predicted nominal strength is examined for instance in (Jirásek et al. 2004). The aim of the present paper is to re-analyze the ability of selected enhanced-continuum models to capture the deterministic size effect in plain concrete specimens under tension and bending.

The numerical study carried in (Grégoire et al. using a non-local (integral type) damage model proposed by (Mazars and Pijaudier-Cabot 1989) in comparison with the authors' own experimental campaign showed that such a model cannot capture properly (in the quantitative sense) the experimental results for both notched and unnotched specimens using the same set of material data. Following this observation, in this paper the performance of selected enhanced-continuum models is examined for both notched (direct tension test) and unnotched (three point bending test) specimens.

Two models belonging to the above-mentioned classes of regularized models are considered. The first is the gradient damage-plasticity model described in (de Borst et al. 1999), and the second is the Hoffman viscoplastic consistency model (Winnicki et al. 2001). Both were implemented by the authors in FEAP (Taylor 2001).

The authors planned to include in the comparison the so-called concrete damaged plasticity model (Lubliner et al. 1989, Lee and Fenves 1998), which is available in the commercial FEA software ABAQUS (SIMULIA Abaqus 2010). Some results of this model for a direct tension test are provided in a companion paper (Szczecina and Winnicki 2018), but the results for the beam bending problem have been inconclusive, so they are not included in this paper.

It is realized that for the considered problems it is enough to analyze two-dimensional models. The considered configurations are based on the works of (Hordijk 1991) and (Grégoire et al. 2013) for the bars and beams, respectively.

2 MATERIAL MODELS

2.1 *Summary of gradient damage model*

In the simplest model of continuum damage mechanics one damage measure ω (Kachanov 1958), which grows from 0 (no damage) to 1 (complete loss of stiffness), is a function of damage history parameter κ^{d} and depends on the deformation of a body. The concept of effective stress $\hat{\boldsymbol{\sigma}}$, which acts on the undamaged material skeleton while actual stress $\boldsymbol{\sigma}$ satisfies equilibrium, is used together with the assumption of strain equivalence in the real and effective (fictitious, undamaged) configuration, see for instance (Simo and Ju 1987). The stress tensors are related by scalar ω:

$$\boldsymbol{\sigma} = (1-\omega)\hat{\boldsymbol{\sigma}}, \quad \hat{\boldsymbol{\sigma}} = \boldsymbol{E} : \epsilon^{e} \tag{1}$$

where $\boldsymbol{E}$ is the Hooke's operator. The elastic strain tensor $\in^{\mathrm{e}}$ is equal to the strain tensor $\in$ when the standard elasto-damage model is considered (this is the case explored in this paper), but the model can easily be coupled with a plastic behaviour of the undamaged material "skeleton" and then $\epsilon^{\mathrm{e}} = \epsilon - \epsilon^{\mathrm{p}}$, see e.g. (de Borst et al. 1999).

Following (Peerlings et al. 1996), the damage evolution in the gradient-enhanced model is governed by the following damage activation function, defined in the strain space:

$$F^{\mathrm{d}}\left(\epsilon, \kappa^{\mathrm{d}}\right) = \bar{\epsilon}\left(\bar{\epsilon}\left(\boldsymbol{\epsilon}\right)\right) - \kappa^{\mathrm{d}} = 0 \tag{2}$$

where $\tilde{\epsilon}$ is an equivalent strain measure and $\bar{\epsilon}$ is an averaged (nonlocal) strain measure which satisfies the following diffusion equation:

$$\bar{\epsilon} - c\nabla^2\bar{\epsilon} = \tilde{\epsilon} \tag{3}$$

and homogeneous natural boundary conditions. The parameter $c > 0$, assumed here to be constant, has a unit of length squared and is related to an internal length scale. During the damage evolution the history parameter κ^{d} is equal to the largest value of $\bar{\epsilon}$ reached in the loading history and obeys the standard loading/unloading conditions.

Although some reservations have been raised with respect to the model, see (Geers 1997, Simone et al. 2003, Poh 2011, Saroukhani et al. 2013), it is used here in its original form called implicit gradient damage (abbreviation GD will further be used to refer to the model), see also (Peerlings et al. 1998). The equivalent strain measure $\tilde{\epsilon}$ can be defined in different ways. In this paper we employ the modified von Mises definition (de Vree et al. 1995), involving the first and second strain invariants, I_1^{ϵ} and J_2^{ϵ}, respectively, and depending on the ratio of compressive and tensile strength $k = f_c'/f_t'$. Although this definition introduces the sensitivity of the model to the sign of strain, the interaction between tensile and compressive response in concrete is not represented properly. In order to improve the description, one would need to use an isotropic version of the damage model

with two damage parameters degrading the tensile and compressive stiffness separately, see for instance in (Mazars and Pijaudier-Cabot 1989).

It is assumed that κ^{d} grows from damage threshold κ_{o} and damage ω asymptotically increases but never reaches 1. We employ an exponential damage growth function according to (Mazars and Pijaudier-Cabot 1989). This relation is well-suited for reproduction of the tensile fracture in concrete, see (Hordijk 1991). In its definition parameter η is responsible for material ductility and related with concrete fracture energy G_f, and parameter α is responsible for residual stress, i.e. it prevents the complete loss of material stiffness to obtain a stable numerical response.

2.2 *Overview of consistency viscoplasticity model*

The second employed model for concrete has been developed within the viscoplasticity theory and follows the idea proposed by (Wang 1997) for metals, named "viscoplastic consistency model" (acronym VP will be used). A similar approach was proposed by (Kleiber 1998) and later developed by (Heeres et al. 2002).

The Burzyński-Hoffman yield surface in its isotropic form is selected, since it was successfully employed in the analysis of concrete structures (Bićanić et al. 1994, Pearce 1993):

$$F^{\mathrm{vp}} = 3J_2^{\boldsymbol{\sigma}} + I_2^{\boldsymbol{\sigma}}\left(f_c - f_t\right) - f_c f_t = 0 \tag{4}$$

where $J_2^{\boldsymbol{\sigma}}$ and $I_2^{\boldsymbol{\sigma}}$ are the usual stress invariants, f_c and f_t are the uniaxial compressive and tensile strengths, respectively. The yield surface can expand or shrink depending on the actual viscoplastic strain rate and the consistency condition is invoked (no overstress is involved).

Two internal variables κ_c and κ_t are used, which are functions of an equivalent viscoplastic strain. They describe the material hardening/softening in compression and tension, respectively. Moreover, two more internal variables η_{c} and η_t are assumed to determine the increase/decrease of compressive and tensile strengths due to an equivalent viscoplastic strain rate. The respective rate-dependent strengths are thus:

$$f_c = f_c(\kappa_c, \eta_c), \quad f_t = f_t\left(\kappa_t, \eta_t\right) \tag{5}$$

The dependence of f_i on κ_i and η_i is formulated in a general way as $f_i = f_i' H_i\left(\kappa_i\right) S_i\left(\eta_i\right)$ for compression ($i = c$) and tension ($i = t$), respectively, where f_i' is the initial compressive/tensile strength. Functions H_i and S_i can be defined in different manners, e.g. as piecewise linear. Some examples, based on experiments performed by (Kupfer 1973, Suaris and Shah 1985), are presented in (Winnicki 2007).

In turn, the rates of the internal variables for compression/tension depend on the current stress and the rates of internal variables κ and η; $\dot{\kappa}_i = g_i(\boldsymbol{\sigma})\dot{\kappa}$ and $\dot{\eta}_i = g_i(\boldsymbol{\sigma})\dot{\eta}$, where subscript i stands for c or t. In the above equations g_c and g_t are scalar functions accounting for independent processes of damage in compression and tension. The functions g_i are selected according to experiments, taking into account the influence of the damage process in compression on the concrete strength in tension and the influence of the damage process in tension on the concrete strength in compression. In (Winnicki 2007) two options are considered: (1) $g_c = g_t = 1$ (damage is assumed to be an isotropic phenomenon) and (2) $g_c + g_t = 1$ (with extreme cases of dominant compressive stress $g_c = 1$, $g_t = 0$ and dominant tensile stress $g_c = 0$, $g_t = 1$).

Next $\dot{\kappa}$ is defined as an equivalent viscoplastic strain rate assuming work hardening, while $\dot{\eta}$ depends on the time derivative of the viscoplastic strain rate:

$$\dot{\kappa} = \frac{1}{\tilde{\sigma}}\boldsymbol{\sigma} : \dot{\epsilon}^{\mathrm{vp}}, \quad \dot{\eta} = \frac{1}{\tilde{\sigma}}\boldsymbol{\sigma} : \dot{\epsilon}^{\mathrm{vp}} \tag{6}$$

where $\tilde{\sigma} = (3J_2^{\boldsymbol{\sigma}})^{\frac{1}{2}}$.

In the course of loading the yield surface can change its shape due to the separate hardening/softening processes of the compressive and tensile strength, but the surface remains convex at all times. The yield surface depends not only on the internal parameter κ, but also on the additional one η. Since the total value of η depends on the first derivatives of viscoplastic strains, the yield surface is rate dependent, i.e. it expands for higher and shrinks for lower viscoplastic strain rates. As a result, this model can correctly predict basic viscoplastic phenomena like creep and relaxation.

The strain rate is decomposed into its elastic and viscoplastic parts and the viscoplastic flow is defined similarly to the classical associated plasticity:

$$\dot{\epsilon} = \dot{\epsilon}^{\mathrm{e}} + \dot{\epsilon}^{\mathrm{vp}}, \ \dot{\epsilon}^{\mathrm{vp}} = \dot{\lambda} n, \ n = \frac{\partial F^{\mathrm{vp}}}{\partial \boldsymbol{\sigma}} \tag{7}$$

In order to establish the viscoplastic multiplier $\dot{\lambda}$ the consistency equation is used, which can be expressed as:

$$n : \dot{\boldsymbol{\sigma}} - h\dot{\lambda} - s\ddot{\lambda} = 0 \tag{8}$$

where h is the classical generalized plastic modulus and s is the generalized viscoplastic modulus (Winnicki 2007). Due to the last term the consistency equation is not an algebraic equation for the viscoplastic multiplier, but a differential equation of the first order, to be solved for an appropriate

initial condition. The generalized plastic and viscoplastic moduli are computed as:

$$h = a_c S_c h_c + a_t S_t h_t, \quad s = a_c s_c H_c + a_t s_t H_t \tag{9}$$

where

$$h_i = \frac{\mathrm{d}H_i}{\mathrm{d}\kappa_i}, \quad s_i = \frac{\mathrm{d}S_i}{\mathrm{d}\eta_i} \tag{10}$$

and the other coefficients are as follows: $a_c = f_c'\left(f_t - \mathrm{tr}\,\boldsymbol{\sigma}\right)\ g_c g,\ a_t = f_t'\left(f_c + \mathrm{tr}\,\boldsymbol{\sigma}\right)\ g t\ g$, and $g = \boldsymbol{\sigma} : n / \tilde{\sigma}$.

When functions S_c and S_t are constant, their derivatives vanish and Equation (8) reduces to the form known from the classical rate independent plasticity. It is shown in (Winnicki 2007) that the model parameters can be linked with fracture energies G_{fc} and G_{fc}, cf. (van Mier 1984, Vonk 1992).

It is finally mentioned that the finite element algorithm for the VP model is similar to the classical rate-independent plasticity, i.e. standard linearization is performed and the weak form of incremental equilibrium equations is discretized. For the gradient damage model a two-field FE model is required with the discretization of the averaging equation (3) and the nonlocal strain measure $\bar{\epsilon}$ as additional unknown.

3 EXAMPLES

3.1 *Specification of tests*

In this paper two examples are considered to verify if the two regularized models described above are capable of representing the size effect.

The first one is a direct tension test. The discretized double-edge notched bar is depicted in Figure 1, cf. (Hordijk 1991, de Borst and Pamin 1996). Three different specimens are considered, the dimensions of which are summarized in Table 1.

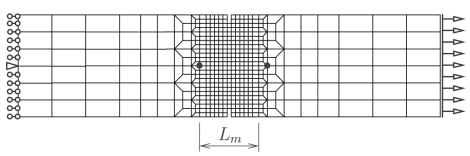

Figure 1. Direct tension test.

Table 1. Direct tension test—geometry.

Specimen	Length L [mm]	Width B [mm]	Measurement base L_m [mm]	Ligament width B_{lig} [mm]
A	500	120	70	100
B	250	60	35	50
C	125	30	17.5	25

However, the mesh density remains the same, i.e. the size of finite element changes together with the dimensions of the specimen. Plane stress conditions and the thickness t = 50 mm are assumed for all simulations. Socalled ligament width B_{lig} is defined, which is the net bar width in the notch region.

The material model data are presented in Table 2. Notice that the internal length scale for gradient damage and the piecewise linear functions $S_c(\eta_c) = S_t(\eta_t)$ for Hoffman viscoplasticity are the same for all specimens. Also, functions $H_c(\kappa_c)$ for compression and $H_t(\kappa_t)$ for tension have a similar character, cf. Figures 2(a) and 2(b). In this test eight-noded finite elements are employed and indirect displacement control algorithm is applied with imposed horizontal displacement at the point marked in Figure 1 on the right hand side of the dense mesh zone.

Next computations are performed for the unnotched beam under three point bending. The configuration, where a half of the domain is considered, is based on (Grégoire et al. 2013) and the finite element mesh is illustrated in Figure 3. Now, four specimens are simulated with the dimensions given in Table 3. As in the previous test, it has been assumed that the mesh density remains unchanged. Again, plane stress holds and thickness $t = 50$ mm is constant for all simulations.

The material data for both models are listed in Table 4. Here, the internal length parameter for the gradient damage model is larger than for the previous test because the specimen dimensions are larger in comparison to the direct tension, the element dimension grows proportionally to the beam size and, to make the regularization active the simulated width of the localization band cannot be smaller than the element size. In this test for the viscoplastic consistency model functions $H_c(\kappa_c)$ and $H_t(\kappa_t)$ are different from that used in direct tension test, but functions $S_c(\eta_c)$ and $S_t(\eta_t)$ remain the same, cf.

Table 2. Direct tension test—material model parameters.

Young's modulus:	$E = 40000$ MPa
Poisson's ratio:	$\nu = 0.15$
GRADIENT DAMAGE (GD)	
Strengths ratio:	$k = 10$
Fracture energy:	$G_f = 0.115$N/mm
Damage threshold:	$\kappa_0 = 8.625 \times 10^{-5}$
Exponential softening	$\alpha = 0.99,\ \eta = 500$
Internal length scale:	$l = 4$ mm, i.e. $c = 8.0$
HOFFMAN VISCOPLASTICITY (VP)	
Work hardening	Equation (6)
Initial tensile strength:	$f_t' = 3.45$ MPa
Initial compressive strength:	$f_c' = 59.3$ MPa
Material functions	Figure 2

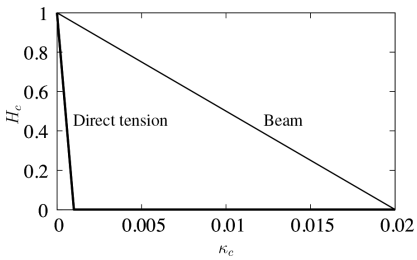

(a) Function H_c.

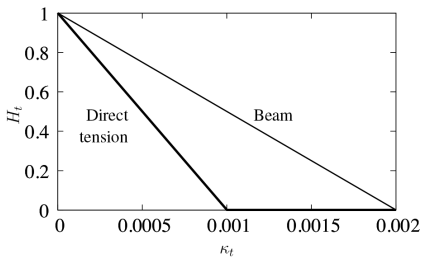

(b) Function H_t.

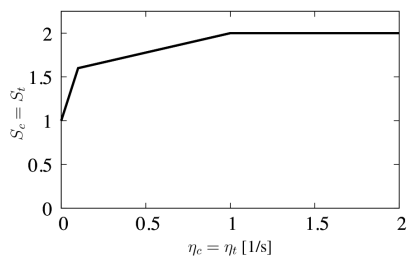

(c) Function $S_c = S_t$.

Figure 2. Material functions for viscoplasticity.

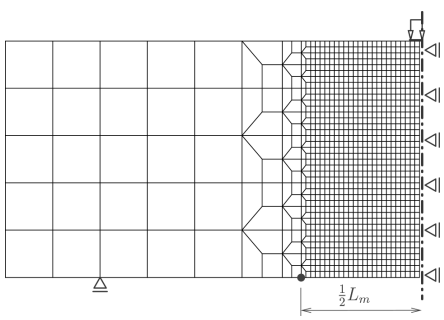

Figure 3. Beam test.

Figures 2(a) and 2(b). Four-noded elements with full integration are introduced similarly to the simulations by (Grégoire et al. 2013). Arc length control is used in the computations.

Table 3. Beam test—geometry.

Specimen	Length L [mm]	Height D [mm]	Span S [mm]	Measurement base L_m [mm]
D1	1400	400	1000	400
D2	700	200	500	200
D3	350	100	250	100
D4	175	50	125	50

Table 4. Beam test—material model parameters.

Young's modulus:	$E = 37000$ MPa
Poisson's ratio:	$\nu = 0.21$
GRADIENT DAMAGE (GD)	
Strengths ratio:	$k = 10$
Fracture energy:	$G_f = 0.100$N/mm
Damage threshold:	$\kappa_o = 1.05 \times 10^{-4}$
Exponential softening	$\alpha = 0.99$, $\eta = 600$
Internal length scale:	$l = 9$ mm, i.e. c = 40.5
HOFFMAN VISCOPLASTICITY (VP)	
Work hardening	Equation (6)
Initial tensile strength:	$f_t' = 3.88$ MPa
Initial compressive strength:	$f' = 42.3$ MPa
Material curves:	Figure 2

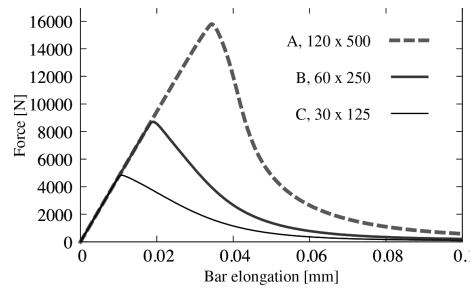

Figure 4. Direct tension test—force-elongation diagrams for GD model.

3.2 *Results for direct tension test*

Figure 4 shows the diagrams of total force at the right-hand edge versus bar elongation for three specimen sizes. This illustrates the global response of the double-edge notched bar under tension. The concept of so-called ligament stress is introduced to observe the size effect:

$$\sigma_{\text{lig}} = \frac{F}{B_{\text{lig}} t} \tag{11}$$

where F is the force, B_{lig} is the ligament width and t is the thickness. Hence, in Figure 5 the results are presented in terms of load divided by the net cross section in the notch area versus average strain

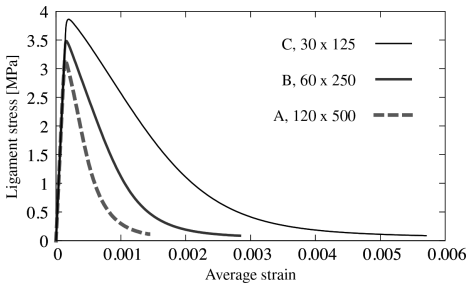

Figure 5. Direct tension test—ligament stress vs average strain diagrams for GD model.

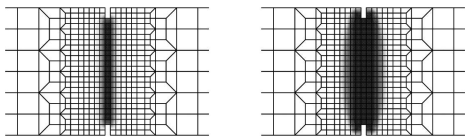

(a) $\bar{\epsilon}$ (on the left) and ω (on the right), specimen A.

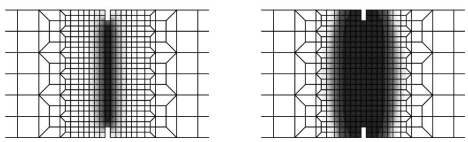

(b) $\bar{\epsilon}$ (on the left) and ω (on the right), specimen B.

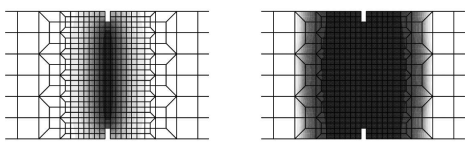

(c) $\bar{\epsilon}$ (on the left) and ω (on the right), specimen C.

Figure 6. Direct tension test—distribution of averaged strain measure $\overline{\epsilon}$ and damage ω in notch vicinity for final states of gradient damage simulations.

calculated as extension of the measurement length over L_m.

In Figure 6 the distributions of the averaged strain measure $\overline{\epsilon}$ and the damage parameter ω are given. Although the damage profile has the unwelcome tendency to broaden with increased bar elongation, it is clearly seen that the width of the damage band (determined by the internal length l) is similar for all specimen sizes, which provides the proper representation of size effect.

Figure 7 shows the results for the GD model, i.e. when all material model parameters are the same as in the previous simulation, but now the internal length scale l is equal to 0, so in fact local damage

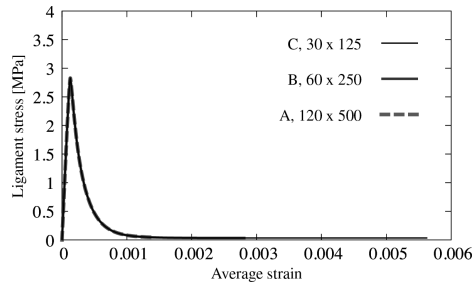

Figure 7. Direct tension test—stress-strain diagrams for damage model without gradient enhancement.

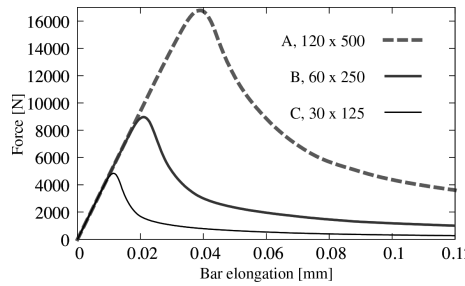

Figure 8. Direct tension test—load-elongation diagrams for VP model.

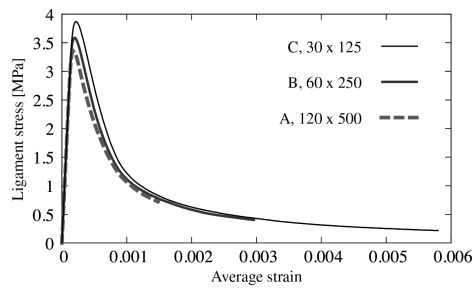

Figure 9. Direct tension test—ligament stress vs average strain diagrams for VP model.

model is adopted. It is observed that the size effect does not occur in this version of the model.

The results presented in Figure 8 for the viscoplastic consistency model and the adopted data set exhibit slightly different limit loads than the GD model and different shape of post-peak equilibrium paths. However, a significantly different response in terms of ligament stress vs average strain is observed in Figure 9, namely the post-critical parts of the diagrams for the three bar sizes are close to one another and the strength values are much closer, so the predicted size effect is smaller.

In Figure 10 the distributions of the internal variable κ_t representing the smeared cracking are provided for the final states on the diagrams from the previous figures. In comparison to the response

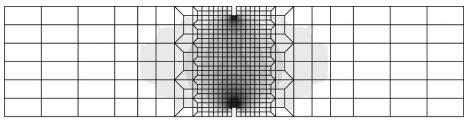

(a) Specimen A.

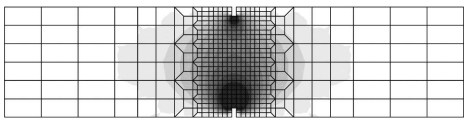

(b) Specimen B.

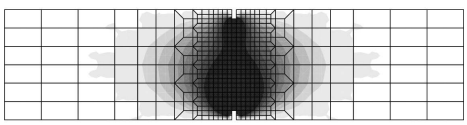

(c) Specimen C.

Figure 10. Direct tension test—final distributions of internal variable κ_t for Hoffman viscoplasticity.

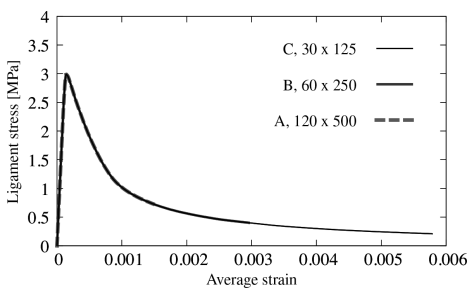

Figure 11. Direct tension test—stress-strain diagrams for Hoffman plasticity without active viscous effects.

of the GD model, the inelastic strains have the tendency to localize at the notches and do not form bands of uniform widths. Symmetry of deformation is also lost.

Analogically to the computations for damage without gradient enhancement, the Hoffman plasticity model without rate dependence (zero viscosity $S_t = S_c \equiv 1$) is also examined. This is the classical version of the model. Figure 11 shows the diagrams where no size effect occurs.

3.3 *Results for unnotched beam*

Figure 12 shows the diagrams of total force applied to the beam versus a pseudo-CMOD measured at the bottom surface between points Lm away from each other, see Table 3. They are plotted for four beam

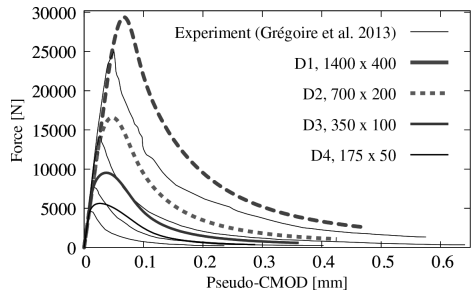

Figure 12. Beam test—load vs pseudo-CMOD diagrams for GD model.

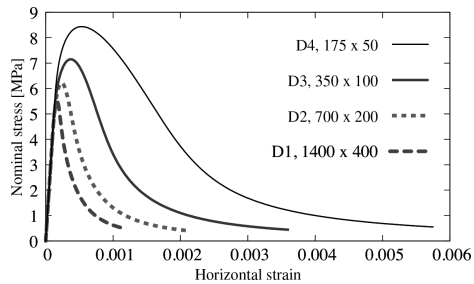

Figure 13. Beam test—nominal stress vs horizontal average strain diagrams for GD model.

sizes marked D1-D4 and compared with experimentally determined diagrams taken from (Grégoire et al. 2013). The numerical response is much different than the experimental one, but no attempts have been made to follow the experiments more closely by taking different material model parameters.

However, as shown in Figure 13, the gradient damage model exhibits a strong size effect. In these computations so-called nominal stress is analyzed:

$$\sigma_{\text{nom}} = \frac{3}{2}\frac{F\,S}{t\,D^2} \tag{12}$$

where F is the force, S is the span, t is the thickness and D is the height of the beam. Averaged strain is derived from the pseudo-CMOD divided by the base L_m. It is noted that for all specimen sizes the adopted value of the internal length scale is constant, while the size of finite element in the densified mesh region grows with the size of the beam (the discretization is the same for all sizes). Figures 14 and 15 show the final distributions of the averaged stain measure $\overline{\epsilon}$ and of damage ω, respectively, for the four beam sizes. Notice that as expected, the widths of the fracture zones are similar because the size of the mesh zone shown grows proportionally with the specimen.

Figure 16 shows the diagrams of total force applied to the beam versus a pseudo-CMOD for the

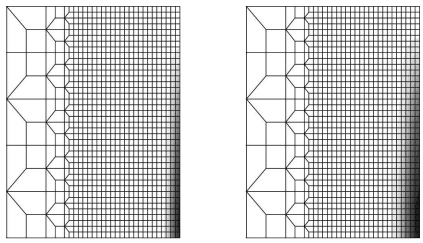

(a) Specimen D_1. (b) Specimen D_2.

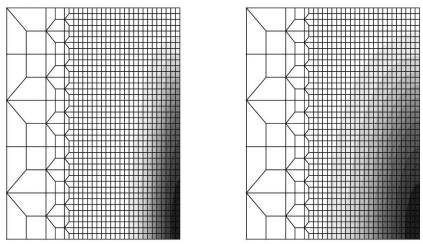

(c) Specimen D_3. (d) Specimen D_4.

Figure 14. Beam test—distribution of averaged stain measure $\overline{\epsilon}$ in final state for GD model.

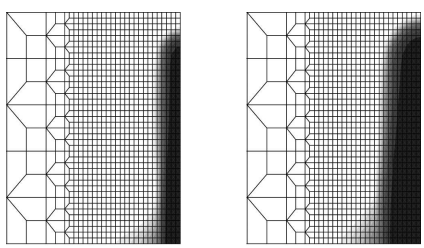

(a) Specimen D_1. (b) Specimen D_2.

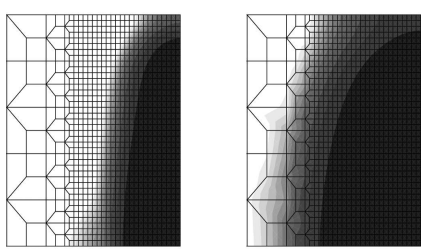

(c) Specimen D_3. (d) Specimen D_4.

Figure 15. Beam test—distribution of damage ω in final state for GD model.

Hoffman consistency viscoplasticity model, compared to the experimental results from (Grégoire et al. 2013). Although the load carrying capacity of the beam is reproduced slightly better than for the

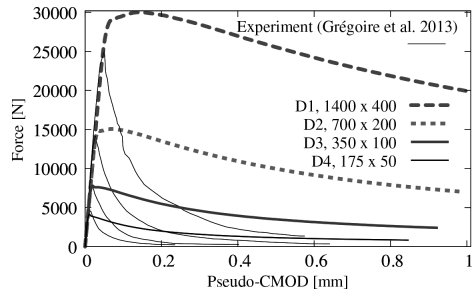

Figure 16. Beam test—load vs pseudo-CMOD diagrams for VP model.

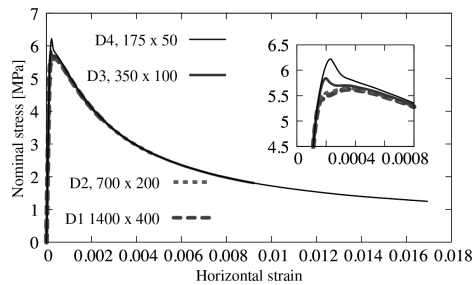

Figure 17. Beam test—nominal stress vs average horizontal strain diagrams for VP model.

other model, the post-peak response is too ductile. Moreover, the diagrams of nominal stress vs average strain in Figure 17 almost overlap for all sizes. It is visible in the zoom that the presence of the viscous term in the model does not affect results significantly. As can be seen in Figure 18 the maps of tensile internal variable κ_t do not represent the expected propagation of the smeared fracture zone upwards, instead a zone of oval shape is formed near the point of first cracking.

When the presented results are analyzed and compared, objections can be raised and differences in the simulation of the bending response are noticed. First, quite large flexural strength of the GD model is seen in Figure 13 for the smallest specimen, which is caused by exaggerated gradient influence. This is not so for the VP model, see Figure 17. Second, for both models the maximum stress is too large for the large specimens, and hence the size effect is underestimated. The physics of the problem is as follows. First cracks occur when the uniaxial tensile strength f_t' is reached in the bottom fibers. Then, as cracking propagates, the force grows until the flexural tensile strength $f_{t,\mathrm{flex}}$ (also called the modulus of rupture) is reached. For small beams $f_{t,\mathrm{flex}}$ is much larger than f_t' since the fracture zone is large in comparison with the specimen. For large beams the fracture band width is

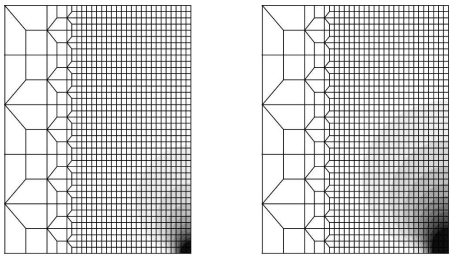

(a) Specimen D_1. (b) Specimen D_2.

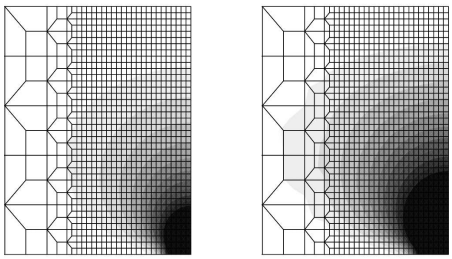

(c) Specimen D_3. (d) Specimen D_4.

Figure 18. Beam test—distribution of internal variable κ_i in final state for VP model.

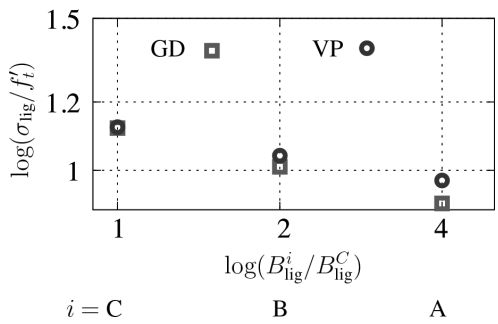

Figure 19. Size effect plot for beam bending test.

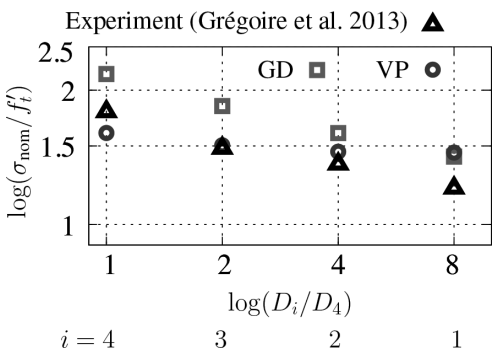

Figure 20. Size effect plot for beam bending test.

relatively small as compared to the specimen size, the response is more brittle and the flexural strength should converge from above to the tensile strength. This is not simulated properly with the employed models.

3.4 *Final remarks*

It is well-known that non-local constitutive models are capable of reproducing the deterministic size effect due to the presence of an internal length parameter. This has been confirmed in the paper using the gradient-enhanced damage model as well as the consistency viscoplasticity model. They behave differently for the tensile bar and beam bending problems. Comparison of the size effect for both models is depicted in Figures 19 and 20. Logarithmic scale is used for both axes. For the three-point bending test the size effect diagram is confronted with experimental data (Grégoire et al. 2013).

The former model exhibits a strong size effect not only in the post-peak regime, but also in the nominal strength. The response of the second model is less obvious. In the direct tension test it clearly seen in the nominal strength, in the beam test the size effect for the adopted data is hardly visible. Further parameter study is therefore necessary, which should also show whether the ability of the viscoplastic model to reproduce size effect depends on the rate of loading.

REFERENCES

Bažant, Z.P. & J. Planas (1998). *Fracture and Size Effect in Concrete and Other Quasibrittle Materials*. CRC Press.

Bažant, Z.P. & Q. Yu (2009). Universal size effect law and effect of crack depth on quasi-brittle structure strength. *ASCE J. Eng. Mech. 135*(2), 78–84.

Bažant, Z.P. (1992). Scaling laws in mechanics of failure. *ASCE J. Eng. Mech. 119*, 1828–1845.

Bažant, Z.P., J. Ožbolt, & R. Eligehausen (1992). Fracture size effect: review of evidence for concrete structures. *ASCE J. Struct. Eng. 120*, 2377–2398.

Bićanić, N., C.J. Pearce, & D.R.J. Owen (1994). Failure predictions of concrete like materials using softening Hoffman plasticity model. In H. Mang, N. Bícaníc, and R. de Borst (Eds.), *Computational modelling of concrete structures, Euro-C 1994*, Volume 1, Swansea, UK, pp. 185–198. Pineridge Press.

de Borst, R. & J. Pamin (1996). Gradient plasticity in numerical simulation of concrete cracking. *Eur. J. Mech. A/Solids 15*, 295–320.

de Borst, R., J. Pamin, & M.G.D. Geers (1999). On coupled gradient-dependent plasticity and damage theories with a view to localization analysis. *Eur. J. Mech. A/Solids 18*(6), 939–962.

de Vree, J.H.P., W.A.M. Brekelmans, & M.A.J. van Gils (1995). Comparison of nonlocal approaches in continuum damage mechanics. *Comput. & Struct. 55*(4), 581–588.

Geers, M.G.D. (1997). *Experimental analysis and computational modelling of damage and fracture*. Ph.D. dissertation, Eindhoven University of Technology, Eindhoven.

Georgin, J.F., L.J. Sluys, & J.M. Reynouard (2004). A coupled damage-viscoplasticity model for the analysis of localization and size effects. *Computers & Concrete 1*(2), 169–188.

Grégoire, D., L.B. Rojas-Solano, & G. Pijaudier-Cabot (2013). Failure and size effect for notched and unnotched concrete beams. *Int. J. Num. Anal. Meth. Geomech. 37*(10), 1434–1452.

Havlásek, P., P. Grassl, & M. Jirásek (2016). Analysis of size effect on strength of quasi-brittle materials using integral-type nonlocal models. *Eng. Fract. Mech. 157*, 72–85.

Heeres, O.M., A.S.J. Suiker, & R. de Borst (2002). A comparison between the Perzyna viscoplastic model and the Consistency viscoplastic model. *Eur. J. Mech. A/Solids 21*, 1–12.

Hordijk, D.A. (1991). *Local approach to fatigue of concrete*. Ph.D. dissertation, Delft University of Technology, Delft.

Jirásek, M., S. Rolshoven, & P. Grassl (2004). Size effect on fracture energy induced by non-locality. *Int. J. Num. Anal. Meth. Geomech. 28*, 653–670.

Kachanov, L.M. (1958). Time of rupture process under creep conditions. *Izd. Akad. Nauk SSSR, Otd. Tekh. Nauk 8,* 26–31. (in Russian).

Kleiber, M. (1998). Plasticity problems. In M. Kleiber (Ed.), *Handbook of Computational Mechanics. Survey and Comparison of Contemporary Methods*, Berlin, Germany, pp. 201–252. Springer Verlag.

Korol, E., J. Tejchman, & Z. Mróz (2017). Experimental and numerical assessment of size effect in geometrically similar slender concrete beams with basalt reinforcement. *Eng. Struct. 141*, 272–291.

Kupfer, H. (1973). *Das Verhalten des Betons unter mehrachsiger Kurzzeitbelastung under besonderer Berücksichtigung der zweiachsigen Beanspruchung*. Number 229. Berlin: Deutscher Ausschuss für Stahlbeton.

Le Bellgo, C., J.F. Dubé, G. Pijaudier-Cabot, & B. Gérard (2003). Calibration of nonlocal damage model from size effect tests. *Eur. J. Mech. A/Solids 22*(1), 33–46.

Lee, J. & G. Fenves (1998). Plastic-damage model for cyclic loading of concrete structures. *ASCE J. Eng. Mech. 124*(8), 892–900.

Lubliner, J., J. Oliver, S. Oller, & E. Oñate (1989). A plasticdamage model for concrete. *Int. J. Solids Struct. 25*(3), 299–326.

Mazars, J. & G. Pijaudier-Cabot (1989). Continuumdamage theory—application to concrete. *ASCE J. Eng. Mech. 115*, 345–365.

Pearce, C.J. (1993). Computational aspects of the softening Hoffman plasticity model for quasi-brittle solids. M.Sc., University Of Wales, College Swansea.

Peerlings, R.H.J., R. de Borst, W.A.M. Brekelmans, & J.H.P. de Vree (1996). Gradient-enhanced damage for quasi-brittle materials. *Int. J. Numer. Meth. Engng 39*, 3391–3403.

Peerlings, R.H.J., R. de Borst, W.A.M. Brekelmans, & M.G.D. Geers (1998). Gradient-enhanced damage modeling of concrete fracture. *Mech. Cohes.-frict. Mater. 3*, 323–342.

Poh, L.H. (2011). *Gradient enhanced plasticity and damage models: adressing the limitations of classical models in softening and hardening*. Ph.D. dissertation, Eindhoven University of Technology, Eindhoven.

Saroukhani, S., R. Vafadari, & A. Simone (2013). A simplified implementation of a gradient-enhanced damage model with transient length scale effects. *Computational Mechanics 51*, 899–909.

Shah, S.P., S.E. Swartz, & C. Ouyang (1995). *Fracture Mechanics of Concrete: Applications of Fracture Mechanics to Concrete, Rock and Other Quasi-brittle Materials*. New York: John Wiley & Sons.

Simo, J.C. & J.W. Ju (1987). Strain- and stress-based continuum damage models—I. Formulation, II. Computational aspects. *Int. J. Solids Struct. 23*(7), 821–869.

Simone, A., H. Askes, & L.J. Sluys (2003). Incorrect initiation and propagation of failure in non-local and gradientenhanced media. *Int. J. Solids Struct. 41*, 351–368.

SIMULIA Abaqus (2010). Abaqus Theory Manual (6.10). Dassault Systemes, Providence, RI, USA.

Suaris, W. & S.P. Shah (1985). Constitutive model for dynamic loading of concrete. *J. of Struct Engng, ASCE 111*(3), 563–576.

Szczecina, M. & A.Winnicki (2018). Analysis of RC frame corners using cdp model. In G. Meschke et al. (Eds.), *Proc. EURO-C 2018 Int. Conf. Computational Modelling of Concrete Structures*, London. CRC Press/Balkema.

Taylor, R.L. (2001). FEAP—A Finite Element Analysis Program, Version 7.4, User manual. University of California at Berkeley, Berkeley.

van Mier, J.G.M. (1984). *Strain-softening of concrete under multiaxial loading conditions*. Ph.D. dissertation, Eindhoven University of Technology, Eindhoven.

van Mier, J.G.M. (2013). *Concrete Fracture: A Multiscale Approach*. Boca Raton: CRC Press.

van Vliet, M.R.A. (2000). *Size effect in tensile fracture of concrete and rock*. Ph.D. dissertation, Delft University of Technology, Delft.

Vonk, R.A. (1992). *Softening of concrete loaded in compression*. Ph.D. dissertation, Eindhoven University of Technology, Eindhoven.

Wang, W.M. (1997). *Stationary and propagative instabilities in metals—a computational point of view*. Ph.D. dissertation, Delft University of Technology, Delft.

Winnicki, A. (2007). Viscoplastic and internal discontinuity models in analysis of structural concrete. Series Civil Engineering, Monograph 349, Cracow University of Technology, Cracow.

Winnicki, A., C.J. Pearce, & N. Bícaníc (2001). Viscoplastic Hoffman consistency model for concrete. *Comput. & Struct. 79,* 7–19.

Computational Modelling of Concrete Structures – Meschke, Pichler & Rots (Eds)
© 2018 Taylor & Francis Group, London, ISBN 978-1-138-74117-1

Numerical investigations on early indicators of fracture in concrete at meso-scale

M. Nitka & J. Tejchman
Gdansk University of Technology, Gdańsk, Poland

ABSTRACT: Fracture is a major reason of the global failure of concretes. The understanding of fracture is important to ensure the safety of structures and to optimize the material behaviour. In particular an early prediction possibility of fracture in concretes is of major importance. In this paper, concrete fracture under bending was numerically analysed using the Discrete Element Method (DEM). The real mesoscopic structure of a concrete beam was modelled based on μCT images. The calculations were performed under 2D and 3D conditions. The special attention was laid on the evolution of a macro-crack and different micro-structural phenomena during fracture before macro-cracking.

1 INTRODUCTION

Fracture is a fundamental phenomenon in quasi-brittle and brittle materials (Bažant & Planas 1997, Lilliu & van Mier 2003, Tejchman & Bobiński 2013). It is characterized by complicated micromechanical processes, including the nucleation, growth and coalescence of micro-cracks which lead to strain localization and later to macro-cracks. It strongly depends upon a heterogeneous structure of materials over many different length scales, changing e.g. in concrete from the few nanometres (hydrated cement) to the millimetres (aggregate particles). At the meso-scale, concrete may be considered as a composite stochastic material wherein four important phases may be separated: cement matrix, aggregate, interfacial transition zones (ITZs) and macro-voids. The presence of highly heterogeneous ITZs with the thickness of about 0–50 μm (depending mainly upon the particle diameter, aggregate shape, roughness and mixing direction) is crucial since they are always the weakest regions in usual concretes (because of their higher porosity) wherein micro-cracking starts ITZs are clear attractors for a crack propagation.

In order to comprehensively study the mechanism of the initiation, growth and formation of localized zones and cracks, mesoscopic concrete models should be used. The advantage of the mesoscopic modelling is the fact that it directly simulates micro-structure and may be used to comprehensively study local phenomena at the micro-level such as the mechanism of the initiation, growth and formation of localized zones and cracks which greatly affect the macroscopic concrete behaviour. The mesoscopic results allow also for a better calibration of continuous, discontinuous and coupled continuous-discontinuous constitutive models for concrete with respect to e.g. characteristic length of micro-structure, crack opening width and occurrence moment of a discrete macro-crack. Discrete models (if they are enough consistent) might progressively replace costly experimental tests to study the influence of concrete meso-structure (aggregates size, aggregate shape, aggregate roughness, aggregate/mortar volume, micro- macro-porosity etc.) on the concrete behaviour. The disadvantages are: enormous computational cost and a difficult calibration procedure with respect to geometric and mechanical properties of ITZs which are still not well recognized.

The discrete element method was chosen in this paper to realistically describe fracture in concrete under bending at the meso-scale (Herrmann et al. 1989, Donzé et al. 1999, Lilliu & van Carol at al. 2001, Mier 2003, Hentz et al. 2004, Kozicki & Tejchman 2008, Dupray et al. 2009, Groh et al. 2011, Nitka & Tejchman 2015, Du et al. 2013, Skarżyński et al. 2015, Suchorzewski et al. 2017). The calculations were performed with the 3-dimensional open-source code YADE that was developed at Grenoble University (Kozicki & Donzé 2008, Šmilauer & Chareyre 2011). Concrete was described as a four-phase material composed of aggregate, cement matrix, interfacial transitional zones and macro-voids.

The calculations were performed under 2D and 3D conditions. The internal structure of concrete (size, shape and location of aggregate and macro-voids, micro-porosity) was directly taken from 3D x-ray images using the very advanced micro-tomography system SkyScan 117 (Skarżyński et al.

2015, Suchorzewski et al 2017). The numerical results were compared with the laboratory experiment. The special attention was laid on the crack propagation connected to normal contact force transmission and fluctuation displacements. The so-called bottleneck method in normal contact force transmission was already successfully used to concrete in order to predict cracks under uniaxial tension (Kahagalage et al. 2017). Macro-cracks may be also predicted based on vortex-structures (Kozicki & Tejchman 2017) that appear in a displacement fluctuation field (Nitka & Tejchman 2015).

2 EXPERIMENTAL RESULTS

The concrete beam was prepared from ordinary Portland cement, aggregate and water. Gravel aggregate and river sand were used. The maximum diameter of aggregate was d_{max} = 16 mm and the average one was d_{50} = 2 mm. The total aggregate volume of specimen was 75% (35% higher than 2 mm in diameter). The beam had the length of 320 mm, height of 80 mm and width of 4 mm. It had a notch at the mid-span) (Fig. 1). The measured uni-axial compressive strength, Young's modulus and Poisson's ratio of concrete were equal to: f_c = 51.81 MPa, E = 36.1 GPa and υ = 0.22, respectively. The quasi-static test on the concrete beam was performed with a controlled notch opening displacement rate (crack mouth opening displacement (CMOD)) of 0.002 mm/min using the loading machine Instron 5569. The maximum vertical force F was equal to 2.25 kN (the tensile strength was 3.91 MPa). After bending tests, the concrete cuboids with the dimensions of 80 mm (height), 50 mm (width) and 40 mm (depth) were cut out from beam in the notch region for scanning by the x-ray micro-tomography Skyscan 1173 in order to obtain the 3D images of concrete meso-structure (in a damaged state).

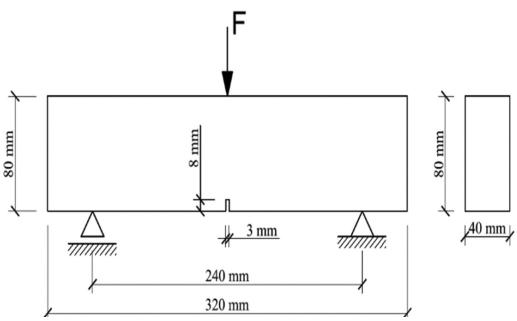

Figure 1. Concrete notched beam under quasi-static three-point bending (F - vertical force).

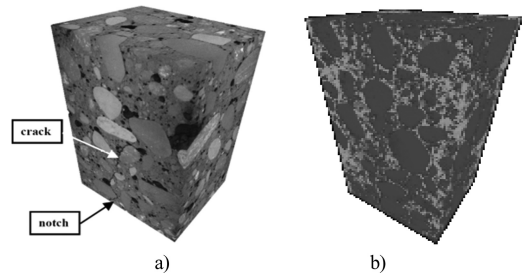

Figure 2. 3D μCT images of cracked cuboidal specimens 80 × 50 × 40 mm^3 obtained by from concrete beam: a) general view and b) with separated phase (blue colour corresponds to aggregates, green colour to cement matrix and red colour to crack and macro-voids).

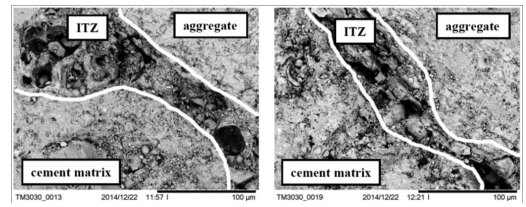

Figure 3. Arbitrary images of ITZs around aggregate particles in concrete specimen by means of scanning electron microscope (Suchorzewski et al. 2016).

Figure 2 shows the 3D images of the cracked region above notch (50 × 80 × 40 mm^3) for CMOD = 0.10 mm when the crack was totally developed.

Concrete was also studied with the aid of the scanning electron microscope (SEM) Hitachi TM3030 with the maximum magnification factor 30'000 to define ITZ's (Fig. 3). The measured width of porous region around aggregate changed between 30–50 μm. It was not dependent upon the aggregate diameter but its roughness (with smoothness of aggregate the ITZ width decrease).

3 DISCRETE ELEMENT METHOD

The 3D discrete element method (DEM) was used in mesoscopic analyses. A simple linear normal contact model under compression was used. Aggregate grains were modelled as clusters composed of spheres (rigid bodies) to reproduce their real shape. The interaction force vector representing the action between two spherical discrete elements in contact was decomposed into a normal and tangential vector, respectively. The normal forces acting on spheres were modelled by an elastic law with a cut-off in tension. The normal and

tangential forces were linked to the displacements through the normal stiffness K_n and the tangential stiffness K_s (Figs. 4a-c) (Kozicki & Donze 2008)

$$\vec{F}_n = K_n U \vec{N}$$
$$\vec{F}_s = \vec{F}_{s,prev} + K_s \Delta \vec{X}_s \quad (1)$$

where U is the overlap between spheres, $\vec{N}$ denotes the normal vector at the contact point, $\vec{X}_s$ is the incremental tangential displacement and $\vec{F}_{s,prev}$ is the tangential force from the previous iteration.

The stiffness parameters were computed with the aid of the modulus of elasticity of the grain contact E_c and two neighbouring grain radii R_A and R_B (to determine the normal stiffness K_n) and with the aid of the modulus of elasticity E_c and Poisson's ratio υ_c of the grain contact and two neighbouring grain radii R_A and R_B (to determine the tangential stiffness K_s), respectively (Kozicki & Donze 2008).

$$K_n = E_c \frac{2R_A R_B}{R_A + R_B}, K_s = \upsilon_c E_c \frac{2R_A R_B}{R_A + R_B} \quad (2)$$

If the grain radius $R_A = R_B = R$, the stiffness parameters were equal to: $K_n = E_c R$ and $K_s = \upsilon_c E_c R$, respectively (thus $K_s/K_n = \upsilon_c$). The contact forces $\vec{F}_n$ and $\vec{F}_s$ satisfied the cohesive-frictional Mohr-Coulomb equation

$$\left\|\vec{F}_s\right\| - F^s_{\max} - \left\|\vec{F}_n\right\| \times \tan\mu \le 0 \quad \text{(before contact breakage)} \quad (3)$$

$$\left\|\vec{F}_s\right\| - \left\|\vec{F}_n\right\| \times \tan\mu \le 0 \quad \text{(after contact breakage)} \quad (4)$$

where μ denotes the inter-particle friction angle and is the cohesive force between spheres. The normal force might be negative down to the minimum value of $F^s_{\max}$ if there was no a geometrical contact between elements. If this minimum normal force between spheres $F^n_{\min}$ was reached, the contact was broken. Moreover, if any contacts between grains re-appeared, cohesion between them was not taken into account. A crack was considered as open if cohesive forces between grains disappeared when a critical threshold was reached.

A choice of a very simple linear elastic normal contact was intended to capture average various contact possibilities in real concrete. One assumed that the cohesive force and tensile force were a function of the cohesive stress C (maximum shear stress at pressure equal to zero), tensile normal stress T and sphere radius (Kozicki & Donze 2008, Ergenzinger et al. 2011):

$$F^s{}_{\max} = C \times R^2, \qquad F^n{}_{\min} = T \times R^2 \quad (5)$$

For two elements in contact, the smaller values of C, T and R were assumed. To dissipate excessive kinetic energy in a discrete system, a simple local non-viscous damping scheme was adopted (Cundall & Hart 1992) which assumed a change of forces by using the damping parameter α

$$\vec{F}^k_{damped} = \vec{F}^k - \alpha \cdot \mathrm{sgn}(\vec{v}^k)\left|\vec{F}^k\right| \quad (6)$$

where $\vec{F}^k$ and $\vec{v}^k$ are the kth components of the residual force and translational velocity, respectively. A positive damping coefficient α is smaller than 1 (sgn(•) returns the sign of the kth component of velocity). The equation can be separately applied to each kth component of a 3D vector x, y and z.

The following five main local material parameters were needed for our discrete simulations: E, υ, μ, C and T which may be successfully calibrated with the aid of real laboratory uniaxial tests on compression and tension of concrete specimens (Nitka & Tejchman 2015, Suchorzewski et al. 2017). In addition, the particle radius R, particle mass density ρ and damping parameters α were required. Note that the material softening was not assumed in the model.

In DEM computations, aggregate grains were modelled as clusters composed of spheres with the diameter of d = 0.5 mm (2D) or d = 2 mm (3D) connected to each other as rigid bodies. One

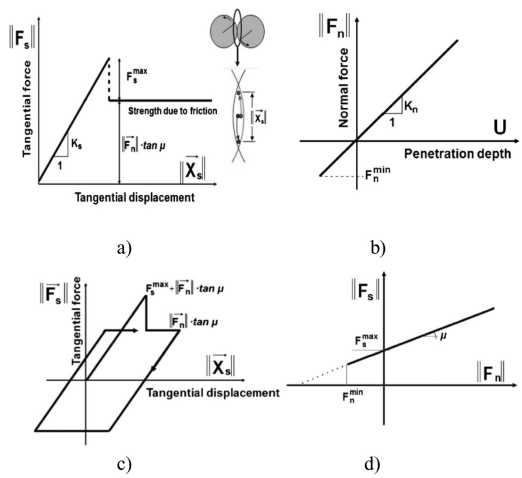

Figure 4. Mechanical response of DEM model: a) tangential contact model, b) normal contact model, c) loading and unloading path in tangential contact model and d) modified Mohr-Coulomb model.

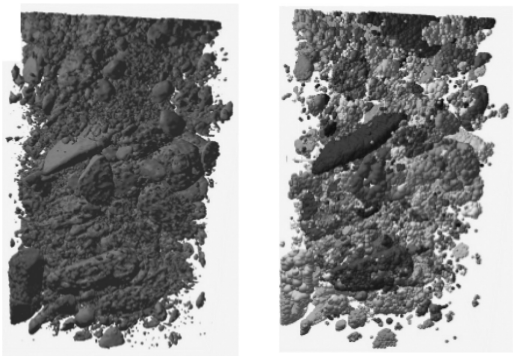

a) b)

Figure 5. Aggregate in concrete sample: a) high density map based on 3D x-ray micro tomographic images and b) clusters composed of spheres in DEM (3D) (each colour corresponds to different aggregate cluster).

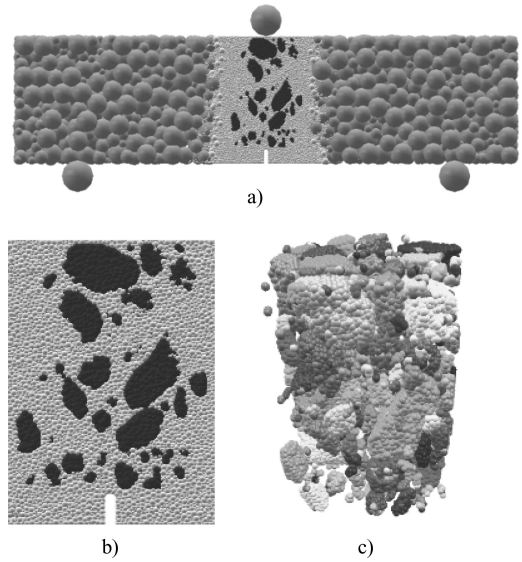

a) b) c)

Figure 6. 3D geometry of concrete model in DEM: a) front view on entire beam, b) 2D meso-region of 50×80 mm^2 close to notch (dark colour corresponds to aggregates and light colour to cement matrix) and c) meso-region of $50 \times 80 \times 40$ mm^3 close to notch composed of aggregate particles with ITZs (each colour corresponds to different aggregate composed of grain clusters of grains).

aggregate might include max. 500 cylinders in 2D calculations and 2200 spheres in 3D calculations. All clusters were considered as aggregate particles if the aggregate diameter was d>2 mm. These particles included ITZs around them. The shape and position of aggregate was taken from density map obtained directly from the x-ray micro tomography images (Fig. 5a). The map of density was changed directly into clusters of spheres and imported to the DEM program (Fig. 5b). The aggregate volume (d>2 mm) was 35% as in the experiment. The macro-voids were also taken directly from the density map (density equal 0). They were simulated as empty spaces.

The cement matrix was modelled with spheres without ITZs (with the diameter of $d = 0.25$–2 mm in 2D simulations and of $d = 0.5$–2 mm in 3D simulations). They pre-filled the concrete specimen in 95%. The minimum grain diameter in 3D calculations was higher due to reduce the computation time. The remaining beam region (outside the meso-region close to the notch) was simulated with spheres of d = 2–8 mm. In 2D calculations only one layer of spheres was modelled along the beam depth (Nitka & Tejchman 2015, Skarżyński et al. 2015, Suchorzewski et al. 2017).

The ITZs were solely simulated as contacts between aggregate and cement matrix grains (without the physical width). The beam included in total about 25'000 cylinders (20'000 cylinders in the meso-region) in 2D analyses and about 230'000 apheres (220'000 elements in the meso-region) in 3D calculations (Fig. 6).

Based on preliminary calculations of uniaxial compression and uniaxial tension tests (Nitka & Tejchman 2015, Suchorzewski et al. 2017), the following parameters of cohesion and tensile strength were used to the particular phase: cement matrix (E_{cm} = 11.2 GPa, C_{cm} = 140 MPa and T_{cm} = 15.0 MPa) and ITZs (E_{ITZ} = 7.8 GPa, C_{ITZ} = 100 MPa and T_{ITZ} = 12.0 MPa) (Xiao et al. 2013). In the remaining region outside the meso-region with large grains was described by the constants: E_{macro} = 12.8 GPa, C_{macro} = 140 MPa and T_{macro} = 15.0 MPa. The remaining parameters were constant for all phases and regions: $\upsilon_c = 0.2$ (Poisson's ratio of the grain contact), $\mu = 18^o$ (inter-particle friction angle), $\alpha_d = 0.08$ (damping parameter) (Kozicki et al. 2013) and $\rho = 2.6$ kG/m^3 (mass density). With the assumed material properties and grain size distribution curve (without clusters, just spherical aggregate, since the microstructure was not studied), the DEM calculations provided the uniaxial compressive strength of 49.5 MPa, elastic modulus of 36 GPa (2D concrete specimen 10×10 cm^2) and tensile strength during bending of 4.40 MPa (2D concrete specimen 4×16 cm^2), i.e. similarly as in experiments (f_c = 51.81 MPa, f_t = 4.04 MPa, E = 36.1 GPa).

The beam was subjected to deformation by prescribing the constant velocity of $v = 2$ mm/s at the place of the vertical force.

4 DEM RESULTS

Figure 7 demonstrate the calculated evolution of the vertical force F against the displacement CMOD from DEM as compared to the experimental one.

The calculated and experimental diagrams were similar in the elastic region and have almost the same peak value (except of one 2D curve wherein the peak was higher by 25%, Fig. 7c). The softening rate was similar in 2D calculations and too small high in 3D calculations as compared to the experiment. This due to the fact that the calibration process was performed on 2D specimens.

The crack propagation path from the experiment and DEM for 3 different cross-sections (at the depth of 10 mm, 20 mm and 30 mm from the beam front side) and CMOD = 0.1 mm is shown in Fig. 8.

The numerical crack trajectory with the real aggregate in the cross-section at the depth of 10 mm (Figs. 8Ba and 8Ca) was almost identical as in the experiment (Fig. 8Aa). In the beam mid-region, the crack propagated in 2D simulations (Fig. 8Bb) in the opposite direction and in 3D simulations enclosed solely one aggregate from another side than in the experiment (Fig. 8Ab). In the cross-section at the depth of 30 mm, the crack initially moved in the different direction in 3D analyses (Fig. 8Cc), but finally ended close to the same aggregate. As compared with 2D calculations the calculated 3D crack path was improved. The crack was strongly curved due to the presence of aggregate and always propagated through the cement matrix and ITZs that were the weakest phases in concrete. Due to the beam notch, the macro-crack was created above the it and then moved upwards due to bending (Fig. 9). The crack

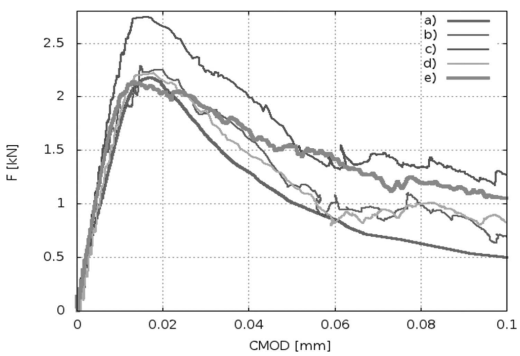

Figure 7. Evolution of vertical force against CMOD: a) experimental curve, b-d) calculated 2D curves in 3 different vertical sections along specimen depth e) calculated 3D curve.

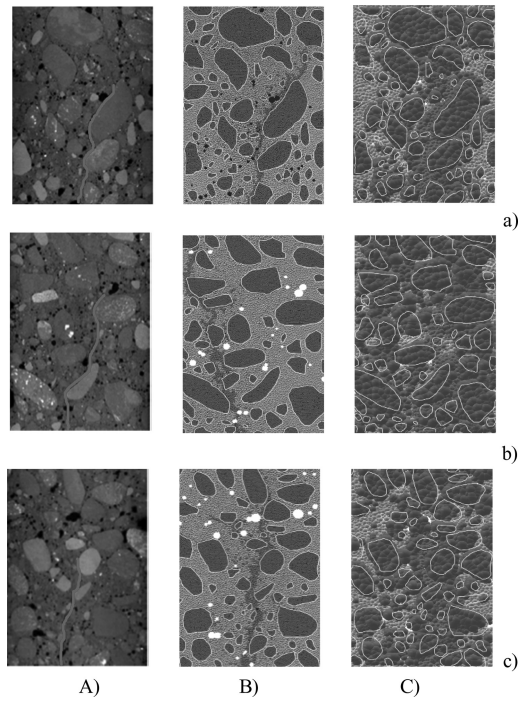

Figure 8. Final crack trajectory in concrete beam above notch after test for CMOD = 0.1 mm: A) μCT-image (red colour shows crack path), B) 2D DEM and C) 3D DEM (red colour denotes elements with broken contacts, dark grey colour denotes aggregate and light grey colour denotes cement matrix) at depth of: a) 10 mm b) 20 mm and c) 30 mm from beam front side.

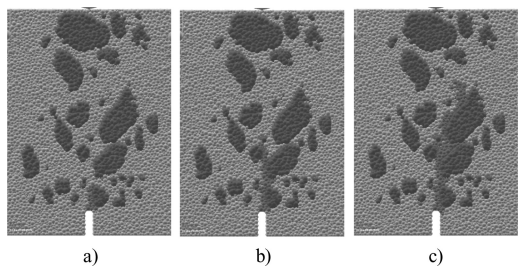

Figure 9. Evolution of crack formation from 3D DEM at depth of 10 mm from front side for CMOD: a) 0.018 mm (after peak load), b) 0.04 mm and c) 0.1 mm (dark grey colour denotes aggregate, light grey colour denotes cement matrix and red colour denotes spheres with broken contacts).

(formed by bridging the interfacial micro-cracks) was strongly curved and its height was different caused by a random spatial distribution of aggregate grains with ITZs (Fig. 9). The ITZs acted as attractors for a macro-crack.

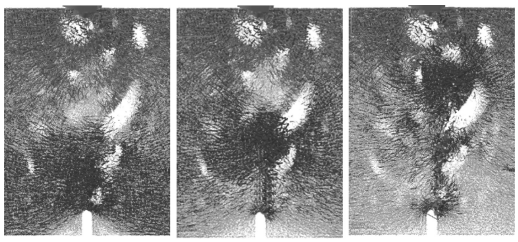

a) b) c)

Figure 10. Evolution of normal contact forces between grains obtained from 3D DEM at depth of 10 mm from front side for CMOD a) CMOD = 0.018 mm (after peak force), b) CMOD = 0.04 mm and c) CMOD = 0.1 mm (test end) (red colour denotes forces larger than average compressive forces, blue colour corresponds to forces lower than average tensile forces, remaining forces are marked in green).

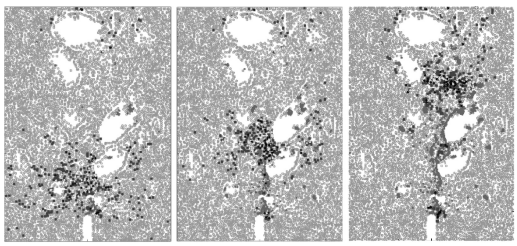

a) b) c)

Figure 11. Contact distribution with their strength from 3D DEM for cross-sections at 10 mm from the face side for CMOD: a) 0.018 mm (after peak force), b) = 0.04 mm and c) CMOD = 0.1 mm (test end) (green colour – all contacts, red colour – broken contacts, blue colour – contacts with strength grade above 50%, yellow colour – contacts with strength grade above 70% and black colour – contacts with strength grade above 90%).

The evolution of the normal contact force network in the concrete beam is demonstrated in Figure 10 (3D calculations). The thickness of the lines represents the magnitude of the normal contact force between two aggregate particles.

The forces were transmitted via a network of contact forces which formed clear force chains. They carried the majority of the loading and transmitted it on the entire system and were the predominant structure of internal forces at meso-scale.

The evolution of the intensity of contact forces for the cross-section at 10 mm from the beam front side is presented in Figure 11.

The high intensive normal contact forces obviously occurred at the front of the macro-crack. Some high intensive normal contact forces

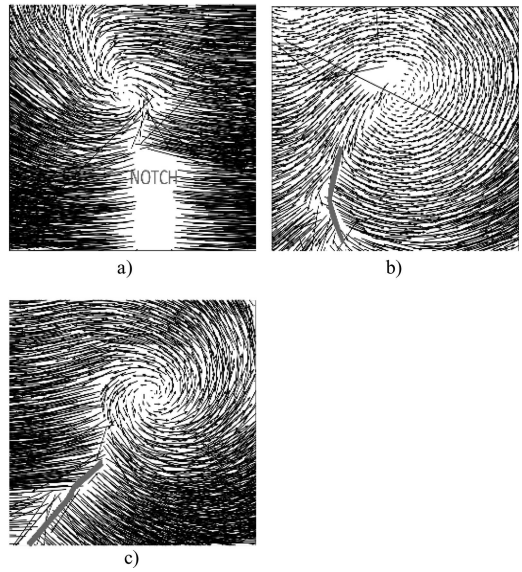

a) b) c)

Figure 12. Displacement fluctuations of particles from 2D DEM (zoomed region): a) 0.016 mm (before peak force), b) = 0.04 mm and c) CMOD = 0.1 mm (test end) with vortices above macro-crack (black vectors are multiplied by factor 1000, red line shows macro-crack crack).

remained along the macro-crack path due to interlocking (Eliáš & Stang 2012, Scholtès & Donzé 2013). It may be seen that some micro-cracks (broken contacts) appeared also far away from the main macro-crack.

Cracks may be early predicted based on the map of displacement fluctuations (Kozicki & Tejchman 2015). Figure 12 presents the spontaneous displacement fluctuations in concrete beam having the form of cells that circulate as quasi-rigid bodies (so-called vortex structures). The individual sphere displacements were able to form the long-range deformation vortex structures that rotated as rigid bodies. A vortex structure appeared above notch (Fig. 12a) or was created just above (about 2–3 mm) the macro-crack (Figs. 12b and 12c). Its radius was between 4–10 mm.

5 CONCLUSIONS

This study presented a numerical 3D mesoscopic approach based on the discrete element method and x-ray μCT images for the characterisation of a quasi-static mechanical behaviour of concrete. It was shown that the characteristic features of fractured concrete may be accurately modelled with the proposed approach. The 3D DEM proved to be

a appealing simulation tool in understanding and predicting the progressive nature of concrete cracking from the mesoscopic to the macroscopic level. It demonstrated a close correlation between numerical and experimental results in terms of strength and fracture propagation. Thus the parametric studies within DEM might be used for the practical design of concrete with the improved desired performance.

Based on our numerical analyses of the concrete beam under 3-point bending which were directly compared to corresponding experiments, the following main conclusions may be drawn:

Both the shape and location of aggregate and presence of ITZs are the key parameters which have to be taken into account in order to obtain a realistic geometry of the macro-crack that propagated by bridging the interfacial micro-cracks.

The beam strength and stiffness increased with increasing strength of ITZs and decreasing microporosity and number of ITZs. The beam brittleness became smaller with increasing number of ITZs and reducing strength of ITZs.

As compared to 2D simulations, the calculated macro-crack's shape and width of FPZ were more realistic in 3D analyses. Relatively less contacts broke in 3D than in 2D calculations that caused the growth of concrete ductility. The calibrated procedure should performed thus with the aid of 3D simulations of laboratory tests on mortar and concrete.

The vortex-structures were the early precursor of macro-cracks since their they concentrated in the region where the macro-crack ultimately later formed. An early prediction possibility of macro-cracks through vortex-structures creates a new perspective for a detection of impending failure in concretes (inherently connected with fracture) within continuum mechanics.

ACKNOWLEDGEMENTS

The research work has been carried out within the project: "*Innovative ways and effective methods of safety improvement and durability of buildings and transport infrastructure in the sustainable development*" financed partly by the European Union POIG.01.01.02-10-106/09-01) and the project "*Experimental and numerical analysis of coupled deterministic-statistical size effect in brittle materials*" financed by the National Research Centre NCN (UMO-2013/09/B/ST8/03598).

REFERENCES

Bažant, Z. and Planas, J. 1997. Fracture and size effect in concrete and other quasi-brittle materials. *CRC Press LLC*, Boca Raton.

Carol, I., López, C.M. and Roa, O. 2001. Micromechanical analysis of quasi-brittle materials using fracture-based interface elements. *International Journal for Numerical Methods in Engineering* **52**: 193–215.

Cundall, P.A. and Hart, R. 1992. Numerical modelling of discontinua. *Engineering Computations* **9**: 101–113.

Donzé, F.V., Magnier, S.A., Daudeville, L. and Mariotti, C. 1999. Numerical study of compressive behaviour of concrete at high strain rates. *Journal for Engineering Mechanics,* 122, **80**: 1154–1163.

Du, C., Sun, L., Jiang, S. and Ying, Z. 2013. Numerical simulation of aggregate shapes of three-dimensional concrete and its applications. *Journal of Aerospace Engineering* 515–527.

Dupray, F., Malecot, Y., Daudeville, L. and Buzaud, E.A. 2009. Mesoscopic model for the behaviour of concrete under high confinement. *International Journal for Numerical and Analytical Methods in Geomechanics* **33:** 1407–23.

Eliáš, J. and Stang, H. 2012. Lattice modeling of aggregate interlocking in concrete, *Int. J. Fracture* **175**: 1–11.

Ergenzinger, C., Seifried, R. and Eberhard, P.A. 2011. Discrete element model to describe failure of strong rock in uniaxial compression. *Granular Matter* **12**(4): 341–364.

Groh, U., Konietzky, H., Walter, K. and Herbst, M. 2011. Damage simulation of brittle heterogeneous materials at the grain size level. *Theoretical and Applied Fracture Mechanics* **55**: 31–38.

He, H., Guo, Z., Stroeven, P., Stroeven, M. and Sluys, L.J. 2009. Influence of particle packing on elastic properties of concrete. *Proc. First International Conference on Computational Technologies in Concrete Structures (CTCS'09),* Jeju, Korea. 1177–1197.

Hentz, S., Daudeville, L. and Donze, F. 2004. Identification and validation of a Discrete Element Model for concrete. *Journal of Engineering Mechanics ASCE* 130 **6**:709–719.

Herrmann, H.J., Hansen, A. and Roux, S. 1989. Fracture of disordered, elastic lattices in two dimensions. *Physical Rev. B,* **39**: 637–647.

Kahagalage, S., Tordesillas, A., Nitka, M. and Tejchman, J. 2017. Predicting cracks from force bottlenecks in a cementitious granular material. *EPJ Web of Conferences 140, Powder and Grains.*

Kozicki, J. and Donzé, F.V. 2008. A new open-source software developer for numerical simulations using discrete modeling methods. *Computer Methods in Applied Mechanics and Engineering* **197**: 4429–4443.

Kozicki, J. and Tejchman, J. 2008. Modelling of fracture processes in concrete using a novel lattice model. *Granular Matter* **10**, 377–388.

Kozicki, J., Niedostatkiewicz, M., Tejchman, J. and Mühlhaus, H.-B. 2013. Discrete modelling results of a direct shear test for granular materials versus FE results. *Granular Matter* **15**(5): 607–627.

Kozicki, J. and Tejchman, J. 2017. Investigations of quasi-static vortex structures in 2D sand specimen under passive earth pressure conditions based on DEM and Helmholtz-Hodge vector field decomposition. *Granular Matter* **19**: 19–31.

Lilliu, G. and van Mier, J.G.M. 2003. 3D lattice type fracture model for concrete. *Engineering Fracture Mechanics* **70**: 927–941.

Nitka, M. and J. Tejchman, J. 2015. Modelling of concrete behaviour in uniaxial compression and tension with DEM. *Granular Matter* **17** (1): 145–164.

Scholtès, L. and Donzé, F.V. 2013. A DEM model for soft and hard rocks: role of grain interlocking on strength. *Journal of the Mechanics and Physics of Solids* **62** (2): 352–369.

Skarżyński, Ł., Nitka, M. and Tejchman, J. 2015. Modelling of concrete fracture at aggregate level using FEM and DEM based on x-ray μCT images of internal structure, *Engineering Fracture Mechanics* **10** (147): 13–35.

Skarżynski, Ł. and Tejchman, J. 2016. Experimental investigations of fracture process in concrete by means of x-ray micro-computed tomography. *Strain* **52**: 26–45.

Suchorzewski, J., Tejchman, J. and Nitka, M. 2017. Discrete element method simulations of fracture in concrete under uniaxial compression based on its real internal structure, *International Journal of Damage Mechanics,* doi: 10.1177/1056789517690915.

Šmilauer, V. and Chareyre, B. 2011. Yade DEM Formulation. Manual.

Tejchman, J. and Bobiński, J. 2013. Continuous and discontinuous modelling of fracture in concrete using FEM. *Springer, Berlin-Heidelberg (eds. W. Wu and R.I. Borja)*.

Xiao, J., Li, W., Suc, Z., Lange, D.A. and Shah, S.P. 2013. Properties of interfacial transition zones in recycled aggregate concrete testes by nanoindentation, *Cement and Concrete Composites* **37**: 276–292.

Computational Modelling of Concrete Structures – Meschke, Pichler & Rots (Eds)
© 2018 Taylor & Francis Group, London, ISBN 978-1-138-74117-1

Incremental sequentially linear analysis of a notched beam

Chenjie Yu, P.C.J. Hoogenboom & J.G. Rots
Department Structural Engineering, Delft University of Technology, Delft, The Netherlands

ABSTRACT: Incremental Sequentially Linear Analysis (ISLA) is a new algorithm for non-linear finite element analysis. It is an extension of Sequentially Linear Analysis (SLA) which has been applied since 2001 as an alternative to the Newton-Raphson method when bifurcation, snap-back or divergence problems arise. ISLA is an incremental procedure with an implicit scheme, which starts and ends with an equilibrium state. The solution search path follows damage steps sequentially with secant stiffness. In each iteration only one element is selected for damaging in the next iteration, which is a similar procedure as used in SLA. In this paper, ISLA is explained and demonstrated for a notched beam test. Because of the incremental procedure, ISLA can be extended to non-proportional loading, geometrically non-linear analysis and transient analysis. The searching path of ISLA is based on physical parameters (damage and history) rather than guided by numerical parameters. In addition, the method keeps the same incremental format throughout the entire analysis, circumventing the need to switch intermittently from incremental to total approaches or vice versa.

1 INTRODUCTION

Nonlinear analysis of quasi brittle materials, such as masonry, reinforced concrete and pre-stressed concrete, has been applied for more than 40 years. However, the robustness of the algorithms is still a serious issue. The load displacement curves of quasi-brittle materials have many little peaks related to initializing and growing of numerous cracks. These peaks are only visible if one zooms in on a curve which is computed with very small load increments. Consequently, the tangent stiffness in the neighborhood of these peaks varies extremely and can lead to divergence of the Newton-Raphson (N-R) iterations at critical load increment.

Many solution methods have been proposed such as the modified Newton-Raphson method with initial stiffnesses (De Borst et al., 2012), LATIN method (Ladeveze, 2012) and sequentially linear analysis (SLA) (Rots, 2001). The saw tooth model has been introduced to make the results independent of the magnitude of the stiffness reduction in a step (Rots et al., 2008) (Rots & Invernizzi, 2004). An orthotropic damage model has been developed based on fixed smeared cracking for SLA (Slobbe et al, 2012). A method called NIEM has been proposed (Graça-e-Costa, 2012), which allows for switching between the incremental and the total approach determined by energy dissipation. Another method has been proposed by Elias (Eliáš et al, 2010) (Eliáš, 2015), who extends SLA to an incremental and non-iterative procedure called Force-Release method. In (DeJong et al., 2008) a method is proposed to perform SLA with non-proportional loading. In the paper (Giardina et al., 2013), it is shown that this method fails when a large overburden force is applied. A simplified method has been proposed for non-proportional loading (Yu et al., 2016). In (Alnaas & Jefferson, 2016), the idea of unloading-reloading is introduced to the solution search path of the traditional Newton–Raphson method. Based on the damage cycle idea in SLA, another concrete analysis method (Al-Sabah & Laefer, 2016) is presented entitled continuous, incremental-only, tangential analysis (CITA) for the Newton–Raphson method. CITA employs piece-wise linear stress-strain curve and a tangent elasticity modulus to calculate stiffness including parts with negative values.

In this paper, a new method is proposed which combines the advantages of the Newton–Raphson method and Sequentially Linear Analysis. The new method is demonstrated on a proportional loading analysis but it can be naturally extended to non-proportional loading, geometrically non-linear analysis, plastic material for cyclic loading and transient analysis because of the incremental procedure.

2 GENERAL PROCEDURE OF THE NEW ALGORITHM

Incremental sequentially linear analysis is an incremental and iterative algorithm, which starts and ends with an equilibrium state. The structure state

is the displacements, velocities and accelerations of the nodes. A step in which the stiffness is reduced is called a cycle. A utilization value is defined. The utilization value is determined at the local by the stress state and the failure surface of an element with the elastic material properties. The critical element is the element that is most close to a first or next damage moment according to a saw tooth stress-strain relation similar to SLA. A utilisation function is defined as the largest utilisation value of all elements (the utilisation value of the critical element), which is a function of the load factors and the stiffness matrix. When the utilization function is larger than 1, the material is overloaded. When the utilization function is smaller than 1, the material can carry more load.

When reaching an equilibrium state, an incremental load is applied for the next load step. If the utilization value is still smaller than 1, the next incremental load is applied. Otherwise, the procedure restarts from the structure state of the previous load step, which means that the displacements are reset to the values of the previous load step. Below are two procedures in one cycle:

– Firstly, the secant stiffness of the critical element of the previous cycle is reduced by the defined stiffness reduction factor, which is the same as SLA. It is noted that the damage procedure is irreversible, which means that all stiffness reductions of the previous cycles are repeated before the current cycle in this load step. Due to these stiffness reduction procedures, the internal forces are updated based on the displacements of the previous load step and the algorithm reaches a temporary equilibrium state, which is automatically calculated by the non-linear implicit scheme with NR iterations.
– Secondly, the incremental load is applied and a linear analysis is performed for the current load step. If the incremental load is prescribed in load steps, it is referred to as *Load control method*. Here load can be both a prescribed force load increment or a prescribed displacement load increment. If the incremental load is scaled based on the reduced stiffness, it is referred to as *Load and damage control method.* The latter is especially suitable in case the problem cannot be handled in displacement control for obtaining the post-peak behavior.

In addition, there is a third algorithm called *Damage control method*. Here, the stiffness is only reduced once in the first cycle no matter how many cycles the load step has. Since the stiffness remains unchanged after the first cycle, the scaling procedure follows a linear interpolation procedure to search for the suitable load factors. It is quite similar to SLA in that the algorithm reaches an equilibrium state for every damage step and the load factors are governed by the utilization value. But the difference is that in ISLA every equilibrium state search starts from the equilibrium state of the previous "load step", which indeed is the previous damage step, instead of the origin in the total scheme of SLA. However, in *Load and damage method* the stiffness is continued to be reduced every cycle. So, the number of stiffness reductions is the same as that of the cycles in the load step.

For the *Load control method* (force control or displacement control loading), a prescribed load schedule is applied and the algorithm below is followed:

1. Save the structure state. (displacements of all nodes initially are all zero)
2. Load the structure state.
3. Apply increment load to the structure based on the loading schedule.
4. Perform a NR analysis (two involved procedures are explained before).
5. Consider all elements and calculate μ. •
6. Store μ_{max}, the maximum μ and the critical element number. •
7. If μ_{max} is smaller than 1, save the structure state and go to step 2 with next load step.
8. Reduce the stiffness of the critical element'
9. Go to step 2 with the same load increment for this load step.

   Follow this loop until all load steps are applied or the stiffness of the structure is extremely small.

For the *Load and damage control method*, a prescribed load schedule is applied and the algorithm below is followed:

1. Save the structure state (displacements of all nodes initially are all zero).
2. Load the structure state.
3. Apply increment, which can be prescribed based on a loading schedule at the beginning and then scaled especially for the post-peak, to the structure.
4. Perform a NR analysis (two involved procedures are explained before).
5. Consider all elements and calculate μ. •
6. Store μ_{max}, the maximum μ and the critical element number. •
7. If μ_{max} is smaller than 1, save the structure state and go to step 2 with next load step.
8. Reduce the stiffness of the critical element. •
9. Go to step 2 with a prescribed or a scaled load increment for this load step based on the utilization value.

   Follow this loop until all load steps are applied or the stiffness of the structure is extremely small.

For the *Damage control method*, the algorithm below is followed:

1. Save the structure state (displacements of all nodes initially are all zero).
2. Load the structure state.
3. Apply increment load to the structure (the initial load increment can be the unity load and then is determined by the utilization value similar to SLA).
4. Perform a NR analysis (two involved procedures are explained before).
5. Consider all elements and calculate μ. •
6. Store μ_{max}, the maximum μ and the critical element number. •
7. If μ_{max} is smaller than 1, save the structure state and go to step 2 with next load step.
8. If the stiffness has already been reduced in this load step, the stiffness remains unchanged, otherwise reduce the stiffness of the critical element. •
9. Go to step 2 with the scaled load factors for this load step based on the utilization value.

   Follow this loop until all load steps are applied or the stiffness of the structure is extremely small.

Step 2 to 9 is one cycle. The main difference of these three algorithms is how to reach the next equilibrium state with the procedure in Step 8 (stiffness changes) and Step 9 (load changes).

3 NOTCHED BEAM TEST

An experiment (Hordijk, 1991) is used for testing, which is a simply supported concrete beam with a notch in the middle (Figure 1). The four-point loading scheme is applied in displacement control, as shown in Figure 2.

The example considers softening for tension (Figure 3). The concrete properties are E = 32000 MPa, Poisson's ratio v = 0.2, tensile strength f_t = 3 MPa, fracture energy G_f = 0.06 N/mm. The compressive behaviour is elastic. Eq. (1) is used to determine the ultimate strain ε_u for different element sizes.

$$\varepsilon_u = \frac{2G_f}{f_t h} \tag{1}$$

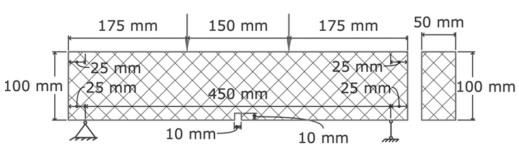

Figure 1. Test model of notched beam.

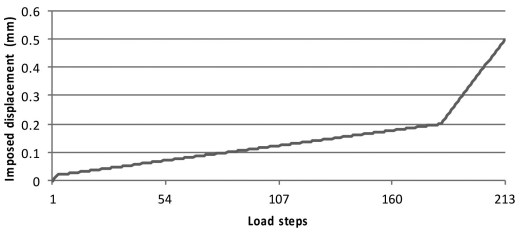

Figure 2. Load schedule (displacement load steps 0.01(2) 0.001(180) 0.01(30)).

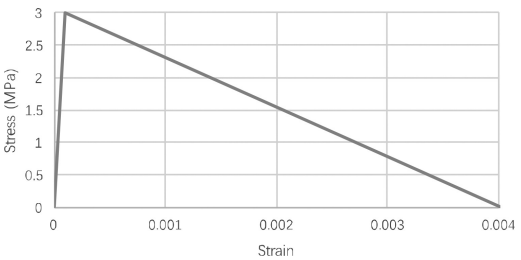

Figure 3. Tensile stress-strain curve for the concrete.

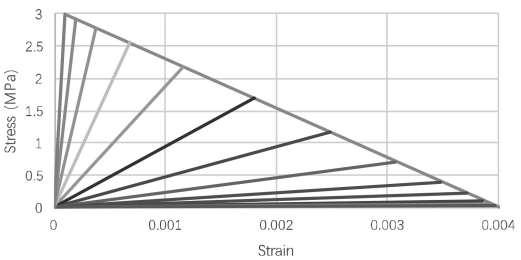

Figure 4. Sequentially reduced stiffness to 50% of the previous value.

where h is the element size.

Figure 4 shows the analysis steps when Young's modulus is sequentially reduced to 50% of the previous value. In the test cases sequential reductions to only 90% of the previous values have been used. This has not been displayed because it makes an unclear picture. The colour range of all principal strain contours below is defined in relation to the concrete's tensile softening behaviour values (Figure 5).

Four-node plane-stress elements are used. The element size is 10 mm. Just one integration point is used in the elements above the notch while the other elements have 4 integration points. Only the elements above the notch can be damaged, and others are kept elastic. Figure 6 identifies 9 elements ahead of the notch. For Element 1, 3, 6 and 8, detailed results will be shown.

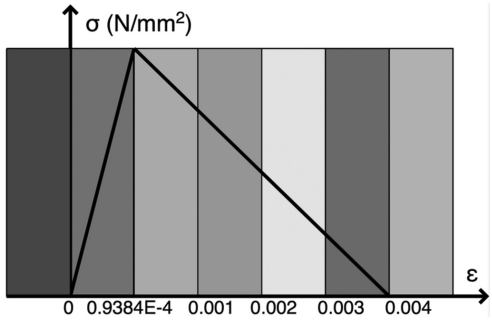

Figure 5. Colour range of principal strain contour.

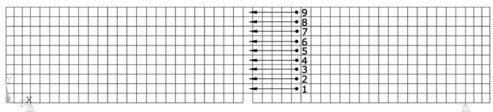

Figure 6. Element numbers.

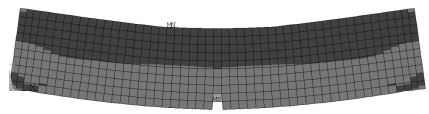

7a. Load step 16 and the maximum displacement is 0.04 mm

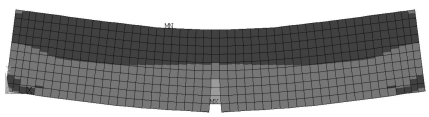

7b. Load step 39 and the maximum displacement is 0.07 mm

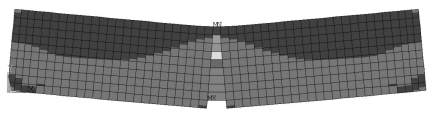

7c. Load step 59 and the maximum displacement is 0.12 mm

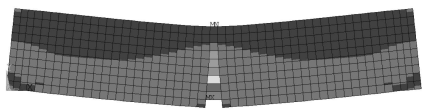

7d. Load step 79 and the maximum displacement is 0.17 mm

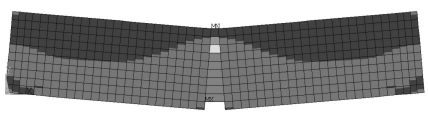

7e. Load step 100 and the maximum displacement is 0.22 mm

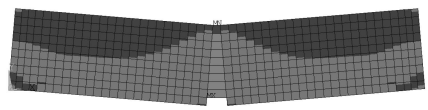

7f. Load step 194 and the maximum displacement is 0.60 mm

Figure 7. X direction strain contour for different load steps.

Figure 7 shows the deformation and damage for 6 values of the load. It is observed that the crack starts at the notch and slowly grows upwards. The x-direction strain contour is used to show the damage process.

Figure 8 shows the force displacement diagram for all 213 load steps (midspan and loading position separately). The selected steps are indicated for the post-processing. Figure 9 shows the stress-strain result for element 1. The blue dots show the principal stress and principal strain in the element integration point for all 213 load steps. Strains larger than 0.005 are not displayed. The red line is the defined envelope of the material tensile stress-strain curve. The dots are sometimes below the curve because the crack grows in small jumps which causes local unloading. If the load steps and sub-steps would be infinitely small, then all blue dots would be exactly on the red curve. In real tests the cracks also grow in small jumps but this is related to material inhomogeneity instead of computational stiffness step size. The boxes labelled a to d are zoomed-in in Figure 10.

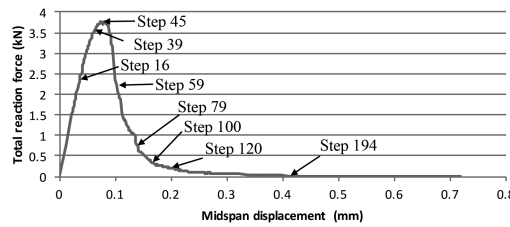

8a. The displacements are selected from the bottom of the beam midspan

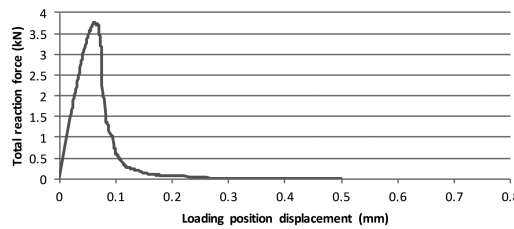

8b. The displacements are selected from the loading position

Figure 8. Load displacement diagram of the notched beam test.

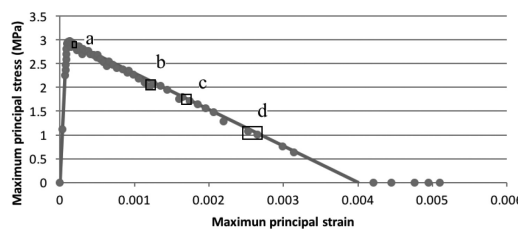

Figure 9. Stress strain results for element 1.

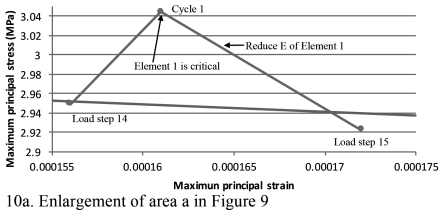

10a. Enlargement of area a in Figure 9

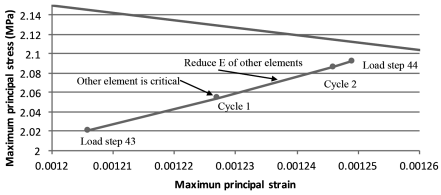

10b. Enlargement of area b in Figure 9

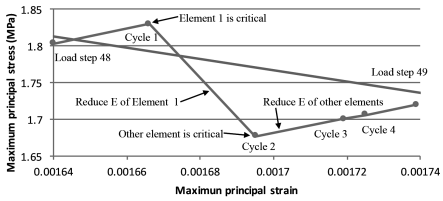

10c. Enlargement of area c in Figure 9

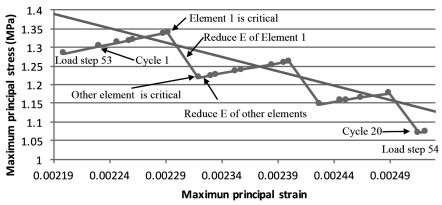

10d. Enlargement of area d in Figure 9

Figure 10. Enlargement of Figure 9.

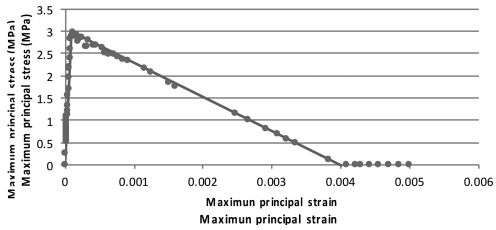

Figure 11. Stress strain results for element 3.

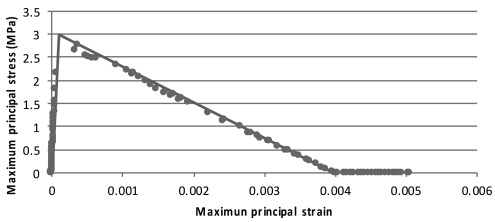

Figure 12. Stress strain results for element 6.

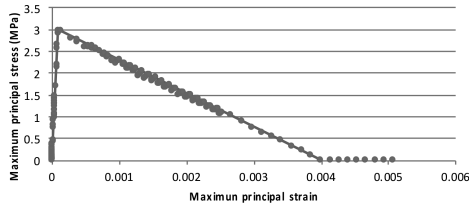

Figure 13. Stress strain results for element 8.

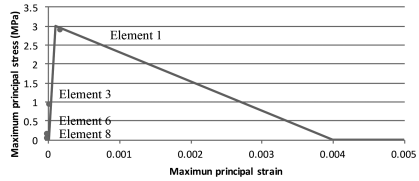

14a. Load step 16

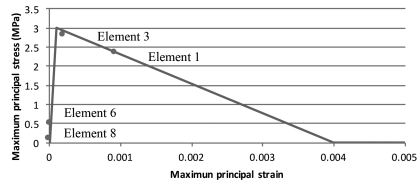

14b. Load step 39

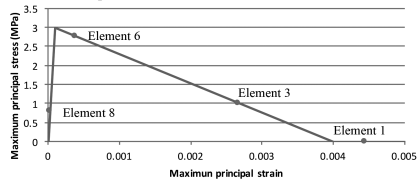

14c. Load step 59

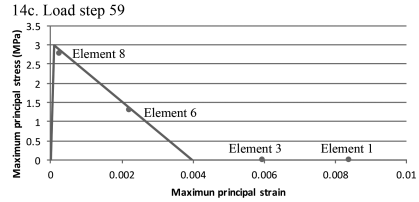

14d. Load step 79

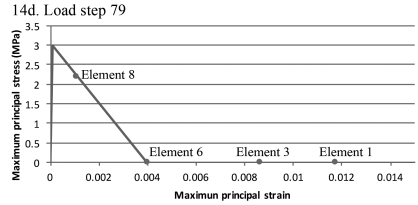

14e. Load step 100

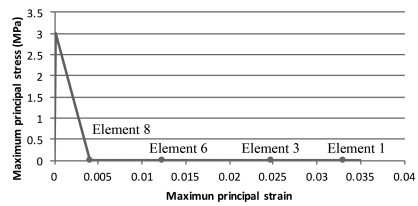

14f. Load step 194

Figure 14. 4 element results for different load steps.

Figure 10 shows the development of cycles in the four load steps indicated as a to d on the stress-strain curve in Figure 9. The Figure shows how the present algorithm works going from one equilibrium state to another. Figure 10 shows the stress redistribution procedure and the difference between a stiffness reduction in element 1 and a stiffness reduction in another element or other elements. When element 1 is the critical element, the stiffness of element 1 is reduced and its stress decreases. When another element is critical, the stiffness of element 1 remains constant and its stress increases. In a similar way, the results of elements 3, 6 and 8 are shown in Figures 11 to 13 respectively.

Figure 14 shows the stress and strain situations of the considered elements at 6 load steps. It can be observed the damaging progresses correctly and sequentially along the material curve. These figures can be compared to the crack patterns in Figure 7.

Figure 15 shows the number of cycles for all load steps. It can be seen that Load step 59 has the maximum number of cycles (162) when the capacity drops from the peak. The critical element number fluctuates from 1 to 6 shown in Figure 16 for Load step 59. Element 1 remains critical in the most of cycles. Figure 17 shows the displacement (midspan and loading position) versus total reaction force curve including results of all cycles in Load step 59. The reaction force keeps decreasing while the midspan displacement remains constant and then descends periodically in Figure 17a and the displacement at the loading position stays the same.

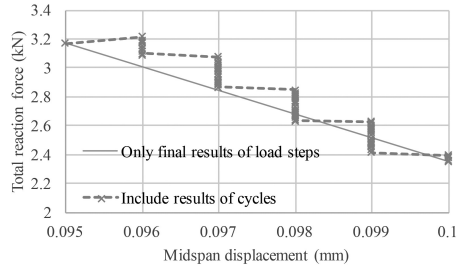

17a. The displacements are selected from the bottom of the beam midspan

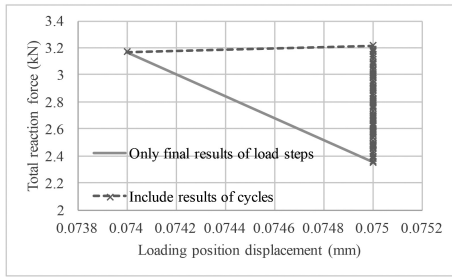

17b. The displacements are selected from the loading position

Figure 17. Displacement force diagram of all cycles in Load step 59.

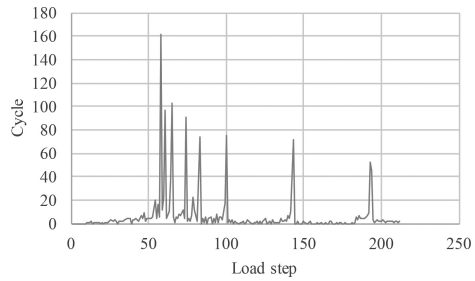

Figure 15. Cycle number of every load step.

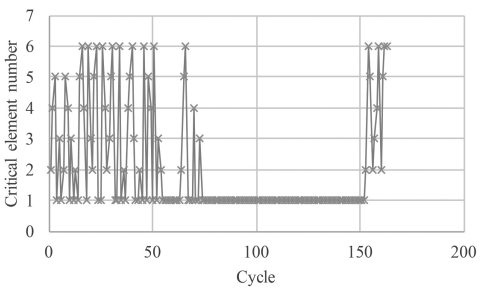

Figure 16. Critical element number of every cycle in Load step 59.

4 CONCLUSIONS

The principle, algorithms and search paths of incremental sequentially linear analysis are shown and demonstrated in this paper. This method is incremental; each increment starts and ends with an equilibrium state. The solution search path follows displacement history and damage cycles sequentially with secant stiffness rather than guidance by numerical parameters. Three methods are described in this paper. Here *Load control method* has been demonstrated for a four-point loaded notched beam. The effectiveness of the scheme with cycles has been illustrated in detail for a number of typical prescribed load steps. Plots of the number of cycles per load step, element criticality and stress-strain jumps illustrate the searching path. For the example considered, the method has a similar high robustness as SLA. Non-proportional loading can be analysed without modifications. There is no

restriction on the load definition; load cases can be applied and removed simultaneously or separately. The method is an incremental procedure and can be extended to include geometrical non-linearity.

REFERENCES

Al-Sabah, A.S. and D.F. Laefer (2016). Use of negative stiffness in failure analysis of concrete beams. Engineering Structures, 126:187–199, 2016.

Alnaas, W.F., A.D. Jefferson (2016). A smooth unloading--reloading approach for the nonlinear finite element analysis of quasi-brittle materials. *Engineering Fracture Mechanics* 152 (2016) 105–125.

Borst, R.D., M.A. Crisfield, J.J.C. Remmers, and C.V. Verhoosel (2012). *Nonlinear finite element analysis of solids and structures*. John Wiley & Sons, 2012.

Chenjie Yu, P.C.J. Hoogenboom, J.G. Rots (2016), Algorithm for non-proportional loading in sequentially linear analysis. 9th International Conference on Fracture Mechanics of Concrete and Concrete Structures, UC Berkeley, 2016.

DeJong, M.J., M.A.N. Hendriks, J.G. Rots (2008). Sequentially linear analysis of fracture under non-proportional loading. *Engineering Fracture Mechanics* 75 (2008) 5042–5056.

Eliáš, J. (2015), Generalization of load–unload and force-release sequentially linear methods. *International Journal of Damage Mechanics* 2015, Vol. 24(2) 279–293.

Eliáš, J., P. Frantík, M. Vořechovský (2010), Improved sequentially linear solution procedure. *Engineering Fracture Mechanics* 77 (2010) 2263–2276.

Giardina, G., A. Graaf, M.A.N. Hendriks, J.G. Rots, and A. Marini (2013). Numerical analysis of a masonry façade subject to tunnelling-induced settlements. *Engineering structures*, 54:234–247, 2013.

Graça-e-Costa, R., J. Alfaiate, D. Dias-da-Costa, L.J. Sluys (2012), A non-iterative approach for the modelling of quasi-brittle materials. *International Journal of Fracture* (2012) 178:281–298.

Hordijk, D.A. (1991), *Local approach to fatigue of concrete*, PhD Dissertation, Delft University of Technology, ISBN 90-9004519-8.

Pierre Ladeveze (2012). Nonlinear computational structural mechanics: new approaches and non-incremental methods of calculation. Springer Science & Business Media, 2012.

Rots, J.G. (2001). Sequentially linear continuum model for concrete fracture. *Fracture Mechanics of Concrete Structures*, 13, 2001.

Rots, J.G. and S. Invernizzi (2004). Regularized sequentially linear saw- tooth softening model. *International Journal for Numerical and Analytical Methods in Geomechanics*, 28(7–8):821–856, 2004.

Rots, J.G., B. Belletti, and S. Invernizzi (2008). Robust modeling of rc structures with an "event-by-event" strategy. *Engineering Fracture Mechanics*, 75(3): 590–614, 2008.

Slobbe, A.T., M.A.N. Hendriks, and J.G. Rots (2012). Sequentially linear analysis of shear critical reinforced concrete beams without shear reinforcement. *Finite Elements in Analysis and Design*, 50:108–124, 2012.



Taylor & Francis
Taylor & Francis Group
http://taylorandfrancis.com

Computational Modelling of Concrete Structures – Meschke, Pichler & Rots (Eds)
© 2018 Taylor & Francis Group, London, ISBN 978-1-138-74117-1

Cohesive crack model in discontinuous Galerkin method

Jan Jaśkowiec
Faculty of Civil Engineering, Institute for Computational Civil Engineering, Cracow University of Technology, Cracow, Poland

ABSTRACT: The crack growth analysis in quasi-brittle material is analysed using discontinuous Galerkin (DG) method. It is natural for the DG methods that traction forces on the mesh skeleton (inter-elements boundaries) have to be applied in the numerical model. The cohesive crack model is directly applied to the skeleton tractions that, in consequence, an enhanced numerical model is obtained for modelling multiple cracks propagations. In the paper the standard traction-separation law is transformed to the adequate softening relation in the traction-strain space. Then the secant Young's modulus is derived which is directly applied to the numerical model. The incremental-iterative scheme is used to model the crack growing through the domain. The method is illustrated with examples where the three-point bending beam is considered.

1 INTRODUCTION

The discontinuous Galerkin method (DG) is applied in this paper for the crack growth analysis in the quasi-brittle material. A cohesive crack model is applied to the numerical model with the help of traction-separation law.

The DG method uses approximation that is discontinuous on the finite element mesh. The discontinuities are located at the mesh skeleton (the interelement boundaries). In spite of the discontinuities the final solution of the DG method is continuous. The DG method require integration along the mesh skeleton to enforce the continuity of the solution. There are many versions of the DG method such as interior penalty DG (IPDG) (Hoppe et al. 2009), local DG (LDG) (Guo et al. 2017) or hybridizable DG (HDG) (Giorgiani et al. 2014) and many others. However, in this paper the DG method with finite difference relations (DGFD) is used which was presented in (Jaśkowiec 2017b, Jaśkowiec et al. 2016). In the DGFD method the compatibility conditions on the mesh skeleton are based on the physical model of the considered material. That is why it is quite easy to apply the physical model of the cohesive crack model at the mesh skeleton and to perform the crack growth analysis. For the sake of clarity the numerical model presented in this paper is called CFDG method, what means cohesive fracture analysis using DG method.

The numerical modelling of the crack growth can be performed using the gradient damage models (Marigo et al. 2016) or using the discrete crack model which usually is applied by XFEM (Jaśkowiec and van der Meer 2014). The numerical model presented in this paper uses the discrete crack description, but also it has a lot of common wit the damage model. There is no need to define criterion for crack growth or the direction of the growth in the FDG method. It is natural for CFDG method to model multiple cracks, branching cracks or mutually crossing cracks.

The DG method has been already used for crack analysis, e.g. (Bird et al. 2017, Engwer and Schumacher 2017, Nguyen 2014, Wu et al. 2014). The CFDG method uses new approach that differs from the other ones known from literature. In the CFDG method the traction-separation law of the cohesive crack model is utilized for evaluation of the secant Young's modulus on the mesh skeleton. It leads to non-linear numerical model in which the secant stiffness matrix is used for incremental-iterative procedure.

The numerical model of the CFDG method has to deal with discontinuous approximation on the mesh skeleton. For the mathematical description of the discontinuities the jumps as well as mean values have to be defined. The value of the discontinuity jump is described by the following discontinuity operators, which are defined with the help of a normal vector $\mathbf{n}^d$ to the mesh skeleton. The discontinuity operators for an arbitrary function g are defined as follows

$$\begin{aligned} [[g]]_\epsilon(\mathbf{x}) &= g(\mathbf{x}+\epsilon\mathbf{n}^d) - g(\mathbf{x}-\epsilon\mathbf{n}^d) \\ [[g]](\mathbf{x}) &= \lim_{\epsilon\to 0}[[g]]_\epsilon(\mathbf{x}) \end{aligned} \quad \text{for } \mathbf{x}\in S^d \qquad (1)$$

where ϵ is an auxiliary scalar parameter.

The mean value of the discontinuity for the same function g are defined as

$$\begin{aligned}&\langle g\rangle_{\epsilon}(\mathbf{x})=\frac{1}{2}\left(g\left(\mathbf{x}+\epsilon\mathbf{n}^{d}\right)+g\left(\mathbf{x}-\epsilon\mathbf{n}^{d}\right)\right) \quad \text{for } \mathbf{x}\in S^{d}\\ &\langle g\rangle(\mathbf{x})=\lim_{\epsilon\to 0}\langle g\rangle_{\epsilon}(\mathbf{x})\end{aligned} \tag{2}$$

The mathematical model of two-dimensional (2D) elasticity problem for the DGFD method is presented in Section 2. In the CFDG method the traction-separation relation has to be transformed in a special way so that the softening model with the secant Young's modulus is evaluated, what is shown in Section 3. In the Section 4 the approximation is constructed that is discontinuous on the mesh skeleton. Some examples are presented in Section 5. The paper ends with some conclusions.

2 MATHEMATICAL MODEL OF DGFD METHOD

The CFDG method, that is used for the crack analysis, is based on the DGFD method which has been developed to solve continuous problems. Thus firstly the scheme for the DGFD method is presented. Subsequently the method will be developed to CFDG method by introduction non-linear relations for the skeleton tractions.

The analysis of the crack growth in the quasi-brittle materials using the discontinuous Galerkin methods starts with the standard equilibrium equation (momentum balance) on the two-dimensional (2D) domain V and the appropriate boundary conditions on the outer boundary S:

$$\begin{aligned}&\operatorname{div}\boldsymbol{\sigma}+\mathbf{b}=\mathbf{0} \qquad \text{in } V\\ &\boldsymbol{\sigma}\mathbf{n}=\hat{\mathbf{t}} \quad \text{on } S^{\sigma}, \quad \mathbf{u}=\hat{\mathbf{u}} \quad \text{on } S^{u}\end{aligned} \tag{3}$$

where $\boldsymbol{\sigma}$ the stress tensor, $\mathbf{b}$ is the body force vector, $\hat{\mathbf{t}}$ is the prescribed traction forces vector, $\mathbf{u}$ is the relative displacement vector and $\hat{\mathbf{u}}$ is the prescribed displacement vector, S^{σ} and S^{u} are the parts of the outer boundary on which the first and second types of the boundary conditions are defined, respectively.

The equation (3) is supplemented by the Hooke's law

$$\boldsymbol{\sigma}=\mathbf{E}:\varepsilon \tag{4}$$

where ε is the Cauchy strain tensor and $\mathbf{E}$ is the fourth order Hooke's tensor for 2D plain-stress state.

In the DG method the approximation discontinuities on the mesh skeleton S^{d} have to be taken into account in the problem formulation. For future calculations the local coordinates associated with S^{d} are specified. They are based on two unit vectors: ($\mathbf{n}^{d}$, $\mathbf{s}^{d}$), where $\mathbf{n}^{d}$ is normal to S^{d} and $\mathbf{s}^{d}$ is unit vectors tangent to S^{d}. The skeleton local coordinates are illustrated in Fig. 1.

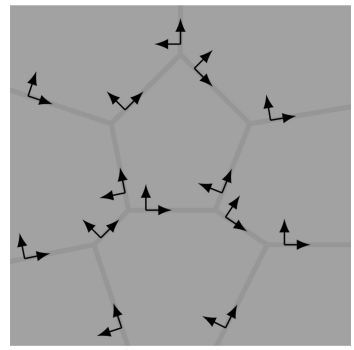

Figure 1. Local coordinates on the skeleton.

The weak form of the mechanical problem from eq. (3) is constructed with the vector test function $\mathbf{v}$

$$\int_{V}\mathbf{v}\cdot\operatorname{div}\boldsymbol{\sigma}\,\mathrm{d}V+\int_{V}\mathbf{v}\cdot\mathbf{b}\,\mathrm{d}V=0 \quad \forall\mathbf{v} \tag{5}$$

The integration by parts of the first term in equation (5) results in the following equation

$$\begin{aligned}&\int_{S^{\sigma}}\mathbf{v}\cdot\hat{\mathbf{t}}\,\mathrm{d}S+\int_{S^{u}}\mathbf{v}\cdot\mathbf{t}\,\mathrm{d}S-\int_{S^{d}}[\![\mathbf{v}]\!]\cdot\mathbf{t}\,\mathrm{d}S\\ &-\int_{V}\nabla\mathbf{v}:\boldsymbol{\sigma}\,\mathrm{d}V+\int_{V}\mathbf{v}\cdot\mathbf{b}\,\mathrm{d}V=0\end{aligned} \tag{6}$$

The integral over the mesh skeleton comes directly from the fact that both the trial and test functions are discontinuous at the skeleton. In consequence the vector of traction forces at the mesh skeleton need to be evaluated. Following the procedure presented in (Jaśkowiec 2017a) it can be shown that the tractions at the skeleton may be expressed as follows

$$\begin{aligned}\mathbf{t}=&\mathbf{E}_{1}^{d}[\![\mathbf{u}]\!]_{w}\\ &+\mathbf{E}_{2}^{d}:\langle\nabla\mathbf{u}\rangle_{w}+\mathbf{E}_{3}^{d}:\langle\nabla\mathbf{u}\rangle\end{aligned} \quad \text{on } S^{d} \tag{7}$$

where $\mathbf{E}_{i}^{d}$ are the appropriate parts of the Hooke's tensor, which definitions are as follows:

$$\mathbf{E}_{1}^{d}=\frac{3}{4w}\left(\frac{E}{1-v^{2}}\mathbf{I}-\frac{Ev}{1-v^{2}}\mathbf{s}^{d}\otimes\mathbf{s}^{d}\right) \tag{8}$$

$$\begin{aligned}\mathbf{E}_{2}^{d}=-\frac{1}{2}\Bigg[&\frac{E}{1-v^{2}}\left(\mathbf{n}^{d}\otimes\mathbf{n}^{d}\otimes\mathbf{n}^{d}\right)\\ &+\frac{E(1-v)}{1-v^{2}}\left(\mathbf{s}^{d}\otimes\mathbf{s}^{d}\otimes\mathbf{n}^{d}\right)\Bigg]\end{aligned} \tag{9}$$

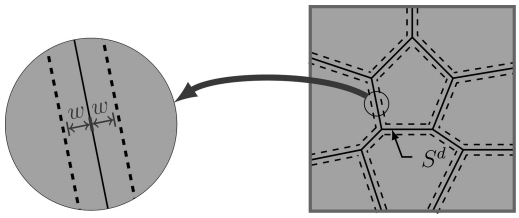

Figure 2. Distance w from the skeleton.

$$\mathbf{E}_3^d = \left[\frac{Ev}{1-v^2}\left(\mathbf{n}^d \otimes \mathbf{I} - \mathbf{n}^d \otimes \mathbf{n}^d \otimes \mathbf{n}^d\right) + \frac{E(1-v)}{1-v^2}\left(\mathbf{s}^d \otimes \mathbf{n}^d \otimes \mathbf{s}^d\right)\right] \tag{10}$$

The scalar parameters w from eqs. (7) and (8) plays a role of stability parameter. The parameters defines the small distance along the whole mesh skeleton, as illustrated in Fig. 2. In calculations the parameter has to be set about $w \approx 10^{-4} h$, where h is the characteristic size of the finite element.

The problem formulation presented in eq. (6) requires also the evaluation of tractions vector on the Dirichlet boundary. That vector has also been proposed in (Jaśkowiec 2017a), and reads as follows

$$\mathbf{t} = \mathbf{E}_1^b \hat{\mathbf{u}} - \mathbf{E}_1^b \mathbf{u} + \mathbf{E}_2^b : \nabla \mathbf{u} - \mathbf{E}_3^b : \nabla \mathbf{u}\left(\mathbf{x}_w\right) - \mathbf{E}_4^b : \nabla \mathbf{u}\left(\mathbf{x}_{2w}\right) \quad \text{on } S^u \tag{11}$$

where the tensors $\mathbf{E}_i^b$ are defined as follows

$$\mathbf{E}_1^b = \frac{3}{w}\left(\frac{E}{1-v^2}\mathbf{I} - \frac{Ev}{1-v^2}\mathbf{s}\otimes\mathbf{s}\right) \tag{12}$$

$$\mathbf{E}_2^b = \left[\frac{Ev}{1-v^2}\left(\mathbf{n}\otimes\mathbf{s}\otimes\mathbf{s}\right) + \frac{E(1-v)}{1-v^2}\left(\mathbf{s}\otimes\mathbf{n}\otimes\mathbf{s}\right)\right] \tag{13}$$

$$\mathbf{E}_3^b = 4\left[\frac{E}{1-v^2}\left(\mathbf{n}\otimes\mathbf{n}\otimes\mathbf{n}\right) + \frac{E(1-v)}{1-v^2}\left(\mathbf{s}\otimes\mathbf{s}\otimes\mathbf{n}\right)\right] \tag{14}$$

$$\mathbf{E}_4^b = \frac{1}{4}\mathbf{E}_3^b \tag{15}$$

In eqs. (8)–(10) and (12)–(14) E is the Young's modulus and v is the Poisson's ratio.

3 COHESIVE ZONE MODEL

The CFDG method is constructed when the cohesive crack model is applied at the mesh skeleton to the DGFD method. In this section the scheme for the secant Young's modulus used in the CFDG method.

In the numerical model presented in this paper the crack propagates along segments of the mesh skeleton. That is why the cohesive crack model has to be applied to the tractions at the mesh skeleton, see eq. (7). The cohesive zone models are usually presented in the form of the traction separation laws where the normal components of crack tractions and crack opening values are given, e.g. (Gálvez et al. 2013, Nagashima and Sawada 2016). Such laws are parametrized by tensile strength f_t and fracture energy G_F. In this paper the traction-separation law has to be transformed to the softening law. In the softening law the values of the normal tractions are described in relation to the normal component of the strain tensor. In Fig. 3 such transformation is illustrated in which $t_n = \mathbf{t}\cdot\mathbf{n}^d$ and $\delta_n = [\![\mathbf{u}]\!]\cdot\mathbf{n}^d$. The softening law is also parametrized by two components: tensile strength and fracture energy density G_f.

For the purpose of the cohesive law, the normal component of the strains on the mesh skeleton can be directly evaluated by the following relation

$$\varepsilon_n = \frac{[\![\mathbf{u}]\!]_w \cdot \mathbf{n}^d}{2w} \tag{16}$$

The strain value ε_n^t can be evaluated directly from the one-dimensional Hooke's relation, while ε_n^c is evaluated with the help of the critical crack opening value δ_n^c :

$$\varepsilon_n^t = \frac{f_t}{E}, \quad \varepsilon_n^c = \varepsilon_n^t + \frac{\delta_n^c}{2w} \tag{17}$$

On the other hand the value δ_n^c can be expressed as

$$\delta_n^c = \frac{2G_F}{f_t} \tag{18}$$

The softening law presented in Fig. 3(b) may be applied with the help of the secant Young's

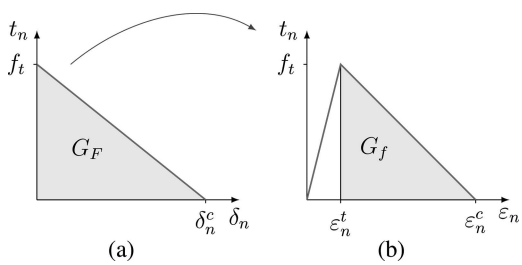

Figure 3. Transformation from the traction-separation law to softening law.

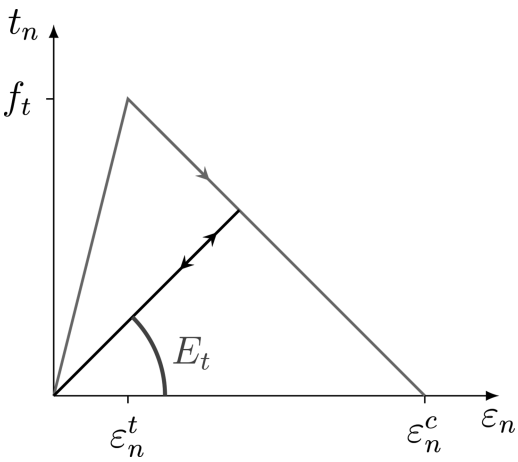

Figure 4. Transformation from the traction-separation law to softening law.

modulus E_t. The E_t depends on the current value of ε_n what is illustrated on Fig. 4. The mathematical description of the secant modulus is expressed as follows

$$E_t = \begin{cases} E & \text{for } \kappa < \varepsilon_n^t \\ E\dfrac{\varepsilon_n^c}{\varepsilon_n^c - \varepsilon_n^t}\cdot\left(\dfrac{\varepsilon_n^c}{\kappa} - 1\right) & \text{for } \kappa \in \left(\varepsilon_n^t, \varepsilon_n^c\right) \\ 0 & \text{for } \kappa > \varepsilon_n^c \end{cases} \tag{19}$$

where κ keeps the maximum value of ε_n from the history of the process. In the crack growth analysis the material Young's modulus has been substituted by the secant modulus in eqs. (8)–(10) and (12)–(14).

4 APPROXIMATION

In DG method arbitrary basis functions for the approximation in finite elements can be applied, see (Jaśkowiec 2017b, Luo, Baum, & Lhner 2008). However, the polynomial approximation is most universal and can be successfully applied to every kind of a problem. In particular, the Chebyshev or Legendre polynomials can be chosen as basis functions for approximation in finite elements. In this work the Chebyshev basis functions are applied to arbitrary polygonal finite elements as well as to rectangular ones (Jaśkowiec et al. 2016).

Approximation in the e-th single finite element is constructed with the help of the element local basis functions and the local degrees of freedom

$$u_\alpha^e(\mathbf{x}) = \sum_{i=1}^{n_e} b_i^e(\mathbf{x})\,(\check{\mathbf{u}}_\alpha^e)_i = \mathbf{b}^e\,\check{\mathbf{u}}_\alpha^e \qquad \text{for } \mathbf{x} \in V^e \text{ and } \alpha = x, y \tag{20}$$

where u_α^e is the displacement in the e-th element into the x or y direction, $\check{\mathbf{u}}_\alpha^e$ is the element degrees of freedom vector for the e-th element for α direction, $\mathbf{b}^e$ is the vector of the e-th element basis functions. The basis functions are defined in the cell local coordinates scaled to the sizes of the cells, i.e.:

$$x^e = \frac{x - x_m^e}{0.5\,h_x^e}, \quad y^e = \frac{y - y_m^e}{0.5\,h_y^e} \tag{21}$$

where the point $\left(x_m^e, y_m^e\right)$ is the centre of gravity of the e-th element cell and h_x^e, h_y^e are the characteristic lengths of the e-th cell in the x and y directions, respectively.

The definition of the Chebyshev functions are well known, but for the sake of clarity the recursive definition of Chebyshev functions is quoted

$$\begin{aligned} &T_0(\xi) = 1, \qquad T_1(\xi) = \xi, \\ &T_{n+1}(\xi) = 2\cdot\xi\cdot T_n(\xi) - T_{n-1}(\xi) \end{aligned} \tag{22}$$

Eq. (20) presents the approximation for one element cell. It can be rewritten for the displacement vector approximation in the whole domain

$$\mathbf{u} = \mathbf{\Phi}\check{\mathbf{u}}, \qquad \text{for } \mathbf{x} \in V \tag{23}$$

where $\check{\mathbf{u}}$ is the vector of displacement degrees of freedom for the whole mesh and $\mathbf{\Phi}$ is the displacement approximation matrix also for the whole mesh.

The jumps and mid-values are approximated using the same vector of degrees of freedom, i.e.

$$[\![\mathbf{u}]\!] = [\![\mathbf{\Phi}]\!]\check{\mathbf{u}}, \quad \langle\mathbf{u}\rangle = \langle\mathbf{\Phi}\rangle\,\check{\mathbf{u}} \qquad \text{on } S^d \tag{24}$$

In the same way the approximation of the jump and mean values at distance ϵ from S^d are defined

$$[\![\mathbf{u}]\!]_\epsilon = [\![\mathbf{\Phi}]\!]_\epsilon\check{\mathbf{u}}, \quad \langle\mathbf{u}\rangle_\epsilon = \langle\mathbf{\Phi}\rangle_\epsilon\,\check{\mathbf{u}} \tag{25}$$

This paper considers the Galerkin formulation, therefore the same approximations as in the equations (23), (24) and (25) are applied to the test function $\mathbf{v}$.

Finally the secant linear system of equations is obtained that has the form

$$\mathbf{K}\check{\mathbf{u}} = \mathbf{F} \tag{26}$$

where

$$\mathbf{K} = \int_V \mathbf{B}^{\mathrm{T}} : \mathbf{E} : \mathbf{B}\, \mathrm{d}V + \int_{S^u} \boldsymbol{\Phi}^{\mathrm{T}} \mathbf{E}_1^b \boldsymbol{\Phi}\, \mathrm{d}S - \int_{S^u} \boldsymbol{\Phi}^{\mathrm{T}} \mathbf{E}_2^b : \mathbf{B}\, \mathrm{d}S + \int_{S^u} \boldsymbol{\Phi}^{\mathrm{T}} \mathbf{E}_3^b : \mathbf{B}(\mathbf{x}_w)\, \mathrm{d}S + \int_{S^u} \boldsymbol{\Phi}^{\mathrm{T}} \mathbf{E}_4^b : \mathbf{B}(\mathbf{x}_{2w})\, \mathrm{d}S + \int_{S^d} [\![\boldsymbol{\Phi}]\!]^{\mathrm{T}} \mathbf{E}_1^d [\![\boldsymbol{\Phi}]\!]_w\, \mathrm{d}S - \int_{S^d} [\![\boldsymbol{\Phi}]\!]^{\mathrm{T}} \mathbf{E}_2^d : \langle \mathbf{B} \rangle_w\, \mathrm{d}S + \int_{S^d} [\![\boldsymbol{\Phi}]\!]^{\mathrm{T}} \mathbf{E}_3^d : \langle \mathbf{B} \rangle \mathrm{d}S \tag{27}$$

$$\mathbf{F} = \int_V \boldsymbol{\Phi}^{\mathrm{T}} \mathbf{b}\, \mathrm{d}V + \int_{S^\sigma} \boldsymbol{\Phi}^{\mathrm{T}} \hat{\mathbf{t}}\, \mathrm{d}S + \int_{S^u} \boldsymbol{\Phi}^{\mathrm{T}} \mathbf{E}_1^b \hat{\mathbf{u}}\, \mathrm{d}S \tag{28}$$

where $\mathbf{B} = \nabla\boldsymbol{\Phi}$.

The solution algorithm for the crack growth analysis require the incremental-iterative scheme. In the scheme in each incremental step the value of the external load is set in such a way, that the required value of the displacement of a specific point is obtained. The secant stiffness matrix depends on the current displacement vector, so the matrix has bo be updated each time the new displacement vector is calculated. In the iterative procedure the equilibrium state has to be found.

5 EXAMPLES

In this paper the three-point bending beam is considered. The geometry and boundary conditions are shown in Fig. 5. The notch in the beams is 25 mm long. The following material parameters have been used in the analysis: E = 37.4 GPa, $\nu = 0.3$, $f_t = 3.5$ MPa and $G_F = 0.16$ N/mm.

The bending beam has been analysed in different contexts where the properties of the CFDG method for fracture analysis have been presented. In the first test, Section 5.1 the numerical test is shown where different values of the Young's modulus for compression and tension have been applied on the mesh skeleton. Subsequently, the single crack growth analysis is presented. In this case the beam is notched, so the crack starts to growth just from the notch. The different situation is shown in Section 5.3 where the beam is not notched. It means that there is no initial source of the failure. In that case multiple cracks appears during the analysis before the one dominant crack starts to propagates.

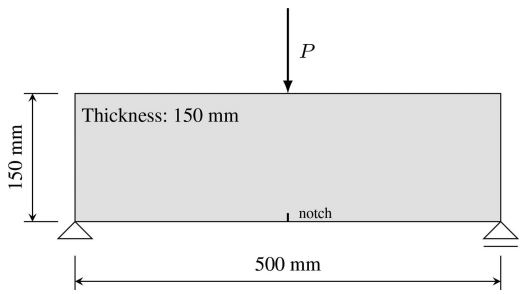

Figure 5. Three-point bending beam.

5.1 *Numerical test example*

It is assumed in this numerical test that the Young's modulus on the mesh skeleton is different for compression and for tension. For the tension the modulus is reduced 10^{-6} times in relation to the compression modulus, see Fig. 6. In calculations the mesh with 500 polygonal elements, Fig. 7, has been used. In each of the element the approximation of the fourth order has been applied.

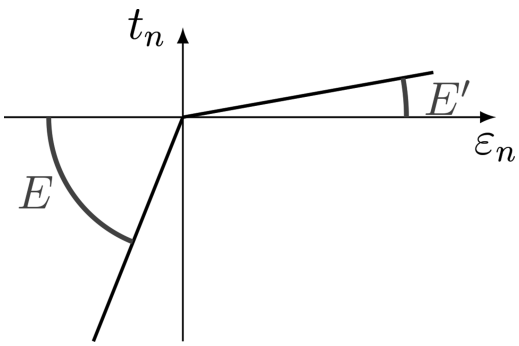

Figure 6. Young's modulus applied in the numerical example: $E' = 10^{-6}E$.

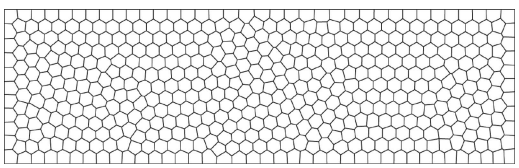

Figure 7. Mesh with 500 polygonal elements.

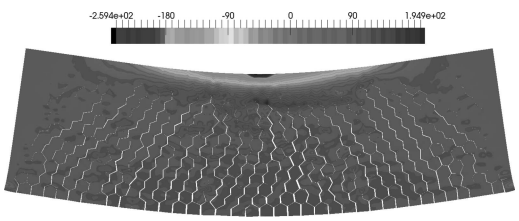

Figure 8. Map of σ_{xx} on the deformed domain in the numerical example.

The results are shown in the form of the σ_{xx} map on the deformed domain, Fig. 8. It can be noticed that due to very soft connections on tensions the deformed beam is cracked all over the domain. It shows that the CFDG method can easily cope with multiple cracks. The cracks may branched or they can cross each other.

5.2 *Crack growth in notched beam*

In this case the beam with a notch is considered. The notch causes the imperfection in the beam and so the single crack starts to grow from the notch. For the calculations the structured mesh with rectangular finite elements is used which is shown in Fig. 9.

The crack starts to growth at the notch and propagates straight up to the loading point. The equilibrium path in relation of the external load P to the vertical displacement at the loading point (LDP) is shown in Fig. 10. The curve has the typical shape for the failure procedure. It reaches the maximum value P = 18 kN for LDP 0.081 mm. The obtained path is with great agreement with the path obtained e.g. in (Asferg, Poulsen, & Nielsen 2007). On the equilibrium path four points are marked; two before and after the curve top, one

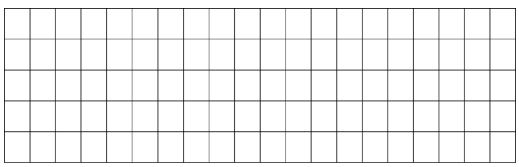

Figure 9. Structured mesh with 100 rectangular finite elements.

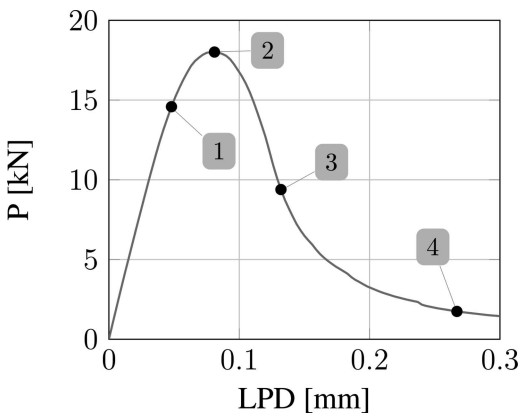

Figure 10. Equilibrium path in load versus LDP for cracking of the notched beam.

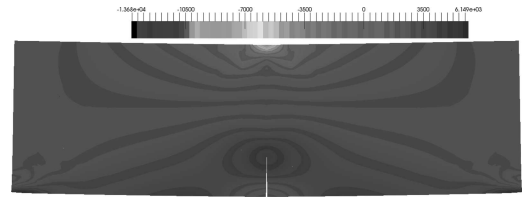

Figure 11. Map of σ_{xx} on the deformed beam at the stage 1 marked in Fig. 10.

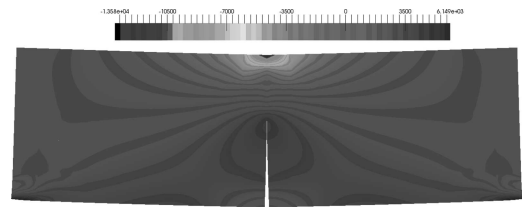

Figure 12. Map of σ_{xx} on the deformed beam at the stage 2 marked in Fig. 10.

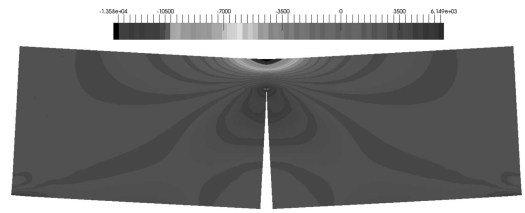

Figure 13. Map of σ_{xx} on the deformed beam at the stage 3 marked in Fig. 10.

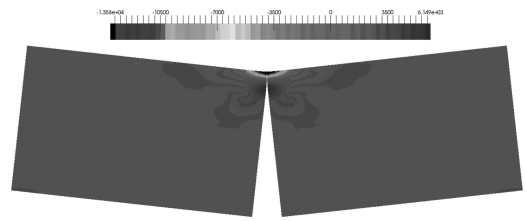

Figure 14. Map of σ_{xx} on the deformed beam at the stage 4 marked in Fig. 10.

at the top of curve and the fourth one close to the final stage of the failure process. The maps of the σ_{xx} stress on the deformed beams for these four points are shown in Figs. 11–14.

5.3 *Crack growth in plain beam*

The failure analysis of the plain three-point bending beam is considered in this example. The beam is not notched, so the crack growth is not a priori ini-

tiated. During the bending process the lower part of the beam is stretched and so the tensile stresses dominates in the part. When the tensile stresses exceed the values of tensile strength the material start to softening. In the numerical model which is based on the CFDG method, the softening of the material is modelled on the mesh skeleton. Eventually, a one discrete crack is initiated that propagates through the beam in the failure process.

The equilibrium path is shown in Fig. 15 where the relation between the external load and the LDP is depicted. The load bearing for the un-notched beam is two times higher in comparison to the notched beam, see Fig. 10. In the curve four characteristic points are marked, for which the the maps of σ_{xx} on the deformed beam are presented in Figs. 16–19.

It can be noticed in Fig. 16 that there are many small cracks in the lower part of the beam. Due to further increment of the external load a single crack path can be distinguished in Fig. 17 that starts to dominate over other small cracks. In another stage of the cracking process the single crack propagates while other small cracks disappear due to decrease of the tensile stress in the other parts of the beam. The tensile stress concentration is observed only

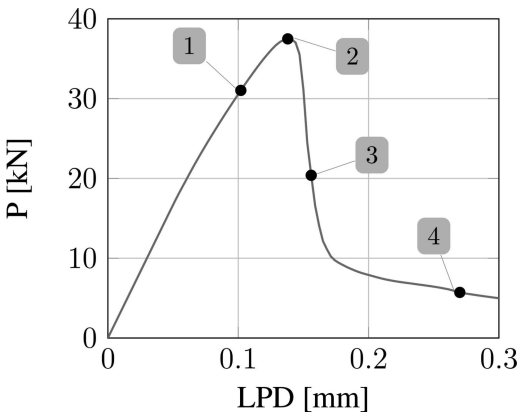

Figure 15. Equilibrium path in load versus LDP for cracking of the plain beam.

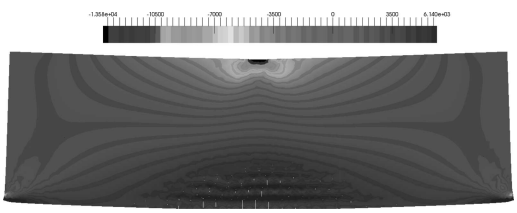

Figure 16. Map of σ_{xx} on the deformed beam at the stage 1 marked in Fig. 15.

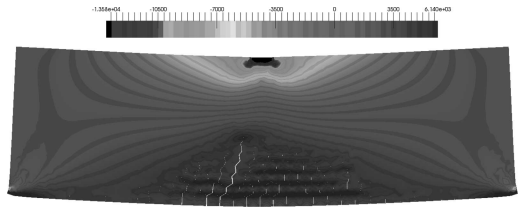

Figure 17. Map of σ_{xx} on the deformed beam at the stage 2 marked in Fig. 15.

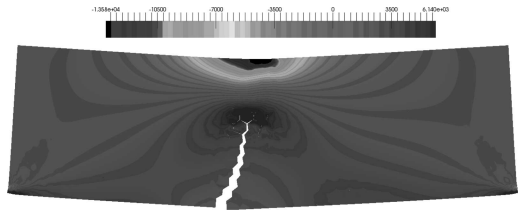

Figure 18. Map of σ_{xx} on the deformed beam at the stage 3 marked in Fig. 15.

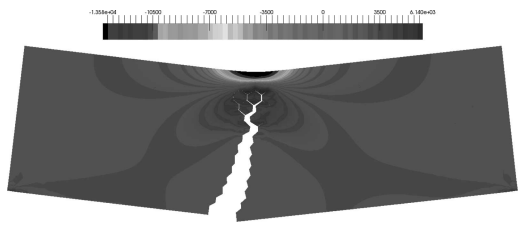

Figure 19. Map of σ_{xx} on the deformed beam at the stage 4 marked in Fig. 15.

near the tip of the crack. The crack tends to reach the loading point on the upper surface of the beam, what is shown in Fig. 19. It can be noticed that the crack tip is not unique since there are few branches at the top of the crack. However, when the crack grows forward only one branch is chosen while other are closed due to uploading.

In this example the crack growth analysis has been shown for un-notched beam. The single crack is initiated at the region that is softened at the first stage of the process. It is a random issue where the crack is formulated in the softened region. A dominant crack path causes that other small cracks are unloaded and the further single crack growth is observed.

6 CONCLUSIONS

A cohesive crack model in the discontinuous Galerkin method has been presented. The DG

method uses approximations that are discontinuous on the mesh skeleton. The algorithm presented in this paper has took advantage of the discontinuous approximation to model the crack growth where the crack propagates along the mesh skeleton. The traction-separation law in the cohesion crack model has been to the softening rule in the traction-strain space. Then the secant Young's modulus has been evaluated that has been applied in the final numerical model. The final numerical method has been called CFDG.

The incremental-iterative scheme has been applied for failure analysis. In the analysis there is no need to defined the criterion for the crack growth nor direction of the crack growth. Therefore the presented algorithm is quite easy for implementation. It is natural for the algorithm to analyse multiple cracks, branching cracks and even the crossing cracks. Not special attention has to be paid in that situations. It may happen that there are two or more cracks in the small neighbourhood. When one crack starts to dominate others crack are unloaded and closed. The closed cracks are 'healed' in compression, it means that they can bear the compression stresses.

The paper has been illustrated with the example where the three-point bending beam has been analysed. Firstly the numerical test has been shown illustrating the ability of the method to model multiple cracks in the domain. Afterwards, the crack growth analysis has been performed for the beam with a notch. Subsequently the crack growth has been analysed but without the notch. In this case some part of the beam has been weakened by tensile stresses. A single crack has been initiated in the weakened region where it has started to propagate.

REFERENCES

Asferg, J.L., P.N. Poulsen, & L.O. Nielsen (2007). A consistent partly cracked XFEM element for cohesive crack growth. *International Journal for Numerical Methods in Engineering 72*(4), 464–485.

Bird, R., W. Coombs, & S. Giani (2017). A quasi-static discontinuous Galerkin configurational force crack propagation method for brittle materials. *International Journal for Numerical Methods in Engineering*. In print.

Engwer, C. & L. Schumacher (2017). A phase field approach to pressurized fractures using discontinuous Galerkin methods. *Mathematics and Computers in Simulation 137*, 266–285.

Gálvez, J., J. Planas, J. Sancho, E. Reyes, D. Cendón, & M. Casati (2013). An embedded cohesive crack model for finite element analysis of quasi-brittle materials. *Engineering Fracture Mechanics 109*, 369–386.

Giorgiani, G., S. Fernndez-Mndez, & A. Huerta (2014). Hybridizable discontinuous Galerkin with degree adaptivity for the incompressible navierstokes equations. *Computers & Fluids 98*, 196–208.

Guo, H., F. Yu, & Y. Yang (2017, May). Local discontinuous Galerkin method for incompressible miscible displacement problem in porous media. *Journal of Scientific Computing 71*(2), 615–633.

Hoppe, R.H.W., G. Kanschat, & T. Warburton (2009). Convergence analysis of an adaptive interior penalty discontinuous Galerkin method. *SIAM Journal on Numerical Analysis 47*(1), 534–550.

Jaśkowiec, J. (2017a). Application of discontinuous Galerkin method to mechanical 2D problem with arbitrary polygonal and very high-order finite elements. *Computer Methods in Applied Mechanics and Engineering 323*, 389–415.

Jaśkowiec, J. (2017b). The discontinuous galerkin method with higher degree finite difference compatibility conditions and arbitrary local and global basis functions. *Computer Assisted Methods in Engineering and Science 23*(2–3), 109–132.

Jaśkowiec, J., P. Pluciski, & A. Stankiewicz (2016). Discontinuous galerkin method with arbitrary polygonal finite elements. *Finite Elements in Analysis and Design 120*, 1–17.

Jaśkowiec, J. & F.P. van der Meer (2014). A consistent iterative scheme for 2d and 3d cohesive crack analysis in xfem. *Computers & Structures 136*, 98–107.

Luo, H., J.D. Baum, & R. Lhner (2008). A discontinuous Galerkin method based on a taylor basis for the compressible flows on arbitrary grids. *Journal of Computational Physics 227*(20), 8875–8893.

Marigo, J.-J., C. Maurini, & K. Pham (2016, Dec). An overview of the modelling of fracture by gradient damage models. *Meccanica 51*(12), 3107–3128.

Nagashima, T. & M. Sawada (2016). Development of a damage propagation analysis system based on level set XFEM using the cohesive zone model. *Computers & Structures 174*, 42–53.

Nguyen, V.P. (2014). Discontinuous Galerkin/extrinsic cohesive zone modeling: Implementation caveats and applications in computational fracture mechanics. *Engineering Fracture Mechanics 128*, 37–68.

Wu, L., G. Becker, & L. Noels (2014). Elastic damage to crack transition in a coupled non-local implicit discontinuous galerkin/extrinsic cohesive law framework. *Computer Methods in Applied Mechanics and Engineering 279*, 379–409.

Computational Modelling of Concrete Structures – Meschke, Pichler & Rots (Eds)
© 2018 Taylor & Francis Group, London, ISBN 978-1-138-74117-1

Mesoscopic simulations of crack propagation in concrete using cohesive elements

W. Trawiński, J. Tejchman & J. Bobiński
Faculty of Civil and Environmental Engineering, Gdansk University of Technology, Gdansk, Poland

ABSTRACT: The paper presents results of two- and three-dimensional meso-scale simulations of fracture in notched concrete beams subjected to three-point bending test. Concrete was assumed as a 3-phase material composed of aggregate grains placed in the cement matrix with Interfacial Transitional Zones (ITZs) between then. In 2D simulations macro-voids were also taken into account. The particle distribution was taken from real concrete beams on the basis of X-ray μCT images. The effect of different properties of ITZs and cement matrix was investigated in parametric studies. A satisfactory agreement in terms of the vertical force versus crack mouth opening displacement evolution and crack geometry was achieved between analyses and laboratory tests.

1 INTRODUCTION

Fracture process in concrete elements is very complex due to the occurrence of phenomena such as branching, coalescence, kinking, tortuousness and interlocking of cracks (Bažant & Planas 1997, Tejchman & Bobiński 2013). To describe them properly, the material heterogeneity should be taken into account. At the meso-scale, concrete can be described as a four-phase material composed of aggregate grains embedded in a cement matrix, macro-voids and a thin porous region of cement paste around aggregate inclusions, namely interfacial transitional zones (ITZs) (Skarżyński & Tejchman 2016). The aforementioned constituents of concrete have different elastic and fracture properties which significantly influence the overall response of a structure.

The aim of the paper was to investigate in detail a complex fracture process in concrete specimens subjected to bending under both 2D and 3D conditions by means of the mesoscopic finite element method (FEM). The material internal structure was taken into account by considering four different phases, namely aggregate, cement matrix, ITZs and macro-voids. The knowledge on the shape and position of aggregates was obtained with the aid of X-ray micro-computed tomography images of concrete specimens (Skarżyński et al. 2015). Besides, random locations of both circular and angular inclusions were also considered. Numerical models were discretized with solid (bulk) elements whereas crack propagation was enabled by embedding cohesive elements in the initial mesh of continuum elements. The process of the mesh modification was carried out using an in-house object-oriented C++ application. Different elastic properties were assumed for bulk finite elements covering aggregate grains, cement matrix and homogeneous region. Different fracture properties (critical traction and fracture energy) were taken for aggregate-cement matrix and cement matrix-cement matrix interfaces. Such a description of concrete eliminated two main drawbacks of usage of interface elements to a fracture process: mesh alignment dependency and convergence problems in simulations of curved cracks. A crack nucleated when a crack initiation criterion was fulfilled whereas the post-peak behavior was governed by a traction-separation law. Crack paths were limited to solid element boundaries and were not allowed for propagating through aggregate.

Two experimentally tested concrete beams under bending were numerically simulated. In the first step, two-dimensional numerical simulations were carried out for several representative cross-sections of specimens (Trawiński et al. 2016). In the second step, three-dimensional analyses were conducted for the same internal concrete structure (Trawiński et al. 2017). The influence of different model parameters (e.g. ITZ/cement matrix strength ratio, aggregate shape) was investigated. In particular, the attention was paid to the dependence of crack paths on fracture properties of ITZs. The outcomes of 2D and 3D analyses were directly compared. The influence of the aggregate shapes and ITZ-width was also analyzed.

2 EXPERIMENTS

The laboratory tests were carried out with two simply-supported concrete beams subjected to three-point bending (Skarżyński et al. 2015). The beam had a rectangular cross-section with the height of $H = 80$ mm and width of $B = 40$ mm. The beam length was $L = 320$ mm ($4 \times H$) and the span between the supports was $3 \times H = 240$ mm. In order to trigger fracture, a notch with the height of $H/10 = 8$ mm and the width of 3 mm was located in the beam bottom mid-span (Figure 1). The concrete mixture was composed of aggregate, sand, cement (CEM I 32.5R) and water. The maximum aggregate diameter was $d_{max} = 16$ mm and mean particle size was $d_{50} = 2.0$ mm. The water/cement, sand/cement and aggregate/cement ratios were 0.42, 0.80 and 1.43, respectively. The total aggregate and sand volumetric content was $V = 75\%$. The average uniaxial compressive strength f_c was equal to $f_c = 51.81$ MPa. The Young modulus E and Poisson's ratio ν were determined as $E = 36.1$ GPa and $\nu = 0.22$, respectively. The measured tensile strength during bending on the concrete beams $4 \times 4 \times 16$ cm^3 was $f_{t,flex} = 3.7$–4.3 MPa. The tests were performed with a constant-controlled notch opening displacement rate of 0.002 mm/min (crack mouth opening displacement (CMOD)). Each test ended for CMOD = 0.10–0.15 mm prior to the unstable failure in order to provide the images of internal micro-structure by means of μCT.

Figure 2 presents two typical experimental diagrams of the vertical force F versus CMOD for the concrete beams (with the displacement CMOD up to 0.15 mm for the beam '1' and up to 0.10 mm for the beam '2'). The ultimate vertical force F was equal to 2.15–2.25 kN. The distribution of aggregate grains and macro-voids in concrete beams was determined based on μCT-images of the concrete cuboids ($80 \times 50 \times 40$ mm^3) extracted from the mid-part of each beam after tests (Skarżyński & Tejchman 2016). Figure 3 shows 3D images of concrete internal structure obtained with the aid of SkyScan 1173 which represents a new generation in high-resolution desktop X-ray micro-computed

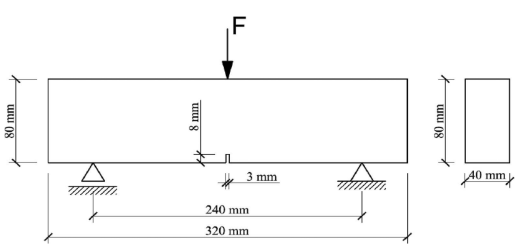

Figure 1. Geometry and boundary conditions of beam subjected to three-point bending test.

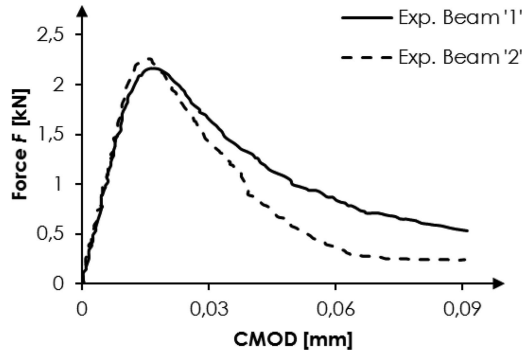

Figure 2. Experimentally measured vertical force F versus CMOD curves for two concrete beams.

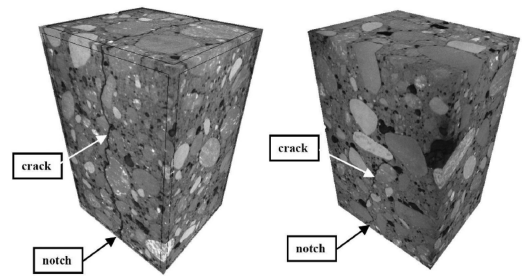

Figure 3. μCT-images of the concrete cracked cuboids cut out from beam '1' (left) and '2' (right).

tomography systems. Aggregate grains and macro-voids might be separated from the cement matrix on images. Interfacial transitional zones (ITZs) occurred around all aggregate grains. The main discrete macro-crack was strongly curved along the beam height and width due to a random presence of aggregate grains and it propagated mainly through the weakest phase in concrete which were interfacial transitional zones (ITZs). Thus micro-cracking occurred first in ITZs. When two interfacial cracks occurred around adjacent aggregates, a crack inside the cement matrix initiated to bridge the interfacial cracks so that a connected crack path was formed. Sometimes the crack propagated through macro-voids and very rarely through a single weak aggregate grain. The crack width changed with the specimen's height in a non-linear way for each beam. For the beam '1' the main crack propagated through the entire specimen's height, whereas it did not reach the top surface in the beam '2'. The scanning electro-microscope (SEM) Hitachi TM3030 was used to measure the width of ITZs. A very non-uniform porous structure of ITZs as well as the presence of separated small sand grains was possible to be observed with the maximum magnification factor 30,000. The

width of porous ITZs did not depend on aggregate particles diameter and changed between 30–50 μm (Skarżyński et al. 2016).

3 CONCRETE MODEL

In order to simulate the fracture process, a cohesive interface finite elements were inserted between solid elements in the beam's mid-region. Two constitutive laws were defined to describe the behavior of concrete in solid and interface finite elements, respectively. In 2D simulations, plane stress 3-node triangular elements and 4-node interface elements were used, while in 3D calculations 4-node tetrahedral solid elements and 6-node interface elements were applied.

3.1 *Solid elements*

A linearly elastic model was assumed for solid elements throughout the entire analysis. The constitutive matrix $\boldsymbol{C}$ linked the stress $\boldsymbol{\sigma}$ with the strain $\boldsymbol{\varepsilon}$ as:

$$\boldsymbol{\sigma} = \boldsymbol{C}\boldsymbol{\varepsilon} \tag{1}$$

The only required material constants for continuum elements were: Young's modulus E and Poisson's ratio v. The Young's modulus of aggregate grains, E_a = 47.2 GPa, was calculated as the weighted average of the moduli of individual components (Trawiński et al. 2016). For the cement matrix bulk elements the value of E_{cm} = 29.2 GPa was chosen and E_h = 36.1 GPa was taken for the homogeneous beam's part wherein a usual 1-phase description was applied. The Poisson's ratio for each material phase was taken as v = 0.22.

3.2 *Cohesive elements*

The behaviour of cohesive elements was governed by the following equation:

$$\begin{bmatrix} t_n \\ t_s \\ t_t \end{bmatrix} = \begin{bmatrix} k_n & 0 & 0 \\ 0 & k_s & 0 \\ 0 & 0 & k_t \end{bmatrix} \begin{bmatrix} \delta_n \\ \delta_s \\ \delta_t \end{bmatrix} \tag{2}$$

where t_n, t_s, t_t = tractions; k_n, k_s, k_t = interface stiffnesses; and δ_n, δ_s, δ_t = relative displacements (index 'n' stands for the normal direction while indices 't' and 's' describe tangential directions). Before cracking, stiffnesses k_n, k_s and k_t were equal to initial stiffnesses k_{n0}, k_{s0}, k_{t0}, respectively. In all simulations all stiffnesses were taken as 10^6 MPa/mm for all interface types (after Caballero et al. 2006, López et al. 2008, Wang et al. 2015, 2016). The assumed penalty stiffness ensured ITZs to be intact (almost without relative displacements) in the elastic deformation range. After cracking all stiffnesses were influenced by a scalar variable D according to:

$$\begin{aligned} k_n &= (1-D)k_{n0} \\ k_s &= (1-D)k_{s0} \\ k_t &= (1-D)k_{t0} \end{aligned} \tag{3}$$

To initiate a cohesive crack, the quadratic nominal stress criterion was assumed:

$$\left\{\frac{\langle t_n \rangle}{t_{n0}}\right\}^2 + \left\{\frac{t_s}{t_{s0}}\right\}^2 + \left\{\frac{t_t}{t_{t0}}\right\}^2 = 1 \tag{4}$$

where t_{n0}, t_{s0}, t_{t0} = critical tractions for the fracture mode I, II and III, respectively; and $\langle\ \rangle$ = the Macaulay bracket. Due to the lack of experimental results, the shear critical tractions t_{s0} and t_{t0} for all cohesive elements were assumed to be the same as the normal ones (similarly as in numerical analyses by Ren et al. 2015, Su et al. 2010 and Yang et al. 2009). Different values were assigned to different interface types. For the inter-phase (aggregate/cement matrix) the value $t_{n0,ITZ}$ = 1.6 MPa was assumed and for the intra-phase (cement matrix/cement matrix) the value $t_{n0,cm}$ = 4.4 MPa was chosen. These values can be interpreted as a tensile strengths of different phases. No cracks were allowed to create between aggregate solid elements.

In order to describe damage under a combination of normal and shear deformations across the interface, the effective relative displacement δ_m was introduced:

$$\delta_m = \sqrt{\langle \delta_n \rangle^2 + \delta_s^2 + \delta_t^2} \tag{5}$$

The exponential softening curve was chosen to describe the behaviour of the interface elements in a post-peak regime. The scalar damage variable D, dependent on the effective relative displacement, was calculated as:

$$D = 1 - \frac{\delta_m^0}{\delta_m^{\max}} \left(1 - \frac{1 - \exp\left(-\alpha \left(\frac{\delta_m^{\max} - \delta_m^0}{\delta_m^f - \delta_m^0} \right) \right)}{1 - \exp(-\alpha)} \right) \tag{6}$$

where δ_m^0 = the effective relative displacement at the crack initiation; δ_m^f = the effective relative displacement at the complete damage; $\delta_m^{\max}$ = the maximum effective relative displacement obtained during the loading history; and α = the parameter

affecting the slope of the softening curve. The displacement δ_m^f was equal to 0.098 mm and 0.071 mm inter-phase (ITZ) and intra-phase (cement matrix) interfaces, respectively. The α parameter was taken as 7.5. These values were chosen in such a way to obtain the fracture energy equal to 20 N/m and 40 N/m for inter-phase and intra-phase interfaces, respectively (Ren et al. 2015, Wang et al. 2015, 2016). Equation (6) is valid only for the displacement $\delta_m^{\max}$ smaller than displacement δ_m^f. If this condition is not fulfilled, the damage parameter $D = 1$ should be used.

4 MESH GENERATION

In the FE mesh generation the real shape and placement of aggregates based on μCT images of the internal structure were taken into account. The open-source software 3D Slicer was used to manually extract aggregate grains from scans. There were around 300 particles described by a very dense triangular surface mesh. Next, the free software Autodesk Meshmixer working with triangle meshes was used in order to smoothen aggregate shapes and to reduce the number of nodes and triangular faces. Each 3D model of a single aggregate particle was reduced to a reasonable mesh accuracy level in order to decrease the computational time of FE analyses (Figure 4). Two mesh accuracy levels were assumed for each particle: a coarse one—described by 100 triangles and a fine one—described by 300 triangles (Figure 5).

The entire generation process of the full 3D FE model consisted of two main stages. In the first stage, the initial FE-mesh without cohesive elements was defined (within Abaqus CAE). In the second stage, cohesive elements were added to the model. The object-oriented application was written to modify the input file and to insert cohesive elements. Different properties were assigned to cement matrix/cement matrix and aggregate/cement matrix interfaces.

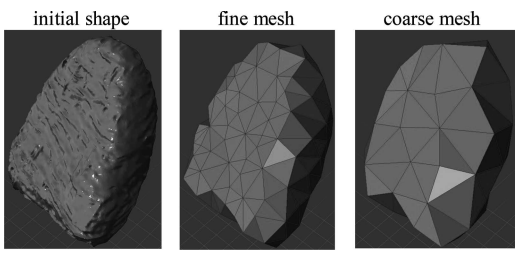

Figure 4. FE surface model of an aggregate grain: initial shape (left), fine mesh (center) and coarse mesh (right).

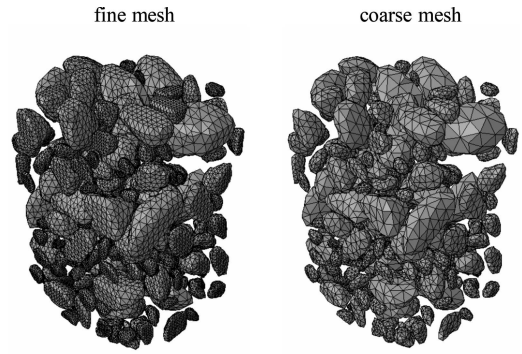

Figure 5. FE surface model of aggregate grains in the middle part of the beam: fine mesh (left) and coarse mesh (right).

5 2D SIMULATIONS

The 2D numerical simulations were carried out under plane stress conditions (Trawiński et al. 2016). The aggregate and void distributions in the concrete beam were taken into account by assigning the different material properties to each phase. The aggregate particles had the diameter 2 mm ≤ d_a ≤ 16 mm. Their location was the same as on the X-ray μCT images. The macro-voids were simulated as the empty spots. The deformation was induced by enforcing the vertical displacement of nodes at the beam top (under the loading plate with the width of 3.0 mm) up to the final value of 0.2 mm.

In order to check the mesh dependence, a convergence analysis was performed for each beam for the selected cross-section. The element size was equal to: s = 2.0 mm, s = 1.5 mm or s = 1.0 mm for a coarse, medium and fine mesh in the heterogeneous beam region, respectively (the medium mesh consisted of 8892 cohesive elements and 8625 solid elements). In the homogeneous beam region, the element size changed from the value of s up to 15 mm. The calculated crack trajectories were always the same independently of the mesh discretization (Figure 6). The force-deflection curves (Figure 7) for the both beams were also independent of the element size. This advantageous effect was achieved by including aggregate particles with ITZs which acted as attractors for the macro-crack.

The calculated force-CMOD curves remained in a good agreement with the experimental ones in terms of the maximum vertical force and the slope of the softening curve (Figure 8). The calculated maximum vertical force $F_{\max}$ varied for the beam '1' from 2.1 kN up to 2.2 kN and for the beam '2' from 2 kN up to 2.25 kN for 3 different cross-sections

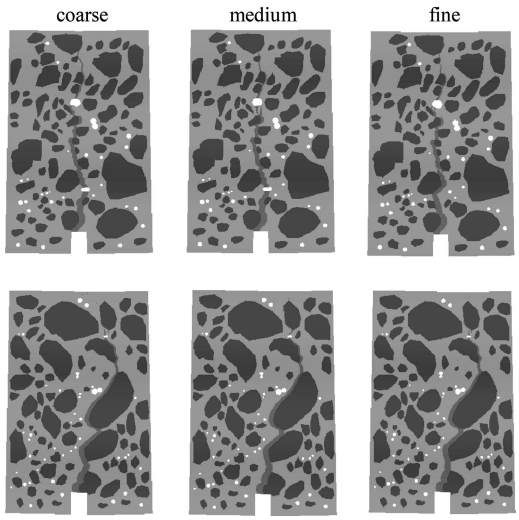

Figure 6. Crack geometry for the coarse mesh (left column), medium mesh (middle column) and fine mesh (right column) for the beam '1' (top row) and the beam '2' (bottom row).

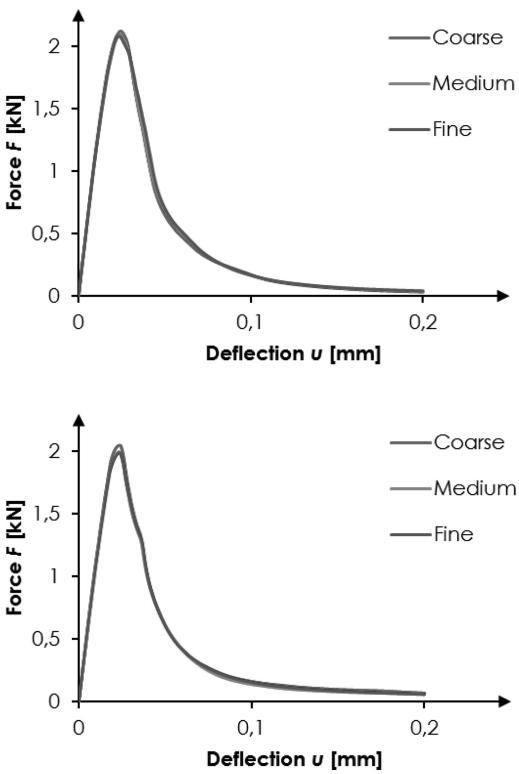

Figure 7. Force-displacement curves for different meshes for the beam '1' (top) and the beam '2' (bottom).

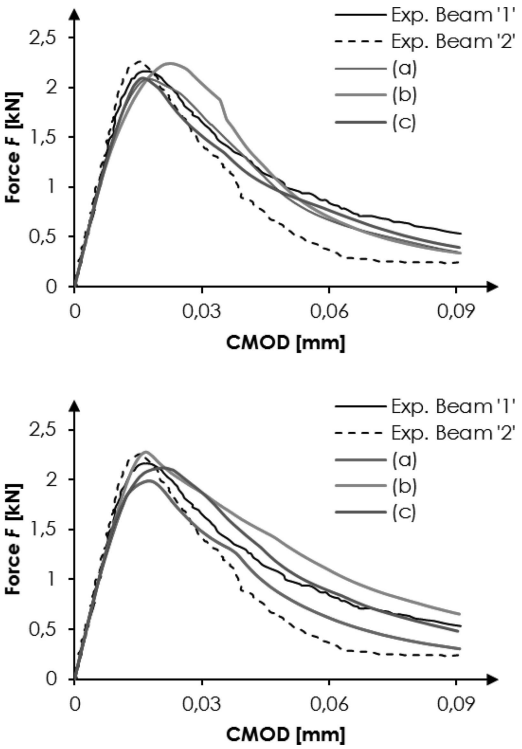

Figure 8. Force-displacement curves for different cross sections: (a) at depth of 3 mm, (b) at depth of 20 cm and (c) at depth of 37 mm compared to experimental outcomes for the beam '1' (top) and the beam '2' (bottom).

that was close to the experiment (F_{max} = 2.15 kN for the beam '1' and F_{max} = 2.25 kN for the beam '2'). The largest difference occurred for the mid-cross-section. The post-peak behaviour in the numerical simulations was slightly softer than in the experiment.

The calculated macro-crack shapes above the notch are shown in Figures 9 and 10 in 3 different vertical-sections along the beam depth as compared to the experiment. The calculated crack height h_c for the beam '1' varied between 63 mm and 70 mm for CMOD = 0.15 mm (in the experiment h_c = 72 mm). The crack length, which indicated the crack tortuosity, was between 75 mm and 80 mm for CMOD = 0.15 mm (in the experiment l_c = 77–80 mm). The crack path for the cross-section at the depth of 3 mm was almost the same as in the experiment. For the remaining beam cross-sections, some deviations from laboratory test outcomes appeared. Sometimes the crack propagated on the other side of aggregate particles than in the experiment. The number of cohesive elements forming a traction-free crack varied from 59 up to 61 at the simulation end. The number of interface

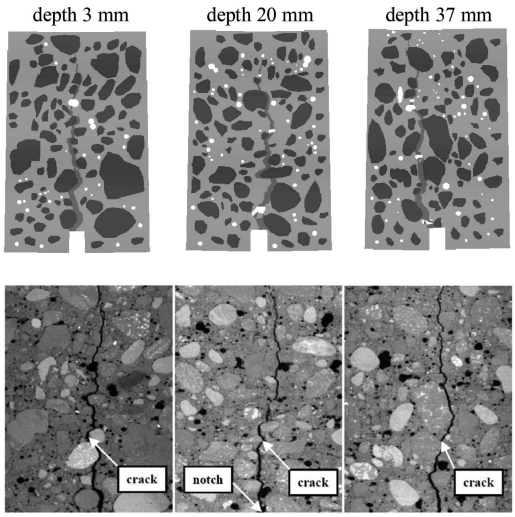

Figure 9. Crack propagation for the beam '1' from FE simulations (top) compared to experiments (bottom) for different cross sections.

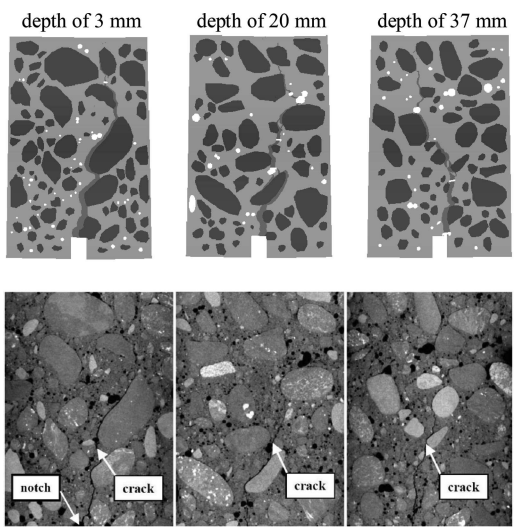

Figure 10. Crack propagation for the beam '2' from FE simulations (top) compared to experiments (bottom) for different cross sections.

elements for the scalar damage parameter $D > 0.95$ changed from 511 up to 645 in the entire model. The calculated width of the crack above the notch was 0.26 mm and was similar as in the experiment (0.24 mm). For the beam '2', the crack height was $h_c = 65$–70 mm (in the experiment $h_c = 45$–56 mm). The crack length varied from 76 up to 94 mm (in the experiment $l_c = 57$–63 mm). The traction-free crack had the height varying between 49 and 52 mm and

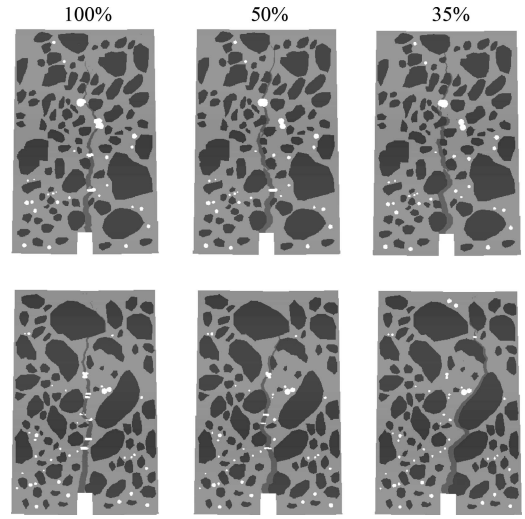

Figure 11. Influence of the strength of the ITZs with respect to the strength of the cement matrix (percentage label in columns) for the beam '1' (top) and the beam '2' (bottom).

the width of 0.06–0.25 mm. The number of cohesive elements forming the crack varied from 60 to 70, whereas the fracture zone was represented by interface elements with $D > 0.95$ (from 416 up to 585 elements). In general, a satisfactory agreement was achieved with the experiment, in particular for the vertical section at the depth of 3 cm. Similarly as in the experiment, the crack mainly propagated through ITZs and rarely through macro-voids.

Some parametric studies were performed. First the influence of the strength of ITZ was investigated. The higher strength of ITZs obviously caused an increase of the beam strength. The macro-crack path changed from an almost straight to a strongly curved one as the strength of ITZs decreased (Figure 11). The increase of the fracture energy of ITZs resulted in higher maximum loads and less brittle response in the post-peak regime. The strength growth of the cement matrix contributed to the increase of both the beam strength and brittleness. The increase of the fracture energy of the cement matrix resulted in the higher beam strength without the influence on the macro-crack geometry.

Next the effect of the shape, content and density of aggregate packing was investigated for the vertical cross-section at the depth of 3 mm for the beam '1'. In order to investigate the aggregate shape, the real angularly-shaped aggregate particles were replaced by the perfectly circularly-shaped aggregate grains (the centre and area of particles were the same). For round particles, the maximum vertical force was slightly higher and the crack path was

less curved and differed from the experimental one in contrast to non-regular particles. Similar results were obtained by Du et al. (2013), He (2010) and Kim & Abu Al-Rub (2011) using mesoscopic continuous FE approaches.

6 3D SIMULATIONS

Initially, in order to check the influence of the mesh density on numerical outcomes, the aggregate particles in the range 2 mm ≤ d_a ≤ 16 mm were described with a coarse and fine meshes (Trawiński et al. 2017). The force-CMOD curves were mesh-independent, but the calculated crack paths slightly depended on the mesh accuracy used for a particle description (Figure 12). For a fine mesh description, the macro-crack path was slightly more curved. A better agreement between the FE results and experimental ones with respect to the crack geometry was achieved for a fine discretization.

Figure 13 shows that the calculated force-CMOD curve was in a satisfactory agreement with

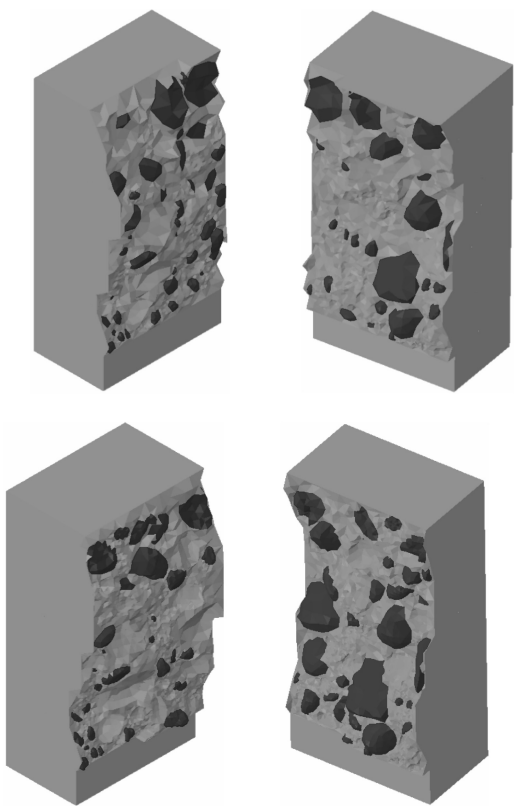

Figure 12. Crack paths for coarse (top) and fine mesh (bottom).

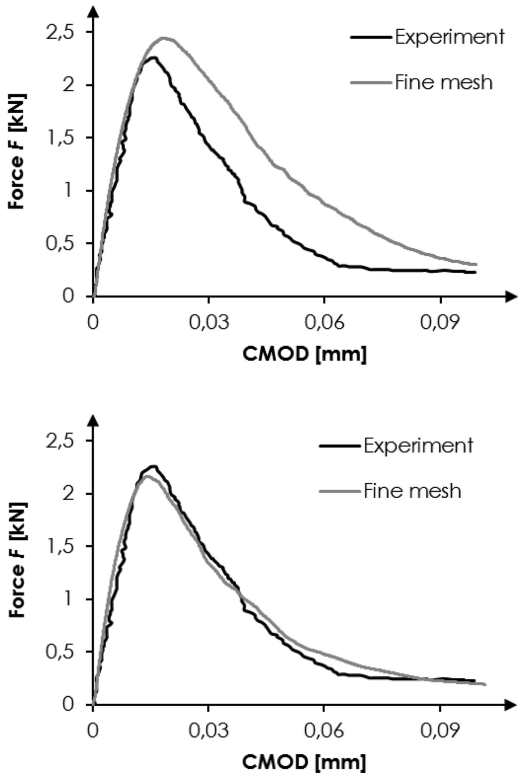

Figure 13. Vertical force-CMOD curves compared to experiment for the standard set of parameters (top) and improved set of parameters (bottom).

the laboratory test result for the same cohesive element properties (called standard parameters) as in the corresponding 2D analyses. The slope of the softening curve obtained from the numerical analysis was the same as in the experiment. It was more realistic as compared to the 2D results. The maximum vertical force F_{max} = 2.45 kN was higher by 10% than the experimental one (F_{max} = 2.25 kN). In order to obtain a better agreement in terms of the force-CMOD curve, the material parameters for cohesive elements (called improved parameters) were updated: $f_{t,ITZ}$ = 1.6 MPa, $f_{t,cm}$ = 3.6 MPa, $G_{F,ITZ}$ = 20 N/m and $G_{F,cm}$ = 25 N/m.

The calculated cracks patterns are presented in Figure 14. In general, a very good agreement was achieved with the experiment. In addition, a better agreement was achieved for 3D numerical analyses than for corresponding 2D simulations. The macro-crack paths obtained from 3D numerical analyses were also closer to the experimental results than outcomes from 2D meso-scale simulations (wherein the calculated crack pattern was identical to the experiment only in a cross-section

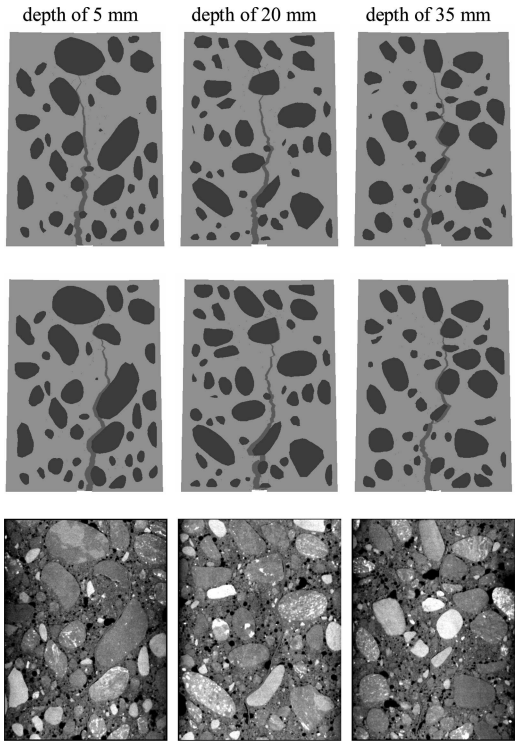

Figure 14. Crack propagation for coarse mesh (top), fine mesh (middle) and from experimental results (bottom) at different depths of the cross sections.

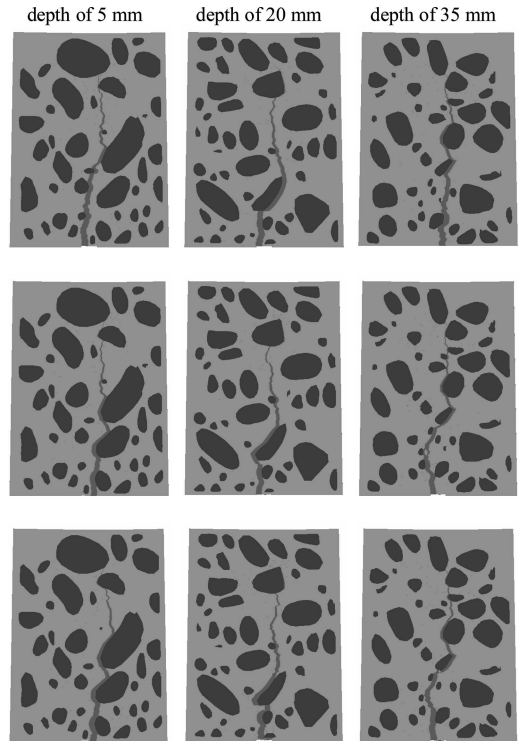

Figure 15. Influence of the strength of the ITZs with respect to the strength of the cement matrix for the 70% (top), 35% (middle) and 35% (bottom) at different depths of the cross sections.

at the depth of 5 mm). The 3D numerical analyses provided a very good agreement regarding the crack geometry in several cross-sections (at the depth of 5, 20 and 35 mm). The calculated crack height h_c varied between 56 mm and 58 mm for CMOD = 0.10 (in the experiment h_c = 45–56 mm). The crack tortuosity, expressed by the crack length l_c, was between 66 and 71 mm (in the experiment l_c = 57–63 mm). The fractured zone (wherein cohesive element stiffness was decreased by more than 95%) included 29 022 cohesive elements while the number of interface elements forming the traction-free crack (D = 1.0) was 6390. Note that in 2D slices obtained from 3D FE analyses some aggregate grains were missing due to a particle mesh simplification prior to the numerical simulations.

The effect of the strength of ITZs was also investigated. The beam's strength and brittleness increased with the higher critical traction of ITZs. The macro-crack changed its shape from an almost straight to a strongly curved one with decreasing tensile strength of ITZs from 1 down to 0.35–0.70 with respect to the cement matrix strength (Figure 15). The calculated geometry of the macro-crack was almost identical with $f_{t,ITZ}/f_{t,cm}$ = 0.35 and $f_{t,ITZ}/f_{t,cm}$ = 0.50 and very similar with $f_{t,ITZ}/f_{t,cm}$ = 0.70. Thus, the calculated crack shape was in agreement with the experiment for the ratio of $f_{t,ITZ}/f_{t,cm}$ = 0.35–0.70.

While manufacturing concrete, its tensile strength may be improved by reducing the porosity in the cement matrix (mainly in the macro-voids and ITZs). This can be done by adding very fine silica particles to the concrete mixture or reducing the water/cement ratio by applying plasticizer. However the concrete brittleness grows at the same time. The concrete tensile strength may be also increased by a reduction of both the thickness of porous ITZs (through applying round smooth aggregate) and number of ITZs (by decreasing the aggregate volumetric content). With respect to the tensile strength, round aggregates are more advantageous than the angular ones and a lower difference between the strength of the cement matrix and ITZs is also more favourable. The concrete brittleness may be diminished by increasing porosity, ITZ-thickness, aggregate volumetric content, aggregate angularity and difference between the

strength of the cement matrix and ITZs in order to lengthen the crack propagation way. Thus it is possible by means of comprehensive mesoscopic calculations (by changing several factors at the same time) to elaborate quantitative recommendations for the optimum aggregate volume content, aggregate shape and mortar macro-porosity (in order to simultaneously obtain both the relatively high strength and ductility of concrete). In the next calculation step, both macro-voids and ITZs with a defined width will be taken into account in 3D simulations. The real shape of cement matrix particles will be also considered. The simulation results will be compared with the experimental ones for the different *w*/*c*-ratio, porosity, aggregate and fine particle volume and aggregate shape.

7 CONCLUSIONS

Considering the real shape and placement of aggregate particles allowed for obtaining a satisfactory agreement between FE outcomes and experimental results in terms of the global (force-displacement) and local (crack pattern) beam response. Three-dimensional numerical results remained in a better agreement with laboratory tests than 2D analyses. The numerical results showed a satisfactory quantitative agreement with the experimental outcomes with respect to the strength and fracture due to the fact that aggregate distribution was realistically reproduced. Due to the presence of aggregate and weak ITZs, the macro-crack was strongly curved and propagated by bridging the initiated interfacial micro-cracks. The higher strength of ITZs and cement matrix caused the increase of the beam strength and its brittleness. The macro-crack path changed from an almost straight to a strongly curved one as the strength of ITZs decreased and the strength of the cement matrix increased.

The force-deflection curves for spherical aggregate grains were very similar for the same aggregate volumetric content. However, the aggregate volume fraction influenced the maximum vertical force (the smaller the aggregate volume fraction, the higher was the vertical force). The averaged beam strength was higher for spherical aggregate than for angular one and the stiffness degradation initiated faster for angular aggregate. Fracture simulations with substitute spherical aggregate are able to predict the beam strength but not the crack geometry. The real shape and placement of aggregate have be taken into account in order to obtain a macro-crack path comparable with the experiment.

The simulations of the concrete behaviour at the meso-scale lead to a better design of a concrete mix. The concrete behaviour can be improved by e.g. increasing the mortar porosity (to make the tensile strength higher) and increasing both aggregate volumetric content and aggregate angularity (to make the brittleness lower through a growth of the number of ITZs and their thickness).

ACKNOWLEDGMENTS

The research work has been carried out within the project "Experimental and numerical analysis of coupled deterministic-statistical size effect in brittle materials" financed by the Polish National Science Centre (NCN) (UMO-2013/09/B/ST8/03598).

The FE calculations were performed at the Academic Computer Centre in Gdansk TASK.

REFERENCES

Bažant, Z. & Planas, J. 1997. *Fracture and size effect in concrete and other quasi-brittle materials*. Boca Raton: CRC Press LLC.

Caballero, A., Carol, I. & López, C.M. 2006. New results in 3D meso-mechanical analysis of concrete specimens using interface elements. In N. Bicanic, H. Mang, G. Meschke & R. de Borst (eds), *Computational Modelling of Concrete Structures*: 43–62. CRC Press, Taylor and Francis Group.

Du, C., Sun, L., Jiang, S. & Ying, Z. 2013. Numerical simulation of aggregate shapes of three-dimensional concrete and its applications. *Journal of Aerospace Engineering* 3; 515–527.

He, H. 2010. *Computational modeling of particle packing in concrete*. PhD thesis. TU Delft.

Kim, S.M. & Abu Al-Rub, R.K. 2011. Meso-scale computational modelling of the plastic-damage response of cementitious composites. *Cement and Concrete Research* 41: 339–58.

López, C.M., Carol, I. & Aguado, A. 2008. Meso-structural study of concrete fracture using interface elements. I: numerical model and tensile behavior. Materials and Structures 41: 583–99.

Ren, W., Yang, Z., Sharma, R., Zhang, Ch. & Withers, P.J. 2015. Two-dimensional X-ray CT image based meso-scale fracture modelling of concrete. *Engineering Fracture Mechanics* 133: 24–39.

Skarżyński, Ł., Nitka. M. & Tejchman, J. 2015. Modelling of concrete fracture at aggregate level using FEM and DEM based on X-ray μCT images of internal structure. *Engineering Fracture Mechanics* 147:13–35.

Skarżyński, Ł. & Tejchman, J. 2016. Experimental investigations of fracture process in concrete by means of X-ray micro-computed tomography. *Strain* 52:26–45.

Su, X.T., Yang, Z.J. and Liu, G.H. 2010. Monte Carlo simulation of complex cohesive fracture in random heterogeneous quasi-brittle materials: A 3D study. *International Journal of Solids and Structures* 47: 2336–45.

Tejchman, J. & Bobiński, J. 2013. *Continuous and discontinuous modeling of fracture in concrete using FEM*. Berlin-Heidelberg: Springer.

Trawiński, W., Bobiński, J. & Tejchman, J. 2016. Two-dimensional simulations of concrete fracture at aggregate level with cohesive elements based on X-ray μCT images. *Engineering Fracture Mechanics* 168:204–26.

Trawiński, W., Tejchman, J. & Bobiński, J. 2017. A three-dimensional meso-scale modelling of concrete fracture based on cohesive elements and X-ray -CT images. *Engineering Fracture Mechanics,* doi: 10.1016/j.engfrac-mech.2017.10.003.

Wang, X., Yang, Z. & Jivkov, A.P. 2015. Monte Carlo simulations of mesoscale fracture of concrete with random aggregates and pores: a size effect study. *Construction and Building Materials* 80: 262–72.

Wang, X., Zhang, M. & Jivkov, A.P. 2016. Computational technology for analysis of 3D meso-structure effects on damage and failure of concrete. *International Journal of Solids and Structures* 80: 310–33.

Yang, Z.J., Su, X.T., Chen, J.F & Liu, G.H. 2009. Monte Carlo simulation of complex cohesive fracture in random heterogeneous quasi-brittle materials. *International Journal of Solids and Structures* 46: 3222–34.

Computational Modelling of Concrete Structures – Meschke, Pichler & Rots (Eds)
© 2018 Taylor & Francis Group, London, ISBN 978-1-138-74117-1

Configurational forces for modelling cohesive fracture in concrete

C.J. Pearce, A. Amar & Ł. Kaczmarczyk
School of Engineering, University of Glasgow, Glasgow, UK

ABSTRACT: The paper presents a formulation for fracture in 3D quasi-brittle solids within the framework of configurational mechanics. A crack front equilibrium condition is derived from the local form of the first law of thermodynamics. The direction of the crack propagation is shown to be given by the direction of the configurational forces on the crack front that maximise the local dissipation. The evolving crack front is continuously resolved by the finite element mesh, without the need for face splitting or the use of enrichment techniques. A monolithic solution strategy is adopted, solving simultaneously for both the material displacements (i.e. crack extension) and the spatial displacements. The dissipative load-displacement path is traced using an arc-length procedure that controls the incremental crack area growth. To maintain mesh quality, smoothing of the mesh is undertaken as a continuous process, together with face flipping, node merging and edge splitting where necessary. The formulation is implemented in MOFEM (www.mofem.gla.ac.uk), which is an open source development platform for finite element analysis, optimised for taking advantage of high performance computing. The formulation is an extension of the previous work of the authors for brittle solids. Performance of the formulation is demonstrated by means of representative numerical simulations, demonstrating the ability accurately resolve complex crack paths in a computationally efficient and robust manner. Examples show the ability of this approach to model propagating cracks using relatively simple finite element meshes, within a robust, efficient and accurate formulation.

1 INTRODUCTION

The pervasive and serious nature of cracks in materials and structures means that the computational modelling of crack propagation continues to be a critical area of research, and a major challenge. This paper presents a finite element based computational framework for modelling crack propagation. It starts with developing the formulation for brittle fracture, based on the work of the authors Kaczmarczyk et al. (2014, 2017) using the concept of configurational mechanics, before extending it to include cohesive cracks. The focus is both the mathematical formulation and the computational framework to model and continuously resolve propagating cracks in a robust and computationally efficient manner.

The concept of configurational mechanics dates back to the original work of Eshelby (1951, 1970) and his study of forces acting on continuum defects. More recently, configurational mechanics has been adopted by, amongst others, Maugin (1993, 2010), Steinmann (2000), Miehe et al. (2007), Gürses and Miehe (2009) and Kaczmarczyk et al. (2014, 2017).

To formulate the crack propagation problem, two related kinematic descriptions are defined in the spatial and material settings. The first description is the classical conservation law of linear momentum balance is described, where Newtonian forces are work conjugate to changes in the spatial position, at fixed material position (i.e. no crack propagation). In the material setting, which represents a dual to the spatial setting, an equivalent conservation law is described, where configurational forces are conjugate to changes in material position but with no spatial motion. This decomposition of the behaviour is proven to be a simple but powerful methodology for describing crack propagation.

The spatial and material displacements fields are both discretised using the same finite element mesh, although we adopt different levels of approximation for the two fields. The meshes comprise 3D tetrahedral elements with arbitrary levels of approximation (Kaczmarczyk et al. (2014, 2017)). The discretised weak form of the two conservation equations represent a set of coupled, nonlinear, algebraic equations that are solved in a monolithic manner using a Newton-Raphson scheme.

In addition, an arc-length method, using crack area rather than displacements as a constraint, is adopted to trace the dissipative load path.

The resulting crack is represented as a displacement discontinuity, requiring the finite element

mesh to resolve the crack and to be continuously adapted as the crack front advances. In contrast to other approaches, we establish an equilibrium condition for the nodal configurational forces acting on the crack front that enables the crack front to advance in a continuous manner. To maintain mesh quality, smoothing of the mesh is undertaken as a continuous process. This is augmented by other local mesh adjustment techniques such as face flipping, node merging and edge splitting where necessary.

In the approach adopted, and unlike other formulations, the configurational forces are calculated at each node as a natural consequence of the analysis and there is no post-processing stage to determine if a crack should propagate. Moreover, the crack front shape is calculated based purely on the physical equations. For brittle fracture, the only material parameters used are elastic modulus, Poisson's ratio and surface energy.

Numerical examples are presented that demonstrate the ability of the formulation to accurately predict crack paths without bias from the original mesh.

2 BODY AND CRACK KINEMATICS

Figure 1 shows an elastic body with an initial crack in the reference material domain. Because of loading, the crack extends and the body deforms elastically. It is convenient to decompose this behaviour into a purely configurational change, i.e. crack extension, which is described by the mapping from the reference material domain to the current material domain, followed by elastic deformation only, described by the mapping from the current material to spatial domain. We utilise these mappings to independently observe the evolution of the crack surface in the material domain and the elastic deformation of solid in the spatial domain.

The material coordinates $\mathbf{X}$ are mapped onto the spatial coordinates $\mathbf{x}$ via the familiar deformation map $\varphi(\mathbf{X}, t)$. The physical displacement is:

$$\mathbf{u} = \mathbf{x} - \mathbf{X} \tag{1}$$

The reference material domain describes the body before crack extension. $\Xi(\boldsymbol{\chi}(t))$ maps the reference material coordinates $\boldsymbol{\chi}$ on to the current material coordinates $\mathbf{X}$, representing a configurational change, i.e. extension of the crack due to advancement of the crack front. Φ maps the reference material coordinates $\boldsymbol{\chi}$ on to the spatial coordinates $\mathbf{x}$. The current material and spatial displacement fields are given as

$$\mathbf{W} = \mathbf{X} - \boldsymbol{\chi} \quad \text{and} \quad \mathbf{w} = \mathbf{x} - \boldsymbol{\chi} \tag{2}$$

$\mathbf{H}$ and $\mathbf{h}$ are the gradients of the material and spatial maps and $\mathbf{F}$ the deformation gradient Kaczmarczyk et al. (2014).

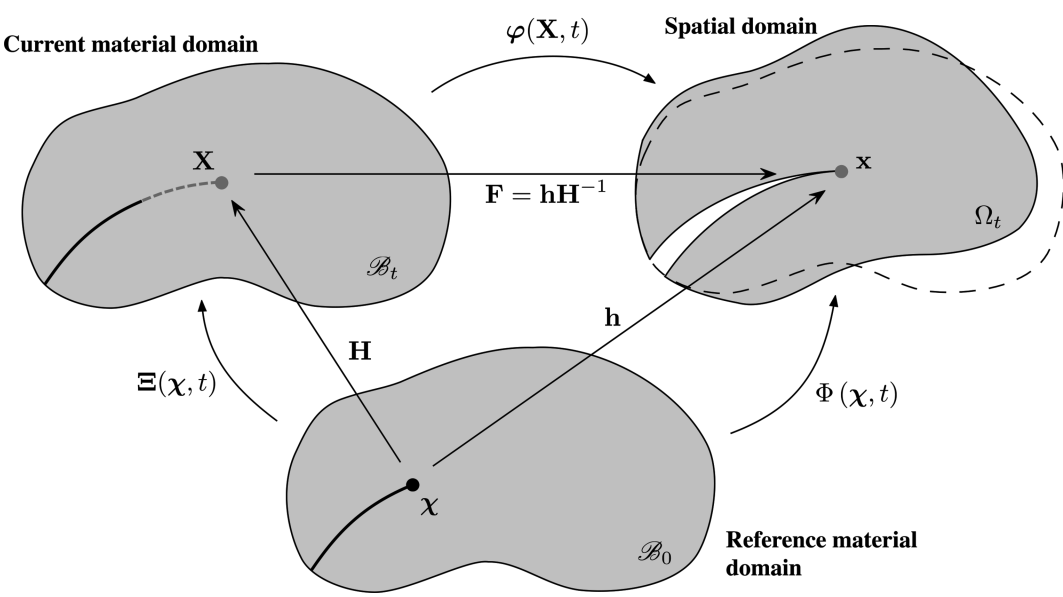

Figure 1. Decomposition of crack propagation in deforming body into material and spatial domains.

3 ENERGY DISSIPATION

Energy dissipation is restricted to an increase in the crack surface area and crack opening. The power of external work on the elastic body is given as:

$$\int_{\partial \mathscr{B}_t} \dot{\mathbf{u}} \cdot \mathbf{t} \, \mathrm{d}S = \int_{\partial \mathscr{B}_t} \left\{ \dot{\mathbf{w}} \cdot \mathbf{t} - \dot{\mathbf{W}} \cdot \mathbf{F}^{\mathrm{T}} \mathbf{t} \right\} \mathrm{d}S \tag{3}$$

where $\mathbf{t}$ is the external traction vector. The rate of change of internal energy of the system can be decomposed as follows:

$$\dot{\mathscr{U}} := \dot{\mathscr{U}}\Gamma + \dot{\mathscr{U}}\mathscr{B}_t \tag{4}$$

where $\mathcal{U}_\Gamma$ is the internal crack energy and $\mathcal{U}_{\mathcal{B}t}$ is the internal body energy. The former is defined as:

$$\mathscr{U}\Gamma := \gamma A_\Gamma \tag{5}$$

where γ is the surface energy and has dimensions N/m. The change of the crack surface internal energy is expressed as:

$$\dot{\mathscr{U}}\Gamma := \frac{\mathrm{d}}{\mathrm{d}t} \mathscr{U}\Gamma = \gamma \dot{A}_\Gamma = \gamma \int_{\partial \Gamma} \mathbf{A} \partial \Gamma \cdot \dot{\mathbf{W}} \mathrm{d}L \tag{6}$$

where $\mathbf{A}_{\partial\Gamma}$ is a dimensionless kinematic state variable that defines the current orientation of the crack front (Kaczmarczyk et al. (2014, 2017)). The change of internal body energy is expressed as

$$\dot{\mathscr{U}}_{\mathscr{B}t} = \frac{\mathrm{d}}{\mathrm{d}t} \int_{\mathscr{B}t} \Psi_V(\mathrm{F}) \mathrm{d}V + \int_{\Gamma t} \Psi_S(\mathrm{g}) \mathrm{d}S \tag{7}$$

where Ψ_V is the free energy of the volume and Ψ_S is free energy of the cohesive crack, which can depend on history variables, and $\mathbf{g}$ is the displacement jump. This can also be expressed as

$$\dot{\mathscr{U}}_{\mathscr{B}t} \int_{\mathscr{B}t} \left\{ \mathbf{P} : \nabla \mathbf{x} \dot{\mathbf{w}} + \Sigma : \nabla \mathbf{x} \dot{\mathbf{W}} \right\} \mathrm{d}V + \int_{\Gamma_t} \mathbf{t} \cdot \dot{\mathbf{g}} \mathrm{d}S \tag{8}$$

where the first Piola-Kirchhoff stress, cohesive traction and Eshelby stress tensors are:

$$\mathbf{P} : \frac{\partial \Psi_V(\mathbf{F})}{\partial \mathbf{F}} \tag{9}$$

$$\mathbf{t} : \frac{\partial \Psi_S(\mathbf{g})}{\partial \mathbf{g}} \tag{10}$$

$$\boldsymbol{\Sigma} : \Psi_V(\mathbf{F}) \mathbf{1} - \mathbf{F}^{\mathrm{T}} \mathbf{P} \tag{11}$$

The Piola-Kirchhoff stress is the familiar driving force for elastic deformation in the spatial domain, whereas the Eshelby stress is its material counterpart and the driving force for local configurational changes.

In this model, energy is dissipated both by the creation of crack surface (configurational change) and crack opening, i.e. due to the work of cohesive forces. The crack propagation criterion is classical, based on Griffith criterion. The crack direction is driven by maximal dissipation of energy, where two phenomena (the creation of crack surface and crack opening) compete with each other.

After some manipulation (Kaczmarczyk et al. (2017)), the first law of thermodynamics,

$$\mathscr{P} = \dot{\mathscr{U}}_\Gamma + = \dot{\mathscr{U}}_{\mathscr{B}t} \tag{12}$$

can be expressed as

$$\dot{\mathbf{W}} \cdot (\gamma \mathbf{A}_{\partial\Gamma} - \mathbf{G}) = 0 \tag{13}$$

where the term $\gamma \mathbf{A}_{\partial\Gamma}$ can be considered the material resistance and

$$\mathrm{G} = \lim_{|\mathcal{L}_\mathrm{n}| \to 0} \int_{\mathcal{L}_\mathrm{n}} \Sigma \mathrm{N} \, \mathrm{d}L \tag{14}$$

the configurational force.

In this model, we are restricted to dissipation at the crack tip and on the crack surface. Crack healing is not permitted, thus the model is restricted to creation of new crack surfaces, it follows that the local forms of the second law is given as

$$\begin{aligned} &\mathscr{D}^G : \gamma \dot{\mathbf{W}} \cdot \mathbf{A}_{\partial\Gamma} \geq 0, \ \mathscr{D}^C := \dot{\mathbf{g}} \cdot \mathbf{t} \geq 0 \\ &\mathscr{D}^G + \mathscr{D}^C \geq 0 \end{aligned} \tag{15}$$

where $\mathscr{D}^G$ and $\mathscr{D}^C$ are the Griffith dissipation of energy per unit length of the crack front and cohesive dissipation per unit of crack surface area. These inequalities restrict evolution of the crack to positive crack area growth at each point of the crack front. Although the first law defines if the crack front is in equilibrium and the second law places restrictions on the direction of crack evolution, it does not determine how $\mathbf{A}_{\partial\Gamma}$ or $\dot{\mathbf{W}}$ evolves. This requires a crack growth criterion.

A straightforward criterion for crack growth, in the spirit of Griffith, is proposed:

$$\phi(\mathbf{G}) = \mathbf{G} \cdot \mathbf{A}_{\partial\Gamma} - g_c / 2 \leq 0 \tag{16}$$

where $g_c = 2\gamma$ is a material parameter specifying the critical threshold of energy release per unit area of the crack surface. For a point on the crack front to be in equilibrium, either $\phi < 0$ and $\dot{\mathbf{W}} = 0$, or $\phi = 0, \dot{\mathbf{W}} \neq 0$ and $\gamma \mathbf{A}_{\partial\Gamma} = \mathbf{G}$ must be satisfied.

To determine the evolution of a point on the crack front we adopt the principle of maximum dissipation. Thus

$$\mathscr{D}_{\max} = (\mathbf{G} - \mathbf{G}^*) \cdot \dot{\mathbf{W}} \geq 0 \tag{17}$$

This can be interpreted as an unconstrained minimisation problem. For a point on the evolving crack front, the crack front orientation is colinear to the configurational force, i.e. $\gamma \mathbf{A}_{\partial\Gamma} = \mathbf{G}$, and the crack extension is given as $\dot{\mathbf{W}} = \dot{\kappa} \mathbf{A}_{\partial\Gamma}$.

4 FINITE ELEMENT RESOLUTION OF CRACK RESOLUTION

The crack front evolves in an implicit, continuous manner (Kaczmarczyk et al. (2017)). The mesh is subsequently moved to resolve the new crack geometry (rather than changing the mesh to create the new crack front). At the end of each load step, equilibrium has been achieved and the configurational forces are parallel to the vector $\mathbf{A}_{\partial\Gamma}$.

In the process of moving the mesh to resolve the moving crack front, the mesh can become distorted, potentially creating poor quality elements leading to numerical errors.

To mitigate this effect, we adopt several strategies:

- *Edge splitting* is applied to elements behind the crack front that have become too elongated. This action will result in the creation of new elements. It is enforced if, for a given node, there exists an adjacent edge with a length greater than 1.5 times the average edge length of all adjacent edges to the node.
- *Node merging* is applied to elements ahead of the crack front that have become too contracted. This action will result in the removal of elements. It is enforced if, for a given node, there exists an adjacent edge with a length less than 1/3 of the length of the longest edge adjacent to the node.
- *Face flipping* is applied to elements in the vicinity of the crack front to ensure that a 3D Delaunay triangulation exists, with optimal internal angles. This is described in more detail below.

These procedures are utilised, if necessary, at the beginning of each load step, before the Newton-Raphson iterations begin, when the solution is already out of equilibrium. Furthermore, in the case when new nodes are added, variables are transferred to the new mesh based upon approximation of the variables using the old mesh.

In addition, the mesh is constantly adapted to maintain mesh quality (Kaczmarczyk et al. (2017)). Figure 2 demonstrates how the crack front evolves using the example of a three-point bending of a beam with an initial corner notch. Crack surface A is an equilibrium solution and the projection of the FE mesh onto the crack surface is shown. Also shown are the configurational forces. Crack surface B shows a subsequent configuration, where the crack front has advanced to a new equilibrium position. The mesh topology has remained the same but the nodes have moved to resolve this new crack geometry. Crack surface C represents a further equilibrium configuration. Here it is clear that the mesh has changed, with new elements being created due to the edge splitting procedure behind the crack front.

4.1 *Face flipping*

At the beginning of each load step, when the solution is out of equilibrium, a patch of elements

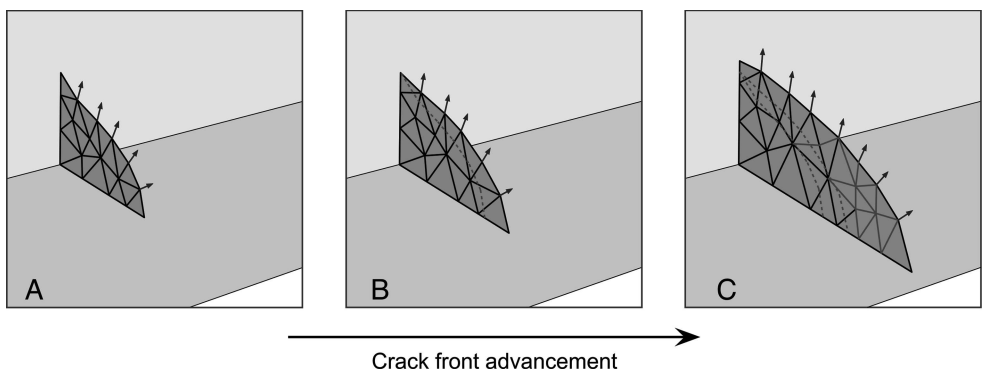

Figure 2. Crack front advancement demonstrated with three-point bending of beam with initial edge notch. The lower images are snapshots of the propagating crack front, with the arrows representing the nodal configurational forces. The projection of the mesh on the crack faces is also shown, including new elements (shown in blue).

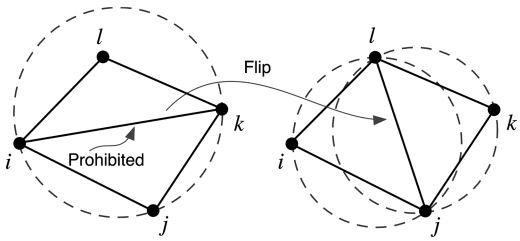

Figure 3. Face flipping in 2D.

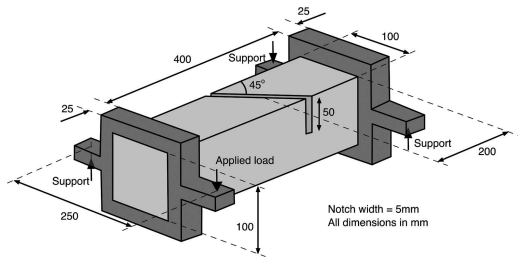

Figure 4. Torsion test geometry.

around the crack front is checked to ensure that it represents a 3D Delaunay triangulation. Figure 3 demonstrates the idea in 2D. Considering the two elements on the left, edge *i-k* is prohibited because it lies in the interior of the circle that intersects the nodes of element *i-j-k* (and element *i-k-l*). Flipping edge *i-k* will address this problem, redefining the two adjacent elements, without affecting the rest of the mesh. Thus, edge *i-k* is removed and replaced by edge *j-l*, and two new adjacent elements are formed that represent a Delaunay triangulation.

5 NUMERICAL EXAMPLES

Kaczmarczyk et al. (2017) have demonstrated the performance of configurational force formulation for linear elastic problems with several numerical examples. Here, two numerical examples are considered. The first illustrates the ability to accurately predict complex crack paths but failure to accurately predict the ultimate load when assuming linear elastic behaviour. The second illustrates the significance of including cohesive cracks to capture size effect of concrete structures.

5.1 *Torsion test*

An experimental study by Brokenshire 1996 of a torsion test of a plain concrete notched prismatic beam (400 mm × 100 mm × 100 mm) is analysed here. The experimental procedure and full details of the boundary conditions and dimensions for the original study are described in Jefferson et al. 2004 and illustrated in Figure 4(a). The notch is placed at an oblique angle across the beam and extends to half the depth. The beam is placed in a steel loading frame, supported at three corners and loaded at the fourth corner. The experiment used aggregates with a maximum size of 10 mm; the characteristic size of the specimen can be considered to be 100 mm.

The beam and steel frame are discretized using tetrahedral elements. The mesh consists of 29,941 nodes. The Young's modulus is 35,000 N/mm^2, Poisson's ratio is 0.2 and fracture energy is 0.08 N/mm.

Figure 5 shows the final crack path. Figure 6 shows the numerically predicted geometry of the

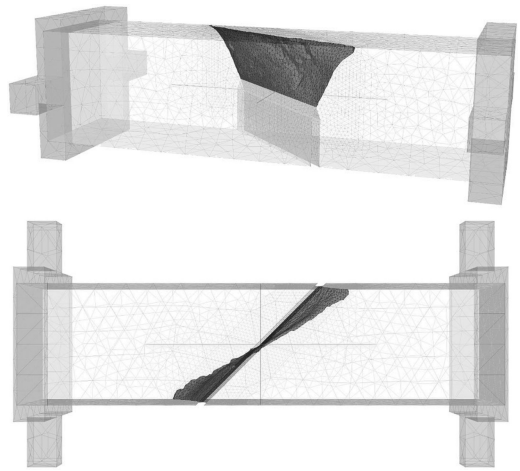

Figure 5. Torsion test crack path.

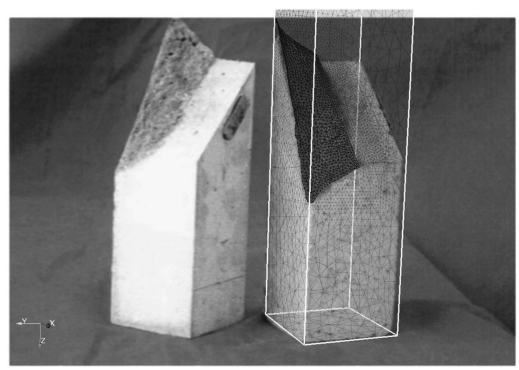

Figure 6. Simulated crack surface superimposed on experimental result, Jefferson et al (2004).

cracked specimen overlain on to the experimentally observed geometry, demonstrating excellent agreement.

Despite the good qualitative predictions, the numerical analyses over predict the experimental

ultimate load by approximately 2.5 times. This difference is a consequence of assuming linear elastic fracture mechanics for a problem where the size of the fracture process zone is significant compared to the size of the problem. This is not an issue for problems where the size of the characteristic size is significantly larger. Even though the crack geometry matches the experimental results very well, the macro-crack has insufficient surface area to match the total amount of dissipated energy.

It is worth noting that Kaczmarczyk et al. (2017) have shown that the ultimate load is accuractly predicted when the test is repeated for nuclear graphite, where the microstructure is signidciantly smaller than for concrete and the assumption of linear elastic fracture mechanics is sufficient.

5.2 *Three-point bending test*

In order to demonstrate the ability to capture size effect through the cohesive elements, a three point bending test is considered where only the crack opening and dissipation due to the crack opening are analysed. The problem is also solved assuming linear elastic fracture mechanics. The span-to-width ratio is 4. The initial crack has a length equal to half the depth. The geometric characteristics are shown on Figure 7. Young's Modulus is 36 GPa, Poisson's ratio is 0.2, tensile strength is 3.8 MPa and the fracture energy 0.0964 N/mm^2.

The characteristic length of the specimen, d, was varied from 200 mm to 5000 mm.

Figure 8 shows the ultimate load vs the characteristic size for both linear elastic and nonlinear fracture mechanics. It can be seen in Figure 8 that as the size decreases, the value of $\log(\sigma_N)$ converges to a horizontal asymptote. As expected, for larger specimen sizes, the two types of analyses converge. It is also shown that, for smaller specimen sizes, the assumption of purely brittle behaviour is not sufficient to correctly capture the strength of the specimen.

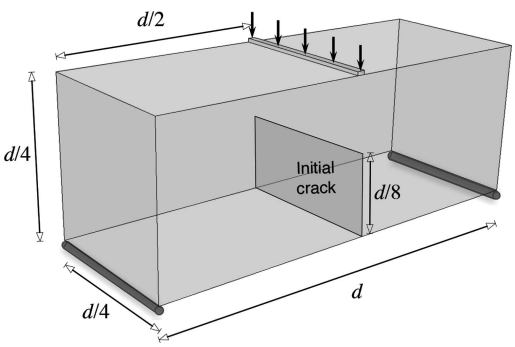

Figure 7. Three point bending test geometry.

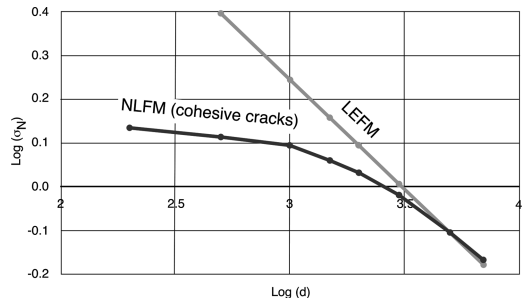

Figure 8. Three point bending test. Size effect for both linear elastic and nonlinear fracture mechanics.

6 CONCLUSIONS

A formulation for cohesive fracture within the context of configurational mechanics has been presented. The linear elastic fracture formulation presented in Kaczmarczyk et al (2017) has been extended to include an additional dissipative mechanism due to cohesive cracks. Configurational forces are the driving force for advancement of the crack front. The local form of the first law of thermodynamics provides a condition for equilibrium of the crack front and the direction of crack propagation is given by the direction of the configurational forces on the crack front. This crack advancement maximises the local dissipation. The moving crack front is continuously resolved by the finite element mesh, without the need for face splitting or the use of enrichment techniques.

To trace the dissipative loading path, an arc-length procedure has been developed that controls the incremental crack area growth. To maintain mesh quality, smoothing of the mesh is undertaken as a continuous process, together with face flipping, node merging and edge splitting where necessary.

Two numerical examples have been presented to demonstrate the significance of including cohesice cracks to capture size effect of concrete structures.

ACKNOWLEDGEMENTS

This work was supported by EDF Energy and The Royal Academy of Engineers (grant number RCSRF1516\2\18). The views expressed in this paper are those of the authors and not necessarily those of EDF Energy.

REFERENCES

Brokenshire, D.R. 1996. *A Study of Torsion Fracture Tests*. Ph.D. Thesis, Cardiff University.

Eshelby, J.D. 1951. The force on an elastic singularity. *Philosophical Transactions of the Royal Society London A*, 224: 87–112.

Eshelby, J.D. 1970. Energy relations and the energy-momentum tensor in continuum mechanics. In M.F. Kanninen et al. (eds), *Inelastic Behavior of Solids*, 77–115.

Gürses, E. & Miehe C. 2009. A computational framework of three-dimensional configurational-force-driven brittle crack propagation. *Computer Methods in Applied Mechanics and Engineering* 198: 1413–1428.

Jefferson, A.D., Barr, B.I.G, Bennett, T. & Hee, S.C. 2004. Three dimensional finite element simulation of fracture test using Craft concrete model, Computers and Concrete, 1: 261–284.

Kaczmarczyk, Ł., Mousavi Nezhad, M. & Pearce, C.J. 2014. Three-dimensional brittle fracture: configurational-force-driven crack propagation. *International Journal of Numerical Methods in Engineering* 97: 531–550.

Kaczmarczyk, Ł., Ullah, Z. & Pearce, C. J. 2017. Energy consistent framework for continuously evolving 3D crack propagation. *Computer Methods in Applied Mechanics and Engineering* 324: 54–73.

Maugin, G.A. 1993. Material Inhomogeneities in Elasticity. Chapman & Hall, London.

Maugin, G.A. 2010. Configurational Forces: Thermomechanics, Physics, Mathematics, and Numerics, Chapman & Hall, London.

Miehe, C., Gürses E. & Birkle M. 2007. A computational framework of configurational-force-driven brittle fracture propagation based on incremental energy minimization. *International Journal of Fracture* 145: 245–259.

Steinmann, P. 2000. Application of material forces to hyperelastic fracture mechanics. I. Continuum mechanical setting. *International Journal of Solids & Structures* 37: 7371–7391.



Taylor & Francis
Taylor & Francis Group
http://taylorandfrancis.com

Computational Modelling of Concrete Structures – Meschke, Pichler & Rots (Eds)
© 2018 Taylor & Francis Group, London, ISBN 978-1-138-74117-1

A constitutive law for concrete with smooth transition from continuous into discontinuous cracks' description

J. Bobiński & J. Tejchman
Faculty of Civil and Environmental Engineering, Gdansk University of Technology, Gdansk, Poland

ABSTRACT: Paper presents a constitutive model for concrete that combines a continuous and discontinuous crack's description to simulate the concrete under tensile dominated loads. In a continuum regime, two different constitutive laws were used. First, a plasticity model with the Rankine failure criterion and an associated flow rule was used. Second, a constitutive law based on isotropic damage mechanics was formulated. Both model alternatives were enriched by a characteristic length of micro-structure with the aid of a integral non-local theory to preserve the mesh-insensitivity of FE-results. Displacement jumps across cracks were captured by applying the eXtended Finite Element Method (XFEM) with cohesive tractions. A transfer function was introduced allowing for a gradual switch from a continuous (smeared) to discontinuous (discrete) softening process. Nodes and elements in the transition zone were doubled. Two benchmarks were numerically simulated with a dominated mode-I (three-point bending test) and under mixed-mode conditions (Nooru-Mohamed test).

1 INTRODUCTION

Cracking is one of the most critical phenomena that should be taken into account in numerical simulations of the concrete behavior. Fracture in concrete is responsible for both the strength and stiffness reduction and it precedes usually the structural failure. At the beginning of loading, a region with several micro-cracks is formed. Upon further loading, a discrete macro-crack emerges from this region of localized deformation. An adequate description of fracture in numerical FE calculations is extremely important to obtain physically realistic results. Within continuum mechanics, there exist two main approaches to describe cracks. The first one describes them in a smeared sense as localized zones of micro-cracks with a non-zero finite width. These approach has to be equipped with one of the regularization methods to properly describe material softening. The alternative approach introduces displacement jumps across cracks while keeping the remaining region as a continuous one. A smeared approach is more proper when describing a micro-crack formation phase while a discontinuous one allows for a better simulation of a macro-crack propagation. Usually, only one approach is used to simulate a crack growth in concrete during the entire deformation process. A combination of continuous and discontinuous approaches makes enables to realistically capture both stages of fracture.

Bobiński & Tejchman (2014, 2016) formulated a constitutive law which combined continuous and discontinuous cracks' description to simulate concrete under tensile dominated loadings. In continuous regime two alternatives were used: elasto-plasticity with the Rankine criterion or isotropic damage mechanics with different definitions of the equivalent strain. In order to obtain mesh independent results, a non-local theory in an integral format was used for both laws as a regularization technique. Displacement jumps across cracks were captured by applying the eXtended Finite Element Method (XFEM) with cohesive tractions. Initially, in all finite elements (integration points), a continuum constitutive law with non-local softening was solely active. A new crack segment was created in the element if the softening driving (state) variable of the constitutive model was greater than assumed the threshold value in element integration points at the front of the crack tip. The direction of the crack segment was calculated from the state variable field. The tractions at the moment of cracking and softening curve parameters were determined from two principles: the dissipated energy balance and stress equilibrium. The formulation proved to be able to simulated different benchmarks but it suffered from some convergence problems and jumps observed on force-displacement curves. Some special techniques had to be proposed in the transition process to obtain a converged solution.

The improvement of the original formulation presented in this paper introduces a smooth transition from continuous (smeared) to a discontinuous (discrete) cracking process via defining a transfer function. It also doubles nodes and finite elements located in a band perpendicular to a newly created discrete crack segment. The width of this doubled zone covers the width of a smeared localized zone. Both doubled element sets share the same nodes along zone boundaries (excluding specimen edges). The problem of the length of the transfer zone along the crack was examined. The computation effectiveness was also analyzed. In addition, an alternative nested scheme (with sub-iterations) was investigated. Two benchmarks were numerically simulated: the first one with a dominated mode-I (three-point bending test) and the second one under mixed-mode conditions (Nooru-Mohamed test).

2 SMEARED CRACKS

2.1 *Elasto-plasticity*

In continuum, an elasto-plastic constitutive law with the standard Rankine criterion was first used. The yield function for 2D case was defined as:

$$f = \max\{\sigma_1, \sigma_2\} - \sigma_t(\kappa_C) \tag{1}$$

where σ_1 and σ_2 = the principal stresses, σ_t = the tensile yield stress and κ_C = the hardening/softening parameter (equal to the maximum principal plastic strain ε_1^p). An associated flow rule was assumed. To define the tensile yield strength σ_t, the exponential softening curve was assumed:

$$\sigma_t(\kappa_C) = f_t \exp\left(-\frac{\kappa_C}{\kappa_u}\right) \tag{2}$$

where f_t = the tensile strength and κ_u = the parameter that controls the slope of the softening curve (it can be interpreted as an intersection point of a tangent line from the peak point with the horizontal axis). This curve was chosen to obtain a perfect match with the exponential softening curve in XFEM (see Section 3). A formulation with this simple exponential softening curve produced very similar results to ones with more sophisticated curves as, e.g. with the experimentally motivated non-linear curve by Hordijk (1991).

2.2 *Continuum damage mechanics*

The second constitutive law was defined within continuum isotropic damage mechanics. The initiation and propagation of micro-cracks was described by a scalar damage parameter D. The virgin state with the elastic stiffness corresponded to the parameter $D = 0$, while a completely cracked material was described by $D = 1$. The damage variable D acted as a stiffness reduction factor:

$$\boldsymbol{\sigma} = (1 - D)\mathbf{C}^e\boldsymbol{\varepsilon} \tag{3}$$

where $\boldsymbol{\sigma}$ = stress vector; $\boldsymbol{C}^e$ = elasticity matrix; and $\boldsymbol{\varepsilon}$ = strain vector. The growth of the variable D was controlled by a monotonically increasing damage history parameter κ_C (no connection with κ_C from Section 2.2) that was defined as the maximum of the equivalent strain measure $\tilde{\varepsilon}$ reached during the entire load history:

$$\kappa_C(t) = \max_{\tau \le t}\{\tilde{\varepsilon}(\tau)\} \tag{4}$$

The equivalent strain $\tilde{\varepsilon}$ is a scalar that takes into account the sensitivity of a degradation process to different principal strain components. Here a definition proposed by Jirásek (2004) for tension (equivalent to the Rankine criterion in plasticity) was used:

$$\tilde{\varepsilon} = \max\{\sigma_i^{eff}\}/E \tag{5}$$

where σ_i^{eff} = principal values of the effective stresses (defined as $\boldsymbol{C}^e\boldsymbol{\varepsilon}$); and E = Young modulus. In order to describe the evolution of the damage variable D, an exponential softening law was used:

$$D = 1 - \frac{\kappa_0}{\kappa_C}\left(1 - \alpha + \alpha e^{-\beta(\kappa_C - \kappa_0)}\right) \tag{6}$$

where κ_0 = the initial value of the damage threshold parameter κ_C; and α and β = the material parameters. The parameters α and β were calibrated based on a force-displacement curve in softening from uniaxial tension tests.

2.3 *Non-local regularization*

Strain softening causes the ill-posedness of the boundary value problem and FE-results become mesh dependent. In order to achieve mesh-independent results, a non-local theory in an integral format was used as a regularization technique.

2.3.1 *Elasto-plasticity*

In elasto-plasticity the rates of the softening parameter $\mathrm{d}\kappa_C$ were treated non-locally according to Brinkgreve (1994):

$$\mathrm{d}\bar{\kappa}_C(\boldsymbol{x}) = (1 - m)\,\mathrm{d}\kappa_C(\boldsymbol{x}) + m\,\mathrm{d}\hat{\kappa}_C(\boldsymbol{x}) \tag{7}$$

with:

$$\mathrm{d}\hat{\kappa}_C(\boldsymbol{x}) = \frac{\int_V \alpha_0\left(\|\boldsymbol{x}-\boldsymbol{\xi}\|\right)\mathrm{d}\kappa_C(\boldsymbol{\xi})\mathrm{d}\boldsymbol{\xi}}{\int_V \alpha_0\left(\|\boldsymbol{x}-\boldsymbol{\xi}\|\right)\mathrm{d}\boldsymbol{\xi}} \tag{8}$$

where $\boldsymbol{x}$ = the coordinates of considered (actual) point; $\boldsymbol{\xi}$ = the coordinates of the surrounding points; and m = the non-locality parameter (it should be greater than 1). As the weighting function α_0, the Gauss distribution was assumed:

$$\alpha_0(r) = \frac{1}{l\sqrt{\pi}} e^{-\left(\frac{r}{l}\right)^2} \tag{9}$$

where r = the distance between points; and l = the characteristic length of micro-structure. The above averaging was restricted only to a small area around each material point (the influence of points at the distance of $r = 3l$ is only of 0.01%).

In FE-simulations, an approximated method was used to evaluate non-local quantities. In the given integration point, the influence of its neighbors was determined using the values from the previous iteration. It enabled us to simplify FE calculations and to preserve the locality of plasticity algorithms. Two splitting methods were used. The first one was based on the proposal by Strömberg & Ristinmaa (1996) and it will be called as the Newton split (superscripts (i) and (i-1) stand for iteration counters):

$$\Delta\bar{\kappa}_C^{(i)}(\boldsymbol{x}) = \Delta\kappa_C^{(i)}(\boldsymbol{x}) + m\left(\Delta\hat{\kappa}_C^{(i-1)}(\boldsymbol{x}) - \Delta\kappa_C^{(i-1)}(\boldsymbol{x})\right) \tag{10}$$

Alternatively the approach proposed by Rolshoven (2003) called the local—non-local split was used:

$$\Delta\bar{\kappa}_C^{(i)}(\boldsymbol{x}) = (1-m)\Delta\kappa_C^{(i)}(\boldsymbol{x}) + m\Delta\hat{\kappa}_C^{(i-1)}(\boldsymbol{x}) \tag{11}$$

In both formulas the terms with the (i–1) iteration counter were taken from the previous global iteration and they were frozen during local iteration at the material point during the global actual iteration (i) while the terms with the superscript (i) were active and they could change their values. Moreover when using the split from Equation (11), a local tangent stiffness matrix was also used:

$$\boldsymbol{C} = \boldsymbol{C}^e - \frac{\boldsymbol{C}^e \frac{\partial f}{\partial \boldsymbol{\sigma}} \left(\frac{\partial f}{\partial \boldsymbol{\sigma}}\right)^T \boldsymbol{C}^e}{\left(\frac{\partial f}{\partial \boldsymbol{\sigma}}\right)^T \boldsymbol{C}^e \frac{\partial f}{\partial \boldsymbol{\sigma}} + (1-m)H} \tag{12}$$

where H = softening (negative) modulus of the tensile yield strength in Equation (2). For $m > 1$, the second term in the denominator was positive (two negative numbers) and the matrix was equivalent to materials with hardening plasticity. As a consequence no numerical problems occurred when solving global system of equations.

2.3.2 *Continuum damage mechanics*

In the simulations within isotropic damage, the equivalent strain measure $\tilde{\varepsilon}$ was replaced by its non-local counterpart $\bar{\varepsilon}$:

$$\bar{\varepsilon}(\boldsymbol{x}) = \frac{\int_V \alpha_0\left(\|\boldsymbol{x}-\boldsymbol{\xi}\|\right)\tilde{\varepsilon}(\boldsymbol{\xi})\mathrm{d}\boldsymbol{\xi}}{\int_V \alpha_0\left(\|\boldsymbol{x}-\boldsymbol{\xi}\|\right)\mathrm{d}\boldsymbol{\xi}} \tag{13}$$

3 DISCRETE CRACKS

The Extended Finite Element Method (XFEM) was used to describe discrete cracks in continuum. It is based on a local partition of the unity (PUM) concept by Melenk & Babuška (1996). It enables adding 'ad hoc' extra terms to a standard FE displacement field interpolation. These extra functions are responsible for capturing displacement jumps. In XFEM cracks do not have to be placed along finite element edges; they may pass through elements without remeshing. Due to a local nature of the enrichment, extra displacement degrees of freedom are solely introduced into finite elements cut by a discontinuity. They are gradually added to subsequent finite elements when a crack propagates. The formulation used in the paper follows (with some improvements and modifications) the original concept by Wells & Sluys (2001). In order to describe jumps in the displacement field, the so-called shifted-basis enrichment proposed by Zi & Belytschko (2003) was used. The shifted-basis enrichment simplifies the implementation of XFEM (two types of the finite elements exist only). Moreover the total nodal displacements are equal to the standard ones.

3.1 *Constitutive laws*

In the bulk continuum, a linear elastic relationship was assumed. An constitutive law between displacement jumps [[$\boldsymbol{u}$]] and tractions $\boldsymbol{t}$ was defined in the crack. The degradation process was controlled by the variable κ_D defined as a maximum value of normal displacement jumps [[u_n]] obtained during loading. During active loading the softening of the normal component of the traction vector t_n was described by the yield curve σ_n using an exponential relationship:

$$\sigma_n(\kappa_D) = D_f f_t \exp\left(-\frac{f_t \kappa_D}{G_F}\right) \tag{14}$$

where G_F = the fracture energy; and D_f = the correction term defined as:

$$D_f = 1 - \exp\left(-\kappa_D \frac{d_f f_t}{G_F}\right) \tag{15}$$

where d_f = the drop factor (Cox 2009). This factor improved the convergence in cases with tension-compression changes. With increasing d_f, the term D_f approached 1. During unloading, the secant stiffness was used with a return to the origin (damage format). In a compressive regime, the penalty stiffness in the normal direction was assumed (it depended on the drop factor d_f). In a tangential direction a constant stiffness T_s was assumed.

3.2 *Crack propagation*

A new crack could be activated or an existing crack could propagate, if the standard Rankine criterion ($\sigma_{\max} > f_t$) was fulfilled at least in one point of the finite element at the front of a crack tip. The direction of a crack extension was assumed to be perpendicular to the direction of the maximum principal stress of the stress vector $\boldsymbol{\sigma}_{tip}$ at the crack tip. These stresses were calculated as the averaged values (Wells & Sluys 2010):

$$\boldsymbol{\sigma}_{tip} = \int_V \boldsymbol{\sigma} w \, \mathrm{d}V \tag{16}$$

where V = the semi-circle domain at the front of the crack tip; and w = the averaging function defined as:

$$w(r) = \frac{1}{(2\pi)^{3/2} l_{av}^3} \exp\left(-\frac{r^2}{2l_{av}^2}\right) \tag{17}$$

where r = the distance from the crack tip; and l_{av} = the averaging length related to the size of finite elements (note that this averaging operation was not intended to introduce an additional characteristic length into a constitutive model). If the direction of the crack propagation is known in advance, a fixed value may be applied. A new crack tip could be placed at the element edge exclusively.

4 COUPLED APPROACH

4.1 *Crack's growth*

Initially, in all finite elements (integration points), a continuum constitutive law with non-local softening was active. A new crack segment was created if the following condition was fulfilled in any of element's integration points at the front of a crack tip:

$$\bar{\kappa}_C > \kappa_{CD} \tag{18}$$

where κ_{CD} = the softening parameter at the transition moment. The parameter $\bar{\kappa}_C$ can be taken for elasto-plasticity (Section 3.1) or continuum damage mechanics (Section 3.2). In some cases, the examination of this condition in the finite element only at the front of the crack tip may cause a locking or crack growth delay. Therefore an extended version of the crack growth criterion was also formulated. In this approach the inequality given by Equation 18 was checked both in all integration points of the finite element at the front of the crack tip and in all integration points in a circle section with the radius l_{crk} and angle φ_{crk}. This section was symmetrically located along the extension of the last crack segment (Figure 1). The direction of a discrete crack propagation $\boldsymbol{p}$ was determined as (Wells et al. 2002):

$$\boldsymbol{p}(\boldsymbol{x}) = \int_V \kappa_p(\xi) w(\|\bar{\boldsymbol{p}}\|) \frac{\bar{\boldsymbol{p}}}{\|\bar{\boldsymbol{p}}\|} \, \mathrm{d}V \tag{19}$$

where $\bar{\mathbf{p}}$ = the direction from the crack tip $\boldsymbol{x}$ to any point $\boldsymbol{\xi}$ in V.

Two conditions had to be fulfilled in the formulation of a coupled continuous-discontinuous constitutive law. The first one is a stress equilibrium. The initial tractions t_n^{init} and t_s^{init} were calculated by projecting continuum stresses onto a crack segment line at the crack creation moment. Based on the known tractions t_n^{init} and t_s^{init}, the initial displacement jumps $[\![u_n^{init}]\!]$ and $[\![u_s^{init}]\!]$ were determined using Equations (14) and (15) (see also Figure 2). The initial displacement jump $[\![u_n^{init}]\!]$ was also added to the value of the parameter κ_x. As a consequence, the XFEM softening in a normal direction started not from the value f_t (at the peak)

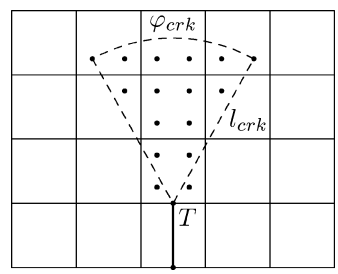

Figure 1. Crack activation criterion with extended method.

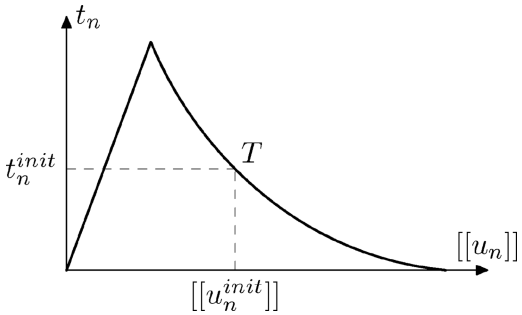

Figure 2. Initial traction and displacement.

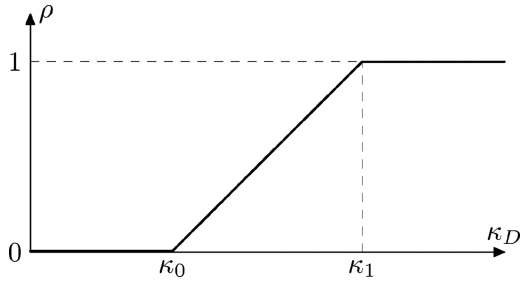

Figure 3. Transfer function ρ: κ approach.

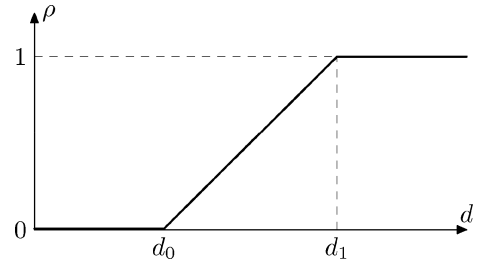

Figure 4. Transfer function ρ: distance approach.

but from a smaller value. A newly inserted crack segment had already accumulated softening.

The second condition required the equivalence of the dissipated energy. The energy not yet dissipated in the continuum softening should be equal to the energy to be dissipated during a discrete softening process (starting from a 'non-peak' configuration). When using elasto-plasticity with non-local softening and XFEM, the dissipated energies for the same yield stress are identical and no special modifications of the softening curve in XFEM are required. To ensure the equivalence of the total dissipated energy in the both approaches, it was sufficient to relate the fracture energy G_F from XFEM with the parameters κ_u, m and l in non-local plasticity (Bobiński & Tejchman 2016). For a continuum damage constitutive law this was not the case. The additional information regarding a stress-displacement curve from the 1D tension test with a damage model had to be provided. Moreover this curve had to be adjusted at the moment of the crack creation to take into account a degradation state in the specimen (Bobiński & Tejchman 2016).

4.2 *Transfer function*

A change of the width of the active localization zone from several finite elements in a non-local model to one finite element in XFEM may cause some convergence problems (Bobiński and Tejchman 2014, 2016). To overcome them an improvement was proposed here. The proposed extension introduced a transfer function ρ that allowed for a gradual switch from a continuous (smeared) to discontinuous (discrete) softening process. It was equal to zero at the tip (no discrete softening) and increased to the maximum value of 1 (no continuum softening). Two possibilities were analyzed. First the transfer function ρ depended on the value of the XFEM variable κ_D (Figure 3). Usually the initial value κ_0 corresponded to κ_D at the transition moment. The κ_1 value controlled the 'transition speed'. Alternatively a dependence on the distance from the crack tip was introduced (Figure 4). Usually the distance d_0 was equal to zero (located at the crack tip).

By extending a crack with a new segment, nodes and finite elements located in a band perpendicular to this segment were doubled. The width of a doubled zone covered the width of a localized zone (it was equal to $6 \times l$ in all simulations). At the bottom layer of finite elements, a continuum law with softening was applied (as in Section 2). At the top layer of finite elements, linear elasticity in bulk and a discrete crack with cohesive softening law were used (as in Section 3). The resultant stresses $\boldsymbol{\sigma}$ were calculated as:

$$\boldsymbol{\sigma} = (1-\rho)\boldsymbol{\sigma}_C + \rho\boldsymbol{\sigma}_D \tag{20}$$

where $\boldsymbol{\sigma}_C$ = the stresses in the continuous layer; and $\boldsymbol{\sigma}_D$ = the stresses in the discontinuous layer. The same formula was used to calculate resultant strains and continuous and discrete state variables. The transfer function ρ was perpendicularly projected from the crack. The doubled element sets shared the same nodes along zone boundaries (Figure 5). As a consequence no special algorithm

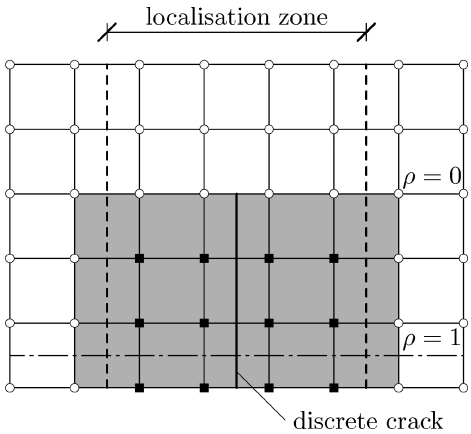

Figure 5. Doubled FE mesh (grey region) with standard (hollow circles) and doubled (black squares) nodes and isolines of function ρ.

was required to force a softening transfer between both approaches.

5 THREE-POINT BENDING TEST

5.1 *Input data*

The geometry of the concrete beam under plane stress conditions is given in Figure 6. Due to a symmetry of the problem, a localized zone and discrete crack were formed along the vertical symmetry axis. The imposed final vertical displacement was $u_{fin} = 0.4$ mm. The Young modulus and Poisson ratio were assumed as $E = 30$ GPa and $\nu = 0.2$. The tensile strength was taken as $f_t = 3.0$ MPa. In plasticity, the exponential softening curve with the parameter $\kappa_u = 2.10 \cdot 10^{-3}$ was chosen. The characteristic length of micro-structure was equal to $l = 5$ mm and the non-locality parameter was $m = 2$. In XFEM, the exponential softening scheme with the fracture energy $G_F = 120$ N/m was assumed and the shear stiffness was $T_s = 0$ N/m^3. The default transition point was $\kappa_{CD} = 14.56 \cdot 10^{-4}$ that corresponded to the 50% of the tensile strength.

5.2 *Results within elasto-plasticity*

5.2.1 *Mesh sensitivity*

First the mesh insensitivity was examined. Three different finite element meshes were defined: coarse, medium and fine with 600, 1260 and 2280 4-node quad elements, respectively. In the mid-region, the refined meshes were assumed with 20, 40 and 80 elements along the vertical symmetry axis for the coarse, medium and fine mesh, respectively. The computed force-displacement curves are presented in Figure 7. In general the obtained

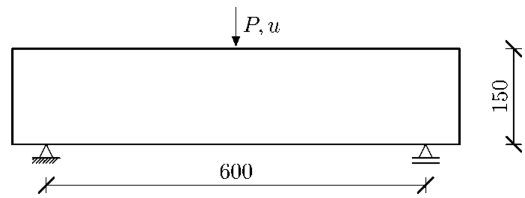

Figure 6. Three-point bending: geometry and boundary conditions.

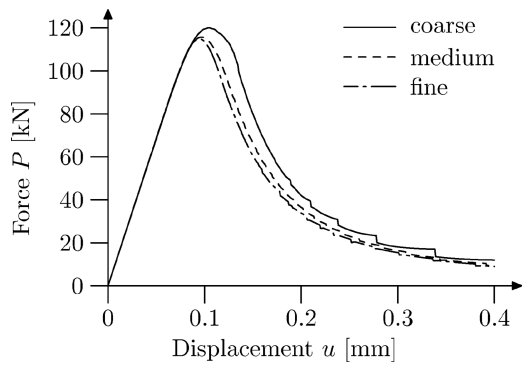

Figure 7. Three-point bending: force-displacement diagrams for different meshes.

curves are similar, although some discrepancies can be observed, especially for the coarse mesh. The finer was mesh, the smaller jumps occurred. The FE-calculations required 2639, 2891 and 5879 iterations to complete the simulation for the coarse, medium and fine mesh, respectively (at least 500 iterations were required). Thus a number of iterations significantly increased for the fine mesh. The simulations with pure XFEM and pure elasto-plasticity required 901 and 2402 iterations only.

5.2.2 *Transfer zone with κ approach*

Next the simulations were performed with different definitions of the mixed zone. The κ approach was used with the different parameters κ_0 and κ_1. A fine mesh was used. Figure 8 shows the force-displacement diagrams for $\kappa_0 = \kappa_{CD}$ with the different κ_1. The values for κ_1 were chosen in such a way to obtain the transfer zone equivalent to the decrease of the yield strength in XFEM equal to $0.1f_t$, $0.2f_t$ and $0.3f_t$. Such a transfer zone was labeled as $[\Delta\rho] = 0.1f_t$ etc. Except of the smallest value $[\Delta\rho] = 0.1f_t$, the almost identical and smooth curves were computed. The total number of iterations was equal to 11270 (0.904), 5879 and 4495 for the $[\Delta\rho]$ equivalent to $0.1f_t$, $0.2f_t$ and $0.3f_t$, respectively. The number in brackets denotes the load part when a simulation failed to converge.

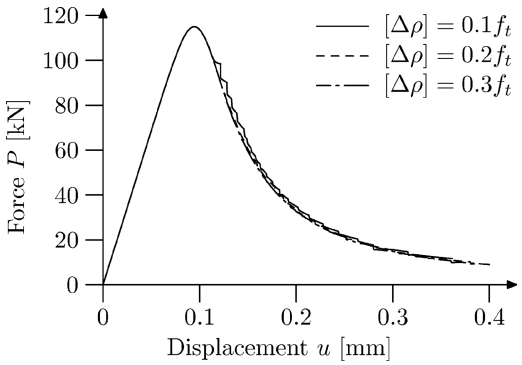

Figure 8. Three-point bending: force-displacement diagrams for κ approach and different definitions of the transfer zone.

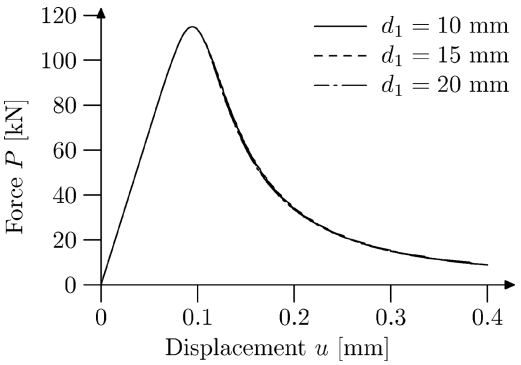

Figure 10. Three-point bending: force-displacement diagrams for distance approach and different definitions of the transfer zone.

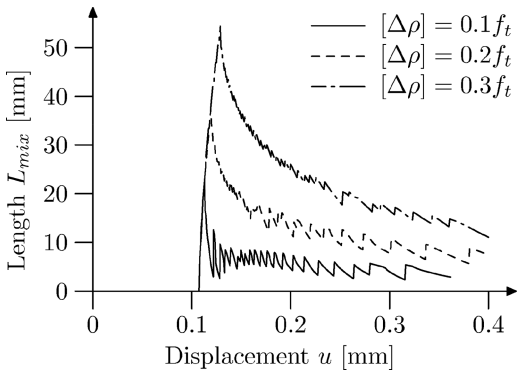

Figure 9. Three-point bending: evolution of lengths of the mixed zone for κ approach and different definitions of the transfer zone.

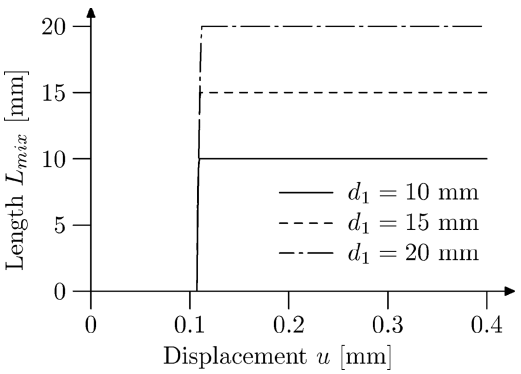

Figure 11. Three-point bending: evolution of lengths of the mixed zone for distance approach and different definitions of the transfer zone.

The calculated lengths (along the crack) of the mixed zone are shown in Figure 9. It can be seen that the larger the value of $[\Delta\rho]$ was assumed, the longer mixed zone was obtained. However this length decreased significantly at the end of the loading. This fact could explain convergence problems observed in simulations during later stages. The creation of a new segment caused usually an increase of the length of the mixed zone (jumps observed on all diagrams).

5.2.3 *Transfer zone with distance approach*

The distance approach to define the transfer zone was also examined. A fine mesh was again used. Figure 10 presents the calculated force—displacement curves for $d_0 = 0$ (start at the crack tip) and the different parameters d_1. The almost identical diagrams were generated. The lengths of the mixed zone are shown in Figure 11.The assumed length was quickly achieved after the start of discrete crack's growth. The total number of iterations was 5973, 4456 and 3728 for the parameter d_1 taken as 6 mm, 9 mm and 12 mm, respectively. The larger the parameter d_1 was assumed, the smaller number of iterations were executed. With the parameter d_0 equal to 6 mm and parameter d_1 assumed as 12 mm, 15 mm and 18 mm (the length of the mixed zone did not change) the total number of iterations was approximately the same for all values of d_1: 3385, 3589 and 3661.

5.2.4 *Sub-iteration algorithms*

Moreover, some simulations with advanced calculation scheme were executed. The iterations within one increment were divided into main iterations and sub-iterations. During sub-iterations the transfer function ρ in nodes was not calculated but values from the last main iteration were used. To update these values, a tolerance of the solution was not allowed to be greater than Tol_S or the number of sub-iterations exceeded $S_{\max}$. Four sets of parameters were analyzed: the set S1

with Tol_S = 0.01 and S_{max} = 200, the set S2 with Tol_S = 0.1 and S_{max} = 20, the set S3 with Tol_S = 0.05 and S_{max} = 10 and the set S4 with Tol_S = 0.025 and S_{max} = 5. The default global error tolerance was equal to 0.01. In the simulations with the set S1, the values of ρ transfer functions were calculated only at the beginning of each increment (and after defining a new crack segment). In simulations for the fine mesh and κ approach with $[\Delta\rho]$ equivalent to $0.2f_t$ the total number of iterations was approximately the same: 5352, 5567, 5662 and 5714 for the parameter sets S1, S2, S3 and S4, respectively. The simulations showed that the use of sub-iterations did not increase the efficiency of the algorithm (almost the same number of iterations was obtained in Section 5.2.1).

5.2.5 *Splitting methods*

Finally different splitting methods and different stiffness matrices were examined. The Newton split with the elastic stiffness matrix, local-non-local split with the elastic stiffness and local tangent matrices were analyzed. A medium mesh was used with the κ approach. For the global tolerance 0.01 the total number of iterations was 7062, 6652 and 2891 for the Newton split with the elastic stiffness matrix, local-non-local split with the elastic stiffness matrix and local-non-local split with the local tangent matrix, respectively. With the larger tolerance of 0.02, the total number of iterations was 4045, 3674 and 2057. For the fine mesh the local-non-local split with the local tangent matrix formulation was solely able to successfully end up the calculations. Therefore this method was chosen as a default approach in all simulations.

5.3 *Results within damage mechanics*

As a companion simulation three-point bending was repeated using a continuum damage model. The following parameter for the isotropic damage constitutive law were assumed: $\kappa_0 = 10^{-4}$, $\alpha = 1.0$, $\beta = 425$. The characteristic length of micro-structure was equal to $l = 5$ mm. The parameter κ_{CD} was taken as $2 \cdot 10^{-3}$. The curve describing softening of the discrete crack was defined based on uniaxial tension. The calculated force-displacement diagram for the medium mesh is presented in Figure 12. A smooth curve was obtained.

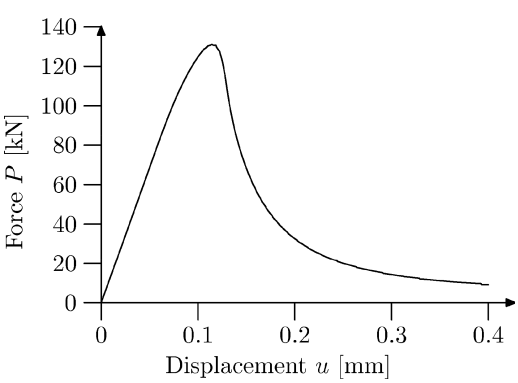

Figure 12. Three-point bending: force-displacement curve within continuum damage mechanics.

6 NOORU-MOHAMED TEST

6.1 *Input data*

As a second benchmark, a double-edge notched (DEN) concrete specimen under combined shear and tension was analyzed (experiment performed by Nooru-Mohamed (1992)). The length and height of the specimen were 200 mm, and the thickness was 50 mm (Figure 13). Two notches with the dimensions of 25×5 mm^2 were located at the mid-points of vertical edges. During the analyzed load scenario, the shear force P_s was applied until it reached a specified value, while the horizontal edges were free. Then the shear force remained constant and the vertical tensile displacement was prescribed. In the experiment, two curved cracks with an inclination depending upon P_s were observed (for the small value of P_s – the cracks were almost horizontal, for the large value of P_s – the cracks were strongly curved), Figure 14. In order to evaluate the quality of cracks, a measure called the crack height h_c was introduced. It was defined as a vertical distance between a horizontal line connecting

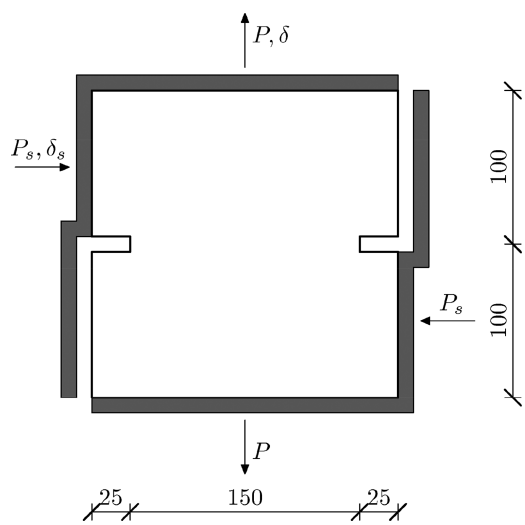

Figure 13. Nooru-Mohamed test: geometry and boundary conditions.

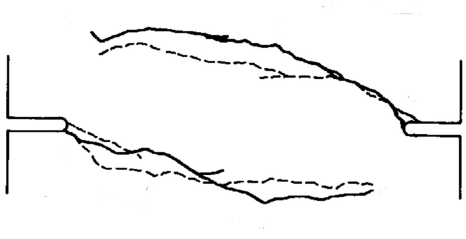

Figure 14. Nooru-Mohamed test: experimental crack geometry for $P_s = 10$ kN.

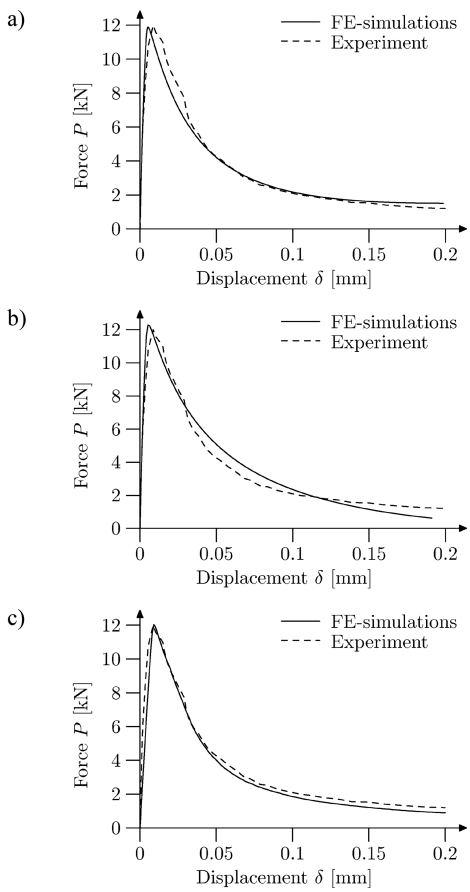

Figure 15. Nooru-Mohamed test: force-displacement curves for: a) pure elasto-plastic model, b) XFEM and c) coupled formulation.

notches and the most far-distant point lying on crack lines. In the experiment, the height h_c, calculated as the average value for 4 cracks, was equal to 3.5 cm (in the range 2.7 = 4.3 cm) for the horizontal shear force of 10 kN.

In calculations the Young modulus and Poisson ratio were assumed as $E = 32.8$ GPa and $v = 0.2$. The tensile strength was taken as $f_t = 2.3$ MPa. In plasticity, the exponential softening curve with the parameter $\kappa_u = 4.20 \cdot 10^{-3}$ was chosen. The characteristic length of micro-structure was $l = 2$ mm and the non-locality parameter was $m = 2$. In XFEM, the exponential softening scheme with the fracture energy $G_F = 75$ N/m was assumed and the shear stiffness was $T_s = 10^{12}$ N/m^3. The default transition point was $\kappa_{CD} = 2.91 \cdot 10^{-3}$ (50% of the tensile strength). The crack growth criterion was checked in the circle section with the angle $\varphi_{crk} = 30°$ and radius $l_{crk} = 5$ mm ahead the crack tip. The k approach with $[\Delta\rho]$ equivalent to $0.2 f_t$ was assumed.

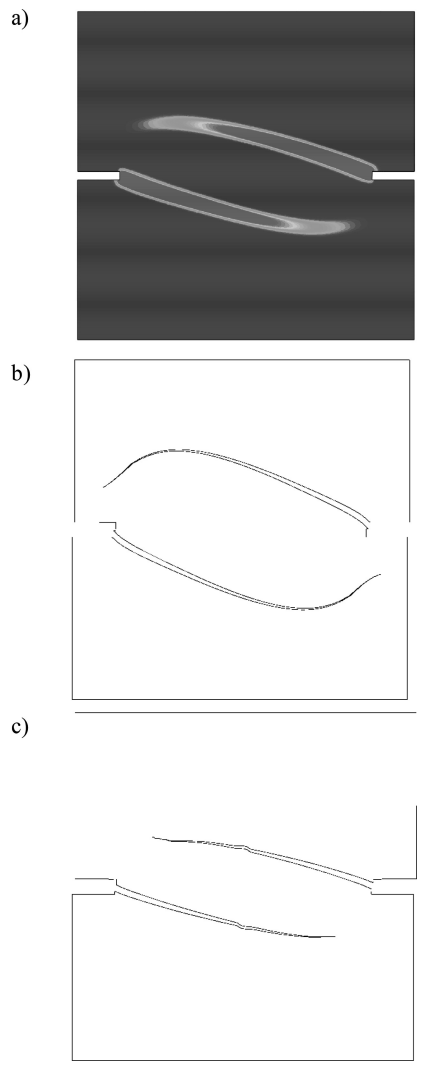

Figure 16. Nooru-Mohamed test: crack patterns for: a) pure elasto-plastic model, b) XFEM and c) coupled formulation.

6.2 *FE-results*

Figure 14 presents the computed force-displacement curves for 3 approaches. Each of them provided the results very similar to the experiment. The calculated crack-patterns are depicted in Figure 15. For the elasto-plastic model the crack height h_c was equal to 2.8 cm (slightly smaller than the experimental value of 3.5 cm). In turn, the XFEM simulations resulted in the too curved cracks (their height was 4.6 cm). In the coupled approach the height h_c was 2.8 cm (similarly as in plasticity).

7 CONCLUSIONS

The presented constitutive law enables a more realistic description of cracks in concrete elements. The formulation is general and it allows for using all constitutive laws in bulk continuum (e.g. isotropic version of a continuum damage mechanics) and all displacement jump-traction relationships along cracks. It may be also easily extended to take into account a decrease of a characteristic length of micro-structure with loading and to obtain more realistic displacement profiles in localized zones. The numerical effectiveness of the proposed formulation was also investigated. The local-non-local split with local tangent stiffness matrix turned out to be the most effective approach within elasto-plasticity. The use of sub-iteration schemes did not improve the formulation robustness.

ACKNOWLEDGMENTS

The research work has been carried out within the project "Experimental and numerical analysis of coupled deterministic-statistical size effect in brittle materials" financed by the Polish National Science Centre (NCN) (UMO-2013/09/B/ST8/03598).

The FE calculations were performed at the Academic Computer Centre in Gdansk TASK.

REFERENCES

Bobiński, J. & Tejchman, J. 2014. A constitutive model for concrete based on continuum theory with non-local softening coupled with eXtended Finite Element Method. In N. Bicanic, H. Mang, G. Meschke & R. de Borst (eds), *Computational Modelling of Concrete Structures*: 117–126. Taylor & Francis Group.

Bobiński, J. & Tejchman, J. 2016. A coupled constitutive model for fracture in plain concrete based on continuum theory with non-local softening and eXtended Finite Element Method. *Finite Elements in Analysis and Design* 114: 1–21.

Brinkgreve, R.B.J. 1994. *Geomaterial models and numerical analysis of softening.* PhD Thesis, TU Delft.

Cox, J.V. 2009. An extended finite element method with analytical enrichment for cohesive crack modelling. *International Journal for Numerical Methods in Engineering* 78: 48–83.

Hordijk, D.A. 1991. *Local approach to fatigue of concrete*. PhD Thesis, TU Delft.

Jirásek, M. 2004. Non-local damage mechanics with application to concrete. *Revue a française de génie civil*, 8: 683–707.

Melenk, J.M. & Babuška, I. 1996. The partition of unity finite element method: basic theory and applications. *Computer Methods in Applied Mechanics and Engineering* 139: 289–314.

Nooru-Mohamed, M.B., 1992. *Mixed mode fracture of concrete: an experimental research.* PhD Thesis, TU Delft.

Rolshoven, S. 2003. *Nonlocal plasticity models for localised failure*. PhD Thesis, EPFL Lausanne.

Strömberg, L. & Ristinmaa, M. 1996. FE-formulation of a nonlocal plasticity theory. *Computer Methods in Applied Mechanics and Engineering*, 136 (1–2): 127–144.

Wells, G.N. & Sluys, L.J. 2001. A new method for modelling cohesive cracks using finite elements. *International Journal for Numerical Methods in Engineering* 50: 2667–2682.

Wells, G.N., Sluys, L.J. & de Borst, R. 2002. Simulating the propagation of displacement discontinuities. *International Journal for Numerical Methods in Engineering* 53: 1235–1256.

Zi, G. & Belytschko, T. 2003. New crack-tip elements for XFEM and applications to cohesive cracks. *International Journal for Numerical Methods in Engineering* 57: 2221–2240.

Computational Modelling of Concrete Structures – Meschke, Pichler & Rots (Eds)
© 2018 Taylor & Francis Group, London, ISBN 978-1-138-74117-1

Nonlocal damage formulation with evolving internal length: The Eikonal nonlocal approach

G. Rastiello
DEN—Service d'études mécaniques et thermiques (SEMT), CEA, Université Paris-Saclay, Gif-sur-Yvette Cedex, France

C. Giry, F. Gatuingt, F. Thierry & R. Desmorat
LMT/ENS Paris-Saclay/CNRS/Université Paris-Saclay, Cachan Cedex, France

ABSTRACT: The proposed contribution presents and investigates the numerical properties of a Eikonal Nonlocal (ENL) continuum damage model. According to this approach, nonlocal interactions between material points are controlled by geodesic distances obtained as solutions of an isotropic time-independent Eikonal equation with a damage dependent metric function. Nonlocal interactions in two-dimensional damaged domains are illustrated first. A numerical formulation for modeling damage dependent non-local interactions within mechanical computations is presented then. It is obtained by using a Fast-Marching Method for updating damage dependent nonlocal interactions throughout the strain localization process. Numerical results of quasi-static simulations involving the failure of quasi-brittle materials in isotropic media are presented. Regularization properties of the proposed model are demonstrated. Furthermore, it is shown that the proposed formulation allows for reducing several parasite effects classically associated with Integral Nonlocal (INL) formulations (damage spreading over large damaged bands, damage diffusion near notches and free-edges, etc).

1 INTRODUCTION

During the development of nonlinearities, the softening behavior of some materials (e.g. ductile failure in metals, quasi-brittle failure in concrete, etc.) leads to the appearance of a localization process zone finite in size. Several theories were proposed to provide a description of these phenomena (G. & Bazant 1987, Pijaudier-Cabot & Benallal 1993, Bažant & Jirásek 2002, Frémond & Nedjar 1996, Peerlings, Geers, de Borst, & Brekelmans 2001, Miehe, Welschinger, & Hofacker 2010, Moës, Stolz, Bernard, & Chevaugeon 2011). Their common feature consists in the introduction of an internal length expressing nonlocal interactions in the localization process zone. Furthermore, these methods allow to avoid problems of non-objective results (mesh dependency) that can appear when using a finite element method for the solution of the quasi-static boundary value problem.

Integral non-local (INL) formulations on the internal variables of the constitutive model (G. & Bazant 1987), in particular, are widely used due to their simplicity of implementation, strong theoretical background and numerical robustness. According to this approach the thermodynamic variable driving the damage evolution process on a material point is computed by weighted averaging of the corresponding local field over the entire domain. Averaging is performed through a nonlocal weighting function (e.g. a Gaussian distribution function), such that the higher is the Cartesian distance between two material points lower is their interaction. A main drawback of this assumption consists however, in nonphysical interactions of material points across damaged bands, cracks and holes. Indeed, any couple of material points such that the Cartesian distance between them is the same interact in the same way. From a numerical viewpoint, this induces some parasite effects, such as damage spreading over a large damaged band, damage diffusion near notches and free-edges, etc. Enhancements of the initial methods were proposed in order to face these limitations and to describe more and more precisely strain localization processes in softening media. Among a lot of papersin the literature, several propose an evolution of the internal length based on phenomenological considerations (Geers, De Borst, Brekelmans, & Peerlings 1998, Pijaudier-Cabot, Haidar, & Dubé 2004, Simone,Wells, & Sluys 2003, Nguyen 2011, Giry, Dufour, & Mazars 2011, Saroukhani, Vafadari, & Simone 2013).

Theoretically derived in (Desmorat, Gatuingt, & Jirásek 2015) and numerically implemented/studied

in (Rastiello, Giry, Gatuingt, & Desmorat 2017), the Eikonal Non-Local (ENL) formulation provides a novel interpretation of damage dependent evolving non-local interactions. From a mathematical point of view, interaction distances between material points are computed by solving an isotropic time-independent Eikonal equation (a stationary Hamilton-Jacobi equation) with a damage dependent Riemannian metric function. From a differential geometry viewpoint, this approach leads to consider that damage induces a curvature of the Riemannian space in which interaction distances are computed. This space is thus no more Euclidean, and distances increase eventually tending to infinity. From a numerical viewpoint, ENL damage models can be implemented by coupling: 1) a nonlinear Finite Element Method (FEM) for solving the continuum damage mechanics problem; 2) a Fast-Marching Method (FMM) (Sethian 1996) for evaluating damage dependent interaction distances over the computed structure. This mathematical/physical framework allows for directly modeling evolving interactions throughout the localization process.

In this paper, a simple ENL Damage model and its numerical implementation are presented first. Then, after discussing on nonlocal interaction in damaged media some simple quasi-static strain localization problems are simulated in order to show the main features of the proposed formulation.

2 ENL DAMAGE FORMULATION

Consider a n-dimensional domain $\mathcal{B}$ and suppose that the mechanical behavior of its constituting material can be described through an isotropic Continuum Damage Model (CDM) with a single scalar variable $d \in [0,1]$. Under small-strain conditions, the second order stress tensor ($\boldsymbol{\sigma}$) is written as:

$$\boldsymbol{\sigma} = \boldsymbol{\sigma}(\boldsymbol{\epsilon}, d) = (1-d)\left[2\mu\boldsymbol{\epsilon} + \lambda(\mathrm{tr}\boldsymbol{\epsilon})\mathbf{I}\right] \tag{1}$$

where tr(•) is the trace operator, (λ, μ) are the homogeneous Lamé parameters, $\boldsymbol{\epsilon}$ is the second order small strain tensor and $\mathbf{I}$ is the second order identity tensor.

The nonlocal damage criterion function is defined as[1]:

$$f^{\mathrm{NL}} = f(\epsilon_{\mathrm{eq}}^{\mathrm{NL}}, \kappa) = \epsilon_{\mathrm{eq}}^{\mathrm{NL}} - \kappa \tag{2}$$

where $\epsilon_{\mathrm{eq}}^{\mathrm{NL}} = \epsilon_{\mathrm{eq}}^{\mathrm{NL}}(\boldsymbol{x})$ is a nonlocal equivalent strain measure (Mazars 1984, de Vree, Brekelmans, & van Gils 1995) and k is an internal variable. This latter starts at a (damage) threshold level k_0 and is updated by requiring that $f^{\mathrm{NL}} = 0$ during damage growth, while $\dot{\kappa} = 0$ at unloading and when $f^{\mathrm{NL}} < 0$. It is therefore updated as:

$$\kappa = \max_{t} \epsilon_{\mathrm{eq}}^{\mathrm{NL}} \tag{3}$$

where $t \in [0,T]$ is a pseudo-time variable. Damage growth is finally supposed to follow the exponential evolution law:

$$d = g(\kappa) = 1 - \frac{\kappa_0}{\kappa}\exp\left\{-\frac{\langle \kappa - \kappa_0 \rangle}{\kappa_c - \kappa_0}\right\} \tag{4}$$

where k_c is the equivalent strain level controlling the shape of the damage evolution function.

2.1 *Nonlocal (NL) strain field*

The nonlocal field $\epsilon_{\mathrm{eq}}^{\mathrm{NL}}$ is computed by weighted averaging of its local couterpart ($\epsilon_{\mathrm{eq}} = \epsilon_{\mathrm{eq}}(\boldsymbol{x})$) over $\mathcal{B}$. Provided a material point occupying the position $\boldsymbol{x}_x$, the averaging formula reads:

$$\epsilon_{\mathrm{eq}}^{\mathrm{NL}} = \epsilon_{\mathrm{eq}}^{\mathrm{NL}}(\boldsymbol{x}_x) = \frac{\int_{\mathcal{B}} \phi(\xi_{xs})\epsilon_{\mathrm{eq}}(\boldsymbol{x}_s)\,\mathrm{d}v}{\int_{\mathcal{B}} \phi(\xi_{xs})\,\mathrm{d}v} \tag{5}$$

where $\phi = \phi(\xi_{xs}) \geq 0$ is a nonlocal weighting function and ξ_{xs} is the ratio of the interaction distance between material points $\boldsymbol{x}_s$ and $\boldsymbol{x}_x$ to the characteristic/internal length ℓ_c. A typical choice of function ϕ is the Gaussian distribution function:

$$\phi = \phi(\xi_{xs}) = \exp(-\xi_{xs}^2/2) \tag{6}$$

2.1.1 *Integral NL model*

In INL formulations, interactions are controlled by Euclidean distances between material points. The length ratio ξ_{xs} thus reads:

$$\xi_{xs} = \xi_{xs}^{\mathrm{INL}} = \frac{\ell_{xs}}{\ell_c} = \frac{\|\boldsymbol{x}_s - \boldsymbol{x}_x\|}{\ell_c} \tag{7}$$

where $\|\bullet\|$ denotes the Euclidean norm. As a consequence of this assumption, any pair of material points ($\boldsymbol{x}_x$, $\boldsymbol{x}_s$) and ($\boldsymbol{x}_x$, $\boldsymbol{x}_s'$) such that $\ell_{xs} = \ell_{xs'}$ interact in the same way. A physical request is, however, that material points across cracks, holes and highly damaged zones do not interact (or at least reduce their interactions).

2.1.2 *Eikonal NL model*

The ENL formulation models this effect by considering that damage induces a curvature of the

1. This represents a simple modeling assumption, introduced for sake of illustration. The proposed ENL formulation can be applied without modifications to different non-local damage models.

Riemannian space in which interaction distances are computed. In this framework, interactions between $\boldsymbol{x}_x$ and other material points $\boldsymbol{x} \in \mathcal{B}$ are controlled by an effective/geodesic distances field $\tilde{\ell}(\boldsymbol{x})$ approximating the viscosity solution of the time-independent isotropic Eikonal equation:

$$\begin{cases} m(\boldsymbol{x}) \| \nabla \tilde{\ell}(\boldsymbol{x}) \| = 1 & \boldsymbol{x} \in \mathcal{B}, \\ \tilde{\ell}(\boldsymbol{x}_x) = 0 \end{cases} \tag{8}$$

where $\nabla(\bullet)$ is the gradient operator and $m(x)$ denotes a damage dependent isotropic Riemannian metric function:

$$m(x) = \sqrt{1 - d(\boldsymbol{x})} > 0 \qquad \boldsymbol{x} \in \mathcal{B} \tag{9}$$

This leads to rewrite the length ratio ξ_{xs} as:

$$\xi_{xs} = \xi_{xs}^{\mathrm{ENL}} = \frac{\tilde{\ell}_{xs}}{\ell_c} \geq \xi_{xs}^{\mathrm{INL}} = \frac{\ell_{xs}}{\ell_c} \tag{10}$$

Uni-dimensional example The influence of damage on nonlocal interactions can be illustrated easily by studying simple one-dimensional (1D) case. Consider an inhomogeneous field $d = d(x)$ defined over a bar $\mathcal{B} = \{x \in \mathbb{R} : x \in (0, L)\}$ and compute the geodesic interaction distance between two material points (x_x and $x_s > x_x$) pertaining to $\mathcal{B}$. Under these conditions, the Eikonal problem (8) reads:

$$\begin{cases} \sqrt{1 - d(x)} \, | \, d_x \tilde{\ell}(x) \, | = 1 & x \in \mathcal{B} \\ \tilde{\ell}(x_x) = 0 \end{cases} \tag{11}$$

where d_x denotes the total derivation with respect to variable x and $|\bullet|$ is the absolute value operator.

Integrating (11) between x_x and x_s leads to write:

$$\tilde{\ell}_{xs} = \int_{x_x}^{x_s} \frac{\mathrm{d}x}{\sqrt{1 - d(x)}} \geq \ell_{xs} = x_s - x_x > 0 \tag{12}$$

According to (12), $\tilde{\ell}_{xs}$ coincides with ℓ_{xs} in undamaged conditions (i.e., the INL setting is recovered) and increases progressively when damaging occurs. As a consequence, material points separated by highly damaged zones could no longer interact (or reduce their interactions).

3 NONLOCAL INTERACTIONS IN TWO-DIMENSIONS

Similar considerations apply to non-local interactions in two-dimensional (2D) domains. When the damage field $d(\boldsymbol{x})$ is not uniform, however, no general closed form viscosity solutions to the Eikonal equation exist. For that reason, numerical solution procedures (Bertsekas 1993, Zhao 2005, Sethian 1996) are needed. In this work, we use a FMM (Sethian 1996) based on a second order approximation of the term $\nabla \tilde{\ell}(\boldsymbol{x})$ over a regular grid of points (Rouy & Tourin 1992).

As a representative example, we consider a square plate $\mathcal{B}$ and compute interaction distances from point x_x under three different conditions: 1) $\mathcal{B}$ is undamaged; 2) $\mathcal{B}$ is crossed by a sharp crack, i.e., $d \to 1^-$ along a line of points and is null elsewhere; 3) $\mathcal{B}$ is a holed plate, i.e., $d \to 1^-$ on points located inside the hole and is null otherwise.

The computed geodesic distances fields and resulting nonlocal weighting functions ϕ are depicted in Figure 1. As expected, one observes that:

1. Geodesic and Cartesian distance fields coincide when damage is null (as in the 1D case). The resulting function ϕ is a Gaussian distribution function with center in $\boldsymbol{x}_x$ (as it is classically assumed in INL formulations);
2. When the domain is damaged (or an hole is present), the Riemannian space in which distances are computed is deformed (i.e., $m(\boldsymbol{x}) \neq 1$). Shortest paths between $\boldsymbol{x}_x$ and points $\boldsymbol{x}_s \in \mathcal{B}$ are no more straight lines and interaction distances increase. As in the 1D case, under some conditions, material points separated by highly damaged zones no-more interact (the resulting weighting functions ϕ are truncated).

4 FEM-FMM NUMERICAL FORMULATION

The implementation of the ENL method into a nonlinear finite element code can be achieved in a non intrusive (as less intrusive as possible) way. The main ingredients of the numerical formulation proposed in (Rastiello, Giry, Gatuingt, & Desmorat 2017) can be summarized as follows:

1. Quasi-static equilibrium equations are solved thanks to a standard FE formulation. Provided the displacement and damage fields at time step t_n, the solution at time $t_{n+1} = t_n + \Delta t_{n+1} > t_n$ is searched iteratively by using a secant algorithm. An explicit integration scheme is adopted for updating the damage field at the Gauss point level throughout global iterations. For the Gauss point occupying the position $\boldsymbol{x}_x$, at the global iteration $k + 1$, one computes:

$$d_{n+1}^{k+1}(\boldsymbol{x}_x) = \max\left(g(\epsilon_{\mathrm{eq},n+1}^{\mathrm{NL},k}), d_{n+1}^{k} \right) \tag{13}$$

where $d_{n+1}^{k} = d_{n+1}^{k}(\boldsymbol{x}_x)$;

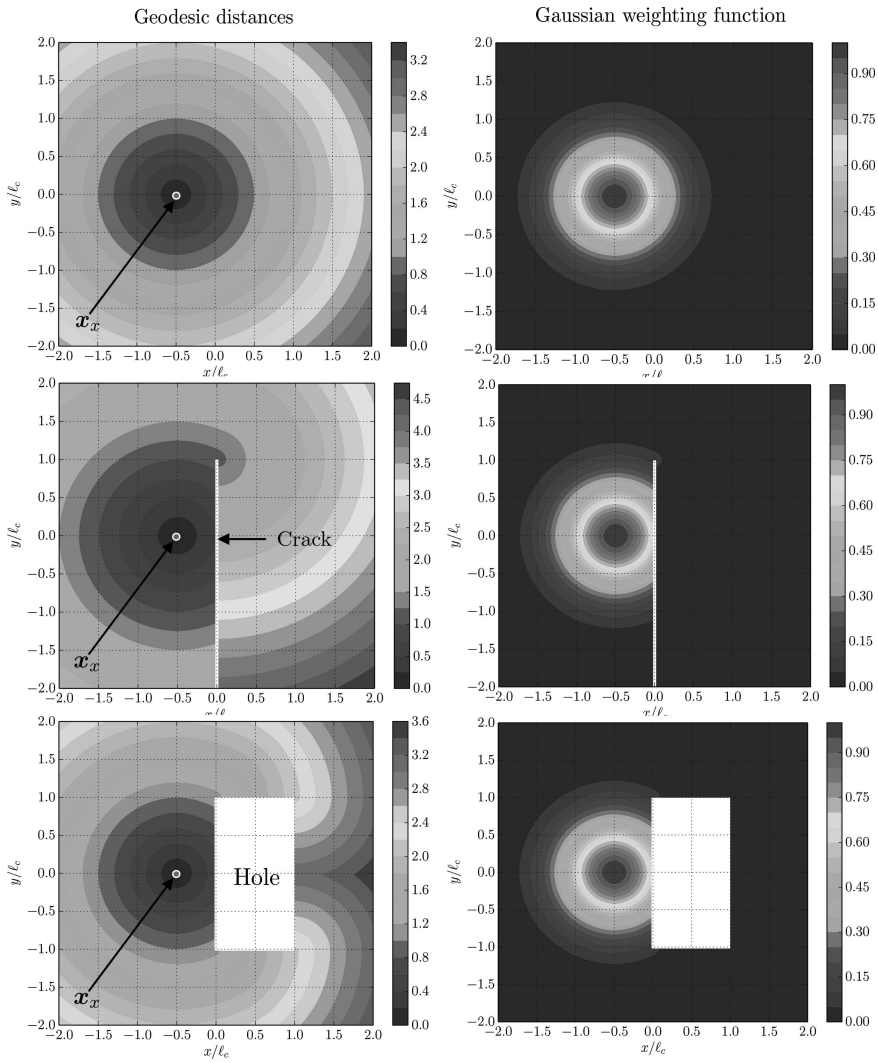

Figure 1. Geodesic distances field $\tilde{\ell}(\boldsymbol{x})$ for a square plate and its influence on the Gaussian weighting function $\phi(\xi)$ centered on the point $\boldsymbol{x}_x$: a) undamaged medium; b) cracked medium; c) holed plate. Geodesic distances are computed over a regular grid comprising 40'401 = 201 × 201 vertex (grid spacing $h = 4\ell_c/200$).

2. Interaction distances between integration points are evaluated through a second-order accurate FMM. For this purpose, independent FM grids are defined gauss point by gauss point. They are centered on the considered Gauss point ($\boldsymbol{x}_x$) and are $2\ell_c \times 2\ell_c$ in size. Provided the finite difference approximation of the gradient term, grid spacing (h) is adapted grid-by-grid in order to ensure minimizing errors in distances computation;
3. The discretized metric function to be used for computing interaction distances is obtained after projection of the damage field from the FE mesh to FM grids;
4. Geodesic distances between gauss points are then computed at the beginning of each time step by solving:

$$\begin{cases} \sqrt{1-d_n(\boldsymbol{x})}\,\|\nabla\tilde{\ell}_{n+1}(\boldsymbol{x})\| = 1, & \boldsymbol{x} \in \mathcal{B} \\ \tilde{\ell}_{n+1}(\boldsymbol{x}_x) = 0 \end{cases} \tag{14}$$

where $d_n(\boldsymbol{x})$ is the damage field a time step t_n;

5. Interaction distances are then kept constant until convergence at time t_{n+1}. They are then used to update the equivalent nonlocal strain field $\epsilon_{\text{eq}}^{\text{NL}}$ driving damage evolution.

5 STRAIN LOCALIZATION EXAMPLES

In this section, 2D quasi-static strain localization problems in quasi-brittle continua are simulated to illustrate the main features (regularization, damage evolution, …) of the ENL damage formulation. In computations, a simple yield criterion function written in the equivalent Mazars strain space is adopted for sake of simplicity.

5.1 *Tie-specimen under tensile loading*

A tie-specimen submitted to a tensile loading is considered first (Figure 2). The domain is discretized through three FE meshes comprising 26, 51 or 101 linear quadrangular FEs to study mesh sensitivity. Strain localization is forced on the center of the specimen by introducing a weak finite element. Provided the chosen material parameters (Figure 2), the resulting structural responses are unstable in the post-peak phase of load for every considered mesh. For that reason, the external load is controlled indirectly using path-following method based upon controlling the mean relative horizontal displacement of two vertical lines of nodes symmetrically placed ($\pm L/20$) with respect to the vertical symmetry axis of the specimen.

5.1.1 *Representative responses*

Computations are performed assuming plane strains conditions and considering the local, standard INL and ENL formulations for sake of comparison. Representative structural responses obtained for a mesh comprising $51 = 51 \times 1$ elements are compared in Figure 2. Damage and equivalent strain distributions along a horizontal line (parallel to the loading direction) for different time stations are depicted in Figure 3. Numerical results evidence that:

- When damage is small, the global and local response provided by the ENL formulation is very close to that obtained using the INL formulation. In this phase, the metric field is approximatively equal to unity and effective geodesic distances do not strongly differ from Euclidean ones.
- When damage increases, geodesic distances increase and become larger than Euclidean distances. Non-local interactions progressively reduce and the ENL global response tends progressively to that obtained through the local damage model.
- When $d \to 1^-$ on the weak finite element, the response provided by the ENL formulation becomes equivalent to that obtained in a local setting. Interaction distances between gauss integration points across the damaged zone tend to infinity and non-local interactions vanish. By this way, no damage evolution occurs even through the sample elongation continues to increase. As it is well known, this effect cannot be modeled through a INL formulation.

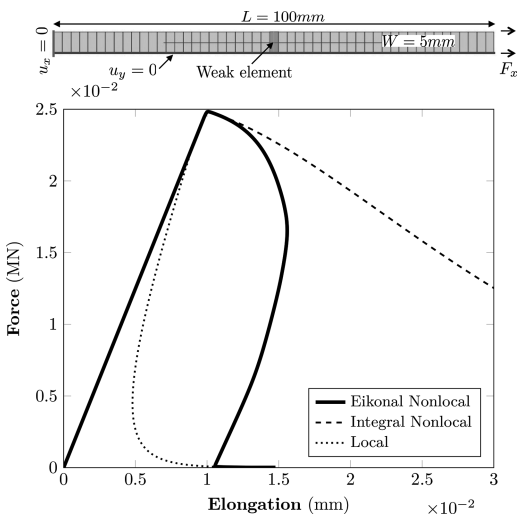

Figure 2. Tensile test. Comparison among representative global force-displacement responses obtained through the local, INL and ENL damage evolution models (FE mesh comprising 51 elements). The specimen in 100 mm in length and 5 mm in width. Constitutive model parameters are as follows: $E = 100$ MPa (Young's modulus), $\nu = 0$, $k_0 = 0.0001$, $k_c = 0.001$ and $\ell_c = 20\,\text{mm}$.

5.1.2 *Regularization features*

As shown in Figure 4, the ENL formulation ensures the objectivity of the obtained solution with respect to the spatial discretization of the computed structure. The global force-displacement responses obtained through three different FE meshes are in good agreement in the whole range of displacements.

Small differences in global responses can be observed only on final simulation phases, when the weaker element is almost fully damaged and no more interacts with its neighbors. A tendency toward a mesh convergence can be however evidenced, thus demonstrating the regularization properties of the proposed ENL formulation. Damage profiles obtained for the three FE meshes are also similar for any damage level (Figure 5).

5.2 *Wedge-splitting test*

A wedge-splitting test (Brühwiler & Wittman 1990) is simulated to study the damage propagation process in a 2D context. A vertically notched sample 100 mm width and 100 mm in height is solicited by imposing increasing horizontal displacements of two vertical bearing surfaces. A sub-vertical damage propagation (form the notch

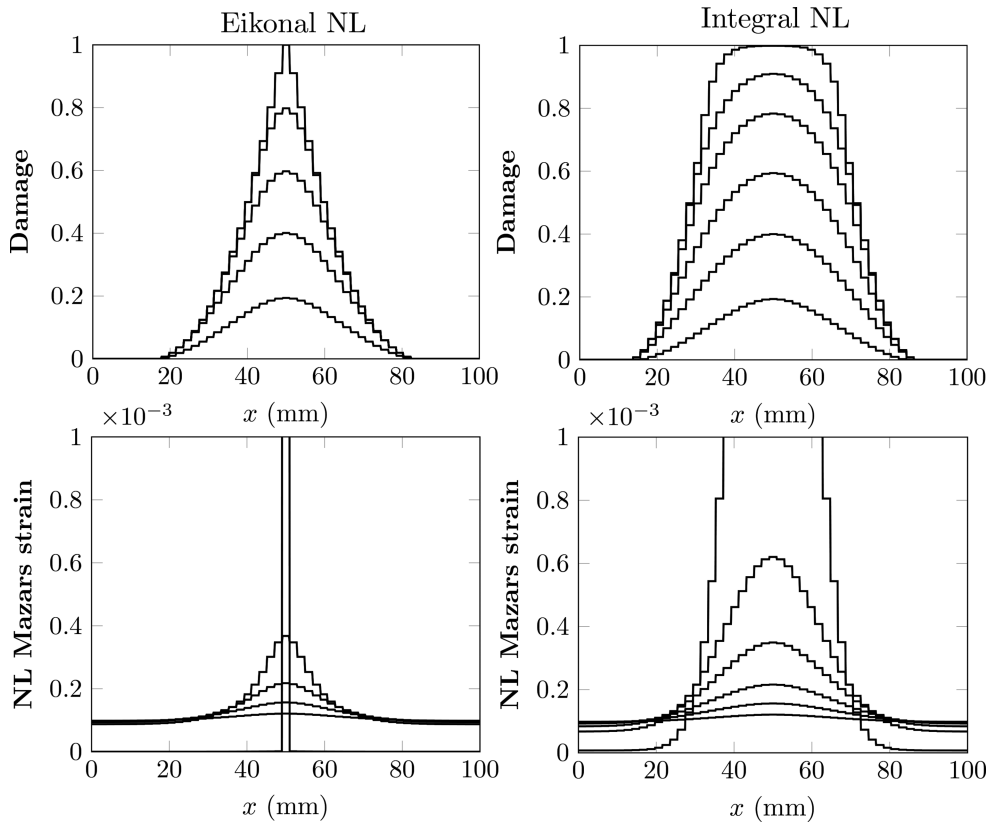

Figure 3. Tensile test, evolution of damage and non-local equivalent strain fields throughout two representative simulations carried out considering ENL (left) and INL (right) damage formulations.

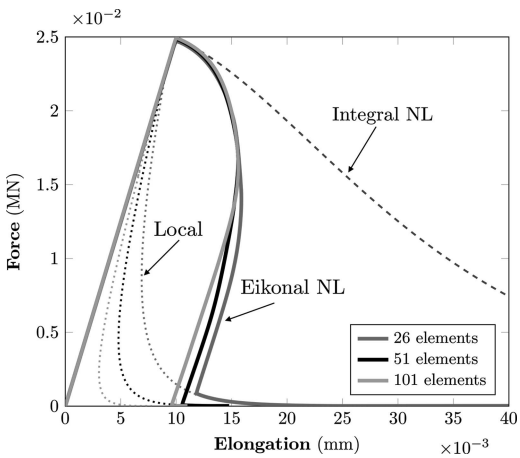

Figure 4. Tensile test, FE mesh sensitivity study. Global responses obtainted through three different FE meshes.

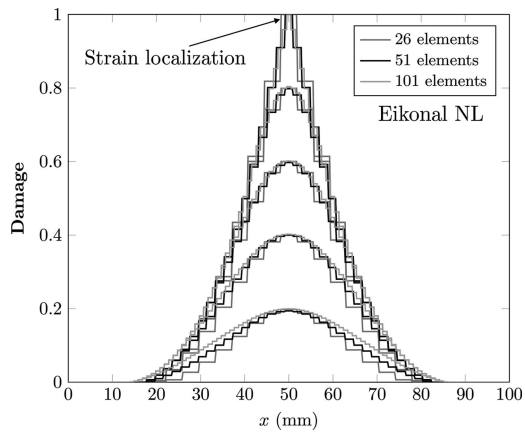

Figure 5. Tensile test, FE mesh sensitivity study. Damage distributions obtainted through three different FE meshes.

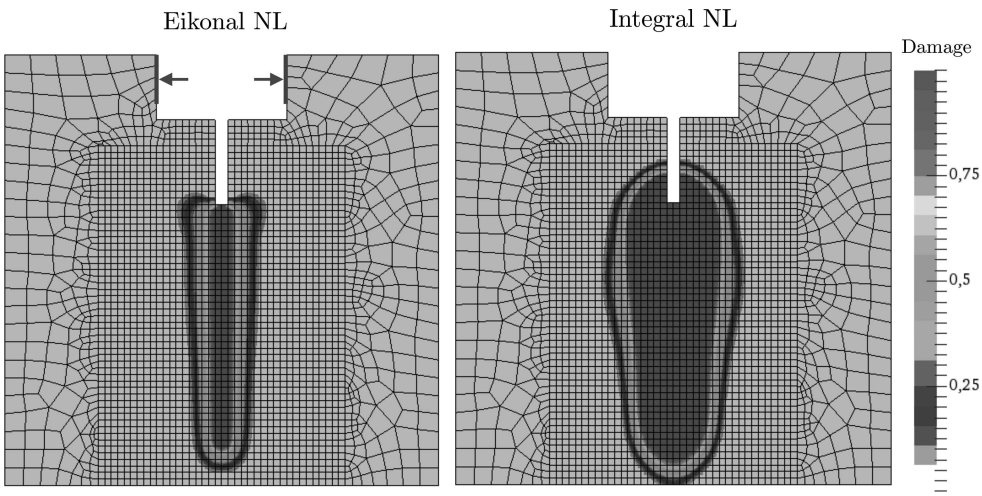

Figure 6. Wedge splitting test: comparison among damage fields computed by considering INL and ENL damage evolution models for the same imposed displacement level. Material parameters are assigned as follows: $E = 100$ MPa, $\nu = 0$, $\epsilon_0 = 0{:}0001$, $\epsilon_c = 0{:}0005$, $\ell_c = 20\,\text{mm}$.

to the bottom of the specimen) is thus induced. The computational domain is discretized by using a finite element mesh comprising 2510 linear quadrilateral finite elements. Computations are performed under plane strain conditions, considering both ENL and INL formulations.

Damage fields obtained corresponding to an advanced phase of the test are compared in Figure 6. This allows showing that the damage field predicted by the INL formulation is spread over a large damaged band, whereas the ENL formulation allows reducing this diffusion. In that case, the damaged band in less wide and d attains unity values on the symmetry axis only. Once this condition is attained, the damage field no more evolves because no interactions occur between integration points located across the symmetry axis. This also ensure that damage diffusion in the backward of the notch is strongly reduced.

6 CONCLUSIVE REMARKS

A simple Eikonal Nonlocal (ENL) continuum damage model was presented in this paper. According to this approach (Desmorat, Gatuingt, & Jirásek 2015, Rastiello, Giry, Gatuingt, & Desmorat 2017), nonlocal interactions between material points are controlled by geodesic distances obtained as solutions of an isotropic time-independent Eikonal equation with a damage dependent metric function. In a differential geometry context, the ENL framework considers that the Riemannian space in which interaction distances are computed is curved due to damage. In otherwords, interaction distances are no more Euclidean, as in the INL formulation, but evolves depending on the damage field evolution. The numerical implementation was obtained by using a Fast-Marching Method (Sethian 1996) for updating damage dependent nonlocal interactions throughout a quasi-static Finite Elements computation (Rastiello, Giry, Gatuingt, & Desmorat 2017). Two simple test-cases were performed in order to show the main features of the ENL formulation. Regularization properties of the proposed model were demonstrated. Furthermore, it was shown that the proposed formulation allows for reducing several parasite effects classically associated with INL formulations (damage spreading over large damaged bands, damage diffusion near notches and free-edges, etc).

REFERENCES

Bažant, Z.P. & M. Jirásek (2002). Nonlocal Integral Formulations of Plasticity and Damage: Survey of Progress. *Journal of Engineering Mechanics 128*(11), 1119–1149.

Bertsekas, D.P. (1993). A simple and fast label correcting algorithm for shortest paths. *Networks 23*(8), 703–709.

Brühwiler, E. & F.H. Wittman (1990). The Wedge splitting test, a new method of performing stable fracture mechanics tests. *Enginnering Fracture Mechanics 35*, 117–125.

de Vree, J., W. Brekelmans, & M. van Gils (1995, may). Comparison of nonlocal approaches in continuum damage mechanics. *Computers & Structures 55*(4), 581–588.

Desmorat, R., F. Gatuingt, & M. Jirásek (2015, jul). Nonlocal models with damage-dependent interactions motivated by internal time. *Engineering Fracture Mechanics 142*, 255–275.

Frémond, M. & B. Nedjar (1996). Damage, gradient of damage and principle of virtual power. *International Journal of Solids and Structures 33*(8), 1083–1103.

G., P.-C. & Z.P. Bazant (1987). Non local Damage Theory. *Asce 113*(10), 1512–1533.

Geers, M., R. De Borst, W. Brekelmans, & R. Peerlings (1998). Strain-based transient-gradient damage model for failure analyses. *Computer methods in applied mechanics and engineering 160*(1–2), 133–153.

Giry, C., F. Dufour, & J. Mazars (2011). Stress-based nonlocal damage model. *International Journal of Solids and Structures 48*(25), 3431–3443.

Mazars, J. (1984). *Application de la mécanique de l'endommagement au comportement non linéaire et à la rupture du béton de structure*. Ph. D. thesis.

Miehe, C., F. Welschinger, & M. Hofacker (2010, sep). Thermodynamically consistent phase-field models of fracture: Variational principles and multi-field FE implementations. *International Journal for Numerical Methods in Engineering 83*(10), 1273–1311.

Moës, N., C. Stolz, P.-E. Bernard, & N. Chevaugeon (2011, apr). A level set based model for damage growth: The thick level set approach. *International Journal for Numerical Methods in Engineering 86*(3), 358–380.

Nguyen, G.D. (2011). A damage model with evolving nonlocal interactions. *International Journal of Solids and Structures 48*(10), 1544–1559.

Peerlings, R., M. Geers, R. de Borst, & W. Brekelmans (2001, nov). A critical comparison of nonlocal and gradient-enhanced softening continua. *International Journal of Solids and Structures 38*(44–45), 7723–7746.

Pijaudier-Cabot, G. & A. Benallal (1993). Strain localization and bifurcation in a nonlocal continuum. *International Journal of Solids and Structures 30*(13), 1761–1775.

Pijaudier-Cabot, G., K. Haidar, & J.-F. Dubé (2004). Non-local damage model with evolving internal length. *International journal for numerical and analytical methods in geomechanics 28*(7–8), 633–652.

Rastiello, G., C. Giry, F. Gatuingt, & R. Desmorat (2017). From diffuse damage to strain localization from a Eikonal Non-Local (ENL) Continuum Damage model with evolving internal length. *Computer Methods in Applied Mechanics and Engineering (under review)*.

Rouy, E. & A. Tourin (1992). A viscosity solutions approach to shape-from-shading. *SIAM Journal on Numerical Analysis 29*(3), 867–884.

Saroukhani, S., R. Vafadari, & A. Simone (2013). A simplified implementation of a gradient-enhanced damage model with transient length scale effects. *Computational Mechanics 51*(6), 899–909.

Sethian, J. a. (1996). A fast marching level set method for monotonically advancing fronts. *Proceedings of the National Academy of Sciences of the United States of America 93*(4), 1591–1595.

Simone, A., G.N. Wells, & L.J. Sluys (2003). From continuous to discontinuous failure in a gradient-enhanced continuum damage model. *Computer Methods in Applied Mechanics and Engineering 192*(41), 4581–4607.

Zhao, H. (2005). A fast sweeping method for eikonal equations. *Mathematics of computation 74*(250), 603–627.

Computational Modelling of Concrete Structures – Meschke, Pichler & Rots (Eds)
© 2018 Taylor & Francis Group, London, ISBN 978-1-138-74117-1

Response scatter control for discrete element models

J. Podroužek
Christian Doppler Laboratory, University BOKU, Vienna
Faculty of Civil Engineering, Brno University of Technology, Brno, Czech Republic

M. Marcon, J. Vorel & R. Wan-Wendner
Christian Doppler Laboratory, University BOKU, Vienna

ABSTRACT: The so-called Lattice Discrete Particle Model (LDPM) naturally accounts for material heterogeneity by random particle placement and size, which is also constrained by a grading curve. This approach captures most microstructural effects of concrete very well, when compared to the continuum framework, however introducing higher order spatial variability enables to control and interpret the response scatter. This paper addresses the effects of various choices of spatially variable material property fields, such as random field described by power spectral functions or gradient based fields, and particle placement schemes, such as those derived from governing random or gradient based fields, in order to account for inherent variability and production processes of several classical concrete tests. These are e.g. cylinder and cube compression test, and unnotched three point bending test. As a consequence, the lattice models become sensitive to a particular choice of spatially variable material property fields and particular particle placement concept, which is no longer independent and random, and the scattering of the response can thus be associated with the physical meaning of an auto-correlation length and particular forms of the spectral function. In particular, the non-monotonous relationship between statistical characteristics of the response, such as the coefficient of variation of the load capacity, and spatial correlation structures, such as power spectral parameters, clearly support the hypotheses on causal relationship between spatial variability, auto-correlation length of the random fields, type of spectral function and meso/micro-structure of the material. By imposing correlated spatial variability the consistency and realism of the LDPM stochastic framework may dramatically increase if objective physical reference for the governing random field and correlation length is established. Since this represents a rather extreme case of high-dimensional problem, simple solutions are not to be expected any time soon. Until then, the presented original framework may serve for the interpretation of different sources and magnitudes of experimental scattering observed in various classical experiments and the illustration of the important implications towards enhanced realism in the reliability based assessment of concrete structures and infrastructure, including fastening systems.

1 INTRODUCTION

Recent developments in particle placement schemes, such as those derived from governing random or gradient based field (J Podroužek et al., 2016), in the context of the lattice discrete particle modelling (LDPM)(Cusatis et al., 2011b, 2011a; Cusatis, 2013), have opened the door for new approaches of investigating the spatial variability of heterogenous materials owing to microstructural features. In this paper, the gradient-based fields and random fields are introduced into the stochastic framework of LDPM to account for inherent variability and production process of several concrete specimen test series (Figures 1 to 3), such as cylinder and cube compression tests and unnotched three point bending test. As a consequence, the lattice models become sensitive to a particular particle placement concept, which is no longer independent and random (Jan Podroužek et al., 2016), and the scattering of the response can thus be controlled and associated with the physical meaning of an auto-correlation length and particular forms of the spectral function. Moreover, particular placement concepts, such as the gradient based fields, may also affect the mean values of the response.

Please note that the applicability of the presented particle placement schemes is not limited to LDPM and can be utilized also in other discrete frameworks. For the overview of currently available particle based models please refer to e.g. the special issue "Advances in Computational Particle Based Methods" in Engineering Computations (Feng et al. 2015).

2 DISCRETE PARTICLE MODELS

A well-established member of the group of discrete concrete constitutive models, the lattice discrete particle model (LDPM) has been extensively calibrated and validated and it has shown superior capabilities in reproducing and predicting concrete behaviour (Cusatis, 2013; Janouchová et al., 2016; Wan-Wendner R. et al., 2016; Wan-Wendner L. et al., 2016; Wan-Wendner L. et al., 2017). It simulates the mesostructure of concrete by a three-dimensional (3D) assemblage of particles (Figs. 1 to 3) that are generated randomly according to a given grain size distribution. Delaunay tetrahedralization and 3D domain

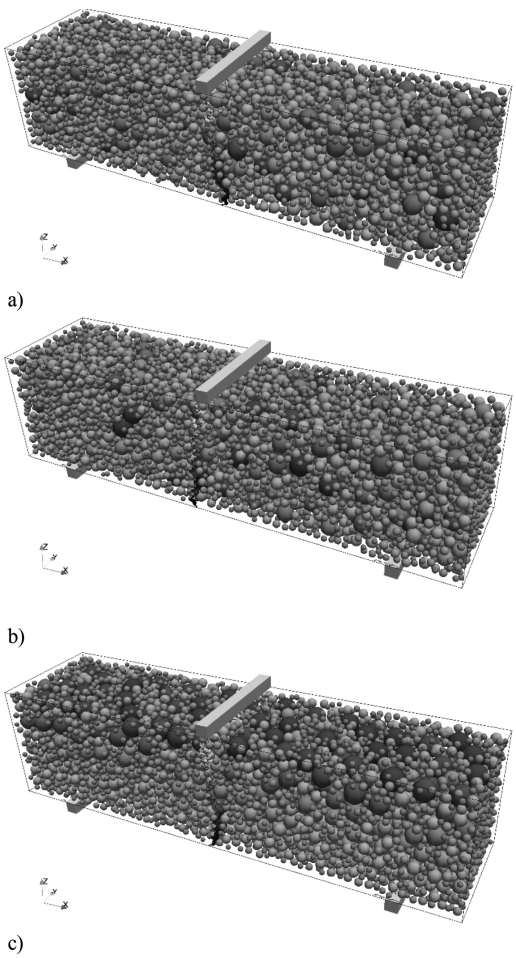

Figure 1. LDPM models of unnotched 3-point-bending test maximizing the COV of load capacity: a) maximum strength realization (PGGFa), b) minimum strength realization (PGGFa), c) maximum strength realization (PGGFb).

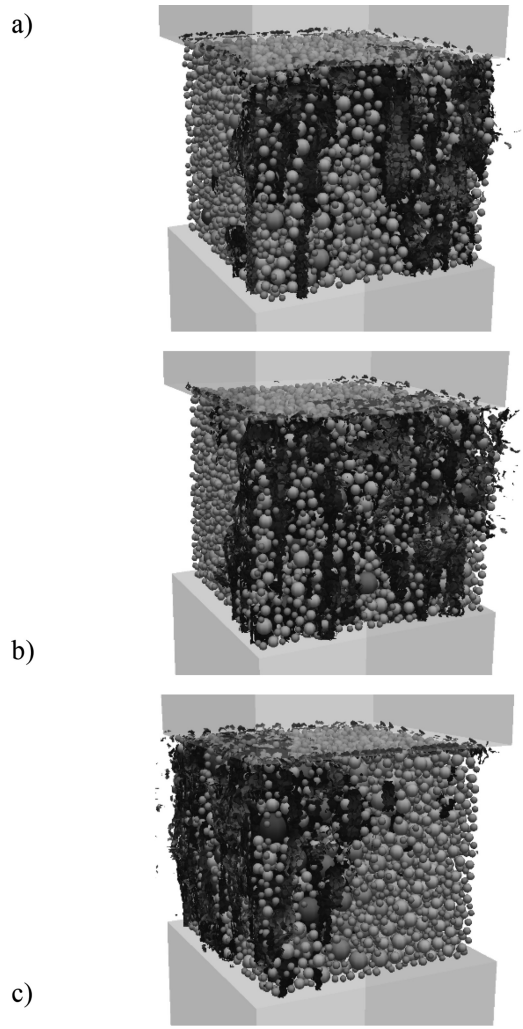

Figure 2. LDPM models of cube compression test maximizing the COV of load capacity: a) maximum strength realization (PGGFa), b) minimum strength realization (PGGFa), c) maximum strength realization (PGGFb).

tessellation are used here to generate a system of cells interacting through triangular facets. Displacements and rotations of such adjacent particles form the discrete compatibility equations in terms of rigid body kinematics. At each cell facet the mesoscale constitutive law is formulated such that it simulates cohesive fracture, compaction due to pore collapse, frictional slip and rate effect. For each single particle, equilibrium equations are finally formulated. An extended version of LDPM is currently developed and simulates various coupled deterioration mechanisms, such as Alkali-Silica reaction (ASR) (Alnaggar et al.,

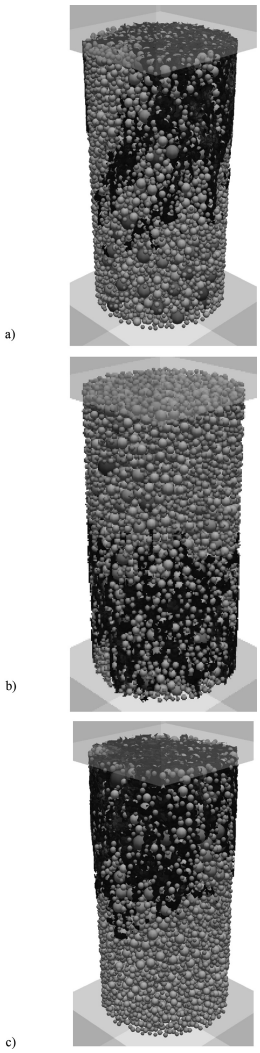

Figure 3. LDPM models of cylinder compression test maximizing the COV of load capacity: a) maximum strength realization (PGGFa), b) minimum strength realization (PGGFa), c) maximum strength realization (PGGFb).

2013; Bažant et al., 2000). A further development is the age-dependent LDPM framework in which the local material properties are derived by chemo-mechanical coupling with a chemo-hygro-thermal model (Wan et al., 2015, Wan-Wendner R. et al., 2016) which also drives the creep and shrinkage analysis in a rate type form (Yu et al., 2012). In regard to the presented numerical investigation of models of classical concrete experiments, important inputs are the maximum and minimum aggregate sizes. The higher bound of the sieve curve is defined by the maximum aggregate size while the minimum aggregate size defines its arbitrary lower bound. The minimum aggregate size affects also the refinement of the discrete mesh and consequently also the computational cost. Please note that the sieve curve is kept constant for all of the presented examples, i.e. only the particle placement schemes are varied. The concrete parameters used for the LDPM in this contribution are taken from (Marcon et al., 2017). Among other parameters which define the concrete properties, minimum and maximum aggregate sizes are chosen as 4 and 18 mm. Friction connection was used to connect the concrete elements to the loading plates. This connection is performed between the plates surface and the LDPM surface nodes which lay inside a domain defined by an arbitrary distance from the plates surface. The nodes connected to the surface can only move in the plane defined by the surfaces and not in its normal direction due to the master slave connection.

Cubes were modelled with an edge length of 150 mm and the cylinder with a length of 300 mm and a diameter of 150 mm. For both cubes and cylinders the plates were modelled as rigid bodies. The unnotched beam was modelled with dimensions $100 \times 100 \times 400$ mm with a span length between the supports at the bottom of 300 mm. Each of the simulations were run in a Vienna Scientific Cluster ("Austrian initiative on high performance computing," 2014) using one node with 16 cores for 3.5 hours. The loading speed for the beams was 2 mm/s, 5 mm/s for the cubes and 20 mm/s for the cylinders. For all the models the kinetic energy has been monitored and it has been verified that it would not influence the results.

3 CHARACTERIZATION OF INTERNAL STRUCTURE

The proposed particle placement schemes may significantly influence the scattering and asymptotic properties of the spatially variable models and thus contribute to the general understanding of the physics and reliability of spatial variability (Podroužek et al., 2017a, 2017a).

The abstraction levels for LDPM are categorized as following (Podroužek et al., 2017b).

3.1 *Independent and Random Particle Placement (IRPP)*

Independent and random particle placement and random diameter according to the size distribution curve and required volume fraction, as proposed by Cusatis et al. (e.g. Cusatis, 2013) in their original publication on LDPM. No conflicting

requirements are to be solved. Overlapping or less than minimum distance particles are resampled.

3.2 *IRPP combined with random or gradient-based field for material characterization only*

The second abstraction level assumes the original particle placement scheme, i.e. the IRPP, combined with one or more random fields, which is used to describe material local fluctuations of material properties resulting from inherent variability (random field) and construction or transport processes (gradient-based fields). Similarly, to the previous case, there are no geometry-related conflicting requirements. Particles which do not satisfy the minimum distance requirement can simply be resampled. Boundary regions may be normally populated by adopting a simple modification to the re-sampling algorithm. Material characterizations derived from random fields must be verified for inadmissible values, such as negative strength, modulus, etc. This may lead to a conflict if the governing probability distribution used for generating the random field is to be maintained. Otherwise, truncated distributions may be used or the realization of random field can be rescaled to fit admissible range (Eliáš et al., 2013; Jan Podroužek et al., 2016; Vořechovský and Novák, 2003). A further shortcoming of this approach is the total lack of (physical) link between micro-structural features captured in the simulation through the particle placement and the spatial variability in the material property fields. This motivated the third group:

3.3 *Particle Generation Governed by a Field (PGGF)*

Here it is assumed that an initial random (PGGFa) or gradient-based (PGGFb) field of choice (or their arbitrary combination) is governing not only the material, but also the particle generation process (i.e. the position and/or the size of each particle). Consequently, modelled micro-structure and material properties would automatically be correlated through the chosen discretisation scheme. In this contribution, only the placement of particles following a field is investigated and compared to the reference, IRPP. Material property fields, linked to the particle placement or not, are not considered at this point. If the particle generation is to be governed not only by granulometric distributions, but also by an initial random (Figures 1 and 2) or gradient-based field (Figure 3), the particle generation becomes a complex problem and has to be approached by balancing trade-offs between conflicting goals. Clearly, the global requirement on particular size distribution can lead to a local conflict with the initial random field, the role of which can be further ambiguous if we consider it to affect both the position and size of the particles (clustering of large particles). Details regarding the associated steps/choices for random fields were published by Podroužek et al. (2016). For higher volume fractions this becomes a computationally expensive procedure, however local conflicts can be resolved in parallel and terminate with the first valid particle. The advantage of the approach lies in the compatibility of the mimicked meso-structure with the material property fields which otherwise cannot be maintained. The use of random fields for particle placement and/ or material property fields implies a causal relationship between spatial variability, auto-correlation length of the random fields, type of spectral function and meso/micro-structure of the material which is an open research question.

4 RESULTS

The presented observations are based on an unique and extensive computational campaign costing 33,600 core-hours (equivalent to 3.8 years on a single core). Each batch (model type, field type and field parameter) is characterized by 20 LDPM realizations. This number does not always ensure a statistically significant characterization of the investigated phenomena, as follows e.g. from the application of gradient-based fields to axially symmetric cube and cylinder compression tests, where the expected symmetry is only partially achieved. The deviation from the expected axial symmetry indicates an insufficient number of LDPM samples. Naturally, this is also a question of structural size and size of characteristic geometrical features compared to the particle size due to the limited resolution of a discrete element framework. The cylinders are better approximated by 20 realizations of LDPM when compared to the cubes, where the mean value of max. stress and COV of max. stress differ by 0.15 MPa and 0.05%, respectively. Nevertheless, given such relatively small deviations and the dimensionality of the associated Monte Carlo (MC) task, introduction of more realizations has not been considered tenable in this stage. There is currently no consensus on the "sufficient" number of LDPM realizations, nor is there an established sampling strategy for spatially variable models, for preliminary work please refer to (Podroužek et al., 2016; Podroužek et al., 2014).

Moreover, it is hard to separate physically or mechanically relevant sources of response scattering from the noise components, owing to model uncertainties (solution and discretiztion artefacts) (e.g. Prabhu et al., 2017).

All presented models utilizing the PGGFa placement scheme share the simplest power form of spectral funtion:

$$distance^{-p} \tag{1}$$

where p is the power spectral parameter (Podroužek et al., 2016).

If the correlated spatial variability models with constant material property fields, i.e. the particle generation governed by random field (PGGFa), (Figure 4), are compared to those with independent and random particle placemenet (IRPP), the scattering of load capacity in terms of COV is generally higher in case of cube and cylinder compression tests (Figures 2 and 3). As of the three point bending test models (beam), in contrary, the scattering in terms of COV is generally lower, when compared to IRPP. Overall, the COV in numerical experiments is a factor 2 to 4 smaller than in comparable real experiments

In terms of mean values of load capacity, the PGGFa models of cube and cylinder show a decreased capacity when compared to the IRPP model. As of the three point bending test models (beam), in contrary, the mean values of load capacity is almost identical, when compared to IRPP.

The investigation of sensitivity to different gradient orientations utilizes models with constant material property fields and particle generation governed by gradient based field (PGGFb). The directions maximizing the COV of load capacity are depicted in Figures 1–3 c). The relationships between peak load range and COV for the investigated models can be found in Figure 5. Here, it can

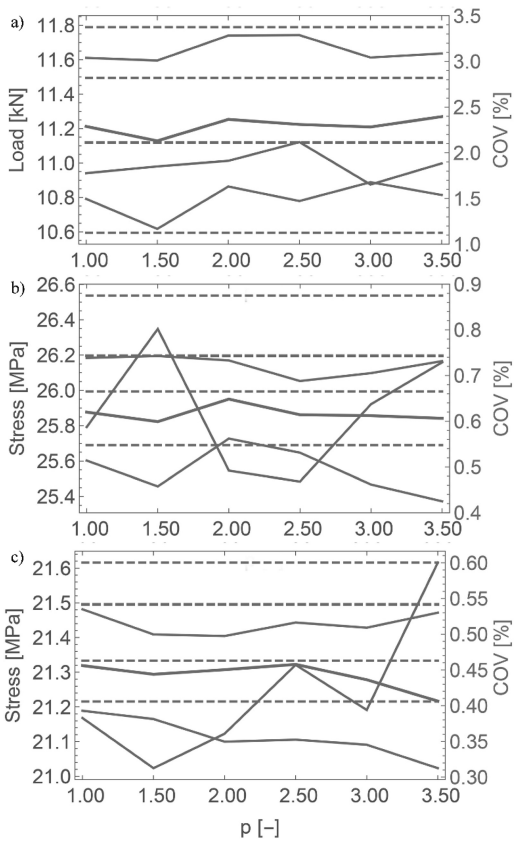

Figure 4. Effect of spectral parameter p on the peak load stress (pls) and COV of peak load; dashed grey lines: IRPP pls (Max., Mean, Min.); solid grey lines: PGGFa pls (Max., Mean, Min.); dashed blue line: IRPP COV of pls; solid blue line: PGGFa COV of pls; a) beams, b) cubes and c) cylinders.

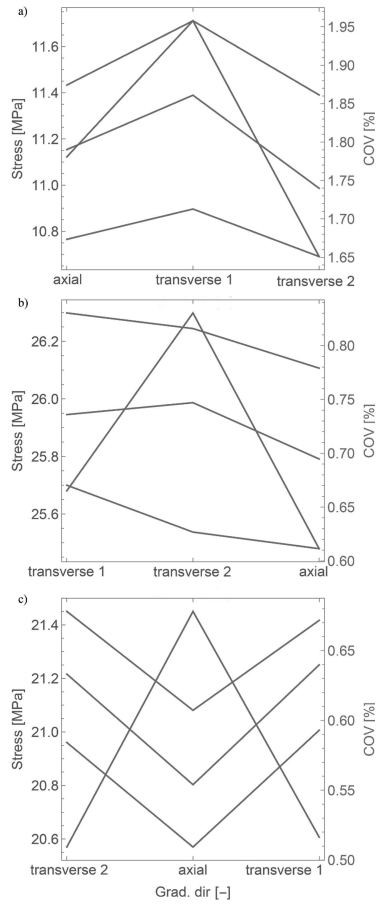

Figure 5. Effect of gradient field orientation (PGGFb) on the peak load stress (pls) and COV of pls; solid grey lines: pls (Max., Mean, Min.); blue line: COV of pls; for gradient directions (Grad. dir) maximizing the COV refer to Figures 1–3 c); a) beams, b) cubes and c) cylinders.

be seen that different field orientations affect not only the COV, but also the load capacity.

In case of cylinder compression tests, the axial gradient field orientation maximizing COV is minimizing the load capacity. In contrary, the bending test shows that the gradient maximizing the COV is also maximizing the load capacity. The cube compression tests yields a mixed effect.

Please note that the different gradient field orientations and random field parameters not only affects the peak load capacity and COV, but also the failure mechanism such as diagonal splitting and crushing (Figures 6 and 7). More details may be found e.g. in (Wan-Wendner et al., 2017).

It should be noted, however, that although the absolute differences in terms of mean and COV are negligible from civil engineering perspective at the presented scales, larger structural components and structures are likely to yield increased absolute differences, both in terms of COV and mean value of load capacity. Please also note the purpose of this study was not to generate (increased or decreased) scatter in LDPM simulations, but to (i) provide a method for a systematic interpretation of the observed scattering in reality, and (ii) build the basis for a thorough investigation of material property random fields linked to the micro-structure with the goal to ultimately provide guidance regarding the best choice of spectral function and a physical meaning of autocorrelation length.

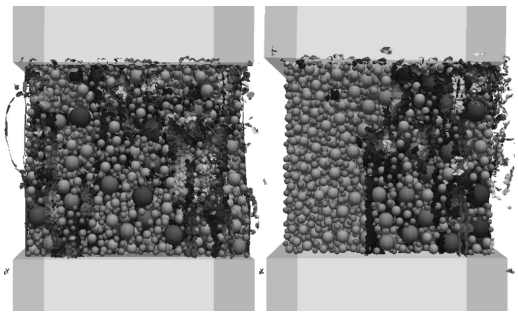

Figure 6. Example of two qualitatively different failure mechanisms from cube compression test realizations.

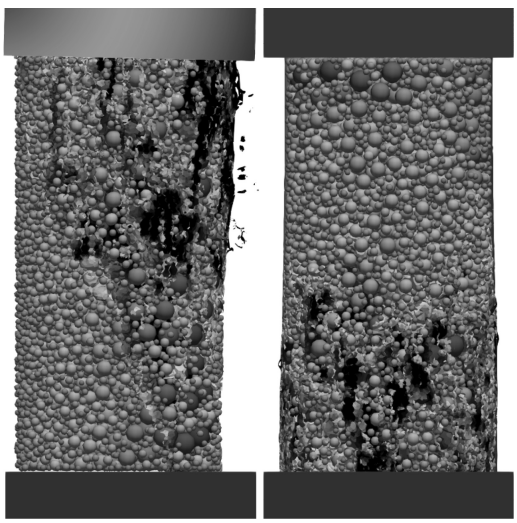

Figure 7. Example of two qualitatively different failure mechanisms from cylinder compression test realizations.

5 OUTLOOK

The proposed particle placement schemes may be further utilized in the extended version of LDPM, where the independent and random particle placement may lead to less conservative degradation evolution as clustering of particles (correlated to initial random field) may speed-up e.g. the particle size dependent ASR process.

The assesment of slender columns is among another application domains, where the production artifacts, such as horizontal casting (prefabrication) can be effectively simulated by the gradient-based fields, together with its consequence on overall stability of the column. Furthermore, a random field may be introduced (e.g. by summation, multiplication, etc.) to reflect the inherent variability in the casting process itself.

The presented spatial variability framework may be more generally utilized towards the assesment of existing structures, where optimization tasks, such as design of experiments (e.g. core samples) need to based on realistic assumptions on spatial variability.

Similarly, the future requirements on computaional mechanics may utilize some of the presented ideas, e.g. in the domain of additive manufactureing (3D printing) of civil structures, where prismatic speciments with solid infills are no longer expected. Instead, lightweight, optimized and bio-inspired structures with complex internal structure (spatial or 3D materials) are suggested (e.g. Benvenuti et al., 2013; Ceccanti et al., 2010), and as such will require a whole new set of tools for the spatial variability based reliability.

6 CONCLUSIONS

A spatial variability package for LDPM has been presented, including two new abstraction levels for the discrete framework, where material characterization and/or particle generation are governed by an initial random field, which increases the consistency

of the LDPM modelling paradigm and potentially enhances the realism of the LDPM simulations, if properly understood.

In order to separate the effects of the particle generation process governed by random or gradient based field from randomized material property fields governed by random or gradient fields, the material property fields have been kept constant for all of the presented results.

Thus, by considering constant material property fields, the presented results are unique in capturing how:

1. directional effects, mimicking the production process (concrete casting) and represented by gradient based fields, may affect the COV of response and thus identify loading directions maximizing the COV;
2. correlated spatial variability models (random fields) governing the particle generation process may increase the COV of response compared to the independent and random generation of particles;
3. functional form for COV and correlation parameters, such as constants in spectral function, could be derived.

Since the presented study concerns only small-scale specimens simulating classical concrete experiments with constant material property fields, the absolute differences resulting from various correlated spatial variability models are rather small. However, the differences will increase if:

1. larger structures or structural components are analysed and/or
2. random fields (inherent variability) are combined with gradient based fields (production, diffusion or transport process) and/or
3. the correlated spatial variability models govern not only the particle generation process but also the material property fields.

This, however, requires addressing several milestones, such as establishing a physical reference for the governing random field model, in particular the choice of spectral function, its parameters and relationship to correlation length. Similarly, objective statistical characterization of spatially variable LDPM models in a small sample Monte Carlo simulation framework is required. Addressing such high-dimensional problems will not be possible in the near future without massive parallelisation of the associated tasks and utilization of scientific clusters. In order to introduce spatial variability into structural reliability, some preliminary work of (Podroužek et al., 2014; Jan Podroužek et al., 2016) on identification strategy for correlated random processes may be further utilized for LDPM models, realizations of which may be further classified by the resulting correlation structure. In this way, various particle placement schemes may not only be statistically benchmarked, but also characterized in terms of first passage probabilities or probability distributions, given a set of critical criteria for a particular model.

ACKNOWLEDGEMENT

The financial support by the Austrian Federal Ministry of Economy, Family and Youth and the National Foundation for Research, Technology and Development is gratefully acknowledged, as well as the support of the project No. LO1408 "AdMaS UP—Advanced Materials, Structures and Technologies", supported by Ministry of Education, Youth and Sports under the "National Sustainability Programme I". The computational results presented have been achieved using the Vienna Scientific Cluster (VSC).

REFERENCES

Alnaggar, M., Cusatis, G., Di Luzio, G., 2013. Lattice Discrete Particle Modeling (LDPM) of Alkali Silica Reaction (ASR) deterioration of concrete structures. Cem. Concr. Compos. 41, 45–59.

Austrian initiative on high performance computing [WWW Document], 2014.. Vienna Sci. Clust. URL http://vsc.ac.at/

Bažant, Z.P., Zi, G., Meyer, C., 2000. Fracture mechanics of ASR in concretes with waste glass particles of different sizes. J. Eng. Mech. 126, 226–232.

Benvenuti, S., Ceccanti, F., De Kestelier, X., 2013. Living on the moon: topological optimization of a 3D-printed lunar shelter. Nexus Netw. J. 15, 285.

Ceccanti, F., Dini, E., De Kestelier, X., Colla, V., Pambaguian, L., 2010. 3D printing technology for a moon outpost exploiting lunar soil, in: 61st International Astronautical Congress, Prague, CZ, IAC-10-D3.

Cusatis, G., 2013. The Lattice Discrete Particle Model (LDPM) for the Numerical Simulation of Concrete Behavior Subject to Penetration. John Wiley & Sons, Inc.

Cusatis, G., Mencarelli, A., Pelessone, D., Baylot, J., 2011a. Lattice Discrete Particle Model (LDPM) for failure behavior of concrete. II: Calibration and validation. Cem. Concr. Compos. 33, 891–905. doi:10.1016/j.cemconcomp.2011.02.010.

Cusatis, G., Pelessone, D., Mencarelli, A., 2011b. Lattice Discrete Particle Model (LDPM) for failure behavior of concrete. I: Theory. Cem. Concr. Compos. 33, 881–890. doi:10.1016/j.cemconcomp.2011.02.011.

Eliáš, J., Vořechovský, M., Le, J.L., 2013. Lattice modeling of concrete fracture including material spatial randomness. Eng. Mech. 20, 413–426.

Feng, Y.T., Xikui, L, Tan, Y. and Ji, S. (editors), 2015. Special Issue: Advances in Computational Particle Based Methods. Engineering Computations, Volume 32 Issue 4.

Janouchová, E., Kucerová, A., Sỳkora, J., Vorel, J., Wendner, R., 2016. Bayesian Calibration of Lattice Discrete Particle Model for Concrete, in: The 7th International Workshop on Reliable Engineering Computing (REC2016). Bochum, Germany.

Marcon, M., Vorel, J., Ninčević, K., Wan-Wendner, R., 2017. Modeling Adhesive Anchors in a Discrete Element Framework. Materials 10, 917.

Podroužek, J., Bucher, C., Deodatis, G., 2014. Identification of critical samples of stochastic processes towards feasible structural reliability applications. Struct. Saf. 47, 39–47.

Podroužek, Jan, Vorel, J., Boumakis, I., Cusatis, G., Wendner, R., 2016. Implications of spatial variability characterization in discrete particle models, in: Proceedings of the 9th International Conference on Fracture Mechanics of Concrete and Concrete Structures. Presented at the FraMCoS-9, Berkeley, CA, USA.

Podroužek, J, Vorel, J., Cusatis, G., Wendner, R., 2016. Imposed Correlation Between Random Field and Discrete Particle Placement, in: 14th International Probabilistic Workshop. Springer, pp. 245–252.

Podroužek, J., Vorel, J., Wan-Wendner, R., 2017a. Discrete particle placement schemes for LDPM. Presented at the EMI 2017, Rio de Janiero, Brazil.

Podroužek, J., Vorel, J., Wan-Wendner, R., 2017b. Random and gradient based fields in discrete particle models of heterogeneous materials. Presented at the UNCECOMP 2017, Rhodes, Greece.

Prabhu, S., Prabhu, S., Atamturktur, S., Atamturktur, S., Cogan, S., Cogan, S., 2017. Model assessment in scientific computing: Considering robustness to uncertainty in input parameters. Eng. Comput. 34, 1700–1723.

Vořechovský, M., Novák, D., 2003. Efficient random fields simulation for stochastic FEM analyses, in: Bathe, K.J. (Ed.),. Presented at the 2nd M.I.T. Conference on Computational Fluid and Solid Mechanics, Elsevier Science Ltd, pp. 2383–2386.

Wan, L., Wendner, R., Cusatis, G., 2015. Behavior of Ultra-High Performance Con-crete at Early Age: Experiments and Simulations. EMI 2015, Jun 16–19, 2015, Stanford, USA.

Wan-Wendner, L., Wan-Wendner, R., Liang, B., Cusatis, G., 2016. Analysis of the Behavior of Ultra High Performance Concrete at Early Age. J Cem Concrete Composites, 74, 120–135.

Wan-Wendner, L.,Wan-Wendner, R., Cusatis, G., 2017. Age-dependent size effect and fracture characteristics of ultra-high performance concrete. J Cem Concrete Composites (in press), arXiv pre-print 1608.08786.

Wan-Wendner, R., Vorel, J., Podroužek, J., Marcon, M., 2017. Gradient Based Fields For Ldpm And Fracture Properties Of Classical Experiments. Presented at the ICF 14 14th International Conference on Fracture, Rhodes, Greece.

Wan-Wendner, R., Nincevic, K., Boumakis, I., Wan, L., 2016. Age-Dependent Lattice Discrete Particle Model for Quasi-Static Simulations, in: Key Engineering Materials. Trans Tech Publ, pp. 1090–1097.

Yu, Q., Bažant, Z.P., Wendner, R., 2012. Improved algorithm for efficient and realistic creep analysis of large creep-sensitive concrete structures. ACI Struct. J. 109, 665–676. doi:10.14359/51684044.

Computational Modelling of Concrete Structures – Meschke, Pichler & Rots (Eds)
© 2018 Taylor & Francis Group, London, ISBN 978-1-138-74117-1

Enhancement of multifiber beam elements in the case of reinforced concrete structures for taking into account the lateral confinement of concrete due to stirrup

N. Khoder
University Grenoble Alpes, CNRS, Grenoble INP, 3SR, Grenoble, France

S. Grange
University Lyon, INSA-LYON, GEOMAS, Villeurbanne, France

Y. Sieffert
University Grenoble Alpes, CNRS, Grenoble INP, 3SR, Grenoble, France

ABSTRACT: Many researches have been conducted in the structural engineering field in order to develop efficient numerical tools able to reproduce the complex nonlinear behavior of reinforced concrete structures. In the case of slender elements, enhanced beam models have been developed to try to introduce shear effects, but in these models, the transverse steel is sometimes taken into consideration with approximated manner or often not at all. However, as shown by some experimental tests, the amount of transverse reinforcement triggers significantly the behavior of beam elements, especially under cyclic loading. The present study adresses this problem by investigating solutions for an enhanced multifiber beam element, accounting for vertical stretching of the cross-section occurring due to the presence of stirrups. A timoshenko beam element with internal degrees of freedom and higher order interpolation functions is selected. Full 3D stresses and strains are obtained and the construction of the element and sectional stiffness matrices is detailed. The element presented hereafter is suitable for an arbitrary shape cross-section made of heterogeneous materials. Numerical applications on a plain concrete cantilever beam subjected to tension and bending tests respectively are presented. Moreover, as a first application, a dilation effect is added to the concrete fibers in order to highlight the role of transversal rebars. All the numerical results are confronted to the outcomes of stantard 3D finite element computations.

1 INTRODUCTION

To study the seismic vulnerability of existing reinforced concrete structures, numerical computations at the structural scale able to account for material nonlinearities are needed. 2D and 3D finite element formulations are too costly, whereas multifiber beam elements combine the advantages of high computational speed with an increased accuracy for nonlinear materials. The principle of multifiber modelling consists on adding a two dimensional section at the Gauss point of the element. Each section is afterwards discretized into several elements presenting Gauss points where stresses and strains are computed. To this end, generalized strains are obtained at the beam Gauss points from the node displacements. Then, based upon Euler-Bernoulli or Timoshenko's theory, they are used to calculate the total strains, and with an adequate constitutive law, stresses are deduced at the Gauss points of the section. The generalized forces are finally derived after an integration made over the cross-section (Guedes et al. 1994).

A variety of approaches have been developed to try to introduce shear effects, such as those proposed by (Le Corvec 2012), but whose model can't be applied to reinforced concrete elements, and the numerical formulation of (Mohr et al. 2010) which is adapted to reinforced concrete applications but works only in 2D. More recently, (Capdevielle et al. 2016) developed a nonlinear multifiber beam model which provides robust results by the introduction of torsional warping in the case of reinforced concrete beams subjected to shear dominating loads.

In the above mentioned works, the transverse steel is sometimes taken into consideration with approximated manner or often not at all. However, as shown by some experimental tests conducted by Cusson & Paultre (1995), the amount of transverse reinforcement triggers significantly the behavior of beam elements, especially under cyclic loading.

Hereafter, a 3D enhanced multifiber beam model able to account for the distortion of the section is presented. It's a displacement-based formulation and higher order interpolation functions are

involved in order to avoid shear locking problems. Moreover, longitudinal and transversal rebars are introduced in the numerical model and their implementation is validated by comparisons performed with results of 3D finite element calculations in the linear elastic framework.

2 PROPOSED MODEL

2.1 *Section kinematics*

A 3D multifiber Timoshenko beam, displacement-based, element has been developed. The main assumption considered herein is that the full displacement of any fiber at the cross-section level is defined by the superposition of the traditional rigid body displacements of the plane section ($\boldsymbol{u^P}$) obtained with Timoshenko's theory, plus an additional displacement field ($\boldsymbol{u^w}$). The latter one has two transversal components, u_y^w and u_z^w, which stand for the distortion of the section in y and z directions respectively. The total displacement ($\boldsymbol{u}$) of any fiber is given by the following equation:

$$\mathbf{u} = \underbrace{\begin{bmatrix} U_x(x) - y\theta_z(x) + z\theta_y(x) \\ U_y(x) - z\theta_x(x) \\ U_z(x) + y\theta_x(x) \end{bmatrix}}_{\boldsymbol{u^P}} + \underbrace{\begin{bmatrix} 0 \\ u_y^w(x,y,z) \\ u_z^w(x,y,z) \end{bmatrix}}_{\boldsymbol{u^w}} \tag{1}$$

U_x, U_y and U_z being the translations in x, y and z directions respectively. As for θ_x, θ_y and θ_z, they denote the three rotations about x, y and z axes respectively, for a standard 3D beam element.

Under the assumption of small displacements, the total strain at any point will be formed by the sum of the plane strain field ($\boldsymbol{\epsilon^P}$) and the distortional strain ($\boldsymbol{\epsilon^w}$) as follows:

$$\boldsymbol{\epsilon} = \frac{1}{2}\left(grad(\boldsymbol{u}) + grad(\boldsymbol{u})\right)^T = \boldsymbol{\epsilon^P}(\boldsymbol{u^P}) + \boldsymbol{\epsilon^w}(\boldsymbol{u^w}) \tag{2}$$

Therefore, the 6 components of the total strain field are defined as:

$$\begin{cases} \epsilon_{xx} = \dfrac{dU_x}{dx} - y\dfrac{d\theta_z}{dx} + z\dfrac{d\theta_y}{dx} \\ \epsilon_{yy} = \dfrac{\partial u_y^w}{\partial y} \\ \epsilon_{zz} = \dfrac{\partial u_z^w}{\partial z} \\ \gamma_{xy} = -\theta_z + \dfrac{dU_y}{dx} - z\dfrac{d\theta_x}{dx} + \dfrac{\partial u_y^w}{\partial x} \\ \gamma_{xz} = \theta_y + \dfrac{dU_z}{dx} + y\dfrac{d\theta_x}{dx} + \dfrac{\partial u_z^w}{\partial x} \\ \gamma_{yz} = \dfrac{\partial u_y^w}{\partial z} + \dfrac{\partial u_z^w}{\partial y} \end{cases} \tag{3}$$

With equation (3), the plane strain field can be expressed in function of the generalized deformation vector $\boldsymbol{e_s}$, and a compatibility matrix $\boldsymbol{a_s}(y,z)$ so that $\boldsymbol{\epsilon^P}$ takes the following form:

$$\boldsymbol{\epsilon^P} = \underbrace{\begin{bmatrix} 1 & 0 & 0 & 0 & +z & -y \\ 0 & 0 & 0 & 0 & 0 & 0 \\ 0 & 0 & 0 & 0 & 0 & 0 \\ 0 & 1 & 0 & -z & 0 & 0 \\ 0 & 0 & 1 & y & 0 & 0 \\ 0 & 0 & 0 & 0 & 0 & 0 \end{bmatrix}}_{\boldsymbol{a_s}(y,z)} \underbrace{\begin{bmatrix} \dfrac{dU_x}{dx} \\ \dfrac{dU_y}{dx} - \theta_z \\ \dfrac{dU_z}{dx} + \theta_y \\ \dfrac{d\theta_x}{dx} \\ \dfrac{d\theta_y}{dx} \\ \dfrac{d\theta_z}{dx} \end{bmatrix}}_{\boldsymbol{e_s}} \tag{4}$$

Also, as can be seen from equation (3), the distortional displacement ($\boldsymbol{u^w}$) contributes to the lateral deformation components (ϵ_{yy}) and (ϵ_{zz}). Therefore, transverse strains are not null, and the additional strains ($\boldsymbol{\epsilon^w}$) play an important role in the description of the vertical stretching of the section. As a consequence, the effect of transversal reinforcement described by lateral expansion and contraction, can be taken into account. Hence, the behavior of confined reinforced concrete elements can be studied.

2.2 *Caillerie's Timoshenko beam element with internal degrees of freedom*

In order to avoid shear locking problems (Stolarski and Belytschko 1982, Ibrahimbergović and Frey 1993) coming from the use of linear interpolation functions, several authors have developed numerical models based on higher order interpolation functions or functions depending on material properties. However, the latter ones present the disadvantage of not being updated after damage. Recently, a new multifiber beam element has been developed by Caillerie et al. (2015) and has been chosen to be introduced in our model. It is presented by Figure 1.

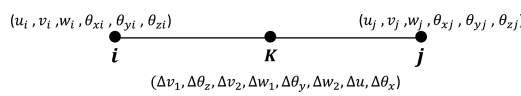

Figure 1. Definition of the degrees of freedom in the 3D version of Caillerie's beam element.

Each of the two nodes (i and j) has 6 degrees of freedom: 3 translations (u,v,w) and 3 rotations $\theta_x,\theta_y,\theta_z$ about x, y and z axes respectively. The proposed element was developed by Caillerie et al. (2015) for 2D applications and was extended in our model to a 3D formulation. Therefore, it presents an internal node K, with 8 internal degrees of freedom ($\Delta v_1,\Delta v_2,\Delta w_1,\Delta w_2,\Delta\theta_x,\Delta\theta_y,\Delta\theta_z$ and Δu).

The generalized displacement field can be therefore written as:

$$\begin{cases} U_x = N_1 u_i + N_2 \Delta u + N_3 u_j \\ U_y = H_R^1 v_i + L_R^1 \Delta v_1 + L_R^2 \Delta v_2 + H_R^2 v_j \\ U_z = H_R^1 w_i + L_R^1 \Delta w_1 + L_R^2 \Delta w_2 + H_R^2 w_j \\ \theta_x = N_1 \theta_{xi} + N_2 \Delta\theta_x + N_3 \theta_{xj} \\ \theta_y = L_R'^1 \theta_{yi} + M_R^3 \Delta\theta_y + L_R'^2 \theta_{yj} \\ \theta_z = L_R'^1 \theta_{zi} + M_R^3 \Delta\theta_z + L_R'^2 \theta_{zj} \end{cases}$$

(N_1, N_2, N_3) and ($L'^1_R, L'^2_R, M^3_R,$) are defined as quadratic interpolation functions, whereas cubic shape functions ($H^1_R, H^2_R, L^1_R, L^2_R$) are used for transverse displacements. It's worth mentioning that these higher order interpolation functions are independent of material properties. They are calculated at the beam Gauss points and take the following form:

$$\begin{aligned} N_1 &= \frac{1}{2}\xi(\xi-1) & L_R^1 &= \frac{(\xi-1)^2(\xi+1)}{4} \\ N_2 &= 1-\xi^2 & L_R^2 &= \frac{(\xi-1)(\xi+1)^2}{4} \\ N_3 &= \frac{1}{2}\xi(\xi+1) & L'^1_R &= \frac{(\xi-1)(3\xi+1)}{4} \\ H_R^1 &= \frac{(\xi-1)^2(\xi+2)}{4} & L'^2_R &= \frac{(\xi+1)(3\xi-1)}{4} \\ H_R^2 &= -\frac{(\xi-2)(\xi+1)^2}{4} & M_R^3 &= 1-\xi^2 \end{aligned} \quad (5)$$

All degrees of freedom are collected in a column vector U^e structured as follows:

$$\boldsymbol{U}^{\mathbf{e}} = \left[\boldsymbol{U}_i^{eT} \quad \Delta\boldsymbol{U}^{eT} \quad \boldsymbol{U}_j^{eT} \right]^T \quad (6)$$

such as:

$$\begin{aligned} \boldsymbol{U}_i^e &= \left[u_i, v_i, w_i, \theta_{xi}, \theta_{yi}, \theta_{zi} \right]^T \\ \Delta\boldsymbol{U}^e &= \left[\Delta v_1, \Delta\theta_z, \Delta v_2, \Delta w_1, \Delta\theta_y, \Delta w_2, \Delta_u, \Delta\theta_x \right]^T \\ \boldsymbol{U}_i^e &= \left[u_j, v_j, w_j, \theta_{xj}, \theta_{yj}, \theta_{zj} \right]^T \end{aligned} \quad (7)$$

As a consequence, the generalized strain field $\boldsymbol{e_s}$ can be written in function of a matrix $\boldsymbol{B_p}$ which gathers the derivatives of the above mentioned interpolation functions related to longitudinal spatial discretization. Then, the new expression of the plane strain field $\boldsymbol{\epsilon^P}$ becomes:

$$\boldsymbol{\epsilon^P} = \boldsymbol{a_s}(y,z)\boldsymbol{B_p}\boldsymbol{U}^e \quad (8)$$

2.3 *Distortional displacement field interpolation*

It is assumed that the distortional displacement ($\boldsymbol{u^w}$) has two non-zero components in y and z directions accounting for the vertical stretching of the cross-section. It is defined as:

$$\boldsymbol{u^w}(x,y,z) = \left[0 \quad u_y^w(x,y,z) \quad u_z^w(x,y,z) \right] \quad (9)$$

where:

$$\begin{cases} u_x^w(x,y,z) = 0 \\ u_y^w(x,y,z) = c_1(x)\varphi_1(y,z) \\ u_z^w(x,y,z) = c_2(x)\varphi_2(y,z) \end{cases} \quad (10)$$

The interpolation is performed independently along the beam axis with the quadratic functions $c_1(x)$ and $c_2(x)$, and on the cross-section with functions $\varphi_1(y,z)$ and $\varphi_2(y,z)$. The latter ones are the classical quadratic functions used for 6 nodes triangular elements TRI6 and they are computed at the section Gauss points.

Distortional strains components can be therefore presented as follows:

$$\begin{cases} \epsilon_{xx}^w = \dfrac{\partial u_x^w}{\partial x} = 0 \\ \epsilon_{yy}^w = \dfrac{\partial u_y^w}{\partial y} = c_1(x)\dfrac{\partial\varphi_1}{\partial y} \\ \epsilon_{zz}^w = \dfrac{\partial u_z^w}{\partial z} = c_2(x)\dfrac{\partial\varphi_2}{\partial z} \\ \gamma_{xy}^w = \dfrac{\partial u_x^w}{\partial y} + \dfrac{\partial u_y^w}{\partial x} = \dfrac{dc_1}{dx}\varphi_1 \\ \gamma_{xz}^w = \dfrac{\partial u_x^w}{\partial z} + \dfrac{\partial u_z^w}{\partial x} = \dfrac{dc_2}{dx}\varphi_2 \\ \gamma_{yz}^w = \dfrac{\partial u_y^w}{\partial z} + \dfrac{\partial u_z^w}{\partial y} = c_1(x)\dfrac{\partial\varphi_1}{\partial z} + c_2(x)\dfrac{\partial\varphi_2}{\partial y} \end{cases} \quad (11)$$

The enhanced strain field can be given by the following expression:

$$\boldsymbol{\epsilon^w} = \boldsymbol{a_w}(y,z)\boldsymbol{e_w} = \boldsymbol{a_w}(y,z)\boldsymbol{B_w}\boldsymbol{W}^e \quad (12)$$

And by the use of a matrix notation, $\boldsymbol{\epsilon^w}$ becomes:

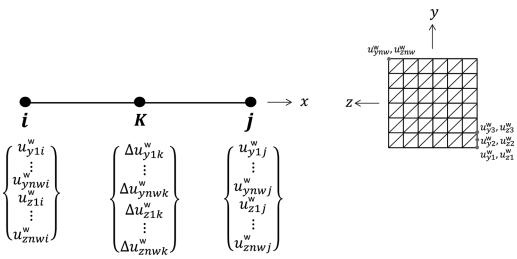

Figure 2. Distribution of the distortional degrees of freedom.

$$\boldsymbol{\epsilon}^{w} = \begin{Bmatrix} \epsilon^{w}_{xx} \\ \epsilon^{w}_{yy} \\ \epsilon^{w}_{zz} \\ \gamma^{w}_{xy} \\ \gamma^{w}_{xz} \\ \gamma^{w}_{yz} \end{Bmatrix} = \underbrace{\begin{bmatrix} 0 & 0 & 0 & 0 \\ 0 & 0 & \dfrac{\partial \varphi_1}{\partial y} & 0 \\ 0 & 0 & 0 & \dfrac{\partial \varphi_2}{\partial z} \\ \varphi_1 & 0 & 0 & 0 \\ 0 & \varphi_2 & 0 & 0 \\ 0 & 0 & \dfrac{\partial \varphi_1}{\partial z} & \dfrac{\partial \varphi_2}{\partial y} \end{bmatrix}}_{\boldsymbol{a}_w(y,z)} \underbrace{\begin{bmatrix} \dfrac{dc_1}{dx} \\ \dfrac{dc_2}{dx} \\ c_1 \\ c_2 \end{bmatrix}}_{\boldsymbol{e}_w} \tag{13}$$

The matrix $\boldsymbol{B}_w$ collects the longitudinal interpolation functions and their derivatives. As for the vector $\boldsymbol{W}^e$, it gathers all the distortional degrees of freedom of the points located on the section i of each element. They are treated as global DOFs of the beam element as shown by Figure 2.

Hence,

$$\boldsymbol{W}^e = \left[\boldsymbol{W}_{yi}^{eT}, \boldsymbol{W}_{zi}^{eT}, \Delta \boldsymbol{W}_{y}^{T}, \Delta \boldsymbol{W}_{z}^{T}, \boldsymbol{W}_{yj}^{eT}, \boldsymbol{W}_{zj}^{eT} \right]^T \tag{14}$$

With:

$$\begin{aligned} \boldsymbol{W}^e_{y(i,j)} &= \left[u^w_{y1(i,j)} \quad \dots \quad u^w_{ynw(i,j)} \right]^T \\ \boldsymbol{W}^e_{z(i,j)} &= \left[u^w_{z1(i,j)} \quad \dots \quad u^w_{znw(i,j)} \right]^T \\ \Delta \boldsymbol{W}^e_{(y,z)} &= \left[\Delta u^w_{(y,z)1} \quad \dots \quad \Delta u^w_{(y,z)nw} \right]^T \end{aligned} \tag{15}$$

n_w being the total number of the nodes per section.

Once, the plane strain $\boldsymbol{\epsilon}^P$ and the distortional strain fields $\boldsymbol{\epsilon}^w$ computed at the Gauss points of the section, the stress distribution at the concrete fibers is deduced.

3 Gauss points per element are needed in order to correctly integrate the higher order polynoms, which means 3 sections per element. Thus, the calculation procedure can be illustrated by Figure 3.

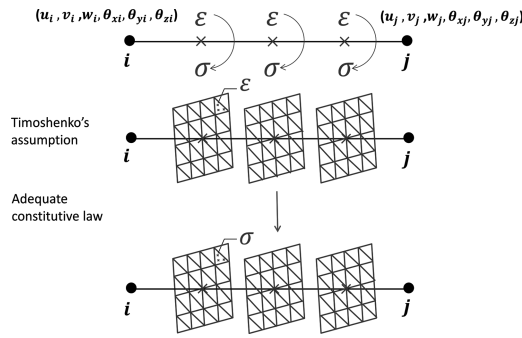

Figure 3. Calculation procedure.

3 GOVERNING EQUATIONS

Beam equilibrium is written in its weak form by equation (16). In addition, the plane section displacement $\boldsymbol{u}^P$ and the distortion one $\boldsymbol{u}^w$ assumed to be orthogonal, the projection of the weak form equilibrium on these two subspaces lead to two equilibrium equations (17). The first one representing the classical equilibrium of the beam element, and the second one being the equilibrium equation of the cross-section. $\boldsymbol{F}$ denotes the external forces and $\boldsymbol{P}^w$ the forces coming from constrained distortion at the beam ends.

$$\int_\Omega \boldsymbol{\varepsilon}^{*T} \boldsymbol{\sigma} d\Omega = \boldsymbol{U}^{*T} \boldsymbol{F}_{ext} \tag{16}$$

$$\Leftrightarrow \begin{cases} \int_\Omega \delta \boldsymbol{\epsilon}^{PT} \hat{\boldsymbol{\sigma}}(\boldsymbol{\epsilon}^P, \boldsymbol{\epsilon}^w) d\Omega = \boldsymbol{F} \\ \int_\Omega \delta \boldsymbol{\epsilon}^{wT} \hat{\boldsymbol{\sigma}}(\boldsymbol{\epsilon}^P, \boldsymbol{\epsilon}^w) d\Omega = \boldsymbol{P}^w \end{cases} \tag{17}$$

At the element level, the beam is discretized into n_e Timoshenko beam elements, of length l_e, each having 3 Gauss points, i.e. 3 sections, whose contribution should be summed in order to compute the terms of the element force vector $\boldsymbol{P}_e$ and the element stiffness matrix $\boldsymbol{K}_e$.

Therefore, the expression of the element stiffness matrix is given by:

$$\boldsymbol{K}_e = \begin{bmatrix} \boldsymbol{K}_{pp} & \boldsymbol{K}_{pw} \\ \boldsymbol{K}_{wp} & \boldsymbol{K}_{ww} \end{bmatrix} \tag{18}$$

where:

$$\begin{aligned} \boldsymbol{K}_{pp} &= \int_{l_e} \boldsymbol{B}_P^T \boldsymbol{a}_S^T \boldsymbol{K}_m \boldsymbol{a}_s \boldsymbol{B}_p dx \\ \boldsymbol{K}_{pw} &= \int_{l_e} \boldsymbol{B}_P^T \boldsymbol{a}_S^T \boldsymbol{K}_m \boldsymbol{a}_w \boldsymbol{B}_w dx \\ \boldsymbol{K}_{wp} &= \int_{l_e} \boldsymbol{B}_w^T \boldsymbol{a}_w^T \boldsymbol{K}_m \boldsymbol{a}_s \boldsymbol{B}_p dx \\ \boldsymbol{K}_{ww} &= \int_{l_e} \boldsymbol{B}_w^T \boldsymbol{a}_w^T \boldsymbol{K}_m \boldsymbol{a}_w \boldsymbol{B}_w dx \end{aligned} \tag{19}$$

$\boldsymbol{P}_e$ being the internal element force vector:

$$\boldsymbol{P}_e = \begin{bmatrix} \int_{l_e} \boldsymbol{B}_p^T \boldsymbol{a}_s^T \hat{\boldsymbol{\sigma}}(\epsilon^P, \epsilon^w) dx \\ \int_{l_e} \boldsymbol{B}_w^T \boldsymbol{a}_w^T \hat{\boldsymbol{\sigma}}(\epsilon^P, \epsilon^w) dx \end{bmatrix} \tag{20}$$

Considering $\boldsymbol{K}_m$ as the stiffness tangent operator, the linearized form of the stress vector $\hat{\boldsymbol{\sigma}}$ is defined as:

$$\hat{\boldsymbol{\sigma}}(x,y) = \boldsymbol{K}_m \boldsymbol{\epsilon} = \boldsymbol{K}_m (\boldsymbol{\epsilon}^P + \boldsymbol{\epsilon}^w) \tag{21}$$

On the other hand, each cross section is discretized into n_s 6 nodes triangular elements. Therefore the section stiffness matrix and the sectional force vector are expressed as follows:

$$\boldsymbol{P}_s = \sum_{S^e=1}^{n_s} \begin{bmatrix} \int_{S^e} \boldsymbol{a}_s^T \hat{\boldsymbol{\sigma}}(\epsilon^P, \epsilon^w) dS^e \\ \int_{S^e} \boldsymbol{a}_w^T \hat{\boldsymbol{\sigma}}(\epsilon^P, \epsilon^w) dS^e \end{bmatrix} = \begin{bmatrix} \boldsymbol{P}_{sp,c} \\ \boldsymbol{P}_{sw,c} \end{bmatrix} \tag{22}$$

$$\boldsymbol{K}_s = \sum_{S^e=1}^{ns} \begin{bmatrix} \boldsymbol{K}_{spp} & \boldsymbol{K}_{spw} \\ \boldsymbol{K}_{swp} & \boldsymbol{K}_{sww} \end{bmatrix} = \begin{bmatrix} \boldsymbol{K}_{spp,c} & \boldsymbol{K}_{spw,c} \\ \boldsymbol{K}_{swp,c} & \boldsymbol{K}_{sww,c} \end{bmatrix} \tag{23}$$

where:

$$\begin{aligned} \boldsymbol{K}_{spp} &= \int_{S^e} \boldsymbol{a}_s^T \boldsymbol{K}_m \boldsymbol{a}_s dS^e \\ \boldsymbol{K}_{spw} &= \int_{S^e} \boldsymbol{a}_s^T \boldsymbol{K}_m \boldsymbol{a}_w dS^e \\ \boldsymbol{K}_{swp} &= \int_{S^e} \boldsymbol{a}_w^T \boldsymbol{K}_m \boldsymbol{a}_s dS^e \\ \boldsymbol{K}_{sww} &= \int_{S^e} \boldsymbol{a}_w^T \boldsymbol{K}_m \boldsymbol{a}_w dS^e \end{aligned} \tag{24}$$

For all the integral calculations, the Gaussian quadrature is applied.

4 IMPLEMENTATION OF LONGITUDINAL AND TRANSVERSAL REBARS

In the case of reinforced concrete elements, the contribution of the longitudinal rebars must be added to that of the concrete fibers. The total section will thus be represented by the sum of the concrete area and the section of the longitudinal reinforcement. The latter one is modelled as point elements intersecting the concrete cross-section. The shape and dimensions of the bar are considered as negligible. Consequently, the warping and distortion of this point element are not taken into account. It follows that the deformations of these elements are composed only by the terms of the plane strain field $\boldsymbol{\epsilon}^P$ defined by Timoshenko's theory.

Regarding the implementation of stirrups, they are modelled as bar elements with linear elastic constitutive law. Each leg of the transversal rebars

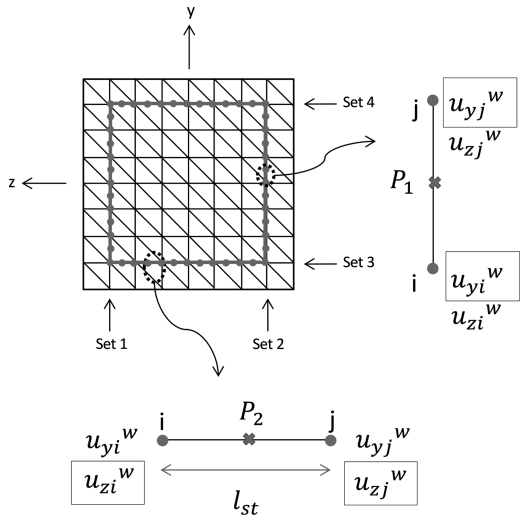

Figure 4. Cross-section discretization: concrete and transversal steel reinforcement mesh.

is discretized into n_{st} sub-elements of length l_{st}, presenting two nodes where the transversal distortional displacements components u_y^w and u_z^w are computed as presented by Figure 4.

Linear Lagrange polynomials N_1 and N_2 are used to interpolate distortion between these two nodes at a single integration Gauss point P. All transversal sub-element rebars colinear to y-direction belong to (Set 1) or (Set 2), whereas those towoards z-direction are attributed to (Set 3) and (Set 4) as seen in Figure 4.

If a Gauss point P_1 belongs to (Set 1) or (Set 2), its total displacement $u_{st}^w(P_1)$ has only one distortional component in y-direction interpolated as follows:

$$u_{y,st}^w(P_1) = N_1 u_{y,i}^w + N_2 u_{y,j}^w \tag{25}$$

As for (Set 3) and (Set 4), a single transversal component along z-axis is assigned to the displacement field $u_{st}^w(P_2)$ such as:

$$u_{z,st}^w(P_2) = N_1 u_{z,i}^w + N_2 u_{z,j}^w \tag{26}$$

Having the expression of the displacement at points P_1 and P_2, the enhanced transversal strain can be deduced.

On the other hand, the contribution of the transversal rebars can be seen at the sectional level, with extra terms added to $\boldsymbol{P}_s$ and $\boldsymbol{K}_s$ such that:

$$\boldsymbol{P}_s = \begin{bmatrix} \boldsymbol{P}_{sp,c} \\ \boldsymbol{P}_{sw,c} + \boldsymbol{P}_{sw,st} \end{bmatrix} \tag{27}$$

$$\boldsymbol{K}_s = \begin{bmatrix} \boldsymbol{K}_{spp,c} & \boldsymbol{K}_{spw,c} \\ \boldsymbol{K}_{swp,c} & \boldsymbol{K}_{sww,c} + \boldsymbol{K}_{sww,st} \end{bmatrix} \tag{28}$$

All the components of the sectional force vector $\boldsymbol{P}_s$ and stiffness matrix $\boldsymbol{K}_s$ with indices c related to concrete fibers are expressed by equations ((22),(23) and (24)). On the other hand, $\boldsymbol{P}_{sw,st}$ and $\boldsymbol{K}_{sww,st}$ referring to transversal steel reinforcements are defined as follows:

$$\begin{aligned} \boldsymbol{P}_{sw,st} &= \sum_{e=1}^{N_{st}} \int_{\Omega^e} A_{st} \times \boldsymbol{a}_{w,st}^T \times \boldsymbol{\sigma}_{st} d\Omega^e \\ \boldsymbol{K}_{sww,st} &= \sum_{e=1}^{N_{st}} \int_{\Omega^e} A_{st} \times \boldsymbol{a}_{w,st}^T \times \boldsymbol{E}_s \times \boldsymbol{a}_{w,st} d\Omega^e \end{aligned} \tag{29}$$

A_{st}, N_{st} and E_s being respectively the area of transversal rebars, the total number of transversal steel sub-elements and the steel tangent stiffness.

Also, in order to attribute a realistic value for the transversal reinforcement area A_{st}, an analogy is done between the enhanced numerical model and a realistic representation of a reinforced concrete beam confined with stirrups equally distributed with a spacing denoted s. Figure 5 presents the analogy made between the numerical beam element and a realistic reinforced concrete beam. Therefore, the adequate numerical rate of stirrups per meter can be obtained by applying the following analogy:

numerical model	analytical representation
$\frac{A_{steel}^{num}}{l_e} = \frac{2 \times A_{st}^{num} \times n_{section}}{l_e}$	$\frac{A_{steel}^{anal}}{s} = \frac{2 \times A_t^{anal}}{s} = \frac{2 \times \pi d^2}{s \times 4}$

$$\Leftrightarrow \frac{2 \times A_{st}^{num} \times n_{section}}{l_e} = \frac{2 \times A_t^{anal}}{s} \tag{30}$$

Hence, the section of transversal steel, A_{st}^{num}, that should be implemented in the numerical model is obtained:

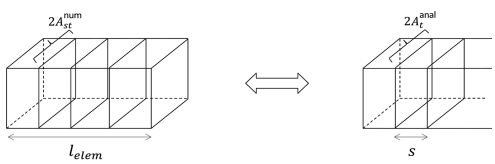

(a) (b)

Figure 5. Analogy between a multifiber element presenting 3 sections (a) with a realistic representation of a reinforced concrete beam confined with stirrups (b).

$$A_{st} = A_{st}^{num} = \frac{A_t \times l_e}{n_{section} \times s} \tag{31}$$

$n_{section}$ being the notation used to refer to the number of sections per element of length l_e in the discretized multifiber beam.

5 VALIDATION PROCESS: NUMERICAL CASE STUDIES

5.1 *Linear elastic cantilever beam without stirrups*

The enhanced multifiber beam element is validated by performing tension and flexure tests on a plain concrete cantilever beam in the linear elastic range. It's a beam of length L = 1 m, modelled using 11 Timoshenko multifiber elements, each having 3 Gauss points. The dimensions of the selected cross-section which is meshed using TRI6 triangular elements are represented in Figure 6. Concrete is modelled using a 3D linear elastic constitutive law and the stress-strain relations are defined as follows:

$$\boldsymbol{\sigma} = \frac{E}{1+\nu}\left[\epsilon + \frac{\nu}{1-2\nu} Tr(\epsilon)\boldsymbol{I}\right] \tag{32}$$

The efficiency of the proposed modelling strategies is tested by confronting the numerically obtained resluts with those of a standard 3D finite element model. To this end, a 3D cantilever beam was meshed with tetrahedral elements. All the computational analysis for both types of models was performed using the library ATLAS (A Tool and Language for Simplied Structural Solution Strategy) developed on the Matlab platform at INSA-Lyon by Prof. S. Grange.

The first aim of the verification process is achieved by plotting the variation of normal transversal stresses σ_{yy} computed at each Gauss point of

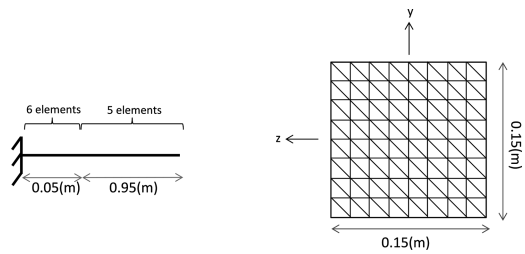

(a) (b)

Figure 6. Longitudinal beam element discretization (a). Cross-section description (b).

the cross-section with respect to the beam length as seen in Figure 7 where a tension test is simulated and Figure 8 which displays the outcomes of a simple flexure test. In both cases, all the enhanced degrees of freedom are restrained at the fixed end, the reason why high gradients of σ_{yy} are observed at this location of the beam. As for the free end, $u_x = 1$ *mm* and $u_y = 1$ *mm* are applied in order to perform respectively the tension (Figure 7) and bending (Figure 8) tests. The beam is free to distort at the free end, hence, the value of σ_{yy} tends to zero. The numerically obtained outcomes prove that the equilibrium state is reached, and a good matching between the results obtained with the 3D enhanced multifiber model and the 3D finite element solution.

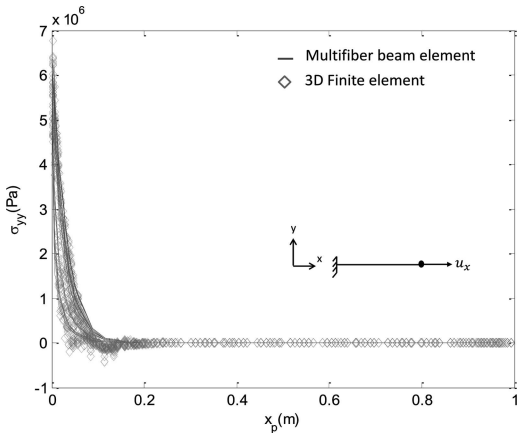

Figure 7. Tension test: Variation of transversal stresses σ_{yy} with respect to the length of the beam.

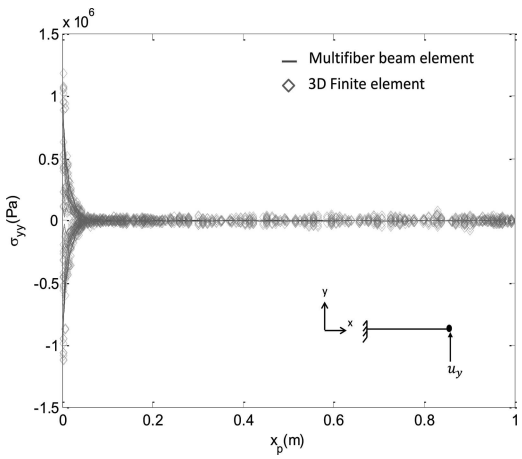

Figure 8. Flexion test: Variation of transversal stresses σ_{yy} with respect to the length of the beam.

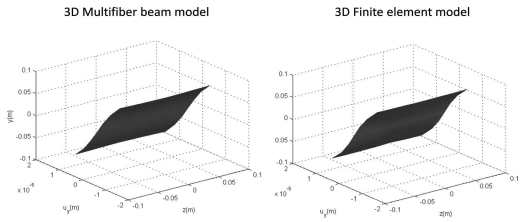

Figure 9. Tension test: Transverse displacement maps obtained with the 3D enhanced multifiber model and the standard 3D FE model.

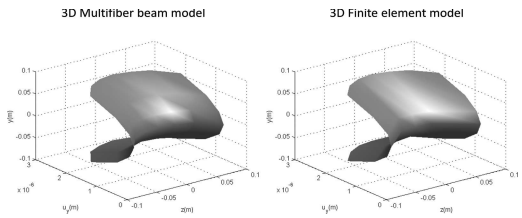

Figure 10. Flexion test: Transverse displacement maps obtained with the 3D enhanced multifiber model and the standard 3D FE model.

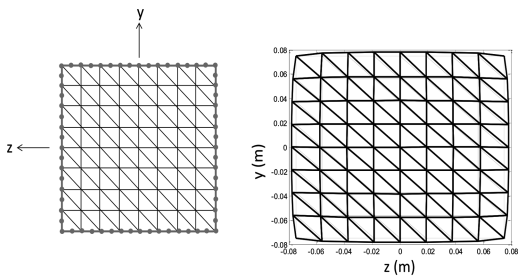

Figure 11. Concrete section confined with stirrups (a). Initial (red) and deformed (black) shape of the cross-section (b).

Moreover, transversal displacement u_y maps are displayed in Figures 9 and 10. By confronting the results provided by the proposed model with those coming from a standard 3D finite element formulation, good agreement can be observed showing the efficiency of the proposed model in reproducing displacements, strains and stresses in the linear elastic framework.

5.2 *Concrete beam element confined with stirrups*

This section highlights the role of stirrups on confining concrete fibers. To this end, dilation effect is simulated by imposing a thermal dilation

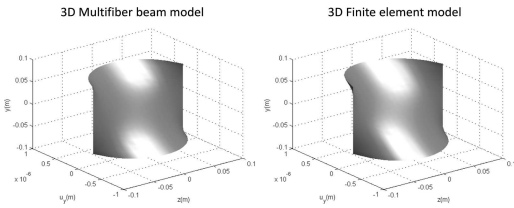

Figure 12. Transversal displacement maps for concrete fibers confined by large section of stirrups.

effect to the concrete fibers in the linear elastic phase. By applying this method and with a large section of stirrups confining the concrete fibers, the initial and deformed shapes of the cross-section are presented in Figure 11. Also, it can be seen in Figure 12 that the comparison between the proposed multifiber model and the 3D FE model presents a reasonable agreement in terms of transversal displacement maps.

6 CONCLUSION

An efficient 3D multifiber beam model was presented aiming at reproducing the vertical stretching of the concrete cross-section confined by stirrups. This distortional effect is taken into account by adding new degrees of freedom to the global level. A novel Timoshenko beam element recently developed by Caillerie et al. (2015) for 2D applications, has been chosen and extended in our model to the 3D formulation in order to avoid shear locking problems. Also, it should be mentioned that the present formulation of the section equilibrium is derived from the one presented by Capdevielle et al. (2016) which takes into account the warping of the cross-section.

The presented model is suitable for an arbitrary cross-section and material. Its efficiency is highlited by comparing the numerically obtained results in terms of stresses and displacement with those coming from 3D finite element modelling. Good matching was observed showing the robustness of the enhanced model and validating its performance in the linear elastic phase.

Furthermore, longitudinal and transversal rebars are modelled. Their implementation was validated by introducing a dilatancy effect to the concrete fibers and confronting the obtained outcomes with those coming from a 3D FE model.

The case studies investigated herein are related to static loadings, although cyclic loadings can take place. A nonlinear dilatant constitutive law is to be implemented and tested on reinforced concrete elements under monotonic and cyclic loadings and hence study the nonlinear response of structural concrete elements subjected to transverse shear. Also, the mass matrix can be implemented in order to conduct dynamic simulation studies, and the warping effect, taken into account by Capdevielle et al. (2016), can be coupled with the distortion of the section in order to obtain a complete 3D enhanced multifiber beam model.

REFERENCES

Caillerie, D., P. Kotronis, & R. Cybulski (2015). A timoshenko finite element straight beam with internal degrees of freedom. *International Journal for Numerical and Analytical Methods in Geomechanics 39*, 1753–1773.

Capdevielle, S., S. Grange, F. Dufour, & C. Desprez (2016). A multifiber beam model coupling torsional warping and damage for reinforced concrete structures. *European Journal of Environmental and Civil Engineering 20,* 914–935.

Cusson, D. & P. Paultre (1995). Stress-Strain model for confined high-strength concrete. *Journal of Structural Engineering 121,* 468–477.

Guedes, J., P. Pegon, & A. Pinto (1994). A fibre/Timoshenko beam element in castem 2000. *Applied Mechanics Unit, Safety Technology Institute, Joint Research Center, European Commision, I-21020 Ispra(VA) Italy, Special Publication Nr. I.94.31.*

Ibrahimbergović, A. & F. Frey (1993). Finite element analysis of linear and non-linear planar deformations of elastic initially curved beams. *International Journal for Numerical Methods in Engineering 36,* 3239–3258.

Le Corvec, V. (2012). *Nonlinear 3d frame element with multiaxial coupling under consideration of local effects.* Ph. D. thesis, University of California, Berkeley.

Mohr, S., J. Bairàn, & A. Mar (2010). A frame element model for the analysis of reinforced concrete structures under shear and bending. *Engineering structures 32,* 3936–3954.

Stolarski, H. & T. Belytschko (1982). Membrane locking and reduced integration for curved elements. *Journal of Applied Mechanics 49,* 172–176.

Analysis of reinforced concrete structures



Taylor & Francis
Taylor & Francis Group
http://taylorandfrancis.com

Computational Modelling of Concrete Structures – Meschke, Pichler & Rots (Eds)
© 2018 Taylor & Francis Group, London, ISBN 978-1-138-74117-1

Modelling of the proof load test on viaduct De Beek

E.O.L. Lantsoght
Politécnico, Universidad San Francisco de Quito, Quito, Ecuador
Concrete Structures, Delft University of Technology, Delft, The Netherlands

A. de Boer
Ane de Boer Consultancy, Arnhem, The Netherlands

C. van der Veen & D.A. Hordijk
Concrete Structures, Delft University of Technology, Delft, The Netherlands

ABSTRACT: In a proof load test, a load corresponding to the factored live load is applied to a bridge, to directly demonstrate that a bridge fulfils the code requirements. The case of viaduct De Beek, a four-span reinforced concrete slab bridge that did not fulfil the requirements for bending moment after an inspection survey is studied. The middle spans, located above highway lanes, which could not be tested in the field, are the critical spans of this structure. Therefore, the observations from the field are used to check the finite element model, and improve the rating of the critical middle spans. The proposed method can be applied and further extended for proof load tests where the access to the site and the critical position of the viaduct is limited. This improvement will allow for an optimized combination of field testing and modelling, reducing the costs of field tests.

1 INTRODUCTION

In the Netherlands, a large number of existing bridges need to be assessed for the load models that are implemented in the Eurocodes, with NEN-EN 1991-2:2003 (CEN 2003) prescribing the traffic loads on bridges. The majority of the existing bridges were built in the decades following the Second World War. Figure 1 gives an overview of the bridge stock in the Netherlands. A considerable part of the Dutch bridge stock consists of reinforced concrete slab bridges, which often rate insufficient for shear. Most of these bridges can be assessed quickly through a spreadsheet-based tool, the Quick Scan (Lantsoght et al. 2013, Vergoossen et al. 2013). Cases that do not fulfil the requirements according to the Quick Scan can be further analysed with linear finite element models (Lantsoght et al. 2017b), non-linear finite element models (Belletti et al. 2013), or probabilistic analyses (Lantsoght et al. 2016). When insufficient information about the structure is available (Aguilar et al. 2015), or when the uncertainty on the capacity is large because of material damage (Lantsoght et al. 2017c), a bridge can be assessed with a proof load test (Lantsoght et al. 2017e).

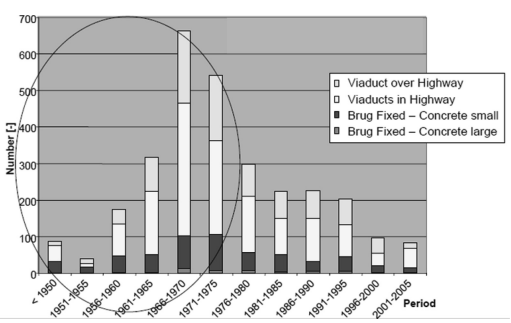

Figure 1. Existing bridges in the Netherlands.

Proof load testing of existing reinforced concrete bridges is becoming increasingly important worldwide as an assessment tool, since the current bridge stock in Europe and North America is ageing and faced with larger loads than what these structures were designed for (Lantsoght et al. 2017i). In a proof load test (Grigoriu and Hall 1984, Juntunen and Isola 1995, Saraf et al. 1996, Ransom and Heywood 1997, Faber et al. 2000, Cai and Shahawy 2003, Anay et al. 2016), a load that corresponds to the factored live load is applied to the bridge structure, to directly demonstrate that the bridge fulfils the code requirements. To optimize the procedures used in proof load tests, it can be interesting to combine field testing and finite element modelling of the bridge under consideration (Halicka et al. in

review). In traditional approaches for proof load testing, linear finite element models are used to determine the most unfavourable position of the load during the field test, and the required magnitude to show that the tested bridge fulfils the code requirements (Lantsoght et al. 2017 g).

Typically, finite element models are not directly used after the proof load test for the assessment of the bridge. Only when the assessment needs to be improved with more accurate restrictions for the passing traffic, further studies are needed. In fact, when a proof load test is successful and the bridge can carry the target proof load at the critical position, it is shown directly that the bridge fulfils the code requirements. As such, further analysis is not required. However, in a number of situations, the combination of a finite element model and the field test results can be interesting. The first situation is when due to constraints related to the site access, the proof load cannot be applied at the critical position. This case is studied in this paper. Another situation is when the bridge owner wants an updated finite element model of the structure for future assessments, such as evaluating if an exceptional superload can be allowed to pass the bridge.

To combine proof load testing with finite element modelling, the concepts used in diagnostic load testing can be used (Bridge Diagnostics Inc. 2012). In a diagnostic load test (Moses et al. 1994, Fu et al. 1997, Velázquez et al. 2000, Kim et al. 2009, Olaszek et al. 2014), a load is applied to a structure and the response of the structure is recorded. The measured response is then used to update the analytical model of the structure, often a finite element model. Ultimately, the structure can be rated based on the improved analytical model.

2 VIADUCT DE BEEK

2.1 *History*

In this paper, the case of viaduct De Beek, built in 1963, is studied (Koekkoek et al. 2016, Lantsoght et al. 2017a, Lantsoght et al. 2017f, Lantsoght et al. 2017h, Lantsoght et al. d). Viaduct De Beek is a four-span reinforced concrete slab bridge with significant flexural cracking. The bridge is located in the Beekstraat, over the highway A67 in the province Noord Brabant.

Upon assessment (Iv-Infra 2015), it was found that the requirements for bending moment are not fulfilled for this structure. As a result, the configuration of the bridge was changed from two lanes (one in each direction) to a single lane, see Figure 2. This viaduct was proof load tested in the end span. The proof load test was used to study if the bridge can carry the loading in two lanes. Proof load testing was interesting given the large cracking present in the structure and the uncertainty related to the capacity.



Figure 2. Traffic restriction on viaduct De Beek.

2.2 *Geometry*

Viaduct De Beek has four spans: two end spans of 10.81 m and two middle spans of 15.40 m. The superstructure is 9.94 m wide, with a carriageway

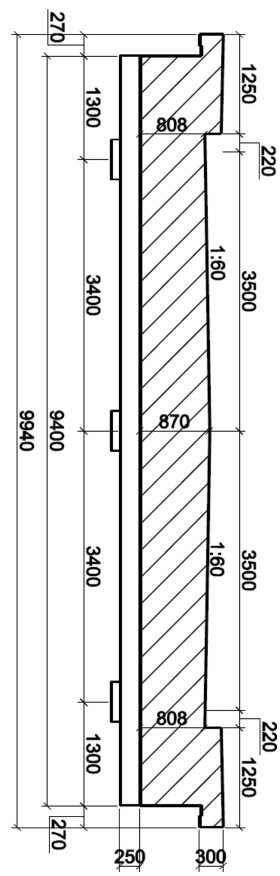

Figure 3. Cross-section of viaduct De Beek at mid support.

of 7.44 m. The height of the slab varies parabolically between 470 mm and 870 mm. A sketch of the cross-section at the mid support between the end span and middle span is shown in Figure 3.

2.3 *Material properties*

The actual concrete compressive strength is determined based on nine core samples as $f_{ck} = 44.5$ MPa, with f_{ck} the characteristic cylinder compressive strength. The resulting design compressive strength is $f_{cd} = 30$ MPa.

Steel samples taken from the viaduct were used to determine the type of steel that was used in the bridge. This steel type turned out to be QR 24, a type of reinforcement steel that was used in the Netherlands until the 1960s. The tested reinforcement has a design yield strength of $f_{yd} = 252$ MPa. The area of reinforcement shown in the available plans of viaduct De Beek is $A_s = 5259$ mm^2/m in the end spans and $A_s = 3506$ mm^2/m in the middle spans. The reinforcement layout of half of the bridge is shown in Figure 4.

Since the middle spans have a larger span length and a smaller amount of reinforcement, the critical sections are found in the middle spans. The critical sections are defined as the sections with the lowest capacity and largest Unity Check (ratio of load effect to capacity). Only the end spans could be tested, because testing of the middle spans would require closing of the highway, which was not permitted. Therefore, a direct assessment through proof load testing was not possible, and the option to use finite element models to improve the assessment of the bridge was explored.

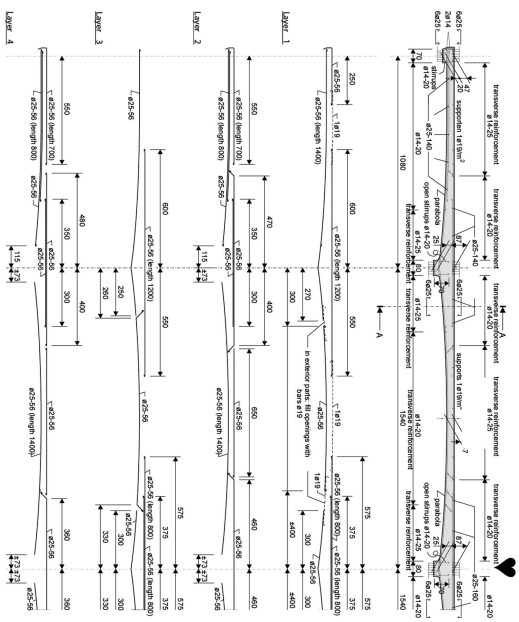

Figure 4. Longitudinal reinforcement layers of viaduct De Beek, showing end span and middle span. The 4 bars of φ 25 mm bars have a spacing of 560 mm. Layers 1 and 3 show extra longitudinal reinforcement at the central support. Layers 2 and 4 show extra longitudinal reinforcement at the intermediate support between the end spans and middle spans.

3 INITIAL FINITE ELEMENT MODEL

In this paper, a finite element model is used to verify if observations from the field with regard to the condition of the bridge and its constraints can be used to update the finite element model. It is then studied if the updated finite element can be used to improve the modelling, and the resulting Unity Check, of the critical middle spans of the structure. The finite element model used in this study was developed in DIANA (DIANA FEA 2017).

The initial finite element model was used for the assessment of the bridge, and to prepare the proof load test. In a first version of the finite element model, the slab is modelled with quadratic shell elements. The size of the elements was 500 mm × 500 mm with a variable thickness of 470 mm to 870 mm. Moreover, the non-structural elements such as sidewalks and barriers are modelled as a representative load and their contribution to the stiffness is neglected. The support conditions are modelled as rigid and ideal. To take into account the present cracking, orthotropy is assumed to a Young's modulus of 14 GPa in the cracked direction, and 36 GPa in the other direction.

The applied load was the combination of the self-weight, layer of asphalt, and load combination from NEN-EN 1991-2:2003 (CEN 2003). The size of the wheel print was enlarged to correspond to a vertical distribution under 45° to the centre of the cross-section.

4 PROOF LOAD TEST

In November 2015, the end span of viaduct De Beek was subjected to a proof load test. All details of the preparation, execution, and analysis of the proof load test can be found in the analysis report of the test (Koekkoek et al. 2016) and in the references describing this test (Lantsoght et al. 2017a, Lantsoght et al. 2017d).

Two tests were carried out: one test at a critical position for bending moment and another test at a critical position for shear. Based on the initial, simplified finite element model, it was found that the

critical position for bending moment is at 3.55 m from the end support, and for shear at 1.1 m from the end support. The critical position for bending moment is the position for which the design tandems of the Eurocode live load model result in the largest sectional moment. The critical position for shear for reinforced concrete slab bridges is taken as $2.5d_l$, with d_l the effective depth to the longitudinal reinforcement.

The tests served a double purpose: 1) gathering experience with proof load testing, in order to develop recommendations for this type of field testing for the Netherlands (Lantsoght et al. 2017g), and 2) evaluating the viaduct De Beek. A system with a steel spreader beam, counterweights, and jacks was used to apply the load, see Figure 5. The use of jacks permitted a cyclic loading protocol. The cyclic loading protocol used at the bending moment position is shown in Figure 6. Such a protocol is recommended for proof load testing as it allows the testing engineer to check linearity and reproducibility during the test, and to verify the stop criteria at different load levels. Stop criteria are criteria defined based on the measurements that indicate that further loading could result in irreversible damage to the structure or even failure. The vertical deformations were measured with laser triangulation sensors and linear variable differential transducers (LVDTs), the strains on the bottom of the concrete with LVDTs applied over 1 m, the increase in crack width with LVDTs, the cracking activity with acoustic emission sensors, the strains in the steel with strain gauges, and the applied load with load cells.

The maximum applied load at the bending moment position was 1751 kN, which corresponds to a sectional bending moment of 6% above that of the Eurocode load combination for the Ultimate Limit State. For the shear position, the maximum applied load was 1560 kN, resulting in a sectional shear force of 2% above the Eurocode Ultimate Limit State. The end span was thus found to fulfill all code requirements for bending moment and shear. However, the results of the proof load test on the end span cannot be directly extrapolated and used for the evaluation of the critical middle span.



Figure 5. Load application with steel spreader beam and counter weights on viaduct De Beek.

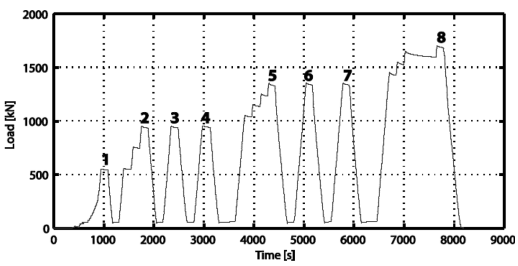

Figure 6. Loading protocol for bending moment test.

5 UPDATING OF FINITE ELEMENT MODEL

To demonstrate that the viaduct has sufficient capacity, an assessment calculation based on the original linear finite element model showed that 7% of plastic redistribution was necessary to obtain Unity Checks smaller than or equal to one (Lantsoght et al. 2017d). This amount of plastic redistribution results in cracking, and possibly corrosion of the reinforcement, which would further reduce the flexural capacity of the critical spans. As such, allowing plastic redistribution would require frequent inspections and would jeopardize the durability of the structure.

The initial model was then refined based on the measurements taken during the field test and inspection of the bridge. Additionally, quadratic solid elements were used in the refined model as compared to quadratic shell elements in the initial model. The size of the elements was 100 mm × 148 mm × 73 mm / 140 mm. To take into account the present cracking, orthotropy is assumed to a Young's modulus of 14 GPa and 36 GPa in the uncracked direction. An overview of the model can be seen in Figure 7, in which solid elements were used to model spans 1, 2, and half of span 3, and shell elements were used for the remaining part of span 3 and for span 4. Figure 8 shows a detail of the meshing of the finite element model. A bottom

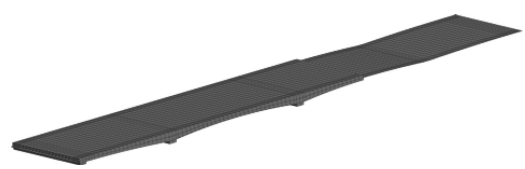

Figure 7. Overview of finite element model.

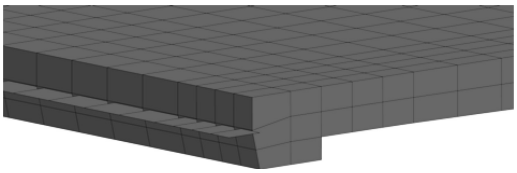

Figure 8. Detail of finite element model.

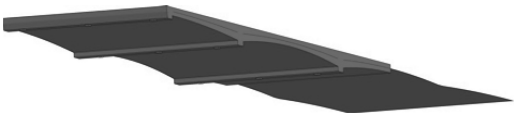

Figure 9. Overview of finite element model, bottom view.



Figure 10. Overview of finite element model, top view.

view of the final model is shown in Figure 9 and a top view in Figure 10. The result of this analysis is an improved model for the entire structure.

Further improvements that were added to the model are a more realistic modelling of the supports, which consists of elastomeric bearings. The elastic properties in the gravity direction of the elastomeric bearings were modelled. In the first model, idealized supports were assumed. The modelled bearings are shown for the end support in Figure 11 and for the mid support in Figure 12. A top view with the correct positions of the bearings is given in Figure 13 and a side view in Figure 14. The result of using a finer modelling of the bearings is that the support beam takes less bending moment in the longitudinal direction and that the bending moment at mid span increases.

In a subsequent refinement, the non-structural elements are taken into account. The stiffness of these elements results in a reduced sectional moment and shear at the critical section. The kerb was built later, so this phased construction should be taken into account. Moreover, only one reinforced bar with $\phi = 14$ mm and one bar with $\phi = 12$ mm fix the kerb to the deck. This limited amount of reinforcement does not warrant full bond between the kerb and the deck.

Finally, the layers of the reinforcement were modelled as in the drawings from Figure 4, see Figure 15.

The applied load was the combination of the self-weight, layer of asphalt, and load combination

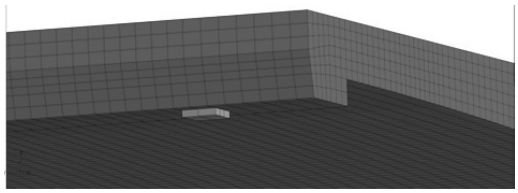

Figure 11. Updated finite element model: detail of end support.

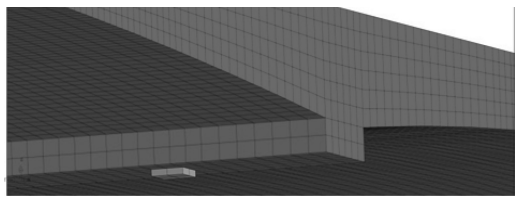

Figure 12. Updated finite element model: detail of middle support.

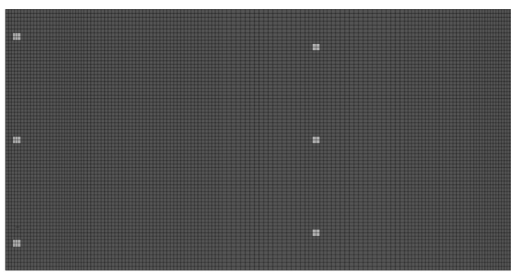

Figure 13. Updated finite element model: positions of elastomeric bearings.



Figure 14. Updated finite element model: side view, showing elastomeric bearings for support.

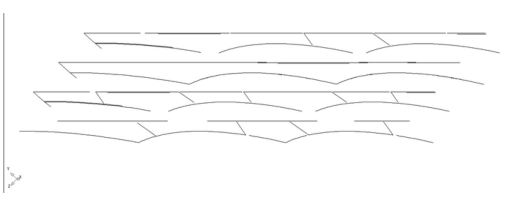

Figure 15. Updated finite element model: modeling of reinforcement layers.

Table 1. Overview of changes to resulting bending moment with refined finite element model for two lanes of traffic.

		M_{Ed} (kNm/m)		
Position	M_{Rd} (kNm/m)	Initial	Updated	OK?
Mid span	307	418	376	No
End span	367	426	335	Yes
Mid support	896	1057	888	Yes

Table 2. Overview of changes to resulting bending moment with refined finite element model for one lane of traffic.

		M_{Ed} (kNm/m)	
Position	M_{Rd} (kNm/m)	Updated	OK?
Mid span	307	343	No
End span	367	303	Yes
Mid support	896	847	Yes

from NEN-EN 1991-2:2003 (CEN 2003). The size of the wheel print was taken as 400 mm × 400 mm, as prescribed by NEN-EN 1991-2:2003 (CEN 2003), since volume elements were used.

The comparison between the assessment based on the initial model and the refined model is given in Table 1. Table 1 shows the bending moment capacity M_{Rd} and the sectional moment M_{Ed} of the initial and the updated finite element model. Comparing the capacity M_{Rd} and the initial sectional moment M_{Ed} shows that none of the considered cross-sections fulfilled the requirements. Comparing the capacity M_{Rd} and the sectional moment M_{Ed} from the updated model shows that only the mid span cross-section does not fulfil the requirements. Therefore, the updated finite element model is further studied with a single lane of traffic, to see if a traffic restriction is warranted. These results are shown in Table 2. Table 2 shows that for the considered case of viaduct De Beek, the bridge does not fulfil the requirements when only one lane of traffic is allowed on the bridge, because the capacity M_{Rd} at the mid span is still smaller than the sectional moment caused by the loads M_{Ed}.

The improved model resulted in an improved Unity Check. For the considered case, the Unity Check is not shown in the tables, but the conclusion from the Unity Check is given in the column "OK?", which contains "yes" if the slab is found to fulfil the code requirements and "no" when the capacity is smaller than the acting sectional moment. With the improved linear finite element model and a traffic restriction, it is found that the code requirements are still not fulfilled for the mid span cross-section. Therefore, a nonlinear finite element analysis is the next evaluation step.

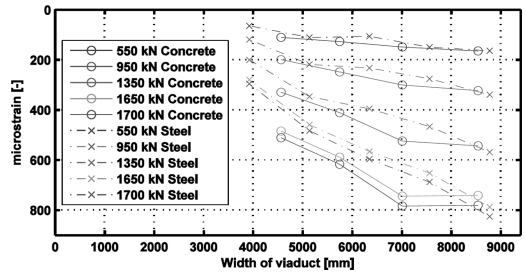

Figure 16. Measured strains in viaduct De Beek.

For the determination of the sectional moment, averaging of the moment in the transverse direction was used. Different widths were analysed for the mid support position: 1.46 m (≈ $2d_l$), 1.74 m, 1.94 m, 2.24 m, and 2.42 m. The result in Table 1 of M_{Ed} = 888 kNm/m is for a transverse distribution of 1.94 m. This value reduces to 841 kNm/m if a distribution width of 2.42 m is used. A larger distribution width than what is typically used ($2d_l$) can be considered, based on the strain measurements from the field test, see Figure 16. The strain measurements show that the strains are distributed over a large width: approximately 2 m for the highest load level, and approximately 4.5 m for the lowest load level. A larger distribution width can thus be used for the interpretation of the results from the finite element model.

6 NONLINEAR FINITE ELEMENT MODEL

Since it is found that the section at the mid support does not fulfil the requirements when a linear finite element analysis is used, a nonlinear analysis is carried out. For the assessment of existing bridges with nonlinear finite element models, the guidelines from RTD 1016-1:2017 (RWS 2017a) with its validation in RTD 1016-2:2017 (RWS 2017b) should be consulted. These guidelines are suitable for reinforced concrete and prestressed concrete, and comprise all bridge types (girder bridges, slab bridges, box girder bridges,…), as well as culverts and tunnels. The guidelines follow the safety format of the *fib* Model Code 2010 (fib 2012). The experience with the use of these guidelines shows that an additional capacity of existing concrete structures of 10–30% can be found when using nonlinear finite element models for the assessment.

In the nonlinear finite element model, one design tandem of 600 kN and a distributed lane load of

9 kN/m^2 are applied. The load is applied as a load factor. According to RTD 1016-1:2017, this factor should be 1.6 in combination with nonlinear finite element models. The value of 1.6 is derived as the product of 1.06 (model factor), 1.2 (geometric and material uncertainties), and 1.25 (partial factor for live loads). For viaduct De Beek, a reduction factor of 0.9, as given in Table NB 4.1 from NEN-EN 1991-2/NA:2011 (Code Committee 351001 2011) for bridges subjected to maximum 20,000 trucks per year, can be added. The required load factor is then 1.44.

The results for a load factor of 0.6 (load step 34) are shown in Figure 17 for the top view and Figure 18 for the side view. A detail of the occurring cracking is shown in Figure 19, in which the maximum crack width is 0.4 mm.

The maximum required load factor in the nonlinear finite element model is 1.44, as explained previously. The results for the load step with the highest load factor of 1.44 (load step 80) are shown in Figure 20 (bottom view) and Figure 21 (top view). The results for the maximum strains are shown in Figure 22 and Figure 23. Figure 24 shows



Figure 17. Top view of results of nonlinear finite element model, showing cracking at the mid support. Load step 34, load factor 0.6.

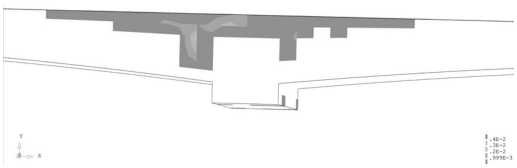

Figure 18. Side view of results of nonlinear finite element model, showing cracking at the mid support. Load step 34, load factor 0.6.

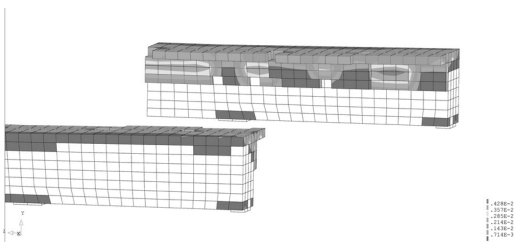

Figure 19. Detail of results of nonlinear finite element model, showing cracking at the mid support. Load step 34, load factor 0.6.

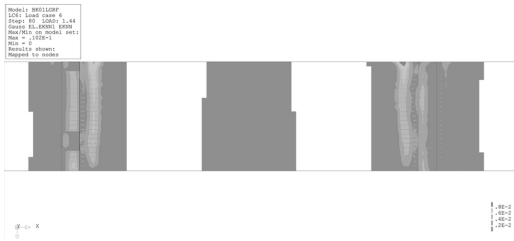

Figure 20. Detail of bottom view of results of nonlinear finite element model. Load step 80, load factor 1.44.

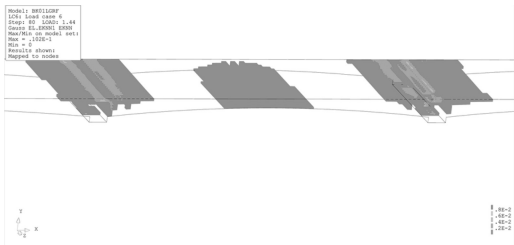

Figure 21. Detail of top view for load step 80, load factor 1.44.

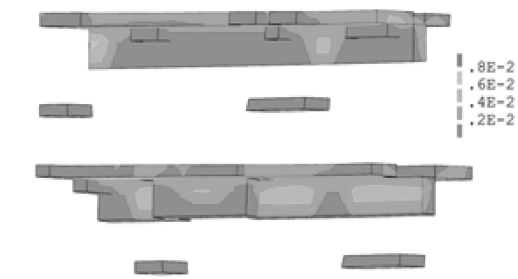

Figure 22. Detail at support 2 (top) and support 3 (bottom) for load step 80, load factor 1.44. ε_{knn} is the cracking strain.

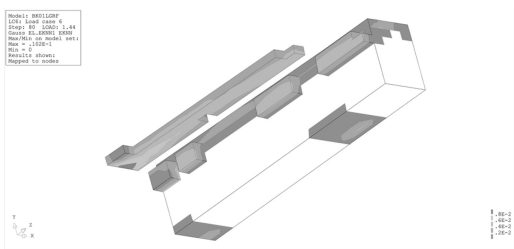

Figure 23. Detail at support 3 (bottom) for load step 80, load factor 1.44, where the maximum strain of 1% occurs and the crack width equals 1 mm.



Figure 24. Result of steel stresses. Red dots indicate yielding of the steel.

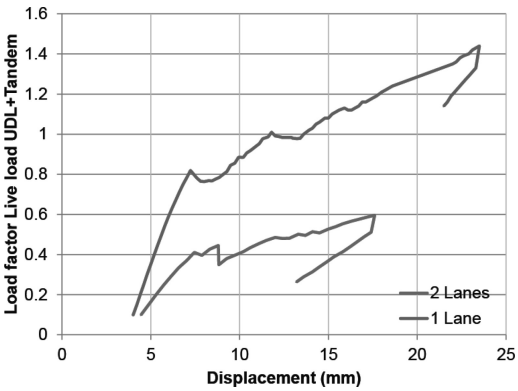

Figure 25. Load-displacement diagram for case with one lane of traffic and case with two lanes of traffic.

where yielding of the steel occurs at the highest load factor. These results show that the bridge fulfils the code requirements for one lane of traffic.

The stiffness of the supports was modified in the model until the cracking pattern in the model corresponds to the cracking observed in the field and during the proof load test, when mostly cracks in the middle spans were observed. To match the cracking in the model and the field, the stiffness of the supports was reduced.

In a next analysis, the nonlinear finite element model is modified to include two lanes of traffic. The results are shown as a load-displacement diagram in Figure 25. For the case with one lane of traffic, it can be seen that the maximum load factor of 1.44 is just reached. For the case with two lanes of traffic, failure occurs for a load factor of 0.6. This result means that the bridge does not fulfill the requirements for two lanes of traffic.

7 DISCUSSION

Further improvement of the model would be to fully calibrate the finite element model to the measurements of the field test (strains and deflections) in the first span. Additionally, measurements of the traffic loads on the bridge have been carried out. The conclusion of these measurements is that 10,000 heavy vehicles pass the bridge annually. These vehicles have axle loads of 100 to 150 kN, and are mostly agricultural vehicles. The measurements of the actual traffic loads can be used to come to an improved evaluation of the structure for its service loads.

The proposed method and its suggested improvements can be applied in the future for proof load tests where the access to the site and the most critical position of the viaduct may be limited. It also allows for an optimized use of the combination of field testing and finite element modelling, in a way that can reduce the costs of field tests. Moreover, with this approach it has been shown that the viaduct De Beek fulfils the requirements when a traffic restriction is used. Since the nonlinear finite element model shows that cracking occurs, continued inspections for the presence of rebar corrosion in the bridge are recommended.

8 SUMMARY AND CONCLUSIONS

A large number of existing bridges in the Netherlands, and most countries in Europe and North America are reaching the end of their originally devised service life, and are subjected to larger live loads than those loads these structures were designed for. As a result, these bridges need to be assessed. Often, an analytical assessment is sufficient to evaluate an existing bridge. In some cases, when the available information is insufficient or when the uncertainties on the capacity are large, field testing by means of proof load testing can be a viable option for the assessment of the bridge.

This paper studies viaduct De Beek, an existing reinforced concrete slab bridge in the Netherlands with insufficient flexural capacity and significant cracking. Viaduct De Beek was subjected to a proof load test in the end span. However, the critical span was the middle span, with a larger span length and smaller amount of reinforcement than the end span. The middle span could not be tested for safety reasons. Therefore, a direct assessment of the viaduct De Beek through a proof load test was not possible.

To evaluate viaduct De Beek, finite element models were used. For the preparation and initial assessment of the bridge, a simplified linear finite element model using shell elements, a coarse mesh, and idealized support conditions was used. For the evaluation and assessment, this initial model was improved and updated based on the observations from the field. Solid elements and a finer mesh were used. The reinforcement was modeled as on the drawings. The properties of the elastomeric bearings in the gravity direction were added

to the model. It was found that even with a traffic restriction, the critical cross-section does not fulfil the code requirements. Therefore, a nonlinear finite element model was used. With this model it was found that the bridge fulfils the code requirements when one lane of traffic is allowed on the bridge.

The assessment based on the initial and updated model is compared. Field data are used, and the most refined model is a nonlinear finite element model. It can be seen that an improved model leads to a sharper assessment. This assessment leads to the conclusion that a traffic restriction on viaduct De Beek is required.

ACKNOWLEDGEMENTS

The authors wish to express their gratitude and sincere appreciation to the Dutch Ministry of Infrastructure and the Environment (Rijkswaterstaat) and the Province of Noord Brabant for financing this research work. The contributions and help of our colleagues Albert Bosman, Sebastiaan Ensink, Rutger Koekkoek, and Yuguang Yang, and of student Werner Vos of Delft University of Technology are gratefully acknowledged. The authors also would like to thank Frank Linthorst and Danny den Boef of Witteveen+Bos, responsible for the logistics and safety, and Otto Illing and the late Chris Huissen of Mammoet, responsible for applying the load, for the fruitful discussions.

REFERENCES

Aguilar, C.V., Jáuregui, D.V., Newtson, C.M., Weldon, B.D. & Cortez, T.M. 2015. Load Rating a Prestressed Concrete Double-Tee Beam Bridge without Plans by Proof Testing. Transportation Research Board Annual Compendium of Papers. Washington DC.

Anay, R., Cortez, T.M., Jáuregui, D.V., Elbatanouny, M.K. & Ziehl, P. 2016. On-Site Acoustic-Emission Monitoring for Assessment of a Prestressed Concrete Double-Tee-Beam Bridge without Plans. Journal of Performance of Constructed Facilities, 30 pp.

Belletti, B., Damoni, C., Hendriks, M.A.N. & Den Uijl, J.A. 2013. Nonlinear finite element analyses of reinforced concrete slabs: comparison of safety formats. In: Van Mier, J.G.M., Ruiz, G., Andrade, C., Yu, R.C. & Zhang, X.X. (eds.) VIII International Conference on Fracture Mecahnics of concrete and Concrete Structures, FraMCoS-8.

Bridge Diagnostics Inc. 2012. Integrated Approach to Load Testing.

Cai, C.S. & Shahawy, M. 2003. Understanding Capacity Rating of Bridges from Load Tests. Practice Periodical on Structural Design and Construction, 8, 209–2016.

Cen 2003. Eurocode 1: Actions on structures – Part 2: Traffic loads on bridges, NEN-EN 1991-2:2003. Brussels, Belgium: Comité Européen de Normalisation.

Code Committee 351001 2011. Eurocode 1 – Actions on structures - Part 2: Traffic loads on bridges, EN 1991-2/NA:2011. Delft, The Netherlands: Civil engineering center for research and regulation, Dutch Normalization Institute.

Diana Fea 2017. Users Manual of Diana, Release 10.1 Delft, The Netherlands.

Faber, M.H., Val, D.V. & Stewart, M.G. 2000. Proof load testing for bridge assessment and upgrading. Engineering Structures, 22, 1677–1689.

FIB 2012. Model code 2010: final draft, Lausanne, International Federation for Structural Concrete.

Fu, G., Pezze III, F.P. & Alampalli, S. 1997. Diagnostic Load Testing for Bridge Load Rating. Transportation Research Record, 1594, 125–133.

Grigoriu, M. & Hall, W.B. 1984. Probabilistic Models for Proof Load Testing. Journal of Structural Engineering, 110.

Halicka, A., Hordijk, D.A. & Lantsoght, E.O.L. (in review). Rating of concrete road bridges with proof loads. ACI SP Evaluation of Concrete Bridge Behavior through Load Testing – International Perspectives, 16.

IV-Infra 2015. 51H-304-01 – De Beek – Recalculation bridge deck (in Dutch).

Juntunen, D.A. & Isola, M.C. 1995. Proof load test of R01 of 61131 M-37 over CSX Railroad, South of Bailey, Michigan. Michigan Department of Transportation.

Kim, Y.J., Tanovic, R. & Wight, R.G. 2009. Recent Advances in Performance Evaluation and Flexural Response of Existing Bridges. Journal of Performance of Constructed Facilities, 23, 190–200.

Koekkoek, R.T., Lantsoght, E.O.L., Yang, Y. & Hordijk, D.A. 2016. Analysis report for the assessment of Viaduct De Beek by Proof Loading. Delft, The Netherlands: Delft University of Technology.

Lantsoght, E., Koekkoek, R., Yang, Y., Van Der Veen, C., Hordijk, D. & De Boer, A. 2017a. Proof load testing of the viaduct De Beek. 39th IABSE Symposium – Engineering the Future. Vancouver, Canada.

Lantsoght, E.O.L., De Boer, A. & Van Der Veen, C. 2017b. Distribution of peak shear stress in finite element models of reinforced concrete slabs. Engineering Structures, 148, 571–583.

Lantsoght, E.O.L., Koekkoek, R.T., Hordijk, D.A. & De Boer, A. 2017c. Towards standardization of proof load testing: pilot test on viaduct Zijlweg. Structure and Infrastructure Engineering, 16.

Lantsoght, E.O.L., Koekkoek, R.T., Veen, C.V.D., Hordijk, D.A. & Boer, A.D. 2017d. Pilot Proof-Load Test on Viaduct De Beek: Case Study. Journal of Bridge Engineering, 22, 05017014.

Lantsoght, E.O.L., Van Der Veen, C., De Boer, A. & Hordijk, D.A. 2016. Probabilistic prediction of the failure mode of the Ruytenschildt Bridge. Engineering Structures, 127, 549–558.

Lantsoght, E.O.L., Van Der Veen, C., De Boer, A. & Hordijk, D.A. 2017e. Proof load testing of reinforced concrete slab bridges in the Netherlands. Structural Concrete, 18, 597–606.

Lantsoght, E.O.L., Van Der Veen, C., De Boer, A. & Hordijk, D.A. 2017f. Required proof load magnitude

for probabilistic field assessment of viaduct De Beek Engineering Structures, 148, 767–779.
Lantsoght, E.O.L., Van Der Veen, C., De Boer, A. & Walraven, J.C. 2013. Recommendations for the Shear Assessment of Reinforced Concrete Slab Bridges from Experiments Structural Engineering International, 23, 418–426.
Lantsoght, E.O.L., Van Der Veen, C., Hordijk, D.A. & De Boer, A. 2017 g. Development of recommendations for proof load testing of reinforced concrete slab bridges. Engineering Structures, 152, 202–210.
Lantsoght, E.O.L., Van Der Veen, C., Hordijk, D.A. & De Boer, A. 2017h. Reliability index after proof load testing: viaduct De Beek. ESREL 2017. Protoroz, Slovenia.
Lantsoght, E.O.L., Van Der Veen, C., Hordijk, D.A. & De Boer, A. 2017i. State-of-the-art on load testing of concrete bridges. Engineering Structures, 150, 231–241.
Moses, F., Lebet, J.P. & Bez, R. 1994. Applications of field testing to bridge evaluation. Journal of Structural Engineering-ASCE, 120, 1745–1762.
Olaszek, P., Lagoda, M. & Casas, J.R. 2014. Diagnostic load testing and assessment of existing bridges: examples of application. Structure and Infrastructure Engineering, 10, 834–842.
Ransom, A.L. & Heywood, R.J. 1997. Recommendations for Proof Load Testing in Australia. Proceedings of the Autostrads 1997 Bridge Conference "Bridging the Milenia". Sydney, Australia.
Rijkswaterstaat 2017. Guidelines for Nonlinear Finite Element Analysis of Concrete Structures. RTD 1016-1:2017.
Rijkswaterstaat 2017b. Validation of the Guidelines for Nonlinear Finite Element Analysis of Concrete Structures – Part: Review of results. RTD 1016-2:2017.
Saraf, V.K., Nowak, A.S. & Till, R. 1996. Proof load testing of bridges. In: Frangopol, D.M. & Grigoriu, M.D. (eds.) Probabilistic Mechanics & Structural Reliability: Proceedings of the Seventh Specialty Conference. Worcester, MA, USA.
Velázquez, B.M., Yura, J.A., Frank, K.H., Kreger, M.E. & Wood, S.L. 2000. Diagnostic load tests of a reinforced concrete pan-girder bridge. Austin, TX, USA: The University of Texas at Austin.
Vergoossen, R., Naaktgeboren, M., 'T Hart, M., De Boer, A. & Van Vugt, E. 2013. Quick Scan on Shear in Existing Slab Type Viaducts. International IABSE Conference, Assessment, Upgrading and Refurbishment of Infrastructures. Rotterdam, The Netherlands.

Computational Modelling of Concrete Structures – Meschke, Pichler & Rots (Eds)
© 2018 Taylor & Francis Group, London, ISBN 978-1-138-74117-1

Organizing an international blind prediction contest for improving a guideline for the nonlinear finite elements analysis of concrete structures

A. de Boer
Ane de Boer Consultancy, Arnhem, The Netherlands

M.A.N. Hendriks
Delft University of Technology, Delft, The Netherlands
Norwegian University of Science and Technology, Trondheim, Norway

C. van der Veen
Delft University of Technology, Delft, The Netherlands

B. Belletti
University of Parma, Parma, Italy

ABSTRACT: At the previous EURO-C conference, a guideline for nonlinear finite analysis and safety assessment of concrete structures was presented. This guideline is a results of a cooperation between the Delft University of Technology, the University of Parma and the Dutch Ministry of Infrastructure and the Environment. The nonlinear finite element results of a workshop around shear failure, held in Rotterdam in 2007, was the starting point for the development of a guideline for nonlinear finite element analysis. The scatter of the results presented in Rotterdam was considered as too large; knowledge of nonlinear finite element analysis of concrete structures should be controlled better in order to make nonlinear finite element analysis an accepted method. In 2012 the first version of the guideline that focussed on girder structures was published.

In 2014, at the concrete structures laboratory of the Delft University of Technology, four almost similar prestressed girders were tested till the ultimate limit load level. This was considered as an opportunity to organise a contest to predict this ultimate load level at failure. The participants were asked to make use of the guideline. A workshop at the University of Parma gave the teams the opportunity to pitch their predictions. This paper presents the following topics: an overview of the content of the guideline, the gain of a controlled blind prediction contest and the main outcomes of the contest in Parma.

1 INTRODUCTION

At the Euro-C in 2014 in Sankt-Anton Austria the first edition of a guideline for the nonlinear finite element analysis (NLFEA) of concrete beams was presented together with an announcement of an international contest for predicting the ultimate limit load of prestressed girders. The aim of the international contest was to get more awareness of the guideline in the concrete mechanics society. The guideline was setup by using two FE codes; in the contest the use of other FE codes were anticipated. The contest was also a test to see if the scatter of the predicted results from the different teams was reasonably small. In a preceding workshop in 2007 in Rotterdam only participants from scientific research institutes were present. In the new contest also practical engineering offices were invited explicitly. The Model Code 2010 and the EC2 code indeed give opportunities to apply nonlinear analysis for concrete structures in practical design and reassessment projects. An important aspect for the practical application was the introduction of the so-called safety formats in both codes. The proof of extra capacity of existing concrete structures by re-examination of these concrete structures with nonlinear analysis has contributed that many structures could remain in operation and be a part of the infrastructure network, instead of being demolished and replaced.

In parallel to the organization of the international contest the NLFEA Guideline was developed further. The application area was extended to reinforced slabs. Besides, all simulations of experiments that were used during the development of

the guideline were documented. This resulted in a set of validation examples for the guideline. All validation examples are reported now in a consistent way, including the process of developing the FE model, the analyses, as well as the reporting of the results. For the future, more validation examples are needed to get a finer coverage of failures of the bearing capacity of existing concrete structures and its failure modes.

2 CONTENT OF THE NLFEA GUIDELINE

2.1 *General*

The NLFEA Guideline includes chapters on Modelling, Analysis, Limit state verification and Reporting of results. In the following sections some items are described in more detail. The guideline has borrowed the layout of the ModelCode2010. In this format the right-hand side pages include the articles and the left-hand side pages include additional information about the articles.

2.2 *Finite elements for concrete*

Elements with quadratic interpolation of the displacement field should be used. Preferably a quadrilateral shape or a hexahedral shape should be used in 2D and 3D, respectively. For large slab structures, modeling with solid brick elements is not practical because of the large amounts of finite elements needed to accurately describe the stresses in the structure. Structural elements such as beam elements and (flat) shell elements can be used to model large-scale structures in cases it is not feasible to model with solid brick elements. However, these types of structural elements are not capable to model shear failure and additional post-analysis checks should be carried out to ensure that a shear failure mode is not overlooked. The preferred elements are also quadratic elements, such as 3-node beams in 2D and 3D, and 6-node triangular and 8-node quadrilateral shell elements for 2.5D analysis. So, models with a combination of structural elements and continuum elements can be considered.

2.3 *Constitutive models*

Material models, in a finite element context, specify the constitutive behavior (the stress-strain relationship) that is assumed for the materials in the structure. The material models are often simplified abstractions of the true material behavior.

For concrete, a total strain-based rotating crack or fixed crack model is preferred, based on linear-elastic properties, extended by tensile behavior, shear behavior, compressive behavior, tension-compression interaction, compression-compression interaction and smearing softening relations using equivalent lengths.

For reinforcement, an elasto-plastic material model with hardening should be used.

2.4 *Convergence tolerances analysis*

The Newton-Raphson iteration method requires a criterion at which equilibrium is supposed to be achieved. In general, the unbalance forces will not be reduced exactly to zero but instead a tolerance has to be set at which convergence is achieved. The criterion is often a norm based on the unbalance force vector, the incremental displacement vector or a norm based on energy. The convergence criterion is often enhanced with a pre-defined maximum number of iterations to avoid excessive number of iterations. The latter, however, should not be considered a convergence criterion.

A suitable convergence criterion has to be used for determining equilibrium. Preferably an energy-norm in combination with a force-norm should be used; a norm based on displacements only should be avoided.

For the type of analyses for which these guidelines are intended, typically 0.01 and 0.001 tolerances are suggested for norms based on unbalance forces and energy norms respectively.

Load increments in which at least one of the two norms is satisfied can be considered as converged. Load increments which do not fully comply the convergence criteria might be still admissible, provided that they are followed by converged load increments and a plausible explanation for the temporarily non-convergence is provided.

2.5 *Reporting aspects*

Thoroughly planning a finite element analysis reduces risks of errors and time and thus costs. Also, the results of a finite element analysis should be reported in a standard fashion to reduce time and costs associated with (peer) reviewing and archiving an analysis. Generally accepted requirements for technical reports, like the consistent use of figure and table captions, consistent referencing to figures, tables, appendices and other reports, an effective structuring in sections and appendices should be followed strictly.

3 A BLIND PREDICTION CONTEST

3.1 *Initiative*

After the publication of the first draft of the NLFEA Guideline in May 2012, which was the

guideline solely dealing with (prestressed) reinforced beams, and after the guideline was in use for a few years, the DIANA Users Association took the initiative for organizing a prediction contest, in close cooperation with the Delft University of Technology and the Dutch Ministry of Infrastructure, Rijkswaterstaat. The contest marked the 30th anniversary of the Association. Four almost similar prestressed beams were to be tested in the second half of 2014 in the lab of the Delft University of Technology. The expected failure was shear force failure. The participants of this International Contest were challenged to predict the failure load. The results were to be presented and discussed in a special contest workshop, which was hosted by the University of Parma in November 2014.

3.2 *Test setup*

The test setup is given in the figure below. The loading jack will be positioned at a distance of 2950 mm from the centre of the support (support type B). The dimensions and material properties of the loading jack and the supports were given in more detail in an appendix, which is downloadable from the website of the Association. The four almost similar precast prestressed girders have been manufactured in May of 2012 and were used for other tests, which were not damaging the girders. The tests of the girders by Sebastiaan Ensink took place from the second half of August until October 2014 in the Stevin Laboratory of Delft University of Technology.

3.3 *Blind predictions*

The participants of the international contest had to provide the following predictions:

1. The maximum (and minimum) load at failure.
2. The failure mechanism.
3. The cracking pattern at SLS (defined as 75% of the failure load) and ULS.
4. The crack width at SLS.
5. The load-displacement diagram at the position of the load.

3.4 *Properties of the T-shaped girders*

Two almost similar types of T-shaped girders were tested, labelled as mid and edge girders. They differ

Table 1. Overview drawings girders.

Girder code	Drawing numbers			
CODE101	100	S100	101	W100
CODE201	200	S200	201	
CODE301	300	S300	301	
CODE401	400	S400	401	

Table 2. Some basic data of T-shaped bridge girders.

Girder code	Type	Height [mm]	Width of top flange [mm]	Length [mm]	Concrete class	Self-weight of girder [kN]
CODE101	mid-beam	1300	750	12000	C53/65	110.75
CODE201	edge beam	1300	875	12000	C53/65	114.55
CODE301	mid-beam	1300	750	12000	C53/65	110.80
CODE401	edge beam	1300	875	12000	C53/65	114.65

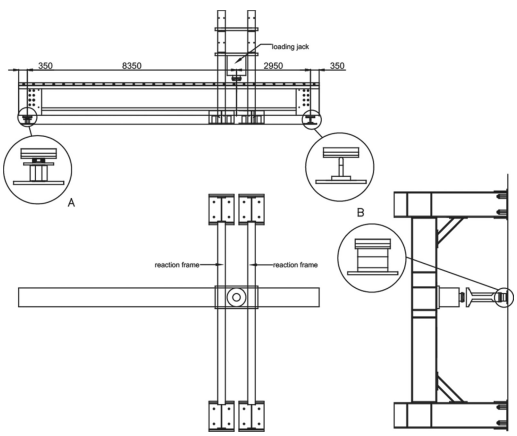

Figure 1. Test setup.

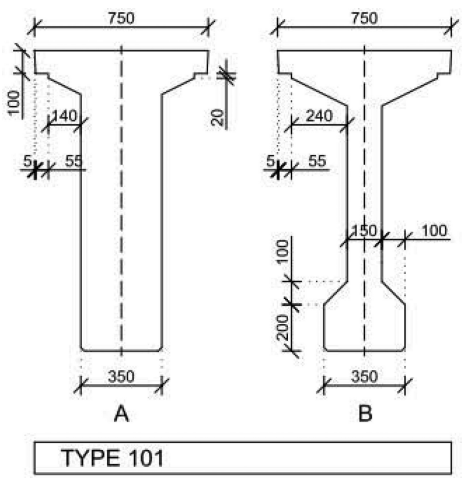

Figure 2. Dimensions of the mid girder 101.

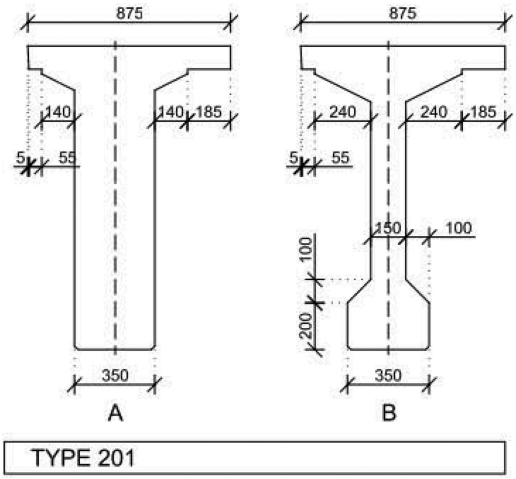

Figure 3. Dimensions of the edge girder 201.

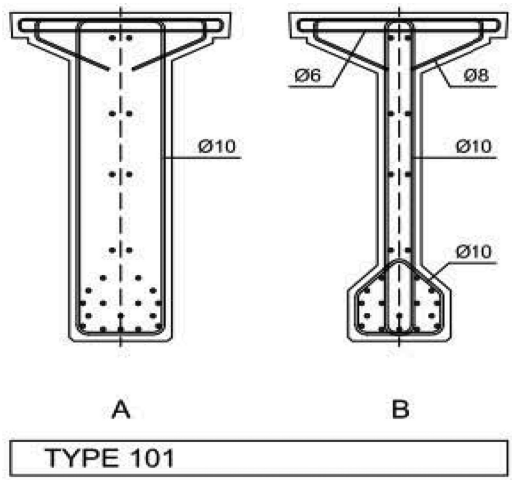

Figure 4. Reinforcement layout of girder 101.

only by width of the top flange (750 mm versus 875 mm). All other properties such as concrete class, amount of prestressing and reinforcement are the same for each girder. Table 1 gives an overview of the four girders.

Table 2 lists the main dimensions and the concrete class. All material properties are designated according to Eurocode 2. Figures 2 and 3 show the cross-sectional dimensions of the mid and edge girders.

In the top flange, in transverse direction, empty ducts are present (Ø45 mm c.t.c. 400 mm). At the ends of the girder in the thickened web also some empty ducts are present (8 × Ø65 mm).

3.5 *Prestressing*

Each girder is pre-tensioned using 24 strands Ø15,7 mm (150 mm^2 per strand) with steel type FeP1860. The measured force per strand before casting of the concrete is 214 kN.

This force needs to be reduced (~8–9%) in order to take into account the elastic deformation of the cross-section to determine the actual prestressing force at t = 0.

The mean cubic concrete strength at time of prestressing was determined at $f_{cm,cube}$ = 54 N/mm^2.

3.6 *Reinforcement*

The shear reinforcement, Figure 4, consist of stirrups (Ø10 mm) with a c.t.c. distance of 120 mm and 80 mm (except for thickened web at both ends) see appendix B (downloadable from the website of the Association), drawings 101, 201, 301, 401 and W100.



Figure 5. Test setup in the lab.

For the manufacturing of the reinforcement cage only some light longitudinal reinforcement is present (10 × Ø8 mm). All reinforcement has steel type B500A (≤Ø6) and B500B (≥Ø8). Figure 5 shows the four girders before testing.

3.7 *Concrete properties*

The mean cubic concrete strength ($f_{cm,cube}$) is continuously monitored and checked by the manufacturer. The mean cubic compressive strength after 28 days is $f_{cm,cube}$ = 83 N/mm^2 and the characteristic cubic compressive strength is $f_{ck,cube}$ = 77 N/mm^2. The concrete mix is a self-compacting concrete.

Also six 150 × 150 × 150 mm^3 cubes have been tested after about 9 months. Three cubes were tested in compression and three in splitting. The results are given in the Table 3 below. The testing

Table 3. Six Concrete cube samples.

Number	Test	$f_{cm,cube}$ [N/mm²]	$f_{ctm,sp}$ [N/mm²]	Age [days]
1	compression	89.92		273
2	compression	91.62		273
3	compression	87.95		267
4	splitting		6.15	273
5	splitting		6.37	273
6	splitting		6.39	273

of the girders took place from the second half of August until October 2014.

3.8 *Workshop in Parma*

The Shear Force Workshop, with contributions of the participants, took place in the first week of November 2014 at the University of Parma. Beatrice Belletti and Cecilia Damoni, of this university, were strongly involved in the validation of the guideline, in close cooperation with Jan Rots, Max Hendriks and Joop den Uijl from the Delft University of Technology. The deadline for submitting the results was originally set to 15th August, and was later extended till the 1st September.

In the workshop every team presented their results in a pitch of 5 minutes. After all team presentations, there was an presentation which summarized all predictions together with the lab results. At the end of the workshop, there was a winner.

4 RESULTS FROM THE CONTEST

Unfortunately only two of the four tests were executed at the moment of the workshop. The failure mode was not a real shear force failure. The influence of the ducts of the transverse prestressing, coming from previous tests on the complete structure clearly influenced the failure mode. Consequently, a revision of the test setup was necessary for the remaining two girders.

All information on the presence of these ducts was available for all participants, All teams were in a position to take this in consideration.

Figures 6 and 7 show the failure of the beams.

In total 14 teams, all from Europe, were present at the workshop at the University of Parma; more than expected by the organization. Eight different countries were represented and 6 different FE packages were used to predict the failure of the girders.

All of the teams presented their results in a condensed format. Aspects like dealing with lacking information and comments or suggestions for improvements of the guideline were presented. This

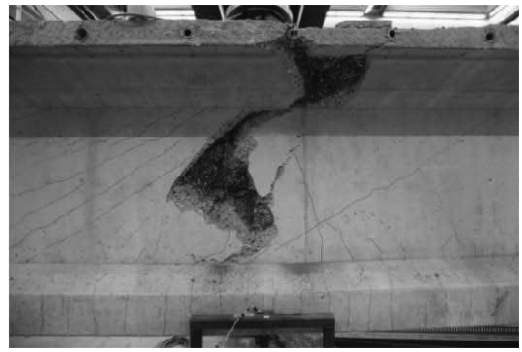

Figure 6. Side view of the failure location.

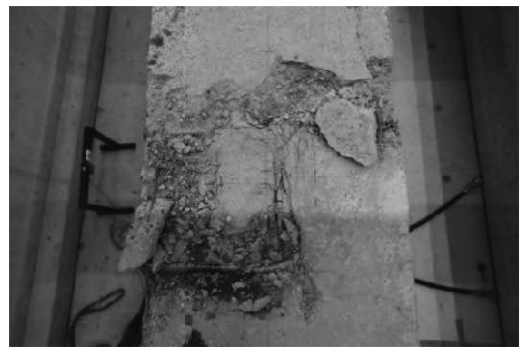

Figure 7. Top view of the flange.

information was used by the organizers and the authors of the guideline for updating the guideline.

The predictions of the failure load ranged from 1824 kN to 2854 kN, which is a 29% undershoot, respectively a 11% overshoot of the experimental result. The mean prediction was 2416 kN, which is 96% of the experimental value and the standard deviation of the predictions is 317 kN which is 13% of the mean prediction. There was a mix of 2D plane stress models and 3D solid models. Various assumptions were used to interpret 2D stress and strain behavior in 3D.

Two teams predicted a failure load which differed 1% from the experimental load of the girder in the lab. The additional questions about crack pattern, crack widths and expected failure mode, were taken into account to appoint the winner of the contest.

5 SUGGESTED IMPROVEMENTS OF THE GUIDELINE

As a results of the workshop the meshing articles in the guideline were refined. For modeling a stand-alone girder such as in the contest, separate

meshing recommendations for subdividing the flange and web are given.

Another observation is the under prediction of the tension stiffening effect and requires an improvement of the guideline. Slipping of reinforcement and an incomplete grouting process of ducts might also be addressed in the guideline. In the test unfilled ducts influenced the failure behavior of the girder. In the subsequent girder test 3 and 4, the ducts were filled with reinforcement bars to get a more realistic failure behavior.

A last improvement concerns the loading sequence. In experiments the load sequence is rather straightforward, the dead weight is followed by a force or uniform load configuration. In practice the design engineer has to deal with dead weights, asphalt, railing and other permanent loads. Additional loads include variable loads, like a uniformly distributed vehicle load and a vehicle tandem load. The permanent and variable loads have in a load combination different load factors. This means that the analyst will have to determine a sequence of load factors within the nonlinear analysis. All loads are incremented till a factor 1.0. Subsequently, all loads are incremented with the lowest additional (0.15) permanent factor (1.15). Finally an extra additional factor (0.10) till the maximum load factor of the variable load factor (1.25) is incremented. When using a safety format based on a global resistance factor an extra load factor of 0.3375 ($= 0.27 \times 1.25$) is required for the variable load, according EC2 and MC2010.

The contest stressed the need of publishing all validation examples in a consistent way. Also, a need was identified to have a report with practical applications of structures based on the NLFEA Guideline.

6 IMPROVEMENTS OF THE GUIDELINE AFTER THE WORKSHOP

After the Parma workshop 5 reports were completed and submitted to the Ministry:

1. Updated NLFEA Guideline
2. Summary of validation experiments
3. Results for reinforced beams
4. Results for prestressed reinforced beams
5. Results for reinforced slabs

There is still a wish and a need to setup a report with results for practical structures. The next section gives an overview of the second report.

7 SUMMARY VALIDATION EXPERIMENTS

7.1 *Model uncertainty*

Table 4 gives an overview of the most important outcomes of the analyses i.e. the ultimate loading capacity. The cases are categorized per failure mode and show the presence of transversal reinforcement. The member name corresponds to the names as used in the titles of the chapters of other parts of the validation: reinforced beams (RB), prestressed beams (PB) and reinforced slabs (RS). The analyses of reinforced slabs have resulted in shear failure mechanisms of a complex nature being typically a combination of one and two-ways shear. Full details have been given in the respective chapters. The table shows the ratio between the maximum experimental load and the resulting maximum load according to the nonlinear finite element analyses with mean properties of material applied.

Table 4. Overview of the case studies categorized per failure mode, showing the ratio of the experimental failure load to the numerical failure load (using mean material properties) and statistical properties of this ratio.

Failure mode		Case	Transversal reinforcement	$P_{max,exp.}/P_{max,NLFEA}$
Bending		RB1	Yes	0.99
		RB3	Yes	1.00
		PB1	Yes	0.93
	Yielding of shear reinforcement	RB3A	Yes	1.14
Flexural-shear	Compressive shear	PB2	Yes	0.94
		PB3	Yes	1.04
		PB4	Yes	0.98
	Diagonal critical crack	RB2	No	0.95
Shear failure in slabs*	Shear	RS1	No	1.62
	Shear	RS2	No	1.36
	Mixed mode	RS3	No	1.29
	One-way shear	RS4	No	1.33
	Mixed mode	RS5	No	1.33
			Mean	1.15
			CoV	0.19

The ratio of the experimental failure load to the numerical failure load (using mean material properties) is a standard way of defining the modelling uncertainty. Safety formats for NLFEA are used to ensure a certain safety level. Within these safety formats, material uncertainty and geometrical uncertainty are usually accounted for directly whereas all other uncertainties are accounted for by the modelling uncertainty. The sources of the modelling uncertainty comprise both the inherent variability of the experiments and the accuracy of the nonlinear finite element models.

Table 5. Statistical properties of the modelling uncertainty per failure mode.

Failure mode	Mean	CoV
Bending	0.97	0.04
Flexural shear in beams	1.01	0.08
Shear in slabs	1.39	0.10
All	1.15	0.19

The table shows a mean value of 1.15 (i.e. on the "safe side" of 1.00) and a coefficient of variation (i.e. the standard deviation divided by the mean value, denoted as CoV) of 0.19. Due to insufficiency of references concerning a similar subject, it is difficult to compare and verify the obtained numbers. In the available references the following can be found. Engen et al. (2016) presents similar values, but for a different modelling approach which is more suited for large scale analyses (with relatively large elements). Schlune et al. (2012) investigated the modelling uncertainty by studying the statistics of various round robin analyses results, i.e. the results of international blind prediction competitions. They reported values of the CoV in the range of 0.03 to 0.39.

As indicated by Schlune, it is reasonable to distinguish easy cases from relatively difficult modelling cases. The round robin analyses usually fall in the latter category, including over-reinforced beams, shear panels and slabs. With this in mind, we calculate the properties of the modelling uncertainty ratio per failure mode. This is presented in Table 5.

We immediately emphasize that the statistics in this table are based on very few case studies. However, although the statistical significance of these properties of the modelling uncertainty is questionable, the table shows that the "difficult cases" are the slabs failing in shear. Following the current guidelines, they give a relatively high coefficient of variation (0.27) in combination with a "safe" mean of 1.35.

7.2 *Comparison of the design resistance using different levels of approximation*

Table 6 summarizes the design resistances. It distinguishes analytical models following the Eurocode and the *fib* Model Code 2010. For the Model Code 2010, different levels of approximations (LoA's) have been considered, where applicable.

The highest level IV in Table 7 of approximation employs nonlinear numerical simulations. Verification of the design resistance according to this method has been executed by means of three safety formats introduced in the Model Code 2010.

The last column in Table 7, shows that increasing the level of approximation indeed reveals an increase of the established design resistance. This column shows the ratio of the highest LoA IV design resistance to the lowest analytical design resistance.

Table 6. Results analytical models.

		MC 2010 [kN]		
Member	EC2 [kN]	LoA I	LoA II	LoA III
RB1	181			
RB3	99			
PB1	1097			
RB3A	85.9	57.67	69.2	97.65
PB2	3859	3275	3968	3968
PB3	668.4	596	761.6	998
PB4	625.4	–	548.8	548.8
RB2	52	35.2	59	–
RS1	43.28			
RS2	636.7	425.4	536.3	–
RS3	232.6	146.3	282.2	–
RS4	224	133	272.6	–
RS5	235.7	157.7	289.3	–

Table 7. Results using different safety formats for LoA IV.

	MC 2010 LoA IV [kN]				
Member	GRF	PF	ECOV	$P_{Rd,\ LoA\ IV}/P_{Rd,min}$	$P_{Rd,\ LoA\ IV}/P_{Rd,max}$
RB1	190	193	203	1.12	1.12
RB3	116	115	120	1.21	1.21
PB1	1352	1376	1514	1.38	1.38
RB3A	110	114	119	2.06	1.22
PB2	4639	4774	5391	1.65	1.36
PB3	1549	1857	1952	3.28	1.36
PB4	809	589	874	1.59	1.4
RB2	54	56	57	1.62	0.97
RS1	–	–	–	–	–
RS2	785	917	890	2.09	1.4
RS3	502	582	588	4.0	2.1
RS4	521	613	607	4.0	2.23
RS5	610	726	677	4.29	2.34

8 CONCLUSION

The impact of the international contest on the further development of the guidelines is substantial. The enthusiastic presentations of blind prediction results at the workshop in a competitive setting, stimulates further research.

ACKNOWLEDGEMENT

The authors wish to thank the Dutch Ministry of Infrastructure and the Environment (Rijkswaterstaat) for financing this research work.

REFERENCES

CEN 2005. Eurocode 2: Design of Concrete Structures – Part 1-1. General Rules and Rules for buildings, EN-1992-1:2005, Brussels, Belgium: Comité European de Normalisation.

de Boer, A., M.A.N. Hendriks, J.A. den Uijl, B. Belletti, C. Damoni 2014. *Nonlinear FEA Guideline for modelling of concrete infrastructure objects*, EURO-C 2014, St. Anton, Austria, pg 977–985.

Engen, M., Hendriks, M.A.N., Overli, J.A. & Aldstedt, E. (2015). Solution strategy for non-linear finite element analyses of large reinforced concrete structures. Structural Concrete, 16(3), 389–397.

fib 2012. ModelCode 2010 Final Draft, Lausanne, International Federation for Structural Concrete (fib).

Hendriks, M.A.N., A. de Boer, B. Belletti, "Guidelines for Nonlinear Finite Element Analysis of Concrete Structures", Rijkswaterstaat Centre for Infrastructure, Report RTD:1016-1:2017, version 2.1.1, 2017 (to be published by Rijkswaterstaat).

Hendriks, M.A.N., A. de Boer, B. Belletti, "Validation of the Guidelines for Nonlinear Finite Element Analysis of Concrete Structures – Part: Overview of results", Rijkswaterstaat Centre for Infrastructure, Report RTD:1016-2:2017, version 1.0, 2017 (to be published by Rijkswaterstaat).

Hendriks, M.A.N., A. de Boer, B. Belletti, "Validation of the Guidelines for Nonlinear Finite Element Analysis of Concrete Structures – Part: Prestressed beams", Rijkswaterstaat Centre for Infrastructure, Report RTD:1016-3B:2017, version 1.0, 2017 (to be published by Rijkswaterstaat).

Hendriks, M.A.N., A. de Boer, B. Belletti, "Validation of the Guidelines for Nonlinear Finite Element Analysis of Concrete Structures – Part: Reinforced beams", Rijkswaterstaat Centre for Infrastructure, Report RTD:1016-3A:2017, version 1.0, 2017 (to be published by Rijkswaterstaat).

Hendriks, M.A.N., A. de Boer, B. Belletti, "Validation of the Guidelines for Nonlinear Finite Element Analysis of Concrete Structures – Part: Slabs", Rijkswaterstaat Centre for Infrastructure, Report RTD:1016-3C:2017, version 1.0, 2017 (to be published by Rijkswaterstaat).

Schlune, H., Plos, M., Gylltoft, K. (2012). Safety formats for non-linear analysis of concrete structures. Magazine of Concrete Research, 64(7), 563–574.

Computational Modelling of Concrete Structures – Meschke, Pichler & Rots (Eds)
© 2018 Taylor & Francis Group, London, ISBN 978-1-138-74117-1

Ultimate limit state design of three-dimensional reinforced concrete structures: A numerical approach

H. Vincent & M. Arquier
Strains, Paris, France

J. Bleyer & P. de Buhan
Ecole des Ponts ParisTech, Champs-sur-Marne, France

ABSTRACT: This contribution is addressing the evaluation of the ultimate bearing capacity of massive reinforced concrete structures. It is based on the finite element implementation of both the lower bound static and upper bound kinematic approaches of yield design, adopting the well-known Rankine criterion for modelling the three-dimensional strength properties of plain concrete, while the reinforcing bars are treated by means of an extended homogenization method. Both yield design approaches lead to optimization problems which are solved by resorting to Semi-Definite Programming (SDP) techniques. The whole computational procedure is finally applied to the design of a bridge pier cap, leading to a fairly narrow bracketing of the exact failure load of this kind of structure.

1 INTRODUCTION

The Ultimate Limit State Design of reinforced concrete structures may be appropriately performed within the theoretical framework of the *yield design* (Salençon, 2013) or *limit analysis* (Chen, 1982) theory. As regards the most frequently encountered situation when the structure to be designed is made of an assemblage of 1D (beams or arches) or 2D (plates or shells) structural members, its ultimate bearing capacity may be evaluated from the previous determination of *interaction yield criteria* involving generalized stresses such as axial-membrane forces and bending moments. This method, which proves particularly attractive from an engineering point of view, has been quite recently used for spatial frame structures (Bleyer & de Buhan, 2013) and reinforced concrete plates (Bleyer et al., 2015) in combination with efficient convex optimization procedures.

On the other hand, assessing the ultimate load bearing capacity of constructions incorporating massive three-dimensional reinforced concrete components, which can no more be modelled as beams or plates, requires a specific analysis, such as the well-known "strut-and-tie" model which, in some way, can be related to the *static approach* of yield design which provides lower bound estimates for the ultimate load bearing capacity of the structure.

With a special attention to evaluating the ultimate shear capacity of reinforced concrete deep beams, both the lower and upper bound methods of yield design have been implemented in the context of a finite element formulation with the help of linear programming techniques (Averbuch & de Buhan, 1999). In this study, reinforced concrete was described according to a *"mixed modelling"* approach, in which plain concrete was modelled as a two-dimensional continuous medium subject to plane stress loading, while the reinforcement bars were treated as one dimensional flexible beams embedded in the surrounding concrete material.

The generalization to the more representative configuration of *linear* reinforcing inclusions placed into *three-dimensional* concrete bodies is posing a somewhat serious challenge as regards the possibility of treating such a case in a "1D-3D" mixed modelling approach. Some attempts to circumvent this problem have already been proposed either in the context of the finite element formulation (Llau et al., 2016) or making use of an implicit homogenization method (Nielsen & Hoang, 2010) or so-called "multiphase model" (Figueiredo et al., 2013).

The present contribution is devoted to applying the previously mentioned multiphase model, initially developed for reinforced soils, to the yield design of three-dimensional reinforced concrete structures. It is based on the combination of the following elements.

- Formulation of the plain concrete three-dimensional strength properties by means of the widely employed *Rankine's* criterion characterized by

the uniaxial tensile and compressive strengths of the concrete.

- Modelling the strength of each individual reinforcement with its surrounding concrete volume as an anisotropic continuum accounting for the axial strength of the reinforcing inclusion.
- Finite element formulation of both the lower bound static and upper bound kinematic approach of yield design based on a discretization of the structure into tetrahedral elements with a piecewise linear variation of the stresses.
- The final optimization procedure is carried out by means of Semi-definite Programming (SDP).

The whole design procedure will be illustrated on the typical example of evaluating the ultimate bearing capacity of a reinforced concrete bridge pier cap subjected to concentrated vertical loads.

2 STRENGTH PROPERTIES OF PLAIN AND REINFORCED CONCRETE

2.1 *Plain concrete strength condition: the Rankine's criterion*

It is generally acknowledged (Chen, 1982; Averbuch & de Buhan, 1999; Bleyer et al., 2015) that the strength of plain concrete under a three-dimensional multi-axial solicitation is adequately described by a "tension cut-off" Mohr-Coulomb criterion of the form:

$$F^c(\underline{\underline{\sigma}}) = \sup\left\{K_p\sigma_M - \sigma_m - f_c; \sigma_M - f_t\right\} \le 0 \qquad (1)$$

where σ_M and σ_m are the major and minor principal components of the stress tensor $\underline{\underline{\sigma}}$, f_t and f_c the uniaxial tensile and compressive strengths of the concrete and:

$$K_p = (1+\sin\varphi)/(1-\sin\varphi) \qquad (2)$$

where φ is the internal friction angle, which is usually taken equal to 37°.

In the following contribution, the simpler *Rankine* criterion defined by:

$$F^c(\underline{\underline{\sigma}}) \le 0 \Leftrightarrow -f_c \le \sigma_m \le \sigma_M \le +f_t \qquad (3)$$

will be adopted. Figure 1 shows that, under plane stress conditions, the Rankine criterion is slightly conservative with respect to the Mohr-Coulomb one, both criteria being even coincident for $f_t = 0$. It may also be represented by means of an intrinsic curve in the Mohr-plane, as shown in Figure 2.

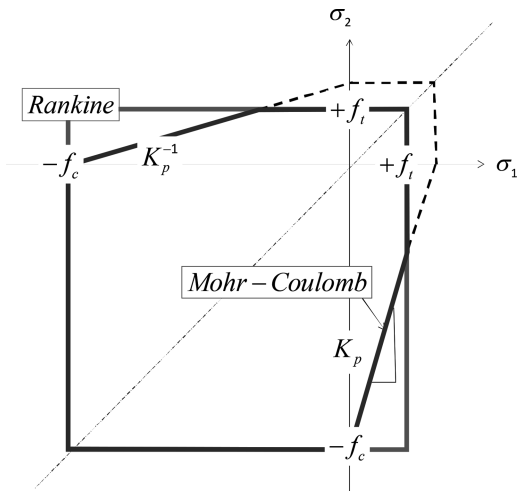

Figure 1. Rankine and tension cut-off Mohr-Coulomb criteria under plane stress conditions.

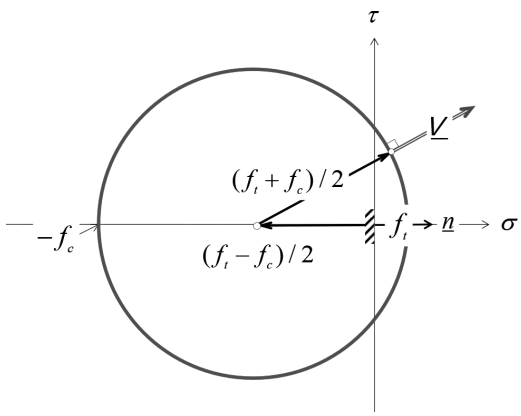

Figure 2. Rankine's intrinsic curve in the Mohr-plane.

2.2 *Reinforcements*

The concrete material is reinforced by one-dimensional steel bars or rods, the strength condition of which may be simply expressed in terms of axial force N only, thereby neglecting any resistance to shear force V and bending moment M:

$$-kN_0 \le N \le N_0, \quad V = M = 0 \qquad (4)$$

where N_0 denotes the tensile resistance of each individual rebar, while k is a non-dimensional parameter ranging from 0 to 1, expressing the reduced resistance of the reinforcement under compression (buckling for instance).

2.3 *Reinforced concrete as homogenized material*

Some significant zones of the reinforced concrete structure (such as deep beams: see for instance: Averbuch & de Buhan, 1999) may be reinforced by such uniformly distributed bars (case of stirrups or open frames). Provided that the spacing between two neighboring reinforcements is sufficiently small as compared with the size of the reinforced zone, the latter may be replaced by a zone where the homogenized constituent material obeys a macroscopic strength condition (see de Buhan & Taliercio, 1991, for composite materials, or Michalowski & Zhao, 1996 for reinforced soils and Averbuch & de Buhan, 1999 for reinforced concrete).

This macroscopic strength condition may be expressed as follows:

$$F^{rc}(\underline{\underline{\sigma}}) \le 0 \Leftrightarrow \begin{cases} \underline{\underline{\sigma}} = \underline{\underline{\sigma}}^c + \sigma^r \underline{e}_1 \otimes \underline{e}_1 \\ \text{with } F^c(\underline{\underline{\sigma}}^c) \le 0 \\ \text{and } -k\sigma_0 \le \sigma^r \le \sigma_0 \end{cases} \tag{5}$$

where $\underline{e}_1$ is the unit vector parallel to the reinforcing bar, and σ_0 is defined as the tensile resistance of the bars *per unit transverse area*:

$$\sigma_0 = N_0 / s^2 \tag{6}$$

which may also be expressed as:

$$\sigma_0 = A^s f_y^s / s^2 = \eta f_y^s \tag{7}$$

where f_y^s denotes the uniaxial strength of the bar constituent material (steel) and A^s the bar cross-sectional area, so that η represents the *reinforcement volume fraction* (see Figure 3 where $s^2 = A^s + A^c$).

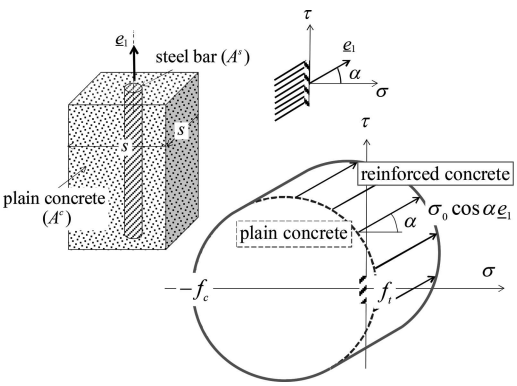

Figure 3. Homogenized strength condition of reinforced concrete relative to an oriented facet.

Figure 3 illustrates the macroscopic strength condition (4) expressed on an oriented facet of the homogenized reinforced concrete in the particular case when $k = 0$ (no compressive resistance of the reinforcements). Such a geometric representation gives a clear evidence of the *strength anisotropy* of the homogenized reinforced concrete in exactly the same way as for fiber composite materials.

It should be noted that, without any reference to the limit analysis or yield design homogenization theory, some authors (Nielsen & Hoang, 2010) did make use of a strength criterion quite similar to (5), that is based on an intuitive additive decomposition of the total stress in reinforced concrete zones into stress components relating to the plain concrete and the reinforcements, each one complying with independently specified strength conditions.

3 MIXED MODELLING OF REINFORCED CONCRETE

3.1 *Limitation of the "mixed modelling" approach*

Referring to the frequently encountered situation where only a small number of differently oriented reinforcements are incorporated in the concrete structure (case of longitudinal reinforcements in deep beams for instance), the above mentioned homogenization method is no more applicable and the so-called "mixed modelling" approach should be advocated. According to this approach, the reinforcements are treated as 1D structural elements with a strength condition defined by (4) embedded in the concrete material modelled as a 3D continuum, the strength of which is specified by (2).

Unfortunately, this 1D-3D *"mixed modelling"* approach faces a serious limitation concerning the establishment of equilibrium equations for such a composite system. Indeed, the equilibrium equation at any point of the reinforcing bar may be written as:

$$\mathrm{d}N(x_1)/\mathrm{d}x_1 + p(x_1) = 0 \tag{8}$$

where p represents the density of axial force exerted by the surrounding concrete material onto the reinforcing bar (Figure 4(a)).

Now, the impossibility of connecting such a 1D distribution p of interaction forces with the three-dimensional stress fields prevailing in the concrete material may be illustrated from the following simple reasoning. Considering a circular cylindrical "control surface" of radius ρ with its axis placed along the reinforcement, as shown in Figure 4(b), the interaction force density p may be obtained

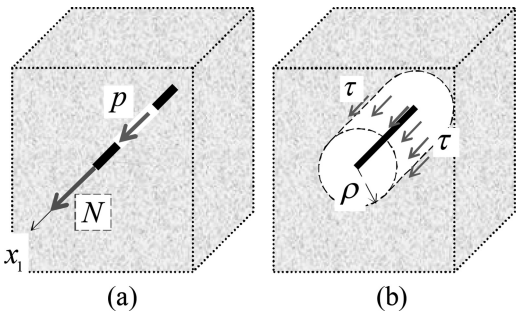

Figure 4. Interaction forces between concrete and reinforcement in the context of 1D-3D mixed modelling.

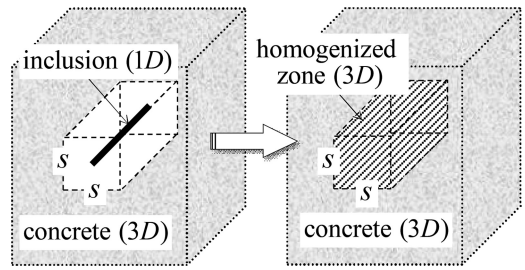

Figure 5. Construction of a homogenized zone around an individual inclusion.

from applying along this surface a longitudinal shear stress τ, the average value of which along the circle drawn on this surface at point x_1, could be expressed as:

$$\langle \tau \rangle (x_1) = p(x_1)/2\pi\rho \tag{9}$$

According to the latter equation, the shear stress which should be developed in the concrete along the control surface for applying a given value of interaction force density p increases to infinity as the radius ρ tends to zero, so that the stress field in the concrete material would tend to infinity along the reinforcement axis. Such a singularity could possibly be taken into account in the context of a linear elastic behavior of the concrete, but definitely not as soon as yielding and failure of the latter is concerned, since in this case the yield strength condition (3) of the concrete would be systematically violated when approaching the 1D reinforcing bar.

3.2 *An extended homogenization model*

Of course, the only fully mechanically consistent and rigorous way of circumventing the above limitation, would be to model each reinforcing bar as a three-dimensional volume body. But, on account of the small diameter of such bars along with the sharp contrast between the reinforcing steel and the surrounding concrete in terms of strength properties, this would undoubtedly imply prohibitive computational costs, due for instance to the highly refined discretization required when employing finite element techniques.

An alternative approach for the finite element modelling of 1D steel inclusions in 3D concrete volumes has been recently proposed by Vincent et al. (2017). Considering one individual 1D-inclusion embedded in a 3D-concrete block, a cylindrical volume of concrete with the inclusion placed along its axis is defined, as shown in Figure 5(a). The intuitive idea is to replace the composite cylindrical volume, thus obtained, by a homogenized cylinder, at any point of which the strength condition is defined by Eqs. (4) and (6), where s represents the side of the squared cross-section of the cylindrical volume.

The advantage of such a modelling procedure, is that the characteristic size of the homogenized zone (namely s) is significantly larger than the inclusion's diameter, thus allowing for example a much easier finite element discretization of the reinforced concrete structure as a 3D-3D composite, since a refinement of the mesh around the inclusion is no more required for obtaining accurate and reliable predictions. Of course, the choice of s being arbitrary, it will be necessary to make sure that the results of the computations performed on the basis of this model, remain rather insensitive to the value of s, which has been checked in (Vincent et al., 2017).

4 NUMERICAL LOWER BOUND APPROACH

4.1 *Statement of the yield design problem*

Assuming that the reinforced concrete structure under consideration is subject to one single loading parameter Q, the ultimate or failure load value Q^+ is defined, in the context of the yield design theory, as the maximum value of Q for which one can exhibit any stress field σ:

- *statically admissible* (S.A.) with Q, *i.e.* verifying the equilibrium equation at any point of the structure Ω:

$$\mathrm{div}\,\underline{\underline{\sigma}}(\underline{x}) + \rho\underline{F}(\underline{x}) = 0,\ \forall \underline{x} \in \Omega \tag{8}$$

where $\rho\underline{F}$ denotes the body force volume density (material specific weight for example), along with

the continuity of the stress-vector across possible stress jump surfaces Σ:

$$\left[\underline{\underline{\sigma}}(\underline{x})\right].\underline{n}(\underline{x}) = 0,\ \forall \underline{x} \in \Sigma \tag{10}$$

as well as the stress boundary conditions associated with the loading Q;

- and complying with the strength conditions assigned to the plain concrete and reinforced concrete zones of the structure, respectively:

$$\begin{aligned} &F^{c}(\underline{\underline{\sigma}}(\underline{x})) \le 0\ \ \forall \underline{x} \in \Omega^{c} \\ &F^{rc}(\underline{\underline{\sigma}}(\underline{x})) \le 0\ \ \forall \underline{x} \in \Omega^{rc},\quad \Omega = \Omega^{c} \cap \Omega^{rc} \end{aligned} \tag{11}$$

where Ω^{c} (respectively Ω^{rc}) represents the part of the structure occupied by the plain concrete (resp. by the homogenized reinforced concrete).

4.2 *Finite element formulation and SDP problem*

Applying the *lower bound static approach* consists in considering S.A. stress fields depending either on a small number of parameters in an analytical approach, or on a large but finite number of stress variables in a numerical approach, such as the finite element method. According to the latter, the geometrical domain Ω occupied by the three-dimensional structure is discretized into N_e tetrahedral finite element Ω^{e}, with a *linear variation* of the stress field inside each element. It is to be noted that there are as many stress tensors attached to any geometrical node of the mesh as there are tetrahedral elements sharing this node as an apex.

It can be shown (Vincent et al., 2017) that the finite element implementation of the lower bound static approach of yield design finally reduces to the following convex optimization problem:

$$\begin{aligned} &Q^{+} \ge Q^{lb} = \underset{\{\Sigma\}}{\text{Max}}\ \ Q = {}^{T}\{A\}\{\Sigma\} \\ &\text{subject to}\ \begin{cases} [B]\{\Sigma\} = \{C\} & \text{equilibrium} \\ F(\{\Sigma\}) \le 0 & \text{strength criteria} \end{cases} \end{aligned} \tag{12}$$

where $\{\Sigma\}$ is a column-vector which collects all the nodal stress variables associated with the mesh discretization of the structure.

Unlike the equilibrium conditions which involve the total stresses only, the strength criteria in the homogenized reinforced zones concern the partial stresses as shown by (5). While the condition relating to the reinforcement writes in the form of a simple *linear* constraint, the strength condition of the plain concrete defined by (3) involves the maximal and minimal principal stress components. The latter thus needs a specific treatment so that the optimization problem (12) may be treated as a *Semi-definite programming* (SDP) optimization problem for which efficient algorithms are available.

5 UPPER BOUND KINEMATIC APPROACH

5.1 *Principle of the approach*

The upper bound kinematic approach of yield design is based upon the dualization of the lower bound static one through the virtual work principle (Salençon, 2013). Thus, given any *kinematically admissible* (K.A.) velocity field $\underline{U}$, the so-called *maximum resisting work* developed in such a field may be calculated as follows:

$$\begin{aligned} P_{mr}(\underline{U}) = &\int_{\Omega^{c}} \pi^{c}(\underline{\underline{d}})\mathrm{d}\Omega^{c} + \int_{\Omega^{rc}} \pi^{rc}(\underline{\underline{d}})\mathrm{d}\Omega^{rc} \\ &+ \int_{\Sigma^{c}} \pi^{c}(\underline{n};\underline{\llbracket V \rrbracket})\mathrm{d}\Sigma^{c} + \int_{\Sigma^{rc}} \pi^{rc}(\underline{n};\underline{\llbracket V \rrbracket})\mathrm{d}\Sigma^{rc} \end{aligned} \tag{13}$$

In the above expression, where d denotes the strain rate tensor and $\underline{\llbracket V \rrbracket}$ the velocity jump across the discontinuity surfaces Σ, the support functions π, defined as:

$$\begin{aligned} &\pi^{c/rc}(\underline{\underline{d}}) = \sup\left\{\underline{\underline{\sigma}} : \underline{\underline{d}};\ F^{c/rc}(\underline{\underline{\sigma}}) \le 0\right\} \\ &\pi^{c/rc}(\underline{n};\underline{\llbracket V \rrbracket}) = \sup\left\{(\underline{\underline{\sigma}}.\underline{n}).\underline{\llbracket V \rrbracket};\ F^{c/rc}(\underline{\underline{\sigma}}) \le 0\right\} \end{aligned} \tag{14}$$

have the following expressions:

$$\begin{aligned} &\pi^{c}(\underline{\underline{d}}) = \sum_{k=1}^{3} \sup\left\{f_t d_k; -f_c d_k\right\} \\ &\pi^{c}(\underline{n};\underline{\llbracket V \rrbracket}) = \frac{f_t + f_c}{2}\left|\underline{\llbracket V \rrbracket}\right| + \frac{f_t - f_c}{2}\underline{\llbracket V \rrbracket}.\underline{n} \end{aligned} \tag{15}$$

for the plain concrete (the second support function relative to a discontinuity may be geometrically calculated from Figure 2), and:

$$\begin{aligned} &\pi^{rc}(\underline{\underline{d}}) = \pi^{c}(\underline{\underline{d}}) + \sup\left\{-k\sigma_0 d_{11}; \sigma_0 d_{11}\right\} \\ &\pi^{rc}(\underline{n};\underline{\llbracket V \rrbracket}) = \pi^{c}(\underline{n};\underline{\llbracket V \rrbracket}) + \sup\left\{-k\sigma_0 n_1 \llbracket V \rrbracket_1; \sigma_0 n_1 \llbracket V \rrbracket_1\right\} \end{aligned} \tag{16}$$

for the reinforced concrete. It is worth noting that, unlike for other criteria such as for instance the tension cut-off Mohr-Coulomb condition (1), the support functions (15) and (16) can be calculated for any velocity field and velocity jumps, without it being necessary to impose kinematic restrictions.

Under these conditions, the yield design upper bound kinematic approach states that the ultimate load must satisfy the following inequality, valid for any K.A. velocity field $\underline{U}$:

$$Q^{+}\dot{q}(\underline{U}) \le P_{mr}(\underline{U}) \tag{17}$$

where the left-hand member of the inequality is the virtual work of the ultimate load, thereby producing the following upper bound estimate:

$$Q^{+} \le Q^{ub} = P_{mr}(\underline{U}) / \dot{q}(\underline{U}), \text{ for } \dot{q}(\underline{U}) > 0 \tag{18}$$

5.2 *Finite element implementation*

Similarly to what has been previously done for the lower bound static approach (section 4.2.), the reinforced structure Ω is discretized into N^e six-nodded tetrahedral finite element Ω^e, with a *quadratic variation* of the velocity field inside each element and *velocity jumps* across the triangular facets separating any two adjacent elements.

As shown in (17) the maximum resisting work is greater than the virtual work of the ultimate load. Thus, finding the best upper bound to the ultimate loading of the reinforced structure Ω can be expressed as the following minimization problem:

$$Q^{+} \le Q^{ub} = \underset{\underline{U}}{\text{Min}} \left\{ P_{mr}(\underline{U}); \dot{q}(\underline{U}) = 1 \right\} \tag{19}$$

Denoting by $\{U\}$ the column-vector collecting all the nodal values of the discretized velocity field, the above minimization problem can be rewritten as:

$$Q^{+} \le Q^{ub} = \underset{\{U\}}{\text{Min}} \left\{ P_{mr}(\{d\}, \{V\}) \right\}$$
$$\text{subject to} \begin{cases} \{d\} = [D]\{U\} \\ \{V\} = [E]\{U\} \\ {}^{T}\{F\}\{U\} = 1 \end{cases} \tag{20}$$

where $\{d\}$ and $\{V\}$ denoted the column-vectors collecting all the nodal values of the strain rates and velocity jumps associated with the velocity field. This minimization problem is also treated by means of *Semi-definite programming* (SDP).

6 PRACTICAL CASE STUDY

The presented numerical procedure for calculating the ultimate load capacity of 3D structures has been implemented. This section provides the example of a three-dimensional reinforced concrete structure for which the ultimate loading capacity is evaluated with a lower bound static approach and an upper bound kinematic approach.

In order to illustrate the efficiency of the implemented 3D yield design procedure, the ultimate bearing capacity of a reinforced concrete bridge pier cap is evaluated.

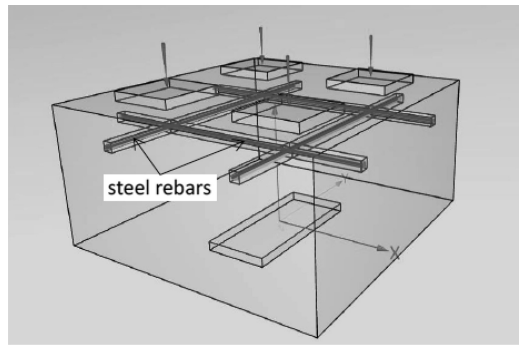

Figure 6. Reinforced concrete pier cap subject to bridge deck loading.

The bridge pier cap is modelled as a $3 \times 3\text{x}1.5$ m^3 parallelepipedic concrete block. The finite element lower bound static approach and the upper bound kinematic approach are performed on this structure subject to four vertical loads representing the action of the overlying bridge deck, as shown in Figure 6.

These loadings are applied in the form of a uniform pressure applied on top of small rigid square pads of 0.7×0.7 m^2. The interaction with the underlying bridge pier is modelled by imposing a rigid connection on a 1.5×0.7 m^2 rectangular area placed at the center of the bottom surface.

The concrete block is made of a homogeneous plain concrete material, with $f_c = 40$ MPa and $f_t = 0.5$ MPa. It is strengthened by four steel rebars of diameter equal to 3 cm, placed just below the loading pads as shown in Figure 6, with a uniaxial strength equal to $f_y^s = 400$ MPa. According to the above described procedure, each of the four rebars is replaced by a homogenized volume of square cross section equal to $s^2 = 0.01$ m^2.

First, a brief parametric study is carried out to illustrate the convergence of the lower and upper bound approaches towards the exact ultimate load. For this purpose, different meshes with an increasing number of finite elements, have been generated. The results of the analysis are shown in Figure 7 which displays the variations of the lower and upper bound estimates as functions of the mesh refinement characterized by the number of tetrahedral finite elements.

It may be clearly seen in this figure that the upper and lower bounds are getting closer as the finite element mesh is refined, which that the evaluation of the ultimate load capacity of the structure is becoming more and more accurate. Indeed, the difference between the upper and lower bounds can

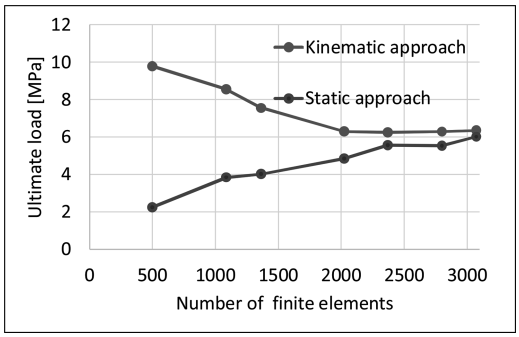

Figure 7. Convergence of the static and kinematic bounds with the increasing number of mesh elements.

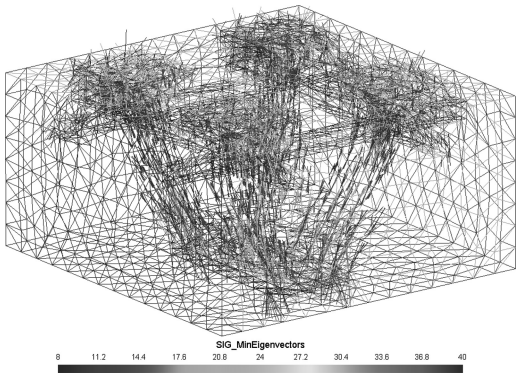

Figure 8. Perspective view of the optimized principal compressive stress field in the concrete.

be interpreted as an error estimator of the result, since the yield design theory ensures that the exact result lies somewhere between the two bounds.

It should be mentioned that the number of tetrahedral finite elements plotted on the horizontal axis corresponds to the kinematic mesh, the static mesh being eight times finer. As the interpolation degree is not the same (linear interpolation for the static approach versus quadratic interpolation for the kinematic approach), the static approach needs to be conducted on finer meshes to converge.

As could be expected, the best results are obtained with the finest meshes, where the structure is discretized in 3073 tetrahedral finite elements for the kinematic approach (24584 for the static approach). However, it is worth noting that the results converge quite rapidly since the relative error is already less than ten percent for kinematic meshes with 2300 elements.

Figure 8 represents the distribution of the principal stresses prevailing in the plain concrete material, while Figure 9 represents the principal tensile

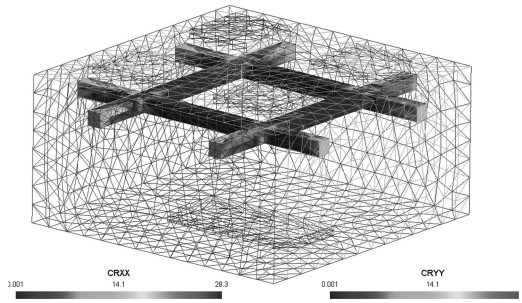

Figure 9. Optimized stress field in the homogenized zone.

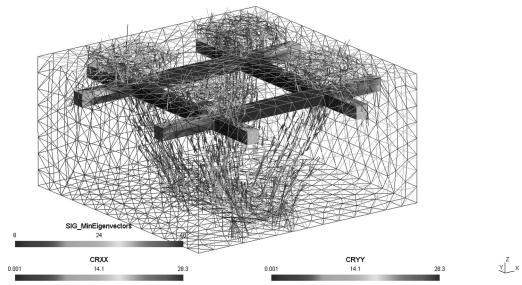

Figure 10. View of the optimized stress field in the whole pier cap.

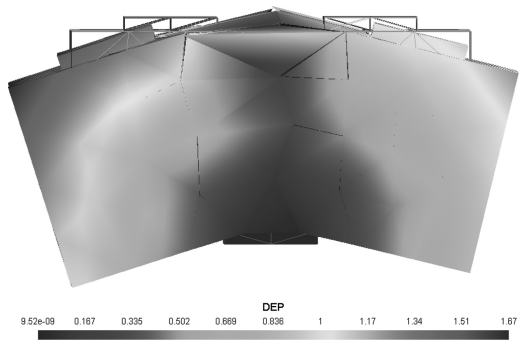

Figure 11. View of the failure mechanism of the pier cap.

stresses in the (homogenized) reinforced zones. Both fields are superimposed in Figure 10.

While the results of the static approach lead to an optimized stress field in the structure which is similar to what the strut and tie method could provide, the kinematic approach gives a clear failure mechanism of the analyzed structure (besides giving an upper bound and thus, an error estimator of the result). The failure mechanism of the reinforced bridge pier cap is shown in Figure 11.

7 CONCLUSION

A specifically dedicated finite element computer code has been set up aimed at producing rigorous lower bound and upper bound estimates for the ultimate load bearing capacity of three-dimensional reinforced concrete structures. It relies upon two recent developments: the numerical formulation of the corresponding optimization problem using Semidefinite Programming, on the one hand, the adoption of a homogenization-based model for describing the mechanical behavior of individual reinforcing inclusions embedded in a surrounding three-dimensional concrete matrix, on the other hand.

The entire procedure may be further extended to other kinds of strength condition for the plain concrete material, such as the already mentioned tension cut-off Mohr-Coulomb criterion (1), which may prove more realistic for capturing the strength properties of concrete, notably under isotropic confining stresses. This will imply to take kinematic restrictions into account in the calculations of the support functions π and thus of the maximum resisting work

REFERENCES

Averbuch D., de Buhan P., 1999. Shear Design of Reinforced Concrete Deep Beams: A Numerical Approach, *Jl. of Structural Engineering*, 125(3): 309–318.

Bleyer J., de Buhan P., 2013. Yield surface approximation for lower and upper bound yield design of 3D composite frame structures, *Computers and Structures*, 129: 86–98.

Bleyer J., Pham D.T., de Buhan P., 2015. Failure design of high-rise concrete panels under fire loading, *Engineering and Computational Mechanics*, 168, EM4: 178–185.

de Buhan P., Taliercio A., 1991. A homogenization approach to the yield strength of composite materials, *European Journal of Mechanics*, A/Solids, 10(2): 129–150.

Chen W.F., 1982. *Plasticity in reinforced concrete*, McGraw-Hill, New-York.

Figueiredo M.P., Maghous S., Filho A.C., 2013. Three-dimensional finite element analysis of reinforced concrete structural elements regarded as elastoplastic multiphase media, *Materials and Structures*, 46: 383–404.

Llau A., Jason L., Dufour F., Baroth J., 2016. Finite element modelling of 1D steel components in reinforced and pre-stressed concrete structures, *Engineering Structures*, 127: 769–783.

Michalowski P.V., Zhao A., 1996. Failure of fibre-reinforced granular soils, *Jl. Geotech. Eng*., ASCE, 122(3): 226–234.

Nielsen M.P., Hoang L.C., 2010. *Limit Analysis and Concrete Plasticity*, CRC Press, Taylor & Francis.

Salençon J., 2013. *Yield Design*, ISTE Ltd, Wiley, London.

Vincent H., Arquier M., Bleyer J., de Buhan P., 2017. Yield design numerical analysis of three-dimensional reinforced concrete structures. *4th Int. Conf. on Mech. Models in Struct. Eng.,* 29 nov-01 dec., Madrid, Spain.

Computational Modelling of Concrete Structures – Meschke, Pichler & Rots (Eds)
© 2018 Taylor & Francis Group, London, ISBN 978-1-138-74117-1

Computational buckling response of reinforcing bars embedded in Hybrid Fiber Reinforced Concrete (HyFRC)

I.D. Williams & C.P. Ostertag
University of California, Berkeley, USA

C.A. Arteta
Universidad del Norte, Colombia

ABSTRACT: This paper presents the development of a model to simulate buckling of a longitudinal reinforcing bar (rebar) embedded in HyFRC. The relatively simple nonlinear 2D model isolates the rebar and distributed lateral support provided by the HyFRC, allowing thorough investigation of the interaction between the bar and cover material. The behavior of the rebar with distributed lateral support provided by HyFRC both with and without lateral reinforcement is compared to a rebar supported solely by lateral ties with discrete spacing. Results indicate that the use of HyFRC delays the onset of rebar buckling, enables strain hardening prior to buckling, and increases the residual post-buckling load-carrying capacity of the rebar. In addition, both model and experimental testing provide evidence that the use of HyFRC continues to improve the response of the rebar with tie spacings up to 12 bar diameters—which doubles what is feasible by current seismic codes.

1 INTRODUCTION

1.1 *Background*

Resisting seismic forces in a reinforced concrete (RC) structure requires the ability to maintain strength and stiffness up to large displacements. Elements subjected to high compressive demands such as columns in special moment frames or the boundary elements in slender special structural walls rely on lateral reinforcement to provide a passive triaxial stress state and prevent buckling of longitudinal reinforcing bars. The combination of these two effects is crucial to the performance of an earthquake-resistant reinforced concrete building. To accomplish this, current design provisions specify necessary lateral reinforcing ratios, ρ_{sh}, and a maximum tie spacing of 6 longitudinal bar diameters, d_b; this last provision is specifically intended to provide sufficient capacity and prevent rebar buckling at high strains.

Recent studies investigating the performance of slender structural walls with high flexural compression demands indicate that failure frequently initiates due to buckling of the longitudinal reinforcement (Segura and Wallace, 2016; Sritharan et al., 2014). One study testing the performance of slender compression elements with seismic-code-compliant detailing under monotonic compressive loading concludes that, in addition to reducing the load-carrying capacity of the longitudinal bars, buckling also reduces the ability of lateral reinforcement to provide confinement (Arteta et al., 2014). Considering these studies, lateral reinforcing bars may not always provide adequate support to longitudinal reinforcing bars at high strain demands, even for high lateral reinforcing ratios.

1.2 *Previous work*

One proposed solution to provide additional confinement and rebar support is through the use of a Hybrid Fiber Reinforced Concrete Composite (HyFRC) in place of conventional concrete. Previous studies on the use of HyFRC in a reinforced concrete section under compression noted that the material does not spall, but remains intact up to high levels of strain. It was suggested that the intact cover may provide additional support to the longitudinal bars and delay the onset of buckling (Nguyen et al., 2017; Panagiotou et al., 2014).

This idea was tested in a continuation of the study by Arteta et al. (2014), investigating the performance of conventional RC special shear wall boundary elements under monotonic compression with various code-compliant reinforcement layouts. One specimen was replicated with exact reinforcement detailing, but with HyFRC in place of conventional concrete. The HyFRC prism was subjected to monotonic uniaxial loading and compared to three conventional reinforced concrete specimens from the previous study, one with the exact same detailing, one with the same lateral

reinforcing ratio, and one with a higher lateral reinforcing ratio. While the conventional RC specimens failed to maintain load following the onset of concrete cover spalling, the HyFRC specimen maintained capacity up to an average section strain of 0.008, where failure occurred due to a construction error. The failed section of one of the conventional RC specimens is shown in Figure 1, showing cover spalling and rebar buckling across multiple ties, with similar failures observed in all three of the control specimens. Rebars directly restrained by the axial stiffness of ties running through the thickness of the section with 135-degree seismic hooks showed buckled lengths up to $9.5d_b$, and longitudinal bars restrained only by the flexural stiffness of the long leg of rectangular hoops had buckled lengths up to $18d_b$.

The failed section for the HyFRC specimen is shown in Figure 2. In contrast to the control specimens, the cover did not spall but remained intact throughout the entire test and had to be forcefully removed to reveal the reinforcement underneath. The buckled length in this specimen was $5d_b$ for both the bars directly tied by 135-degree seismic hooks and those only in contact with the rectangular hoops. Further investigation of the rebar strains revealed that the longitudinal rebars in the control specimens buckled at a section strain between 0.003 and 0.005, and no buckling was apparent in the HyFRC at a strain of 0.008 (which corresponds to the strain at the point of failure). Although buckling was observed to have taken place upon completion of the test, it was unclear at what strain level it occurred due to the rapid shear failure (Williams et al., 2017).

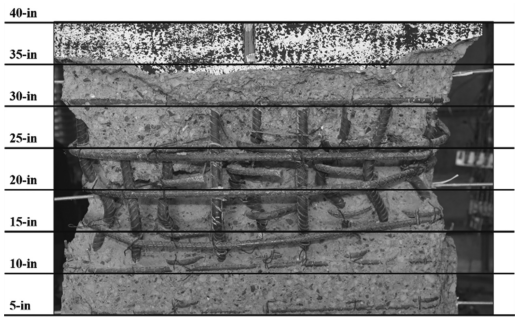

Figure 1. Failed region of control specimen C3.



Figure 2. Failed region of HyFRC specimen H1.

1.3 *Inelastic buckling*

Buckling of an element under compressive loading is an ever-present issue in structural engineering. Euler's classical solution shown in Equation 1 relates the critical elastic buckling load, P_{cr}, to the modulus of elasticity of the material, E, the second moment of area of the cross section, I, and an effective length corresponding to the inflection points of the displaced shape of the element, L_e.

$$P_{cr} = \frac{\pi^2 EI}{L_e^2} \tag{1}$$

While this solution is elegant in its simplicity, it is rarely applicable in reinforced concrete design, as code provisions are put in place to prevent elastic buckling from taking place. It was originally proposed that as the material enters the nonlinear range of response, the critical buckling load becomes dependent on the instantaneous tangent modulus of the material, E_T (Engesser, 1891). It was later noted that the tangent modulus gives a lower bound. As buckling progresses in the nonlinear range of material response, the region of the section placed in further compression as the element deforms takes on the tangent material modulus, while the region on the other side of the neutral axis begins unloading with original stiffness, E, as shown in Figure 3.

Due to this behavior a reduced modulus, E_R, was proposed. The formula for the reduced modulus of a circular cross section is given in Equation 2 (Timoshenko and Gere, 1961).

$$E_R = \frac{4E_s E_T}{\left(\sqrt{E_s} + \sqrt{E_T}\right)^2} \tag{2}$$

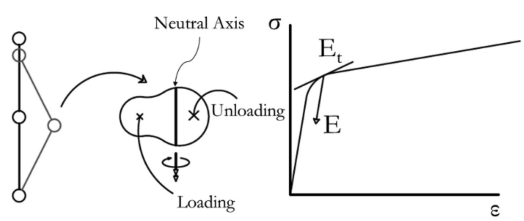

Figure 3. Illustration of material behavior during plastic buckling for an arbitrary cross section.

This theory is effective for predicting the point of buckling initiation for a rod with simple end conditions. Other theories exist for predicting the behavior of a bar restrained with lateral springs along the length, as is the case for a longitudinal rebar restrained by ties. Full analysis of bar buckling and the interactions associated with lateral ties and strain hardening cover material requires nonlinear, iterative solutions. To achieve this, a model is developed using the software package OpenSees (McKenna et al., 2000) that simulates geometric instability of an embedded steel bar in compression considering inelastic material behavior.

1.4 *HyFRC*

The composite material used in the previous study on shear wall boundary elements is a HyFRC developed by Blunt and Ostertag (Blunt & Ostertag, 2009a). A characteristic of HyFRC that is essential to this study is the strain hardening behavior of the material (Blunt & Ostertag, 2009b). This behavior is achieved at relatively low fiber volume fraction through fiber hybridization, that is, using a blend of fibers for multi-scale crack control. Microfibers made of polyvinyl alcohol arrest microcracks, causing diffuse microcracking rather than early formation of a localized macrocrack; and larger, hooked-end fibers begin to control the behavior as crack width increases. Details of the fibers used in the HyFRC mix design used in this investigation are given in Table 1, with mix proportions given in Table 2. Steel fibers S1 and S2 are hooked-end fibers.

Table 1. Fiber properties.

Designation	Material	Length mm	Strength MPa	Modulus GPa	Aspect Ratio
PA	PVA	8	1600	24	200
S1	Steel	30	1100	200	55
S2	Steel	60	1050	200	80

Table 2. HyFRC mix weight proportions.

Cement*	Water	Coarse agg.**	Fine agg.***	SP****	Fiber dosage V_f [%] PA	S1	S2
1	0.54	1.83	2.07	0.0017	0.2	0.5	0.8

**ASTM C150 Type II,*
***pea gravel, MSA = 10 mm,*
****coarse sand, FM = 3.2,*
***** Superplasticizer: Glenium 7500 (weight of solids).*

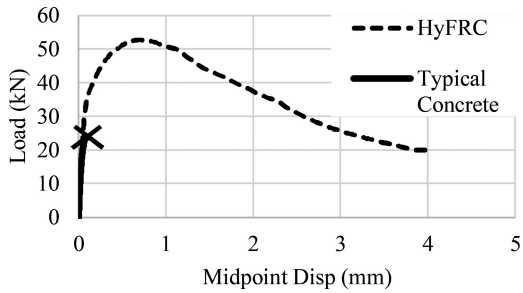

Figure 4. 4-point bending test of HyFRC and typical concrete.

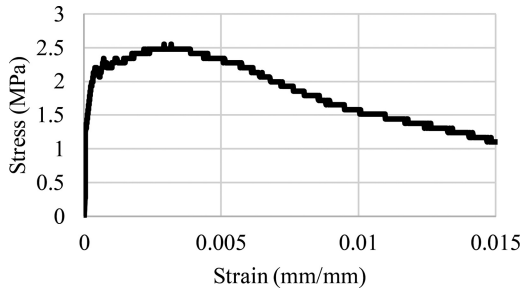

Figure 5. HyFRC uniaxial tension test.

Flexural results of four-point beam tests conducted on HyFRC and typical concrete specimens tested according to ASTM C1609/C1609M – 12 are given in Figure 4 (ASTM, 2005). Beams tested are 6 × 6 × 24 in. with 18 in. clear span between supports. The deflection hardening properties of HyFRC can be seen clearly by comparing these two plots. While typical concrete displays brittle failure in flexure, the HyFRC specimen continues to increase in load-carrying capacity following initial cracking of the cementitious matrix, and continues to harden up to a capacity more than double that of the typical concrete specimen. Slow displacement softening follows the ultimate load capacity. Results of a uniaxial tensile test of a HyFRC dogbone specimen with a 4 × 4-in. cross-section and gage length of 13.25-in. are given in Figure 5. These results indicate that HyFRC displays some amount of strain hardening in direct tension, with ductile strain softening following peak load.

2 OPENSEES MODEL

2.1 *Buckling model*

The schematic shown in Figure 6 illustrates key components of the bar model without cover. No cover is modeled for the control specimens as

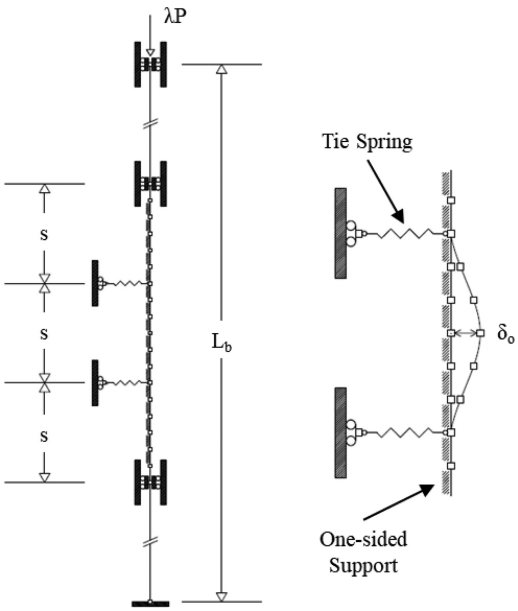

Figure 6. OpenSees buckling model.

spalling is typically observed at a strain of 0.002, which is near or below the strain at which inelastic buckling is expected to occur. To remain consistent with previous shear wall experiments the bar length, L_b, is set to 183 cm. Lateral tie elements are placed at an interval, s, that is varied for the different test cases. These tie elements are free to move in the vertical direction consistent with the movement of the longitudinal rebar at that point. This ensures that the resulting force from the tie remains horizontal. Buckling is expected to remain within a region of 3s, referred to as the Region of Interest (ROI). Elements within the ROI are free to displace laterally in one direction, with movement restricted in the other direction to represent stabilization from the concrete core and prevent the bar from buckling in an S-shape (i.e. a higher-mode shape). Rotation and lateral movement are restricted at the ends of the ROI and at the top node, with vertical displacement free. Vertical, lateral, and rotational displacement are fixed at the bottom node. Vertical load, P, with load factor, λ, are imposed on the top node. The ROI is divided into 36 elements. A corotational displacement formulation is used at the element-level to accommodate large expected displacements and rotations of the model. The elements use a force-based state determination with a Gauss-Lobatto curvature scheme using five integration points along the length of each element. A circular fiber section is assigned to each integration point to ensure accurate state determination. The Giuffré-Menegotto-Pinto (GMP) steel model with isotropic strain hardening is used for state determination of each fiber in the section. This steel model features a rounded transition from elastic to inelastic response, which is important for numerical stability of the model (Filippou F.C., Popov E.P., 1983).

A displacement-controlled integrator is chosen to accommodate sudden load drops often exhibited by compressive bifurcation and the residual equations are solved with the Newton-Raphson algorithm (Leon et al., 2011). This model is designed to allow buckling to progress as naturally as possible, however a slight flaw must be included to initiate instability. This is accomplished by imposing deformed shape with initial eccentricity, δ_o, to the node at mid-height of the bar.

2.2 *Cover model*

Strain hardening column cover materials are modeled simply as nonlinear springs placed at each node along the height of the buckling bar model. The procedure for assigning cover spring properties is outlined in Figure 7. Each spring is assigned a tributary area and material properties equivalent to the cover material being investigated. Tributary cover areas assigned to each spring are taken from dimensions of the reinforcement layout typical in a special shear wall boundary element (Figure 7(a)). The width of the tributary area is equal to the center-to-center spacing between adjacent longitudinal bars, and the height is equal to the length of the

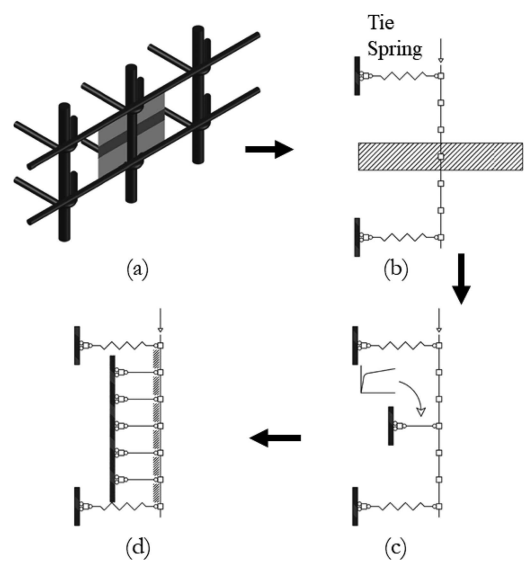

Figure 7. Cover spring development—(a) Reinforcement layout, (b) tributary area of cover spring, (c) material assignment, (d) repetition along length of longitudinal bar model.

element in the analysis model (Figure 7(b)). Equivalent tributary area and material model are assigned to each spring (Figure 7(c)), and springs are placed at each node along the length of the longitudinal bar (Figure 7(d)). Cover springs free to translate vertically along with nodes of the longitudinal bar model, which ensures cover forces remain horizontal. Cover material is added along the entirety of the ROI.

The constitutive model of the cover is based on test results of a HyFRC dogbone specimen tested in uniaxial tension under displacement control shown in Figure 5. The material behavior in tension is characterized by brief tension hardening following crack formation in the cementitious matrix from 0.06% strain to peak stress at 0.31% strain, followed by tension softening up to failure. Following acquisition of test data, a suitable material model was chosen. OpenSees contains a trilinear material model intended to represent fiber reinforced cementitious composites such as HyFRC called ECC0. This model can be accurately calibrated to fit test data. When tested with the buckling model, however, the sharp corners of this material model cause instability in the state determination of the cover spring elements. In order to mitigate this issue, the more stable GMP model is used to model spring behavior. Although this is intended to model steel materials, it can be modified to represent the behavior of HyFRC up to the point of strain softening. Comparison of the GMP and ECC0 models is shown in Figure 8.

2.3 *Test specimens*

Steel material properties and geometry for this investigation are chosen to match those from the previous shear wall study. The material is modeled as ASTM A706 Gr60 rebar with a tested yield strength of 468 MPa. Longitudinal bars have a diameter of 22.2 mm, and lateral ties a diameter of 12.7 mm. Ties

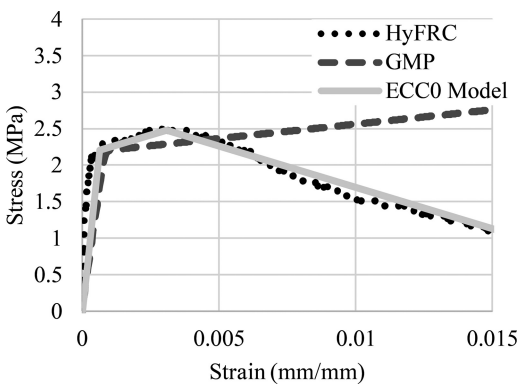

Figure 8. Calibration of HyFRC cover material model.

Table 3. Buckling model control specimen parameters.

ID	s/d_b –	s mm	δ_o mm	Cover –
C1	3	66.7	2.54	off
C2	4	88.9	0.254	off
C3	4.6	101.6	0.254	off
C4	6	133.4	0.254	off
C5	8	177.8	0.254	off
C6	10	222.3	0.254	off
C7	12	266.7	0.254	off

Table 4. Buckling model with HyFRC cover springs parameters.

ID	s/d_b –	s mm	δ_o mm	Cover –
F1	3	66.7	2.54	on
F2	4	88.9	1.27	on
F3	4.6	101.6	1.27	on
F4	6	133.4	1.27	on
F5	8	177.8	1.27	on
F6	10	222.3	1.27	on
F7	12	266.7	3.81	on

are placed at spacing, s, corresponding to s/d_b ranging from 3 to 12 as shown in Tables 3 and 4. The tie spacing of $s/d_b = 4.6$ is taken from the previous shear wall study and is included here for comparison. Initial eccentricity, δ_o, is not consistent for all test cases. In some cases, the value is increased to initiate buckling and prevent the solver from missing the lowest energy mode. Further study to investigate the bar's sensitivity to this eccentricity is required, but is not included here. Two series of tests are conducted in this study. The C-series (shown in Table 3) is the control, representing bars embedded in conventional RC with no cover modeled (as it is assumed to have spalled prior to rebar buckling) and the only restraint coming from lateral ties. The F-series (given in Table 4) includes distributed springs representative of the HyFRC cover in addition to lateral ties.

3 RESULTS AND DISCUSSION

3.1 *Test results*

C-Series and F-Series models are run up to a strain of 7.5%. Step sizes are adjusted for each model to achieve convergence. Given the unstable nature of this model, step sizes on the order of $L_o \times 10^{-5}$ are required to capture the buckling mode. Larger step sizes fail to converge or miss the lowest energy

buckling mode. Resulting Normalized Force vs. Normalized Displacement plots for each case in the C- and F-Series are given in Figure 9 and Figure 10, respectively. Each plot contains the steel response without buckling as a dotted line. The buckling stress as a function of tie spacing ratio for each case is shown in Figure 11 with a dotted line showing the

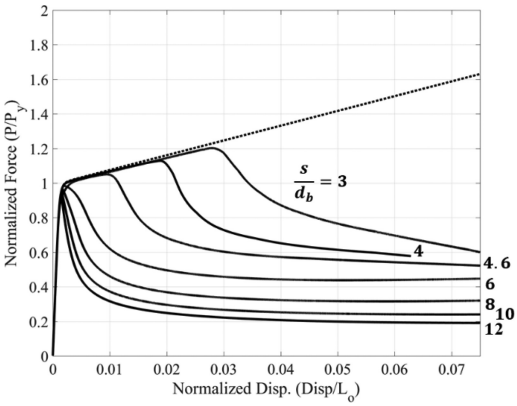

Figure 9. C-series – normalized force vs. normalized disp.

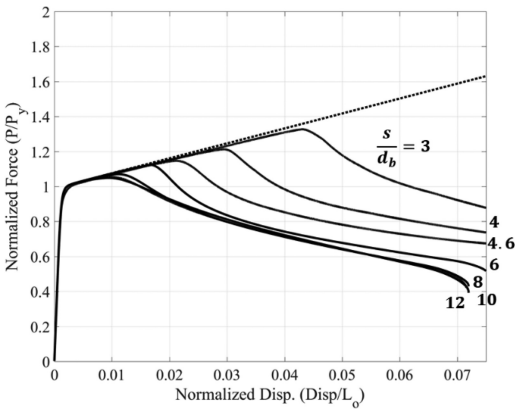

Figure 10. F-series – normalized force vs. normalized disp.

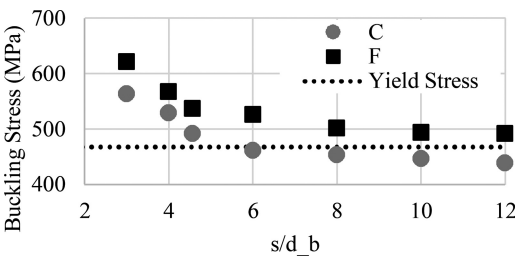

Figure 11. Buckling stress vs. tie spacing.

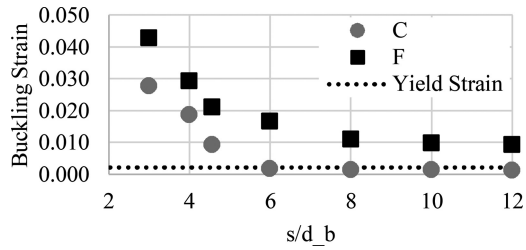

Figure 12. Buckling strain vs. tie spacing.

material yield stress. The buckling strain as a function of tie spacing ratio is given in Figure 12 with a dotted line showing the material yield strain.

3.2 *Discussion*

It is clear from Figure 9 that the lateral ties delay buckling and enable strain hardening for specimens C1, C2, and C3 with $s/d_b \leq 4.6$. Those specimens with $s/d_b \geq 6$, however, buckle right as the steel begins to yield and does not achieve hardening. This is not the case for the F-series, as shown in Figure 10. Here buckling is delayed past yield for all specimens, and as the tie spacing increases there appears to be a lower limit to the behavior. Comparing the stress at buckling in Figure 11 highlights the increased strength capacity of the F-series for all tie spacings. More importantly, Figure 12 shows the increase in ductility capacity of the F-series for all tie spacings. The data for the F-series appears to approach an asymptote at a strain of 1%, indicating that at some point the ties are no longer crucial in delaying buckling, but the cover is doing the majority of the work in stabilizing the bar.

4 CONCLUSIONS

The goal of restraining buckling is not to completely prevent bifurcation, but to delay it to the largest possible strains to take advantage of the hardening properties of the steel and maintain capacity up to high levels of strain. The results show that the conventional method of using ties achieves this to some extent for tight tie spacings. Important findings from this study are:

- In conventional RC, ties only delay rebar buckling for very short s/d_b ratios.
- The addition of a strain-hardening cover increases the buckling load for all specimens.
- The strain-hardening cover increases the buckling strain for all specimens, and shows an asymptote at a strain of 1%.
- The HyFRC cover alone may be sufficient to delay rebar buckling up to high strains.

The point of buckling onset in the model appears sensitive to the initial eccentricity given to the model. This eccentricity is increased in the HyFRC test cases to induce buckling. Parametric study on the eccentricity, number of elements, HyFRC tensile stiffness, rebar diameters, and other factors still needs to be conducted to construct a full understanding of the phenomena at play.

REFERENCES

Arteta, C.A., To, D.V, Moehle, J.P., 2014. Experimental response of boundary elements of code-compliant reinforced concrete shear walls, in: Tenth U.S. National Conference on Earthquake Engineering. Earthquake Engineering Research Institute, Anchorage, Alaska. doi:10.4231/D37H1DN29.

ASTM, 2005. C 1609/C 1609M-05 Standard Test Method for Flexural Performance of Fiber-Reinforced Concrete (Using Beam With Third-Point Loading) 1. *Astm* i, 1–8. doi:10.1520/C1609.

Blunt, J., Ostertag, C.P., 2009. Performance-Based Approach for the Design of a Deflection Hardened Hybrid Fiber-Reinforced Concrete. *J. Eng. Mech. 1*35, 978–986. doi:10.1061/(ASCE)0733–9399(2009)135: 9(978).

Blunt, J.D., Ostertag, C.P., 2009. Deflection Hardening and Workability of Hybrid Fiber Composites. *ACI Mater. J.* 106, 265–272.

Engesser, F., 1891. *Die Knickfestigkeit gerader Stäbe*. W. Ernst & Sohn, Berlin.

Filippou F.C., Popov E.P., B.V.V., 1983. Effects of Bond Deterioration on Hysteretic Behaviour of Reinforced Concrete Joints. Earthq. Eng. Res. Cent.

Leon, S.E., Paulino, G.H., Pereira, A., Menezes, I.F.M., Lages, E.N., 2011. A Unified Library of Nonlinear Solution Schemes. *Appl. Mech. Rev.* 64, 40803. doi:10.1115/1.4006992.

McKenna, F., Fenves, G.L., Scott, M.H., Jeremic, B., 2000. Open system for earthquake engineering simulation (OpenSees).

Nguyen, W., Trono, W., Panagiotou, M., Ostertag, C.P., 2017. Seismic response of a rocking bridge column using a precast hybrid fiber-reinforced concrete (HyFRC) tube. *Compos. Struct.* 174, 252–262. doi:10.1016/j.compstruct.2017.04.058.

Panagiotou, M., Trono, W., Jen, G., Kumar, P., Ostertag, C.P., 2014. Experimental Seismic Response of Hybrid Fiber-Reinforced Concrete Bridge Columns with Novel Longitudinal Reinforcement Detailing. *ASCE J. Bridg. Eng.* 20. doi:10.1061/(ASCE) BE.1943–5592.0000684.

Segura, C.L., Wallace, J.W., 2016. Deformation capacity of thin reinforced concrete shear walls (pp. O-64), in: 2016 NZSEE Conference. New Zealand Society for Earthquake Engineering Inc., pp. 1–8.

Sritharan, S., Beyer, K., Henry, R.S., Chai, Y.H., Kowalsky, M., Bull, D., 2014. Understanding poor seismic performance of concrete walls and design implications. *Earthq. Spectra* 30, 307–334. doi:10.1193/021713EQS036M.

Timoshenko, S., Gere, J.M., 1961. *Theory of elastic stability*. Dover Publications.

Williams, I.D., Arteta, C.A., Ostertag, C.P., 2017. Experimental Response of a HyFRC Boundary Element Under Pure Compression, in: 16th World Conference on Earthquake Engineering. Santiago, Chile, p. Paper 1092.



Taylor & Francis
Taylor & Francis Group
http://taylorandfrancis.com

Computational Modelling of Concrete Structures – Meschke, Pichler & Rots (Eds)
© 2018 Taylor & Francis Group, London, ISBN 978-1-138-74117-1

Analysis of RC frame corners using CDP model

M. Szczecina
Faculty of Civil Engineering and Architecture, Kielce University of Technology, Kielce, Poland

A. Winnicki
Faculty of Civil Engineering, Cracow University of Technology, Cracow, Poland

ABSTRACT: The paper presents results of computations of reinforced concrete frame corners under opening bending moment. Such corners require an optimal and carefully thought reinforcement, which fulfils both ULS and SLS. The paper is a continuation of research which was presented at the previous Euro-C 2014 Conference. Authors decided to analyze both corners with the same and with different section heights of elements joining in corner. FEM analyses in Abaqus were performed using CDP model. Efficiency factors of corners were established and, moreover, history of loading, yielding of steel and crack development were recreated. Finally, the authors compared efficiency factors of the corner for different reinforcement details in plane stress and plane strain state to recommend the most preferable reinforcement detail.

1 INTRODUCTION

Reinforced concrete corners under opening bending moment are a very common case in structural design, for example in frames, retaining walls and tanks. In these corners the Bernoulli's principle is not fulfilled and distributions of both strain and stress are non-linear and complicated even for elastic material, so a designer should base the choice of reinforcement detail on handbook rules, on results of laboratory tests (Mayfield 1972, Skettrup et al. 1984) and also on numerical models. There are also strong evidences (McGregor 2004, Campana et al. 2013) that the use of too large reinforcement ratio leads to a significant decrease of efficiency factor of a corner.

The paper is a continuation of research which was presented at the previous Euro-C 2014 Conference (Szczecina & Winnicki 2014). Authors decided to perform numerical calculations of frame corners in FEM in Abaqus using Concrete Damaged Plasticity (CDP) model for concrete. Thanks to this analysis it was possible to check both ULS and SLS. Efficiency factors of each detail of corner reinforcement were established and, moreover, history of loading, yielding of steel and crack development were recreated. Finally, the authors analyzed the influence of reinforcement ratio on the gained efficiency factor.

In order to make reliable computations authors analyzed some input material parameters of CDP model, first of all dilation angle ψ for plastic flow in the p-q plane and relaxation time. These parameters were calibrated in Abaqus in simple numerical tests, namely in uniaxial tension and biaxial compression and then compared with result of laboratory tests of (Woliński 1991, Kupfer 1973). Additionally, the following issues were analyzed in tension test:

- size effect,
- mesh size sensitivity,
- use of notched and unnotched specimens.

One of the most important parameters which describes the effectiveness of used reinforcement detail is the efficiency factor. Authors of the paper focused on two issues:

- calculation of the efficiency factor for each reinforcement detail,
- conclusion which of the details is the most preferable.

The second issue is particularly important for corners with different section heights of elements joining in corner, because this situation is not described in Eurocode 2 and is very rarely presented in handbooks for designers.

Authors of the paper selected some reinforcement details of the corners, namely:

- the corner without any additional stirrups and diagonal bars,
- one diagonal bar as additional reinforcement,
- one diagonal stirrup as additional reinforcement,
- the corner with three parallel diagonal stirrups,
- the corner with three fan-shaped stirrups,
- combination of a diagonal bar and three diagonal stirrups.

2 CDP MODEL IN ABAQUS

Authors of the paper decided to perform FEM calculations in Abaqus. In this code there are three different models for definition of the tensile and compressive behavior of concrete:

- Concrete Damaged Plasticity (CDP),
- cracking model for concrete,
- concrete smeared cracking.

Authors decided to choose the Concrete Damaged Plasticity (CDP) Model. The CDP was theoretically described by Lubliner et al. (1989, 1990) as so called "Barcelona model" and developed by Lee and Fenves (1996, 1998).

The main assumptions of this model are listed as follows:

- there are two damage mechanisms: tensile cracking and compressive crushing of concrete,
- material stiffness is reduced by two damage parameters, d_t for tension and d_c for compression,
- the yield function is specified according to Lubliner (1989) and the flow potential is a hyperbolic function (Abaqus User Manual),
- the plastic flow is nonassociated.

The postfailure stress-displacement curve of concrete for uniaxial tension can be defined in Abaqus in the following ways:

- by specifying the relationship between cracking strain and yield stress in uniaxial tension,
- by specifying the relationship between cracking displacement (crack width) and yield stress,
- by defining the fracture energy G_f and yield stress.

The equations of the multiaxial behavior, the yield function in CDP model and the flow potential function are listed below respectively:

$$\boldsymbol{\sigma} = (1-d)\mathbf{D}_{\mathbf{0}}^{\mathbf{el}} : (\varepsilon - \varepsilon_{pl}) \tag{1}$$

$$F = \frac{1}{1-\alpha}\left(\bar{q} - 3\alpha\bar{p} + \beta(\tilde{\varepsilon}_{pl})\left\langle\hat{\bar{\sigma}}_{\max}\right\rangle - \gamma\left\langle -\hat{\bar{\sigma}}_{\max}\right\rangle\right) - \bar{\sigma}_c(\tilde{\varepsilon}_{pl}) = 0 \tag{2}$$

$$G = \sqrt{(\varepsilon\sigma_{t0}\tan\psi)^2 + \bar{q}^2} - \bar{p}\tan\psi \tag{3}$$

where $\boldsymbol{\sigma}$ is a stress tensor, $\mathbf{D}_{\mathbf{0}}^{\mathbf{el}}$ denotes initial elasticity matrix, d is the damage parameter, α, β and γ are parameters of the yield surface, $\bar{p}$ is the hydrostatic equivalent pressure stress, $\bar{q}$ is von Mises equivalent effective stress, ε is flow potential eccentricity and ψ is dilation angle.

The yield function is presented in the plane stress state in the Figure 1, the plastic potential function is shown in the Figure 2.

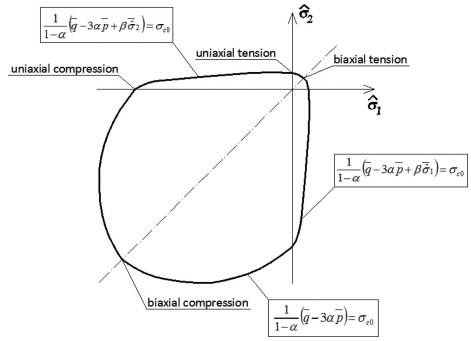

Figure 1. Yield function in the plane stress state.

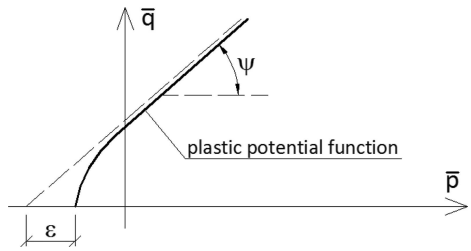

Figure 2. Plastic potential function in meridian plane.

It is also possible to apply the viscoplastic regularization in CDP model according to Duvaut-Lions (1976) approach. Rate of change of plastic viscous strains can be derived from formula (4):

$$\dot{\varepsilon}_v^{pl} = \frac{1}{\mu}\left(\varepsilon^{pl} - \varepsilon_v^{pl}\right) \tag{4}$$

where μ denotes relaxation time (in Abaqus called "viscosity parameter").

It is easy to establish a majority of CDP parameters except the dilation angle and the relaxation time. The choice of values of ψ and μ is still an open scientific issue. A proper calibration of these two parameters should be performed to gain realistic results for RC elements. The following section of the paper is fully dedicated to this issue.

3 CALIBRATION OF CDP PARAMETERS

As pointed out in the Section 2, there is a need to establish proper values of two crucial parameters of CDP Model, namely relaxation time and dilation angle. As regards the dilation angle of concrete there are many different values which were proposed, some of them are listed in the Table 1.

Similar situation occurs for the value of relaxation time. Some authors (Genikomsou & Polak

Table 1. Values of dilation angle assumed in works of different authors.

Author	Dilation angle [degrees]
Jankowiak 2010	49
Polak, Genikomsou 2014	38
Mostafiz et al. 2017	38
Malm 2009	25÷38
Menetrey 1994	10
Mostofinejad and Saadatmand 2010	0
Marzec 2008	8 or 10
Rodriguez et al. 2013	30

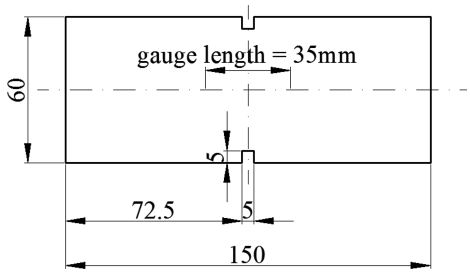

Figure 3. Specimen in uniaxial tension test.

2014, 2015, Pereira et al. 2015) suggest values from 10^{-5} s to 10^{-4} s. Both relaxation time and dilation angle should be properly calibrated and therefore authors of the paper performed numerically two simple tests:

– uniaxial tension test to establish the value of relaxation time,
– uniaxial and biaxial compression test to establish the value of dilation angle.

3.1 *Uniaxial tension test*

The geometry of specimen in uniaxial tension test is presented in the Figure 3. The specimen was modeled with 2D elements in plane stress state. Two notches allowed to impose one crack localized in a vertical symmetry axis of specimen. Properties and geometry of the specimen were taken from Woliński's research (1991). Displacement was imposed at the right edge whereas the left edge was fixed. The material properties for the specimen were as follows: $f_c = 34.30$ MPa, $f_t = 3.5$ MPa, $E_c = 35$ GPa, $\nu_c = 0.167$.

For the specimen under tension the tensile behavior of concrete was assumed in four different manner, namely:

– version 1. – as a set of points on σ–u_{cr} curve taken from Woliński's research,

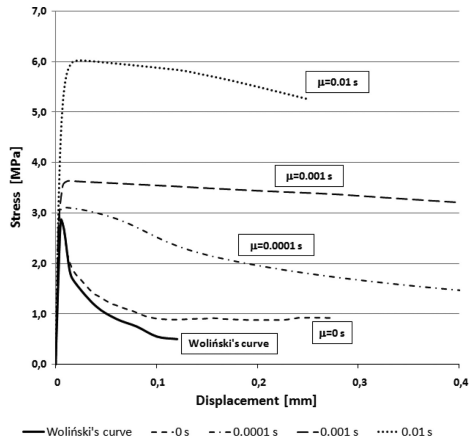

Figure 4. Stress vs displacement in uniaxial tension test.

– version 2. – as a bilinear relationship between crack width and stress according to Model Code (2010),
– version 3. – as a set of points on σ–u_{cr} curve after authors' modification for better fit to Wolinski's curve,
– version 4. – value of fracture energy $G_f = 120.7$ Nm^{-1} according to Wolinski's results.

For the sake of brevity in the paper results only for versions 1. and 4. are presented. The obtained results for versions 2. and 3. are quite similar in the qualitative sense.

The value of relaxation time was assumed from 0 through 0.0001s, 0.001 s until 0.01 s. The loading time was assumed as 1 s.

3.1.1 *Results of uniaxial tension test for various relaxation time*

The relationship between stress and displacement for the notched specimen and various relaxation time is presented in the Figure 4 and compared with Woliński's experimental curve. These results are gained form 1 mm mesh size and the version 1. of concrete tension behavior. The relatively large values of relaxation time, namely 0.001 s and 0.01 (for loading time t = 1 s) cause too optimistic results for tension strength. Therefore authors of the paper recommend the value of relaxation time not larger than 0.0001s for loading time t = 1 s.

3.1.2 *Results of uniaxial tension considering size effect*

Authors of the paper considered also a size effect for specimens under tension. Stress-displacement curves for version 1. and 4. are presented

in the Figures 5 and 6 respectively. The curves corresponding to original size and two or four times larger specimen are labeled. For both versions a peak of stress is the same and the only differences appear in the post-critical range. Authors' numerical results confirm that for local material formulation, which is the case of CDP model in Abaqus, size effect cannot be properly reproduced.

3.1.3 *Results of uniaxial tension considering mesh sensitivity*

Stress-displacement relationship for different mesh size in the versions 1 and 4 is presented in the Figures 7 and 8 respectively. The original mesh size was 1 mm, then 2 mm and 5 mm meshes were analyzed. There are some slight differences between all three curves gained in Abaqus for both versions, nevertheless the mesh-independent results are obtained in uniaxial tension in Abaqus.

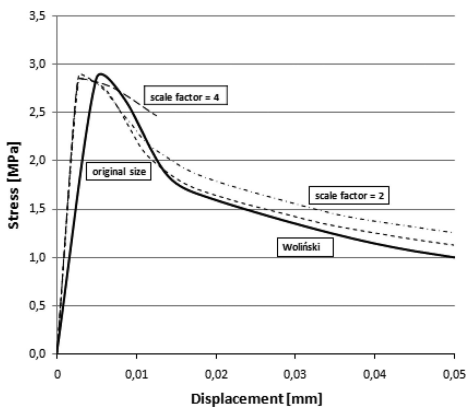

Figure 5. Stress-displacement relationship in tension test for different specimen size in version 1.

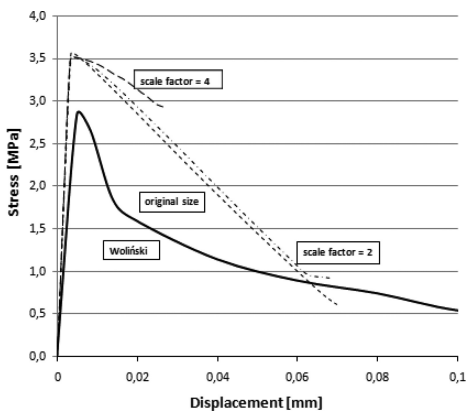

Figure 6. Stress-displacement relationship in tension test for different specimen size in version 4.

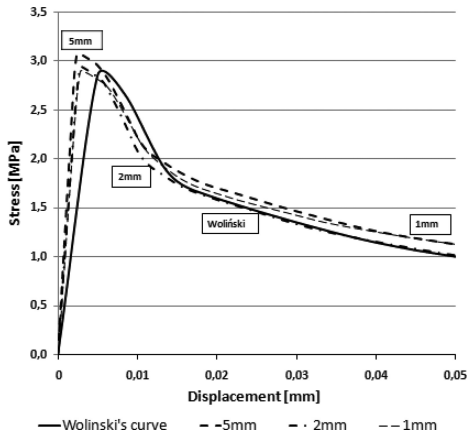

Figure 7. Stress-displacement relationship in tension test for different mesh size in version 1.

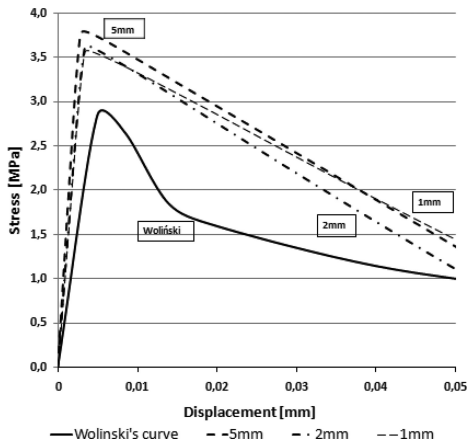

Figure 8. Stress-displacement relationship in tension test for different mesh size in version 4.

3.1.4 *Results of uniaxial tension for notched and unnotched specimen*

Authors of this paper performed also calculations for the unnotched specimen to find out what are the values of stress in this case. Finite elements in the middle of the specimen close to the edge had a tensile strength 0.9 f_t in order to force a crack in the middle of the specimen. Stress-displacement relationships are compared for notched and unnotched specimens in the Figures 9 and 10 for version 1 and 4 respectively. There is no clear difference between both curves and the peak of stress is the same for both versions.

3.2 *Uniaxial and biaxial compression test*

The geometry and boundary conditions of specimen under compression is shown in the Figure 11.

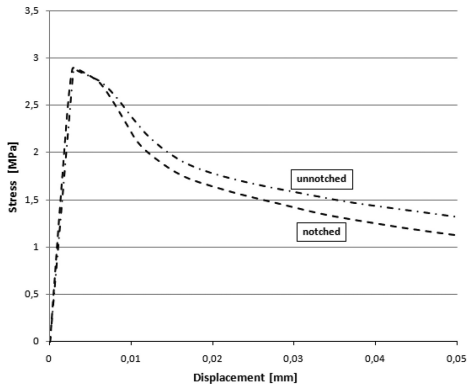

Figure 9. Stress-displacement relationship for notched and unnotched specimen—version 1.

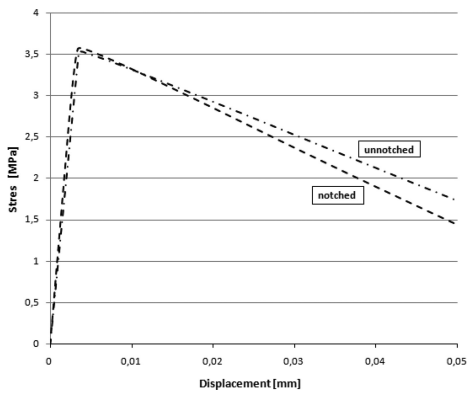

Figure 10. Stress-displacement relationship for notched and unnotched specimen—version 4.

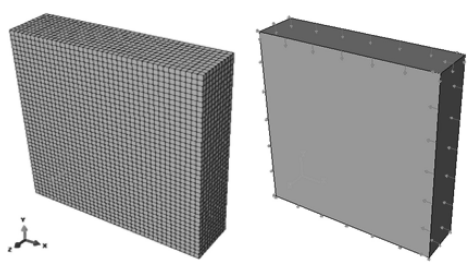

Figure 11. Specimen in compression test.

Displacement was imposed either at the top edge (for uniaxial compression) or at both the top and right edges (for biaxial compression). Stress-strain curve in uniaxial compression was calibrated to match experimental results of Kupfer.

The material properties for the specimens were as follows: f_c = 34.30 MPa, f_t = 3.5 MPa, E_c = 35 GPa, ν_c = 0.167. Authors of the paper tested various values of dilation angle, namely: 0, 5, 15 and 30 degrees. The other values of CDP parameters were assumed as follows: fracture energy 120.7 Nm^{-1}, eccentricity ε = 0.1, fb0/fc0 = 1.16, K = 0.667. The main goal of this test it to establish a reasonable value of dilation angle. For biaxial test two different cases were taken into consideration, namely 1:1 and 1:0.5 tests, where ratios 1:1 and 1:0.5 mean proportion between imposed displacements in two perpendicular directions in a loading plane.

In the Figures 12 to 14 the relationship between volumetric strain ε_v and linear strain ε_{11} is presented. Each graph contains also the relationship obtained in Kupfer's laboratory tests. In numerical computations volumetric strains remain negative for dilation angle in range 0–15 degrees. For dilation angle equal to 30 degrees excessive dilatancy is observed (large positive values of volumetric strains in postcritical range). Therefore authors of the paper recommend to set low values of dilation angle, for example 5 degrees.

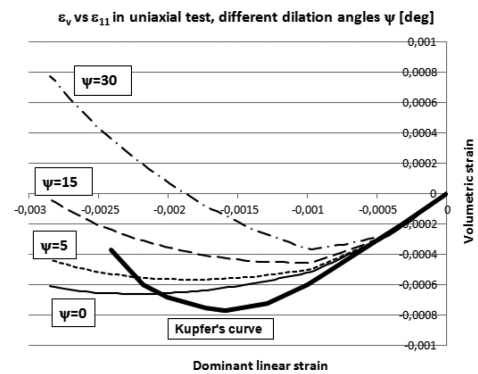

Figure 12. Volumetric strain in uniaxial compression test.

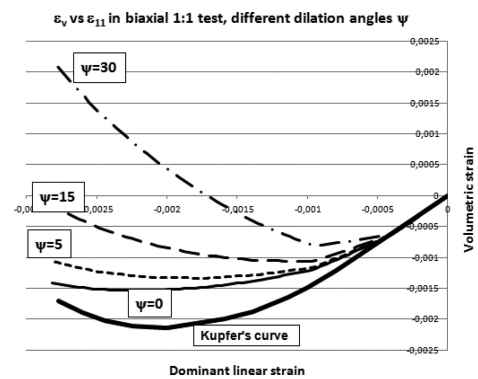

Figure 13. Volumetric strain in biaxial 1:1 compression test.

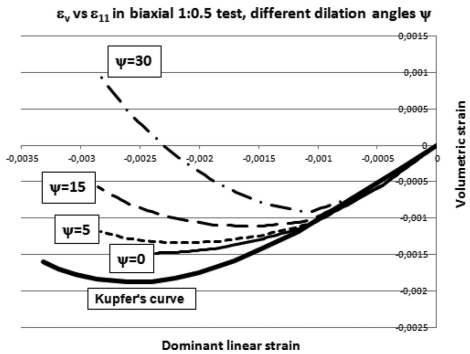

Figure 14. Volumetric strain in biaxial 1:0.5 compression test.

4 RC FRAME CORNERS TAKEN TO ANALYSIS

Two different cases of RC corners were taken into consideration, namely with the same and different cross sections of a beam and a column joining in the corner—see Figs. 15 and 16, dimensions are in [mm]. The main reinforcement of columns and beams was assumed as follows:

- four bars ϕ20 in the beam and the same in the column for the case of the same cross sections,
- four bars ϕ12 in the beam and four bars ϕ20 in the column for the case of the different cross sections.

All corners are made of concrete C40/50 and reinforced with steel B500SP. The material constants were taken according to Eurocode 2 or Model Code 2010:

- concrete: $f_c = 34.30$ MPa, $E_c = 35$ GPa, $\nu = 0.167$, $f_{ct} = 3.5$ MPa, $G_f = 146.5$ N/m,
- steel: $f_y = 434.8$ MPa, $E_s = 200$ GPa, $\nu = 0.3$.

Authors of the paper considered seven different reinforcement details, which are shown in the Fig. 17. The setup of reinforcement in detail 7. is an original idea of authors, and the rest of details were taken from laboratory tests of Mayfield et al. (1972) and Skettrup et al. (1984). In this paper the details were applied for both cases of cross sections.

All the corners were subjected to an opening bending moment M = 30 kNm. Calculations were performed in FEM in Abaqus and the assumed model for concrete was Concrete Damaged Plasticity (CDP) and for reinforcing steel—classical metal plasticity (von Mises yield criterion). Concrete corner was modeled with 2D quadrilateral elements and reinforcing steel was modeled with 1D beam elements. Size of finite elements for concrete varied from 5 and 10 to 20 mm (see Fig. 18). For reinforcing steel it was constant and equal to

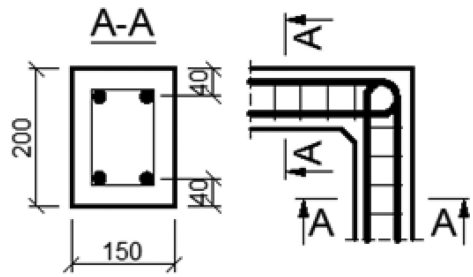

Figure 15. Geometry and reinforcement of RC corner in the case of the same cross sections.

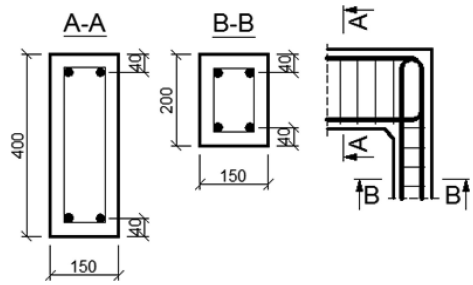

Figure 16. Geometry and reinforcement of RC corner in the case of the same cross sections.

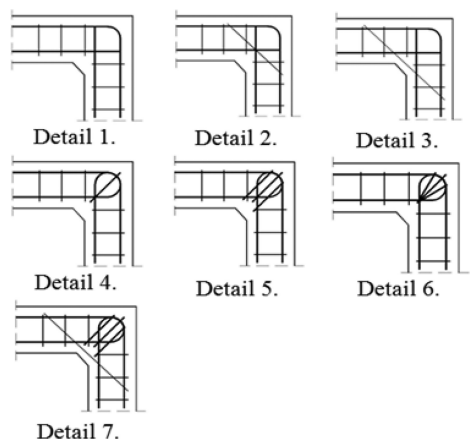

Figure 17. Reinforcement details taken to analysis.

10 mm (Fig. 19). The full bond of steel and concrete was assumed, which is called "embedded region" in Abaqus code.

Solution of non-linear problem was performed with incremental Newton-Raphson method. Maximal load parameter was assumed as $\lambda = 2$, where $\lambda = 1$ corresponds to bending moment M = 30 kNm. Calculations were performed both in plane stress

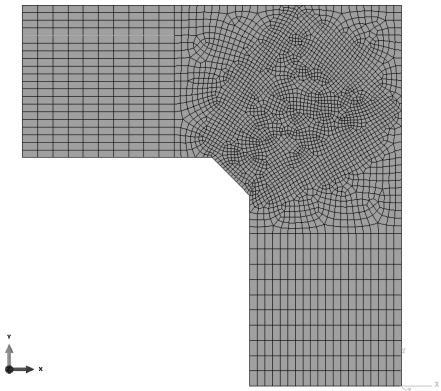

Figure 18. Reinforcement details taken to analysis.

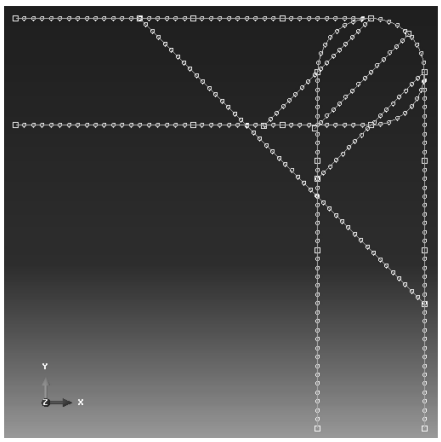

Figure 19. Reinforcement details taken to analysis.

and plane strain state. Tensile behavior of concrete was defined by the fracture energy $G_f = 146.5$ N/m and yield stress 3.5 MPa. After the calibration of CDP parameters the value of relaxation time was assumed as 0.0001s and the value of dilation angle as 15 degrees.

5 RESULTS OF FEM CALCULATIONS

As mentioned above, calculations in FEM in Abaqus allow to check both ULS and SLS. It is also possible to calculate efficiency factor of each reinforcement detail of the corner. This factor can be obtained according to the formula:

$$\eta = \frac{M_{failure}}{M_{capacity}} \tag{5}$$

where $M_{failure}$ denotes opening bending moment causing failure of the corner and $M_{capacity}$ is bearing capacity of the corner in bending.

In the Fig. 20 to 23 equivalent plastic strains in tension for reinforcement details 3. and 7. and the same cross sections are presented. Those details were selected deliberately to show the difference between crack propagation if diagonal stirrups are used (detail 7.) or not. Note that PEEQT output variable in Abaqus denotes not only equivalent plastic strains in tension, but also indicates propagation of cracks in concrete. It can be observed that the use diagonal stirrups is preferable to reduce the propagation of cracks. Furthermore, PEEQT are shown both in plane stress and plane strain state and there is no greater difference between crack patterns in both states.

Figures 24 to 27 present also PEEQT for details 3. and 7. but this time for the case of different cross sections. The overall effect of the use of diagonal stirrups is the same as for the case of the same cross sections, namely a significant reduction of crack propagation. Note that in plane strain state for both details the crack propagation appears on a larger

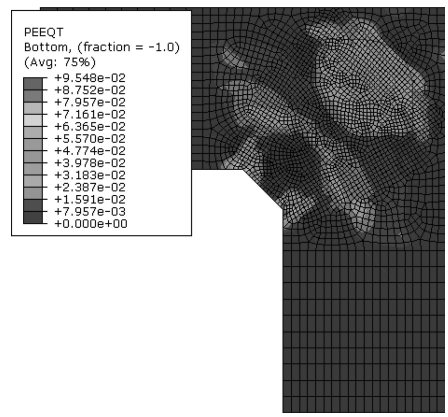

Figure 20. PEEQT for detail 3. in plane stress state—the same heights.

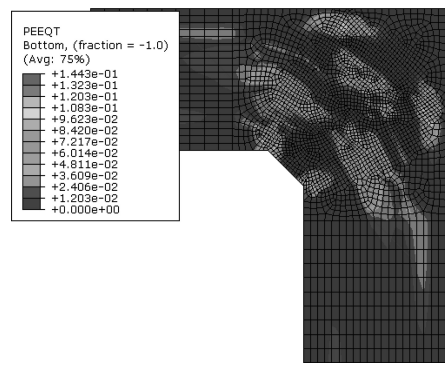

Figure 21. PEEQT for detail 3. in plane strain state—the same heights.

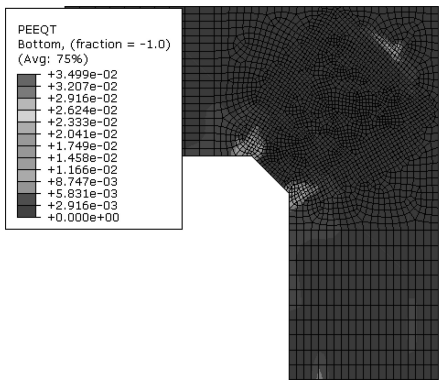

Figure 22. PEEQT for detail 7. in plane stress state—the same heights.

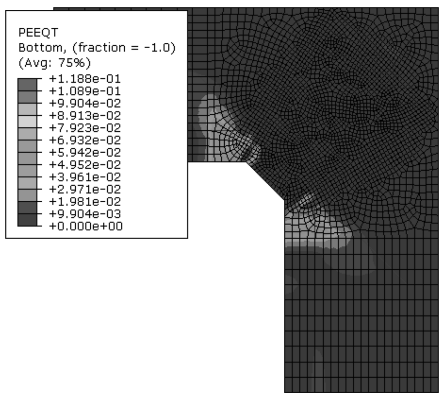

Figure 23. PEEQT for detail 7. in plane strain state—the same heights.

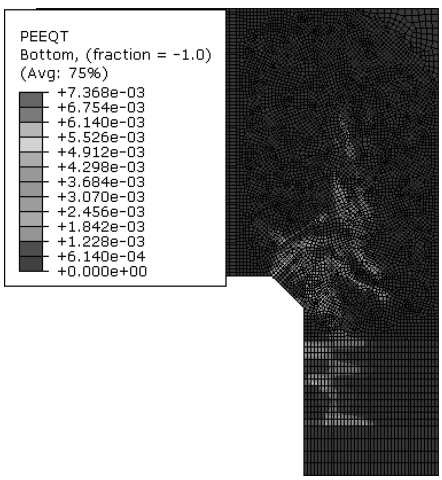

Figure 24. PEEQT for detail 3. in plane stress state—different heights.

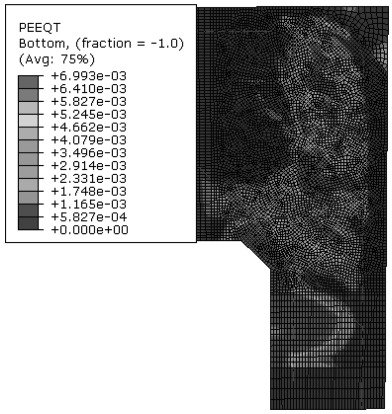

Figure 25. PEEQT for detail 3. in plane strain state—different heights.

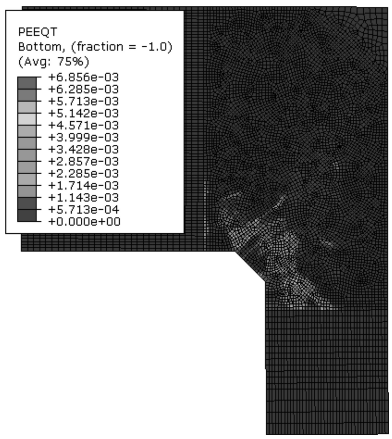

Figure 26. PEEQT for detail 7. in plane stress state—different heights.

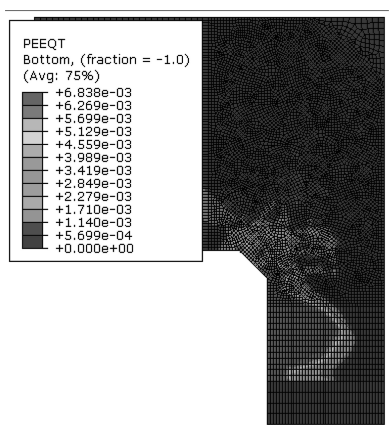

Figure 27. PEEQT for detail 7. in plane strain state—different heights.

area, especially for detail 3., where many diagonal cracks occur in the reflex angle and in the corner. For detail 7. in plane strain state a very strong cracking occurs indeed, but mainly outside the corner (in column). That is also an evidence that the use of diagonal stirrups is advisable.

Thanks to PEEQT it is possible to calculate crack width in each step of FEM analysis. The relationship between crack width and load parameter λ is presented in the Fig. 28 to 31. A vertical solid line represents a very common value of permissible crack width according to codes. It is clear that the use of diagonal stirrups allows to reduce the crack width.

In the Table 2. efficiency factors for all reinforcement details are presented. The factors obtained in the plane stress state for both cases confirm that the use of diagonal stirrups ensures very favorable efficiency factors. In plane strain state, however, efficiency factors are greater than 1 also for details 1. to 3. It means that for those details crack width is decisive to calculate required reinforcement.

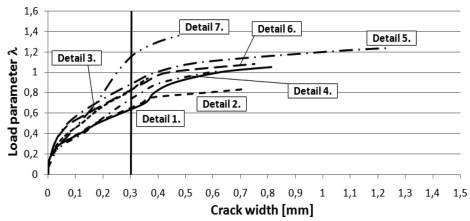

Figure 28. Crack width vs load parameter in plane stress state and the same cross sections case.

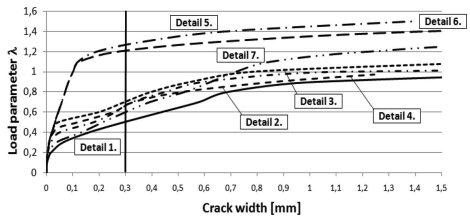

Figure 29. Crack width vs load parameter in plane strain state and the same cross sections case.

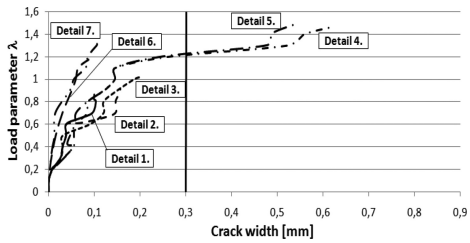

Figure 30. Crack width vs load parameter in plane stress state and different cross sections case.

In the Table 3. authors of the paper compared efficiency factors obtained in FEM with factors taken from laboratory tests of other authors. Concerning experimental results it is worth noticing that for details 1., 2., 4. and 5. the obtained efficiency factors are considerably smaller than those obtained from FEM. For details 3., 6. and 7. the efficiency factors coming from experiments are fairly close to those from FEM.

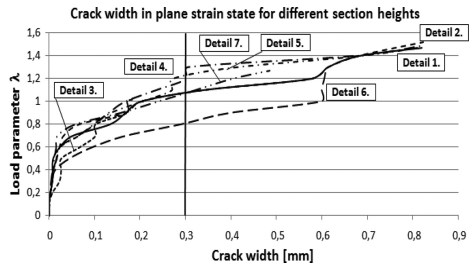

Figure 31. Crack width vs load parameter in plane strain state and different cross sections case.

Table 2. Efficiency factors of reinforcement details obtained in FEM calculations.

Detail No	The same cross sections case		Different cross section case	
	FEM plane stress	FEM plane strain	FEM plane stress	FEM plane strain
1.	0.81	1.20	0.86	1.20
2.	0.79	1.17	0.63	1.25
3.	0.83	1.26	0.81	1.24
4.	1.21	1.32	1.21	1.47
5.	1.25	1.35	1.23	1.38
6.	1.27	1.32	1.17	1.22
7.	1.23	1.49	1.20	1.26

Table 3. Efficiency factors obtained in laboratory tests and FEM calculations for the same cross sections.

Detail No	Laboratory tests	FEM plane stress	FEM plane strain
1.	0.43 (Mayfield et al. 1972) 0.66 (Kordina & Wiedemann 1978)	0.81	1.20
2.	0.58 (Mayfield et al. 1972) 0.55 (Skettrup et al. 1984)	0.79	1.17
3.	1.07 (Moretti & Tassios 2011)	0.83	1.26
4.	0.88 (Mayfield et al. 1972)	1.21	1.32
5.	0.78 (Mayfield et al. 1972)	1.25	1.35
6.	1.32 (Kordina & Wiedemann 1978) 1.13 (Skettrup et al. 1984)	1.27	1.32
7.	1.12 (Moretti & Tassios 2011)	1.23	1.49

6 CONCLUSIONS

Results of calculations presented in the paper allow to draw the following conclusions:

– some parameters of CDP model in Abaqus code, e.g. dilation angle and relaxation time demand a proper calibration,
– authors of the paper determined the proper values of those parameters as follows: relaxation time not larger than 0.0001s for loading time t = 1 s and dilation angle not larger than 15 degrees,
– CDP model reproduces well the behavior of corners under opening moment both for the same and different cross sections cases,
– the use of diagonal stirrups (details 4. to 7.) is recommendable because of relatively high values of the efficiency factor as well a significant reduction of crack propagation and crack width.

REFERENCES

2010. *The fib Model Code for Concrete Structures 2010*, Ernst&Sohn (A Wiley Brand): Berlin.

Abaqus/CAE ver. 6–12.2, Dassault Systemes Simulia Corp., 2012.

Abaqus 6.12 Analysis User's Manual, 2012.

Campana, S., Ruiz Fernandez, M., Muttoni, A. 2013. Behaviour of nodal regions of reinforced concrete frames subjected to opening moments and proposals for their reinforcement, *Engineering Structures*, 51: 200–210.

EN1992-1-1 (2004) Eurocode 2 – Concrete structure – Part 1–1: General rules and rules for buildings.

Genikomsou, A., Polak M.A., 2015. Finite element analysis of punching shear of concrete slabs using damaged plasticity model in ABAQUS, *Engineering Structures*, 98: 38–48.

Genikomsou, A., Polak, M.A., 2014. FEA of RC slabs under static and cyclic loadings based on damage plasticity model, *Proceedings 8th International Conference AMCM 2014*: 210–218, Wrocław.

Jankowiak, T., 2010. *Kryteria zniszczenia betonu poddanego obciążeniom quasi-statycznym i dynamicznym (Damage criteria of concrete under dynamic and quasi-static load*, in Polish), PhD thesis, Poznań University of Technology: Poznań.

Kordina K., Wiedemann G., 1978. *Forschungsvorhaben V 112. 1 A/DAfStb. Bewehrungsführung in Rahmenecken*. Technische Universitat Braunschweig: Braunschweig.

Kupfer, H. 1973. *Das Verhalten des Betons Unter Mehrachsiger Kurzzeitbelastung Unter Besonderen Berücksichtigung der Zweiachsigen Beanspruchung*. Verlag von Wilhelm Ernst und Sohn: Berlin.

Lee, J., 1996. *Theory and implementation of plastic-damage model for concrete structures under cyclic and dynamic loading*. PhD thesis, University of Berkeley: Berkeley.

Lee, J., Fenves, G.L., 1998. *Plastic-Damage Model for Cyclic Loading of Concrete Structures*. Journal of Engineering Mechanics, 124: 892–900.

Lubliner, J., Oliver, J., Oller, S., Oñate, E., 1989. *A plastic-damage model for concrete*, International Journal of Solids Structures, 25: 229–326.

Lubliner, J., Oliver, J., Oller, S., Oñate, E., 1990. *Finite element nonlinear analysis of concrete structures using a "plastic-damage model"*, Engineering Fracture Mechanics, 35: 219–321.

MacGregor, J. 2004. *Reinforced Concrete. Mechanics and Design*. Prentice Hall: New Jersey.

Malm, R., 2009. *Predicting shear type crack initiation and growth in concrete with non-linear finite element method*, PhD thesis, Royal Institute of Technology: Stockholm.

Marzec, I., 2008. *Zastosowanie modelu sprężysto-plastycznego betonu z degradacją sztywności i nielokalnym osłabieniem do modelowania elementów betonowych cyklicznie obciążonym (Application of elastic-plastic model of concrete with stiffness degradation and non-local softening to model concrete elements under cyclic load*, in Polish). PhD, Gdańsk University of Technology: Gdańsk.

Mayfield, B., Kong, F.K. & Bennison, A. 1972. Strength and Stiffness of Lightweight Concrete Corners, *ACI Journal* 69(7): 420–427.

Menetrey, P., 1994. *Numerical analysis of punching failure in reinforced concrete structures*, PhD, Ecole Polytechnique Federale de Lausanne: Lausanne.

Moretti, M., Tassios, T.P., 2011. Detailing of Corner Joints Under Opening Moment. *Proceedings of fib Symposium*, Prague.

Mostafiz, E., Al Azad, A., Shahin, H.M., Al Shafian, S., 2017. Numerical Analysis of a Reinforced Concrete Slab Column Connection Subjected to Lateral & Vertical Loading, *Proceedings of the International MultiConference of Engineers and Computer Scientists IMECS 2017*, Hong-Kong.

Mostofinejad, D., Saadatmand, H. 2010. *A Procedure for Predicting the Behavior of FRP Confined Concrete Using the FE Method*. Transaction A: Civil Engineering, Sharif University of Technology, 17(6): 471–481.

Pereira, H.F.S.G., Cunha, V.M.C.F., Sena-Cruz, J., 2015. *Numerical simulation of galvanized rebars pullout*. Frattura ed Integrità Strutturale, 31: 54–66, Gruppo Italiano Frattura: Cassino.

Rodríguez, J., Martínez, F., Martí, J., 2013. *Concrete Constitutive Model, Calibration and Applications*. 2013 SIMULIA Community Conference: Wien.

Skettrup, E., Strabo, J., Andersen, J.H. & Brondum-Nielsen, T. 1984. Concrete Frame Corners, *ACI Journal* 81(6): 587–593.

Szczecina, M., Winnicki, A. 2014. FEM and Strut-and-Tie analysis of RC frame corners under opening bending moment. *Computational Modelling of Concrete Structures: Proceedings of EURO-C 2014, St. Anton Am Arlberg, Austria, 24–27 March 2014,* 2: 1041–1050.

Woliński, Sz. 1991. *Własności betonu rozciąganego i ich zastosowania w nieliniowej mechanice pękania (Properties of concrete under tension and their use in non-linear fracture mechanics*, in Polish). Rzeszów University of Technology: Rzeszów.

Computational Modelling of Concrete Structures – Meschke, Pichler & Rots (Eds)
© 2018 Taylor & Francis Group, London, ISBN 978-1-138-74117-1

Probabilistic cracking model for macrocrack propagation in reinforced concrete structures

P. Rossi, C. Nader & J.L. Tailhan
Institut Français des Sciences et Technologies des Transports, de l'Aménagement et des Réseaux (IFSTTAR), Université Paris-Est, France

ABSTRACT: This paper presents the numerical modelling (finite elements) of the macrocrack propagation in a very large Double Cantilever Beam specimen (DCB specimen usually used in the framework of Fracture Mechanics studies) containing rebars. This numerical modelling is based on three non-linear models: a probabilistic semi-explicit model for concrete cracking, the use of interface elements with a Morh-Coulomb law for steel/concrete bond and an elastic perfect plastic behaviour for the rebars. Relevant results in terms of global behaviour, macrocracking of the DCB specimen and of macrocraking information are obtained

1 INTRODUCTION

IFSTTAR, the French Institute of Science and Technology for Transports, Development and Networks, has been developing recently a probabilistic semi-explicit cracking model for concrete. But, this model has not been still validated for studying macrocrack propagation in a reinforced concrete structure. Concerning the modelling of the concrete/steel bond, two modelling strategies were also recently introduced (Phan & et al. (2013 a, b), Phan, Tailhan & Rossi (2015)):

1. The concrete-rebar bond is represented by interface elements. Their behaviour is described with a simple deterministic damage model with only two parameters, cohesion and slip (i.e. relative tangential displacement between steel and concrete).
2. The notches/indentations are explicitly modeled along the whole length of the rebar with a perfect bond between concrete and rebar.

Both of these modelling strategies analyze cracking behaviour in reinforced concrete structures by explicitly modelling the rebar and the steel-concrete bonds (whether via interface elements or explicitly modeled notches/indentations). The second modeling strategy, which is more local, is very interesting because it yields reliable information about the cracking process of a tie-beam in case of lack of p experimental data.

2 THE PROBABILISTIC SEMI-EXPLICIT CRACKING MODEL AND THE STEEL-CONCRETE BOND MODEL

2.1 *The probabilistic semi-explicit cracking model*

The probabilistic cracking model was first developed at IFSTTAR (formerly LCPC) by Rossi & Richer (1987) and Rossi & Wu (1992) and recently improved by Tailhan, Dal Pont & Rossi (2010). It describes the behaviour of concrete via its two major characteristics: heterogeneity, and sensitivity to scale effects (Rossi & et al. (1994)). The physical basis of the model (presented in detail in Rossi & Richer (1987) and Rossi & Wu (1992) can be summarized as follow:

- The heterogeneity of concrete is due to its composition. The local mechanical characteristics (tensile strength f_t, shear strength τ_c) are randomly distributed.
- The scale effects are a consequence of the heterogeneity of the material. The mechanical response directly depends on the volume of material that is stressed.
- The cracking process is controlled by defects in the cement paste, by the heterogeneity of the material, and by the development of tensile stress gradients.

The following points specify how the numerical model accounts for these physical evidences:

- The model is developed in the framework of the finite element method, each element representing a given volume of (heterogeneous) material.
- The tensile strength is distributed randomly on all elements of the mesh using a Weibull distribution function whose characteristics depend on the ratio: *volume of the finite element*/*volume of the largest aggregate*, and the compressive strength (as a good indicator of the quality of the cement paste). The volume of the finite element depends on the mesh, while the volume of the largest aggregate is a property of the concrete (Rossi & Richer (1987) and Rossi & Wu (1992) and Tailhan, Dal Pont & Rossi (2010)).
  Remark: a Weibull distribution function is the best to take into account the rupture in tension of a brittle and heterogeneous material as concrete.
- The shear strength is also distributed randomly on all elements using a distribution function: (1) its mean value is independent of the mesh size and is assumed equal to the half of the average compressive strength of the concrete and (2) its deviation depends on the element's size, and is the same (for elements of same size) as that of the tensile strength (Rossi, Ulm & Hachi (1996)).
- Concerning the cracks representation, it is possible to use a semi-explicit approach, it means, in the present case, to use linear volume elements. The problem, with this type of elements, is that it is not capable to catch correctly the stresses concentrations at the macrocrack tip during its propagation. One solution is then to introduce some dissipation energy in the cracking criteria associated to this volume element. By this way, the error made in determining the crack initiation in the volume element is well compensated by the good modeling of the crack propagation within the element. Concerning the present model, the energetic effect associated to the elementary cracking process is represented through a simple isotropic damage law with a single scalar parameter (Lemaitre & Chaboche (1994)). A probabilistic energetic regularization is also retained.

Without going into details of numerical implementation of the model, its main features can be summarized as follows:

- A bilinear stress–strain relationship is used to represent elementary cracking (Figure 1). The elementary dissipative process (i.e. crack propagation inside the FE itself) starts when the major principal stress at a given Gauss point equals the material tensile strength. Dissipation is then driven by the positive part of the projection of the strain along the normal direction of the major principal stress. When the total energy available for the FE is dissipated, it is declared cracked and its elementary stiffness matrix is set to zero (Tailhan, Dal Pont & Rossi (2010)). This allows avoiding stress-locking phenomena.
- The model is numerically implemented using a rotating crack approach (Rots & et al. (1985) and Jirasek & Zimmermann (1998)). During the dissipative phase, the stress is allowed to evolve according to any changes in the stress state in the material.
- Differently from smeared-cracking approaches (de Borst & Nauta (1985), Jirasek (2011) and Meschke & et al. (2011)), no additive decomposition is introduced in the constitutive law to distinguish between elastic deformation and crack contributions. An elementary crack is supposed to exist only after the condition the damage parameter equal 1 is achieved (Rossi & Tailhan (2012). The elementary crack opening is then computed from the projection of the elementary displacements along the normal direction of the major principal stress.
- For sake of simplicity, crack re-closure is not explicitly treated. The model assumes that the dissipative process does not influence the elementary stiffness in compression. So, for reclosed cracks, the elementary stiffness matrix in compression is completely recovered while the elementary tensile strength is set to zero.
- The constitutive law of the model is completely defined by two parameters: the tensile strength and the volumetric density of dissipated energy. An energetic regularization technique allows computing the volumetric density of dissipated energy from the surface cracking energy by dividing this last energy by an elementary characteristic length (Bazant & Oh (1983)). This elementary characteristic length, l_e, is here computed from elementary volume, V_e, as $l_e = V_e^{1/3}$. More complex definitions are possible, depending on the FE shape and the order of interpolation of the displacement field. This choice can influence the predicted crack paths, however due to the probabilistic aspects of the model this effect is strongly reduced. The volumetric density of dissipated energy is defined element-by element according to spatially uncorrelated lognormal statistical law (Feller (2008)). This choice of a lognormal statistical law is an arbitrary one (the use of a Weibull law is no more relevant as for the tensile strength distribution due to the fact that, in this approach, the rupture is no more considered as perfectly brittle). As for the tensile strength parameters, the standard deviation related to the volumetric density of dissipated energy depend on the elementary volume. In contrary, the mean value of the energy distribution is assumed independent of elementary volume. Its value is estimated as 2γ where γ is the specific fracture energy per unit area (which is

an intrinsic material parameter) according Griffith's theory (Irwin (1968)).

Note that, in this modelling approach, the creation and the propagation of a crack is the result of the creation of elementary holes that randomly appear and can coalesce to form the macroscopic cracks (*semi-explicit cracking approach*). As output of the numerical simulation, the representation of the cracks direction is related to the perpendicular directions of the principal tensile strengths at the origin of the cracks initiation.

2.2 *Concrete/steel bond model*

A simple and robust model has been developed and validated at IFSTTAR [2, 3, and 4]. It takes into account the nonlinear behaviour of the concrete-rebar bond in the frame of damage mechanics. It can represent physical phenomena such as interface sliding, cracks appearance and degradation process. The concrete-rebar bond is modeled as interface elements. Their role is to:

- Ensure the displacement continuity between the concrete and the steel before the slip of the interface and before the cracking of the concrete, thus ensuring the transfer of stresses between steel and concrete.
- Represent the macroscopic mechanical effect of the rebar at the ribs—which is not explicitly represented in the mesh.
- Simulate a local failure between steel and concrete along the rebar resulting from a loss of the local adhesion due to shear cracking.
- Simulate the local friction between the concrete and the steel after the interface failure.

The model is implemented in 2D and 3D (Phan & et al. (2013 a, b). It models the concrete-rebar bond as a material zone that progressively degrades

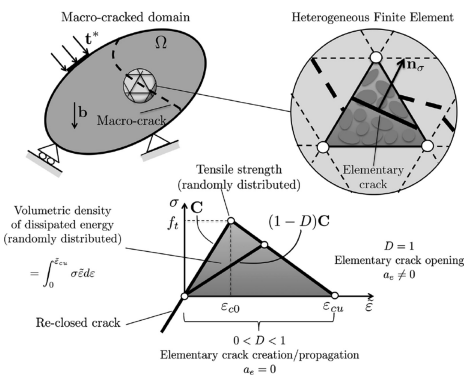

Figure 1. Probabilistic concrete cracking model—Semi-explicit approach.

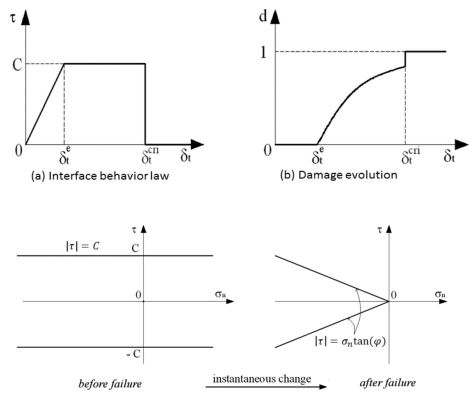

Figure 2. Steel-concrete interface behaviour law.

in shear (the tensile failure is neglected). Prior to total failure, stresses are continuously transmitted through the interface.

The interface model is based on a damage model that maintains a constant level of stress when the critical shear has been reached (Figure 2). When the relative tangential displacement between the concrete and the rebar exceeds a critical value, the interface element is declared broken (Rossi (1993)). After failure, a Mohr-Coulomb type of friction behaviour is maintained.

The interface model is deterministic. This is a valid approximation because the cracking process around the rebar is governed by the presence of the ribs (rather than the heterogeneity of concrete) (Lundgren (2005)).

Only the values of the maximum shear stress, and of the tangential critical relative displacement, have to be determined. It is usually realized by performing a numerical inverse analysis, it means by fitting tie-beam test results obtained with the rebar and the concrete concerned (Phan & et al. (2013 a), Phan, Tailhan & Rossi (2015)).

3 MODELLING OF THE CRACK PROPAGATION IN A REINFORCED DCB SPECIMEN

The structural problem here concerned is the macrocrack propagation in a Double Cantilever Beam (DCB) concrete specimen. This type of specimen and study are very current in the framework of Linear Fracture Mechanics theory. The specificity of the specimen concerned by this paper is related to two points: the first one concerns the fact that the dimensions of the specimen are very (unusually) important (3.5 meters length and 1.1 meters width) and the second concerns the fact that the

specimen contains rebars along of the potential propagation of the macrocrack (Rossi (1988)).

So, this structural problem is clearly related to the propagation of a macrocrack over a long distance and crossing rebars. It is then an interesting case to treat with the non-linear models presented above.

3.1 *Some details about the validation test*

The dimensions of the specimen and the loading conditions related to the test are presented in Figure 3. The steel bars used were ribbed ones with 6 mm diameter. The distance between the rebars was 10 cm and the first rebar was located at 30 cm from the front tip of the notch (Figure 4).

Note that the specimen contained a narrowed section in its center part to force the propagation of the macrocrack along this reduced section (Figure 3). For the same reason and objective, prestressing cables were used and placed along the flanges of the specimen (Figure 3).

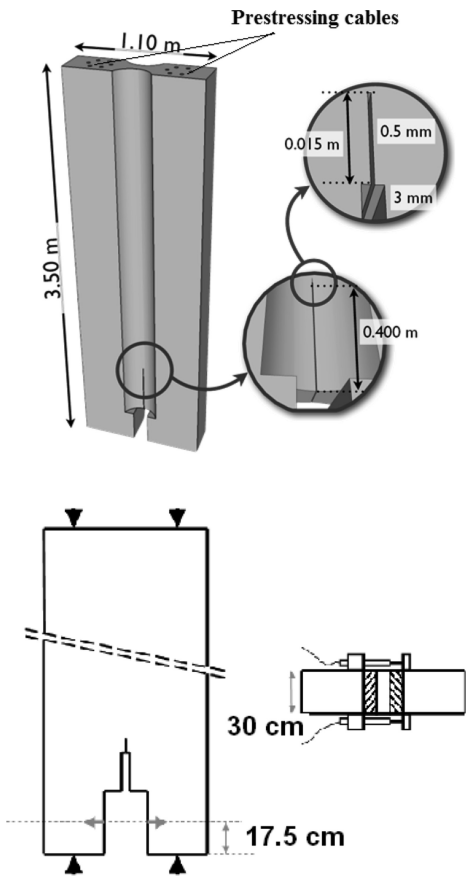

Figure 3. DCB dimensions and loading conditions.

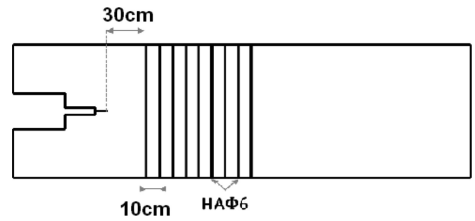

Figure 4. Position of the rebars in the DCB specimen.

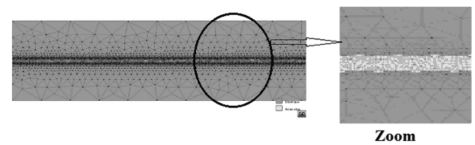

Figure 5. 2D finite element mesh of the numerical tie-beams (rebar with indentations).

3.2 *Numerical simulations*

To model the crack propagation in the reinforced DCB specimen, it is more relevant to use interface elements to model concrete/steel bonds than to take into account all the indentations of the rebars (see section 1, introduction).

The problem with the experimental study chosen to perform the validation of the numerical modelling strategy is that no tie-beam tests (see section 2.2) were performed in parallel to DCB test. So, the solution is to use the micro-scale level strategy (see section 1, introduction) developed and validated in previous work (Phan, Tailhan & Rossi (2015)) and to consider, by this way, a numerical tie-beam. To be clearer the tie-beam test is replaced by the numerical tie-beam (numerical test) as reference to determine the values of the parameters related to the interface elements. Of course, this solution is computational time consuming, but it consists to replace experimental tests which are also time consuming.

The numerical tie-beam chosen contains the same rebar than used in the DCB test surrounded by 10 cm of concrete (the distance between two rebars in the DCB specimen). So, the dimensions of the numerical tie-beam chosen are: 10 cm of high, 10 cm of width and 140 cm of length.

The 2D finite elements mesh (plane stresses plane conditions) of the numerical tie-beam (rebar with indentations) is presented in Figure 5.

The parameters of the concrete (semi-explicit approach) and the steel behaviours in the framework of the local models, presented in section 2, are given in Table 1.

Remark: the value of 2γ used for the numerical simulations is the one obtained by the experimental analysis (Rossi (1988)).

Table 1. Model parameters values related to the concrete (semi-explicit approach) and the steel behaviours in the framework of the local 2D approach (tie-beams simulations).

Material	Parameter	Value	Unit
	Tensile strength		MPa
	Scale parameter	8.0	
	Shape parameter	1.0	
Concrete	dissipated energy		
	Mean value	1.3	10^{-4}MN mm^{-2}
	Deviation	8.4	10^{-4}MN mm^{-2}
	Compressive strength	55	MPa
	Young modulus	35000	MPa
Steel	Young modulus	191000	MPa
	Elastic limit	400	MPa

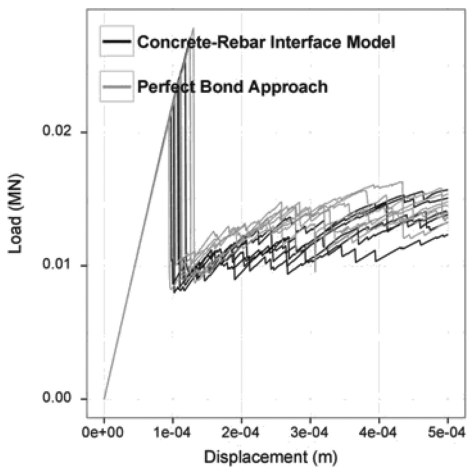

Figure 6. Load-Displacement curves related to the numerical tie-beam and to the two strategies to model it.

Table 2. Model parameters values related to the 2D concrete/steel bond behavior (2D simulations).

Cohesion	C	10	MPa
Critical tangent displacement	δ_t^{cri}	4	10^{-6} m

Figure 6 presents load-displacement curves related respectively to the two strategies of modelling the concrete/steel bond evocated in section 1 (introduction). In this figure are presented several curves for each modelling strategy. It is of course the result of the probabilistic models chosen.

Table 2 presents the values of the parameters related to the concrete/steel bond modeled with the interface elements and obtained by performing the fitting procedure evocated in section 2.2.

Figures 7 and 8 present examples of cracking process of the numerical tie-beam obtained with the two strategies of modelling the concrete/steel bond.

In Figure 9 is presented the 2D (plane stresses conditions) finite elements mesh of the reinforced DCB specimen. It can be noted that, due to the geometry of the DCB specimen considered, the realization of the numerical simulations in plane stresses conditions seems very relevant.

In Figure 10 are presented load-notch opening displacement curves related to the numerical simulations and the one obtained by experience (Rossi (1988)).

In Figure 11 is presented an example of cracking pattern obtained with the numerical simulations.

A look of Figures 10 and 11 leads to the following conclusions: the non-linear models presented in this paper and especially that related to the concrete cracking (which can be considered from the same family of smeared crack models) are relevant to model a localized macrocrack propagation in a reinforced concrete structure.

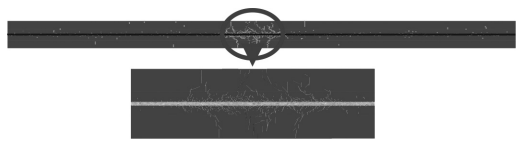

Figure 7. Example of cracking process of the numerical tie-beams—without interface elements.

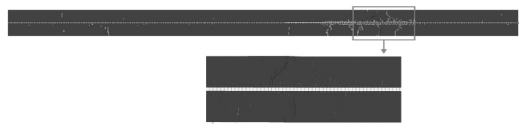

Figure 8. Example of cracking process of the numerical tie-beams—with interface elements.

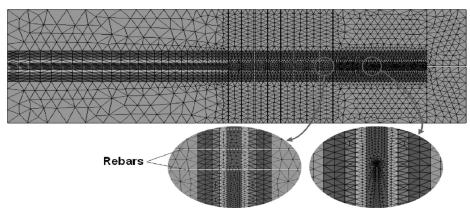

Figure 9. 2D Finite elements mesh of the DCB specimen.

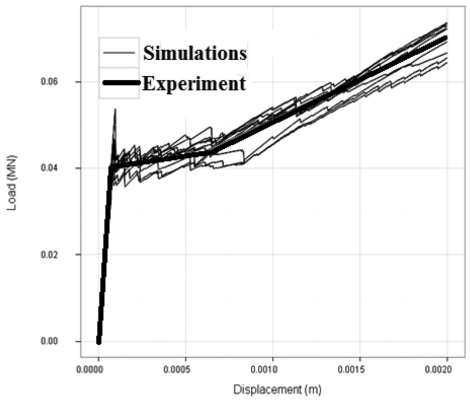

Figure 10. Crack mouth opening displacement (CMOD) versus loading curves related to the DCB specimen—Comparison between numerical simulations and experience.

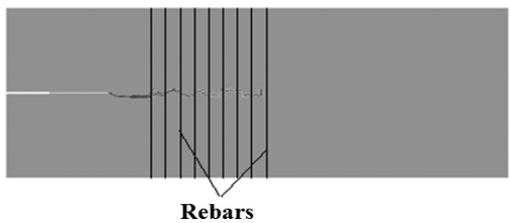

Figure 11. Example of cracking pattern of the DCB specimen obtained with 2D simulations.

4 CONCLUSION

This paper presents the numerical modelling (finite elements) of the macrocrack propagation in a very large Double Cantilever Beam specimen containing rebars. This numerical modelling is based on three non-linear models: a probabilistic semi-explicit model for concrete cracking, the use of interface elements with a Morh-Coulomb law for steel/concrete bond and an elastic perfect plastic behaviour for the rebars. It appears clearly that these models are relevant to give interesting information in terms of global behaviour and macrocracking of the DCB specimen without using a classical non-linear fracture mechanics approach.

REFERENCES

Bazant, Z. & Oh, B. 1983. Crack band theory for fracture of concrete. *Mater struct* 16(3):155–177.

de Borst, R. & Nauta, P. 1985. Non-orthogonal cracks in a smeared finite element model. *Eng Comput* 2(1):35–46.

Feller, W. 2008 An introduction to probability theory and its applications, *vol 2. Wiley, New York*.

Irwin, G. 1968. Linear fracture mechanics, fracture transition, and fracture control. *Eng Fract Mech* 1(2):241–257.

Jirasek, M. & Zimmermann, T. 1998. Rotating crack model with transition to scalar damage. *J Eng Mech* 124(3):277–284.

Jirasek, M. 2011. Damage and smeared crack models. In: Hofstetter G, Meschke G (ed) Numerical modeling of concrete Ann. Solid Struct. Mech. cracking. CISM International Centre for Mechanical Sciences, vol. 532. Springer, Vienna, pp. 1–49.

Lemaitre, J. & Chaboche, J.L. 1994. Mechanics of solid materials. *Cambridge University press*, Cambridge.

Lundgren K. 2005. Bond between ribbed bars and concrete. Part 1: Modified model, *Magazine of Concrete Research*, 57(7): 371–382.

Meschke, G. & et al. 2011. Numerical modeling of concrete cracking. *Springer, chap Smeared Crack and X-FEM Models in the Context of poromechanics*, pp. 265–327.

Phan, T.S., & et al. 2013 a. Numerical modeling of the rebar/concrete interface: case of the flat steel rebars, *Materials and structures* 46.6: 1011–1025.

Phan, T.S., Rossi, P. and Tailhan, J-L. 2015. Numerical modelling of the concrete/rebar bond, *Cement and Concrete Composites* 59: 1–9.

Phan, T.S., Tailhan, J-L & Rossi, P. 2013 b. 3D numerical modelling of concrete structural element reinforced with ribbed flat steel rebars. Structural Concrete 14.4: 378–388.

Rastiello & et al. 2015. Macroscopic probabilistic cracking approach for the numerical modelling of fluid leakage in concrete, *Annals of Solid and Structural Mechanics* (2015), 7(1–2):1–16.

Rossi, P. & Richer, S. 1987. Numerical modelling of concrete cracking based on a stochastic approach, *Materials and Structures* 20.5: 334–337.

Rossi, P., et al., Scale effect on concrete in tension, *Materials and Structures* 27.8: 437–444.

Rossi, P., Tailhan, J.L. 2012. Cracking of concrete structures: interest and advantages of the probabilistic approaches. In: Rilem international conference on numerical modelling strategies for sustainable concrete structures, SSCS'2012. Aix-en-Provence, France.

Rossi, P., Ulm, F-J & Hachi, F. 1996. Compressive behaviour of con crete: physical mechanisms and modeling, *Journal of Engineering Mechanics* 122.11: 1038–1043.

Rossi, P., Wu, X., Probabilistic model for material behaviour analysis and appraisement of concrete structures, *Magazine of concrete research* 44.161 (1992): 271–280.

Rossi, P. 1986. Fissuration du béton: du matériau à la structure. Application de la mécanique linéaire de la rupture. PhD Thesis, Ecole Nationale des Ponts et Chaussées, p. 228, (in french), published in *LPC Research Reports*, n°150, 1988 (in french).

Rossi, P. 1993. Comportement dynamique des bétons: du matériau à la structure. *Annales de l'Institut technique du bâtiment e des travaux publics*. No. 511. Institut technique du bâtiment et des travaux publics, (in french).

Rots, J.G. & et al. 1985. Smeared crack approach and fracture localization in concrete, *HERON* 30(1).

Tailhan, J-L., Dal Pont, S. & Rossi, P. 2010. From local to global probabilistic modeling of concrete cracking, *Annals of Solid and Structural Mechanics* 1.2: 103–115.

Computational Modelling of Concrete Structures – Meschke, Pichler & Rots (Eds)
© 2018 Taylor & Francis Group, London, ISBN 978-1-138-74117-1

Numerical simulation of shear strength in a short reinforced concrete corbel strengthened with composite material compared with experimental results

I. Ivanova & J. Assih
University of Reims Champagne-Ardenne, France

V. Stankov & D. Dontchev
University of Chemical Technology and Metallurgy, Bulgaria

ABSTRACT: This paper describes a numerical analysis carried out to assess the shear strength of strengthened short reinforced concrete corbel by using Carbon Fiber Reinforced Fabrics (CFRF). To extend the life and shear strength of the reinforced concrete structures often used technique for external bonding of composite materials. This study provides a comparison of curves obtained with numerical model and experimental curves of corbels. Results show that in general, ultimate load, crack patterns and deformation capacity were satisfactorily reproduced. The Finite element model results are successful compared and validated by experimental results.

1 INTRODUCTION

Composite Fiber Reinforced Fabrics (CFRF) have many advantages: lightweight, flexibility, implementation easier and also physicochemical properties anti corrosion interesting. The shear strength and the ultimate capacity of strengthened short reinforced concrete corbel (Corry, 2001), (Bourget, 2001), (Li, 2001) with prediction requires nonlinear analysis. In the numerical simulations, the shear strength is mainly influenced by the tensile softening behavior and the shear stiffness of cracked concrete. Sensitivity analyses on different input parameter, crack and material models were performed to investigate their effect on the shear strength.

The study involves using three different configurations of strengthening using CFRF, using finite element and nonlinear dynamic analysis method. The strengthening by CFRF wrapping method, bonding directly the CFRF on both faces of corbel and bonded inclined CFRF on both face of corbel are examined and compared to experimental results of strengthened and reinforced concrete corbels. Comparative analysis results of reinforced concrete corbel model show a 82% increase in load-carrying capacity of strengthened reinforced concrete corbel models compared to reference model (without CFRF strengthening).

This article provides a comparison of curves obtained with numerical model and experimental curves of corbels. Results show that in general, ultimate load, crack patterns and deformation capacity were satisfactorily reproduced. The Finite element model results are successful compared and validated by experimental results.

2 EXPERIMENTAL STUDY

2.1 *Experimental model*

The column supporting two short trapezoidal corbels cantilevering on either side was 150 by 300 mm in cross section and 1000 mm long. Corbels had cantilever projection length of 200 mm, with thicknesses of 150 mm at both faces of column and the free end. All reinforced concrete corbel specimens have the same dimensions and are reinforced in the same way.

2.2 *Bending test*

All corbels were tested on a test slab in the civil engineering laboratory of the University of Reims Champagne-Ardenne. This test Machin has a hydraulic jack with a nominal capacity of one thousand (1000) kN. The three-point flexion bending test was applied for all samples. But noted that, the corbel, Figure 1, is thus subjected to a bending test in reverse position compared to reality.

The corbels were tested using a single patch load with (a) shear span to depth (d) ratio equal to 0.45.

The load is applied to the test body by the base of the pole by means of a jack supplied by

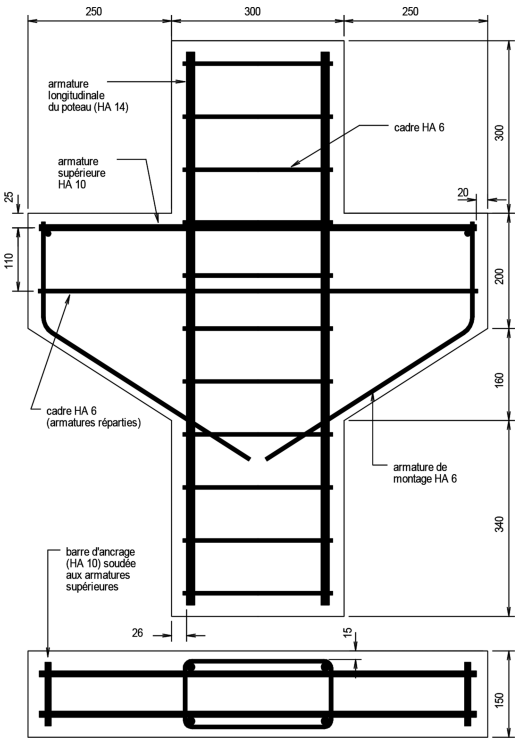

Figure 1. Reinforced concrete corbel Model [Ivanova, 2013].

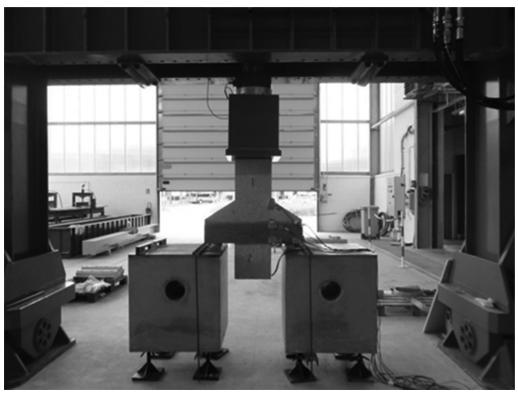

Figure 2. Experimental device.

the hydraulic unit. The average loading speed is 0.02 kN/s. Each console of the test body is subjected to a vertical load equivalent to the reaction of the support device, i.e. half the load of the cylinder. To avoid local crushing of the concrete under the support, is interposed between the console and support a hardwood plate thickness 3 mm.

Table 1. Proprieties of used materials.

Materials	Young's modulus (GPa)	Ultimate strength (MPa)	Poisson's ratio
Concrete	30 ± 2	33.2 ± 2	0.25
Steel bar	200 ± 1	610 ± 10	0.30
Adhesive	4.1 ± 1	36 ± 1	0.41
Fabrics	86 ± 1	775 ± 65	0.45

2.3 *Mechanical characteristics of the materials used*

The mechanical characteristics of materials used are presented on Table1.

2.4 *Experimental results*

The control reinforced concrete corbel without strengthening is noted "C0" with the letter "C" means the Corbel and (zero) "0" means without reinforcement. For other specimens, the second letter represents the type of reinforcement like "B" means Bandage. Afterwards, the number of layer of fabrics is indicates by 1, 2, 3 and 5. At the end, the small letter indicates the type of composite material, u for unidirectional.

From the large amount of data obtained from testing, only typical data are reported here in Table 2. This paper present the results on the type of strengthening on bending and shear, bonding directly carbon fiber fabrics on either surfaces or full wrapping of short reinforced concrete corbel.

Four concrete corbels were tested. Three of them are strengthened bonding carbon fiber fabric as in Table 2 and one control specimen without reinforcing.

The results show that there is a very significant increase in capacity loading for the three types of reinforcement 41 to 82%.

The obtained ultimate load of control corbel was F_0, equal to 357 kN. And when comparing to strengthened corbels, the results showed an increase in the load F_R/F_0 of 1.41 for CI2b and of 1.82% for CB3u. In the former case, the inclined composite fabrics of 45 are bonded perpendicular to the diagonal crack. The bonded inclined fabric of CI2b area represents 32.5% of corbel total area. While the second case with CP3u represents 51, 6%, and in the last case with CB3u represents 60.0%.

In fact, the results show that strengthening is more effective wrapping through the containment effect of concrete and a resumption of strength by carbon fiber fabrics. Doubling the bonding area, the ultimate load increased by 14%. While, of course, in the case of reinforcement corbels

Table 2. Design of testing specimen [Ivanova, 2013].

Notification		Design	F_R/F_0
CI2b	Strengthened corbel by bonded Inclined bidirectional carbon fiber fabrics on both sides	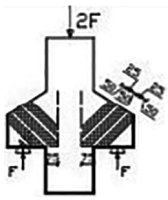	1,41%
CP3u	Strengthened corbel by bonded unidirectional carbon fiber fabrics on both sides.	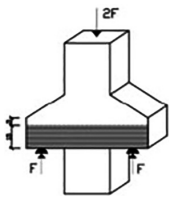	1,55%
CB3u	Wrapping strengthened corbel by bonded composite plates on both sides.	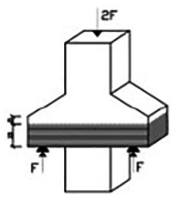	1,82%

F_R: ultimate load of strengthened reinforced concrete corbel.
F_0: ultimate load of reinforced concrete corbel.

by wrapping, means by containment, the ultimate load grows up to twice. Accordingly, the test results shows, that composite fabrics judiciously suitable on surface more effectively, the ultimate load capacity is increased.

2.5 *Influence of layer of carbon fiber fabrics on ultimate strength of Corbels*

Four of reinforced concrete corbels were strengthened by wrapping carbon fiber fabrics by varying the thickness of fabrics from 1, 2, 3, and 5 layers. The composition materials used are unidirectional carbon fiber fabrics. The experimental results of ultimate loads Fu are presented in Figure 3.

The results show an optimal value of fabrics thickness for three layers. So the ultimate load capacity of the structure growing when the number of fabrics layer increases. But after three fabric layers, the reinforced bracket becomes stiffer and prematurely causes compression failure at low loads

Considering the last corbel tested, the ultimate load drops by 7% from the previous one. In fact, the results show that the strengthened reinforced concrete corbel with a 3-layer carbon fibre fabrics

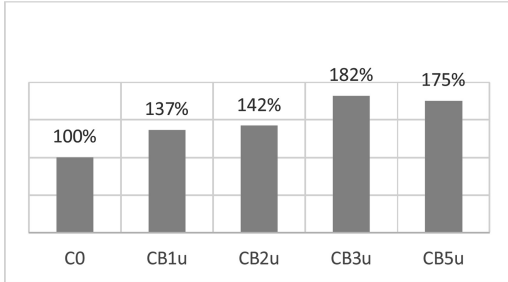

Figure 3. Influence of number of carbon fabric layer on ultimate load of corbels strengthened fabric wrapping [Ivanova, 2015].

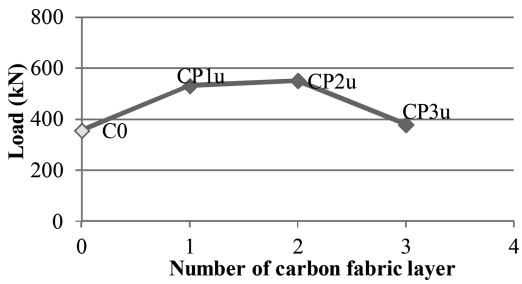

Figure 4. Effect of carbon fabric layer on ultimate load of corbels strengthened by fabric sheets on front and rear faces [Ivanova, 2015].

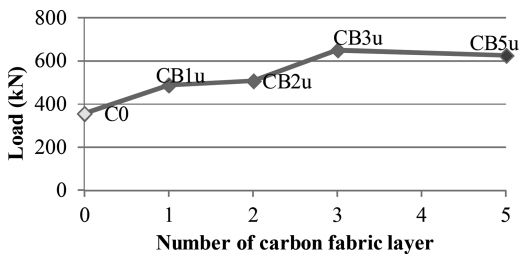

Figure 5. Influence of number of carbon fabric layer on ultimate load of corbels strengthened RC corbels [Ivanova, 2015].

offered better results (82% more than control reinforced concrete corbel without strengthening).

Figure 4 shows the influence of the thickness of carbon fabric sheet on the failure load of the corbels. The reinforced concrete corbels were strengthened by bonded on front and rear faces the carbon fabric sheet. In fact, the results shown an optimum value of the thickness from which the ultimate load decreased. Increasing the thickness caused premature rupture of the carbon fabric sheet.

Figure 5 presents the influence of the thickness on the failure load of the corbels. The reinforced

concrete corbels were strengthened by wrapping carbon fiber fabrics. The results show an optimum value of the thickness from which the failure load decreases. Increasing the thickness caused premature collapse of the corbel.

2.6 *Effect of type of reinforcement with composite materials*

2.6.1 *Specimen CP3u*

This specimen was strengthened with externally bonded three fabric layers on horizontal area face of corbel. The results showed one major diagonal crack started at the bearing point and propagated towards the embedding between the column and the corbel. This crack appeared at a load of 310 kN could be caused the collapse of the strengthened reinforced concrete corbel at an ultimate load of 380 kN. However, when the number of layer increases, the results showed the typical failure called the peeling off the sheet at the end. The accumulation of several strips of fabric on top of each other results in a thickening of the plate as a whole, and therefore, they peeled off easily and cannot reach to the maximum load-bearing capacity of the composite. There was no apparent damage on the composite plate, just concrete cracked major diagonal shear crack beneath the sheet. In fact, the concrete crack caused of debonding of the sheets on the front and rear face of the corbel.

2.6.2 *Specimen CB3u*

The first flexural cracks appeared at 140 kN and bearing load at 365 kN for this specimen. So, the latest of appearance of diagonal cracks could be because of the containment effect by wrapping. It shows by the results of curves obtained with strain gauges "G1" (steel tie local deformation) for four different corbels. These curves are compared to reference reinforced concrete corbel without strengthening. The results show that curves were similar and the ultimate load increased with a third reduction of strain. In all four cases, first micro cracks is started at the same loads between 130 and 140 kN. There was one main diagonal shear crack almost at an angel 45 degrees and this crack started at the bearing point. This crack caused failure of the specimens. Corbel failed at ultimate loads at 651 kN.

2.6.3 *Specimen CI2b*

First flexural crack was appeared at 116 kN little more than the previous specimen. Like the above specimen CP3u, only one major diagonal crack was started at the bearing point, and propagated towards the embedding of the column and the corbel. This crack appeared at 380 kN and caused specimen failure at 520 kN. There was no apparent damage of the fabric sheets. But the concrete would appear to be the weak material of this dovetailing with this major diagonal shear crack.

2.7 *Mechanical behavior of strengthened RC corbels using strain gauges*

To study the local mechanical behavior of Strengthened RC corbels, the strain gauges with extensometer technique was used. Of course, this technique allows evaluating the local strains at a point of measurement of carbon fiber sheet, concrete and steel bar with the help of electric gauges glued to their specific area.

This measurement point is chosen to obtain the maximum strain in the strengthened RC corbel.

2.8 *Effect of fabric thickness*

Figure 4 shows the influence of the thickness of carbon fiber fabric plates in the local strain of the tie steel bar of each strengthened reinforced concrete corbel using strain gauge G1 in the embedding section. The high deformation values around 6000 μm/m of the tie steel bars of CB1u corbel at a load of 325 kN (Figure 4) corresponds to the appearance of the diagonal crack and the plasticization of the bar. Probably, it was the result of an excessive local deformation of the steel reinforcement. So, this plasticization of the steel is characterized by a bearing at 325 kN and would produce the recovery of strength and strains by the carbon fiber cloth sheets. These deformations are important like 6000 μm/m. In Figure 4, the sudden return to constant deformation of the CB1u curve attests to the failure of the composite fabric. In fact, strains should be not transmitted.

The effect of the bonded by wrapping obviously reduces the rigidity of the structure with lower deformations than 2000 μm/m. The CB3u configuration

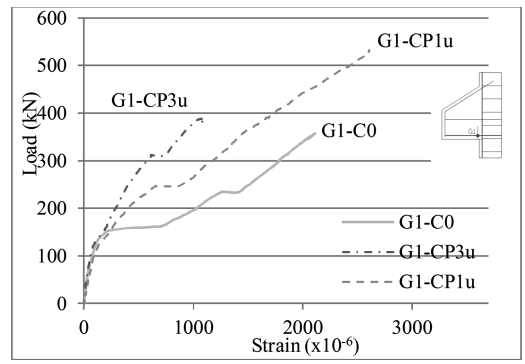

Figure 6. strain versus strain of tie steel bar at point G1 in the section embedding of CB1u, CB2u, CB3u, CB5u and C0 corbels. [Ivanova, 2014].

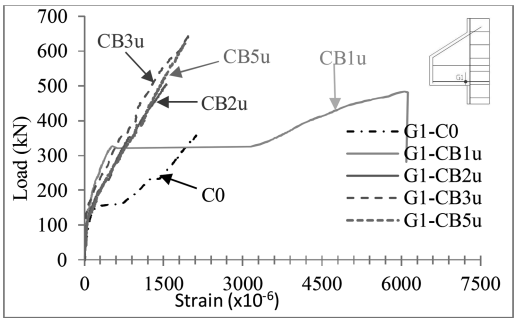

Figure 7. strain versus strain of tie steel bar at point G1 in the section embedding of CB1u, CB2u, CB3u, CB5u and C0 corbels. [Ivanova, 2014].

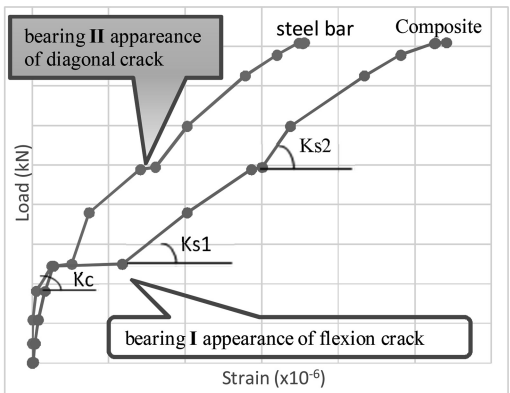

optimal experimental result.

Figure 8. Characteristic mechanical behavior of strengthened RC corbels.

remains for the tests carried out the optimal experimental result.

The results obtained using strain gauges in Figures 8 and 9, mainly show the appearance of bearings corresponding to flexion and oblique cracks, and three different behavior domains.

The elastic area where the strains of steel bar, concrete and carbon fiber fabric grow linearly according to the load applied.

The second area is characterized by the appearance of the first cracks in the concrete in the tensile zone.

In the third area, the test showed the appearance of diagonal cracks due to the effect of shear strength

The appearance of the bearings also marked the change of behavior of the structure as shown by the angles Ks1 and Ks2. They are represented the changing of slope. These changes of slope is illustrating either by the opening of diagonal cracks (Ks2), by the appearance of new cracks (Kc) or by the propagation of cracks (Ks1).

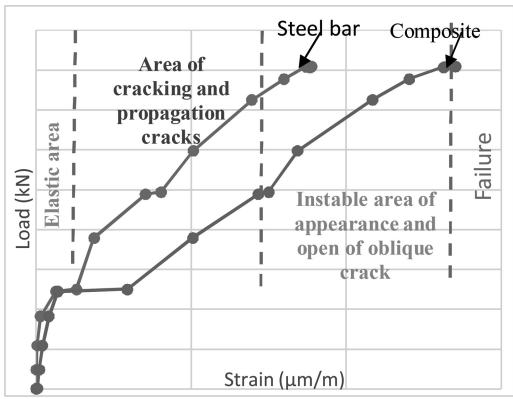

Figure 9. Different mechanical behavior of strengthened RC corbels.

3 NUMERICAL STUDY

For modeling in ABAQUS software, we should consider suitable behavioral models for materials. The selection of behavioral models has great impact on the outcomes and the conditions should be considered as the model reaches reality.

ABAQUS software uses suitable parameters to simulate the damage mechanics for tensile and compression effects within the Concrete Damaged Plasticity (CDP) analytical framework (Abaqus, 2013), (Hansen, 2001). Numerical values of five plastic parameter and specific parameters of concrete behavior in tensile and compression are used in the software to simulate full behavior of concrete, besides elastic parameters (elasticity module and Poisson coefficient). The first parameter introduced in concrete plastic features is dilation angle. Internal dilation angle is volume strain ratio to shear strain of materials. Internal dilation angle that is considered here ranges between 20 to 40 degrees for concrete with considerable impact on materials ductility. By increasing the angle, ductility value is correspondingly increased. This angle is 25 degree in this study (Hansen, 2001), (Rafati, 2016).

Second parameter is eccentricity, which is a small positive value that expresses the rate of approach of the plastic potential hyperbola to its asymptote.

So the higher flexure value was in low potentials. This parameter is considered as 0.1 in software as default value. The third in CDP[1] model was f_{bo}/f_{bc} parameter, the two-surface yield stress to compressive one-surface yield stress as obtained 1.1 to 1.16 in tests (Hansen, 2001). The value of

1. Concrete damaged plasticity.

dimension-less parameter in Abaqus parameter was 1.16, which is taken as a criterion in this study. The fourth parameter in plasticity definition of CDP model was parameter K defining the form of yield surface which use of 0.5 to 1.

K value in software is 0.667 and is suitable for concrete modeling based on references (Taqieddin, 2008). The last parameter of CDP model in plasticity parameters is viscosity parameter showing visco-plastic resting time. Some of the convergence problems can be eliminated by standardization and regulation of visco-plastic equations. Thus, the stresses can exit yield level. The elasticity module parameter in this study is 23.49 GPa and Poisson coefficient is 0.2.

Table 1. is based on behavioral model of Mander and Park for confined concrete, to introduce concrete behavior in compression phase. Table 2 was used to introduce concrete behavior in tensile phase [Mander, 1988]. The numerical values of equivalent compressive plastic strain and equivalent tensile plastic strain are used to show damage extension. As can be seen in Figure 10, equivalent plastic strains can be attained by compressive or tensile strain and stress values, damage parameters and elasticity elastic module.

Two different three dimensional, 8 and 20 node quadratic brick elements are used to model the concrete, while the reinforcing bars are modeled as axial members embedded within the concrete brick elements. For concrete modeling, C3D8R element of solid type with eight nodes and three degrees of freedom in each node are applied. To model steel bars inside corbel and the column, T3D2 element of beam elements with and nodes is used. To model composite coverage CFRF, shell element S4R with four nodes and six degree of freedom in each node.

3.1 *Concrete characteristics*

In fact, in simulating, concrete behavior is a synthesis of the plasticity and damaged models. There is the combination of isotropic behavior of elastic damage with the plastic isotropic behavior under compression and tensile conditions. The compressive behavior of concrete (Figure 10) is considered as elastic-plastic work-hardening model followed by a perfectly plastic response, which terminate at the onset of crushing.

Concrete is a material having complex non-linear behaviors even at low-level stresses The underlying causes of the concrete's non-linear responses of the concrete are not only linked to its material characteristics, but arise from the environmental factors, cracking, bi-axial stiffness and softening of strains [Hanson, 2001].

Two principal theories of plasticity and damage mechanism are highly consistent with real behavior of concrete, although each of which often predicts reinforced concrete behavior, some cases of which nonetheless, does not explain the realities with high accuracy. The plausible way in simulating concrete behavior is a synthesis of the plasticity and damage models. Such model combines the isotropic behavior of elastic damage with the plastic isotropic behavior under compression as in Figure 10 and tensile conditions as in Figure 11.

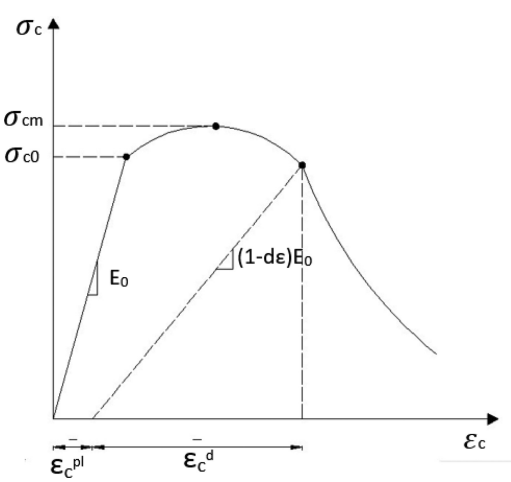

Figure 10. Concrete behavior in uniaxial compression load (Plastic strain and non-elastic strain in concrete response curve) [Abaqus, 2013].

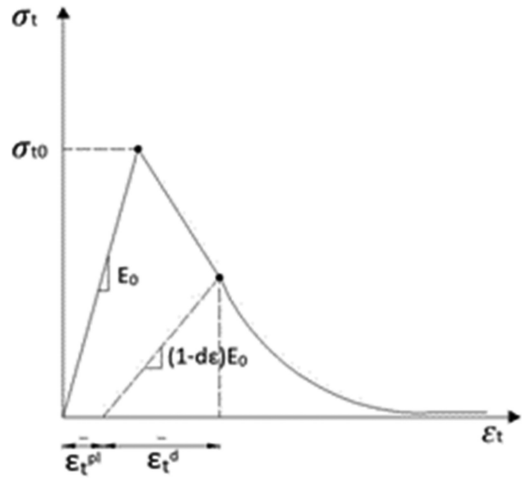

Figure 11. Concrete behavior in uniaxial tensile load (Plastic strain and non-elastic strain in concrete response curve) [Abaqus, 2013].

3.2 *Steel characteristic*

Steel behavior is idealized and the tensile and compressive behavior of this matter is equal without having specific effect on the results. Two-linear ideal curve is used for modeling in order to reduce analysis time and avoid the problems of non-convergence of elastic-fully plastic models. The volume mass for steel materials is 7850 kg/m^3, elasticity model is 200 GPa, Poisson coefficient was 0.3 and yield stress is 360 MPa.

The behavior curve of steel materials (bar) is bi-linear with slope 0.01 and elasticity module in stiffening region is similar to those in Figure 12.

Elastic perfectly plastic material in both tension and compression in Abaqus simulation, Figure13.

In this study, steel was assumed to behave as an elastic perfectly plastic material in both tensile and compression.

3.3 *CFRP characteristics*

Carbon fiber fabric sheet mechanical features are different in various directions and carbon fibers form a carbon fiber reinforced sheets as multi-layer with Epoxy resin. It is a brittle material and there is no need to define damage evolution and just need to define Hashin Damage [Hanson, 2001].

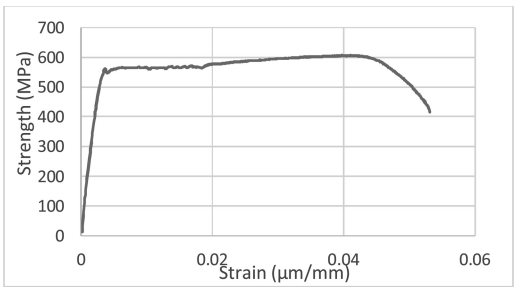

Figure 12. Steel bar behavior in tensile test.

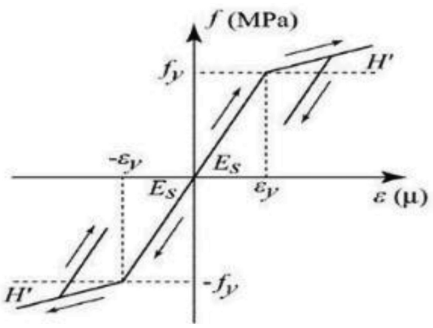

Figure 13. Bi-linear curve of steel materials behavior.

The Figure 14 shows the mechanical characteristics obtained during a tensile test carried out on the used carbon fiber fabrics. However, for simplification of the calculations we used the Abaqus data to perform the calculations.

The features polymer composite sheets reinforced with carbon fiber fabrics are introduced in accordance with the extracted features of lab specimen to Abaqus software. The mechanical and strength features of CFRP sheets are shown in Tables 3, 4.

The CFRF are a brittle material, so there is no need to define damage evolution. The behavior of CFRF was elastic-linear until rupture as shows the Figure 14.

3.4 *Modeling in Abaqus*

3.4.1 *Materials interaction*

As in modeling we have different materials, to show the boundary between the materials and correct

Table 3. Strength features of CFRP sheets [Abaqus, 2013].

Longitudinal tensile strength (Mpa)	Longitudinal compressive strength (Mpa)	Transverse tensile strength (Mpa)	Transverse compressive strength (Mpa)	Longitudinal shear strength (*Mpa*)	Transverse shear strength (*Mpa*)
3100	2300	3100	2300	3	3

Table 4. Mechanical specifications of CFRP sheets [Abaqus, 2013].

ρ (kg/m^3)	E1 (MPa)	E2 (MPa)	Nu12	G12 (MPa)	G13 (MPa)	G23 (MPa)
1800	165000	82500	0.3	1019	2038	2038

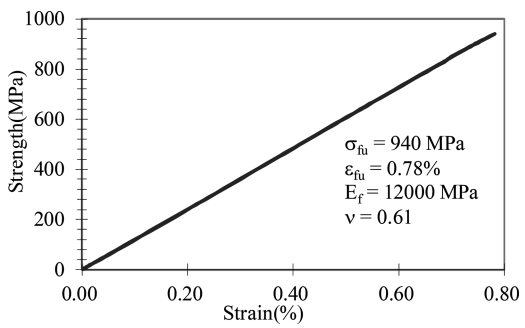

Figure 14. Results of tensile test of Carbon fiber fabric.

performance of analysis, we should define interaction. Among the terms in ABAQUS software, Embedded region is used as interaction between steel (rebar) and concrete. To define interaction between CFRP and concrete surface, there is a difference between defining interaction between rebar and concrete and we can use Tie to define interaction between concrete and CFRP. Resin is also defined among them and to reduce analysis time, steel bar tie is used in this study.

3.4.2 *Dividing the model to finite elements (Meshing)*

Different elements of various parts are selected based on elements performance. For concrete modeling, C3D8R element of solid type with eight nodes and three degrees of freedom in each node are applied. This element can apply plastic deflections and big deflections and can model cracking in three orthogonal directions in all eight integrating points. To model steel bars inside corbel and concrete column, T3D2 element of beam elements with two end nodes is used. This element is a 3-D first order linear element. To model composite coverage CFRP, shell element S4R with four nodes and six degree of freedom in each node (three translational degrees of freedom and three rotational degrees of freedom). The above shell element can have one-layer isotropic section and single-layer or multi-layer orthotropic with various angular configurations of layers.

Mesh sensitivity analysis is applied to achieve suitable mesh for analysis and achieving exact answer. Based on required outputs, meshing dimensions are reduced as the output parameter changes are ignored in two meshing. Partitioning operation is used in order to apply regular meshing on models, in connection site of corbel to column. The mesh results are shown in Figure 15.

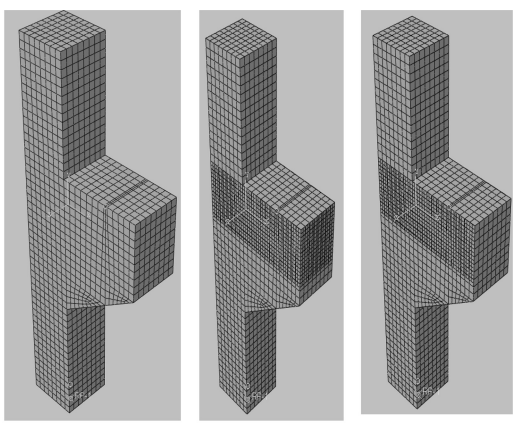

Figure 15. Mesh of corbels. (a) Reinforced concrete corbel, (b): strengthened reinforced concrete corbel by wrapping and (c): reinforced corbel strengthened by bonded composite sheet on front and rear faces.

3.4.3 *Definition of boundary conditions and loading*

Possible to create joint support, by creating reference point in two ends of column, joint support is dedicated to these points.

An axial force Nu (horizontal force) and a shear force Vu (vertical force) are applied on concrete bracket. As the beam is placed directly on bracket, beam support is provided as the horizontal movement of beam is free. Thus, Nu = 0 and based on specimen test method (corbel) in lab, vertical force Vu is imposed as extended to bracket loading plane. Two ways can be considered for applying load on corbel. Loading can either be done as force control or by strain control in the embedding section on corbel. All models are loaded based on controlling maximum displacement 1 cm.

3.4.4 *Analysis results*

Because of the non-linear features of concrete, any analysis should therefore be done within the non-linear theoretical framework. The method has static nature and as some static issues are encountered with non-convergence, non-linear dynamic analysis is used to explain the realities. Application of dynamic analysis instead of static analysis is likely to yield more realistic results under circumstances where the ALLKE ratio (kinetic energy) to ALLIE (internal energy) in each time of loading is less than 0.1 [Rafati, 2016].

For the numerical results, first, we present the global behavior of the reinforced concrete corbel without strengthening as shown in Figure 16.

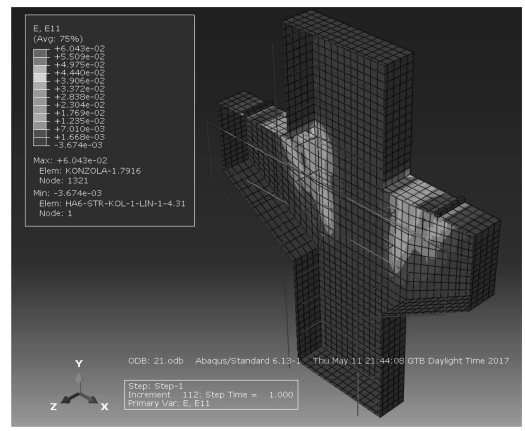

Figure 16. Numerical representation of the experimental model.

The results showed the stress peaks at the embedding section between the column and the two corbels. Result was consistent with the experimental result.

Considering the symmetry and by gain time for the saving of calculation time, the results of a band-reinforced beam are presented in Figure 17. The recovery of strengths by the composite fiber reinforced fabrics was modified the stress distributions in corbel, Figure 18.

Indeed, the influence of the thickness of composite carbon fiber fabrics is presented in the Figure 19, representing the optimal reinforcement of reinforced concrete corbel. The Figure 20 presented the strain in the embedding section of the corbel reinforced with a composite plate of three layer fabrics.

The numerical elements used in this work seem to correspond to the observations made experimentally. But a finer mesh would improve the results off. The laws of behavior of materials used also seem to approach the experimental results. Figure 20 shows the results of an reinforced concrete corbel strengthened by two carbon fiber fabric sheets bonded on its front and rear faces.

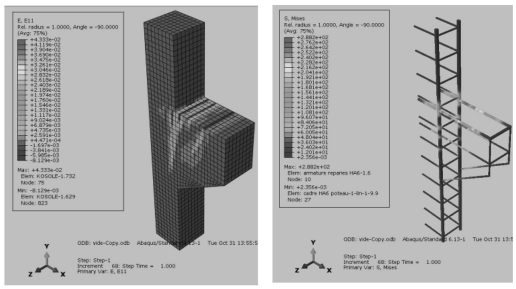

(a) (b)

Figure 17. Stresses in concrete (a) and steel bars (b) of reinforced concrete corbel.

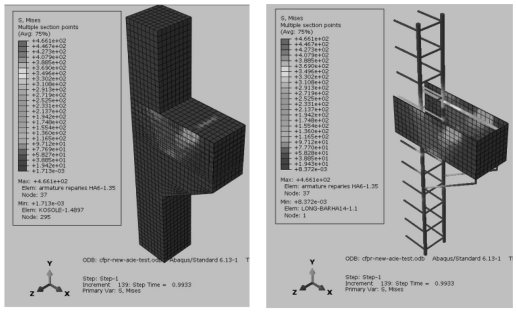

(a) (b)

Figure 18. Stresses in composite plate (a) and stresses in composite plate and steel bars (b) in reinforced concrete corbel bonded by wrapping with three layers of fabrics.

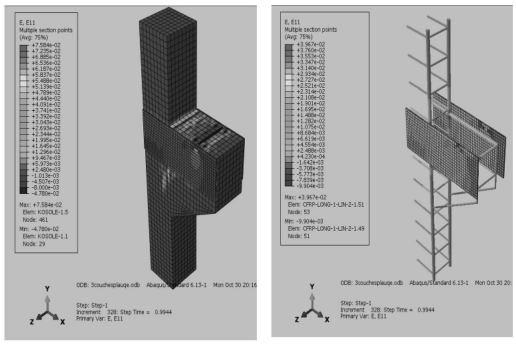

(a) (b)

Figure 19. Stresses in composite plate (a) and stresses in composite plate and steel bars (b) in reinforced concrete corbel bonded with three layers of fabrics on face and rear area of reinforced concrete corbel.

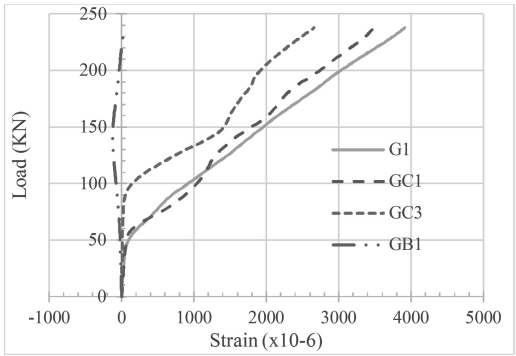

Figure 20. Strains in the embedding section of strengthened reinforced concrete corbel by wrapping one layer of carbon fiber fabrics.

4 CONCLUSIONS

It is clear that the cleaning of the surface conditions of the concrete and composite materials must be carefully executed. The method used in this study was sandblasting. The choice of carbon fiber composite materials is justified by their very interesting mechanical and flexibility properties.

The thickness of the composite material has a very sensible effect on the ultimate loading. In fact, the optimum value found was 3 layers for a maximum ultimate load or of 82% more compared to corbels without strengthening.

The results show also a one-third reduction in rigidity of the strengthening RC corbels by

wrapping Fiber fabrics. Three main areas were appeared in the highlighted behavior: elastic area, begin and propagation cracks area and the latest the unstable area with the diagonal crack which mainly caused the collapse of corbel.

This article provides a comparison of curves obtained with numerical model and experimental curves of corbels. Results show that in general, ultimate load, crack patterns and deformation capacity were satisfactorily reproduced. The Finite element model results are successful compared and validated by experimental results

REFERENCES

ABAQUS V6.13 Manuals, 2013. Providence, RI: Dassault Systemes.

Bourget M., Delmas Y. and Toutlemende T., 2001. Experimental study of the behavior of reinforced high-strength concrete short corbel, *Materials and Structures*, April 2001, Vol. 34: 155–162.

Corry R.W. and Dolan C.W. 2001. Strengthening and Repair of a Column Bracket Using a Carbon Fiber Reinforced Polymer (CFRP) Fabric, *PCI Journal*, vol 46, 54–63,

Hansen E., Willam K., Carol I., 2001, A two-surface anisotropic damage/plasticity model for plain concrete, *Proceedings of Framcos-4 Conference Paris, Fracture Mechanics of Concrete Materials.*

Ivanova I., 2013. Comportement mécanique des consoles courtes en béton armé renforcées ou réparées par collage de matériaux composites. *Thèse de doctorat*, Université de Reims.

Ivanova I., Assih J., Li A., Delmas Y. 2014. Influence of fabric layers on strengthened reinforced concrete short corbels *International Journal of Civil Engineering and Technology*, Vol. 5 (10) pp. 33–43.

Ivanova I., Assih J., Li A., Dontchev D., Delmas Y. 2015 Experimental investigation into strengthened short reinforced concrete corbels by bonding carbon fiber fabrics *Journal of Adhesion Science and Technology*— 29 (20), pp. 2176–2189.

Li A., Assih J., Delmas Y., 2001. Shear strengthening of RC beams with externally bonded CFRP sheets *Journal of Structural Engineering,* 127: 4, 374–380.

Mander J.B., Priestley M.J.N., Park R., 1988, Theoretical Stress-Strain Model for Confined Concrete, Fellow, ASCE.

Mehdi Rezaei, Osman S. A. Shanmugam N.E. 2010. Finite element analysis of reinforced concrete corbels, *EMESEG'10 Proceedings of the 3rd WSEAS international conference on Engineering mechanics, structures, engineering geology, Corfu Island, Greece — July 22–24, 2010, pp. 448–452.*

Rafati A., Razavi S.V., 2016. Finite Element Analysis of Reinforced RC Bracket Using CFRP Plates*, Journal of Solid Mechanics, Vol.8* (4) pp. 734–743.

Taqieddin Z., 2008, Elasto-Plastic and Damage Modeling of Reinforced Concrete, Ph.D. Dissertation, Louisiana State University, Baton Rouge, LA.

Computational Modelling of Concrete Structures – Meschke, Pichler & Rots (Eds)
© 2018 Taylor & Francis Group, London, ISBN 978-1-138-74117-1

Computational modeling and experimental testing of shear and flexure performance of prestressing concrete T-shaped beams—safety formats

A. Strauss & B. Krug
University of Natural Resources and Life Sciences, Vienna, Austria

O. Slowik, D. Novák & L. Novák
Brno University of Technology, Brno, Czech Republic

ABSTRACT: A complex approach to probabilistic analysis and design of precast prestressed concrete girders failing in shear is presented. Experimental studies have been performed on full scale prestressed concrete roof elements and scaled laboratory tested elements, they served as basis for deterministic nonlinear modelling with model updating of precast members and subsequent probabilistic evaluation of structural response variability. The results are used as thresholds for loading of produced structural elements and probabilistic design procedure as less conservative method compared to classical partial safety factor based design and alternative ECOV method.

1 INTRODUCTION

Shear strength of concrete beams has been the subject of many controversies and debates and it has been extensively studied over the last five decades, e.g. (Bairan et al. 2006, Bažant & Yu 2003, Bažant & Planas 1998, Ceresa et al. 2007, Mari et al. 2015, Russo et al. 2005). The ultimate capacity of reinforced concrete beams subjected to combined shear and flexure is affected by many phenomena and uncertainties, such as existing multi-axial states of stresses, the anisotropy induced by the diagonal concrete cracking, the interaction between concrete and reinforcement (bond) and the brittleness of the failure mode. A large number of shear tests have been performed during the last decades, as summarized (Collins et al. 2008) in order to obtain valuable information about the shear transfer mechanisms.

The comprehensive experimental study of material parameters was performed first (Řoutil et al. 2014, Strauss et al. 2014, Zimmermann et al. 2014). It was understood from the early beginning that to develop very good numerical model for comparison with experiment of real structure would be impossible without the proper knowledge of fracture-mechanical parameters. The aim was to include in the database results for specified type of concretes the time of testing, the mean values, the standard deviations of the fracture mechanical concrete parameters and the most suitable mathematical model for probability distribution functions. In particular, three-point bending (3PB) tests have been conducted on specimens made of C50/60 and C40/50 (Řoutil et al. 2014), with a central edge notch and analyzed via the effective crack approach and work-of-fracture method (Elices et al. 1992). By means of an advanced identification approach based on artificial neural network modelling (Lehký et al. 2014, Novák & Lehký 2006), the following three fundamental parameters of concrete were identified: modulus of elasticity E_c, tensile strength f_{ct}, and specific fracture energy G_f. The compressive strength of concrete f_c was measured by means of standard cubic compression tests.

Main goal of this paper is to present here the complex approach to computational modeling of destructive test based on data obtained from fracture mechanical experiments. Whole approach will be presented on the benchmark of scaled T shaped roof girder. Described girder was produced by Franz Oberndorfer GmbH & Co KG as the part of broth experimental study (Strauss et al. in press) aimed to support advanced development process of produced precast structural members. Beam represent scaled version of full scale TT shaped roof LDE7 girder produced by mentioned company. The shear destructive test under laboratory conditions were performed on ten scaled girders. Presented example represents the most complex one (in terms of geometry) and it was marked as T30 150/V2. One of the goals was to create accurate numerical models of destructive tests and perform subsequent stochastic simulation in order to determine statistic of the shear response behavior. Obtained results helped to establish basic deterministic and stochastic modelling procedure which

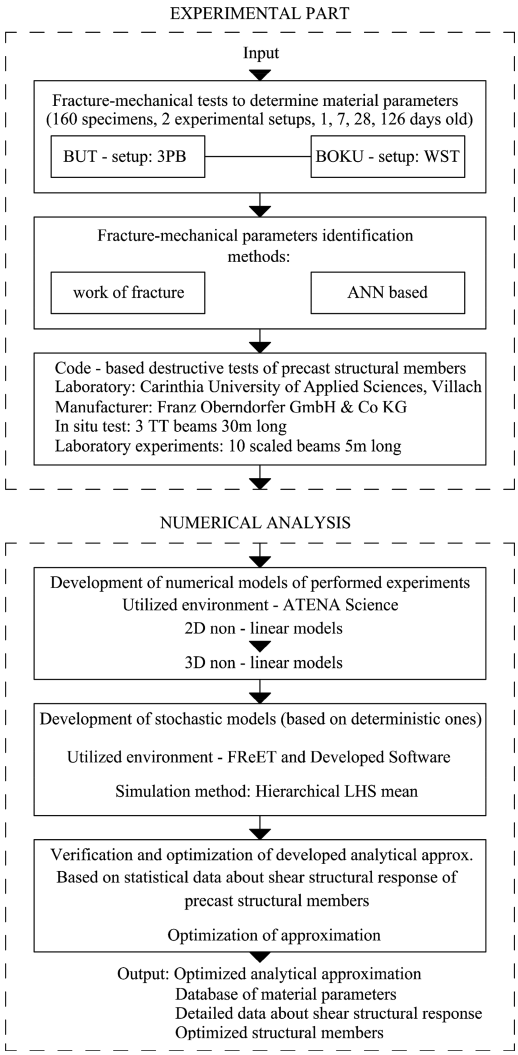

Figure 1. Scheme of the experimental and numerical studies associated with the research project on shear—normal force interactions of prestressed concrete girders.

is now being applied for full scale girders from production of Franz Oberndorfer GmbH & Co KG. Figure 1 displays whole developed procedure.

2 ANYLYSED STRUCTURE AND EXPERIMENT PROPERTIES

2.1 *Geometrical and prestressing properties of the analyzed beam T30/150 V2*

The beam has a T-shaped cross section, a total length of 5.00 m and a total height of 0.30 m. The web width is 0.14 m (This is the bottom dimension – web is slightly conical). The plate has a dimension b/h of 1.50 m/0.07 m. The beam is continuously prestressed to 898 MPa via 8 × 7-wire 1/2-inch strands with a wire quality of ST 1570/1770. The top two of all eight wires are isolated at a distance of 2.00 m from the beam end (only on one side), that is, they are not connected to the concrete. The isolation of those wires results in an asymmetrical load which is caused by the prestressing. In addition to the pretensioner wires, two reinforcement bars with a diameter of 20 mm are located in the lower reinforcement layer and six reinforcement bars with a diameter of 14 mm are located in the upper reinforcement layer. The lower reinforcement layer was anchored using four horizontal rebars in U-bolt shape with a diameter of 12 mm per side. Even though basically no stirrup reinforcement was planned according to the reinforcement layout, 10 rebars in U-bolt shape with a diameter of 6 mm were mounted in order to attach electrical strain gauge sensors (ESGs) at a distance of 0.50 m to each other along the bar. The plate of the beam was equipped with orthogonal reinforcement of 8 mm in diameter at a distance to each other of 0.20 m in the longitudinal and transverse directions. More detailed description of girders geometry along with the drawings can be found in (Strauss et al. in press).

2.2 *Destructive experiment setup*

Figure 2 shows the load path of the T30/150 V2 laboratory tested beam, which treats information for the nonlinear modeling procedure as essential. The displacement-controlled loading processes applied to the laboratory-tested beams were divided into four loading and unloading cycles. More details can be found in (Stoerzel et al. 2015).

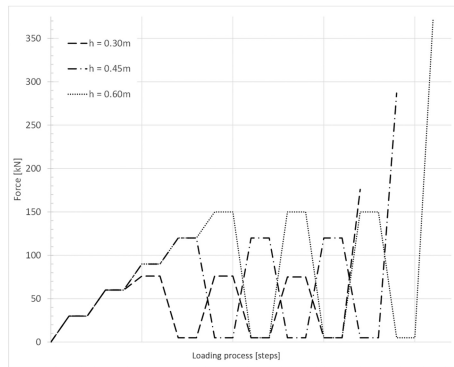

Figure 2. Loading scheme during the destructive testing of beam T30 150/V2.

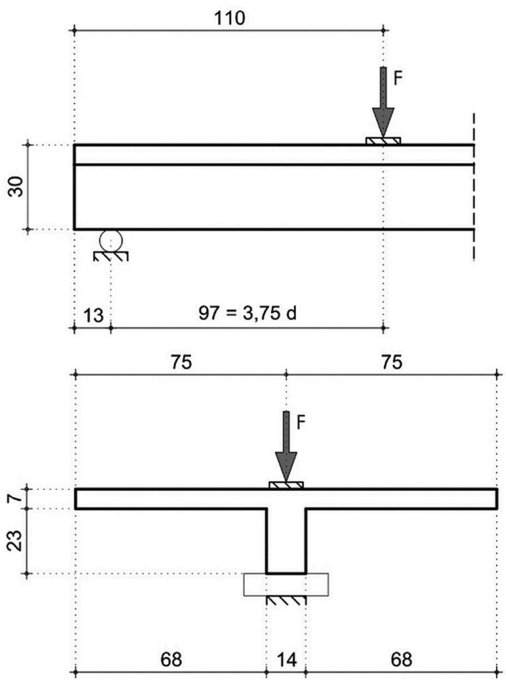

Figure 3. Layout of performed destructive test.

As shown in Figure 3, the girder was subjected to structural analysis in the laboratory and stored in a linear array on rolls. The loading was initiated via a test cylinder equipped with a calotte, which was mounted onto a 150 × 150 mm bearing plate at a height *d* of the bar at a distance of 3.75 m from the bearing line. More details about monitoring setup can be found in (Strauss et al. in press).

3 DETERMINISTIC COMPUTATIONAL MODEL

Non-linear computational model of destructive test of scaled T-shaped pre-stressed girder was created using GID-ATENA Science software environment (Červenka et al. 2007). Geometry of beam and reinforcement was modelled exactly according to drawings provided by manufacturer. Two linear supports were used for the model, since rollers were used during test. Regular hexagonal FE mesh composed of 16728 finite elements was generated in the program GID. The mesh has been condensed in the area of assumed shear failure. The FE mesh generated along with support conditions is shown in Figure 4. Detailed model of reinforcement (including tendons) is visible in Figure 5. The steel reinforcement was modelled

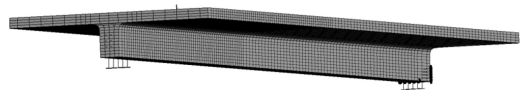

Figure 4. Finite element mesh and support conditions.

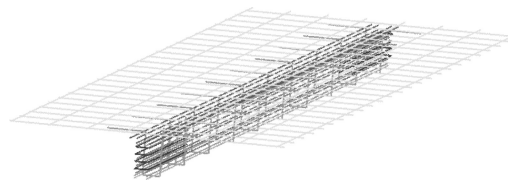

Figure 5. Reinforcement layout.

using 1D reinforcement material defined by strain vs. stress multilinear diagram. Prestressing tendons were also modelled using 1D reinforcement material, but working diagram of tendons was idealized as bilinear material with hardening.

Neglecting losses of prestressing could cause a significant inaccuracy of numerical model. Models without losses of prestressing have almost same ultimate capacity as models with consideration of losses. However, they underestimate final deflection of beam and resulting Load—Displacement (hereinafter LD) curve did not correspond to experimental one.

Prestressing is applied as initial strain for reinforcement line. This application will ensure that loss of prestressing due to elastic deformation of concrete is calculated explicitly. However, prestressing force was applied to concrete with age of only 14 hours during manufacturing process. This means that elastic modulus of concrete was different than elastic modulus after 28 days of hardening. Initial strain for reinforcement line should be reduce by the difference between strain of concrete with age 14 hours and strain of concrete with age 28 days exposed to prestressing force. Second loss of prestressing which should be applied by reduction of initial strain for reinforcement line is loss due to relaxation of tendons. Creep and shrinkage deformation leads to losses of prestressing. Test of girder was performed after 41 days of hardening. FIB model code 2010 was used for calculation of creep and shrinkage deformation. This deformation was recalculated to corresponding temperature load in order to influence stress state in reinforcement and tendons.

The LD experimental diagrams were fundamental for model updating process (see Figure 6). Note, that model of experiment represents from statistical point of view model of one realization, as discussed in (Novák et al. 2015). For advanced

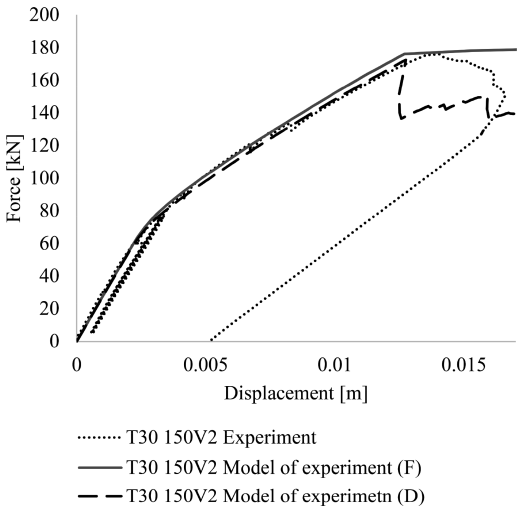

Figure 6. LD curves—Experiment vs. created numerical models: (D) – displacement loaded, (F) – force loaded.

Table 1. Identified material parameters of concrete.

Parameter	Mean	COV	PDF
Compressive strength	77 MPa	6.4%	GMB min EV1
Tension strength	3.9 MPa	10.6%	GMB max EV 1
E-module	34.8 GPa	10.6%	WBL min (3par)
Fracture energy	219.8 Jm^{-2}	12.8%	GMB max EV 1

modelling of concrete 3D Nonlinear Cementitious 2 (Červenka et al. 2007) material model was utilized. Table 1. shows the mean values and the corresponding probability distribution function of material parameters identified in (Lehký et al. 2014). Stochastic model of the concrete material properties based on the identified parameters was utilized to estimate material parameters of experimental realization using knowledge of compressive strength of the concrete. More detailed information about this procedure, deterministic models and theirs updating may be found in (Novák et al. 2015, Slowik et al. 2015).

4 VERIFICATION OF THE NON-LINEAR FINITE ELEMENT MODEL (NLFEM)

The following criteria divided into four levels of approximation (LoA) according to the basic philosophy of the Model Code 2010 allow a gradual adaptation and verification of the model set-up for NLFEM considerations.

4.1 *Macro—Verification (LoA-1)*

Verification of the NLFEM model set up on a macro or global level corresponds to the first level of approximation, including: (a) Examination of the boundary conditions, e.g. the support types and load application (support conditions and load introduction on the model) based on quantitative evaluation of the deformation behaviour or the deformation lines (deflection, rotation, curvature etc.) for a moderate stress situation, which is highly likely to cause a linear elastic model behaviour; (b) Examination of model homogeneity, avoidance of zones of crack formation, high stress gradients due to rigidity leaps, support conditions and plasticisation areas for a moderate load situation. The avoidance of the above can be achieved through the adaptation of the material models, the discretization, the detailed formation of the material properties, e.g. of the stiffness (modulus of elasticity); (c) Comparison of the deformation behaviour of the NLFEM model set-up with the deformation behaviour of comparable already verified NLFEM models or verified experiments. These comparative variables can be derived from their own verified NLFEM model set-ups and experiments as well as from verified data sets from the literature; (d) The findings on the deformation properties of scale models from tests and NLFEM together with the findings of conformity tests provide a significant basis for the verification of the deformation behaviour of unscaled and scaled model set-ups.

4.2 *Meso-Verification—Load Displacement Curves (LoA-2)*

Verification of the NLFEM model set up on a meso level corresponds to the second level of approximation, including:

Development and examination of the LD curves, e.g. distinction: (a) In linearly elastic regions or linearly elastic model behaviour; (b) In nonlinear quasi-elastic regions with controlled low steady stiffness changes e.g. due to micro-cracks (moderately curved regions); (c) In nonlinear regions with progressive stiffness changes (e.g., localization of fracture process zones); (c) In nonlinear regions with sudden stiffness changes in the LD curves (e.g., failure of reinforcing elements—connection zones, etc.); (d) These regions must be clearly identified in the load levels and the deformation levels and should be checked on their plausibility. The LD curves are essential elements of the model evaluation in the third LoA level.

Classification of the NLFEM model set up with respect to a brittle/ductile model behaviour: (a) An abrupt decrease in the LD curves of the NLFEM after the maximum load is interpreted as a

brittle failure of the model. By means of comparable tests from the literature or from own laboratory activities allow the verification of the LD curves with respect to their brittle behaviour. Possible deviations can be resulted due to the inappropriate choice of material laws, the inappropriate choice of solution algorithm (Newton Rapson method vs. Arc Length method), the inadequate detail formation e.g. reinforcement and bond behaviour; (b) A moderate decrease in the LD curves of the NLFEM with pronounced deformation behaviour after the maximum load is interpreted as a ductile failure of the model. By means of comparable tests from the literature or from own laboratory activities allow the verification of the LD curves with respect to the ductile behaviour; (c) Possible deviations can be caused due to the inappropriate choice of material laws, the inappropriate choice of the solution algorithm (Newton Rapson method vs. Arc Length method), the inadequate detail formation e.g. modelling of the reinforcement as a BI-linear material law with an unlimited flow plateau can lead to a pronounced unrealistic ductile behaviour of the NLFEM model. An unsuitable selection of the boundary conditions are also causes of the unrealistic ductile behaviour of the models.

4.3 *Meso Verification—Standard models (LoA-3)*

Verification of NLFEM model set up on a meso level corresponds to the third level of approximation, including: (a) The evaluation of the LD curves using the analytical models of load-bearing capacity (ULS) anchored in the standards. The standard models are equipped with security formats and they are based on linear approaches. The results of the analytical models should therefore have a significant distance to the bearing load (mean value based) determined by means of the NLFEM and, in the main case also lie in the linearly elastic or moderately nonlinear elastic range of the LD curves outlined above; (b) The evaluation of the LD curves using the analytical models of serviceability (SLS) anchored in the standards – "deflection, crack width, oscillation". The standard models of serviceability should have a significant distance from the serviceability characteristics (mean value based) determined by means of the NLFEM and also lie in the linearly elastic or moderately nonlinear elastic range of the LD curves outlined above. These considerations can usually be limited to the consideration of the displacement axis of the LD diagram.

4.4 *Micro Verification—Crack images (LoA-4)*

Verification of NLFEM model set up on a micro level corresponds to the fourth level of approximation, including the examination of the crack pattern development for a continuous increase of the load up to the failure of the model. The following sources can be used as a reference for the evaluation of crack development: (a) State of the Art: Findings of the crack image development from the professional world; (b) Findings from preliminary tests in a 1:1 scale for the model set up; (c) Findings from preliminary tests on scaled measurements for the model set up; (d) Findings from the literature; (e) Inspection and monitoring findings from accompanying 1:1 tests.

5 PROBABILISTIC DESIGN AND SAFETY FORMATS

5.1 *Semi-probabilistic approach*

In practical applications are nonlinear finite element models huge and stochastic models contain a high number of random input variables. In such cases, computational requirements are significantly reduced by semi-probabilistic methods, where design value of response R is evaluated instead of the probability of failure. If R is lognormal distributed independent random variable, the design value of R is defined as:

$$R_d = \mu_R \cdot \exp(-\alpha_R \beta_n \upsilon_R) \tag{1}$$

where υ_R is coefficient of variation (CoV), α_R represents sensitivity factor and recommended value is $\alpha_R = 0.8$. The reliability index β is another way to express the probability of failure p_f, and it is defined by:

$$\beta = -\phi_N^{-1}(p_f) \tag{2}$$

where ϕ_N^{-1} is the inverse of the standard normal probability distribution function. The target reliability index for ultimate limit state, moderate consequences of failure and reference period of 50 years is set as $\beta_n = 3.8$ according to (JCSS 2001).

Obviously, for determination of design value by semi-probabilistic approach is crucial to correctly estimate the mean value and CoV, this can be done by various reliability methods. Besides full probabilistic method using Monte Carlo type sampling, it is possible to use for example the simple numerical quadrature method proposed by (Rosenblueth 1975).

5.2 *Partial safety factor*

According to EN 1990, NLFEA is computed with design values of input random variables and result is assumed to be design value of resistance R_d:

$$R_d = R(f_{yd}, f_{cd}, ...) \tag{3}$$

Partial safety factor (PSF) method may lead to an unrealistic redistribution of internal forces and different failure mode of structure because of extremely low design values of input variables. Due to the possibility of the different behaviour of finite element model, it is recommended to compute NLFEA with mean value and apply global safety factor on the result.

5.3 *EN 1992-2*

The only global safety factor approach defined in EN is the global safety factor concept according to EN 1992-2, the design value is estimated as follows:

$$R_d = \frac{R(f_{ym}, f_{cm}, ...)}{\gamma_R} \tag{4}$$

where $f_{ym} = 1.1 * f_{yk}$ is mean value of steel reinforcement, $f_{cm} = 0.843 * f_{ck}$ is reduced mean value of concrete property because of its higher variability and idea that design values should correspond to the same probability. These values are derived from characteristic values (5% percentile) χ_k. The global safety factor for resistance is set as $\gamma_R = 1.27$. For concrete the Eurocode 2 allows only compressive type of failure, however the study presented by (Červenka 2013) extends its applications also to brittle modes of failure. As can be seen, PSF and EN 1992-2 methods need just one NLFEA simulation.

5.4 *ECoV by Červenka*

The ECoV methods are based on semi-probabilistic approach, the difference is in the way how to estimate the coefficient of variation and mean value of the response. It is assumed lognormal distribution for response variable R in proposal by (Červenka 2013) and (Holický 2006), thus coefficient of variation υ_R can be estimated as:

$$\upsilon_R = \frac{1}{1.65} \ln\left(\frac{R_m}{R_k}\right) \tag{5}$$

Note that, in ECoV by Červenka are just 2 simulations of NLFEA needed, first one with mean values of input random variables $R_m = R(f_{ym}, f_{cm}, \alpha_{nom}, \ldots)$ and the second simulation R_k using characteristic values. Described concept was adopted in the FIB Model Code 2010 and design value R_d was later decreased by another factor $\gamma_{Rd} = 1.06$:

$$R_d = \frac{R_m}{\gamma_R \gamma_{Rd}}, \gamma_R = \exp(\alpha_R \beta \upsilon_f) \tag{6}$$

5.5 *ECoV by Schlune et al.*

The extended ECoV method proposed by (Schlune et al. 2012), where υ_R is composed of the variability of the numerical model υ_m, geometrical uncertainties υ_g, and material uncertainties υ_f:

$$\upsilon_R = \sqrt{\upsilon_g^2 + \upsilon_m^2 + \upsilon_f^2} \tag{7}$$

Recommended values for the variability of NLFEM and geometrical uncertainties can be found in the literature. The coefficient of variation of material υ_f, if material parameters are not correlated, can be calculated as:

$$\upsilon_f \approx \frac{1}{R} \sqrt{\sum_{i=1}^{N} \left(\frac{R_m - R_{\Delta fi}}{\Delta_{fi}} \sigma_{fi} \right)^2} \tag{8}$$

where the response of construction $R_{\Delta fi}$ is determined by NLFEA using reduced mean values of material variables by Δ_{fi} and σ_{fi} is standard deviation of *i-th* variable. If the lognormal distribution of material variables is assumed, the reduced values of f_i can be calculated as:

$$f_{\Delta fi} = f_{mi} \cdot \exp(-c \cdot \upsilon_{fi}) \tag{9}$$

where f_{mi} is mean value of material characteristic and the step size parameter is defined as $c = (\alpha_R \beta)/\sqrt{2}$ Note that, this approach requires $N+1$ simulations of NLFEA, where N is the number of material random variables. The extension of the the method for correlated material variables can be found in (Schlune et al. 2012) as well.

5.6 *Sampling points in 2D*

Representation of above described methods can be seen in Figure 7.

Single approaches define sampling points in N-dimensional space, where their coordinates represent values of input random material characteristics. The difference is in the number and position of sampling points. Generally, more sampling points lead to the more accurate estimation of CoV and the choice of most efficient method depends on the size of NLFEM and stochastic model.

Note that, the computational requirements the ECoV method by (Schlune et al 2012). and Numerical quadrature by (Rosenblueth 1975) are strongly dependent on the size of the stochastic model.

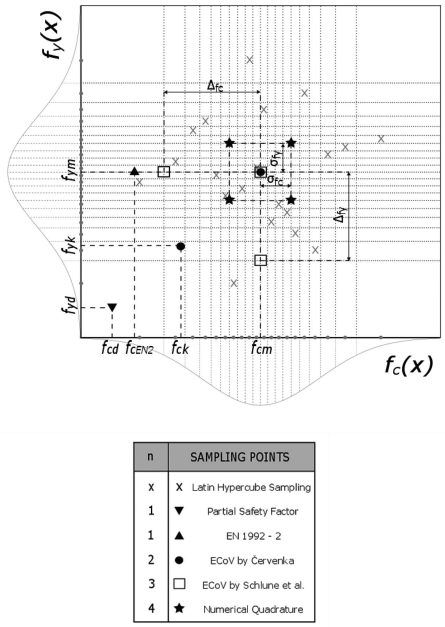

Figure 7. Results of investigated safety format concepts.

Thus, the sensitivity analysis should be performed to reduce the number of random input variables.

6 STOCHASTIC MODELLING

6.1 *Stochastic model*

The aim was to estimate statistical variability of shear capacity of prestressed girders and to propose probabilistically based design values or resistances. For the purpose of stochastic analysis, the SARA software package with solver ATENA and reliability tool FReET (Novák et al. 2014) were utilized. Sensitivity analysis performed at the beginning of the whole process showed the most decisive/dominating parameters of nonlinear modelling. A set of 12 parameters was utilized for stochastic evaluation of structural response variability. Stochastic model of concrete was based on data presented in (Řoutil et al. 2014) obtained by ANN based identification (Novák et al. 2015, Lehký et al. 2014).

Identified material parameters of concrete were obtained from laboratory test under perfect condition – resulting in quite small variability of material parameters of concrete. In order to ensure realistic results, it was necessary to introduce higher variability for obtained material parameters and to randomize also density of concrete mixture. Stochastic models of steel reinforcement (Bst 550B) and tendons (cables – ST 1570/1770) were based at recommendations of

Table 2. Identified material concrete parameters.

Parameter	Mean	COV	PDF
E	34.8 GPa	20.6%	WBL min (3 par)
f_t	3.9 MPa	20.6%	GMB max EV I
f_c	–77 MPa	16.4%	GMB min EV I
G_f	219.8 J.m^{-2}	32.8%	GMB max EV I
ρ	0.0023 kton/m^3	4%	Normal
E_s	200 GPa	2%	Normal
f_{ys}	610 MPa	4%	Normal
E_t	195 GPa	2.5%	Normal
f_{yt}	1387.88 MPa	2%	Normal
P	0.0835 MN	6%	Normal
I. L.	1	10%	Lognormal
L. T. L.	1	10%	Lognormal

(JCSS 2001) (variability) and information from manufacturer (mean value). Prestressing force was randomized according to the recommendation of (JCSS 2001). For each realization also prestressing losses were calculated according to FIB model code 2010. It was decided to introduce uncertainty of calculated losses of prestressing with variability corresponding to recommendations in (JCSS 2001).

The stochastic model of destructive test of girder T30 150/V2 is shown in Table 2. Parameters are: E – Young's modulus (E – concrete, E_s – steel reinf., E_t – tendons), f_t – tensile strength, fc – compressive strength, G_f – fracture energy, ρ – density of concrete mixture, f_{ys} – yield strength of steel reinforcement, f_{yt} – yield strength of tendons, IL – uncertainty for immediate losses of prestressing and LTL – uncertainty for long term losses of prestressing. Also, statistical correlations were considered (Novák et al. 2015). In order to introduce required statistical correlations, the simulated annealing optimization method (Vořechovský et al. 2012) was utilized.

Utilized correlation matrix may be found in (Slowik et al. 2015).

6.2 *Simulation*

Stochastic analysis of beam T30 150V2 described in this paper is the first from scheduled probabilistic assessments of laboratory tested girders. Due to enormous computational demands it was decided to utilize efficient HSLHS method (Vořechovský 2014). The aim is to perform analysis with lower number of samples at the beginning and to use this set of samples for sensitivity analysis (Novák et al. 2017), to fix possible errors and to use previous simulations in consequent analysis. Statistics of response using set of 10 simulations was extended in second run of HSLHS by another 20 simulations so the total amount of performed simulations is so far 30. Figure 7 captures calculated LD curves for Performed simulations.

6.3 *Ultimate limit state*

Ultimate limit state is represented by critical value of force applied during experiment (peak of LD diagram). Subsequently the comparison of fully probabilistic approach, numerical quadrature (Rosenblueth 1975), classical calculation of response using partial safety factors and various versions of so called ECOV methods (Holický 2006, Červenka 2013, Schlune et al 2012) to estimate design value was performed. In case of fully probabilistic design, calculated percentile of shear resistance corresponds to probability 0.0012 according to recommendations in (EN 1990 2002) (based on separation of resistance and action of load variables) is performed. The estimated probability distribution function (PDF) of shear resistance is shown in Figure 8. Lognormal probability distribution function is utilized in order to demonstrate results and to compare calculated structural response with alternative approaches. Final results are demonstrated in Figure 8, as could be expected, the results of deterministic methods PSF and EN 1992-2 are most conservative. Also note that the results of stochastic methods, except the ECoV by Červenka which significantly underestimated the variation of response R, are quite close: from 110 to 130 kN. If the result of semi-probabilistic approach based on Latin Hypercube Sampling (LHS) is considered as the reference, the most efficient method is ECoV modified by Schlune.

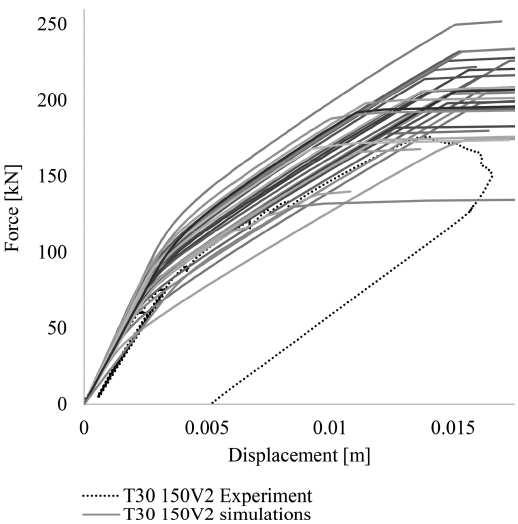

Figure 8. LD curves of 30 performed simulations.

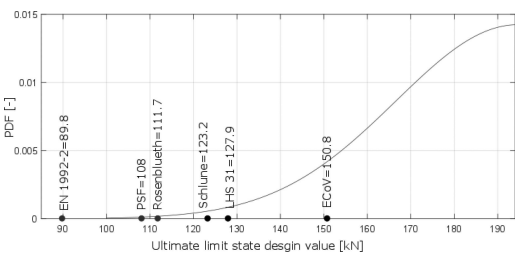

Figure 9. PDF (lognormal) of applied force at ultimate limit state.

7 CONCLUSION

The paper describes integration/application of the modelling of nonlinearity and uncertainty to predict shear failure behaviour of prestressed concrete girders in the light of advanced design possibilities. The approach is complex, going from fracture-mechanical parameters determination and advanced deterministic 3D computational modelling of girders to stochastic modelling. The aim was to assess the variability of shear response and to present and verify alternative design procedures in comparison with fully probabilistic design. The paper describes this complex way, first results of stochastic analysis were presented for beam T30 150V2, more extensive studies will continue.

ACKNOWLEDGEMENT

The authors give thanks for the financial support of the Czech Science Agency project No. 17-02862S ("PROMOSS") also from project of the specific university research at Brno University of Technology, registered under the number FAST-J-17-4786.

REFERENCES

Bairan, G., J.M. & Mari, B., A.R. 2006, Coupled model for the non-linear analysis of anisotropic sections subjected to general 3D loading. Part 1: Theoretical formulation. *Computers and Structures*, 84 (31–32), pp. 2254–2263.

Bažant Z. P., Planas J. 1998, Fracture and size effect in concrete and other quasibrittle materials, *CRC Press LLC*, Boca Raton.

Bažant Z. P., Yu Q. 2003, Designing against size effect on shear strength of reinfoced concrete beams without stirrups, *Struct. Eng*. Report, No. 03-02/A466 s.

Ceresa, P., Petrini, L. & Pinho, R. 2007, Flexure-shear fiber beam-column elements for modeling frame structures under seismic loading – State of the art. *Journal of Earthquake Engineering*, 11 (SUPPL. 1), pp. 46–88.

Červenka, V. 2013, Reliability-based non-linear analysis according to fib model code 2010, in *Struct Concr J* fib, 14:19–28.

Červenka, V., Jendele, L. & Červenka, J. 2007, ATENA Program Documentation – Part 1: Theory, Cervenka Consulting, Prague, Czech Republic.

Collins, M.P., Bentz, E.C. & Sherwood, E.G. 2008, Where is shear reinforcement required? Review of research results and design procedures. *ACI Structural Journal*, 105 (5), pp. 590–600.

Comité Euro-International du Beton (Hrsg.) 2012, CEB-FIP Model Code 2010: "Design Code", *fib Bulletin* No. 65/66, Lausanne.

Elices, M., Guinea, G. V. & Planas, J. 1992, Measurement of the fracture energy using three-point bend tests: Part 3–Influence of cutting the P–δ tail. *Material and Structures*, 25 (6): 327–334.

EN 1990 2002, Eurocode – Basis of structural design, 87 pp.

EN 1992 2005, Eurocode: design of concrete structures, Brussels: *European Comitee for Standardization.*

Holický, M. 2006, Global resistance factors for concrete members, *Acta Polytechnica*, CTU, Prague.

JCSS, 2001, JCSS Probabilistic Model Code. Zurich: J*oint Committee on Structural Safety*, ISBN 978-3-909386-79-6.

Lehký, D., Keršner, Z. & Novák, D. 2014, FraMePID-3PB Software for Material Parameters Identification Using Fracture Test and Inverse Analysis. *Advances in Engineering Software*, Vol. 72, 147–54.

Mari, A., Bairan, J., Cladera, A., Oller, E. & Ribas, C., 2015, Shear-flexural strength mechanical model for the design and assessment of reinforced concrete beams. *Structure and Infrastructure Engineering*, 11 (11),1399–1419.

Novák, D. & Lehký, D. 2006, ANN inverse analysis based on stochastic small-sample training set simulation. *Engineering Application of Artificial Intelligence,* 19:731–40.

Novák, D., Řoutil L., Novák L., Slowik, O., Strauss, A. & Krug, B., 2015, Database of fracture-mechanical concrete parameters and its implementation into reliability software FReET. *Proceedings of IPW2015 13th International Probabilistic Workshop*, 4–6 November 2015, Liverpool, Great Britain.

Novák, D., Slowik, O., Novák, L., Strauss, A., Lehký, D., 2017, Statisical and sensitivity analyses of prestressed concrete girders failing in shear, *Proceedings of 12th International Conference on Structural Safety & Reliability*, Vienna, Austria.

Novák, D., Vořechovský, M., Teplý, B., 2014, FReET: Software for the statistical and reliability analysis of engineering problems and FReET-D: Degradation module. *Advances in Engineering Software* (Elsevier) 7: 179–192.

Rosenblueth, E., 1975, Point estimates for pro bability moments, in *Proc. Natl. Acad Sci*, USA, 72:38124.

Řoutil, L., Lehký, D., Šimonová, H., Kucharczyková, B., Keršner, Z., Novák, T., Zim-mermann, T., Strauss, A. & Krug B., 2014, Experimental-computational determination of mechanical fracture parameters of concrete for probabilistic life-cycle assessment. *Proceedings of IALCCE 2014 – Fourth International Symposium on Life-Cycle Civil Engineering*, Tokyo, Japan.

Russo, G., Somma, G. and Mitri, D., 2005, Shear strength analysis and prediction for reinforced concrete beams without stirrups. *J. Struct. Eng.*, 131(1), 66–74.

Schlune, H., Gylltoft, K., Plos, M., 2012, Safety formats for non-linear analysis of concrete structures, *in Mag Concrete Res*, 64:563–74.

Slowik, O., Novák, D., Krug, B. & Strauss, A., 2015, Shear failure of pre-stressed concrete T-shaped girders: Experiment and nonlinear modeling. *Proceedings of IABSE 2015 conference of International Association for Bridge and Structural Engineering*, September 23–25, Geneva, Switzerland.

Slowik, O., Novák, N., Novák, L., 2016, Shear resistance of prestressed girders: Probabilistic design, *Proceedings of International Probabilistic Workshop,* Ghent, Netherlands.

Stoerzel J., Randl N., Strauss A., 2015, Monitoring shear degradation of reinforced and pre-tensioned concrete members. In: *IABSE Conference 2015: Structural Engineering*. Geneva: International Association for Bridge and Structural Engineering.

Strauss A, Krug B, Slowik O, Novak D., in press, Combined shear and flexure performance of prestressing concrete T-shaped beams: Experiment and deterministic modeling. *Structural Concrete.* 2017;1–20. https://doi.org/ 10.1002/suco.201700079.

Strauss, A., Zimmermann, T., Lehký, D., Novák, D. & Keršner, Z., 2014, Stochastic fracture-mechanical parameters for the performance-based design of concrete structures. *Struct. Concr*. 15(3), 380–394.

Vořechovský, M., 2012, Correlation control in small sample Monte Carlo type simulations II: Analysis of estimation formulas, random correlation and perfect uncorrelatedness. *Probabilistic Engineering Mechanics*, 29, 105–120.

Vořechovský, M., 2014, Hierarchical refinement of Latin Hypercube Samples. *Computer-Aided Civil and Infrastructure Engineering*, volume 00, 2014: 1–18.

Zimmermann, T., Strauss, A., Lehký, D., Novák, D. & Keršner, Z., 2014, Stochastic fracture-mechanical characteristics of concrete based on experiments and inverse analysis. *Constr build mater* 73: 535–543.



Taylor & Francis
Taylor & Francis Group
http://taylorandfrancis.com

Computational Modelling of Concrete Structures – Meschke, Pichler & Rots (Eds)
© 2018 Taylor & Francis Group, London, ISBN 978-1-138-74117-1

Characterising the shear behaviour of steel fibre-reinforced concrete

S. Zeranka & G.PA.G. van Zijl
Stellenbosch University, Stellenbosch, Western Cape, South Africa

ABSTRACT: The Mode I and Mode II fracture of steel fibre-reinforced self-consolidating concrete is investigated experimentally at two scales of observation, namely at the scale of a single fibre (Micro-scale) and at the scale of a single localised crack (Meso-scale). The Meso-scale data is used to calibrate and validate a material model implemented in a numerical procedure via a user material (UMAT) in the commercial finite element package Abaqus. An empirical model reconciles the fibre component characterised via a single fibre transverse pull-out test with the composite Iosipescu shear test.

1 MODELLING CONCEPT

In the smeared crack concept, a cracked solid remains a continuum and the effect of the crack(s) is distributed or "smeared" over the entire element area. This concept was originally proposed by Rashid (1968). Isotropy is assumed prior to cracking with orthotropic behaviour after crack formation. The total strain $\{\varepsilon\}$ is decomposed into two components, the strain in the uncracked material $\{\varepsilon_c\}$ and the strain in the crack $\{\varepsilon_{cr}\}$ (Eq. 1). The uncracked material and the crack are assumed to work in series (Fig. 1).

$$\{\varepsilon\} = \{\varepsilon_c\} + \{\varepsilon_{cr}\} \tag{1}$$

The membrane element in Figure 2 is subject to general in-plane stresses. In the uncracked stage the axes of the local coordinate system (n-t) are coincident with the principal stress directions, oriented with an angle with respect to the global coordinate system (x–y). As soon as the maximum principal tensile stress exceeds the concrete tensile strength, crack formation occurs perpendicular to the principal tensile stress direction. At this point the crack orientation (Φ) is assumed to be fixed according to the smeared-fixed crack concept. The axes of orthotropy (n–t) are normal and parallel to the crack surface (Fig. 2).

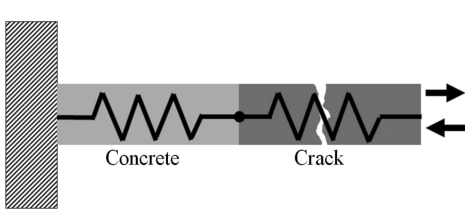

Figure 1. Uncracked concrete and crack working in series (Bernardi et al. 2012).

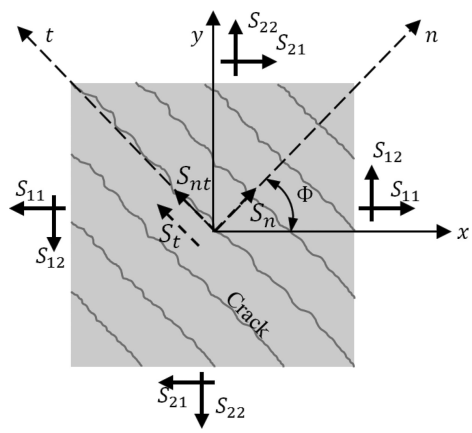

Figure 2. Cracked plane stress element subject to general in-plane stresses (Notation: global stress S_{11}, S_{22} and S_{12}).

2 ANALYTICAL FORMULATION OF MATERIAL MODEL

Prior to cracking, the material is assumed to be isotropic linear elastic. The only parameters for this state are the Young's modulus (E) and Poisson's ratio (ν). At crack initiation, when the positive principal tensile stress is equal to or exceeds the tensile strength of the material at an integration point, the formulation changes from isotropic to orthotropic in the local crack coordinate system (n–t), which remains fixed for the duration of the analysis.

According to Equation 1, the strain increment is decomposed into its uncracked and crack portions. The uncracked material is assumed to remain isotropic linear elastic. The crack traction increment Δt^{cr} is related to the crack strain increment $\Delta\varepsilon_{nt}^{cr}$ via the crack tangent stiffness matrix D^{cr} (Eq. 2). Equation 2 is derived in Subsection 3.1.2 to follow.

$$\Delta t^{cr} = D^{cr} \Delta \varepsilon_{\mathrm{nt}}^{cr} \tag{2}$$

The crack tangent stiffness matrix is assumed to take the form:

$$D^{cr} = \begin{bmatrix} D^{I} & 0 \\ 0 & D^{II} \end{bmatrix}, \tag{3}$$

where D^{I} and D^{II} are the Mode I and II stiffness moduli respectively.

The assumption of zero off-diagonal terms in Equation 3 implies that direct shear-normal coupling is ignored. This effect can be obtained indirectly, by relating the shear modulus D^{II} to the crack normal strain. The implication of this simplification will be discussed in the analysis output and conclusions.

2.1 *Mode I parameters*

2.1.1 *Strength parameters and fracture initiation*

A simple Rankine-type tension-cut off condition (Fig. 3a) is assumed in the principal stress space (σ_1-σ_2). Only one strength parameter, namely the uniaxial tensile strength f_{ct} is therefore needed to represent this model. This assumption requires that tensile cracking is not accompanied by significant lateral compression as justified by Kupfer et al. (1969). With regard to crack initiation, the crack is assumed to be orientated perpendicular to the direction of the major principal tensile stress only in the absence of significant lateral compression.

2.1.2 *Fracture propagation*

Several Mode I fracture softening functions have been proposed in the literature e.g. Hillerborg et al. (1976) and Bazant & Oh (1983). The parameters, which are assumed to be fixed material properties, include the tensile fracture energy, G_{ft}, which is the amount of energy required to create one unit of area of a Mode I crack and the shape of the softening diagram e.g. linear, multi-linear, exponential or some other nonlinear function. An exponential function, such as the one illustrated in Figure 3b is used. For smeared cracks, the fracture is assumed to be distributed over a crack band width *h* (Bazant & Oh 1983). The crack band width is related to the specific Finite Element (FE) configuration. It is assumed that the energy is released over this width in order to obtain results that are objective with regard to mesh refinement. A uniform strain distribution is also assumed over the crack band. The local Mode I crack traction-strain ($t_n^{cr} - \varepsilon_n^{cr}$) relation has the form given by Equation 4. The fracture energy G_{ft}/h corresponds to the area under the softening curve for a discrete crack.

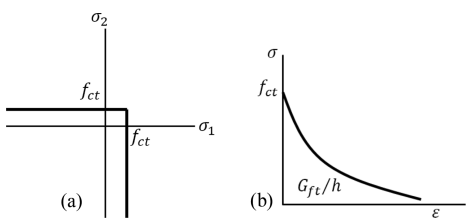

Figure 3. (a) Rankine-type tension cut-off model, (b) Mode I exponential fracture softening function.

$$t_n^{cr} = f_{ct} e^{-\frac{f_{ct} h}{G_{ft}} \varepsilon_n^{cr}} \tag{4}$$

2.1.3 *Crack tangent stiffness modulus*

The crack tangent stiffness is the derivate of the softening function and is therefore also expressed in terms of the strength and energy parameters, as well as the shape of the softening diagram (Eq. 5).

$$D^{I} = \frac{d}{d\varepsilon_n^{cr}}\left(t_n^{cr}\right) = \frac{-f_{ct}^{\,2} h}{G_{ft}} e^{-\frac{f_{ct} h}{G_{ft}} \varepsilon_n^{cr}} \tag{5}$$

2.2 *Mode II parameters*

The Mode II response has a limit function of the same type as for Mode I, namely

$$t_{nt}^{cr} = f_{cs} e^{-\frac{f_{cs} h}{G_{fs}} \gamma_{nt}^{cr}} \tag{6}$$

The shear stiffness for initial Mode II loading as well as unloading and reloading is a function of the normal strain in the crack (Eq. 7). The crack width therefore determines the initial shear stiffness and hence the peak shear stress reached. Loading along the limit function is a function of shear strain only (Eq. 6). Stated differently, the crack shear stress is a function of the crack normal and shear strain during loading and unloading. Once the Mode II limit function is reached, the shear stress and tangent stiffness is only a function of the crack shear strain.

$$D^{II} = \max\left(\left[1 - \frac{\varepsilon_n^{cr} h}{w_m}\right] G \cdot f_i, G_{min}\right) \cdot h \tag{7}$$

where t_{nt}^{cr} is the crack shear traction, γ_{nt}^{cr} is the crack shear strain, f_{cs} is the peak shear stress on the limit function (where $\varepsilon_n^{cr} = 0$ and $\gamma_{nt}^{cr} = 0$), G_{fs} is the shear fracture energy, w_m and f_i are calibrated model parameters, G is the elastic shear modulus and G_{min} is a minimum shear modulus.

3 NUMERICAL PROCEDURE

Abaqus user subroutine UMAT is called for each integration point at each iteration of every increment. It is provided with the material state at the start of the increment (stress, solution-dependent

state variables, temperature, and any predefined field variables) and with the increments in temperature, predefined state variables, strain, and time.

3.1 *Material state: Uncracked and cracked*

The positive principal tensile strain governs the material state. The first task is therefore to compute the principal strain values from the given total global strain.

If the positive principal tensile strain is less than the specified cracking strain, linear elastic isotropy is assumed. However, if this is not the case, the material is considered to be cracked or damaged and nonlinear orthotropic behaviour is assumed. Because this material model considers strain reversals accompanied with unloading, it is important to establish a state variable which stores the cracked state of the material.

3.1.1 *Elastic domain: Linear elastic isotropy*

Provided the positive principal tensile strain does not equal or exceed the prescribed strain at which cracking initiates and the state variable which tracks the status of the material, does not equate to a "cracked" status, the material will be treated as a linear elastic isotropic material.

3.1.2 *Cracked domain: Derivation of stress-strain relation*

An incremental strain formulation is used in the derivation of the stress-strain relation in the cracked domain (Rots 1989). As stated before, the total strain of the cracked material is decomposed into the strain in the crack and the strain in the uncracked material. Expressed in incremental form this is

$$\Delta\varepsilon_{xy} = \Delta\varepsilon_{xy}^{cr} + \Delta\varepsilon_{xy}^{co} \tag{8}$$

where

$\Delta\varepsilon_{xy}$– total strain of cracked material (in global coordinates)

$\Delta\varepsilon_{xy}^{cr}$ – strain in crack (in global coordinates)

$\Delta\varepsilon_{xy}^{co}$ – strain of uncracked material (in global coordinates)

Considering the strain increment in the local crack coordinates n–t,

$$\Delta\varepsilon_{\mathrm{nt}}^{cr} = \left[\Delta\varepsilon_{\mathrm{n}}^{cr}\ \Delta\gamma_{\mathrm{nt}}^{cr}\right]^T \tag{9}$$

where

$\Delta\varepsilon_{\mathrm{n}}^{cr}$ – local strain normal to the crack (Mode I)

$\Delta\gamma_{\mathrm{nt}}^{cr}$ – local shear strain parallel to the crack (Mode II)

The local crack strains can be expressed in the global coordinate system x–y.

$$\Delta\varepsilon_{xy}^{cr} = N\Delta\varepsilon_{\mathrm{nt}}^{cr} \tag{10}$$

where

$$N = \begin{bmatrix} c^2 & -sc \\ s^2 & sc \\ 2sc & c^2 - s^2 \end{bmatrix} \tag{11}$$

with $c = \cos\Phi$ and $s = \sin\Phi$.

In the same way, the incremental tractions on the crack surface can be expressed as

$$\Delta t^{cr} = \left[\Delta t_{\mathrm{n}}^{cr}\ \Delta t_{\mathrm{nt}}^{cr}\right]^T \tag{12}$$

where

$\Delta t_{\mathrm{n}}^{cr}$ – Mode I normal traction increment

$\Delta t_{\mathrm{nt}}^{cr}$ – Mode II shear traction increment

The relationship between the global stress increment and the local traction increment is

$$\Delta t^{cr} = N^T\Delta\sigma \tag{13}$$

where $\Delta\sigma$ is the total global stress increment.

To complete the system of equations, a constitutive model for the uncracked material (between cracks) is needed, as well as traction-strain/displacement relations for the smeared cracks i.e.

$$\Delta\sigma = D^{co}\Delta\varepsilon^{co} \tag{14}$$

$$\Delta t^{cr} = D^{cr}\Delta\varepsilon_{\mathrm{nt}}^{cr} \tag{15}$$

where

D^{co} is the tangent stiffness matrix for the uncracked material and

D^{cr} is the tangent stiffness matrix for the cracked material

The overall stress-strain relation for the cracked material with respect to the global coordinate system can now be derived. First substitute the relation for the global crack strain increment in terms of the local crack strain increment into the decomposition relation i.e.

Substitute Equation 10 into Equation 8, which yields:

$$\Delta\varepsilon = N\Delta\varepsilon_{12}^{cr} + \Delta\varepsilon^{co} \tag{16}$$

Substitute Equation 16 into Equation 14, which yields:

$$\Delta\sigma = D^{co}\left(\Delta\varepsilon - N\Delta\varepsilon_{12}^{cr}\right) \tag{17}$$

Pre-multiplying with N^T yields:

$$N^T\Delta\sigma = N^T D^{co}(\Delta\varepsilon - N\Delta\varepsilon_{12}^{cr}) \tag{18}$$

Substitute Equation 15 and 13 into the LHS of above, which yields:

$$D^{cr}\Delta\varepsilon_{12}^{cr} = N^T D^{co}\left(\Delta\varepsilon - N\Delta\varepsilon_{12}^{cr}\right) \tag{19}$$

This provides the link between local crack strain and total global strain:

$$\left(D^{cr} + N^T D^{co} N\right)\Delta\varepsilon_{12}^{cr} = N^T D^{co}\Delta\varepsilon \tag{20}$$

$$\Delta\varepsilon_{12}^{cr} = \left(D^{cr} + N^T D^{co} N\right)^{-1} N^T D^{co}\Delta\varepsilon \tag{21}$$

Finally, the overall relation between global stress and strain by substituting above into Equation 19, which yields

$$\Delta\sigma = D^{crco}\,\Delta\varepsilon \tag{22}$$

where the total stiffness matrix for the cracked material is

$$D^{crco} = D^{co} - D^{co} N \left(D^{cr} + N^T D^{co} N\right)^{-1} N^T D^{co}$$

3.1.3 *Cracked domain: Procedure*

The positive principal tensile strain is greater than or equal to the cracking strain or the state variable which tracks the material state is set to a "cracked" state. The first step in the cracked state is to determine the crack orientation. The crack orientation is only determined once at the onset of cracking and is then stored.

3.1.3.1 Compute incremental and total local strain

The material model implemented, is expressed in terms of the local total strains, as well as the local strain increment, in the case of unloading or reloading. The next step in the procedure is therefore to transform the global total strain tensor and the global strain increment, to the crack basis using the following transformations (Eqs. 23–24).

$$\begin{bmatrix} \varepsilon_1 \\ \varepsilon_2 \\ \gamma_{12} \end{bmatrix} = \begin{bmatrix} c^2 & s^2 & sc \\ s^2 & c^2 & -sc \\ -2sc & 2sc & c^2 - s^2 \end{bmatrix} \begin{bmatrix} \varepsilon_x \\ \varepsilon_y \\ \gamma_{xy} \end{bmatrix} \tag{23}$$

$$\begin{bmatrix} \Delta\varepsilon_1 \\ \Delta\varepsilon_2 \\ \Delta\gamma_{12} \end{bmatrix} = \begin{bmatrix} c^2 & s^2 & sc \\ s^2 & c^2 & -sc \\ -2sc & 2sc & c^2 - s^2 \end{bmatrix} \begin{bmatrix} \Delta\varepsilon_x \\ \Delta\varepsilon_y \\ \Delta\gamma_{xy} \end{bmatrix} \tag{24}$$

3.1.3.2 Local stress and tangent stiffness

Compute the local stresses and corresponding local tangent stiffness as per material model defined in Section 2, then assemble the global tangent stiffness matrix for cracked material as per Subsection 3.1.2. Transform local stresses to global basis and return stress and cracked material tangent stiffness matrix to Abaqus.

4 MODEL VERIFICATION FOR A SINGLE FINITE ELEMENT

Testing and verification of the user subroutine is done for a single element, where the only complex part of the model is the UMAT and the boundary conditions can be isolated easily.

4.1 *Element type and dimensions*

A 4-node bilinear plane stress quadrilateral is used in all cases.

4.2 *Boundary conditions*

The boundary conditions tested are illustrated in Figure 4. The element is first subjected to uniaxial tensile loading (Fig. 4a) and repeated unloading (Fig. 4b) and reloading. In the unloading step, the prescribed displacement is removed linearly over the step time, while the other boundary conditions are retained. These two boundary conditions serve to test and validate the Mode I material model directly, as well as the unloading and reloading functions of the Mode I response. The unloading and reloading capability of the material model is not elaborated here.

The next boundary condition tested is the Mode II response without initial loading in Mode I (Fig. 4d). Even though this load case is not implemented in the Meso-scale test, it demonstrates the case for a diagonal crack in the element. An equation constraint ($_o$) is applied to the two loading nodes (in Fig. 4c&d) to ensure that both nodes undergo the same horizontal displacement. This

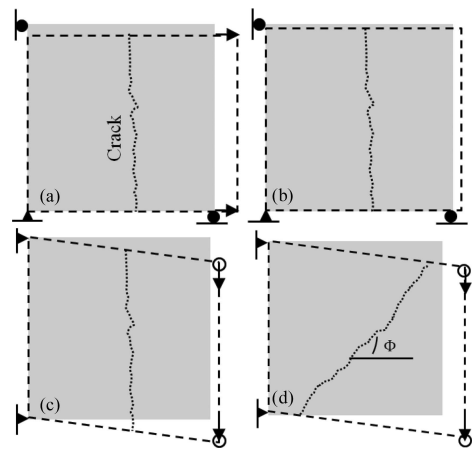

Figure 4. Single element boundary conditions (a) tensile loading, followed by (b) tensile unloading and (c) shear loading; (d) Shear/Mode II loading only (diagonal cracking).

way the element edges remain parallel and the strains and stresses observed for all four integration points in the element remain uniform.

The final boundary condition executes Mode I loading (Fig. 4a), Mode I unloading (Fig. 4b), followed by Mode II loading only (Fig. 4c). In this case the crack is fixed vertically in the Mode I step and is subjected to shear loading.

4.3 *Analysis output*

The analysis results for the single element validation will only be discussed and not illustrated. Illustrations of model performance will be provided for the Meso-scale analysis in Section 6.

Mode I loading and repeated unloading and reloading: The Abaqus output stress agrees with the model limit function.

Mode II loading only: The local normal stress to the crack follows the prescribed Mode I model. Similarly the local shear stress also adheres to the prescribed Mode II model.

Mode I loading and unloading, followed by Mode II loading: The normal stress adheres to the Mode I model during loading along the limit function and unloading produces the prescribed permanent deformation. The strain normal to the crack does not increase again in the shear/Mode II step and hence no reloading takes place normal to the crack. This is anticipated for this model where the Mode I and Mode II responses are decoupled and dilatancy is not accounted for. The only link between the Mode I and Mode II response is the shear stiffness during initial shear loading, as well as shear unloading and reloading, where the shear stiffness is a function of the crack width. Increasing the initial crack width reduces the initial shear stiffness and consequently also the peak shear stress. The global shear stress adheres to the Mode II model.

In conclusion, the Mode I and Mode II material models are successfully verified by the single element test for the boundary conditions considered.

5 MODEL CALIBRATION WITH MESO-SCALE DATA

5.1 *Experimental investigation: Mode I & II fracture*

Zeranka (2018) designed (Table 1) and classified several steel fibre-reinforced self-consolidating mortars (SCM) and concretes (SCC). Subsequent experimental programs designed, fabricated and executed Meso-scale tests for Mode I and II fracture of these composites. The data from the uniaxial tension test (Fig. 6) and Iosipescu (1967) shear test (Fig. 5) is used as input to calibrate and validate the material model.

Table 1. Composite designs.

Composite	Constituent	kg/m^3
SCM	OPC CEM II 52.5 N	357
	Fly ash	178
	Mineral filler	178
	Water	237
	Malmesbury sand	927
	Philippi sand	397
	MAPEI Dynamon SX	4.43
SCC-450	Greywacke stone 9 mm	450
SCC-600	Greywacke stone 9 mm	600
	$f_{c,cube\ 28\text{-}day}$ [MPa]	54.1
	Fibre type (Bekaert Dramix)	RC-65/35-BN

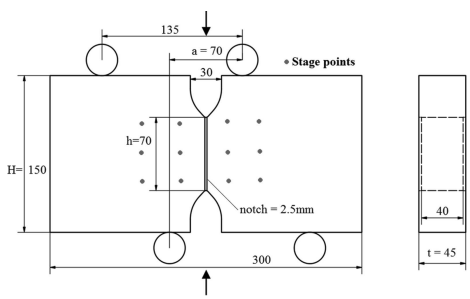

Figure 5. Iosipescu shear test configuration (Zeranka 2018).

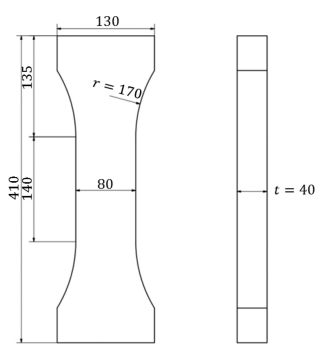

Figure 6. Uniaxial tension test specimen geometry (Zeranka 2018).

5.2 *Calibration of Mode I model*

Only two material parameters are required for the Mode I material model, namely the peak tensile strength f_{ct} and the Mode I fracture energy G_{ft}. These parameters are summarised in the Table 2.

Table 2. Mode I material parameter values.

Composite	SCM			SCC-450		
V_f [%]	0.5%	0.75%	1.0%	0.5%	0.75%	1.0%
f_{ct} [N/mm²]	2.85	2.99	2.61	4.40	3.40	3.65
G_{ft} [N/mm]	3.23	3.79	3.51	2.11	2.75	3.55

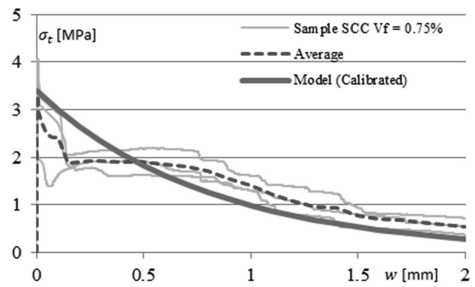

Figure 7. Typical uniaxial tension stress (σ_t) in [MPa] vs. crack width (w) in [mm].

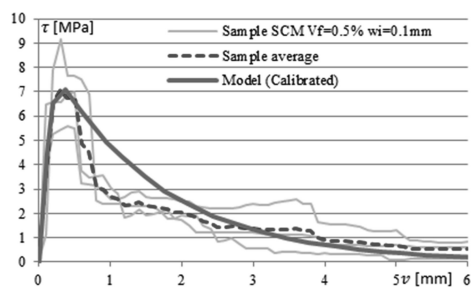

Figure 8. Typical Iosipescu shear stress (τ) in [MPa] vs. shear displacement (v) in [mm].

Figure 7 is a typical plot of the calibrated model (Eq. 4) with the sample and average uniaxial tensile response determined experimentally. Given the simplicity of the model, it adequately represents the experimental data.

5.3 *Calibration of Mode II model*

Four parameters are used to describe and calibrate the Mode II material model. The calibrated values are provided in Table 2 for each composite type (SCM, SCC-450 & SCC-600), fibre dosage (V_f) and pre-crack width (w_i). Apart from the shear fracture energy G_{fs}, which is the average from the experimental data, the other parameters f_{cs}, w_m and f_i are adjusted to fit the experimental average data. A typical calibrated curve is shown in Figure 8. Again, given the simplicity of the model, it adequately represents the experimental data.

Table 3. Mode II material and model parameter values.

Comp.	V_f %	w_i mm	f_{cs} N/mm²	G_{fs} N/mm	w_m mm	f_i –
SCM	0.5	0.1	9.0	14.12	0.50	0.005
		0.3	4.0	10.90	0.48	0.018
	0.75	0.1	9.5	13.95	0.60	0.007
		0.3	6.0	12.47	0.55	0.006
	1.0	0.1	10.0	16.10	0.50	0.007
		0.3	8.0	21.74	0.65	0.006
SCC-450	0.5	0.1	7.0	15.94	0.60	0.007
		0.3	4.3	7.87	0.65	0.0035
	0.75	0.1	8.7	21.24	0.60	0.007
		0.3	7.2	18.78	0.60	0.0065
	1.0	0.1	12.2	25.91	0.52	0.015
		0.3	10.2	24.06	0.60	0.015
SCC-600	0.5	0.1	6.0	14.64	0.55	0.006
		0.3	6.0	13.84	0.56	0.014

Note that w_m and f_i are currently defined as model parameters and not material parameters. Although it is likely that these parameters have physical significance, this will not be investigated further in this study. The values of w_m and f_i are also not unique, but can vary in certain ranges. All that can be said of these parameter values is that the specific combination given in Table 3 adequately calibrates the model for the experimental average data.

6 MODEL VALIDATION VIA MESO-SCALE IOSIPESCU SHEAR TEST

6.1 *Model details*

6.1.1 *Model dimensions*

The model dimensions are shown in Figure 9. The wedge notch geometry is simplified to a rectangular notch. The impact of this simplification is believed to be minimal. All other dimensions are the same as the experimental specimen. The roller supports are assumed to bear over a width of 3 mm. The region outside the notch is assumed to remain linear elastic, with the same elastic properties as the notch.

6.1.2 *Boundary conditions*

The model regions (a1–a2) and edges (e1–e4) to which the boundary conditions are applied are shown in Figure 9. In the tension/pre-crack step, region a1 is restrained against horizontal and vertical translation, while a prescribed horizontal translation is applied to region a2. The following boundary conditions (BC1) are applied to the specimen edge locations (e1–e4) during the shear step and are used for all analyses. Edge e1 and e2 are restrained against vertical translation and edge e3 and e4 undergo a prescribed vertical

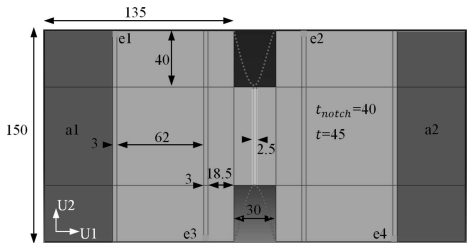

Figure 9. Model dimensions and boundary conditions.

displacement. The inner supports (e2 and e3) are restrained against horizontal translation during the shear step. An alternative boundary condition (BC2) where only one inner support (e2 or e3) is restrained against horizontal translation is also discussed in terms of the deformed shape and stresses.

6.1.3 *Mesh configuration*

A 4-node bilinear plane stress quadrilateral is used in all analyses. Each element in the notch is 2.5 × 2.5 mm. There are 28 elements over the height of the notch.

6.2 *Analysis output*

6.2.1 *Deformed shape*

The typical deformed shapes are given in Figure 10 for the model and experiment respectively. It is clear from the comparison between the two deformed shapes, that the model overestimates the crack opening for BC1. From the experiment it is also clear that horizontal translation does occur at the inner supports, which is assumed to be zero in the model. If one of the inner supports is allowed to translate freely in the horizontal direction (BC2), the deformed shape in Figure 8b is obtained.

Figure 8b has a closer resemblance to the experimental deformation and the associated boundary condition is believed to be a better approximation compared to that of BC1. However, some issues arise when using BC2 with a material model where the Mode I and Mode II responses are decoupled and dilatancy is not accounted for. This will be addressed in the analysis of the Abaqus stresses that follow.

6.2.2 *Stresses*

All stresses are the average centroid element stresses of all 28 elements over the height of the notch.

6.2.2.1 Abaqus normal stress S_{11}

In the case of a vertical crack, the crack coordinate system coincides with the global coordinate system and the global stress S_{11} matches the local normal stress (S_n). Figure 11 illustrates the model performance. In all cases, after initial loading and unloading in Mode I, reloading in Mode I occurs

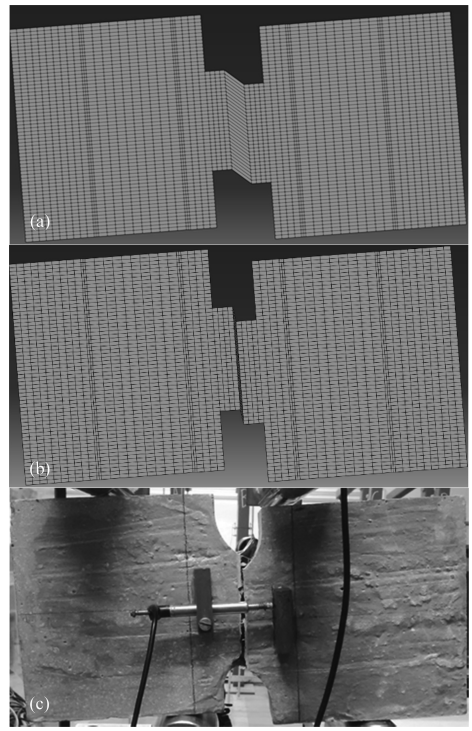

Figure 10. Model deformation for (a) BC1 and (b) BC2 and (c) typical experimental deformation.

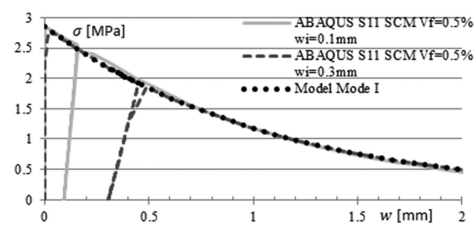

Figure 11. Typical stress (σ) normal to crack vs. crack width, w for w_i = 0.1 mm and 0.3 mm (SCM V_f = 0.5%).

during the Iosipescu shear step. This is contrary to what is observed for a single element, where no further crack opening is observed or expected for a vertical crack subjected to pure shear loading. This increased crack widening is not due to the material model, as dilatancy is not accounted for and the Mode I and Mode II actions are decoupled. Due to the simulated boundary conditions of the Iosipescu shear test, the crack width continues to increase during shear loading. As observed for the deformed shape in Figure 10a, the crack width is overestimated in all cases (also see Figure 15).

The alternative boundary condition BC2 (Fig. 10b) results in the normal crack strain becoming negative

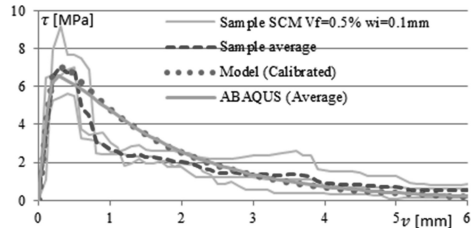

Figure 12. Typical shear stress (τ) parallel to crack vs crack shear displacement, v for w_i = 0.1 mm (SCM V_f = 0.5%).

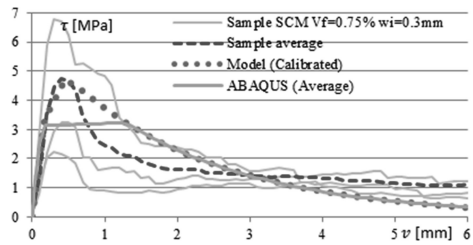

Figure 13. Typical shear stress (τ) parallel to crack vs crack shear displacement, v for w_i = 0.3 mm (SCM V_f = 0.75%).

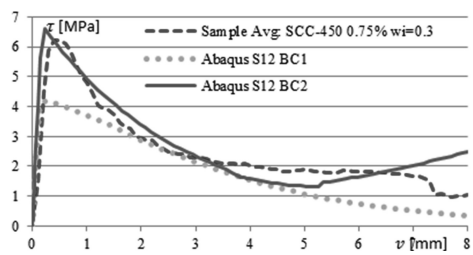

Figure 14. Typical shear stress (τ) vs crack shear displacement, v for BC1 and BC2 (SCC-450 V_f = 0.75% w_i = 0.3 mm).

and no reloading takes place normal to the crack during the shear step.

6.2.2.2 Abaqus shear stress S_{12}

In all analyses, the Abaqus global shear stress S_{12} matches the calibrated model. The only discrepancy that occurs between the calibrated model and the Abaqus output, is in the computation of the initial shear stiffness and consequently the peak shear stress. This is attributed to the fact that the initial shear stiffness is a function of the crack width, which is overestimated by the Abaqus model for BC1. As a result a softer response occurs initially, as can be seen in the typical results in Figures 12 and 13. This error is less prevalent for the smaller initial crack width w_i = 0.1 mm, which is expected.

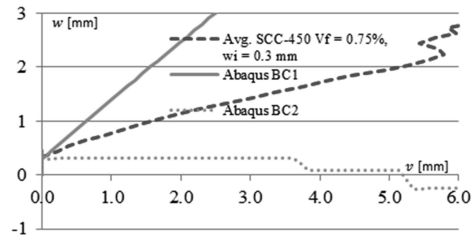

Figure 15. Typical crack width w vs. shear displacement v for BC1 and BC2 compared to experimental data.

A comparison is made between the two boundary conditions analysed in Figure 14 for one composite. Recall that 'BC2' is the boundary condition where only one of the inner supports is restrained against horizontal translation. 'BC2' gives a better approximation of the peak shear stress compared to 'BC1', but at larger shear displacements, the shear stress increases again and deviates from the material model. This phenomenon has been characterised by Rots (ICF7, 1989) as "stress-locking", which occurs in continuum and smeared crack modelling when fixed cracks with significant shear retention lead to stress rebuild.

Figure 15 shows the typical discrepancy between the experimental and Abaqus shear vs. crack opening displacement. In the case of the alternative boundary condition (BC2), the normal strain and stress parallel to the crack becomes unrealistically high.

7 EMPIRICAL LINK BETWEEN MICRO AND MESO-SCALE DATA

An empirical model which utilises the data obtained at the Micro and Meso-scale of observation, as well as an analysis of the fibre distribution, simulates the fibre component of the composite Mode II response.

7.1 *Micro-scale: Single fibre transverse pull-out*

The Ohno-beam (Arakawa & Ohno, 1957) shear test method is adapted to investigate the transverse pull-out response of a single hooked-end steel fibre (Fig. 16). Five fibre orientations are investigated in Zeranka (2018) as defined in Figure 17. Two fibre embedded lengths (L_{fe}) are considered, $L_f/4$ and $L_f/2$ (L_f – fibre length). $L_f/4$ is selected here to be representative of the average embedded length and the data for this embedded length will be used in the empirical model.

7.2 *Model description*

Figure 18 show the transverse pull-out load vs. transverse pull-out displacement. A simple empirical

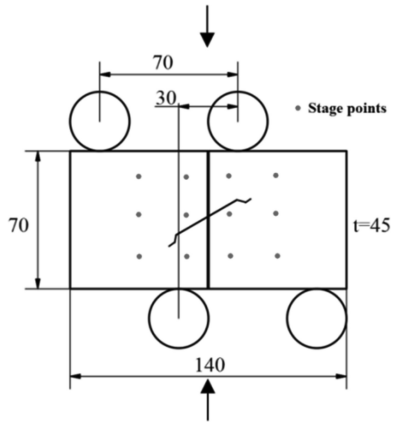

Figure 16. Experimental configuration of single fibre test.

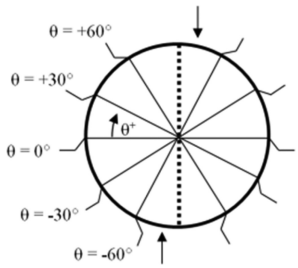

Figure 17. Definition of fibre orientation, θ with respect to loading configuration.

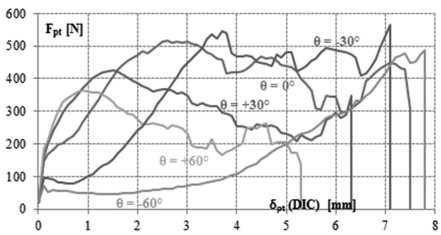

Figure 18. Transverse pull-out load (F_{pt}) vs. transverse pull-out displacement (δ_{pt}) for average response θ = –60° to +60°, $L_{fe} = L_f/4$.

model can be derived from the experimental data obtained at the Meso and Micro-scale of observation. The main principle of the model is to superimpose/reconcile and validate the fibre component (Micro-scale) and the composite (Meso-scale) fracture response. Given the total fibre count and fibre orientation distribution, the number of fibres that fall inside each defined orientation interval can be determined. The average transverse pull load vs. normal displacement response (Fig. 19) for each fibre orientation (θ = –60°, –30°, 0°, +30° and +60°) is then multiplied by the number of fibres

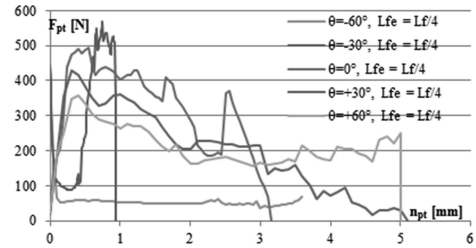

Figure 19. Transverse pull-out load (F_{pt}) vs. normal pull-out displacement (n_{pt}) for average response θ = –60° to +60°, $L_{fe} = L_f/4$.

in each corresponding orientation interval and added together to estimate the total fibre contribution to the composite response (in the form of total shear load vs. normal displacement/crack opening). Finally, for each composite and fibre volume fraction, the average shear displacement (δ_v) – crack width (w_c) relation at the Meso-scale is used to estimate the shear load vs. shear displacement relation.

7.3 *Model input*

The model therefore requires the following input:

1. The shear/transverse pull-out load (F_{pt}) vs. normal displacement (n_{pt}) for each of the fibre orientations considered (Fig. 19). Only the results from the embedded length $L_f/4$ are used.
2. The fibre count, i.e. the number of fibres in the shear plane of the Meso-scale test. The fibre count is determined from destructive and non-destructive (CT-scan) methods.
3. The fibre orientation distribution (CT-scan) for each fibre dosage (V_f = 0.5%, 0.75% & 1.0%).
4. The shear displacement (δ_v) – crack width (w_c) relation at the Meso-scale for each composite (SCM, SCC-450 and SCC-600) and fibre dosage (V_f = 0.5%, 0.75% and 1.0%)

7.4 *Model validation*

Figures 20 and 21 compare the model of the fibre component to the composite response at the Meso-scale. Only V_f = 0.75% is shown for the composite SCC-450. The model is compared with respect to the shear load (F_v) vs. normal displacement/crack opening (w_c) and shear displacement (δ_v), for both initial crack widths $w_i \approx$ 0.1 mm and 0.3 mm. Comparisons are made in terms of peak shear load, residual response and initial stiffness (prior to peak load).

7.4.1 *Peak shear load*

In general, a better approximation is made for an initial crack width, $w_i \approx$ 0.3 mm. Recall that the model only considers the fibre component. It is

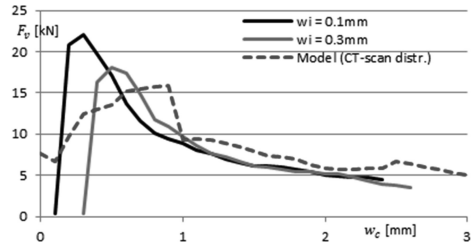

Figure 20. Shear load vs crack opening for SCC-450 0.75%.

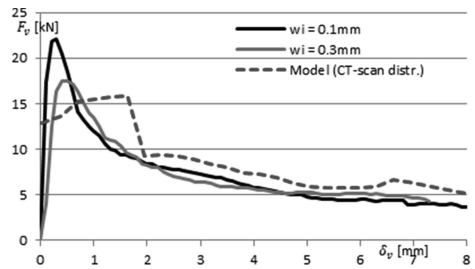

Figure 21. Shear load vs shear displacement for SCC-450 0.75%.

therefore postulated that at smaller initial crack width, $w_i \approx 0.1$ mm, shear interface cohesion and roughness/friction is still present, contributing to peak shear load. As the crack width, w_c increases, the model closely simulates the Meso-scale response, as the majority of the shear interface cohesion and friction is no longer present. Only the fibre component provides resistance at this stage.

7.4.2 *Residual tail end response*

In general, the fibre only model simulates the residual/tail end response reasonably well.

7.4.3 *Initial stiffness*

The model does not simulate the initial stiffness before and up to peak shear load. The stiffness is underestimated and in most cases, the modelled peak shear load is offset from the actual peak shear load with a significant margin. This is however to be expected for a model that only simulates the fibre component and does not account for the composite stiffness provided by the shear interface cohesion and shear interface roughness or aggregate interlock.

7.5 *Discussion*

The empirical 'fibre-only' model can be improved with a larger sample size at the Micro and Meso-scale. The fibre pull-out response should also be investigated for other fibre orientations and embedment lengths. With respect to the fibre distribution (fibre count and orientation) determined via CT-scanning, a larger sample size is also recommended.

8 SUMMARY AND CONCLUSIONS

The numerical and empirical models developed simulate the composite response well, given their relative simplicity and limited experimental data. In structural applications, continuum elements are the most appropriate for analysis. Limitations are however encountered for continuum elements and this particular application due to unstable/unreliable results at larger shear-slip (observed for BC2). This behaviour is mitigated in this instance by choosing different boundary conditions (BC1). Alternatively, this can also be resolved via the use of discrete/interface elements and a corresponding interface material model instead of continuum elements. However, the general application of discrete elements requires complex and computational demanding re-meshing algorithms to be implemented correctly. Future research should attempt to link the Mode I and Mode II response and account for dilatancy and confinement across the shear interface.

REFERENCES

Abaqus 6.10 Finite Element Analysis software, SIMULIA™ by Dassault Systèmes ®.

Arakawa, T. & Ohno, K. 1957. Shear Tests of Reinforced Concrete Beams by Special Type of Loading (In Japanese), *Transactions of the Architectural Institute of Japan*, 57: 581–584.

Bazant, Z. P. & Oh, B. H., 1983. Crack band theory for fracture of concrete. *Materials and Construction,* May, 16(3): pp. 155–177.

Bernardi P., Cerioni R., Michelini E., 2012. Prediction of post-cracking behaviour in SFRC elements under in-plane stresses. *Proceedings: 4th International conference on crack paths (CP 2012)*, Gaeta, Italy. pp. 651–659.

Hillerborg, A., Modéer, M., Petersson, P. E., 1976. Analysis of crack formation and crack growth in concrete by means of fracture mechanics and finite elements. *Cement Concrete Res*, 6, pp. 773–782.

Iosipescu, N., 1967. New accurate method for single shear testing of metals, *J. Materials*, 2(3): 537–566.

Kupfer, H., Hilsdorf, H. K., and Rusch, H., 1969. Behaviour of concrete under biaxial stresses. *ACI Journal*, 66(8), pp. 656–666.

Rashid, Y. R., 1968. Analysis of prestressed concrete pressure vessels. *Nuclear Engineering and Design*, 7(4), pp. 334–344.

Rots, J. G., 1989. Crack models for concrete: Discrete or smeared? Fixed, multi-directional or rotating? *Heron*, Vol. 34 no.1.

Rots, J. G., 1989. Various crack concepts for curved fracture in concrete. *ICF7*, Houston (USA).

Zeranka, S., 2018. Steel Fibre-Reinforced Concrete: Multi-scale Characterisation towards Numerical Modelling. PhD-thesis, Stellenbosch University.

Computational Modelling of Concrete Structures – Meschke, Pichler & Rots (Eds)
© 2018 Taylor & Francis Group, London, ISBN 978-1-138-74117-1

Shear behavior of full-scale RC slabs without shear stirrups in nuclear buildings: Experimental and numerical modeling

W.S.A. Nana, S. Limam & T.T. Bui
INSA Lyon, SMS-ID, University of Lyon, Lyon, France

A. Limam
University of Lyon, Lyon, France

S. Abouri
EDF-SEPTEN, France

ABSTRACT: The following study analyzes the shear behavior of full-scale slabs without shear reinforcement (the design of slabs used in nuclear buildings) under a concentrated load near a linear support. Experimental tests were conducted to quantify the shear strength and the associated failure modes. A series of 16 tests on 16 full-scale slabs are presented (fourteen slabs measuring 4 m × 2.6 m × 0.3 m; one slab of 4 m × 2.6 m × 0.35 m and another of 4 m × 2.6 m × 0.4 m). We addressed the influence of several variables, such as bottom longitudinal reinforcement, bottom transverse reinforcement, compressive strength, concrete aggregate size, slab depth and loading plate length on the slabs' shear strength. The influence of axial tension and compression loads on the shear resistance of one-way reinforced concrete slab was also addressed. The experiments are firstly used to evaluate the pertinence of Eurocode 2 for the shear design of reinforced concrete slabs without shear reinforcement in comparison with the French approach, and then to make comparisons with the ACI 318-14 code and fib Model Code 2010 formulations using the levels of approximation LoA I and LoA II. Then concrete damaged plasticity (CDP) in Abaqus software was used for three-dimensional (3D) modelling and calibration.

1 INTRODUCTION

A wide range of reinforced concrete (RC) structures such as buildings, infrastructures, industrial facilities and protective structures may be subjected to several types of forces acting, most often bending and shearing forces. The latter type of shear force is of particular concern. Indeed, the shear failure of reinforced concrete slabs not containing shear reinforcements is generally brittle. Unlike bending failure, shear failure is sudden and catastrophic, which makes its occurrence highly undesirable. This is especially the case for reinforced concrete slabs subjected to concentrated loads near their supports.

There is no consensus that one standard is better than another in the estimation of the shear strength of reinforced concrete structures. While it is true that there is some similarity of design provisions to estimate the contribution of shear reinforcement (if present) on shear strength, these standards differ in their approach to the concrete's contribution to shear strength. Depending on the standards (ACI Comittee 318, 2014) (Fib Model Code 2010, 2012), (FD P 18–717. Eurocode 2, 2013), (CEN. Eurocode 2, 2005) the influence of some materials' involved in the shear resistance mechanism is ignored or considered only partially, therefore neglecting a shear effect in the resistance estimation. Therefore the experimental tests which will be presented had as primary objective a better understanding of the phenomenon of shear.

The non-linear finite element analysis used in modelling the engineering structures is currently an advanced numerical tool which can provide a very good prediction. However, the modelling of the nonlinear behaviour for reinforced concrete structures under shear loading is generally difficult, especially for thick slabs when the 3D effect in the thickness increases. There are many non-linear concrete models from different theories: nonlinear elasticity, plasticity, damage mechanics and coupled damage and plasticity models. However, no model can reproduce all the failure mechanisms for reinforced concrete structures. Therefore, the verification of the robustness of the numerical model applied for the non-linear behaviour of the reinforced concrete is still necessary.

2 EXPERIMENTAL PROGRAM

2.1 *Tests specimens*

All slabs had no shear reinforcement. The slabs were designed to study the shear resistance subjected to a concentrated load near the support. The distance from the loading plate to the support should be more than twice the slab's effective depth, according to the traditional rule that seeks to prevent the direct transmission of loads to the supports. This is equivalent to choosing a shear span a_v/d ratio greater than or equal to 2.0 (Kani, 1964) (a_v is the side-to-side horizontal distance between the load and the support, d is the effective depth of the slab). In the present case, a constant value $a_v/d = 2.1$ (equivalent to $a/d = 2.52$) was chosen for all slabs, except for the S6 and S7 specimens.

The tests were carried out with a slab structure simply supported on four sides. Transverse and longitudinal reinforcements were also designed to ensure that the shear failure occurs prior to bending. The experimental program consisted of sixteen slabs: fourteen slabs measuring 4 m × 2.6 m × 0.3 m (S1 to S5, S8 to S10, ST1 to ST4, SC1, SC2); one slab (slab S6) measuring 4 m × 2.6 m × 0.35 m and another (slab S7) measuring 4 m × 2.6 m × 0.40 m. The slabs are grouped by series. In each series we study the influence of a given parameter involved in the shear resistance mechanism.

In Series I (S2, S8) the influence of concrete compressive strength, in Series II (S2, S6 and S7) the influence of a_v/d ratio, in Series III (S1, S4, and S5) the influence of longitudinal reinforcement ratio, in Series IV (S1–S3) the transverse reinforcement ratio, in Series V (S2, S2B) the concrete maximum aggregate size, in Series VI (S2, S9) the compressive axial stress and finally in Series VIII (S2, ST1, ST2, ST3 and ST4) the tension axial stress (Table 1 and Table 2).

The reinforcement layout of specimens is illustrated in Figure 1 for slabs without axial load.

2.2 *Materials*

The concrete used to design the slabs is a ready-mixed normal strength class C20/25 concrete except for slab S8 with a class C40/50 concrete. The maximum aggregate size was 11.2 mm for all specimens, except for specimen S2B with a maximum aggregate size of 20 mm. An overview of the concrete properties of the slabs tested is given in Table 1 and Table 2.

High adherence (HA) steel bars used to reinforce the slabs were Fe500 B with guaranteed 500 MPa yield strength and >540 MPa resistance at failure. A 20 mm concrete cover provided the effective depths to the longitudinal reinforcement.

1.3 *Test setup for slabs*

The mechanical loading system consists of a hydraulic actuator with a maximum load capacity of 2000 KN. Vertical displacements were measured using six displacement sensors (LVDT) placed at different points on the slab. Strains were measured using electrical strain gauges (LG and TG) placed at multiple positions, as indicated also in Figure 1.

For slabs with axial load, the tensile and compressive forces were applied via 12 hydraulic jacks on one side. The test setup with axial load is illus-

Table 1. Properties of slabs without axial load.

Series	Slabs	ρl (%)	ρt (%)	d_l [mm]	d_t [mm]	a_v [mm]	a_v/d_l	Concrete class [MPa]	Maximum aggregate size [mm]	Loading plate length [mm]
I	S2	1.223	1.106	267.5	242.5	560	2.1	C20/25	11.2	60 × 15
	S8	1.223	1.106	267.5	242.5	560	2.1	C40/50	11.2	60 × 15
II	S2	1.223	1.106	267.5	242.5	560	2.1	C20/25	11.2	60 × 15
	S6	1.030	0.917	317.5	292.5	560	1.8	C20/25	11.2	60 × 15
	S7	0.890	0.783	367.5	342.5	560	1.5	C20/25	11.2	60 × 15
III	S1	1.223	0.854	267.5	245.0	560	2.1	C20/25	11.2	60 × 15
	S4	1.003	0.854	267.5	245.0	560	2.1	C20/25	11.2	60 × 15
	S5	1.551	0.837	270.0	250.0	560	2.1	C20/25	11.2	60 × 15
IV	S1	1.223	0.854	267.5	245.0	560	2.1	C20/25	11.2	60 × 15
	S2	1.223	1.106	267.5	242.5	560	2.1	C20/25	11.2	60 × 15
	S3	1.223	1.349	267.5	242.5	560	2.1	C20/25	11.2	60 × 15
V	S2	1.223	1.106	267.5	242.5	560	2.1	C20/25	11.2	60 × 15
	S2B	1.223	1.106	267.5	242.5	560	2.1	C20/25	20.0	60 × 15
VI	S2	1.223	1.106	267.5	242.5	560	2.1	C20/25	11.2	60 × 15
	S9	1.167	1.056	267.5	242.5	560	2.1	C20/25	11.2	70 × 15

Table 2. Properties of slabs with axial load.

Series	Slabs	ρl (%)	ρt (%)	d_l [mm]	d_t [mm]	a_v/d_l	Axial load Nu [kN]	Axial stress σ_{cp} [MPa]	Concrete class [kN]	Maximum aggregate size [mm]	Loading plate length [mm]
VII	S2	1.223	1.106	267.5	242.5	2.1	0.0	0.00	C20/25	11.2	60 × 15
	SC1	1.223	1.106	267.5	242.5	2.1	1200	1.00	C20/25	11.2	60 × 15
	SC2	1.223	1.106	267.5	242.5	2.1	1800	1.50	C20/25	11.2	60 × 15
VIII	S2	1.223	1.106	267.5	242.5	2.1	0.0	0.00	C20/25	11.2	60 × 15
	ST1	1.223	1.106	267.5	242.5	2.1	–600	–0.50	C20/25	11.2	60 × 15
	ST2	1.223	1.106	267.5	242.5	2.1	–780	–0.65	C20/25	11.2	60 × 15
	ST3	1.223	1.106	267.5	242.5	2.1	–1200	–1.00	C20/25	11.2	60 × 15
	ST4	1.223	1.106	267.5	242.5	2.1	–1440	–1.20	C20/25	11.2	60 × 15

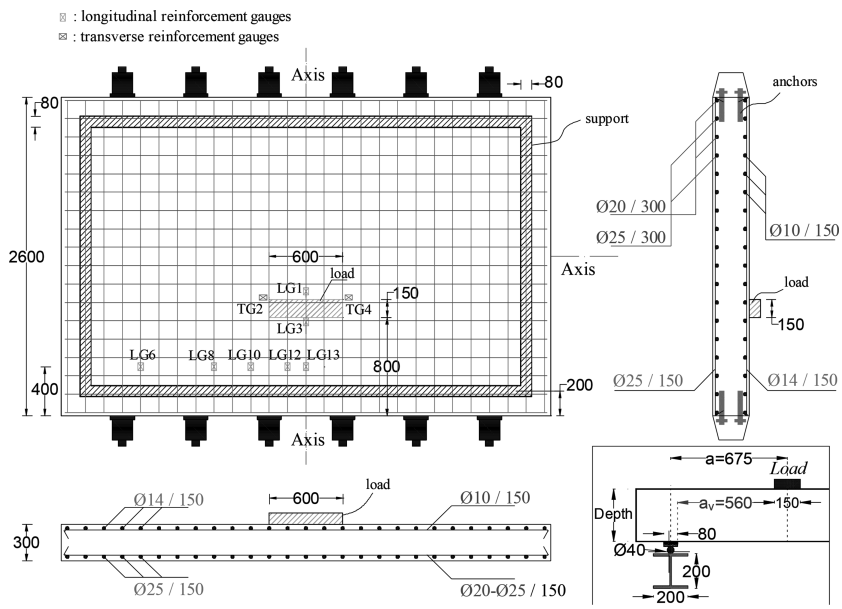

Figure 1. Reinforcement layout of slabs with axial load.

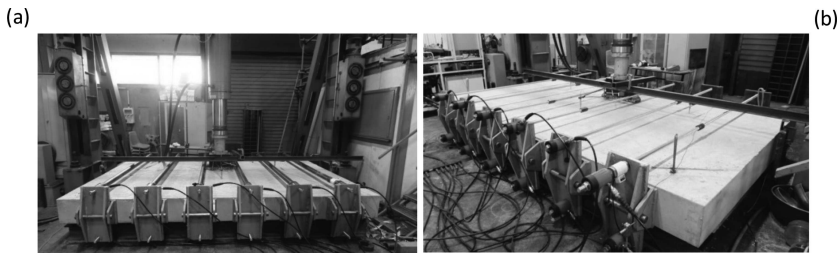

Figure 2. Test setup of slabs with: a) tension axial load; b) compression axial load.

trated in Figure 2. The axial compression or tension was applied in each test before vertical loading was applied.

The detail of test setup for slabs with and without axial load is given in (Bui et al., 2017a), (Bui et al. 2017b).

3 EXPERIMENTAL RESULTS AND DISCUSSION

3.1 *Shear strength*

For slabs subjected to a concentrated load, the shear resistance should not be calculated over its entire width b_w but over a certain effective width b_{eff}. A first method was used by the Dutch with a 45° horizontal load spreading from the center of the load ($b_{eff,1}$) (Figure 3). The second method used in the present study is according to the French recommendation (FD P 18-717, 2013) with a 45° horizontal load spreading from the far edges of the load ($b_{eff,2}$). Test results showed that the shear load determined by the French practices had a good ability to predict the experimental results.

The values of the peak loads Pu and the ultimate shear loads Vexp of the slabs are summarized in Table 3.

3.2 *Failure modes*

The same type of cracks was observed for all slabs. The cracking patterns of slab S2 is presented in Figure 4. Three types of crack were observed on the bottom side. Firstly, the flexural cracks with the cracking line perpendicular or parallel to four sides of slab were well controlled by longitudinal and transverse reinforcement. These flexural cracks were located at the same locations of the bottom transverse and longitudinal reinforcement bars embedded in the slab. Secondly, the cracks generated by the mechanism of two-way shear slab with perimeter cracks surrounded the loading area.

Although cracks were generated by the mechanism of two way slab shear, the final failure was due to the shear failure. In complement to the observations during the test, where first overload fracture is observed near the support characterized by a cracking line (third type of crack), a post mortem analysis is conducted for each slab to confirm that the failure is from shear (one way) and not from punching shear (two way) (Limam et al. 2017).

3.3 *Influence of concrete compressive strength*

In a first approach, the influence of the compressive strength $f_{cm,meas}$ on the failure load was studied using the variability of the compressive strength of concrete. There was a variation between 18 and

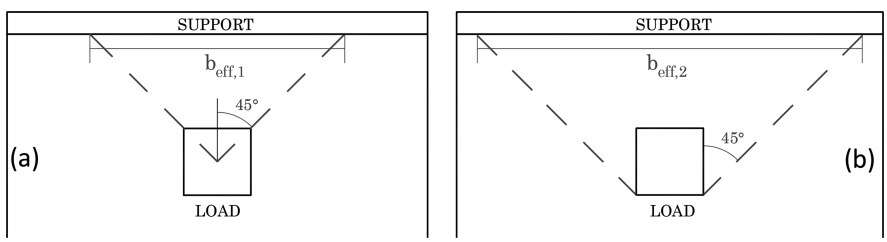

Figure 3. Methods for determining the effective shear width beff; (a) Dutch code; (b) French code.

Table 3. Peak loads obtained for slabs.

Slabs	a_v/d_l	ρl [%]	ρt [%]	$f_{cm,meas}$ [MPa]	b_{eff} [mm]	P_u [kN]	Failure mode	V_{100kN} [kN] corresponding to $P_{u=100kN}$	V_{exp} [kN]	$V_{exp}/\sqrt{f_{cm}}$	$V_{exp}/b_{eff}\times d\times\sqrt{f_{cm}}$ [MPa]
S1	2.1	1.223	0.854	24.1	2100	1111	Shear	61.21	680	139	0.247
S2	2.1	1.223	1.106	30.9	2100	1220	Shear	61.21	747	134	0.239
S2B	2.1	1.223	1.106	30.5	2100	1353	Shear	61.21	828	150	0.267
S3	2.1	1.223	1.349	18.8	2100	1032	Shear	61.21	632	146	0.259
S4	2.1	1.003	0.854	23.9	2100	1050	Shear	61.21	643	132	0.234
S5	2.1	1.551	0.837	34.6	2100	1257	Shear	61.21	769	131	0.231
S6	1.8	1.030	0.917	33.2	2100	1427	Shear	62.22	888	154	–
S7	1.5	0.890	0.783	34.2	2100	1796	Shear	63.19	1135	194	–
S8	2.1	1.223	1.106	51.7	2100	1632	Shear	61.21	999	139	–
S9	2.1	1.167	1.056	30.4	2200	1350	Shear	61.10	825	150	–
SC1	2.1	1.223	1.106	35.6	2100	1309	Shear	61.21	801	134	0.239
SC2	2.1	1.223	1.106	33.3	2100	1294	Shear	61.21	792	137	0.244
ST1	2.1	1.223	1.106	34.0	2100	1162	Shear	61.21	711	122	0.217
ST2	2.1	1.223	1.106	34.7	2100	1212	Shear	61.21	742	126	0.224
ST3	2.1	1.223	1.106	34.2	2100	881	Shear	61.21	539	92	0.164
ST4	2.1	1.223	1.106	34.2	2100	906	Shear	61.21	555	95	0.169

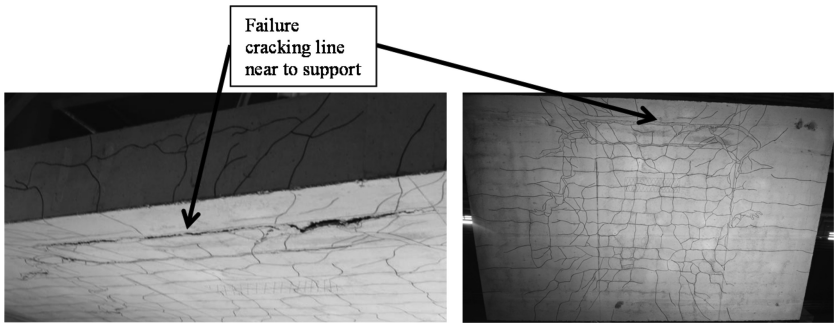

Figure 4. Failure mode of slab S2.

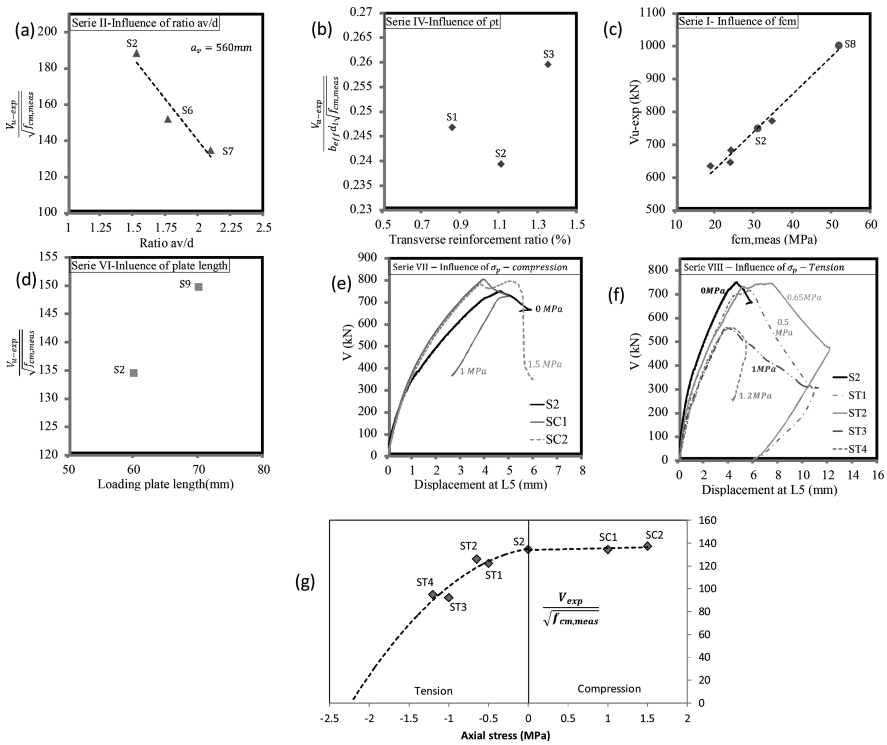

Figure 5. Influence of parameters involving in shear resistance mechanism.

35 MPa of the concrete compressive strength for the class C20/25 concrete used to design the slabs. From the experimental observations, it was found that shear strength increased with increasing compressive strength (Table 3 and Figure 5c).

3.4 *Influence of the effective depth d_l*

The results obtained for series II (S2, S6, and S7) are presented in Table 3 and Figure 5a. For shear capacity comparison, the shear strengths were normalized by the square-root of the compressive strength $f_{cm,meas}$. The results show a clear increase in the normalized shear strength with decreases in the ratio a_v/d_l (from 747 kN to 1135 kN). These experimental results confirm that an arching action is present in the slabs with free shear spans between $0.5d_l$ and $2d_l$. The experimental data agree with the theoretically expected increase in strength.

3.5 *Influence of the longitudinal and transverse reinforcement*

Slabs of serie III (S1, S4, and S5) and serie IV (S1, S2 and S3) were used to evaluate the influence of longitudinal and transverse reinforcement respec-

tively. We varied the diameter of the bars and kept constant the spacing between them. The shear strengths were normalized by the square-root of $f_{cm,meas}$, the effective depth and width. These results (Table 3 and Figure 5b) indicate that the trend of influence of longitudinal or transverse reinforcement on the shear capacity of the slabs is unclear.

3.6 *Influence of maximum aggregate size Dmax*

To evaluate the influence of the maximum aggregate size on shear strength slabs of serie V (S2 and S2B) were used. The results obtained (Table 3) show that the use of a maximum aggregate size of 20 mm improved the shear strength by 10% compared with the smaller maximum aggregate size of 11.2 mm.

3.7 *Influence of loading plate length*

To evaluate the influence of loading plate length on slab shear behaviour, series VI (S2 and S9) was used. The experiments demonstrate that as the length of the loading plate increased from L = 60 cm to L = 70 cm, the shear capacity increased (Figure 5d). A 12% shear gain was obtained.

3.8 *Influence of compression and tension axial stress*

The influence of the axial stress on the ultimate shear capacity obtained from the experimental slab tests is shown in Table 3 and Figure 5e, Figure 5f and Figure 5g. As expected, specimens with axial tensions reduced the shear strength and specimens with axial compressions increased the shear strength. The gain in shear capacity from the axial compression was very small due to the low compressive axial stress applied (1 MPa and 1.5 MPa) in comparison to the compressive resistance of concrete (35.6 MPa and 33.3 MPa).

Contrary to the effect of axial compression, the application of axial tension loads sharply decreased the shear strength by more than 30% with 1 MPa and 1.2 MPa tensile stresses (equal to $0.28f_{ctm,meas}$ and $0.34f_{ctm,meas}$) (Figure 5g). When the ultimate load was reached, the specimens demonstrated a softening response, with a large reduction in the applied force for increasing deflections (Figure 5f).

For the tests with axial compression (SC1 and SC2), the same elastic stiffness with the test without axial load (S2) in the force/displacement response was obtained (Figure 5e). After cracking, a strong reduction of stiffness was observed in the test without axial load, while for the tests with axial compression, this stiffness was kept constant and reduced slightly later. This can be explained by the fact that the compression forces have a tendency to delay crack development. When the slab was subjected to large axial compression (1.5 MPa) after the post-peak phase, a sudden drop was observed in the force/displacement curve corresponding to the brittle shear failure.

Table 4. Shear design models: EC2, French approach, EC2-punching, ACI 318-14 and fib Model Code 2010.

Shear design models	Formulas
Eurocode 2 (EC2) (CEN. Eurocode 2, 2005)	$V_{Rd,c} = Max\begin{cases}\left[C_{Rd,c}\cdot k\cdot\sqrt[3]{100\cdot\rho_l\cdot f_{ck}}+k_1\cdot\sigma_{cp}\right]\cdot b_{eff}\cdot d\\ \left[\nu_{min}+k_1\cdot\sigma_{cp}\right]\cdot b_w\cdot d\end{cases}$ $\nu_{min} = 0.035k^{3/2}\sqrt{f_{ck}}$
French National Annex (FDP 18-717, 2013)	$\nu_{min} = \begin{cases}0.23\sqrt{f_{ck}} & (2)\\ 0.035k^{3/2}\sqrt{f_{ck}} & (3)\end{cases}$ (2) For slabs with transverse redistribution of loads and walls, (3) For beams and other types of slab.
ACI 318-14 (ACI Committee 318, 2014)	$V_{ACI_simplified} = 0.17\sqrt{f_{ck}}\,b_{eff}\,d_l$ $V_{ACI} = \left(0.16\sqrt{f_{ck}}+17\rho_l\frac{V_u d_l}{M_u}\right)b_w d_l \le 0.29\sqrt{f_{ck}}\,b_{eff}$
Fib Model Code 2010 (Fib Model Code 2010, 2012)	$V_{Rd,c} = k_v\times\frac{\sqrt{f_{ck}}}{\gamma_c}\times b_w\times d$ $k_v\left(LoA\ I\right) = \frac{180}{1000+1.25d}$ and $k_v\left(LoA\ II\right) = \frac{0.40}{(1+1500\varepsilon_x)}\times\frac{1300}{(1000+k_{dg}d)}$ $k_{dg} = \frac{32}{(16+dg)} \ge 0.75$ and $\varepsilon_x = \left(\frac{\frac{M_{Ed}}{d}+V_{Ed}+N_u\left(\frac{1}{2}+\frac{\Delta e}{d}\right)}{2E_s\times A_s}\right)$

3 SHEAR DESIGN MODELS

The formulas for calculating the shear strength of slabs according to (CEN. Eurocode 2, 2005), (FD P 18-717. Eurocode 2, 2013), (ACI Comittee 318, 2014) and (Fib Model Code 2010, 2012), are given in Table 4. These formulas have been largely detailed in (Bui et al., 2017a), (Bui et al. 2017b), (Bui et al. 2017c) and (Limam et al. 2017).

4 SHEAR STRENGTHS PREDICTED BY SHEAR DESIGN MODELS VERSUS EXPERIMENTAL RESULTS

For slabs without axial load, the comparison between the experimental results and the shear design code is illustrated in Figure 6. Calculations using the measured $f_{cm,meas}$ were conducted, and these are compared to the experimental results. These results indicate that the French approach uses the optimal formula to calculate shear in slabs under concentrated loads close to the support. The shear capacity V_{EC2} from EN 1992-1-1:2005 led to an underestimation in all experiments (AVG = 1.23; STD = 0.09). When the French approach with $\nu_{min} = 0.23\sqrt{f_{ck}}$ was used, the shear capacity V_{France} improved the predictions, which were closer to the experimental results (AVG = 1.11; STD = 0.06). The shear capacity from ACI 318-14 (AVG = 1.33; STD = 0.07) and ACI simplified (AVG = 1.45; STD = 0.07) also underestimated the results in all experiments. The results also show that the Model Code 2010 with the second level of approximation (LoA II) predicts very well the shear capacity of specimens. A best safety margin was obtained (AVG = 1.08; STD = 0.10). However, the Model Code 2010 with the first level of approximation (LoA I) seems to be very conservative (AVG = 1.85; STD = 0.11).

For slabs with axial load, our experimental results are combined with the results from the 92 beam tests with axial tension found in literature. Only the results of the tests with and without axial tension were presented. The compression tests were not investigated in this paper. The comparison of test results to the EC2, ACI 318-04 and ETC-C was drawn as Figure 7. The EC2 give many overestimated results (unconservative) for the beams and some slab tests. The shear capacity V_{ACI} from ACI 318-04 leads to the better results and conservative

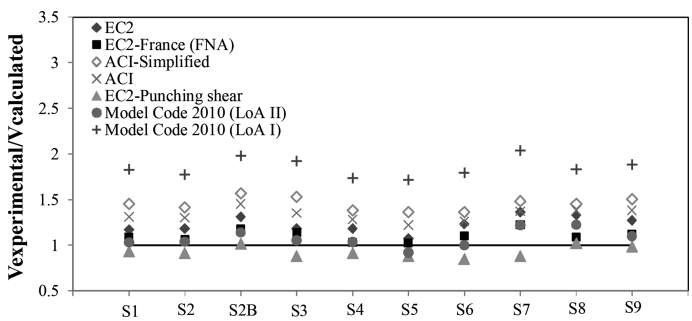

Figure 6. Slabs without axial loads: Comparisons of test results from EC2, French National Annex, ACI 318-14 and fib Model Code 2010.

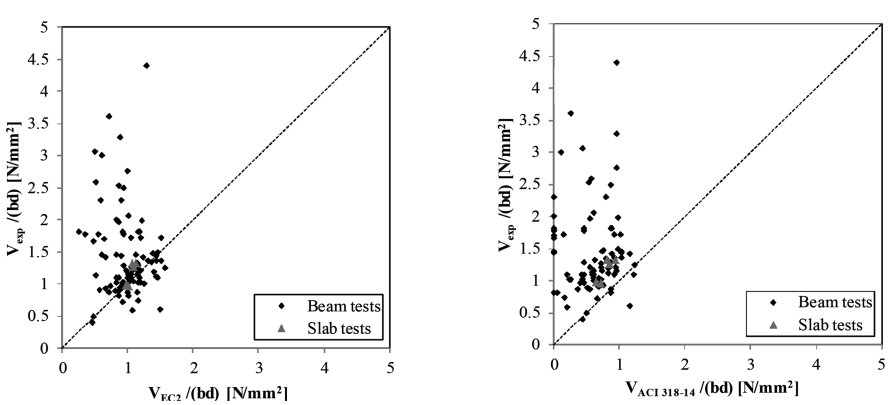

Figure 7. Slabs with axial loads: Comparison of test results to EC2 and ACI 318-14.

for most of experiments. However, for the slab tests, ACI 318-04 gives the results exceeding underestimation (AVG = 1.493; STD = 0.110) compared to EC2 (AVG = 1.086; STD = 0.134). Noted that AVG and STD were calculated for the $V_{exp}/V_{calculated}$ from four slab tests with axial tension (ST1-ST4). The ACI 318-14 should be used for the security situation of shear strength with axial tension even that it is too conservative for the reinforced concrete slab members.

6 FINITE ELEMENT MODEL

In this research, the numerical investigations to study the structural response of slabs and their failure mode were conducted using the FEM in Abaqus. The simulations were conducted with an explicit quasi-static solution technique in Abaqus/Explicit. The explicit methods require very small time increments to satisfy the stability limits.

6.1 *Concrete damage plasticity model*

The CDP model in Abaqus which combines plasticity and damage is based on the models proposed by (Lubliner et al, 1989) for monotonic loading and was later developed by (Lee et Fenves, 1998) to consider dynamic and cyclic loadings.

In the model, the uniaxial stress–strain relationship of steel reinforcement was modelled as elastic-plastic behaviour. The yield strength fy = 500 MPa and the ultimate strength fu = 540 MPa were used. The Young modulus and Poisson ratio were assumed to be 210 GPa and 0.3, respectively.

7 MODELLING, RESULTS AND DISCUSSION

7.1 *Description of the FE model*

By considering the specimens' symmetry in the transverse direction, only half of the slabs were modelled in three dimensions. The concrete region is meshed by eight-noded hexahedral elements (C3D8R) with a reduced integration scheme to avoid the shear locking effect (ABAQUS Version 6.12 Documentation, 2013), and the reinforcements were meshed by two-noded linear beam elements (B31). The mesh size is 20 mm, chosen through a mesh convergence study. The reinforcements were modelled as the rebars embedded in the concrete with a perfect bond. The load was applied in the vertical direction over the entire surface of the load distribution plate with the displacement control. The slabs were simply supported on four sides by modelling four rigid supports.

7.2 *Results and discussion*

7.2.1 *Calibration of the FE model*

First the numerical model has been calibrated through a reference experimental test on slab S2. The tensile strength and the compression strength have been identified from the experiments. The parameters of ratio of tensile/the compressive meridian ($K_c = 0.6667$); eccentricity ($\epsilon = 0.1$); ratio of biaxial compressive strength/uniaxial compressive strength ($\sigma_{b0}/\sigma_{c0} = 1.16$) have been taken from the recommended values in the literature). The energy Gf according to the MC1990 Fracture Energy was retained compared to the MC2010. A calibrated dilation angle of 37° was used (Nana et al, 2017).

7.2.2 *Comparison of the experimental and numerical results*

Based on the calibrated numerical model presented above, non-linear FE modelling of the experimental specimens without axial load was conducted. The comparison of the load/displacement responses between the experimental results and the numerical analysis for some slabs are shown in Figure 9, showing that the prediction of ultimate loads by the FE model shows good agreement with the experimental results. The trends of the load–displacement responses in experimental tests and numerical analysis were similar. However, the stiffness in the load–displacement responses predicted by the FE model is slightly stiffer than the experimental results. In the experiment, the displacement measured is taken relative to the reference of the laboratory floor.

As can be seen in Figure 8, the predictions of the FEM (AVG = 1.03, STD = 0.03) are less conservative compared to the FNA predictions. Consequently, the FEM predictions are closer to reality. Nevertheless, the FNA approach predicts the shear capacity of slabs with a reasonable safety margin (AVG = 1.10, STD = 0.06).

Figure 10 shows the cracking patterns obtained from the FE analysis. In the numerical models, the crack patterns were visualized through the maximum principal plastic strains. Compared to the crack patterns observed in the experimental tests, the proposed non-linear FE model shows an accurate prediction of the locations and the directions of the crack propagations.

7.2.3 *Parametric study*

In this section, the calibrated FE model was used to study the effect of several factors such as the influence of the longitudinal and transverse reinforcement ratio, slab depth, the concrete aggregate size and finally the influence of the loading plate length on slab shear strength. The compressive characteristic strength $f_{ck} = 20$ MPa was used and

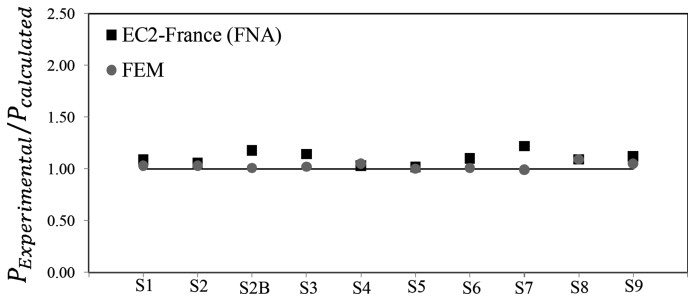

Figure 8. Comparison of the experimental, numerical (FEM) and analytical (EC2) ultimate load for all slabs.

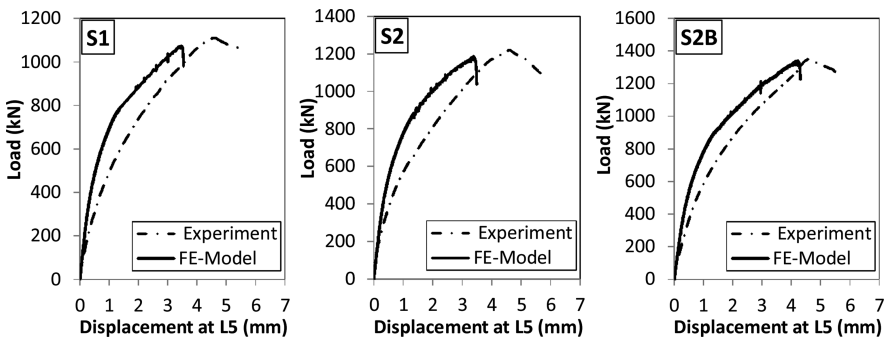

Figure 9. Experimental and numerical load/deflection responses for slabs without axial load.

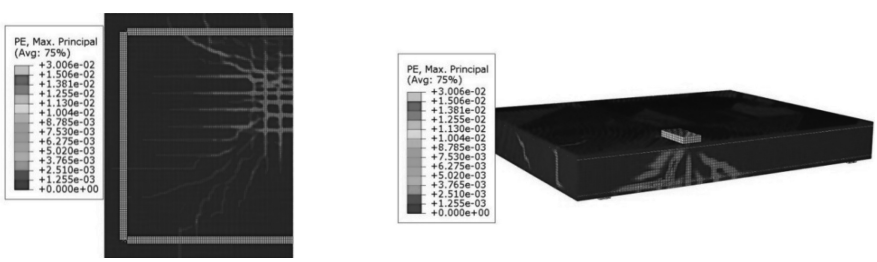

Figure 10. Cracking pattern at ultimate load visualized through the maximum principal plastic strain.

Table 5. Classes concrete characteristics according to EN 1992-1-1 (CEN. Eurocode 2, 2005).

Concrete class (NF EN 1992-1-1)	f_{ck} [MPa]	f_{ctm} [MPa]	Young modulus [GPa]
C20/25	20	2.20	30

the corresponding mechanical properties necessary for the simulations are given in Table 5 below.

a. *Effect of longitudinal and transverse reinforcement, slab depth, maximum aggregate diameter*

It was found that the increase of the transverse or longitudinal reinforcement ratio gives a slightly stiffer rigidity in the post-elastic phase and gives an increase of the shear capacity. For the effect of the slabs' depth on shear strength, it was found that the greater the slab's depth, the more the elastic stiffness increased. As the a_v/d_l ratio decreased, a significant increase in the shear capacity of the slabs was observed as expected. In addition, it was found that the a_v/d_l ratio varied in a linear relationship with the shear capacity. For the effect of the maximum aggregate diameter on shear strength, it was found that the increase in the maximum aggregate diameter gives an increase in shear capacity and the stiffer behaviour in the post-elastic phase.

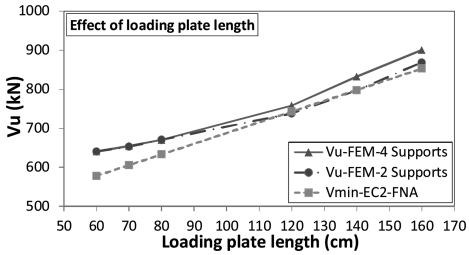

Figure 11. Influence of the different loading plate lengths on shear strength: comparison between slabs: four supports—FEM, two supports—FEM, and two supports—FNA.

b. *Effect of loading plate length*

To study the effect of loading plate length on shear strength, the configurations of Series VI (S2 = 60 cm, S9 = 70 cm) were re-modelled with the same concrete strength. Furthermore, the four loading plate lengths – 80 cm, – 120 cm, 140 cm and 160 cm – were also modelled to evaluate their influence on shear strength. As can be seen in Figure 11, the numerical results show that the shear capacity increased when the loading plate length was extended.

8 CONCLUSIONS AND PROSPECTS

The following conclusions can be drawn from the results obtained in this study:

- The experiments show that the concrete compressive strength has a significant influence on the shear capacity. The maximum aggregate size can improve the shear strength of slabs. A clear increase in normalized shear strength with decreasing a_v/d ratio was observed.
- The axial tension force decreases at once the shear strength and the stiffness of force/displacement response. However, the ductility after ultimate shear strength was improved substantially. The large axial compression improves the ultimate shear strength but it will cause the failure in a brittle manner.
- For slabs without axial loads: The EC2 approach with the value $\upsilon_{min} = 0.23\sqrt{f_{ck}}$ proposed by the French National Annex resulted in the best correlation with the experimental results of mean shear capacity.
- For slabs with axial loads: The ACI 318-14 should be used for the security situation of shear strength with axial tension even that it is too conservative for the reinforced concrete slab members.
- The proposed numerical model is capable of predicting the shear strength and failure modes of reinforced concrete slabs. A 37° dilatation angle combined with the Model Code 1990 fracture energy approach was recommended in the numerical model for the concrete with grade C20/25.

REFERENCES

ABAQUS Version 6.12 Documentation. (2013).

ACI Comittee 318. Building code requirements for structural concrete (ACI 318-14) and commentary. Am Concr Inst, SP 2014:520.

Bui, T.T., Limam, A., Nana, W.S.A., Ferrier, E., Bost, M., & Bui, Q.B. (2017c). Evaluation of one-way shear behaviour of reinforced concrete slabs: experimental and numerical analysis. *European Journal of Environmental and Civil Engineering*, 1–27.

Bui, T.T., Abouri, S., Limam, A., NaNa, W.S.A., Tedoldi, B., Roure, T., 2017a. Experimental investigation of shear strength of full-scale concrete slabs subjected to concentrated loads in nuclear buildings. *Eng. Struct.* 131, 405–420. doi:10.1016/j.engstruct.2016.10.045

Bui, T.T., Nana, W.S.A., Abouri, S., Limam, A., Tedoldi, B., Roure, T., 2017b. Influence of uniaxial tension and compression on shear strength of concrete slabs without shear reinforcement under

CEN. Eurocode 2: design of concrete structures—Part 1–1: general rules and rules for buildings. EN 1992-1-1. Bruss Belg Com Eur Norm 2005; 2005: 229.

concentrated loads. *Constr. Build. Mater*. 146, 86–101. doi:10.1016/j.conbuildmat.2017.04.068

FD P 18-717. Eurocode 2 - calcul des structures en béton—Guide d'application des normes NF EN 1992; 2013.

Fib Model Code 2010: final draft Lausanne Int Fed Struct Concr 2012.

Kani GNJ. The riddle of shear failure and its solution. *J Proc* 1964; 61:441–68.

Lee J, Fenves G. Plastic-damage model for cyclic loading of concrete structures. *J Eng Mech* 1998;124(8):892–900.

Limam, S., Nana, W.S.A., Bui, T.T., Limam, A., & Abouri, S. (2017). Experimental investigation and analytical calculations on shear strength of full-scale RC slabs with shear reinforcement for nuclear power plants. *Nuclear Engineering and Design*, *324*, 143–157.

Lubliner J, Oliver J, Oller S, Oñate E. A plastic-damage model for concrete. *Int J Solids Struct* 1989;25(3):299–326.

Nana, W.S.A., Bui, T.T., Limam, A., & Abouri, S. (2017, May). Experimental and Numerical Modelling of Shear Behaviour of Full-scale RC Slabs Under Concentrated Loads. In *Structures* (Vol. 10, pp. 96–116). Elsevier.

Computational Modelling of Concrete Structures – Meschke, Pichler & Rots (Eds)
© 2018 Taylor & Francis Group, London, ISBN 978-1-138-74117-1

Numerical lower bound analysis of plate bending problems containing requirements on shear capacity and shear-bending interaction

T.W. Jensen
Bridge Scandinavia, COWI A/S, Denmark

P.N. Poulsen & L.C. Hoang
Department of Civil Engineering, Technical University of Denmark, Denmark

ABSTRACT: The load carrying capacity of reinforced concrete slabs without shear reinforcement under concentrated loads are often limited by the shear capacity. In the last decades, numerical limit analysis have shown to be efficient methods to determine the load carrying capacity of slabs. However, most of the elements have only been used with yield criteria considering the moments. In this paper, an element with linear moment fields and an element with quadratic moment fields for numerical limit analysis of slabs are presented. The elements can handle limitation on both moment and shear forces. The moments are limited by Nielsen conic yield criteria combined with yield criteria for shear forces and moment-shear interaction. The elements are shown to converge from below. The moment, shear and moment-shear yield criteria are shown to work with the elements on benchmark plate examples and for plates with concentrated loads. Furthermore, the effects of limitation on shear forces on the yield mechanism are presented and a clear difference between the yield mechanism for moment and shear failure is shown.

1 INTRODUCTION

The load carrying capacity of reinforced concrete slabs without shear reinforcement is often limited by the shear capacity and the capability of the structure to redistribute the internal forces. The shear problem arises when e.g. concentrated loads are close to the support and for wide slabs where redistribution of forces perpendicular to the span direction are needed. Limit analysis based on the assumption of perfect plastic material behaviour have been used for assessment of existing concrete slab bridges for the last decades. The most prominent methods for hand calculations are the upper bound yield line method (Johansen 1943) and the lower bound strip method (Hillerborg 1974). The yield line method considers only flexural collapse mechanisms and can therefore not handle limitations on shear forces. The strip method assumes zero twisting moment, which limits the extent of redistribution of internal forces.

Within the last decades, it has been demonstrated that finite element limit analysis (*FELA*) is an extremely efficient approach to analyse plate bending problems. In the early development (Chan 1972, Faccioli & Vitiello 1973, Anderheggen & Knöpfel 1972), the non-linear yield criteria were linearised. The development of efficient non-linear convex optimization algorithms initiated the development of elements which involve non-linear yield criteria (Krabbenhøft & Damkilde 2002, Nielsen & Poulsen 2009), such as the Nielsen conical criteria for concrete slabs (Nielsen 1963). However, the lower bound finite elements, that are often adopted, do not allow for limitations of the shear forces. The reason is that these elements, developed to comply with Kirchhoff thin-plate theory, do not have requirements of continuity of the twisting moments along the edges. To be able to determine admissible distributions of internal forces with account for limitations of the shear capacity, it is necessary to work with lower bound elements which have bending, twisting as well as shear continuity along the edges. Such an element was presented in (Bleyer & Buhan 2014) with quadratic moment fields with full continuity and the von Mises yield criteria with limitation on shear. In (Larsen, Poulsen, & Olesen 2011) a shell element with Mohr-Coulomb criteria for concrete was presented which also can handle limitation on shear and moments.

In this paper, equilibrium elements with linear and parabolic moment fields are presented. The elements are used to analyse plate bending problems where the Nielsen conical yield criteria are imposed in combination with a criterion for transverse shear actions as well as moment-shear interaction criteria. The performances of the linear and quadratic elements are compared-with focus on

the issue of shear limitations and boundary conditions. The comparison includes well-known plate bending problems. The dual variables for both elements are presented based on which the yield mechanisms can be extracted. The yield mechanisms can in this context be interpreted as bending failure or "shear failure". The full continuity elements perform very well and converge, from below, toward the analytical exact solutions when the number of elements is increased. Convergence is observed for all elements in benchmark plate bending problems.

2 EQUILIBRIUM ELEMENTS

In the lower bound method, all moment, shear forces and loads must be in equilibrium. The equilibrium equations for a plate are given as

$$\frac{\partial v_x}{\partial x} + \frac{\partial v_y}{\partial y} + p = 0 \tag{1}$$

$$\frac{\partial m_{xx}}{\partial x} + \frac{\partial m_{yx}}{\partial y} + v_x = 0 \tag{2}$$

$$\frac{\partial m_{yy}}{\partial y} + \frac{\partial m_{xy}}{\partial x} + v_y = 0 \tag{3}$$

where m is the moment, v is the shear force and p is a surface load.

In finite element limit analysis, the equilibrium is ensured internal in the element and between the element edges (or surfaces for solid elements). In this section, two plate equilibrium elements are presented.

2.1 *Linear element*

A triangle element, with linear moment fields varying between the nodes, is shown in Figure 1. The shear forces in the linear triangle are, according to

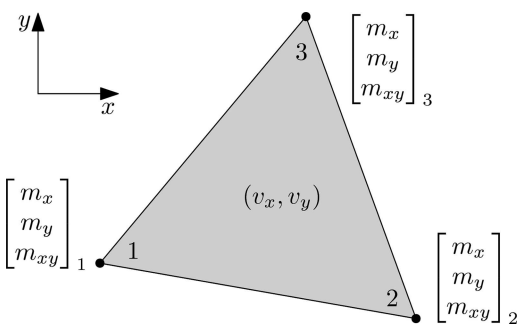

Figure 1. Moments and shear forces in linear triangle element, *Lin*.

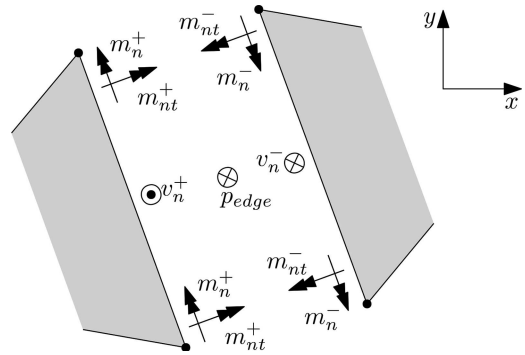

Figure 2. Linear element: Edge equilibrium.

equations (2) and (3), constant. This implies that it is not possible to apply a surface load. Surface loads are approximated as uniform line loads on each edge of the element.

Equilibrium between the elements is obtained along the edges as shown in Figure 2. The edge moments are obtained by transforming the moments in the corners to the direction normal or tangent to the connected sides which can be written as

$$\begin{bmatrix} m_n \\ m_{nt} \end{bmatrix}_{j,i} = \mathbf{T}_{\mathbf{m}j} \begin{bmatrix} m_x \\ m_y \\ m_{xy} \end{bmatrix}_i, [v_n]_{j,i} = \mathbf{T}_{\mathbf{v}j} \begin{bmatrix} v_x \\ v_y \end{bmatrix}_i \tag{4}$$

where j refer to the side, i refer to the node, $\mathbf{T}_\mathbf{m}$ is the transformation matrix for moments and $\mathbf{T}_\mathbf{v}$ is the transformation matrix for shear forces. The transformation matrices can easily be obtained by using area coordinates, see (Krabbenhøft & Damkilde 2002). The load placed on the edge of the element must be in equilibrium with the shear forces on the edge, i.e. the edge load is equal to the jump in shear forces. This is written as

$$v_n^+ + v_n^- + p_{edge} = 0 \tag{5}$$

where "+" and "–" indicate the shear forces from two connected elements.

2.2 *Quadratic element*

The triangle element, with quadratic moment fields, is defined the same way as the linear element shown in Figure 1, but with three additional nodes on the middle of each side. These 6 nodes define the moment fields. The shear fields for the quadratic element are linear with maxima in the corner nodes. On this element, a constant surface load can be applied due to the linear shear fields.

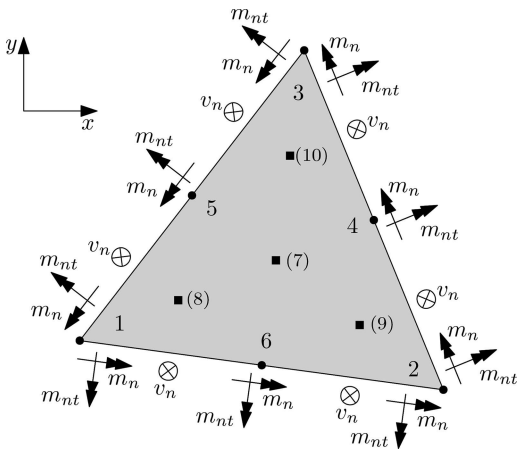

Figure 3. Quadratic element: Edge moments and shear forces.

The moments and shear forces on the edges are shown in Figure 3 with the 6 defining nodes, 1–6. The moments and shear forces on the edges are obtained from equation (4).

3 YIELD CRITERIA

The section forces in the elements are limited by yield criteria. The most common yield criteria for reinforced concrete slabs in bending are Nielsens conic yield criteria which is given as

$$\begin{aligned}(m_{Px}-m_x)(m_{Py}-m_y)-m_{xy}^2\geq 0\\ (m'_{Px}-m_x)(m'_{Py}-m_y)-m_{xy}^2\geq 0\end{aligned} \tag{6}$$

where m_{Px} and m_{Py} are the positive plastic moment capacities, and m'_{Px} and m'_{Py} are the negative plastic moment capacities.

To demonstrate the ability of the developed elements to account for limitation of shear actions, the following relationships for moment-shear interaction will be investigated:

$$\begin{aligned}&\left(\frac{\tilde{m}_P}{m_P}\right)^n+\left(\frac{|\upsilon|}{\upsilon_P}\right)^n=1\Rightarrow\\ &\tilde{m}_P(\upsilon)=m_P\left(1-\left(\frac{|\upsilon|}{\upsilon_P}\right)^n\right)^{\frac{1}{n}}\end{aligned} \tag{7}$$

where $\tilde{m}_P$ is the reduced moment capacity due to the shear force υ and υ_P is the plastic shear capacity. For $n = 1$ we get a linear interaction, $n = 2$ a quadratic and $n = \infty$ no interaction (see Figure 4).

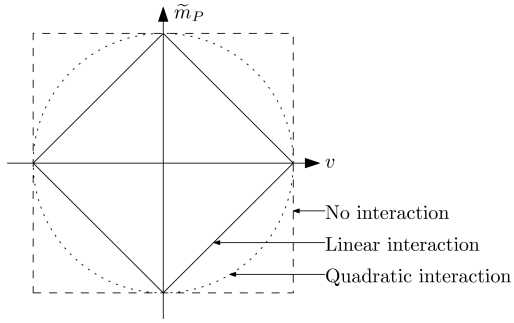

Figure 4. Schematic graph of investigated moment and shear interaction.

By applying the equilibrium conditions in (7) to all moment capacities in the yield criteria in (6), the combined moment and shear yield criteria can be written as

$$\begin{aligned}(\tilde{m}_{Px}(\upsilon_x)-m_x)(\tilde{m}_{Py}(\upsilon_y)-m_y)-m_{xy}^2\geq 0\\ (\tilde{m}'_{Px}(\upsilon_x)+m_x)(\tilde{m}'_{Py}(\upsilon_y)+m_y)-m_{xy}^2\geq 0\end{aligned} \tag{8}$$

It should be noted that in shear reinforced concrete beams, $n = \infty$ is usually valid. However, for members without shear reinforcement which at the same time contains casting joints, there will in some way, be a need to introduce moment-shear interaction. In this context, it is noted that $n = 1$ will always constitute a conservative choice. A more adequate interaction relationship should of course be based on a mechanical model taking into account the structural layout in question. This is, however, not within the scope of this paper. Yield criteria for reinforced slabs are further treated in (Marti 1990) and (Nielsen & Hoang 2011).

3.1 *Check point for the elements*

The yield criteria are checked at the nodes of the elements. The maximum moment for a linear moment field is found at the corner of the element. The maximum moment for elements with non-linear moment fields can occur anywhere on the element. The yield criteria can therefore be violated if they are only checked at the nodes.

The basic quadratic element, referred to as *Quad6*, have 6 nodes as shown in Figure 3. Additional yield check point can be added to minimize the violation of the yield criteria. When an extra point is added, the element is referred to as *Quad7*. When four extra points are added to the element, it is referred to as *Quad10*. The extra nodes are shown in Figure 3, where the first extra node is node 7. The coordinates of the nodes, as area coordinates, are

Table 1. Maximum possible violation of yield criterion $-m_P \le m \le m_P$ in element.

Element	Lin	Quad6	Quad7	Quad10
Number of nodes, [–]	3	6	7	10
Error, $\frac{m_{max}-m_p}{m_p}$ [%]	0.0	66.7	33.3	25.0

$$\mathbf{z}^7 = \begin{bmatrix} \frac{1}{3} & \frac{1}{3} & \frac{1}{3} \end{bmatrix}, \quad \mathbf{z}^8 = \begin{bmatrix} \frac{2}{3} & \frac{1}{6} & \frac{1}{6} \end{bmatrix}$$
$$\mathbf{z}^9 = \begin{bmatrix} \frac{1}{6} & \frac{2}{3} & \frac{1}{6} \end{bmatrix}, \quad \mathbf{z}^{10} = \begin{bmatrix} \frac{1}{6} & \frac{1}{6} & \frac{2}{3} \end{bmatrix} \tag{9}$$

The quadratic element is analysed with respect to the maximum possible violation of the yield criterion $-m'_P \le m \le m_P$, given that the moments at the nodes are within the yield criterion. The results are shown in Table 1 for $m_P = m'_P$. The results shows maximum possible violations between 25–67%. These violations occur when there is a large variation of the moments between the nodes. For *Quad6*, the maximum violation occur when moments at the corner nodes are equal to $-m'_P$ and the moments at the side nodes are equal to m_P. Such a moment distribution is very unlikely even for a coarse mesh. Furthermore, when the shear forces, i.e. the variation of the moment, are limited, the possible violation is also limited. The size of the actual violation can be expected to me much less for dense meshes, which is shown in the numerical examples.

4 OPTIMIZATION PROBLEM FOR THE LOWER BOUND METHOD

The objective of the lower bound methods is to find the maximum load, where the stress distribution is in equilibrium and within the yield criteria, i.e. an admissible stress field. The equilibrium conditions can be formulated in a discrete general form as

$$\mathbf{H}\beta = \mathbf{R}_c + \lambda\mathbf{R} \tag{10}$$

where β is a vector with all the stress components, $\mathbf{H}$ is the equilibrium matrix, $\mathbf{R}_c$ is a constant load vector and $\mathbf{R}$ is a load vector which is scaled with the load factor λ.

The maximum load carrying capacity is found by maximizing the load factor λ. When maximizing the load, all the stresses must be within the yield criteria which can by written in a general form as

$$f_i(\beta) \le 0 \quad i = 1,2\ldots n \tag{11}$$

where n is the total number of yield criteria.

The lower bound method can now be written as a optimization problem given as

$$\begin{aligned} &\text{max imize} && \lambda \\ & && \mathbf{H}\beta = \mathbf{R}_c + \lambda\mathbf{R} \\ &\text{subject to} && f_i(\beta) \le 0 \quad i = 1,2\ldots n \end{aligned} \tag{12}$$

The optimization problem will always be convex since yield criteria are convex. Convex optimization problems have an unique solution and are fast to solve with modern optimization algorithm. The plate problem with yield criteria given in equation (7) and (8) can be solved with second order cone programming (SOCP) which is a special kind of convex programming. Lower bound problems with other well known yield criteria, such as Mohr-Coulomb and von Mises, can also be solved with convex programming, see (Krabbenhøft, Lyamin, & Sloan 2007).

The optimization problem in (12) is very useful for assessment of existing structures. However, the problem can be reformulated to a design situation where the objective is to minimize the amount of material given a constant design load. The optimization problem can be written as

$$\begin{aligned} &\text{min imize} && \mathbf{w}^T\mathbf{c} \\ & && \mathbf{H}\beta = \mathbf{R}_c \\ &\text{subject to} && \mathbf{c}_{\min} \le \mathbf{c} \\ & && f_i(\beta, \mathbf{c}) \le 0 \quad i = 1,2\ldots n \end{aligned} \tag{13}$$

where $\mathbf{c}$ is the capacities used in the yield criteria, $\mathbf{w}$ is the weight/cost of the each capacity variable and $\mathbf{c}_{\min}$ is a minimum required capacity. If there is no requirement on the minimum material amount, the minimum amount of material is $\mathbf{c}_{\min} = 0$.

4.1 *Yield mechanism*

In the optimization process of the problem in (12), two set of dual variables are calculated. The two set of dual variables are related to the equality constraints and the inequality constraints respectively. The dual variables related to the equality constraints can be interpreted as the strain rates related to the equilibrium equations in the virtual work equations, see (Krenk, Damkilde, & Høyer 1994). The equilibrium equations (1) and (5) are related to vertical displacement rate.

The displacement rates related to (1) and (5) are given as displacement rates per length or area. The displacement rates related to (1) must therefore be scaled by $\frac{1}{2A}$ where A is the area of the element. The displacement rate is placed on the centroid of the triangle for a constant load. The displacement rate related to (5) must be scaled by $\frac{1}{l_j}$ where l_j is the length of the element side j. For the linear element, where the load and shear forces

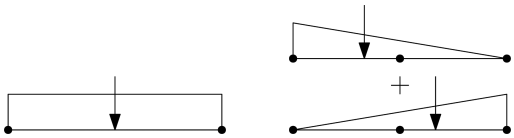

Figure 5. Edge displacement rate position. a) Linear element. b) Quadratic element.

are constant on the element edge, the displacement rate is placed in the middle of the edge as shown in Figure 5a. For the quadratic element, where the load and shear forces are linear varying on the element edge, the displacement rates are placed $\frac{1}{3}l_j$ away from the related node as shown in Figure 5b.

5 NUMERICAL EXAMPLES

The presented elements are investigated with respect to convergence and capability to limit shear forces. The linear element is referred to as *Lin* and the quadratic elements are referred to as *Quad*, where the yield criteria in *Quad6* are checked in node 1–6 shown in Figure 3. *Quad7* and *Quad10* are checked in node 1–7 and 1–10 respectively.

The optimization algorithm for SOCP from Mosek (MOSEK 2015) are used in all examples. The meshes are generated with the MESH2D package (Engwirda 2017) for Matlab, which generate an unstructured mesh.

5.1 *Simple one span plate*

A simple supported one span plate with uniform surface load is analysed with limitation on shear forces and moments. The exact solution is given as

$$p_{max} = \begin{cases} \dfrac{8m_p}{l_x^2} & \text{for} \quad v_p \geq \dfrac{4m_p}{l_x} \\ \dfrac{2v_p}{l_x} & \text{for} \quad v_p < \dfrac{4m_p}{l_x} \end{cases} \tag{14}$$

The plate is analysed with a shear capacity $v_p > \frac{4m_p}{l_x}$ which should result in a moment yield mechanism and a shear capacity $v_p < \frac{4m_p}{l_x}$ which should result in a shear yield mechanism. The yield mechanisms for the two cases are shown in Figure 6. The figure shows that the quadratic element *Quad* fails due to moment limitation in the first case, which is seen as a hinge in the middle of the plate. In the second case, the plate is failing due to shear limitation as expected. This is seen as a vertical drop of the whole beam from each end.

The linear element produces similar results. However, it should be noted that the load placed on a supported element edge does not effect the shear forces in the element. The surface load on the linear element is placed on the edges of the element. On a supported element, this results in $\frac{1}{3}$ of the surface load on the element is going directly in the supported without effecting the element.

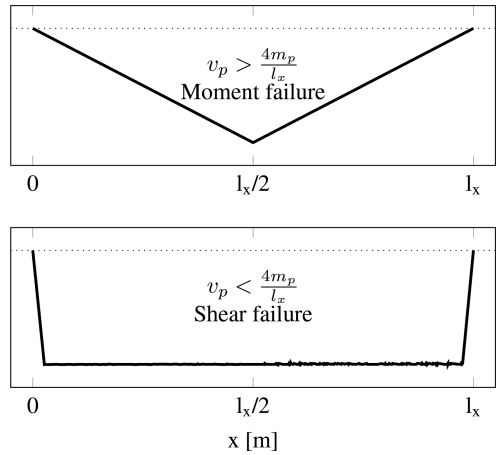

Figure 6. Yield mechanism for simple support one span uniformed loaded plate $l_y = l_x$. Number of quadratic elements, $N = 240$.

5.2 *Clamped square plate*

The clamped square plate with uniform surface load is an benchmark example for convergence test in finite element limit analysis. The exact solution is found in (Fox 1974) and is $p = 42.851\frac{m_p}{l^2}$. The results of the different elements are shown in Figure 7. The figure shows that the linear element *Lin* and the quadratic element with 10 yield check points *Quad10* converge from an lower value than the exact. The elements must converge from a lower value to be a true lower bound element. The quadratic elements with 6 and 7 yield check points, *Quad6* and *Quad7*, overestimate the exact capacity. However, the overestimates are very small compared with the maximum possible violation of the yield criteria for the elements shown in Table 1. However, they are decreasing with an increasing number of elements.

The convergence rates of the quadratic elements are significant faster than the linear element. The quadratic element have more degrees of freedom and a quadratic moment fields, which is a better fit for the squared plate problem compared to the element with linear moment fields. The yield criteria in the *Quad10* element are checked at 10 nodes while it is only checked at 3 nodes for the linear element, which results in a longer computation time. It should be noted that all computation times for the clamped plate still are within seconds.

To investigate the effect of shear limitation and moment-shear interaction, shown in equation (7) and (8), the clamped plate is analysed with all momentshear interaction yield criteria with 232 *Quad7* elements and an increasing shear strength. The error of 232 *Quad7* elements with Nielsen conic yield criteria is 0.03%. The results for the moment-shear interactions are shown in Figure 8. The figure shows that the load increases with the shear capacity increasing for all moment-shear interaction yield criteria. For the yield criteria with no interaction between moment and shear, the capacity is within 5% of the exact solution without shear limitations when the shear capacity is $\upsilon_p = 11.5\frac{m_p}{l}$. It is within 1% for $\upsilon_p = 19\frac{m_p}{l}$. If we assume a quadratic interaction the shear capacity has to be $\upsilon_p = 30\frac{m_p}{l}$ for the load to be within 5% of the exact solution.

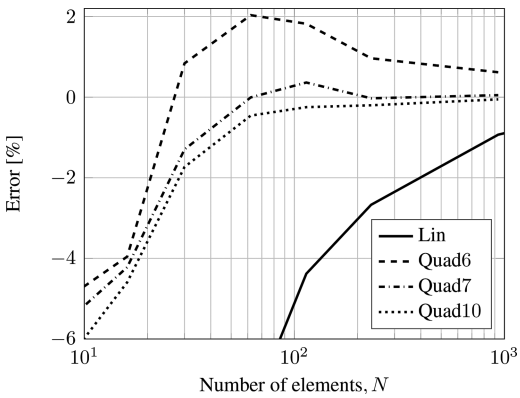

Figure 7. Convergence of squared clamped plate with uniform load. Analytical solution: $p = 42.851\frac{m_p}{l^2}$.

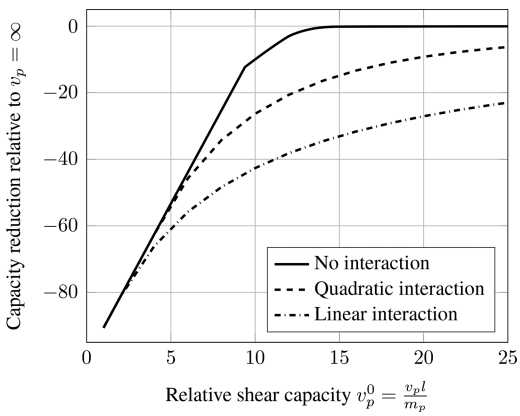

Figure 8. Squared clamped plate with uniform load and limitation on shear forces. Three different moment-shear interactions. Analytical solution for $\upsilon_p = \infty$: $p = 42.851\frac{m_p}{l^2}$. Element: *Quad7*, $N = 232$.

5.3 *Wide bridge with axle loads*

A wide bridge with axle loads is analysed with and without shear limitations. The bridge is shown in Figure 9. The purposes of the example are to demonstrate the effect of the shear limitations on the yield mechanism and the distribution of shear forces. The bridge has the same capacities for positive and negative moments. The moment capacity in the x direction is 5 times larger than in the y direction, $m_{px} = 5m_{py}$.

The yield mechanism for the moment yield criteria in equation (6) is shown in Figure 10. The figure shows that the bridge experience a local collapse and forms an approximate half envelop yield mechanism. The analysis is made with both the linear element and the quadratic elements and give the same load carrying capacity.

The shear capacity in the y direction is now reduced to $\upsilon_{py} = \frac{m_{py}}{1[m]}$. The reduction of the load

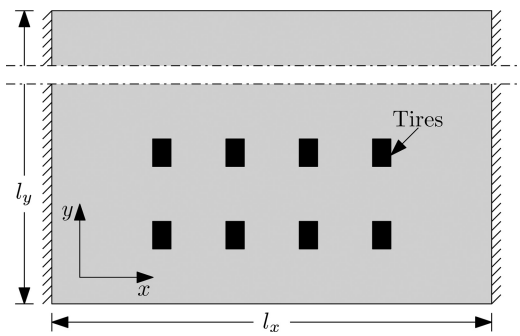

Figure 9. Single span wide bridge load with three axles. $l_x = 8$ [m] and $l_y = 12$ [m].

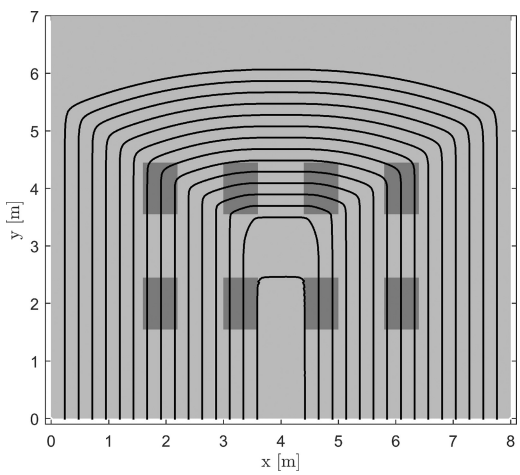

Figure 10. Contour lines of yield mechanism for moment yield criteria only.

carrying capacity due to the reduction of the shear capacity is 12% for no interaction between moment and shear, and 23% for linear interaction. The yield mechanisms along $\frac{l_x}{2}$ are shown in Figure 11. The figure shows that the slab fails in shear when the reduced shear capacity is taken into account. This is seen from the the lines between 3 and 6 meters, where the line is inclined for the moment failure and almost vertical for the shear failures. The same is seen for the simple supported plate in Figure 6.

The yield mechanism is a visualization of where the moments and shear forces are at the limit of the yield criteria. Moments and shear forces not on the limit of the yield criteria, or not considered in the yield criteria, are therefore not restricted to a unique value. In the following, it is shown how forces can vary when they are not at the limit of the yield criteria or not con sidered in the yield criteria.

The reaction forces along the sides are shown in Figure 12a and 12b for the linear element and the quadratic element. The figure shows very different reaction forces. The reaction forces for the analysis with the quadratic element vary extremely and have very high peak values compared with the reaction forces from the analysis with the linear element. The extreme variations of the shear forces are possible, because the shear forces are only required to be continuous normal to the element edges, as shown in Figure 2. It is seen that it is not possible to get the maximum required shear forces from an analysis, where only the moments are included in the yield criteria.

In Figure 12c the reaction forces are shown for an analysis, where the shear forces are limited to $\upsilon_{px} = \frac{m_{px}}{0.5[m]}$ and $\upsilon_{py} = \frac{m_{py}}{0.5[m]}$. The limitation of shear forces have not reduced the load carrying capacity, compared with the analyses with limitation on moments only. Nor has it changed the yield mechanism. However, the reaction forces have been reduced significantly and are similar to the reactions from the analysis with the linear element shown in Figure 12a. In both cases, a peak is seen where the one row of tires are placed at $y = 2$ [m]. Next to the other row of tires, there are still a fluctuation of the reaction forces. This is where the yield mechanism ends as shown in Figure 10.

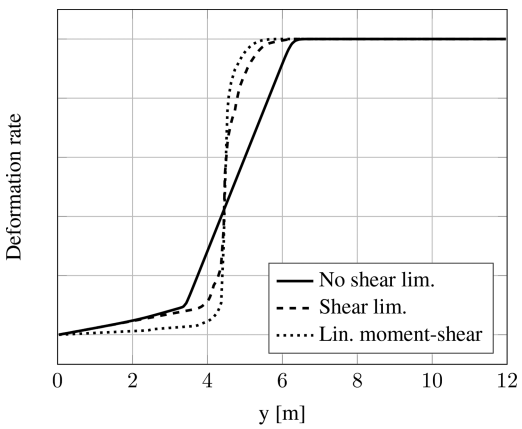

Figure 11. Yield mechanisms of wide bridge along $\frac{l_x}{2}$. with different moment-shear interactions.

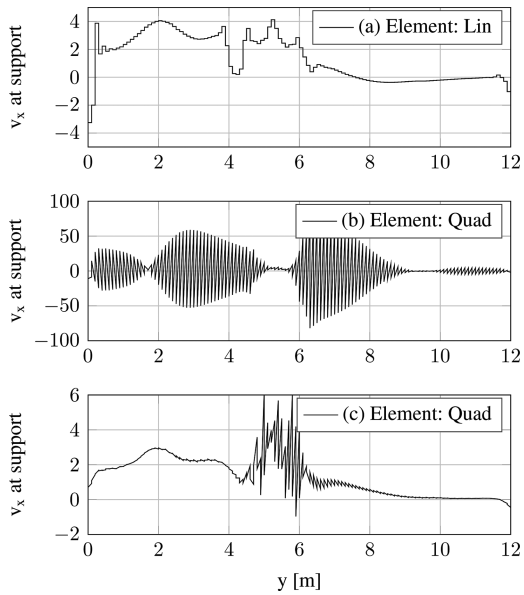

Figure 12. Shear forces at support. All analyses return the same load carrying capacity. a) Linear element and moment yield condition only. b) Quadratic element and moment yield criteria only. c) Quadratic element with moment yield criteria and shear limitation of $\upsilon_{px} = \frac{m_{px}}{0.5[m]}$ and $\upsilon_{py} = \frac{m_{py}}{0.5[m]}$.

It should be noted that all shear forces shown in Figure 12 are within the admissible moment and shear field given by the equilibrium conditions and yield criteria. However, when moments and shear forces are not near the yield surface and the system is underdetermined, the optimization algorithms have the freedom to choose higher values than necessary to carry the load.

6 CONCLUSION

Two equilibrium elements have been presented for finite element limit analysis of reinforced concrete slabs. It have been shown that both elements can

handle limitation on shear forces, which is not possible with the widely used Kirchhoff element.

The element with linear moment fields and the element with quadratic moment fields have been compared. The linear element converges from below in the clamped plate benchmark problem, while the quadratic element with 6 nodes overestimate the load carrying capacity. The overestimate is possible because the element can violate the yield criteria inside the element, due to the non-linear moment fields. By adding extra points to the element, where the yield criteria are checked, the overestimate can be reduced and even removed by adding four extra points, even though it is still possible for the element to violate the yield criteria. Furthermore, the overestimate is reduced with an increasing number of elements.

The elements have been used to calculate an one span simple supported plate with uniform load. Both elements can be limited by shear forces and showed a bending failure mechanism and a shear failure when the shear capacity is reduced.

The quadratic element has been used to calculated the load carrying capacity of the squared clamped plate where different moment-shear interactions are imposed. The element perform well with no interaction, linear interaction and quadratic interaction between moments and shear forces. It has been shown that a shear capacity of at least $v_p = 11.5\frac{m_p}{l}$ is needed to obtain the exact solution of the clamped plate from (Fox 1974) within 5%.

The yield mechanism is presented for both bending failure and shear failure. The yield mechanism gives a visualization of where the moments and shear forces are at the limit of the yield criteria. The yield mechanism for shear forces at the limit is recognized by a vertical displacement rate discontinuity, while the bending failure is more continuous with clear hinges in simple cases.

The optimization algorithms finds the maximum load for an admissible stress field. The moments and shear forces, which are not at the limit of the yield criteria, can therefore take any value as long as the stresses are admissible.

REFERENCES

Anderheggen, E. & H. Knöpfel (1972). Finite element limit analysis using linear programming. *International Journal of Solids and Structures 8*(12), 1413–1431.

Bleyer, J. & P. Buhan (2014). Lower bound static approach for the yield design of thick plates. *International Journal for Numerical Methods in Engineering 100*(11), 814–833.

Chan, H. (1972). The collapse load of reinforced concrete plate. *International Journal for Numerical Methods in Engineering 5*(1), 57–64.

Engwirda, D. (2017). Mesh2d.

Faccioli, E. & E. Vitiello (1973). A finite element, linear programming methods for the limit analysis of thin plates. *International Journal for Numerical Methods in Engineering 5*(3), 311–325.

Fox, E.N. (1974). Limit analysis for plates: the exact solution for a clamped square plate of isotropic homogeneous material obeying the square yield criterion and loaded by uniform pressure. *Philosophical Transactions of the Royal Society of London A: Mathematical, Physical and Engineering Sciences 277*(1265), 121–155.

Hillerborg, A. (1974). *Strip method of design*. Number Monograph.

Johansen, K.W. (1943). *Brudlineteorier*. Jul. Gjellerups Forlag.

Krabbenhøft, K. & L. Damkilde (2002). Lower bound limit analysis of slabs with nonlinear yield criteria. *Computers & structures 80*(27), 2043–2057.

Krabbenhøft, K., A. Lyamin, & S. Sloan (2007). Formulation and solution of some plasticity problems as conic programs. *International Journal of Solids and Structures 44*(5), 1533–1549.

Krenk, S., L. Damkilde, & O. Høyer (1994). Limit analysis and optimal design of plates with equilibrium elements. *Journal of Engineering Mechanics 120*(6), 1237–1254.

Larsen, K.P., P.N. Poulsen, & J.F. Olesen (2011). *Numerical Limit Analysis of Reinforced Concrete Structures: Computational Modeling with Finite Elements for Lower Bound Limit Analysis of Reinforced Concrete Structures*. Ph. D. thesis, Technical University of Denmark (DTU).

Marti, P. (1990). Design of concrete slabs for transverse shear. *Structural Journal 87*(2), 180–190.

MOSEK (2015). *The MOSEK optimization toolbox for MATLAB manual. Version 7.1 (Revision 32)*.

Nielsen, L.O. & P. Poulsen (2009). Computational limit analysis of perfectly plastic plate bending based on lower bound optimization.

Nielsen, M. (1963). Flydebetingelser for jernbetonplader (english summary: Yield conditions for reinforced concrete slabs). pp. 61–82.

Nielsen, M.P. & L.C. Hoang (2011). *Limit analysis and concrete plasticity*. CRC press.

Computational Modelling of Concrete Structures – Meschke, Pichler & Rots (Eds)
© 2018 Taylor & Francis Group, London, ISBN 978-1-138-74117-1

Simulation of reinforced HPFRCC deformation capacity under flexure- and shear-dominated stress states

M. Pokhrel & M.J. Bandelt
Department of Civil and Environmental Engineering, New Jersey Institute of Technology, Newark, NJ, USA

ABSTRACT: High-Performance Fiber-Reinforced Cementitious Composites (HPFRCCs) have a high material toughness that allow them to sustain compressive strains without spalling beyond that of normal concrete. Recent experimental findings have shown that unlike ordinary reinforced concrete elements that often fail in flexure due to concrete crushing, reinforced HPFRCCs can undergo high inelastic deformations resulting in tensile reinforcement fracture before crushing of the cementitious material. Experimental results to date have shown that reinforcement ratio strongly influences member deformation capacity due to rebar fracture. Specifically, by increasing reinforcement ratio in HPFRCCs, the reinforcement strains decrease for a given level of deformation, providing high deformation capacity in members that are more heavily reinforced. In this paper, the deformation capacity of reinforced HPFRCC structural elements subjected to various stress states has been investigated through numerical simulation. Of particular interest is the influence of flexure and shear stress states on member deformation capacity. Computational simulations are conducted on members with two different shear span-to-depth ratios and three different reinforcement ratios. For the same reinforcement ratio, simulation results show that there is a 5 to 20% reduction in the deformation capacity of shear dominated beams compared to flexure dominated beams. The observed dominant crack patterns are used to investigate reinforcement strain distribution and rebar fracture in different beams. The simulation results show similar damage pattern and strain localization phenomenon that has been observed in recent experimental studies.

1 INTRODUCTION

High-performance fiber-reinforced cementitious composites (HPFRCCs) are a special type of cement-based composite that are characterized by pseudo-strain hardening behavior under uniaxial tensile loading with multiple distributed cracking prior to crack localization (Li 2003, Naaman and Reinhardt 2006). The unique tensile properties of HPFRCC at the material level improves structural response when HPFRCCs are combined with reinforcement. Reinforced HPFRCCs have been observed to have higher damage tolerance, ductility and energy absorption capacity compared to ordinary reinforced concrete elements (Fischer and Li 2002, Parra-Montesinos 2005, Canbolat et al. 2005). These characteristics make them ideal construction materials for resilient and durable structures, especially in regions with high seismic demands.

Although HPFRCCs provide numerous opportunities to improve various aspects of structural performance, recent tension stiffening experiments have shown that reinforced HPFRCCs had lower deformation capacity than reinforced concrete when loaded in direct tension (Moreno et al. 2014) since HPFRCCs were able to resist splitting cracks better than concrete. The high resistance of HPFRCCs to splitting cracks has been observed in bond-slip experiments as well for a variety of fiber types and experimental setups (Chao et al. 2010, Bandelt and Billington 2016a). As an extension of the work by Moreno et al. (2014) on reinforcement fracture, Bandelt and Billington (2016b) found that reinforced HPFRCCs loaded in flexure predominantly fail due to reinforcement fracture, and that deformation capacity of reinforced HPFRCCs increases with reinforcement ratio.

Bandelt and Billington (2016b) also found that there is significant dispersion in deformation capacity of HPFRCC beams for a given reinforcement ratio. This wide variability in deformation could be due to a number of factors, such as fiber type, tensile properties of the HPFRCC, geometry of the experimental setup, or shear span-to-depth ratio (i.e. effect of shear) for different beams.

The research conducted herein aims to identify how shear span-to-depth ratio influences deformation capacity due of HPFRCC beams to reinforcement fracture. Quantitative and qualitative results in terms of HPFRCC damage patterns, reinforcement strain, and deformation capacity are explored to understand how shear span-to-depth ratio influences behavior of reinforced HPFRCC components.

In this study, Engineered Cementitious Composites (ECC) were used for simulation of all of the beams. ECC has been developed based on the principle of micromechanics such that it exhibits multiple fine cracking (Li and Leung 1992), and typically does not contain coarse aggregate. ECC was chosen for this study because its deformation capacity with varying reinforcement ratios has been experimentally investigated under monotonic and cyclic loading conditions (Bandelt and Billington 2016b). The result from this previous study are used to validate simulation results presented herein.

2 FINITE ELEMENT MODEL

2.1 *Model geometry*

Two dimensional finite element models of two different length beams were used for the simulation as shown in Figure 1. The geometric cross section and material parameters were based on the experimental study conducted by Bandelt and Billington (2016b). The beam with shear-span-to-depth ratio (a/d) of 4.06 has a center-to-center length of 1300 mm with a width of 130 mm and height of 180 mm. And, the beam with shear span-to-depth ratio (a/d) of 6.75 has a length of 2160 mm with same cross section dimensions. Support plates of 80 mm length and 20 mm height were used at the two ends and loading plates of the same dimension were used in both beams. Loading plates and support plates were modeled with linear elastic material property. Vertical compression-only springs of stiffness 1.0×10^4 N/mm were used at the two supports to reproduce softness of the supports (Bandelt and Billington 2017). The horizontal spring had tension and compression stiffness of 5.0×10^3 N/mm.

A total of six beams, with cross section details outlined in Table 1, were simulated in this study with variations in shear span-to-depth ratio and longitudinal reinforcement ratio. The notation of beams were based on the dominant stress state and reinforcement ratio; for e.g., SHEAR-0.70 refers to a shear-stress state dominant beam with a shear span-to-depth ratio of 4.06 and longitudinal reinforcement ratio of 0.70%. In this study, beams with shear span-to-depth ratio of 4.06 are considered shear dominated (Wight 2015) and will be referred from this point onward as shear beams. And, beams with shear span-to-depth ratio of 6.75 are considered as flexure dominated beams (Wight 2015) and will be referred to as flexure beams from this point onward. Longitudinal reinforcement of area 142 mm^2, 258 mm^2 and 398 mm^2 corresponding to reinforcement ratios of 0.70%, 1.25% and 1.90% were used at the top and bottom sides of beams. Transverse reinforcement of area 16 mm^2 was provided at spacing of 75 mm in all beams.

2.2 *Material models and nonlinear properties*

A total strain based fixed crack model proposed by Feenstra et al. (1998) was used as the constitutive model for simulating ECC material behavior. A shear retention factor (β) of 0.01 was used (Moreno-Luna 2014). ECC was modeled using eight-noded quadratic plane stress elements with a mesh size of 10×10 mm. Quadratic interpolation and a 3×3 gauss integration scheme was utilized. A multi-linear tensile stress-strain curve was used for modeling tension behavior of ECC as shown in Figure 2. The initial stiffness (E), maximum tensile stress (f_t) and peak tensile strain (ε_{tp}) before softening were obtained from experimental data of

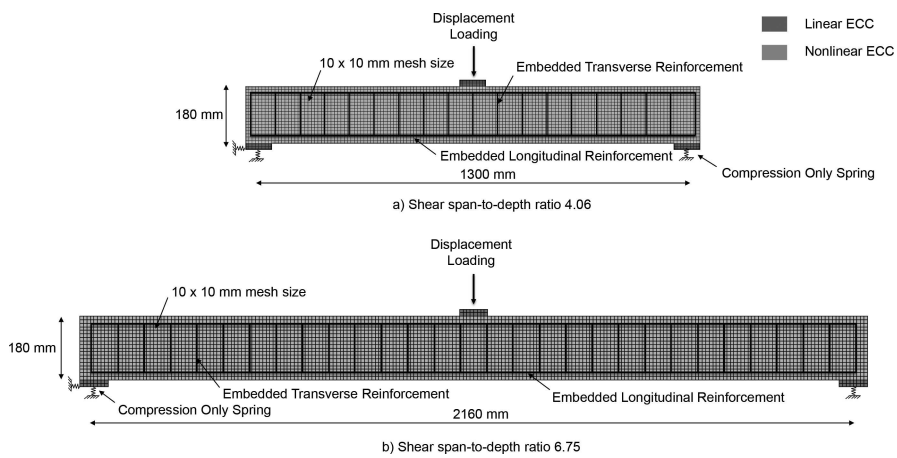

Figure 1. Finite element models with different shear span-to-depth ratios.

Table 1. Details of beam cross section.

Beam		Cross section		Depth	Longitudinal steel			Transverse steel		
		b	h	d	d_b		Area	d_s	Area	Spacing
Notation	a/d	[mm]	[mm]	[mm]	[mm]	No. of Bars	[mm^2]	[mm]	[mm^2]	[mm]
SHEAR-0.70	4.06	130	180	160	10	142	3	2	16	75
SHEAR-1.25	4.06	130	180	160	13	258	3	2	16	75
SHEAR-1.90	4.06	130	180	160	16	398	3	2	16	75
FLEX-0.70	6.75	130	180	160	10	142	3	2	16	75
FLEX-1.25	6.75	130	180	160	13	258	3	2	16	75
FLEX-1.90	6.75	130	180	160	16	398	3	2	16	75

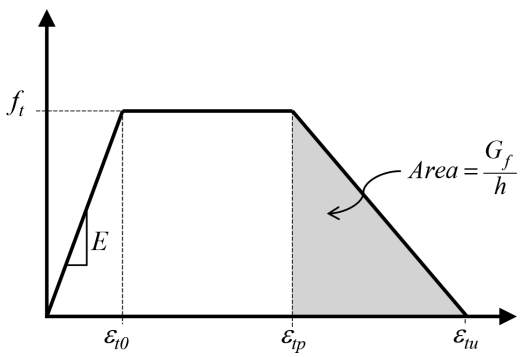

Figure 2. Multilinear tensile property of ECC.

Table 2. Material properties.

Description	ECC	Longitudinal steel	Transverse steel
f_t [Mpa]	2.9	–	–
ε_{t0} [%]	0.0169	–	–
ε_{tp} [%]	0.75	–	–
G_f [Mpa-mm]	6.1	–	–
f_c' [Mpa]	55	–	–
G_c [Mpa-mm]	52.5	–	–
E [Gpa]	17.2	200	205
v	0.15	0.3	0.3
β	0.01	–	–
f_y [Mpa]	–	455	690
f_u [Mpa]	–	675	–
ε_u [%]	–	16	–

Moreno-Luna (2014) and is summarized in Table 2. The ultimate tensile strain (ε_{tu}) of the ECC is based on tensile fracture energy (G_f) as shown in Equation 1 (Bandelt and Billington 2017).

$$\varepsilon_{tu} = 2\frac{G_f}{h}\frac{1}{f_t} + \varepsilon_{tp} \quad (1)$$

In the above equation, h is the crack bandwidth which is equal to $\sqrt{A}$, where A is the area of eight-noded ECC element. The uniaxial compression property of ECC material was modeled using a parabolic stress-strain curve based on compressive fracture energy (Feenstra 1993). Compressive strength (f_c'), compressive fracture energy (G_c) and Poisson's ratio (v) were all based on data from Moreno-Luna (2014) and are tabulated in Table 2.

Longitudinal and transverse reinforcements were modeled as embedded reinforcement elements with mesh size of 10 mm. Perfect bond was assumed to exist between longitudinal reinforcement and ECC material. Although there are different bond-slip models (Chao et al. 2010, Harajli 2009, Bandelt and Billington 2017) available to accurately model interface between longitudinal reinforcement and the HPFRCC material surrounding it, there is a relatively small difference in the predicted ultimate deformation capacity between beams simulations using bond-slip model and perfect-bond model when beams are subjected to monotonic loading (Bandelt and Billington 2017).

Longitudinal reinforcement was modeled using Von Mises plasticity model with strain hardening. Uniaxial tensile response data such as modulus of elasticity, yield stress, ultimate stress and ultimate strain were based on test conducted by Bandelt and Billington (2016b) and are summarized in Table 2. Transverse reinforcement was modeled using Von Mises plasticity model without strain hardening. The values of modulus of elasticity and yield stress listed in Table 2 were obtained from experimental data of Bandelt and Billington (2016b).

2.3 *Loading and analysis parameters*

An incremental displacement of 0.25 mm was applied at each load step in the finite element simulation. Nonlinear static analyses were conducted using the commercial finite element software, DIANA 10.1 (DIANAFEA 2016). The

equilibrium criteria was based on a regular Newton-Raphson scheme. The numerical solution was assumed to converge when force or displacement or energy norm was equal to 1% or 0.1% or 0.01% respectively. A line search algorithm was used to minimize the norm and achieve quick convergence.

3 SIMULATION RESULTS AND DISCUSSION

3.1 *Moment-drift response*

The applied moment versus drift response of flexure and shear dominated beams for different reinforcement ratios are shown in Figure 3. Drift is expressed in percentage (%) and is calculated by normalizing deformation by shear span length. The shear span length for shear beams and flexure beams are 650 mm and 1080 mm, respectively.

The initial elastic response of shear beams and flexure beams are similar. For the three reinforcement ratios studied, shear beams and flexure beams exhibit the same elastic stiffness before yielding. The yield criteria for beams was defined based on the average yield strain in the longitudinal reinforcement over three integration points (Bandelt and Billington 2017), which corresponds to a gage length of 30 mm. Beams were assumed to yield and undergo inelastic deformation once the strain in longitudinal reinforcement reached 0.2275% strain based on yield stress and modulus of elasticity listed in Table 2. Shear beams SHEAR-0.70, SHEAR-1.25 and SHEAR-1.90 started to yield at drift of 0.93%, 1.19% and 1.45% respectively. In the case of flexure beams, FLEX-0.70, FLEX-1.25 and FLEX-1.90 started to yield at drift of 0.93%, 1.05%

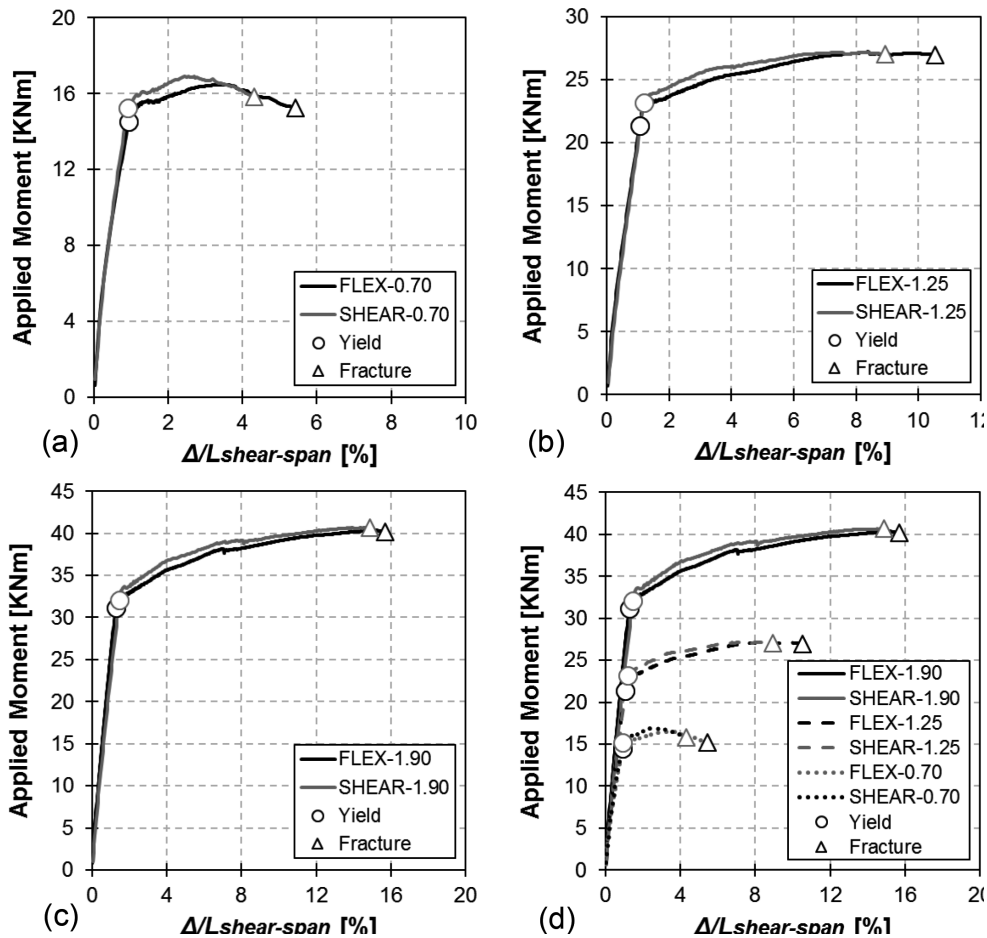

Figure 3. Applied moment vs. drift response of beams with (a) $\rho = 0.70\%$ (b) $\rho = 1.25\%$ (c) $\rho = 1.90\%$ (d) all reinforcement ratios.

and 1.25% respectively. The drift levels are almost the same in both types of beams for the same reinforcement ratio, i.e. drift capacity of SHEAR-070 and FLEX-070 are approximately equal. And, the yield moment for both types of beams are nearly equal because of the use of the same reinforcement ratio in the finite element models.

The post-yield behavior of shear beams and flexure beams in all three cases are similar with all showing positive stiffness. The peak moment and drift capacity of the beams were based on the fracture strain in the longitudinal reinforcement as described in Sec. 3.3. The moment capacity of shear beams and flexure beams are nearly equal due to the use of the same reinforcement ratio.

The drift capacity of the shear beams SHEAR-0.70, SHEAR-1.25 and SHEAR-1.90 are 4.31%, 8.93% and 14.87%, respectively, and that of flexure beams are FLEX-0.70, FLEX-1.25 and FLEX-1.90 are 5.43%, 10.53% and 15.71%, respectively. The drift capacity ofthe shear beams are lower than flexure beams for the same reinforcement ratio, although the material level and cross section level properties are exactly same. This reduction in deformation capacity in shear beams is due to the influence of increased shear which is discussed in Sec. 3.4.

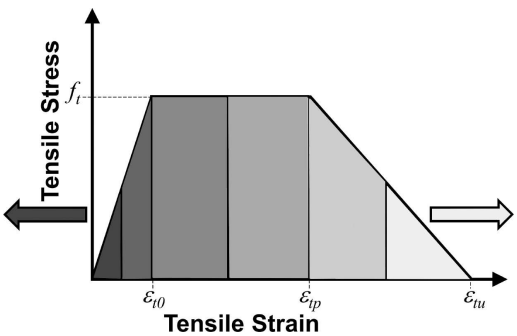

Figure 4. Tensile strain contour color range.

3.2 *Damage pattern*

The damage pattern in the beams are shown in terms of contour color range (Figure 4) for different stages of deformation: elastic, multiple fine cracking, pseudo-strain hardening (two ranges), softening and dominant crack formation. Contours are based on principal tensile strain. Figures 5 and 6 show tensile strain at three drift levels for shear beams and flexure beams respectively to show the damage progression rate and final damage state before fracture of the longitudinal reinforcement.

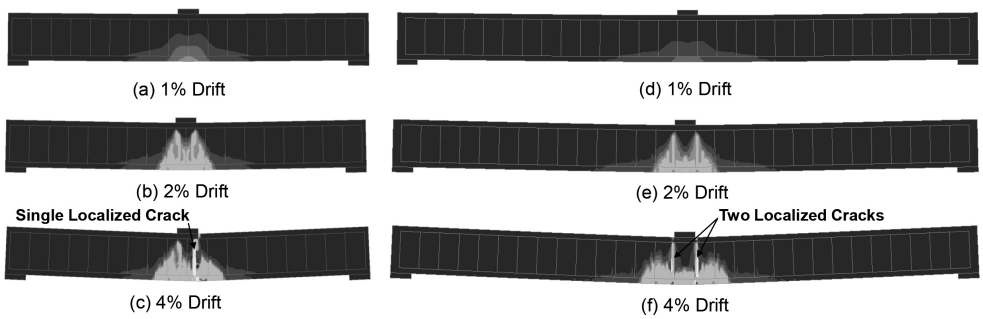

Figure 5. Principal tensile strain in beams with $\rho = 0.70\%$ (a-c) SHEAR-0.70, (d-f) FLEX-0.70.

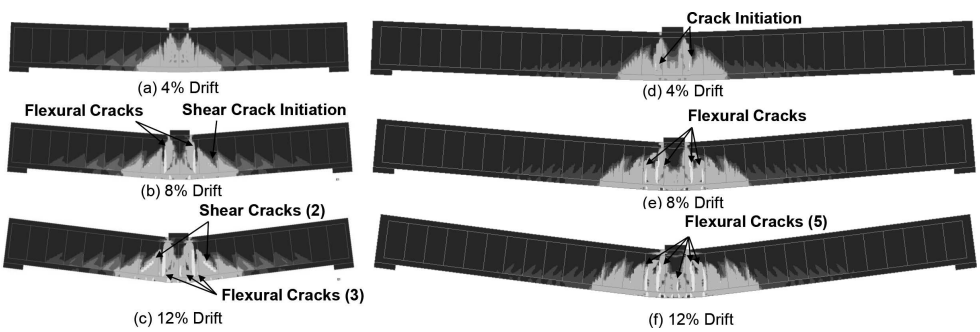

Figure 6. Principal tensile strain in beams with $\rho = 1.90\%$ (a-c) SHEAR-1.90, (d-f) FLEX-1.90.

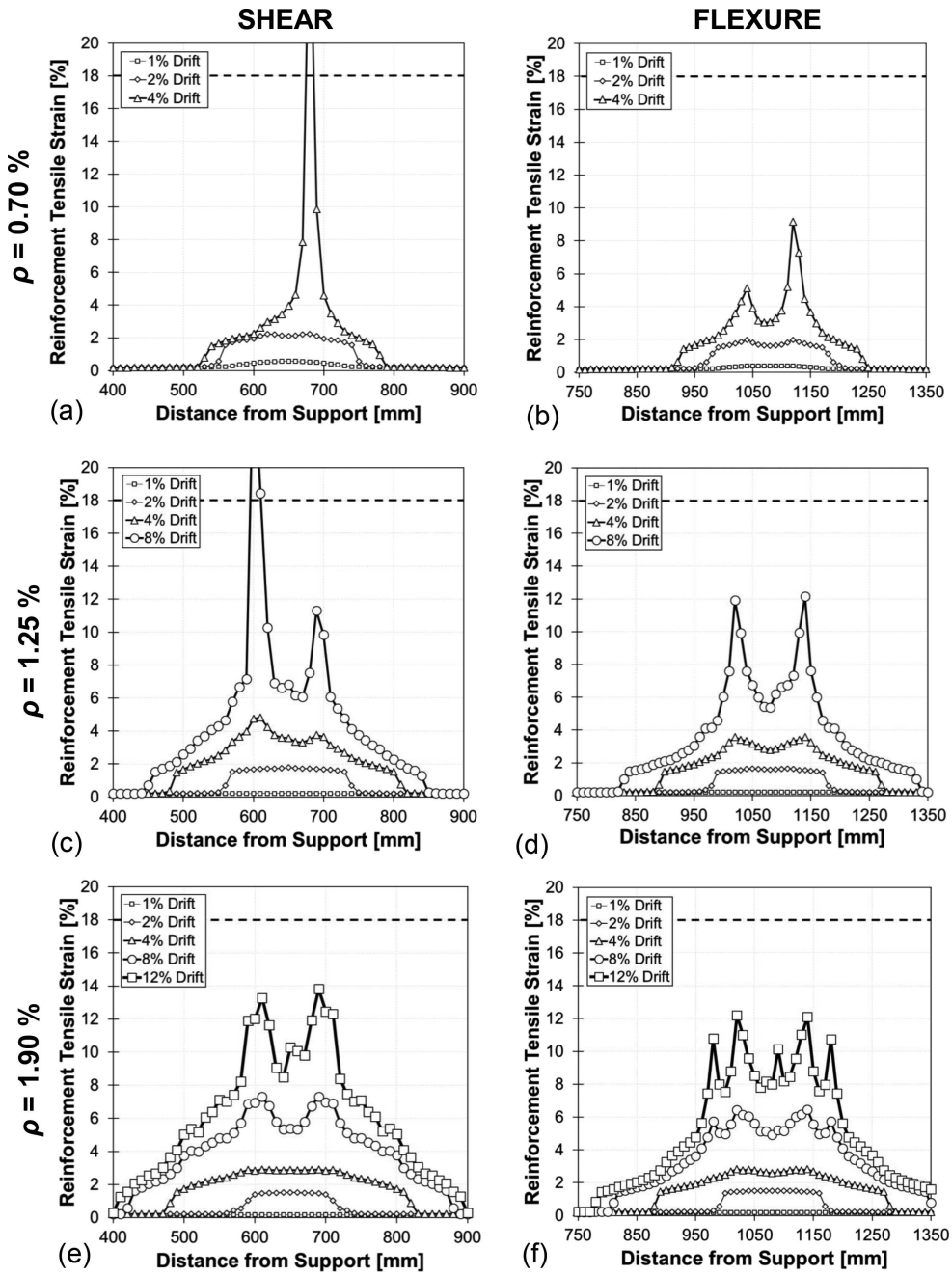

Figure 7. Strain in longitudinal reinforcement along the span of beam at different drifts (a) SHEAR-0.70, (b) FLEX-0.70, (c) SHEAR-1.25, (d) FLEX-1.25, (e) SHEAR-1.90, (f) FLEX-1.90.

There are two major differences in the damage pattern observed in shear beams compared to flexure beams. The first difference is the number of dominant cracks as shown in Figure 5(c) and (f). SHEAR-070 beam has a single dominant localized crack whereas FLEX-070 has two dominant localized cracks at the same drift of 4%. The deformation capacity of FLEX-070 is 25% higher than

SHEAR-070 beam because the damage was divided between two cracks in FLEX-070 compared to SHEAR-070 in which damage was concentrated over one large crack. The second difference in damage patterns is the type of dominant cracks as shown in Figure 6(c) and (f). SHEAR-190 beam has diagonal tension, or shear, cracks in addition to flexural cracks; however, FLEX-190 beam has only one type of crack (i.e. flexural cracks) at 12% drift level. The occurrence of shear cracks decreases the deformation capacity in ECC beams as observed experimentally by Bandelt and Billington (2016b).

3.3 *Strain in reinforcement*

The failure mechanism of reinforced HPFRCC beams is different than that of a conventional reinforced concrete beam. Reinforced HPFRCC beams fail due to fracture of reinforcement rather than crushing of compression zone material as observed experimentally (Fischer and Li 2002, Parra-Montesinos and Chompreda 2007, Frank, Lepech, and Billington 2017, Bandelt and Billington 2016b). The strength and drift capacity was determined by checking the average strain in the longitudinal reinforcement over three integration points (Bandelt and Billington 2017), which corresponds to a gage length of 30 mm. Beams were assumed to fail once the strain in longitudinal reinforcement reached an 18% strain value.

The inelastic deformation in beams is concentrated in the region where longitudinal reinforcement has yielded. To quantify this length, strain in longitudinal reinforcement along the span of all the beams at different drift levels were plotted as shown in Figure 7. In Figure 7, the horizontal axis is the distance from the left hand support. It can be seen that for the same drift level, shear beams undergo less inelastic deformation compared to flexure beams; for example longitudinal reinforcement in SHEAR-070 (Figure 7 (a)) undergoes plastic deformation for a length of 270 mm whereas FLEX-070 (Figure 7 (b)) undergoes plastic deformation for a length of 350 mm for 4% drift. This implies that inelastic strain is distributed over a longer length in flexure beams compared to shear beams, and thus, flexure beams undergo more inelastic deformation and therefore have higher deformation capacity than shear beams. The peaks in strain plots are locations of strain localization, and the beams failed by fracture of longitudinal reinforcement at these dominant crack locations as shown in Figures 5 and 6.

3.4 *Influence of flexure and shear on* $\Delta_{capacity}$

The experimental study by Bandelt and Billington (2016b) showed that deformation capacity of ECC beams tend to increase with an increase in reinforcement ratio. The maximum deformation capacity result, presented in Figure 8, shows the same trend for shear and flexure beams. The deformation in flexure beams is due to pure bending (flexural deformation) whereas the deformation in shear beams is mostly due to angular distortion (shear deformation). The crack pattern seen from experiments conducted by Bandelt and Billington (2016b) clearly shows the sign of shear deformation in beams of the same material and cross-sectional properties as the shear beams in this study. The deformation capacity of shear beams is lower than flexure beams by 20.6%, 15.2% and 5.3% corresponding to reinforcement ratios of 0.70%, 1.25% and 1.90% respectively. Thus, the stress state influences deformation capacity more at lower reinforcement ratios.

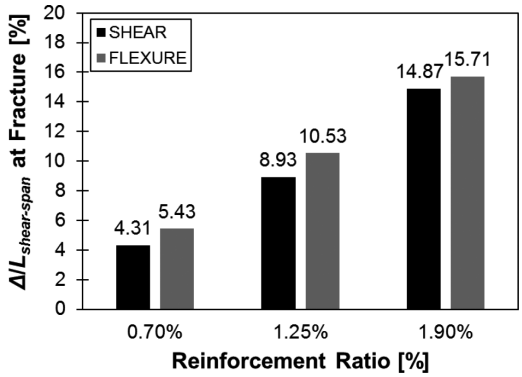

Figure 8. Effect of variation in ρ [%] and a/d ratio in $\Delta/L_{shear\text{-}span}$ [%].

4 CONCLUSION

Two dimensional continuum finite element simulations of six simply supported ECC beams with flexure dominant (three beams) and shear dominant (three beams) behavior were analyzed to investigate the damage pattern and ultimate deformation capacity under monotonic loading. The numerical simulations showed that there is a 5% to 20% reduction in the deformation capacity due to the influence of shear. Larger discrepancies between shear and flexure dominated deformation capacity were observed at lower reinforcement ratios. The difference in the deformation capacity is mainly due to formation of a smaller number of dominant cracks in shear beams compared to flexure beams. A lower number of cracks resulted in strain localization over a smaller gage length of longitudinal reinforcement and early failure of shear beams due to fracture of reinforcement. Furthermore, as the reinforcement ratio increased,

cracking patterns in shear beam consisted of diagonal tension cracks along with vertical cracks which aided in early exhaustion of load carrying ability of shear beams compared to flexure beams.

Additional simulations are being carried out to study additional sources of deformation capacity variability in high-performance fiber-reinforced cementitious composites. Experimental investigations will also be conducted to validate the simulation results.

ACKNOWLEDGMENT

The simulations were performed using finite element software DIANA Version 10.1 (DIANAFEA 2016). The authors gratefully acknowledge the support of John A. Reif, Jr., Department of Civil and Environmental Engineering at New Jersey Institute of Technology.

REFERENCES

Bandelt, M.J. and S.L. Billington (2016a). Bond behavior of steel reinforcement in high-performance fiber-reinforced cementitious composite flexural members. *Materials and Structures 49*(1), 71–86.

Bandelt, M.J. and S.L. Billington (2016b). Impact of reinforcement ratio and loading type on the deformation capacity of high-performance fiber-reinforced cementitious composites reinforced with mild steel. *Journal of Structural Engineering 142*(10), 04016084.

Bandelt, M.J. and S.L. Billington (2017, August). Simulation of displacement capacity of reinforced HPFRCC flexural members. Submitted to *Journal of Structural Engineering*.

Canbolat, B.A., G.J. Parra-Montesinos, and J.K. Wight (2005). Experimental study on seismic behavior of high-performance fiber-reinforced cement composite coupling beams. *ACI Structural Journal 102*(1), 159–166.

Chao, S.-H., A.E. Naaman, and G.J. Parra-Montesinos (2010). Local bond stress-slip models for reinforcing bars and prestressing strands in high-performance fiber-reinforced cement composites. *ACI Special Publication SP-272*(8), 151–172.

DIANAFEA (2016). Diana release 10.1. http://www.dianafea.com.

Feenstra, P.H. (1993). *Computational Aspects of Biaxial Stress in Plain and Reinforced Concrete*. Ph. D. thesis, Delft University of Technology.

Feenstra, P.H., J. Rots, A. Arnesen, J. Teigen, and K. Hoiseth (1998). A 3D constitutive model for concrete based on a con-rotational concept. In D. Borst, Bicanic, Mang, and Meschke (Eds.), *Computational Modelling of Concrete Structures, Proceedings of EURO-C 1998*, Rotterdam, pp. 13–22. Balkema.

Fischer, G. and V. Li (2002). Effect of matrix ductility on deformation behavior of steel-reinforced ECC flexural members under reversed cyclic loading conditions. *ACI Structural Journal 99*(6), 781–790.

Frank, T.E., M.D. Lepech, and S.L. Billington (2017). Experimental testing of reinforced concrete and reinforced ECC flexural members subjected to various cyclic deformation histories. *Materials and Structures 50*(5), 232.

Harajli, M.H. (2009). Bond Stress Slip Model for Steel Bars in unconfined or Steel, FRC, or FRP confined concrete. *Journal of Structural Engineering 135*(5), 509–518.

Li, V. (2003). On engineered cementitious composites (ECC) a review of the material and its applications. *Journal of Advanced Concrete Technology 1*(3), 215–230.

Li, V. and C. Leung (1992). Steady-state and multiple cracking of short random fiber composites. *Journal of Engineering Mechanics 118*(11), 2246–2264.

Moreno, D.M., W. Trono, G. Jen, C. Ostertag, and S.L. Billington (2014). Tension stiffening in reinforced high performance fiber reinforced cement-based composites. *Cement and Concrete Composites 50*(2014), 36–46.

Moreno-Luna, D. (2014). *Tension stiffening in reinforced high performance fiber reinforced cement based composites*. Ph.d., Stanford University.

Naaman, A. and H. Reinhardt (2006). Proposed classification of hpfrc composites based on their tensile response. *Materials and Structures 39*(5), 547–555.

Parra-Montesinos, G. and P. Chompreda (2007). Deformation capacity and shear strength of fiber-reinforced cement composite flexural members subjected to displacement reversals. *Journal of Structural Engineering 133*(3), 421–431.

Parra-Montesinos, G.J. (2005). High-performance fiber-reinforced cement composites: An alternative for seismic design of structures. *ACI Structural Journal 102*(5), 668–675.

Wight, J.K. (2015). *Reinforced Concrete: Mechanics and Design*. Hoboken, New Jersey: Pearson.

Computational Modelling of Concrete Structures – Meschke, Pichler & Rots (Eds)
© 2018 Taylor & Francis Group, London, ISBN 978-1-138-74117-1

Computer-aided stress field analysis of discontinuity concrete regions

J. Mata-Falcón, D.T. Tran & W. Kaufmann
Institute of Structural Engineering, Swiss Federal Institute of Technology (ETH), Zurich, Switzerland

J. Navrátil
IDEA RS s.r.o., Brno, Czech Republic
VŠB—Technical University of Ostrava, Czech Republic

ABSTRACT: Strut-and-tie models and stress fields are widespread methods in engineering practice for the design of discontinuity regions. They are powerful tools that give the engineer control over the design, but they are not directly applicable for checking serviceability criteria and their use for the dimensioning of real-life structures often requires tedious iterative hand calculations. This paper presents a method for the design and assessment of discontinuity regions in concrete structures aiming at overcoming these limitations. The method consists of a FE-based computer-aided stress field analysis that implements uniaxial constitutive laws for reinforcement and concrete in compression. The tensile strength of concrete is neglected except for its stiffening effect on the reinforcement, and the effective compressive strength is automatically evaluated based on the principal tensile strain. The correlation with experimental results is excellent in terms of failure modes, ultimate loads as well as stiffness and crack widths.

1 INTRODUCTION

Changes in geometry and concentrated loads cause discontinuities in concrete structures. The resulting discontinuity regions such as e.g. corbels, deep beams, walls with openings and dapped beam-ends are typically the most critical elements of concrete structures. In spite of the evolution of computational tools over the past decades, designers continue using classic tools as strut-and-tie models (Schlaich et al. 1987) and stress fields (Marti 1985) for the design of discontinuity regions in engineering practice, because they yield direct insight into the load carrying behaviour and allow dimensioning the reinforcement according to practical considerations. However, these tools are typically applied as hand calculations, making their application tedious and time-consuming since iterations are required and several load-cases need to be considered in real-life structures. Furthermore, while strut-and-tie models and stress fields share a consistent mechanical basis through plasticity theory, the resulting designs may, strictly speaking, only be considered as conservative lower bound solutions if sufficient deformation capacity is available. While adequate ductility can easily be guaranteed in the design of new structures by appropriate detailing and providing minimum reinforcement, this is often impossible for existing structures and hinders the application of classic tools for assessment purposes. In addition, serviceability criteria (deformations, crack widths, etc.) cannot be reliably verified by using these methods.

Several attempts to develop programs for computer-aided truss modelling were made in the past decades. While there are many existing applications implementing strut-and-tie models for specific regions such as e.g. corbels and pile caps, these solutions lack of generality. Some tools as e.g. CAST (Tjhin & Kuchma 2002) and AStrutTie (2017) solve this limitation and allow the design of any discontinuity region. Although these tools are very interesting, they did not find widespread application so far in engineering practice, presumably because the user has to (i) propose a truss model and (ii) assign the "correct" effective concrete compressive strength to the individual truss members and nodes. This process can be time-consuming, affecting user friendliness and efficiency. This problem can be overcome by considering continuous stress fields (by means of simplified nonlinear elastic-plastic FE-analysis) and determining the effective concrete compressive strength from the transverse strains as defined by modern design codes (e.g. *fib* Model Code 2010). Fernández Ruiz & Muttoni (2007) developed EPSF, a first model following this approach, which yields excellent failure load predictions (Muttoni et al. 2015) but with limited user-friendliness since it was not developed as a commercial program. Moreover, since EPSF neglects tension stiffening, it can be generally applied neither for serviceability checks nor for elements with insufficient deformation capacity.

This paper presents a method for the design and assessment of discontinuity regions in concrete

structures aiming at overcoming the mentioned limitations of classic design tools and existing computer-aided models, while keeping the advantages of truss models (i.e. use of material parameters perfectly known during design and clear understanding of the force flow of the solution). The method, similarly as EPSF, consists of a continuous stress field FE-based analysis that automatically computes the effective compressive strength of concrete. Simple uniaxial constitutive laws provided in concrete standards for concrete and reinforcement are considered, without the need for additional material properties as required for nonlinear FE-analyses, making the presented method suitable for engineering practice. The consideration of tension stiffening allows covering all design code prescriptions including serviceability and load-deformation aspects, not consistently addressed by previous approaches.

This method is currently being implemented in *IDEA StatiCa Detail*, a new user-friendly software developed jointly by ETH Zürich and the software company IDEA RS in the framework of the DR-Design Eurostars-10571 project.

2 DISCONTINUITY REGION DESIGN (DRD) METHOD

Discontinuity Region Design (DRD) is a computer-aided stress field analysis carried out by means of a simplified nonlinear FE-calculation that automatically satisfies strain compatibility and explicitly allows accounting for strain limitations of concrete and reinforcement. The reinforcement's design and the safety format factor will be later discussed in section 2.4, while the following sections present the verification model for a given concrete geometry and reinforcement considering average material properties.

2.1 *Main assumptions*

DRD assumes fictitious rotating stress-free cracks opening without slip (see Figure 1a) and considers the equilibrium at the cracks together with average strains of the reinforcement. Hence, the model considers maximum concrete (σ_{c3r}) and reinforcement stresses (σ_{sr}) at the cracks, while concrete tensile strength is neglected ($\sigma_{c1r} = 0$) except for its stiffening effect on the reinforcement. The consideration of tension stiffening allows capturing the average strains of the reinforcement (ε_m).

According to the assumptions of the model, the principal directions of stresses and strains coincide and the behaviour of the main directions in the cracked state is decoupled except for the compression softening effect (see section 2.2.1). This justifies the use of the simple uniaxial laws presented in the following sections.

In spite of their simplicity, similar assumptions have been demonstrated to yield accurate predictions for reinforced members subjected to in-plane loading (Kaufmann 1998) if the provided reinforcement avoids brittle failures at cracking. However, the method is excessively conservative for slender elements without transverse reinforcement,

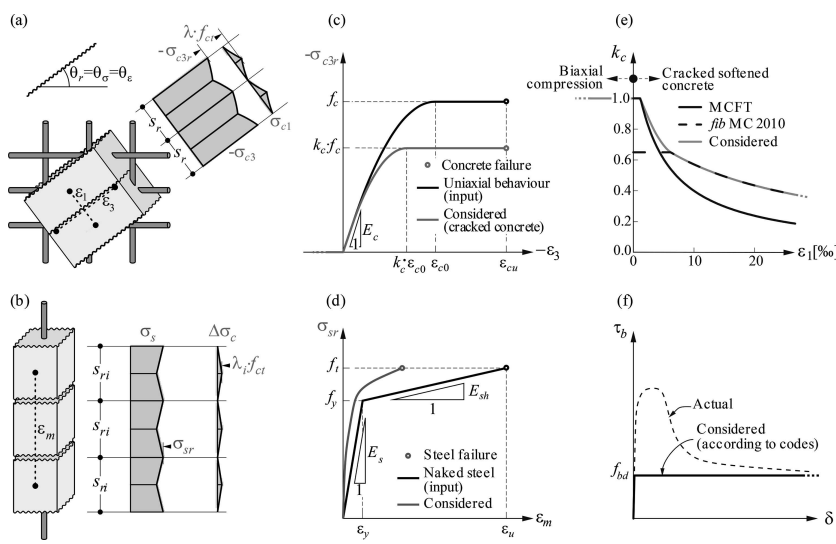

Figure 1. Verification model: (a) principal stresses in concrete and reinforcement; (b) stresses in the reinforcement direction; (c) stress-strain diagram of concrete in terms of maximum stresses and considering compression softening; (d) stress-strain diagram of reinforcement in terms of stresses at the cracks and average strains; (e) compression softening law; (f) bond shear stress-slip relationship.

since relevant mechanisms for such elements as aggregate interlock, residual tensile stresses at the crack tip and dowel action are not considered.

2.2 *Constitutive models*

2.2.1 *Concrete*

The model implements the uniaxial compression constitutive laws prescribed by design codes for the design of cross sections, which only depend on the compressive strength. In this study, the parabola-rectangle diagram of EN1992-1-1 is used (Fig. 1c). As previously indicated, as in classic reinforced concrete design, the tensile strength is neglected.

The effective compressive strength is automatically evaluated for cracked concrete based on the principal tensile strain (ε_1) by means of the k_c reduction factor, as shown in Figures 1c, e. The reduction relationship implemented (Fig. 1e) is a generalisation of the *fib* Model Code 2010 proposal for shear verifications that contains a minimum reduction of the concrete compressive strength not suitable for other actions. This compression softening law is consistent with the main assumptions (see section 2.1), since it is also derived in terms of maximum stresses at the cracks. As outlined in Kaufmann et al. (in press), the reduction of the concrete compressive strength derived in terms of average stresses, as e.g. in the Modified Compression Field Theory (MCFT) by Vecchio & Collins (1986) (Fig. 1e), may be excessive when applied to models such as DRD which consider maximum stresses.

The concrete failure in compression is defined by the ultimate strain limit allowed by design codes (ε_{cu}). Design codes reducing this strain limit depending on the strength (e.g. EN1992-1-1) consider the increasing brittleness of higher strength concretes. The strain limit in compression is imposed to the average strain over a characteristic crushing band length to avoid the local mesh size dependency intrinsic to the finite element method used. The characteristic crushing band length is defined as the depth of the compression zone or the thickness of the section, using the smaller of these values.

2.2.2 *Reinforcement*

By default, the idealized bilinear stress-strain diagram for the naked reinforcement bars as defined in design codes (Fig. 1d) is considered. The definition of this diagram only requires basic properties of the reinforcement known during the design phase (strength and ductility class). Whenever known, the actual stress-strain relationship of the reinforcement (hot-rolled, cold-worked…) can be considered. While an elastic ideal plastic formulation would also be possible, it would not allow verifying deformation capacity due to the lack of explicit failure criteria.

Tension stiffening is introduced by modifying the input stress-strain relationship of the naked reinforcing bar in order to capture the average stiffness of the bars embedded in concrete (ε_m). The implementation of tension stiffening will be presented in section 2.2.4.

2.2.3 *Bond (anchorage)*

Bond-slip between reinforcement and concrete is introduced in the finite element model considering the simplified stepped perfectly plastic constitutive relationship presented in Figure 1f, with f_{bd} being the design value of the ultimate bond stress specified by the design code for the specific bond conditions. This is a simplified model with the sole purpose of verifying bond prescriptions according to design codes (i.e. anchorage of reinforcement). A different bond model is considered for tension stiffening (section 2.2.4) and crack width calculations (section 2.3) in which an average bond response is required.

2.2.4 *Tension stiffening*

The implementation of tension stiffening distinguishes between the cases of stabilized and non-stabilized crack patterns.

In fully developed crack patterns, tension stiffening is introduced using the Tension Chord Model (TCM) (Marti et al. 1998, Alvarez 1998) – Fig. 3a – which has been shown to yield excellent response predictions in spite of its simplicity (Burns 2012). However, in the TCM tension

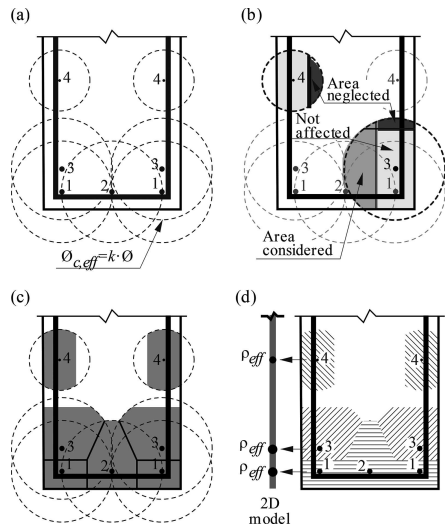

Figure 2. Effective area of concrete in tension for stabilized cracking: (a) maximum concrete area that can be activated; (b) cover and global symmetry condition; (c) resultant effective area; (d) definition of the effective amount of reinforcement per layer.

stiffening depends on the reinforcement ratio and assigning to each rebar the appropriate concrete area acting in tension between the cracks is crucial. To this end, an automatic procedure to define the corresponding effective reinforcement ratio (ρ_{eff}) for any configuration is proposed in Figure 2. The procedure consists of the following steps: (i) definition of the maximum area of concrete that each rebar can activate in tension (Fig. 2a), (ii) verification of the symmetry condition of the tensile stress field of each rebar considering the interaction with adjacent bars (as described in Figure 2b), (iii) assignment of the effective concrete area to each rebar (Fig. 2c) and (iv) calculation of a single effective reinforcement ratio per layer of bars (Fig. 2d). This procedure requires the three-dimensional consideration of the reinforcement in spite of the bi-dimensional stress field being analysed. Assuming a uniform stress f_{ct} throughout the activated concrete area, the diameter of the maximum area of concrete in tension ($\varnothing_{c,eff}$) follows from:

$$\varnothing_{c,eff} = \varnothing \sqrt{\frac{f_t}{f_{ct}}} \tag{1}$$

where $\varnothing$ = bar diameter.

Non-stabilized crack pattern is considered for (i) local cracks triggered by geometric discontinuities – e.g. dapped-end beams and frame corners with opening moments presented in Figure 4d – as well as (ii) areas with low amount of reinforcement. The amount of reinforcement ρ_{cr} given in Equation (2) defines the minimum amount for which the reinforcement carries the cracking load without yielding.

$$\rho_{cr} = \frac{f_{ct}}{f_y - (n-1) f_{ct}} \tag{2}$$

where f_y = reinforcement yield strength; f_{ct} = concrete tensile strength; and $n = E_s/E_c$ = modular ratio.

The cracks existing in regions with reinforcement ratios lower than ρ_{cr} are either generated by non-mechanical actions (e.g. shrinkage) or progression of cracks controlled by other reinforcement. For these cases, cracking is non-stabilized and tension stiffening is considered using the Pull-Out Model (POM) described in Figure 3b. This model analyses the behaviour of a single crack (i) considering no mechanical interaction between cracks, (ii) neglecting the deformability of concrete in tension and (iii) assuming the same bond shear stress-slip relationship used by the TCM (stepped, rigid-perfectly plastic with $\tau_b = \tau_{b0} = 2 f_{ct}$ for $\sigma_s \le f_y$ and $\tau_b = \tau_{b1} = f_{ct}$ for $\sigma_s > f_y$). This allows obtaining the reinforcement strain distribution (ε_s) nearby the crack for any maximum steel stress at the crack (σ_{sr}) directly from equilibrium. Given the fact that the crack spacing is unknown for a non-fully developed crack pattern, the average strain (ε_m) is computed for any load level over the distance between points with zero slip when the rebar reaches its

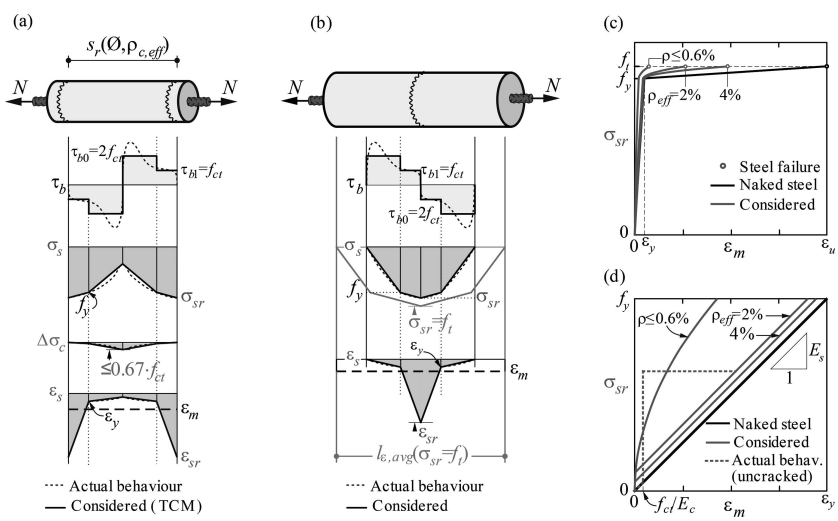

Figure 3. Tension-stiffening model: (a) tension chord element for stabilized cracking with distribution of bond shear, steel and concrete stresses, and steel strains between cracks; (b) pull-out assumption for non-stabilized cracking with distribution of bond shear and steel stresses and strains around the crack; (c) resulting tension chord behaviour in terms of reinforcement stresses at the cracks and average strains for B500B steel; (d) detail of the elastic part of the tension chord response.

tensile strength (f_t) at the crack ($l_{\varepsilon,avg}$ in Figure 3b), leading to the following relationships:

$$\varepsilon_m = \frac{\sigma_{sr}^2 \cdot \frac{\tau_{b1}}{\tau_{b0}}}{2 \cdot E_s \left[f_t + f_y \left(\frac{\tau_{b1}}{\tau_{b0}} - 1 \right) \right]} \quad \text{for } \sigma_{sr} \le f_y \tag{3}$$

$$\varepsilon_m = \frac{\frac{f_y}{E_s}\left[\sigma_{sr} + f_y \left(\frac{\tau_{b1}}{2\tau_{b0}} - 1 \right) \right] + \frac{\left(\sigma_{sr} - f_y\right)^2}{2E_{sh}}}{f_t + f_y \left(\frac{\tau_{b1}}{\tau_{b0}} - 1 \right)} \tag{4}$$

for $\sigma_{sr} > f_y$

where $E_{sh} = (f_t - f_y)/(\varepsilon_u - f_y / E_s)$ = steel hardening modulus.

The proposed models allow computing the behaviour of bonded reinforcement, which is finally considered in the analysis. The behaviour including tension stiffening for the most common European reinforcing steel (B500B, with $f_t/f_y = 1.08$ and $\varepsilon_u = 5\%$) is illustrated in Figures 3c-d. It can be observed that the consideration of tension stiffening does not affect the strength of the reinforcement, but increases its stiffness and significantly reduces its ductility. This reduction of the ductility can limit the strength of the members as discussed in section 3.2.

2.3 *Crack width calculation*

The crack widths are calculated with the methodology described in Figure 4. A crack kinematic without slip is considered (Fig. 4a), which is consistent with the main assumptions of the model (section 2.1). The principal directions of stresses and strains define the inclination of the cracks ($\theta_r = \theta_\sigma = \theta_\varepsilon$). According to Figure 4b the crack width (w) can be projected in the direction of the rebar (w_b), leading to:

$$w = \frac{w_b}{\cos\left(\theta_r + \theta_b - \pi/2\right)} \tag{5}$$

where θ_b = bar inclination.

The component w_b is consistently calculated based on the presented tension stiffening models by integrating the reinforcement strains. For those regions with fully developed crack patterns (see section 2.2.4), the calculated average strains (ε_m) along the rebars are directly integrated along the crack spacing (s_r) as indicated in Figure 4c, leading to:

$$w_b = \int_{s_r} \left(\varepsilon_m - \varepsilon_{cm} \right) \cdot dx = \int_{s_r} \left(\varepsilon_m - \frac{\lambda \cdot f_{ctm}}{2E_s} \right) \cdot dx \tag{6}$$

where s_r may vary by a factor of 2, i.e. $s_r = \lambda s_{r0}$, with $\lambda = 0.5 \ldots 1.0$; and $s_{r0} = s_{r0} = \varnothing f_{ctm} (1 - \rho_{eff})/(2\tau_{b0} \rho_{eff})$ = theoretical maximum value of the crack spacing according to TCM.

For the case of non-stabilized cracking w_b is calculated according to the procedure described in Figure 4c based on the results of maximum stresses in the reinforcement (σ_{sr}), which in this case are more reliable than the average strains.

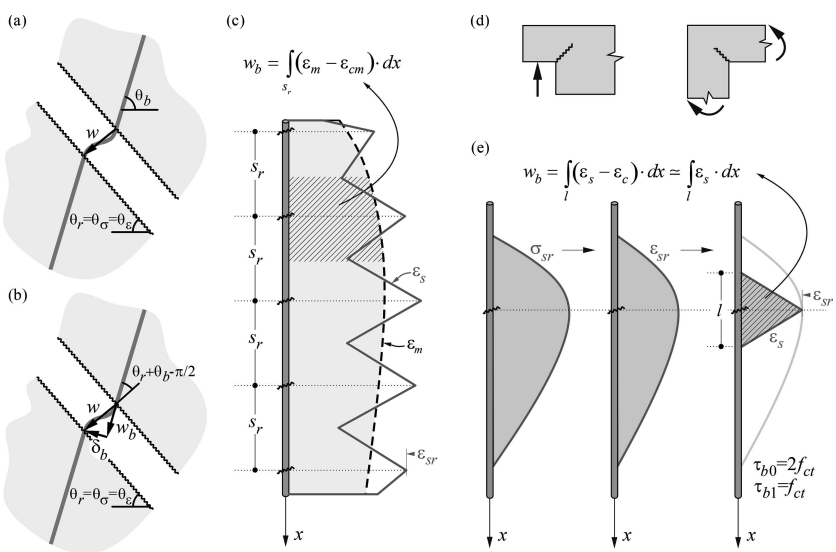

Figure 4. Crack width calculation: (a) considered crack kinematics; (b) projection of crack kinematics into principal directions of the rebar; (c) crack width in the direction of the rebar for stabilized cracking; (d) cases with local non-stabilized cracking regardless the reinforcement amount; (e) crack width in the direction of the rebar for non-stabilized cracking.

2.4 *Design process*

While the details of reinforcement design are beyond the scope of this paper, a brief description of the design process is given in the following (see also Navrátil et al. (2017)). In a first step, the user introduces the geometry and loading of the region of interest. Subsequently, the user can define the reinforcement layout based on his experience or by making use of linear elastic stress trajectories and a topology optimisation algorithm. In the next step, the program performs an ultimate limit state analysis, adjusting the reinforcements that the user wants to be dimensioned. Finally, serviceability checks (deformations and crack widths) are carried out. The partial safety factor approach, typically used in engineering practice, is also considered in DRD.

2.5 *Finite element implementation*

The finite element model is composed of the following element types: (i) 1D reinforcement element, (ii) 2D concrete element, (iii) special 2D bond element and (iv) rigid body and interpolation constraints between elements. The last two are used for bond modelling. Furthermore, the latter enable the concrete and reinforcement finite element mesh to be created independently. The first type consists of two-node rod elements for which only axial stiffness is considered. The second type consists of four-node and three-node isoparametric flat plate elements considering a plane state of stresses. Full Newton-Raphson algorithm is used to solve the set of nonlinear equations.

3 EXPERIMENTAL VALIDATION

This section presents examples of application of the DRD calculation model. Based on a selection of existing experiments from the literature, the suitability of the model for analysing RC structural members is explored with respect to ultimate strength, failure mechanism, load-displacement response and crack width estimation. The discussion focuses on the influence of tension stiffening. If not stated otherwise, the analysis uses the default parameters described in the previous section.

3.1 *Ultimate strength and load-deformation response under combined loading – application to shear walls*

Bimschas (2010) and Hannewald et al. (2013) studied the force-deformation response of cantilever wall-type bridge piers under quasi static-cyclic loading. Figure 5 shows the experimental setup, leading to a combined axial, bending and shear loading. Bimschas et al. (2015) showed that the cyclic envelope of these experiments can be reasonably approximated using a monotonic analysis as in DRD.

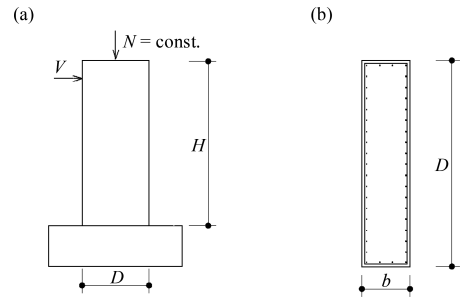

Figure 5. VK-Series: (a) experimental setup; (b) cross-section.

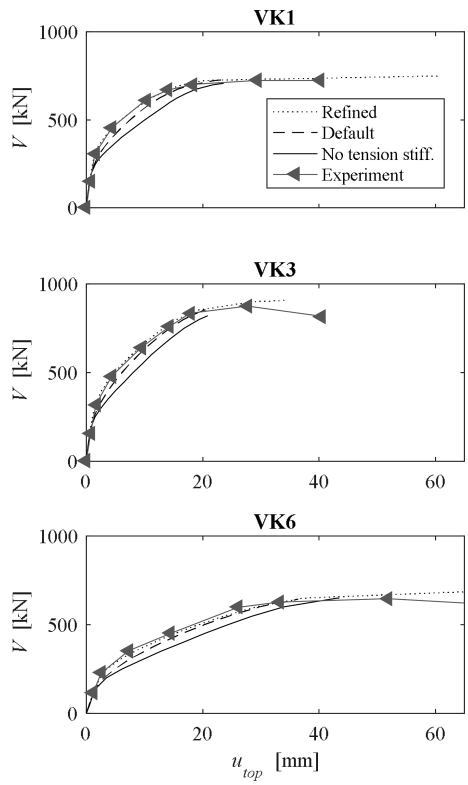

Figure 6. VK-Series: results of load-deformation response.

In this context, the experimental envelope of the cyclic response is re-evaluated for three specimens (VK1, VK3 and VK6) and compared with the numerical results. The experimental force-displacement curves in Figure 6 are calculated as average values of the push and pull direction of

the first cycle of each load level. The displacement component is obtained by subtracting the part due to anchorage slip from the total measured displacement at height of load application since the foundation is not modelled in the numerical analysis. The contribution of anchorage slip is estimated following the assumptions given in Bimschas et al. (2015).

Table 1 summarises the parameters relevant for the analysis in which ρ and ρ_{eff} indicate the geometric and effective reinforcement ratio, respectively. The three analysed specimens differ in the amount of longitudinal reinforcement and the effective depth.

As described in section 2.2.4, tension stiffening is included by means of the TCM and the POM in longitudinal and transverse direction, respectively.

Figure 6 compares the experimental load-deformation response to analyses with and without tension stiffening. While the influence on the deformation behaviour is pronounced, the peak load estimations are accurate in both cases. The analyses cannot capture the uncracked stiffness after decompression, since tensile strength is neglected; however, the consideration of tension stiffening leads to a reasonable estimation of the deflections in the cracked regime. For the three experiments, the numerical model develops its maximum capacity when concrete reaches its peak strength in the base wall corner (2‰ average strain over crushing band length), which agrees with the experimental observations. At this point, the numerical analysis is stopped since post-peak behaviour cannot be captured by model definition.

A refined analysis is also performed considering the actual stress-strain relationship of the reinforcement (hot-rolled, cold-worked…) as well as the uncracked stiffness of the reinforcement. The latter can equivalently be considered in the constitutive law of the reinforcement. The results of the refined analysis are also presented in Figure 6; note that strain limit criteria were omitted in these analyses. For the three analysed specimens, the load-deformation results of the refined model show excellent agreement with the experimental data until ultimate strength.

Table 1. VK-Series: parameters of analysis.

Specimen			VK1	VK3	VK6
Eff. height	H	[m]	3.30	3.30	4.50
Section depth	D	[m]	1.50	1.50	1.50
Section width	b	[m]	0.35	0.35	0.35
Longitudinal reinforcement					
	ρ	[%]	0.82	1.23	1.23
	ρ_{eff}	[%]	1.9	2.7	2.7
	f_y	[MPa]	515	515	521
	ε_y	[‰]	2.6	2.6	2.6
	f_t	[MPa]	630	630	609
	ε_u	[‰]	126	126	126*
Transverse reinforcement					
	ρ	[%]	0.08	0.08	0.08
	f_y	[MPa]	518	518	528
	ε_y	[‰]	2.6	2.6	2.6
	f_t	[MPa]	681	681	680
	ε_u	[‰]	84	84	84
	f_{cm}	[MPa]	35	34	34*

*Assumed.

3.2 *Shear strength – application to beams with low amount of transverse reinforcement*

Huber et al. (2016) tested simply supported beams with and without a minimum amount of transverse reinforcement according to the experimental setup shown in Figure 7. While DRD neglects shear transfer mechanisms relevant for slender elements (see 2.1), similar assumptions have been observed (e.g. Campana (2013)) to be suitable for beams in the same range of slenderness even without transverse reinforcement. In this context, four experiments of this campaign failing by rupture of the transverse reinforcement are analysed in this section: specimen R1000 m60 and R500 m351 designed with one-leg hooks (alternately placed) and specimen R1000 m35 and R500 m352 with two-leg stirrups. Table 2 summarizes the parameters relevant for the analysis. Tension stiffening is included by means of the TCM and the POM in the longitudinal and transversal direction, respectively. As in the previous section, an analysis neglecting tension stiffening is also carried out.

Detailed results of specimen R1000 m35 are presented in Figure 8 (continuous stress fields) and Table 3 (local results for the governing steel and concrete finite elements). The comparison to the

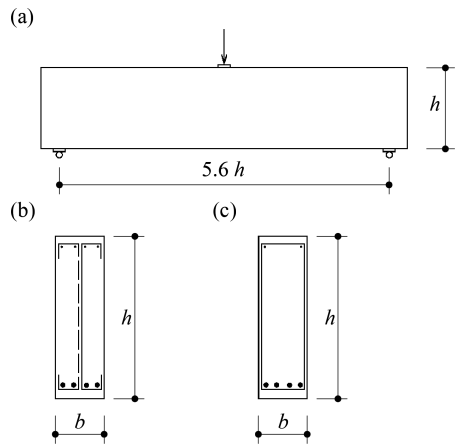

Figure 7. R-Series: (a) experimental setup; (b) specimens R1000 m60/R500 m351; (c) specimens R1000 m35/R500 m352.

Table 2. R-Series: parameters of analysis.

Specimen		R1000 m35	R1000 m60	R500 m352	R500 m351
Section height	h [m]	1.00	1.00	0.50	0.50
Section width	b [m]	0.30	0.30	0.15	0.15
Transverse reinforcement					
	ρ [%]	0.09	0.09	0.08	0.09
	f_y [MPa]	569	552	653	569
	ε_y [‰]	2.9	2.8	2.8	2.9
	f_t [MPa]	638	654	710	638
	ε_u [‰]	31	34	49	31
	f_{cm} [MPa]	30	61	36	38

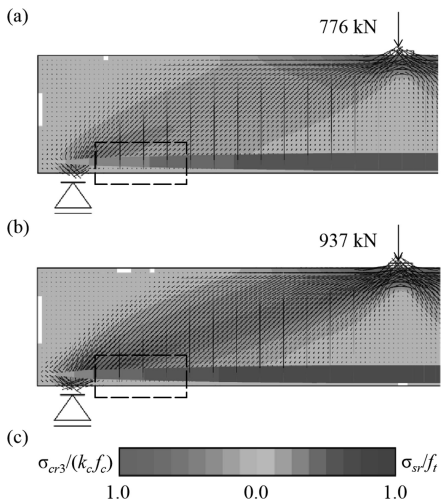

Figure 8. Results of continuous stress fields for R1000 m35: (a) tension stiffening considered; (b) tension stiffening neglected.

Table 3. R1000 m35: results in governing nodes of steel and concrete finite elements (vicinity of the support highlighted in Figure 8).

		Figure 8 (a)	Figure 8 (b)
ε_{mz}	[‰]	5.4	20
σ_{srz}	[MPa]	638 (= f_t)	600
ε_1	[%]	6.4	23.0
k_c	[–]	0.64	0.41
σ_{cr3}	[MPa]	7.7	12.0
$\sigma_{cr3}/(k_c f_c)$	[–]	0.42	1.00

observed failure mode ('stirrup rupture') and load (V_{exp} = 768 kN) clearly shows that the analysis without tension stiffening considerably overestimates the shear capacity (more than 20%) due to inaccurate treatment of stiffness and deformation capacity of the stirrups. Moreover, the experimental failure mode is not captured and, eventually, the model is limited by 'concrete crushing' ($\sigma_{cr3}/(k_c f_c)$ = 1). The analysis with tension stiffening allows a reasonable estimation of the shear strength and the corresponding failure mode to be captured. In this analysis, the effective utilisation ratio of concrete at failure ($\sigma_{cr3}/(k_c f_c)$ = 0.42) shows that concrete is far from crushing. The consideration of tension stiffening also impacts the resulting k_c factor, showing the relevance of using compression softening relationships consistent with the model assumptions.

These observations of R1000 m35 also apply to the other examples. This is summarized in Figure 9 where the safety factor (ratio of experimental load and numerical estimation) and the effective utilisation factor of concrete are presented for all the analysed tests. When neglecting tension stiffening the numerical model is not able to capture the experimental failure mode and allows significant redistributions that lead to excessive compressive stresses in concrete contradicting the experimental evidence.

These examples show that tension stiffening, in spite of not affecting the strength of the reinforcement, has a significant impact in the ultimate load of members failing due to insufficient ductility of the reinforcement. While the overestimation of the capacity when neglecting tension stiffening could be partly compensated using a different compression softening relationship formulated in terms of average stresses (e.g. MCFT), this approach (i) would be inconsistent with the model assumptions, (ii) would not capture the failure of the reinforcement and (iii) could lead to excessive reductions of the compressive strength for other failure modes.

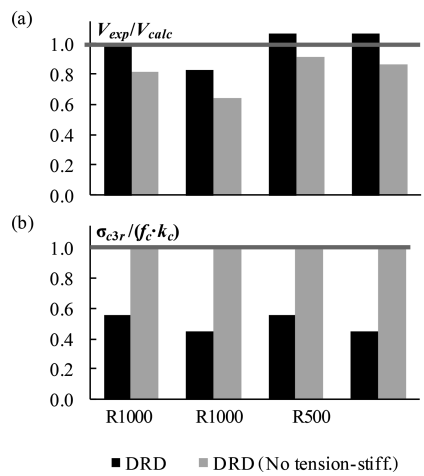

Figure 9. R-Series: main numerical results: (a) ratio of experimental and predicted load; (b) effective utilisation ratio of concrete – (black: tension stiffening considered; grey: tension stiffening neglected).

3.3 *Crack width estimation – application to members subjected to pure bending*

Franz & Breen (1978) investigated the influence of skin reinforcement on the crack width distribution on the side face of large RC beams by means of pure bending tests as described in Figure 10. Herein, specimen RS-3 is selected to explore the crack width estimation of the DRD model. Table 4 summarizes the parameters used for analysis. The longitudinal reinforcement is modelled according to the TCM assuming distributed cracking. For simplicity, the main reinforcement is lumped to one layer.

Figure 11 compares the numerical results with the reference experimental data at three load levels in the cracked-elastic regime. The reference experimental crack widths are calculated as average values over the element length l. The numerical results are presented as a range to account for the natural scatter in crack spacing (λ = 0.5–1). It is noted that the maximum crack width in the tests occurred in the web, where the crack spacing is larger, and not at the main reinforcement, where the strain is highest. This effect is well covered by the DRD model, in which the crack widths are highly influenced by the effective reinforcement ratio (ρ_{eff}). In this case, the resultant ρ_{eff} from the proposed method is very similar to the proposal of Franz & Breen (1978).

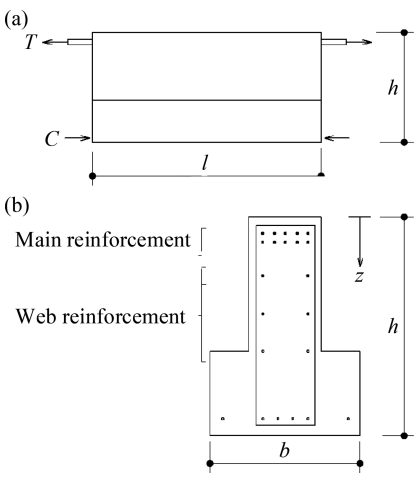

Figure 10. RS-3: (a) experimental setup; (b) cross section.

Table 4. RS-3: parameters of analysis.

RS-3			
Section height	h	[mm]	885
Section width	b	[mm]	600
Element length	l	[mm]	1830
Main reinforcement (2 × ∅ 15.9 mm; 8 × ∅ 12.7 mm)			
	f_y	[MPa]	429
	ε_y	[‰]	2.2
	ρ_{eff}	[%]	3.3
Web reinforcement (6 × ∅ 6 mm)			
	f_y	[MPa]	531
	ε_y	[‰]	2.7
	ρ_{eff}	[%]	0.6
	f_{cm}	[MPa]	34

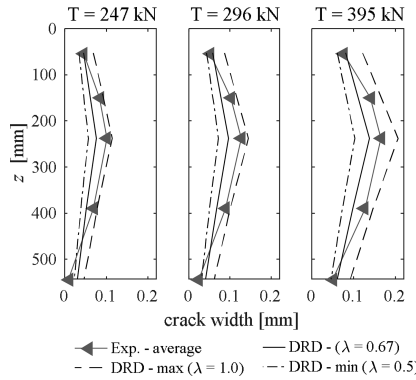

Figure 11. RS-3: crack width distribution at three load levels in the cracked-elastic regime.

4 CONCLUSIONS

This paper presents Discontinuity Region Design (DRD), a computer-aided method for the design and assessment for members subjected to in-plane loading, i.e. beams, walls and particularly discontinuity regions. DRD is suitable for engineering practice since it implements simple constitutive relationships according to design codes. The proposed Pull-Out Model allows estimating the stiffness and ductility of areas with low amounts of reinforcement.

The comparison with experimental results has shown an excellent agreement in bearing capacity and failure mode. The consideration of tension stiffening is essential to capture failures due to insufficient ductility of the reinforcement in low reinforced areas. In such cases, the capacity may be significantly overestimated when neglecting tension stiffening (20% on average for the analysed cases). The consideration of tension stiffening also leads to reasonable estimations of the load-displacement behaviour and crack widths even considering a fully cracked state.

5 FURTHER RESEARCH

While this work defines the tension stiffening behaviour independently for each reinforcement

direction, existing models (Kaufmann 1998, Seelhofer 2009) couple this behaviour in the different reinforcing directions for the case of homogeneously reinforced panels in which all the concrete is assumed to be activated in tension. Further research is required to understand this interaction in non-homogeneously reinforced elements as well as in elements in which not all the concrete area is activated in tension.

The proposed automatic procedure to define the effective area of concrete in tension is applied to the full area of concrete, which could underestimate in some cases the effective reinforcement ratio; while this is conservative in terms of bearing and deformation capacity, the proposed procedure should be extended to neglect the concrete in compression in this calculation.

Finally, the implementation of a model to estimate the cracking load for the different parts and resistance mechanisms of the analysed structures in DRD would allow checking whether the provided reinforcement avoids brittle failures at cracking. Consequently, in addition to the implementations described in this paper, all the functions typically assumed by the so-called "minimum reinforcement" could be automatically verified in DRD.

ACKNOWLEDGMENTS

This work is part of the DR-Design Eurostars-10571 project and has received partial funding from the Eurostars-2 joint programme with co-funding from the European Union Horizon 2020 research and innovation programme. The authors gratefully acknowledge this financial support as well as the contribution of the different members of the project. They would also like to express their gratitude to Nils Schriber for his work on the implementation of tension stiffening.

REFERENCES

Alvarez, M. 1998. *Einfluss des Verbundverhaltens auf das Verformungsvermögen von Stahlbeton*. Doctoral thesis, Institute of Structural Engineering, ETH Zurich, IBK report nº236. Basel: Birkhäuser Verlag.

AStrutTie 2017. HanGil IT. Available from: http://astrut-tie.aroad.co.kr/ accessed 31 Oct. 2016.

Bimschas, M. 2010. *Displacement based seismic assessment of existing bridges in regions of moderate seismicity*. Doctoral thesis, Institute of Structural Engineering, ETH Zurich, IBK Report nº326. Zurich: vdf Hochschulverlag.

Bimschas, M., Chatzi, E. & Marti, P. 2015. Inelastic Deformation Analysis of Reinforced Concrete Bridge Piers, Part 2: Application and Verification, *ACI Structural Journal*, vol. 112, no. 3: 277–286.

Burns, C. 2012. *Serviceability Analysis of Reinforced Concrete Members Based on the Tension Chord Model*. Doctoral thesis, Institute of Structural Engineering, ETH Zurich, IBK Report nº342. Zurich: vdf Hochschulverlag.

Campana, S. 2013. *Éléments en béton armé soumis à une combinaison de flexion, effort tranchant et forces de déviation*. Doctoral thesis, École Polytechnique Fédérale de Lausanne, Thesis nº5574, Lausanne.

CEN European Committee for Standardization 2004. *Eurocode 2. Design of concrete structures – general rules and rules for buildings*. EN 1992-1-1, Brussels.

Fernández Ruiz, M. & Muttoni, A. 2007. On development of suitable stress fields for structural concrete. *ACI Structural Journal*, vol. 104, no. 4: 495–502.

Fédération Internationale du Béton, 2013. *fib Model Code for Concrete Structures 2010*. Berlin: Ernst & Sohn.

Franz, G.C. & Breen, J.E. 1978. *Control of cracking on the side faces of large reinforced concrete beams*. Center for Highway Research, The University of Texas at Austin.

Hannewald, P., Bimschas, M. & Dazio, A. 2013. *Quasi-static cyclic tests on RC bridge piers with detailing deficiencies*. Institute of Structural Engineering, ETH Zurich, IBK Report nº352. Zurich: vdf Hochschulverlag.

Huber, P., Huber, T. & Kollegger, J. 2016. Investigation of the shear behavior of RC beams on the basis of measured crack kinematics, *Engineering Structures*, vol. 113: 41–58.

Kaufmann, W. 1998. *Strength and deformations of structural concrete subjected to in-plane shear and normal forces*. Doctoral thesis, Institute of Structural Engineering, ETH Zurich, IBK report nº234. Basel: Birkhäuser Verlag.

Kaufmann, W., Mata-Falcón, J. & Beck, A. (in press) *Future directions for research on shear in structural concrete*. fib Bulletin of the WP 2.2.1, Workshop on Beam Shear, 5–6 Sept 2018, Zurich.

Marti, P. 1985. Truss models in detailing, *Concrete International*, vol. 7, no. 12: 66–73.

Marti, P., Alvarez, M., Kaufmann, W., Sigrist, V. 1998. Tension Chord Model for Structural Concrete. *Structural Engineering International*, vol. 8, no. 4: 287–298.

Muttoni, A., Ruiz, M.F. & Niketic, F. 2015. Design versus Assessment of Concrete Structures Using Stress Fields and Strut-and-Tie Models, *Structural Journal*, vol. 112, no. 05: 605–616.

Navrátil, J., Ševčík, P., Michalčík, L. et al. 2017. Řešení stěn a detailů betonových konstrukcí (In Czech: A Solution for Walls and Details of Concrete Structures). *Proceedings 24th Czech Concrete Days, 22–23 Nov 2017*, Litomyšl: ČBS ČSSI.

Schlaich, J., Schäfer, K. & Jennewein, M. 1987. Toward a consistent design of structural concrete. *PCI Journal*, vol. 32, no. 3: 74–150.

Seelhofer, H. 2009. *Ebener Spannungszustand im Betonbau: Grundlagen und Anwendungen*. Doctoral thesis, Institute of Structural Engineering, ETH Zurich, IBK Report nº320. Zurich: vdf Hochschulverlag.

Tjhin, T.N. & Kuchma, D.A. 2002. Computer-based tools for design by strut-and-tie method: advances and challenges. *ACI Structural Journal*, vol. 99, no. 5: 586–594.

Vecchio, F.J. & Collins, M.P. 1986. The Modified Compression-Field Theory for Reinforced Concrete Elements subjected to Shear. *ACI Journal*, vol. 83, no. 2: 219–231.

Computational Modelling of Concrete Structures – Meschke, Pichler & Rots (Eds)
© 2018 Taylor & Francis Group, London, ISBN 978-1-138-74117-1

Investigations on strength and fracture in RC beams scaled along height or length

J. Suchorzewski, I. Marzec, J. Tejchman & E. Korol
Gdansk University of Technology (GUT), Gdansk, Poland

ABSTRACT: The objective of the present paper is to identify experimentally and theoretically differing failure mechanisms in reinforced concrete beams subjected to four-point bending for a separate variation of the depth and length at the constant thickness. Experiments were performed on reinforced concrete beams under four-point bending. Different failure mechanisms included steel yielding, diagonal tension or shear-compression depending upon the ratio of the shear to the beam depth a/D. The shear strength of beams evidently decreased with increasing a/D-ratio. The experimental results were numerically simulated using two-dimensional finite element analyses under plane stress conditions, based on a coupled elasto-plastic-damage constitutive model for concrete that was enhanced by non-locality in the softening regime. The numerical calculation results satisfactorily captured both the experimental shear strength and failure mechanisms.

1 INTRODUCTION

The size effect in concrete elements is ascribed to a reduction of nominal structural strength corresponding to the maximal load value reached in the loading process composed of the load increasing phase, critical state and post critical phase of the decreasing load. The nominal strength is then expressed in terms of the local or averaged stress at the critical state, specified from the elastic analysis. Usually the size effect has been specified for geometrically similar elements, differing only by the value of the size factor. The other important size dependent effect is a growth of brittleness with increasing size factor. It may be characterized by the ratio of the loading force work in the post critical state to the total dissipated loading work in the deformation process until ultimate failure. Alternatively, the equivalent softening modulus value may be used to characterize element brittleness. These two loading process parameters are fundamental for the assessment of the element safety and its interaction with adjacent structural elements.

The extensive experimental studies and analytical formulae were presented in order to specify the dependence of the critical stress value on the size factor for plain and reinforced concrete beams subjected to bending, tension or compression (e.g. Carpinteri 1989, Bažant & Planas 1998, Duan and Hu 2004, Bazant et al. 2007, Hoover & Bazant 2014, Korol et al. 2013, 2014, 2017). Most experimental tests were conducted for geometrically concrete beams of varying size and reinforcement ratio. However, only several papers were devoted to the analysis of the size effect in beams for an independent variation of height and length in reinforced concrete (e.g. Zhang & Tan 2007). This class of the variation of geometric parameters is typical in the engineering design and requires a separate study.

The objective of the present paper is to identify experimentally and numerically differing failure mechanisms in reinforced concrete beams subjected to four-point bending for a separate variation of the depth and length at the constant thickness. Special attention was paid to a description of a fracture process (inherently related to the size effect). The two-dimensional (2D) finite element (FE) analyses under plane stress conditions were performed with a coupled elasto-plastic-damage constitutive model for concrete (with non-local softening) and compared with the experimental outcomes.

2 EXPERIMENTAL PROGRAME

The laboratory tests of four-point bending were conducted on rectangular concrete beams with horizontal steel ribbed bars without shear (vertical) reinforcement (Suchorzewski et al. 2017). The beams were scaled along either the depth D (series '1') or length l_{eff} (series '2') (Fig. 1A). The thickness of all beams was t = 0.25 m to avoid differences in the hydration heat effects (that are proportional to the member thickness). Referring to Fig. 1 it may be seen that there are two shear

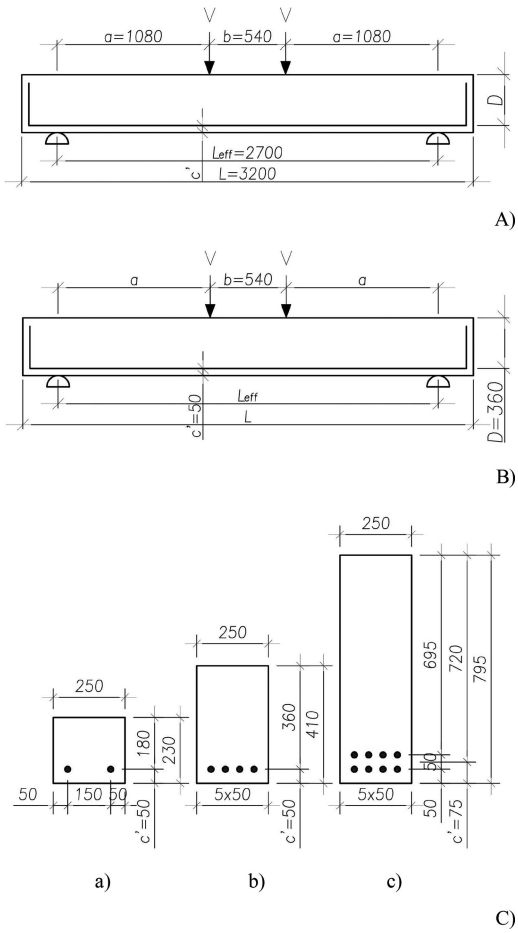

Figure 1. Experimental reinforced concrete beams under four-point bending: A) loading scheme for series '1' (l_{eff} = 2700 mm, a = 1080 mm, b = 540 mm) with varying D, B) loading scheme for series '2' (D = 360 mm, b = 540 mm) with varying a and l_{eff}, C) cross-section of: a) beam S1D18a108 (D = 180 mm), b) beams: S1D36a108, S2D36a36, S2D36a72, S2D36a108 (D = 360 mm) and c) beam S1D72a108 (D = 720 mm) (D - effective beam height, l_{eff} - distance between beam supports, l - total beam length, V - vertical concentrated force applied, a - shear zone span, b - bending zone span, dimensions are in [mm]).

regions of the length a and the bending region of the length b in the central beam portion. The beam deformation and failure was characterized by two non-dimensional geometric parameters and one size parameter: $\eta_a = a/D$, $\eta_b = b/D$, $\eta_l = l_{eff}/D = 2\eta_a + \eta_b$. As the length parameter η_l depends on η_a and η_b, we selected two independent parameters (η_a and η_b) and the size parameter D in order to describe the shear or bending strength evolution. Let us note that in most papers only the strength dependence on the size D was analyzed at fixed parameters η_a and η_b. The reinforcement ratio $\eta_r = A_r/A_b$ was constant for the varying cross-sectional area A_b of the beam. The concrete cover (c = 4 mm) was large enough to prevent the bond failure of a splitting type. Thus the distance from the bar centre to beam bottom was always $c' = h\text{-}D$ = 50 mm (Fig. 1C). For two reinforcement layers this distance was c' = 75 mm (Fig. 1Cc). The reinforcement location parameter $\eta_c = c'/D$ varied between 0.10–0.28 (series '1') or was fixed at 0.14 (series '2').

The beams of the series '1' were scaled along the effective height D in the proportion 1:2:4 with the constant effective span length l_{eff} = 2700 mm. The beams were denoted as S1D18a108, S1D36a108 and S1D72a108, where the symbol *S1* denotes the series '1', D - the effective beam depth in [cm] and a - the shear zone length in [cm]. Note that the beam S1D36a108 (D = 360 mm) had the same dimensions as the concrete beam (denoted as SL40) used in the size effect experiments (Korol & Tejchman 2014) and was twice as high as the beam S1D18a108 (D = 180 mm) and twice as small as the beam S1D72a108 (D = 720 mm). Thus, the shear zone length a and bending zone length b (distance between two concentrated forces V) were constant a = 1080 mm and b = 540 mm, respectively (Fig. 1A). The shear span parameter $\eta_a = a/D$ was 1.5, 3 and 6, the length parameter $\eta_l = l_{eff}/D$ was 3.75, 7.5 and 15 and the bending span parameter $\eta_b = b/D$ was 0.75, 1.5 and 3. Each beam height h included 3 identical concrete specimens in order to verify the result repeatability (indicated as: S1D18 A108_1 - S1D18a108_3, S1D36a108_1 - S1D36a108_3 and S1D72a108_1 - S1D72a108_3).

The beams of the series '2' had the same height (D = 360 mm) but the varying effective span length l_{eff} and shear span a (the latter scaled in the proportion 1:2:3) (Fig. 1B). The beams were denoted as S2D36a36 (a = 360 mm), S2D36a72 (a = 720 mm) and S2D36A108 (a = 1080 mm) with the length parameter $\eta_l = l_{eff}/D$ = 3.5, 5.5 and 7.5, the shear span parameter $\eta_a = a/D$ = 1.0, 2.0 and 3.0 and the bending span parameter $\eta_b = b/D$ = 1.5. The longest beam from the series 2 (S2D36a108) had the same dimensions as the beam from the series '1' denoted as S1D36a108. The beam S2D36a36 was as twice as short as the beam S2D36a72 and the beam S2D36a108 was as twice as long as the beam S2D36a72. Each beam included 2 identical specimens (denoted as: S2D36a36_1-S2D36a36_2, S2D36a72_1-S2D36A72_2, S2D36a108_1-S2D36a36_2).

In total 15 beams (series '1': 9 beams and series '2': 6 beams) were subjected to four-point bending. The ratio of the shear span a to the effective

height D varied from $\eta_a = a/D = 1$ up to $\eta_a = 6$, thus different failure modes were expected to be developed (Walraven 1978). The ratio of the bending span b to the effective height D varied from $\eta_b = b/D = 0.75$ up to $\eta_b = 3$ (series '1') and $\eta_b = 1.5$ (series '2').

The reinforcement of all beams consisted of ribbed bars of the diameter $\phi = 20$ mm with the mean yielding stress of 560 MPa (class B500) and the modulus of elasticity of 205 GPa. The longitudinal reinforcement ratio was designed as 1.4%. Each beam size required a different number of bars depending on the effective depth D. The beams of $D = 18$ cm and $D = 36$ cm had 2 and 4 bars in one layer, respectively whereas the beam of $D = 72$ cm had two layers with 4 bars i.e. 8 bars in total (Fig. 1C). In order to avoid the anchorage zone failure, hooked steel bars were used (Fig. 1) with the anchorage length of 130 mm, 310 mm or 670 mm, depending on the beam height.

The specimens from the series '1' and series '2' were casted separately, however the concrete recipe was similar. The maximum aggregate diameter was $d_{max} = 16$ mm and the water to cement ratio was 0.41. Three accompanying tests were performed, including uniaxial compression on cubes ($150 \times 150 \times 150$ mm^3) and splitting tension and elastic compression on cylinders ($\phi = 150$ mm and $L = 150$ mm). The measured average compressive strength on cubes $f_{cm,1}$ was 59.26 MPa (series '1') and $f_{cm,2} = 63.81$ MPa (series '2') (the mean value $f_{cm} = 61.5$ MPa). Thus the corresponding concrete class was C45/55. The average characteristic splitting tensile strength was 2.81 MPa (series '1') and 3.61 MPa (series '2') (the average value - 3.21 MPa). The measured average elastic modulus was $E = 33.1$ GPa (series '1') and $E = 35.3$ GPa (series '2'). The tests were performed under displacement-controlled conditions. Steel loading plates were used in order to avoid local concrete crushing. Their area was always the same, i.e. 100×250 mm^2 ($l_a \times t$). The area of support (bearing) plates ($l_b \times t$) had also the same size. During the test, the vertical force and displacements were measured. The true deflection at the mid-span and support displacement were registered by means of linear variable displacement transducers (LVDT's). The steel strains were traced with strain gauges placed on reinforcement bars at the beam mid-span.

3 EXPERIMENTAL RESULTS

3.1 *Failure modes and nominal strength (series '1': varying effective depth D and bending zone span b at constant shear zone span a)*

The varying effective depth $D = 0.18$, 0.36 and 0.72 m and constant shear span $a = 1.08$ m contributed to the variation of the parameter η_a from 1.5 through 3.0 up to 6.0, the parameter η_b from 0.75 up to 3 and the parameter η_l from 3.75 up to 15. It was experimentally observed that these parameters had a great effect on the beam failure mode and ultimate load.

The smallest beams S1D18a108 with $\eta_a = 6.0$ ($\eta_b = 3$, $\eta_l = 15$) reached their limit state in the flexural failure mechanism developing in the central beam zone, inducing concrete cracking and longitudinal reinforcement yielding combined with concrete crushing in the upper beam portion. This failure mode was preceded by growth and opening of bending cracks leading to the localized failure combined with a significant increase of the beam deflection. The effective stress used for the expression of beam strength was the elastic stress value at the external beam layer $\sigma_{eff} = (3P_{max}/tD)a/D$.

The medium high beams S1D36a108 for $\eta_a = 3$ ($\eta_b = 1.5$, $\eta_l = 7.5$) failed in shear with dominant normal diagonal crack displacements (so-called diagonal shear-tension failure (Sato et al. 2004)) and this type of failure was sudden and brittle. The highest beams S1D72a108 with $\eta_a = 1.5$ ($\eta_b = 0.75$, $\eta_l = 3.75$) failed in shear with significant both tangential and normal diagonal crack displacements (so-called diagonal shear-compression failure (Sato et al. 2004)) and with a huge increase of the ultimate shear strength supported by an internal arch action. This failure mode was also sudden and brittle. The vertical-force-deflection diagrams were similar for beams with the similar geometry. All curves after first cracking changed their slope and behave almost linearly up to the yield plateau and/or up to the peak force (for the beams S1D36a108 and S1D72a108, the yield plateau was not reached). The post-peak softening was not observed due to a sudden loss of the beam stability during failure.

3.2 *Failure modes and nominal strength (series '2': varying shear zone span a at constant effective depth D and bending zone span b)*

The varying shear span $a = 0.36$ m, 0.72 m and 1.08 m and constant beam depth $D = 0.36$ m provided the varying shear span parameter η_a from 1.0 through 2.0 up to 3.0 and constant bending span parameter $\eta_b = 1.5$, ($\eta_l = 3.5$–7.5). The effect of the varying shear span on the nominal strength and failure mode was very strong. The longest beam S2D36a108 with $\eta_a = 3.0$ failed due to diagonal shear failure with the dominant tension. The shortest beams S2D36a36 with $\eta_a = 1.0$ ($\eta_l = 3.5$) failed due to the shear failure combined with the dominant compression. The failure was characterized by a high shear strength and relatively low deflection. The shear span parameter $\eta_a = 2$ in the beam S2D36a72 ($\eta_l = 5.5$) turned out to be a transitional

limit value between high beams and low beams where the failure changed its mode. The first beam S2D36a72_1 failed in shear with dominant normal diagonal crack displacements and the second one S2D36a72_2 failed in shear with significant both normal and tangential diagonal crack displacements. Due to a varying failure mode, the ultimate vertical forces and corresponding deflections strongly varied. The beam S2D36a72_1 reached P_{max} = 320.17 kN and u/D = 1.86% whereas the beam S2D36a72_2: P_{max} = 439.43 kN and u/D = 3%. The difference in the ultimate force was 35% while in the deflection was 60%. The force-deflection diagrams were nearly linear up to the peak force and had similar shapes. The post-peak softening was not registered because of the sudden failure.

The effective ultimate shear stress representing beam strength was assumed as its mean cross-sectional value $\tau_c = V_{max}/(tD)$. In the series '1' (l_{eff} = 2700 mm, a = 1080 mm), its mean value was τ_c = 1.34 MPa, τ_c = 1.35 MPa and τ_c = 2.86 MPa for the beam S1D18a108 (D = 180 mm, η_a = 6, η_b = 3), S1D36a108 (D = 360 mm, η_a = 3, η_b = 1.5) and S1D72a108 (D = 720 mm, η_a = 1.5, η_b = 0.75), respectively (Fig. 2). Thus the effective failure stress τ_c increased with increasing depth D due to a different failure mode but decreased with increasing span ratio η_a (Figs. 2A-2B). In the series '2' (η_b = 1.5, D = 360 mm), the measured shear strength $\tau_c = V_{max}/(tD)$ decreased with increasing shear span a and effective length l_{eff} from τ_c = 7.39 MPa (η_a = 1, η_l = 3.5) to τ_c = 2.11 MPa (η_a = 2, η_l = 5.5) and next down to τ_c = 1.31 MPa (η_a = 3, η_l = 7.5) (Fig. 2A). Thus with the decrease of η_a from 3 down to 1.5 (η_l = 7.5–3.75), the shear strength increased 2.2 times but with the decrease of η_a from 3 down to 1 (η_l = 7.5–3.5), the shear strength increased 6 times. Figure 2C presents the shear strength evolution for increasing parameter η_a based on own experimental data (Fig. 2Ca) and compared with results obtained by Słowik & Smarzewski (2012) (Fig. 2Cb) wherein the beams were scaled along their length. Both experimental data show good agreement.

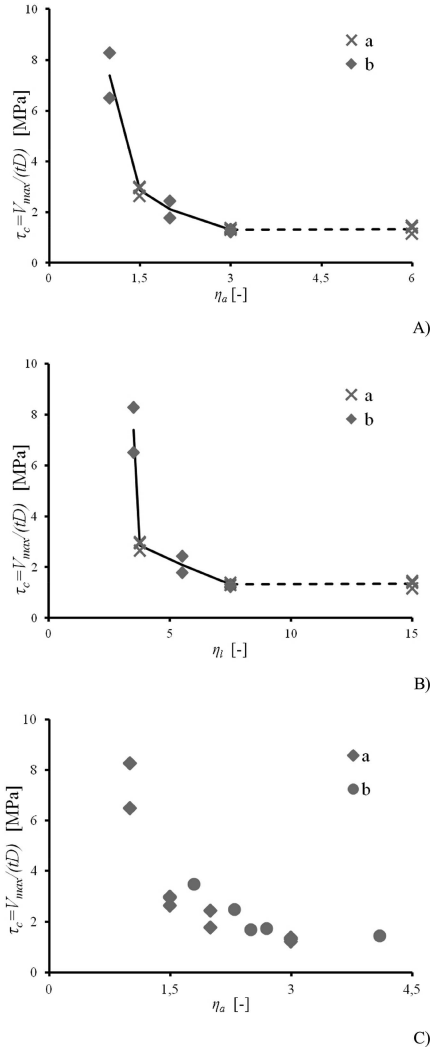

Figure 2. Experimental results presenting evolution of shear strength: A) for varying length parameter $\eta_l = l/D$ and shear span parameter $\eta a = a/D$, B) for varying bending span parameter $\eta_b = b/D$ (a) series '1' with varying effective depth D and bending span b at constant shear span a and b) series '2' for varying with constant effective depth D and bending span b) and C) as compared with experiments by Slowik & Smarzewski (2012) for different η_a (a) our experiments and (b) experiments by Slowik and Smarzewski (2012)) (note that beams for η_a = 6 failed in flexural mechanism).

3.3 *Crack patterns*

The crack evolution was similar for all the specimens up to 50% of the ultimate load value. First, the vertical flexural cracks appeared in the beam mid-span region (12% of the failure force) wherein the bending moment was constant. Later inclined cracks formed in the shear zone due to shear stress action close to both supports. A further evolution of the crack pattern was different: the low beams (η_a = 6, η_l = 15) failed in bending by reinforcement yielding and the high beams ($\eta_l \leq$ 7.5) failed in brittle diagonal shear. The shape and location of the critical diagonal crack from the nearest support depended upon the failure type. The critical diagonal crack ($\eta_a \leq 3$) was significantly steeper for the smaller ratio of η_a and η_l. The mean failure diagonal crack inclination to the horizontal changed from 30° up to 42° for η_a = 1–3 (Fig. 3).

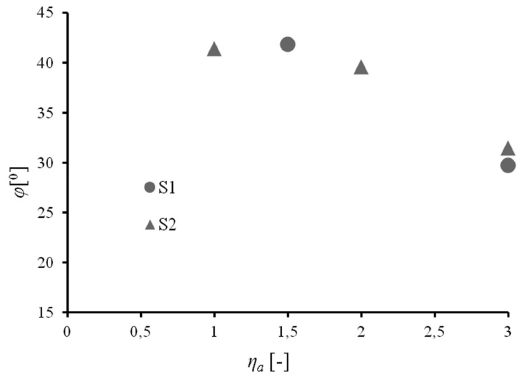

Figure 3. Diagonal failure crack inclination to horizontal φ in RC beams for experiment series '1' (S1, triangular markers) and '2' (S2, diamond markers) versus ratio $\eta_a = a/D$ = 1–3 (a - shear domain span, D - effective height).

In the beam S1D18a108 (a/D = 6), the vertical cracks stabilized after reaching 12% of the beam height for 80% of the peak force P_{max}. Next the crack width in the bending span domain b continuously increased. The critical diagonal crack for low beams (η_a = 3) initiated near the mid-point of the shear span a and after reaching the ⅓ of the beam height turned to the direction of the vertical force point with the angle between 16.8° and 19.4°, whereas in the bottom part, where the crack propagated through reinforcement, the angle varied between 42.2° and 43.6°. The distance between the critical diagonal crack and beam support d_c related to the shear span a varied between $d_c/a = 0.5$ (η_a = 3) for low beams up to as $d_c/a = 0$ for high beams (η_a = 1). The dominant inclined crack propagated towards a beam compression zone and support, reaching at the failure first the beam top and next the beam bottom. The formation of a critical diagonal crack for high beams (η_a = 1 and η_a = 1.5) was sudden. Shortly after the appearance, the critical diagonal crack stabilized at the 65% of the beam height. The further growth towards a compression zone was very slow and stable. Just before the failure a new diagonal crack appeared in concrete by connecting the support and vertical force point. The crack evolution for the beam S2D36a72_1 was similar to the one for low beams with the ratio a/D = 3 while the second beam S2D36a72_2 had a crack pattern typical for high beams. For η_a = 2–3 the critical diagonal cracks were strongly curved to the horizontal in the compressive region opposite to the cases with $\eta_a < 2$ where they were almost straight. In general the crack geometries were approximately in agreement with the direction of compressive principal stresses.

The average number of main cracks decreased with decreasing shear span ratio a/D and changed from 4 cracks in the beam S1D18a108 up to 8 for the beam S1D72a108. The crack spacing increased from 14 cm (beams S1D18a108 and S1D36a108) up to 20 cm for the highest beam S1D72a108. In the beam series '2' it was constant - 12.5 cm. The crack width w was the largest for the beam S1D18a108 due to steel yielding (w = 0.35 mm) and the smallest for the highest beam S1D72a108 (w = 0.20 mm).

Summing up, the limit load P_l in experiments depended on two non-dimensional geometric parameters $\eta_a = a/D$ and $\eta_b = b/D$ and the scale parameter D, thus $P_l = P_l(\eta_a, \eta_b, D)$. The length parameter $\eta_l = l_{eff}/D = 2\eta_a + \eta_b$ was affected then by η_a and η_b. Depending upon $\eta_a = a/D$, two failure mechanisms occurred, namely the flexural mechanism in the central beam zone and the shear mechanism developed through a combined shear-tension or shear-compression mode in exterior beam zones. Two shear failure modes were distinguished depending on the dominance of tension or compression acting on the progressive shear crack interface.

4 NUMERICAL SIMULATIONS

4.1 *Constitutive model for concrete*

The experimental results were numerically simulated using FE analyses under 2D plane stress conditions, based on a coupled elasto-plastic-damage constitutive concrete model with non-local softening for (Marzec & Tejchman 2012). The model showed its capability to describe a mixed failure mode in reinforced concrete beams (Marzec et al. 2013, Marzec & Tejchman 2013, Korol et al. 2017).

The plasticity and scalar damage were combined assuming the so-called strain equivalence hypothesis. The elasto-plasticity was defined in terms of effective stresses as

$$\sigma_{ij}^{eff} = C_{ijkl}^{e} \varepsilon_{kl} \,. \tag{1}$$

In an elasto-plastic regime, the failure surface as a combination of two surfaces was assumed. The linear isotropic Drucker-Prager criterion with a non-associated flow rule in compression and the Rankine criterion with an associated flow rule in tension (Malecki at al. 2007, Marzec at al. 2007) defined by the effective stresses were used. The material degradation was calculated within isotropic damage mechanics, independently in tension and compression using one equivalent strain measure $\tilde{\varepsilon}$ by Mazars (1986) (ε_i - principal strains)

$$\tilde{\varepsilon} = \sqrt{\sum_i \langle \varepsilon_i \rangle^2} \ . \tag{2}$$

The equivalent strain measure $\tilde{\varepsilon}$ may be defined in terms of elastic or total strains. The stress-strain relationship was represented by the following formula

$$\sigma_{ij} = (1 - D)\,\sigma_{ij}^{eff}. \tag{3}$$

with the term '1-D' defined as:

$$(1 - D) = (1 - s_c D_t)(1 - s_t D_c), \tag{4}$$

where

$$D_t = 1 - \frac{\kappa_0}{\kappa}\left(1 - \alpha + \alpha e^{-\beta(\kappa - \kappa_0)}\right), \tag{5}$$

$$D_c = 1 - \left(1 - \frac{\kappa_0}{\kappa}\right)\left(0.01\frac{\kappa_0}{\kappa}\right)^{\eta_1} - \left(\frac{\kappa_0}{\kappa}\right)^{\eta_2} e^{-\delta(\kappa - \kappa_0)}, \tag{6}$$

$$s_t = 1 - a_t \omega\left(\sigma_{ij}^{eff}\right) \ \text{ and } \ s_c = 1 - a_c\left(1 - \omega\left(\sigma_{ij}^{eff}\right)\right), \tag{7}$$

$$\omega\left(\sigma_{ij}^{eff}\right) = \begin{cases} 0 & \text{if } \sigma_{ij}^{eff} = 0 \\ \dfrac{\sum \langle \sigma_i^{eff} \rangle}{\sum \left|\sigma_i^{eff}\right|} & \text{otherwise} \end{cases}. \tag{8}$$

The damage functions D_t and D_c describe the damage evolution under tension (Peerlings et al. 1998) and compression (Geers 1997) with the material constants: α, β, η_1, η_2 and δ. The splitting factors are denoted by a_t and a_c and $\omega\left(\sigma_{ij}^{eff}\right)$ denotes the stress weight function (Lee and Fenves 1998). The Macauley bracket in Eq. 8 is defined as $\langle x \rangle = (x + |x|)/2$. The constitutive model with a different stiffness in tension and compression and a positive-negative stress projection operator to simulate crack closing and crack re-opening is thermodynamically consistent. It shares main properties of the model by Lee and Fenves (1998), which was proved to not violate thermodynamic principles (plasticity is defined in the effective stress space, isotropic damage is used and the stress weight function is continuous).

In the case of linear hardening model requires the following 16 material constants: E, υ, κ_0, α, β, η_1, η_2, δ, a_t, a_c, ψ, φ, initial yield stresses $\sigma_{yt}^{\ 0}$ (tension) and $\sigma_{yc}^{\ 0}$ (compression) and plastic hardening moduli H_p (in compression and in tension). The quantities $\sigma_y^{\ 0}$ (initial yield stress during hardening) and κ_0 are responsible for the peak location on the stress-strain curve and a simultaneous activation of the plasticity and damage criteria. The shape of the stress-strain-curve in softening is influenced by the constant β in tension, and by the constants δ and η_2 in compression. In turn, the stress-strain curve at the residual state is affected by the constant α in tension and by the constant η_1 in compression. Since, the compressive stiffness is recovered upon the crack closure as the load changes from tension to compression and the tensile stiffness is not recovered due to compressive micro-cracks, the parameters a_c and a_t can be taken for the sake of simplicity as $a_c = 1.0$ and $a_t = 0$. However, the parameters a_c and a_t directly influence the splitting functions s_t and s_c. Thus, as a consequence the damage growth under tension may be influenced by the evolution of both the damage functions D_c and D_t (Eqs. 4–8). In order to improve the model (to properly reproduce two characteristic failure modes in shear: diagonal shear-tension and diagonal shear-compression), a model modification was proposed by differentiating the damage growth under tension and compression. The growth of the functions D_t and D_c (Eqs. 5 and 6) were controlled by two independent threshold parameters κ_t and κ_c. Both the parameters were calculated based on the parameter κ as

$$\kappa_t = \kappa\omega\left(\sigma_{ij}^{eff}\right) \ \text{ and } \ \kappa_c = \kappa\left(1 - \omega\left(\sigma_{ij}^{eff}\right)\right), \tag{9}$$

where the threshold parameter κ was defined as the maximum of the equivalent strain measure $\tilde{\varepsilon}$ reached during the load history up to time t: $\kappa = \max \tilde{\varepsilon}(\tau)$. The damage under tension was thus controlled by the threshold parameters κ_t and the damage under compression by the threshold parameters κ_c. Thus, under pure tension the stress weight function was $\omega = 1$ and the growth of damage under pure tension was solely influenced by the evolution of D_t.

The material constants were fitted to the uniaxial compressive strength for concrete cubes equal to f_{cm} = 61.5 MPa and splitting tensile strength for concrete cylinders equal to f_{ctm} = 3.2 MPa. The following set of the material constants was assumed for FE calculations (with $\tilde{\varepsilon}$ in Eq. 2 defined in terms of total strains): E = 34 GPa and ν = 0.2, $\sigma_{yt}^{\ 0}$ = 3.3 MPa, $\sigma_{yc}^{\ 0}$ = 60 MPa, H_p = 17 GPa, $\kappa_0 = 9 \times 10^{-5}$, $\phi = 14°$, $\psi = 8°$, $\beta = 75$, $\alpha = 0.95$, $\eta_1 = 1.15$, $\eta_2 = 0.15$, $\delta = 150$, $a_t = 0$ and $a_c = 1$. Using the assumed material constants, the fracture energies were: G_f = 100 N/m in tension and G_c = 3150 N/m in compression.

4.2 *Non-local approach*

A non-local theory was used as a regularization technique (Bažant and Jirásek 2002). In this approach, the principle of a local action does not hold any more. The introduction of non-locality does not violate thermodynamic principles (Borino et al. 2003). In the calculations the equivalent strain measure the $\tilde{\varepsilon}$ in damage region was replaced by

its non-local definition $\bar{\varepsilon}$ (Pijauder-Cabot and Bažant 1987)

$$\bar{\varepsilon} = \frac{\int_V \omega(\|\boldsymbol{x}-\boldsymbol{\xi}\|)\,\tilde{\varepsilon}(\boldsymbol{\xi})\,\mathrm{d}\boldsymbol{\xi}}{\int_V \omega(\|\boldsymbol{x}-\boldsymbol{\xi}\|)\,\mathrm{d}\boldsymbol{\xi}}. \tag{10}$$

As a weighting function ω, the Gauss distribution function was used (Bažant and Jirásek 2002)

$$\omega(r) = \frac{1}{l_c\sqrt{\pi}} e^{-\left(\frac{r}{l_c}\right)^2}, \tag{11}$$

where l_c is the characteristic length of microstructure and the parameter r denotes the distance between material points. The averaging in Eq. 11 was restricted to a small representative area around each material point (the influence of points at the distance of $r = 3 \times l_c$ was only of 0.01%). The characteristic length is mainly determined with an inverse identification process of experimental data (Skarżyński et al. 2011). The characteristic length l_c of micro-structure within isotropic elasto-plasticity and isotropic damage mechanics is about 2 mm (fine-grained concrete) and 5 mm (usual concrete), based on measurements of a localized zone width on the concrete surface under bending by means of the digital image correlation (DIC) technique (Skarżyński et al. 2011) and comparative non-linear FE analyses with non-local softening. In our FE calculations we always assumed $l_c = 5$ mm.

4.3 *Reinforcement*

In order to simulate the behaviour of steel bars (modelled as one-dimensional truss elements), an elasto-perfect plastic constitutive law was assumed with the modulus of elasticity of $E_s = 205$ GPa and yield stress of $\sigma_{ys} = 560$ MPa (class B500). For describing the interaction between concrete and reinforcement, a bond relationship was defined. In general, this relationship is complex and depends on several factors (e.g. concrete class, concrete cover, bar diameter, bar rib height and bar rib spacing). Two different bond-failure mechanisms may appear connected to a pull-out or splitting mode. Since the bond behaviour was not experimentally investigated, the analyses were carried out with a relationship between the bond shear stress τ_b and slip u using the simple bond law by Dörr (1980) with 2 parameters only. It neglects softening and assumes a yield plateau

$$\tau_b = \begin{cases} f_t\left[0.5(u/u_0) - 4.5(u/u_0)^2 + 1.4(u/u_0)^3\right] & \text{if } 0 < u \le u_0 \\ 1.9 f_t & \text{if } u > u_0 \end{cases}. \tag{12}$$

The parameter and u_0 is the displacement at which perfect slip occurs. In order to consider bond-slip, the interface with a zero thickness was assumed along a contact surface where the relationship between the shear traction and the slip was introduced. The assumed value of u_0 was 0.06 mm.

The model was implemented into the commercial finite element code *Abaqus* (2004). with the aid of the subroutine UMAT (user constitutive law definition) and UEL (user element definition). The non-local averaging was performed in the current configuration. This choice was governed by the fact that element areas in this configuration were automatically calculated by *Abaqus* (2004).

In the FE calculations, some simplifications were assumed. The half part of beams was analyzed only in order to strongly reduce the computation time. Thus, a symmetric failure mode was taken into account in contrast to the experimental results (Figs. 9–13). The meshes consisting of 57'700–203'500 plane stress triangular elements with a linear shape function in the so-called 'union jack pattern' were used. The element size was $e = 5$ mm ($e = l_c = 5$ mm).

4.4 *FE results*

The results of numerical simulations as compared to experiments are described in Figs. 4–13. The calculated ultimate vertical forces were in good agreement with the experimental ones (Table 1). The difference was about 0.5–24.1%. The largest difference was for beams S2D36a72 (24.1%). In contrary, for the beam S2D36a72_2 the difference was 8%. For other beams the difference was not larger than 13.3%. The difference increased with the beam size (except of S2D36a72).

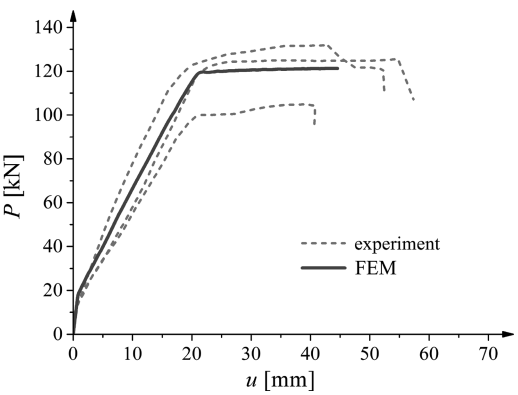

Figure 4. Experimental and calculated force-deflection diagrams for beams S1D18a108.

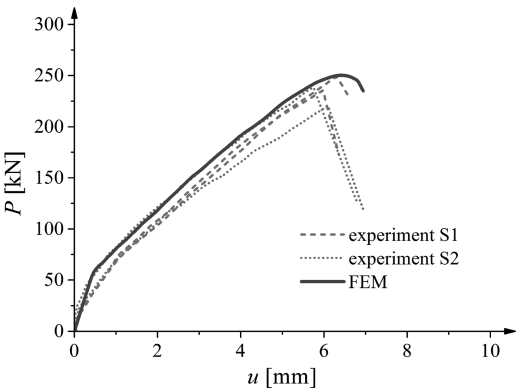

Figure 5. Experimental and calculated force-deflection diagrams for beams S1-S2D36a108.

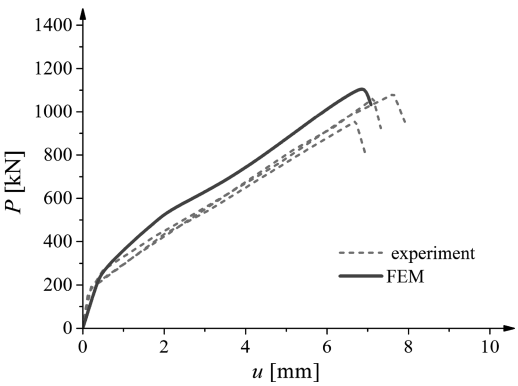

Figure 6. Experimental and calculated force-deflection diagrams for beams S1D72a108.

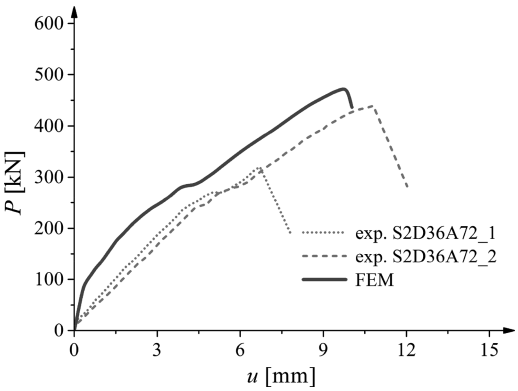

Figure 7. Experimental and calculated force-deflection diagrams for beams S2D36a72.

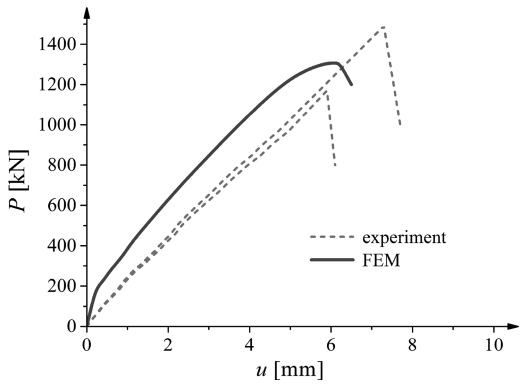

Figure 8. Experimental and calculated force-deflection diagrams for beams S2D36a36.

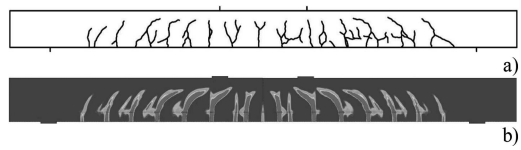

Figure 9. Comparison of contours of non-local equivalent strain measure $\overline{\varepsilon}$ with cracks pattern for beams S1D18a108: a) experiment and b) FEM.

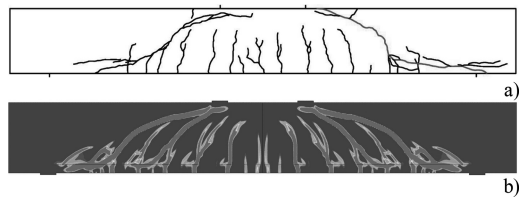

Figure 10. Comparison of contours of non-local equivalent strain measure $\overline{\varepsilon}$ with cracks pattern for beam S1D36a108: a) experiment and b) FEM.

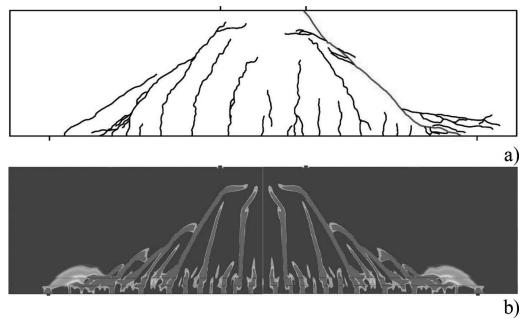

Figure 11. Comparison of contours of non-local equivalent strain measure $\overline{\varepsilon}$ with cracks pattern for beams S1D72a108: a) experiment and b) FEM.

The geometry of localized zones matched the experimental crack pattern (Figs. 9–13), although some differences existed, as e.g. the number of localized zones in experiments was smaller than in FEM. The calculated spacing of localized zones versus experimental data is given in Table 2. The average spacing of localized zones (main and secondary) was smaller by about 9–27% as compared with the experimental average crack spacing (main and secondary). The highest difference was about 27% (beam S2D36a36).

The calculated vertical and inclined main localized zones were close to the experimental crack pattern (location and inclination). The calculated crack pattern is obviously symmetric in contrast to the experimental one. However the overall characteristic of the failure mode was satisfactorily reflected in calculations. The location, inclination and distance from the support of the critical inclined localization zone for both diagonal shear tension and diagonal shear compression failure modes were in satisfactory agreement with experimental outcomes (Figs. 9–13). In the case of the beam S2D36a72 the numerical results reflected rather shear failure in concrete with dominant tangential diagonal crack displacements than with dominant normal diagonal crack displacements (Figs. 7 and 12).

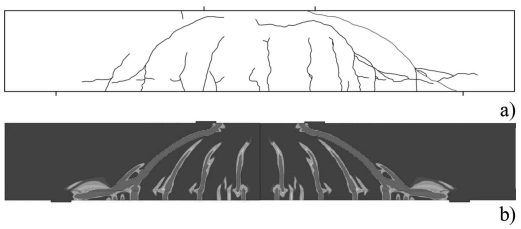

Figure 12. Comparison of contours of non-local equivalent strain measure $\bar{\varepsilon}$ with cracks pattern for beams S2D36a72: a) experiment and b) FEM.

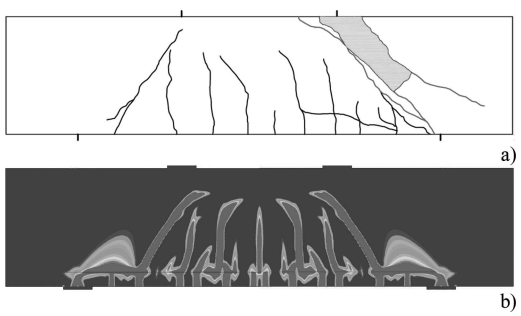

Figure 13. Comparison of contours of non-local equivalent strain measure $\bar{\varepsilon}$ with cracks pattern for beams S2D36a36: a) experiment and b) FEM.

Table 1. Failure force in FEM and experiments.

Beam size	Mean failure vertical force (experiment) [kN]	Failure vertical force (FEM) [kN]	Difference [%]
S1D18a108	120.7	120	0.5
S1D36a108	235.9	250	6.0
S1D72a108	1029.7	1106	7.4
S2D36a72	379.8	472	24.1
S2D36a36	1330.5	1307	–1.8

Table 2. Crack spacing in FEM and experiments.

Beam size	Crack spacing (experiment) [mm]	Spacing of localized zones (FEM) [mm]
S1D18a108	110–130	108
S1D36a108	110–157	126–157
S1D72a108	135–210	87–189
S2D36a72-1	132–200	95–207
S2D36a72-2	108–160	
S2D36a36	110–157	75–120

5 CONCLUSIONS

The following basic conclusions may be derived from our novel size effect experiments on RC beams being scaled along either the depth or length with the size parameters $\eta_a = a/D = 1$–6, $\eta_b = 0.75$–3 and $\eta_l = l_{eff}/D = 3.5$–15.

The shear strength of beams evidently decreased with increasing both parameters $\eta_a = a/D$ and $\eta_l = l_{eff}/D$. It also decreased with increasing parameter η_b from 0.75 up to 1.5 in beams with varying effective depth and constant effective length. The shear strength's increase was extremely large (250%) in the range of $\eta_a = 1.0$ ($\eta_l = 3.5$) and $\eta_a = 1.5$ ($\eta_l = 3.75$).

Two different failure modes were observed in RC beams: plastic flexural expressed by reinforcement yielding for $a/D = 6$ ($\eta_l = 15$, $\eta_b = 3$) and brittle shear in concrete with dominant normal diagonal crack displacements (so-called shear-tension failure) for $\eta_a = 2$–3 ($\eta_l = 5.5$–7.5, $\eta_b = 1.5$) or with simultaneous significant normal and tangential diagonal crack displacements (so-called shear-compression failure) for $\eta_a = 1$–2 ($\eta_l = 3.5$–5.5, $\eta_b = 0.75$–1.5). The distance between the critical diagonal crack and beam support d_c related to the shear span a

varied between $d_c/a = 0.5$ for low beams ($\eta_a = 3$) up to as $d_c/a = 0$ for high beams ($\eta_a = 1$).

The good accordance between the numerical and experimental outcomes was achieved with respect to the failure mode, shear strength, deflection, location and inclination of the critical diagonal localized shear zone.

ACKNOWLEDGMENTS

The research works have been carried out within the project: "Innovative ways and effective methods of safety improvement and durability of buildings and transport infrastructure in the sustainable development" financed by the European Union (POIG.01.01.02-10-106/09-01) and within the project: "Experimental and numerical analysis of coupled deterministic-statistical size effect in brittle materials" financed by the National Science Centre NCN (UMO-2013/09/B/ST8/03598). The numerical calculations were performed on supercomputers of the Academic Computer Centre in Gdańsk TASK.

REFERENCES

Abaqus. Theory Manual, Version 5.8, 2004, Hibbit, Karlsson & Sorensen Inc.

Bažant, Z.P. and J. Planas. 1998. *Fracture and size effect in concrete and other quasibrittle materials.* CRC Press LCC, Boca Raton.

Bažant, Z.P. & Jirasek, M. 2002. Non-local integral formulations of plasticity and damage: survey of progress. *Journal of Engineering Mechanics* 128: 1119–1149.

Bažant, Z.P. et al. 2007. Energetic-statistical size effect simulated by SFEM with stratified sampling and crack band model. *International Journal of Numerical Methods in Engineerings* 71(11): 1297–320.

Borino, G., Failla, B. & Parrinello, F. 2003. A symmetric nonlocal damage theory. *Int. J. Solids Struct.* 40: 3621–3645.

Carpinteri, A. 1989. Decrease of apparent tensile and bending strength with specimen size: two different explanations based on fracture mechanics. *Int. J. Solids and Structures* 25(4): 407–29.

Dörr, K. 1980. Ein Beitag zur Berechnung von Stahlbetonscheiben unter Berücksichtigung des Verbundverhaltens. *Phd Thesis*, Darmstadt University, Germany.

Duan, K. & Hu, X. 2004. Specimen boundary induced size effect on quasi-brittle fracture. *Strength Fract. Complexity* 2(2): 47–68.

Geers, M.G.D. 1997. *Experimental analysis and computational modeling of damage and fracture.* PhD Thesis, Eindhoven University of Technology.

Hoover, C.G. & Bazant, Z.P. 2014. Universal size-shape effect law based on comprehensive concrete fracture tests. *J. Eng. Mech.* 473–479.

Korol, E. & Tejchman, J. 2014. Experimental investigations of size effect in reinforced concrete beams failing by shear. *Engineering Structures* 58:63–78.

Korol, E., Tejchman, J. & Mróz, Z. 2013. FE calculations of a deterministic and statistical size effect in concrete under bending within stochastic elasto-plasticity and non-local softening. *Engineering Structures* 8: 205–219.

Korol, E. Tejchman, J. & Mróz, Z. 2014. FE analysis of size effects in reinforced concrete beams without shear reinforcement based on stochastic elasto-plasticity with non-local softening. *Finite Elements in Analysis and Design* 88: 25–41.

Korol, E., Tejchman, J. & Mróz, Z. 2017. Experimental and numerical assessment of size effect in geometrically similar slender concrete beams with basalt reinforcement. *Eng. Struct.* 141: 272–291.

Lee, J. & Fenves, G.L. 1998. Plastic-damage model for cyclic loading of concrete structures. *Journal of Engineering Mechanics* 124(8): 892–900.

Malecki, T., Marzec, I., Bobiński, J. & Tejchman, J. 2007. Effect of a characteristic length on crack spacing in a reinforced concrete bar under tension. *Mechanics Research Communications* 34(5–6): 460–465.

Marzec, I. & Tejchman, J. 2012. Enhanced coupled elasto-plastic-damage models to describe concrete behaviour in cyclic laboratory tests: comparison and improvement. *Archives of Mechanics* 64(3): 227–259.

Marzec, I., & Tejchman, J. 2013. Computational modelling of concrete behaviour under static and dynamic conditions. *Bulletin of the Polish Academy of Sciences-Technical Sciences* 61(1): 85–96.

Marzec, I., Bobinski, J. & Tejchman, J. 2007. Simulations of crack spacing in reinforced concrete beams using elastic-plasticity and damage with non-local softening. *Computers and Concrete* 4(5): 377–403.

Marzec, I., Skarżyński, Ł., Bobiński, J. & Tejchman, J. 2013. Modelling reinforced concrete beams under mixed shear-tension failure with different continuous FE approaches. *Computers and Concrete* 12(5): 585–612.

Mazars, J. 1986. A description of micro- and macroscale damage of concrete structures. *Engineering Fracture Mechanics* 25(5–6): 729–737.

Peerlings, R.H.J., de Borst, R., Brekelmans, W.A.M. & Geers, M.G.D. 1998. Gradient enhanced damage modelling of concrete fracture. *Mechanics of Cohesive-Frictional Materials* 3: 323–342.

Pijauder-Cabot, G. & Bažant, Z.P. 1987. Non-local damage theory. *ASCE Journal of Engineering Mechanics* 113: 1512–1533.

Sato, Y., Tadokoro, T. & Ueda, T. 2004. Diagonal Tensile Failure Mechanism of Reinforced Concrete Beams. *Journal of Advanced Concrete Technology* 2(3): 327–341.

Słowik, M. & Smarzewski, P. 2012. Study of the scale effect on diagonal crack propagation in concrete beams. *Computational Material Science* 64: 216–220.

Suchorzewski, J., Korol, E., Tejchman, J. & Mróz, Z. 2017. Experimental study of shear strength and failure mechanisms in RC beams scaled along height or length. *Engineering Structures* (under review).

Walraven, J.C. 1978. The Influence of Depth on the Shear Strength of Lightweight Concrete Beams without Shear Reinforcement. *Stevin Laboratory Report* No. 5-78-4, Delft University of Technology.

Zhang N. & Tan K. 2007. Direct strut-and-tie model for single span and continuous deep beams. *Engineering Structures* 29: 2987–3001.

Computational Modelling of Concrete Structures – Meschke, Pichler & Rots (Eds)
© 2018 Taylor & Francis Group, London, ISBN 978-1-138-74117-1

Modeling of quasi-brittle materials cracking using a lattice discrete element approach

E. Zafati, C. Oliver-Leblond & F. Ragueneau
LMT-Cachan ENS Paris-Saclay/CNRS/PRES Université Paris Saclay, Cachan, France

ABSTRACT: In the context of sustainable development, the study of durability of concrete structures is considered as one of the major challenge of the 21th century. Although, the concrete material is viewed as complex heterogeneous medium at the fine scales, it has been well established that the prediction of the durability of reinforced concrete structures is strongly correlated to the prediction of the degradations caused by cracking. But the cracks have different impacts at different observation scales. At the microscopic scale, permeability is directly correlated to the cracks characteristics such as their spacing, length, opening or tortuosity. At the macroscopic scale, the degradation of concrete influences the stiffness, the load distribution and the bearing capacity. Therefore, it is crucial to develop efficient numerical models adapted to the observation scale in order to represent correctly the cracking of concrete. Continuum damage mechanics, developed to analyze the damage evolution in continuum media, cannot describe finely the cracking process. Consequently, the macroscopic continuous models, widely used in engineering problems, represent major drawback concerning the physical representation of discrete features of cracking and the difficulty to identify the material parameters for complex loading. Considered as an alternative to experimental testing, the beam-particle approach, labeled LDEM (Lattice Discrete Element Method), has proven to be a powerful tool to describe a more realistic quasi-brittle behavior for materials such concrete. The model is built using polygonal particles linked by brittle beams with frictional contact forces developed after failure of the beams. The method has been used to establish equations of a macroscopic model, on the basis of damage and plasticity theories. The integration algorithm is based on implicit time scheme enabling a large range of applications involving complex loadings paths such multi-axial and cyclic loadings. In this study, a global/local computational strategy, proposed previously by Oliver-Leblond et al., is assessed on a three-points bending test. A continuous damage model is used to compute the full solution at the global scale is given for cyclic. However, the local reanalysis of the damaged parts, by means of the LDEM method, has been carried numerically for monotone loads. The purpose is to describe the failure mechanisms and to validate the robustness of the approach using comparisons with the experimental results.

1 INTRODUCTION

An accurate description of damage process of concrete materials is essential to assess efficiently the durability of concrete structures. It is well-known that the concrete failure is manifested by the development of multiple crack branches. Thus, the numerical prediction of the main features characterizing a crack (pattern, opening, rugosity,...) is of major interest.

Lattice discrete element method (LDEM) is considered as one of the promising approaches able to describe efficiently the fracture mechanisms of quasi-brittle materials such as the concrete. The LDEM method, adopted in this work, developed by Delaplace () and enhanced later by Vassaux et al. (2015) Vassaux et al. (2016), consists on a network of rigid particles interacting each other via cohesive and contact-friction laws. The cohesive interactions are allowed by brittle-elastic beams where the failure is controlled by random failure thresholds in order to obtain a more realistic representation of the heterogeneity of the concrete material. The contact forces are computed using the same law as for cohesive force with slight modifications following the work of Vassaux et al. (2016).

In the present paper, a failure structure analysis in the case of cyclic loads is performed using a combination of two numerical techniques: the finite element method and the lattice discrete element method labeled the global/local technique in this paper. This novel approach has been initially developed for monotone loads Oliver-Leblond et al. (2013) and consists of two main steps: in the first step, the global response is computed using the finite element method and a continuum

damage constitute law. Then, using the nodal displacement obtained from the finite element model, a second local analysis is addressed on pre-selected parts from the structure in order to describe the cracking pattern at the fine scale and to evaluate more accurately the crack opening values.

The paper is reorganized as follows: the first part is devoted to the description of the global/local method. The continuum damage model used in the global analysis, developed in Vassaux et al. (2016), is characterized by its suitable features to reproduces the unilateral effects as well as the hysteresis effects due the crack closure and the friction mechanisms. The fundamental equations of the lattice discrete element approach used for the local analysis are also presented. In the second part, a virtual cyclic three-points bending test is performed using the global/local approach with an emphasis on the comparison with the experimental results. It should be stressed that only numerical results for the monotone loads are considered for the local analysis. The purpose is to assess the robustness of the numerical approach, especially the discrete element approach, by comparing with the experimental field measurements around the cracks.

2 DESCRIPTION OF THE METHOD

As pointed out in the introduction, the method used here is quite simple and consist in a global analysis of the structure by the finite element method and a local analysis of the Region of Interest (ROI) by the discrete element method. The boundary conditions applied to the local analysis are exactly the interpolated displacements obtained from the global analysis.

The local analysis can be viewed as a post-processing tool providing information at the scale of the crack. It has the advantage of giving a fine representation of the local behavior of the crack and related features such as the opening cracks. The computation procedure can be splitted into the following steps:

- Global analysis of the whole structure with a non-linear finite element model including damage;
- Identification and cutting of the ROI, which is the region of damage concentration;
- Extraction and interpolation of the displacements from the global mesh to the local mesh;
- Local analysis of the ROI with a discrete element model.

The boundary conditions applied to the local computation are easily deduced from the global computation at the non-free surfaces of the ROI via an interpolation relation. Indeed, let u_l^p be the imposed displacement at the particle l picked out from the discrete element model. The displacement u_l^p can be expressed as:

$$u_l^p = \sum_i N_i(\zeta_l, \eta_l)\mathcal{U}_i^e \tag{1}$$

where e refers to the element picked out from the finite element model in such a way that the particle l belongs to the element e. The couple (ζ_l, η_l) stands for the coordinates of the particle l in the reference element, N_i are the shape functions and $\mathcal{U}_i^e$ are the nodal displacement related to the element e.

2.1 *Fundamental equations for a continuum damage model*

The continuum damage model adopted in this work has been proposed in Vassaux et al. (2016). It is characterized by its capabilities of reproducing the progressive stiffness recovery and the hysteresis effects caused respectively by crack closure and friction. The macroscopic model is described using a decomposition technique of the total stress $\boldsymbol{\sigma}$ into two independent parts as follows:

$$\boldsymbol{\sigma} = \boldsymbol{\sigma}^m + \boldsymbol{\sigma}^f \tag{2}$$

where $\boldsymbol{\sigma}^m$ is the stress tensor in the cracked continuum medium and $\boldsymbol{\sigma}^f$ is the stress tensor driving the behavior of the crack once it is closed.

In order to model the fracture processes, the following Helmholtz free energy is introduced in the following form:

$$\Psi^m(\epsilon, d, z) = \frac{1}{2}(1-d)\epsilon : C : \epsilon + \Psi^{m,d}(z) \tag{3}$$

Here d is the isotropic damage variable, ϵ is the strain tensor, $\boldsymbol{C}$ is the fourth order Hooke's tensor and $\Psi^{m,d}$ is the consolidation function depending on the isotropic hardening variable z.

The non-associated pseudo-potential of dissipation φ^m is similar to the Mazar failure criterion and is defined by:

$$\varphi^m = \overline{Y} - (Y_0 + Z) \tag{4}$$

where Z refers to the thermodynamic force associated with the variable z, Y_0 the elastic limit energy rate and $\overline{Y}$ is the energy rate defined by $Y = \frac{1}{2}E\epsilon_0\epsilon^{eq}$ where E is the Young's modulus, ϵ_0 is the elastic limit strain and ϵ^{eq} is the Mazars equivalent strain.

Using the consistency conditions the damage variable evolves according to the following relation:

$$d = 1 - \frac{\overline{Y}}{Y_0}\exp\left\{-\frac{B_0}{\kappa}\left(\overline{Y} - Y_0\right)\right\} \tag{5}$$

where B_0 is a parameter controlling the softening behavior and κ is defined by:

$$\kappa = 1 + k_0\left(\frac{\langle \boldsymbol{C}:\boldsymbol{\epsilon}\rangle : \langle \boldsymbol{C}:\boldsymbol{\epsilon}\rangle}{(\boldsymbol{C}:\boldsymbol{\epsilon}):(\boldsymbol{C}:\boldsymbol{\epsilon})}\right)^{1/2} \tag{6}$$

where k_0 is a parameter taking into account the confining pressure.

As mentioned above, the tensor σ^f has been introduced to describe the behavior of the crack in order to reproduce the stiffness recovery and the hysteresis effects by means of a plastic model. Moreover, the following assumption in terms of the rates has been adopted:

$$\dot{\boldsymbol{\sigma}} = \vartheta\left(\epsilon^f\right)\mathbf{C} : \boldsymbol{\epsilon}^f \tag{7}$$

where $\boldsymbol{\epsilon}^f = d\boldsymbol{\epsilon}$ is called the homogenized contribution of crack openings to the total strain. The function ϑ is a scalar function which can be interpreted as the proportion of the closed cracks and is assumed to be depending on $\boldsymbol{\epsilon}^f$ as follows:

$$\vartheta\left(\boldsymbol{\epsilon}^f\right) = 1 - \frac{1}{1 + \exp\left(-\frac{\alpha_0}{I_1\left(\epsilon^f_{max}\right)} I_1\left(\boldsymbol{\epsilon}^f\right)\right)} \tag{8}$$

where ε^f_{max} at the time T is given by $\varepsilon^f_{max}(T) = \varepsilon^f(t_m)$ and $t_m = \arg\left(\max_{0<t<T} I_1\left(\epsilon^f(t)\right)\right)$.

According to ref, the hysteresis effects are induced by frictional sliding at the surface of cracks which can be described by a plastic constitutive law. Therefore, a perfectly plastic model

$$\varphi^f\left(\boldsymbol{\sigma}^f\right) = \sqrt{J_2\left(\boldsymbol{\sigma}^f\right)} + \mu_0 I_1\left(\boldsymbol{\sigma}^f\right) \tag{9}$$

The parameter μ_0 plays the role of the friction coefficient.

A non-associated dissipation potential has been adopted in ref following the relation:

$$\overline{\varphi}^f\left(\boldsymbol{\sigma}^f\right) = \sqrt{J_2\left(\boldsymbol{\sigma}^f\right)} \tag{10}$$

One may notice that the equation (10) entails that the plastic strain introduces an isochoric transformation.

2.2 *Fundamental equations for the lattice discrete element method*

The lattice discrete element method adopted in this work is a combined beam-particle-based model. With this approach, the material is described by polygonal particles linked by brittle beams with the possibility of frictional contact after the failure of the beams. Therefore, the crack pattern is naturally created once one or several beams linking particles are removed.

The mesh is generated using a combination of the Delaunay's triangulation to obtain the set of beams linking the particles and the Voronoi tessellation to compute the polygonal particles. The centroids of the particles are fixed randomly using a grid technique as described in Vassaux et al. (2015).

The cohesion between particles are represented by Euler-Bernoulli beams (see Figure 1) linking the centroids of the particles (lattice model). Moreover, four parameters have to be identified: the length l_b, the cross section area A_b are given the mesh geometry and are different for each beam while the Young's modulus E_b and the inertia coefficient $\alpha = 64 I_b \pi / A_b^2$ (I the moment of inertia) are equal to all beams. The last two parameters are identified in such a manner to recover the elastic properties of the material, E and ν, respectively Youngs modulus and Poissons ratio.

The contact interaction is activated when two separated particles, no more linked by a cohesive beam, overlap. The magnitude of the contact forces, as well as their direction and their point of application, depend only on the overlapping areas. The normal force $\underline{F}_n$ between the two particles is then computed as:

$$\underline{F}_n = -\frac{E_b S_r}{l_c}\underline{n} \tag{11}$$

where $\underline{n}$ is the contact normal vector, S_r is the overlap area and l_c is a characteristic length equal

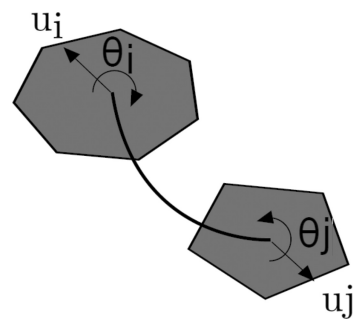

Figure 1. Euler-Bernoulli beam in a deformed state.

to the harmonic mean of the diameters of both particles in contact. The friction force $\underline{F}_t$ follows a Coulomb's type friction as follows:

$$\underline{F}_t = \min\left\{\begin{array}{l}\dfrac{E_b I_c}{l_c^3}\left[\left(u(i)-u(j)\right).\underline{t}-\Delta u_{s,ij}\right],\\ \mu\left\|\underline{F}_n\right\|\end{array}\right\} \tag{12}$$

where μ is the friction coefficient and $I_c = \frac{l_c^3}{12}$.

The cohesive beam are endowed with brittle behavior. The breaking threshold P_{ij} of the beam linking two particles i and j is expressed in terms of the axial strain ϵ_{ij} of the beam and the rotations θ_i and θ_j related to both particles as follows:

$$\left\{\frac{\epsilon_{ij}}{\epsilon_{ij}^r}\right\} + \frac{\left|\theta_i - \theta_j\right|}{\theta_{ij}^r} \geq 1 \tag{13}$$

Here, the critical strain ϵ_{ij}^r and the critical rotation θ_{ij}^r of the concerned beam i-j are assigned random values according to the Weibull distribution defined by two parameters: the scale factor λ and the shape factor k.

The procedure to compute the numerical solution by the LDEM method follows an implicit algorithm is not presented here. Further details can be found in Vassaux et al. (2015).

3 APPLICATION: THREE POINT BENDING TEST

In this section, the global/local analysis presented above is applied to a reinforced concrete beam under cyclic load.

3.1 *Experimental set-up description*

The beam considered here has been tested under vertical load within the framework of the project CEOS.fr supported by the French national agency for research. The experimental results may be found in Lebon (2011). The specimen is characterized by the length 1650 mm and the section 200 × 150 (width × thickness). It has been reinforced by 4 steel bars (4HA12) (two in the top part and two in the bottom part). 15 stirrups with the diameter 6 mm have also been included with a maximal spacing equal to 150 mm. The time evolution of the imposed displacement is shown in Figure 2.

The Digital Image Correlation (DIC) technique has been employed to describe experimental results characterizing the cracks. Indeed, the fine description of the experimental displacement field through DIC allows us to pick out the crack patterns, tip and opening.

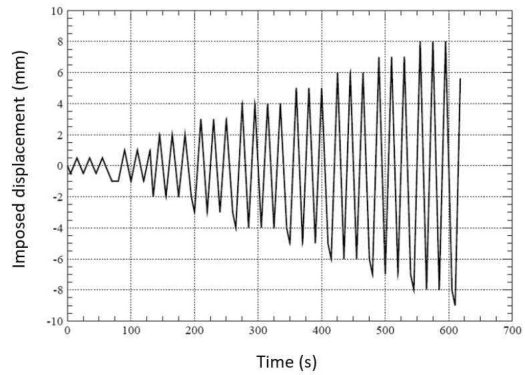

Figure 2. Time evolution of the imposed displacement.

Figure 3 depicts the three-dimensional mesh adopted for the different parts of the beam. The concrete structure is modeled using eight-noded hexahedral finite elements characterized by the average size $h = 0.02m$. The constitutive law assigned to the concrete part is the one described in section 2 where the inelastic parameters are summarized in Table 1. Fracture energy regularization method depending on elements size is employed.

The vertical rebars are modeled by one-dimensional bar elements. The steel rebars are assigned isotropic Hooke's model, which parameters are as follows: the Young's modulus and the Poisson's ratio are equal to 200 GPa and 0.3 respectively.

The longitudinal reinforcements are modeled by the three-dimensional eight-noded hexahedral finite elements characterized by the size $h = 0.02m$. An isotropic plastic model is adopted for the longitudinal steels with the same Hooke's parameters as the vertical rebars while the elastic stress limit is equal to 450 *MPa*. In the whole model, a perfect steel-concrete interface is assumed.

3.2 *Global analysis*

The comparison of the numerical response, obtained by the finite element model, and the experimental one (one may refer to Lebon (2011)) is depicted in Figure 4. It is seen that the order of magnitudes are well estimated, i.e., the load is approximately equal to 60 kN when the displacement is equal to 5 mm. Moreover, one may observe that the global stiffness diminishes as long as the load magnitude increases due to the cracking process. The global response is also symmetrical and the stiffness recovery is observed when the loading switches from one direction to the opposite direction.

Figure 5 shows the damage contours obtained when the imposed displacement reaches the value 8 *mm*, compared with the experimental strain

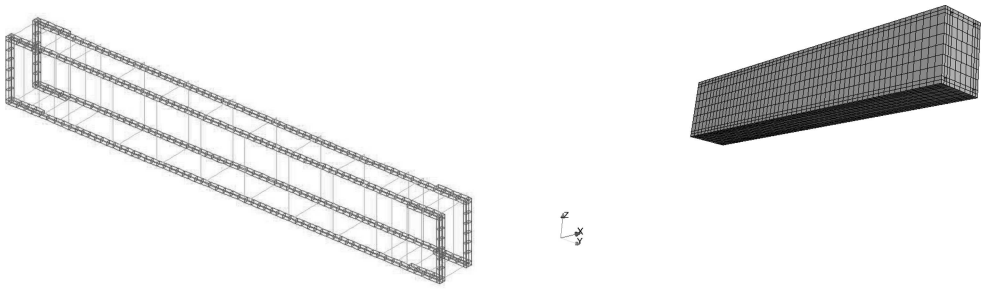

(a) Reinforced cage (b) Concrete structure

Figure 3. Finite element mesh of the reinforced cage and the concrete beam.

Table 1. Values of the continuum model's parameters for the beam's test simulation.

E (GPa)	ϵ_0	$B_0\left(kJ^{-1}*m^3\right)$	k_0	α_0	μ_0
27 (GPa)	1×10^{-3}	4	5	6.5	2.89

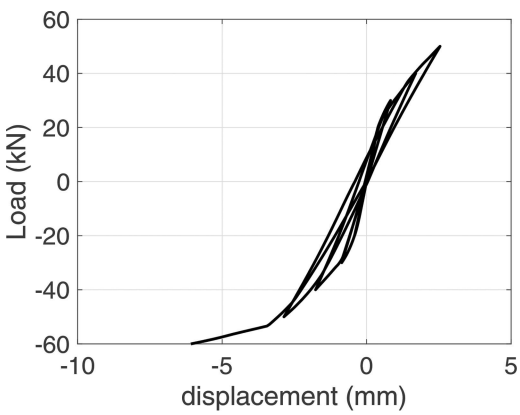

(a) Numerical

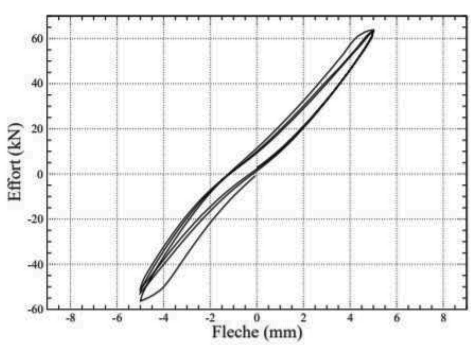

(b) Experimental

Figure 4. Numerical load-displacment curve (left) vs experimental load-displacement curve (right).

contours obtained by the The Digital Image Correlation method. From a qualitative point of view, it is seen that the numerical results are in agreement with the experimental one in term of the crack profiles. Moreover, the number of the cracks are almost identical.

One may notice that the representation of hysteresis loops, due to frictional sliding, slightly differs from experimented one (see Figure 4). Such discrepancy may be explained by mechanisms unrelated to concrete's behavior, namely steel-concrete interface degradation and friction.

3.3 *Discrete element local analysis*

As pointed out in the introduction, the local analysis in this paper has been carried numerically for monotonic loads. More precisely, the imposed displacement is progressively increased until the maximal value that is 8 *mm*. On the basis of the damage contours, the damaged zone is splitted into five regions are identified to be reanalyzed by the discrete element method.

The classical method to represent the steel bar for the discrete element method consists of a mesh composed of particles aligned along the steel bars (Meguro & Hakuno (1989)). In this case, further constitutive laws should be introduced in order to reproduce the steel behavior as well as the steel-concrete interface. The global/local analysis proposed in Oliver-Leblond et al. (2013), used in this work, does not require the modification of the discrete model to take into account of such behaviors. Indeed, the steel and the concrete-steel interface behaviors are only studied at the global scale. Therefore, the steel bars are removed from the mesh and replaced by the Dirichlet boundary conditions applied to the concrete-steel interface.

Figure 6 depicts the discrete element mesh as well as the boundary regions where the displacement is applied. The parameters identified for the concrete are summarized in Table 2.

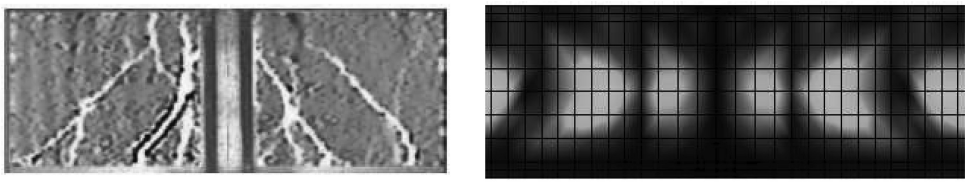

(a) Numerical (b) Experimental

Figure 5. Numerical load-displacment curve (left) vs experimental load-displacement curve [] (right).

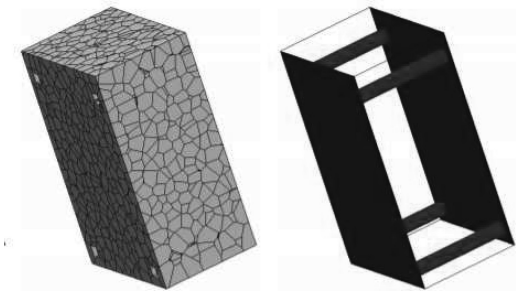

Figure 6. The discrete element mesh and the boundary conditions.

Table 2. Identified parameters for the local analysis.

	Physical signification	Value	Unit
E	Young's modulus	23	GPa
α	Inertial coefficient	0.75	–
λ_{ε_r}	Critical strain threshold	2×10^{-4}	–
λ_{θ_i}	Critical rotation threshold	1×10^{-3}	–
k	Shape factor	5	–

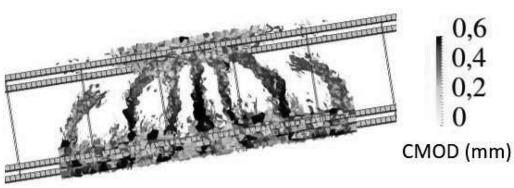

Figure 7. Cracking patterns for the maximal imposed displacement (8 mm).

The crack patterns obtained for the imposed displacement 8 *mm* are shown in Figure 7. It is seen that the crack profiles are in a good agreement with the ones presented in Figure 5 (a). Indeed, the number of the cracks is the same and the positions of the cracks are almost identical.

For the same reanalyzed zone, the opening profile is presented in Figure 8 before yielding (for

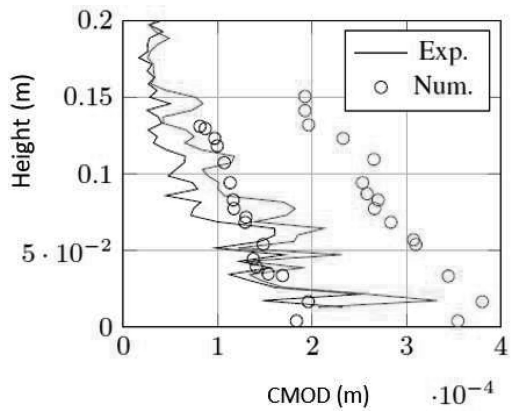

Figure 8. The crack opening mouth displacement with respect to the height.

the imposed displacement equal to 4 mm in black color) and after yielding (the maximal imposed displacement 8 mm in red color). Before yielding, the experimental results are correctly reproduced. Moreover, the experimental curves shows that the crack opening displacement slightly increases between the imposed displacements 4 mm and 8 mm whereas the same displacement increases two times in the numerical results.

4 CONCLUSIONS

In this paper, a global/local strategy has been used, following the line of Oliver-Leblond et al. (2013), to study the cracking mechanisms for reinforced concrete structures. An approach based on the continuum damage mechanics to reproduce the nonlinear behavior at the scale of the structure. Then, a lattice discrete element method is used to describe the properties of the cracks at the fine scale.

A three point bend test on a reinforced beam have been studied. The global/local strategy adopted in this paper enables a quantitative description of the failure patterns as well as the crack mouth opening

displacement. Therefore, this novel strategy is considered valuable for concrete failure analysis.

Since the local reanalysis has been carried out for the monotone loads. It would be interesting to extended the local reanalysis to cyclic loads using the recent developments carried out by Vassaux et al. (2015).

REFERENCES

Delaplace, A. *Modélisation discrète appliquée au comportement des matériaux et des structures.* France: Mémoire d'habilitation á diriger des recherches de l'Ecole Normale Supérieure de Cachan.

Lebon, G. (2011). *Analyse de l'endommagement des structres de génie civil: Techniques de sous-structuration hybride couplées à un modéle de l'endommagement anisotrope.* France: Thèse de doctorat de l'Ecole Normale Supérieure de Cachan.

Meguro, K. & M. Hakuno (1989). Fracture analyses of concrete structures by the modified dsitinct element method. *Stuctural Engineering/Earthquake Engineering. 6*, 283–294.

Oliver-Leblond, C., A. Delaplace, F. Ragueneau, & B. Richard (2013). Nonintrusive global/local analysis for the study of fine cracking. *International Journal for Numerical and Analytical Methods in Geomechanics. 37*, 973–992.

Vassaux, M., C. Oliver-Leblond, B. Richard, & F. Ragueneau (2016). Beam-particle approach to model cracking and energy dissipation in concrete: Identification strategy and validation. *Cement and Concrete Composites 70*, 1–14.

Vassaux, M., B. Richard, F. Ragueneau, & A. Millard (2016). Regularised crack behaviour effects on continuum modeling of quasi-brittle materials under cyclic loading. *Engineering Fracture Mechanics 149*, 18–36.

Vassaux, M., B. Richard, F. Ragueneau, A. Millard, & A. Delaplace (2015). Lattice models applied to cyclic behavior description of quasi-brittle materials: advantages of implicit integration. *International Journal for Numerical and Analytical Methods in Geomechanics. 39*, 775–798.



Taylor & Francis
Taylor & Francis Group
http://taylorandfrancis.com

Computational Modelling of Concrete Structures – Meschke, Pichler & Rots (Eds)
© 2018 Taylor & Francis Group, London, ISBN 978-1-138-74117-1

Evaluation of safety formats for structural assessment based on nonlinear analysis

J. Červenka & V. Červenka
Červenka Consulting s.r.o., Prague, Czech Republic

M. Sýkora & J. Mlčoch
Klokner Institute, Czech Technical University in Prague, Prague, Czech Republic

ABSTRACT: *fib* Model Code 2010 introduced for the first time a comprehensive system for the treatment of safety and uncertainty for structural assessment and design based by nonlinear analysis. The paper analyzes a selected example from the literature with shear failure when two different failure modes are observed depending on the choice of material parameters. This issue is critical for the global assessment by nonlinear analysis since it often involves assumptions about the statistical distribution of structural strength. When different failure modes are involved, i.e. by steel yielding or concrete failure, these assumptions may not be valid and the calculated design strength may not be on the safe side. The influence of different failure modes on the structural strength is evaluated mainly for the ECOV method, where the assumption of log-normal distribution is used. The global assessment by nonlinear analysis is compared with the analytical solutions based on standard Eurocode and Model Code 2010 shear formulas. The results show that even though the ECOV methods provides higher design strength values, the difference is not significant especially if one takes into account the overall uncertainties involved in reinforced concrete analysis and design.

1 INTRODUCTION

The Model Code 2010 of *fib* (2013) (MC2010) introduced for the first time a comprehensive system for the treatment of safety and model uncertainty for structural assessment and design based on nonlinear analysis. On the basis of MC2010, new safety formats are being proposed also in relation to the ongoing revisions of Eurocodes and evolution of the new *fib* Model Code, *fib* (2016).

Focusing on resistance variables only, non-linear analysis can be based on one of the following safety formats:

1. Partial factor method (PSF)—the use of design values of material properties. This approach is allowed in EN 1992-1-1 (2004)—"EC2"—and is also advocated for instance in the draft of ISO 22111 as a bases for design of structures and general requirements. Annex A of this draft emphasizes the importance of:
   - assessment whether a low or high design value is unfavorable.
   - inclusion of model uncertainty.
2. Global resistance methods—MC2010 makes distinction between two approaches:
   2a. The analysis based on mean properties of reinforcement, modified characteristics of concrete and a single value of global partial factor deemed to cover all failure modes. This approach is also adopted in EN 1992-2 (2005).
   2b. Method of estimation of a coefficient of variation of resistance ECoV described e.g. by Červenka (2008). This method was later extended by Schlune et al. (2011, 2012). In principle ECoV requires two or more structural analyses to estimate coefficient of variation of resistance and then global partial factor.
3. Fully probabilistic method—is the most accurate, but also the most complicated and computationally demanding approach, where the design resistance is calculated either by advanced sampling approaches or by searching for a solution with given probability along an approximated response surface.

This study analyses the test of an ordinary beam with shear failure by Anderson & Ramirez (1989), for which two different failure modes can be observed depending on the choice of material parameters. Numerical models are based on FEM and simplified shear models according to EC2 and MC2010 with three levels of approximation (LoA). Mean shear strength predictions are critically compared and design values are estimated for each of the numerical models using the selected safety formats 1, 2b and 3.

2 NONLINEAR ANALYSIS

The nonlinear finite element analyses presented in this paper are performed with the software ATENA (Červenka et al. 2017) using the combined fracture-plastic model for concrete of Červenka & Pappanikolaou (2008).

The constitutive model formulation assumes small strains, and is based on the strain decomposition into elastic (ε_{ij}^{e}), plastic (ε_{ij}^{p}) and fracture (ε_{ij}^{f}) components. The stress development is described by the rate equations reflecting the progressive damage (concrete cracking) and plastic yielding (concrete crushing):

$$\dot{\sigma}_{ij} = D_{ijkl} \cdot (\dot{\varepsilon}_{kl} - \dot{\varepsilon}_{kl}^{p} - \dot{\varepsilon}_{kl}^{f}) \tag{1}$$

Flow rules govern the evolution of plastic and fracturing strains:

$$\text{Plastic model: } \dot{\varepsilon}_{ij}^{p} = \dot{\lambda}^{p} \cdot m_{ij}^{p}, \quad m_{ij}^{p} = \frac{\partial g^{p}}{\partial \sigma_{ij}} \tag{2}$$

$$\text{Fracture model: } \dot{\varepsilon}_{ij}^{f} = \dot{\lambda}^{f} \cdot m_{ij}^{f}, \quad m_{ij}^{f} = \frac{\partial g^{f}}{\partial \sigma_{ij}} \tag{3}$$

where $\dot{\lambda}^{p}$ is the plastic multiplier rate and g^{p} is the plastic potential function, $\dot{\lambda}^{f}$ is the inelastic fracturing multiplier and g^{f} is the potential defining the direction of inelastic fracturing strains. The multipliers are evaluated from the consistency conditions.

The model of Menetrey-Willam (1995) is used for plasticity of concrete in multiaxial stress state in compression (Figure 1) with nonlinear hardening (Figure 2) and linear softening (Figure 3).

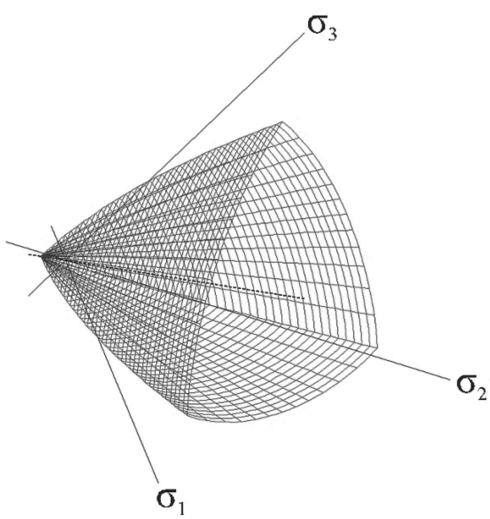

Figure 1. Visualization of the three-parameter Menetrey & Willam (1995) three-parameter concrete failure criterion.

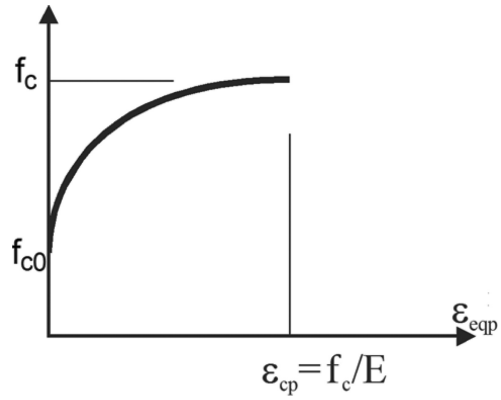

Figure 2. Hardening law for the plasticity model for concrete in compression.

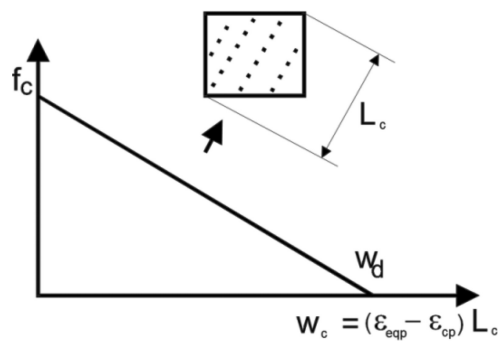

Figure 3. Softening law for the plasticity model for concrete in compression.

In tension, Rankine criterion for tensile fracture with exponential softening of Hordijk (1991)—see Figure 4—is used, where w_t stands for the crack width.

The stress softening in tension is determined using the crack band approach of Bažant & Oh (1983) and analogically in compression according to Červenka et al. (2014). The crack band L_t as well as the crush band size L_c are adjusted with regard to the crack orientation approach proposed by Červenka & Margoldová (1995). This method is illustrated in Figure 5 and described by Eq. (4):

$$\begin{aligned} &L_t' = \alpha\gamma L_t \quad \text{and} \quad L_c' = \gamma L_c \\ &\gamma = 1 + (\gamma_{max} - 1)\frac{\theta}{45}, \quad \theta \in \langle 0;45 \rangle, \quad \gamma_{max} = 1.5 \end{aligned} \tag{4}$$

The crack angle θ is taken as the average angle between crack direction and element sides.

The above formulation controls the strain localization accounting for the mesh size and the crack orientation. Parameter α is introduced to cover the localization effect due to the element type

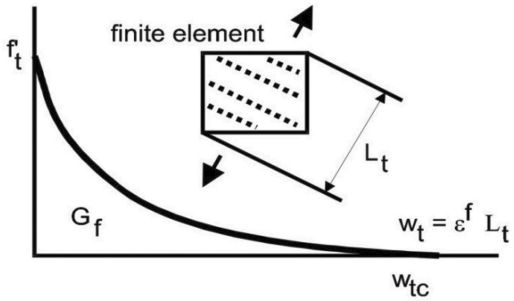

Figure 4. Crack opening law according to Hordijk (1991).

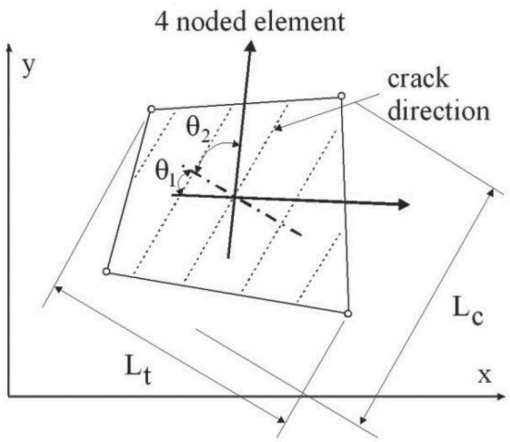

Figure 5. Crack band formulation.

as reported recently in the work of Slobbe et al. (2013). In this study $\alpha = 1$ is used for low order elements with 2×2 integration scheme and $\alpha = 0.6$ for quadratic elements with 3×3 integration scheme.

Some additional features of cracked concrete included in the model, namely the reduction of compressive strength and shear stiffness degradation, often referred as a shear retention effect, should be mentioned due to their importance in problems dominated by shear failure.

The damage of concrete by cracks is reflected according to Bentz et al. (2006) in the reduction factor r_c of the compressive strength f_c as follows:

$$\sigma_c = r_c f_c$$
$$r_c = \frac{1}{0.8 + 170\,\varepsilon_1}, \quad r_c^{\lim} \le r_c \le 1.0 \tag{5}$$

where ε_1 is the tensile strain normal to the crack. The largest maximal fracturing strain is used for ε_1 and the compressive strength reduction is limited by $r_c^{\lim}$. In this work $r_c^{\lim} = 0.8$ is considered.

The shear strength of the cracked surface is also considered according to the modified compression field theory (MCFT) by Bentz et al. (2006):

$$\sigma_{ij} \le \frac{0.18\sqrt{f_c'}}{0.31 + \dfrac{24w}{a_g + 16}}; \quad i \ne j \tag{6}$$

Taking into account the crack width w and aggregate size a_g. Since MCFT does not offer shear stiffness, the authors proposed to relate the shear stiffness K_t^{cr}, oriented tangentially to the crack face, to the normal stiffness K_n^{cr} already defined by a crack opening law:

$$K_t^{cr} = s_F\, K_n^{cr} \tag{7}$$

The normal stiffness comes directly from the tensile softening law in Figure 4 as:

$$K_n^{cr} = f_t(w_t)/w_t \tag{8}$$

This makes the shear stiffness dependent on the crack opening displacement and independent of the mesh size. The scaling factor $S_F = 50$ was used in the presented analyses.

3 SAFETY FORMATS FOR NONLINEAR ANALYSIS

The design condition is formulated as:

$$E_d < R_d \tag{9}$$

where E_d represents the design actions and R_d the design resistance. They include required safety margins, whereas for simplicity the probabilities of actions and resistance are considered separately.

The verification of safety by the condition (9) in the standard design practice is applied to cross sections and actions that are obtained by a linear analysis. It is well known that this concept is not consistent, since different methods are used for the calculation of:

- Actions—linear analysis and
- The resistance of cross sections—nonlinear material behavior.

In statically indeterminate systems the section forces may change due to force redistribution at the ultimate limit state. Furthermore, only local safety check is exercised and a global safety assessment is not performed, and is unknown. That is

why a global safety format is preferred in case of nonlinear analysis.

The action E_d in condition (9) is considered on the global level (for example it can represent the intensity of the investigated load combination) and the resistance R_d is an ultimate load intensity at failure for the given load combination obtained by the nonlinear analysis.

The Model Code 2010 introduces four methods for global assessment using nonlinear analysis as described in Section 1. This paper concentrates on mainly on the partial factor (PSF) and ECoV method. The full probabilistic approach is used mainly as a comparative and reference solution.

3.1 *ECoV method—estimate of coefficient of variation*

ECoV method proposed by Červenka (2008) is based on the idea that the random distribution of resistance due to material, which is described by the coefficient of variation V_m, can be estimated from mean R_m and characteristic values R_k of resistance. The underlying assumption is that the distribution of resistance is according to the lognormal distribution, which is however typical for the structural resistance. Considering these assumptions the coefficient of variation V_m can be expressed as:

$$V_m = \frac{1}{1.65} \ln\left(\frac{R_m}{R_k}\right) \tag{10}$$

Then the global safety factor γ_R of resistance can be calculated as:

$$\gamma_R = \exp(\alpha_R \beta V_R), \quad V_R = \sqrt{V_m^2 + V_{Rd}^2} \tag{11}$$

where α_R is the sensitivity factor for resistance (as defined by FORM) and β is the reliability index. V_{Rd} is the model uncertainty. Eq. (11) assumes unbiased model predictions—unity mean of model uncertainty.

The above procedure enables to estimate the safety of resistance in a rational way, based on the principles of reliability accepted by the codes. Appropriate code provisions can be used to identify these parameters. For instance, typical values in EN 1990 are $\beta = 3.8$ (50 years) and $\alpha_R = 0.8$, which leads to a 1.12‰ fractile as a design value of resistance. The global resistance factor is then:

$$\gamma_R \cong \exp(3.04\, V_R) \tag{12}$$

and the design resistance is calculated as:

$$R_d = R_m / \gamma_R \tag{13}$$

The main task in this method is the determination of the mean and characteristic values of resistance R_m, R_k. They can be calculated by two separate nonlinear analyses using mean and characteristic values of the input material parameters, respectively.

The method is very general and reliability level β and distribution type can be changed if required. It can capture different types of failure and the sensitivity to a random variation of the material parameters is automatically included. The slight disadvantage of this method is the need for two separate non-linear analyses.

3.2 *Partial Safety Factor method (PSF)*

This approach is the natural extension of the standard partial safety factor method, which is used in the most design codes. In this method, the design condition is identical to Eq. (9), where the design action $E_d = E(F, \gamma_G, \gamma_Q, \gamma_P, ...)$ is a function of the representative load F, which is multiplied by the partial safety factors $\gamma_G, \gamma_Q, \gamma_P, ...$ for permanent loads, live loads, pre-stressing, etc. The resistance $R_d = (f_d)$ is calculated by a nonlinear analysis using design values of the material parameters $f_d = f_k / \gamma_M$, where f_k are characteristic values and γ_M partial safety factors of materials.

4 CASE STUDY

The presented analysis is focused on beam W1 tested by Anderson & Ramirez (1989). Beam of cross-section 406 × 406 mm was subjected to a four-point bending test with a shear span a = 0.91 m. The beam was designed to fail in shear, i.e. to comply with the condition for shear stress $V_{test}/(b_w d) > 6$. The following input parameters describe material and geometrical properties (cf. Table 1):

- Concrete compressive strength f_c = 29.1 MPa
- Effective cross-sectional width b_w = 406 mm
- Effective depth d = 344 mm (thus a/d = 2.15)
- Yield strength of shear reinforcement f_y = 455 MPa
- Shear reinforcement ratio ρ_w = 3.9‰
- Longitudinal reinforcement ratio ρ_l = 2.31%.

The load-deflection curve for the tested beam is shown in Figure 6. The obtained shear resistance was V_{test} = 460 kN.

Table 1. Models of basic variables.

Variable	Sym.	Dist.	μ_X/X_k	V_X
Concrete comp. strength	f_c	LN	29.1/21.1 MPa	0.2
Yield strength of reinf.	f_y	LN	455/414 MPa	0.058
Modul. elasticity reinf.	E_s	det	200 GPa	–
Shear reinf. ratio	ρ_w	det	0.0039	–
Longitudinal reinf. ratio	ρ_l	det	0.0231	–
Beam width	b_w	det	0.406 m	–
Effective depth	d	det	0.344 m	–

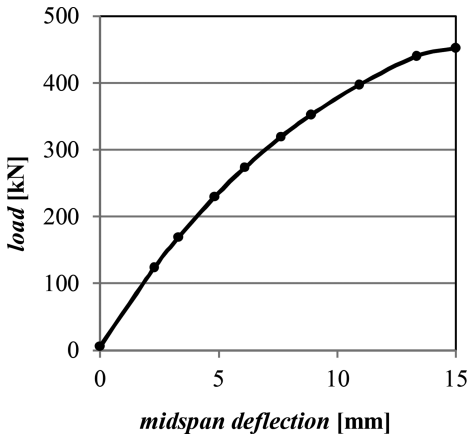

Figure 6. Experimental load-deflection curve for the beam under investigation Anderson & Ramirez (1989).

Annex D of EN 1990 (2002) allows estimating of design resistance R_d from an only test result provided that coefficient of resistance V_R is known. Assuming a lognormal distribution, two alternative approaches can be used:

$$R_d = \eta_d \exp(m_{\ln R} - k_{n=1;5\%} \times V_R)/\gamma_M = \\ = 1 \times \exp(\ln 460 - 2.31 \times 0.1)/1.15 = 317 \text{ kN}$$

$$R_d = \eta_d \exp(m_{\ln R} - k_{n=1;1‰} \times V_R) = \\ = 1 \times \exp(\ln 460 - 4.36 \times 0.1) = 297 \text{ kN}$$

where $\eta_d = 1$ is the design value of the conversion factor that could cover the difference between test and real-structure conditions; and k_n = coefficient given by EN 1990 (2002) for one test, known CoV and characteristic (5% fractile) or design (1.12‰) values. The CoV of resistance is estimated for stirrups yielding—the failure mode observed in the test. This is commonly associated with $V_R < 0.1$. However, EN 1990 (2002) assumes using "a conservative upper estimate of V_R", which is deemed here to be reflected by $V_R = 0.1$. As only one test is available and the V_R-value is likely conservative, the design value indicated in relationships (1) needs to be considered as a rough approximation, probably leading to a lower bound on a true design resistance.

5 DESIGN STRENGTHS ACCORDING SIMPLIFIED MODELS

5.1 *Models under investigation*

For the sake of comparison, the broadly used analytical shear models EC2 and the three levels of approximation in MC2010 (LoA) are applied to compare unbiased model predictions with the test result and to estimate design shear strength considering commonly assumed scatter of material properties (Table 1). Variability of geometrical properties is neglected; additional numerical verifications reveal that the effect of this simplification on design values is insignificant in the case under investigation. This is attributable to small dispersion of geometrical data for ordinary-sized beams and large coefficients of variation for uncertainty in shear models (Table 2).

For EC2, LoA1 and LoA2, the model resistance is obtained as:

$$R_{\text{model}} = \min[R_{\text{model,s}}(f_y),\ R_{\text{model,c}}(f_c)] \quad (14)$$

where the subscripts s and c denote stirrups and concrete, respectively. Real resistance is estimated by considering model uncertainties, Holicky et al. (2016):

$$R = \min[\theta_s\ R_{\text{model,s}}(f_y),\ \theta_c\ R_{\text{model,c}}(f_c)] \quad (15)$$

For LoA3 no distinction between the stirrups and concrete contributions is made. Numerical integration is used in probabilistic analysis.

5.2 *Design strengths for beam W1*

Table 3 provides model resistances based on mean strengths, i.e. best estimates using the models, but ignoring the effect of model uncertainty. Whilst LoA2 and LoA3 lead to the resistances close to the test result, LoA1 provides an overly conservative value (as expected) and EC2 overestimates shear strength.

The difference between the LoA1 and EC2 predictions may be explained by the difference in the limits of the strut angle. The lower bound for LoA1 is 30° and 21.8° is for EC2; both limits govern the $R_{\text{model}}(f_{ym}, f_{cm})$—values. When the

Table 2. Probabilistic description of resistance model uncertainty θ (lognormal distribution).

Model	μ_θ/V_θ	Ref.
Stirrups yielding		
EC2	1.275/0.2*	Sykora et al. (2015)
LoA1	1.86/0.24*	Krejsa et al. (2014), Sykora et al. (2017)
LoA2	1.47/0.21*	Sykora et al. (2017)
Concrete crushing		
EC2	1.4/0.25	*fib* COM3 TG3.1 (2016)
LoA1	1.55/0.27**	–
LoA2	1.3/0.27**	–
Combined—sum of stirrups and concrete contributions		
LoA3	1.15/0.225	Sykora et al. (2017)

*For moderately reinforced beams (1 MPa $< \rho_w f_{yw} \leq$ 2 MPa).
**Estimate based on the model uncertainty characteristics for EC2 and comparison of EC2 and the model under investigation.

Table 3. Comparison of mean and design strengths according to EC2 and levels of approximation (LoA) (in kN).

Model	$R_{model}(f_{ym}, f_{cm})$	μ_R*	$R_{d,prob}$	$R_{d,PFM}$	$R_{d,ECoV}$
EC2	558	676	363	395	394
LoA1	387	669	332	306	273
LoA2	436	620	327	363	327
LoA3	477	550	306	366	327

*Obtained as the mean value of the probabilistic model, including the effect of model uncertainties.

strut angle is fixed to 30°, the EC2 model leads to 387 kN. The test configuration (a/d = 2.15) likely leads to the so-called shear-bond failure, O'Brien and Dixon (2012), for which the alternative EC2 approach for short shear spans with direct strut action may be used.

Also provided in Table 3 are the mean values μ_R of the probabilistic model that include the effect of model uncertainties. It is immediately realized that except for LoA3, these are less informative indications due to the mixture of two failure models.

For each shear model, Table 3 further gives the set of estimates of design values:

- $R_{d,prob}$ obtained from the probabilistic model as a fractile corresponding to probability $p_d = \Phi(-\alpha_R \beta_t) = \Phi(-0.8 \times 3.8) = 0.00112$ with Φ denoting the cumulative distribution function of the standardized normal distribution.
- $R_{d,PFM} = R_{model}(f_{yk}/\gamma_S, f_{ck}/\gamma_C)$ in which model uncertainties are not explicitly accounted for; they are deemed to be indirectly considered through the partial factors γ_S and γ_C.
- $R_{d,ECoV}$ obtained using the approach outlined in Section 3. In this case, the inclusion of model uncertainty is less straightforward. The resistances based on mean or characteristic and more importantly on design values may relate to different failure modes (see the following section). This is why the effect of model uncertainty is approximated by applying the model uncertainty factor γ_{Rd} = 1.08 according to *fib* COM3 TG3.1 (2016) and the coefficient of variation V_{Rd} is neglected in Eq. (11). Detailed analysis of this issue is beyond the scope of the submitted contribution.

The results obtained in this section can be summarized as follows:

- LoA2 and LoA3 provide unbiased estimates—$R_{model}(f_{ym}, f_{cm})$—close to the test result and seem to well describe the shear capacity of the tested beam. These two models leads to 'probabilistic' design values, $R_{d,prob}$, in the range from 306–327 kN that well correspond to the first estimates of the design value obtained in Section 4.
- For these two models, the partial factor method, $R_{d,PFM} \approx 365$ kN, seem to overestimate the design value by about 10–20%. The ECoV leads in this case to a realistic estimate of the design value.
- LoA1 as a simplified alternative to the upper levels is expected to yield conservative estimates which is confirmed by this example, particularly by the $R_{d,ECoV}$ –value.
- All the EC2 predictions, $R_{d,prob}$ - $R_{d,PFM}$ - $R_{d,ECoV}$, overestimate the design value, likely due to the low a/d ratio and possible shear-bond failure.

5.3 *Parametric study for shear reinforcement ratio—pilot investigations*

A parametric study is further conducted to compare the design values obtained by the partial factor method, $R_{d,PFM}$, and the ECoV, $R_{d,ECoV}$, with the design value assessed as a 1.12‰ fractile, $R_{d,prob}$. Using the models of basic variables given in Table 1, shear reinforcement ratio ρ_w is varied to analyse the beams failing by stirrups yielding (low values of ρ_w) or by concrete crushing (high ρ_w). In this pilot investigation, the EC2 model is applied only.

Figure 7 displays the probability density function of shear resistance based on the EC2 model and the individual contributions of stirrups and concrete. It can be observed that low shear strengths, R < 500 kN—that are of interest in design in this case—are dominated by concrete properties while the resistances around the mean value and upper values tend to follow the probability density function of stirrups yielding.

Figure 8 shows the ratios of design values, $R_{d,PFM}/R_{d,prob}$ and $R_{d,ECoV}/R_{d,prob}$, as a function of shear reinforcement ratio, 1‰ ≤ ρ_w ≤ 1%. The

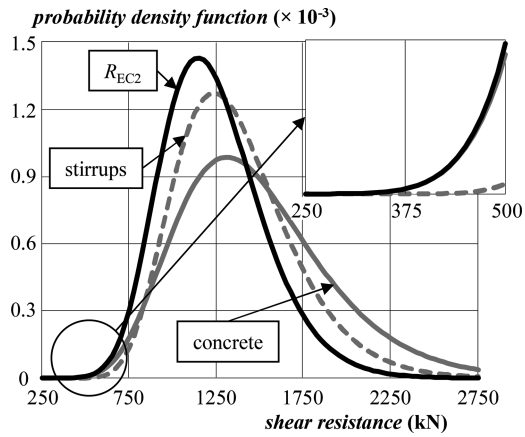

Figure 7. Probability density function of shear resistance according to EC2 and the contributions of stirrups and concrete (ρ_w = 1.5%).

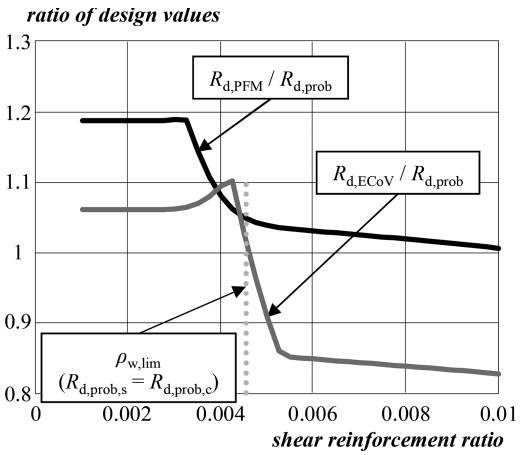

Figure 8. Ratios of design values as a function of shear reinforcement ratio.

EC2 model seems to overestimate the design value by ~20% for low ρ_w and provides estimates very close to $R_{d,prob}$ for high ρ_w's. This finding, however, should not be generalised as the test for which the EC2 model overestimates shear strength is intentionally selected.

Also the ECoV yields to non-conservative estimates for stirrups yielding (up to 10%) and tends to become conservative for concrete crushing (up to 15%). Particularly for the latter case, the difference between $R_{d,ECoV}$ and $R_{d,prob}$ is attributable to the different model uncertainty characteristics; the simplified treatment of the ECoV using $\gamma_{Rd} = 1.08$ adopted in Section 5.2 insufficiently accounts for vast model uncertainties related to concrete crushing (Table 2).

Figure 8 clearly portrays the transition zone, $4‰ \le \rho_w \le 6‰$, in which the ECoV changes from the stirrups to concrete failure mode. It is interesting to note that an incorrect failure mode is detected by the ECoV for a wide range of ρ_w:

- The analysis based on mean values: the concrete crushing dominates for $\rho_w > 1.8\%$ whilst the limiting value of 4.5‰ is indicated by comparing the 1.12‰ fractiles of resistances based on a separate contributions of stirrups and concrete.
- The analysis based on characteristic values: the concrete crushing dominates for $\rho_w > 1.1\%$ and, again, a wrong failure mode is indicated for the range 0.45–1.1%.

These observations suggest that a due care needs to be taken to adequately include model uncertainties that may differ for various failure modes while the effect of the transition area in which some of failure modes are identified incorrectly is less important. Further investigations are necessary, however.

It is important to keep in mind that all the results are sensitive to the changes in the alpha factor that reflects the importance of uncertainties in resistance and load parameters on structural reliability.

6 DESIGN STRENGTH BY NONLINEAR FE ANALYSIS

In order to evaluate the performance of the investigated safety formats for structural assessment by nonlinear analysis, the same example is analyzed using nonlinear simulation software ATENA (Červenka et al. 2017). The used finite element mesh and the reinforcement model are shown in Figure 9. The mesh size in this model is approximately 40 mm, which corresponds to minimal size, for which concrete can be still treated as a homogeneous material. For smaller mesh sizes it would be questionable to use the macroscopic material properties.

Embedded reinforcement approach is used to model reinforcement using truss elements. The finite element mesh is composed of linear isoparametric brick elements for the beam. For the load and support plates elastic material is assumed with tetrahedral finite elements.

First the design strength is calculated by nonlinear analysis using the ECoV method and PSF method. For ECoV method two analyses are necessary with mean and characteristic properties. For PSF method the material parameters used in the nonlinear analysis are divided by the appropriate safety factors (1.5 for concrete and 1.15 for steel). The used material parameters are listed in Table 4. The calculated load-displacement curves are shown in Figure 13.

It is interesting to note that the mean analysis shows a very good agreement with the experiment for both the strength (475 kN vs. 460 kN exp.) as well deflection (15/15 mm) at failure. Figure 11 shows that for the mean analysis the dominant failure mode is yielding of reinforcement, while for

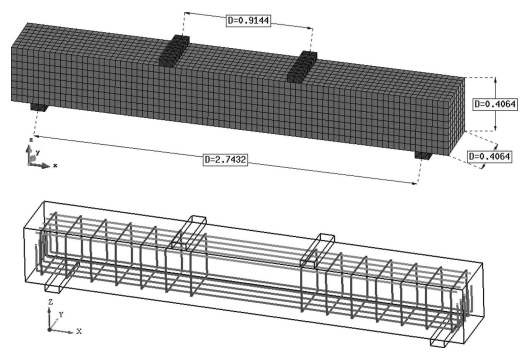

Figure 9. FE mesh and reinforcement model in the beam W1 tested by Anderson & Ramirez (1989).

Table 4. ECoV evaluation by ATENA nonlinear analysis.

Concrete	Mean	Char	Design
E [MPa]	30718	30718	30718
ft [MPa]	2.3	1.61	1.07
f_c [MPa]	29.2	21.2	14.1
G_F [N/m]	134	126	84
Steel			
E [MPa]	200 000	200 000	200 000
f_y [MPa]	455	414	360
f_t [MPa]	569	518	450
εlim [–]	0.14	0.14	0.14
Beam W1—peak load values			
V_{ATENA} [kN]	475	411	340
Experiment	460		
ECoV evaluation based on Eq. (10) to (13)			
V_R		0.0877	
γ_R		1.31	
$V_{d\text{-}ECOV}$ [kN]		362	

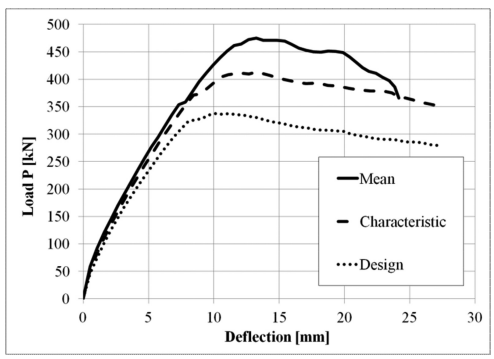

Figure 10. Comparison of mean, characteristic and design load-displacement curves.

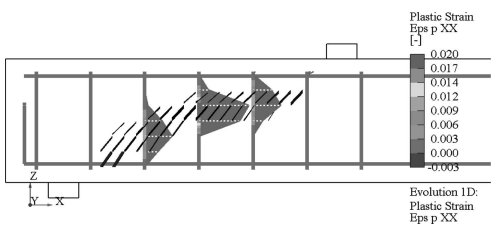

Figure 11. Stirrups yielding at maximal load for mean analysis.

characteristic and design analyses the failure mode is dominated by crushing of concrete as can be seen from Figure 12.

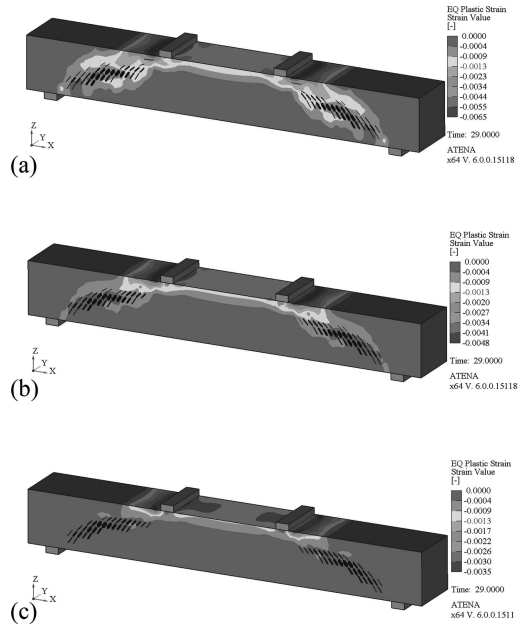

Figure 12. Extend of concrete compressive crushing at peak load for design (a), characteristic (b) and mean (c) analyses.

This indicates that the selected example exhibits the expected switch between the failure mode by steel and concrete depending on the assumptions made about the material parameters. However, the failure mode separation is not as strong as it was indicated by the simplified approaches in Section 5. For the mean analysis the failure mode is dominated by stirrups yielding however the compressive crushing is present as well. Similar behavior was observed in characteristic and PSF analyses where concrete crushing is dominant, but stirrup yielding takes place as well.

The results obtained by ECoV method and PSF method were compared with a fully probabilistic analysis using the probabilistic extension of ATENA, i.e. software SARA (Bergmeister et al. 2009). This software uses a probabilistic sampling approach based on LHS to perform effective evaluation of structural reliability assuming the randomness and uncertainty in the input parameters. Table 5 summarizes the selected material parameters for this randomization process.

Only the most important strength parameters are considered to have a statistical distribution. The other material parameters are considered to be deterministic. The coefficient of variation was selected such that the characteristic value (i.e. 95% probability quantile) corresponds to the value assumed in the previous ECoV analysis (see Table 4). The LHS analysis was performed with

Table 5. Statistical parameters for probabilistic analysis.

Parameter	Mean	CoV	Distribution
Concrete			
f_t [MPa]	2.3	0.207	Lognormal (2 par.)
f_c [MPa]	29.2	0.186	Lognormal (2 par.)
G_F [N/m]	134	0.325	Weibul (2 par.)
Steel			
fy	455	0.057	Lognormal (2 par.)

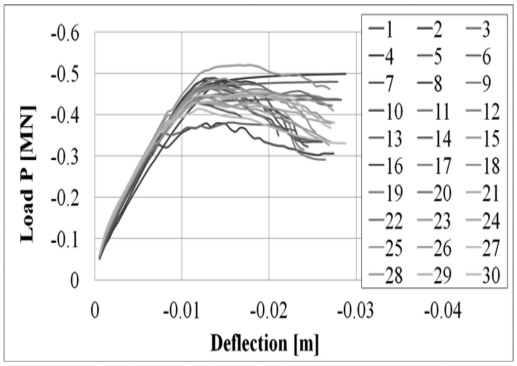

Figure 13. Load-displacement diagrams for fully probabilistic assessment.

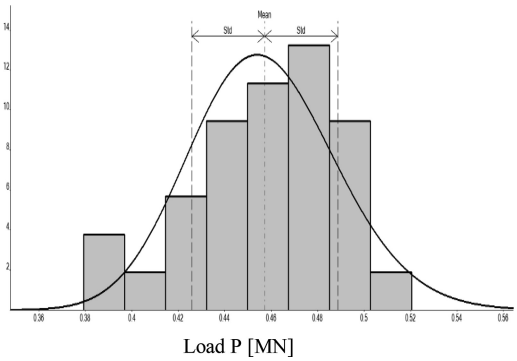

Figure 14. Histogram of beam strength (i.e. peak loads *P*) from probabilistic analysis.

30 samples, which is the minimum value proposed in SARA software. The calculated load-displacement curves are shown in Figure 13. It is possible to observe that some of the analyses clearly show a ductile behaviour indicating a failure by reinforcement yielding while other analyses show softening behavior, which is an indication of concrete crushing failure or combination of both failure modes.

Figure 14 shows the histogram of peak loads calculated by the probabilistic analyses as well as its approximation by lognormal distribution.

Table 6. Design strength calculated by probabilistic analysis.

Strength	Values
Mean [kN]	457
Char [kN]	407
Experiment [kN]	460
Design [kN]—10-3 probability	369
Design [kN]—ECOV method (see Table 4)	362
Design [kN]—PSF method	340

From this approximated lognormal distribution the design strength can be calculated assuming the design resistance probability of 10^{-3}, which corresponds the overall probability of failure 10^{-6} as it is assumed by Eurocode EN 1990.

The final comparison of the design strength values for the investigated beam by the probabilistic approach as well as ECoV and PSF methods is summarized in Table 6. It is possible to observe that the mean value obtained by the probabilistic analysis is again very close to the experimental value. The design strength calculated by the probabilistic analysis is very close to the value from ECoV method. The PSF approach provides the lowest value of the design strength.

7 CONCLUSIONS

The global assessment by nonlinear analysis is compared with analytical solutions based on standard Eurocode and Model Code 2010 shear formulas for the beam for which different failure modes are predicted using mean and characteristic values. The study indicates that different failure modes, either due to failure of concrete or due to reinforcement yielding, do not have significant effects on the design value of resistance calculated by ECoV method. This is especially true considering the overall uncertainties involved in reinforced concrete analysis and design. Furthermore in case of resistance models based on nonlinear FE analysis a clear identification of an obtained failure mode may not be always straightforward due to the common interaction of various failure modes involved.

The partial factor approach (PSF) for the global structural assessment by nonlinear analysis provides the most conservative results even in this investigated example involving various failure modes (Table 6). This is in agreement with the previous investigations reported in Červenka (2008). The comparison of the design values obtained by the various approaches reveals the benefit gained when using an advanced FEM model even for the example relatively well suited for applications of simplified methods:

– The analysis using ATENA leads to design values in the range of 340–360 kN (Table 6).
– The design values estimated directly from the test result along with a conservative estimate of CoV of resistance (Section 4) or by a full probabilistic model based on *fib* Levels of Approximation 2 and 3 seem to vary from 300–330 kN.

The pilot study suggests that it is necessary to adequately take into consideration model uncertainties that may differ for various failure modes while the effect of the transition area in which some of failure modes are identified incorrectly is less important.

Further investigations are necessary, however. It is important to keep in mind that all the results are sensitive to the changes in the sensitivity factor that reflects the importance of uncertainties in resistance and load parameters on structural reliability.

ACKNOWLEDGEMENTS

This work has been supported by the Czech Science Foundation within the project 16-04132S "Epistemic uncertainties in crack models in reinforced concrete structures".

REFERENCES

Anderson, N.S. & Ramirez, J.A. 1989. Detailing of stirrup reinforcement. *ACI Structural Journal* 86(5): 507–515.

Bažant, Z.P. & Oh, B.H., 1983. Crack band theory for fracture of concrete. *Materials and Structures, RILEM* 16 (3), 155–177.

Bentz, E.C., Vecchio, F.J., Collins, M.P. 2006. Simplified Modified Compression Field Theory for Calculating Shear Strength of Reinforced Concrete Elements. ACI Material Journal, Jul/Aug 2006.

Bergmeister, K., Novák, D., Pukl, R., Červenka, V., 2009, Structural assessment and reliability analysis for existing engineering structures, theoretical background, Structure and Infrastructure Engineering, Vol. 5, Issue 4, August 2009, pp. 267–275.

Červenka, J., Červenka, V., Laserna, S., 2014, On finite element modelling of compressive failure in brittle materials, *Computational Modeling of Concrete Structures*. Bicanic et al. (Eds), Euro-C 2014, St. Anton, Austria, Tazlor & Francis Group, London, ISBN 978-1-138-00145-9, pp. 273–281.

Červenka J. & Papanikolaou V. 2008. Three Dimensional Combined Fracture-Plastic Material Model for Concrete. *Int Journal of Plasticity*. 24:2192–220.

Červenka, V., 2008, Global Safety Format for Nonlinear Calculation of Reinforced Concrete. Beton- und Stahlbetonbau 103, Special Edition, Ernst & Sohn. pp. 37–42.

Červenka, V., Červenka, J. & Jendele, L. 2017. *ATENA Program Documentation, Part 1: Theory, 2017*, Cervenka Consulting s.r.o., 2013, www.cervenka.cz.

Červenka, V., Margoldová, J., 1995, Tension Stiffening Effect in Smeared Crack Model, *Engineering Mechanics*, Stain F(Sture (Eds), Proc. 10th Conf., Boulder, Colorado, pp. 655–658.

Cervenka, V. 2013. Reliability-based non-linear analysis according to *fib* Model Code 2010. *Structural Concrete* 14(1): 19–28.

EN 1990: 2002. *Eurocode - Basis of structural design*. Brussels: CEN.

EN 1992-1-1: 2004. *Design of concrete structures - Part 1-1: General rules and rules for buildings*. Brussels: CEN.

EN 1992-2: 2005. *Eurocode 2 - Design of concrete structures - Part 2: Concrete bridges - Design and detailing rules*. Brussels: CEN.

fib 2013. *fib Model Code for Concrete Structures 2010*. Lausanne: *fib*.

fib 2016. *fib*-news: Structural Concrete 1/2016. *Structural Concrete* 17(1): 125–131.

fib COM3 TG3.1 2016. *Partial Factor Methods for Existing Structures (fib bulletin 80, recommendation). fib*.

Holicky, M., Sykora, M. & Retief, J.V. 2016. Assessment of Model Uncertainties for Structural Resistance. *Probabilistic Engineering Mechanics* 45(-): 188–197.

Hordijk, D.D. 1991. *Local Approach to Fatigue of Concrete.* Ph.D. Thesis. Delft University of Technology.

Krejsa, J., Holicky, M. & Sykora, M. 2014. Uncertainty in shear resistance of reinforced concrete beams with stirrups – comparison of EN 1992-1-1 and *fib* MC 2010 approaches. *Transactions of the VSB - Technical University of Ostrava, Civil Engineering Series* 14(1): 1–9.

Menetrey, P. & Willam, K.J. 1995. Triaxial Failure Criterion for Concrete and its Generalization. *ACI Structural Journal*. 1995;92:311–8.

Model Code 2010. *First complete draft. Volume 1 - fib bulletin 55. Volume 2 - fib bulletin 56*. ISSN 1562-3610. ISBN 978-2-88394-095-6. International Federation for Structural Concrete (*fib*), Lausanne, Switzerland. 2010.

O'Brien E., Dixon A. & Sheils E. 2012. Reinforced and Prestressed Concrete Design to EC2, CRC Presss.

Schlune, H., Plos, M. & Gylltoft, K. 2011. Safety formats for nonlinear analysis tested on concrete beams subjected to shear forces and bending moments. *Engineering Structures* 33(8): 2350–2356.

Schlune, H., Plos, M. & Gylltoft, K. 2012. Safety formats for non-linear analysis of concrete structures. *Magazine of Concrete Research* 64(7): 563–574.

Slobbe A.T., Hendriks M.A.N., Rots J.G., 2013, Systematic assessment of directional mesh bias with periodic boundary conditions: Applied to the crack band model. Engineering Fracture Mechanics, V. 109, September 2013, Pages 186–208.

Sykora, M., Holicky, M., Prieto, M. & Tanner, P. 2015. Uncertainties in resistance models for sound and corrosion-damaged RC structures according to EN 1992-1-1. *Materials and Structures* 48(10): 3415–3430.

Sykora, M., Krejsa, J., Mlcoch, J., Prieto, M. & Tanner, P. 2018. Uncertainty in shear resistance models of reinforced concrete beams according to fib MC2010 (in press); *In: Structural Concrete* – Journal of fib.

Computational Modelling of Concrete Structures – Meschke, Pichler & Rots (Eds)
© 2018 Taylor & Francis Group, London, ISBN 978-1-138-74117-1

Modelling boundary conditions imposed by loads and supports in 3D D-regions

C. Meléndez & P.F. Miguel
Instituto de Ciencia y Tecnología del Hormigón, Universitat Politècnica de València, València, Spain

ABSTRACT: The analysis and design of D-regions has traditionally been contentious and their behaviour misunderstood; this is specially true for D-regions exhibiting a 3D behaviour. Finite element analysis has become a valuable tool to understand better the response of these critical regions, which ultimately has led to more efficient designs. The fact that D-regions are characterised by complex internal stress fields gives special relevance to the definition of certain aspects of the finite element model. In particular, the imposed boundary conditions to account for loads and supports significantly affects the global results and, therefore, their definition must be done with care and as realistically as possible. The solution of including load and support elements into the finite element model is tedious and may result in the distortion of the preferred mesh. An alternative approach is presented in this document based on the work undertaken by the authors in the development of a nonlinear finite element-based tool oriented towards the analysis and design of 3D D-regions. Special load and support models were implemented permitting to omit these elements from the model but considering their effect on the global response by imposing appropriate boundary conditions. These models are based on the principles of finite element modelling and static condensation. One example of their application to a pile cap foundation is shown at the end of the document to highlight the influence of the defined boundary conditions on the predicted response; results show strength variations of up to 100% depending on which model is adopted.

1 INTRODUCTION

Concrete structures can be subdivided into two types of regions: (i) those in which the Bernoulli hypothesis of plane strain distribution is assumed to be valid (known as B or Bernoulli regions) and (ii) those in which the strain distribution is nonlinear (referred to as D- or discontinuity regions).

D-regions are caused by abrupt changes in the geometry of the structure and/or concentrated loads and are characterised by complex stress fields. The design of D-regions was traditionally contentious and mainly supported on rules of thumb or judgement based on past experience. Two alternative methods, the strut-and-tie method (Schlaich, Schafer, & Jennewein 1987) and the stress field method (Muttoni, Schwartz, & Thürlimann 1997), shed some light on the design of these critical regions. However, their application is not always straightforward and free from difficulties (Tjhin & Kuchma 2002). Additional barriers are found when the element has a 3D behaviour (Reineck, Lourenço, Almeida, & Haugerud 2011).

Finite element analysis can complement and facilitate the application of the strut-and-tie and the stress field method, especially when dealing with those more complex D-regions and/or when more refined predictions or designs are required. Linear-elastic stress fields can be helpful to propose initial strut-and-tie and stress field models; and nonlinear stress fields facilitate a better understanding of the resisting mechanism and the internal stress flow near the ultimate limit state from which strut-and-tie and stress field models can be derived. Nonlinear finite element analysis alone is a promising alternative for the design of D-regions (Amini Najafian & Vollum 2013) having advantages over the strut-and-tie and stress field methods, such as permitting a greater level of detail and the prediction of the nonlinear response.

Finite element analysis of reinforced concrete structures has spread in the last decades with the development of more versatile and user-friendlier finite element software packages. In most cases these tools are used for the analysis and/or design of B-regions; differences between B- and D-regions are such that some additional aspects must be acknowledged and considered when developing a finite element model for the latter. In particular, the effect of the boundary conditions due to loads and supports on the final analysis results differs significantly: in B-regions they affect the stress field in the vicinity of loads and supports, but do not influence significantly the global results as long as the locations and principal restraint directions are defined appropriately; in D-regions they affect the stress field in the vicinity of the boundary surfaces, but also the stress field inside the

entire element and, hence, its response. Therefore, the definition of the boundary conditions must be done with care when modelling D-regions.

While concrete material modelling has gained the interest of many researchers over the years, the definition of boundary conditions has attracted less attention. Simplified approaches such as fixing the degrees of freedom at support locations or assuming concentrated (point) loads are frequent. These approaches can be adequate when analysing relatively large elements or structures where the stress field induced near loads and supports is dimmed with distance, but not for D-regions. One approach that can be followed to properly consider the boundary conditions imposed by loads and supports is to include these elements explicitly in the finite element model. This solution can be tedious, cannot be considered as user-friendly and may involve modifying the original, preferred mesh of the region object of study.

This document describes an approach to account for the boundary conditions imposed by loads and support elements in D-regions in a comprehensive and realistic manner, without having to define them explicitly and, hence, facilitating the development of the finite element model. Loads and support models implemented into the nonlinear finite element-based tool FESCA 3D (Meléndez 2017) will be described. Principles of finite element modelling and static condensation are applied to obtain the different models proposed. Load modelling is treated first: the procedure to determine the equivalent nodal forces of a distributed load and the condensed stiffness matrix of a loading substructure, regardless of the geometry of the finite element mesh, is described. Support modelling is considered afterwards: the fundamentals of the implemented uniform-stress support model and flexible support model are presented. One example of its application to a pile cap foundation is shown at the end of the document to highlight the influence of load and support modelling on the predicted response; results show strength variations of up to 100% depending on which model is adopted.

2 D-REGIONS AND IMPORTANCE OF BOUNDARY CONDITIONS

D-regions appear near abrupt changes in geometry (geometrical discontinuity) and/or concentrated loads (static discontinuity). The disturbed stress field caused by these discontinuities is "stabilised" at further sections. According to St. Venantś principle the length of the dispersion zone is approximately equal to the width or depth of the element, which delimits the extension of the D-region from the source of discontinuity and where the Bernoulli hypothesis is valid again. Axial forces, shear forces and bending moments at the boundary surfaces constitute actual loads for the D-region. The stress field resulting from these forces at the boundary sections can be determined considering that the hypothesis of plane strain distribution is valid.

In some cases the discontinuity is such compared to the dimensions of the whole element that the entire structural element is a D-region in itself (generalised discontinuity). That is the case of deep beams, deep pile caps or walls with openings. In these cases the hypothesis of plane strain distribution is not valid in any section of the element. For these elements loads are in general transferred by other structural elements supported on them (e.g. slabs, columns,...). The stress field resulting at the contact surfaces depends on the magnitude and geometry of the loading substructure, but also on the stiffnesses of both structural elements.

In both cases described above the dimensions of the boundary surfaces are of the same order of magnitude as the whole D-region. Therefore, the stress fields at these sections have an important effect on the stress flow resulting inside the element and, hence, on the global response. This effect can be seen clearly by analysing a strut-and-tie model and how much the displacement of a node affects the forces of struts and ties through the variation of the strut angles; a variation of the stress field induced by the boundary conditions is equivalent to a variation of the resultant locations and the disposition of the truss nodes.

3 LOAD MODELLING

External loads in finite element modelling are considered by means of nodal forces. Loads can be considered as (i) punctual or (ii) distributed. The former is a simple approach that permits the direct introduction of loads into the nodal force vector, butis not recommended in general when using 2D and 3D finite elements as it leads to stress concentration in the vicinity of the load; moreover, it does not account for the load dimensions, an important parameter in D-regions.

If the load is considered as distributed, the total applied force needs to be transformed first into a system of equivalent nodal forces. The value of these nodal forces depends not only on the magnitude and geometry of the load, but also on the geometry of the finite element mesh. A simple approach to obtain the value of these nodal forces is to assume that the total load is divided equally by the number of nodes located inside the loading area; this method does not necessarily lead to the desired stress field at the loading surface. A more precise approach is necessary for modelling D-regions to guarantee that the stress field induced at the loading surface by the obtained nodal forces

simulates the actual stress condition. This involves considering not only the geometry of the loading substructure, but also its stiffness.

3.1 *Determination of the equivalent nodal forces of a distributed load*

Principles of the finite element method can be used to calculate the magnitude of the nodal forces equivalent to a distributed load. Given a distributed load $q(x,y)$ acting over an area S_q, the equivalent nodal forces for a particular finite element placed inside this area $\{f^e_{ext}\}$ can be calculated as:

$$\{f^e_{ext}\} = \int\int_{S^e_q} q(x,y)\{N(x,y)\}dxdy \tag{1}$$

where $\{N\}$ is a vector containing the shape functions of the finite element and S^e_q the portion of the loading area placed inside the finite element.

If the load is uniformly distributed as it is common in practice and the integration is undertaken in the natural coordinate system of the finite element (Figure 1) equation 1 can be written as:

$$\{f^e_{ext}\} = q\int\int_{S^e_q} \{N(\xi,\eta)\}|J(\xi,\eta)|d\xi d\eta \tag{2}$$

where ξ,η are the natural coordinates of the finite element, and $|J(\xi,\eta)|$ is the determinant of the Jacobian matrix given by:

$$[J] = \begin{bmatrix} \frac{\partial x}{\partial \xi}\frac{\partial y}{\partial \xi} \\ \frac{\partial x}{\partial \eta}\frac{\partial y}{\partial \eta} \end{bmatrix} = \begin{bmatrix} x_i\frac{\partial N_i}{\partial \xi} y_i\frac{\partial N_i}{\partial \xi} \\ x_i\frac{\partial N_i}{\partial \eta} y_i\frac{\partial N_i}{\partial \eta} \end{bmatrix} \tag{3}$$

The integration domain S^e_q is delimited by the edges of the finite element and the external perimeter of the load area. The latter must be expressed in the natural coordinate system (ξ,η): for rectangular areas the integration domain in the natural coordinate system can be obtained from the transformation of the intersecting points between the finite element edges and the perimeter of the load area; for circular geometries a transformation of the circumferential equation is needed (Figure 2). The latter can be derived considering that the coordinates of any point inside the finite element can be expressed

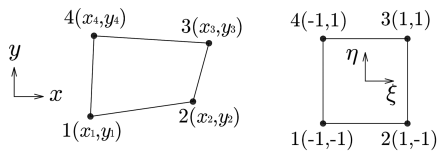

(a) Physical coordinates (b) Natural coordinates

Figure 1. Coordinates mapping for quadrilateral element.

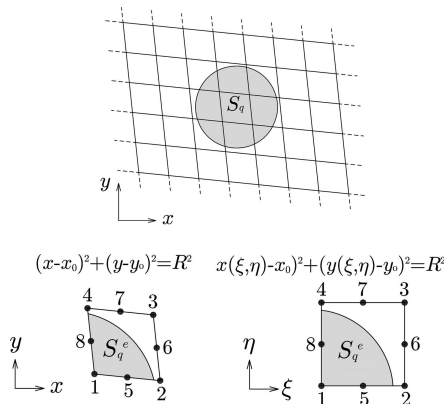

Figure 2. Determination of equivalent nodal forces of a distributed load.

as a function of the finite element nodal coordinates (x_i,y_i) and the finite element shape functions $N_i(\xi,\eta)$ as:

$$\begin{aligned} x &= N_i(\xi,\eta)x_i = x(\xi,\eta) \\ y &= N_i(\xi,\eta)y_i = y(\xi,\eta) \end{aligned} \tag{4}$$

Therefore, the equation of a circumference can be written in terms of the natural coordinates (ξ,η) as:

$$\left(x(\xi,\eta) - x_0^2\right) + \left(y(\xi,\eta) - y_0\right) = R^2 \tag{5}$$

The integration domain can then be obtained by solving ξ as a function of η in equation 5, or vice versa.

For reference, the finite element equivalent nodal forces for an 8-node quadrilateral subjected to a uniform load q which acts on its entire area are equal to:

$$\begin{aligned} f^{e,i}_{ext} &= -\frac{1}{12}A^e q \text{ for corner nodes } i = 1,2,3,4 \\ f^{e,i}_{ext} &= \frac{1}{3}A^e q \text{ for midside nodes } i = 5,6,7,8 \end{aligned} \tag{6}$$

where A^e is the area of the eight-node quadrilateral. Negative values of the nodal forces at the corners must be noticed.

Equivalent nodal forces computed for every finite element which is located fully or partly inside the loading area are then assembled into the global nodal force vector.

3.2 *Consideration of the stiffness of loading substructures through static condensation*

When the load is applied through an auxiliary element (e.g. a stub column), the stress distribution

which is actually being transmitted to the main element/structure can differ from the one applied at the free extreme. The difference between both distributions depends on the stiffnesses of the loading element and the main element and must be considered if a sound internal stress field is to be obtained inside the D-region. This statement seems to indicate that it is necessary to include loading substructures into the finite element model. An alternative, more straightforward approach based on the principles of static condensation can be proposed.

The concept of static condensation permits the reduction of the number of degrees of freedom of a system and is useful when dealing with structural systems which can be subdivided into different substructures. For a certain substructure *sub*, degrees of freedom can be classified as primary (master), *m*, or secondary (to-be-condensed), *c*. The former will be in general the degrees of freedom which connect the substructure to the other elements. The stiffness system of equation can be written as:

$$\begin{bmatrix} \{F_m^{sub}\} \\ \{F_c^{sub}\} \end{bmatrix} = \begin{bmatrix} K_{mm}^{sub} & K_{mc}^{sub} \\ K_{cm}^{sub} & K_{cc}^{sub} \end{bmatrix} \begin{bmatrix} \{r_m^{sub}\} \\ \{r_c^{sub}\} \end{bmatrix} \tag{7}$$

from which:

$$\{F_m^{sub}\} = [K_{mm}^{sub}]\{r_m^{sub}\} + [K_{mc}^{sub}]\{r_c^{sub}\} \tag{8}$$

$$\{F_c^{sub}\} = [K_{cm}^{sub}]\{r_m^{sub}\} + [K_{cc}^{sub}]\{r_c^{sub}\} \tag{9}$$

The to-be-condensed displacement vector $\{r_c^{sub}\}$ can be solved from equation 9:

$$\{r_c^{sub}\} = [K_{cc}^{sub}]^{-1}\left(\{F_c^{sub}\} - [K_{cm}^{sub}]\{r_m^{sub}\}\right) \tag{10}$$

and can then be substituted into equation 8 giving the reduced system of equations:

$$\{F_m^{sub}\} = \left([K_{mm}^{sub}] - [K_{mc}^{sub}][K_{cc}^{sub}]^{-1}[K_{cm}^{sub}]\right)\{r_m^{sub}\} + [K_{mc}^{sub}][K_{cc}^{sub}]^{-1}\{F_c^{sub}\} \tag{11}$$

where the displacements of the condensed degrees of freedom $\{r_c^{sub}\}$ have been eliminated. Equation 11 can also be written as:

$$\{\overline{F}_m^{sub}\} = [\overline{K}^{sub}]\{r_m^{sub}\} \tag{12}$$

If needed, the displacements of the condensed degrees of freedom $\{r_c^{sub}\}$ can be obtained from equation 10 once the displacements of the master degrees of freedom $\{r_m^{sub}\}$ have been determined.

The concept of static condensation can be used to account for the effect of the loading substructure in the stiffness and stress field of a D-region without having to introduce it explicitly into the finite element model. This approach was considered in FESCA 3D (Meléndez 2017), where in addition the nonlinear behaviour of loading substructures during the loading history was neglected; this assumption is appropriate in many cases for elements which are expected to be under compression and permits the use of the same condensed stiffness matrix and condensed force vector throughout the whole analysis.

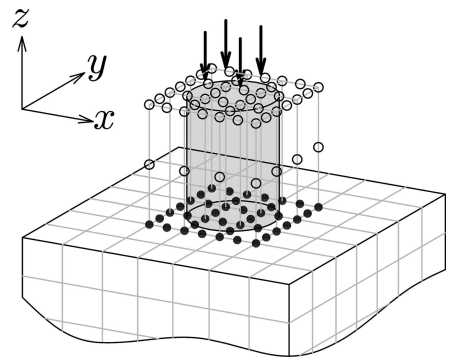

Figure 3. Static condensation of circular loading substructure.

FESCA 3D proceeds as follows. First, it builds an internal finite element mesh for the loading substructure, which considers the defined load area, the input height of the substructure and the geometry of the finite element mesh of the main element (Figure 3). Then the stiffness of the internally-generated finite elements is computed, assuming that the material is isotropic; the actual dimensions of the load element are considered and, thus, numerical integration is only performed in the load area domain. Nodal forces are applied at the upper degrees of freedom of the substructure; the magnitude of these forces is determined assuming a uniform distribution as described in the previous section. After this the stiffness matrices and force vectors of the internally-generated finite elements are assembled into the stiffness system of equations of the substructure. Then the condensed stiffness matrix and the condensed force vector can be determined; the master nodes are those in contact with the main element. Finally $[\overline{K}^{sub}]$ and $\{\overline{F}^{sub}\}$ are assembled accordingly into the global stiffness matrix and the global external nodal force vector, respectively.

4 SUPPORT MODELLING

Supports induce reaction forces on the structure, the magnitude of which can only be determined after free displacements are obtained. Similarly to loads, the resultant stress distribution at support areas due to reaction forces affects the internal

stress field and hence the predicted results, especially when the dimensions of the support areas are of the same order of magnitude as the dimensions of the whole element. To obtain a realistic prediction it is important that the stress distribution induced by the defined support condition is similar to the actual one.

It is a common approach in finite element analysis to define the support conditions just by setting the displacements of the corresponding degrees of freedom of the nodes located inside the support area to zero. This implies treating supports as perfectly rigid elements. This assumption is realistic in only very few cases, but can be admissible for elements where the stress distribution at the supports is not of importance for the global response of the element. Otherwise, consideration of the stiffnesses of the support elements and its effect on the stress field is relevant and should be considered in the finite element model. Special support models were integrated in FESCA 3D to permit a simple, but realistic modelling of the boundary conditions imposed by them.

4.1 *Uniform-stress support condition*

This support type enforces a uniform stress distribution at the support area, regardless of the geometry of the finite element mesh. To obtain this the global stiffness matrix of the system is modified to enforce proportionality between nodal reactions.

If the stress at the support area is to be uniform, the induced nodal reactions must be proportional to the equivalent nodal forces which would be obtained for a uniform load with the same geometry as the support. The concept of nodal tributary area can be used to enforce this. The tributary area of a node is defined as the ratio between the nodal equivalent force caused by a uniform load, and the total load. This ratio is a function of the geometry of the load and the finite element mesh and does not depend on the magnitude of the load. The tributary area of a node i can be obtained similarly to the equivalent nodal forces of a uniform load (equation 1) as:

$$A^i_{trib} = \sum_{e=1}^{n} \int\int_{S^e_b} N^e_i(\xi,\eta)\left|J^e(\xi,\eta)\right| d\xi d\eta \qquad (13)$$

where n is the number of finite elements the node belongs to and that are "touched" by the support area, S^e_b refers to the support area located inside the corresponding finite element and N^e_i is the shape function of the node whose tributary area is being obtained.

The nodal tributary area needs to be obtained for all nodes which form part of the finite elements which are "touched" by the support area, even if that particular node is not enclosed inside the support perimeter. This calculation can derive in negative values of A^i_{trib}.

Once the tributary nodal areas are obtained, the global stiffness matrix of the system is modified to enforce proportionality between nodal reactions and, hence, induce a uniform stress distribution at the support area. This modification is done as follows:

$$F_{3(i-1)+j} = K_{3(i-1)+j,k} r_k + \frac{A^i_{trib}}{A_{sup}} C_j r_k \approx$$
$$\approx \frac{A^i_{trib}}{A_{sup}} \left(C_j r_k\right) \propto \frac{A^i_{tri}}{A_{sup}} \qquad (14)$$

where A_{sup} is the total area of the support, i is the node number, j the degree of freedom to which the support restrain applies, C_j is a constant large enough to dismiss the term $K_{3(i-1)+1,k} r_k$, and r_k is the displacement of a degree of freedom of reference. If the node of reference is the centre of the support, the constant C_j in equation 14 gains a physical meaning: it is the stiffness of an equivalent spring which substitutes the support. Indeed, the displacement of the central node multiplied by the stiffness value C_j gives the total reaction. This reaction is distributed between the support nodes according to the ratio A^i_{trib}/A_{sup}, enforcing a uniform stress distribution. Taking the centre of the support as reference also permits the simulation of the rotation around the centre of the support, which is a typical condition of pinned supports.

In general the adoption of any arbitrary, relatively large value for C_j is appropriate. Three stiffness values can be defined for every support. Furthermore, directions of action do not necessarily need to coincide with the global directions (x, y, z), because the stiffness matrix is transformed into the global coordinate system before being assembled into the global stiffness matrix.

4.2 *Flexible support condition*

This approach is based on the automatic development of an internal finite element mesh for the support elements which is then assembled into the global finite element model (Figure 4). The procedure is similar to that presented for modelling loading substructures, although in this case the concept of static condensation cannot be used because reactions and, hence, $\{F_c\}$ and $\{F_m\}$ are unknown a priori. Therefore, the stiffness calculated for the support substructure is assembled into the global stiffness system, whose size is increased to incorporate the new degrees of freedom.

The stiffness matrix of the support substructure is obtained by assembling accordingly the stiffness matrices of the internally-generated finite elements. The actual dimensions of the load element are considered and numerical integration is only performed in the support area domain. An isotropic, elastic material constitutive model is assumed, which is a

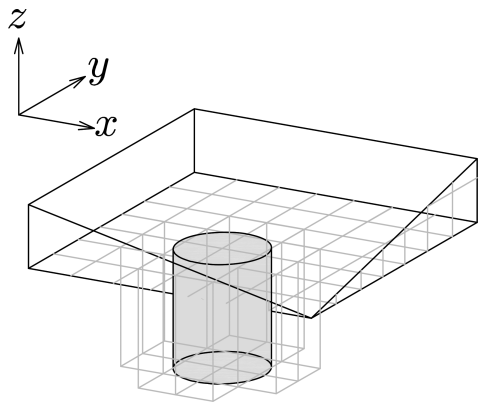

Figure 4. Automatic generation of auxiliary finite elements to consider circular pile.

rather realistic assumption for elements which are expected to be under compression.

This approach actually implies to include the support elements into finite element model, but this is done automatically by the program and permits the adoption of support geometries that do not fit with the geometry of the finite element mesh thanks to the undertaken numerical integration. As shown later, this can facilitate the definition of some finite element models, such as the introduction of a circular support in a model which is meshed with quadrilateral finite elements.

5 EXAMPLE OF APPLICATION AND RESULT COMPARISON

The purpose of this section is to highlight the importance of a proper definition of the boundary conditions imposed by loads and supports in the analysis of D-regions. A deep four-pile cap tested by Suzuki, Otsuki, & Tsubata (1998) was taken as reference. Load and support models described in previous sections were adopted in different analysis cases. Results obtained from linear elastic finite element analysis and nonlinear finite element analysis are presented: the former shows the effect on the elastic stress field of the different load and support models; the latter outlines the influence of the adopted boundary conditions on the predicted strength and the importance of an adequate modelling of loads and supports elements in D-regions.

Deep pile cap specimen BPC-30-30-1 from reference (Suzuki, Otsuki, & Tsubata 1998) was considered. The dimensions of this element were $800 \times 800 \times 300$ mm. A $300 \times 300 \times 200$ mm stub column was cast on its top. The specimen was supported on four 150 mm-diameter supports, with almost zero resistance to rotation and horizontal displacement; the distance between support centres was

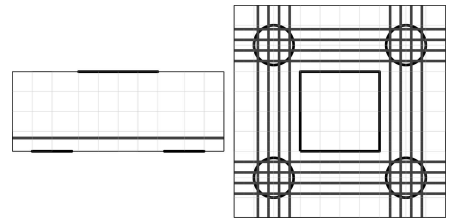

Figure 5. FE mesh for pile cap BPC-30-30-1. Column omitted.

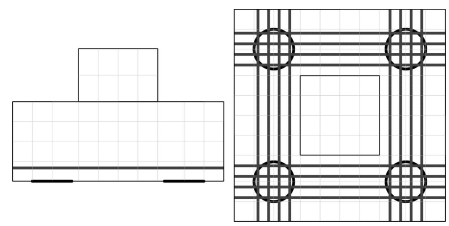

Figure 6. FE mesh for pile cap BPC-30-30-1. Column included.

500 mm. The load was applied through the supports to make the four reactions equal. This column was fixed at its top to the testing machine. Reinforcement was bunched over the piles forming a square; each band was formed by $4\phi 10$; yield and ultimate stress of steel was 405 MPa and 592 Mpa, respectively. The concrete compressive strength was 28.9 MPa.

Two alternative meshes were adopted. In the first one only the pile cap was modelled, using a $10 \times 10 \times 4$ twenty-node hexahedron mesh (Figure 5). In the second one, the stub column was also included with $4 \times 4 \times 2$ additional twenty-node hexahedrons (Figure 6). Hereafter these meshes are referred as Mesh 1 and Mesh 2, respectively.

Following engineering instinct the load was applied at the top of the cap in Mesh 1 and at the top of the column in Mesh 2, and supports were defined at the bottom of the cap regardless of the adopted mesh type. This implies turning upside down the actual experimental setup. Despite this inversion, flexibility given by the implemented load and support models permits the simulation of similar conditions as those in the test.

5.1 *Linear elastic finite element analysis*

5.1.1 *Load models*

The capabilities of the implemented model and the influence of considering or not the effect of the stub column on the stress distribution induced underneath is assessed in this subsection through the representation of the contour plots of the compressive vertical stress field on the upper horizontal cap plane. Three different approaches were considered

to model the load for assessing the differences: (i) neglect the importance of the stub column and adopt Mesh 1, (ii) adopt Mesh 1 but consider the effect of the column by static condensation and (iii) adopt Mesh 2. All results presented here were obtained for a vertical column load of 500 kN.

Results obtained with the first approach are shown in Figure 7. The stress distribution corresponding to the original load geometry is plotted in Figure 7a. Two variations were proposed in addition to demonstrate the flexibility of the model in representing typical load geometries regardless of the finite element mesh: firstly, a 300 mm-diametre column geometry was adopted (Figure 7b); and secondly, a 300 mm-diametre column geometry was adopted and the regular finite element mesh was distorted (Figure 7c). The resultant stress field is not corrupted even for distorted and arbitrarily-oriented meshes. This permits the definition of the finite element mesh without having to attend to geometric details of the loads. It should be noted that these plots were generated by linear interpolation of the stress values obtained at the closest integration points, which explains why lower stress levels are observed near the load perimeter.

Neglecting the effect of the load element (the stub column in this case) is a common approach in practice, but inadequate for the analysis of D-regions. The resultant stress distribution varies importantly when considering the effect of the

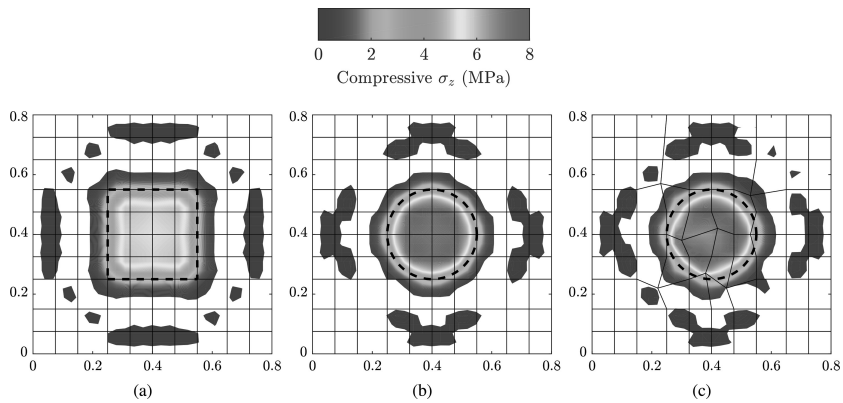

Figure 7. FE vertical stress field at loading area. Column effect not included: (a) uniform square load, (b) uniform circular load with regular mesh, (c) uniform circular load with distorted mesh.

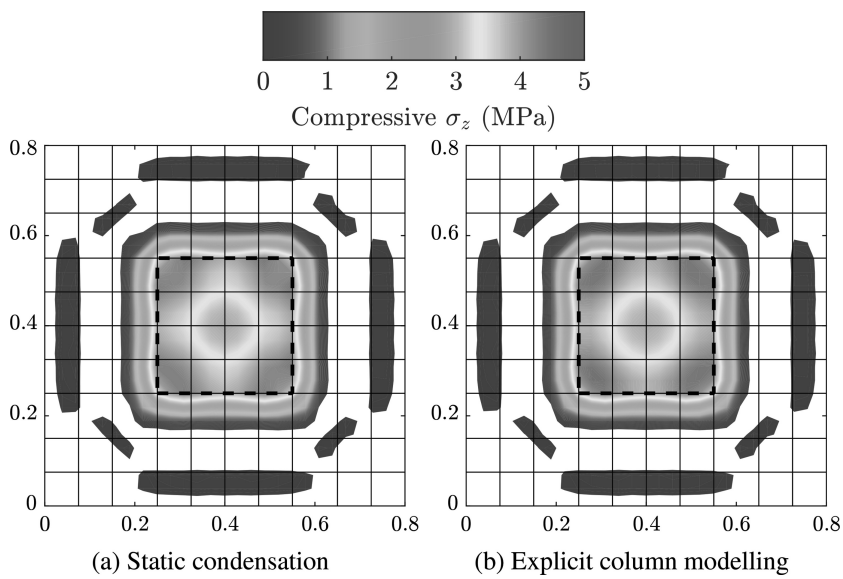

Figure 8. FE vertical stress field at loading area. Column effect included.

column (Figure 8). Stresses concentrate at the column corners because the uniform stress distribution at the top of the column is deviated on the way to the cap. As discussed later in section 5.2, this stress concentration has a notable effect on the resultant strength and stiffness of the element. Almost identical results are obtained with the simple model based on static condensation (Figure 8a) and the more complete finite element Mesh 2 (Figure 8b).

5.1.2 *Support models*

The influence of different support models on the stress distribution induced over the support areas is assessed similarly through the representation of the contour plots of the compressive vertical stress fields on these planes. Only the support model was varied from case to case while the support geometry remained unaltered (150 mm-diameter bearings). Fixed, uniform-stress and flexible supports were considered. All results were obtained for a vertical column load of 500 kN.

Figure 9 shows four contour plots of the vertical compressive stress field σ_z at the bottom section of the cap obtained by adopting: (i) the fixed support model (Figure 9a), (ii) the uniform-stress support model (Figure 9b), (iii) a flexible support model consisting of 50 mm-thick steel plates (Figure 9c) and (iv) a flexible support model consisting of 200 mm-high concrete piles (Figure 9d).

Stress concentration at the inner corners of the piles is observed for the fixed support model (Figure 9a) and, to a lesser extent, for the flexible support model with steel plates (Figure 9c). The stress is not perfectly uniform for the uniform-stress support model, with slightly higher values around the centre of the pile (Figure 9b); this is a consequence of the coarse mesh adopted because although the internal forces at the support base are forced to be equivalent to a uniform stress distribution, with few integration points inside the support area it cannot be guaranteed that stresses at integration points will reflect a uniform stress. More

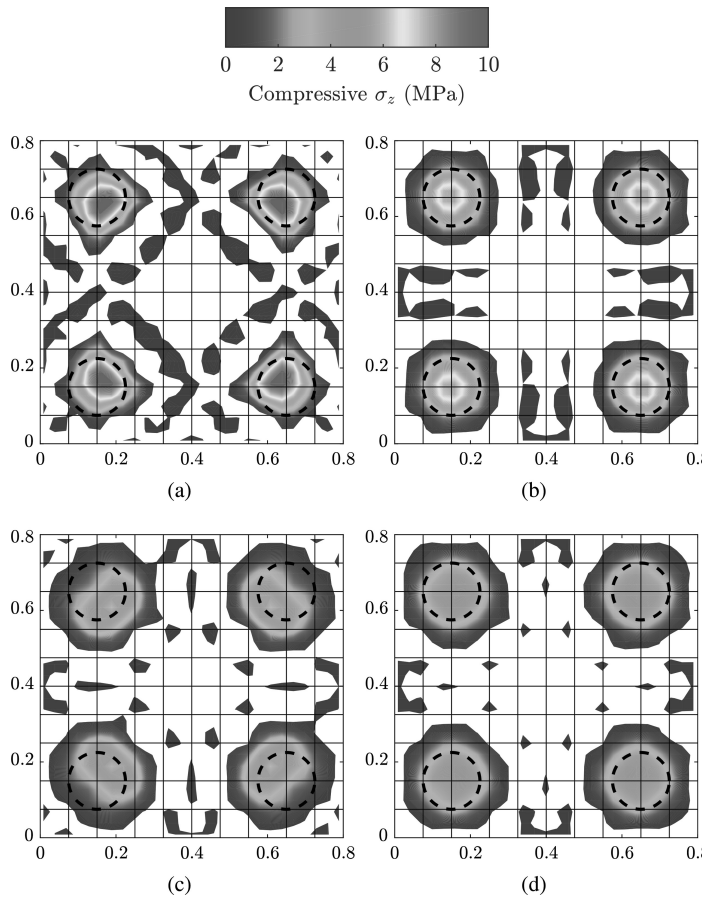

Figure 9. FE vertical stress field at support areas: (a) Fixed supports, (b) Uniform-stress supports (c) Flexible supports (steel plates), (d) Flexible supports (concrete piles).

accurate results could have been obtained with little refinement of the mesh.

The effect of the support stiffness on the stress distribution can be observed by comparing Figure 9c and 9d: results obtained for the steel plate supports (stiffer) show stress concentration at the inner corners, similar to the fixed supports; results obtained for the concrete pile supports (more flexible) show a fairly uniform stress distribution.

5.2 *Nonlinear finite element analysis*

As shown in the previous subsection induced stress fields at the column and support areas are influenced by the adopted load and support models. The effect of this variation of the stress field on the predicted strength and stiffness of the element is assessed in this subsection. Nonlinear finite element analyses were run for a more realistic comparison of the predictions considering the following simplified assumptions for concrete material modelling: tensile strength of concrete was neglected; an elastic-perfectly plastic response was adopted for concrete in compression (f_{cp} = 25.4 MPa); enhancement of concrete strength due to confinement was taken into account through a Drucker-Prager yield surface; concrete strength softening due to transverse cracking was not considered as tensile strains are to be unrealistic due to the low reinforcement quantities and the neglection of the tensile strength of concrete (more detailed information of the adopted material model can be found in (Meléndez, Miguel, & Pallarés 2016)).

Before presenting the finite element results, a simple strut-and-tie model may facilitate the understanding of the influence of the load and support models through the stress field on the predicted strength and stiffness. Finite element models leading to stress concentration around the column corners and/or the support inner-corners result in more inclined equivalent strut angles than those giving a uniform stress distribution. Steeper struts result in lower forces at strut and ties for the same vertical load. Therefore, if the strength is limited by yielding of the ties or failure of the strut, those models leading to more inclined strut angles will predict higher strengths. Considering this, a higher strength must be expected:

- for fixed supports than for uniform-stress supports
- the more rigid the support is
- if the column stiffness is taken into account

Obtained finite element results can be presented after this discussion. The experimental and finite element load-deflection curves obtained for the considered pile cap specimen are plotted in Figure 10; predicted yielding loads $P_{y,FE}$ are given and compared with the experimental yielding load $P_{y,test}$ in Table 1.

The following conclusions can be obtained regarding load modelling:

- If the column effect is disregarded, the response is more flexible and the yielding load is lower than the ones observed in the test (Figure 10a).
- Significantly stiffer and stronger predictions are obtained if the effect of the column is considered (Figure 10b, 10c).
- Very similar results are obtained by using static condensation (Figure 10b) and by including the column explicitly in the finite element mesh (Figure 10c).

The following conclusions can be obtained regarding support modelling:

- The variation of the finite element results with the support models can be up to around 50%.
- As expected, uniform-stress supports lead to the weakest and more flexible response, and the response obtained with steel plate supports is stiffer and stronger than with the concrete piles.
- Fixed supports did not lead to the strongest and stiffest response in this case as it should be expected. The reason is found in the adopted finite element mesh, which left a significant portion of the support area unrestraint as not many nodes were located inside the defined area. This evidences the inadequacy of the fixed support

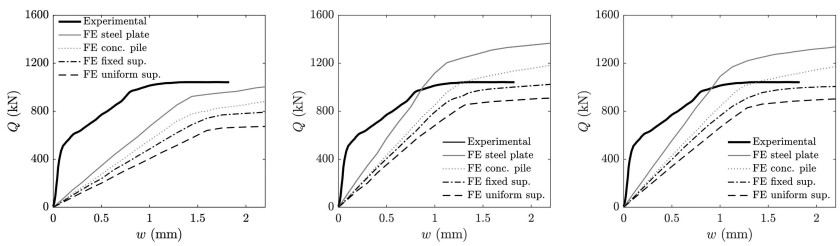

(a) Column effect disregarded (b) Column effect considered by static condensation (c) Column effect considered by explicit modelling

Figure 10. FE load-deflection curves for pile cap BPC-30-30-1 obtained under diffferent load and support assumptions. Tensile strength of concrete neglected.

Table 1. FE yielding loads for pile cap BPC-30-30-1 obtained under different load and support assumptions. Tensile strength of concrete neglected.

$P_{y,FE}$(kN)| $P_{y,test}/P_{y,FE}$	No column	With column	
		Implicit	Explicit
Uniform-stress sup.	660|1.56	860|1.20	860|1.20
Concrete flex. sup.	825|1.25	1050|0.98	1035|0.99
Steel flex. sup.	930|1.11	1210|0.85	1180|0.87
Fixed sup.	775|1.33	970|1.06	955|1.08

condition because a small variation of the support geometry can lead to large variations in the results depending on the number of nodes that are "captured" by the defined area.

These results show the importance of a proper modelling of load and support elements. Results can vary about 100% depending on the adopted assumptions. Considering the experimental setup, the most appropriate assumption in this case would have been considering the column effect (either by static condensation or by including it in the finite element model) and adopting a uniform-stress support model for the supports. Based on the results plotted in Figure 10b-10c it is seen that under these conditions the predicted strength is lower than the experimental one. To obtain more realistic predictions the tensile strength needs to be accounted for (Meléndez 2017).

6 CONCLUSIONS

Boundary conditions imposed by loads and supports have an important effect on the response of D-regions and, hence, if sound predictions are to be obtained they must be defined appropriately in the finite element model.

This document presented the fundamentals of the load and support models developed and integrated in the nonlinear finite element tool FESCA 3D developed by the authors and oriented for the analysis of 3D D-regions.

Principles of static condensation were used to account for the effect of the loading substructure without having to include it explicitly in the finite element mesh. Principles of the finite element method were considered for the development of the uniform-stress distribution support model and the flexible support model. These models cover realistically most situations in engineering practice and experimental testing.

An example of application to a four-pile cap specimen was presented at the end of the document where different load and support models were adopted. Although it was known before the analyses that some of these models were not appropriate for the existing conditions, none of them could have been classified as absurd a priori. Comparison of the results demonstrated the importance of an adequate definition of the boundary conditions in the analysis of D-regions, with result variations of up to 100% depending on the adopted assumptions. These results also showed that the frequently used fixed support model is inappropriate for the analysis of D-regions.

REFERENCES

Amini Najafian, H. & R.L. Vollum (2013). Design of planar reinforced concrete D regions with nonlinear finite element analysis. *Engineering Structures 51*, 211–225.

Meléndez, C. (2017). *A finite element-based approach for the analysis and design of 3D reinforced concrete elements and its application to D-regions*. Ph.D. thesis, Universitat Politècnica de València.

Meléndez, C., P.F. Miguel, & L. Pallarés (2016). A simplified approach for the ultimate limit state analysis of three-dimensional reinforced concrete elements. *Engineering Structures 123*, 330–340.

Muttoni, A., J. Schwartz, & B. Thürlimann (1997). *Design of concrete structures with stress fields*. Birkhäuser Verlag.

Reineck, K., M.S. Lourenço, J.F. Almeida, & S. Haugerud (2011). Gaining Experience with Strut and Tie Models for the Design of Concrete Structures. In *Design Examples for Strut-and-Tie Models, fib bulletin 61*, pp. 197–216.

Schlaich, J., K. Schafer, & M. Jennewein (1987). Toward a Consistent Design of Structural Concrete. *PCI Journal 32*(May-June), 74–150.

Suzuki, K., K. Otsuki, & T. Tsubata (1998). Influence of Bar Arrangement on Ultimate Strength of Four-Pile Caps. *Transactions of the Japan Concrete Institute 20*, 195–202.

Tjhin, T.N. & D.A. Kuchma (2002). Computer-Based Tools for Design by Strut-and-Tie Method: Advances and Challenges. *ACI Structural Journal 99*(5), 586–594.

Computational Modelling of Concrete Structures – Meschke, Pichler & Rots (Eds)
© 2018 Taylor & Francis Group, London, ISBN 978-1-138-74117-1

Parameter identification as the basis for finite element simulations of ultimate limit states of concrete hinges

J. Kalliauer & T. Schlappal
Institute for Mechanics of Materials and Structures, TU Wien—Vienna University of Technology, Vienna, Austria

H.A. Mang
Institute for Mechanics of Materials and Structures, TU Wien—Vienna University of Technology, Vienna, Austria
College of Civil Engineering, Tongji University, Shanghai, China

B. Pichler
Institute for Mechanics of Materials and Structures, TU Wien—Vienna University of Technology, Vienna, Austria

ABSTRACT: Reinforced concrete hinges, subjected to eccentric compression, are failing in a ductile fashion (Schlappal et al. 2017). Three-dimensional Finite Element simulations are prime candidates for a more detailed analysis of this interesting structural behavior. Such nonlinear simulations, however, typically require pocedures for updating of the underlying models. They involve fitting of input parameters such that the output of the simulations agree with experimental measurements (Kalliauer et al. 2017). In the present contribution, it is investigated to which extent fitting procedures, involving time-consuming *nonlinear three*-dimensional Finite Element simulations, can be avoided. Therefore, input parameters are identified by combining (i) results from destructive and nondestructive compression tests on plain concrete specimens, (ii) results from centric and eccentric compression tests on concrete hinges subjected to serviceability loads, (iii) a multiscale model for tensile failure of concrete, and (iv) *linear*-elastic *two*-dimensional Finite Element simulations. Parameter identification aims of (i) quantifying the influence of damage of concrete (resulting from restrained shrinkage prior to structural testing) on the elastic stiffness, the tensile strength, and the fracture energy, and of (ii) determination of the characteristic triaxiality of the compressive stress states, prevailing in the neck region, in order to ensure modeling of the triaxial compressive strength of concrete in accordance with regulations of Eurocode 2. After parameter identification, a nonlinear three-dimensional Finite Element simulation of the bearing capacity tests by Schlappal et al. (2017) is carried out. The obtained numerical results agree well with experimental observations. This underlines the usefulness of the presented parameter identification strategy.

1 INTRODUCTION

Concrete hinges were invented by Freyssinet in the first half of the 20th century (Freyssinet 1923, Freyssinet 1954). They represent necks of monolithically produced reinforced concrete structures (Marx & Schacht 2010a, Schacht & Marx 2010). In order to allow these necks to act as structural hinges, their bending stiffness must be significantly smaller than that of the connected reinforced concrete parts. Therefore, only a few pairs of inclined steel bars run across the center of the neck, which is their crossover point. In addition, as part of the concept, concrete hinges may exhibit bending-induced tensile cracking under regular service loads (Leonhardt & Reimann 1965, Leonhardt 1986, Marx & Schacht 2010a, Marx & Schacht 2010b, Marx & Schacht 2010c). Concrete hinges are used as supports in integral bridge construction (Sallenbach 1967, Marx & Schacht 2010a, Schacht & Marx 2010, Schacht & Marx 2015, Morgenthal & Olney 2016) and as segment-to-segment interfaces of segmented linings in mechanized tunnelling (Janßen 1983, Hordijk et al. 1996, De Waal 2000, Blom 2002, Maidl et al. 2012, Jusoh et al. 2015).

Pioneering design guidelines for concrete hinges were developed in the 1960s by Leonhardt and Reimann (1965). More recently, they were improved in order to be applicable within the presently used semi-probabilistic safety concept (Marx & Schacht 2010a, Marx & Schacht 2010b, Marx & Schacht 2010c, Schacht & Marx 2010). Still, it is noteworthy that the original guidelines refer to Serviceability-Limit-States rather than to Ultimate-Limit-States. This was the motivation to carry out experiments (Schlappal et al. 2017) and to re-analyze them by means of Finite Element simulations (Kalliauer et al. 2017). These simulations were based on default input parameters. The latter were derived from the uniaxial compressive strength and from Young's modulus,

measured on plane concrete specimens 28 days after their production. Corresponding simulation results overestimated the load bearing capacity of concrete hinges by 80%. This resulted in the need for a model updating procedure, involving the fitting of input parameters such that the output from simulations agreed with experimental measurements. The number of fitting parameters could be reduced significantly by involving a recently developed multiscale model for tensile failure of plain concrete (Hlobil et al. 2017).

The aim of the present contribution is to check to which extent a thorough analysis of experiments, carried out on plane concrete prisms and on reinforced concrete hinges, allows for *identification* of material properties of concrete that yield satisfactory Finite Element simulation results *without* the need of a fitting procedure on the level of nonlinear three-dimensional structural analyses. To this end, the contribution is structured as follows. Section 2 contains a collection of experimental data on plain concrete prisms and on concrete hinges subjected to centric and eccentric compression. In Section 3, a thorough analysis of the experimental data is carried out in order to quantify input parameters for subsequent Finite Element simulations. Section 4 is devoted to the Finite Element simulation of the bearing capacity of concrete hinges subjected to eccentric compression. Conclusions drawn from this study are presented in Section 5.

2 EXPERIMENTAL DATA

Schlappal et al. (2017) carried out compression experiments on plain concrete specimens and reinforced concrete hinges.

2.1 *Properties of reinforced concrete hinges*

The shape of the tested concrete hinges and the arrangement of the steel reinforcement (Fig. 1) were designed in accordance with guidelines by Leonhardt and Reimann (1965). The reinforcement ratio amounted to

$$\rho = \frac{A_s}{A} = 1.3\%, \tag{1}$$

where A_s and $A = 7.5\ \text{cm} \times 30\ \text{cm} = 225\ \text{cm}^2$, respectively, denote the cross-sectional area, occupied by steel and the reinforced neck (Fig. 1). Young's modulus of the structural steel amounted to (British Standards Institution and CEN European Committee for Standardization 2015b)

$$E_s = 210\ \text{GPa}. \tag{2}$$

To avoid that the concrete hinges, subjected to compressive line loads, will crush locally in the immediate vicinity of the load application system, steel plates were welded onto the top and bottom reinforcement cages before casting (Fig. 1). Three nominally identical concrete hinges were tested, one after the other.

In order to quantify structural creep of concrete hinges, they were subjected, for four hours each, to centric compression, amounting to 200 kN. The changes of the opening of the lateral notches were measured by six inductive displacement sensors (Schlappal et al. 2017). Test results have indicated that the experiments could be reproduced satisfactory, see the thick solid lines in Fig. 2 for the creep strain evolution under sustained loading, normalized with respect to the creep strain reached at the end of the loading process.

In order to quantify bending-induced tensile cracking, each of the three concrete hinges were subjected to three consecutive eccentric compression tests, using line loads, incrementally increased by 25 kN up to 200 kN. The three tests for each specimen referred to three different load eccentricities:

$$e = \{20\ \text{mm},\quad 22\ \text{mm},\quad 24\ \text{mm}\}. \tag{3}$$

After each load increment, the tests were interrupted for 10 seconds, in order to take images of the

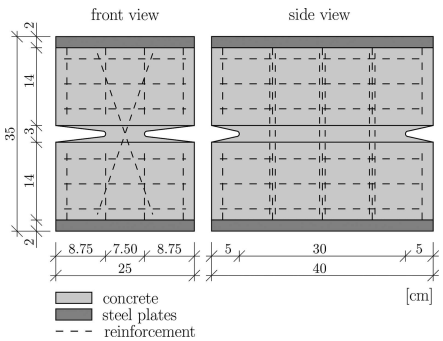

Figure 1. Formwork drawing of the analyzed concrete hinges; after (Schlappal et al. 2017).

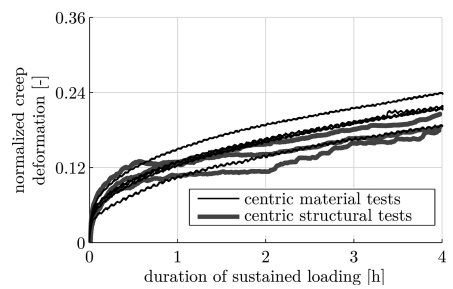

Figure 2. Evolution of creep deformations under sustained loading, normalized by the averaged deformation at the end of the loading process; after (Schlappal et al. 2017).

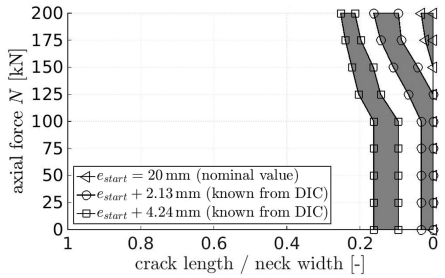

Figure 3. Bending-induced cracking of concrete hinges under eccentric compression: crack length as a function of eccentricity and load level; after (Schlappal et al. 2017).

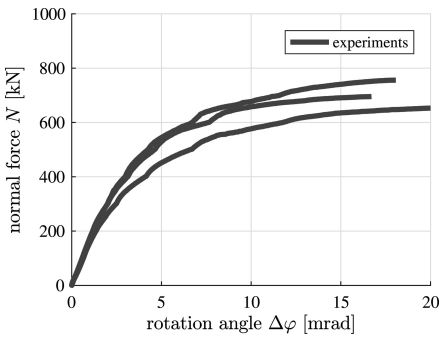

Figure 4. Rotation angles across the neck regions of three concrete hinges, as a function of eccentric loading (e = 25 mm) up to the load-carrying capacity; after (Schlappal et al. 2017).

front-side and the back-side notches, using cameras of a Digital Image Correlation system. This way, the crack length could be determined as a function of the eccentricity and the load level, see Fig. 3.

In order to quantify the bearing capacity of the concrete hinges, they were subjected to eccentric compression with an eccentricity of e = 25 mm. Ultimate load levels amounted to 654 kN, 695 kN and 756 kN, see Fig. 4.

2.2 *Properties of plain concrete specimens*

The cube compressive strength, $f_{c,cube}$, and the Young's modulus, E_c, were determined 28 days after production, following the Austrian standards for testing of concrete (Austrian Standards Institute 2010):

$$f_{c,cube} = 56.25\ \text{MPa}, \quad E_c = 34.75\ \text{GPa}. \tag{4}$$

As for characterization of creep, concrete prisms were subjected, for four hours each, to centric compression, equal to nearly 20% of the short-term uniaxial compressive strength. Five tests on nominally identical specimens were carried out. Three tests delivered nearly the same creep response, bounded by the results from the other two tests. The thin solid lines in Fig. 2 refer to the evolution of the creep strains under sustained loading, normalized with respect to the creep strain reached end the end of the loading process.

3 INPUT PARAMETERS FOR STRUCTURAL SIMULATIONS

Reinforced concrete hinges are prone to develop shrinkage-induced damage in the neck region (Leonhardt and Reimann 1965), reducing the elastic stiffness, the tensile strength, and the fracture energy of concrete. In addition, concrete hinges are known to exhibit triaxial compressive stress states in the neck region. This calls for realistic modeling of the triaxial compressive strength of concrete.

As for material modeling of concrete, the "CC3DNonLinCementitious" model (Červenka and Papanikolaou 2008) of the Finite Element software "Atena Science" (Červenka Consulting et al. 2016) was used. It is based on a Menétrey–Willam failure surface (Menétrey and Willam 1995). Corresponding input values for Finite Element simulations of the bearing capacity tests (Fig. 4) requires identification of input values for the mentioned concrete model.

3.1 *Identification of the elastic stiffness of damaged concrete*

On average the plain concrete prisms exhibited a creep activity which was by 12.7% larger than that of the reinforce concrete hinges (Fig. 2). This experimental observation will be used for identification of the damaged elastic stiffness of concrete in the neck region of the concrete hinges. It is based on considerations regarding stress-concentration, see Ross (1958) for a similar approach.

Consider that (i) the plain concrete prisms were subjected to a compressive stress σ, and that (ii) the reinforced neck region is subjected to the same *average* stress, such that the compressive force F amounts to $\sigma \cdot A$, where A denotes to total cross-section of the neck of the concrete hinges. Decomposing A into the areas occupied by concrete, A_c, and the one by steel, A_s, delivers

$$A = A_c + A_s. \tag{5}$$

Introducing the average stress within the concrete, σ_c, and the steel, σ_s, respectively, and formulating force equilibrium in loading direction yields

$$\sigma A = \sigma_c A_c + \sigma_s A_s. \tag{6}$$

In order to establish a relation between σ_c and σ_s, firm bond between concrete and steel is assumed.

This results in the following strain compatibility condition

$$\varepsilon_c = \varepsilon_s. \tag{7}$$

Considering elastic deformations, the strains in Eq. (7) are linked to the stresses in Eq. (6) by means of Hooke's law, such that Eq. (7) can be re-written as

$$\frac{\sigma_c}{E_{cd}} = \frac{\sigma_s}{E_s}, \tag{8}$$

where E_{cd} denotes the damaged stiffness of concrete in the neck region. Solving Eq. (8) for σ_s, inserting the resulting expression into Eq. (6), and solving the obtained expression for the stress ratio σ/σ_c delivers

$$\frac{\sigma}{\sigma_c} = \frac{A_c}{A} + \frac{E_s}{E_{cd}}\frac{A_s}{A}. \tag{9}$$

Using Eqs. (1) and (5), Eq. (9) can be reformulated as follows:

$$\frac{\sigma}{\sigma_c} = (1-\rho) + \frac{E_s}{E_{cd}}\rho. \tag{10}$$

Eq. (10) underlines that the average stress in the neck region is by a factor of σ/σ_c larger than the average stress within the creeping concrete.

The experimental results of Fig. 2 are interpreted as follows: creeping of the reinforced concrete neck was smaller than in the plane concrete prisms, because the average stress level of the creeping concrete is by a factor of σ/σ_c smaller than the average stress of the reinforced neck region. This is the motivation to set σ/σ_c in Eq. (10) equal to the experimentally observed normalized creep strain ratio, amounting to 1.127, see Fig. 2. Solving the resulting expression for the stiffness of damaged concrete and specializing the results for Eqs. (1) and (2), delivers

$$E_{cd} = \frac{E_s\rho}{1.127-(1-\rho)} = 19.5\ \text{GPa}. \tag{11}$$

3.2 *Identification of the crack density parameter*

The elastic stiffness of undamaged concrete, see Eq. (4), and of damaged concrete, see Eq. (11) allows for estimation of Budiansky and O'Connel's crack density parameter ω. To this end, concrete is considered to be damaged by parallel open cracks. Young's modulus in the direction normal to the crack plane is estimated, using a multiscale model for damaged concrete, see (Pichler et al. 2007, Hlobil et al. 2017), as

$$E_{cd} = E_c\left[1+\frac{16\omega}{3}(1-\nu_c^2)\right]^{-1}. \tag{12}$$

Solving Eq. (12) for the damage variable ω and consideration of Eqs. (4) and (11) as well as the standard value of Poisson's ratio of concrete, $\nu_c = 0.20$, see British Standards Institution and CEN European Committee for Standardization (2015a), delivers

$$\omega = \left(\frac{E_c}{E_{cd}}-1\right)\frac{3}{16(1-\nu_c^2)} = 15.3\%. \tag{13}$$

3.3 *Identification of the damaged uniaxial tensile strength of concrete*

Bounds of the damaged tensile strength of concrete can be determined, based on the experimental observation that tensile cracking of the concrete hinges starts between the compressive load levels

$$N \in [150\ \text{KN};\quad 175\ \text{KN}], \tag{14}$$

acting with an eccentricity of $e = 20$ mm, see Fig. 3. The maximum tensile stress, max σ_t, resulting from the combined action of a normal force N and a bending moment $M = Ne$, was quantified by Schlappal et al. (2017), by means of results from linear-elastic plane-strain Finite Element analyses of the investigated concrete hinges:

$$\max\ \sigma_t = 2.77\frac{N}{ab} - 2.00\frac{6(Ne)}{a^2b}, \tag{15}$$

where ab denotes the cross-sectional area of the neck and $a^2b/6$ stands for beam theory-related elastic section modulus. Furthermore, 2.77 and 2.00 are numerically determined stress increase factors relative to the stress levels according to beam theory. Specializing Eq. (15) for $e = 20$ mm, $a = 75$ mm, $b = 300$ mm, and for the two bounds of the normal force given in (14), delivers experimentally-derived bounds of the damaged tensile strength of concrete, amounting to

$$f_{t,dam} \in [2.87\ \text{MPa};\ 3.34\ \text{MPa}]. \tag{16}$$

A more precise estimate of the damaged tensile strength is determined by means of a multiscale analysis of tensile failure of concrete by Hlobil et al. (2017). This model is based on the following relation between the tensile strength of the undamaged and damaged material:

$$f_{t,dam} = \frac{f_t}{\sqrt{1+1.223\omega}}. \tag{17}$$

The tensile strength of undamaged concrete, f_t, is estimated by the following standard relation (fib 2013)

$$f_t = 0.3\,\text{MPa} \cdot \left(\frac{0.85\left(f_{c,cube} - 8\,\text{MPa}\right)}{1\,\text{MPa}} \right)^{2/3}. \quad (18)$$

Specializing Eq. (18) for the value of $f_{c,cube}$ from Eq. (4), delivers

$$f_t = 3.57\,\text{MPa}. \quad (19)$$

Specializing Eq. (17) for Eqs. (13) and Eq. (19) yields

$$f_{t,dam} = 3.28\,\text{MPa}. \quad (20)$$

Notably, Eq. (20) satisfies the corresponding bounds, see Eq. (16).

3.4 *Identification of the fracture energy of damaged concrete*

Atena science (Červenka et al. 2016) suggest the following value of the fracture energy for concrete with a cube compressive strength according to Eq. (4):

$$G_f = 147\,\text{J/m}^2. \quad (21)$$

Shrinkage-induced cracking reduces this value by an increment ΔG_f. The latter is quantified on the basis of a smeared crack model as

$$\Delta G_f = \int_0^{w_d} \sigma \text{dw}, \quad (22)$$

where σ and w denote the cohesive stress and the smeared crack opening displacement, respectively. The relation between these two quantities is given by Hordijk (1991) as

$$\sigma = f_t \cdot \left\{ \left[1 + \left(c_1 \frac{\text{w}}{\text{w}_c} \right)^3 \right] \exp\left(-c_2 \frac{\text{w}}{\text{w}_c} \right) - \frac{\text{w}}{\text{w}_c}\left(1 + c_1^3\right)\exp\left(-c_2\right) \right\}, \quad (23)$$

with (Červenka et al. 2016)

$$c_1 = 3, \quad c_2 = 6.93, \quad \text{w}_c = 5.14\, G_f / f_t. \quad (24)$$

The smeared crack opening displacement w_d, related to shrinkage-induced damage, is determined by specializing Eq. (23) for Eqs. (24), $\sigma = f_{t,dam}$, and $\text{w} = \text{w}_d$, and inserting Eqs. (19)–(21) into the resulting expression, followed by solving the latter for w_d as:

$$\text{w}_d = 2.6\,\mu\text{m} \quad (25)$$

Inserting of the functions of Eqs. (23)–(25) into Eq. (22) and consideration of Eqs. (19)–(21) yields

$$\Delta G_f = 8.893\,\text{J/m}^2. \quad (26)$$

Subtracting ΔG_f from G_f, see Eqs. (21) and (26), yields the value of the effective fracture energy of the damaged concrete as

$$G_{fd} = G_f - \Delta G_f = 138.1\,\text{J/m}^2. \quad (27)$$

3.5 *Identification of the stress triaxiality in the neck region*

Concrete hinges exhibit triaxial compressive stress states in the neck region (Leonhardt & Reimann 1965). In order to quantify a characteristic principal stress ratio, a linear-elastic plane-strain Finite Element simulation is carried out with an load eccentricity e amounting to 25 mm. The principal stress ratios are evaluated in the smallest cross-section of the neck. Averaging them in the region between the surface of the root of the compressed notch and a distance from that surface, amounting to the maximum aggregate size of 16 mm, delivers the average principal stress ratio as

$$\sigma_1 : \sigma_2 : \sigma_3 = 1.00 : 0.45 : 0.30. \quad (28)$$

The stress ratios in Eq. (28) allow for calculating corresponding Haigh–Westergaard coordinates as (Menétrey & Willam 1995, Grassl & Jirásek 2006)

$$\xi = 1.01\sigma_1, \quad \rho = 0.521\,|\,\sigma_1\,|, \quad \vartheta = 0.842\,\text{rad}, \quad (29)$$

where σ_1 denotes the compressive principal normal stress in loading direction and ξ, ρ, and ϑ stand for the hydrostatic and deviatoric component of the characteristic stress state and for its Lode angle, respectively.

3.6 *Eurocode-based description of the triaxial strength of concrete*

The triaxial-to-uniaxial strength ratio of concrete, F, is estimated on the basis of recommendations for partially loaded areas according to Eurocode 2-1-1 (British Standards Institution and CEN European Committee for Standardization 2015a), see also (Marx and Schacht 2010a, Marx and Schacht 2010b, Marx and Schacht 2010c, Kalliauer et al. 2017). The strength ratio F depends on geometric dimensions and reads as:

$$F = \sqrt{A_{c1}/A_{c0}}, \quad (30)$$

where A_{c1} is equal to the thickness of the concrete hinge (40 cm) times three times the neck width, 3_{b1},

see (British Standards Institution and CEN European Committee for Standardization 2015a), and A_{c0} denotes the loaded neck-area that is equal to the thickness of the neck (30 cm) times the neck width b_1, see Fig. 5. Therefore, the triaxial-to-uniaxial compressive strength ratio of concrete amounts to

$$F = \sqrt{\frac{40\ \text{cm} \cdot 3\, b_1}{30\ \text{cm} \cdot b_1}} = 2. \tag{31}$$

3.7 *Identification of the slope of the Menétrey–Willam failure surface in the Haigh–Westergaard stress space*

The Menétrey–Willam failure surface is defined as (Menétrey and Willam 1995, Červenka and Papanikolaou 2008, Červenka and Červenka 2013)

$$F_{3P}^{p}(\xi,\rho,\vartheta) = \frac{3}{2}\left(\frac{\rho}{f_c'}\right)^2 + \frac{m}{f_c'}\left(\rho\frac{r(\vartheta)}{\sqrt{6}} + \frac{\xi}{\sqrt{3}}\right) - c = 0, \tag{32}$$

where m and $r(\vartheta)$, respectively, are defined as

$$m = \frac{3e_\sigma}{e_\sigma + 1}\frac{f_c'^2 - f_t'^2}{f_c' f_t'}, \tag{33}$$

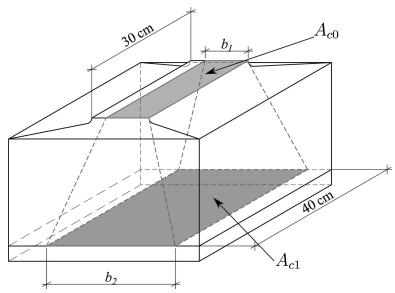

Figure 5. Application of regulations of Eurocode 2 regarding partially loaded areas to concrete hinges; after (Kalliauer et al. 2017).

and

$$r(\vartheta) = \frac{4\left(1-e_\sigma^2\right)\cos^2\vartheta + (2e_\sigma - 1)^2}{2\left(1-e_\sigma^2\right)\cos\vartheta + (2e_\sigma - 1)\,H} \tag{34}$$

with

$$H = \sqrt{4\left(1-e_\sigma^2\right)\cos^2\vartheta + 5e_\sigma^2 - 4e_\sigma}. \tag{35}$$

see also Fig. 6.

The initial value of the hardening/softening parameter c is given as $c_{ini} = 1$ (Červenka et al. 2016). The "eccentricity" $e_\sigma = 0.52$ controls the shape of the failure surface in the deviatoric planes. The elastic limit stress under uniaxial compression, f_c', increases—during strain hardening—from its initial value, f_{c0}, up to the uniaxial compressive strength, f_c. The uniaxial tensile strength of the Menétrey–Willam failure surface, f_t', is an auxiliary value, because it is larger than the *actual* uniaxial tensile strength, f_t. The latter is modeled by a Rankine criterion. The ratio of the auxiliary-toreal uniaxial tensile strength

$$\lambda_t = \frac{f_t'}{f_t}, \tag{36}$$

is another input parameter for Finite Element simulations with Atena science. In order to obtain a triaxial-to-uniaxial strength ratio $F = 2$, see Eqs. (31), for the characteristic triaxial compressive stress state defined in Eq. (28), the numerical value of λ_t must amount to

$$\lambda_t = 8.9, \tag{37}$$

see also Fig. 6.

4 STRUCTURAL SIMULATIONS BY MEANS OF THE FINITE ELEMENT METHOD

The bearing capacity tests described in Section 2 are simulated by Atena science, the material model

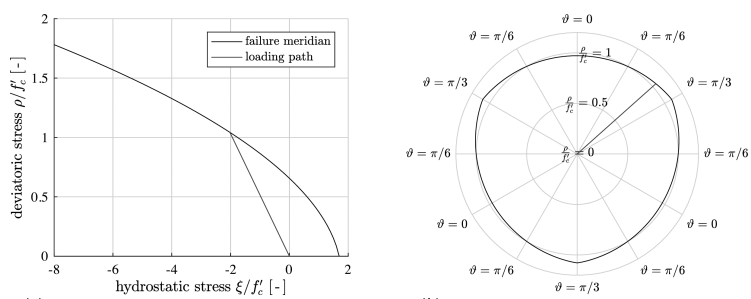

Figure 6. Representation of the Menétrey–Willam failure surface in the Haigh–Westergaard stress space (a) section containing the hydrostatic axis (see abscissa), and (b) deviatoric plane; the blue graph represents (the projection of) the stress path resulting from proportional increase of a triaxial compressive stress state with principal stress ratios given in Eq. (28).

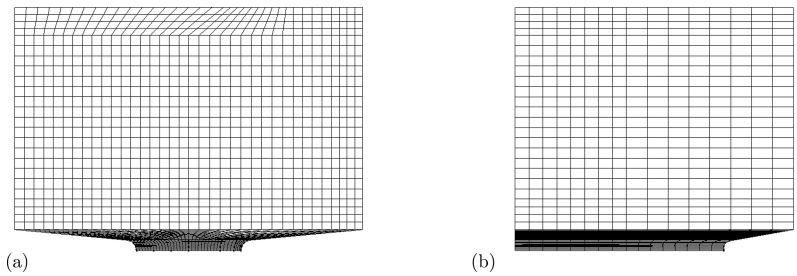

Figure 7. Three-dimensional Finite Element mesh consisting of 27 776 hexahedral elements with a characteristic element size of 1.25 mm in the neck region: (a) front view, (b) lateral view; exploiting double symmetry of the problem, only one fourth of the reinforced concrete hinge is discretized.

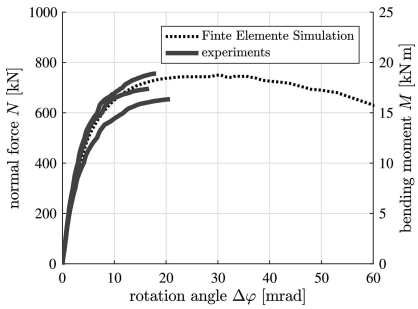

Figure 8. Behavior of concrete hinges subjected to eccentric compression (e = 25 mm) up to their bearing capacity: comparison of experimental observations (see the blue graphs) with results from nonlinear three-dimensional Finite Element simulations using Atena science, the material model "CC3DNonLinCementitious", and the input parameters derived above.

"CC3DNonLinCementitious", and the previously derived input parameters. Default values are used for those input values that have not been discussed above.

The Finite Element mesh shown in Fig. 7, consists of 27 776 hexahedral elements with trilinear displacement interpolation, 31 730 nodes, and 95 190 degrees of freedom. This mesh was the result of a convergence study, documented in (Kalliauer 2016).

The numerical simulations reproduce the experimentally observed behavior both qualitatively and quantitatively in a satisfactory fashion, and they provide insight into the post-peak softening behavior of the concrete hinges, which was not quantified experimentally, see Fig. 8.

5 DISCUSSION AND CONCLUSIONS

The bearing capacity of reinforced concrete hinges, subjected to eccentric compression, was investigated by means of experiments and three-dimensional Finite Element simulations. The required input parameters for nonlinear numerical simulations were identified *a priori*, by combining (i) results from destructive and nondestructive compression tests on plain concrete specimens, (ii) results from centric and eccentric compression tests on concrete hinges subjected to serviceability loads, (iii) a multiscale model for tensile failure of concrete, and (iv) linear-elastic plane-strain Finite Element simulations. In other words, identification of input parameters was carried out *without* fitting the results from nonlinear structural simulations to the experimentally observed behavior. Therefore, the described nonlinear three-dimensional numerical simulation represents a nontrivial quantitative test of the predictive capabilities of the developed Finite Element model. This test was passed successfully. Hence, the developed Finite Element model is validated. This is useful for the future development of *nonlinear* interface laws that are necessary prerequisites for the analysis of Ultimate Limit States of integral bridges and of segmented tunnel rings.

FUNDING AND ACKNOWLEDGMENTS

Financial support by the Austrian Science Fund (FWF) provided within the project P 281 31-N32 "Bridging the Gap by Means of Multiscale Structural Analysis" and corresponding discussions with Yong Yuan (Tongji University) and Jiaolong Zhang (TU Wien/Tongji University) are gratefully acknowledged.

Additional interesting discussions, carried out within the VIF-project 845681 "Optimierte Bemessungsregeln für dauerhafte bewehrte Betongelenke [Optimized Rules for the Design of Permanent Reinforcement Concrete Hinges]", with Markus Vill (Vill Ziviltechniker GmbH), Michael Schweigler (TU Wien), Susanne Gmainer and Martin Peyerl (Smart Minerals GmbH), Alfred Hüngsberg (ÖBB-Infrastruktur AG), as well as Erwin Pilch and Michael Kleiser (ASFINAG Bau Management GmbH) are also gratefully acknowledged.

REFERENCES

Austrian Standards Institute (2010). ONR 23303:2010-09-01 *Prüfverfahren Beton (PVB) – Nationale Anwendung der Prüfnormen für Beton und seiner Ausgangsstoffe [Test protocol concrete – National application of testing standards for concrete and its raw materials]*. Austrian Standards Institute. In German.

Blom, C.B.M. (2002). *Design philosophy of concrete linings for tunnels in soft soils*. Ph. D. thesis, Delft University of Technology.

British Standards Institution & CEN European Committee for Standardization (2015a). EN 1992-1-1:2015-07-31 *Eurocode 2: Design of concrete structures – Part 1–1: General rules and rules for buildings*. London: British Standards Institution and CEN European Committee for Standardization.

British Standards Institution & CEN European Committee for Standardization (2015b). EN 1993-1-1:2005+A1:2014 *Eurocode 3. Design of steel structures. – Part 1–1: General rules and rules for buildings*. London: British Standards Institution and CEN European Committee for Standardization.

Červenka, J. & V. Červenka (2013). Three dimensional combined fracture-plastic material model for concrete including creep and rate effect for dynamic loading. Technical report, Červenka Consulting. http://www.cervenka.cz/assets/files/papers/3D Fracture-Plastic Model v5.pdf last access: November 08, 2017.

Červenka, J. & V.K. Papanikolaou (2008). Three dimensional combined fracture–plastic material model for concrete. *International Journal of Plasticity 24*(12), 2192–2220.

Červenka, V., L. Jendele, & J. Červenka (2016). *ATENA program documentation Part 1 – Theory* (February 5, 2016 ed.). Červenka Consulting s.r.o.

Červenka Consulting, V. Červenka, L. Jendele, J. Červenka, et al. (2016). Build 12562 & ATENA 5.1.3. Internet source.

De Waal, R.G.A. (2000). *Steel fibre reinforced tunnel segments – for the application in shield driven tunnel linings.* Ph. D. thesis, Delft University of Technology.

fib (2013). *fib Model Code for Concrete Structures 2010*. Ernst & Sohn, Wiley.

Freyssinet, E. (1923). Le pont de Candelier [The bridge of Candelier]. *Annales des Ponts et Chaussées* 1, 165f. In French.

Freyssinet, E. (1954). Naissance du béton précontraint et vues d'avenir [Birth of prestressed concrete and future outlook]. *Travaux* (236), 463–474. In French.

Grassl, P. & M. Jirásek (2006, nov). Damage-plastic model for concrete failure. *International Journal of Solids and Structures 43*(22–23), 7166–7196.

Hlobil, M., M. Göstl, J. Burrus, C. Hellmich, & B. Pichler (2017). Molecular-to-macro upscaling of concrete fracture: theory and experiments. *Journal for the Mechanics and Physics of Solids*. under revision.

Hordijk, D.A. (1991). *Local approach to fatigue of concrete*. Ph. D. thesis, Delft University of Technology. ISBN 90/9004519-8.

Hordijk, D.A., F. Gijsbers, & P. Boortunnels (1996). Laboratoriumproeven tunnelsegmenten [Laboratory testing of tunnel segments]. Technical Report Reporte Interno K100-W-026, Nederlands kenniscentrum voor ondergronds bouwen en ondergronds ruimtegebruik (COB), Delft. In Dutch.

Janßen, P. (1983). *Tragverhalten von Tunnelausbauten mit Gelenkstübbings [Structural behavior of segmented tunnel linings]*. Ph.D. thesis, Technical University of Braunschweig. In German.

Jusoh, S.N., H. Mohamad, A. Marto, N.Z.M. Yunus, & F. Kasim (2015). Segment's joint in precast tunnel lining design. *Jurnal Teknologi 77*(11), 91–98.

Kalliauer, J. (2016). Insight into the structural behavior of concrete hinges by means of Finite Element simulations. Master thesis, TU Wien.

Kalliauer, J., T. Schlappal, M. Vill, H. Mang, & B. Pichler (2017). Bearing capacity of concrete hinges. *Acta Mechanica*. Accepted for publication.

Leonhardt, F. & H. Reimann (1965). *Betongelenke: Versuchsbericht, Vorschläge zur Bemessung und konstruktiven Ausbildung. Kritische Spannungszustände des Betons bei mehrachsiger, ruhender Kurzzeitbelastung [Concrete hinges: Test report, recomendations for structural design. Critical stress states of concrete under multiaxial static short-term loading]*, Volume 175. Ernst und Sohn. In German.

Leonhardt, F. (1986). Mainbrücke Gemünden – Eisenbahnbrücke aus Spannbeton mit 135 m Spannweite [Bridge over the river Main at Gemünden – prestressed railway bridge with a span of 135 m]. *Beton- und Stahlbetonbau 81*(1), 1–8. In German.

Maidl, B., M. Herrenknecht, U. Maidl, & G. Wehrmeyer (2012). *Mechanised Shield Tunnelling*. Wiley-Blackwell.

Marx, S. & G. Schacht (2010a). *Betongelenke im Brückenbau [Concrete hinges in bridge construction]*, Volume 18. Deutscher Beton- und Bautechnik-Verein e.v. In German.

Marx, S. & G. Schacht (2010b). Concrete hinges – historical development and contemporary use. *3rd fib International Congress – 2010 3*, 2822–2843.

Marx, S. & G. Schacht (2010c). Gelenke im Massivbau [Hinges in concrete structures]. *Beton- und Stahlbetonbau 105*(1), 27–35. In German.

Menétrey, P. & K.J. Willam (1995). Triaxial failure criterion for concrete and its generalization. *ACI structural Journal 92*(3), 311–318.

Morgenthal, G. & P. Olney (2016). Concrete hinges and integral bridge piers. *Journal of Bridge Engineering 21*(1), 06015005.

Pichler, B., C. Hellmich, & H.A. Mang (2007). A combined fracture-micromechanics model for tensile strain-softening in brittle materials, based on propagation of interacting microcracks. *International Journal for Numerical and Analytical Methods in Geomechanics 31*(2), 111–132.

Ross, A. (1958). Creep of concrete under variable stress. In *Journal Proceedings*, Volume 54, pp. 739–758.

Sallenbach, H.H. (1967). Betongelenke beim Hardturm-Viadukt [Concrete hinges for the Hardturm-Viadukt]. *Schweizer Bauzeitung 85*, 615–619. In German.

Schacht, G. & S. Marx (2010). Unbewehrte Betongelenke – 100 Jahre Erfahrung im Brückenbau [Unreinforced concrete hinges – 100 years experience in bridge constructions]. *Beton- und Stahlbetonbau 105*(9), 599–607. In German.

Schacht, G. & S. Marx (2015). Concrete hinges in bridge engineering. *Proceedings of the Institution of Civil Engineers-Engineering History and Heritage 168*(2), 65–75.

Schlappal, T., M. Schweigler, S. Gmainer, M. Peyerl, & B. Pichler (2017). Creep and cracking of concrete hinges – insight from centric and eccentric compression experiments. *Materials and Structures*. Accepted for publication.

Computational Modelling of Concrete Structures – Meschke, Pichler & Rots (Eds)
© 2018 Taylor & Francis Group, London, ISBN 978-1-138-74117-1

Rotational capacity of concrete beams using a crack process band

Jens Peder Ulfkjaer
Aarhus University, Aarhus, Denmark

ABSTRACT: Rotational capacity of a reinforced concrete structure is a measure of structural robustness. Here the rotational capacity of reinforced concrete beams is based on modelled and experimentally determined load-deflection curves. The modeling of the moment-curvature relationship in a cross section is based on an iterative process. The modeling of the load-displacement curve is divided into two parts. First a model for the pre-peak and then the second curvature interval will be the post-peak. This division of the model is made because the beam will be subjected to a de-loading zone around the beam middle which will have increasing curvature while the cross sections outside the band will have decreasing curvature. By using both the pre-peak and the post-peak models, the whole load-displacement curve can be modelled. It is seen from that the rotational capacity of a reinforced concrete beam is dependent on the beam size and the reinforcement ratio.

1 INTRODUCTION

Robustness is in generally considered a property of the system that can be interpreted on deterministic or probability based methods.

On a probabilistic level this performed on an engineering system where the system can refer to both a structural system and as well as its associate inspection, maintenance and repair Baker et al. (2008).

On a structural level, the robustness of a reinforced concrete structure is a measure of the ability to obtain deformations prior to failure, Beeby A.W (1997).

On a deterministic level there exists indices such as the deterministic reserve strength, Frangopol and Curley (1987).

The rotational capacity of a reinforced concrete structure is another measure of robustness. In many aspects, this makes rotational capacity an important factor of reinforced concrete structures, i.e. redistribution of internal forces, robustness and warning before failure, R. Eligehausen (1987), H. Eifler (1987).

In the determination of the rotational capacity it is important to take the descending branch into consideration as a large amount of energy is dissipated in that phase, J.E. Daniel et al (2008), B. Sungjin et al (2009).

The rotational capacity is dependent on many factors including reinforcement ratio, see Figure 1, concrete quality but also size, Hillerborg A. (1990).

The subject of rotational capacity has been the subject of wide research over the last couple of decades and a nice overview of the development is given by, Carpinteri et al (2009).

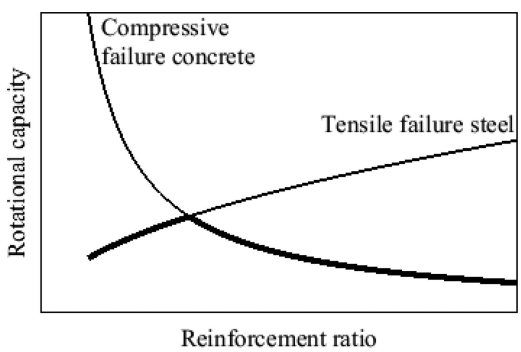

Figure 1. Rotational capacity as a function of the reinforcement ratio for two different failure modes.

Here the rotational capacity of reinforced concrete beams is determined based on modelled load-deflection curve and from experiments. The model is based on a method with a crack band developed for plain and lightly reinforced concrete beams combined with virtual work, Christensen and Lykkegård (1995), Ulfkjær et al. (1995), Ulfkjaer and Brincker (1996), Henriksen et al. (1996).

The rotational capacity is in general dependent on many factors and in Figure 1 the dependence on the reinforcement ratio is illustrated, changing with the failure mode.

2 NUMERICAL MODEL

The model to determine the force-displacement curve for a reinforced concrete beam will be based

on the use of non-linear stress-strain relationships for both concrete and reinforcement.

Before modeling the load-displacement curve a moment-curvature relationship will be modeled and then be used in the determination of the load-displacement curve.

The method is separated into two procedures called **pre-peak** and **post-peak**. The peak-value is the curvature value which gives the highest moment value in the moment-curvature relation. The pre-peak procedure will be based on the use of virtual work. In the post-peak procedure a process band will be introduced in the modeling of the descending part of the load-displacement curve.

2.1 *Basic assumptions*

When modeling the load-displacement curve for a reinforced concrete beam, the following assumptions will be used.

The static system is three-point bending. Only the tensile reinforcement has been taken into consideration. This means that no compressive reinforcement or stirrups has any influence on the modeled load-displacement curve.

The following set of complete conditions have been applied.

The static condition: Equilibrium between external and internal loads. Virtual work is used in the modeling of the load-displacement curve.

The geometrical condition: plane cross sections remains plain.

The constitutive conditions: for concrete and steel are as follows:

2.1.1 *Concrete*

The stress-strain curve for concrete compression is based on a function from CEB (1990). This function gives a non-linear stress-strain curve as shown in Figure 2.

The stress-strain curve for concrete in tension is based on a linear elastic stress-strain curve with linear softening. To determine the rupture strain the fracture energy described by, Hillerborg, (1985) has been taken in consideration. This gives at stress-strain curve as shown in Figure 3.

2.1.2 *Steel*

The stress-strain curve for the reinforcement is modeled so it matches the stress-strain curve for hot rolled steel with a parabolic hardening from Berkeley, (2006). The stress-strain curve is shown in Figure 4.

2.2 *Modeling the moment-curvature relationship*

The modeling of the moment-curvature relationship in a cross section is based on an iterative

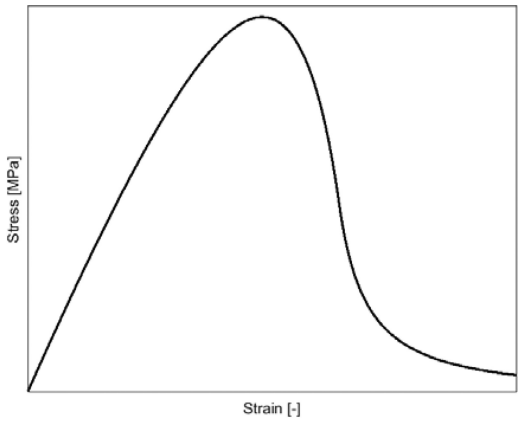

Figure 2. Stress-strain curve for concrete in compression.

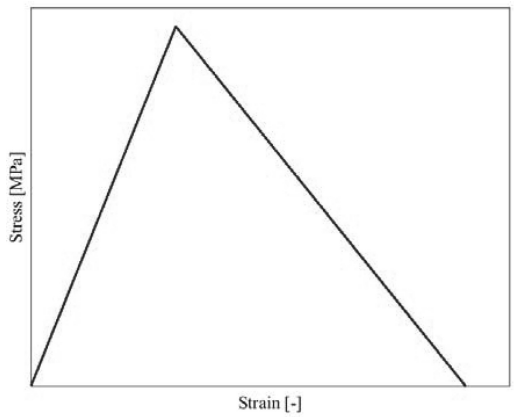

Figure 3. Stress-strain curve for concrete in tension.

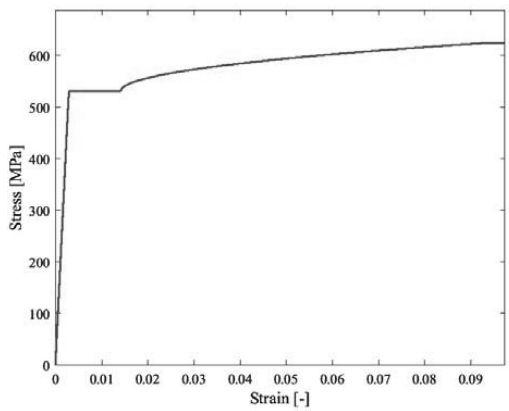

Figure 4. Stress-strain relationship for the steel in tension.

process, and is used as a basis to calculate the load-displacement curve.

Basically the bending moment in the cross section is determined corresponding to a number of curvatures between zero and the curvature at rupture in either reinforcement or concrete.

The geometry of the cross section as well as the characteristics of the materials must be defined prior to the calculation. Subsequently the first curvature level (for which the bending moment is requested) is chosen, and the iterative process begins by guessing a neutral axis depth. Then the strain distribution in the cross section is calculated based on the chosen curvature level and an assumption that plane cross sections remain plane.

This assumption through the constitutive conditions also provides a stress distribution in the cross section as the stress-strain diagram was defined a priori. The resultant forces in the cross section are calculated and the equation of equilibrium in the cross section is written.

In the case that equilibrium is not found a new neutral axis depth is chosen and the above mentioned procedure is repeated until equilibrium occurs. At the equilibrium state the bending moment is calculated and additional it is controlled that neither the strain in the concrete or reinforcement exceeds the materials ultimate strain, as rupture thereby would have occurred.

Using this method a single point on the moment-curvature relationship is determined. Finally, this method can be repeated a sufficient number of times to estimate the full moment-curvature relationship.

2.3 *Modeling of the load-displacement curve*

The modeling of the load-displacement curve is divided into two parts. First a model for the pre-peak which is for the curvature interval $0 \leq \kappa \leq \kappa_{Peak}$. The second curvature interval will be the post-peak $\kappa_{Peak} \leq \kappa \leq \kappa_{Rupture}$. This division of the model is made because the beam will be subjected to a de-loading. This will mean increasing deformations due to decreasing load. At de-loading a band around the beam middle will have increasing curvature while the cross sections outside the band will have decreasing curvature. By using both the pre-peak and the post-peak models the whole load-displacement curve can be modeled.

2.4 *Pre-Peak modeling of the load-displacement curve*

The load-deflection curve for the pre-peak interval $0 \leq \kappa \leq \kappa_{Peak}$ is modeled after the following procedure.

The moment-curvature relationship for the chosen geometry of the cross section will be the input for modeling the load-displacement curve.

1. Decide for which curvature level the deformations must be calculated for. The associated load level can be defined on the basis of the moment curvature relationship.
2. The beam is divided into intervals. The size of the intervals indicates the distance between each point on the load moment curve. The curvature variation along the beam axis and the virtual moment curve values will be calculated.
3. The moment distribution along the beam axis to the chosen load level, M, is determined. The moment curve is depending on the static system. In this case straight lines.
4. Define the curvature variation along the beam axis to the chosen load level. The curvature variation along the beam axis can be defined by using the moment curvature relationship. Hereby the curvature in each cross section along the beam axis can be determined for a specific bending moment.
5. The virtual moment curve M_1 is determined along the beam axis.
6. Virtual work is used to determine a single point on the load-displacement, δ, curve corresponding to the curvature level:

$$\delta_{center} = \int_0^L \frac{MM_1}{EI} dx = \int_0^L M_1 \kappa dx \tag{1}$$

Note that this only gives one point on the load-displacement curve. By starting again from point 1 and choosing a new curvature level another point can be calculated.

2.5 *Post-Peak modeling of the load-displacement curve*

To estimate the load-deflection curve for the post-peak interval $\kappa_{peak} \leq \kappa \leq \kappa_{rupture}$ a fracture process band is introduced at the middle of the beam in which the distribution of curvature is assumed being constant.

The deformation is then divided into two parts: a plastic and an elastic contribution.

$$\delta_{process} = \delta_{band,elastic} + \delta_{band,process} \tag{2}$$

2.5.1 *Plastic deformation*

The plastic contribution to the deformation is calculated on the basis of the curvature in the plastic band, and the estimated size of the plastic band. Theoretically, the deflection across the band

follows an ideal circular shape, as the distribution of the curvature is assumed being constant within the band. The beam segments outside the band is here assumed being rectilinear (without any elastic contributions). The following equations have been used to calculate the plastic distributions to the deformation:

$$R_{zero} = \frac{1}{\kappa_{process}} \tag{3}$$

The total plastic deformation is then given by:

$$\delta = \delta_{elastic} + \delta_{process} \tag{4}$$

Note that the plastic deformation increases despite that the beam in this subjected to de-loading.

2.5.2 *Elastic deformation*

The previously assumed rectilinear beam segments in the elastic part are now having an elastic distribution of curvature, and will as a result provide an elastic deformation.

A spring constant, is introduced, and the elastic deformation is then formulated as a function of the load:

$$\delta_{elastic} = \frac{1}{48}\frac{PL^3_{reduced}}{EI} \tag{5}$$

Were P is the external load and $L_{reduced}$ is the length of the elastic part of the beam. It should be noticed that the elastic deformation will decrease during the de-loading, while the distribution of curvature outside the plastic band is decreasing. However, the curvature in the process band will increase leading to an increase in $\delta_{process}$.

3 EXPERIMENTAL INVESTIGATION

3.1 *Introduction*

This article is based on a test program consisting of 117 beams in three-point bending, 54 plain concrete beams for determination of the fracture energy and 324 concrete cylinders for determination of the concrete strength parameters, Henriksen, M.S. (2004). In this paper 27 of these beams have been considered.

In the test program full load-deflection curves, the curvature variation along the beam axis and the mutual angular rotation has been measured. These data has been used to determine the plastic rotational capacity for all 27 beams.

Nine different beam types have been considered and each type has been repeated three times. Beam sizes and reinforcement ratios are listed in Table 1.

The 27 beams have the same slenderness ratio ($L/h = 12$).

To insure the beam failure is in bending stirrups along the beam axis were used. To secure that the stirrups and the compression reinforcement had no influence on the compression zone, no stirrups were placed in the middle of the beam.

3.2 *Test set-up*

The reinforced concrete beams were all subjected to three-point bending in a specially designed

Table 1. Naming of the beams with sizes and reinforcement ratios.

	L	Reinforcement ratio		
Type: $b \times h$	mm	0.14%	0.39%	1.57%
B: 100×100	1200	1ø4	2ø5	8ø5
E: 100×200	2400	1ø6	1ø10	4ø10
H: 200×400	4800	1ø12	1ø20	4ø20

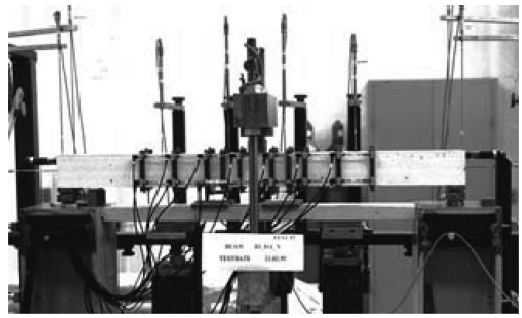

Figure 5. The test set-up. The two steel columns can be moved to adjust for different beam length.

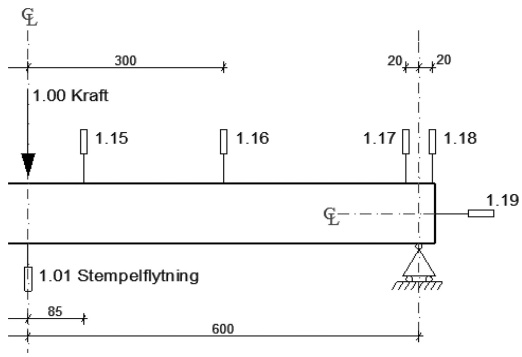

Figure 6. The measurement system allowing for measuring rotations vertical displacements and rotations at the supports.

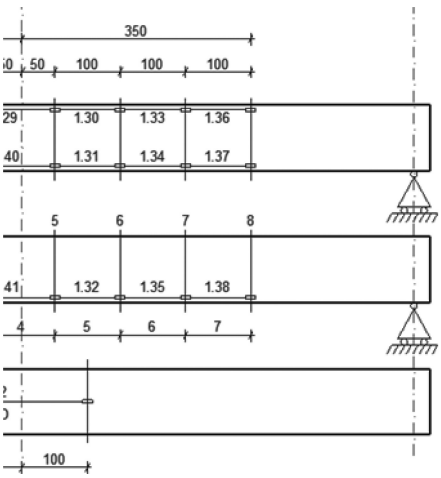

Figure 7. The measurement system allowing for measuring rotations along the beam axis.

servo-controlled material testing system, which was built as to allow testing of different beam sizes, see Figure 1.

3.3 *Boundary conditions*

Horizontal displacements and rotations were partially allowed at both supports. Rotations around the beam axis were only allowed at one support. At the load point rotations were allowed around all axes.

3.4 *Measurements*

The vertical displacements of the beam were measured at eight points along the beam axis, of which four LVDT's were used to determine the rotations at the ends of the beams. The stroke was measured using the built-in LVDT, see Figure 2. By using a number of specially designed measuring frames, it was possible to measure the mutual rotation of the cross-section along the beam axis. Then the average curvature between the measuring frames could be estimated by dividing the mutual rotations by the distance between the frames, see Figure 3.

3.5 *Materials*

Concrete

A normal strength concrete was used. The concrete was delivered from a commercial manufacturer (ISO 9002 certificate). The mechanical properties of the concrete were obtained by national standard tests, and these parameters are listed in. Concrete cylinders with a diameter of 100 mm and a depth of 200 mm, were used to determine the compressive strength, the tensile splitting strength and the modulus of elasticity. In addition, notched RILEM beams with a span of 800 mm, a depth of 100 m mm and a thickness of 100 mm were used to determine the bending tensile strength and the bending fracture energy. See Table 2.

Table 2. Mechanical properties of the concrete.

	Mean	S. Dev
Compressive strength	64.0 [MPa]	6.12 [MPa]
Splitting Strength	4.09 [MPa]	0.54 [MPa]
Modulus of elasticity	4.23E4 [MPa]	3.10 [GPa]
Bending tensile strength	5.51 [MPa]	0.34 [MPa]
Bending fracture energy	126 [J/m^2]	8.30 [J/m^2]

Table 3. Mechanical properties of the steel.

Diameter	E_s	f_y	f_u	$\Delta\varepsilon_{sy}$ [%]	ε_{su} [%]	f_u/f_y
ø4	2.01E5	740	0	740	1.41	–
ø5-1	1.94E5	701	0	701	2.20	–
ø5-2	2.01E5	708	0	708	2.94	–
ø6	2.09E5	600	3.44	664	13.1	1.11
ø10	2.06E5	611	2.27	681	11.2	1.11
ø12	2.01E5	555	2.56	642	11.5	1.16
ø20	1.82E5	531	1.13	624	9.27	1.18

Reinforcement

In this test program, two types of reinforcement and six different diameters have been used. This has been necessary in order to match the reinforcement ratios in the different beam sizes. The two types of reinforcement (ø4 and ø5) are the cold drawn and (ø6, ø10, ø12 and ø20) are hot rolled steel. The cold drawn steel has a relative small deformation capacity whereas the hot rolled steel has a large yield capacity and a clear strain hardening. Table 3 shows the Youngs Modulus, E_s, the yield strength, f_y, the ultimo strength, f_u, the length of the yield plateau, $\Delta\varepsilon_{sy}$ and the ultimo strain, ε_{su}.

The results of selected tests will be shown in the next section together with the modelling results.

4 PARAMETER INVESTIGATION

4.1 *Definition of rotational capacity*

The following measure has been used as the rotational capacity, θ, for both the model and the experiments and is based on load displacement curves.

$$\theta = \frac{4}{L}\int_0^{\infty} \frac{F}{F_y}\, d\delta \tag{1}$$

where, F_y, is the maximum load.

4.2 *Results*

An example of a model result is shown in Figure 8 where the modelled curve is shown together with the three experimental results. In the particular case the length of the band is chosen as 970 mm.

For the remaining beams the length of the band has also been estimated.

In Figure 9 is seen that the rotational capacity of a reinforced concrete beam is very dependent on the reinforcement ratio. In the figure below it is seen that the rotational capacity is increasing until a reinforcement ratio of about 0.4%. After this point the rotational capacity decreases to a more or less a steady level at a reinforcement ratio at about 1.5%. It should be noted that Figure 9 is not based on experiments but using the model described.

This trend is very similar to the theoretical figure shown in the introduction.

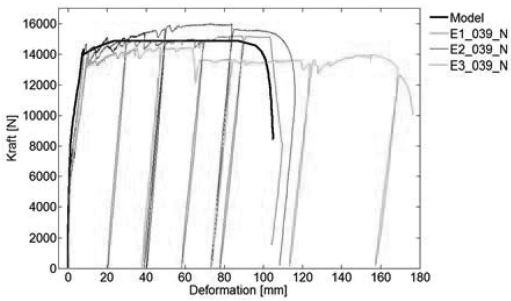

Figure 8. Model and experimental determined curve for E3_039_1-3.

Table 4. Rotational capacities for the 27 beams.

	Experimental		Model	
Beam	Mean	S.Dev	Mean	S.Dev
B_014	0.0230	3.7E-3	0.025	4.1E-3
B_039	0.0334	7,8E-3	0.021	7.4E-3
B_157	0.0649	6.0E-3	0.046	4.7E-3
E1_014	0.0517	9.2E-3	0.208	1.1E-2
E1_039	0.2260	5.1E-2	0.025	3.7E-3
E1_157	0.0795	2.5E-2	0.063	2.3E-2
H1_014	0.0152	1.0E-3	0.029	1.1E-3
H1_039	0.1070	1.7E-2	0.067	9.8E-3
H1_157	0.0719	8.0E-3	0.060	7.0E-3

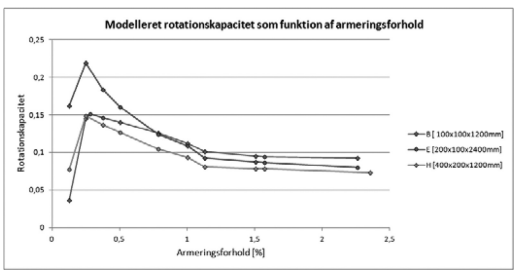

Figure 9. Modelled rotational capacity as a function of the reinforcement ratio for varying beam dimensions.

5 CONCLUSIONS

A model for determination of complete load deflection curves for reinforced concrete beam has been developed. The method is separated into two procedures called **pre-peak** and **post-peak**. The peak-value is the curvature value which gives the highest moment value in the moment-curvature relation. The modeling of the moment-curvature relationship in a cross section in the pre-peak is based on an iterative process, and by use of virtual work the displacements can be calculated from the curvature. In the post-peak procedure a process band is introduced in the modeling of the descending part of the load-displacement curve.

This article is based on a test program consisting of 117 beams in three-point bending, 54 plain concrete beams for determination of the fracture energy and 324 concrete cylinders for determination of the concrete strength parameters. In this paper 27 of these beams have been considered. The test set-up was specially developed for testing beams at very different load scales. There was large scatter of the rotational capacity determined in the test.

The load displacement corves from the model fits very well with the experimentally determined.

For the descending branch it was necessary to fit the size of the band, and additional work is needed for a consistent model. Also the results from the remaining 80 beams should be analyzed with the model.

ACKNOWLEDGEMENTS

The implementation of the model in Matlab© has mainly been performed by Lise K. Andersen and Mikkel S. Jensen during qualifying dissertation for the bachelor's degree, L. Andersen and M S. Jensen (2011).

REFERENCES

Andersen, L and M S. Jensen, *Rotationskapacitet i armerede betonbjælker,* Aarhus University, In danish (2011).

Bae Sungjin and Oguzhan Bayrak: *Plastic Hinge Length of Reinforced Columns*, ACI Structural Journal, Title no. 105-S28, May-June, 2008.

Baker, J.W., Schubert, M. and Faber, M.H: *On the Assesment of Robustness,* Structural Safety, Volume 30, Issue 3, May 2008, Pages 253–267.

Beeby A.W.: *Ductility in reinforced concrete: why is it needed and how is it achieved?*, The Structural Engineer, Volume 75/No 18, September 16, 1997.

Berkeley, California, Computers and Structures, Inc.,: *Technical Note Material Stress-Strain Curves,* April 2006.

Carpinteri A, Corrado M, Mancini G. and Paggi M (2009). *Size Scale Effects on Rotational Capacity of Reinforced Concrete Beams*, ACI Structural Journal, November—December 2009, 887–896.

CEB-FIP Bulletin 242 – *Ductility of Reinforced Concrete Structures*, Synthesis Report and Individual Contributions, Bulletin d'Information Nº 242, May 1998.

CEB-FIP Model Code 1990 – *Final draft*, The Euro-International Committee for Concrete and the International Federation for Prestressing, Bulletin d'Information Nº 203, July 1991.

CEB-FIP—Model Code 2010, *First complete draft*, Volume 1, March 2010.

CEB-FIP—Model Code 2010, *First complete draft*, Volume 2, April 2010.

Christensen F and Løkkegaard T.: *Post-Peak Behaviour of Reinforced Concrete Beams,* M.Sc. Study Programme Civil Engineering, Department of Building Technology and Structural Engineering University of Aalborg, January 1995.

Daniell, J.E., Oehlers, D.J., Griffith, M.C., Mohamed M.S. and Ozbakkaloglu, AliT. *The softening rotation of reinforced concrete members*, Engineering Structure, Volume 30, Issue 11, November 2008, Pages 3159–3166.

Eligehausen R., Langer P: *Rotation capacity of plastic hinges and allowable degree of moment redistribution*, Universität Stuttgart, January 12, 1987

Frangopol, B.R. and Curley, J.P, *Effects of damage and redundancy on structural reliability*, Journal of Structural Engineering 113 (7), 1533–1549.

Eifler, H.G. Plauk: *Drehfähigkeit plastischer Gelenke in biegebeanspruchten Stahlbetonkonstruktionen*. Bericht der Bundesanstalt für Materialeprüfung (BAM) zum Forschungsvorhaben BAM: vh 221.2.221, Berlin, 1974.

Henriksen M.S., Ulfkjær J.P and Brincker R.*: Scale effects and transitional failure phenomena of reinforced concrete beams in flexure. Part 1*, Department of Building Technology and Structural Engineering, Aalborg University, Aalborg, Denmark, August 1996.

Henriksen M.S: *Deformation Capacity and Cracks of Reinforced Concrete Beams*, Ph.D. Thesis, Department of Building Technology and Structural Engineering, Aalborg University, Aalborg, Denmark, 2004.

Hillerborg, A.: *Fracture mechanics concepts applied to moment capacity and rotational capacity of reinforced concrete beams*, Division of Building Materials, Lund Institute of Tecknology, 1990.

Hillerborg, A.: *The theoretical basis of a method to determine the fracture energy GF of concrete*, Materials and Structures, Volume 18, Number 4, Rilem Technical Committees, July, 1985.

Ulfkjaer J.P, Krenk S and Brincker R., *Analytical Model for Fictitious Crack Propagation in Concrete Beams*, Journal of Engineering Mechanics, ASCE Vol 121, No.1, January 1995, 7–15.

Ulfkjær, J. P., & Brincker, R. (1996). *Analytical Model for Fictitious Crack Propagation in Reinforced Concrete Beams without Debonding*. In A. Carpinteri (Ed.), Proceedings of the International Union of Theoretical and Applied Mechanics (IUTAM) Symposium on Size-Scale Effects in the Failure Mechanisms of Materials and Structures: Politecnico di Torino, Turin, Italy, 3–7 October, 1994, 357–370.



Taylor & Francis
Taylor & Francis Group
http://taylorandfrancis.com

Computational Modelling of Concrete Structures – Meschke, Pichler & Rots (Eds)
© 2018 Taylor & Francis Group, London, ISBN 978-1-138-74117-1

An embedded rebar model for computational analysis of reinforced concrete structures with applications to longitudinal joints in precast tunnel lining segments

V.E. Gall, S.N. Butt, G.E. Neu & G. Meschke
Institute for Structural Mechanics, Ruhr-University Bochum, Germany

ABSTRACT: In this contribution, a high-resolution structural model employing the Finite Element Method (FEM) is developed and used to investigate the crack distributions and local failures in reinforced concrete structures, with specific focus on the longitudinal joint of individual tunnel segments. A two-pronged approach for the modeling of reinforced concrete is proposed. Firstly, in order to correctly take into account the fracture behavior of the concrete, the concrete itself is modeled using non-zero thickness interface elements placed between finite bulk elements. The interface elements control the fracture behavior, and the bulk elements contribute to the compressive behavior of the concrete through means of an elasto-plastic constitutive law. Secondly, in order to account for the reinforcement bars, the rebar itself is modeled as a simple linear truss and coupled with the concrete matrix using a constraint condition between control points located on the rebar elements and their respective projection points within the elements in which they are embedded. As a consequence of this, the degrees of freedom of the bulk and rebar elements are not condensed at the element level and therefore rebar slip, and the resulting bond-stress response (as is given in the model code for example), can be explicitly accounted for. It is not necessary that the constituent truss and bulk meshes be compatible. Furthermore, because the constraint condition is only defined between the linear bulk elements and the rebar truss elements, rebar slip and interfacial damage remain independent, and are only coupled on the structural level. Examples are provided for the validation of this approach. The developed simulation technique is finally used to predict the cracking response of the longitudinal joints of reinforced concrete tunnel lining segments.

1 INTRODUCTION

Reinforced concrete (RC) is one of the mostly widely used building materials in the construction industry. Its adaptability to most constructions is due on one hand to its cost, as it is relatively inexpensive to produce, and on the other hand, due to its mechanical properties, as it possesses high compressive and tensile strengths. Reinforced concrete's high compressive strength is naturally inherited from its concrete bulk, whereas its high tensile strength is due not only to the steel reinforcement bars cast within the concrete matrix, but also to the interface properties between the steel and concrete. When predicting the structural response of reinforced concrete structures, it is therefore not only important to the accuracy with which the material behavior of the steel and concrete constituents is modeled, but also to which extent the bond-slip behavior of the steel-concrete interface is taken into account.

Numerical methods offer many techniques with which to model composite reinforced concrete structures. Using numerical methods, the complex interactions between different structural constituents such as the bond-slip behavior between the concrete and the rebar, the rebar plasticity, and the concrete damage mechanisms can be explicitly taken into account. The following provides a brief overview of some common approaches used to model embedded reinforcement within the Finite Element Method (FEM).

Explicit reinforcement: The simplest manner in which to model reinforcement bars is to explicitly incorporate the reinforcement as truss elements or beam elements into the mesh. This method, however simple and intuitive, offers multiple drawbacks. The largest drawback is that the mesh must be modified to account for the reinforcement nodes. This can be numerically costly as, in the case of reinforcement near to the structure's surface, the domain must be very finely meshed in order to account forthe minimum concrete cover needed. If bond-slip characteristics are to be considered, this scheme must be augmented with other modeling techniques, such as the introduction of a contact algorithm between the reinforcement and the concrete (Rumanus 2009).

Smeared reinforcement: Using the basic concepts of mixture theory (Truesdell & Toupin 1960), the reinforcement bars can be embedded within the concrete matrix and treated macroscopically as a single material. The global macroscopic strain is split at the material point level and a homogenization scheme, e.g. (Mori & Tanaka 1973) is used to regain the global macroscopic stresses. Using this method, it is difficult to explicitly account for rebar slip unless the slip is implicitly accounted for as a function of the steel strain as in (Rumanus 2009). Additionally, it is difficult to incorporate discrete cracking of the concrete into such methods. A method using the Strong Discontinuity approach has, however, been presented in (Oliver, Linero, Huespe, & Manzoli 2008).

Embedded reinforcement: Embedded methods, as first introduced by e.g. (Phillips & Zienkiewicz 1976), for modeling reinforced concrete are those in which, on the basis of displacement constraints, a formulation of the global stiffness matrix is developed in which only the degrees of freedom of the concrete elements appear. Such methods are appealing as the orientation of the rebar within the concrete mesh plays a subordinate role and complex reinforcement geometries can therefore be easily modeled. Generally, such methods are used if a stiff bond-slip behavior is to be modeled, however the method has been extended to account for slip by first (Elwi & Hrudey 1989) and more recently by (Hartl 2002, Jendele & Cervenka 2006).

The method proposed in this contribution is a composite of the embedded and Explicit methods. Using a penalty-based constraint condition between the nodes of the concrete bulk elements and the rebar element, the reinforcement bars, represented by truss elements, can be arbitrarily meshed and included with in the concrete bulk. This contact condition is further enhanced using concepts from plasticity theory in order to account for the bond-slip mechanism as provided in the *fib* model code 2010 (International Federation for Structural Concrete (fib) 2013). The concrete compressive behavior is controlled by an elasto-plastic constitutive law and concrete tensile behavior is controlled using modified high-aspect-ratio interface elements as proposed by Manzoli, Gamino, Rodrigues, & Claro 2012) and (Zhan & Meschke 2016). The steel material behavior is described as isotropic elastic-plastic. The proposed method is numerically robust and is able to account for the independent crack development in the concrete, the plastification and failure of the reinforcement bars, and is able to provide a correct crack-spacing estimation in multiple-cracking phenomena. The method is applied to the analysis of a flexural beam test and to the analysis of concrete tunnel lining segments under compression.

2 COMPOSITE NUMERICAL MODEL OF REINFORCED CONCRETE

In order to model the reinforced concrete, cohesive interface elements as proposed by Manzoli Gamino, Rodrigues, & Claro 2012, in conjunction with standard small-strain triangular Finite Elements (i.e. Bulk elements) and a penalty based tying algorithm between standard truss elements and the bulk elements are used. The interface solid elements (ISE's) are used to simulate the cracking behavior, and consequent loss of strength, of the concrete and the standard elements control the compressive behavior of the structure. The ISE's are formulated as per Zhan & Meschke 2016. The truss elements that are used to represent the reinforcement bars are tied to the bulk elements in order to enable the reinforcement to bridge cracked areas. The interface elements are of a discrete thickness and therefore the FE mesh is processed such that each standard element is surrounded by interface elements. The mesh of the truss elements, because of the tying algorithm, is independent of that of the others (see Figure 1). In what follows, a description is given of the mechanics of the constituent parts.

2.1 *Interface solid elements*

The ISEs are based on degenerated 2D and 3D solid elements as presented in (Zhan & Meschke 2016). The material properties of these elements are modified to include a displacement based damage formulation derived from a fiber-pullout law (Zhan & Meschke 2014), in order to describe the stress state of the concrete after cracking. The element formulation is based upon the principles of the continuum strong discontinuity approach for the representation of cracks in finite elements.

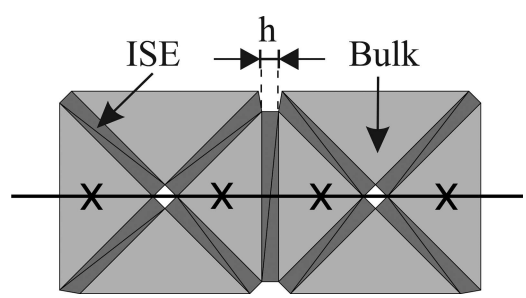

Figure 1. Mesh composition: ISE's are dark grey, bulk elements are light grey, and the truss is represented by the horizontal line. The ×'s mark the location of the truss nodes.

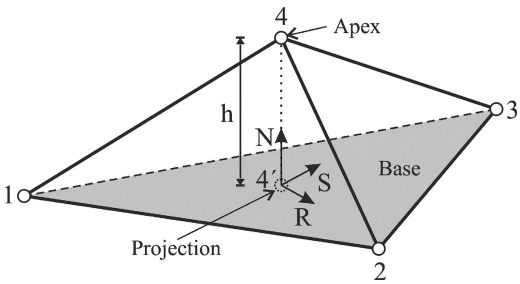

Figure 2. Degenerated 3D solid element characterized by its "base" surface, an "apex" point (Node-4), and the projection of the apex point onto its base (point 4′) along N.

The ISE elements used to model the cracks can, in the general 3D case, be represented as shown in Figure 2:

Here h is the height of the elements, which is usually taken to be a value of approximately 1/1000 of the average side length of the element's base. Because of this the strain in the ISE's is almost exclusively related to the (regularized) unbounded strain $\hat{\varepsilon}$ defined as:

$$\varepsilon \approx \hat{\varepsilon} = \frac{1}{h}(\llbracket \mathbf{u} \rrbracket \otimes \mathbf{N})^s. \tag{1}$$

The displacement jump, $\llbracket \mathbf{u} \rrbracket$ is determined from the relative displacement of the apex node with respect to its projection on the base (Fig. 2).

The inelastic constitutive behavior of ISE is formulated as:

$$\boldsymbol{\sigma} = (1-d)\mathbb{C}_e : \varepsilon \approx (1-d)\frac{1}{h}\mathbb{C}_e : \left(\llbracket \mathbf{u} \rrbracket \otimes \mathrm{n}\right)^s, \tag{2}$$

where d is the scalar damage variable and $\mathbb{C}_e$ denotes the elastic stiffness tensor. A Poisson's ratio of $\nu = 0$ is chosen to decouple the stresses parallel and normal to the interface surface. The loading criterion, $f(\sigma,\alpha)$ isdefined in terms of the equivalent stress $\tilde{\sigma}$ and the displacement-like internal parameter α:

$$f(\boldsymbol{\sigma},\alpha) = \tilde{\sigma} - t(\alpha) \le 0, \tag{3}$$

where the equivalent stress $\tilde{\sigma}$ is defined as:

$$\tilde{\sigma} = \sqrt{\sigma_n^2 + \left(\frac{\sigma_r}{\beta}\right)^2 + \left(\frac{\sigma_s}{\beta}\right)^2}. \tag{4}$$

Here β is a constant that defines the ratio between the strength of the interface element in the normal and shear directions, similar to (Carol, Prat, & Lopez 1997, Grassl & Rempling 2008). If $\beta = 1$ this corresponds to a spherical yield surface in stress space, whereas if $\beta \neq 1$ the failure surface is ellipsoidal.

The softening behavior of interface is determined based on degenerated form of of a so-called "crack bridging model" used to describe SFRC behavior, in which the SFRC contribution is neglected (Zhan & Meschke 2016):

$$t(\alpha) = (f_t)\exp\left\{-\frac{\alpha}{w_{\mathrm{ref}}}\right\}, \tag{5}$$

where f_t represents the tensile strength of the fiber reinforced concrete composite and $w_{ref} = G_f / f_t$, where G_f is the fracture energy. The internal parameter α is defined based on the maximum value of equivalent separation experienced during the loading history as

$$\alpha = \max(\tilde{u}) - \tilde{u}_0. \tag{6}$$

The equivalent crack separation, $\tilde{u}$, is defined as

$$\tilde{u} = \sqrt{\llbracket u \rrbracket_n^2 + \left(\frac{\llbracket u \rrbracket_r}{2\beta}\right)^2 + \left(\frac{\llbracket u \rrbracket_s}{2\beta}\right)^2}, \tag{7}$$

where β is the same as in Eqn. (4) and $\tilde{u}_0$ corresponds to the limit state of the elastic interface:

$$\tilde{u}_0 = \frac{f_t}{K_0} = \frac{h f_t}{E} \approx 0, \tag{8}$$

with K_0 and E representing the "rigid" elastic stiffness and the Young's modulus of the equivalent interface behavior, respectively. The scalar damage variable $d(\alpha)$ is obtained by comparing the secant stiffness K^{sec} with the elastic stiffness of the equivalent interface behavior as

$$d(\alpha) = 1 - \frac{K^{\mathrm{sec}}}{K_0} = 1 - \frac{ht}{E(\alpha + \tilde{u}_0)}. \tag{9}$$

Lastly it should be noted that damage is only allowed to occur if the ISE is in tension, i.e. if $(\llbracket u \rrbracket_n - \tilde{u}_0 \ge 0)$. Hence, no damage occurs if the interface is in compression. For this reason the elastic properties of the ISE must be chosen in such a manner as to match those of the bulk elements.

2.2 *Rebar*

The rebar in the composite is modeled using linear truss elements. In principle the rebar could be modeled using a beam element, i.e. with a bending stiffness, but here it is assumed that the bending stiffness of the rebar is negligible compared to the bulk concrete which justifies the use of truss elements for modeling rebars. The trusses are modeled as an elastic-perfectly plastic material using a Von-Mises yield criterion.

2.3 *Interfacial constraint formulation*

To model the interaction between the rebar and concrete, the internal force contribution of the rebar slip with respect to the bulk matrix is penalized to enforce a displacement constraint between the rebar and the concrete bulk. In order to do so, a "gap" function between the two domains must be established. The gap, as defined in the global coordinate system, is here taken to be:

$$g = \mathbb{N}_{truss}(\xi_0) \cdot \mathbf{u}_{\text{truss}} - \mathbb{N}_{\text{bulk}}(\xi'_{0,\text{bulk}}) \cdot \mathbf{u}_{\text{bulk}}, \tag{10}$$

where $\mathbf{u}_{\text{truss/bulk}}$ is the displacement vector describing the nodal displacements of the truss or bulk element, $N_{truss/bulk}(\xi)$ is the shape function matrix of the truss/bulk elements, ξ_0 is an arbitrary control point located on the truss and $\xi'_{0,\text{bulk}}$ is the projection of ξ_0 within the bulk element expressed in the local coordinate system of the bulk element.

In order to decompose the gap vector into directions parallel and perpendicular to the truss, an orientation matrix $\mathbb{T}$, to describe the local coordinate system of the truss is defined:

$$\mathbb{T} = \begin{bmatrix} \hat{\mathbf{n}} \\ \hat{\mathbf{r}} \\ \hat{\mathbf{s}} \end{bmatrix}, \tag{11}$$

where $\hat{\mathbf{n}}$ is the unit vector that describes the direction parallel to the truss, and $\hat{\mathbf{r}}$ and $\hat{\mathbf{s}}$ are arbitrarily defined unit vectors in directions normal to $\hat{\mathbf{n}}$ and to each other. The gap function, $\mathbf{g}$, can therefore be expressed in the local coordinates of the truss as $\mathbf{g}'$:

$$\mathbf{g}' = \mathbb{T}^{\mathbf{T}}\mathbf{g} = \begin{bmatrix} s_{\parallel} \\ g_{r,\perp} \\ g_{s,\perp} \end{bmatrix}. \tag{12}$$

Here the first component of the gap vector, $s_{\parallel}$, can be interpreted as being the slip between the truss and bulk that occurs parallel to $\hat{\mathbf{n}}$, i.e. along the direction of the truss.

In order to ensure that no interpenetration of the truss and the bulk matrix occurs, The gaps and slips must be penalized. By defining a penalization matrix $\mathbb{E}$ as:

$$\mathbb{E} = \begin{bmatrix} \epsilon_n & 0 & 0 \\ 0 & \epsilon_r & 0 \\ 0 & 0 & \epsilon_s \end{bmatrix}. \tag{13}$$

The contact force resulting from the penalization of the local gap function becomes:

$$\mathbf{F} = \mathbb{E}\mathbf{g}'. \tag{14}$$

Here $\epsilon_n, \epsilon_r, \epsilon_s$, are chosen to be sufficiently high to guarantee a displacement constraint. For similar problems, it is suggested to use a value of ε as 50 to 100 times of the bulk material properties (Ninić, Stascheit, & Meschke 2014). The first component of the contact force can be interpreted as the bond force between rebar and concrete. Explicitly, the bond force is therefore given as:

$$F_{bond} = [\mathbb{E}\mathbb{T}\mathbf{g}]_1 = \epsilon_{\mathbf{n}}\mathbf{s}_{\parallel}. \tag{15}$$

2.4 *Interface slip*

The model presented so far is equivalent to a fully rigid displacement constraint, assuming the penalty values are taken to be sufficiently high. In order to accurately model rebar pull-out along the concrete-rebar interface, a mechanical formulation must be chosen that accounts for non-recoverable slip and for the permanent degradation of the bond properties of the interface. The given problem is therefore formulated as an isotropic softening elasto-plasticity problem. First a constitutive relationship must be defined. This is obtained by defining a bond stress τ_{bond}, i.e. the stress at the rebar-concrete interface. To do so, a strain measure for the rebar slip must be defined, here $\varepsilon_{slip} = s_{\parallel}/l_r$ is used, where l_r is the length of the truss element. This definition corresponds to a linear slip and a constant strain in each interface. A higher order approximation of the slip and slip strain is also possible by using multiple control points ξ_0 along the interface. Finally, an elastic constitutive relation for the rebar slip is given by:

$$\tau_{bond} = \frac{\epsilon_n s_{\parallel}}{\pi \varnothing_r l_r} = \frac{\epsilon_n}{\pi \varnothing_r} \varepsilon_{slip}. \tag{16}$$

Here $\varnothing_r$ and l_r are the diameter and length of the rebar, respectively.

This elastic constitutive relationship defined in Eq.(16) can be extended to take into account the bond degradation and the non-recoverable slip deformation. To do so, the total slip strain ε_{slip} is additively decomposedinto an elastic ε^{e}_{slip} and non-elastic ε^{p}_{slip} part as:

$$\tau_{bond} = \frac{\epsilon_n}{\pi \varnothing_{rebar}} (\varepsilon^{e}_{slip} - \varepsilon^{p}_{slip}). \tag{17}$$

With the addition of a flow rule, an isotropic hardening law, and the corresponding Kuhn-Tucker loading/unloading conditions

$$\begin{aligned} &\dot{\varepsilon}^{p}_{slip} = \gamma sign(\tau), \\ &\dot{\alpha} = \gamma, \\ &f(\tau,\alpha) \le 0 \qquad \gamma \ge 0 \qquad \gamma f(\tau,\alpha) = 0. \end{aligned} \tag{18}$$

the plasticity problem is complete. The yield and softening functions are chosen so as to be a function of the bond-slip properties of reinforcement.

2.5 *Interfacial bond properties*

In order to obtain correct structural response, a correct bond-slip relationship must be used. If special rebar types are to be investigated, relationships for the bond-slip characteristics of the concrete-rebar interface can be derived from uni-axial pull-out tests, such as those provided in (Ruiz, Elices, & Planas 1998). However, as many rebar designs are standardized, direct bond-slip relationships are provided in the literature for standard rebar and concrete types, e.g. (Bigaj 1999). The bond-slip characteristic curve used in this contribution is a modified form of the law provided by the ModelCode2010 (see Figure 3), as research has shown this relationship to be sufficient in describing the structural behavior of reinforced concrete structures (Jendele & Cervenka 2006).

What is of interest here is the pull-out relationship. If a good bond quality is assumed between the rebar and concrete, the fit parameters are defined as in Table 1:

Here f_{cm} is the compressive strength of the concrete and c_{clear} is the distance between parallel consecutive reinforcement ribs.

In order to obtain a stress strain relationship from the bond slip curve, the slip is normalized over the surface area of the truss. Additionally, as it has been observed that, in structures that are primarily controlled by concrete fracture, the assumption of a stiff bond is sufficient (Rumanus 2009) to model material behavior, the first ascending section of the bond-slip relationship is simplified by an elastic-perfectly plastic envelope as seen in Figure 4, where the "elastic" slope of the interface is controlled by the penalty parameter.

Using the modified shear stress-strain curve, the yield function and hardening parameter can be defined as:

Table 1. Bond slip parameters used to define the control points of the bond-slip relationship as given by the International Federation for Structural Concrete (fib) 2013.

Bond-slip parameters				
$\tau_{b,max}$	$\tau_{b,f}$	S_1	S_2	S_3
$2.5\sqrt{f_{cm}}$	$0.4\tau_{b,max}$	1.0[*mm*]	2.0[*mm*]	c_{clear}

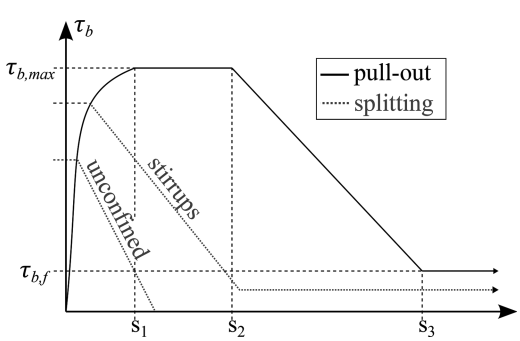

Figure 3. General form of the analytical bond stress–slip relationship as given by the International federation for Structural Concrete (fib) 2013.

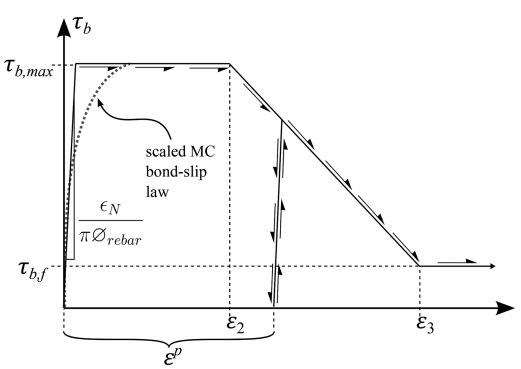

Figure 4. Regularized stress-strain form of bond stress–slip relationship as given by the International federation for Structural Concrete (fib) 2013 with loading path. The dotted line represents the original curve whereas the solid line represents the simplified version adopted in this contribution.

$$f(\tau,\alpha) = |\tau| - (2.5\sqrt{f_{cm}} + H(\varepsilon_{slip})\alpha), \tag{19}$$

and the hardening variable is defined as a piecewise function of the maximum previously experienced strain:

$$H = \begin{cases} 0 & if\ |\varepsilon_{max}| \in [0, \varepsilon_2) \\ \dfrac{-2.5\epsilon_N \sqrt{f_{cm}}}{\epsilon_N \Delta\varepsilon + 2.5\varnothing_r l\sqrt{f_{cm}}} & if\ |\varepsilon_{max}| \in [\varepsilon_2, \varepsilon_3] \\ 0 & if\ |\varepsilon_{max}| \in (\varepsilon_2, \infty) \end{cases} \tag{20}$$

3 ASSESSMENT OF THE PROPOSED MODELING CONCEPT

In order to investigate the acceptability of the proposed approach in modeling the fracturing process of reinforced concrete, flexural tests as carried out by (Leonhardt & Walther 1962) were simulated. The experimental setup is shown in Figure 5 and material properties are provided in Tables 2 and 3. The simulated crack progression is shown in Figure 6, the final simulated shear crack in Figure 7 and the experimentally observed crack distribution is shown in Figure 8.

The interface properties are determined according to the (International Federation for Structural Concrete (fib) 2013) as described in the previous section.

The predominant feature of the fractured beam is the large shear crack that develops upon failure.

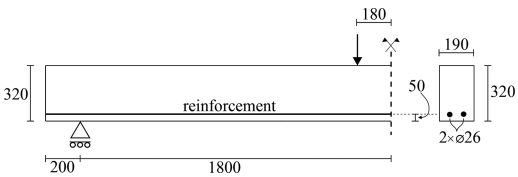

Figure 5. Experimental setup of simulation; front view of beam on right and cross section left. All units are given in [mm].

Table 2. Properties of linear elastic (bulk) and interface solid elements (ISE) used to model the Leonhardt Beam.

Concrete			
Property	bulk	ISE	Unit
Young's modulus, E	32000	32000	N/mm^2
Poisson ratio, v	0.2	0.0	–
Tensile strength, f_t	–	1.64	N/mm^2
Fracture energy, G_f	–	0.062	N/mm

Table 3. Properties of reinforcement.

Reinforcement		
Young's modulus, E	32000	N/mm^2
Poisson ratio, v	0.0	–
Yield Stress, σ_y	456	N/mm^2
Hardening modulus, H	2.0	N/mm^2

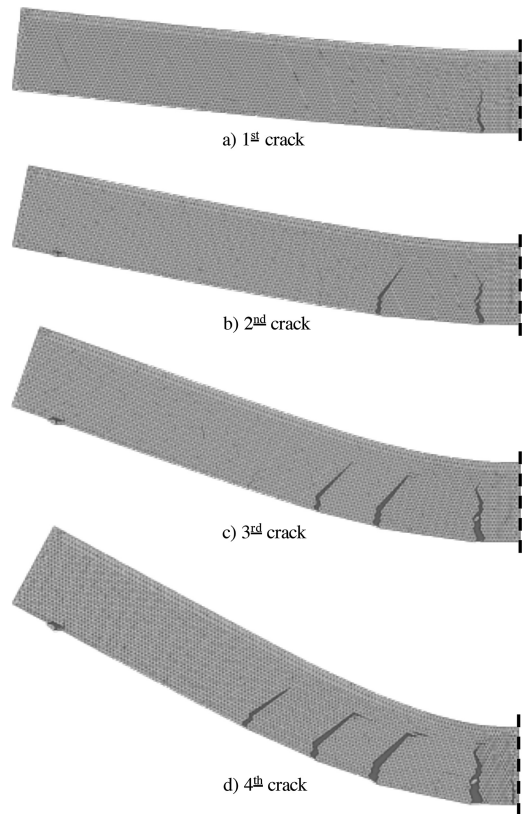

Figure 6. Simulated progression of crack development (100x displacement magnification).

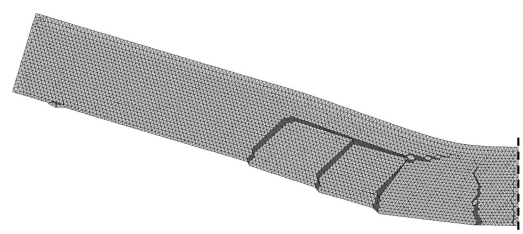

Figure 7. Predicted final crack distribution in simulation at failure (50x displacement Magnification). The experimentally observed shear failure is captured using the proposed method.



Figure 8. Observed fracture pattern as reported in *Leonhardt and Walther*, 1962.

the crack propagates from a mid-section of the beam, intersects with another pre-existing crack, and then propagates further towards the loading point as can be seen in Figure 8. The finite element simulation is able to capture this phenomenon at failure 7. As is readily observed, the major crack occurs in approximately the same position as that observed in the experiment, intersects with other cracks and, as observed in the experiment, leads to failure due to the shear crack along the top section of the beam.

What is also of interest is the capability of the proposed method in predicting the crack development along the length of the rebar. As can be seen in Figure 6, the first crack occurs at the point at which bending stresses are the highest, specifically below the loading area. Du to unloading in the surrounding concrete matrix, the tensile stresses then progress along the rebar and initiate the second crack further along the reinforcement. This pattern of cracking and followed by a load redistribution continues until the shear crack as observed in 7 leads to failure. As is evident by both the ability to simulate the governing shear crack at failure as well as the crack progression, the proposed method offers a powerful framework for the investigation of traditionally reinforced concrete structures.

4 LOADING OF SEGMENTAL TUNNEL LINING

Typically, segmental linings used in mechanized tunneling are designed as reinforced concrete structures. A complete tunnel lining ring is composed of several segments that interact along longitudinal joints and ring joints to form the tunnel tube. According to experience, these linings are highly susceptible to fracture at the center of the lining along their longitudinal direction, i.e. in direction of the length of the tunnel, and at the inner corners of the longitudinal joints, i.e. at the corners of their inner radius (Sugimoto 2006). This second failure phenomenon, chipping at the segment corner, is particularly common. It leads to rebar exposure which makes the steel susceptible to corrosion damage. Although not always immediately structurally relevant, these chipping effects can, over time, lead to serviceability issues. For reasons such as this, design codes provide maximum allowable crack widths in tunnel lining segments (Deutsches Institut für Normung 2011).

In order to investigate damage during tunneling at the segment level, and specifically the effects of the loadings on the longitudinal joint, radial deformations obtained by a full 3D FE simulation of the mechanized tunneling process (Smarslik, Putke, Marwan, Gall, Meschke, & Mark 2017) are applied to a finely meshed plane-strain model of a lining segment. The geometry of the lining segment can be seen in Figure 9.

The investigated segment is assumed to be at the tunnel crown. This placement of the segment has been chosen because most observed segment damages in TBM driven tunnels tend to occur at the crown (Sugimoto 2006). The reaction of the adjoining segments are taken into account by the linear elastic segments at both ends of the modeled segment. Interface elements are placed between the modeled segment and the adjacent segment to enable the opening of the longitudinal joint.

The lining segment simulation performed, although realistic, does not represent a distinct tunnel project. For this reason, the representative concrete material properties provided in Table 4 have been chosen.

The chosen reinforcement layout does not correspond to a specific tunnel project, but, has been chosen so as to represent an exemplary reinforcement layout (Putke, Bergmeister, & Mark 2016). Reinforcement for the splitting stresses and a standard cage reinforcement around the perimeter of the segment are modeled (Figure 10). All rebars and

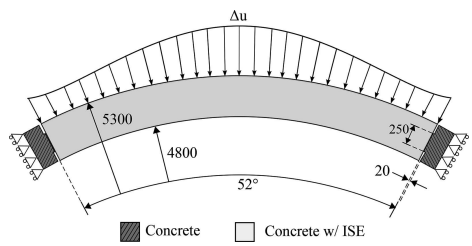

Figure 9. Setup for the numerical simulation. All units are given in [mm].

Table 4. Properties of linear elastic (bulk) and interface solid elements (ISE) used to model plain concrete in the presented lining simulations.

Property	bulk	ISE	Unit
Young's modulus, E	36000	36000	N/mm^2
Poisson ratio, v	0.2	0.0	–
Tensile strength, f_t	–	3	N/mm^2
Fracture energy, G_f	–	0.1	N/mm

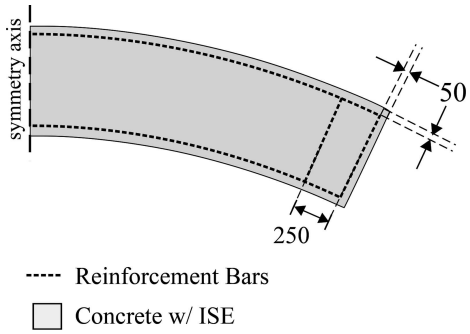

Figure 10. Layout for the reinforcement bars. All units are given in [mm].

interface properties are modeled as described in the section above. It is assumed that rebar cages are placed at 10 cm intervals. To investigate the effect of increasing reinforcement on the crack distribution of the segment, two representative calculations are performed, one using a reinforcement diameter of $\varnothing = 10$ *mm* and one in which $\varnothing = 20$ *mm*.

4.1 *Predcted crack width*

Figures 11, 12, and 13 display the predicted crack distribution for an unreinforced plain concrete segment (PC), a standard reinforced segment, and an over-reinforced segment, respectively. The unreinforced segment is intended as a reference case, and the over-reinforced segment is intended to show the non-linear effects of increasing reinforcement. The predicted crack widths are shown in Table 5.

What can be seen in the the unreinforced segment is that the primary failure mechanism corresponds to "chipping" at the segment corner, and not to a splitting stress failure due to load spreading, as is the case which is designed for. The shape, or rather size, of the load transfer area between two segment joints inhibits the formation of stresses in the corner of the segment. This leads to a type of shearing strain developing between the strained and unstrained areas of the segment at bottom corner of the joint that in turn leads to crack development. Interestingly, because of the effect of the confinement due to the grout, this effect is not observable along the outer edge of the segment.

The conventionally reinforced segment ($\varnothing = 10$ *mm*) displays, as would be expected, a much smaller cracked zone. The observed failure phenomenon corresponds to a splitting type failure as would be expected due to unconfined load spreading. The presence of the reinforcement bars effectively redistribute the stresses so that cracking at the corner is prevented. It should be noted that a diagonal crack is present immediately at the contact area of the longitudinal joint, but does propagate to the

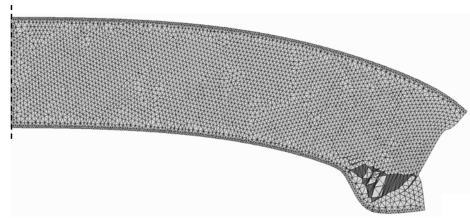

Figure 11. Predicted crack distribution for an unreinforced concrete segment; intended as a reference case (cracked area in red; 200x magnification of displacements).

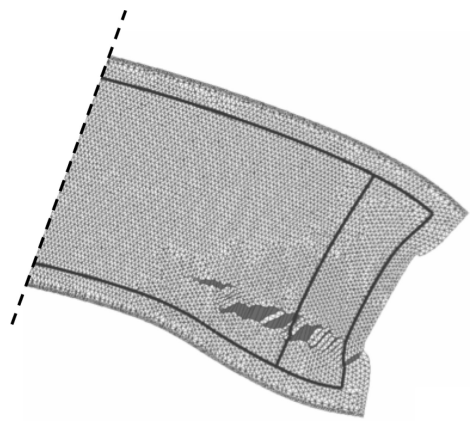

Figure 12. Predicted crack distribution in the tunnel segment assuming a rebar diameter of $\varnothing = 10$ *mm* (cracked area in red; 200x magnification of displacements).

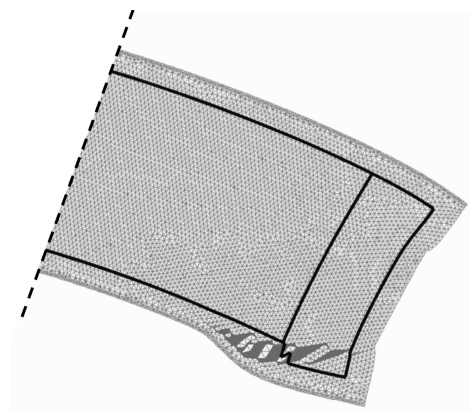

Figure 13. Predicted crack distribution in the tunnel segment assuming a rebar diameter of $\varnothing = 20$ *mm* (cracked area in red; 200x magnification of displacements).

inner edge of the segment. Additionally, the calculated crack width (see Table 5) is within the allowable range i.e. ≤ 0.3 mm (Deutsches Institut für Normung 2011). The strongly reinforced segment

Table 5. Predicted crack widths for the unreinforced segment (PC) and the two variations of reinforced segments (RC).

	PC	RC ∅ 10 mm	RC ∅ 20 mm
Crack [mm]	0.57	0.18	0.38

displays a significantly different crack pattern, as only the "chipping" type of failure is observed. Because the reinforcement bars are significantly stiff due to the increased area, the reinforcement redistributes the stresses to to the stiffest area of the segment, which occurs at its inner corner. The resulting maximum crack width is slightly above the allowable crack widths of 0.3 mm as given in (Deutsches Institut für Normung 2011).

What the presented examples show is that the investigated segment is structurally stable with respect to the applied loads. Cracking is local and does not propagate throughout the segment in a manner so as to compromise the the load bearing capacity of the structure. The expected crack width, however, is not always within an acceptable range, depending on the choice of reinforcement. The design case for which the splitting reinforcement is designed is based on predicted load spreading in an unconfined loading case (German Tunnelling Committee (DAUB) 2013, Deutsches Institut für Normung 2011). The loading scenario that occurs beneath longitudinal joints of tunnel linings is, however, not unconfined, as the grouting confines another area of the joint. The load eccentricity coupled with the one-sided confinement leads to the often observable "chipping" phenomena. This may only be true at the investigated location. The moment at the springline of the tunnel lining is typically negative, and therefore the segment bends in the opposite direction than it does at the tunnel crown. Consequently, a different failure mode would be expected. However, it can be seen that the reinforcement has a significant effect on crack distribution as a more strongly reinforced segment leads to a different failure pattern than a more weakly reinforced segment. Design criteria are typically based on linear load spreading analyses which can often overlook such phenomena.

5 CONCLUSIONS

Within this contribution, a novel concept for the modeling of traditionally reinforced concrete structures has been proposed. Interface Solid Elements (ISE's) are used to model the fracture response of concrete and kinematically linear standard finite elements are used to model the bulk response of the concrete matrix. The reinforcement bars are modeled as elastoplastic truss elements, whose discretization is independent of that of the concrete. The trusses and concrete interact on the basis of a penalty based contact constraint, which has been modified to account for interfacial slip along the length of the rebar. The interfacial slip law is derived from that proposed in International Federation for Structural Concrete (fib) 2013. In analogy to plasticity theory, a measure of non-recoverable plastic slip is defined in order to reproduce the permanent degradation of the concrete rebar interface.

Experiments performed by Leonhardt & Walther 1962 are simulated using the proposed method. It is shown that the method is able to qualitatively simulate the various failure phenomena observed in the experiment, characterized by first opening of bending cracks, followed by a shear crack, which eventually leads to structural collapse. Further, the developed modeling technique is applied for the damage analysis of segmental tunnel linings. Specifically, damage at the longitudinal joint is investigated. It is shown that, different degrees of reinforcement significantly effect the predicted failure phenomena. A larger amount of reinforcement leads to an unfavorable redistribution of stresses that is no longer represents design assumptions, i.e. that a splitting type of failure is to be expected. Rather, when using more reinforcement a "chipping" type of failure, as is often observed, dominates.

ACKNOWLEDGEMENT

Financial support for this work was provided by the German Science Foundation (DFG) in the framework of the sub-project B2 of the Collaborative Research Center SFB 837 "Interaction modeling in mechanized tunneling". This support is gratefully acknowledged.

REFERENCES

Bigaj, A.J. (1999). *Structural dependence of rotation capacity of plastic hinges in RC beams and slabs*. Ph. D. thesis, Department of Civil Engineering, Delft University of Technology.

Carol, I., P.C. Prat, & C.M. Lopez (1997). Normal/shear cracking model: Application to discrete crack analysis. *Journal of Engineering Mechanics 123*(8), 765–773.

Deutsches Institut für Normung (2011). DIN EN 1992-1-1: 2011-01: *Eurocode 2 – Bemessung und Konstruktion von Stahlbeton und Spannbetontragwerken—Teil 1-1: Allegemeine Bemessungsregeln und Regeln für den Hochbau*. Beuth Verlag GmbH, Berlin, Germany. in German.

Elwi, A. & T. Hrudey (1989). Finite element model for curved embedded reinforcement. *Journal of Engineering Mechanics* (115), 740–754.

German Tunnelling Committee (DAUB) (2013). Recommendations for the design, production and installation of segmental rings. Technical report, Deutscher Ausschuss für unterirdisches Bauen e. V. (DAUB).

Grassl, P. & R. Rempling (2008). A damage-plasticity interface approach to the meso-scale modelling of concrete subjected to cyclic compressive loading. *Engineering Fracture Mechanics 75*, 4804–4818.

Hartl, H. (2002). *Developement of a Continuum-Mechanics-Based Tool for 3D Finite Element Analysis of Reinforced Concrete Structures and Application to Problems of Soil-Structure Interaction*. Ph. D. thesis, Institut for Structural Concrete, Graz University of Technology.

International Federation for Structural Concrete (fib) (2013). *fib Model Code for Concrete Structures 2010*. Ernst & Sohn. Jendele, L. & J. Cervenka (2006). Finite element modeling of reinforcement with bond. *Computers and Structures 84*, 1780–1791.

Jendele, L. & J. Cervenka (2006). Finite element modelling of reinforcement with bond. *Computers and Structures 84*, 1780–1791.

Leonhardt, F. & R. Walther (1962). Beiträge zur Behandlung der Schubprobleme im Stahlbetonbau. In *Schubversuche an einfeldrigen Stahlbetonbalken mit und onhe Schubbewehrung zur Ermittlung der Schubtragfähigkeit und der oberen Schubspannugsgrenze*, Volume 151. Deutscher Ausschuss für Stahlbeton.

Manzoli, O., A. Gamino, E. Rodrigues, & G. Claro (2012). Modeling of interfaces in two-dimensional problems using solid finite elements with high aspect ratio. *Computers and Structures 94–95*, 70–82.

Mori, T. & K. Tanaka (1973). Average stress in the matrix and average elastic energy of materials with misfitting inclusions. *Acta Metallica 21*(5), 571–574.

Ninić, J., J. Stascheit, & G. Meschke (2014). Beam-solid contact formulation for finite element analysis of pile-soil interaction with arbitrary discretization. *International Journal for Numerical and Analytical Methods in Geomechanics 38*(14), 1453–1476.

Oliver, J., D. Linero, A. Huespe, & O. Manzoli (2008). Twodimensional modeling of material failure in reinforced concrete by means of a continuum strong discontinuity approach. *Computer Methods in Applied Mechanics and Engineering 197*(5), 332–348.

Phillips, D.V. & O.C. Zienkiewicz (1976). Finite element nonlinear analysis of concrete structures. In *Institution of Civil Engineers Proceedings 61*, pp. 59–88.

Putke, T., K. Bergmeister, & P. Mark (2016). Wirtschaftliches Konstruieren und Bewehren. In K. Bergmeister, F. Fingerloos, and J.D. Wörner (Eds.), *Beton-Kalender 2016*, pp. 695–739.

Ruiz, G., M. Elices, & J. Planas (1998). Experimental study of fracture of lightly reinforced concrete beams. *Materials and Structures 31*, 683–691.

Rumanus, E. (2009). *Ein mikromechanisch orientiertes numerisches Schädigungsmodell für Stahlbeton unter Einbeziehung von hygro-mechanischen Einwirkungen*. Ph. D. thesis, Ruhr-Universität Bochum.

Smarslik, M., T. Putke, A. Marwan, V.E. Gall, G. Meschke, & P. Mark (2017). Berechnungsmodelle für Bau—und Endzustände von Tübbingtunneln. In Deutsche Gesellschaft fur Geotechnik e. V. (Ed.), *Taschenbuch für den Tunnelbau 2018*. Ernst & Sohn GmbH & Co. KG. (In Print).

Sugimoto, M. (2006, February). Causes of shield segment damages during construction. In *International Symposium on Underground Excavation and Tunnelling,* Bangkok, Thailand, pp. 67–74.

Truesdell, C. & R. Toupin (1960). *Handbuch der Physik*, Chapter The classical field theories, pp. 226–793. Springer, Berlin.

Zhan, Y. & G. Meschke (2014). Analytical model for the pullout behavior of straight and hooked-end steel fibers. *Journal of Engineering Mechanics (ASCE) 140(12)*, 04014091(1–13).

Zhan, Y. & G. Meschke (2016). Multilevel computational model for failure analysis of steel-fiber-reinforced concrete structures. *Journal of Engineering Mechanics (ASCE) 142*(11), 04016090(1–14).

Computational Modelling of Concrete Structures – Meschke, Pichler & Rots (Eds)
© 2018 Taylor & Francis Group, London, ISBN 978-1-138-74117-1

Robust design of hybrid steel fiber reinforced concrete tunnel lining segments

G.E. Neu, V.E. Gall, S. Freitag & G. Meschke
Institute for Structural Mechanics, Ruhr-Universität Bochum, Bochum, Germany

ABSTRACT: The circular lining in mechanized tunneling consists of several concrete segments which are exposed to different loading cases during tunnel construction. The loading scenarios can be divided into longitudinal loads caused by the jacks and circumferential loads resulting from soil and grouting pressure. This contribution is focused on the analysis of Steel Fiber Reinforced Concrete (SFRC) segmental linings under circumferential loads, where the area around the longitudinal joints is of particular importance. The occurrence of splitting stresses due to the partial area loading in combination with imperfections, conditioned by the construction process, often leads to a chipping of segment corners. In order to find a robust segment design, the influence of misalignments between adjoining segments on the crack pattern is investigated. In addition, a hybrid segment design is proposed and optimized with respect to robustness under consideration of uncertain parameters.

1 INTRODUCTION

Precast tunnel lining segments are subjected to various complex loading conditions during the mechanized tunneling process. In order to design a segment, these loading scenarios are simplified and often do not reflect the complexity of the true conditions. In case of the longitudinal joints, subjected to the critical partial area loading case, often damages, mainly a chipping of the segment corners, occurs during the construction (Sugimoto 2006). There are several possible causes, primarily inaccuracies during the construction, which result in an exceedance of the assumed loads in the design stage and the development of not tolerable cracks in consequence of critical splitting stresses. Due to the geometry of the longitudinal joint in combination with the required concrete cover, the performance of conventional reinforcement is limited. Steel Fiber Reinforced Concrete (SFRC) can be used to improve the post cracking behavior of the segmental lining and helps to meet the requirements of the serviceability state (SLS). A discrete crack model based on interface elements is used to predict the resulting crack patterns and the corresponding crack width in SFRC and Plain Concrete (PC) (Zhan & Meschke 2016). The aim of this contribution is to find a robust segment design, which ensures a sufficient performance of the segment under all considered boundary conditions and loading scenarios. To emphasize the influence of imperfections on the structural behavior, different segment designs subjected to realistic loading conditions and misalignments are analyzed.

A robust segment design, going along with the reduction of damages, is only employable in tunneling projects, if the economic feasibility is given. Mechanized tunneling is a highly automated process, which requires a prefabrication of the segments. Thousands of segments have to be produced during a tunnel construction and therefore, the lining segment design has a great influence on the economic success of the project. For this reason, hybrid PC-SFRC segment concepts has been proposed (Gall, Neu, Zhan, & Meschke 2017). In this paper, the hybrid PC-SFRC segments will be optimized to obtain robust and economic designs. This optimization task should account for uncertainties on the material scale (fiber orientation, strength of the concrete), because these parameters could cause a perceivable variation of the structural response. In order to do so, the concept of robust optimization (Taguchi 1989) is applied to ensure that the calculated optimum leads to a sufficient performance and a low variability of the solution. The optimization task is solved by the Particle Swarm Optimization (PSO) (Kennedy & Eberhart 1995).

2 NUMERICAL MODELING OF CONCRETE AND STEEL REINFORCED CONCRETE BEHAVIOR

In this contribution, cohesive interface elements, as proposed by (Manzoli, Gamino, Rodrigues, & Claro 2012), in conjunction with standard small-strain Finite Elements (FE), are used in order to

model cracking in plain and steel fiber reinforced concrete. The Interface Solid Elements (ISE) are used in order to capture the cracking and consequent loss of strength of the concrete. The standard elements control the compressive behavior of the structure until the surrounding interfaces are damaged. As the ISE's have a discrete thickness, the FE mesh is processed such that each standard element is surrounded by interface elements. The ISEs are based on degenerated 2D and 3D solid elements as presented in (Zhan & Meschke 2016). The material properties of these elements are modified to include a displacement based damage formulation derived from a fiber-pullout law (Zhan & Meschke 2014), in order to describe the stress state of the concrete after cracking. The element formulation is based upon the principles of the continuum strong discontinuity approach for the representation of cracks in finite elements.

2.1 *Interface material model*

The inelastic constitutive behavior of ISE is formulated in terms of damage mechanics as:

$$\begin{aligned}\sigma &= (1-d)\,\mathbb{C}_{\mathbf{e}} : \varepsilon \\ &\approx (1-d)\,\frac{1}{h}\mathbb{C}_{\mathbf{e}} : \left(\llbracket \mathbf{u} \rrbracket \otimes \mathbf{n}\right)^{s},\end{aligned} \tag{1}$$

where d is the scalar damage variable, h the height of the ISE and $\mathbb{C}_{\mathbf{e}}$ denotes the elastic stiffness tensor. A Poisson's ratio of $\nu = 0$ is chosen to decouple the stresses parallel and normal to the interface surface. The damage variable d is given as:

$$d(\alpha) = 1 - \frac{h\, t(\alpha)}{E^{*}(\alpha + \tilde{u}_0)} \tag{2}$$

$$\tilde{u}_0 = \frac{h\, f_t^{*}}{E^{*}} \approx 0 \tag{3}$$

Here, $\tilde{u}_0$ corresponds to the limit state of the elastic interface and α is an internal parameter defined based on the maximum value of equivalent separation experienced during the loading history. The softening behavior of an interface $t(\alpha)$ (see Figure 1c) is determined based on the parameterized function obtained from a so-called "crack bridging model" (Zhan & Meschke 2016):

$$\begin{aligned}t(\alpha) = (f_t^{*} - t_1)\exp\left(-\frac{\alpha}{w_{\text{ref}}}\right) + t_1\frac{w_u - \alpha}{w_u} \\ + t_2 \exp\left(c_1 - c_2\alpha\right)\alpha,\end{aligned} \tag{4}$$

where f_t^{*} represents the tensile strength of the fiber reinforced concrete composite and the remaining parameters are appropriately determined according to numerical results of crack bridging response obtained for a specific fiber cocktail. A detailed explanation of the material model is given in (Zhan 2016).

2.2 *Crack bridging law*

The crack bridging model Eq. (4) is proposed so that, using an analytical model predicting the pullout force-displacement relation of single fibers (Zhan & Meschke 2014) and taking an anisotropic fiber orientation into account,the integration of the pullout response of all the fibers intercepting the crack provides the traction-separation relation for an open crack (Zhan & Meschke 2016).

A unit area of an opening crack and the corresponding volume element of the composite material, containing a number of distributed fibers crossing the crack, is considered (Figure 1b). The pullout response of each fiber is dependent on the position $\tilde{x}$ and the inclination θ of the fiber with respect to the crack plane (Figure 1a). With increasing crack width w, the integration of the individual fiber pullout forces with respect to the position and inclination results in the fiber bridging stress (Wang, Backer, & Li 1989):

$$t^{\text{fib}}(w) = \frac{c_f}{A_f} \cdot \ldots \int_{\tilde{x}=0}^{L_f/2} \left[\int_{\theta=0}^{\arccos(2\tilde{x}/L_f)} F(\tilde{x},\theta,w)\, p(\theta)\, \mathrm{d}\theta \right] p(\tilde{x})\, \mathrm{d}\tilde{x} \tag{5}$$

In Eq. (5), c_f is the volume fraction of the fibers and A_f is the cross-section area of one fiber. The single fiber pullout force $F(\tilde{x},\theta,w)$ is dependent on $\tilde{x}$ and θ. The spatialdispersion characteristics $p(\theta,\tilde{x})$ of the fiber cocktail in the composite is represented by the probability density p as a function of the inclination angle θ and the position $\tilde{x}$ of the fiber. The probability density regarding the inclination angle $p(\theta)$ incorporates the anisotropic fiber orientation and the boundary effect as a general result of the casting process.

A global sensitivity analysis is performed with COSSAN (Patelli 2016) to illustrate the influence of all composite parameters on the traction-separation law, which is evaluated by the required energy E resulting in a specific crack width (Figure 1c). Crack widths w_{crack} of 0.2 mm and 10 mm are investigated representing the service and ultimate limit state (SLS & ULS) in accordance to (Eurocode 2–2011). The results in terms of First Order Sobol indices are shown in Figure 2. First Order Sobol indices can be calculated by

$$S_i = \frac{Var(E(Y \mid X_i))}{Var(Y)}, \tag{6}$$

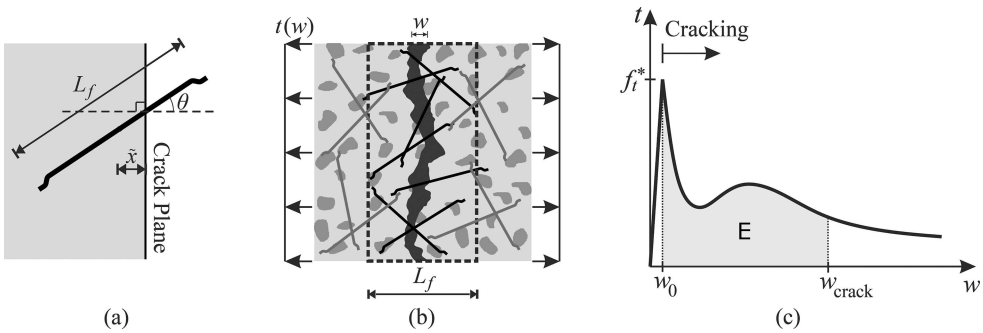

Figure 1. Crack bridging model: (a) Position and inclination of a fiber with respect to the crack; (b) Unit area of an open crack in SFRC intercepted by fibers with length L_f; (c) Equivalent traction-separation relation for the cohesive solid interface model.

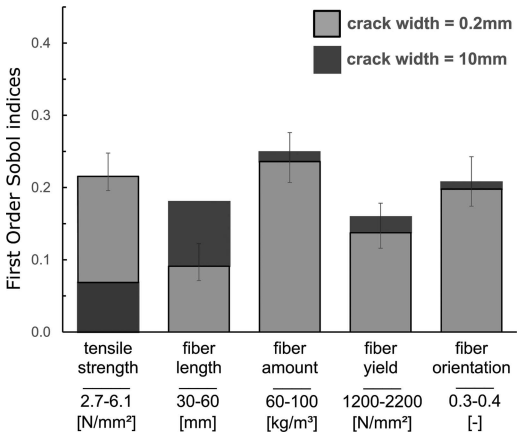

Figure 2. Sensitivity of parameters on the post-cracking response—First Order Sobol Indices and parameter range.

where Y is the output and X_i are the input factors (Saltelli, Ratto, Andres, Campolongo, Cariboni, Gatelli, Saisana, & Tarantola 2008). The post cracking behavior in both cases is sensitive to the fiber orientation and the amount of fibers. For the SLS, the tensile strength of the concrete is one of the main determining factors. With increasing crack width, the influence of the tensile strength on the post cracking behavior is decreasing and the properties of the fiber cocktail define the post cracking response. For a crack width of 10 mm, the fiber length is one of the most important parameters because of its influence on the crack bridging abilities of the SFRC.

3 ROBUST OPTIMIZATION

A general optimization task under uncertainty can be stated by the following mathematical terms:

$$\begin{aligned} &\text{optimize:} && (\mathbf{x}, \boldsymbol{\theta}) \\ &\text{subject to:} && g_i(\mathbf{x}, \boldsymbol{\theta}) \le 0, \qquad i = 1,\ldots,I \\ &&& h_j(\mathbf{x}, \boldsymbol{\theta}) = 0, \qquad j = 1,\ldots,J \end{aligned} \tag{7}$$

where, $\mathbf{x}$ is the vector of deterministic and/or uncertain design variables, which leads to the optimal solution (minimum or maximum of Z), $\boldsymbol{\theta}$ represents the vector of uncertain a priori variables, $Z(\mathbf{x}, \boldsymbol{\theta})$ is the objective function, $g_i(\mathbf{x}, \boldsymbol{\theta})$ and $h_j(x, \boldsymbol{\theta})$ are functions that define inequality and equality constraints.

A multi-objective optimization with ψ objectives can be replaced by a surrogate problem.

$$\bar{Z} = \sum_{\psi=1}^{\psi} \varphi_\psi \cdot \frac{Z_\psi}{R_\psi} \qquad with \sum_{\psi=1}^{\psi} \varphi_\psi = 1, \tag{8}$$

where φ_ψ are the weights of the single objectives and R_ψ are reference values to normalize the single objectives. The weights can be chosen in accordance to the desired significance of each single objective. In order to solve the optimization task stated in Eq. (7), many algorithms based on different concepts can be used. An overview can be found in (Amaran, Sahinidis, Sharda, & Bury 2016). Incorporating uncertainties within the optimization task is described in (Schuëller & Jensen 2008).

3.1 *Concept of robust optimization*

Robust optimization is strongly related to uncertainty modeling. A conventional, deterministic optimal design may not always lead to an optimal product, if uncertainties in design and a priori parameters are considered. There are multiple sources of uncertainties, which result in a variance or at least ranges of the assumed geometrical and material parameters. In this work, uncertain

parameters are modeled as stochastic numbers. Robust optimization incorporates the variances for finding an optimal design,which provides a sufficient performance under all considered conditions and not only for a specific parameter combination. Figure 3 illustrates exemplary the methodology of robust optimization.

In general, the objective of a robust design is to optimize the mean and to minimize the variability that results from uncertainty, represented by uncertain a priori parameters θ and/or uncertain design variables $\mathbf{x}$. The objective function for a robust optimization can be expressed with Eq. (8) by

$$\bar{Z} = \varphi_{\mu} \cdot \frac{\mu(Z(\mathbf{x},\theta))}{R_{\mu}} + \varphi_{\sigma} \cdot \frac{\sigma(\mathrm{Z}(x,\theta))}{R_{\sigma}} \tag{9}$$

where μ is the mean value and σ is the standard deviation of the objective function. Depending on the chosen weights $(\varphi_{\mu},\varphi_{\sigma})$, the mean value of the objective function is optimized under consideration of the corresponding standard deviation. A survey of robust optimization concepts and approaches can be found in (Beyer & Sendhoff 2007, Zang, Friswell, & Mottershead 2005).

3.2 *Particle swarm optimization*

The Particle Swarm Optimization (PSO), proposed by (Kennedy & Eberhart 1995), is a global optimization algorithm that is, similar to the Evolutionary Algorithms (EA), based on the simulation of animal social behavior. It tries to simulate the movements of birds in a flock, which are capable of finding a feeding ground fast and efficient. N particles are randomly placed in the design space, where every particle i contains its position $\mathbf{P}_i$ and the corresponding value of the objective function $Z(i) = Z(P_i)$. For every iteration step, the new position of every particle i in the next increment $k+1$ is calculated by:

$$\mathbf{P}_i^{k+1} = \mathbf{P}_i^{k} + \Delta\mathbf{P}_i^{k+1} \tag{10}$$

where, $\Delta\mathbf{P}_i^{k+1}$ is a combination of the old position update $\Delta\mathbf{P}_i^{k}$, the individual best position of the particle in search history $\mathbf{P}_i^{best}$ and the best position one particle of the whole swarm archived $\mathbf{G}^{best}$:

$$\begin{aligned}\Delta\mathbf{P}_i^{k+1} = {} & c_1 \cdot \Delta\mathbf{P}_i^{k} + \mathbf{r}_{individual} \cdot c_2 \cdot (\mathbf{P}_i^{best} - \mathbf{P}_i^{k}) \\ & + \mathbf{r}_{global} \cdot c_3 \cdot (\mathbf{G}^{best} - \mathbf{P}_i^{k})\end{aligned} \tag{11}$$

c_1, c_2 and c_3 are constants which are chosen to c_1 = 0.729 and $c_2 = c_3$ = 1.434 in accordance to (Shi & Eberhart 1998). The diagonal matrices $\mathbf{r}_{individual}$ and $\mathbf{r}_{global}$ contain random numbers uniformly distributed in the interval [0; 1], which are sampled new in each increment k to balance the attraction of each particle towards the individual and global best solution. The calculation of the new position is visualized in Figure 4.

Termination criterion's can be either based on a predefined value of the objective function, the velocity of particles or the density of the swarm. To avoid local minimums, it is recommend to restart the PSO multiple times and compare the resulting optima. An overview of the PSO algorithm and numerous modifications can be found in (Yang 2009).

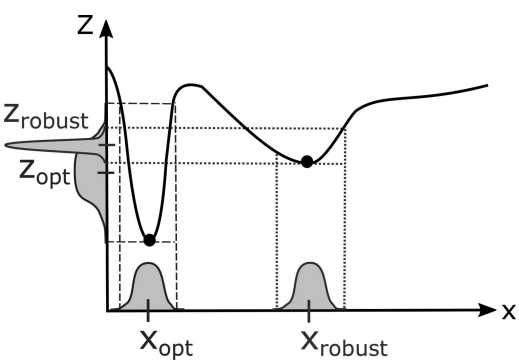

Figure 3. Example of a robust optimization: Two uncertain design variables, one for the robust (x_{robust}) and one for an conventional optimization (x_{opt}), lead to different solutions. The minimum of the conventional optimization has a smaller mean value (Z_{opt}) than the minimal mean value resulting from a robust optimization (Z_{robust}), but as well a higher variance.

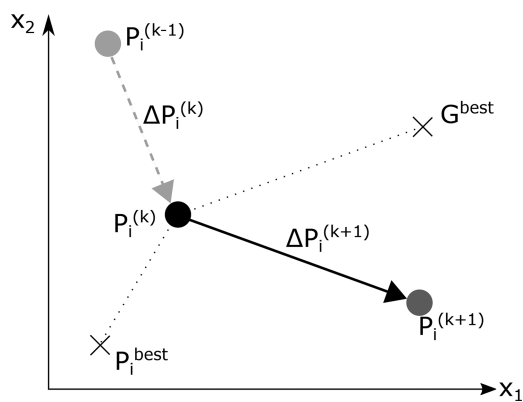

Figure 4. Influences on the calculation of the new position of one particle $\mathbf{P}_i^{k+1}$ in a two-dimensional design space (see Eq. (10), (11)).

4 ROBUST OPTIMIZATION OF A LINING SEGMENT

4.1 *FE-model*

The numerical model for the analysis of a lining segment consists of the hybrid segment itself, the grouting layer and parts of the adjoining segments (Figure 5). A radial displacement Δu is applied on the grouting layer in accordance to the final ground deformations.

The displacement is predicted by a process oriented tunnel simulation model (Marwan, Alsahly, Gall, & Meschke 2017) and transfered to the segment model. The consideration of the structural scale is necessary to incorporate the interdependency between machine advancement and the surrounding soil as well as the time dependent behavior of the grout. The optimization and investigation regarding imperfections is performed for a segment placed in the tunnel crown. The prescribed deformation decreases from 9.32 *mm* in the middle of the segment to 4.96 *mm* at the joint area. The elasticity modulus of the grout layer will be assumed to $E = 250 \frac{N}{mm^2}$ with a Poisson ratio of 0.2.

In order to accurately predict realistic segmental lining response, a correct quantification of concrete material properties is necessary. To this end, a series of loading tests were performed on typical lining concrete in order to determine its material properties based on DIN EN 12390 (Table 1).

The properties of the hybrid SFRC cap are calculated using the formulas from (Eurocode 2–2011) depending on the concrete strength. The coefficients for the t-w-relationship (Eq. (4)) are calculated depending on the chosen amount, geometry, material properties and orientation of the fibers. For simplification, all calculations are carried out with a consistent fiber geometry ($fiber_{length} = 60\ mm$).

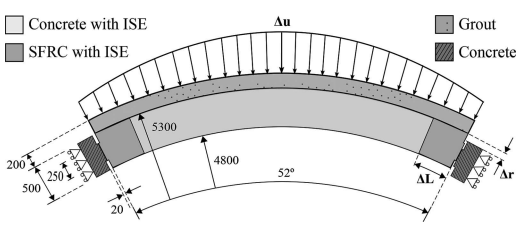

Figure 5. Setup for the numerical simulation of a hybrid segment. All units are given in [mm].

Table 1. Properties of Linear Elastic (LE) and Interface Solid Elements (ISE) used to model plain concrete (PC).

	Units	LE	ISE
Elasticity Modulus, E	N/mm^2	35545	35545
Poisson Ratio, ν	–	0.2	0.0
Tensile Strength, f_t	N/mm^2	–	4.05
Fracture Energy, G_f	Nmm	–	0.1
Beta, β	–	–	1.25

4.2 *Influence of imperfections*

The effect of imperfections, in this case misalignments between adjoining segments Δr, on the crack width and pattern of a lining segment is investigated. The misalignment results in an eccentricity of the contact stress resultant towards the inner radius and simultaneously a reduction of the load transferring area. To illustrate the variation of system performance due to imperfections, four representative designs are be compared. In addition to segments consisting entirely of PC and SFRC, two hybrid designs with a SFRC cap width of $\Delta L = 500\ mm$ (see Figure 5), but different concrete strengths and fiber amounts are examined. The material parameters are listed in Table 2.

The performance of these segment designs subjected to different misalignment levels are shown in Figure 6. A crack width of 0.2 mm is chosen as

Table 2. Properties of concrete and fibers for the fiber reinforced segment designs. The properties of the PC segment are shown in Table 1.

	Units	Full SFRC	Hybrid A	Hybrid B
E	N/mm^2	37191	41770	44095
f_t	N/mm^2	4.18	5.43	6.11
G_f	N_{mm}	0.11	0.13	0.15
fib_{yield}	N/mm^2	1400	1400	2200
fib_{amount}	kg/m^3	60	60	100

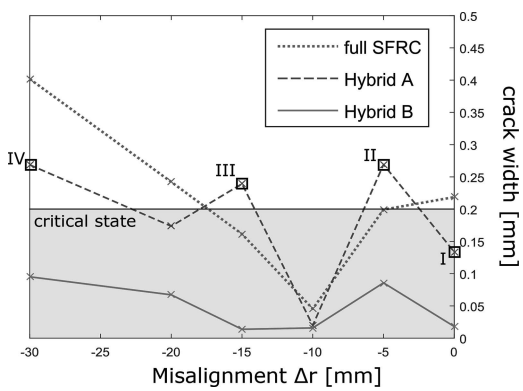

Figure 6. Correlation between the maximum crack width and misalignments Δr for different segment designs.

the maximal tolerable crack width in accordance to (Eurocode 2–2011). The PC segment is not displayed because of its poor performance.

For the considered loading scenario, the use of a hybrid design instead of a whole segment reinforced by steel fibers is not connected to any noticeable decrease in performance. The *Hybrid A*-design would meet the requirements if misalignments arenot considered, but in fact, it is vulnerable to unavoidable misalignments due to tunnel construction. In contrast, a sufficient hybrid design (*Hybrid B*) performs well for all considered imperfections.

Different than expected, the crack width is not constantly increasing with the misalignment. It is observed that different misalignment levels changes the crack pattern (see Figure 7), which is strongly connected to the evolving splittingstresses due to partial area loading. With increasing misalignment, the position of the splitting stresses moves from the inner segment boundary towards the centroidal axis, which interfere with the increasing stresses transfered at the longitudinal joint. In case of a perfect segment installation ($\Delta r = 0$ *mm*), a chipping at the segment corner occurs. A misalignments up to 5 *mm* tends to a crack pattern similar to a classical partial area loading case, where one big splitting crack occurs. The main crack moves towards the middle of the segment without any noticeable inclination, which is the result of increasing stresses together with a still unfavorable position of the splitting stresses. At a misalignment of $\Delta r = 10$ *mm* no critical cracks appear, because the increase of stress due to the misalignments is compensated through a much less critical position of the splitting stresses. With increasing misalignment ($\Delta r = 15$ *mm*, 30 *mm*), there is only a slightly favorable change in the position of splitting stresses whereas the increasing stress becomes the dominant factor influencing the crack width.

Furthermore, the efficiency of SFRC highly depends on the orientation of the fibers and should be accounted for in a robust segment design. The influence of fiber orientation and the misalignment on the maximum crack width for the *Hybrid A*-designis shown in Figure 8. A fiber orientation with a value of 0.4 represents a favorable orientation whereas a value of 0.3 can be interpreted as a unfavorable orientation. The critical state is defined as the exceedance of the tolerated crack width in the SLS. If a favorable fiber orientation, corresponding to a value of 0.4, is assumed, the *Hybrid A*-design fulfills the requirements regarding the maximum crack width. However, a combination of unfavorable fiber orientation and specific misalignments canresult in a undesirable performance of the segment design.

4.3 *Optimization of a lining segment*

The previous section showed that hybrid segments are able to prevent critical cracking if a proper segment design is defined. In this section, an optimization based on the major design parameters (see Figure 2) is performed to determine a robust hybrid segment design with a minimal SFRC material usage. The optimization is limited to the

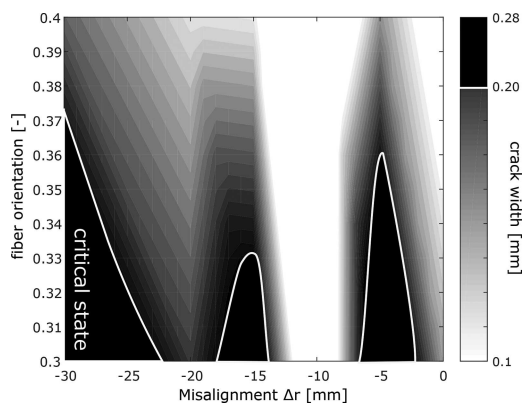

Figure 8. Contour plot of the crack width depending on the fiber orientation and the misalignment Δr for the *Hybrid A*-design. The critical state is specified by a crack width of 0.2 *mm*.

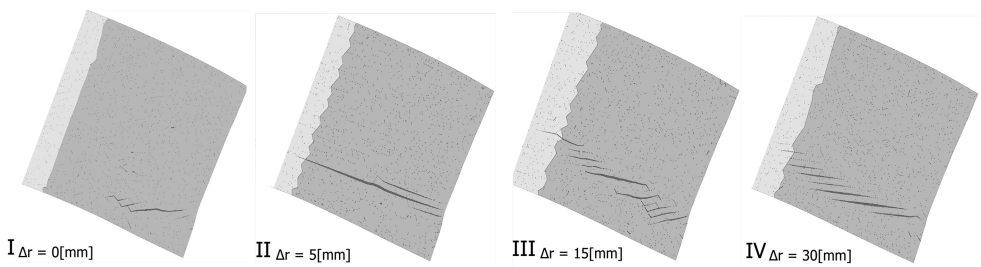

Figure 7. Crack patterns for different misalignment levels for the Hybrid A-design with a fiber orientation of 0:3 and a magnification factor of 20.

properties of the SFRC cap, why the remaining segment consists of PC defined by Table 1.

Optimization tasks, especially if stochastic variables are considered, need a high amount of model evaluations in order to find the optimal solution. For an already complex finite element model, the computational costs would be too high and therefore an approximation of the structural model is necessary. A two layer feed-forward Artificial Neural Network (ANN) with back-propagation training (Hagan & Menhaj 1994) is used to approximate the structural response of the lining segment. An explanation of artificial neural networks functionality and other meta modeling techniques can be found in (Simpson, Poplinski, Koch, & Allen 2001).

The meta model should be able to predict the maximum crack width depending on the chosen input parameters (Table 3). The ANN was trained with 832 samples, generated by Latin Hypercube Sampling, to obtain a good approximation of the structural model.

The objective of the optimization is the minimization of the SFRC cap width ΔL and the required amount of fibers fib_{amount}. Beside the savings on material costs, the minimization of the fiber amount reduces the likelihood of fiber clumping and therefore contribute to a more consistent performance. A maximum tolerable crack width of 0.2 mm is employed as inequality condition to ensure a sufficient performance of the segment. In addition, the variance of the crack width $\sigma_{crack\ width}$ isincluded as objective in the optimization in order to account for the robustness of the structural response (see Section 3.1). The yield stress of a fiber fib_{yield} and the concrete strength f_c are stated as design variables in which the compression strength of concrete is modeled as stochastic parameter with a Gaussian distribution (μ_{f_c} to be optimized with $\sigma_{f_c} = 8 N/mm^2$). The elasticity modulus as well as the tensile strength of concrete arecalculated depending on the compressive strength. The fiber orientation $fib_{orientation}$ is included as uncertain a priori parameter modeled by a uniform distribution.

Table 3. Variables and their ranges for ANN surrogate training and the optimization task. The variable types are also included (Design Variable—DV and uncertain a priori parameter—AP).

Variables	Range	Distribution
ΔL (DV)	250–600 [mm]	–
fib_{amount} (DV)	60–100 [kg/m^3]	–
μf_c (DV)	75–95 [N/mm^2]	Gaussian (μ, σ)
fib_{yield} (DV)	1200–2200 [N/mm^2]	–
fib_{orient} (AP)	0.25–0.4 [–]	Uniform

The multi-objective optimization task can be stated as:

$$\begin{aligned} \text{optimize}: & Z_1 = \min \Delta L \\ & Z_2 = \min fib_{amount} \\ & Z_3 = \min \sigma_{crack\ width} \\ \text{subject to}: & \mu_{crack\ width} \leq 0.2 \text{ mm} \end{aligned}$$

The range of all parameters and their distribution is shown in Table 3.

The resulting objective function in terms of Eq. (8) is given by

$$\bar{Z} = \varphi_1 \cdot \frac{\Delta L}{R_1} + \varphi_2 \cdot \frac{fib_{amount}}{R_2} + \varphi_3 \cdot \frac{\sigma_{crack\ width}}{R_3}, \qquad (12)$$

where the reference values $R_{\psi\ =\ [1,2,3]}$ for the normalization of the single objectives were chosen in accordance to the optimum of each individual objective (R_1 = 290.16 mm, R_2 = 60 kg/m^3, and $R_3 = 0.022\ mm$). To analyze the effect of the weights $\varphi_{\psi=[1,2,3]}$, the Pareto front between the SFRC cap width and the amount of fibers as well as the variance of the crack width is plotted in Figure 9.

It can be observed, that a further increase of the SFRC cap width above approx. 350 mm, corresponding to a weight of $\varphi_1 \approx 50\%$, has no influence on the minimization of the fiber amount (see Figure 9a). On the other hand, the robustness of the structural response is increasing in relation with the SFRC cap width (see Figure 9b). Above a SFRC cap width of approx. 400 mm, there is only a slightly improvement of the robustness. Based on this observation, two optimizations with different priorities are performed. For one optimization, the minimization of the material usage is of major importance ($\varphi_1/\varphi_2/\varphi_3$ = 50/25/25 [%]), whereas the other optimization is more focused on the robustness rather than the minimization of the material usage ($\varphi_1/\varphi_2/\varphi_3$ = 30/30/40 [%]). The resulting optimal design variables for both cases are listed in Table 4.

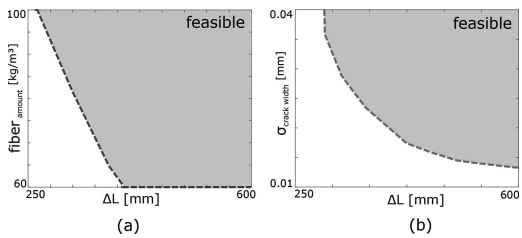

Figure 9. (a) Pareto front between the SFRC cap width ΔL and the amount of fibers; (b) Pareto front between the SFRC cap width ΔL and the variance of the crack width.

Table 4. Optimal designs for the minimization of the material usage focused optimization (50/25/25) and for the optimization regarding the robustness (30/30/40).

$\varphi_1/\varphi_2/\varphi_3$ [%]	50/25/25	30/30/40
ΔL [mm]	363.5	407.8
μf_c [N/mm^2]	95	95
$f_t(\mu_{fc})$ [N/mm^2]	5.89	5.89
$G_f(\mu_{fc})$ [N/mm]	0.15	0.15
$E(\mu_{fc})$ [N/mm^2]	43348	43348
fib_{amount} [kg/m^3]	82.1	89.4
fib_{yield} [N/mm^2]	2043.2	2200

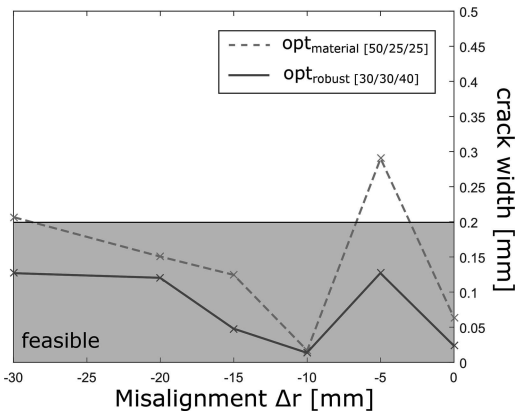

Figure 10. Correlation between the maximum crack width and misalignments Δr for both optimized designs.

In order to verify the solutions, numerical FE simulations with these parameters are performed. The deviation between the maximum crack width computed by the FE model (0.0613 mm) and the crack width predicted by the ANN (0.0587 mm) for the (50/25/25) optimized segment is smaller than 5%. It can be assumed that the predictions of the ANN are reliable at the objective function close to the optimum.

In Addition, numerical simulations were performed to investigate the performance of the optimized designs exposed to imperfections (see Section 4.2). The performance of both optimized designs is shown in Figure 10. It can be observed that the on material usage optimized segment $opt_{material}$ performs well for most misalignment levels apart a misalignment of $\Delta r = 5$ mm, where the maximum crack width reaches a critical value of 0.3 mm. The variation of the crack width subjected to misalignments is relatively high. In comparison, the maximum crack width of the robust segment design opt_{robust} at all misalignment levels is still lower than the defined critical crack width of 0.2 mm and shows a lower variance.

5 CONCLUSION

The results presented in this paper demonstrate that the proposed hybrid segment designs are capable of resisting the splitting behavior observed due to partial area loadings. The investigation of misalignments between adjoining segments indicates that the chipping of the segment corners may not necessarily result from imperfections but rather develop due to stress distributions resulting from the segment geometry. Nevertheless, misalignments up to 30 mm can result in a duplication of the maximum crack width connected with the exceedance of the tolerable crack width. A robust segment design is able to perform well under unfavorable fiber orientations and high misalignment levels. In order to find such a robust segment design, an optimization with consideration of uncertainties and the robustness of the lining response was performed. Two optimized hybrid segment designs for different objectives were proposed. The overall performance of both segment designs is sufficient, but only the robust optimized design is less vulnerable in regard to imperfections and uncertain a priori parameters.

ACKNOWLEDGEMENTS

Financial support was provided by the German Research Foundation (DFG) in the framework of project B2 of the Collaborative Research Center SFB 837 Interaction modeling in mechanized tunneling. This support is gratefully acknowledged.

REFERENCES

Amaran, S., N.V. Sahinidis, B. Sharda, & S.J. Bury (2016). Simulation optimization: a review of algorithms and applications. *Annals of Operations Research 240*(1), 351–380.

Beyer, H.-G. & B. Sendhoff (2007). Robust optimization – a comprehensive survey. *Computer Methods in Applied Mechanics and Engineering 196*(33), 3190–3218.

DIN EN 1992-1-1 (2011). Eurocode 2 – Bemessung und Konstruktion von Stahlbeton und Spannbetontragwerken – Teil 1-1: Allgemeine Bemessungsregeln und Regeln für den Hochbau.

Gall, V., G. Neu, Y. Zhan, & G. Meschke (2017). Computer aided steel-fiber reinforced segment design using a multiscale modeling framework. In W. Press (Ed.), *Proceedings of the World Tunnel Congress,* Bergen, Norway, pp. 1942–1948.

Hagan, M.T. & M.B. Menhaj (1994). Training feedforward networks with the marquardt algorithm. *Transactions on Neural Networks 5*(6), 989–993.

Kennedy, J. & R.C. Eberhart (1995, November-December). Particle swarm optimization. In I. Press (Ed.), *Proceedings of the IEEE International Con-*

ference on Neural Networks, Piscataway, NJ, USA, pp. 1942–1948.

Manzoli, O., A. Gamino, E. Rodrigues, & G. Claro (2012). Modeling of interfaces in two-dimensional problems using solid finite elements with high aspect ratio. *Computers and Structures 94–95*, 70–82.

Marwan, A., A. Alsahly, V. Gall, & G. Meschke (2017). Computational modelling for segmental lining installation in mechanized tunneling. In G. Hofstetter, K. Bergmeister, J. Eberhardsteiner, G. Meschke, and H. F. Schweiger (Eds.), *Proceedings of the 4th International Conference on Computational Methods in Tunneling and Subsurface Engineering (EURO:TUN 2017)*, pp. 153–160.

Patelli, E. (2016). Cossan: A multidisciplinary software suite for uncertainty quantification and risk management. In *Handbook of Uncertainty Quantification*, pp. 1–69. Springer International Publishing.

Saltelli, A., M. Ratto, T. Andres, F. Campolongo, J. Cariboni, D. Gatelli, M. Saisana, & S. Tarantola (2008). *Global Sensitivity Analysis. The Primer*, pp. 155–182. Wiley.

Schuëller, G. & H. Jensen (2008). Computational methods in optimization considering uncertainties—an overview. *Computer Methods in Applied Mechanics and Engineering 198*(1), 2–13.

Shi, Y. & R. Eberhart (1998). Parameter selection in particle swarm optimization. In V. W. Porto, N. Saravanan, D. Waagen, and A. E. Eiben (Eds.), *Evolutionary Programming VII: 7th International Conference, EP98 San Diego, California, USA, March 25–27, 1998 Proceedings*, Berlin, Heidelberg, pp. 591–600. Springer Berlin Heidelberg.

Simpson, T., J. Poplinski, P. N. Koch, & J. Allen (2001). Metamodels for computer-based engineering design: Survey and recommendations. *Engineering with Computers 17*(2), 129–150.

Sugimoto, M. (2006, February). Causes of shield segment damages during construction. In *International Symposium on Underground Excavation and Tunnelling*, Bangkok, Thailand, pp. 67–74.

Taguchi, G. (1989). Introduction to quality engineering. Technical report, American Supplier Institute.

Wang, Y., S. Backer, & V. Li (1989). A statistical tensile model of fibre reinforced cementitious composites. *Composites 20*(3), 265–274.

Yang, B. (2009). *Modified Particle Swarm Optimizers and their Application to Robust Design and Structural Optimization*. Ph. D. thesis, Fakultät Bauingenieur- und Vermessungswesen der Technischen Universität München, Munich, Germany.

Zang, C., M. Friswell, & J. Mottershead (2005). A review of robust optimal design and its application in dynamics. *Computers & Structures 83*(4), 315–326.

Zhan, Y. (2016). *Multi-level Modeling of Fiber Reinforced Concrete and Application to Numerical Simulations of Tunnel Lining Segments*. Ph. D. thesis, Ruhr University Bochum.

Zhan, Y. & G. Meschke (2014). Analytical model for the pullout behavior of straight and hooked-end steel fibers. *Journal of Engineering Mechanics (ASCE) 140(12)*, 04014091(1–13).

Zhan, Y. & G. Meschke (2016). Multilevel computational model for failure analysis of steel-fiber-reinforced concrete structures. *Journal of Engineering Mechanics (ASCE) 142(11)*, 04016090(1–14).



Taylor & Francis
Taylor & Francis Group
http://taylorandfrancis.com

Computational Modelling of Concrete Structures – Meschke, Pichler & Rots (Eds)
© 2018 Taylor & Francis Group, London, ISBN 978-1-138-74117-1

Structural analysis of segmented tunnel rings: A combination of transfer relations with an interface law

J.L. Zhang & H.A. Mang
Institute for Mechanics of Materials and Structures, TU Wien—Vienna University of Technology, Vienna, Austria
College of Civil Engineering, Tongji University, Shanghai, China

X. Liu & Y. Yuan
College of Civil Engineering, Tongji University, Shanghai, China

B. Pichler
Institute for Mechanics of Materials and Structures, TU Wien—Vienna University of Technology, Vienna, Austria

ABSTRACT: Structural analysis of segmented tunnel rings is challenging, because displacement discontinuities and relative rotation angles develop at segment-to-segment interfaces. To meet this challenge, a hybrid method was recently developed by Zhang et al. (2017). It uses the known external loading and *measured* interfacial discontinuities as input for structural analysis. The latter is based on analytical transfer relations, representing solutions of the governing equations of the linear theory of slender circular arches. The present contribution goes one step further. In order to enable structural analysis *without* measured interfacial discontinuities, the transfer relations are combined with an interface law. The latter represents a mathematical relation between the bending moment transmitted across a typical segment-to-segment interface and the resulting relative rotation angle. The proposed approach is applied to linear structural analysis of the first four load steps of a real-scale test on a segmented tunnel ring. Corresponding results are compared with the output of the aforementioned hybrid method. This way, it is shown that the presented method delivers reasonable estimates of the inner forces. However, the displacements are predicted less accurately, because rigid body motions of the segments cannot be quantified by interface laws.

1 INTRODUCTION

In hybrid methods, monitored data are used as input for structural simulations. Concerning the analysis of tunnel linings, Rokahr (Rokahr and Zachow 1997) and Hellmich (Hellmich 1999, Hellmich et al. 1999, Hellmich et al. 2001) developed the first hybrid methods for the New Austrian Tunneling Method. They are nowadays frequently applied in construction of tunnels (Brandtner et al. 2007), in order to quantify stress levels in shotcrete tunnel shells on the basis of measured displacements. Follow-up research activities were concerned with the development of modern multiscale material models for hydrating shotcrete (Pichler et al. 2008). This allowed for (i) reducing the required experimental activities to calorimetry testing of the binder of the shotcrete (Ullah et al. 2012), (ii) assessing the robustness of safety analyses of shotcrete tunnel shells with respect to rebound-related uncertainties of the effective composition of shotcrete, finally arriving at the tunnel wall (Ullah et al. 2012), and for (iii) identifying a non-trivial mode of arching thrustline behavior of young top-heading shotcrete tunnel shells, subjected to both ground pressure and ground shear (Ullah et al. 2013).

As for mechanized tunneling, the first hybrid method was recently presented by Zhang et al. (2017). The authors re-analyzed the first four load steps of a real-scale laboratory test on a segmented tunnel ring. The structure was subjected to 24 hydraulic jack forces, simulating the ground pressure. In the experiment, the displacement discontinuities and the relative rotation angles at all six segment-to-segment interfaces were monitored (Liu et al. 2016). These measurements were used as input for hybrid analysis of the structural behavior of the tested tunnel ring (Zhang et al. 2017). During regular service of segmented tunnel linings, however, interfacial discontinuities of displacements and rotation angles are *unknown*. This provides the motivation to apply interface laws to structural analysis of segmented tunnel rings.

$$\begin{bmatrix} u(\varphi) \\ v(\varphi) \\ \theta(\varphi) \\ M(\varphi) \\ N(\varphi) \\ V(\varphi) \\ 1 \end{bmatrix} = \begin{bmatrix} \cos\varphi & \sin\varphi & T_{13}(\varphi) & T_{14}(\varphi) & T_{15}(\varphi) & T_{16}(\varphi) & \sum u^L(\varphi) \\ -\sin\varphi & \cos\varphi & T_{23}(\varphi) & T_{24}(\varphi) & T_{25}(\varphi) & T_{26}(\varphi) & \sum v^L(\varphi) \\ 0 & 0 & 1 & T_{34}(\varphi) & T_{35}(\varphi) & T_{36}(\varphi) & \sum \theta^L(\varphi) \\ 0 & 0 & 0 & 1 & T_{45}(\varphi) & T_{46}(\varphi) & \sum M^L(\varphi) \\ 0 & 0 & 0 & 0 & \cos\varphi & -\sin\varphi & \sum N^L(\varphi) \\ 0 & 0 & 0 & 0 & \sin\varphi & \cos\varphi & \sum V^L(\varphi) \\ 0 & 0 & 0 & 0 & 0 & 0 & 1 \end{bmatrix} \cdot \begin{bmatrix} u_i \\ v_i \\ \theta_i \\ M_i \\ N_i \\ V_i \\ 1 \end{bmatrix}. \quad (1)$$

Interface laws are mathematical functions relating the originally unknown relative rotation angles at segment-to-segment interfaces to the normal force and the bending moment transmitted across these interfaces. Popular interface laws were developed by Leonhardt and Reimann (1965), Gladwell (1980), and Janßen (1983). As for the special case of interfaces subjected to eccentric compression, these state-of-the-art interface laws suggest that relative rotation angles increase *linearly* with increasing loading (Schlappal et al. 2017). This allows for a reliable description of Serviceability Limit States, but does not account for the *nonlinearities* associated with Ultimate Limit States concerning the bearing capacity of the interfaces (Schlappal et al. 2017). As regards the desirable development of nonlinear interface laws, only first steps are documented in the open literature, see e.g. (Liu et al. 2017) and references therein. Generally applicable models are still lacking.

In this paper, a linear interface law taken from (Liu et al. 2017) is combined with transfer relations representing analytical solutions of the governing equations of the linear theory of slender circular arches (Zhang et al. 2017). Because of the *linear* nature of the performed structural analyses, the present focus is resting on segmented tunnel rings subjected to external loads which are significantly smaller than the bearing capacity. This was the motivation to restrict the analyses to the first four load steps of the aforementioned real-scale laboratory test on a segmented tunnel ring. Notably, the segments showed no sign of bending-induced tensile cracking during the analyzed initial phase of the test (Liu et al. 2016). Therefore, linear elastic behavior of the reinforced concrete segments and a linear interface law are reasonable assumptions.

The experimentally applied hydraulic jack forces enter the structural analysis as input, while the interfacial discontinuities are *predicted* by the interface law. This results in classical load-controlled simulations. Corresponding numerical results are compared with available results from the hybrid method. This allows for assessing both qualitatively and quantitatively to which extent a classical structural analysis, i.e. one without use of measured displacements, can provide insight into the structural behavior of a segmented tunnel ring.

The paper is structured as follows. Section 2 refers to analytical solutions for segmented tunnel rings. The transfer relations for such structures and the proposed interface law are briefly summarized. In addition, analytical solutions for integration constants and relative rotation angles are derived. In Section 3, the proposed mode of analysis is applied to the first four load steps of a real-scale test on a segmented tunnel ring. Section 4 contains the conclusions drawn from the present research.

2 ANALYTICAL SOLUTIONS FOR SEGMENTED TUNNEL RINGS

2.1 *Transfer relations (Zhang et al. 2017)*

In this paper, structural analysis of segmented tunnel rings is based on transfer relations, representing analytical solutions of the governing equations of the linear theory of slender circular arches (Zhang et al. 2017). Eq. (1), see above, contains the matrix-vector representation of the transfer relations, following the notation used by Rubin and Vogel (1993). The components T_{13} to T_{46} of the transfer matrix read as (Zhang et al. 2017)

$$T_{13}(\varphi) = R\sin\varphi, \quad (2)$$

$$T_{14}(\varphi) = \frac{R^2}{EI}(\cos\varphi - 1), \quad (3)$$

$$T_{15}(\varphi) = \frac{R}{EA}\frac{1}{2}\varphi\sin\varphi + \frac{R^3}{EI}\left(\frac{1}{2}\varphi\sin\varphi + \cos\varphi - 1\right), \quad (4)$$

$$T_{16}(\varphi)=\frac{R}{EA}\left(\frac{1}{2}\varphi\cos\varphi-\frac{1}{2}\sin\varphi\right)+\frac{R^3}{EI}\left(\frac{1}{2}\varphi\cos\varphi+\frac{1}{2}\sin\varphi\right), \tag{5}$$

$$T_{23}(\varphi)=R\,(\cos\varphi-1), \tag{6}$$

$$T_{24}(\varphi)=\frac{R^2}{EI}(\varphi-\sin\varphi), \tag{7}$$

$$T_{25}(\varphi)=\frac{R}{EA}\left(\frac{1}{2}\varphi\cos\varphi+\frac{1}{2}\sin\varphi\right)+\frac{R^3}{EI}\left(\varphi-\frac{3}{2}\sin\varphi+\frac{1}{2}\varphi\cos\varphi\right), \tag{8}$$

$$T_{26}(\varphi)=\frac{R}{EA}\left(-\frac{1}{2}\varphi\sin\varphi\right)+\frac{R^3}{EI}\left(1-\cos\varphi-\frac{1}{2}\varphi\sin\varphi\right), \tag{9}$$

$$T_{34}(\varphi)=-\frac{R}{EI}\varphi, \tag{10}$$

$$T_{35}(\varphi)=\frac{R^2}{EI}(\sin\varphi-\varphi), \tag{11}$$

$$T_{36}(\varphi)=\frac{R^2}{EI}(\cos\varphi-1), \tag{12}$$

$$T_{45}(\varphi)=R\,(1-\cos\varphi), \tag{13}$$

$$T_{46}(\varphi)=R\sin\varphi. \tag{14}$$

In Eqs. (1)–(14), R, EA, and EI denote the radius of the neutral axis of the arch, the extensional stiffness, and the bending stiffness, respectively. The vector on the left-hand-side of Eq. (1) contains the kinematic and static variables, referring to the cross-section at an arbitrary value of the angular coordinate φ, i.e. the radial displacement u, the circumferential displacement v, the cross-sectional rotation θ, the bending moment M, the normal force N, and the shear force V. The summation symbols in the last column of the transfer matrix in Eq. (1) refer to the superposition of so-called "load integrals". The latter represent analytical solutions for (i) radial point loads and (ii) relative rotation angles at segment-to-segment interfaces. The load integrals for a radial point load P, acting at position φ_p, read as (Zhang et al. 2017):

$$u_P^L(\varphi)=\frac{1}{2}\left(\frac{PR}{EA}+\frac{PR^3}{EI}\right)\left[(\varphi-\varphi_p)\cos(\varphi-\varphi_p)-\sin(\varphi-\varphi_p)\right]\;H(\varphi-\varphi_p), \tag{15}$$

$$v_P^L(\varphi)=\left\{-\frac{PR}{EA}\left[\frac{1}{2}(\varphi-\varphi_p)\sin(\varphi-\varphi_p)\right]-\frac{PR^3}{EI}\left[\frac{1}{2}(\varphi-\varphi_p)\sin(\varphi-\varphi_p)+\cos(\varphi-\varphi_p)-1\right]\right\}\;H(\varphi-\varphi_p), \tag{16}$$

$$\theta_P^L(\varphi)=\frac{PR^2}{EI}\left[\cos(\varphi-\varphi_p)-1\right]H(\varphi-\varphi_p) \tag{17}$$

$$M_P^L(\varphi)=R\,P\sin(\varphi-\varphi_p)H(\varphi-\varphi_p), \tag{18}$$

$$N_P^L(\varphi)=-P\sin(\varphi-\varphi_p)H(\varphi-\varphi_p), \tag{19}$$

$$V_P^L(\varphi)=P\cos(\varphi-\varphi_p)H(\varphi-\varphi_p), \tag{20}$$

where $H(\varphi-\varphi_p)$ stands for the Heaviside function. The load integrals for a relative rotation angle, $\Delta\theta_j$, across an interface positioned at the angular coordinate φ_j, read as (Zhang et al. 2017):

$$u_{\Delta\theta}^L(\varphi)=-R\Delta\theta_j\sin(\varphi-\varphi_j)H(\varphi-\varphi_j), \tag{21}$$

$$v_{\Delta\theta}^L(\varphi)=R\Delta\theta_j\left[1-\cos(\varphi-\varphi_j)\right]H(\varphi-\varphi_j), \tag{22}$$

$$\theta_{\Delta\theta}^L(\varphi)=\Delta\theta_j H(\varphi-\varphi_j), \tag{23}$$

$$M_{\Delta\theta}^L(\varphi)=N_{\Delta\theta}^L(\varphi)=V_{\Delta\theta}^L(\varphi)=0. \tag{24}$$

The state vector on the right-hand-side of Eq. (1) refers to the initial cross-section, marked by the index "i". The corresponding kinematic and static variables, u_i, v_i, θ_i, M_i, N_i, and V_i, represent unknown integration constants (Zhang et al. 2017). Further unknowns are the relative rotation angles at the interfaces. They intervene in the interface law, introduced next.

2.2 *Linear interface law*

In the present contribution, a simple interface law is used for the description of the six segment-to-segment interfaces of a segmented tunnel ring. The interface law relates the bending moments transmitted across the six interfaces, M_j, $j = 1, 2, \ldots, 6$, to the resulting relative rotation angles of the interfaces, $\Delta\theta_j$, $j = 1, 2, \ldots, 6$, using a rotational spring stiffness as the proportionality factor. In this context, it is emphasized that the analyzed segment-to-segment interfaces is unsymmetric with respect to the horizontal middle axis of the cross-section of the segment. This is the consequence of eccentric

bolts, used to connect neighboring segments. Therefore, the effective rotational spring stiffnesses of the interfaces depends on the orientation of the bending moments transmitted across the interfaces. The designations K^+ and K^- are used for a positive and a negative bending moment, respectively. Thus, the interface law reads as

$$\left.\begin{aligned} M_j &= K^+ \Delta\theta_j, \text{ if } M_j > 0 \\ M_j &= K^- \Delta\theta_j, \text{ if } M_j < 0 \end{aligned}\right\} \; j = 1,2,\ldots,6. \tag{25}$$

2.3 *Derivation of a linear system of equations allowing for the analytical calculation of the integration constants and the relative rotation angles*

Identification of the six integration constants u_i, v_i, θ_i, M_i, N_i, and V_i and of the six relative rotation angles at the six interfaces of a segmented tunnel ring requires

The remaining six equations are obtained from formulating the interface law (25) for all six interfaces. To this end, the fourth line of the transfer relations (1) is specified for the position of the interfaces, i.e. for $\varphi = \varphi_j$, $j = 1,2,\ldots,6$. The obtained expression for the six bending moments M_j, $j = 1,2,\ldots,6$, are inserted into the interface law (25). This delivers additional six linear equations for the nine unknowns.

The described nine linear equations can be solved *analytically*, see Eq. (47). Therein, K_1, K_2, …, K_6 stand for the rotational spring stiffnesses of the six interfaces. They are either equal to K^+ or to K^-, depending on the sign of the corresponding bending moments M_1, M_2, …, M_6, see Eq. (25). Notably, these signs are originally *unknown*.

2.4 *Solution strategy for the system of equations (26)*

Generally, a typical trial-and-error approach is required for solving the system of equations (26).

$$\begin{bmatrix} M_i \\ N_i \\ V_i \\ \Delta\theta_1 \\ \Delta\theta_2 \\ \vdots \\ \Delta\theta_6 \end{bmatrix} = -\begin{bmatrix} 0 & 0 & \frac{R\pi}{EA}+\frac{R^3\pi}{EI} & -R\sin\varphi_1 & -R\sin\varphi_2 & \cdots & -R\sin\varphi_6 \\ \frac{2R^2\pi}{EI} & \frac{R\pi}{EA}+\frac{R^3\pi}{EI} & 0 & R(1-\cos\varphi_1) & R(1-\cos\varphi_2) & \cdots & R(1-\cos\varphi_6) \\ -\frac{2R\pi}{EI} & -\frac{2R^2\pi}{EI} & 0 & 1 & 1 & \cdots & 1 \\ 1 & R(1-\cos\varphi_1) & R\sin\varphi_1 & K_1 & 0 & \cdots & 0 \\ 1 & R(1-\cos\varphi_2) & R\sin\varphi_2 & 0 & K_2 & \cdots & 0 \\ \vdots & \vdots & \vdots & \vdots & \vdots & \vdots & \vdots \\ 1 & R(1-\cos\varphi_6) & R\sin\varphi_6 & 0 & 0 & \cdots & K_6 \end{bmatrix}^{-1} \cdot \begin{bmatrix} \sum u_P^L(2\pi) \\ \sum v_P^L(2\pi) \\ \sum \theta_P^L(2\pi) \\ \sum M_P^L(\varphi_1) \\ \sum M_P^L(\varphi_2) \\ \vdots \\ \sum M_P^L(\varphi_6) \end{bmatrix}, \tag{26}$$

twelve equations. Notably, the kinematic variables u_i, v_i, and θ_i refer to rigid body motions of the segmented tunnel ring. Without loss of generality, they may be set equal to zero, i.e.

$$u_i = v_i = \theta_i = 0, \tag{27}$$

reducing the number of required equations to nine.

As for the identification of the three static variables M_i, N_i, and V_i, three geometric continuity conditions are formulated for the *closed* segmented tunnel ring (Zhang et al. 2017). To this end, the transfer relations are specified for $\varphi = 2\pi$, resulting in a relation between the state variables at the initial and the final (index "f") cross-section. Since the final cross-section is equal to the initial cross-section, the geometric compatibility conditions are obtained as $u_f = u_i$, $v_f = v_i$, and $\theta_f = \theta_i$. This delivers three linear equations for the nine unknowns.

As for the examples presented in the sequel, such a trial-and-error approach could be completed in two steps. As for the first step, the stiffnesses of all six interfaces is set equal to the arithmetic mean of K^+ and K^-:

$$K_1 = K_2 = \cdots = K_6 = \frac{K^+ + K^-}{2}. \tag{28}$$

After the solution of Eq. (26), the integration constants and the relative rotation angles are known. Inserting them into the transfer relations (1), allows for calculation of the bending moments transmitted at the interfaces. The mathematical signs of these bending moments allows for assigning either K^+ or K^- to each one of the interfaces. These updated values are inserted into Eq. (26).

The second solution of Eq. (26), based on the updated values of the spring stiffnesses, delivers updated values of the integration constants and the relative rotation angles. Inserting them into the transfer relations (1), allows for calculation of the bending moments transmitted at the interfaces. As for the examples presented in the sequel, the signs of the bending moments did not change from the first to the second solution. This proves that *proper* values of the spring stiffnesses were used for the second step. The obtained transfer relations allow for computation of the state vector at an arbitrary cross-section of interest simply by multiplying the known transfer matrix with the known vector of kinematic and static variables of the initial cross-section.

3 STRUCTURAL ANALYSIS OF A REAL-SCALE TEST OF A SEGMENTED TUNNEL RING

3.1 *Application of the proposed analysis method*

The proposed mode of structural analysis is applied to re-analysis of the initial phase of a real-scale test of a segmented tunnel ring (Liu et al. 2016), see Fig. 1. The structural analysis focuses on the first four load steps, during which the reinforced concrete segments remained uncracked. Therefore, linear elastic behavior of the reinforced concrete segments and a linear interface law appear as reasonable assumptions.

The radius of the tested ring, R, is equal to 2.925 m see Fig. 2(a). The ring is an assembly of six precast reinforced concrete segments, named K, A, B, C, D, E. The segment-to-segment interfaces were positioned at angular coordinates $\varphi_{j=1,2,\ldots,6}$ = [8°, 73°, 138°, 222°, 287°, 352°], whereby the angular coordinate φ is measured from the crown of the segmented tunnel ring, i.e. from the cross-section in the middle of segment K. The thickness and the axial length of the segments amount to 0.35 m and 1.2 m, respectively. The extensional stiffness EA and the bending stiffness EI of the steel-reinforced concrete segments are given as 18,260 MN and 186 MNm^2, respectively. Compressive loading was imposed by 24 equally distributed hydraulic jacks, see Fig. 2(b). The point loads were imposed at angular positions $\varphi_{p=1,2,\ldots,24}$ = [0°, 15°, 30°, … 345°]. They simulate the anisotropic ground pressure,

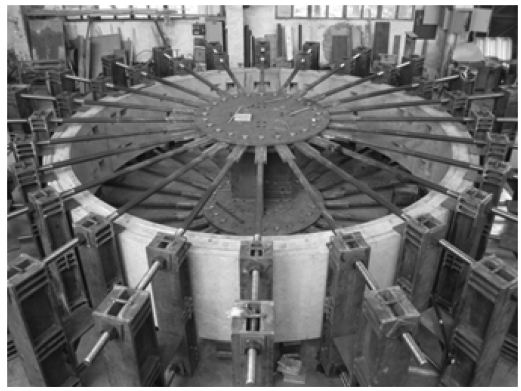

Figure 1. Setup of the analyzed real-scale experiment on a segmented tunnel ring (Liu et al. 2016).

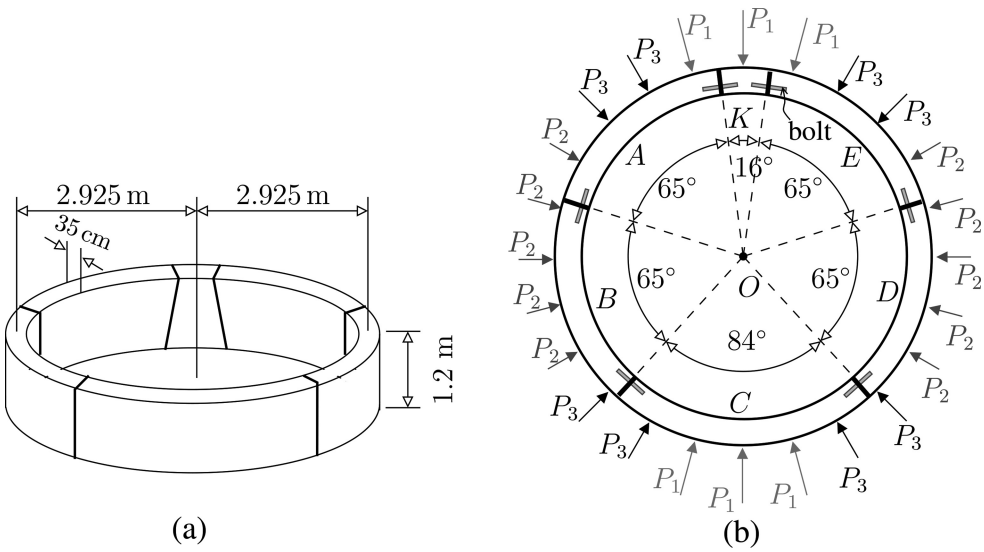

Figure 2. Geometric dimensions of the analyzed segmented tunnel ring and its external loading: (a) axonometric sketch of the ring, (b) top view of the ring, illustrating the layout of the hydraulic jacks (Zhang et al. 2017).

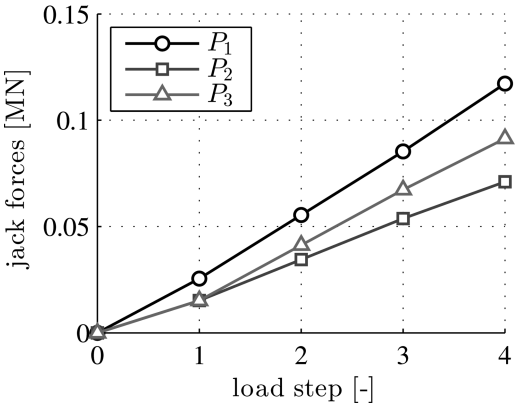

Figure 3. Numerical values of the hydraulic jack forces imposed onto the segmented tunnel ring during the first four load steps of the test (Zhang et al. 2017).

see Fig. 3. The numerical values of the rotational spring stiffnesses of the interfaces are taken from (Liu et al. 2017). They read as

$$K^{-} = 11.0\,\mathrm{MNm/rad}, \tag{29}$$

$$K^{+} = 6.5\,\mathrm{MNm/rad}. \tag{30}$$

For each one of the four considered load steps, the solution strategy described in Subsection 2.4 is used. In this context, Eq. (26) is evaluated for (i) the load integrals concerning the point loads, taken from Eqs. (15)–(18), (ii) the numerical input values from Table 1, (iii) the hydraulic jack forces from Fig. 3, and (iv) the assigned spring stiffnesses $K_{1,2,\ldots,6}$. Table 2 summarizes the obtained numerical results for the three integration constants and the six relative rotation angles. After the two-step solution of Eq. (26), described in Subsection 2.4, the transfer relations (1) are specified (i) for the expressions (2)–(14), (ii) the load integrals (15)–(24), (iii) the numerical input values from Table 1, (iv) the hydraulic jack forces illustrated in Fig. 3, (v) the vanishing kinematic variables at the initial cross-section, see (27), and (vi) the results obtained from the solution of Eq. (26), see Table 2. The obtained transfer relations may be evaluated for any angular position φ of interest. The computed kinematic variables allow for illustrating the deformed configuration (Fig. 4), following the formula (Zhang et al. 2017).

$$\begin{aligned}\mathbf{u}(\varphi,r) &= u(\varphi)\mathbf{e}_r(\varphi) \\ &+\left[v(\varphi)-(r-R)\theta(\varphi)\right]\mathbf{e}_\varphi(\varphi),\end{aligned} \tag{31}$$

where $\mathbf{u}$, $\mathbf{e}_r$, and $\mathbf{e}_\varphi$ stand for the displacement vector and for the unit base vectors in the radial and the circumferential directions, respectively. The distribution of the normal stresses (Fig. 4) follows from (Melan 1913).

$$\sigma_{\varphi\varphi}(\varphi,r) = \frac{N(\varphi)}{A} + \frac{M(\varphi)}{I}(r-R), \tag{32}$$

where A and I denote the cross-sectional area and the moment of inertia, respectively.

Table 1. Properties of the segmented tunnel ring, occurring in the transfer relations.

quantity	Numerical value
radius of the axis of the ring	$R = 2.925$ m
bending stiffness	$EI = 186$ MNm^2
extensional stiffness	$EA = 18{,}260$ MN
position of interface 1	$\varphi_1 = 8°$
position of interface 2	$\varphi_2 = 73°$
position of interface 3	$\varphi_3 = 138°$
position of interface 4	$\varphi_4 = 222°$
position of interface 5	$\varphi_5 = 287°$
position of interface 6	$\varphi_6 = 352°$
position of the *kth* hydraulic jack	$\varphi_k = (k-1)\cdot 15°$

Table 2. Numerical values of (i) the internal forces at the crown of the ring and (ii) the relative rotation angles at the interfaces, obtained from the numerical evaluation of Eq. (26).

Loadstep	1	2	3	4
M_i [MNm]	–0.0172	–0.0383	–0.0594	–0.0864
N_i [MN]	–0.0627	–0.1489	–0.2351	–0.3158
V_i [MN]	0.0128	0.0277	0.0427	0.0586
$\Delta\theta_1$ [10^{-3} rad]	–1.25	–2.84	–4.43	–6.50
$\Delta\theta_2$ [10^{-3} rad]	2.01	4.62	7.25	10.64
$\Delta\theta_3$ [10^{-3} rad]	–0.64	–1.53	–2.42	–3.56
$\Delta\theta_4$ [10^{-3} rad]	–0.64	–1.53	–2.42	–3.56
$\Delta\theta_5$ [10^{-3} rad]	2.01	4.62	7.25	10.64
$\Delta\theta_6$ [10^{-3} rad]	–1.25	–2.84	–4.43	–6.50

3.2 *Comparison of results from the presented analysis with results from hybrid analysis of the same structural test*

It is interesting to compare the results from the presented structural analysis with the corresponding results from hybrid analysis of the same test, where both the imposed jack forces *and* the measured interfacial discontinuities were used as input (Zhang et al. 2017). The results obtained from structural analysis, described in Subsection 3.1, refer to a *symmetric answer* of the *symmetrically loaded* segmented tunnel ring. Results from the

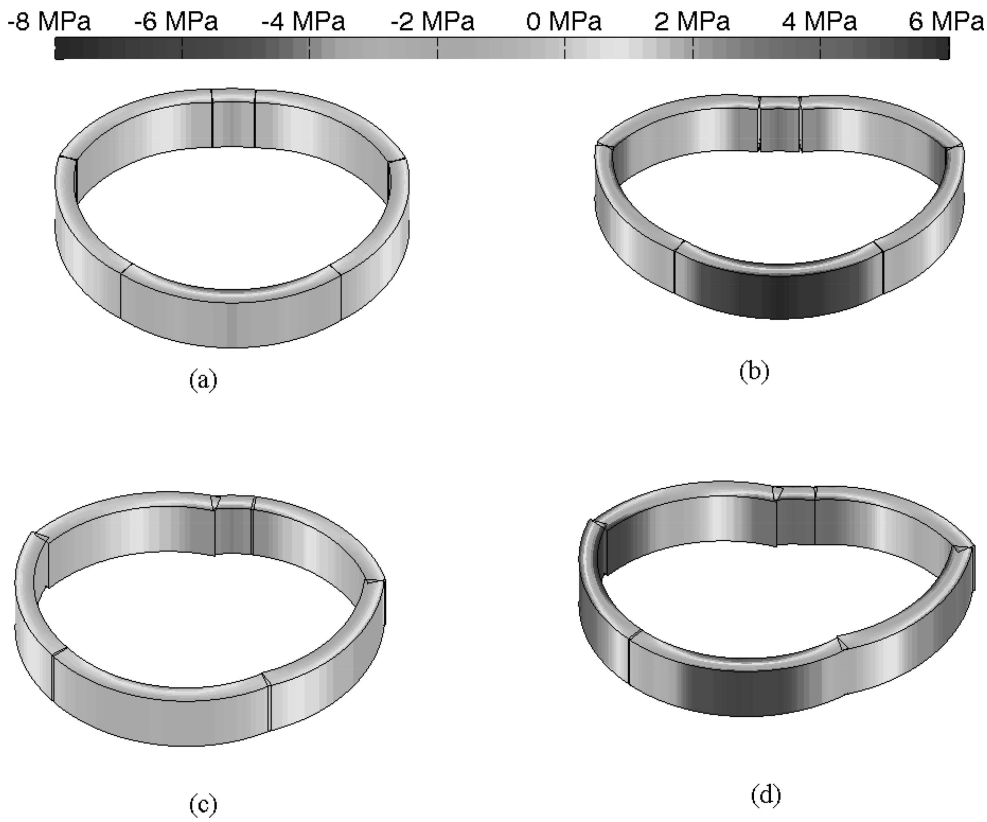

Figure 4. Deformed configuration of the analyzed segmented tunnel ring and distribution of the normal stresses according to Eqs. (31) and (32): (a) load step 2 and (b) load step 4, analyzed by the presented approach, where the interfacial discontinuities are predicted by the interface model (25); (c) load step 2 and (d) load step 4, analyzed by the hybrid method (Zhang et al. 2017), where the measured interfacial discontinuities were used as input; the magnification factor of the displacements amounts to 50.

hybrid analysis, in turn, indicate a *nonsymmetric answer* of the *symmetrically loaded* segmented tunnel ring.

The differences concerning the inner forces and the corresponding stresses are rather small. The largest differences were obtained for the bending moment, compare Figs. 5(a) and (d). The differences between the normal stresses were insignificant (Fig. 4), because the stress states are dominated by the compressive normal forces.

The computed displacements, in turn, show quite significant differences, compare Figs. 4(a) and (c) as well as Figs. 4(b) and (d). This is because the tested ring exhibited initial geometric imperfections. The latter resulted in nonsymmetric *measured* interfacial discontinuities (Zhang et al. 2017). Notably, the nonsymmetric part of the measured displacement discontinuities refers mostly to rigid body motions. This explains why the present analysis delivers reliable estimates of the inner forces, but underestimates the displacements.

4 SUMMARY AND CONCLUSIONS

A linear interface law, see (25), was combined with transfer relations (1). This allowed for performing design-like structural simulations of a segmented tunnel ring, subjected to known external loading. The conceptual advantage of the presented analysis method over the competing hybrid method, see (Zhang et al. 2017), is that the latter requires measurements of interfacial discontinuities, while the former does not need such measurements.

In the context of the analyzed real-scale test, it was shown that the presented method delivers good estimates of the inner forces. Thus, the interface law (25) accounted reasonably well for the

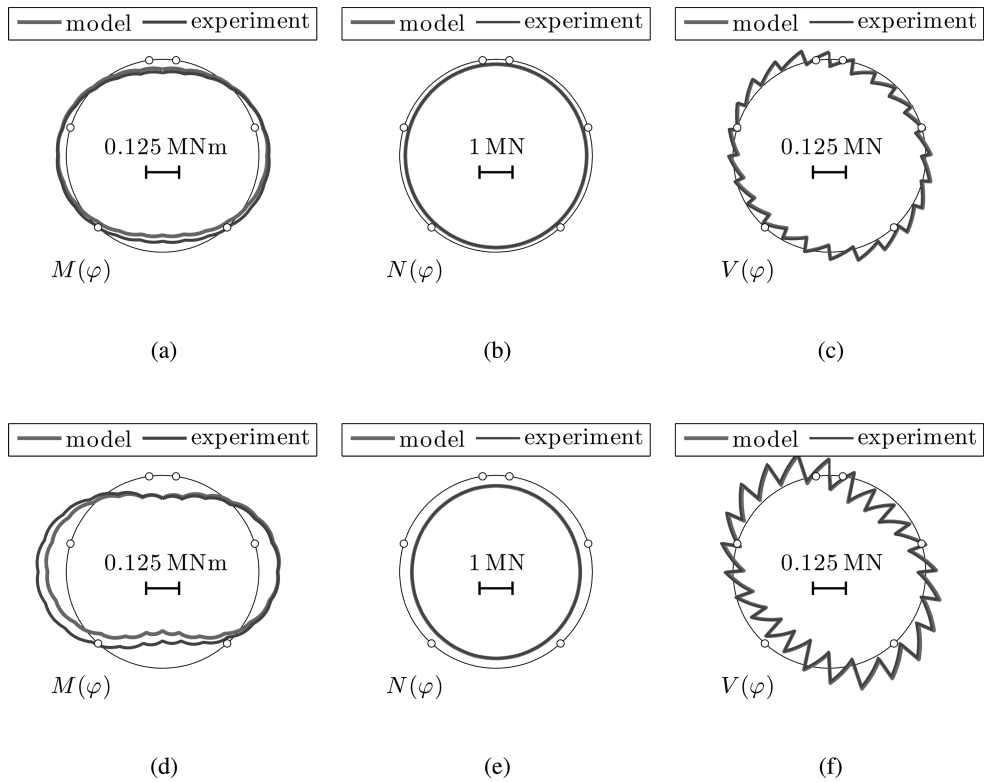

Figure 5. Distributions of internal forces of the analyzed segmented tunnel ring: (a)–(c) load step 2, (d)-(f) load step 4; the red graphs are obtained from the presented approach, where the interfacial discontinuities are predicted by the interface model (25); the blue graphs are obtained from hybrid analysis (Zhang et al. 2017), where the measured interfacial discontinuities were used as input.

discontinuities induced by the inner forces, transmitted across the interfaces. The displacements of the analyzed tunnel ring, however, were predicted with less accuracy. They consist of two parts, one of which is caused by the inner forces, while the other one is the consequence of discontinuities due to rigid body motions, which are not considered by the proposed interface law.

As for the analysis of Serviceability Limit States, both the inner forces *and* the displacements must be quantified reliably. For such states, the hybrid method remains the "gold standard", because interface models cannot predict rigid body motions of the segments.

As for the analysis of Ultimate Limit States, a reliable quantification of the inner forces is necessary, while accurate values of the displacements are less important. In this context, it seems that the proposed approach may be useful for engineering practice. Anyhow, this requires the development of (i) transfer relations, capable of accounting for the *nonlinear* behavior of reinforced concrete segments, and of (ii) *nonlinear* interface laws. The latter should be supported by real-scale tests on so-called "concrete hinges" (Schlappal et al. 2017) and corresponding numerical re-analyses, based on the Finite Element method (Kalliauer et al. 2017).

ACKNOWLEDGMENT

Financial support by the Austrian Science Fund (FWF), provided within project P 281 31-N32 "Bridging the Gap by Means of Multiscale Structural Analyses", and interesting discussions with Thomas Schlappal (TU Wien) are gratefully acknowledged. In addition, the first author gratefully acknowledges financial support by the China Scholarship Council.

REFERENCES

Brandtner, M., B. Moritz, & P. Schubert (2007). On the challenge of evaluating stress in a shotcrete lining:

Experiences gained in applying the hybrid analysis method. *Felsbau 25*(5), 93–98.

Gladwell, G.M.L. (1980, June). *Contact problems in the classical theory of elasticity*. Springer Science & Business Media.

Hellmich, C. (1999). *Shotcrete as part of the new Austrian tunneling method: From thermochemomechanical material modeling to structural analysis and safety assessment of tunnels*. Ph. D. thesis, Vienna University of Technology, Vienna, Austria.

Hellmich, C., J. Macht, & H.A. Mang (1999). Ein hybrids Verfahren zur Bestimmung der Auslastung von Spritzbetonschalen [A hybrid method for determination of the degree of utilization of shotcrete tunnel shells]. *Felsbau 17*(5), 422–425. In German.

Hellmich, C., H.A. Mang, & F.-J. Ulm (2001). Hybrid method for quantification of stress states in shotcrete tunnel shells: combination of 3D in situ displacement measurements and thermochemoplastic material law. *Computers & Structures 79*(22), 2103–2115.

Janßen, P. (1983, December). *Tragverhalten von Tunnelausbauten mit Gelenkstübbings [Structural behavior of segmented tunnel linings]*. Ph. D. thesis, Technical University of Braunschweig. In German.

Kalliauer, J., T. Schlappal, M. Vill, H.A. Mang, & B. Pichler (2017). Bearing capacity of concrete hinges subjected to eccentric compression: Multiscale structural analysis of experiments. *Acta Mechanica*. accepted for publication.

Leonhardt, F. & H. Reimann (1965). *Betongelenke: Versuchsbericht, Vorschläge zur Bemessung und konstruktiven Ausbildung. Kritische Spannungszustände des Betons bei mehrachsiger, ruhender Kurzzeitbelastung [Concrete hinges: test report, recommendations for structural design. Critical stress states of concrete under multiaxial static short-term loading]*, Volume 175. Ernst und Sohn. In German.

Liu, X., Y. Bai, Y. Yuan, & H.A. Mang (2016). Experimental investigation of the ultimate bearing capacity of continuously jointed segmental tunnel linings. *Structure and Infrastructure Engineering 12*(10), 1364–1379.

Liu, X., C. Zhang, C. Zhang, & Y. Yuan (2017). Ultimate loadcarrying capacity of the longitudinal joints in segmental tunnel linings: Illustrated with the typical segment joints of the Shanghai Metro rapid transit system. *Structural Concrete 18*(5), 693–709. 10.1002/suco.201600070.

Melan, J. (1913). *Theory of arches and suspension bridges*. Chicago, Clark.

Pichler, B., S. Scheiner, & C. Hellmich (2008). From micronsized needle-shaped hydrates to meter-sized shotcrete tunnel shells: Micromechanical upscaling of stiffness and strength of hydrating shotcrete. *Acta Geotechnica 3*(4), 273–294.

Rokahr, R. & R. Zachow (1997). Ein neues Verfahren zur täglichen Kontrolle der Auslastung einer Spritzbetonschale [A new method for the daily monitoring of the stress intensity of a sprayed concrete lining]. *Felsbau 15*(6), 430–434. In German.

Rubin, H. & U. Vogel (1993). *Baustatik ebener Stabwerke [Frameworks for structural analysis]*. Köln: Stahlbau Handbuch Für Studium und Praxis BAND 1 Teil A, Stahlbau-Verlagsgesellschaft mbH. In German.

Schlappal, T., M. Schweigler, S. Gmainer, M. Peyerl, & B. Pichler (2017). Creep and cracking of concrete hinges—Insight from centric and eccentric compression experiments. *Materials and Structures*. accepted for publication.

Ullah, S., B. Pichler, & C. Hellmich (2013). Modeling ground-shell contact forces in NATM tunneling based on three-dimensional displacement measurements. *Journal of Geotechnical and Geoenvironmental Engineering 139*(3), 444–457.

Ullah, S., B. Pichler, S. Scheiner, & C. Hellmich (2010). Shellspecific interpolation of measured 3D displacements, for micromechanics-based rapid safety assessment of shotcrete tunnels. *Computer Modeling in Engineering and Sciences (CMES) 57*(3), 279–315.

Ullah, S., B. Pichler, S. Scheiner, & C. Hellmich (2012). Influence of shotcrete composition on load-level estimation in NATM-tunnel shells: Micromechanics-based sensitivity analyses. *International Journal for Numerical and Analytical Methods in Geomechanics 36*(9), 1151–1180.

Zhang, J.-L., C. Vida, Y. Yuan, C. Hellmich, H.A. Mang, & B. Pichler (2017). A hybrid analysis method for displacement-monitored segmented circular tunnel rings. *Engineering Structures 148*, 839–856.



Taylor & Francis
Taylor & Francis Group
http://taylorandfrancis.com

Steel-concrete interaction, fiber-reinforced concrete, and masonry



Taylor & Francis
Taylor & Francis Group
http://taylorandfrancis.com

Computational Modelling of Concrete Structures – Meschke, Pichler & Rots (Eds)
© 2018 Taylor & Francis Group, London, ISBN 978-1-138-74117-1

Investigation of dowel action on a steel-concrete bond model for reinforced concrete structures

C. Turgut
DEN-Service d'Études Mécaniques et Thermiques (SEMT), CEA, Université Paris-Saclay, Gif-sur-Yvette, France
LEME, UPL, Université Paris Nanterre, Ville d'Avray, France

L. Jason
DEN-Service d'Études Mécaniques et Thermiques (SEMT), CEA, Université Paris-Saclay, Gif-sur-Yvette, France
IMSIA, CEA, EDF, CNRS, ENSTA ParisTech, Université Paris Saclay, Palaiseau, France

L. Davenne
LEME, UPL, Université Paris Nanterre, Ville d'Avray, France

A. Pirard
DDN, ENGIE, Paris La Défense Cedex, France

ABSTRACT: Steel-concrete bond modeling has a vital importance to examine the crack properties in reinforced concrete structures. Different finite element models exist to represent this bond behavior in numerical simulations. A recent developed bond-slip model for large scale simulations is represented and tested with several simulations data on deep beams by using different reinforcement models. The Shear behavior of the reinforced concrete structures is investigated by using bond-slip model especially focusing on dowel action. Additionally, the new model is compared with the perfect bond hypothesis for the experimental test cases.

1 INTRODUCTION

Cracking in reinforced concrete structures is generally influenced by the stress distribution along the interface between steel and concrete. A deeper understanding of steel-concrete interface is thus essential to predict the cracking of these structures. Different finite element models e.g. [1, 2, 3 and 4] exist to represent this bond behavior in numerical simulations. Though, these models are rarely compatible with the large scale simulations due to meshing difficulties, heavy computational cost etc. In order to overcome these difficulties, a perfect relation between steel and concrete, which assumes the same displacement between both materials (perfect bond), is generally used for structural numerical applications. But, the perfect relation is unable to predict the significant disorders, and especially the crack pattern (repartition and opening of the cracks), which is directly linked to the steel—concrete bond behavior.

A new bond slip model for large scale simulations was successively developed and applied to the finite element code Cast3M [5] by Casanova et al. [6, 7, 8] and Mang et al [9, 10, 11] to predict the crack pattern in reinforced concrete structures with a reasonable calculation time. But the model focused only on the tangential behavior of the bond. However the normal behavior of the bond may have also a significant effect on crack initiation and concrete failures. Indeed, when there is shear transfer through the crack, especially for deep beams or shear walls, the 'Dowel Action', which involves the normal interaction between steel and concrete, needs to be taken into account.

In this contribution, the normal behavior of the bond-slip model is investigated, through the dowel effect, by comparing 1D beam or truss elements for steel model, to the perfect relation hypothesis. Its influence is especially demonstrated on bending tests on continuous deep beams. It is shown that the proposed simulation strategy enables to reproduce experimental results and predicts transfer of bond stresses from reinforcement to concrete.

2 BOND-SLIP MODEL

The proposed bond-slip model is a new approach for steel-concrete bond behavior modeling which

is adapted for large scale simulations. It improves the cracking description during the active cracking phase (beginning of crack apparition) and influences the local behavior of the structure especially around the steel reinforcement by taking into account mechanical interactions between concrete (generally in 3D) and steel reinforcement (represented by 1D elements). It is not necessary to define additional mesh for the interface, the bond-slip model which comprises the calculation time quite reasonable for the numerical applications.

2.1 *Description of the model*

Bond-slip model is based on a zero thickness interface element between the steel bar (1D) and a segment (strictly superimposed to the steel bar) which is perfectly bounded to the concrete element. A schematic representation can be seen in Figure 1. The superimposed element is bounded to the concrete element by kinematic relations as in case of perfect bonding model and the kinematic relations of the bond are defined for the interface element according to the adhesion characteristics.

2.2 *Kinematic relations of the model*

As it can be seen in Figure 1 the interface element consists of 4 nodes and each node has 3 degrees of freedom. Displacement [u] of the interface element nodes can be written as Eq. 1 below where t denotes the tangential direction along the steel bar, n1 and n2 denote the normal directions of interface nodes.

$$[u]^{\mathrm{T}} = \{u_{1t}, u_{1n1}, u_{1n2}, u_{2t}, u_{2n1}, u_{2n2}, u_{3t}, u_{3n1}, u_{3n2}, u_{4t}, u_{4n1}, u_{4n2}\} \tag{1}$$

The slip (δnd) between steel and concrete can be calculated directly from the displacement difference of interface element nodes which is represented in Figure 2.

The slip between the nodes is calculated by the following equation (Eq. 2):

$$[\delta_{\mathrm{nd}}] = \begin{bmatrix} \mathrm{I}_3 & 0_3 & -\mathrm{I}_3 & 0_3 \\ 0_3 & \mathrm{I}_3 & 0_3 & -\mathrm{I}_3 \end{bmatrix} [u] \tag{2}$$

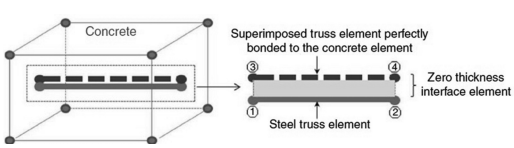

Figure 1. Representation of the interface element [10].

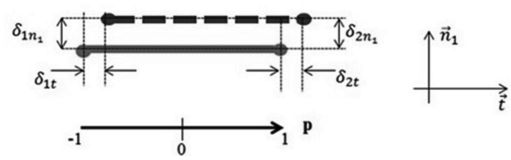

Figure 2. Definition of the slips between steel and concrete in the interface element [10].

where

$$\mathrm{I}_3 = \begin{bmatrix} 1 & 0 & 0 \\ 0 & 1 & 0 \\ 0 & 0 & 1 \end{bmatrix} \tag{3}$$

$$0_3 = \begin{bmatrix} 0 & 0 & 0 \\ 0 & 0 & 0 \\ 0 & 0 & 0 \end{bmatrix} \tag{4}$$

From Eq. 2 the slip can be represented as in Eq. 5.

$$[\delta_{\mathrm{nd}}]^{\mathrm{T}} = \{\delta_{1t}, \delta_{1n1}, \delta_{1n2}, \delta_{2t}, \delta_{2n1}, \delta_{2n2}\} \tag{5}$$

The total sliding of the interface element is calculated as in Eq. 6.

$$\{\delta(p)\} = \begin{Bmatrix} \delta_t(p) \\ \delta_{n1}(p) \\ \delta_{n2}(p) \end{Bmatrix} = [B_1(p)\ B_2(p)][\delta_{nd}] \tag{6}$$

where

$$B_1(p) = 0.5(1-p)I_3 \tag{7}$$

$$B_2(p) = 0.5(1+p)I_3 \tag{8}$$

$$-1 \le p \le 1 \tag{9}$$

Combining equations 2 and 6, the slip can be written as in terms of displacement as in Eq. 10:

$$\{\delta(p)\} = B(P)\{u\} \tag{10}$$

The generalized stresses $\{\sigma(p)\}$ can be written as in Eq. 11 which contains again 3 different components for 1 tangential and 2 normal directions.

$$\{\sigma(p)\} = \begin{Bmatrix} \sigma_t \\ \sigma_{n1} \\ \sigma_{n2} \end{Bmatrix} \tag{11}$$

Stresses on the interface element can be calculated from the slip values for a defined normal stiffness value chosen linear, and from a defined adhesion law for the tangential direction regarding equations 12 and 13 respectively.

$$\begin{Bmatrix} \sigma_{n1}(p) \\ \sigma_{n2}(p) \end{Bmatrix} = k_n \begin{Bmatrix} \sigma_{n1}(p) \\ \sigma_{n2}(p) \end{Bmatrix} \tag{12}$$

$$\sigma_t = f_{ad}(\delta_{nd}) \tag{13}$$

The adhesion law in the tangential direction is based on the study of Casanova et al. [6, 7, and 8]. The adhesion law is presented on Figure 3.

2.3 *Calculation of the nodal forces on the interface element*

The nodal forces on the interface element for the 4 different nodes can be represented as in Eq. 14.

$$\left\{F_{interface}\right\}^T = [F_1^T \; F_2^T \; F_3^t \; F_4^T] \tag{14}$$

The forces on each interface element nodes can be calculated with Eq. 15 and Eq. 16 below by integrating the stress values of each node.

$$F_1 = \begin{bmatrix} F_{1t} \\ F_{1n1} \\ F_{1n2} \end{bmatrix} = \frac{\ell_{int}}{2} \int_{-1}^{0} \bar{\bar{A}} \{\sigma(p)\} dp \tag{15}$$

and

$$F_2 = \begin{bmatrix} F_{2t} \\ F_{2n1} \\ F_{2n2} \end{bmatrix} = \frac{\ell_{int}}{2} \int_{0}^{1} \bar{\bar{A}} \{\sigma(p)\} dp \tag{16}$$

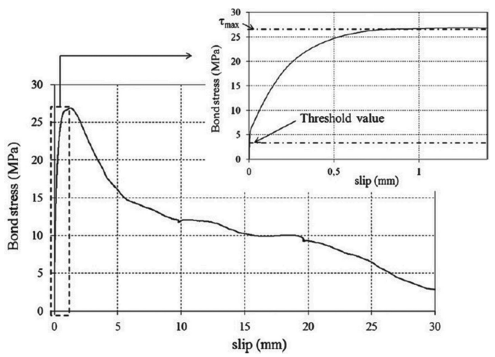

Figure 3. Adhesion law between steel and concrete (global curve and zoom on the pre-peak behavior) [8].

where ℓ_{int} is the length of the interface element and

$$\bar{\bar{A}} = \begin{bmatrix} \pi d_s & 0 & 0 \\ 0 & d_s & 0 \\ 0 & 0 & d_s \end{bmatrix} \tag{17}$$

with d_s the diameter of steel bar.

The following equations 18 and 19 can be obtained from the force equilibrium.

$$F_3 = \begin{bmatrix} F_{3t} \\ F_{3n1} \\ F_{3n2} \end{bmatrix} = -F_1 \tag{18}$$

$$F_4 = \begin{bmatrix} F_{4t} \\ F_{4n1} \\ F_{4n2} \end{bmatrix} = -F_2 \tag{19}$$

3 DOWEL ACTION

3.1 *Definition*

Shear transfer in cracked reinforced concrete structures is generally governed by three mechanisms as presented in Figure 4.

1. Shear resistance of un-cracked concrete,
2. Aggregate interlock,
3. Dowel action.

After the crack occurrence, the concrete blocks on both sides of the crack slide against each other and the bar embedded inside the concrete is subjected to a relative transverse displacement. The bending of the two ends of the embedded bar is called dowel action. This can be defined as the bearing capacity of the reinforcement against the perpendicular forces applied on it. As it can be seen in Figure 5, only a specific length of the steel

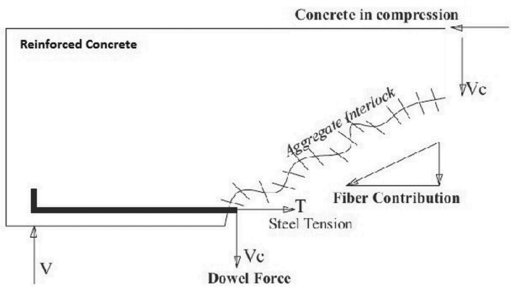

Figure 4. Shear transfer mechanisms in RC structures [16].

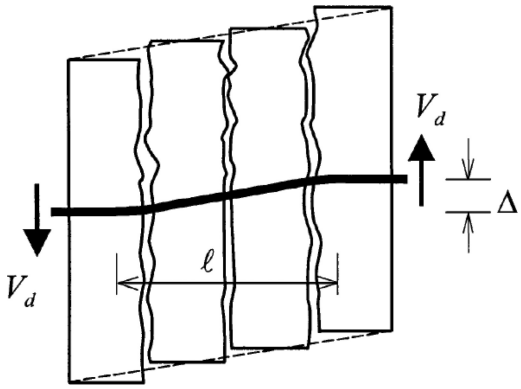

Figure 5. Representation of the dowel action [13].

bar is subjected to this deformation and it can only occur when the crack widens to a certain amount. Dowel action becomes significant around the peak loading stage of the structure. Dowel strength across the shear plane is a combination of shear, kinking and bending of the reinforcement.

Dowel action thus contributes to the shear strength of a RC structure combined with the other shear transfer mechanisms. In literature, several experimental and numerical studies were performed in order to investigate the dowel effect like [12–16] etc. They underlined different influent parameters (reinforcement layout, geometry, loads etc.) but also came to different conclusions regarding the relative importance of the dowel action. Since it depends on many parameters, it is not easy to investigate the dowel action separately among the other transfer components. Furthermore, the contributions of these parameters keep on changing when the applied loads increase due to the internal stress distribution. Even though the flexural behavior of reinforced concrete structures can be quite accurately predicted by using simple bending theories, the prediction of shear behavior remains a challenging task even with the sophisticated finite element methods.

In this contribution, dowel effect is analyzed, regarding the simulation of the bond between steel and concrete by using bond-slip model in order to evaluate its performance compared to the perfect bond assumption. Four-point bending test on continuous deep beams which is a rather common geometry in the structural area is chosen for this specific analysis. The simulations are performed by perfect bond assumption and bond-slip model for the steel-concrete interface. The numerical results are then compared with experimental ones to determine the general behavior of the both models. Besides the dowel action, the effect of reinforcement and concrete parameters to the general behavior is also investigated.

4 BENDING TESTS ON CONTINUOUS DEEP BEAMS

4.1 *Experimental setup*

Four-point bending tests on a continuous deep beam from the experimental study of Zang et al. [16] are chosen for the reference geometry. Deep beam with the horizontal reinforcement geometry is analyzed to observe the effect of dowel action. Experimental test setup (Figure 6), reinforcement layout (Figure 7), specimen details (Table 1),

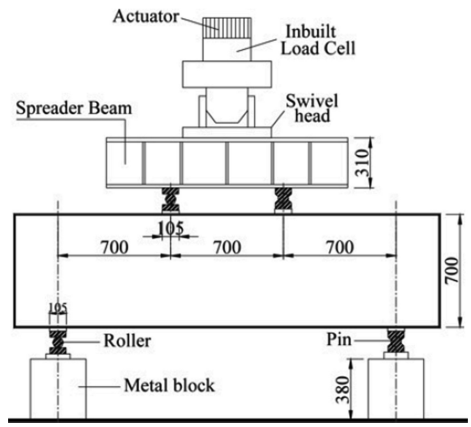

Figure 6. Experimental test setup of continuous deep beam [17].

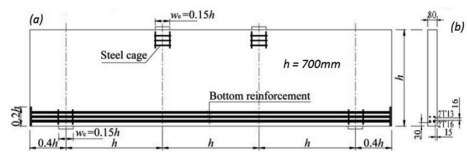

Figure 7. (a) Reinforcement layout of the specimen. (b) Cross section of the beam [17].

Table 1. Details of the specimen [17].

Beam Width b (mm):	80
Overall Height h (mm):	73
Width of Loading & Support Plate w (mm):	105
Effective Depth d (mm):	650
Bottom Reinforcement As (mm)²:	668 (T13 + T16)
Reinforcement Ratio ρ (%):	1.28
Concrete Compressive Strength $f_c'(MPa)$	24.8

Table 2. Material properties of the reinforcement [17].

	Types of steel bars	
	T13	T16
Diameter $\phi\,(mm)$	13	16
Nominal Yield Stress $f'_y(MPa)$:	520	499
Nominal Ultimate Stress $f'_u(MPa)$:	611	648
Young Modulus $E\,(GPa)$:	190	611

Table 3. Experimental results [17].

Failure Load $Vn\,(kN)$:	311
Initial Flexural Cracking Load $Vcr\,(kN)$	70
Initial Diagonal Cracking Load $Vd\,(kN)$:	160
Serviceability Load $Vser\,(kN)$:	160
Failure Mode:	Shear Compression

material properties (Table 2), experimental results (Table 3) and crack distribution after loading (Figure 8) are respectively presented as following.

4.2 *Simulation properties*

Different models are used for the numerical analysis in order to analyze proper representation of the structural behavior under shear loading. Due to the symmetry in four-point bending test, the simulation is made for ¼ geometry of the whole specimen. The series of simulations are focused on the reinforcement model and also the steel-concrete interface representation. The horizontal steel bars are modeled with elastoplastic 1D beam or truss element models. Bond-slip model or perfect bond assumption of steel-concrete interface are used in the simulations. 3D solid elements with Mazars damage model [18] are used for concrete. Then the results are compared among themselves and with the experimental ones in order to analyze different representation of the structural behavior under shear loading. The properties of the simulations are presented in Table 4 and the mesh geometry is shown in Figure 9.

4.3 *Numerical results*

Four different series of simulations have been performed on continuous deep beams under shear loading which contain horizontal steel bars. Concrete is modelled with 3D solid elements with Mazars dam-

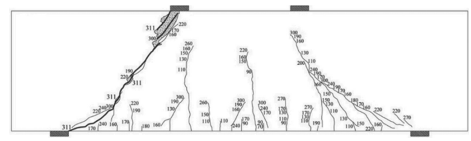

Figure 8. Crack pattern of the specimen at the end of loading [17].

Table 4. Simulation properties.

Simulation Name:	Truss_bond	Truss_perfect
Concrete:	3D solid elements	3D solid elements
Reinforcement:	1D Truss elements	1D Truss elements
Steel-concrete bond:	Bond-slip model	Perfect bond
Mesh Density (spacing of nodes in m):	0.02 for concrete 0.01 for steel	0.02 for concrete 0.01 for steel
Simulation Name:	**Beam_bond**	**Beam_Perfect**
Concrete:	3D solid elements	3D solid elements
Reinforcement:	1D beam elements	1D beam elements
Steel-concrete bond:	Bond-slip model	Perfect bond
Mesh Density (spacing of nodes in m):	0.02 for concrete 0.01 for steel	0.02 for concrete 0.01 for steel

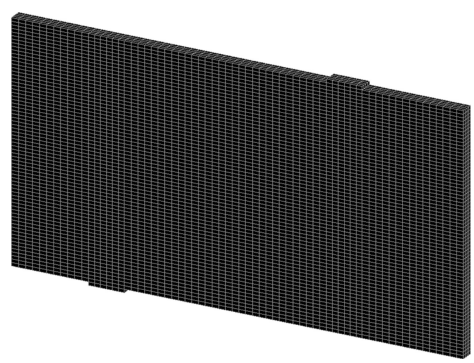

Figure 9. Mesh geometry.

age model [18]. In the first simulation case, which is denoted by the name "truss_perfect", horizontal steel bars are represented 1D truss elements and the perfect bond assumption is assumed for the steel-concrete interface. In the second simulation case, which is denoted by the name "truss_bond", the reinforcement is again represented with 1D truss elements but bond-slip model is used for the steel-concrete interface. The third and fourth simulation

cases focus on 1D beam element representation for the steel, using perfect bond and bond-slip model for the steel-concrete interface. They are denoted by the names "beam_perfect" and "beam_bond" respectively.

Figure 10 shows the force-displacement comparison between experimental and numerical results of the four different simulations. In order to show the effect of shear cracks in the numerical simulations, Figure 11 gives the damage shapes at the important time steps for the "beam-perfect" and the "beam_bond" simulations, along with the corresponding force-displacement curves. Figure 12 shows the tangential slip between steel and concrete in the interface elements along the reinforcement for "truss_bond" and "beam_bond" simulations. It should be remarked that there is no slip between steel and concrete in case of perfect bond ("truss_perfect" and "beam_perfect" simulations) since the same displacement is assumed in reinforcement and concrete. Finally, the magnified deformed shapes at the end of the four simulations are presented in Figure 13 to analyze the mechanisms that lead to the ruin and/or the end of convergence in the simulations.

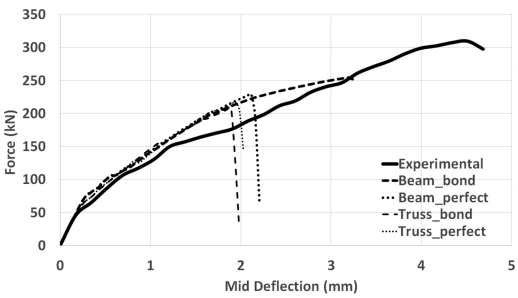

Figure 10. Force-displacement curves of numerical and experimental results.

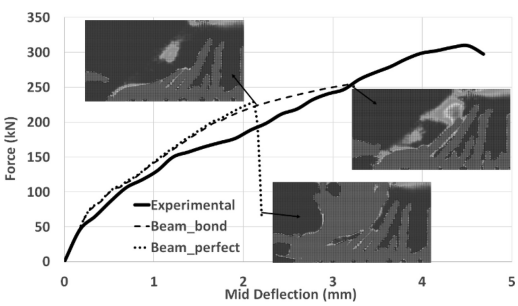

Figure 11. "Beam_perfect" and "beam_bond" simulations: Force-displacement curves and damage shapes at important time steps.

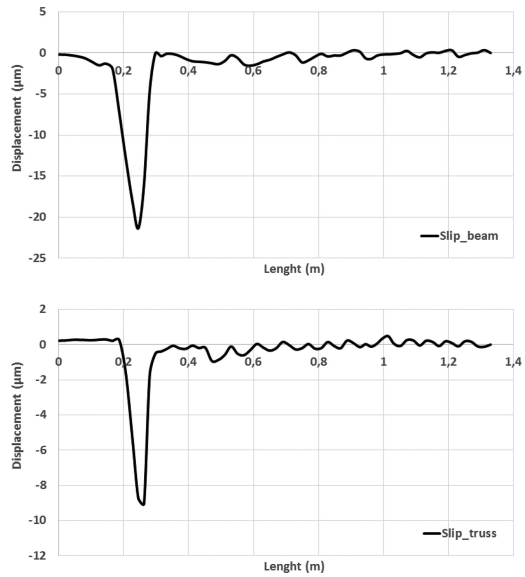

Figure 12. Tangential slip between steel and concrete along the horizontal steel bars.

4.4 *Evaluation of the results*

Concerning the global behavior, one can see on Figure 10 that the simulation curves are close to the experimental one. But for three simulations ("Truss_perfect", "Truss_bond" and "Beam_perfect") there is a huge force drop along with an apparition of a shear crack between the support and the loading point (Fig. 13b, c and d). The drop is about at the same level for "Truss_perfect" and "Truss bond" simulations. For the "Beam_perfect" simulation, the simulation goes a little further because of the bending stiffness of beam elements which delays the damage evolution in the concrete under shear. But there is still a premature shear crack in the simulation with the perfect bond assumption. One can observe the quick growth of damage, in one time step, before and after the drop, on Figure 11. On the contrary, the combination of bond-slip model for steel concrete interface and beam element approach for the reinforcement model ("Beam_bond" simulation) can go much further in the force displacement graph compared to the other simulations and gives yet coherent results with the experimental ones. Moreover, this later simulation still converges, and is still running when writing this paper. But one can see in Figure 11 that the shear crack may be about to appear.

Both truss and beam models have a force drop at the time of the shear crack occurrence. One can see that the drop is higher in truss element compared to the beam element model. It is a manifestation

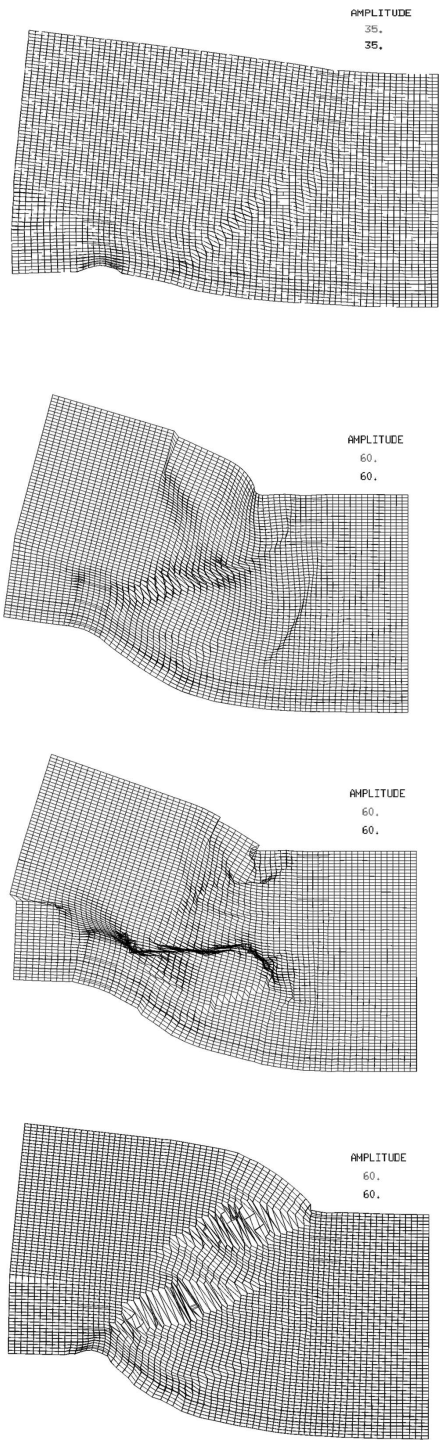

Figure 13. Final deformed shapes of (a) beam_bond, (b) beam_perfect, (c) truss_bond and (d) truss_perfect simulations at the end of simulation.

of the dowel effect. Indeed, truss elements cannot withstand transverse shear forces. On contrary beam elements can take a part of the global shear force. The remaining force (drop) which is not observed in experimental curve is probably taken by the aggregate interlock which is not explicitly modeled in the damage model.

It can be seen that the maximum slip is always observed on the bottom support due to stress concentration when the slips of bond-slip model simulations for truss and beam element steel bar representations are considered (Figure 12). Moreover the slip of beam element approach is relatively high compared to the truss element approach. This discrepancy may originate from the consideration of the all forces (both tangential and normal directions) in beam element model contrary to the truss element model which considers only the tangential forces along the steel bar. The truss element approach for the steel representation can only represent a certain amount forces even if the bond-slip model is used.

There is a close interaction between damage in concrete and bond slip behavior. Indeed it is observed that the last simulation ("Beam_bond") go much further before shear crack appearing. The sliding introduces some relaxations and the stress distributions are different, especially near the support where the shear crack starts. All these observations reveal the extreme dependence of the behavior on boundary conditions in such simulations. Mesh density, concrete damage model, symmetry properties, location of the applied force, blockage methodology of the bottom support, material properties and the exact location of the cage reinforcement around the supports may cause the stress concentration on the supports and lead to a sudden failure of the support in such finite element analysis. Thus, the boundary conditions should be defined meticulously by considering all of the parameters which may affect the numerical calculations in order to avoid this kind of consequences.

5 CONCLUSION

The shear behavior of the reinforced concrete structures is investigated by focusing on dowel action. The finite element analyses are performed with the proposed bond slip model for the steel concrete interface and compared with the experimental values plus the perfect bond assumption models which is most commonly used in industrial area. 1D reinforcement models (truss and beam) are also examined within the scope of this study.

Four-point bending test of a continuous deep beam is modeled with truss element or beam

element approaches using bond-slip or perfect bond interface models for the numerical analyses. Results revealed that the truss element representation of the reinforcement is not sufficient to reflect global behavior after the shear crack occurrence due to its lack of ability to consider transverse behavior response of the steel when a shear load is applied. The stress drop is quite smaller in beam element representation of the steel bars with perfect bond model compared to the truss element approach. However the general behavior is not totally representing the reality when it is compared with the experiments. Since the bond-slip model is considering different displacements on both steel and concrete materials, it successfully represents the shear transfer mechanism like the dowel action which appears after shear crack occurrence if the reinforcement model considers all the forces.

Finally, the bond-slip model represents global (force-displacement relation) and local behavior (crack pattern) of the reinforced concrete structures under shear loading better than the perfect bond assumption model.

REFERENCES

[1] Gattesco N. 1999. Analytical modeling of nonlinear behavior of composite beams with deformable connection. *Journal of Constructional Steel Research* vol. 52 p. 195–218.

[2] Gooranorimi O. & Suaris W. & Nanni A. 2017. A model for the bond-slip of a GFRP bar in concrete. *Engineering Structures* vol. 146 p. 34–42.

[3] Ranzi G. & Ansourian P. & Gara F. & Leoni G. & Dezi L. 2005. Displacement-based Formulations for Composite Beams with Longitudinal Slip and vertical Uplift. *University of Sydney, Department of Civil Engineering, Research Report No: R837* Sydney/Australia.

[4] Queiroz F. D. & G. Queiroz G. & Nethercot D. A. 2009. Two-dimensional FE model for evaluation of composite beams, I: Formulation and validation. *Journal of Constructional Steel Research* vol. 65 p. 1055–1062.

[5] Cast3M, 2017. Site officiel Cast3M - Commissariat à l'Energie Atomique et aux énergies alternatives. [En ligne]: http://www-cast3m.cea.fr/

[6] Casanova, A. & Jason, L. & Davenne, L. 2012. Bond slip model for the simulation of reinforced concrete structures. *Engineering Structures* 39: 66–78.

[7] Casanova, A. & Jason, L. & Davenne, L. 2013. Prise en Compte de la Liaison Acier-Béton pour le Calcul de Structures Industrielles. *RAPPORT CEA-R-632*.

[8] Casanova, A. & Jason, L. & Davenne, L. & Pinelli X. 2013. Confinement effects on the steel–concrete bond strength and pull-out failure. *Engineering Fracture Mechanics* Vol. 97 p.92–104.

[9] Mang, C. & Jason, L. & Davenne, L. 2015. A new bond slip model for reinforced concrete structures validation by modelling a reinforced concrete tie. *Engineering Computations* 32: 1934–1958.

[10] Mang, C. & Jason, L. & Davenne, L. 2016. Crack opening estimate in reinforced concrete walls using a steel-concrete bond model. *Archives of Civil and Mechanical Engineering* 16: 422–436.

[11] Mang, C. & Jason, L. & Davenne, L. 2016. Modélisation de La Liaison Acier-Béton dans Le Calcul de Structures en Béton Armé. *RAPPORT CEA-R-6428*.

[12] Kotsovos, M.D. & Jelic, I. & Pavlovic. M.N. 1999. Study of Dowel Action in Reinforced Concrete Beams. *Concrete Research* 51: 131–141.

[13] Kwan, A.K.H. & He, X.G. 2001. Modeling dowel action of reinforcement bars for finite element analysis of concrete structures. *Computers and Structures* 79: 595–604.

[14] Kwan, A.K.H. & Ng, P.L. 2013. Modeling dowel action of discrete reinforcing bars for finite element analysis of concrete structures. *Computers and Concrete* 12: 19–36.

[15] Ince, R. & Erhan Yalcin, E. & Arslan, A. 2006. Size Dependent Response of Dowel Action in R.C. Members. *Engineering Structures* 29: 955–961.

[16] Xia J. & Xiao Y. & Mackie K. R. & Al-Ramahee M. & Mirmiran A. 2015. Dowel action and shear strength contribution of high strength rebar embedded in ultra-high performance fiber reinforced concrete. *Engineering Structures* vol. 83 p. 223–232.

[17] Zhang, N. & Tan, H.T. 2007. Size effects in RC deep beams: Experimental investigation and STM verification. *Engineering Structures* 29: 3241–3254.

[18] Mazars J. 1986. A description of micro and macro scale damage of concrete structures. *Engineering Fracture Mechanics* 25: 729–737.

Computational Modelling of Concrete Structures – Meschke, Pichler & Rots (Eds)
© 2018 Taylor & Francis Group, London, ISBN 978-1-138-74117-1

Multi-scale tension stiffening approach for the minimum reinforcement of hybrid concrete beams

A.P. Fantilli, A. Gorino & B. Chiaia
Department of Structural, Building and Geotechnical Engineering, Politecnico di Torino, Torino, Italy

ABSTRACT: To reinforce cementitious matrix, a combination of steel rebar and fibers can be used in massive concrete members, e.g., tunnel linings. Due to their large cross-sections, and to the moderate state of stress, these Hybrid Reinforced Concrete (HRC) elements typically contain the minimum reinforcement to prevent the brittle failure. Thus, a model capable to predict the flexural behavior of such HRC members is of practical interest. The multi-scale approach proposed herein is based on the flexural response of both Lightly Reinforced Concrete (LRC) and Fiber-Reinforced Concrete (FRC) beams, containing only rebar and fibers, respectively. As for LRC and FRC elements, the model provides the so-called Ductility Index (DI), used to define the minimum reinforcement of HRC beams. According to the results of several tests, the transition between the brittle ($DI < 0$) and ductile ($DI > 0$) response indicates the optimal value of the hybrid reinforcement.

1 INTRODUCTION

Hybrid Reinforced Concrete (HRC), where steel reinforcing bars are combined with short fibers randomly dispersed in the cementitious matrix, is often adopted in massive structures, e.g., precast and cast-in-situ tunnel linings (Caratelli et al. 2012, Chiaia et al. 2007, de la Fuente et al. 2012, Plizzari and Tiberti 2006). The aim is to reduce the amount of rebar necessary to satisfy static requirements, through the addition of the fibers.

Indeed, in Lightly Reinforced Concrete (LRC) elements containing only rebar, a minimum reinforcement $A_{s,min}$ is traditionally required to avoid the brittle failure (Levi 1985). In other words, the ultimate bending moment of the concrete cross-section M_u has to be greater than the effective cracking moment M_{cr*}, i.e., the maximum bending moment reached during the growth of the first crack (Maldague 1965), in order to guarantee a ductile failure:

$$M_u \geq M_{cr*} \tag{1}$$

Similarly, in Fiber-Reinforced Concrete (FRC) beams, the minimum fiber volume fraction $V_{f,min}$ can be identified. For such fiber content, the transition between the deflection-softening (i.e., the brittle response) and the deflection-hardening (i.e., the ductile response) occurs (Naaman 2003).

Referring to HRC elements, despite the several research works presented until now (de Montaignac et al. 2012, di Prisco et al. 2014, Facconi et al. 2016, Falkner and Henke 2005), a simple and univocal criterion for evaluating the minimum hybrid reinforcement, consistent with those of LRC and FRC, cannot be found in the literature.

With the aim to fill this research gap, a multi-scale general model able to predict the brittle/ductile transition of HRC beams in bending is introduced herein. This model combines the flexural response of LRC and FRC beams, as studied by Fantilli et al. (2016a,b). Specifically, at the scale of the fiber-reinforcement, an ideal tie composed by a fiber and the surrounding matrix is analyzed. The pull-out mechanism of this element, which includes both the bond-slip between fiber and concrete and the fracture mechanics of concrete in tension (Bažant and Cedolin 1991), provides the cohesive stress vs. crack width relationship of FRC. Then, at the beam scale, the flexural response of an HRC member can be evaluated. Specifically, the previous stress vs. crack width relationship becomes a boundary condition in the tension-stiffening problem of a FRC beam in bending containing steel rebar. The present model is similar to that recently proposed by Barros et al. (2015), even if the strain localization of concrete in compression is neglected, due to the low amount of reinforcement.

The numerical results of this new multi-scale model, and some experimental data as well, show that the design-by-testing procedure proposed to assess the brittle/ductile flexural behavior (and the minimum reinforcement) of LRC and FRC elements (Fantilli et al. 2016a,b,c) can be extended also to HRC members.

2 A NEW GENERAL MODEL

2.1 *At the scale of the fiber*

According to Fantilli et al. (2016b), the fiber-reinforcement is modelled herein by means of an ideal tie defined by a single straight steel fiber surrounded by the cross-sectional area of cementitious matrix A_m (Fig. 1a):

$$A_m = \frac{A_f}{V_f} = \frac{\pi \cdot \phi_f^2}{4 \cdot V_f} \tag{2}$$

where A_f, ϕ_f = area and diameter of the fiber cross-section, respectively; V_f = fiber volume fraction used in the FRC mixture.

As in the case of an ordinary reinforced concrete tie (Fantilli et al. 1999), only a portion of the element is investigated. Specifically, such portion is delimited by the cracked cross-section (i.e., the cross-section 0–0 in Fig. 1a), and the so-called Stage I cross-section (i.e., the cross-section 1–1 in Fig. 1a). The cross-section 0–0 is assumed to be in midspan and orthogonal to the fiber, whereas in the cross-section 1–1 the perfect bond between steel fiber and concrete is re-established. Within this portion of length l_{tr} (i.e., the transfer length), as the horizontal coordinate z increases, stresses (and strains) move from steel fiber to concrete in tension, due to the bond-slip mechanism acting at the interface of the materials. The slip s between fiber and concrete vanishes in Stage I cross-section (Fig. 1b), where the strains of fiber ε_f and concrete matrix ε_m are the linear elastic values $\varepsilon_{f,1}$ and $\varepsilon_{m,1}$ (Fig. 1c).

Within the transfer length, the interaction between fiber and matrix is described by the following equilibrium and compatibility equations:

$$\frac{d\sigma_f}{dz} = -\frac{p_f}{A_f} \cdot \tau\left[s(z)\right] = -\frac{4}{\phi_f} \cdot \tau\left[s(z)\right] \tag{3}$$

$$\frac{ds}{dz} = -\left[\varepsilon_f(z) - \varepsilon_m(z)\right] \tag{4}$$

where σ_f = stress in the fiber; p_f = perimeter of the fiber cross-section; τ = bond stress corresponding to the slip s between fiber and concrete matrix.

The resultant N of the axial stresses in fiber and matrix (i.e., σ_f and σ_m, respectively), acting in each cross-section of the ideal tie, can be computed as:

$$N = \sigma_f \cdot A_f + \sigma_m \cdot A_m \tag{5}$$

To solve the system composed by Eqs.(3)–(5), the following boundary condition is needed in order to fix the value of the slip s_0 in the cracked cross-section, as a function of the crack width w:

$$s_0 = \frac{w}{2} \tag{6}$$

Moreover, at a distance l_{tr} from the midsection, the absence and the stationary state of slip need to be imposed. This statement corresponds to fix $\varepsilon_f = \varepsilon_m$ in Eq.(4). Only when $l_{tr} < L_f/2$ (L_f = fiber length), these conditions can be considered valid.

The cohesive tensile stress on the crack surfaces of the ideal tie can be defined by the stress vs. crack width relationship proposed by Model Code 2010 (*fib* 2012) and depicted in Fig. 2. Moreover,

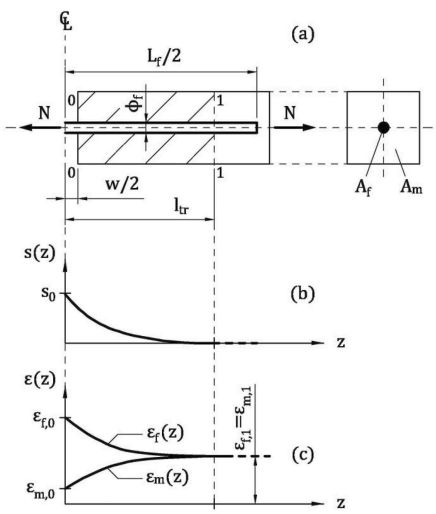

Figure 1. Modeling the fiber pull-out: (a) portion of the ideal tie composed by a straight fiber and the surrounding cementitious matrix in presence of a single crack; (b) slip between fiber and matrix; (c) strains in fiber and matrix.

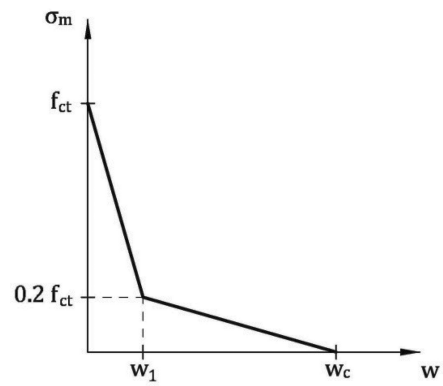

Figure 2. Fictitious crack model proposed by Model Code 2010 (*fib* 2012) for evaluating the stresses of the cementitious matrix on the crack surface.

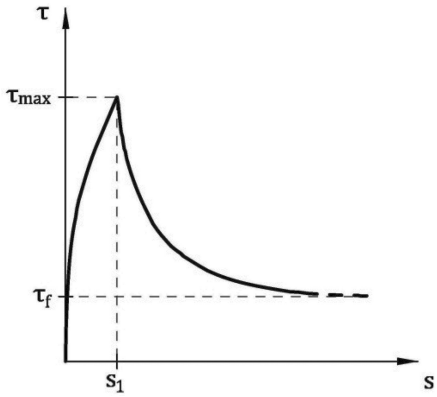

Figure 3. Bond-slip model proposed by Fantilli and Vallini (2003) for evaluating the stresses at the interface between fiber and matrix.

the interaction between fiber and concrete matrix is studied through the model proposed by Fantilli and Vallini (2003), originally developed for smooth steel fibers in a cementitious matrix (Fig. 3).

2.2 *Numerical evaluation of* $\sigma_c(w)$

To study the pull-out of the ideal tie depicted in Fig. 1a, the so-called tension-stiffening problem needs to be solved within the one-dimensional domain of length l_{tr}. The proposed numerical solution (Fig. 4) is based on the following iterative procedure (Fantilli et al. 2016b):

1. Assign a value to the crack width w in the midsection of the ideal tie.
2. Compute the slip s_0 in the midsection (Fig. 1b) through Eq.(6).
3. By means of the stress vs. crack width relationship depicted in Fig. 2, calculate the tensile stress of the matrix in the midsection $\sigma_{m,0}$.
4. Under the hypothesis of linear elastic behavior of the concrete matrix, calculate the strain in midsection $\varepsilon_{m,0}$ (Fig. 1c).
5. Assume a trial value to the axial load N (Fig. 1a).
6. According to Eq.(5), evaluate the stress of the fiber in midsection $\sigma_{f,0}$. As the failure of the fiber is not considered herein, $\sigma_{f,0}$ must be lower than f_u (where f_u = ultimate strength of fiber).
7. Assuming the linear elastic behavior of the fiber, calculate the strain in midsection $\varepsilon_{f,0}$ (Fig. 1c).
8. Considering Δl as a small portion of the unknown $l_{tr} < L_f/2$, define $z_i = i \cdot \Delta l$ (where $i = 1, 2, 3, \ldots$).
9. For each i (or z_i) calculate:
   - The bond stress τ_i, related to the slip s_{i-1}, with the bond-slip relationship represented in Fig. 3.
   - The strain of the fiber $\varepsilon_{f,i}$ through Eq.(3), based on the finite difference method and assuming the linear elastic behavior of the fiber.
   - The strain $\varepsilon_{m,i}$ of the matrix according to Eq.(5) and assuming the linear elastic behavior of the uncracked matrix.
   - The slip s_i by means of Eq.(4) and by applying the finite difference method.
10. When $s_i \cong 0$, verify if $\varepsilon_{f,i} \cong \varepsilon_{m,i}$, [i.e., the slip is in stationary state in Eq.(4)], otherwise change N and go back to step 6.
11. Calculate the tensile stress σ_c referred to the cross-sectional area of the ideal tie (i.e., $A_m + A_f$ in Fig. 1a):

$$\sigma_c = \frac{N}{A_m + A_f} \tag{7}$$

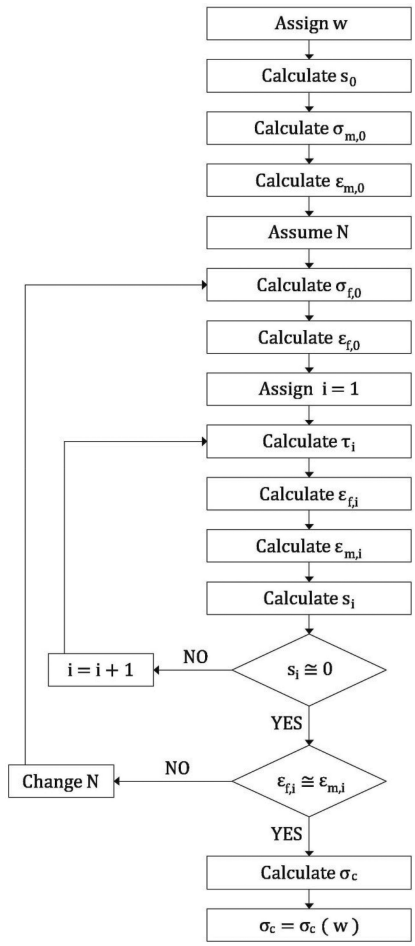

Figure 4. Flow-chart of the numerical procedure for evaluating $\sigma_c(w)$.

For a given w, such numerical procedure calculates the corresponding stress of the cracked FRC. The complete σ_c-w curve can be obtained by varying the assigned crack width, in order to describe the tensile behavior of the concrete matrix after cracking in an HRC member.

2.3 *At the scale of the beam*

As in the case of LRC members (Fantilli et al. 2016a), a block of HRC beam in three point bending is modelled (Fig. 5a). It fails in presence of a single flexural crack, due to the low amounts of reinforcement considered herein. Similarly to the previous ideal tie, such block of beam is delimited by the cracked cross-section (i.e., the midsection 0–0) and the Stage I cross-section (i.e., the cross-section 1–1), in which the perfect bond between steel rebar and FRC matrix in tension is re-established. Moreover, in analogy with the ideal tie, stresses (and strains) move from rebar to cementitious matrix when the horizontal coordinate z increases from zero to the transfer length of the beam, due to the bond-slip mechanism. At the level of reinforcement, the slip s between rebar and FRC vanishes in Stage I cross-section (Fig. 5b), where

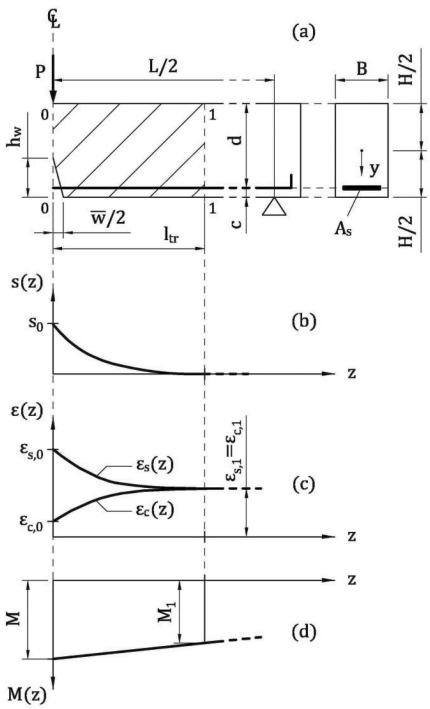

Figure 5. Modelling the flexural response of an HRC beam: (a) portion of the beam in presence of a single crack; (b) slip between rebar and FRC matrix in tension; (c) strains of rebar and FRC matrix in tension; (d) diagram of bending moment.

concrete strain ε_c equates rebar strain ε_s (Fig. 5c). In the cross-section 0–0, a linear strain profile between uncracked FRC and rebar in tension is assumed (Fig. 6a). Conversely, in the cracked zone of depth h_w, crack width w decreases linearly from the bottom of the beam (where $w = \overline{w}$) to the crack tip (where $w = 0$), in spite of the presence of rebar. On the other hand, due to the perfect bond, steel and concrete strain at level of reinforcement are equal in Stage I cross-section, where $\varepsilon_{s,1} = \varepsilon_{c,1}$ (Fig. 6b)

Within the transfer length (Fig. 5d), $M_1 = M$ is assumed (where M_1 = bending moment in the Stage I cross-section, M = bending moment in the cracked cross-section). In the same zone of the beam, the interaction between steel rebar and FRC in tension is described by the equilibrium and compatibility equations, formally identical to Eqs.(3)–(4):

$$\frac{d\sigma_s}{dz} = -\frac{p_s}{A_s}\cdot\tau\left[s(z)\right] = -\frac{4}{\phi_s}\cdot\tau\left[s(z)\right] \tag{8}$$

$$\frac{ds}{dz} = -\left[\varepsilon_s(z) - \varepsilon_c(z)\right] \tag{9}$$

where σ_s = stress in the rebar; p_s, A_s, ϕ_s = area, perimeter and diameter of the rebar cross-section.

In the absence of an external axial load ($R = 0$), the resultant of axial stresses in cross-section 0–0 is:

$$R = \int_{A_c}\left(\sigma_{c,0}\right)dA + \sigma_{s,0}\cdot A_s = 0 \tag{10}$$

where $\sigma_{c,0}$, $\sigma_{s,0}$ = stresses of concrete and rebar in cross-section 0–0; A_c = area of concrete.

Assuming y as the vertical coordinate of the beam cross-section (Fig. 5a), the internal bending moment M can be computed as follows:

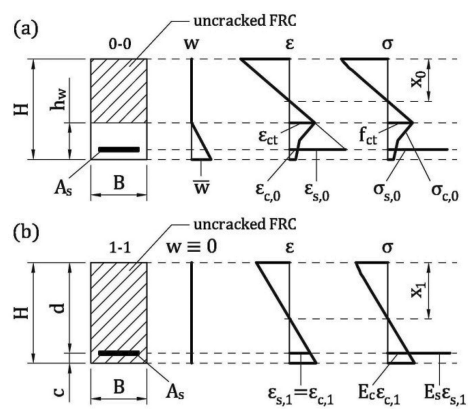

Figure 6. State of strain and stress at boundaries of a portion of HRC beam: (a) cracked cross-section 0–0; (b) Stage I cross-section 1–1.

$$M = \int_{A_c} \left(\sigma_{c,0} \cdot y\right) dA + \sigma_{s,0} \cdot A_s \cdot \left(\frac{H}{2} - c\right) \tag{11}$$

where H = beam depth; c = distance between the centroid of the rebar and the bottom level.

In accordance with Fantilli and Chiaia (2013), rebar strain decrements and concrete strain increments at the level of reinforcement are assumed as similar:

$$\varepsilon_s(z) = \varepsilon_{s,0} - \chi(z) \cdot \left(\varepsilon_{s,0} - \varepsilon_{s,1}\right) \tag{12}$$

$$\varepsilon_c(z) = \varepsilon_{c,0} - \chi(z) \cdot \left(\varepsilon_{c,0} - \varepsilon_{c,1}\right) \tag{13}$$

where $\varepsilon_{s,0}$, $\varepsilon_{c,0}$ = steel rebar and concrete strains at level of reinforcement in the cracked cross-section; χ = similarity coefficient.

To solve Eqs.(8)–(13), it is necessary to use as a boundary condition the value of the slip s_0 in the cracked cross-section, which is a function of the crack width at bottom level $\overline{w}$:

$$s_0 = \frac{\overline{w}}{2} \cdot \frac{h_w - c}{h_w} \tag{14}$$

In addition, in the Stage I cross-section, it is necessary to impose, respectively, the absence of slip and its stationary state [i.e., $\varepsilon_s = \varepsilon_c$ in Eq.(9)].

To define the stress vs. strain relationship σ_c-ε_c of concrete in compression, the ascending branch of the Sargin's parabola (*fib* 2012) is used. Moreover, the linear elastic constitutive law is adopted for the uncracked concrete in tension (Fig. 7).

The stress vs. strain relationship σ_s-ε_s of the steel rebar is modeled with the elastic-perfectly plastic constitutive law of Fig. 8. To describe the interaction at the interface between rebar and concrete, the bond-slip relationship proposed by Model Code 2010 (*fib* 2012) for ribbed bars is used (Fig. 9). Finally, the stress vs. crack width relationship obtained in the previous sections (Fig. 10) is adopted for describing the tensile behavior of cracked FRC.

2.4 *Numerical evaluation of $M(\overline{w})$*

The problem previously formulated can be solved by applying the iterative procedure described by the flow-chart reported in Fig. 11 (Fantilli et al. 2016a). The same procedure is also summarized by the following points:

1. Assign a value to the crack width $\overline{w}$ in the cross-section 0–0.
2. Assume a trial value for the crack depth h_w (where $c < h_w < H$).

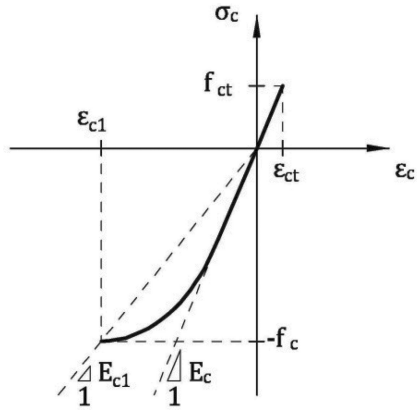

Figure 7. Constitutive relationship for uncracked concrete in tension and compression (*fib* 2012).

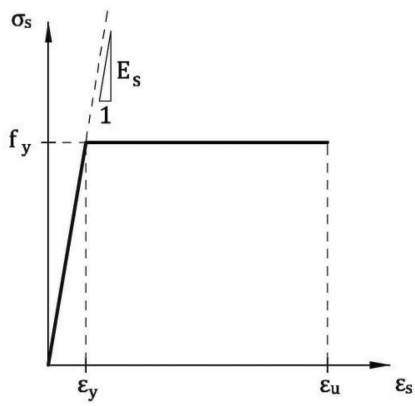

Figure 8. Constitutive relationship for steel rebar in tension (*fib* 2012).

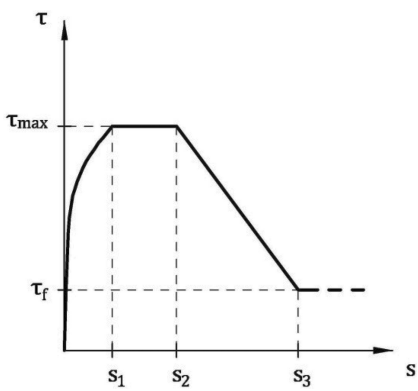

Figure 9. Bond-slip model proposed by Model Code 2010 (*fib* 2012) for evaluating the stresses at the interface between rebar and concrete in tension.

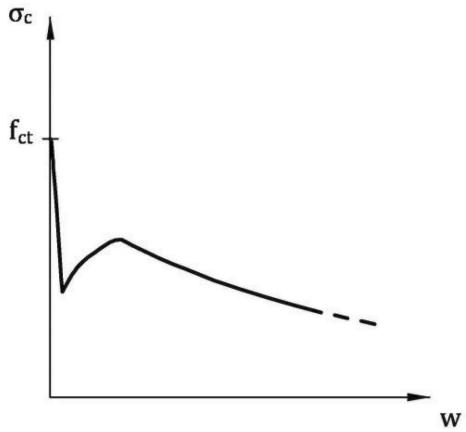

Figure 10. Stress vs. crack width relationship obtained from the fiber pull-out for evaluating the stresses of the FRC matrix on the crack surface.

3. Calculate the slip s_0 in cross-section 0–0 with Eq.(14) (Fig. 5b).
4. Assuming a linear crack profile, calculate the cohesive stress in cracked FRC of cross-section 0–0 by means of the stress vs. crack opening relationship previously obtained from the ideal tie (Fig. 10).
5. Assume a trial value for x_0 (i.e., the distance from the top edge to the neutral axis in the cracked cross-section of Fig. 6a).
6. Define the state of stress of uncracked FRC and steel rebar in cross-section 0–0 through the constitutive relationships of concrete and steel (Fig. 7 and Fig. 8).
7. Calculate the resultant R in the cracked cross-section [Eq.(10)].
8. Verify if the resultant $R \cong 0$. If not, change x_0 and go back to step 6.
9. Compute the internal bending moment M in the cracked cross-section [Eq.(11)].
10. Considering Δl as a small portion of the transfer length, define $z_i = i \cdot \Delta l$ (where $i = 1, 2, 3, \ldots$).
11. For each i (or z_i) calculate:
    - The bond stress τ_i, related to the slip s_{i-1} with the bond-slip relationship of Fig. 9.
    - The strain $\varepsilon_{s,i}$ in the reinforcement through Eq.(8), by using the finite difference method.
    - The similarity coefficient of the strains χ_i, by inverting Eq.(12).
    - The strain of concrete $\varepsilon_{c,i}$ at the level of reinforcement with Eq.(13).
    - The slip s_i by means of Eq.(9) and of the finite difference method.
12. When $s_i \cong 0$, verify whether $\varepsilon_{s,i} \cong \varepsilon_{c,i}$, otherwise change h_w and go back to step 3.

The previous numerical procedure calculates the internal bending moment corresponding to a given crack width and, consequently, the complete M-$\overline{w}$ curve of an HRC beam can be obtained by varying the assigned $\overline{w}$.

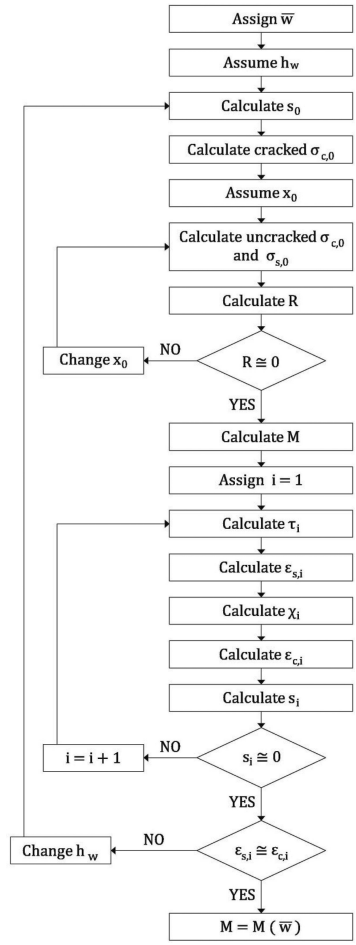

Figure 11. Flow-chart of the numerical procedure for evaluating $M(\overline{w})$.

3 VALIDATION OF THE MODEL

3.1 *Numerical analyses*

The numerical procedures illustrated in Section 2 are adopted to describe the M-$\overline{w}$ curves of 108 ideal HRC beams in three point bending. They are divided into 36 groups of 3 beams, having the same geometrical and material properties, but with different amounts of rebar or fibers. For all the groups, the width B and the span L of the beams are 0.5 and 6 times the depth H (assuming the values of 200 and 400 mm), respectively. Three compressive strengths of concrete are considered (i.e., f_c = 30, 45, and 60 MPa). The same properties of

steel rebar are assumed in all the groups (i.e., the yielding strength f_y = 450 MPa, and the modulus of elasticity E_s = 210 GPa), whereas the steel fibers (L_f = 60 mm, f_u = 1,000 MPa, and E_f = 210 GPa) have the aspect ratio L_f/ϕ_f = 40, 60, and 80. These values of geometrical and material properties are the same previously investigated for LRC and FRC beams by Fantilli et al. (2016a,b). Hence, for each group of HRC members, the minimum amounts of rebar $A_{s,min}$ and fibers $V_{f,min}$ which would be necessary to respect Eq.(1) are already known. The values of A_s and V_f referred to each ideal member are reported in the Appendix 1 as Table A1. In this Table, the beams are designated with the label HX_CY_AZ_ϕW_K (where X = beam depth in mm, Y = concrete strength in MPa, Z = fiber aspect ratio, W = rebar diameter in mm, and K = progressive number inside the homogeneous group of three beam).

As an example, the M-$\bar{w}$ curves of the three beams of a group are reported in Fig. 12. Two stationary points, concerning the effective cracking moment (M_{cr*}) and the ultimate bending moment (M_u), are clearly evident in each curve. The curve of the ideal beam H200_C45_A60_ϕ5_1 shows a brittle flexural response, because $M_u < M_{cr*}$, whereas the reinforcement of H200_C45_A60_ϕ5_2 is close to the minimum value as $M_u \cong M_{cr*}$. Finally, the M-$\bar{w}$ curve of H200_C45_A60_ϕ5_3 describes a typical ductile behavior with $M_u > M_{cr*}$.

3.2 *Comparison with experimental results*

To compare the large set of numerical results with a more limited number of experimental data, it is convenient to analyze all them through a non-dimensional approach. Specifically, due to the similar flexural response, the brittle/ductile behavior of HRC beams can be evaluated by means of the following ductility index (DI), as in the case of LRC and FRC beams (Fantilli et al. 2016a,b,c):

$$DI = \frac{M_u - M_{cr*}}{M_{cr*}} \tag{15}$$

The definition of DI is in agreement with the traditional way to study the problem of the minimum reinforcement in LRC beams (Bosco et al. 1990, Fantilli et al. 1999, Ruiz et al. 1999). Based on Eq.(1), DI is positive for beams showing a ductile response, whereas under-reinforced members exhibit $DI < 0$. As a result, the minimum amount of hybrid reinforcement (and the brittle/ductile transition) can be identified by imposing $DI = 0$.

Since both M_u and M_{cr*} depend on the amount of reinforcement, DI should be in turn a function of A_s and V_f. Accordingly, the following reinforcement ratio r can be introduced as the parameter governing the brittle/ductile transition (Gorino et al. 2016):

$$r = \frac{A_s}{A_{s,min}} + \frac{V_f}{V_{f,min}} \tag{16}$$

It should be remarked that the minimum reinforcements $A_{s,min}$ and $V_{f,min}$, both referred to an HRC beam, are those of the associated LRC and FRC members. As $A_{s,min}$ and $V_{f,min}$ are defined for the specific type of beam, all the related parameters (e.g., concrete strength, rebar and fiber properties, beam size, etc.) are taken into account. In such a way, r is independent of any geometrical and mechanical property.

The values of DI and r computed for the ideal beams investigated herein are reported Table A1. It is worth noting that, within each group of beams (e.g., Fig. 13), a linear relationship between DI and r is attained. Moreover, the intersection between the line DI-r and the horizontal axis (i.e., DI = 0) falls around the value r = 1, corresponding to the minimum hybrid reinforcement.

By plotting in a single diagram all the [DI-r] couples computed for the 108 ideal HRC beams, an approximately linear trend can be observed between the two non-dimensional variables (Fig. 14):

$$DI = \zeta \cdot (r - 1) \tag{17}$$

The slope ζ of the line which better approximates the numerical data, obtained with the least square method, is equal to 0.8. It is worth noting that such value is comprised between the slopes referred to LRC and FRC beams, which are 1 and 0.7, respectively (Fantilli et al. 2016a,b,c).

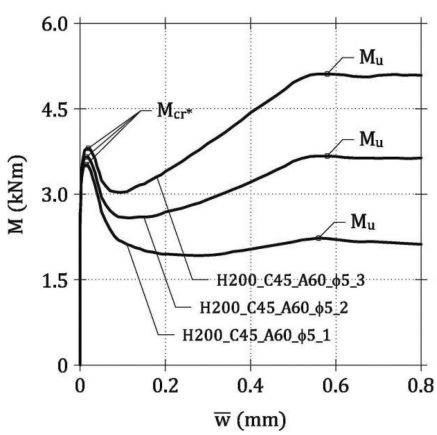

Figure 12. M-$\bar{w}$ curves referred to the three ideal HRC beams of an homogeneous group.

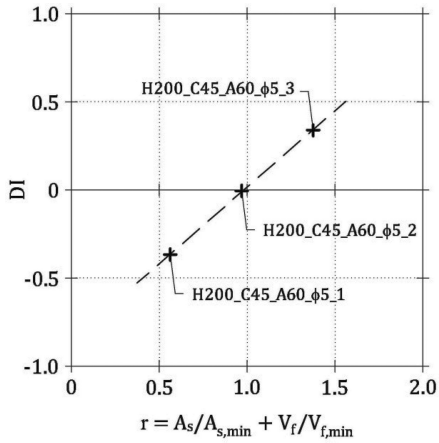

Figure 13. *DI-r* relationship referred to the three ideal HRC beams of an homogeneous group.

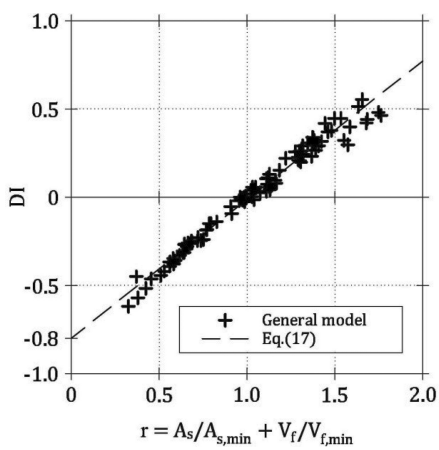

Figure 14. *DI-r* relationship referred to the 108 ideal beams.

With the aim of validating the proposed model, the general results given by Eq.(17) are compared to the experimental values of *DI* obtained from three point bending tests on HRC beams (Gorino et al. 2016). Specifically, they are plotted as a function of *r* in the non-dimensional diagram depicted in Fig. 15. As this diagram exhibits good agreement between Eq.(17) and the experimental points, the validity of the proposed multi-scale general model seems to be confirmed.

Moreover, since both numerical and experimental results provide the minimum hybrid reinforcement by imposing $r = 1$ into Eq.(16), the minimum amount of rebar and fibers used to reinforce HRC members is given by the linear combination of $A_{s,min}$ and $V_{f,min}$, as represented in Fig. 16 (Gorino et al. 2016):

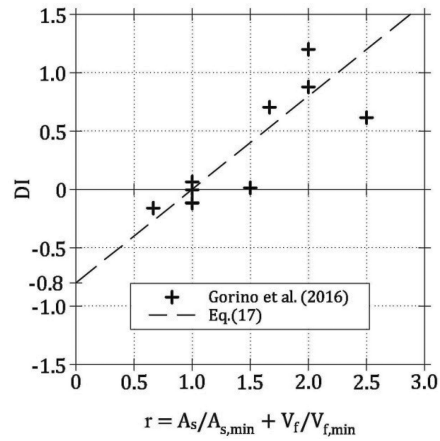

Figure 15. *DI-r* relationship referred to the beams experimentally tested by Gorino et al. (2016).

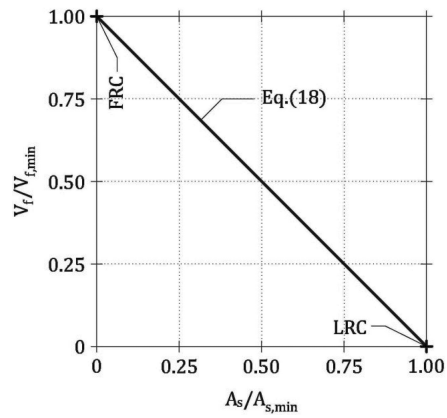

Figure 16. Eq.(18) for combining rebar and fibers in order to attain the condition of minimum ductility (i.e., $DI = 0$).

$$\frac{A_s}{A_{s,min}} + \frac{V_f}{V_{f,min}} = 1 \tag{18}$$

All the results here supported by the experimental data reported in Fig. 15 are also in agreement with those of other theoretical models (Chiaia et al. 2009, Liao et al. 2016, Mobasher et al. 2015) and with the recent recommendations of Model Code 2010 (*fib* 2012) regarding the minimum reinforcement for crack control in HRC members.

4 CONCLUSIONS

According to the numerical and experimental investigations previously described, the following conclusions can be drawn:

i. A new multi-scale general model can be adopted to predict the brittle/ductile behavior of HRC beams in bending, by combining the fiber pull-out and the flexural response of HRC beams. This model is validated by the comparison with experimental results.
ii. The reinforcement of HRC beams can be represented by the reinforcement ratio r, i.e., a linear combination of the area of rebar A_s and of the fiber content V_f, both normalized with respect to their minimum amounts $A_{s,min}$ and $V_{f,min}$, respectively [Eq.(16)].
iii. The brittle/ductile flexural response of HRC beams can be described by the ductility index DI [Eq.(15)], which is proportional to the difference between the ultimate bending moment, M_u, and the effective cracking moment, M_{cr*}.
iv. Both theoretical and experimental results suggest the existence of a linear trend between DI and r [Eq.(17)].
v. The minimum hybrid reinforcement which satisfies the condition $M_u = M_{cr*}$ (i.e., $DI = 0$) is defined by any linear combination of $A_{s,min}$ and $V_{f,min}$ [Eq.(18)].

Further theoretical and experimental studies should be developed to extend the present approach for evaluating the brittle/ductile flexural response to statically indetermined structures (e.g., slabs on ground, frames, etc.).

REFERENCES

Barros, J.A.O., Taheri, M. & Salehian, H. 2015. A model to simulate the moment–rotation and crack width of FRC members reinforced with longitudinal bars. Engineering Structures 100: 43–56.

Bažant, Z.P., & Cedolin, L. 1991. Stability of Structures: Elastic, Inelastic, Fracture and Damage Theories. Oxford University Press, New York.

Bosco, C., Carpinteri, A. & Debernardi, P.G. 1990. Minimum reinforcement in high-strength concrete. ASCE Journal of Structural Engineering 116(2): 427–437.

Caratelli, A., Meda, A. & Rinaldi, Z. 2012. Design according to MC2010 of a fibre-reinforced concrete tunnel in Monte Lirio, Panama. Structural Concrete 13: 166–173.

Chiaia, B., Fantilli, A.P. & Vallini, P. 2007. Evaluation of minimum reinforcement ratio in FRC members and application to tunnel linings. Materials and Structures 40: 593–604.

Chiaia, B., Fantilli, A.P. & Vallini, P. 2009. Combining fiber-reinforced concrete with traditional reinforcement in tunnel linings. Engineering Structures 31: 1600–1606.

de la Fuente, A., Pujadas, P., Blanco, A. & Aguado, A. 2012. Experiences in Barcelona with the use of fibres in segmental linings. Tunnelling and Underground Space Technology 27: 60–71.

de Montaignac, R., Massicotte, B. & Charron, J.P. 2012. Design of SFRC structural elements: flexural behaviour prediction. Materials and Structures 45: 623–636.

di Prisco, M., Colombo, M., Bonalumi, P. & Beltrami, C. 2014. FRC structural applications according to the *fib* Model Code 2010: A unified approach. In: Proc. FRC 2014 Joint ACI-fib International Workshop: 224–234. Montreal.

Facconi, L., Plizzari, G.A. & Minelli, F. 2016. Hybrid reinforcement (rebars + fibers) for elevated slabs. In: Proc. 9th RILEM International Symposium on Fiber Reinforced Concrete (BEFIB 2016): 969–979. Vancouver.

Falkner, H. & Henke, V. 2005. Steel fibre reinforced concrete, from research to standards. Concrete Structures 6: 39–46.

Fantilli, A.P. & Chiaia, B. 2013. Golden Ratio in the Crack Pattern of Reinforced Concrete Structures. ASCE Journal of Engineering Mechanics 139(9): 1178–1184.

Fantilli, A.P., Chiaia, B. & Gorino, A. 2016a. Minimum reinforcement and ductility index of lightly reinforced concrete beams. Computers and Concrete 18(6): 1175–1194.

Fantilli, A.P., Chiaia, B. & Gorino, A. 2016b. Fiber volume fraction and ductility index of concrete beams. Cement and Concrete Composites 65: 139–149.

Fantilli, A.P., Chiaia, B. & Gorino, A. 2016c. Unified Approach for Minimum Reinforcement of Concrete Beams. ACI Structural Journal 113(05): 1107–1116.

Fantilli, A.P., Ferretti, D., Iori, I. & Vallini, P. 1999. Behaviour of R/C Elements in Bending and Tension: The Problem of Minimum Reinforcement Ratio. European Structural Integrity Society 24: 99–125.

Fantilli, A.P. & Vallini, P. 2003. Bond-slip relationship for smooth steel reinforcement. In: Proc. Computational Modelling of Concrete Structures (EURO-C 2003): 215–224. St. Johann Im Pongau.

fib (International Federation for Structural Concrete) 2012. Model Code 2010 - Final draft, Volume 1, *fib* Bulletin, 65. Lausanne, Switzerland.

Gorino, A., Fantilli, A.P., Chiaia, B., Zampini, D., Guerini, A. & Volpatti, G. 2016. Brittle vs. ductile behavior of concrete beams reinforced with steel rebars and fibers. In Proc. 9th Rilem Int. Symp. on Fiber Reinforced Concrete (BEFIB 2016): 1263–1274. Vancouver.

Levi, F. 1985. On Minimum Reinforcement in Concrete Structures. ASCE Journal of Structural Engineering 111(12): 2791–2796.

Liao, L., de la Fuente, A., Cavalaro, S. & Aguado, A. 2016. Design procedure and experimental study on fibre reinforced concrete segmental rings for vertical shafts. Materials and Design 92: 590–601.

Maldague, J.C. 1965. Établissement des Lois Moments-Courbures. Annales de l'Institut Technique du Batiment et des Travaux Publics 213: 1170–1218.

Mobasher, B., Yao, Y. & Soranakom, C. 2015. Analytical solutions for flexural design of hybrid steel fiber reinforced concrete beams. Engineering Structures 100: 164–177.

Naaman, A.E. 2003. Strain hardening and deflection hardening fiber reinforced cement composites. In: Proc. 4th Int. RILEM Workshop on High Performance Fiber Reinforced Cement Composites: 95–113. Ann Abor.

Plizzari, G.A. & Tiberti, G. 2006. Steel fibres as reinforcement for precast tunnel segments. Tunnelling and Underground Space Technology 21 (3–4): 438–439.

Ruiz, G., Elices M. & Planas, J. 1999. Size Effect and Bond-Slip Dependence of Lightly Reinforced Concrete Beams. European Structural Integrity Society 24: 67–97.

APPENDIX 1

Table A1. Parameters of the 108 ideal HRC beams adopted for the numerical analyses.

Beam	A_s (mm²)	V_f (%)	r	DI
H200_C30_A80_ϕ4_1	13	0.15	0.68	–0.25
H200_C30_A80_ϕ4_2	25	0.15	1.03	0.06
H200_C30_A80_ϕ4_3	38	0.15	1.38	0.31
H200_C30_A80_ϕ5_1	20	0.05	0.65	–0.26
H200_C30_A80_ϕ5_2	20	0.20	0.98	0.00
H200_C30_A80_ϕ5_3	20	0.35	1.32	0.24
H200_C30_A60_ϕ4_1	13	0.25	0.77	–0.19
H200_C30_A60_ϕ4_2	25	0.25	1.11	0.11
H200_C30_A60_ϕ4_3	38	0.25	1.46	0.37
H200_C30_A60_ϕ5_1	20	0.15	0.79	–0.15
H200_C30_A60_ϕ5_2	20	0.30	1.04	0.04
H200_C30_A60_ϕ5_3	20	0.45	1.29	0.21
H200_C30_A40_ϕ4_1	13	0.30	0.68	–0.26
H200_C30_A40_ϕ4_2	25	0.30	1.02	0.04
H200_C30_A40_ϕ4_3	38	0.30	1.37	0.29
H200_C30_A40_ϕ5_1	20	0.10	0.64	–0.27
H200_C30_A40_ϕ5_2	20	0.40	0.98	–0.02
H200_C30_A40_ϕ5_3	20	0.70	1.31	0.20
H200_C45_A80_ϕ5_1	20	0.15	0.72	–0.23
H200_C45_A80_ϕ5_2	39	0.15	1.13	0.13
H200_C45_A80_ϕ5_3	59	0.15	1.53	0.45
H200_C45_A80_ϕ6_1	28	0.10	0.79	–0.15
H200_C45_A80_ϕ6_2	28	0.25	1.11	0.10
H200_C45_A80_ϕ6_3	28	0.40	1.42	0.32
H200_C45_A60_ϕ5_1	20	0.10	0.56	–0.37
H200_C45_A60_ϕ5_2	39	0.10	0.97	0.00
H200_C45_A60_ϕ5_3	59	0.10	1.38	0.34
H200_C45_A60_ϕ6_1	28	0.05	0.66	–0.26
H200_C45_A60_ϕ6_2	28	0.25	0.98	–0.01
H200_C45_A60_ϕ6_3	28	0.45	1.29	0.23
H200_C45_A40_ϕ5_1	20	0.15	0.56	–0.37
H200_C45_A40_ϕ5_2	39	0.15	0.97	–0.01
H200_C45_A40_ϕ5_3	59	0.15	1.37	0.34
H200_C45_A40_ϕ6_1	28	0.10	0.69	–0.25
H200_C45_A40_ϕ6_2	28	0.40	0.99	–0.01
H200_C45_A40_ϕ6_3	28	0.70	1.30	0.21
H200_C60_A80_ϕ5_1	20	0.15	0.64	–0.31
H200_C60_A80_ϕ5_2	39	0.15	0.97	–0.01
H200_C60_A80_ϕ5_3	59	0.15	1.31	0.26
H200_C60_A80_ϕ6_1	28	0.10	0.69	–0.25
H200_C60_A80_ϕ6_2	28	0.25	1.00	0.00
H200_C60_A80_ϕ6_3	28	0.40	1.31	0.23
H200_C60_A60_ϕ5_1	20	0.25	0.72	–0.25
H200_C60_A60_ϕ5_2	39	0.25	1.05	0.06
H200_C60_A60_ϕ5_3	59	0.25	1.38	0.32
H200_C60_A60_ϕ6_1	28	0.10	0.63	–0.31
H200_C60_A60_ϕ6_2	28	0.35	1.02	0.02
H200_C60_A60_ϕ6_3	28	0.60	1.41	0.29
H200_C60_A40_ϕ5_1	20	0.30	0.64	–0.32
H200_C60_A40_ϕ5_2	39	0.30	0.97	–0.01
H200_C60_A40_ϕ5_3	59	0.30	1.30	0.26
H200_C60_A40_ϕ6_1	28	0.10	0.58	–0.35
H200_C60_A40_ϕ6_2	28	0.50	0.99	–0.03
H200_C60_A40_ϕ6_3	28	0.90	1.39	0.27
H400_C30_A80_ϕ8_1	50	0.10	0.59	–0.36
H400_C30_A80_ϕ8_2	101	0.10	0.95	–0.02
H400_C30_A80_ϕ8_3	151	0.10	1.32	0.29
H400_C30_A80_ϕ10_1	79	0.05	0.69	–0.26
H400_C30_A80_ϕ10_2	79	0.20	1.03	0.00
H400_C30_A80_ϕ10_3	79	0.35	1.37	0.23
H400_C30_A60_ϕ8_1	50	0.15	0.62	–0.33
H400_C30_A60_ϕ8_2	101	0.15	0.98	–0.01
H400_C30_A60_ϕ8_3	151	0.15	1.34	0.31
H400_C30_A60_ϕ10_1	79	0.05	0.66	–0.28
H400_C30_A60_ϕ10_2	79	0.20	0.91	–0.09
H400_C30_A60_ϕ10_3	79	0.35	1.17	0.08
H400_C30_A40_ϕ8_1	50	0.35	0.75	–0.24
H400_C30_A40_ϕ8_2	101	0.35	1.12	0.07
H400_C30_A40_ϕ8_3	151	0.35	1.48	0.38
H400_C30_A40_ϕ10_1	79	0.10	0.69	–0.26
H400_C30_A40_ϕ10_2	79	0.50	1.13	0.04
H400_C30_A40_ϕ10_3	79	0.90	1.57	0.30
H400_C45_A80_ϕ8_1	50	0.15	0.58	–0.38
H400_C45_A80_ϕ8_2	151	0.15	1.12	0.11
H400_C45_A80_ϕ8_3	251	0.15	1.66	0.55
H400_C45_A80_ϕ10_1	79	0.10	0.64	–0.32
H400_C45_A80_ϕ10_2	79	0.35	1.16	0.10
H400_C45_A80_ϕ10_3	79	0.60	1.68	0.44
H400_C45_A60_ϕ8_1	50	0.10	0.42	–0.52
H400_C45_A60_ϕ8_2	151	0.10	0.96	0.00
H400_C45_A60_ϕ8_3	251	0.10	1.50	0.45
H400_C45_A60_ϕ10_1	79	0.10	0.58	–0.37
H400_C45_A60_ϕ10_2	79	0.45	1.13	0.06
H400_C45_A60_ϕ10_3	79	0.80	1.68	0.42
H400_C45_A40_ϕ8_1	50	0.10	0.37	–0.45
H400_C45_A40_ϕ8_2	151	0.10	0.91	–0.05
H400_C45_A40_ϕ8_3	251	0.10	1.44	0.42
H400_C45_A40_ϕ10_1	79	0.10	0.53	–0.42
H400_C45_A40_ϕ10_2	79	0.60	1.04	–0.01
H400_C45_A40_ϕ10_3	79	1.10	1.55	0.32
H400_C60_A80_ϕ8_1	50	0.25	0.74	–0.25
H400_C60_A80_ϕ8_2	151	0.25	1.19	0.15
H400_C60_A80_ϕ8_3	251	0.25	1.63	0.51
H400_C60_A80_ϕ10_1	79	0.10	0.56	–0.39
H400_C60_A80_ϕ10_2	79	0.35	1.07	0.03
H400_C60_A80_ϕ10_3	79	0.60	1.59	0.40
H400_C60_A60_ϕ8_1	50	0.10	0.38	–0.57
H400_C60_A60_ϕ8_2	151	0.10	0.83	–0.14
H400_C60_A60_ϕ8_3	251	0.10	1.28	0.26
H400_C60_A60_ϕ10_1	79	0.10	0.51	–0.44
H400_C60_A60_ϕ10_2	79	0.50	1.13	0.06
H400_C60_A60_ϕ10_3	79	0.90	1.75	0.48
H400_C60_A40_ϕ8_1	50	0.10	0.32	–0.62
H400_C60_A40_ϕ8_2	151	0.10	0.77	–0.18
H400_C60_A40_ϕ8_3	251	0.10	1.22	0.22
H400_C60_A40_ϕ10_1	79	0.10	0.46	–0.46
H400_C60_A40_ϕ10_2	79	0.75	1.11	0.03
H400_C60_A40_ϕ10_3	79	1.40	1.76	0.46

(Continued).

Table A1. (*Continued*).

Computational Modelling of Concrete Structures – Meschke, Pichler & Rots (Eds)
© 2018 Taylor & Francis Group, London, ISBN 978-1-138-74117-1

Investigation of effect of local bond model on crack propagation in RC using 3D RBSM

L. Eddy, K. Matsumoto & K. Nagai
Institute of Industrial Science, The University of Tokyo, Tokyo, Japan

Z. Wang
Korea Advanced Institute of Science and Technology (KAIST), Daejeon, South Korea

ABSTRACT: In this study, local bond model using 3D RBSM is proposed in which the reinforcing bar with its ribs in 3D shape is modeled accurately. In 3D RBSM, the local failure including cracks is predicted by checking for the discontinuous deformation of concrete and interaction between concrete and the reinforcing bar at the meso-scale. To verify the availability of the proposed approach, the simulations of a massive concrete specimen with a single reinforcing bar and under tension loading are conducted. The simulation results are compared with the experimental results which show a good agreement in terms of the strain distribution of the reinforcement. Other simulations of the tension stiffening behavior in a RC element are also conducted. The results of these simulations are also discussed through the comparison with the experimental results with good agreement in terms of macroscopic responses and the strain distributions of the reinforcing bar. The effect of porous concrete adjacent to the reinforcing bar is taken into the consideration. The simulation results indicate that the macroscopic responses are not affected by the bond model, but the internal stresses and cracks are different due to different bond models. The proposed approach is a suitable method when the effect of the local bar ribs-concrete interaction needs to be considered, while the conventional bond stress-slip relationship is applicable for the conventional structural analysis when the element size is over 10 cm.

1 INTRODUCTION

One of the important factors affecting the behavior of a reinforced concrete (RC) is the bond between concrete and the reinforcement. Stresses can be transferred between concrete and the reinforcement in a RC member because of the presence of the bond. Shima et al. (1987) successfully modeled the bond between concrete and a reinforcing bar by a unique bond-stress-slip relationship through the experimental work in which specimens with a reinforcing bar embedded in massive concrete were used. Cracks formed around deformed steel bars in a RC member were successfully observed by Goto (1971) in which the specimens with a single deformed steel bar embedded in a long concrete prism were loaded with axial tension. The specimens were injected with ink, and the cracks were examined after the specimens were split longitudinally along the bar.

To model the bond between concrete and the reinforcement in the numerical simulation of a RC, some researchers used a bond stress-slip relationship. In the previous researches, Suga et al. (2001) and Gedik et al. (2011) modified the bond stress-slip relationship proposed by Shima et al. (1987) to simulate the bond between concrete and a reinforcing bar in RC members having thin concrete cover. Meanwhile, Bolander et al. (1998, 1999, 2000, 2002) followed the bond stress-slip relationship recommended for confined concrete obtained through experimentation conducted by Eligehausen et al. (1983). However, the bond stress-slip relationship derives from the integration of the stress-strain fields over a certain distance on average. The relationship is strongly affected by the mechanical action of bar ribs against concrete. It seems that the bond stress-slip relationship has some limitations to be used in some cases.

In this study, a 3D rigid body spring model (3D RBSM) which is a discrete numerical method at meso-scale is proposed to accurately model the reinforcing bar with its ribs in 3D shape. 3D RBSM can predict the local failure including cracks by checking for the discontinuous deformation of concrete and the interaction between concrete and the reinforcing bar at the meso-scale. In our research group, 3D RBSM has been used to study the behavior of reinforced concrete members by directly modeling the shape of the reinforcement

in 3D, including its ribs. Authors (2016a, b) and Hayashi et al. (2017) have successfully simulated variations in crack pattern due to different reinforcement arrangements in the beam-column joints. In addition, the applicability of this simulation method to the confinement effect of stirrups has been confirmed by Nagai et al. (2014).

There are two ultimate aims of this study. The first is to investigate the applicability of 3D RBSM to model the bond behavior between concrete and reinforcement through the comparison with the experimental results (Shima et al. 1987). The second is to compare the proposed approach with the conventional bond stress-slip relationship and to discuss when each bond model is suitable to be used.

2 NUMERICAL METHOD AND CONSTITUTIVE MODELS

2.1 *Numerical method*

In this study, simulations are carried out by 3D RBSM, as proposed by Kawai et al. (1978). A three-dimensional RC model is formed from a mesh of rigid bodies. Each rigid body has six degrees of freedom, consisting of three translational degrees of freedom and three rotational degrees of freedom around certain points within its interior. Each is connected to other rigid bodies by three springs which are two shear springs and one normal springs as shown in Figure 1. To model a RC member in 3D, two types of element are used which are concrete and steel. As the propagation of cracks in RC is one of the most important factors affecting RC behavior, the mesh arrangement in RBSM is important. To prevent cracks propagation in a non-arbitrary direction, a random geometry in the form of a Voronoi diagram is used for element meshing. Concrete elements are modeled with a size of approximately $10 \times 10 \times 10 \sim 20 \times 20 \times 20$ mm^3, which is similar to the aggregate size, in order to ensure a similar cracking pattern to actual concrete. The geometry of steel elements is modeled accurately, with full 3D modeling of the reinforcement bar arrangement, in order to properly account for the interlocking between reinforcement and concrete. The meso-scale mesh arrangement used of concrete and steel in this study is shown in Figure 2. The properties of springs are determined such that the elements, when combined together, are able to predict accurately the response determined in laboratory scale material tests. The simulation system developed by Nagai et al. (2005) is used.

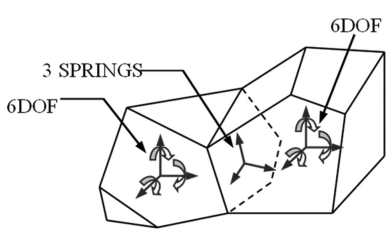

Figure 1. 3D RBSM mechanical model.

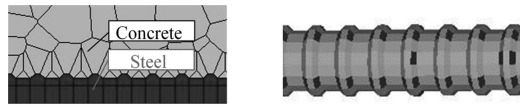

(a) Cross section. (b) 3D model of re-bar

Figure 2. Mesh arrangement for concrete and re-bar.

2.2 *Constitutive model of elements*

Two types of elements are used to represent the behavior of RC in this study.

1. Concrete elements

As mentioned above, the shape of concrete elements is determined randomly using a Voronoi diagram. However, elements near steel elements are constructed manually in order to follow the actual 3D geometry of the reinforcing bars.

Random element generation is thought to lead to accurate replication of the concrete fracture process. The constitutive models for the normal and shears spring of the concrete elements are shown in Figure 3. In the compression zone, the normal spring of the concrete elements behave elastically, since compressive failure is not allowed at the meso-scale. A crack, between two rigid bodies occurs when the tensile stress of the normal springs exceeds the tensile strength of the concrete elements (f_t). After the tensile strength (f_t) is exceeded, the tensile stress of the normal spring is assumed to decrease bilinearly depending on the crack width between the two rigid bodies where the crack width is defined as the relative displacement between two rigid bodies. When a crack occurs, concrete tends to spring back and the deformation in the concrete is negligibly small. In this study, the maximum crack width (w_{max}) is assumed to be 0.3 mm (Fig. 3a). On the other hand, an elasto-plastic behavior is assumed for the shear springs of the concrete elements (Fig. 3b), where the maximum value of the shear stress is calculated based on Equation 1 (Fig. 3c).

$$\tau_{max} = \pm(1.6 f_{telem}{}^2(-\sigma+f_{telem})^{0.4}+0.15 f_{telem}) \; if \; (\sigma \geq 3 f_{telem})$$

$$\tau_{max} = \pm(1.6 f_{telem}{}^2(-4 f_{telem})^{0.4}+0.15 f_{telem}) \; if \; (\sigma < 3 f_{telem}) \quad (1)$$

where τ_{max} = maximum value of shear stress (MPa); f_{telem} = tensile strength of concrete elements (MPa); σ = normal stress of concrete elements (MPa).

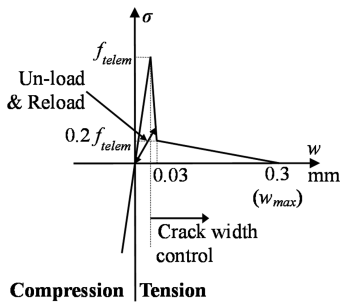

(a) Normal spring of concrete.

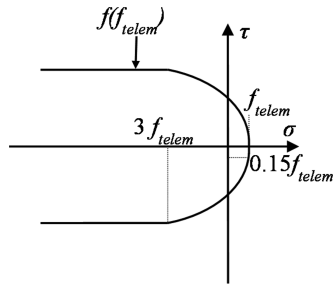

(c) τ_{max} criterion for concrete.

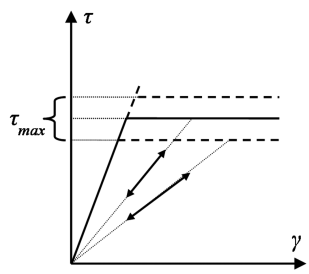

(b) Shear spring of concrete.

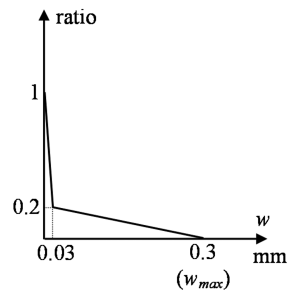

(d) Shear reduction factor.

Figure 3. Constitutive models of concrete.

Equation 1 is determined such that the elements, when combined together, are able to predict accurately the normal concrete response in the experimental material tests which are uniaxial tension, uniaxial compression, and biaxial compression tests (Eddy, 2015). When a fracture occurs in the normal springs, the calculated shear stress is reduced according to the reduction in normal stress. As the result, the shear spring cannot carry the shear stress when the crack width of the normal springs exceeds w_{max} (Fig. 3d).

For the models with interfacial transition zone, for regions within one diameter (1D) from the surface of the reinforcement, the constitutive models for normal springs and the maximum value of the shear stress of the concrete elements are modified to account for the interfacial transition zone between the reinforcement and concrete (Salem & Maekawa, 2004). In this zone, because aggregate particles do not come too close to the bar due to the wall effect and water/cement ratio is higher, the elastic modulus and the tensile strength for the normal springs in this zone are assumed to be half of that of the concrete element (Fig. 4). In addition, the maximum value of the shear stress for the shear springs in this zone is also reduced to be half of that of the concrete element.

2. Steel elements

The geometry of steel elements is modeled in an accurate manner to properly account for the interlocking between concrete and a reinforcing bar (Fig. 2). The normal springs of steel bars are modeled based on the stress-strain relationship of steel bars proposed by Shima et al. (1987). The stress-strain relationship used for the normal springs is represented by Equation 2. Meanwhile, the shear springs used for the steel elements are assumed to be perfectly elastic.

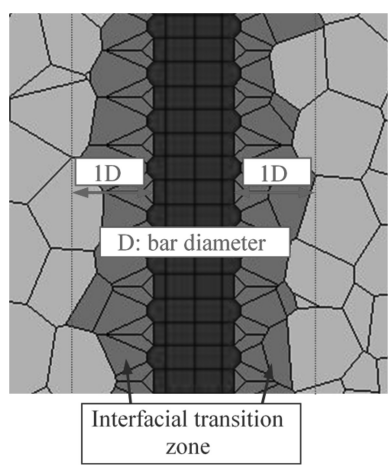

Figure 4. Interfacial transition zone.

$$\sigma_s = E_s \varepsilon_s \quad if\ (\varepsilon_s < \varepsilon_y)$$
$$\sigma_s = f_y \quad if\ (\varepsilon_y < \varepsilon_s < \varepsilon_{sh}) \tag{2}$$

$$\sigma_s = f_y + (1 - e^{((\varepsilon sh - \varepsilon s)/k)})\ (1.01 f_u - f_y) \qquad if\ (\varepsilon_s > \varepsilon_{sh})$$

where k = 0.032 $(400/f_y)^{1/3}$; σ_s = steel stress (MPa); ε_s = steel strain; f_y = yield strength (MPa); f_u = tensile strength (MPa); ε_{sh} = initial strain hardening assumed to be 1.5%.

3. Concrete-steel interface

At the concrete-steel interface, the constitutive models of the normal springs and shear springs have the same behavior as those of concrete elements (Fig. 3a). However, to consider the concrete-steel interface as a weak region, the tensile strength of the interface elements is assumed to be half that of concrete elements.

3 DETAIL OF NUMERICAL SIMULATIONS

3.1 *Numerical models*

The numerical study is divided into three series listed in Table 1. The first and second series are intended to verify the applicability of 3D RBSM in modeling the bond behavior between concrete and reinforcement through the comparison with the experimental results conducted by Shima et al. (1987). Meanwhile, the objective of the third series is to compare the proposed approach with the conventional bond stress-slip relationship and to discuss when each bond model is suitable to be used. The first series is the simulations of pull-out of a reinforcing bar embedded in a massive concrete. Four numerical models are considered in the first series which are selected from among those used in the experiments by Shima et al. (1987). They are signified by EM-S-WOI, EM-S-WI, EM-A-WOI, EM-A-WI. In the cases of EM-S-WOI and EM-S-WI, a steel bar is used as the reinforcing bar. EM-S-WOI means that the interfacial transition zone is not modeled, while EM-S-WI means that the interfacial transition zone is considered. Meanwhile, in the cases of EM-A-WOI and EM-A-WI, an aluminium bar which has much smaller Young's modulus than that of a steel bar is used as the reinforcing bar. EM-A-WOI means that the interfacial transition zone is

Table 1. Detail of numerical models.

Series	Case	Description	Material properties of concrete			Number of elements
			Compressive strength (MPa)	Tensile strength (MPa)	Modulus of elasticity (MPa)	
1	EM-S-WOI	Steel bar is embedded in massive concrete without interfacial zone	34.3	2.43	29,290	82,846
	EM-S-WI	Steel bar is embedded in massive concrete with interfacial zone	34.3	2.43	29,290	82,835
	EM-A-WOI	Aluminium bar is embedded in massive concrete without interfacial zone	34.3	2.43	29,290	82,846
	EM-A-WI	Aluminium bar is embedded in massive concrete with interfacial zone	34.3	2.43	29,290	82,835
2	TS-610-WOI	Tension stiffening (fy = 610 MPa) without interfacial zone	25.0	1.50	25,500	94,360
	TS-610-WI	Tension stiffening (fy = 610 MPa) with interfacial zone	25.0	1.50	25,500	93,442
	TS-350-WOI	Tension stiffening (fy = 350 MPa) without interfacial zone	25.0	1.50	25,500	94,360
	TS-350-WI	Tension stiffening (fy = 350 MPa) with interfacial zone	25.0	1.50	25,500	93,442
3	TS-RBSM	Tension stiffening modeled using 3D RBSM with interfacial zone	25.0	1.50	25,500	61,759
	TS-BONDSLIP	Tension stiffening modeled using conventional bond stress-slip	25.0	1.50	25,500	53,087

not modeled, while EM-A-WI means that the interfacial transition zone in modeled.

In the second series, the simulations of the tension stiffening behavior in RC are conducted where a reinforcing bar is arranged in the center of the concrete prism for the tension test. The yield strength of the reinforcing bar is varied. Four numerical models based on the experiments by Shima et al. (1987) are considered in the second series which are signified by TS-610-WOI, TS-610-WI, TS-350-WOI, TS-350-I. In TS-610-WOI and TS-610-WI, the yield strength of the reinforcing bar is 610 MPa. In TS-610-WOI, the interfacial transition zone is not modeled, while in TS-610-WI the interfacial transition zone is modeled. Meanwhile, In TS-350-WOI and TS-350-WI, the yield strength of the reinforcing bar is 350 MPA. The interfacial transition zone is not considered in TS-350-WOI, while in TS-350-WI, the interfacial transition zone is considered.

To compare the proposed approach with the conventional bond stress-slip relationship, additional two numerical models of the tension stiffening simulation are conducted which are named by TS-RBSM and TS-BONDSLIP. TS-RBSM means that the reinforcing bar with its ribs in 3D shape is modeled directly, while in TS-BONDSLIP, the reinforcing bar is modeled as a plain bar where the bond between concrete and the reinforcing bar is modeled using the slip-stress relationship.

3.2 *Geometry of numerical models*

Figure 5 shows the geometries of the numerical models. Numerical models in Series 1 and Series 2 are the same as those in the experimental specimens (Shima et al. 1987). For comparison, details of the original experimental specimens are included in Figure 6.

The geometries of the numerical models in Series 1 are shown in Figure 5a. A reinforcing bar is arranged vertically in the center of a massive concrete having a cross-sectional size of 500 × 500 mm which is large enough to prohibit a splitting crack. One deformed bar of 17.7 mm nominal diameter is embedded at the center of the model. The development length of the reinforcing bar is 40 D. A 10 D un-bonded length is included. Here, D is the diameter of the reinforcing bar. Material properties of the reinforcing bar are given in Table 2. Meanwhile, Figure 5b shows the geometries of the numerical models in Series 2. The models have a cross-sectional size of 200 × 250 mm and length of 3000 mm with an un-bonded length of 150 mm at both ends. The reinforcement consisted of one reinforcing bar with a 19.1 mm nominal diameter that resulted in a reinforcement ratio of 0.6%. The material properties of the reinforcing bar are also included in Table 2.

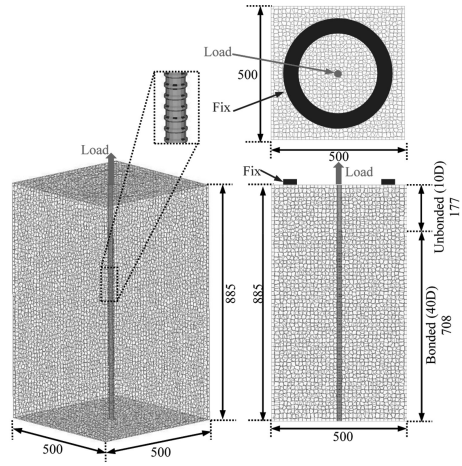

(a) Simulation of pullout of a reinforcing bar embedded in a massive concrete in Series 1.

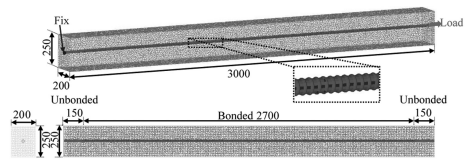

(b) Tension stiffening simulation in Series 2.

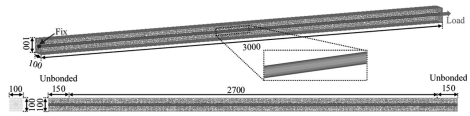

(c) Tension stiffening simulation in Series 3 (TS-BONDSLIP).

Figure 5. Geometries of numerical models (Units: mm).

The models in Series 3 as shown in Figure 5c have a cross-sectional size of 100 × 100 mm and length of 3000 mm with an un-bonded length of 150 mm at both ends. The reinforcement consisted of one reinforcing bar with a 19.1 mm nominal diameter. The material properties of the reinforcing bar are listed in Table 2.

3.3 *Boundary conditions*

Figure 5 also shows the boundary conditions of the numerical models. For the comparison details of experiment arrangement are shown in Figure 6. In Series 1, to model the support plate in the experimental set up, fix condition in all directions is assumed at the top models. Pull-out displacement is applied to the steel elements at the loaded end face of the longitudinal reinforcing bar. Displacement is increased 0.005 mm at each loading step. 200 steps of displacement are applied in the simulation.

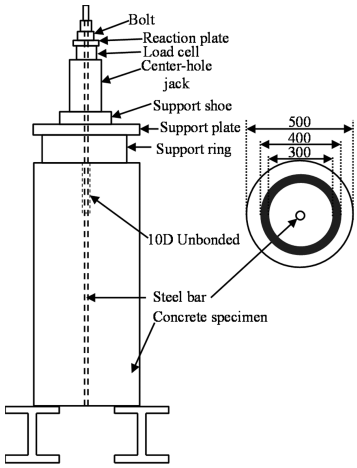

(a) Pullout of a reinforcing bar embedded in a massive concrete (Units: mm)

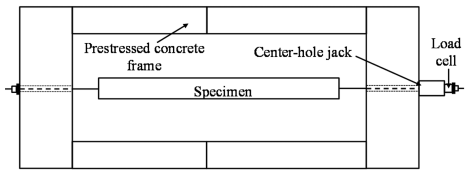

(b) Tension stiffening in RC.

Figure 6. Experimental set up (Shima et al. 1987).

Table 2. Material properties of reinforcing bar.

Type of bar	Nominal Diameter (mm)	Modulus of elasticity (MPa)	Yield strength (MPa)
Steel bar in Series 1	17.7	190,000	480
Aluminium bar in Series 1	17.7	72,000	450
Steel bar of TS-350-WOI and TS-350-WI in Series 2	19.1	190,000	350
Steel bar of TS-610-WOI and TS-610-WI in Series 2	19.1	190,000	610
Steel bar in Series 3	19.1	190,000	610

In Series 2 and Series 3, fix condition in all directions is assumed at one end of the reinforcing bar, while monotonic displacement is applied to another end of the reinforcing bar. Displacement is increased 0.015 mm at each loading step. 2000 steps of displacement are applied in the simulation.

4 SIMULATION RESULTS AND DISCUSSIONS

4.1 *Simulation of pullout of a reinforcing bar embedded in a massive concrete.*

The reinforcement strain distributions predicted by the simulation results are compared with those of Shima model (Shima et al. 1987). Figure 7a shows the comparison between the simulation results and Shima model when the strain at the loaded end is 800 micron, while Figure 7b shows the comparison between the simulation results and Shima model when the strain at the loaded end is 2000 micron.

The strain decreases from peak at the loaded end to the free end, and the strain is greater with higher loading. In the cases of EM-S-WOI and EM-A-WOI, the simulation results overestimate the bond stresses which is indicated by the steeper slope of the reinforcement strain distribution. When the interfacial transition zone is assumed (EM-S-WOI and EM-A-WOI), the computed strain distributions become closer to the Shima model. The experimental data shows that with smaller Young's modulus of the reinforcing bar (aluminium case), the bond stress becomes smaller. The smaller bond stress of the aluminium bar is resulted from the larger strain of the aluminum bar compared with the steel bar at the same slip (Shima et al. 1987). The tendency for the bond stress to become smaller with a smaller Young's modulus of the reinforcing bar could be captured by the simulation. As shown in Figure 7, the simulation results (EM-S-WOI & EM-A-WOI) are in good agreement with Shima model (steel & aluminium). The applicability of 3D RBSM to simulate variations in bond stress due to different Young's modulus is confirmed.

Figure 8 shows the internal stresses and cracks in the vicinity of the reinforcing bar for the first 150 mm of bonded length in all cases when the strain at the loaded end is 2000 microns. Here, the stresses represent the normal stresses of springs between rigid bodies. These internal stresses and cracks in the numerical models show that there is bonding along the reinforcing bar indicated by the compressive bearing stresses at the contact faces between ribs and surrounding concrete. As shown in Figure 8, by modeling the shape of the ribs, it is possible to take into consideration those stresses which are in the off-axis direction of the reinforcing bar. The model of deformed reinforcing bar can reproduce the conical shape of stresses pattern. As shown in Figure 9, the local cracks predicted by the simulation results are comparable to the Goto cracks (Goto 1971).

Because the interfacial transition zone is assumed in EM-S-WI and EM-A-WI, cracks

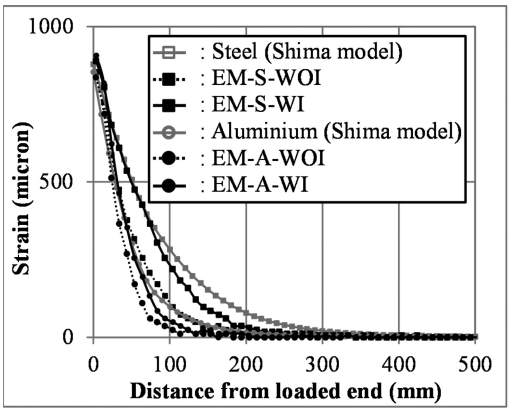

(a) Strain distributions when the strain at the loaded end is 800 microns.

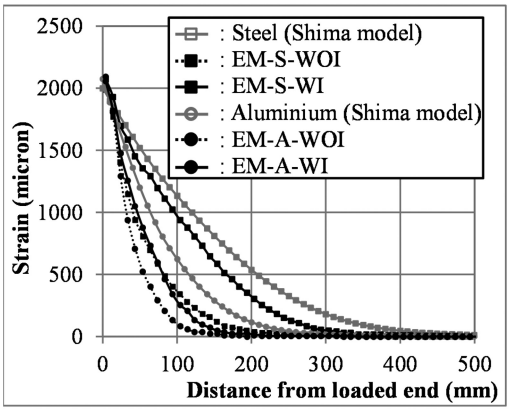

(b) Strain distributions when the strain at the loaded end is 2000 microns.

Figure 7. Reinforcement strain distributions predicted by the simulation results for all cases in Series 1 compared with Shima model (Shima et al. 1987).

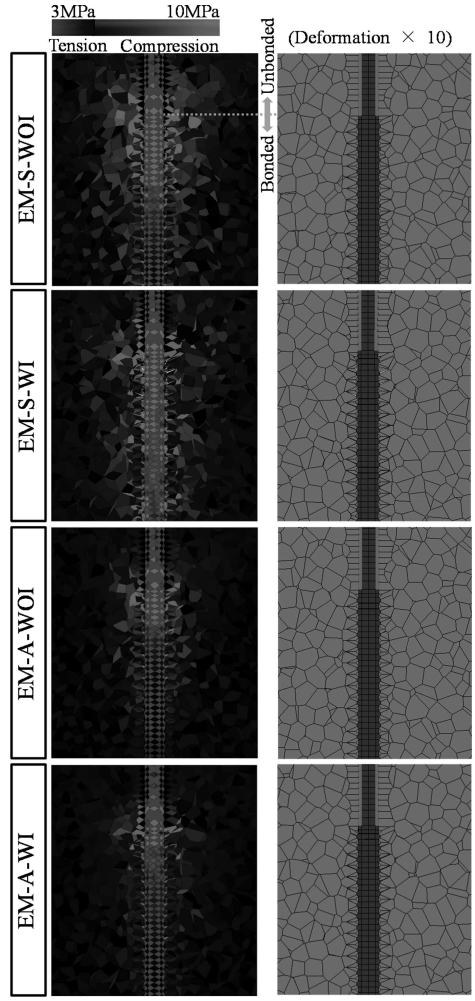

Figure 8. Internal stresses and cracks in the vicinity of the reinforcing bar when the strain at the loaded end is 2000 microns for all numerical models in Series 1.

occur easily in vicinity of the reinforcing bar. As the result, the strains along the reinforcing bar in EM-S-WI and EM-A-WI (with interfacial transition zone) are larger than those in EM-S-WOI and EM-A-WOI (without interfacial transition zone), resulting in weaker bond stresses in EM-S-WI and EM-A-WI. The effect of the local bond behavior on the RC behavior is investigated further in the simulation of tension stiffening.

4.2 *Simulation of tension stiffening in RC*

The simulation results are compared with the experimental observations (Shima et al. 1987) in terms of the load-average strain relationship, the average stress-strain relationship of the reinforcing bar, and the average stress-strain relationship of concrete. Figure 10 shows the simulation and experimental results when the yield strength of the reinforcing bar is 610 MPa, while Figure 11 shows the simulation and experimental results when the yield strength of the reinforcing bar is 350 MPa. Generally, the simulation results are roughly the same as the experimental results. By means of the bond stress between the reinforcing bar and concrete, the concrete is still able to develop the tensile stress away from the crack section. As the result, the tensile stiffness of a RC element is higher than that of a bare bar. Furthermore, concrete can carry tensile load even after the bar has yielded. It can be

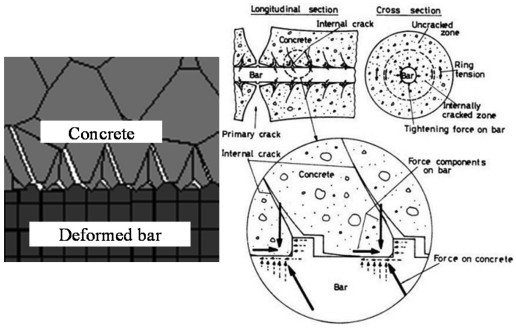

Figure 9. Close-up view of interaction between ribbed reinforcing bar and concrete (Deformation × 10). Comparison is made experimentally observed results of Goto (1971).

concluded that 3D RBSM can simulate the tension stiffening behavior in a RC element.

Based on the average stress-strain of the reinforcing bar, the yielding point of the average stress-strain relationship of the reinforcing bar is lower than that of the bare bar.

It is because when the reinforcing bar at the crack section yields, the stress of the reinforcing bar between two cracks should be less than the yield stress. This tendency can be captured by the simulation. Although the simulation overestimates the yielding point of the average stress-strain relationship of the reinforcing bar in TS-350-WOI and TS-350-WI cases, the tendency for the yielding point of the average stress-strain relationship of the reinforcing bar becomes lower with a lower yield strength of the reinforcing bar is captured. Simulation results predict that the macroscopic responses are not significantly affected because of the presence of the artificial transition zone. The numerical models exhibit a similar response irrespective the presence of the artificial transition zone.

Crack patterns and reinforcement strain distributions for TS-610-WOI and TS-610-WI cases are shown in Figure 12, while crack patterns and reinforcement strain distributions for TS-350-WOI and TS-350-WI cases are shown in Figure 13. The reinforcement strain distributions of the simulation results are compared with those of the experimental measurement. The simulation results confirm that under increasing load, more cracks form because of the presence of the bond between concrete and the reinforcing bar. The tendency for the number of cracks to become more with higher yield strength of the reinforcing bar is captured in the simulation. The simulation results also show

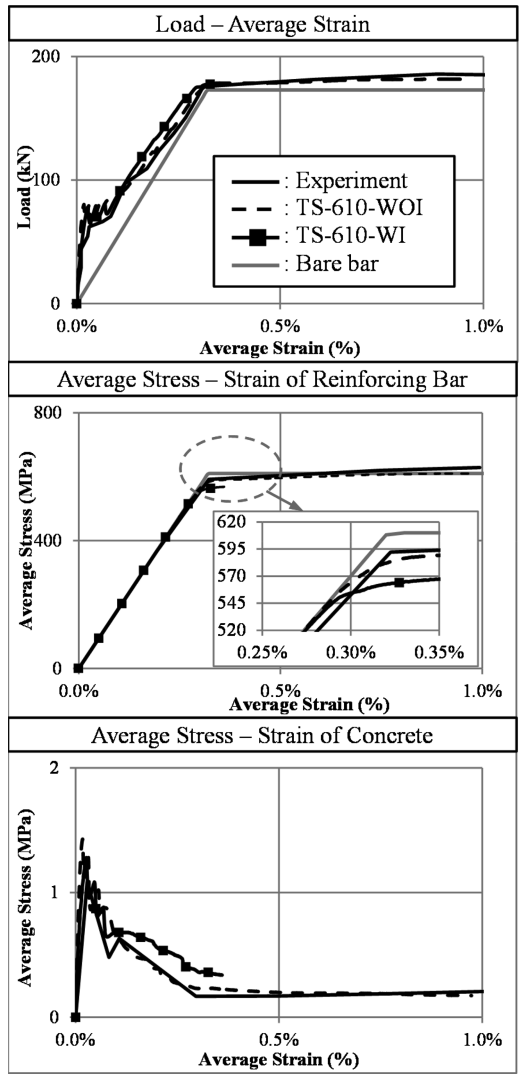

Figure 10. Load-average strain relationships and average stress-strain relationships of reinforcing bar and concrete of TS-610-WOI and TS-610-WI cases.

that as the bond stresses becomes stronger (TS-610-WOI and TS-350-WOI), the number of cracks becomes more and the width of cracks becomes smaller when they are compared with TS-610-WI and TS-350-WI cases. If the interfacial transition zone is considered which is weaker bond strength, the numbers of cracks and strain distributions along the reinforcing bar in TS-610-WI and TS-350-WI show a good agreement with the observed cracks and strain distributions in the experiment.

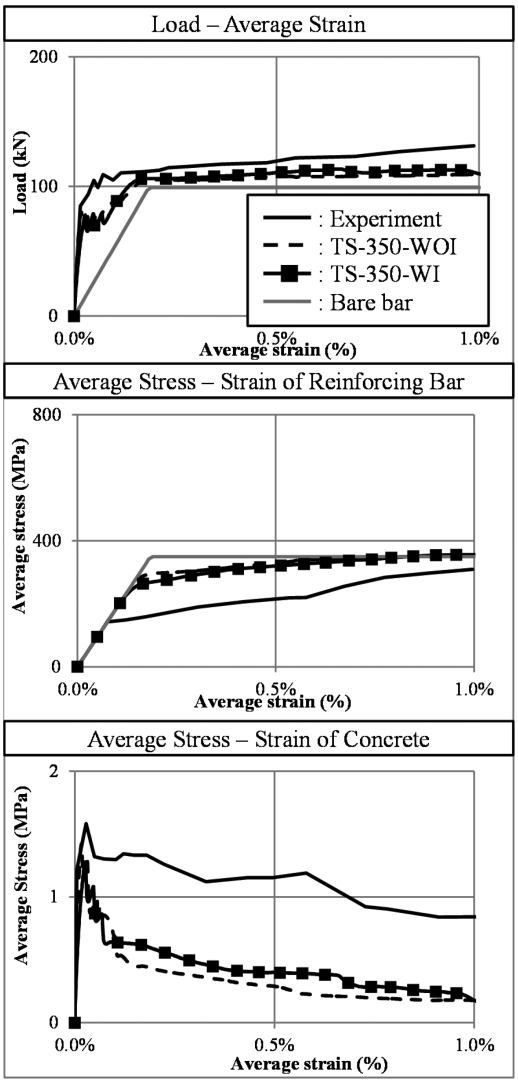

Figure 11. Load-average strain relationships and average stress-strain relationships of reinforcing bar and concrete of TS-350-WOI and TS-350-WI cases.

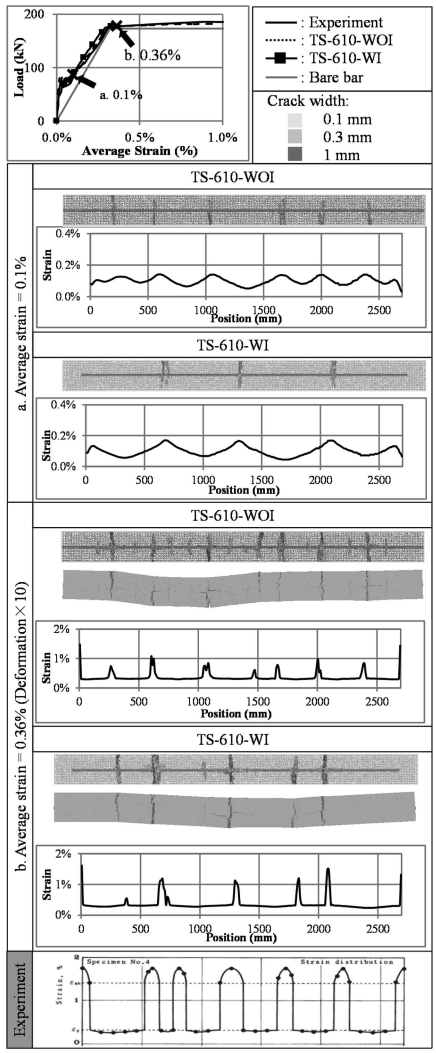

Figure 12. Crack patterns and reinforcement strain distributions for TS-610-WOI and TS-610-WI cases.

Eventually, it also can be concluded that although the macroscopic responses are not significantly affected by the local bond, but the local behavior, number of cracks, width of cracks are different.

4.3 *Comparison between 3D RBSM model and conventional bond stress-slip relationship.*

The proposed approached is compared with the conventional bond stress-slip relationship. In the case of the conventional bond stress-slip relationship (TS-BONDSLIP), the reinforcing bar is modeled as the plain bar. The spring parallel to the reinforcing bar represents the bond action between the bar and the concrete material.

The bond stress-slip relationship used for the constitutive model of the shear spring is similar to that used by Gedik et al. (2001) which is shown in Figure 14, where the relationship up to the maximum shear strength is defined by Equation 3 (Suga et al. 2001).

$$\tau = 0.36 f_c'^{2/3}\{1-\exp(-40(s/D)^{0.5})\} \quad (3)$$

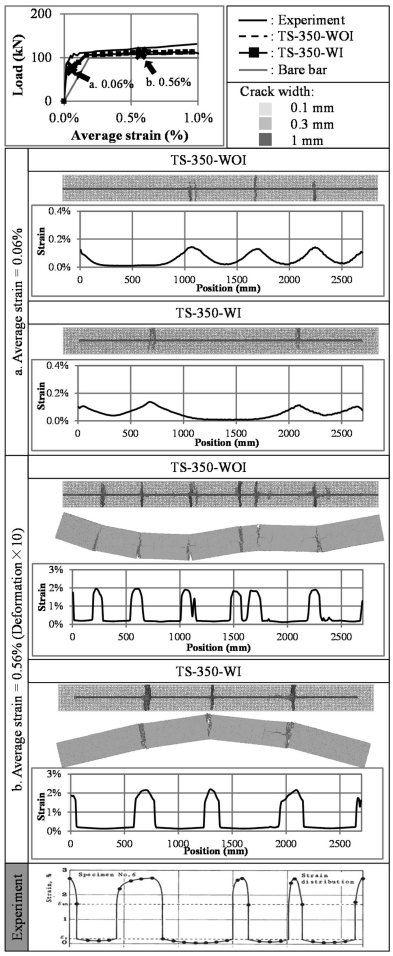

Figure 13. Crack patterns and reinforcement strain distributions for TS-350-WOI and TS-350-WI cases.

where τ = bond stress (MPa); f_c' = compressive strength of concrete (MPa); s = slip (mm); D = diameter of the reinforcing bar (mm).

The load-average strain relationships for the numerical models in Series 3 are shown in Figure 15. Simulation results predict that the macroscopic responses of a RC element are the same in both cases irrespective of the bond model. The bond model does not affect the macroscopic response of a RC element. Furthermore, the difference of the average stress-average strain relationships of concrete for both models is not significant as shown in Figure 16. Although the macroscopic responses are similar in both bond models, the internal stresses and cracks are different between both bond models.

Figure 17 shows the internal stresses and cracks for all numerical models in Series 3 at an average strain of 0.28%, while Figure 18 shows the internal stresses and cracks for all numerical models in Series 3 at an average strain of 0.83%. Simulation results show that only primary transversal cracks occur at a certain distance in the case of the conventional bond slip-stress relationship (TS-BONDSLIP). Meanwhile, if the 3D shape arrangement of a reinforcing bar including its ribs is modeled directly (TS-RBSM), local cracks radiating from the bar ribs, as well as the primary transversal cracks are predicted in the numerical model.

As shown in Figure 19, by modeling the shape of the ribs, it is possible to take into consideration

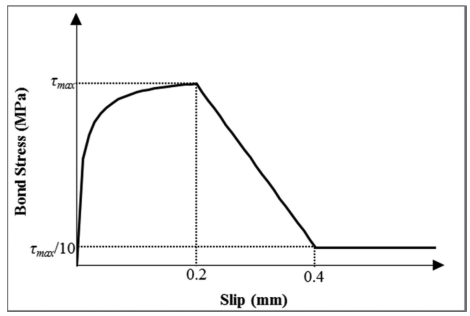

Figure 14. Bond stress-slip relationship.

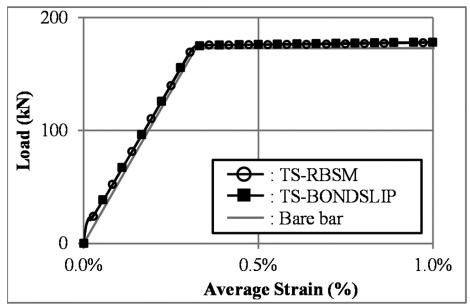

Figure 15. Load-average strain relationships for the numerical models in Series 3.

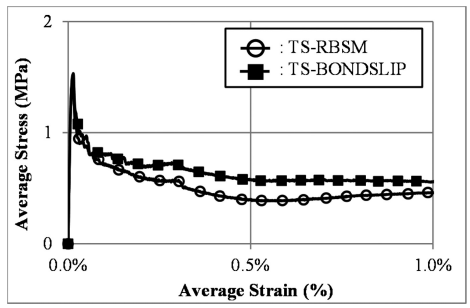

Figure 16. Average stress-average strain relationships of concrete for the numerical models in Series 3.

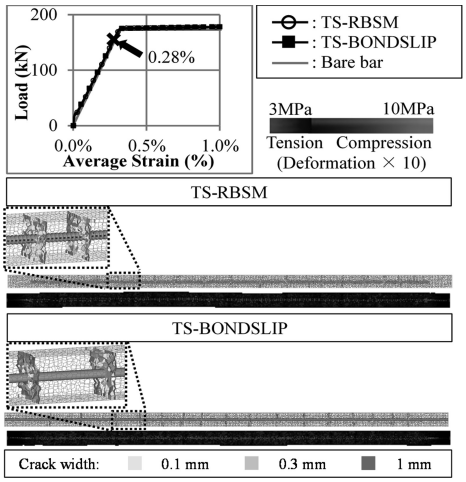

Figure 17. Internal stresses and cracks for numerical models in Series 3 at an average strain of 0.28%.

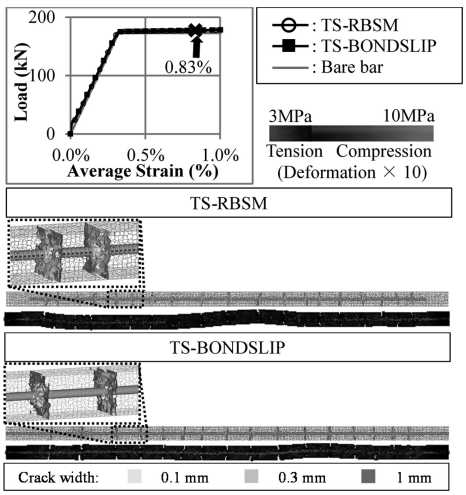

Figure 18. Internal stresses and cracks for numerical models in Series 3 at an average strain of 0.83%.



(a) Goto cracks (b) TS-RBSM (c) TS-BONDSLIP

Figure 19. Comparison of internal cracks near the primary cracks of numerical models in Series 3 at an average strain of 0.83% with Goto cracks.

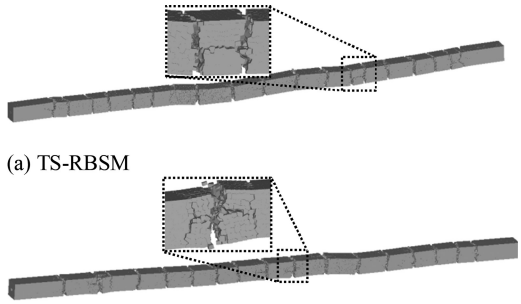

(a) TS-RBSM

(b) TS-BONDSLIP

Figure 20. Surface cracks for the numerical models in Series 3 at an average strain of 1.0% (Deformation × 10).

those stresses which are in the off-axis direction of the reinforcing bar. TS-RBSM can reproduce the conical shape of stresses pattern. In addition, the local cracks predicted in TS-RBSM are comparable to the Goto cracks (Goto 1971). Because TS-RBSM can reproduce the conical shape of stresses pattern, the splitting cracks near the primary cracks in TS-RBSM are more visible than those in TS-BONDSLIP as shown in the surface cracks of numerical models (Fig. 20). Therefore, if the effect of the local bar ribs-concrete interaction needs to be considered, the proposed approach is a suitable method, while the conventional bond stress-slip relationship is applicable for the conventional structural analysis when the element size is over 10 cm.

5 CONCLUSIONS

In order to investigate the availability of the 3D discrete element numerical method called 3D Rigid Body Spring Model (RBSM) in modeling the local bond behavior in a reinforced concrete member and to compare the proposed approach with the conventional bond stress-slip relationship, numerical simulations of the pull-out of a reinforcing bar embedded in a massive concrete and the tension stiffening model are conducted. The conclusions obtained from this research are as follows.

1. Simulations of a massive concrete specimen with a single reinforcing bar and under tension loading give a good agreement of strain values along the reinforcing bar. If the effect of porous concrete adjacent to the reinforcing bar is taken into the consideration where the stiffness and tensile strength of concrete within a distance of 1.0D measured from the bar face are reduced, the computed strain distributions become closer to the Shima model. The applicability of 3D RBSM to simulate variations in bond

stress due to different Young's modulus is also confirmed. The tendency for the bond stress to become smaller with a smaller Young's modulus of the reinforcing bar could be captured by the simulation. In addition, the local cracks predicted by the simulation results are comparable to the Goto cracks.

2. In the simulations of tension stiffening behavior in a RC, the simulation results are roughly the same as the experimental results. The tendencies for the yielding point of the average stress-strain relationship of the reinforcing bar becomes lower with lower yield strength of the reinforcing bar and the number of cracks to become more with higher yield strength of the reinforcing bar are captured by the simulations. The simulation results show that although the macroscopic responses are not significantly affected by the presence of the artificial transition zone, but it affects the number of cracks along the RC, the width of cracks, and the reinforcement strain distribution.
3. Simulation results show that the macroscopic response in term of the load-average strain relationship of the proposed approach is the same as that of the conventional bond stress-slip relationship. However, the internal stresses and cracks are different between both bond models. In the case of the conventional bond stress-slip relationship, only primary transversal cracks occur at a certain distance. Meanwhile, if the 3D shape arrangement of a reinforcing bar including its ribs is modeled directly, local cracks radiating from the bar ribs as well as the primary transversal cracks are predicted in the numerical model. Because the proposed approach can reproduce the conical shape of stresses pattern, the splitting cracks near the primary cracks are more visible than the conventional bond stress-slip model. The proposed approach is a suitable method when the effect of the local bar ribs-concrete interaction needs to be considered, while the conventional bond stress-slip relationship does not simulate well the local cracking behavior. The conventional bond stress-slip relationship is good enough to simulate the macroscopic behavior and major cracks. Therefore, the bond stress-slip relationship is applicable for the conventional structural analysis when the element size is over 10 cm, but it is not suitable for the meso-scale analysis.
4. The proposed approach is a unified model. It does not depend on the confinement conditions, while the conventional bond stress-slip relationship should be changed under different confinement conditions.

REFERENCES

Bolander, J.E. & Saito, S. 1998. Fracture analysis using spring networks with random geometry. *Engineering Fracture Mechanics* 61(5): 569–591.

Bolander, J.E. & Le, B.D. 1999. Modeling crack development in reinforced concrete structures under service loading. *Construction and Building Materials* 31(1): 23–31.

Bolander, J.E., Hong, G.S., & Yoshitake, K. 2000. Structural concrete analysis using rigid-body-spring networks. *Computer-Aided Civil and Infrastructure Engineering* 15(2): 120–133.

Bolander, J.E. & Hong, G.S. 2002. Rigid-body-spring network modeling of prestressed concrete members. *ACI Structural Journal* 99(5): 595–604.

Eddy, L. 2015. Numerical simulation of failure of RC beam-column joint by 3D RBSM. In *Ph.D. Thesis*. The University of Tokyo, Tokyo.

Eddy, L. & Nagai, K. 2016a. Numerical simulation of beam-column knee joints with mechanical anchorages by 3D rigid body spring model. *Engineering Structures* 126: 547–558.

Eddy, L., Matsumoto, K., & Nagai, K. 2016b. Effect of perpendicular beams of failure of beam-column knee joints with mechanical anchorages by 3D RBSM. *Journal of Asian Concrete Federation* 2(1): 56–66.

Eligehausen, R., Popov, E.P., & Bertero, V.V. 1983. Local bond stress-slip relationships of deformed bars under generalized excitations. In *Earthquake Engineering Research Center Report* 82/83. University of California, Berkeley.

Gedik, Y.H., Nakamura, H., Yamamoto, Y., & Kunieda, M. 2011. Evaluation of three-dimensional effects in short deep beams using a rigid-body-spring-model. *Cement and Concrete Composites* 33(9): 978–991.

Goto, Y. 1971. Cracks formed in concrete around deformed tension bars. *ACI Journal* 68(4): 244–251.

Hayashi, D., Nagai, K., & Eddy, L. 2017. Mesoscale analysis of RC anchorage performance in multidirectional reinforcement using a three-dimensional discrete model. *Journal of Structural Engineering* 143(7): 04017059.

Kawai, T. 1978. New discrete models and their application to seismic response analysis of structures. *Nuclear Engineering and Design* 48(1): 207–229.

Nagai, K., Sato, Y., & Ueda, T. 2005. Mesoscopic simulation of failure of mortar and concrete by 3D RBSM. *Journal of Advanced Concrete Technology* 3(3): 385–402.

Nagai, K., Hayashi, D., & Eddy, L. 2014. Numerical simulation of failure of anchorage with shifted mechanical anchorage bars by 3D discrete model. *Advances in Structural Engineering* 17(6): 861–869.

Salem, H.M. & Maekawa, K. 2004. Pre-and postyield finite element method simulation of bond of ribbed reinforcing bars. *Journal of Structural Engineering* 130(4): 671–680.

Shima, H, Chou, L.L., & Okamura, H. 1987. Micro and macro models for bond in reinforced concrete. *Journal of the Faculty of Engineering* 39(2): 133–194.

Suga, M., Nakamura, H., Higai, T., & Saito, S. 2001. Effect of bond properties on the mechanical behavior of RC beam. *Proceedings of Japan Concrete Institute* 23: 295–300. (in Japanese).

Computational Modelling of Concrete Structures – Meschke, Pichler & Rots (Eds)
© 2018 Taylor & Francis Group, London, ISBN 978-1-138-74117-1

Modeling of bond fatigue in reinforced concrete based on cumulative measure of slip

A. Baktheer & R. Chudoba
Institute of Structural Concrete, RWTH Aachen University, Aachen, Germany

ABSTRACT: In this paper we introduce a thermodynamically consistent bond-interface pressure-sensitive damage model with cumulative sliding strain measure as a fundamental source of fatigue damage. The modeling approach provides a clear physical interpretation of the dissipative mechanisms governing the propagation of fatigue damage within the concrete-steel interface so that it is possible to reproduce both the monoutonic and the cyclic behavior of the bond with a consistent set of material parameters. The model has been applied for simulation of the degradation process in the bond between concrete and reinforcement under pullout fatigue loading. The paper presents numerical studies of the fatigue pullout behavior with detailed analysis of the damage propagation during loading and unloading stages, and at different levels of imposed lateral pressure. To validate the ability of the model, pullout simulations of tests published in the literature have been conducted.

1 INTRODUCTION

An increased interest in detailed description and characterization of fatigue behavior of reinforced concrete (RC) members has developed during the last decade due to the enhanced requirements on the fatigue resistance of structures exposed to up to 10^7 number of cycles, e.g. wind turbine towers or bridges. The behavior of RC members subjected to fatigue loading can only be appropriately described if the local degradation processes affecting the bond strength under fatigue loading are captured. It significantly affects the structural deformation, the width and distribution of the cracks in the RC members and, certainly, the ultimate failure. Besides extensive experimental investigations, several attempts have been made to develop reliable numerical models. Theoretical characterization of RC fatigue behavior is a challenging task that has attracted attention of researchers during the past decades as documented by our brief survey of existing modeling approaches.

For plain concrete, several models addressing the fatigue damage propagation have been proposed. Pragmatic approaches to modeling use the number of performed loading cycles directly as a damage driving variable (Chaboche and Lesne 1988, Pfanner 2003, Pfister et al. 2006, Theil 2016). More advanced approaches to simulation of fatigue damage process cycle by cycle at subcritical load levels with damage related either to total strain (Marigo 1985, Alliche 2004, Mai et al. 2012), or to the inelastic strain (Wu et al. 2006, Kindrachuk et al. 2015). In order to reflect the opening/closure and growth of microcracks and/or the frictional sliding along their lips, the formulation of the dissipative mechanisms has been refined by introducing the internal sliding strain as a damage driving variable within the same framework of isotropic damage and internal sliding strain. In this way, a unified model for monotonic and low cycle fatigue loads has been proposed by (Desmorat et al. 2007). An approach relating the dissipative terms owing to fatigue damage even closer to the observable disintegration mechanisms within the material structure appeared recently in (Kirane and Bažant 2015). The key idea of this model is to relate the damage evolution to the cumulative measure of volumetric strain.

Little amount of research studying the effect of the fatigue loading on the bond between the concrete and reinforcement has been reported so far (Rteil et al. 2011). The complex bond behavior between concrete and reinforcement can be represented using volumetric bodies with an appropriate constitutive relationship. However for large structures and fatigue loading such treatment becomes too time consuming. Less computational demanding approaches involve 1D elements or zero thickness interface elements. As demonstrated in (Ayoub and Filippou 1999), the models of the cyclic loading of bond must have independent field for slip between the steel and concrete. A slip based thermodynamic formulation of zero thickness interface model capable of capturing pressure sensitive bond behavior, interaction of damage and sliding at the interface was presented in (Ragueneau et al. 2006). Another cyclic model based on directly addressed slip in the concrete steel bond has been presented

in (Kwak and Kim 2006). There is also a number of cyclic models focused on general cohesive contact, not addressing explicitly the bond between concrete and steel reinforcement (Roe and Siegmund 2003, Harper and Hallett 2010). More recent work (Carrara and De Lorenzis 2015) introduces a thermodynamically consistent model coupling damage and plasticity for the behavior of interfaces under shear cyclic loading conditions used to simulate the bond fatigue of FRP sheets externally bonded to concrete.

In the present paper we propose a cumulative measure of slip as a fundamental damage driving mechanism. Based on this assumption, we introduce the link between damage rate and absolute value of the microsliding rate and incorporate also the effect of pressure sensitivity. The thermodynamic framework coupling several interacting effects of the damage, cumulative sliding and lateral pressure constitutes the basis for an efficient numerical solver for initial boundary value problem representing the pullout test.

The present paper is organized as follows: After presenting the bond interface model formulated within the thermodynamic framework in Sec. 2 we evaluate and discuss the behavior of the model at the level of a material point in Sec. 3. Then, in Sec. 4 we describe the issues related to the pullout simulation. In Sec. 5 and Sec. 6 we present the calibration and validation of the model based on the results offatigue pullout tests published in the literature. Finally, we present numerical investigations focused on the effect of the lateral confinement on the bond fatigue behavior and the effect of the loading sequence with variable amplitudes on the fatigue life.

2 BOND SLIP INTERFACE MODEL FORMULATION

2.1 *Thermodynamic framework*

2.1.1 *Helmholtz free energy and state variables*

Considering the coupling between the damage and inelastic sliding slip the thermodynamic potential of the bond interface is postulated as

$$\rho\psi = \frac{1}{2}(1-\omega)E_{\mathrm{b}}(s-s^{\pi})^2 + \frac{1}{2}\gamma\alpha^2 + \frac{1}{2}Kz^2, \qquad (1)$$

where ψ is the Helmholtz free energy, ρ is the material density, E_b is the bond stiffness, s is the slip, K and γ are the isotropic and kinematic hardening moduli respectively. The thermodynamic internal variables are inelastic sliding s^{π} defining the irreversible slip, damage variable ω ranging from 0 to 1, the internal variables of isotropic hardening z and kinematic hardening α. The state equations linking the thermodynamic forces with the internal variables are obtained by differentiating the thermodynamic potential of the bond interface (1) with respect to each internal variable. The derivative with respect to slip s defines the bond stress as

$$\tau = \frac{\partial\rho\psi}{\partial s} = (1-\omega)E_{\mathrm{b}}(s-s^{\pi}). \qquad (2)$$

The sliding bond stress related to the irreversible part of slip s^{π} is obtained as

$$\tau^{\pi} = -\frac{\partial\rho\psi}{\partial s^{\pi}} = (1-\omega)E_{\mathrm{b}}(s-s^{\pi}). \qquad (3)$$

As apparent from this equation, the sliding bond stress depends both on inelastic sliding and on the damage state variables. This reveals the thermodynamic coupling between the two dissipative mechanisms.

The back stress associated with kinematic hardening is given by

$$X = \rho\frac{\partial\psi}{\partial\alpha} = \gamma\alpha, \qquad (4)$$

and the thermodynamic force associated with isotropic hardening reads

$$Z = \rho\frac{\partial\psi}{\partial z} = Kz. \qquad (5)$$

The energy release rate owing to the damage development is defined as

$$Y = -\rho\frac{\partial\psi}{\partial\omega} = \frac{1}{2}E_{\mathrm{b}}(s-s^{\pi})^2. \qquad (6)$$

To separate the elastic and inelastic domains of the material state, we introduce a threshold function defining the bounds of the sliding stress. For this purpose, we introduce the effective stress as

$$\tilde{\tau}^{\pi} = \frac{\tau^{\pi}}{1-\omega}. \qquad (7)$$

With regard to (3) the state equation for the effective sliding bond stress reads

$$\tilde{\tau}^{\pi} = E_{\mathrm{b}}(s-s^{\pi}). \qquad (8)$$

The threshold function is defined similarly to the yield function in plasticity theory as

$$f = |\,\tilde{\tau}^{\pi} - X\,| - Z - \bar{\tau} + \frac{a}{3}\sigma_N, \qquad (9)$$

where $\bar{\tau}$ is the reversibility limit, σ_N is the lateral pressure and a is a material parameter controlling

the pressure sensitivity. The threshold function governs the loading/unloading conditions using the effective sliding bond stress and accounts for the effect of lateral pressure in a similar way as the Drucker-Prager yield function.

The flow potential governing the damage evolution extends the threshold function (9) by a non-associative term as

$$\phi = f + \frac{S(1-\omega)^c}{(r+1)}\left(\frac{Y}{S}\right)^{r+1}\left(\frac{\overline{\tau}}{\overline{\tau} - a\,\sigma_N}\right), \tag{10}$$

where S is material parameter denoted as the damage strength, and $c \geq 1$,r are material parameters controlling the damage accumulation.

2.1.2 *Evolution equations*

The evolution laws are obtained by differentiating the flow potential (10) with respect to the thermodynamic forces

$$\dot{s}^\pi = \dot{\lambda}\frac{\partial \phi}{\partial \tau^\pi} = \frac{\dot{\lambda}}{1-\omega}\,\mathrm{sign}(\tilde{\tau}^\pi - X), \tag{11}$$

$$\dot{z} = -\dot{\lambda}\frac{\partial \phi}{\partial Z} = \dot{\lambda}, \tag{12}$$

$$\dot{\alpha} = -\dot{\lambda}\frac{\partial \phi}{\partial X} = \dot{\lambda}\,\mathrm{sign}(\tilde{\tau}^\pi - X), \tag{13}$$

$$\dot{\omega} = \dot{\lambda}\frac{\partial \phi}{\partial Y} = (1-\omega)^c\left(\frac{Y}{S}\right)^r\left(\frac{\overline{\tau}}{\overline{\tau} - a\,\sigma_N}\right)\dot{\lambda}. \tag{14}$$

The consistency condition can then be written as follows

$$\dot{f} = \dot{\tilde{\tau}}^\pi\frac{\partial f}{\partial \tilde{\tau}^\pi} + \dot{X}\frac{\partial f}{\partial X} + \dot{Z}\frac{\partial f}{\partial Z} = 0. \tag{15}$$

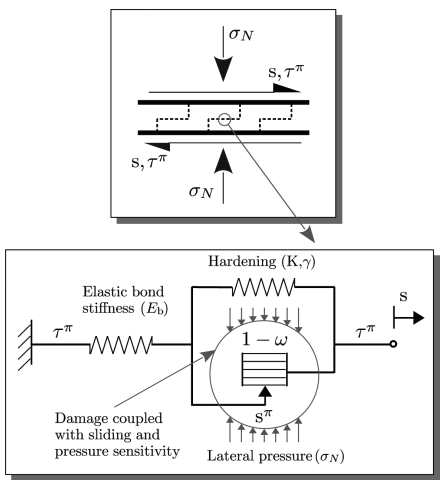

Figure 1. Schematic representation of the bond slip interface.

Using the evolution equation (11) the incremental multiplier can be resolved as

$$\dot{\lambda} = (1-\omega)|\,\dot{s}^\pi\,|. \tag{16}$$

By substituting for $\dot{\lambda}$ in (14), the relation between the damage rate and the absolute value of sliding rate is obtained as

$$\dot{\omega} = (1-\omega)^{c+1}\left(\frac{Y}{S}\right)^r\left(\frac{\overline{\tau}}{\overline{\tau} - a\,\sigma_N}\right)|\,\dot{s}^\pi\,|. \tag{17}$$

Realizing that

$$s^\pi_{\mathrm{cum}}(t) = \int_0^t |\,\dot{s}^\pi\,|\,\mathrm{d}t \tag{18}$$

we recognize that the evolution law (17) actually introduces the cumulative sliding slip as the fundamental source of damage.

2.1.3 *Thermodynamic admissibility*

The constitutive bond model developed within the thermodynamic framework implicitly satisfies the so called Clausius-Duhem inequality ($\mathcal{D} \geq 0$) for any kind of loading scenarios. The energy dissipation is defined as

$$\mathcal{D} = -\frac{\partial \rho\psi}{\partial \boldsymbol{q}}\cdot\dot{\boldsymbol{q}}, \tag{19}$$

where $\boldsymbol{q} = \{s^\pi, \alpha, z, \omega\}$ is the vector of the internal variables. By substituting the state functions (2)–(6) into (19) we get

$$\mathcal{D} = \tau^\pi\dot{s}^\pi - X\dot{\alpha} - Z\dot{z} + Y\dot{\omega}. \tag{20}$$

By further substituting the evolution equations (14) into equation (20) the overall energy release rate reads after small rearrangements

$$\begin{aligned}\mathcal{D} &= \tau^\pi\frac{\dot{\lambda}}{1-\omega}\,\mathrm{sign}(\tilde{\tau}^\pi - X)\\ &\quad - X\dot{\lambda}\,\mathrm{sign}(\tilde{\tau}^\pi - X) - Z\dot{\lambda} + Y\dot{\omega}\\ &= \left[(\tilde{\tau}^\pi - X)\,\mathrm{sign}(\tilde{\tau}^\pi - X) - Z\right]\dot{\lambda} + Y\dot{\omega}\\ &= \left[|\,\tilde{\tau}^\pi - X\,| - Z\right]\dot{\lambda} + Y\dot{\omega}.\end{aligned} \tag{21}$$

To reflect the effect of lateral pressure on the energy release rate we rephrase the threshold function (9) in the form

$$|\,\tilde{\tau}^\pi - X\,| - Z = \overline{\tau} - \frac{a}{3}\sigma_N. \tag{22}$$

By substituting the left hand side into (20) we obtain the particular form of the Clausius-Duhem inequality as

$$\mathcal{D} = \left(\overline{\tau} - \frac{a}{3}\sigma_N\right)\dot{\lambda} + Y\dot{\omega} \geq 0. \tag{23}$$

Recalling that $\bar{\tau}$, a, $\dot{\lambda}$, Y and $\dot{\omega}$ are all positive by definition, we can conclude that the admissible range of lateral stress is $\sigma_N \leq 3\bar{\tau}/a$.

2.2 *Numerical implementation*

The introduced material model has been implemented into the standard finite element framework as an implicit time-stepping algorithm incrementally integrating the evolution equations (14). The derived numerical integration algorithm follows the standard scheme (Simo and Hughes 2006). An incremental step showing the evaluation of admissible state variables for the given increment of the control slip is shown in Algorithm 25. The incremental multiplier at each time step is computed numerically from the consistency condition (15) which is used for the return mapping procedure to correct the internal variables after elastic trial prediction. By substituting evolution equations (11)–(14) into the consistency condition (15) the inelastic multiplier is obtained as

$$\dot{\lambda} = \frac{E_\mathrm{b}\, \dot{s}\, \mathrm{sign}(\tilde{\tau}^\pi - X)}{E_\mathrm{b}/(1-\omega) + \gamma + K}, \tag{24}$$

and its increment as

$$\Delta\lambda = \frac{f_{n+1}^{\mathrm{trial}}}{E_\mathrm{b}/(1-\omega) + \gamma + K}. \tag{25}$$

Due to the implicit form of the damage evolution equations (14) one has to perform local newton iterations. This might be too costly for fatigue simulations. Similarly to (Desmorat et al. 2007) we apply an assumption of a damage quasi-constant over a time increment, which significantly accelerates the simulation without a loss of accuracy.

To ensure a robust and efficient numerical implementation of the proposed model, the consistent algorithmic stiffness is required. The algorithmic stiffness relates the rates of the stress and slip as follows

$$\dot{\tau} = E_\mathrm{b}^{\mathrm{alg}} \dot{s}. \tag{26}$$

With regard to (2) we can express the stress rate as

$$\dot{\tau} = (1-\omega) E_\mathrm{b} (\dot{s} - \dot{s}^\pi) - \dot{\omega} E_\mathrm{b} (s - s^\pi). \tag{27}$$

After substituting the evolution equations for damage and sliding slip, including the incremental multiplier (24) and rearranging terms, we obtain the algorithmic stiffness as

$$E_\mathrm{b}^{\mathrm{alg}} = (1-\omega)E_\mathrm{b} - \frac{(1-\omega)E_\mathrm{b}^2}{E_\mathrm{b} + (\gamma + K)(1-\omega)} - \frac{(1-\omega)^c E_\mathrm{b}^2 (s - s^\pi)\left(\frac{\bar{\tau}}{\bar{\tau} - a\,\sigma_N}\right)\left(\frac{Y}{S}\right)^r}{\left(E_\mathrm{b}/(1-\omega) + \gamma + K\right)\mathrm{sign}(\tilde{\tau}^\pi - X)}. \tag{28}$$

3 BEHAVIOR OF A SINGLE MATERIAL POINT

3.1 *Cumulative fatigue damage*

The degradation of the bond behavior under monotonic and cyclic loading controlled by the level of slip is presented in Fig. 2a. The cyclic slip loading with increasing amplitude demonstrates the link between the damage rate and the absolute value of the inelastic sliding rate resulting in damage accumulation at the sub-critical load levels. The damage accumulation during both loading and unloading stages is shown separately in Fig. 2b.

3.2 *Pressure sensitivity*

The effect of lateral pressure on the bond behavior between concrete and steel for monotonic loading has been reported in the literature (Eligehausen et al. 1982, Torre-Casanova et al. 2013) showing an increase of the maximum bond stress for increasing level of lateral pressure. In Fig. 2c the bond slip behavior subjected to cyclic slip loading with increasing amplitude is shown for different levels of lateral pressure. The dissipated energy is increasing proportionally with the level of the lateral pressure as shown in Fig. 2d.

Algorithm 1: Bond-slip time-stepping scheme

Data: $s_n,\ \Delta s,\ \omega_n,\ s_n^\pi,\ \tau_n,\ \tau_n^\pi,\ \alpha_n,\ z_n$
Result: $s_{n+1}^\pi,\ \omega_{n+1},\ \tau_{n+1}^\pi,\ \alpha_{n+1},\ z_{n+1}$
Constants: $\gamma,\ K,\ \bar{\tau},\ E_\mathrm{b},\ S,\ r,\ c,\ a$

$s_{n+1} = s_n + \Delta s$

$\tau_{n+1}^{\pi,trial} = E_\mathrm{b}(1-\omega_n)(s_{n+1} - s_n^\pi)$

$\tilde{\tau}_{n+1}^{\pi,trial} = E_\mathrm{b}(s_{n+1} - s_n^\pi)$

$f_{n+1}^{trial} = |\tilde{\tau}_{n+1}^{\pi,trial} - \gamma\alpha_n| - Kz_n - \bar{\tau} + \frac{a}{3}(\sigma_N)$

if $f_{n+1}^{trial} \leq 0$ **then**
  $\longrightarrow$ Elastic step
  $\tau_{n+1}^\pi = \tau_{n+1}^{\pi,trial}$ $\qquad$ $\omega_{n+1} = \omega_n$
else
  $\longrightarrow$ Return mapping
  $\Delta\lambda = \frac{f_{n+1}^{trial}}{E_\mathrm{b}/(1-\omega_n) + \gamma + K}$

(*Continued*)

Algorithm 1: (*Continued*)

$$s^{\pi}_{n+1} = s^{\pi}_{n} + \frac{\Delta\lambda}{1-\omega_n}\text{sign}(\tilde{\tau}^{\pi,trial}_{n+1} - X_n)$$

$$Y_{n+1} = \frac{1}{2}E_b(s_{n+1} - s^{\pi}_{n+1})^2$$

$$\omega_{n+1} = \omega_n + \Delta\lambda\frac{\bar{\tau}(1-\omega_n)^c}{\bar{\tau} - a\,\sigma_N}\left(\frac{Y_{n+1}}{S}\right)^r$$

$$\tau^{\pi}_{n+1} = (1-\omega_{n+1})E_b(s_{n+1} - s^{\pi}_{n+1})$$

$$z_{n+1} = z_n + \Delta\lambda$$

$$\alpha_{n+1} = \alpha_n + \Delta\lambda\,\text{sign}(\tilde{\tau}^{\pi,trial}_{n+1} - X_n)$$

end

This highlits the fact that the sensitivity of the bond with respect to lateral pressure is based on a sound representation of the underlying physical phenomenon.

4 PULLOUT BOUNDARY VALUE PROBLEM

The described material model is embedded into the initial boundary value problem in a usual way following the weak formulation of the equilibrium condition on an infinitesimal element of the interface (see Fig. 3)

$$A_f\sigma_{f,x} - p\tau(s) = 0, \tag{29}$$

where τ denotes the shear stress and s the slip between the reinforcement and matrix. The index $(.)_{,x}$ denotes the derivative with respect to the spatial coordinate x, A_f and p are the cross-sectional area and the perimeter of the reinforcement, respectively. Similarly, the equilibrium of an infinitesimal element of the matrix can be given as

$$A_m\sigma_{m,x} + p\tau(s) = 0, \tag{30}$$

in which A_m is the cross-sectional area of the matrix. A liner elastic behavior is assumed for the reinforcement and the matrix. The boundary conditions shown in Fig. 3 can be summarized as follows

$$\begin{aligned} u_m &= \bar{u}_m(\theta) \text{ on } \Gamma_{u_m}, \sigma_m A_m = \bar{t}_m(\theta) \text{ on } \Gamma_{t_m}, \\ u_f &= \bar{u}_f(\theta) \text{ on } \Gamma_{u_f}, \sigma_f A_f = \bar{t}_f(\theta) \text{ on } \Gamma_{t_f}, \end{aligned} \tag{31}$$

in which $\Gamma_{u_m}, \Gamma_{t_m}, \Gamma_{u_f}$ and Γ_{t_f} denote the boundary points where the corresponding boundary conditions are applied. The essential boundary conditions $\bar{u}_{mf}$ and the natural boundary conditions $\bar{t}_{mf}$ are prescribed as functions of the intrinsic time variable θ which is used to control the loading history. Denoting the integration of the product of two functions u, v over the domain $\Omega := [-L, 0]$ as $(u,v)_\Omega$, the weak formulation can be expressed as

$$\begin{aligned} &\left(\tilde{u}_m, A_m\sigma_{m,x} + p\tau\right)_\Omega + \left(\tilde{u}_f, A_f\sigma_{f,x} - p\tau\right)_\Omega \\ &\quad - \left(\tilde{u}_m, A_m\sigma_m - \bar{t}_m(\theta)\right)_{\Gamma_{t_m}} - \left(\tilde{u}_f, A_f\sigma_f - \bar{t}_f(\theta)\right)_{\Gamma_{t_f}} \\ &\quad + \left(\tilde{u}_m, u_m - \bar{u}_m(\theta)\right)_{\Gamma_{u_m}} + \left(\tilde{u}_f, u_f - \bar{u}_f(\theta)\right)_{\Gamma_{u_f}} = 0. \end{aligned} \tag{32}$$

Here $\tilde{u}_m$ and $\tilde{u}_f$ denote the test functions that are assumed to have continuous first derivatives, are L^2 integrable and implicitly fulfill the essential boundary

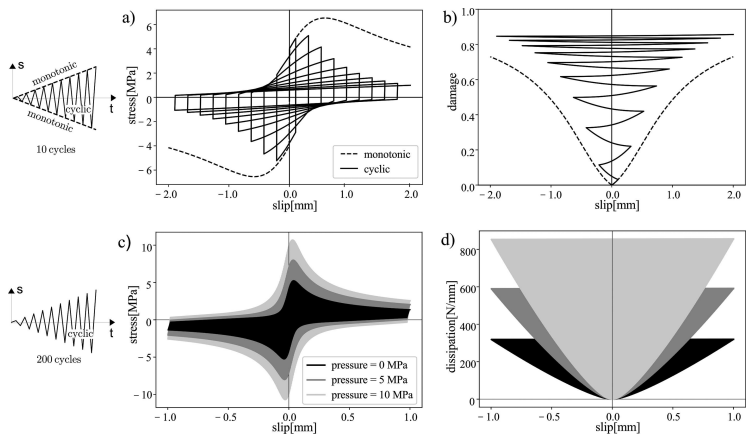

Figure 2. Cyclic bond behavior of the model: a) bond slip response for monotonic envelope and cyclic loading; b) damage evolution; c) cyclic bond slip response under different levels of lateral pressure; d) dissipation under cyclic loading of different levels of lateral pressure.

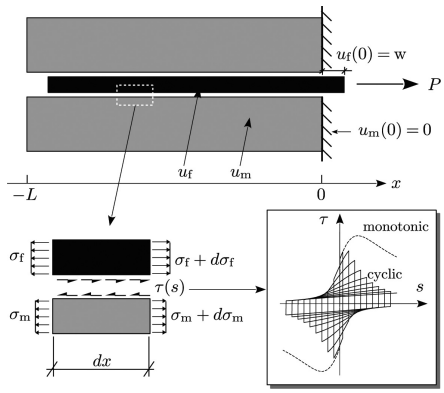

Figure 3. Mechanical model of the pullout problem.

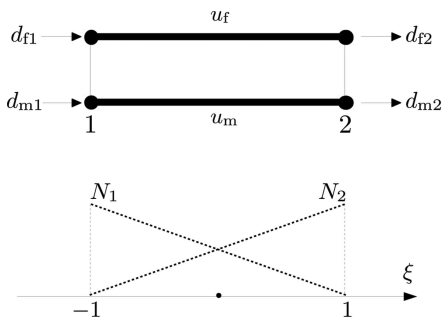

Figure 4. Linear 1D finite element with two displacement fields.

conditions. (see e.g. (Zienkiewicz et al. 2005)). Since $\tilde{u}_m = 0$ on Γ_{u_m} and $\tilde{u}_f = 0$ on Γ_{u_f}, the last two terms in equation (32) vanish. Using integration by parts, the order of the stress derivatives $\sigma_{m,x}$ and $\sigma_{f,x}$ in the above integration can be reduced as follows

$$\left(\tilde{u}_{(.)}, A_{(.)}\sigma_{(.),x}\right)_\Omega = \left(\tilde{u}_{(.)}, A_{(.)}\sigma_{(.)}\right)_\Gamma - \left(\tilde{u}_{(.),x}, A_{(.)}\sigma_{(.)}\right)_\Omega. \quad (33)$$

Then, by substituting equation (33) for both matrix and reinforcement into (32), the following variational formulation of the pullout problem is obtained

$$\left(\tilde{u}_{m,x}, A_m\sigma_m\right)_\Omega + \left(\tilde{u}_f - \delta u_m, p\tau\right)_\Omega + \left(\tilde{u}_{f,x}, A_f\sigma_f\right)_\Omega - \left(\tilde{u}_m, \bar{t}_m(\theta)\right)_{\Gamma_{tm}} - \left(\tilde{u}_f, \bar{t}_f(\theta)\right)_{\Gamma_{tf}} = 0. \quad (34)$$

The resulting functional is prepared for discretization using the finite element method. By choosing linear shape functions to approximate the displacement fields u_m and u_f (see Fig. 4) and the test functions $\tilde{u}_m$ and $\tilde{u}_f$ we obtain the known finite element models of a pullout problem, e.g. (Goodman et al. 1968, Herrmann 1978, Grande and Imbimbo 2016). Details of the generic implementation using high-level open-source libraries for scientific computing are provided in (Li et al. 2017) based on an index notation and the Einstein summation convention to obtain a compact form of the system equations that can be directly translated to a highly efficient, executable code.

5 MODEL CALIBRATION

The model parameters for a common combination of steel reinforcement with bar diameter of $d_s = 14$ mm and concrete matrix C25/30 have been identified using the test program performed by (Rehm and Eligehausen 1979). The setup of the pullout test is depicted in Fig. 5a. The bond length was set to $3d_s$ and the displacement was measured at the unloaded end. The test results show a pullout failure under fatigue loading.

The bond model parameters are summarized in Table 1. The bond stiffness E_b has been set equal to the shear stiffness of concrete. The parameters $\bar{\tau}, K, \gamma, S, r$ and c have been identified using the momotonic pullout reponse shown in Fig. 5b as dashed line and the experimentally determined Wöhler curve depicted in Fig. 5d. The Wöhler curve represents the fatigue life for different levels of the normalized loading level $S = F_{max} / F_u$, where F_{max} and F_u denote the upper load level in the fatigue test and the ultimate load level in the monotonic test, respectively (see Fig. 5b). For all tests, a constant mininum load level $F_{min} = 0.1F_u$ has been set.

The fatigue creep curves, i.e. the slip versus fatigue life, corresponding to the individual loading levels included in the test program are compared with the numerically obtained curves in Fig. 5c. Apparently, the model shows the ability to reproduce both the monotonic and cyclic behavior of the bond with a single set of material parameters. Also, the endurance limit for low load levels with no fatigue failure could be reproduced.

In Fig. 5e the damage evolution at the loaded and unloaded ends is plotted for both monotonic and cyclic loadings. The results reveal the nonlinear accumulation of damage during fatigue life. To illustrate the ability of the model to reproduce the typical shape of the fatigue creep curve, the pullout slip at the loaded end calculated for the load level $S = 0.8$ is plotted in Fig. 5f. The shape of the curve reveals three stages of fatigue development: rapid growth in the first and last stages, and stabilized, quasi-linear growth in the middle stage. This agrees well with the shape of the fatigue creep curves observed experimentally for comparable material combinations reported in (Lindorf et al. 2009) and (G. L. Balazs 1998).

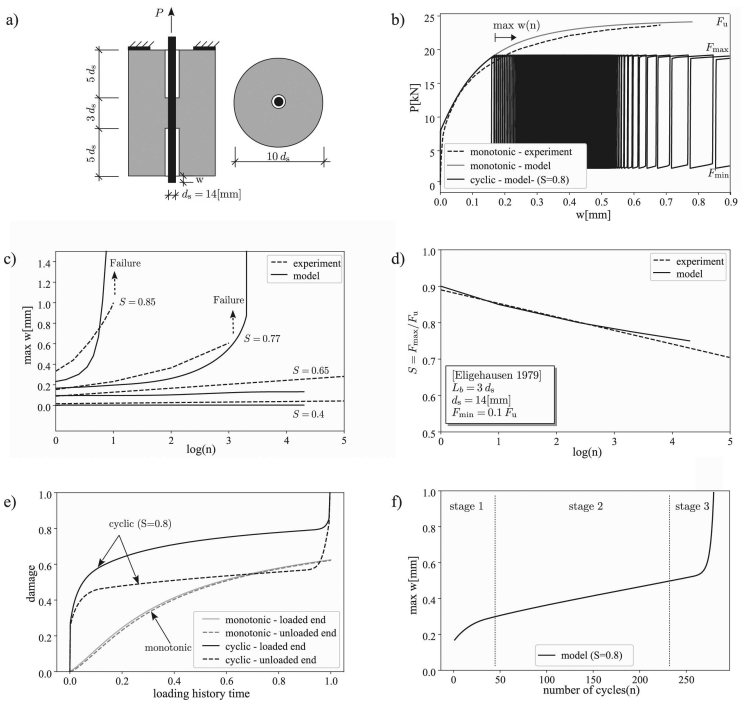

Figure 5. Model calibration with (Rehm and R. Eligehausen 1979) test program: a) test setup; b) displacement vs. pull-out force curve for monotonic and cyclic loading; c) fatigue creep curve for different load levels; d)Wöhler curve; e) damage evolution at the loaded and unloaded ends of the pullout simulation; f) fatigue creep curve for the load level (S = 0.8).

Table 1. Model parameters.

E_b	Elastic bond modulus	12900	[MPa]
$\overline{\tau}$	Reversibility limit	4.2	[MPa]
K	Isotropic hardening modulus	11.0	[MPa]
γ	Kinematic hardening modulus	55.0	[MPa]
S	Damage strength	4.8×10^{-4}	[MPa]
r	Damage accumulation parameter	0.51	[–]
c	Damage accumulation parameter	2.8	[–]
a	Pressure sensitivity	0.2	[–]

6 MODEL VALIDATION

To validate the described modeling approach, we need to check the ability of the model to predict the fatigue behavior for changed bond length. Because, the test series used for calibration only considered one value of bond length, the model validation can only be performed using experimental data from other sources. Obviously, this is far from ideal as the tests conducted by other authors are not perfectly comparable. However, a consistent set of tests with varied bond length has not been available at the time of writing this paper.

The tests performed by (G. L. Balazs 1998) were conducted with the bond length of $5d_s$ and reinforcement diameter $d_s = 16$ mm. The test results are plotted in form of data points representing the fatigue life up to the bond failure in Fig. 6a. The numberically predicted Wöhler curve is plotted as the solid line.

Another comparison has been performed for fatigue experiments presented by (Basquin 1910) with the bond length set to $10d_s$. The Wöhler curve presented in this paper has not been defined as the bond failure, but by a criterion that the slip growth Δs with respect to the slip s_0 at the first cycle gets larger than by 0.1 mm. The comparison with the predicted fatigue life curve is provided in Fig. 6b.

7 NUMERICAL STUDIES

7.1 *Effect of the lateral pressure/tension*

RC members are frequently subjected to biaxial load under cyclic loading, e.g. non-prestressed bridge decks. The tensile stresses in the longitudinal direction lead to crack development along the transverse reinforcement which influence the bond behavior along the reinforcement. For that reason the bond fatigue behavior under transverse tension represents a highly relevant issue in structural

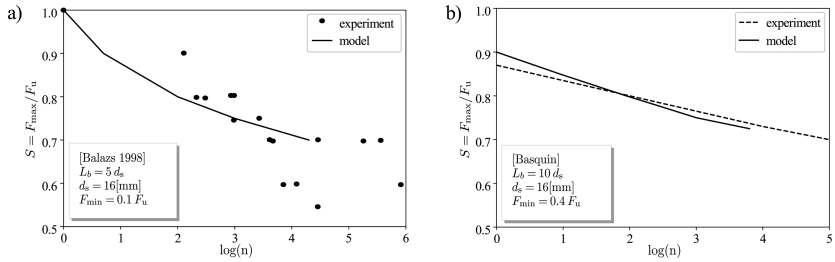

Figure 6. Model validation in terms of Wöhler curves: a) [Balazs] test; b) [Basquin] test.

assessment (Lindorf et al. 2009). Therefore, the effect of lateral confinement on the pullout fatigue has been also studied using the present model. The load levels were the same as in the case without confinement.

The Wöhler curves obtained for three levels of lateral action, i.e. pressure, neutral, tension, are plotted in Fig. 7a. In Fig. 7b the corresponding fatigue creep curves for the load level S = 0.75 are shown. The obtained results reproduce plausible trends in the fatigue life response, e.g. the lifetime reduction for transverse tension experimentally documented by (Lindorf et al. 2009).

7.2 *Effect of variable loading range*

Another parametric study demonstrating the feasibility of the modeling approach addresses the effect of variable fatigue loading. The most familiar and simplest method used to predict the fatigue life for variable amplitudes is the linear damage accumulation hypothesis according to (Palmgren 1924, Miner et al. 1945). In this hypothesis, the sequence of the loading levels has no relevance and the damage accumulation is assumed to be linear. This contradicts with the experimental results reported by (Holmen 1982) and shows limited validity as discussed e.g. by (Roggendorf and Goralski 2014).

By capturing the fundamental dissipative effects driving the fatigue damage evolution the model should be able to account for the effect of the loading sequence and variable amplitudes in a more realistic way. In Fig. 8a numerical study of the pullout behavior under two loading scenarios is presented. In particular, the fatigue response is compared for high-low (H-L) and low-high (L-H) loading scenarios with H corresponding to $S = 0.75$ and L to $S = 0.7$ load levels. The lower bound of the load was kept constant $F_{min} = 0.1F_u$ all the time. The number of loading cycles applied for the first loading level in both cases (H-L and L-H) was $N_1 < N_1^f$, where N_1^f represents the fatigue life of the first loading level under constant amplitude. Then the second loading level has been applied until failure N_f. The number of cycles for the second loading level was then recorded as $N_2 = N_f - N_1$. Examples of the calculated pullout force vs. displacement curves for two loading scenarios is presented in Fig. 8e and Fig. 8f.

Fatigue creep curves obtained for the studied six loading scenarios are depicted in Figs. 8cd. Uniform loading scenarios, showing early failure for (H) and late failure for (L) loadings. These curves represent the upper and lower bounds for all possible creep curves with combined loading levels (H) and (L). Considering the (H-L) loading sequence with 60% and 80% of consumed lifetime N_1^f at the first, higher level of cyclic loading (H), we obtain the two creep curves shown in Fig. 8c denoted as load scenarios (1) and (2). Apparently, during the second phase of loading with the load level (L) the slip first remains constant and the fatigue creep curve travels towards the lower bound (L) but the slip starts to increase well before reaching the bound, intiating an earlier the pullout failure. This means, that the initial phase of loading has been remembered within the state representation of the bond.

For the inverse loading sequence (L-H) 10% and 20% of lifetime has been consumed at the first loading level (L). The fatigue creep curves shown in Fig. 8d as scenarios (3) and (4) reveal a sudden jump of slip from the lower bound curve (L) upon the switch to the higher load level (H). During further cycling, the curve stays slightly belows the upper bound and follows its shape until failure.

The comparison of the detailed study with the P-M model is summarized for all four scenarios in Fig. 8b. While the (H-L) loading sequence shows more conservative prediction of (P-M) rule in comparison to the calculated results, the (L-H) loading sequence shows that the (P-M) rule leads to strongly unsafe prediction. In particular, the scenario (4) with $0.2N_1^f$ number of cycles applied for the (L) level failed after $\approx 0.23N_2^f$ number of cycles with (H) loading level whereas the linear (P-M) rule would give the prediction for failure in $= 0.8N_2^f$ number of cycles.

This result stresses the importance of more realistic treatment of loading sequence and variable amplitudes in the fatigue assessment of structures which is far from the proportionality assumption

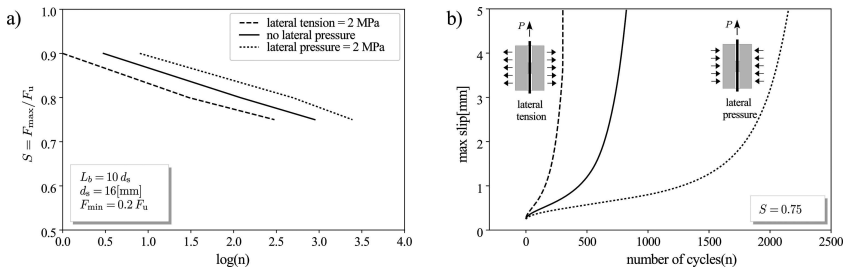

Figure 7. The effect of the lateral pressure/tension on the bond fatigue behavior: a) Wöhler curves; b) slip increase during fatigue life for loading level S = 0.75.

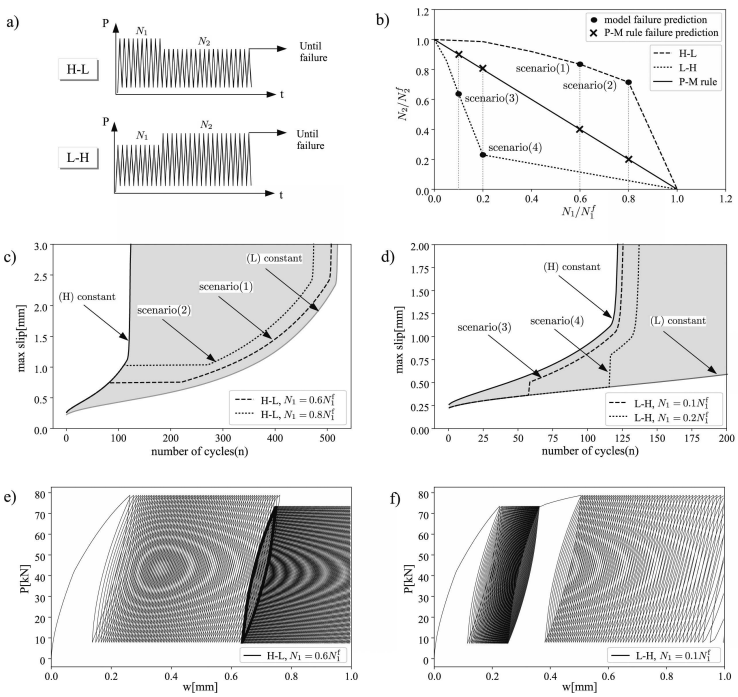

Figure 8. Study of the bond fatigue under different loading sequences and variable amplitudes: a) loading scenarios; b) the sensitivity of the model to the loading sequence effect of the fatigue life in comparison with Palmgren-Miner rule; c,d) fatigue creep curves for the (H-L) loading scenario; d) fatigue creep curves for the (L-H) loading scenario; e) pullout load v.s displacement curve for the (H-L) loading scenario; f) pullout load v.s displacement curve for the (L-H) loading scenario.

postulated by the (P-M) rule and applied in the engineering practice. By ignoring this effect, the safety factors may be set uneconomically large or dangerously low (Kirane and Bažant 2015).

8 CONCLUSIONS

The proposed model gives a realistic prediction of bond fatigue behavior up to several thousands of load cycles for different experimental results published in the literature. The model shows the ability to simulate both monotonic and cyclic behavior of the bond between reinforcement and concrete using a consistent set of material parameters.

The studies testing the ability of the model to include the effect of lateral pressure/tension and the effect of loading sequence provide promising results demonstrating the potential of the proposed damage accumulation hypothesis for realistic prediction of the fatigue behavior of RC structural members.

ACKNOWLEDGEMENTS

The work was supported by the Bundesministerium für Bildung und Forschung and the Deutscher Ausschuss für Stahlbeton, project number F-2013-021. This support is gratefully acknowledged.

REFERENCES

Alliche, A. (2004). Damage model for fatigue loading of concrete. *International Journal of Fatigue 26*(9), 915–921.

Ayoub, A. & F.C. Filippou (1999). Mixed formulation of bondslip problems under cyclic loads. *Journal of Structural Engineering 125*(6), 661–671.

Basquin, O. (1910). The exponential law of endurance tests. In *Proc Astm,* Volume 10, pp. 625–630.

Carrara, P. & L. De Lorenzis (2015, December). A coupled damage-plasticity model for the cyclic behavior of shearloaded interfaces. *Journal of the Mechanics and Physics of Solids 85,* 33–53.

Chaboche, J. & P. Lesne (1988). A non-linear continuous fatigue damage model. *Fatigue & fracture of engineering materials & structures 11*(1), 1–17.

Desmorat, R., F. Ragueneau, & H. Pham (2007, February). Continuum damage mechanics for hysteresis and fatigue of quasi-brittle materials and structures. *International Journal for Numerical and Analytical Methods in Geomechanics 31*(2), 307–329.

Eligehausen, R., E.P. Popov, & V.V. Bertero (1982). Local bond stress-slip relationships of deformed bars under generalized excitations.

G.L. Balazs (1998, October). Bond under Repeated Loading. *Special Publication 180.*

Goodman, R.E., R.L. Taylor, & T.L. Brekke (1968). A model for the mechanics of jointed rock. *Journal of Soil Mechanics & Foundations Div.*

Grande, E. & M. Imbimbo (2016). A simple 1d-finite element approach for the study of the bond behavior of masonry elements strengthened by frp. *Composites Part B: Engineering 91,* 548–558.

Harper, P.W. & S.R. Hallett (2010). A fatigue degradation law for cohesive interface elements–development and application to composite materials. *International Journal of Fatigue 32*(11), 1774–1787.

Herrmann, L.R. (1978). Finite element analysis of contact problems. *Journal of the Engineering Mechanics Division 104*(5), 1043–1057.

Holmen, J.O. (1982). Fatigue of concrete by constant and variable amplitude loading. *Special Publication 75,* 71–110.

Kindrachuk, V.M., M. Thiele, & J.F. Unger (2015). Constitutive modeling of creep-fatigue interaction for normal strength concrete under compression. *International Journal of Fatigue 78,* 81–94.

Kirane, K. & Z.P. Bažant (2015). Microplane damage model for fatigue of quasibrittle materials: Sub-critical crack growth, lifetime and residual strength. *International Journal of Fatigue 70,* 93–105.

Kwak, H.-G. & J.-K. Kim (2006). Implementation of bond-slip effect in analyses of rc frames under cyclic loads using layered section method. *Engineering structures 28*(12), 1715–1727.

Li, Y., J. Bielak, J. Hegger, & R. Chudoba (2017). An incremental inverse analysis procedure for identification of bondslip laws in composites applied to textile reinforced concrete. *Composites Part B: Engineering,–.*

Lindorf, A., L. Lemnitzer, & M. Curbach (2009). Experimental investigations on bond behaviour of reinforced concrete under transverse tension and repeated loading. *Engineering Structures 31*(7), 1469–1476.

Mai, S.H., F. Le-Corre, G. Forêt, & B. Nedjar (2012). A continuum damage modeling of quasi-static fatigue strength of plain concrete. *International Journal of Fatigue 37,* 79–85.

Marigo, J. (1985). Modelling of brittle and fatigue damage for elastic material by growth of microvoids. *Engineering Fracture Mechanics 21*(4), 861–874.

Miner, M. et al. (1945). Cumulative fatigue damage. *Journal of applied mechanics 12*(3), A159–A164.

Palmgren, A. (1924). Die lebensdauer von kugellagern (durability of ball bearings). *ZDVD 68,* 339.

Pfanner, D. (2003). Zur degradation von stahlbetonbauteilen unter ermüdungsbeanspruchung. konstruktiven ingenieurbau. ruhr-universität bochum.

Pfister, T., Y. Petryna, & F. Stangenberg (2006). Damage modelling of reinforced concrete under multi-axial fatigue loading. *Computational modelling of concrete structures. Balkema, Mayrhofen,* 421–429.

Ragueneau, F., N. Dominguez, & A. Ibrahimbegovic (2006, November). Thermodynamic-based interface model for cohesive brittle materials: Application to bond slip in RC structures. *Computer Methods in Applied Mechanics and Engineering 195*(52), 7249–7263.

Roe, K. & T. Siegmund (2003). An irreversible cohesive zone model for interface fatigue crack growth simulation. *Engineering fracture mechanics 70*(2), 209–232.

Roggendorf, T. & C. Goralski (2014). Ermüdungsverhalten von beton unter zyklischer beanspruchung aus dem betrieb von windenergieanlagen. *Beton- und Stahlbetonbau 109*(11), 824–828.

Rteil, A., K. Soudki, & T. Topper (2011). Mechanics of bond under repeated loading. *Construction and Building Materials 25*(6), 2822–2827.

Simo, J.C. & T.J. Hughes (2006). *Computational inelasticity,* Volume 7. Springer Science & Business Media.

Theil, N. (2016). Fatigue life prediction method for the practical engineering use taking in account the effect of the overload blocks. *International Journal of Fatigue 90,* 23–35.

Torre-Casanova, A., L. Jason, L. Davenne, & X. Pinelli (2013). Confinement effects on the steel–concrete bond strength and pull-out failure. *Engineering Fracture Mechanics 97,* 92–104.

Wu, J.Y., J. Li, & R. Faria (2006). An energy release rate-based plastic-damage model for concrete. *International Journal of Solids and Structures 43*(3), 583–612.

Zienkiewicz, O.C., R.L. Taylor, & J. Zhu (2005). *The finite element method for solid and structural mechanics,* pp. 69–71. Butterworth-heinemann.

Computational Modelling of Concrete Structures – Meschke, Pichler & Rots (Eds)
© 2018 Taylor & Francis Group, London, ISBN 978-1-138-74117-1

Fatigue life assessment of reinforced concrete members considering bond-slip

Sonali Bhowmik & Sonalisa Ray
Indian Institute of Technology Roorkee, Roorkee, India

ABSTRACT: In the present work, an analytical model has been developed to predict the crack propagation and fatigue life in reinforced concrete members under the action repetitive loading. The analytical model is developed from the fundamental principles using the theory of dimensional analysis in conjunction with the concept of selfsimilarity. The presence of reinforcement is taken into account by incorporating a pair of closing force in steel. Further, the effect of bond-slip phenomenon on crack propagation and fatigue life estimation has been considered and the variation in steel stresses at different level of slip has been incorporated in the analytical formulation. Various important material and loading parameters which influence the crack propagation behavior are considered in the present analytical formulation. The parameters are, critical energy dissipation, change in energy release rate, initial crack length, maximum size of the aggregate and the reinforcement ratio. The proposed model has been implemented for the prediction of fatigue life and crack growth behavior for the experimental data available in the literature.

1 INTRODUCTION

Conventional design methods for reinforced concrete members assumes zero tensile strength of concrete and ignores the stiffness variation and stress concentration due to the presence of crack. The internal stress distribution in reinforced concrete member varies considerably due to the existence of cracks and flaws. In fact, in concrete a large size process zone exists ahead of the crack tip and considerable amount of energy is consumed in overcoming this zone. Therefore, use of fracture mechanics in reinforced concrete member can provide a realistic solution for studying crack growth behavior. Reinforced concrete members being a heterogeneous material, the crack propagation behavior is controlled by concrete toughness and elasticity of steel. Generally, the effect of reinforcement in the concrete member is simulated by incorporating a pair of closing force exerted by steel. Under the action of repetitive loading, the crack grows in a progressive manner up to yielding and therefore the bridging action also changes continuously. A perfect bonding between the reinforcing bar and the surrounding concrete is considered in the fatigue analysis of reinforced concrete members. It is responsible for the transmission of stresses from the reinforcing bar to the surrounding concrete. A lacking in the perfect bonding between the reinforcing bar and the concrete matrix is a common phenomenon in and leads to the failure of the composite action of the concrete and reinforcing bar thereby, accelerating the slipping of bars. Further, this leads to the variation in the bridging action in the reinforcing bar and influencing the overall crack growth behavior and fatigue life. Therefore, such a behavior must be taking into consideration under the action of repetitive loading.

One of the most earliest study was done by Eligehausen et al. (Eligehausen et al. 1983) to investigate the stress-bond relationship of deformed bars under monotonic as well as cyclic loading. The results from their experimental studies have been further used to develop an analytical model and this model was able to predict the behavior of deformed bars for various loading and bond conditions. From the experimental study it has been concluded that, the degradation of bond stiffness and bond strength in case of cyclic loading depends upon the maximum value of peak slip along with other significant parameter like number of cycles. Manfredi and Pecce (Manfredi & Pecce 1998) have been developed an model for analysis of reinforced concrete beams which includes an straightforward formulation of bond-slip relationship. The model developed using the concept of matrix method allows to understand the distribution of slip, bond stress, stress and strain of the steel bar and the curvature along the beam. To know the applicability of the method a case study has been conducted together with the theoretical-experimental comparisons.

Lee and Watanabe (Lee and Watanabe 2003) have proposed a model which predicts axial strain in the plastic hinge region of reinforced concrete structure subjected to reversed cyclic loading of different patterns. The model consists of four path type whichincludes, pre-flexural yielding or unloading region, post-flexural yielding region, slip region and repeated loading region. Twelve beams have been tested under reversed cyclic loading to verify the developed model and found in good agreement with those calculated longitudinal axial strains values. Oh et al. (Oh and Kim 2007) have proposed a realistic model considering the bond-stress behavior under repetitive loading by conducting a series of experiments. The model has been derived for slip and residual slip as a function of bond stress-slip relationship and the number of load cycles. An increment of slip and residual slip values has been observed with the increase of repetitive load cycles. A formulation based on safe fatigue criterion has been established and recommends that, bond failure occurs for slip at ultimate bond stress. Hong and Park (Hong and Park 2012) developed an analytical model based on the principles of stress-slip theories and the characteristics of deformed bar together with concrete cross-sectional area. This model has been developed specially for reinforced concrete member subjected to axial tension loadings in order to estimate bond stress-slip relationship effectively. The proposed model has been validated by using the experimental data available in literature the JSCE design codes. Fernandes et al. (Fernandes et al. 2013) has developed a numerical model for beam-column joint specimen with plain bars under cyclic response by including the effect of slippage. They have used seismoStruct software to perform the numerical analyses. Firstly, the analysis was carried out without considering the effects of bar slippage. Secondly effect of bondslip was considered in the analysis of the joint specimen with plain bars. Lee et al. (Lee et al. 2015) has proposed a method for assessment of the structural behavior of reinforced concrete members under reverse cyclic loading. This method considers the bond deterioration after flexural yielding. The formulation of bond stress and bond force has been established using the fundamental concepts of bond failure in their proposed method and illustrated in equation 1 and 2. Further, the predicted results were validated using the experimental results available in literature.

$$\tau_f = \frac{A_b\left(1.7 f_y\right)}{\left(l - 2lp\right)p} \tag{1}$$

$$V_f = \tau_f p j_d \tag{2}$$

where, τ_f and V_f are bond stress and bond force. p is the perimeter of steel section. A_b is the cross-sectional area of the steel bar. lp and jd are the plastic hinge length and lever arm respectively. Isojeh et al (Isojeh et al. 2017) were conducted Experimental investigations to study the fatigue behaviour of reinforced concrete deep beams. From their research, it has been found that, the rate of deformation increases as the stress range is increased. The beams having increased longitudinal reinforcement ratios shows higher fatigue life, which is in agreement with the fatigue behaviour of reinforced concrete structures. The most oldest study of incorporating the effect of reinforcement was attempted by Carpinteri (Carpinteri 1985) as a pair of eccentric axial force estimated by the rotation congruence condition. In this study the dependency of mechanical and geometrical properties of reinforced members on fracturing process and plastic flow of reinforced concrete structures has been confirmed.

This model further improved by Bosco and Carpinteri (Bosco and Carpinteri 1992) by applying reinforcement forces directly to the crack surface. Further rigorous investigations has been carried out by Carpinteri (Carpinteri 1991, Carpinteri 1992) and (Carpinteri 1985) in order to address the shakedown phenomenon on reinforced concrete structures subjected to cyclic loadings. Similar type of study has been performed by Carpinteri et al (Carpinteri et al. 2004) to analyze the flexure behaviour of reinforced concrete beam with multiple reinforcements under cyclic loading. This fracture mechanics based analytical model considers the effect of crack bridging reactions from reinforcements. Sain and Chandra Kishen (Sain and Chandra Kishen 2008) have proposed a method to predict the unstable crack propagation in reinforced concrete beam subjected to cyclic loading. Effect of reinforcement has been considered as a closing force produced by the external moment. Instead of considering the assumption of steel yielding this method accounts the formation of FPZ at the crack tip. Ray and Chandra Kishen (Ray and Kishen 2014) developed a fatigue crack propagation law by using the concept of dimensional analysis for plain concrete members. Effect of reinforfement in terms of closing force has been considered in the model along with the crack growth characterizing parameters such as, fracture toughness, crack length, loading ratio and structural size. Many researchers have attempted to develop analytical models for the prediction of crack propagation under the action of fatigue loading

using the fundamental principles of dimensional analysis and the theory of intermediate asymptotics. One of the most earliest fatigue crack growth model using the above concept has been proposed by Barenblatt and Botvina (Barenblatt and Botvina 1980). On this line, various researchers (Carpinteri and Spagnoli 2004, Spagnoli 2005, Carpinteri and Paggi 2007) have derived the closed form expression of the mathematical model for the prediction of crack growth rate in metalic and quasibrittele materials. Ciavarella et al. (Ciavarella et al. 2008) have proposed a unified fatigue crack propagation law using the concepets of dimensional analysis. The correlation between the Paris law constants m and C for concrete like materials are found to be considerable different than metals. Further, Carpinteri and Paggi (Carpinteri and Paggi 2009) have applied dimensional analysis approach and concepts of complete and incomplete self-similarity to the Paris curve and Wohler curve on the similar line of study proposed by Barenblatt and Botvina (Barenblatt and Botvina 1980) on dimensional analysis. The incomplete self-similarity used in dimensionless variable gives a unified description of fatigue. Paggi (Paggi 2011) has developed a fatigue crack growth model to depict a clear picture of classical power law equations which are being used to predict fatigue behaviour of quasi-brittle materials like concrete. Theoretically, it has been shown that parameters used in Paris law are dependent of micro-structural size, crack-sizeand size-scale. Ray and Chandra Kishen (Ray and Chandra Kishen 2011) have developed an dimensionally homogeneous analytical model to predict fatigue crack propagation in plain concrete. This model incorporates different parameters, such as, the tensile strength, fracture energy, loading ratio, initial crack length and structural size. Further, this model has been improved in order to predict fatigue crack propagation of plain concrete under the action of variable amplitude loading (Ray and Chandra Kishen 2012). Le and Bazant (Le and Bazant 2011) in their study, attempted to explain the physical mechanisms in the Paris law developed for fatigue crack growth by considering damage accumulation in the cyclic FPZ at the tip of the crack. Based on this theory, it has been concluded that S-N curve must be size dependent for quasi-brittle structure. Further, a modified form of Paris-Erdogan model for the estimation of crack growth rate under the action of fatigue loading for rocks has been proposed by Le et al. (Le et al. 2014). Through experimental and theoretical investigations, the authors have concluded that observed size effect can be explained by incorporating critical energy dissipation for fatigue crack growth. According to the authors, a larger size fractue processzone is observed in the case of fatigue loading than the monotonic loading. The model proposed by Le et al. (Le et al. 2014) has been modified by Kirane and Bazant (Kirane and Bazant 2016) for quasi-brittle materials using dimensional analysis approach. Based on the evidences of experimental and numerical study, on contrary to the studies by Bazant and Xu (Bazant and Xu 1991) and Le et al. (Le et al. 2014 the authors have observed a smaller size fracture process zone under cyclic loading than the monotonic one.

2 DIMENSIONAL ANALYSIS APPROACH AND SELF-SIMILARITY

The theory of dimensional analysis and intermediate asymptotic can be used for the development of mathematical formulation in a given physical problem. Firstly, Dimensional analysis considers various variables that governs the physical phenomenon under consideration and converts them into dimensionless numbers having total physical dimension equal to unity. Use of dimensionless numbers is advantageous as it reduces the number of variables which are needed to define a physical problem and provides physical meaning of the parameters which leads to a better understanding of the phenomenon if formed correctly. Moreover, the use of dimensionless number can reduce the quantity of experimental data required. Secondly, the application of theory of self-similarity to this dimensionless numbers can eliminate either too small or large terms. However, depending on the physical problem considered, different self-similar solutions can be derived.

3 ANALYTICAL FORMULATION

In this section the model developed by (Bhowmik & Ray 2016) have been used and further improved by incorporating the effect of bond-slip and closing force due to reinforcement. The closed form of expression for the crack growth rate represented as (da/dN) under the action of fatigue loading is derived using the theory of dimensional analysis in conjunction with the theory of intermediate asymptotic as described by (Bhowmik & Ray 2016).

The governing variables which affect the fatigue crack propagation are listed with their physical dimensions in Table 1. The final mathematical formulation for crack growth rate can be expressed in terms of the governing variables as below.

$$\frac{da}{dN} = \left(\frac{U_C}{\sigma_t}\right)\left(\frac{\Delta G_I}{U_C}\right)^{\gamma_1}\left(\frac{G_{Imax}}{U_C}\right)^{\gamma_2}\left(a\frac{\sigma_t}{G}{}_C\right)^{\gamma_3} \quad \Phi(\Pi_4) \tag{3}$$

Where, coefficients γ_1, γ_2 and γ_3 and the function Φ was obtained as 0.064, 1.316, 1.303 and 0.65 respectively using experimental results. The simplified from of the proposed fatigue crack propagation model in Equation 3 is given below.

$$\frac{da}{dN} = U_C^{1-\gamma_1-\gamma_2-\gamma_3}\Delta G_I^{\gamma_1} G_{Imax}^{\gamma_2}\sigma_t^{\gamma_3-1}a^{\gamma_3}\Phi_2\left(\Pi_4\right) \tag{4}$$

Comparing the proposed model described in Equation 4 with the well known Paris law and using the linear elastic fracture mechanics relation $\Delta G_I = \frac{(\Delta K_I)^2}{E}$ and $G_{Imax} = \frac{\Delta G_I}{1-R}$, The Paris law constants can be written as:

$$m = 2(\gamma_1 + \gamma_2)$$
$$C = U_C^{1-\gamma_1-\gamma_2-\gamma_3}\Delta K_I{}^{2(\gamma_1+\gamma_2)}E^{-\gamma_1-\gamma_2}(1-R)^{-\gamma_2}\sigma_t^{\gamma_3-1}a^{\gamma_3}\Phi_2$$

Where, E is the modulus of elasticity, R is the loading ratio and ΔK_I is the stress intensity factor range.

As mentioned earlier the effect of reinforcement is considered in this work by incorporating a pair of closing force as proposed by Carpinteri (Carpinteri 1992). The proposed crack propagation model for plain concrete is further improved by considering the effect of bond-slip when subjected to fatigue type of loading. The unknown steel force has been calculated by considering a beam cross section subjected to bending moment M and axial closing force F transmitted by the reinforcement as shown in Figure 1 (Ray and Kishen 2014). Applying the congruence condition as shown in Equation 5, the axial closing force was obtained by using the equation 6.

$$\varphi = \lambda_{MM}\left[M - F\left(\tfrac{h}{2} - c\right)\right] + \lambda_{MM}\left|-F\right| = 0 \tag{5}$$

$$\frac{Fd}{M} = \frac{1}{\left(\frac{1}{2} - \frac{c}{h}\right) + r(\xi)} \tag{6}$$

with, $r(\xi) = \frac{\int_0^{\xi} Y_M(\xi)Y_F(\xi)d\xi}{\int_0^{\xi} Y_M^2(\xi)d\xi}$

where, ξ is relative crack depth, Y_M and Y_F are geometric functions as illustrated in Equations 7 and 8.

$$Y_M(\xi) = 6(1.99\xi^{1/2} - 2.47\xi^{3/2} + 12.97\xi^{5/2} - 23.17\xi^{7/2} + 24.80\xi^{9/2}) \tag{7}$$

$$Y_M(\xi) = 1.99\xi^{1/2} - 0.41\xi^{3/2} + 18.70\xi^{5/2} - 38.48\xi^{7/2} + 53.85\xi^{9/2} \tag{8}$$

Now using the obtained unknown steel force, stress intensity factor can be calculated by using Equations 9 and 10.

$$K_I = \frac{M^*}{h^{3/2}b}Y_M(\xi) + \frac{F^*}{h^{1/2}b}Y_F(\xi) \tag{9}$$

For $M < M_p$

$$K_I = \frac{M}{h^{3/2}b}Y_M(\xi) - \frac{F_p}{h^{1/2}b}Y_F(\xi) \tag{10}$$

For $M > M_p$

Here, M_p is the moment at which reinforcement yields and expression for M* and F* can be expressed as

$$M^* = M - F\left(\tfrac{h}{2} - c\right) \quad and \quad F^* = -F$$

The quantity ΔG_I was computed using the Equations 9 and 10 in conjunction with the bond force. The Equations 1 and 2 was used to obtain the bond force.

Table 1. Governing parameters with their dimensions.

ΔG_I	Change in energy release rate	FL^{-1}
G_{Imax}	Maximum value of energy release rate	FL^{-1}
D	Structural size	L
d_{max}	Size of the aggregate	L
σ_t	Tensile strength	FL^{-2}
U_C	Fatigue fracture energy	FL^{-1}
a	Crack length	L

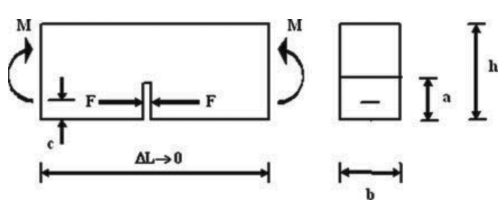

Figure 1. RC beam under bending moment.

4 EFFECT OF CLOSING FORCE AND BOND SLIP IN FATIGUE CRACK PROPAGATION

In this current work, fatigue crack propagation law has been developed considering the effect of reinforcement (Carpinteri 1992) in combination

with the bondslip (Lee et al. 2015). The experimental data of Baluch et al. (Baluch et al. 1990) and Isojeh et al. (Isojeh et al. 2017) has been used to compute fatigue crack propagation rate as well as fatigue life for various load ranges. Baluch et al. (Baluch et al. 1990) had tested a series of beams subjected to three point bend test with different percentage of steel to study the frecture process. The beam specimens are considered to be lighly reinforced with a span of 1400 *mm*. The fatigue test data of three beams of Isojeh et al. (Isojeh et al. 2017) has been used in this work to study the crack growth rate bahaviour. The parameter U_c has estimated using the empirical Equation 11as per CEB Model code 90.

$$U_c = \gamma f_c'^{0.7} \tag{11}$$

where, f_c' is the compressive strength and γ is a coefficient depends upon the maximum size of the aggregate d_{max} and can be expressed as $\gamma = 2.828e^{0.0454 d_{max}}$. The stress intensity factor range due to bond-slip has been calculated using the method of carpinteri (Carpinteri 1992) and Lee et al. (Lee, Kim, Kim, & Choi 2015). The total SIF was obtained by combining the SIF due to bond-slip and the SIF due to application of both moment and axial force acting on the beam. ΔG_I was computed using this combined stress intensity factor range and used in the proposed model. The material properties and geometry of beams are given in Table 2 illustrates the results generated by the proposed model using the experimental data of Isojeh et al. (Isojeh et al. 2017). The case of both perfect bonding and consideration of slip behavior between the reinforcement bars and surrounding matrix have analyzed for varying reinforcement ratios (ρ).

In Figure 2 the stress intensity factor range is plotted with fatigue crack growth rate to study the behaviour of crack growth rate when bond-slip is taken into consideration. Figure 3 and 4 shows the plot of ΔP versus the number of cycles as obtained by the developed model together with Paris law. Similarly in Figure 5, ΔP versus the number of cycles has plotted with considering bond-slip and perfect bonding for the results generated by the proposed model. An improvement in results are indicated in these plots which reflects the feasibility of incorporation of bond-slip phenomenon in the proposed model.

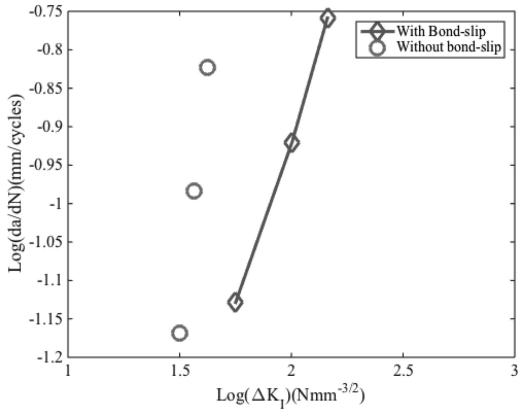

Figure 2. Variation of crack growth rate (*da/dN*) as a fucntion of stress intensity factor range (ΔK_I) (Baluch et al. 1990).

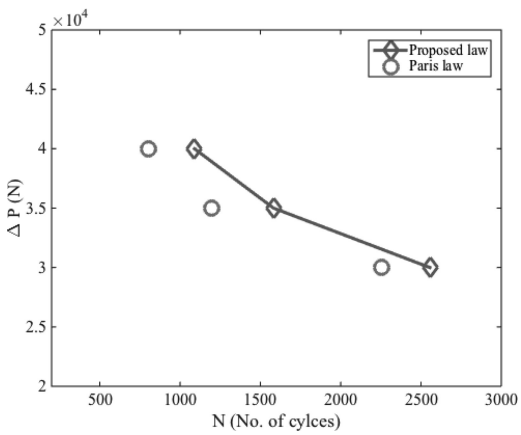

Figure 3. Computed fatigue life using proposed model and Paris law for different applied load ranges with considering bond-slip (Baluch et al. 1990).

Table 2. Material properties and geometry of the specimen.

Specimen	Depth *D (mm)*	Span *S mm*	Thickness *B (mm)*	Notch size *a (mm)*	U_c *(N/mm)*	*E (MPa)*	σ_t *(MPa)*
Beam1 (Baluch et al. 1990)	380	1400	102	38	43.82	2062.207	3.36
Beam2 (Isojeh et al. 2017)	250	700	175	25	68.8528	33446.150	4.45

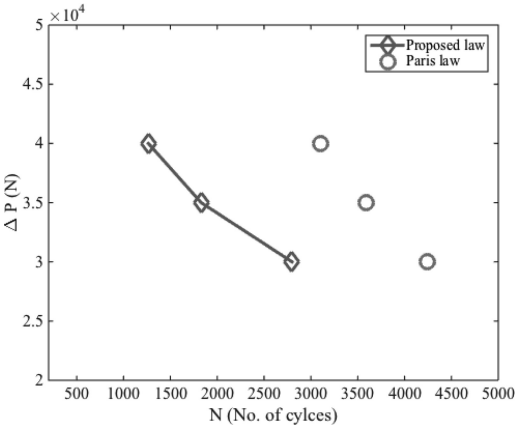

Figure 4. Computed fatigue life using proposed model and Paris law for different applied load ranges considering perfect bonding (Baluch et al. 1990).

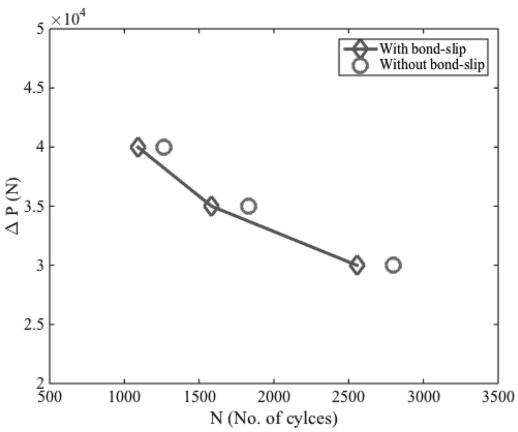

Figure 5. Computed fatigue life using proposed model with considering bond-slip and perfect bonding (Baluch et al. 1990).

Table 3. Comparison of results of Isojeh et al. with and without bond-slip.

		Number of cycles to failure (N_f)	
Beam	ρ (%)	With bond-slip	Without bond-slip
C80-20-0	0.45	186745	205591
C75-0-1	0.90	3051	132544
C75-0-2	1.40	661	132544

5 CONCLUSIONS

In this present work, an analytical model has been proposed to predict crack propagation in plain concrete member under the action of repetitive loading. This model has been developed using the concept of dimensional analysis in conjunction with intermediate asymptotic and self-similarity. This model considers the influence of effect of reinforcement through closing force exerted by steel and bond slip, with other fatigue crack growth parameters such as the size dependent fracture energy, change in energy release rate, frequency, initial crack length, structural size, maximum size of the aggregate. Further this model has been used to predict the fatigue crack growth rate and fatigue life using the data available in literature. A strong influence of closing force and bond-slip on fatigue life has been captured and justified by the results produced by the proposed model.

REFERENCES

Baluch, M.H., A.K. Azad, & W. Ashmawi (1990). Fracture mechanics application to reinforced concrete members in flexure. *In: International workshop on the application of fracture mechanics to reinforced concrete*, 413–436.

Barenblatt, G.I. & L.R. Botvina (1980). Incomplete selfsimilarity of fatigue in the linear range of fatigue crack growth. *Fatigue and Fracture of Engineering Materials and Structures, 3*, 193–202.

Bazant, Z.P. & K. Xu (1991). Size Effect in Fatigue Fracture of Concrete. *ACI Materials Journal, 88*(4), 390–399.

Bhowmik, S. & S. Ray (2016). Effects of fracture process zone on fatigue crack growth in concrete. *In proceedings of 9th International Conference on Fracture Mechanics of Concrete and Concrete Structures.*

Bosco, C. & A. Carpinteri (1992). Fracture behavior of beam cracked across reinforcement. *Theoretical and Applied Fracture Mechanics 17*(1), 61–68.

Carpinteri, A. (1991). Energy dissipation in R.C. Beams under cyclic loadings. *Engineering Fracture Mechanics 39*(2), 177–184.

Carpinteri, A. & A. Paggi (2007). Self-similarity and Crack Growth Instability in the Correlation between the Paris Constants. *Engineering Fracture Mechanics, 74*, 1041–1053.

Carpinteri, A. & M. Paggi (2009). A unified interpretation of the power laws in fatigue and the analytical correlations between cyclic properties of engineering materials. *International Journal of Fatigue, 31*, 1524–1531.

Carpinteri, A. & A. Spagnoli (2004). A fractal analysis of size effect on fatigue crack growth. *International Journal of Fatigue, 26*(4), 125–133.

Carpinteri, A., A. Spagnoli, & S. Vantadori (2004). A fracture mechanics model for a composite beam with multiple reinforcements under cyclic bending. *International Journal of Solids and Structures 41*(20), 5499–5515.

Carpinteri, B.A. (1985). Hysteretic behaviour of RC beams. *Journal of Structural Engineering ASCE 110*(9), 2073–2084.

Carpinteri, B.A. (1992). Reinforced concrete beam behavior under cyclic loadings. *In: Applications of fracture mechanics to reinforced concrete*, 547–578.

Ciavarella, M., M. Paggi, & A. Carpinteri (2008). One, No One and One hundred thousand crack propagation laws: A generalized Barenblatt and Botvina dimensional analysis approach to fatigue crack growth. *Journal of the Mechanics and Physics of Solids, 56*, 3416–3432.

Eligehausen, R., E. Popov, & V. Bertero (1983). Local bond stress-slip relationship of deformed bars under general ized excitations. *Report no. UCB/EERC*, 83–23.

Fernandes, C., H. Varum, & A. Costa (2013). Importance of the bond-slip mechanism in the numerical simulation of the cyclic response of RC elements with plain reinforcing bars. *Engineering Structures 56*, 396–406.

Hong, S. & S.K. Park (2012). Uniaxial bond stress-slip relationship of reinforcing bars in concrete. *Advances in Materials Science and Engineering 2012*.

Isojeh, B., M. El-Zeghayar, & F.J. Vecchio (2017). Engineering structures high-cycle fatigue life prediction of reinforced concrete deep beams. *Engineering Structures 150*, 12–24.

Issa, M.A., M.S. Islam, & A. Chudnovsky (2000). Size effects in concrete fracturePart II: Analysis of test results. *International Journal of Fracture*, 25–42.

Keerthy, M.S. & J.M. Chandra Kishen (2016). Influence of aggregate bridging on the fatigue behaviour of concrete. *International Journal of Fatigue, 90*, 200–209.

Keerthy, M.S. & J.M. Chandra Kishen (2017). A multiscale approach for modeling fatigue crack growth in concrete. *International Journal of Fatigue, 98*, 1–13.

Kirane, K. & Z.P. Bazant (2016). Size effect in Paris law and fatigue lifetimes for quasibrittle materials: Modified theory, experiments and micro-modeling. *International Journal of Fatigue, 83*, 209–220.

Le, J.L. & Z.P. Bazant (2011). Unified nano-mechanics based probabilistic theory of quasibrittle and brittle structures: II. Fatigue crack growth, lifetime and scaling. *Journal of the Mechanics and Physics of Solids, 59*(7), 1322–1337.

Le, J.L., J. Manning, & J.F. Labuz (2014). Scaling of fatigue crack growth in rock. *International Journal of Rock Mechanics and Mining Sciences, 72*, 71–79.

Lee, J.-Y., K.H. Kim, S.W. Kim, & H. Choi (2015). Bond Strength Deterioration of Reinforced and Prestressed Concrete Members at Reversed Cyclic Loads. *Strength of Materials 47*(1), 177–185.

Lee, J.Y. & F. Watanabe (2003). Predicting the longitudinal axial strain in the plastic hinge regions of reinforced concrete beams subjected to reversed cyclic loading. *25*, 927–939.

Manfredi, G. & M. Pecce (1998). A refined R.C. beam element including bondslip relationship for the analysis of continuous beams. *Computers & Structures 69*(1), 53–62.

Nallathambi, P., B.L. Karihaloo, & B.S. Heaton (1984). Effect of specimen and crack sizes, water/cement ratio and coarse aggregate texture upon fracture toughness of concrete. *Magazine of Concrete Research, 36*, 227–236.

Oh, B.H. & S.H. Kim (2007). Advanced Crack Width Analysis of Reinforced Concrete Beams under Repeated Loads. *Journal of Structural Engineering 133*(3), 411–420.

Paggi, M. (2011). Modeling fatigue in quasi-brittle materials with incomplete self-similarity concept. *Materials and Structures, 44*, 659–670.

Ray, S. & J.M. Chandra Kishen (2011). Fatigue crack propagation model and size effect in concrete using dimensional analysis. *Mechanics of Materials. 43*(129), 75–86.

Ray, S. & J.M. Chandra Kishen (2012, feb). Fatigue crack growth due to overloads in plain concrete using scaling laws. *Sadhana, Indian Academic of Sciences 37*(1), 107–124.

Ray, S. & J.M.C. Kishen (2014). Analysis of fatigue crack growth in reinforced concrete beams. pp. 183–198.

Sain, T. & J.M. Chandra Kishen (2008). Probabilistic assessment of fatigue crack growth in concrete. *International Journal of Fatigue 30*(12), 2156–2164.

Spagnoli, A. (2005). Self-similarity and fractals in the Paris range of fatigue Crack growth. *Mechanics of Materials, 37*, 519–529.



Taylor & Francis
Taylor & Francis Group
http://taylorandfrancis.com

Computational Modelling of Concrete Structures – Meschke, Pichler & Rots (Eds)
© 2018 Taylor & Francis Group, London, ISBN 978-1-138-74117-1

Simulation of interface behavior between steel and concrete to study loss of bond due to reinforcement corrosion

B. Sanz & J. Planas
Departamento de Ciencia de Materiales, Universidad Politécnica de Madrid, Madrid, Spain

J.M. Sancho
Departamento de Estructuras de Edificación, Universidad Politécnica de Madrid, Madrid, Spain

ABSTRACT: Corrosion of steel in reinforced concrete structures leads to a decrease in the cross-sectional area of the reinforcement, cracking of the concrete cover, and loss of bond between the steel and the concrete. In order to calculate the remaining service life of affected structures it is essential to model those effects. Focusing on bond, previous studies in the literature have shown that the maximum bond stress increases for small corrosion levels but then decreases after a given critical amount of corrosion. However, different values for the maximum stress and critical corrosion are reported, due to the differences in the test conditions and the geometry of the specimens, which determine the resisting mechanisms contributing to bond. Moreover, research on the effect of corrosion on each resisting mechanism is needed. In this work loss of bond has been studied by means of numerical simulations. Adherence tests consisting in push-out of the reinforcement have been simulated. The specimens are concrete slices cut from prisms reinforced with a calibrated steel tube. Those were corroded in such a manner that uniform corrosion occurred along the tube length. From the test, the maximum bond stress and residual stress transmitted for a large displacement are determined. Tests were conducted also for slices of non-corroded specimens, in order to analyze the response of bare specimens. Simulations of the tests have been carried out within the finite element framework COFE (continuum oriented finite element). For the behavior of the interface between the steel and the concrete, joint elements have been programmed with a cohesive behavior and several softening laws. Three-dimensional models of the concrete slices have been used and the behavior of bare specimens has been examined. From the simulations, it has been assessed that uniform stress is transmitted between the steel and the concrete, demonstrating the ability of the tests to determine the stress during push-out of the tube. In addition, it has been disclosed that a cohesive frictional behavior between the steel and the concrete is adequate to reproduce the actual behavior of the specimens.

1 INTRODUCTION

Corrosion of steel in reinforced concrete structures involves generation of an oxide layer. It leads to a decrease in the cross-sectional area of the reinforcement, cracking of the concrete cover, and loss of bond between the steel and the concrete (Andrade, Alonso, & Molina 1993). In order to calculate the remaining life of affected structures it is essential to model those effects.

Regarding loss of bond, previous studies in the literature have shown that for specimens with a low degree of corrosion, maximum bond stress increases, due to an increase in the roughness of the steel surface and in the reactionary confinement of the bar in the concrete, while for high corrosion levels, bond stress decreases, due to development of a thick oxide layer, which has a lubricating effect, degradation of bar ribs, and formation of longitudinal cracks, which diminishes confinement (Al-Sulaimani, Kaleemullah, Basunbul, & Rasheeduzzafar 1990, Almusallam, Al-Gahtani, Aziz, & Rasheeduzzafar 1996). Moreover, degradation of stirrups might also influence bond strength, since they are the main mechanism of confinement after cracking of the cover (Hanjari, Coronelli, & Lundgren 2011, Juarez, Guevara, Fajardo, & Castro-Borges 2011). However, different values for the maximum stress and critical corrosion are reported. This is due to the differences in the test conditions and geometry of the specimens, which determine the resisting mechanisms contributing to bond. Thus, values obtained from a given test may not be adequate to reproduce the behavior for other conditions. Moreover, research on the effect of corrosion on each resisting mechanisms is necessary.

In order to investigate loss of bond between the steel and the concrete due to reinforcement corrosion, an experimental and numerical study has

been carried out. This paper focus on the numerical part of the study. Adherence tests consisting in push-out of the reinforcement were carried out and are simulated. The specimens are concrete slices, which are cut from concrete prisms reinforced with a smooth steel tube. With such a geometry, interlocking of bar deformations against the concrete is avoided, and bond stress is due only to adhesion and friction. Thus, the material behavior at the steel-concrete interface can be sought. For details in the experimental design, see (Sanz 2014). The prisms were corroded in such a manner that uniform corrosion is expected to occur along the tube length, using the experimental setup presented in (Sanz, Planas, & Sancho 2015). Tests were also carried out using slices of prisms not subjected to accelerated corrosion in order to analyze the response of bare specimens.

Simulations of the tests have been carried out within the finite element framework **COFE** *(Continuum Oriented Finite Element)*. This program implements elements with an embedded adaptable crack (Sancho, Planas, Cendón, Reyes, & Gálvez 2007, Sancho, Planas, Fathy, Gálvez, & Cendón 2007) which reproduce fracture of concrete according to the standard cohesive model (Hillerborg, Modéer, & Petersson 1976). However, in the simulations presented in the current paper elastic behavior was assumed for the concrete, since their results are compared to experimental results of uncracked specimens. For the interface behavior, joint elements were programmed with a cohesive behavior and several softening laws. The behavior of bare specimens was sought, using three dimensional models of the specimens. From the simulations, the maximum shear stress and residual stress after a large displacement of the tube were analyzed and compared to those obtained in the experiments. In addition, the map of stress at the steel-concrete interface was examined.

In the paper, Section 2 reviews the context of the current study and main aspects of the experiments, Section 3 presents the numerical model, the programmed elements and materials for interface behavior, and the characteristics of the simulations, Section 4 discusses the main results, and, finally, Section 5 presents the conclusions of this work.

2 CONTEXT OF THE STUDY

2.1 *Specimens and materials*

The specimens of push-out tests were concrete slices which were obtained from concrete prisms. The prisms had a cross-section as that indicated in Figure 1 and were 90 mm in height. They were reinforced with a calibrated steel tube compliant with the EN 10305–1standard (EN-10305 2010), which was 1 mm thick and was centered at the prism height.

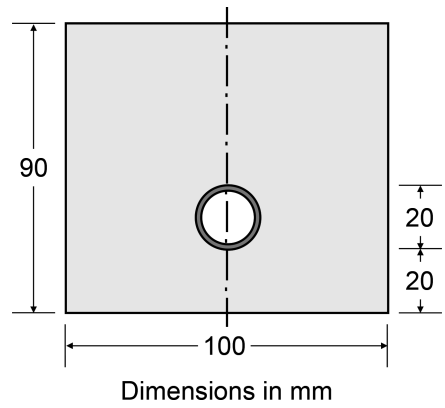

Figure 1. Cross-section of the specimens.

The prisms were subjected to accelerated corrosion, using the experimental device presented in (Sanz, Planas, & Sancho 2015). A constant current of 400 μA/cm^2 was applied using the impressed current technique (Andrade, Alonso, & Molina 1993, El Maaddawy & Soudki 2003). The conditions were such that uniform corrosion was expected to occur along the tube length, as demonstrated by gravimetric measurements and from the tubes inspection. It is essential for the comparison of the experimental results with those of the current simulations. The nominal corrosion depth, which is the amount of steel that is transformed into oxide, at the end of the test was 38 μm, calculated according to Faraday's law. During the tests, a main crack developed through the cover, as well as several secondary cracks, as assessed in slices of the prisms impregnated with fluorescent resin. It should be noticed that the current density is much higher than the values observed in the nature, which may affect the type of oxide generated (Andrade, Alonso, Rodríguez, & García 1996) and, thus, the value of bond strength (Prieto, Tanner, & Andrade 2011); however, it falls within the range for which Faraday's law has been shown to hold for chlorinated concrete (El Maaddawy & Soudki 2003, Caré & Raharinaivo 2007). For details in the experiments, see (Sanz, Planas, & Sancho 2015, Sanz 2014).

After corrosion, the prisms were cut into slices following the method described in (Sanz, Planas, & Sancho 2013). Normally the central slice was used in push-out tests, which was cut with an average thickness of 20 mm. It was sandpapered to eliminate burrs produced during cutting. Other slices were used in other post-corrosion tests, but are out of the scope of this paper.

The concrete was fabricated using Portland Cement type I 52,5 R, with siliceous aggregate and sand with a maximum size of 8 mm, and 3% of calcium chloride by cement weight was added to

produce depassivation of the steel. Prior to casting, the tubes were cleaned using the method described in (Kayafas 1980), to re move any oxide developed at the steel surface, which is essential to ensure the same initial adherence conditions in push-out tests. The ends of the tube were coated with enamel, to prevent them from corrosion during casting and curing, while keeping a length of 80 mm free to corrode centered at the tube. See (Sanz, Planas, & Sancho 2013, Sanz, Planas, & Sancho 2015) for details in the fabrication of specimens.

For each batch, specimens for mechanical characterization were fabricated, to determine the fracture behavior of concrete at the age of 28 days. In particular, standard cylinders 150 mm in diameter and beams 100 × 100 × 500 mm^3 were fabricated. All the specimens were fabricated in laboratory conditions and kept and cured in a bath of lime saturated water in a temperature-controlled chamber at 20°C until testing time.

2.2 *Push-out tests*

Since the specimens for adherence tests are concrete slices and anchoring of the tube is not possible, an experimental setup was designed to push the tube out of the concrete. Figure 2 shows a sketch of the experiment. The main aspects of the tests are described next. For details in the experimental devices, see (Sanz 2014).

The load was applied to the steel by means of a cylindric part centered at the steel tube, with the maximum outer diameter compatible with the tube dimensions. The slices rested on another cylindric part, also centered at the tube, which transmitted the load to the concrete over a ring with the minimum outer diameter. The dimensions of the loading devices were calculated according to the tube dimensions, hence the importance of using calibrated tubes as a reinforcement in this study. The displacement of the steel with respect to the concrete was recorded using a linear variable displacement transducer, called *lvdt* in the following.

The test was run under displacement control, using the *lvdt* output as the feed-back signal, with monotonic displacement of the steel tube. The test

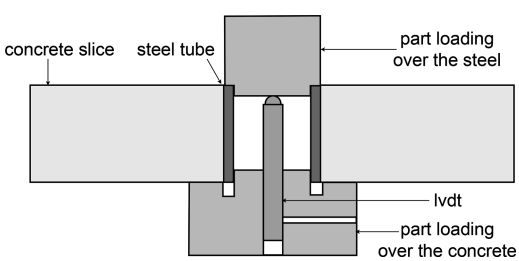

Figure 2. Sketch of push-out tests.

was stopped at approximately 2 mm of displacement of the tube. The shear stress at the steel-concrete interface was computed from the records of load and displacement, assuming uniform stress and taking into account the actual surface of concrete contacting the tube, as:

$$\tau = \frac{P}{\pi D\left(L - \delta\right)} \tag{1}$$

where P is the load, D is the outer diameter of the tube (i.e., 20 mm), L is the average length of the tube, and δ is the displacement of the tube.

3 SIMULATIONS

3.1 *Numerical model*

Finite-element simulations of push-out tests were carried out using models of the specimens described in Section 2.1, to analyze the response of bare specimens in the adherence tests.

The simulations were carried out within the finite element framework COFE *(Continuum Oriented Finite Elements)*. It implements elements with an embedded adaptable cohesive crack (Sancho, Planas, Cendón, Reyes, & Gálvez 2007, Sancho, Planas, Fathy, Gálvez, & Cendón 2007), which reproduce concrete cracking according to the standard cohesive model introduced by (Hillerborg, Modéer, & Petersson 1976). However, in this study concrete behavior was assumed to be linear elastic, since concrete is assumed to be uncracked in the non-corroded specimens.

3.2 *Joint elements*

To simulate the behavior of the steel-concrete interface, interface elements have been used, which are an extended version of the joint elements presented in (Sanz, Planas, Fathy, & Sancho 2008, Sanz, Planas, & Sancho 2013). Those are zero-thickness elements that transmit stress only between pairs of nodes, thus each pair of nodes behaves independently of the other pairs of the element.

At their original version, the joint elements had four nodes and were defined only for two-dimensional problems. In the current version, the formulation of the elements has been generalized, leading to two families of elements, prisms and hypercubes, both working in two and three dimensions. They are defined by the dimensions of their section and by the external unitary normal vector **n**, as shown in Fig. 3.

For a relative displacement **w** of the nodes of a given pair, the traction vector t at those nodes depends on the displacement and on the constitutive law of the material, as:

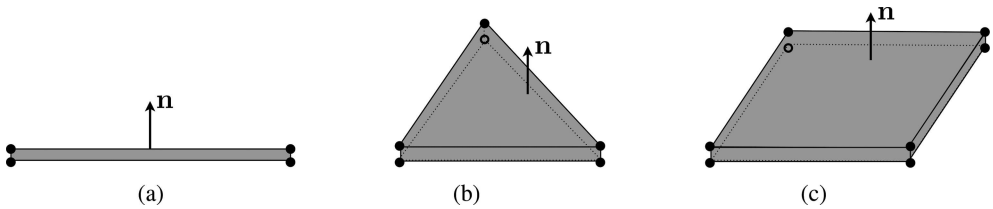

Figure 3. Joint elements: two-dimensional element (a), prismatic element (b) and hexahedral element (c).

$$\mathbf{t} = \mathbf{K}_n \mathbf{w} \tag{2}$$

where $\mathbf{K}_n$ is a second order stiffness tensor that depends on the unitary normal $\mathbf{n}$ of the element, and can be split into its normal and shear components as:

$$\mathbf{K}_n = k_n \mathbf{n} \otimes \mathbf{n} + k_t \left(\mathbf{1} - \mathbf{n} \otimes \mathbf{n} \right) \tag{3}$$

where k_n and k_t are the normal and shear stiffnesses, respectively, and $\mathbf{1}$ is the second order identity tensor. Therefore, the traction vector is calculated as follows:

$$\mathbf{t} = k_n \left(\mathbf{w} \cdot \mathbf{n} \right) \mathbf{n} + k_t \left[\mathbf{w} - \left(\mathbf{w} \cdot \mathbf{w} \right) \mathbf{n} \right] \tag{4}$$

3.3 *Materials for the interface*

Three types of cohesive materials have been programmed for the interface with several softening laws: linear softening, linear softening plus residual friction, and exponential softening plus residual friction. Their main characteristics are explained next.

The cohesive material with linear softening (*L*) is based on the model from Camanho and Davila (Camanho & Davila 2002). Figure 4(a) shows a sketch of its constitutive law. It follows a traction-separation law, in which the separation $\mathbf{w}_m$ is computed as the module of the tangential displacement and the positive normal displacement (i.e., the normal displacement in the case of tension):

$$\mathbf{w}_m = \mathbf{w}_t + \langle \mathbf{w}_n \rangle \tag{5}$$

In this material, for a positive monotonic separation, the traction increases following the curve 0 A shown in Fig. 4(a), until the tensile strength is reached. Then the traction decreases following the curve AB, occurring degradation of the stiffness, until it is zero for a separation larger than a given critical value w_c. The same applies for a negative separation and curve ODFG. For a negative normal displacement, the stiffness k_n is constant and the normal component of the traction vector follows the curve 0E. Unloading to the origin is implemented.

The second material (*LF*) is a variant of the previous one, with a residual constant friction f_{fr} for large separations. Figure 4(b) shows a sketch of the positive part of the traction-separation law.

Finally, the third material (*E*) follows an exponential softening law in which the exponent is proportional to a given factor c and to $w–w_0$, where w is the actual separation and w_0 is the separation corresponding to the tensile strength, and the stress decreases asymptotically to the friction stress. Figure 4(c) shows a sketch of that material.

3.4 *Parameters in the simulations*

Finite element simulations of push-out tests have been carried out using three-dimensional models of the specimens, with the dimensions of the cross-section shown in Figure 1, and a thickness of 20 mm.

Figure 5(a) shows a 3D view of the mesh, and Fig. 5(b) a cross-section. A structured mesh was generated using the pre-post Finite Elements mesh processor Gmsh (Geuzaine & Remacle 2009). Hexahedral elements with assumed enhanced strain were used for the steel and the concrete, and interface hexahedral elements for the interface, as marked in the figure. The number of hexahedra in the direction of the z-axis, i.e., in the thickness of the slice, was eight. In the plane $x – y$, the number of interface and steel elements per quarter of circumference was sixteen, with one layer of elements for the interface, and three layers for the steel. The mesh in the concrete matched the mesh in the tube, and the size of the elements was increased to be ten times that of interface elements at the outer boundary of the concrete.

The properties of the materials were as follows. For the concrete, linear elastic behavior was assumed, with elastic modulus E = 30 GPa and Poisson's ratio $\nu = 0.2$. For the steel, linear elastic behavior was also assumed, with E = 200 GPa and $\nu = 0.3$. For the interface, three cohesive behaviors were simulated, according to the three models described in Section 3.3: linear, linear with residual friction, and with exponential softening ans residual friction. The properties of the cohesive materials are displayed in Table 1. In the case of the exponential softening, the exponent was assumed initially as displayed in the table, and then

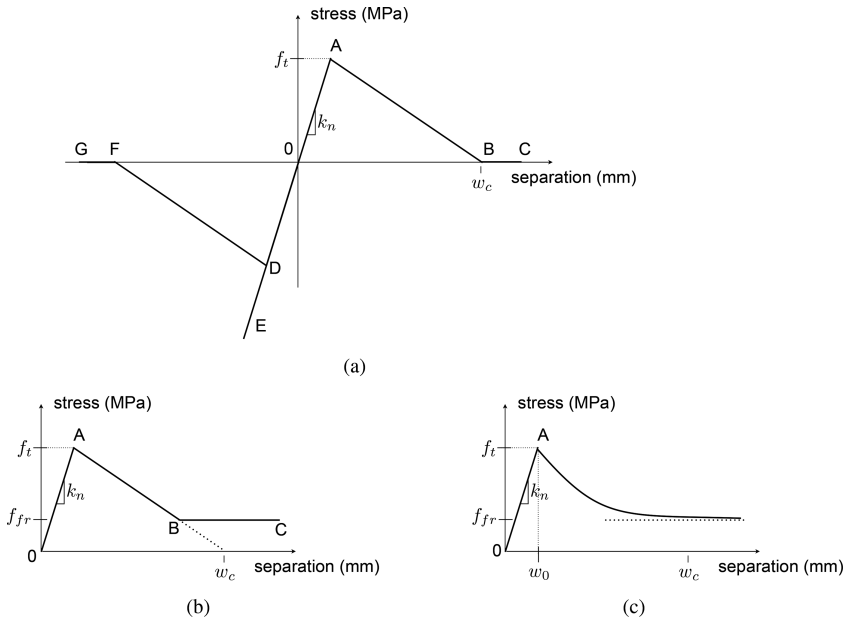

Figure 4. Cohesive material with linear softening, based on the model of Camanho and Davila, 2002 (a), material with linear softening and residual friction (b), and material with exponential softening and residual friction (c).

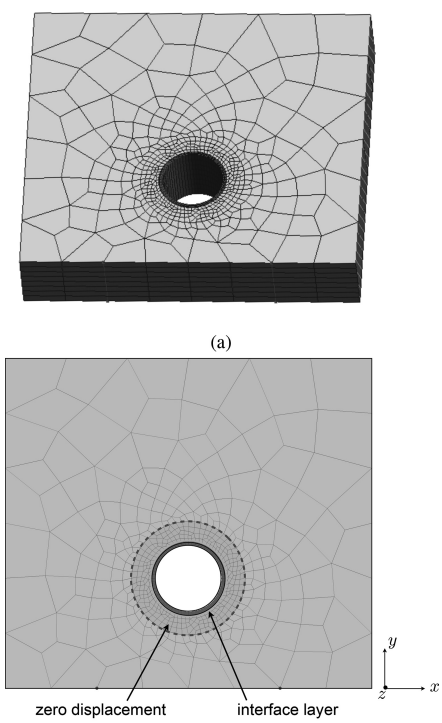

Figure 5. Mesh of three-dimensional models of the specimens used in numerical simulations.

Table 1. Parameters of the materials in the simulations, where k_n is the initial stiffness, f_t the tensile strength, w_c the critical separation at which stress of the cohesive law is zero, f_{fr} the frictional stress, c the factor of the exponent, L stands for 'linear', LF for 'linear with friction´, and E for 'exponential softening with friction'.

	k_n (N/mm^3)	f_t (MPa)	w_c (mm)	f_{fr} (MPa)$_r$	c (mm^{-1})
L	10^6	3:0	0.05	–	–
LF	10^6	3:0	0.05	1.0	–
E	10^6	3:0	–	1.0	100

was diminished logarithmically, with values 50, 25, and 12.5 mm–1.

A total displacement of 0.2 mm was applied to the upper nodes of steel in the axis direction in 20 steps of 0.4 µm followed by 96 steps of 2 µm. The movement of the concrete nodes within the shadowed ring in Figure 5 was restricted, which correspond to the support ring in the experiments.

4 RESULTS AND DISCUSSION

4.1 *Experimental results*

The main experimental results are explained next. Figure 6(a) shows the results of corroded specimens,

with 38 μm of corrosion depth. In particular, the curves of nominal shear stress versus displacement of the tube are displayed. The curves are plotted up to a displacement of 1000 μm, although the tests were run up to 2000 μm, since no significant changes occurred from that displacement on. It is observed that the curves display an initial steep slope, a peak, and then a progressive descent, which indicates that there is a residual bond stress due to friction.

Figure 6(b) shows the results for specimens not subjected to accelerated corrosion. The curves of shear stress display a behavior similar to that of corroded specimens, except for a sudden drop after the peak with a marked instability, as indicated in the curves by the dotted lines. Complementarily, unloads and reloads were carried out in two specimens, from which it was observed that displacement of the tube was permanent; it indicates that after debonding of the tube occurs, bond stress might be due mainly to friction.

For completeness of the presented results, Table 2 displays the stress and the displacement corresponding to the peak, and the stress at 1000 μm of displacement of the tube.

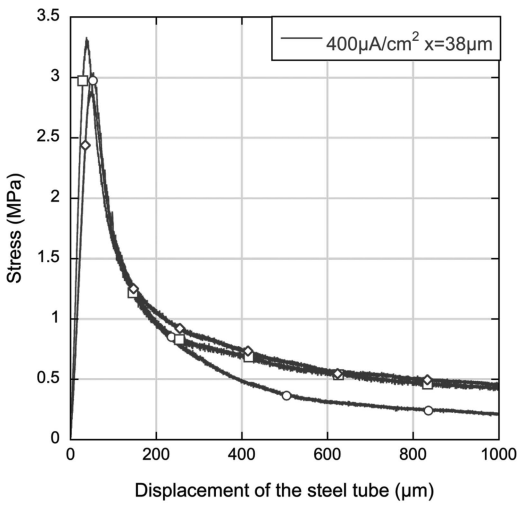

(a)

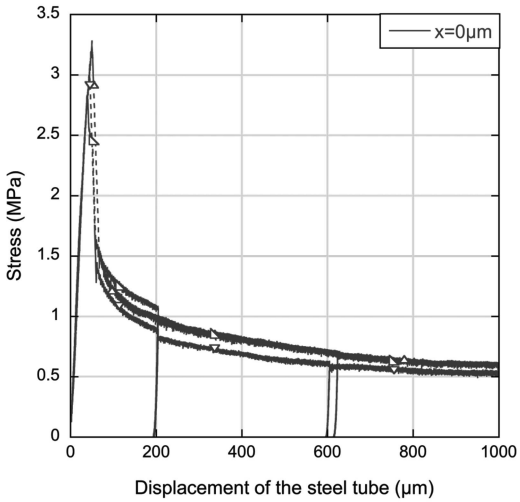

(b)

Figure 6. Experimental results of push-out tests for specimens with 38 m of corrosion depth (a) and for specimens not subjected to accelerated corrosion (b).

4.2 *Numerical results*

The results of the simulations are explained next.

Firstly, the mean stress was computed from the total reaction of the steel, assuming uniform stress at the interface and considering the displacement of the tube, as in the experiments. Figure 7 shows the curves of mean shear stress versus displacement of the tube for the cases with linear softening and linear softening with friction (solid symbols, with circles and squares, respectively), and the four cases with exponential softening with friction (open symbols). In order to compare the experimental and numerical results, the curves of experimental stress versus inelastic displacement of the tube are drawn, which were computed by subtracting for each point the displacement of the curve-fit of the initial nearly-linear part of the stress-displacement curves. It is observed that the simulations using a material with exponential softening are the best reproducing the experimental results, in particular that with coefficient c = 25 mm–1. Thus, we will focus in this simulation in the following. It should be noticed that no attempt has been made in this work to determine accurately the best values of the interface parameters, since these simulations are intended to assess the distribution of shear stresses at the interface during push-out.

Then the map of stress at the steel-concrete interface was analyzed. Figure 8 shows the map of shear stress at the interface elements for the selected simulation and selected values of displacement of the tube. For each diagram, the

Table 2. Results of push-out tests: nominal corrosion depth x of the specimens, mean and standard deviation of the stress τ_u and displacement u corresponding to the peak, and of the stress τ_{1000} corresponding to 1000 μm of displacement of the tube.

x (μm)	τ_u (MPa)	δ_u (μm)	τ_{1000} (MPa)
38	3.09 ± 0.23	43.6 ± 5.5	0.364 ± 0.13
0	3.03 ± 0.23	44.4 ± 5.4	0.589 ± 0.035

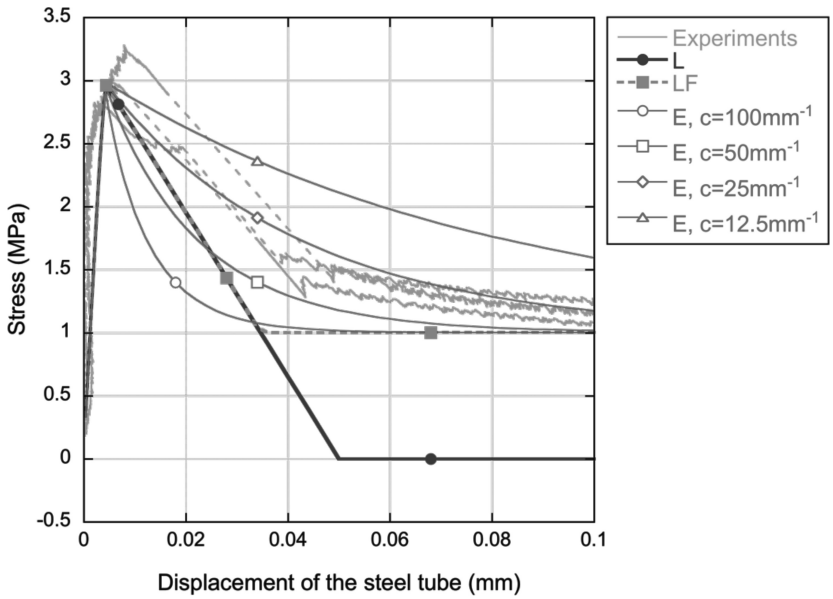

Figure 7. Numerical curves of mean shear stress versus displacement and comparison to the experimental results, where L stands for linear softening, LF for linear softening with friction, E for exponential softening with friction, and c is the coefficient of the exponent in the exponential law.

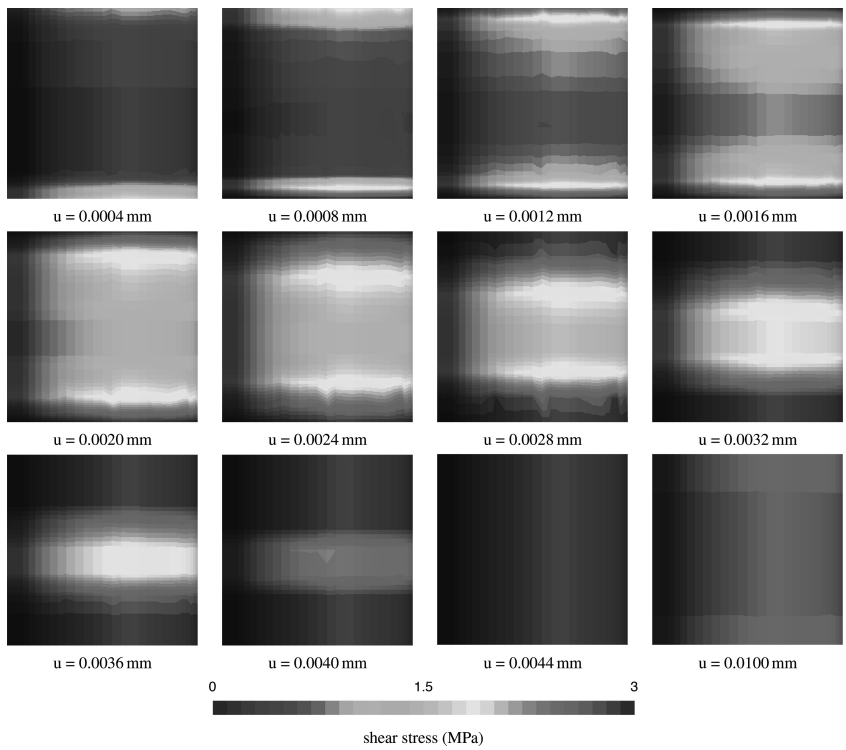

Figure 8. Map of shear stress of interface element for various values of displacement of the tube, for a simulation with exponential softening and exponent factor $c = 25$ mm^{-1}.

displacement of the tube is indicated in mm below. The scale of stress in MPa is displayed on the bottom of the figure. As shown in the first diagram, for a displacement u = 0.4 μm, the shear stress is not uniform, and presents differences greater than 1.4 MPa between the minimum, which occurs at the center, and the maximum, which occurs at the bottom end. For u = 0.8 μm, the tensile strength is reached at the bottom end, while the stress on the top is still smaller than 1.9 MPa, and the minimum stress at the center is 0.29 MPa. This is the step with the greatest gradient of tension. In the following diagram, the stress continues growing at the top of the tube, until for u = 1.6 μm the tensile strength is reached at the top of the tube. As seen in the next diagrams, the maximum stress propagates through horizontal bands from the ends of the tube to the central part, until the tensile strength is reached in all the tube for a displacement u = 4.4 μm, which corresponds to the peak in the curve of mean stress (see Figure 7). From that displacement on, the difference between the maximum and minimum stress for a given displacement is smaller than 0.1 MPa; thus, shear stress can be assumed to be uniform in the length of the tube. As the displacement increases, as shown in the last diagram, the stress decreases in the tube, following the curve in Figure 7 corresponding to this simulation.

5 CONCLUSIONS

In this work, simulations of adherence tests have been carried out within the framework of a general study to investigate loss of bond due to reinforcement corrosion. The specimens are prisms reinforced with a calibrated steel tube. Therefore, influence of the reinforcement geometry is avoided, and adhesion and friction can be investigated. In order to simulate the behavior of the steel-concrete inteface, joint elements have been programmed with a cohesive behavior and several softening laws.

Simulations of the tests assuming elastic behavior for the steel and the concrete, and a cohesive behavior with exponential softening for the interface are able to reproduce overall the experimental curves of shear stress versus displacement of the tube of specimens not subjected to accelerated corrosion.

From the simulations it has been assessed that stress of the tube is uniform from the displacement corresponding to the peak on. Thus, the maximum and residual values of shear stress determined in these experiments are reliable, and the experimental setup can be applied to study loss of bond due to reinforcement corrosion.

ACKNOWLEDGEMENTS

The authors gratefully acknowledge the *Secretaría de Estado de Investigación, Desarrollo e Innovación of the Spanish Ministerio de Economía y Competitividad* for providing financial support for this work under the projects BIA2010-18864 and BIA2014-54916-R. The authors also acknowledge *Oficemen, Grupo Cementos Portland Valderrivas* for donating the cement used to fabricate the specimens of this work.

REFERENCES

Almusallam, A.A., A.S. Al-Gahtani, A. Aziz, & Rasheeduzzafar (1996). Effect of reinforcement corrosion on bond strength. *Construction and Building Materials 10*(2), 123–129.

Al-Sulaimani, G.J., M. Kaleemullah, I.A. Basunbul, & Rasheeduzzafar (1990). Influence of corrosion and cracking on bond behavior and strength of reinforced concrete members. *Structural Journal 87*(2), 220–231.

Andrade, C., C. Alonso, & F.J. Molina (1993). Cover cracking as a function of bar corrosion: Part i-experimental test. *Materials and Structures 26*(8), 453–464.

Andrade, C., C. Alonso, J. Rodríguez, & M. García (1996). Cover cracking and amount of rebar corrosion: importance of the current applied in accelerated tests. In R.K. Dhir and M.R. Jones (Eds.), *Concrete in the Service of Mankind, Concrete Repair, Rehabilitation and Protection,* pp. 263–273.

Camanho, P.P. & C.G. Davila (2002). Mixed-mode decohesion finite elements for the simulation of delamination in composite materials. Technical report, NASA/TM-2002–211737, pp.1–37.

Caré, S. & A. Raharinaivo (2007). Influence of impressed current on the initiation of damage in reinforced mortar due to corrosion of embedded steel. *Cement and Concrete Research 37*(12), 1598–1612.

E&FN Spon, London, UK.

El Maaddawy, T.A. & K.A. Soudki (2003). Effectiveness of impressed current technique to simulate corrosion of steel reinforcement in concrete. *J. Mater. Civil Eng. 15*(1), 41–47.

EN-10305 (2010). Steel tubes for precision applications. Technical delivery conditions. seamless cold drawn tubes. Technical Report 10305–1.

Geuzaine, C. & J.-F. Remacle (2009). Gmsh: a three dimensional finite element mesh generator with built-in pre- and post-processing facilities. *International Journal for Numerical Methods in Engineering 79*(11), 1309–1331.

Hanjari, K.Z., D. Coronelli, & K. Lundgren (2011). Severely corroded reinforced concrete with cover cracking: Part 2. anchorage capacity. In C. Andrade and G. Mancini (Eds.), *Modelling of Corroding Concrete Structures: Proceedings of the Joint fib-RILEM Workshop held in Madrid, Spain, 22–23 November 2010,* Volume 5, Dordrecht, pp. 207–217. Springer Netherlands.

Hillerborg, A., M. Modéer, & P.-E. Petersson (1976). Analysis of crack formation and crack growth in

concrete by means of fracture mechanics and finite elements. *Cem. Concr. Res. 6*(6), 773–781.

Juarez, C.A., B. Guevara, G. Fajardo, & P. Castro-Borges (2011, 12). Ultimate and nominal shear strength in reinforced concrete beams deteriorated by corrosion. *Eng. Struct. 33*(12), 3189–3196.

Kayafas, I. (1980, 8). Technical note: Corrosion product removal from steel fracture surfaces for metallographic examination. *Corrosion, NACE 36*(8), 443–445.

Prieto, M., P. Tanner, & C. Andrade (2011). Bond response in structural concrete with corroded steel bars. experimental results. In C. Andrade and G. Mancini (Eds.), *Modelling of Corroding Concrete Structures: Proceedings of the Joint fib-RILEM Workshop held in Madrid, Spain, 22–23 November 2010,* Dordrecht, pp. 231–241. Springer Netherlands.

Sancho, J.M., J. Planas, A.M. Fathy, J.C. Gálvez, & D.A. Cendón (2007). Three-dimensional simulation of concrete fracture using embedded crack elements without enforcing crack path continuity. *International Journal for Numerical and Analytical Methods in Geomechanics 31*(2), 173–187.

Sancho, J.M., J. Planas, D.A. Cendón, E. Reyes, & J.C. Gálvez (2007). An embedded crack model for finite element analysis of concrete fracture. *Eng. Fract. Mech. 74*(1–2), 75–86.

Sanz, B. (2014). *Experimental and numerical study of cracking of concrete due to reinforcement corrosion.* Ph. D. thesis, E.T.S.I. Caminos, Canales y Puertos (U.P.M.).

Sanz, B., J. Planas, & J.M. Sancho (2013, 12). An experimental and numerical study of the pattern of cracking of concrete due to steel reinforcement corrosion. *Eng. Fract. Mech. 114,* 26–41.

Sanz, B., J. Planas, & J.M. Sancho (2015). A closer look to the mechanical behavior of the oxide layer in concrete reinforcement corrosion. *Int. J. Solids Struct. 62,* 256–268.

Sanz, B., J. Planas, A.M. Fathy, & J.M. Sancho (2008). Modelización con elementos finitos de la fisuración en el hormigón causada por la corrosión de las armaduras. *Anales de Mecánica de la Fractura 25*(2), 623–628.



Taylor & Francis
Taylor & Francis Group
http://taylorandfrancis.com

Computational Modelling of Concrete Structures – Meschke, Pichler & Rots (Eds)
© 2018 Taylor & Francis Group, London, ISBN 978-1-138-74117-1

Modeling of localization and softening behavior of passively confined concrete using coupled RBSM and nonlinear shell FEM

R. Mendoza Jr., Y. Yamamoto, H. Nakamura & T. Miura
Department of Civil Engineering, Nagoya University, Nagoya, Japan

ABSTRACT: A newly developed coupled numerical model which combines the use of RBSM and nonlinear shell FEM is introduced. The model was used to investigate the effect of steel tube confinement in the localization and softening behavior of concrete. Analysis of steel-tube confined concrete columns showed that by increasing the level of confinement (expressed in terms of steel percentage ratio), the strain-softening behavior of concrete can be transitioned into strain-hardening behavior. Evaluation of local axial strains in concrete further showed that when localized deformation in concrete is present, the axial-displacement curve exhibits strain-softening, whereas when the entire height of column is under constantly increasing local axial strain, the axial-displacement curve exhibits strain-hardening. The analysis also showed that by increasing the confinement in concrete, the length of localized damage is also increased. This suggests that localized deformation and softening behavior in concrete may coexist even in concrete confined by thick steel tubes.

1 INTRODUCTION

When concrete fails in compression, damage becomes localized. This phenomenon has been well-documented in unconfined concrete specimens (e.g. van Mier 1997, Nakamura & Higai 2001) which showed that the compression failure of concrete is a localized phenomenon. The tests performed by these authors showed similar tendencies, that is, (1) the post-peak stress-averaged strain diagrams of specimens with different slenderness (height-to-diameter ratio, H/D) show an increase in ductility with decreasing slenderness; and (2) when these stress-averaged strain diagrams are converted into stress-post peak displacements, the diagrams are more or less coincident with one another which indicates that the same amount of displacement is needed to fracture the specimens.

The consequences of this phenomenon are also well-recognized. When localization occurs, the stress-averaged strain diagram becomes size-dependent which invalidates the use of information from short column test to long columns which experiences localization. This means that for test data from columns with strain localization to be useable, the length of compressive fracture zone has to be defined or the stress-strain curve must be obtained directly from the compressive fracture zone. Conversely, in numerical analysis, simulation of specimens which experiences localization becomes sensitive to element discretization. Thus, the compressive fracture energy must be considered to obtain reliable solutions independent of mesh size.

Under passive confinement, the strain-softening and localization behavior of concrete is less studied. To date, only limited research was performed to investigate these behaviors, and among this are the works of Caner and Bazant (2002), and Wu and Wei (2016). The study of Caner and Bazant (2002) investigated the amount of critical steel reinforcement ratio ρ_{cr} (ratio of the steel tube area and combined area of the concrete and steel tube) needed to eliminate the post-peak softening behavior of confined concrete. Using combined experimental and numerical results, the critical confining reinforcement ratio was determined to be 14.2% which is said to be the ratio needed for the effective tangential stiffness to transitions to a non-negative value. When long columns are used, it was found numerically that a higher steel reinforcement ratio equal to 16% is needed. The works of Wu and Wei (2016), on the other hand, investigated the localization of concrete under FRP confinement. They tested FRP-confined cylinders with varying slenderness from H/D = 2.0 to up to 4.6. The effect of increasing level of confinement was also investigated by varying the thickness of FRP sheets. To measure the localization zone, strain gauges were attached to the surface of FRP strips to measure vertical and lateral strains in combination with digital image correlation (DIC) measurements. They concluded that localization occurs in FRP-confined concrete with low level of confinement,

in which the post-peak curve exhibits softening response. The localization length was also found to increase with increasing level of confinement. Together, although these two past studies contributed on the understanding of softening and localization behavior of concrete under passive confinement, further investigations are required. In particular, the study of Caner and Bazant (2002) has not qualitatively assessed the effect of localization length on the elimination of softening behavior in concrete. Also, the experiment performed by Wu and Wei (2016) has not evaluated the gradual elimination of localization under increasing confinement. It should be noted that experimentally evaluating the localization of concrete under confinement is such challenging task as concrete is encased by the confining material. Thus, a numerical simulation method that can qualitative evaluate the localized deformation of concrete under confinement provides a viable alternative.

In this paper, we present a newly developed coupled numerical method to simulate localization, softening, and confinement behavior of concrete passively confined by steel tube. The coupled method combines the use of Rigid Body Spring Model (RBSM) to simulate the salient features of concrete and nonlinear finite shell element to simulate the behavior of steel tube. In RBSM, concrete is idealized as an assemblage of rigid particles interconnected by normal and shear springs. The constitutive models for concrete in compression, tension, and shear are assigned on these springs which then dictate the interaction between particles. The authors have already utilized RBSM in a wide application of concrete engineering problems—ranging from material (e.g., corrosion-induced cracking in concrete) to structural member analysis (e.g., shear failure mechanism), and plate analysis subject to impact—and have shown that the method can well simulate cracking, localization and post-peak softening behavior of concrete. The confining steel tube, on the other hand, is modeled using a four-node, isoparametric shell finite element method (FEM). The element is capable of simulating large displacement and large rotation intended to capture local buckling effects. The model has been verified with some benchmark models for geometrically nonlinear shell and has shown good agreement. The coupling of RBSM and shell is performed by introducing discrete interface link elements (one normal and two shear springs) which are pre-assigned on RBSM surfaces in contact with shell elements. Constitutive models which consist of linear normal and bilinear shear model are assigned on these springs to simulate the composite interaction between concrete and steel.

This paper will first present the performance of the newly developed coupled RBSM-shell model in simulating the behavior of thick and thin-walled circular concrete-filled steel tubes (CFST). In particular, we would like to show the performance of the coupled model in simulating softening in low-confined concrete. The capability of the model to simulate behavior of CFST with varying slenderness is then presented. A parametric study which aims to qualitatively investigate the presence of localization zone in low-confined concrete and the elimination of this localized zone in high confined concrete is presented.

2 CONCRETE MODELING USING RBSM

In modeling concrete using RBSM, the following steps are utilized: (1) the target of the simulation is first defined; (2) the appropriate scale is selected (macro, meso, and micro-scale); (3) constitutive models are developed based on the target of the simulation; and (4) parameters are calibrated with experimental data. The RBSM utilized in the proposed coupled RBSM-shell model is based on the formulation of Yamamoto (2008). The formulation is based on a meso-scale, single phase averaging model of concrete which aims to simulate meso-scale concrete behavior such as softening and localization fractures of concrete such as cracking and failure behaviors of reinforced concrete members. The idealization of concrete using RBSM discretized using Voronoi diagram is presented in Figure 1. At the boundary surface of any two given particles, the integration points are set by dividing the boundary the surface into sets of triangles. In the centroid of each triangle, one normal and two shear springs are assigned. This arrangement automatically captures the effects of bending and torsional behavior without the need of introducing rotational springs. The material constitutive models for concrete are then assigned on these springs which simulate the behavior of concrete. From this two-particle assembly, the system stiffness matrix can be readily derived. The complete element formulation of RBSM can be found in the works of Yamamoto (2008).

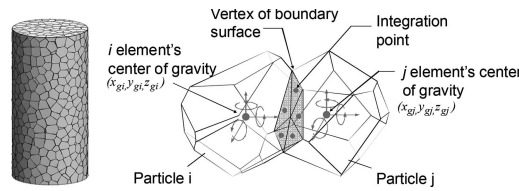

Figure 1. Idealization of concrete using RBSM and two-rigid particle assembly discretized using Voronoi diagram.

The material constitutive models of concrete for tension, compression, and shear are presented in Figure 2. The tension model (Figure 2a) for normal spring consists of a tri-linear model that is linear up to the tensile strength, σ_t, and transitions into a bilinear softening branch defined by a quarter (1/4) model. The strain parameters ε_{tu} and ε_{tl} are defined based on the tensile fracture energy, g_f, and the distance between RBSM nuclei, h. An S-shape curve (Figure 2b) model describes the compression model for normal spring, which was derived by combining two quadratic functions. The parameters ε_c and ε_{cl} are described in Figure 2b and are given by Equations 1a to 1 g. Parameters ε_{c2}, ε_{c1}, and ε_{c2} are derived constants based on the model calibrations performed (See Yamamoto, 2008). These parameters define the nonlinearity in the compression behavior of the normal spring.

$$\sigma = \begin{cases} a_0\varepsilon^2 + b_0\varepsilon & (\varepsilon > \varepsilon_{c1}) \\ a_1\varepsilon^2 + b_1\varepsilon + c_1 & (\varepsilon \le \varepsilon_{c1}) \end{cases} \tag{1a}$$

$$\varepsilon_{c1} = -\frac{2\sigma_c}{E(1+\alpha_{c1})} \tag{1b}$$

$$a_0 = -\frac{E(1-\alpha_{c1})}{2\varepsilon_{c1}} \tag{1c}$$

$$b_0 = E \tag{1d}$$

$$a_1 = \frac{E(\alpha_{c2}-\alpha_{c1})}{2(\varepsilon_{c2}-\varepsilon_{c1})} \tag{1e}$$

$$b_1 = \frac{E(\alpha_{c1}\varepsilon_{c2}-\alpha_{c2}\varepsilon_{c1})}{\varepsilon_{c2}-\varepsilon_{c1}} \tag{1f}$$

$$c_1 = -a_1\varepsilon_{c1}^2 - b_1\varepsilon_{c1} - \sigma_c \tag{1g}$$

The shear stress-strain relation represents the combination of two shear springs. The resultant strain is defined using Equation 2a, and from this, the resultant shear stress is derived from the stress-strain relation with components defined using Equation 2b. Figure 2c describes the envelop of the shear stress-strain relation together with Equations 2a to 2h. The parameters, τ_f and γ_f, are the shear strength and its corresponding shear strain, respectively. γ_{max} refers to the maximum shear strain in the loading history. Parameters G and K refer to the elastic shear modulus and shear-softening coefficient, respectively. The latter depends on the magnitude of normal stress described in Figure 2d and Equation 2d. The Mohr-Coulomb criterion (Figure 2e) was chosen as the failure envelop for the shear springs. A shear deterioration coefficient was also introduced to account for the decrease in shear stress due to increasing crack width.

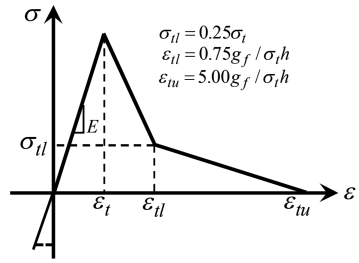

(a) Tension model of normal spring

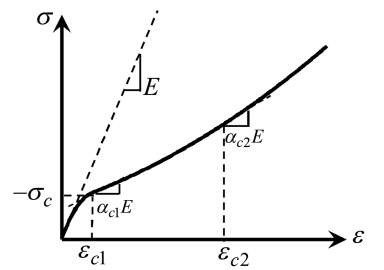

(b) Compression model of normal spring

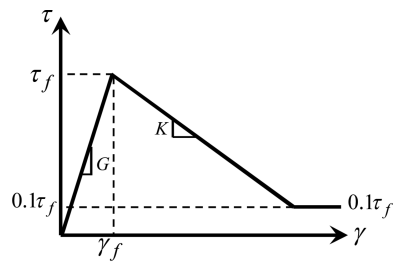

(c) Shear spring model

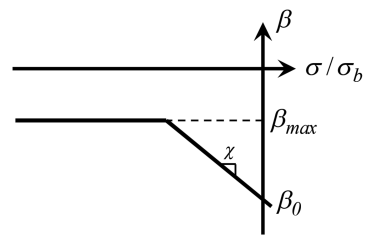

(d) Softening coefficient of shear spring

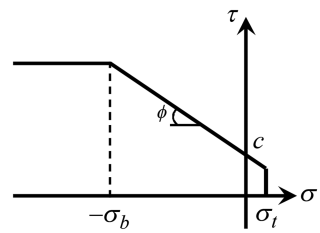

(e) Mohr-Coulomb type criterion

Figure 2. Material models for concrete (Yamamoto 2008).

Table 1. Parameters for modeling concrete using RBSM (Yamamoto 2008, 2014).

Normal spring							Shear spring							
Elastic modulus	Tensile response		Compressive response				Elastic modulus	Fracture criterion			Softening behavior			
E	σ_t	g_f	σ_c	ε_{c2}	α_{c1}	α_{c2}	$\eta = G/E$	c	ϕ	σ_b	β_0	β_{max}	χ	κ
N/mm²	N/mm²	N/mm²						N/mm²	degree	N/mm²				
1.4 E*	0.8 f_t*	0.5 G_f*	1.5 fc'*	–0.02	0.15	0.25	0.35	0.14 fc'*	37	fc'*	–0.05	–0.02	–0.01	–0.3

*Macroscopic material parameters obtained from concrete specimen tests.
E*: Young's modulus, ft*: Tensile strength, Gf*: Fracture energy, fc'*: compressive strength.

This is described in Equation 2h and is dependent on the cracking and ultimate strain, ε_t and ε_{tu}, of the normal spring.

$$\gamma = \sqrt{\gamma_l^2 + \gamma_m^2} \tag{2a}$$

$$\tau_l = \tau\frac{\gamma_l}{\gamma}, \tau_m = \tau\frac{\gamma_m}{\gamma} \tag{2b}$$

$$\tau = \begin{cases} G\gamma & (\gamma < \tau_{f,soft}/G) \\ \tau_{f,soft} & (\gamma \geq \tau_{f,soft}/G) \end{cases} \tag{2c}$$

$$\tau_{f,soft} = \max(\tau_f + K\langle\gamma_{\max} - \gamma_f\rangle, 0.1\tau_f) \tag{2d}$$

$$K = \beta G \tag{2e}$$

$$\beta = \min(\beta_0 + \chi(\sigma/\sigma_b), \beta_{\max}) \tag{2f}$$

$$\tau_f = \begin{cases} c - \sigma\tan\varphi & (\sigma > -\sigma_b) \\ c + \sigma_b\tan\varphi & (\sigma \leq -\sigma_b) \end{cases} \tag{2g}$$

$$\beta_{cr} = \frac{\varepsilon_t}{\varepsilon}\exp\left\{\frac{\kappa}{\varepsilon_{tu}}(\varepsilon - \varepsilon_{tu})\right\} \tag{2h}$$

The derived constants for the parameters described above were determined through calibration of experiments of uniaxial tension and compression, hydrostatic compression, and triaxial compression. The calibration process considered a range of test specimens with varying size, shape, mesh size, and concrete strength. The calibrated parameters are given in Table 1.

3 MODELING OF STEEL TUBE

The confining steel tube is modeled using a degenerated, four-node, isoparametric shell FEM. The development of the nonlinear shell program follows closely the formulation of Noguchi and Hisada (1993). The element consist of five degrees of freedom per node and capable of capturing large displacement and large rotation effects, but small strains.

Figure 3 shows the geometry of the element at initial configuration, $t = 0$. The position vector of

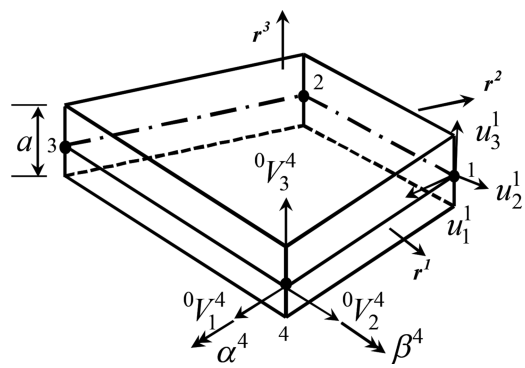

Figure 3. Four-node isoparametric nonlinear shell element for modeling steel tube.

any point within the element at time t is described as follows:

$${}^t\mathrm{x} = \sum_{k=1}^{4} \mathrm{N_k}\,{}^t\mathrm{x}^k + \frac{\mathrm{r}^3}{2}\mathrm{a}\sum_{k=1}^{4}\mathrm{N_k}\,{}^t\mathrm{V}_3^k \tag{3a}$$

where the left subscripts t represents the current time t, and $\mathrm{N_k}(r^1,r^2)$ are the interpolation functions at node k. With Equation 3a, the incremental displacement vector, $\boldsymbol{u}$, of the same point from time t to t' $(t + \Delta t)$ is obtained as follows:

$$\boldsymbol{u} = {}^{t'}\boldsymbol{x} - {}^t\boldsymbol{x} \tag{3b}$$

$$\mathbf{u} = \sum_{k=1}^{4}\mathrm{N_k}\,\mathbf{u}^k + \frac{\mathrm{r}^3}{2}\mathrm{a}\sum_{k=1}^{4}\mathrm{N_k}({}^{t'}\mathbf{V}_3^k - {}^t\mathbf{V}_3^k) \tag{3c}$$

$\boldsymbol{V}_3^k$ is the unit vector normal to the shell mid-surface in the direction of r^3 at nodal point k. The normal vector is commonly referred as the shell director vector. In order to simulate large rotations, the shell director vector is updated by the finite rotation tensor ${}_t^{t'}\boldsymbol{R}$ as

$${}^{t'}\boldsymbol{V}_3^k = {}_t^{t'}\boldsymbol{R}\,{}^t\boldsymbol{V}_3^k \tag{3d}$$

The finite rotation ${}^{t'}_{t}\boldsymbol{R}$, according to Noguchi and Hisada (1993), can be expressed by means of the Taylor series expansion as follows:

$$ {}^{t'}_{t}\boldsymbol{R} = \boldsymbol{I} + {}^{t'}_{t}\boldsymbol{\Phi}^{k} + \frac{1}{2!}({}^{t'}_{t}\boldsymbol{\Phi}^{k})^{2} + ..., \tag{3e} $$

$\boldsymbol{I}$ is a unit tensor and ${}^{t'}_{t}\boldsymbol{\Phi}^{k}$ is the skew-symmetric spin tensor whose axial vector is ${}^{t'}_{t}\boldsymbol{\theta}^{k}$ described in Equation 3 g. It should be noted that the norm of the axial vector ${}^{t'}_{t}\boldsymbol{\theta}^{k}$ is equal to the finite rotation angle ω.

$$ {}^{t'}_{t}\boldsymbol{\Phi}^{k} = \begin{bmatrix} 0 & -{}^{t'}_{t}\theta^{k}_{3} & {}^{t'}_{t}\theta^{k}_{2} \\ {}^{t'}_{t}\theta^{k}_{3} & 0 & -{}^{t'}_{t}\theta^{k}_{1} \\ -{}^{t'}_{t}\theta^{k}_{2} & {}^{t'}_{t}\theta^{k}_{1} & 0 \end{bmatrix} \tag{3f} $$

$$ {}^{t'}_{t}\boldsymbol{\theta}^{k} = {}^{t'}_{t}\theta^{k}_{i}\boldsymbol{e}_{i} \tag{3g} $$

The axial vector is further decomposed into two orthonormal vectors that are orthogonal to the shell director vector, $\boldsymbol{V}_3^k$, as

$$ {}^{t'}_{t}\boldsymbol{\theta}^{k} = \alpha^{k}\,{}^{t}\boldsymbol{V}_{1}^{k} + \beta^{k}\,{}^{t}\boldsymbol{V}_{2}^{k} \tag{3h} $$

Applying Equations 3d to 3f, (using only the linear and quadratic terms of Equation 3e) we have

$$ \mathbf{u} = \sum_{k=1}^{4} \mathrm{N_k}\mathbf{u}^{k} + \frac{r^3}{2}a\sum_{k=1}^{4} \mathrm{N_k}({}^{t'}_{t}\mathbf{R} - \mathbf{I})\,{}^{t}\mathbf{V}_{3}^{k} \tag{3i} $$

$$ \mathbf{u} = \sum_{k=1}^{4} \mathrm{N_k}\mathbf{u}^{k} + \frac{r^3}{2}a\sum_{k=1}^{4} \mathrm{N_k}\,{}^{t'}_{t}\mathbf{\Phi}^{k}\,{}^{t}\mathbf{V}_{3}^{k} + \frac{r^3}{2}a\sum_{k=1}^{4} \mathrm{N_k}\frac{1}{2!}({}^{t'}_{t}\mathbf{\Phi}^{k})^{2}\,{}^{t}\mathbf{V}_{3}^{k} \tag{3j} $$

The operation ${}^{t'}_{t}\boldsymbol{\Phi}^{k}\boldsymbol{V}_3^k$ can be expressed as the cross product of the axial vector, ${}^{t'}_{t}\boldsymbol{\theta}^{k}$, and the shell director, $\boldsymbol{V}_3^k$, which further simplify Equation 3 j into:

$$ \mathbf{u} = \sum_{k=1}^{4} \mathrm{N_k}\mathbf{u}^{k} + \frac{r^3}{2}a\sum_{k=1}^{4} \mathrm{N_k}\,{}^{t'}_{t}\boldsymbol{\theta}^{k} \times {}^{t}\mathbf{V}_{3}^{k} + \frac{r^3}{2}a\sum_{k=1}^{4} \mathrm{N_k}\frac{1}{2!}\{{}^{t'}_{t}\boldsymbol{\theta}^{k} \times ({}^{t'}_{t}\boldsymbol{\theta}^{k} \times {}^{t}\mathbf{V}_{3}^{k})\} \tag{3k} $$

Applying the decomposition of axial vector from Equation 3h, and noting that $\boldsymbol{V}_1^k, \boldsymbol{V}_2^k$, and $\boldsymbol{V}_3^k$ are orthonormal unit vectors, the incremental displacement vector can be rewritten as

$$ \mathbf{u} = \sum_{k=1}^{4} \mathrm{N_k}\mathbf{u}^{k} + \frac{r^3}{2}a\sum_{k=1}^{4} \mathrm{N_k}(-\alpha^{k}\,{}^{t}\mathbf{V}_{2}^{k} + \beta^{k}\,{}^{t}\mathbf{V}_{1}^{k}) + \frac{r^3}{2}a\sum_{k=1}^{4} \mathrm{N_k}\frac{1}{2!}\{(-\alpha^{k})^{2} + (\beta^{k})^{2}\}\,{}^{t}\mathbf{V}_{3}^{k} \tag{3l} $$

With the geometry and displacement vector defined, the element stiffness matrix can be readily developed. Here, the covariant and contravariant components in the convected coordinate system were used to define the Green-Lagrange strain tensor and the second Piola-Kirchhoff stress tensor, respectively. Additionally, the shear locking problem commonly encountered in shell elements is solved using a selective reduced integration scheme where the transverse shear strains $2\varepsilon_{23}$ and $2\varepsilon_{13}$ are evaluated at in-plane natural coordinates (0, 0). The steel material modeling uses a von Mises yield criterion with an isotropic hardening. The element has been verified (see Mendoza et al. 2018) with benchmark model for geometrically nonlinear shell and has been found to perform well.

4 MODELING OF RBSM-SHELL INTERFACE

A representation of the proposed coupled RBSM-shell model is given in Figure 4, where concrete is idealized as an assemblage of rigid particles discretized using Voronoi diagram with random geometry and the steel tube using shell finite elements.

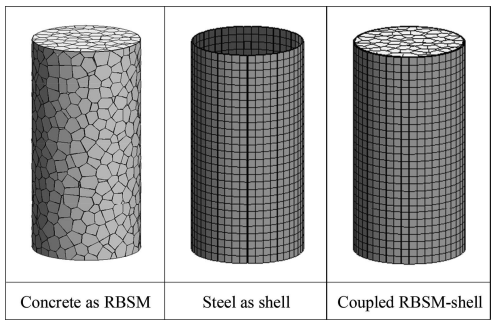

Figure 4. A representation of RBSM-shell model.

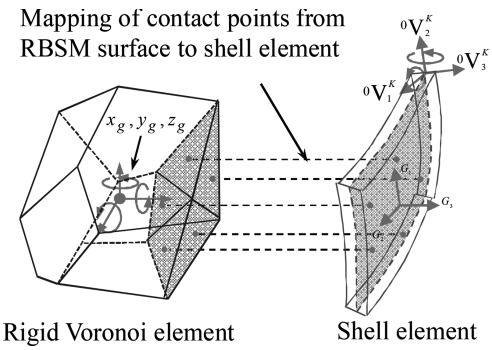

Figure 5. RBSM particle-shell element interface elements.

Figure 5 illustrates the interaction of a RBSM particle and shell element.

Similar to the boundary surface of any two given RBSM particles, the surfaces of RBSM particles in contact with shell elements are divided into triangles as shown in Figure 5. The corresponding centroids of these triangles act as discrete contact points between RBSM and shell. Since these points are generated at random, the isoparametric coordinates of contact points on shell element surface are initially unknown. To calculate these values, an inverse mapping algorithm was introduced utilizing Equation 4 where the Jacobian matrix $\boldsymbol{J}$ represent the covariant base vectors of the shell element (at time $t=0$). Vectors $\boldsymbol{X}_u$ and $\boldsymbol{X}_0$ are position vectors of the unknown and known (reference point taken as the center of shell element) contact points, and $\boldsymbol{r}_u^i$ and $\boldsymbol{r}_0^i$ are the target and initial isoparametric coordinates. The target values are determined using the iterative Newton-Raphson solution scheme.

$$\boldsymbol{r}_u^i = \boldsymbol{r}_0^i + \boldsymbol{J}^{-}(\boldsymbol{X}_u - \boldsymbol{X}_0) \tag{4}$$

The constitutive models for the interface elements are presented in Figure 6. The normal spring is limited to compression to allow the separation of RBSM and shell under tension loading. A bilinear model is adopted for the shear springs which exhibit hardening when the normal is under compression, and softening when the normal is under tension. The slope of the normal spring is assumed to be equal to the modulus of elasticity of concrete and that of the shear springs equal to concrete shear modulus.

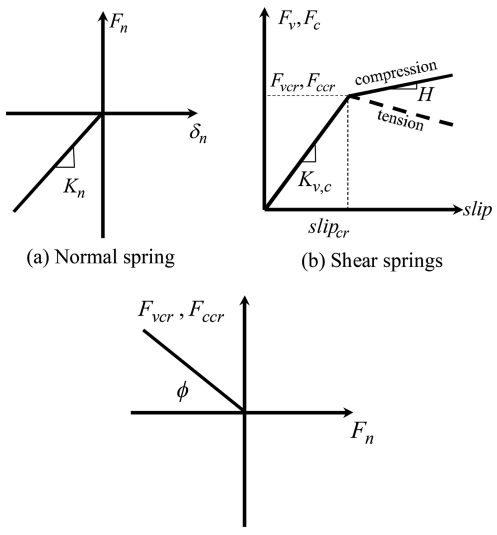

Figure 6. Constitutive models for normal and shear interface elements with Mohr-Coulomb envelop.

The slope of the hardening and softening coefficient is taken as 1/100. Failure envelop for the shear springs is defined by a Mohr-Coulomb failure criterion where the coefficient of friction was assumed to be equal to 0.25.

5 MODELING OF RBSM-SHELL INTERFACE

The capability of RBSM-shell model in simulating the uniaxial compressive behavior of concrete-filled steel tubes is presented in this section. In particular, the model's capability to simulate softening in low-confined CFST and hardening in high-confined CFST is presented. CFST experiments with varying slenderness (H/D ratio) are also analyzed to show that the model can capture the influence of slenderness in the compressive behavior of CFST. The experiments used for comparison are from the works of O'Shea & Bridge (2000), Hu & Teng (2011), Schneider (1998), Huang et al. (2002), and Tomii et al. (1977).

Limited test have been conducted to investigate the compressive behavior of thin-walled CFST. Test data were sought for specimens with evident post-peak softening response. Specimen S10CS50A was selected from the test performed by O'shea & Bridge (2000) in which the diameter-to-tube thickness ratio (D/t) is equal to 220, whereas specimen F0-202 was selected from the work of Hu & Teng (2011) with a reported D/t ratio of 202. The properties of these specimens are given in Figure 7. For both specimens, the load was applied simultaneously on concrete and steel tube section. In the experiments performed by O'shea & Bridge (2000), the reported axial strength is based on the axial strength carried by the concrete core section. This was determined by subtracting the load carried by the steel tube using an incremental analysis in which the data are based on measured strains on steel tube combined with the determined (from tension coupon test) stress-strain relationship of steel. For the test of Hu & Teng (2011), the reported axial load is the total load carried by concrete and steel obtained directly from a data logger. In both specimens, the axial shortening was measured using three axial displacement transducers, and the reported axial strains were calculated by dividing the measured axial displacement by the height of the specimens. In the simulation, the axial load was applied using axial displacement increments. A rigid plate was introduced to apply displacement increments on the concrete core, whereas for the steel tube, the load was applied directly on top shell nodes. This allows the easy decoupling of the axial contribution of steel and concrete. Both rigid plate and top shell nodes were subjected to same displacement increments of 0.01 mm. Pinned boundary

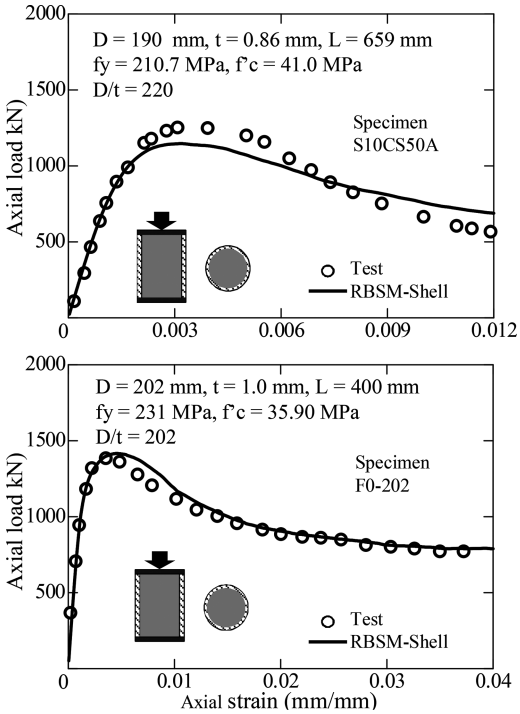

Figure 7. Axial load-strain comparison of test and simulation results of low-confined CFSTs.

conditions were assumed on top and bottom of the specimens. The solution was performed using modified Newton-Raphson iterative solution scheme and the convergence is set to attained when the error becomes less than 10^{-3} or when the maximum iteration limit is reached (max iteration = 200). Input mesh size for RBSM and shell is 12.5 mm and 10 mm, respectively. In all the analysis performed in this paper, the RBSM-to-shell mesh size ratio of 1.25 was maintained.

Comparisons of axial load-strain diagram between test and simulation results for specimen S10CS50 and F0-202 are given in Figure 7. The vertical axis represents the axial load (carried by concrete for specimen S01CS50A, and by concrete and steel for specimen F0-202) while the horizontal axial represents the average axial strains. The experimental results are shown as circular marker points while the simulation results are plotted as solid lines. For both specimens, a good agreement can be observed with the prediction of initial modulus, peak axial strength, and the corresponding axial strains.

The simulations of post-peak softening curve also show an excellent agreement with the test results. The results demonstrate the capability of RBSM-shell model in simulating the axial load-displacement behavior of low-confined CFST. A particular note is the good fit in the axial prediction of specimen S10CS50A which represent the axial-strain diagram of concrete. The good agreement between test and simulation results suggests that the RBSM-shell model can also well-represent the axial contribution of sole concrete and that of concrete and steel tube combined.

The simulation for high-confined CFST follows the same procedure described for low-confined CFST. Here, the test specimens selected for comparisons are from the experiments of Schneider (1998) and Huang et al. (2002). The specimens have a D/t ratio of 21 (for specimen C2) and 40 (for specimen CU-040). The properties of these specimens are given in Figure 8. Axial shortening reported in the test were measured using four axial displacement transducers while the reported axial loads—concrete and steel combined—were obtained directly from compression test machines.

Figure 8 shows the comparison between test and simulation results. Once again, the experimental results are shown as circular marker points while the simulation results are plotted as solid lines. It is clear from the comparison that the RBSM-shell model is capable of simulating the compressive behavior of thick-walled CFST. The strain-hardening behavior observed in the tests is well-simulated by the proposed model. Together, the

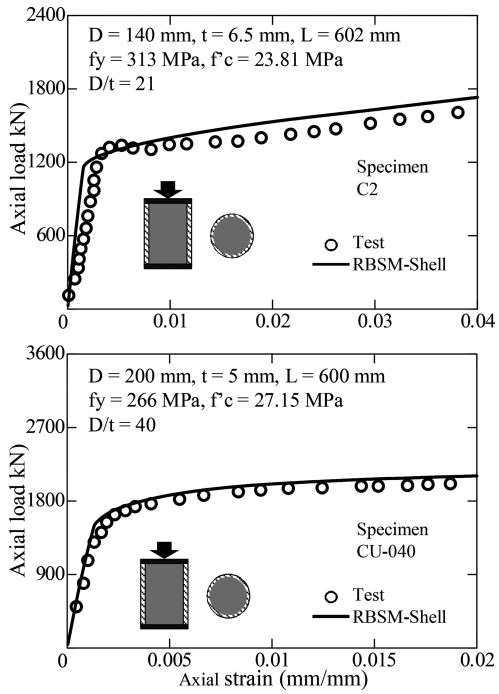

Figure 8. Axial load-strain comparison of test and simulation results of high-confined CFSTs.

results for thin and thick-walled CFST demonstrate the performance of the RBSM-shell model in simulating the axial load-strain curves of low-confined and high-confined CFST cases. This was done without any performed parameter optimization or calibration with test results of CFST, i.e. the coupling of RBSM-shell is a direct combination of the individual performance of each numerical model.

Validations to show the performance of the RBSM-shell model in simulating CFST with varying height is presented in Figure 9. The test specimens are from the experiments of Tomii et al. (1977). The specimens have similar material and geometric properties (as shown in Figure 9) except for the height which is 300 (H/D = 2), 450 (H/D = 3), and 600 mm (H/D = 4) for specimen 4MN30, 4MN45, and 4MN60, respectively.

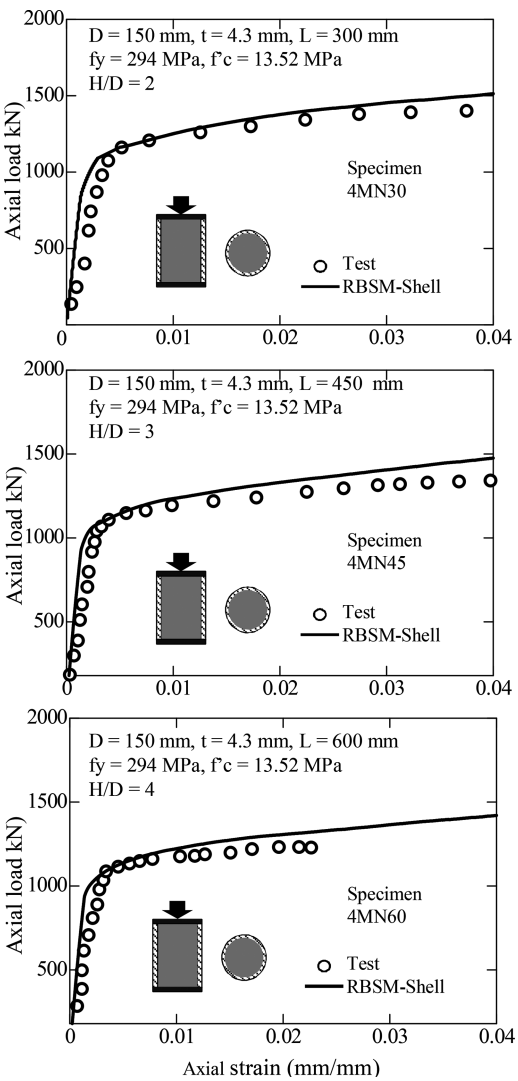

Figure 9. Axial load-strain comparison of test and simulation results of CFSTs with different height.

Axial displacements in the test were measured using four dial indicators and the reported axial strains were calculated by dividing these measurements by the specimen height. For the simulation models, a similar procedure as described above was followed. Comparison of axial load-strain diagrams between test and simulation results are presented in Figure 9. Test results are represented by circular markers and simulation results by solid lines. A good fit can be generally observed between test and simulation results. In all the tests, a strain-hardening behavior was observed with no defined peak. This observation was also captured by the simulation models. Overall, the comparison suggests that the RBSM-shell model can simulate the axial-load displacement response of CFST irrespective of height.

6 LOCALIZATION AND SOFTENING IN STEEL-TUBE CONFINED CONCRETE

Yamamoto (2008) already presented the capability of RBSM in simulating localization and strain-softening behavior in unconfined concrete specimens subjected to uniaxial compression. In this section, we extend and evaluate this capability of RBSM to steel-tube confined concrete specimens. The objective is to determine the effect of passive confinement in the localization of deformation in concrete. Specifically, the relation between softening and the length of localization damage in concrete under increasing confinement (expressed in terms of steel reinforcement ratio) is studied. Four numerical models were analyzed which represents four levels of steel confinement which are expressed in terms of increasing steel tube thickness. The thicknesses considered are 0.6 mm, 1.30 mm, 2.65 mm, and 5.0 mm representing 1.80%, 4.0%, 8.0%, and 14.8% steel reinforcement ratios ρ, respectively. Material properties for all the simulation specimens are the same, i.e., concrete compressive strength $f'c$ = 40 MPa, and steel yield strength fy = 250 MPa. The diameter and length of the specimens are 130 mm and 520 mm, respectively. Input RBSM mesh size was set at 12 mm while a 10 mm mesh size was used for shell elements. Pinned boundary condition was assumed on top and bottom of the specimens.

The axial load-strain diagram for the four specimens representing 1.80%, 4.0%, 8.0%, and 14.8% steel reinforcement ratio are shown in Figure 10. The presented axial load represents the load carried by both concrete and steel. The axial strains are the ratio of applied displacement and specimen height. The axial load-displacement diagram

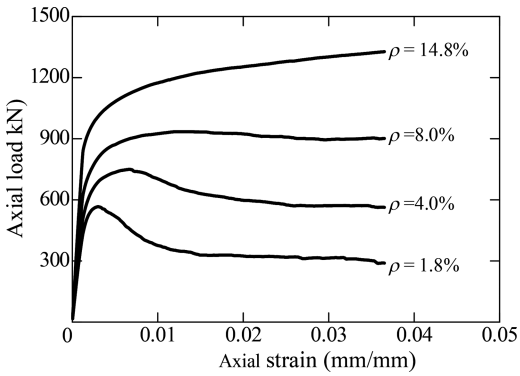

Figure 10. Axial load-strain diagram of steel-tube confined concrete columns under increasing confinement.

for specimen with ρ = 1.80% and 4.0% shows an evident post-peak softening response. In contrast, an almost perfect plastic and a strain hardening response can be observed for specimen with ρ = 8.0% and 14.8%, respectively. The results show the effect of increasing the passive confinement provided by steel tube in transitioning the behavior of confined concrete from softening into hardening response. These results are consistent with those observations of Caner and Bazant which mentioned that at 8% steel ratio, a mild softening can be observed which can be considered as the transition zone between softening and hardening behavior.

To relate these simulation results with the localization of deformation in concrete. The same specimens were used to measure the local axial strains within the concrete core. The measurement of local axial strains within the concrete provides a quantitative way of measuring the region of localized damage in concrete. The procedure was first introduced in the experiments performed by Nakamura and Higai in which they embedded strain gauges attached on an acrylic bar in concrete cylinder and prism specimens. This approach allowed them to distinguish portion of concrete that are under increasing strain (localized zone) and those that under decreasing strain (unloading zone).

In the numerical modeling of concrete using RBSM, a similar concept can be applied. By defining displacement control points (representing strain gauges) along the height of the specimen, local vertical displacements can be extracted.

The local axial strains are then determined by taking the relative vertical displacement between two adjacent points and dividing it by the distance between the two points. A representation of this method is shown in Figure 11. The displacement control points were defined at 40 mm interval along the height of the specimens. In Figure 12, the extracted local axial strains from the analysis are shown for all the simulation models (in the order of 1.80%, 4.0%, 8.0%, and 14.80% steel ratio). The left hand side plot in each figure represents the local axial strain at four post-peak or post-yield average strain values. For specimen with evident peak axial strength (specimen with 1.80% and 4.0% steel ratio), the reported local axial strain values are at loadings corresponding to average strain at peak ε_p, $2\varepsilon_p$, $3\varepsilon_p$, and $4\varepsilon_p$. For specimen with 8.0% and 14.80% steel ratio, the local axial strain values are at loadings corresponding to average strain value at yield ε_y (taken as 0.2% offset), and at average strains ε_{ave} equal to 1%, 2%, and 3%. The localized zone is determined by comparing the four measured local axial strains at a specific height of the specimen. Increasing strains are assigned as part of localized zone, whereas decreasing strains are assigned as part of unloading zone. From the results, it can be observed that the length of localized zone increases as the level of confinement increases. Specimen with 1.80% steel ratio has the most localized region while specimen with 14.8% steel ratio shows constantly increasing local axial strains along the height. The deformed behavior for concrete and steel are also provided in Figure 12. These simulated deformed behaviors are consistent with the measured length of localized region. The results are also consistent with the presented load-displacement curves in Figure 10. A softening response can be observed for specimens with defined localized region, whereas for specimen with mild softening (specimen with 8% steel ratio), a small region along the height of the specimen unloads, and for Specimen with 14.8% steel ratio with strain-hardening response, local axial strains constantly increase. This suggests that localization of deformation and softening behavior of concrete co-exist in the compressive behavior of steel-tube confined concrete, that is, when localized deformation in concrete occurs, one should expect that the axial-displacement curve will exhibit a softening response.

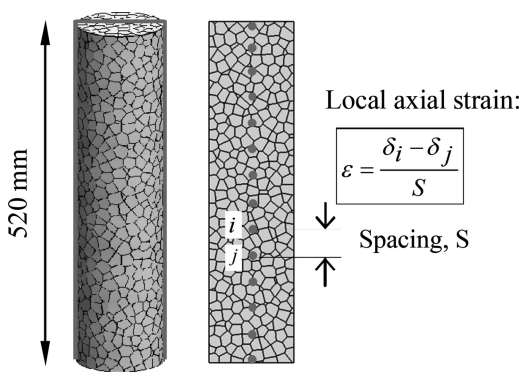

Figure 11. Locations of local axial displacement control points for measurement of local axial strains.

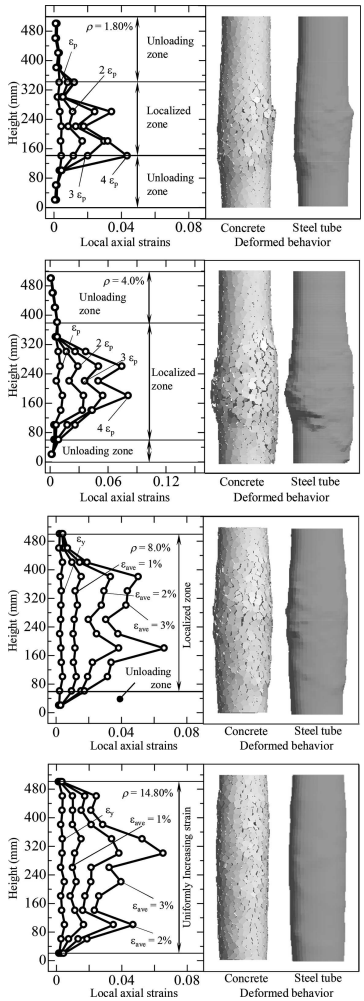

Figure 12. Simulation of localization length and deformation behavior of concrete core and steel tube under increasing confinement.

7 CONCLUSION

A newly developed coupled numerical model which combines the use of RBSM and nonlinear shell FEM in the analysis of steel-tube confined concrete columns was introduced. The presented model can accurately simulate the axial stress-strain softening behavior of low-confined CFST and the strain-hardening behavior of high-confined CFST. Simulations of axial-displacement diagram of specimens with different height showed good agreement with experimental results. This suggests that the model can provide an accurate prediction of the axial stress-strain behavior of CFST irrespective of height. A numerical study was performed to investigate the localization and softening behavior of concrete under increasing steel tube confinement. It was found that (1) the length of localized deformation in steel tube confined concrete increases with increasing confinement (increasing steel ratio); and (2) for specimen with strain softening response, localization zone was observed, whereas for specimen with strain hardening response, the entire specimen height was under a constantly increasing local axial strain. These results suggest that when localized deformation in concrete is observed, a strain-softening response should always be expected.

REFERENCES

Caner, F.C. & Bazant, Z.P. 2002. Lateral confinement needed to suppress softening of concrete in compression. *J. Eng. Mech.,* 128(12): 1304–1313.

Hu, Y.M. Yu, T. & Teng, J.G. 2011. FRP-confined circular concrete-filled thin steel tubes under axial compression, *J. Compos. Constr.,* 15(5):850–860.

Huang, C.S., Yeh, Y.K., Liu, G.Y., Hu, H.T., Tsai, K.C., Weng, Y.T. Wang, S.H., Wu, M.H. 2002. Axial load behavior of stiffened concrete-filled steel columns. *J. Struct. Eng.*, 128(9): 1222–1230.

Mendoza, R.J., Yamamoto, Y., Nakamura, H., & Miura, T. 2018. Numerical simulation of compressive failure behaviors of concrete-filled steel tube using coupled discrete model and shell finite element. *High Tech Concrete: Where Technology and Engineering Meet*, Springer Intl.

Nakamura, H. & Higai, T. 2001. Compressive fracture energy and fracture zone length of concrete. In P.B. Shing & T. Tanabe (eds), *Modeling of Inelastic Behavior of RC Structures under Seismic Loads*. 471–487. ASCE.

Noguchi, H. & Hisada, T. 1993. Sensitivity analysis in post-buckling problems of shell structures. *Comp. & Struct.*, 47: 699–710.

O'Shea, M.D. & Bridge, R.Q. 2000. Design of circular thin-walled concrete-filled steel tubes. J. Struct. Eng., 126(11):1295–1303.

Schneider, S.P. 1998. Axially loaded concrete-filled Steel Tubes, *J. Struct. Eng.*,124(10):1125–1138.

Tomii, M., Yoshimura, K. & Morishita, Y. 1977. Experimental studies on concrete filled steel tubular stub columns under concentric loading, *Stability of Structures under Static and Dynamic Loads*, ASCE.

van Mier, J.G.M. 1997. *Fracture processes of concrete: assessment of material parameters for fracture models*. CRC Press, Inc.

Wei, Y. & Wu, Y.F. 2016. Experimental study of concrete columns with localized failure. *J. Compos. Constr.*, 20(5).

Yamamoto, Y. 2008. *Evaluation of failure behaviors under static and dynamic loadings of concrete members with mesoscopic scale modeling*. D.Eng. Dissertation, Nagoya University. [in Japanese].

Yamamoto, Y., Nakamura, H., Kuroda, I., Furuya, N., 2014. Crack propagation analysis of reinforced concrete wall under cyclic loading using RBSM. *European J. Civil Engineering*, 18 (7): 780–792.

Computational Modelling of Concrete Structures – Meschke, Pichler & Rots (Eds)
© 2018 Taylor & Francis Group, London, ISBN 978-1-138-74117-1

Simulation of reinforced ductile cement-based composite beams under cyclic loads

S.L. Billington & Y. Shao
Department of Civil and Environmental Engineering, Stanford University, Stanford, CA, USA

T.E. Frank
U.S. Air Force, Arlington, VA, USA

M.J. Bandelt
Department of Civil and Environmental Engineering, New Jersey Institute of Technology, Newark, NJ, USA

D.M. Moreno
Jensen Hughes, Washington, DC, USA

ABSTRACT: High Performance Fiber-Reinforced Cement-based Composites (HPFRCCs) exhibit pseudo-strain hardening behavior in tension and little to no spalling in compression. HPFRCC has been proposed for use in earthquake- and blast-resistant structural design due to its high damage tolerance. Tension-stiffening, bond-slip behavior, and reinforcement fracture failure in reinforced HPFRCC components have been experimentally investigated. Numerical modeling approaches to predict these unique experimental responses have also been developed and are further explored and validated here with a cyclically loaded cantilever beam experiment. Simulation results are able to capture the test strength, stiffness, and hysteretic energy dissipation with reasonable accuracy. With the help of a recently developed bond-slip model for reinforced HPFRCCs, reinforcing strains are also well simulated up to drifts of 6%. At large drifts of 12% when the experiment fails, the simulated steel strains are below the expected failure strain of the reinforcing bar, and two possible causes are discussed.

1 INTRODUCTION

High-performance fiber-reinforced cement-based composites (HPFRCCs) are ductile cementitious materials that exhibit multiple cracking in uniaxial tension, retain residual strength in compression, and show high levels of damage tolerance when subjected to large deformations in reinforced structural members. These materials have been proposed for use in building and infrastructure systems to improve the seismic performance of reinforced concrete structures in a range of flexure-dominated and shear-dominated designs as well as seismic retrofit applications.

While many proof-of-concept applications have shown that reinforced HPFRCC systems have higher ductility and strength compared to that of ordinary reinforced concrete members, limited data is available on fundamental reinforced composite behavior from which to develop design guidelines and advance their use in practice. Some design codes have adopted approaches for the design of reinforced HPFRCC using models similar to those for reinforced concrete. However, there are several modes of failure observed in experiments that are not accurately modeled by traditional reinforced concrete mechanics. For example, the strain hardening and fracturing of reinforcing steel prior to concrete crushing was observed in 16 out of 25 reported experiments on cyclically-loaded reinforced HPFRCC components summarized in Bandelt & Billington (2016a). This failure mode is not accurately represented by strength predictions that assume steel yielding is maintained up to crushing of the cementitious material.

This paper presents several recent experimental investigations and the development of numerical modeling tools and approaches to predict the unique performance of reinforced HPFRCC materials, including reinforcement strain hardening and fracture, to support the development of new design approaches for reinforced HPFRCC materials. Modeling methods are needed to capture the experimentally observed hardening of reinforcement that is not considered in traditional reinforced concrete strength predictions.

2 BACKGROUND

In reinforced HPFRCC components, compression failures are significantly less common than fracture of the reinforcing steel, due to the damage tolerance and residual strength of HPFRCC materials in compression (summary in Bandelt & Billington 2016a). Flexural failure of reinforced HPFRCC members is more likely to occur due to reinforcement fracture, and as members become more tension controlled (i.e., members with lower reinforcement ratios), deformation capacity appears to decrease (Fig. 1). Although members with high reinforcement ratios, such as bridge columns, and those with diagonal reinforcement, such as coupling beams, are not presented in Figure 1, reinforcement fracture has occurred in these types of members as well.

Understanding the mechanics of the strain-hardening and fracture response of reinforced HPFRCC flexural elements has been the subject of several recent experimental investigations, including tension-stiffening experiments (Moreno et al. 2014), bond-slip experiments (Bandelt & Billington 2016b) and investigations into the impact of cyclic loading protocol on failure (Frank et al. 2017) in reinforced HPFRCC components. These experiments are briefly summarized here followed by modeling methods proposed to assist in predicting the cyclic behavior of reinforced HPFRCC components.

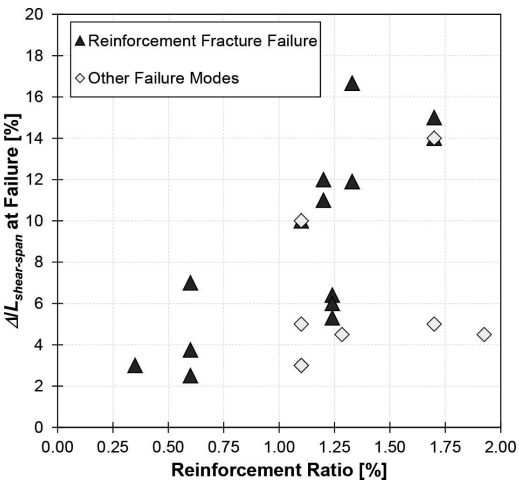

Figure 1. Deformation vs. reinforcement ratio of reinforced HPFRC components indicating high rates of failure by fracture of tension reinforcement.

3 UNIQUE EXPERIMENTAL RESPONSE OF REINFORCED HPFRCC MATERIALS

3.1 *Tension stiffening behavior*

Tension stiffening experiments have demonstrated a unique tension-stiffening effect provided to mild steel reinforcement by HPFRCC materials in tension and flexure, wherein the HPFRCC materials carry tension beyond the yield strain of the mild steel reinforcement (Fischer & Li 2002, Bischoff 2003, Blunt & Ostertag 2009, Jansson et al. 2012, Moreno et al. 2012, Lee et al. 2013). Moreno et al. (2014) demonstrated that the multiple cracking of various HPFRCC materials led to uniform bar yielding and early hardening of the reinforcement at the location of dominant cracks relative to reinforced concrete. The reinforcement fractured within the HPFRCC at lower specimen strain levels than when embedded in traditional concrete (Fig. 2, left).

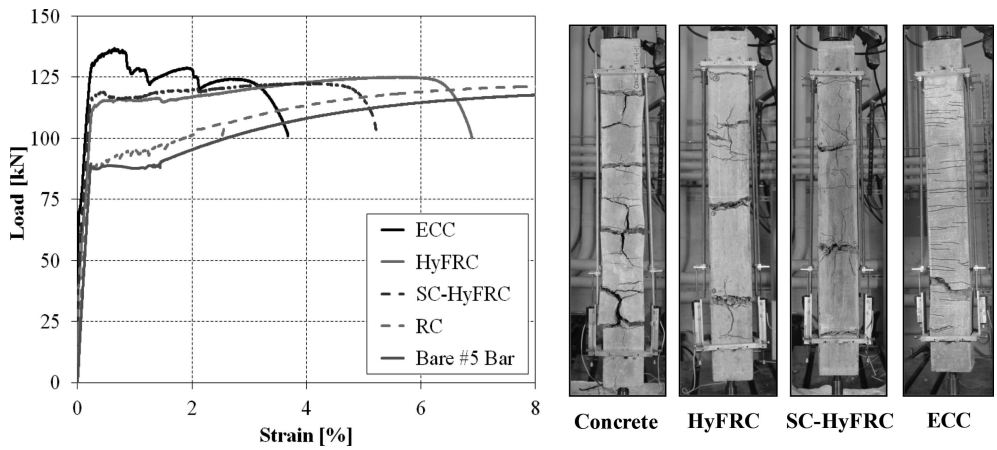

Figure 2. Uniaxial load vs. specimen strain for three reinforced HPFRCC materials, traditional reinforced concrete, and a bare reinforcing bar (left) and failure of the tension stiffening specimens (right).

The ultimate fracture strain of the tension stiffening experiments was found to be a function of the HPFRCC's ability to resist or restrain splitting cracks and to prevent or allow additional dominant transverse cracks to form at specimen strains beyond 1%. The formation of transverse and splitting cracks at failure in reinforced concrete, and three HPFRCC materials (Hybrid Fiber Reinforced Concrete (HyFRC), Self-compacting Hybrid Fiber Reinforced Concrete (SC-HyFRC), and Engineered Cementitious Composites (ECC)) are shown in Figure 2 on the right. If the formation of splitting cracks is prevented and if no additional transverse cracks are formed along the length of the specimen, strain will localize in the first dominant transverse crack leading to fracture of the steel reinforcement at low overall specimen strains, as exhibited in the reinforced ECC. If splitting cracks occur before the fibers are pulled out in a transverse crack, as with HyFRC materials, strains are more evenly spread and several of the multiple transverse cracks can grow wider together, delaying reinforcement fracture and exhibiting higher specimen deformation levels.

3.2 *Bond-slip behavior*

Bond-slip experiments have demonstrated that HPFRCC normalized bond strengths of mild reinforcement are on average 37% higher than those in traditional reinforced concrete. Furthermore, the bond-slip behavior of reinforcement in HPFRCCs have a higher toughness than observed for traditional concrete specimens (Fig. 3) (Bandelt & Billington 2016b). Under cyclic loading, it has been found that cyclic displacement reversals cause the interface between the reinforcement and an HPFRCC material to degrade significantly, resulting in a more rapidly degrading bond strength relative to monotonic bond-slip response (Fig. 4). This bond degradation is attributed to a combination of splitting cracks near the longitudinal tension reinforcement, and internal crushing of the interface between the reinforcement and cementitious matrix.

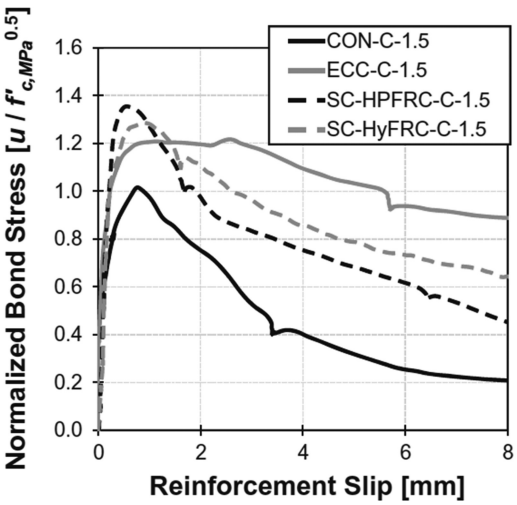

Figure 3. Normalized bond stress vs. reinforcement slip of mild reinforcement in four cementitious materials determined by lap splice beam tests in flexure. CON = Concrete; ECC = Engineered Cementitious Composites; SC-HPFRC = Self-compacting High Performance Fiber Reinforced Concrete; SC-HyFRC = Self-compacting Hybrid Fiber Reinforced Concrete. (From Bandelt & Billington 2014).

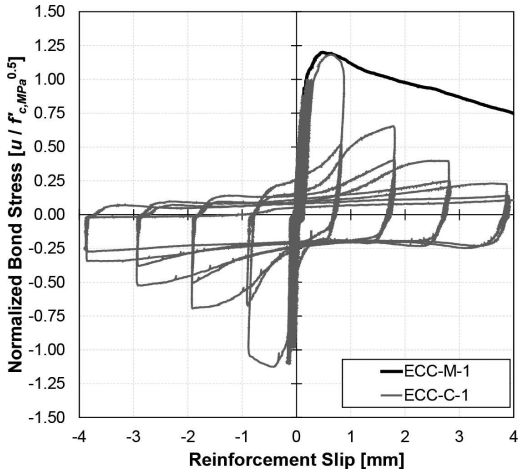

Figure 4. Monotonic and cyclic bond-slip response from flexural beam-end experiments for ECC. M = monotonic loading and, C = Cyclic loading (From Bandelt et al. 2017).

3.3 *Reinforcement fracture failure*

Fracture failure in reinforced HPFRCC component is reviewed in Bandelt & Billington (2016a) where it is noted that failure due to reinforcement fracture rather than crushing of the HPFRCC material is common. This behavior has been observed in flexure and shear-dominated elements as well as members with large axial loads such as bridge columns. Their review of literature also identified that reinforcement fracture failure has also occurred in members with varying drift capacities (i.e., from 2.5 to 15% drift) with the deformation capacity strongly affected by longitudinal reinforcement ratio. Adding to this literature review, a new study confirmed that the impact of load cycling on deformation capacity is

strongly affected by changes in longitudinal reinforcement ratio. Unlike traditional reinforced concrete, deformation capacity is shown to increase under monotonic and cyclic loading by increasing the reinforcement ratio of a reinforced HPFRCC flexural element. In addition, it was found that load cycling can decrease deformation capacity of flexural members by up to 67% when compared to their monotonic deformation capacity (Bandelt & Billington 2016a).

4 MODELING CYCLIC RESPONSE OF REINFORCED HPFRCC COMPONENTS TO CAPTURE STEEL FRACTURE

The combination of the unique tension stiffening response as well as bond-slip response of reinforced HPFRCC materials necessitates design methods that represent the expected failure mechanisms. Traditional methods based on mechanics of slender beams often underestimate the strength of reinforced HPFRCC components subjected to bending, even when accounting for the tensile capacity of the HPFRCC material. Most importantly, the high compressive strains reached by flexural reinforced HPFRCC elements allow the reinforcement to strain harden and fracture before the matrix material fails in compression. Significant differences in monotonic vs. cyclic response particularly at low reinforcement ratios also requires careful attention for accurate simulation. Simulation tools that can predict how the HPFRCC and reinforcement interface deteriorates under cyclic loading are needed to design, detail, and predict the behavior of reinforced HPFRCC components.

To capture the experimentally observed behaviors described above requires simulation of the bond behavior between reinforced HPFRCC both under monotonic and cyclic loading. A 2D bond-slip model for both monotonic and cyclic simulations was developed by Bandelt (2015) based on the bond-slip experiments described in Section 3. The envelope of the bond-slip response serves as the basis for the model development, and the calibrated cyclic bond-slip curve for the simulations to be presented are shown in Figure 5. The ascending portion of the bond-slip curve is defined by a power law function based on experimental observations. A secant unloading and reloading path through the origin is used to simulate the cyclic behavior during the ascending portion of the bond-slip function. Details and demonstrations of predicting monotonic and cyclic response of reinforced HPFRCC beams are given in Bandelt (2015). It was found that this bond-slip model improved predictions of deformations at which fracture of the

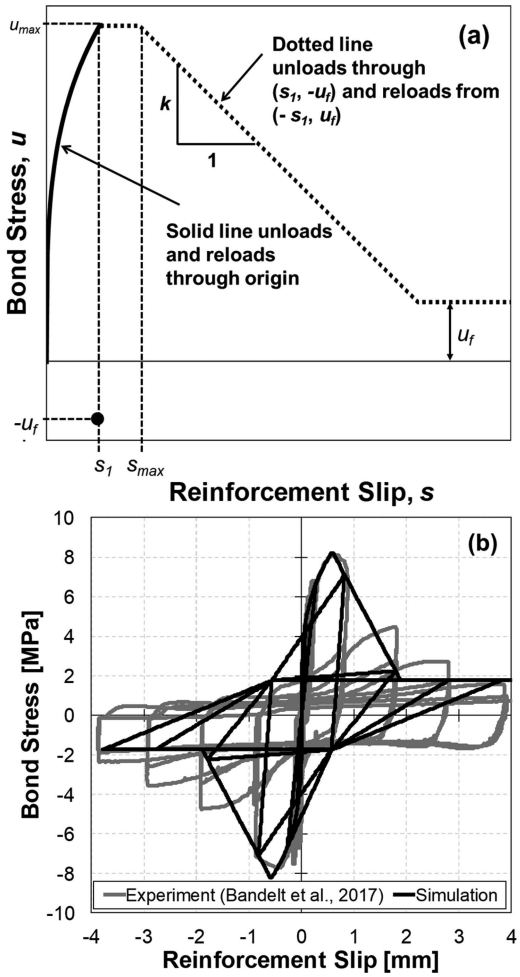

Figure 5. Bond stress vs. reinforcement slip (a) material model envelope, and (b) calibration for cyclic simulations.

reinforcement occurred relative to models simulating perfect bond between the HPFRCC and reinforcement. Hysteretic response of the cyclically loaded beams was also well simulated.

This bond-slip modeling approach was applied herein to another cyclically loaded type of reinforced HPFRCC specimen. The specimen geometry is a vertical cantilever with an enlarged base clamped to a strong floor. The numerical model geometry is shown in Figure 6. The ECC and steel plates were modeled with eight-noded plane stress elements using a 3×3 Gaussian integration scheme. The ECC was modeled using a total strain based fixed crack model in tension, and a total

strain based parabolic model in compression. The steel reinforcement was modeled with directly integrated two-noded truss elements. The transverse steel was modeled as perfectly bonded, embedded reinforcement in the eight-noded ECC elements. The bond-slip behavior between the longitudinal steel reinforcement and ECC was modeled with four-noded interface elements with zero thickness. A two-point Newton-Coates integration scheme was used for the interface elements.

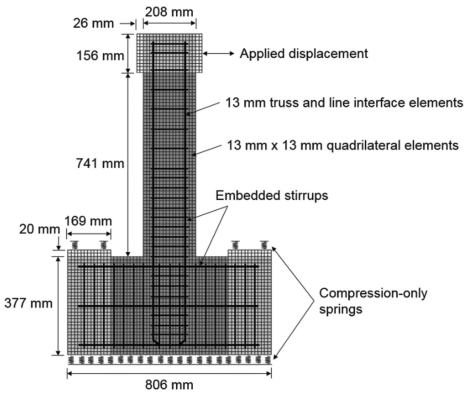

Figure 6. Finite element mesh for cyclically loaded cantilever reinforced HPFRCC beam (Frank 2016).

Material properties and model parameters are shown in Table 1 and were selected based on values used in previous numerical studies or the results of material property test results reported in Frank (2016). Initial tensile strength (f_t), cracking strain (ε_{to}), Young's modulus (E), and fracture energy (G_f) of the ECC were estimated from an inverse analysis of four monotonic third point bending tests on ECC beams wherein a multi-linear material model was assumed. The compressive fracture energy was determined from experimental results of Moreno et al. (2014), and the compressive strength was determined from experimental results in Frank (2016). Steel properties were determined experimentally (Frank 2016) and cyclic behavior, which included the Bauschinger effect, was governed by a

Table 1. Material properties and model parameters.

ECC			
Variable	Description	Value	Units
E	Young's modulus	7.0	GPa
f'_c	Compressive strength	46	MPa
G_c	Compressive fracture energy	52.5	MPa-mm
ε_{to}	Cracking strain	0.000571	mm/mm
f_t	Tensile strength	4.0	MPa
σ_{tp}	Stress at onset of softening	4.0	MPa
ε_{tp}	Strain at onset of softening	0.011	mm/mm
G_f	Tensile fracture energy	2.3	MPa-mm
ν	Poisson's ratio	0.15	–
β	Shear retention factor	0.1	–
13 mm longitudinal steel			
Variable	Description	Value	Units
E	Young's modulus	200	GPa
F_y	Yield strength	455	MPa
F_u	Ultimate strength	675	MPa
ε_{sh}	Strain at onset of strain hardening	0.014	mm/mm
ε_u	Strain at fracture	0.18	mm/mm
ν	Poisson's ratio	0.3	–
Transverse steel			
Variable	Description	Value	Units
E	Young's modulus	200	GPa
F_y	Yield strength	690	MPa
ν	Poisson's ratio	0.3	–

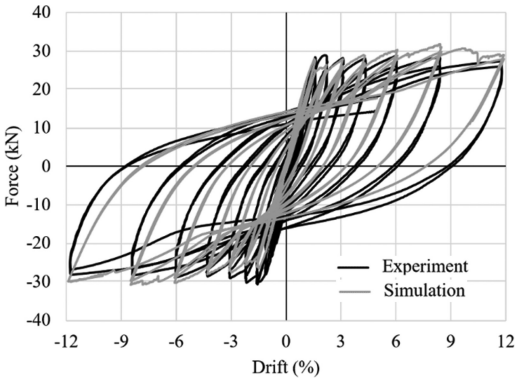

Figure 7. Hysteretic response of the experiment and simulation (Frank 2016).

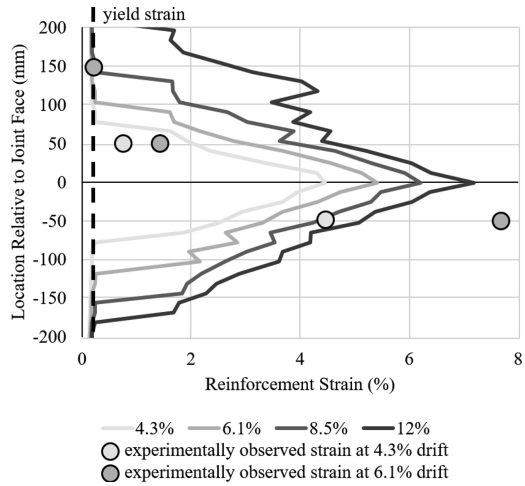

Figure 8. Reinforcement strain profile in the experiment and simulation around the joint face.

set of rules calibrated through experimental results and described in (Shen et al. 1993).

The hysteretic responses of the specimen and the simulation are shown in Figure 7. In both cases the beam has been subjected to a cyclic protocol proposed by the Federal Emergency Management Agency in FEMA (2007). This protocol consists of two cycles at each amplitude beginning with 0.15% drift and increasing by 40% with each subsequent drift up to failure of the specimen. As seen in Figure 7, the strength and stiffness simulated were within 10% of that recorded experimentally. Hysteretic energy dissipation in the simulation was within 17% of that observed experimentally. In the experiment, the steel fractured in a negative drift cycle after having reached 12% drift in the positive direction. Fracture strains were not reached in the simulated reinforcement.

As a goal of the simulations is to predict the fracture failure of the reinforcement, the strains in the reinforcement are compared across the experiment and the simulation. Using numerical models, strain in the steel reinforcement could be monitored at 6.5 mm intervals (i.e., the distance between integration points). In the experiment, there were three strain gages affixed to the steel reinforcing bars roughly 100 mm apart centered at 50 mm above the joint.

Figure 8 shows reinforcement strain profiles of the simulation from 200 mm below to 200 mm above the joint face along the longitudinal steel in tension at the peak of the first excursion to four levels of drift: 4.3%, 6.1%, 8.5%, and 12%. Strain in the steel reinforcement was highest near the base of the beam where the applied moment was highest. Both the magnitude of strain and the length of reinforcing bar that underwent strain hardening increased with drift. In the simulation, the steel reinforcement strain 150 mm above the joint remained at or below yield strain through 8.5% drift, in agreement with reinforcement strain experimentally observed at 6.1% drift. The magnitude of the reinforcement strains simulated at 50 mm above and 50 mm below the joint face were reasonably close to experimentally observed strain gage data. A vertical shift up in the beam of the experimentally observed reinforcement strain data, as opposed to inaccuracies in the model, likely account for the difference between observed and simulated reinforcement strains. Overall, the trends observed in the simulation were similar to those in the experiment in terms of measured strains and cracking behavior. It is noted that at 12% drift the simulated strains did not exceed 8% strain, well below the anticipated strain at which fracture of the steel would occur.

Figure 9 shows the relationship of the reinforcement strain versus drift in the experiment and simulation. The recorded strain history from the strain gauge located 5 mm below the joint face is compared with the simulated strain extracted from the integration point 6.5 mm below joint face. In the experiment, the strain gauge failed during the cycles of 6.0% drift. The simulated strain in the reinforcement approximates the overall behavior of recorded strain up to ~6.0% drift. The strain accumulation during cyclic load is also well captured by the finite element model. In the experiment, the specimen fails due to reinforcement fracture during the cycles of 12% drift. At 12% drift, the simulated reinforcement strain reaches 0.061, which is below the anticipated fracture strain of 0.14–0.18. Two possible causes may lead to this low value simulated when fracture is expected. First, very low

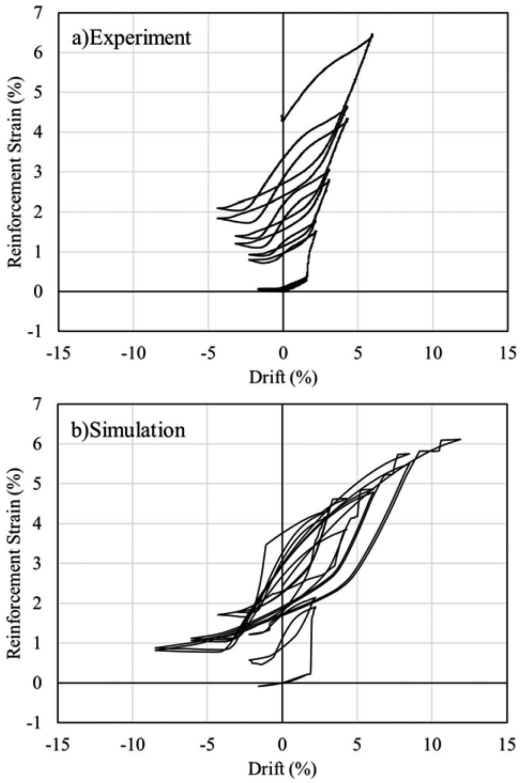

Figure 9. Specimen drift vs. reinforcement strain for the (a) experiment and (b) simulation.

cycle fatigue may have occurred during the cyclic loading of the experiment, which was loaded at a quasi-static strain rate of 0.00002/s. According to Mander et al. (1994), strain amplitudes around 0.03 caused early fracture to mild steel reinforcement bars within 2–5 cycles at strain rates of 0.005/s. In the simulation reported here, the strain amplitude exceeds 0.03 when the drift exceeds 8.5%, so it is possible that very low cycle fatigue could have occurred. Second, in the current model, the reinforcement is simulated using truss elements. Shear sliding of ECC along the dominant crack was observed and would likely cause bending in the reinforcement, which is not captured in truss elements. This bending would cause additional strain accumulation leading to fracture. Generally, the simulation captures the reinforcement strain behavior up to 6.0% drift. Future research is needed to explore the effect of very low cycle fatigue of reinforcement in ECC and the effect of shear sliding.

In the larger set of experiments conducted by Frank (2016), it was also observed that strain increases in the steel occurred in some cases before or after splitting cracks, leading to a hypothesis that bond degradation can be caused by two different mechanisms, not individually captured by a 2D analysis. While it was found that altering the bond-slip model in 2D did not capture these differences well phenomenologically (Frank 2016), 3D modeling of this behavior was captured with reasonable accuracy (Bandelt et al. 2017). Further investigation is needed to evaluate steel fracture strain prediction in 3D modeling approaches.

5 DISCUSSION

Finite element modeling of individual designs to predict their performance under over loads, is always possible yet may be impractical. For design purposes, an approach that replicates that of ultimate strength design for reinforced concrete will be more acceptable. An approach that uses numerical modeling to simulate the tension stiffening of the reinforcement and combines this information with a traditional reinforced concrete mechanics approach for calculating ultimate strength is proposed (Moreno et al. 2014). Others have proposed to use mechanics of traditional fiber reinforced concrete to predict ultimate strength. These methods do not account for the strain hardening of the reinforcement often observed prior to matrix crushing. Currently, a design approach that accounts for reinforcing ratio is being developed. Reinforcement ratio impacts whether the ultimate capacity is reached prior to crack localization, wherein matrix strength and steel yield strength dominate the ultimate capacity of a flexural member, or after crack localization wherein strain hardening of the reinforcement will dominate the ultimate capacity of the flexural member.

6 SUMMARY AND CONCLUSIONS

The unique behavior of reinforced HPFRCC in terms of tension stiffening and bond-slip that has been observed to lead to strain accumulation and fracture in reinforcing steel necessitates design methods that represent the expected failure mechanisms. Most importantly, the high compressive strains reached by flexural reinforced HPFRCC elements allow the reinforcement to strain harden and fracture before the matrix material fails in compression. Significant differences in monotonic vs. cyclic response particularly at low reinforcement ratios also require attention for accurate simulation of reinforcement strain. Simulation tools that can predict how the HPFRCC and reinforcement interface deteriorates under cyclic loading are needed to design, detail, and predict the behavior of reinforced HPFRCC components.

A new bond-slip model has been applied to a cantilever beam test of reinforced HPFRCC subjected to a cyclic loading protocol with stepwise increasing deformations. By adopting experimentally observed material properties both directly and through inverse analysis, hysteretic response of the beam was simulated within 10% of the strength and stiffness of the experiment and within 17% of the hysteretic energy dissipation. Reinforcing strains are also well simulated to moderate drifts (6%, or half the ultimate drift capacity). The simulations are able to reach the drifts when the experiments failed by reinforcement fracture without the simulated steel strains being in the range expected for fracture. Two possible reasons for this under-prediction of strain that are not captured in the simulations are very low cycle fatigue of the reinforcing bars and bending of the reinforcement due to shear sliding.

Finite element modeling of individual designs to predict their performance under over loads may be impractical for design purposes. An approach that replicates that of ultimate strength design for reinforced concrete is needed that accounts for reinforcing ratio as the reinforcing ratio impacts whether the ultimate capacity is a function of matrix strength and steel yield strength or rather a function of strain hardening of the reinforcement.

REFERENCES

Bandelt, M.J. & Billington S.L. 2014. Simulation of High-Performance Fiber-Reinforced Cementitious Composites with Bond-Slip Effects. *Proceedings of EURO-C 2014, Computational modeling of concrete and concrete structures*, St. Anton am Alberg, Austria.

Bandelt, M.J. 2015. Behavior, Modeling, and Impact of Bond in Steel Reinforced High-Performance Fiber-Reinforced Cement-Based Composites. *Ph.D. Thesis*, Stanford University.

Bandelt, M.J. & Billington, S.L. 2016a. Impact of Reinforcement Ratio and Loading Type on the Deformation Capacity of High-Performance Fiber-Reinforced Cementitious Composites Reinforced with Mild Steel. *Journal of Structural Engineering,* 142, 14.

Bandelt, M.J. & Billington, S.L. 2016b. Bond behavior of steel reinforcement in high-performance fiber-reinforced cementitious composite flexural members. *Materials and Structures,* 49, 71–86.

Bandelt, M.J., Frank, T.E., Lepech, M.D. & Billington, S.L. 2017. Bond behavior and interface modeling of reinforced high-performance fiber-reinforced cementitious composites. *Cement and Concrete Composites,* 83, 188–201.

Bischoff, P.H. 2003. Tension stiffening and cracking of steel fiber-reinforced concrete. *Journal of materials in civil engineering,* 15, 174–182.

Blunt, J.D. & Ostertag, C.P. 2009. Deflection hardening and workability of hybrid fiber composites. *ACI Materials Journal,* 106, 265–272.

FEMA 2007. Interim Testing Protocols for Determining the Seismic Performance Characteristics of Structural and Nonstructural Components. *Federal Emergency Management Agency*, Washington, DC.

Fischer, G. & Li, V.C. 2002. Influence of matrix ductility on tension-stiffening behavior of steel reinforced engineered cementitious composites (ECC). *ACI Structural Journal,* 99, 104–111.

Frank, T.E. 2016. Response of Reinforced Engineered Cementitious Composite Flexural Members Subjected to Various Cyclic Deformation Histories. *Ph.D. Thesis*, Stanford University.

Frank, T.E., Lepech, M.D. & Billington, S.L. 2017. Experimental testing of reinforced concrete and reinforced ECC flexural members subjected to various cyclic deformation histories. *Materials and Structures,* 50, 232.

Jansson, A., Flansbjer, M., Löfgren, I., Lundgren, K. & Gylltoft, K. 2012. Experimental investigation of surface crack initiation, propagation and tension stiffening in self-compacting steel-fibre-reinforced concrete. *Materials and structures,* 45, 1127–1143.

Lee, S.-C., Cho, J.Y. & Vecchio, F.J. 2013. Tension-stiffening model for steel fiber-reinforced concrete containing conventional reinforcement. *ACI Structural Journal,* 110, 639.

Mander, J., Panthaki, F. & Kasalanati, A. 1994. Low-cycle fatigue behavior of reinforcing steel. *Journal of Materials in Civil Engineering,* 6, 453–468.

Moreno, D., Trono, W., Jen, G., Ostertag, C. & Billington, S. 2012. Tension-stiffening in reinforced high performance fiber-reinforced cement-based composites under direct tension. *High Performance Fiber Reinforced Cement Composites 6*. Springer.

Moreno, D.M., Trono, W., Jen, G., Ostertag, C. & Billington, S.L. 2014. Tension stiffening in reinforced high performance fiber reinforced cement-based composites. *Cement and Concrete Composites,* 50, 36–46.

Shen, C., Mizuno, E. & Usami, T. 1993. A generalized two-surface model for structural steels under cyclic loading. *Doboku Gakkai Ronbunshu,* 1993, 23–33.

Computational Modelling of Concrete Structures – Meschke, Pichler & Rots (Eds)
© 2018 Taylor & Francis Group, London, ISBN 978-1-138-74117-1

The use of trilinear softening functions for modelling the cracking of fibre reinforced concrete

A. Enfedaque, M.G. Alberti & J.C. Gálvez
Departamento de Ingeniería Civil, Construcción, E.T.S I. de Caminos, Canales y Puertos, Universidad Politécnica de Madrid, Madrid, Spain

ABSTRACT: The relevance of fibre reinforced cementitious materials (FRC) has increased due to the appearance of regulations that establish the requirements needed to take into account the contribution of the fibres in the structural design. However, in order to exploit the properties of such materials it is a key aspect being able to simulate their behaviour under fracture conditions. Considering a cohesive crack approach, several authors have studied the suitability of using several softening functions. However, none of these functions can be directly applied to FRC. The present contribution analyses the suitability of multilinear softening functions in order to obtain simulation results of fracture tests of a wide variety of FRC. The implementation of multilinear softening functions has been successfully performed by means of a material user subroutine in a commercial finite element code obtaining accurate results in a wide variety of FRC. Such softening functions were capable of simulating a ductile unloading behaviour as well as a rapid unloading followed by a reloading and afterwards a slow unloading. Moreover, the implementation performed has been proven as versatile, robust and efficient from a numerical point of view.

1 INTRODUCTION

Concrete has remarkable compressive strength but also shows quasi-brittle behaviour under tensile and flexural loads (Bazant & Planas, 1997). Concrete tensile behaviour has been enhanced by adding randomly distributed short fibres, creating a material commonly termed fibre-reinforced concrete (FRC) and allowing partial or total substitution of traditional reinforcement (Zollo, 1996, Serna et al., 2009).

Various models have been postulated that deal with the physical process of cracking in concrete. The smeared crack approach (Polanco-Loria, 1997) has been commonly used when there is no localisation of the cracks and when the crack opening is reduced. When crack is localized, the so-called discrete approach has provided more accurate results. One of the most used cracking models for plain concrete was developed by Hillerborg (Hillerborg et al, 1976) and named the cohesive crack model. This model has been successful applied not only to plain concrete, but also to other brittle or quasi-brittle materials such as brick masonry (Gálvez et al., 2013, Reyes et al., 2009, Sancho et al 2007). A more detailed explanation of this model may be found in any of the references provided.

The cohesive crack model reproduces the fracture behaviour of plain concrete by using as an input the tensile strength (obtained by means of the indirect tensile strength test, EN 12390-6) and the fracture energy (RILEM TC-187-SOC, 2007). The type of softening function should be selected (Slowik et al, 2006). Diverse softening functions have been proposed, which may vary from an exponential function to a linear or bilinear one. The latter has been profusely used due both to its simplicity and the accurate results that it provides. However, none of these functions can be directly applied to reproduce the fracture behaviour of FRC produced nowadays. Some researchers have made an extensive analysis of the constitutive models of steel FRC and one type of plastic FRC in standard and high-strength concretes (Kang et al, 2010). Other authors have studied the influence of the fibre length made of steel and the placement method in the tension softening curves of ultra-high-strength concrete. These have been also analysed by other authors in examining FRC made with steel fibres in normal and high-strength concrete and even when using recycled steel fibres (Kang et al, 2011). Nevertheless, the application of these results to polyolefin fibre reinforced concrete (PFRC) is a question that deserves being studied to a deeper extent. Moreover, the changes of the softening function that should be implemented when the dosage of polyolefin fibres varies had not been assessed at the time of writing.

Based on the post-cracking response of the experimental results of FRC it would be possible to perform an inverse analysis and hence obtain the parameters that define the material softening function as previously performed in various types of FRC: PFRC (Alberti et al, 2014a, 2014b, 2015), SFRC (Kooiman et al, 2000) and GRC (Enfedaque et al, 2017).

In this paper the fracture behaviour of FRC is replicated in a finite element method (FEM) programme by implementing the softening function deduced from the experimental campaigns by means of a user material subroutine. Two types of FRC are used for the numerical simulation: PFRC (Alberti et al, 2014a, 2015) and GRC (Enfedaque et al, 2017).

2 SOFTENING BEHAVIOUR OF FRC

The softening function of plain concrete is considered as a material property (Bazant & Planas, 1997), starting at the maximum stress and being the area below the curve named as cohesive fracture energy and computed by expression (1), with w_c being the critical crack opening where cohesive stress becomes zero (Elices et al, 1996) and $f(w)$ the tensile stress at w crack opening.

$$G_F = \int_0^{w_c} f(w)\,dw \tag{1}$$

The bulk material is modelled as an isotropic linear elastic material. The maximum strength of the material equals the tensile strength (f_{ct}) the cracking behaviour onsets and expression (2) is validated.

$$f_{ct} = f(0) \tag{2}$$

Consequently, the softening function is the main characteristic of the material while fracturing and therefore the one that defines the behaviour while cracking. In this regard it has to be outlined that when dealing with plain concrete cracking there are several types of functions that have been used successfully. For instance, linear, bilinear or exponential curves have been used obtaining accurate results (Hillerborg et al, 1976, V. Slowik et al, 2006, Roelfstra & Wittmann, 1986, Guinea et al 1994, Kooiman et al, 2000). One possibility of an exponential softening function can be seen in (3):

$$\sigma = f_{ct} \cdot e^{\left(-\frac{f_t \omega}{G_F}\right)} \tag{3}$$

where G_F is the specific fracture energy and f_{ct} is the tensile strength. A way of obtaining such softening functions is by what has been termed inverse analysis, adjusting experimental response of a notched specimen by trial-and-error optimisation through

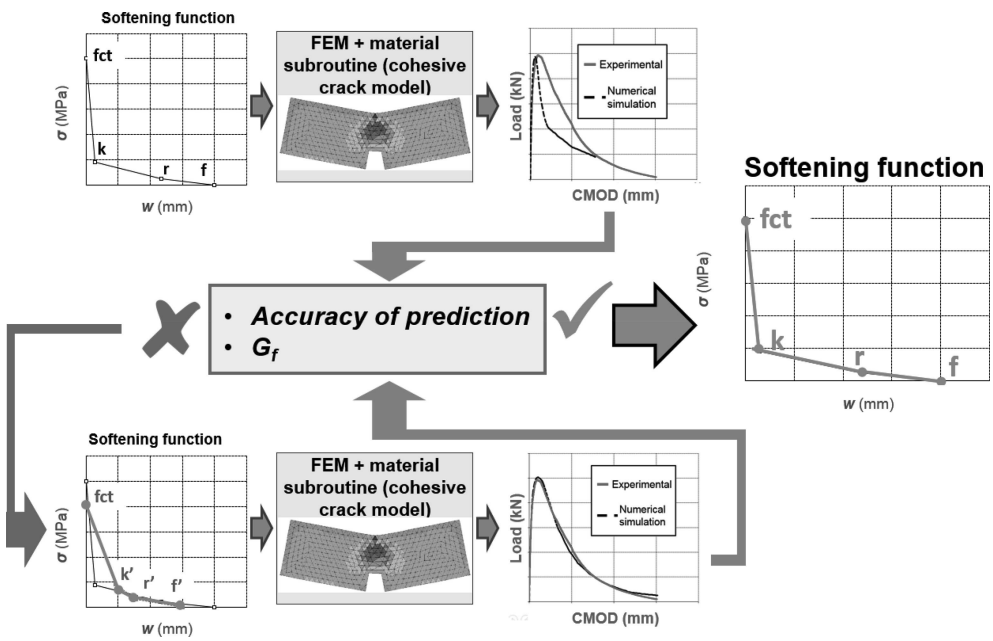

Figure 1. Inverse analysis used to reproduce the fracture test results.

use of finite element methods (De Oliveira et al., 2006). Based on the promising results obtained using a bilinear softening function both in accuracy to the experimental results and in numerical calculus efficiency, the material improvements provided by the presence of fibres has been introduced in several studies as modifications of multilinear functions (Alberti et al, 2017). Such relations were implemented in a commercial finite element programme by means of a user subroutine for material. Hence, the numerical simulations were performed using ABAQUS code and one UMAT subroutine to model the fracture behaviour of PFRC and GRC. In such a sense, the non-linear fracture process zone emerges in the elements placed on the crack. Given that the behaviour of the fracturing elements depends on a constitutive relation that needs to be iteratively fit the scheme that can be seen in Figure 1 was followed.

Applying the multilinear approach to the softening functions that are capable of introducing the effect in the fracture behaviour of PFRC and GRC such functions can be defined as in expressions (4) and (5) respectively. In these expressions the only difference can be observed in the first unloading part. In this regard, both approaches; the one related with PFRC using an exponential function and the one related with GRC which uses a linear function provide a remarkable degree of accuracy.

$$\begin{cases} \sigma = f_{ct} \cdot e^{\left(-\frac{f_{ct} w}{G_F}\right)} & if \quad 0 < w \le w_k \\ \sigma = \sigma_k + \left(\frac{\sigma_r - \sigma_k}{w_r - w_k}\right)(w - w_k) & if \quad w_k < w \le w_r \\ \sigma = \sigma_r + \left(\frac{-\sigma_r}{w_f - w_r}\right)(w - w_r) & if \quad w_r < w \le w_f \\ \sigma = 0 & if \quad w > w_f \end{cases} \tag{4}$$

$$\begin{cases} \sigma = f_{ct} + \left(\frac{\sigma_k - f_{ct}}{w_k}\right) w & if \quad 0 < w \le w_k \\ \sigma = \sigma_k + \left(\frac{\sigma_r - \sigma_k}{w_r - w_k}\right)(w - w_k) & if \quad w_k < w \le w_r \\ \sigma = \sigma_r + \left(\frac{-\sigma_r}{w_f - w_r}\right)(w - w_r) & if \quad w_r < w \le w_f \\ \sigma = 0 & if \quad w > w_f \end{cases} \tag{5}$$

3 DISCUSSION

Several experimental results of fracture tests performed in cementitious materials were reproduced using the aforementioned implementation. The test reproduced in the case of the PFRC tests had been conducted in $100 \times 100 \times 430$ mm^3 specimens. The span of the three-point bending tests was $3D$ and the notch $1/3D$, being D the height of the square cross section (100 mm). Such specimens had been manufactured adding 3, 4.5, 6 and 10 kg/m^3 of 60 mm-long polyolefin fibres to a self-compacting concrete. The details of the manufacturing process as well as the testing setup and procedure followed can be found in (Alberti et al, 2014). The recommendation followed was RILEM-TOC 187 (2007). The curves shown are the average of at least three successful tests. Although it could be argued that a larger amount of test would be required to provide sound conclusions it has to be highlighted that the careful handling and preparation of the test setup provided results with a limited degree of scatter. Regarding the simulations, if Figure 2 is observed it can be seen how the softening function implemented was capable of reproducing with a remarkable accuracy the behaviour of PFRC. This implementation was found both robust and numerically efficient besides of the great adaptability that it boasts. This can be clearly perceived in Figure 2. By changing the points that define each stretch of the softening functions the several implementations were able to reproduce all the features of the experimental results. The latter is of high relevance because the minimum post-peak registered changes noticeably between the formulations. Similarly, the values of the maximum post peak loads of the simulations appear in similar values in the simulated curves. Not only these values were reproduced but also the slopes of the unloading and reloading branches of the experimental curves are accurately obtained.

In order to check the adaptability of the multilinear softening curves another fibre reinforced cementitious material of a totally different nature was simulated. In this case the material chosen was a glass fibre reinforced cement (GRC). This material is manufactured by merging cement mortar and randomly distributed short glass fibres. Similarly to the case previously explained of PFRC the multilinear softening functions were implemented in this case for reproducing the fracture test results obtained in previous research (Enfedaque et al, 2015). Three GRC formulations were manufactured, being among them the use of some chemical additives the only difference. Such additives seek to prevent the change of mechanical properties that undergo the traditional GRC formulations as times passes. Such formulations were named GRC, GRC-M and GRC-P which correspond to traditional GRC, GRC with a Metaver additive and a GRC with Powerpozz additive. In contrast to PFRC the fracture tests conducted with the several formulations of GRC could not be performed following

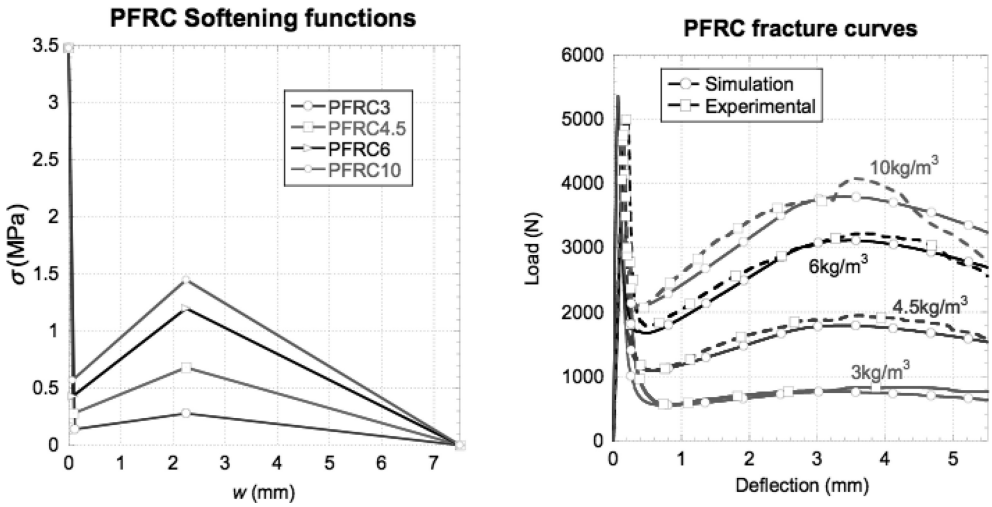

Figure 2. Softening functions (left) and comparison between simulated and experimental results (right) of PFRC.

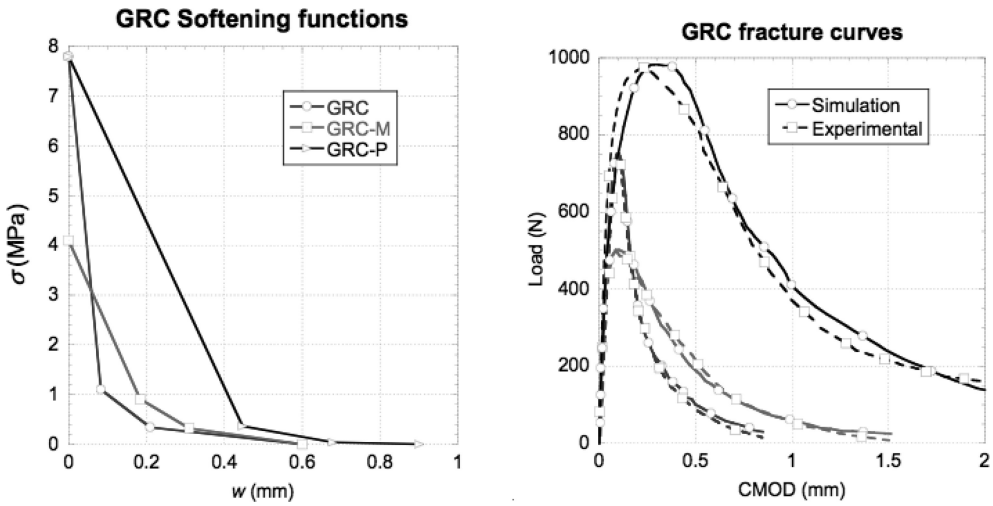

Figure 3. Softening functions (left) and comparison between simulated and experimental results (right) of GRC.

any recommendation as at the time of such research there was no one available. Nevertheless, the closest adaptation of the previously mentioned RILEM-TOC 187 recommendation was followed. Similarly to PFRC the curves shown in Figure 3 are the average of at least three successful tests and a remarkably low degree of scatter was registered.

As in the previous case of PFRC, the multilinear softening functions implemented were divided into three stretches. However, in the case of GRC the slope of the stretches were in all cases negative. The changes in the values that define the stretches of the softening functions were able to reproduce with remarkable accuracy the fracture behaviour of GRC including the noticeable changes in the maximum load sustained, ductility and in the unloading rate that the material boasted. In the first case it can be seen that there is no clear connection between the maximum load obtained in the test and the tensile strength of the material. It seems that the slope of the material in the first unloading branch is also of high importance to determine the maximum load of the test. This can be seen comparing the behaviour of GRC-P

and GRC. Both softening functions have the same tensile strength but on the contrary the slope of the first unloading branch of the GRC-P provides the material a higher loading capacity.

Regarding the changes in the ductility, the crack width of the softening functions is the major factor that define it. However there is also influence of the slope of the third stretch of the softening function because as can be seen in Figure 3, GRC-M and GRC have the same maximum crack width but the maximum crack mouth opening displacement (CMOD) is different in both formulations.

Comparing the features of the softening functions implemented it can be stated that when the first unloading branch has a great negative slope the maximum load that the material can sustain in the fracture tests is mainly determined by the tensile strength of the material as can be seen in all the cases of PFRC and also in GRC formulation. Nevertheless, as in the case of GRC-P when there is a more gradual loss of stiffness the material is still able to increase its capacity of sustaining load although the closer parts of the tip of the notch are already damaged and the stiffness of the sample decreased noticeably before reaching the maximum load. This phenomenon was also perceived in the numerical models performed where several elements closer to the notch tip were already damaged when the maximum load was reached.

4 CONCLUSIONS

4.1 *Text and indenting*

The implementation of multilinear softening functions has been performed successfully in a material user subroutine in a commercial finite element code. Using this implementations, fracture tests of PFRC and GRC have been reproduced with a remarkable degree of accuracy. The implementation has been proven as versatile, robust and efficient from a numerical point of view.

The changes in the tensile strength of the material and the points that define the stretches of the softening functions have been shown suitable to simulate the progressive unloading that appear in the GRC formulations fracture tests and the reload events that take place in the PFRC ones.

The variations of the length and slope of the parts of the softening functions enable to analyse the changes of the material behaviour that are introduced by several the amount of fibres in PFRC and the effects of the chemical additives in the case of GRC. It has to be underlined that this approach was able to simulate a ductile unloading behaviour, such the one that appears in GRC, as well as the rapid unloading followed by a reloading and afterwards a slow unloading as the one that appears in PFRC.

When there is a first unloading branch with a high slope the peak load registered in the tests is mainly determined by the tensile strength of the material. Nevertheless, if such slope is more gradual the combination of the slope and tensile strength of the material determine the peak load registered experimentally. In what regards the material ductility, it is mainly influenced by the maximum crack width that the material sustains.

ACKNOWLEDGEMENTS

The authors gratefully acknowledge the financial support provided by the Ministry of Economy and Competitiveness of Spain by means of the Research Fund Project BIA 2016-78742-C2-2-R. They also offer their gratitude to SIKA SAU for supporting the Enterprise University Chair: Cátedra Sika-UPM.

REFERENCES

Alberti MG, Enfedaque A & Gálvez JC, "On the mechanical properties and fracture behavior of polyolefin fiber-reinforced self-compacting concrete," *Construction and Building Materials,* vol. 55, pp. 274–288, 2014a.

Alberti MG, Enfedaque A, Gálvez JC, Cánovas MF & Osorio IR, "Polyolefin fiber-reinforced concrete enhanced with steel-hooked fibers in low proportions," *Materials & Design,* vol. 60, pp. 57–65, 2014b.

Alberti MG, Enfedaque A & Gálvez JC, "Comparison between polyolefin fibre reinforced vibrated conventional concrete and self-compacting concrete," *Construction & Building Materials,* vol. 85(15), pp. 182–194, 2015.

Alberti MG, Enfedaque A, Gálvez JC & E. Reyes "Numerical modelling of the fracture of polyolefin fibre reinforced concrete using a cohesive fracture approach", *Composites Part B: Engineering*, 111, pp. 200–210, 2017.

Bazant ZP & Planas J, Fracture and size effect in concrete and other quasibrittle materials, CRC press, 1997.

De Oliveira JLA, Sousa E & Gettu R, "Determining the tensile stress-crack opening curve of concrete by inverse analysis," *Journal of engineering mechanics,* vol. 132(2), pp. 141–148, 2006.

Elices M & Planas J, "Fracture mechanics parameters of concrete: An overview," *Advanced Cement Based Materials,* vol. 4, pp. 116–127, 1996.

Enfedaque A., Romero H.L., Gálvez J.C. 2014, Fracture energy evolution of two concretes resistant to the action of freeze-thaw cycles. *Materiales de Construcción*, 64(313), 2014.

Enfedaque A, Alberti MG & Gálvez JC, "Application of trilinear softening functions based on a cohesive crack approach to the simulation of the fracture behaviour of fibre reinforced cementitious materials", IOP Conf. Series: *Materials Science and Engineering* 246, 2017.

Enfedaque A., Gálvez J.C., Suárez F. 2015, Analysis of fracture tests of glass fibre reinforced cement (GRC) using digital image correlation 2015. *Construction and Building Materials* (75), 472–487, 2015.

Gálvez JC, Planas J, Sancho JM, Reyes E, Cendón DA, Casati MJ, An embedded cohesive crack model for finite element analysis of quasi-brittle materials, *Engineering Fracture Mechanics,* (109), 369–386, 2013.

Guinea GV, Planas J & Elices M, "A general bilinear fit for the softening curve of concrete," *Materials and Structures,* vol. 27(2), pp. 99–105, 1994.

Hillerborg A, Modéer., Petersson PE, Analysis of crack formation and crack growth in concrete by means of fracture mechanics and finite elements, *Cement and Concrete Research,* 6(6), 773–78, 1976.

Kang ST, Lee Y, Park YD & Kim JK, "Tensile fracture properties of an Ultra High Performance Fiber Reinforced Concrete (UHPFRC) with steel fiber," *Composite Structures,* vol. 92(1), 61–71, 2010.

Kang ST & Kim JK, "The relation between fiber orientation and tensile behavior in an Ultra High Performance Fiber Reinforced Cementitious Composites (UHPFRCC)," *Cement and Concrete Research,* 41(10), 1001–1014, 2011.

Kooiman A.G., Van Der Veen C., Walraven J.C. 2000, Modelling the post-cracking behaviour of steel fibre reinforced concrete for structural design purposes, *HERON,* 45(4), 275–308, 2000.

Polanco-Loria M. 1997, Numerical modelling of plain and reinforced concrete by damage mechanics, Trondheim: Department of Structural Engineering, Norwegian University of Science and Technology, 1997.

Powerpozz: http://www.bigfreshcontrol.com/documents/act_documents/10.150MetakaolinPhys&ChemWhite.pdf.

Reyes E, Gálvez JC, Casati MJ, Cendón DA, Sancho JM & Planas J, An embedded cohesive crack model for finite element analysis of brickwork masonry fracture, *Engineering Fracture Mechanics,* 76(12), 1930–44, 2009.

RILEM TC-187-SOC, "Indirect test for stress-crack opening curve," 2007.

Roelfstra PE & Wittmann FH, "Numerical methods to link strain softening with failure of concrete," *Fracture Toughness and Fracture Energy,* pp. 163–175, 1986.

Sancho JM, Planas J, Cendón DA, Reyes E, Gálvez JC, An embedded crack model for finite element analysis of concrete fracture, *Engineering Fracture Mechanics,* 74(1), 75–86, 2007.

Serna P, Arango S, Ribeiro T, Núñez AM & Garcia-Taengua E, "Structural cast-in-place SFRC: Technology, control criteria and recent applications in Spain," *Materials & Structures, 42(9),* p. 1233–1246, 2009.

Slowik V, Villmann B, Bretschneider & Villmann T, "Computational aspects of inverse analyses for determining softening curves of concrete," *Computer Methods in Applied Mechanics and Engineering,* vol. 195(52), p. 7223–7236, 2006.

Zollo R, "Fiber-reinforced concrete: an overview after 30 years of development," *Cement & Concrete Composites,* vol. 19, pp. 107–122, 1996.

Computational Modelling of Concrete Structures – Meschke, Pichler & Rots (Eds)
© 2018 Taylor & Francis Group, London, ISBN 978-1-138-74117-1

Model comparisons for a shell structure made of textile reinforced concrete

T. Senckpiel & U. Häussler-Combe
Department of Civil Engineering, Institute of Concrete Structures, Technische Universität Dresden, Dresden, Germany

ABSTRACT: Textile Reinforced Concrete (TRC) is an innovative composite material which is suitable for slender shell structures. Lightweight and load-bearing ceiling elements made of TRC with spans of 3 and 4.3 m and slendernesses of 15 and 21.5 were developed and tested in 6 point bending tests with regard to their load carrying capacity, usability and type of failure. The curved cross-sectional shape and a component thickness of merely 1.3 cm requires the finite element method as calculation method. To model the geometry of the structure conventional layered shell elements were taken. The presented numerical simulations show the usage of two different material models. They are compared in terms of accuracy and the required input data. By comparing the experimental and numerical results, several application possibilities for the respective models can be derived and for each of them the advantages and disadvantages can be obtained.

1 INTRODUCTION

Carbon concrete is being used increasingly in the case of reinforcing existing constructions (Curbach et al. 2011) and for new carbon concrete applications (Scheerer et al. 2017). The project partners, who are involved in the presented project, have set themselves the goal of developing a real alternative to established construction: A precast ceiling element, which is economically and technically competitive through the application of a newly developed innovative composite material. Not only the design and the production technology should be redesigned because of using the new materials efficiency, but also the simulation of the material behavior should be considered and rethought.

In the research project, the Technische Universität Dresden and their partners dealt comprehensively with all aspects of designing a completely new component: A totally new material was invented and investigated. In addition a new cross-sectional design of ceiling elements was used to deal with the given requirements. And at least the material and components were tested to verify simulation models and to do studies for changing conditions. Thus, material models were chosen and compared. All these mentioned parts are presented in the following sections of this article.

2 MATERIALS

One part of the project was the development and investigation of a new material composite. It consists of a nonwoven which is soaked with a mineral matrix and is called Fleece Concrete Composite (FCC) by the inventor Eisewicht (2015). A further developed material composite is a combination of FCC and Textile Reinforced Concrete (TRC) with the name of Nonwoven-Textile Reinforced Concrete (N-TRC), which can be seen in Figure 6 and was used for the ceiling elements.

To impregnate the nonwoven successfully with the mineral matrix, the concrete mixes should be harmonize with the nonwovens fabrics. The concrete mixture was adjusted with regard to composition, rheological behavior and largest particle size what was made by the project partner BCS Natur- und Spezialbaustoffe GmbH (BCS). The partner Sächsisches Textilforschungsinstitut e.V.

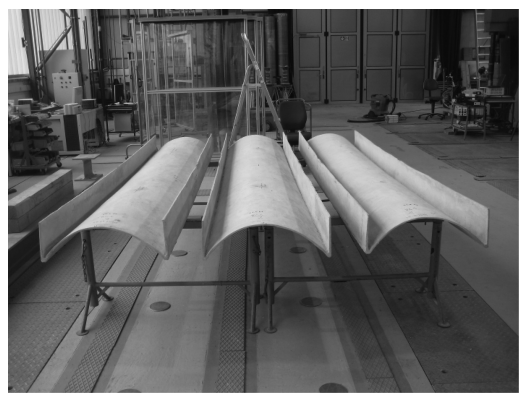

Figure 1. 3 ceiling elements.

(STFI) developed the nonwovens with regard to their fiber geometry, type and structure.

2.1 *Concretes*

The mineral matrix which is modified for soaking the nonwoven is called Texton-C and is a fine-grained concrete from BCS. It has a maximum grain size of 200 micrometers and can be assigned to concrete strength class 42.5. Another fine-grained concrete is used to achieve a good bond between the matrix and the textile. The name of the second mentioned concrete is Texton-D and it has a strength of 61 MPa.

2.2 *Carbon textiles*

The carbon textiles which were used for the ceiling elements were produced by the TUDATEX GmbH Dresden. A heavy-tow textile (HT) was used for the minimum reinforcement of the component and has already a general building inspectorate approval (DIBt 2017). It has a fineness of 3300 tex in the warp direction and 800 tex in the weft direction. In regard to the distance of 10.71 mm between the yarns in the warp direction and 14.28 mm in the weft direction this corresponds to a reinforcement area of 1.71 cm²/m in first mentioned direction and to a 0.31 cm²/m in the second one. The Young's modulus is 170000 MPa according to the old inspectorate approval (DIBt 2014).

A low-tow textile (LT) was used in addition for the most stressed areas in the gussets between the webs and the arch. This textile has in each direction a fineness of 800 tex and a yarn distance of 7.14 mm, which results in a cross-sectional area of 0.62 cm²/m or 0.44 mm² per yarn. The Young's modulus of one yarn was measured in tensile tests by the TUDATEX GmbH and is 193000 MPa. The values of the elastic modulus of one yarn is used as input data for the second of the two material models, which were presented in the article.

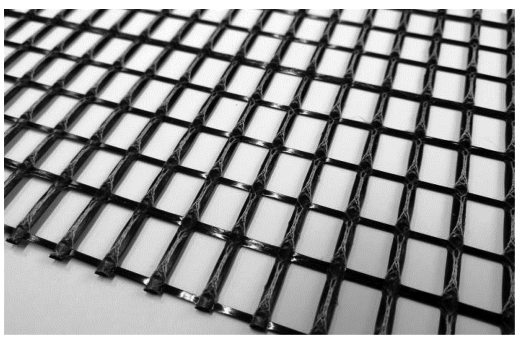

Figure 2. Carbon textile with 3300 tex.

2.3 *Concrete soaked nonwoven*

In order to achieve and apply a more effective manufacturing process in comparison to the common laminating one, which would have to be done laborious by hand for the curved ceiling elements, the partners decided to use concrete soaked nonwovens. The benefits are mentioned in section 4. Therefor different nonwovens were produced or procured from the partner STFI and were tested in combination with the fine concrete matrix. The material of the nonwoven, which was used for the presented second of three developed generation of ceiling elements is polyester, but due to other conditions it was not used anymore for the third generation. The nonwovens were chosen in regard to have good properties in their strength and ductility.

Various FCC specimens were tested in uniaxial tensile tests to carry out the stress-strain behavior. The investigations were done according to the experimental setup after Schütze et al. (2015) in the Otto-Mohr-Laboratory of the Technische Universität Dresden and the gained experimental results were used again as input data for the second material model.

2.4 *Composite material*

The properties of the N-TRC were tested in small-scale material tests. The compressive strength and the Young's modulus under compressive stress was carried out at specimens, which were cut out of the tested ceiling elements with the dimensions of L/W/H: 60 mm/10–16 mm/40 mm. Because of the used nonwovens, which softens the material, the compressive strength had just a reduced value of 32 MPa. The Young's modulus was 11486 MPa. The corresponding stress-strain curves can be seen in Figure 5.

Like the FCC the composite material N-TRC was investigated in uniaxial tensile tests according

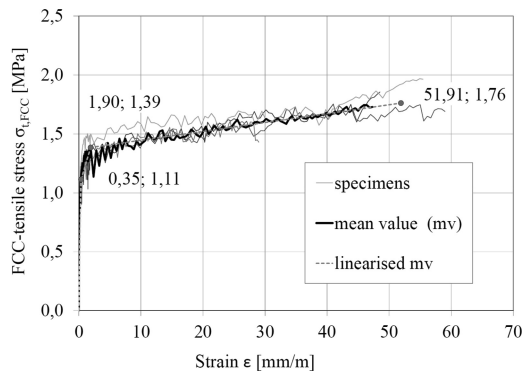

Figure 3. Uniaxial tensile test results of concrete soaked nonwoven specimens.



Figure 4. Application of a nonwoven to a TRC specimen.

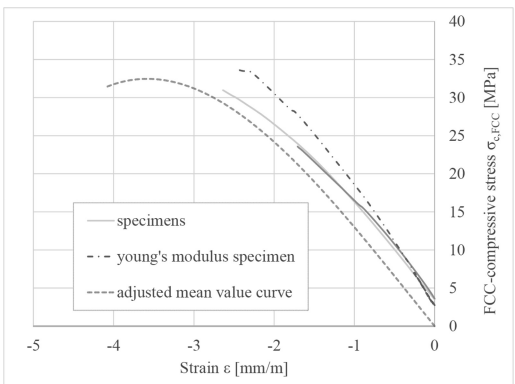

Figure 5. Compression test of the compound material.

to Schütze et al. (2015), too. The stress strain behavior in the longitudinal direction can be seen in the Figure 7. Each type of textile, which is described in the section 2.2, was tested with four single-layered reinforced specimens (L/W/H: 1100 mm/55 mm/9 mm).

The stress-strain curves of these tested specimens and the resulting mean-value curves can be clearly divided into 3 states: an uncracked state, a state of crack formation and a final cracking state.

In contrast to the conventional procedure the tensile stress is determined by referencing it to the entire cross-sectional area of the N-TRC specimen and not to the cross-sectional area of all yarns.

The significant points of the curves are used for the input data for a first material model. The Young's modulus at the first branch of the curves is with 12300 MPa approximately the same. The mean value of the cracking strength of the two

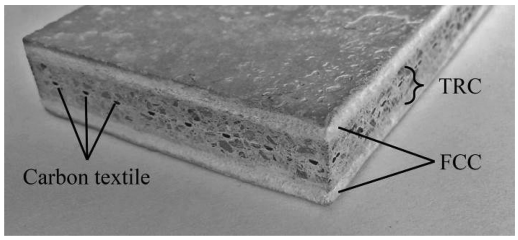

Figure 6. Fine grained concrete with a reinforcement of carbon textiles and a layer of concrete soaked nonwovens on each side.

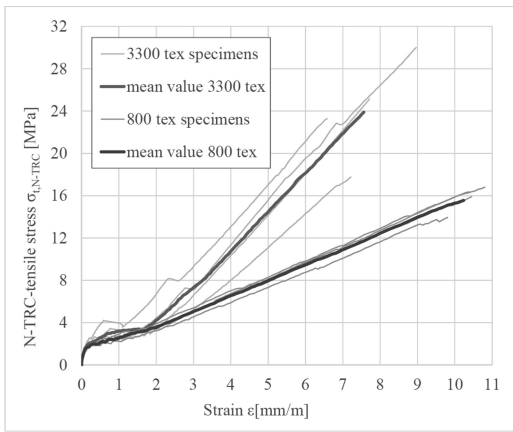

Figure 7. Material tension tests of the composite N-TRC material where the stress refers to the cross-section of the specimen.

curves is with 2.3 MPa for the heavy-tow and with 1.7 MPa for the low-tow slightly different. The modulus of elasticity of the post-cracking state IIb is $E_{c,HT,IIb}$ = 3485 MPa for heavy tow textile related to the cross-section of the entire composite material. The Young's modulus based only on the cross-section of the textile is $E_{tex,HT,IIb}$ = 218,000 MPa. Its reinforcement ratio is ρ_{HT} = 1.49% and the mean thickness of the four tested specimens was t_{HT} = 10.69 mm.

These material parameters for the test specimens of the low tow textile are: $E_{c,LT,IIb}$ = 1459 MPa, $E_{tex,LT,IIb}$ = 237,000 MPa, ρ_{LT} = 0.61% and t_{LT} = 9.8 mm. This data is important for the calculation of material behavior when using material model above in case of textile combinations and thickness changes in the load-bearing structure.

3 DESIGN AND CONSTRUCTION

The ceiling elements were designed to replace wooden beam ceilings in need of renovation. The

loads to be carried remain the same: the dead load, additional dead loads and the service load.

During the project time three different design variants of the ceiling elements were developed. In the present paper the second generation is introduced. In the component tests of the lightweight ceiling elements of the first generation, the values for the deflections were close to or even above the maximum permissible l/250 (EC 2 2010) deflection for the quasi-permanent load combination (EC 1 2010). To decrease theses high deflections of the ceiling elements, which had a component thickness of 1.7 cm in all parts, the project partners decided to increase the thickness in the middle of the element over a length of 1.5 m for the second generation presented here, where it has the greatest effect. The enlarging of the cross-section and hence the moment of inertia was easily done using additional layers of FCC.

The shape of the ceiling elements was originally based on the idea to design the load-bearing behavior in longitudinal direction by means of two webs and laterally with an arch. The components have a cross-section height of 20 cm and the arch of 18 cm. The width of a ceiling element is 60 cm (see Figure 8). The length can be specified as 320 cm and the span as 300 cm. However, experiments and simulations have shown that the load-bearing structure works as a whole during load transfer. This is mainly due to the equal moments of inertia of the arch and the webs. Another advantage is that there are no large shear stresses in the reinforcement plane between the webs and the shell in the longitudinal direction of the ceiling elements.

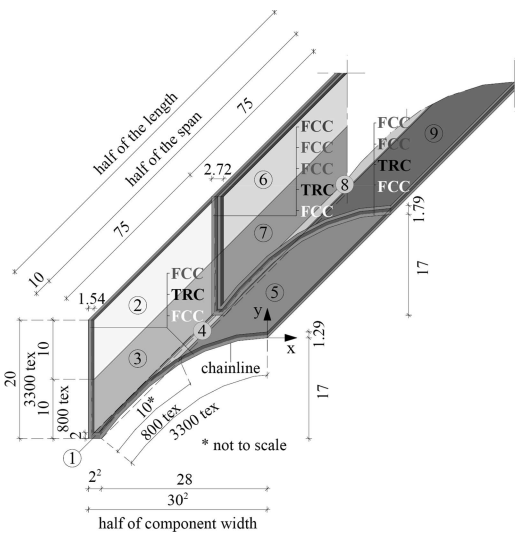

Figure 8. Ceiling element design, geometry and cross-sectional compositions.

The arched shape is based on a chain line with the equation:

$$y(x) = -25.4cm^{*}\cosh\frac{x}{25.4cm} + 25.4cm \qquad (1)$$

In order to be able to achieve longer spans and still keep the deflection as low as possible, a reinforced concrete infill was used for the third and 4.5 m long generation of ceiling elements. These were also successfully examined in experimental tests.

4 MANUFACTURING PROCESS

The ceiling elements of the second generation were manufactured in layers. As the first layer, a layer of FCC was placed on the formwork, which is shown in Figure 9. Next, a thin layer of Texton-D concrete was applied to the FCC layer to place the two layers of textile on top of it. The heavy tow fabric over the entire width of the component and the low tow fabric in the gusset areas. The fabrics were then laminated with Texton-D concrete to ensure a good bond. A layer of FCC has been laid up again. As already mentioned in section 3, additional FCC layers have been applied in the center of the element like it can be seen on Figure 4. On a length of

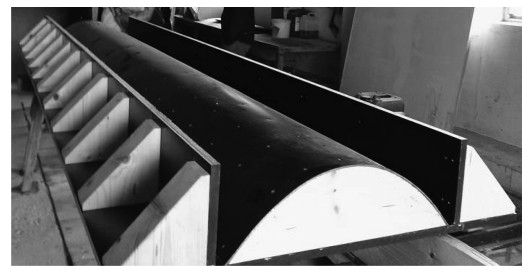

Figure 9. Formwork for the ceiling element production.



Figure 10. Experimental six point element bending test.

1.5 m, an additional FCC layer has been laid over the entire element width and the webs have been equipped with a second FCC strip.

5 EXPERIMENTAL COMPONENT TESTS

A total of 20 elements have been produced, where out of 16 have been tested and 4 are used as demonstrators. The elements have been subjected to 6-point bending tests. The test setup can be seen in Figure 10. The steel profiles of the load distribution structure had a fixed and a movable bearing and were thus statically determined. The four wooden load distribution templates, whose geometry corresponded to the arched shape of the ceiling

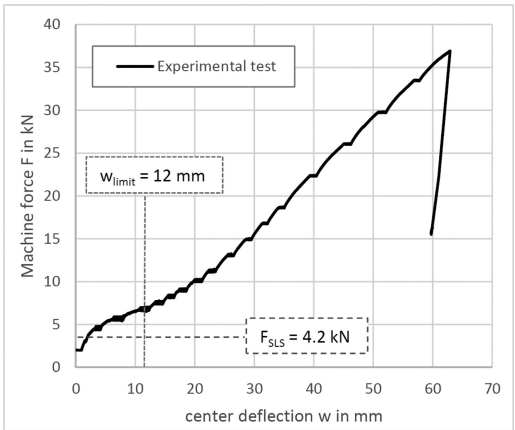

Figure 11. Experimental machine force vs. center deflection curve of an element test.

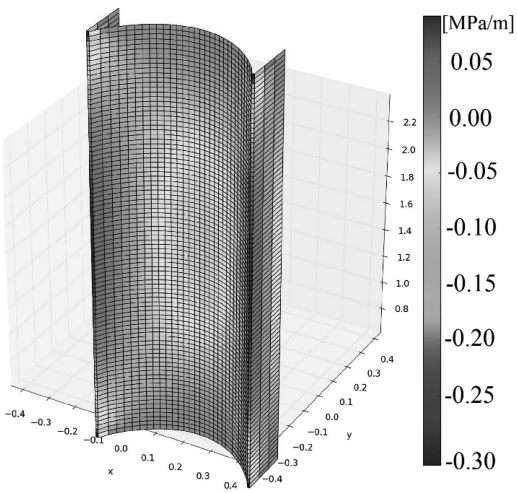

Figure 12. Membrane forces in longitudinal direction.

elements, transferred the force into the component. During the test, the force and various displacements and strains were measured. The force-center deflection of a load test is shown in Figure 11.

In addition, Figure 11 shows that the maximum permissible deflection of 12 mm for a calculated load in the serviceability limit state of 4.2 kN has been achieved by the ceiling element.

6 CALCULATION AND ASSESSMENT

The results and observations from the component test were used to develop and validate suitable calculation models and procedures with which both the load bearing capacity and the relevant deformations of the ceiling elements can be predicted sufficiently accurate.

6.1 *Loads and calculation of internal forces*

The determination of the internal forces and deformations of the bearing members were performed with the help of the FEM program ConFem (Häussler-Combe 2017). For the determination of the bearing capacity and the deformations, the following three loadings relevant for the calculation of the test and the assessment are considered:

- Dead loads of the floor construction, a dry substructure according to DIN EN 1991-1-1 and of the arch filling consisting of a lightweight concrete are in total $gE_{,substructure} = 2.1$ kN/m²,
- Dead load of one ceiling element is $gE_{,Element} = 0.46$ kN/m² and
- Service loads in buildings of domestic and residential areas according to DIN EN 1991-1-1 are $q = 2$ kN/m².

For the initial dimensioning, the normal forces n in the center of the ceiling element were determined with an elastic material model and a first, simplier version (see Figure 12) of the structural model described in the following section 7.1.

To assess the structure of the first ceiling element generation for the ultimate limit state, the ceiling element was divided into two parts: the arch and the web, whereby the gusset belongs to the web. The loadings were considered by superposition taking into account the partial factors for actions ($\gamma_G = 1.35$ and $\gamma_Q = 1.5$) and combinations of actions $\Psi_{2,Q} = 0.3$), which were obtained from DIN EN 1991 (2010).

The largest calculated membrane tensile forces with an orientation in the longitudinal direction of the arch is located 3.5 cm away from the gusset in the center of the element and has a value of: $n_{shell} = 30$ kN/m. At these mentioned 3.5 cm the author has defined the transition between the web

respectively the gusset and the shell and as this is the lowest point of the shell, the highest tensile stress is also here. The maximum membrane tensile forces at the bottom of the webs or in the gussets are: $n_{gusset} = 90$ kN/m.

6.2 *Initial dimensioning*

A common measure for the distance between the weft yarns of carbon textiles is due to production factors $a_{weft} = 10.7$ mm. Therewith, the yarn force in the shell can be calculated to $F_{yarn,shell} = n_{shell} \cdot a_{weft} = 0.321$ kN.

Furthermore it can be seen from the simulation results that the lower 7.5 cm (= $z_{tension\ zone}$) of the web is stressed under tension. Starting from a conservative rectangular stress profile, the tensile force on the web can be calculated to $F_{web} = n_{web} \cdot z_{tension\ zone} = 6.7$ kN. The design strength of the heavy to fabric presented in section 2.2 is according to DIBt (2014) $f_{tex} = 750$ N/mm². For the low tow fabric the same value was assumed with the knowledge at that time. This leads to the required yarn cross-sectional area in the shell: $A_{req,shell} = F_{yarn,shell} / f_{tex} = 0.43$ mm², which corresponds to the low tow fabric with its yarn fineness of 800 tex. The required reinforcement area for the web can be calculated in the same way: $A_{req,web} = F_{web} / f_{tex} = 8.9$ mm². One heavy tow yarn has a cross-sectional area of $A_{heavy\ tow\ yarn} = 1.83$ mm² what results to the minimum number of required yarns: $n_{req,web} = A_{req,web} / A_{heavy\ tow\ yarn} = 4.9 \approx 5$.

Based on the results of the initial dimensioning, the project partners decided to use the low tow fabric as minimum reinforcement in all parts of the ceiling elements of the first generation and the heavy tow fabric as additional reinforcement in the gusset. As mentioned in section 3, due to the high deflection the second generation has been geometrically adapted. In addition, the fabrics have also changed their intended use. This was done for reasons of price and stiffness improvements for the cracked condition. The heavy tow fabric was used for the second generation over the entire cross-sectional width and the low tow fabric is only used as additional reinforcement in the gusset area.

7 SIMULATION MODELS

7.1 *Structural model*

To verify the correct implementation of the continuum based MITC4 shell elements according to Bathe (2002) in ConFem and the development of different material models applied with ConFem, the FEM software Abaqus was used for comparative computations.

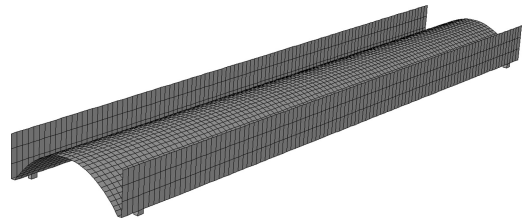

Figure 13. Structural model with shell and solid elements made with Abaqus CAE.

The structural model shown in Figure 13 consists of four-noded shell elements and is explained in (Häussler-Come 2014 & Bathe 2006). The shell elements assumed strain to avoid locking and describe the geometry shown in Figure 8 with their mid-surface. The model also takes into account the different thicknesses of the shell structure.

In order to minimize concentrated loads on the bearings, the structural model is supported by 3D eight-noded solid elements. This avoids local stress peaks, which would predict an unrealistic failure too early. A comparatively low modulus of elasticity of 1000 MPa was assumed for the solid elements. To avoid side effects, the Poisson's ratio of the solid elements has been set to 0. In the longitudinal direction of the ceiling element, the lower nodes of the solid elements are movable on one side and fixed on the other. In the transverse direction, all nodes of the solid elements and all nodes within the load application areas are fixed. The total load has been applied in small steps using nodal loading with an incrementally iterative approach.

7.2 *Material models*

In the following two material models are presented, which on the one hand offer a fast and easy application of the parameters obtained from the experimental material tests and thus a fast way to a simulation result. On the other hand, the implementation of a further material model is presented, which captures more input parameters and allows more variation possibilities for the simulation in this way.

7.2.1 *Material model 1: isotropic mises elastoplasticty*

The first material model uses the relatively simple approach of an isotropic mises elastoplasticity. The model uses only the stress-strain curves of the diagram shown in Figure 7 as a material equation.

For the different cross section compositions with their different thicknesses and reinforcement contents as shown in Figure 8, calibrations have been

made for the material behavior in the final cracking state. The first calibration process must be carried out due to the difference in thickness between the tensile test specimens and the different thicknesses in the ceiling element. The average thickness of the tensile test specimens is 10.69 mm. But the average thickness for the cross-sectional section number 2 Figure 8 is 15.4 mm. In the stress-strain diagram, which refers to the entire material cross-section, it is ignored that the load-bearing effect in the final cracking state is only achieved by reinforcement. Consequently, in the case of a thicker but equally reinforced cross-section, the curve section of the uncracked state should not differ in the same diagram and the curve section of the final cracking state should be flatter. The curve gradient for a 15.4 mm/10.69 mm thicker cross-section has been adjusted in inverse proportion by the authors. This can be seen in Table 1 and Figure 14.

Another calibration was done with the modulus of elasticity in the final cracking state for a tensile specimen with both reinforcements. It can be determined with the average modulus of elasticity of the textiles and the sum of the reinforcement ratios:

$$\bar{E}_{c,HT+LT,IIb} = \left(\rho_{HT} + \rho_{LT}\right) \times \bar{E}_{tex} \tag{2}$$

The above described calibration of the Youung's modules has also been carried out for the sections of different thicknesses with the combined reinforcement.

Although the experimental data come from uniaxial tensile tests, no distinction is made in material model 1 for compression and tension. Furthermore, the test specimens contain the mentioned biaxial textile fabrics, but in the material model 1 isotropic behavior is assumed. These apparently too coarse simplifications need to be taken into account when evaluating the results and offer the possibility of interpreting the entire load-bearing behavior of the structure. Figure 15 shows the simulation result, which was achieved with Abaqus and the trilinear curves stress-strain curves. In the elastic, non-cracked state and in the state of crack formation, the correspondence between the results of the experimental test and the simulation results of material model 1 is very high. In the final cracking state, there is an underestimation of the structural rigidity of the load-bearing structure, whereby the difference between the two force-deflection curves becomes greater as the force increases.

Table 1. Cross-sections and their calibrated parameters.

cross section	thickness [mm]	reinforcement [tex]	*cal.* E_{IIb} [MPa]
tensile test LT	9,8	800	1459
tensile test HT	10,69	3300	3485
cal. combi.	10,24	800+3300	4792
1	20	800+3300	*1862*
2	15,4	3300	*2419*
3	15,4	800+3300	*3187*
4	12,9	800+3300	*3805*
5	12,9	3300	*2887*
6	27,2	3300	*1369*
7	27,2	800+3300	*1805*
8	17,9	800+3300	*2742*
9	17,9	3300	*2081*

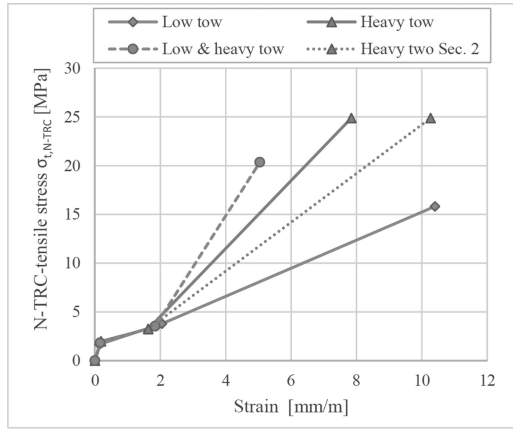

Figure 14. Mean value curves of the composite stress-strain relation of a heavy tow and low tow reinforced specimen and two calibrated relations.

7.2.2 *Material model 2: isotropic damage elasticity and reinforcement layers*

In comparison to the elastoplasticity, where permanent strains occur and material stiffness behavior remains unchanged, the damage of the second material model is based on the decreasing material stiffness, without permanent plastic deformations remaining upon unloading. Here, the cross section of the shell elements represents only the concrete or the FCC behavior, respectively with the ability to distinguish between compressive and tensile regime. Thus, the authors have tried to take into account the experimental stress-strain curves from the compressive and tensile tests of pure concrete soaked nonwovens (see Figure 3 and Figure 5) using the homogeneous, isotropic strain based damage material model, which is basically triaxial and suitable for the shell element described in section 7.1 (see Häussler-Combe & Hartig 2008).

This means that the behavior from the compression tests (see Figure 5) can be simulated very well.

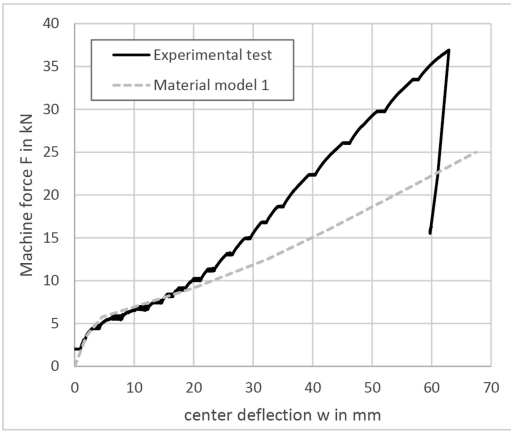

Figure 15. Comparison of the experimental and the with the smeared material model calculated machine force vs. center deflection curve of an element test.

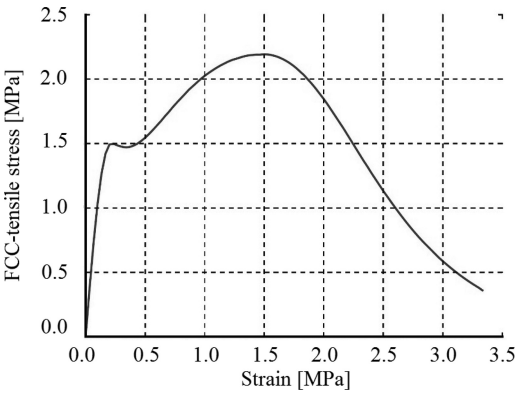

Figure 16. Tensile stress-strain relation of an adjusted concrete material model to simulate an FCC layer.

The tensile behavior of the FCC (see Figure 3) was also attempted to be mapped using isotropic damage elasticity. The simulation result of a uniaxial tensile test of an FCC specimen can be seen in Figure 16.

In material model 2, the textile reinforcement layers were considered using the layer model. This makes it possible to explicitly integrate several reinforcement layers into the shell element. The height, orientation and area of the reinforcement layers can be freely selected.

Because the stress in the uncracked state is almost exclusively absorbed by the FCC material and the reinforcement is only activated in the multiple cracking state, a bilinear stress-strain curve has been used as the material law. In this way, the slip between the two materials is also represented (see Figure 17).

Currently only one material law can be defined for all reinforcement layers. The authors decided to use the Young's modulus of the heavy tow textile, because it is the most widely used textile in the ceiling element.

The structural model uses up to six different layers. In the cross-sections, in which only one bi-directional mesh has been installed, the reinforcement has been considered by using two layers. These are located at the same cross-section, but differ in orientation (0° and 90°). In the other, double-reinforced sections, another four layers are used and the two first mentioned ones are disregarded.

In the elastic and uncracked state of the component, the calculation results shown in Figure 17

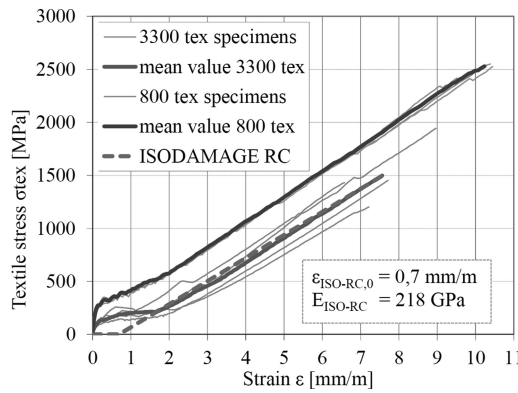

Figure 17. Stress strain curves of the heavy tow and low tow tensile specimens related to the textile cross-sections with the bilinear stress strain curve assumed for the material modell 2.

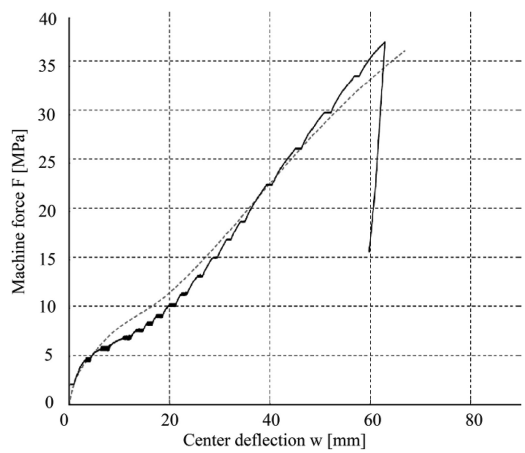

Figure 18. Comparison of the experimental and the with the machine force calculated isodamage material model vs. center deflection curve of an element test.

are again very close to those of the experimentally determined results. With the start of the multiple cracking state, however, the curves deviate slightly from each other in order to cross again in the final cracking state. For the most part, the differences can be regarded as very small.

7.2.3 *Material model comparison*

If one compares the two material models, it can be stated that model 1 needs less experimental data as input parameters and thus requires less time and less experimental costs in advance. This also means that the implementation of a trilinear material curve is also less costly for the modeler than the layer-accurate consideration of the reinforcement. On the other hand, there is of course a higher degree of accuracy for the second material model when approximating a real structure to a computational model.

Further advantages of the second material model are the possible consideration of the damage of a normal concrete or the FCC material (see Figure 19) in individual stress states, which can also be used for the consideration of a stress history.

In addition, with material model 2 it is also possible to test other materials in different combinations in a simulation. Thus, other concrete soaked nonwoven can be tested by directly using the results from unreinforced specimen results. Therefore, no reinforced tensile specimen must be produced. However, it should be noted that the combination of different matrices with different reinforcements also leads to different bond characteristics. In order to take this into account in both model 1 and 2, an experimental data base with reinforced tensile specimens is required.

In the experimentally carried out load-bearing capacity test of the ceiling elements, the maximum chargeable force was limited by a compressive failure in the upper part of the web at the transition to the thicker component cross-section. Currently, failure in simulation can only be achieved by reaching the maximum tensile strength in composite material on model 1 or by reaching the maximum damage induced by tensile stresses in model 2. Model 2 has at least the potential to show the real failure. However, this further development is still in progress.

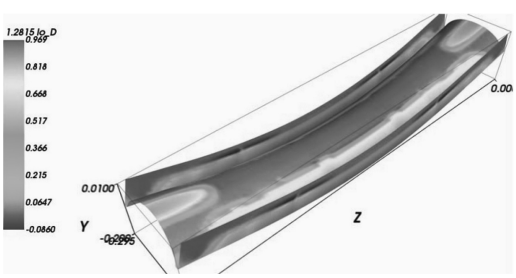

Figure 19. Damage visualization of a ceiling element.

Last but not least, model 1, in comparison to model 2, can very well represent the important part of the load-bearing behavior of the ceiling element and in the rest of the part the load-bearing behavior is underestimated on the safe side.

8 CONCLUSION

The first model is more accurate within the serviceability limit state in terms of deformation behavior (compare Figure 11, Figure 15 and Figure 18). Therefore, the recommendation for Model 1 is applicable if a ceiling element with comparable dimensions is to be designed for usability. For a better estimation of the whole structural behavior and for more flexibility for variation of material and reinforcement, the second model is recommended. However, it must be taken into account for which purpose the models are needed.

In the case that the influence of the reinforcement layer or the simulation of component failure because of compression is more decisive for completely different ceiling elements or if a parameter study of other concrete soaked nonwovens is to be carried out, the use of the second model can be recommended. However, the use of the first model is preferable if parameter studies are to be undertaken in order to optimize the structure for different requirements of the construction industry. This is because model 1 shows the correct determination of the first crack force and a very good representation of the force-deflection curve in the area of the for lightweight structures important serviceability limit state.

REFERENCES

Bathe, K.-J. 2002. Finite element procedures. Springer-Verlag Berlin Heidelberg New York.

Curbach, M., Ortlepp, R., Scheerer, S. & Frenzel, M., 2011. Von der Vision zur Anwendung: Verstärken mit textilbewehrtem Beton. In *Der Prüfingenieur* 39 (2011), H. 39, p. 32–44.

DIBt, Deutsches Institut für Bautechnik, Zulassungsstelle für Bauprodukte und Bauarten. 2014. *Verfahren zur Verstärkung von Stahlbeton mit TUDALIT (Textilbewehrter Beton)*. Allgemeine Bauaufsichtliche Zulassung Nr. Z–31.10–182, Juni.

DIBt, Deutsches Institut für Bautechnik, Zulassungsstelle für Bauprodukte und Bauarten. 2017. *Verfahren zur Verstärkung von Stahlbeton mit TUDALIT (Textilbewehrter Beton)*. Allgemeine Bauaufsichtliche Zulassung Nr. Z-31.10–182, Juni.

DIN EN 1015-3. 2007. *Prüfverfahren für Mörtel für Mauerwerk – Teil 3: Bestimmung der Konsistenz von Frischmörtel*. Deutsche Fassung EN 1015-3:1999+A1:2004+A2: 2006. Mai 2007.

Eisewicht, G. 2015. Fleece Concrete Composite (FCC) und Textile Reinforced Concrete (TRC) – Synergien und Möglichkeiten. In TUDALIT e.V. (ed.), *TUDALIT-Magazin* No. 13: 25. Dresden.

EN 1991-1-1 (EC 1). 2010. *Einwirkungen auf Tragwerke – Teil 1-1: Allgemeine Einwirkungen auf Tragwerke – Wichten, Eigengewicht und Nutzlasten im Hochbau*. Deutsche Fassung EN 1991-1-1:2002 + AC:2009. Dezember 2010.

EN 1992-1-1 (EC 2) 2011. *Nationaler Anhang – National festgelegte Parameter – Eurocode 2: Bemessung und Konstruktion von Stahlbeton- und Spannbetontragwerken – Teil 1-1: Allgemeine Bemessungsregeln und Regeln für den Hochbau*; Deutsche Version EN 1992-1-1:2004 + AC:2010. Januar 2011.

Häussler-Combe, U. 2014. *Computational methods for reinforced concrete structures*. John Wiley Sons.

Häussler-Combe, U. 2017. *http://concrete-fem.com/*. Retrieved 26th October 2017.

Häussler-Combe, U. & Hartig, J. 2008. Formulation and numerical implementation of a constitutive law for concrete with strain-based damage and plasticity. In *International Journal of Non-Linear Mechanics* 43 (5): 399–415.

Schütze, E., Lorenz, E. & Curbach, M. 2015. Static and Dynamic Fatigue Strength of Textile Reinforced Concrete. In *IABSE (Ed.): Elegance in Structures, Poceedings of IABSE Conference Nara.* 13.-15.5.2015 in Nara (Japan). Printed in Japan. pp. 332–333 (abstract; full paper on CD: 8 pp.) – ISBN 978-3-85748-138-3.

Scheerer, S., Chudoba R., Garibaldi M. P. & Curbach, M. 2017. Shells Made of Textile Reinforced Concrete – Applications in Germany. In *IASS Journal of the International Association for Shell and Spatial Structures*. Vol. 58, No. 1, 79 93.

Computational Modelling of Concrete Structures – Meschke, Pichler & Rots (Eds)
© 2018 Taylor & Francis Group, London, ISBN 978-1-138-74117-1

Finite element research of reinforced concrete structures strengthened with Textile Reinforced Concrete (TRC)

A. Schumann, R. Zobel & M. Curbach
Institute of Concrete Structures, Technische Universität Dresden, Dresden, Germany

ABSTRACT: Nowadays, most structures are made of Reinforced Concrete (RC). But many of them have to be strengthened sometimes. One efficient method for strengthening RC structures is the use of Textile Reinforced Concrete (TRC). Besides the flexural strengthening, TRC can rise the shear capacity, too. To investigate the shear strengthening of RC structures with TRC few experimental tests were conducted. These tests are the basis for numerical investigations of the shear strengthening with TRC, which is described in this paper. At first, the experimental setup will be described, afterwards the simulation of the several components of a RC structure strengthened with TRC is shown. The next step is the comparison between unstrengthened and strengthened beams. All simulations show a good conformity between numerical and experimental results. Based on these simulations, further investigations can be done to achieve more information about the complex behavior of a shear strengthening with TRC.

1 INTRODUCTION

In the last decades, reinforced concrete (RC) had been the predominant construction material for buildings, bridges or hydraulic structures. But nowadays many of those structures have to be strengthened in consequence of rising loads, damages, material aging or in terms of new use. A new method for strengthening existing buildings is the use of textile reinforced concrete (TRC). TRC consists of the two components: textile grid and fine-grained concrete. For a general overview of textile reinforced concrete and the various types of usable textiles as reinforcement in concrete see Brameshuber (2006), Peled et al. (2017), Scheerer et al. (2017), Schladitz et al. (2016), Scheerer et al. (2015). In the past, much research had been done in terms of strengthening of reinforced concrete structures with TRC. Most of the investigations are based on experimental tests, e.g. on the flexural behavior of RC slabs strengthened with TRC (Schladitz et al. (2012), Triantafillou (2016)) or investigations of the shear-rising capacity of RC beams strengthened with TRC (Brückner et al. (2008), Brückner et al. (2006)). With those experimental tests the principal behavior of the interaction of the different composite materials can be determined clearly. But the disadvantage of those experimental tests, especially if large scale tests were used, are the high costs. Therefore in the most cases only a few large scale tests can be conducted. But the investigation of the behavior of strengthened RC structures with TRC with a few numbers of tests is not a solution because with it not all parameters or effects can be researched. To achieve an overview of the full behavior of concrete structures besides the experimental investigations, the finite element method (FEM) is a approved alternative for those kinds of problems. Moreover, researches by using the FEM have the big advantage, that no costs occur, e.g. for the materials or the testing of the large scale samples. In general only a few experimental tests for calibrating the numerical model have to be available.

In this paper the numerical investigations of the shear strengthening of different RC beams with TRC are shown. Thereby the complex behavior of the shear strengthening of RC structures with TRC should be investigated further. The basis for the FE simulations are the experimental tests of Brückner (2011).

2 BASICS OF RC ELEMENTS STRENGTHENED WITH TRC

The shear failure of steel reinforced concrete structures without any strengthening applications can be divided in:

- concrete compression failure caused by combined bending and shear forces,
- tensile failure of the shear steel reinforcement,
- compression failure of highly reinforced concrete webs,
- failure of the end anchorage of the longitudinal flexural steel reinforcement,

- splitting of the web caused by the longitudinal steel reinforcement, wich where bended up at the end.

Compression failure of the concrete caused by combined bending and shear forces occurs, if the critical shear crack rises in the compression zone. If the remaining compression zone is too small, the concrete crushes and the whole structure collapses. This failure mode indicates the yielding of the steel shear reinforment. At RC beams with less shear reinforcement, the ultimate tensile strength of the steel stirrups can be exceeded before a concrete compression failure occurs. Besides the two main failure criteria for shear, an insufficient end anchorage of the longitudinal reinforcement and the collapse of the concrete web caused by the compression force can lead to an failure of the whole structure. Additionally, if the longitudinal reinforcement is bended up in the end, the splitting of the web caused by the tensile forces of the up-bending can lead to an shear failure.

There are even more failure types when RC beams were strengthened with TRC, e.g. Brückner (2011), Brückner et al. (2006) and Ortlepp (2007):

- tensile failure of the textile grids,
- debonding between the strengthening layer and the surface of the RC element,
- insufficient end anchorage of the textile grid,
- delamination between the textile grid and fine-grained concrete.

Analogous to the tensile failure of steel stirrups, the textile grids can break up if the maximum tensile strength is reached. All other failure modes of shear strengthening of RC structures depend on the bond behavior of the textile grids and the connection between the RC surface and the strengthening layer.

3 NUMERICAL MODELLING OF THE SHEAR STRENGTHENING OF RC STRUCTURES WITH TRC

3.1 *Experimental tests*

The shear strengthening of RC structures with TRC was investigated at the Technische Universität Dresden by a few large-scale tests on three types of beams. These tests are the basis for the numerical investigations and will be described in this chapter in a nutshell. For a description in detail see Brückner (2011).

Figure 1 shows the cross-sections of the unstrengthened steel reinforced beams. In this paper, according to Brückner (2011), following notations of the beams will be used:

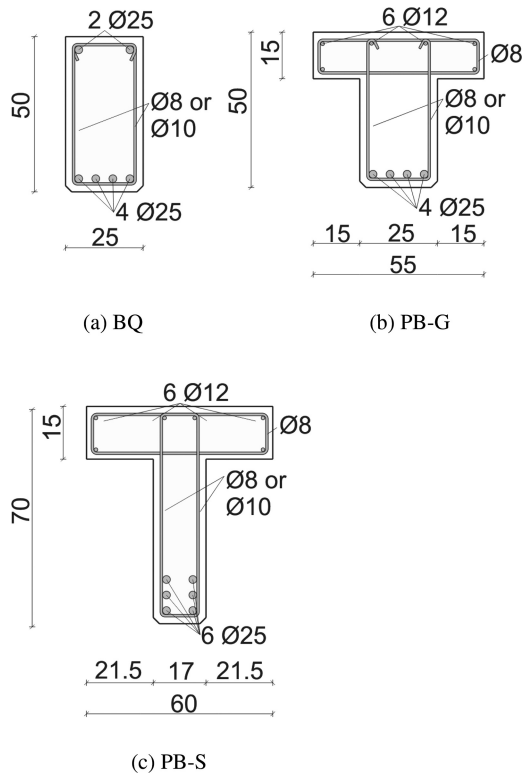

Figure 1. Principal drawing of the cross-sections [cm] after Brückner (2011), graphics: Alexander Schumann.

- beam 1 = BQ (rectangular beam),
- beam 2 = PB-G (compact T-beam),
- beam 3 = PB-S (slim T-beam),
- 1-BQ-0 = unstrengthened rectangular beam with higher concrete strength,
- 2-BQ-3 = rectangular beam with lower concrete strength and 3 layers of TRC.

The RC beams had a length of 5.0 m resp. 8.4 m. The arrangement of the shear reinforcement is illustrated in Figure 2. Because of the symmetric order of the shear reinforcement, only the halfs of the beams are shown. The T-beams were tested in 3-point bending tests. During the experiments, the beams had been loaded and supported in two different ways, as it can be seen in Figure 3. So each beam was tested twice.

At first, 10 beams should be manufactured ($3 \times$ BQ, $4 \times$ PB-G and $3 \times$ PB-S), but the concrete strength of the first beams was higher than expected. Therefore the shear capacity was higher than previously calculated. Moreover a flexure failure of the RC beams without and with TRC strengthening could not be excluded. Therefore the first beams of each type had to be manufactured again with a

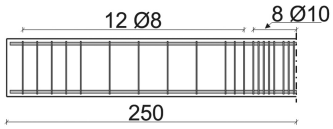

(a) BQ

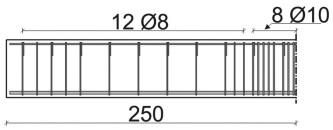

(b) PB-G

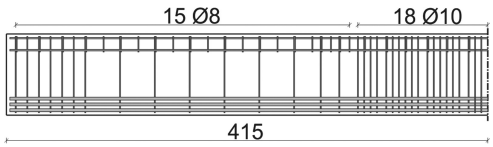

(c) PB-S

Figure 2. Principial drawing of the shear reinforcement [cm] after Brückner (2011), graphics: Alexander Schumann.

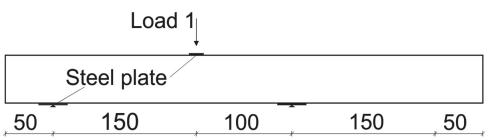

(a) test setup 1

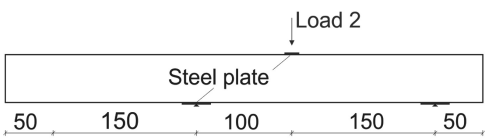

(b) test setup 2

Figure 3. Principal drawing of the test setups [cm] after Brückner (2011), graphics: Alexander Schumann.

lower concrete strength. In summary 13 reinforced concrete beams with and without TRC strengthening were produced and tested. These 13 elements are the basis for the numerical investigations. More information about the tested beams can be found in the following sections and tables.

3.2 *FE discretisation*

The simulation of the large-scale tests on RC beams strengthened with TRC was executed in ANSYS. To achieve a realistic material behavior of strengthened RC structures and to investigate the influence of different parameters on the load-carrying capacity the large scale tests are modeled three-dimensionally with solid elements with eight nodes for the concrete and beam elements for the steel reinforcement with a rigid bond behavior between both element types. Rigid bond means, that the elements share the same node. The used geometry, reinforcement and material data for the FE simulation are described in section 3.1 respectively 3.3. In the experimental testing of the large-scale structures all specimen were loaded twice. In the numerical investigations the RC beams had just been loaded once, because during the second loading of the experimental tests unexpected problems occured. For all calculations only the first load and support applications (Figure 3) are used.

The mesh of the unstrengthened beam PB-G is exemplary shown in Figure 4 (a) and the corresponding reinforcement in Figure 4 (b). Considering the symmetry of the specimen, just the half of the structures were modeled in ANSYS. The

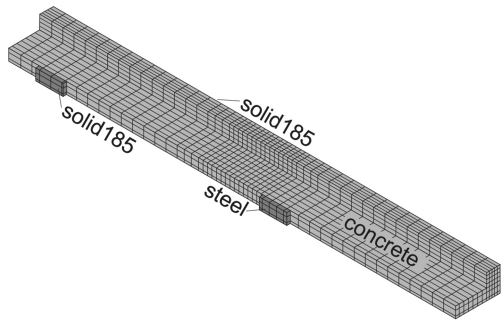

(a) mesh

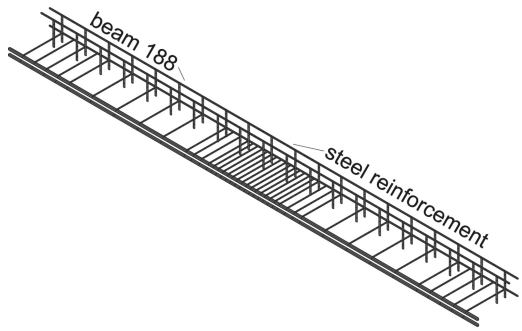

(b) reinforcement

Figure 4. Exemplary graphics of the unstrengthened model of beam PB-G, from ANSYS, modified by Alexander Schumann.

structures had been loaded in two loadsteps in ANSYS. At first, the beams were loaded by their self-weight. In the second loadstep, the structures were loaded with a defined displacement until their ultimate bending or shear capacity was reached.

For the simulation of the strengthened RC beams with TRC, additionally layers have been applied. The TRC layers for the shear strengthening were added on the vertical surfaces of the webs as it can be seen in Figure 5. Analogous to the experimental tests the beams in ANSYS had not been strengthened over the whole structure lengths. The beam BQ, which could be strengthened over the whole outer area of the cross-section, was strengthened analogous to the T-beams: the upper areas of the cross-sections remained unstrengthened. The strengthening layers were simulated with solid elements for the fine-grained concrete and a smeared reinforcement for the textile grids. According to the experimental tests the smeared reinforcement was modeled with an angle of 45° respectively 135° between the longitudinal direction of the beam and fiber orientation in the textile. The connection between the RC structure and the strengthening TRC layer was modeled with a *Surface-to-Surface* contact in ANSYS with a full bond (ANSYS Inc. (2014)). With this setting the *Surface-to-Surface* contact is able to transer compression and tensile forces.

3.3 *Materials*

After the whole FE model was shown, the single components will be described. With simulating each component of a RC beam strengthened with TRC, the different used material models in ANSYS should be calibrated and the suitability of those material behaviors should be proved.

For the simulation of the non-linear material behavior of the concrete, the *Menetrey-Willam* model from DYNARDO according to Dynardo (2015) is used. The *Menetrey-Willam* model in *multiPlas* is based on the *Willam-Warnke* yield surface. For further information see Dynardo (2015). As input parameters for the concrete model in ANSYS the values in Table 1 are used. Because of missing stress-strain curves of the concrete, the strains for the simulation are defined according to DIN EN 1992-1-1:2011-01 (2011).

In the large-scale tests, four different diameters for the steel rebars were used. The strength of each diameter was investigated by three experimental tests each according to DIN EN 488-3:2009-08 (2009). The results of the experimental tensile tests (mean curves) for the steel rebars are shown in Figure 6 (a). As a numerical calibration those tensile tests were simulated. For the material behavior a bilinear model had been used in ANSYS (ANSYS Inc. (2014)). Figure 6 (b) shows exemplary the comparison between FE simulation and experiment of two tensile tests with different diameters and Table 2 shows the input parameters of the different steel rebars in ANSYS.

Textile reinforced concrete consists of the two components fine-grained concrete and textile fibers. Thousands of those textile fibers were combined to yarns, for getting e.g. a textile grid. Additionally, the fibers are impregnated to increase the tensile strength. The tensile stress of TRC is characterized by tensile tests, see e.g. Schütze et al. (2015). The stress-strain curves of the used glass fiber grid are shown in Figure 7. The strength of the used fine-grained concrete is listed in Table 3. In summary, two, three and four layers of textiles had been tested with tensile tests. The cross-section

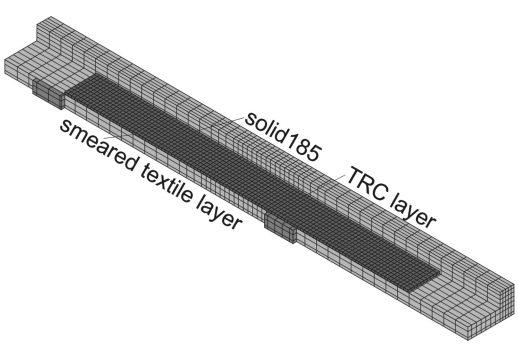

Figure 5. FE model of the RC beam PB-G strengthened with TRC, graphic from ANSYS, modified by Alexander Schumann.

Table 1. Experimental data of the used concretes for the RC (mean values) from Brückner (2011).

No.	Cylindrical compressive strength $f_{cm,zyl}$ [N/mm²]	Young's modulus E_{cm} [N/mm²]	Splitting tensile strength $f_{ct,sp}$ [N/mm²]
1-BQ-0	49.3	31780	3.32
2-BQ-0	31.0	27410	2.85
2-BQ-2	31.3	28540	2.68
2-BQ-3	30.7	28250	2.50
1-PB-G-0	47.5	34580	3.45
2-PB-G-0	27.3	27600	2.40
2-PB-G-2	29.0	26810	2.50
2-PB-G-3	33.0	25260	2.41
2-PB-G-4	36.8	31240	2.83
1-PB-S-0	37.8	32980	2.98
2-PB-S-0	32.6	31170	2.78
2-PB-S-3	29.8	27640	2.72
2-PB-S-4	28.8	28270	2.30

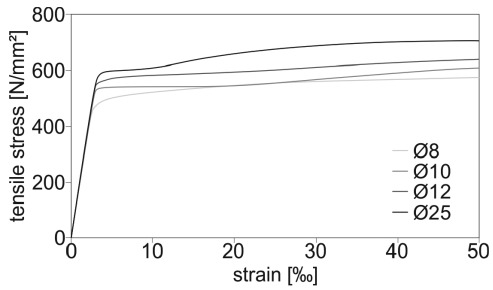

(a) Experimental tests

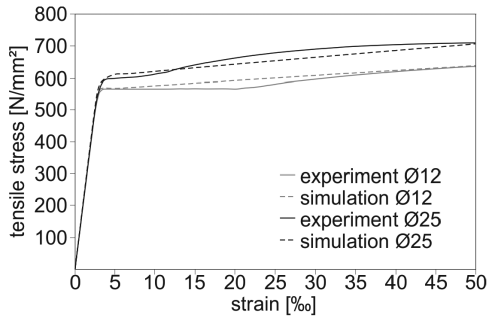

(b) Comparison of two experimental and numerical tests

Figure 6. Tensile tests of the steel rebars after Brückner (2011) and own numerical simulations.

Table 2. Numerical input parameters for the steel rebars.

No.	Young's modulus[1] $E_{s,I}$ [N/mm²]	Poisson's ratio ν_s [–]	Yielding strength f_y [N/mm²]	Young's modulus[2] $E_{s,II}$ [N/mm²]
Ø8	190000	0.3	500	2500
Ø10	210302	0.3	572	2300
Ø12	202482	0.3	566	2300
Ø25	198829	0.3	608	3000

[1]before steel yielding.
[2]after steel yielding.

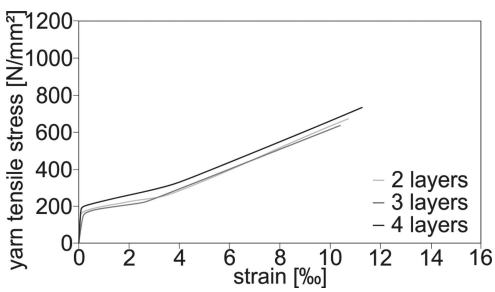

Figure 7: Experimental tensile tests of TRC, after Brückner (2011).

Table 3. Experimental datas of the fine-grained concrete from Brückner (2011).

No.	Compressive strength[1] R_c [N/mm²]	Tensile flexural strength[2] R_f [N/mm²]
2-BQ-2	69.8	4.30
2-BQ-3	76.3	4.93
2-PB-G-2	81.3	4.75
2-PB-G-3	75.1	4.43
2-PB-G-4	81.2	5.64
2-PB-S-3	70.2	4.60
2-PB-S-4	63.7	5.12

[1]compressive strength, tested after DIN EN 196-1:2016-11 (2016).
[2]tensile flexure strength, tested after DIN EN 196-1:2016-11 (2016).

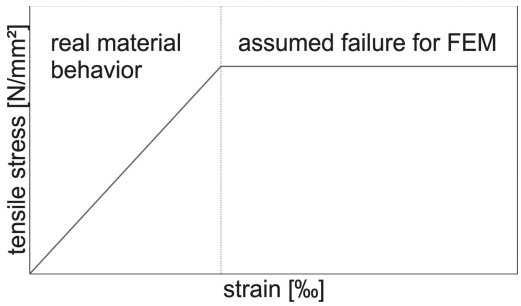

Figure 8. Principial drawing of the numerical assumption of the stress-strain behavior for a tensile load in longitudinal direction for fibers made of glass, graphic: Alexander Schumann.

of each textile layer was 121.8 mm²/m (Brückner (2011)). For calibrating the strengthening layers with TRC the tensile tests had been simulated. In this experiment only fibers made of glass had been used. The specimens were modeled with hexahedral shaped solid elements with eight nodes (ANSYS Inc. (2014)). The textile grid was modeled as a smeared reinforcement with a rigid bond between the concrete elements and the reinforcement layer. Glass fibers show an almost linear elastic stress-strain behavior with a brittle failure, see e.g. Abdkader (2004), Füllsack-Köditz (2004). For the FE-simulation a bilinear material model with a yielding strength for the textile grid of 660 N/mm² and the second Young's modulus of 0 N/mm² had been used (Figure 8). This assumption was used to see the failure of the textiles by displaying the plastic strains in ANSYS. Figure 9 shows the comparison between an experimental tensile test with two layers of textile grids and the FE simulation. With

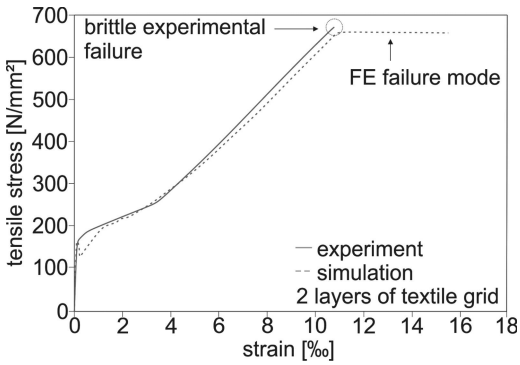

Figure 9. Comparison between an experimental (after Brückner (2011)) and a numerical tensile test for TRC.

this comparison it can be proved, that the mechanical behavior of a TRC structure can be simulated with the defined material model. But it can be seen, that the failure mode between experimental and numerical test is the same, but in the experiment the structures collapse brittle, whereas the collapse of the TRC specimen in ANSYS is ductile.

3.4 *Comparison between simulation and FEM for the unstrengthened reinforced beams*

Figures 10 (a)–(c) show the comparison between the experimental and the numerical tests of the RC beams without TRC strengthening. On the x-axes the vertical displacement of the beams and on the y-axes the concentrated load are indicated. The self-weights of the structures are excluded.

With Figures 10 (a)–(c) it can be proved, that the experimental tests can be simulated with the material properties shown in section 3.1 and 3.3 in ANSYS. The uncracked stages, the cracking of the beams, the final cracked stage and the failure modes can be illustrated. Compared to the experimental displacementload curves the FE solutions are at the early stages always a bit stiffer. This additional stiffness of the FE model can be justified by the way of modeling the RC beams. The large-scale tests were simulated with solid elements for the concrete and beam elements for the steel reinforcement. Therefore the cross-sections of the numerical concrete beams are higher than in reality and this leads to a higher stiffness until the beams start cracking. After the crack initiation is completed the numerical structures show almost the same stiffness as the real beams. Besides the way of modeling the beam with solid and beam elements, further reasons for the higher stiffness of the FE model are e.g. not considering of internal stresses caused by creep and shrinkage interaction, or of possible predamages during the manufactoring of the beams.

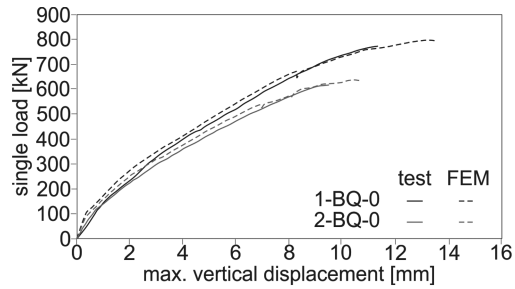

(a) BQ

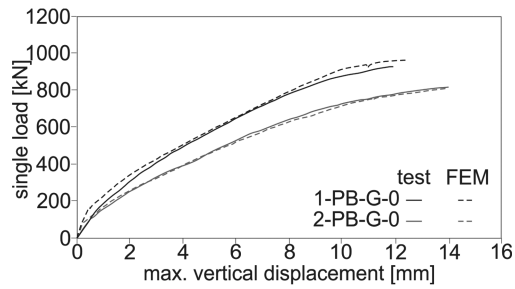

(b) PB-G

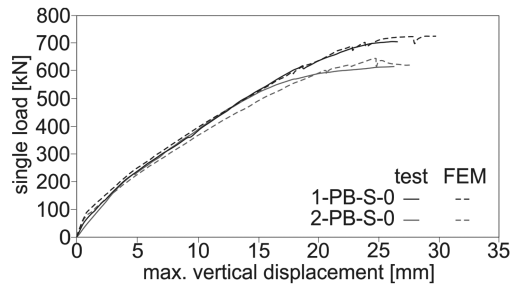

(c) PB-S

Figure 10. Comparison between experimental (after Brückner (2011)) und numerical tests: unstrengthened beams.

3.5 *Comparison between simulation and FEM for the strengthened reinforced beams with TRC*

The comparisons between the FE simulations and the experimental tests are shown in Figures 11 (a)–(c). For each beam two comparisons with different numbers of TRC grids had been performed. The results of the T-beam 2-PB-G-3 are not shown in Figure 11 (b). This test setup has a significant deviation between the experimental and the numerical solution. Moreover the experimental displacement-load curve for the beam 2-PB-G-3 show a deviation between beam 2-PB-G-2 and 2-PB-G-4, too. Therefore the differences between the numerical

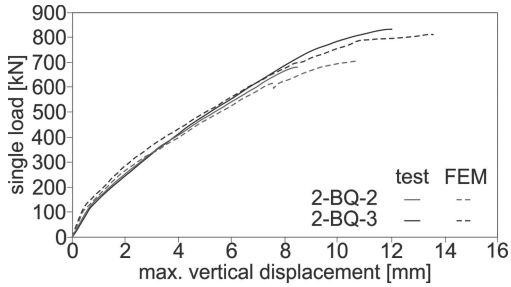

(a) BQ

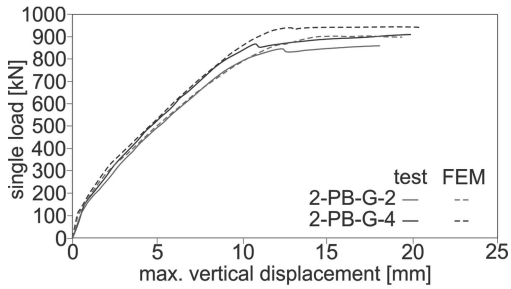

(b) PB-G

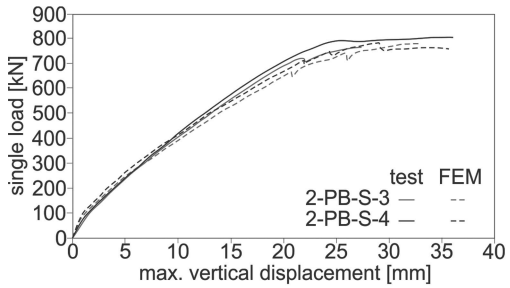

(c) PB-S

Figure 11. Comparison between experimental (after Brückner (2011)) und numerical tests: strengthened beams with TRC.

and the experimental tests can be lead back to the deviation of the experimental tested structure.

Besides the T-beam 2-PB-G-3, all numerical calculations show a good behavior, compared to the experimental tests. With the FE models the principal material behavior of unstrengthened and strengthened RC beams with TRC can be simulated. The loaddisplacement curves of the different specimen show almost the same behavior than the experimental ones. Moreover the ultimate loads of the FEM solutions offer only small deviations compared to the experimental setups, which can be lead back to inevitable scattering of the different material components.

Table 4. Overview of the experimental loads (from Brückner (2011)) and own FE simulations.

No.	TRC layers	$F^{1}_{u,e}$	$F^{2}_{u,n}$
1-BQ-0	–	771	799
2-BQ-0	–	617	642
2-BQ-2	2	679	714
2-BQ-3	3	833	806
1-PB-G-0	–	927	957
2-PB-G-0	–	813	810
2-PB-G-2	2	855	906
2-PB-G-3	3	842	–
2-PB-G-4	4	907	947
1-PB-S-0	–	700	730
2-PB-S-0	–	615	639
2-PB-S-3	3	745	779
2-PB-S-4	4	808	782

[1]ultimate experimental load.
[2]ultimate numerical load.

An overview of the ultimate loads in experiment and FEM is shown in Table 4. Besides the comparison between the ultimate load of the FEM and the experiment, the failure modes of the numerical and experimental tests were a crucial criterion of the suitability of the FE model. In all FE investigations the same failure mode as in the experimental setup occured. Therefore it can be proved, that the shear strengthening of RC structures with TRC can be simulated with ANSYS. But, analogous to section 3.4, all FE solutions have a slightly stiffer behavior than the experimental structures, caused by the way of modeling the RC beams.

4 DISCUSSION

The simulations of the RC beams with or without TRC strengthening can be performed with the finite element method. With the calibrated FE model new investigations of the shear strengthening of RC structures with TRC are available. At first the experimental conclusions can be confirmed with the simulations. The shear capacity of RC structures can be increased by strengthening those elements with TRC. On the one hand the crack initiations of a strengthened beam starts at a higher loading, compared to an unstrengthened structure. On the other hand the ultimate load can be, in some investigations signify cantly, increased. Furthermore with the numerical researches it can be proved, that the strengthening layers with TRC leads to smaller crack widths compared to the same structure without any strengthening layers at the same load level. Because of that, the failure of the structure caused by the shear stresses can be protracted, which leads to higher ultimate loads. Figure 12 shows a comparisons of the first principal plastic strains between an

unstrengthened and a strengthened RC structure with four layers of TRC. To compare both structures only the first principal strain in the RC structure by the same load is plotted.

With Figure 12 (a) the typical failure mode of most of the investigated beams can be described. In the most cases, analogous to the experimental studies, the concrete in the compression zone failures caused by the shear forces. The shear cracks rise until the force in the remaining compression zone is too big and the concrete collapses. Besides the concrete failure caused by the shear forces the tensile strength of the textile grids are reached in some numerical researches. In those cases the failure of the whole structure is not induced by the RC elements. This kind of failure can be prevented if textile grids with higher tensile strength, e.g. carbon instead of glass, is used. Therefore a strengthening with carbon reinforced concrete can lead to a further increase compared to a TRC strengthening with glass fibers.

Besides the previous described failure modes for a shear strengthened RC beam, compression failure and reaching the tensile strength of the strengthening layers, the collapse of the structure can be caused by exceeding the ultimate strains of the steel shear reinforcement. But in all FE investigations this failure mode has not occurred because of the used steel reinforcement with an ultimate strain of about 50 ‰ in the experiments. Additionally to the previous described shear failure modes the structure can collapse by reaching the flexure capacity. This failure mode occurs, if the shear capacity is highly increased by the TRC strengthening. Therefore the shear strengthening cannot achieve their full potential. In the FE and experimental investigations this failure mode appeared by the beam PB-S by strengthening with 3 or 4 layers. Therefore only a negligible increase in the ultimate load had been reached by increasing the number of textile grids (Figure 11 (c) and Table 4).

With these numerical investigations of the shear strengthening of RC structures with TRC it should be proved, that the complex shear behavior can be simulated. But for this simulations some assumptions had been made. The two significant assumptions are the used material model for the textile grid and the modeling of the bond behavior between the RC structure and the strengthening layers. The material model for the textile grids made of glass fibers is a bilinear model without a failure criterion. But in reality glass fibers show a linear elastic material behavior with a brittle failure. This assumption had been made for getting a better convergence of the solution. But in the next step the used material model will be replaced with a more realistic model. The second assumption which had been made for the simulations is the full bond behavior between the TRC layers and the surface of the RC structure. For the simulations these assumptions decrease the time for calculating. But, especially if carbon is used instead of glass for the fibers, the bond behavior has a huge influence on the efficacy of the strengthening with TRC for shear (Brückner (2011), Brückner et al. (2008)). Therefore the next step of the simulations should obtain the real bond behavior of the used textile grid.

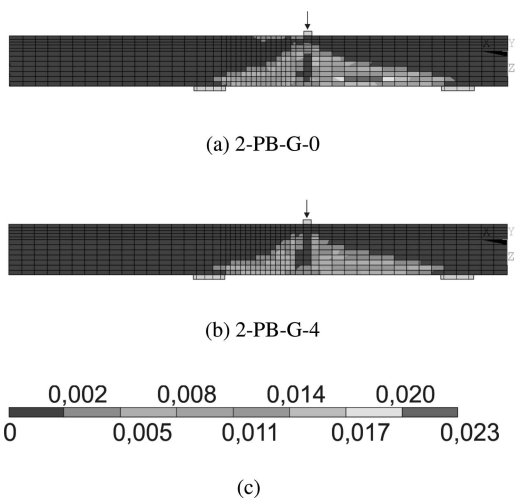

Figure 12. Principal showing of the positive influence of a shear strengthening by ploting the first principal plastic strains (blue = zero plastic strains, red = maximum plastic strains) in the RC structure at a force of 786 kN, graphics from ANSYS, modified by Alexander Schumann.

5 OUTLOOK AND FURTHER RESEARCH

Now, by having a full calibrated and checked FE model further investigations will be made to achieve new scientific findings for the shear strengthening. The shear capacity of shear strengthened RC structures with TRC is influenced by a large number of parameters. Therefore selected parameters will be investigated in the future. One crucial part of further investigations contain the textile grid in the TRC layers. On the one hand fibers made of carbon instead of glass will be used. Moreover a realistic material model for the carbon fibers with different stress-strain curves for each direction (longitudinal, radial and tangential) should be used. On the other hand the influence of the angle of the textile grid according to the load direction will be investigated. Besides the effects on the shear behavior caused by the textile grid, parameter studies will be obtained to determine the influence of the fine-grained concrete. At first the tensile and compressive strength of the fine-grained concrete will be changed. Afterwards the effect of the thickness of the strengthening layers will be investigated, too.

Another important influence which should be investigated in further researches is a predamage of the RC structures before the strengthening TRC layers are applied. By now, the TRC strengthening is applied on the undamaged RC beams, but in reality the shear strengthening will be used for predamaged structures. Therefore this influence must be considered and the shear capacity of an undamaged and a predamaged strengthened RC structure must be compared.

On the basis of these FE investigations a new experimental setup for future large-scale tests for the shear strengthening of RC structures with carbon reinforced concrete will be developed. Those tests will be conducted in the common research project *C3-V1.2: Verification and testing concepts for standards and approvals* (C3-V1.2 (2017)), which is C^3: *Carbon Concrete Composite* (Schladitz et al. (2016)).

6 CONCLUSION

The potential of the shear strengthening of RC structures with TRC had been shown by a few experimental large-scale tests in the past. With a TRC strengthening, the shear capacity can be increased, compared to an unstrengthened RC beam, up to 35% (Brückner (2011) (Table 4). Because of the high costs of those large-scale tests, only a few investigations could be made. Therefore those RC structures were modeled by using the finite element method to get a better understanding of the principal behavior of the interaction between the RC and the strengthening layers. Moreover, by the use of numerical researches important influences and parameters of the shear capacity with a TRC strengthening can be done.

The modeling of the large-scale tests proceeded in three steps. In the first step the several components of a strengthened beam had been simulated. Afterwards the unstrengthened RC structures were recalculated to calibrate the FE model. The next step was the simulating of the strengthened RC beams with TRC. All comparisons between experimental and numerical tests showed a good conformity. Thus, it can be proved, that the shear strengthening of RC elements with TRC can be simulated.

REFERENCES

Abdkader, A. (2004). *Charakterisierung und Modellierung der Eigenschaften von AR-Glasfilamentgarnen für die Betonbewehrung*. Dissertation, Technische Universität Dresden, Fakultät fur Maschinenwesen.

ANSYS Inc. (2014). Documentation for release 15.0.

Brameshuber, W. (Ed.) (2006). *State-of-the-Art report of RILEM Technical Committee TC 201-TRC 'Textile Reinforced Concrete'*, Volume 36. RILEM Publ.

Brückner, A. (2011). *Querkraftverstärkung von Bauteilen mit textilbewehrtem Beton*. Dissertation, Technische Universität Dresden, Fakultät für Bauingenieurwesen.

Brückner, A., R. Ortlepp, & M. Curbach (2006). Textile reinforced concrete for strengthening in bending and shear. *Materials and Structures, Vol. 39*, 741–748.

Brückner, A., R. Ortlepp, & M. Curbach (2008). Anchoring of shear strengthened for T-beams made of TRC. *Materials and Structures, Vol. 41*, 407–418.

C3-V1.2 (2017). https://www.bauen-neudenken.de/vorhaben/v1-2-nachweis-und-pruefkonzeptefuer-normen-und-zulassungen/ (02.08.2017).

DIN EN 196-1:2016-11 (2016). DIN EN 196-1:2016-11: Methods of testing cement—Part 1: Determination of strength; German version EN 196–1:2016.

DIN EN 1992-1-1:2011-01 (2011). Eurocode 2: Design of concrete structures—Part 1–1: General rules and rules for building; German version EN 1992-1-1:2004+AC:2010.

DIN EN 488-3:2009-08 (2009). Reinforcing steels – Reinforcing steel in coils, steel wire.

Dynardo (2015). User's Manual multiPlas: Release 5.1.0 for ANSYS 14.5.7 and 15.0.

Füllsack-Köditz, R. (2004). *Verbundverhalten von GFKBewehrungsstäben und Rissentwicklung in GFKstabbewehrten Betonbauteilen*. Dissertation, Bauhaus-Universität Weimar, Institut für Konstruktiver Ingenieurbau.

Ortlepp, R. (2007). *Untersuchungen zur Verbundverankerung textilbewehrter Feinbetonverstärkungsschichten*. Dissertation, Technische Universität Dresden, Fakultät für Bauingenieurwesen.

Peled, A., A. Bentur, & B. Mobasher (2017). *Textile Reinforced Concrete (Modern Concrete Technology)*. CRC Press.

Scheerer, S., F. Schladitz, & M. Curbach (2015). Textile Reinforced Concrete-from the idea to a high performance material. pp. 15–33.

Scheerer, S., E. Schütze, & M. Curbach (2017). Strengthening and Repair with Carbon Concrete Composites – the First General Building Approval in Germany. *International Conference: Strain-Hardening Cement-Based Composites (SHCC 4)*.

Schladitz, F., M. Curbach, M. Tietze, & M. Lieboldt (2016). Carbon and Concrete—The Future of Construction. *IABSE Conference—Bridges and Structures Suistainability—Seeking Intelligent Solutions. Guangzhou: IABSE*, 242–523.

Schladitz, F., F.M., & M. Ehlig, D. Curbach (2012). Bending load capacity of reinforced concrete slabs strengthened with textile reinforced concrete. *Engineering Structures, Vol. 40*, 317–326.

Schütze, E., E. Lorenz, & M. Curbach (2015). Test Methods for Textile Reinforced Concrete. *11th International Symposium on Ferrocement and Textile Reinforced Concrete 3rd ICTRC (ed. Brameshuber, W.), Aachen*, 307–318.

Triantafillou, T. (2016). *Textile Fibre Composites in Civil Engineering*. Woodhead Publishing.



Taylor & Francis
Taylor & Francis Group
http://taylorandfrancis.com

Computational Modelling of Concrete Structures – Meschke, Pichler & Rots (Eds)
© 2018 Taylor & Francis Group, London, ISBN 978-1-138-74117-1

Probabilistic multiple cracking model of elastic-brittle matrix composite reflecting randomness in matrix, reinforcement and bond

M. Vořechovský
Institute of Structural Mechanics, Brno University of Technology, Brno, Czech Republic

R. Chudoba & Y. Li
Institute of Structural Concrete, RWTH Aachen University, Aachen, Germany

R. Rypl
Honeywell, Brno, Czech Republic

ABSTRACT: The paper describes a semi-analytical multiscale model of the tensile response of unidirectional brittle-matrix composites with heterogeneous reinforcement. A probabilistic multiple cracking model is proposed, and we apply a probabilistic crack bridge model to simulate the behavior of a representative crack bridge within proposed model, which simulates the strain-hardening response of a multiply cracked composite subjected to tensile loading. In order to reflect the random nature of matrix cracks emerging during the loading process, we apply the random strength approach and represent the matrix strength by a random field. A robust algorithm is formulated for determining initiation loads and positions of matrix cracks for an arbitrary formulation of the fiber-matrix interface. The developed model is calibrated and validated against experiments with textile reinforced concrete.

1 INTRODUCTION

Multiple cracking of matrix and/or fibers in uniaxially loaded brittle matrix composites (BMCs) increases the toughness and ductility of the composite material. Composites with these favorable properties have a higher impact resistance and stress redistribution capacity. Moreover, the multiple cracking behavior is of great importance for the serviceability limit state as it is closely related to deformations and crack widths.

The response of fibrous composites to tensile loading depends on the material properties of both the matrix, and the fibers, and their interface (Marshall et al., 1985; Curtin, 1993a). The typical form of such a response includes an initial linear stage with the stiffness defined by the rule of mixtures as

$$E_c = E_f V_f + E_m (1 - V_f) \tag{1}$$

with E_f and E_m denoting the fiber and matrix moduli of elasticity, respectively, and V_f denoting the fiber volume fraction. With the inception of the first matrix crack marking the beginning of multiple cracking (matrix fragmentation), the stiffness starts to decrease. During the following phase of multiple cracking, stress redistributions both between and within the constituents take place. This second phase continues up to the state where all fibers are fully debonded so that the composite is saturated with cracks, which marks the start of the third phase—a linear response with stiffness equal to $E_f V_f$. The vertical offset between the composite stress in the third phase and an equivalent reinforcement response $E_f V_f \varepsilon_c$, with ε_c being the global strain, is due to the tensile stress accumulated in the matrix fragments, see Fig. 1.

1.1 *Intermediate state*

Analytical solutions to the tensile response of BMCs are only possible for special cases regarding the assumptions about constituents and their

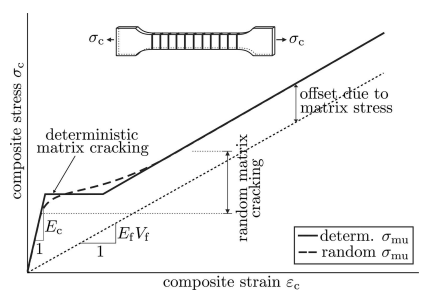

Figure 1. Response of a unidirectional composite subjected to tensile load: deterministic matrix strength σ_{mu} (solid line); random matrix strength σ_{mu} (dashed line).

interface. In particular, a number of models have been formulated under the assumption of a constant bond stress vs. fiber slip and linear-elastic behavior of both fibers and matrix, with brittle failure upon reaching a deterministic strength. The first model with these assumptions is the ACK model developed by Aveston et al. (1971), where a trilinear representation of the composite tensile response was introduced; see Fig. 1 (solid line). After the first crack, which denotes the end of the linear response, the multiple cracking is assumed to be driven by a constant applied stress. This assumption results in a horizontal branch in the stress-strain behavior. It involves the process of matrix fragmentation, which has been thoroughly studied by Kimber and Keer (1982). For its simplicity, this model has been utilized for the simulation of tensile response of cementitious composites (Larrinaga et al., 2013; Cuypers and Wastiels, 2006).

The need to enhance models of the matrix fragmentation process so that they fit the experimentally observed smooth transition between the initial composite stiffness E_c and the saturated state stiffness $E_f V_f$ (see dashed line in Fig. 1) led to the consideration of the energy balance during the process of matrix cracking and fiber debonding (Aveston and Kelly, 1973; Budiansky et al., 1986). A few years later, the randomness of matrix strength became involved as another source of the increasing stress during the multiple cracking stage (Cho et al., 1992; Curtin, 1993a; Hui et al., 1995).

According to a review article by Castelier et al. (2010), three modeling approaches to multiple cracking with random matrix strength have been considered so far: the random strength approach (Curtin, 1993b; Harlow and Phoenix, 1978a,b; Kang and Bolander, 2016); the random crack approach Netravali et al. (1989); Henstenburg and Phoenix (1989); Curtin (1993a) and the continuous approach (Curtin, 1991; Hui et al., 1995). All of these models are analytical or semi-analytical and incorporate both matrix and fiber strength randomness. In the present model, we adopt a version of the random strength approach which is modified in order to account for the interaction of crack bridges, see Sec 2.

The primary goal of the present article, which serves as a promotion of a journal paper by the authors (Chudoba et al., 2018), is to introduce a *generic algorithm for the matrix fragmentation process* that can be easily combined with several different types of crack bridge models

- analytic models with constant frictional bond
- finite-element crack bridge models with nonlinear material laws for reinforcement and bond
- micromechanical probabilistic crack bridge models reflecting random properties of the reinforcement and of the bond in arbitrary combinations

The development of the algorithm has been motivated by the need to accurately characterize the behavior of textile-reinforced concrete, a composite material with heterogeneous material structure of matrix, reinforcement and bond at overlapping scales of resolution.

1.2 *Ultimate state*

The failure process of BMC is governed by the interacting reinforcement and bond within a fragmented matrix. Both the reinforcement and the bond characteristics exhibit scatter that has a significant effect on the ultimate strength. A well established approach to the evaluation of the composite strength is the probabilistically based chain-of-bundles (CHOB) model (Zweben and Rosen, 1970; Rosen, 1964; Smith, 1982; Chudoba et al., 2011). It accounts for the contribution of broken fibers to the stress transmission, which increases with growing distance from the failure position. Beyond the stress transfer length δ_c away from the point of rupture, broken fibers contribute to the stress transmission to the same degree as intact fibers. This effect makes the fiber stress at position z independent of fiber breaks beyond distance $z \pm \delta_c$.

In the present model, we consider a variable stress transfer length, which originates from the variability in bond properties among individual fibers. This variable length prevents the classical CHOB from being directly applied because there is no unique bundle size. In addition, the strength does not depend only on the material properties, but also on the crack spacing. In the past, *probabilistic* interaction between the crack spacing and the composite strength has been identified by Phoenix and Raj (1992); Phoenix (1993); Curtin (1993b). These models consider homogeneous bond and they predict strength reduction for decreasing crack spacing. However, for the studied material with high scatter of bond strength, the effect of *fiber strain homogenization* due to increasing crack density has been observed by the authors in (Rypl et al., 2013; Vořechovský et al., 2017). The strain homogenization causes a considerable strength increase in composites with heterogeneous reinforcement as the crack spacing decreases. Both these kinds of interaction are incorporated in the present model.

2 PROBABILISTIC MULTIPLE CRACKING MODEL

This section presents an informal illustration of the of the proposed crack tracing algorithm. Robust mathematical description as a guide for its generic implementation is available in (Chudoba et al., 2018). In the remainder of this section, a little more specific description of the algorithm follows. The class of

methods generally referred to as "random strength approach" (Castelier et al., 2010) can be illustrated using the graphical representation of stress states at several selected load levels shown in Fig. 3.

The first diagram (Fig. 3a) shows the matrix stress along the specimen after the first crack has appeared at the location of minimum matrix strength. Upon further loading, the matrix stress is growing until the matrix strength is reached at some other point of the specimen (Fig. 3b). New crack is then inserted into the numerical representation of the specimen by updating the stress profile (Fig. 3b) in accordance with the considered crack bridge model summarized in Fig. 2.

During this *intermediate state of cracking*, the goal of the crack tracing algorithm is to find the next crack (see Fig. 4), i.e. to determine the load level corresponding to the configuration with a new crack.

The *cracking condition* is based on comparison of the local field of matrix strength along the specimen (see the wavy function in Figs. 3 and 4) and the current matrix tensile stress (see the serrated profiles below the strength profiles in the figures). Numerical examples presented in this article assume that the matrix tensile strength is a Gaussian random field. The matrix stress state respecting the existing cracks is known and the load σ_c initiatinga new crack at any point x of the tensile specimen can be obtained by seeking the minimum load level yielding the equality of local matrix strength and the stress.

The crack bridge model delivers the local profile of the matrix stress in the vicinity of the crack. The stress profile depends on the underlying bond law describing the stress transfer between the reinforcement and the matrix and on the instantaneous crack spacing. In the shown example a simple crack bridge model with constant bond has been used. For this model, expressions for matrix stress (σ_m), reinforcement strain (ε_f), and of crack width w required by the crack-tracing algorithm are available in a closed form as summarized in Fig. 2.

The incorporation of a *crack bridge model* exploits the concepts of stress field symmetry about the midpoint between adjacent crack planes, see Fig. 4b, in a multiply cracked composite. At an intermediate state, each of the K crack bridges can be regarded independently. With the assumption of stress field symmetry, the description of individual crack bridges can be conveniently centered at the crack position given by the local coordinate $z = 0$. The domain of a crack bridge is then defined within the range $L_l \le z \le L_r$, where L_l and L_r denote the midpoints of distances to the nearest left- and right-hand side cracks, respectively. Within this domain, the local crack bridge formulation represents an initial boundary value problem governed by the uniaxial equilibrium condition

$$\sigma_c = V_f\ \sigma_f(z) + (1 - V_f)\ \sigma_m(z), \qquad (2)$$

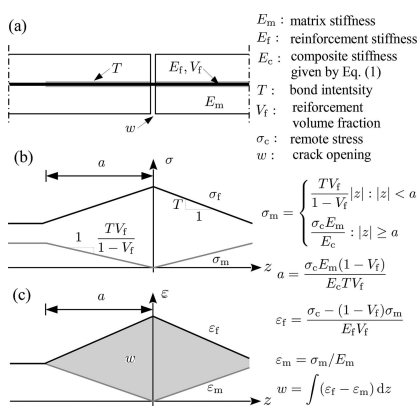

Figure 2. Analytical solution of a crack bridge with constant bond: (a) the crack bridge; (b,c) the reinforcement and matrix stress and strain profiles, respectively.

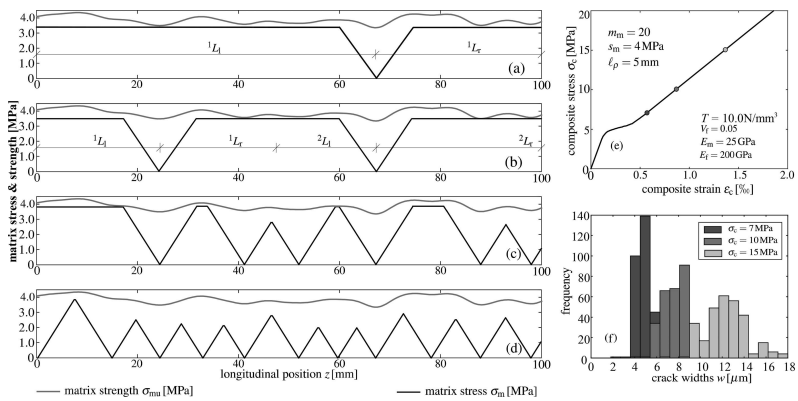

Figure 3. Computational example with random matrix strength and random bond strength (uniform distribution between 0.2 and 0.8 N/mm^2 with average $\mu_\tau = 0.6$ N/mm^2): evolution of matrix cracking in a composite with random bond and strength (a) – (d); stress-strain diagram (e); crack width histograms (f).

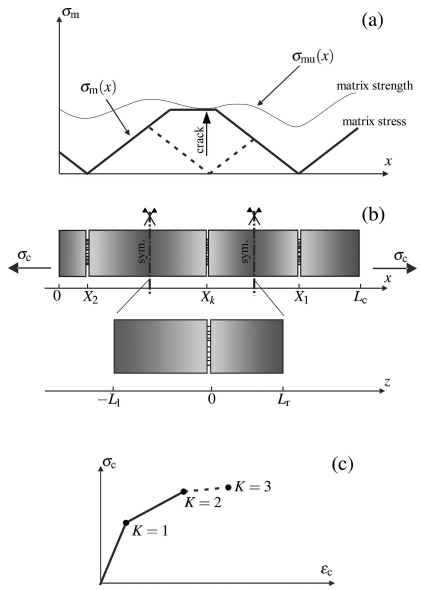

Figure 4. The interim state of cracking after the initiation of the *Kth* crack: (a) matrix stress profile and matrix strength; (b) composite with detail of the *Kth* crack bridge; (c) stress-strain diagram.

where $\sigma_f(z)$ is the fiber stress, and by the compatibility conditions at the transitions between two neighboring crack bridge domains.

The full *cracking history* is obtained by repeated evaluation of preceding conditions for an incremented crack counter $K = K + 1$. In the initial state $K = 0$ without a crack, the matrix stress is constant along the specimen and can be obtained explicitly using the rule of mixtures. The algorithm ends if no solution to the equality of stress and strength is found for any load σ_c indicating a saturated cracking state with K_{sat} cracks. The ultimate failure is determined by attaining the fiber strength in the weakest crack bridge.

With the identified history of the matrix cracking states $K = 1, 2,\ldots,K_{sat}$ at hand, the *composite strains*, ε_c, corresponding to the load σ_c can be evaluated for the given crack positions $X^{(K)}$ as

$$\varepsilon_c^{(K)}(\sigma_c) = \frac{1}{L_c}\left[\sum_{k=1}^{K} w_k^{(K)}(\sigma_c) + \frac{1}{E_m}\int_0^{L_c} \sigma_m^{(K)}(\sigma_c, x)\,dx\right],$$

where the first term sums the crack widths and the second term accounts for elastic deformation of the matrix. The matrix stress $\sigma_m^{(K)}$ is known from the solution of the cracking history and the K crack openings $w_k^{(K)}$, $k = 1,2,\ldots,K$ have to be provided by a crack bridge model.

The process of crack detection, stress update and strain evaluation is repeated until the saturated crack state has been achieved. The simulation delivers the relation between the composite stress and strain as shown in Fig. 3e. At the same time, the matrix crack widths in all crack bridges are evaluated at individual levels of composite stress; see Fig. 3f. This detailed output allows the user to analyze the sensitivity of the composite behavior to the input parameters and their statistical variability. Parameters used for the present example are summarized in Fig. 3e. The stress-strain diagram and the crack widths were simulated for a composite specimen with a length of 3000 mm. For brevity, the matrix stress profiles are shown on a 100 mm long segment of the simulated tensile specimen.

The abstract formulation of the crack tracing algorithm can be combined with various types of crack bridge models, either analytical formulations or numerical finite element models or probabilistic fiber-bundle based models.. In such a way, different types of composites can be covered, including short-fiber composites (engineered cementitious composites), or composites using continuous homogeneous reinforcement (GFRP, CFRP) bars, as well as and multi-filament reinforcement (textile-reinforcement concrete). The crack bridge model can be inserted as a plug-that provides the mapping between the remote composite stress as a control variable to the matrix stress profile in the crack bridge vicinity, and to the crack opening w. It is important to note, that the algorithm identifies the cracks one by one without the need to specify the size of a load step as needed e.g. in (Lu et al., 2017). This paper uses a particular type of crack bridge model relevant for textile-reinforced concrete (TRC).

3 PROBABILISTIC CRACK BRIDGE MODEL

In order to investigate some salient features of TRC tensile behavior a series of test setups has been conducted with three variants of cross-sectional layout. The focus was on TRC composites with dry (non-impregnated) carbon yarns that exhibit a high degree of heterogeneity owing to the imperfect penetration of the cement-based matrix into the multi-filament yarn structure. It is important to note that the heterogeneity of the matrix, yarn and of the bond appear at a comparable scale. The heterogeneity has a significant effect on the overall behavior of the composite that needs to be reflected in the models and design codes.

3.1 *Crack bridge test*

Five prismatic specimens of the size $40 \times 100 \times 1000$ mm were produced for the single crack bridge test. The specimens contained a single carbon fabric ply with 11 parallel yarns (Toho Tenax Co., Ltd, 12k, 800 tex) in the longitudinal direction and the

matrix was notched in the middle of the longitudinal dimension in order to initiate a matrix crack. The notch was produced by a thin steel plate coated with a mold release agent to avoid adhesion to the matrix. The ratio between the cross-sectional areas ≈ 3995 mm^2 (matrix) and ≈ 5 mm^2 (fibrous reinforcement) has been chosen in order to ensure that the matrix does not crack anywhere but in the notch. The rather long embedded length of the yarns (500 mm at each side of the centered crack) was chosen to provide a long process zone.

The results of the single crack bridge tests are shown in terms of force F vs. crack opening w diagrams in Fig. 5. The high initial stiffness of the specimens corresponds to the contribution of filaments with strong bond (sleeve filaments). When the response approaches the maximum force, individual filaments start to break. During the descending branch, a combination of debonding of filaments with weak bond and pullout of broken filaments occurs.

In order to model the test, a crack bridge model has to be selected and calibrated. We have selected the probabilistic crack bridge model PCBM presented by Rypl et al. (2013). For the calibration of the model, we use a representative experimental curve obtained by averaging the measured forces for each measured crack opening; see the dashed curve in Fig. 5a. This representation is equivalent to the simultaneous testing of all five specimens in parallel with the measured force normalized to a single experiment.

3.2 *Calibration of the PCBM parameters*

The experimental observation presented before indicates the high amount of material heterogeneity in both material components and in the bond. This imperfection results in significant bond strength variations among individual filaments and must be reflected in the model formulation.

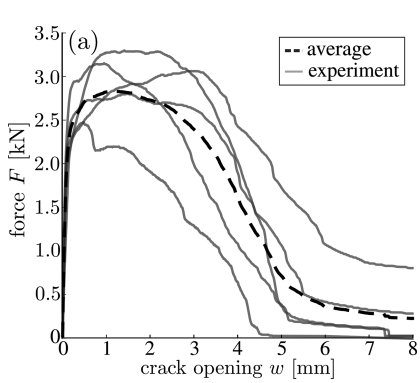

Figure 5. Results of the tensile tests on single crack bridges: Crack opening vs. force curves of five tested specimens and their average, $A_c = 4000$ mm.

There are seven parameters that need to be provided as input for the combined, multiscale PMCM-PCBM if all of them are considered as deterministic. However, some of the parameters are inherently random, which introduces additional unknowns into the model formulation – descriptors of their statistical distributions.

Carbon fibers have a random tensile 1) breaking strain ξ determined by the weakest flaw in the material structure. The 2) bond strength τ is random due to the irregular matrix penetration into the yarn structure and the 3) effective matrix tensile strength is random due to its heterogeneous material structure and (quasi) brittle failure mode. The remaining parameters are assumed to be deterministic: From the product specifications. The matrix modulus of elasticity, fiber radius, and fiber modulus of elasticity were set deterministic based on based on tests performed at RWTH Aachen, see the model parameters are summarized in Table 1.

While the values of the deterministic parameters are obtained in a straightforward way from standardized experiments, the statistical distributions of sets of random parameters related to random breaking strength and bond strength are to be identified by statistical inference based on experiments performed for this purpose. The description of these tests follow. The parameters related to the effective matrix tensile strength σ_{mu} must be obtained with unnotched tests and the model used for calibration is not the PCBM alone, but the combination of PCBM with PMCM, see Section 4.

Fiber breaking strain

We use the common assumption of a compound Poisson process for the spatial and severity distribution of fiber flaws with the distribution-parameters shape m_f and scale s_f related to the reference volume $V_0 = 1\ mm^3$. It can be derived that the breaking strain of a fiber embedded in matrix with constant frictional stress at their interface follows the two-parameter Weibull distribution. The calibration of the two parameters of strength distribution is based on previous experimental work by the authors (tensile tests on carbon yarns and single carbon filaments Rypl et al. (2015)). It can be found e.g. in Rypl et al. (2015) and references therein that the mean breaking strain of a fiber of length L is given by

$$\mu^*_{\varepsilon_f}(L, s_f, m_f) = (\pi r^2 L)^{-1/m_f}\, s_f \Gamma(1 + 1/m_f), \tag{3}$$

where s_f is the characteristic breaking strain of a reference unit volume $V_0 = 1\ mm^3$, and m_f is the shape parameter of the breaking strain distribution. The tests at two different gauge lengths yielded $s_f = 7.6 \cdot 10^{-3}$ [-] and $m_f = 6.7$ [-]. More details can be found in (Chudoba et al., 2018).

Table 1. Parameters of the probabilistic multiple cracking model.

parameter		value	unit
fiber breaking strain	ξ	random	[-]
bond strength	τ	random	[MPa]
eff. matrix strength	σ_{mu}	random	[MPa]
fiber radius	r	3.5	[μm]
fiber Young's modulus	E_f	182	[GPa]
matrix Young's modulus	E_m	25	[GPa]
fiber vol. fraction	V_f	set	[%]

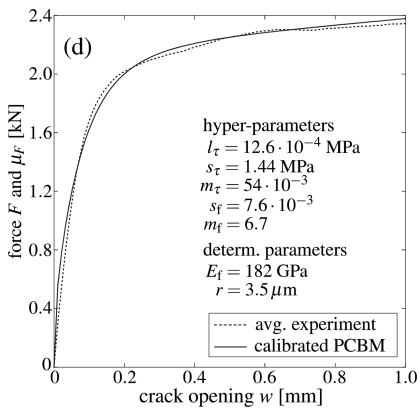

Figure 6. PCBM with calibrated parameters of τ distribution.

Bond strength

Observing the microscopic structure of the yarn cross-section, one can distinguish that the contact between the majority of filaments in the core of the yarn and the matrix is poor. These core filaments will transfer only a minor part of the bridging force. A much smaller fraction of filaments – sleeve filaments – are fully covered by the matrix around the whole perimeter and will thus have a much stronger bond. One possible mathematical function that describes this distribution of the effective bond strength is the gamma distribution with parameters for shape m_τ, scale s_τ and location l_τ given by

$$\tau \sim G_\tau(\tau; m_\tau, s_\tau) = \frac{\gamma\left(m_\tau, (\tau - l_\tau)/s_\tau\right)}{\Gamma(m_\tau)} \qquad (4)$$

with $\gamma(x, y)$ being the lower incomplete gamma function and $\Gamma(x)$ the complete gamma function. If $m_\tau < 1$, the probability density is highest at the lower bond l_τ, which represents the core filaments, and its right tail with much lower density represents the bond strength of sleeve filaments by higher values of τ and a large variability.

The three parameters $\{s_\tau, m_\tau, l_\tau\}$ describing the distribution of the bond strength s_τ, m_τ and l_τ can be *calibrated* independently of the matrix strength parameters by fitting the single crack bridge experiment responses with the PCBM. Fig. 6d shows the match between the experiment and the PCBM response calculated with the calibrated set of parameters: $s_\tau = 1.44$ [MPa], $m_\tau = 0.054$ [–] and $l_\tau = 12.6 \cdot 10^{-4}$ [MPa].

4 THE FRAGMENTATION MODEL

The only missing parameter in the PMCM is the spatial distribution of the effective matrix strength. In order to calibrate it, the multiple cracking experiments with $V_f = 1.0\%$ were used. Validation of the model is performed via comparison of the (i) model prediction with the calibrated parameters and (ii) experiments on the multiple cracking experiments with $V_f = 1.5\%$.

4.1 *TRC tensile test*

The specimens with a higher fiber volume fraction had a cross-sectional area of 100 × 20 mm and a length of 1000 mm and contained carbon fabrics of the same type as the notched crack bridge specimens (see Fig. 7). Five specimens contained four plies and another five contained six plies resulting in the respective fiber volume fractions of $V_f = 1.0\%$ and $V_f = 1.5\%$. Displacement fields were recorded within the 120 × 100 mm surface area of each specimen using the digital image correlation system ARAMIS. The measured displacement histories were post-processed by the crack detection tool delivering crack initiation, evolution, widths and spacing of cracks as a function of the load, see Fig. 7c. In addition, two displacement transducers were placed along the sides of the specimen to measure the displacement over 250 mm of the gauge length (see Fig. 7a).

The results of the multiple cracking tests are shown in Fig. 9b in terms of force F vs. composite strain ε_c diagrams (look only at the experimental curves at the moment). The corresponding measured fiber strengths $\sigma_f^* = F^*/A_{f,tot}$ ranged between 1038 and 1340 MPa for specimens with $V_f = 1.0\%$ and between 1307 and 1419 MPa for specimens with $V_f = 1.5\%$. It can be observed that the fiber strength grows with increasing fiber volume fraction by 96% and 124% for the respective V_f values of 1.0% and 1.5% compared to the single crack bridge experiments. An explanation of this phenomena is given in Section 6.

4.1.1 *Effective matrix strength model*

Although the tensile strength of a pristine cement-based matrix can be assumed to follow rules of the weakest link model and thus be simulated by the Weibull distribution, its effective *in-situ* properties in TRC differ significantly from this idealization.

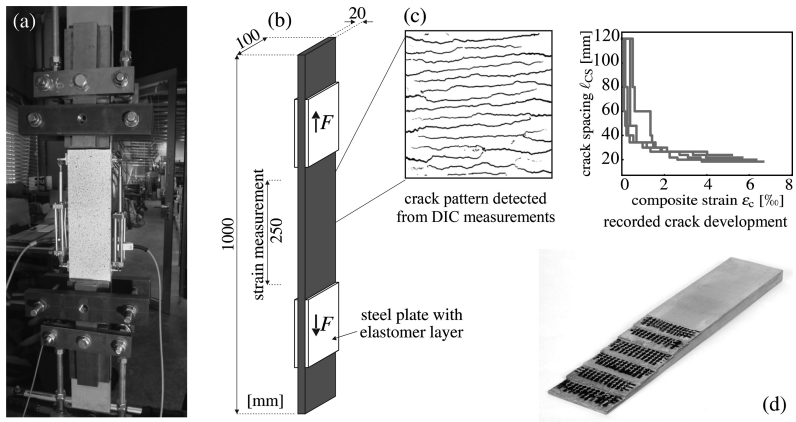

Figure 7. Textile reinforced concrete tensile specimens: (a) clamped specimen before tensile test; (b) diagram of the clamped specimen; (c) detected matrix cracks; (d) cross-sectional layout.

The bridging fibers restrain crack propagation and thus eliminate flaw sensitivity of the matrix rendering the weakest link features incorrect. Instead of a serial coupling of independent links the structural system is of the series-parallel type (Harlow and Phoenix, 1978a,b) and its strength is described by a Gaussian distribution (close to mean values and spreading far towards the tails if the number of parallel microbonds is high) with a smooth transition towards Weibullian tails (with variable shape and scale parameters).

Since the current model is a 1D representation of the composite, we have to lump all effects that influence the two-dimensional *in-situ* fiber-bridged crack propagation in TRC into a single random variable which represents the *in-situ* effective matrix strength. We are aware of the fact that such an effective matrix strength is also dependent on the cross-sectional area of the composite and, therefore, cannot be regarded as a material parameter without a proper scaling to arbitrary geometries.

Given the assumptions described above, we model the one-dimensional effective matrix strength by a two-parameter Gaussian distribution: $\sigma_{mu} \sim \mathcal{G}_{\sigma_{mu}}(\sigma_m; m_m, s_m)$, where m_m is the mean value, s_m is the standard deviation and this couple is related to the autocorrelation length ℓ_ρ. The autocorrelation length ℓ_ρ has been shown to have a rather minor effect on the cracking process (Rypl, 2014) in a composite specimen loaded in tension, and is therefore set to $\ell_\rho = 1\,\text{mm}$, which corresponds to the maximum aggregate size in the cement-based matrix of TRC.

The selection of Gaussian distribution can be advocated by a fact that the effective matrix strength can be viewed as a result of parallel coupling of many microbonds in the material structure (including the interfaces between many grains in each cross section and also the reinforcing action of fibers). Such an additive mechanism of strength generation with many sources of variability leads to Gaussian distribution of cross sections even if the strength distributions of the constituents are different.

Calibration

In order to identify the two parameters defining the effective matrix tensile strength distribution, $\{s_m, m_m\}$, we utilize the force-strain curves of the multiple cracking experiments with $V_f = 1.0\%$. The simulation was performed with the calibrated parameters for fiber breaking strain and bond strength written in Fig. 6. In order to unify the units, we have to multiply the load σ_c introduced in the PMCM formulation with the composite cross-sectional area $A_c = 2000\ \text{mm}^2$ so that $\mu_F = \sigma_c A_c$.

The identified mean value and standard deviation of Gaussian random effective matrix strength are written in Fig. 8e. There are five pairs $\{s_m, m_m\}$ – each for an individual specimen tested. One can observe a low value of the coefficient of variation (s_m/m_m) of the Gaussian effective matrix strength. This might be surprising as cement-based matrix is usually reported to have greater variability in strength. However, in TRC, the matrix is reinforced with fibers and one has to consider effective matrix strength. The bridging fibers arrest crack initiation and propagation and thus diminish the flaw-sensitivity of the cement-based matrix, which in its pristine state has a much greater relative variability.

A notable variability in the effective matrix strength is, however, present among individual specimens. Such a global variability can be caused by the positions of reinforcing textiles, initial specimen deformations that cause bending moment during the tensile test, position of clamps etc.

The responses of the model with the calibrated vectors of PCBM and the five sets of calibrated

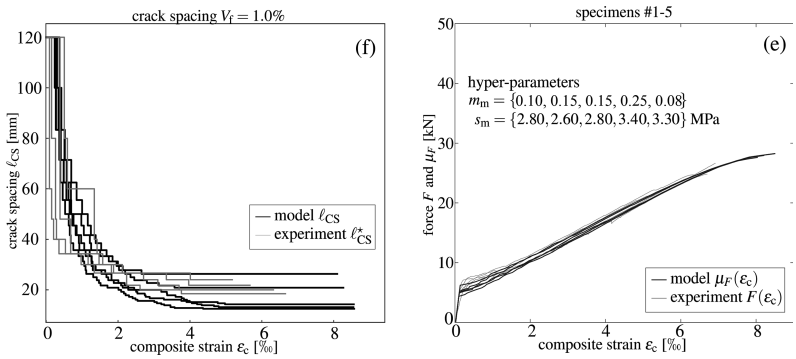

Figure 8. Calibration hyper-parameters of the σ_{mm} distribution: (e) five PMCM simulations (black curves) with effective matrix strength parameters calibrated on five experiments (gray curves); (f) predicted evolution of crack spacing compared to measured values.

parameters for the matrix strength are depicted in Fig. 8e. In Fig. 8f, the evolution of the crack spacing during the loading process is shown. Since the present model is a 1D representation of this 2D crack propagation problem, we only consider the crack spacing at the specimen margins, where the 2D effect discussed in Section 3 is least pronounced. Let us emphasize that while the lack-of-fit with respect to the force-strain response was minimized in the course of the calibration, the model is purely predictive in terms of crack spacing and strength. The average of the saturated crack spacings measured experimentally was 20.1 mm and the average saturated crack spacing from the five simulations of the PMCM was 20.6 mm indicating a 2.5% difference (see Fig. 8f). Regarding the composite strength, the model tends to overestimate the ultimate performance of the composite by about 20% (see Fig. 8e).

It can be concluded that the crack spacing at failure, the first cracking stress and the optimum of the lack of fit intersect in this case of averaged experiments and identify the optimum of the s_m and m_m hyper-parameters. However, this was not the case for all experiments when considered individually. We therefore calibrated the effective matrix strength hyper-parameters based on the minimum lack of fit and ignored the discrepancies in the crack spacing and the first cracking stresses for individual test specimens. As stated above, the lack of fit was evaluated for the computationally feasible five samples of the random field, whose average results in jagged isolines. We have used a mathematical smoothing method on the isolines (see Fig. 8c), which makes the isomaps appear as if they have been averaged from a large number of simulations. Again, this was performed only for demonstration purposes and was not included in the calibration process in any way.

5 PREDICTION OF COMPOSITE TENSILE RESPONSE

We now proceed to the prediction of the response of a composite with $V_f = 1.5\%$. It has been observed experimentally and studied theoretically that the first cracking stress rises with increased fiber volume fraction (Budiansky et al., 1986; Marshall et al., 1985; Marshall and Cox, 1987). In the cited references, researchers have related the (deterministic) matrix strength to fiber volume fraction in the following way

$$\sigma_{mu} = \left[\frac{6\tau\Gamma_m V_f^2 E_f E_c^2}{r(1-V_f)E_m^2} \right]^{1/3} \tag{5}$$

with Γ_m denoting the specific matrix fracture energy. This formula is the result of an energy balance analysis involving matrix crack propagation and fiber debonding.

In the present calibration, the mean value of the effective matrix strength distribution, m_m, approximately equals the deterministic matrix strength because the standard deviation s_m is very low. We can therefore use Eq. (5) for the scaling of m_m and assume that the s_m remains unaffected by the increased V_f (replace σ_{mu} by m_m in Eq. 5). With this assumption, we can evaluate the scaling factor for the effective mean matrix strength $\hat{m}_m$ corresponding to an arbitrary fiber volume fraction $\hat{V}_f$ if we know a pair of mean values m_m and the corresponding fiber volume fraction V_f. The scaling factor reads, using Eq. (5),

$$\frac{\hat{m}_m}{m_m} = \left[\frac{\hat{V}_f^2 \hat{E}_c^2 (1-V_f)}{V_f^2 E_c^2 (1-\hat{V}_f)} \right]^{1/3}, \tag{6}$$

where $\hat{E}_c = E_f \hat{V}_f + E_m(1-\hat{V}_f)$. For the particular case of fiber volume fractions 1.5% and 1.0%, the ratio of the two scale parameters ≈ 1.34, which

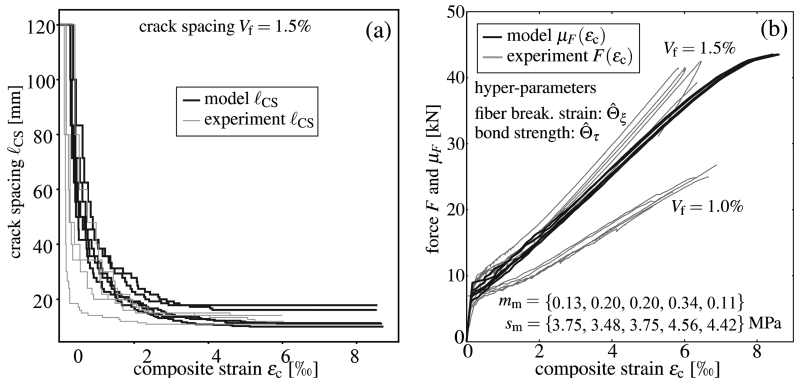

Figure 9. Validation of the model: (a) predicted crack spacing evolution (black curves) compared to measured saturated crack spacing (gray curves); (b) predicted force-strain responses for a composite with fiber volume fraction $V_f = 1.5\%$.

defines the scaling factor for the effective matrix strength distribution according to the described theory.

Our assumption is that the matrix Gaussian strength has the same cov for 1.5% as calibrated for the 1% volume fraction of fibers. That is we multiply both the mean values m_m and the standard deviations s_m by the same factor of 1.34.

It is obvious from the table in Fig. 8 that the parameters m_m, s_m vary randomly among individual specimens. This variability is likely to result from uncertainties at the specimen scale and not from the variability of the matrix micro-structure. As described above, possible causes of this variability include specimen deformations (curvature) due to shrinkage, the position of the clamps during the tensile test, and the position of textile fabrics.

The force-strain curves and crack spacing evolution evaluated by the PMCM with the calibrated distributions are depicted in Fig. 9. Note that the sampled s_m were multiplied by the factor 1.34 as described in the above paragraph.

Observing the force-strain response in Fig. 9b, the agreement between the model's prediction and the experiments seems to be acceptable. The first cracking stresses and multiple cracking stage are captured with good accuracy, but in the third (linear) range there is a discrepancy in stiffness. While the model predicts the composite stiffness as $E_f V_f$, the experimentally measured stiffness increases during the loading process by a higher amount than that predicted by the model for an increased fiber volume fraction.

Fig. 9a depicts the prediction of the crack spacing evolution and its validation with the experimentally measured crack spacing. The averages of the measured and predicted saturated crack spacing are 13.6 mm and 16.5 mm, rendering a difference of 1.9 mm or ≈ 20%.

6 DISCUSSION AND CONCLUSIONS

It has been demonstrated that the multiscale probabilistic multiple cracking model introduced in this paper is able to predict the behavior of fibrous composites with heterogeneous reinforcement subjected to tensile loading given the material parameters and their distribution. The model only requires parameters with a physical interpretation and does not require *a-priori* information concerning the composite response such as the saturated crack spacing or ultimate strength.

With the calibrated parameters, we have predicted the crack spacing, ultimate strength and force-strain response of textile reinforced concrete with an extrapolated fiber volume fraction. Without claiming that the present study provides a complete validation of the model, the predicted trends have proved to be consistent with the behavior of the performed experiments.

The probabilistic multiple cracking model is capable of reproducing and predicting the force-strain response of the composite, the process of multiple cracking and the saturated state, which includes crack spacing (and the closely related crack widths); see Figs. 8 and 9. These predictive capabilities imply that the model reflects the random bond structure and the resulting stress transfer between the fibrous reinforcement and the matrix in a fairly accurate manner.

In the accompanying experiments, the average measured fiber strength of the crack bridge experiments and the multiple cracking experiments with $V_f = 1.0\%$ and $V_f = 1.5\%\%$ correspond to a respective 96% and 124% increase in fiber strength in the multiple cracking experiments compared to the fiber strength measured in the crack bridge experiments. Strength variations of this magnitude are significant and have to be taken into account when

designing composites with heterogeneous reinforcement. We have provided a brief explanation of this phenomenon based on differences in crack spacing in (Rypl et al., 2013).

ACKNOWLEDGMENTS

This work was supported by the Czech Science Foundation GAČR under the project No. GA16-22230 and by the German Federal Ministry of Education and Research (BMBF) as part of the Carbon Concrete Composite (C^3) project, subproject C-V1.2. This support is gratefully acknowledged.

REFERENCES

Aveston, J., G. Cooper, & A. Kelly (1971). Single and multiple fracture, the properties of fibre composites. In *Proc. Conf. National Physical Laboratories*, pp. 15–24. IPC Science and Technology Press Ltd. London.

Aveston, J. & A. Kelly (1973). Theory of multiple fracture of fibrous composites. *J. Mater. Sci. 8*(3), 352–362.

Budiansky, B., J. Hutchinson, & A. Evans (1986). Matrix fracture in fiber-reinforced ceramics. *Journal of the Mechanics and Physics of Solids 34*(2), 167–189.

Castelier, E., L. Gélébart, C. Lacour, & C. Lantuéjoul (2010, December). Three consistent approaches of the multiple cracking process in 1D composites. *Composites Science and Technology 70*(15), 2146–2153.

Cho, C., J. Holmes, & J. Barber (1992). Distribution of matrix cracks in a uniaxial ceramic composite. *J. Am. Ceram. Soc. 2*(75), 316–324.

Chudoba, R., R.R., M. Vořechovský, & X. Li (2018). Probabilistic multiple cracking model of brittle matrix composite reflecting randomness in matrix, reinforcement and bond. *Composites Part B: Engineering* (in review).

Chudoba, R., M. Vořechovský, & R. Rypl (2011). Identification of the effective bundle length in a multifilament yarn from the size effect response. *Journal of Composite Materials 45*(25), 2659–2668.

Curtin, W. (1991). Exact theory of fiber fragmentation in a single-filament composite. *Journal of Materials Science 26*, 5239–5253.

Curtin, W. (1993a). Multiple matrix cracking in brittle matrix composite. *Acta metall. mater. 41*(5), 1369–1377.

Curtin, W. (1993b). The tough to brittle transition in brittle matrix composites. *Journal of the Mechanics and Physics of Solids 41*(2), 217–245.

Cuypers, H. & J. Wastiels (2006). Stochastic matrix-cracking model for textile reinforced cementitious composites under tensile loading. *Materials and Structures 39*(8), 777–786.

Harlow, D. & S. Phoenix (1978a). The chain-of-bundles probability model for the strength of fibrous materials I: Analysis and conjectures. *Journal of Composite Materials 12*(2), 195–214.

Harlow, D. & S. Phoenix (1978b). The chain-of-bundles probability model for the strength of fibrous materials II: a numerical study of convergence. *Journal of Composite Materials 12*(3), 314–334.

Henstenburg, R. & S. Phoenix (1989). Interfacial shear strength studies using the single-filament-composite test. part II: a probability model and Monte Carlo simulation. *Polymer Composites 10*(5), 389–408.

Hui, C.-Y., S. Phoenix, M. Ibnabdeljalil, & R. Smith (1995). An exact closed form solution for fragmentation of Weibull fibers in a single filament composite with applications to fiberreinforced ceramics. *Journal of the Mechanics and Physics of Solids 43*(10), 1551–1585.

Kang, J. & J.E. Bolander (2016). Multiscale modeling of strainhardening cementitious composites. *Mechanics Research Communications 78, Part B*, 47–54.

Kimber, A. & J. Keer (1982, August). On the theoretical average crack spacing in brittle matrix composites containing continuous aligned fibres. *Journal of Materials Science Letters 1*(8), 353–354.

Larrinaga, P., C. Chastre, J. San-Jos, & L. Garmendia (2013, December). Non-linear analytical model of composites based on basalt textile reinforced mortar under uniaxial tension. *Composites Part B: Engineering 55*, 518–527.

Lu, C., C.K. Leung, & V.C. Li (2017). Numerical model on the stress field and multiple cracking behavior of engineered cementitious composites (ecc). *Construction and Building Materials 133*(Supplement C), 118–127.

Marshall, D. & B. Cox (1987, November). Tensile fracture of brittle matrix composites - influence of fiber strength. *Acta Metallurgica 35*(11), 2607–2619.

Marshall, D., B. Cox, & A. Evans (1985). The mechanics of matrix cracking in brittle-matrix fiber composites. *Acta Metallurgica 33*(11), 2013–2021.

Netravali, A., R. Henstenburg, S. Phoenix, & P. Schwartz (1989). Interfacial shear strength studies using the single-filament composite test. i: Experiments on graphite fibers in epoxy. *Polymer Composites 10*(4), 226–241.

Phoenix, S. (1993). Statistical issues in the fracture of brittlematrix fibrous composites. *Composites Science and Technology 48*(1–4), 65–80.

Phoenix, S. & R. Raj (1992). Scalings in fracture probabilities for a brittle matrix fiber composite. *Acta Metallurgica et Materialia 40*(11), 2813–2828.

Rosen, B. (1964). Tensile failure of fibrous composites. *AIAA Journal 2*(11), 1985–1991.

Rypl, R. (2014). *Probabilistic approach to the mechanics of composites with heterogeneous reinforcement*. Ph. D. thesis, RWTH Aachen University.

Rypl, R., R. Chudoba, U. Mörschel, S. Stapleton, T. Gries, & G. Sommer (2015). A novel tensile test device for effective testing of high-modulus multi-filament yarns. *Journal of Industrial Textiles 44*(6), 934–947.

Rypl, R., R. Chudoba, A. Scholzen, & M. Vořechovský (2013). Brittle matrix composites with heterogeneous reinforcement: Multi-scale model of a crack bridge with rigid matrix. *Composites Science and Technology 89*, 98–109.

Smith, R. (1982). The asymptotic distribution of the strength of a series-parallel system with equal load-sharing. *The Annals of Probability 10*(1), 137–171.

Vořechovský, M., R. Rypl, & R. Chudoba (2017). Probabilistic crack bridge model reflecting random bond properties and elastic matrix deformation. *Composites Part B: Engineering in press*.

Zweben, C. & B. Rosen (1970). A statistical theory of material strength with application to composite materials. *Journal of the Mechanics and Physics of Solids 18*(3), 189–206.

Computational Modelling of Concrete Structures – Meschke, Pichler & Rots (Eds)
© 2018 Taylor & Francis Group, London, ISBN 978-1-138-74117-1

Numerical modelling of textile reinforced concrete sandwich panels

Isabella G. Colombo, Matteo Colombo & Marco di Prisco
Department of Civil and Environmental Engineering, Politecnico di Milano, Milan, Italy

ABSTRACT: The paper is aimed at predicting the behavior of lightweight textile reinforced concrete (TRC) sandwich panels tested in bending. Panels are characterized by thin external TRC layers cast on an expanded polystyrene (EPS) layer used as thermal insulation (12 + 100 + 12 mm). Each panel is 3.03 m long and 1.5 m wide. Displacement controlled tests up to failure have been performed on two full-scale panels and the experimental results are used as a benchmark for the analysis shown in this paper. A 3D non-linear finite element model built in Abaqus is proposed. The model includes both material and geometry non-linearity. The numerical analysis performed on full-scale panel allows to predict the specimen global response and to investigate the failure modes that involve the sandwich solution.

1 INTRODUCTION

In the two thousands, Hegger & Horstmann (2009) proposed lightweight textile reinforced concrete (TRC) sandwich panels; in these panels, shear connectors have been introduced to obtain a durable and proper sandwich action (Shams et al. 2014). In other cases, advanced cementitious composite sandwich panels without shear connectors have been investigated (Müller et al. 2012, Zani et al. 2014).

The sandwich panel investigated in the paper has been developed in the framework of the European project EASEE—Envelope Approach to improve Sustainability and Energy Efficiency in existing multi-storey multi-owner residential buildings (2012–2016) - financed in the seventh Framework Program of the European Commission.

Among the goals of the project, there was the design and development of a solution that could be a more durable alternative to the exterior insulation and finishing system (EIFS), which is now the most widespread energy retrofitting method adopted on existing buildings.

The developed multi-layer precast sandwich panel shows many advantages if compared with the EIFS: a lower impact on occupant life (no scaffolding required), the possibility to obtain the desired finishing, the increase in impact resistance, the higher quality of finishing and the higher durability.

The panel has already been applied in some demo buildings, including a three-story residential building in Cinisello Balsamo (Colombo et al. 2016), which was completely retrofitted with this solution.

More details concerning the investigation on the panel carried out within the project can be found in Colombo et al. (2014, 2015a, 2015b, 2016a, 2016b, under review) and in Colombo (2015).

The main aim of the paper is modelling the behavior of a full-scale EASEE sandwich panel by means of a finite element analysis.

Concerning finite elements, in literature TRC has been modelled discretizing the fabric as a grid reinforcement embedded in the matrix (Larringa et al. 2014, Miccoli et al. 2015) or considering it as homogeneous (di Prisco & Zani 2012). Regarding foam materials, in Abaqus Masso-Moreu & Mills (2004) and Ozturk & Anlas (2011) modelled them through crushable foam model with volumetric hardening.

The finite element model—here applied on the full-scale panel—has been previously validated through experimental results obtained testing sandwich beams with dimensions of $1200 \times 500 \times 120$ mm^3 and $550 \times 150 \times 120$ mm^3 (Colombo 2015, Colombo et al. under review). The main assumptions of that model are: considering textile reinforced concrete as a homogeneous material, considering perfect bond at TRC/EPS interfaces and deriving parameters, which are necessary for the definition of material constitutive laws, through simple tests on EPS and TRC specimens. In that case, a good prediction of the bending behavior was achieved. According to the numerical results, it was possible to state that the sandwich beam response is governed by polystyrene non-linear behavior and by membrane and bending behavior of textile reinforced concrete.

2 REFERENCE EXPERIMENTAL TESTS

2.1 *Experimental campaign*

The model presented in this paper refers to four-point displacement-controlled tests performed on two textile reinforced concrete full-scale sandwich panels (Colombo et al. 2016b).

The panel (Figure 1) is characterized by the following stratigraphy: two external layer 12 mm thick made of textile reinforced concrete (TRC) and an internal insulation layer 100 mm thick in expanded polystyrene (EPS). The length of the panel is equal to 3030 mm and its width is equal to 1500 mm.

Shear forces are mainly transferred through EPS to the TRC layers; in any case, in order to avoid the detachment of the layers in extreme conditions (e.g. fire), four stainless steel AISI 310S bent bars

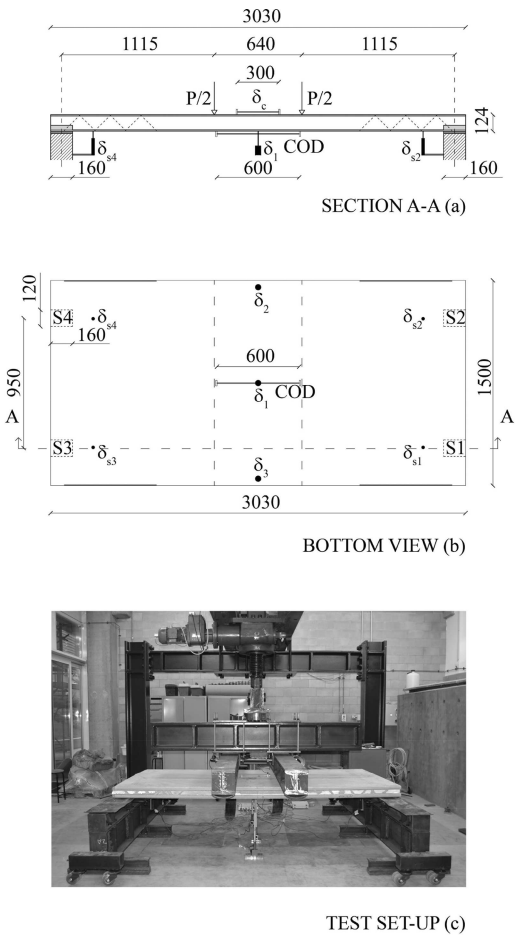

Figure 1. Test set-up and instrumentation of the panel: lateral view (a), bottom view (b) and picture of panel V2 during test (c) - measures in mm.

(ϕ5) were embedded in both the longitudinal panel edges at the upper and lower ends (Figure 1a).

At the four corners, in correspondence of regions S1-S2-S3-S4 (see Figure 1b), four high-performance fiber reinforced concrete (HPFRC) thickenings 160 × 120 × 42 mm have been cast; this portions of mortar allow the fastening of the panel to the exiting façade in real application.

Panels were cast using a vertical formwork, which allows to: minimize voids and defects in the mortar layers, guarantee a proper thickness of these layers, and ensure a high level of surface finishing.

The TRC layers were obtained reinforcing high strength fine grain mortar with one alkali-resistant (AR) glass fabric.

The matrix mix design is shown in Table 1; the mortar is characterized by a high flowing capability, thus guaranteeing good matrix-fabric and matrix-EPS bond. The average cubic compressive strength (f_{ccm}) - determined according to EN 196-1 Standard for mortar—is equal to 87.7 MPa (STD = 15.6% on 10 specimens) at 28 days.

The characteristics of the fabric selected as reinforcement are collected in Table 2. Fabrics are placed with warp yarns along the panel longitudinal direction.

The expanded polystyrene—commercially known as "EPS250" - has a density of 35 kg/m^3 and a thermal conductivity of 0.034 W/mK (UNI EN 13163). According to the test results

Table 1. Matrix mix design.

Component	Content
Cement I 52.5 (kg/m^3)	600
Quartz sand 0–2 mm (kg/m^3)	847
Water (l/m^3)	207
Superplasticizer (kg/m^3)	33
Slag (kg/m^3)	500

Table 2. Characteristics of the fabric.

Fabrication technique	Leno weave
Material	AR-glass
Coating	SBR*-based water resin
Warp yarn spacing (mm)	10.0
Weft yarn spacing (mm)	14.3
Warp (Tex)	2 × 2400
Weft (Tex)	2 × 1200
Coating weight (g/m$^2_{fabric}$)	100
Max. tensile load on 70 mm (kN)	9.15

*Styrene-Butadine Rubber.

(Colombo et al. under review), it is characterized by an elastic modulus in compression of 13.7 MPa, a uniaxial compressive yield stress of 0.19 MPa, a uniaxial tensile yield stress of 0.39 MPa, a shear yield stress of 0.16 MPa and a shear modulus of 5.04 MPa.

Two nominally identical tests (named V1 and V2) were performed. The test set-up is shown in Figure 1: a schematic view is plotted in subfigures (a) and (b) and a picture of panel V2 during test is provided in subfigure (c).

The panel is simply supported on four points, under HPFRC thickenings, over elastomeric bearing plates S (160 × 120 × 10 mm).

In the same figure, the instrumentation of the panel is shown. In particular, four linear variable differential transformers (LVDTs) were vertically placed on the bottom surface of the panel to measure the specimen vertical displacement next to the supports (δ_{S1}, δ_{S2}, δ_{S3} and δ_{S4}). On the same surface, at mid-span, three potentiometric transducers were placed in vertical position in order to measure the specimen vertical displacement respectively in the center and on the border of the panel (δ_1, δ_2 and δ_3). Two other LVDTs were placed on the bottom and upper surfaces astride the mid-span with a gauge length respectively equal to 300 mm and 600 mm: the first one is aimed at measuring the displacement δ_c on the compressed side, and the latter is instrumental at measuring the crack opening displacement (COD). An electronic measurement system SPIDER8 by HBM is used for data acquisition.

A contrast frame equipped with an electromechanic actuator with a maximum capacity of 1000 kN (Figure 1c) is used to perform the displacement-controlled tests; a constant increase of jack cross-head displacement (stroke, 15 μm/sec) was imposed.

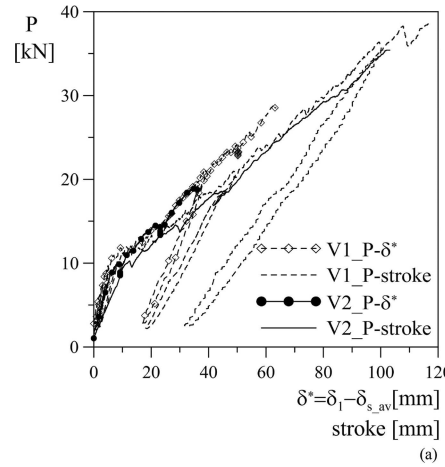

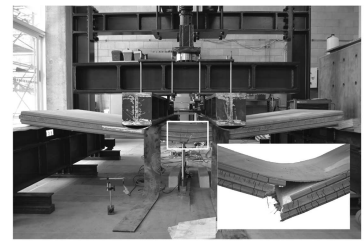

PANEL V1 - FAILURE (b)

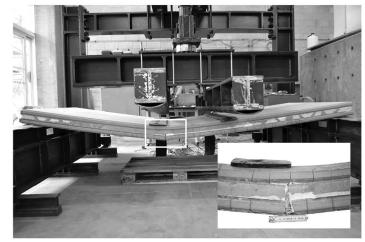

PANEL V2 - FAILURE (c)

Figure 2. Test results: load vs. stroke and load vs. vertical displacement δ* curves (a), failure of panel V1 (b) and failure of panel V2 (c).

2.2 *Experimental results*

The test results are shown in Figure 2. In Figure 2a the load (P) versus stroke and load versus vertical displacement δ* curves are plotted. δ* is the relative displacement, which is obtained detracting the average displacement at the supports δ_S from the value of the mid-point vertical displacement δ_1. P-δ* curves stopped before the test ending as instruments were removed before the failure of the specimens for safety reasons. In the first test (V1), four un-loading reloading cycles (dashed lines) were imposed to monitor permanent deflections.

In both panels, failure occurred due to the achievement of the maximum tensile deformation of the lower TRC layer. This failure caused the consequent failure of EPS and, hence, the debonding between expanded polystyrene and the upper TRC layer. This is clearly visible in the zoom proposed in Figure 2b. The maximum load reached in the tests is equal to 38.98 kN and 35.92 kN respectively for panel V1 and V2.

Looking at Figure 2a, it is possible to state that a very good repeatability has been obtained in the tests, in particular considering the vertical displacement δ*, which is free of any influence of the neoprene crushing.

During both tests, a widely extended multicracking pattern characterized the bottom TRC layer. Local bending under the loading knives

caused also a multi-cracking on the upper TRC layer, but just close to the load application points.

3 NUMERICAL MODEL

3.1 *Description of the model*

The model of the panel was implemented in Abaqus /CAE 6.13-1 and is shown in Figure 3. In order to reduce the numerical effort, a quarter of the panel has been reproduced exploiting both *xy* and *yz* symmetries.

As visible in Figure 3a, the panel layers (TRC and EPS), the HPFRC thickening, the neoprene supports and the loading knife are modelled as solid and homogeneous, while the bent bar is modelled as a truss.

Perfect bond is assumed at EPS/TRC interfaces and between the panel and neoprene supports. The interaction between the loading knife and the upper neoprene layer is characterized by a hard contact in the normal direction and by a friction with coefficient equal to 0.6 in the tangential direction. The

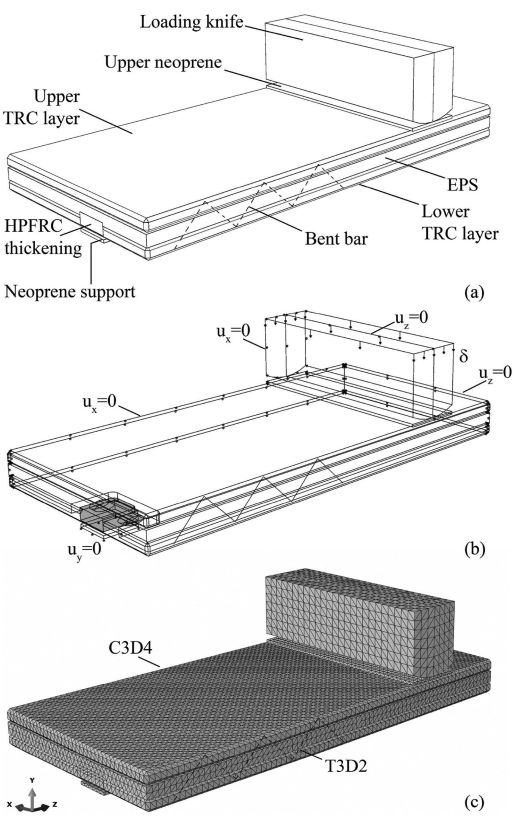

Figure 3. Model of the panel: geometry (a), constrains (b) and mesh (c).

Table 3. Mesh characteristics.

	Nodes	Elements	Elements over the thickness	Max. aspect ratio
Loading knife	1774	8104 (C3D4)	–	2.7
Upper neoprene	885	2450 (C3D4)	1	3.9
Upper TRC layer	6415	19,253 (C3D4)	1	5.0
EPS	20,042	98,352 (C3D4)	6	3.6
Lower TRC layer	6818	20,300 (C3D4)	1	3.0
HPFRC	370	1288 (C3D4)	3	5.0
Neoprene support	98	216 (T3D2)	1	3.0
Bent bar	103	102 (T3D2)	–	–
Whole model	29,354	150,065	–	–

bent bar is embedded in the whole model. As in the real panel the bent bar is embedded only in concrete, the numerical response should be stiffer than the real one. However, as shown in Section 4.2, the influence of bent bar on the global behavior of the panel is negligible; hence, this approximation is acceptable.

Concerning constraints (Figure 3b), displacement orthogonal to the symmetry planes are prevented, the lower neoprene support is constrained in the vertical direction on the bottom face and a vertical displacement δ of the loading knife is imposed on the whole upper surface of the knife. In order to prevent improper motion of the loading knife, the displacement in *z*-direction of some nodes is prevented as shown in the figure.

The mesh is shown in Figure 3c. Four-node linear tetrahedral elements (C3D4 - Continuum, 3-D, 4-node) are used in the case of solid homogeneous sections, and two-node linear truss elements (T3D2 - Truss, 3-D, 2-node) are used for trusses. The mesh characteristics are collected in Table 3.

3.2 *Constitutive laws*

In the following, the constitutive laws adopted for each materials are described.

The elastic phase of textile reinforced concrete is defined introducing a Young's modulus of 30 GPa (according to literature results on cement matrix characterized by similar compressive strength and maximum aggregate size, Brameshuber et al. 2006) and a Poisson's ratio of 0.2.

The plastic behavior of TRC is introduced using Abaqus Concrete Damage Plasticity model. No damage curves are introduced; hence, the model simply behaves as a plasticity model. An elastic-perfectly plastic behavior is assumed

in compression, considering a yield strength of 87.7 MPa according to the values already discussed in Section 2.1. In tension, the stress-irreversible strain relationship shown in Figure 4 is introduced. Point T1 indicates that TRC starts to multi-crack; after point T2 only the contribution of fabric and tension stiffening remain active; when T3 is reached, the brittle failure of the fabric occurs.

This stress-strain relationship is obtained starting from the experimental tensile behavior of TRC specimens tested according to the set-up described in Colombo et al. (2013). Three nominally identical specimens with dimension of $400 \times 70 \times 10$ mm were tested. These specimens were cast using the same matrix of the panels and were reinforced with one AR-glass fabric (see Section 2.1). The stress values are obtained dividing the measured load by the specimen cross-section. As no displacement transducer was applied on the specimens, it was not possible to directly obtain strains; hence, an identification procedure of the actual strains was performed based on the results already presented in Colombo et al. (under review).

It is worth to note that TRC tensile behavior is assumed homogeneous over the layer thickness; the reliability of this assumption was discussed and proved in Colombo et al. (under review).

Concerning expanded polystyrene (EPS), the following elastic parameters have been used: a Young's modulus of 13.7 MPa—defined according to the experimental results shown in Colombo et al. (under review) - and a Poisson's ratio of 0.1.

Crushable Foam model with volumetric hardening is used to define the plastic behavior. It is necessary to introduce three main parameters: the yield stress in uniaxial compression (σ_c^0), the ratio k between the uniaxial (σ_c^0) and the hydrostatic (p_c^0) compressive strength and the ratio k_t between the hydrostatic tensile (p_t) and the hydrostatic compressive (p_c^0) strength. According to the procedure proposed in Colombo et al. (under review), the adopted values are respectively 0.19 MPa for σ_c^0, 1.59 for k and 54.3 for k_t.

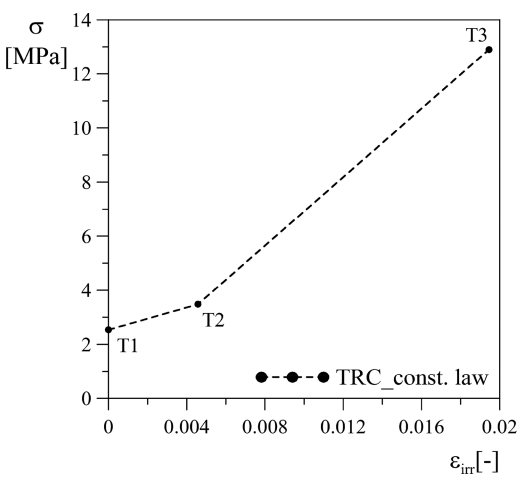

Figure 4. Plastic tensile constitutive law adopted for TRC.

As this material model is hardening in uniaxial tension, it is not able to catch the brittle tensile failure of EPS; hence, a verification of the maximum stresses reached in expanded polystyrene is necessary in order to exclude the tensile failure of this layer.

The HPFRC is considered elastic (Young's modulus equal to 47,500 MPa and Poisson's ratio equal to 0.2) (Zani et al. 2014, MC2010).

Neoprene rubber is supposed to be elastic with a Young's modulus of 0.7 MPa and a Poisson's ratio of 0.49 MPa (Materials Data Book 2003).

The steel constituting the loading knife is considered elastic with a Young's modulus of 210,000 MPa and a Poisson's ratio of 0.3.

The stainless steel constituting bent bar (310S) is modeled in elastic phase with the same parameters already mentioned for steel (E = 210,000 MPa and $\nu = 0.3$), and plasticity is accounted considering an hardening behavior characterized by a yield strength of 205 MPa, an ultimate tensile strength of 515 MPa and an elongation in 50 mm of 40% (ASTM A473 – 17a).

4 NUMERICAL RESULTS

4.1 *Comparison between numerical response and experimental behavior*

In Figure 5, the numerical response is shown in terms of load P versus relative mid-point vertical displacement δ*. The numerical curve is compared with the experimental curves obtained for both panels V1 and V2. As the measure of δ_i was stopped before reaching the failure, in the Figure also the ultimate values of load sustained by both panels is indicated ("V1 failure" and "V2 failure").

A very good correlation between numerical and experimental curves is obtained.

On the numerical response, the relevant points of the constitutive laws of textile reinforced concrete, expanded polystyrene and reinforcing steel are highlighted. Points T refers to the points already discussed in Figure 4 on the TRC constitutive law; subscript "inf" refers to the lower TRC layer, and subscript "sup" refers to the upper TRC layer. Point E1 indicates the yielding of the compressive strut in the EPS layer (Figure 6a; see also Colombo et al. under review).

Point S1 indicates the bent bar yielding.

Looking at the numerical curve it is possible to identify a tri-linear behavior mainly governed by

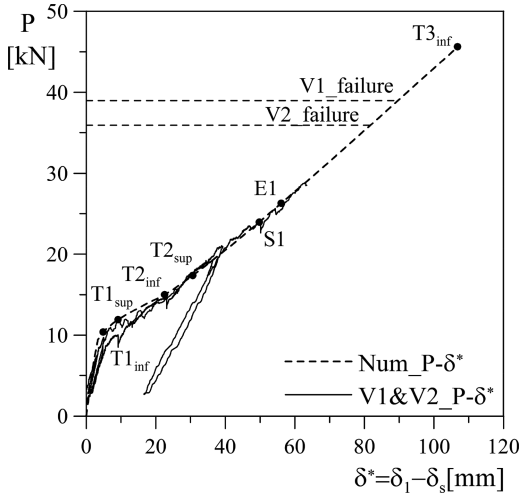

Figure 5. Numerical response in terms of load vs mid-point vertical displacement.

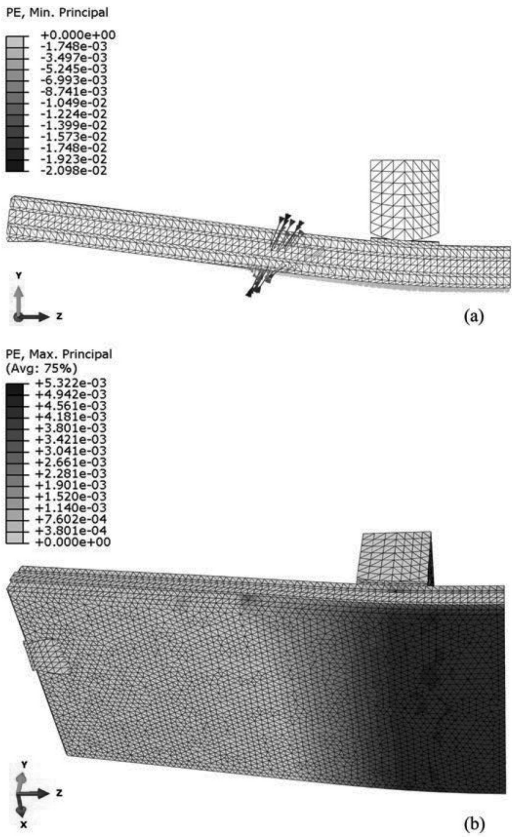

Figure 6. Yielding of the compressive strut in EPS layer at point E1 (a) and multi-cracking of the lower TRC layer at point $T2_{inf}$ (b).

the tensile behavior of the lower TRC layer. The first linear branch ends when the lower TRC layer starts its multi-cracking phase (point $T1_{inf}$); the second branch extends up to point $T2_{inf,}$ ending of the multi-cracking of the lower TRC layer (Figure 6b); finally, the panel failure is due to the achievement of the maximum tensile strength at the lower TRC layer (point $T3_{inf}$).

The failure mode obtained in the finite element analysis complies with what happened during tests (failure due to the tensile failure of the lower TRC layer) even if the ultimate load is overestimated of about 20%.

This overestimation could be due to the fact that, in experimental tests, at a certain load level close to failure, local EPS-TRC debonding may occur, thus leading to greater tensile strain in the lower TRC layer than that obtained in the numerical analysis. In addition, local effects on TRC due to the presence of load must be taken into account. Once the ultimate strain is reached in TRC, the failure occurs at a load level that is lower than the ultimate load estimated through the FE analysis.

4.2 *Evaluation of the influence of the bent bar on the panel behavior*

In order to evaluate the influence of the bent bars on the global response of the panel, a numerical model without bent bars has been developed. In this case, the shear transfer between TRC layers is entrusted exclusively to expanded polystyrene layer. It is worth noting that bent bars have been introduced in the panel only to guarantee that a

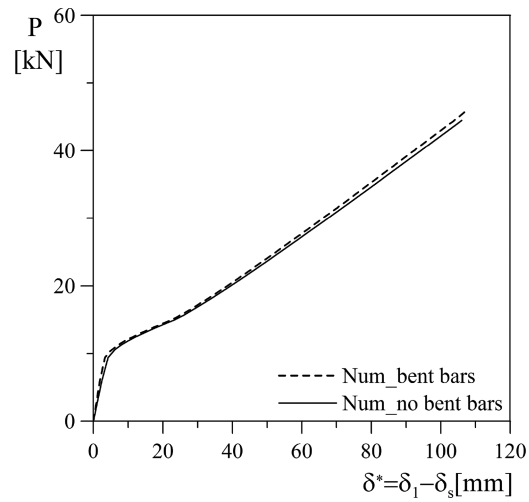

Figure 7. Numerical load vs. mid-point vertical displacement: comparison between responses obtained with and without bent bars.

shear connector will act in extreme conditions, under which EPS could sublimate.

The numerical curve obtained in this simulation is plotted in Figure 7 (continuous line), where it is compared with the response obtained in the case of panel with bent bars (dashed line – curve already shown in Figure 5).

Looking at the figure it is possible to state that the presence of the steel connectors does not affect the global behavior of the panel in standard conditions and that the shear transfer between the two external layers is mainly governed by the EPS. However, it should be useful not only in extreme conditions, but also when long-term cyclic stresses may affect TRC/EPS bond, thus leading to an increase in the durability of the panel.

5 CONCLUSIONS

The finite element model developed in Abaqus and discussed in the paper allows the designer to perfectly estimate the bending behavior and the mode of failure of the multilayer panel designed in the European EASEE project as energy retrofitting solution for existing building.

As already verified in Colombo et al. (under review), in which sandwich beams were modeled, the main assumptions of the model are reliable. In particular:

- considering perfect bond at EPS/TRC interfaces;
- defining material parameters through proper experimental tests on TRC and EPS specimens;
- modelling textile reinforced concrete as a homogeneous material.

The ultimate load is overestimated of about 20%. The main reason could be a local debonding between expanded polystyrene and the lower TRC layer at mid-span at ultimate limit state in full-scale panel, leading to higher tensile strain than numerical ones, and hence a lower failure load. Hence, the assumption of perfect bond could be restrictive at ultimate limit state.

The identification of relevant points on the numerical curve allows to understand that the panel behavior is mainly governed by the tensile behavior of the lower TRC layer.

Considering the slenderness of the panel, the yielding of the compressive strut in EPS layer does not affect the global response; on the contrary, this failure mechanism was relevant in the case of sandwich beams characterized by the same stratigraphy and smaller dimensions (Colombo 2015, Colombo et al. under review).

In standard conditions, the behavior of the panel is scantly affected by the presence of bent bars.

REFERENCES

ASTM International A473 – 17a: Standard Specification for Stainless Steel Forgings.

Brameshuber, W., Brockmann, T., Curbach, M., Meyer, C., Vilkner, G., Mobasher, B., … Wastiels, J. 2006. Textile Reinforced Concrete - State-of-the-art. In W. Brameshuber (ed) *Report of RILEM Technical Committee 201-TRC. RILEM Publications*.

Colombo, I.G. 2015. *Multilayer precast façade panel: structural optimization for energy retrofitting*. PhD thesis. PhD in Structural, Seismic and Geotechnical Engineering, Politecnico di Milano (Department of Civil and Environmental Engineering).

Colombo, I.G., Magri, A., Zani, G., Colombo, M. & di Prisco, M. 2013. Textile Reinforced Concrete: Experimental investigation on design parameters. *Materials and Structures* 46(11): 1933–1951.

Colombo, I.G., Colombo, M. & di Prisco, M. 2014. Multilayer Precast Façade Panel: structural optimization for the energy retrofitting and for sustainable constructions. In J. Bastien, N. Rouleau, M. Fiset & M. Thomassin (eds), *Proceedings of the 10th fib International PhD Symposium in Civil Engineering*: 291–296.

Colombo, I.G., Colombo, M. & di Prisco, M. 2015a. Bending behaviour of Textile Reinforced Concrete sandwich beams. *Construction and Building Materials* 95: 675–685.

Colombo, I.G., Colombo, M. & di Prisco, M. 2015b. TRC precast façade sandwich panel for energy retrofitting of existing buildings. In *Proceedings of DSCS 2015 - International Workshop on Durability and Sustainability of Concrete Structures*, *ACI SP-305, Bologna, October 1st – 3rd, 2015*, pages 30.1–30.10.

Colombo, I.G., Colombo, M. & di Prisco, M. 2016a. TRC multilayer precast façade panel: structural behavior in freezing-thawing condition. In *Proceedings of the II International Conference on Concrete Sustainability ICCS16, Madrid, June 13th – 15th, 2016,* 10 pages.

Colombo, I.G., Colombo, M. & di Prisco, M. 2016b. Mechanical characterization of TRC precast façade sandwich panel for energy retrofitting of existing buildings, *Studies and Researches* 34, *Graduate School in Concrete Structures - Fratelli Pesenti - Politecnico di Milano, Italy*.

Colombo, I.G., Colombo, M. & di Prisco, M. (**under review**). Analytical and numerical prediction of the bending behaviour of textile reinforced concrete sandwich beams. Submitted to *Journal of Building Engineering*.

di Prisco, M. & Zani, G. 2012. Experimental and numerical analysis of advanced cementitious composites for sustainable roof elements. In *Proceedings of the "Numerical modeling - Strategies for Sustainable Concrete Structures - Aix-en-Provance, France"*.

EN 196-1 (2005). Methods of testing cement - Part 1: Determination of strength.

Hegger, J. & Horstmann, M. (2009) Light-weight TRC sandwich building envelopes. *Excellence in Concrete Construction through Innovation*: 187–194.

Larrinaga, P., Chastre, C., Biscaia, H.C. & San-Josè, J.T. 2014. Experimental and numerical modeling of basalt textile reinforced mortar behavior under uniaxial tensile stress. *Materials & Design* 55: 66–74.

Masso-Moreu, Y. & Mills, N. 2004. Rapid hydrostatic compression of low-density polymeric foams. *Polymer Testing* 23(3): 313–322.

Materials Data Book 2003, Cambridge University Engineering Department.

MC2010 (2013). fib Model Code for Concrete Structures 2010.

Miccoli, L., Fontana, P., Johansson, G., Zandi, K., Williams Portal, N. & Müller, U. 2015. Numerical modelling of UHPC and TRC sandwich elements for building envelopes. In *Proceedings of the "IABSE Conference - Structural Engineering: Providing Solutions to Global Challenges" Geneva, Switzerland*: 195–203.

Müller, F., Kohlmeyer, C. & Schnell, J. 2012. Load-Bearing Behaviour of Sandwich Strips with XPS-Core and Reinforced HPC-Facings. In *Proceedings of Hipermat 2012 – 3rd International Symposium on UHPC and Nanotechnology for High Performance Construction Materials*, Kassel University Press, p. 781–788.

Ozturk, U.E. & Anlas, G. 2011. Finite element analysis of expanded polystyrene foam under multiple compressive loading and unloading. *Materials & Design* 32(2): 773–780.

Shams, A., Horstmann, M. & Hegger, J. 2014. Experimental investigations on Textile-Reinforced Concrete (TRC) sandwich sections. Composite Structures 118: 643–653.

UNI EN 13163 (2009). Thermal insulation products for buildings - Factory made products of expanded polystyrene (EPS) – Specification.

Zani, G., Colombo, M. & di Prisco, M. 2014. High performance cementitious composites for sustainable roofing panels. In J. Bastien, N. Rouleau, M. Fiset & M. Thomassin (eds), *Proceedings of the 10th fib International PhD Symposium in Civil Engineering*: 333–338.

Computational Modelling of Concrete Structures – Meschke, Pichler & Rots (Eds)
© 2018 Taylor & Francis Group, London, ISBN 978-1-138-74117-1

A two-phased and multi-scale finite element analysis of the tensile creep behavior of polypropylene fiber reinforced concrete

R. Vrijdaghs, E. Verstrynge & L. Vandewalle
Department of Civil Engineering, KU Leuven, Leuven, Belgium

M. di Prisco
Department of Structural Engineering, Politecnico di Milano, Milan, Italy

ABSTRACT: Polymeric fibers can be used in concrete elements to improve the properties in the fresh or hardened state. In the latter case, structural macrofibers can be added to increase the residual load-bearing capacity after matrix cracking, and as such, can partially or entirely replace traditional reinforcement. Polymeric fiber reinforced concrete (PFRC) can be designed according to the Model Code 2010, but no design guidelines are given to take creep behavior into account, limiting the usage of FRC in structural applications.

The tensile creep behavior of cracked PFRC is dependent on the creep deformation of individual fibers and on the creep behavior of the interface between fiber and matrix. Because of the different factors involved, a fundamental understanding of FRC creep can only be obtained by taking both mechanisms into account. Therefore, a numerical model with discrete treatment of individual fibers is set up. The results of the finite element analysis (FEA) is compared against experimental tests. In the experiments, the concrete cores are precracked to localize crack formation and growth and the time-dependent crack widening is measured over the crack. To calibrate the material models used in the FEA, the creep behavior of individual fibers as well as the pull-out behavior (short-term and creep) of the fiber is determined for a range of different embedded lengths and angles.

In the finite element model, polypropylene fibers are randomly generated in an FRC beam. In a next step, a core is taken from the beam, and subsequently notched during which the effect of fiber cutting is simulated. The location of the crack in the numerical model is known (i.e. in the notched section) and fibers crossing this crack contribute to the load-bearing capacity of the element. An algorithm is implemented in MATLAB that calculates the embedded length of each crack-crossing fiber at both its ends. The material model governing pull-out behavior is then assigned to every load-bearing fiber based on its embedded length and angle, as determined by the multi-scale testing. The fibers are assigned a creep behavior model based on the experimental tests. Because of the low stresses involved, a linear elastic material model for concrete is adopted.

The load, expressed as a percentage of the residual capacity, is imposed for 180 days on both the physical test specimen and on the numerical model and the crack widening is compared. Good agreement can be obtained and the model is able to capture crack growth of PFRC. Furthermore, the use of finite element modelling allows to determine the fiber stress in a cracked section of FRC, and based on the results presented here, an average fiber stress was obtained of 10% and 15% of the fibers ultimate strength for the two considered load ratios.

1 INTRODUCTION

1.1 *State of the art*

Fiber reinforced concrete (FRC) has recently been introduced in the Model Code 2010 (MC10) (federation internationale du beton (fib) 2010), opening the door to structural applications. Despite being an important step towards greater usage of FRC, some key aspects of structural design are not yet taken into account in the design approach of MC10. Long-term behavior and deferred deformations due to creep are not yet accounted for, and the Model Code specifies that long-term behavior of cracked FRC under tension has to be taken into account but fails to provide design rules. While the design approach of MC10 considers FRC to be a single-phased material, a full understanding of the creep behavior of FRC needs to take into account the interaction between fibers and concrete, leading to a

two-phase material with the discrete treatment of fibers. Such a two-phased model can be readily implemented in finite element modeling (FEM) and can serve as an important tool in the understanding of FRC creep. In such models, at least three different materials are considered: concrete (Neville 1970), fiber and fiber-matrix interface (Nieuwoudt & Boshoff 2015, Babafemi & Boshoff 2015). Recently, a number of research papers have been published using the two-phased approach to steel FRC (Cunha, Barros, & Sena-Cruz 2012, Kang, Kim, Lim, & Bolander 2014). In the two cited papers, a smeared-crack approach is adopted for the concrete and the fiber pull-out and interfacial behavior is based on experimental results of single-fiber pull-out. In literature, such a two-phased approach is then used to predict the post-cracking behavior and residual strength. However, to the author's knowledge, no papers are published to determine the creep behavior of FRC using a two-phased material approach. This paper presents the experimental results and numerical simulation of a two-phased model of the uniaxial tensile creep of polymeric FRC.

1.2 *Problem statement and aim*

The creep behavior of FRC is still poorly understood but it is of great importance in structural design. While MC2010 considers FRC to be a single-phase material for design purposes, the individual behavior of fibers and interface plays and important role in the response of the composite. Therefore, a multi-scale, two-phased model with discrete treatment of the fibers is proposed and built to explain FRC creep behavior. In this multi-scale approach, the experiments of the lower scale are used to calibrate the material models in the finite element model and to predict the creep behavior of the composite.

2 EXPERIMENTAL PROGRAM

2.1 *Overview*

In order to identify the creep behavior of polymeric FRC, an extensive multi-scale experimental program has been set up, consisting of short and long-term tests on individual fibers, pull-out tests and uniaxial tests on FRC. All tests are performed in a climate controlled room at 20 °C and 60% relative humidity. In this section, a short summary of the different experimental setups will be given, and further details can be found in literature. (Vrijdaghs, di Prisco, & Vandewalle 2016, Vrijdaghs, di Prisco, & Vandewalle 2017a, Vrijdaghs, di Prisco, & Vandewalle 2017b).

2.2 *Material properties*

In the experimental program, one type of commercially available polypropylene (PP) fiber is considered. The fiber is an embossed fiber with a nominal length of 45 mm and an equivalent diameter of 0.9 mm. Short-term characterization tests were performed in accordance with the European Standard EN 14889-2 to determine the tensile strength f_t, the strain at failure ε_{ft} and the cord's modulus E. Based on 5 test specimens, it was found that f_t = 451 MPa, ε_{ft} = 16% and E = 4400 MPa, placing the fiber at the lower end of the spectrum in terms of strength and stiffness.

The concrete used in the experimental program is a normal-strength concrete with a 28-days cube compressive strength f_c = 43 MPa, determined in accordance with EN 12390-5. The post-peak residual strength is assessed in the displacement-controlled three-point bending test as described in EN 14651, yielding a class of 1c based on 16 specimens. The average bending tensile strength f_L, SLS residual strength f_{R1} and ULS residual strength f_{R3} are 3.70 MPa, 1.78 MPa and 2.05 MPa, respectively.

2.3 *Fiber creep and pull-out (creep) test*

The individual fiber and pull-out creep tests are performed in a climate room at constant temperature and relative humidity. In both cases, the samples are placed into a creep frame, consisting of welded and bolted steel profiles and subjected to sustained loading. During the test, the deformation is recorded at a rate of 1 Hz for one week after the moment of loading, and subsequently lowered until 0.1 Hz until the end of the test. The recorded deformation is either the total fiber elongation in the case of the single fiber creep test, or the total pull-out displacement during the pull-out creep tests. All deformations are recorded contact lessly using optical laser sensors. The laser sensors have a declared accuracy of at least ± 0.1 mm, which is well below the measured deformations, and can measure up to 250 mm.

For the fiber creep tests, uncut fibers with an initial length of 200 mm are subjected to tensile creep loading at 5 different load ratios (LR) (the ratio between the applied creep stress and the fiber strength f_t), in this case 22%, 36%, 43%, 53% and 63%. In total, 12 samples were tested and the creep load was sustained for 180 days, after which the samples that did not fail were unloaded.

In addition to the single fiber creep tests, pull-out tests were performed as well. All pull-out creep tests were done on perpendicularly embedded fibers in a concrete matrix with an embedded length of 15 mm. 5 different load ratios were considered for the sustained loading: 25%, 40%, 50%, 60%

and 75%. The LR is expressed as a percentage of the average short-term peak load $F_{max} = 201$ N with a coefficient of variation of 6.3% as determined from a short-term pull-out tests on 6 specimens. The recorded creep deformations include both time-dependent fiber pull-out as well as single fiber creep. The tests were performed until failure was observed, or until 60 days after load application, whichever comes first. The short-term pull-out tests were performed on a univeral test machine in a displacement controlled test whereby a displacement rate of $\dot{\delta} = 10$ mm/min is applied and the resulting force is measured.

2.4 *FRC creep test*

Creep tests are performed on cylindrical FRC specimens with a nominal diameter and height of 100 mm and 300 mm, respectively. The specimens are cored from a prism used in the short-term post-peak characterization test according to EN 14651. Coring from a prism ensures that the wall effect and preferential fiber orientation is mitigated as much as possible. After coring, the samples are notched at mid-height and the core's diameter is decreased to 80 mm in order to localize the crack formation. The samples are then placed in a precracking setup in which a tensile load can be applied eccentrically in order to achieve uniform crack width growth over the notched section. The crack width is measured by three LVDTs placed around the circumference of the notch and record the total deformation due to tensile loading at a rate of 10 Hz during the precracking. The samples are precracked to an initial crack width of 0.2 mm, after which the cores are unloaded and the irreversible crack width w_{irr} is recorded. The cores are then placed in a creep frame consisting of a cantilevered system. In the creep frame, a uniaxial tensile load is applied to the specimen and two load levels are considered, 30% and 45% of the residual strength at the initial precrack width of 0.2 mm. The load is sustained for 180 days and time-dependent crack growth is measured at a rate of 1 Hz in the first week after loading, and subsequently lowered to 0.1 Hz until unloading.

3 NUMERICAL MODEL

3.1 *Overview*

In order to fully understand the mechanisms behind FRC creep, the composite material cannot be considered homogeneous and the fibers and matrix need to be considered separately. While this two-phased approach will be too computationally intensive for nearly all design applications, it can provide a deeper understanding of the stress redistribution and the effect of fiber creep in FRC creep. Therefore, a numerical model is developed in which the fibers are generated separately from the matrix, and different properties are assigned to the fibers, the fiber-matrix interface and the concrete matrix itself. The fibers are procedurally generated in a MATLAB algorithm. Based on fiber orientation and embedded length, unique material model parameters are assigned to each individual contributing fiber and a finite element input file is generated. This input file can be imported in the commercial finite element software packet DIANA after which a non-linear time-dependent analysis is ran. This is done for 20 different fiber sets, each with a random number of fibers crossing the crack and randomly distributed embedded lengths and angles. The results of the Monte-Carlo analysis are then extracted and discussed. All simulations are ran on a desktop pc with a 6-core, 12-thread Xeon processor with 32 GB RAM.

3.2 *Fiber generation algorithm*

A fiber generation algorithm is developed in MATLAB, in which fibers are randomly generated in a predefined volume. The algorithm requires the geometry of the volume in which the fibers need to be generated as well as the fiber geometry and volume fraction. An outline of the fiber generation algorithm is given in Fig. 1.

The algorithm starts with the first fiber of which the start point, i.e. one end of the fiber, is randomly generated in the predefined volume. It will check if that randomly generated point is sufficiently far from all up-until-then generated fibers. The minimum distance required is twice the largest dimension of the cross-section of the fiber: the diameter in case of a circular cross section or the largest dimension of a rectangle. If that is the case, the algorithm will randomly pick two angles θ and ψ, the angle of the fiber in the xy-plane and the angle between the xy-plane and the fiber, respectively, see the inset in Figure 1. These angles define the end point, i.e. the other end of the fiber, as well as the fiber itself. Similarly, a check will be performed whether the end point (1) lies within the volume and (2) is sufficiently far from all fibers. Additionally, a check is done to see whether (3) the minimal distance between fiber i and all up-until-then generated fibers $1..i-1$ is greater than the required minimum, defined before. If either of the three preconditions fail, two new angles are chosen and the process is repeated until all checks are fulfilled, unless it has already tried that 100 times. If that is the case, a new start point is generated in order to prevent an endless loop at one very difficult start point. If all checks succeed, the fiber is successfully

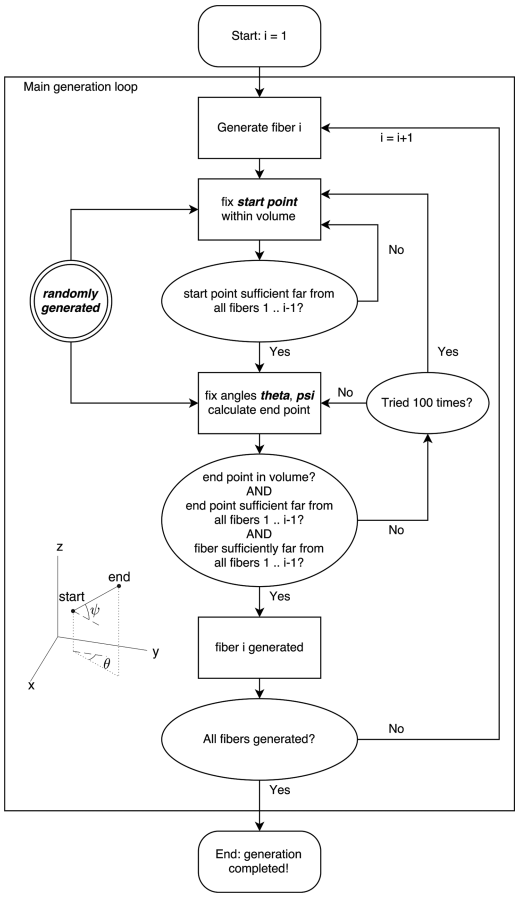

Figure 1. Outline of the fiber generation algorithm.

generated. If that was the last fiber, a complete set is generated and the algorithm ends. If not, a new fiber is generated and the process starts anew.

Because every additional fiber needs to be checked against all other already generated fibers, the computational cost of the marginal fiber increases every step. In Fig. 2, the average time to generate a complete fiber set in a volume of $150 \times 150 \times 400$ mm ^{3} is shown on the left hand side on a logarithmic scale. It is clear that the time to calculate all fibers increases greatly with increasing fiber fraction. At fiber fractions greater than 0.5 V%, the time to calculate all fibers increases exponentially with V%. On the right hand side of the figure, the average number of calculations to generate an additional fiber is shown. Despite the high variability owing to the random nature of the process, the required number of iterations seem to follow an exponential curve at V% > 0.5% as well. Extrapolating the results, it is possible to calculate that for volume fractions exceeding 1.25%,

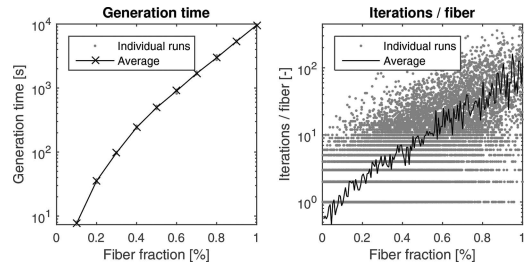

Figure 2. Computational Complexity of the fiber generation algorithm (left) calculation time (right) number of iterations.

the required generation time would be at least 10 hours. Therefore, it is suggested that the computational cost of the algorithm becomes prohibitively expensive at fiber volume fractions exceeding 1.25 V%.

Following the generation of a fiber set, a virtual core is taken from the predefined volume. The dimensions of this core are equal to the core's dimensions used in the test, i.e. 300 mm high with a diameter of 100 mm. Since all fibers are generated in a 400 mm high beam-shaped volume, this step not only includes coring to a cylindrical shape but also cutting off parts of the cylinder. During this step, fibers can be partly cut, such that not all fibers in the virtual core have a length equal to the initial fiber length of 45 mm.

Once the cored cylinder is generated, the next step is to notch the specimens as this will have an impact on the fibers as well. In Fig. 3, various fibers are shown with different results due to notching. The majority of all generated fibers (0) in the core will not intersect the notched section, and these fibers are not changed during notching. However, the fibers that cross the notched section can be cut by the notching procedure and as such, the embedded length before and after notching is not necessarily equal. These fiber can either be fully intact (1), completely cut (2) or partly cut (3). In the first case, the fibers are intact due to the limited notch depth and/or width. Fibers can also be completely cut because they are entirely inside the notched part of the core. In the last case, fibers can be partly cut because part of the fibers lies within the notched part of the core. In the case of fully intact or partially cut fibers, (parts of) the fibers are contributing to the load bearing capacity and unique pull-out and creep model parameters are assigned to these fibers. In the other case, i.e. completely cut fibers, no parts of these fibers are taking up forces in the notched sections. These fibers behave then identical as the fibers that are not near the notched part.

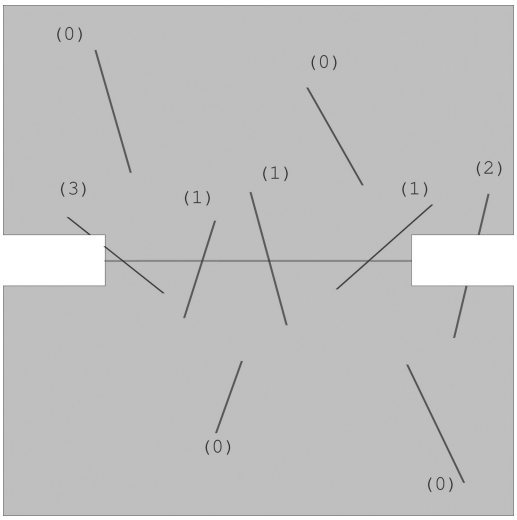

Figure 3. Different fiber orientation and the notching effect (note: the notch depth is exaggerated by 10 mm).

To summarize, fibers are randomly generated in a beam shaped element ensuring that no fibers overlap or intersect. This approach ensures that the wall effect and preferential fiber orientation is not a factor in the core itself. Due to the nature of the fiber generation algorithm, the computational complexity increases with every fiber such that the approach is feasible up to a fiber volume fraction of 1.25 V%. After the fibers are generated, a virtual core is taken from the beam, which causes some fibers to be cut. After coring, the virtual core is notched, thereby causing some fibers to be cut in the notched section. After the notching, a fiber set is obtained and the embedded length and angle of all fibers is known, both at the notched section and elsewhere. The whole procedure takes about 2.5 hour for 1 V%.

3.3 *Finite element model*

Once the fiber set is generated, a finite element model (FEM) can be built. The model consists of two phases, namely the concrete matrix phase and the discrete fibers phase, and the model is used to simulate the creep behavior of PFRC. Since the creep experiments consider only a cracked section, the numerical model is built with the crack already present. The initial crack width that is retained in the FEM is equal to the average irreversible crack width measured in the experiments, i.e. $w_{irr} = 0.13$ mm as discussed further. The advantage of this approach is that the concrete cracking does not need to be simulated, significantly simplifying the calculations. However, by ignoring matrix cracking, the effect of matrix spalling cannot be taken into account but given the low stress levels (see further), it is argued that the simplification is valid. The fibers can be divided into two different types: embedded fibers and bond-slip fibers. The former category consists of fibers that are perfectly bonded with the concrete matrix. These fibers do not cross the cracked section and as such do not take up the tensile force. The latter type of fibers are connected to the matrix through an interface that allows relative displacements. These fibers are located near the cracked section.

The model is built in the dedicated finite element program DIANA. The main advantage of using DIANA is that so-called reinforcement elements can be defined independently from the matrix itself. The reinforcement elements need to be embedded in so-called mother elements and internally, the stiffness of the mother elements is then adapted based on the properties of the reinforcement element in it. This feature is particularly interesting in the case of two phased materials such as FRC as the solid 3D mesh that represents the concrete matrix remains identical for different fiber sets. The fibers are then modeled using reinforcement elements that can be defined independently of the concrete matrix.

The FEM consists in total of 4 different element types: (1) 3D solid elements, (2) embedded reinforcements, (3) bond-slip reinforcement elements and (4) beam elements. All element types use quadratic interpolation functions. The 3D solid elements are ten-node, three-side isoparametric solid tetrahedrons and are used to represent the concrete matrix. The embedded reinforcement elements are used to define fibers that are not crossing the crack. These fibers contribute to the stiffness of the material, but since they are not crossing any crack, they take up only very limited forces and are therefore assumed to be perfectly bonded. The third element type is a bond-slip reinforcement to model fibers crossing the crack. As these fibers take up significant parts of the tensile load, they cannot be assumed to be perfectly bonded. Therefore, a interfacial bond-slip behavior is defined for every fiber crossing the crack. The fibers can then slide with respect to the concrete matrix at load application. Finally, beam elements are used to model the fibers in the cracked section itself. In the crack, no mother elements are present in which reinforcement element could be embedded. Therefore, bond-slip reinforcement elements are connected by beam elements in the crack. In total, the model consists of nearly 50,000 nodes and 32,000 elements, with most of the nodes (58%) and elements (55%) located in a 20 mm wide zone around the notched section to ensure adequate accuracy in that area.

Similar to the experimental work, the tensile force is applied uniaxially to the top of specimen. In the FEM, the average experimentally observed residual strength is used to determine the applied load for both load ratios. In-plane translations at the top are fixed, but rotations are not prevented such that the top part can rotate and translate along the specimen axis. Similarly, at the bottom end of the specimen, no rotations are prevented, but all translation of the sample are fixed.

DIANA uses a linear stiffness solver and convergence is reached once the relative error of both displacement and forces simultaneously is less than 2%.

3.4 *Material models*

In the FEM, 4 different element types are used, and a material model needs to be assigned to every element. In this section, an overview of the different material models will be given.

3.4.1 *Concrete*

In the analysis, it is assumed that the concrete behaves linearly-elastic and no concrete cracking or creep is taken into account. The advantage of linearizing concrete behavior is that the computations are significantly simplified, but some degree of accuracy is lost. However, the simplification is justified for a number of reasons. Firstly, the crack width is explicitly modeled during the FEM construction so no matrix cracking during the precracking needs to be taken into account. Secondly, neglecting matrix cracking implies that matrix spalling cannot be taken into account either. However, short-term pull-out tests on individual fiber pull-out have shown that matrix spalling is only signficant at high loads ($> 50\%$ of f_t) and high embedded angles($\theta > 60°$) for the type of fiber and the concrete strength used in this research. In reality, given the high fiber volume percentage and the low applied creep loads involved, the fiber stresses at highly inclined fibers rarely, if ever, reach these stress levels. Therefore, matrix spalling is very rarely an issue and can thus be safely neglected with only limited loss of accuracy. Thirdly, in uniaxial tension softening materials, nearly all deformations during a tensile creep test are localized in the cracked section. Furthermore, given the low matrix stresses, it is reasonable to assume that concrete tensile creep is negligible. Lastly, drying shrinkage tests on companion specimens have shown that the deformations due to drying are several orders of magnitude smaller than the creep deformations. Based on these arguments, a linear elastic material model for concrete is adopted.

3.4.2 *Fibers*

Secondly, creep of the individual fibers is of high importance in the overall creep behavior of FRC and should therefore be taken into account. The fiber material model is defined in both the beam and the reinforcement elements, but not all material models are available for the reinforcement elements. Therefore, a different model is implemented for the two element types.

For the reinforcement elements, a linear-plastic material model is used. Plasticity can occur in the fibers and irreversible deformations remain upon unloading from stress levels exceeding 20% in a short-term test. This plasticity is implemented for both the bond-slip and embedded fibers. While plastic deformations can be readily implemented, DIANA does not allow a material model that takes into account creep to be assigned to reinforcement elements. Therefore, for both the embedded and bond-slip fibers, creep cannot be accounted for. However, the creep of the fibers in concrete can be lumped in the creep deformations of the beam elements, as discussed further.

For the beam elements, creep is taken into account in a viscoelastic material model through a time-dependent Young's modulus as this can be readily implemented in DIANA. The creep of the reinforcement elements can be lumped in the beam element creep by further decreasing the stiffness in time. This results in a (virtual) increase of the free length of the fiber, thereby taking the creep deformations of the reinforcement elements into account as well. Furthermore, the fiber creep tests have shown that fibers can exhibit creep rupture after a certain time under load. Fiber creep rupture is implemented in the beam elements as well, by effectively zeroing the stiffness once creep rupture would be observed in the creep test.

3.4.3 *Interface*

Finally, an interface material model is implemented for both types of reinforcement elements. As discussed before, the embedded fibers do not cross the crack and are therefore assumed to be perfectly bonded to the matrix. In DIANA, the default setting is a perfect bond between the reinforcement and mother element so no special material models need to be defined. For the bond-slip reinforcement elements near the notched section, the fiber can undergo displacements relative to the matrix. Therefore, a bond-slip model needs to be defined. This model is calibrated on a series of short-term pull-out tests at varying embedded lengths and angles. The measured load $P(\delta)$ during the pull-out tests is rescaled to a bond stress $\tau(\delta)$ as a function of the pull-out displacement δ, in accordance with Eq. 1 where in d is the equivalent fiber diameter and ℓ_0 the initial embedded length. From the fiber generation algorithm, the embedded length and angle at both sides of the cracked section for every bond-slip fiber is known. Therefore, two unique

multi-linear bond-slip curves (one above andone below the crack) can be calculated for every bond-slip fiber based on the individual embedded length and angle. Furthermore, fiber fracture due to pull-out is stochastically simulated as some test specimens at high embedded angles and lengths exhibited fiber failure. In the material model, the bond strength τ is effectively zeroed at a certain displacement, corresponding to the displacement at maximum load as observed in the pull-out tests.

$$\tau(\delta) = \frac{P(\delta)}{\pi \cdot d \cdot (\ell_0 - \delta)} \quad (1)$$

For the bond-slip fibers, pull-out creep should be taken into account as well as fibers can gradually slide out of the matrix in time. However, research on these fibers has shown that individual fiber creep is the driving mechanism behind pull-out creep as Poisson contractions during fiber creep cause a decrease in bond strength in time (Vrijdaghs, di Prisco, & Vandewalle 2017b). Furthermore, in the same research, it was shown that the fiber creep closely follows the pull-out curve as well and that only small errors are made when neglecting pull-out creep and taking only fiber creep in the concrete into account. This is already done in the beam elements by decreasing the time-varying stiffness. In that way, fiber pull-out creep is lumped in individual fiber creep as well.

3.4.4 *Summary*

To conclude, Fig. 4 shows an overview of the different materials models that are used in the FEM: (1) a linear elastic model for concrete, (2) embedded reinforcement elements behaving elastoplastically with a perfect bond with the concrete, (3) elasto-plastic bond-slip reinforcements with a bond-slip behavior allowing slippage from the concrete and (4) viscoelastic beam elements with fiber creep failure and lumped pull-out and bond-slip reinforcements creep.

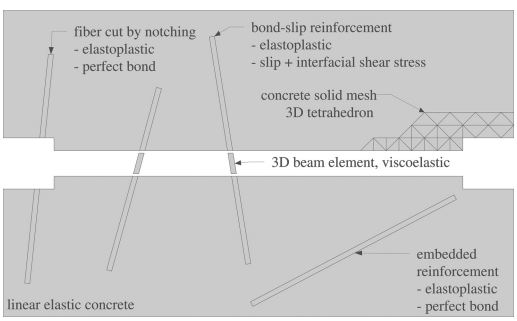

Figure 4. Summary of the different material models in the FEM.

4 RESULTS AND DISCUSSION

4.1 *Experimental results and material model calibration*

4.1.1 *Sile fiber creep*

The single fiber creep deformations are shown in Fig. 5(a) together with the implemented fiber creep model in terms of the compliance, i.e. strain over applied stress. Note that the model is mainly based on the lowest loaded fibers as the results have shown that the fibers are not highly stressed during the creep test. It is acknowledged that the total strain at failure for the higher loaded fibers is not accurately captured but fiber creep rupture was not observed during the FRC creeptest (180 days). A comparison between the experimental failure times of the samples loaded at 43%, 53% and 63% and the failure times implemented in the model can be found in 5(b). A good agreement is found and this fiber failuremodel is extended for all load ratios in the model.

4.1.2 *Fiber pull-out*

In Fig. 6, the results of the single fiber short-term pull-out tests are shown for varying embedded lengths and angles. The results of the implemented single fiber pull-out model are superimposed on the experimental results. It is clear that the interfacial model can accurately capture the pull-out behavior for the (θ, ℓ) combinations shown here. This model is implemented for every bond-slip fiber and yields a unique material model based on individual (θ, ℓ) combinations. As discussed before, fiber fracture during pull-out is stochastically taken into account as well as can be seen in subfigure (d) wherein fiber fracture was observed for some samples. In this particular case, the model implements complete fiber pull-out.

4.1.3 *FRC creep*

Finally, the FRC creep results are shown in Fig. 7 for the (a) 4 samples loaded at 30% and (b) 7 samples at 45%. In this figure, only the deformations during the

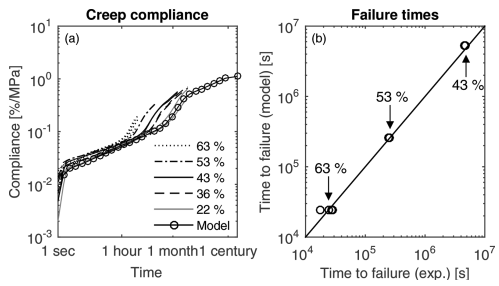

Figure 5. (a) Single fiber creep results together with the implemented creep model (b) comparison of the failure times.

creep test are shown and not the total crack widths, i.e. $w - w_{irr}$. It is clear that there is a very large difference between the two load ratios, with the highest loaded samples showing excessive crack formation exceeding the limits imposed by Eurocode 2 within hours or days. Also note that the scatter of the 45% loaded samples is very high while the lower loaded samples all behave relatively similarly.

4.2 *Numerical results*

4.2.1 *Fiber generation algorithm*

The most important outcome of the fiber generation algorithm is the location, length and angle of all bond-slip fibers, as these take up the tensile forces. In order to highlight the performance of the algorithm, 20 different fiber sets were completed at 1 V% and the results show that 57 fibers cross the crack on average at that volume percentage with an coefficient of variation of 12%. Simulations at varying volume fractions show that the number of fibers in the crack increases linearly with the volume fraction, as would be expected. The results of all fibers are shown in Fig. 8. In subfigure (a) and (b), a histogram of the minimum embedded length and angle is shown, respectively. While the embedded length is reasonably uniformly distributed between 0 mm and $\ell/2 = 22.5$ mm, it is clear that the contributing fibers show a clear tendency towards lower embedded angles. This is to be expected since the notching procedure and the non-zero initial crack width decrease the chances of highly angled fibers to cross the cracked section. Figure (c) shows the length-angle combination for all fibers together with the global average of all 1134 fibers. The average fiber is inclined at a 30° angle and has a minimum embedded length of 10 mm.

The results of the 20 runs can be compared to a uniform distribution in a cumulative distribution function (CDF) as is shown in Fig. 9. The figure shows the CDF for the 1134 fibers in the notched section of the 20 runs, of the cylinder as a whole and a uniform distribution. It is clear that while the embedded angle for the fibers at the notched section is very skewed towards lower angles, the angle of all fibers in the cylinder is very close to a uniform distribution. The CDF of the minimum length on the other hand shows the same trend for the fibers in the notched section and elsewhere in

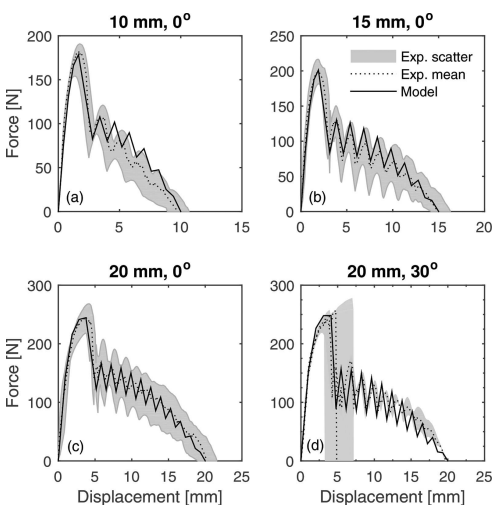

Figure 6. Experimental pull-out results at different embedded lengths and angles together with the results of the implemented model.

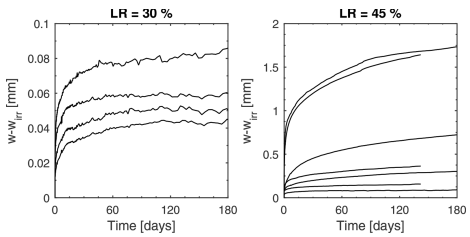

Figure 7. Creep deformations of the FRC samples at (a) 30% and (b) 45%.

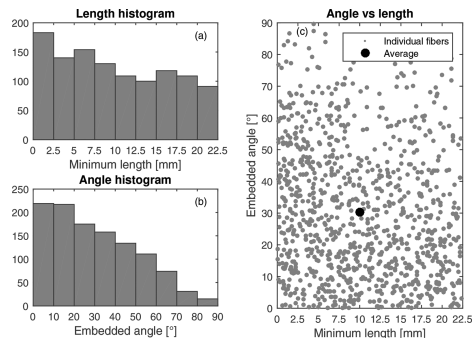

Figure 8. Results of 20 different fiber sets at 1 V%: (a) histogram of the minimum embedded length (b) embedded angle (c) length-angle combination for all fibers.

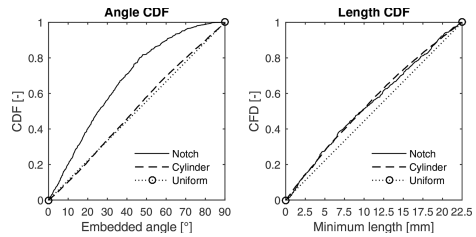

Figure 9. CDF of the embedded angle and minimum length for the notched section, the whole specimen and a uniform distribution.

the cylinder. This can be attributed to the fact that not all fibers in the cylinder have the same length due to coring and therefore, the distribution is skewed towards lower embedded lengths.

4.2.2 *Finite element analysis*

Running the finite element analysis for the 20 fiber sets discussed in Fig. 8 yields the results shown in Fig. 10 and Fig. 11 for 30% and 45% respectively. In these figures, the crack width increase as a function of time is shown, i.e. $w - w_{irr}$. The average numerical result is presented together with the 10% and 90% quantile limits of the 20 simulations. Furthermore, the minimum and maximum observed crack width is also shown. Finally, the observed experimental results are superimposed as well to assess the predictive capabilities of the model.

By comparing the numerical and the experimental results, it is clear that the model can accurately predict the slope and crack width growth of the test specimens, barring excessive crack width observed for two specimens at 45%. However, the initial crack width upon loading is overestimated for both load ratios. This is attributed to the fact that the initial fiber stiffness at $t = 0$ seconds is likely too small in the model, thereby causing the instantaneous crack opening to be too large. This is attributed to the fact that the stiffness is derived from an experiment whereby the load cannot be applied instantaneously. However, in the numerical model, this is the case and therefore a higher stiffness needs to be implemented than the stiffness observed in the fiber characterization test. Nevertheless, a good agreement is found between the experimental and numerical results based on a two-phased model calibrated on the fiber and interface behavior.

4.3 *Discussion*

The stress of the fibers in the cracked section is very important to assess the creep deformations of polymeric FRC, as individual fiber creep will be the main contributing mechanism to time-dependent crack widening. The results of the evolution of the stresses as a function of time for the 30% and 45% loaded samples is shown in Fig. 12 and Fig. 13, respectively. Similarly as for the deformations, the average stress level of all fibers in all 20 simulations is shown in black while the absolute minimum and maximum stresses are presented in gray. Furthermore, the 10% and 90% quantile limits are indicated with gray shading. It is quite remarkable that at these volume concentrations, 90% of all

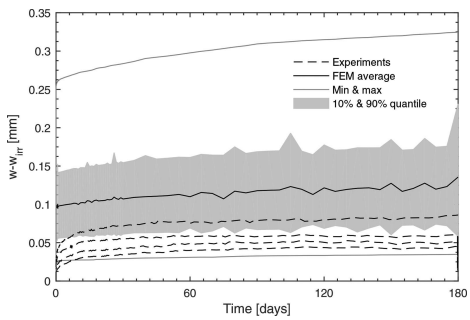

Figure 10. Finite element results of the creep of 20 simulations at 30%.

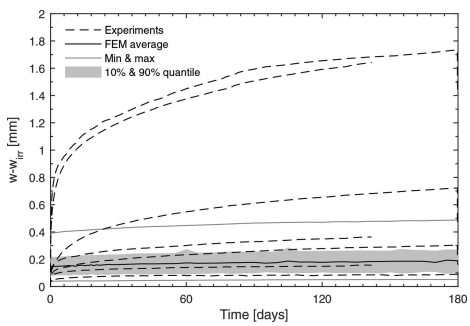

Figure 11. Finite element results of the creep of 20 simulations at 45%.

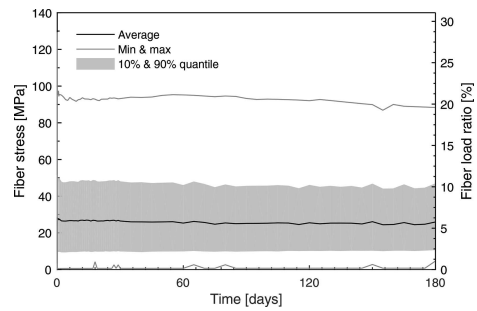

Figure 12. Evolution of the fiber stresses as a function of time for 20 simulations at 30%.

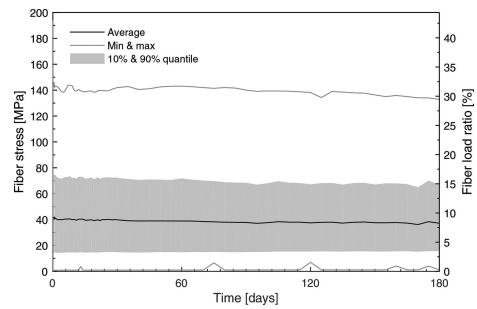

Figure 13. Evolution of the fiber stresses as a function of time for 20 simulations at 45%.

fibers experience stress levels well below 10% and 15% of the uniaxial fiber strength during the entire duration of the test for the 30% and 45% loaded samples, respectively. Only the highest loaded fiber experiences stress levels of around 20% and 30%. Furthermore, the evolution of the stresses in time reveals that the highest loaded fiber unloads in time and stress of the lowest loaded fiber increases. There seems to be a redistribution of stresses in time, and it is reasonable to assume that at infinite time, all fibers will experience the same stress, barring fiber fracture and pull-out. The latter two phenomena (fracture and pull-out) are taken into account but given the low crack width at 180 days and the low stress levels involved, neither phenomenon was observed in the numerical model.

5 CONCLUSIONS

In this paper, the results of a multi-scale experimental campaign and numerical model into the uniaixial tensile creep behavior of polypropylene fiber reinforced concrete are presented and discussed. The experiments included short-term characterization tests on single fibers and FRC specimens as well as a series of tests on the individual fiber pull-out behavior under various embedded lengths and angles. Furthermore, creep tests were conducted on single fibers and fiber pull-out specimens. The aim of the experiments was to serve as input for the material models in a multi-scale numerical model with a discrete treatment of fibers. The experiments on the creep of FRC considered precracked, cored FRC specimens that were subjected to 30% and 45% of the residual strength for 180 days. In the finite element model, the fibers are randomly generated throughout a fixed volume and, just as in practice, virtual cores were taken from this beam to ensure no wall effects were present in the specimens. In total, 20 different fiber sets and corresponding specimens were generated and simulated in the dedicated finite element software suite DIANA.

The results of the fiber generation algorithm showed that a random distribution was obtained but at the notched section, the average minimum embedded length for all 20 simulations was lower than a quarter of the fiber length. This is attributed to the fact that not all fibers in the core have a length equal to the initial fiber length anymore due to coring and notching. Furthermore, the results showed that there was a clear skewness towards lower embedded angles due to the notching.

From the results of the numerical analyses, the following conclusions can be drawn:

1. The numerical model, calibrated on the fiber and interfacial behavior can be used to determine creep deformations and a good agreement in the curve's shape was obtained. However, given the instantaneous load application in the FEM, the initial crackopening was overestimated and the fiber stiffness should be adapted accordingly.
2. Fiber stresses are quite low in the cracked section: 90% of all fibers were subjected to stresses lower than 10% and 15% of the tensile strength, for the 30% and 45% loaded samples respectively. While fiber fracture was taken into account, it was not observed given the low fiber stresses involved. Additionally, the effect of fiber pull-out upon loading was almost negligible as well at these stress levels.
3. The numerical results further underline the importance of single fiber creep behavior on the uniaxial tensile creep at the FRC scale. In order to control crack widths in polymeric FRC, the results suggest to improve the single fiber creep behavior.

Further research can include a study of the effects of pull-out creep by explicitly taking it into account, rather than lumping it in fiber behavior. Additionally, concrete cracking and non-linear concrete behavior can be included and might contribute to the excessive large crack widths that were observed for some specimens.

REFERENCES

Babafemi, A.J. & W.P. Boshoff (2015). Tensile creep of macrosynthetic fibre reinforced concrete (msfrc) under uni-axial tensile loading. *Cement and Concrete Composites 55*(0), 62–69.

Cunha, V.M.C.F., J.A.O. Barros, & J.M. Sena-Cruz (2012). A finite element model with discrete embedded elements for fibre reinforced composites. *Computers And Structures 9495*, 22–33.

federation internationale du beton (fib) (2010).Model code 2010 first complete draft.

Kang, J., K. Kim, Y.M. Lim, & J.E. Bolander (2014). Modeling of fiber-reinforced cement composites: Discrete representation of fiber pullout. *International Journal of Solids and Structures 51*(10), 1970–1979.

Neville, A.M. (1970). Creep of concrete: plain, reinforced, and prestressed. Amsterdam: North-Holland.

Nieuwoudt, P. & W.P. Boshoff (2015). *Modelling the Time-Dependent Pull-Out Behaviour of Hooked Steel Fibres*, pp. 1485–1494. American Society of Civil Engineers. doi:10.1061/9780784479346.174.

Vrijdaghs, R., M. di Prisco, & L. Vandewalle (2016). Creep of cracked polymer fiber reinforced concrete under sustained tensile loading.

Vrijdaghs, R., M. di Prisco, & L. Vandewalle (2017a). *Creep Deformations of Structural Polymeric Macrofibers*, pp. 53–61. Dordrecht: Springer Netherlands.

Vrijdaghs, R., M. di Prisco, & L. Vandewalle (2017b). Short-term and creep pull-out behavior of polypropylene macrofibers at varying embedded lengths and angles from a concrete matrix. *Construction and Building Materials 147*, 858–864.

Computational Modelling of Concrete Structures – Meschke, Pichler & Rots (Eds)
© 2018 Taylor & Francis Group, London, ISBN 978-1-138-74117-1

Numerical simulation of the fracture behaviour of glass fibre reinforced cement: A cohesive crack approach

A. Enfedaque, M.G. Alberti & J.C. Gálvez
Departamento de Ingeniería Civil, Construcción, E.T.S I. de Caminos, Canales y Puertos, Universidad Politécnica de Madrid, Madrid, Spain

ABSTRACT: The exceptional mechanical characteristics that Glass Fibre Reinforced Cement (GRC) shows are obtained by merging the properties of the glass fibres and the brittle matrix. Cement mortar provides a notable compressive strength and correspondingly the presence of glass fibres enhances the material toughness. Moreover, the fracture energy is also increased due to the presence of the glass fibres that add a multiple cracking damage pattern and, hence, a large damaged surface. In order to provide available resources that may ease and widen the structural design of GRC, the assessment and verification of its constitutive relations is of high significance, given that such relations may reproduce the fracture behaviour. The softening function of GRC under flexural tensile fracture tests in an in-plane disposition has been obtained by combining numerical simulations with an inverse analysis. The application of tri-linear softening functions reproduces with notable accuracy the fracture behaviour of GRC. The constitutive relations found can be used for future modelling and structural design and, therefore have widened the feasible applications and reliability of GRC in the construction industry.

1 INTRODUCTION

In the last five decades glass fibre reinforced cement (GRC) has been extensively used in the building industry, especially since the first alkali-resistant fibres became available (Proctor et al. 1982). In such period, GRC has been suitable for a wide range of applications, such as telecommunication towers (Ferreira & Branco, 2007), permanent formworks (Shah et al. 1988), cladding panels (Correia et al. 2006), sewers and even in certain ornamental uses. The use of GRC in these applications has been based not only on cost-reduction concepts and the final appearance of the structures, but also on the remarkable mechanical behaviour of the composite material. Indeed, GRC is one example of the utilisation of the best performance of its two constituents: glass fibre and the cement mortar matrix. In most occasions, such properties can be obtained by combining a mortar cement matrix and a 5% volumetric fraction of chopped glass fibres. While the stiffness and the compressive properties are provided by the cement mortar, the presence of the fibres contributes to improving the ductility and tensile and flexural strength of the material (Majumdar & Laws 1991).

However, it was detected that the GRC properties were strongly affected as time passed and consequently the use of GRC in structural application has been limited to non-structural applications (Grutzeck 1981, Majumdar 1975, Mobasher & Shah 1989, Shah et al. 1988, Purnell et al. 2001, Marikunte et al 1997, Enfedaque et al. 2010). In order to widen the use of GRC the fracture energy of several GRC formulations was determined as well as the damage mechanism and patterns that appeared. Such properties were found in GRC by applying a modification of RILEM TC-187 SOC, which corresponds to a recommendation successfully used for obtaining the fracture energy of concrete (Enfedaque et al. 2014, Fathy et al. 2008).

In order to achieve a reliable structural design of GRC members it is important to reproduce the fracture behaviour of GRC by using numerical or analytical methods. Such importance lies on the fact that GRC members are not performed with any type of reinforcement. Consequently if any GRC member collapses human or material damage may occur.

The fracture behaviour of concrete, when there is no localisation of the cracks and when the crack opening is reduced, has been replicated by means of the smeared crack approach (Polanco-Loria 1997). However, when there is a clear cracking zone in the material the discrete approach has provided more accurate results. In this case one behaviour model developed by Hillerborg which was termed the cohesive crack model (Hillerborg et al. 1976) is one of the most used. Such approach was found successful when applied to plain concrete fracture

tests. Not only has this model been applied successfully to plain concrete, but also to other brittle or quasi-brittle materials such as brick masonry (Galvez et al. 2013, Reyes et al. 2009, Sancho et al. 2007). In addition, in certain circumstances this model represents with accuracy not only fracture evident in Mode I, but also a fracture process generated under a Mode II without the need of using a tracking algorithm (Sancho et al. 2006). Moreover, the fracture behaviour of steel and polyolefin fibre reinforced concrete have been simulated by means of the cohesive crack approach with a notable degree of accuracy (Kooiman et al. 2000, Albert et al. 2016). Nevertheless, the suitability of the cohesive crack approach when applied to GRC deserves thorough study.

The accurate results of the numerical calculus will help structural designers to take full advantage of the properties that GRC boasts, enabling a confident use of the model proposed and widening the application of GRC both in the building industry and in civil engineering applications. It is worth noting that the inverse analyses shown in this paper allowed the achievement of constitutive relations that can be used in future modelling and design procedures, providing engineers with relevant possibilities and innovative knowledge in the field. In order to achieve such goals the fracture behaviour of GRC was simulated in a finite element method (FEM) program by implementing a material user subroutine. Such user-defined behaviour boasted a tri-linear softening function. By modifying the characteristic points that define the tri-linear function the fracture behaviour of two different GRC compositions has been performed. This shows the ability of the tri-linear softening curve to reproduce the fracture behaviour of several formulations of GRC

2 EXPERIMENTAL RESULTS

2.1 *Material manufacturing and test setup*

Test boards were manufactured with dimensions of 1200 mm in length, 1200 mm in width and approximately 10 mm in thickness. These boards were produced using the same process as that used in the GRC industry by simultaneous projection of cement mortar and chopped long glass fibres with a length of 38 mm. An extensive description of the manufacturing process and the specimen preparation can be seen in reference (Enfedaque et al. 2015). The boards were manufactured using three formulations; one control formulation (GRC), another one where the thermal treated pure kaolin Metaver® has been added (Metaver) (GRC-M), and another that had a Powerpozz® (Powerpozz) addition (GRC-P). All the cement mortar preparations can be seen in Table 1.

Table 1. Cement mortar formulations (kg).

	GRC	GRC-M	GRC-P
Cement	50	50	50
Sand	50	50	50
Water	17	23	23
Platiciser	0.5	0.5	0.5
Addition	–	12.5	12.5

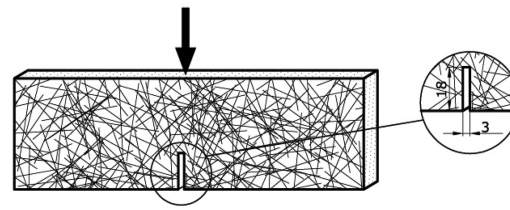

Figure 1. Sketch of the fibres orientation in the GRC specimen. Measures in mm.

As Figure 1 shows, the fracture tests were carried out in the in-plane orientation, with the fibres being almost fibres parallel to the loading direction. The notch of the specimens were performed using a water-cooled circular saw equipped with a diamond disk with a thickness of 3 mm.

Fracture tests were performed in a universal testing machine equipped with a 10 kN load cell. Instrumented with two LVDT extensometers placed at each side of the respective specimen and a crack mouth open displacement (CMOD) gauge. The CMOD gauge was fixed to the notch lips by using a pair of steel blades that were glued to the specimens. An image of the test setup can be seen in Figure 2. The damage patterns were obtained by means of a high-definition camera and a commercial software.

All tests were controlled by the CMOD gauge opening speed. The CMOD opening velocity used during the tests can be seen for both perpendicular and parallel orientation of the fibres in Table 2.

2.2 *Fracture test results and damage patterns*

In Figure 3 the behaviour of the specimens of GRC without any addition and loaded in the parallel direction of the fibres can be seen. The curves boast a shape similar to the one that might appear in a concrete fracture test. The curves of Figure 3 show a first a linear loading branch followed by a soft unloading branch that resembles an exponential curve. Between the limit of proportionality (LOP) and the maximum load there were only minor changes of stiffness between the limit of proportionality (LOP) and the maximum load

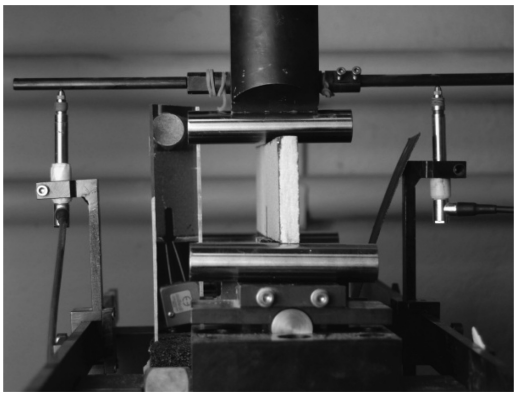

Figure 2. Test setup.

Table 2. CMOD opening steps.

CMOD speed (μm/min)	w (μm)
0.012	0–300
0.024	300–550
0.048	550–750
0.072	750-end of test

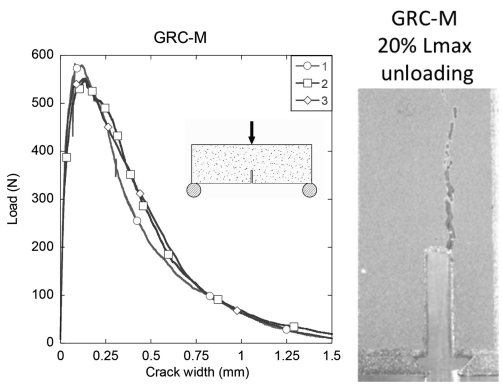

Figure 3. GRC-M fracture test results and damage pattern at 20% of maximum load after peak load.

reached up to almost 850 N. The specimens failed, in all the tests, with an opening of the crack close to 1.5 mm and there was hardly any scatter in the test results. Figure 3 shows the damage pattern generated during the fracture test. In this figure the red area shadows the zone where the cracks appeared. As can be easily deduced from this image, during the fracture test all the damage was concentrated in only one crack.

The results of the fracture tests performed on GRC-M in the in-plane orientation can be

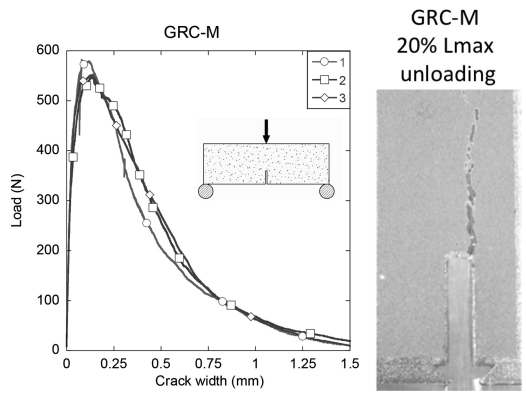

Figure 4. GRC-M fracture test results and damage pattern at 20% of maximum load after peak load.

seen in Figure 4. The same characteristics as the aforementioned GRC without additions curves can be seen in the curves that appear in this figure. Nevertheless, the unloading branch of the curve is more gradual after the peak load was reached. The peak load in these curves were around 560 N in all cases. The GRC-M fracture curves show that the specimen was losing a significant part of its stiffness and the opening of the notch increased but the material was still capable of withstanding load. This characteristic developed from this point until 0.65 mm of CMOD where there was a final change of curvature. Once this had taken place, an exponential unloading could be seen until a crack width of 1.5 mm was reached. There was hardly any scatter among the behaviour of the specimens tested similarly to what happened in the GRC samples. From the image in the right part of Figure 4, where the damage pattern can be seen, it can be clearly perceived that the reddish colours which shown the damage produced during the test appear to be focused on the crack that starts in the notch and is bound to the loading point.

A noticeable scatter that appeared in the fracture tests performed in the GRC-P specimens that can be seen in Figure 5. Some important information can be obtained in spite of the cited scatter. A first zone with linear elastic behaviour that ended with the LOP before reaching the maximum load appeared in all curves. Subsequently, and in contrast with the curves of GRC and GRC-M previously shown in Figure 4 there was a clear distinction between the LOP and the maximum load recorded in the tests. Those ones ranged between 900 and 1100 N. moreover, before reaching the maximum load a notable loss of stiffness appeared in the specimens where some scatter can be observed. These differences among the curves

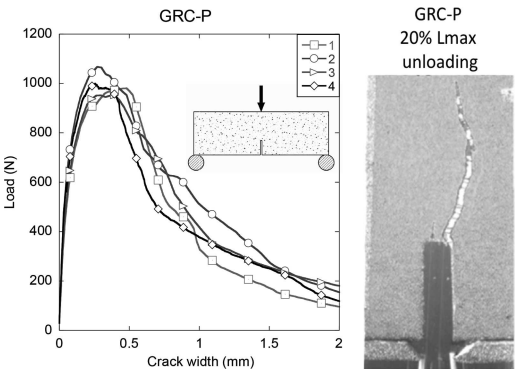

Figure 5. GRC-M fracture test results and damage pattern at 20% of maximum load after peak load.

are more notorious after the maximum load, in the first part of the unloading branch,. Therefore the appearance of the curves up to this point could be considered similar.

Another point that is worth to highlight is that there were clear differences in the CMOD recorded at the same load for each of the specimens. The curves begin to show a similar behaviour from a 1.5 mm CMOD onwards where a load bearing capacity comparable in all the specimens until CMOD reached 3 mm and the tests ended could be observed. As discussed in (Enfedaque et al. 2015), the damaged area in one representative specimen of GRC-P was distributed during the test in a more extensive area than in the GRC-M and GRC specimens. However, in Figure 5 it can be seen that in the last stages of the test the fractured area is concentrated in an area that emerges from the right part of the notch.

From the damage patterns shown in Figure 3, Figure 4 and Figure 5 it would seem that a numerical simulation that uses cohesive crack modelling can be suitable for GRC because the damage produced is concentrated in a limited portion of the bulk of the specimens.

3 NUMERICAL MODELLING

In this work, a simple generalization of the cohesive crack to mixed mode is used which assumes that the traction vector **t** transmitted across the crack faces is parallel to the crack displacement vector **w** (central forces model). For monotonic loading in which the magnitude of the crack opening vector |**w**| is never decreasing, the relationship reads:

$$\mathbf{t} = \frac{f(|\mathbf{w}|)}{|\mathbf{w}|}\mathbf{w} \tag{1}$$

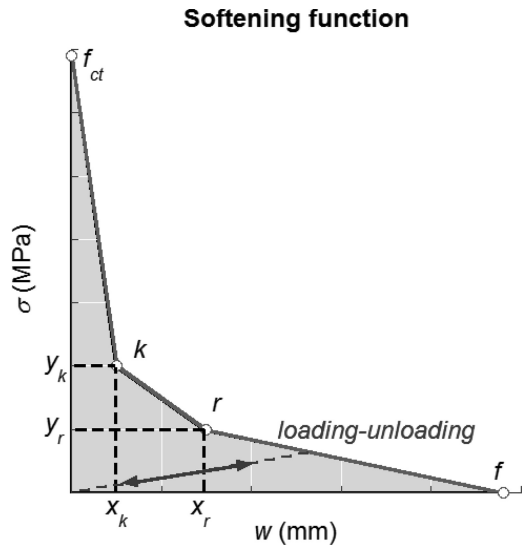

Figure 6. Tri-linear softening function proposed for GRC.

where $f(|\mathbf{w}|)$ is the softening function for pure opening mode that can be seen in Figure 6 and formulated in equation (2).

$$\begin{cases} \sigma = \left(\dfrac{\sigma_k - f_{ct}}{w_k}\right) w & if \quad 0 > w > w_k \\ \sigma = \left(\dfrac{\sigma_r - \sigma_k}{w_r - w_k}\right) w & if \quad w_k > w > w_r \\ \sigma = \left(\dfrac{-\sigma_r}{w_f - w_r}\right) w & if \quad w_r > w > w_f \end{cases} \tag{2}$$

To take into account a possible unloading process it is assumed that the cohesive crack unloads to the origin, as it appears in the blue dashed line that appear in Figure 6 and (1) is rewritten as:

$$\mathbf{t} = \frac{f(|\tilde{\mathbf{w}}|)}{|\tilde{\mathbf{w}}|}\mathbf{w} \quad being\ \tilde{\mathbf{w}} = \max(|\mathbf{w}|) \tag{3}$$

where $\tilde{\mathbf{w}}$ is an equivalent crack opening defined as the historical maximum of the magnitude of the crack displacement vector.

This behaviour can be implemented in an arbitrary finite element defined by a node design as shown in Fig. 7a. If a straight crack is embedded in it and one of the faces of the crack as the reference, its normal **n** pointing towards the other face can be considered as the positive normal. Let **w** be the displacement jump across the crack of the opposite

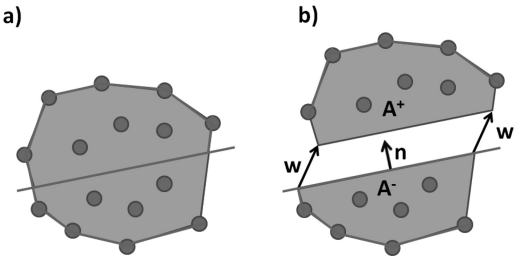

Figure 7. Finite element with a crack with uniform opening: (a) generic element with nodes and crack line and (b) displacement jump across the crack line.

side of the crack with respect to the reference side (see Fig. 7b).

The crack splits the element in two sub-domains $\mathbf{A}^+$ and $\mathbf{A}^-$. Following the strong discontinuity approach [29], the approximated displacement field within the element can be written as:

$$\mathbf{u}(\mathbf{x}) = \sum_{\alpha \in A} N_\alpha(\mathbf{x})\mathbf{u}_\alpha + \left[H(\mathbf{x}) - N^+(\mathbf{x})\right]\mathbf{w} \tag{4}$$

where α is the element node index, $N_\alpha(\mathbf{x})$ the traditional shape function for node α, $\mathbf{u}_\alpha$ the corresponding nodal displacement, $H(\mathbf{x})$ the Heaviside jump function across the crack plane [i.e., $H(\mathbf{x}) = 0$ for $\mathbf{x} \in \mathbf{A}^-$, $H(\mathbf{x}) = 1$ for $\mathbf{x} \in \mathbf{A}^+$], and

$$N^+(\mathbf{x}) = \sum_{\alpha \in A^+} N_\alpha(\mathbf{x}) \tag{5}$$

The strain tensor is obtained from the displacement field as a continuous part ε^c plus a Dirac's δ function on the crack line. The continuous part, which determines the stress field on the element on both sides of the crack, is given by

$$\varepsilon^c(\mathbf{x}) = \varepsilon^\alpha(\mathbf{x}) - \left[b^+(\mathbf{x}) \otimes \mathbf{w}\right]^S \tag{6}$$

$$\mathbf{b}^+(\mathbf{x}) = \sum_{\alpha \in A^+} \mathbf{b}_\alpha(\mathbf{x}) \tag{7}$$

with $\mathrm{b}_\alpha(\mathrm{x}) = grad\ N_\alpha(\mathbf{x})$ and superscript indicating symmetric part of a tensor. Obviously, $\boldsymbol{\varepsilon}^\alpha(\mathbf{x})$ is the *apparent* strain tensor of the element computed from the nodal displacements.

Along the cohesive crack line, the jump vector $\mathbf{w}$ and the traction vector $\mathbf{t}$ are to be related by Eq. (3). For the exact solution, the traction vector is computed locally as $\mathbf{t} = \boldsymbol{\sigma} \cdot \mathbf{n}$. For the finite element, however, we must deal with approximate tractions and crack jump vectors, and there is not a single way to determine the relationship between the approximate stress field and the tractions. To simplify the reasoning, we approximate the traction field along the crack line by a constant traction $\bar{\mathbf{t}}$. The determination of $\mathbf{t}$ is approximate, and can be done in two different ways: (1) as an average along the crack line of the local traction vector $\boldsymbol{\sigma} \cdot \mathbf{n}$, or (2) by forcing the global equilibrium of either $\mathbf{A}^+$ or A^- (which is equivalent, in this case, to using the principle of virtual work). The corresponding equations read:

$$\bar{\mathbf{t}} = \frac{1}{L}\int_L \boldsymbol{\sigma}\,\mathbf{n}\,dl \tag{8}$$

$$\bar{\boldsymbol{t}} = \frac{1}{L}\int_A \boldsymbol{\sigma}\,\boldsymbol{b}^+ dA \tag{9}$$

In which the stress tensor is that corresponding to the classical Finite Element approximation based on the continuous strain in Eq. (6). In general, the two equations do not coincide, as shown next for constant strain triangles with embedded crack.

The reasoning that has been previously mentioned was implemented in a constant strain triangle. If in such triangle a strong discontinuity line (crack) such as shown in Fig. 8a, is considered, and select the positive normal pointing towards the solitary node. Therefore it can be shown that

$$\mathbf{b}^+ = \frac{1}{h}\mathbf{n}^+ \tag{10}$$

where h is the height of the triangle over the side opposite to the solitary node and $\mathbf{n}^+$ the unit normal to that side. With this, and the fact that the stresses are uniform, Eqs. (8) and (9) reduce to

$$\bar{\mathbf{t}} = \boldsymbol{\sigma}\,\mathbf{n} \tag{11}$$

$$\bar{\mathbf{t}} = \frac{A}{hL}\boldsymbol{\sigma}\,\mathbf{n}^+ \tag{12}$$

where A is the area of the element and L the length of the crack. This shows that for local and global equilibrium to hold, it is required that $\mathbf{n}^+ = \mathbf{n}$ and $hL = A$ This reduces to the following two conditions: (1) the discontinuity (crack) line must

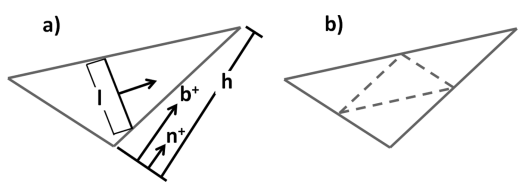

Figure 8. Constant stress triangle: (a) geometrical definitions and (b) potential crack paths satisfying both local and global equilibrium (dashed lines).

be parallel to one of the sides of the triangle, and (2) the discontinuity line must be located at mid height. Thus the potential crack lines satisfying both local and global equilibrium are those indicated by dashed lines in Fig 8b.

In our approach the local equilibrium Eq. (11) is used in conjunction with the strain approximant (9). This leads to a non-symmetric formulation. If Eq. (12) is imposed then a symmetric formulation is obtained. However, that both formulations tend to coincide when the crack runs parallel to one side of the element and at mid height (*not* through the centroid).

The implementation assumes linear elastic behaviour of the material outside the crack. The crack displacement vector **w** is handled as two internal degrees of freedom which are solved at the level of the crack within the finite element (assumed to be a constant strain triangle).

One of the main tasks of the implementation is to compute the stress tensor in the element, which follows an algorithm similar to plasticity, since the stress tensor is given, from Eq. (9) and the hypothesis of elastic bulk material behaviour, as

$$\boldsymbol{\sigma} = \mathbf{E} : \left[\varepsilon^{\alpha} - \left(\mathbf{b}^{+} \otimes \mathbf{w} \right)^{S} \right] \tag{13}$$

where **E** is the tensor of elastic moduli. Before computing the result for the stress, the crack displacement must be solved for. The corresponding equation is obtained by substituting the foregoing expression for the stress into Eq. (11) and the result into the cohesive crack Eq. (6). The resulting condition is

$$\frac{f\left(|\tilde{\mathbf{w}}|\right)}{|\tilde{\mathbf{w}}|}\mathbf{w} = \left[\mathbf{E} : \varepsilon^{\alpha}\right] \cdot \mathbf{n} - \left[\mathbf{E} : \left(\mathbf{b}^{+} \otimes \mathbf{w} \right)^{S} \right] \mathbf{n} \tag{14}$$

which can be rewritten as

$$\frac{f\left(|\tilde{\mathbf{w}}|\right)}{|\tilde{\mathbf{w}}|}\mathbf{w} = \left[\mathbf{E} : \varepsilon^{\alpha}\right] \cdot \mathbf{n} - \left[\mathbf{n} \cdot \mathbf{E} : \mathbf{b}^{+}\right] \mathbf{w} \tag{15}$$

or else

$$\left[\frac{f\left(|\tilde{\mathbf{w}}|\right)}{|\tilde{\mathbf{w}}|} 1 + \left[\mathbf{n} \cdot \mathbf{E} : \mathbf{b}^{+}\right] \right] \mathbf{w} - \left[\mathbf{E} : \varepsilon^{\alpha}\right] \cdot \mathbf{n} \tag{16}$$

where 1 is the second-order unit tensor. This equation is solved for **w** using Newton Raphson's method given the nodal displacements (and so ε^{α}) once the crack is formed and thus **n** and $\mathbf{b}^{+}$ are also given.

One of the key points in the proposed method is how the crack is introduced in the element, i.e., how **n** and $\mathbf{b}^{+}$ are determined.

As long as the tensile strength of the material has not been reached the crack opening $\mathbf{w} = 0$ in the element, and **n** and $\mathbf{b}^{+}$ are undefined. Therefore, the element loads elastically and $\boldsymbol{\sigma} = \mathbf{E}:\varepsilon^{\alpha}$ until the maximum principal stress exceeds the tensile strength. Then a crack is introduced perpendicular to the direction of the maximum principal stress, and **n** is computed as a unit eigenvector of $\boldsymbol{\sigma}$.

Next, the solitary node and the vector $\mathbf{b}^{+}$ are determined by requiring the angle between **n** and $\mathbf{b}^{+}$ to be the smallest possible (see Fig. 8). This is equivalent to selecting the solitary node so that the side opposite to it be as parallel as possible to the crack. This procedure was devised based on the observation of (Borja 2000) that the behaviour of this type of element is best when the crack meets such condition, and also based on the analysis in the previous section showing that the local and global equilibrium are simultaneously met only when **n** is parallel to $\mathbf{b}^{+}$.

As the cracking process takes place at the element level, and is strictly local no crack continuity is enforced or crack exclusion zone defined. This leads in many circumstances to locking after a certain crack growth. Such locking seems to be due to a bad prediction of the cracking direction in the element ahead of the pre-existing crack. To overcome this problem without introducing global algorithms (crack tracking and exclusion zones), an adaptability criterion is introduced and a certain amount of crack adaptability within each element is enabled. The crack is allowed to adapt to later variations in principal stress direction *while its opening is small*. This crack adaptation is implemented very easily by stating that while the equivalent crack opening at any particular element is less than a threshold value $\mathbf{w}_{th}$, the crack direction is recomputed at each step as if the crack were freshly created. After $\mathbf{w} \geq \boldsymbol{w}_{th}$, no further adaptation is allowed and the crack direction becomes fixed. Threshold values must be related to the softening properties of the material, and values of the order of 0.1–0.2 G_f/f_t are usually satisfactory as has been shown in [21, 22, 23].

4 INVERSE ANALYSIS AND DISCUSSION

In order to perform the simulations the described model has been introduced in a commercial finite element programme by means of a user subroutine for material. Hence, this paper develops numerical simulations by using ABAQUS and one UMAT subroutine to model the behaviour of GRC. In such a sense, the non-linear fracture process zone emerges in the elements placed on the crack. Given that the behaviour of the fracturing elements depends on a constitutive relation that needs to be iteratively fit, if the behaviour of equation

(2) is used the values of t, k, r, and f have to be defined. In addition to these values a constant elasticity modulus of 22.5 GPa has been used for the two formulations. This value is in the range that appears in previous studies (Majumdar 1991).

The results that have been shown in Figure 3, Figure 4 and Figure 5 and in reference (Enfedaque et al. 2015) were reproduced by iteratively modifying the values of t, k, r, and f. In Table 3 the values of t, k, r, and f that were used to reproduce the fracture tests of GRC, GRC-M and GRC-P can be observed.

The values of the parameters used in the numerical simulations that can be seen in Table 3 have been used to reproduce the experimental results that can be seen in Figure 9, Figure 10 and Figure 11. As can be easily perceived from the curves of Figure 9 and 10 by modifying the four characteristic points that define the tri-linear softening function a remarkable good correlation can be found between the experimental and the numerical curves. In the case of the curves of Figure 11 there is a certain degree of disparity probably caused by the scattering of the experimental tests.

From the softening functions that are compared in Figure 12 it can be observed that the presence of Metaver causes a reduction of the tensile strength when added to GRC. It is also notable that the ductility of the two formulations is analogue being in both cases equal to 0.6 mm. Thus, as the crack progresses there are changes in the fracture

Table 3. Characteristic points of the tri-linear softening functions used.

	GRC		GRC-M		GRC-P	
	(mm)	(MPa)	(mm)	(MPa)	(mm)	(MPa)
t	0.000	7.80	0.000	4.10	0.000	7.80
k	0.083	1.10	0.184	0.91	0.447	0.36
r	0.210	0.34	0.310	0.32	0.679	0.04
f	0.600	0.00	0.600	0.00	0.900	0.00

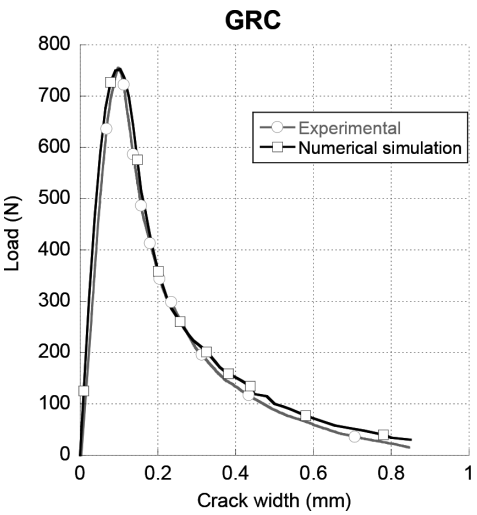

Figure 9. Experimental results versus simulation results in GRC.

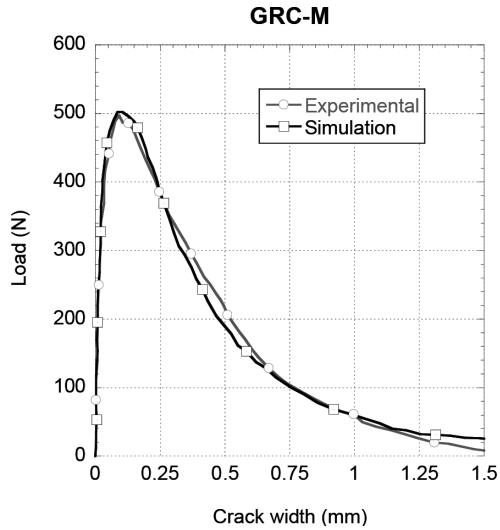

Figure 10. Experimental results versus simulation results in GRC-M.

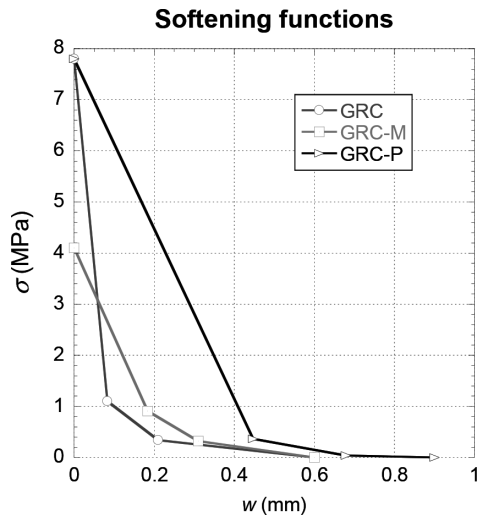

Figure 11. Softening functions obtained by inverse analysis.

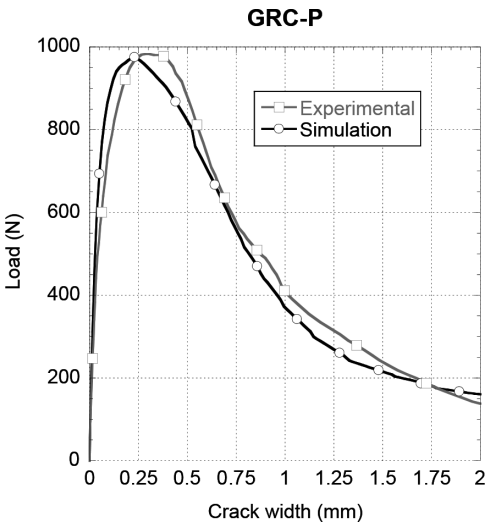

Figure 12. Experimental results versus simulation results in GRC-P.

behaviour which might be caused by the reduction of the load bearing capacity at different rates

The fracture energy that is dissipated in the material in the simulation when the elements are subjected to tensile stresses can be obtained by integrating the areas that appear under the σ-w curves of Figure 12. The values obtained can be seen in Table 4. If such values are compared with those obtained in the experimental campaign (Enfedaque et al. 2015) it can be clearly seen that although the mechanical behaviour of the two formulations have been accurately reproduced there are around a 15% difference between the experimental fracture energy and the simulated one. This 15% reduction of the fracture energy in the numerical model can be explained by the different compressive behaviour of the material and the numerical model. While in the numerical model no compressive damage has been considered, in the tests, and due to the great ductility of the material, the compressive stresses that appear in the upper part of the samples might exceed its compressive strength and consequently some energy may be consumed in the plasticity damage mechanism.

5 CONCLUSIONS

A cohesive model based on the emergence of a discrete crack has been programmed in a commercial finite element numerical code. Such code included an implementation of a cohesive crack model with a tri-linear softening function which substitutes the traditional exponential function used for concrete. By means of an inverse analysis the representative values that define the softening function for the three formulations of GRC studied have been obtained. An accurate reproduction of the fracture behaviour of GRC has been obtained.

The softening functions obtained show that the presence of Metaver causes a reduction of the tensile strength when added to GRC. Moreover, it can be argued that the fracture behaviour of GRC and GRC-M change due to the reduction of the load bearing capacity at a different rate. In addition, it should be also highlighted that the ductility of the two formulations is comparable being in both cases equal to 0.6 mm.

Based on the experimental data available in previous studies [27] a comparison between the numerical and experimental values of fracture energy obtained has been performed. Based on such comparison it has been observed that the experimental fracture energy is around a 15% greater than those obtained by integrating the area under the softening functions. Such differences can be attributed to the absence of damage in the compressed elements of the numerical model. This issue is a matter that should be addressed in future developments of the constitutive relations.

The constitutive model proposed provides a significant tool for structural designers that is capable of reproducing with reasonable accuracy the fracture behaviour of GRC. Therefore, designers might take full advantage of the improvement of properties that glass fibres added to the cement mortar widening the application of GRC in everyday building industry. Additionally, it should be pointed out that reproducing the fracture behaviour of GRC is a key task to increase the use of GRC due to the potential damage that can occur in case of a material failure.

REFERENCES

Alberti M.G., Enfedaque A., Gálvez J.C., Agrawal V. 2016, Reliability of polyolefin fibre reinforced concrete beyond laboratory sizes and construction procedures,. *Composite Structures*, (140), 506–524.

Borja R.I. 2000, A finite element model for strain localization analysis of strongly discontinuous fields based on standard Galerkin approximation. *Computer Methods in Applied Mechanics and Engineering*, (190), 1529–1249.

Correia J.R., Ferreira J., Branco F.A. 2006 A rehabilitation study of sandwich GRC façade panels. *Construction and Building Materials,* 20(8):554–61.

Enfedaque A., Sánchez Paradela L., Sánchez-Gálvez V. 2010. The effect of silica fume and metakaolin on glass-fibre reinforced concrete (GRC) ageing time. *Materiales de Construccion* (300), 67–82.

Enfedaque A., Romero H.L., Gálvez J.C. 2014, Fracture energy evolution of two concretes resistant to the action of freeze-thaw cycles. *Materiales de Construcción*,64 (313).

Enfedaque A., Gálvez J. C., Suárez F. 2015, Analysis of fracture tests of glass fibre reinforced cement (GRC) using digital image correlation 2015. *Construction and Building Materials* (75), 472–487.

Fathy A.M., Sanz B., Sancho J.M., Planas J. 2008 Determination of the bilinear stress crack opening curve for normal- and high-strength concrete. *Fatigue & Fracture of Engineering Materials & Structures* 31(7), 539–48.

Ferreira J.G., Branco F.A. 2005, Structural application of GRC in telecommunication towers. *Construction and Building Materials,* 21(1), 19–28.

Gálvez J.C., Planas J., Sancho J.M., Reyes E., Cendón D.A., Casati M.J. 2013, An embedded cohesive crack model for finite element analysis of quasi-brittle materials, *Engineering Fracture Mechanics,* (109), 369–386.

Hillerborg A., Modéer M., Petersson P.E. 1976, Analysis of crack formation and crack growth in concrete by means of fracture mechanics and finite elements, *Cement and Concrete Research,* 6(6), 773–78.

Kooiman A.G., Van Der Veen C., Walraven J.C. 2000, Modelling the post-cracking behaviour of steel fibre reinforced concrete for structural design purposes, *HERON,* 45(4), 275–308.

Majumdar A.J 1975. Fiber reinforced cement and concrete. Construction Press, 279–314.

Majumdar A.J. 1991, Laws V. Glass fiber reinforced cement. Oxford: BSP Professional Books.

Marikunte S., Aldea C., Shah S.P. 1997, Durability of glass fiber reinforced cement composites. *Advanced Cement Materials.* 5,100–8.

Metaver: http://catalogue.newchem.org/finlandstore/Up_files%5CMDS%20Metaver%20I.pdf.

Mobasher B., Shah S.P. Test parameters for evaluating toughness of glass fiber reinforced concrete panels 1989. *ACI Materials Journal*. 86:448–58.

Polanco-Loria M. 1997, Numerical modelling of plain and reinforced concrete by damage mechanics, Trondheim: Department of Structural Engineering, Norwegian University of Science and Technology.

Powerpozz: http://www.bigfreshcontrol.com/documents/act_documents/10.150MetakaolinPhys&ChemWhite.pdf.

Purnell P., Short N.R., Page C.L. 2001. A static fatigue model for the durability of glass fiber reinforced cement. *Journal of Materials Science*; 36:5385–90.

Reyes E., Gálvez J.C., Casati M.J., Cendón D.A., Sancho J.M. and Planas J. 2009, An embedded cohesive crack model for finite element analysis of brickwork masonry fracture, *Engineering Fracture Mechanics,* 76(12), 1930–44.

Sancho J.M., Planas J., Gálvez J.C., Reyes E. and. Cendón D.A, 2006. An embedded cohesive crack model for finite element analysis of mixed mode fracture of concrete, 2006 *Fatigue & Fracture Engineering Materials & Structures*, 29 (12), 1056–1065.

Sancho J.M., Planas J., Cendón D.A., Reyes E., Gálvez J.C. 2007, An embedded crack model for finite element analysis of concrete fracture, *Engineering Fracture Mechanics,* 74(1), 75–86.

Shah S.P., Ludirdja D., Daniel J.I., Mobasher B. Toughness-durability of glass fiber reinforced concrete systems. *ACI Materials Journal*, 85, 352–60.



Taylor & Francis
Taylor & Francis Group
http://taylorandfrancis.com

Computational Modelling of Concrete Structures – Meschke, Pichler & Rots (Eds)
© 2018 Taylor & Francis Group, London, ISBN 978-1-138-74117-1

Multiscale modeling of steel fiber reinforced concrete based on the use of coupling finite elements and mesh fragmentation technique

L.A.G. Bitencourt Jr., Y.T. Trindade & T.N. Bittencourt
Department of Structural and Geotechnical Engineering, Polytechnic School at the University of Sao Paulo, Sao Paulo, Brazil

O.L. Manzoli & E.A. Rodrigues
Department of Civil Engineering, Sao Paulo State University, Bauru, Brazil

ABSTRACT: A multiscale model is proposed based on the use of coupling finite elements recently developed by the authors. This feature allows the use of the same strategy to deal with two problems of non-matching meshes addressed in this work. One is regarding the coupling of discrete steel fibers into the bulk finite elements (overlapping meshes), and the other corresponds to the coupling of different subdomains of a concurrent multiscale model (non-overlapping meshes). Thus, for problems where the material failure concentrates in a specific region, the numerical model with a discrete treatment of fibers can be applied only in this region of interest, increasing the performance in terms of computation time. Using this approach for coupling non-matching meshes, a non-rigid coupling procedure is proposed to describe the complex nonlinear behaviour of the fiber-concrete interaction by adopting an appropriate damage constitutive model. To avoid the necessity of the widely used crack tracking schemes, a technique based on the insertion of special interface finite elements (three-node triangular or four-node tetrahedral elements) in between all regular finite elements of the mesh was applied. It can be shown that, as the aspect ratio of the interface element increases (ratio of the largest to the smallest dimension), the element's strains also increase approaching the same kinematics as the continuum strong discontinuity approach. As a consequence, standard continuum constitutive models, which tend toward discrete constitutive relations as the aspect ratio increases, can be applied to describe fracture process. Several tests are performed to show the applicability of the proposed scheme to build multiscale models and to predict the fracture process in steel fiber reinforced concrete.

1 INTRODUCTION

Concrete is one of the most widely used construction material. This material is classified as quasi-brittle materials, i.e., material with low tensile strength and strain capacities. To overcome these main drawbacks, discontinuous steel fibers have been added to concrete cimentitious matrices, resulting in so-called Steel Fiber Reinforced Concrete (SFRC). Despite the wide use of SFRC in recent years, the addition of fibers for improving material properties comes from ancient times.

The main benefits of the addition of steel fibers in concrete are directly related to their ability to transfer stresses across cracks. Before the addition of steel fibers and after matrix cracking, the tensile stress immediately decreases. However, after the addition of a certain volume of fibers and after matrix cracking, the fibers are able to maintain a certain load bearing capacity, avoiding an abrupt failure of the composite.

According to Bentur & Mindess (2007), this process of stress transfer depends on the internal structure of the composite, and the main factors that influence the composite's behavior are (i) the structure of the bulk cementitious matrix, (ii) the shape and distribution of the fibers, and (iii) the structure of the fiber-matrix interface. Therefore, a numerical model with a discrete treatment of the fibers seems to be a natural way to simulate the behavior of this material, taking into account all the factors aforementioned, in a totally independent way.

Recently, a number of numerical models adopting this strategy have been proposed (Radtke et al. 2010, Cunha et al. 2011, Cunha et al. 2012, Etse et al. 2012, Pros et al. 2012). As an alternative to existing numerical models with this type of approach a new numerical model for modeling the behavior of SFRC has been developed. This model is based on the use of coupling finite elements (CFEs) (Bitencourt Jr. et al. 2015), recently

developed by the authors to couple non-matching finite element meshes. Thus the independent meshes of the concrete bulk and a cloud of steel fibers can be modeled in a totally independent way, including the fiber-concrete interaction by the use of an appropriate constitutive model.

For modeling the crack initiation and propagation, a mesh fragmentation technique (Manzoli et al. 2016) based on the use of interface finite element with high aspect ratio (Manzoli et al. 2012) is employed. The main advantage of this approach consists that the fracture process can be modeled entirely in the continuum framework, composed of standard finite elements usually available in FEM codes and continuum constitutive models. In this work, a tensile damage constituive model, compatible with Continuum Strong Discontinuity Approach (CSDA) is used (Oliver et al. 1999, Oliver et al. 2002).

2 DISCRETE AND EXPLICIT REPRESENTATION OF STEEL FIBERS

A discrete and explicit representation of steel fibers based on the use of coupling finite elements (CFEs) is adopted. The procedure to construct the numerical model is depicted in Figure 1. Initially, a cloud of steel fibers is generated based on the geometry of the problem. In this work an uniform isotropic random distribution is used. Then, concrete (Figure 1(a)) and steel fibers (Figure 1(b)) are discretized in finite elements in a totally independent way (non-conforming meshes). Finally, coupling finite elements are introduced in order to couple the independent meshes (Figure 1(b)).

As can be seen in Figure 1(d), each CFE has the same nodes of an underlying finite element of the existing mesh and an extra node, coinciding with the loose node (this node is called the coupling node) that belongs to its domain. As a consequence, the CFEs overlap the finite elements of the original mesh around the coupling nodes "c_i". Note that for each loose node, one coupling finite element is required. An example of the addition of a coupling finite element can be seen in Figure 1(d), where the coupling finite element $CFE_1 = \{j,k,l,c_1\}$ is introduced, whose c_1, is the coupling node.

These elements that share nodes with both non-matching meshes can then be used to ensure the compatibility of displacements and to transfer interaction forces between non-matching meshes. The interaction forces between the non-matching meshes may also be described by an appropriate constitutive model applied in the CFEs. This is one of the major advantages of the technique, since a rigid (full compatibility of displacements) or non-rigid (degrading interface) coupling can be considered easily. Thus, the use of this technique for modeling SFRC is very appealing, since steel fibers, concrete and steel fibers-concrete interface can be modeled independently.

After the application of the coupling procedure (Figure 1(c)), the global internal force vector and the stiffness matrix can be written as:

$$\mathbf{F}^{int} = \overset{nel_{\Omega^C}}{\underset{e=1}{A}} \left(\mathbf{F}_e^{int}\right)_{\Omega^C} + \overset{nel_{\Omega^{SF}}}{\underset{e=1}{A}} \left(\mathbf{F}_e^{int}\right)_{\Omega^{SF}} + \overset{nel_{CFE}}{\underset{e=1}{A}} \left(\mathbf{F}_e^{int}\right)_{CFE} \tag{1}$$

$$\mathbf{K} = \overset{nel_{\Omega^C}}{\underset{e=1}{A}} \left(\mathbf{K}_e\right)_{\Omega^C} + \overset{nel_{\Omega^{SF}}}{\underset{e=1}{A}} \left(\mathbf{K}_e\right)_{\Omega^{SF}} + \overset{nel_{CFE}}{\underset{e=1}{A}} \left(\mathbf{K}_e\right)_{CFE} \tag{2}$$

where A stands for the finite element assembly operator, the first and second terms of the Equations 1 and 2 are related to the subdomains from the concrete Ω^C and steel fibers Ω^{SF}, respectively, and the third term is tied to the introduction of the CFEs.

2.1 *Coupling finite element formulation*

Consider a standard isoparametric finite element of domain Ω^e, with number of nodes equal to nn, and shape functions $\overline{N}_i(\mathbf{X})$ $(i = 1, nn)$, which are defined for the material points $\mathbf{X} \in \Omega^e$, such that the displacement $\overline{\mathbf{U}}$ at any point in its domain can be approximated in terms of its nodal displacements $\mathbf{D}_i$ $(i = 1, nn)$, as follows:

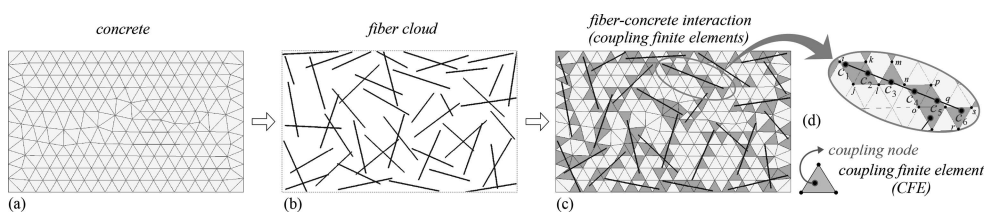

Figure 1. Coupling procedure for non-matching finite element meshes: (a) discretization of the concrete in FEs; (b) generation and discretization of the could of steel fibers; (c) creation and insertion of the CFEs; (d) detail of the coupling in overlapping meshes.

$$\overline{\mathbf{U}}(\mathbf{X}) = \sum_{i=1}^{nn} \overline{N}_i(\mathbf{X})\mathbf{D}_i. \tag{3}$$

The CFE is a finite element which has the above described nodes of the standard isoparametric finite element as well as an additional node, $nn + 1$, called coupling node (C_{node}), situated at the material point $\mathbf{X}_c \in \Omega^e$, as illustrated in Figure 2 for 3-node triangle + C_{node} and 4-node tetrahedral + C_{node}.

The relative displacement, $[\![\mathrm{U}]\!]$, defined as the difference between the displacement of the C_{node} and the displacement of the material point $\mathbf{X}_c$, can be evaluated using the shape functions of the underlying finite element, $\overline{N}_i(\mathbf{X}_c)$ $(i = 1, nn)$, as follows:

$$\begin{aligned}[\![\mathrm{U}]\!] &= \mathbf{D}_{nn+1} - \overline{\mathbf{U}}(\mathbf{X}_c) \\ &= \mathbf{D}_{nn+1} - \sum_{i=1}^{nn} \overline{N}_i(\mathbf{X}_c)\mathbf{D}_i = \mathbf{B}_e\mathbf{D}_e,\end{aligned} \tag{4}$$

where the matrix $\mathbf{B}_e = [-\overline{\mathbf{N}}_1(\mathbf{X}_c) - \overline{\mathbf{N}}_2(\mathbf{X}_c) \ldots - \overline{\mathbf{N}}_{nn}(\mathbf{X}_c)\mathbf{I}]$, $\overline{\mathbf{N}}_i = \overline{N}_i\mathbf{I}$, $\mathbf{I}$ is the identity matrix of order 2 or 3, for 2D and 3D problems, respectively, and $\mathbf{D}_e = \{\mathbf{D}_1\, \mathbf{D}_2 \ldots \mathbf{D}_{nn+1}\}$ stores the displacement components of the coupling finite element.

Thus, the internal virtual work of the CFE is given by

$$\delta W_e^{int} = \delta[\![\mathrm{U}]\!]^T\, \mathbf{F}([\![\mathrm{U}]\!]), \tag{5}$$

where $\mathbf{F}([\![\mathrm{U}]\!])$ is the reaction force owing to the relative displacement $[\![\mathrm{U}]\!]$ and $\delta[\![\mathrm{U}]\!]$ is an arbitrary virtual relative displacement, compatible with the boundary conditions of the problem. Using the same approximation for the virtual relative displacement as that used for the relative displacement given by Equation 4, i.e., $\delta[\![\mathrm{U}]\!] = \mathbf{B}_e\delta\mathbf{D}_e$, the internal force vector of the coupling finite element can be expressed as follows:

$$\mathbf{F}_e^{int} = \mathbf{B}_e^T\mathbf{F}([\![\mathbf{U}]\!]). \tag{6}$$

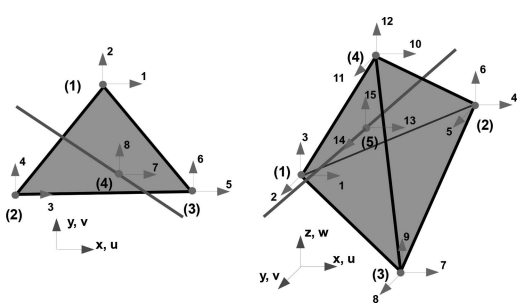

Figure 2. 2D and 3D coupling finite elements with linear interpolation functions of displacements: (a) 3-node triangle + C_{node} and 4-node tetrahedral + C_{node}.

Accordingly, the corresponding tangent stiffness matrix of the CFE can be obtained by the following expression:

$$\mathbf{K}_e = \frac{\partial\mathbf{F}_e^{int}}{\partial\mathbf{D}_e} = \mathbf{B}_e^T\mathbf{C}_{tg}\mathbf{B}_e \tag{7}$$

where $\mathbf{C}_{tg} = \partial\mathbf{F}([\![\mathrm{U}]\!]) / \partial[\![\mathrm{U}]\!]$ is the tangent operator of the constitutive relation between reaction force and the relative displacement.

2.1.1 *Perfect adherence*

Assuming a linear elastic model to describe the relation between the reaction force and the relative displacement:

$$\mathbf{F} = \mathbf{C}[\![\mathbf{U}]\!] = \mathbf{C}\mathbf{B}_e\mathbf{D}_e \tag{8}$$

where $\mathbf{C}$ is the matrix of elastic constants. The perfect adherence or a rigid coupling enforcing displacement compatibility of two non-matching meshes, can be imposed by assuming a very high value for the elastic stiffness, such that the matrix of elastic constants is expressed as follows:

$$\mathbf{C} = \begin{bmatrix} \tilde{C} & 0 & 0 \\ 0 & \tilde{C} & 0 \\ 0 & 0 & \tilde{C} \end{bmatrix} \tag{9}$$

where $\tilde{C}$ stands for a high elastic stiffness value, which plays the role of a penalty variable on the relative displacement. It is important to note that, because of the equilibrium conditions, the interaction force $\mathbf{F}$ in 8 must be bounded. Hence, when the elastic constants tend towards a very high value, the relative displacement components $[\![\mathbf{U}]\!]$ must tend to zero.

2.1.2 *Example 01: Non-matching meshes of a concurrent multiscale model*

In this example, the strategy developed for coupling non-matching meshes is applied to couple the macro and mesoscale subdomains of an embedded concurrent multiscale model and to account the fiber-matrix interaction in the mesoscale region. Two numerical analyses of a reduced model of a three-point bending beam are performed assuming linear elastic material behavior, first considering a concurrent multiscale model and then, for comparison, a full mesoscale model. A load of $F = 5 \times 10^4$ N is applied in both analyses. Figure 3 illustrates the geometry, boundary conditions and the finite element mesh employed for both tests. The analyses were performed considering a plane stress state with an out-of-plane thickness of 40 *mm*.

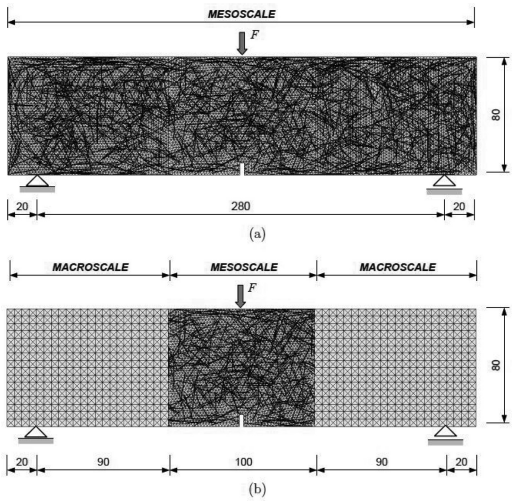

Figure 3. Three-point bending beam simulated numerically using: (a) a mesoscale model, and (b) a concurrent multiscale model (dimensions in mm).

The mesoscale region is composed of two phases, steel fibers and cementitious matrix. The volume fraction of steel fibers is 0.5%, with fiber diameter of 0.5 mm and length of 20 mm. The steel fibers are distributed randomly in the mortar matrix (see Figure 3). For the macroscale subdomains, the SFRCC is considered as a homogeneous isotropic material characterized by effective material parameters. In this example, the Mixture Theory (Trusdell & Toupin 1960) was used to calculate these parameters (Young's modulus and Poisson's ratio). So, the effective parameters are obtained by:

$$P_{ef} = V_f P_f + V_c P_c \tag{10}$$

where P_{ef} is the effective Young's modulus (E_{ef}) or the Poisson's ratio (ν_{ef}); V_f and V_c are the volume fractions of the fibers and cementitious matrix, respectively; while P_f and P_c are the Young's modulus or the Poisson's ratio of the fibers and matrix, respectively. The material parameters adopted for each phase of the composite are given in Table 1.

Cementitious matrix and steel fibers are discretized by three-node triangular finite elements and two-node (one-dimensional) truss finite elements, respectively (see Figure 3). For each fiber, eight elements are used. As can be noted, because of the different scales, the discretization in the mesoscale subdomains is significantly finer than in the macroscale regions. This refinement in the region of interest is very important to reduce the analysis time, because an analysis considering full mesoscale models increases the computational effort considerably. In this example, the full mesoscale model has 38,449 degrees of freedom (DOF), while the multiscale model has only 14,775 DOF.

Table 1. Material parameters.

SFRCC	E_{ef}(MPa)	20,950
	υ_{ef}	0.18
Cementitious Matrix	E_c(MPa)	20,000
	υ_c	0.18
Steel fibers	E_f(MPa)	210,000
	υ_f	0.30

With regard to the coupling procedure adopted for the multiscale model, the finite elements of the macroscale mesh around the non-matching interface were used as base elements to construct the CFEs, while the nodes from the mesoscale mesh at the macro-mesoscale interface were selected to act as the fourth node of the CFEs. Details of the coupling procedure between the macro and mesoscale subdomains using the four-node triangular finite elements are illustrated in Figure 4. A total of 82 CFEs were employed to couple the macro and mesoscale regions. In the mesoscale subdomains, the same procedure were adopted, being one coupling finite element for each truss node. For the mesoscale model, a total of 11,367 elements were introduced, while in the multiscale model, 3,468 were added in the mesoscale region. Note that one finite element may be the base for more than one CFE, since more than one node that is being coupled may belong to the domain of this finite element (see Figure 4(b)). To achieve complete displacement compatibility between the non-matching meshes, the rigid coupling procedure (perfect adherence) described in Section 2.1.1 was applied assuming an elastic stiffness of $\tilde{C} = 10^9$ N/mm.

Table 2 compares the meso and multiscale models. As expected, owing to the size of the system equations to be solved for each model, the performance of the multiscale model in terms of computing time was more efficient. The multiscale model was solved about three times faster, and a very minor difference in the vertical displacement at midspan was obtained. It is important to note that part of this difference is attributed to the homogenization technique employed here.

Figure 5 illustrates the total displacement contour field obtained in both models. As can be also noted, the proposed technique for coupling non-matching meshes is able to ensure the continuity of the displacement fields. Although this newly developed technique does not enforce continuity of the stress field, Figure 6 shows that, owing to equilibrium conditions, the stress fields for the meso and multiscale models are in good agreement.

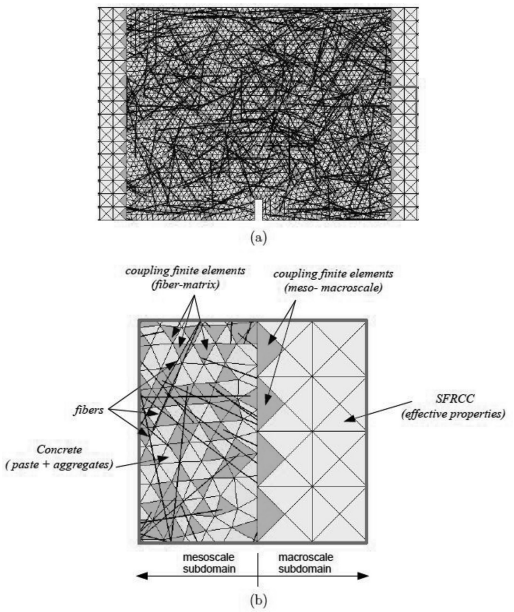

Figure 4. Non-matching meshes: (a) coupling procedure; (b) detail of the coupling finite elements.

Table 2. Comparison of the data of the mesoscale and multiscale models.

	Mesoscale	Multiscale
DOF's	38,449	14,775
Assembly time (stiffness matrix)	1.880 s	0.854 s
Solving time (linear equations)	36.293 s	10.394 s
Total elapsed time	48.1745 s	17.954 s
Vertical displacement at midspan	–0.9480 mm	–0.9407 mm

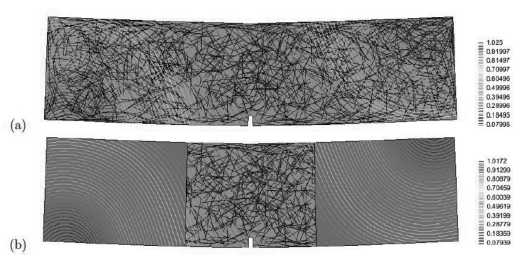

Figure 5. Total displacement contour field (mm): (a) mesoscale model; (b) multiscale model (with scaling factor of 5.).

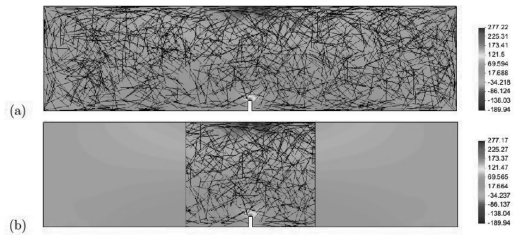

Figure 6. Horizontal normal stress in concrete (in MPa): (a) mesoscale model; (b) multiscale model.

2.1.3 *Loss of adherence*

The loss of adherence is represented through a non-rigid coupling between the non-matching meshes, allowing a relative displacement between the steel fiber and concrete, and insert an interaction force between these two components.

Since the relative movement of the reinforcement with respect to the concrete matrix is in essence a sliding in the direction of the reinforcement axis, it is necessary to use a local coordinate system, (**n**, **s**, **t**), oriented such that the axis **n** coincides with the reinforcement axial orientation. Thus, the relative displacement and its corresponding reaction force can be expressed as $[\![\mathbf{u}]\!] = \mathbf{R}[\![\mathbf{U}]\!]$ and $\mathbf{f} = \mathbf{RF}$, respectively, where $\mathbf{R}$ is the orthogonal rotation matrix between the local and global reference systems.

The loss of adherence model can be easily represented by assuming an elastic constitutive model with distinct elastic constants, according to the local coordinate system:

$$\mathbf{c} = \begin{bmatrix} c_n & 0 & 0 \\ 0 & c_s & 0 \\ 0 & 0 & c_t \end{bmatrix} = \begin{bmatrix} c_n & 0 & 0 \\ 0 & \tilde{c} & 0 \\ 0 & 0 & \tilde{c} \end{bmatrix}, c_n \ll \tilde{c}. \tag{11}$$

In general, these models are described by a relationship between the local (shear) stress, τ, acting at the reinforcement-matrix interface, and the relative displacement (interface slip), s.

Since the CFE introduces into the problem an interaction force between the concrete matrix and the steel reinforcement, at coupling node, one may consider that this force results from the bond (shear) stress, τ, on the bond area (reinforcement-matrix interface) in the vicinity of the couplig node. Therefore, by assuming that the bond (shear) stress is constant in the vicinity of the node and that the size of the vicinity (influence length) that contributes to the resultant force in a specific node corresponds to the average of the half distances between the node "i" and its adjacent nodes of the reinforcement "j" e "k", the interaction force may be expressed as:

$$f_n = \tau\left([\![u_n]\!]\right) P L, \tag{12}$$

where $L = (L_{ij} + L_{jk})/2$ is the influence length and P is the perimeter of the reinforcement cross-section. Note that the slip, s, is given by the relative displacement in direction n, i.e., $s = [\![u_n]\!]$. The remaining transverse components of the resultant force can be expressed as:

$$f_s = \tilde{c}\,[\![u_s]\!]\,P\,L \tag{13}$$

and

$$f_t = \tilde{c}\,[\![u_t]\!]\,P\,L. \tag{14}$$

2.1.4 *Continuum damage model to describe bond slip*

In the case of partial bond, a constitutive model based on the continuum damage theory may be used to describe the constitutive relationship between the shear stress (adherence stress) and the relative sliding. Thus, the damage model can be described by the following equations:

$$\tau = (1-d)\,\bar{\tau} \quad \text{(constitutive relation)} \tag{15}$$

$$\bar{\tau} = c_n\,[\![u_n]\!] \quad \text{(effective shear stress)} \tag{16}$$

$$\phi = \|\bar{\tau}\| - r \le 0 \quad \text{(damage criterion)} \tag{17}$$

$$r = max[\bar{\tau}] \quad \text{(evolution law of the internal variable)} \tag{18}$$

$$d = 1 - \frac{q(r)}{r} \quad \text{(evolution of the damage variable)} \tag{19}$$

where c_n is the elastic stiffness constant (unit of stress per unit of length), $d \in [0,1]$ is the scalar damage variable, $\bar{\tau}$ is the effective shear stress, and r is the strain-like internal variable that assumes the maximum value reached by $\bar{\tau}$ during the load process. The function $q(r)$ represents the hardening/softening law of the constitutive model, and it may be adjusted to fit any bond slip model of type $\tau(s)$, considering the relationship $q(r) = \tau(r/c_n)$.

Taking as an example the bond-slip relationship proposed by the CEB *fib* Model Code, depicted in 7 and described by the equations:

$$\tau(s) = \begin{cases} \tau_{max}\left(\dfrac{s}{s_1}\right)^{\alpha} & \text{if} \quad s \le s_1 \\ \tau_{max} & \text{if} \quad s_1 \le s \le s_2 \\ \tau_{max} - \dfrac{(\tau_{max} - \tau_f)(s - s_2)}{s_3 - s_2} & \text{if} \quad s_2 \le s \le s_3 \\ \tau_f & \text{if} \quad s > s_3 \end{cases}, \tag{20}$$

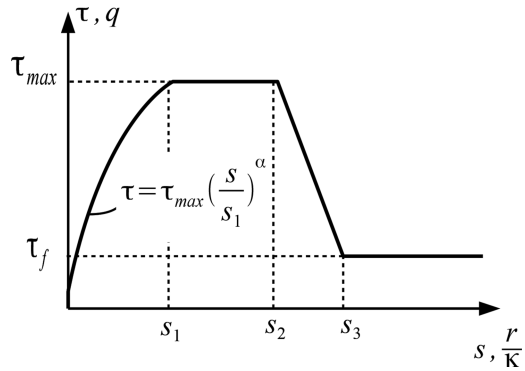

Figure 7. Interface stress bond-slip relationship (monotonic loading) proposed by CEB *fib* Model Code.

the corresponding hardening/softening law is defined in terms of the stress- and strain-like internal variable as:

$$q(r) = \begin{cases} \tau_{max}\left(\dfrac{r/c_n}{s_1}\right)^{\alpha} & \text{if} \quad r/c_n \le s_1 \\ \tau_{max} & \text{if} \quad s_1 \le r/c_n \le s_2 \\ \tau_{max} - \dfrac{(\tau_{max} - \tau_f)(r/c_n - s_2)}{s_3 - s_2} & \text{if} \quad s_2 \le r/c_n \le s_3 \\ \tau_f & \text{if} \quad r/c_n > s_3 \end{cases} \tag{21}$$

where α, τ_{max}, τ_f and $s_i (i = 1,2,3)$ are the parameters of the model, which depend on the concrete strength f_{ck}, the bar geometry (ribbed or smooth), the confining situation (confined or unconfined) and bond condition (good or poor), according to the CEB *fib* Model Code.

In order to avoid problem of convergence, the IMPL-EX integration scheme is used for the integration of the damage constitutive model described above. More details can be found in (Oliver et al. 2008, Prazeres et al. 2015).

2.1.5 *Example 02: Pullout behavior of steel fiber*

This example consists of a single straight fiber with a circular cross section embedded on one side. A bilinear bond stress-slip relationship between the fiber and the concrete matrix was assumed, with frictional pullout strength of $\tau_{f,max} = 3.0$ MPa and slip at frictional pullout strength of $s_f = 0.1$ mm. Additionally, the tributary area of concrete considered effective was based on a prism diameter of 15 times the fiber diameter. It is used a straight steel fiber of length $l_f = 30$ mm, diameter $d_f = 0.565$ mm, whose behavior is described by

an elastic perfectly plastic model, with Young's modulus of $E_f = 210{,}000$ MPa and yield stress of $\sigma_y = 345$ MPa. The fiber is embedded in a linear elastic matrix material, with Young's modulus of $E_c = 32{,}617$ MPa and Poisson's ratio of $\nu_c = 0.18$.

The numerical model constructed is illustrated in Figure 8. The fiber is discretized using 10 two-node (truss) elements, embedded in the cylindrical specimen discretized with 608 four-node tetrahedral finite elements. The fiber and matrix are modeled using an elastoplastic and elastic material model, respectively. The coupling between these two independent meshes are performed employing 6 five-node tetrahedral coupling finite elements, as shown in Figure 8(b). A non-rigid coupling procedure with the damage material model presented in the 2.1.4 to describe the bond-slip behavior was employed. The bilinear bond-slip adopted may be described by the equations:

$$\tau(s) = \begin{cases} \tau_{max}\left(\dfrac{s}{s_1}\right) & \text{if} \quad s \le s_1 \\ \tau_{max} & \text{if} \quad s > s_1 \end{cases}, \tag{22}$$

and considering the relationship $q(r) = \tau(r/c_n)$, may be also described in terms of the stress- and strain-like internal variable as:

$$q(r) = \begin{cases} \tau_{max}\left(\dfrac{r/c_n}{s_1}\right) & \text{if} \quad r/c_n \le s_1 \\ \tau_{max} & \text{if} \quad r/c_n > s_1 \end{cases}. \tag{23}$$

The following values were adopted for the interface parameters: $c_n = 10^3$ MPa/mm, $\tau_{max} = 3.0$ MPa, and $s_1 = 0.1$ mm. To avoid the separation and penetration between the fiber and matrix in the direction normal to fiber $c_s = 10^9$ N/mm and $c_t = 10^9$ N/mm were also adopted.

In the numerical analysis, a prescribed vertical displacement was imposed at the free end of the fiber (see Figure 8(a)), and a fixed boundary condition at the bottom of the cylindrical specimen. Figure 9 illustrates the results obtained in terms of fiber stress at crack against the fiber slip at crack. As can be seen, the result obtained by numerical analysis is identical to that obtained using the analytical formulas of the Diverse Embedment Model (DEM) (Lee et al. 2011), what proves that the strategy adopted for the interface was able to reproduce the fiber-concrete interaction. Moreover, the variation of the slip along the fiber obtained numerically is also identical to that obtained by the DEM, as shown in Figure 10.

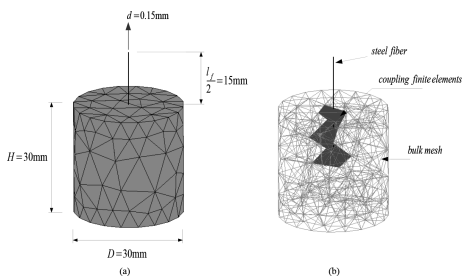

Figure 8. 3D numerical model of the pullout test of single straight fiber embedded on one side: (a) setup of the pullout tests, and (b) detail of the coupling procedure.

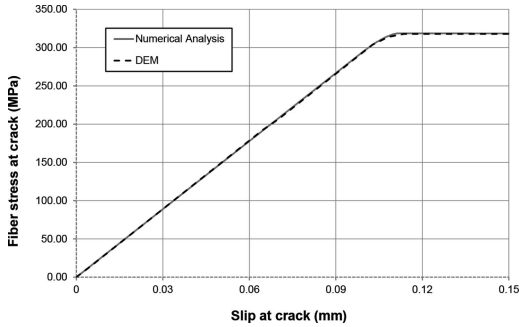

Figure 9. Fiber stress at crack with $l_a = 0.5\, l_f$ for straight fiber.

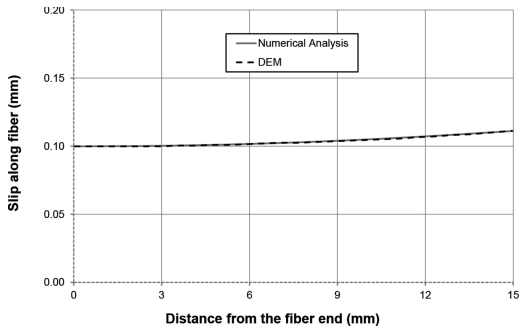

Figure 10. Variation of the slip along the fiber when end slip is 0.1 *mm*.

3 MESH FRAGMENTATION TECHNIQUE

In this work, the crack initiation and propagation in SFRC is simulated using a mesh fragmentation technique (Manzoli et al. 2016) based on the use of interface finite element (Manzoli et al. 2012). The procedure consists in reassembling the original mesh (Figure 11(a)) in such a manner that the regular elements are first transformed into independent elements by replicating

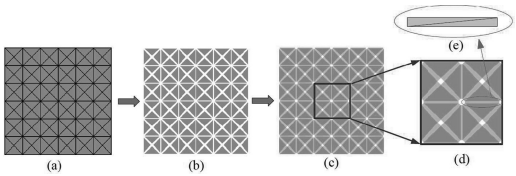

Figure 11. Mesh fragmentation technique.

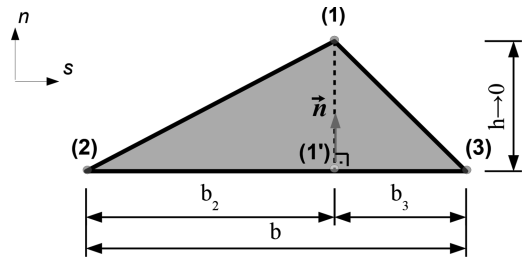

Figure 12. Interface finite element.

the shared nodes, and then a very small reduction is imposed on each element, creating narrow spaces between them (Figure 11(b)). After that the gaps between two neighboring modified elements are filled out by pairs of triangular finite elements (Figure 11(e)) with high aspect ratio (Figures 11(c) and (d)). For 3D examples, the same procedure can be applied using tetrahedral finite elements.

3.1 *Interface finite element with high aspect ratio*

Let us consider the three-nodes triangular FE depicted in Figure 12(c), with height h, given by the distance between the node (1) and its projection on the element base, (1′).

$$\varepsilon = \tilde{\varepsilon} + \underbrace{\frac{1}{h}(\mathbf{n} \otimes [\![\mathbf{u}]\!])}_{\hat{\varepsilon}} \tag{24}$$

where $(\bullet)^S$ refers to the symmetric part of $(\bullet)$, $\mathbf{n}$ is the unit vector normal to the element base, $\otimes$ denotes a dyadic product and $[\![\mathbf{u}]\!]$ is a vector that stores the components of the relative displacement; $\hat{\varepsilon}$ collects the components of the strain tensor which depends on h and $\tilde{\varepsilon}$ contains the rest of the components.

It is important to note that, when the height h tends to zero, the strain component $\tilde{\varepsilon}$ remains bounded while the component $\hat{\varepsilon}$ is no longer bounded. Therefore, in the limit situation of h tending to zero, the element strains are related almost exclusively to the relative displacement between node (1) and its projection on the element base, (1′), implying that node (1) and its projection (1′) tend to the same material point. Consequently, the relative displacement $[\![\mathbf{u}]\!]$ becomes a measure of the displacement discontinuity (strong discontinuity). The structure of the strain field in equation 24 corresponds to the typical kinematics of the Continuum Strong Discontinuity Approach (CSDA) (Oliver et al. 1999, Oliver 2000, Oliver and Huespe 2004). As a consequence, the analyses can be performed integrally in the context of the continuum mechanics, which represents a clear advantage of this method.

3.1.1 *Tensile damage model*

The crack formation and propagation processes is described by a continuum tension damage model, in which the damage criterion iis written in terms of the tension stress component normal to the base of the interface element, only if the normal stress is positive ($\bar{\sigma}_n > 0$). Thus, the damage model can be described by the following equations:

$$\sigma = \begin{cases} (1-d)\,\bar{\sigma} & \text{if } \bar{\sigma}_n > 0 \\ \bar{\sigma} & \text{if } \bar{\sigma}_n \le 0 \end{cases} \quad \text{(constitutive relation)} \tag{25}$$

$$\bar{\sigma} = \mathbf{C} : \varepsilon \quad \text{(effective stress tensor)} \tag{26}$$

$$\phi = \bar{\sigma}_n - r \le 0 \quad \text{(damage criterion)} \tag{27}$$

$$r = max[\bar{\sigma}_n] \quad \text{(evolution law of the internal variable)} \tag{28}$$

$$d = 1 - \frac{f_t}{r} e^{\frac{f_t^2}{EG_f} h\left(1 - \frac{r}{f_t}\right)} \quad \text{(evolution of the damage variable)} \tag{29}$$

where $\mathbf{C}$ is fourth order elastic tensor, f_t is the material tensile strength, E is the Young's modulus and G_f is the fracture energy of the material, $d \in [0, 1]$ is the scalar damage variable and r is the strain-like internal variable.

As crack propagations usually induce numerical instability, since multiple cracks could simultaneously be formed in the nonlinear zone of the material. To circumvent this problem and improve the performance and robustness of the constitutive tensile damage model, the implicit-explicit (IMPL-EX) integration scheme is adopted (Oliver et al. 2008, Prazeres et al. 2015).

4 FINAL EXAMPLE: DIRECT TENSION TESTS

A series of experimental direct tension tests carried out by (Baez 2014) on notched specimens with steel fiber volume fractions of 0.5, 1.0 and 1.5% are numerically analyzed. For all the analyses per-

formed, the fiber-matrix interaction is described by the relation depicted in Figure 13 and given by the following equations:

$$\tau(s) = \begin{cases} \tau_{max}\left(\dfrac{s}{s_1}\right)^{\alpha} & \text{if} \quad s \le s_1 \\ \tau_{max} - \dfrac{(\tau_{max} - \tau_f)(s - s_1)}{s_2 - s_1} & \text{if} \quad s_1 \le s \le s_2 \\ \tau_f & \text{if} \quad s > s_2 \end{cases}. \tag{30}$$

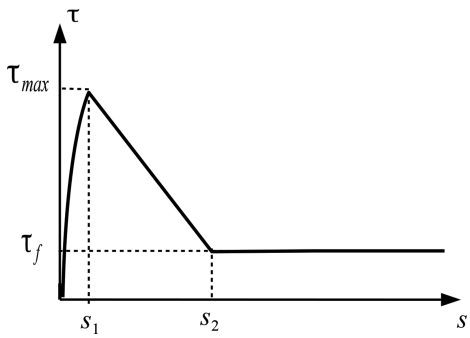

Figure 13. Bond-slip relation adopted to described the fiber-matrix interaction.

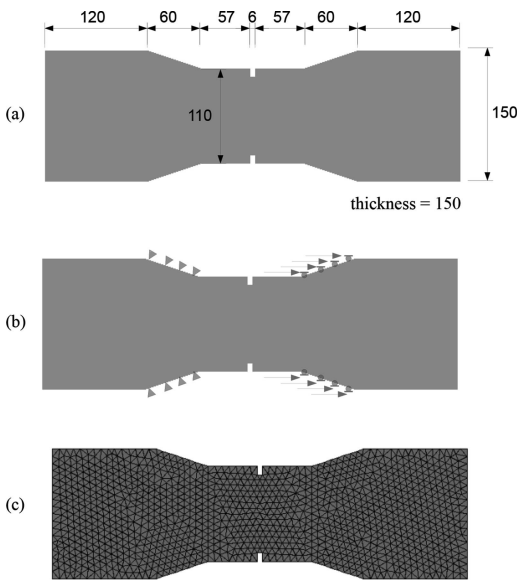

Figure 14. 2D numerical model: (a) geometrical properties (dimensions in mm), (b) boundary conditions and loading, and (c) finite element mesh of the concrete sample.

Figure 14 shows the geometrical properties, boundary conditions, and FE mesh employed for the 2D numerical analyses performed. The analyses were carried out considering plane stress conditions with an out-of-plane thickness of 150 mm. An incremental horizontal displacement of $\delta = 3.3$ mm on the right side of the specimen was imposed, as illustrated in Figure 14(b).

The hooked steel fibers used in the experimental tests were the Dramix ® RL 45/50 BN with length of $l_f = 50.0$ mm and diameter of $d_f = 1.05$ mm. The steel fibers were discretized using two-node (one-dimensional) truss finite elements. For each fiber 5 finite elements were used. An elastic perfectly plastic constitutive model, with Young's modulus of $E_s = 200$ GPa and yield stress of $\sigma_y = 520$ MPa was used to describe their behavior. The distribution of the fibers for the three cases are depicted in Figure 15. As can be noted in this figure, only the fibers bridging the cracks were considered in the analyses. Therefore, a total of 300, 600 and 900 fibers were employed in the models with steel fiber volume fractions of 0.5, 1.0 and 1.5%, respectively. A previous study of this example demonstrated that the fibers outside the fracture plane have almost no influence on final response. Thus, fibers outside the fracture plane were removed to avoid high computational costs.

The concrete bulk is discretized in 3,760 three-node triangular finite elements for all the cases.

The coupling between the independent meshes of the concrete bulk and steel fibers are carried out by four-node triangular coupling finite elements

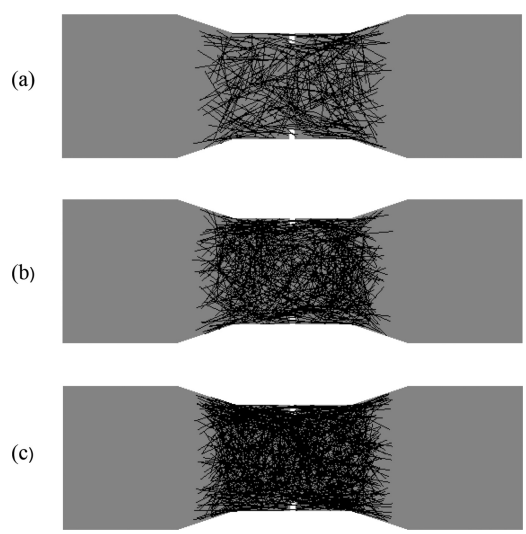

Figure 15. Fiber distribution in the direct tension test specimens for: (a) $V_f = 0.5\%$, (b) $V_f = 1.0\%$ and (c) $V_f = 1.5\%$.

with the non-rigid procedure outlined in ???. For this coupling procedure, the following parameters were adopted: $\tau_{max} = 6.5$ MPa, $\tau_f = 1.5$ MPa, $\alpha = 0.4$, $s_1 = 0.01$ mm, $s_2 = 7.0$ mm, $c_n = 10^3$ MPa/mm, and $c_s = 10^9$ N/mm.

For the tensile damage model employed to describe the behavior of the interface finite elements, the following parameters were used: Young's modulus $E = 18{,}101$ MPa; Poisson's ratio $\nu = 0.0$; fracture energy $G_f = 0.100$ N/mm and tensile strength $f_t = 1.72$ MPa. Since the failure is described exclusively by the interfaces, the concrete bulk is assumed linear elastic with Young's modulus of $E = 18{,}101$ MPa and Poisson's ratio of $\nu = 0.23$.

Figure 16 to Figure 18 illustrate the force × displacement curves obtained for the different fiber volume fractions using the mesh fragmentation technique. The results obtained are in good agreement with those obtained experimentally by (Baez 2014).

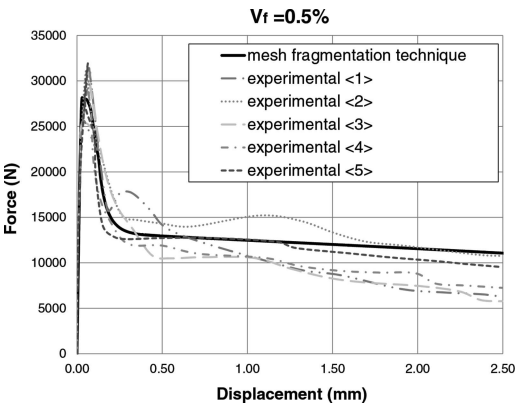

Figure 16. Force × displacement curves. Comparison between numerical and experimental responses for $V_f = 0.5\%$.

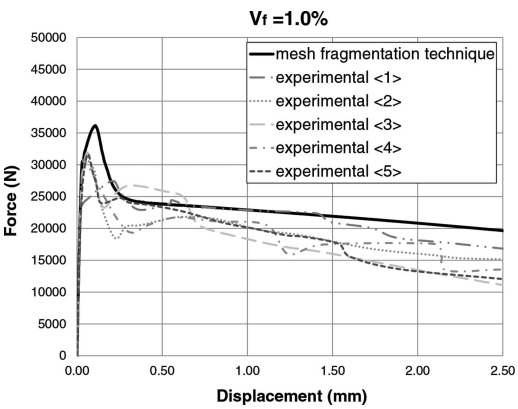

Figure 17. Force × displacement curves. Comparison between numerical and experimental responses for $V_f = 1.0\%$.

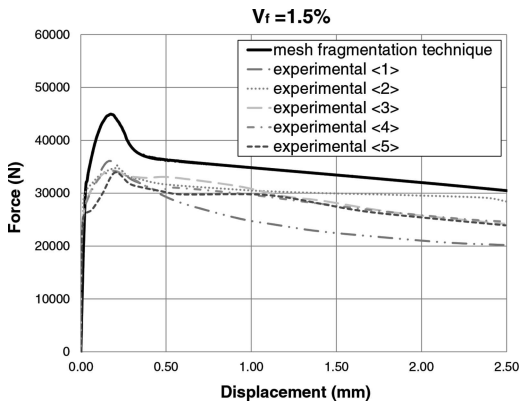

Figure 18. Force × displacement curves. Comparison between numerical and experimental responses for $V_f = 1.5\%$.

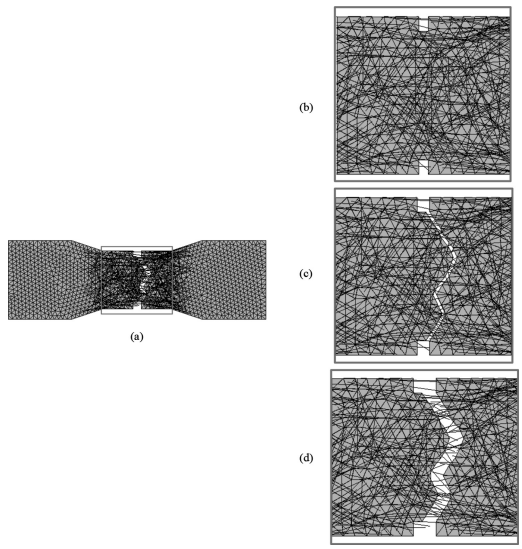

Figure 19. Failure pattern obtained using mesh fragmentation technique for $V_f = 0.5\%$: (a) deformed mesh at final load, and detail of the failure process for horizontal displacements (b) $\delta = 0.24$ mm, (c) $\delta = 0.9$ mm and (d) $\delta = 3.3$ mm (figures with scaling factor of 3).

The failure pattern for $V_f = 0.5\%$ in different load stages can be seen in Figure 19.

3D numerical analyses were also performed for the specimen with $V_f = 0.5\%$. Figure 20 shows the finite element mesh used for the concrete bulk and the distribution of fibers employed in the analyses. In addition, to evidence the effect of the fibers,

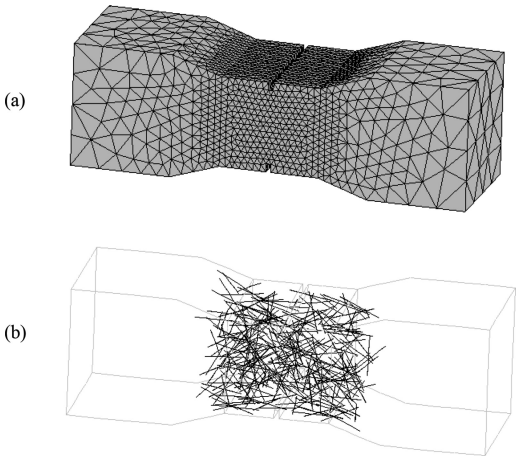

Figure 20. 3D finite element mesh of the direct tension test: (a) concrete phase and (b) fiber phase for $V_f = 0.5\%$.

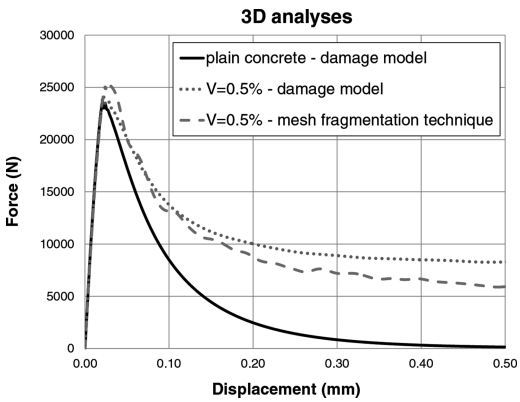

Figure 21. 3D numerical analyses of plain concrete and steel fiber concrete with fiber volume fraction of $V_f = 0.5\%$.

the specimen of plain concrete was also simulated. The responses in terms of force × displacement curves are illustrated in Figure 21. The results for $V_f = 0.5\%$ are in good agreement and the effect of the fibers becomes clear in the post-peak regime.

The failure patterns obtained for the case with $V_f = 0.5\%$ are depicted in Figure 22.

5 CONCLUDING REMARKS

A numerical model for modeling the behavior of SFRC has been proposed. The advantage of the use of a model with a discrete treatment of fibers is that the fiber's effect on the composite behavior

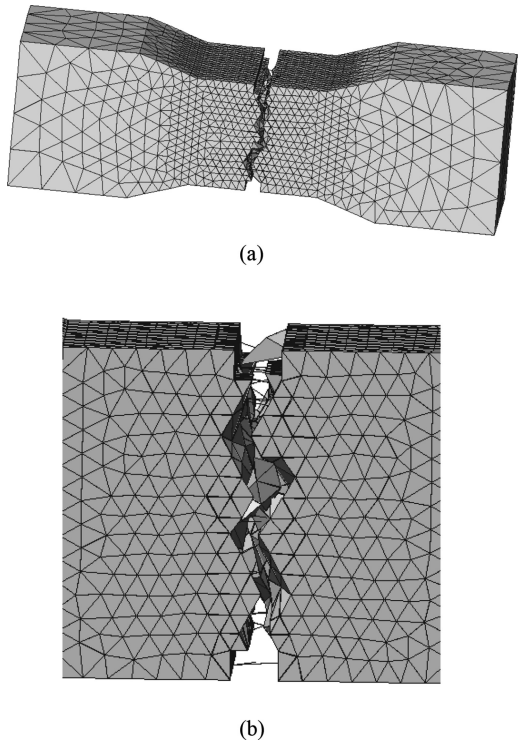

Figure 22. Failure pattern obtained using mesh fragmentation technique for $V_f = 0.5\%$: (a) specimen tested and (b) detail of the failure (with a scaling factor of 25).

can be modeled separately. Thus, the material has been modeled as a composite made up by three phases: concrete, discrete discontinuous steel fibers and steel fiber-matrix interface. To obtain this model, coupling finite elements recently developed by the authors have been used.

The first three examples have been performed to show the characteristics of important components of the model, such as, coupling non-matching meshes, fiber-concrete interface and mesh fragmentation technique. Then, all these ingredientes were used to simulate the fracture process in SFRC (with steel fiber volume fractions of 0.5, 1.0 and 1.5%) elements under tension. In general, the load × deflection curves show that the numerical strategy is able to capture the effect of steel fibers on the behavior of the composite. Moreover, for all the cases the mesh fragmentation technique was able to capture the crack propgation process in SFRC.

ACKNOWLEDGMENTS

The authors wish to acknowledge the financial support of the National Council for Scientific

and Technological Development (CNPq), Coordination for the Improvement of Higher Education Personnel (CAPES) and Sao Paulo Research Foundation (FAPESP).

REFERENCES

Baez, F.A.L. (2014). *Modelo numerico del comportamiento inelastico del concreto reforzado con fibras cortas de acero*. Ph. D. thesis, Universidad Nacional de Colombia.

Bentur, A. & S. Mindess (2007). *Fibre Reinforced Cementitious Composites*. Modern Concrete Technology Series.

Bitencourt Jr., L.A.G., O.L. Manzoli, P.G.C. Prazeres, E.A. Rodrigues, & T.N. Bittencourt (2015). A coupling technique for non-matching finite element meshes. *Computer Methods in Applied Mechanics and Engineering 290*, 19–44.

Cunha, V., J. Barros, & J. Sena-Cruz (2011). An integrated approach for modelling the tensile behaviour of steel fibre reinforced self-compacting concrete. *Cement and Concrete Research 41*(1), 64–76.

Cunha, V., J. Barros, & J. Sena-Cruz (2012). A finite element model with discrete embedded elements for fibre reinforced composites. *Computers & Structures 94–95*(0), 22–33.

Etse, G., A. Caggiano, & S. Vrech (2012). Multiscale failure analysis of fiber reinforced concrete based on a discrete crack model. *International Journal of Fracture 178*(1–2), 131–146.

Lee, S.-C., J.-Y. Cho, & F. Vecchio (2011). Diverse embedment model for steel fiber-reinforced concrete in tension: Model development. *ACI Materials Journal 108*(5), 516–525.

Manzoli, O., A. Gamino, E. Rodrigues, & G. Claro (2012). Modeling of interfaces in two-dimensional problems using solid finite elements with high aspect ratio. *Computers and Structures 94–95*(0), 70–82.

Manzoli, O.L., M.A. Maedo, L.A. Bitencourt, & E.A. Rodrigues (2016). On the use of finite elements with a high aspect ratio for modeling cracks in quasi-brittle materials. *Engineering Fracture Mechanics 153*, 151–170.

Oliver, J. (2000). On the discrete constitutive models induced by strong discontinuity kinematics and continuum constitutive equations. *International Journal of Solids and Structures 37*(48–50), 7207–7229.

Oliver, J., M. Cervera, & O.L. Manzoli (1999). Strong discontinuities and continuum plasticity models: the strong discontinuity approach. *Int. J. of Plasticity 15*(3), 319–351.

Oliver, J., A. Huespe, & J. Cante (2008). An implicit/explicit integration scheme to increase computability of non-linear material and contact/friction problems. *Computer Methods in Applied Mechanics and Engineering 197*(21–24), 1865–1889.

Oliver, J., A. Huespe, M. Pulido, & E. Chaves (2002). From continuum mechanics to fracture mechanics: the strong discontinuity approach. *Engineering Fracture Mechanics 69*(2), 113–136.

Oliver, J. & A.E. Huespe (2004). Continuum approach to material failure in strong discontinuity settings. *Computer Methods in Applied Mechanics and Engineering 193*(30–32), 3195–3220.

Prazeres, P.G.C., L.A.G. Bitencourt Jr., T.N. Bittencourt, & O.L. Manzoli (2015). A modified implicit-explicit integration scheme: an application to elastoplasticity problems. *Journal of the Brazilian Society of Mechanical Sciences and Engineering*, 1–11.

Pros, A., P. Diez, & C. Molins (2012). Modeling steel fiber reinforced concrete: numerical immersed boundary approach and a phenomenological mesomodel for concrete-fiber interaction. *International Journal for Numerical Methods in Engineering 90*(1), 65–86.

Radtke, F., A. Simone, & L. Sluys (2010). A computational model for failure analysis of fibre reinforced concrete with discrete treatment of fibres. *Engineering Fracture Mechanics 77*(4), 597–620.

Trusdell, C. & R. Toupin (1960). *The classical field theories. Handbuch der Physik*. Springer Verlag.

Computational Modelling of Concrete Structures – Meschke, Pichler & Rots (Eds)
© 2018 Taylor & Francis Group, London, ISBN 978-1-138-74117-1

Nonlinear finite element analysis of steel fiber-reinforced concrete coupling beams

S.-W. Kim, H.-D. Yun, S.-J. Jang, W.-S. Park & Y.-I. Jang
Chungnam National University, Daejeon, South Korea

C.-S. Choi
Hanyang University, Seoul, South Korea

ABSTRACT: This paper describes a nonlinear finite element analysis of steel Fiber-Reinforced Concrete (FRC) coupling beams. In this study, to reduce and simplify the reinforcement details in the coupling beams, Steel Fiber-Reinforced Concretes (SFRCs) were used. The analysis procedure was performed to assess the validity of modeling techniques for simulating the cyclic behavior of the FRC coupling beams. The coupling beam specimens were modeled using nonlinear, two-dimensional plane stress analysis with DIANA. In constitutive model, Thorenfeldt model in compression and Hordijk model in tension were used for concrete model, and the SFRC was modeled with Fiber-Reinforced Concrete model. A cyclic analysis was performed on the specimens to determine whether the curves could be produced and to verify whether the correct failure modes and sequence of damage was seen in the simulation. The analytical results showed that improvements in the finite element model could lead to improvements in the simulation results.

1 INTRODUCTION

As an effective structural element for multistory buildings, structural walls have been used. Because of existence of openings, two structural walls are interconnected by short and deep beams called coupling beams. Therefore the coupling beam is very important structural element representing a reliable earthquake-resistant system.

In recent, high-strength concrete (HSC) is widely applied in the construction industry due to engineering characteristics and economic advantages. By using HSC to a high-rise building, unacceptable oversized columns on the lower floors could be avoided. In addition to the column size, HSC could allow large column spacing and usable floor space (Swamy 1987). However, HSC generally shows marked brittleness with low tensile strength and strain capacities.

To overcome the shortage of HSC, steel fiber-reinforced concrete (SFRC) can be proposed as an alternative to concrete in coupling beams between shear walls.

The use of SFRC has been proposed in order to reduce the level of reinforcing required while maintaining or even improving strength, ductility and energy dissipation, in addition to improving damage tolerance (Balaguru *et al.* 1992, Batson 1976, Kwak *et al.* 2002, Otter & Naaman 1988, Song & Hwang 2004). In this study, a large-scale experimental investigation was conducted in which concrete and SFRC coupling beams with various reinforcing details were subjected to quasi-static, cyclic lateral loading to failure.

The purpose of this study is to assess the validity of modeling techniques for simulating the cyclic behavior of these SFRCC coupling beams. Presented in this paper are results from nonlinear finite element analyses performed on the coupling beam specimens containing diagonal reinforcing.

2 TEST SPECIMEN AND ANALYTICAL MODEL OF COUPLING BEAM

2.1 *Coupling beam test specimens*

To evaluate behavior of RC coupling beams with steel fiber, structural tests were conducted with vari-able fiber volume fractions and steel reinforcement details. The coupling beams had an aspect ratio of 2.0, meaning that the behavior was shear dominated rather than flexural. The specimens had a cross section of 200 mm by 300 mm and a height of 600 mm. The primary reinforcing consisted of diagonal D10 bars with accompanying confining reinforcement.

Full reinforcing details, including longitudinal and transverse reinforcing, can be seen in Figure 1. SC80 specimen is a diagonally reinforced concrete coupling beam with crossties in the beam section.

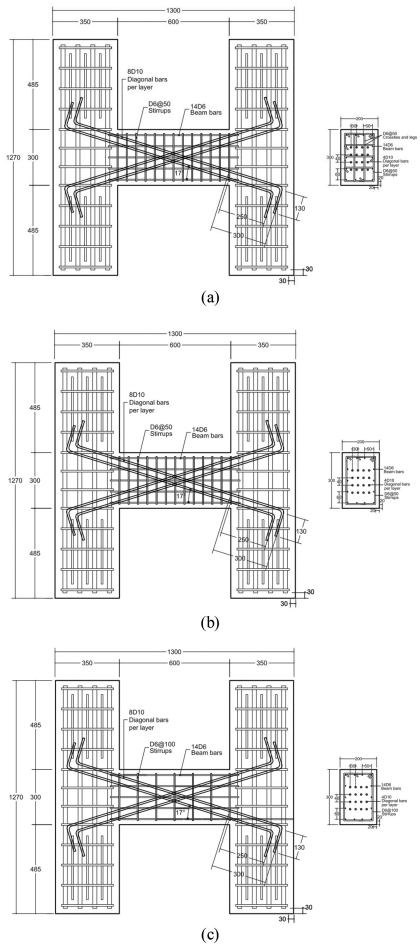

Figure 1. Coupling beam test specimens. (a) SC80 specimen; (b) SC80f-1.0 specimen; (c) SC80f-1.25 specimen.

Table 1. Details of test specimens.

Specimen	Fiber volume fraction (%)	Shear reinforcement	
		Stirrup	Crosstie
SC80	–	D6@50	D6@50
SC80f-1.0	1.00	D6@50	–
SC80f-1.25	1.25	D6@100	–

For SC80f-1.0 specimen, steel fiber-reinforced concrete ($V_f = 1.0\%$) was used and crossties and legs in the beam section was eliminated. For SC80f-1.25 specimen ($V_f = 1.25\%$), the amount of stirrup in the beam section was reduced compared to the other specimens. The details of the coupling beam specimens are listed in Table 1.

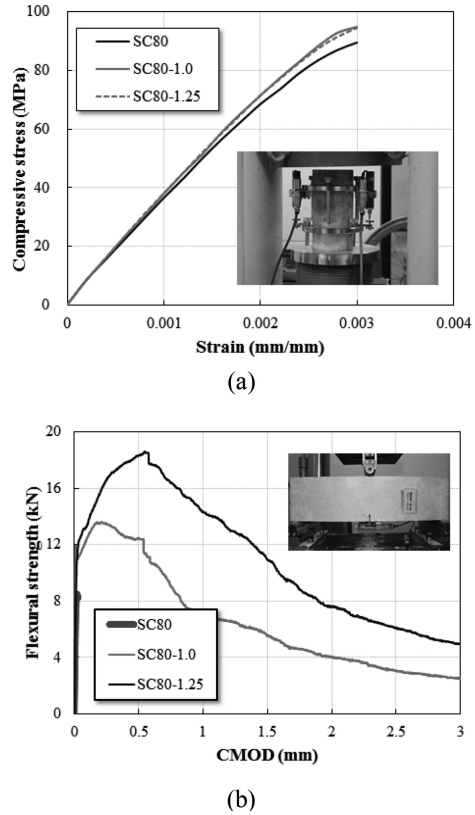

Figure 2. Plot of mechanical properties of concrete and FRC. (a) compressive test results; (b) bending test results.

The concrete and FRC had a specified compressive strength of 80 MPa. The concrete and FRC were high strength concretes and had unconfined compressive strengths of 85–93 MPa. Compressive and bending stress-strain plot for the concrete and FRC can be seen in Figure 2.

2.2 *Finite element model of coupling beam*

For efficiency of analysis, the coupling beam specimens were modeled using nonlinear, two-dimensional plane stress analysis with the commercial finite element code Diana (Version 10.1).

Figure 3 shows material models used for coupling beam in this study. The coupling beam segment was modeled with nonlinear constitutive models for both the concrete and the FRC as well as the steel reinforcing. For compression, Thorenfeldt model was used to consider descending curve after peak stress. For tension, Hordijk and Fiber-Reinforced Concrete models of Total strain based crack model in DIANA software were respectively used for concrete and FRC.

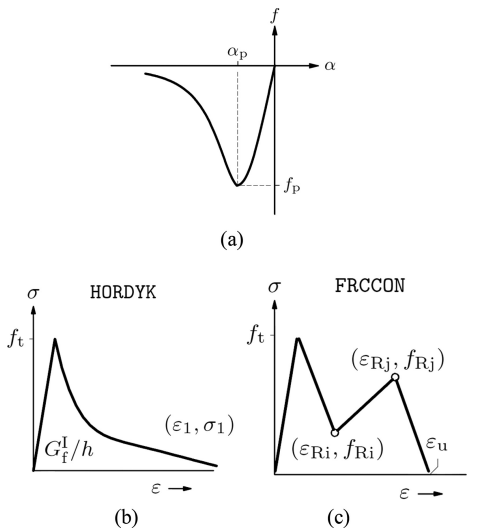

Figure 3. Material modes used for coupling beam. (a) Thorenfeldt model for compression; (b) Hordijk model for tension of concrete; (c) Fiber reinforced model for tension of SFC.

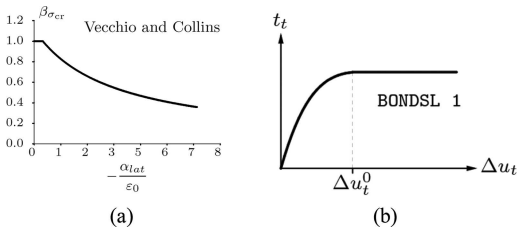

Figure 4. Reduction and bond model used. (a) Vecchio and Collins model; (b) Doerr bond-slip model.

Plane stress analysis is applicable for these specimens due to fact that out-of-plane stress are minimal. Nonlinear behavior is incorporated through material nonlinearity; geometric nonlinear behavior is not considered as its effect are negligible. The concrete was modeled using 8-noded quadrilateral, isoparametric plane stress elements with a 2×2 Gauss integration scheme. Out-of-plane thickness were defined accordingly for the coupling beam and wall segments.

The model for the steel reinforcing was based on the Su & Zhu (1994) model which incorporates the Bauschinger effect for cyclic loading and was calibrated and implemented in Diana by Kwan & Billington (2001). The steel reinforcing bars were modeled with 2-noded, embedded reinforcing elements. Embedded reinforcing elements are assumed to have perfect bond with the mother plane stress elements. To describe the relationship for reduction due to lateral cracking, Vecchio and Collins model [Figure 4(a)] was used. To describe bond behavior between steel and concrete Doerr model [Figure 4(b)] was used.

3 EXPERIMENTAL PLAN AND ANALYSIS METHOD

3.1 *Experimental plan*

During testing, specimens were rotated 90 degrees and both of the wall segments were bolted to the hinged loading frame. The specimens were subjected to quasi-static loading through applied displacement cycles with a 1000 kN-capacity hydraulic actuator. The actuator was connected to the steel loading frame that was bolted to the top and bottom wall segments. A photograph of the testing setup can be seen in Figure 5.

3.2 *Analysis method*

Figure 6 shows a finite element mesh. All nodes along the bottom edge of the model were constrained in the X and Y directions to represent the base fixity of the specimen. To model the effect of the connection detail between the steel loading frame and the top segment wall supports,

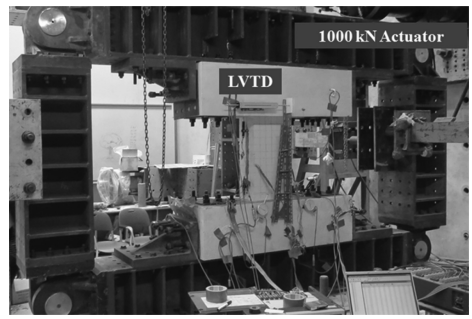

Figure 5. Test setup for coupling beam specimen.

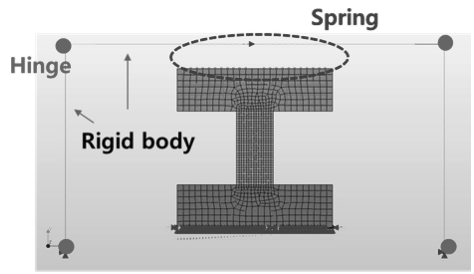

Figure 6. Finite element mesh for coupling beam specimen.

two-noded spring element were used, which provided stiffness in the vertical direction while providing none in the horizontal direction.

To represent the true behavior of the roller supports, a nonlinear elastic spring stiffness was used, in which a stiffness equivalent to the axial stiffness of the threaded rods was assigned in compression, and an essentially zero stiffness was assigned in tension.

The zero stiffness in tension was meant to correspond to the fact that the test setup did not prevent the specimen from losing contact with the roller during testing.

4 EXPERIMENTAL AND ANALYSIS RESULTS

A cyclic analysis was performed on coupling beam specimens to determine whether the load-displacement curves could be produced and to verify whether the correct failure modes and sequence of damage was seen in the simulation. The experimental and analytical load-chord rotation results for the cyclic analyses are shown in Figure 7.

For the coupling beam specimens, the load-chord rotation behavior of the simulation matches the experimental data well. The degradation of strength and stiffness with increasing cycles is captured well.

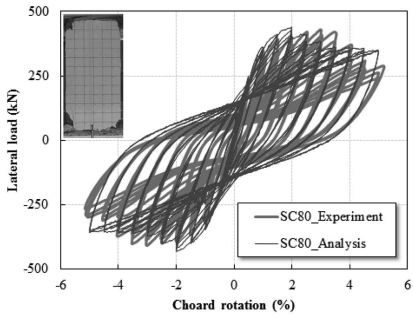

(a)

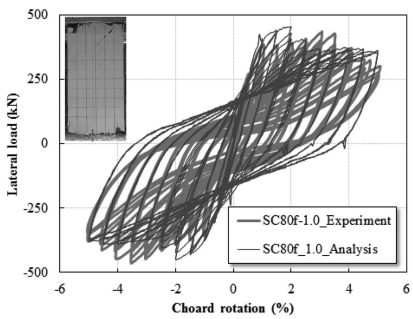

(b)

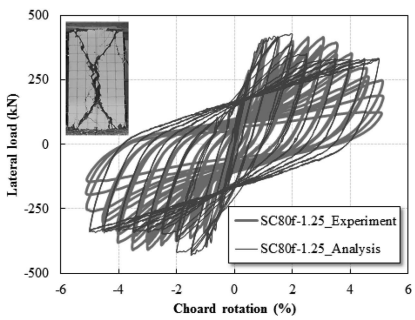

(c)

Figure 7. Experimental load-chord rotation response and analysis results from simulation. (a) SC80; (b) SC80f-1.0; (c) SC80f-1.25.

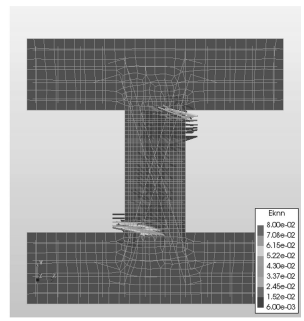

(a)

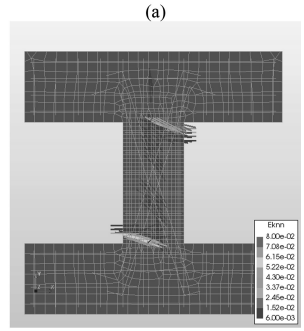

(b)

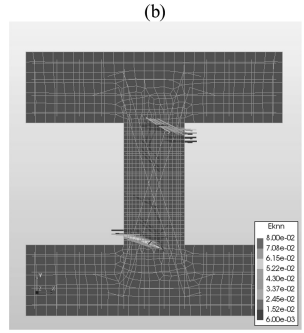

(c)

Figure 8. Contour plot of cracking. (a) SC80; (b) SC80f-1.0; (c) SC80f-1.25.

Figure 8 shows a photograph and results from the simulation of the coupling beam specimens at final failure. The localization of cracking can be easily seen in the lower left hand corner of the specimen, with other distributed cracking occurring throughout the remainder of the specimen. In the simulation, the peak strength is reached as the compressive strength of the SFRC is reached and a flexural plastic hinge forms at the bottom of the specimen. The contour plots of cracking show that relatively larger widths of crack are concentrated in the lower left hand corner and have localized there.

5 CONCLUSIONS

A total strain-based rotating crack model developed specifically for SFRC materials was used to simulate the cyclic behavior of coupling beams for shear walls. The simulation method is shown to adequately capture the load-chord rotation behavior of the specimens, as well as the progression and location of damage in the specimens.

Experimental results showed that for shear controlled coupling beams, SFRC materials can lead to large increases in strength before shear failure occurs. In addition to strength increase, reinforcement details confining concrete and preventing buckling of primary reinforcement through use of SFRC materials.

The SFRC material has the ability to change the failure mode from shear to flexural. Further improvements in the finite element model, such as incorporation of bond-slip effects, more detailed modeling of the support conditions, and improvement in the SFRC constitutive model (such as changing the compression failure envelope from bilinear to trilinear or even polynomial) could lead to improvements in the simulation results.

Further parameter studies could lead to proposed modifications of reinforcing and other specimen details in order to optimize performance.

ACKNOWLEDGEMENT

This research was supported by Basic Science Research Program through the National Research Foundation of Korea (NRF) funded by the Ministry of Education (NRF-2016R1D1A3B02008179) and by the Ministry of Science, ICT & Future Planning (NRF-2015R1C1A1A02036481).

REFERENCES

Balaguru, P., Narahari, R., & Patel, M. 1992. Flexural toughness of steel fiber reinforced concrete. *Materials Journal* 89(6): 541–546.

Batson, G. 1976. Steel fiber reinforced concrete. *Materials Science and Engineering* 25: 53–58.

Kwak, Y.K., Eberhard, M.O., Kim, W.S., & Kim, J. 2002. Shear strength of steel fiber-reinforced concrete beams without stirrups. *ACI Structural Journal* 99(4): 530–538.

Kwan, W.P. & Billington, S.L. 2001. Simulation of Structural Concrete Under Cyclic Load. *Journal of Structural Engineering* 127(12): 1391–1401.

Otter, D.E., & Naaman, A.E. 1988. Properties of steel fiber reinforced concrete under cyclic load. *Materials Journal* 85(4): 254–261.

Song, P.S. & Hwang, S. 2004. Mechanical properties of high-strength steel fiber-reinforced concrete. *Construction and Building Materials* 18(9): 669–673.

Su, X. & Zhu, B. 1994. Algorithm for hysteresis analysis of prestressed-concrete frames. *Journal of Structural Engineering* 120(6): 1732–1744.

Swamy, R.N. 1987. *High-strength concrete-material properties and structural behaviors*. ACI SP-87. Detroit: American Concrete Institute.



Taylor & Francis
Taylor & Francis Group
http://taylorandfrancis.com

Computational Modelling of Concrete Structures – Meschke, Pichler & Rots (Eds)
© 2018 Taylor & Francis Group, London, ISBN 978-1-138-74117-1

Micromechanics based modelling of fibre reinforced cementitious composites

I.C. Mihai & A.D. Jefferson
Cardiff University, Cardiff, UK

P. Lyons
LUSAS, Kingston Upon Thames, UK

ABSTRACT: A constitutive model for fibre reinforced cementitious composites based on micromechanical solutions is presented. The model employs a two-phase composite based on the Eshel by matrix-inclusion solution and the Mori-Tanaka homogenization scheme and also simulates directional microcracking. An exterior point Eshelby based criterion is employed to model crack-initiation in the matrix-inclusion interface. Microcrack surfaces are assumed to be rough and able to regain contact under both normal and shear displacements. Once cracks start to develop, the crack-bridging action of fibres is simulated using a local constitutive equation that accounts for the debonding and pull-out of fibre groups with different orientations. It is shown that the combination of the rough microcrack and fibre-bridging sub-models allows microcracking behaviour deriving from both tensile and compressive loads to be modelled in a unified manner. Numerical results obtained with the proposed micromechanical constitutive model are compared with experimental data. Good correlation between numerical and experimental responses demonstrates the potential of the model to capture key characteristics of the mechanical behaviour of fibre reinforced cementitious composites.

1 INTRODUCTION

Fibres have been added to cementitious materials since ancient times but their use has expanded greatly over past half century (Naaman 2008). They endow brittle cement-bound materials with enhanced tensile strength, and their inclusion in cementitious matrices can delay the onset of macrocracking and enhance both ductility and durability (Naaman 2008).

The behaviour of cementitious composites reinforced with randomly distributed and oriented discontinuous fibres is largely governed by fibre pull-out. This may or may not be accompanied by fibre rupture, depending on the fibre geometry and fibre-cement matrix interface properties. When a crack opens, the fibres crossing the crack plane begin to debond and are subsequently pulled out (i.e. the fibres slide relative to the concrete matrix). In this process, they can be considered to apply closure tractions to the crack faces thus stabilising the crack growth. Via these crack-bridging mechanisms, the fibres continue to transfer stresses between the two crack faces until their complete pull-out.

Constitutive models for fibre reinforced concrete (FRC)—and in general modelling for cement based composites—can be classified in two main categories: macroscopic models that follow a phenomenological approach and models based on micromechanical solutions. Phenomenological models generally employ theories based on plasticity and/or damage mechanics in order to simulate the macroscopic behaviour and their formulation often makes use of functions obtained by fitting experimental data. By contrast, micromechanical models aim to relate the microstructure of concrete, and the physical mechanisms that govern its evolution, to the macroscopic behaviour observed in experiments.

The present model builds on a series of micromechanical constitutive models for plain concrete proposed by Jefferson & Bennett (2007, 2010) and Mihai & Jefferson (2011) which are extended to capture the mechanical behaviour of fibre reinforced concrete (Mihai & Jefferson, 2017).

The micromechanical constitutive model for FRC which employs Budiansky & O'Connell's (1976) solution for an elastic solid containing penny-shaped microcracks, the Eshelby matrix-inclusion solution and which features a microcrack initiation criterion based on the exterior point Eshelby solution as well as a rough crack contact component that accounts for the recovery of stiffness when

microcrack surfaces regain contact. The influence of fibres after cracks are initiated is addressed in a crack-plane constitutive relationship making use of the crack-bridging stress of Lin & Li (1997). The model components are presented in Section 2. Results from single-point and finite element simulations employing the proposed constitutive model for fibre reinforced concrete, compared against experimental data, are presented in Section 3.

2 MICROMECHANICS BASED CONSTITUTIVE MODEL FOR FIBRE REINFORCED CONCERTE

2.1 *Model concepts*

A full account of the constitutive model for fibre reinforced concrete is presented in Mihai & Jefferson (2017), however the main assumptions and key equations of the model are provided below. The general concepts of the model are presented in Figure 1. The concrete matrix of the fibre reinforced material is modelled as a two-phase solid material that comprises series of penny-shaped microcracks which can have various orientations, defined by ψ and θ (Figure 1b). It is assumed that the effect of each series of cracks with the same orientation is equivalent to that of a thin band of material containing these cumulated microcracks (Figure 1c) and, as damage progresses, they can coalesce and form macro-cracks. The mid-plane of the thin band is referred to as a 'crack-plane'. Moreover, in each direction, the corresponding crack-plane is crossed by randomly distributed and oriented short fibres. The model also assumes that cracks have rough surfaces that can regain contact.

2.2 *Two-phase composite*

The elastic constitutive relationship for the two-phase composite is obtained by making use of the micromechanics Eshelby matrix-inclusion solution and the Mori-Tanaka homogenisation scheme (Mura, 1987) for a non-dilute distribution of inclusions:

$$\bar{\boldsymbol{\sigma}} = \mathbf{D}_{m\Omega} : \bar{\boldsymbol{\varepsilon}} \tag{1}$$

where $\bar{\boldsymbol{\sigma}}$ and $\bar{\boldsymbol{\varepsilon}}$ are the average far-field stress and strain respectively. $\mathbf{D}_{m\Omega}$ is the elasticity tensor of the composite:

$$\mathbf{D}_{m\Omega} = \left(f_m \mathbf{D}_m + f_\Omega \mathbf{D}_\Omega \cdot \mathbf{T}_\Omega\right) \cdot \left(f_m \mathbf{I}^{4s} + f_\Omega \mathbf{T}_\Omega\right)^{-1} \tag{2}$$

in which $\mathbf{D}_\beta$ represents the elasticity tensor and f_β the volume fraction of β-phase (β = m or Ω), $f_m + f_\Omega = 1$. $\mathbf{I}^{4s}$ is the fourth order identity tensor and

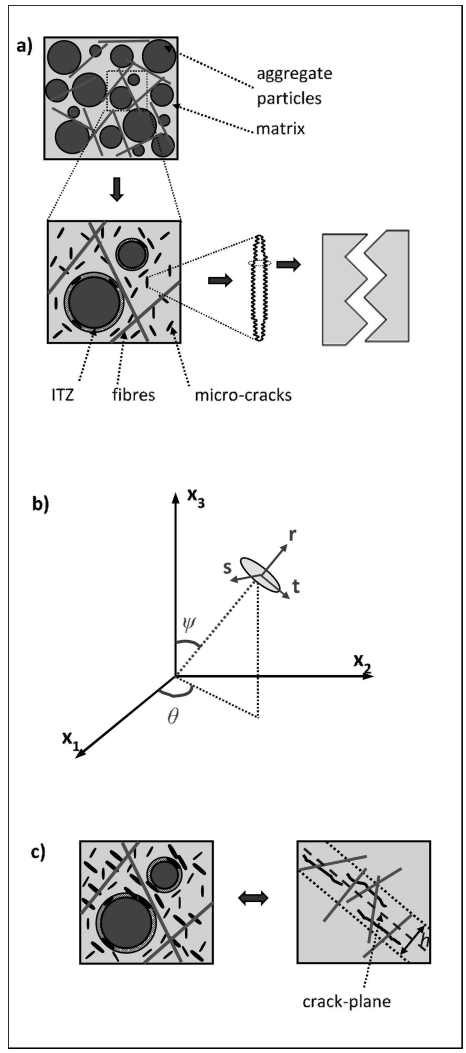

Figure 1. a) Model concepts. b) Local coordinate system. c) Schematic representation of the crack-plane.

$$\mathbf{T}_\Omega = \mathbf{I}^{4s} + \mathbf{S}_\Omega \cdot \left[\left(\mathbf{D}_\Omega - \mathbf{D}_m\right) \cdot \mathbf{S}_\Omega + \mathbf{D}_m\right]^{-1} \cdot \left(\mathbf{D}_m - \mathbf{D}_\Omega\right) \tag{3}$$

$\mathbf{S}_\Omega$ is the Eshelby tensor for spherical inclusions (Nemat-Nasser & Hori, 1993).

2.3 *Directional microcracking*

A solution based on the work of Budiansky & O'Connell (1976) is employed to address microcracking by evaluating the added strain $\boldsymbol{\varepsilon}_a$ from series of penny-shaped microcracks of various orientations distributed according to a crack

density function f(θ, ψ). The added strains resulting from the microcracks are superimposed on the composite such that the constitutive Equation 1 becomes:

$$\bar{\boldsymbol{\sigma}} = \mathbf{D}_{m\Omega} : (\bar{\boldsymbol{\varepsilon}} - \boldsymbol{\varepsilon}_a) \tag{4}$$

The added strain are as follows (Budiansky & O'Connell, 1976):

$$\boldsymbol{\varepsilon}_{\mathrm{a}} = \left(\frac{1}{2\pi} \int_{2\pi} \int_{\pi/2} \mathbf{N}_{\varepsilon} : \mathbf{C}_a : \mathbf{N} f(\theta,\psi) \, \sin(\psi) \mathrm{d}\psi \mathrm{d}\theta \right) : \bar{\boldsymbol{\sigma}} \tag{5}$$

in which $\mathbf{C}_a$ is the local compliance tensor in the local coordinate system of a microcrack (**r**, **s**, **t**) and **N** the stress transformation tensor. The crack density parameter is related to a directional damage parameter $\omega\,(0 \le \omega \le 1)$ such that:

$$f(\theta,\psi)\boldsymbol{C}_a = \frac{\omega(\theta,\psi)}{1-\omega(\theta,\psi)} \boldsymbol{C}_L = \boldsymbol{C}_{\alpha}(\theta,\psi) \tag{6}$$

where $\mathbf{C}_{\mathrm{L}} = \frac{1}{E_m} \begin{bmatrix} 1 & 0 & 0 \\ 0 & \frac{4}{2-\nu_m} & 0 \\ 0 & 0 & \frac{4}{2-\nu_m} \end{bmatrix}$ is the local elastic compliance tensor, with ν_m and E_m being Poisson's ratio and Young's modulus of the matrix phase respectively. Introducing Equation 5 and Equation 6 into Equation 4 and rearranging gives:

$$\bar{\boldsymbol{\sigma}} = \left(\mathbf{I}^{4s} + \frac{\mathbf{D}_{\mathrm{m}\Omega}}{2\pi} \int_{2\pi} \int_{\frac{\pi}{2}} \mathbf{N}_{\varepsilon} : \mathbf{C}_{\alpha}(\theta,\psi) : \mathbf{N} \cdot \sin(\psi) \mathrm{d}\psi \mathrm{d}\theta \right)^{-1} \cdot \mathbf{D}_{\mathrm{m}\Omega} : \bar{\boldsymbol{\varepsilon}} \tag{7}$$

2.4 *Microcrack initiation criterion*

The crack initiation criterion proposed by Mihai & Jefferson (2011) is employed here; microcracking in each direction is assumed to initiate in a band of matrix material within the interfacial transition zone (ITZ), when the local principal stress in this band reaches the tensile strength of the interface (f_{ti}). The initial damage surface, F_s is given by:

$$F_s(\boldsymbol{\sigma}_L, f_{ti}) = \sigma_I(\boldsymbol{\sigma}_L) - f_{ti} = 0 \tag{8}$$

where $\boldsymbol{\sigma}_L$ is the local stress which is related to the average far-field stress as follows:

$$\boldsymbol{\sigma}_L(\psi,\theta) = \mathbf{N}(\psi,\theta) : \bar{\boldsymbol{\sigma}} \tag{9}$$

The local stresses in the thin band of matrix material in the ITZ are evaluated based on the exterior point Eshelby solution (Eshelby, 1959) which gives the expression of the total stress field outside an ellipsoidal inclusion embedded in an infinite elastic matrix (Ju & Sun, 1999). The Mori-Tanaka homogenization scheme is applied in order to account for the interaction between inclusions and the total stress field in the matrix outside an inclusion is obtained as:

$$\begin{aligned} \boldsymbol{\sigma}_{\mathrm{m}\Omega}(\mathbf{x}) = \mathbf{D}_{\mathrm{m}} \cdot \left[\mathbf{I}^{4s} + \mathbf{S}_{\mathrm{E}}(\mathbf{x}) \cdot \mathbf{B}_{\Omega} \right] \\ \cdot \left[f_{\Omega} \mathbf{T}_{\Omega} + f_m \mathbf{I}^{4s} \right]^{-1} : \left(\bar{\boldsymbol{\varepsilon}} - \boldsymbol{\varepsilon}_{\mathrm{a}} \right) \end{aligned} \tag{10}$$

in which $\mathbf{B}_{\Omega} = -\left[\mathbf{S}_{\Omega} + \left(\mathbf{D}_{\Omega} - \mathbf{D}_{\mathrm{m}} \right)^{-1} \cdot \mathbf{D}_{\mathrm{m}} \right]^{-1}$.

$\mathbf{S}_{\mathrm{E}}(\mathbf{x})$ is the exterior point Eshelby tensor for spherical inclusions, derived in a dimensionless form in Li et al. (2007) and **x** is the position vector relative to the centre of inclusion. A local damage function was subsequently derived from the local crack initiation criterion in Equation 8 and is given by:

$$F_{\zeta}(\boldsymbol{\varepsilon}_L, \zeta) = \left(\varepsilon_{Lrr} \frac{1+\alpha_L}{2} + \sqrt{\varepsilon_{Lrr}{}^2 \left(\frac{1-\alpha_L}{2} \right)^2 + r_L^2 \left(\varepsilon_{Lrs}^2 + \varepsilon_{Lrt}^2 \right)} \right) - \zeta \tag{11}$$

in which $\alpha_L = \frac{\nu_{\mathrm{m}}}{1-\nu_{\mathrm{m}}}$, $\mathrm{r}_L = \frac{\nu_{\mathrm{m}} - 1/2}{\nu_{\mathrm{m}} - 1}$, and noting that the following loading/unloading conditions apply:

$$F_{\zeta} \le 0; \quad \dot{\zeta} \ge 0; \quad F_{\zeta} \dot{\zeta} = 0 \tag{12}$$

2.5 *Rough crack contact*

A rough crack closure component is also implemented to simulate the recovery of stress on microcracks that regain contact. In each direction the local stress was written as a summation of the average stress on intact material and the recovered stress on debonded material that regains contact:

$$\mathbf{s}_{\alpha} = \mathbf{D}_{\mathrm{L}} \left[(1-\omega)\mathbf{I}^{2s} + \omega H_f(\boldsymbol{\varepsilon}_{\mathrm{L}}) \boldsymbol{\Phi}(m_g, \boldsymbol{\varepsilon}_{\mathrm{L}}) \right] : \boldsymbol{\varepsilon}_{\mathrm{L}} \tag{13}$$

H_f is a reduction function that decreases from 1 to 0 as the potential for shear transfer reduces with increasing crack opening. This is given by $H_f(\boldsymbol{\varepsilon}_{\mathrm{L}}) = e^{-c_1 \frac{\varepsilon_{Lrr} - \varepsilon_{lm}}{\eta \varepsilon_0}}$ with $\mathrm{c}_1 = 3$. Parameter β is the normalised asperity height, $\eta = \mathrm{h_t}/\mathrm{u_0}$, $\mathbf{D}_{\mathrm{L}} = \mathbf{C}_{\mathrm{L}}{}^{-1}$ and $\boldsymbol{\varepsilon}_{\mathrm{L}}$ is the local strain tensor.

$\boldsymbol{\Phi}(m_g, \boldsymbol{\varepsilon}_{\mathrm{L}})$ is a contact matrix that depends upon the contact state (see Figure 2) as follows:

$\boldsymbol{\Phi} = \mathbf{0}$ if crack surfaces are not in contact (open region)

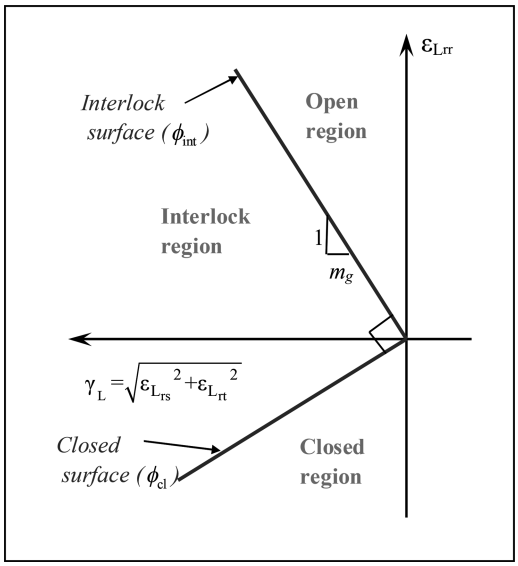

Figure 2. Contact model concepts.

$\mathbf{\Phi} = \mathbf{\Phi}_g$ if crack surfaces are in contact (interlock region)
$\mathbf{\Phi} = \mathbf{I}$ if are in fully closed region.

The expression of the contact matrix in the interlock region is:

$$\mathbf{\Phi}_g = \frac{1}{1+\mathrm{m}_g^2}\left(\left(\frac{\partial \phi_{\mathrm{int}}}{\partial \boldsymbol{\varepsilon}_L}\right)\left(\frac{\partial \phi_{\mathrm{int}}}{\partial \boldsymbol{\varepsilon}_L}\right)^T + \phi_{\mathrm{int}}\frac{\partial^2 \phi_{\mathrm{int}}}{\partial \boldsymbol{\varepsilon}_L^2}\right) \tag{14}$$

where:

$$\begin{aligned}\phi_{\mathrm{int}}(\boldsymbol{\varepsilon}_{\mathrm{L}}, m_g) &= m_g \varepsilon_{\mathrm{Lrr}} - \sqrt{\varepsilon_{\mathrm{Lrs}}{}^2 + \varepsilon_{\mathrm{Lrt}}{}^2} \\ \phi_{\mathrm{cl}}(\boldsymbol{\varepsilon}_{\mathrm{L}}, m_g) &= \varepsilon_{\mathrm{Lrr}} + m_g \sqrt{\varepsilon_{\mathrm{Lrs}}{}^2 + \varepsilon_{\mathrm{Lrt}}{}^2}\end{aligned} \tag{15}$$

m_g is the slope of the interlock contact surface and, in a physical sense, it represents the slope of the asperity, thus being a measure of the crack surface roughness.

2.6 *Crack bridging action of fibres. local constitutive relationship*

The influence of fibres is taken into account in the crack-plane stress-strain expression assuming that the fibre contribution develops after crack initiation. This is illustrated in Figure 3. In the case of fibre reinforced concrete Equation 13 becomes:

$$\begin{aligned}\mathbf{s}_{\alpha} = \big[&(1-\omega)\mathbf{D}_{\mathrm{L}} + \omega(1-\omega_f)\mathbf{D}_{\mathrm{fL}} \\ &+ \omega H_f(\boldsymbol{\varepsilon}_{\mathrm{L}})\mathbf{D}_{\mathrm{L}} \cdot \mathbf{\Phi}(m_g, \boldsymbol{\varepsilon}_{\mathrm{L}})\big] : \boldsymbol{\varepsilon}_{\mathrm{L}}\end{aligned} \tag{16}$$

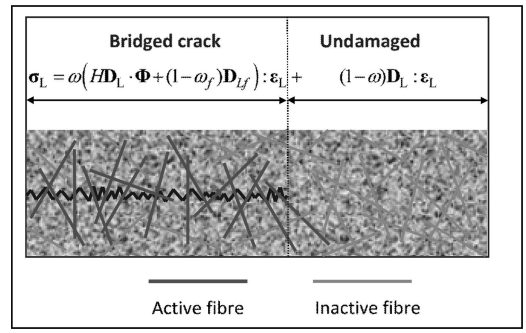

Figure 3. Crack-plane model with rough contact and fibre-bridging.

where ω_f is a fibre effective damage parameter that characterises the crack-bridging state of fibres and varies from 0, for a state before any fibre pull-out occurs, to 1, for a case in which all fibres are completely pulled out from the matrix. $\mathbf{D}_{\mathrm{Lf}} = E_{df} \cdot \mathbf{I}^{2s}$ is a local elastic stiffness given by the interface bond of the fibres crossing the crack-plane, before the start of pull-out, assuming a linear debonding behaviour.

The evolution of the fibre effective damage parameter ω_f is obtained from the following 1-D relation:

$$(1-\omega_{\mathrm{f}})E_{\mathrm{df}}\zeta_{\mathrm{f}} = \sigma_{\mathrm{cb}} \tag{17}$$

in which ζ_f is a resultant crack opening parameter that takes into account the normal and shear components of the crack-plane strain tensor and is governed by the effective fibre damage function given in Equation 18 and the loading/unloading conditions given in Equations 19:

$$F_{\zeta f}(\boldsymbol{\varepsilon}_L, \zeta_f) = \frac{1}{2}\left(\varepsilon_{Lrr} + \sqrt{\varepsilon_{Lrr}{}^2 + 4\left(\varepsilon_{Lrs}{}^2 + \varepsilon_{Lrt}{}^2\right)}\right) - \zeta_f \tag{18}$$

$$\mathrm{F}_{\zeta f} \le 0; \quad \dot{\zeta}_f \ge 0; \quad F_{\zeta f}\dot{\zeta}_f = 0 \tag{19}$$

σ_{cb} in Equation 17 is the crack bridging stress that is transferred between two opposing faces of a fully formed crack subjected to normal opening displacements, through the pull-out action of the fibres that cross the crack. The crack-bridging model of Lin & Li (1997) is employed in which a crack-bridging stress-crack opening relationship was obtained by averaging the contributions from all fibres that cross the crack-plane during the debonding and the pull-out phases respectively:

$$\sigma_{\mathrm{B}}(\delta) = \frac{4V_f}{\pi d_f^2}\int_{\varphi=0}^{\pi/2}\int_{z=0}^{(L_f/2)\cos\varphi} P(\delta)p(\varphi)p(z)\mathrm{d}z\mathrm{d}\varphi \tag{20}$$

in which V_f is the volume fraction of fibres, L_f and d_f are the length and diameter of the fibres respectively. $P(\delta)$ describes the debonding and pull-out force-displacement behaviour of a single fibre embedded in a concrete matrix, in a direction along the fibre axis. $p(\varphi)$ and $p(z)$ are probability density functions of the orientation angle φ and centriodal distance z respectively. The single fibre P-δ relation was derived assuming a linear slip-hardening interface constitutive relation between the fibre-matrix interface shear stress τ and the interface S:

$$\tau = \tau_0(1+\beta S/d_f) \tag{14}$$

in which τ_0 is the frictional sliding shear stress at the tip of the debonding zone before any slip takes place and β is a nondimensional hardening parameter. The two fibre-matrix interface parameters, τ_0 and β can be obtained from an experimental single fibre pull-out P-δ curve as detailed in Lin & Li (1997).

Incormporating the rough crack contact and the crack-bridging effect of fibres, the final stress-strain model is:

$$\bar{\boldsymbol{\sigma}} = \left(\mathbf{I}^{4s} + \frac{\mathbf{D}_{m\Omega}}{2\pi} \int_{2\pi}\int_{\frac{\pi}{2}} \mathbf{N}_{\varepsilon} : \mathbf{C}_{add}(\theta,\psi) : \mathbf{N} \cdot \sin(\psi) d\psi d\theta \right)^{-1} \cdot \mathbf{D}_{m\Omega} : \bar{\boldsymbol{\varepsilon}} \tag{21}$$

where:

$$\mathbf{C}_{add} = \left[\mathbf{C}_L^{-1} \left[(1-\omega)\mathbf{I}^{2s} + \omega \sum_i p_{ci} H_i \boldsymbol{\Phi}_i \right] + \omega(1-\omega_f)\mathbf{D}_{fl} \right]^{-1} - \mathbf{C}_L \tag{22}$$

and in which the contact component was expanded and written as a weighted summation to account for the variability of the crack roughness. p_{ci} is the proportion, or the probability of the occurrence, of a certain type of asperity. The integration over a hemisphere in Eq. (21) is evaluated numerically by employing McLaren integration rule with 29 sample directions.

3 NUMERICAL RESULTS

3.1 *Uniaxial tension*

Numerical results for a uniaxial tension strain path obtained with the proposed micromechanical model and using a single set of realistic material properties (Table 1) are compared with experimental data of Li et al. (1998) and presented in Figure 4. The numerical simulations compare well with experimental results; the model is able to predict the increase of strength and ductility of the composite with the increase of the fibre dosage.

3.2 *Uniaxial compression*

Numerical results for a uniaxial compression strain path are next compared with experimental data of Cachim et al. (2002) and presented in Figure 5. The material properties employed for the numerical simulations are presented in Table 2. Numerical predictions lie between experimental bounds and

Table 1. Material properties (Uniaxial tension test).

L_f (mm)	d_f (mm)	τ_0 (MPa)	β	E_m (GPa)	E_Ω (GPa)	f_{ti} (MPa)
30	0.5	0.8	0.1	25	60	1.5

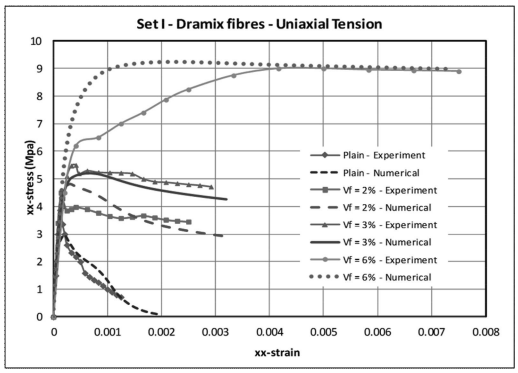

Figure 4. Numerical predictions of uniaxial tensile tests of Li et al. (1998).

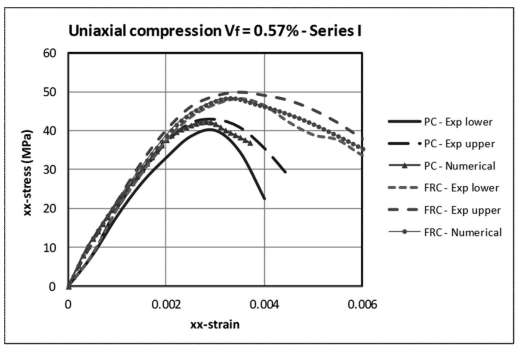

Figure 5. Numerical predictions of uniaxial compression tests of Cachim et al. (2002).

Table 2. Material properties (Uniaxial compression test).

L_f (mm)	d_f (mm)	τ_0 (MPa)	β	E_m (GPa)	E_Ω (GPa)	f_{ti} (MPa)
30	0.5	1.0	0.1	17	44	1.5

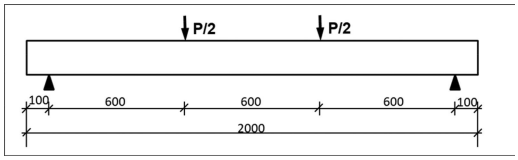

Figure 6. Experimental setup.

the model captures the slight increase in strength and an enhanced ductility of the FRC relative to plain concrete.

3.3 *FE simulations*

The fibre model has been implemented in the commercial finite element software LUSAS and a numerical study based on a set of experimental 4-point bending tests carried out at Cardiff University is presented below. Full details of the experimental study are presented in a forthcoming journal publication.

3.3.1 *Experimental tests*

Reinforced concrete beams ($120 \times 150 \times 2000$ mm) with conventional reinforcement and varying fibre content were tested using the experimental setup shown in Figure 6 in which all dimensions are in mm. Varying volume fractions of Dramix steel fibres ($L_f = 60$ mm and $d_f = 0.71$ mm) were used in manufacturing the specimens as presented in Table 4. All beams were provided with 1ϕ10 mm rebar flexural reinforcement and ϕ6 mm shear links 50 mm c/c. Beams were subjected to 4-point bending under mid-point displacement control and tests were monitored throughout with Digital Image Correlation (DIC) equipment.

3.3.2 *Numerical simulations*

Numerical analyses were carried out to simulate the experimental tests with the three types of specimens given in Table 4. In this work geometric properties from industrial data sheets for Dramix fibres were employed along with the set of material properties given in Table 5.

The finite element mesh with the boundary conditions used for the numerical analysis is presented in Figure 7. Finite element predictions of the load-deflection curves are compared with the experimental curves for the three sets of tests (Figure 8).

Table 4. Experimental test specimens.

Batch code	V_f (by volume)
Control	0%
SFRC1	1%
SFRC2	2%

Table 5. Material properties (4 point bend test).

L_f (mm)	d_f (mm)	τ_0 (MPa)	β	E_m (GPa)	E_Ω (GPa)	f_{ti} (MPa)
60	0.71	1.1	0.04	21	30	1.5

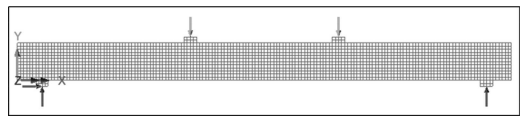

Figure 7. Finite element mesh.

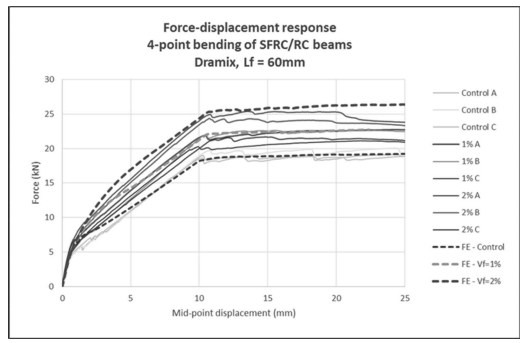

Figure 8. Force-displacement results.

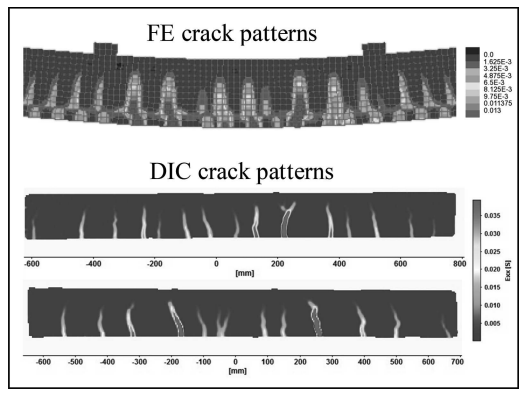

Figure 9. Numerical and experimental crack patterns. Control specimens.

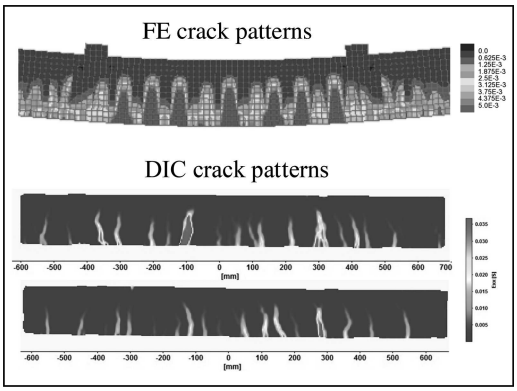

Figure 10. Numerical and experimental crack patterns. SFRC2 $V_f = 2\%$.

The proposed model is able capture accurately the increase in capacity with increasing fibre content.

Plots of the major principal strains obtained from the finite element simulations showing the regions of localised damage are presented in Figures 9 and 10 for a mid-point displacement of 15 mm. Plots of the experimental crack patterns obtained from the DIC monitoring are also presented in Figures 9 and 10.

It can be seen that with the addition of fibres cracking becomes more distributed and the model captures this characteristic well.

4 CONCLUSIONS

A constitutive model for fibre-reinforced cementitious composites based on micromechanical solutions was proposed. Good correlation between numerical results—obtained from both single-point and finite element simulation—and experimental data indicates that the proposed model captures correctly key characteristics of the overall macroscopic mechanical behaviour of fibre reinforced cement based composites, such as the increase of ductility and overall toughness of the fibre reinforced composite relative to the plain concrete matrix.

ACKNOWLEDGEMENTS

The authors gratefully acknowledge the support of the finite element company LUSAS.

REFERENCES

Budiansky, B. & O'Connell, R.J. 1976. Elastic moduli of a cracked solid. *International Journal of Solids and Structures*, 12: 81–97.

Cachim, P.B., Figueiras, J.A. & Pereira, P.A.A. 2002. Fatigue behaviour of fiber-reinforced concrete in compression. *Cement & Concrete Research*, 24: 211–217.

Eshelby, J.D. 1959. The elastic field outside an ellipsoidal inclusion. *Proceedings of the Royal Society A: Mathematical, Physical & Engineering Sciences*, 252(1271): 561–569.

Jefferson, A.D. & Bennett, T. 2007. Micro-mechanical damage and rough crack closure in cementitious composite materials. *International Journal for Numerical and Analytical Methods in Geomechanics* 31: 133–146.

Jefferson, A.D. & Bennett, T. 2010. A model for cementitious composite materials based on micro-mechanical solutions and damage-contact theory. *Computers and Structures* 88: 1361–1366.

Ju, J.W. & Sun, L.Z. 1999. A Novel Formulation for the Exterior-Point Eshelby's Tensor of an Ellipsoidal Inclusion. *Journal of Applied Mechanics, ASME*, 66: 570–574.

Li, Z., Li, F., Chang, T.-Y.P. & Mai, Y.-W. 1998. Uniaxial tensile behaviour of concrete reinforced with randomly distributed short fibres. *ACI Materials Journal* 95(5): 564–574.

Li, S., Sauer, R.A. & Wang, G. 2007. The Eshelby Tensors in a Finite Spherical Domain—Part I: Theoretical Formulations. *Journal of Applied Mechanics, ASME*, 74: 770–783.

Lin, Z & Li, V.C. 1997. Crack bridging in fiber reinforced cementitious composites with slip-hardening interfaces. *Journal of the Mechanics and Physics of Solids* 45(5): 763–787.

Mihai, I.C. & Jefferson, A.D. 2011. A numerical model foe cementitious composite materials with an exterior point Eshelby microcrack initiation criterion. *International Journal of Solids and Structures*, 48: 3312–3325.

Mihai, I.C. & Jefferson, A.D. 2017. A Micromechanics Based Constitutive Model for Fibre Reinforced Cementitious Composites. *International Journal of Solids and Structures,* 110: 152–169.

Mura T. 1987. *Micromechanics of Defects in Solids. Second, revised edition*, Martinus Nijoff Publishers, The Netherlands.

Naaman, A.E. 2008. Development and evolution of tensile strain-hardening FRC composites. *7th RILEM International Symposium on Fibre Reinforced Concrete: Design and Applications—BEFIB 2008*, 1–28.

Nemat-Nasser, S. & Hori, M. 1993. *Micromechanics: Overall Properties of Heterogeneous Materials*. Amsterdam: North-Holland.



Taylor & Francis
Taylor & Francis Group
http://taylorandfrancis.com

Computational Modelling of Concrete Structures – Meschke, Pichler & Rots (Eds)
© 2018 Taylor & Francis Group, London, ISBN 978-1-138-74117-1

Tensile viscous response of Strain Hardening UHPFRC under high restraint and isothermal conditions

M.A. Hafiz & E. Denarié
Division of Maintenance and Safety of Structures (MCS-IIC-ENAC), Ecole Polytechnique Fédérale de Lausanne (EPFL), Lausanne, Switzerland

ABSTRACT: Strain Hardening Ultra High Performance Fiber Reinforced Concretes (SH-UHPFRC) have a high elastic limit (around 10 MPa) and high tensile strength (upto 20 MPa) and exhibit significant strain hardening (1 to 4 ‰) under tensile loads. These appealing features make them extremely effective materials for strengthening and improving the durability of existing structures. However, their cast on site application induces significant eigenstresses due to restraint conditions. In this paper, the effects of various restraint conditions on the tensile viscous response of SH-UHPFRC was determined experimentally using a Temperature Stress Testing Machine and was modelled. Tests were done at partial and full restraint conditions to study the eigenstresses development. The ageing linear viscoelastic response of the material was modeled using an ageing generalized Maxwell model, fitted on the experimental data of eigenstresses. The influence of the scatter of free shrinkage measurements on the model prediction was studied through a sensitivity analysis.

1 INTRODUCTION

Ultra High Performance Fiber Reinforced Concrete (UHPFRC) are materials with very low permeability, outstanding durability and excellent mechanical properties including high tensile strength (over 10 MPa). They can exhibit significant strain hardening behavior (1 to 4 ‰) with a suitable fibrous mix. Because of these excellent properties, they are very well suited for rehabilitation and strengthening of existing structures.

A new layer of cementitious materials applied on an existing structure undergoes volume changes due to autogenous shrinkage, drying shrinkage and thermal effects. In case of UHPFRC, the autogenous shrinkage usually dominates and the thermal effects are only significant for thick layers (more than 50 mm depth). The existing structure as well as the reinforcement bars in the new layer if any, tend to restrain these early age volume changes, which lead to the development of tensile eigenstresses in the new layer. The magnitude of the eigenstresses developed due to such restraint conditions depends on the relationship between the flexural and axial stiffness of the existing structure and that of the new layer. A stiff structure with a thin new layer can therefore lead to full restraint conditions, thereby leading to the highest possible magnitudes of eigenstresses in the new material.

Depending on the stiffness of the structure, even more than 90% of the free deformations can be hindered, thereby leading to a situation which is close to full restraint conditions as can be seen in Denarie et al. (2011). Not much attention has been given to studying the development of eigenstresses in UHPFRC in the early age right after setting. Especially, no work has been done until now to study the influence of full restraint conditions on the development of eigenstresses in cementitious materials.

However, the strain hardening capacity of the UHPFRC helps to reduce the effect of the eigenstresses except in very special cases of unfavorable fiber orientations in which it can be severely reduced. Moreover, the viscoelastic potential in tension of UHPFRC also plays a favorable role in relaxing the eigenstresses.

Altoubat and Lange (2001), Atrushi (2003), Bissonnette et al. (2001) studied about the tensile creep behavior of early age concrete. Kovler (1994) developed a testing system for determining the mechanical behavior of early age concrete under restraint and free uniaxial shrinkage. Igarashi et al. (2000) investigated the autogenous shrinkage and the induced restraining stresses in high strength concrete. Habel (2004) studied the mechanical response of composite UHPFRC/concrete members at early age and long term. Kamen et al. (2008) developed a Temperature Stress Testing Machine (TSTM) at MCS/EPFL to investigate the early age behavior of UHPFRC. Kamen et al. (2009), Switek et al. (2009), Switek-Rey et al. (2016) investigated

the tensile creep of UHPFRC at early age which confirmed a significant creep potential due to the high paste volume in the UHPFRC.

Bažant and Prasannan (1989) proposed the solidification theory to model the basic creep of concrete. Loukili (1996) discussed numerical modelling of basic creep, including the coupling with time independent material damage. Berthollet (2003) proposed a model that takes into account all the different mechanisms relative to the creep kinetics and the effect of loading rates.

This paper presents experimental tests carried out to study the development of eigenstresses in UHPFRC under two different restraint conditions. Two tests were carried out at full restraint conditions and one test was conducted at a partial restraint condition with a degree of restraint of approximately 54%. The eigenstresses development in partial restraint conditions was modelled using a linear ageing viscoelastic model that was later applied to the case of full restraint. The effects of scatter in the measurements were studied using a sensitivity analysis.

2 MODELLING

An ageing linear viscoelastic generalized Maxwell model was used to predict the development of eigenstresses under various restraint conditions. The model is represented schematically in the Figure 1.

with,

E_k = the stiffness of the spring element in Maxwell unit k;

$E_k\tau_k$ = the viscosity of the dashpot in Maxwell unit k, where τ_k is the retardation time;

In an ageing Maxwell model, these material properties are age dependent. As such, an incremental constitutive relation must be derived to predict the development of the stresses.

Let us first consider the incremental procedure for a single Maxwell chain. Assuming a constant incremental strain rate of $\Delta\varepsilon^i$ in a time interval from t^i to t^{i+1}, the stress at the end of the interval is given by the sum of the stress at the beginning of step i, decaying according to a Maxwell model, and the stress due to the effect of a strain increment $\Delta\varepsilon^i$ applied linearly from time t^i to time t^{i+1}.

$$\sigma_k^{i+1} = \frac{\tau_k}{\Delta t}.E_k.\left(1 - e^{-\frac{\Delta t}{\tau_k}}\right).\Delta\varepsilon^i + \sigma_k^i.e^{-\frac{\Delta t}{\tau_k}} \quad (1)$$

where,

σ_k^{i+1} = stress in Maxwell unit k at the end of the time interval Δt;

σ_k^i = stress in Maxwell unit k at the beginning of the time interval Δt;

$\Delta\varepsilon^i$ = total strain increment

Δt = duration of the time interval.

Hence, for a generalized Maxwell model with m Maxwell units, the total stress is given by,

$$\sigma^{i+1} = \sum_{k=1}^{m}\left[\frac{\tau_k}{\Delta t}.E_k.\left(1 - e^{-\frac{\Delta t}{\tau_k}}\right)\right].\Delta\varepsilon^i + \sum_{k=1}^{m}\sigma_k^i.e^{-\frac{\Delta t}{\tau_k}} \quad (2)$$

In order to implement the effect of the different degrees of restraint in the system, an additional spring with a stiffness of E_0 was introduced in series after the Maxwell model as shown in Figure 2.

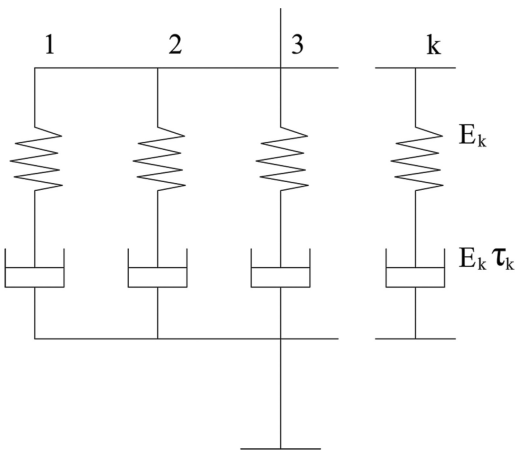

Figure 1. Schematic representation of a generalized Maxwell model (adapted after FEMMASSE (2006)).

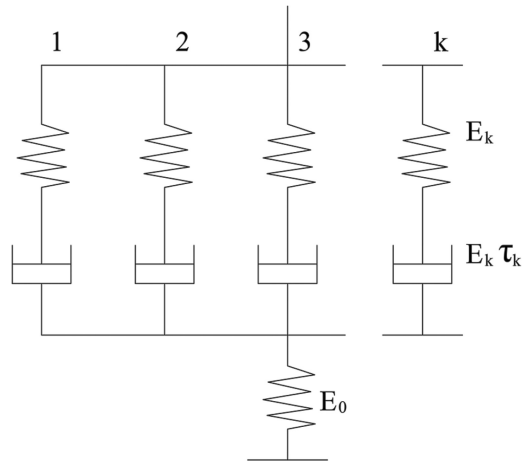

Figure 2. Schematic representation of a generalized Maxwell model with an additional spring E_0 (adapted after FEMMASSE (2006)).

Let us consider the total strain increment acting on the model as the strain increment due to autogenous shrinkage, $\Delta\varepsilon^{i,sh}$. Assume that the strains induced in the Maxwell model and the additional spring, due to this strain increment, are $\Delta\varepsilon_1^i$ and $\Delta\varepsilon_0^i$ respectively. If σ_0^i and σ_0^{i+1} are the stresses in the additional spring at t^i and t^{i+1} respectively, then we have,

$$\Delta\varepsilon^{i,sh} = \Delta\varepsilon_1^i + \Delta\varepsilon_0^i \tag{3}$$

$$\sigma_0^{i+1} = \sigma_1^{i+1} \tag{4}$$

Now for the additional spring and from equation (4) we have,

$$\sigma_0^{i+1} = E_0.\Delta\varepsilon_0^i = \sigma_1^{i+1} \tag{5}$$

$$\Delta\varepsilon_0^i = \frac{\sigma_1^{i+1}}{E_0} \tag{6}$$

The total stress at the end of the time interval Δt in the Maxwell model is therefore given by,

$$\sigma_1^{i+1} = \sum_{k=1}^{m}\left[\frac{\tau_k}{\Delta t}.E_k.\left(1-e^{-\frac{\Delta t}{\tau_k}}\right)\right] \cdot\left(\Delta\varepsilon^{i,sh}-\Delta\varepsilon_0^i\right)+\sum_{k=1}^{m}\sigma_k^i.e^{-\frac{\Delta t}{\tau_k}} \tag{7}$$

Using (6), we have,

$$\sigma_1^{i+1} = \sum_{k=1}^{m}\left[\frac{\tau_k}{\Delta t}.E_k.\left(1-e^{-\frac{\Delta t}{\tau_k}}\right)\right] \cdot\left(\Delta\varepsilon^{i,sh}-\frac{\sigma_1^{i+1}}{E_0}\right)+\sum_{k=1}^{m}\sigma_k^i.e^{-\frac{\Delta t}{\tau_k}} \tag{8}$$

Rewriting equation (8) yields,

$$\sigma_1^{i+1} = \frac{\sum_{k=1}^{m}\left[\frac{\tau_k}{\Delta t}.E_k.\left(1-e^{-\frac{\Delta t}{\tau_k}}\right)\right].\Delta\varepsilon^{i,sh}+\sum_{k=1}^{m}\sigma_k^i.e^{-\frac{\Delta t}{\tau_k}}}{1+\frac{\sum_{k=1}^{m}\left[\frac{\tau_k}{\Delta t}.E_k.\left(1-e^{-\frac{\Delta t}{\tau_k}}\right)\right]}{E_0}} \tag{9}$$

Hence, comparing equations (2) and (9), it can be seen that, the stress in a finite restraint system can be obtained by multiplying the stress in the case of an infinitely restrained system by a factor μ corresponding to the degree of restraint, given by,

$$\mu = \frac{1}{1+\frac{\sum_{k=1}^{m}\left[\frac{\tau_k}{\Delta t}.E_k.\left(1-e^{-\frac{\Delta t}{\tau_k}}\right)\right]}{E_0}} \tag{10}$$

As such, by varying the spring stiffness E_0, the eigenstresses development under the influence of autogenous shrinkage in different restraint conditions, can be predicted.

3 EXPERIMENTAL

3.1 *Material*

The strain hardening UHPFRC type CM22-TKKb, from the CEMTEC$_{multiscale}$® family was used for the experimental tests. The composition of the mix is shown in Table 1. Straight steel fibers of length 10 mm and diameter 0.2 mm were added to the compact matrix.

3.2 *Vibration Resonance Frequency Test (VRFT)*

The development of elastic modulus was studied using Vibration Resonance Frequency tests in order to develop the linear viscoelastic models to predict the eigenstresses development.

The tests were carried out using a special testing setup which was developed in MCS/EPFL by Kazemi Kamyab (2013) and was setup inside a climate chamber maintained at 20°C. Cylindrical specimens of dimensions 140 mm × 70 mm were kept on a support in front of a special system consisting of a steel sphere suspended using a steel thread. The specimens were hit with the steel sphere at the center, which produced longitudinal vibrations in the specimen. The longitudinal vibrations were measured using an accelerometer at the other end of the cylinder. Using an analytical procedure developed by Kolluru et al. (2000), the development of elastic modulus was calculated from the first two longitudinal resonant frequencies of the specimen obtained though a Fourier analysis.

3.2 *Temperature Stress Testing Machine (TSTM)*

The Temperature Stress Testing Machine (TSTM) was developed at MCS during the thesis of Kamen

Table 1. UHPFRC recipe.

Material	[kg/m³]
Cement	1467.0
Silica fume	381.4
*Steel fibers (straight macro fibers, slightly torqued and microfibers/steel wool)	706.5
Total water	225.8
Superplasticizer (total)	20.5

*Detailed fibrous mix is patent protected.

(2008). It is a thermo-mechanical testing machine, which is setup inside a climate room with a temperature of 20 +/–1°C. The test setup is used to conduct mechanical tests on cementitious specimens at very early age, at different temperatures, directly after casting. A cooling fluid circulates in copper pipes attached to the moulds, which helps in maintaining a fixed temperature around the specimen. A schematic representation of the TSTM is shown in Figure 3.

The test setup consists of two devices; the Free Setup (FS) helps to measure the free autogenous deformation whereas the Restrained Setup (RS) helps in measuring the eigenstresses developing under various restraint conditions, as well as the associated free deformations.

The stresses in the material were calculated by dividing the force measured by the load cell of the RS setup with the cross sectional area of the specimen. In both the devices, fully sealed specimens of cross sectional dimensions 50 mm × 100 mm were used. Two types of tests were conducted at 20°C on the UHPFRC specimens; full restraint tests and partial restraint tests.

The full restraint tests (named FR_1 and FR_2) were started under stroke control (passive restraint, stroke idle), but when the stress in the material reached about 0.2 MPa, the control was switched to closed loop deformation control. During this stage, the deformations were controlled in such a way that the relative displacements between two points A and B 750 mm apart, remained constant whereas the partial restraint tests were conducted under stroke control. This was therefore an active control and fulfilled full restraint conditions in the material.

In the partial restraint test (named PR_1 test), the entire test was controlled through stroke control and the stroke was kept in the same relative position without any movement. It is not a 100% restraint test because of the finite stiffness of the machine parts. The partial restraint imposed in the test was calculated to be approximately 54% on the basis of the free deformations in the free and restrained setups.

Depending on the restraint conditions, the autogenous deformations led to different magnitudes of the eigenstresses. It was assumed that the autogenous shrinkage occurring in the RS setup was the same as that of the FS setup.

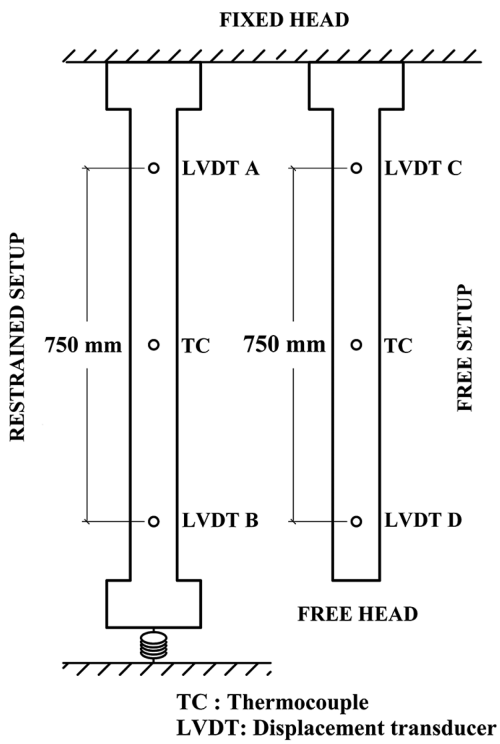

Figure 3. Schematic representation of TSTM testing setup.

4 TEST RESULTS AND MODELLING

4.1 *Overview*

As can be seen from the equation (10), the stresses predicted by the model will depend on the Maxwell chain parameters like E_k and τ_k as well as the autogenous shrinkage strains $\Delta\varepsilon^{i,sh}$ acting on the model. The retardation times τ_k were considered in such a way so as to cover the entire duration of the test. As such, five Maxwell chains were selected with the respective retardation times of 1, 10, 100, 1000 and 10000 hours.

Now the main aim of the modelling was to determine the parameters E_k of the Maxwell chains. The sum of the individual E_k values at any particular time is equal to the elastic modulus of the material E_{tot} at that particular time. The evolution of the elastic modulus with age was determined by VRFT. The other main input of the model was the development of the autogenous shrinkage $\Delta\varepsilon^{i,sh}$.

A least square fitting procedure was adopted to find the parameters of the Maxwell chain, in order to have an ageing linear viscoelastic generalized Maxwell model, which can predict the development of eigenstresses in the TSTM under different various restraint conditions.

The temperature in the center of all specimens was monitored continuously for all TSTM tests. All the tests were carried out at a temperature of 20°C, imposed by the thermal bath linked to the cooling circuits. For all tests, both free and restrained specimen had the same temperature history, and

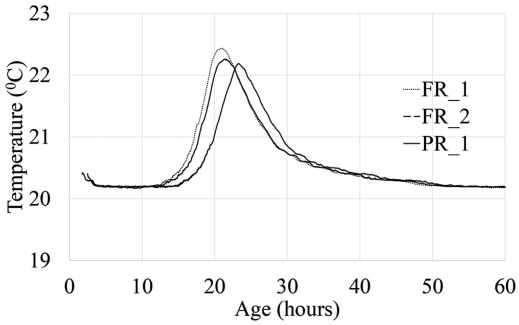

Figure 4. Temperature history in the three tests.

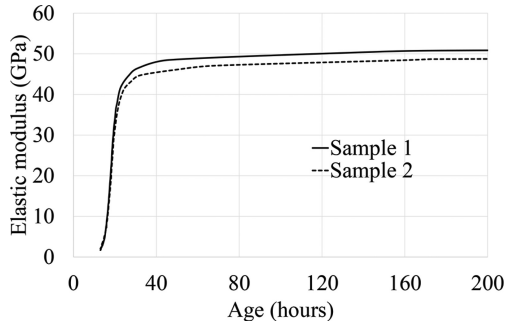

Figure 5. Development of elastic modulus from VRFT.

there was an increase in the temperature of about 2 to 2.2°C in all the three specimens during the setting of the UHPFRC. As seen in Figure 4, the temperature began to increase around 13 to 15 hours and the maximum temperature in the specimens occurred around 21 to 23 hours. However, after the maximum temperature, it decreased and stabilized around 20°C again. As such, the tests can be considered as quasi-isothermal at 20°C.

4.2 *Elastic modulus development from VRFT*

The development of elastic modulus was studied using the VRFT and the results of two specimens are shown in Figure 5.

In both the specimens, the elastic modulus stabilized around 50 GPa after around 7 days. There is a slight difference in the final stabilized value of the elastic modulus of the two specimens. This may be due to slight experimental differences between the two batches or due to the slight difference in the orientation of the fibers and its volume in the two specimens. The difference could also be due to a change in the components in the meantime between the two batches, as the second sample was made from a new delivery of cement and silica fume.

4.3 *Autogenous shrinkage at 20°C*

The early age autogenous deformations in the UHPFRC were measured using the FS setup of the TSTM. It was assumed that the autogenous deformations vary linearly from one end to the other and between the points D and C in Figure 3. The autogenous shrinkage was calculated by subtracting the deformations measured at two points, which are 750 mm apart. Figure 6 shows the development of autogenous shrinkage in the FS setup corresponding to the two full restraint (FR) tests and one partial restraint (PR) test. It can be seen that there is a swelling phase in each

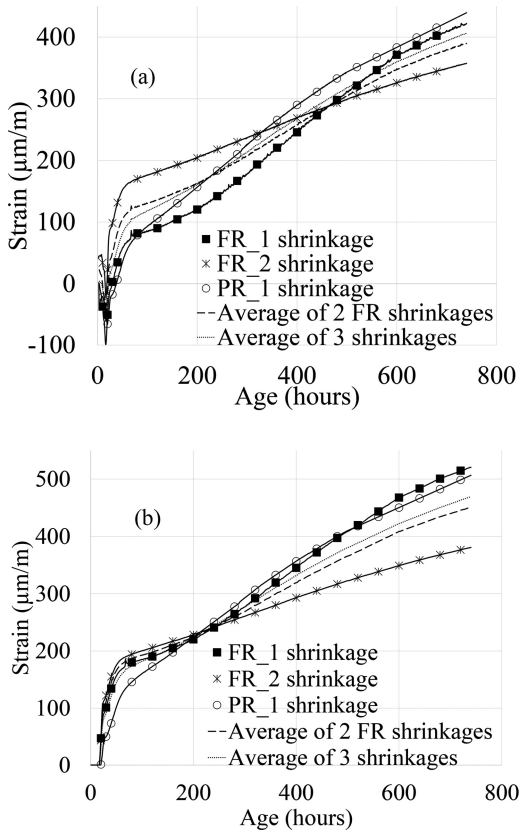

Figure 6. Evolution of autogenous deformations in the free (FS) setup, (a) without zeroing (b) zeroed after swelling. (Shrinkage is shown as positive).

of the shrinkage curves, but it is the autogenous shrinkage after the end of the swelling phase that leads to the development of the eigenstresses in the material. More discussions on the development of autogenous shrinkage can be found in Hafiz and Denarié (2017).

4.4 *Eigenstresses development at 20°C*

The development of eigenstresses was studied along with the measurement of the evolution of the free shrinkage deformations. The development of the eigenstresses under these different conditions are shown in the Figure 7.

As expected, the magnitude of the eigenstresses developed in the case of the full restraint tests were much higher than that in the partial restraint tests as can be seen from Figure 7. The stresses even reached around 12 MPa after one month, which is higher than the elastic limit of the material, which usually ranges between 8 MPa and 10 MPa at 28 days, for similar curing conditions. As such, the stress levels clearly reached the strain hardening domain of the tensile response of the material.

Fracture tests conducted on these full restraint specimens later, showed that the eigenstresses had almost reached the ultimate strength of the specimens. Fracture test on FR_1 specimen showed an ultimate strength of 12.8 MPa, whereas that on the FR_2 specimen showed an ultimate strength of 16.6 MPa. The ultimate strength results were consistent with the values shown by Switek (2010), who obtained an average ultimate tensile strength of 15.5 MPa for specimens loaded at 10 days. The authors of the present paper also conducted uniaxial tensile tests on dumbbell specimens, with cross sections of 50 mm × 30 mm, in an electromechanical test setup at very low strain rates of 10^{-8} 1/s, which showed an average ultimate tensile strength of 15.4 MPa at 14 days age.

Moreover, it could reasonably be assumed that, under full restraint, the eigenstresses will continue to increase along the stress-deformation path of the strain hardening response of the material until the ultimate tensile strength, as long as the autogenous shrinkage increases. But it is also possible that the eigenstresses start decreasing before the ultimate tensile strength, as the effect of additional shrinkage increment beyond a certain time may be offset by the relaxation effects due to the viscous response of the UHPFRC. This will be confirmed by conducting the tests for longer durations. More discussions regarding the development of the eigenstresses in the full and partial restraint tests can be found in Hafiz and Denarié (2017).

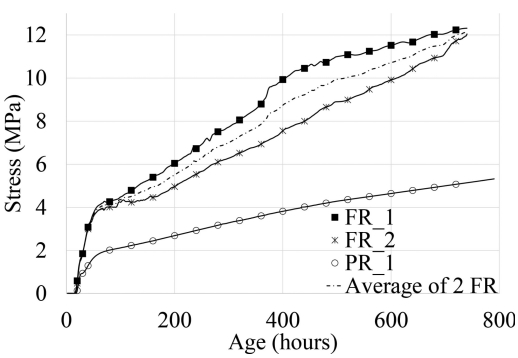

Figure 7. Development of eigenstresses under different restraint conditions.

4.5 *Modelling*

In Figure 7, it can be seen that the stress levels in the full restraint test went above 12 MPa whereas that in the partial restraint test was below 6 MPa after about 720 hours (one month). As such, we can see that the stress level in the partial restraint test is still within the elastic range. However, in order to model the stress development in the partial restraint test, it was necessary to know the value of the degree of restraint imposed on the material in such a test.

Let us assume that the autogenous deformation occurring in the FS setup is $\varepsilon_{free}^{free}$. In a partial restraint test, in the RS setup, a part of the autogenous deformation is restrained whereas the remaining part of the autogenous deformation is free. Let us call the former as $\varepsilon_{restra\,int}^{restra\,int}$ and the latter as $\varepsilon_{restra\,int}^{free}$. Now we have, from the RS and FS setup,

$$\varepsilon_{restra\,int}^{restra\,int} + \varepsilon_{restra\,int}^{free} = \varepsilon_{free}^{free} \tag{11}$$

For a full restraint test, all of the autogenous deformation is restrained in the RS setup. As such, $\varepsilon_{restra\,int}^{free}$ is zero in a full restraint test and therefore the stress at any time t, in the elastic case, is given by,

$$\sigma_{full}(t) = E_{tot}(t).\varepsilon_{restra\,int}^{restra\,int}(t) = E_{tot}(t).\varepsilon_{free}^{free}(t) \tag{12}$$

The stress in the case of a partial restraint test is given by,

$$\begin{aligned}\sigma_{partial}(t) &= E_{tot}(t).\varepsilon_{restra\,int}^{restra\,int}(t) \\ &= E_{tot}(t).\left(\varepsilon_{free}^{free}(t) - \varepsilon_{restra\,int}^{free}(t)\right)\end{aligned} \tag{13}$$

Now, the degree of restraint is defined as the ratio of the stress occurring in a material to the stress that could have occurred in the material under full restraint conditions. That is,

$$\text{Degree of restraint,} \quad \mu = \frac{\sigma_{partial}(t)}{\sigma_{full}(t)} \tag{14}$$

Using equations (12), (13) and (14), we can find,

$$\mu = 1 - \frac{\varepsilon_{restra\,int}^{free}(t)}{\varepsilon_{free}^{free}(t)} \tag{15}$$

The evolution of the $\varepsilon_{free}^{free}(t)$ was described in section 4.3. The evolution of $\varepsilon_{restra\,int}^{free}(t)$ was also determined in a similar way in the RS setup. Using equation (15), Figure 8 was obtained to determine the degree of restraint in the system.

The asymptotic value in the Figure 8 is an indication of the degree of restraint in the partial restraint test. It can be seen that the asymptotic value is around 0.54. As such, the degree of restraint in the system was taken as 54%.

Once we have determined the degree of restraint, the next step was to fix the value of machine stiffness E_0 in the model in order to have a degree of restraint of 54%. It was found that a value of 59000 MPa for E_0 gives the required degree of restraint in the system.

Now for the actual modelling, there were three main set of parameters, that could influence the prediction of the stresses.

1. The development of the elastic modulus, E_{tot}.
2. The Maxwell chain parameters E_k and τ_k.
3. The autogenous shrinkage development, $\Delta\varepsilon^{i,sh}$

Since the development of elastic modulus was almost similar in both of the VRF tests as shown in Figure 5, it was decided to consider the average of them for the modelling. It was assumed that the Elastic modulus development remain similar in all the tests. For the autogenous shrinkage, it was decided to consider the average of the autogenous shrinkage curves from the three tests; two full restraint tests and the partial restraint test, as the input.

Using a least square regression analysis, the parameters of the Maxwell chains were determined which are shown in Table 2, along with the elastic modulus development and average autogenous shrinkage development used in the model.

The corresponding prediction of the eigenstresses development is shown in Figure 9. It can be seen that the model very well predicts the development of the eigenstresses in the partial restraint test.

Table 2. Parameters of the Maxwell model.

τ_1 Hour	τ_2 Hour	τ_3 Hour	τ_4 Hour	τ_5 Hour
1	10	100	1000	10000

Age Hour	E_{tot} GPa	$\frac{E_1}{E_{tot}}$	$\frac{E_2}{E_{tot}}$	$\frac{E_3}{E_{tot}}$	$\frac{E_4}{E_{tot}}$	$\frac{E_5}{E_{tot}}$	ε^{sh} μm/m
0	0.0	0.30	0.20	0.10	0.40	0.00	0
16	2.8	0.30	0.20	0.10	0.40	0.00	0
20	14.2	0.30	0.20	0.10	0.40	0.00	30
22	26.5	0.30	0.20	0.10	0.40	0.00	58
24	34.7	0.20	0.20	0.20	0.20	0.20	75
26	38.2	0.20	0.20	0.20	0.20	0.20	82
28	40.6	0.20	0.20	0.20	0.20	0.20	86
30	42.2	0.20	0.20	0.20	0.20	0.20	91
32	43.5	0.20	0.20	0.20	0.20	0.20	96
34	44.2	0.20	0.20	0.20	0.20	0.20	102
36	44.9	0.20	0.20	0.20	0.20	0.20	108
40	46.0	0.20	0.20	0.20	0.20	0.20	121
43	46.4	0.06	0.30	0.10	0.18	0.36	128
46	46.6	0.06	0.30	0.10	0.18	0.36	135
50	46.8	0.06	0.30	0.10	0.18	0.36	144
60	47.4	0.01	0.05	0.31	0.38	0.24	158
80	48.4	0.01	0.05	0.31	0.38	0.24	173
100	49.3	0.01	0.05	0.31	0.38	0.24	181
150	50.2	0.01	0.00	0.51	0.23	0.24	202
300	51.0	0.01	0.00	0.51	0.23	0.24	276
480	51.7	0.01	0.00	0.45	0.23	0.31	371
740	52.5	0.00	0.00	0.25	0.33	0.41	469

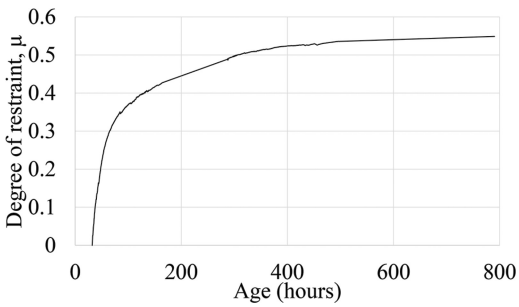

Figure 8. Degree of restraint, μ.

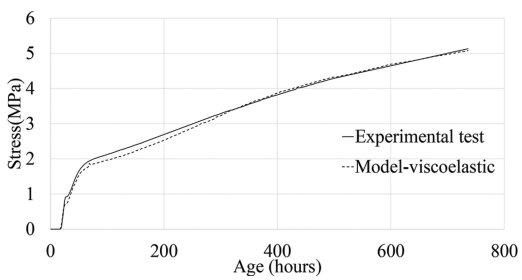

Figure 9. Comparison of the experimental and predicted values of eigenstresses in the partial restraint test.

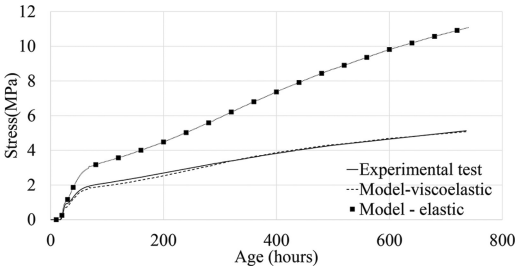

Figure 10. Comparison of the experimental and predicted values of the eigenstresses in the partial restraint test using elastic and viscoelastic incremental models.

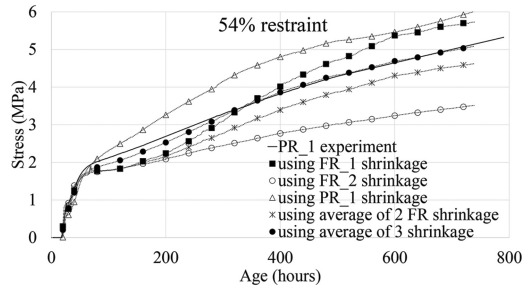

Figure 11. Sensitivity analysis at 54% restraint.

Another important capability of the modelling, is that it can also predict the response of the material, if it was purely elastic ageing, by considering only the Maxwell chain with the largest response time. Accordingly, a value of 1 was assigned to all the rows of the column E_s/E_{tot} in Table. As indicated earlier, the viscoelastic property of UHPFRC helps a lot in relaxing the eigenstresses in the material. As it is clear from the Figure 10, the predicted eigenstresses that would have been around 11 MPa if the material was elastic, was relaxed to a stress of 5 MPa in the actual case. As such, the viscoelasticity of UHPFRC helped in relaxing more than 50% of the eigenstresses developing in the material.

4.6 *Sensitivity analysis*

A sensitivity analysis was carried out in order to predict the effect of the scatter in the autogenous shrinkage values measured, on the development of the eigenstresses. In this analysis, the development of the elastic modulus was kept same as before and the Maxwell chains obtained from the previous step of the modelling was used. Unlike the initial modelling, in which the average of three autogenous shrinkage was used, the autogenous shrinkage developments from the individual tests were input separately into the model. The scatter of the eigenstresses predicted was then analyzed and discussed. The sensitivity analysis was also carried out to predict the eigenstresses development under full restraint conditions and the results were compared with the experimental full restraint tests.

4.6.1 *Partial restraint conditions*

In the first step, the sensitivity analysis was carried out for partial restraint condition of 54% restraint. Figure 11 shows the prediction of the eigenstresses under different autogenous shrinkage developments.

The sensitivity analysis gives an idea about the scatter of the magnitude of eigenstresses that could develop in the material, because of the scatter in the shrinkage values. It can be seen from Figure 6, that the scatter of the shrinkage values is approximately 30% of the average value of the 3 shrinkage curves at 720 hours. The scatter in the eigenstresses predicted at 720 hours is 46% of the average eigenstresses predicted and is slightly higher than that of the autogenous shrinkage.

4.6.2 *Full restraint conditions*

The sensitivity analysis was also carried out to predict the eigenstresses development under full restraint conditions. The full restraint conditions were achieved in the model by setting a very high value for E_0 of 1×10^8 MPa. The predicted eigenstresses development under full restraint conditions are shown in Figure 12.

It can be seen from the Figure 12, that the experimental eigenstresses under full restraint conditions remain well within the range of the prediction of the model until around 8–10 MPa. The experimental FR_1 test starts deviating away from the model prediction just above 8 MPa whereas that of the FR_2 test goes out of the prediction above 11 MPa. We assume that this deviation is because, beyond 8–10 MPa, the material goes beyond its elastic range and therefore the effects of non-linearity comes into picture. Once the material enters the strain hardening zone of the tensile response, then there is not only the effects of linear viscoelasticity but also that of non-linear viscoelasticity. On top of that the effects of damage in the material also affects the tensile response of the material. As such, there is a complex interaction of linear viscoelasticity, non-linear viscoelasticity and fracture mechanics in the strain hardening zone.

Hence, a model incorporating the interaction of the linear viscoelasticity, non-linear viscoelasticity and damage is needed, in order to predict the complex time dependent tensile response of the UHPFRC until the end of the strain hardening zone. This can be done by considering a threshold for the linear viscoelasticity above which non-linear viscoelasticity starts acting. Along with that,

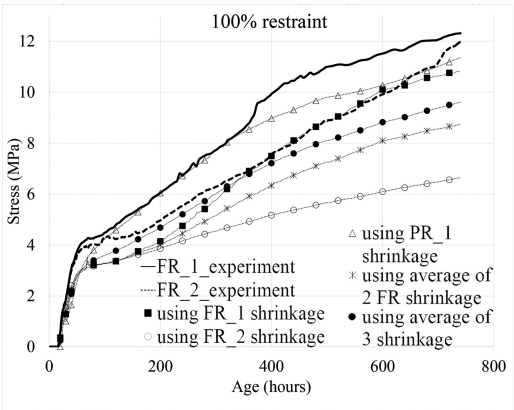

Figure 12. Sensitivity analysis at 100% restraint.

in the strain hardening domain, a decrease in the elastic modulus should be considered using a damage factor. Such a model would then be able to account for the complex interactions of the above mentioned phenomena in order to predict the overall tensile response until the ultimate tensile strength of the material.

5 CONCLUSIONS

- TSTM tests on SH-UHPFRC under full restraint conditions showed that the eigenstresses could reach values higher than the elastic limit and even close to the ultimate strength of the material. It highlighted the necessity of using a strain hardening material for overlaying applications, in order to avoid localized macrocracking and meet the serviceability criterion associated to the protective function.
- Linear viscoelastic models can very well predict the development of eigenstresses in UHPFRC, if the stress levels are below the elastic limit of the material.
- UHPFRC viscoelasticity helps in relaxing the eigenstresses by more than 50%.
- Modelling incorporating the influence of interaction of non-linear viscoelasticity, viscoplasticity and damage is required for modelling the eigenstresses beyond the elastic limit.

ACKNOWLEDGEMENT

The project was financially supported by the Swiss National Science Foundation (grant 200021_153394/1). The authors would like to appreciate the help given by the technicians of GIC-ENAC-EPFL in performing the experimental works with the TSTM.

REFERENCES

Altoubat, S.A. & Lange, D.A. 2001. Tensile basic creep: measurements and behavior at early age. *ACI Materials Journal,* 98(5), 386–393.

Atrushi, D.S. 2003. *Tensile and Compressive Creep of Early Age Concrete: Testing and Modelling.* PhD thesis, Norwegian University of Science and Technology, Noruega.

Bažant, Z.P. & Prasannan, S. 1989. Solidification theory for concrete creep. I: Formulation. *Journal of engineering mechanics,* 115, 1691–1703.

Berthollet, A. 2003. *Contribution à la modélisation du béton vis-à-vis du vieillissement et de la durabilité: interaction des déformations de fluage et du comportement non-linéaire du matériau*. PhD thesis, INSA de Lyon.

Bissonnette, B., Boily, D., Bastien, J. & Fafard, M. 2001. Tensile creep of concrete repair materials: recent experimental findings towards optimization. *Concreep 6,* 6, 599–604.

Denarie, E., Silfwerbrand, J. & Beushausen, H. 2011. Structural behaviour. *Bonded Cement-Based Material Overlays for the Repair, the Lining or the Strengthening of Slabs or Pavements*. Springer.

Habel, K. 2004. *Structural behaviour of composite UHPFRC–concrete elements.* Doctoral thesis, Swiss Federal Institute of Technology, Lausanne, Switzerland.

Hafiz, M.A. & Denarié, E. 2017. Experimental Study of Tensile Response of Strain Hardening UHPFRC at Early Age. *International Conference on Strain-Hardening Cement-Based Composites*, 308–315.

Igarashi, S.-I., Bentur, A. & Kovler, K. 2000. Autogenous shrinkage and induced restraining stresses in high-strength concretes. *Cement and Concrete Research,* 30, 1701–1707.

Kamen, A. 2007. *Comportement au jeune âge et différé d" un BFUP écrouissant sous les effets thermomécaniques*. PhD thesis, École polytechnique fédérale de Lausanne.

Kamen, A., Denarié, E., Sadouki, H. & Brühwiler, E. 2008. Thermo-mechanical response of UHPFRC at early age—Experimental study and numerical simulation. *Cement and Concrete Research,* 38, 822–831.

Kamen, A., Denarié, E., Sadouki, H. & Brühwiler, E. 2009. UHPFRC tensile creep at early age. *Materials and Structures,* 42, 113.

Kazemi Kamyab, M. 2013. *Autogenous Shrinkage and Hydration Kinetics of SH-UHPFRC under Moderate to Low Temperature Curing Conditions*. PhD thesis, École polytechnique fédérale de Lausanne.

Kolluru, S.V., Popovics, J.S. & Shah, S.P. 2000. Determining elastic properties of concrete using vibrational resonance frequencies of standard test cylinders. *Cement, concrete and aggregates,* 22, 81–89.

Kovler, K. 1994. Testing system for determining the mechanical behaviour of early age concrete under restrained and free uniaxial shrinkage. *Materials and Structures,* 27, 324–330.

Loukili, A. 1996. *Etude du retrait et du fluage de Bétons à Ultra-Hautes Performances*. PhD thesis, Ecole Centrale de Nantes, France.

Switek-Rey, A., Denarié, E. & Brühwiler, E. 2016. Early age creep and relaxation of UHPFRC under low to high tensile stresses. *Cement and Concrete Research,* 83, 57–69.

Switek, A., Denarié, E. & Brühwiler, E. 2009. Tensile creep of UHPFRC under low and high stresses. *4th International Conference on Construction materials: Performance, Innovations and Structural Implications ConMat" 09*, 1, 432–437.

Switek, A.E. 2010. *Time-dependent response of ultra high performance fibre reinforced concrete (UHPFRC) under low to high tensile stresses*. PhD thesis, École polytechnique fédérale de Lausanne, Switzerland.

Computational Modelling of Concrete Structures – Meschke, Pichler & Rots (Eds)
© 2018 Taylor & Francis Group, London, ISBN 978-1-138-74117-1

A beam-particle model to identify constitutive laws for quasi-brittle materials under complex loading: From concrete to masonry

C. Oliver-Leblond, C. Giry, C. Limoge, M. Vassaux, E. Anglade & F. Ragueneau
LMT (ENS Cachan, CNRS, Universit Paris Saclay), Cachan, France

ABSTRACT: In recent years, macroscopic continuous damage models have been used to simulate large civil engineering structures subjected to seismic loadings. Those models are often chosen for their ability to capture mechanical non-linearities due to the fracture process with relatively reasonable computational costs. However, they tend to be limited because of the complexity of this fracture process. Classical limitations are for example, the oversight of important phenomena, the omission of the interactions between different mechanisms and the difficulty to identify the numerous parameters. To overcome those limitations, a virtual testing approach has been proposed. A discrete model is used to provide various material responses under simple as well as complex loadings which are needed for the formulation and the calibration of a macroscopic continuous damage model. The discrete media is described with rigid particles and beam elements between them reproducing the cohesion of the material. Contact and friction laws are also introduced in the model in order to describe the behavior during crack closure and sliding. It has been shown that this discrete model is able to reproduce the complex fracture process of quasi-brittle materials and thus complement experimental campaigns. Therefore, it was validated and used as a virtual testing tool to establish equations of the macroscopic model, on the basis of damage and plasticity theories. The macroscopic model has then been calibrated entirely with the microscopic model (e.g. formulation of the function defining the closure of microcracks). Finally, it has been employed to simulate the response of structural elements as reinforced concrete wall under alternate shear loading. In this paper, the extension of this work to assess the behavior of old masonry is exposed. Indeed, seismic assessment of historical masonry structures is a crucial field of architectural heritage. However, for this kind of structures, it may be difficult to get information relative to the mechanical properties of the masonry itself. Indeed, as the structures may generally be protected as cultural heritage, no sample of the material can be extracted in order to characterize it. Furthermore, some loadings can be difficult to reproduce experimentally (e.g. pure tension test on old masonry wall). First, the use of the beam-particle model to reproduce the behavior of old masonry is validated through published results of an experimental campaign performed on old-liked masonry walls. In a second part of the paper, the behavior of old masonry is discussed according to the results obtained from numerical experimental campaign. Several loading states are considered in order to observe the shape of the elastic domain as well as the non-linear behavior. In accordance with the results exposed, the parameters of a simple damage model are identified in order to go up to the computation at the structural scale. In the last part, through a case study dealing with baroque religious heritage in French Savoy, a continuous damage model which parameters are identified from numerical experiments is used in order to analyze the response of a church under seismic loading. An analysis of the non-linearities observed in the simulation is proposed with a comparison with "classical" failure mechanism of masonry churches under seismic loading.

1 INTRODUCTION

Recent events have shown that the preservation of historical masonry structures against seismic hazard is of main concern and needs preventive assessments. In this context, it is necessary to propose efficient tools capable of taking into account all the possible ruin mechanisms of the studied structure. However this problem still represent a challenge as old masonry displays complex mechanical behaviors. In fact it is characterized by its composite nature, formed by discrete units of stones or bricks, separated by dry or mortared joints, and possibly infilling materials. Its tensile strength is almost null, providing a brittle tensile response, explained by the low tensile strength of its materials and of the connection between its components. Its shear response is frictional due to cracking and separation along joints once the limited bond between units and mortar is lost. It is also an anisotropic material whose response highly depends on the load orientation. These complex

failure modes will be magnified when the structure is subjected to complex loads, such as earthquake.

Old masonry is most often very heterogeneous and irregular, even in a single structure, because it has often been repaired along the structure's life, with various materials. Moreover, its components can hardly be characterized in order to respect the integrity of the protected masonry structure. Protection rules limit the possible tests, pits and cores, on the structure. Therefore the available information that can be collected is very limited. In this context, virtual testing strategy has to be considered to investigate the complex behavior of old masonry material.

Recent works of some of the authors have proposed a virtual testing tool to identify the response of quasi-brittle material as concrete under cyclic loadings. This tool, based on discrete element method, provides a framework allowing to represent explicitly the multiple and anisotropic crack openings and their closure as well as the friction between solids. By considering some adjustments of this tool and based on similar works as the one of Lemos (2007), this approach can be derived for the assessment of the behavior of old masonry.

In order to describe efficiently and with a limited computational time the response of old masonry at structural scale without making too much hypothesis and loosing too much information, a nonlinear continuous homogenized model seems to be still the better choice. However, this kind of model can introduce several parameters that need to be identified. Due to the fact that a few data are available and that some experimental tests can be tricky to manage, the virtual testing tool represents a good candidate to do this task. Combining general data on the real masonry (i.e. compressive strength) and this virtual testing tool, one can get an overall view of the behavior of the material.

In a first part, the beam-particle modeling technique is presented and its capacity to reproduce the behavior of old masonry is investigated. Then, this model is used as a virtual testing tool to identify the parameters of a simple continuous model for which the main equations are described. At the end, a structural application of the identified continuous model is performed, considering the response of a French baroque church under an Alpine recent earthquake.

2 MESOSCOPIC SIMULATIONS OF OLD MASONRY

2.1 *Modeling technique*

In order to provide a representative response of samples at the material scale, virtual testing needs the introduction of a microscopic model. The framework considered in this work is a 2D particle-based model made of a combination of a Euler-Bernoulli beams network, which is used to reproduce cohesion and the fracture mechanisms between the particles, and of the DEM framework, which allows to describe realistic interactions between the cracks thanks to the integration of contact and friction mechanisms. Unlike classical DEM or Contact Dynamics models, the microscopic model is developed within a quasi-static framework to enable reasonable computational costs and to avoid the introduction of arbitrary dynamic effects. The integration algorithm is an incremental version of classic event driven integration schemes, to allow the computation of the solution as a succession of stable equilibrium states, while accounting for other non-linearities than fracture, namely contact and friction, which cannot be solved in a event driven fashion.

The cohesion forces and moment between two connected particles i and j are given in equation 1. Two parameters are introduced to describe the beams behavior: their coefficient of inertia α and their Young modulus $\bar{E}$.

$$\begin{cases} F_{N,ij} = \dfrac{\bar{E}A_{b,ij}}{l_{b,ij}}(\mathbf{u}_i - \mathbf{u}_j).\mathbf{n}_{b,ij} \\ F_{T,ij} = \dfrac{12\bar{E}I_{b,ij}}{l_{b,ij}^3}(\mathbf{u}_i - \mathbf{u}_j).\mathbf{t}_{b,ij} - \dfrac{6\bar{E}I_{b,ij}}{l_{b,ij}^2}(\theta_i - \theta_j) \\ M_{Z,ij} = \dfrac{6\bar{E}I_{b,ij}}{l_{b,ij}^2}(\mathbf{u}_j - \mathbf{u}_i).\mathbf{t}_{b,ij} + \dfrac{4\bar{E}I_{b,ij}}{l_{b,ij}}\left(\theta_i - \dfrac{\theta_j}{2}\right) \end{cases} \quad (1)$$

where

- $F_{N,ij}, F_{T,ij}$ and $M_{Z,ij}$ stand for, respectively, the normal force, the tangent force and the bending moment in the beam linking particles i and j;
- α and E are the coefficient of inertia and the Young modulus of the beams respectively;
- $\mathbf{u}_i$ is the displacement vector of the particle i and θ_i its rotation;
- $\mathbf{n}_{b,ij}$ and $\mathbf{t}_{b,ij}$ are the normal and tangent vectors to the cross-section of the beam linking particles i and j;
- $A_{b,ij}$ is the cross-section, $I_{b,ij}$ the moment of inertia and $l_{b,ij}$ the length of the beam.

A brittle behavior is imposed to the beams and the failure criterion is expressed in function of the beam elongation and the relative rotation of its ends.

$$\frac{\epsilon_{ij}}{\epsilon_{cr,ij}} + \frac{|\theta_i - \theta_j|}{\theta_{cr,ij}} > 1 \quad (2)$$

where $\epsilon_{cr,ij}$ is the critical elongation of the beam $i-j$ and $\theta_{cr,ij}$ is the critical relative rotation.

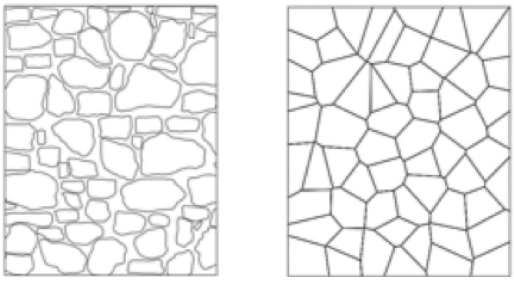

Figure 1. Masonry wall: experimental sample (left) and its associated virtual sample (right).

When this breaking threshold is reached, the beam is removed and a crack appears at the common edge of the particles i and j formerly linked by this beam.

The original particle-based model considered for this work is originally developed for quasi-brittle material such as concrete. For this kind of material, phases are generally not distinctly described, thus statistically distributed failure properties are considered. When employed to model masonry, a simplification can be made due to the distinct me so-structure of masonry (distinction between stones and mortar). Experimental observations show that cracks rarely propagate through stones thus one can assume that each discrete polygonal particle (i.e. rigid particle) obtained using a random Voronoi diagram of the masonry structure represents a distinct stone (see Figure 1).

When two stones separated by a crack interact, contact forces are generated:

$$\mathbf{F}_{cont,ij} = \frac{\bar{E} S_{r,ij}}{l_{c,ij}} \mathbf{n}_{c,ij} \tag{3}$$

where $\mathbf{F}_{cont,ij}$ is for the normal contact force between the particles i and j, $\mathbf{n}_{c,ij}$ is a normal vector to the contact direction, $S_{r,ij}$ is the overlap area and $l_{c,ij}$ a characteristic length defined as the harmonic mean of the diameter of the particles.

In addition, a friction force can be generated in between two contacting particles following Coulomb friction model:

$$\begin{cases} \left\| \mathbf{F}^{el}_{fricij} \right\| = \dfrac{\bar{E} I_{c,ij}}{l^3_{c,ij}} \left\| \left[\left(\mathbf{u}_{c,ij} - \mathbf{u}_{c,ji} \right) \cdot \mathbf{t}_{c,ij} - \Delta u_{s,ij} \right] \right\| \\ \left\| \mathbf{F}_{fricij} \right\| = \min\left(\left\| \mathbf{F}^{el}_{fricij} \right\|, \mu \left\| \mathbf{F}_{cont,ij} \right\| \right) \end{cases} \tag{4}$$

where $\Delta u_{s,ij}$ is the tangential relative displacement between the two particles and μ is the friction coefficient of the stone.

This beam-particle model as well as its integration algorithm are thoroughly described in (Vassaux, Richard, Ragueneau, Millard, & Delaplace 2015). The validation of the model under multi-axial and cyclic loading—and therefore with respect to mixed-mode fracture and contact activation—has been presented in (Vassaux, Oliver-Leblond, Richard, & Ragueneau 2016).

2.2 *Calibration*

The model features only six parameters to be calibrated: the size of the particles, the beam Young modulus and coefficient of inertia, the extension and rotation failure thresholds, and the friction coefficient. The adaptation of the model for old masonry leads to the calibration of these parameters with only a single compression test, while in its original application to quasi-brittle materials, several non-elastic tests were required (Vassaux, Oliver-Leblond, Richard, & Ragueneau 2016).

2.3 *Valiation for three-leaf stone masonry*

Tests conducted by Silva (2012) on three-leaf stone masonry wall of 1.20 m height, 1.00 m width and 0.50 m thickness are used as reference in order to validate the ability of the present model to reproduce masonry behavior. Stress-strain curves provided by a monotonic compression test are used to calibrate the elastic and failure parameters. Validation is completed checking the efficiency of the model to reproduce the shear behavior of a similar wall.

In practice, the dimension of the particles is chosen to obtain the same number of stones than in the real masonry wall. The present reference wall has ten stories of six stones in the wall surface. Since the mesoscopic model is only 2D, simulated results correspond to a one-meter thick wall. These results are linearly converted to be compared with the experimental results of the half-meter thick wall.

The parameters identified for the mesoscopic model are given in Table 1, as well as the experimental properties provided in (Silva 2012) and

Table 1. Experimental data and parameters of the mesoscopic model.

Experimental		Model	
Parameter	Value	Parameter	Value
ν_L	0.19	α	0.80
E	2.9 GPa	$\bar{E}$	2.5 GPa
$\boldsymbol{\sigma}^{1,cr}$	0.4 MPa	ϵ_{cr}	10^{-4}
$\boldsymbol{\sigma}^{max}$	2.1 MPa	θ_{cr}	7.10^{-4}

used to calibrate the model: the longitudinal Poisson ratio, the initial Young modulus, the first-crack appearance stress and the peak-load stress.

As the last parameter of the mesoscopic model (i.e. the friction coefficient) can not be identified from the experiments, its value is taken from the literature. Stones friction coefficient is classically assessed to 0.6.

A first verification of the model efficiency lies in checking the monotonic compression response. The simulated and experimental responses are compared in Figure 2. The model is able to reproduce qualitatively and quantitatively the overall response up to the peak-load, before a complete brittle failure of the wall occurs.

Of course, the validation is not complete because part of the experimental compression response has been used to calibrate the mesoscopic model. Therefore, validation is pursued with a shear test under a constant axial compression stress of 1 MPa. The simulated and experimental responses are compared in 3. Masonry used for this test is supposed to be identical to the masonry used for the compression test, therefore we used the same parameters for the mesosocopic model. The simulated response is quantitatively similar to the experimental response up to an applied displacement of 4 mm. Beyond this applied displacement, experimental and simulated responses slightly part ways, brittle failure is observed at 5 mm numerically, while it is observed at 6 mm experimentally.

As an additional confirmation of the efficiency of the mesoscopic model, the numerical crack pattern at the peak-load is given in figure... No comparison can be made with experimental results provided in (Silva 2012). Nevertheless orientation of cracksis relevant to a shear test, implying that the correct failure mechanisms are captured.

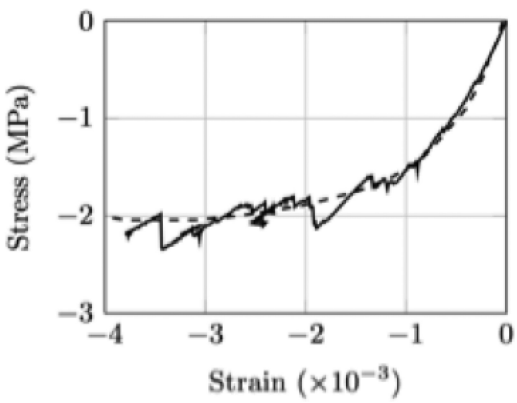

Figure 2. Response of the masonry wall under compressive loading (exp. vs mesoscopic model).

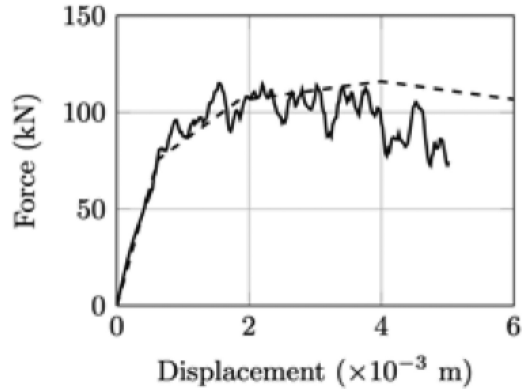

Figure 3. Response of the masonry wall under shear loading (exp. vs mesoscopic model).

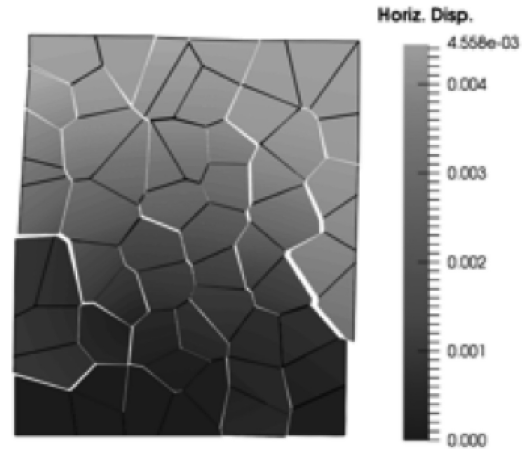

Figure 4. Simulated crack pattern under shear loading with 1 MPa compression.

3 CONTINUOUS MODEL FOR STRUCTURAL ANALYSIS

3.1 *Isotropic continuous damage model*

At the structural level, a simple isotropic damage model is used to describe the old masonry. The main equations are recalled. Its formulation can be seen as a simplified version of the one proposed by Faria, Oliver, & Cervera (1998). Despite its simplicity, this model reproduces the dissymmetrical behavior in tension and compression as well as the unilateral effect for cyclic loading. Furthermore, the damage variable is driven by strain quantity providing through an explicit formulation.

The damage occurring in the masonry is decomposed in two process: one for tension d^t and one for

compression d^c. The Helmholtz free energy of the model is expressed as:

$$\begin{cases} \rho\psi = (1-d^t)\psi_0^t + (1-d^c)\psi_0^c \\ \psi_0^t = \mathcal{H}[\mathrm{Tr}\,\tilde{\sigma}]\epsilon : \mathbf{C}_0 : \epsilon \\ \psi_0^c = \mathcal{H}[-\mathrm{Tr}\,\tilde{\sigma}]\epsilon : \mathbf{C}_0 : \epsilon \end{cases} \tag{5}$$

where $\mathbf{C}_0$ is the fourth-order isotropic linear-elastic constitutive tensor, is the effective stress and $\mathcal{H}[\cdot]$ is the Heaviside function.

By deriving the Helmholtz free energy according to the strain tensor ϵ, one can get the expression of the state law:

$$\sigma = \left((1-d^t)\mathcal{H}[\mathrm{Tr}\,\tilde{\sigma}] + (1-d^c)\mathcal{H}[-\mathrm{Tr}\,\tilde{\sigma}]\right)\mathbf{C}_0 : \epsilon \tag{6}$$

In order to verify the thermodynamical consistency of the model, we have to respect the Clausius-Duhem inequality:

$$\sigma : \dot{\epsilon} - \rho\dot{\psi} \geq 0 \tag{7}$$

This inequality can be verified if we achieve to respect:

$$\begin{cases} \dfrac{\partial \psi}{\partial d^t}\dot{d}^t = \psi_0^t \dot{d}^t \geq 0 \\ \dfrac{\partial \psi}{\partial d^c}\dot{d}^c = \psi_0^c \dot{d}^c \geq 0 \end{cases} \tag{8}$$

By definition, ψ_0^t and ψ_0^c are always positive. As a consequence, we only have to ensure a positive evolution of the damage variables d^t and d^c to verify the Clausius-Duhem inequality. This condition can be simply imposed on the damage evolution law.

The damage thresholds are defined according to the equivalent strain criteria. As the nonlinear behavior is decoupled in two parts in order to reproduce the unilateral effect, two equivalent strains are defined:

$$\begin{cases} \epsilon_{eq}^t = \sqrt{\sum_{i=1}^{3} \langle \epsilon_i^t \rangle_+^2} \\ \epsilon_{eq}^c = \sqrt{\sum_{i=1}^{3} \langle \epsilon_i^c \rangle_+^2} \end{cases} \tag{9}$$

with ϵ_i^t the eigenvalues of the tensile strain tensor $\mathcal{H}[\mathrm{Tr}\,\tilde{\sigma}]\epsilon$ and ϵ_i^c the eigenvalues of the compressive strain tensor $\mathcal{H}[-\mathrm{Tr}\,\tilde{\sigma}]\epsilon$.

The loading surfaces are defined for each nonlinear domains:

$$\begin{cases} f^t = Y^t - \epsilon_0^t \\ f^c = Y^c - \epsilon_0^c \end{cases} \tag{10}$$

where $Y^t = \max(\epsilon_{eq}^t, \epsilon_0^t)$ and $Y^c = \max(\epsilon_{eq}^c, \epsilon_0^c)$.

The masonry exhibits a softening behavior under tensile loading and a hardening behavior followed by a softening behavior under compressive loading. For these reasons, the evolution laws initially proposed for concrete are used:

$$\begin{aligned} d^t &= 1 - \frac{\epsilon_0^t}{Y^t}\exp\left[-B^t(Y^t - \epsilon_0^t)\right] \\ d^c &= 1 - (1-A^c)\frac{\epsilon_0^c}{Y^c} - A^c\exp\left[-B^c(Y^c - \epsilon_0^c)\right] \end{aligned} \tag{11}$$

where A^c, B^c and B^t are the model parameters which control the evolution shape of d^c and d^t and ε_0^t (resp. ε_0^c) the equivalent strain threshold associated to the apparition of the first cracks under tension (resp.compression).

In order to ensure mesh objectivity even during the softening phase, the Hillerborg energy based regularization technique is used. The parameter B^t is adjusted in order to dissipate the same energy in every element independently on their characteristic size h:

$$B^t = \frac{hf^t}{G_f^t} \tag{12}$$

where G_f^t stands for the energy dissipation identified by uniaxial tension test and f^t stands for the peak stress in tension.

For the proposed application, a plane stress condition is considered (i.e. shell element formulation). In order to get this plane stress state, the out-of-plane component is imposed directly equal to zero.

3.2 *Numerical calibration process*

The parameters to be calibrated are the Young modulus, the tensile strength, the compressive limit strain, the energy dissipation, and the coefficients A^c and B^c which are controlling the evolution of damage in compression.

The elastic parameters (i.e. the Young modulus and the Poisson ratio) have been taken identical to the experimental ones. The other parameters have been identified thanks to a virtual compression test and a virtual tension test performed with discrete mesoscopic model through an optimized calibration technique.

An error function, which describes the distance gap between the discrete model curve $\mathbf{f}^{DEM}$ and the continuous one $\mathbf{f}^{CON}$, is defined:

$$F_{error}(\mathbf{x}) = \sum_{i=0}^{n_{end}} \sqrt{\frac{|f_i^{DEM} - f_i^{CON}(\mathbf{x})|}{|f_i^{DEM}|}} \quad (13)$$

The error function depends only on the five nonlinear parameters of the damage model which are stored in $\mathbf{x}$. The identification of theses parameters is then performed with the a minimization process using the GRENAT tool (Laurent, Boucard, & Soulier 2013). It provides a very inexpensive approximate responses of the objective function and enables to achieve a global optimization and to obtain the global minimum. The process only require to test 2^5 parameter combinations, which represents only 2 hours for the tensile test with a simple 12 Go memory and 64 bits computer.

The parameters identified for the continuous damage model are given in Table 2.

As a first verification of the efficiency of the continuous damage model, one can check the monotonic responses used for the calibration process. Thus, Figure 5 gives a comparison between the continuous responses in compression and Figure 6 in tension. The experimental response is given when available. One can notice that the overall behavior is well reproduced and the limit strengths are correctly estimated in both cases.

For further validation, the responses of the shear test under a constant axial compression stress of 1 MPa are presented in Figure 7. The responses are similar in the elastic phase but they start diverging around 1 m. Nevertheless, the observed gaps between the two models and the experiments remain acceptable especially since no calibration of the shear process has been performed for the continuous damage model.

It has to be pointed out that even if a simple continuous damage model is considered here, this calibration procedure can be easily used to identify more complex model with a larger set of parameters.

Table 2. Parameters of the continuous damage model.

Parameter	Value
ε_0^t	$6{,}67.10^{-5}$
ε_0^c	$1{,}56.10^{-4}$
G_f^t	10 J.m
B^c	1500
A^c	0.185

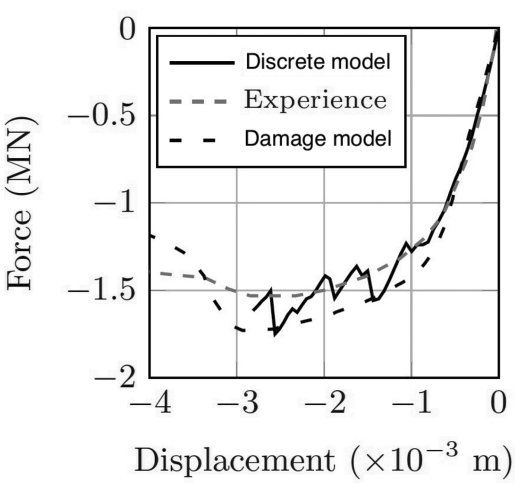

Figure 5. Response of the masonry wall in compression.

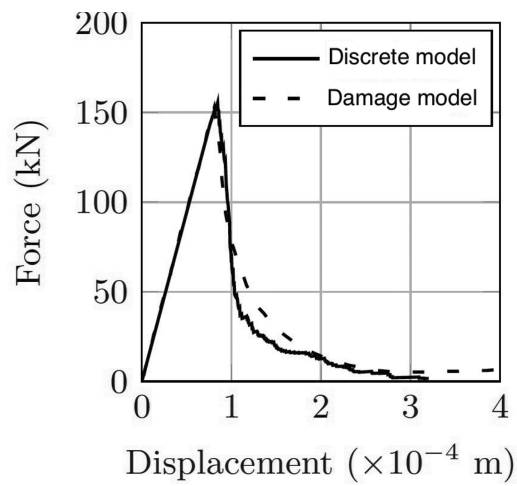

Figure 6. Response of the masonry wall in tension.

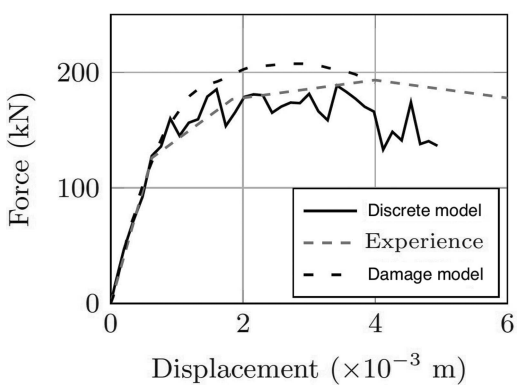

Figure 7. Response of the masonry wall in shear.

4 ANALYSIS OF AN OLD MASONRY CHURCH

An application of the continuous damage model, and thus of the virtual testing method to identify the masonry, to a complete old masonry structure is now presented. One should note that it because it is not possible to know the values of the material parameters for this specific church, the parameters identified previously are conserved. To take into account the specificities of each church and the characteristics of its materials, we only modify the elastic parameters, according to in-situ modal data.

4.1 *Description of the church*

The Notre-Dame de la Gorge church (NDG) is located in the Chamonix—Mont Blanc Valley in the French Alps, at 1250 meters above the sea level. The ground slope between the entrance facade and the choir is greater than 15 %. This church has been built between 1699 and 1701, and exposes some precious baroque cultural assets: statues, reredos, paintings (Limoge-Schraen, Giry, Desprez, & Ragueneau 2015). As shown in Figure 8, NDG has a single nave, with a rectangular tribune above the first span of the nave. The choir and the sacristy are 3.5 m narrower than the nave, and 3 steps above it. They are covered by a roof lower than the one over the nave, which is ended by an important cantilevered part over the entrance facade. The bell tower is placed along the nave, and covered by an onion shaped roof. During the Revolution it has been transformed into a stable which explains the structural evolution such as modifications of the openings or the add of a small lintel. The church has been very little maintained during the 19th century,

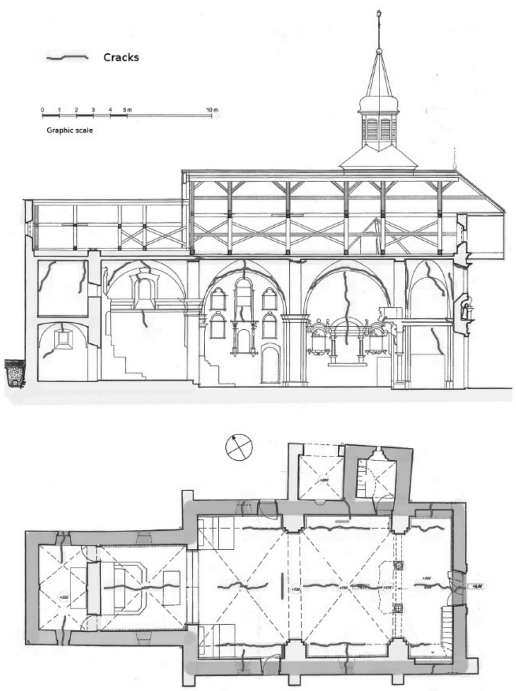

Figure 8. Plan and longitudinal section of NDG church. Cracks noticed during the field survey.

The masonry is very rustic, with an important proportion of mortar and small irregular stones. No data was available regarding its mechanical characteristics but the disposition of the stones and the materials are considered to be close to the ones in studied by Silva (2012). As a consequence, the nonlinear parameters considered are the ones identified previously. The only paired stones are in the basement of the bell tower and in the corner of the entrance facade. As showed in Figure 8, cracks are numerous, especially around the openings, between the nave and the choir, and in the vaults. Some of them are opened through the entire wall, such as the one in the entrance facade.

4.2 *Numerical study*

The mesh of the structure has been developed from plans and in-situ measurements (i.e. laser pointing and photogrammetry). The elastic parameters of the different parts of the church have been identified thanks to modal updating. The proposed method for the modeling of the whole building and the modal updating of the global model is explained in (Limoge-Schraen, Giry, Desprez, & Ragueneau 2015). All computations have been performed with the finite element code Cast3M.

Pilasters, buttresses, arches and structural elements of the framework such as the belfry, the onion shaped bulb and the inferior purlins in the choir and the nave, are modeled with beam elements. For the masonry elements multifiber beam elements with nonlinear material laws are considered.

Walls, vaults and tribune are described with multilayer shell elements. Even if it is a strong assumption, Casarin (2006) has shown with parametric tests that shell elements give relevant results for an entire structure under seismic loading. The masonry of each substructure of NDG is characterized by a tensile strength $f' = E\epsilon_0'$ and the Young modulus has been identified during the modal updating.

The Vallorcine earthquake (2005) is considered as a loading because it is representative of the seismic activity in the studied area. Indeed, it is the strongest earthquake recorded in the area since the establishment of the instrumentation and it is well-below the reference accelerations.

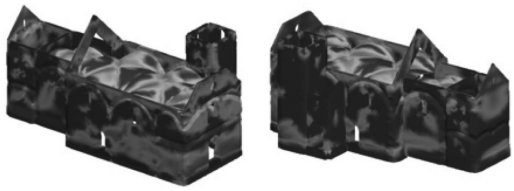

Figure 9. Damage field at the end of the Vallorcine earthquake (2005).

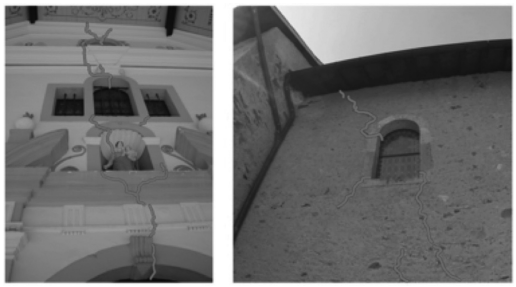

Figure 10. Surveyed damage in NDG.

Figure 9 shows the tensile damage field d^t at the end of the 22 seconds signal. One can notice the concentration of the damage in the vaults. The computed damage areas are consistent qualitatively with the history of the disorders observed in the studied churches, as shown by the comparison with Figure 10.

5 CONCLUSIONS

In this work a global methodology for the seismic vulnerability assessment of an entire non-paired masonry structure from the material behavior up to the structural response has been proposed. At the material scale, a virtual testing tool, initially developed for concrete, has been adapted for non-paired old masonry. A comparison with experimental data from the literature has shown the capacity of this tool to efficiently reproduce the nonlinear behavior of the masonry.

At the structural scale, it stays necessary to have a material model which allows taking into account the highly nonlinear behavior of masonry under seismic loading while keeping a relatively small computational time. To fulfill this requirement, an isotropic continuous damage model has been considered. In order to identify the parameters of this model and to investigate different loading paths, the virtual testing tool has been used. This identification process is a very interesting answer to many problems encountered in historical masonry structures assessment, particularly the difficulty to manage in-situ tests and to replicate the real loadings in laboratory tests. In order to illustrate the whole process, the response of a church under seismic loading has been studied. The main damages observed on the structure have been retrieved considering a historical earthquake in the region of interest.

As perspectives, the development of a full 3D version of the virtual testing tool could allow to describe out-of-plane crack and additional ruin mechanisms of the masonry wall. Furthermore, the influence of the out-of-plane heterogeneity of the wall could be investigated. Concerning the macroscopic model, more complex models can be identified. Indeed, the capacities of the virtual testing tool have not been fully used as the description of friction during cyclic loading. It has been shown for application son concrete that hysteretic phenomena can be efficiently identified with this virtual testing tool.

REFERENCES

Casarin, P. (2006). *Structural assessment and seismic vulnerability analysis of a complex historical building*. Ph. D. thesis, University of Trento.

Faria, R., J. Oliver, & M. Cervera (1998). A strain-based plastic viscous-damage model for massive concrete structures. *International Journal of Solids and Structures. 35*(4), 1533–1558.

Laurent, L., P.-A. Boucard, & B. Soulier (2013). A dedicated multiparametric strategy for the fast construction of a cokriging metamodel. *Computers and Structures. 124*, 61–73.

Lemos, J. (2007). Modeling of historical masonry with discrete elements. *International Journal of Architectural Heritage: Conservation, Analysis, and Restoration. 1*(2), 190–213.

Limoge-Schraen, C., C. Giry, C. Desprez, & F. Ragueneau (2015). Toward a large-scale seismic assessment method for heritage building: Vulnerability of masonry baroque churches. *European Journal of Environement and Civil Engineering. 20*(6), 680–710.

Silva, B. (2012). *Diagnosis and strengthening of historical masonry structures: numerical and experimental analyses*. Ph. D. thesis, University of Padova.

Vassaux, M., C. Oliver-Leblond, B. Richard, & F. Ragueneau (2016). Beam-particle approach to model cracking and energy dissipation in concrete: Identification strategy and validation. *Cement and Concrete Compositions*. *70*, 1–14.

Vassaux, M., B. Richard, F. Ragueneau, A. Millard, & A. Delaplace (2015). Lattice models applied to cyclic behavior description of quasi-brittle materials: advantages of implicit integration. *International Journal for Numerical and Analytical Methods in Geomechanics. 39*(7), 775–798.

Computational Modelling of Concrete Structures – Meschke, Pichler & Rots (Eds)
© 2018 Taylor & Francis Group, London, ISBN 978-1-138-74117-1

The adobe delta damage model

T. Li Piani
Civil Engineering Faculty, Structural Mechanics Section, TU Delft, Delft, The Netherlands
TNO, Defence, Safety and Security, Rijswijk, The Netherlands
Netherlands Defence Academy, Faculty of Military Sciences, Den Helder, The Netherlands

J. Weerheijm
Civil Engineering Faculty, Structural Mechanics Section, TU Delft, Delft, The Netherlands
TNO, Defence, Safety and Security, Rijswijk, The Netherlands

L. Koene
Netherlands Defence Academy, Faculty of Military Sciences, Den Helder, The Netherlands

L.J. Sluys
Civil Engineering Faculty, Structural Mechanics Section, TU Delft, Delft, The Netherlands

ABSTRACT: A local damage model has been developed for interpreting the dynamic performance of Adobe, a traditional form of masonry whose components are made of sun-dried and unpressed soil possibly reinforced with fibres. This paper presents a numerical model to assess the static performance of bricks and mortar of Adobe. It has been validated with reference to the results of a characterization campaign performed in 2016 on Adobe bricks and mortar produced in Germany. Although Adobe buildings are among the oldest examples of masonry constructions, spread in all continents of the world, the properties of the material and the overall mechanical performance are still poorly understood, especially with respect to the influence of the adopted mixture on the mechanical properties. As a consequence, very few numerical models are developed for Adobe. The assessment of Adobe structures is becoming a priority task because they are often spread in areas of the world prone to a wide range of dynamic hazards, whose disastrous consequences must be prevented. As for masonry, the overall performance of Adobe structures depends on the properties of bricks and mortar. Three types of bricks and one type of mortar with different element mixture compositions were tested in compression and bending tests and their behaviour was analysed. The interpretation of experimental results classifies Adobe as a quasi brittle material, with special reference to concrete. Moreover, it was found out that for the same mineralogical family, the amount of fibres in the mixture of Adobe controls the deformation capacity of Adobe. Overall, a numerical model for Adobe was cast within a damage concept originally defined for concrete. A modified version of the last damage model by Mazars was developed. In order to avoid the typical mesh dependency that characterizes simulations of softening materials, a local regularization algorithm was implemented, starting from the damage delay model developed by Allix. Overall, only two mechanical parameters in compression and tension are required to calibrate the loading evolution laws of the model. In fact, the initial damage strains and elastic moduli in tension and compression were derived directly from the mean values experimentally associated to each mixture. For each type of mixture, numerical simulations on resulting bricks were performed in statics for uniaxial compression and three point bending tests using the strength and strain values experimentally derived. The mechanical parameters of the model were calibrated in order to match the experimental force displacement curves. The Adobe delta damage model proves to constitute a suitable tool to predict the material performance of Adobe. This paper resumes the experimental campaign, presents the algorithmic details of the model and the comparisons with respect to experimental data and mesh dependence.

1 INTRODUCTION

This paper presents an isotropic damage model for the mechanical performance assessment of quasi brittle materials characterized by softening laws in tension and compression. This model proposes to solve mesh dependence, a typical pathology of these materials, that leads to progressive damage

concentration upon mesh refinement, by means of a local regularization algorithm. The numerical model presented herein takes its roots from a modified version (Pereira, Weerheijm, & Sluys 2017) of the last local damage model developed by Mazars (Mazars, Hamon, & Grange 2015). Instead of emplacing a non local regolarization algorithm like in the original model, mesh objectivity was proposed to be solved by means of a rate dependent model (Van Der Meer & Sluys 2009). On the other hand, it was recently shown that not always strain rate models are effective at solving mesh dependency (Pereira, Weerheijm, & Sluys 2017). Therefore, in the present model mesh objectivity was aimed to be obtained incorporating local damage loading laws with "delta" functions, implemented using Allix's damage delay formulations for composites (Allix & Deu 1997). The results obtained with the presented model show that rate dependent damage models are a valuable strategy to obtain mesh objective simulations in 1D and 2D using isotropic damage models developed for brittle materials (Ortiz, Deletombe, & Chuzel-Marmot 2015). The mechanical parameters of the model have been calibrated with respect to the results of static tests on bricks and mortar of Adobe. It connotes one of the most ancient form of masonry on Earth, constituted by unpressed sun dried earthen bricks joint together by mud mortar (Houben & Guillaud 1994). Neglected for centuries since the adoption of modern building materials, Adobe has been gaining serious attention among Western countries in the last decades (Thompson 2015). In fact, Adobe buildings offer high thermal and acoustic performances and they constitute a class of eco-friendly materials, theoretically completely recyclable (Parra-Saldivar & Batty 2006). Moreover, they are easy to produce and cheap to build; for these reasons, they are largely spread in developing countries (Agarwal 1975). Unfortunately, the mechanical properties of these buildings, often spread in areas of the world prone to earthquakes, are still not completely addressed (Arya, Boen, & Ishiyama 1986). Thus, a common approach in literature is to simulate the performance of entire structures using modelling techniques and material models already available in libraries of commercial software (Angelillo, Lourenço, & Milani 2014). Therefore, the current research on this masonry started from an experimental campaign on its components, namely brick and mortar (Li Piani, Krabbenborg, Weerheijm, Koene, & Sluys 2017). Two types of bricks made of different mixture and one type of mortar were physically and mechanically characterized for static loading. The results obtained classify Adobe components within the class of quasi brittle materials: softening force displacement curves characterize failure in tension and compression, whose slope is controlled by the amount of fibres present in the mixture. The results of the campaign are resumed in the second section of this article. Experimental tests were used as a starting point to calibrate the numerical model developed for Adobe. The algorithm presented in section 3 was developed with the main goal of keeping it as intuitive and simple as this ancient building technology is. Only two mechanical parameters are necessary in tension and compression. They are calibrated with respect to the static tests on Adobe components in pure compression and bending tests. The numerical simulations and the experimental-numerical comparisons are reported in section 4. It also contains the evidence of mesh objectivity by means of numerical simulations for mesh refinement.

2 AN EXPERIMENTAL CAMPAIGN ON ADOBE BRICKS AND MORTAR

Two types of bricks with different mixture composition (Type A-B) and one mud mortar (Type M) used to assemble Adobe walls were physically and mechanically characterized at the military engineering laboratory in Breda, in the Netherlands. Physical and mechanical tests were performed. For an extensive reading of the experimental campaign, please be referred to the article of the authors (Li Piani, Krabbenborg, Weerheijm, Koene, & Sluys 2017).

Ranges of soil mixture element percentages and mean density values are reported in Table 1 for each type. In the following, only the main observations from the mechanical tests are resumed.

2.1 *Preparation and test setup*

Compressive tests were performed on at least six samples per type according to UNI EN 772-1. Displacement controlled analyses at a speed rate of 2 mm/min were performed. Samples extracted from six bricks and rectified in order to assure plane parallelism of surfaces were put in contact with the steel plates of the Universal Testing machine (Figure 1a). Furthermore, three point

Table 1. Physical properties of the tested Adobe.

Type	Clay %	Silt %	Sand %	Fibre %bw	Density kg/m^3
A	24–25	47–48	27–28	17–18	1230
B	18–19	43–46	30–33	32–37	800
M	11–12	66–68	21–22	3–5	1410

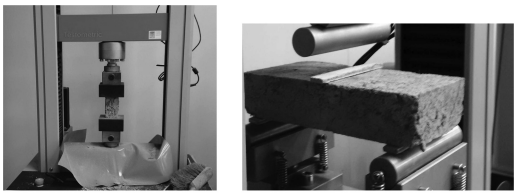

(a) (b)

Figure 1. Test setup in compression (a) and bending (b).

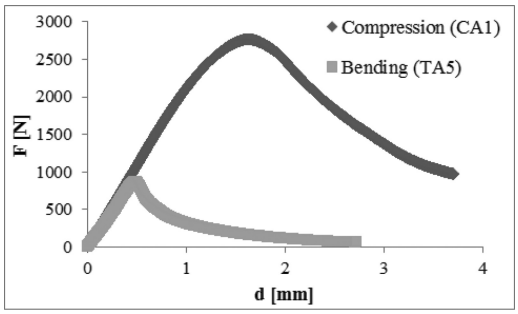

Figure 2. Typical F-d shape in compression and tension (Type A).

bending tests were performed on at least four samples per type according to UNI EN 12390-5. Displacement controlled analyses at a speed rate of 1 mm/min were performed. Entire bricks were rectified when necessary prior to testing. In order to avoid possible indentation, the direct contact between both the two inferior and the superior steel rolls was prevented through interposition with stripes of wood (Figure 1b).

2.2 *Observations and test results*

The force displacement plots in compression reveal three phases in the material response of Adobe to uniaxial compressive loading (Figure 2).

The initial response of bricks and mortar is linear and the brick is supposed to be intact. At a stress level between 55% (mainly for Type B) and 85% (mainly for Type M) of the strength pre-peak hardening behaviour is observed. At this phase, internal microcracking processes are supposed to start in the material but the external surfaces of the samples remain intact until peak load is reached. After the peak load, diagonal macro-cracks become visible starting from the corners of the samples (Figure 3a), and a softening behaviour is shown in the force displacement curve (Figure 2). The force displacement plots in three point bending tests reveal two distinct phases in the material response of air dried Adobe (Figure 2). The material response is linear until approximately the peak load (95–100% of the peak load for Type A and M, slightly lower for Type B), when a single crack is formed at the mid span of the bottom side (Figure 3b), that anticipates an immediate post peak softening behaviour (Figure 2). The crack quickly propagates and the attainment of the residual strength tail in the force displacement curve corresponds to a crack length of about 83–90% of the specimen height (Figure 3b).

For each force-displacement curve in compression, the compressive strength (f_b), the strain at peak stress (ε_{f_b}), the elastic stiffness (E) and the ratio between the displacement at 20% of decay of strength over the peak load displacement (d_u) are

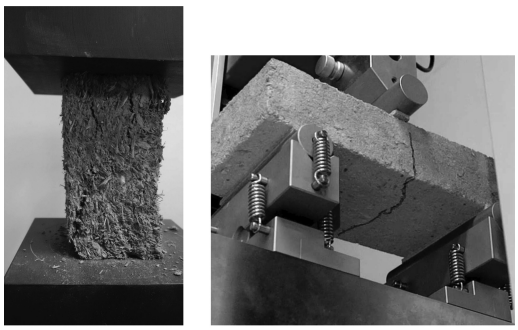

(a) (b)

Figure 3. Typical cracking patterns for Adobe bricks in compression (a) and bending.

Table 2. Mechanical parameter in compression.

Type	f_b MPa	E MPa	ε_{f_b} %	d_u –
A	1.3(0.1)	101(16)	1.9(0.3)	1.4(0.2)
B	0.2(0.0)	12(2)	3.1(0.3)	1.5(0.1)
M	1.6(0.1)	210(56)	0.9(0.2)	1.4(0.1)

Table 3. Mechanical parameters in tension.

Type	f_{fl} MPa	E_{fl} MPa	ε_{fl} %
A	0.7(0.1)	100(25)	0.7(0.2)
B	0.2(0.3)	21(4)	1.1(0.1)
M	0.7(0.1)	195(24)	0.4(0.1)

reported in Table 2. In tension the flexural strength (f_{fl}), the flexural modulus (E_{fl}) and the strain at peak stress (ε_{fl}) are shown in Table 3. The experimental campaign revealed that the mechanical

parameters strongly depend on the adopted soil mixture. Within a same mineralogical family, an increase in the ratio of clay enhances strength and elastic modulus, while fiber reinforcement governs the deformation performance.

3 THE ADOBE DELTA DAMAGE MODEL

As a consequence of the depicted failure patterns, the research of a numerical tool for Adobe was performed within models for concrete-like materials. In particular, the modified version of the last isotropic damage model developed by Mazars (Mazars, Hamon, & Grange 2015) was adopted as starting point (Pereira, Weerheijm, & Sluys 2017). The model is characterized by the definition of two different damage evolution laws for tensile cracking and compression crushing, calculated through separated loading functions and properly combined. On the other hand, it is well known that numerical simulations of softening materials like Adobe using damage models suffer of mesh dependence, a numerical pathology that leads to localization of damage in a single element for mesh refinement (Sluys & de Borst 1992). In order to avoid this issue, different approaches are suitable. In the original Mazars', a so called non-local model was implemented (Mazars, Hamon, & Grange 2015). Despite their efficiency, these algorithms usually imply non obvious code developments (Pijaudier Cabot & Bazant 1988). Instead for Adobe, a simpler approach capable of maintaining the model local was preferred. Thus, rate dependent models were investigated (Van Der Meer & Sluys 2009). Few models in literature have proved to be capable of solving mesh dependency using artificial viscosity (Sluys & de Borst 1992) (Suffis, Lubrecht, & Combescure 2003). Among them, a damage delay framework initially adopted by Allix in 1997 was chosen (Allix & Deu 1997). The features of the final model and the implementation aspects are described in the following paragraph. The code was developed in C++ using an implicit Newton-Raphson solution algorithm.

3.1 *Model description*

The stress tensor of an isotropic damage model is usually expressed:

$$\sigma = (1-\omega)\tilde{\sigma} \quad \text{with} \quad \tilde{\sigma} = E : \varepsilon, \tag{1}$$

where ε is the strain vector, E the elastic stiffness tensor w is the damage scalar, that ranges between 0 and 1 and $\tilde{\sigma}$ is the effective stress vector. In order to avoid numerical issues, the maximum value of damage in each integration point is limited to 0.9995. The damage is built starting from the definition of the loading functions.

As in Mazars (Mazars, Hamon, & Grange 2015), two equivalent strain formulations depending on the first invariant and second deviatoric invariant of strain are implemented for tension and compression. In eq. (2), they are though developed within the octahedral space, to derive a direct link with pressure (p) and deviatoric stress tensor (q) according to relations in eq. (3)

$$\begin{cases} \varepsilon_{eq_t} = \dfrac{1}{(1-2\nu)} * \varepsilon_{oct} + \dfrac{1}{2(\sqrt{2}*(1+\nu))}\gamma_{oct} \\ \varepsilon_{eq_c} = \dfrac{3}{(2\nu-1)} * \varepsilon_{oct} + \dfrac{3}{2(\sqrt{2}*(1+\nu))}\gamma_{oct} \end{cases} \tag{2}$$

where ε_{oct} and γ_{oct} respectively are the normal and tangential strain components with reference to the octahedral plane, related to the stress space as in eq. (3):

$$\begin{cases} \varepsilon_{oct} = \dfrac{1-2\nu}{E} p \\ \gamma_{oct} = \dfrac{2(\nu+1)}{3E} q \end{cases} \tag{3}$$

The evolution of the nonlinear response is directly related to the growth of two monotonic internal variables k_t and k_c which account for the historical maximum equivalent strain reached during loading, implemented in eq. (4) according to (Pereira, Weerheijm, & Sluys 2015).

$$\begin{cases} k_c(i) = \max[\varepsilon_{eq_c}(1-r^{\alpha}), k_c(\tau)] \quad \text{for all} \quad i \geq \tau \\ k_t(i) = \max[\varepsilon_{eq_t} r^{\alpha}, k_t(\tau)] \quad \text{for all} \quad i \geq \tau \end{cases} \tag{4}$$

where r is the triaxiality factor proposed by Lee and Fenves (Lee & Fenves 1998) for multiaxial loading states, α is a constant set to 0.1 and the mechanical parameters k_{0t} and k_{0c} are the damage initiation strains in tension and compression (Pereira, Weerheijm, & Sluys 2015).

The equivalent strain values enter the damage evolution law, which combines two internal functions independently developed for compression crushing (ω_c) and tension cracking (ω_t) as in eq. (5).

$$\omega = 1-(1-\omega_t)(1-\omega_c) \tag{5}$$

In turn, the local evolution laws are pure softening functions after damage initiation (Ortiz, Deletombe, & Chuzel-Marmot 2015). They are calculated as in eq. (6).

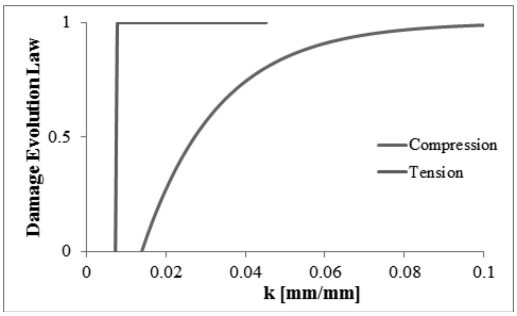

Figure 4. Damage profiles in tension and compression (using calibrated parameters for Type A).

$$\begin{cases} (\omega_c)^L = 1 - \dfrac{1}{e^{C(k_c - k_{0c})}} \\ (\omega_t)^L = 1 - \left(\dfrac{k_{0t}}{T k_t} \right) \end{cases} \tag{6}$$

where C and T are material parameters in compression and tension (Figure 4) and L denotes local.

Given a generic prescribed displacement ($d = \frac{u}{N} i$), where u is a displacement function with unit meter (in statics) or time (in dynamics), N is the number of steps the displacement is subdivided in and i is the iteration step number. Both the loading evolution laws in compression and tension are updated at each iteration after damage initiation in order to account a "delta" increment according to eq. (7):

$$\omega_i = \delta\omega_i + \omega_{i-1} \tag{7}$$

where the delta functions $\delta\omega$ at each step are calculated using the exponential function of the damage bounded rate of damage developed by Allix et al. at the "*Laboratorie de mecanique e technologie de Cachan*" in 1997 (Ladevéze, Allix, Deü, & Lévêque 2000).

$$\begin{cases} \delta\omega_c = \dfrac{\Lambda_c}{N}(1 - e^{-(w_{c_i}^L - w_{c_{i-1}})}) \\ \delta\omega_t = \dfrac{\Lambda_t}{N}(1 - e^{-(w_{t_i}^L - w_{t_{i-1}})}) \end{cases} \tag{8}$$

where Λ_t and Λ_c are two non-dimensional material parameters that accelerate damage and N is needed to make the results independent of load discretization.

3.2 *Numerical simulations of adobe subjected to uniaxial compressive tests and three points bending tests*

Before performing numerical simulations with the developed model, some preliminary hypotheses on the material parameters and simulation goals are made:

- The mean values of elastic stiffness experimentally derived for each type are used in the model for compression tests. Not all curves are considered for the analysis but only those which fit the Interquartile Range method (IQR) for compressive strength and strain at compressive strength.
- A 0.1 value for the Poisson ratio is assumed, which is equal to the value referred in the only known research devoted to the issue for Adobe (Silveira, Varum, & Costa 2013)
- For sake of simplicity, the value of Λ is initially assumed constant for bricks and mortar in tension and compression
- All material parameters used in compression are taken the same in bending tests
- The calibrated value of initial damage strain in compression (k_{0c}) is imposed to lie in the range between 0.5 and 0.8 of the mean compressive strength value resulting from experimental evidence for each type.
- The elastic stiffness and the initial damage strain in tension (k_{0t}) are determined in agreement with the sigma-epsilon method proposed by the RILEM standard for steel fibre reinforced concrete (RILEM TC 162-TDF 2003). The model is linear elastic with a modulus same as in compression until the attainment of the stress level associated to the first crack in bending. Consistently with experiments, the cracking stress level is approximated with the flexural strength in the Adobe model.

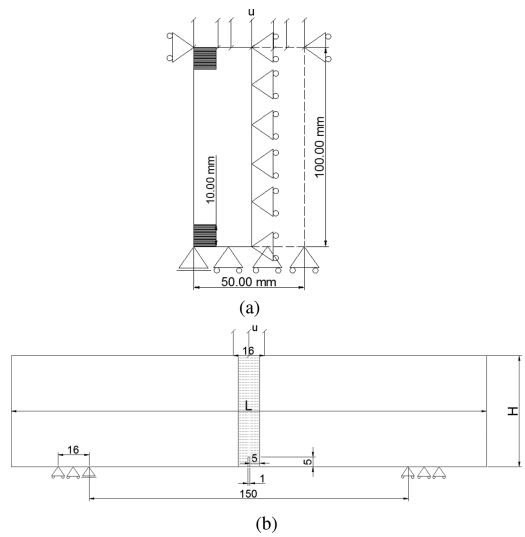

Figure 5. Numerical setup in compression (a) and bending (b) tests.

- The numerical simulations are meant to replicate the real geometry and setup of the tested samples. In compression, the value of height over cross side ratio is maintained and approximate geometrical dimensions are chosen for the sample. In order to trigger localization consistently with the experimental observations, a mechanical defect (initial damage strain equal to 0.1%) is imposed at corners of the specimen. For sake of simplicity, only half of the brick is modelled numerically (Figure 5(a)). For bending simulations, the mean geometrical measures of the tested samples are taken for each type. A geometrical imperfection is used to trigger localization (Figure 5(b)).
- The numerical simulations in compression and bending are performed in order to match as closely as possible the slope of the mean force displacement relations built averaging the experimental curves using parabolic-linear functions in compression and exponential in tension, at least until ultimate displacement levels (larger deformation levels are not experimentally available for all tests in compression).
- A mesh with bilinear quadrilateral element with four integration points is used. Selective quadrilateral mesh refinement of 1 mm is imposed for 5 cm at the right and left end side of the notch (in grey in Figure 5(b)) in the bending test. 2.5 mm mesh is used for tests in compression.
- Displacement controlled analyses are imposed at the upper side of the brick in compression (Figure 5(a)) and at the mid span in tension (Figure 5(b)). A precision of $(1*10^{-4})$ was imposed.

The best fit simulations are shown for each Type in Figure 6 in terms of force displacement plots. They are presented together with the mean experimental curves associated to each Type and within its experimental envelopes. Also an example of a typical experimental F-d curve is presented in the same graph. The list of calibrated numerical parameters in compression and tension for bricks and mortar are reported in Table 4. From each numerical curve both in tension and compression, values of mechanical parameters were deducted and graphically compared with the mean experimental ones reported in Tables 2–3 (Figure 10).

In compression (Figure 6(a-c)), with all the aforementioned assumptions for all the types, the best fit numerical curves matched the slope of the experimental ones until at least ultimate displacement. In this sense, it was possible to set a fixed value for Λ_c for all types, leaving only C as the mechanical calibrating parameter. Moreover, the best fit for initial damage strain levels in Table 4 are consistent with experimental observations: the attainment of

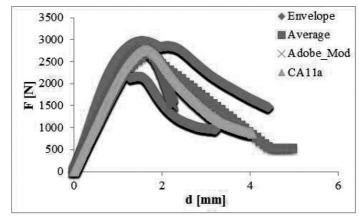

(a)

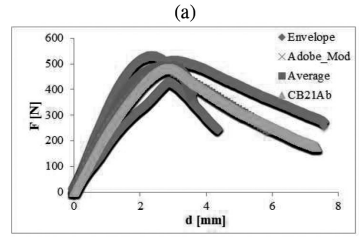

(b)

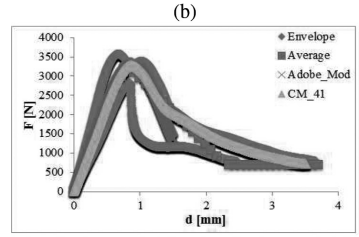

(c)

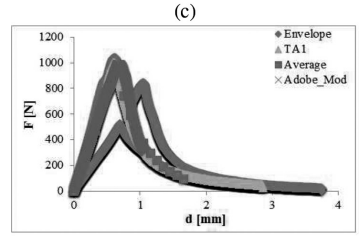

(d)

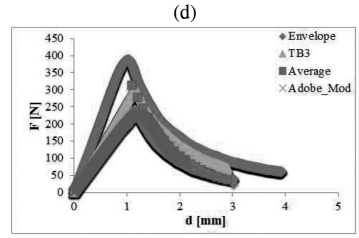

(e)

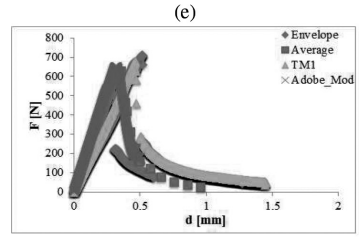

(f)

Figure 6. Experimental-numerical comparisons in compression (a-c) and flexure (d-f) for Type A (a;d), Type B (b;e) and M (c;f).

Table 4. List of best fit parameters for Adobe bricks and mortar.

Type	C –	Λ_c –	T –	Λ_t –	k_{0_c} %	k_{0_t} %
A	55	4.0	1000	160	1.3	0.7
B	25	4.0	1000	70	1.5	1.1
M	160	4.0	1000	440	0.7	0.4

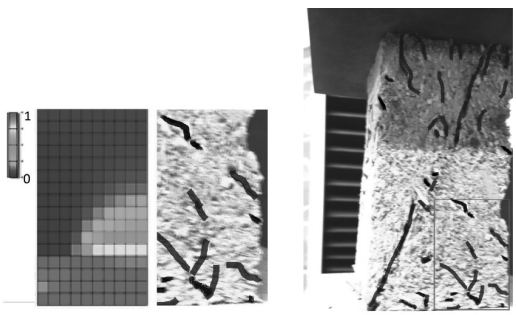

(a) (b)

Figure 7. Damage in a quarter of brick using the Adobe delta damage model in compression and zoom on experimental cracking pattern (a) of CA11a cracking pattern in uniaxial compression (b).

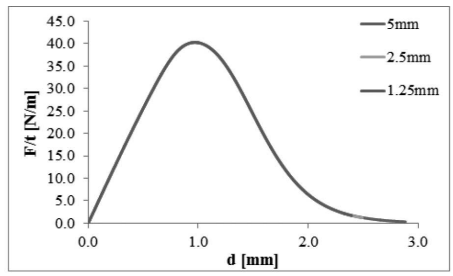

(a)

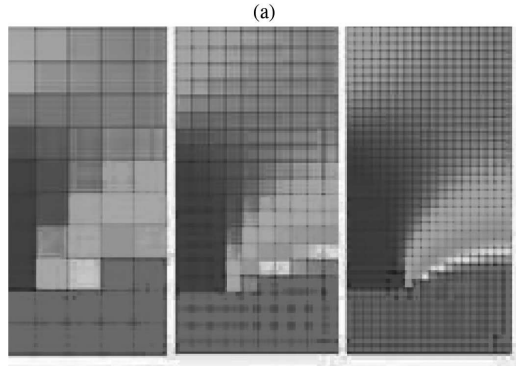

(b)

Figure 8. Force displacement curve in compression for Type A for different meshes and related failure pattern at d = 2.1 mm.

the pre-peak non linear branch happens at highest stress levels for Type M (0.8 times the compressive strength) and lowest for Type B (0.5). As a result of its simple formulation, at larger deformations, the loading functions are not sufficient to capture the slope of the post peak experimental curve, despite the numerical curve remains within the experimental envelope until at least 50% of the compressive strength. Also the comparison with experiments in terms of mechanical parameters reveals a good match, with relative errors smaller than 5% (Figure 10). Moreover, despite the numerical setup and the three dimensionality of the problem, the model could recall some features of the diagonal cracking typical of many tested samples (Figure 7).

Two dimensional tests in compression and tension were performed with different meshes using the best fit calibrated mechanical parameters (Table 4). A wide range of parameter combinations were tested and the results prove the mesh independence of the model (Figure 8). In particular, for all tested cases, the convergency to the mesh independent solution is already achieved using the 2.5 mm mesh.

Next, the bending tests have been analysed. Also for three point bending tests, the numerical simulations accomplished the desired goal (Figure 6(d-f)). Using the material parameters derived in compression and the flexural strain as given in RILEM, it was possible to match the elastic and post peak softening curves derived for bricks and mortar. It was not possible to keep the Λ_t value constant as in compression, because the F-d curve in bending, for all types of Adobe, required the adoption of very high values of T (Table 4). The average curve of each type was matched calibrating the values of Λ_t in eq. 8. Its value resulted maximum for Type M and lowest for B. For both Type A and Type M, the numerical simulations matched most of the average experimental curves. Only for Type B the numerical F-d plot is located in the inferior bound of the envelope. This may confirm the finding in the previous paper that cutting and rectification processes can result in a pre-damage state of soft Adobe bricks. Moreover, the mechanical parameters deducted from each numerical analysis according to elastic calculations lie within the standard deviations of each experimental parameter experimentally determined (Figure 10). Also in terms of failure pattern, the numerical simulations were similar to Adobe's experimental response (Figure 9). For both the bricks and the mortar, a single crack

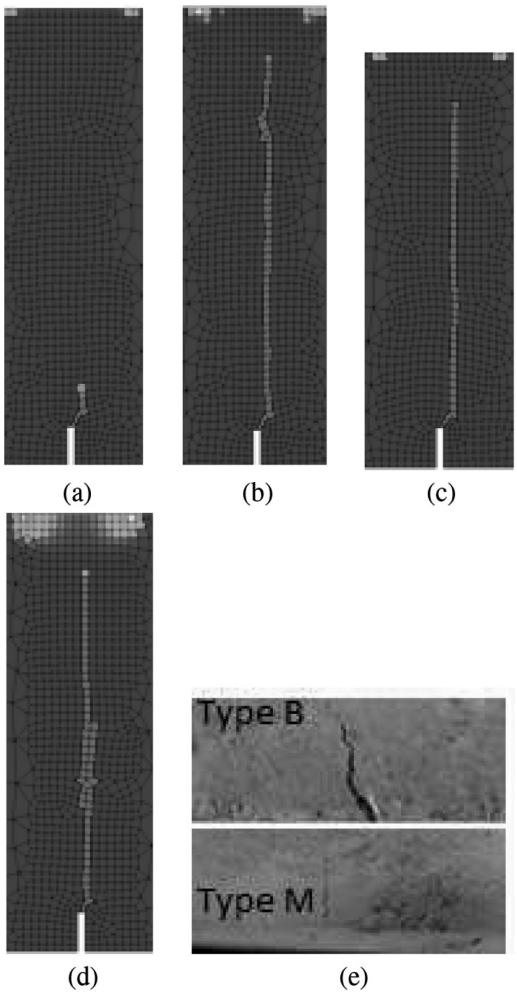

Figure 9. Crack propagation at d = 0.7 mm(a) and d = 1.2 mm (b) for Type A, at d = 2.2 for Type B (c) and at d = 0.5 mm for Type M (d); crack comparison between Type B and M (e).

is formed in the middle of the brick just before the attainment of the peak load (Figure 9(a)). After peak load, it grows very fast (Figure 9b-d). The crack width itself numerically derived is consistent with the observed physics: wider cracks characterize many samples of Type B with respect to Type A and Type M (Figure 9(e)). For Type A and M, the indentation effect is numerically negligible (Figure 9(b,c)), while in case of the soft Adobe (Type B), damage propagation is starting from an early stage of loading. In the experiment, damage was prevented by using wooden stripes on the top of each brick corresponding to the steel roll.

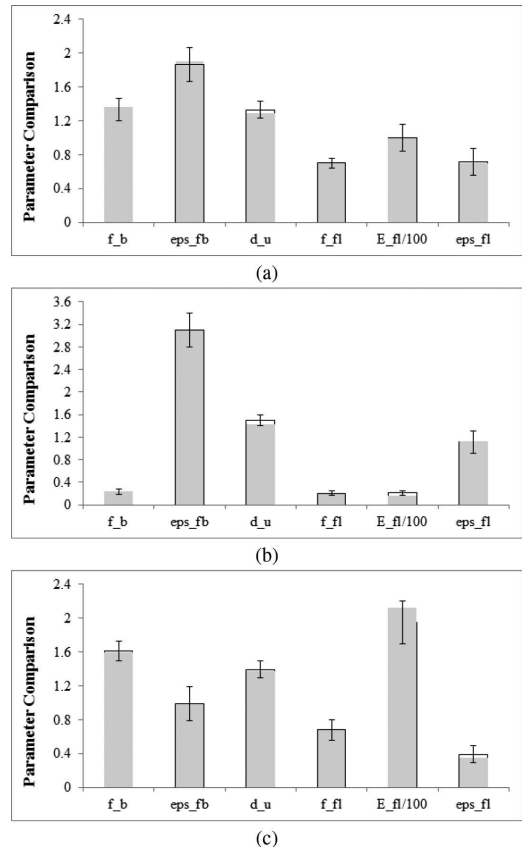

Figure 10. Experimental-numerical comparisons for each mechanical parameters in Chapter 3 in compression and tension for Type A(a), B(b) and M(c).

4 CONCLUSIONS

In this paper, a modified version of the last Mazars isotropic damage model solves the pathological mesh dependence of softening law-materials in mode I by means of a local regularization algorithm. In particular, an adaptation of rate dependent damage models in statics lead to the definition of a generic delta formulation included in the damage evolution laws of the model. In recent studies it was shown that the same local model could not be regularized by means of strain rate inclusion. Instead damage delay models, originally developed for composites materials, can be suitable tools also to address the response of brittle materials such as Adobe through the retardation of damage. In the delta functions, Λ are mechanical parameters of the model which control the ductility of the model. These parameters have been calibrated for address-

ing the static response of Adobe components. Bricks and mortar have been identified in the class of quasi brittle materials and their response in tension and compression is characterized by softening laws in the force displacement graphs. Therefore, mesh objectivity is a priority task also in the modelling of Adobe. The numerical model developed for Adobe proved to be capable of assessing the static performance of bricks and mortar made of different clay and fiber content, that was already proved to significantly influence the strength and deformation capacity of this material. Despite the symplifing hypotheses, the simulations performed were consistent with the physics of the material experimentally observed. Not only in terms of the main mechanical parameters in tension and compression needed to identify the material, but also recalling some typical features of failure modes experimentally observed in compression and bending tests. All the implemented mechanical parameters of the model have a physical relation to the physics. The calibration confirmed that mortar is more brittle than bricks of similar soil mixtures but different fibre reinforcement, which in turn enhances ductility to the specimen. For all the types, using the same material parameters calibrated with respect to pure compression tests and the elastic modulus and damage initiation strain in tension according to RILEM guideline, it was possible to address in bending the experimental force displacements curves by means of a single parameter calibration. That was larger (less brittle) for high straw reinforced bricks and smaller for mortar. This opens an interesting debate on the similarities between the performance of SFRC and Adobe, both characterized by the inclusion of fibres in the production process to prevent an elsewhise brittle behaviour. The model constitute a good starting point toward the dynamic assessment of Adobe. The model will be improved in future research in order to make it capable of addressing complex failure patterns typical of high strain rates induced loadings.

REFERENCES

Agarwal, A. (1975). Mud as a Traditional Building Material. *The Changing Rural Habitat; edited by Brian Brace Taylor. Singapore: Concept Media/Aga Khan Award for Architecture 1*, 137–146.

Allix, O. & J.-F. Deu (1997). Delayed-Damage Modelling for Fracture Prediction of Laminated Composites under Dynamic Loading. *Engineering Transactions 45*(1).

Angelillo, M., P.B. Lourenço, & G. Milani (2014). Masonry behavior and modelling. In *Mechanics of Masonry Structures*, pp. 341.

Arya, A., T. Boen, & Y. Ishiyama (1986). *Guidelines for earthquake resistant non-engineered construction*. Number iv. UNESCO.

Houben, H. & H. Guillaud (1994). *Earth construction: a comprehensive guide*. ITDG Publishing.

Ladevèze, P., O. Allix, J.F. Deü, & D. Lévêque (2000). A mesomodel for localisation and damage computation in laminates. *Computer Methods in Applied Mechanics and Engineering 183*(1–2), 105–122.

Lee, J. & G.L. Fenves (1998). Plastic-Damage Model for Cyclic Loading of Concrete Structures. *Journal of Engineering Mechanics 124*(8), 892–900.

Li Piani, T., D. Krabbenborg, J. Weerheijm, L. Koene, & L. Sluys (2017). The Mechanical Performance of Traditional Adobe Masonry Components: An experimental-analytical characterization of soil bricks and mud mortar (in submission).

Mazars, J., F. Hamon, & S. Grange (2015). A new 3D damage model for concrete under monotonic, cyclic and dynamic loadings. *Materials and Structures*, 3779–3793.

Ortiz, R., E. Deletombe, & Y. Chuzel-Marmot (2015). Assessment of damage model and strain rate effects on the fragile stress/strain response of ice material. *International Journal of Impact Engineering 76*, 126–138.

Parra-Saldivar, M.L. & W. Batty (2006). Thermal behavior of adobe constructions. *Building and Environment 41*(12), 1892–1904.

Pereira, L., J. Weerheijm, & L.J. Sluys (2015). Simulation of dynamic behaviour of quasi brittle materials with new rate dependent damage model. In *9th International Conference on Fracture Mechanics of Concrete and Concrete Structures (FraMCos-9)*, pp. 14.

Pereira, L.F., J. Weerheijm, & L.J. Sluys (2017). A new effective rate dependent damage model for dynamic tensile failure of concrete. *Engineering Fracture Mechanics 176*, 281–299.

Pijaudier-Cabot, G. & Z. Bazant (1988). Nonlocal damage theory. *Engineering Mechanics 113*(10), 1512–1533.

RILEM TC 162-TDF (2003). RILEM TC 162-TDF: Test and design methods for steel fibre reinforced concrete. Sigmaepsilon design method. Final Recommendation. *Materials and Structures 36*(October 2003), 560–567.

Silveira, D., H. Varum, & A. Costa (2013). Influence of the testing procedures in the mechanical characterization of adobe bricks. *Construction and Building Materials 40*(March), 719–728.

Sluys, L.J. & R. de Borst (1992). Wave propagation and localization in a rate-dependent cracked medium-model formulation and one-dimensional examples. *International Journal of Solids and Structures 29*(23), 2945–2958.

Suffis, A., T.A.A. Lubrecht, & A. Combescure (2003). Damage model with delay effect analytical and numerical studies of the evolution of the characteristic damage length. *International Journal of Solids and Structures 40*(13–14), 3463–3476.

Thompson, C. (2015, sep). This insane 40 foot tall 3D printer could help solve the global housing crisis. *Business Insider*.

Van Der Meer, F. & L. Sluys (2009). Continuum Models for the Analysis of Progressive Failure in Composite Laminates. *Journal of Composite Materials 43*(20), 2131–2156.



Taylor & Francis
Taylor & Francis Group
http://taylorandfrancis.com

Computational Modelling of Concrete Structures – Meschke, Pichler & Rots (Eds)
© 2018 Taylor & Francis Group, London, ISBN 978-1-138-74117-1

Non-proportional loading for 3-D stress situations in sequentially linear analysis

M. Pari & J.G. Rots
Faculty of Civil Engineering and Geosciences, Delft University of Technology, Delft, The Netherlands

M.A.N. Hendriks
Faculty of Civil Engineering and Geosciences, Delft University of Technology, Delft, The Netherlands
Norwegian University of Science and Technology, Trondheim, Norway

ABSTRACT: This article presents a new non-proportional loading strategy for Sequentially Linear Analysis (SLA), which is a robust secant stiffness based procedure for nonlinear finite element analysis of quasi-brittle materials, like concrete and masonry. The strategy is based on finding the principal planes for a total strain based fixed cracking model, by searching for the critical plane where the normal stresses due to the scaled combination of two non-proportional loads is equal to the allowable strength. For a plane stress situation (2D), the scaling factor λ is expressed as a function of θ, the inclination of an arbitrary plane to the reference coordinate system, and a one dimensional (θ) optimization of λ is done to determine the principal plane and the resulting fixed crack coordinate system. This approach has been illustrated to match up to the closed form solution, obtained previously based on the principal stress theory, using single element tests and a quasi-static test pushover test on a masonry shear wall. Finally, the concept for the 3-D stress situation is presented, where the optimization problem becomes two-dimensional, with respect to *l* and *m* (two-directional cosines).

1 INTRODUCTION

The Sequentially Linear Analysis (SLA) procedure is a total approach, in the context of total strain based fixed cracking models, wherein a sequence of scaled linear analyses is performed coupled with decreasing secant stiffness and strength at the critical integration point of a finite element model. In contrast to the traditional incremental-iterative nonlinear finite element analyses, the key aspect of the SLA approach is the departure from using the tangent stiffness, which significantly affects the stability of FE solutions in softening regions, to the secant stiffness which would yield numerically favourable positive definite stiffness matrices. The constitutive law is discretized into the so-called saw tooth laws with decreasing positive secant stiffness and has undergone improvements over the years to have mesh objective results (Rots et al. 2009).

The procedure was initially developed for a proportional loading scheme, where the rate of change of all loads is the same. The extension of SLA to non-proportional loading, closer to real life loading situations, was rather difficult and was initially confined to plane stress situations (2-D) in a fixed cracking model approach. When there are multiple non-proportional loads, problems arise with respect to finding the critical integration point and the scaling of the loads. The approach initially was based on expressing global stresses as the superposition of stresses due to constant and (non-proportional) variable loads. Subsequently, using the principal stress theory, a closed form solution (DeJong et al. 2008) for the critical load multiplier was found and the crack coordinate system was established for the secondary cracking to follow. The Force-release (F-R) method (Elias et al. 2010), another alternative for the non-proportional loading problem, additionally aimed to address the dynamic phenomenon due to a damage event, that could lead to a series of subsequent failures in the vicinity of a damaged element, by redistributing the unbalanced forces gradually. Since it could not handle snap backs because of not being able to alter the previously applied load (constant load), the General method was proposed (Elias 2015) of which the F-R and the load-unload (L-U) methods (like SLA) are extreme cases, depending on time scales for the redistribution. Simultaneously, a constrained maximization analogy with a double load multiplier strategy (Van de Graaf 2017), one for constant and the other for variable loads was also conceived to address the redistribution phenomenon and was illustrated using continuum

models for larger scale simulations like settlement of a building and pushover of masonry walls. This approach is used as reference in this study.

For a 3-D stress situation, as in the case of solid/brick finite elements, a fixed cracking model allowing for 3-D cracking had already been proposed (Voormeeren 2011) in the context of SLA, however, only for a proportional loading scheme. Thus, there was a need for a non-proportional loading strategy suitable for 3-D stress situations in SLA. Using the approach of principal stress evaluation for 3-D stress situations, as done in the plane stress case by DeJong, results in cubic equations in the load multiplier λ and the resulting closed form solution for λ is very complex. Thus, alternatives were sought to avoid the necessity for a closed form solution of the critical load multiplier and this forms the crux of the study.

In this article, we present a new non-proportional loading strategy based on finding the principal planes, and thus the fixed crack coordinate system, by searching for the plane where the normal stresses due to the scaled combination of two non-proportional loads is equal to the allowable strength. This is done by optimization of the critical load multiplier, expressed as a function of the inclination of an arbitrary plane, and the normal stresses on the plane due to a constant and a (non-proportional) variable load.

2 BACKGROUND THEORY

2.1 *General workflow*

The procedure for SLA is as follows:

1. Set up the saw-tooth laws as shown in Figure 1.
2. Run a linear analysis with full value of the constant load.
3. In case of damage already in this stage (nonlinearity):
   a. Identify the critical integration point with the least ratio of (σ_1/f_t), where σ_1 is the maximum principal stress and f_t is the allowable strength.
   b. Scale the constant load.
   c. Reduce the strength and stiffness of the critical integration point based on the saw-tooth law.
   d. Return to step 2 and repeat until the scaled value of the constant load is the same as the original full value.
4. Once the constant load is fully applied, add the variable load as a unit load and perform a linear analysis.
5. Construct the global stresses as a superposition of the stresses due to the constant and variable load (indicated with indices 'c' and 'v' respectively) and find a closed form solution for the critical load multiplier from the principal stress theory (plane stress situation) as shown below:

$$\sigma_{xx} = \sigma_{xx,c} + \lambda^* \sigma_{xx,v} \tag{1}$$

$$\sigma_{xx} = \sigma_{xx,c} + \lambda^* \sigma_{xx,v} \tag{2}$$

$$\sigma_{xx} = \sigma_{xx,c} + \lambda^* \sigma_{xx,v} \tag{3}$$

$$\sigma_{(1,2)}(\lambda) = \frac{1}{2}(\sigma_{xx} + \sigma_{yy}) \pm \sqrt{\frac{1}{4}(\sigma_{xx} - \sigma_{yy})^2 + \sigma_{xy}^2} \tag{4}$$

6. Determine the integration point for which the load multiplier λ is critical. In principle, solving for the inequality $\sigma_{(1,2)}(\lambda) \leq f$, where 'f' is the allowable strength, sets of values of λ per integration point per failure direction are found and the maximum value of the common subset is chosen as the critical λ. In the event of an empty solution set, wherein the stress states in no integration point allows for a constitutively admissible scaled combination of the constant and variable loads, a return to an 'intermediate proportional scheme' is done. The 'last successful load combination' is scaled in a proportional way thereby reducing the constant load and also partly retaining the scaled variable load. (Van de Graaf 2017).
7. Once the critical integration point and load multiplier is determined, scale the stresses and

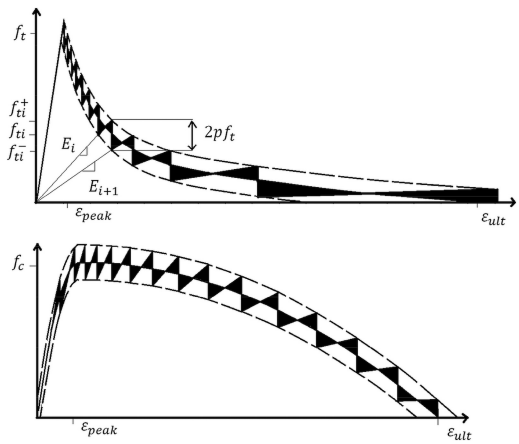

Figure 1. Saw-tooth curves for exponential tension softening (top) and parabolic compressive softening bottom in the ripple curve formulation. The dashed curves represent the delimiting curve at an offset to the 'mother/base' constitutive curve (by a percentage 'p' of the allowable strength) to allow for a formulation with regularized fracture energy to ensure mesh objectivity.

strains as well accordingly and obtain the new stress state.

8. Remove all loads and update the strength and stiffness of the critical integration point based on the saw tooth law and return to step 2 until the element/structure is completely damaged.

2.2 *Fixed cracking model in SLA*

SLA has thus far been based on a total strain based smeared cracking model. As soon as the principal stress violates the allowable strength at an integration point, the isotropic stress strain relation $\sigma = D\varepsilon$, transforms into an orthotropic relation at the *n-t* cracked coordinate system as $\sigma_{nt} = D_{nt}\varepsilon_{nt}$. The normal direction's Young's modulus and strength are damaged according to the saw tooth law. In the event of stress rotations that lead to stresses in the tangential direction violating the allowable strength, the damage is introduced similarly. So every integration point essentially requires two uniaxial saw tooth laws in the 2-D plane stress situation. This aside, the shear behaviour in the fixed cracking model is represented using a variable step wise shear retention function that takes into account the reduction of shear stiffness with increasing damage in normal direction of the cracked plane. Also, the Poisson's ratio is reduced at the same rate as the associated Young's modulus.

2.3 *Motivation for a new non-proportional strategy*

Determining the critical load multiplier in a plane stress situation is straightforward as shown in the previous section. Substitution of the global stresses, i.e. Equation 1, 2, and 3, into the expression for the principal stress (Equation 4), would yield a quadratic equation in λ thereby resulting in a closed form solution. So the existence of a rather simple expression for the principal stress is key to this approach and this is primarily because the characteristic equation for a 2-D stress situation is also a quadratic equation.

However, for a 3-D stress situation the principal stresses would be the roots of a cubic characteristic equation (Equation 7).

$$\det(\Sigma - \Lambda\mathbf{I}) = 0 \tag{5}$$

$$\begin{vmatrix} \sigma_{xx} - \Lambda & \sigma_{xy} & \sigma_{zx} \\ \sigma_{xy} & \sigma_{yy} - \Lambda & \sigma_{yz} \\ \sigma_{zx} & \sigma_{yz} & \sigma_{zz} - \Lambda \end{vmatrix} = 0 \tag{6}$$

$$\Lambda^3 - I_1\Lambda^2 + I_2\Lambda - I_3 = 0 \tag{7}$$

where Σ is the 3-D stress tensor, Λ are the principal values, $\mathbf{I}$ is the Identity matrix and I_1, I_2 and I_3 are the stress invariants. An analytical expression for the principal values from Equation 7 would not be as simple as Equation 4. It is well documented in literature about mathematical procedures like Cardano's method (Birkhoff & MacLane 1997) involving transformation to get reduced cubic equations and subsequent reduction to a quadratic equation to find analytical solutions, but such an approach for solving Equation 7 would prove rather complex and cumbersome. Since the superposed stresses as in Equation 1, 2 and 3 would introduce a new variable λ, finding a closed form solution, to be able to implement in a finite element framework, becomes rather unrealistic.

This motivated the need for a new non-proportional strategy suitable for the 3D stress situations. Numerical algorithms were considered as a possible solution to solve the cubic equation with the additional variable λ, but to reduce the complexity of the problem, reformulation of the problem statement was regarded to be more pragmatic and this led to the new approach described in the next section. The problem is reduced to that of a two-dimensional optimization problem, the directional cosines, in the 3-D case but is first elucidated in the 2-D plane stress situation to match up to the existing closed form solution.

3 REFORMULATION OF NON-PROPOPORTIONAL LOADING IN SLA

3.1 *Concept*

The non-proportional loading strategy being considered retains the concept of superposition of stresses due to the two non-proportional loads, referred to as constant and variable loads hereon, to obtain global stresses. Instead of resorting to the principal stress theory to find the closed form solution for λ, the normal stress on an arbitrary plane is now expressed as a function of the inclination of the plane to the reference axes.

The normal stresses due to the constant and the variable loads (denoted by the subscripts *c* and *v*) would be functions of θ:

$$\sigma_{nn,c} = \frac{1}{2}\left(\sigma_{xx,c} + \sigma_{yy,c}\right) + \frac{1}{2}\left(\sigma_{xx,c} - \sigma_{yy,c}\right)\cos(2\theta) + \sigma_{xy,c}\sin(2\theta) \tag{8}$$

$$\sigma_{nn,v} = \frac{1}{2}\left(\sigma_{xx,v} + \sigma_{yy,v}\right) + \frac{1}{2}\left(\sigma_{xx,v} - \sigma_{yy,v}\right)\cos(2\theta) + \sigma_{xy,v}\sin(2\theta) \tag{9}$$

The scaled combination of the stresses shown, σ_{nn}, above would have to be equal to the allowable strength, from which the load multiplier λ, is expressed as a function of θ as shown below:

$$\lambda(\theta) = (f - \sigma_{nn,c}(\theta)) / \sigma_{nn,v}(\theta) \quad (10)$$

where f is the allowable strength.

The idea is to find the minimum value of λ, at which the slope of the function is zero, and the corresponding value of θ will determine the inclination of the failure (cracking/crushing) plane. This was initially verified for simple stress states by comparing against the analytically derived closed form solution for λ and the inclination of the crack plane as formulated by DeJong et al. (2008).

The function of the load multiplier may be continuous or discontinuous for different stress states but is periodic every π radians. Thus, it is sufficient to evaluate the function over a range of $\theta = [-\pi/2, \pi/2]$ to evaluate the critical λ and the corresponding critical cracking plane. Typical functions are shown in Figure 3.

It is observed that the maxima or minima of this function correspond to 'critical' values of λ for which the scaled combination of the normal stresses due to constant and variable loads, σ_{nn}, approach the allowable strength. The physical meaning of the expression for λ as a function of the cracking inclination θ is that there several combinations of λ and θ for a certain kind of loading (stress state). However, there are only two critical admissible values in the interval $\theta = [-\pi/2, \pi/2]$, the maxima and the minima, for a certain stress state which could be seen as upper and the lower bound

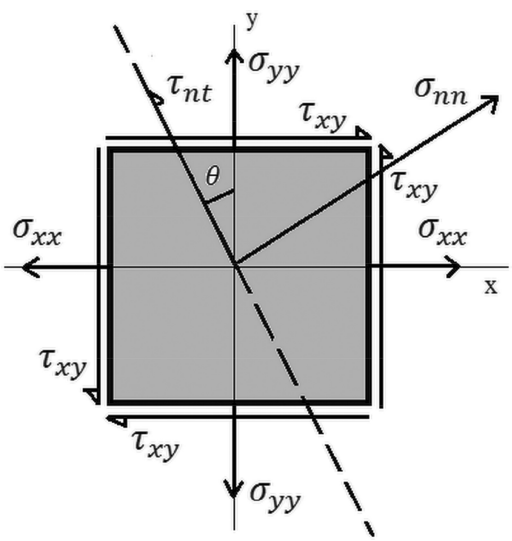

Figure 2. Plane stress situation: Normal stress σ_θ and Shear stress τ_θ, on a plane at an inclination θ to the reference axes.

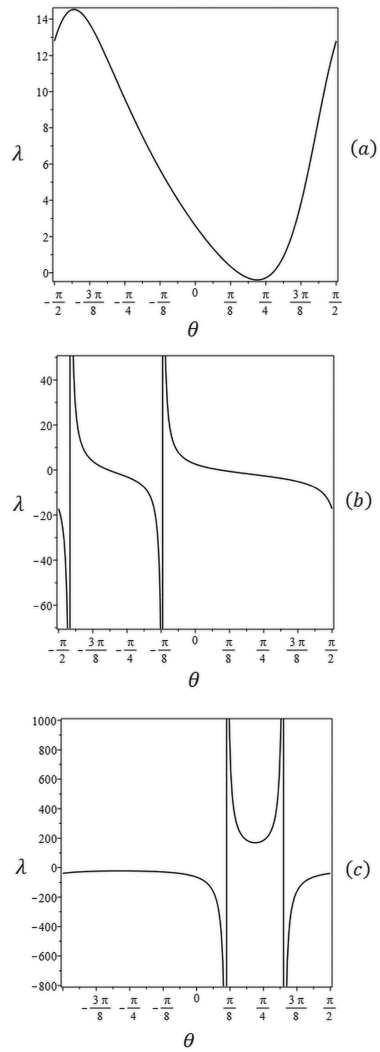

Figure 3. Example of functions of λ with respect to the inclination of an arbitrary plane at an inclination θ to the reference axes where: (a) there are global critical points, (b) there are 'no' critical points (infinite real set) and (c) there are local critical points, that can result in a possible load combinations to initiate failure.

solutions. These bounds are analogous to the λ_{min} and λ_{max} of the sets of admissible lambda values found per integration point as described by Van de Graaf (2017). Therefore, along the same lines, the critical values for each integration point are used to set up the 'sets' of λ values, and the maximum of the common subset is chosen as the global critical load multiplier λ_{crit}. In the event of an empty common subset, the strategy to temporarily reduce the constant load by proportionally scaling the 'last

successful' load combination as mentioned in section 2.1 is adopted (Van de Graaf 2017).

In case of functions such as those shown in Figure 3(b), there appears to be only global extreme values at certain θ and no local critical points. This would mean that critical bounding solutions where failure can be initiated are infinite and so such cases can be neglected. In other words, the range of admissible values of the scaled variable load to initiate failure at an integration point is the infinite real set.

Additionally, it is to be noted that for the new crack coordinate system at an inclination θ with respect to the reference coordinate system, there will also be a normal stress σ_{tt} which is not to be neglected. For the critical λ evaluated by finding the optimum θ with respect to σ_{nn}, the corresponding σ_{tt} at an angle (θ +π/2) should be lesser than the maximum principal stress or greater than minimum principal stress, for tensile or compressive failure along σ_{nn} respectively. Thereby we ensure that the derived λ also results in the normal stresses which are in accordance to the principal stress theory. Depending on these aspects of the function, we can address the non-proportional loading strategy now as an optimization problem.

3.1.1 *Minimization of the λ function using optimization algorithm*

With the knowledge of typical functions within the interval [–π/2, π/2], the choice to utilize optimization techniques, to find the minimum for every integration point per linear analysis, was made. In this study, the minimization of the function is carried out in two stages if the function is smooth and parabolic near the minima as shown in Figure 3(a) and Figure 3(c). Firstly, the minimum is bracketed using the inverse parabolic interpolation. Subsequently, the golden section search algorithm (Kiefer 1953) is used to find a functional minimum. This method is the optimization counterpart of the root finding bisection method. The idea is to successively narrow down the set of values to a small interval where the minimum exists. The convergence towards the minimum is linear but the method is always guaranteed to converge. The maximum can be found by adopting the same strategy but with the negative of the function. In scenarios wherein no minima occurs as shown in Figure 3(b) or there are global minimum (extreme values) alongside the critical local minimum as in the case of Figure 3(c), the algorithm has to be modified, to appropriately find the critical points or neglect the integration point with such stress states on the whole. The knowledge of the first derivative of the function can make it possible to use faster optimization routines to find the desired critical points and this is being currently investigated. Nevertheless, as explained in the following sections, the strategy matches up to the existing closed-form solution based strategy and also in terms of computational effort (time).

4 VALIDATION STUDIES (2D)

4.1 *Single element test*

The concept for the reformulated non proportional strategy, hereon referred to as the Sequentially linear 'theta-based' non-proportional strategy (SLTHNP) was implemented and validated in the commercial FEA program DIANA FEA. Several single element tests were performed and one such is presented in this paper. The scheme of the test on the linear plane stress element is as shown in Figure 4. The plane stress element is assigned unit material properties as shown in Table 1. The test is performed with both the SLTHNP and the closed

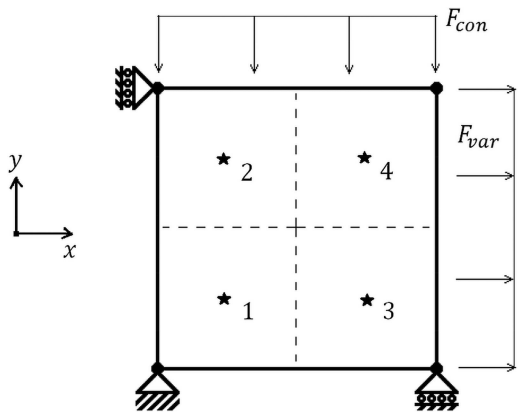

Figure 4. A Linear plane stress element, with boundary conditions as shown, is subject to constant load F_{con} in the negative-y direction followed by the unit proportional load F_{var} in the positive-x direction. In-plane Gaussian integration scheme 2 × 2 is used (demarked as stars).

Table 1. Material properties for the test.

Property	Value	Units
Young's Modulus (E)	1000	N/m²
Poisson's ration (*v*)	0	–
Tensile strength (f_t)	1	N/m²
Tensile Mode-I fracture energy (G_{fI})	1	N/m
Compressive strength (f_c)	1	N/m²
Compressive fracture energy (G_c)	1	N/m
Number of Saw-tooth*	20	–

*Linear Tensile and parabolic compressive Saw-tooth as shown in Figure 1 with a 'p' factor of 0.1.

form solution based non-proportional strategy of DeJong later improved by Van de Graaf (2017), hereon referred to as SL2DNP.

The constant load is kept low to about 0.01 N/m so that damage in an integration point happens only when the variable load is applied and the non-proportional loading strategy, as the case may be, determines the cracking plane and the load multiplier. The stress strain evolution in all 4 integration points is observed for both simulations with SL2DNP and SLTHNP.

Since the loading is such that damage will occur only in tension along the X-direction, the corresponding stress strain relations in X-direction alone are presented in Figure 5. It can be seen for integration points 1 and 2 that at certain load steps an integration point may lie on the secant branch (as another point becomes critical) or at the upper limit point of the saw tooth, depending on whether or not the point under consideration is critical, and vice versa. As expected, in line with similarities observed for simple stress states as mentioned in the previous section (analytical comparisons), the approaches match. A similar test with constant tension load in Y (but small enough to avoid damage) and the variable compression load in X directions also show good agreement between the approaches. This validates the SL2DNP at element level but there was need for an assessment at a structural level involving stress redistributions and this is shown in the next section.

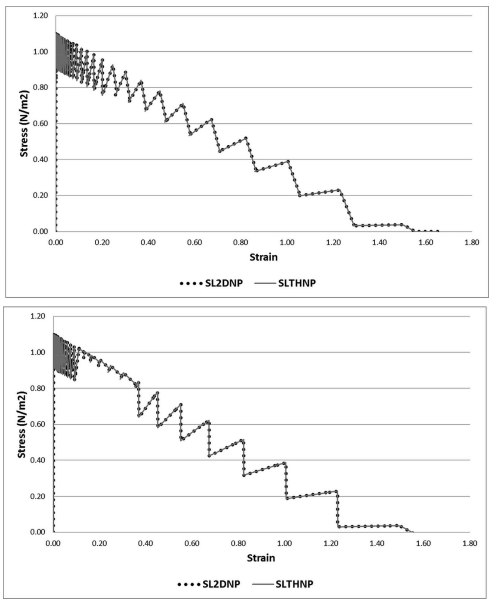

Figure 5. Stress strain evolution along the x-direction which is subject to tension as observed using the closed form solution based SL2DNP strategy and the theta based new SLTHNP strategy for integration points 1 & 2 - (top) and (bottom) respectively.

4.2 *Quasi-static cyclic pushover test—High wall*

To demonstrate the SLTHNP strategy, the benchmark of a calcium silicate masonry shear wall test is chosen. Several in-plane quasi-static cyclic tests were performed on calcium-silicate and clay brick walls at TU Delft in the Stevin Lab as a part of the extensive research campaign addressing the induced seismic situation in Groningen, The Netherlands (Rots et al. 2016). Of these, one of the high walls is tested using SLA with the SL2DNP and SLTHNP strategies.

The constitutive relationship combining a linear tension softening and a parabolic compression softening behaviour in uniaxial direction, similar to that presented in Figure 1, is used. The wall is slender, around 2.75 m × 1.1 m in size. It is a single wythe wall of thickness 0.1 m and is subject to a vertical precompression of 0.7 MPa. The experimental setup has double clamped boundary conditions (top edge remains straight but is free to move vertically in the direction of overburden). After application of precompression, a lateral load is applied in a cyclic fashion. The experimental setup is shown in Figure 6 and the end stage damage pattern was a combination of flexure (rocking failure), toe crushing and sliding failures. For further details refer Ravenshorst et al. (2016). Although the test is cyclic in nature, the test could be used as a benchmark in a monotonic approach to make qualitative comparisons between the experimental backbone/envelope curve and the SL2DNP and SLTHNP non-proportional strategies.

The force displacement curves from the SL2DNP and SLTHNP simulations, in comparison

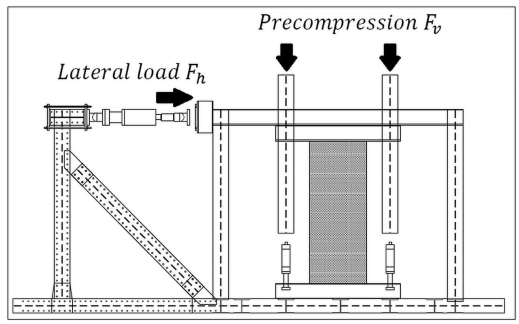

Figure 6. Experimental setup of shear wall with dimension 2.75*1.1 m^2 with thickness 0.102 m. The pre-compression and lateral loads are applied using hydraulically controlled actuators as shown (Ravenshorst et al. 2016).

to the experimental backbone curve are shown in Figure 8. There is a slight deviation in the numerical result from the experiment and this can attributed to calibration of material properties which were obtained from material level tests which were also done as a part of the campaign. These are shown in Table 2.

Nevertheless, the aim of the study is to demonstrate the applicability of the proposed non-proportional strategy for Sequentially linear analysis and therefore in-depth comparisons are made only between the SL2DNP and SLTHNP approaches and only an overall/global comparison to the experimental benchmark in terms of the damage patterns and the failure modes is made. For the same reasons, the comparison between the approaches is stopped at 7.0 mm for the simulations while the experiment was continued to around 25 mm top displacement.

The results from both the simulations are in agreement until the top displacement of 7.0 mm until which the analysis has been investigated. Since the results from SL2DNP match exactly with those from SLTHNP, the evolution of the maximum principal strain ε_1 is shown only for the SLTHNP simulations in Figure 7. The rocking/flexure failure that was observed in the experiment is seen in both simulations and the strain contours are in agreement.

However, there are a couple of points to be noted. The optimization routine to find critical λ, the golden search algorithm, is dependent on a certain tolerance for convergence to the solution and the solution is sensitive to this parameter. Varying the tolerance further may alter the proximity to the closed form solution; however beyond a certain value this would not be the case. The sensitivity of the SLTHNP with respect to this tolerance is currently being investigated with this benchmark and the one discussed in the next section.

It has to be pointed out that compressive softening was not observed for the displacements considered. This is due to the choice of comparing simulations until a net top displacement of 7.0 mm. Also, the combined tension-compression biaxial failure model that has been used in this study has an intrinsic problem that in a uniaxial case, if an integration point softening in tension unloads locally (is possible for monotonic analysis also due to stress redistributions (Van de Graaf 2017)) it carries over the damaged stiffness into compressive regime and this could affect the results. This aspect of the biaxial failure envelope is also being currently investigated.

4.3 *Quasi-static cyclic pushover test—Low wall*

The benchmark presented in the previous section exhibits a rather simple damage pattern, a rocking mode. In order to authenticate the validity of the SLTHNP strategy in comparison to SL2DNP for another failure mode, the benchmark of low wall that exhibited a brittle failure by diagonal cracking is investigated.

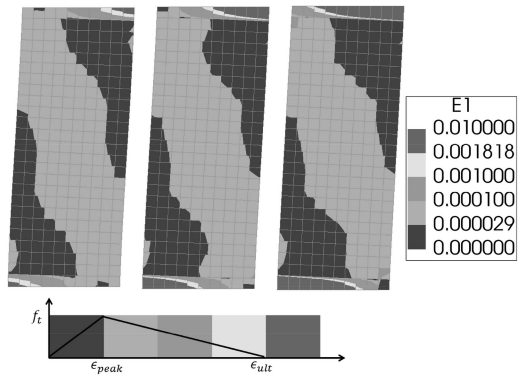

Figure 7. Maximum principal strain ε_1 evolution at A, B and C points of Figure 8 for SLA using SLTHNP non-proportional loading strategy.

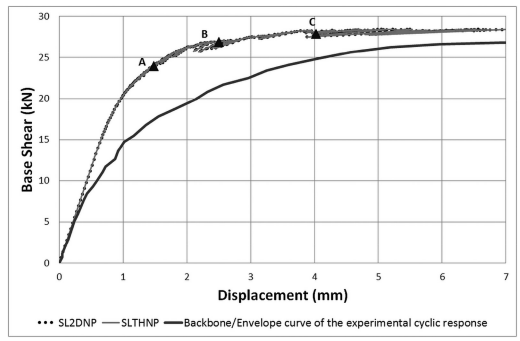

Figure 8. Comparison of the monotonic SLA simulations of the shear wall test using SL2DNP and SLTHNP non-proportional loading strategies and the envelope curve of the cyclic experimental curve.

Table 2. Material properties for the shear wall test *.

Property	Value	Units
Young's Modulus (E)	5.091E+09	N/m^2
Poisson's ration (v)	0.2	–
Tensile strength (f_t)	0.15E+06	N/m^2
Tensile Mode-I fracture energy (G_{fI})	15	N/m
Compressive strength (f_c)	5.93E+06	N/m^2
Compressive fracture energy (G_c)	31300	N/m
Number of Saw-tooth	30	–

*Properties obtained from material level tests on calcium silicate masonry (Esposito et al. 2016).

The wall considered is rather squat in comparison to the previous benchmark, around 1.35 m(high) × 1.1 m in size. The experimental setup has double clamped boundary conditions and after application of precompression of 0.6 MPa, a lateral load is applied in cyclic fashion similar to the previous benchmark. The experimental setup is shown in Figure 9. The material properties for the constitutive relationship combining a linear tension softening and a parabolic compression softening behaviour in uniaxial direction, similar to that presented in Figure 1, is presented in Table 3.

The only point to be noted is that the elements in the middle of the wall in Figure 9 are assigned a higher Mode-I fracture energy than the extreme row of elements (grey-coloured) in order to account for the relatively larger energy dissipation in a shear failure as against a rocking failure. Diagonal shear failure was observed in the experiment subsequent to reaching the peak force. For further details about the experiment refer Anthoine et al. (1995). Monotonic simulations are made to make qualitative comparisons between the SL2DNP and SLTHNP non-proportional strategies.

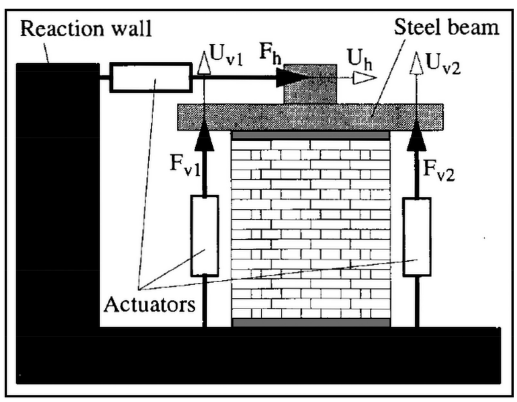

Figure 9. Experimental setup of low-shear wall, Anthoine et al. (1995).

Table 3. Material properties for low-wall test*.

Property	Value	Units
Young's Modulus (E)	1.491E+09	N/m^2
Poisson's ration (ν)	0.15	–
Tensile strength (f_t)	0.15E+06	N/m^2
Tensile Mode-I fracture energy (G_{fI})	150	N/m
Compressive strength (f_c)	6.20E+06	N/m^2
Compressive fracture energy (G_c)	40000	N/m
Number of Saw-tooth	30	–

*Properties calibrated after sensitivity analysis for tensile mode-I fracture energy and tensile strength. Additionally for continuum elements (extreme rows) G_{fI} = 100 N/m.

The results from the SLTHNP and SL2DNP simulations exactly match thereby validating the new strategy for the non-proportional loading problem. In contrast to the previous benchmark, here a return to the 'intermediate proportional scheme' proposed by Van de Graaf (2017) is also

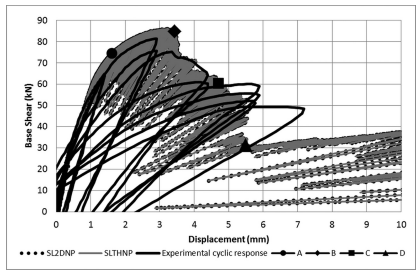

Figure 10. SL2DNP and SLTHNP simulations of the low wall test and the characteristic points A, B, C and D.

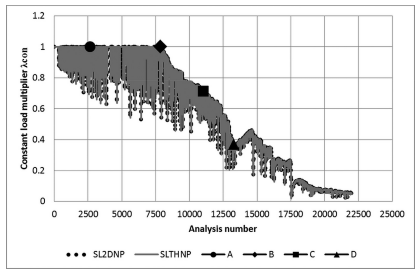

Figure 11. Evolution of λ_{con} in the two simulations of the low wall test and the characteristic points from Figure 10.

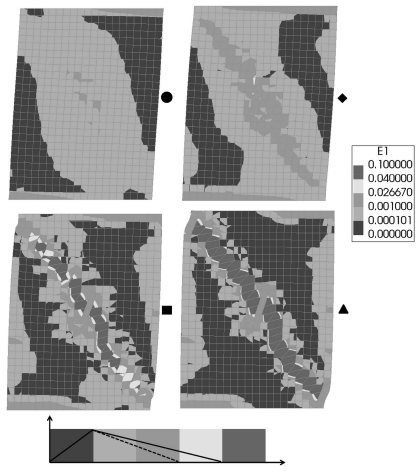

Figure 12. Evolution of principal strain 1 (dotted softening branch—extreme elements, whole—middle elements).

observed. This is seen in Figure 11, where the load multiplier associated with the constant load (in this case the precompression) λ_{con} reduces below 1.0 over the number of linear analysis steps. It regains the initial value of precompression most often but post step 7850, there seems to be a gradual decrease up until step 13300 where the value reaches almost 0.3. Physically this would mean that the precompression on the wall cannot be recovered and the gradual decrease could be interpreted as the wall nearing collapse state. Damage pattern for 4 characteristic points A, B, C and D in Figure 10 are shown in Figure 12 and a comparison between damage patterns of both approaches (exact match) is not made here owing to triviality.

5 EXTENSION OF THE NEW NON-PROPORTIONAL LOADING STRATEGY TO 3-D STRESS SITUATIONS

5.1 *Concept*

The purpose of introducing and demonstrating the theta based non-proportional strategy at a 2-D level was to prove the validity of the method. However, the aim of the strategy is ultimately to have 3-D SLA simulations with non-proportional loading or in other words simulations with a constant and variable load. Due to the aforementioned problems with finding closed form solution in a 3-D stress situation, in line with the 2-D reformulation of the non-proportional problem based on theta—the inclination of the arbitrary plane to the reference axes, the 3-D non-proportional loading problem is reformulated based on directional cosines.

In the 3-D stress situation, an arbitrary plane can be related to the reference coordinate system by means of the directional cosines *l*, *m* and *n*, of which only two may be considered independent variables since they are related as $l^2 + m^2 + n^2 = 1$. The normal stresses acting on this plane due to the constant and variable loads can thus be expressed as

$$\sigma_{nn,c} = \sigma_{xx,c} l^2 + \sigma_{yy,c} m^2 + \sigma_{zz,c} n^2 + (2\sigma_{xy,c} lm) + (2\sigma_{yz,c} mn) + (2\sigma_{xz,c} nl) \quad (11)$$

$$\sigma_{nn,v} = \sigma_{xx,v} l^2 + \sigma_{yy,v} m^2 + \sigma_{zz,v} n^2 + (2\sigma_{xy,v} lm) + (2\sigma_{yz,v} mn) + (2\sigma_{xz,v} nl) \quad (12)$$

The load multiplier is now expressed as a function of only two of the directional cosines, rewriting the third as $n = \sqrt{(1 - l^2 - m^2)}$, as shown below:

$$\lambda(l,m) = (f - \sigma_{nn,c}(l,m)) / \sigma_{nn,v}(l,m) \quad (13)$$

The idea is to find the critical values of λ, the maxima or minima of this function, at which the slope of the function is zero, make sets of admissible values of λ per integration point and choose the maximum λ of the common subset similar to the 2D case. The values of *l*, *m* and *n* corresponding to the λ_{crit} will determine the inclination of the failure (cracking/crushing) plane. The function of the load multiplier may be continuous or discontinuous for different stress states similar to those observed in the 2-D plane stress situation and are shown in Figures 13 and 14. Additionally, analogous to the 2-D case, for the new crack coordinate system at an inclination *l*, *m* and *n,* with respect to the reference coordinate system, there will also be a normal stress σ_{tt} and σ_{ss} which are to be considered. For the critical λ evaluated by finding the optimum *l*, *m* and *n*, with respect to σ_{nn}, the corresponding σ_{tt} and σ_{ss} should be such that $\sigma_1 > \sigma_2 > \sigma_3$.

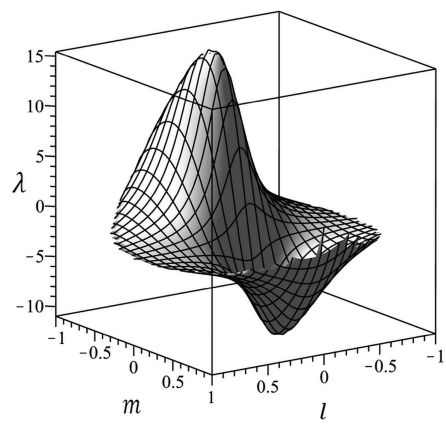

Figure 13. Example of a smooth continuous function of λ with respect to the inclination of an arbitrary plane defined by directional cosines *l* and *m*.

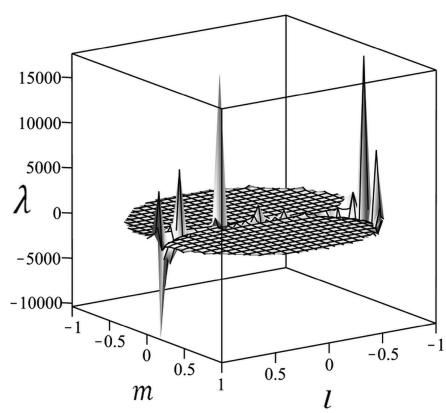

Figure 14. Example of a discontinuous λ with respect to the inclination of an arbitrary plane at an inclination defined by directional cosines *l* and *m*.

In addition to the non-proportional loading strategy the fixed crack approach for the 3-D stress situation to allow for an additional tertiary cracking is necessary. The idea for the change from isotropic to orthotropic formulation upon damage in 2D plane stress situation were extended to the 3D-stress state by Voormeren (2011). Here the transformation of the original isotropic formulation into the *n*-s-*t* orthotropic formulation expressed as $\sigma_{nst} = D_{nst}\ \varepsilon_{nst}$, allowing for tertiary cracking as well, is done. The associated variable shear retention functions and poisson ratio reductions were also considered. The damaged integration point will have 3 each of Young's moduli, shear moduli and poisson's ratio.

The extrema (bounds) of the critical load multiplier was determined in the 2-D stress situation numerically using a one-dimensional optimization routine. In the reformulated 3-D non-proportional loading problem, the optimization has to be done with respect to 2 variables *l* and *m*. So a multidimensional optimization routine is required and preliminary investigations have been made with the rather basic downhill simplex method, the 3-D version of the golden section search. The limitation in multi-dimensional optimization is that the initial bracketing of the extremum is not possible and emphasis has to be laid on possibly restarting the optimization routine from a 'converged solution' repeatedly to ensure that the extremum is indeed global and not a local one. Investigations are also ongoing for the choice of a faster optimization routine like the Conjugate gradient method.

6 CONCLUSIONS

A new strategy for Sequentially linear analysis with a view to address the 3-D non-proportional loading has been presented in this study. This was motivated by the lack of a simple closed form expression for the critical load multiplier λ in the 3-D case as in the 2-D plane stress situation. The problem statement for non-proportional loading has been proposed to be reformulated to first express the normal stress on an arbitrary plane, at an inclination θ with respect to the reference coordinate system, as the scaled combination of the normal stresses due to the constant and variable loads. This was equated to the allowable strength based on the saw-tooth constitutive law and ultimately the load multiplier was expressed as a function of θ. It has been shown in this study that the θ corresponding to extreme/critical values of the aforementioned function would result in inclination of the principal planes, using an optimization routine. First, the approach was presented for a 2-D stress situation and demonstrated using single element tests and quasi-static pushover tests on a slender calcium silicate masonry wall and a squat brick masonry wall. It has been shown to be in agreement with the closed form solution based non-proportional loading strategy as presented by DeJong (2008) and later readapted by Van de Graaf (2017). Furthermore, the concept for the 3-D stress situation has been presented and is currently being investigated with single element tests and benchmarks. Also investigations are ongoing to improve the biaxial tension compression failure model used in this study, to address the crack closure problem; and to extend SLA to cyclic loading applications.

ACKNOWLEDGEMENTS

The research is funded as a part of the author's PhD Program by Nederlandse Aardolie Maatschappij B.V. (NAM) and is gratefully acknowledged. Also, the author is thankful for the contribution of DIANA FEA towards the development of SLA and the additional new implementations.

REFERENCES

Anthoine, A., Magonette, G. & Magenes, G. 1995. Shear compression testing and analysis of brick masonry walls. *10th European conference on earthquake Engg.,* Balkema.

Birkhoff, G. & Maclane, S. 1997. A survey of Modern Algebra. 5th edition, London: A.K. Peters.

DeJong, M.J., Hendriks, M.A.N. & Rots, J.G. 2008. Sequentially linear analysis for fracture under non-proportional loading. *Engineering Fracture Mechanics,* 75, 5042–5056.

Elias, J., Frantik, P. and Vorechovsky, M. 2010. Improved sequentially linear solution procedure. *Engineering Fracture Mechanics,* 77, 2263–2276.

Elias, J. 2015. Generalization of load-unload and force-release sequentially linear methods. *International Journal of Damage Mechanics,* 24(2), 279–293.

Esposito, R., Messali, F., Crielaard R., Rots, J.G. 2016. Tests for the material characterization of replicated masonry and wall ties, *Final Report*, Delft University of Technology.

Kiefer, J. 1953. Sequential minimax search for a maximum. *Proc. American Mathematical Society*, 4 (3): 502–506.

Ravenshorst, G., Messali, F., 2016a. In-of-plane tests on replicated masonry walls. *Final report*, Delft University of Technology.

Rots, J.G., Belletti, B. & Invernizzi, S. 2004. Robust modelling of RC structures with an "event-by-event" strategy. *Engineering Fracture Mechanics,* 75, 590–614.

Rots, J.G, Messali, F., Esposito, R., Jafari, S. & Mariani, V. 2016. Computational modelling of masonry with a view to Groningen induced seismicity. *Proc. of the International conference on SAHC*, Leuven, Belgium.

Van de Graaf, A.V. (2017). Sequentially linear analysis for simulating brittle failure. PhD thesis, Delft University of Technology.

Voormeeren, A.V. (2011). Extension and verification of sequentially linear analysis to solid elements. Master's thesis, Delft University of Technology.

Computational Modelling of Concrete Structures – Meschke, Pichler & Rots (Eds)
© 2018 Taylor & Francis Group, London, ISBN 978-1-138-74117-1

Shear-sliding behavior of masonry: Numerical micro-modeling of triplet tests

F. Ferretti & C. Mazzotti
DICAM Department, University of Bologna, Bologna, Italy

R. Esposito & J.G. Rots
Department of Structural Engineering, Delft University of Technology, Delft, The Netherlands

ABSTRACT: Masonry is a composite material, whose behavior is strongly influenced by the presence of vertical and horizontal mortar joints, weak elements along which the shear failure usually occurs. The scope of the present work was to investigate factors that could affect the shear-sliding behavior of masonry, by performing numerical simulations of triplet tests conducted on calcium silicate brick masonry specimens with two different bond patterns. In the numerical analyses, a simplified micro-modeling strategy was adopted. A composite interface model was used, including a tension cut-off, a Coulomb friction criterion and a compressive cap. The numerical models were validated through comparisons with results from experimental tests, in terms of failure load, post-peak behavior and specimen deformability. Moreover, factors that could influence the shear-sliding behavior of masonry were analyzed by performing parametric studies. The simplified-micro modeling confirmed to be a very efficient strategy to capture the nonlinear behavior of masonry.

1 INTRODUCTION

The shear failure modes of a masonry structural element—toe crushing associated to rocking, sliding or diagonal cracking—depend mainly on its geometry, boundary conditions, level of compression applied, quality of the component materials and texture (Magenes & Calvi 1997). Regarding brick masonry, the presence of horizontal and vertical mortar joints surely affects the shear response of a masonry pier. Indeed, in many cases, they represent planes of weakness along which the failure can occur (Lourenço 1996, Rots 1997). When dealing with the shear-sliding failure mode of masonry panels, it can be described by the Coulomb friction criterion. In this case, the local properties of the mortar-brick interface, in terms of initial shear strength and friction coefficient, are the most important parameters to be defined.

Experimental laboratory tests may be performed for the evaluation of the mortar joint shear strength. To ensure the reliability of the results in a compression-shear test, various aspects have to be taken into account (Riddington et al. 1997). First of all, normal and shear stress distributions should be uniform along the sliding mortar joint. Secondly, the failure should initiate far away from the joint edges and should propagate quickly on the entire length of the joint. Finally, the presence of tensile stresses should be checked and avoided since they could affect the test outcomes.

Due to the difficulty in finding a testing procedure satisfying all the previous aspects, many different test methods have been proposed and studied in the past (Drysdale et al. 1979, Stöckl et al. 1990, Riddington & Jukes 1994, Van der Pluijm 1999). They basically differed one from another in the geometry of the specimen—e.g. considering one or more bed joints—and in the loading arrangement. Few test methods included the presence of head joints (Atkinson 1989). Finite element analyses were also carried out to investigate peculiar aspects of the different methodologies, highlight their advantages and disadvantages and propose new test methods (Jukes & Riddington 2000, Popal & Lissel 2010, Montazerolghaem & Jaeger 2014).

A particular focus is here devoted to the triplet test, as proposed by the standard EN 1052-3 (Fig. 1). During the test, the specimen is subjected to a constant axial pre-compression, while a shear load is applied to the central brick to produce its sliding. This test is really common since it does not need any specific or complex equipment (if compared to other testing methods) and, above all, it was found to be adequate to provide for reliable results (Vermeltfoort, 2010). However, the main

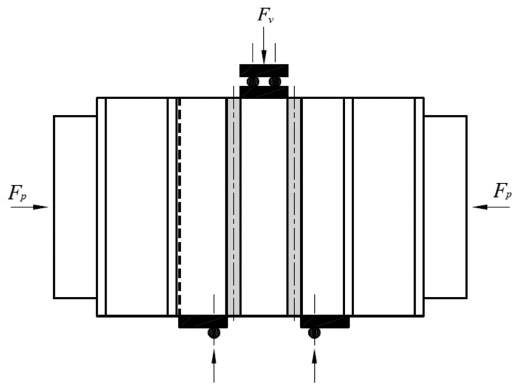

Figure 1. Triplet test setup, EN1052-3.

issues of this test are: (i) stress concentrations close to the loading points; (ii) presence of bending moment along the joint, which causes non-uniform stress distributions and can lead to undesired failure, especially for very low value of pre-compression. To partially overcome these problems, the position of the supports in the standard setup ensure the minimum bending moment inside the joints (Jukes & Riddington 2001). By performing the triplet test using a displacement controlled procedure, all properties characterizing the shear-sliding behavior of mortar joints, according to a Coulomb friction model, can be derived: shear strength, cohesion and friction softening, mode-II fracture energy, dilatancy.

The scope of the present work was to investigate factors that could affect the shear-sliding behavior of masonry. In particular, the influence of the boundary conditions and the role of dilatancy were studied in detail. Attention was also paid to the development of the stress distribution along the mortar joints and the cracks formation and evolution. To these purposes, numerical simulations of triplet tests conducted on calcium silicate brick masonry were performed. The mechanical parameters to be used in the numerical models were obtained from experimental tests on standard triplet specimens. Comparisons between numerical and experimental results were carried out to validate the numerical model, which was also applied to the case of a modified triplet test geometry, as will be explained in the following sections.

2 TRIPLET TEST

In the triplet test (EN 1052-3), a sliding failure is reproduced, in which the mortar joints are subjected to a prescribed level of axial compression (orthogonal to the bed joints) and to an increasing tangential shear load.

With the objective of investigating the shear properties of bed joints in calcium silicate brick masonry, a laboratory experimental campaign was carried out at Delft University of Technology on replicated masonry samples (Jafari & Esposito 2016). The triplet test setup is presented in Figure 2. Specimens were built using calcium silicate bricks (dimensions: $214 \times 102 \times 72$ mm^3) and cementitious mortar (joint thickness: 10 mm). At the beginning of the test, the pre-compression was applied by means of a manually operated hydraulic jack (load controlled) and kept constant. The lateral steel plates ensured the diffusion of the compressive load on the entire lateral surfaces of the sample. The shear load was then applied, along the vertical direction, to the intermediate brick, by using a displacement controlled apparatus composed of a 100 kN hydraulic jack and of a spherical joint. The assigned shear displacement rate was equal to 0.005 mm/s during the loading phase and to 0.05 mm/s in the unloading phase. During the test, displacements tangential and orthogonal to the mortar joints were continuously measured with Linear Variable Differential Transformers (LVDT), positioned on both sides of the specimen. Nine specimens were tested at three levels of pre-compression: 0.20 N/mm^2, 0.60 N/mm^2 and 1.20 N/mm^2. Moreover, one sample was tested with a pre-compression equal to 0.05 N/mm^2, to better estimate the initial shear strength.

The typical shear load-slip (tangential relative displacement) relationship was characterized by an initial almost linear behavior up to the peak load, followed by a softening branch and a residual tail, corresponding to a dry friction condition.

By performing the test with different levels of pre-compression, and plotting the peak shear strength τ against the normal compressive stress σ, it was possible to calibrate the Coulomb friction failure criterion:

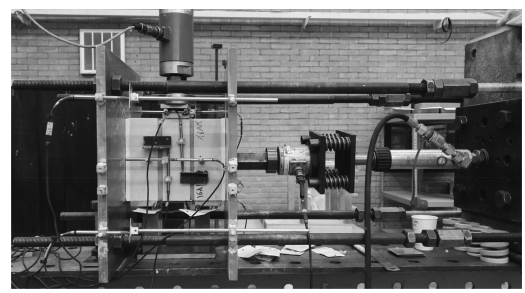

Figure 2. Triplet test experimental setup.

$$\tau = c_0 + \sigma \tan \phi_0, \quad (1)$$

where c_0 is the cohesion or initial shear strength, and ϕ_0 is the friction angle. In a similar way, by plotting the residual shear strength τ_{res} against the normal compressive stress σ and performing a linear interpolation, the residual failure criterion could be evaluated as well. It is characterized by a residual shear strength c_{res} and by a residual friction angle ϕ_{res}.

The mode-II fracture energy G_f^{II} was calculated for each test and its linear dependence on the pre-compression level can be described by the following equation (Rots 1997, Van der Pluijm 2000):

$$G_f^{II} = a\sigma + b, \quad (2)$$

where a and b were determined from linear regression of experimental data.

Transverse expansion upon shearing was observed during experimental tests. Therefore, parameters governing the dilatant behavior of mortar joints were evaluated by least-squares fitting of experimental data, according to the variable formulation for dilatancy (Van Zijl 2004):

$$\tan \psi = \tan \psi_0 \left\langle 1 - \frac{\sigma}{\sigma_u} \right\rangle e^{-\delta v_p}, \quad (3)$$

where v_p is the plastic shear displacement, ψ_0 is the dilatancy angle at zero confining stress and shear slip, σ_u is the pre-compression level at which the dilatancy goes to zero, and δ is the dilatancy shear-slip degradation coefficient. It was found in previous researches (Van der Pluijm 2000, Van Zijl 2004) that, during the sliding failure, the dilatancy is arrested at high pre-compression and large plastic shear displacement.

The determined mechanical properties are reported in Table 1 and were used as input parameters for the numerical simulations. The Young's moduli and Poisson's ratios for bricks and mortar were determined through uniaxial compression tests on the single components and on masonry wallets.

The standard triplet specimen, according to the European Standard (EN 1052-3), is composed by three bricks, arranged with a stacked bond pattern (Fig. 3a). However, considering a typical masonry pattern, the situation in which two bricks slide one over the other is not common. A more representative condition is the one in which also head joints are included. In order to study the influence of the vertical mortar joints on the sliding failure of masonry, modified triplet specimens were tested also, characterized by a running bond pattern (Fig. 3b).

Table 1. Input parameters for masonry.

	Description	Symbol	Units	Value
Parameters from tests	Elastic modulus of brick	E_b	[N/mm^2]	10000
	Poisson's ratio of brick	ν_b	–	0.16
	Elastic modulus of mortar	E_m	[N/mm^2]	1088
	Poisson's ratio of mortar	ν_m	–	0.20
	Cohesion	c_0	[N/mm^2]	0.13
	Friction angle	ϕ_0	[rad]	0.463
	Residual friction angle	ϕ_{res}	[rad]	0.463
	Compressive strength	f_c	[N/mm^2]	6.35
	Compr. fracture energy	G_f^c	[N/mm]	20
	Equiv. plastic shear displ.	κ_p	–	0.005
Calibrated parameters	Interface normal stiffness	k_n	[N/mm^3]	122.1
	Interface shear stiffness	k_t	[N/mm^3]	50.7
	Tensile strength	f_t	[N/mm^2]	0.09
	Mode-I fracture energy	G_f^I	[N/mm]	0.01
	Dilatancy angle	ψ_0	[rad]	0.374
	Confining normal stress	σ_u	[N/mm^2]	0.58
	Exp. degradation coeff.	δ	–	9.63
	Mode-II fracture energy	a	[mm]	0.114
	$(G_f^{II} = a\sigma + b)$	b	[N/mm]	0.011

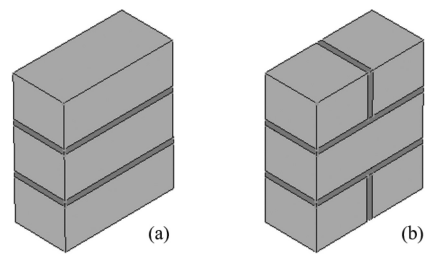

Figure 3. Specimen geometry: (a) standard triplet specimen (stacked bond); (b) modified triplet specimen (running bond).

3 SIMPLIFIED MICRO-MECHANICAL MODELING

Several modeling strategies can be used for masonry, depending on the way in which the constituents (units and mortar) and their interactions are considered. In general, it is possible to distinguish between a micro-modeling strategy, in which the single components are individually taken into account, and a macro-modeling strategy, in which masonry is modeled as a composite (Lourenco et al. 1995, Rots 1997). In the numerical analyses here presented, a micro-mechanical model was chosen, given the high level of accuracy needed to study the sliding failure along the mortar joint and considering the small dimensions of the samples.

In the framework of micro-modeling, it is also possible to distinguish between detailed and simplified

strategies, as classified in previous researches (Lourenço et al. 1995, Rots 1997). Differently from the detailed strategy, which implies the use of continuum elements for both units and mortar joints and of interface elements for adhesion surfaces (Fig. 4a), in the simplified micro-modeling, the mortar joints are modeled as zero-thickness interface elements and the units are modeled using continuum elements with expanded geometry, so to maintain the overall dimensions of the sample unchanged (Fig. 4b). The simplified micro-modeling strategy was considered adequate to capture the shear behavior observed in the tests, also allowing for the reduction of the computational effort, and was adopted in this research.

The details of the mesh used in the numerical models are shown in Figure 5a, b for the two different triplet specimen typologies. 2D models were adopted and, making use of symmetry, only half of the sample was considered. According to the simplified micro-modeling approach, bricks were modeled using quadratic 8-noded plane stress elements, while line 3-noded interface elements were adopted to model the zero-thickness mortar joints.

A linear elastic behavior was considered for plane stress elements (bricks), with the typical stress-strain relations for continuum elements. For interface elements, the constitutive behavior can

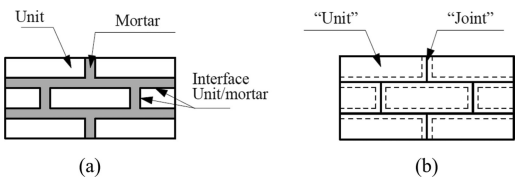

Figure 4. Modeling strategies for masonry structures: (a) detailed micro-modeling; (b) simplified micro-modeling. (Lourenco 1996).

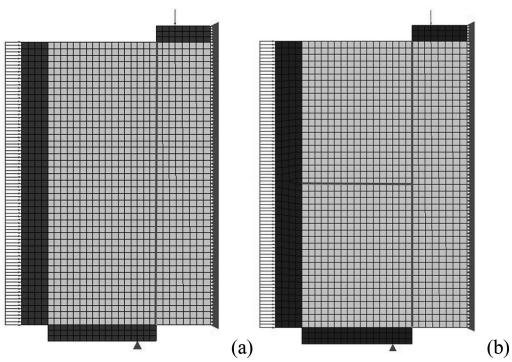

Figure 5. Finite element model: (a) standard triplet specimen; (b) modified triplet specimen.

be described through a relationship between the stresses and the relative displacements along the interface, which in the linear elastic range reads:

$$\begin{bmatrix} \sigma \\ \tau \end{bmatrix} = \begin{bmatrix} k_n & 0 \\ 0 & k_t \end{bmatrix} \cdot \begin{bmatrix} \Delta u \\ \Delta v \end{bmatrix}, \tag{4}$$

where σ and τ are the compressive and shear stresses along the interface, k_n and k_t are the normal and the shear stiffness, respectively, and Δu and Δv are the normal and tangential relative displacements.

In the simplified micro-modeling, the elastic stiffness parameters of the brick-mortar interfaces were evaluated considering the actual dimensions of units and mortar joints and their mechanical properties (Rots 1997):

$$k_n = \frac{E_b E_m}{t_m \left(E_b - E_m\right)} \tag{5}$$

$$k_t = \frac{G_b G_m}{t_m \left(G_b - G_m\right)} = \frac{E_b E_m}{2t_m \left(E_b \left(1+\nu_m\right) - E_m \left(1+\nu_b\right)\right)}, \tag{6}$$

where E_b and G_b are the elastic and shear modulus of the bricks, E_m and G_m are the elastic and shear modulus of the mortar, and t_m is the mortar joint thickness.

Since the sliding failure was expected to take place along the bed joint, the nonlinear behavior was only assigned to this failure plane. A composite interface model was used, including a tension cut-off, a Coulomb friction criterion and a compressive cap (Fig. 6).

Exponential softening for both tension and shear failure (mode-I and mode-II failure types, respectively) was included, while a hardening/softening behavior was introduced for compression. The complete description of the numerical implementation is not reported here, but the reader can refer to Lourenco (1996).

With reference to the Coulomb friction model, which describes the shear-sliding behavior

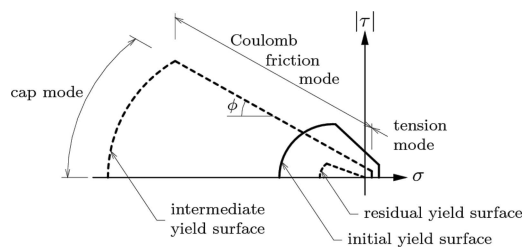

Figure 6. Composite interface model for nonlinear interface elements.

observed in experimental tests, the yielding function reads:

$$f(\sigma,\kappa_2) = |\tau| + \sigma\tan\phi(\kappa_2) - c(\kappa_2). \quad (7)$$

The cohesion and friction softening are defined according to the following expressions:

$$c(\kappa_2) = c_0 \cdot \exp\left(-\frac{c_0}{G_f^{II}}\kappa_2\right) \quad (8)$$

$$\tan\phi(\kappa_2) = \tan\phi_0 + (\tan\phi_{res} - \tan\phi_0)\frac{c_0 - c(\kappa_2)}{c_0}. \quad (9)$$

In the previous equations, c_0 is the cohesion of the brick-mortar interface, ϕ_0 and ϕ_{res} are the initial and the residual friction angle, respectively, G_f^{II} is the mode-II fracture energy, and κ_2 is a scalar indicating the amount of softening, assumed equal to the plastic shear displacement.

A non-associated plastic potential is considered:

$$g_2 = |\tau| + \sigma\tan\psi - c_0 \quad (10)$$

with a variable dilatancy angle ψ, depending on the normal stress and the plastic shear displacement, according to Equation 3.

The input parameters used in the numerical models for masonry are reported in Table 1, where distinction is made between parameters obtained directly from tests and calibrated ones. Concerning calibrated parameters, tensile strength and mode-I fracture energy were determined as a fraction of the cohesion and mode-II fracture energy, respectively (Rots 1997). The parameters for the Coulomb friction model were calibrated from standard triplet tests results, as explained in Section 2, and then used also in the numerical simulations for modified triplets.

To entirely reproduce the test setup, the loading steel plates were also modeled using quadratic plane stress elements, with a linear elastic behavior. The elastic modulus E_s and the Poisson's ratio ν_s for steel were equal to 210000 N/mm^2 and 0.30, respectively. Interface elements were adopted for the brick-to-steel contact surfaces. These elements were modeled as a no-tension material, with a dummy value for the normal stiffness in compression, to allow both the transfer of compressive stress and the separation between steel plates and bricks in presence of tensile stresses. A very low value (10 N/mm^3) was given to the shear stiffness to avoid lateral confinement of bricks.

Numerical simulations were performed with the finite element software DIANA FEA (Release 10.1), at 4 different pre-compression levels σ_p (0.05–0.20–0.60–1.20 N/mm^2), to reproduce the loading conditions of the experimental tests. The numerical simulations were carried out by imposing an increasing vertical displacement to the top plate. Regular Newton-Raphson method was adopted to solve the nonlinear problem.

4 NUMERICAL RESULTS

In this section, results of the numerical simulations are presented for standard and modified triplet tests, and compared with experimental results. The experimental results obtained from standard triplet tests were used to calibrate the parameters governing the previously described model.

4.1 *Standard triplet test*

The results of the numerical simulations for standard triplet tests, at each pre-compression level, are reported in Figure 7 and Figure 8 in terms of shear stress τ *vs* tangential displacement δ_v and normal displacement δ_u *vs* tangential displacement δ_v, respectively. They are compared with experimental

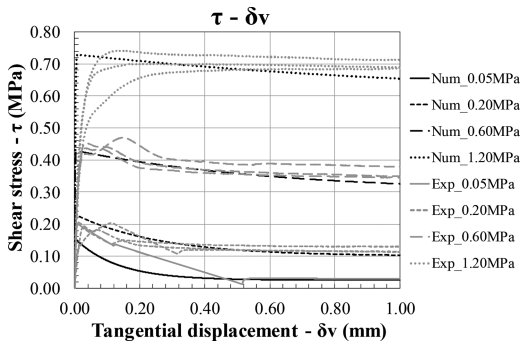

Figure 7. Standard triplet test, shear stress *vs* tangential displacement.

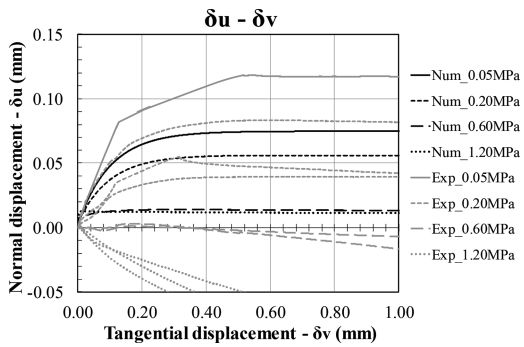

Figure 8. Standard triplet test, normal displacement *vs* tangential displacement.

results. Concerning τ-δ_v diagram, it can be noticed how numerical results are in good agreement with the experimental ones, for all pre-compression levels. The presence of multiple peaks in some of the experimental curves could indicate that the failure was not activated at the same time on both mortar joints. However, given the symmetric model considered, this aspect is not studied here. Looking at Figure 8, it can be noticed that, for pre-compression levels of 0.60 N/mm^2 and 1.20 N/mm^2, the experimental curves show a compression orthogonal to the bed joint which is not well captured by the numerical results. This can be explained by some setup features—e.g. lateral loading plate not free to displace at high pre-compression stress levels—or by considering that the failure mode observed in these experimental tests, especially for the pre-compression level of 1.20 N/mm^2, was not a pure sliding failure along the brick-mortar interface but involved the mortar itself. Indeed, cracking in the mortar occurred along the compression lines, especially close to the upper joint edge. In order to capture the very low—even negative—values of normal displacements δ_u, variations to the numerical model could be made. On the one hand, a modification of the boundary conditions could be considered, as will be discussed in detail in Section 5.1. On the other hand, to properly describe the mortar failure, a detailed micro-modeling strategy, not reported in this work, could be adopted.

The principal stress distributions in Figure 9, reported as an example for a pre-compression level of 0.20 N/mm^2, show high stress concentrations close to the loading plates and the presence of a compressed strut.

Considering the results of the nonlinear analyses for standard triplet specimens, it is interesting to investigate the development of the stress distributions along the joint and the propagation of the failure, given that they could influence the reliability of the results, as mentioned at the beginning.

In Figure 10 and Figure 11 the stress evolution along the sliding failure plane is shown, both for normal and tangential stresses, at pre-compression equal to 0.20 N/mm^2. It can be noticed that the stress distributions are not uniform along the joint and that concentrations of stresses occur at the joint edges, as already observed. Due to the diffusion of the shear load, in the first part of test, the normal compression increases at the joint extremities (always greater at the top), while it decreases in the middle of the specimen. In the post-peak phase, instead, the normal compression is greater at mid-height than at the extremities. The shear stress distributions develop accordingly.

Failure did not initiate far away from the joint edges but close to the bottom extremity and then propagated upwards. Nevertheless, a shear displacement increase of less than 0.01 mm was

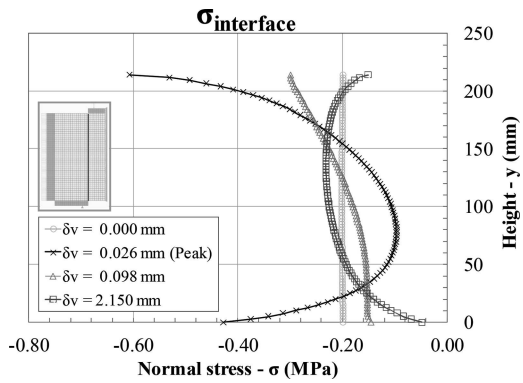

Figure 10. Standard triplet test at pre-compression 0.20 N/mm^2, normal stress evolution along the nonlinear interface.

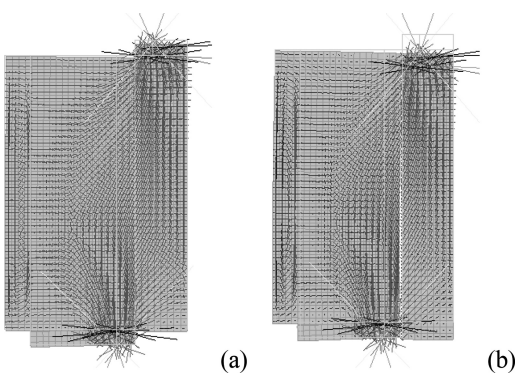

Figure 9. Standard triplet test at pre-compression 0.20 N/mm^2 – Principal stress distributions: (a) pre-peak (δ_v = 0.02 mm); (b) post-peak (δ_v = 0.08 mm).

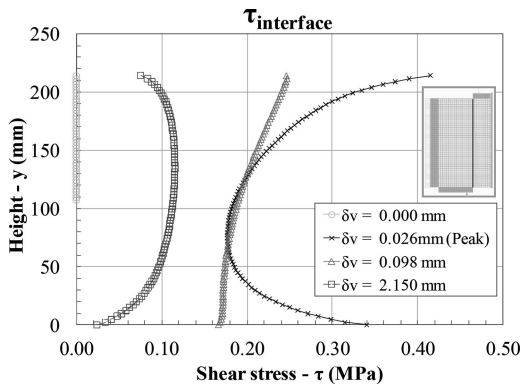

Figure 11. Standard triplet test at pre-compression 0.20 N/mm^2, tangential stress evolution along the nonlinear interface.

needed for it to propagate along the entire joint length.

Similar results were obtained in previous researches, where finite element analyses of different shear tests were performed and stress distributions compared (Riddington et al. 1997, Stöckl et al. 1990). In almost all shear tests, except the one proposed by Van der Pluijm (1999), non-uniform stress distributions were observed and peak stresses at the joint extremities were quite high.

4.2 *Modified triplet test*

The results of the numerical simulations for modified triplet tests are reported in terms of shear stress τ *vs* tangential displacement δ_v (Fig. 12) and in terms of normal displacement δ_u *vs* tangential displacement δ_v (Fig. 13). Experimental results are also included. It can be noticed a good agreement between numerical and experimental results, especially in the τ-δ_v diagram. In the δ_u-δ_v diagram, their agreement is quite good for almost all pre-compression levels, especially in correspondence of low tangential displacement values. Exceptions

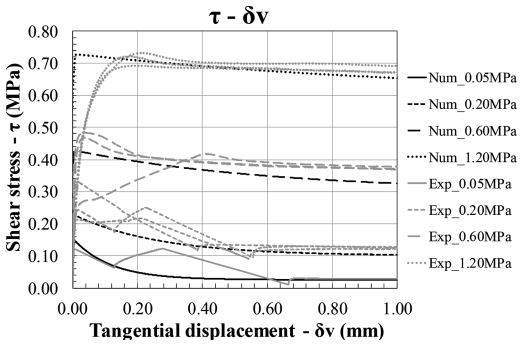

Figure 12. Modified triplet test, shear stress *vs* tangential displacement.

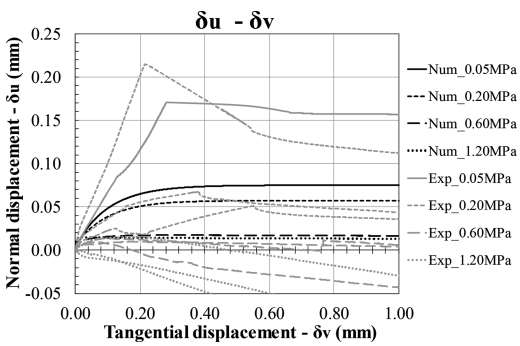

Figure 13. Modified triplet test, normal displacement *vs* tangential displacement.

are represented by the sample tested at 0.05 N/mm^2 and by one specimen at 0.20 N/mm^2, which showed a great expansion upon shearing. The issue previously highlighted for standard triplets—which registered negative δ_u values for high pre-compression stresses—is here present only for two samples at pre-compression equal to 1.20 N/mm^2.

The results of the numerical analysis for modified triplet specimens are satisfactory if compared with experimental results, even if the numerical model was calibrated with results from standard triplet tests. This fact could be explained by considering the failure modes observed in modified triplet tests. Indeed, in the majority of the cases, the sliding failure involved the brick-mortar interface close to the central brick. Only in few cases, the mortar continuity between the head and bed joint was damaged. Therefore, the presence of the head joint, for the masonry typology investigated, did not seem to have a great influence on the outcomes of the tests, especially in terms of peak and residual shear loads.

Figure 14 and Figure 15 show the stress evolution along the sliding failure plane of the vertical joint for increasing values of shear slip, both for normal and tangential stresses, at a pre-compression of 0.20 N/mm^2. As already observed for standard triplet tests, the stress distributions are not uniform along the joint and concentrations of normal stresses are present at the joint extremities. The jump in the stress distributions in correspondence of the head joint can be explained by considering that the upper left brick was subjected to a variable lateral shortening (prevalent at the top) and a clockwise rotation. With respect to the stress distributions for the standard triplet tests (Figs. 10, 11), these movements caused, along the upper portion of the sliding surface, higher peak stresses at the top and reduced stresses in the

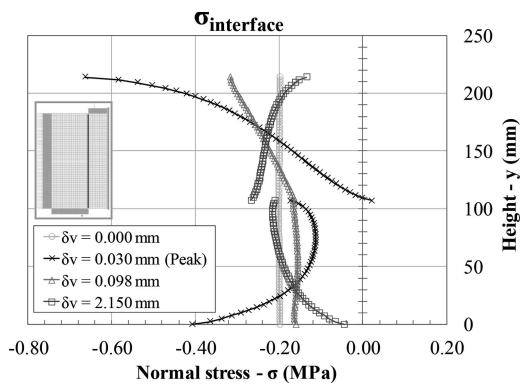

Figure 14. Modified triplet test at pre-compression 0.20 N/mm^2, normal stress evolution along the nonlinear interface.

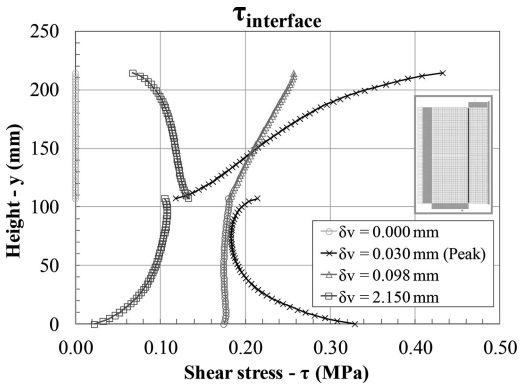

Figure 15. Modified triplet test at pre-compression 0.20 N/mm^2, tangential stress evolution along the non-linear interface.

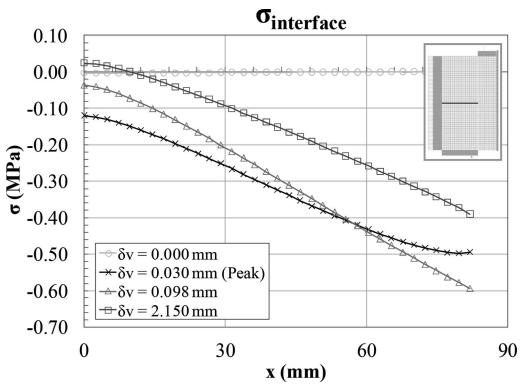

Figure 16. Modified triplet test at pre-compression 0.20 N/mm^2, normal stress evolution along the head joint.

middle, even leading to tensile normal stresses in a small portion of the sliding interface.

The normal stress evolution on the head joint is presented in Figure 16. Maximum values of compressive stresses are located at the right-end side, close to the sliding failure plane. This is consistent with the diffusion of the shear load inside the specimen and with the clockwise rotation of the upper left brick. With the failure propagation, the reduction of the compressive stresses along the head joint can be related to the reduction of the upper left brick deformation due to the lateral relaxation of the sample in the softening phase.

5 PARAMETRIC STUDIES

In this section, some modifications to the numerical models are introduced with the aim of studying the influence of different parameters and testing conditions on the shear-sliding behavior of calcium silicate masonry.

5.1 *Influence of boundary conditions (standard triplet test)*

Dilatancy is one of the most important parameters governing the sliding failure of mortar joints. Indeed, the dilatant behavior of masonry could affect the results in two different ways, depending on the boundary conditions of the triplet tests. It could either produce an increase in the peak load, in case of restrained lateral displacement, or an increase in the displacements orthogonal to the bed joint, if the specimen is free to displace laterally. In particular, an increase in the shear capacity is determined by the fact that, during the sliding, when the transverse expansion is restrained, the pre-compression level on the joint increases, which consequently leads to higher peak loads. Therefore, the way in which the pre-compression is applied to the sample plays a crucial role in the outcomes of the test.

To study the influence of the boundary conditions, additional numerical simulations were performed, in which the pre-compression load was applied as a constant lateral displacement, i.e. to reproduce the restrained displacements condition. The mechanical properties and the pre-compression levels considered were the same of the previous analyses. The results of the numerical simulations for the laterally restrained model are here reported for standard triplet tests only.

The shear stress τ *vs* tangential displacement δ_v diagrams are reported in Figure 17. It can be stated that the laterally restrained condition is not representative of standard triplet tests at low pre-compression stress levels, i.e. 0.05 N/mm^2 and 0.20 N/mm^2. Indeed, differently to what can be observed in Figure 7, the numerical curves do not correspond at all to the experimental ones.

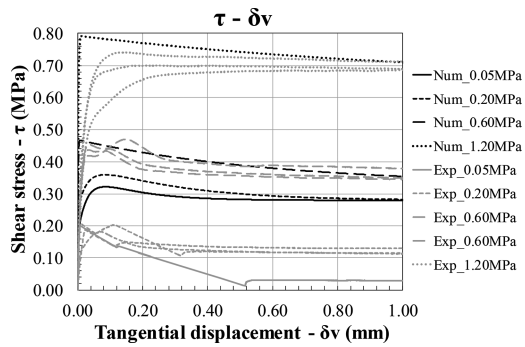

Figure 17. Standard triplet test with restrained lateral displacement, shear stress *vs* tangential displacement.

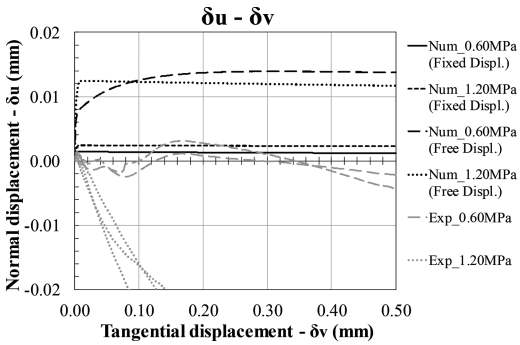

Figure 18. Standard triplet test, shear stress *vs* tangential displacement—Free *vs* restrained lateral displacement conditions.

On the opposite, for higher pre-compression levels (0.60 N/mm^2 and 1.20 N/mm^2), there is a good agreement between numerical and experimental results. This is related to the fact that, in these latter cases, dilatancy is playing a very marginal role, given the high compression acting on the joint.

The normal displacement δ_u *vs* tangential displacement δ_v diagrams are reported in Figure 18 for triplet tests at 0.60 N/mm^2 and 1.20 N/mm^2. Here, the results already presented for standard triplets with free lateral displacements are reported as well. The portion of the diagram for low values of tangential displacements is considered, since it is the most interesting part, corresponding to the activation of the sliding failure and the reaching of the peak load. It can be noticed that for the restrained displacement condition, the normal displacement is considerably low. However, the behavior of the samples at high pre-compression levels is still not properly captured. Indeed, as already observed, the simplified micro-modeling seems to be not adequate to reproduce the failure modes observed in these tests, and detailed micro modeling is probably needed.

5.2 *Influence of dilatancy parameters (modified triplets test)*

The uplift upon shearing is governed by the dilatancy function (Eq. 3) and, therefore, by the parameters ψ_0, σ_u and δ. In this context, parametric studies were performed for models with free lateral displacements, varying the values of these parameters. In the followings, results of numerical simulations for modified triplet tests are shown, where increased values of ψ_0 and σ_u were considered (Table 2). Indeed, experimental results showed that modified triplet specimens were characterized by higher normal displacements δ_u with respect to

Table 2. Modified dilatancy parameters.

Parameter	Symbol	Value
Dilatancy angle	ψ_0 [rad]	0.561 (+50%)
Confining normal stress	σ_u [N/mm^2]	0.70 (+20%)
Exp. degradation coeff.	δ	9.63

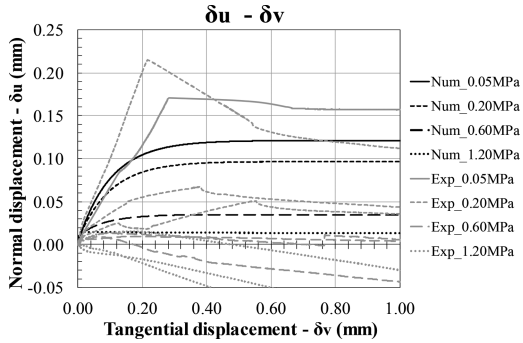

Figure 19. Modified triplet test, normal displacement *vs* tangential displacement.

standard triplets. Given the observations reported in Section 5.1, the results were not expected to be different from the previous models in terms of shear capacity, but in terms of normal displacements. Figure 19 shows an increase in the normal uplift for all tests, except for the case with pre-compression equal to 1.20 N/mm^2. Comparing it with Figure 13, it is possible to observe that a better agreement between numerical and experimental results is found, especially at low pre-compression levels.

5.3 *Influence of the elastic properties of head joint (modified triplets test)*

With reference to the modified triplet specimens, parametric studies were carried out on the elastic stiffnesses of the head joint. Indeed, in the engineering practice, it is quite common to deal with masonry structures in which head joints have lower mechanical properties than bed joints. This is due to construction reasons and, moreover, to the fact that head joints are not subjected to compression during the curing. Therefore, imperfections or microcracks are often present. To simulate this situation, the elastic modulus of mortar was reduced by 50% and the elastic stiffness parameters of the interface elements were modified accordingly. Results are here reported in terms of normal stresses for the pre-compression level of 0.20 N/mm^2 (Fig. 20). Distributions at peak load and in the residual phase are shown and

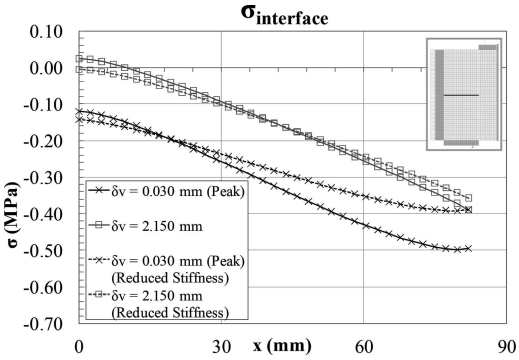

Figure 20. Modified triplet test at pre-compression 0.20 N/mm^2, normal stress evolution—Intact *vs* weak head joint.

results from Figure 16 are also included. In presence of weak head joint, a 20% compressive stress reduction can be observed on the right-end side of the joint, in correspondence of the peak load ($\delta_v = 0.030$ mm), as expected. In the residual phase, instead, where the shear load has already been transferred and a pure friction behavior can be observed, the two stress distributions are almost coincident.

Differences were not observed neither in terms of peak and residual shear load nor in terms of orthogonal displacements. Similar observations can be done for the other pre-compression levels, which are not reported here, for sake of brevity.

The variation of the elastic properties of the head joint was not sufficient to influence the sliding failure during the triplet test. In order to consider different behaviors, e.g the failure within the head joint or in the contact point between head and bed joint, the use of a detailed micro-modeling strategy could be useful, in which nonlinearities could be assigned to the head joint. However, these variations were not considered here, given that the head joint was not involved in the sliding failure during experimental tests.

6 CONCLUSIONS

The numerical simulations of triplet tests presented in this paper were carried out to study the shear-sliding behavior of calcium silicate brick masonry. Two different geometries were considered: the standard triplet specimen and the modified one, characterized by a running bond pattern. A simplified micro-modeling strategy was adopted. The models were calibrated with results of standard triplet tests and then validated through comparisons between numerical and experimental results.

The obtained numerical results allowed to understand which aspects could most affect the outcomes of the triplet tests. In particular, the influence of dilatancy and the boundary conditions were analyzed.

The influence of dilatancy on the results of the triplet test is strongly associated to the boundary conditions of the test itself. On the one hand, in case of restrained lateral displacements, an overestimation of the shear capacity was observed for samples at pre-compression equal to 0.05 N/mm^2 and 0.20 N/mm^2. At higher pre-compression levels, instead, the restrained displacements condition could partially capture the very low values registered for normal displacements. On the other hand, in case of free lateral displacements, the dilatancy can affect the values of the normal displacements along the sliding failure plane. To investigate this aspect, parametric studies were performed on the variables defining the dilatancy function. In particular, for modified triplet tests, in which the registered transverse displacement upon shearing was higher than in standard triplet tests, these parametric studies allowed to better capture the behavior of the samples, at least for low pre-compression levels.

The presence of a head joint did not have a great influence on the tests outcomes. This was confirmed both by numerical and experimental results and can be related to the specific masonry typology investigated. Indeed, the head joint was almost never involved in the failure process. Parametric studies were performed, reducing the normal and shear stiffness values, and the only difference in the results was represented by a change in the stress distributions along the head joint. In order to include failure modes involving the head joint, it is advisable to use a detailed micro-modeling strategy.

Aspects related to the triplet test setup and execution were analyzed and briefly discussed, such as the presence of non-uniform stress distributions along the sliding bed joint, the concentration of stresses at its extremities, the failure initiation and propagation. Even if the objective of the research was not to reduce or eliminate the influence that these aspects have on the test outcomes, they all represents intrinsic issues in the triplet test, which is important to be aware of.

In conclusion, the numerical simulations here presented allowed to gain a better understanding of the sliding failure in triplet tests. Future works can be done with the objective of better capturing the shear failure within the mortar at high pre-compression level. The detailed micro-modeling approach could be used to this purpose, in which failure inside the mortar can be included.

ACKNOWLEDGMENTS

The experimental tests used in this paper were performed at Delft University of Technology within the "Testing program 2016 for Structural Upgrading of URM Structures" financed by Nederlandse Aardolie Maatschappij (NAM) under contract number UI63654. The first author would like to acknowledge the "Marco Polo" mobility program of the University of Bologna, that provided funding for her visiting period at Delft University of Technology.

REFERENCES

Atkinson, R.H., Amadei, B., Saeb, S. & Sture, S. 1989. Response of masonry bed joints in direct shear. *Journal of Structural Engineering*, 115(9):2276–2296.

Drysdale, R.G., Vanderkeyl, R. & Hamid, A.A. 1979. Shear strength of brick masonry joints. *Proc. 5th Int. Brick and Block Mas. Conf., Washington D.C., 5–10 October 1979*.

EN 1052-3:2002. Method of test masonry—Part 3: Determination of initial shear strength. *European Standards (EN)*.

Jafari, S. & Esposito, R. 2016. Material tests for the characterisation of replicated calcium silicate brick masonry. *Delft University of Technology, Report number C31B67WP1-9, 14 November 2016*.

Jukes, P. & Riddington, J.R. 2000. Finite element prediction of block triplet shear strength. *Proc. 12th Int. Brick and Block Mas. Conf., Madrid, 25–28 June 2000*.

Jukes, P. & Riddington, J.R. 2001. The failure of brick triplet test specimens. *Masonry International*, 15(1).

Lourenco, P.B., Rots, J.G. & Blaauwendraad, J. 1995. Two approaches for the analysis of masonry structures: micro and macro-modeling. *Heron*, 40(4):313–340.

Lourenco, P.B. 1996. Computational strategies for masonry structures, PhD thesis, Delft University of Technology.

Magenes, G. & Calvi G.M. 1997. In-plane seismic response of brick masonry walls. *Earthquake Engineering and Strucural Dynamics*, 26:1091–1112.

Montazerolghaem, M. & Jaeger, W. 2014. A comparative numerical evaluation of masonry initial shear test methods and modifications proposed for EN 1052-3. *Proc. 9th International Masonry Conference, Guimaraes, 2014*.

Popal, R. & Lissel, S.L. 2010. Numerical evaluation of existing mortar joint shear tests and a new test method. *Proc. 8th International Masonry Conference, Dresden, 2010*.

Riddington, J.R., Fong, K.H. & Jukes, P. 1997. Numerical study of failure initiation in different joint shear tests. *Masonry International*, 11(2).

Riddington, J.R. & Jukes, P. 1994. A masonry joint shear strength test method. *Proc. Instn Civ. Engrs Structs & Bldgs*, 104:267–274.

Rots, J.G. 1997. *Structural Masonry—An experimental/numerical basis for practical design rules*, Rotterdam: Balkema.

Stöckl, S., Hofmann, P. & Mainz, J. 1990. A comparative finite element evaluation of mortar joint shear tests. *Masonry International*, 3(3).

Van der Pluijm, R. 1999. Out of plane bending of masonry. *Ph.D. Thesis. Eindhoven University of Technology, The Netherlands*.

Van der Pluijm, R., Rutten, H. & Ceelen, M. 2000. Shear behaviour of bed joints. *Proc. 12th Int. Brick and Block Mas. Conf., Madrid, 25–28 June 2000*.

Van Zijl, G. 2004. Modeling masonry shear-compression: role of dilatancy highlighted. *Journal of Engineering Mechanics*, 130(11):1289–1296.

Vermeltfoort, A.T. Variation in shear properties of masonry. *Proc. 8th International Masonry Conference, Dresden, 2010*.



Taylor & Francis
Taylor & Francis Group
http://taylorandfrancis.com

Dynamic behavior: From seismic retrofit to impact simulation



Taylor & Francis
Taylor & Francis Group
http://taylorandfrancis.com

Computational Modelling of Concrete Structures – Meschke, Pichler & Rots (Eds)
© 2018 Taylor & Francis Group, London, ISBN 978-1-138-74117-1

Mechanical model of adhesive post-installed anchor subjected to combined force

Y. Takase & M. Mizoguchi
Muroran Institute of Technology, Hokkaido, Japan

T. Wada
Department of Architecture, Hokkaido Polytechnic College, Hokkaido, Japan

ABSTRACT: In seismically retrofitted structures, seismically retrofitting members are generally connected to existing members by post-installed anchors and roughening the concrete surface. This study aimed at verifying behaviors of post-installed anchors subjected to tensile force and shear force. First, we conducted the experimental test. As a result of this test, the shear force was decreasing with tensile force increasing. In addition, we modified our mechanical model using the relation between T/T_a and Q/Q_a (T; allowable tensile force, Q; allowable shear force, T_a; specific tensile force, Q_a; specific shear force). To the end, it was shown that the modified model could be estimate reasonably the experimental results.

1 INTRODUCTION

In seismically active countries such as Japan, it is important to improve the ability of buildings to withstand earthquakes through seismic retrofits. A common method of retrofitting uses post-installed anchors which connect strengthening members to existing members. During an earthquake, shear stress is transferred through the post-installed anchors, making them a vital support for load-bearing elements in reinforced concrete structures.

It is most common for the retrofit members to be connected inside the frame of an existing structure; however, having them connected on the outside is becoming an increasingly popular option. The main advantage of external connections is that there is very little disruption to the internal functions of the building as compared to an internal connection. Unfortunately, considerable research has not been conducted on the shear and tensile forces experienced by externally connected, post-installed members.

In this paper, we conducted shear loading tests on post-installed anchors subjected to constant tensile force. Furthermore, we modified our proposed mechanical model (Takase et al. 2013) that can predict the relationship between shear force Q and slip δ under a combined stress.

2 EXPERIMENTAL PROGRAM

2.1 *Test parameters*

Table 1 shows the individual characteristics of 13 specimens tested in this study. Experimental parameters include diameter ϕ, concrete compressive strength f_c, and tensile stress f_t. The diameters of the deformed bars used as anchor bolts are 13 mm, 16 mm, and 19 mm; a designed concrete strength F_c is set at 9, 15 and 21 N/mm^2 as would be found in older buildings; and f_N is set at about 0, 0.33f_y, and 0.66f_y N/mm^2, where f_y is the yield strength of the anchor bolt. Due to a lack of specimens, those with an F_c of 9 and 21 N/mm^2 are only tested at $f_N = 0$

Table 1. Specimen parameters of this experimental test.

Specimen No.	ϕ (mm)	r_N	F_c (N/mm^2)	L_e (mm)	Grouting mortal
D13-000T-15	13	0	15	10ϕ	Prop.-1
D13-033T-15	13	0.33	15	10ϕ	Prop.-1
D13-066T-15	13	0.66	15	10ϕ	Prop.-1
D16-000T-9	16	0	9	10ϕ	Prop.-2
D16-056T-9	16	0.56	9	10ϕ	Prop.-2
D16-000T-15	16	0	15	10ϕ	Prop.-1
D16-033T-15	16	0.33	15	10ϕ	Prop.-1
D16-066T-15	16	0.66	15	10ϕ	Prop.-1
D16-000T-21	16	0	21	10ϕ	Prop.-2
D16-056T-21	16	0.56	21	10ϕ	Prop.-2
D19-000T-15	19	0	15	10ϕ	Prop.-1
D19-033T-15	19	0.33	15	10ϕ	Prop.-3
D19-066T-15	19	0.66	15	10ϕ	Prop.-1

ϕ: Diameter of anchor bolt, r_N: Ratio of f_y and f_N, f_y: Yield strength, f_N: Tensile stress, F_c: Design compressive strength of concrete, E_c: Young's modulus of concrete, L_e: Embedded length of anchor bolt.

and 0.56f_y N/mm^2. After that, the tensile stress ratio $r_N = f_N/f_y$ is used as the index instead of f_N.

The specimens are named according to their specifications. The number that follows the first letter D indicates the diameter ϕ, followed by the parameter values for r_N and F_c.

2.2 *Test specimens*

Figure 1 shows details of the specimens. Table 2 outlines the material properties of the concrete and the mortar, while Table 3 shows those of the anchor bolts. Three grouting mortal properties are prepared in this test because of difference of the loading date.

The specimens used to model the existing members are 440 mm × 400 mm × 250 mm reinforced concrete blocks and those used to model the supporting members are 350 mm × 170 mm × 160 mm grouting mortar blocks with 10 mm reinforcing bars. Post-installed anchors are adhered to the freshly formed concrete blocks and the grouting mortar blocks are constructed around them. Normal-weight concrete is used to cast the specimens. The joining surfaces between the concrete and grouting mortar are greased in order to minimize the effects of friction. When connecting the post-installed anchors, a rotary drill is used for drilling, and injectable epoxy adhesives are applied for anchoring.

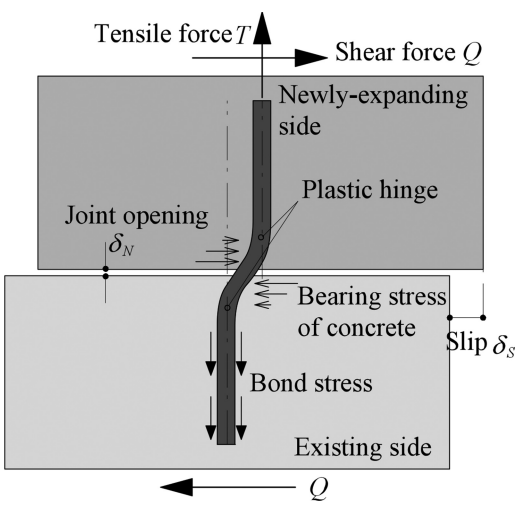

Figure 1. Mechanical behaviour of post-installed anchor under combined stress.

Table 2. Material properties of concrete and grouting mortal.

	f_c (N/mm^2)	E_c (kN/mm^2)	f_t (N/mm^2)
F_c = 10 N/mm^2	12.5	18.1	1.43
F_c = 20 N/mm^2	20.5	23.8	1.93
F_c = 30 N/mm^2	30.5	25.9	1.93
Grouting mortal-1	59.07	23.59	3.30
Grouting mortal-2	62.66	25.63	3.00
Grouting mortal-3	72.58	23.94	3.35

f_c: Compressive strength, E_c: Young's modulus, f_t: Splitting strength.

Table 3. Material properties of anchor bolts.

ϕ (mm)	f_y (N/mm^2)	f_u (N/mm^2)	E_s (kN/mm^2)	δ (%)
13	375	582	193	26
16	396	582	194	24
19	402	600	189	23

ϕ: Diameter of anchor bolt, f_y: Yielding strength, f_u: Ultimate strength, E_s: Young's modulus of anchor bolt, δ: Elongation after fracture.

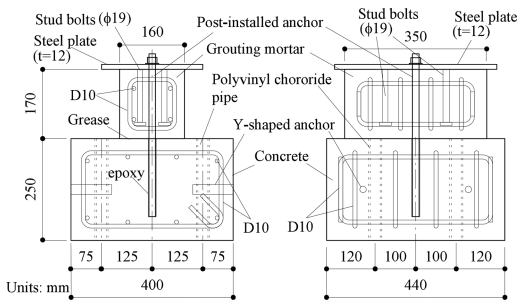

Figure 2. Test specimen used for loading test under combined stress.

2.3 *Loading and measurement method*

Figure 3 shows the loading equipment. The measurement method is illustrated in Figure 4. The test specimens are subjected to a cyclic shear force and constant tensile force from the loading equipment in Figure 3. The two hydraulic jacks and the one center-hall jack are used for shear loading and tensile loading, respectively. The test specimens are fixed to the reaction beam and the loading beam. The loading beam is attached to the loading frame through a pantograph allowing it to be displaced horizontally during shear loading.

The slip δ_S and the gap δ_N are an average value of the relative horizontal displacement and the vertical displacement, respectively.

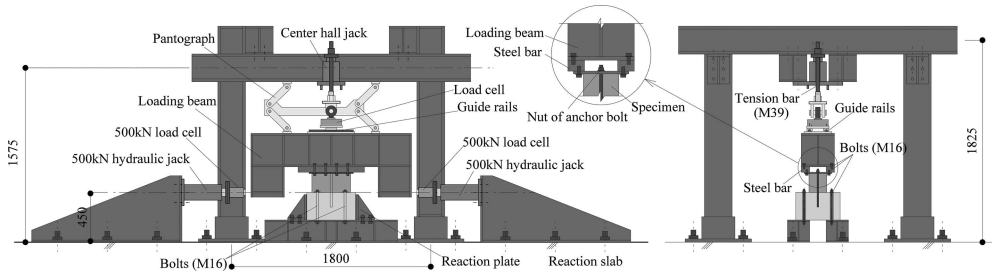

Figure 3. Loading equipment used for cyclic shear loading test subjected to constant tensile force.

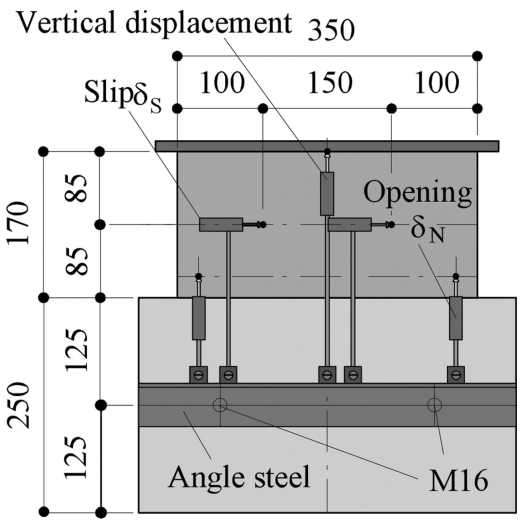

Figure 4. Mesurement method of shear loading test under combined stress.

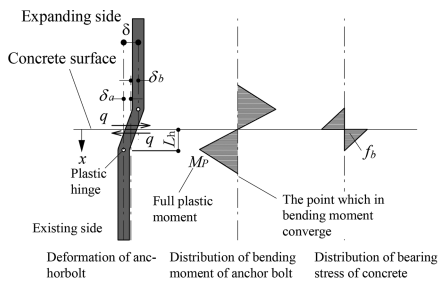

(a) Plastic hindge of anchor bolt and bearing stress of concrete

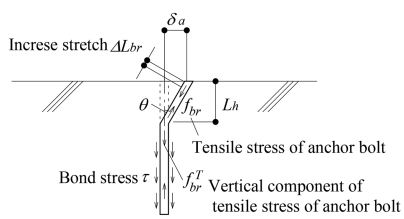

(b) Bond behaviour between anchor bolt and concrete

Figure 5. Demonstrates the technique of dowel-action modelling.

3 PROPOSED MODEL

We constructed a mechanical model of an adhesive post-installed anchor subjected to shear loading using the piles theory (Takase et al. 2013). The failure modes of post-installed anchors explored in this paper are i) the yielding of the anchor bolt and ii) the bearing failure of concrete. Of course, this model could not evaluate behaviours with being applied to tensile force. Then, we modify this model to evaluate the behaviour under combined stress. Because the details of proposed model was presented in previous literature, the modified points is mainly explained in this chapter.

3.1 *Equilibrium of shear force*

Figure 5 demonstrates the technique of dowel-action modelling for a post-installed anchor. When the displacement is small, it is possible to apply the elastic beam theory to a post-installed anchor.

But, elastic beam theory cannot be extended to the case where the anchor bolt or concrete are within their plastic range. Therefore, we proposed the model as shown in Figure 5 to better describe the behaviour in a nonlinear zone.

In the proposed model, initially the plastic behaviour of the anchor bolt at the bending point (the hinge) is calculated. Assuming that the anchor bolt deforms in a linear manner around the plastic hinge, the bearing stress acts on the concrete. Furthermore, the anchor bolt will tend to elongate between the concrete surface and the plastic hinge. Thus, the anchor bolt is subject to tensile stress, with a significant shear component. As above, the shear force q_a equated to i) the bending moment of the plastic hinge q_s, ii) the bearing stress of the concrete q_b, and iii) the shear component of the tensile stress of the anchor bolt q_T^s.

$$q_a = q_s + q_b + q_T^s \tag{1}$$

3.2 *Depth of plastic hinge*

The depth of the plastic hinge influences the three components of the shear force. According to the elastic beam theory, the depth of the largest moment L_M can be calculated. However, when concrete is in its plastic range, L_h becomes smaller, and thus, L_M gets larger. Therefore the following equation is used in the proposed model.

$$L_h = \frac{3\pi}{8}\sqrt[4]{\frac{4E_s I_z}{\kappa\phi}} \tag{2}$$

Here, κ is the reaction modulus of the concrete. The Maekawa model (1996) was used in this equation to obtain the reaction modulus of concrete.

$$\kappa = \frac{150 f_c}{\phi} \tag{3}$$

Here, f_c is the compressive stress applied on the concrete (N/mm^2). From Equations (2) and (3), the shear force q_s that causes the anchor bolt to yield is obtained as follows.

$$q_s = \frac{M_p}{L_h} \tag{4}$$

M_P is the plastic moment of anhor bolt.

3.3 *Bearing stress of concrete*

The concrete strain from the deformation of an anchor bolt is influenced by any slippage of the anchor bolt. Assuming that the anchor bolt deforms linearly around the plastic hinge, the slip δ_a is described as follows.

When $0 < x < L_h$,

$$\delta_a(x) = \delta_a(0) - \frac{\delta_a(0)}{L_h} \cdot x \tag{5}$$

When $L_h < x$,

$$\delta_a(x) = 0 \tag{6}$$

Here, x is the depth from joint surface.

Concrete strain is considered to be the greatest near the anchor bolt, decreasing with the distance from the anchor bolt. However, it is difficult to provide evidence of this phenomenon. Here, the concrete strain is described as the average strain.

$$\varepsilon_b = \delta_a / L_{\varepsilon b} \tag{7}$$

Here $L_{\varepsilon b}$ is the effective length to calculate concrete strain and assuming $L_{\varepsilon b}$ is 5ϕ.

The bearing force of the concrete is calculated by multiplying the circumference of the semicircle of the anchor bolt by the integral of the compressive stress from $x = 0$ to $x = L_h$.

3.4 *Tensile stress of anchor bolt*

When the anchor bolt deforms around the plastic hinge, it is stretched between the hinge point and the concrete surface. The increase in length ΔL_{br} is as follows.

$$\Delta L_{br} = \sqrt{\Delta\delta_a^2 + L_h^2} - L_h \tag{8}$$

The strain ε_{br} is obtained from ΔL_{br}. Moreover, its shear component force q_T^s can be obtained.

In addition, because the adhesion bond between the plastic hinge and the concrete surface is hardly damaged, the bond properties may not be affected.

3.5 *Mechanical behavior of the three components*

Figure 6 shows the mechanical behaviours of three components in compliance with Equation (1).

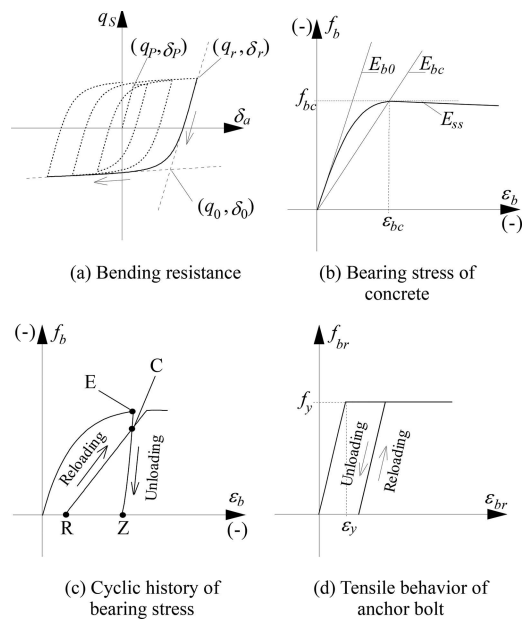

Figure 6. Mechanical behaviors used in the proposed model.

1. Bending Resistance of Plastic Hinge

In this model, the bending resistance behaviour of the plastic hinge is considered the same as the behaviour of a reinforcing bar subjected to tensile stress. As a constitutive equation, the Menegotto–Pinto model (Menegotto & Pinto 1973) is used here replacing stress and strain with force q_s and displacement δ_a.

2. Bearing Stress of Concrete

The bearing stress is related to the local compressive stress within the concrete. This likeness allows for the constitutive laws of compressive stresses to be applied to the bearing stress up to the maximum stress (Saenz 1983).

$$f_b = \frac{E_{b0} \cdot \varepsilon_b}{1 + \left(\frac{E_{b0}}{E_{bc}} - 2\right)\left(\frac{\varepsilon_b}{\varepsilon_{bc}}\right) + \left(\frac{\varepsilon_b}{\varepsilon_{bc}}\right)^2} \tag{9}$$

Here, we modified the bearing stress model in post-peak behaviour from the previous model. After the maximum stress is reached, the stress remained because the anchor bolt is restrained in the previous model. But, we consider the stress softening in the modified model. The stress softening modulus E_{ss} is 0.3% of Young's modulus. This value was determined from the experimental results.

Moreover, the maximum bearing stress exceeds the maximum compressive stress. In this model, the following equation is used for the maximum bearing stress f_{bc}.

$$f_b c = 18 \times f_c^{\frac{1}{3}} \tag{10}$$

Figure 6(c) shows behaviour during unloading and reloading. An unloading curve is expressed by parabolic function (Naganuma & Ohkubo 2000) through the point Z (Karsan & Jirsa 1969). A reloading curve is also expressed by linear function through the point R and C (Naganuma & Ohkubo 2000).

3. Tensile Stress of Anchor bolt

The resulting behaviour when tensile stress is applied to a bilinear model is shown in Figure 6(d).

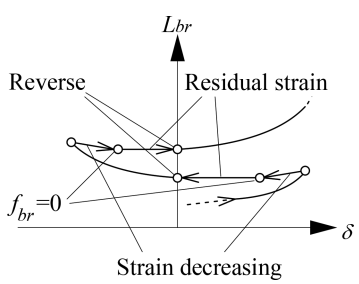

Figure 7. Behavior of anchor bolt.

Moreover, the behaviour of L_{br} subjected to cyclic loading is presented in Figure 7.

3.6 *Relationship between tensile force ratio and shear force ratio*

Generally, the following formula is used in structural members subjected to combined forces.

$$\left(T/T_a\right)^{\alpha} + \left(Q/Q_a\right)^{\alpha} = 1 \tag{11}$$

Here, T_a and Q_a are a specific tensile strength and shear strength of an anchor bolt, respectively. T and Q are the allowable tensile force and shear force under a combined stress. α is an experimental coefficient that generally takes a value between 1 and 2.

We can express T_a with the following equation.

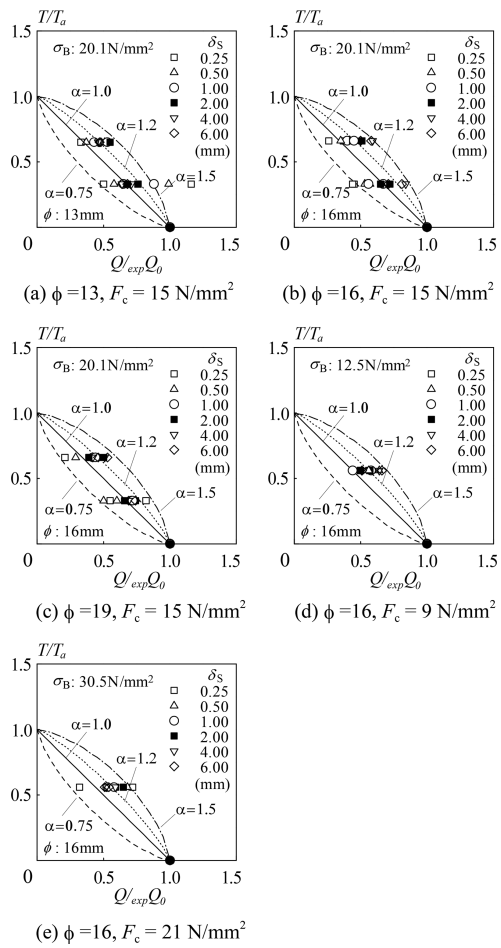

(a) ϕ =13, F_c = 15 N/mm²
(b) ϕ =16, F_c = 15 N/mm²
(c) ϕ =19, F_c = 15 N/mm²
(d) ϕ =16, F_c = 9 N/mm²
(e) ϕ =16, F_c = 21 N/mm²

Figure 8. Relationship between ratio of tensile force T/T_a and ratio of shear force Q/Q_a.

$$T_a = \sigma_y \times A_s \tag{12}$$

Here a_s is the cross-sectional area of an anchor bolt.

A shear strength formula for an anchor bolt can be used to determine Q_a; however, these formulas can vary considerably from test results. Therefore, we apply the shear force Q when $r_N = 0$ to Q_a instead of a shear strength formula.

Figure 8 shows the relationship between T/T_a and Q/Q_a obtained from the tests. According to the test results, it is found that the range of α is 0.75 to 1.5.

Here, Q, when the bolt is subjected to constant tensile force T, can be expressed by transforming Equation (13).

$$Q = \sqrt[\alpha]{1-(T/T_a)^{\alpha}} \times Q_a \tag{13}$$

In this modified model, α is set to 1 as the midium value from 0.75 to 1.0.

4 ADAPTABILITY OF PROPOSED MODEL TO EXPERIMENTAL RESULTS

Figures 9 (a)–(i) show comparisons of the test and analysis results of the Q–δ_S curves in the case of $F_c = 15$ N/mm^2. Figures 10 (a)–(d) show comparisons of the test and analysis results of the Q–δ_S curves in the case of $F_c = 9$ and 21 N/mm^2.

When we calculate the Q–δ_S curves using proposed model, it is necessary to consider the deformation of the joint side. But, we have here assumed to deform as a rigid body due to precise calculation.

According to Figure 9, the bigger the diameter of the anchor bolt, the bigger the value of Q. In addition, the bigger the tensile stress ratio r_N, the smaller the value of Q.

Observing the results of D13-000T-15 and D16-000T-15, the proposed model estimates a slightly lower peak force than the test results. However, the test behaviours beyond $\delta_S = 1$ mm are predicted reasonably well. As mentioned above, the proposed model can estimate the test results well overall.

Unlike D13-000T-15 and D16-000T-15, the analytical stiffness was found to be higher than the test results for D19-000T-15. Although, the proposed model still evaluates the test behaviour for this specimen after $\delta_S = 1$ mm as well as D13-000T-15 and D16-000T-15.

Next, we observe the test results of the specimens subjected to a tensile force illustrated in Figures 9 (b), (c), (e), (f), (h) and (i), those with $r_N = 0.33$ and 0.66. A similar degree of accuracy was achieved in these tests as for the specimens

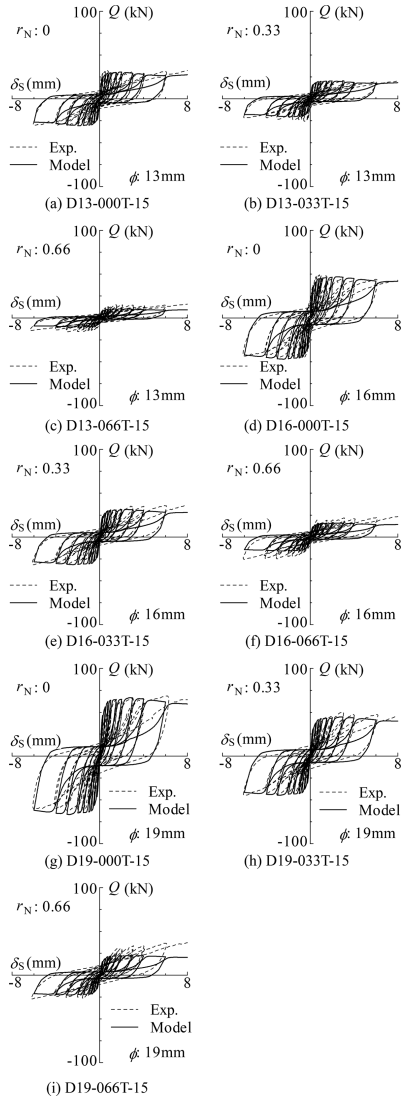

Figure 9. Comprarison test results with proposed model in the case of $F_c = 15$ N/mm^2.

with $r_N = 0$. However, the analytical results are a bit lower than the test results in the specimens with $r_N = 0.66$. This tendency is especially noticeable in D19-066T-15 on a positive side.

Observing Figure 10 illustrating the results of $F_c = 9$ and 21 N/mm^2, the modified model can reasonably estimate the test results as well as $F_c = 15$ N/mm^2.

As above mentioned, the modified model is capable of evaluating the overall behaviours of the specimens. Thus, it is thought that this model will be useful in an engineering field such as seismic design.

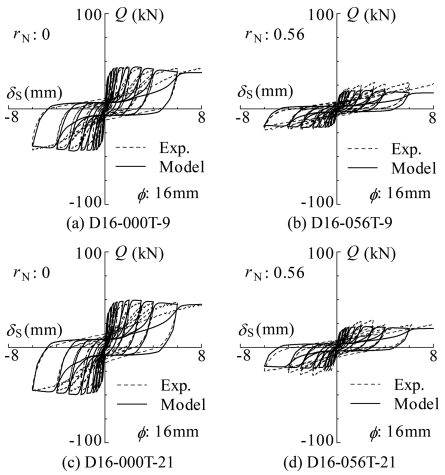

Figure 10. Comprarison test results with proposed model in the case of $F_c = 9$ and 21 N/mm^2.

5 CONCLUSIONS

In this study, we conducted shear loading tests on concrete specimens subjected to cyclic shear force and constant tensile force; we then modified a mechanical model of a post-installed anchor seismic retrofit. In this model, the shear force is equal to the sum of the bending resistant force q_s, the bearing stress of concrete q_B, and the shear component of the tensile stress q_T^s. Moreover, Equation (13) was applied to the proposed model in order to evaluate the behaviour under combined force.

Findings obtained in this study are as follows:

1. The shear force decreased as the tensile force increased.
2. For the relationship between T/T_a and Q/Q_a, the test results were reasonably estimated by choosing α in the range 0.75 to 1.5.
3. By setting $\alpha = 1$ in Equation (13), the modified model can predict test results reasonably well.

Improvements to the proposed model in future studies will focus on considering bond stress–slip behaviour of adhesives and separation of joint.

ACKNOWLEDGMENT

This work was supported by JSPS KAKENHI Grant Number 16K18195.

REFERENCES

Ando, Y. & Nakano, K., 2008, Influence of edge distance for shear capacity of post-installed bonded anchor, *Proceedings of annual research meeting, AIJ*, No. 51: 77–80. (in Japanese).

Fukumoto, K., Kiyohara, T., Nakano, K. & Matsuzaki, Y., 1998, Experimental study on structural performance of post installed bonded anchors, *Summaries of technical papers of Annual Meeting, AIJ, C-2*: 719–720. (in Japanese).

Hofbeck, J.A., Ibrahim, I.O. & Mattock, A.H., 1969, Shear transfer in reinforced concrete, *Journal of ACI*, No. 66: 119–128.

Jimenez, R., White, R.N. & Gergely, P., 1982, Cyclic shear and dowel action models in R/C, *Journal of ASCE, Vol. 108, No. ST5*: 1106–1123.

Karsan, I.D. & Jirsa, J.O., 1969, Behavior of Concrete under Compressive Loading, *Journal of ASCE*, Vol. 95*, No. ST2*: 2543–2563.

Maekawa, K. & Qureshi, J., 1996, Ccomputational model for reinforcing bar embedded in concrete under combined axial pullout and transverse displacement, *Journal materials, Conc. Struct., Pavements, JSCE(532)*: 227–239. (in English).

Menegotto, M. & Pinto, P.E., 1973, Method of analysis for cyclically loaded R.C. plane frame including changes in geometory and non-elastic behavior of elements under combined normal force and bending, *Pfoceedings of IABSE, Symposiium on Resistance and Ultimate Deformability of Structures Acted on by Well Defined Repeated Loads*; pp. 15–22.

Naganuma, K. & Ohkubo, M., 2000, An analytical model for reinforced concrete panels under cyclic stresses, *Journal of strutural engneering, AIJ*, No. 536: 135–142.

Ollgaard, J.G., Slutter, R.G. & Fisher, J.W., 1971, Shear strength of stud connectors in lightweight and normal-weight concrete, *AISC Engineering Journal*: 55–64.

Sadasue, K., Hosokawa, Y., Oka, K. & Minami, K., 2009, Experimantal study of shear strength of disk anchor, *Proceedings of the Japan Concrete Institute, Vol. 31, No. 2*: 1009–1014.(in Japanese).

Saenz, L.P., 1983, Discussion of Equation for Stress - Strain Curve of Concrete, by Desayi P. and Krishnan S., *ACI Journal, Vol. 61, No. 9*: 1227–1239.

Sakai, J. & Kawashima, K., 2003, Modification of the Gtuffre, Menegotto and Pinto Model for Unloading and Reloading Paths with Small Strain Variations, *Proceedings of JSCE, No. 738, Vol. 1-64, JSCE(738)*: 159–169. (in Japanese).

Takase Y., Wada, T., Ikeda T. & Shinohara Y., 2013, Mechanical Model of Adhesive Post-installed Anchor Subjected to Cyclic Shear Force, *Proceedings of Fracture Mechanism of Concrete and Concrete Structures,* P445.

Takase Y., Abe T., Ikeda T., Wada T., Katori K. & Shinohara Y., 2014, Discussion on Mechanical Behavior of Joints Using Post-installed Anchor and Concrete Surface Roughening for Seismic Retrofitting, *Proceedings of JCompurational Modeling of Concrete Structures*: 837–846.

Tsuyoshi, M., Sadasue, K., Ishimura, M. & Minami, K., 2010, Experimental study on post-installed diagonal anchor, *Proceedings of the Japan Concrete Institute, Vol. 32, No. 2*: 985–990.(in Japanese).

Vintzeleou, E.N. & Tassios, T.P., 1986, Mathematical models for dowel action under monotonic and cyclic conditions, *Magazine of concrete research*, *Vol. 38, No. 134*: 13–22.



Taylor & Francis
Taylor & Francis Group
http://taylorandfrancis.com

Computational Modelling of Concrete Structures – Meschke, Pichler & Rots (Eds)
© 2018 Taylor & Francis Group, London, ISBN 978-1-138-74117-1

FEM analysis of post-installed adhesive anchors under combined stress

Y. Ishida & H. Sakata
Tokyo Institute of Technology, Meguro-ku, Tokyo, Japan

Y. Takase
Muroran Institute of Technology, Muroran-shi, Hokkaido, Japan

Y. Maida
Chiba University, Chiba-shi, Chiba, Japan

Y. Shirai
Kanagawa University, Yokohama-shi, Kanagawa, Japan

T. Sato
TOBISHIMA Corporation, Minato-ku, Tokyo, Japan

ABSTRACT: In order to investigate the mechanical behavior of the post-installed adhesive anchor under combined stress, this study constructs a three-dimensional FEM analysis model which can reproduce the experiment conducted in the past. A total of 13 test specimens of varying parameters were studied. From the analysis result, the influence of each parameter on the stress distribution inside the material was grasped, and the mechanical behavior of the post-installed adhesive anchors was studied. The analysis results showed that the shear strength and stiffness are greatly affected by anchor diameter and axial stress ratio; whereas the influence of the concrete strength is relatively small. In addition, the dowel effect was confirmed from the Mises stress distribution of the anchor bolt, and it was confirmed that the range where the Mises stress reaches the yield strength is 4 to 5 times of the anchor diameter d_a.

1 INTRODUCTION

Post-installed adhesive anchors are used for external seismic retrofitting joint for existing reinforced concrete building. As a structural characteristic of external seismic retrofitting, existing frame and reinforcing frame are eccentric. Thus, in addition to the shear force, compressive force and tensile forces due to the eccentric bending moment act on the joint, so that a combined stress appears at the joint of external seismic retrofitting.

However, there are few studies on post-installed adhesive anchors under combined stress, and it is difficult to grasp in detail its mechanical behavior when subjected to combined stress. For that reason, Japan's current design method (Japan Building Disaster Prevention Association 2002), suggests the use of reduction factor which is based on engineering judgment.

This paper, therefore, investigates the mechanical behavior of the post-installed adhesive anchors under combined stress by constructing a three-dimensional (3-D) analysis model of the experiment conducted by Takase et al. (2016) using finite element method (FEM).

From the analysis, the influence of each parameter (i.e. anchor diameter d_a, axial stress ratio η and concrete strength σ_B) on the stress distribution inside the material is grasped, and the mechanical behavior of the post-installed adhesive anchors under combined stress is studied.

2 OUTLINE OF EXPERIMENT

2.1 *Details of specimens*

The details of specimens are shown in Figure 1. For the specimen, an epoxy injection type post-installed

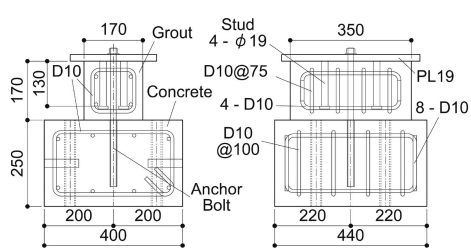

Figure 1. Details of specimens (unit: [mm]).

adhesive anchor was applied to the concrete member corresponding to the existing frame. After that, grease was applied to the joint surface. Then, the steel plate with the welded stud and the reinforcements were installed–this steel plate assumes the flange of the steel frame in the external seismic retrofitting. The grout was then press-fitted between the joint surface and the steel plate.

For the construction of the post-installed adhesive anchor, a wet core drill was used as piercing device and pierced the concrete downward.

2.2 *Loading device*

The loading device is shown in Figure 2. Hydraulic jacks were attached to the left and right by the height of the joint surface, then the shear force was applied by pressing either one. In addition, a center hole jack was attached in the vertical direction. The influence of the weight of the loading jig etc. was removed. Furthermore, in the specimen with the tensile force, shear force was applied after giving a tensile force according to the axial stress ratio.

The relative horizontal displacement and the relative vertical displacement were measured at two positions as shown in Figure 3, and the average value thereof was used.

The loading plan in Figure 4 shows cyclic loading in the positive and negative directions. Each positive and negative load was applied up to the relative horizontal displacement of 0.5 [mm], and then it was loaded repeatedly twice in each direction up to 4.0 [mm] relative horizontal displacement. Finally, the specimen was loaded once up to the relative horizontal displacement of 6.0 [mm] in the positive and negative directions, and it was pushed to the positive side until failure.

2.3 *Target specimens*

The parameters of the specimen are indicated in Table 1, and the specifications of the materi-

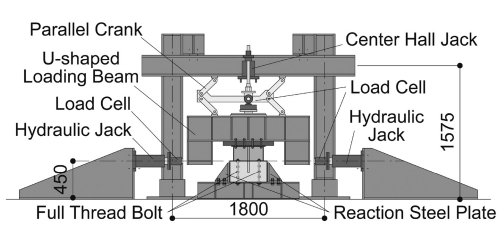

Figure 2. Loading device (unit: [mm]).

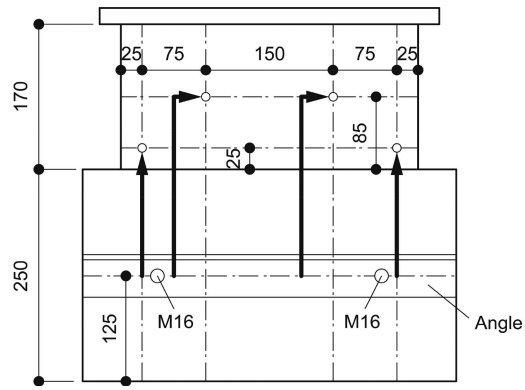

Figure 3. Measurement plan (unit: [mm]).

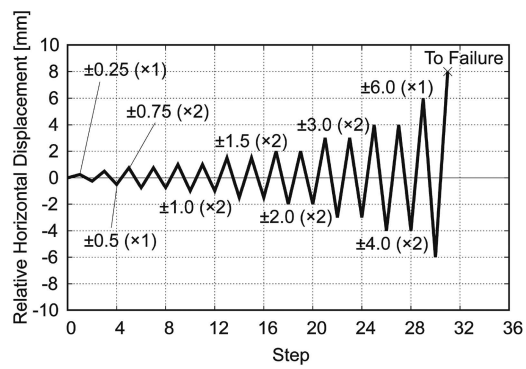

Figure 4. Loading plan (unit: [mm]).

Table 1. Parameters of specimen.

	d_a	η	F_c
Specimen	mm	–	N/mm^2
D13-0-15	12.7 (D13)	0	15.0
D13-0.33T-15		0.33	
D13-0.66T-15		0.66	
D16-0-9	15.9 (D16)	0	9.0
D16-0-15			15.0
D16-0-21			21.0
D16-0.33T-15		0.33	15.0
D16-0.56T-9		0.56	9.0
D16-0.56T-15			15.0
D16-0.56T-21			21.0
D19-0-15	19.1 (D19)	0	15.0
D19-0.33T-15		0.33	
D19-0.66T-15		0.66	

d_a: Anchor diameter.
η: Axial stress ratio (tensile force).
F_c: Design strength of concrete.

Table 2. Materials specifications.

	For concrete			For grout			For anchor bolt	
	σ_B	σ_t	E_c	σ_{Gc}	σ_{Gt}	E_G	σ_y	E_s
Specimen	N/mm^2	N/mm^2	N/mm^2	N/mm^2	N/mm^2	N/mm^2	N/mm^2	N/mm^2
D13-0-15								
D13-0.33T-15	19.0	1.93	23.7×10^3	59.1	3.30	23.4×10^3	375	193×10^3
D13-0.66T-15								
D16-0-9	12.5	1.43	18.1×10^3	70.7	3.00	24.6×10^3		
D16-0-15	19.0		23.7×10^3	59.1	3.30	23.4×10^3		
D16-0-21	30.5	1.93	25.9×10^3	70.7	3.00	24.6×10^3		
D16-0.33T-15	19.0		23.7×10^3	59.1	3.30	23.4×10^3	396	194×10^3
D16-0.56T-9	12.5	1.43	18.1×10^3					
D16-0.56T-15	17.4	1.46	19.8×10^3	70.7	3.00	24.6×10^3		
D16-0.56T-21	30.5		25.9×10^3					
D19-0-15	19.0	1.93	23.7×10^3	59.1	3.30			
D19-0.33T-15	21.1		22.6×10^3	72.6	3.28	23.4×10^3	402	189×10^3
D19-0.66T-15	19.0		23.7×10^3	59.1	3.30			

σ_B: Compressive strength of concrete.
σ_t: Tensile strength of concrete.
σ_{Gc}: Compressive strength of grout.
σ_{Gt}: Tensile strength of grout.
σ_y: Yield strength of anchor bolt.
E_c: Young's Modulus of concrete.
E_G: Young's Modulus of grout.
E_s: Young's Modulus of anchor bolt.

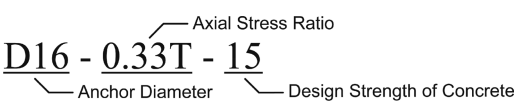

Figure 5. Definition of specimen name.

als are indicated in Tables 2. In this paper, a total of 13 specimens are targeted in a combination of parameters with three anchor diameters, three axial stress ratios, and three concrete strengths.

Here, the axial stress ratio η is the ratio of the tensile stress to the yield strength of the anchor bolt. So, T in the specimen name refers to the tensile stress.

The definition of the specimen name is given in Figure 5. As an example, D16 refers to a 16-mm diameter anchor bolt, 0.33T refers to the axial stress ratio, and 15 refers to the design strength of concrete in [N/mm^2].

3 OUTLINE OF ANALYSIS

3.1 *Construction of 3-D FEM analysis model*

A general nonlinear FEM analysis program (named FINAL) was used for analysis. The outline of the FEM analysis model is shown in Figure 6. In this analysis model, due to symmetry, only half

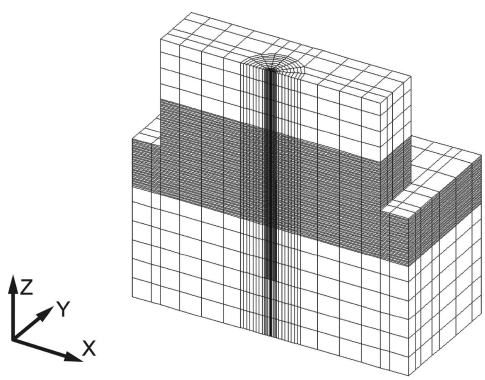

Figure 6. Outline of FEM analysis model.

is modeled against the vertical plane (X-Z plane) passing through the force axis.

The boundary conditions are shown in Figure 7. On the cut surface, only Y-translation was restrained. All the degrees of freedom were restrained on the lower surface of the concrete, and the upper surface of the grout and the U-shaped loading beam were kept parallel. In addition, X-translational degree of freedom of the concrete ends in the Y-Z plane were restrained. Then, the total support reaction forces in the X direction was doubled and taken as the shear force.

The concrete, the grout, and the anchor bolt were modeled as hexahedral elements (eight-node isoperimetric elements), and the epoxy resin between concrete and anchor bolt was modeled as joint element with thickness as shown in Figure 8(a). Finally, depending on the interface, joint element without thickness were inserted to model the bonding properties between the materials as shown Figure 8(b).

For loading, forced displacement was applied to the force application points on the right and left of the U-shaped loading beam modeled with beam elements of large stiffness. In addition, the tensile force was given as an initial stress to the element at the top end of the anchor bolt. In this analysis, loading was applied in one direction until the relative horizontal displacement reached 4.0 [mm].

3.2 *Material configuration rule*

3.2.1 *Concrete and grout*

The material configuration rule of concrete and grout is shown in Figure 9. The modified Ahmad model (Naganuma 1995) was used to determine the characteristics of concrete and grout until compressive strength was reached. Then, the Nakamura-Higai model (Nakamura & Higai 1999), which is based on fracture energy, was used for the characteristic of the compression softening zone. In addition, for the failure condition under tri-axial stress, the five-parameter model by William-Warnke and the coefficients of Ohnuma et al. (Naganuma 1995) was used.

On the other hand, the tensile side was assumed linear until reaching the tensile strength. In this analysis model, anchor bolt was modeled with hexahedral elements, and the joint elements described below were used. The reinforcements were modeled as embedded reinforcements in concrete and grout elements, and the tension stiffening characteristics were reproduced using the Izumo model (Izumo et al. 1987). Thus, the parameter C was set to 1.0 so as not to double count the adhesion property.

The Poisson's ratio of concrete and grout were set to 0.2.

3.2.2 *Anchor bolt and reinforcement rebars*

The material constitution rule of the anchor bolt and the reinforcements is shown in Figure 10.

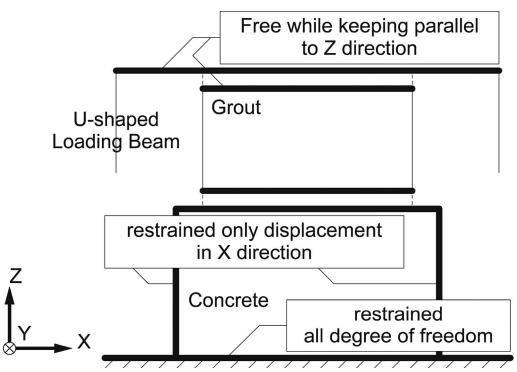

Figure 7. Boundary conditions.

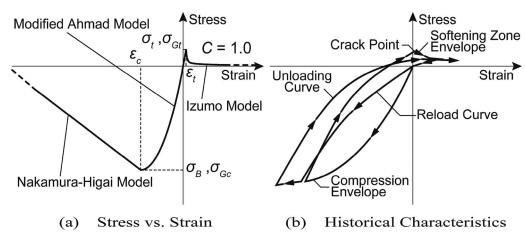

Figure 9. Material configuration rule (concrete and grout).

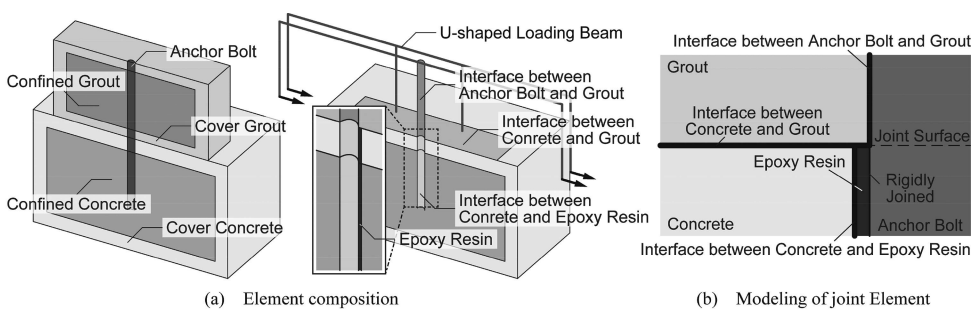

Fiugre 8. Element modeling outline.

Both the compression side and the tensile side were modeled as bi-linear. The stiffness after yielding was 1/100 E_s based on the material test results (where E_s is the Young's modulus of anchor bolt). In addition, the yielding condition of von Mises was used for the yield condition under the multi-axial stress of the anchor bolt.

The Poisson's ratio of anchor bolt was set to 0.3.

3.3 *Characteristics of joint elements*

3.3.1 *Interface between concrete and epoxy resin*

The characteristics in the shear direction is shown in Figure 11(a). The characteristics was determined based on adhesion performance experiments of the post-installed adhesive anchors constructed using the same materials and construction method as the test specimen of the experiment covered in this study (Setoguchi et al. 2010).

On the other hand, the vertical characteristics was modeled to have large stiffness in compression and not to transmit tension stress as shown in Figure 11(b).

3.3.2 *Epoxy resin between concrete and anchor bolt*

Past studies (Setoguchi et al. 2010, Nakano et al. 2009) reported that adhesion sliding occurs at the interface between concrete and epoxy resin. For this reason, the adhesion property of Figure 11(a) was inserted between concrete and epoxy resin, and the epoxy resin and the anchor bolt were rigidly joined as shown in Figure 8(b).

The characteristics in the shear direction of the epoxy resin are already included in the adhesion property in Figure 11(a). Therefore, in this part, the characteristic in the shear direction has large stiffness as shown in Figure 12(a).

Material specifications of the epoxy resin are: specific gravity d_b is 1.2; compressive strength σ_{bc} is 109 [N/mm^2]; tensile strength σ_{bt} is 75.7 [N/mm^2], and; Young's modulus E_b is 2,730 [N/mm^2]. In this study, the diameter for piercing the concrete of the existing frame is assumed to be one size larger than the anchor diameter d_a. Therefore, the thickness of the epoxy resin was set to 1.5 [mm].

The characteristic in the vertical direction is assumed to be bi-linear as shown in Figure 12(b). The coordinates of the break points were calculated from the specifications of the epoxy resin stated above and the condition that the thickness of epoxy resin is 1.5 [mm].

3.3.3 *Interface between Anchor Bolt and Grout*

The characteristics in shear direction was determined with reference to the results of the adhesion performance experiment between concrete and deformed rebar (Nakano et al. 2009) as shown in Figure 13(a).

The vertical characteristics were modeled in the same way as the interface between concrete and epoxy resin (Figure 13(b)).

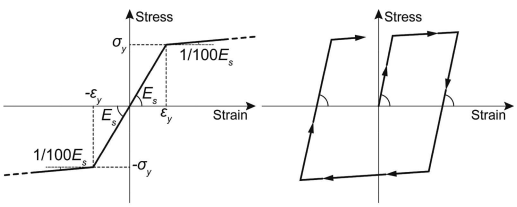

Figure 10. Material configuration rule (anchor bolt and reinforcements).

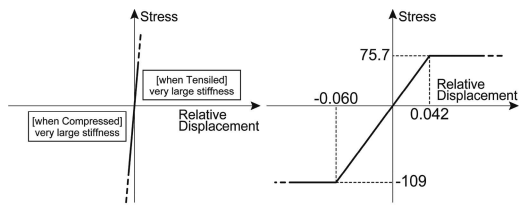

Figure 12. Characteristics of joint element (Epoxy resin between concrete and anchor bolt).

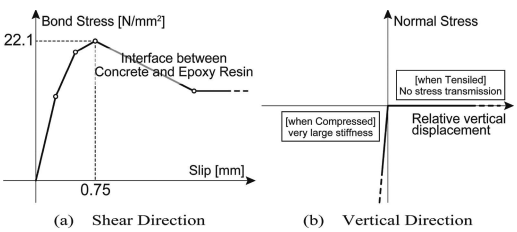

Figure 11. Characteristics of joint element (Interface between concrete and epoxy resin).

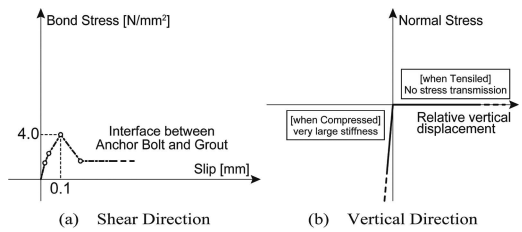

Figure 13. Characteristics of joint element (Interface between anchor bolt and grout).

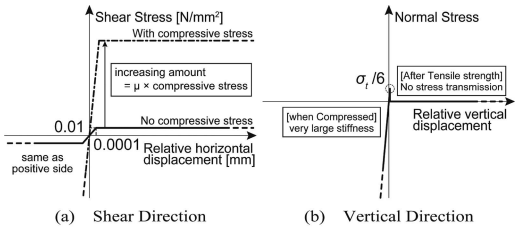

Figure 14. Characteristics of joint element (Interface between concrete and grout).

3.3.4 *Interface between concrete and grout*

The shear direction characteristics is shown in Figure 14(a). The shear stress by adhesion between concrete and grout was set to 0.01 [N/mm^2] so as not to affect the overall shear strength. When compressive stress acted, the amount of increase in shear stress due to friction was taken into consideration. The friction coefficient μ was set to 0.974 which is the apparent shear friction coefficient by the mechanical mechanism such as shear friction force of the joint surface and meshing of the aggregate from reference (Katori et al. 1998).

The vertical characteristics is shown in Figure 14(b). When a compressive stress was applied, the interface provided large stiffness. The tensile side also had the same stiffness up to the tensile strength. After reaching the tensile strength, the bond was released and the normal stress and the shear stress of the joint element were zero. From the study of Kimu et al. (2008), the tensile strength was set to 1/6 of the tensile strength σ_t of concrete.

4 ANALYSIS RESULTS AND DISCUSSIONS

4.1 *Shear force vs. relative horizontal displacement*

The analysis results of shear force vs. relative horizontal displacement relationship of all 13 specimens are shown in Figures 15–17. The solid line is the analysis result, and the dotted line is the experiment result. Here, the relative horizontal displacement is the average value of the relative horizontal displacement of concrete and grout measured at two points, same as the experiment of reference (Takase et al. 2016). According to the current Japanese design method (Japan Building Disaster Prevention Association 2002), the horizontal deformation amount of the post-installed anchor is provided until 2.0 [mm]. Therefore, in this study, the range up to 4.0 [mm] which is twice that in this research was set as the scope of analysis.

The analysis results of the shear force vs. relative horizontal displacement relationship show generally good agreement with the experimental results, except for some specimens. In this paper, we consider that this analysis model is effective, and discuss the consideration based on the analysis results below.

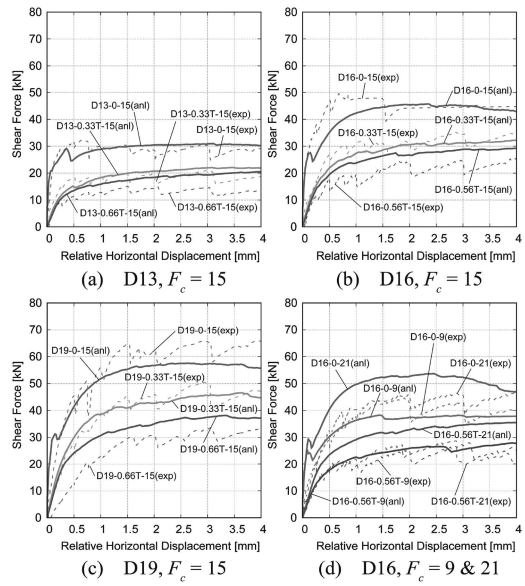

Figure 15. Shear force vs. relative horizontal displacement (Comparison by axial stress ratio η).

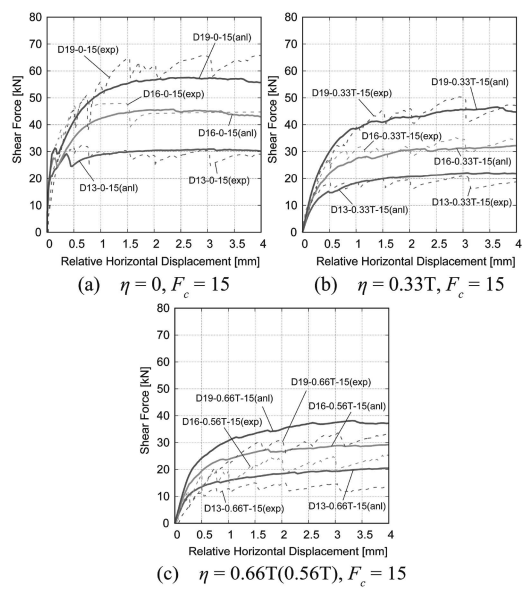

Figure 16. Shear force vs. relative horizontal displacement (Comparison by anchor diameter d_a).

Considering the axial stress ratio η, both the analysis result and the experiment result show that the specimen subjected to shear force only has larger initial stiffness than the specimen subjected to shear force and tensile force. It was caused by the shear stress due to friction of the joint surface. In addition, when comparing the analysis results of two specimens subjected to shear force and tensile force in Figure 15, initial stiffnesses are approximately equal. However, from the relative horizontal displacement of about 0.25 [mm], gradually the stiffness and the shear strength tend to decrease as the axial stress ratio increases. In the specimens subjected to shear force and tensile force, when the predetermined tensile stress was applied to the top end of the anchor bolt, the separation of the joint surface could be confirmed. Therefore, it can be said that there is no shear resistance of the joint surface.

Next, a comparison by anchor diameter d_a is carried-out; results are shown in Figure 16. Comparing the rate of decrease in the shear strength of the specimen with axial stress ratio of 0.66T(0.56T) to the shear strength of the specimen with axial stress ratio of 0.33T at each anchor diameter, it was 6% for D13, 9% for D16 and 18% for D19. From this, as the anchor diameter d_a increases, the rate of decrease in shear strength due to the axial stress ratio tends to increase. For large anchor diameter d_a with large axial stress ratio η, the entire cross-section tends not to yield; only the tensile side of the cross-section yields because the tensile stress dominates.

Finally, the influence of the concrete strength σ_B is compared in Figure 17. In any of the axial stress ratios, as the concrete strength σ_B increases, the stiffness and the shear strength tend to increase. However, when compared with the influence of the axial stress ratio η and the anchor diameter d_a, the influence of the concrete strength is smaller.

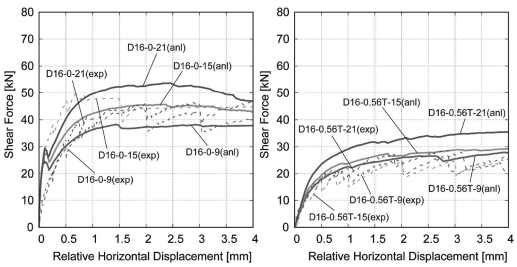

(a) D16, $\eta = 0$ (b) D16, $\eta = 0.56$T

Figure 17. Shear force vs. relative horizontal displacement (Comparison by concrete strength σ_B).

4.2 *Minimum principal stress distribution*

Figure 18 shows the minimum principal stress distribution that acts on concrete and grout when the relative horizontal displacement is 2.0 [mm]. Here, based on D16-0-15, in order to compare the influence due to the axial stress ratio η, the anchor diameter d_a and the concrete strength σ_B, analysis results of 7 out of 13 specimens are shown. Furthermore, Table 3 and Table 4 indicate the analysis results of the minimum principal stress and the increase rate to the uni-axial compressive strength of all specimens.

In all of the specimens, the maximum absolute value of the minimum principal stress is generated where the grout contacts the anchor bolt and is subjected to bearing pressure. Additionally, Figure 19

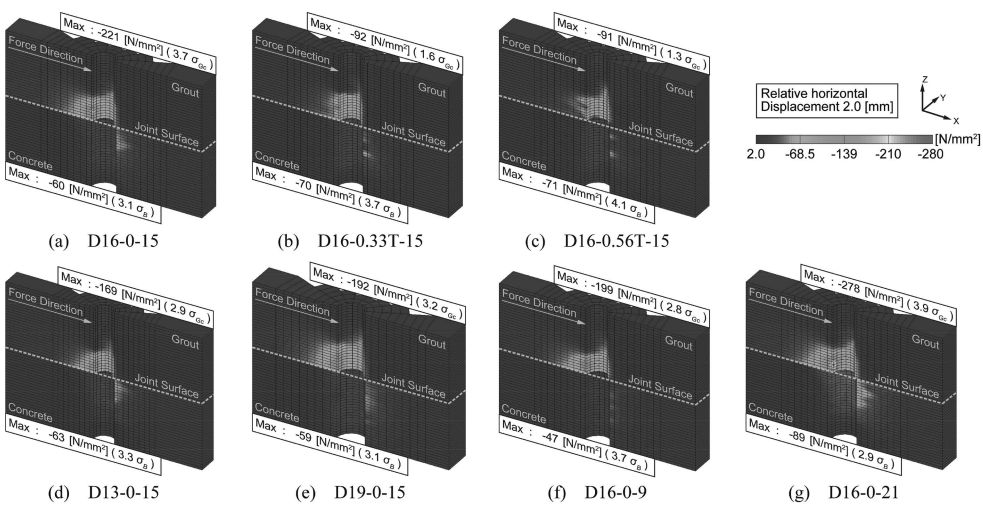

(a) D16-0-15 (b) D16-0.33T-15 (c) D16-0.56T-15

(d) D13-0-15 (e) D19-0-15 (f) D16-0-9 (g) D16-0-21

Figure 18. Minimum principal stress distribution acting on concrete and grout.

Table 3. Minimum principal stress inside concrete.

Specimen	$\sigma_{min,p}$ N/mm^2	σ_B N/mm^2	$\sigma_{min,p}/\sigma_B$ –
D13-0-15	–63		3.3
D13-0.33T-15	–79	–19.0	4.1
D13-0.66T-15	–60		3.1
D16-0-9	–47	–12.5	3.7
D16-0-15	–60	–19.0	3.1
D16-0-21	–89	–30.5	2.9
D16-0.33T-15	–70	–19.0	3.7
D16-0.56T-9	–40	–12.5	3.2
D16-0.56T-15	–71	–17.4	4.1
D16-0.56T-21	–90	–30.5	3.0
D19-0-15	–59	–19.0	3.1
D19-0.33T-15	–46	–21.1	2.2
D19-0.66T-15	–61	–19.0	3.2

$\sigma_{min,p}$: Minimum principal stress inside concrete.
σ_B: Uni-axial compressive strength of concrete.
$\sigma_{min,p}/\sigma_B$: Increase rate.

Table 4. Minimum principal stress inside grout.

Specimen	$\sigma_{min,p}$ N/mm^2	σ_{Gc} N/mm^2	$\sigma_{min,p}/\sigma_{Gc}$ –
D13-0-15	–169		2.9
D13-0.33T-15	–145	–59.1	2.4
D13-0.66T-15	–97		1.6
D16-0-9	–199	–70.7	2.8
D16-0-15	–221	–59.1	3.7
D16-0-21	–278	–70.7	3.9
D16-0.33T-15	–92	–59.1	1.6
D16-0.56T-9	–138		2.0
D16-0.56T-15	–91	–70.7	1.3
D16-0.56T-21	–147		2.1
D19-0-15	–192	–59.1	3.2
D19-0.33T-15	–107	–72.6	1.5
D19-0.66T-15	–94	–59.1	1.6

$\sigma_{min,p}$: Minimum principal stress inside grout.
σ_{Gc}: Uni-axial compressive strength of grout.
$\sigma_{min,p}/\sigma_{Gc}$: Increase rate.

shows the minimum principal stress distribution generated inside concrete. In all specimen, concrete receives a bearing pressure from the anchor bolt, so the minimum principal stress is concentrated near the joint surface. Then, it can be confirmed that there is a radial three dimensional stress distribution. In addition, it is conceivable that in a portion where the anchor bolt is locally deformed, it becomes a multi-axial compressive stress field. Comparing the minimum principal stress acting on concrete with the uni-axial compressive strength σ_B of concrete, it tends to increase to about 3 to 4 times.

Comparing Figures 19(a), (b), and (c), the maximum absolute value of the minimum principal stress is generated in the vicinity of the joint surface in the specimen subjected to shear force only. On the other hand, in the specimen subjected to shear force and the tensile force, there is a tendency that the maximum absolute value occurs at the position on the concrete side about 1.0 d_a from the joint surface.

Next, comparing Figures 19(a), (d), and (e), stress distributions are stereoscopically radial in all specimens, but tend to be distributed over a wider range as the anchor diameter d_a becomes larger. This is probably because the bearing pressure area increases as the anchor diameter increases.

Finally, when comparing Figure 19(a), (f), and (g), the distribution range of the minimum principal stress is approximately equal since the anchor diameter d_a is the same. However, as the concrete strength σ_B increases, the maximum absolute value of the minimum principal stress tends to increase.

4.3 *Mises stress distribution*

Figure 20 shows the Mises stress distribution acting on the anchor bolt when the relative horizontal displacement is 2.0 [mm]. Here, the analysis results of 9 of the 13 specimens are shown for comparison of the difference by axial stress ratio η for each anchor diameter d_a. Furthermore, Table 5 indicates the maximum value of Mises stress and the ratio to the yield strength of all the specimens.

From the distribution state of Mises stress of these 9 specimens (Figure 20), it can be inferred that local bending deformation of the anchor bolt occurs near the joint surface. This analysis result confirms the occurrence of dowel effect.

The amount of deformation in the horizontal direction of the node on the material axis of the anchor bolt at the position of 30.0 [mm] above and below relative to the position of the joint surface is also shown in Figure 20. From these results, in all test specimens, the center of dowel deformation tends to be slightly on the concrete side rather than joint surface position. This is because the concrete strength σ_B is smaller than the grout strength σ_{Gc}, so that the fixed end position of the dowel deformation of the anchor bolt is deeper than the grout side on the concrete side from the joint surface.

In addition, the section of dowel deformation tends to be wider as the anchor diameter d_a increases. Focusing on the range where the Mises stress reaches the yield strength of the anchor bolt σ_y, it is about 4 to 5 times of the anchor diameter d_a.

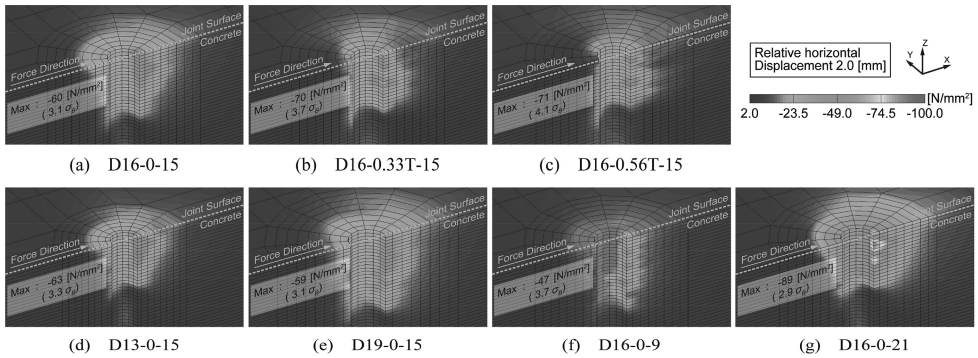

Figure 19. Minimum principal stress distribution acting on concrete.

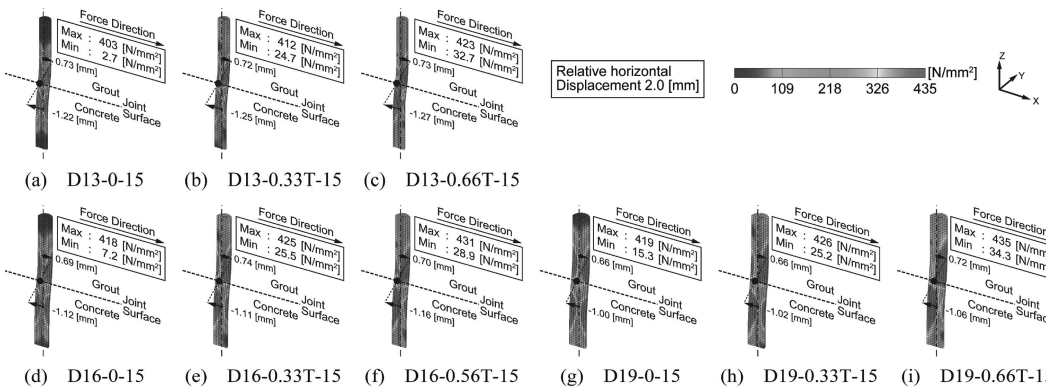

Figure 20. Mises stress distribution acting on anchor bolt.

Table 5. Mises stress inside anchor bolt.

Specimen	σ_{Mises} N/mm²	σ_y N/mm²	σ_{Mises}/σ_y –
D13-0-15	403		1.07
D13-0.33T-15	412	375	1.10
D13-0.66T-15	423		1.13
D16-0-9	417		1.05
D16-0-15	418		1.06
D16-0-21	421		1.06
D16-0.33T-15	425	396	1.07
D16-0.56T-9	430		1.09
D16-0.56T-15	431		1.09
D16-0.56T-21	437		1.10
D19-0-15	419		1.04
D19-0.33T-15	426	402	1.06
D19-0.66T-15	435		1.08

σ_{Mises}: Mises stress inside anchor bolt.
σ_y: Yield strength of anchor bolt.
σ_{Mises}/σ_y: Increase rate.

In the specimen subjected to shear force only, Mises stress is symmetrically distributed on the compression side and the tensile side with respect to the material axis when the anchor bolt undergoes dowel deformation. On the other hand, in the specimen subjected to shear force and the tensile force, the Mises stress on the tensile side tends to increase due to the application of the tensile force.

Also, paying attention to the maximum value of each Mises stress, it increases higher than the yield strength σ_y of the anchor bolt, and it tends to increase as the anchor diameter d_a and axial stress ratio η are larger. From this, it can be inferred that distortion has occurred to the strain hardening region in the anchor bolt because tensile strain is increased by applying tensile force.

5 CONCLUSIONS

In this study, a 3-D FEM analysis model was constructed based on experiments of post-installed

adhesive anchor under combined stress and analyzed. Based on the results, the following findings were obtained.

1. 3-D FEM analysis model was constructed using the material configuration rules of concrete, grout and steel, and the characteristics of joint elements according to the past literature. As a result, it was adequate to reproduce the experimental results almost accurately in the deformation zone up to the relative horizontal displacement of 4.0 [mm] which is twice the allowed horizontal deformation amount of the post-installed anchor in current design method.
2. In relation to shear force vs. relative horizontal displacement, the shear characteristic of the anchor bolt is greatly affected by the anchor diameter d_a and axial stress ratio η. On the other hand, the effect of concrete strength is relatively small. This tendency agreed well with the experimental results, and the influence due to the difference in parameters could also be reproduced with high accuracy.
3. It was confirmed that the minimum principal stress acting on concrete is a radial three-dimensional distribution, and the range tends to be wider as the anchor diameter becomes larger. In addition, when the anchor diameters are equal and the concrete strengths are different, the distributions of the minimum principal stresses are substantially equal, but as the concrete strength increases, the maximum absolute value of the minimum principal stress increases. Also, the concrete is under multi-axial compressive stress near the joint surface and tends to increase to about 3 to 4 times the uni-axial compressive strength.
4. From Mises stress distribution of anchor bolt, dowel effect was confirmed. Furthermore, the range where the Mises stress reaches the yield strength differs depending on the anchor diameter d_a and is in the range of about $4d_a$ to $5d_a$. Moreover, as the tensile force was applied, the increase in the Mises stress was confirmed, and the influence of the strain hardening of the anchor bolt also remarkably occurred.

ACKNOWLEDGMENTS

In constructing the analytical model of this research valuable advice was received from Professor Kazuhiro Naganuma in Nihon University and Professor Takahiro Yamada in Yokohama National University. In addition, this research was carried-out after technical cooperation from Tobishima Corporation. We express deep appreciation here.

REFERENCES

Izumo, J., Shima, H. & Okamura, H. 1987. Analysis Model of Reinforced Concrete Board Element Subjected to In-plane Force (in Japanese). *Concrete Journal*, Vol. 25, No. 87.9-1: 107–120.

Japan building disaster prevention association. 2002. External seismic retrofitting manual (in Japanese).

Katori, K., Hayashi, S., Ushigaki, K. & Norimono, T. 1998. Effects of Surface Roughness on Shear Behavior of Construction Joint Arranging Connecting Bars Perpendicularly: Studies on shear behavior of joint. *Journal of Structural and Construction Engineering*, No. 508: 101–110.

Kimu, H., Noguchi, T., Yoneda, N. & Hamasaki, H. 2008. Construction of Adhesion Constitutive Law between Repair Mortar and Frame Concrete by FEM inverse analysis (in Japanese). *Proceedings of the Japan Concrete Institute*, Vol. 30, No. 2: 577–582.

Naganuma, K. 1995. Stress-Strain Relationship for Concrete Under Triaxial Compression. *Journal of Structural and Construction Engineering*, No. 474: 163–170.

Nakamura, H. & Higai, T. 1999. Compressive Fracture Energy and Fracture Zone Length of Concrete. *Seminar on Post-peak Behavior of RC Structures Subjected to Seismic Load*, Vol. 2: 259–272.

Nakano, K., Mastuzaki, Y. & Sugiyama T. 2009. Average Bond Strength of Post-installed Bonded Anchor. *Summaries of Technical Papers of Annual Meeting Architectural Institute of Japan*: 149–150.

Setoguchi, H., Abe, T., Takase, Y., Sato, S., Takahashi, M. & Sato, T. 2010. Experimental Study to Confirm the Performance of Post-installed Anchor that Uses Core Drill Method: Part 2. Test of Bond Strength that Uses Injection Type Anchor. *Summaries of Technical Papers of Annual Meeting Architectural Institute of Japan*: 149–150.

Takase, Y., Wada, T. & Shinohara, Y. 2016. A Study on Mechanical Behavior of Post-installed Adhesive Anchor Receiving Repeated Shear Force under Consist Tensile Force. *Proceedings of the Japan Concrete Institute*, Vol. 38, No. 2: 1105–1110.

Computational Modelling of Concrete Structures – Meschke, Pichler & Rots (Eds)
© 2018 Taylor & Francis Group, London, ISBN 978-1-138-74117-1

Mechanical model of shear stress transfer of roughened concrete surface for R/C existing member

Tsubasa Isozaki, Ukyo Musya & Yuya Takase
College of Environmental Technology Muroran Institute of Technology, Japan

Takahide Abe & Keita Sakamoto
Seismic Solution Department, Tobishima Corporation, Japan

Takeshi Hiwatashi
Research and Development Center, Toa Corporation, Japan

Keiichi Katori
Department of Architecture, Faculty of Science and Engineering, Toyo University, Japan

ABSTRACT: When buildings undergo seismic retrofitting, reinforcement members are connected to existing members by roughening the concrete surfaces (via chipping) and applying post-installed anchors. According to the Japanese guidelines for structural seismic retrofitting, the shear strength of post-installed anchors must be evaluated, but there is no standard for concrete roughening. Therefore, in this paper, a mechanical model of a roughened concrete surface is constructed based on the Bujadaham model, which can estimate the stress transfer mechanism of a cracked concrete surface. The results of the investigation show that even when the area of roughened concrete varies the shear stress–shear displacement relation and the normal stress–shear displacement relations can be reasonably estimated by the proposed model with considering the angle density function, $\Omega(\theta)$, and the proposed contact stress model.

1 INTRODUCTION

In Japan, an area where earthquakes occur frequently, buildings are required to have high seismic performance. Recently, seismic retrofitting of buildings with low seismic performance has become an important solution for utilizing existing buildings effectively. When seismic retrofits are performed on reinforced concrete structures, supporting members are added to the existing building using post-installed anchors to enhance earthquake resistance. For effective transfer of shear force from the existing skeleton to the seismic retrofit members during an earthquake, it is very important to properly integrate the new members with the existing structure. The most common method for this integration is to chip the concrete surfaces using a vibration drill. The roughened concrete creates shear resistance at the joint surface due to the meshing effect of the uneven surface. However, the concrete roughening process is dependent on the technique and awareness of the vibration drill operator, making exactly defining the outcome of surface roughening difficult.

In addition, due to the potential for variance in concrete roughening, there is no unified specification for the process (e.g., depth, dimension).

As far as the preliminary research went for this study, there was no previous literature that theoretically pursued the shear resistance performance of roughened concrete from vibration drilling. On the other hand, some research about the shear stress transfer mechanism of a cracked surface does exist.

Specifically, three representative cracking models have been studied. The first is the "experimental cracking model," which is created by simulating experimental results. The second is the "virtual crack model," which models the shape of the cracked surface based on the maximum size and particle size distribution of the aggregate in the concrete and uses this information to develop a constitutive law. The third is the "physical contact model," which incorporates the shape characteristics calculated from a shape measurement experiment for the actual cracked surface into the constitutive law. The physical contact model is regarded as the most reliable among the three models. According to previous

literature, we can estimate the shear stress and normal stress interacting on the entire cracked surface by integrating the contact stress with the area of the entire interface. In other words, it is inferred that the shear resistance performance can be evaluated quantitatively. Thus, in this paper, the first objective is to conduct shape measurement and analysis to determine the shape characteristics of the roughened concrete. Next, we conduct shear loading tests to verify the shear resistance performance; and finally, we construct a mechanical model to evaluate the experiment results.

2 EXPERIMENTAL PROGRAM

When connecting new and existing members during a seismic retrofit, both post-installed anchors and concrete roughening are generally implemented, and it is thought that the two have a mutual interaction. However, in this study, we focused on the shear resistance performance by concrete roughening alone and conducted shear loading tests without post-installed anchors.

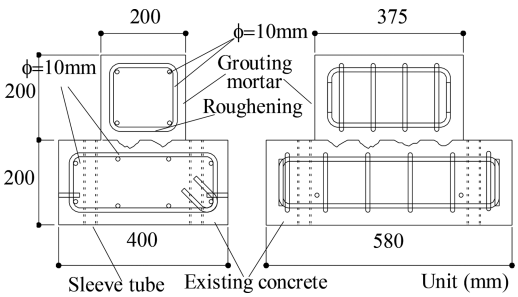

Figure 1. Dimension specification of specimen.

2.1 *Experimental parameter*

The experimental specimen is shown in Figure 1, and the associated properties are given in Table 1. The characteristics of the grout and the concrete surface of the specimen are chosen to simulate the joint and existing beam in a seismic retrofit connection. Both the shape measurement and the shear loading test are performed on this specimen. Table 2 lists the material properties of the concrete and grout used in the experiment. The compressive strengths of the concrete and grouting mortar are 17.1 and 64.6 N/mm^2 or 19.9 and 68.7 N/mm^2 respectively, due to the difference in loading timing. The existing member was modelled by a rectangular block with dimensions 580 mm × 400 mm × 200 mm. A 375 mm × 200 mm roughened concrete section is designated as the test area and represents the joint surface. The roughened concrete surface ratio r_{cr} is given by the ratio of joint surface area A_j to horizontal projected area A_{cr}; this value as well as the roughened concrete depth are used as experimental parameters. Five values for r_{cr} were tested in the experiment: 0.1, 0.2, 0.3, 0.5 and 0.75. Because the profile of the roughened concrete is irregular, the shape

Table 1. Specimen parameters.

Specimen	Area ratio of roughening	Measured value	Depth	Maximum depth
CH-10N	0.100	0.099	Normal	17.1 mm
CH-10D		0.117	Deep	23.9 mm
CH-20N	0.200	0.213	Normal	10.7 mm
CH-20D		0.182	Deep	20.7 mm
CH-30N	0.300	0.290	Normal	14.7 mm
CH-30D		0.308	Deep	20.5 mm
CH-50N	0.500	0.499	Normal	18.3 mm
CH-75N	0.750	0.777	Normal	18.5 mm

r_{cr}: Area ratio of roughening.

Table 2. Material properties.

Specimen	Material	Compressive strength (N/mm^2)	Young's modulus (kN/mm^2)	Splitting strength (N/mm^2)
CH-10M,CH-30M	Concrete	17.1	24.7	1.83
CH-50M,CH-75M	Grouting mortar	64.6	26.2	2.10
CH-10D,CH-20D	Concrete	19.9	29.1	1.90
CH-20M,CH-30D	Grouting mortar	68.7	26.3	3.42

characteristic may possibly be different even with the same roughing area ratio r_{cr}. For this reason, two specimens each having an r_{cr} of 0.1, 0.2, and 0.3 were prepared with different chipping depth, and their shape characteristics were compared.

2.2 *Manufacturing method of test specimens*

First, the formwork for the existing concrete member was set, and the concrete was cast vertically. A piece of plywood for concrete surface processing was used on the upper surface of the test specimen to give the joining surface an initial smooth finish. Next, the joint surface was roughened with a vibration drill, with r_{cr} being determined by image analysis. To accomplish this analysis, a black paint was applied to the smooth joining surface before roughening was performed. As roughening took place, the black surface concrete was removed, revealing a profile with two distinct visual properties. Image analysis was performed based on the color difference, which confirmed the area ratio. The construction condition of the roughened surface of the specimens are shown in Photograph 1. The results of the image analysis can bbe found in Table 1. Comparing the image analysis result to the intended r_{cr} shows that a fairly accurate r_{cr} can be obtained using a vibration drill. After con—firming r_{cr}, shape measurement of roughened surface was performed using a high-sensitivity spot laser displacement meter. Next, the formwork for an indirect joint member of dimensions 375 mm × 200 mm × 200 mm was placed on the joining surface. Finally, the reinforcement bars were arranged and the grout was cast on the surface. A premixed grout was used and the amount of water to be added was specified by the material. In addition, grease was applied to the smooth surface areas to minimalize the influence of fixation and friction.

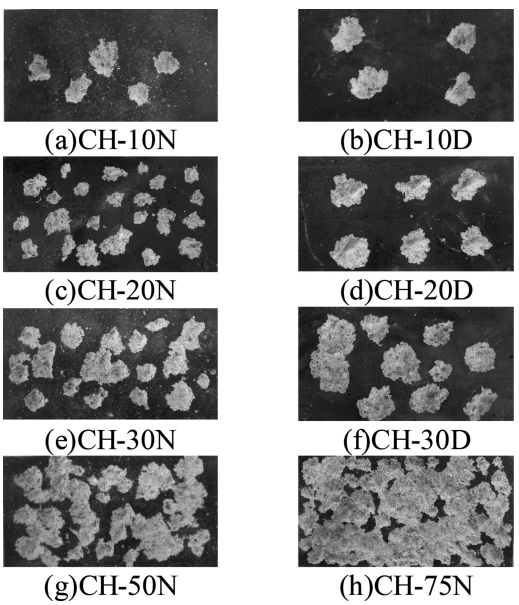

Photograph 1. Roughened concrete surface.

2.3 *Shape measurement of roughened*

The shape measurement device is shown in Figure 2. As shown in the figure, a three-dimensional coordinate measurement system is constructed using a high-sensitivity spot laser displacement meter and linear encoder, which measures the uneven profile of the roughened concrete surface. An H-section steel beam fitted with a linear guide is fixed around the test specimen, and on this linear guide, a high-sensitivity spot laser displacement meter is installed. The three-dimensional shape data of the roughened concrete surface are acquired by measuring the height of the uneven portion with the displacement meter while scanning on the x and y planes along the rail. The measurement intervals are set at 0.04 mm in the x-direction and 0.5 mm in the y-direction.

2.4 *Loading and measurement method of shear loading experiment*

The equipment for the shear loading experiment is described in Figure 3. A hydraulic jack with a maximum load of 500 kN was used for vertical axis force control, and two identical jacks were used for bi-directional horizontal loading. The compressive stress acting on the joint surface was set at a constant 0.48 N/mm^2, while the horizontal loading acted cyclically to control shear displacement. Previous studies report that the axial stress generated

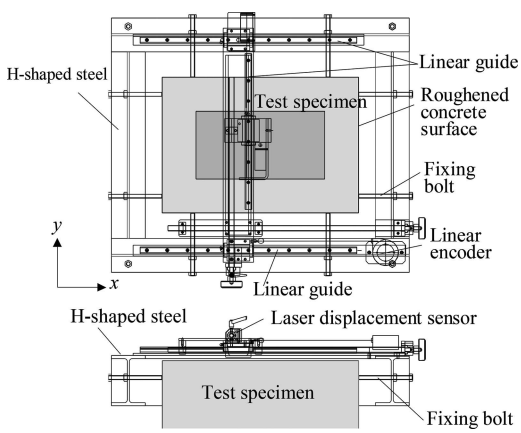

Figure 2. Shape measurement equipment.

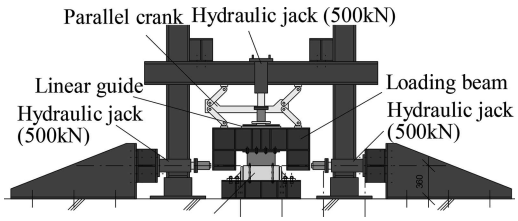

Figure 3. Loading equipment.

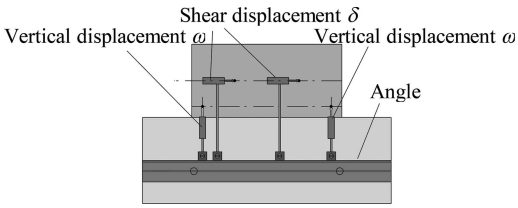

Figure 4. Measurement method of shear loading test.

in the joint surface of internally reinforced concrete was approximately 0.4 N/mm^2. Furthermore, according to a trial calculation of axial stress, the average axial stress for external reinforcement was between 0.5 and 1.5 N/mm^2. Therefore, in this experiment, axial force is applied such that 0.48 N/mm^2 is constant on the joint surface. The horizontal loading jacks were aligned with the joint surface to minimize the eccentricity moment. The axial force was controlled such that the loading beam remained horizontal and the target axial force was achieved with one hydraulic jack.

The measurement method is shown in Figure 4. An angle was placed on the existing concrete, and the displacement meter was extended to the new member side from the angle. Using this displacement gauge, vertical displacements, ω, and relative horizontal displacements, δ, for the existing and reinforcement members were measured.

3 MODELING OF SHEAR STRESS TRANSFER MECHANISM OF ROUGHENED CONCRETE SURFACE

As mentioned in Chapter 1, various existing models have been proposed for a constitutive law representing the shear stress transfer mechanism on a concrete crack surface. Among them, the Li and Maekawa model and the Bujadaham model of physical contact are clear, compatible, and reliable in relation to an uneven surface profile and shear stress. In a previous study, we built a mechanical model of concrete roughness based on the Li–Maekawa model. Although the resulting experimental values could be estimated until maximum concrete strength was reached, the stress-decreasing behavior after the peak could not be evaluated completely. Therefore, in this paper, we describe the shear stress transfer mechanism for a roughened concrete surface with higher accuracy based on the Bujadaham model that considers friction.

3.1 *Contact stress acting on local uneven surface*

The conceptual diagram of the contact stress acting on a local crack surface when considering friction is shown in Figure 5. According to the stress transfer model based on physical contact theory, the way to calculate the shear and vertical stress on a concrete crack surface is as follows: i) calculate the shear component and the vertical component of the contact stress σ_{con} occurring on the local uneven surface, ii) multiply each component by the angle density function, $\Omega(\theta)$, and the effective contact area ratio, K, iii) integrate over the whole cracked region. Furthermore, since the Bujadaham model considers friction, the stress of friction is added to the shear component and subtracted from the horizontal component, as can be seen from the conceptual image in Figure 5.

$$\tau = \int_{-\pi/2}^{\pi/2} K \cdot \sigma_{con} \cdot \Omega(\theta) \cdot (\sin\theta + \mu\cos\theta) d\theta \quad (1)$$

$$\sigma = \int_{-\pi/2}^{\pi/2} K \cdot \sigma_{con} \cdot \Omega(\theta) \cdot (\cos\theta - \mu\sin\theta) d\theta \quad (2)$$

Here, θ is the angle of inclination and μ is the friction coefficient (μ = 0.6). In the Bujadaham model, a friction coefficient of 0.4 on the contact surface is used. However, it must be questioned whether this coefficient can be used for the roughened concrete surface in the present study. In the precast guidelines, the coefficient of friction used is 0.6 when surface treatment is not applied to the mating surface. In addition, when an artificial uneven surface is provided, the coefficient of friction used is 1.0. In this study, as shown in Figure 5, friction is acting on a local uneven surface, and can

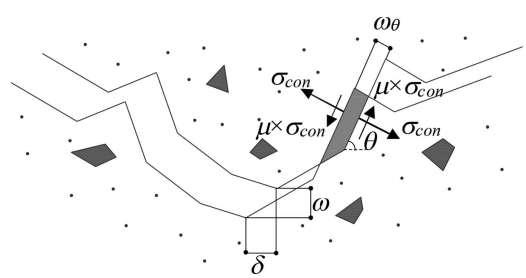

Figure 5. Image of contact on local roughness.

therefore be taken as friction between flat surfaces, so $\mu = 0.6$ is chosen.

Furthermore, as the crack width increases, the uneven surfaces lose contact with each other, thereby decreasing the stress. The extent of contact loss is expressed with the effective contact area ratio, K. Therefore, the maximum depth of the uneven surface is defined as D_{max}, and the contact area effective ratio, K, is expressed by the following equation.

$$K = 1 - 2\omega / D_{\max} \tag{3}$$

3.2 *Angle density function* $\Omega(\theta)$

The angle density function $\Omega(\theta)$ used in the Li–Maekawa and Bujadaham models intended for a cracked concrete surface is $\Omega(\theta) = 0\ 5\ \cos\theta$. However, it is unknown whether this equation can be applied to a roughened concrete surface. This is especially pertinent to this experiment, which uses multiple concrete specimens prepared with different levels of roughness, because it can be predicted with certainty that the angle density distributions will vary between specimens. Furthermore, because the roughened concrete profile will vary depending on the skill and attentiveness of the drill operator, there is a possibility for variance in roughness between specimens with the same roughened concrete surface area ratio. The angle density distribution is obtained from the angle of the roughened concrete surface using the three-dimensional data found during shape measurement. The shape analysis method is shown in Figure 6. A specimen installation error caused the three-dimensional shape measurement data to be taken at a slight incline, implying that all acquired data must be corrected. As shown in Figure 6, the coordinate reference plane is calculated using the least-squares method with respect concrete surface before roughening. Then, the measurement data are converted to coordinate values and the shape of the roughened surface is analyzed.

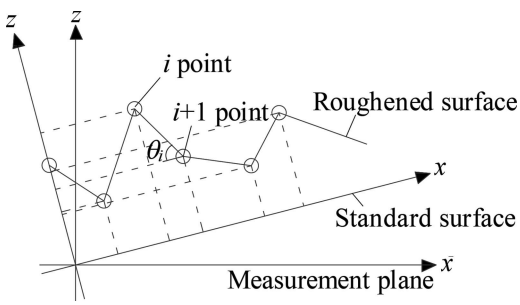

Figure 6. Shape analysis method.

The angle θ_i of the roughened surface can be expressed by the following equation using the coordinate values, x_{i+1}, z_{i+1}, of contiguous points, i+1.

$$\theta_i = \tan^{-1}\left\{\left(z_{i+1} - z_i\right) / \left(x_{i+1} - x_i\right)\right\} \tag{4}$$

The angle density $\Omega(\theta)$ is obtained by integrating the frequency distribution of the angle θ_i over the entire roughened surface and setting the area to 1 and $\Omega(\theta)$ satisfies the following equation.

$$\int_{-\pi/2}^{\pi/2} \Omega(\theta) d\theta = 1 \tag{5}$$

The angle density distribution of specimens with r_{cr} from 0.1 to 0.75 are shown in Figure 7. In this figure, all specimens show a peak density value at an angle of $\theta = 0$ (rad.), which decreases proportionally with surface roughness as the angle approaches $\pm\pi/2$ (rad.). A comparison of the angle density distribution of specimens with an r_{cr} of 0.2 and 0.3 does not show any great differences.

Next, the repeated specimens with an r_{cr} of 0.1 to 0.3 are compared amongst themselves and also do

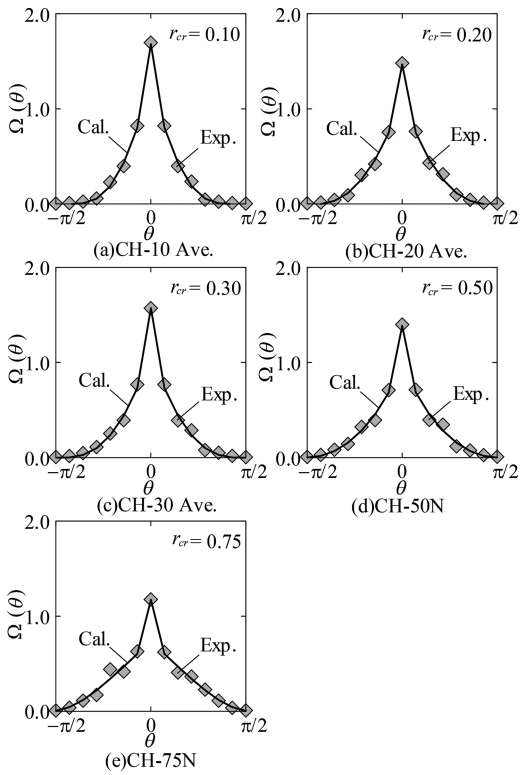

Figure 7. Inclined density distribution.

not show any great differences in the angle density distribution. As described above, chipping concrete can result in a random surface roughness profile, so it follows that differences in angle density distribution may occur even with the same r_{cr}. When incorp-orating this information in the mechanical model, the average value for each r_{cr} is used for the angle density distribution. This is an acceptable assumption because there was no significant difference in the maximum strength and stress—slip curves of specimens with the same roughened concrete area ratio, which was not the case for the shear loading test described in Section 4.2.

3.3 *Simulation of angle density function* $\Omega(\theta)$

The values of the angle density distribution $\Omega(\theta)$ for each roughened concrete area ratio and the simulation formula of the proposed angle density function are also shown in Figure 7. It is necessary to determine a formula for the angle density distribution using shape analysis to substitute $\Omega(\theta)$ into Equations (1) and (2).

$$\Omega(\theta) = \frac{4}{3}(a_0 + a_1 \cdot |\theta|^n) \cdot \cos^m \theta \tag{6}$$

The values used for expressing the angle density function of each specimen are described in Table 3 with analysis coefficients a_0, a_1, n, and m. The analysis coefficients are calculated with respect to the angle density distribution for each specimen using the least squares method. Figure 7 demonstrates that $\Omega(\theta)$ of a roughened surface can be estimated using Equation (6).

3.4 *Modeling of contact stress*

The contact stress-contact displacement ($\sigma_{con} - \omega_\theta$) relation of the Bujadaham model for a cracked concrete surface incorporates compression softening in an elasto-plastic model. We will instead construct our model to adapt to the stress transmission mechanism of the roughened concrete surface.

Table 3. Coefficients of angle density function.

	Coefficient for Equ.(6)			
Roughened area	a_0	a_1	n	m
10% average	1.26	−1.18	0.42	3.40
20% average	1.10	−1.00	0.42	1.70
30% average	1.18	−1.06	0.36	2.25
50%	1.04	−0.90	0.36	1.25
75%	0.88	−0.54	0.18	1.90

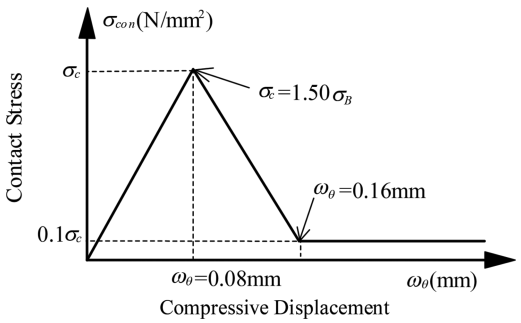

Figure 8. Modeling of Contact stress on local roughness shape.

The model of contact stress for a local uneven plane is shown in Figure 8. The contact displacement of the local uneven plane in the contact normal stress direction is defined as $\Omega(\theta)$ and it is expressed as the following equation.

$$\omega_\theta = \delta \sin\theta - \omega \cos\theta \quad (\omega_\theta \geq 0) \tag{7}$$

As mentioned above, since this study is intended for a roughened concrete surface, it is unknown whether the past model can be applied. Therefore, the model of contact stress is constructed from the relation of uniaxial compression softening characteristics of Darwin Pecknold. To use this model as the contact model of the roughened concrete surface, the compressive strain and compressive stress degree are replaced with the contact displacement and contact stress. The proposed model is constructed such that the stress softening behavior through the point where contact stress is 0.1 σ_c and is twice the contact displacement ω_θ. This represents the large load reduction behavior after the peak experimental value in the shear stress–shear displacement relation obtained from the shear loading experiment described in Section 4.2.

4 CONSISTENCY TO THE EXPERIMENT RESULT OF THE PROPOSED MODEL

In this chapter, we compare the proposed model with the results of a shear loading experiment and verify its suitability. In the shear loading tests, cyclic loading is performed, but to perform basic verification, we compare with the load envelope curve.

4.1 *Failure mode*

The failure modes and conceptual diagrams of the roughened concrete specimens are shown in Figure 9. There were two distinct results observed

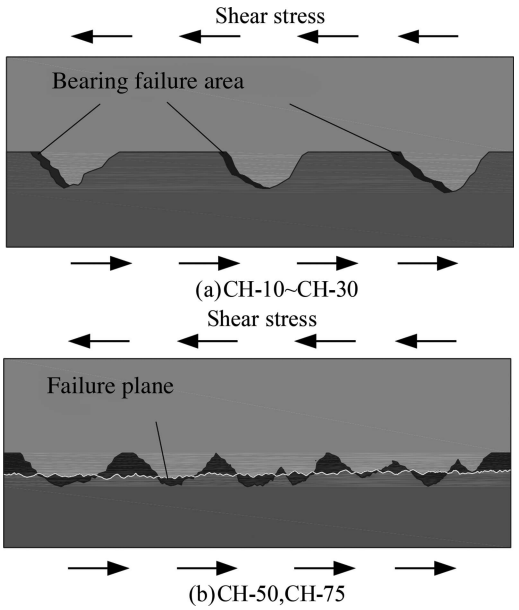

Figure 9. Failure mode.

during the shear loading experiment. In the specimens with an r_{cr} of 0.1 to 0.3, bearing failure occurred in the existing concrete member along the uneven surface profile as shown in Figure 9(a). In the specimens with r_{cr} of 0.5 and 0.75, the existing and reinforcing members experienced shear failure simultaneously. Based on this result, it can be said that a roughened surface area ratio greater than 0.5 provides adequate integration of a reinforcing member. However, there are additional necessary considerations within the scope of this experiment. Furthermore, more detailed verification is required, such as experiments on specimens with r_{cr} = 0.3–0.5, where the compressive strength, axial stress, and failure mode of concrete are switched. In fact, the bearing pressure fracture and the shear fracture may be mixed so creating a mechanical model that incorporates the failure mode becomes important.

4.2 *Shear loading test results*

The shear displacement, δ, and shear stress, τ_{max}, at maximum stress is shown in Table 4 and the experimental results of the τ–δ relation of each specimen are shown in Figure 10. First, we compare the specimens with different roughened concrete area ratios. The maximum stress tends to rise with increasing r_{cr}.

However, when r_{cr} exceeds 0.5, there is no difference the maximum strength. After the peak stress,

Table 4. Experimental results of maximum strength.

Specimen	$+\delta$ (mm)	$+\tau_{max}$ (N/mm^2)	$-\delta$ (mm)	$-\tau_{max}$ (N/mm^2)	$-\tau_{max}/+\tau_{max}$
CH-10N	+0.39	+1.04	–0.24	–1.07	1.03
CH-10D	+0.46	+1.13	–0.41	–1.08	0.95
CH-20N	+0.20	+1.36	–0.22	–1.20	0.88
CH-20D	+0.32	+1.35	–0.21	–1.09	0.80
CH-30N	+0.43	+1.58	–0.20	–1.39	0.88
CH-30D	+0.47	+1.57	–0.50	–1.56	0.99
CH-50N	+0.43	+1.69	–0.48	–1.62	0.96
CH-75N	+0.47	+1.66	–0.47	–1.64	0.99
				Average	0.94

δ: Shear displacement.
τ_{max}: Maximum strength.

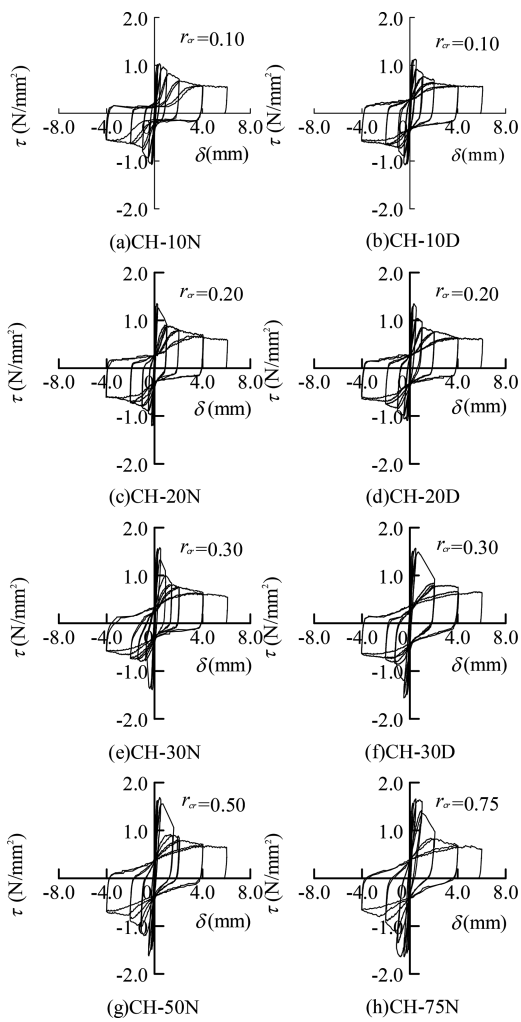

Figure 10. Experimental results.

all specimens exhibit brittle behavior and the load becomes constant. Next, a comparison is made between the specimens with multiples (r_{cr} = 0.1, 0.2, 03). Differences in the τ–δ relation due to the roughed concrete depth are not found. In other words, these results indicate that the shear stress–shear displacement relationship is hardly affected by the roughened concrete depth.

4.3 *Comparison of experimental results and proposed model*

The results of the shear loading tests are compared with the proposed model to verify their consistency. The results of the proposed model can also be found in the shear loading experiment results shown in Figure 11. Observing Figure 11, there is no big difference in ω due to r_{cr} even in the same fracture mode, until the shear displacement, which is the peak stress, approaches 0.2–0.5 mm. However, after the peak, it does not depend on the magnitude of r_{cr}, but ω varies. Therefore, δ–ω relations used in this analysis are classified into r_{cr} = 0.1 to 0.3, r_{cr} = 0.5, 0.75 for each destruction formulas, and the average values of them are approximated by least squares method, and the equations (8) and (9) and approximate curve is used.

$$\omega = 0.005\delta^3 - 0.076\delta^2 + 0.527\delta \quad (8)$$

$$\omega = 0.006\delta^3 - 0.122\delta^2 + 0.891\delta \quad (9)$$

The experimental values τ and σ are calculated by dividing the shear load, Q, and the vertical load, N, by the joint surface area, A_j.

$$\tau = Q/A_j \quad (10)$$

$$\sigma = N/A_j \quad (11)$$

The data shown in Figure 12 indicates that the test results for specimens with an r_{cr} from 0.1 to 0.3 can be roughly predicted. In the proposed model, the specimen with r_{cr} = 0.2 had a maximum strength higher than that of the specimen with r_{cr} = 0.3. This discontinuity is considered to be due to the relationship between strength and the angle density distribution; for an r_{cr} of 0.2, the density of larger inclination angles is larger than that for an r_{cr} of 0.3. In the specimens with roughened concrete area ratios of 0.5 and 0.75, the analysis values exceed the experimental values. As described above, the specimens with an r_{cr} of 0.5 and 0.75 experienced simultaneous failure of the existing concrete and the roughened surface, but in the proposed model, the shear strength is instead calculated from the contact stress of the local uneven surface. Furthermore, it is not possible to evaluate the experimental failure mode with this model. In other words, until the roughened concrete area ratio where the failure mode changes is reached (r_{cr} = 0.3 in this experiment), it can be evaluated with the proposed model, but not beyond that point. Thus, it is necessary to evaluate the shear failure on the existing side using other models or to reconstruct the proposed model.

Finally, the vertical stress, σ, is compared with the experimental value. The vertical stress–shear displacement (σ–δ) relation is shown in Figure 13. For the test specimens with an r_{cr} of 0.1 to 0.3,

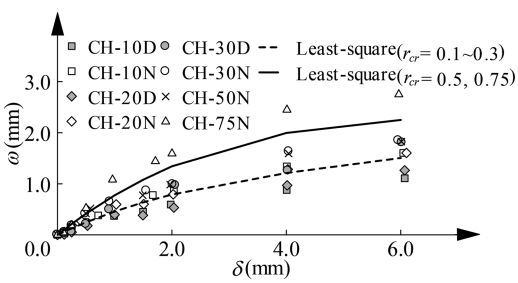

Figure 11. ω–δ relations.

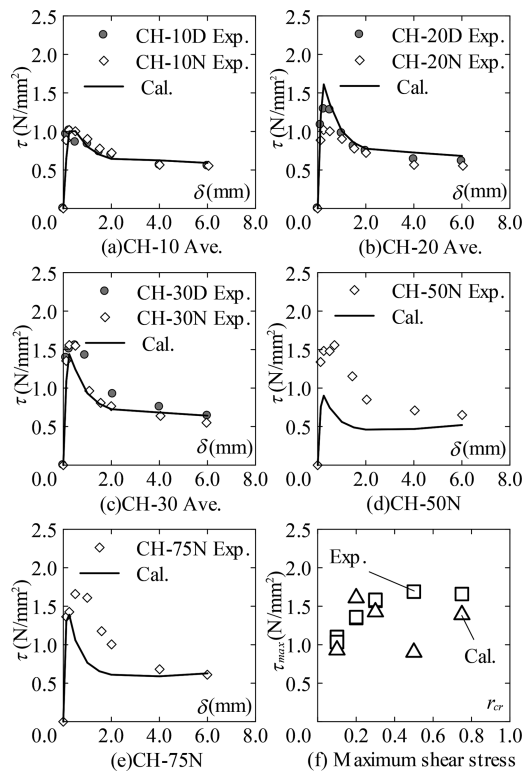

Figure 12. τ–δ relations.

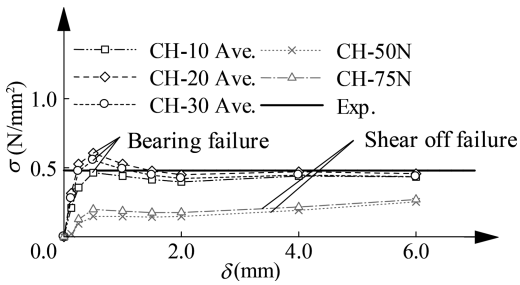

Figure 13. σ–δ relations.

the experimental values are evaluated satisfactorily. However, as with the shear stress, the calculated values for specimens with r_{cr} = 0.5 and 0.75 are much larger than the experimental values. It is inferred that the vertical stress increased for the same reasons that caused the shear stress to be overvalued.

5 CONCLUSION

In this study, we conducted a shear loading test and shape measurement of a seismically retrofitted concrete specimen to evaluate the stress transfer mechanism of a roughened concrete surface. In addition, we constructed a mechanical model representing the roughened concrete surface and compared experimental and analytical values. The findings of this study are as follows:

i. The angle density distribution varies depending on the roughened concrete area ratio. As the roughened concrete area ratio increases, $\Omega(\theta)$ at the peak (0 rad.) tends to decrease, and $\Omega(\theta)$ for large angles tends to increase.
ii. By comparing the experimental values with the proposed model from the shear loading experiment, the experimental values can be evaluated satisfactorily for specimens with an r_{cr} from 0.1 to 0.3. However, the analytical values of the specimens with an r_{cr} of 0.5 or 0.75 were significantly higher than the experimental values.
iii. Regarding the vertical stress, the experimental values can be evaluated satisfactorily for specimens with an r_{cr} of 0.1 to 0.3, but for specimens with an r_{cr} of 0.5 or 0.75, they are overevaluated.

In this paper, the shear resistance performance of a roughened concrete surface was verified using a previous theory that describes the shear stress transfer mechanism of a cracked concrete surface. By using the constitutive equation that expresses the shear transfer mechanism of a cracked concrete surface and considers the contact stress and friction of the local uneven surface, the shear and vertical stress of specimens with a roughened concrete area ratio of up to 0.3 can be evaluated. However, for specimens with a roughened concrete area ratio of 0.5 or 0.75, the shear stress and vertical stress are overestimated. In the proposed model, we could not express the failure modes for the latter specimens. This problem will be a focus of future research.

REFERENCES

Architectural Institute of Japan: Structural Design of Precast Concrete Connection Emulating Cast-in-place Reinforced Concrete, 2002.

Bazant, Z.P., Gambarova, P. Rough Cracks in Reinforced Concrete, J. of Structure Div., ASCE, Vol. 106, No.4, pp. 819–842, 1980.

Bujadaham Buja. The Universal Model for Transfer across Crack in Concrete, Department of Civil Engineering, The Graduate School of The University of Tokyo, March 1991.

Darwin, D., D.A. Pecknold. Analysis of RC Shear Panels under Cyclic Loading, J. of Structure Div., ASCE, Vol. 102 No.ST2, pp. 355–369, February 1976.

Fenwick,R.C., Pauly,T. Mechanisms of Shear Resistance of Concrete Beams, J. of Stractur Div., ASCE, Vol. 94, No.10, pp. 2325–2350, 1968.

Isozaki, T., Takase, Y., Abe, T., Katori, K. Fundamental Study on Shear Resistance of Roughened Concrete Surface for Existing Members, Proceedings of the Japan Concrete Institute, Vol. 39 No. 2, pp. 919–924, 2017.6 (in Japanese).

Katori, K., Abe, T., Kubota, M., Takase, Y., Sakazaki, T., Hiwatashi. T., Murata, T., and Hirata, S. Development of Concrete Surface Roughening Method having Minimal Vibration and Noise. Part7. Evaluation of Indirect Connection Shear Strength, Summaries of Technical Papers of Annual Meeting Architectural Institute of Japan, Structures IV, pp. 293–294, 2013.8 (in Japanese).

Li, B., Maekawa, K. & Okamura, H. Contact density model for stress transfer across cracks in concrete. J. of the faculty of Eng. University of Tokyo(B), Vol. 40, No. 1, pp. 9–52, 1989.

Nakano, K., Matsuzaki., Y.: Additional Method of Shear Resistances in Precast Concrete Connections, J. Struct. Constr. Eng., AIJ, No. 550, 151–158, 2001.12.

Tsuyoshi, M., Ishimura, Y., Sadasue, K., Minami, K. Study on Shear Strength of Diagonal Post-installed Anchor, Proceedings of the Japan Constitute Institute, Vol. 32, pp. 985–990, 2010.6 (in Japanese).

Walraven, J.C. Fundamental Analysis of Aggregate Interlock, J.of Structure Div., ASCE, Vol. 107, No. 11, pp. 2245–2270, 1981.

Watanabe, F., Kouno, S., Muguruma, H. Aggregate Interlock along a Cracked Surface and Its Modeling, Proceedings of the Japan Concrete Institute, Vol. 11 No. 2, pp. 311–316, 1989.



Taylor & Francis
Taylor & Francis Group
http://taylorandfrancis.com

Computational Modelling of Concrete Structures – Meschke, Pichler & Rots (Eds)
© 2018 Taylor & Francis Group, London, ISBN 978-1-138-74117-1

A practical design method to retrofit existing RC buildings with viscous dampers

R. Gobirahavan & A.C. Wijeyewickrema
Tokyo Institute of Technology, Tokyo, Japan

ABSTRACT: Many existing RC buildings have been designed using older versions of seismic standards and such buildings may be severely damaged due to earthquakes that may occur in the future. New buildings are designed to achieve a higher seismic performance compared to existing buildings, using updated seismic design maps. Hence, seismic performance enhancement is necessary for existing buildings, corresponding to the current earthquake design level. In this study, a non-iterative design procedure is proposed to determine the mechanical characteristics of additional linear viscous dampers that are needed, to achieve an enhanced seismic performance of existing RC buildings. The enhanced seismic performance of the buildings is based on the maximum Inter-story Drift Ratio (IDR) of the buildings. The viscous damper forces are calculated relative to the story shear forces in the unretrofitted buildings. The proposed design procedure is validated by considering 4-, 8-, and 12-story RC buildings, which were designed using IBC 2009, ASCE 7-05, and ACI 318-08. Seismic performance is enhanced according to the design level of IBC 2015. PERFORM-3D (CSI 2011) software is used for modeling and analysis of the buildings.

1 INTRODUCTION

In recent years, many existing buildings have been severely damaged due to strong ground motions around the world. New buildings designed using current earthquake design levels that have been updated due to large magnitude earthquake events in recent years, achieve a higher seismic performance than existing buildings. Therefore, it is necessary to enhance the performance of existing buildings by increasing damping and/or stiffness of the buildings corresponding to the current earthquake design level.

Passive energy dissipation devices can be used to enhance the seismic performance of existing buildings. Viscous dampers are velocity dependent passive energy dissipation device. Therefore, the forces generated by linear viscous dampers in a structure "out-of-phase" with force generated by the structural system. This is a significant advantage that viscous damping systems have over hysteretic damping systems that generate their maximum forces when structural system is at its maximum displacements (Christopoulos & Filiatrault 2006).

Recently, simple and convenient design methods have been proposed to calculate the supplemental viscous damper parameters for practicing engineers. Silvestri et al. (2010) developed a five step design procedure to calculate the viscous damping constants to reach the target performance level of the buildings. Zhou et al. (2012) proposed a practical design method to retrofit existing RC buildings, where a simplified relationship was developed between the maximum force of additional nonlinear viscous damper and story shear force, based on the required additional damping ratio.

The distribution of the viscous damping constants is an issue along the height of the buildings, because only the required equivalent single degree of freedom system viscous damping can be calculated from most of the proposed procedures. There are a few studies about the distribution of viscous damping constants along the height of the building, where the effectiveness of the simple and advanced damper placement techniques along the height of the building were compared based on building performance and cost due to additional viscous dampers (Whittle et al. 2012, Hwang et al. 2013, Landi et al. 2015).

In this study, a non-iterative practical design procedure is proposed for dimensioning the additional viscous dampers to reach the target performance of existing RC buildings. The proposed procedure is mostly applicable for practicing engineers in the preliminary design. The maximum force of the viscous dampers are calculated relative to the story shear forces along the height of the unretrofitted building. In addition, the effectiveness of the distribution of the damping constants proportional to story mass, maximum story shear force, and maximum inter-story drift ratio (IDR) along the height of the RC building is investigated by keeping the total viscous damping force constant.

2 VISCOUS DAMPERS

2.1 *Viscous damping force*

A viscous damper dissipates energy by fluid orificing due to the piston head movement in the cylinder. Fluid flow through the piston results in a resisting force $P(t)$ which depends on the velocity of the piston movement through the cylinder, defined by,

$$P(t) = C\left|\frac{dx_i(t)}{dt}\right|^{\alpha} \operatorname{sgn}\left(\frac{dx(t)}{dt}\right), \tag{1}$$

where C = viscous damping constant, α = velocity coefficient, $P(t)$ = axial force, and $x(t)$ = the displacement of the viscous damper. When $\alpha = 1$, the device acts as a linear viscous damper (Christopoulos & Filiatrault 2006).

2.2 *Maximum linear viscous damping force relative to the story shear force for a damper aligned horizontally*

The maximum viscous damping force P_i^{max} in the ith story is,

$$P_i^{max} = C_i \max_t \left|\frac{dx_i(t)}{dt}\right|^{\alpha}, \tag{2}$$

and in terms of the maximum displacement x_i^{max} at the ith story using the equivalent pseudo-velocity is,

$$P_i^{max} = C_i(\omega_1 x_i^{max})^{\alpha}, \tag{3}$$

where ω_1 = fundamental circular frequency of the building. The maximum linear viscous damping force $P_i^{L\text{-}max}$ is,

$$P_i^{L-max} = C_i^L \omega_1 x_i^{max}, \tag{4}$$

where C_i^L = linear viscous damping constant which is proportional to the story stiffness K_i of the ith story of the building,

$$C_i^L = \frac{2\xi}{\omega_1} K_i, \tag{5}$$

where ξ = damping ratio of the first mode of the building. Therefore, the linear maximum damping force $P_i^{L\text{-}max}$ can be approximated with respect to the maximum story shear force V_i^{max} as,

$$P_i^{L-max} = 2\xi K_i x_i^{max} = 2\xi V_i^{max}. \tag{6}$$

3 PROPOSED DESIGN PROCEDURE

The design procedure consists of four steps.

Step 1: Determine the maximum IDR and story shear forces along the height of the unretrofitted building for the current earthquake design level

Nonlinear response history analysis (NLRHA) is used to find the maximum IDR and story shear forces V_i^{max} along the height of the unretrofitted RC building for the current earthquake design level.

Step 2: Define the displacement profile for the corresponding allowable IDR at the enhanced performance level

The first mode displacement shape is used to define the displacement profile along the height of the building for the allowable IDR by considering higher mode effects and the empirical relationship is,

$$\Delta_i^R = \omega_\theta \theta_c h_i \frac{(4H - h_i)}{(4H - h_1)}, \tag{7}$$

$$\omega_\theta = 1.15 - 0.0034H < 1,$$

where Δ_i^R = retrofitted (target) displacement in i^{th} floor, h_i = height of the ith floor, ω_θ = reduction factor to account for the higher mode, θ_c = allowable IDR, and H = height of the building (Sullivan et al. 2012, Sullivan & Lago 2012).

Step 3: Determine the equivalent single degree of freedom system displacements

The retrofitted (target) displacement Δ^R and unretrofitted displacement Δ^{UR} of the equivalent single degree of freedom system can be calculated from,

$$\Delta^R = \sum_1^n m_i \left(\Delta_i^R\right)^2 \Big/ \sum_1^n m_i \Delta_i^R, \tag{8}$$

$$\Delta^{UR} = \sum_1^n m_i \left(\Delta_i^{UR}\right)^2 \Big/ \sum_1^n m_i \Delta_i^{UR}, \tag{9}$$

where m_i = mass of the ith floor n = number of stories, and Δ_i^{UR} = unretrofitted displacement in i^{th} floor (Sullivan et al. 2012, Sullivan & Lago 2012). The unretrofitted displacement in i^{th} floor Δ_i^{UR} can be calculated from the IDR profile in Step 1.

Step 4: Calculate the maximum forces of viscous dampers and damping constants along the stories

The required equivalent viscous damping ξ_{req} is calculated by scaling the displacement spectrum at the current earthquake design level as,

$$\xi_{req} = \left(\left(\frac{\Delta^{UR}}{\Delta^R}\right)^2 \times 10\right) - 10, \tag{10}$$

where the viscous damping of the unretrofitted building is assumed as 5%. The required maximum viscous damping forces $P_i^{L\text{-}max}$, viscous damping constants C_i^L, and maximum damper displacement Δ_i^d can be calculated using the Eq. 6 as,

$$P_i^{L-max} = 2\xi_{req} V_i^{max}, \tag{11}$$

$$C_i^L = \frac{\xi_{req} V_i^{max} T_1}{\pi \Delta_i^R}, \tag{12}$$

$$\Delta_i^d = \Delta_i^R - \Delta_{i-1}^R. \tag{13}$$

4 APPLICATION OF THE PROCEDURE

4.1 *Building description and modeling*

The proposed design procedure is applied to 4-, 8-, and 12-story RC buildings (Fig. 1). The 3-bay by 3-bay buildings are symmetric. The bay width is 6.1 m in the both directions and the story height is 3.9 m. The buildings are designed using the equivalent lateral force procedure, following the provisions of IBC 2009, ASCE 7–05, and ACI 318–08. The design response spectrum is constructed for an arbitrary location in California (33.99 N, 118.162 W) and the soil is characterized as stiff soil (Site class D). Design floor dead load (slab, partitions, finishes), live load, and self-weight of the concrete are 8.28 kN/m^2, 2.37 kN/m^2, and 25 kN/m^3, respectively.

Three-dimensional finite element modelling was carried out using PERFORM-3D (CSI 2011). Beam and column members are divided into three elements along the length and each element is modeled using inelastic fiber segments. A section is discretized into unconfined concrete fibers, confined concrete fibers, and steel fibers. Uniaxial material models with a nonlinear constitutive relationship are assigned to the fibers. Mander model (Mander et al. 1988) and Manegotto and Pinto model (Mangetto et al. 1973) are used for concrete and steel, respectively. Rigid diaphragms are used for floors to have same horizontal displacement and rotation about vertical axis. The viscous damper and supporting brace are modeled as Maxwell spring-dashpot system (elastic bar and dashpot are connected in series).

4.2 *Nonlinear Response History Analysis (NLRHA)*

The current earthquake design level is defined from U.S. Seismic design maps based on the provisions of IBC 2015 at the same location of the building. A total of seven far-fault ground motions (Table 1) are selected from the Pacific Earthquake Engineering Research Centre database (PEER 2017). In the selection process, the following criteria are employed: (i) magnitude of the earthquake $M_W \geq 6.5$; (ii) the closest distance to the fault rupture $10 < R_{rup} \leq 100$ km; (iii) the site class for recording station is D. The selected ground motions are scaled to the current earthquake design spectrum in the period range of $0.2T_1$ to $1.5T_1$ (Fig. 2). For the buildings considered in this study, the period range is 0.18 s to 3.38 s (the fundamental period T_1 of the 4-, 8-, and 12-story buildings are 0.89 s, 1.74 s, and 2.25 s, respectively). The ground

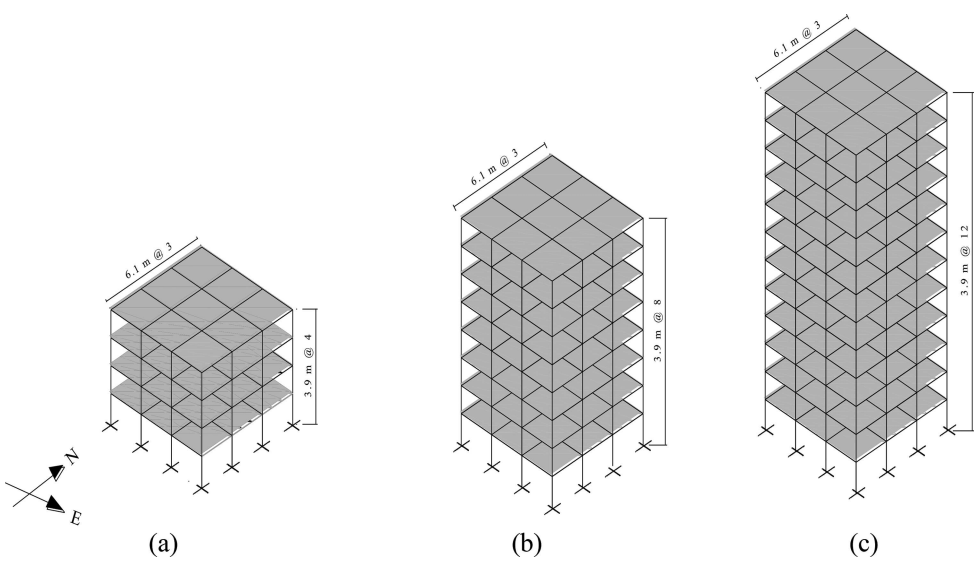

Figure 1. The RC buildings used in this study: (a) 4-story (b) 8-story (c) 12-story.

Table 1. Ground motions used in this study.

No	Event	Year	Station	M_w	Source-site distance (km)	Shear wave velocity (m/s)	Scaling factor
1	Imperial Valley-06	1979	Delta	6.53	22.03	242.05	2.29
2	Corinth_ Greece	1981	Corinth	6.60	10.27	361.40	2.61
3	Taiwan SMART1(45)	1986	SMART1 O02″	7.30	57.13	285.09	3.20
4	Superstition Hills-02	1987	El Centro Imp. Co. Cent	6.54	18.20	192.05	2.01
5	Northridge-01	1994	Canyon Country – W Lost Cany	6.69	12.44	325.60	1.56
6	Kobe_ Japan	1995	Sakai	6.90	28.08	256.00	3.42
7	El Mayor-Cucapah_ Mexico	2010	RIITO	7.20	13.00	242.05	1.62

motions are applied in the N-S direction of the building.

The mean values of the peak IDR and story shear forces of the unretrofitted building is used (Step 1 of design procedure). The allowable IDR of the building is θ_c = 1% to enhance the performance to immediate occupancy level based on FEMA-356 guidelines at the current earthquake design level. The visous damper is connected diagonally with a supporting brace in series as shown in Fig. 3. The maximum viscous damping forces $P_i^{L\text{-}max}$, viscous damping constants C_i^L, and maximum damper displacement Δ_i^d can be converted from the simple geometric relationship,

$$P_i^{L-max} = \frac{2\xi_{req} V_i^{max}}{\cos\theta}, \tag{14}$$

$$C_i^L = \frac{\xi_{req} V_i^{max} T_1}{\pi \Delta_i^d \cos\theta}, \tag{15}$$

$$\Delta_i^d = (\Delta_i^R - \Delta_{i-1}^R)\cos\theta. \tag{16}$$

The viscous damper characteristics calculated from the proposed procedure are given in Tables 2–4.

The response indicators for the buildings with and without additional linear viscous dampers obtained from NLRHA are shown in Figs. 4–7. The mean values of the peak IDR of the buildings without dampers (Step 1 of design procedure) and with dampers is shown in Fig. 4. The peak IDR of the buildings reduce to 1%, which indicates that the proposed procedure can be used to estimate the required additional viscous damper characteristics to set the target performance. There is no significant difference in the peak IDR profile pattern along the height of the building due to the additional viscous dampers. Fig. 5 shows that

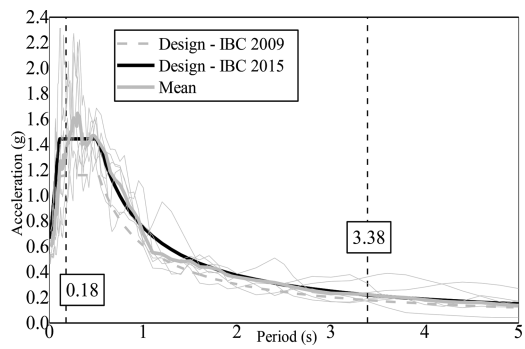

Figure 2. Comparison of 5%-damped mean acceleration response spectrum of scaled ground motions with design acceleration response spectrum.

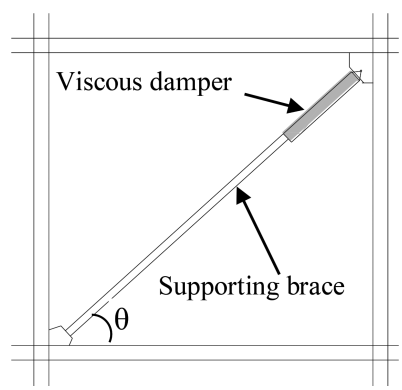

Figure 3. Schematic of viscous damper and supporting brace.

the estimated displacement profile based on the allowable IDR (Step 2 of design procedure) are close to the peak floor displacement profile of the

Table 2. Estimation of viscous damper characteristics for the 4-story building.

Story	m_i (t)	V_i^{max} (kN)	IDR^{max}	Δ_i^{UR} (mm)	Δ_i^R (mm)	Δ_i^d (mm)	$P_i^{L\text{-}max}$ (kN)	C_i^L (kN.s/m)
1	495	5,401	0.016	64.0	40.0	33.5	2,032	8,587
2	470	4,856	0.020	144.9	74.7	29.0	1,827	8,908
3	470	4,430	0.017	214.3	104.0	24.6	1,667	9,605
4	444	3,149	0.011	258.4	128.1	20.1	1,185	8,345

*Δ^{UR} = 209.5 mm, Δ^R = 98.2 mm, and ξ = 31.5%.

Table 3. Estimation of viscous damper characteristics for the 8-story building.

Story	m_i (t)	V_i^{max} (kN)	IDR^{max}	Δ_i^{UR} (mm)	Δ_i^R (mm)	Δ_i^d (mm)	$P_i^{L\text{-}max}$ (kN)	C_i^L (kN.s/m)
1	495	6,405	0.017	70.0	39.8	33.3	3,007	24,984
2	470	6,043	0.021	163.0	77.0	31.2	2,837	25,199
3	470	5,758	0.018	245.5	111.7	29.0	2,704	25,790
4	470	5,375	0.016	315.9	143.8	26.9	2,524	25,999
5	470	4,913	0.016	380.5	173.4	24.7	2,307	25,833
6	470	4,735	0.015	444.5	200.3	22.6	2,223	27,270
7	470	4,206	0.012	502.4	224.7	20.4	1,975	26,774
8	444	2,773	0.008	541.8	246.6	18.3	1,302	19,727

*Δ^{UR} = 403.4 mm, Δ^R = 181.5 mm, and ξ = 39.3%.

Table 4. Estimation of viscous damper characteristics for the 12-story building.

Story	m_i (t)	V_i^{max} (kN)	IDR^{max}	Δ_i^{UR} (mm)	Δ_i^R (mm)	Δ_i^d (mm)	$P_i^{L\text{-}max}$ (kN)	C_i^L (kN.s/m)
1	527	9,589	0.010	40.0	36.2	32.9	3,898	42,544
2	501	8,997	0.017	107.6	76.9	31.5	3,658	41,161
3	501	8,410	0.019	183.8	112.8	30.1	3,419	40,784
4	501	8,083	0.021	268.2	147.1	28.7	3,286	41,112
5	501	7,795	0.017	337.8	179.7	27.3	3,169	41,679
6	501	7,321	0.017	405.8	210.6	25.9	2,976	41,262
7	501	6,634	0.016	470.5	239.9	24.5	2,697	39,527
8	501	5,854	0.016	535.8	267.5	23.1	2,381	36,993
9	469	4,559	0.016	601.8	293.4	21.7	2,069	34,241
10	469	4,005	0.016	667.6	317.6	20.3	1,854	32,783
11	469	4,005	0.014	726.0	340.2	18.9	1,629	30,937
12	444	2,500	0.008	764.8	361.1	17.5	1,017	26,774

*Δ^{UR} = 546.1 mm, Δ^R = 260.1 mm, and ξ = 34.0%.

building. The reduction in the story shear forces due to additional viscous dampers is more in the upper stories of the buildings. The reduction in the base shear is about 25% in the buildings. The additional linear viscous dampers reduce the peak floor accelerations along the height of the buildings (Fig. 7). The reduction is considerably less in the 12-story building. The reduction in the roof acceleration decreases with increasing height of the building, the 12-story building shows the same acceleration for both retrofitted and unretrofitted cases.

4.3 *Supporting brace for the viscous damper*

The stiffness of the supporting brace can significantly affect the performance of the viscous damper. However, it is necessary that the braces

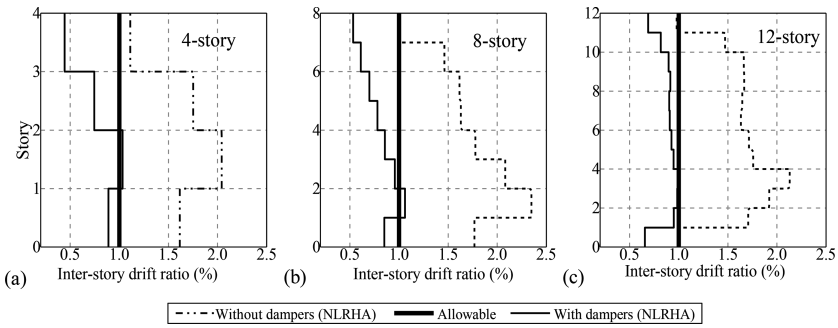

Figure 4. Mean values of the peak IDR of the buildings: (a) 4-Story (b) 8-Story (c) 12-Story.

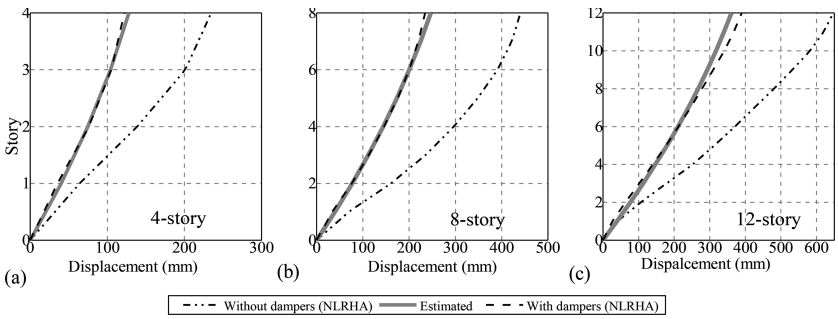

Figure 5. Mean values of the peak floor displacment of the buildings: (a) 4-Story (b) 8-Story (c) 12-Story.

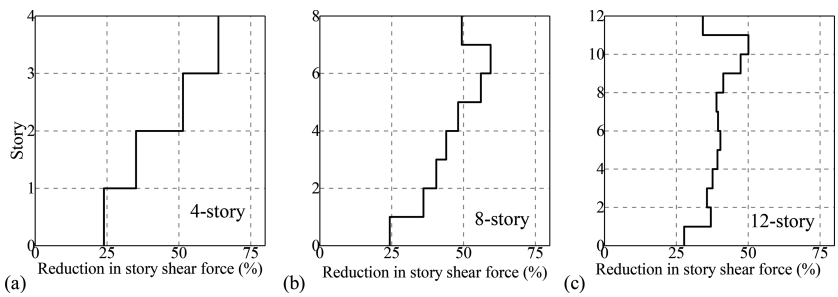

Figure 6. Mean values of the reduction in the peak story shear force of the buildings: (a) 4-Story (b) 8-Story (c) 12-Story.

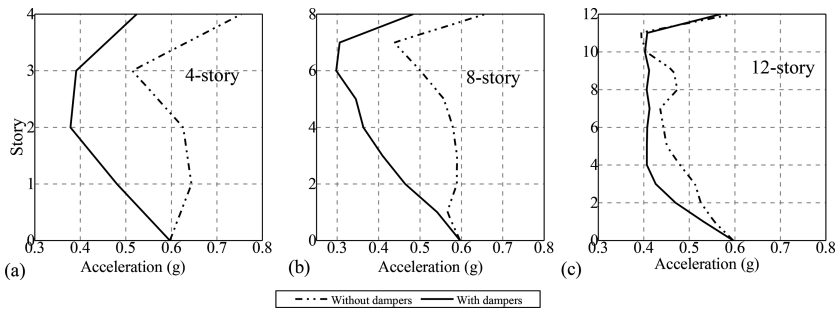

Figure 7. Mean values of the peak floor acceleration of the buildings: (a) 4-Story (b) 8-Story (c) 12-Story.

should be as stiff as possible to increase the efficiency of the viscous dampers. The braces were assumed as rigid in the proposed design procedure (dynamic effect from supporting braces are neglected). Londoño et al. (2014) proposed a relationship to calculate the required minimum axial stiffness of supporting braces to provide a specific efficiency by linear viscous dampers,

$$k_i^b = \left(\frac{1}{\varepsilon^2} - 1\right)^{-\frac{1}{2}} C_i^L \quad \omega_1, \tag{17}$$

where ε = efficiency and k_i^b = minimum axial stiffness of the brace in i^{th} story of the building. In the present study, the axial stiffness of the supporting brace in the ith story is taken as, $10{*}k_i^b$ with ε = 98%. Table 5 shows the stiffness of the supporting bars. The peak deformation of the viscous damper is compared with the peak deformation of the viscous damper and brace compound component in Fig. 8. Both deformations coincide with each other, hence, the axial stiffness of the supporting braces can be calculated from $10{*}k_i^b$ in the proposed procedure.

Table 5. The stiffness of the supporting braces.

Story	4-Story (kN/m)	8-Story (kN/m)	12-Story (kN/m)
1	2,897,202	4,437,232	5,829,918
2	3,005,677	4,475,335	5,713,046
3	3,240,575	4,580,236	5,588,700
4	2,815,673	4,617,407	5,633,603
5		4,587,905	5,711,320
6		4,843,111	5,654,259
7		4,755,008	5,416,481
8		3,503,467	5,069,205
9			4,692,184
10			4,492,400
11			4,239,433
12			2,857,745

5 EFFECTIVENESS OF THE DISTRIBUTION OF VISCOUS DAMPING CONSTANTS

Keeping the total viscous damping forces calculated in Section 4 constant, the effectiveness of distribution of viscous damping constants proportional to story parameters p_i^s, viz., story mass (SM), story shear force (SS), and IDR is considered in this section. A simplified relationship is used to calculate the viscous damping characteristics based on Landi et al. (2015). The viscous damping constant C_i^L is proportional to the story parameter p_i^s is,

$$C_i^L = k_p p_i^s, \tag{18}$$

where k_p is a constant. Hence, the sum of the viscous damping constants are proportional to the sum of the story parameters,

$$\sum_{i=1}^{n} C_i^L = k_p \sum_{i=1}^{n} p_i^s, \tag{19}$$

From Eq. 18 and Eq. 19,

$$C_i^L = p_i^s \left(\sum_{k=1}^{n} C_k^L \Big/ \sum_{k=1}^{n} p_k^s \right). \tag{20}$$

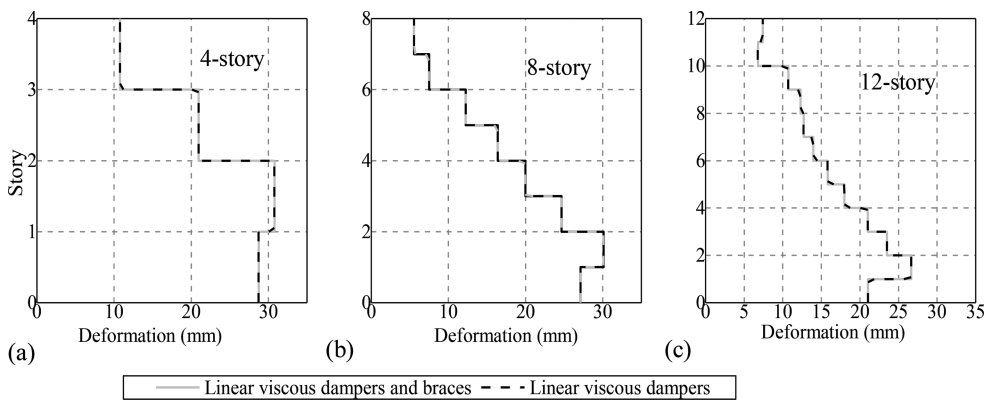

Figure 8. Mean values of the peak deformation of the dampers of the buildings: (a) 4-Story (b) 8-Story (c) 12-Story.

Substituting C_i^L from Eq. 20 into the Eq. 4 the maximum viscous damping force in the ith story is,

$$P_i^{L-max} = \frac{2\pi p_i^s}{T_1}\left(\sum_{k=1}^{n} C_k^L \Delta_k^d \Big/ \sum_{k=1}^{n} p_k^s\right). \quad (21)$$

The sum of the maximum viscous damper forces is,

$$\sum_{k=1}^{n} P_k^{L-max} = \frac{2\pi}{T_1}\left(\sum_{k=1}^{n} p_k^s \Delta_k^d \sum_{k=1}^{n} C_k^L \Big/ \sum_{k=1}^{n} p_k^s\right). \quad (22)$$

Using Eq. 20, the sum of the viscous damper forces can be simplified as,

$$\sum_{k=1}^{n} P_k^{L-max} = \frac{2\pi C_i^L}{T_1 p_i^s} \sum_{k=1}^{n} p_k^s \Delta_k^d. \quad (23)$$

Finally, from Eq. 11, Eq. 12, and Eq. 23 the viscous damping constant C_i^L and maximum viscous damping force $P_i^{L\text{-}max}$ at the each story is,

$$C_i^L = \frac{\xi_{req} p_i^s T_1}{\pi}\left(\sum_{k=1}^{n} V_k^{max} \Big/ \sum_{k=1}^{n} p_k^s \Delta_k^d\right), \quad (24)$$

$$P_i^{L-max} = 2\xi_{req} p_i^s \Delta_i^d \left(\sum_{k=1}^{n} V_k^{max} \Big/ \sum_{k=i}^{n} p_k^s \Delta_k^d\right). \quad (25)$$

Tables 6–8 show the damping constant C_i^L and maximum viscous damping force $P_i^{L\text{-}max}$ using different methods.

The seismic performances are compared in Figs. 9–10 using NLRHA. In all cases, the peak IDR satisfy the target performance (Fig. 9), while the peak floor accelerations using the different methods are nearly the same (Fig. 10). There is no significant difference in the seismic performance of the buildings due to different methods used to calculate damping constants.

Table 6. Viscous damping constants and forces calculated using different methods for 4-Story building.

	Proposed procedure		Damping constant proportional to story mass (SM)		Damping constant proportional to peak story shear force (SS)		Damping constant proportional to peak IDR	
Story	$P_i^{L-\max}$ (kN)	C_i^L (kN.s/M)	$P_i^{L-\max}$ (kN)	C_i^L (kN.s/M)	$P_i^{L-\max}$ (kN)	C_i^L (kN.s/M)	$P_i^{L-\max}$ (kN)	C_i^L (kN.s/M)
1	2,032	8,587	2,195	9,276	2,458	10,348	2,032	8,585
2	1,827	8,908	1,806	8,803	1,915	9,338	2,235	10,847
3	1,667	9,605	1,527	8,803	1,478	8,519	1,616	9,312
4	1,185	8,345	1,183	8,330	860	6,059	838	5,909
Sum	6,711	35,445	6,711	35,212	6,711	34,299	6,711	34,653

Table 7. Viscous damping constants and forces calculated using different methods for 8-Story building.

	Proposed procedure		Damping constant proportional to story mass (SM)		Damping constant proportional to peak story shear force (SS)		Damping constant proportional to peak IDR	
Story	$P_i^{L-\max}$ (kN)	C_i^L (kN.s/M)	$P_i^{L-\max}$ (kN)	C_i^L (kN.s/M)	$P_i^{L-\max}$ (kN)	C_i^L (kN.s/M)	$P_i^{L-\max}$ (kN)	C_i^L (kN.s/M)
1	3,007	24,984	3,199	26,582	3,737	31,045	3,047	25,316
2	2,837	25,199	2,840	25,227	3,298	29,292	3,784	33,608
3	2,704	25,790	2,644	25,227	2,926	27,911	3,124	29,805
4	2,524	25,999	2,449	25,227	2,529	26,053	2,470	25,444
5	2,307	25,833	2,253	25,227	2,127	23,816	2,085	23,344
6	2,223	27,270	2,057	25,227	1,872	22,954	1,886	23,133
7	1,975	26,774	1,861	25,227	1,503	20,390	1,554	20,928
8	1,302	19,727	1,576	23,872	887	13,442	939	14,231
Sum	18,879	201,576	18,879	201,816	18,879	194,904	18,879	195,809

Table 8. Viscous damping constants and forces calculated using different methods for 12-Story building.

Story	Proposed procedure		Damping constant proportional to story mass (SM)		Damping constant proportional to peak story shear force (SS)		Damping constant proportional to peak IDR	
	$P_i^{L-\max}$ (kN)	C_i^L (kN.s/M)	$P_i^{L-\max}$ (kN)	C_i^L (kN.s/M)	$P_i^{L-\max}$ (kN)	C_i^L (kN.s/M)	$P_i^{L-\max}$ (kN)	C_i^L (kN.s/M)
1	3,898	42,544	3,714	40,533	4,800	52,382	2,168	23,658
2	3,658	41,161	3,386	38,591	4,312	49,148	3,510	40,005
3	3,419	40,784	3,235	38,591	3,851	45,941	3,774	45,019
4	3,286	41,112	3,085	38,591	3,529	44,157	3,988	49,894
5	3,169	41,679	2,934	38,591	3,238	42,582	3,130	41,171
6	2,976	41,262	2,784	38,591	2,885	39,995	2,897	40,160
7	2,697	39,527	2,633	38,591	2,473	36,242	2,612	38,277
8	2,381	36,993	2,483	38,591	2,057	31,980	2,481	38,560
9	2,069	34,241	2,185	36,147	1,681	27,808	2,358	39,022
10	1,854	32,783,	2,044	36,147	1,408	24,906	2,201	38,934
11	1,629	30,937	1,903	36,147	1,152	21,883	1,816	34,492
12	1,017	26,774	1,667	34,205	666	13,658	1,117	22,922
Sum	32,053	417,014	32,053	453,316	32,053	430,682	32,053	452,510

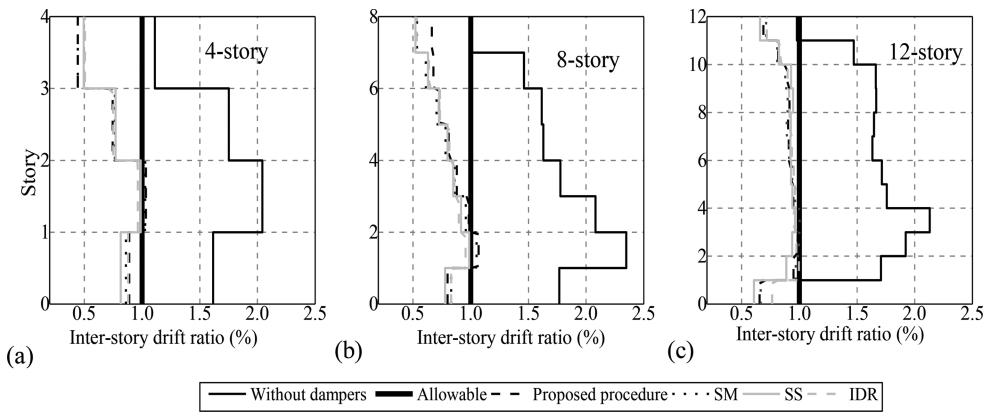

Figure 9. Mean values of the peak IDR of the buildings: (a) 4-Story (b) 8-Story (c) 12-Story.

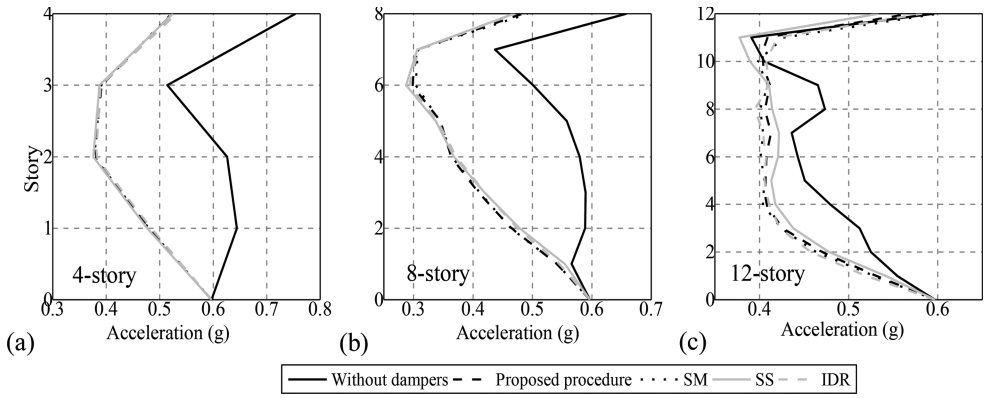

Figure 10. Mean values of peak floor acceleration of the buildings: (a) 4-Story (b) 8-Story (c) 12-Story.

6 CONCLUSIONS

In this paper, a non-iterative design procedure is proposed to calculate the mechanical characteristics of additional linear viscous dampers needed to enhance the seismic performance of existing buildings to correspond to the current earthquake design level.

The proposed design procedure is applied to 4-, 8-, and 12-story buildings. Results from NLRHA show that the retrofitted buildings satisfy the allowable IDR and that the proposed procedure can be used to estimate the linear viscous damper characteristics. The estimated displacement profile for the corresponding allowable IDR (Step 2 of the proposed procedure) is close to the peak displacement profile along the height of the buildings from NLRHA. Peak story shear forces reduce due to the additional viscous dampers, the reduction in the base shear is about 25%, and the reduction increases along the height of the buildings. There is a reduction in the peak floor accelerations due to additional viscous dampers and the reduction is more in the 4- and 8- story buildings.

The effectiveness of the distribution of viscous damping constants proportional to story mass, story shear force, and IDR were investigated. The buildings satisfy the target performance when the different methods are used to obtain the damping constants and there is no significant difference in the performance of the buildings.

REFERENCES

ACI Committee 318 2008. *Building code requirements for structural concrete (ACI 318-08),* Farmington Hills, USA.

American Society of Civil Engineers 2005. *Minimum Design Loads for Buildings and Other Structures (ASCE 7-05),* Reston, VA, USA.

Christopoulos, C. & Filiatrault, A. 2006. *Principles of Passive Supplemental Damping and Seismic Isolation.* IUSS Press, Pavia, Italy.

Computers and Structures, Inc. 2011. *PERFORM-3D, Nonlinear analysis and performance assessment of 3D structures,* Version 5, Berkeley, California.

Federal Emergency Management Agency 356 2000. *Prestandard and Commentary for the Seismic Rehabilitation of Buildings (FEMA-356),* Washington, DC, USA.

Hwang, J.S., Lin, W.C., & Wu, N.J. 2013. Comparison of distribution methods for viscous damping coefficients to buildings. *Structure and Infrastructure Engineering*, 9(1), 28–41.

International Code Council 2009. *International Building Code*, *(IBC 2009)*, Country Club Hills, IL, USA.

International Code Council 2015. *International Building Code*, *(IBC 2015)*, Country Club Hills, IL, USA.

Landi, L., Conti, F., & Diotallevi, P.P. 2015. Effectiveness of different distributions of viscous damping coefficients for the seismic retrofit of regular and irregular RC frames. *Engineering Structures*, 100, 79–93.

Londoño, J.M., Wagg, D.J., & Neild, S.A. 2014. Supporting brace sizing in structures with added linear viscous fluid dampers: A filter design solution. *Earthquake Engineering and Structural Dynamics*, 43(13), 1999–2013.

Mander, J.B., Priestley, M.J., & Park, R. 1988. Theoretical stress-strain model for confined concrete. *Journal of Structural Engineering*, 114(8), 1804–1826.

Menegotto, M., & Pinto, P. 1973. Methods of Analysis for Cyclically Loaded R/C Frames Including Changes in Geometry and Non-elastic Behavior under Combined Normal Force and Bending, *Symposium of Resistance and Ultimate Deformability of Structure Acted by Well Defined Repeated Load*, Lisbon, Portugal, 15–22.

PEER (Pacific Earthquake Engineering Research) 2017. *PEER NGA Database*. PEER, University of California, Berkeley. [accessed on Feb 2017].

Silvestri, S. Gasparini, G. & Trombetti, T. 2010. A five-step procedure for the dimensioning of viscous dampers to be inserted in building structures. *Journal of Earthquake Engineering,* 14(3), 417–447.

Sullivan, T.J., & Lago, A. 2012. Towards a simplified direct DBD procedure for the seismic design of moment resisting frames with viscous dampers. *Engineering Structures*, 35, 140–148.

Sullivan, T.J, Priestley, M.J.N, & Calvi, G.M. 2012. *A Model Code for the Displacement Based Seismic Design of Structures*: DBD12, IUSS Press, Pavia, Italy.

Whittle, J.K., Williams, M.S., Karavasilis, T.L., & Blakeborough, A. 2012. A comparison of viscous damper placement methods for improving seismic building design. *Journal of Earthquake Engineering*, 16(4), 540–560.

Zhou, Y., Lu, X., Weng, D., & Zhang, R. 2012. A practical design method for reinforced concrete structures with viscous dampers. *Engineering Structures*, 39, 187–198.

Computational Modelling of Concrete Structures – Meschke, Pichler & Rots (Eds)
© 2018 Taylor & Francis Group, London, ISBN 978-1-138-74117-1

An improved RSA procedure to compute shear force in tall RC shear wall buildings

K. Khy & C. Chintanapakdee
Department of Civil Engineering, Chulalongkorn University, Thailand

A.C. Wijeyewickrema
Department of Civil Engineering, Tokyo Institute of Technology, Tokyo, Japan

ABSTRACT: The Response Spectrum Analysis (RSA) procedure is widely used to compute the seismic design forces of a structure. However, previous studies have demonstrated that the RSA procedure underestimates the design shear force in the wall and have proposed the Higher Mode Elastic RSA (HME-RSA) method to compute the design shear force in the wall. For tall buildings, higher modes may not behave elastically. In this study, the accuracy of the HME-RSA method is evaluated and the Higher Mode Inelastic RSA (HMI-RSA) method is proposed to compute the design shear force in tall RC shear wall buildings. Four tall buildings with 15, 20, 31 and 39 stories subjected to earthquake excitations in Bangkok, Thailand, were first designed by the RSA procedure, then Nonlinear Response History Analysis (NLRHA) was conducted to compute more accurate results. It was found that the HME-RSA method overestimates shear force in the 31- and 39-story buildings. The HMI-RSA method could significantly improve the accuracy of the HME-RSA method in computing the design shear force in all four buildings that were considered.

1 INTRODUCTION

Reinforced concrete (RC) shear walls are commonly used as the lateral force resisting system in tall buildings. To design such structures to resist earthquakes, the response spectrum analysis (RSA) procedure is widely used in practice to compute the seismic design forces of the structure. To compute the design forces of inelastic RC walls with an acceptable ductility demand in the conventional RSA procedure, the elastic responses computed from many vibration modes are combined and then reduced by a single response modification factor (R), assuming that all modes are equally affected by inelastic action. The structural wall is normally designed to experience flexural yielding by reducing elastic bending moment by the R factor, but RSA procedure reduces elastic shear force by the same R factor, which assumes that shear force is reduced by the same factor as bending moment, or in other word, flexural yielding of the wall limits shear force in the same way as it limits bending moment. However, previous studies have shown that the shear force in the wall subjected to dynamic loading keeps increasing after flexural yielding occurs at the base of the wall (Ghorbanirenani et al., 2011, Panagiotou et al., 2011), that inelasticity of each mode is not identical, and that higher modes are not significantly affected by inelasticity as much as the first mode (Eibl & Keintzel, 1988, Priestley, 2003, Calugaru & Panagiotou, 2012, Munir & Warnitchai, 2012, Maniatakis et al., 2013, Najam & Warnitchai, 2017). Therefore, using a single R factor to reduce elastic shear force of all modes in the RSA procedure, is the primary source of underestimation of shear force contributed from higher modes. As demonstrated in recent studies, shear force computed from nonlinear response history analysis (NLRHA) is significantly larger than the design shear force computed from RSA (Khy & Chintanapakdee, 2017, Najam & Warnitchai, 2017).

To estimate this large shear force in inelastic RC walls, previous studies have proposed the higher-mode elastic RSA (HME-RSA) method, which combines inelastic first mode with elastic higher modes to compute the design shear force in the walls (Priestley, 2003, Chopra et al., 2004, Calugaru & Panagiotou, 2012). The inelastic first-mode shear can be computed by direct displacement method (Priestley, 2003), by modal pushover analysis (Chopra et al., 2004), or by reducing elastic first mode with the first-mode force response reduction factor (Calugaru & Panagiotou, 2012). However, most of them focused on RC cantilever walls designed to yield at the base region. For a real building, inelasticity may occur in RC beams or coupling beams throughout the height of the building and the higher modes may not behave elastically for tall buildings. The accuracy of the RSA and HME-RSA methods is evaluated in this paper by using four tall RC shear wall buildings

with 15, 20, 31, and 39 stories. Then a higher mode inelastic RSA (HMI-RSA) method is proposed, which uses different force reduction factors to reduce the elastic force contributed from each mode and combines the reduced modal force with modal combination rule, e.g. SRSS, to compute the seismic design shear force in tall RC shear wall buildings. The accuracy of the RSA, HME-RSA and HMI-RSA methods is evaluated by comparing the computed demands to the benchmark results computed from NLRHA.

2 CASE STUDY BUILDINGS

Four existing tall RC shear wall buildings located in Bangkok, Thailand, were employed. These 15-, 20-, 31-, and 39-story buildings are denoted by BL1, BL2, BL3, and BL4, respectively. BL2, BL3, and BL4 have a podium at the first few stories and one tower continues up to the top floor, which is typical for tall buildings in Bangkok. The primary lateral force resisting system consists of RC core walls and shear walls. The gravity load carrying system is RC columns with post-tensioned flat slabs. The typical floor plans and three dimensional models of the selected buildings are shown in Figure 1. The basic characteristics of the buildings are summarized in Table 1.

Because the design demands of these existing buildings are not known, the reinforcement of structural members of these existing buildings were re-designed with flexural demands computed by RSA, in order to evaluate the accuracy of the RSA and HME-RSA procedures.

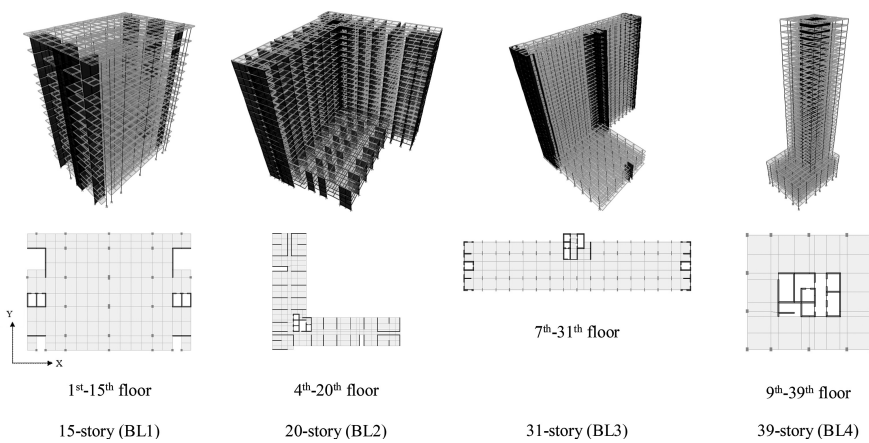

Figure 1. Plans and three dimensional models of the shear wall buildings.

Table 1. Basic characteristics of the shear wall buildings.

Building			BL1	BL2	BL3	BL4
No. of stories			15	20	31	39
Total height (m)			55.40	54.50	89.95	125.55
Podium height (m)			NA	10.05	15.3	26.50
Typical story height (m)			3.2	2.75	2.85	3.2
RC wall section area/floor area			0.012	0.022	0.012	0.015
RC column section area/floor area			0.012	NA	0.013	0.013
Maximum wall thickness (m)			0.25	0.20	0.30	0.35
Maximum column size (m × m)			1.2 × 0.6	NA	1.8 × 0.5	1.8 × 0.8
Natural periods of the first-three translational modes (sec)	X direction	T_1	2.76	1.38	4.29	4.63
		T_2	0.53	0.32	1.12	1.06
		T_3	0.21	0.14	0.51	0.48
	Y direction	T_1	2.24	1.58	2.86	4.84
		T_2	0.44	0.36	0.71	0.96
		T_3	0.18	0.16	0.35	0.37

3 EARTHQUAKE GROUND MOTIONS

The maximum considered earthquake (MCE) ground motions were employed. The Conditional Mean Spectrum (CMS) ground motions were obtained for six periods of interest: 0.2, 0.5, 1, 1.5, 2, and 3 sec. Since Bangkok is located on soft soil layers, three pairs of ground motions were selected and scaled to the target spectrum on rock site, and then they were simulated to propagate through soft soil layers underlying downtown Bangkok by using SHAKE2000 (Ordonez, 2012) for each of the six periods of interest. The six sets of output ground motions are considered as CMS soft soil ground motions. Detailed information of these ground motions and soil properties can be found in Poovarodom et al. (2017). The average spectrum of six records in each set of period of interest represents the Uniform Hazard Spectrum (UHS) spectral ordinate at that period of interest, as CMS usually matches UHS at the period of interest. The UHS and CMS for 2.5% damping ratio soft soil ground motions are shown in Figure 2.

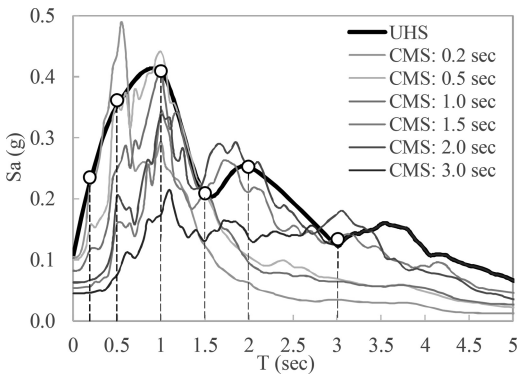

Figure 2. Uniform Hazard Spectrum (UHS) and Conditional Mean Spectrum (CMS) conditioned at 0.2, 0.5, 1.0, 1.5, 2.0 and 3.0 sec for 2.5% damping ratio soft-soil ground motions.

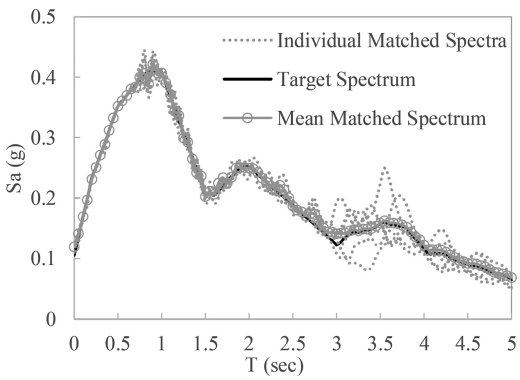

Figure 3. Individual matched spectra and target spectrum for 2.5% damping ratio soft-soil ground motions.

In the analysis, the RSA, HME-RSA, and HMI-RSA procedures used the UHS, while the NLRHA used the CMS ground motions. To ensure that the analysis results for different methods are compatible for comparison, the CMS ground motions in the set for period of interest of 3 sec were modified by using SeismoMatch (SeismoSoft, 2016) to have a spectral shape fitted to the UHS. The individual matched spectra, and the mean matched spectrum to the UHS for 2.5% damping ratio are shown in Figure 3.

4 METHODOLOGY

The procedure adopted in this study is outlined as follows:

- Analyze the structures by the conventional RSA in ASCE 7-10 using ETABS (CSI 2015).
- Design the structural systems according to ACI 318M-14 such that the design strength is approximately equal to the factored demands computed from RSA.
- Analyze the structures by NLRHA using PERFORM-3D (CSI 2011) to evaluate the accuracy of the conventional RSA.
- Compute the force response reduction factor of each mode, which is determined by using modal pushover analysis (MPA).
- Compute force demands from the higher mode elastic RSA (HME-RSA) and the higher mode inelastic RSA (HMI-RSA) methods.
- Evaluate the accuracy of the conventional RSA, HME-RSA, and HMI-RSA by comparing the computed demands to the benchmark results computed from NLRHA.

5 ANALYSIS METHODS

5.1 *Response Spectrum Analysis (RSA)*

The RSA procedure in ASCE 7–10 is adopted in this study. A linear elastic structural model considering the cracked cross section of structural members was constructed using ETABS (CSI 2015) for the RSA. In the RSA procedure, the elastic responses computed from many modes are combined to get the total elastic responses, which are then divided by the response modification factor (R) to compute the design forces. The analysis shall include a sufficient number of modes to obtain a combined modal mass participation of at least 90 percent of the total mass in the direction of response considered. According to ASCE 7–10, it is required that modal base shear (V_t) determined

from the RSA procedure is at least equal to 85% of the static base shear (V_s) computed from the equivalent lateral force (ELF) procedure. For story drifts, ASCE 7-10 employs the deflection amplification factor (C_d) to scale up the story drifts computed from the RSA after reducing by R factor. The UHS as shown in Figure 2 was used in the RSA. The design bending moment, design shear force and design displacement demands in the RSA procedure are computed from

$$M = \frac{SF \cdot I}{R}\sqrt{M_{1e}{}^2 + M_{2e}{}^2 + M_{3e}{}^2 + \cdots} \quad (1)$$

$$V = \frac{SF \cdot I}{R}\sqrt{V_{1e}{}^2 + V_{2e}{}^2 + V_{3e}{}^2 + \cdots} \quad (2)$$

$$\Delta = \frac{C_d}{R}\sqrt{\Delta_{1e}{}^2 + \Delta_{2e}{}^2 + \Delta_{3e}{}^2 + \cdots} \quad (3)$$

where M_{ie}, V_{ie}, and Δ_{ie} are the elastic bending moment, shear force, and story drift contributed from mode i, respectively, I is the importance factor, and SF is the scaling factor required to make the modal base shear (V_t) at least equal to 85% of the static base shear (V_s). SF is computed by $0.85V_s/V_t$ and is not less than one.

5.2 *Higher Mode Elastic RSA (HME-RSA)*

To compute shear force in inelastic RC walls, previous studies have proposed to use a higher mode elastic RSA (HME-RSA) method which assumes that the higher mode responses behaved elastically and the inelasticity affected only the first-mode response. The method combines inelastic first-mode force response with elastic higher mode force responses by using the SRSS combination rule. The inelastic first-mode force in the present study is computed by reducing the elastic first-mode force response with the force response reduction factor of the first mode R_1, which is determined by pushover analysis as described in Section 8. In the HME-RSA method, shear force in the structures is computed by Eq. (4). Bending moment and story drift can be computed by the conventional RSA.

$$V = \sqrt{\left(\frac{V_{1e}}{R_1}\right)^2 + V_{2e}{}^2 + V_{3e}{}^2 + \cdots} \quad (4)$$

5.3 *Nonlinear Response History Analysis (NLRHA)*

The NLRHA was carried out by using PERFORM-3D (CSI 2011). The UHS spectrally matched ground motions were used (see Fig. 3). A modal damping ratio of 2.5% was assigned to every significant vibration mode for the NLRHA. The ground motions were applied in each direction separately for all the analyses considered. By these considerations, the ground motion intensity and damping ratio among analysis methods are equivalent for the purpose of comparison.

6 NONLINEAR STRUCTURAL MODEL

Nonlinear structural models were created in PERFORM-3D. The RC walls were modeled using inelastic fiber shear wall elements. Nonlinear fiber modeling was used over the entire height since flexural yielding may occur at any location due to higher-mode effects. The material stress-strain relationship for concrete proposed by Mander et al. (1988) was adopted and for steel, a bilinear inelastic model was used. The expected material strength was used to account for the fact that actual material strengths are generally greater than nominal strengths specified by designers. The RC columns were modeled by linear elastic elements with nonlinear plastic hinge zone at both ends. The plastic zones were modeled by inelastic fiber elements in a manner similar to that used for RC wall. The RC beams included a middle elastic portion and rotational plastic hinge elements at both ends. Plastic hinge properties were defined by a tri-linear moment-hinge rotation relationship. Joints between members were considered to be rigid connections. The slabs were assumed to be elastic and modeled by elastic shell elements. The rigid floor diaphragm constraint was assigned to each floor level.

7 COMPARISON OF DESIGN DEMANDS BY RSA AND NLRHA

For NLRHA, the results presented are the mean values of peak responses to the ground motions used in the NLRHA. Here, shear force is normalized by the weight of the building, V/W; bending moment is normalized by the product of the weight and the height of the building, $M/(WH)$; story displacement is normalized by the building height, δ/H; and story drift is normalized by the story height, Δ/L.

As shown in Figure 4, story displacement and story drift ratio computed from RSA are similar to that computed from NLRHA, but Figure 5 shows that the force demands computed from RSA are significantly lower than the demands computed from NLRHA throughout the entire height of the building. However, for slender walls to achieve ductile flexural yielding at the wall base, the maximum bending moment computed

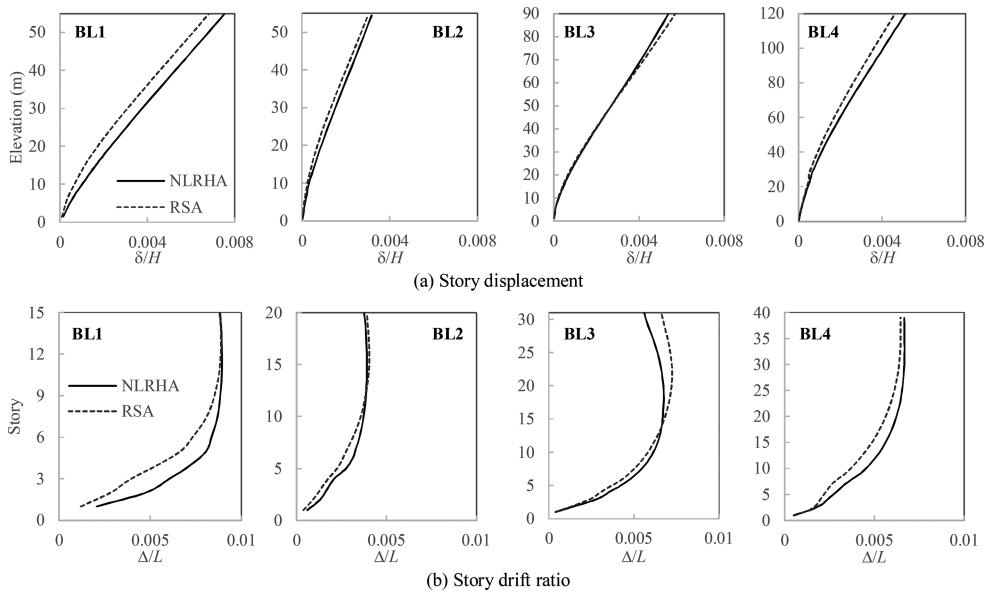

Figure 4. (a) Story displacement; and (b) story drift ratio computed from RSA and NLRHA for X direction seismic excitation.

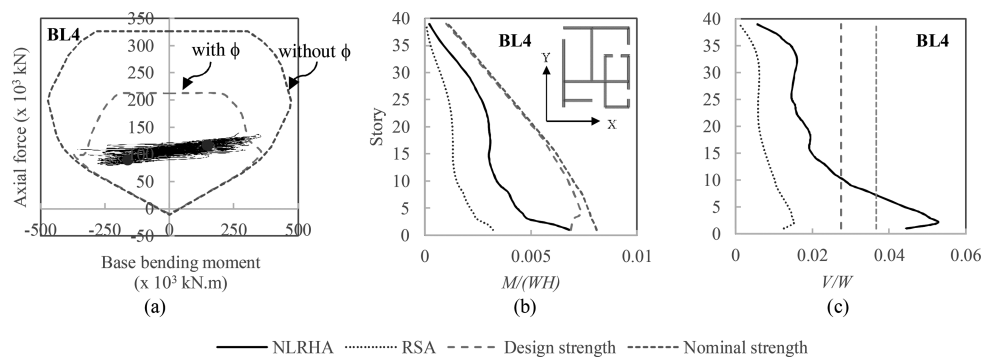

Figure 5. Provided strengths and force demands computed from RSA and NLRHA of core wall in 39-story building (BL4) for X direction seismic excitation.

from NLRHA cannot be larger than the provided flexural strength, which is larger than the design bending moment computed from RSA due to flexural over-strength. As shown in Figure 5(a), axial force and bending moment of the wall computed from NLRHA are located inside the design P-M interaction surface. Due to the minimum reinforcement of the RC wall required by ACI 318M-14, the flexural over-strength is about two at the base of the wall, and bending moment computed from NLRHA is two times larger than the bending moment computed from RSA. The provided flexural strength according to the minimum reinforcement ratio was larger than the bending moment computed from NLRHA along the height of the wall as shown in Figure 5(b). Unlike bending moment, shear response can lead to brittle failure thus should be practically designed to be elastic. The design shear strengths obtained from the shear demands computed from RSA were considerably smaller than the actual shear demands computed from NLRHA for the core wall at the first few stories as seen in Figure 5(c), which can cause shear failure in structural walls. The underestimation in computing the shear forces in the walls using RSA is the main problem that this study attempts to improve to avoid shear failure in structural walls.

8 INELASTICITY OF EACH MODE

To investigate the inelasticity of each mode, modal pushover analysis was conducted using both linear elastic and nonlinear inelastic structural models. The stiffness of the linear elastic structural model was equal to the initial stiffness of the nonlinear inelastic structural model. The target roof displacement of the first mode was computed using the displacement coefficient method in ASCE 41-13, while the target roof displacements of the higher modes were taken equal to elastic demands computed by linear modal analysis of the structural model considering cracked cross section of structural members. The first-three translational modes were considered in this study. The force response reduction factor was defined as the ratio between the elastic base shear and the inelastic base shear computed from modal pushover analysis at the specified target roof displacement.

The base shear-roof drift relationship computed from linear and nonlinear pushover analysis along with the specified target roof drift is shown in Figure 6. The base shear is normalized by the building weight, V_b/W. The force response reduction factor of each mode is summarized in Table 2. It was found that the inelasticity of each mode was different. The force response reduction factor decreased with increasing mode order. The force response reduction factor of the first mode was about two for most of the cases, which is lower than the response modification factor ($R = 5$) used in the design of these buildings because of the scaling factor required by ASCE 7–10 and the flexural over-strength inherent in the design process. For the 15- and 20-story buildings, higher modes behaved elastically as the force response reduction factors of the 2nd and 3rd modes were equal to one. For the 31- and 39-story buildings, the force response reduction factors of higher modes were larger than one indicating that higher modes did not act elastically. Therefore, using elastic higher modes is appropriate for 15- and 20-story buildings and is overly conservative for 31- and 39-story buildings.

Table 2. Force response reduction factors of the first-three translational modes in the X direction.

Building	1st mode	2nd mode	3rd mode
15-story (BL1)	2.09	1.00	1.00
20-story (BL2)	1.59	1.00	1.00
31-story (BL3)	1.98	1.49	1.00
39-story (BL4)	2.00	1.79	1.21

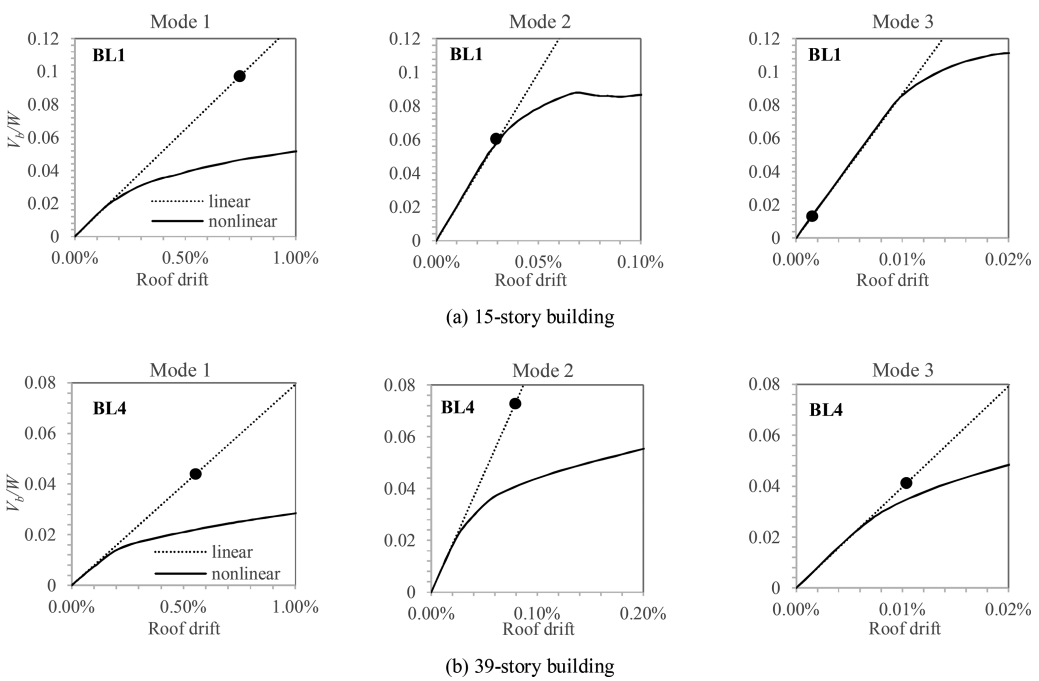

(a) 15-story building

(b) 39-story building

Figure 6. Pushover curves along with the specified roof drift of the first-three translational modes in the X direction: (a) 15-story building (BL1); and (b) 39-story building (BL4).

9 HIGHER MODE INELASTIC RSA (HMI-RSA)

As discussed in Section 7, the underestimation of the RSA procedure in computing shear force in structural walls is the main focus of the present study. An improved higher mode inelastic RSA (HMI-RSA) method is proposed to compute the design shear force in tall RC shear wall buildings. As investigated in the preceding section, the level of inelasticity of each mode is different and higher modes of tall buildings do not remain in the elastic range as assumed by the HME-RSA method, HMI-RSA method is developed by modification from the HME-RSA method such that inelasticity of higher modes is considered by reducing elastic forces contributed from each mode by different force response reduction factors. The HME-RSA method combines the reduced modal forces using the SRSS combination rule. The force response reduction factor of each mode is determined as described in the preceding section. The first-three translation modes of the building in the direction considered are reduced by different force response reduction factors, and modes higher than the third mode are assumed to be elastic. In the HMI-RSA method, shear force of the structure is computed by

$$V = \sqrt{\left(\frac{V_{1e}}{R_1}\right)^2 + \left(\frac{V_{2e}}{R_2}\right)^2 + \left(\frac{V_{3e}}{R_3}\right)^2 + V_{4e}^2 + \cdots} \tag{5}$$

where R_i is the force response reduction of mode i.

10 EVALUATION OF RSA, HME-RSA AND HMI-RSA METHODS

The accuracy of the RSA, HME-RSA and HMI-RSA methods is evaluated by comparing the computed demands to the benchmark results computed from NLRHA. The story shear force and shear force in local members are normalized by the weight of the building and the bending moment in local members is normalized by the product of the weight and the height of the building.

The normalized story shear is shown in Figure 7. It is seen that RSA underestimates the story shear force computed from NLRHA throughout the height of the building. The underestimation of the RSA procedure is mainly due to the use of a single R factor to reduce elastic forces contributed from all the modes. The HME-RSA method could predict story shear force for the 15- and 20-story buildings, but it provided conservative results for the 31- and 39-story buildings comparing to the

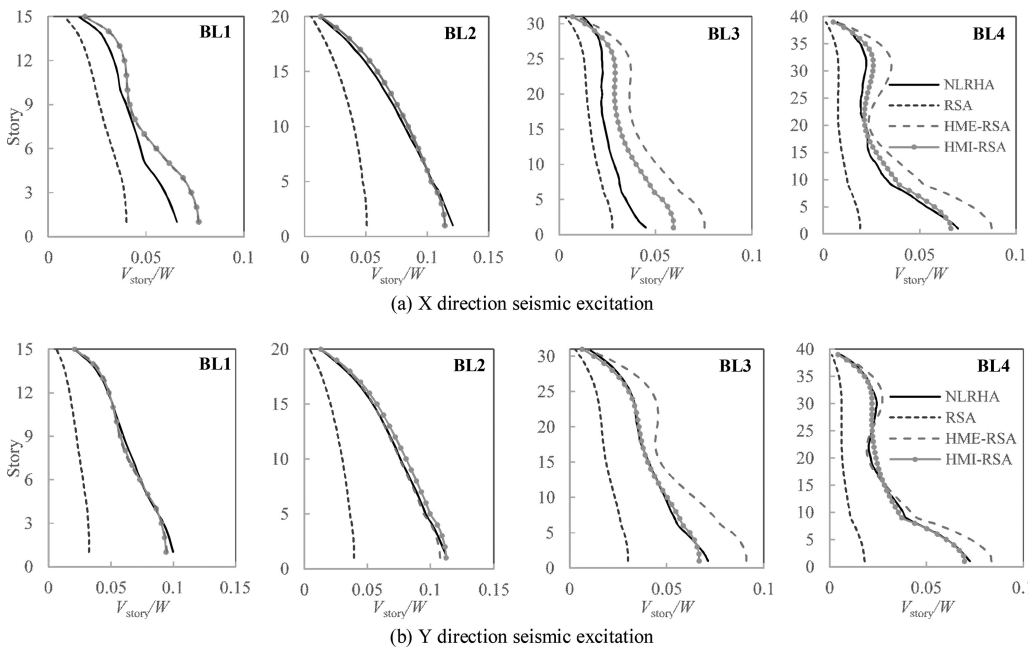

Figure 7. Comparison of story shear force computed by RSA, HME-RSA, HMI-RSA, and NLRHA: (a) X direction; and (b) Y direction seismic excitation.

NLRHA because higher modes did not behave elastically for these two buildings as noted in Section 8. Including inelasticity of higher modes as considered in the HMI-RSA method could significantly improve the accuracy of the HME-RSA method; as the HMI-RSA method provides good accuracy in computing story shear force for all the case study buildings. The accuracy of the HME-RSA and HMI-RSA methods is the same for the 15- and 20-story buildings because their higher mode responses are in elastic range as found in Section 8.

The HMI-RSA method can also compute shear force in the local components with reasonable accuracy. As shown in Figure 8, the shear forces in RC shear wall and core wall computed from HMI-RSA are similar to those computed from NLRHA for all the case study buildings. However, the accuracy of the HMI-RSA method for local component-force demands is not as good as for the story-force demands. This is because the force distribution from story demands to structural members in that story is different between the HMI-RSA and NLRHA methods. For HMI-RSA, the force distribution is based on initial elastic stiffness of structural members, while NLRHA accounts for more accurate distribution of nonlinear seismic demands.

Despite the use of the SRSS modal combination rule in computing force demands, the HMI-RSA could well predict story shear force and shear force in local members. However, the accuracy of the HMI-RSA method in computing bending moment is not as good as in computing shear force because when flexural yielding occurs in the wall, the bending moment computed by using the SRSS combination rule can be larger than the provided flexural strength and bending moment computed from NLRHA, which is limited by the provided capacity as shown in Figure 5a. As shown in Figure 9, HMI-RSA provides larger bending moment than NLRHA for the core wall in 31- and 39-story buildings. However, bending moment computed by NLRHA or by HMI-RSA should not be used in design because the bending moment computed from these methods already includes flexural over-strength in the design. Bending moment can be computed by conventional RSA as shear wall is usually designed to yield and experience ductile failure. For shear force which is brittle failure, RSA procedure provides inadequate shear demands for design. The HMI-RSA method is suggested to compute shear force for design.

The shortcoming of using HMI-RSA is that it requires modal pushover analysis to compute the force response reduction factor of each

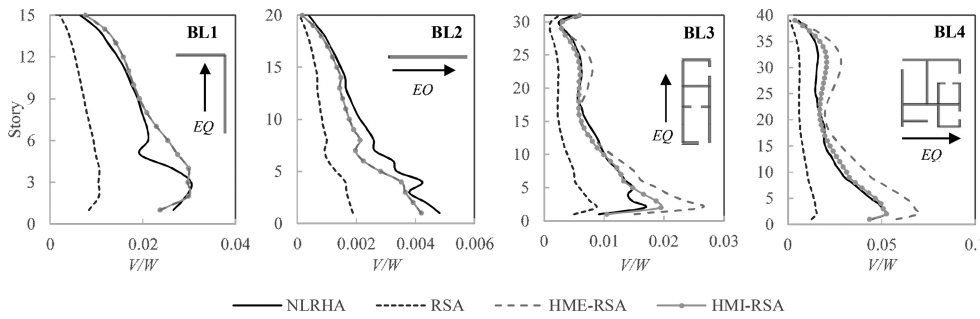

Figure 8. Shear force in RC walls computed by RSA, HME-RSA, HMI-RSA, and NLRHA.

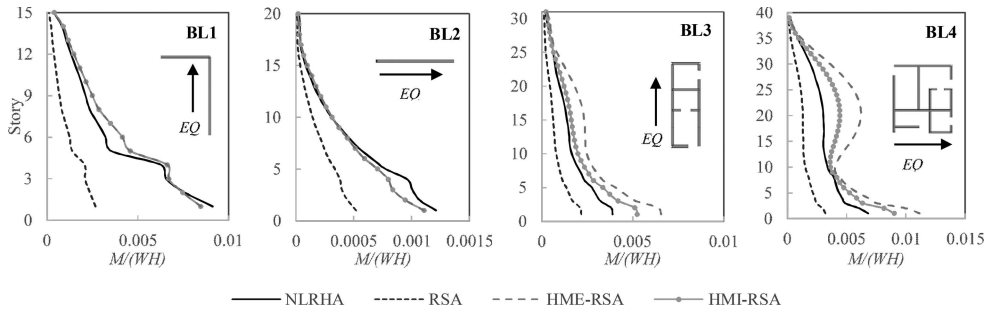

Figure 9. Bending moment in RC walls computed by RSA, HME-RSA, HMI-RSA, and NLRHA.

mode. Once the force response reduction factors are determined and because most commercial software provide an option for user-defined scaling factors for each vibration mode response, the HMI-RSA method can be used in available commercial software similar to the RSA procedure.

11 CONCLUSIONS

Four tall RC shear wall buildings were used to evaluate the accuracy of the conventional RSA and HME-RSA methods. An improved RSA procedure referred to as the higher mode inelastic RSA (HMI-RSA) method was proposed in this study to compute design shear force of RC walls in tall building. The core findings of this study are summarized as follows:

- The RSA procedure can be used to compute story displacement and story drift ratio for design as it can provide good estimates of inelastic story displacement and story drift ratio computed from NLRHA. As structural walls is normally design to experience ductile flexural yielding, bending moment computed by RSA procedure can be used for design, but it should not be used to compute shear force for design because it significantly underestimates shear force obtained from NLRHA, which is mainly due to the use of a single response modification factor to reduce elastic forces contributed from all the modes.
- The HME-RSA method can be used for short buildings, but it should not be used for tall buildings because higher modes in tall buildings do not behave elastically. As found in this study, HME-RSA could well predict shear force in 15- and 20-story buildings, but it provided conservative results for 31- and 39-story buildings comparing to NLRHA.
- The HMI-RSA method is recommended to compute design shear force in tall RC shear wall buildings as it can provide good accuracy comparing with NLRHA in computing story shear force and shear force in RC shear walls and core walls for all the case study buildings.

ACKNOWLEDGEMENTS

The authors gratefully acknowledge the financial support of Thailand Research Fund (TRF), JICA through the ASEAN University Net-work/ Southeast Asia Engineering Education Development Network (AUN/SEED-Net) program, and Chulalongkorn University through the Center of Excellence in Earthquake Engineering and Vibration. The helpful suggestions for this study provided by Prof. Pennung Warnitchai at Asian Institute of Technology are highly appreciated.

REFERENCES

ACI (American Concrete Institute) 2014. *Building code requirements for structural concrete (ACI 318M-14) and commentary (ACI 318RM-14)*. Farmington Hills, USA.

ASCE (American Society of Civil Engineers) 2010. *Minimum design loads for buildings and other structures.* ASCE/SEI 7-10. Reston, Virginia.

ASCE (American Society of Civil Engineers) 2013. *Seismic Evaluation and Retrofit of Existing Buildings.* ASCE/SEI 41-13. Reston, Virginia.

Calugaru, V. & Panagiotou, M. 2012. Response of tall cantilever wall buildings to strong pulse type seismic excitation. *Earthquake Engineering and Structural Dynamics* 41(9): 1301–1318.

Chopra, A.K., Goel, R.K. & Chintanapakdee, C. 2004. Evaluation of a modified MPA procedure assuming higher modes as elastic to estimate seismic demands. *Earthquake Spectra* 20(3): 757–778.

Computers and Structures, Inc. 2011. *PERFORM-3D, Nonlinear analysis and performance assessment of 3D structures, Version 5.0.1*. Berkeley, California.

Computers and Structures, Inc. 2015. *ETABS, Integrated building design software, Version 15.2.2*. Berkeley, California.

Eibl, J. & Keintzel, E. 1988. Seismic shear forces in RC cantilever shear walls. *9th World Conference on Earthquake Engineering*, *1988*, Tokyo-Kyoto, Japan.

Ghorbanirenani, I., Tremblay, R., Léger, P. & Leclerc, M. 2011. Shake table testing of slender RC shear walls subjected to eastern North America seismic ground motions. *Journal of Structural Engineering* 138(12): 1515–1529.

Khy, K. & Chintanapakdee, C. 2017. Evaluation of Seismic Shear Demands of RC Core Walls in Thailand Determined by RSA Procedure. *Engineering Journal* 21(2): 151–172.

Mander, J.B., Priestley, M.J. & Park, R. 1988. Theoretical stress-strain model for confined concrete. *Journal of Structural Engineering* 114(8): 1804–1826.

Maniatakis, C.A., Psycharis, I.N. & Spyrakos, C.C. 2013. Effect of higher modes on the seismic response and design of moment-resisting RC frame structures. *Engineering Structures* 56: 417–430.

Munir, A. & Warnitchai, P. 2012. The cause of unproportionately large higher mode contributions in the inelastic seismic responses of high-rise core-wall buildings. *Earthquake Engineering and Structural Dynamics* 41(15): 2195–2214.

Najam, F.A. & Warnitchai, P. 2017. A modified response spectrum analysis procedure to determine nonlinear seismic demands of high-rise buildings with shear walls. *The Structural Design of Tall and Special Buildings*.

Ordonez, G.A. 2012. SHAKE2000-*A computer program for the 1-D analysis of geotechnical earthquake engineering problems*. GeoMotion, LLC; Lacey, Washington, USA.

Panagiotou, M., Restrepo, J.I. & Conte, J.P. 2011. Shake-table test of a full-scale 7-story building slice. Phase I: Rectangular wall. *Journal of Structural Engineering* 137(6): 691–704.

Poovarodom, N., Jirasakjamroonsri, A. & Warnitchai, P. 2017. Development of new design spectral accelerations for Bangkok considering deep basin effects. *16th World Conference on Earthquake Engineering*, *2017*, Santiago Chile.

Priestley, M.J.N. 2003. Does capacity design do the job? An examination of higher mode effects in cantilever walls. *Bulletin of the New Zealand Society for Earthquake Engineering* 36(4): 276–292.

SeismoSoft 2016. *SeismoMatch, A computer application capable of adjusting earthquake accelerograms to match a specific target response spectrum, Version 2016*. http://www.seismosoft.com.

Computational Modelling of Concrete Structures – Meschke, Pichler & Rots (Eds)
© 2018 Taylor & Francis Group, London, ISBN 978-1-138-74117-1

Introduction of shear warping in fibre beam elements for the computation of the nonlinear behaviour of concrete beams

S. Capdevielle
LMT, ENS Cachan, CNRS, Université Paris-Saclay, Cachan, France

S. Grange
INSA-Lyon, University Lyon, GEOMAS, Lyon, France

F. Dufour
CNRS, Grenoble INP, University Grenoble Alpes, Grenoble, France

C. Desprez
MAST, SDOA, IFSTTAR, Université Paris-Est, Marne-la-Vallée, France

ABSTRACT: The present paper deals with modelling the nonlinear behaviour of concrete using the fibre element method. Proved to be efficient for slender structural elements mainly subject to normal stresses, the method lacks in accuracy when modelling the effect of shear. The present contribution proposes to enhanced a Timoshenko fibre beam element by adding shear warping deformations in the formulation. Transverse shear as well as torsion warping is taken into account, enabling the computation of the response to a complex loading. Warping degrees of freedom are computed simultaneously with the beam degrees of freedom by a fully implicit solution procedure. Concrete is modelled using a 3D damage model. Due to the coupling of warping and global beam degrees of freedom, the warping displacements in the beam element can evolve with the evolution of concrete damage. The beam element enhancement is validated at the cross-section scale considering a linear elastic behaviour. Enhanced beam elements are then used to model experimentally-tested structural elements. Both the linear and non-linear parts of the structural response are investigated.

1 INTRODUCTION

Modelling a structure using fibre beam elements is proved to be an efficient approach (Grange et al. 2008, Kotronis and Mazars 2005, Kotronis and Grange 2010). The method enables the modeller to carry out computations at the structural scale, taking into account the nonlinear behaviour of concrete, at a relatively low computational cost. Based on beam elements, the fibre beam element approach avoids the use of a generalized constitutive law by adding the cross-section scale. From the generalized strains, strains in the cross section are computed according to a kinematics assumption. Stresses are obtained from the strains at each integration point of the cross section by a chosen constitutive law. By integrating the stresses over the cross-section, generalized forces are eventually computed (Spacone and El-Tawil 2004). The results are convincing for structural elements subject to normal stresses. However, the computed behaviour lacks in accuracy in the case of large shear stresses. Indeed, the plane cross-section assumption used to compute the strains is not precise enough to convey the effect of shear.

Several authors have proposed to address this problem by introducing warping in the kinematics of fibre beam elements (Mazars et al. 2006, Bairan and Mari 2007, Le Corvec and Filippou 2011, Capdevielle et al. 2016). Based on these approaches, an improved fibre beam element is developed in the present paper. Warping degrees of freedom, accounting for both torsion and shear warping are introduced in the formulation. The warping degrees of freedom are computed along with the global beam degrees of freedom by satisfying the structure equilibrium through an implicit solution procedure. The concrete behaviour is represented by the Mu model (Mazars et al. 2014). Through the nonlinear solution procedure, warping evolution is fully coupled with the damage evolution inthe cross section.

After a summary of the main equations of the enhanced element formulation, the numerical behaviour of the beam element is investigated at the cross-section scale. The behaviour of a cantilever

beam subject to a vertical end-load is computed using a linear elastic material behaviour. The warping strains in the beam are compared to the analytical solution. To investigate the effect of warping coupled with the material nonlinearities, the response of a reinforced concrete structure subject to a dynamic load is eventually simulated.

2 FORMULATION OF THE ENHANCED ELEMENT

A 3D displacement-based Timoshenko fibre beam element is enhanced by the addition of warping degrees of freedom. This part presents the main equations of the enhancement. The modified kinematics is described first, followed by the variation-alformulation of the equilibrium equations. Some specificities of the shape functions required by the enhancement are eventually presented.

2.1 *Enhancement of the kinematics*

The vector $\mathbf{u}$ of displacements in the beam is additively decomposed into a plane displacement part $\mathbf{u}^p$ and a part coming from the cross-section warping $\mathbf{u}^w$. The two parts are assumed to be orthogonal (Bairan and Mari 2006), which means that warping displacements are free from any rigid body motion of the cross-section. $\mathbf{u}^p$ contains the classical displacements in Timoshenko's cross section. Warping displacements are assumed to occur only in the longitudinal x direction. u, v and w represent the mean translations of the cross section, respectively in the x, y and z directions. θ_x, θ_x and θ_x are the mean rotations.

$$\mathbf{u} = \mathbf{u}^p + \mathbf{u}^w + = \begin{bmatrix} u - y\theta_z + z\theta_y \\ v - z\theta_x \\ w + y\theta_x \end{bmatrix} + \begin{bmatrix} u_x^w(x,y,z) \\ 0 \\ 0 \end{bmatrix} \tag{1}$$

From the displacements described in equation 1, the linearized strain tensor $\boldsymbol{\varepsilon}$ can be computed as follows:

$$\boldsymbol{\varepsilon} = \frac{1}{2}\left(\mathbf{grad}(\mathbf{u}) + \mathbf{grad}(\mathbf{u})^T\right) = \boldsymbol{\varepsilon}^p + \boldsymbol{\varepsilon}^w \tag{2}$$

The strain vector ϵ used in the beam formulation is thus computed as described in equation 3.

$$\boldsymbol{\epsilon} = \begin{bmatrix} \epsilon_{xx} \\ 2\epsilon_{xy} \\ 2\epsilon_{xz} \end{bmatrix} = \underbrace{\begin{bmatrix} \frac{du}{dx} - y\frac{d\theta_z}{dx} + z\frac{d\theta_y}{dx} \\ -z\frac{d\theta_x}{d} + \frac{dv}{d} - \theta_z \\ y\frac{d\theta_x}{dx} + \frac{dw}{dx} + \theta_y \end{bmatrix}}_{\epsilon^p} + \underbrace{\begin{bmatrix} \frac{\partial u_x^w}{\partial x} \\ \frac{\partial u_x^w}{\partial y} \\ \frac{\partial u_x^w}{\partial z} \end{bmatrix}}_{\epsilon^w} \tag{3}$$

2.2 *Variational form of the equilibrium equation*

Assuming that there is no body force, the variational form of the beam equilibrium equation is given in equation 4. $\boldsymbol{\sigma}$ denotes Cauchy's stress tensor and $\boldsymbol{\delta}\mathbf{u}$ the virtual displacements. Ω represents the beam integration domain.

$$\int_\Omega \boldsymbol{\delta}\mathbf{u}^T \mathrm{div}(\sigma) d\Omega = 0 \tag{4}$$

The virtual displacements are assumed to be decomposed in a plane-section part and a warping part, like the real displacement field.

$$\int_\Omega \left(\boldsymbol{\delta}\mathbf{u}^{pT} + \boldsymbol{\delta}\mathbf{u}^{wT}\right) \mathrm{div}\left(\sigma\right) d\Omega = 0 \tag{5}$$

Taking into account the orthogonality of the plane-section displacement field and the warping displacement field, equation 5 is projected on the corresponding subspaces. This leads to two sets of equations (6). By integrating by part each integral in equation 6, we get the final weak form of the equilibrium equations (7).

$$\begin{cases} \int_\Omega \boldsymbol{\delta}\mathbf{u}^{pT} \mathrm{div}\left(\sigma\right) d\Omega = 0 \\ \int_\Omega \boldsymbol{\delta}\mathbf{u}^{wT} \mathrm{div}\left(\sigma\right) d\Omega = 0 \end{cases} \tag{6}$$

$$\begin{cases} \int_\Omega \boldsymbol{\delta}\epsilon^{pT} \sigma \, d\Omega = \int_{\partial\Omega} \boldsymbol{\delta}\mathbf{u}^{pT} (\sigma\mathbf{n}) dS \\ \int_\Omega \boldsymbol{\delta}\epsilon^{wT} \sigma \, d\Omega = \int_{\partial\Omega} \boldsymbol{\delta}\mathbf{u}_x^{wT} (\sigma_{xx} n_x) dS \end{cases} \tag{7}$$

2.3 *Beam finite element formulation*

A Timoshenko beam element with linear longitudinal shape functions is enhanced. In the transverse directions, the cross-section is discretized using linear triangles.

To enforce the orthogonality of plane section and warping displacements, rigid-body motions of the cross section need to be removed from the shape functions used to interpolate warping displacements. The transverse shape functions N_i are thus projected on the subspace orthogonal to the plane displacement field (Le Corvec 2012). The resulting shape functions $\tilde{N}_i$, given in equation 8 are used for warping displacements. The derivatives of the projected shape functions (equation 10) also need to be computed for the beam element formulation (Capdevielle et al. 2017).

$$\tilde{N}_i = N_i - \int_{\mathcal{S}} N_i \begin{bmatrix} \frac{1}{a_1} & \frac{y}{a_2} & \frac{z}{a_3} \end{bmatrix} d\mathcal{S} \begin{bmatrix} 1 \\ y \\ z \end{bmatrix} \tag{8}$$

where $\mathcal{S}$ represents the cross-section integration domain, and a_1, a_2 and a_3 are computed as follows:

$$
\begin{aligned}
a_1 &= \int_{\mathcal{S}} 1 \, d\mathcal{S} \\
a_2 &= \int_{\mathcal{S}} y^2 d\mathcal{S} \\
a_3 &= \int_{\mathcal{S}} z^2 d\mathcal{S}
\end{aligned}
\tag{9}
$$

$$
\begin{cases}
\dfrac{\partial \tilde{N}_i}{\partial y} = \dfrac{\partial N_i}{\partial y} - \int_{\mathcal{S}} N_i \dfrac{y}{a_2} d\mathcal{S} \\
\dfrac{\partial \tilde{N}_i}{\partial z} = \dfrac{\partial N_i}{\partial z} - \int_{\mathcal{S}} N_i \dfrac{z}{a_3} d\mathcal{S}
\end{cases}
\tag{10}
$$

In the longitudinal direction, the warping degrees of freedom of each cross section are interpolated to the nodes of the beam element using the beam shape functions.

2.4 *Solution procedure*

Let the matrices B_p and B_w contain the derivatives of the longitudinal shape functions, and the matrices $\mathbf{a}_s$ and $\mathbf{a}_w$ the transverse shape functions and there derivatives. After discretisation of the variational form of the equilibrium equations (7), we obtain the following non-linear system of equations to solve:

$$
\underbrace{\mathop{\mathbf{A}}_{e=1}^{n_{el}} \begin{bmatrix} \int_{\Omega^e} {B_p^T}{\mathbf{a}_s}^T \hat{\sigma}(\epsilon^p, \epsilon^w) d\Omega^e \\ \int_{\Omega^e} B_w^T {\mathbf{a}_w}^T \hat{\sigma}(\epsilon^p, \epsilon^w) d\Omega^e \end{bmatrix}}_{\mathbf{P}_{\text{el}}} = \begin{bmatrix} \boldsymbol{F}_{\text{ext}} \\ \boldsymbol{F}^w \end{bmatrix}
\tag{11}
$$

In equation 11, $\boldsymbol{F}_{\text{ext}}$ represents the external forces. $\boldsymbol{F}^{\text{w}}$ are the forces due to restrained warping boundary conditions. The longitudinal interpolation of warping degrees of freedom enables to take into account a variation of warping due to the boundary conditions in the longitudinal direction. The warping nodal degrees of freedom are added to the global beam degrees of freedom in the final system of equations.

The nonlinear system of equations (11) is solved using a fully nonlinear solution procedure based on Newmark's method. The enhanced element is implemented in the finite element code ATL4S (Grange 2015). This code is used to compute the numerical examples presented in the next paragraphs.

3 WARPING PROFILE AT THE CROSS-SECTION SCALE

The enhanced fibre beam element built in the previous part is tested here under transverse shear. The case study is presented in Figure 1. A cantilever beam of 1 m length is subject to a vertical load of 1 N applied at its free end. The cross-section is rectangular with dimensions 0.1 m × 0.2 m. The beam is discretized in 10 enhanced fibre elements. This relatively high number of beam elements is chosen to reduce the error linked to the longitudinal interpolation with linear shape functions. Two cross-section meshes are used, displayed in Figure 2. A linear elastic material is considered, with a Young's modulus of 30 GPa and a Poisson's ratio of 0.2.

The strains obtained with the enhanced fibre beam computation are displayed in Figure 3. They

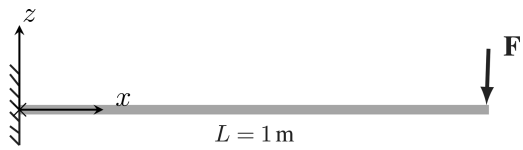

Figure 1. Considered case study for the analytical validation of the enhanced fibre beam element in transverse shear.

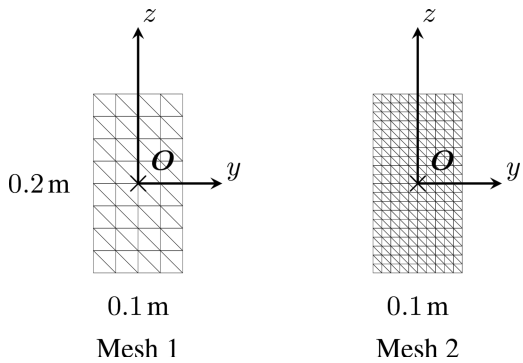

Figure 2. Cross-section meshes used for the analytical validation of the enhanced fibre beam element.

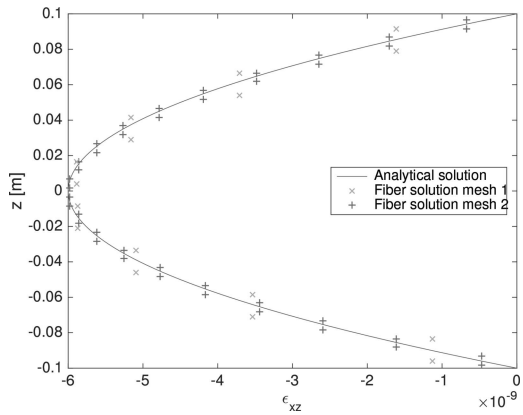

Figure 3. Results for the bended cantilever beam case-study: comparison of the computed shear strains to the analytical shear strains for the bended cantilever beam.

are compared to the analytical strains obtained by Jourawski's theory. These results are extracted from (Capdevielle et al. 2017). They show that the linear elastic strains accounting for transverse shear warping are well computed by the enhanced fibre beam element.

Since the warping degrees of freedom are linked at the nodes through the longitudinal interpolation, it is possible to take into account the effect of restrained warping at the boundary conditions. The results of the cantilever beam case study are further investigated here. Warping is assumed to be prevented at the fixed end. Figure 4 displays the warping displacements in both the cross-sections closest and furthest to the fixed boundary condition.

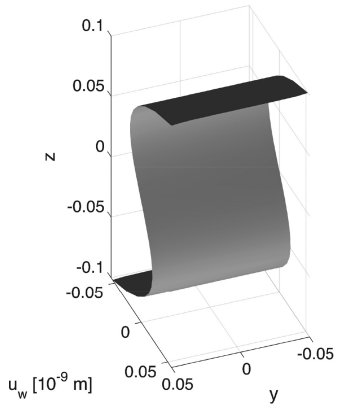

(a)

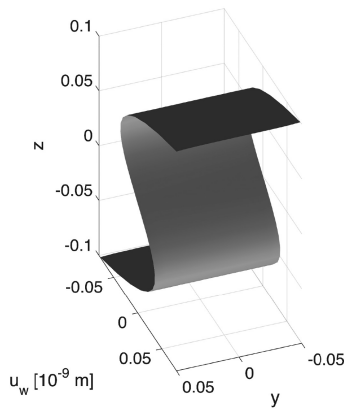

(b)

Figure 4. Warping displacements in different cross-sections of the beam displayed in figure 1. 4(a): Closest cross-section to the fixed boudary conditions. 4(b) Closest cross-section to the beam's free end.

The warping displacements are greater close to the free end of the beam than close to the fixed boundary condition (see Figure 4). This result confirms the fact that the longitudinal interpolation of warping displacements enables the solution to account for constrained warping conditions.

More results on the linear elastic validation of the transverse shear and coupled shear/torsion behaviour are presented in (Capdevielle et al. 2017).

4 INFLUENCE OF WARPING ON THE STRUCTURAL DYNAMIC BEHAVIOUR

Once the linear elastic behaviour of the enhanced beam element is validated, the effect of warping at the structural scale with a damaging material is investigated. The CAMUS mock-up (CEA 1998), shown in Figure 5(a) is studied here. It is a reinforced concrete structure, representing a 5-story building. It comprises two walls of section 1,70 m × 0,06 m. The walls are connected by reinforced concrete slabs representing the floors and supporting the added weight. Each story is 0.90 m high, and the basement is 0,6 m high. The mock-up is fixed on a shaking table. Seismic signals of increasing intensity have been applied to the structure in the direction of the wall plane.

The study aims at investigating the effect of including warping in the formulation on the numerical response of the structure. The fibre beam element model used here is based on (De Biasio 2014). Each story is discretized into 3 fibre beam elements. The floor mass is lumped at the corresponding nodes. The cross-section mesh is displayed in Figure 4. Each wall is discretised into 12 triangular elements.

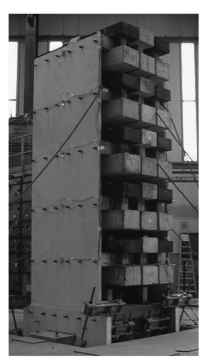

(a)

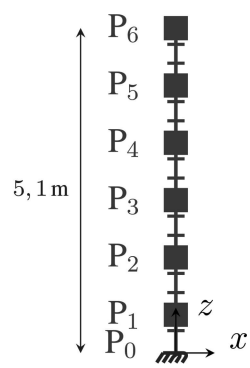

(b)

Figure 5. CAMUS mock-up (De Biasio 2014) and fibre element numerical model.

A simplified mesh for the steel rebars is used, with 3 triangular elements in each wall.

The first fundamental frequencies of the structure are computed, without and with the warping enhancement in the fibre elements. The shaking table is not modelled here. The results are given in Table 1.

The fundamental frequencies corresponding to flexural modes are shifted by 5% by adding warping in the model. The model without warping is stiffer. This is consistent with results obtained in torsion, for which adding warping in the model reduces the initial stiffness of the torque-twist curve (Mazars et al. 2006, Capdevielle et al. 2016).

A dynamic time-analysis of the CAMUS structure is then carried out. Concrete is modelled using the Mu damage model (Mazars et al. 2014). The steel rebars are modelled using the Menegott Pinto model (Menegotto and Pinto 1973). The accelerogram applied to the structure is given in Figure 7. A Rayleigh damping of 2% is considered in the model.

The resulting top displacements of the structure, respectively computed without and with the warping enhancement, are given in Figure 8. It can be seen that the difference in the fundamental frequencies induces aprogressive shifting of the two response curves. It can also be noted that the model without warping results in a residual displacement at the end of the computation, whereas there is no residual displacement for the model with warping. This is probably due to the yielding of the reinforcing rebars in the case of the model without warping. These results need more investigation before a definitive conclusion can be assessed.

This case-study clearly demonstrates the effect of warping on the structural behaviour. Though, it does not show the importance of including warping in the formulation to represent the real behaviour of a structure, even if accounting for warping is physically relevant. Indeed, by suitably calibrating the shaking table model, both models without and with warping are able to represent the experimental behaviour. A further study needs to be conducted to assess the importance of taking warping into account. A set of beams experimentally tested in torsion has been modelled with the enhanced element and will be presented at the conference.

Table 1. First fundamental frequencies of the CAMUS structure obtained by a numerical modal analysis without modelling the shaking table.

Frequencies [Hz]	Mode 1	Mode 2	Mode 3
Without warping	9.45	44.55	46.11
With warping	9.01	43.29	43.87
Relative difference	5%	3%	5%

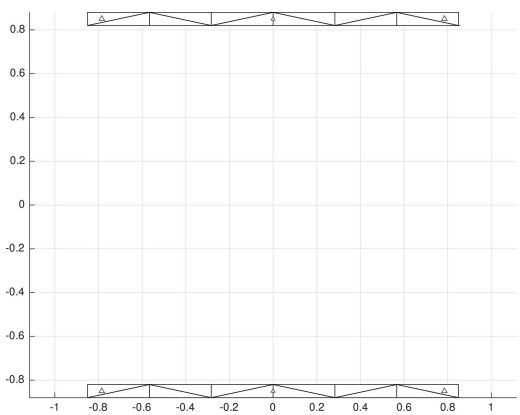

Figure 6. Mesh of the cross-section.

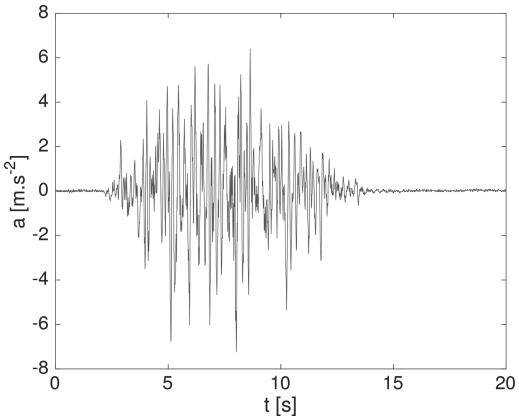

Figure 7. Accelerogram of the signal applied to the CAMUS structure.

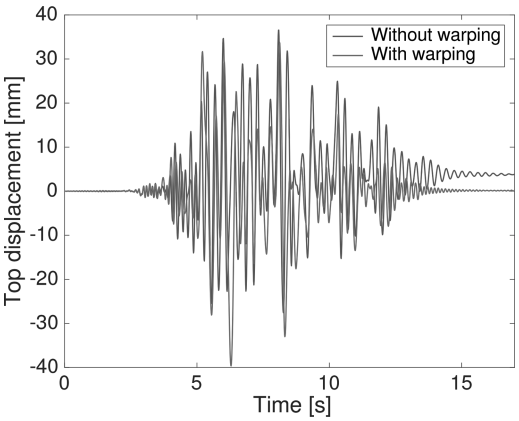

Figure 8. Top displacement of the mock-up during the seismic loading; comparison of the numerical results using the enhanced element without and with warping.

5 CONCLUDING REMARKS

An enhanced fibre beam element with additional warping degrees of freedom has been presented. The enhancement is formulated by adding warping displacements to the kinematics of a Timoshenko fibre beam element. The warping shape functions to interpolate warping displacements in the transverse directions are set to be free of the rigid-body motions of the cross-section. A first numerical example has been presented on a cantilever beam subject to a vertical load. With a linear elastic material, an analytical solution is available. The numerically computed strains have been successfully compared to the analytical strains in the cross section. Then, the enhanced element has been used to model a structure under dynamic loading. Although the difference in fundamental frequencies between the model without and with the warping enhancement is small, it induces a remarkable difference in the nonlinear dynamic response of the structure. This study has been carried out to compare both numerical models. Further case-studies need to be presented to compare the numerical results to an experimental structural behaviour. They will prove the importance of taking warping into account to represent the real behaviour of a structure.

Using the element with warping is about two times more computationally demanding than the plain Timoshenko fibre beam element. Nevertheless, a computation at the structural scale is still possible with the enhanced element. For an efficient model, enhanced fibre beam elements should be associated with classical elements and used only where necessary. The warping degrees of freedom need to be condensed out to the global beam degrees of freedom to enable the connection to different beam elements.

ACKNOWLEDGEMENTS

The authors would like to thank the PIA-SINAPS@ project (Séisme et Installation Nucléaire: Améliorer et Pérenniser la Sureté), approved and funded by the National Agency of Research (ANR) following the RSNR 2012 call for projects on future investments post-Fukoshima. (SINAPS@ ANR-11-RSNR-0022).

REFERENCES

Bairan, J.M. & A.R. Mari (2006). Coupled model for the nonlinear analysis of anisotropic sections subjected to general 3d loading. part 1: Theoretical formulation. *Computers & structures 84*(31), 2254–2263.

Bairan, J.M. & A.R. Mari (2007). Multiaxial-coupled analysis of rc cross-sections subjected to combined forces. *Engineering structures 29*(8), 1722–1738.

Capdevielle, S., S. Grange, F. Dufour, & C. Desprez (2016). A multifiber beam model coupling torsional warping and damage for reinforced concrete structures. *European Journal of Environmental and Civil Engineering 20*(8), 914–935.

Capdevielle, S., S. Grange, F. Dufour, & C. Desprez (submitted 2017). A fiber beam element with warping due to shear and torsion for the non-linear computation of concrete beams under multiaxial loadings. *Submitted to Engineering Structures, under review.*

CEA (1998). Camus international benchmark. experimental results. synthesis of the participant reports. Technical report, CEA Saclay, France.

De Biasio, M. (2014). *Ground motion intensity measures for seismic probabilistic risk analysis*. Ph. D. thesis, Université de Grenoble.

Grange, S. (2015). Modéles multi-échelles et algorithmes pour les simulations dynamiques: application ‘a la vulnérabilité sismique des structures. Habilitation á diriger des recherches, Université de Grenoble-Alpes.

Grange, S., P. Kotronis, & J. Mazars (2008, December). Numerical modelling of the seismic behaviour of a 7-story building: NEES benchmark. *Materials and Structures 42*(10), 1433–1442.

Kotronis, P. & J. Mazars (2005). Simplified modelling strategies to simulate the dynamic behaviour of r/c walls. *Journal of Earthquake Engineering 9*(2), 285–306.

Kotronis, P. & S. Grange (2010). Simplified modelling strategies for reinforced concrete structures. *European Journal of Environmental and Civil Engineering 14*(6–7), 823–838.

Le Corvec, V. & F. Filippou (2011). Enhanced 3d fiber beamcolumn element with warping displacements. In *Proceedings of the 3rd ECCOMAS Thematic Conference on Computational Methods in Structural Dynamics and Earthquake Engineering*.

Le Corvec, V. (2012). *Nonlinear 3d frame element with multiaxial coupling under consideration of local effects*. Ph. D. thesis, University of California, Berkeley.

Mazars, J., F. Hamon, & S. Grange (2014). A new 3d damage model for concrete under monotonic, cyclic and dynamic loadings. *Materials and Structures*, 1–15.

Mazars, J., P. Kotronis, F. Ragueneau, & G. Casaux (2006). Using multifiber beams to account for shear and torsion: Applications to concrete structural elements. *Computer Methods in Applied Mechanics and Engineering 195*(52), 7264–7281.

Menegotto, M. & P. Pinto (1973). Method of analysis for cyclically loaded reinforced concrete plane frames including changes in geometry and non-elastic behavior of elements under combined normal force and bending. In *IABSE Symposium on the Resistance and Ultimate Deformability of Structures Acted on by Well-Defined Repeated Loads, Lisbon*.

Spacone, E. & S. El-Tawil (2004). Nonlinear analysis of steelconcrete composite structures: State of the art. *Journal of Structural Engineering 130*(2), 159–168.

Computational Modelling of Concrete Structures – Meschke, Pichler & Rots (Eds)
© 2018 Taylor & Francis Group, London, ISBN 978-1-138-74117-1

Characterization of cracks of damaged concrete structures in dynamics

R. Akiki, C. Giry & F. Gatuingt
LMT, ENS Paris-Saclay, CNRS, Université Paris-Saclay, Cachan, France

ABSTRACT: The analysis and prediction of the degradation process and cracking of concrete structures with numerical models is an important issue in the field of civil engineering. In order to describe the global behavior of a structure composed of quasi-brittle material as well as local fields, a continuous approach using nonlinear constitutive law (e.g. damage, plasticity, …) remains the most efficient one regarding the computational time. However, one has to consider additional tools to extract discrete information about cracks like spacing and openings from these computations. The objective of this research is to propose tools capable of extracting local information such as cracking using two post-treatment methods of a global finite element analysis.

These methods are applied to a dynamic one-point bend test case and results show the capability of both methods to give a good estimation of crack path and openings.

1 INTRODUCTION

1.1 *Context*

This research work is part of the safety of packaging used to confine radioactive wastes. In order to assess the capacity of a package made of concrete to avoid the leakage of waste contained in it, one has to quantify its properties of permeability and more particularly the cracking in case of accident. Among the possible loading inducing damage and cracking in the context of waste containment, the falling of a package is a critical situation. The current methodologies for qualifying packages are based entirely on experimental analyzes carried out on structures at full scale. As a consequence, associating the experimental procedure with a step of simulation using a numerical tool is an interesting alternative.

1.2 *Modeling strategies of cracking in quasi-brittle media*

The modeling of the cracking in quasi-brittle materials can be tackled through different strategies. A first approach consists in a diffuse description of the cracking with a continuous description of the displacement field. Then the progressive degradation is described through a field of internal variable like damage. Another approach consists in an explicit description of the cracking with the use of a discontinuous displacement field through a kinematic enrichment. This enrichment can be introduced at the finite element scale like E-FEM, for instance, or as additional degrees of freedom like X-FEM, for instance. Despite the advantage of getting a direct information on the crack opening and crack location with the second approach, the continuous description of degradation remains the most efficient technic to deal with the response of a full scale structure.

In order to quantify cracking (location, opening) from a continuous field, an additional post-treatment needs to be introduced. In this work, two post-treatment methods have been considered.

The first method combines a topological search method used to locate cracks developed by (Bottoni et al. 2015) and a continuous/discontinuous approach used to compute the crack opening initially proposed by (Dufour et al. 2008). It consists in comparing the computed strain fields, with the analytical one derived from the displacement profile described as a strong discontinuity. Both strain fields are regularized using a Gaussian function. The crack opening can then be adjusted so as to reduce the gap between the regularized strain field and the regularized strong discontinuity strain field. Furthermore, a general formulation of these tools for 2D and 3D problem is proposed in this work. The direction of the mode I crack at a point is determined as the one which maximizes the crack opening along the associated 1D profile.

The second method is a non-intrusive re-analysis at the local scale performed with a discrete model in order to extract fine information about crack opening. A region of interest (ROI) corresponding to the damaged area obtained from the global analysis is defined. Then, the loading steps corresponding to the steps of re-analysis are determined, where boundary conditions are extracted from the continuous displacement field and applied on the non-free surfaces of the ROI. The material is

described with a discrete element approach based on an assembly of polyhedral particles linked by Euler-Bernoulli beams with brittle behavior. Further details concerning the discrete model used at the local scale can be found in (Oliver-Leblond et al. 2013).

2 EXPERIMENTAL CAMPAIGN

In order to understand the mechanisms of deformation and cracking of fiber concrete (the quasi-brittle material considered in this study) under mechanical stresses close to those encountered by the packages during the impact and in order to identify the most appropriate behavior law to use in the simulations as well as its parameters, an experimental campaign has been performed. The main results obtained are summed up in this part.

2.1 *Quasi-static loading*

Three different types of test have been performed under quasi-static conditions: compression test, splitting test and 3-point bending test. Two types of fibers were considered for the industrial context: FRC1 (amorphous cast iron flat fiber) and FRC2 (steel fiber). The mean mechanical properties obtained are given for each concrete in Table 1.

A noticeable gain for the fracture energy is observed with the steel fibers. Indeed, the hooks of these fibers highly improve the ductile behavior of the concrete. With the flat fibers, only the yield strength is increased compared to standard concrete but only a small improvement of the ductile behavior is observed.

2.2 *Dynamic loading*

In order to quantify the sensitivity of our fiber reinforced concrete to the strain rate, several dynamic loadings have been performed thanks to a split Hopkinson bar device. Compressive and splitting loading have been applied in order to identify the compressive and tensile behavior of the material and a one-point bending test has been developed (Akiki, Gatuingt, Giry, Schmitt, & Stéfan 2016) to identify the flexural behavior and the dynamic fracture energy. Classical post-treatment thanks to strain gauges placed along the bars has been considered as well as Digital Image Correlation (DIC) to quantify cracking at the surface of the specimen tested. These last results are used later for comparison with the results obtained numerically.

Table 1. Mechanical properties of the fiber reinforced concretes.

Parameter	Unit	FRC1	FRC2
Tensile strength (splitting test)	MPa	6.9	7.4
Tensile strength (flexural test)	MPa	11.3	12.9
Compressive strength	MPa	75	87.4
Fracture energy	N/m	900	9000
Young modulus	GPa	42	40

Fig. 1 shows the classical evolution of the forces at the input and output bar/specimen interfaces during the compressive test.

One can see for the compressive test that the equilibrium is reached in the sample as the evolution of the force obtained at the input and the output faces of the specimen are superposed.

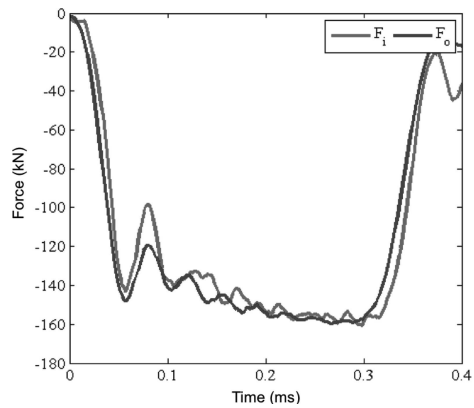

Figure 1. Evolution of the forces at the input and output bar/specimen interfaces during the compressive test.

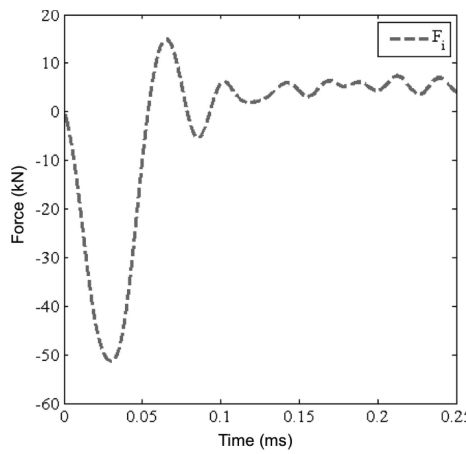

Figure 2. Experimental evolution of the force at the input interface bar/specimen during the one-point bending test.

2.3 *Identification of the parameters of the continuous model*

In order to identify the parameters of the material model driving the linear and nonlinear behavior, an inverse analysis including the global response measured experimentally is considered. A minimization process of an error fonction comparing the experimental results and the one obtained from the FE modeling of the test is used. For this identification, the MATLAB® function *lsqnonlin* (i.e. nonlinear least-square solver) is considered. The error function r is defined according to Eq. 1 and includes the response of the compressive test under quasi-static loading $f^{i,c}$, the tensile strength y^t and the evolution of the force at the input interface bar/specimen during the one-point bending test $F^{i,f}$ (see Fig. 2). The indice $\cdot i$ stands for the time step i.

$$r = \sqrt{\sum_{i=1}^{n}\left(\frac{f_s^{i,c}(\underline{x})-f_e^{i,c}}{\sum_{i=1}^{n} f_e^{i,c}}\right)^2+\left(\frac{y_s^t(\underline{x})-y_e^t}{y_e^t}\right)^2+\sum_{i=1}^{n}\left(\frac{F_s^{i,f}(\underline{x})-F_e^{i,f}}{\sum_{i=1}^{n} F_e^{i,f}}\right)^2}, \quad (1)$$

3 CONTINUOUS DESCRIPTION OF THE DEGRADATION

The modeling of the degradation of the structure is managed thanks to a continuous approach. The material's behavior used in our FE simulations is described by an elasto-plastic constitutive law including damage and rate effect: model MAT-159 in LS-DYNA (Murray 2007).

The parameters of the model have been identified according to the method exposed in the previous section. In order to test the method exposed in the next section regarding the cracking quantification, a finite element model of the full Hopkinson bar device for 1-point bending test has been used. The main characteristics of the mesh are given in Table 2 and Fig. 3 gives the an overview of the modeling.

Figs. 4 and 5 show the damage field D and the strain component ε_{yy} during the failure process of the beam. One can see classical fracture process zone propagating from the notch up to the side of the beam in contact with the impactor. These fields allow to characterize the global degradation of the specimen and provide diffuse information at the local scale.

Table 2. Characteristics of the mesh for the one-point bending test.

Entity	Number of nodes	Number of elements
Impactor	4329	3680
Incoming bar	22126	20700
Specimen	115816	107100

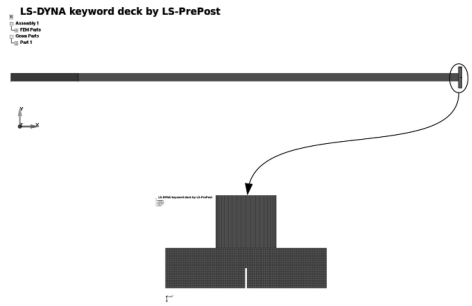

Figure 3. FE mesh of the one-point bending test: global view and zoom over the contact between the bar and the specimen.

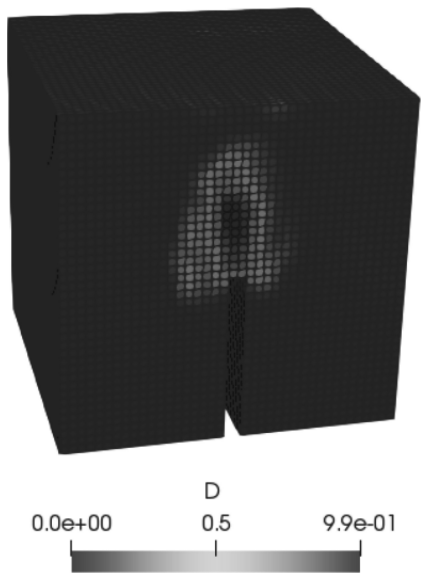

Figure 4. Damage field obtained during the failure of the specimen.

4 EXTRACTION OF CRACKING FROM CONTINUOUS COMPUTATION

The continuous description of degradation based on damage and/or plasticity model allow to describe the global behavior but does not provide information on crack. As a consequence, additional tools need to be introduced in order to get discontinuous information like crack location and opening. In this work, two approaches have been considered to post-treat the continuous fields.

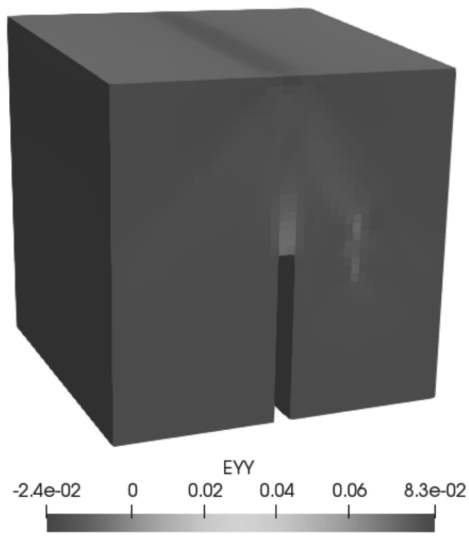

Figure 5. Strain component ε_{yy} field obtained during the failure of the specimen.

4.1 *Topological search and continuous-discontinuous approach for crack opening*

Let's consider an isotropic material with a non-linear behavior which state is characterized by a strain tensor ε and a corresponding stress tensor σ. By considering that the linear part of the material keeps the same properties as the ones of the virgin material, one can express an anelastic strain ε^{an} according to Eq. 2.

$$\varepsilon^{an} = \varepsilon - \mathbf{C}^{-1} : \sigma, \tag{2}$$

with $\mathbf{C}$ the elasticity tensor.

In the analysis of quasi-brittle materials, by considering that the nonlinearities fully participate to the cracking process, one can associate the anelastic strain tensor to the cracking. As a consequence, the crack location and crack opening are obtained from the post-treatment of this field.

This first method proposed is dedicated to the quantification of mode I crack opening. The main idea behind locating the direction of the crack and evaluating its opening is to consider that the crack opens in mode I in the direction that maximizes the crack opening. In order to quantify the crack opening at a point in a given direction from a continuous field, the method proposed by (Dufour et al. 2008) is used. The main equations are recalled hereafter.

For a given direction $\mathbf{n}$, the projection of the strain tensor obtained from the finite element computation ε_N^{FE} is defined by:

$$\varepsilon_N^{FE} = \mathbf{n}^T . \varepsilon . \mathbf{n} \tag{3}$$

One can get a scalar field $\varepsilon_N^{FE}(s)$ over a 1D profil parameterized by the direction $\mathbf{n}$ and a distance to the center s. (Dufour et al. 2008) propose to quantify the crack opening from this scalar field by comparing it with the 1D strain profil corresponding to a strong discontinuity $\varepsilon_N^{SD}(s)$. As this last field is a Dirac like function, a direct comparison is not possible. As a consequence, the authors propose to compare the convolution product of both profils with a filter function $\phi(x_0 - s)$ (x_0 defining the crack location on the 1D profil). By considering that the convoluted strain field are equal at the crack location (i.e. location of the maximum of $\phi \star \varepsilon_N^{FE}(x_0)$), the crack opening $\|u\|$ writes:

$$\|u\|(x_0) = \int_\ell \varepsilon_N^{FE}(s).\phi(x_0 - s)\mathrm{d}s \tag{4}$$

From this equation, the location x_0 and the crack opening $\|u\|$ are obtained.

From this quantification of the crack opening, the identification of the direction of mode I opening at a given point along the crack is obtained by maximimizing $\|u\|$ according to $\mathbf{n}$. This direction is parameterized in 2D by an angle θ. Finally, the maximization problem is defined by Eq.5.

$$\theta_{crack} = \max_{\theta} \left\{ \theta \in [0, \pi[; \|u\|(\theta, \varepsilon^{an}) \right\} \tag{5}$$

The formulation of the problem can easily be generalized to 3D field by defining the orientation of $\mathbf{n}$ with two angles: θ and φ.

From a given point and a direction of opening, the definition of the next searching point along the crack is defined according to the topological method proposed by (Bottoni et al. 2015). A new point of search P_{search}^{i+1} is defined by Eq.6.

$$\begin{aligned} \left\| P_{crack}^{i} P_{search}^{i+1} \right\| &= h, \\ \left(\overline{P_{crack}^{i} P_{search}^{i+1}} \right).\mathbf{n} &= 0, \\ \left(\overline{P_{crack}^{i-1} P_{crack}^{i}} \right).\left(\overline{P_{crack}^{i} P_{search}^{i+1}} \right) &> 0 \end{aligned} \tag{6}$$

4.2 *Global/local approach for the description of cracking*

In this section the global/local method used in a reanalysis of the continuous calculation is described. This approach allows to give local information relative to cracking (e.g. location, opening, …) by reanalyzing the damaged areas of the structure studied in a continuous framework (Oliver-Leblond et al. 2013). Fig. 6 gives the evolution process of analysis of the method. At the global scale, the nonlinear behavior of the structure is described thanks to the continuous model. The obtained damage pattern is studied and several Regions of Interest (ROIs) can be defined corresponding to distinct areas of

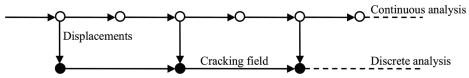

Figure 6. Global/Local sequential analysis.

damage if necessary. Then, the loading steps for the extraction of crack features are determined and will correspond to the steps of re-analysis. For those loading steps, boundary conditions are extracted from the continuous displacement field and applied on the non-free surfaces of the ROIs – namely the ones which cut the whole domain. The natural way to transfer the displacement field from the global scale to the local scale is to use the shape functions of the finite elements used for the global computation. Then, the displacement $u_L(x_L)$ applied at a local node x_L of a non-free surface of a ROI is directly obtained with Eq. 7.

$$u_L(x_L) = \sum_{j=1}^{N_{FE}} N_j(x_L) u_j, \tag{7}$$

where N_j are the shape functions of the finite element model, u_j is the displacement vector computed at the global scale and N_{FE} is the number of finite element nodes. The cracking pattern obtained at the previous step will be retrieved at the current step of the local re-analysis in order to follow the crack propagation accurately. The discrete computation of the chosen ROIs can be parallelised.

4.3 *Discrete local model*

The discrete model used at the local scale has been proposed by (Delaplace 2005) and offers a reliable description of concrete behaviour for tensile loadings. The material is described as an assembly of polyhedral particles linked by Euler-Bernoulli beams. The quasi-brittle behaviour of the material is obtained through a brittle behaviour for the beams. The breaking threshold P_{ab} of $a - b$, the beam linking the particles a and b, not only depends on the beam extension ε_{ab} but also on the rotations of the two particles θ_a and θ_b (Eq.8).

$$P_{ab} = \left(\frac{\varepsilon_{ab}}{\varepsilon^{cr}}, \frac{|\theta_b - \theta_a|}{\theta^{cr}} \right) > 1, \tag{8}$$

The six "material" parameters of the beam $a - b$ need to be calibrated. First, the length and the area are imposed by the geometry. Then, the inertia and the elastic modulus are identified in order to retrieve the elastic behaviour of the global computation. Finally, the calibration of the breaking thresholds ε^{cr} and θ^{cr} of the beam allow us to fit the peak and post-peak behaviour of the global model. The calibration is performed on an independent case study

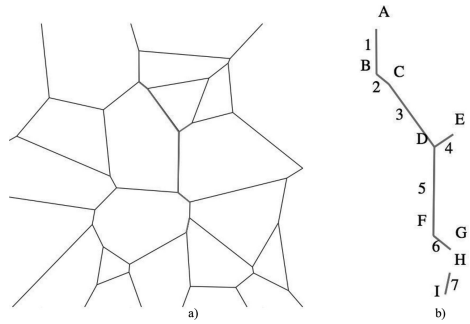

Figure 7. Discrete elements description of the media with micro cracks a) Representation of microcracks in graph theory b).

(Oliver-Leblond et al. 2013). Our study focuses on a fine description of crack pattern and on the measurement of the crack opening. The crack pattern is defined as the common side of the particles initially linked by the breaking beams. The opening of the crack is computed by considering the relative displacement $u_b - u_a$ of the unlinked particles a and b. The measure of the opening between those particles e_{ab} is projected on the normal n_{ab} of the local discontinuity (Eq.9).

$$e_{ab} = \langle (u_b - u_a).n_{ab} \rangle +, \tag{9}$$

4.4 *Quantification of cracks properties*

In order to get information on cracking from the discrete element re-analysis, additional tools have been considered. The micro cracked domain obtained from the discrete element re-analysis is described in graph theory (Fig. 7).

Using the Bellman-Ford algorithm (Moore 1959) in this framework, an identification of the macro-crack in the domain reanalyzed is obtained. In order to choose the right crack path at a crossroad, the crack opening associated to each discrete element is used as a weight.

5 DYNAMIC ONE-POINT BENDING TEST

In this last part, the methods of quantification of the crack opening exposed in the previous sections are applied to the case of a dynamic one-point bending test with a split Hopkinson bar apparatus.

The specimen is a notched beam with a square section of size $d = 4$ cm and length $L = 4d$. The height of the notch is equal to $0.5d$. The characteristics of the fiber reinforced concrete are: $E = 41$ GPa, $f'_c = 75$ MPa and $\nu = 0.23$. The speed

of the impactor of the input bar of the Hopkinson bar apparatus is limited to 8 m/s.

The results obtained numerically for cracking are compared to the experimental ones obtained by Digital Image Correlation (DIC) thanks a high-speed camera and the software CORRELI RT3 (Tomicevic et al. 2013). For the first approach (i.e. Topological search and continuous-discontinuous approach for crack opening), the anelastic strain ε^{an} is directly used to identify the crack location and crack opening obtained on the surface of the specimen. For the second approach (i.e. global/ local approach for the description of cracking) an area of post-treatment associated to the location of the FPZ is defined. Fig. 8 gives the ROI and the discrete element mesh used for the re-analysis. 3500 particles are used to describe the area of re-analysis. The red lines defined the boundary where displacements are imposed. As the area of interest is sufficiently small, the kinetic energy is considered as homogeneous over the region of interest and an equivalent quasi-static analysis introducing only the displacement at the boundaries seems to be reasonable.

Fig. 9 shows the residual field of the DIC which is a good indicator of the crack path obtained experimentally.

Fig. 10 shows the crack pattern obtained with the first approach. One can see a good prediction

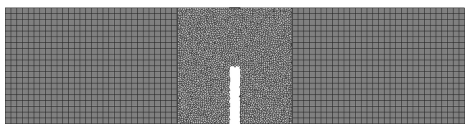

Figure 8. Discrete element mesh used for the re-analysis.

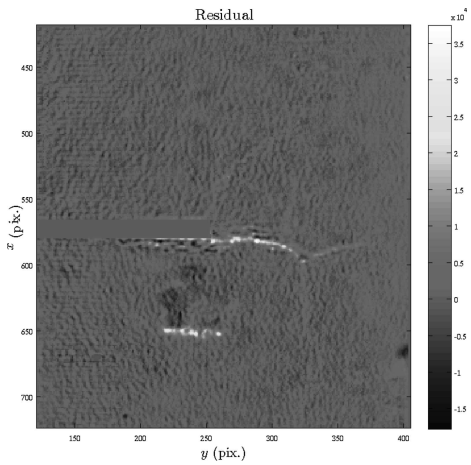

Figure 9. Experimental crack path obtained by DIC.

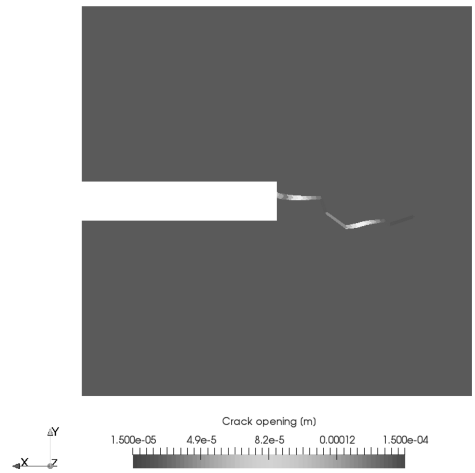

Figure 10. Crack pattern obtained with the second approach.

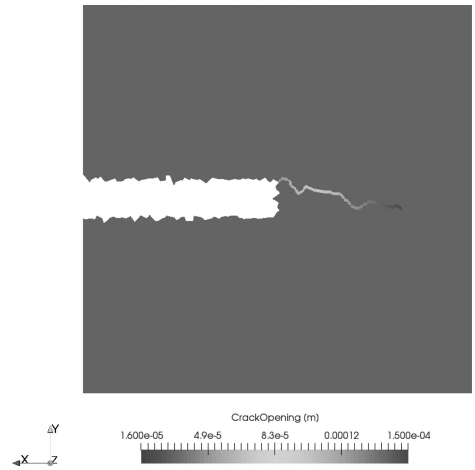

Figure 11. Crack pattern obtained with the second approach.

of the crack path compared to the one experimentally obtained.

Fig. 11 shows the crack pattern obtained with the second approach. One can see that the second approach also gives in average a good prediction of the crack path compared to the one obtained experimentally.

Furthermore, the crack opening for both methods is in the same order of magnitude and corresponds to the experimental data. In particular, the maximum crack opening along the crack path is around 150 μm for both modeling.

Regarding the definition of the crack tip, it may be not well capture with the first approach but as this data is not relevant for the final application

and as this information still is a tricky experimental measurement (e.g. order of magnitude of the opening versus noise). In conclusion, both approaches show good prediction of crack pattern from a continuous computation.

6 CONCLUSION

Two different methods have been proposed in this work to characterize the crack pattern from a continuous computation. The first one exploits directly the fiels obtained from a FE simulation (stress and strain) to locate the crack and quantify the opening. The second one considers a reanalysis of the FPZ through a discrete element modeling. Both methods are not dependent of the model used for the continuous modeling and can be considered in a general purpose to quantify cracking. In the work presented, this is a first application of these methods to quantify cracking in the case of dynamic loading. It has been shown that both methods are capable of quantifying precisely the location and the opening of the crack for a dynamic one-point bending test on a fiber-reinforced concrete beam with a split Hopkinson bar apparatus. Further investigation and validation of the methods, more particularly for 3D post-treatments are in progress.

ACKNOWLEDGMENTS

The authors would like to thank New AREVA for its financial support.

REFERENCES

Akiki, R., F. Gatuingt, C. Giry, N. Schmitt, & L. Stéfan (2016). Modeling and simulation for an optimized design of a dynamic bending test. In *ECCOMAS Congress 2016 — Proceedings of the 7th European Congress on Computational Methods in Applied Sciences and Engineering*, Volume 1, pp. 242–253.

Bottoni, M., F. Dufour, & C. Giry (2015). Topological search of the crack pattern from a continuum mechanical computation. *Eng. Struc. 99*, 346–359.

Delaplace, A. (2005). Fine description of fracture by using discrete particle model. In *11th International Conference on Fracture*.

Dufour, F., G. Pijaudier-Cabot, M. Choinska, & A. Huerta (2008). Extraction of a crack opening from a continuous approach using regularized damage models. *Computers and Concrete 5(4)*, 375–388.

Moore, E.F. (1959). The shortest path through a maze. In *Proc. Internat. Sympos. Switching Theory*, Volume 2, pp. 285–292.

Murray, Y. (2007). Users manual for ls-dyna concrete material model 159. Technical report.

Oliver-Leblond, C., A. Delaplace, F. Ragueneau, & B. Richard (2013). Non-intrusive global/local analysis for the study of fine cracking. *Int. J. for Numer. Anal. Meth. Geomech. 37(8)*, 973–992.

Tomicevic, Z., F. Hild, & S. Roux (2013). Mechanics-aided digital image correlation. *The Journal of Strain Analysis for Engineering Design. 48(5)*, 330–343.



Taylor & Francis
Taylor & Francis Group
http://taylorandfrancis.com

Computational Modelling of Concrete Structures – Meschke, Pichler & Rots (Eds)
© 2018 Taylor & Francis Group, London, ISBN 978-1-138-74117-1

High-dynamic strengthening of cementitious materials subjected to uniaxial compression

E. Binder & H.A. Mang
Institute for Mechanics of Materials and Structures, TU Wien—Vienna University of Technology, Vienna, Austria
College of Civil Engineering, Tongji University, Shanghai, China

Y. Yuan
College of Civil Engineering, Tongji University, Shanghai, China

B. Pichler
Institute for Mechanics of Materials and Structures, TU Wien—Vienna University of Technology, Vienna, Austria

ABSTRACT: Infrastructures made of reinforced concrete such as e.g. tunnels and bridges, must withstand exceptional loads, caused by earthquakes, car impacts, accidential blast loads, etc. The latter two belong to the high-dynamic loading regime where strain rates are typically larger than 1/s. In this regime, the strength of concrete specimens increases significantly with increasing loading rate. The reason for this strengthing effect is still debated. This provides the motivation for the present contribution which is devoted to the analysis of high-dynamic compression tests on cement pastes, mortars, and concretes. An elasto-brittle model for high-dynamic strengthening is employed, which was proposed by Fischer et al. (2014) and extended towards consideration of the scatter of the quasi-static strength values by Binder et al. (2017). The aim of the present contribution is twofold. At first, the quantitative assessment of the predictive capabilities of the described model is extended towards consideration of experimental data from Hao & Hao (2013). Secondly, the question is tackled how to represent high-dynamic strength values of *different* materials (cement pastes, mortars, and concretes) in *one* diagram, such that a meaningful direct comparison becomes possible. The latter goal is achieved by comparing two independent measures of the increase of the compressive strain during the failure process of a specimen: the first one refers to the measured Dynamic strength Increase Factor (DIF), the quasi-static strength, and Young's modulus and the second one to the the strain rate, the characteristic crack propagation length, and the crack propagation speed.

1 INTRODUCTION

Current safety standards demand that tunnels and bridges must withstand exceptional load cases such as impact and blast loads. The latter may result from traffic accidents, e.g. from cars crashing into a tunnel lining, or from the detonation of so-called Improvised Explosive Devices (Ngo, Mendis, Gupta, & Ramsay 2007, Solz & Ruiz-Ripoll 2016). This provides the motivation to investigate concrete subjected to high-dynamic loading.

It was shown in many high-dynamic experiments that the strength of cementitious materials increases with increasing loading rate, see, e.g., (Bischoff and Perry 1991, Gary and Bailly 1998, Grote et al. 2001, Tedesco and Ross 1998, Xu et al. 2012, Zhang et al. 2009). This strengthening is significant in the high dynamic testing regime, where strain rates are typically larger than 1/s.

The available experimental database has resulted in several modeling attempts. The CEB-recommendation (1993) as well as the models of Tedesco and Ross (1998) and of Grote et al. (2001) provide empirical formulae for the high-dynamic compressive strength of cementitious materials. Mihashi and Wittmann (1980) as well as Bažant et al. (2000) have developed models based on the assumption that micro-cracking depends on the strain rate. Cotsovos and Pavlovic (2008), Li and Meng (2003), and Gary and Bailly (1998) have attributed the strength increase with increasing strain rate to inertial confinement which is a structural effect. Fischer et al. (2014) related the dynamic strength increase to the quasi-static strength and to

the duration of the failure process, lasting from the start of crack propagation to the final disintegration of the tested specimen. Thereby, it was considered that loading of the specimen increases during the evolution of the failure process. The load level reached at the end of the failure process is the high-dynamic strength of the tested specimen.

The aim of the present contribution is twofold. At first, the exemplary validation of the model by Fischer et al. (2014) is extended towards consideration of experimental data from Hao & Hao (2013). Secondly, the question is tackled how to represent high-dynamic strength values of *different* materials (cement pastes, mortars, and concretes) in *one* diagram, such that a reasonable direct comparison becomes possible.

The present paper is structured as follows. Section 2 contains a brief overview over the necessary prerequisites for the present analysis. Section 3 is devoted to the assessment of the predictive capabilities of the investigated DIF model. Section 4 establishes the sought *direct* compability of high-dynamic strength values of *different* cementitious materials. Section 5 contains a summary and conclusions. Throughout the entire manuscript, a positive sign in mathematical expressions relates to compression.

2 ELASTO-BRITTLE PREDICTION OF HIGH-DYNAMIC STRENGTH, BASED ON QUASI-STATIC STRENGTH DATA

In this section, the developments of Fischer et al. (2014), Pichler et al. (2014), and Binder et al. (2017) are briefly summarized. The respective elasto-brittle model for the dynamic increase factor (DIF) of the compressive strength of cementitious materials was derived, based on the following considerations:

- Cracking is considered to start also under high-dynamic loading, once the quasi-static strength is reached.
- The failure process of the specimen starts at the onset of cracking and ends once the first crack splits the specimen such that it disintegrates into pieces.
- During the failure process, it is possible to further increase the loading.
- Cracks are considered to propagate along nanoscopic interfaces at a speed, estimated to be equal to the shear wave velocity v_s. Notably, v_s is only by a few percent greater than the Rayleigh wave speed, and the latter is frequently considered to be a good estimate of the crack propagation velocity (Freund 1998).
- The shear wave velocity can be quantified, based on known values of the shear modulus G and the mass density ρ, as $v_s = \sqrt{G/\rho}$. The shear modulus, in turn, is related to the Young's modulus E and Poisson's ratio ν as $G = E/[2(1+\nu)]$.
- The loading reached at the end of the failure process, i.e. immediately before disintegration of the specimen, is equal to its high-dynamic strength.

This line of arguments has led to the follwoing closed-form expression of the DIF, defined as the dynamic-to-static strength ratio, see Fischer et al. Fischer et al. (2014).

$$DIF = \frac{f_{dyn}}{f_{stat}} = 1 + \frac{E\,\dot{\varepsilon}}{f_{stat}}\frac{l_c}{v_s} \quad . \tag{1}$$

In Eq. (1), f_{dyn}, f_{stat}, $\dot{\varepsilon}$, and l_c stand for the dynamic strength, the quasi-static strength, the strain rate, and the relevant crack propagation length. In the context of elasto-brittle modeling, the products $E\,\dot{\varepsilon}$ and l_c/v_s can be interpreted as the elastic stress rate and the duration of the failure process, respectively.

2.1 *Uncertainty regarding the position of crack nucleation*

The crack length, l_c, is equal to the distance along which a crack must propagate in order to split the specimen. Therefore, l_c depends on the geometrical properties of the tested specimen and on the (*a priori* unknown) position at which the first crack nucleates. Lack of knowledge of the latter is a source of uncertainty. Still, considering that axial splitting is the typical failure mode under uniaxial compression, l_c is bounded as follows:

- The smallest value of l_c is obtained, if the crack nucleates in the middle of the specimen, such that both crack tips have to propagate along half of the specimen height. Therefore, the lower bound is given as $l_c = h/2$.
- The largest value of l_c is obtained if the crack nucleates right at one of the interfaces between the specimen and the adjacent load application system, such that the crack tip has to propagate along the total height of the specimen. Therefore, the upper bound is given as $l_c = h$.

2.2 *Uncertainty regarding the quasi-static strength*

As regards quantification of the statistical scatter of the quasi-static strength, see f_{stat} in Eq. (1), the estimation of statistical quantiles is desirable. Unfortunately, this is often impossible, because experimentalists frequently only communicate the *mean value* of the quasi-static strenght. As a remedy,

Binder et al. (2017) combined the statistical scatter considered by Eurocode 2 (EN 1992-1-1 (2011)), which refers to a Gaussian distribution, with quantiles of a corresponding lognormal distribution.

Eurocode 2 defines the characteristic strength for ultimate limit state design as the 5%-quantile of the strength distribution. Concerning the compressive strength of concrete, the 5%-quantile is set equal to a value which is by 8 MPa smaller than the mean strength determined by laboratory testing. Considering a Gaussian distribution, this approach is related to a standard deviation of the uniaxial compressive strength amounting to $\hat{s} = 4.865\ MPa$.

A lognormal distribution appears to be more appropriate to describe the statistical properties of the compressive strength, which is a strictly positive quantity. In order to convert the standard deviation from Eurocode 2 to the one from the envisioned lognormal distribution, it is proposed to set the 5%-quantile of the Gaussian distribution equal to the 5%-quantile of the lognormal distribution. Denoting the value of the mean strength from the experiments as $\hat{f}$ and the standard deviation of the Eurocode as $\hat{s}$, the proposed approach from Binder et al. (2017) yields the sought standard deviation of the natural logarithm of the quasi-static compressive strength distribution as,

$$\overline{s} = u_{5\%} + \sqrt{(u_{5\%})^2 - 2\ln\left(1 + \frac{\hat{s}\cdot u_{5\%}}{\hat{f}}\right)}, \qquad (2)$$

where $u_{5\%} = -1.645$ is the value that cuts an area of 5% of the standardized normal distribution, exhibiting a vanishing mean value.

Using the standard deviation of the natural logarithm of the quasi-static compressive strength distribution according to Eq. (2), any p-quantile of the lognormal distribution can be calculated according to the following standard relation:

$$f_p = \exp\left(\ln(\hat{f}) + \overline{s}\cdot u_p\right). \qquad (3)$$

In the following, the 5% and 95%-quantiles of the lognormal distribution will be used as upper and lower bounds of the quasi-static compressive strength. To this end, p in Eq. (3) is set equal to 5% and to 95%, respectively, noting that $u_{95\%}$ amounts to +1:645.

3 QUANTITATIVE ASSESSMENT OF THE INVESTIGATED DIF MODEL

The investigated DIF model is applied to cement pastes, mortars, and concretes. In order to assess the predictive capabilities of the model, experimental material was selected that provides the necessary input for the model, such that no parameter needs to be fitted.

3.1 *Cement paste tested by Fischer et al. (2014)*

Fischer et al. (2014) crushed cement paste cylinders under quasi-static conditions and with a Split Hopkinson Pressure Bar (SHPB), see Table 1 for the experimental data. Corresponding model predictions agree qualitatively and quantitatively very well with the experimental data, see Fig. 1.

3.2 *Mortar tested by Zhang et al. (2009)*

Zhang et al. (2009) crushed mortar cylinders with two different sizes: one group exhibited $h_1 = 18$ mm and $\varnothing_1 = 37$ mm, the other one $h_2 = 25$ mm and $\varnothing_2 = 50$ mm, see Table 2 for the experimental data. Corresponding model predictions agree both qualitatively and quantitatively very well with

Table 1. Experimental data regarding high-dynamic strength testing by Fischer et al. (2014) from cement paste cylinders: $f_{stat} = 48.16$ MPa; $E = 14.24$ GPa; $G = 5.53$ GPa; $\varnothing = 10$ mm; $h = 6.6$ mm; $\rho = 1593$ kg/m^3.

f_{dyn} [MPa]	$\dot{\varepsilon}$ [s^{-1}]	f_{dyn} [MPa]	$\dot{\varepsilon}$ [s^{-1}]
74.15	700	132.73	1900
42.01	200	164.39	2100
74.41	500	156.36	2100
48.60	500	133.73	2100
65.40	500	152.64	2100
114.26	5000	143.78	1900

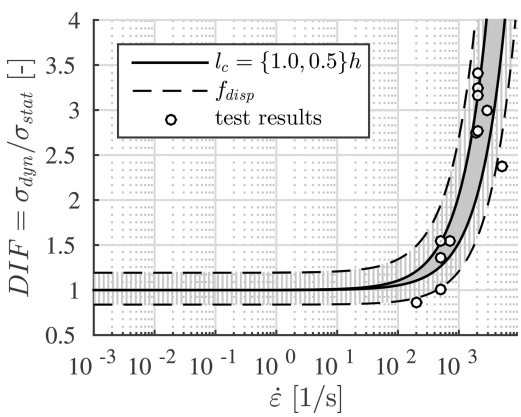

Figure 1. Comparison of increase of the model-predicted high-dynamic strength according to Eq. (1) with measured dynamic strength increase factors from Fischer et al. (2014), see Table 1.

the experimental data, see Fig. 2 as well as Wang et al. (2017).

3.3 *Concrete tested by Hao and Hao (2013)*

In this contribution, exemplary model validation is extended to high-dynamic strength tests performed by Hao & Hao (2013). They tested plain concrete cylinders with a diameter of 50 mm and a height of 80 mm, see Table 3 for the experimental data. Because they have neither reported the shear modulus nor Poisson's ratio of the tested concrete, the latter is estimated as the standard value of concrete: $\nu = 0.2$. Corresponding model predictions agree both qualitatively and quantitatively very well with the experimental data, see Fig. 3.

Table 2. Experimental data regarding high-dynamic strength testing by Zhang et al. (2009) from mortar cylinders: f_{stat} = 51 MPa; E = 23.1 GPa; ν = 0.19; ρ = 2116 kg/m^3; (a) h = 18 mm; ∅ = 37 mm, and (b) h = 25 mm; ∅ = 50 mm.

f_{dyn} [MPa]	$\dot{\varepsilon}$ [s^{-1}]	f_{dyn} [MPa]	$\dot{\varepsilon}$ [s^{-1}]
70.56	49	86.57	205
73.82	71	90.44	295
74.75	85	96.52	338
75.11	131	98.16	346
75.69	153	99.45	323
79.67	184	101.67	330
81.66	220	109.04	453
64.45	37	79.14	126
71.22	69	82.03	165
71.47	76	88.80	192
75.02	86	93.34	165
72.13	89	93.75	229
76.01	126	98.62	261
77.00	153		

Table 3. Experimental data regarding high-dynamic strength testing by Hao & Hao (2013) from concrete cylinders: f_{stat} = 35.5 MPa; E = 28.29 GPa; ∅ = 75 mm; h = 37.5 mm; ρ = 2201 kg/m^3.

f_{dyn} [MPa]	$\dot{\varepsilon}$ [s^{-1}]	f_{dyn} [MPa]	$\dot{\varepsilon}$ [s^{-1}]
36.57	1.31 10^{-4}	68.52	99.4
34.44	1.35 10^{-4}	58.93	103.8
53.25	65.4	63.55	131.3
45.09	70.5	64.61	135.6
53.96	79.1	62.84	141.9
46.51	79.2	90.53	163.6
57.16	90.2	81.65	177.3
65.68	98.7	81.65	175.4
61.77	99.1		

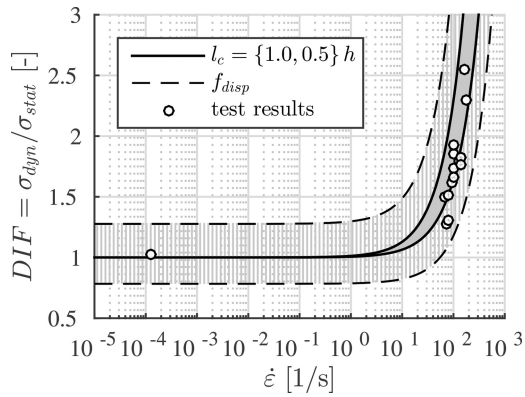

Figure 3. Comparison of increase of the model-predicted highdynamic strength according to Eq. (1) with measured dynamic strength increase factors from Hao & Hao (2013) see Table 3.

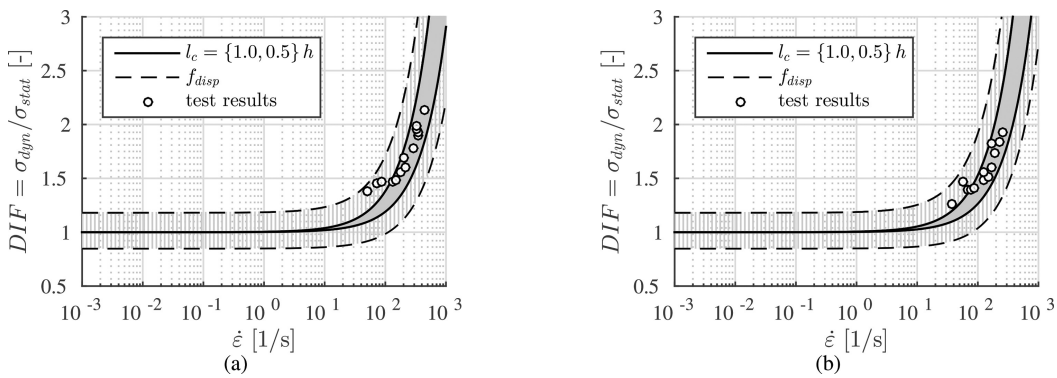

Figure 2. Comparison of increase of the model-predicted high-dynamic strength according to Eq. (1) with measured dynamic strength increase factors from Zhang et al. (2009): (a) h = 18 mm, and (b) h = 25 mm, see Table 2.

4 COMPARISON OF HIGH-DYNAMIC STRENGTH VALUES OF DIFFERENT CEMENTITIOUS MATERIALS

The analyzed cement pastes, mortars, and concretes are based on different elastic stiffnesses, quasi-static strengths, and specimen dimensions. This renders a direct comparison of the different test results a challenging task. In order to compare data from all analyzed high-dynamic testing series in *one* diagram, Eq. (1) is rearranged as

$$(DIF-1)\frac{f_{stat}}{E}=\frac{\dot{\varepsilon}l_c}{v_s}. \tag{4}$$

The left-hand-side of Eq. (4) can be interpreted as the increase of dynamic strain during the failure process. It is based on the measured DIF values, the quasi-static strength, and on Young's modulus. The right-hand-side of Eq. (4) represents the increase of the dynamic strain, predicted by means of the strain rate, the crack propagation length, and the crack propagation speed.

When it comes to displaying the experimental data summarized in Tables 1, 2, and 3 according to Eq. (4), each one of the high dynamic compression tests is represented by two points: one obtained for $l_c = h/2$, the other one for $l_c = h$, see Fig. 4. All of these data points form a quite dense data cloud. This underlines that Eq. (4) is indeed well suited to compare high-dynamic strength data referring to different materials.

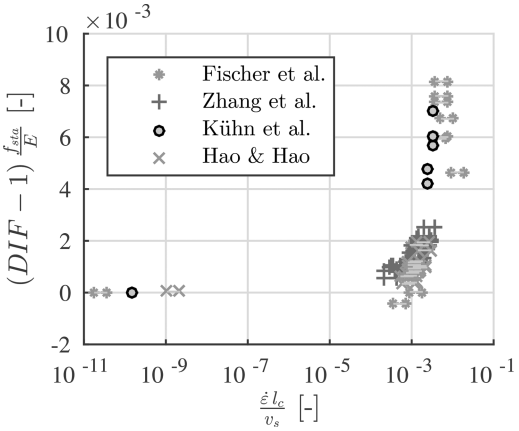

Figure 4. Dimensionless diagram relating two different expressions for the increase of strains during the failure process, see Eq. (4), thus allowing for a direct comparison of high-dynamic strength values of *different* materials: strength values from high-dynamic testing, taken from Tables 1–3.

5 SUMMARY AND CONCLUSIONS

The model used in the present contribution considers that the duration of a compressive strength tests consists of (i) the period of time until crack nucleation and (ii) the duration of the failure process. In the quasi-static regime, the latter is negligibly short compared to the former period of time. In the high-dynamic regime, however, both contributions are of the same order of magnitude.

The good qualitative and quantitative agreement between model predictions and independent experimental data corroborates the essential modeling assumptions that (i) cracking starts, independent of the loading rate, once the quasi-static strength is reached, (ii) cracks propagate approximately at a speed which can be estimated on the basis of the shear wave speed, and (iii) the maximum load of a specimen is reached, once the first crack has propagated such that it splits the specimen.

It is concluded that the high-dynamic strengthening effect of cementitous materials is directly proportional to the duration of the failure process. This was exploited in the context of developing a strategy that allows for a *direct* comparison of high-dynamic strength tests carried out on *different* cementitious materials. It is based on the comparison of two independent modes of quantifying the increase of the strain during the failure process.

As for bridges and tunnels, it is concluded that concrete will be damaged if the quasi-static strength is reached or exceeded, no matter how fast the loading is applied. Therefore, infrastructural facilities must be inspected very carefully, even after non-catastrophic high-dynamic loading events.

ACKNOWLEDGMENT

Financial support by the Austrian Science Fund (FWF), provided within project P 281 31-N32 "Bridging the Gap by Means of Multiscale Structural Analyses", is gratefully acknowledged.

REFERENCES

Bažant, Z., F. Caner, M. Adley, & S. Akers (2000). Fracturing rate effect and creep in microplane model for dynamics. *Journal of Engineering Mechanics 126*, 962–970.

Binder, E., H. Mang, Y. Yuan, & B. Pichler (2017). Impact and blast loads in tunneling: does the strength of concrete indeed increase with the loading rate? In *Proceedings of the IV International Confrence on Computational Methodes in Tunneling and Subsurface Engineering*, pp. 773–780. Univercity Innsbruck.

Bischoff, P. & S. Perry (1991). Compressive behaviour of concrete at high strain rates. *Materials and Structures 24*(6), 425–450.

Comite Euro-International du Beton (1993). CEB-FIP Model Code.

Cotsovos, D. & M. Pavlovic (2008). Numerical investigation of concrete subjected to compressive impact loading. part 1: A fundamental explanation for the apparent strength gain at high loading rates. *Computers and Structures 86*, 145–163.

European Committee for Standardization (2011). Eurocode 2: Design of concrete structures—part 1–1: General rules and rules for buildings.

Fischer, I., B. Pichler, E. Lach, C. Terner, E. Barraud, & F. Britz (2014). Compressive strength of cement paste as a function of loading rate: Experiments and engineering mechanics analysis. *Cement and Concrete Research 13*(58), 186–200.

Freund, L. B. (1998). *Dynamic fracture mechanics*. Cambridge University Press.

Gary, G. & P. Bailly (1998). Behaviour of quasi-brittle material at high strain rate. experiment and modelling. *European Journal of Mechanics-A/Solids 17*(3), 403–420.

Grote, D. L., S. W. Park, & M. Zhou (2001). Dynamic behavior of concrete at high strain rates and pressure: I. experimental characterization. *International Impact Engineering 25*(9), 869–886.

Hao, Y. & H. Hao (2013). Dynamic compressive behaviour of spiral steel fibre reinforced concrete in split hopkinson pressure bar tests. *Construction and Building Materials 48*, 521–532.

Li, Q. & H. Meng (2003). About the dynamic strength enhancement of concrete-like materials ina slpit hopkinson pressure bar test. *Solids and Structures 40*, 343–360.

Mihashi, H. & F.Wittmann (1980). Stochastic approach to study the influence of rate of loading on strength of concrete. *Heron 25*, 54.

Ngo, T., P. Mendis, A. Gupta, & J. Ramsay (2007). Blast loading and blast effects on structures—an overview. *Structural Engineering 7*, 76–91.

Pichler, B., I. Fischer, E. Lach, C. Terner, E. Barraud, & F. Britz (2014). The influence of loading rate on the compressive strength of cementitious materials: experiemnts and "separation of time scales" -based analysis. *Conference Paper 13*(58), 0.

Solz, A. & M. Ruiz-Ripoll (2016). Experimental and computational characterization of dynamic loading and structural restistance of tunnels in blast scenarios. *Fire Technology 52*, 1595–1618.

Tedesco, J. & C. Ross (1998). Strain-rate-dependent constitutive equations for concrete. *Journal of Pressure Vessel Technology 120*(4), 398–405.

Wang, H., E. Binder, H. Mang, Y. Yuan, & B. Pichler (2017). Exeptional load cases for tunnel linings. *Manuscript in preparation*.

Xu, Z., H. Hao, & H. Li (2012). Experimental study of dynamic compressive properties of fibre reinforced concrete material with different fibres. *Materials & Design 33*, 42–55.

Zhang, M., H. Wu, Q. Li, & F. Huang (2009). Further investigation on the dynamic compressive strength enhancement of concrete-like materials based on split hopkinson pressure bar tests. part i: Experiments. *International Journal of Impact Engineering 36*(12), 1327–1334.

Computational Modelling of Concrete Structures – Meschke, Pichler & Rots (Eds)
© 2018 Taylor & Francis Group, London, ISBN 978-1-138-74117-1

Modelling of reinforced concrete members for high impulsive loading

Y. Lu & J. Xu
School of Engineering, Institute for Infrastructure and Environment, The University of Edinburgh, Edinburgh, UK

ABSTRACT: RC components subjected to high dynamic loadings tend to undergo two main phases of response, namely a shock and stress wave phase, and structural response phase. The structural response phase may be further divided into three consecutive stages represented respectively by intense shear near the support, intense shear over a relatively small shear span, and global bending. Because the governing mechanisms are very different in different phases and stages of the response, modelling of the response of concrete components under such impulsive load becomes particularly challenging, and it requires the modelling of the concrete material to be capable of simulating confined compression, tension, shear and the interaction between concrete and steel within the same model framework. This paper presents an overview of the development of a general model for RC components (beams in particular) for the analysis under impulsive loads. To cater for the complex and high nonlinearity involved in the responses, the analysis is carried out using general purpose dynamic analysis software (LS-DYNA) with an explicit scheme. The constitutive model for concrete is evaluated and calibrated comprehensively for various stress conditions, and its behaviour in terms of preserving a realistic concrete-reinforcing bar interaction is scrutinised. A representative RC beam/slab is then modelled and analysed with a particular interest in looking into the development of the shear forces during the transient stage of the response and the shear resistance. The trends of decreasing shear span and increasing shear resistance are observed based on the numerical simulation results.

1 INTRODUCTION

Advanced numerical simulation techniques are increasingly used in the investigation of the response of concrete structures subjected to extreme dynamic loading, complementary to or replacing physical testing which is generally difficult to conduct and is costly. Examples of the use of this category of numerical simulations include projectile penetration and perforation on hardened targets, impact, as well as blast to hardened and normal reinforced concrete structures.

As far as the structural response of concrete structures are concerned, a particular challenge to numerical modelling of the high impulsive load response is the ability to cover both the stress wave dominated phase of the response to the final global deformation phase with a realistic representation of the residual structural state. As the governing mechanisms change between the two phases of the response, a concrete material model which has shown sound performance in high-intensity dynamic stress applications may not necessarily perform as well in a reinforced concrete environment under a global deformation scenario. However, this issue has not received enough attention in the numerical simulation literature concerning RC structural response to impulsive load. In some cases this is due to a focus of analysis on the direct impulsive response where softening detail may not show a marked influence, and in some other cases though this could be due to a lack of appreciation on the potential significance of such a modelling consideration.

This paper discusses the modelling of reinforced concrete structure subjected to blast-type of loading in a "hydrocode" environment, where dynamic phenomena and complex stress state including the involvement of hydrostatic pressure constitute the major requirements on a model framework and the material descriptions. In particular, the application and performance of representative concrete material models in hydrocodes are examined.

2 OVERVIEW OF NUMERICAL SIMULATION STUDIES ON RC MEMBERS UNDER BLAST OR IMPACT LOAD

There has been a large body of literature concerning impact and blast effects on concrete structures and the associated numerical modelling using hydrocodes. These may broadly be divided into the following categories:

a. Modelling for penetration and perforation

when a concrete object is subjected to ultra-high intensity dynamic load, high intensity stress waves will develop upon the arrival of pressure wave and as a result localised material failure could occur prior to any significant global structural response (Lu and Wang, 2006). In this case the FE description of bond interaction would not significantly influence the response, and in most studies a perfect-bond assumption for the rebar and concrete is adopted. Typical scenarios in this load regime include projectile penetration and perforation, impact and close-in blast. The immediately affected concrete often experiences highly confined triaxial compressive state and the modelling of such effects requires a proper description of the concrete behaviour in the medium and high pressure regime. Damage plasticity based models that incorporate a pressure dependent failure surface and rate dependency, for instance, RHT (Riedel et al. 2009), JHC (Holqmuist and Johnson 1993) and K&C model (Malvar and Crawford 1997; Magallanes et al. 2010) are generally suited for this type of applications and the relevant model behaviour has been tested and calibrated extensively (Tu and Lu 2009).

b. Structural response and failure under far-field blast and general impulsive loading

If a structural member survives from the initial shock and stress wave effects, it enters into a structural response phase with effects closely related to the global deflection in much the same way as in a quasi-static loading situation. The pressure would largely diminish, and instead the response turns to be governed by bending, shear and the integrity between steel rebar and concrete. The change of the response mode requires the material model to be capable of accommodating tension, shear, and complex multi-axial stress conditions in the low pressure regime. In high shear force region, the shear stress (or "bond" stress on the actual physical interface) between rebar and concrete will tend to play an important role in determining the residual state of the overall structural member.

A perfect-bond assumption is widely adopted in numerical simulation of the response of RC members to impact and blast loading. Besides simplicity, a prevailing justification for this approach is based on a recognition that "bond" failure between steel reinforcement and concrete can always be replicated by the failure of the concrete elements, which are attached to the rebar elements and hence subject to an interface stress state similar to bond. In this way, the macroscopic reinforcement-concrete composite effect and the global response of the RC member is maintained. What is less recognised, however, is the fact that the stress condition in the layer of concrete attached to the rebar is altered and this in turn requires the concrete material model to be less sensitive to a certain degree of variation of the stress condition, especially in a damaged tension-shear state around the steel rebar. Depending upon the loading and structural conditions, this factor may or may not introduce a noticeable effect. Therefore, this potential issue has not been discussed sufficiently in the numerical simulation community.

3 DISCUSSION ON ESSENTIAL DAMAGE FEATURES IN CONCRETE MATERIAL MODELS

While the majority of the hydrocode models for concrete materials have been validated to a varying extent in applications where high pressure and localised material response plays a dominant role, detailed examination of the performance of such material models in the global deformation phase, and potential issues therein, is limited. For reinforced concrete structures, the demand on the material model to exhibit appropriate behaviour in tension and shear regime becomes particularly important as these properties determine the vital transfer of stresses between concrete and reinforcing bars to make a realistic "reinforced concrete" structural behaviour. Some of the key features of K&C and CSC models that relate closely to the behaviour in a typical reinforced concrete application under blast are briefly discussed here.

3.1 *K&C model*

In K&C concrete model, the current strength surface is defined as a linear interpolation between the maximum and either the yielding or residual failure surfaces (Crawford et al. 2012), depending on the cumulative damage level:

$$\Delta\sigma(=\sqrt{3J_2}) = \begin{cases} \eta\Delta\sigma_m + (1-\eta)\Delta\sigma_y & for \quad \lambda < \lambda_m \\ \eta\Delta\sigma_m + (1-\eta)\Delta\sigma_r & for \quad \lambda \geq \lambda_m \end{cases} \tag{1}$$

where $\Delta\sigma_y, \Delta\sigma_m$ and $\Delta\sigma_r$ are three separate failure surfaces, representing yielding, maximum and residual surfaces, respectively. All three failure surfaces are pressure dependent and the corresponding material parameters are determined by calibrating against experimental material test results

The interpolation factor η is a function of the modified effective plastic strain measure. λ is calculated as a factored effective plastic strain from $\overline{\varepsilon^p} = \sqrt{(2/3)\varepsilon_{ij}^p \varepsilon_{ij}^p}$, where ε_{ij}^p is the total plastic strain tensor. For the convenience of discussion,

we employ β_1 and β_2 to denote the modification factors, thus according to the original definition, λ can be expressed as:

$$d\lambda = \begin{cases} (\beta_1)\overline{d\varepsilon^p} & for \quad p \geq 0 \\ (\beta_2)\overline{d\varepsilon^p} & for \quad p < 0 \end{cases} \tag{2}$$

with

$$\beta_1 = \frac{1}{r_f(1+p/f_t)^{b_1}}, \beta_2 = \frac{1}{r_f(1+p/f_t)^{b_2}} \tag{3}$$

where f_t, r_f are the tensile strength and a rate scaling factor, respectively. p is the hydrostatic pressure; positive is compression and negative is tension. b_1 and b_2 are exponential weighting factors to control different rate of accumulation of incremental plastic strain in the hydrostatic compression ($p \geq 0$) and tension regime ($p < 0$).

K&C model also generates an indicative scaled damage factor (SDF) which is calculated from the modified effective plastic strain measure as:

$$SDF = \frac{2\lambda}{\lambda + \lambda_m} \tag{4}$$

In the pre-peak phase where $0 \leq \lambda \leq \lambda_m$, SDF varies from 0 to 1.0. After entering into the post-peak or softening phase, SDF varies from 1.0 to 2.0. It should be noted SDF so-defined is rather insensitive to changes of plastic strain in the advanced damage states, and therefore less indicative of the damage severity.

3.2 *CSC model*

The strength surface in this model is a cap model (Murray 2007) with a smooth/continuous intersection between a shear failure surface $F_f(I_1)$ and hardening cap $F_c(J_1,\kappa)$, as follows:

$$f(I_1, J_2, J_3, \kappa) = J_2 - \Re^2 F_f F_c \tag{5}$$

With failure surfaces defined above, the model uses a scalar damage index d to transform the undamaged (effective) stress tensor into damaged one in a proportionate manner, i.e. $\sigma_{ij}^{\text{damaged}} = (1-d)\sigma_{ij}^{\text{undamaged}}$. The damage is applied to the stresses after being updated by a visco-plasticity algorithm. The damage index d ranges from 0 for no damage to 1 for complete failure, and is defined in accordance with two strain-based energy terms and is separated into two parts, namely, brittle damage index d_b for tensile stress state, and ductile damage index d_d for compressive stress state,

$$d_b = \frac{1}{D}\left[\frac{1+D}{1+D\exp^{-C\tau_b}} - 1\right] \qquad \text{(Tensile)}$$

$$d_d = \frac{d_{\max}}{D}\left[\frac{1+B}{1+B\exp^{-A\tau_d}} - 1\right] \qquad \text{(Compressive)} \tag{6}$$

Parameter A, B, C and D control the shape of the softening function. The brittle damage accumulation depends on the maximum principal strain term, $\tau_b = \sqrt{E\varepsilon_{\max}^2}$, and it accumulates when τ_b exceeds a threshold. The ductile damage depends on the total strain components, $\tau_d = \sqrt{1/2\sigma_{ij}\varepsilon_{ij}}$, and it accumulates when τ_d exceeds its respective threshold.

The model has a capacity to recover from tensile damage when the stress state becomes compressive again, simulating crack closure. This is achieved by discarding the accumulated tensile damage such that $d = d_d$ for a compression state, otherwise $d = \max(d_b, d_d)$.

3.3 *Fracture energy and mesh convergence*

The general considerations of crack softening in both K&C and CSC models stem from the crack band theory (Bazant and Oh 1983). To enable a mesh-objective solution and general mesh convergence, both K&C and CSC models essentially incorporate a length factor, albeit in a different manner. The strain energy in the softening phase of the material response is evaluated over a characteristic "band width", L_c, to match target fracture energy, G_f, which is considered as a material property. In CSC model, L_c is simply tied to the characteristic element size L_e (cubic root of the element volume), implying that the softening (crack) is always localised within a single layer of elements. On the other hand, K&C model provides a possibility of dealing with softening to spread (in the band width direction) over multiple elements, and this is achieved by introducing a user specified localisation width L_w. When the element size L_e is larger than L_w, the standard treatment prevails such that the characteristic length L_c is made equal to the element size L_e. In case the element size is smaller than L_w, the stress-strain relation is then adjusted based on the presumption that the facture energy is dissipated over the localisation width L_w (user defined) rather than a single element length L_e.

4 DISCUSSION ON THE BEHAVIOUR OF CONCRETE MATERIAL MODELS CONCERNING REBAR-CONCRETE INTERACTION

A sound representation of the rebar-concrete interaction is crucial in the modelling of RC structures

in a global mode of response, and failing this could result in unrealistic premature structural failure in the numerical simulation.

To allow for a direct assessment of the rebar-concrete interaction behaviour resulting from the use of K&C and CSC concrete material models, a series of simple bending and pull-out simulations have been conducted with comparison to relevant experimental data. In addition, a RC beam with transverse reinforcement (stirrups) is also analysed to demonstrate how the presence of stirrups may help alleviate the demand on concrete material model in capturing concrete-rebar interaction behavior.

4.1 *Rebar-concrete interaction in a quasi-static bending test*

A simple RC beam involving only longitudinal rebar, originally tested by Janney et al (1956) under static loading, has been selected for this verification simulation. The test beam was 305 × 152 mm in cross section with an effective depth of 211 mm. The length of the beam was 3.05 m with a clear span of 2.74 m. The longitudinal reinforcement ratio was 1.87%. Under 4-point loading, the shear span-to-depth ratio was about 4.3. The rebar had a yield strength of 333 MPa, and concrete had a compressive strength of 36.2 MPa. The tensile strength of concrete was assumed to be 2.8 MPa. As reported from the experiment, the beam developed multiple cracks in the region of pure bending. Finally the beam failed in a flexural mode without any apparent shear or bond problem.

The numerical simulation is carried out using LS-DYNA. To reduce the computation cost, one-third of the beam cross-section width which contains a single reinforcing bar is modelled, maintaining the original reinforcing ratio. In the FE model, 8-node solid elements are used for concrete. Steel bars are modelled by either beam elements or solid elements, respectively, for a comparison. It is noted that the results between using the above two rebar models are generally in line with each other although quantitative differences exist. Considering that for generally modelling of RC components the use of beam elements for rebar is more viable in terms of computing cost, only the results with beam rebar elements are presented here.

The predicted load (in terms of the mid-span moment) vs. central deflection relationships using the two concrete models are compared with the experimental result in Figure 2. It can be observed that the simulations using the K&C model tend to fail prematurely with an abrupt loss of the global resistance at a deflection of 12 mm (1/250 of the net span). On the other hand, the simulations using the CSC model appear to match well the experimental curve with a slightly higher strength.

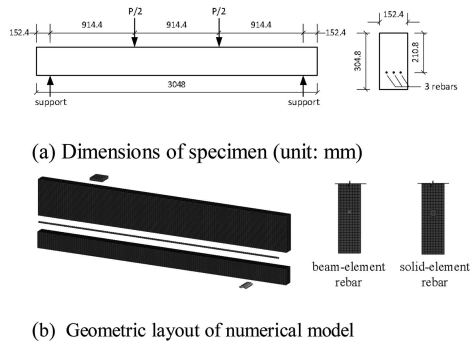

(a) Dimensions of specimen (unit: mm)

(b) Geometric layout of numerical model

Figure 1. Experimental RC beam and its FE model.

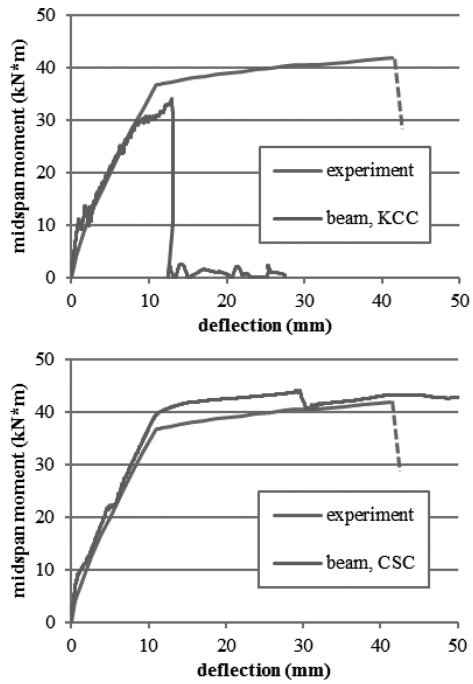

Figure 2. Comparison of central deflection—mid-span moment curves.

It is noted that the experimental failure point was recorded at around 42 mm.

The crack patterns at selected deflection levels are shown in Figure 3. The failure patterns in the K&C model demonstrate that the premature failure in these cases is attributable to the failure of concrete elements to which the rebar elements are attached, leading to the loss of the reinfrocement effect (analogous to the rebar being pulled out or sliding in the concrete). On the other hand, the CSC model also developed damage along the longitudinal rebar but the effect is not catastrophic

and the overall behaviour matches well the experiment as mentioned earlier.

4.2 *Rebar-concrete interaction in a quasi-static pull-out test*

The interaction between rebar and concrete in the numerical models has been further examined in a classical pull-out scenario, using the test specimens conducted by Eligehausen et al. (1983) as a benchmark.

Figure 4 shows the relationship between the inferred bond stress vs. end slip from the numerical simulations as compared with the experiment.

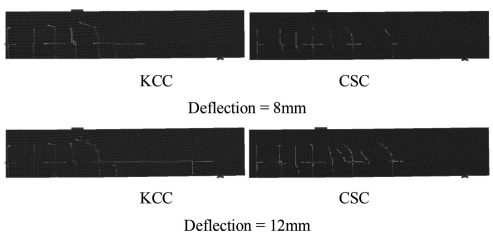

Figure 3. Crack profiles of RC beam under quasi-static load.

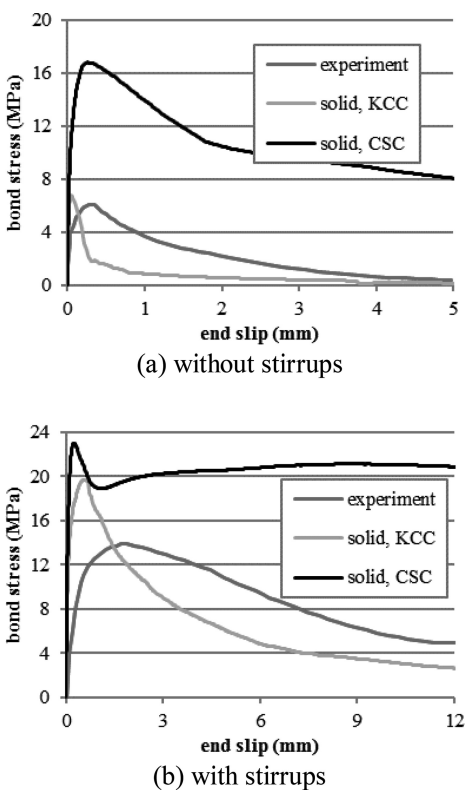

Figure 4. Comparison of global bond-slip relations.

For the specimen without stirrups, the K&C model exhibits overly brittle pull-out behaviour and the specimen fails abruptly when the maximum stress was attained. For the case with stirrups (Figure 32(b)), the K&C model behaved in a similar manner as in the case without stirrups, with much less ductility comparing with the experiment. On the other hand, it can be observed that the CSC model ends to considerably over-predict the bond strength as well as the overall slip deformability. In the specimen with stirrups, the CSC model exhibits an unrealistically ductile behaviour with almost a plastic response phenomenon.

4.3 *Rebar-concrete interaction in the presence of stirrups*

The issue with the K&C model concerning rebar-concrete interaction is apparent from the simulation of the RC slab response to blast in the previous section. However, seldom has such a problem been noticed in previous modelling simulations of RC response to blast and impact loads in the literature. Besides the fact that many of the simulations did not actually involve substantial global response, as commented in the review section, the reinforcement usually consisted of both longitudinal and transverse/shear links. In the numerical model such intersecting reinforcement is commonly modelled as rigidly jointed, which would effectively prevent catastrophic failure in the rebar-concrete interaction to occur in the analysis. The following case example will illustrate such a combination of incorrect representation in both the orthogonal reinforcement (stronger than should be) and the concrete (more fragile than should be) that tends to cancel out each other and thus mask the true issue in the representation of the rebar-concrete interaction that needs to be rectified.

A typical simply-supported RC beam under quasi-static load is considered (Miyamoto et al. 1989). The RC beam had a rectangular cross-section of 160 × 150 mm and a span of 1.2 m. The longitudinal reinforcement consisted of 5 deformed bars of 10 mm in diameter, two in the compression zone and three in the tension zone, giving a tensile reinforcement ratio of about 1.12%. The transverse reinforcement was made of 6-mm stirrups with a spacing of 50 mm. The reinforcement had yield and ultimate strength of 352 MPa and 468 MPa, respectively. The compressive strength of concrete was 29.4 MPa.

The tested beam experienced significant plateau stage, and eventually collapsed at the deflection of 5 mm (4% of span) due to propagation of diagonal cracks towards the loading plate, exhibiting a global bending-shear mode of failure.

In the numerical models, one third of the cross-section width and a half span are simulated. The

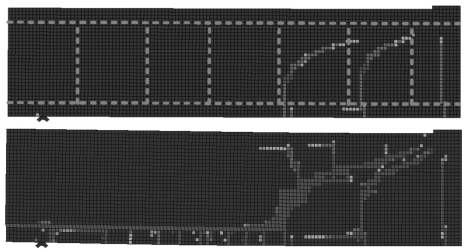

Without stirrups (deflection 2mm / 5mm)

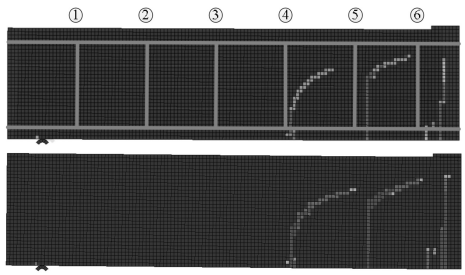

With stirrups (deflection 2mm / 5mm)

Figure 5. Crack patterns of RC beam with and without stirrups.

beam is placed on a simply fixed support at one end, and loaded with a rigid plate in the mid-span in a deformation controlled way. Beam elements are employed for all the reinforcing steel bars.

The simulated damage pattern indicates a diagonal tension failure mode similar to the experiment, as shown in Figure 5. The results suggests that the presence of stirrups effects to reduce the demand on the direct rebar-concrete interaction (bond) and thus helps alleviate demands on the concrete material model in terms of tension-softening behaviour. In this respect, caution should be exercised when evaluating the material model performance from the simulation of concrete structures with full steel cages.

5 MODIFICATION FOR TENSION-SOFTENING

The phenomenon associated with the premature failure in the numerical simulation with the K&C concrete model is deemed to be resulting from a premature and complete loss of strength in the concrete elements surrounding the rebar. Noting that these elements are generally in a shear/tension state, it is be reasonable to consider modifying the softening or descending phase of the material model in the tension regime. In the current implementation of the K&C model in LS-DYNA, such an effect can be realised by modifying the damage accumulation curve. The default η-λ relation, which is basically a linear function, generates a uniaxial stress-strain curve with a very steep softening response under both uniaxial tension and compression, with a cut-off strain limit beyond which the strength becomes zero. The proposed modification is to modify the second branch of the η-λ curve with an exponential function, thus resulting a more gradual softening and a prolonged residual state. Figure 6 shows a set of the exponential functions with a different termination limit of the λ_{max} values.

The above modification is aimed for improving of the softening behaviour in tension, therefore measures should be taken to ensure the modification does not cause significant changes in the model behavioru under compression. In K&C model the same η-λ is used for both tension and compression regimes, but it allows a control of different softening features in compression and tension through the plastic strain accumulation factor b_1 and b_2, respectively. Therefore the b_1 factor is adjusted so as to compensate the unwanted stretching of the softening behaviour in the general compression. Calibration analyses suggest that an exponential η-λ curve with $\lambda_{max} = 0.004$ and an adjusted $b_1 = 1.2$ are suitable. Figure 7 shows the corresponding behaviour of the resulting

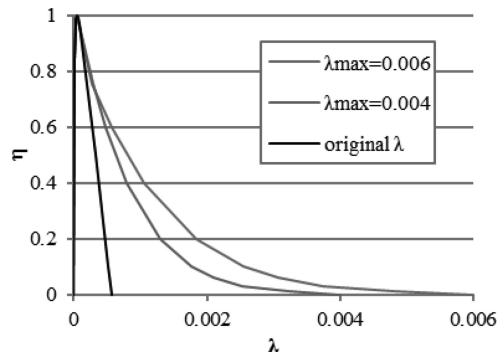

Figure 6. Modified η–λ curve.

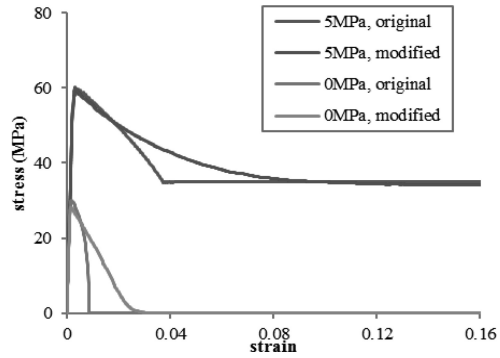

Figure 7. Stress-strain curves under confined compression after modification.

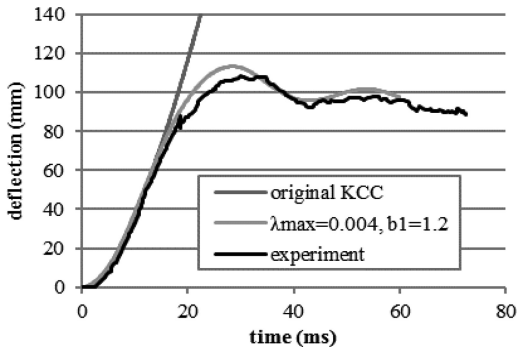

Figure 8. Predicted response using the modified softening scheme.

material model under general confined compression. The comparison with the original K&C model in the confined compression region do not differ significantly, indicating that the recommended modifications for rectifying the tension/shear softening behaviour would not introduce significant side effect when it comes into general compression regime.

The above parameterisation has been adopted in the revised simulation of the RC slab response to blast loading. Figure 8 shows the new deflection response time histories, where a significant improvement is observed. The simulated crack distributions also match well the experiment, as well as those obtained from the simulation with the CSC model (not shown).

From the above analyses and discussion it can be generally established that for a damage-plasticity concrete material model like K&C to extend its satisfactory performance into applications where the global deformation regime plays an important role, an appropriate description of the detailed softening behaviour in shear/tension can be crucial. This is particularly true in terms of a reaslitic representation of the rebar-concrete interaction (or "bond"), even though the tension softening of plain concrete itself may not be of significant interest.

6 SIMULATION OF SHORTENED DURATPION LOADING AND HIGH SHEAR RESPONSE

The RC slab/beam model is further subjected to impulsive load with shortened duration and increased peak load, which simulate near field blast, to observe high shear responses and the corresponding failure modes. For simplicity, the same load pattern as used in Section ** is adopted with shortened duration from ~50 ms to ~20 ms and 5 ms, and increased peak pressure from 0.33 MPa to 1.34 and 5.35 MPa, respectively, as shown in Figure 9.

Under the impulsive blast loading with peak pressure of 1.34 MPa and time duration of 20 ms, despite of similar deflection response (not shown), the failure modes using the modified K&C model suggests a combined bending and shear failure with clear diagonal shear cracks.

Under the impulsive blast loading with peak pressure of 5.35 MPa and time duration of 5 ms, the failure pattern shown in Figure 11 suggests that the member fails in a direct shear mode, in which transient failure takes place and forms a vertical or steeply inclined shear crack near the end support,

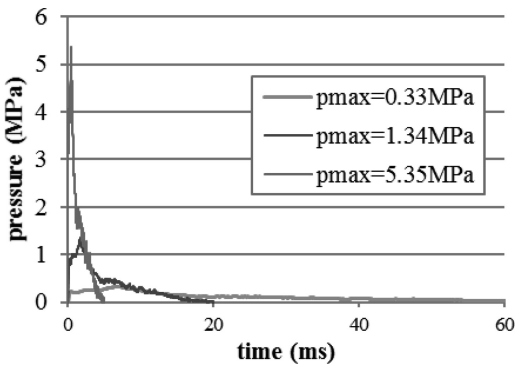

Figure 9. Numerical simulation with modified blast loadings.

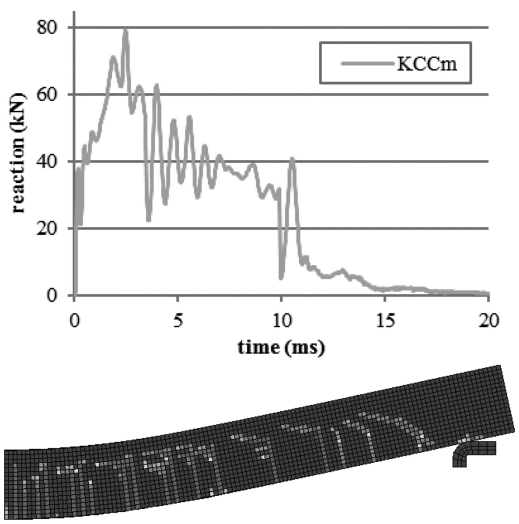

Figure 10. Simulated response with 20 ms duration loading.

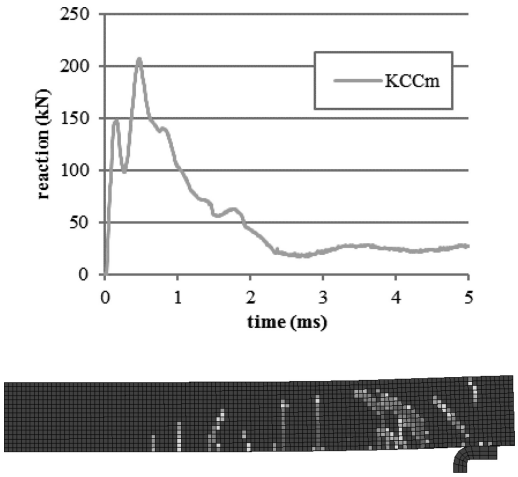

Figure 11. Simulated response with 5 ms duration loading.

without develops significant global flexural deflection. The maximum shear response (and hence shear resistance) exhibited considerable increase as compared to the 20-ms loading case.

7 CONCLUDING REMARKS

This paper has been concerned with numerical modelling of reinforced concrete components subjected to high impulsive loading, especially for cases where both the stress wave and global structural responses are important. It is demonstrated that the rebar-concrete interaction is a key factor affecting the global response simulation, and therefore particular care should be exercised in ensuring a realistic representation of the tension softening behaviour of concrete, in addition to the general requirements on pressure and dynamic rate representation in the material descriptions. Two concrete material models are discussed in this respect, and in particular, the K&C which is widely used in the numerical modelling of concrete for high dynamic loadings, has been examined in detail. A modification scheme is proposed to rectify the softening behaviour, and this type of modification is deemed to be applicable in similar damage-plasticity models for a more realistic simulation of the concrete behaviour in simulation of the global structural regime of the responses.

REFERENCES

Bažant, Z.P., and Oh, B.H. 1983. Crack band theory for fracture of concrete. Matériaux et Constructions, 16, 155–77.

Crawford, J.E., Wu, Y., Choi, H., Magallanes, J.M., and Lan, S. 2012. Use and validation of the release iii k&c concrete material model In LS-DYNA." Technical Report TR-11-36.5, Karagozian & Case, Glendale, CA, 2012.

Eligehausen, R., Popov, E.P., and Bertero, V. V. 1983. Local bond stress-slip relationships of deformed bars under generalized excitations. Berkeley: UCB/EERC-83/23, Earthquake Engineering Research Center.

Holqmuist, T.J., and Johnson, G.R. 1993. A computational constitutive model for concrete subjected to large strains, high strain rate, and high pressures. 14th international symposium on ballistics, Vol. 9, 591–600.

Janney, J.R., Hognestad, E. and McHenry, D. 1956. Ultimate flexural strength of prestressed and conventionally reinforced conrete beams." Journal of the American Concrete Institute Proceedings, 52, 601–620.

LS-DYNA. 2007. keyword user's manual version 971. Livermore Software Technology Corporation.

Lu, Y., and Wang, Z. 2006. Characterization of structural effects from above-ground explosion using coupled numerical simulation. Computers & Structures, 84(28),1729–42.

Magallanes, J.M., Wu, Y., Malvar, L.J., and Crawford, J.E. 2010. Recent improvements to release iii of the k&c concrete model." Eleventh International LSDYNA Users Conference, 37–48.

Malvar, L.J., and Crawford, J.E. 1997. A plasticity concrete material model for DYNA3D. International Journal of Impact Engineering, 19(97), 847–73.

Miyamoto, A., King, M., and Fujii, M. 1989. Non-linear dynamic analysis and design concepts for rc beams under impulsive loads." Bulletin of the New Zealand National Society for Earthquake Engineering, 22(2), 98–111.

Murray, Y.D. 2007. Users Manual For LS-DYNA Concrete Material Model 159. FHWA-HRT-05-062, Federal Highway Administration, McLean, VA.

Riedel, W., Thoma, K., Hiermaier, S., and Schmolinske, E. 1999. Penetration of reinforced concrete by beta-b-500 numerical analysis using a new macroscopic concrete model for hydrocodes. Proceedings of the 9th International Symposium on the Effects of Munitions with Structures.

Tu, Z., and Lu, Y. 2009. Evaluation of typical concrete material models used in hydrocodes for high dynamic response simulations. International Journal of Impact Engineering, 36(1), 132–46.

Computational Modelling of Concrete Structures – Meschke, Pichler & Rots (Eds)
© 2018 Taylor & Francis Group, London, ISBN 978-1-138-74117-1

Author index

Abe, T. 973
Abouri, S. 615
Adams, M.P. 421
Akiki, R. 1009
Alberti, M.G. 813, 867
Alex, A. 109
Amar, A. 491
Anglade, E. 913
Antonelli, A. 55
Arquier, M. 553
Arteta, C.A. 561
Assih, J. 585

Baktheer, A. 767
Balabanić, G. 387
Bandelt, M.J. 421, 633, 805
Baroth, J. 237
Bažant, Z.P. 15, 73
Belletti, B. 545
Benboudjema, F. 209
Benedetto, M. 403
Bentz, D.P. 203
Bhowmik, S. 777
Billington, S.L. 805
Binder, E. 1017
Bitencourt Jr., L.A.G. 127, 877
Bittencourt, T.N. 127, 877
Bleyer, J. 553
Bobiński, J. 481, 499
Bolander, J. 289
Bouhjiti, E.M. 237
Boulant, G. 215
Boumakis, I. 197
Bousikhane, F. 305
Briffaut, M. 249
Bui, T.T. 615
Butt, S.N. 705

Caggiano, A. 403
Capdevielle, S. 1003
Carol, I. 363
Červenka, J. 669
Červenka, V. 669
Charpin, L. 215
Chaves Figueiredo, S. 295
Chiaia, B. 745
Chintanapakdee, C. 993
Choi, C.-S. 889
Chudoba, R. 767, 839
Colombo, I.G. 849
Colombo, M. 849
Cordes, T. 189
Curbach, M. 829
Cusatis, G. 93, 203, 305
Czernuschka, L. 197

Dadi, Y. 275
Dave, M. 275
Davenne, L. 737
Davies, R.E. 285
de Boer, A. 535, 545
de Buhan, P. 553
Denarié, E. 903
Desmorat, R. 509
Desprez, C. 1003
Di Luzio, G. 93, 203, 305
di Prisco, M. 849, 857
Divet, L. 377
Dodhiya, A. 275
Dontchev, D. 585
Dufour, F. 237, 1003

Eddy, L. 755
Eliáš, J. 429
Enfedaque, A. 813, 867
Eriksson, D. 317
Esposito, R. 941
Etse, G. 403

Fantilli, A.P. 745
Ferretti, F. 941
Frank, T.E. 805
Freitag, S. 715

Gal, E. 137, 149
Gall, V.E. 705, 715
Gálvez, J.C. 813, 867
Gambarelli, S. 229
Gasch, T. 317
Gatuingt, F. 209, 509, 1009
Gawin, D. 327
Ghosh, P. 109
Giry, C. 509, 913, 1009
Gobirahavan, R. 983
Gong, F. 335
Gorino, A. 745
Grange, S. 249, 525, 1003
Grassl, P. 55
Grigorovitch, M. 149

Haelewyn, J. 215
Hafiz, M.A. 903
Hamon, F. 215
Han, T.-S. 141, 311
Häussler-Combe, U. 819
Hénault, J.-M. 215
Hendriks, M.A.N. 545, 931
Hirthammer, V. 155
Hiwatashi, T. 973
Hoang, L.C. 625
Hofstetter, G. 189
Hoogenboom, P.C.J. 465
Hordijk, D.A. 535

Ishida, Y. 963
Iskhakov, T. 345
Isozaki, T. 973
Ivanova, I. 585

Jang, S.-J. 889
Jang, Y.-I. 889
Jaśkowiec, J. 473
Jason, L. 737
Jayasuriya, A. 421
Jefferson, A.D. 285, 895
Jensen, T.W. 625
Jirásek, M. 25
Jourdain, X. 209

Kaczmarczyk, Ł. 491
Kaliske, M. 413
Kalliauer, J. 689
Kang, J. 289
Karihaloo, B.L. 173
Katori, K. 973
Kaufmann, W. 641
Keremidis, K. 3
Khoder, N. 525

Khy, K. 993
Kim, J.-S. 141, 311
Kim, S.-W. 889
Kindrachuk, V. 155
Koene, L. 921
Kolařík, F. 113
Kollegger, J. 43
Koniorczyk, M. 327
Korol, E. 651
Krč, R. 165
Kromoser, B. 43
Krug, B. 595
Kulasegaram, S. 173
Kwapisz, M. 395

Langhi, M. 275
Lantsoght, E.O.L. 535
Lavaud, S. 377
Lechner, A. 395
Li Piani, T. 921
Li, W. 305
Li, Y. 839
Liaudat, J. 363
Lifshitz Sherzer, G. 137
Limam, A. 615
Limam, S. 615
Limoge, C. 913
Liu, X. 725
Lolli, F. 87
López, C.M. 363
Louhghalam, A. 265
Lu, Y. 1023
Luo, W. 73
Lyons, P. 895

Maekawa, K. 335, 353
Maida, Y. 963
Malbois, M. 377
Maňák, J. 113
Mang, H.A. 257, 689, 725, 1017
Manzoli, O.L. 127, 877
Marcon, M. 517
Marzec, I. 651
Masoero, E. 87, 93, 203
Masson, B. 237
Mata-Falcón, J. 641
Mathieu, J.-P. 215
Matsumoto, K. 755
Mazars, J. 249
Mazzotti, C. 941
Meléndez, C. 679
Mendoza Jr., R. 795
Meschke, G. 345, 705, 715
Michel-Ponnelle, S. 215
Middendorf, B. 103
Miguel, P.F. 679
Mihai, I.C. 895
Miura, T. 795
Mizoguchi, M. 955
Mlčoch, J. 669
Modi, P. 275
Moreno, D.M. 805
Mungule, M. 275
Musya, U. 973

Nader, C. 579
Nagai, K. 755
Nakamura, H. 795
Nana, W.S.A. 615
Navrátil, J. 641
Nedjar, B. 371, 377
Němeček, J. 113
Němeček, J. 113
Neu, G.E. 705, 715
Neuner, M. 189
Nincevic, K. 197
Nitka, M. 457
Novák, D. 595
Novák, L. 595

Ogawa, S. 353
Oliver-Leblond, C. 661, 913
Ostertag, C.P. 561
Ožbolt, J. 229, 387

Pamin, J. 447
Pari, M. 931
Park, W.-S. 889
Pathirage, M. 203
Pearce, C.J. 491
Pellenq, R.J.-M. 3
Pereira, L. 63
Pesavento, F. 327
Petersen, T. 79, 265
Pichler, B. 257, 689, 725, 1017
Pirard, A. 737
Planas, J. 785
Podroužek, J. 165, 517
Pokhrel, M. 633
Poulsen, P.N. 625

Qomi, M.J.A. 3

Ragueneau, F. 661, 913
Rahimi-Aghdam, S. 15
Rastiello, G. 509
Ray, S. 777
Rebhan, M. 395
Rodrigues, E.A. 127, 877
Romero Rodríguez, C. 295
Rospars, C. 371
Rossi, P. 579
Rots, J.G. 465, 931, 941
Rypl, R. 839

Sakamoto, K. 973
Sakata, H. 963
Salah Uddin, K.M. 103
Sánchez, M. 127
Sancho, J.M. 785
Sanz, B. 785
Sato, T. 963
Šavija, B. 121
Schlangen, E. 121, 137, 295
Schlappal, T. 689
Schreter, M. 189
Schumann, A. 829
Sémété, P. 215
Senckpiel, T. 819
Shao, Y. 805
Shirai, Y. 963
Shvab, I. 93
Sieffert, Y. 525
Slowik, O. 595
Sluys, L.J. 63, 921
Šmilauer, V. 113
Snoeck, D. 295
Sola, E. 387
Soleilhet, F. 209
Stankov, V. 585
Strauss, A. 595
Suchorzewski, J. 437, 651
Suza, D. 43
Sýkora, M. 669
Szczecina, M. 569

Tailhan, J.L. 579
Taillade, F. 215
Takahashi, Y. 335, 353
Takase, Y. 955, 963, 973
Tanaka, Y. 353
Tao, Y. 183
Tejchman, J. 437, 457, 481, 499, 651
Thierry, F. 509
Timothy, J.J. 345
Titscher, T. 155
Torrenti, J.-M. 225, 377
Toulemonde, C. 215
Tran, D.T. 641
Trawiński, W. 481
Trindade, Y.T. 877
Turgut, C. 737

Ulfkjaer, J.P. 697
Ulm, F.-J. 3, 79, 265
Unger, J.F. 155

van der Veen, C. 535, 545
van Zijl, G.PA.G. 605
Vandewalle, L. 857
Vassaux, M. 913

Verstrynge, E. 857
Vincent, H. 553
Vořechovský, M. 839
Vorel, J. 517
Vorwagner, A. 395
Vrijdaghs, R. 857

Wada, T. 955
Wang, H. 257
Wang, Z. 755
Wan-Wendner, L. 197
Wan-Wendner, R. 165, 197, 517
Weerheijm, J. 63, 921
Wieczorek, A. 327
Wijeyewickrema, A.C. 983, 993
Williams, I.D. 561
Winnicki, A. 447, 569
Wosatko, A. 447

Xu, J. 1023

Yamamoto, Y. 795
Ye, G. 137
Yu, C. 465
Yuan, Y. 183, 257, 725, 1017
Yun, H.-D. 889

Zafati, E. 661
Zeranka, S. 605
Zhang, H. 121
Zhang, J.L. 725
Zobel, R. 829
Zreid, I. 413